CODEN: JASMAN

ISSN: 0001-4966

The Journal of the Acoustical Society of America

Vol. 127, No. 4 April 2010

JASA EXPRESS LETTERS

LETTERS TO THE EDITOR

(Continued)

CONTENTS—*Continued from preceding page*

(Continued)

CONTENTS—*Continued from preceding page*

(Continued)

CONTENTS—*Continued from preceding page*

PSYCHOLOGICAL ACOUSTICS [66]

SPEECH PRODUCTION [70]

SPEECH PERCEPTION [71]

BIOACOUSTICS [80]

(Continued)

CONTENTS—*Continued from preceding page*

Initialization method for speech separation algorithms that work in the time-frequency domain

Auxiliadora Sarmiento, Iván Durán-Díaz, and Sergio Cruces[a)]
Departamento de Teoría de la Señal y Comunicaciones, University of Seville, Camino de los Descubrimientos S/N, 41092 Seville, Spain
sarmiento@us.es, iduran@us.es, sergio@us.es

Abstract: This article addresses the problem of the unsupervised separation of speech signals in realistic scenarios. An initialization procedure is proposed for independent component analysis (ICA) algorithms that work in the time-frequency domain and require the prewhitening of the observations. It is shown that the proposed method drastically reduces the permuted solutions in that domain and helps to reduce the execution time of the algorithms. Simulations confirm these advantages for several ICA instantaneous algorithms and the effectiveness of the proposed technique in emulated reverberant environments.

PACS numbers: 43.60.Pt, 43.60.Gk, 43.60.Np [DOS]
Date Received: December 7, 2009 **Date Accepted:** January 11, 2010

1. Introduction

This article considers the problem of the blind separation of speech signals that are recorded in a real room, assuming the same number of microphones and speakers. It is well known that any acoustic signal acquired from microphones in a real recording environment suffers from reflections on the walls and surfaces inside the room. Therefore, the recorded signals can be accurately modeled as a convolutive mixture, where the mixing filter is usually considered a high-order finite impulse response filter.

We focus on the time-frequency domain approach for blind source separation (BSS). In this approach, the convolutive mixture is approximated by a set of parallel instantaneous mixing problems for each frequency, being each of these problems solved independently with a suitably chosen independent component analysis (ICA) algorithm. Since the separated sources can have an arbitrary ordering, with this technique, a postprocessing to align the solutions before reconstructing them in time domain is necessary. The ordering ambiguity for each frequency, which is known as the permutation problem, is ubiquitous when working in the time-frequency domain and is especially important in real recordings, where the length of the room impulse response can be very long (greater than 250 ms) and can contain strong peaks corresponding to the echoes. Several methods have been proposed to overcome the permutation problem, which can be divided into two groups. Some methods solve independently, for each frequency, the instantaneous mixture and then a known property of the signals or of the mixing filter are used in order to fix the permutation ambiguity. Examples of these properties are the following: the assumption of similarity among the envelopes of the source signal waveforms, the estimation of the direction of arrival, and the continuity on the frequency response of the mixing filter. A second group of methods tries to avoid permuted solutions by choosing a suitable initialization of the ICA algorithms for each of the frequencies. Our proposal belongs to this second group of methods and suggests an initialization procedure for those ICA algorithms that use the whitening of the observations in the time-frequency domain. The experiments show

[a)]Author to whom correspondence should be addressed.

that this initialization, which exploits the local continuity of the demixing filter in such domain, reduces drastically the number of the solutions that are permuted and also may be used to reduce the execution time of the ICA algorithms while keeping intact the quality of the separation.

2. Problem formulation

We model the microphone observations $x_i(n)$, $i=1,\ldots,N$, of a real room recording by a convolutive mixture of the speech sources $s_i(n)$, $i=1,\ldots,N$, in a noiseless situation, i.e.,

$$x_i(n)=\sum_{j=1}^{N}\sum_{k=0}^{P-1}h_{ij}(k)s_j(n-k),\quad i=1,\ldots,N, \tag{1}$$

where $h_{ij}(n)$ is the impulse response (of P taps) from the source j to the microphone i. In order to blindly recover the original speech signals (sources), one can apply a matrix of demixing filters to the observations $x_i(n)$ that yields an estimate of each of the sources

$$y_i(n)=\sum_{j=1}^{N}\sum_{k=0}^{M-1}b_{ij}(k)x_j(n-k),\quad i=1,\ldots,N, \tag{2}$$

where $b_{ij}(k)$ denotes the (i,j) demixing filter of M taps. Let $X_i(f,t)$ and $S_i(f,t)$ be, respectively, the short-time Fourier transform (STFT) of $x_i(n)$ and $s_i(n)$. The time-domain convolutive mixture in Eq. (1) can be approximated in the time-frequency domain by a set of parallel instantaneous mixing problems:

$$\mathbf{X}(f,t)=\mathbf{H}(f)\mathbf{S}(f,t), \tag{3}$$

where $\mathbf{X}(f,t)=[X_1(f,t),\ldots,X_N(f,t)]^T$ and $\mathbf{S}(f,t)=[S_1(f,t),\ldots,S_N(f,t)]^T$ are the observation and source vectors for each time-frequency point, respectively, and $\mathbf{H}(f)$ is the frequency response of the mixing filter whose elements are $H_{ij}(f)=[\mathbf{H}(f)]_{ij}\,\forall\, i,j$. The separation model is given by

$$\mathbf{Y}(f,t)=\mathbf{B}(f)\mathbf{X}(f,t), \tag{4}$$

where $\mathbf{Y}(f,t)=[Y_1(f,t),\ldots,Y_N(f,t)]^T$ is the vector of outputs or estimated sources, and $\mathbf{B}(f)$ are the separating matrices to be estimated for each frequency f.

Due to the decoupled nature of the solutions across different frequencies, the correspondence between the true sources and their estimates suffers from ambiguities in the scaling, phase, and order. Thus, the vector of source estimates can be modeled approximately as

$$\mathbf{Y}(f,t)\approx\mathbf{P}(f)\mathbf{D}(f)\mathbf{S}(f,t), \tag{5}$$

where $\mathbf{P}(f)$ is a permutation matrix and $\mathbf{D}(f)$ is a diagonal matrix of complex scalars. $\mathbf{P}(f)$ and $\mathbf{D}(f)$ constitute ambiguities for each frequency that need to be determined before being able to recover the estimated sources in time domain.

3. Initialization procedure for ICA algorithms

The ICA algorithms used for estimating the optimal separation system $\mathbf{B}(f)$ in each frequency are often started at any arbitrary point. However, a suitable initialization of the algorithm has several advantages. For instance, when the algorithm is initialized near the optimal solution, a much faster convergence of the algorithm will be obtained. Furthermore, the initialization can exploit prior information on the mixture in order to avoid permutation ambiguity. One interesting initialization approach considers the continuity of the frequency response of the mixing filter $\mathbf{H}(f)$ and its inverse. Under this assumption, the initialization of the separation system $\mathbf{B}(f)$ from the optimal value of the separation system at the previous frequency $\mathbf{B}_o(f-1)$ seems reasonable. However, we cannot directly apply $\mathbf{B}(f)=\mathbf{B}_o(f-1)$ in those ICA algorithms that whiten

the observations. The whitening is performed by premultiplying the observations vectors with an $N \times N$ matrix $\mathbf{W}(f)$. After that, the new observations $\mathbf{Z}(f,t)$ can be expressed as another mixture of the sources:

$$\mathbf{Z}(f,t) = \mathbf{W}(f)\mathbf{X}(f,t) = \mathbf{U}_*(f)\mathbf{S}(f,t), \tag{6}$$

where the new mixing matrix $\mathbf{U}_*(f) = \mathbf{W}(f)\mathbf{H}(f)$ is unitary. Then, the separation matrix $\mathbf{B}(f)$ can be decomposed as the product of a unitary matrix and the whitening matrix,

$$\mathbf{B}(f) = (\mathbf{U}(f))^H \mathbf{W}(f). \tag{7}$$

Due to the variability of the sources spectra, in general, the whitening matrices $\mathbf{W}(f)$ and $\mathbf{W}(f-1)$ in contiguous frequencies are different. Consequently, when solving $\mathbf{B}(f) = \mathbf{B}_o(f-1)$ directly to obtain $(\mathbf{U}(f))^H = \mathbf{B}_o(f-1)\mathbf{W}^{-1}(f)$, there is no longer guarantee that this matrix is still unitary.

A *classical initialization* technique avoids the previously described problem in the following way. First, it multiplies the observations $\mathbf{X}(f,t)$ by the optimal separation matrix at the previous frequency. Then, it determines the matrix $\mathbf{W}(f)$ which whitens these new observations. Therefore, the overall separation matrix is calculated as

$$\mathbf{B}(f) = (\mathbf{U}(f))^H \mathbf{W}(f)\mathbf{B}_o(f-1). \tag{8}$$

In this work, we propose a new initialization procedure that consists in initializing the separation matrix $\mathbf{B}(f)$ trying to minimize the weighted distance with several of the optimal separation systems previously calculated for nearby frequencies, while the matrix $\mathbf{U}(f)$ is constrained to be unitary. This leads to the constrained minimization problem,

$$\sum_i \alpha_i \|\mathbf{B}_o(f-i) - \mathbf{B}(f)\|_F^2 \quad s.t. \quad (\mathbf{U}(f))^H \mathbf{U}(f) = \mathbf{I}_N, \tag{9}$$

where $\|\cdot\|_F$ denotes the Frobenius norm and α_i are non-negative weighting scalars. The solution of this problem is given by $\mathbf{U}(f) = \mathbf{Q}_L \mathbf{Q}_R^H$, where $\mathbf{Q}_L$ and $\mathbf{Q}_R$ are, respectively, the left and right singular vectors of the singular value factorization which follows:

$$[\mathbf{Q}_L, \mathbf{D}, \mathbf{Q}_R] = \mathrm{svd}(\mathbf{W}(f) \sum_i \alpha_i (\mathbf{B}_o(f-i))^H). \tag{10}$$

4. Experimental results

In this section, we present several experiments illustrating that the proposed initialization produces good quality separation with convolutive mixtures of speech signals by using different ICA algorithms. In addition, we will discuss the ability of the initialization procedure to reduce the permuted solutions, as well as its effectiveness to guarantee a high convergence speed of the ICA algorithm in such reverberant conditions. In order to have the possibility to determine the number of permuted solutions and some objective measures of quality of the separation, it is needed to know the exact room impulse response and the sources without errors. For this reason, we emulated real room recordings by means of synthetic mixtures. Therefore we created 25 synthetic mixtures of two speech sources. The sources were chosen from male and female speakers in a database[1] of 12 individual recordings of 5 s duration and sampled at 10 kHz. Those sources were mixed using a simulated room mixing system, shown in Fig. 1, determined using the ROOMSIM toolbox.[2] We computed the STFT with a finite Fourier transform of 2048 points, 90% overlapping, and Hanning windows of length 1024 samples. Then, we estimated the separation system $\mathbf{B}_o(f)$ by initializing the ICA algorithms with both the *classical initialization* and the proposed initialization. After that, we fixed the permutation and scale ambiguities applying the method described in Ref. 3, and finally filtered the observations to obtain the time-domain estimated sources.

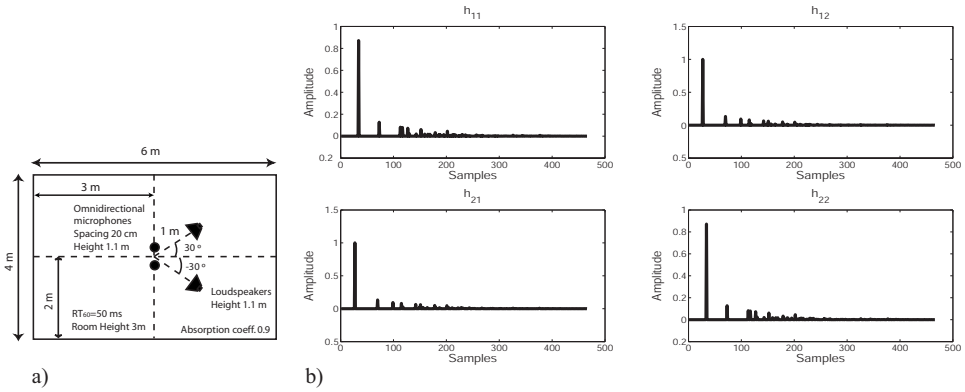

Fig. 1. (a) Microphone and loudspeaker positions for the simulated room recordings and (b) channel impulse responses of the considered filter.

We applied our initialization method to various ICA algorithms which have been proved to be efficient to estimate the separation system $\mathbf{B}_o(f)$. Since speech signals are highly nonstationary, we used two popular ICA algorithms based on nonstationarity of signals, SOBI (Ref. 4) and THINICA (Ref. 5). THINICA was used in two different configurations, by first extracting one source and then reconstructing the other, and by the simultaneous extraction of the two sources, referred hereinafter as THINICA-SIM. To quantify the quality of the estimated sources, each output was decomposed, by the BSS_EVAL toolbox,[6] into three terms $y_i(t)=s_{\text{tar}}+e_{\text{int}}+e_{\text{art}}$, which represent, respectively, the target source, the interference from other sources, and a last component of artifacts. Then, we calculated three performance measures: the source to interference ratio (SIR), the source to artifact ratio (SAR), and the source to distortion ratio (SDR),

$$\text{SIR} = 10\log_{10}\frac{\|s_{\text{tar}}\|^2}{\|e_{\text{int}}\|^2}, \quad \text{SAR} = 10\log_{10}\frac{\|s_{\text{tar}}+e_{\text{int}}\|^2}{\|e_{\text{art}}\|^2}, \quad \text{SDR} = 10\log_{10}\frac{\|s_{\text{tar}}\|^2}{\|e_{\text{int}}+e_{\text{art}}\|^2}. \tag{11}$$

The obtained results, presented in Table 1, show that for the THINICA case the initialization improves up to 8 dB the SAR and SDR in comparison with the classical method. In the other cases, the initialization does not achieve a significant improvement of the estimated sources quality.

As an example, two sources can be listened to in Mm. 1 and Mm. 2. Mixtures from these sources by means of a mixing system like that described in Fig. 1 are in Mm. 3 and Mm. 4. Finally, in Mm. 5 and Mm. 6, the sources recovered by the algorithm THINICA-SIM (Ref. 4) with the proposed initialization can be listened to.

Mm. 1. [First source: female voice sampled at 10 kHz. This is a file of type "wav" (99 kbytes).]

Mm. 2. [Second Source: male voice sampled at 10 kHz. This is a file of type "wav" (99 kbytes).]

Mm. 3. [First observation of the mixture of the two sources. This is a file of type "wav" (99 kbytes).]

Mm. 4. [Second observation of the mixture of the two sources. File of type "wav" (99 kbytes).]

Mm. 5. [First recovered source. This is a file of type "wav" (99 kbytes).]

Mm. 6. [Second recovered source. This is a file of type "wav" (99 kbytes).]

Table 1. Comparison of the average SIR, SAR, and SDR for different ICA algorithms by initializing with both the classical and the proposed initialization method.

	SIR (dB)		SAR (dB)		SDR (dB)	
	Classic	Ini-1	Classic	Ini-1	Classic	Ini-1
THINICA	20.16	22.03	0.86	9.32	0.70	8.92
THINICA-SIM	21.97	22.15	12.70	12.79	12.02	12.13
SOBI	22.48	22.15	13.02	12.83	12.43	12.16

In order to prove the effectiveness of the initialization to guarantee a high convergence speed of the algorithm, we calculated the average CPU time that each algorithm uses to solve the separation in each frequency. We also analyzed the performance of our initialization procedure in terms of the number of permutations. The results, summarized in Fig. 2, corroborate that the proposed initialization reduces both the computational effort of the ICA algorithms and the number of permutations. The reduced number of permutations is particularly very interesting because it allows us to design new algorithms to solve the permutations based on this reduction. Also, it could be used to alleviate the computational burden of the algorithms that solve the permutation problem.

We investigated those frequencies in which our initialization is not able to preserve the permutation order. Without loss of generality, we considered the simulation results provided by the THINICA-SIM algorithm using the proposed initialization. In Fig. 3, we represent the normalized modulo of the frequency response of the optimal demixing filter from source 1 to microphone 1 (upper plot), and the normalized histogram of the frequencies in which the solutions remained permuted (lower plot). It could be noted that echoes in the impulse response of the mixing filter introduce rapid oscillations on the frequency response, so our main assumption about the continuity of the mixing filter is not valid in all the frequencies. For this reason, it can be observed that frequencies presenting a high number of permutations correspond to those in which the frequency response of the optimal demixing filter exhibits strong peaks. However, there are also a set of frequencies in which, although the mixing filter does not exhibit those oscillations, the solutions are still permuted. This can be explained when the source separation problem is ill determined at these frequency bands or when the profiles across time of the second order statistics used by the chosen algorithms are similar for both sources, since they can fail to separate the sources in these situations.

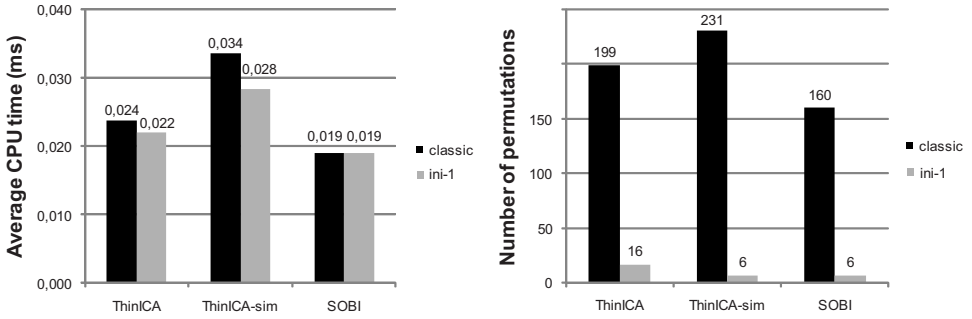

a) b)

Fig. 2. (a) Average CPU time (ms) to run different ICA algorithms in each frequency by initializing with both the classical and the proposed initialization method. (b) Number of permutations for different ICA algorithms by initializing with both the classical and the proposed initialization method.

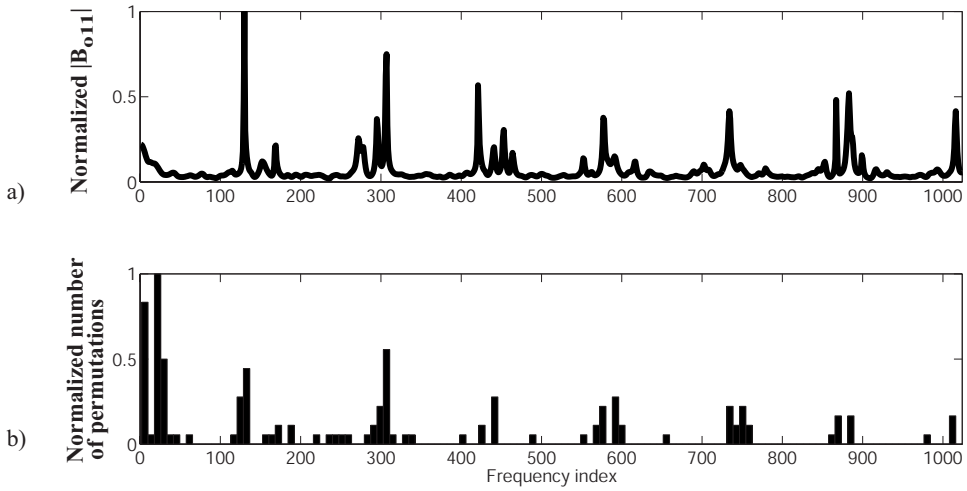

Fig. 3. (a) Normalized modulo of the frequency response of the optimal demixing filter from source 1 to microphone 1 and (b) normalized histogram of the number of permutations for 25 experiments and using THINICA-SIM algorithm.

5. Conclusions

In this article we have considered the problem of the blind separation of speech signals in reverberant scenarios. We have presented an initialization procedure for those ICA algorithms that work in the time-frequency domain and use a whitening of the observations as a preprocessing step. Computer simulations show that this initialization, when incorporated to the existing ICA algorithms, reduces drastically the number of permutations. In addition, the proposed initialization helps to alleviate the computational execution time of the ICA algorithms that solve the separation in each frequency, while preserving the quality of the separated speech sources.

Acknowledgments

This work was supported by MCYT Spanish Project No. TEC2008-06259.

References and links

[1]M. S. Pedersen, D. Wang, J. Larsen, and U. Kjems, "Two-microphone separation of speech mixtures," IEEE Trans. Neural Netw. **19**, 475–492 (2008).
[2]D. Campbell, ROOMSIM toolbox, http://media.paisley.ac.uk/~campbell/Roomsim/ (Last viewed Dec. 7, 2009).
[3]A. Sarmiento, S. Cruces, and I. Durán, "Improvement of the initialization of time-frequency algorithms for speech separation," in Proceedings of the 8th International Conference on ICA and Signal Separation, Paraty, Brazil (2009), pp. 629–636.
[4]A. Belouchrani, K. Abed-Meraim, J. F. Cardoso, and E. Moulines, "A blind source separation technique using second-order statistics," IEEE Trans. Signal Process. **45**, 434–444 (1997).
[5]S. Cruces, A. Cichocki, and L. De Lathauwer, "Thin QR and SVD factorizations for simultaneous blind signal extraction," in Proceedings of the European Signal Processing Conference (EUSIPCO), Vienna, Austria (2004), pp. 217–220.
[6]C. Fèvotte, R. Gribonval, and E. Vincent, BSS_EVAL Toolbox User Guide, Technical Report No. 1706, IRISA, Rennes, France (2005).

Graded activation of the intrinsic laryngeal muscles for vocal fold posturing

Dinesh K. Chhetri,[a] Juergen Neubauer, and David A. Berry
The Laryngeal Dynamics and Physiology Laboratories, Division of Head and Neck Surgery, David Geffen School of Medicine, UCLA, 62-132 CHS, Los Angeles, California 90095
dchhetri@mednet.ucla.edu

Abstract: Previous investigations using *in vivo* models to study the role of intrinsic laryngeal muscles in phonation have used neuromuscular stimulation to study voice parameters. However, these studies used coarse stimulation techniques using limited levels of neuromuscular stimulation. In the current investigation, a technique for fine control of laryngeal posturing was developed using graded stimulation of the laryngeal nerves. Vocal fold strain history to graded stimulation and a methodology for establishing symmetric laryngeal activation is presented. This methodology has immediate applications for the study of laryngeal paralysis and paresis, as well as general questions of neuromuscular control of the larynx.

PACS numbers: 43.70.Gr, 43.70.Jt, 43.70.Bk [AL]
Date Received: December 8, 2009 **Date Accepted:** January 18, 2010

1. Introduction

Study of voice production and control mechanisms of the larynx is critical to furthering our understanding of human speech, communication, and phonatory pathology. Neuromuscular control of the larynx plays a critical role in phonation and has been investigated in animal (Choi *et al.*, 1993a, 1993b, 1995), human (Kempster *et al.*, 1988; Atkinson 1978; Faaborg-Andersen 1965), and computer models (Farley 1994; Story and Titze 1995). However, such studies in animals and humans have been limited, due to the difficulty in using laryngeal stimulation techniques to obtain fine control of laryngeal posturing. Animal studies have primarily used *in vivo* canine models to provide neuromuscular stimulation to laryngeal nerves. Unfortunately, however, only coarse "on/off" or "low/medium/high" settings have been utilized in these studies (Choi *et al.*, 1993a, 1993b, 1995).

The work of Nasri *et al.* (1995) shows the difficulty encountered in achieving fine control of laryngeal posturing (Choi *et al.*, 1993a, 1993b, 1995). Although Nasri *et al.* (1995) did not explicitly study laryngeal posturing, they showed that the compound nerve action potential and electromyographic signals of the thyroarytenoid (TA) muscle were sigmoid functions of the recurrent laryngeal nerve (RLN) stimulation current (or voltage). Similarly, Gorman and Mortimer (1983) measured muscle force upon electrical stimulation of the nerve to the medial gastrocnemius muscle in cats, observed a sigmoidal force response, and concluded these sigmoidal responses to be a consequence of muscle recruitment responses, first from activation of large then small diameter nerve fibers. They noted that "the current level between threshold excitation (I_0) and maximal recruitment (I_{max}) is not large." However, they also noted a number of variables, which could assist in maximizing the difference in current levels between I_0 and I_{max}, including a reduction in the pulse width of the electrical stimulus. Consequently, any method that attempts to achieve fine control of laryngeal posturing must take in account these known sigmoidal responses of muscles to the stimulation current.

Human studies have measured laryngeal electromyographic signals to correlate with the fundamental frequency (Atkinson 1978; Faaborg-Andersen 1965). However, multiple la-

[a]Author to whom correspondence should be addressed.

ryngeal muscles are concurrently activated in human voice production, and thus, the effect of individual muscle could not be evaluated. Kempster *et al.* (1988) applied direct stimulation to the intrinsic muscles via electromyographic electrodes while the subject phonated. However, fine control of laryngeal muscles was not attempted in this experiment. Finally, while computer modeling would be useful in conceptualizing laryngeal control mechanisms, neuromuscular data must first be obtained, on which to base such computational models.

Controlled activation of the intrinsic laryngeal muscles in a graded fashion is crucial for a variety of investigations in voice physiology, including investigations of asymmetric laryngeal pathologies (e.g., laryngeal paralysis and paresis), glottal posturing, and control of voice parameters such as fundamental frequency, phonation onset, and laryngeal aerodynamics. In order to facilitate such future investigations, the purpose of the present study is to develop a methodology, which uses graded stimulation of laryngeal nerves to achieve fine control of both symmetric and asymmetric laryngeal posturing.

2. Methods

An *in vivo* canine phonation model was used. The canine larynx is a close match to the human larynx in terms of its gross, microscopic, and histologic anatomy, and the utility of this model in voice research is well established (Berke *et al.*, 1987; Garrett *et al.*, 2000). The Institutional Animal Research Committee approved the experimental protocol. The animal was anesthetized and placed on an operating table. A vertical midline skin incision was then made on the anterior neck to widely expose the larynx and the trachea. Bilateral RLNs and superior laryngeal nerves (SLNs) were isolated. A low tracheotomy was performed for intra-operative ventilation, and the oral endotracheal tube was removed. The larynx was exteriorized into the neck by first performing an infrahyoid pharyngotomy and then by dividing the pharynx circumferentially at this level. A supraglottic laryngectomy was performed, removing bilateral false vocal folds, epiglottis, and thyroid cartilage above the level of the ventricles. This allowed the larynx to be slightly lifted off the neck and improved the exposure and access to the larynx for experimental manipulation and measurements. The nerve branch to the posterior cricoarytenoid (PCA) muscles was divided bilaterally to remove the effects of PCA contraction during RLN stimulation. Knots of fine diameter nylon sutures were placed at various locations on the thyroid cartilage, arytenoids, and vocal folds for automated tracking of laryngeal landmarks such as the vocal process.

The four laryngeal nerves were electrically stimulated independently using cathodal stimulation pulse trains applied by monopolar, flexible, carbon-elastomer electrodes. The common ground electrodes were connected to surrounding tissue. The nerve stimulation pulse trains were generated with a C computer program that programmed two peripheral component interconnect (PCI) bus-based AD/DA boards (PowerDAQ PD2-MFS-8–500/16, United Electronics Industries, Walpole, Massachusetts) to generate four different stimulation pulse trains simultaneously. The digital timer of one board (accuracy of 1 μs) was used as a reference clock to simultaneously trigger the pulse train generation, analog signal acquisition, and a high-speed digital camera. The computer-generated voltage pulse trains were transformed into current pulse trains with a constant current stimulus isolator (A-M Systems Analog Stimulus Isolator Model M 2200, A-M Systems, Sequim, Washington).

The threshold current for neuromuscular activation of laryngeal muscles was established by visually observing the onset of vocal fold twitches as pulse train amplitudes (stimulation levels) increased. A high-speed camera was used to display and record a superior view of the larynx. Care was needed to either electrically insulate the monopolar stimulation electrodes from the surrounding tissue or to decrease the electrode-nerve contact impedance. This critically affected the activation threshold. For electrical insulation, small strips of plastic foil were placed between the monopolar electrode and the surrounding tissue, thus preventing shunting of the stimulation current to the surrounding tissue. Decreasing the electrode-nerve contact impedance by filling the gap between electrode and nerve with water based lubricating jelly as an electrical conductor (Surgilube, Fougera, Melville, New York) also decreased the relative impedance of the nerve tissue versus the surrounding tissue.

Each stimulation pulse train consisted of rectangular monophasic pulses, with constant amplitude, pulse width of 0.1 ms, in contrast with a pulse width of 1.5 ms used previously in Choi *et al.* (1993a, 1993b, 1995), and pulse repetition rate of 200 Hz for both the RLN and SLN stimulation. These stimulation pulse parameters were based on preliminary tests to achieve a fused muscle contraction above stimulation threshold. The stimulation duration per pulse train was 1500 ms, which contained 300 rectangular pulses. To allow muscle recovery, each pulse train was followed by 3.5 s pause, prior to the next pulse train. The high-speed camera was typically triggered 2 ms after the onset of each pulse train to capture the geometric change in the larynx, due to intrinsic muscle activation. All four nerves were concurrently stimulated with different pulse train amplitudes.

With the AD/DA boards, analog signals could be recorded simultaneously, along with the generation of the stimulation pulse trains at a sampling rate of 125 kHz. Typical signals recorded include subglottal mean pressure, subglottal mean flow rate, subglottal acoustic pressure fluctuations, and acoustic pressure fluctuations downstream of the exposed canine larynx. The same C program that generated the pulse train sequences triggered the high-speed camera (Photron FASTCAM Ultima APX, Photron, San Diego, California). All camera settings were controlled using the DaVis software (LaVision Inc., Goettingen, Germany). The camera frame rate for these geometric posturing studies was 100 or 500 frames per second (fps) at a spatial resolution of 512×512 or 1024×1024 pixels per image.

Strain histories as a function of graded nerve stimulation were measured from high-speed digital frames using cross-correlation image processing (MATLAB image processing toolbox) that tracked laryngeal suture landmarks. The suture positions identified by MATLAB program were visually verified for accuracy. Time to maximum vocal fold length change was measured from the strain histories. To calculate vocal fold strain, the suture landmarks at the anterior commissure and the vocal processes were used. The reference length L_0 was measured at zero stimulation. Strain was calculated as $(L_i - L_0)/L_0$, where L_i is vocal fold length upon graded stimulation. This digital frame analysis also allowed for observation of the trajectories of vocal fold movement to graded stimulation.

3. Results and discussion

In vivo experiments were performed in three canines, and data were similar in all animals. Therefore, representative examples are presented. Figure 1 shows the strain of the left and right vocal folds to (a) 23 levels of graded stimulation of the left RLN, and (b) 26 levels of graded stimulation of the left SLN. For low levels of stimulation, a linear change was observed, which demonstrates graded laryngeal muscle activation to graded nerve stimulation. For higher levels of stimulation, the strain reached a plateau, which likely results from geometric constraints of the laryngeal muscles and framework. Figure 1 also demonstrates the mechanical connection of both vocal folds, as activation of the left vocal fold also resulted in similar length change in the non-stimulated right vocal fold. However, the trajectories of the vocal processes were different (see high-speed digital image inserts in Fig. 1). Results were similar between RLNs and SLNs on either side of the larynx.

The onset of vocal fold movement to stimulation could be observed within the first few high-speed frames. The maximal vocal fold strain magnitude was reached around 60 ms for RLN stimulation and around 150 ms after SLN stimulation. These results were similar for the three larynges and are similar to the results of Titze *et al.* (1997). Maximum vocal fold strain for the three larynges ranged from −20% to −30% for RLN stimulation, and +10% to +15% for SLN stimulation. These values are similar to those reported by Titze *et al.* (1997) for RLN, but not for SLN stimulation, where they reported maximal strain range from +26% to +71%. The reason for this discrepancy is unclear. During stimulation of the SLN, some lateral flaring of the thyroid cartilage occurred that may have reduced the lengthening stress of the cricothyroid muscle [see high-

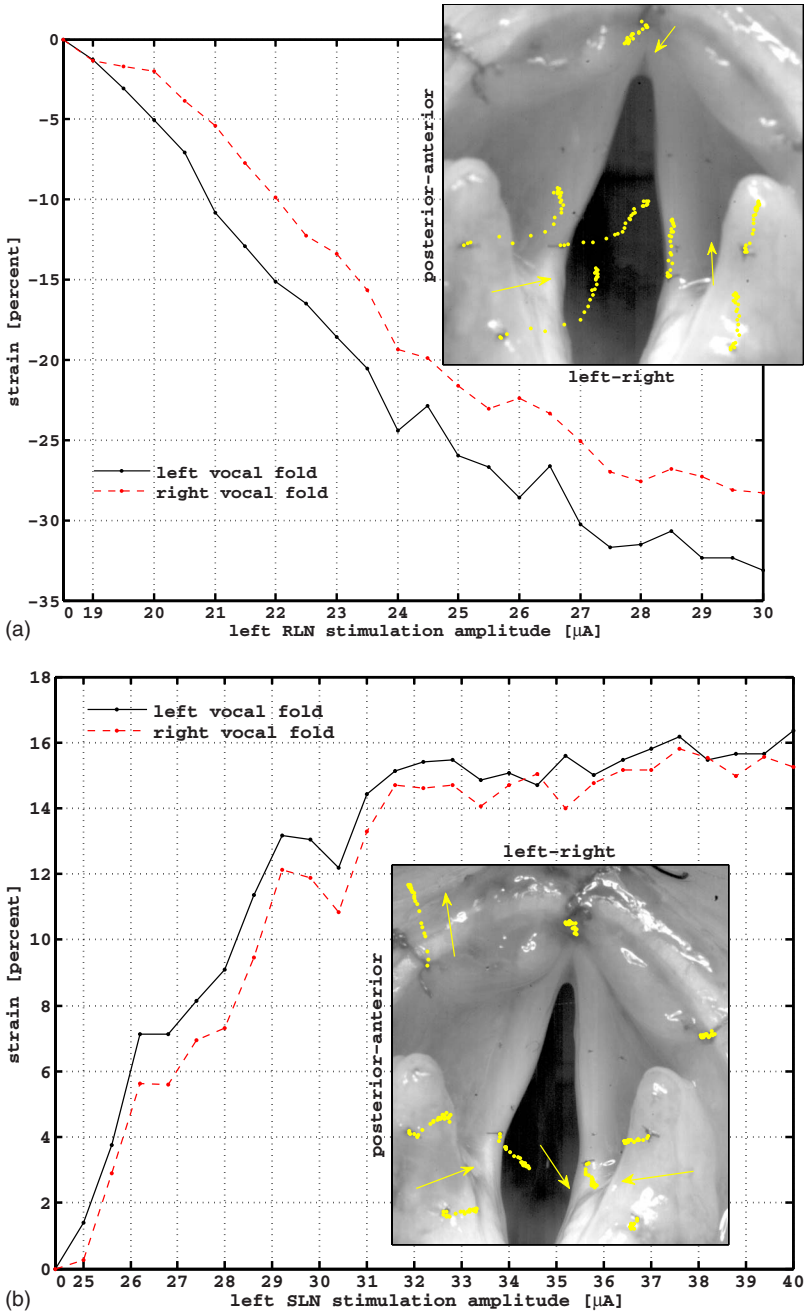

Fig. 1. (Color online) (a) Strain of the left and right vocal folds to 23 levels of graded stimulation of the *left* RLN and (b) 26 levels of graded stimulation of the left SLN. Reference length (L_0) was at zero stimulation amplitude (baseline). The strain values (percentage change in length) were measured at 1.0 s after the onset of the stimulation pulse train (pulse train duration 1.5 s, pulse width 0.1 ms, repetition rate 100 Hz). The figure insert shows individual changes in position of the suture landmarks at each level of graded stimulation (dots) and the overall direction of movement (arrows) plotted on the digital high-speed video frame obtained at baseline. Note the difference in trajectories between the stimulated *left* vocal fold and the non-stimulated *right* vocal fold, as well as the as the flaring movement of the left thyroid cartilage with ipsilateral SLN stimulation.

speed digital image insert in Fig. 1(b)]. The flaring of the thyroid cartilage was likely due to larynx preparation (exteriorization of the larynx in the neck, division of the strap muscles, and supraglottic laryngectomy) for improved visualization and measurements. However, our surgical technique appears similar to that of Titze *et al.* (1997). The effect of thyroid cartilage flaring on maximal strain of the vocal fold during SLN stimulation will need to be evaluated in future studies.

For investigations of laryngeal asymmetries, parameter values for symmetric muscle activation must first be established. Because laryngeal muscles exhibit a known sigmoidal response to stimulation current or voltage (Gorman and Mortimer, 1983; Nasri *et al.*, 1995), the range of threshold excitation current (I_0) to maximal recruitment current (I_{max}) was determined for each nerve (left RLN, right RLN, left SLN, right SLN) of each larynx. More specifically, I_0 was determined as the minimum stimulation current at which weak vocal fold twitches were observed. This was a reliable observation, and I_0 values were similar between the left and right vocal folds when electrical isolation of the electrode-nerve contact was carefully maintained during the experiment. A non-conducting material isolated the electrode-nerve contact area from touching adjacent tissue, and fluid build-up around the electrode-nerve contact points was prevented. I_{max} was determined as the minimum input current at which no further change in strain was observed.

Once I_0 and I_{max} were established for each nerve, graded stimulation was performed within that range. Symmetry of stimulation parameters was determined from the vocal fold strain and the distance between the vocal processes as a function of graded stimulation. Figures 2(a)–2(c) illustrate the left vocal fold strain [Fig. 2(a)], right vocal fold strain [Fig. 2(b)], and distance between the vocal processes [Fig. 2(c)] as a function of 11 levels of graded stimulation of the left and right RLNs (total 121 left/right conditions). The symmetry of the isocontour lines with respect to the diagonal reveals the symmetric response of vocal fold strain and vocal process distance to graded stimulation, implying symmetric graded activation of the larynx. Figures 2(d)–2(f) demonstrate the effect of adding low levels of bilaterally symmetric SLN stimulation. The results on the left vocal fold strain [Fig. 2(d)], right vocal fold strain [Fig. 2(e)], and distance between vocal processes [Fig. 2(f)] are similar to Figs. 2(a)–2(c), although there is a more abrupt transition in the measured variables at mid levels of graded stimulation of RLNs. Interestingly, the abrupt transition from a gradual change in strain to final strain levels occurred when strain had reached zero strain (resting length) as the lengthening effect on the vocal fold (positive strain) of SLN stimulation was countered by the shortening effect on the vocal fold by the gradual increase in RLN stimulation levels. The mechanism for this transition may be explained by muscle length versus force characteristics, but is a topic for further investigation.

The effect of TA stimulation is medial bulging of the mid-portions of the vocal folds (Choi *et al.*, 1993a). Figure 3 is photomontage of vocal fold postural change to symmetric graded stimulation [along the diagonal of Fig. 2(c)] of the left and right RLNs. With increasing stimulation, more medial bulging is observed until glottic closure is achieved in the mid-membranous area. This medial bulging effect to TA contraction has not been replicated in *ex vivo* or current computer models. The effects of medial bulging of the vocal folds on phonatory parameters, such as fundamental frequency, phonation onset pressures, and glottal geometry, are subjects of further research and can be studied using graded stimulation.

4. Conclusions

A methodology for graded stimulation of laryngeal nerves (left and right RLNs and SLNs) was developed, which yielded fine control of both symmetric and asymmetric laryngeal posturing. Once the threshold excitation current and maximal recruitment current were established for each nerve, a symmetric postural response of the larynx was established. Similarly, a wide range of asymmetric states was also established. In the future, this methodology will be used to study laryngeal paralysis and paresis, as well as more general questions of neuromuscular control of the larynx.

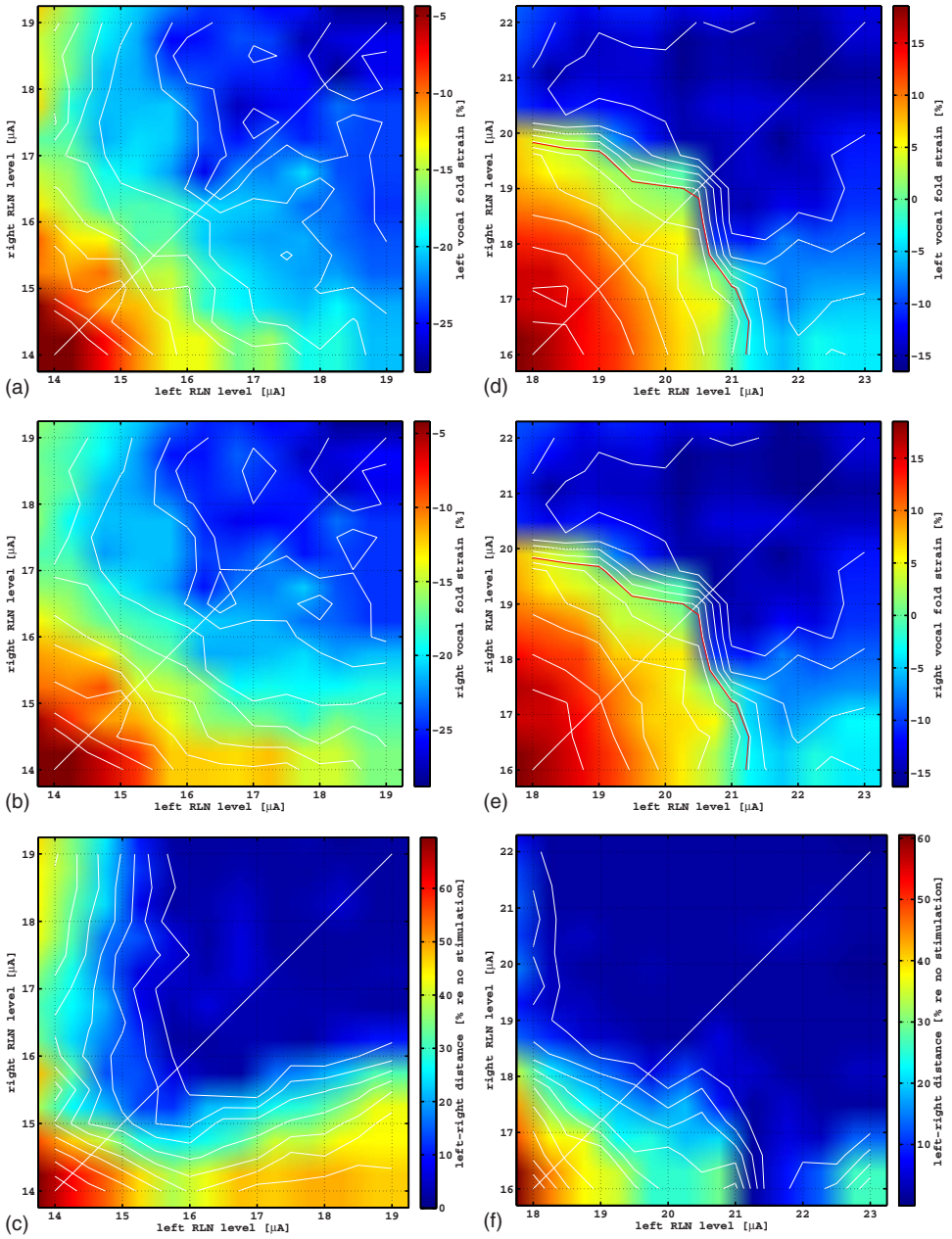

Fig. 2. (Color online) Symmetry of stimulation parameters was determined from analysis of left vocal fold strain (a),(d), right vocal fold strain (b),(e), and distance between vocal processes (c),(f), as a function of 11 levels of graded stimulation of the right and left RLNs (total 121 conditions). Zero SLN stimulation was applied in (a),(b),(c), and in (d),(e),(f) a low level of SLN stimulation amplitude was applied that was close to the excitation threshold (left SLN 24 μA, right SLN 34 μA). The symmetry of the isocontour lines with respect to the diagonal (straight diagonal white line) demonstrates symmetric response of the vocal folds, implying symmetric graded activation of the larynx. However, in presence of SLN activation (d)–(f) there was an abrupt transition in strain of the vocal folds when zero strain was reached. The percentage strain values at the stimulated conditions are with respect to reference length measured at zero stimulation. (Measurements for stimulated conditions taken at 404 ms after onset of stimulation pulse train; pulse train repetition rate 200 Hz; camera frame rate 500 fps with resolution 512 $\times$512 pixels.)

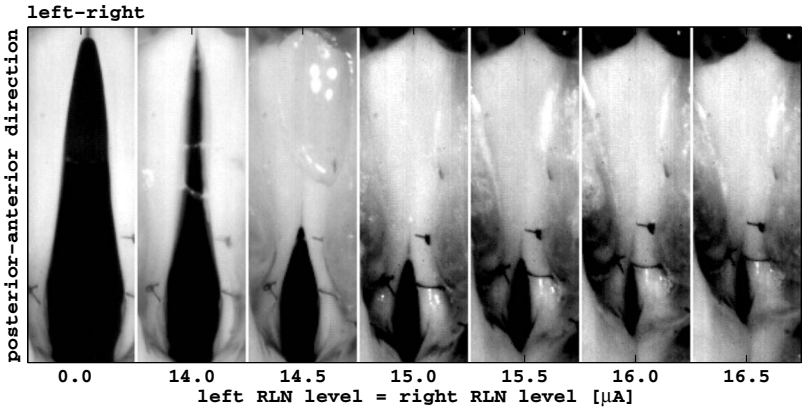

Fig. 3. Photomontage of vocal fold postural change to symmetric graded stimulation. The experimental conditions are identical to Fig. 2 and the photomontage is taken from images along the diagonal in Fig. 2(c). The medial bulging effect of the vocal folds is seen first, followed by closure of the posterior commissure.

Acknowledgments

This study was supported by Grant No. R01 DC003072-S1 from the National Institutes of Health.

References and links

Atkinson, J. E. (**1978**). "Correlation analysis of the physiological factors controlling fundamental voice frequency," J. Acoust. Soc. Am. **63**, 211–222.

Berke, G. S., Moore, D. M., Hantke, D. R., Hanson, D. G., Gerratt, B. R., and Burstein, F. (**1987**). "Laryngeal modeling: Theoretical, in vitro, in vivo," Laryngoscope **97**, 871–881.

Choi, H. S., Berke, G. S., Ye, M., and Kreiman, J. (**1993a**). "Function of the thyroarytenoid muscle in a canine laryngeal model," Ann. Otol. Rhinol. Laryngol. **102**, 769–776.

Choi, H. S., Berke, G. S., Ye, M., and Kreiman, J. (**1993b**). "Function of the posterior cricoarytenoid muscle in phonation: In vivo laryngeal model," Otolaryngol.-Head Neck Surg. **109**, 1043–1051.

Choi, H. S., Ye, M., and Berke, G. S. (**1995**). "Function of the interarytenoid (IA) muscle in phonation: In vivo laryngeal model," Yonsei Med. J. **36**, 58–67.

Faaborg-Andersen, K. (**1965**). "Electromyography of laryngeal muscles in humans: Techniques and results," Folia Phoniatr (Basel) **3**, 1–71.

Farley, G. R. (**1994**). "A quantitative model of voice F0 control," J. Acoust. Soc. Am. **95**, 1017–1029.

Garrett, C. G., Coleman, J. R., and Reinisch, L. (**2000**). "Comparative histology and vibration of the vocal folds: Implications for experimental studies in microlaryngeal surgery," Laryngoscope **110**, 814–24.

Gorman, P. H., and Mortimer, J. T. (**1983**). "The effect of stimulus parameters on the recruitment characteristics of direct nerve stimulation," IEEE Trans. Biomed. Eng. **BME-30**, 407–414.

Kempster, G. B., Larson, C. R., and Kistler, M. K. (**1988**). "Effects of electrical stimulation of cricothyroid and thyroarytenoid muscles on voice fundamental frequency," J. Voice **2**, 221–229.

Nasri, S. N., Dulguerov, P., Damrose, J., Ye, M., Kreiman, J., and Berke, G. S. (**1995**). "Relation of recurrent laryngeal nerve compound action potential to laryngeal biomechanics," Laryngoscope **105**, 639–643.

Story, B. H., and Titze, I. R. (**1995**). "Voice simulation with a body-cover model of the vocal folds," J. Acoust. Soc. Am. **97**, 1249–60.

Titze, I. R., Jiang, J. J., and Lin, E. (**1997**). "The dynamics of length change in canine vocal folds," J. Voice **11**, 267–76.

A new adaptive resonance frequency of piezoelectric components used for vibration damping

A. Faiz[a)]
Laboratoire de Biophysique Audioprothèse, Faculté de Pharmacie, Nancy University, Nancy 54000, France
adil.faiz@pharma.uhp-nancy.fr

L. Petit and D. Guyomar
Laboratoire de Génie Electrique et Ferroélectricité, Institut National des Sciences Appliquées de Lyon, Lyon University, Villeurbanne 69621, France
lionel.petit@insa-lyon.fr, daniel.guyomar@insa-lyon.fr

J. Ducourneau
Laboratoire de Biophysique Audioprothèse, Faculté de Pharmacie, Nancy University, Nancy 54000, France
joel.ducourneau@pharma.uhp-nancy.fr

Abstract: This paper describes two methods for vibration damping in a broad band frequency range using a piezoelectric patch. The first method, applied to an adaptive device, uses a bias (static voltage control), which applies stresses or releases stresses in a piezoelectric component to modify its mechanical characteristics and thereby its resonance frequency. The second method is based on a semipassive approach [synchronized switch damping (SSD)], developed to control structural vibration damping using a piezoelectric component. Attenuations of 10 and 4.8 dB in vibration velocity have been obtained using the adaptive frequency and SSD methods.

PACS numbers: 43.50.Hg, 43.55.Wk [JM]
Date Received: May 12, 2009 **Date Accepted:** December 2, 2009

1. Introduction

Vibration damping has become a priority research area in a number of industries including car manufacturing, aerospace, and sports equipment manufacturing. Faced with this diversity of potential applications, various damping methods have been designed based on piezoelectric materials. These components (patch, piezofiber composite, and thick or thin layer) are bonded on or embedded in the structure and are used as sensors, actuators, or combined sensors and actuators. When the structure vibrates, the piezoelectric components are stressed and respond by creating an electric field based on the piezoelectric effect. Electrical energy degradation or transfer leads to control and vibration attenuation.

A complex system integrating at least one sensor, a control unit, and a feedback actuator is required for active vibration control. External power sources and amplifiers are additionally required for the control unit and actuators.

Passive techniques are more adaptable because of their simplicity and compactness. The piezoelectric component is connected to a specific electrical system incorporating a dissipative shunt (Hagood and Flotow, 1991). The most effective method is the tuned shunt, in which a circuit incorporating an inductor (L) and a resistor (R) in series is connected to a piezoelectric component capacitor (C_0). Optimum damping is achieved by tuning the electrical resonance to the frequency of the unwanted structural mode. This method gives good results but has several

[a)]Author to whom correspondence should be addressed.

Table 1. Resonance frequency, coupling coefficient and the vibration damping for different static voltage applied.

Static voltage applied	−5 V	0 V	5 V
Resonance frequency	350 Hz	400 Hz	450 Hz
Coupling coefficient k^2	52%	48.7%	44%
Attenuation (dB)	10 dB	7.6 dB	4.4 dB

disadvantages:

(1) Multimodal damping requires the use of complex shunt circuits (Wu, 1998).
(2) At low frequency modes, the optimum inductance is very high and may reach tens or hundreds of henry.

Several semipassive or active-passive techniques had been proposed to overcome these drawbacks. In the active-tuned solid state piezoelectric absorber developed by Davis and Lesieutre (1998), a passive capacitive shunt circuit is used for electrically adjusting the effective stiffness and consequently the resonance frequency of the piezoelectric components. In the approach suggested by Morgan and Wang (2002), an arrangement comprising an adaptive tuning inductor, a negative resistance, and a coupling creates a system with multimodal damping capacity.

More recently, switched shunt techniques have been developed, which introduce a nonlinear approach by modifying piezoelectric component properties or boundary conditions in synchrony with structural movement. The state-switching method proposed by Clark (2000) is a variable stiffness technique, in which piezoelectric components are periodically maintained in the open-circuit state, then switched and maintained in the short-circuit state in synchrony with structural movement. In a rather different way, Cunefare *et al.* (2000) successfully adapted the earlier work of Larson *et al.* (1998) on the state-switching concept to vibration damping and has proposed the state-switching absorber (SSA) (Cunefare *et al.*, 2000).

Richard *et al.* (1999) suggested previously the synchronized switch damping (SSD) technique, which is the approach considered in this paper. The SSD technique (Richard *et al.*, 2000) involves modifying the voltage on a piezoelectric component bonded to the structure a simple switch actuated for short periods in synchrony with structural movement. This switch connects the piezoelectric component to a small inductor (SSDI). The process involves a phase shift between the piezoelectric component strain and the resulting voltage; this causes energy dissipation. The SSD method offers several advantages: it is unaffected by environmental changes because of its self-adaptive broad band behavior, it does not require a large tuning inductor at low and very low frequencies, it achieves multimodal damping without the need for complex circuitry and it only requires a very low power supply for switch control. The adaptive resonance frequency and the SSD methods are described in Sec. 2 of this paper. Section 3 then describes the experimental setup and results.

2. Anechoic termination principle

2.1 Adaptive resonance frequency of the piezoelectric component absorber

To obtain a smart panel broad band frequency range, it would be necessary to use various piezoelectric components with different resonance frequencies. This could be achieved by integrating piezoelectric components into the various dimensional specifications and/or mechanical characteristics.

To make this panel type more flexible, we can conceivably modify the resonance frequency of the piezoelectric component without radically changing these physical properties.

The adaptive resonance frequency method involves changing the stiffness of the system by modifying the electric conditions and thus varying the resonance frequency (Table 1).

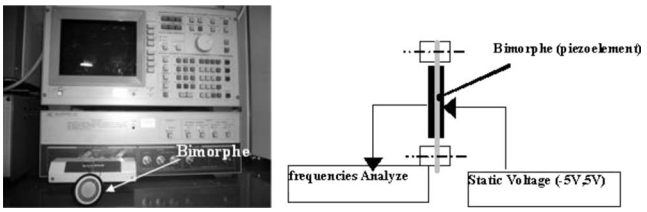

Fig. 1. Experimental device for adaptive resonance frequency of piezoelectric components.

Stiffness can be changed by applying a static voltage to the piezoelectric component. It can be increased or decreased based on the piezoelectric component polarity and the static voltage.

The experimental device shown in Fig. 1 is a piezoelectric component, specifically a 50 mm diameter MURATA Ceramitone VSB50EW-0701B buzzer, connected to a spectrum analyzer (4194A HP). The control bias allows a static voltage to be applied the piezoelectric component. Impedance analysis yields the variation in this component's characteristic parameters (resonance and antiresonance frequency, quality factor, and coupling factor) with respect to static voltage.

Figure 2(a) illustrates the admittance spectrum variation for the piezoelectric component with respect to static voltage.

Figures 2(b)–2(d) illustrate the resonance and antiresonance frequencies (f_0,f_1), the coupling factor k^2, and the mechanical quality factor Q for the piezoelectric component with respect to applied voltage (−5 to 5 V).

We note that the resonance and antiresonance frequencies in Fig. 2(b) increase with respect to the static voltage. This variation causes the specific characteristics of the piezoelectric component to be modified. Increasing flexibility of the piezoelectric component with respect to

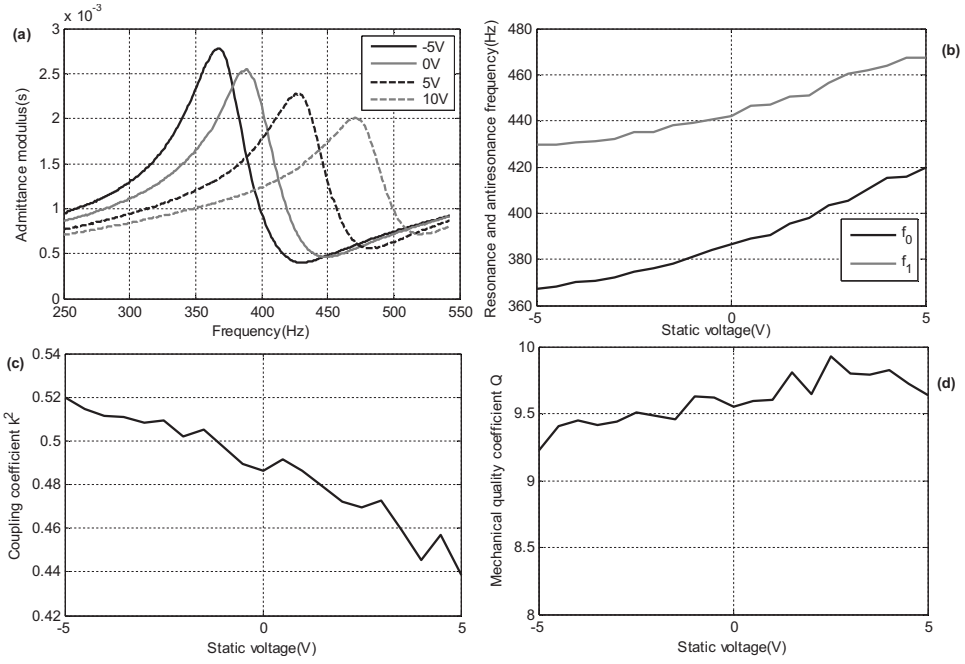

Fig. 2. Admittance modulus (a) and mechanical proprieties of piezoelectric component with respect to static voltage [(b)–(d)].

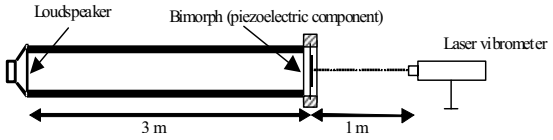

Fig. 3. Experimental device for vibration damping.

negative voltage leads to decreasing resonance frequency. Conversely, the positive voltage stiffens the piezoelectric component and leads to increasing resonance frequency.

Figure 2(c) illustrates the variation in electromechanical coupling coefficient with respect to voltage. Increased voltage reduces the coupling coefficient and this reduction is caused by greater stiffness according to Eq. (1). The coupling coefficient is approximately 10% for the voltage used in this experiment (5 V).

$$k^2 = \frac{f_1^2 - f_0^2}{f_1^2}. \tag{1}$$

The mechanical quality factor for the piezoelectric component remains practically constant for all applied voltages. Figure 2(d) illustrates this variation; this parameter is conventionally calculated from the bandwidth of the real part of the admittance.

These results show that the first bending mode resonance frequency for the piezoelectric component is controlled and this enables the first bending mode frequency to be adjusted for the excitation frequency.

2.2 The nonlinear technique

The principle involves intermittently switching piezoelectric components to a specific shunt circuit (resistor R_s and inductor L_s) to discharge the piezoelectric component capacitance each time the strain [or displacement $u(t)$] reaches a maximum. The SSDI device is used to control the piezoelectric component voltage. A specific analog processing box detects the voltage $V(t)$ extremum and actuates the switch control. An oscillating capacitance discharge is induced through the inductor. Pulse ω_s of this oscillation is directly related to the piezoelectric component blocked capacitance C_0 and L_s based on the equation

$$\omega_s = \frac{1}{2\pi\sqrt{L_s C_0}}. \tag{2}$$

If the switching control pulse width t_s is equivalent to the half-oscillation period, the voltage $V(t)$ is precisely reversed at each maximum value. The voltage is then distorted, resulting in a magnification and a quasi-$\pi/2$ phase between the voltage $V(t)$ and the displacement $u(t)$. The piezoelectric effect causes the voltage to exert a force, which is invariably opposed to the speed. This method is described in another paper (Faiz *et al.*, 2006 Guyomar *et al.*, 2006).

3. Experimental setup

The experimental setup shown in Fig. 3 comprises a 3 m long, 28 mm internal diameter brass pulse tube. A loudspeaker fitted to one end of this tube generates a tone sweep acoustic wave (200–800 Hz). An active end featuring a piezoelectric buzzer (50 mm diameter MURATA Ceramitone VSB50EW-0301B buzzer) is connected to the other end of the pulse tube. A vibrometer laser monitoring the vibration velocity is positioned 1 m from the buzzer terminals, which are connected to a SSDI-type controller for switched nonlinear processing of the piezoelectric voltage.

Figure 4 illustrates the vibration velocity with and uncontrolled (SSD on, SSD off) of the buzzer in three cases: voltage static=−5, 0, and 5 V.

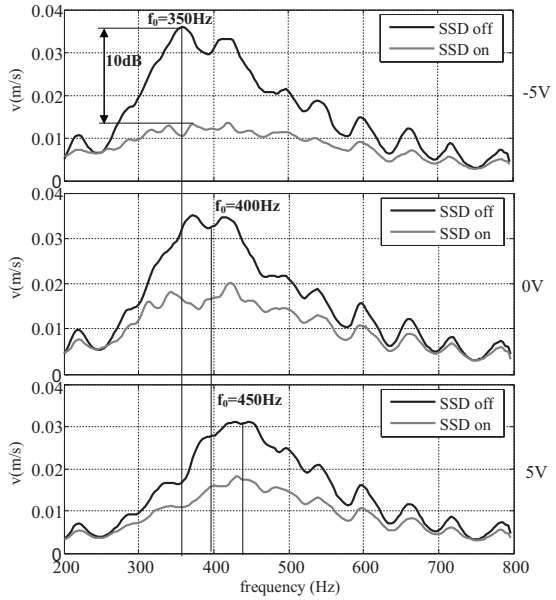

Fig. 4. The vibration velocity is plotted with the uncontrolled (SSD off) and then the controlled (SSD on) buzzer termination in three cases: voltage static=−5, 0, and 5 V.

The buzzer resonance frequency is successively 350 Hz when the static buzzer voltage $V=-5$ V, 400 Hz when $V=0$ V, and 450 Hz when $V=5$ V. This adaptation frequency and the SSD on control ensure satisfactory attenuation at different frequencies.

For the controlled buzzer when the applied static voltage is −5 V, the maximum vibration velocity is one-fifth of the case without control. This corresponds to a 10 dB attenuation of the vibration velocity. This attenuation is specified in Fig. 4.

4. Conclusion

Both the SSD control and adaptation resonance frequency methods offer to be high performance in relation to solving vibration damping problems. High attenuation is obtained for different resonance frequencies (10–4.4 dB).

The control device described in this study is simple, lightweight, and compact. It requires only little energy to control a resonance frequency. Moreover, the SSDI-related device can be self-powered using vibration energy to start and continue the damping function.

The ongoing aim of current research into acoustic control architecture is to extend this technique to associate various skin panels on a large surface. One of the main advantages of the proposed technique is its potential for high performance at low frequency using a very low profile, thin, lightweight panel device. Another research aim is controlling large panels combining a number of piezoelectric patches designed for different modes.

References and links

Clark, W. W. (**2000**). "Vibration control with state-switching piezoelectric materials," J. Intell. Mater. Syst. Struct. **11**, 263–271.

Cunefare, K. A., De Rosa, S., Sadegh, N., and Larson, G. (**2000**). "State-switched absorber for semi-active structural control," J. Intell. Mater. Syst. Struct. **11**, 300–310.

Davis, C. L., and Lesieutre, G. A. (**1998**). "An actively-tuned solid state piezoelectric vibration absorber," Proc. SPIE **3327**, 169–182.

Faiz, A., Guyomar, D., Petit, L., and Buttay, C. (**2006**). "Wave transmission reduction by piezoelectric semipassive technique," Sens. Actuators, A **128**, 230–237.

Guyomar, D., Faiz, A., Petit, L., and Richard, C. (**2006**). "Wave reflection and transmission reduction using a piezoelectric semipassive nonlinear technique," J. Acoust. Soc. Am. **119**, 285–298.

Hagood, W. N. and Flotow, A. V. (**1991**). "Damping of structural vibrations with piezoelectric materials and

passive electrical networks," J. Sound Vib. **146**, 243–268.
Larson, G. D., Rogers, P. H., and Munk, W. (**1998**). "State switched transducers: A new approach to high-power low frequency, underwater projectors," J. Acoust. Soc. Am. **103**, 1428–1441.
Morgan, R. A. and Wang, K. W. (**2002**). "Active-passive piezoelectric absorbers for systems under multiple non-stationary harmonic excitations," J. Sound Vib. **255**, 685–700.
Richard, C., Guyomar, D., Audigier, D., and Bassaler, H. (**2000**). "Enhanced semipassive damping using continuous switching of a piezoelectric device on an inductor," Proc. SPIE **3989**, 288–299.
Richard, C., Guyomar, D., Audigier, D., and Ching, G. (**1999**). "Semipassive damping using continuous switching of a piezoelectric device," Proc. SPIE **3672**, 104–111.
Wu, S. Y. (**1998**). "Method for multiple shunt damping of structural vibration using a single PZT transducer," Proc. SPIE **3327**, 159–168.

Wavefield extraction using multi-channel chirplet decomposition

Grégoire Le Touzé,[a] Paul Cristini, and Nathalie Favretto-Cristini
Laboratoire de Mécanique et d'Acoustique-CNRS, 31 chemin Joseph-Aiguier, 13402 Marseille Cedex 20, France
le_touze@lma.cnrs-mrs.fr, cristini@lma.cnrs-mrs.fr, favretto@lma.cnrs-mrs.fr

Jacques Blanco
PhySeis Consultant, 23 route de Burosse, 64350 Lalongue, France
jacques.blanco@orange.fr

Abstract: In acoustical and seismic fields, wavefield extraction has always been a crucial issue to solve inverse problem. Depending on the experimental configuration, conventional methods of wavefield decomposition might no longer likely to hold. In this paper, an original approach is proposed based on a multichannel decomposition of the signal into a weighted sum of elementary functions known as chirplets. Each chirplet is described by physical parameters and the collection of chirplets makes up a large adaptable dictionary, so that a chirplet corresponds unambiguously to one wave component.

PACS numbers: 43.60.Fg, 43.60.Mn [CG]
Date Received: December 2, 2009 **Date Accepted:** January 26, 2010

1. Introduction

In most acoustical and seismic applications, the wavefield is a combination of waves (e.g., direct arrival and reflections, normal modes, and compressional and shear waves) As knowledge of wave characteristics (i.e., time arrival, waveform, amplitude, and phase) is useful for solving the inverse problem (e.g., source localization and characterization, and estimation of environment parameters), wavefield extraction has always been a crucial issue. Wavefield decomposition can be achieved in different ways. A common way consists in projecting the signal on a set of functions. This set can be a basis of functions (e.g., time, frequency, time-frequency, Tau-P, frequency-wavenumber, and basis of matrix methods) where wave components overlap is small and upon which the filter is applied. For instance, the frequency domain achieved by the Fourier representation corresponds to the projection of the signal based on sinusoids. The set can also be a frame (overcomplete). In this case, the functions often correspond to a well-studied type (e.g., Gabor functions and wavelets) forming a dictionary of atoms and the projection is called atomic decomposition. The decomposition can be either adaptive, by searching a collection of different atoms in order to best match the inner structure of the signal, or not adaptive (i.e., fixed) as the well known continuous wavelet transform. After the decomposition, the signal can be written as a linear combination of atoms selected in the dictionary. Depending on the chosen method, this processing has limitations. First, changing the basis often requires a receiver configuration which consists of many sensors generally aligned and regularly spaced along an array. It is the case for frequency-wavenumber filtering,[1] Tau-P decomposition,[2] and matrix method of decomposition.[3] Moreover, the new basis is not always successful to avoid overlap between wave components. This is particularly true for frequency and time-frequency domains, even if some methods attempt to prevent these intrinsic drawbacks.[4] Those limitations prevent decomposition for numerous applications. For instance, in the case of reservoir monitoring using information derived from induced microseismicity, despite the short distance between the sources and the sensors positioned in boreholes, because the array is limited to a small

[a]Author to whom correspondence should be addressed.

number of sensors not necessarily regularly spaced, it is difficult to go beyond the classical location map. Moreover, the surrounding zone of microseismic sources is the place where body waves and dispersive waves are greatly interfering.

We propose in this paper a method to overcome these limitations. The objective is that after the decomposition each atom corresponds unambiguously to one wave component. For this reason, an adaptive decomposition on a large overcomplete dictionary is chosen. Two issues are linked to this type of methods: the choice of elementary functions (called atoms) that build up the dictionary and the algorithm of decomposition that selects from the dictionary the atoms that best suit and that calculates the projection coefficient. We use a dictionary of seven-parameter chirplets initially developed by Bardainne *et al.*,[5] which allows a great adaptability. This dictionary is described in Sec. 2. The algorithm of decomposition that we have developed includes an array processing based on the matching pursuit (MP) algorithm followed by an optimization step. It is described in Sec. 3. Results on synthetic data are presented in Sec. 4.

2. Seven-parameter chirplet dictionary

In order to associate unambiguously one atom to one wave component, we sought a dictionary with two constraints. First, a wave component can be perfectly described by one atom of the dictionary. Then, the combination of several wave components (two or more) cannot be described by only one atom. The first assumption requires a dictionary extremely flexible and thus very large. We chose a seven-parameter chirplet dictionary, a chirplet being a time-limited function which corresponds to a piece of chirp. Like wavelets, chirplets are based on a mother function generally Gaussian. The two-parameter Gabor dictionary (i.e., time translated and frequency shift version of the mother function) or the wavelet dictionary (i.e., time translated and dilated/contracted) are the most conventional chirplet dictionaries.

A third parameter (i.e., the linear coefficient of modulation) has been introduced.[6] Acoustic or seismic wave components can vary not only in arrival time (depending on travel path for a given wave source), in frequency (depending on source bandwidth and filtering attenuation by the medium), in duration (depending on source and dispersion), in linear or nonlinear frequency modulation (depending on source and dispersion) but also in overall waveform which characterizes the type of waves (e.g., body waves, guided waves, or interface waves). The symmetric Gaussian envelope of the mother wavelet is unsuitable for most of these waves. As a consequence, Gabor, wavelet, and even four-parameter dictionaries are not flexible enough to fully describe physical events and to fulfill assumptions formulated above. This is the reason why we used a normalized chirplet dictionary introduced by Bardaine *et al.*[5] in a seismic context where atoms are described by seven appropriate parameters to suit the physical configuration, i.e., the time delay τ_i and six morphological parameters. The first four parameters f_i, o_i, $q1_i$, and $q2_i$ represent, respectively, the frequency shift, the chirplet duration (i.e., number of oscillations), the linear frequency modulation coefficient, and the nonlinear modulation coefficient. The last two parameters $e1_i$ and $e2_i$ control the envelope shape by acting, respectively, on the symmetry and on the duration of the constant flat shape between the left and right Gaussian halves. Once established the range of definition for each parameter, we build up the dictionary by accounting for all the possible combinations of the parameters. For details on the formulation of the chirplet dictionary, see Ref. 5. Finally, note that the larger the number of parameters and the range of solutions, the larger the computational complexity and time, but the more the assumptions can be fulfilled.

3. Proposed algorithm

A decomposition associating unambiguously one atom to one wave component corresponds to a "sparse" problem because the number of atoms involved in the decomposition is "small" in comparison to the number of sample points needed to store the signals. Over the last years the signal processing community has been interested in this problem and algorithms have been developed to find sparse solutions. Unfortunately, the problem of constructing the best approximation of a signal as a linear superposition of K atoms drawn from a coherent dictionary becomes an intractable combinatorial problem, even if the dictionary is finite. As a general rule,

we face a trade-off between signal approximation and constraint relaxation. Therefore, it is addressed by heuristic stepwise algorithms which do not seek the optimal solution. The selected atoms and their coefficient of projection depend on the choice of the decomposition method. The well known MP algorithm introduced by Mallat *et al.*[7] determines iteratively a set of atoms. Numerous methods have been developed to improve or to complete the MP method (e.g., basis pursuit[8] and method of frames[9]). All these methods fail when one signal (i.e., one single sensor) is only considered. The originality of our decomposition method consists in taking advantage of the common information provided by a same wave (corresponding to the same physical phenomenon) at each sensor, leading us to extend the MP to the multi-component array configuration. Indeed, the basis pursuit is not extensible to array processing and the method of frames is not efficient in the case of sparse problem.

We first detail the decomposition of observed signals into a linear combination of K chirplets by the MP. The starting point of the first iteration ($k=0$) is the signal itself: $x_0=x$. For each iteration, the MP finds the best match between the signal and the atom dictionary $\mathcal{D}^{\text{chirp}}=\{h_i\}$, $i=1,\ldots,M$, by computing the maximum modulus inner product (i.e., the projection) of the signal among all atoms:

$$|i_k| = \arg\max_i |\langle x_k, h_i \rangle| \tag{1}$$

with the coefficient A_k given by

$$A_k = \langle x_k, h_{i_k} \rangle \tag{2}$$

and where x_k is the residual after the kth iteration $x_k=x_{k-1}-A_{k-1}h_{k-1}$. After K iterations, the signal is described by the linear combination:

$$x = \sum_{k=0}^{K-1} A_k h_{i_k} + R_K x, \tag{3}$$

where $R_K x$ is the residual. This iterative procedure is performed until some predefined requirements are satisfied. The stopping criterion is generally the percentage of energy given by the residual between the decomposition result and the original signal. The MP is easy to implement besides being the fastest algorithm of decomposition. Note that if the seven-parameter chirplet dictionary is used, each selected atom k is fully described by nine parameters, i.e., the seven of the associated chirplet h_k plus two parameters of the decomposition coefficient A_k (i.e., the amplitude and the phase). To take into account the mutual information shared by sensor and component signals while preserving a degree of freedom to reflect wave changes, we propose the following two-step algorithm: a multi-component array MP process followed by an optimization process.

3.1 Step 1: Multi-component array matching pursuit

We first assume that a same wave is present on the whole array. The fulfillment of this assumption depends on the configuration of propagation and reception. This array can be divided into several parts to make sure this assumption stays valid. Depending on the configuration, we also assume that some of the seven parameters of chirplets describing the same wave across the array and some of the two projection parameters (i.e., amplitude and phase) are fixed, whereas the others vary independently. Still considering the wave, the same assumption is made for the outputs of a three-component sensor. The repartition between fixed and varying parameters is not necessarily identical but the set of fixed-sensor parameters must be included into the set of fixed-component parameters. The choice of fixed and varying parameters depends on the way of propagation of the waves through the complex media. Note that the amplitude and the phase are always supposed to be varying parameters across the array (for sensors and components). Parameters can thus be divided into three classes: the sensor and the component fixed parameters F, the sensor and component varying parameters V, and the mixed parameters M. By assumption all the M parameters are component fixed and sensor varying. The chirplet dictionary in-

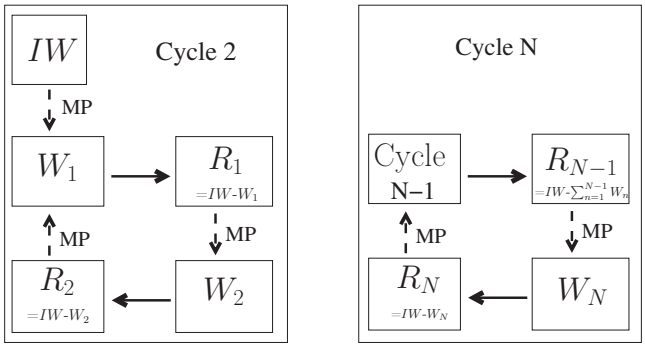

Fig. 1. Diagram of the recursive cycles (step 2).

dexed by these classes of parameters is written $\mathcal{D}^{\text{chirp}}=\{h_{F,M,V}\}$. For instance, in a seismic context the chirplet is assumed to possess the same six morphological parameters across the array, whereas time delay and both the projection parameters are allowed to vary. For the outputs of a three-component geophone, only the projection parameters are allowed to vary. Finally, we can write $F=\{f,o,q1,q2,e1,e2\}$, $M=\tau$, and $V=\{|A_p|,\arg(A_p)\}$.

The multi-component array matching pursuit (MAMP) algorithm implements the MP across the array, through the assumption on fixed and varying parameters. At the kth iteration, the algorithm selects the chirplet which maximizes the double sum of projections:

$$F_k, \quad \{M_{k,l}\}_{l=1}^{L}, \quad \{V_{k,l,j}\}_{l=1,j=1}^{L,J} = \arg\max_{F} \sum_{l=1}^{L} \arg\max_{M} \sum_{j=1}^{J} \arg\max_{V} |\langle x_{k,l,j}, h_{F,M,V}\rangle|, \tag{4}$$

where L is the number of sensors and J is the number of components at each sensor. The projection coefficient is given by

$$A_{F_k,M_{k,l},V_{k,l,j}} = \langle x_{k,l,j}, h_{F_k,M_{k,l},V_{k,l,j}}\rangle.$$

MAMP proceeds by iterating the same way as the conventional MP. The extracted wave components are characterized by their nine parameters and the relevant part of the signal is fully characterized in a sparse way by 9 K information.

3.2 Step 2: Optimization

Overlap between two independent wave components, which may skew the decomposition, is different at each sensor, making the array processing particularly relevant for this situation. The summation gets partially rid of this problem and makes the result more reliable. To converge toward a more reliable result, we propose a recursive process. We first explain the subroutine cycle 2 described in Fig. 1. The starting point is the initial wavefield (IW) on which the MAMP process is applied with two iterations to determine a first approximation of the two first wave components (noted W_1 and W_2). This corresponds to the conventional MAMP process. To improve the MAMP efficiency, W_2 is subtracted from the initial wavefield IW and an additional MAMP iteration is applied on the residual ($R_2=\text{IW}-W_2$), giving a more reliable approximation of W_1. Then, this new estimate W_1 is subtracted from the IW and again, another MAMP iteration is applied on the residual ($R_1=\text{IW}-W_1$), giving in turn a more reliable approximation of W_2. This process is iterated until the energy of the residual, $R_{12}=W_I-W_1-W_2$, no longer decreases. This ends cycle 2 which corresponds to the decomposition of the IW into two atoms. Similarly, the process can be extended to a finite number of atoms. For N atoms, the recursive process is a generalization of cycle 2 by replacing W_1 by cycle $N-1$ and W_2 by W_N (Fig. 1). After this optimized step, all significant wave components are supposed to be extracted.

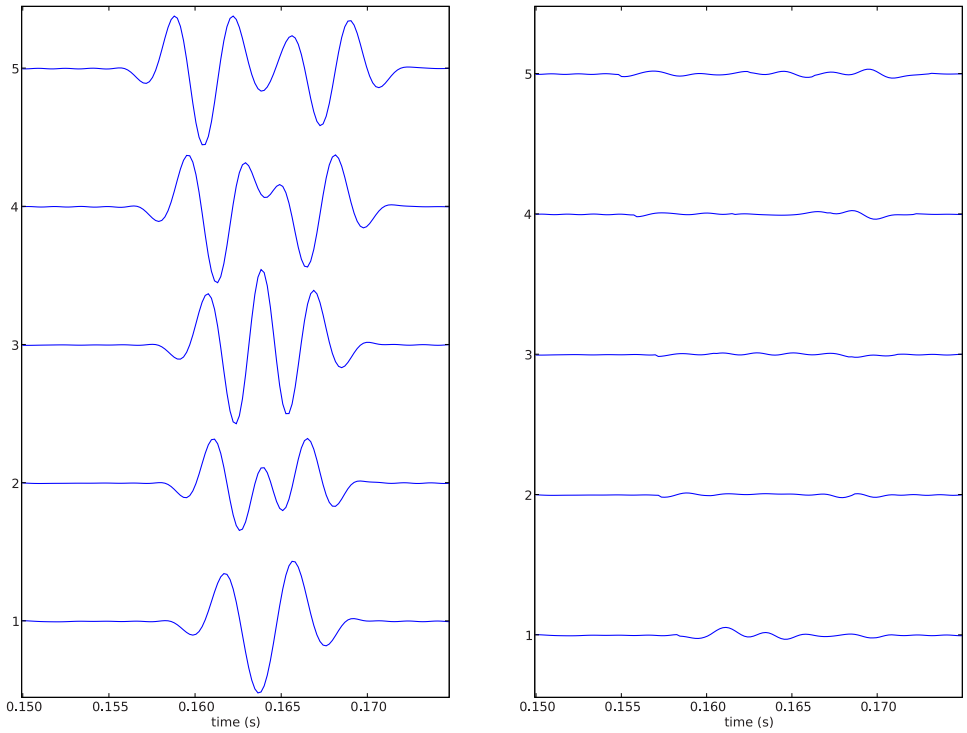

Fig. 2. (Color online) Synthetic data. Left panel: data of the vertical component. Right panel: residual after the optimized MAMP decomposition.

4. Applications

The original method of wavefield decomposition described in this paper was applied on a synthetic seismic data set. Observations were simulated by the OASES software[10] for a simple configuration where an omnidirectional source emitted a pulse in a three homogeneous layer medium. The advantage of using the OASES code instead of real data in a first test is that the code provides exact solutions of wave components. The signal to be filtered is recorded in the vicinity of the interface between layers 1 and 2. It is composed of two compressional waves, up-P and down-P. The two-component (vertical and radial) sensors were vertically aligned but not regularly spaced. Some parameters of the wavefield model were variables, so that the interference between the two wave components might sufficiently change across the array (Fig. 2). The decomposition performances have been evaluated by measuring the percentage of energy to rebuild the true wavefield by the extracted one. Table 1 shows the variations of the average percentage on both components for the five sensors for each method used [here, MP, MAMP, and optimized MAMP (OMAMP)]. Thanks to the array processing and the optimization step, the optimized MAMP significantly improves the efficiency of separation process. The optimization step is particularly efficient in the case of a large overlap between wave components (traces 1 and 2).

Table 1. Percentage of energy of reconstruction as a function of decomposition methods.

	1	2	3	4	5
MP	17.2	45.5	16.1	23.6	49.4
MAMP	31.5	71.5	67.6	95.3	97.0
OMAMP	63.9	96.2	96.0	97.2	98.3

When the two wave components overlap so much that they visually seem to be single, the performances of the method are expected to be lower, as it is the case for the trace 1 (down trace of the Fig. 2). Nevertheless, the OMAMP algorithm still gives satisfactory results.

5. Conclusions

In this article, we have presented an original method of wavefield decomposition based on a chirplet decomposition within a two-step algorithm. This algorithm accounts for the array configuration to better constrain the uniqueness of the solution while optimizing the conventional decomposition algorithms. Results show a large improvement of the decomposition efficiency, even in the case of a large overlap between signals. Beyond the wavefield separation aspect, this signal decomposition is a key to an effective compact representation for signal compression when signals may be repeated over time as in acoustics or seismicity.

Acknowledgment

This work was supported by the Agence Nationale de la Recherche (ANR) under the EMSAPCO2 project.

References and links

[1]M. Bath, *Spectral Analysis in Geophysics* (Elsevier, Amsterdam, 1974).
[2]J. Blanco and G. Canadas, "Wavefield decomposition by 3-D/3-C inversion process in tau-p domain," in 65th Conference & Exhibition, EAGE, Stavanger (2003), p. 103.
[3]E. Shang, "Source depth estimation in waveguide," J. Acoust. Soc. Am. **77**, 1413–1418 (1985).
[4]G. Le Touzé, B. Nicolas, J. Mars, and J.-L. Lacoume, 2009, "Matched representations and filters for guided waves," IEEE Trans. Signal Process. **57**(5), 1783–1795.
[5]T. Bardainne, P. Gaillot, N. Dubos-Sallée, J. Blanco, and G. Sénéchal, "Characterization of seismic waveforms and classification of seismic events using chirplet atomic decomposition. Example from the Lacq gas field (Western Pyrenees, France)," Geophys. J. Int. **166**, 699–718 (2006).
[6]S. Mann and S. Haykin, "The chirplet transform: Physical considerations," IEEE Trans. Signal Process. **43**, 2745–2761 (1995).
[7]S. Mallat and Z. Zhang, "Matching pursuit with time-frequency dictionaries," IEEE Trans. Signal Process. **41**, 3397–3415 (1993).
[8]S. Chen, D. Donoho, and M. Saunders, "Atomic decomposition by basis pursuit," J. Soc. Ind. Appl. Math. **43**, 129–159 (2001).
[9]I. Daubechies, "Time-frequency localization operators: A geometric phase space approach," IEEE Trans. Inf. Theory **34**, 605–612 (1988).
[10]H. Schmidt, "Seismo-acoustic fast field algorithm for range independent environments," User's Guide, SR 113, SACLANT ASW Research Centre, La Spezia, Italy Vol. **77**, pp. 1413–1418 (1987).

Identification of synthetic vowels based on a time-varying model of the vocal tract area function

Kate Bunton and Brad H. Story[a)]
Speech Acoustics Laboratory, Department of Speech, Language, and Hearing Sciences, University of Arizona, Tucson, Arizona 85721
bunton@email.arizona.edu, bstory@u.arizona.edu

Abstract: The purpose of this study was to conduct an identification experiment with synthetic vowels based on the same sets of speaker-dependent area functions as in Bunton and Story [(2009) J. Acoust. Soc. Am. **125**, 19–22], but with additional time-varying characteristics that are more representative of natural speech. The results indicated that vowels synthesized using an area function model that allows for time variation of the vocal tract shape and includes natural vowel durations were more accurately identified for 7 of 11 English vowels than those based on static area functions.

PACS numbers: 43.70.Aj, 43.70.Bk [JH]
Date Received: November 11, 2009 **Date Accepted:** January 19, 2010

1. Introduction

The vocal tract area function is a representation of the collective effect of the positions of the articulators at some instant in time, and is a primary component in the development of certain types of speech production models and speech synthesizers. The typical aim in using such models is to compute the acoustic characteristics of various structural and kinematic variations of the vocal tract, and compare them to similar measurements of natural speech. An equally important, but less common aim is to assess the perceptual relevance of speech sounds produced by such models. Toward this goal, a vowel identification experiment was reported by Bunton and Story (2009) in which synthetic vowel samples were based on vocal tract area functions of eight different speakers. A particular vowel was generated by specifying a static area function that had been derived from previously published measurements based on magnetic resonance imaging (MRI) (Story *et al.*, 1996, 1998; Story, 2005a, 2008). Vowels were synthesized with a one-dimensional wave-reflection type of vocal tract model coupled to a voice source. Considerable variability was noted in the identification accuracy of individual vowels based on the simulated productions. These results were not surprising given the large body of research that has suggested that vowel inherent spectral changes, such as time-varying formant transitions and vowel duration, are important for identification accuracy (Nearey and Assmann, 1986; Nearey, 1989; Hillenbrand and Nearey, 1999; Hillenbrand *et al.*, 2000; Nittrouer, 2007). Thus, it is hypothesized that identification accuracy of synthetic vowels based on vocal tract area functions would be enhanced if the shape defined by the area function was allowed to change over the duration of each vowel, and that duration was vowel dependent.

2. Method

2.1 Acoustic analysis of recorded vowels

To obtain spectro-temporal information for the vowel synthesis, time-varying formant frequencies were obtained from productions of 11 American English vowels ([i, ɪ, e, ɛ, æ, ʌ, ɑ, ɔ, o, ʊ, u]) spoken in citation form by an adult male speaker. The vowels were digitally recorded with a

[a)]Author to whom correspondence should be addressed.

Kay Elemetrics CSL4400 using an AKG CS1000 microphone. The first two formant frequencies were estimated over the time course of each vowel with the formant analysis module in PRAAT (Boersma and Weenink, 2009). Formant analysis parameters were manually adjusted so that the formant contours of $F1$ and $F2$ were aligned with the centers of their respective formant bands in a simultaneously displayed wide-band spectrogram. Fundamental frequency and intensity contours for each vowel were also extracted with the appropriate PRAAT modules and were transferred to vector form in MATLAB (The Mathworks, 2008) for further processing. This collection of trajectories was not intended to be representative of American English in general, but rather to capture the natural temporal variation of formant frequencies for one speaker that could be emulated in synthetically generated vowels.

2.2 Formant-to-area function mapping

A technique for mapping area functions to formant frequencies, and vice versa, was developed by Story and Titze (1998) and further described in Story (2005a, 2005b, 2009). With this technique a time-varying area function can be generated by

$$A(x,t) = \frac{\pi}{4}[\Omega(x) + q_1(t)\phi_1(x) + q_2(t)\phi_2(x)]^2, \quad (1)$$

where x is the distance from the glottis and t is time. The $\Omega(x)$, $\phi_1(x)$, and $\phi_2(x)$ are the mean vocal tract diameter function and shaping functions (referred to as "modes") as obtained from principal component analysis (PCA) of a speaker-specific set of static area functions. The $q_1(t)$ and $q_2(t)$ are scaling coefficients that determine the vocal tract shape at a given instant of time. As shown in Story and Titze (1998), within a limited range any given pair of $[q_1, q_2]$ coefficients corresponds to a unique pair of $[F1, F2]$ formants, thus forming a one-to-one mapping.

Eight different coefficient-to-formant mappings were generated based on the same sets of area functions for the eight speakers studied in Bunton and Story (2009). These included four male (mean age 33 years; range 29–40 years) and four female (mean age 26 years; range 23–39 years) speakers. Speakers will be identified in this study as they were previously as SF0, SF1, SF2, SF3, SM0, SM0-2, SM1, SM2, and SM3, where "F" denotes female and "M" male. The SM0-2, SM1, SM3, SF1, SF2, and SF3 contained area functions for the 11 American English vowels ([i, ɪ, e, ɛ, æ, ʌ, ɑ, ɔ, o, ʊ, u]), whereas the SM0 and SF0 sets do not have an area function for the [e] vowel, and the SM2 set does not have an [ɛ]. Hence these latter sets represent only ten vowels each.

As an example, the coefficient-to-formant mapping calculated for speaker SM0-2 is shown in Fig. 1 where the coefficient mesh [Fig. 1(a)] is mapped to the $[F1, F2]$ formant mesh [Fig. 1(b)]. The $[F1, F2]$ trajectories superimposed on the formant mesh in Fig. 1(b) are those from the analysis described in Sec. 2.1, except that they have been slightly rescaled so that they fit entirely within the mesh. Transforming these trajectories to the coefficient domain results in the (q_1, q_2) trajectories superimposed on the mesh in Fig. 1(a). When used in Eq. (1), each coefficient trajectory will generate a time-varying area function whose $F1$ and $F2$ frequencies will emulate the original formant contours.

For the other seven speakers, the $[F1, F2]$ trajectories were rescaled so that they fit entirely within a given speaker's formant mesh, similar to Fig. 1(b) for SM0-2, and then transformed to that speaker's coefficient space so that a time-varying area function could be produced with Eq. (1). In total, 88 time-dependent area functions were generated across 8 speakers and 11 vowels. Note that even though 3 of the original area function sets (for SF0, SM0, and SM2) contained only 10 vowels, 11 vowels could be generated with the formant-to-coefficient mapping technique.

2.3 Synthetic vowel samples

A synthetic vowel sample was generated for each time-varying area function with a voice source model acoustically and aerodynamically coupled to a wave-reflection model of the tra-

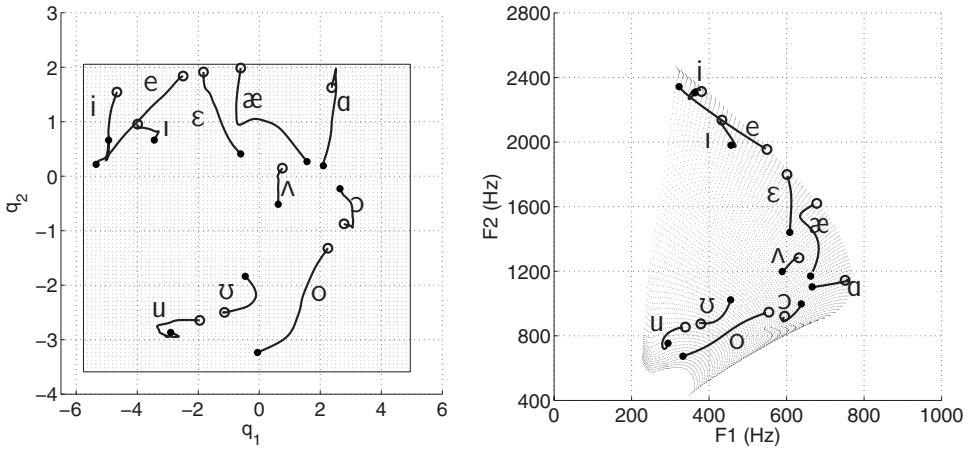

Fig. 1. Demonstration of the formant-to-coefficient mapping based on speaker SM0-2. (a) The mesh in the background, bounded by the thin line, represents the mode coefficient space generated from the PCA of SM0-2's original 11 vowels, and the trajectories correspond to the formant trajectories in (b). (b) The deformed mesh in the background represents the $[F1, F2]$ space generated from the coefficient mesh in (a), and the formant trajectories are those measured with formant analysis but slightly rescaled so that they fit entirely within the mesh. In both (a) and (b), the open and closed circles at the end points of each trajectory denote the onset and offset of the vowel, respectively.

chea and vocal tract (Liljencrants, 1985; Story, 1995). The vocal tract shape, which extended from glottis to lips, was dictated at every time sample by the given area function $A(x,t)$. The wave propagation algorithm included energy losses due to yielding walls, viscosity, heat conduction, and radiation at the lips (Story, 1995), and accommodated the different vocal tract lengths of each speaker.

The voice source model was based on a kinematic representation of the medial surface of the vocal folds (Titze, 1984, 2006). Control parameters for this study consisted of fundamental frequency, degree of posterior adduction, and respiratory pressure. The fundamental frequency ($F0$) for each male vowel sample was varied according to the contours extracted in the acoustic analysis described in Sec. 2.1. For the female vowels, each measured $F0$ contour was multiplied by a factor of 2. For example, the peak $F0$ in the contour for the male [i] vowels was 112 Hz whereas for the female it was 224 Hz. The respiratory pressure for each sample, male or female, was ramped from 0 to 7840 $\mathrm{dyn/cm^2}$ in the initial 50 ms with a cosine function, and then maintained at a constant pressure for the remaining duration of the utterance. The posterior adduction of the vocal folds was varied slightly over the time course of each synthetic vowel according to the shape of the intensity contour measured in the acoustic analysis of the recorded vowels. That is, the adduction was greatest (vocal folds closest together) at the point where the intensity of a particular recorded vowel was highest. Because of the somewhat more breathy quality of female speakers (e.g., Klatt and Klatt, 1990), the posterior separation of the vocal folds was set to be 30% greater for the vowels generated from the female area functions. Other model parameters were set to constant values throughout the time course of each utterance.

The output of the vocal fold model is a glottal area signal. This was coupled to the propagating pressures and air flows in the trachea and vocal tract through aerodynamic and acoustic considerations as described by Titze (2002). The glottal flow was determined by the interaction of the glottal area with the time-varying pressures present just inferior and superior to the glottis. In addition, a noise component was added to the glottal flow signal if the calculated Reynolds number within the glottis exceeded 1200. The sound pressure signal radiated at the lip termination was converted to an audio file for later presentation in the listening experiment.

The durations of each synthetic vowel were based on the measurements reported for

Table 1. Percentage of vowels identified correctly for each speaker across listeners. The bottom row indicates the mean identification accuracy *across all vowels for each speaker*, and the rightmost column indicates the mean identification accuracy *across all speakers for each vowel*.

	Speaker									
Vowel	SM0	SM0-2	SM1	SM2	SM3	SF0	SF1	SF2	SF3	Mean
i	92	74	78	88	94	86	88	50	90	82
ɪ	42	68	88	78	80	80	84	82	80	76
e	100	98	100	100	98	98	94	94	98	98
ɛ	68	92	84	82	90	98	88	98	100	89
æ	94	62	84	92	92	92	58	92	74	82
ʌ	90	96	96	92	94	66	94	98	92	91
ɑ	52	40	48	68	52	22	52	32	50	46
ɔ	82	88	80	76	80	86	76	80	82	81
o	98	94	94	98	100	76	92	94	90	93
ʊ	64	80	92	76	90	88	86	88	76	82
u	82	86	86	92	86	70	66	68	78	79
Mean	79	80	85	86	87	78	80	80	83	

male and female speakers by Hillenbrand *et al.* (1995, p. 3103). However, because they were measured for vowels embedded within "hVd" words, the durations were increased by 50% so that the resulting isolated vowels would be similar to the length of an hVd word.

2.4 Listeners

Ten listeners (five males and five females) with a mean age of 28.1 years served as participants. Listeners were native speakers of American English, native to Arizona, and passed a hearing screening at 25 dB hearing level (HL) for frequencies of 0.5, 1, 2, and 4.0 kHz bilaterally.

2.5 Listening task

Vowel samples were presented via loudspeaker placed 1 m in front of individual listeners seated in a sound treated room. Sample presentation was controlled using the ALVIN interface (Hillenbrand and Gayvert, 2005). Prior to the experimental task, listeners completed a training task with naturally produced vowel samples from an adult male speaker to assure that listeners were able to identify all 11 English vowels and to familiarize them with the computer interface. Mean identification accuracy was 97.4% across listeners for this training task. For the experimental task, following presentation of the target vowel, listeners were asked to use the computer mouse to select one of the buttons displaying the 11 English vowels on the computer screen. Each button listed the phonetic symbol for the vowel and a corresponding hVd word. Listeners were allowed to replay each sample once. Each listener heard five repetitions of each vowel sample blocked by speaker sex in random order. Listening sessions lasted 30–40 min. A confusion matrix based on listener identification was calculated separately for each speaker and then compiled across speakers to form a composite confusion matrix.

3. Results

Percent correct identifications of each vowel based on each speaker are shown in Table 1. The mean identification accuracy across all vowels for individual speakers ranged from 79% to 87% (see bottom row of table). For individual vowels, the mean identification accuracy was greater than 70% with the exception of [ɑ], which was identified correctly 46% of the time.

A composite confusion matrix including the identification data based on all speakers (across listeners) is shown in the upper half of Table 2. Correct identification of target vowels can be seen along the diagonal in boldface cells. Vowel confusions were typically between

Table 2. Composite confusion matrix of the vowels identified across speakers. The values in each cell are shown as percent. The upper half of the table shows data from the present study and the lower half shows identification databased on the static vowel experiment reported in Bunton and Story (2009).

		Listeners' identification										
		i	ɪ	e	ɛ	æ	ʌ	ɑ	ɔ	o	ʊ	u
Vowel intended by speaker (time-varying)	i	**82**	11	1	6	0	0	0	0	0	0	0
	ɪ	1	**76**	2	21	0	0	0	0	0	0	0
	e	0	0	**98**	0	1	0	0	0	0	0	0
	ɛ	0	0	0	**89**	9	1	2	0	0	0	0
	æ	0	0	2	10	**82**	2	3	1	0	0	0
	ʌ	0	0	0	3	2	**91**	4	1	0	0	0
	ɑ	0	0	0	0	16	1	**46**	37	0	0	0
	ɔ	0	0	0	0	0	1	17	**81**	0	0	0
	o	0	0	0	0	0	0	2	2	**93**	3	0
	ʊ	0	0	0	0	0	6	1	0	2	**82**	9
	u	0	0	0	0	0	1	0	0	2	18	**79**
Vowel intended by speaker (static)	i	**93**	6	0	1	0	0	0	0	0	0	0
	ɪ	2	**25**	39	22	1	9	0	0	0	0	0
	e	2	27	**34**	35	1	0	0	0	0	0	0
	ɛ	0	2	12	**36**	35	2	0	0	0	10	2
	æ	0	0	0	2	**97**	0	1	1	0	0	0
	ʌ	0	0	0	0	0	**34**	20	14	5	24	4
	ɑ	0	0	0	0	12	6	**50**	28	4	0	0
	ɔ	0	0	0	0	0	1	25	**61**	13	1	0
	o	0	0	0	0	0	9	7	7	**39**	28	11
	ʊ	0	0	0	0	0	2	7	8	12	**40**	32
	u	0	0	0	0	0	0	0	0	1	11	**88**

adjacent vowel categories in the vowel space. For the vowel [i], confusions occurred with [ɪ] and [ɛ], and [ɪ] and [ɛ] were frequently confused with each other. Accuracy for the vowel [e] was the highest at 99% across speakers. For the male speakers, the identification accuracy for target vowel [ɛ] was 83% and was most frequently confused with [æ]. In contrast, the identification accuracy for [ɛ] was 96% across female speakers. For all speakers, the central vowel [ʌ] was confused with both [æ] and [ɑ]. For the back vowels, accuracy for [ɑ] was the lowest of any vowel (46%), and was most frequently confused with [ɔ]. The vowels [u] and [ʊ] were confused by listeners for all speakers.

To compare the results for the time-varying vowels in the present study to those for static vowels, a composite confusion matrix was calculated from the individual speaker confusion matrices reported in Bunton and Story (2009). This is shown in the lower half of Table 2. Based on a two-way analysis of variance (ANOVA), the main effects of synthesis condition (time-varying vs static), $F(1,176)=117.88$, $p<0.001$, and vowel, $F(10,176)=9.86$, $p<0.001$, were statistically significant. The interaction was also significant, $F(10,176)=13.88$, $p<0.001$.

It can be seen in Table 2 that seven of the vowels ([ɪ,e,ɛ,ʌ,ɔ,o,ʊ]) synthesized with a time-varying vocal tract shape were identified more accurately than the vowels based on static vocal tract shapes reported by Bunton and Story (2009). With the exception of [ɔ], the increase in accuracy over the static cases was 50% or more. For [ɔ] the increase was 20%. Identification accuracy of the [ɑ] vowel was similarly poor for the time-varying compared to the static case (46% vs 50%, respectively). In both studies the [ɑ] vowel was primarily confused with the [ɔ], which is likely because these two categories tend to be collapsed in the southwest United States

(Labov *et al.*, 2006). The other corner vowels [i, æ, u] were less accurately identified when the vocal tract shape varied in time than when it was static. The differences for these three vowels ranged from 9% to 16%.

Audio samples of the 11 vowels in the static and time-varying conditions for speaker SM0-2 are available for listening in Mm. 1 and Mm. 2. The order of presentation in each condition is identical to that listed in the first column of Table 2.

Mm. 1. [SM0-2_static.wav (792 KB). This is a file of type "wav."]

Mm. 2. [SM0-2_timevary.wav (1 MB). This is a file of type "wav."]

4. Discussion

The hypothesis of this study was that identification accuracy of synthetic vowels based on vocal tract area functions would be enhanced if the shape defined by the area function was allowed to change over the duration of each vowel, and duration was vowel dependent. Demonstrating improvement in identification of some vowels by incorporating additional time-varying cues is, of course, not unexpected. Time-varying formant transitions and vowel duration are well known to be important cues for improved identification accuracy (Nearey and Assmann, 1986; Nearey, 1989; Hillenbrand and Nearey, 1999; Hillenbrand *et al.*, 2000; Nittrouer, 2007). The question remains, however, as to why the identification accuracy of the time-varying vowels is still well below those reported for similarly time-varying vowels generated with a formant synthesizer (e.g., Hillenbrand and Nearey, 1999). A major difference is that formant synthesis allows precise control of the formant frequencies and bandwidths over the time course of a vowel, whereas the method of synthesis used in the present study is based on generating movement of the vocal tract. Although formants extracted from natural speech were mapped into movement information (i.e., $[q_1, q_2]$ coefficients) to drive the vocal tract model, this was based only on $F1$ and $F2$ (see Fig. 1). That is, when coupled to the voice source and trachea, the time-varying area functions produced sound samples that contained $[F1, F2]$ formant trajectories based on the original recording, but there was no direct control of the formants higher than $F2$ even though higher formants existed in the signal due to the resonant structure of the vocal tract shape. Thus it is possible that for some of the vowels generated, the pattern of formants $F3$ and higher created information that conflicted with the target vowel. An example is the time-varying [i] based on SM-02's vocal tract (the first sample in the accompanying Mm. 2). The $[F1, F2]$ trajectory for this synthetic vowel is precisely that shown in the upper left corner of Fig. 1(b), and indicates little movement of either $F1$ or $F2$. There is, however, a downward glide of $F3$ such that the distance between $F2$ and $F3$ decreased over the duration of the vowel, and perhaps contributed to its confusion with [ɪ]. Interestingly, the length of the corresponding $[q_1, q_2]$ trajectory for this vowel in the coefficient space [Fig. 1(a)] indicates that there was a change occurring in vocal tract shape, but in this case the change primarily affected $F3$.

It is not surprising that time-varying changes in the area function intended to move $F1$ and $F2$ in some specific pattern might also have unintended effects on the upper formant frequencies. Acoustic modeling of the vocal tract shape has shown that even subtle changes in cross-sectional area may have large effects on some formants (e.g., Stevens, 1989; Story *et al.*, 2001; Story, 2006), especially when such changes occur in a part of the vocal tract that is already fairly constricted. Thus, it can be predicted that the vowels [i,ɑ,u] would be particularly susceptible to these effects because, compared to other vowels, they typically are produced with the most constricted vocal tract shapes. Perhaps this is at least a partial explanation of why these vowels were not identified with greater accuracy than the static versions. It is not clear why the time-varying [æ] vowel was identified less accurately than its static counterpart. A next step in this process is to build in more control of the upper formant frequencies via the area function model.

From the results of the present study it is concluded that (1) time-varying area functions produce vowels that are more identifiable than those produced with static area functions

(with the exceptions noted previously) and (2) a model of the vocal tract area function can serve as the basis for future studies to assess the perceptual relevance of various structural and kinematic variations of the vocal tract.

Acknowledgment

This research was supported by NIH Grant No. R01-DC04789.

References and links

Boersma, P., and Weenink, D. (**2009**). PRAAT, Version 5.1, www.praat.org (Last viewed 2/2/2009).
Bunton, K., and Story, B. H. (**2009**). "Identification of synthetic vowels based on selected vocal tract area functions," J. Acoust. Soc. Am. **125**, 19–22.
Hillenbrand, J., Clark, M., and Houde, R. (**2000**). "Some effects of duration on vowel recognition," J. Acoust. Soc. Am. **108**, 3013–3022.
Hillenbrand, J., and Gayvert, R. T. (**2005**). "Open source software for experiment design and control," J. Speech Lang. Hear. Res. **48**, 45–60.
Hillenbrand, J., Getty, L. A., Clark, M. J., and Wheeler, K. (**1995**). "Acoustic characteristics of American English vowels," J. Acoust. Soc. Am. **97**, 3099–3111.
Hillenbrand, J., and Nearey, T. (**1999**). "Identification of resynthesized /hVd/ utterances: Effects of formant contour," J. Acoust. Soc. Am. **105**, 3509–3523.
Klatt, D. H., and Klatt, L. C. (**1990**). "Analysis, synthesis, and perception of voice quality variations among male and female talkers," J. Acoust. Soc. Am. **87**, 820–857.
Labov, W., Ash, S., and Boberg, C. (**2006**). *The Atlas of North American English: Phonetics* (Mouton de Gruyter, Berlin).
Liljencrants, J. (**1985**). "Speech synthesis with a reflection-type line analog," DS Dissertation, Department of Speech Communication and Music Acoustics, Royal Institute of Technology, Stockholm, Sweden.
Nearey, T. M. (**1989**). "Static, dynamic, and relational properties in vowel perception," J. Acoust. Soc. Am. **85**, 2088–2113.
Nearey, T. M., and Assmann, P. F. (**1986**). "Modeling the role of vowel inherent spectral change in vowel identification," J. Acoust. Soc. Am. **80**, 1297–1308.
Nittrouer, S. (**2007**). "Dynamic spectral structure specifies vowels for children and adults," J. Acoust. Soc. Am. **122**, 2328–2339.
Stevens, K. N. (**1989**). "On the quantal theory of speech," J. Phonetics **17**, 3–45.
Story, B. H. (**1995**). "Speech simulation with an enhanced wave-reflection model of the vocal tract," Ph.D. thesis, University of Iowa, Iowa City, IA.
Story, B. H. (**2005a**). "Synergistic modes of vocal tract articulation for American English vowels," J. Acoust. Soc. Am. **118**, 3834–3859.
Story, B. H. (**2005b**). "A parametric model of the vocal tract area function for vowel and consonant simulation," J. Acoust. Soc. Am. **117**, 3231–3254.
Story, B. H. (**2006**). "A technique for 'tuning' vocal tract area functions based on acoustic sensitivity functions," J. Acoust. Soc. Am. **119**, 715–718.
Story, B. H. (**2008**). "Comparison of magnetic resonance imaging-based vocal tract area functions obtained from the same speaker in 1994 and 2002," J. Acoust. Soc. Am. **123**, 327–335.
Story, B. H. (**2009**). "Vocal tract modes based on multiple area function sets from one speaker," J. Acoust. Soc. Am. **125**, EL141–EL147.
Story, B. H., and Titze, I. R. (**1998**). "Parameterization of vocal tract area functions by empirical orthogonal modes," J. Phonetics **26**, 223–260.
Story, B. H., Titze, I. R., and Hoffman, E. A. (**1996**). "Vocal tract area functions from magnetic resonance imaging," J. Acoust. Soc. Am. **100**, 537–554.
Story, B. H., Titze, I. R., and Hoffman, E. A. (**1998**). "Vocal tract area functions for an adult female speaker based on volumetric imaging," J. Acoust. Soc. Am. **104**, 471–487.
Story, B. H., Titze, I. R., and Hoffman, E. A. (**2001**). "The relationship of vocal tract shape to three voice qualities," J. Acoust. Soc. Am. **109**, 1651–1667.
The Mathworks (**2008**). MATLAB, Version 7.6.0.324.
Titze, I. R. (**1984**). "Parameterization of the glottal area, glottal flow, and vocal fold contact area," J. Acoust. Soc. Am. **75**, 570–580.
Titze, I. R. (**2002**). "Regulating glottal airflow in phonation: Application of the maximum power transfer theorem to a low dimensional phonation model," J. Acoust. Soc. Am. **111**, 367–376.
Titze, I. R. (**2006**). *The Myoelastic Aerodynamic Theory of Phonation* (National Center for Voice and Speech, Iowa City, IA), pp. 197–214.

Detecting Atlantic herring by parametric sonar

Olav Rune Godø
Institute of Marine Research, P.O. Box 1870 Nordnes, 5817 Bergen, Norway
olavrune@imr.no

Kenneth G. Foote
Woods Hole Oceanographic Institution, Woods Hole, Massachusetts 02543
kfoote@whoi.edu

Johnny Dybedal
Kongsberg Defence and Aerospace AS, P.O. Box 55, Strandveien 1, 7501 Stjørdal, Norway
johnny.dybedal@kongsberg.com

Eirik Tenningen and Ruben Patel
Institute of Marine Research, P.O. Box 1870 Nordnes, 5817 Bergen, Norway
eirik.tenningen@imr.no, ruben.patel@imr.no

Abstract: The difference-frequency band of the Kongsberg TOPAS PS18 parametric sub-bottom profiling sonar, nominally 1–6 kHz, is being used to observe Atlantic herring. Representative TOPAS echograms of herring layers and schools observed *in situ* in December 2008 and November 2009 are presented. These agree well with echograms of volume backscattering strength derived simultaneously with the narrowband Simrad EK60/18- and 38-kHz scientific echo sounder, also giving insight into herring avoidance behavior in relation to survey vessel passage. Progress in rendering the TOPAS echograms quantitative is described.

PACS numbers: 43.30.Sf, 43.80.Jz, 43.80.Nd, 43.30.Lz [JL]
Date Received: December 16, 2009 **Date Accepted:** February 2, 2010

1. Introduction

Remote detection of fish by acoustics was demonstrated by Sund in 1935,[1] and ultrasonic acoustic surveys have been an integral part of scientific surveys of pelagic[2] and benthopelagic[3,4] fish stocks for over 30 years. Acoustic surveys are normally carried out at discrete frequencies in the band from 18 to 300 kHz.

Norwegian spring-spawning herring (*Clupea harengus*) is the largest existing herring stock, with an annual catch exceeding 1×10^6 tonnes.[5] The stock is monitored annually with multiple-frequency acoustics using the Simrad EK60 scientific echo sounder operating at 18, 38, 70, 120, and 200 kHz. During the period November–January, the herring winters off the northwest continental shelf of Norway, where the present study took place in 2008 and 2009.

Availability of the Kongsberg TOPAS PS18 Parametric Sub-bottom Profiler on board R/V "G. O. Sars" has encouraged examination of its potential for surveying herring[6] as well as other fishes. This parametric sonar, with total difference-frequency band 0.5–6 kHz, may have several advantages. At its long wavelengths, 25–300 cm, scattering is less sensitive to orientation effects, which are strong at the short wavelengths of ordinary ultrasonic frequencies used in surveying.[7,8] It may also be possible to exploit strong or resonance scattering by the swimbladder-bearing herring, as has been done in other studies,[9–13] to determine fish size,[14] contributing to remote classification and avoiding biases associated with physical capture, as by pelagic trawling.

The immediate objectives of this study are (1) to demonstrate the ability of the TOPAS parametric sonar to detect herring in the water column and (2) to investigate the influence of the transmit signal waveform on the detection process. The larger project goal is to use parametric

sonar to quantify pelagic fish such as herring. This involves determination of numerical density, as by echo integration,[2] and the swimbladder-resonance frequency for remote sizing and other classification.

It is noted that the TOPAS echo data presented here have not been reduced to values of volume backscattering strength. This reduction is sufficiently complicated to require additional processing, which is outlined.

2. Materials

In December 2008 and November 2009, wintering of Norwegian spring-spawning herring was observed in the area (N71–72, E14–17). The behavior was different in the two years: the herring formed layers, or shoals, in December 2008, but distinct schools in November 2009. The difference can be attributed to the one-month difference in time, with associated maturation effects.

The principal acoustic instrument used in this study was the Kongsberg TOPAS PS18 Parametric Sub-bottom Profiler.[15] This parametric sonar, as a parametric acoustic array,[16,17] is based on collinear transmission of powerful signals in the band 15–21 kHz. Because of the acoustic nonlinearity of water, the waves interact in the water column, forming a virtual endfire array that generates new waves, especially at the sum and difference frequencies. The difference-frequency wave is often exceptionally directional, with broad bandwidth and significant apparent secondary source level too, e.g., 204 dB re 1 μPa at 1 m. In the case of TOPAS, the nominal difference-frequency band is 0.5–6 kHz, with beamwidths in the approximate range 3–5 deg. The beam can also be steered over a wide sector. Scattered difference-frequency waves are received and detected conventionally with part of the TOPAS transducer.

In December 2008, the presence of herring in a shoal or layer enabled the acoustic measurements to be made without the need for hunting tactics. In November 2009, the presence of herring in rather small compact schools required use of a horizontal multibeam sonar, the Simrad SP70 Fish Finding Sonar, operating in the band 20–30 kHz, to track schools, and vessel-maneuvering to pass over them.

During both cruises, the observed herring was sampled with a pelagic trawl. Conductivity-temperature-depth profiles were also taken to obtain information about sound speed. The observation and sampling platform during both cruises was R/V "G. O. Sars," a 4000-gross-tonne research vessel built in 2003.

3. Methods

Herring have been observed routinely by sonar including echo sounders operating at ultrasonic frequencies since the 1950s,[18] with well-developed methodology for measuring its numerical density. This methodology has been applied here based on the Simrad EK60 scientific echo sounder operating at 18, 38, 70, 120, 200, and 333 kHz.[19] The split-beam transducer beamwidths at 18 and 38 kHz were 11 and 7 deg, respectively, with both transmitting sinusoidal signals in 1-ms bursts.

The initial observations were made on 7 December 2008 at position (N71.4, E16.3) with bottom depth exceeding 1000 m. The TOPAS and EK60 were operated simultaneously at a nominal, constant ping rate of 1 ping/s, but without use of an external trigger signal. The phase of the TOPAS was adjusted to avoid interference in the vicinity of the herring layer. The observations were made both with the vessel drifting freely and with the vessel sailing at its ordinary survey speed of 5 m/s.

During the period 13–18 November 2009, the herring was observed in the middle of the ongoing fishery at roughly (N71, E15). The TOPAS and EK60 were again operated simultaneously, but with use of an external trigger signal and phasing sufficient to avoid interference in the upper 500 m. Because of the presence of herring in rather small schools, the SP70 was used for tracking, and the vessel was maneuvered to maximize the chances of passing directly over the schools. The vessel speed was typically in the range 1.5–4 m/s. The bottom depth was approximately 1500–2500 m.

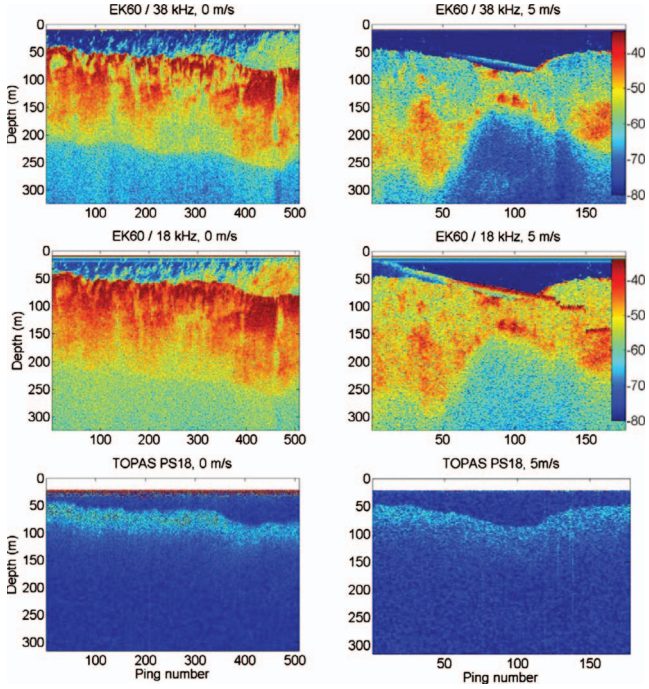

Fig. 1. Two sets of concurrent echograms of Norwegian spring-spawning herring in its wintering area near (N71.4, E16.3) observed from R/V "G. O. Sars" on 7 December 2008. The left set was obtained while the vessel was drifting freely; the right set was obtained with the vessel sailing at the ordinary survey speed of 5 m/s. Echograms obtained with the Simrad EK60 scientific echo sounder display values of the volume backscattering strength in decibels according to the attached color bar. The echograms derived with the Kongsberg TOPAS PS18 Parametric Sub-bottom Profiler involved transmission of a 16-ms FM signal with linear frequency dependence over the band 1–6 kHz, with sampling at 30 kHz after a 20-ms trigger delay, represented by the blank area at the top of the echogram. These data have not been processed, lacking both range compensation and calibration. All echograms were derived from measurements made with proximate transducers with vertically downward oriented beams. In the EK60 echograms collected at 5 m/s, there are extraneous signals, probably second bottom echoes, appearing at the surface and descending through the herring records.

4. Results and discussion

4.1 First cruise, December 2008

Representative echograms of herring collected simultaneously with the TOPAS parametric sonar and EK60/18- and 38-kHz scientific echo sounders on 7 December 2008 are shown in Fig. 1. A pelagic trawl taken at the same position yielded a catch dominated by herring, lengths 28–36 cm, with mean 32.5 cm. The basic similarity in corresponding echograms, especially with respect to the upper surface of the herring layer, demonstrates that the difference-frequency band of TOPAS can detect herring aggregations in the midwater column. Other echo data collected simultaneously during this cruise with the EK60 and TOPAS demonstrate the detection of herring by TOPAS at least to 200 m.

The similarity in detected upper surfaces of the herring layers is also revealing of herring behavior. Typically, herring respond to the passage of survey vessels by diving and moving away from the vessel path.[20,21] Given that the beamwidth of the TOPAS difference-frequency beam is of order 3–5 deg, while the beamwidths of the EK60/18 and 38 kHz transducers are 11 and 7 deg, respectively, a differential effect in diving and horizontal movement should be detectable, at least to the order of the narrowest beam diameter at the upper surface, about 4 m. The absence of an effect suggests that the behavior is largely unaffected by passage of the vessel.

There are also differences in the TOPAS echograms relative to the EK60 echograms. A major difference is the apparently weaker echo response with increasing depth in the herring layer. This is interesting because the difference-frequency pressure field is still developing at ranges where the herring layer is being measured, while the beamwidth is decreasing. However, the TOPAS echograms have not been compensated for range, while the EK60 echograms have been increased according to the ordinary function used for volume backscattering, discussed further in Sec. 4.3.

It may be wondered whether the observed TOPAS echo response is consistent with the phenomenon of swimbladder resonance, with enhanced frequency-selective scattering at the kilohertz difference-frequencies of TOPAS. Since herring cannot inflate its swimbladder underwater, the gas-filled sac will decrease with increasing pressure. Effects on backscattering are relatively well known at ultrasonic frequencies,[22] but much less so at the mentioned kilohertz frequencies, although the swimbladder is expected to dominate the scattering in both frequency regimes.[9,14,23] The depth and depth history are expected to influence the backscattering to a significant degree. At higher, ultrasonic frequencies, the elongated form of the herring swimbladder, with flattened deformation against the spinal vertebrae under compression,[24] precludes strong resonance scattering.[25]

As an aside, the EK60 echograms in Fig. 1 reveal an interesting phenomenon. Strong, patchy scattering above the upper surface of the layer is believed to be due to individual herring migrating to the sea surface to fill their swimbladder.[26]

4.2 Second cruise, November 2009

During the period 13–18 November 2009, the TOPAS PS18 parametric sonar was used with the EK60 scientific echo sounder to observe herring in small schools off the northwest coast of Norway. To aid the process of detection with vertically oriented transducer beams, the SP70 sonar was used to track schools from horizontal ranges extending to about 1500 m.

The schools were so numerous at the beginning of the cruise that it was a relatively simple matter of following an arbitrary transect to pass over these. Later, the schools dispersed, and the opportunity was seized to observe the same school repeatedly. Detections with four different TOPAS waveforms are demonstrated in Fig. 2: a 20 ms duration frequency-modulated (FM) pulse spanning the frequency band 1–6 kHz, and three continuous-wave (cw) pulses, each with four cycles, at 6, 3, and 1.5 kHz, respectively. Herring schools were also detected at intermediate frequencies as well as at 1.2 kHz. A pelagic trawl taken in the vicinity of the observations reported in Fig. 2 yielded exclusively herring, length 15.5–37.5 cm, mean 30.5 cm.

Detection at lower frequencies, which could be useful vis-à-vis swimbladder-resonance excitation, requires further work. The ambient noise is rather high at such frequencies, while the parametric array itself is less efficient at generating low difference-frequency signals, since the intensity varies as the fourth power of the difference frequency.[17]

Again, a basic similarity in form, especially with respect to the upper surface of the schools, is evident when comparing TOPAS echograms with the corresponding EK60/18-kHz echograms. As in the case of the herring layers in 2008, the herring schools do not display differential avoidance effects to within the width of the narrow TOPAS beam at the upper surface of the schools.

4.3 Future work

The accomplishment of this work is demonstration of the ability of the TOPAS parametric sonar to detect herring in the water column using a variety of transmit signals. The larger goal of the work, using the parametric sonar to quantify pelagic fish such as herring, is now being pursued. The envisioned quantification involves determination of numerical density, as by echo integration,[2] and determination of the swimbladder-resonance frequency for remote sizing and other classification.

The two essential requirements for quantification have already been defined.[27,28] The parametric sonar echoes must be compensated for range to remove simple geometric scattering effects, as is done routinely with conventional sonars.[2,29,30] This is relatively complicated in the

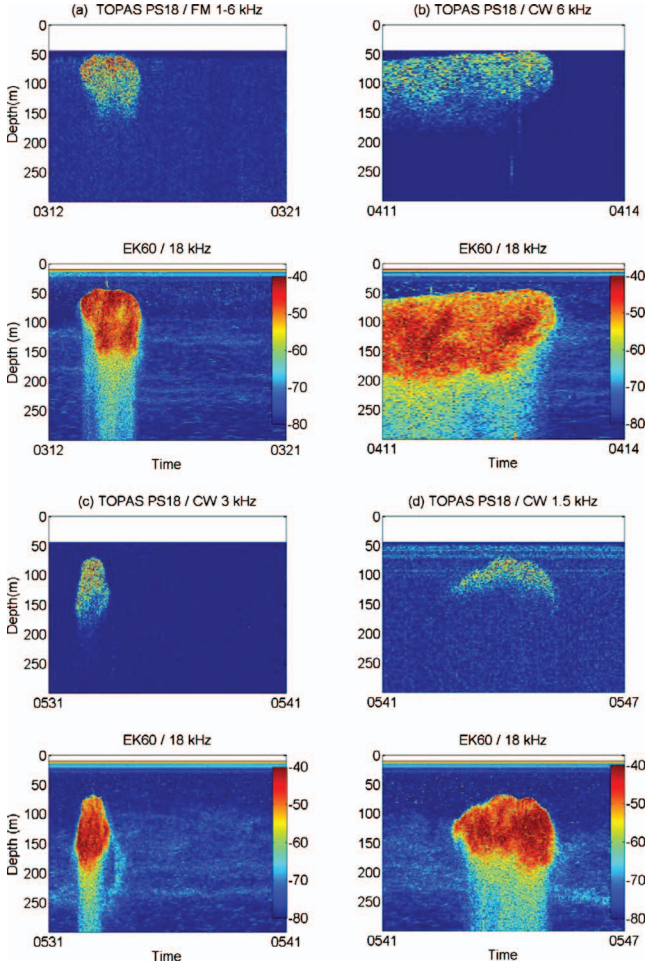

Fig. 2. Echograms collected on the same school of Norwegian spring-spawning herring in its wintering area near (N71.3, E15) on 15 November 2009 during repeated passes with R/V "G. O. Sars" while sailing at 5 m/s. Upper panel: Echograms obtained with the TOPAS PS18 parametric sonar, expressed as raw values without range compensation, for each of four transmit signals, with frequency band indicated for the 20-ms duration linear FM signal and with center frequency indicated for the 4-cycle cw burst. Echo data were sampled at 25 kHz following a 50-ms trigger delay, represented by the blank area at the top of the echogram. The TOPAS echoes have been processed by matched filtering for the FM signal and bandpass filtering for the cw signals. Lower panel: Respective echograms obtained with the EK60/18-kHz scientific echo sounder, with 1-ms duration transmission at 18-kHz, expressed as values of volume backscattering strength.

case of parametric sonar because the difference-frequency field increases with range in the nearfield, while the difference-frequency beamwidth decreases.[28] The range compensation function for expression of TOPAS data as relative values of volume backscattering strength has been described and evaluated numerically in a separate study.

The parametric sonar also requires calibration. The standard-target method[31,32] is being adapted for parametric sonar. The first calibration trial was conducted on 10 December 2008. Echoes from a 280-mm-diameter solid sphere of an aluminum alloy[33] were measured at each of three depths with a variety of transmit signal waveforms.[27] The target position is being determined by simultaneous observations with the EK60/18- and 38-kHz scientific echo sounder, whose split-beam transducers are located in the vicinity of the TOPAS transducer. This will enable TOPAS echoes to be expressed in physical scattering units of volume backscattering

When the range compensation function and calibration data from TOPAS are available, the echo spectrum will be examined. The use of both broadband FM signals and a series of narrowband CW signals will enable a strong comparison to be made.

The same TOPAS data will also be compared with data collected simultaneously with the ultrasonic EK60 scientific echo sounder. This will prove the consistency and potential usefulness of parametric sonar for quantification of swimbladder-bearing fish in the very region where the parametric beam is being formed.

Acknowledgments

Work supported by the Norwegian Research Council under Grant No. 184705 and the Office of Naval Research under Award No. N000140910482.

References and links

[1]O. Sund, "Echo sounding in fisheries research," Nature (London) **135**, 953 (1935).
[2]D. N. MacLennan, "Acoustical measurement of fish abundance," J. Acoust. Soc. Am. **87**, 1–15 (1990).
[3]O. R. Godø and V. G. Wespestad, "Monitoring changes in abundance of gadoids with varying availability to trawl and acoustic surveys," ICES J. Mar. Sci. **50**, 39–51 (1993).
[4]W. A. Karp and G. E. Walters, "Survey assessment of semi-pelagic gadoids: The example of walleye pollock, *Theragra chalcogramma*, in the Eastern Bering Sea," Mar. Fish. Rev. **56**, 8–22 (1994).
[5]R. Toresen and O. J. Østvedt, "Variation in abundance of Norwegian spring-spawning herring (*Clupea harengus, Clupeidae*) throughout the 20th century and the influence of climatic fluctuations," Fish Fish. **1**, 231–256 (2000).
[6]O. R. Godø, K. G. Foote, J. Dybedal, and E. Tenningen, "Observing Atlantic herring by parametric sonar," J. Acoust. Soc. Am. **125**, 2718 (2009).
[7]O. Nakken and K. Olsen, "Target strength measurements of fish," Rapp. P.-V. Reun.-Cons. Int. Explor. Mer **170**, 52–69 (1977).
[8]L. Midttun, "Fish and other organisms as acoustic targets," Rapp. P.-V. Reun.-Cons. Int. Explor. Mer **184**, 25–33 (1984).
[9]D. V. Holliday, "Resonance structure in echoes from schooled pelagic fish," J. Acoust. Soc. Am. **51**, 1322–1332 (1972).
[10]O. Diachok, "Effects of absorptivity due to fish on transmission loss in shallow water," J. Acoust. Soc. Am. **105**, 2107–2128 (1999).
[11]O. Diachok, "Absorption spectroscopy: A new approach to estimation of biomass," Fish. Res. **47**, 231–244 (2000).
[12]N. C. Makris, P. Ratilal, D. T. Symonds, S. Jagannathan, S. Lee, and R. W. Nero, "Fish population and behavior revealed by instantaneous continental shelf-scale imaging," Science **311**, 660–663 (2006).
[13]J. S. M. Rusby, M. L. Somers, J. Revie, B. S. McCartney, and A. R. Stubbs, "Experimental survey of a herring fishery by long-range sonar," Mar. Biol. (Berlin) **22**, 271–292 (1973).
[14]A. Løvik and J. M. Hovem, "Experimental investigation of swimbladder resonance in fishes," J. Acoust. Soc. Am. **66**, 850–854 (1979).
[15]J. Dybedal, "TOPAS: Parametric end-fire array used in offshore applications," in *Advances in Nonlinear Acoustics*, edited by H. Hobæk (World Scientific, Singapore, 1993), pp. 264–275.
[16]P. J. Westervelt, "Parametric acoustic array," J. Acoust. Soc. Am. **35**, 535–537 (1963).
[17]M. B. Moffett and W. L. Konrad, "Nonlinear sources and receivers," in *Encyclopedia of Acoustics*, edited by M. J. Crocker (Wiley, New York, 1997), pp. 607–617.
[18]O. Dragesund, J. Hamre, and Ø. Ulltang, "Biology and population dynamics of the Norwegian spring-spawning herring," Rapp. P.-V. Reun.-Cons. Int. Explor. Mer **177**, 43–71 (1980).
[19]L. N. Andersen, "The new Simrad EK60 scientific echo sounder system," J. Acoust. Soc. Am. **109**, 2336 (2001).
[20]E. Ona, O. R. Godø, N. O. Handegard, V. Hjellvik, R. Patel, and G. Pedersen, "Silent research vessels are not quiet," J. Acoust. Soc. Am. **121**, EL145–EL150 (2007).
[21]K. Olsen, J. Angell, F. Pettersen, and A. Løvik, "Observed fish reactions to a surveying vessel with special reference to herring, cod, capelin and polar cod," FAO Fish. Rep. **300**, 131–138 (1983).
[22]E. Ona, X. Zhao, I. Svellingen, and J. E. Fosseidengen, "Seasonal variation in herring target strength," in *Herring: Expectations for a New Millenium*, edited by F. Funk, J. Blackburn, D. Hay, A. J. Paul, R. Stephenson, R. Toresen, and D. Witherell (University of Alaska Sea Grant College Program, Fairbanks, AK, 2001), pp. 461–487.
[23]K. G. Foote, "Importance of the swimbladder in acoustic scattering by fish: A comparison of gadoid and mackerel target strengths," J. Acoust. Soc. Am. **67**, 2084–2089 (1980).
[24]E. Ona, "Physiological factors causing natural variations in acoustic target strength of fish," J. Mar. Biol. Assoc. U.K. **70**, 107–127 (1990).
[25]D. T. I. Francis and K. G. Foote, "Depth-dependent target strengths of gadoids by the boundary-element method," J. Acoust. Soc. Am. **114**, 3136–3146 (2003).

[26]J. H. S. Blaxter and R. S. Batty, "The herring swimbladder—Loss and gain of gas," J. Mar. Biol. Assoc. U.K. **64**, 441–459 (1984).
[27]K. G. Foote, J. Dybedal, and E. Tenningen, "Standard-target calibration of a parametric sonar over the difference-frequency band, 1-6 kilohertz (A)," J. Acoust. Soc. Am. **125**, 2718 (2009).
[28]K. G. Foote, "Range compensation function for echo integration in transducer near fields, with special reference to parametric sonar (A)," J. Acoust. Soc. Am. **125**, 2718 (2009).
[29]S. T. Forbes and O. Nakken, "Manual of methods for fisheries resource survey and appraisal. Part 2. The use of acoustic instruments for fish detection and abundance estimation," FAO Man. Fish. Sci. **5**, 1–138 (1972).
[30]R. B. Mitson, *Fisheries Sonar* (Fishing News Book Ltd., Farnham, Surrey, UK, 1983).
[31]K. G. Foote, "Maintaining precision calibrations with optimal copper spheres," J. Acoust. Soc. Am. **73**, 1054–1063 (1983).
[32]K. G. Foote, H. P. Knudsen, G. Vestnes, D. N. MacLennan, and E. J. Simmonds, "Calibration of acoustic instruments for fish density estimation: A practical guide," ICES Coop. Res. Rep. **144**, 1–69 (1987).
[33]K. G. Foote, D. T. I. Francis, and P. R. Atkins, "Calibration sphere for low-frequency parametric sonars," J. Acoust. Soc. Am. **121**, 1482–1490 (2007).

8-kHz bottom backscattering measurements at low grazing angles in shallow water

Hyoungsul La[a] and Jee Woong Choi[b]
Department of Environmental Marine Sciences, Hanyang University, 1271 Sa-3-dong, Ansan, Gyeonggi-do 426-791, Korea
hsla@kopri.re.kr, choijw@hanyang.ac.kr

Abstract: 8-kHz bottom backscattering measurements at low grazing angles (6°–31°) are presented. The experiment was performed at a very shallow water site with a silty bottom on the south coast of Korea. Backscattering strengths between −42 and −30 dB were obtained and were compared to a theoretical backscattering model and Lambert's law. The fit of the theoretical model to the measurements suggests that sediment volume scattering is dominant over scattering from bottom interface roughness. Combining these results with previous measurements found in the published literature implies that backscattering strengths from silty sediment increase slightly as the frequency increases.

PACS numbers: 43.30.Gv, 43.30.Hw, 43.30.Ma [WS]
Date Received: May 15, 2009 **Date Accepted:** February 1, 2010

1. Introduction

This paper presents the results of bottom backscattering measurements at low grazing angles and a frequency of 8 kHz. The bottom backscattering strengths, as a function of grazing angle within the range 6°–31°, were extracted from monostatic reverberation data measured at an experimental site with silty sediment off the south coast of Korea. Measuring bottom backscattering signals at low grazing angles is difficult due to possible contamination by signals scattered from the sea surface and subsequent multi-path reverberation. However, it is essential to investigate the scattering mechanisms for low grazing angles, as the scattering of low-grazing-angle acoustic waves from the seafloor dominates long-range reverberation in shallow water.

A number of efforts have been made to measure bottom backscattering strengths at low grazing angles for frequencies less than 1 kHz (Refs. 1 and 2) and higher than 10 kHz.[3,4] However, few measurements have assessed the backscattering strengths for low grazing angles at intermediate frequencies (1–10 kHz) owing to the difficulty of measurement. Holland *et al.*[5] showed that sub-bottom scattering is significant on a seafloor with a layered structure using backscattering strengths measured in the 1–4 kHz frequency band. Soukup and Gragg[6] presented scattering data for rocky bottoms in the 2–3.5 kHz band and conducted geoacoustic inversion with comparisons to the interface scattering model. Hines *et al.*[7] presented low-grazing-angle bottom backscattering measurements taken at frequencies of 4 and 8 kHz, and reported that backscattering strengths from sandy sediments lie within a range of −50 to −20 dB for grazing angles between 3° and 15°, showing that backscattering strength increases with increasing grazing angle. This result provides a good comparison with that reported here, which are performed on a silty bottom.

In this paper, the properties of backscattering for an acoustically soft bottom are investigated via comparisons with Lambert's law[8] and the theoretical backscattering model developed by Mourad and Jackson[9] (referred to as "theoretical model" from here on). Lambert's law

---

[a]Present address: Korea Polar Research Institute, Incheon, Korea.
[b]Author to whom correspondence should be addressed.

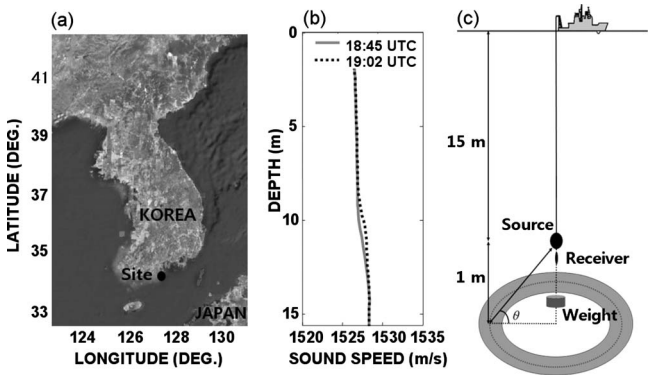

Fig. 1. (a) Location of the experimental site (34°29.45′ N, 127°49.13′ E). (b) The sound speed profile of the water column measured by conductivity-temperature-depth casts. (c) Experimental geometry for measurements of bottom backscattering strengths.

is expressed as a function of bottom grazing angle and an empirical coefficient equal to −27 dB, which is typically used as a default value. The theoretical model was developed by combining scattering from interface roughness with volume scattering. The roughness scattering model consists of the Kirchhoff approximation for steeper grazing angles and the composite roughness model for other grazing angles, and it was suggested to be applied over the frequency range 10–100 kHz. Although 8-kHz bottom backscattering strengths are presented here, we compare our results directly to the predictions obtained from the theoretical model without any modifications.

2. Experimental description and observations

The bottom backscattering measurements were taken in September 2007 at a very shallow water site (34°29.45′ N, 127°49.13′ E) off the coast of Ando in the south of Korea in water 16 m deep [Fig. 1(a)]. A DT-X split-beam transducer (Biosonics, Inc., Seattle, WA) with a center frequency of 420 kHz was used to survey the seafloor at the experimental site. This instrument provides high resolution bathymetry, showing that the bottom is flat in the north-south direction, with a small slope of less than 1.0° in the east-west direction. Analysis of sediment cores collected by divers shows that the mean grain size at depths up to 20 cm was 5.6ϕ [where $\phi=-\log_2(d/d_0)$, d is the grain diameter in millimeters, and d_0 is the reference length, equal to 1 mm], corresponding to medium silt. The standard deviation was estimated to be 1.9ϕ using the graphic method suggested by Folk and Ward.[10] Conductivity-temperature-depth casts were made twice, before and after acoustic observations, to measure the sound speed profile in the water column [Fig. 1(b)]. The sound speed structure was very stable (in the range 1526–1528 m/s) over the course of the acoustic measurements. Wind speeds were in the range 0–3.5 m/s, and the sea state was very calm.

An omni-directional acoustic source (D-17, RESON, Slangerup, Denmark) was deployed at 1 m above the bottom interface from a small boat, which drifted with the currents and waves. The transmitted signals were received by an omni-directional hydrophone (TC-4014, RESON), which was placed 0.1 m from the acoustic source to receive the signals backscattered from the ocean bottom at low grazing angles without any interaction from the sea surface [Fig. 1(c)]. An 8-kHz continuous wave pulse with a length of 0.6 ms was transmitted every 0.5 s, and repeated 100 times. The received signals were sampled at 300 kHz and band-pass filtered with a 3-dB bandwidth of 3 kHz centered at 8 kHz for noise removal. Figure 2(a) shows the received levels for 100 realizations (thin lines) and their average intensity (thick line). The first arriving contribution is associated with the direct path, the echo returned from the weight, and the normal-incidence bottom reflected signal, which is characterized by very small intensity fluctuations. Note that portions of the data with travel time corresponding to the direct path exceed the dynamic range of the receiving system owing to the very close proximity of the source.

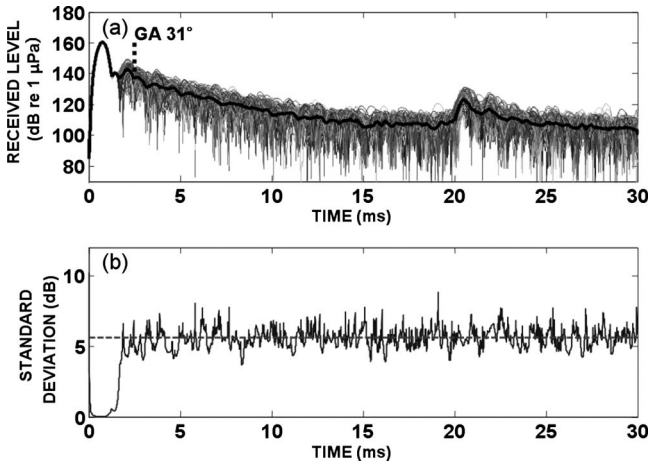

Fig. 2. (a) Received intensity levels for 100 realizations (thin lines) and their averaged intensity (thick line). (b) Standard deviation (expressed in decibels) for 8-kHz bottom backscattering signals.

Subsequent arrivals ($>\sim 2$ ms) consist of backscattered signals from the bottom, which are interrupted by scattered signals from the sea surface arriving after ~ 20 ms; the intensities of these signals fluctuate greatly, as might be expected from rough surface scattering. The minimum grazing angle of the bottom backscattered signal is limited by the signals arriving prior to the sea surface-reflected arrival, referred to as a fathometer return. Assuming that the refraction effect is negligible (owing to the iso-speed profile in the water column), the lower bound of the grazing angle is set at about 6°; the corresponding slant range is ~ 10 m. In order to determine the upper bound, we consider a range that is in the acoustic far-field region and is sufficiently far from the source to avoid contamination from the direct path and echo returned from the weight. For a spherical wave the acoustic far-field is defined as $kr \gg 1$, where k and r are the acoustic wave number and the distance from the source, respectively.[11] To satisfy this criterion, we take $kr = 60$, for which the slant range is estimated to be ~ 2 m for 8 kHz, corresponding to a grazing angle of about 31°. The region of the time series of the reverberation level corresponding to the upper bound is marked by the vertical dashed line in Fig. 2(a). Figure 2(b) shows the standard deviation (expressed in decibels), which is ~ 5.6 dB for bottom and sea surface scattering, and is consistent with the standard deviation of instantaneous intensity measurements based on a time-bandwidth product equal to unity.[12,13] However, the first arrival is an exception, as it is not subject to random intensity fluctuations, and thus its standard deviation is much smaller than that of random fluctuations.

3. Measurement results

The sonar equation for estimating the bottom backscattering strength as a function of grazing angle is given by[14]

$$\mathrm{BS}(\theta) = \mathrm{RL} - \mathrm{SL} + 2\mathrm{TL} - 10 \log A, \tag{1}$$

where $\mathrm{BS}(\theta)$ is the bottom scattering strength in dB re 1 m^2 over the insonified area (A) at a grazing angle θ, RL is the received level in dB re 1 μPa, SL is the source level (which is 174 dB re 1 μPa at 1 m for these measurements), and TL is the one-way transmission loss (in dB) from the source to the bottom interface, corresponding to the grazing angle θ. TL is predicted by estimating the spherical spreading loss, which is $20 \log(c_w T/2)$ where c_w and T are the compressional wave speed in water and the arrival time, respectively. Absorption loss is negligible because the absorption coefficient predicted using the formula suggested by Francois and Garrison[15] is $\sim 0.5 \times 10^{-3}$ dB/m for 8 kHz. The insonified area is associated with the beam patterns of the source and receiver and the pulse length of the source signal. For the omni-directional source and receiver, the insonified area is assumed to be a circular annulus, and its size is given by

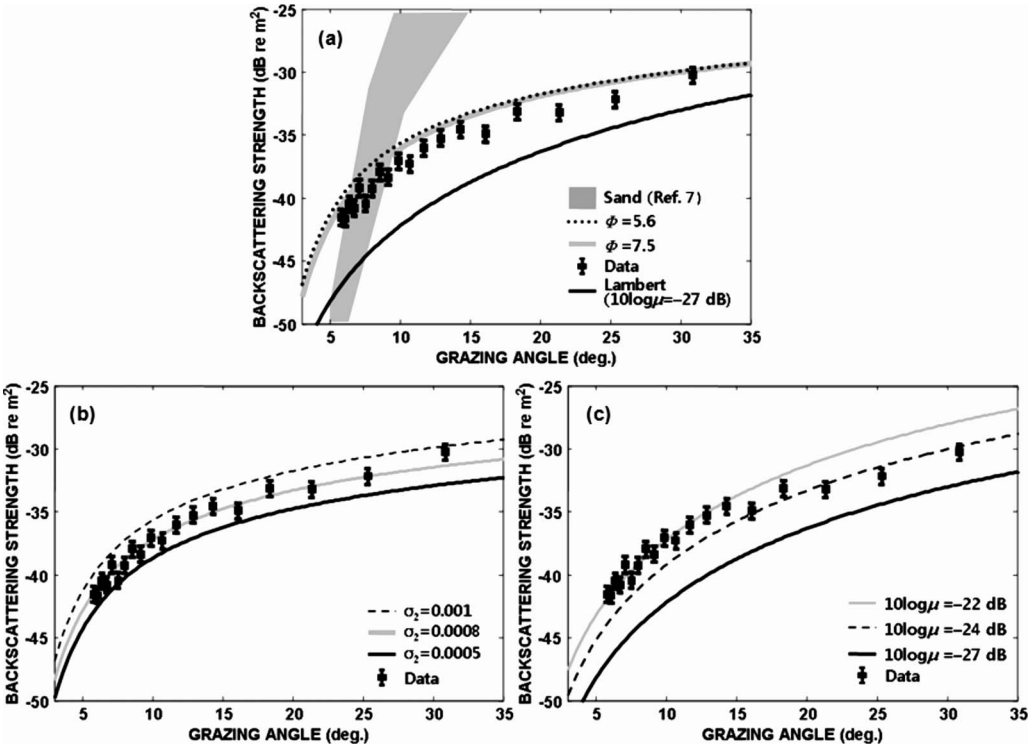

Fig. 3. (a) Comparisons of the measured backscattering strengths with the model predictions. Dotted line and thick gray line indicate the predictions obtained from the theoretical model for grain sizes of ϕ=5.6 and 7.5, respectively. The black line indicates Lambert's law with 10 log μ=−27 dB. The shaded region represents the range of backscattering strengths measured on a sandy bottom in Ref. 7. (b) and (c) show the predictions obtained from the theoretical model for the mean grain size of ϕ=5.6 and Lambert's law, respectively, and their comparisons with the measured data. The dashed line, gray line, and black line in (b) are the model predictions for σ_2=0.001, 0.0008, and 0.0005, respectively. The gray line, dashed line, and black line in (c) are the model outputs from Lambert's law with 10 log μ=−22, −24, and −27 dB, respectively.

$$A = \tfrac{1}{2}\pi \cos^2\theta c_w^2 T\tau, \tag{2}$$

where τ is the pulse length of the source signal, which is similar to the expression in Ref. 16.

Figure 3 shows the backscattering strengths, calculated using Eq. (1), as a function of grazing angle and their comparisons with the model predictions. The backscattering strengths were measured at time intervals in the scattering signal corresponding to the slant range intervals of $c_w\tau/2$. For grazing angles from 6° to 31°, the backscattering strengths are approximately −42 to −30 dB, showing an increase with grazing angle. The error bars represent the uncertainty range of the backscattering strengths. For a random signal with an amplitude distribution that follows a Rayleigh probability density function, the intensity average for 100 realizations (expressed in decibels) has a Gaussian distribution with a standard deviation of ~0.6 dB. The systematic error, including the uncertainties in the source level and the receiving sensitivity, was estimated to be less than ±0.5 dB via the calibration experiment performed at the calibration water tank located at Hanyang University in Ansan, Korea. The error associated with transmission loss is negligible, as the sound speed was very stable over the course of the acoustic measurements. The total error reflected in the error bars is thus expected to be approximately ±0.8 dB.

The measured backscattering strengths are compared to the model predictions obtained from the theoretical backscattering model and Lambert's law. To predict the scattering strengths with the theoretical model, input parameters that include the sediment sound speed, density, attenuation, and bottom roughness spectrum must be determined. Unfortunately, aside

from grain size, quantitative geoacoustic parameters were not measured at the site. The input parameters were therefore estimated using the geoacoustic relationships with grain size.[17] The dotted line shown in Fig. 3(a) indicates the model predictions obtained from the theoretical model for the mean grain size of $\phi=5.6$; these predictions are 1–3 dB greater than the measured backscattering strengths. The shaded area denotes the range of backscattering strengths measured on a sandy bottom in Ref. 7, which shows a more rapid increase with grazing angle than our experimental data, as well as much higher values than the backscattering strengths presented here for grazing angles greater than $\sim 10°$. The thick gray line shows that the model predictions for $\phi=7.5$ (which corresponds to the mean minus one standard deviation) are nearly identical to those for the mean grain size, which implies that scattering from volume inhomogeneities is dominant. Meanwhile, the experimental data are about 3–6 dB greater than the predictions made using Lambert's law, given by[8]

$$\mathrm{BS}_{LL} = 10\log(\sin^2\theta) + 10\log\mu, \tag{3}$$

where μ is a scattering constant associated with the insonified area. For a comparison to the measured backscattering strengths, $10\log\mu=-27$ dB reported by Mackenzie is used.[8]

For the acoustically soft bottom, sediment volume scattering is dominant over scattering from the interface roughness. Accordingly, the theoretical model for this sediment type is most sensitive to the volume parameter σ_2, defined as the ratio of the sediment volume scattering cross section to the sediment attenuation coefficient; typical values range from 0.0001 to 0.004.[17] Figure 3(b) shows the theoretical results obtained using $\sigma_2=0.0005$, 0.0008, and 0.001, which is a default value suggested in Ref. 9 for $5.0\leq\phi\leq 9.0$, and was used in the model predictions in Fig. 3(a). The measured backscattering strengths fall within the range of the theoretical model outputs predicted with σ_2 values between 0.0005 and 0.001, showing the best fit to the model predictions obtained with $\sigma_2=0.0008$.

Finally, the measured backscattering strengths are compared to the predictions obtained from Lambert's law for various values of $10\log\mu$ [Fig. 3(c)]. The model-data comparisons indicate that the model curve for $10\log\mu=-22$ dB agrees reasonably well with the measured backscattering strengths for grazing angles less than 15°. However, the experimental data for grazing angles between 15° and 31° tend to be closer to the model predictions obtained using a value of −24 dB for $10\log\mu$.

4. Summary and conclusions

Measurements of 8-kHz bottom backscattering strengths for low grazing angles (less than 31°) made in shallow water off the south coast of Korea have been presented. The seafloor at the experimental site had a flat, silty bottom with a mean grain size of 5.6ϕ. The measured signals were converted to backscattering strengths as a function of grazing angle, and were compared to model predictions obtained from Lambert's law and the theoretical scattering model of Ref. 9. Overall backscattering strengths for grazing angles between 6° and 31° fell between −42 and −30 dB. When compared with Lambert's law, the best-fit curve was found in the −22 to −24 dB range for $10\log\mu$. Although the theoretical model was developed for use with higher frequencies (10–100 kHz), the roughness scattering cross section for lower grazing angles is calculated via the composite roughness model, in which the small-roughness perturbation approximation is used with corrections for shadowing by the large-scale surface and its rms slope. This approximation is valid for cases in which the interface relief is much smaller than the acoustic wavelength.[18] Mourad and Jackson[19] applied this model to low-frequency (<1 kHz) bottom backscattering. For a soft bottom such as our experimental seafloor, the theoretical model is most sensitive to the volume parameter σ_2, and the model predictions provided the best fit to the measured backscattering strengths at $\sigma_2=0.0008$.

Holland and Neumann[1] collected low-frequency (100–1000 Hz) bottom scattering strengths for grazing angles less than 25° on a silty-clay seafloor and reported values between −45 and −40 dB. Jackson and Briggs[3] presented low grazing angle bottom scattering measurements for frequencies higher than 20 kHz. They reported that the backscattering strengths measured on a silty-clay bottom with a mean grain size of 5.2ϕ ranged between −43 and −27 dB at 20

kHz and between −35 and −25 dB at 35 kHz. Combining these results with the backscattering strengths reported here, one may conclude that backscattering strength increases slightly with increasing frequency. The increase in scattering strength with increasing frequency appears to be consistent with the 3-dB increase for each decade increase in frequency reported in Ref. 17.

Acknowledgments

This research was supported by the Agency for Defense Development, Korea (Grant No. UD080001DD) and the National Research Foundation of Korea (Grant No. 2008-0058752).

References and links

[1]C. W. Holland and P. Neumann, "Sub-bottom scattering: A modeling approach," J. Acoust. Soc. Am. **104**, 1363–1373 (1998).
[2]R. J. Greaves and R. A. Stephen, "Seafloor acoustic backscattering from different geological provinces in the Atlantic Natural Laboratory," J. Acoust. Soc. Am. **101**, 193–208 (1997).
[3]D. R. Jackson and K. B. Briggs, "High-frequency bottom backscattering: Roughness versus sediment volume scattering," J. Acoust. Soc. Am. **92**, 962–977 (1992).
[4]S. Stanic, R. R. Goodman, K. B. Briggs, N. P. Chotiros, and E. T. Kennedy, "Shallow-water bottom reverberation measurements," IEEE J. Ocean. Eng. **23**, 203–210 (1998).
[5]C. W. Holland, R. Hollett, and L. Troiano, "Measurement technique for bottom scattering in shallow water," J. Acoust. Soc. Am. **108**, 997–1011 (2000).
[6]R. J. Soukup and R. F. Gragg, "Backscatter from a limestone seafloor at 2–3.5 kHz: Measurements and modeling," J. Acoust. Soc. Am. **113**, 2501–2514 (2003).
[7]P. C. Hines, J. C. Osler, and D. J. MacDougald, "Acoustic backscattering measurements from littoral seabeds at shallow grazing angles at 4 and 8 kHz," J. Acoust. Soc. Am. **117**, 3504–3516 (2005).
[8]K. V. Mackenzie, "Bottom reverberation for 530- and 1030-cps sound in deep water," J. Acoust. Soc. Am. **33**, 1498–1504 (1961).
[9]P. D. Mourad and D. R. Jackson, "High frequency sonar equation models for bottom backscatter and forward loss," Proceedings: Oceans'89 (1989), pp. 1168–1175.
[10]R. L. Folk and W. C. Ward, "Brazos River bar: A study in the significance of grain size parameters," J. Sediment. Petrol. **27**, 3–26 (1957).
[11]P. H. Dahl, "High-frequency underwater sound," in *Encyclopedia of Electrical and Electronic Engineering*, edited by J. G. Webster (Wiley, New York, 2007), pp. 1–19.
[12]N. C. Makris, "The effect of saturated transmission scintillation on ocean acoustic intensity measurements," J. Acoust. Soc. Am. **100**, 769–783 (1996).
[13]J. W. Choi and P. H. Dahl, "Measurement and simulation of the channel intensity impulse response for a site in the East China Sea," J. Acoust. Soc. Am. **119**, 2677–2685 (2006).
[14]R. J. Urick, *Principles of Underwater Sound* (McGraw-Hill, New York, 1983).
[15]R. E. Francois and G. R. Garrison, "Sound absorption based on ocean measurements: Part II: Boric acid contribution and equation for total absorption," J. Acoust. Soc. Am. **72**, 1879–1890 (1982).
[16]R. P. Chapman and J. H. Harris, "Surface backscattering strengths measured with explosive sound sources," J. Acoust. Soc. Am. **34**, 1592–1597 (1962).
[17]D. R. Jackson and M. D. Richardson, *High-Frequency Seafloor Acoustics* (Springer, New York, 2007).
[18]E. I. Thorsos and D. R. Jackson, "The validity of the perturbation approximation for rough surface scattering using a Gaussian roughness spectrum," J. Acoust. Soc. Am. **86**, 261–277 (1989).
[19]P. D. Mourad and D. R. Jackson, "A model/data comparison for low-frequency bottom backscatter," J. Acoust. Soc. Am. **94**, 344–358 (1993).

Judgments of intensity for brief sequences

Frederick J. Gallun
VA RR&D National Center for Rehabilitative Auditory Research, Portland VA Medical Center, 3710 SW US Veterans Hospital Road, Portland, Oregon 97239
frederick.gallun@va.gov

Abstract: The ability to make intensity judgments for sequential stimuli was examined with an intensity-discrimination task involving three 50-ms noise bursts with non-overlapping frequency ranges. Targets (single bursts) presented in three-burst sequences were required to be as much as 5 dB more intense than targets presented as single bursts in isolation, especially for the later targets. Randomizing target position in the sequence did not reliably reduce performance, nor were thresholds for younger and older listeners reliably different. These increases in increment detection threshold are indications of a specific intensity-processing deficit for stimuli occurring later in a sequence.

PACS numbers: 43.66.Fe, 43.66.Mk [QF]
Date Received: January 5, 2010 **Date Accepted:** February 18, 2010

1. Introduction

Older listeners' reduced ability understand speech in complex environments has been associated with a specific temporal processing deficit (e.g., Gordon-Salant and Fitzgibbons, 1999; Wingfield *et al.*, 1999; Salthouse, 1992). Listeners of all ages asked to make judgments about stimuli embedded in rapidly changing sequences tend to do worse for longer sequences and later arriving stimuli (e.g., Vachon and Tremblay, 2005; Cousineau *et al.*, 2009). If aging is associated with specific temporal impairments, then it becomes very important to understand the baseline ability of listeners to make temporal judgments for sequential stimuli.

The ability to make intensity judgments is usually tested by asking the listener to compare an isolated standard of a known frequency and level with a target matched in duration and frequency and varying only in level (e.g., McGill and Goldberg, 1968; Jesteadt *et al.*, 1977). Such paradigms provide stable estimates of threshold and extremely precise performance (thresholds of 2 dB or less).[1] Embedding standard and target in a sequence, however, can greatly increase thresholds. Watson (2005) found that the intensity of targets presented in sequences of distractor tones needed to be as much as 7 dB more intense than when those same targets were presented in isolation. Uncertainty about the target or confusions about which stimulus was target and which was distractor are the usual explanations for these effects (e.g., Watson *et al.*, 1975; Leek and Watson, 1984; Watson, 2005). Nonetheless, some data are consistent with a reduction in performance associated merely with temporal position. The current experiment had as its goal the establishment of the size of such effects and the dissociation of problems due to impaired temporal processing from the impacts of age and/or uncertainty. In addition, a simultaneous condition was included in order to establish baseline performance for a condition in which it was more likely that all of the elements would be perceived as a single auditory object.

2. Methods

Five "younger" listeners (4 females, mean age: 31.0 years, range: 28–36 years) and seven "older" listeners (3 females, mean age: 56.0 years, range: 51–60 years) participated. All had pure-tone hearing thresholds of 25 dB hearing level (HL) or better (re ANSI, 2004) at octave frequencies between 0.25 and 8 kHz in the left ear—the test ear in all conditions. All were paid for their participation and all procedures were reviewed and approved by the Institutional Review Boards of both the Portland VA Medical Center and the Oregon Health Sciences University.

Stimuli were 50-ms noise bursts with 5 ms $\cos^2$ onset and offset ramps. Bursts were presented in three frequency ranges: low (400–560 Hz), middle (1620–2400 Hz), or high (4080–6100 Hz). Noise was generated digitally (sampling rate of ~50 kHz) in the MATLAB environment (Mathworks, Inc., Natick, MA) from 20-Hz spaced equal-amplitude tones with randomized starting phase. Tucker-Davis Technologies digital-to-analog converters, anti-aliasing filters, and attenuators (TDT System 3 RP2.1, PA5, and HB7 hardware) generated an analog signal that was presented to the left ear through a Sennheiser HD280 headphone.[2]

Detection thresholds (DTs) were obtained for each noise burst (low, middle, and high frequencies) in a same/different task. Two intervals were presented, each marked with a visual display and separated by 500 ms of silence. Each interval had a 50% chance of containing a signal. Listeners were to respond "same" when a signal or silence had been presented on both intervals (50% chance) and "different" when one interval contained silence and one interval contained a signal (50% chance). Feedback was given after each trial, and the rms level of the noise burst was increased or decreased following a three-down/one-up adaptive tracking procedure (Levitt, 1971). The initial level of 40 dB sound pressure level (SPL) was raised or lowered in 4-dB steps until the first reversal, 2-dB steps until a second reversal, and then 1-dB steps for eight more reversals, which were averaged to give the DT estimate. Three estimates of DT were collected for each frequency.

Increment-detection thresholds (ITs) were obtained for each listener for bursts presented alone and in sequences. Two intervals were presented with the same visual marking and 500 ms separation, and listeners reported "same" if the stimulus in the second interval had the same intensity (or set of intensities) as the stimulus in the first interval (as was done in Cousineau *et al.*, 2009). Differences were always an increment in the intensity of only one of the bursts in the second interval. ITs were estimated using a same/different tracking procedure similar to that employed in the detection task.

Baseline burst level (to which the increment could be added) was roved on each trial from a nominal level of 35 dB sensation level (SL) by ±5 dB in order to encourage comparison of the two intervals rather than judgments of the second (see Green, 1988). When multiple bursts were presented in a single interval, each was roved independently to discourage listeners from comparing across bursts in a sequence. The increment was initially set to 10 dB and changed by 4 dB until the first reversal, 2 dB until the second reversal, and 1 dB for eight more reversals, which were averaged to estimate threshold. Increments never exceeded 25 dB and in general the maximum level of the incremented stimulus rarely exceeded 85 dB SPL.

Four conditions were tested in an interleaved fashion to preclude learning effects. In the "single-burst" condition, one fixed frequency burst was presented in each interval for the entire adaptive track. In the "simultaneous" condition, all three bursts were presented with simultaneous onsets. In the "adjacent" condition, the onsets of the bursts were delayed by 50 ms (the duration of the preceding burst), while in the "delayed" condition, the onsets of the bursts were delayed by 200 ms (the duration of the preceding burst plus 150 ms). For each of the three conditions with multiple bursts, either the burst to which the increment was added was fixed for an entire adaptive track (low, middle, or high) or was randomly changed on each trial ("random"). In the sequential conditions with multiple bursts (adjacent and delayed), the order of the bursts was fixed (low, then middle, then high) in order to reduce uncertainty in the fixed target conditions. This leads to a potential confound of frequency and order effects, and thus the second condition (simultaneous presentation) was included to examine the effects of frequency alone.

It was hypothesized that the uncertainty introduced by randomizing the target burst would have the greatest effect for conditions 3 and 4, where both temporal and frequency uncertainty were introduced. Listeners were expected to require larger increments to reliably detect that a change had occurred when the target was random, and the impacts were expected to be greatest for the older listeners.

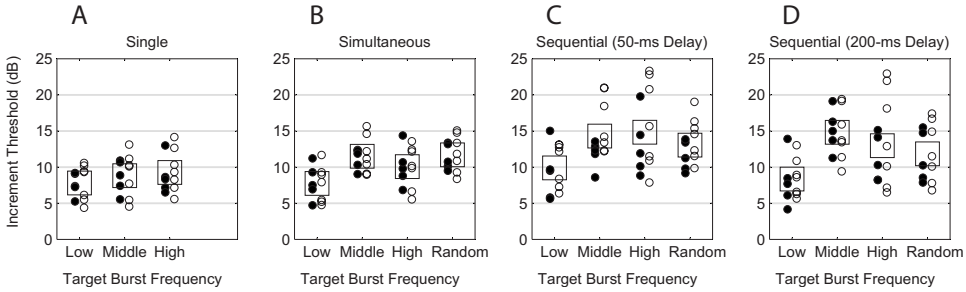

Fig. 1. Panels show average ITs for five listeners younger than 37 years (filled circles) and seven listeners older than 50 years (unfilled circles) in condition 1 [single burst, panel (A)], condition 2 [simultaneous bursts, panel (B)], condition 3 [50-ms delay between onsets, adjacent, panel (C)], and condition 4 [200-ms delay between onsets, delayed, panel (D)]. Unfilled squares indicate the mean across all listeners for that condition.

3. Results

Mean DTs in dB SPL were 20.3, 15.8, and 24.5 dB SPLs for low, middle, and high frequency bursts, respectively. All listeners had individual thresholds between 3 and 36 dB SPL. These values are consistent with the audiometric thresholds for these listeners after conversion to dB SPL. A mixed-measures analysis of variance (ANOVA)[3] with age group as a between-subjects variable and frequency as a within-subjects variable showed that the differences among thresholds for the three frequencies were statistically significant ($F_{2,20}=6.07$, $p<0.01$), but there was no significant main effect of age group ($F_{1,10}=2.26$, $p=0.16$) or interaction ($F_{2,20}=0.68$, $p=0.52$). *Post-hoc* t-tests showed that the effects of frequency were due to the difference between the middle frequency burst and the high frequency burst.

The average IT in the single-burst condition was similar across noise bursts: 7.8 (low), 8.8 (middle), and 9.3 dB (high). Average performance across listeners is plotted as the large open squares in Fig. 1, panel (A), with the smaller filled circles indicating mean performance for the five younger listeners and the smaller open circles the seven older listeners. These values are higher than those reported for tonal stimuli (3.5 dB; Cousineau *et al.*, 2009) or even for roving-level noise bursts (4 dB; Heinz and Formby, 1999). A mixed-measures analysis of variance showed that the differences among bursts were statistically significant ($F_{2,20}=4.66$, $p<0.05$) but there was no significant main effect of age group ($F_{1,10}=2.26$, $p=0.164$) or interaction ($F_{2,20}=0.32$, $p=0.73$). *Post-hoc* t-tests showed that the effects of frequency were due to the significant differences ($p<0.05$) between the low burst and the middle and high bursts, while the middle and high did not differ significantly ($p>0.05$). Average IT for each burst was not significantly correlated with detection threshold (for all correlation analyses throughout, each subject contributed one pair of values per frequency; thus 12 points per correlation).

When the bursts were all presented simultaneously, with no differences in onset or offset, average IT for the low was 7.7 dB, while the middle was 11.5 dB and the high was 10.2 dB. Randomizing the target burst within an adaptive track resulted in an increment threshold of 11.6 dB. Performance is plotted in Fig. 1, panel (B). A mixed-measures analysis of variance revealed that the differences among the burst thresholds were statistically significant ($F_{1.8,18.1}=14.19$, $p<0.001$) but there was no significant main effect of age group ($F_{1,10}=0.07$, $p=0.80$) or interaction ($F_{1.8,18.1}=0.34$, $p=0.70$). *Post-hoc* t-tests showed that the thresholds of all of the frequency bursts differed significantly from each other ($p<0.05$), with the exception of the middle burst, which was not significantly different from the high burst or the random frequency condition ($p>0.05$). Average IT for each burst was not significantly correlated with detection threshold. This suggests that frequency range alone had an impact on performance when all three bursts were presented simultaneously in each interval. In the absence of a clear model distinguishing sequential and simultaneous masking (which are known to differ in important ways), it is still useful

to consider the two as simply additive in order to reveal the minimum changes in performance that are likely to be due to the onset differences alone. This analysis is applied below.

When all three bursts were presented on each interval, delayed in onset by the duration of the preceding burst so that onsets and offsets were adjacent, average IT for the low was 10.0 dB, while the middle was 14.3 dB and the high was 14.8 dB. Randomizing the target burst resulted in an increment threshold of 13.0 dB. Performance for the younger and older listeners is plotted in Fig. 1, panel (C). A mixed-measures analysis of variance revealed that the differences among the burst thresholds were statistically significant ($F_{3,30}=8.82$, $p<0.001$) but there was no significant main effect of age group ($F_{1,10}=2.19$, $p=0.18$) or interaction ($F_{3,30}=0.71$, $p=0.55$). *Post-hoc* t-tests showed that the thresholds of all of the frequency bursts differed significantly from each other ($p<0.05$), with the exception of the middle burst, which was not significantly different from the high burst or the random frequency condition ($p>0.05$), and the random frequency threshold, which did not differ from the thresholds for the middle or high frequency bursts ($p>0.05$). Average IT for each burst was not significantly correlated with detection threshold. Even assuming that the changes in threshold found in the simultaneous condition would have occurred in the burst conditions, these ITs represent increases of 2–4.5 dB for each burst that were a direct result of the sequential presentation. Thus, delaying the onsets of the bursts *hurt* performance, even when the target burst was fixed for the entire adaptive run.

When all three bursts were presented on each interval delayed by 200 ms (i.e., creating a 150 ms gap between bursts), average IT for the low was 8.4 dB, while the middle was 14.8 dB and the high was 13.0 dB. Randomizing the target burst resulted in an increment threshold of 11.8 dB. Performance is plotted in Fig. 1, panel (D). A mixed-measures analysis of variance revealed that the differences among the burst thresholds were statistically significant ($F_{1.7,16.9}=10.67$, $p<0.001$) but there was no significant main effect of age group ($F_{1,10}=0.25$, $p=0.63$) or interaction ($F_{1.7,16.99}=0.79$, $p=0.45$). *Post-hoc* t-tests showed that the thresholds for the low, high, and random frequency bursts did not differ significantly from each other ($p>0.05$), but that the middle burst was significantly higher than the low and random burst ($p<0.05$). The middle and high burst thresholds were not significantly different ($p>0.05$). Average IT for each burst was not significantly correlated with detection threshold. As with the previous data, even assuming that these ITs represent the additive combination of frequency and order effects, they represent increases of 2–3 dB for each burst that were a direct result of the sequential presentation, suggesting that delaying the onsets of the bursts by 200 ms did not remove the impacts of sequential presentation shown in condition three.

As a final statistical test of the differences among conditions, the ITs for conditions 2–4 were entered into a repeated-measures ANOVA with condition and frequency as within-subject variables. The main effect of condition was significant ($F_{2,22}=14.50$, $p<0.001$) as was the main effect of frequency ($F_{1.99,21.94}=15.33$, $p<0.001$) and the interaction ($F_{6,66}=3.965$, $p<0.01$). *Post-hoc* t-tests showed that the simultaneous and delayed conditions differed significantly from each other ($p<0.01$), but that the 50- and 200-ms delays were not significantly different from each other ($p=0.23$). The random frequency ITs were significantly different from the low burst ITs ($p<0.01$), but not from the middle or high ITs. The low ITs were significantly lower than the middle and high burst ITs ($p<0.05$), but the middle and high were not different from each other ($p=1.00$).

4. Discussion

The hypothesis that listeners have a reduced ability to make intensity judgments about targets embedded in a temporal sequence is supported by these results. The detrimental effect of presenting three bursts and asking listeners to judge only one of them was shown in the absence of temporal variation (in condition 2), but this could not account for all of the results. The impacts of age and uncertainty reported previously (e.g., Salthouse, 1992; Watson, 2005; Kidd *et al.*, 2008) were not found for this particular combination of listeners and conditions. Previous data

(Hafter *et al.*, 1998) have shown that a sensory-trace representation appears to be resistant to the costs of dividing attention, and listeners in this experiment may have been relying on a sensory-trace representation, which reduced the effects of age and uncertainty.

Thresholds for the single-burst stimuli were much greater than usually reported, even for noise stimuli roved in level (8 dB rather than the 4 dB shown by Heinz and Formby, 1999). One possibility is that listeners made level judgments of the second stimulus as a group rather than comparing the levels of the individual bursts to memories of the first presentation. A simple model simulating the impact of roving on ITs based on an overall loudness strategy predicts single-burst thresholds of roughly 8 dB. This model also predicts a reduction in performance for the multiple burst conditions and no impact of randomizing the target. However, it predicts no difference based on whether the multiple bursts are presented sequentially or simultaneously, and so cannot account for these results. The finding that performance was not worse in the simultaneous case, where subjects would have been more likely to hear all three bursts as a single object with a single intensity, suggests that auditory grouping might actually be able to reduce interference for stimuli like these.

Sequential processing deficits have primarily been modeled in the visual domain, where the suggestion is that sequential presentation impairs processing due to an inherent time-dependence of the underlying short-term memory consolidation process (Vogel and Luck, 2002; Tremblay, *et al.*, 2005; Vachon and Tremblay, 2005). Essentially, early elements of a to-be-remembered sequence are encoded accurately, but later elements must wait in a sensory "buffer" where they degrade in a time-dependent manner until they can be encoded. The general pattern of results described here, in which the first element was more accurately discriminated than the later elements, is consistent with the general predictions of such a model. One potential explanation for the lack of an effect of onset timing is that the integration time into short-term memory is on the order of 200–600 ms (as suggested by Vogel and Luck, 2002), and that the delays used were simply too short to show a release from temporal interference.

Acknowledgments

This work was supported by the Department of Veterans Affairs and by the NIH. Stephen Fausti, Anna Diedesch, Michelle Molis, Marjorie Leek, Chris Mason, Virginia Best, Gerald Kidd, and Barbara Shinn-Cunningham provided helpful comments and guidance. Matthew Marble, Kelly Reavis, and Marc Caldwell helped with data collection. The greatest debt is to the participants.

References and links

[1]Level difference is reported as the decibel change in the overall level of the stimulus ($[10 \log(\Delta I+I)]$-$10 \log I$) that would result from a given increment in intensity (ΔI) being added to a standard level (I). This measure has been shown to be very compressive for small values of ΔI (Green, 1988), despite the good detectability of such increments in some paradigms, leading to the use of the ratio of increment to standard ($10 \log \Delta I/I$) when small increments are being detected. As these two units are approximately linearly related for changes greater than 3 dB (Green, 1988), the more familiar measure has been used here.

[2]Frequency response of the headphones was not flat, but the overall level of each stimulus was digitally calibrated prior to amplification and attenuation such that the rms level of each stimulus was equated at the output of the headphone speaker. Any variations in the relative levels of frequency components within each stimulus were allowed to remain, since randomization of component phase introduces such variations in effective level.

[3]All mixed-measures tests were corrected for significant violations of the assumption of sphericity (when they occurred) by adjusting the degrees of freedom using a Greenhouse–Geisser correction. All *post-hoc* tests were Bonferroni corrected.

ANSI (**2004**). *Methods for manual pure-tone threshold audiometry* (ANSI S3.21-2004), American National Standards Institute, New York, NY.

Cousineau, M., Demany, L., and Pressnitzer, D. (**2009**). "What makes a melody: The perceptual singularity of pitch sequences," J. Acoust. Soc. Am. **126**, 3179–3187.

Gordon-Salant, S., and Fitzgibbons, P. J. (**1999**). "Profile of temporal processing in older listeners," J. Speech Lang. Hear. Res. **42**, 300–311.

Green, D. M. (**1988**). *Profile Analysis* (Oxford University Press, New York).

Hafter, E. R., Bonnel, A.-M., Gallun, E., and Cohen, E. (**1998**). "A role for memory in divided attention between two independent stimuli," in *Psychophysical and Physiological Advances in Hearing*, edited by A. R. Palmer, A. Rees, A. Q. Summerfield, and R. Meddis, (Whurr, London), pp. 228–238.
Heinz, M. G., and Formby, C. (**1999**). "Detection of time- and bandlimited increments and decrements in random-level noise," J. Acoust. Soc. Am. **106**, 313–326.
Jesteadt, W., Wier, C. C., and Green, D. M. (**1977**). "Intensity discrimination as a function of frequency and sensation level," J. Acoust. Soc. Am. **61**, 169–177.
Kidd, G., Jr., Mason, C. R., Richards, V. M., Gallun, F. J., and Durlach, N. I. (**2008**). "Informational masking," in *Auditory Perception of Sound Sources*, edited by W. A. Yost, A. N. Popper, and R. R. Fay (Springer, New York), pp. 143–190.
Leek, M. R., and Watson, C. S. (**1984**). "Learning to detect auditory pattern components," J. Acoust. Soc. Am. **76**, 1037–1044.
Levitt, H. (**1971**). "Transformed up-down methods in psychoacoustics," J. Acoust. Soc. Am. **49**, 467–477.
McGill, W. J., and Goldberg, J. P. (**1968**). "Pure-tone intensity discrimination and energy detection," J. Acoust. Soc. Am. **44**, 576–581.
Salthouse, T. A. (**1992**). "Influence of processing speed on adult age differences in working memory," Acta Psychol. **79**, 155–170.
Tremblay, S., Vachon, F., and Jones, D. M. (**2005**). "Attentional and perceptual sources of the auditory attentional blink," Percept. Psychophys. **67**, 195–208.
Vachon, F., and Tremblay, S. (**2005**). "Auditory attentional blink: Masking the second target in necessary, delayed masking is sufficient," Can. J. Exp. Psychol. **59**, 279–286.
Vogel, E. K., and Luck, S. J. (**2002**). "Delayed working memory consolidation during the attentional blink," Psychon. Bull. Rev. **9**, 739–743.
Watson, C. S. (**2005**). "Some comments on informational masking," Acta Acust. Acust. **91**, 502–512.
Watson, C. S., Wroton, H. W., Kelly, W. J., and Benbassat, C. A. (**1975**). "Factors in the discrimination of tonal patterns. I. Component frequency, temporal position, and silent intervals," J. Acoust. Soc. Am. **57**, 1175–1185.
Wingfield, A., Tun, P. A., Koh, C. K., and Rosen, M. J. (**1999**). "Regaining lost time: Adult aging and the effect of time restoration on the recall of time-compressed speech," Psychol. Aging **14**, 380–389.

An improved method to determine the onset timings of reflections in an acoustic impulse response

John Usher
Barcelona Media – Innovation Centre, Avenida Diagonal 177, 08018 Barcelona, Spain
john.usher@barcelonamedia.org

Abstract: Determining the absolute onset time of reflections in an acoustic impulse response (IR) has applications for both subjective and physical acoustics problems. Although computationally simple, a first-order energetic analysis of the IR can lead to false-positive identification of reflections. This letter reports on a method to determine reflection onset timings using a modified running local kurtosis analysis to identify regions in the IR where the distribution is non-normal. IRs from both real and virtual rooms are used to validate the method and to find optimum analysis window sizes.

PACS numbers: 43.55.Br, 43.55.Mc, 43.58.Gn, 43.60.Cg [NX]
Date Received: November 4, 2009 **Date Accepted:** February 18, 2010

1. Introduction

The absolute timings of early reflections in a room impulse response (RIR) can be used to solve a variety of problems relating to both subjective and physical acoustical phenomena in the corresponding environment (be it real or virtual). Although slight imprecision in the timing detection will not dramatically change coloration nor spatial impression, since both are evaluated at a more global level, the initial time-delay gap (ITDG) can affect perceptual integration of the direct and reflected sound (i.e., the precedence effect) and may affect speech intelligibility or musical timbre. Physical characteristics of a space can also be determined from precise timings of reflections in an acoustic IR; a process commonly used in SONAR, seismic exploration, and medical diagnosis.

The most computationally simple method to identify the reflection onset timings (ROTs) in a RIR is from an analysis of the energy envelope. There are a variety of approaches to this first-order energy profile analysis for onset detection within an audio signal, such as using tuned edge-detection wavelet filters or spectral-domain energy fluctuations (for instance, this has been applied to finding the onset of transient events in music audio signals[1]). It is the goal of this short letter to first describe the short-comings of using an energy profile analysis to determine ROTs in a RIR, and to second introduce an improved method based on a local running statistical analysis of the RIR. The analysis is particularly directed toward identifying low-order early reflections after the direct-sound.

2. Characterizing a room impulse response by ROTs

2.1 Energy profile analysis vs statistical energy analysis

To demonstrate the short-coming of using a first-order energetic analysis to determine ROTs, we refer to the RIR described in Fig. 1 that was measured in an open-ended room of dimensions $1.10 \times 2.73 \times 4.9$ m (w, h, d). By analysis of an image-source model constructed using the same acoustic measurement parameters, we can verify that the "true" first reflection actually corresponds to the peak marked with the box symbol in Fig. 1. However, using a simple analysis of the energy envelope of the RIR, the "false" reflection peak marked with the cross symbol shortly after the direct-sound peak would be mistaken as the first reflection. Such false reflections in the energy profile may be a result of distortion from anti-aliasing filters in the analog to digital converter system or from nonlinearities in the excitation and measurement transducer systems. Precise reflection onset

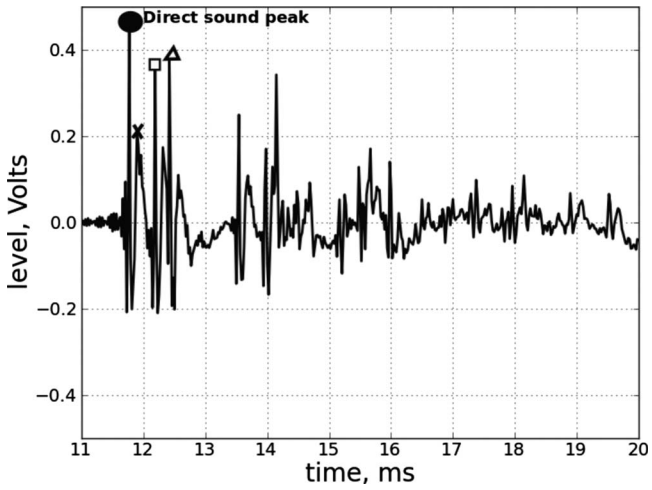

Fig. 1. RIR measured in an open-ended room of dimensions $1.10 \times 2.73 \times 4.9$ m (w,h,d). The true first and second arriving reflections were determined using a room model and are marked with the square and the triangle. The false reflection peak is marked with a cross, clearly indicating the problem of using an energy profile analysis to determine the timing onset of reflections in a RIR.

detection in a RIR is a problem further compounded by scattering effects from room surfaces, which can introduce a Poisson-like distribution for early reflections from averaged acquisition methods (such as maximum length sequence or swept-sine techniques).[2]

Statistical approaches to identifying reflection timings in an acoustic impulse response can overcome the problems with an energy analysis by utilizing the second-order statistics of a RIR. Reverberation is generally defined as a physical phenomenon where the sound reflections impinging on a point are such that the pressure can be modeled as a stochastic function with a normal distribution and a mean of zero, and that part of a RIR that has a normal distribution is called the reverberant part.[3] The degree to which a part of a RIR has a normal distribution (the "degree of normality") has been used before to determine the onset of the reverberation. Two such measures of normality are "average rms response fluctuation" and kurtosis. Schroeder's frequency-domain stochastic model[3] predicts that 68.26% of the response curve will lie within about 10 dB of the average level. Similarly, the Abel and Huang criterion[4] for the reverberant part of a RIR is based on the well-known phenomenon that 68.26% of the observations of a normal population will be found within 1 standard deviation of its mean.[5]

Another well established and understood measure of the degree of normality is *kurtosis*. Kurtosis can be considered as a measure of the degree of peakedness of a distribution, or more correctly as the degree of bi-modality. The kurtosis k of a data series x is defined as the ratio of its fourth central moment to its standard deviation raised to the power of 4 (hence kurtosis is always positive) as follows:

$$k = \frac{E\{x-\mu\}^4}{\sigma^4}, \tag{1}$$

where $E\{\bullet\}$ is the statistical expectation operator, μ is the mean, and σ is the standard deviation of the data series x.

To develop a running kurtosis analysis of data x, consider a block of samples centered about discrete time sample n as follows:

$$\mathbf{x} = [x_{n-m/2}, x_{n-m/2+1}, \ldots, x_{n+m/2-1}].$$

The running kurtosis of $\mathbf{x}_n$ is now defined as

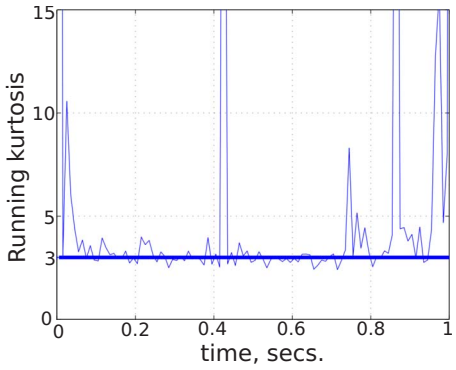

Fig. 2. (Color online) Sliding kurtosis echogram of a RIR from a 3000 m^3 concert hall. The reverberant component is defined when the kurtosis is equal to 3. Strong late individual reflections can be discerned, but fine-structure in the early part cannot. A sliding 10 ms rectangular window was used to calculate kurtosis according to Eq. (2).

$$k_n = \frac{(x_n - \mu_n)^4}{\sigma_n^4}, \tag{2}$$

where μ_n and σ_n are the mean and standard deviation of the m-length vector $\mathbf{x}_n$. If sample x_n is large compared with the local samples $\mathbf{x}_n$ then the kurtosis will be high (*leptokurtic*); a flat distribution in $\mathbf{x}_n$—a low peakedness—will have a low kurtosis (*platykurtic*); and a normal distribution has a kurtosis of 3. However, a bi-modal distribution will also give a low kurtosis; so therefore low kurtosis values are not necessarily an indication of low peakedness.[6] Kurtosis has been used before for acoustic IR analysis: for determining the optimum length of adaptive filters for applications such as blind audio upmixing[7] and for determining the onset of musical instruments in an audio signal.[1] In a RIR, spurious large-value samples from strong individual reflections will clearly have a leptokurtic distribution, giving a kurtosis greater than 3. It is this principle that forms the basis of the proposed method for identifying the onset of early reflections in a RIR.

2.2 Modified kurtosis method

Similar to the "echogram" or "reflection diagram" of Kuttruff,[8] which shows the absolute strength (i.e., acoustic power) of reflections impinging on a point over time, we can show a plot of the RIR kurtosis as a function of time (though the magnitude of the kurtosis is not necessarily related directly to the strength of the reflections). Such a "kurtosis echogram" for a RIR measured in a concert hall is shown in Fig. 2, where the onset of the strong first-order reflection from the rear of the concert hall can be discerned about 0.4 s after the direct-sound. However, fine-structure detail of the early impulse response is unclear and individual early reflections cannot be discerned.

The temporal resolution of the running kurtosis echogram is affected by two parameters: the range over which the local kurtosis is calculated (i.e., the window size m) and the overlap between successive kurtosis frames. As we saw in Fig. 2, a long temporal window smears the fine-structure of the early impulse response. This can be understood analytically by considering the reflection density of the RIR. The reflection density (reflections/s) can be approximated by

$$\frac{\mathrm{d}N}{\mathrm{d}T} = 4\pi\frac{c^3 t^2}{V}, \tag{3}$$

where c is the speed of sound, V is the room volume, and t is the time since the RIR onset. It has been reported that this relationship holds not just for rectangular rooms but also for any room shape.[8] Using Eq. (3), we can determine that for the first 6 ms of our 15 m^3 test room the

echo-density is approximately 1 arrival/ms, corresponding to 1 reflection arriving every 5 samples for a 48 kHz sample-rate system. If the kurtosis analysis window is less than the inter-reflection time then the expected difference between the instant RIR sample value x and the local mean μ may be lower than the RIR mean (or the RIR mean calculated with a larger local window) and likewise the kurtosis will be low even when a reflection is within the analysis window. Alternatively, if the kurtosis window is too large then the temporal resolution for kurtosis will be smeared, and a bi-modal distribution from double peaks within the analysis window can also give a low kurtosis.[6] We therefore introduce a modified kurtosis metric that is a function of two analysis windows: a first small window to estimate a "fast" local estimate of the RIR level [this replaces the single sample value x in Eq. (1)], and a second longer local window over which a "slower" mean and standard deviation are calculated. The modified kurtosis estimate is now defined as

$$k_{n,l,m} = \frac{(\mu_{n,l} - \mu_{n,m})^4}{\sigma_{n,m}^4}, \tag{4}$$

where l and m are the lengths of a first and second data window, both centered about sample n of the data series $\mathbf{x}$; $\mu_{n,l}$ and $\mu_{n,m}$ are the means of the l-length and m-length local data windows ($m > l$); and $\sigma_{n,m}$ is the standard deviation of the m-length window. An empirical investigation was conducted to find optimum window lengths l and m.

3. Results and discussion

The short window size for the estimate of the fast running-average, i.e., the length l, was four samples. This gave sufficient temporal resolution to capture a single reflection; and yet the time of arrival between two consecutive reflections in the early part of a RIR is generally at least four samples for small rooms, as discussed previously with reference to the Kuttruff echo-density trend in Eq. (3). The window size for the longer local IR window, i.e., the length m, was varied from being 2 to 16 times the length of the four-sample window. Figure 3 show that as the ratio of the long to small window (i.e., m/l) is increased, then the resulting "kurtosis echogram" becomes less noisy and the kurtosis peaks can be more easily discerned. However, for m/l ratios greater than 16, the width of these peaks increases, making it difficult to precisely identify the timing of peak maxima.

The criterion for selecting the optimum m/l ratio was by a difference between the ROTs of the measured RIR using the new two-window running kurtosis method, compared with the true ROTs as determined using the analytic image-source room model. The empirical ROTs were determined by analysis of the kurtosis echograms shown in Fig. 3 using a peak-picking inspection of the kurtosis data for peaks greater than a value of 3. The measurement was repeated with six different source-receiver locations (in the same room), and the real-world ROTs were compared with the virtual ROTs determined from the corresponding room model. For the first six ROTs, there was a 100% correspondence between the real and virtual ROTs for six different source-receiver test configurations when the m/l ratio was equal to 16. However, these exploratory findings used source-receiver locations that were chosen to be non-symmetrical about the room axes. For source-receiver locations centered near the central room axes, we would find that ROTs nearly coincided and would therefore decrease the inter-reflection time to a value less than the smallest analysis window yielding a bi-modal distribution with a low kurtosis; hence the reflection onsets may not be detected. Accordingly, we conclude that the kurtosis analysis method is effective for RIR echo-densities less than approximately 1-per-ms, which corresponds to approximately the first 80 ms of the RIR for a 3000 m^3 concert-hall sized room [predicted using Eq. (3)]. Although the analysis was conducted on full-band audio signals, the method for identifying ROTs is applicable for filtered IRs, such as octave of third-octave filtered time signals.

4. Conclusion

A new method has been proposed to determine the onset of individual reflections in the early part of a RIR. The method is based on a running local kurtosis analysis with two analysis win-

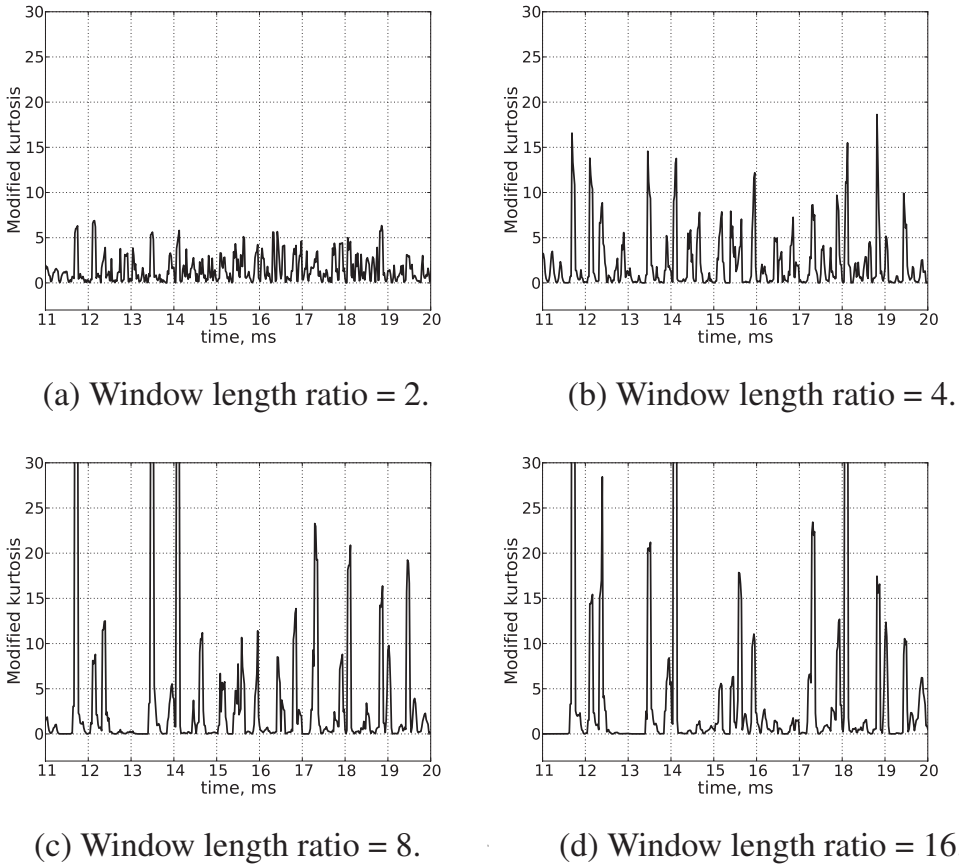

Fig. 3. Modified running kurtosis analysis of the RIR in Fig. 1. The window length ratio corresponds to m/l in the modified kurtosis equation [Eq. (4)], where the short window length l was always equal to four samples. Note that the false peak identified with the cross symbol in Fig. 1 was not detected.

dows to identify regions in the RIR where the distribution is non-normal. RIRs determined from both real and virtual rooms were used to validate the new method and to find optimum analysis window sizes, where a first window size of 0.8 ms and a second of 12.8 ms were found to accurately identify reflection onsets for the early part of the RIR. The effectiveness of identifying reflection onsets was found to be related to the relative length of the smaller window and the reflection density: The new method was reliable for densities less than 1-per-ms.

Acknowledgments

This work was partly supported by grants from iMP, Call No. FP7-ICT-2007-3 and Objective ICT-2007.4.4. The author is grateful for the comments from three anonymous reviewers.

References and links

[1]J.-P. Bello, L. Daudet, S. Abdallah, C. Duxbury, M. Davies, and M. Sandler, "A tutorial on onset detection in music signals," IEEE Trans. Speech Audio Process. **13**, 1035–1047 (2005).
[2]G. Defrance, L. Daudet, and J.-D. Polack, "Finding the onset of a room impulse response: Straightforward?," J. Acoust. Soc. Am. **124**, EL248–EL254 (2008).
[3]M. R. Schroeder, "Statistical parameters of the frequency response curves of large rooms," J. Audio Eng. Soc. **35**, 299–305 (1987).
[4]J. S. Abel and P. Huang, "A simple, robust measure of reverberation echo density," in Proceedings of the 121st AES Convention, preprint 6985 (2006), pp. 1–10.

[5]A. Papoulis and S. U. Pillai, *Probability, Random Variables and Stochastic Processes*, 4th ed. (McGraw-Hill, New York, 2002).
[6]R. B. Darlington, "Is kurtosis really peakedness?," Am. Stat. **24**, 19–22 (1970).
[7]J. Usher and J. Benesty, "Enhancement of spatial sound quality: A new reverberation-extraction audio upmixer," IEEE Trans. Audio, Speech, and Lang. Process. **15**, 2141–2150 (2007).
[8]H. Kutruff, *Room Acoustics*, 3rd ed. (Elsevier Science, Essex, UK, 1991).

LETTERS TO THE EDITOR

This Letters section is for publishing (a) brief acoustical research or applied acoustical reports, (b) comments on articles or letters previously published in this Journal, and (c) a reply by the article author to criticism by the Letter author in (b). Extensive reports should be submitted as articles, not in a letter series. Letters are peer-reviewed on the same basis as articles, but usually require less review time before acceptance. Letters cannot exceed four printed pages (approximately 3000–4000 words) including figures, tables, references, and a required abstract of about 100 words.

Comments on "On pore fluid viscosity and the wave properties of saturated granular materials including marine sediments" [J. Acoust. Soc. Am. 122, 1486–1501 (2007)] (L)

Nicholas P. Chotiros and Marcia J. Isakson
Applied Research Laboratories, The University of Texas at Austin, Austin, Texas 78713-8029

(Received 15 February 2008; revised 31 July 2009; accepted 22 December 2009)

The ability of the grain shearing (GS) and viscous grain shearing (VGS) models to relate geophysical and acoustic properties is tested by a method based on the claimed tight coupling between compressional and shear wave speeds and attenuations, which allows the test result to be quantified in a single parameter. The VGS model is claimed to provide a better fit to the measured sound speed and attenuation in sandy sediments below 10 kHz. *In situ* measurements of wave speeds and attenuations from the Sediment Acoustics Experiment 1999 (SAX99) and published laboratory measurements by Prasad and Meissner [Geophysics **57**, 710–719 (1992)] on a number of sand samples were used to test the models. By this metric, the SAX99 data show that the VGS model is no better than the original GS model because the improved agreement of compressional wave speeds at low frequencies is achieved at the expense of gross overestimation of the shear wave attenuation. When applied to the measurements by Prasad and Meissner, it is shown that the GS models are not applicable at any significant confining pressures, and at zero pressure they may only be applicable to a small subset of the sand samples.
 [DOI: 10.1121/1.3337240]

PACS number(s): 43.20.Jr, 43.30.Ma [ADP] Pages: 2095–2098

I. INTRODUCTION

The grain shearing (GS) model[1] may be categorized as a nearly constant Q (NCQ) model. These models, as a class, have been successfully applied to the modeling of seismic wave propagation.[2] In the GS model, the Q of the shear wave is actually constant and that of the compressional wave is nearly constant, changing by a factor of 2 over approximately 4 decades of frequency. It is an attractive model because it has a relatively small number of input parameters, but it was unable to track the steep sound speed dispersion observed below 10 kHz measured in the West Florida sand sheet during the Sediment Acoustics Experiments (SAXs) in 1999 and in 2004. At SAX99, there were relatively few measurements[3] below 10 kHz and those data points had been regarded with some skepticism. However, since that time, they have been reinforced by more recent measurements[4] from SAX04 and the trend is undeniable. In the viscous grain shearing[5] (VGS) model, an additional mechanism was introduced to allow the model to accommodate the observed dispersion. The purpose of this letter is to show that the GS and VGS equations may be rearranged to cleanly separate the acoustic and geophysical parameters on opposite sides of the equal sign, and thus test the ability of the GS models to predict acoustic properties from geophysical measurements, and vice versa, using data available in the open literature. By this means, the validity of the GS models may be tested.

II. THEORY

For the GS model, Eq. (6) in Ref. 5 gives a relationship between the complex wave number of the compressional wave and the geophysical parameters. This equation is rewritten below in a form that is applicable to both GS and VGS.

$$\frac{c_o}{c_p} - j\frac{c_o\alpha_p}{\omega_p} = [1 - \chi g(\omega_p)(j\omega_p nT)^n]^{-1/2}, \tag{1}$$

where c_p and α_p are the speed and attenuation of the compressional wave at frequency ω_p, c_o is Wood's equation sound speed, χ is the grain shearing coefficient, n is the material exponent, and T is an arbitrary time constant. In Eqs. 45–47 of Ref. 1, c_o is defined entirely in terms of the geophysical parameters,

$$c_o^2 = \frac{\kappa_o}{\rho_o}, \quad \frac{1}{\kappa_o} = N\frac{1}{\kappa_w} + (1-N)\frac{1}{\kappa_g}, \quad \rho_o = N\rho_w + (1-N)\rho_g, \tag{2}$$

where N is porosity, κ_w, κ_g, ρ_w, and ρ_g are the bulk moduli and densities of the pore fluid and grains, respectively.

The function $g(\omega_p)$ is the viscous dissipation term, introduced in Eq. (35) of Ref. 5 to convert the GS model into the VGS model. It is rewritten below in terms of a magnitude and a phasor, in which the phase angle ϕ_p is a function of frequency ω_p and the viscoelastic time constant τ. Note that by making τ equal to infinity, $g(\omega_p)$ becomes unity and the VGS model reverts to the GS model.

$$g(\omega_p) = \left(1 + \frac{1}{j\omega_p\tau}\right)^{n-1} = \left(1 + \frac{1}{\omega_p^2\tau^2}\right)^{(n-1)/2} e^{j\phi_p}. \tag{3}$$

Following a similar procedure as Eqs. (6)–(11) of Ref. 5, the two sides of Eq. (1) are squared and inverted. Using the identity

$$(j)^n = \cos\left(\frac{n\pi}{2}\right) + j\,\sin\left(\frac{n\pi}{2}\right), \tag{4}$$

the real and imaginary parts may be separated to give the following equations, which are comparable to Eqs. (10) and (11) of Ref. 5 from GS theory,

$$\chi(\omega_p T)^n\left(1 + \frac{1}{\omega_p^2\tau^2}\right)^{(n-1)/2}\cos\left(\phi_p + \frac{n\pi}{2}\right) = \left(\frac{c_p}{c_o}\right)^2\frac{[1-X^2]}{[1+X^2]^2} - 1, \tag{5}$$

$$\chi(\omega_p T)^n\left(1 + \frac{1}{\omega_p^2\tau^2}\right)^{(n-1)/2}\sin\left(\phi_p + \frac{n\pi}{2}\right) = \left(\frac{c_p}{c_o}\right)^2\frac{2X}{[1+X^2]^2}, \tag{6}$$

where $X = c_p\alpha_p/\omega_p$.

Dividing one by the other to get a tangent function, the result is an equation that is valid for VGS and GS, and comparable to Eq. (12) of Ref. 5.

$$\tan\left(\phi_p + \frac{n\pi}{2}\right) = \frac{2X}{[1-X^2] - \left(\frac{c_o}{c_p}\right)^2[1+X^2]^2}. \tag{7}$$

By a similar process to Eqs. (13)–(15) in Ref. 5, but including a viscous dissipation term, $g(\omega_s)$, a corresponding tangent identity is obtained for the shear wave.

$$\tan\left(\phi_s + \frac{n\pi}{2}\right) = \frac{2Y}{1-Y^2}, \tag{8}$$

where $Y = c_s\alpha_s/\omega_s$, c_s and α_s are the shear speed and attenuation at frequency ω_s, and ϕ_s is the phase shift due to VGS viscous dissipation at ω_s, as defined by

$$g(\omega_s) = \left(1 + \frac{1}{j\omega_s\tau}\right)^{n-1} = \left(1 + \frac{1}{\omega_s^2\tau^2}\right)^{(n-1)/2} e^{j\phi_s}. \tag{9}$$

Comparing the left-hand sides of Eqs. (7) and (8), it is evident that the two tangent terms would be equal if ϕ_p and ϕ_s were equal. In the case of GS, τ is infinite, the values of both ϕ_p and ϕ_s are exactly zero, and equality is always obtained. In the case of VGS, equality may be achieved if the frequencies of the compressional and shear waves, ω_p and ω_s, are equal, since both ϕ_p and ϕ_s are identical functions of frequency, as defined in Eqs. (3) and (9). Equality may be approximately achieved if both ω_p and ω_s were very much larger or smaller than $1/\tau$ because in those cases their values would asymptotically tend toward 0 or $(1-n)\pi/2$, respectively. Given equality, the tangent terms may be eliminated from Eqs. (7) and (8), and after some rearrangement, the result is

$$c_o^2 = c_p^2\frac{X(Y^2-1) - Y(X^2-1)}{Y(1+X^2)^2}. \tag{10}$$

A similar derivation may be found in Ref. 7. It appears that c_o^2 can be calculated in two different ways: (a) by using the bulk sediment properties via Wood's equation as defined in Eq. (2) or (b) by using measured wave parameters as defined in Eq. (10). It is proposed that the GS models be tested by comparing the values of c_o^2 obtained by these two different expressions. To avoid confusion, the value defined by Eq. (2) will be called c_{ob}^2, where the subscript b denotes that the value depends only on the bulk sediment properties (κ_w, κ_g, ρ_w, ρ_g, and N). The value obtained by Eq. (10) will be called c_{ow}^2, the subscript w referring to its dependence only on the wave parameters (c_p, X, Y).

$$c_{ow}^2 = c_p^2\frac{(1-X^2)Y - X(1-Y^2)}{Y(1+X^2)^2}, \tag{11}$$

$$c_{ob}^2 = \frac{\kappa_o}{\rho_o}. \tag{12}$$

To make the comparison simpler, let us define R as the ratio,

$$R = \frac{c_{ow}^2}{c_{ob}^2}. \tag{13}$$

An R ratio of one supports the GS model, and by making all wave measurements at the same frequency ($\omega_p = \omega_s$) the result would also apply to VGS models. The beauty of this method is that the wave properties are cleanly separated from the bulk properties; c_{ow}^2 is exclusively a function of the wave properties and c_{ob}^2 of the bulk properties. The difference between them is a direct indication of the GS models' ability to connect bulk and wave properties, and this connection may be quantified in terms of just one variable, R.

III. APPLICATION TO PUBLISHED DATA

At SAX99, the *in situ* measured shear wave speed and attenuation[3] at 1 kHz were 120 m/s (with a range of 97–147 m/s) and 30 dB/m (with a range of 21–40 dB/m). The *in situ* compressional wave speed and attenuation measurements were simultaneously made at a number of frequencies between 2 and 200 kHz, in addition to core measurements at 400 kHz, as shown in Figs. 3 and 4 of Ref. 3. These data points are identified in Figs. 1(a) and 1(b). A couple of curves representing the upper and lower bound GS models from the same reference are also shown. From the same reference, the relevant geophysical parameter values for calculating c_{ob}^2 are $\kappa_w = 2.395$ GPa, $\kappa_g = 32$ GPa, ρ_w

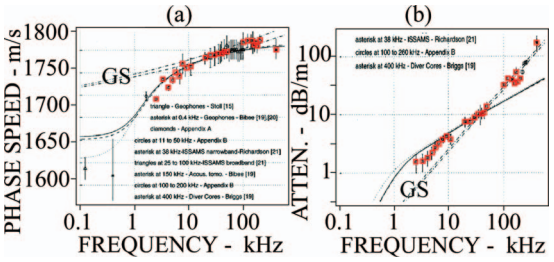

FIG. 1. Measured (a) sediment sound speeds and (b) attenuations as a function of frequency from SAX99 and GS model curves from Ref. 3. Points that have simultaneous speed and attenuation measurements marked in red. The significance of the other model curves and detailed descriptions of the data sources may be found in the Ref. 3. Adapted from Figs. 3 and 4 of Ref. 3, with permission.

$=1023\ \mathrm{kg/m^3}$, $\rho_g=2690\ \mathrm{kg/m^3}$, and $N=0.385$. With the shear wave frequency ω_s set at 1 kHz, the R ratio was computed as a function of the compressional wave frequency ω_p, and the result is shown in Fig. 2. The range of acceptable values of R is a function of the uncertainty in the values of the input parameters. The uncertainty in the values of bulk properties κ_w, κ_g, ρ_w, and ρ_g will be ignored because they are negligible compared to those of the experimentally measured values of N, c_p, X, and Y. Assuming that the errors follow a normal distribution, and assigning a conservative rms error of 2% to each of c_p, X, and Y, and a rms error of 0.02 to N, it is found by numerical simulation that the acceptable range of values of R is within ± 0.1 of 1, at the 80% level. Specifically, 80% of the experimental values of R should lie between 0.9 and 1.1. In Fig. 1(a), it is evident that the measured wave speeds below 10 kHz are not in agreement with the GS model, and in Fig. 2, the corresponding values of R are less than 0.9. Between 10 and 400 kHz, the R ratios are within the acceptance zone, indicating that the shear measurements at 1 kHz, in combination with the compressional measurements in this frequency band, are compatible with the GS model, most likely because their behavior in this region is consistent with a nearly constant Q model. There is a discernible trend in the values of R and a second order polynomial least-squares fit is superimposed as a plausible trend, and as a way of interpolating its value at 1 kHz, the frequency at which the shear wave parameters were measured. At this frequency, the test is also applicable to VGS, but the interpolated value of R is far from the acceptable region. This seems to be inconsistent with the purpose of VGS,

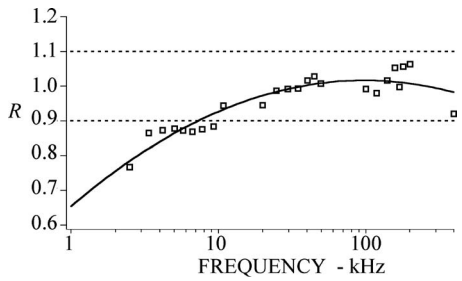

FIG. 2. R ratios from SAX99 data as a function of the frequency at which the compressional wave parameters were measured ($\omega_p/2\pi$), with shear wave parameters measured at 1 kHz. Least-squares error second order polynomial fit. Upper and lower bounds of acceptance zone (dashed lines).

which is to improve model-data agreement at the lower frequencies as stated in Ref. 5. In fact, there is no inconsistency because VGS achieves improved agreement with compressional wave speed and attenuation at the expense of the shear wave. It is a simple matter to run the VGS model with the parameter values provided in Ref. 5 to find that it predicts a shear wave attenuation coefficient that is an order of magnitude greater than the measured value at 1 kHz, as given on p. 417 of Ref. 3 and with a slope that is no longer consistent with the first power of frequency. When one is intent on fitting a particular set of wave parameters, it is easy to lose sight of the other parameters. The R ratio test does not favor any particular set of subset of parameters, but it gives a robust indication of the model-data compatibility that includes all the relevant parameters. By this measure, VGS is no better than GS.

To properly test the VGS model, measurements of all four wave parameters at the same frequency are needed. In fact, there are very few published experiments in which all four parameters are measured at the same frequency. The measurements published by Prasad and Meissner[6] are the only ones to our knowledge. They were made at 100 kHz as a function of confining pressure, in both dry air-saturated and water-saturated well-sorted quartz sands. The measurement procedure involves placing the sample, in its natural state, in a cylindrical test cell between two porous pistons, in which compressional and shear wave transducers were embedded. Since the pistons were porous, the pore fluid was not pressurized. The confining pressure between the pistons was increased in discrete steps. After each step, the sample was allowed to settle for 6 hours, to ensure that steady-state had been reached, before taking measurements of porosity, and wave speeds and attenuations. The attenuation was presented in the form of $1/Q$. It is easily shown that the X and Y parameters in the GS model and the compressional and shear Q values, Q_p and Q_s, are related by the following identities:

$$2X=\frac{1}{Q_p} \quad \text{and} \quad 2Y=\frac{1}{Q_s}. \tag{14}$$

The details of the experimental process and the pitfalls to be avoided are described in Prasad's dissertation.[7] The sand samples are labeled in the form "xM." The prefix "x" may be either "a" or "p" indicating angular or rounded grains, respectively. The number "M" distinguishes different effective grain sizes. Porosity measurements as a function of confinement pressure, available from Ref. 7, were given for samples p2, p3, p4, and p6. The porosities of the remainder were interpolated from these values according to effective grain size. In fact, the changes in porosity were so small that substantially the same results would have been obtained if an approximate value of porosity, i.e., 0.42, were used. Since these were quartz sand samples, the usual values of density and bulk modulus for quartz sand may be used in the calculation of c_{ob}^2: $\kappa_g=36$ GPa and $\rho_g=2650\ \mathrm{kg/m^3}$. The bulk properties for the water and dry atmospheric air are $\kappa_w=2.3$ GPa, $\rho_w=1000\ \mathrm{kg/m^3}$, and $\kappa_w=0.145$ MPa, $\rho_w=1.29\ \mathrm{kg/m^3}$, respectively. The wave parameters for the calculation of c_{ow}^2 are found in Figs. 2–5 of Ref. 6.

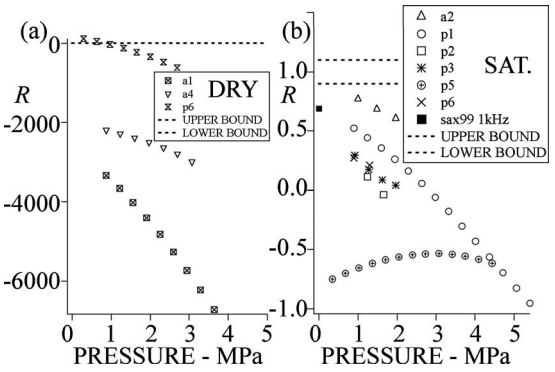

FIG. 3. *R* ratios from (a) dry air-saturated and (b) water-saturated quartz sand samples as a function of confinement pressure using measurements from Ref. 6. Upper and lower bounds of acceptance zone (dashed lines).

For the GS model,[1] it was claimed that the fluid films between asperities are "highly incompressible." Therefore, the fact that these measurements were made under pressure should be immaterial. The values of the wave parameters measured by Prasad and Meissner showed varying degrees of pressure dependence; therefore, c_{ow}^2 was calculated as a function of confining pressure, at all pressure samples for which all four wave parameters are available. The computed *R* ratios for the dry air-saturated sand samples are shown in Fig. 3(a). Contrary to common assumptions, air should be considered as a saturating fluid and its influence is not negligible.[8] Of the three sand samples, the *R* ratio of sample p6 crosses the acceptance zone at a pressure of approximately 1 MPa. One might say that, for this particular type of sand and at this pressure, the GS models are valid, but this is likely to be just coincidence. With the remaining two sand samples, there is no agreement at all because the *R* ratio does not come close to the acceptance zone. The fact that most of the *R* ratio values are negative is very interesting because it is entirely incompatible with the GS models, from which *R* is defined as the ratio of two positive quantities.

The results for the water-saturated sand samples are shown in Fig. 3(b). Most of the water-saturated samples have positive *R* ratio values at low confining pressures. The one exception is sample p5: Its grain size is in between those of p3 and p6. Their wave properties are all very similar, except that the compressional wave attenuation of p5 is significantly greater than those of p3 and p6. This suggests that the water-saturated p5 sample may contain a significant concentration of gas bubbles; therefore, p5 will be ignored from this point on. If the *R* ratio values may be extrapolated to zero pressure, it appears that the curve for a2 may intersect the *y*-axis within the acceptance zone, while the remainder may do so at values that are significantly lower. This suggests that the GS models may be acceptable at zero or low confinement pressures, and only for some sediments. It is interesting to note that a2 is the only sample with "angular grains." All the other samples have "rounded grains." The interpolated *R* ratio from SAX99 at 1 kHz is also shown in Fig. 3(b). It appears to be consistent with the laboratory data because the curves for p1, p2, p3, and p6 appear to converge on it at zero confinement pressure.

IV. CONCLUSIONS

There are three main conclusions: (1) The GS and VGS equations may be rewritten in a way that puts all the geophysical parameters on one side of the equation sign and all the acoustic parameters on the other. This allows the ability of the GS and VGS models to connect bulk and wave properties to be quantified in just one parameter, the *R* ratio. (2) The VGS model achieves better agreement with the compressional wave measurements from SAX99, but at the expense of grossly overestimating the shear wave attenuation. It is observed that the GS models are compatible with combinations of shear and compressional wave parameters only within certain frequency bands in which the wave behavior may be approximated as constant *Q*. Outside these frequency bands, particularly in the strongly dispersive band for compressional waves, i.e., between 1 and 10 kHz, both GS and VGS are problematic. (3) When compared to laboratory measurements of compressional and shear waves in sands at 100 kHz by Prasad and Meissner, the GS and VGS models are found to be completely incompatible with wave propagation in air-saturated sand, and possibly compatible with measurements from just one water-saturated sand sample out of the five that were tested, and only when the results are interpolated to zero confinement pressure. It is likely that the proposed tight coupling between compressional and shear wave speeds and attenuations is not valid and different material exponents may be required for shear and compressional waves.

ACKNOWLEDGMENT

This work is sponsored by the Office of Naval Research, Code 321 OA, under the management of Robert Headrick.

[1]M. J. Buckingham, "Wave propagation, stress relaxation, and grain-to-grain shearing in saturated, unconsolidated marine sediments," J. Acoust. Soc. Am. **108**, 2796–815 (2000).
[2]E. Kjartansson, "Constant Q wave propagation and attenuation," J. Geophys. Res. **84**, 4737–4748 (1979).
[3]K. L. Williams, D. R. Jackson, E. I. Thorsos, D. Tang, and S. G. Schock, "Comparison of sound speed and attenuation measured in a sandy sediment to predictions based on the Biot theory of porous media," IEEE J. Ocean. Eng. **27**, 413–428 (2002).
[4]P. C. Hines, J. C. Osler, J. Scrutton, and A. P. Lyons, "Time-of-flight measurements of acoustic wave speed in sandy sediments from 0.6–20 kHz," *Boundary Influences in High Frequency*, Shallow Water Acoustics, 5th–9th eds., edited by N. G. Pace and P. Blondel (University of Bath, Bath, UK, 2005), pp. 49–56.
[5]M. J. Buckingham, "On pore-fluid viscosity and the wave properties of saturated granular materials including marine sediments," J. Acoust. Soc. Am. **122**, 1486–1501 (2007).
[6]M. Prasad and R. Meissner, "Attenuation mechanisms in sands: Laboratory versus theoretical (Biot) data," Geophysics **57**, 710–719 (1992).
[7]M. Prasad, "Experimental and theoretical considerations of attenuation and velocity interactions with physical parameters in sands," der Mathematisch-Naturwissenschaftlichen Fakultät, Doctorate dissertation, Christian-Albrechts-Universität, Kiel (1988), 122 pp.
[8]M. Kimura, "Frame bulk modulus of porous granular marine sediments," J. Acoust. Soc. Am. **120**, 699–710 (2006).

Response to "Comments on 'Pore fluid viscosity and the wave properties of saturated granular materials including marine sediments [J. Acoust. Soc. Am. 127, 2095–2098 (2010)]' " (L)

Michael J. Buckingham[a)]
Marine Physical Laboratory, Scripps Institution of Oceanography, University of California, San Diego, 9500 Gilman Drive, La Jolla, California 92093-0238

(Received 19 January 2010; revised 28 January 2010; accepted 2 February 2010)

Chotiros and Isakson [J. Acoust. Soc. Am. **127**, 2095–2098 (2010)] raised three main issues concerning the grain-shearing and viscous-grain-shearing (VGS) theories of wave propagation in saturated marine sediments. (1) They introduced the *R*-ratio as a test of the two theories, (2) they then used the *R*-ratio to compare the theories with published measurements of compressional and shear wave properties of laboratory sediments under high confinement pressures, and (3) they pointed out that the VGS theory overestimates the shear attenuation measured during the Sediment Acoustics Experiment 1999 (SAX99) by about an order of magnitude. With regard to the *R*-ratio, it provides an incomplete test of the theories and, moreover, it returns ambiguous results. As for the tests against measurements made under high confinement pressures, they are invalid because the theories are not applicable under such conditions. The third point is correct, but a minor modification to the VGS theory resolves the difficulty.
 [DOI: 10.1121/1.3337241]

PACS number(s): 43.30.Ma [ADP] Pages: 2099–2102

I. INTRODUCTION

Chotiros and Isakson[1] provided a critique of Buckingham's grain-shearing[2] (GS) and viscous-grain-shearing[3] (VGS) theories of sound wave and shear wave propagations in saturated granular media. They reached three main conclusions: (1) the dispersion relations for the compressional and shear waves, as predicted by each of the two theories, may be expressed in terms of a single variable, which they designated the *R*-ratio; (2) the GS and VGS theories do not fit the high-pressure data of Prasad and Meissner[4] for either dry or saturated sands; and (3) the VGS model overestimates the shear wave attenuation measured during the ONR-supported Sediment Acoustics Experiment 1999 (Ref. 5) (SAX99) at a frequency of 1 kHz by about an order of magnitude. Each of these three issues is discussed below.

II. THE *R*-RATIO

Chotiros and Isakson's *R*-ratio,[1] their Eq. (13), is based on a reduction of the GS and VGS dispersion relations for compressional and shear waves into a single equation in which all the geophysical parameters appear on one side of the equality sign while all the acoustic parameters appear on the other side. A notable point about the *R*-ratio is that it does not involve the grain-shearing parameters n, γ_p, and γ_s, which characterize the grain-shearing process,[3] but depends only on the wave properties (speeds and attenuations) and the spot frequencies at which they were measured. Chotiros and Isakson's[1] method of analysis follows a similar development to that in Secs. IIB and IIC of Buckingham,[3] and their Eq. (10), which is the central component of the *R*-ratio, is the same as Buckingham's Eq. (16). Chotiros and Isakson[1] asserted that the *R*-ratio makes a comparison of theory with data easy, since the dispersion relations are reduced to a single parameter, whose value is unity in the event of a satisfactory match between theory and data. The *R*-ratio, however, has certain undesirable characteristics, which limit its utility.

For instance, if *R* were to deviate from unity, representing a mismatch between theory and data, the cause of the departure would be unknown. It could be due to a mismatch of the sound speed, the sound attenuation, the shear speed or the shear attenuation, or any combination of all four, since they are blended together in the expression for *R*. To identify the source of the departure from $R=1$, it would be necessary to revert to direct comparisons of the original dispersion relations with experimental data. At high frequencies, where the GS and VGS theories are essentially the same, such comparisons between the theories and extensive data sets taken from the open literature have already been performed by Buckingham,[6] and in all the cases examined, the theories show a satisfactory fit to the data.

Another limitation of the *R*-ratio is that, even if it were evaluated over a range of spot frequencies, it would yield no explicit information on the frequency dependencies of the wave speeds and attenuations. Its usefulness as a test of the GS and VGS theories is therefore quite restricted, since the frequency dispersion of the wave speeds and the frequency dependencies of the attenuations are important factors when it comes to assessing the validity of any theory of sound propagation in saturated granular media. Moreover, since the *R*-ratio is just a compressed form of the GS and VGS equa-

a)Electronic mail: mbuckingham@ucsd.edu

tions, it is incapable of providing any insights beyond those available from the original dispersion relations themselves. The computational effort required to make direct comparisons between the theories and data is negligible, since the GS and VGS dispersion relations take the form of simple algebraic equations.

A more serious objection to the R-ratio is that it may return a misleading result, because the condition $R=1$ does not correspond to a unique X, Y pair. (X and Y are defined in Refs. 1 and 3.) Thus, it is possible for R to be unity even when the theory does not match the data, since an infinite number of X, Y combinations return a value of $R=1$. To be specific, R takes a value of unity whenever

$$Y=\frac{c_{0b}^2(1+X^2)^2-c_p^2(1-X^2)^2+\sqrt{[c_{0b}^2(1+X^2)^2-c_p^2(1-X^2)^2]^2+4c_p^4X^2}}{2c_p^2X}, \tag{1}$$

as may easily be established from Eqs. (11) and (13) in Ref. 1. In effect, the R-ratio may return false positives.

But this is not the only type of ambiguity associated with the R-ratio: It cannot distinguish between the GS theory and the VGS theory when the wave variables in the latter are all measured at the same frequency. Under this condition, the expression for R, as given by Eqs. (11)–(13) in Ref. 1, is exactly the same in the two cases. Even if a genuine (i.e., non-false positive) value of $R=1$ were returned, it would not be possible to tell whether it referred to the GS theory or the VGS theory. A value of $R=1$ is a necessary but not sufficient condition for the theories to match the data.

III. PRASAD AND MEISSNER'S DATA

Prasad and Meissner[4] investigated the effects of high confining pressures on the speeds and attenuations of compressional and shear waves in various samples of oven-dried sands and water-saturated sands. Their measurements were made using a pulse transmission technique in which the center frequency was about 100 kHz, with the samples subjected to confining pressures extending up to approximately 6 MPa (equivalent to 60 atm). Porous pistons were used to compress the samples, allowing the pore fluid to remain unpressurized. Inevitably under such conditions, the grains will have been crushed together, significantly altering the nature of the grain-to-grain contacts. That the grain contacts were indeed modified in the high-pressure experiments is indicated by the fact that, in all the cases reported, the wave speeds and the attenuations at 100 kHz exhibited pronounced dependencies on the confining pressure (see Figs. 2–5 in Ref. 4). Since no dispersion curves were reported by Prasad and Meissner,[4] it is not known whether the compressional and shear wave attenuations in their pressurized sand samples conformed to the near-linear dependence on frequency predicted by the GS theory.

Chotiros and Isakson[1] took Prasad and Meissner's[4] measurements of the compressional and shear wave speeds and attenuations and computed the corresponding R-ratio for each sand sample. They found that in all but one case the R-ratio deviates significantly from unity, and in some cases the R-ratio computed using their Eqs. (11)–(13) turns out to be negative, even though R is defined as the ratio of two real, squared quantities. Chotiros and Isakson[1] concluded that the GS and VGS theories are incompatible with Prasad and Meissner's[4] high-confinement-pressure data.

The GS and VGS theories were developed specifically for water-saturated marine sediments under natural conditions in the sea bed, not for laboratory sand samples under extremely high confinement pressures. The dissipation mechanism that is a central component of the GS and VGS theories is a particular form of inter-granular shearing, which is based on a molecularly thin layer of pore fluid at grain contacts. Under the high confinement pressures of Prasad and Meissner's[4] experiments, the grain contacts may have suffered significant damage and distortion, to the extent that completely new and unknown physical mechanisms governed the wave properties. Since there is no reason to believe that the GS and VGS theories would hold under such extreme conditions, it is inappropriate to use Prasad and Meissner's[4] high-pressure data as a test of the two theories.

IV. SAX99 DATA INCLUDING SHEAR ATTENUATION

Chotiros and Isakson[1] criticized the VGS theory on the grounds that it overestimates the attenuation of the shear wave, as measured during the SAX99 experiments[5] on a medium-sand marine sediment, by about an order of magnitude. The SAX99 data set[5] is unusual, if not unique, in that it contains data on the four wave properties, the compressional and shear wave speeds and both attenuations, along with detailed information on the physical properties of the medium. Using a variety of techniques, the SAX99 compressional wave properties were measured over more than three decades of frequency, from 125 Hz to 400 kHz, resulting in dispersion curves that are extremely well characterized by the experimental data. By comparison, the SAX99 data on the shear wave properties are much more meagre, due to the difficulties of making *in-situ* shear wave measurements: Richardson *et al.*,[5] using bimorph bender elements mounted on the In Situ Sediment geoAcoustic Measurement System (ISSAMS), was able to measure the shear speed and attenuation but at just a single frequency of approximately 1 kHz.

Because of the dearth of data on the shear wave, it received relatively little attention in Buckingham's development of the VGS theory,[3] which, in retrospect, was an oversight. Chotiros and Isakson[1] are correct in noting that the VGS theory yields a shear attenuation that exceeds the value observed in SAX99 by a factor of about 10. A simple resolution of this problem, which should have been incorporated into the original discussion of the VGS theory, is given below.

To take account of the viscosity of the pore fluid, the VGS theory includes the function

$$g(\omega\tau)=\left(1+\frac{1}{j\omega\tau}\right)^{-1+n}, \tag{2}$$

where the variables are as defined by Buckingham.[3] The viscoelastic time constant in Eq. (2) may be expressed as

$$\tau=\frac{1}{2\pi f_t}, \tag{3}$$

where f_t is a threshold frequency above which the effect of pore fluid viscosity decays to a negligible level. In the original VGS theory,[3] it is implicit that the threshold frequency is the same for the compressional wave and the shear wave, and therein lies the origin of the mismatch to the shear attenuation.

Rather than a threshold frequency, a more plausible criterion is that the onset of pore fluid viscosity is governed by wavelength. Letting λ_t be the threshold wavelength, below which the effect of pore fluid viscosity decays to zero, then the viscoelastic time constants for the compressional and shear waves will be different. For the compressional wave

$$\tau = \tau_p = \frac{\lambda_t}{2\pi c_p} \tag{4a}$$

and for the shear wave

$$\tau = \tau_s = \frac{\lambda_t}{2\pi c_s}, \tag{4b}$$

from which it follows that the viscoelastic time constants for the compressional and shear waves are related as follows:

$$\tau_s = \frac{c_p}{c_s}\tau_p. \tag{5}$$

Thus, τ_s is larger than τ_p by a factor equal to the ratio of the wave speeds, which is of the order of ten.

The VGS dispersion relations may now be expressed in terms of the new viscoelastic time constants. For the compressional wave, the speed and attenuation are

$$c_p(\omega) = \frac{c_0}{\mathrm{Re}[1 + \chi(j\omega T)^n g(\omega\tau_p)]^{-1/2}}, \tag{6a}$$

$$\alpha_p(\omega) = -\frac{\omega}{c_0}\mathrm{Im}[1 + \chi(j\omega T)^n g(\omega\tau_p)]^{-1/2}, \tag{6b}$$

and for the shear wave

$$c_s(\omega) = \frac{\sqrt{\gamma_s/\rho_0}}{\mathrm{Re}[(j\omega T)^n g(\omega\tau_s)]^{-1/2}}, \tag{7a}$$

$$\alpha_s(\omega) = -\omega\sqrt{\frac{\rho_0}{\gamma_s}}\,\mathrm{Im}[(j\omega T)^n g(\omega\tau_s)]^{-1/2}, \tag{7b}$$

where the notation is the same as that used by Buckingham.[3]

To distinguish the four dispersion relations in Eqs. (6) and (7) from the original VGS theory, they will be referred to as the VGS(λ) version of the theory. It should be noted that the grain-shearing parameters, n, γ_p, and γ_s (and hence χ) in the VGS(λ) theory, are determined using the same matching technique introduced by Buckingham[3] in connection with the VGS theory, and thus, for a given data set such as SAX99, n and χ will be exactly the same in the two versions. If τ_p is taken to be equal to τ, then the compressional wave dispersion curves predicted by the two versions of the theory are identical. Thus, the effects of introducing $\tau_s \neq \tau_p$ are only apparent in the shear wave dispersion curves.

For a comparison of the VGS(λ) theory with the SAX99 experimental measurements, all four expressions in Eqs. (6) and (7) have been evaluated as functions of frequency using the parameter values shown in Table I. The resultant VGS(λ) wave speeds and attenuations are plotted in Fig. 1, with the SAX99 data included for comparison. Since $\tau_p = \tau$, and n and χ have the same values as previously,[3] the VGS(λ) curves in Figs. 1(a) and 1(b) for the compressional wave are identical to their counterparts from the VGS theory (shown as the red curves in Figs. 1a and 1b of Ref. 3). The shear speed and attenuation curves from the two theories differ, however, as illustrated in Figs. 1(c) and 1(d), respectively. The single data point represented by the solid green circle in Fig. 1(d) is Richardson's value of 30 dB/m for the shear attenuation,[5] with the error bars denoting the spread in his measurements, ranging from 21 to 40 dB/m. Clearly, the black VGS line in Fig. 1(d) overestimates the shear attenuation, as noted by Chotiros and Isakson,[1] whereas the red VGS(λ) curve is consistent with Richardson's[5] data point.

TABLE I. Parameter values used in VGS(λ) theory for comparison with SAX99 experimental data.

Material parameter	Symbol	SAX99
Density of pore fluid (kg/m^3)	ρ_w	1023
Bulk modulus of pore fluid (Pa)	K_w	2.395×10^9
Sound speed in pore fluid (m/s)	c_w	1530.1
Density of grains (kg/m^3)	ρ_s	2690
Bulk modulus of grains (Pa)	K_g	3.2×10^{10}
Porosity	N	0.385
Bulk density of sediment (kg/m^3)	ρ_o	2048.2
Bulk modulus of sediment (Pa)	κ_o	5.557×10^9
Wood's speed (m/s)	c_o	1647.1
Material exponent	n	0.0617
Grain-shearing coefficient	χ	0.0724
Compressional coefficient (Pa)	γ_p	3.796×10^8
Shear coefficient (Pa)	γ_s	1.711×10^7
Compressional viscoelastic time constant (ms)	τ_p	0.12
Shear viscoelastic time constant (ms)	τ_s	1.77
Matching parameters		
Sound speed (m/s)/frequency (kHz)		1770.1/38
Sound attenuation (dB/m)/frequency (kHz)		10.12/38
Shear speed (m/s)/frequency (kHz)		120/1

V. CONCLUDING REMARKS

In the final sentence of their Conclusions, Chotiros and Isakson[1] stated that the tight coupling between the compressional and shear wave speeds and attenuations, which is a fundamentally important feature of the GS and VGS theories [and also, of course, the VGS(λ) version], is not valid and that different material exponents (the parameter n in Table I) may be needed for shear and compressional waves. Such a suggestion, that the compressional and shear waves are not correlated, is inconsistent with the large body of evidence that has been accumulating in the open literature for several decades.

Hamilton[7,8] and Richardson[9] both developed regression relations linking the compressional wave speed to the shear wave speed; and Buckingham[6] presented numerous plots of data taken from literature, for instance, compressional speed

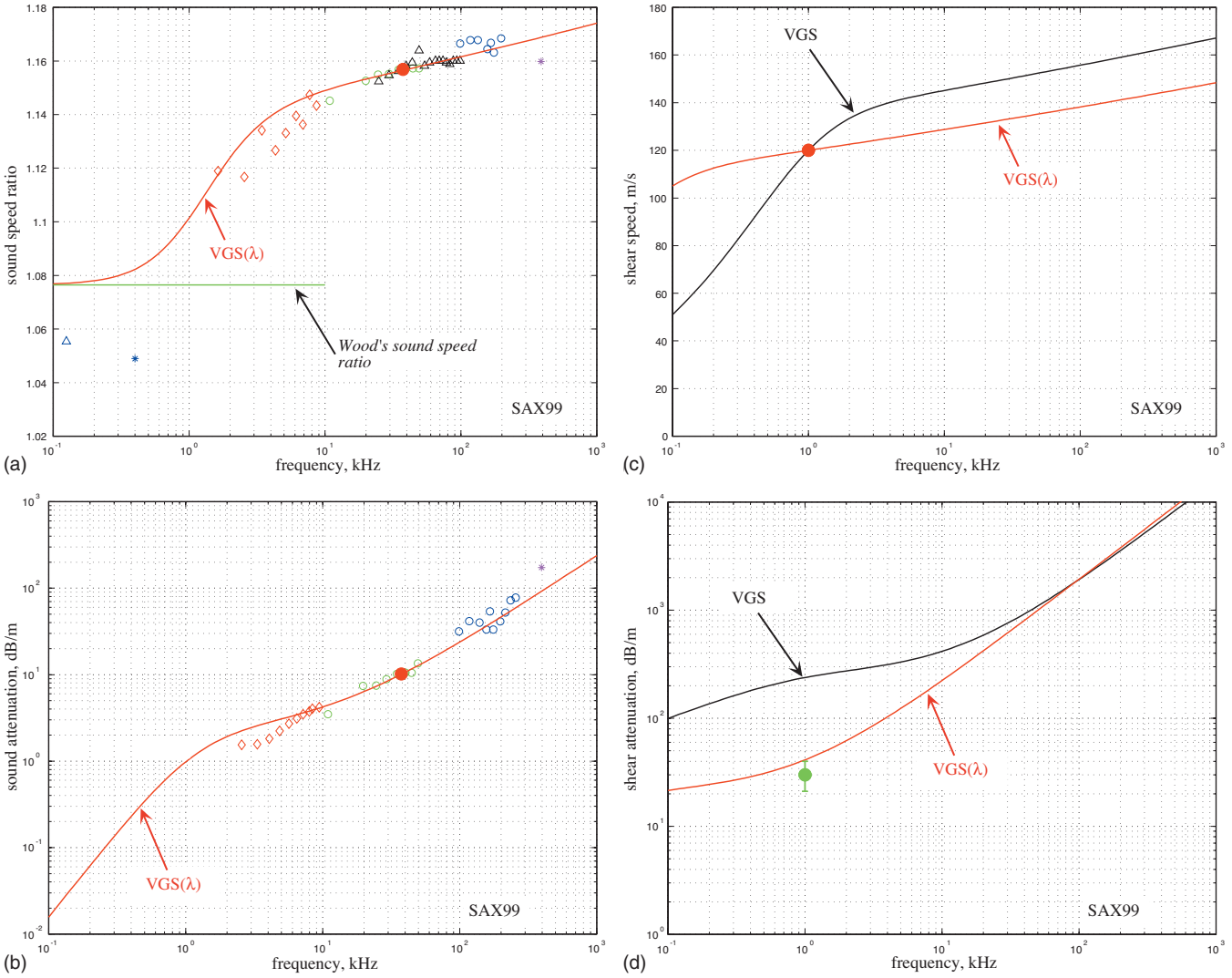

FIG. 1. VGS(λ) theory (red line) evaluated from Eqs. (6) and (7), and VGS theory (black line), for the SAX99 sediment: (a) sound speed ratio, (b) sound attenuation, (c) shear speed, and (d) shear attenuation. The large solid red circles in (a)–(c) are the points at which the theories were matched to the data. The large solid green circle in (d) is the measurement of the shear attenuation.

versus porosity and shear speed versus porosity, from which it may be inferred that the two wave speeds are strongly coupled. It is difficult to understand how Chotiros and Isakson[1] can reconcile their assertion that the compressional and shear waves are not tightly coupled with the overwhelming experimental evidence to the contrary.

Moreover, the idea that different material exponents are required for the compressional and shear waves, as suggested by Chotiros and Isakson,[1] is unnecessary, as exemplified in the analysis of the VGS(λ) version of the viscous-grain-shearing theory developed above. In any case, such arbitrary tampering with the material exponent n is not in the spirit of the GS and VGS theories, which are based as far as possible on physical mechanisms rather than *ad-hoc* data-fitting techniques.

ACKNOWLEDGMENT

The research was supported by the Office of Naval Research, Ocean Acoustics Code 321 OA, under Grant No. N00014-07-1-0109, sponsors Dr. Ellen Livingston and Dr. Robert Headrick.

[1]N. P. Chotiros and M. J. Isakson, "Comments on "Pore fluid viscosity and the wave properties of saturated granular materials including marine sediments" [J. Acoust. Soc. Am. 122, 1486–1501 (2007)]," J. Acoust. Soc. Am. **127**, 2095–2098 (2010).
[2]M. J. Buckingham, "Wave propagation, stress relaxation, and grain-to-grain shearing in saturated, unconsolidated marine sediments," J. Acoust. Soc. Am. **108**, 2796–2815 (2000).
[3]M. J. Buckingham, "On pore-fluid viscosity and the wave properties of saturated granular materials including marine sediments," J. Acoust. Soc. Am. **122**, 1486–1501 (2007).
[4]M. Prasad and R. Meissner, "Attenuation mechanisms in sands: Laboratory versus theoretical (Biot) data," Geophysics **57**, 710–719 (1992).
[5]M. D. Richardson, K. B. Briggs, D. L. Bibee, *et al.*, "Overview of SAX99: Environmental considerations," IEEE J. Ocean. Eng. **26**, 26–53 (2001).
[6]M. J. Buckingham, "Compressional and shear wave properties of marine sediments: Comparisons between theory and data," J. Acoust. Soc. Am. **117**, 137–152 (2005).
[7]E. L. Hamilton, "Vp/Vs and Poisson's ratios in marine sediments and rocks," J. Acoust. Soc. Am. **66**, 1093–1101 (1979).
[8]E. L. Hamilton, "Acoustic properties of sediments," in *Acoustics and the Ocean Bottom*, edited by A. Lara-Saenz, C. Ranz Cuierra, and C. Carbo-Fité (Consejo Superior de Investigacions Cientificas, Madrid, 1987), pp. 3–58.
[9]Richardson, M. D., "In-situ, shallow-water sediment geoacoustic properties," in *Shallow-Water Acoustics*, edited by R. Zhang and J. Zhou (China Ocean, Beijing, China, 1997), pp. 163–170.

Third- and fourth-order elasticities of biological soft tissues (L)

Michel Destrade and Michael D. Gilchrist
School of Electrical, Electronic, and Mechanical Engineering, University College Dublin, Belfield, Dublin 4, Ireland

Raymond W. Ogden
Department of Mathematics, University of Glasgow, University Gardens, Glasgow G12 8QW, Scotland, United Kingdom

(Received 13 October 2009; revised 3 February 2010; accepted 4 February 2010)

In the theory of weakly nonlinear elasticity, Hamilton *et al.* [J. Acoust. Soc. Am. **116**, 41–44 (2004)] identified $W=\mu I_2+(A/3)I_3+DI_2^2$ as the fourth-order expansion of the strain-energy density for incompressible isotropic solids. Subsequently, much effort focused on theoretical and experimental developments linked to this expression in order to inform the modeling of gels and soft biological tissues. However, while many soft tissues can be treated as incompressible, they are not in general isotropic, and their anisotropy is associated with the presence of oriented collagen fiber bundles. Here the expansion of W is carried up to fourth order in the case where there exists one family of parallel fibers in the tissue. The results are then applied to acoustoelasticity, with a view to determining the second- and third-order nonlinear constants by employing small-amplitude transverse waves propagating in a deformed soft tissue.
 [DOI: 10.1121/1.3337232]

PACS number(s): 43.25.Ba, 43.25.Zx, 43.25.Ed [ROC] Pages: 2103–2106

I. INTRODUCTION

Due to their high fluid content, many soft biological tissues and gels exhibit nearly *incompressible* behavior: they are constrained to undergo essentially volume-preserving deformations and motions. This has long been known and, in fact, can be traced back to the experiments of Swammerdam[1,2] in 1758. Mathematically, the internal constraint of incompressibility is expressed by imposing the condition $\det \boldsymbol{F}=1$ at all times, where $\boldsymbol{F}$ is the deformation gradient. In *exact* nonlinear isotropic elasticity theory, the strain-energy density W is written in fullest generality as a function of I, II, and III, the first three principal invariants of the right Cauchy–Green strain tensor $\boldsymbol{C}=\boldsymbol{F}^T\boldsymbol{F}$, which are defined by

$$I=\operatorname{tr}\boldsymbol{C},\quad II=\tfrac{1}{2}[(\operatorname{tr}\boldsymbol{C})^2-\operatorname{tr}(\boldsymbol{C}^2)],\quad III=\det\boldsymbol{C}=(\det\boldsymbol{F})^2. \tag{1}$$

It is then easy to enforce incompressibility, which requires that $III=1$ at all times and hence that $W=W(I,II)$ only.

In *weakly* nonlinear isotropic elasticity theory, W is expanded in terms of invariants of the Green–Lagrange strain tensor $\boldsymbol{E}=\frac{1}{2}(\boldsymbol{C}-\boldsymbol{I})$, either using the set

$$i_1=\operatorname{tr}\boldsymbol{E},\quad i_2=\tfrac{1}{2}[(\operatorname{tr}\boldsymbol{E})^2-\operatorname{tr}(\boldsymbol{E}^2)],\quad i_3=\det\boldsymbol{E} \tag{2}$$

(this is the choice of Murnaghan[3]) or the set

$$I_1=\operatorname{tr}\boldsymbol{E},\quad I_2=\operatorname{tr}\boldsymbol{E}^2,\quad I_3=\operatorname{tr}\boldsymbol{E}^3 \tag{3}$$

(this is the choice of Landau and Lifshitz[4]). In each case the respective terms are of orders 1, 2, and 3 in $\boldsymbol{E}$.

Then, in *third-order* elasticity theory, W is expanded as a linear combination of i_1, i_2, i_3, i_1i_2, and i_1^3 (or, equivalently, I_1, I_2, I_3, I_1I_2, and I_1^3) and higher-order terms are neglected; thus, five elastic constants are required to describe third-order solids. (Note that some authors refer to this as second-order elasticity since the stress is second order in the strain; a similar comment applies to fourth-order versus third-order elasticity.) In *fourth-order* elasticity theory, terms linear in i_1^4, i_2^2, i_1i_3, and $i_1^2i_2$ (or, equivalently, I_1^4, I_2^2, I_1I_3, and $I_1^2I_2$) are also retained; thus, nine elastic constants are required to describe fourth-order solids. Now, however, it is slightly more complicated to enforce incompressibility because the constraint involves a combination of invariants of $\boldsymbol{E}$, rather than a single invariant of $\boldsymbol{C}$. Nevertheless, this can be achieved because of obvious connections between the sets (1)–(3). This was done long ago by Rivlin and Saunders[5] in 1951 and by Ogden[6] in 1974, for third- and fourth-order incompressible solids, respectively. In particular, these authors showed that the number of elastic constants drops from 5 to 2 for third-order solids, and from 9 to 3 for fourth-order solids compared with the compressible case.

Recently, Hamilton *et al.*,[7] unaware of these previous contributions, rediscovered the latter result, and wrote W in the form

$$W=\mu I_2+\frac{A}{3}I_3+DI_2^2, \tag{4}$$

where μ, A, and D are the respective second, third-, and fourth-order elasticity constants of weakly nonlinear incompressible isotropic elasticity. Subsequently, several papers[8–23] have been devoted to the study of the theoretical and experimental implications of this expansion for linearized and nonlinear waves and vibrations in incompressible solids. Experiments have been conducted on isotropic gels and phantoms to measure the nonlinear elastic coefficients, and good progress has been achieved in the understanding and implementation of elastographic techniques.[12–14,16,17]

Now, the ultimate goal of elastography is the imaging of biological soft tissues, and it is therefore important to be able

to evaluate μ, A, and D experimentally. At the same time, it must be kept in mind that soft tissues are anisotropic solids, in contrast to gels and phantoms. This anisotropy is due to the presence of oriented collagen fiber bundles, which are three orders of magnitude stiffer than the surrounding tissue in which they are embedded (this surrounding tissue consists of a network of elastin fibers, smooth muscle cells, and proteoglycans, *inter alia*, which collectively form an essentially isotropic "matrix"). The natural conclusion of this consideration is that there is a need for expansions of W up to the third or, depending on the context, fourth order for incompressible anisotropic solids. For the particular application considered in Sec. III of the present paper, however, it suffices to pursue the analysis only up to the third order.

II. FOURTH-ORDER TRANSVERSELY ISOTROPIC SOLIDS

Here we consider soft tissues with one preferred direction, associated with a family of parallel fibers of collagen. We denote by $\boldsymbol{A}$ the unit vector in that direction when the solid is unloaded and at rest. The theory of Spencer[24] tells us that in all generality, W is a function of at most five invariants in exact nonlinear compressible elasticity theory. One valid choice for these quantities is

$$W = W(I_1, I_2, I_3, I_4, I_5) \quad \text{where } I_4 \equiv \boldsymbol{A}\cdot\boldsymbol{E}\boldsymbol{A},\ I_5 \equiv \boldsymbol{A}\cdot\boldsymbol{E}^2\boldsymbol{A}. \tag{5}$$

Now we expand W up to terms of order 4 in the Green–Lagrange strain. This involves a linear combination of the following quantities:

$$\text{order 2: } I_1^2, I_2, I_4^2, I_5, I_1I_4,$$

$$\text{order 3: } I_1^3, I_1I_2, I_3, I_1I_4^2, I_1I_5, I_1^2I_4, I_2I_4, I_4^3, I_4I_5,$$

$$\text{order 4: } I_1^4, I_1^2I_2, I_1I_3, I_2^2, I_1I_4^3, I_1^2I_5, I_1^2I_4^2, I_1^3I_4, I_2I_4^2, I_2I_5, I_4^4, I_5^2, I_1I_2I_4, I_1I_4I_5, I_3I_4. \tag{6}$$

Note that the first-order terms are omitted from the list because they give rise to constant stresses. Hence there are 29 elastic constants for fourth-order, transversely isotropic, compressible solids.

In incompressible solids, however, the isotropic invariants are not independent. They are connected by the incompressibility condition, which can be written in terms of the invariants (2) exactly as[6] $i_1 = -2i_2 - 4i_3$, or equivalently, in terms of the invariants (3), as

$$I_1 = I_2 - \frac{4}{3}I_3 - I_1^2 + 2I_1I_2 - \frac{2}{3}I_1^3, \tag{7}$$

so that the number of independent quantities in Eq. (6) is greatly reduced. For instance, I_1^2 is of fourth order, and $I_1I_2 = I_2^2$ and $I_1^3 = 0$ at fourth order. This allows the list to be shortened to

$$\text{order 2: } I_2, I_4^2, I_5,$$

$$\text{order 3: } I_3, I_2I_4, I_4^3, I_4I_5,$$

$$\text{order 4: } I_2^2, I_2I_4^2, I_2I_5, I_4^4, I_5^2, I_3I_4, \tag{8}$$

which are associated with 13 elastic constants *in toto*.

For third-order, transversely isotropic, incompressible, nonlinear elastic solids, for example, the strain-energy density is thus expressible in the form

$$W = \mu I_2 + \frac{A}{3}I_3 + \alpha_1 I_4^2 + \alpha_2 I_5 + \alpha_3 I_2 I_4 + \alpha_4 I_4^3 + \alpha_5 I_4 I_5, \tag{9}$$

where μ, α_1, and α_2 are second-order elastic constants and A, α_3, α_4, α_5, and α_6 are third-order elastic constants. A lengthier expansion is required at fourth order, which requires a linear combination of the six additional terms listed in Eq. (8). We do not include these here. Indeed, it suffices for our present purposes to restrict attention to second- and third-order terms in W since at this order the speed of infinitesimal plane waves depends linearly on the strain through the third-order constants, even for the specialization to an isotropic material.

III. ACOUSTOELASTICITY

We now consider the propagation of small-amplitude plane body waves in a deformed soft tissue with one family of parallel fibers. We assume that the solid has been prestressed by the application of the Cauchy stress $\boldsymbol{\sigma}$, say, giving rise to a predeformation with corresponding deformation gradient $\boldsymbol{F}$.

Let $\boldsymbol{u} = \boldsymbol{u}(\boldsymbol{x}, t)$ denote the mechanical displacement associated with the wave motion, ρ the (constant) mass density, and p the incremental Lagrange multiplier due to the incompressibility constraint. Then the incremental equations of motion and of incompressibility read[25]

$$\mathcal{A}_{0piqj}u_{j,pq} - p_{,i} = \rho\partial^2 u_i/\partial t^2, \tag{10a}$$

$$u_{i,i} = 0, \tag{10b}$$

respectively, where the comma signifies partial differentiation with respect to the current coordinates $\boldsymbol{x} \equiv x_i$ and $\boldsymbol{\mathcal{A}_0}$ is the fourth-order tensor of instantaneous moduli, with components

$$\mathcal{A}_{0piqj} = F_{p\alpha}F_{q\beta}\delta_{ij}\frac{\partial W}{\partial E_{\alpha\beta}} + F_{p\alpha}F_{q\beta}F_{j\nu}F_{i\gamma}\frac{\partial^2 W}{\partial E_{\alpha\gamma}\partial E_{\beta\nu}}. \tag{11}$$

This expression is exact, while to compute the derivatives of W with respect to Eq. (9), the following quantities are needed:

$$\frac{\partial I_2}{\partial E_{\alpha\beta}} = 2E_{\alpha\beta}, \quad \frac{\partial^2 I_2}{\partial E_{\alpha\gamma}\partial E_{\beta\nu}} = \delta_{\alpha\beta}\delta_{\gamma\nu} + \delta_{\alpha\nu}\delta_{\gamma\beta},$$

$$\frac{\partial I_3}{\partial E_{\alpha\beta}} = 3E_{\alpha\gamma}E_{\gamma\beta},$$

$$\frac{\partial^2 I_3}{\partial E_{\alpha\gamma}\partial E_{\beta\nu}} = \frac{3}{2}(\delta_{\alpha\beta}E_{\nu\gamma} + \delta_{\alpha\nu}E_{\beta\gamma} + \delta_{\gamma\nu}E_{\alpha\beta} + \delta_{\gamma\beta}E_{\alpha\nu}),$$

$$\frac{\partial I_4}{\partial E_{\alpha\beta}} = A_\alpha A_\beta, \quad \frac{\partial^2 I_4}{\partial E_{\alpha\gamma}\partial E_{\beta\nu}} = 0,$$

$$\frac{\partial I_5}{\partial E_{\alpha\beta}} = A_\alpha A_\gamma E_{\beta\gamma} + A_\beta A_\gamma E_{\alpha\gamma},$$

$$\frac{\partial^2 I_5}{\partial E_{\alpha\gamma}\partial E_{\beta\nu}} = \frac{1}{2}(A_\alpha A_\nu \delta_{\beta\gamma} + A_\alpha A_\beta \delta_{\gamma\nu} + A_\beta A_\gamma \delta_{\alpha\nu} + A_\gamma A_\nu \delta_{\alpha\beta}). \tag{12}$$

Let us now consider the propagation of homogeneous plane body waves, in the form

$$\boldsymbol{u} = \boldsymbol{a}\mathrm{e}^{\mathrm{i}k(\boldsymbol{n}\cdot\boldsymbol{x}-vt)}, \quad p = \mathrm{i}kP\mathrm{e}^{\mathrm{i}k(\boldsymbol{n}\cdot\boldsymbol{x}-vt)}, \tag{13}$$

where $\boldsymbol{a}$ is the unit vector in the direction of linear polarization, k is the wave number, v is the phase speed, and P is a scalar. Then the incremental incompressibility condition (10b) gives $\boldsymbol{a}\cdot\boldsymbol{n}=0$, and the wave is thus *transverse*. The incremental equations of motion (10a) can be written in the form

$$\boldsymbol{Q}(\boldsymbol{n})\boldsymbol{a} - P\boldsymbol{n} = \rho v^2 \boldsymbol{a}, \quad \text{where} \quad [\boldsymbol{Q}(\boldsymbol{n})]_{ij} = \mathcal{A}_{0piqj} n_p n_q. \tag{14}$$

Taking the dot product of this equation with $\boldsymbol{n}$ gives an expression for P. Substituting this back into Eq. (14) and using the orthogonality of the propagation and polarization vectors, we end up with the symmetric eigenvalue problem,

$$[\boldsymbol{I} - \boldsymbol{n}\otimes\boldsymbol{n}]\boldsymbol{Q}(\boldsymbol{n})[\boldsymbol{I} - \boldsymbol{n}\otimes\boldsymbol{n}]\boldsymbol{a} = \rho v^2 \boldsymbol{a} \tag{15}$$

for the wave speed and polarization for any given direction of propagation. The wave speed v is given simply by $\rho v^2 = \mathcal{A}_{0piqj} n_p n_q a_i a_j$.

As a simple example of the application of the above equations, consider the case where a sample of soft tissue is under uniaxial tension or compression with the direction of tension parallel to the fibers. We denote by e the elongation of the sample in the direction (x_1, say) of the uniaxial stress and discard all terms equal to or higher than e^2 in the expansions. In particular, we obtain the approximations

$$\boldsymbol{F} = \mathrm{diag}[1+e, 1-e/2, 1-e/2],$$

$$\boldsymbol{E} = \mathrm{diag}[e, -e/2, -e/2]. \tag{16}$$

Also, we find that there are only 15 nonzero components of $\boldsymbol{\mathcal{A}_0}$ in the (x_1,x_2,x_3) coordinate system because, in this special case, the principal axes of stress and strain are aligned. Now let θ be the angle between the direction of propagation and the x_1 axis. Then the *secular equation*, which gives the wave speed in terms of the elastic moduli, has the same form as in the isotropic case,[26] with the difference that the moduli depend not only on the isotropic elastic constants μ and A but also on the anisotropic elastic constants α_1, α_2, α_3, α_4, and α_5. It reads[26]

$$\rho v^2 = (\alpha + \gamma - 2\beta)\cos^4\theta + 2(\beta - \gamma)\cos^2\theta + \gamma, \tag{17}$$

where

$$\alpha = \mathcal{A}_{01212}, \quad 2\beta = \mathcal{A}_{01111} + \mathcal{A}_{02222} - 2\mathcal{A}_{01122} - 2\mathcal{A}_{01221},$$

$$\gamma = \mathcal{A}_{02121}. \tag{18}$$

Lengthy, but straightforward, calculations reveal that

$$2\beta - \alpha - \gamma = 2\alpha_1 + 2(4\alpha_1 + 3\alpha_2 + 3\alpha_3 + 3\alpha_4 + 2\alpha_5)e,$$

$$2(\beta - \gamma) = 2\alpha_1 + (3\mu + 10\alpha_1 + 8\alpha_2 + 6\alpha_3 + 6\alpha_4 + 4\alpha_5)e,$$

$$4\gamma = 4\mu + 2\alpha_2 + (A + 2\alpha_2 + 4\alpha_3 + 2\alpha_5)e. \tag{19}$$

Clearly, Eq. (17) provides a direct means of evaluating the elastic constants by measuring the transverse wave speed for a variety of e and θ combinations.

IV. CONCLUSION

We have shown that seven elastic constants are required to describe third-order incompressible solids with one family of parallel fibers, and we have indicated that these constants may be determined by using the acoustoelastic effect. We have also noted that 13 constants are needed for fourth-order solids.

In closing this letter, we remark that although many biological soft tissues exhibit transverse isotropy (one family of parallel fibers), many more must be modeled as orthotropic materials (two families of parallel fibers). Then, the list of invariants is increased from 4 (I_1, I_2, I_4, I_5) to 7, with the following three additions:

$$I_6 \equiv \boldsymbol{B}\cdot\boldsymbol{E}\boldsymbol{B}, \quad I_7 \equiv \boldsymbol{B}\cdot\boldsymbol{E}^2\boldsymbol{B}, \quad I_8 \equiv (\boldsymbol{A}\cdot\boldsymbol{E}\boldsymbol{B})\boldsymbol{A}\cdot\boldsymbol{B}, \tag{20}$$

where $\boldsymbol{B}$ is the unit vector in the direction of the second family of parallel fibers. In that case, an expansion of W up to third or fourth order yields such a large number of elastic constants to be determined, that it defeats its own usefulness. We would argue that it is more advantageous to turn to the exact nonlinear theory, where constitutive anisotropic models have been successfully evaluated against experimental test data to capture well the mechanics of orthotropic soft tissues. For instance, the Holzapfel–Gasser–Ogden model for arteries[27] is now implemented in many finite element analysis software packages. It requires the experimental determination of only three elastic constants per layer of arterial wall.

ACKNOWLEDGMENTS

This work is supported by a Senior Marie Curie Fellowship awarded by the Seventh Framework Programme of the European Commission to the first author and by an E.T.S. Walton Award, given to the third author by Science Foundation Ireland. This material is based on works supported by the Science Foundation Ireland under Grant No. SFI 08/W.1/B2580.

[1] J. Swammerdam, *The Book of Nature II* (Seyffert, London, 1758), pp. 122–132.
[2] M. Cobb, "Exorcizing the animal spirits: Jan Swammerdam on nerve function," Nature (London) **3**, 395–400 (2002).
[3] F. D. Murnaghan, *Finite Deformation of an Elastic Solid* (Wiley, New York, 1951).
[4] L. D. Landau and E. M. Lifshitz, *Theory of Elasticity*, 3rd ed. (Pergamon, New York, 1986).
[5] R. S. Rivlin and D. W. Saunders, "Large elastic deformations of isotropic

materials. VII. Experiments on the deformation of rubber," Philos. Trans. R. Soc. London, Ser. A **243**, 251–288 (1951).
[6]R. W. Ogden, "On isotropic tensors and elastic moduli," Proc. Cambridge Philos. Soc. **75**, 427–436 (1974).
[7]M. F. Hamilton, Y. A. Ilinskii, and E. A. Zabolotskaya, "Separation of compressibility and shear deformation in the elastic energy density," J. Acoust. Soc. Am. **116**, 41–44 (2004).
[8]E. A. Zabolotskaya, Y. A. Ilinskii, M. F. Hamilton, and G. D. Meegan, "Modeling of nonlinear shear waves in soft solids," J. Acoust. Soc. Am. **116**, 2807–2813 (2004).
[9]E. A. Zabolotskaya, Y. A. Ilinskii, and M. F. Hamilton, "Nonlinear surface waves in soft, weakly compressible elastic media," J. Acoust. Soc. Am. **121**, 1873–1878 (2007).
[10]L. Ostrovsky, A. Sutin, Y. Il'inskii, O. Rudenko, and A. Sarvazyan, "Radiation force and shear motions in inhomogeneous media," J. Acoust. Soc. Am. **121**, 1324–1331 (2007).
[11]C. Vanhille and C. Campos-Pozuelo, "Numerical analysis of strongly nonlinear extensional vibrations in elastic rods," IEEE Trans. Ultrason. Ferroelectr. Freq. Control **54**, 96–106 (2007).
[12]J.-L. Gennisson, M. Rénier, S. Catheline, C. Barrière, J. Bercoff, M. Tanter, and M. Fink, "Acoustoelasticity in soft solids: Assessment of the nonlinear shear modulus with the acoustic radiation force," J. Acoust. Soc. Am. **122**, 3211–3219 (2007).
[13]M. Rénier, J.-L. Gennisson, M. Tanter, S. Catheline, C. Barrière, D. Royer, and M. Fink, "Nonlinear shear elastic moduli in quasi-incompressible soft solids," Proc.-IEEE Ultrason. Symp. 554–557 (2007).
[14]X. Jacob, S. Catheline, J.-L. Gennisson, C. Barrière, D. Royer, and M. Fink, "Nonlinear shear wave interaction in soft solids," J. Acoust. Soc. Am. **122**, 1917–1926 (2007).
[15]M. S. Wochner, M. F. Hamilton, Y. A. Ilinskii, and E. A. Zabolotskaya, "Cubic nonlinearity in shear wave beams with different polarizations," J. Acoust. Soc. Am. **123**, 2488–2495 (2008).
[16]M. Rénier, J.-L. Gennisson, C. Barrière, D. Royer, and M. Fink, "Fourth-order shear elastic constant assessment in quasi-incompressible soft solids," Appl. Phys. Lett. **93**, 101912 (2008).
[17]M. Renier, J.-L. Gennisson, C. Barriere, S. Catheline, M. Tanter, D. Royer, and M. Fink, "Measurement of shear elastic moduli in quasi-incompressible soft solids," *Nonlinear Acoustics Fundamentals and Applications, Book Series*, 18th International Symposium on Nonlinear Acoustics, Stockholm, Sweden, 7–10 July 2008 [AIP Conf. Proc. **1022**, 303–306 (2008)].
[18]M. S. Wochner, M. F. Hamilton, Y. A. Ilinskii, and E. A. Zabolotskaya, "Nonlinear torsional wave beams," *Nonlinear Acoustics Fundamentals and Applications, Book Series*, 18th International Symposium on Nonlinear Acoustics, Stockholm, Sweden, 07–10 July 2008 [AIP Conf. Proc. **1022**, 335–338 (2008)].
[19]M. Mironov, I. Konopatskaya, P. Pyatakov, G. Clement, and N. Vykhodtseva, "Parametric excitation of shear waves in soft solids," *Nonlinear Acoustics Fundamentals and Applications, Book Series*, 18th International Symposium on Nonlinear Acoustics, Stockholm, Sweden, 07–10 July 2008 [AIP Conf. Proc. **1022**, 448–451 (2008)].
[20]W. Domański, "Propagation and interaction of non-linear elastic plane waves in soft solids," Int. J. Non-Linear Mech. **44**, 494–498 (2009).
[21]L. A. Ostrovsky, "Radiation force in nonlinear, focused beams," J. Acoust. Soc. Am. **124**, 1404–1407 (2008).
[22]M. A. Mironov, P. A. Pyatakov, I. I. Konopatskaya, G. T. Clement, and N. I. Vykhodtseva, "Parametric excitation of shear waves in soft solids," Acoust. Phys. **55**, 567–574 (2009).
[23]E. A. Zabolotskaya, Y. A. Ilinskii, and M. F. Hamilton, "Weakly nonlinear oscillations of a compliant object buried in soil," J. Acoust. Soc. Am. **125**, 2035–2040 (2009).
[24]A. J. M. Spencer, *Deformations of Fibre-Reinforced Materials* (University Press, Oxford, 1972).
[25]R. W. Ogden, *Non-Linear Elastic Deformations* (Ellis Horwood, Chichester, 1984).
[26]R. W. Ogden, "Incremental statics and dynamics of pre-stressed elastic materials," in *Waves in Nonlinear Pre-Stressed Materials*, CISM Lecture Notes Vol. **495**, edited by M. Destrade and G. Saccomandi (Springer, New York, 2007).
[27]G. A. Holzapfel, T. C. Gasser, and R. W. Ogden, "A new constitutive framework for arterial wall mechanics and a comparative study of material models," J. Elast. **61**, 1–48 (2000).

Are urban noise pollution levels decreasing? (L)

M. Arana
Department of Physics, Acoustics Laboratory, Public University of Navarre, 31006 Pamplona, Spain

(Received 5 August 2009; revised 14 December 2009; accepted 4 February 2010)

The majority of acoustic impact studies developed over the last 50 years have used a similar acoustic parameter (L_{eq}, L_{dn}) but the noise mapping methodology has been very uneven. The selection of the measurement points, the measurement periods, or the evaluation indices have not followed a unique criterion. Therefore, it is not possible to compare the sound pollution levels between different cities from those studies, at least in a rigorous sense. Even more, different studies carried out in the same city by different researchers during different years and using different methodologies are not conclusive whether the acoustic pollution increases or decreases. The present paper shows results, with statistical significance, about the evolution of the acoustic pollution obtained for two Spanish cities, Pamplona and Madrid. In both cases, it can be concluded that noise pollution decreases over time ($P<0.01$).
 [DOI: 10.1121/1.3337228]

PACS number(s): 43.50.Rq [BSF] Pages: 2107–2109

I. INTRODUCTION

In science, not all questions are valid. Only questions which are set out in well defined terms and whose answers can be verified quantitatively are deemed appropriate. In order to be able to give a rigorous answer to questions such as "Is city A noisier than city B?" or "Has noise pollution fallen in city A over the last few years?," it is necessary to have an objective evaluation parameter for noise pollution in a city, in addition to a methodology for evaluating it. The majority of acoustic impact studies developed over the last 50 years have used a similar acoustic parameter ($L_{Aeq,T}$), which is related to the acoustic energy during the evaluation period T, typically day L_d, evening L_e, and night L_n periods as well as the combined parameter L_{den} or L_{dn},[1] but the noise mapping methodology has been very uneven. This work analyses the main results obtained when producing noise maps for Pamplona and the measurement records from the environmental monitoring network set up by Madrid City Council, both cases involving Spanish cities. In the case of Pamplona, the corresponding noise maps were made in 1987–1988, 1997–1998, and 2007–2008. In the case of Madrid, the measurement period is from 1999 to 2003, inclusive.

Pamplona is a city with approximately 200 000 inhabitants in the north of Spain. Three noise maps were made for the city in 1987–1988, 1997–1998,[2] and 2007–2008. In all three cases, a total of 162 measuring stations were used, located in the nodes of a cross-linked 220×220 m^2, covering the whole consolidated urban area. The measurement station selection can therefore be considered as random. The noise pollution level was characterized by the daytime L_{Aeq} parameter, meaning the equivalent sound level to the time period between 8 a.m. and 10 p.m. All measurements were taken at street level using type I sound level meters during working days (from Monday to Friday) in favorable atmospheric conditions. The measurement stations were assigned to the district of the city where they were located. The most important aspect to highlight is that the methodology used to make these three noise maps (measurement stations, duration, and length of the measurements, parameters measured, etc.) were exactly the same in all three cases.

The Madrid City Council Environmental Department for noise control installed remote control measurement stations in 1998 throughout the city's urban area. Each of them recorded the hourly equivalent sound levels, $L_{Aeq,h}$. Twenty stations continually recorded sound levels over 5 complete years, from 1999 to 2003, inclusive. In total, 876, 480 measurements were recorded for the $L_{Aeq,1h}$ parameter. All commonly established parameters for evaluating noise pollution[3] could be obtained for this work: L_d, L_e, L_n, and L_{den}.

II. RESULTS

Figure 1(A) shows the average noise pollution levels in each district for the three measurement campaigns, as well as the average value of the city's noise pollution. The values indicated for each district correspond to the energy average from the values obtained in all the stations belonging to the district in question. The decrease in noise pollution observed in the district 9, mainly due to the implementation of pedestrian areas, is particularly remarkable

Figure 1(B) shows the evolution of the results for the different parameters (average value of the 20 stations, averaged in terms of energy) from 1999 to 2003.

III. DISCUSSION

As we can see in Fig. 1, a decreasing tendency in noise pollution can be perceived. We should now focus on whether this tendency is significant or not. This should be resolved using the appropriate statistical test. When the data are normal, analysis methods are more efficient than methods based on rank tests. In the case of Pamplona, the measuring stations covered the whole consolidated urban area in detail and their selection was random. The distribution could therefore be considered as normal. However, for the case of Madrid, the data were obtained from fixed measuring stations set up by the City Council without random criteria over a cross-

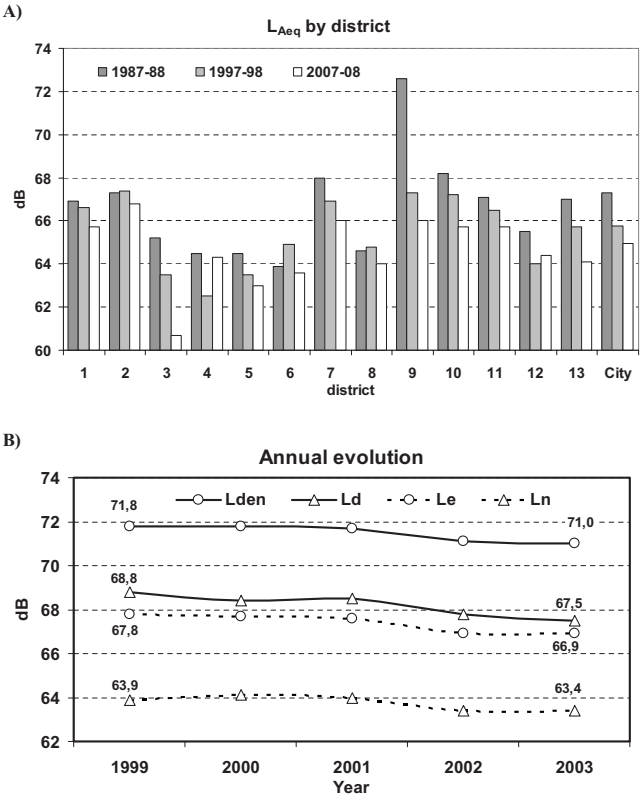

FIG. 1. (A) Noise pollution levels by district and for the whole city of Pamplona (Spain). (B) Annual evolution of the L_d, L_e, L_n, and L_{den} parameters in the city of Madrid (Spain).

linked area. On the other hand, these results are completely solid given that they represent exactly the noise pollution for each measuring station.

The methods based on ranks require less strict assumptions about the population distributions and they are almost as efficient as their normal equivalents when the data follow normal distribution, and they are more efficient when the data do not follow normal distribution. Taking the random block model,

$$Y_{ij} = \mu + \tau_i + \gamma_i + \varepsilon_{ij} \quad (i = 1, \ldots, k;\ j = 1, \ldots, b)$$

where k is the number of populations, b is the number of blocks, μ is the total average, τ_i is the effect due to the population, and γ_j is the effect due to the blocks and ε_{ij} are the random errors.

Tables I and II show the results for the two cities. In the case of Madrid, each value represents the exact noise pollution $-L_{\mathrm{Aeq,24h}}$ averaged annually—in each measurement station. In the case of Pamplona, each value represents the daytime noise pollution on workdays $-L_{\mathrm{Aeq,8–22h}}$ averaged annually—in each district of the city.

In our case, $k=20$ stations and $b=5$ years (Madrid) and $k=13$ districts and $b=3$ decades (Pamplona). To evaluate population differences in the model, the most appropriate ranks-based test (similar to the F-test for normal populations) is the Friedman test. The hypotheses to test are that not all the population effects, τ_I, are null. This means that there is a significant drop in the total noise pollution in both cities. The chi-squared values (from Tables I and II) are 18.27 for four degrees of freedom (Madrid) and 10.54 for two degree of freedom (Pamplona). In both cases, we can conclude that noise pollution decreases over time ($P<0.01$). A decrease in the percentage of people exposed to noise has been also observed in a 1 decade noise climate research.[4]

We must finally remember that the dB measurement is relative to a logarithmic scale. It is more intuitive to assess the reduction in terms of acoustic energy existing in the environment. From this point of view, noise pollution dropped by 17% from 1999 to 2003 in Madrid and by 41% from 1998 to 2008 in Pamplona.

TABLE I. Evolution of noise over time ($L_{\mathrm{Aeq,24h}}$ parameter) in Madrid, Spain.

Madrid, Spain. $L_{\mathrm{Aeq,24h}}$					
	Year				
Station	1999	2000	2001	2002	2003
1	70.3	70.3	70.4	70.3	70.0
2	69.9	69.7	69.5	69.3	69.9
3	66.6	66.8	68.3	67.9	66.3
4	63.0	63.1	63.2	63.2	62.6
5	73.4	73.2	72.7	72.6	73.0
6	67.9	67.3	70.5	66.9	66.9
7	66.8	67.1	67.4	67.5	66.9
8	67.7	67.2	67.2	67.1	67.0
9	71.2	70.6	70.8	70.9	70.8
10	68.0	67.3	66.8	65.8	66.3
11	63.8	62.5	61.6	61.9	62.1
12	70.4	69.3	69.3	68.8	69.4
13	71.2	70.8	70.3	69.7	69.7
14	61.8	63.5	63.6	62.4	62.7
15	64.5	65.2	63.9	63.8	63.7
16	65.1	65.0	65.5	64.6	64.5
17	70.2	70.3	70.2	69.6	68.6
18	69.6	67.6	66.7	66.4	65.8
19	63.6	63.7	64.1	63.9	64.1
20	69.8	70.7	71.1	69.8	69.1

TABLE II. Evolution of noise over time ($L_{\mathrm{Aeq,8–22h}}$ parameter) in Pamplona, Spain.

Pamplona, Spain $L_{\mathrm{Aeq,8–22h}}$			
	Year		
District	1987–1988	1997–1998	2007–2008
1	66.9	66.6	65.8
2	67.3	67.4	66.9
3	65.2	63.5	60.8
4	64.5	62.5	64.4
5	64.5	63.5	63.1
6	63.9	64.9	63.7
7	68	66.9	66.1
8	64.6	64.8	64.1
9	72.6	67.3	66.1
10	68.2	67.2	65.8
11	67.1	66.5	65.8
12	65.5	64	64.5
13	67	65.7	64.2

ACKNOWLEDGMENTS

Support from the Spanish Dirección General de Investigación Científica y Técnica (Grant Nos. PA86/0292 and BIA2003-09306-C04-03) and the Government of Navarra is gratefully acknowledged.

[1]T. J. Schultz, "Synthesis of social surveys on noise annoyance," J. Acoust. Soc. Am. **64**, 377–405 (1978).

[2]M. Arana and A. Garcia, "A social survey on the effects of environmental noise on the residents of Pamplona, Spain," Appl. Acoust. **53**, 245–253 (1998).

[3]Directive 2002/49/EC of the European Parliament and of the Council of 25 June 2002 relating to the assessment and management of environmental noise (2002).

[4]C. J. Skinner and C. J. Grimwood, "The UK noise climate 1990–2001: Population exposure and attitudes to environmental noise," Appl. Acoust. **66**, 231–243 (2005).

Masked speech priming: Neighborhood size matters (L)

Chris Davis, Jeesun Kim,[a] and Angelo Barbaro
MARCS Auditory Laboratories, University of Western Sydney, New South Wales 1797, Australia

(Received 3 June 2009; revised 6 February 2010; accepted 10 February 2010)

The current study investigated the robustness of priming from a masked speech priming method introduced by Kouider and Dupoux [(2005). Psychol. Sci. **16**, 617–625]. In this procedure, a compressed spoken prime is embedded in auditory masking stimuli and presented immediately prior to an uncompressed auditory target. The degree to which spoken stimuli could be compressed without significant data loss was first determined. Using this compression level, repetition and form priming were measured for the target words with a high versus low number of phonological neighbors. The results indicated that robust masked speech priming occurred only for word targets that had few neighbors. © *2010 Acoustical Society of America.* [DOI: 10.1121/1.3353116]

PACS number(s): 43.71.Sy [RSN] Pages: 2110–2113

I. INTRODUCTION

In the visual masked priming paradigm (e.g., Forster and Davis, 1984), a pattern masked written stimulus (the prime) precedes a clearly visible target word. A typical finding is that lexical decisions made to target words preceded by same word primes are faster than those made to unrelated primes, even though the participant is unaware of the masked primes. The advantage of this procedure is that it minimizes the involvement of conscious response strategies while also producing a range of effects not usually found in unmasked priming paradigms. Moreover, patterns of masked priming arising from manipulations of prime-target relationships have provided important data for topics ranging from type of lexical access mechanism to the development of such mechanisms.

The usefulness of masked priming as a probe of written word processing has encouraged researchers to attempt to develop an auditory version of masked priming in order to investigate speech processing. Recently Kouider and Dupoux (2005) developed a method that has produced reliable masked speech repetition priming even when the prime is embedded among other speech-like signals. Critically, this method does not involve an attentional manipulation whereby primes are unattended (since unattended processing might eliminate lexical processing altogether, Lachter *et al.*, 2004). What was done was that auditory primes were time compressed and hidden within a noise mask (a stream of spectrally speech-like but unintelligible noise). Immediately following the prime, a target dubbed over the noise mask was presented for lexical decision (targets were 15 dB louder than masks and primes, see Fig. 1).

In the study, Kouider and Dupoux (2005) examined priming effects for four types of prime-target relationship (repetition, morphological, phonological, and semantic) against matched unrelated control prime conditions. They also measured priming effects using four different prime compression rates: 35%, 40%, 50%, and 70%. They found that when primes were compressed to 35% or 40% of their original duration participants had little awareness of them. At these prime compression rates, a robust repetition priming effect (30–40 ms) was found but there was no significant phonological, morphological, or semantic priming. Furthermore, at these compression rates, there was no repetition or phonological priming for nonword targets.

Kouider and Dupoux (2005) proposed that their demonstration of the feasibility of subliminal priming for spoken word processing had opened up a line of investigation by which the functional architectures of the written and auditory word processing can be compared using parallel tasks and masking techniques. This claim raises a number of questions that will be addressed in the current research: How robust is the masked auditory priming effect (can it be readily replicated)? This is an interesting issue since to our knowledge there has been no published replication of Kouider and Dupoux (2005) results. Does using a fixed compression rate of 35% for all prime stimuli degrade the data of some stimuli (will all the primes be "intact" as is the case for written primes)? Finally, given the idiosyncratic nature of speech (in contrast to nonidiosyncratic written words), can a standardized auditory masked priming method be developed?

In addition, there are several other aspects of the Kouider and Dupoux study that can be extended. For instance, in their study, the repeated and form priming contrast was tested using different target items, but a more powerful demonstration of any differences between these prime types would be had by using the same targets (with an across participant design). Furthermore, given that it is a general assumption of spoken word recognition models (see McQueen, 2007 for a review) that word recognition entails the parallel evaluation of multiple lexical hypotheses/candidates with a process of competition among these, it is of considerable interest to test how priming may be affected by phonological neighborhood (*N*) size.[1] Testing how priming is affected by this variable is additionally important since recently it has been shown that masked repetition priming of written targets is affected by target *N* size (Kinoshita *et al.*, 2008).

[a]Author to whom correspondence should be addressed. Electronic mail: j.kim@uws.edu.au

 0001-4966/2010/127(4)/2110/4/$25.00

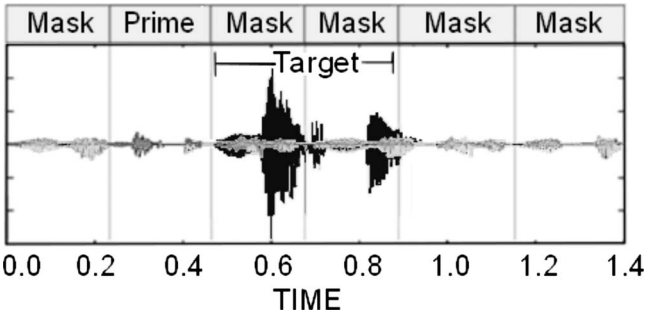

FIG. 1. Illustration of the masked speech paradigm used by Kouider and Dupoux (2005) and in the current study. The target (in black) is dubbed over the reversed-speech masking sounds (gray) and presented immediately after the prime (the masks and prime are time compressed and attenuated −15 dB compared to the target).

II. EXPERIMENT

To address the above issues, the experiment consisted of three parts: The first examined whether the set of words chosen (selected to vary in phonological *N* size) could all be reliably identified at compression rates of 35% (it is possible that this rate, which was used for the French stimuli of Kouider and Dupoux, 2005, is not suitable for English). In the second part, repetition and form priming were measured using the same target items (the compression of which was adjusted according to the outcome of part 1). The third part of the study assessed the degree to which the masked primes were able to be consciously perceived by using the prime lexical decision procedure used by Kouider and Dupoux. In order to provide a means of standardizing the materials, so that other researchers can use them, a commercially available high quality text to speech synthesized voice was used.

A. Method

The current experiments used the masked auditory priming technique developed by Kouider and Dupoux (2005) (see Fig. 1). To ensure uniformity and standardization of materials we used a text to speech program (TEXTALOUD program from Nextup.com). To create the speech stimuli, we chose the Nuance text to speech Australian Lee voice. This very natural sounding synthesized speech is generated by concatentative synthesis that uses a unit-selection approach (where small segments of recorded speech are selected and joined together using flexible unit-selection algorithms). This program allows manipulation of the speech rate without changing pitch.

The COOL EDIT 2000 program was used to edit and additionally adjust (where needed, see below) the compression of the experimental stimuli. That is, any further time compression of primes was achieved through the pitch synchronous overlap and add (PSOLA) technique (see Moulines and Charpentier, 1990) as used by Kouider and Dupoux (2005). The program was also used to time-reverse the background speech masks and for the embedding of prime and target items within the background masks. The intensity of the primes, targets, and masking items was adjusted by the computer software PRAAT (Boersma, 2001). DMDX (Forster and Forster, 2003) was used to present the stimuli in each of the three parts of the experiment. Lexical statistics (spoken word frequency and phonological *N* size) were selected from the Celex database (Baayen *et al.*, 1995) and checked with the HAL corpus (Balota *et al.*, 2007).

TABLE I. Summary of target lexical statistics for the word targets. Phonological *N* statistics were calculated using an average of the HAL (Balota *et al.*, 2007) and Celex (Baayen *et al.*, 1995) corpora.

Condition	Mean phonological *N* size (HAL-Celex)	Mean Celex frequency
Low *N* targets	2.4	960
High *N* targets	15.2	830

1. Participants

For part 1 (the compression test), 17 participants (10 men and 7 women, mean age=25.2 years) were recruited. In parts 2 and 3 (priming and prime availability) the same 52 participants (21 men and 31 women, mean age=23.7) were employed (these people had not participated in part 1). All participants were native speakers of Australian English with no self-reported hearing impairment.

2. Materials

The target items in the priming experiment consisted of 60 words and 60 nonwords, each ranging from one to three syllables (average length=1.75). 30 targets were selected to have relatively few phonological neighbors (mean *N* size =2.4; range=0–6, mean number of phonemes=3.9, and SD=0.63) and 30 targets to have many neighbors (mean *N* size=15.2; range=5–31, mean number of phonemes=3.6, and SD=0.62). There was a significant difference in *N* size between the low and high *N* groups, $t(58)=9.64$, $p<0.05$ [there was no difference in the number of phonemes between the *N* groups, $t(58)=1.45$, $p>0.05$]. The low *N* group had a mean spoken word frequency of 968 per million and the high *N* group a mean of 830 per million (see Table I). The difference in spoken word frequency between low and high *N* groups was not significant, $t(58)=0.43$, $p>0.05$. The nonword targets were constructed to closely resemble word targets (e.g., /tʉːdæɪ/ - /tʉːfæɪ/) given that neither the Celex nor Hal corpuses provide *N* density statistics for nonwords. It was presumed that the *N* statistics for these nonwords would trend with the *N* densities of the matched real words.

Three types of primes were constructed for each target: repetition primes, form primes (e.g., phonologically related primes and targets), and control primes (these were unrelated words and nonwords). The form primes were selected so that the different phoneme(s) typically did not occur in the onset, and the percentage of cases when this did occur was similar for the low and high *N* primes and targets (36% and 33%, respectively). All the primes for word targets were words and the primes for nonword targets were nonwords. Three experimental lists were constructed so that each target would appear in each prime condition without being repeated in any list. Target items were produced by using TEXTALOUD text to speech interface set at the speed setting of −5.0. The compressed prime items (and masks) were produced by using the maximum speed setting (30). This resulted in a rate that was

on average approximately 40% of original (target) duration and a further time compression adjustment was made using COOL EDIT 2000. The PRAAT program was used to normalize the amplitude of all sound files.

3. Procedure

Part 1: Compression test. Participants were tested individually in a quiet testing booth. Each participant listened to the compressed prime materials presented one at a time over a set of headphones (Sennheiser PC 131). Participants were asked to listen to 4 practice items and 60 test words (nonwords were not tested) and to identify the rapidly spoken word by typing what they thought they had heard. The order of items was counterbalanced across participants. After each identification, participants were then asked to rate their confidence in the decision by typing a number ranging from 1 (not very) to 5 (very) confident.

Part 2: Priming test. Participants were tested individually. Three versions of the experiment were constructed, so that each type of prime would precede each target, but within a version no target would be repeated. Each participant was assigned to one of the three versions of the experiment. Participants were required to perform an auditory lexical decision task on the loud target item that was embedded in the babble speech. Participants were not informed about the presence of the prime. They placed their index fingers on the right (for the YES response) and the left (for the NO response) hand buttons of a button box connected to the PC via a Parallel Input/Output (PIO) card for record of accurate response timing. A set of 12 practice items was constructed in the same fashion as the experimental items and this practice set preceded each version of the experiment. The first two practice items were provided with feedback via DMDX identifying the correct response, and the participant was then required to request the next item (using a foot pedal). The remaining practice items played immediately after one another, and there was no feedback. Following this practice set, the participants listened to the 120 test items and performed a lexical decision task on each target item. Response data were trimmed so that responses that were less than 160 ms and those greater than 1200 ms (set due to the nature of the presentation conditions) were discarded from the analysis (this affected less than 0.5% of the data).

Part 3: Prime availability test. Part 3 was conducted with the same people who participated in part 2 and was conducted immediately after it. Participants were told that they would hear similar items to those that they heard in experiment 2. The structure of each item was explained to participants and they were told to ignore the loud word and concentrate on the prime word that was presented just before it. Participants were instructed to classify the prime as either a word or a nonword using the same response options as part 2. Participants first performed lexical decision for three practice items for which the prime compression was 60% and feedback about the correctness of the response was provided. After each item, the participant was required to press a foot pedal to request the next item. Following these items, five more practice items were presented at the 35% compression rate; these items were presented immediately after one another and no feedback was provided. Participants were presented 80 test items (prime-target repetition trials were not used) for lexical decision on the masked primes.

TABLE II. Mean lexical response time (in milliseconds) and error rates with standard error in parentheses for low and high *N* word targets for the three priming conditions (repetition prime, form prime, and control prime).

Target *N* size	Condition	RT	% error
Low	Repetition	856 (22)	6.3 (1)
	Form	889 (22)	8.1(1.2)
	Control	891 (27)	7.3 (1)
High	Repetition	888 (24)	6.9(1.2)
	Form	863 (21)	10.0(1.3)
	Control	873 (21)	8.8(1.3)

B. Results

Part 1: Compression test. An analysis of the percentage of words correctly identified (exact spelling) indicated that on average participants identified 80.2% (range=6%–100%; SE=3.36) of the target words time compressed at 35%. The mean confidence rating of participants was 3.92 (range =2.3–4.7). There were nine words for which the accuracy rates were less than 70% with a mean accuracy rate of 25% (range=6%–53%; SE=5.13), indicating that the compression rate of 35% was not suitable for all words. The compression of these words was done by hand (generally by compressing the vowels more than the consonant) and by this way a compression level of approximately 35% was achieved.

Part 2: Priming test. Mean reaction times for high and low *N* word targets as a function of prime type are shown in Table II. Two analyses of variance (ANOVAs) were conducted on the response latency data (one for the participant data, $F1$, and one for the item data, $F2$) to examine difference due to target *N* size (high and low) and priming condition (repetition, form, and control).

Overall, the effect of target *N* size was not significant; both $Fs<1$. The effect of prime type was also not significant; both $Fs<1$. There was, however, a significant interaction between target *N* size and prime type for the participant analysis, $F1(2,98)=5.92$, $p<0.05$, that was borderline for the item analysis, $F2(2,54)=3.00$, $p=0.06$. To investigate

TABLE III. Mean lexical response time (in milliseconds) and error rates with standard error in parentheses for low and high *N* nonword targets for the three priming conditions (repetition prime, form prime, and control prime).

Target *N* size	Condition	RT	% error
Low	Repetition	972(27.0)	16.5(1.9)
	Form	978(29.0)	15.8(1.4)
	Control	990(27.1)	15.6(1.6)
High	Repetition	958(30.0)	18.6(1.6)
	Form	994(29.0)	15.4(1.8)
	Control	960(30.8)	17.0(1.8)

the basis of this interaction between target *N* size and prime type, the data for the low and high *N* targets were analyzed separately. There was repetition priming effect for the low *N* targets (contrasting the repetition and control conditions), $F1(1,48)=6.15$, $p<0.05$; $F2(1,27)=3.7$, $p<0.05$. There was no difference among these prime types for the high *N* targets, $F1(1,48)=1.41$, $p>0.05$; $F2(1,27)=1.08$, $p>0.05$.

An analysis of the error rates for target words showed that there was no significant difference between the low and high target *N* groups, $F1(1,96)=1.92$, $p>0.05$; $F2<1$, no differences as a function of prime type, $F1(2,96)=2.92$, $p>0.05$; $F2(2,54)=2.23$, $p>0.05$, and no interaction between target *N* size and prime type; both $Fs<1$.

Mean response times and percentage of errors for the nonword targets are shown in Table III. Once again ANOVAs were conducted to determine whether there were differences as a function of *N* size and prime type. There was no significant difference between the target *N* size groups, both $Fs<1$, no difference between prime types, $F1(2,98)=2.24$, $p>0.05$; $F2(2,52)=1.77$, $p>0.05$, nor an interaction between prime type and target size, $F1(2,98)=2.29$, $p>0.05$; $F2<1$. An analysis of the error rates for nonwords indicated that there was no significant difference between the target *N* conditions, both $Fs<1$, no difference between the prime types, both $Fs<1$, nor a significant interaction between target *N* size and prime type, both $Fs<1$.

Part 3: Prime availability test. As the prime lexical decision task entailed making a forced-choice between two alternatives (word or nonword) chance performance was 50% correct. If participants performed at this level it can be assumed that they had no awareness of the lexical status of the masked primes. The results showed that the mean percentage of correct responses at identifying the masked primes was similar for words 50.87% (SD=15.15) and nonwords 50.97% (SD=14.25). Two one-sample t tests were conducted to determine if these response rates differed from chance; they did not, for words $t(51)=0.415$, $p>0.05$ and for nonwords $t(51)=0.493$, $p>0.05$.

C. Discussion

This study investigated the robustness of the auditory masked priming method introduced by Kouider and Dupoux (2005) using a high quality commercially available text to speech voice (so other researchers can readily test the same or similar materials). The initial experiment evaluated the integrity of the compressed words at a fixed compression rate (35%). The subsequent masked priming experiment examined whether priming would be affected by phonological *N* size, following which the degree of prime availability was determined.

The results of the compression test (part 1) indicated the following: (1) The majority of words compressed to 35% are still sufficiently intact so as to reliably identified. (2) Not all words can be time compressed to the same level and still be identified. This result means that some care needs to be taken in conducting auditory masked priming studies in order to avoid problems with the intactness of primes.

The results of the priming test (part 2) indicated that this masking method does not interfere with the production of a robust priming effect. Indeed, in general, the pattern of results replicated those of Kouider and Dupoux (2005), i.e., repetition priming (but no form priming) for word targets and no priming for nonword targets. The null priming effect for nonword targets suggests that this type of priming is based on the lexical activation of abstract word forms, and so would not occur for nonwords (Kouider and Dupoux, 2005).

The current results also indicated that target *N* size is an important moderator of masked repetition priming: When a target word had many phonological neighbors, it showed no repetition priming at all. Kinoshita *et al.* (2008) found a similar trend in their results with written stimuli and attributed it to a mechanism in which the strength of any priming effect is divided by the number of neighbors, so that the net benefit will be smaller priming for words that have high-density *Ns*. However, the influence of phonological *N* size on repetition priming appears to be stronger with spoken than for written words (where high *N* words still showed a repetition priming effect, although this was about half the size of low *N* target words, Kinoshita *et al.*, 2008). A reason why high *N* targets might not show repetition priming at all is that in this paradigm the registration of the masked priming may be rather weak and so any activation (or evidence) the prime triggers is offset by competition from the targets neighbors. Given this, it is important that researchers investigating auditory masked priming effects are aware of the influence that phonological *N* size has on repetition priming.

ACKNOWLEDGMENT

We acknowledge ARC support (DP0453143).

[1]In the current study, phonological neighborhood size is defined as the number of words that differ from a given target by one phoneme substitution, addition, or deletion (e.g., Luce and Pisoni, 1998).

Baayen, R. H., Piepenbrock, R., and Gulikers, L. (**1995**). The Celex Lexical Database (Version 2.0) (computer software), Linguistic Data Consortium, University of Pennsylvania, Philadelphia, PA.

Balota, D. A., Yap, M. J., Cortese, M. J., Hutchison, K. A., Kessler, B., Loftis, B., Neely, J. H., Nelson, D. L., Simpson, G. B., and Treiman, R. (**2007**). "The English lexicon project," Behav. Res. Methods **39**, 445–459.

Boersma, P. (**2001**). "Praat, a system for doing phonetics by computer," GLOT **5**, 341–345.

Forster, K. I., and Davis, C. (**1984**). "Repetition priming and frequency attenuation in lexical access," J. Exp. Psychol. Learn. Mem. Cogn. **10**, 680–698.

Forster, K. I., and Forster, J. C. (**2003**). "DMDX: A Windows display program with millisecond accuracy," Behav. Res. Methods Instrum. Comput. **35**, 116–124.

Kinoshita, S., Castles, A., and Davis, C. (**2008**). "The role of neighbourhood density in transposed-letter priming," Lang. Cognit. Processes **24**, 506–526.

Kouider, S., and Dupoux, E. (**2005**). "Subliminal speech priming," Psychol. Sci. **16**, 617–625.

Lachter, J., Forster, K. I., and Ruthruff, E. (**2004**). "Forty-five years after Broadbent (1958): Still no identification without attention," Psychol. Rev. **111**, 880–913.

Luce, P. A., and Pisoni, D. B. (**1998**). "Recognising spoken words: The neighbourhood activation model," Ear Hear. **19**, 1–36.

McQueen, J. (**2007**). "Eight questions about spoken-word recognition," in *The Oxford Handbook of Psycholinguistics*, edited by M. Gaskell (OUP, Oxford), Chap. 3, pp. 37–53.

Moulines, E., and Charpentier, F. (**1990**). "Pitch-synchronous waveform processing techniques for text-to-speech synthesis using diphones," Speech Commun. **9**, 453–467.

Accuracy of formant measurement for synthesized vowels using the reassigned spectrogram and comparison with linear prediction (L)

Sean A. Fulop[a)]
Department of Linguistics, California State University, Fresno, 5245 N. Backer Avenue, Fresno, California 93740-8001

(Received 19 September 2009; revised 13 January 2010; accepted 13 January 2010)

This brief report describes a small study which was undertaken with nine synthetic vowel tokens, in an effort to demonstrate the validity of the reassigned spectrogram as a formant measurement tool. The reassigned spectrogram's performance is also compared with that of a typical pitch-asynchronous linear predictive analysis and is found to be superior. In this study, reassigned spectrograms were further processed to highlight the formants and then were used to measure these synthetic vowel formants generally to within 0.5% of their known true values, far surpassing the accuracy of a typical linear predictive analysis procedure which was inaccurate by as much as 17%. The overall accuracy of reassigned spectrographic formant measurement is thus demonstrated in these cases. © *2010 Acoustical Society of America.* [DOI: 10.1121/1.3308476]

PACS number(s): 43.72.Ar [SSN] Pages: 2114–2117

I. INTRODUCTION AND BACKGROUND

The *reassigned* or time-corrected instantaneous frequency spectrogram has been advocated occasionally[1–3] as a tool for making spectral measurements of speech signals and, in particular, for the measurement of formants. Indeed, one study[4] tried automatic formant tracking with the reassigned power spectrum (essentially a reassigned spectrogram frame-by-frame) and concluded that the performance was superior to that of typical linear predictive methods. This study only tested the performance on real vowels, for which the true formants cannot be known, and the assessment of superiority was made based on purely subjective and qualitative grounds such as "the formant trajectories are smoother" and "formants are more clearly visible" than with the linear predictive methods.

If the reassigned spectrogram is very good for measurement and tracking of formants, and given that the early studies cited date from up to 15 years ago, one might wonder why everyone has not adopted it by now. The study by Plante *et al.*[1] showed qualitatively that the reassigned spectrogram looks clearer than the conventional one but did not prove it to be accurate in its placement of frequency components such as formants. If the "clearly visible" formants in a reassigned spectrogram were wrong by 50 or 100 Hz, or were entirely spurious, how would anyone know?

The present study also applies a "pruning" technique which attempts to isolate components, such as formants, in a sparse plot of the reassigned spectrogram which excludes other information. This additional layer of postprocessing can only decrease the degree of confidence which applied researchers may have in the methodology. This report describes a small study which was undertaken with nine synthetic vowel tokens, in an effort to definitively demonstrate for the first time the accuracy of the "pruned" reassigned spectrogram as a formant measurement tool, particularly when compared to linear predictive analysis. Indeed, in this study the technology was used to measure these vowel formants generally to within 0.5% of their known true values, far surpassing the accuracy of a typical pitch-asynchronous linear predictive analysis procedure. Being as it is a small study, it is not intended in this report to provide a statistically valid measure of the overall accuracy of the reassigned spectrogram or of linear predictive analysis. The methods here also do not involve automatic tracking or peak picking. It is only intended to demonstrate that the reassigned spectrogram is indeed accurate for measuring formants manually, and that in this small study it improves upon manual application of linear prediction by an order of magnitude.

A. Reassigned spectrograms and pruning

The reassigned spectrogram[2,5] and algorithms for its computation have been treated thoroughly in the literature,[6] so only a brief digression is provided here. It is assumed that a subject signal $f(t)$ can be modeled as the sum of general AM/FM components:

$$f(t) = \sum_n A_n(t) e^{i(\Omega_n(t)+\phi_n)} \tag{1}$$

and that the short-time Fourier transform (STFT) is defined in the following way:

$$\mathrm{STFT}_h(\omega, T) \overset{\mathrm{def}}{=} \int_{-\infty}^{\infty} f(t+T) h(-t) e^{i\omega t} dt. \tag{2}$$

The method of reassignment exploits information contained within the partial derivatives of the STFT complex phase, with respect to time and frequency, in the following way. The *channelized instantaneous frequency* (CIF) of a signal as a function of time and frequency is defined thusly as

[a)]Electronic mail: sfulop@csufresno.edu

 0001-4966/2010/127(4)/2114/4/$25.00

$$\mathrm{CIF}(\omega,T) \overset{\mathrm{def}}{=} \frac{\partial}{\partial T}\arg(\mathrm{STFT}_h(\omega,T)), \tag{3}$$

where STFT_h is the short-time Fourier transform using window function h. If there is just one AM/FM component dominant in the neighborhood of a frequency bin, then the CIF spectrum will show the instantaneous frequency of that component with arbitrary precision (i.e., not quantized by the discrete time-frequency grid).

Dual to the above, the *local group delay* (LGD) of a signal is given by

$$\mathrm{LGD}(\omega,T) \overset{\mathrm{def}}{=} -\frac{\partial}{\partial \omega}\arg(\mathrm{STFT}_h(\omega,T)). \tag{4}$$

The LGD at a time-frequency point (ω_0,T_0) on the STFT matrix may be interpreted as the average true time of $\mathrm{STFT}_h(\omega_0,T_0)$; this is an estimate of the "time correction" to the maximum energy point of the dominant AM/FM signal component observed at (ω_0,T_0). Now, the reassigned spectrogram plots each STFT magnitude at the new location of its computed CIF and at a time point corrected by its LGD. The method of reassignment applied to a spectrogram thus yields a new representation, which remaps all spectrographic magnitudes to the instantaneous frequency of the nearest signal component that could be resolved in the original and also corrects the time smearing of the spectrogram by reassignment to nearest times where the group delay is concentrated.[6]

The further processing technique, which is herein called *pruning* of the reassigned spectrogram, was first theoretically outlined by Nelson,[2,7] and involves the computation of the second-order mixed partial derivative of the STFT phase. Algorithms for performing the pruning as in the present paper were presented in other literature.[8] Nelson (op. cit.) argued that the nearly stationary AM/FM components of a signal $x(T)$ satisfy

$$\frac{\partial^2}{\partial\omega\,\partial T}\arg(\mathrm{STFT}_h(\omega,T)) = \frac{\partial}{\partial\omega}\mathrm{CIF}_x(\omega,T) \approx 0. \tag{5}$$

The precise threshold for the above partial derivative condition can be empirically determined and will in practice depend on the degree of deviation from a pure sinusoid that is tolerable in the application at hand. This means that greater tolerance in this threshold will be required where line components having high chirp rates are expected—for speech signals in which the relevant components are formants, an absolute value of the derivative on the order of <0.1 has been found to work well.

B. Accuracy of formant estimation

The most complete study of formant measurement accuracy for synthesized vowels seems to be that of Monsen and Engebretson.[9] Their study pitted spectrographic manual measurement against a linear predictive analysis procedure of a sort typically used in speech science at that time. The spectrographic measurement procedure was rather flexible but did not use wideband analysis directly; three experts were provided with a wideband spectrogram "for orientation," paired with a single narrowband power spectrum for each vowel token. The readers could only use the narrowband power spectrum to measure the formant values, which they would have to do by manually smoothing the spectrum to locate the peaks by eye.

The linear predictive analysis was performed manually as well. The procedure was inadequately described but seems to have involved deliberately overfitting the power spectrum using a linear prediction filter having 22 poles. The values of the first three formants would have to have been extracted from the expected 10 or 11 spectral peaks by manual inspection. No mention was made of the specific means for deciding on the formant values from the overfit analysis, although it was mentioned that smoother linear prediction spectra having a smaller number of poles yielded decreased measurement accuracy.

Monsen and Engebretson found that the linear prediction-estimated F_1, F_2, and F_3 of their synthesized vowels were only accurate to within ± 60 Hz, and that manual spectrographic measurement performed comparably on the lower two formants and less well on F_3. They further suggested that this margin of error is contained within the difference limens for formant perception, but this is apparently not correct. Kewley-Port and Watson's[10] later comprehensive study of formant perception in synthesized vowels reports difference limens of 14 Hz for formants below 800 Hz and 1.5% for higher formants.

II. MATERIALS AND METHODS

For the test materials, nine vowels were synthesized using the formant synthesizer included with the PRAAT (Ref. 11) speech analysis software. The PRAAT "vowel editor" function was used to set the F_1 and F_2 values by listening, so that eight of the vowels have a quality recognizable as American English. Additionally, the vowel [ɔ̲] was synthesized with an overly back (low) F_2 value which yields an unrealistic quality and is very close to F_1. The lower two formants of the vowels are listed with the results in Table I. The F_3 and F_4 values were set to 2500 and 3500 Hz, respectively, in all of the vowels. There were no formants other than these four. Each vowel sound was synthesized for a 300 ms span, using a fundamental frequency which began at 120 Hz and descended at a rate of 2 octaves/s. This yielded a reasonable baritone falling intonation which would be commonplace in real speech. The vowel sounds were created with a 44.1 kHz sampling rate.

To obtain complete formant data from linear prediction, the following procedure was undertaken for each synthesized vowel sound. The vowel sound was first downsampled to 10 kHz sampling frequency, which facilitates simple selection of the filter order for the linear prediction. Then, the PRAAT function "To formant (Burg)" was invoked seeking four formants, which performed a standard linear predictive smoothing (by the BURG algorithm) using a filter order of 8 and 50 ms Gaussian windows (which effectively capture only the central 25 ms). The resulting formant estimates were computed by solving the roots of the predictor polynomial and recorded for all analysis frames through the duration of the vowel.

TABLE I. Synthesized and measured formant values (Hz) by linear prediction (BURG) and reassigned spectrogram.

			LP			Spgm		
Vowel	F_1	F_2	F_1	F_2	F_3	F_1	F_2	F_3
i	306	2241	319–397	2139	2453	306	2262	2467
e	415	2137	433–490	2068	2439	415	2151	2475
ɛ	559	1794	593–615	1773	2422	559	1795	2488
æ	731	1768	753–783	1752	2422	732	1769	2488
u	325	689	337–384	713–745	2406–2415	324	680	2498
o	454	715	468–518	740–769	2406–2416	455	705	2498
ɔ	602	884	618–657	910–936	2408–2420	605	870	2495
ɔ̱	635	715	634–678	736–801	2406–2417	628	714	2498
ɑ	714	1008	733–762	1034–1053	2415	722	1000	2496

The values obtained from this procedure were the best that could be obtained using linear prediction in the PRAAT software system. As a comparison check, several vowels were also analyzed using the covariance algorithm in a pitch-asynchronous fashion and again using the covariance algorithm on a small window encompassing only the closed phase of the glottal cycle. Formant estimates were extracted from these analyses by solving the roots of the predictor polynomial. The formant estimates obtained from the covariance algorithm in a pitch-asynchronous mode were within a few Hz of those obtained by the BURG method and were not significantly different. Both pitch-asynchronous linear prediction (LP) procedures benefited from signal pre-emphasis, which is intended to cancel out the spectral tilt of the glottal source and increase the accuracy of the formant estimates.[12] The formant estimates obtained using the covariance algorithm only on the closed phase with or without pre-emphasis were considerably less accurate, despite the occasional advocacy of this latter technique as the most accurate.[13] Closed phase linear prediction analysis is extremely sensitive to properly locating the analysis window, and it appears that it is not possible to overcome these problems using a manual system such as PRAAT.

Reassigned spectrograms were computed for a brief excerpt from the middle of each vowel encompassing five or six glottal cycles. These were computed in MATLAB using 7 ms (308 point) Hann windows, zero-padded to 2048 points for the fast Fourier transform computations. This method is not highly sensitive to the sampling rate of the signal. The reassigned spectrograms were further pruned by the procedure outlined in Sec. I A to show only points closely associated with line components in the signal. Formant values were measured by magnifying the image, as shown in Fig. 1, and placing the mouse pointer over the line showing the formant during the middle of the glottal cycle. Figure 2 shows a conventional spectrogram of the same vowel for comparison. The corresponding frequency value was automatically reported by a MATLAB routine. In the case of the vowel [ɔ̱] with unrealistically close formants, the spectrogram was barely able to resolve them, and they were connected by vertical interference lines.

III. RESULTS

Table I shows the results of the measurements by reassigned spectrogram and linear prediction using the BURG algorithm, compared with the known values of F_1 and F_2 for the vowels. F_3 is 2500 Hz in every case. The linear prediction formant values frequently varied considerably over the course of the vowel; when this variation was more than a few Hz, a range is reported. This phenomenon is due to the changing fundamental frequency of the vowel, showing how the linear prediction formant estimates depend on this value.

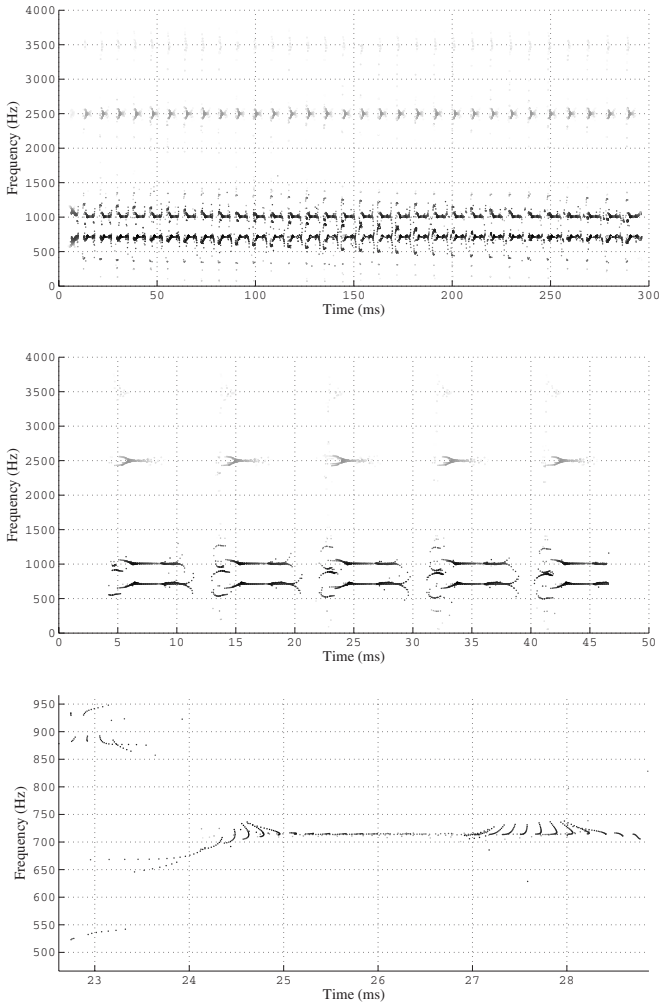

FIG. 1. Three reassigned spectrograms of synthesized [ɑ], computed with 7 ms Hann windows and pruned to highlight components only. Top panel shows the entire vowel; middle panel shows 50 ms from the middle of the vowel; bottom panel simply magnifies our view of the middle panel to show F_1 in one glottal cycle.

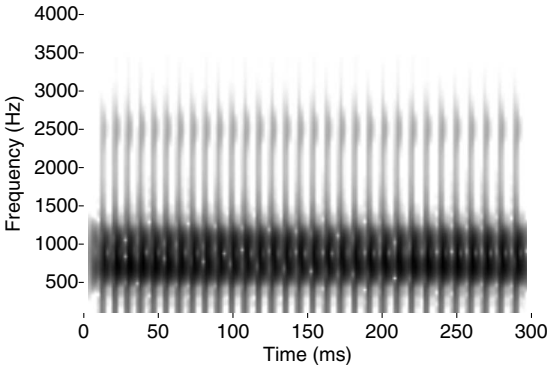

FIG. 2. Conventional spectrogram of synthesized [ɑ], computed using the same windows and other parameters from the reassigned spectrograms.

The reassigned spectrographic measurements were independent of the fundamental and were consistent from cycle to cycle.

The linear prediction formant values for F_1 and F_2, which are the most important in speech analysis, were usually too high by a considerable amount. For the case of [i], for instance, the middle of the range of values is 17% too high. The only accurate linear prediction estimate was the F_2 of [æ], which differed by just 4 Hz from the true value. The F_3 values were always too low, usually by 3% or more. The reassigned spectrographic measurements, by contrast, were within 3 Hz of seven different F_1 values and within 10 Hz of six different F_2 values. The largest error was the F_2 of [ɔ], which was measured 1.6% too low.

IV. CONCLUSION

This small study of synthetic vowels demonstrates that not only is the reassigned spectrogram a very good tool for measuring formants when suitably pruned but it also far exceeds the performance of a standard type of linear prediction analysis. This is surprising, given that the vowels were generated by a basic sort of formant synthesizer that adheres perfectly to the source-filter theory of speech production, the assumptions of which underlie the procedure of linear predictive speech analysis.[13] Since speech *in vivo* is guaranteed to stray from the perfect source-filter model due to aeroacoustic and coupling effects which are not found in the synthetic vowels, one can only induce that the formant estimates of linear prediction analysis in real vowels can only be less accurate than those reported here. On the other hand, the reassigned spectrogram is not a parametric analysis and makes no modeling assumptions other than the separability of the line components. It can be expected to make accurate formant estimates for real spoken vowels, to the extent that the formants are prominently excited by the glottal pulses. It would be useful for a future study to measure the errors in linear prediction formant estimates from real vowels. Since there is no way to know the true formant values of a spoken vowel, unlike a synthetic one, it is suggested that the formants measured from reassigned spectrograms could be used as a substitute gold standard for such a study.

ACKNOWLEDGMENTS

Thanks to Kelly Fitz for pointing out the need for a paper like this and to Paul Boersma for always answering pesky questions about PRAAT.

[1]F. Plante, G. Meyer, and W. A. Ainsworth, "Improvement of speech spectrogram accuracy by the method of reassignment," IEEE Trans. Speech Audio Process. **6**, 282–287 (1998).
[2]D. J. Nelson, "Cross-spectral methods for processing speech," J. Acoust. Soc. Am. **110**, 2575–2592 (2001).
[3]S. A. Fulop, "Phonetic applications of the time-corrected instantaneous frequency spectrogram," Phonetica **64**, 237–262 (2007).
[4]F. Plante and W. A. Ainsworth, "Formant tracking using reassigned spectrum," in EUROSPEECH '95—Fourth European Conference on Speech Communication and Technology (ISCA) (1995), pp. 741–744.
[5]F. Auger and P. Flandrin, "Improving the readability of time-frequency and time-scale representations by the reassignment method," IEEE Trans. Signal Process. **43**, 1068–1089 (1995).
[6]S. A. Fulop and K. Fitz, "Algorithms for computing the time-corrected instantaneous frequency (reassigned) spectrogram, with applications," J. Acoust. Soc. Am. **119**, 360–371 (2006).
[7]D. J. Nelson, "Instantaneous higher order phase derivatives," Digit. Signal Process. **12**, 416–428 (2002).
[8]S. A. Fulop and K. Fitz, "Separation of components from impulses in reassigned spectrograms," J. Acoust. Soc. Am. **121**, 1510–1518 (2007).
[9]R. B. Monsen and A. M. Engebretson, "The accuracy of formant frequency measurements: A comparison of spectrographic analysis and linear prediction," J. Speech Hear. Res. **26**, 89–97 (1983).
[10]D. Kewley-Port and C. S. Watson, "Formant-frequency discrimination for isolated English vowels," J. Acoust. Soc. Am. **95**, 485–496 (1994).
[11]P. Boersma and D. Weenink, PRAAT: Doing phonetics by computer (2009).
[12]J. Harrington and S. Cassidy, *Techniques in Speech Acoustics* (Kluwer, Dordrecht, 1999).
[13]J. D. Markel and A. H. Gray, Jr., *Linear Prediction of Speech* (Springer-Verlag, Berlin, 1976).

The direct field boundary impedance of two-dimensional periodic structures with application to high frequency vibration prediction

Robin S. Langley
Department of Engineering, University of Cambridge, Trumpington Street, Cambridge CB5 8HU, United Kingdom

Vincent Cotoni
ESI US R&D, 12555 High Bluff Drive, Suite 250, San Diego, California 92130

(Received 22 April 2009; revised 11 January 2010; accepted 21 January 2010)

Large sections of many types of engineering construction can be considered to constitute a two-dimensional periodic structure, with examples ranging from an orthogonally stiffened shell to a honeycomb sandwich panel. In this paper, a method is presented for computing the boundary (or edge) impedance of a semi-infinite two-dimensional periodic structure, a quantity which is referred to as the direct field boundary impedance matrix. This terminology arises from the fact that none of the waves generated at the boundary (the direct field) are reflected back to the boundary in a semi-infinite system. The direct field impedance matrix can be used to calculate elastic wave transmission coefficients, and also to calculate the coupling loss factors (CLFs), which are required by the statistical energy analysis (SEA) approach to predicting high frequency vibration levels in built-up systems. The calculation of the relevant CLFs enables a two-dimensional periodic region of a structure to be modeled very efficiently as a single subsystem within SEA, and also within related methods, such as a recently developed hybrid approach, which couples the finite element method with SEA. The analysis is illustrated by various numerical examples involving stiffened plate structures. [DOI: 10.1121/1.3314254]

PACS number(s): 43.20.Gp, 43.40.Dx, 43.40.Ey [DF] Pages: 2118–2128

I. INTRODUCTION

A two-dimensional periodic structure is a special form of construction in which a number of identical units are connected in a regular pattern to cover a two-dimensional surface. One example is an orthogonally stiffened plate or shell, in which the basic unit is a rectangular panel with edge stiffeners; this type of arrangement is used extensively in ship and aircraft structures. On a smaller scale, another example is a honeycomb panel, in which the basic unit is a repeating section of the honeycomb core, together with the attached region of the faceplates. As part of the design process, it is often required to predict the vibration of an engineering structure over a wide frequency range, and any periodic region of the structure might be excited by acoustic noise, or through physical connections to items of equipment or to other parts of the structure. In the latter case, the structural connections are likely to be along one or more of the boundaries (i.e., the edges) of the periodic region, and thus, the behavior of a periodic structure under boundary excitation is an important part of the vibration prediction process. As described in what follows, analytical and numerical methods that are directed at mid- and high frequency vibrations require knowledge of the boundary *impedance* of the various structural components; the relevant impedance equations have not previously been derived for two-dimensional periodic components, and this issue is addressed in the present work.

A well known method for the analysis of high frequency vibrations is the statistical energy analysis (SEA) approach (see, for example, Lyon and DeJong, 1995). The motivation for this approach arises from the fact that, at high frequencies, the number of degrees of freedom required by standard analysis methods, such as the finite element method, becomes prohibitive, and furthermore, the response becomes sensitive to random structural imperfections, meaning that statistical considerations are important. These issues are addressed in SEA by considering the structure to be an assembly of a relatively small number of subsystems. The method yields the ensemble average of the vibrational energy of each subsystem, and expressions can also be derived for the ensemble variance of the subsystem energies (Langley and Cotoni, 2004). Relatively, little previous research has considered the application of SEA to systems having periodic structural components, and differing approaches have been taken by authors who have addressed this issue. For example, Keane and Price (1989) studied the effect of structural periodicity in a one-dimensional system by modeling a periodic region of the system as a single SEA subsystem. In contrast, Langley *et al.* (1997) modeled a two-dimensional periodic plate as a coupling element between two non-periodic plates, rather than as a subsystem. Tso and Hansen (1998) applied the periodic subsystem approach of Keane and Price (1989) to a two-dimensional plate with uni-directional stiffeners, and considered an SEA model in which this plate was coupled to an isotropic plate. More general two-dimensional periodic structures have been considered as SEA subsystems by Cotoni *et al.* (2008), although in this case, the concern was with the intrinsic properties of the subsystem and with

 0001-4966/2010/127(4)/2118/11/$25.00

coupling to an acoustic volume, rather than with boundary coupling to other structural components. Other work on the application of SEA to periodic structures has taken a different approach, in which the periodic component is considered to be an assembly of homogeneous subsystems, rather than a single subsystem (Sum *et al.*, 2003; Choi, 2004); in addition, periodicity in a structural connection between two homogeneous structural subsystems has been considered by Bosmans and co-workers (1997, 2001), who studied line junctions with regular bolt spacings. Given the existing literature, it is clear that there remains a need for a methodology, whereby a general periodic component can be incorporated into an SEA model as a subsystem and coupled to other structural subsystems. Central to the SEA approach is the calculation of a set of coupling loss factors (CLFs), which govern the flow of energy between the various subsystems, and these are commonly derived by considering the boundary impedances of the components, which meet at a structural joint [see, for example, Langley and Heron (1990) or Bosmans and Nightingale (2001)]. The required boundary impedance is that of a "semi-infinite" component, in the sense that waves generated at the boundary are not considered to be reflected back to the boundary; this is also sometimes referred to as the "direct field" boundary impedance (Shorter and Langley, 2005a). The present work derives the direct field impedance matrix at the boundary of a general two-dimensional periodic system, thus allowing a wide range of CLFs to be calculated, and therefore enabling the use of general two-dimensional periodic subsystems in SEA models. It can be noted that similar ideas, directed toward a different end, have been developed by Duhamel (2008) in the development of absorbing boundary conditions for acoustic wave propagation. The present work is implemented within the framework of the finite element method, and the combination of this method with periodic structure theory has been the subject of research for many years. Early work on free wave propagation [for example, Orris and Petyt (1974)] has been extended to waveguides and forced vibration [for example, Manconi and Mace (2009) and Waki *et al.* (2009)], although the edge impedance of a structure has not previously been considered.

The present work also has application to enhanced versions of SEA, which are directed at the prediction of mid-frequency vibrations; the need for such enhancements arises from the fact that the conditions required for the successful application of SEA tend to limit the method to the prediction of high frequency vibrations. One recently developed approach for the analysis of mid-frequency vibrations (referred to as the hybrid method) couples the finite element method to SEA within a single vibration model of the structure [see, for example, Shorter and Langley (2005b) and Cotoni *et al.* (2007)]. Parts of the structure (for example, stiff frames and joints) are modeled by using the finite element method, whereas components that have a high modal density (for example, thin panels) are modeled as SEA subsystems. To include a component as a SEA subsystem, it is necessary to compute the direct field dynamic stiffness at the boundaries of the component, and (as in the case of SEA) the present work extends the capability of the method by allowing two-dimensional periodic subsystems to be considered.

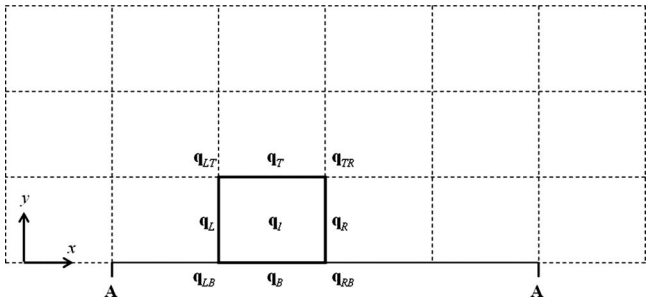

FIG. 1. A two-dimensional semi-infinite periodic system, with the partition of the degrees of freedom of a single periodic cell. The edge of the structure is along the x axis, and the structure extends over the plane $y>0$.

The boundary impedance for a semi-infinite two-dimensional periodic structure (corresponding to the direct field impedance) is derived in Sec. II. A number of benchmark studies and example applications are then described in Sec. III, including the application of the method to an SEA model, in which an orthogonally stiffened panel is treated as a single subsystem.

II. CALCULATION OF THE BOUNDARY IMPEDANCE

A. General remarks

A schematic of a semi-infinite two-dimensional periodic structure is shown in Fig. 1. The structure is composed of a basic cell, which is repeated in both the x- and y- directions to fill the half-plane $y>0$, so that the line $y=0$ represents the system boundary. One of the basic periodic cells is highlighted in Fig. 1; there is no restriction on the detailed geometry or complexity of this cell, which would typically be an edge stiffened panel for a marine or aeronautical structure, an extruded panel for a train floor structure, or a repeating tile for either a honeycomb sandwich panel or a panel with an isogrid of stiffening elements. Furthermore, the structure may have curvature in either the x- or the y- direction, in which case the concept of a semi-infinite system remains a useful paradigm, although the system would technically be infinitely "wrapped" around the axis of curvature. The aim of the present work is to derive the frequency dependent impedance matrix associated with the degrees of freedom of a finite region of the boundary, labeled A-A in Fig. 1. In order to do this, it is necessary to impose conditions on the remaining part of the boundary, which could, for example, be considered to be either restrained or free, and the present analysis allows any set of conditions to be applied. The analysis proceeds below by: (i) deriving the impedance matrix for the special case in which any two cells, which are adjacent in the x-direction, have a response which is identical apart from a specified phase shift; (ii) extending this result to the case in which the motion of the boundary section A-A is repeated periodically along the boundary; (iii) considering the case in which general boundary conditions are applied outside of the region A-A.

B. The impedance matrix under a specified boundary-wise phase shift

The following analysis is concerned with harmonic vibration of the system at a specified frequency ω, so that a typical response variable $q(t)$ can be written in the form $q(t)=\mathrm{Re}[q(\omega)\exp(i\omega t)]$, where $q(\omega)$ is referred to as the complex amplitude of the response. The terminology "complex amplitude of the response" is abbreviated simply to "response" in what follows, so that all response quantities are considered to be complex functions of frequency. The first stage in deriving the impedance matrix of the boundary region A-A shown in Fig. 1 is to consider the dynamics of the system under a specified cell-wise phase shift ε_x in the x-direction. Thus, the response of any particular cell is taken to be $\exp(-i\varepsilon_x)$ times that of the left hand neighboring cell. It can be noted that this is the periodic structure equivalent of assuming a wavenumber dependency k in the x-direction, as would be done in a Fourier transform analysis of the response of a homogeneous system.

The degrees of freedom associated with a single periodic cell are shown in Fig. 1, and these are taken to consist of the displacements $\mathbf{q}$ associated with the left (subscript L) and right (subscript R) hand edges, the top and bottom edges (subscripts T and B), the four corners (subscripts LB, RB, RT, and LT), and the interior (subscript I) of the cell. Typically, the cell could be modeled by using the finite element method, in which case each nodal degree of freedom can readily be assigned to one of the various displacement groups shown in Fig. 1 (it can be noted that the cell must be meshed so that the nodes on opposite edges mirror each other). If a cell-wise phase shift $\exp(-i\varepsilon_x)$ is taken to apply in the x-direction, then it follows that

$$\begin{pmatrix} \mathbf{q}_I \\ \mathbf{q}_B \\ \mathbf{q}_T \\ \mathbf{q}_L \\ \mathbf{q}_R \\ \mathbf{q}_{LB} \\ \mathbf{q}_{RB} \\ \mathbf{q}_{LT} \\ \mathbf{q}_{RT} \end{pmatrix} = \begin{pmatrix} \mathbf{0} & \mathbf{0} & \mathbf{0} & \mathbf{0} & \mathbf{I} & \mathbf{0} \\ \mathbf{0} & \mathbf{I} & \mathbf{0} & \mathbf{0} & \mathbf{0} & \mathbf{0} \\ \mathbf{0} & \mathbf{0} & \mathbf{0} & \mathbf{I} & \mathbf{0} & \mathbf{0} \\ \mathbf{0} & \mathbf{0} & \mathbf{0} & \mathbf{0} & \mathbf{0} & \mathbf{I} \\ \mathbf{0} & \mathbf{0} & \mathbf{0} & \mathbf{0} & \mathbf{0} & \mathbf{I}e^{-i\varepsilon_x} \\ \mathbf{I} & \mathbf{0} & \mathbf{0} & \mathbf{0} & \mathbf{0} & \mathbf{0} \\ \mathbf{I}e^{-i\varepsilon_x} & \mathbf{0} & \mathbf{0} & \mathbf{0} & \mathbf{0} & \mathbf{0} \\ \mathbf{0} & \mathbf{0} & \mathbf{I} & \mathbf{0} & \mathbf{0} & \mathbf{0} \\ \mathbf{0} & \mathbf{0} & \mathbf{I}e^{-i\varepsilon_x} & \mathbf{0} & \mathbf{0} & \mathbf{0} \end{pmatrix} \begin{pmatrix} \mathbf{q}_{LB} \\ \mathbf{q}_B \\ \hline \mathbf{q}_{LT} \\ \mathbf{q}_T \\ \hline \mathbf{q}_I \\ \mathbf{q}_L \end{pmatrix}, \tag{1}$$

$$\mathbf{q}_{\mathrm{full}} = \mathbf{R}\mathbf{q}_{\mathrm{red}}. \tag{2}$$

Equation (2) represents an abbreviated form of Eq. (1), so that $\mathbf{R}$ is the matrix that appears in Eq. (1), $\mathbf{q}_{\mathrm{full}}$ is the full set of degrees of freedom of the cell, and $\mathbf{q}_{\mathrm{red}}$ is the reduced set required to describe the cell response given the constraints imposed by the specified phase shift. The partitions that appear in $\mathbf{q}_{\mathrm{red}}$ in Eq. (1) are used to highlight the fact that the reduced degrees of freedom fall into three groups: those on the bottom edge of the cell, those on the top edge, and those elsewhere in the cell. In the absence of damping, the equations of motion of the cell can be written in the form

$$(-\omega^2\mathbf{M}+\mathbf{K})\mathbf{q}_{\mathrm{full}} = \mathbf{F}_{\mathrm{full}}, \tag{3}$$

where $\mathbf{M}$ is the mass matrix, $\mathbf{K}$ is the stiffness matrix, and $\mathbf{F}_{\mathrm{full}}$ is the set of forces acting on the cell. It follows from Eq. (2) that Eq. (3) can be rewritten in terms of the reduced set of degrees of freedom to give

$$\mathbf{R}^{*T}(-\omega^2\mathbf{M}+\mathbf{K})\mathbf{R}\mathbf{q}_{\mathrm{red}} = \mathbf{R}^{*T}\mathbf{F}_{\mathrm{full}}. \tag{4}$$

The right hand side of this equation can be developed by noting that: (i) no external loads are applied to the interior of the cell or to the left and right hand edges, (ii) the equilibrium condition at the right hand edge of the cell involves the force $\mathbf{F}_R$, together with the force $\mathbf{F}_L\exp(-i\varepsilon_x)$, which corresponds to the force at the left hand edge of the neighboring cell. It thus follows that

$$\mathbf{F}_R + \mathbf{F}_L e^{-i\varepsilon_x} = \mathbf{0}, \tag{5}$$

$$\mathbf{R}^{*T}\mathbf{F}_{\mathrm{full}} = \begin{pmatrix} \mathbf{F}_{LB} + \mathbf{F}_{RB}e^{i\varepsilon_x} \\ \mathbf{F}_B \\ \hline \mathbf{F}_{LT} + \mathbf{F}_{RT}e^{i\varepsilon_x} \\ \mathbf{F}_T \\ \hline \mathbf{0} \\ \mathbf{0} \end{pmatrix}. \tag{6}$$

It is now convenient to label the partitions of $\mathbf{q}_{\mathrm{red}}$ with the notation

$$\mathbf{q}_b = \begin{pmatrix} \mathbf{q}_{LB} \\ \mathbf{q}_B \end{pmatrix}, \tag{7}$$

$$\mathbf{q}_t = \begin{pmatrix} \mathbf{q}_{LT} \\ \mathbf{q}_T \end{pmatrix}, \tag{8}$$

$$\mathbf{q}_o = \begin{pmatrix} \mathbf{q}_I \\ \mathbf{q}_L \end{pmatrix}, \tag{9}$$

so that Eq. (4) can be written as

$$\begin{pmatrix} \mathbf{C}_{bb} & \mathbf{C}_{bt} & \mathbf{C}_{bo} \\ \mathbf{C}_{tb} & \mathbf{C}_{tt} & \mathbf{C}_{to} \\ \mathbf{C}_{ob} & \mathbf{C}_{ot} & \mathbf{C}_{oo} \end{pmatrix} \begin{pmatrix} \mathbf{q}_b \\ \mathbf{q}_t \\ \mathbf{q}_o \end{pmatrix} = \begin{pmatrix} \mathbf{F}_b \\ \mathbf{F}_t \\ \mathbf{0} \end{pmatrix}, \tag{10}$$

where the matrix $\mathbf{C}$ is the matrix product that appears on the left hand side of Eq. (4), and $\mathbf{F}_b$ and $\mathbf{F}_t$ represent the first two force partitions in Eq. (6). It follows from Eq. (10) that

$$\mathbf{q}_o = -\mathbf{C}_{oo}^{-1}\mathbf{C}_{ob}\mathbf{q}_b - \mathbf{C}_{oo}^{-1}\mathbf{C}_{ot}\mathbf{q}_t, \tag{11}$$

$$\begin{pmatrix} \mathbf{C}_{bb} - \mathbf{C}_{bo}\mathbf{C}_{oo}^{-1}\mathbf{C}_{ob} & \mathbf{C}_{bt} - \mathbf{C}_{bo}\mathbf{C}_{oo}^{-1}\mathbf{C}_{ot} \\ \mathbf{C}_{tb} - \mathbf{C}_{to}\mathbf{C}_{oo}^{-1}\mathbf{C}_{ob} & \mathbf{C}_{tt} - \mathbf{C}_{to}\mathbf{C}_{oo}^{-1}\mathbf{C}_{ot} \end{pmatrix} \begin{pmatrix} \mathbf{q}_b \\ \mathbf{q}_t \end{pmatrix} = \begin{pmatrix} \mathbf{F}_b \\ \mathbf{F}_t \end{pmatrix}, \tag{12}$$

and further that

$$\begin{pmatrix} \mathbf{D}_{bb} & \mathbf{D}_{bt} \\ \mathbf{D}_{tb} & \mathbf{D}_{tt} \end{pmatrix} \begin{pmatrix} \mathbf{q}_b \\ \mathbf{q}_t \end{pmatrix} = \begin{pmatrix} \mathbf{F}_b \\ \mathbf{F}_t \end{pmatrix}, \tag{13}$$

$$\begin{pmatrix} -\mathbf{D}_{bt}^{-1}\mathbf{D}_{bb} & -\mathbf{D}_{bt}^{-1} \\ \mathbf{D}_{tb}-\mathbf{D}_{tt}\mathbf{D}_{bt}^{-1}\mathbf{D}_{bb} & -\mathbf{D}_{tt}\mathbf{D}_{bt}^{-1} \end{pmatrix}\begin{pmatrix} \mathbf{q}_b \\ -\mathbf{F}_b \end{pmatrix}=\begin{pmatrix} \mathbf{q}_t \\ \mathbf{F}_t \end{pmatrix}. \tag{14}$$

Equation (13) is a restatement of Eq. (12), using the notation $\mathbf{D}_{rs}$ $(r,s=b,t)$ to represent the entries of the matrix (a dynamic stiffness matrix), which appears in the equation. Equation (14) is a rearrangement of Eq. (13), in which the displacement and force at the top edge of the cell are related to those at the bottom edge, so that the matrix, which appears in Eq. (14), represents the transfer matrix of the cell for a translation in the y-direction.

In order to derive the impedance matrix associated with the boundary of the periodic structure, the system response to an arbitrary set of forces applied to the boundary must be computed. This can be done by first deriving the set of all possible free wave motions of the system, and then imposing the relevant boundary conditions. To this end, Floquet's theorem [see, for example, Brillouin (1953)] can be applied, which states that (for wave motion) any two cells, which are adjacent in the y-direction must have a motion, which is identical apart from a multiplying factor $\exp(-i\varepsilon_y)$. Whereas the phase shift ε_x is specified in the present analysis, the admissible values of the phase shift ε_y are initially unknown, and must be found from the equations of motion of the system. For any particular cell, it follows from Floquet's theorem that

$$\begin{pmatrix} \mathbf{q}_t \\ \mathbf{F}_t \end{pmatrix}=e^{-i\varepsilon_y}\begin{pmatrix} \mathbf{q}_b \\ -\mathbf{F}_b \end{pmatrix}, \tag{15}$$

so that Eq. (14) yields

$$\left\{\begin{pmatrix} -\mathbf{D}_{bt}^{-1}\mathbf{D}_{bb} & -\mathbf{D}_{bt}^{-1} \\ \mathbf{D}_{tb}-\mathbf{D}_{tt}\mathbf{D}_{bt}^{-1}\mathbf{D}_{bb} & -\mathbf{D}_{tt}\mathbf{D}_{bt}^{-1} \end{pmatrix}-\mathbf{I}e^{-i\varepsilon_y}\right\}\begin{pmatrix} \mathbf{q}_b \\ -\mathbf{F}_b \end{pmatrix}=\mathbf{0}. \tag{16}$$

It follows that the admissible values of ε_y can be found from the eigenvalues of the cell transfer matrix. In practice, Eq. (16) can be ill-conditioned if the term $\mathbf{D}_{bt}^{-1}$ is near-singular, and the equation can be rearranged to yield

$$\left[\begin{pmatrix} \mathbf{D}_{bb} & \mathbf{I} \\ \mathbf{D}_{tb} & \mathbf{0} \end{pmatrix}-e^{-i\varepsilon_y}\begin{pmatrix} -\mathbf{D}_{bt} & \mathbf{0} \\ -\mathbf{D}_{tt} & \mathbf{I} \end{pmatrix}\right]\begin{pmatrix} \mathbf{q}_b \\ -\mathbf{F}_b \end{pmatrix}=\begin{pmatrix} \mathbf{0} \\ \mathbf{0} \end{pmatrix}, \tag{17}$$

which avoids the use of the inverse of the matrix partition $\mathbf{D}_{bt}$. If the vector $\mathbf{q}_b$ contains N degrees of freedom, then Eq. (17) will yield $2N$ eigenvalues and eigenvectors representing various types of wave motion within the system. The wave motion may either be propagating, in which case ε_y is real, or evanescent, in which case ε_y has an imaginary component leading to a change in the wave amplitude from cell to cell in the y-direction. Furthermore, propagating waves may propagate energy either toward or away from the boundary, and evanescent waves may either grow or decay with increasing distance from the boundary. Only those waves, which propagate energy away from the boundary, or which decay with increasing distance from the boundary, are valid solutions for the case of boundary excitation, and symmetry implies that N of the $2N$ waves will meet these conditions. Valid evanescent waves can be identified from the condition

$$\mathrm{Im}(\varepsilon_y)<0, \tag{18}$$

and valid propagating waves can be identified from the condition

$$\mathrm{Im}(\varepsilon_y)=0 \quad \text{and} \quad P=(i\omega/4)\boldsymbol{\phi}^{*T}\begin{pmatrix} \mathbf{0} & \mathbf{I} \\ -\mathbf{I} & \mathbf{0} \end{pmatrix}\boldsymbol{\phi}>0, \tag{19}$$

where P is the power propagated away from the boundary and $\boldsymbol{\phi}$ is the mode shape yielded by Eq. (17). Having identified the relevant N waves, the boundary motions and forces can be expanded as a linear combination of these waves in the form

$$\mathbf{q}_b=\sum_{n=1}^{N}a_n\mathbf{q}_{bn}=\mathbf{Q}\mathbf{a}, \tag{20}$$

$$\mathbf{F}_b=\sum_{n=1}^{N}a_n\mathbf{F}_{bn}=\mathbf{P}\mathbf{a}, \tag{21}$$

where a_n is the amplitude of the nth wave, $\mathbf{q}_{bn}$ and $\mathbf{F}_{bn}$ are the boundary displacements and forces per unit amplitude, respectively, arising from this wave (which can be identified from the nth mode shape $\boldsymbol{\phi}_n$), and the matrices $\mathbf{Q}$ and $\mathbf{P}$ are defined accordingly. The wave amplitudes a_n can be eliminated from Eqs. (20) and (21) to yield

$$\mathbf{P}\mathbf{Q}^{-1}\mathbf{q}_b=\mathbf{D}\mathbf{q}_b=\mathbf{F}_b, \tag{22}$$

$$\mathbf{Z}=-(i/\omega)\mathbf{D}, \tag{23}$$

where $\mathbf{D}$ is the dynamic stiffness matrix of the boundary under the imposed x-wise phase shift $\exp(-i\varepsilon_x)$, and $\mathbf{Z}$ is the associated impedance matrix. This result is extended to more general boundary motions in the following sections.

C. The impedance matrix of a periodically repeating boundary

The case is now considered in which the boundary region A-A is composed of M cells. The motion of the whole boundary is specified as a periodic repetition of the motion of A-A, so that an identical motion is obtained in any two cells that are separated by $M-1$ intermediate cells. Under this condition, the x-wise phase parameter ε_x must be restricted to the set ε_{xr}, where

$$\varepsilon_{xr}=\frac{2\pi(r-1)}{M}, \quad r=1,2,\ldots,M, \tag{24}$$

so that the resulting motion is repeated every M cells. The response of the boundary region A-A can be expressed as a linear combination of the motion associated with each of these phase parameters, so that

$$\mathbf{q}_{bs}=\sum_{r}\mathbf{q}_b^{(r)}e^{-i\varepsilon_{xr}s}, \tag{25}$$

where $\mathbf{q}_{bs}$ is the boundary motion of cell s of the region A-A $(s=1,2,\ldots,M)$, and $\mathbf{q}_b^{(r)}$ is the motion component associated with the phase parameter ε_{xr}. Equation (25) can be expressed in the form

$$\mathbf{q}_{\mathrm{AA}} = \begin{pmatrix} \mathbf{q}_{b1} \\ \mathbf{q}_{b2} \\ .. \\ \mathbf{q}_{bM} \end{pmatrix} = \begin{pmatrix} \mathbf{I}e^{-i\varepsilon_{x1}} & \mathbf{I}e^{-i\varepsilon_{x2}} & .. & \mathbf{I}e^{-i\varepsilon_{xM}} \\ \mathbf{I}e^{-i2\varepsilon_{x1}} & \mathbf{I}e^{-i2\varepsilon_{x2}} & .. & \mathbf{I}e^{-i2\varepsilon_{xM}} \\ .. & .. & .. & .. \\ \mathbf{I}e^{-iM\varepsilon_{x1}} & \mathbf{I}e^{-iM\varepsilon_{x2}} & & \mathbf{I}e^{-iM\varepsilon_{xM}} \end{pmatrix} \begin{pmatrix} \mathbf{q}_b^{(1)} \\ \mathbf{q}_b^{(2)} \\ .. \\ \mathbf{q}_b^{(M)} \end{pmatrix} = \mathbf{S} \begin{pmatrix} \mathbf{q}_b^{(1)} \\ \mathbf{q}_b^{(2)} \\ .. \\ \mathbf{q}_b^{(M)} \end{pmatrix}, \tag{26}$$

where $\mathbf{q}_{\mathrm{AA}}$ represents the motion of the region A-A, and the matrix $\mathbf{S}$ is defined accordingly. Similarly, the forces on the boundary region A-A can be written in the form

$$\mathbf{F}_{\mathrm{AA}} = \mathbf{S} \begin{pmatrix} \mathbf{F}_b^{(1)} \\ \mathbf{F}_b^{(2)} \\ .. \\ \mathbf{F}_b^{(M)} \end{pmatrix} = \mathbf{S} \begin{pmatrix} \mathbf{D}^{(1)} & \mathbf{0} & .. & \mathbf{0} \\ \mathbf{0} & \mathbf{D}^{(2)} & .. & \mathbf{0} \\ .. & .. & .. & .. \\ \mathbf{0} & \mathbf{0} & & \mathbf{D}^{(M)} \end{pmatrix} \begin{pmatrix} \mathbf{q}_b^{(1)} \\ \mathbf{q}_b^{(2)} \\ .. \\ \mathbf{q}_b^{(M)} \end{pmatrix}, \tag{27}$$

where $\mathbf{F}_b^{(r)}$ is the force associated with the phase parameter ε_{xr}, and $\mathbf{D}^{(r)}$ represents the dynamic stiffness matrix associated with this phase parameter, as calculated from Eq. (22) with $\varepsilon_x = \varepsilon_{xr}$. It follows from Eqs. (26) and (27) that

$$\mathbf{F}_{\mathrm{AA}} = \mathbf{S} \begin{pmatrix} \mathbf{D}^{(1)} & \mathbf{0} & .. & \mathbf{0} \\ \mathbf{0} & \mathbf{D}^{(2)} & .. & \mathbf{0} \\ .. & .. & .. & .. \\ \mathbf{0} & \mathbf{0} & & \mathbf{D}^{(M)} \end{pmatrix} \mathbf{S}^{-1} \mathbf{q}_{\mathrm{AA}} = \mathbf{D}_{\mathrm{AA}} \mathbf{q}_{\mathrm{AA}}, \tag{28}$$

where $\mathbf{D}_{\mathrm{AA}}$ is the dynamic stiffness matrix of the boundary region A-A under the stated conditions. The impedance matrix then follows as $\mathbf{Z}_{\mathrm{AA}} = -(i/\omega)\mathbf{D}_{\mathrm{AA}}$. This result is extended to a wider class of boundary motion in Sec. II D.

D. The impedance matrix for more general boundary motions

This section is concerned with the impedance matrix associated with a region A-A of the boundary when general boundary conditions are applied outside of this region. Taking the region A-A to consist of M cells, the first step in the analysis is to consider an extended region of $M+M'$ cells, which is repeated periodically. The dynamic stiffness matrix of this extended region can be derived by using the analysis of Sec. II C, and general boundary conditions can then be applied over the additional M' cells. To this end, the dynamic stiffness relation for the periodically repeating extended region can be written in the form

$$\begin{pmatrix} \mathbf{D}_{11} & \mathbf{D}_{12} \\ \mathbf{D}_{21} & \mathbf{D}_{22} \end{pmatrix} \begin{pmatrix} \mathbf{q}_{\mathrm{AA}} \\ \mathbf{q}_{\mathrm{BB}} \end{pmatrix} = \begin{pmatrix} \mathbf{F}_{\mathrm{AA}} \\ \mathbf{F}_{\mathrm{BB}} \end{pmatrix}, \tag{29}$$

where the boundary region containing the additional M' cells is labeled B-B, and the matrix in Eq. (29) is obtained by applying Eq. (28) to the extended region (A-A)∪(B-B). If the boundary B-B is *clamped*, so that $\mathbf{q}_{\mathrm{BB}}=0$, then Eq. (29) yields

$$\mathbf{D}_{11}\mathbf{q}_{\mathrm{AA}} = \mathbf{F}_{\mathrm{AA}}. \tag{30}$$

Conversely, if the boundary B-B is *free*, so that $\mathbf{F}_{\mathrm{BB}}=0$, then Eq. (29) yields

$$(\mathbf{D}_{11} - \mathbf{D}_{12}\mathbf{D}_{22}^{-1}\mathbf{D}_{21})\mathbf{q}_{\mathrm{AA}} = \mathbf{F}_{\mathrm{AA}}. \tag{31}$$

Other boundary conditions over the region B-B can also be considered, and the resulting dynamic stiffness matrix over the region A-A can be deduced from Eq. (29). If the region B-B is sufficiently large, then waves emanating from each periodic repetition of the boundary A-A will have very little interaction, meaning that the results yielded by the present approach will closely approximate the dynamic stiffness matrix of a single region A-A embedded in an infinite boundary with specified boundary conditions. The impedance matrix then follows by dividing the dynamic stiffness matrix by $i\omega$.

E. The dynamic stiffness matrix in wavenumber space

In certain applications, there may be a requirement to couple the boundary of a periodic system to the boundary of a homogenous system. The dynamic stiffness matrix of the boundary of a semi-infinite homogeneous system can normally be expressed in analytical form in wavenumber space [see, for example, Langley and Heron (1990), for the case of a plate], and it is therefore convenient to also consider the dynamic stiffness matrix of the periodic system in wavenumber space. To consider the specific example of a periodically stiffened plate, which is to be coupled to an unstiffened homogeneous plate, the coupling lies along a line (the x-axis), which forms the edge of each plate. For a given wavenumber k in the x-direction, the displacements of this line can be expressed in the form

$$\begin{aligned} &[u_x(x), u_y(x), u_z(x), \theta(x)]^T \\ &\quad = [U_x(k), U_y(k), U_z(k), \Theta(k)]^T e^{-ikx} \\ &\quad = \mathbf{U}(k)e^{-ikx}, \end{aligned} \tag{32}$$

where $u_x(x)$, $u_y(x)$, and $u_z(x)$ are the displacements at position x, and $\theta(x)$ is the edgewise rotation (i.e., θ_{yy} in standard notation). The degrees of freedom at the edge of the periodically stiffened plate, $\mathbf{q}_{\mathrm{AA}}$, will include plate nodes that lie on the coupling line, but may also include nodes associated with stiffeners that do not lie on this line. The nodes, which do not lie on the boundary line, are taken to be "free" (i.e., uncoupled), and under these conditions, the dynamic stiffness matrix $\mathbf{D}_{\mathrm{AA}}$ (computed with $\varepsilon_x = kL$, where L is the cell width) can be reduced to a matrix which involves only the coupling line freedoms, following a process analogous to that employed in the derivation of Eq. (31). Denoting the reduced degrees of freedom by $\mathbf{q}_r$ and the reduced dynamic

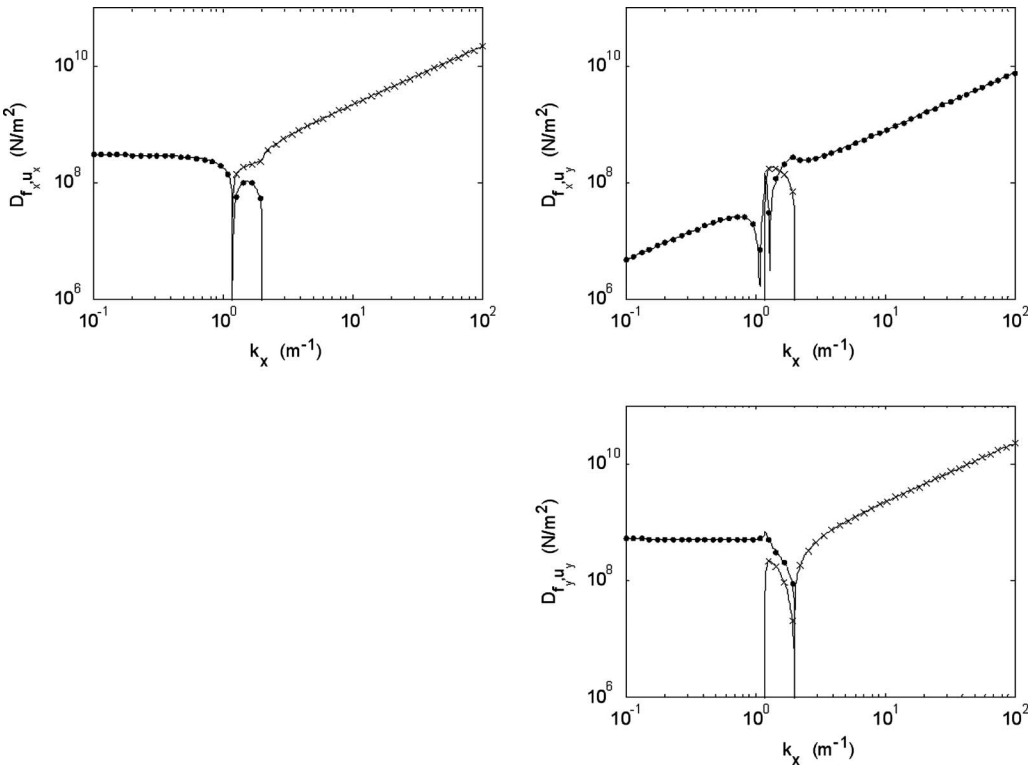

FIG. 2. Absolute value of real part (cross) and imaginary part (dot) of the wave dynamic stiffness for the in-plane degrees of freedom (u_x and u_y) along the edge of a semi-infinite thin plate, as a function of trace wavenumber. Solid lines: reference results from Langley and Heron (1990); dots and crosses: Eq. (34) of the present theory.

stiffness matrix by $\mathbf{D}_r$, the 4×4 dynamic stiffness matrix associated with wavenumber k can be then derived as

$$\mathbf{q}_r = \mathbf{A}(k)\mathbf{U}(k), \tag{33}$$

$$\mathbf{D}(k) = \mathbf{A}(k)^T\mathbf{D}_r\mathbf{A}(k), \tag{34}$$

where the matrix $\mathbf{A}(k)$ is a compatibility matrix relating the nodal degrees of freedom $\mathbf{q}_r$ to the boundary line degrees of freedom represented by Eq. (32). As required, Eq. (34) can be used to couple the periodic system to a homogeneous system whose stiffness properties are described in wavenumber space.

III. NUMERICAL EXAMPLES

A. Benchmark studies for a homogeneous plate

As an initial validation of the foregoing analysis the method is applied to a homogeneous plate, since various benchmark analytical results are available for this case. The considered plate is 2 mm thick and constructed from steel, with Young's modulus $E=1.98\times10^{11}$ N/m^2, Poisson's ratio $\nu=0.3$, and density $\rho=7700$ kg/m^3. The first problem investigated is the computation of the wavenumber dynamic stiffness along the edge of a semi-infinite plate, for which analytical results have been given by Langley and Heron (1990). To this end, a finite element model consisting of a 2×2 grid of CQUAD four-noded plate elements has been taken as the basic periodic unit; in principle, a single element could have been considered, but this would not exercise the internal freedoms $\mathbf{q}_I$ and the edge freedoms (such as $\mathbf{q}_L$) employed in the theory. The aim is to compute the wavenumber dynamic stiffness matrix at 1 kHz for projected wavenumbers k_x between 0.1 and 100 m^{-1} (the wavenumbers for shear, longitudinal, and bending waves at this frequency are 2.01, 1.19, and 45.42 m^{-1}, respectively). The periodic unit is taken to have dimension 5×5 mm^2 (so that $\varepsilon_x=0.005k_x$), and the boundary is modeled as a single cell ($M=1$), with periodic repetitions, as described in Secs. II C and II E. Results for the in-plane dynamic stiffness matrix and out-of-plane (bending) dynamic stiffness matrix are shown in Figs. 2 and 3, respectively. As would be expected, the results are real (representing a reactive stiffness) when k_x exceeds the relevant free wavenumber, in which case, a propagating wave cannot be generated by the boundary motion. The numerical results show very good agreement with the analytical results due to Langley and Heron (1990), although at low values of k_x, there are some slight discrepancies in the real part of the bending coupling term $D_{u_z,\theta_{yy}}$ shown in Fig. 3. A convergence study for this case is shown in Fig. 4, where results are presented for periodic units with successive dimensions of 20 mm, 10 mm, 5 mm, 2.5 mm, 1.25 mm, and 0.0625 mm. Letting Δ represent the finite element side length, the Helmholtz number $k_x\Delta$ at the largest wavenumber $k_x=100$ m^{-1} ranges from 1 for the coarsest model, to 0.0313 for the finest model. Normally, in the finite element analysis of vibration, it is recommended that $k\Delta$ is in the region of 1 or less to yield accurate results, where k is the wavenumber of vibration. In the present case however, at $k_x=100$ m^{-1} the projected wavenumber along the x-axis is accompanied by exponential decay in the y-direction, and for the coarsest model, this produces an exponential decay in vibration level

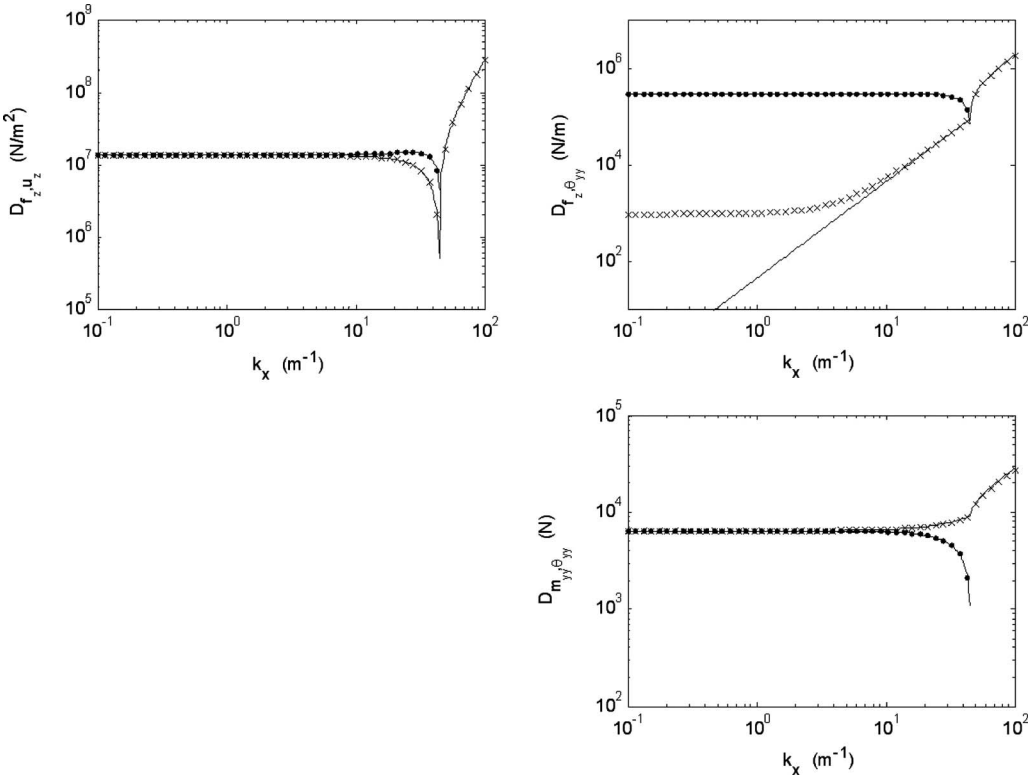

FIG. 3. Absolute value of real (cross) and imaginary (dot) parts of the wave dynamic stiffness for the bending degrees of freedom (u_z and θ_{yy}) along the edge of a semi-infinite thin plate, as a function of trace wavenumber. Solid lines: reference results from Langley and Heron (1990); dots and crosses: Eq. (34) of the present theory.

of 67% across a single element, which is not well modeled by the element shape functions. This accounts for the relatively poor result yielded by the coarsest model at $k_x = 100$ m^{-1} in Fig. 4. At the lowest projected wavenumber, $k_x = 1$ m^{-1}, the predicted real part of the dynamic stiffness exceeds the theoretical prediction even for the finest model, but the value is less than 0.2% of the imaginary part of the stiffness, and is therefore negligible. Waki *et al.* (2009) have recently presented a comprehensive study of the numerics of combining the finite element method with periodic structure theory, and the findings of that work are consistent with the foregoing results and can be used to guide the choice of mesh size in the present application area.

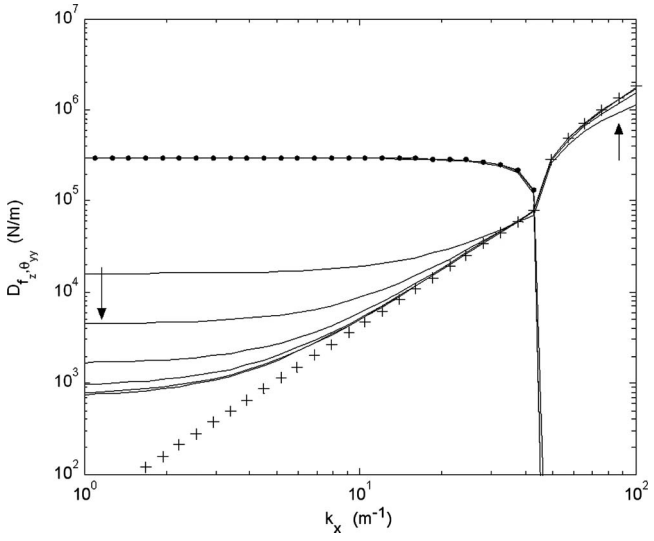

FIG. 4. Absolute value of real (cross) and imaginary (dot) parts of the force-rotation wave dynamic stiffness along the edge of a semi-infinite thin plate, as a function of trace wavenumber. Dots and crosses: reference results from Langley and Heron (1990); solid lines: prediction from the present theory with models of different mesh density (the arrows indicate the evolution of the curves with increasing mesh density).

The second example considered concerns a problem where it is known in advance that the numerical method will not be able to produce the exact analytical solution: the out-of-plane point mobility at the edge of a semi-infinite plate. The analytical solution for this problem contains infinities, and it is of interest to see how the numerical method might perform for this case. The same plate as in the previous example is considered, and the same periodic unit consisting of a 5×5 mm^2 patch of four CQUAD elements is adopted. The boundary is taken to consist of $M = 1$ cells, augmented by a boundary extension having $M' = 500$ cells, as described in Sec. II D. The extended boundary is considered to be free, and by employing Eq. (31), the dynamic stiffness of a single node can be derived under this condition. By inverting the resulting dynamic stiffness matrix for the three out-of-plane degrees of freedom ($u_z \theta_{xx} \theta_{yy}$), the receptance matrix, and hence, the mobility matrix, can be derived. The results obtained are shown as a function of frequency in Fig. 5, where a comparison is made with analytical results due to Su and Moorhouse (2004). Considering the diagonals of the matrix, the present method yields a good approximation for the real part of the mobility, but not for the imaginary part: For $Y_{\theta_{xx},\theta_{xx}}$ and $Y_{\theta_{yy},\theta_{yy}}$, the analytical result for the imaginary part is infinite, while for Y_{u_z,u_z} it is zero. In the first two

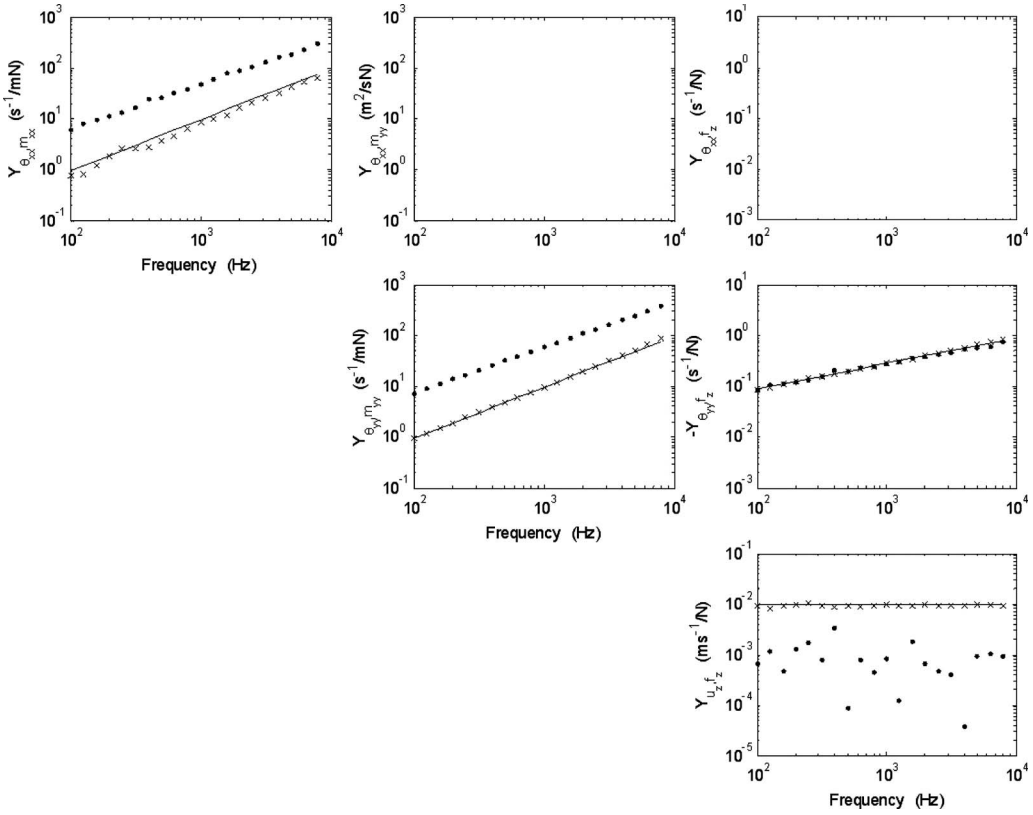

FIG. 5. Real (cross) and imaginary (dot) parts of the point mobility on the free edge of a semi-infinite thin plate, as a function of frequency. Solid lines: reference results from Su and Moorhouse (2004); dots and crosses: Eq. (31) of the present theory. The vertical scale of the graphs for the cross mobilities is set in accordance with the scales of the corresponding graphs for the self mobilities.

cases, the numerical method yields values which are an order of magnitude greater than the real parts, while in the latter case, the computed value is relatively small and numerically erratic. It has been found that as the mesh size is reduced, the predicted real parts are relatively unchanged, while the imaginary part becomes larger in the first two cases and smaller in the second. The present approach therefore captures the essential features of the analytical results, but is of course unable to fully resolve the singularities resulting from the continuum equations. In contrast to the diagonal entries of the mobility, the off-diagonal entries contain no singularities and are well predicted by the numerical method. The two off-diagonal components, which are theoretically zero due to symmetries, were computed to have values between 10^{-10} and 10^{-8}; this is clearly numerical noise and well below the order of magnitude of the nonzero terms in the matrix.

B. Wave transmission between a periodic plate and a homogeneous plate

Tso and Hansen (1998) have considered elastic wave transmission between a periodically stiffened plate and a bare plate, which are coupled at a right angle. The stiffeners on the stiffened plate run parallel to the junction line, with the first being 100 mm from the junction, and subsequent stiffeners having a 100 mm spacing. Each plate is 2 mm thick and made out of steel, and the stiffeners are 6 mm thick steel plates, which are 14 mm in height and symmetrically centered on the plate neutral axis. In the present work, the stiffened plate has been analyzed by using the periodic unit shown as an inset in Fig. 6. The method described in Sec. II E has been used to calculate the dynamic stiffness matrix of the stiffened plate at the junction, and these results have been augmented with the corresponding analytical results for the bare plate. The wave transmission coefficient of the junction for bending waves has been calculated as follows: (i) An

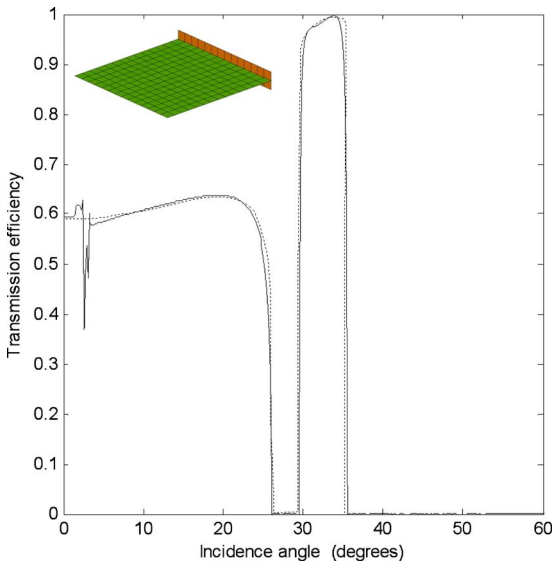

FIG. 6. (Color online) Transmission efficiency as a function of angle of incidence for the flexural waves of a bare plate connected at right angle to a simply stiffened plate. Dotted line: reference results by Tso and Hansen (1998); solid line: Eq. (34) of the present theory, using the finite element mesh of the cell shown in the top-left corner.

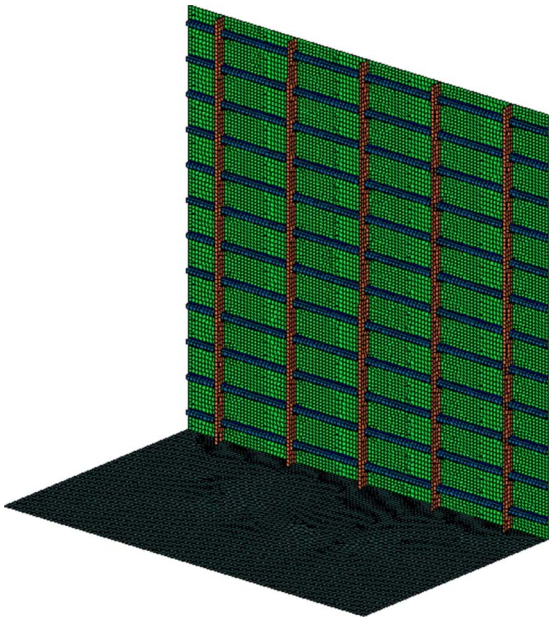

FIG. 7. (Color online) Finite element model of two panels connected at right angle along an edge (the model with 25 000 nodes is valid up to 1000 Hz).

incident bending wave of projected wavenumber k and frequency ω is considered in the bare plate; (ii) the forces arising from this wave when the boundary is held fixed are calculated, i.e., when the wave is reflected from a blocked boundary; (iii) these forces are applied to the junction of the coupled plates (the stiffness matrix of the complete junction is the sum of the stiffness matrices of the two plates) and the junction response is calculated; (iv) given the junction response and the dynamic stiffness matrix of the stiffened plate, the power transmitted to the stiffened plate can be calculated; (v) the power transmission coefficient τ is then the ratio of the transmitted power to the incident power. Results obtained in this way are shown in Fig. 6, where a comparison is made with the results scanned from the paper by Tso and Hansen (1998). The results relate to a frequency of 1 kHz and are presented in terms of the angle of incidence of the bending wave, $\sin\theta = k/k_b$, where k_b is the bending wavenumber. Very good agreement between the two sets of results is obtained, with the transmission coefficient dropping to zero in the stop bands of the stiffened plate (between 26° and 30°, and above 36°), and rising to almost unity in a pass band. There is some disagreement between the two sets of results at low angles of incidence, arising from the fact that the present results include in-plane motions of the plates, while those of Tso and Hansen (1998) do not. Below 1.5°, the incident bending wave can produce a propagating longitudinal wave, and below 2.54°, a propagating shear wave can be generated.

C. Forced response of a plate assembly

As a demonstration of the potential use of the foregoing analysis for predicting the high frequency response of complex systems, a structure, which consists of an orthogonally stiffened panel attached at right angles to a homogeneous panel, is now considered. A detailed finite element model of the structure is shown in Fig. 7: the vertical panel is representative of an aircraft fuselage section (although the panel is kept flat for simplicity), with z-section frames and "omega" stringers connected to a thin skin. The horizontal panel is a flat thin plate. Interest lies in using the foregoing theory to efficiently develop a SEA model of the system, in which the vertical and horizontal panels are each considered to be SEA subsystems. The frequency range of interest is 50 Hz to 1 kHz

The panels are made of aluminum with material properties $E=71\times10^9$ N/m^2, $\rho=2700$ kg/m^3, and $\upsilon=0.33$, and a loss factor of 1% is adopted. Each panel is rectangular, and the dimensions of the ribbed panel are 2.5×2.4 m^2 with a skin thickness of 1 mm; the stringers are 2 mm thick and the frames are 3 mm thick. The thickness of the elements employed in the finite element model is increased in the vicinity of the connections between the ribs and skin, to allow for overlapping structural components. The bare panel is of dimension 2.5×1.5 m^2 with a 1.5 mm skin thickness. The junction between the two panels is 2.5 m long and for the purposes of example only, the skins are connected, i.e., the frames are not connected to the horizontal panel.

A two subsystem SEA model of the structure has been developed by using the foregoing theory in conjunction with earlier work. The SEA equations have the form (Lyon and DeJong, 1995)

$$\begin{pmatrix} \omega\eta_1 n_1 + \omega\eta_{12} n_1 & -\omega\eta_{12} n_1 \\ -\omega\eta_{21} n_2 & \omega\eta_2 n_2 + \omega\eta_{21} n_2 \end{pmatrix} \begin{pmatrix} E_1/n_1 \\ E_2/n_2 \end{pmatrix} = \begin{pmatrix} P_1 \\ P_2 \end{pmatrix}, \tag{35}$$

where E_j is the vibrational energy of subsystem j and η_j is the loss factor. The SEA model requires: (i) the modal density n_j of each subsystem; (ii) the CLF η_{12} between the two subsystems; (iii) the power input P_j to each subsystem from external excitation. The modal density of the bare panel is available from standard texts [for example, Lyon and DeJong (1995)], while the modal density of the stiffened panel can be found by employing two-dimensional periodic structure theory, as described by Cotoni *et al.* (2008). To this end, the periodic cell used to analyze the stiffened panel is shown as an inset in Fig. 8; the finite element model of this cell consists of 346 elements. The coupling loss factor between the two panels can be expressed in terms of the junction dynamic stiffness matrices as follows (Shorter and Langley, 2005b):

$$\omega\eta_{12} n_1 = (2/\pi)\sum_{r,s} H\{D_{rs}^{(1)}\}(\mathbf{D}_{\text{tot}}^{-1} H\{\mathbf{D}^{(2)}\}\mathbf{D}_{\text{tot}}^{-1*T})_{rs}. \tag{36}$$

Here, $\mathbf{D}^{(j)}$ is the dynamic stiffness matrix of subsystem j, $\mathbf{D}_{\text{tot}}$ is the sum of the two subsystem dynamic stiffness matrices, and n_1 is the modal density of subsystem 1. The notation $H(\mathbf{D})$ represents the Hermitian part of the matrix $\mathbf{D}$, i.e., $(\mathbf{D}-\mathbf{D}^{*T})/2$, which reduces to the imaginary part when $\mathbf{D}$ is symmetric. The matrices $\mathbf{D}^{(j)}$ can be expressed in either wavenumber coordinates or physical coordinates; in the present work, physical coordinates have been used, and the method described in Sec. II has been employed for the stiffened plate, with analytical results used for the bare plate. The

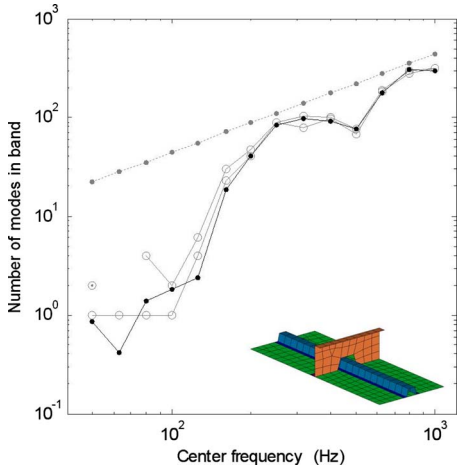

FIG. 8. (Color online) Number of modes of the cross-wise stiffened panel in the third octave frequency bands from 50 to 1000 Hz. Solid gray lines: reference energy flow results for two sets of boundary conditions; solid black line: prediction from the periodic theory as implemented by Cotoni *et al.* (2008) using the finite element mesh of a cell shown in the bottom-right corner; dotted gray line: analytical formula for the same unribbed panel.

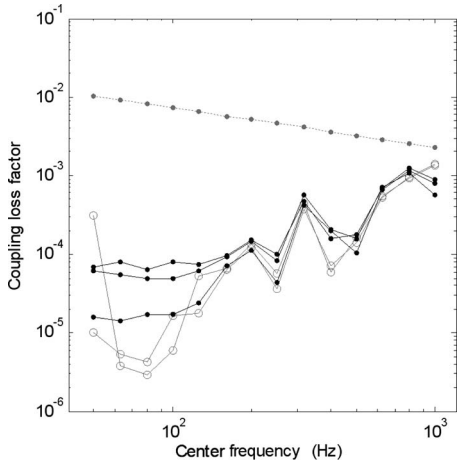

FIG. 9. Coupling loss factor from the flat bare panel to the cross-wise stiffened panel connected at right angle along an edge. Solid gray lines: reference energy flow results for two sets of boundary conditions; solid black lines: predictions from the periodic theory with three sets of boundary condition outside the junction region A-A; free, periodic, and clamped correspond, respectively, to the lower, middle, and higher curves at low frequency; dotted gray line: analytical formula for the same unribbed panel.

excitation applied to the system is taken to be rain-on-the-roof loading of the bare panel, and standard results are available for the power input arising from this loading (Lyon and DeJong, 1995).

Reference results for the forced response of the system have been obtained by using the detailed finite element model shown in Fig. 7, which comprises approximately 25 000 nodes. The model has been solved using modal synthesis, and around 2600 modes were computed below 1350 Hz for use in the analysis. The energy flow post-processing technique described by Mace and Shorter (2000) and implemented in the software package VA One (The ESI Group, 2008) has been used to derive benchmark SEA quantities from the detailed finite element model. With this approach, each panel is defined as a single subsystem, and the post-processing yields: (i) the number of modes in each subsystem in 1/3 octave frequency bands; (ii) the CLF between the subsystems; (iii) the power input from rain-on-the-roof excitation for each subsystem; (iv) the energy response of each subsystem under rain-on-the-roof excitation. These results have been obtained for two different sets of boundary conditions applied to the outer edges of the panels: all nodes were either constrained to zero motion (clamped) or zero forces (free).

The number of modes of the stiffened panel in the third octave frequency bands between 50 and 1000 Hz is shown in Fig. 8. Good agreement is seen between the prediction using periodic structure theory (black solid line) and the energy flow post-processing results obtained under the two different sets of boundary conditions (gray solid lines). It can be noted that there are very few modes in the bands below 100 Hz. The straight line shows the analytical value of modes in band for the same panel without the stringers and frames: it can be seen that these members significantly stiffen the structure and reduce the modal density. This is particularly true at low frequencies; for higher frequencies, the modal density of the stiffened panel approaches that of an unstiffened panel, and periodic structure effects are less important.

The coupling loss factor from the bare panel to the stiffened panel, as computed by the post-processing energy flow model and by the present theory, is shown in Fig. 9. Two results are shown for the benchmark post-processing model, corresponding to the two sets of boundary conditions applied to the structure. Three sets of results are shown for the present theory, which correspond to different ways in which the physical junction can be imposed on the theoretically infinite boundary of a semi-infinite system. In the first case, the physical junction has been taken to be repeated periodically (Sec. II C); in the second case, the boundary has been clamped beyond the physical junction (Sec. II D); in the third case, the boundary has been taken to be free beyond the physical junction (again, Sec. II D). All the predictions are in reasonably good agreement above 100 Hz; below this frequency, the structure has a very low mode count (see Fig. 8), and furthermore, the vibrational wavelength is long compared to dimensions of the junction, meaning that the SEA results are sensitive to the way in which the physical junction is extended along the infinite boundary. As a reference, the coupling loss factor between two bare plates is also shown in the figure—it can be seen that effect of the stiffening on vibration transmission is very significant, and it is correctly predicted by the present theory.

Finally, Fig. 10 shows the energy response of both panels when rain-on-the-roof excitation is applied to the bare panel. For the SEA prediction obtained using the present method, the average value of the three coupling loss factors shown in Fig. 9 was used. In line with the preceding results, the SEA predictions agree well with the energy flow model above 100 Hz. In particular, the SEA model is able to capture the oscillations of the energy response of the ribbed plate above 200 Hz, which arise mainly due to the coupling properties, which are predicted using the present theory. It is emphasized that this SEA model has been constructed using the unit shown as an inset in Fig. 8, and all the required parameters have been extracted using periodic structure theory. It

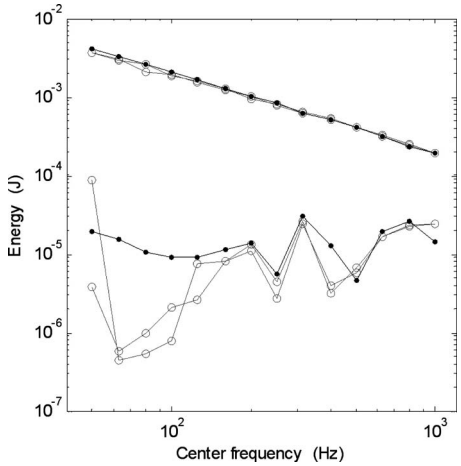

FIG. 10. Energy response of the connected flat bare panel and the crosswise stiffened panel to rain-on-the-roof excitation of the bare panel. The top curves correspond to the driven bare panel, and the bottom curves to the transmitted stiffened panel. Solid gray lines: reference energy flow results for two sets of boundary conditions; solid black lines: SEA predictions using the modal density and coupling loss factor from the periodic theory.

should be noted that SEA is a statistical theory, and the results obtained represent an average taken over an ensemble of randomly perturbed structures. For this reason the theory will not agree perfectly with response results for any one realization of the structure, unless the ensemble variance is zero, and this is clearly not the case for the present structure. A method of predicting the response variance within the context of SEA has been presented by Langley and Cotoni (2004).

IV. CONCLUSIONS

A method has been presented for computing the direct field impedance (or dynamic stiffness matrix) of the boundary of a two-dimensional periodic structure, which is based on a model of a single periodic cell. It has been shown that the method can be used to develop structural coupling loss factors for use in SEA and related methods, and potential applications include the medium and high frequency vibration analysis of aerospace and marine structures. The method enables "periodic" subsystems to be considered so that, for example, an aircraft fuselage could be considered to be an assembly of relatively few subsystems. Coupling between such subsystems and an acoustic space has been considered by Cotoni *et al.* (2008), while structural coupling between the subsystems is covered by the present analysis. The application of the method to a system involving an orthogonally stiffed panel has shown good agreement with benchmark finite element results, and the further application of the method to more complex systems is warranted.

Bosmans, I., and Nightingale, T. R. T. (**2001**). "Modeling vibrational energy transmission at bolted junctions between a plate and a stiffening rib," J. Acoust. Soc. Am. **109**, 999–1010.
Bosmans, I., and Vermeir, G. (**1997**). "Diffuse transmission of structure-borne sound at a periodic junction of semi-infinite plates," J. Acoust. Soc. Am. **101**, 3443–3456.
Brillouin, L. (**1953**). *Wave Propagation in Periodic Structures*, 2nd ed. (Dover, New York).
Choi, S. (**2004**). "The SEA approach to vibration localization in a nearly periodic structure," Mech. Based Des. Struct. Mach. **32**, 235–252.
Cotoni, V., Langley, R. S., and Shorter, P. J. (**2008**). "A statistical energy analysis subsystem formulation using finite element and periodic structure theory," J. Sound Vib. **318**, 1077–1108.
Cotoni, V., Shorter, P. J., and Langley, R. S. (**2007**). "Numerical and experimental validation of a finite element—Statistical energy analysis method," J. Acoust. Soc. Am. **122**, 259–270.
Duhamel, D. (**2008**). "Computation of absorbing boundary conditions from wave finite elements for general media," in Proceedings of the Eurodyn 2008, Seventh European Conference on Structural Dynamics, Southampton, July 7–9.
Keane, A. J., and Price, W. G. (**1989**). "Statistical energy analysis of periodic structures," Proc. R. Soc. London **423**, 331–360.
Langley, R. S., and Cotoni, V. (**2004**). "Response variance prediction in the statistical energy analysis of built-up systems," J. Acoust. Soc. Am. **115**, 706–718.
Langley, R. S., and Heron, K. (**1990**). "Elastic wave transmission through plate/beam junctions," J. Sound Vib. **143**, 241–253.
Langley, R. S., Smith, J. D., and Fahy, F. J. (**1997**). "Statistical energy analysis of periodically stiffened damped plate structures," J. Sound Vib. **208**, 407–426.
Lyon, R. H., and DeJong, R. G. (**1995**). *Theory and Application of Statistical Energy Analysis* (Butterworth-Heinemann, Boston).
Mace, B. R., and Shorter, P. J. (**2000**). "Energy flow models from finite element analysis," J. Sound Vib. **233**, 369–389.
Manconi, E., and Mace, B. R. (**2009**). "Wave characterization of cylindrical and curved panels using a finite element method," J. Acoust. Soc. Am. **125**, 154–163.
Orris, R. M., and Petyt, M. (**1974**). "A finite element study of harmonic wave propagation in periodic structures," J. Sound Vib. **33**, 223–236.
Shorter, P. J., and Langley, R. S. (**2005a**). "On the reciprocity relationship between direct field radiation and diffuse reverberant loading," J. Acoust. Soc. Am. **117**, 85–95.
Shorter, P. J., and Langley, R. S. (**2005b**). "Vibro-acoustic analysis of complex systems," J. Sound Vib. **288**, 669–699.
Su, J. X., and Moorhouse, A. T. (**2004**). "A closed form solution for the mobility of an edge-excited, semi-infinite plate," J. Acoust. Soc. Am. **115**, 2075–2082.
Sum, K. S., Khoo, P., Peng, S. Z., and Pan, J. (**2003**). "Statistical energy analysis of the distribution of flexural energy in asymmetric-periodic plates," in Proceedings of the Tenth International Congress on Sound and Vibration 2003, Stockholm, Sweden.
Tso, Y. K., and Hansen, C. H. (**1998**). "The transmission of vibration through a coupled periodic structure," J. Sound Vib. **215**, 63–79.
VA One 2008 User's Guide (ESI Group, Paris, France, **2008**).
Waki, Y., Mace, B. R., and Brennan, M. J. (**2009**). "Numerical issues concerning the wave and finite element method for free and forced vibrations of waveguides," J. Sound Vib. **327**, 92–108.

A detailed analysis about penumbra caustics

Régis Marchiano[a)]
Université Pierre et Marie Curie-Paris 6, and CNRS, UMR 7179, Institut Jean le Rond d'Alembert, 4 Place Jussieu, 75252 Paris Cedex 05, France

(Received 5 March 2009; revised 1 October 2009; accepted 31 December 2009)

A penumbra caustic is an interrupted fold caustic. It looks like a fold caustic but with a finite size. This kind of caustic results from the focusing of a semi-infinite concave wavefront. The pressure around the extremity of the penumbra caustic can be expressed analytically in terms of incomplete Airy function for linear monochromatic waves. Using asymptotic expansions in the vicinity of the extremity, that classical result is rederived. It can be matched with the classical Fresnel diffraction before the extremity and with the classical diffraction catastrophe theory after the extremity. Nevertheless the linear modeling is not valid for incoming shock waves. A theoretical description of the phenomenon of focusing of shock waves at a penumbra caustic is given. It relies on the Zabolotskaya–Khokhlov equation. Numerical simulations are used to compute the behavior of this phenomenon. In particular, the numerical simulations show the presence of a triple point inside the pressure field. Finally, the theory and the numerical simulations are applied to explain the apparent paradox of non-causality around fold caustic.
 [DOI: 10.1121/1.3298432]

PACS number(s): 43.25.Cb, 43.25.Jh [ADP] Pages: 2129–2140

I. INTRODUCTION

A caustic is a surface (in three dimensional medium) or a line [in two-dimensional medium (2D)] of amplification of a wavefield corresponding to the zone where rays are tangent in the framework of the geometrical approximation. There exist various kinds of caustics depending on their shapes. The theory of catastrophes[1,2] classifies caustics. The simplest ones are the fold and cusp caustics, which can be described in a two-dimensional space. Caustics are generic features of any wavefield (optics, acoustics, etc.) and correspond to stable focuses.[3] They are singularities of amplitude in the framework of a geometrical ray approximation. To avoid this singularity, one has to introduce the diffraction around the caustics. This is the basis of the theory of catastrophes applied to a wavefield also known as diffraction catastrophe theory. This theory predicts the field around the caustics thanks to special integral functions.[4] For instance, the field in the vicinity of the fold caustics can be expressed in terms of Airy function,[5] and the field in the vicinity of the cusp caustic can be expressed in terms of Pearcey function.[4,6]

Nevertheless, the theory of catastrophes is restricted to ideal caustics with infinite size. In the real world, caustics have a finite size. A penumbra caustic is an interrupted fold caustic (see Fig. 1 for a geometrical illustration of the differences between a fold caustic, a penumbra caustic, and a cusp caustic). It can be engendered either by a concave wavefront with a finite size or by an infinite wavefront diffracted by a screen. Consequently, one can say that all fold caustics are, in fact, penumbra caustics as they have to be of finite size and so possess an extremity. Nevertheless, it is generally assumed that the size of fold caustics is large enough, and the effects of their finite size are neglected.

Even if such a caustic does not enter the classification of the theory of catastrophes, it can be viewed as a degenerated fold caustic. In particular, it is possible to express the field near the penumbra caustic in terms of the incomplete Airy function, which is related to the Airy function. These results have been derived for linear electromagnetic waves,[4,7–9] but are also valid for linear monochromatic acoustic waves. For transient linear or nonlinear waves, no models have been derived to our knowledge. Although nonlinear regime could provide special behavior.

In several cases the classical diffraction laws have to be modified in nonlinear acoustics. Thus, the simple case of diffraction of a plane wave by a semi-infinite rigid screen is different in linear acoustics from nonlinear acoustics. In linear regime, after the screen, the illuminated zone and the shadow zone are matched by the Fresnel function.[10,11] The thickness of the region of matching, called the penumbra zone, grows proportionally to the square root of the propagation distance. In the nonlinear regime, the penumbra zone grows differently depending on the temporal shape of the incoming signal: a step shock or an "N" wave does not diffract with the same laws as a saw-tooth shock wave.[12] Focusing of shock waves on caustics is another example where diffraction laws have to be modified. If the incoming waves are shock waves, the field around the caustic cannot be described in terms of the special integral function any longer. Indeed, this formulation predicts infinite pressure on caustics. As proposed by Guiraud[13] for the fold caustic, another physical limiting mechanism, namely, the local nonlinear effects, is required to describe the acoustical field. This result

[a)]Author to whom correspondence should be addressed. Electronic mail: regis.marchiano@upmc.fr

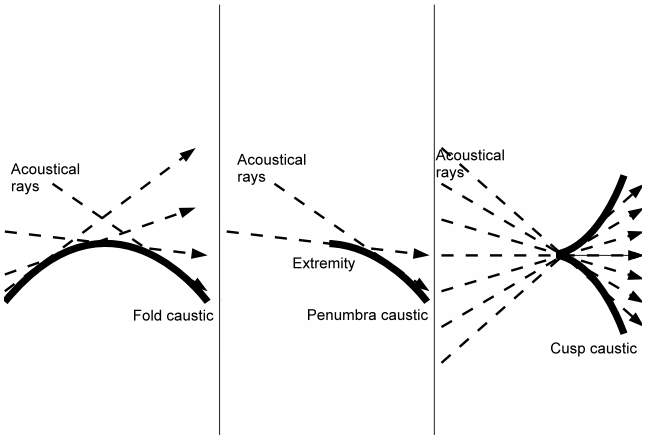

FIG. 1. Three different caustics: the fold, the penumbra, and the cusp caustic.

has been numerically[14,15] and experimentally checked[16] and extended to the cusp caustic[17–20] for which it has also been validated.[21]

The focusing of shock waves on a penumbra caustic exhibits the main characteristic for these two situations (nonlinear Fresnel diffraction and nonlinear diffraction around caustics). Indeed, before the extremity of the caustic, the main phenomenon is the diffraction of an unfolded wavefront as for the nonlinear Fresnel diffraction. After the extremity of the caustic, the main phenomenon is the focusing of shock waves on a caustic. From a theoretical point of view this problem is very appealing as it seems to be at the boundary between various kinds of diffraction problems.

The study of the focusing of waves (linear or not) on a penumbra caustic is interesting to know the behavior in the neighborhood of the extremity of the caustic. Another interest is to study the wavefield near classical fold caustics with an alternative point of view. That complementary approach can be used to revisit some open questions as the apparent non-causality around fold caustics.[22]

The first part presents an alternative derivation of the modeling for monochromatic waves in terms of the incomplete Airy function. Special attention is paid to the matching of the incomplete Airy function with the Fresnel integral for the unfolded wavefront and to the Airy integral around the caustic. That matching is an original result consistent with the different regimes of diffraction. The characteristic lengths of diffraction are deduced from this first part. The second part is devoted to the detailed derivation of the modeling for transient linear and nonlinear waves. Again, special attention is paid to the study of the theoretical consistency of this new model with the description of the nonlinear Fresnel diffraction and the focusing of shock waves on a fold caustic. To our knowledge, that theoretical model has never been derived previously for penumbra caustics. The third part deals with the numerical investigation of this phenomenon. Examples of pressure fields along the penumbra caustic for incoming shock waves are presented. Finally, the model is used to give numerical evidence to a new explanation of the paradox of causality around the fold caustics.

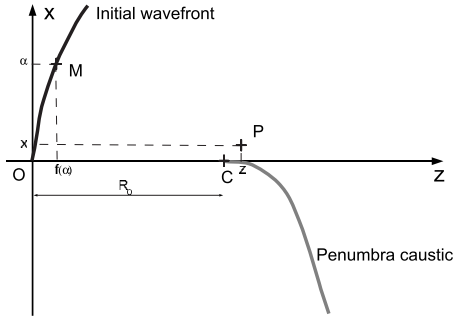

FIG. 2. Geometry of a penumbra caustic.

II. LINEAR THEORY: FOCUSING OF SMOOTH WAVES ON PENUMBRA CAUSTICS

In this section, the modeling of the focusing of smooth monochromatic waves on a penumbra caustic is derived. First of all, a study of the geometry of the caustic in the neighborhood of its extremity is presented. That is an alternative derivation of previous works.[4,7] Knowing the local equation of the caustic, it is possible to obtain an asymptotic solution valid around the extremity of the caustic by using classical diffraction theory. Along the composite shadow boundary, this solution is then compared to Fresnel diffraction and the Airy function. This study about the matching between the various regimes of diffraction is original and permits to have a unified description between the Fresnel diffraction and the diffraction around caustics.

A. Geometry of the penumbra caustic

Let us consider a wave traveling in a two-dimensional, homogeneous, and inviscid medium. That wave comes from an initial semi-infinite wavefront, as depicted in Fig. 2. The coordinate system is denoted as (Oxz); it is orthonormal. The origin O is attached to the extremity of the initial wavefront. The x-axis is tangent to the initial wavefront at point O (it is oriented toward the wavefront), and the z-axis is normal to the initial wavefront at point O. It is oriented toward the concavity of the wavefront. In that coordinate system, the equation of the semi-infinite wavefront is written as

$$z_w = f(x). \tag{1}$$

The choice of that coordinate system implies several properties for the function describing the wavefront. First of all, the choice of the origin implies that $f(0)=0$. Then, the position of the two axes (x-axis tangent and z-axis normal to the wavefront) implies that $f'(0)=0$. The radius of curvature of the wavefront is denoted as $R(x)$. At the origin, the sense of the z-axis toward the concavity implies that it has a positive value: $R_0=R(x=0)=1/f''(0)>0$. Consequently, the coordinates of the extremity of the caustic, labeled as C, are $(x=0,\ z=R_0)$. Finally, we assume that the third derivative with respect to x is nonzero: $f'''(0)\neq 0$.

The distance r between a point of the wavefront M, whose coordinates are $(\alpha, f(\alpha))$, and the current listening point P, whose coordinates are (x,z), is

$$r = \sqrt{(x-\alpha)^2 + (z-f(\alpha))^2}. \tag{2}$$

With the medium of propagation being assumed homogeneous and the traveling waves having a small amplitude, the traveling time between the point of the wavefront M and the current listening point P is r/c_0, with c_0 the linear speed of sound. That function is also referred to the phase function. That result is due to Fermat's principle, which states that the travel time between points M and P has to be extremal. Consequently, acoustical rays are the lines satisfying $\partial r/\partial\alpha = 0$. A caustic is the locus of points, where the first and second derivatives of r are simultaneously zero:

$$\frac{\partial r}{\partial \alpha} = 0,$$

$$\frac{\partial^2 r}{\partial \alpha^2} = 0. \tag{3}$$

These equations mean that a caustic is formed of rays (the first derivative is zero), which are intersecting each other (second derivative is also zero). As outlined, the first condition is a consequence Fermat's principle and leads to the ray equation

$$x + f'(\alpha)z - \alpha - f(\alpha)f'(\alpha) = 0. \tag{4}$$

Note that equation identifies each acoustical ray passing through the point (x,z) by parameter α. As the medium is homogeneous, the acoustical rays are straight lines.

The second condition is due to the fact that the adjacent rays intersect at the caustic [injecting Eq. (2) in Eq. (3)]:

$$f''(\alpha)z - 1 - f(\alpha)f''(\alpha) - f'^2(\alpha) = 0. \tag{5}$$

We seek to describe the geometry of the caustic in the vicinity of its extremity located at $(x=0,\ z=R_0)$. Such a caustic is created by a set of rays emanating from a region close to the origin. With the rays being indexed by parameter α, only the acoustical rays corresponding to a small parameter α are considered. Let us introduce parameter $\delta = z - R_0$, which measures the longitudinal distance to the extremity of the caustic. Starting from Eqs. (4) and (5) and using expansions in power series of α for function f and its first, second, and third derivatives, the parametric equations of the caustic's geometry are obtained as

$$\delta = -\alpha R_0^2 f'''(0) + O(\alpha^2) \quad \text{with} \quad \alpha \geq 0,$$

$$x = \frac{\alpha^2}{2} R_0 f'''(0) + O(\alpha^3) \quad \text{with} \quad \alpha \geq 0. \tag{6}$$

Those two equations show that the local shape of the caustic, in the neighborhood of its extremity, is a semiparabola whose radius of curvature is $a/2$:

$$x = -\frac{\delta^2}{a} \quad \text{with} \quad \delta > 0. \tag{7}$$

The parameter $a = -2R_0^3 f'''(0)$ takes into account the geometry of the initial wavefront.

B. Characteristic scales of diffraction

According to Huygens' principle, the pressure field can be decomposed into a sum of cylindrical diverging waves emanating from the wavefront. Far away from the initial wavefront, the Hankel function describing the acoustical field can be approximated by its asymptotic expansion

$$p(x,z,t) = e^{-i\omega_0 t} \int_0^{+\infty} r^{-1/2} A(\alpha) e^{ik_0 r} d\alpha, \tag{8}$$

with $k_0 = \omega_0/c_0$ the characteristic wave number of the wave, ω_0 the characteristic angular frequency of the wave, and $A(\alpha)$ a regular function, slowly varying, describing the amplitude of the field.

To express the field around the extremity of the caustic, only the field emanating from the initial wavefront close to the origin has to be taken into account. An asymptotic expression of the equation describing the field around the extremity of the caustic can be derived by substituting the Taylor expansion of Eq. (2) into Eq. (8). The Taylor expansion is truncated at the fourth order in the phase term and at the third order in the amplitude term. According to the scales found in Sec. II A, the expansion in a power series of α at the fourth order of function r is

$$r = z - x\left(\frac{\alpha}{R_0}\right) - \frac{\delta}{2}\left(\frac{\alpha}{R_0}\right)^2 + \frac{a}{12}\left(\frac{\alpha}{R_0}\right)^3 + O(\alpha^4). \tag{9}$$

So, around the extremity of the caustic, the integral describing the acoustical field [Eq. (8)] can be approximated by

$$p(x,z,t) = A_0 e^{-i\omega_0(t-z/c_0)} \int_0^{+\infty} \exp\left[i\left(-xk_0\left(\frac{\alpha}{R_0}\right) - \frac{\delta k_0}{2}\left(\frac{\alpha}{R_0}\right)^2 + \frac{ak_0}{12}\left(\frac{\alpha}{R_0}\right)^3 \right)\right] d\alpha, \tag{10}$$

with $A_0 = A(0)/R_0^{1/2}$.

That formulation leads to introduce the following dimensionless variables:

- the dimensionless delayed time:

$$\bar{t} = \omega_0(t - z/c_0), \tag{11}$$

- the dimensionless variable indexing the acoustical ray:

$$\bar{\alpha} = \left(\frac{12}{k_0 a}\right)^{-1/3} \frac{\alpha}{R_0}, \tag{12}$$

- the dimensionless transverse variable:

$$\bar{x} = \left(\frac{12k_0^2}{a}\right)^{1/3} x, \tag{13}$$

- the dimensionless longitudinal variable:

$$\bar{z} = \frac{1}{2}\left(\frac{12^2 k_0}{a^2}\right)^{1/3} \delta. \tag{14}$$

Introducing the dimensionless parameter of diffraction η:

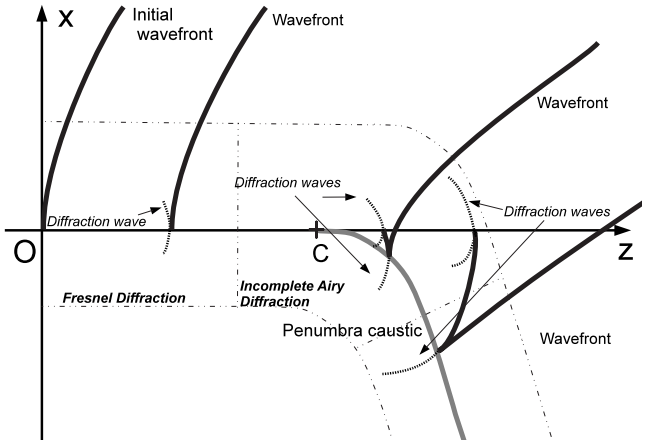

FIG. 3. Matching between the various areas of diffraction.

$$\eta = \left(\frac{12}{k_0 a}\right)^{1/3} \ll 1, \tag{15}$$

it is obvious that the diffraction mechanism acts on layers with different widths in the longitudinal and transverse directions. Indeed, the transverse dimensionless variable is varying with the power of -2 of η:

$$\bar{x} = \frac{12x}{a\eta^2}, \tag{16}$$

while the longitudinal dimensionless variable is varying with the power of -1:

$$\bar{z} = \frac{6\delta}{a\eta}. \tag{17}$$

Combining Eqs. (16) and (17), we obtain the local dimensionless equation of the caustic around its extremity:

$$\bar{x} = -\frac{\bar{z}^2}{3}. \tag{18}$$

Expressed with the dimensionless variables, the pressure field around the extremity of the caustic is

$$p(\bar{x},\bar{z},\bar{t}) = A_0 e^{i\bar{t}} \int_0^{+\infty} \exp[i(-\bar{x}\bar{\alpha} - \bar{z}\bar{\alpha}^2 + \bar{\alpha}^3)] d\bar{\alpha}. \tag{19}$$

The formulation of this expression differs from those obtained previously in the literature;[4,7–9] nevertheless, as it is demonstrated in Sec. II C, the former results can be rederived from Eq. (19). Moreover, it is possible to derive also the classical Fresnel diffraction before the wavefront reaches the caustic. Far away from the extremity but still around the caustic, the expression derived below is consistent with the classical theory for the fold caustic.

C. From the Fresnel diffraction to the theory of catastrophes

1. Matching with the classical Fresnel diffraction

Far away from the caustic, and in the vicinity of the extremity of the wavefront, the wavefront can be considered locally as a plane wave (Fig. 3). Consequently, it has to diffract into the shadow region, as predicted by the Fresnel diffraction law.[11] Indeed, far enough from the caustic in the side of the negative $\bar{z}$ and near the axis of propagation ($\bar{z} \to -\infty$), the term of order $\bar{\alpha}^3$ in Eq. (19) becomes negligible in comparison with the term of order $\bar{z}\bar{\alpha}^2$ and Eq. (19) becomes

$$p(\bar{x},\bar{z},\bar{t}) = \tilde{A}_0 e^{i\bar{t}} \int_0^{+\infty} \exp[i(-\bar{x}\bar{\alpha} - \bar{z}\bar{\alpha}^2)] d\bar{\alpha}. \tag{20}$$

It is possible to introduce a new variable

$$u = \sqrt{-\bar{z}}\left(\bar{\alpha} + \frac{\bar{x}}{2\bar{z}}\right). \tag{21}$$

Note that this formulation is correct since the quantity $\bar{z}$ is strictly negative. Introducing that new variable into Eq. (20), it becomes

$$p(\bar{x},\bar{z},\bar{t}) = \frac{\tilde{A}_0}{\sqrt{-\bar{z}}} \exp\left[-i\left(\frac{\bar{x}^2}{4\bar{z}} - \bar{t}\right)\right] \int_{\bar{x}/2\sqrt{-\bar{z}}}^{+\infty} \exp[iu^2] du. \tag{22}$$

That last equation can be recast in terms of Fresnel integral

$$p(\bar{x},\bar{z},\bar{t}) = \frac{\tilde{A}_0}{\sqrt{-\bar{z}}} \exp\left[-i\left(\frac{\bar{x}^2}{4\bar{z}} - \bar{t}\right)\right] \left[F\left(\frac{-\bar{x}}{2\sqrt{-\bar{z}}}\right) + \left(\frac{1+i}{2}\right)\right], \tag{23}$$

with F the Fresnel integral[23]

$$F(\nu) = \int_0^{\nu} \exp[iu^2] du. \tag{24}$$

So, the classical diffraction law is recovered in the area where the wavefront is not yet folded ($\bar{z} < 0$) (Fig. 3). The field in the sounded zone ($\bar{x} > 0$) is matched to the field in the shadow zone with a continuous transition thanks to the Fresnel function. The width of the diffraction layer changes as $\bar{x}/\sqrt{-\bar{z}}$. Moreover, the amplitude of the field increases as $1/\sqrt{-\bar{z}}$. That effect is due to the focusing induced by the presence of the penumbra caustic. Because of that amplitude term, it is obvious that this description fails in the vicinity of the caustic extremity located in $\bar{z}=0$.

2. The incomplete Airy function

In the neighborhood of the extremity of the caustic (Fig. 3), the pressure field has to be described by Eq. (19). Nevertheless, this equation can be recast in a more usual form, namely, the incomplete Airy function. Therefore, it is necessary to use a new scaling in the equation by introducing the following parameter:

$$\tilde{\alpha} = 3^{1/3}\bar{\alpha} - \frac{\bar{z}}{3^{2/3}}. \tag{25}$$

The pressure field becomes

$$p(\bar{x},\bar{z},\bar{t}) = \tilde{A}_0 \exp\left[-i\left(\bar{t}+\frac{\bar{z}}{3}\left(\bar{x}+\frac{2\bar{z}^2}{9}\right)\right)\right] I\left(\left(\frac{-1}{3^{1/3}}\right)\left[\bar{x}+\frac{\bar{z}^2}{3}\right], \frac{-\bar{z}}{3^{2/3}}\right), \tag{26}$$

with the new amplitude factor $\tilde{A}_0 = A_0/3^{1/3}$ and where $I(\zeta,\eta)$ is the incomplete Airy function:[23]

$$I(\zeta,\eta) = \int_{\eta}^{+\infty} \exp[i(\nu\zeta + \nu^3/3)]d\nu. \tag{27}$$

That formula is in agreement with previous works.[4,7–9] It describes the pressure field at the extremity of the penumbra caustic without any singularities. Note that the argument of the incomplete Airy function is given by the equation of the caustic.

3. Matching with the catastrophe theory

Looking at the pressure field far from point $C(\bar{z}\to+\infty)$, but near the caustic $(\bar{x}+\bar{z}^2=O(1))$ (Fig. 3), Eq. (19) can be approximated by

$$p(\bar{x},\bar{z},\bar{t}) = \tilde{A}_0 \exp\left[-i\left(\bar{t}+\frac{\bar{z}}{3}\left(\bar{x}+\frac{2\bar{z}^2}{9}\right)\right)\right] \times \mathrm{Ai}\left(\frac{-1}{3^{1/3}}\left(\bar{x}+\frac{\bar{z}^2}{3}\right)\right), \tag{28}$$

with Ai the Airy function:[23]

$$\mathrm{Ai}(\zeta) = \int_{-\infty}^{+\infty} \exp\left[i\left(\frac{\nu^3}{3}+\nu\zeta\right)\right]d\nu. \tag{29}$$

The Airy function is the canonical function in the classification of the theory of catastrophes describing the field in the neighborhood of a fold caustic. This result is physically consistent since far from the extremity of the caustic, the field is not influenced by the finite size of the wavefront and has the same behavior as prescribed by the theory of catastrophes for an infinite fold caustic. This situation is depicted in Fig. 3. The extremity of the wavefront does not interact with the fold made by the wavefront. Consequently, it is possible to describe the acoustical pressure along the composite shadow boundary by those three classical diffraction integrals (Fig. 3), starting from the classical Fresnel diffraction to the theory of catastrophes. Nevertheless, these theories are linear and break if the incoming signal carries shocks as it has already been demonstrated for fold[13] and cusp caustics.[17] In that last case, nonlinear effects cannot be neglected and play an important role by acting as a physical limiting mechanism.

III. NONLINEAR THEORY: FOCUSING OF SHOCK WAVES AT A PENUMBRA CAUSTIC

In this section, the problem of focusing of shock waves at a penumbra caustic is studied. Using the results issued from the linear study, a nonlinear equation governing the pressure is derived. Then, the associated boundary conditions are derived thanks to a matching with the geometrical acoustics.

A. The KZ equation

Propagation of acoustical finite amplitude waves through a homogeneous medium is described by the Kuznetsov equation[24]

$$\frac{\partial^2\phi}{\partial t^2} - c_0^2\left(\frac{\partial^2\phi}{\partial x^2}+\frac{\partial^2\phi}{\partial z^2}\right) = \frac{\partial}{\partial t}\left[\frac{1}{c_0^2}\frac{B}{2A}\left(\frac{\partial\phi}{\partial t}\right)^2 + (\nabla\phi)^2\right], \tag{30}$$

where ϕ is the acoustic velocity potential, and $B/2A$ is the nonlinear parameter of the medium. This equation is exact up to the second order and takes into account diffraction and nonlinear effects. Considering the geometry of the problem, it is possible to reduce the Kuznetsov equation to Khokhlov–Zabolotskaya (KZ) equation.[25] Let us introduce the dimensionless acoustical potential $\bar{\phi}$ defined from the physical potential by the following relation:

$$\bar{\phi}(\bar{x},\bar{z},\bar{t}) = \frac{\omega_0}{U_0 c_0}\phi(x,z,t), \tag{31}$$

where U_0 is the characteristic amplitude of the velocity of the fluid particles. Introducing the dimensionless potential and the dimensionless variables defined above [Eqs. (11), (13), and (14)], the dimensionless formulation of the Kuznetsov equation is

$$\frac{\partial^2\bar{\phi}}{\partial\bar{z}\,\partial\bar{t}} - \frac{\partial^2\bar{\phi}}{\partial\bar{x}^2} - \mu\frac{\partial}{\partial\bar{t}}\left(\frac{\partial\bar{\phi}}{\partial\bar{t}}\right)^2 = \frac{\eta^2}{4}\frac{\partial^2\bar{\phi}}{\partial\bar{z}^2} + \epsilon\frac{\partial}{\partial\bar{t}}\left[\left(\frac{\partial\bar{\phi}}{\partial\bar{x}}\right)^2 + \frac{\eta^2}{4}\left(\frac{\partial\bar{\phi}}{\partial\bar{z}}\right)^2 - \frac{a\eta^3}{12}\frac{\partial\bar{\phi}}{\partial\bar{z}}\frac{\partial\bar{\phi}}{\partial\bar{t}}\right], \tag{32}$$

where the coefficient $\mu=\epsilon/\eta^2(1+(B/2A))$ compares the nonlinear and diffraction effects, and $\epsilon=U_0/c_0$ is the acoustical Mach number.

The terms on the right hand side of that equation can be neglected if the Mach number and the diffraction parameter are small in comparison to unity. Under these assumptions, $\epsilon\ll 1$ and $\eta\ll 1$, Eq. (32) is reduced to the KZ equation for potential

$$\frac{\partial^2\bar{\phi}}{\partial\bar{z}\,\partial\bar{t}} - \frac{\partial^2\bar{\phi}}{\partial\bar{x}^2} - \mu\frac{\partial}{\partial\bar{t}}\left(\frac{\partial\bar{\phi}}{\partial\bar{t}}\right)^2 = 0. \tag{33}$$

The classical formulation of the KZ equation[25] is obtained by introducing the dimensionless pressure $(\bar{p}=\partial\bar{\phi}/\partial\bar{t})$:

$$\frac{\partial^2\bar{p}}{\partial\bar{z}\,\partial\bar{t}} - \frac{\partial^2\bar{p}}{\partial\bar{x}^2} - \mu\frac{\partial^2\bar{p}^2}{\partial\bar{t}^2} = 0. \tag{34}$$

To close the mathematical formulation of the problem, boundary conditions have to be derived; this is the purpose of Sec. III B.

Far from the extremity of the caustic, the field can be described by the geometrical acoustics but that approximation fails near the extremity where the field has to be described by the KZ equation. Nevertheless, far enough from

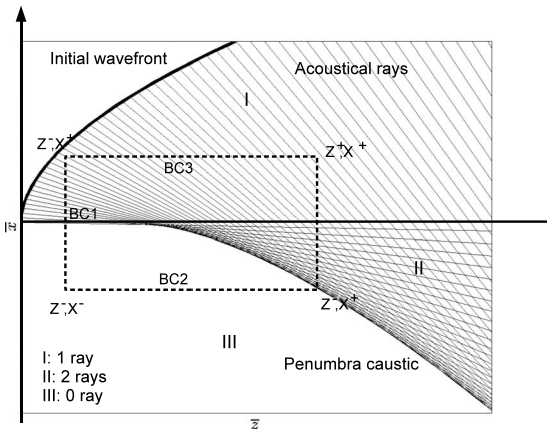

FIG. 4. Penumbra caustic and acoustical rays.

the extremity of the caustic, it is possible to match the two descriptions. The inner solution given by the KZ equation is matched asymptotically to the solution coming from the geometrical acoustics by applying the stationary phase method. By using Eqs. (4) and (9) under their dimensionless form [see Eqs. (12)–(14)], it yields the dimensionless equation for the acoustical rays:

$$-3\bar{\alpha}^2+2\bar{\alpha}\bar{z}+\bar{x}=0. \tag{35}$$

An acoustical ray corresponds to a positive real root of that equation; for a given position $(\bar{x},\bar{z})$, the number of real positive roots indicates the number of rays passing through that position (see Fig. 4). The study of Eq. (35) shows that there exist three different zones in the domain $(\bar{x},\bar{z})$.

- In zone I $(\bar{x}>0,\forall\bar{z})$, there is only one positive real root:

$$\bar{\alpha}_+=\frac{\bar{z}+\sqrt{\bar{z}^2+3\bar{x}}}{3} \quad \text{if } \bar{x}>0, \quad \forall\,\bar{z}. \tag{36}$$

Only one ray passes through each point in this area.
- In zone II $(\bar{x}\in[0,-\bar{z}^2/3],\bar{z}>0)$, there are two real positive roots:

$$\bar{\alpha}_\pm=\frac{\bar{z}+\sqrt{\bar{z}^2+3\bar{x}}}{3} \quad \text{if } \bar{x}\in\left[0,-\frac{\bar{z}^2}{3}\right], \quad \bar{z}>0. \tag{37}$$

There are two different rays which pass through each point of zone II. They correspond to one ray which has already tangented the caustic, and another one which has not tangented it yet. Consequently, the boundary conditions cannot involve this zone.
- In zone III $(\bar{x}<-\bar{z}^2/3,\bar{z}>0)$, there is no real positive root. That zone is the shadow zone where no acoustical ray passes.

The amplitude of the field is recovered by applying the stationary phase method to geometrical acoustics. Thus, the amplitude near the extremity is approximated by the inverse of the square root of the second derivative of function $\bar{r}$ in relation to $\bar{\alpha}$. The boundary conditions, which close the formulation of the problem, are as follows.

- In zone I, the pressure near the extremity of the caustic is

$$\bar{p}(\bar{x},\bar{z},\bar{t}) \underset{\sqrt{\bar{x}^2+\bar{z}^2}\to\infty}{\to} \frac{1}{\sqrt{|2\bar{z}-6\bar{\alpha}_+|}} \times F(\bar{t}+\bar{\alpha}_+\bar{x}+\bar{z}\bar{\alpha}_+^2-\bar{\alpha}_+^3) \quad \text{with } \bar{x}>0, \tag{38}$$

where F is the temporal shape of the incoming signal and $\bar{\alpha}_+$ is the only real positive root associated with the incoming ray.
- In zone III, there is no signal and consequently no pressure:

$$\bar{p}(\bar{x},\bar{z},\bar{t}) \underset{\sqrt{\bar{x}^2+\bar{z}^2}\to\infty}{\to} 0 \quad \text{with } \bar{x}<0. \tag{39}$$

The derivation of the boundary conditions achieves the formulation of the problem. It is now possible to look for solutions either analytically, such as similarity laws, or numerically.

From a numerical point of view, the KZ equation is solved in a box around the extremity of the penumbra caustic (see Fig. 4). The coordinates of the corners of the box are labeled by X^-, X^+, Z^-, and Z^+. Three boundaries of that box are imposed. The first one is $\bar{p}(\bar{x},\bar{z}=Z^-,\bar{t})$ (see BC1 in Fig. 4). According to the derived boundary conditions, $\bar{p}(\bar{x},\bar{z}=Z^-,\bar{t})=0$ is applied from $\bar{x}=X^-$ to $\bar{x}=0$, and Eq. (38) is applied from $\bar{x}=0$ to $\bar{x}=X^+$. The second imposed boundary condition is $\bar{p}(\bar{x}=X^-,\bar{z},\bar{t})=0$ (see BC2 in Fig. 4). The last imposed condition is given by Eq. (38) used for $\bar{p}(\bar{x}=X^+,\bar{z},\bar{t})$ with $\bar{z}\in[Z^-,Z^+]$ (see BC3 in Fig. 4).

B. Solution for transient signals in linear regime

The previous analysis shows that the pressure has to satisfy the KZ equation [Eq. (34)] associated with the boundary conditions derived above [Eqs. (38) and (39)]. If nonlinearities are negligible in comparison with diffraction effects, then parameter μ tends toward zero. Thus, we obtain the linear KZ equation

$$\frac{\partial^2\bar{p}}{\partial\bar{z}\,\partial\bar{t}}-\frac{\partial^2\bar{p}}{\partial\bar{x}^2}=0. \tag{40}$$

That equation only takes into account the diffraction effects. The boundary conditions [Eqs. (38) and (39)] are unchanged. So, the problem to solve is linear and admits an analytical solution based on the incomplete Airy function:

$$\bar{p}(\bar{x},\bar{z},\bar{t})=\frac{1}{\sqrt{4\pi}}\mathrm{TF}^{-1}\left\{|\bar{\omega}|^{1/2}\hat{F}(\bar{\omega})(1-i\,\mathrm{sgn}(\bar{\omega}))\times\int_0^{+\infty}\exp[i\bar{\omega}(-\bar{\alpha}\bar{x}-\bar{\alpha}^2\bar{z}+\bar{\alpha}^3)]d\bar{\alpha}\right\}, \tag{41}$$

where TF^{-1} is the inverse Fourier operator, $\bar{\omega}=\omega/\omega_0$ is the dimensionless angular frequency, and $\hat{F}$ is the Fourier transform of the incoming waveform.

That solution is valid for any incoming smooth wave. But if the incoming signal is carrying shock waves, that solution is no more valid because it leads to a singularity as-

sociated with the incoming shocks. For an incoming N wave, the calculations (not reproduced here) show the existence of two singularities of type $(1-\bar{t})^{-1/6}$ associated with each incoming shock. Note that this is the same law as for the fold caustic.[26] With infinite pressure being physically meaningless, the conclusion is that the linear theory is inconsistent in this case. Then, following Guiraud[13] for the fold caustic or Coulouvrat[17] for the cusp caustic, it is necessary to introduce the nonlinear effects as a new limiting physical phenomenon to recover a physical solution. Nevertheless, in this case, the problem is nonlinear and only a numerical resolution is possible.

C. Similarity law

As outlined in Sec. III B, the focusing of shock waves on a penumbra caustic is an intrinsically nonlinear phenomenon. Consequently, this phenomenon cannot be described by a linear modeling, and Eq. (34) and its associated boundary conditions [Eqs. (38) and (39)] have to be solved. For the fold caustic, It has been shown that there exists a nonlinear similarity rule characteristic of this intrinsically nonlinear behavior.[13,27] In this section, it is shown that such a law exists also for this problem. By introducing the following new scaling:

$$\bar{p} = \mu^{-1/5}\tilde{p}, \tag{42}$$

$$\bar{t} = \mu^{6/5}\tilde{t}, \tag{43}$$

$$\bar{x} = \mu^{4/5}\tilde{x}, \tag{44}$$

$$\bar{z} = \mu^{2/5}\tilde{z}, \tag{45}$$

$$\bar{\alpha} = \mu^{2/5}\tilde{\alpha}, \tag{46}$$

the KZ equation becomes

$$\frac{\partial^2\tilde{p}}{\partial\tilde{z}\,\partial\tilde{t}} = \frac{\partial^2\tilde{p}}{\partial\tilde{x}^2} + \frac{\partial}{\partial\tilde{t}}\left(\frac{\partial\tilde{p}}{\partial\tilde{t}}\right)^2, \tag{47}$$

and the associated boundary conditions.

- In zone I,

$$\tilde{p}(\tilde{x},\tilde{z},\tilde{t}) \underset{\sqrt{\tilde{x}^2+\tilde{z}^2}\to\infty}{\to} \frac{1}{\sqrt{|2\tilde{z}-6\tilde{\alpha}_+|}} \times F(\mu^{6/5}(\tilde{t}+\tilde{\alpha}_+\tilde{x}+\tilde{z}\tilde{\alpha}_+^2-\tilde{\alpha}_+^3)) \quad \text{with } \tilde{x}>0, \tag{48}$$

where $\tilde{\alpha}_+=(\tilde{z}+\sqrt{\tilde{z}^2+3\tilde{x}})/3$.

- In zone III,

$$\tilde{p}(\tilde{x},\tilde{z},\tilde{t}) \underset{\sqrt{\tilde{x}^2+\tilde{z}^2}\to\infty}{\to} 0 \quad \text{with } \tilde{x}<0. \tag{49}$$

Parameter μ does not appear anymore in the KZ equation. Nevertheless, it appears now in the phase of boundary conditions in zone I. Consequently, for an incoming signal that would be unchanged by a temporal dilatation like a step shock [$F(t)=0$ if $t<0$ and $F(t)=1$ if $t>0$], the problem does not depend on the nonlinear parameter μ. Then, the variables denoted with a tilde have to be constant. In particular, at the extremity of the penumbra caustic ($\bar{x}=0$ and $\bar{z}=0$), the amplitude of the incoming wave scales as the power of $-1/5$ of μ and the time has to dilate with the power of 6/5 of μ. These similarity laws are exactly the same as those of the problem of the fold caustic.

That result is not obvious. Indeed, the fold caustic model of Guiraud[13] is based on the nonlinear Tricomi equation, which is of mixed type: hyperbolic in the zone of rays and elliptic in the shadow zone. Moreover, the fold caustic model is unidimensional, and the boundary conditions deal with both an incoming and an outgoing ray. This is very different from the present theory based on the KZ equation, which is a hyperbolic equation, and the boundary conditions deal only with incoming rays. Our results show that there is a deep matching between the focusing on a penumbra caustic and on a fold caustic even in nonlinear regime.

IV. NUMERICAL INVESTIGATIONS OF THE FOCUSING OF SHOCK WAVES ON A PENUMBRA CAUSTIC

Numerical investigations are made with the numerical solver of the KZ equation previously described.[21] The code solves the problem for the potential and then the pressure field is computed. It is based on a fractional step procedure. On each step, diffraction and nonlinear effects are solved separately. The diffraction is solved in the time domain following the TEXAS code procedure.[28] Nonlinear effects are solved also in the time domain by the Burgers–Hayes method.[15,29] That method is based on a semi-analytical solution of the nonlinear equation. Hence, shock waves are computed very quickly and accurately without any assumptions (numerical or artificial viscosity).

Two situations are investigated. The first one is the focusing of a transient signal in linear regime. The transient signal is chosen to be a sinusoidal wave nested in a rectangular window. The second situation studied is the focusing of a shock wave in nonlinear regime. The shock wave is a step shock.

A. Numerical investigation of the focusing of smooth transient signals in linear regime

To simulate the focusing of smooth transient signals in linear regime, we choose to simulate the propagation of a sinusoidal wave nested in a rectangular window. Consequently, the function F of Eq. (38) is $F(u)=W(u)\sin(\pi u)$, where $W(u)$ is the rectangular window (in this example, the size of the window is equal to four periods of the sinusoid). The coefficient of nonlinearity μ is zero; only the linear effects of propagation and diffraction are taken into account.

Figure 5 shows the pressure field at five different distances along the $\bar{z}$-axis from the extremity of the penumbra caustic: (a) $\bar{z}=-1$, (b) $\bar{z}=-0.5$, (c) $\bar{z}=0$, (d) $\bar{z}=1$, and (e) $\bar{z}=2$ (the extremity of the caustic is located in $\bar{z}=0$). Far from the extremity of the caustic [Fig. 5(a)] the wavefront is concave but not folded yet, no diffraction waves are visible anymore. It is the incoming wavefront. Before the extremity of the caustic [Fig. 5(b)], a cylindrical wave due to diffraction is

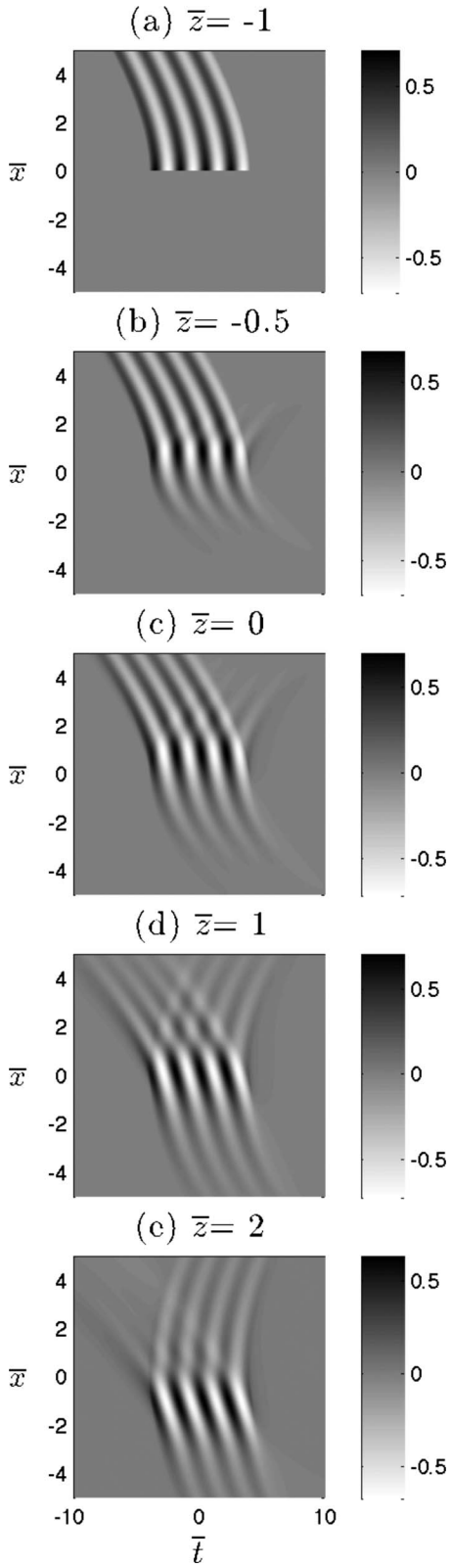

FIG. 5. Spatio-temporal pressure fields in $\bar{z}=-1$, -0.5, 0, 1, and 2 for an incoming burst in linear regime ($\mu=0$).

visible. This is in agreement with the behavior described in Fig. 3. At the extremity of the penumbra caustic [Fig. 5(c)], there is a diffraction wave emanating from the end of the wavefront, which penetrates into the shadow zone and into the sounded zone. Theoretically, the wavefront is not yet folded but it is the location of the extremity of the penumbra caustic. In $\bar{z}=+1$ [Fig. 5(d)], the wavefront is now theoretically folded, and the diffraction effect due to the finite size also induces diffraction. The main result is the presence of a pattern of interferences. This pattern looks like the patterns already observed for the fold caustic.[15,16] Indeed, the different lobes (oscillations of the amplitude between $\bar{x}=0$ and $\bar{x}=4$) correspond to the lobes of the Airy function. In this case, they correspond to the lobes of the incomplete Airy function. In $\bar{z}=+2$ [Fig. 5(e)], the same physical phenomena are visible. The rotation of the pattern of interference is due to the relative position of this pattern in comparison with the position of the caustic (the pattern has to be perpendicular to the caustic). The weak amplitude of the incoming signal is due to the decreasing behavior of the boundary conditions as function of $\bar{z}$ [Eq. (48)].

B. Numerical investigation of the focusing of shock waves in nonlinear regime

To investigate the focusing of shock waves in nonlinear regime, we choose to simulate the propagation of a step shock. Indeed, this kind of shock wave is very convenient to visualize the deformation of the wavefield during the propagation. Function F is a step shock (0 or 1 depending on the argument of the function). The coefficient of nonlinearity μ is chosen equal to 1.

Figure 6 presents the pressure field at five different locations from the extremity of the penumbra caustic: (a) $\bar{z}=-1$, (b) $\bar{z}=-0.5$, (c) $\bar{z}=0$, (d) $\bar{z}=1$, and (e) $\bar{z}=2$. At the initial position [$\bar{z}=-1$, Fig. 6(a)], the wavefront (which corresponds to the sharp transition between white and black) is not yet folded. Before the extremity of the caustic [Fig. 6(b)], a cylindrical wave due to diffraction is visible. This is in agreement with the behavior described in Fig. 3. At the extremity of the caustic $\bar{z}=0$, the diffraction wave is visible again: there is a cylindrical wave emanating from the end of the wavefront. This wave is different in Figs. 6(d) and 6(e) because its shape is not a perfect cylinder. This is due to the competitive effect between the diffraction at the end of the wavefront and the fold of the wavefront, as illustrated in Fig. 3. Note that this effect is not due to nonlinear effects. It exists also for the focusing of smooth waves in linear regime. But it is difficult to visualize (see Fig. 5). A nonlinear effect is the presence of a triple point inside the pressure at $\bar{z}=2$ [Fig. 6(e)]. A triple point is a point where three shocks are merging: the incoming and the outgoing shocks are merging into a third shock.

Figure 7 provides a zoom of the area with the triple point and a simulation of the pressure in linear regime. From these two visualizations we can see that the third shock resulting from the merging of the incoming and outgoing shocks is due to an intrinsically nonlinear effect. This pattern is not visible if the simulation is only linear: there is no shock after the merging point of the incoming and outgoing shocks. This conclusion is similar to the conclusion made for the von Neumann reflection.[32] That result is in agreement with the experimental observation of a triple shock made by Sturtevant and Kulkarny.[30] This is analogous to the situation

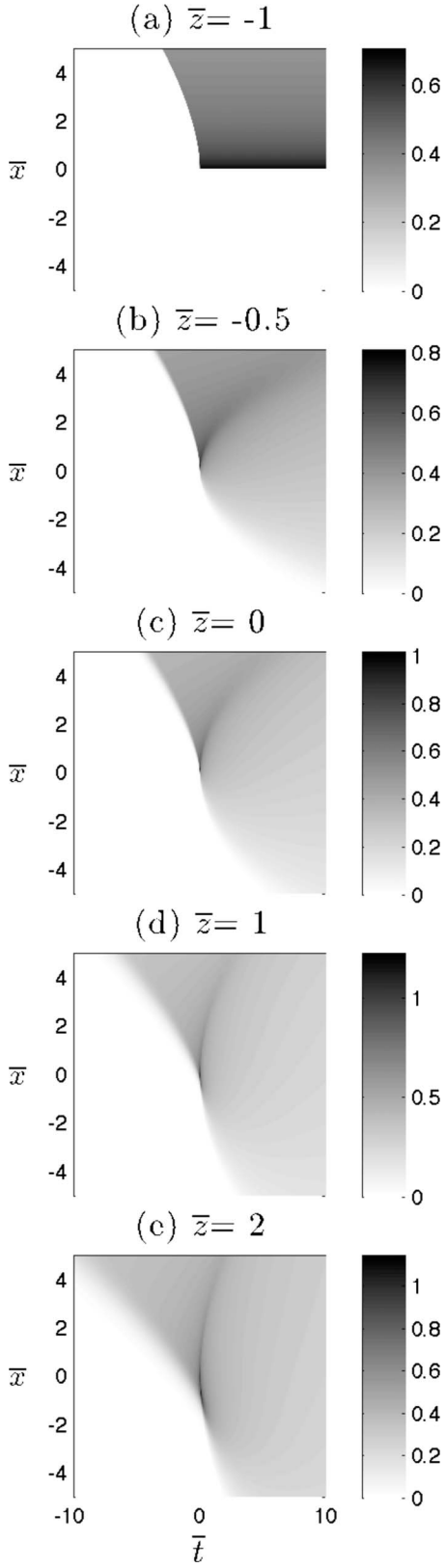

FIG. 6. Spatio-temporal pressure fields in $\overline{z}=-1$, -0.5, 0, 1, and 2 for an incoming step function in nonlinear regime ($\mu=1$).

observed for the von Neumann reflection in acoustics[31–33] or to the Mach reflection in aerodynamics.[34–36] Note that the presence of a triple point near a fold caustic is theoretically impossible as triple points are incompatible with the nonlinear Tricomi equation.[37]

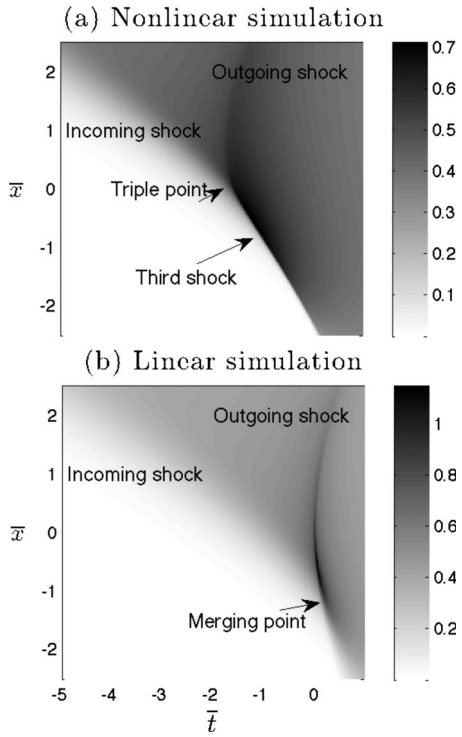

FIG. 7. Pressure fields for an incoming step function in $\overline{z}=2$ simulated with (a) the nonlinear model ($\mu=1$) and (b) the linear model.

V. AN EXPLANATION OF THE APPARENT PARADOX OF NON-CAUSALITY AROUND FOLD CAUSTICS

Penumbra caustics are related to fold caustics. Even though around the extremity of the penumbra caustic the acoustical field is different from the one around a fold caustic, far enough from the extremity of the caustic, the fields have to be the same for both caustics. This assumption is supported by the matching between the diffraction integrals in linear regime but also by the same similarity laws in nonlinear regime. In a sense, penumbra caustics provide an alternative and a good way to study fold caustics. In this paragraph, it is proposed to use that property to revisit the problem of apparent non-causality around fold caustics.

The description of the focusing of transient linear waves on a fold caustic within the diffraction catastrophe theory is well-established. The pressure field is computed in terms of the Airy function [with an expression analogous to Eq. (41)]. But with this formulation, precursors exist on the temporal signals (see, for instance, Fig. 1 in Ref. 22). The presence of these precursors seems to be in contradiction with the causality principle. The same phenomenon occurs for the focusing of shock waves. Using the nonlinear Tricomi equation, it is possible to compute the signal on the caustic. For an incoming N wave, the signal on the caustic is a U wave. The amplitude of the U wave tends toward zero asymptotically toward the decreasing values of time. This behavior also seems to break the principle of causality. Brown and Tappert[22] proposed an explanation for the linear transient waves. Their explanation is based on the fact that such caustics are a part of certain higher dimensional caustics.

The aim of this section is to provide an alternative explanation, which seems easier to understand even if this is

not necessarily in contradiction with the pioneering works of Brown and Tappert. The focusing of an N wave on a penumbra caustic is computed numerically with the code described in Sec. III. Then, the pressure field is analyzed along the caustic farther and farther from the extremity to study the shape of the pressure signals. The simulation is made in nonlinear regime to avoid any singularities. Figure 8 shows the temporal profile of the waves in five different locations of the computed domain [see Fig. 8(a)]. One location is situated before the caustic at the extremity of the wavefront in $\bar{z}=-0.5$, $\bar{x}=0$ [Fig. 8(b)], and the other four ones are situated along the caustic at $\bar{z}=0$, $\bar{z}=1$, $\bar{z}=2$, and $\bar{z}=3$ [respectively, Figs. 8(c)–8(f)]. At the initial position [Fig. 8(b)], the signal is a perfect N wave. It is obvious that the signal begins in $T=-1$, and there are no precursors before that time. At the extremity of the caustic [Fig. 8(c)], the signal is still an N wave even if diffraction effects slightly affect the shape of the signal. Again, no precursors are visible. As we move away from the extremity of the caustic, the transition between no signal/signal becomes smoother. In particular, in $\bar{z}=3$, the pressure tends smoothly to zero before the first shock at decreasing times. This behavior is in agreement with the assumption that far away from the extremity, the field is similar to the field of a fold caustic. Figure 9 shows a zoom on the first shock of the N wave for the different locations. All the signals are time shifted to have their maximum located at $t=0$. It is clear from this figure that the farther the signal is located, the longer the return to a zero pressure is. Again, this behavior is expected as it is characteristic of the fold caustic. As mentioned above, the causality seems not to be respected: there is a signal before the main signal (shock front).

Nevertheless, the modeling used to compute the above results is different from the classical diffraction catastrophe theory. In the classical theory of catastrophes, the modeling is based on the linear or nonlinear Tricomi equations. The linear and nonlinear Tricomi equations are mixed type equations (hyperbolic/elliptic). The hyperbolic part corresponds to zones where rays propagate while the elliptic part corresponds to the shadow zone. This equation results from a very elegant modeling involving only one spatial dimension to take into account propagation and diffraction along the fold caustic. The elliptic nature of the linear and nonlinear Tricomi equations allows non-causal behavior. With the modeling proposed in that paper, the equation is fully hyperbolic. Hence, illuminated and shadow zones are not distinguished and the behavior has to be causal. Consequently, the interpretation of the form of the signals, as those presented in Figs. 8 and 9, cannot involve non-causality.

The proposition made in the present paper is that the apparent non-causality of the signal is due to the arrival of diffracted waves propagating through the shadow zone. This situation is depicted in Fig. 10. Diffracted waves are produced by the interrupted wavefront. These waves propagate through the shadow zone (which is a hyperbolic zone in this description) and contribute to a nonzero pressure before the arrival of the main signal on the caustic. This interpretation

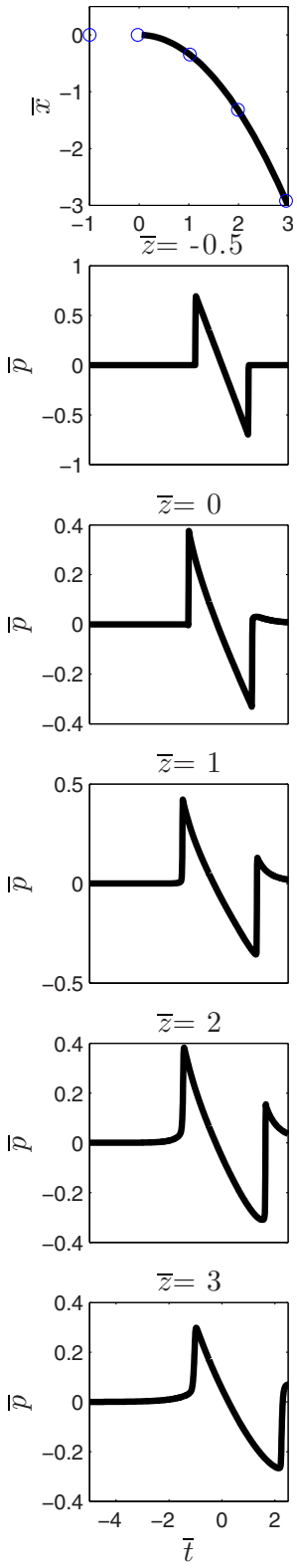

FIG. 8. (Color online) Pressure signals before, at the extremity, and along the penumbra caustic. The top figure shows the positions from which pressure signals are extracted.

is supported by the numerical simulations made in Sec. III, where diffracted waves are clearly visible. Note that this explanation is not necessarily in contradiction with the theory of Brown and Tappert.[22] Indeed, their explanation is an interpretation of the caustic as a projection of another caustic

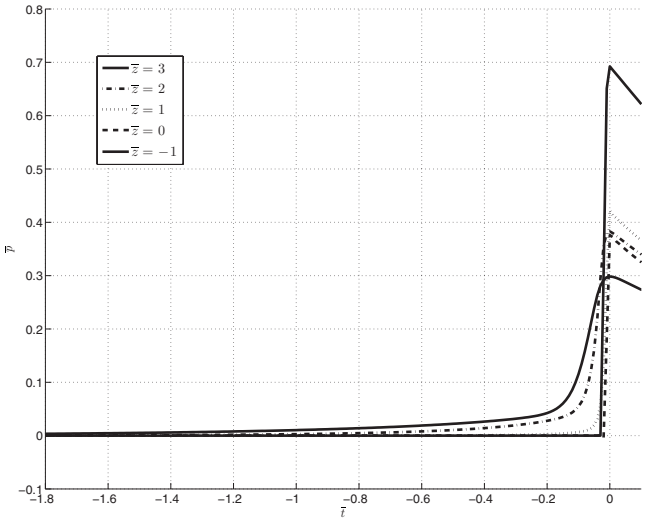

FIG. 9. Zoom on the first shock of the pressure signals in Fig. 8.

of higher dimension. Our explanation is based on a two-dimensional visualization of a phenomenon usually described by a one-dimensional analysis.

VI. CONCLUSIONS

For linear waves, the pressure field is described by the incomplete Airy function. This result already derived in the literature is consistent with the Fresnel diffraction before the extremity of the penumbra caustic and the theory of catastrophes far enough from the extremity. For incoming shock waves, local nonlinearities have to be taken into account. Thus, it is possible to describe the focusing of shock waves on a penumbra caustic with the KZ equation. Numerical simulations show that after the extremity of the caustic, triple points may occur. Far enough from the extremity, results match those of the fold caustic. Using this property, an original explanation of the apparent non-causality has been proposed. This apparent paradox could be explained in terms of diffracted waves propagating through the shadow zone. This phenomenon is not an intrinsically acoustical phenomenon. Therefore, this explanation is still valid for other branches of wave physics for which the non-causality paradox arises.

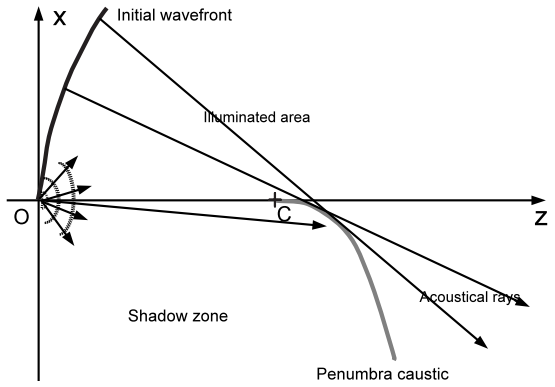

FIG. 10. Simple description of the explanation of the apparent paradox of non-causality around fold caustics.

ACKNOWLEDGMENTS

The author is very grateful to Dr. F. Coulouvrat [Institut Jean le Rond d'Alembert, UPMC and CNRS (UMR 7190)] and Dr. J.-L. Thomas [Institut des Nanosciences de Paris, UPMC and CNRS (UMR 7588)] for their fruitful discussions about this paper.

[1]R. Thom, *Structural Stability and Morphogenesis* (Benjamin, Reading, MA, 1975).
[2]T. Poston and I. Stewart, *Catastrophe Theory and Its Applications* (Dover, New York, 1996).
[3]M. V. Berry, "Waves and Thom's theorem," Adv. Phys. **25**, 1–26 (1976).
[4]Y. A. Kravtsov and Y. I. Orlov, *Caustics, Catastrophes and Wave Fields* (Springer, New York, 1993).
[5]G. B. Airy, "On the intensity of light in the neighourhood of a caustic," Trans. Cambridge Philos. Soc. **6**, 379–401 (1838).
[6]T. Pearcey, "The structure of field diffracted by a curvilinear wedge in the presence of caustics," Philos. Mag. **37**, 311–317 (1946).
[7]L. Levey and L. B. Felsen, "On transitions functions occurring in the theory of diffraction in inhomogeneous media," J. Inst. Math. Appl. **3**, 76–97 (1967).
[8]L. Levey and L. B. Felsen, "On incomplete Airy functions and their application to diffraction problems," Radio Sci. **4**, 959–969 (1969).
[9]Y. I. Orlov, "A uniform asymptote of field diffracted by a curvilinear wedge in the presence of caustics," Radio Eng. Electron. Phys. **20**, 8–13 (1975).
[10]A. J. Fresnel, *Oeuvres completes (Complete Works)* (Imprimerie Impériale, Paris, 1866).
[11]A. D. Pierce, *Acoustics, An Introduction to Its Physical Principles and Applications* (Acoustical Society of America, Melville, NY, 1989).
[12]F. Coulouvrat and R. Marchiano, "Nonlinear Fresnel diffraction of weak shock waves," J. Acoust. Soc. Am. **114**, 1749–1757 (2003).
[13]J.-P. Guiraud, "Acoustique géométrique, bruit balistique des avions supersoniques, focalisation (Geometrical acoustics, balistic noise of supersonic aircraft and focusing)," J. Mec. **4**, 215–267 (1965).
[14]T. Auger and F. Coulouvrat, "Numerical simulation of sonic boom focusing," AIAA J. **40**, 1726–1734 (2002).
[15]R. Marchiano, F. Coulouvrat, and R. Grenon, "Numerical simulation of shock wave focusing at fold caustics, with application to sonic boom," J. Acoust. Soc. Am. **114**, 1758–1771 (2003).
[16]R. Marchiano, J.-L. Thomas, and F. Coulouvrat, "Experimental simulation of supersonic superboom in a water tank: Nonlinear focusing of weak shock waves at a fold caustic," Phys. Rev. Lett. **91**, 184301 (2003).
[17]F. Coulouvrat, "Focusing of shock waves at a caustic cusp," Wave Motion **32**, 233–245 (2000).
[18]M. S. Cramer, "Focusing of weak shock waves at an axisymmetric arête," J. Fluid Mech. **110**, 249–253 (1981).
[19]M. S. Cramer, "Focusing of weak three-dimensional shock waves," AIAA J. **19**, 1363–1365 (1981).
[20]M. S. Cramer and A. R. Seebass, "Focusing of weak shock waves at an arête," J. Fluid Mech. **88**, 209–222 (1978).
[21]R. Marchiano, F. Coulouvrat, and J. L. Thomas, "Nonlinear focusing of acoustic shock waves at a caustic cusp," J. Acoust. Soc. Am. **117**, 566–577 (2005).
[22]M. G. Brown and F. D. Tappert, "Causality, caustics and the structure of transient wave fields," J. Acoust. Soc. Am. **80**, 251–255 (1986).
[23]M. Abramowitz and I. Stegun, *Handbook of Mathematical Functions* (Dover, New York, 1965).
[24]V. P. Kuznetsov, "Equation of nonlinear acoustics," Sov. Phys. Acoust. **16**, 467–470 (1970).
[25]E. A. Zabolotskaya and R. V. Khokhlov, "Quasi-plane waves in the nonlinear acoustics of confined beams," Sov. Phys. Acoust. **15**, 35–40 (1969).
[26]A. R. Seebass, "Nonlinear acoustic behavior at a caustic," in Proceedings of the 3rd Conference on Sonic Boom Research (1971), pp. 87–120.
[27]W. D. Hayes, "Similarity rules for nonlinear acoustic propagation through a caustic," in Proceedings of the 2nd Conference on Sonic Boom Research (1968), pp. 165–171.
[28]Y. S. Lee and M. F. Hamilton, "Time-domain modeling of pulsed finite-amplitude sound beams," J. Acoust. Soc. Am. **97**, 906–917 (1995).
[29]F. Coulouvrat, "A quasi-analytical shock solution for general nonlinear progressive waves," Wave Motion **46**, 97–107 (2009).
[30]B. Sturtevant and V. Kulkarny, "The focusing of weak shock waves," J.

Fluid Mech. **73**, 651–671 (1976).
[31]S. Baskar, F. Coulouvrat, and R. Marchiano, "Nonlinear reflection of grazing acoustic shock waves: Unsteady transition from von Neumann to mach to snell-descartes reflections," J. Fluid Mech. **575**, 27–55 (2007).
[32]R. Marchiano, F. Coulouvrat, S. Baskar, and J. L. Thomas, "Experimental evidence of deviation from mirror reflection for acoustical shock waves," Phys. Rev. E **76**, 056602 (2007).
[33]E. Tabak and R. R. Rosales, "Focusing of weak shock waves and the von Neumann paradox of oblique shock reflection," Phys. Fluids **6**, 1874–1892 (1994).
[34]G. Ben-Dor, *Shock Wave Reflection Phenomena* (Springer, New York, 1992).
[35]E. Mach, "Über den Verlauf von Funkenwellen in der Ebene und im Raume (Study on the waves generated in air by electric sparks)," Sitzungsbr. Akad. Wiss. Wien **78**, 819–838 (1878).
[36]J. von Neumann, "Oblique reflection of shocks," in *John von Neumann Collected Work*, edited by A. H. Taub (Pergamon, New York, 1943), Vol. **6**, pp. 238–299.
[37]R. R. Rosales and E. G. Tabak, "Caustics of weak shock waves," Phys. Fluids **10**, 206–222 (1998).

Characteristics of second harmonic generation of Lamb waves in nonlinear elastic plates

Martin F. Müller and Jin-Yeon Kim
School of Civil and Environmental Engineering, Georgia Institute of Technology, Atlanta, Georgia 30332-0355

Jianmin Qu
G. W. Woodruff School of Mechanical Engineering, Georgia Institute of Technology, Atlanta, Georgia 30332-0405

Laurence J. Jacobs[a)]
School of Civil and Environmental Engineering and G. W. Woodruff School of Mechanical Engineering, Georgia Institute of Technology, Atlanta, Georgia 30332-0360

(Received 1 October 2009; revised 30 December 2009; accepted 30 December 2009)

This paper investigates the characteristics of the second harmonic generation of Lamb waves in a plate with quadratic nonlinearity. Analytical asymptotic solutions to Lamb waves are first obtained through the use of a perturbation method. Then, based on a careful analysis of these asymptotic solutions, it is shown that the cross-modal generation of a symmetric second harmonic mode by an antisymmetric primary mode is possible. These solutions also demonstrate that modes showing internal resonance—nonzero power flux to the second harmonic mode, plus phase velocity matching—are most useful for measurements. In addition, when using finite wave packets, which is the case in most experimental measurements, group velocity matching is required for a cumulative increase in the second harmonic amplitude with propagation distance. Finally, five mode types (which are independent of material properties) that satisfy all three requirements for this cumulative increase in second harmonic amplitude—nonzero power flux, plus phase and group velocity matching—are identified. These results are important for the development of an experimental procedure to measure material nonlinearity with Lamb waves.
 [DOI: 10.1121/1.3294714]

PACS number(s): 43.25.Dc, 43.20.Mv, 43.35.Cg [YHB] Pages: 2141–2152

I. INTRODUCTION

Recent research has demonstrated that nonlinear ultrasonic waves can be used to detect fatigue damage in its early stages.[1–4] This second harmonic generation describes a nonlinear acoustic effect where components are generated at twice the frequency of the excitation wave. These second harmonic acoustic components can be directly attributed to the nonlinear elastic properties of a material. As opposed to its linear elastic properties, these nonlinear elastic properties are much more sensitive to changes in the microstructure, such as those caused by fatigue damage. Experimental measurements of these second harmonic components[1–4] potentially enable the direct characterization of the nonlinear elastic properties and the associated damage state of a material.

The objective of this research is to determine the conditions for the second harmonic generation of Lamb waves in a plate with quadratic nonlinearity. Following the solution to this problem derived by de Lima and Hamilton,[5] analytical asymptotic solutions to Lamb waves are first obtained through the use of a perturbation method. Then, based on a careful analysis of these asymptotic solutions, it is shown that the cross-modal generation of a symmetric second harmonic mode by an antisymmetric primary mode is possible. This clarifies contradictory statements between de Lima and Hamilton,[5] Deng,[6] and Srivastava and di Scalea.[7] These solutions also demonstrate that modes showing internal resonance—nonzero power flux to the second harmonic mode, plus phase velocity matching—are most useful for measurements. In addition, when using finite wave packets, which is the case in most experimental measurements, group velocity matching is required for a cumulative increase in the second harmonic amplitude with propagation distance. Note that phase velocity matching requires that the phase velocities for the excitation mode at frequency ω and for the second harmonic mode at the double frequency, 2ω, be the same. Group velocity matching requires the same, but for the group velocity.

Finally, this paper identifies five mode types (which are independent of material properties) that satisfy all three requirements for this cumulative increase in second harmonic amplitude—nonzero power flux, plus phase and group velocity matching. The identification of these mode combinations is critical for the development of an experimental procedure to measure material nonlinearity with Lamb waves, which is important for material characterization and nondestructive evaluation (NDE) applications.

[a)]Author to whom correspondence should be addressed. Electronic mail: laurence.jacobs@coe.gatech.edu

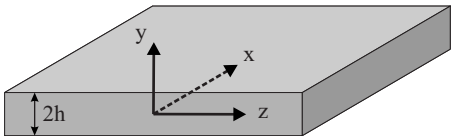

FIG. 1. Coordinate system of the infinite plate.

II. SECOND HARMONIC GENERATION

Consider an elastic, homogeneous, isotropic, infinite plate with quadratic nonlinearity. Guided Lamb waves propagate in the positive z-direction of this $2h$ thick plate, while the upper and lower surfaces at $y=\pm h$ are assumed to be stress free, as seen in Fig. 1.

Following the solution derived by de Lima and Hamilton,[5] consider a perturbation approach that expresses the overall solution of the displacement field as the sum of a primary wave $\boldsymbol{u}^{(1)}$, which is associated with the wave launched into the plate at frequency ω, and a secondary wave $\boldsymbol{u}^{(2)}$, which arises at twice the primary frequency, 2ω, and is the second harmonic wave generated by the quadratic nonlinearities in the plate, or

$$\boldsymbol{u}=\boldsymbol{u}^{(1)}+\boldsymbol{u}^{(2)}. \tag{1}$$

The perturbation condition,

$$|\boldsymbol{u}^{(2)}| \ll |\boldsymbol{u}^{(1)}|, \tag{2}$$

states that the nonlinear effect of second harmonic generation is very small compared to the primary wave. This method reduces the nonlinear boundary value problem to two linear boundary value problems: a homogeneous one for the primary wave and an inhomogeneous one for the secondary wave, which is forced by the primary wave.

The solution for the primary wave is given by linear Lamb mode theory.[8,9] Ignoring shear horizontal (SH) modes, the mode solution assumes the form

$$\boldsymbol{u}(y,z,t)=\tilde{\boldsymbol{u}}(y)e^{i(\kappa z-\omega t)}, \tag{3}$$

where the mode shape $\tilde{\boldsymbol{u}}(y)$ propagates harmonically in the z-direction. The Lamb mode $\tilde{\boldsymbol{u}}(y)$ can be either symmetric or antisymmetric, which is specified by the y-symmetry of the in-plane component $\tilde{u}_z(y)$. That is, for a symmetric (antisymmetric) Lamb mode, the in-plane component $\tilde{u}_z(y)$ is a symmetric (antisymmetric) function in y, while the out-of-plane component $\tilde{u}_y(y)$ is an antisymmetric (symmetric) function in y.

For symmetric Lamb modes, one obtains

$$\tilde{u}_y=i\frac{D}{h}\left(-\frac{(\bar{\kappa}^2-\bar{\beta}^2)\sin\bar{\beta}}{2\bar{\kappa}\sin\bar{\alpha}}\sin\left(\frac{\bar{\alpha}y}{h}\right)+\bar{\kappa}\sin\left(\frac{\bar{\beta}y}{h}\right)\right), \tag{4a}$$

$$\tilde{u}_z=-\frac{D}{h}\left(\frac{(\bar{\kappa}^2-\bar{\beta}^2)\sin\bar{\beta}}{2\bar{\alpha}\sin\bar{\alpha}}\cos\left(\frac{\bar{\alpha}y}{h}\right)+\bar{\beta}\cos\left(\frac{\bar{\beta}y}{h}\right)\right), \tag{4b}$$

where $\bar{\kappa}=\kappa h$ is the normalized Lamb wave number and $\bar{\omega}=\omega h$. Moreover,

$$\bar{\alpha}=\sqrt{(\bar{\omega}/c_L)^2-\bar{\kappa}^2},\quad \bar{\beta}=\sqrt{(\bar{\omega}/c_T)^2-\bar{\kappa}^2}, \tag{5}$$

where c_L is the longitudinal wave speed and c_T the shear wave speed in an unbounded medium. The complex coefficient D determines the amplitude of the mode and depends on the actual excitation of the mode. For antisymmetric Lamb modes, the solution is

$$\tilde{u}_y=i\frac{C}{h}\left(-\frac{(\bar{\kappa}^2-\bar{\beta}^2)\cos\bar{\beta}}{2\bar{\kappa}\cos\bar{\alpha}}\cos\left(\frac{\bar{\alpha}y}{h}\right)+\bar{\kappa}\cos\left(\frac{\bar{\beta}y}{h}\right)\right), \tag{6a}$$

$$\tilde{u}_z=\frac{C}{h}\left(\frac{(\bar{\kappa}^2-\bar{\beta}^2)\cos\bar{\beta}}{2\bar{\alpha}\cos\bar{\alpha}}\sin\left(\frac{\bar{\alpha}y}{h}\right)+\bar{\beta}\sin\left(\frac{\bar{\beta}y}{h}\right)\right), \tag{6b}$$

with the complex amplitude C. An important feature of Lamb modes is given by the dispersion relations between frequency and wave number, which allows for only modes with certain combinations of frequencies and wave numbers to propagate.

For the secondary boundary value problem, de Lima and Hamilton[5] employed a modal expansion technique. The secondary solution is written as

$$\boldsymbol{u}^{(2)}(y,z,t)=\sum_{n=1}^{N}A_n(z)\tilde{\boldsymbol{u}}_n(y)e^{-2i\omega t}, \tag{7}$$

which displays the sum of the N propagating linear modes at twice the primary frequency, 2ω, weighted by the respective amplitude coefficient $A_n(z)$ for each mode n in the expansion. This means that $A_n(z)$ determines how strong a certain secondary mode in the expansion is excited. Some manipulations, including a reciprocity relation and the orthogonality condition for linear modes, lead to an ordinary differential equation for $A_n(z)$, whose solution is given by

$$A_n(z)=\frac{f_n^{\mathrm{vol}}+f_n^{\mathrm{surf}}}{4\mathcal{P}_{nn}}\begin{cases}\dfrac{i}{\kappa_n^*-2\kappa}(e^{2i\kappa z}-e^{i\kappa_n^* z}) & \text{if } \kappa_n^*\neq 2\kappa\\ ze^{2i\kappa z} & \text{if } \kappa_n^*=2\kappa\end{cases}, \tag{8}$$

where κ is the Lamb wave number of the primary mode, κ_n is the Lamb wave number of the nth secondary mode in the expansion, the superscript " *" denotes the complex conjugate, and

$$\mathcal{P}_{nn}=-\frac{1}{2}\Re e\int_{-h}^{h}\tilde{\boldsymbol{v}}_n^*\cdot\tilde{\boldsymbol{\sigma}}_n\cdot\boldsymbol{n}_z dy \tag{9}$$

is the power carried by the nth secondary mode. $\boldsymbol{n}_z$ is the unit normal vector in z, $\tilde{\boldsymbol{v}}$ is the particle velocity, and $\tilde{\boldsymbol{\sigma}}$ is the linear stress tensor. It is seen that $A_n(z)$ is proportional to the sum of the terms

$$f_n^{\mathrm{vol}}=\int_{-h}^{h}\tilde{\boldsymbol{v}}_n^*\cdot\tilde{\boldsymbol{f}}^{2\omega}dy, \tag{10a}$$

$$f_n^{\text{surf}} = -\boldsymbol{n}_y \cdot \bar{\boldsymbol{S}}^{2\omega} \cdot \tilde{\boldsymbol{v}}_n^* \big|_{-h}^{h}, \tag{10b}$$

where $\boldsymbol{n}_y$ is the unit normal vector in the y-direction. f_n^{vol} and f_n^{surf} are interpreted physically as the power fluxes from the primary wave to the nth secondary mode due to material nonlinearities via volume body forces and surface tractions, respectively. This means that the stronger the power flux from the primary to the nth secondary mode, the stronger the secondary mode is excited. The power flux is caused by the body force $\bar{\boldsymbol{f}}^{2\omega}$ and surface tractions due to the stress tensor $\bar{\boldsymbol{S}}^{2\omega}$. These terms represent the complex 2ω-harmonic amplitude of the real quantities $\bar{\boldsymbol{f}}$ and $\bar{\boldsymbol{S}}$, which are given as

$$\begin{aligned}\bar{S}_{ij} = {} & \bar{B}\frac{\partial u_k}{\partial a_k}\frac{\partial u_i}{\partial a_j} + \frac{\bar{A}}{4}\frac{\partial u_i}{\partial a_k}\frac{\partial u_k}{\partial a_j} + (\lambda + \bar{B})\frac{\partial u_k}{\partial a_k}\frac{\partial u_j}{\partial a_i} + \left(\mu + \frac{\bar{A}}{4}\right) \\ & \times\left(\frac{\partial u_j}{\partial a_k}\frac{\partial u_i}{\partial a_k} + \frac{\partial u_k}{\partial a_j}\frac{\partial u_k}{\partial a_i} + \frac{\partial u_j}{\partial a_k}\frac{\partial u_k}{\partial a_i}\right) + \left(\frac{\lambda}{2}\frac{\partial u_k}{\partial a_l}\frac{\partial u_k}{\partial a_l}\right. \\ & \left. + \bar{C}\frac{\partial u_k}{\partial a_k}\frac{\partial u_l}{\partial a_l}\right)\delta_{ij} + \frac{\bar{B}}{2}\left(\frac{\partial u_k}{\partial a_l}\frac{\partial u_k}{\partial a_l} + \frac{\partial u_k}{\partial a_l}\frac{\partial u_l}{\partial a_k}\right)\delta_{ij}\end{aligned} \tag{11a}$$

in index notation, and

$$\bar{\boldsymbol{f}} = \nabla \cdot \bar{\boldsymbol{S}}. \tag{11b}$$

The quantities in Eq. (11a) are the real primary displacement field u_i, Lamé's constant λ, the shear modulus μ, the third-order elastic material constants[10] $\bar{A}$, $\bar{B}$, and $\bar{C}$, and the coordinates in the reference configuration $(a_1, a_2, a_3) = (x, y, z)$. Equation (11) is obtained by the perturbation of the nonlinear boundary value problem, when keeping up to quadratic terms of displacements in the constitutive relation.

III. SYMMETRY PROPERTIES

Based on the modal solution presented above, both de Lima and Hamilton[5] and Deng[6] concluded contradictory symmetry properties of the second harmonic wave. de Lima and Hamilton stated that a primary mode can generate a secondary mode only of the same symmetry, e.g., an antisymmetric primary mode can excite an antisymmetric, but not a symmetric second harmonic mode, and vice versa. In contrast, Deng stated that the second harmonic wave must be purely symmetric, thus contradicting de Lima and Hamilton. Note that Deng did not conclude explicitly that a symmetric secondary mode can be generated by an antisymmetric primary mode.

This section clarifies this symmetry issue by the use of the modal solution presented in Sec. II employing generic y-symmetric functions, similar to Srivastava and di Scalea.[7] Equations (7) and (8) show that a secondary mode n can be excited only if the power flux from the primary to the secondary mode is nonzero, i.e., if $f_n^{\text{vol}} + f_n^{\text{surf}} \neq 0$. In general, the computations of f_n^{vol} and f_n^{surf} are very lengthy. Conclusions on symmetries can be achieved, however, by utilizing simple symmetry properties of functions.

In preparation for demonstrating the symmetry properties of the forcing terms $\bar{\boldsymbol{f}}$ and $\bar{\boldsymbol{S}}$, the expression for $\bar{\boldsymbol{S}}$ in Eq. (11a) is expanded for the two dimensions y and z, since the x-component of the displacement field for Lamb modes is zero when plane strain is assumed, i.e., $\partial/\partial x = 0$. This result is shown in the Appendix.

Now, let the primary mode be a symmetric Lamb mode whose displacement field is given in Eq. (4). In order to investigate symmetries along the y-axis, the following notation is introduced: $\mathcal{S}(y)$ is a generic, unspecified element of the set of symmetric functions in y, while $\mathcal{A}(y)$ is a generic, unspecified element of the set of antisymmetric functions in y. As discussed earlier, $u_y = \mathcal{A}(y)$ and $u_z = \mathcal{S}(y)$ hold for a symmetric mode. It is also seen that a derivative of u_i with respect to y changes the type of symmetry in y, while a derivative with respect to z does not change the type of symmetry in y. Moreover, the following rules are known:

(1) $\mathcal{S}(y) \cdot \mathcal{S}(y) = \mathcal{S}(y)$ and $\mathcal{A}(y) \cdot \mathcal{A}(y) = \mathcal{S}(y)$.
(2) $\mathcal{A}(y) \cdot \mathcal{S}(y) = \mathcal{A}(y)$ and $\mathcal{S}(y) \cdot \mathcal{A}(y) = \mathcal{A}(y)$.
(3) $\mathcal{S}(y) + \mathcal{S}(y) = \mathcal{S}(y)$ and $\mathcal{A}(y) + \mathcal{A}(y) = \mathcal{A}(y)$.

Using these results, the symmetry of the first term of Eq. (A1) is calculated as

$$\frac{\partial u_y}{\partial y}\frac{\partial u_y}{\partial y} = \mathcal{S}(y) \cdot \mathcal{S}(y) = \mathcal{S}(y).$$

In the same way, it is easily shown that all the terms on the diagonal of $\bar{\boldsymbol{S}}$ are $\mathcal{S}(y)$, while all the off-diagonal terms are $\mathcal{A}(y)$; hence

$$\bar{\boldsymbol{S}}_{\text{sym}} = \begin{pmatrix} \mathcal{S}(y) & \mathcal{A}(y) \\ \mathcal{A}(y) & \mathcal{S}(y) \end{pmatrix}. \tag{12a}$$

Furthermore, by Eq. (11b),

$$\bar{\boldsymbol{f}}_{\text{sym}} = \begin{pmatrix} \frac{\partial}{\partial y} & \frac{\partial}{\partial z} \end{pmatrix} \cdot \begin{pmatrix} \mathcal{S}(y) & \mathcal{A}(y) \\ \mathcal{A}(y) & \mathcal{S}(y) \end{pmatrix} = \begin{pmatrix} \mathcal{A}(y) \\ \mathcal{S}(y) \end{pmatrix}, \tag{12b}$$

where the subscript stands for the type of symmetry of the primary mode.

If the primary mode is antisymmetric, Eq. (6) shows that $u_y = \mathcal{S}(y)$ and $u_z = \mathcal{A}(y)$. Application to the same exemplary term above

$$\frac{\partial u_y}{\partial y}\frac{\partial u_y}{\partial y} = \mathcal{A}(y) \cdot \mathcal{A}(y) = \mathcal{S}(y)$$

yields the same result for that of a symmetric primary mode. This is explained by the fact that products of displacements are involved—even though each single term changes its symmetry in y, as compared to the analysis of a symmetric primary mode, the product rules lead back to the same result. Hence,

$$\bar{\boldsymbol{S}} = \begin{pmatrix} \mathcal{S}(y) & \mathcal{A}(y) \\ \mathcal{A}(y) & \mathcal{S}(y) \end{pmatrix}, \tag{13a}$$

and

$$\bar{\boldsymbol{f}} = \begin{pmatrix} \mathcal{A}(y) & \mathcal{S}(y) \end{pmatrix}^T, \tag{13b}$$

independent of the primary mode's symmetry. Since $\bar{\boldsymbol{f}}^{2\omega}$ and $\bar{\boldsymbol{S}}^{2\omega}$ are the complex harmonic amplitudes of $\bar{\boldsymbol{f}}$ and $\bar{\boldsymbol{S}}$, they show the same symmetry properties.

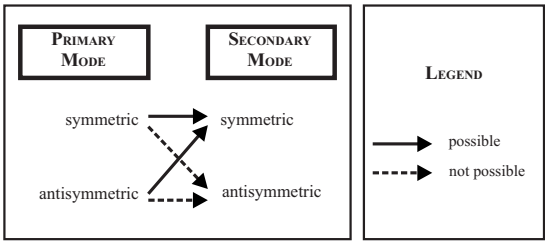

FIG. 2. Symmetry scheme of the second harmonic Lamb wave generation.

Recalling Eq. (10), the result for the power fluxes f_n^{vol} and f_n^{surf} depend on the symmetry properties of the secondary mode n. From $\tilde{\boldsymbol{v}}=i\omega\tilde{\boldsymbol{u}}$, one concludes

$$\tilde{\boldsymbol{v}}_{\mathrm{sym}}=\begin{pmatrix}\mathcal{A}(y) & \mathcal{S}(y)\end{pmatrix}^T \tag{14a}$$

for a symmetric mode, and

$$\tilde{\boldsymbol{v}}_{\mathrm{asym}}=\begin{pmatrix}\mathcal{S}(y) & \mathcal{A}(y)\end{pmatrix}^T \tag{14b}$$

for an antisymmetric mode. Finally, with $\mathbf{n}_y=(1,\ 0)$ and the secondary mode being symmetric, Eq. (10) becomes

$$f_n^{\mathrm{surf}}=\begin{pmatrix}1, & 0\end{pmatrix}\cdot\begin{pmatrix}\mathcal{S}(y) & \mathcal{A}(y)\\ \mathcal{A}(y) & \mathcal{S}(y)\end{pmatrix}\cdot\begin{pmatrix}\mathcal{A}(y)\\ \mathcal{S}(y)\end{pmatrix}\Bigg|_{y=-h}^{h}$$
$$=\mathcal{A}(y)\big|_{y=-h}^{h}\neq 0, \tag{15a}$$

$$f_n^{\mathrm{vol}}=\int_{y=-h}^{h}\begin{pmatrix}\mathcal{A}(y)\\ \mathcal{S}(y)\end{pmatrix}^T\cdot\begin{pmatrix}\mathcal{A}(y)\\ \mathcal{S}(y)\end{pmatrix}dy=\int_{y=-h}^{h}\mathcal{S}(y)dy\neq 0. \tag{15b}$$

It is noted that the inequality to zero holds in general, but there might be special frequencies and pairs of primary and secondary modes, for which at least one of these terms or their sum can be zero. Thus, if the secondary mode is symmetric, $A_n(z)\neq 0$ holds generally.

For the secondary mode being antisymmetric, one obtains

$$f_n^{\mathrm{surf}}=\begin{pmatrix}1, & 0\end{pmatrix}\cdot\begin{pmatrix}\mathcal{S}(y) & \mathcal{A}(y)\\ \mathcal{A}(y) & \mathcal{S}(y)\end{pmatrix}\cdot\begin{pmatrix}\mathcal{S}(y)\\ \mathcal{A}(y)\end{pmatrix}\Bigg|_{y=-h}^{h}$$
$$=\mathcal{S}(y)\big|_{y=-h}^{h}=0, \tag{16a}$$

$$f_n^{\mathrm{vol}}=\int_{y=-h}^{h}\begin{pmatrix}\mathcal{S}(y)\\ \mathcal{A}(y)\end{pmatrix}^T\cdot\begin{pmatrix}\mathcal{A}(y)\\ \mathcal{S}(y)\end{pmatrix}dy=\int_{y=-h}^{h}\mathcal{A}(y)dy=0, \tag{16b}$$

implying that $A_n(z)=0$ according to Eq. (8).

Summarizing these results, it is concluded that both a symmetric and an antisymmetric primary mode can excite a symmetric mode at twice the primary frequency. In contrast, neither a symmetric nor an antisymmetric primary mode can excite an antisymmetric mode at twice the primary frequency. Figure 2 displays this result graphically. Other authors[6,7,11] stated that the secondary wave is purely symmetric at the double frequency. However, they do not mention explicitly that the cross-modal excitation from an antisymmetric primary mode to a symmetric secondary mode is possible.

IV. INTERNAL RESONANCE

Recalling the modal solution in Sec. II, de Lima and Hamilton[5] observed that the amplitude coefficient $A_n(z)$ in Eq. (8) shows two fundamentally different behaviors depending on the relation between the wave numbers of the primary mode and the nth secondary mode. Noting the definition of the phase velocity

$$c_{\mathrm{ph}}=\frac{\omega}{k}, \tag{17}$$

the second case in Eq. (8) is referred to as phase velocity matching, since $\kappa^{(2\omega)}=2\kappa$ and $\omega^{(2\omega)}=2\omega$ imply that

$$c_{\mathrm{ph}}^{(2\omega)}=\frac{\omega^{(2\omega)}}{\kappa^{(2\omega)}}=\frac{\omega}{\kappa}=c_{\mathrm{ph}}, \tag{18}$$

where the superscript (2ω) denotes the terms associated with the second harmonic mode. Also note from Eq. (5) that for the case of phase velocity matching, $\bar{\alpha}^{(2\omega)}=2\bar{\alpha}$ and $\bar{\beta}^{(2\omega)}=2\bar{\beta}$.

If in addition to phase velocity matching, nonzero power flux from the primary to the secondary wave is assumed, the secondary mode shows internal resonance. In this case, the solution for the nth mode in the expansion takes the form

$$\boldsymbol{u}_n^{(2)}=\frac{f_n^{\mathrm{vol}}+f_n^{\mathrm{surf}}}{4\mathcal{P}_{nn}}z\tilde{\boldsymbol{u}}_n^{(2)}(y)\,e^{2i(\kappa z-\omega t)}. \tag{19}$$

The term internal resonance[5] is motivated by the linearly growing amplitude with propagation distance, z. This proportionality between the amplitude and the propagation distance suggests that the secondary mode can grow without any bounds. However, this behavior is prohibited by the perturbation condition of Eq. (2), which means that the perturbation solution is valid only up to a certain propagation distance.

de Lima and Hamilton[5] also mentioned that the nonresonant solution in Eq. (8), where $\kappa^{(2\omega)}\neq 2\kappa$, results in the sinusoidal behavior

$$\boldsymbol{u}_n^{(2)}=\frac{f_n^{\mathrm{vol}}+f_n^{\mathrm{surf}}}{2\mathcal{P}_{nn}\kappa_d}\sin\left(\frac{1}{2}\kappa_d z\right)\tilde{\boldsymbol{u}}_n^{(2)}(y)\,e^{i((1/2)(2\kappa+\kappa^{(2\omega)})z-2\omega t)}, \tag{20}$$

where $\kappa_d=\kappa^{(2\omega)}-2\kappa$ is interpreted as the deviance from exact phase velocity matching. In general, this nonresonant solution is not desirable, since displacements are bounded, and there are distances z where the amplitude is identically zero. However, a special case not mentioned in de Lima and Hamilton[5] is practically relevant; if κ_d is very small, the nonresonant solution approaches the resonant solution. In this case of approximate phase velocity matching, the second harmonic solution grows at an almost linear rate with propagation distance. Figure 3 shows the qualitative behavior of the amplitude depending on phase velocity matching.

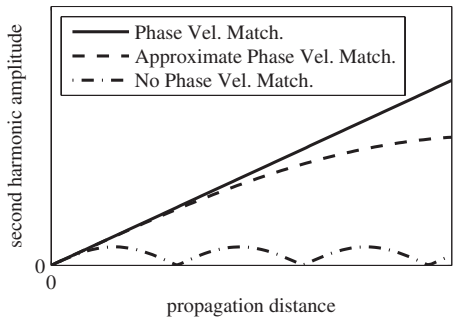

FIG. 3. Qualitative behavior of the second harmonic amplitude depending on phase velocity matching.

For material's characterization applications in NDE, exact or approximate internal resonance has several advantages. First, the growing amplitude results in large displacements after some propagation distance, improving the signal-to-noise ratio for measurements. In addition, other modes that are not in internal resonance may be disregarded as small when compared to the mode in resonance, after some distance, so that they do not interfere with the resonant mode under consideration.

V. GROUP VELOCITY MATCHING

Knowing that exact or approximate internal resonance is a desirable feature, finally, consider the additional importance of group velocity matching for practical measurements. In practice, the group velocity

$$c_g = \frac{d\omega}{d\kappa} = \frac{d\bar{\omega}}{d\bar{\kappa}} \tag{21}$$

plays an important role, since the group velocity—and not the phase velocity—is the propagation velocity of the energy of finite "wave packets" with similar frequencies. It follows that signals of different group velocities will shift relative to each other with propagation distance. Thus, if the primary and the secondary modes have different group velocities, the initial secondary mode generated at the beginning will separate locally from the primary mode, making the power flux from the primary to the initial secondary mode zero. This results in a bounded secondary wave whose amplitude does not show a linear increase with propagation distance. Therefore, for practical applications which employ finite wave packets, group velocity matching is required. Group velocity matching is defined as $c_g^{(2\omega)} = c_g$.

While it is commonly agreed that phase velocity matching is a necessary condition, the concept of group velocity matching is more controversial. Deng *et al.*,[12] for instance, did not believe that group velocity matching is a necessary condition, while Lee *et al.*[13] supported the argument given above. The analytical complexity to describe the influence of the group velocity on time-domain signals makes analytical arguments difficult to prove. The physical interpretation given above suggests group velocity matching at least as an adjuvant condition, if not necessary.

Two expressions of the group velocity in terms of the variables $\bar{\omega}$, $\bar{\kappa}$, and c_{ph} will be stated for future reference. Note that according to Eq. (17), only two of these variables are independent. First, the frequency equations from the linear elastic theory[8] for symmetric and for antisymmetric modes, respectively, are

$$\Phi_{\mathrm{sym}}(\bar{\omega},\bar{\kappa}) = \cos\bar{\alpha}\sin\bar{\beta}\,(\bar{\kappa}^2-\bar{\beta}^2)^2 + \sin\bar{\alpha}\cos\bar{\beta}\,4\bar{\alpha}\bar{\beta}\bar{\kappa}^2 = 0 \tag{22}$$

and

$$\Phi_{\mathrm{asym}}(\bar{\omega},\bar{\kappa}) = \sin\bar{\alpha}\cos\bar{\beta}\,(\bar{\kappa}^2-\bar{\beta}^2)^2 + \cos\bar{\alpha}\sin\bar{\beta}\,4\bar{\alpha}\bar{\beta}\bar{\kappa}^2 = 0, \tag{23}$$

representing implicit functions of $\bar{\omega}$ and $\bar{\kappa}$. Following Pilarski *et al.*,[14] if $\bar{\omega}$ is regarded as $\bar{\omega}=\bar{\omega}(\bar{\kappa})$, the group velocity is written as

$$c_{g,\mathrm{sym}} = -\frac{\partial\Phi_{\mathrm{sym}}/\partial\bar{\kappa}}{\partial\Phi_{\mathrm{sym}}/\partial\bar{\omega}} = \frac{N_{\mathrm{sym}}}{D_{\mathrm{sym}}} \tag{24}$$

and

$$c_{g,\mathrm{asym}} = -\frac{\partial\Phi_{\mathrm{asym}}/\partial\bar{\kappa}}{\partial\Phi_{\mathrm{asym}}/\partial\bar{\omega}} = \frac{N_{\mathrm{asym}}}{D_{\mathrm{asym}}}, \tag{25}$$

according to Eq. (21) and the rules of derivatives of implicit functions. By carrying out these derivatives, one obtains

$$\begin{aligned} N_{\mathrm{sym}} = {} & \cos\bar{\alpha}\cos\bar{\beta}\,[\bar{\alpha}\bar{\kappa}(\bar{\kappa}^2-\bar{\beta}^2)^2 + 4\bar{\alpha}\bar{\beta}^2\bar{\kappa}^3] \\ & - \sin\bar{\alpha}\sin\bar{\beta}\,[\bar{\beta}\bar{\kappa}(\bar{\kappa}^2-\bar{\beta}^2)^2 + 4\bar{\alpha}^2\bar{\beta}\bar{\kappa}^3] \\ & + \sin\bar{\alpha}\cos\bar{\beta}\,[4\bar{\beta}^2\bar{\kappa}^3 + 4\bar{\alpha}^2\bar{\kappa}^3 - 8\bar{\alpha}^2\bar{\beta}^2\bar{\kappa}] \\ & - \cos\bar{\alpha}\sin\bar{\beta}\,8\bar{\alpha}\bar{\beta}\bar{\kappa}(\bar{\kappa}^2-\bar{\beta}^2), \end{aligned} \tag{26a}$$

$$\begin{aligned} D_{\mathrm{sym}} = {} & \cos\bar{\alpha}\cos\bar{\beta}\left[\bar{\alpha}\frac{\bar{\omega}}{c_T^2}(\bar{\kappa}^2-\bar{\beta}^2)^2 + 4\bar{\alpha}\bar{\beta}^2\bar{\kappa}^2\frac{\bar{\omega}}{c_L^2}\right] \\ & - \sin\bar{\alpha}\sin\bar{\beta}\left[\bar{\beta}\frac{\bar{\omega}}{c_L^2}(\bar{\kappa}^2-\bar{\beta}^2)^2 + 4\bar{\alpha}^2\bar{\beta}\bar{\kappa}^2\frac{\bar{\omega}}{c_T^2}\right] \\ & + \sin\bar{\alpha}\cos\bar{\beta}\left[4\bar{\beta}^2\bar{\kappa}^2\frac{\bar{\omega}}{c_L^2} + 4\bar{\alpha}^2\bar{\kappa}^2\frac{\bar{\omega}}{c_T^2}\right] \\ & - \cos\bar{\alpha}\sin\bar{\beta}\,4\bar{\alpha}\bar{\beta}\frac{\bar{\omega}}{c_T^2}(\bar{\kappa}^2-\bar{\beta}^2) \end{aligned} \tag{26b}$$

for symmetric modes, and

$$\begin{aligned} N_{\mathrm{asym}} = {} & \cos\bar{\alpha}\cos\bar{\beta}\,[\bar{\beta}\bar{\kappa}(\bar{\kappa}^2-\bar{\beta}^2)^2 + 4\bar{\alpha}^2\bar{\beta}\bar{\kappa}^3] \\ & - \sin\bar{\alpha}\sin\bar{\beta}\,[\bar{\alpha}\bar{\kappa}(\bar{\kappa}^2-\bar{\beta}^2)^2 + 4\bar{\alpha}\bar{\beta}^2\bar{\kappa}^3] \\ & - \sin\bar{\alpha}\cos\bar{\beta}\,8\bar{\alpha}\bar{\beta}\bar{\kappa}(\bar{\kappa}^2-\bar{\beta}^2) \\ & + \cos\bar{\alpha}\sin\bar{\beta}\,[4\bar{\beta}^2\bar{\kappa}^3 + 4\bar{\alpha}^2\bar{\kappa}^3 - 8\bar{\alpha}^2\bar{\beta}^2\bar{\kappa}], \end{aligned} \tag{27a}$$

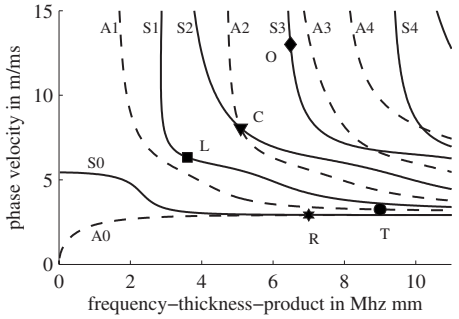

FIG. 4. Dispersion curves for an aluminum plate with matching mode pairs: C—crossing, L—symmetric modes at longitudinal phase velocity, O—cutoff frequency, T—nonzero order modes with a high wave number, and R—quasi-Rayleigh wave.

$$D_{\text{asym}} = \cos\bar{\alpha}\cos\bar{\beta}\left[\bar{\beta}\frac{\bar{\omega}}{c_L^2}(\bar{\kappa}^2-\bar{\beta}^2)^2+4\bar{\alpha}^2\bar{\beta}\bar{\kappa}^2\frac{\bar{\omega}}{c_T^2}\right] - \sin\bar{\alpha}\sin\bar{\beta}\left[\bar{\alpha}\frac{\bar{\omega}}{c_T^2}(\bar{\kappa}^2-\bar{\beta}^2)^2+4\bar{\alpha}\bar{\beta}^2\bar{\kappa}^2\frac{\bar{\omega}}{c_L^2}\right] - \sin\bar{\alpha}\cos\bar{\beta}\,4\bar{\alpha}\bar{\beta}\frac{\bar{\omega}}{c_T^2}(\bar{\kappa}^2-\bar{\beta}^2) + \cos\bar{\alpha}\sin\bar{\beta}\left[4\bar{\beta}^2\bar{\kappa}^2\frac{\bar{\omega}}{c_L^2}+4\bar{\alpha}^2\bar{\kappa}^2\frac{\bar{\omega}}{c_T^2}\right] \tag{27b}$$

for antisymmetric modes. It should be noted that both $\bar{\alpha}$ and $\bar{\beta}$ are functions of $\bar{\omega}$ and $\bar{\kappa}$. Rose[15] presented a description of the group velocity in terms of $\bar{\omega}$ and c_{ph}.

$$c_g = c_{\text{ph}}^2\left(c_{\text{ph}}-\bar{\omega}\frac{dc_{\text{ph}}}{d\bar{\omega}}\right)^{-1}. \tag{28}$$

VI. CHARACTERISTICS OF MATCHING MODE PAIRS

Finally, five mode types (which are independent of material properties) that satisfy all three requirements for a cumulative increase in second harmonic amplitude with propagation distance—nonzero power flux, plus phase and group velocity matching—are identified. Figure 4 shows an example for each type in the dispersion curves for an aluminum plate (c_L=6320 m/ms, c_T=3130 m/ms), featuring crossing points (C), symmetric modes at the longitudinal phase velocity (L), nonzero order modes near cutoff frequencies (O), nonzero order modes with a high wave number (T), and the fundamental modes $A0$ and $S0$ with a high wave number (quasi-Rayleigh wave) (R). Each matching pair is considered in detail to determine their usefulness for practical measurements, with an emphasis on conditions for specific frequencies and wave numbers, plus the amplitudes of surface displacements, particularly out-of-plane motion, which tends to be easier to experimentally measure.

A. Crossing points

A crossing point is defined as a $(\bar{\omega},\bar{\kappa})$-pair for which a symmetric and an antisymmetric mode cross in the dispersion curves. It turns out that this is possible in the region $c_{\text{ph}}>c_L$, where both $\bar{\alpha}$ and $\bar{\beta}$ are real and positive. Thus, at a crossing point, both Eqs. (22) and (23) need to be satisfied simultaneously. By subtraction of Eq. (22) from Eq. (23), one obtains

$$(\sin\bar{\alpha}\cos\bar{\beta}-\cos\bar{\alpha}\sin\bar{\beta})((\bar{\kappa}^2-\bar{\beta}^2)^2-4\bar{\alpha}\bar{\beta}\bar{\kappa}^2)=0. \tag{29}$$

Solving for the term $(\bar{\kappa}^2-\bar{\beta}^2)^2-4\bar{\alpha}\bar{\beta}\bar{\kappa}^2=0$ reduces to the Rayleigh wave speed c_R, which is not the solution sought, since $c_R<c_L$. Hence, from Eq. (29),

$$\sin\bar{\alpha}\cos\bar{\beta}-\cos\bar{\alpha}\sin\bar{\beta}=\sin(\bar{\alpha}-\bar{\beta})=0 \tag{30}$$

or

$$\bar{\alpha}-\bar{\beta}=n\pi,\quad n\in\mathbb{N} \tag{31}$$

is inferred. Substituting this condition into Eq. (22) yields

$$\cos\bar{\beta}\sin\bar{\beta}\,(\bar{\kappa}^2-\bar{\beta}^2)^2+\sin\bar{\beta}\cos\bar{\beta}\,4\bar{\alpha}\bar{\beta}\bar{\kappa}^2=0; \tag{32}$$

hence one concludes

$$\bar{\beta}=n\pi/2,\quad n\in\mathbb{N}^+. \tag{33}$$

Recalling Eq. (31), it is proved that at a crossing point, either case I

$$\bar{\beta}=n_\beta\pi,\quad \bar{\alpha}=n_\alpha\pi,\quad n_\beta,n_\alpha\in\mathbb{N}^+, \tag{34}$$

or case II

$$\bar{\beta}=\frac{(2n_\beta-1)\pi}{2},\quad \bar{\alpha}=\frac{(2n_\alpha-1)\pi}{2},\quad n_\beta,n_\alpha\in\mathbb{N}^+ \tag{35}$$

must hold. Note that $n_\beta>n_\alpha$ by the definition of $\bar{\alpha}$ and $\bar{\beta}$. Using Eq. (5), these conditions allow for the computation of the corresponding frequencies as

$$\bar{\omega}=\sqrt{\frac{n}{c_L^2-c_T^2}}c_Lc_T\pi, \tag{36}$$

where $n=n_\beta^2-n_\alpha^2$ for case I and $n=n_\beta(n_\beta-1)-n_\alpha(n_\alpha-1)$ for case II.

Assuming phase velocity matching, it is concluded for both cases that

$$\bar{\beta}^{(2\omega)}=\bar{n}_\beta\pi,\quad \bar{\alpha}^{(2\omega)}=\bar{n}_\alpha\pi,\quad \bar{n}_\beta,\bar{n}_\alpha\in\mathbb{N}^+, \tag{37}$$

at frequency $2\bar{\omega}$. For case I, both $\bar{n}_\beta$ and $\bar{n}_\alpha$ are even, and odd for case II. This fulfills Eq. (34) and it follows that $(\bar{\omega}^{(2\omega)},\bar{\kappa}^{(2\omega)})$ is a crossing point of case I, which matches phase velocity with the point $(\bar{\omega},\bar{\kappa})$. By the definition of a crossing point, it is obvious that there is phase velocity matching from the symmetric as well as from the antisymmetric mode to both the symmetric and antisymmetric modes at the double frequency.

For the group velocities, the results from Eqs. (24), (25), (26a), (26b), (27a), and (27b) are recalled. For case I, using Eq. (34), the group velocities are

$$c_{g,\text{sym}}^{\text{I}}=\frac{\bar{\kappa}(\bar{\kappa}^2-\bar{\beta}^2)^2+4\bar{\beta}^2\bar{\kappa}^3}{(\bar{\omega}/c_T^2)(\bar{\kappa}^2-\bar{\beta}^2)^2+4\bar{\beta}^2\bar{\kappa}^2(\bar{\omega}/c_L^2)}, \tag{38}$$

TABLE I. Phase velocity matching mode pairs at crossing points.

From mode at $\bar{\omega}$				To mode at $2\bar{\omega}$				
Sym.	Case	$\tilde{u}_y(h)$	$\tilde{u}_z(h)$	Sym.	Case	$\tilde{u}_y(h)$	$\tilde{u}_z(h)$	Group match.
Sym	I	0	$\neq 0$	Sym	I	0	$\neq 0$	Yes
Asym	II	0	$\neq 0$	Sym	I	0	$\neq 0$	Yes
Sym	II	$\neq 0$	0	Sym	I	0	$\neq 0$	No
Asym	I	$\neq 0$	0	Sym	I	0	$\neq 0$	No
Asym	I	$\neq 0$	0	Asym	I	$\neq 0$	0	Yes
Sym	II	$\neq 0$	0	Asym	I	$\neq 0$	0	Yes
Asym	II	0	$\neq 0$	Asym	I	$\neq 0$	0	No
Sym	I	0	$\neq 0$	Asym	I	$\neq 0$	0	No

$$c^{\mathrm{I}}_{g,\mathrm{asym}} = \frac{\bar{\kappa}(\bar{\kappa}^2 - \bar{\beta}^2)^2 + 4\bar{\alpha}^2\bar{\kappa}^3}{(\bar{\omega}/c_L^2)(\bar{\kappa}^2 - \bar{\beta}^2)^2 + 4\bar{\alpha}^2\bar{\kappa}^2(\bar{\omega}/c_T^2)}, \tag{39}$$

while for case II, using Eq. (35), one arrives at

$$c^{\mathrm{II}}_{g,\mathrm{sym}} = \frac{\bar{\kappa}(\bar{\kappa}^2 - \bar{\beta}^2)^2 + 4\bar{\alpha}^2\bar{\kappa}^3}{(\bar{\omega}/c_L^2)(\bar{\kappa}^2 - \bar{\beta}^2)^2 + 4\bar{\alpha}^2\bar{\kappa}^2(\bar{\omega}/c_T^2)}, \tag{40}$$

$$c^{\mathrm{II}}_{g,\mathrm{asym}} = \frac{\bar{\kappa}(\bar{\kappa}^2 - \bar{\beta}^2)^2 + 4\bar{\beta}^2\bar{\kappa}^3}{(\bar{\omega}/c_T^2)(\bar{\kappa}^2 - \bar{\beta}^2)^2 + 4\bar{\beta}^2\bar{\kappa}^2(\bar{\omega}/c_L^2)}. \tag{41}$$

Note that $c^{\mathrm{I}}_{g,\mathrm{sym}} = c^{\mathrm{II}}_{g,\mathrm{asym}}$ and $c^{\mathrm{II}}_{g,\mathrm{sym}} = c^{\mathrm{I}}_{g,\mathrm{asym}}$.

Regarding the crossing point at the double frequency, it was stated already that it can be only of case I. Since phase velocity matching is shown, the group velocities of the crossing point at frequency $2\bar{\omega}$ are obtained with Eqs. (38) and (39) for case I. Then, the factors of 2 cancel and it is shown that

$$c^{\mathrm{I}}_{g,\mathrm{sym}} = c^{\mathrm{I},(2\omega)}_{g,\mathrm{sym}}, \tag{42}$$

$$c^{\mathrm{I}}_{g,\mathrm{asym}} = c^{\mathrm{I},(2\omega)}_{g,\mathrm{asym}}. \tag{43}$$

Thus, the following conclusions are made.

- If the crossing point $(\bar{\omega},\bar{\kappa})$ is case I, then there is group velocity matching from the symmetric mode at $(\bar{\omega},\bar{\kappa})$ to the symmetric mode at $(2\bar{\omega},2\bar{\kappa})$, i.e., $c^{\mathrm{I}}_{g,\mathrm{sym}} = c^{\mathrm{I},(2\omega)}_{g,\mathrm{sym}}$, as well as from the antisymmetric mode at $(\bar{\omega},\bar{\kappa})$ to the antisymmetric mode at $(2\bar{\omega},2\bar{\kappa})$, i.e., $c^{\mathrm{I}}_{g,\mathrm{asym}} = c^{\mathrm{I},(2\omega)}_{g,\mathrm{asym}}$.
- If the crossing point $(\bar{\omega},\bar{\kappa})$ is case II, then there is group velocity matching from the symmetric mode at $(\bar{\omega},\bar{\kappa})$ to the antisymmetric mode at $(2\bar{\omega},2\bar{\kappa})$, i.e., $c^{\mathrm{II}}_{g,\mathrm{sym}} = c^{\mathrm{I},(2\omega)}_{g,\mathrm{asym}}$, as well as from the antisymmetric mode at $(\bar{\omega},\bar{\kappa})$ to the symmetric mode at $(2\bar{\omega},2\bar{\kappa})$, i.e., $c^{\mathrm{II}}_{g,\mathrm{asym}} = c^{\mathrm{I},(2\omega)}_{g,\mathrm{sym}}$.

Table I itemizes each possible combination along with the results about the displacements at the surface, which are explored in the following.

Regarding case I crossing points, the displacements at the surface follow by substitution of Eq. (34) into Eqs. (4) and (6), setting $y=h$. For symmetric modes, one obtains

$$\tilde{u}^{\mathrm{I}}_y(h) = 0, \tag{44a}$$

$$\tilde{u}^{\mathrm{I}}_z(h) = Dh\bar{\beta}\frac{\bar{\kappa}^2 + \bar{\beta}^2}{\bar{\kappa}^2 - \bar{\beta}^2}\cos\bar{\beta}, \tag{44b}$$

where the frequency equation, Eq. (22), is applied to simplify the expression. The displacements at the surface for the antisymmetric modes take the form

$$\tilde{u}^{\mathrm{I}}_y(h) = iCh\frac{\bar{\kappa}^2 + \bar{\beta}^2}{2\bar{\kappa}}\cos\bar{\beta}, \tag{45a}$$

$$\tilde{u}^{\mathrm{I}}_z(h) = 0, \tag{45b}$$

where the frequency equation Eq. (23) is used.

Similarly, using Eq. (35) for case II crossing points yields

$$\tilde{u}^{\mathrm{II}}_y(h) = iDh\frac{\bar{\kappa}^2 + \bar{\beta}^2}{2\bar{\kappa}}\sin\bar{\beta}, \tag{46a}$$

$$\tilde{u}^{\mathrm{II}}_z(h) = 0 \tag{46b}$$

for symmetric modes, and

$$\tilde{u}^{\mathrm{II}}_y(h) = 0, \tag{47a}$$

$$\tilde{u}^{\mathrm{II}}_z(h) = -Ch\bar{\beta}\frac{\bar{\kappa}^2 + \bar{\beta}^2}{\bar{\kappa}^2 - \bar{\beta}^2}\sin\bar{\beta} \tag{47b}$$

for antisymmetric modes.

Summarizing these results with reference to Table I, either the symmetric or the antisymmetric mode at a crossing point matches phase and group velocity with the symmetric mode of the crossing point at the double frequency. Two observations deserve special mention. First, only the first two entries in Table I satisfy all the conditions required above. The other entries have either an antisymmetric secondary mode making the power flux from the primary wave zero or do not match group velocity. Second, for all the relevant pairs, the normal displacements at the surface are identically zero.

B. Symmetric modes at the longitudinal velocity

An investigation of symmetric Lamb modes at the longitudinal phase velocity c_L with regard to the out-of-plane displacement at the free surface and group velocity was pre-

sented by Pilarski *et al.*[14] They provide frequency-thickness products, where phase velocity equals longitudinal velocity. Then, they prove that the normal displacement at the surface vanishes and that all modes at these points have the same group velocity, which depends on the linear material properties only. This section considers these results in terms of phase and group velocity matching.

Using the condition $c_{\mathrm{ph}}=c_L$, one obtains

$$\bar{\alpha}=0, \quad \bar{\beta}=n\pi, \quad n\in\mathbb{N}^+ \tag{48}$$

to satisfy the frequency relation. The corresponding frequencies

$$\bar{\omega}=\frac{n\pi c_T}{\sqrt{1-(c_T/c_L)^2}}, \quad n\in\mathbb{N}^+ \tag{49}$$

are obtained from Eqs. (5) and (48). Assuming phase velocity matching yields

$$\bar{\alpha}^{(2\omega)}=0, \quad \bar{\beta}^{(2\omega)}=2n\pi, \quad n\in\mathbb{N}^+, \tag{50}$$

which satisfies Eq. (48). Thus, there is phase velocity matching from each symmetric mode at the frequencies described in Eq. (49) to another symmetric mode at the double frequency both having the longitudinal phase velocity.

Substitution of Eq. (48) into the relation for the group velocity Eq. (24) results in

$$c_g=\frac{\bar{\kappa}(\bar{\kappa}^2-\bar{\beta}^2)^2+8\bar{\beta}^2\bar{\kappa}^3}{(\bar{\omega}/c_T^2)(\bar{\kappa}^2-\bar{\beta}^2)^2+8\bar{\beta}^2\bar{\kappa}^2(\bar{\omega}/c_L^2)}, \tag{51}$$

where the limit $\sin(\bar{\alpha})\approx\bar{\alpha}$ is used, since $\bar{\alpha}$ is very small. This is simplified as

$$c_g=\frac{c_L c_T^2(c_L^4+4c_L^2c_T^2-4c_T^4)}{12c_L^2c_T^4-4c_L^4c_T^2+c_L^6-8c_T^6} \tag{52}$$

and thus depends only on the material's properties. Consequently, the group velocity is constant for all symmetric modes at the longitudinal phase velocity. This means, for each phase velocity matching pair, group velocity matching is fulfilled as well. Note that Pilarski *et al.*[14] obtained another value for the group velocity. Confidence in the value presented here is gained by comparison to numerical results from the software DISPERSE.[16]

The displacement field in Eq. (4) yields

$$\tilde{u}_y(h)=0, \tag{53}$$

if the conditions of Eq. (48) are satisfied, i.e., the normal displacement at the surface is zero. Using the frequency Eq. (22), the in-plane displacement at the surface becomes

$$\tilde{u}_z(h)=Dh\bar{\beta}\frac{\bar{\kappa}^2+\bar{\beta}^2}{\bar{\kappa}^2-\bar{\beta}^2}\cos\bar{\beta}, \tag{54}$$

which is nonzero.

In summary, each symmetric mode at the longitudinal phase velocity shows phase and group velocity matching to another symmetric mode at the double frequency. The respective frequencies and the common group velocity are given above. As is the case for crossing points, the out-of-plane displacement at the surface is zero, while the in-plane displacement at the surface is nonzero.

C. Nonzero order modes near cutoff frequencies

Graff[8] provided a concise introduction to cutoff frequencies, which are obtained for the low wave number limit $\bar{\kappa}\to 0$. This section relates Graff's results to phase and group velocity matching.

In the low wave number limit $\bar{\kappa}\to 0$,

$$\bar{\alpha}\to\frac{\bar{\omega}}{c_L}, \quad \bar{\beta}\to\frac{\bar{\omega}}{c_T}, \tag{55}$$

hold, which leads to the conditions

$$\text{case SI:} \quad \bar{\alpha}\to\frac{(2n-1)\pi}{2}, \quad n\in\mathbb{N}^+ \tag{56a}$$

or

$$\text{case SII:} \quad \bar{\beta}\to n\pi, \quad n\in\mathbb{N}^+, \tag{56b}$$

for symmetric modes, and

$$\text{case AI:} \quad \bar{\alpha}\to n\pi, \quad n\in\mathbb{N}^+ \tag{56c}$$

or

$$\text{case AII:} \quad \bar{\beta}\to\frac{(2n-1)\pi}{2}, \quad n\in\mathbb{N}^+, \tag{56d}$$

for antisymmetric modes. From Eqs. (55) and (56), the respective cutoff frequencies are obtained as

$$\text{case SI:} \quad \bar{\omega}\to\frac{(2n-1)\pi}{2}c_L, \quad n\in\mathbb{N}^+, \tag{57a}$$

$$\text{case SII:} \quad \bar{\omega}\to n\pi c_T, \quad n\in\mathbb{N}^+, \tag{57b}$$

$$\text{case AI:} \quad \bar{\omega}\to n\pi c_L, \quad n\in\mathbb{N}^+, \tag{57c}$$

$$\text{case AII:} \quad \bar{\omega}\to\frac{(2n-1)\pi}{2}c_T, \quad n\in\mathbb{N}^+. \tag{57d}$$

To show phase velocity matching for a case SI mode in the limit $\bar{\kappa}\to 0$, the phase velocity matching conditions are applied to Eq. (56a) to obtain

$$\bar{\alpha}_{\mathrm{SI}}^{(2\omega)}=(2n-1)\pi\in\text{case AI}, \tag{58a}$$

where the subindex indicates the type of the mode at frequency $\bar{\omega}$. This means that there is phase velocity matching from every case SI mode to the case AI mode at the double frequency. Similarly, the phase velocity matching conditions for the other cases

$$\bar{\beta}_{\mathrm{SII}}^{(2\omega)}=2n\pi\in\text{case SII}, \tag{58b}$$

$$\bar{\alpha}_{\mathrm{AI}}^{(2\omega)}=2n\pi\in\text{case AI}, \tag{58c}$$

$$\bar{\beta}_{\mathrm{AII}}^{(2\omega)}=(2n-1)\pi\in\text{case SII} \tag{58d}$$

are obtained. In other words, in the limit $\bar{\kappa}\to 0$ there is phase

TABLE II. Phase velocity matching mode pairs at cutoff frequencies.

From mode at $\bar{\omega}$				To mode at $2\bar{\omega}$			
Case	$\bar{\alpha}$, $\bar{\beta}$	$\tilde{u}_y(h)$	$\tilde{u}_z(h)$	Case	$\bar{\alpha}$, $\bar{\beta}$	$\tilde{u}_y(h)$	$\tilde{u}_z(h)$
SII	$\bar{\beta}=n\pi$	0	$\neq 0$	SII	$\bar{\beta}=2n\pi$	0	$\neq 0$
AII	$\bar{\beta}=\frac{(2n-1)\pi}{2}$	0	$\neq 0$	SII	$\bar{\beta}=(2n-1)\pi$	0	$\neq 0$
SI	$\bar{\alpha}=\frac{(2n-1)\pi}{2}$	$\neq 0$	0	AI	$\bar{\alpha}=(2n+1)\pi$	$\neq 0$	0
AI	$\bar{\alpha}=n\pi$	$\neq 0$	0	AI	$\bar{\alpha}=2n\pi$	$\neq 0$	0

velocity matching:

- from every case SI symmetric mode to a case AI antisymmetric mode,
- from every case SII symmetric mode to a case SII symmetric mode,
- from every case AI antisymmetric mode to a case AI antisymmetric mode, and
- from every case AII antisymmetric mode to a case SII symmetric mode.

Note that $c_{\mathrm{ph}}\to\infty$ as $\bar{\kappa}\to 0$, and thus, phase velocity matching in this limiting case means that both phase velocities of the mode pair approach infinity.

The group velocities for all the modes described above converge to zero, i.e.,

$$c_g^i \to 0, \quad i=\mathrm{SI,SII,AI,AII} \tag{59}$$

as $\bar{\kappa}\to 0$, which is observed by Eqs. (24) and (25). Using the relations for the cutoff frequencies above, all the terms in the nominator tend to zero, while there is always a term in the denominator that does not vanish. Hence, each phase velocity matching pair shows group velocity matching with the group velocity tending to zero.

Graff's[8] results are presented for the surface displacements. The displacements of symmetric modes become

$$\tilde{u}_y(y) \to -\frac{A}{h}\bar{\alpha}\sin\bar{\alpha}\frac{y}{h}, \tag{60a}$$

$$\tilde{u}_z(y) \to -\frac{D}{h}\bar{\beta}\cos\bar{\beta}\frac{y}{h}, \tag{60b}$$

as $\bar{\kappa}\to 0$, where A is another arbitrary complex constant. For case I, the boundary conditions require $D=0$, thus

$$\tilde{u}_y^{\mathrm{SI}}(h) \to -\frac{A}{h}\bar{\alpha}\sin\bar{\alpha}, \quad \tilde{u}_z^{\mathrm{SI}}(h)\to 0 \tag{61}$$

with $\bar{\alpha}\to(2n-1)\pi/2$. For case SII, on the other hand, $A=0$ is required, resulting in

$$\tilde{u}_y^{\mathrm{SII}}(h) \to 0, \quad \tilde{u}_z^{\mathrm{SII}}(h) \to -\frac{D}{h}\bar{\beta}\cos\bar{\beta} \tag{62}$$

with $\bar{\beta}\to n\pi$.

Regarding antisymmetric modes, the displacement field reduces to

$$\tilde{u}_y(y) \to \frac{B}{h}\bar{\alpha}\cos\bar{\alpha}\frac{y}{h}, \tag{63a}$$

$$\tilde{u}_z(y) \to \frac{C}{h}\bar{\beta}\sin\bar{\beta}\frac{y}{h} \tag{63b}$$

with the complex constant B. For case AI, the boundary conditions yield $C=0$, or

$$\tilde{u}_y^{\mathrm{AI}}(h) \to \frac{B}{h}\bar{\alpha}\cos\bar{\alpha}, \quad \tilde{u}_z^{\mathrm{AI}}(h)\to 0 \tag{64}$$

with $\bar{\alpha}\to n\pi$, while case AII requires $B=0$, and thus

$$\tilde{u}_y^{\mathrm{AII}}(h) \to 0, \quad \tilde{u}_z^{\mathrm{AII}}(h) \to \frac{C}{h}\bar{\beta}\sin\bar{\beta}, \tag{65}$$

where $\bar{\beta}\to(2n-1)\pi/2$.

Table II shows all the possible combinations with their displacements at the surface. Again, only symmetric modes at double frequencies are useful for second harmonic generation, i.e., the first two entries in the table. One observes—as in Secs. VI A and VI B—that the out-of-plane displacement at the surface for these modes is zero, while the in-plane component is nonzero. For $\bar{\kappa}=0$, the group velocity is zero, meaning that no energy is carried and the wave does not propagate. For this reason, these modes are practically relevant only in the approximation where $\bar{\kappa}$ is small, but nonzero. Then, phase velocity matching holds approximately, and the group velocity and the normal displacement at the surface is small, but nonzero.

D. Nonzero order modes with high wave number

For high wave numbers, i.e., $\bar{\kappa}\to\infty$, nonzero order modes show a nondispersive behavior. It will be shown that both the phase and the group velocity converge to the shear wave speed c_T for all nonzero order modes, and thus satisfy approximately the matching conditions.

In this section, the region $c_T<c_{\mathrm{ph}}<c_L$ is considered. It follows that $\bar{\alpha}=\bar{\alpha}'i$, where

$$\bar{\alpha}' = \sqrt{\bar{\kappa}^2-\left(\frac{\bar{\omega}}{c_L}\right)^2}, \tag{66}$$

and thus, the frequency equations are

$$\Phi_{\mathrm{sym}}(\bar{\omega},\bar{\kappa}) = \sin\bar{\beta}\left[1-\left(\frac{\bar{\beta}}{\bar{\kappa}}\right)^2\right]^2 - 4\tanh\bar{\alpha}'\cos\bar{\beta}\,\frac{\bar{\alpha}'\bar{\beta}}{\bar{\kappa}^2} = 0 \tag{67}$$

and

$$\Phi_{\mathrm{asym}}(\bar{\omega},\bar{\kappa}) = \cos\bar{\beta}\left[1-\left(\frac{\bar{\beta}}{\bar{\kappa}}\right)^2\right]^2 + 4\coth\bar{\alpha}'\sin\bar{\beta}\,\frac{\bar{\alpha}'\bar{\beta}}{\bar{\kappa}^2} = 0. \tag{68}$$

In the high wave number limit $\bar{\kappa}\to\infty$, requiring

$$\bar{\beta}\to n\pi, \quad n\in\mathbb{N}^+ \tag{69}$$

satisfies Eq. (67) for symmetric modes. Similarly, Eq. (68) for antisymmetric modes holds for

$$\bar{\beta}\to\frac{(2n-1)\pi}{2}, \quad n\in\mathbb{N}^+. \tag{70}$$

In these cases, since

$$\frac{\bar{\beta}}{\bar{\kappa}} = \sqrt{\left(\frac{c_{\mathrm{ph}}}{c_T}\right)^2 - 1}\to 0, \tag{71}$$

one concludes $c_{\mathrm{ph}}\to c_T$, and

$$\bar{\alpha}' = \bar{\kappa}\sqrt{1-\left(\frac{c_{\mathrm{ph}}}{c_L}\right)^2}\to\bar{\kappa}\gamma\to\infty, \tag{72}$$

where $\gamma=\sqrt{1-(c_T/c_L)^2}$. That is, the phase velocity of all the nonzero order modes converges to the shear velocity for $\bar{\kappa}\to\infty$. Furthermore, since $\bar{\omega}\to c_T\bar{\kappa}\to\infty$, the frequency increases with wave number.

Since all the nonzero order modes converge to the same phase velocity, there is phase velocity matching from each of these modes to every nonzero order mode in the high wave number limit $\bar{\kappa}\to\infty$. This also implies that the modes show a nondispersive behavior, meaning that $\partial c_{\mathrm{ph}}/\partial\bar{\omega}=0$. From Eq. (28),

$$c_g\to c_{\mathrm{ph}}\to c_T \tag{73}$$

follows, i.e., the group velocities of all the nonzero order modes converge to the shear velocity. Thus, group velocity matching from each to every nonzero order mode is concluded for the limit $\bar{\kappa}\to\infty$.

For the subsequent investigation of the displacements, the limits

$$\frac{(\bar{\kappa}^2-\bar{\beta}^2)}{\bar{\kappa}} = \bar{\kappa}\left[1-\left(\frac{\bar{\beta}}{\bar{\kappa}}\right)^2\right]\to\bar{\kappa} \tag{74}$$

and

$$\frac{(\bar{\kappa}^2-\bar{\beta}^2)}{\bar{\alpha}} = \frac{1}{\gamma}\bar{\kappa}\left[1-\left(\frac{\bar{\beta}}{\bar{\kappa}}\right)^2\right]\to\frac{\bar{\kappa}}{\gamma} \tag{75}$$

will be helpful. Another limit for symmetric modes is obtained using the frequency relation, Eq. (67),

$$\bar{\kappa}\sin\bar{\beta}\to 4\tanh\bar{\alpha}'\cos\bar{\beta}\,\frac{\bar{\alpha}'\bar{\beta}}{\bar{\kappa}}\to 4\gamma\bar{\beta}\cos\bar{\beta}<\infty, \tag{76}$$

which is used to calculate the displacements at the surface from Eq. (4),

$$\tilde{u}_y^{\mathrm{sym}}(h)\to 2iDh\gamma\bar{\beta}\cos\bar{\beta}<\infty, \tag{77a}$$

$$\tilde{u}_z^{\mathrm{sym}}(h)\to Dh\bar{\beta}\cos\bar{\beta}<\infty. \tag{77b}$$

Equation (77) suggests that the displacements at the surface are nonzero. Yet, if the depth $y^n=h/(2n)$ is considered, for example, one term in the normal displacement of Eq. (4) tends to infinity, since

$$\bar{\kappa}\sin(\bar{\beta}y^n/h)\to\bar{\kappa}\sin(\pi/2)=\bar{\kappa}\to\infty. \tag{78}$$

Thus, D has to approach zero in order to obtain a physically reasonable, finite displacement field, and the out-of-plane displacement at the surface $u_y(h)$ becomes infinitesimally small compared to the displacement $u_y(h/(2n))$, i.e.,

$$\tilde{u}_y^{\mathrm{sym}}(h)\to 0. \tag{79}$$

For the in-plane displacement $u_z(y)$, there is no depth y to make any term unbounded, so that

$$\tilde{u}_z^{\mathrm{sym}}(y)\to 0 \quad \text{for all } y \tag{80}$$

follows, i.e., the wave tends to become a pure shear wave as $\bar{\kappa}\to\infty$, propagating at the shear wave speed.

Regarding antisymmetric modes, Eqs. (68) and (70) yield the limit

$$\bar{\kappa}\cos\bar{\beta}\to -4\coth\bar{\alpha}'\sin\bar{\beta}\,\frac{\bar{\alpha}'\bar{\beta}}{\bar{\kappa}}\to -4\gamma\bar{\beta}\sin\bar{\beta}<\infty, \tag{81}$$

which is used to calculate the displacements of Eq. (6) at the surface,

$$\tilde{u}_y^{\mathrm{asym}}(h)\to -2iCh\gamma\bar{\beta}\sin\bar{\beta}<\infty, \tag{82a}$$

$$\tilde{u}_z^{\mathrm{asym}}(h)\to -Ch\bar{\beta}\sin\bar{\beta}<\infty. \tag{82b}$$

If the middle layer $y^n=0$ is considered in Eq. (6), the normal displacement tends to infinity because

$$\bar{\kappa}\cos(\bar{\beta}y^n/h)\to\bar{\kappa}\cos(0)=\bar{\kappa}\to\infty, \tag{83}$$

while there is no y that makes the in-plane displacement unbounded. Hence, with the same argument as above,

$$\tilde{u}_y^{\mathrm{asym}}(h)\to 0 \tag{84}$$

and

$$\tilde{u}_z^{\mathrm{asym}}(y)\to 0 \quad \text{for all } y. \tag{85}$$

Thus, as $\bar{\kappa}\to\infty$, both symmetric and antisymmetric modes tend to become pure shear waves at the shear velocity with zero displacements at the surface.

In summary, as $\bar{\kappa}\to\infty$ in the region $c_T<c_{\mathrm{ph}}<c_L$, it is shown that all nonzero order modes approach the shear ve-

locity c_T in both the phase and the group velocity. Hence, phase and group velocity matching is concluded from each to every mode in the high wave number limit. Furthermore, the out-of-plane displacement at the surface and the in-plane displacement over the whole cross section converge to zero, so that the motion becomes pure shear. From a practical perspective, the results may be applied approximately, i.e., as $\bar{\kappa}$ becomes large but not infinity. Then, depending on the wave number and the approximation tolerance applied, the results hold for a certain number of modes.

E. Fundamental modes with high wave number (quasi-Rayleigh surface wave)

In the region $c_{\mathrm{ph}}<c_T<c_L$ for $\bar{\kappa}\to\infty$, the fundamental modes take the form of a Rayleigh surface wave, called a quasi-Rayleigh wave for plates. The additional term *quasi* indicates that this is not the original Rayleigh wave—as defined for a semi-infinite half-space—but the Lamb modes that behave like a Rayleigh wave in the high frequency domain. As $\bar{\kappa}$ increases, the wavelength becomes much smaller than the plate's thickness, so that the plate appears approximately as a semi-infinite half-space.

The condition $c_{\mathrm{ph}}<c_T$ implies that $\bar{\alpha}$ and $\bar{\beta}$ are complex and written as $\bar{\alpha}=i\bar{\alpha}'$ and $\bar{\beta}=i\bar{\beta}'$, where $\bar{\alpha}'$ as in Eq. (66) and

$$\bar{\beta}' = \sqrt{\bar{\kappa}^2 - \left(\frac{\bar{\omega}}{c_T}\right)^2}. \tag{86}$$

The frequency equations (22) and (23) reduce to the Rayleigh wave equation

$$(\bar{\kappa}^2 + \bar{\beta}'^2)^2 - 4\bar{\alpha}'\bar{\beta}'\bar{\kappa}^2 = 0, \tag{87}$$

whose solution is the Rayleigh wave speed c_R with the property $c_R<c_T$. Hence, the limits

$$\bar{\alpha}' = \bar{\kappa}\sqrt{1 - \left(\frac{c_R}{c_L}\right)^2} \to \bar{\kappa}\gamma_\alpha \to \infty, \tag{88}$$

$$\bar{\beta}' = \bar{\kappa}\sqrt{1 - \left(\frac{c_R}{c_T}\right)^2} \to \bar{\kappa}\gamma_\beta \to \infty \tag{89}$$

are concluded, where $\gamma_\alpha=\sqrt{1-(c_R/c_L)^2}$ and $\gamma_\beta=\sqrt{1-(c_R/c_T)^2}$.

Since both fundamental modes $A0$ and $S0$ converge to the Rayleigh wave speed in the high wave number limit $\bar{\kappa}\to\infty$, there is phase velocity matching from each fundamental mode to itself and to the other one. As in Sec. VI D, group velocity equals phase velocity, i.e.,

$$c_g \to c_{\mathrm{ph}} \to c_R \tag{90}$$

due to the nondispersive behavior and Eq. (28). Hence, group velocity matching for the fundamental modes is concluded.

Substituting the limits obtained above in the displacement fields, Eqs. (4) and (6) result in

$$\tilde{u}_y^{S0}(y) = \frac{D\bar{\kappa}}{h}\left(\frac{(1+\gamma_\beta^2)\sinh\bar{\beta}'}{2\sinh\bar{\alpha}'}\sinh\left(\bar{\alpha}'\frac{y}{h}\right) - \sinh\left(\bar{\beta}'\frac{y}{h}\right)\right), \tag{91a}$$

$$\tilde{u}_z^{S0}(y) = \frac{iD\bar{\kappa}}{h}\left(\frac{(1+\gamma_\beta^2)\sinh\bar{\beta}'}{2\gamma_\alpha\sinh\bar{\alpha}'}\cosh\left(\bar{\alpha}'\frac{y}{h}\right) - \gamma_\beta\cosh\left(\bar{\beta}'\frac{y}{h}\right)\right) \tag{91b}$$

for the symmetric fundamental mode $S0$, and

$$\tilde{u}_y^{A0}(y) = \frac{iC\bar{\kappa}}{h}\left(-\frac{(1+\gamma_\beta^2)\cosh\bar{\beta}'}{2\cosh\bar{\alpha}'}\cosh\left(\bar{\alpha}'\frac{y}{h}\right) + \cosh\left(\bar{\beta}'\frac{y}{h}\right)\right), \tag{92a}$$

$$\tilde{u}_z^{A0}(y) = \frac{C\bar{\kappa}}{h}\left(\frac{(1+\gamma_\beta^2)\cosh\bar{\beta}'}{2\gamma_\alpha\cosh\bar{\alpha}'}\sinh\left(\bar{\alpha}'\frac{y}{h}\right) - \gamma_\beta\sinh\left(\bar{\beta}'\frac{y}{h}\right)\right) \tag{92b}$$

for the antisymmetric fundamental mode $A0$. These equations show—according to the theory of Rayleigh waves—that the energy is concentrated at the surface and that displacements vanish exponentially with depth. As $\bar{\alpha}'$ and $\bar{\beta}'$ become large, the $\sinh(\cdot)$ and $\cosh(\cdot)$ terms grow with a faster exponential rate as y approaches h. In the very limit $\bar{\alpha}', \bar{\beta}'\to\infty$, the displacement is concentrated entirely in an infinitesimally small layer beneath the surface. Therefore, large out-of-plane and in-plane displacements are observed at the plate's surface.

In summary, for large wave numbers and frequencies, both the phase and the group velocity of the fundamental modes $S0$ and $A0$ converge to the Rayleigh surface wave speed $c_R<c_T$. Due to its nondispersive behavior, both phase and group velocity matching are concluded. The displacements at the surface are large as compared to the inner part of the plate, since energy is concentrated in a thin layer beneath the surface.

VII. CONCLUSION

This research considers the conditions for the second harmonic generation of Lamb waves using these results to determine five different types of matching pairs of Lamb modes with internal resonance. These matching mode pairs all satisfy the conditions of nonzero power flux to the second harmonic wave, phase velocity matching, and group velocity matching. The first condition is shown to be satisfied if symmetric second harmonic modes are considered. For the velocity matching conditions, two mode types match phase and group velocity exactly (crossing points and symmetric modes at the longitudinal velocity), while three mode types match

approximately (modes near cutoff frequencies, nonzero order modes for high wave numbers, and quasi-Rayleigh wave). The analysis of these matching mode pairs provides critical information for their experimental generation and detection such as excitation frequencies, and related quantities such as phase and group velocity. In addition, it is shown that all these mode pairs (except for the quasi-Rayleigh pair) that satisfy internally resonant second harmonic generation also display zero out-of-plane displacements at the surface.

These results provide a suite of potential mode combinations that can be used to experimentally measure a second harmonic amplitude that is linearly increasing with propagation distance, potentially with a higher signal-to-noise ratio. These measured second harmonic amplitudes enable the direct characterization of a material's nonlinear elastic components and the associated damage state.

ACKNOWLEDGMENTS

This work was partially supported by the National Science Foundation under Contract No. CMMI-0653883 and the Air Force Office of Scientific Research under Contract No. FA9550-08-1-0241. The Deutscher Akademischer Austauschdienst (DAAD) provided partial support to Martin F. Müller.

APPENDIX: EXPANSION OF FORCING TERM

$$\bar{S}_{yy} = \left(\frac{3\lambda}{2} + 3\mu + \bar{A} + 3\bar{B} + \bar{C}\right)\frac{\partial u_y}{\partial y}\frac{\partial u_y}{\partial y} + \left(\frac{\lambda}{2} + \mu + \frac{\bar{A}}{4} + \frac{\bar{B}}{2}\right)\left(\frac{\partial u_y}{\partial z}\frac{\partial u_y}{\partial z} + \frac{\partial u_z}{\partial y}\frac{\partial u_z}{\partial y}\right) + \left(\frac{\lambda}{2} + \bar{B} + \bar{C}\right)\frac{\partial u_z}{\partial z}\frac{\partial u_z}{\partial z} + (\lambda + 2\bar{B} + 2\bar{C})\frac{\partial u_y}{\partial y}\frac{\partial u_z}{\partial z} + \left(\mu + \frac{\bar{A}}{2} + \bar{B}\right)\frac{\partial u_y}{\partial z}\frac{\partial u_z}{\partial y}, \tag{A1}$$

$$\bar{S}_{zz} = \left(\frac{3\lambda}{2} + 3\mu + \bar{A} + 3\bar{B} + \bar{C}\right)\frac{\partial u_z}{\partial z}\frac{\partial u_z}{\partial z} + \left(\frac{\lambda}{2} + \mu + \frac{\bar{A}}{4} + \frac{\bar{B}}{2}\right)\left(\frac{\partial u_y}{\partial z}\frac{\partial u_y}{\partial z} + \frac{\partial u_z}{\partial y}\frac{\partial u_z}{\partial y}\right) + \left(\frac{\lambda}{2} + \bar{B} + \bar{C}\right)\frac{\partial u_y}{\partial y}\frac{\partial u_y}{\partial y} + (\lambda + 2\bar{B} + 2\bar{C})\frac{\partial u_y}{\partial y}\frac{\partial u_z}{\partial z} + \left(\mu + \frac{\bar{A}}{2} + \bar{B}\right)\frac{\partial u_y}{\partial z}\frac{\partial u_z}{\partial y}, \tag{A2}$$

$$\bar{S}_{yz} = \left(\lambda + 2\mu + \frac{\bar{A}}{2} + \bar{B}\right)\left(\frac{\partial u_y}{\partial y}\frac{\partial u_z}{\partial y} + \frac{\partial u_z}{\partial z}\frac{\partial u_z}{\partial y}\right) + \left(\mu + \frac{\bar{A}}{2} + \bar{B}\right)\left(\frac{\partial u_y}{\partial y}\frac{\partial u_y}{\partial z} + \frac{\partial u_z}{\partial z}\frac{\partial u_y}{\partial z}\right), \tag{A3}$$

$$\bar{S}_{zy} = \left(\lambda + 2\mu + \frac{\bar{A}}{2} + \bar{B}\right)\left(\frac{\partial u_y}{\partial y}\frac{\partial u_y}{\partial z} + \frac{\partial u_z}{\partial z}\frac{\partial u_y}{\partial z}\right) + \left(\mu + \frac{\bar{A}}{2} + \bar{B}\right)\left(\frac{\partial u_y}{\partial y}\frac{\partial u_z}{\partial y} + \frac{\partial u_z}{\partial z}\frac{\partial u_z}{\partial y}\right). \tag{A4}$$

[1]J.-Y. Kim, L. J. Jacobs, J. Qu, and J. W. Littles, "Experimental characterization of fatigue damage in a nickel-base superalloy using nonlinear ultrasonic waves," J. Acoust. Soc. Am. **120**, 1266–1273 (2006).
[2]J. Herrmann, J.-Y. Kim, L. J. Jacobs, J. Qu, J. W. Littles, and M. F. Savage, "Assessment of material damage in a nickel-base superalloy using nonlinear Rayleigh surface waves," J. Appl. Phys. **99**, 124913 (2006).
[3]C. Pruell, J.-Y. Kim, J. Qu, and L. J. Jacobs, "Evaluation of plasticity driven material damage using Lamb waves," Appl. Phys. Lett. **91**, 231911 (2007).
[4]C. Pruell, J.-Y. Kim, J. Qu, and L. J. Jacobs, "Evaluation of fatigue damage using nonlinear guided waves," Smart Mater. Struct. **18**, 035003 (2009).
[5]W. J. de Lima and M. F. Hamilton, "Finite-amplitude waves in isotropic elastic plates," J. Sound Vib. **265**, 819–839 (2003).
[6]M. Deng, "Analysis of second-harmonic generation of Lamb modes using a modal analysis approach," J. Appl. Phys. **94**, 4152–4159 (2003).
[7]A. Srivastava and F. L. di Scalea, "On the existence of antisymmetric or symmetric Lamb waves at nonlinear higher harmonics," J. Sound Vib. **323**, 932–943 (2009).
[8]K. F. Graff, *Wave Motion in Elastic Solids* (Oxford University Press, London, 1975).
[9]J. D. Achenbach, *Wave Propagation in Elastic Solids* (Elsevier Science B.V, Amsterdam, 1975).
[10]L. D. Landau and E. M. Lifshitz, *Theory of Elasticity* (Pergamon, New York, 1986).
[11]M. Deng, "Cumulative second-harmonic generation of Lamb-mode propagation in a solid plate," J. Appl. Phys. **85**, 3051–3058 (1999).
[12]M. Deng, P. Wang, and X. Lv, "Experimental observation of cumulative second-harmonic generation of Lamb-wave propagation in an elastic plate," J. Phys. D: Appl. Phys. **38**, 344–353 (2005).
[13]T.-H. Lee, I.-H. Choi, and K.-Y. Jhang, "The nonlinearity of guided wave in an elastic plate," Mod. Phys. Lett. B **22**, 1135–1140 (2008).
[14]A. Pilarski, J. J. Ditri, and J. L. Rose, "Remarks on symmetric Lamb waves with dominant longitudinal displacements," J. Acoust. Soc. Am. **93**, 2228–2230 (1993).
[15]J. L. Rose, *Ultrasonic Waves in Solid Media* (Cambridge University Press, Cambridge, 1999).
[16]B. Pavlakovic and M. Lowe, DISPERSE, User's Manual Version 2.0.11, Software Version 2.0.15e, Imperial College, London, England (2001).

Limiting factors in acoustic separation of carbon particles in air

David Karpul,[a] Jonathan Tapson, Michael Rapson, Adrian Jongens, and Gregory Cohen
Department of Electrical Engineering, University of Cape Town, Rondebosch, Cape Town 7701, South Africa

(Received 26 May 2009; revised 17 January 2010; accepted 19 January 2010)

Particles suspended in a fluid that is exposed to an acoustic standing wave experience a time-averaged force that drives them to either the pressure nodes or anti-nodes of the wave. Several filter designs have been successfully implemented using this force to filter small particles in liquids with low flow rates and small cross-sectional areas. It has been suggested that the filtration of small solid particles out of a gas, such as carbon in air (smoke), would be a possible application of acoustic standing wave based particle separation. This study shows the limiting factors, in both power requirements and design factors, of an acoustic filter designed for filtering smoke particles across large cross-sectional areas. It is shown that while filtration is possible, the power needed is impractical. It is also shown that operating the filter within certain settling time parameters optimizes the energy usage of the filter.
 [DOI: 10.1121/1.3311883]

PACS number(s): 43.25.Qp, 43.20.Ks, 43.25.Gf [OAS] Pages: 2153–2158

I. INTRODUCTION

Kundt and Lehmann[1] were the first to describe the acoustic force exerted on small particles (relative to the applied wavelength) suspended in a fluid [e.g., spirulina cells in water[2] or carbon in air (smoke)[3]], by an acoustic standing wave. This time-averaged force was first used to visualize the wavelength of sound by making acoustic fields visible, such as in the well-known Kundt's tube apparatus (which traditionally uses lycopodium powder in air). The effective result of this force is to drive the particle to either the pressure node or anti-node of the standing wave. The sign of the acoustic contrast factor (ACF) indicates whether the force will be in the direction of the nearest pressure node, or the nearest pressure anti-node.[4,5] The ACF is a parameter calculated using the densities of sound and speed of sound in the fluid and the particle material, respectively. For example, a water particle in air would be driven to the nearest pressure node, whereas an air bubble in water would be driven to the nearest pressure anti-node.

In more recent years, this force has been used in filtering small particles in flowing fluids. While using this acoustic force for filtration may prove to be useful in many applications across diverse media, there is not as yet a significant amount of research being done into practical applications of the technology.[2,6] The black carbon released from the burning of fossil fuels and biomasses in industrial processes has been identified as possibly being the second largest cause of global warming.[7] It has been suggested that using acoustic force fields to filter the carbon particles from air would be a possible application.[2,3,6] A practical example of a useful situation for such a design would be to remove the smoke and fly ash being released into the atmosphere by industrial smoke stacks. This study reveals the limiting factors, in both power requirements and design factors, of a single half-wavelength acoustic filter designed for filtering smoke particles across large cross-sectional areas for practical industrial applications.

II. CURRENT WORK

The backgrounds to several different successfully implemented filter designs are discussed below, the most conceptually straightforward being a single half-wavelength filter (Fig. 1). The design applies a single half-wavelength standing wave across a cavity through which a suspension flows. As the particles flow through the tube, they are drawn to the center and flow inline. They can then be filtered out by separating them from the clearer fluid toward the perimeter of the cross-section.[5,8]

The most popular filter design is the h-shape separator.[2,9] Named after the shape of the flow channels, the conceptual operation of the h-shape separator is straightforward (Fig. 2).

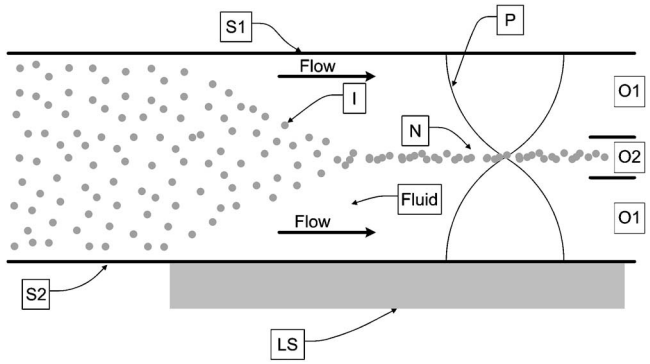

FIG. 1. Diagram demonstrating how a single half-wavelength acoustic filter uses a standing wave to force particles to flow inline so they can be filtered off separately. *O*1 is the clear fluid outlet; *O*2 is the particle enriched fluid outlet; *S*1 and *S*2 are acoustically reflecting surfaces; *P* is the acoustic pressure amplitude envelope; *I* is an impurity particle; *N* is the nodal plane of acoustic pressure; and LS is a planar wave generating line source, normally achieved through the use of a piezoceramic plate transducer.

[a]Author to whom correspondence should be addressed. Electronic address: david@karpul.com

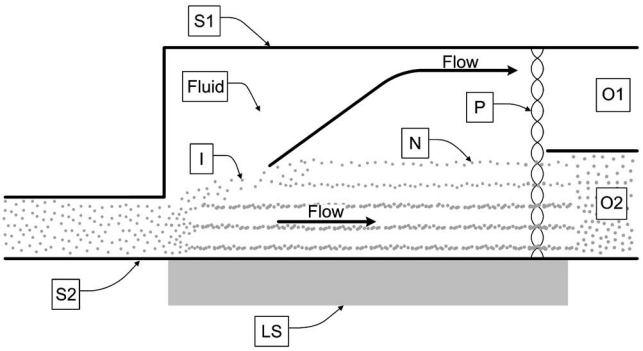

FIG. 2. Diagram demonstrating how the multiple nodes created in an h-shaped separator trap the particles and prevent them from exiting through the low particle concentration output. *O*1 is the clear fluid outlet; *O*2 is the particle enriched fluid outlet; *S*1 and *S*2 are acoustically reflecting surfaces; *P* is the acoustic pressure amplitude envelope; *I* is an impurity particle; *N* is a nodal plane of acoustic pressure; and LS is a planar wave generating line source.

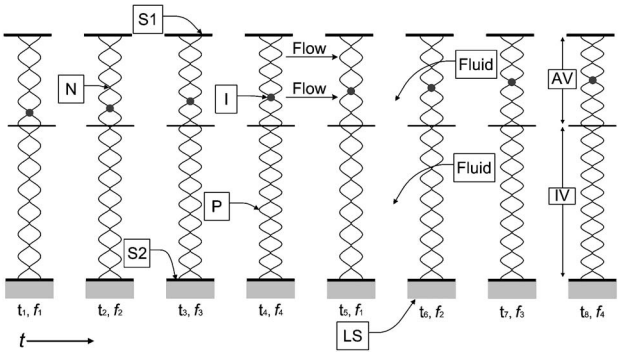

FIG. 3. Diagram of the basic operating principle of a drifting resonance field separation device, demonstrating how progressive harmonics of the fundamental resonant frequency drift a particle from one side of the active volume to the other. *S*1 and *S*2 are acoustically reflecting surfaces; *P* is the acoustic pressure amplitude envelope; *I* is the impurity particle; *N* is a nodal plane of acoustic pressure; LS is a planar wave generating line source; AV is the active volume, and IV is the inactive volume.

A fluid containing suspended particles is allowed to flow through a small pipeline. The pipeline then opens into a larger cavity across which an acoustic force field is exerted. Higher order harmonics of the fundamental resonant mode are applied across the cavity to create multiple pressure nodes running parallel to the flow of the fluid. The particles tend to be "captured" by the multiple nodes close to the inlet, therefore remaining in the lower portion of the cavity, while the fluid is free to fill the whole cavity. The particles can then be filtered out using a separate outlet for the clearer fluid.

Much work has been done to optimize the energy density within the cavities of h-filters and to adjust the relative size of the output pipelines for optimization of maximum removal of particles or maximum concentration of particles.[9,10]

A typical h-filter operates at frequencies in the order of MHz and has a cavity diameter of 10 mm, operating with fluid flow rates in the order of 100 l/day.[6]

A drifting resonance field separation device controls the position of the particles rather than simply allowing them to follow a constant trajectory or to move toward a static location.[11] Instead of applying the acoustic field directly to the flowing fluid, it is applied through an inactive layer of fluid (Fig. 3). This allows the position of the nodes to be controlled by using varying higher order harmonics of the fundamental resonant frequency. By stepping through these modes, a drifting resonant field is created and the particles are swept to one side of the active volume.

III. BACKGROUND TO SMOKE STACKS

A. Introduction

Smoke stacks are industrial chimneys and take the form of a tall vertical pipe or channel, often made from steel or reinforced concrete. They were originally designed to enhance the combustion process by creating a draft of air into the combustion zone, but now serve mainly to spread the pollution created by the process over a larger area to comply with government standards.

B. Volume flow rate of smoke stacks

Smoke stacks vary dramatically from application to application. They can have internal diameters larger than 2 m, and vary in height from tens of meters high to over three hundred.

Many smoke stacks today employ a fan-assisted forced draft to ensure the correct flow of air into the combustion zone. Designs without such a fan make use of the "stack effect," which is a phenomenon in gases that creates a flow proportional to the square root of the height of the stack and the temperature difference between the exhaust gas and the outside air. Calculating the flow created by the stack effect for a small smoke stack, operating at a relatively low temperature, would result in a conservative value for the flow rates in smoke stacks.

Equation (1) provides an approximation of the volume flow rate of a smoke stack using this thermal draft.[12] The equation neglects frictional resistance and heat losses. It also assumes that the molar mass of the gas inside the stack and the outside air are the same.

$$\Phi = CA\sqrt{2gl\frac{T_i - T_o}{T_i}}, \tag{1}$$

where Φ is the volume flow rate in $m^3\ s^{-1}$, C is the discharge coefficient, usually between 0.65 and 0.7, A is the cross-sectional area in m^2, g is the acceleration due to gravity, l is the length of the smoke stack, T_i is the average absolute temperature inside the smoke stack, and T_o is the ambient absolute temperature outside the smoke stack.

Hence, the flow rate q in $m\ s^{-1}$ can be given by

$$q = \frac{\Phi}{A} = C\sqrt{2gl\frac{T_i - T_o}{T_i}}. \tag{2}$$

In order to establish the minimum power needed for acoustic filtration in smoke stacks, a typical value of a low flow rate is needed. It is shown below that higher flow rates result in higher power requirements. For a small smoke stack, 30 m long, operating at 373 K (100 °C, i.e., steam), with any internal diameter, Eq. (2) produces an approximation of

7.3 m s^{-1}. Thus, the flow rate of smoke stacks in general can be reasonably modeled around this value.

C. Fly ash

Combustion processes produce a wide range of chemical byproducts, both gaseous and particulate matter. The combustion of coal to create electricity produces fly ash, which contains *inter alia* carbon in various forms, diverse organic compounds, and sulfur compounds.

The effects of this particulate matter on people have been widely studied and include asthma, lung cancer, cardiovascular issues, and premature death.[13] The release of carbon and carbon compounds into the atmosphere is strongly associated with global warming, and industry is facing serious regulation concerning emission control.

While fly ash takes the form of many compounds with a range of sizes, from microns to nanometers, it may reasonably be modeled as spherical carbon particles with an average radius of 1 μm.

IV. CALCULATING ACOUSTIC RADIATION FORCE ON A SINGLE PARTICLE

Yisioka *et al.*,[14–16] and later, Gor'kov,[17] presented the first analysis of the acoustic force exerted on a single small compressible sphere (relative to the wavelength). Previous analysis had considered a simpler situation of noncompressible spheres.[18] Gor'kov gives the time-averaged force on a single, small, compressible sphere in an arbitrary sound field as

$$\mathbf{F} = -\nabla\left(\frac{2}{3}\pi R^3\left[\frac{\overline{P^2}}{\rho_f c_f^2} - \frac{\overline{P^2}}{\rho_p c_p^2} - \frac{3\rho_f(\rho_p-\rho_f)}{2\rho_p-\rho_f}\overline{v^2}\right]\right), \tag{3}$$

where $\overline{P^2}$ is the temporal mean square of the acoustic pressure, $\overline{v^2}$ is the temporal mean square of the fluid displacement velocity, R is the particle radius, ρ_f and ρ_p are the densities of the fluid medium and the particle, respectively, and c_f and c_p are the velocities of sound through the fluid medium and the particle, respectively.

Since only the pressure and the acoustic displacement velocity are spatially dependant, Eq. (3) can be rewritten for a one-dimensional longitudinal wave in the x-direction as

$$F = -\frac{2}{3}\pi R^3 \times \left(\left[\frac{1}{\rho_f c_f^2} - \frac{1}{\rho_p c_p^2}\right]\frac{\partial \overline{P^2}}{\partial x} - \left[\frac{3\rho_f(\rho_p-\rho_f)}{2\rho_p-\rho_f}\right]\frac{\partial \overline{v^2}}{\partial x}\right). \tag{4}$$

Using the equation for adiabatic gases that states

$$P = -\rho_f c_f^2 \frac{\partial \xi}{\partial x}, \tag{5}$$

where P denotes the pressure fluctuations and ξ is the displacement of a fluid particle from its equilibrium position, and given a standing wave of the form

$$P(x,t) = A\cos(\omega t - kx) + A\cos(\omega t + kx), \tag{6}$$

where $P(x,t)$ denotes the pressure at any given point in space and time along a single dimension x, ω is the angular frequency of the wave, the amplitude of the standing wave is given by $2\times A$ [A denotes pressure amplitude and not area as in Eq. (1) and Eq. (2)] and k is the wave number, which is equal to ω/c_f, it can be shown that

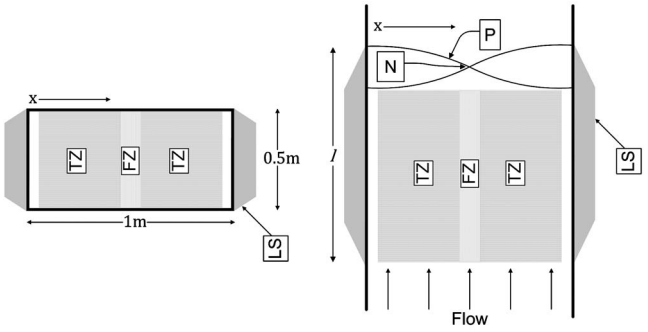

FIG. 4. Diagram of modeling parameters for acoustic filtration over a large cross-section. The side view on the right shows how the acoustic field is applied over a fixed length. P is the acoustic pressure amplitude envelope; N is the nodal plane of acoustic pressure; LS is the planar wave generating line source; TZ is the target zone; FZ is the filtration zone; and l is the length of the filter.

$$v(x,t) = \frac{A}{\rho_f c_f}\cos(\omega t - kx) - \frac{A}{\rho_f c_f}\cos(\omega t + kx), \tag{7}$$

where $v(x,t)$ denotes the acoustic displacement velocity at any given point in space and time along a single dimension x. Herewith, we obtain for the spatial gradient of the temporal average of the square of acoustic pressure P

$$\frac{\partial \overline{P^2}}{\partial x} = -2A^2 k\sin(2kx), \tag{8}$$

and similarly for the temporal average of the square of the fluid displacement velocity

$$\frac{\partial \overline{v^2}}{\partial x} = \frac{2A^2 k}{\rho_f^2 c_f^2}\sin(2kx). \tag{9}$$

By inserting Eqs. (8) and (9) into Eq. (4), it can be shown that for a planar standing wave in air, Eq. (3) can be reduced to

$$\mathbf{F} = A^2 \omega C\sin(2kx), \tag{10}$$

where

$$C = -\frac{4}{3}\pi R^3 \frac{-5\rho_p^2 c_p^2 + 2\rho_p c_p^2 \rho_f + 2\rho_f c_f^2 \rho_p + \rho_f^2 c_f^2}{c_f^3 \rho_f c_p^2 \rho_p (2\rho_p + \rho_f)}. \tag{11}$$

V. MODELING OF SMOKE STACK FILTRATION

A. Theoretical configuration

There are many possible applications of smoke filtration. This study focuses on addressing the pollution caused by smoke stacks, and thus, the theoretical scenario is largely based on typical operating parameters of an industrial smoke stack.

For this study, a simplified model of smoke stack filtration is put forward. The smoke stack is assumed to have a rectangular cross-section of 1×0.5 m^2 as depicted in Fig. 4. A rectangular cross-section is used for simplicity. A single

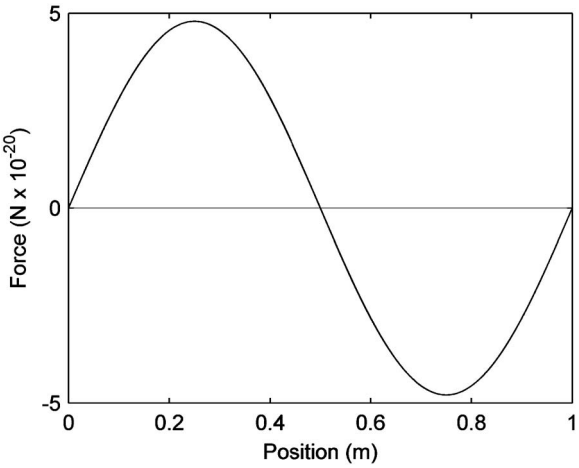

FIG. 5. Graph of the one-dimensional force exerted on a small particle of graphite across a single half-wavelength acoustic standing wave, showing that particles to the left of the center experience a positive force pushing them toward the center, and particles to the right of the center experience a negative force, also toward the center.

half-wavelength standing wave is excited along the longer dimension, with the goal of driving particles to the center. This creates a layer of agglomerated impurities in the center that can be filtered out separately to the clearer gas toward the outside, as in Fig. 1.

The region in the center of the longer dimension where particles could be filtered out separately will be referred to as the *filtration zone*. The region where particles are to be moved out of the flow, and toward the filtration zone, will be referred to as the *target zone*. The particles in the target zone must be moved into the filtration zone before exiting the filter for effective filtration to occur. The amount of time taken for a particle on the outside of the target zone to move into the filtration zone will be referred to as $\tau_{\max}$. Arbitrarily, the goal will be to move approximately 90% particles into 10% of the cross-section. The 10% dead band is created because the low magnitudes of acoustic force at the outside of the smoke stack (Fig. 5) would cause very large $\tau_{\max}$ values and distort the measure of the effectiveness of the filter. The target zone thus extends from 0.05 m from the edges to 0.05 m from the center, and the filtration zone extends 0.05 m in both directions, outwards from the center.

A smoke particle is modeled as carbon (graphite) with a particle radius of 1 μm. A model of polystyrene foam would more readily be verified by experiment, thus, particles of polystyrene foam, 2 mm in diameter, are also considered.

The model assumes two sound sources creating the opposing sound waves described in Eq. (6). Each source contributes half of the required power. This is done as the resonant characteristics of a chimney or filter design are variable. This model can only be applied directly if the acoustic quality factor (Q) of the chimney is 1. In order to take into account the acoustic quality factor Q of the system, the power required should be divided by the Q-value to obtain the total power needed.

B. Modeling of particle motion

The parameters of Eq. (11) are shown in Table I for graphite in air and polystyrene foam in air.

TABLE I. Table of properties of air, graphite, and polystyrene foam used to calculate the acoustic force on a particle.

Substance	Density ρ (kg m^{-3})	Speed of sound c (m s^{-1})	Particle radius R (m)	C (m^3 s^3 kg^{-1})
Air	1.21	343	N/A	N/A
Graphite	2200	3800	1×10^{-6}	2×10^{-25}
Polystyrene foam	17	760	1×10^{-3}	2×10^{-16}

Figure 5 shows the one-dimensional force exerted on graphite for an intensity of 1 W m^{-2} or 120 dB referred to as 1×10^{-12} W m^{-2}, which latter is the threshold of acoustic pain in humans. For a half wavelength of 1 m in air, $\omega=1077.6$ rad s^{-1}. Acoustic intensity can be calculated from acoustic pressure using the equation: $I=(P_{\rm rms})^2/\rho_f c_f$, where I is acoustic intensity in W m^{-2}. The graph clearly shows that particles to the left of the center experience a positive force pushing them toward the center, and particles to the right of the center experience a negative force, also toward the center.

Several other forces act on the particles, such as Konig and Bjerknes forces.[19] These forces will not be taken into account in this analysis. The Stokes drag force affects $\tau_{\max}$ significantly and must be taken into account. The Stokes drag force is given as[11]

$$\mathbf{F_d} = -6\mu RV, \tag{12}$$

where μ is the dynamic viscosity of the fluid medium and V is the velocity of the particle that must not be confused with the acoustic displacement velocity v of the medium, as in Eq. (3).

Combining Eqs. (10) and (12), the acceleration a of the particle is

$$a = \frac{F(x) + F_d(V)}{m}, \tag{13}$$

where m is the mass of the particle and is calculated for a spherical particle from its density and radius.

This can be expressed as a set of first order differential equations in terms of position (x) and velocity (V), where

$$\dot{x} = V,$$

$$\dot{V} = \frac{F(x) + F_d(V)}{m}. \tag{14}$$

Using this set of first order differential equations, a fourth order Runge–Kutta approximation can accurately simulate the position of the particle over time. Figure 6 shows the particle trajectories for both graphite ($R=1$ μm) and polystyrene foam ($R=1$ mm) calculated using this Runge–Kutta approximation. It demonstrates the relative intensities required for a $\tau_{\max}$ of 4 s for both materials.

C. Modeling of power requirements

It is easiest to consider a section of the smoke stack with length l as part of the filter with the assumption that any sound that escapes this section, be it down the length of the

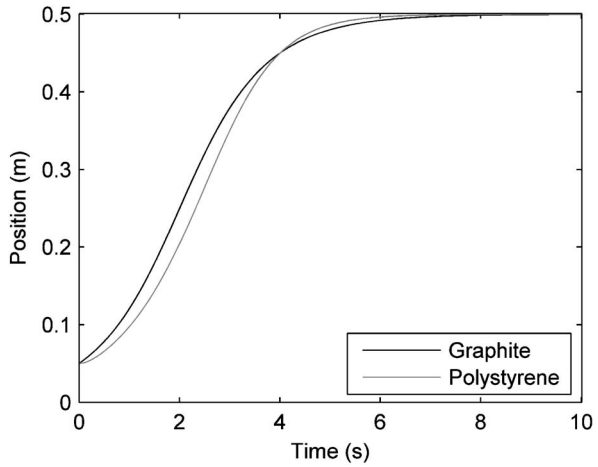

FIG. 6. Particle position against time for a single particle starting from rest on the outside of the target zone for both graphite ($R=1$ μm, $I=1.03\times10^{9}$ W m^{-2}) and polystyrene foam ($R=1$ mm, $I=1.15\times10^{3}$ W m^{-2}).

smoke stack or in another form of dissipation, does not contribute to the forcing function. For effective filtration to occur, the maximum settling time is given as

$$\tau_{\max}=\frac{l}{q}, \tag{15}$$

where q is the flow rate of the fluid in m s^{-1}.

It was observed in simulation that $\tau_{\max}$ and acoustic intensity have an inverse relationship for $\tau_{\max}$ values above a threshold (Fig. 7). For very low values of $\tau_{\max}$, or very high values of intensity, this relationship is no longer true, and a higher intensity would be required for the same value of $\tau_{\max}$ than that given by the inverse relationship.

Above this threshold value, the required intensity for a given $\tau_{\max}$ is given by

$$\frac{I}{I_r}=\frac{\tau}{\tau_{\max}}, \tag{16}$$

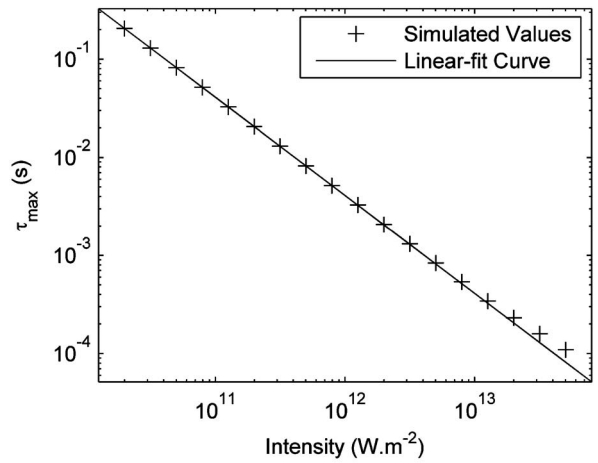

FIG. 7. Graph demonstrating the inverse relationship between $\tau_{\max}$ and acoustic intensity for graphite, and the deviation from the linear-fit curve for high acoustic field intensities and low $\tau_{\max}$ values.

where I is acoustic intensity in W m^{-2}, and τ is the settling time corresponding to a reference intensity $I_r=1$ W m^{-2} (i.e., the y-axis intercept of Fig. 7).

It was shown in simulation that the relationship holds true for polystyrene foam on the same interval with a different value of τ. The values of τ for graphite and polystyrene foams are 4.1×10^{9} s and 4.4×10^{3} s, respectively.

The acoustic power required with a Q of 1 is

$$P=I\times A=I\times0.5\times l, \tag{17}$$

where A is the area perpendicular to the wave direction.

By combining Eqs. (15)–(17), it can be shown that the minimum power for effective filtering is given by

$$P=\frac{\tau}{\frac{l}{q}}\times0.5\times l=q\frac{\tau}{2}. \tag{18}$$

This gives the minimum acoustic power needed for effective filtering in a smoke stack with a conservative flow rate of 7.3 m s^{-1} as approximately 15 GW and 16 KW for graphite and polystyrene foam, respectively.

VI. DISCUSSION OF RESULTS

A. Total power required for effective filtration

The minimum power required for effective filtration of carbon particles at a conservative flow rate of 7.3 m s^{-1} in this arrangement is given as 15 GW. It can be seen through the relationships developed above that mildly changing some of the basic parameters of the arrangement will not reduce this number sufficiently for it to enter the realm of feasibility.

For comparison, the required power for a $\tau_{\max}$ of 2 s for polystyrene foam was calculated for a longitudinal standing wave in a tube with diameter of 5 cm. This is a common arrangement and is known as the Kundt's tube experiment. The tube inherently has a Q of approximately 2 because of the near perfect reflection off one of its ends, and the minimal losses through the sides of the tube. The required acoustic power was computed using Eq. (18) as 2.2 W, which is in the correct order of magnitude for this type of apparatus. This suggests that the model is reasonably grounded in reality.

While it is true that raising the Q of the system will reduce the required power proportionally, a large Q is not expected due to the losses incurred due to the cavity having open ends. Furthermore, the efficiencies of high power acoustic transducers in this range are very low, and serve to increase dramatically the amount of electrical power required by the system.

B. Optimizing the length of the filter

Figure 7, coupled with Eq. (18) above, represent a very significant result. It demonstrates that the amount of power needed for a given flow rate as a function of l is constant until reaching a particular threshold. Reducing l further forces $\tau_{\max}$ into the non-linear region of Fig. 7.

If one were to ignore the Stokes drag force, this result would be expected. Applying a smaller acoustic force over a

longer flow distance would have the same effect on τ_{max} as a larger acoustic force over a shorter flow distance. Hence, the total power would remain constant.

Considering the Stokes drag force, one would expect that increasing l would cause a reduction in the necessary average velocity of the particle, and thus, a reduction in the energy lost through drag. Equation (18) simply shows that for velocities below a certain threshold, the reduction in velocity caused by further increasing l would be insignificant in terms of saving energy.

An examination of Fig. 7 in the non-linear region shows that for a given τ_{max}, a larger intensity is needed than that given by the linear-fit curve. Hence, it is more energy efficient to use a filter with a longer l in order to increase the required τ_{max} (further into the linear region) than it would be to operate in the non-linear region of the graph.

VII. CONCLUSIONS

It has been shown that acoustic filtering is a working form of filtration, but the power needed in the industrial smoke stack environment, for the configuration discussed above, is unfeasibly large. The implication of this is if acoustic filtration is to be applied to environments with large volume flow rates, a new configuration of acoustic filtration is needed.

It has also been shown that proper design of the wavefront length of the applied standing wave in acoustic filtration affects the power required for effective filtration. This parameter can be optimized to a particular value for a given material simply by operating above a defined threshold of τ_{max} for a given scenario.

ACKNOWLEDGMENTS

The authors wish to acknowledge the important role of the University of Cape Town, its facilities and technical staff, without whom this research would not be possible. In particular, D. Karpul thanks the Sensors and Actuators Group, the Acoustics Group, Cesarina Edmonds-Smith, Steven Schrire, and Samuel Ginsberg.

[1] A. Kundt and O. Lehmann, "Longitudinal vibrations and acoustic figures in cylindrical columns of liquids," Ann. Phys. Chem. **229**, 1–12 (1874).
[2] E. Benes, M. Gröschl, H. Nowotny, H. Bohm, S. Radel, C. Hauser, J. Power, K. Lowe, L. Briarty, and M. Davey, "The ultrasonic h-shape separator: Harvesting of the alga spirulina platensis under zero-gravity conditions," Proceedings of the World Congress of Ultrasonics (2003), pp. 1631–1638.
[3] E. Riera, J. A. Gallego-Juarez, and T. J. Mason, "Airborne ultrasound for the precipitation of smokes and powders and the destruction of foams," Ultrason. Sonochem. **13**, 107–116 (2006).
[4] M. Gröschl, "Ultrasonic separation of suspended particles–Part I: Fundamentals," Acust. Acta Acust. **84**, 432–447 (1998).
[5] G. Goddard and G. Kaduchak, "Particle concentration in a line-driven tube," J. Acoust. Soc. Am. **117**, 3440–3447 (2005).
[6] E. Benes, M. Gröschl, H. Nowotny, F. Trampler, T. Keigzer, H. Bohm, S. Radel, L. Gherardini, J. Hawkes, R. Konig, and C. Delouvroy, "Ultrasonic separation of suspended particles," Proc.-IEEE Ultrason. Symp. 649–659 (2001).
[7] M. Z. Jacobson, "Strong radiative heating due to the mixing state of black carbon in atmospheric aerosols," Nature (London) **409**, 695–697 (2001).
[8] J. Hawkes, W. Coakley, M. Groschl, E. Benes, S. Armstrong, P. Tasker, and H. Nowotny, "Single half-wavelength ultrasonic particle filter: Predictions of the transfer matrix multilayer resonator model and experimental filtration results," J. Acoust. Soc. Am. **111**, 1259–1266 (2002).
[9] H. Böhm, L. Briarty, K. Lowe, J. Power, E. Benes, and M. Davey, "Quantification of novel h-shaped ultrasonic resonator for separation of biomaterials under terrestrial gravity and microgravity conditions," Biotechnol. Bioeng. **82**, 74–85 (2003).
[10] J. Hawkes, M. Gröschl, E. Benes, H. Nowotny, and W. Coakley, "Positioning particles within liquids using ultrasonic force fields," Proceedings of the Forum Acusticum 2002, Special Session PHA-01: Acoustics of Dispersed Particulate Matter, Sevilla, Spain, Sept. 16–20, 2002.
[11] B. Handl, M. Gröschl, F. Trampler, E. Benes, S. Woodside, and J. Piret, "Particle trajectories in a drifting resonance field separation device," J. Acoust. Soc. Am. **3**, 1957–1958 (1998).
[12] V. V. Baturin, *Fundamentals of Industrial Ventilation*, 3rd ed. (Pergamon, New York, 1972), p. 400.
[13] G. M. Masters, *Introduction to Environmental Engineering and Science*, 2nd ed. (Prentice-Hall, Upper Saddle River, NJ, 1998), pp. 351–355.
[14] K. Yosioka and Y. Kaisima, "Acoustic radiation pressure on a compressible sphere," Acustica **5**, 167–173 (1955).
[15] T. Hasegawa and K. Yosioka, "Acoustic radiation force on a solid elastic sphere," J. Acoust. Soc. Am. **46**, 1139–1143 (1969).
[16] K. Hasegawa and K. Yosioka, "Acoustic radiation force on fused silica spheres and intensity determination," J. Acoust. Soc. Am. **58**, 581–585 (1975).
[17] L. P. Gor'kov, "On the forces acting on a small particle in an acoustical field in an ideal fluid," Sov. Phys. Dokl. **6**, 773–775 (1962).
[18] L. V. King, "On the acoustic radiation on spheres," Proc. R. Soc. London, Ser. A **147**, 212–240 (1933).
[19] A. Doinikov, "Acoustic radiation interparticle forces in a compressible fluid," J. Fluid Mech. **444**, 1–21 (2001).

Multimode radiation from an unflanged, semi-infinite circular duct with uniform flow

Samuel Sinayoko, Phillip Joseph, and Alan McAlpine
Institute of Sound and Vibration Research, University of Southampton, Southampton SO17 1BJ, United Kingdom

(Received 30 January 2009; revised 25 January 2010; accepted 30 January 2010)

Multimode sound radiation from an unflanged, semi-infinite, rigid-walled circular duct with uniform subsonic mean flow everywhere is investigated theoretically. The multimode directivity depends on the amplitude and directivity function of each individual cut-on mode. The amplitude of each mode is expressed as a function of cut-on ratio for a uniform distribution of incoherent monopoles, a uniform distribution of incoherent axial dipoles, and for equal power per mode. The directivity function of each mode is obtained by applying a Lorentz transformation to the zero-flow directivity function, which is given by a Wiener–Hopf solution. This exact numerical result is compared to an analytic solution, valid in the high-frequency limit, for multimode directivity with uniform flow. The high-frequency asymptotic solution is derived assuming total transmission of power at the open end of the duct, and gives the multimode directivity function with flow in the forward arc for a general family of mode amplitude distribution functions. At high frequencies the agreement between the exact and asymptotic solutions is shown to be excellent.
 [DOI: 10.1121/1.3327814]

PACS number(s): 43.28.Py, 43.20.Mv, 43.50.Cb [AH] Pages: 2159–2168

I. INTRODUCTION

A. Background: Duct power estimation from limited far-field data

Various common noise sources radiate sound into finite length ducts containing a uniform mean flow, from which the sound escapes into the far field via radiation from an unbaffled open end. Examples are exhaust mufflers, large exhaust stacks, and aircraft turbofan engines. Often one wishes to determine the sound power radiated from the duct opening, either as an index of insertion loss in order to assess silencer performance, or as a means of quantifying and ranking the total noise output for predicting community annoyance. The sound power may, in principle, be determined by integrating the normal component of sound intensity over a surface enclosing the duct exit at a large distance from the duct where the flow is quiescent. However, sometimes not all measurement locations required to perform the integration are easily accessible, as in the case of large exhaust stacks, which may be tens of meters high. In this example, the only measurements that are easy to make are close to the ground, corresponding to the rear arc or backward-radiated sound radiated at angles approaching 180° to the duct axis. It is clear that a method of inferring the radiated power, at any frequency, from a small number of far-field mean square pressure measurements would be extremely useful to the noise control engineer.

B. Scope of investigation

This paper presents a theoretical and numerical study of the non-dimensional directivity function $Q(ka,\theta)$ for multimode sound radiation from the open end of an unflanged, semi-infinite, rigid-walled circular duct, in the presence of a uniform subsonic mean flow. This paper extends earlier work by Joseph and Morfey in which the effects of flow were neglected.[1] The directivity function $Q(ka,\theta)$ relates the far-field mean square pressure, at any polar angle θ to the duct axis including the rear arc and at any flow Mach number, to the net sound power transmitted along the duct. The non-dimensional frequency ka equals $2\pi fa/c$, where f is the frequency, a is the duct radius, and c is the sound speed.

To calculate the modal radiation in the presence of uniform flow, a Lorentz transform is applied to the exact theoretical zero-flow modal directivity functions for sound radiation from an unflanged, semi-infinite, rigid-walled circular duct, as given by Homicz and Lordi.[2] This single-mode analysis is applied in what follows to a particular family of mode amplitude distribution functions, which includes the following three special cases: (a) excitation of incident modes by incoherent monopoles uniformly distributed over a duct cross section, (b) excitation by incoherent axial dipoles uniformly distributed over a duct cross section, and (c) equal in-duct power per incident mode above cut-off. In each case, the individual modes are incoherently excited, and the contribution of evanescent modes is neglected.

This paper also presents high-frequency asymptotic expressions for $Q(ka,\theta)$ for the three source models that explicitly include the effect of uniform mean flow. Since scattering at the edge of the duct opening is neglected in the high-frequency model, this analysis is limited to the forward arc.

Simulations of $Q(ka,\theta)$ as a function of θ are presented in this article, for the three incident-mode source models, at a number of representative Mach numbers (positive and negative representing exhaust and inlet conditions) in both the forward and rear arcs. Results showing Q for $ka=50$ calculated from the exact result and from the high-frequency

asymptotic result are compared with generally excellent agreement in the forward arc, not too close to the sideline directions.

This approach is used for the first time to assess the sensitivity of multimode radiation from ducts to the effects of air flow. The derivation of analytic expression for multimode far-field radiation, in which the effects of flow are included, allows decisions to be made about when flow effects should be included in numerical prediction schemes such as finite element (FE) and computational fluid dynamics (CFD) analyses. It also provides insight into the relative sensitivity of different sources (and therefore mode amplitude distributions) to the effects of flow. In particular, the analytic solutions presented here for the multimode directivity functions permit a rapid assessment of the far-field radiation angles that are most affected by flow.

C. Previous work

1. Multimode radiation

As outlined above, the problem of high-frequency radiation from ducts in which the sound field comprises many acoustic modes is common to a number of situations in which noise is a serious issue, such as the broadband noise from ducted fans and exhaust stacks. Yet almost no work has been published dealing with the characteristics and level of the noise field transmitted along the duct and its subsequent radiation to the far field. Only Rice[3] in the 1970s, and more recently Joseph and Morfey,[1] explicitly addressed some of these issues for multimode sound radiation from ducts. However, both studies neglect the potentially important effect of the uniform mean flow. Rice[3] derived an expression for the high-frequency mean square pressure directivity by (effectively) replacing the expression for mean square pressure involving a summation over two modal indices with a single integral over modal cut-off ratio. This simplification is based on the principle that the angles of the main radiation lobes for different modes with the same cut-off ratio are identical. Rice[3] assumed a distribution of mode amplitudes that varies as the cut-off ratio raised to some exponent. Although there is no physical justification for such a mode distribution function, the situation in which the total sound power is shared equally among the propagating modes is a special case. His analysis is restricted to the forward arc, and the effects of mean flow are neglected.

Joseph and Morfey[1] presented a more general formulation for the multimode mean square pressure directivity in the absence of flow that is valid in both forward and rear arcs. The analysis was undertaken for a general family of mode distributions in which incoherent monopoles and axial dipoles uniformly distributed over the duct cross section are special cases, as is also the case of "equal energy per mode." Following a similar procedure to that adopted by Rice,[3] closed-form expressions were derived for the mean square pressure directivity non-dimensionalized on the total sound power for the above source distributions that are restricted to the high-frequency limit in the forward arc.

The present paper extends the work of Joseph and Morfey[1] to include the effects of a uniform mean flow that is everywhere the same. Flow effects are shown to substantially distort the directivity for some mode amplitude distributions. The analysis shows that, despite the amplification effects on the sound power (convective amplification) and the distortion of the directivity function by the mean flow, the mean square pressure normalized on sound power in the high-frequency limit can be still expressed in closed form.

2. Single-mode radiation

There is far more published work associated with single-mode radiation from ducts (compared to work reported on multimode radiation). In the absence of mean flow, Homicz and Lordi[2] gave the exact modal directivity functions for sound radiation from an unflanged, semi-infinite, rigid-walled circular duct. These are derived using the Wiener–Hopf technique. Homicz and Lordi[2] outlined how the corresponding directivity functions with a uniform flow everywhere can be determined from the no flow solutions. Their approach is utilized in this current work (see Sec. II A).

We note here that other Wiener–Hopf solutions of sound radiation from flow ducts have been reported since the work by Homicz and Lordi.[2] In Ref. 4 the far-field sound radiation from a semi-infinite duct is derived for the case when the (uniform) flow velocities inside and outside the duct are different. Munt[4] modeled the separation between the two fluids by a vortex sheet. In Ref. 4 a comparison between experimental measurements and predictions of the far-field pressure showed excellent agreement. He later extended his result to give the near-field solution.[5] Rienstra[6] examined sound radiation from a semi-infinite annular duct immersed in a uniform flow, where the centerbody extends downstream from the open end of the duct. More recently these solutions have been extended by Gabard and Astley,[7] who derived the sound radiated from a semi-infinite annular duct for the case when the (uniform) flow velocities inside and outside the duct are different. In addition to providing the exact solution for the single-mode directivity, Gabard and Astley[7] also gave an example of multimode directivity for equal power per mode. However, they did not derive any simple analytical expressions for the far-field multimode directivity with flow, which is the objective of the work reported in this paper.

D. Summary of simplifying assumptions used in the modeling of the multimode radiation from ducts with uniform flow

In this work, a number of important simplifications are made in the analysis of the multimode sound radiation from ducts with uniform flow. The main simplifying assumptions are listed as follows.

(1) The duct is assumed to be straight, circular, and of semi-infinite length.
(2) The duct walls are rigid and have zero thickness.
(3) The duct is assumed to be free of absorbing liners and other forms of dissipation.
(4) The mean flow is assumed to be steady, inviscid, and isentropic. The mean flow is assumed to be uniform ev-

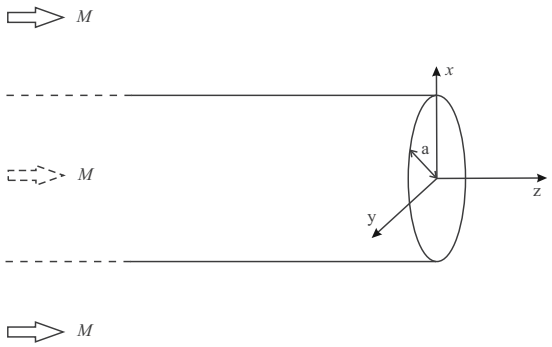

FIG. 1. Circular duct of radius a immersed in a uniform flow of Mach number M.

erywhere so that no shear layers exist downstream of the duct, and there are no boundary layers at the duct walls.

A sketch of the semi-infinite, circular duct of radius a immersed in a uniform mean flow of Mach number M is shown in Fig. 1. As a consequence of (1), axial standing waves can be neglected. Assumption (2) allows the effects of diffraction and scattering to be neglected in the high-ka analytic radiation models developed in this paper. We emphasize, however, that the full effects of diffraction at the duct lip are included in the general model formulation to allow the prediction of rear arc radiation. As a consequence of (3) and (4) energy is conserved, so that in-duct sound power equals the sound power radiated to the far field. In the absence of any jet shear layers (since the flow is everywhere uniform), energy dissipation mechanisms identified by, for example, Bechert,[8] in which acoustic energy is dissipated by the vorticity in the jet shear layers, are not included. Also as a consequence of (4), complications in the prediction of far-field radiation arising from shear layer refraction, and scattering owing to unsteady, turbulent flow in jet shear layers, therefore, do not arise. Thus, in this work, the consequences of including the mean flow are limited to convection effects.

II. FAR-FIELD PRESSURE DIRECTIVITY WITH FLOW

Consider an unflanged, semi-infinite, rigid-walled circular duct of radius a, immersed in a uniform flow of Mach number M, which is assumed to be identical inside and outside the duct. Inside the duct, the position is specified in terms of cylindrical polar coordinates (r,ϕ,z), as sketched in Fig. 2. Outside the duct, the position is specified in terms of

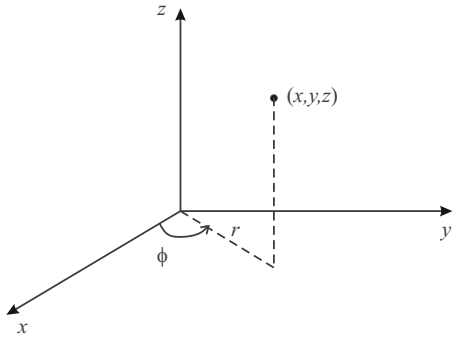

FIG. 2. Cylindrical polar coordinate system (r,ϕ,z).

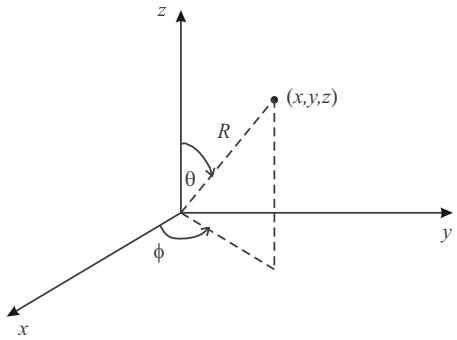

FIG. 3. Spherical polar coordinate system (R,θ,ϕ).

spherical polar coordinates (R,θ,ϕ), as sketched in Fig. 3.

At a single frequency ω, the acoustic pressure field propagating toward the open end of a semi-infinite duct containing a uniform mean flow may be expressed in the form

$$p(r,\phi,z,t)=\sum_{(m,n)\in\mathcal{O}} A_{mn}\Psi_{mn}(r,\phi)e^{j(\omega t-k_{z,mn}z)}, \tag{1}$$

where the mode order (m,n) is restricted to the set of cut-on modes, denoted by $\mathcal{O}$. In Eq. (1) A_{mn} is the modal pressure amplitude at the source plane (say, $z=0$), Ψ_{mn} is the orthonormal mode shape function of the duct defined such that

$$\frac{1}{S}\int_0^{2\pi}\int_0^a \Psi_{mn}(r,\phi)\Psi^*_{m'n'}(r,\phi)r\mathrm{d}r\mathrm{d}\phi = \begin{Bmatrix} 0 & (m,n)\neq(m',n') \\ 1 & (m,n)=(m',n') \end{Bmatrix}, \tag{2}$$

where $S=\pi a^2$ is the cross-sectional area of the duct, and $k_{z,mn}$ denotes the axial wavenumber of mode (m,n) given by

$$k_{z,mn}=\frac{(\alpha_{mn}-M)k}{\beta^2} \quad \text{where} \quad \alpha_{mn}=\sqrt{1-\left(\frac{\kappa_{mn}}{k}\right)^2\beta^2}. \tag{3}$$

In Eq. (3), $k=\omega/c$ denotes the free field acoustic wavenumber, $\beta=\sqrt{1-M^2}$, α_{mn} is the modal cut-on ratio, and $\kappa_{mn}=j_{mn}/a$ is the mode transverse wavenumber where j_{mn} equals the value of the nth turning point of the Bessel function of the first kind of order m. The modal cut-on ratio α_{mn} is in the range $0\leq\alpha_{mn}\leq 1$ for propagating modes, where $\alpha_{mn}=0$ is the cut-on/cut-off transition point.[9] For evanescent modes, α_{mn} is purely imaginary, and the modes transport no sound power to the far field. Therefore, in this paper, evanescent modes are neglected, and in Eq. (1) the sum is restricted to the set of cut-on modes.

Also at a single frequency ω, we define an in-duct to far-field non-dimensional transfer function $H_{mn}(ka,\theta)$, such that the far-field pressure may be written as

$$p_f(R,\theta,\phi,t)=\frac{a}{R}\sum_{(m,n)\in\mathcal{O}} A_{mn}H_{mn}(ka,\theta)e^{j(\omega t-m\phi-kR)}. \tag{4}$$

We now assume that the excitation is broadband in origin such that the modal amplitudes are random variables with respect to time t. This is a realistic assumption in the case of, for example, excitation by the incoherent sources distributed over the rotor blades and stator vanes in a turbofan engine

arising from interaction with turbulent flow. In practice, a single realization of the modal amplitudes A_{mn} may be obtained by taking the Fourier transform of the pressure at the source plane over a short time interval. For broadband excitation, the modes are assumed to be incoherent; i.e.,

$$E\{A_{mn}A^*_{m'n'}\}=0 \quad \text{if} \quad (m,n)\neq(m',n'), \tag{5}$$

in which case the mean square pressure becomes

$$\overline{p_f^2}(R,\theta)=\frac{1}{2}\left(\frac{a}{R}\right)^2\sum_{(m,n)\in\mathcal{O}}|H_{mn}(ka,\theta)|^2E\{|A_{mn}|^2\}, \tag{6}$$

where for broadband noise $\overline{p_f^2}$ is the far-field mean square pressure in a small specified frequency bandwidth, and similarly $E\{|A_{mn}|^2\}$ is the expectation of the modulus squared of the modal amplitudes in the same frequency bandwidth. Assuming incoherent modes Eq. (5) simplifies the expression for the far-field mean square pressure $\overline{p_f^2}$, and ensures that the radiated field is axisymmetric; i.e., there is no dependence on azimuthal angle ϕ.

A. Transfer function for modal radiation from ducts with flow

In this section, the modal radiation transfer function H_{mn} for ducts immersed in a uniform flow is related to that for modal radiation in the absence of flow, denoted by H^0_{mn}. Homicz and Lordi[2] gave the far-field expression for H^0_{mn}, which is derived using the Wiener–Hopf technique. We note that an approximate zero-flow transfer function may also be obtained using the Rayleigh integral, whose validity is restricted to the forward arc, which has been formulated previously, for example, by Tyler and Sofrin.[10]

Following the procedure in Ref. 2, H_{mn} is obtained by Lorentz transformation of the zero-flow transfer function H^0_{mn}. This type of approach, previously used by Homicz and Lordi,[2] has been recently examined in more detail by Chapman.[11] In essence, $M>0$ represents an exhaust problem, where sound is radiated in the direction of the flow, whereas $M<0$ represents an inlet problem, where sound is radiated against the oncoming flow.

In the case of $M>0$, following the procedure outlined in Ref. 2, in our notation we obtain

$$H_{mn}(ka,\theta)=\frac{\beta}{\sqrt{1-M^2\sin^2\theta}}H^0_{mn}(ka/\beta,\tan^{-1}(\beta\tan\theta)), \tag{7}$$

where H^0_{mn} is the far-field transfer function of mode (m,n) in the absence of flow $(M=0)$.

In the case of $M<0$, the singularity in pressure on the leading edge of the open end of the duct requires that the Lorentz transformation is applied instead to the zero-flow velocity potential solution. The pressure solution is then obtained from the velocity potential via the acoustic momentum equation. Again following the procedure in Ref. 2, in our notation we obtain

TABLE I. Details of source models in a circular duct with uniform flow. Note that $P^2_{\mu\nu\gamma}$ has dimensions of pressure squared in a small specified frequency bandwidth. In this small frequency bandwidth, $\overline{Q_s^2}$ is the mean square volume velocity per unit area due to the monopole distribution, $\overline{F_s^2}$ is the mean square force per unit area due to the dipole distribution, and in the case of equal power per mode, W_0 is the power transmitted by each mode.

	Monopole	Dipole	Equal power per mode
(μ,ν,γ)	(0,1,2)	(1,0,2)	(0,1,1)
$P^2_{\mu\nu\gamma}$	$(\rho_0c_0)^2\overline{Q_s^2}/2$	$\overline{F_s^2}/2$	$2\rho_0c_0W_0/S$

$$H_{mn}(ka,\theta)=\frac{\beta}{1-M\alpha_{mn}}\frac{\sqrt{1-M^2\sin^2\theta}-M\cos\theta}{1-M^2\sin^2\theta}\times H^0_{mn}(ka/\beta,\tan^{-1}(\beta\tan\theta)), \tag{8}$$

where it is noted that this equation differs slightly from the equation given by Homicz and Lordi, most likely due to a typographical error in Ref. 2. Our result is recovered by replacing $\cos\psi$ in the expression in Ref. 2 with $\cos\tilde{\psi}$.

B. Modal amplitude distributions

In this paper the behavior of the far-field mean square pressure $\overline{p_f^2}$ is investigated for a particular family of mode distribution functions $E\{|A_{mn}|^2\}$. The mode amplitude distribution function may be obtained by generalizing the approach taken by Joseph *et al.*[12] The result is

$$E\{|A_{mn}|^2\}=P^2_{\mu\nu\gamma}\left(\frac{M-\alpha_{mn}}{1-M^2}\right)^{2\mu}\left(\frac{1-\alpha_{mn}M}{1-M^2}\right)^{2\nu}\frac{1}{\alpha^\gamma_{mn}}, \tag{9}$$

where $P_{\mu\nu\gamma}$ is a measure of source strength, and (μ,ν,γ) denotes a trio of indices that define the source model. Written in full, $E\{|A_{mn}|^2\}$ is listed below in Eq. (10) for the following special cases: (a) a uniform distribution of incoherent monopoles $(\mu,\nu,\gamma)=(0,1,2)$, (b) a uniform distribution of incoherent axial dipoles $(\mu,\nu,\gamma)=(1,0,2)$, and (c) equal power per mode $(\mu,\nu,\gamma)=(0,1,1)$.

$$\text{(a)}\quad E\{|A_{mn}|^2\}=P^2_{012}\left(\frac{1-\alpha_{mn}M}{1-M^2}\right)^2\frac{1}{\alpha^2_{mn}}, \tag{10a}$$

$$\text{(b)}\quad E\{|A_{mn}|^2\}=P^2_{102}\left(\frac{M-\alpha_{mn}}{1-M^2}\right)^2\frac{1}{\alpha^2_{mn}}, \tag{10b}$$

$$\text{(c)}\quad E\{|A_{mn}|^2\}=P^2_{011}\left(\frac{1-\alpha_{mn}M}{1-M^2}\right)^2\frac{1}{\alpha_{mn}}. \tag{10c}$$

The source strength term and indices (μ,ν,γ) for each mode amplitude distribution are summarized in Table I.

Equation (9) is more general than the source models derived previously by Joseph *et al.*,[12] but at the expense of having to include an additional exponent, γ, which allows for the equal power per mode model to be included in the general family of mode amplitude distribution functions.

III. MULTIMODE DIRECTIVITY FACTOR $Q(ka,\theta)$ WITH FLOW

As in Ref. 1 the non-dimensional multimode directivity function is defined by

$$Q(ka,\theta)=\frac{4\pi R^2}{\rho_0 c_0 E\{W_f\}}\overline{p_f^2}(R,\theta), \tag{11}$$

where $E\{W_f\}$ denotes the expected value of the radiated acoustic power. Following the definition of generalized acoustic intensity given by, for example, Morfey,[13] it can be shown that the radiated power is given by

$$E\{W_f\}=\frac{4\pi R^2}{\rho_0 c_0}\int_0^\pi \overline{p_f^2}(R,\theta)F(\theta)\sin\,\theta \mathrm{d}\theta, \tag{12}$$

where, after considerable algebra, $F(\theta)$ is given by

$$F(\theta)=\frac{\beta^4\sqrt{1-M^2\sin^2\,\theta}}{2(\sqrt{1-M^2\sin^2\,\theta}-M\cos\,\theta)^2}. \tag{13}$$

Note that for zero-flow, $F(\theta)=1/2$, and Eq. (12) reduces to the classical result for radiated sound power in a medium at rest. The function F incorporates two effects on the intensity by the mean flow. One is that it resolves the intensity in the radial direction, since in the presence of flow the intensity vector is no longer radially orientated. The second is that it includes the effects of convective amplification in which the sound intensity is modified by the presence of flow.

Combining Eqs. (11) and (12) shows that Q satisfies the normalization condition

$$\int_0^\pi Q(ka,\theta)F(\theta)\sin\,\theta\,\mathrm{d}\theta=1. \tag{14}$$

Evaluation of Eq. (11) using Eqs. (6)–(8) and (10) is a computationally intensive procedure for large ka and M. For example, at $ka=50$, there are approximately 650 cut-on modes at $M=0$. This number increases as $(1-M^2)^{-1/2}$ as M increases. Thus, there is a need for a simple analytic formula that provides a good approximation to $Q(ka,\theta)$ in the high-frequency limit, for the family of sound sources described in Sec. II B.

IV. ANALYTIC EXPRESSION FOR $Q(ka,\theta)$ IN THE HIGH-ka LIMIT

In this section, analytic expressions are derived for the non-dimensional multimode directivity function Q (11) in the presence of flow for the general family of source distributions given in Sec. II B.

In order to determine the radiated sound power $E\{W_f\}$ for use in the evaluation of Q, we make the assumption that the incident transmitted sound power in the duct and that radiated from the open end are equal. Thus, we first consider the sound power $E\{W_{mn}\}$ transmitted by a single-mode wave traveling along the duct with flow. Following Morfey,[13]

$$E\{W_{mn}\}=\frac{S}{2\rho_0 c_0}\frac{\beta^4\alpha_{mn}}{(1-\alpha_{mn}M)^2}E\{|A_{mn}(\alpha_{mn})|^2\}, \tag{15}$$

where $E\{|A_{mn}|^2\}$ is a function of α_{mn} given by Eq. (9) and is defined by the indices (μ,ν,γ).

A. In-duct sound power transmission between θ and $\theta+\delta\theta$

Rice *et al.*[14] examined how duct modes' propagation angles are related to sound radiation. They derived the angle of propagation with respect to the duct axis of the wavefronts connected to modes in a circular duct with uniform mean flow. In this paper the modal propagation angle θ is equivalent to what Rice *et al.*[14] referred to as the "resultant axial propagation angle in the duct." This angle is not normal to the wavefronts owing to the convective effect of the mean flow.

The in-duct sound power transmitted along the duct by modes between propagation angles θ and $\theta+\delta\theta$ is the sum of the modal powers transmitted by each mode whose propagation angle θ_{mn} lies between θ and $\theta+\delta\theta$; i.e.,

$$\delta W(\theta)=\sum_{(m,n)\in\mathcal{O}_\theta} W_{mn}, \tag{16}$$

where

$$\mathcal{O}_\theta=\{(m,n)\in\mathcal{O}|\theta\le\theta_{mn}\le\theta+\delta\theta\}. \tag{17}$$

Combining Eqs. (15) and (16) gives

$$E\{\delta W(\theta)\}=\frac{S}{2\rho_0 c_0}\sum_{(m,n)\in\mathcal{O}_\theta}\frac{\beta^4\alpha_{mn}}{(1-\alpha_{mn}M)^2}E\{|A_{mn}(\alpha_{mn})|^2\}. \tag{18}$$

The propagation angle θ_{mn} can be related to α_{mn} (and M) using the following result from Ref. 14:

$$\cos\,\theta_{mn}=\frac{\alpha_{mn}\beta}{\sqrt{1-M^2\alpha_{mn}^2}}. \tag{19}$$

For each mode $(m,n)\in\mathcal{O}_\theta$, since $\delta\theta\ll 1$, we have $\theta_{mn}\approx\theta$, and Eq. (19) may be rearranged giving

$$\alpha(\theta)\approx\frac{\cos\,\theta}{\sqrt{1-M^2\sin^2\,\theta}}. \tag{20}$$

Substituting Eq. (20) into Eq. (18) gives

$$E\{\delta W(\theta)\}=\frac{S}{2\rho_0 c_0}\frac{\beta^4\alpha(\theta)}{(1-\alpha(\theta)M)^2}E\{|A_{mn}(\alpha(\theta))|^2\}\delta N(\theta), \tag{21}$$

where $\delta N(\theta)$ denotes the number of modes with propagation angle between θ and $\theta+\delta\theta$, such that $\delta N/N$ is small, where N is the total number of propagating modes.

We now take the limit as $ka\to\infty$ to obtain an asymptotic expression for δN to enable Eq. (21) to be evaluated analytically. The derivation of $\delta N(\theta)$ is presented in the Appendix. It is shown that as $ka\to\infty$,

$$\delta N(\theta) = \left(\frac{1}{2}ka\right)^2 \frac{\sin 2\theta}{(1 - M^2 \sin^2 \theta)^2}\delta\theta. \tag{22}$$

Substituting this asymptotic expression for $\delta N(\theta)$ in Eq. (21) leads to the following analytic expression for the in-duct sound power transmitted between the range of angles θ and $\theta + \delta\theta$:

$$E\{\delta W(\theta)\} = \frac{S}{2\rho_0 c_0}\left(\frac{1}{2}ka\right)^2 \frac{\sin 2\theta}{(1 - M^2 \sin^2 \theta)^2} \times \frac{\beta^4 \alpha(\theta)}{(1 - \alpha(\theta)M)^2} E\{|A_{mn}(\alpha(\theta))|^2\}\delta\theta, \tag{23}$$

which is valid in the high-ka limit. Thus the total transmitted power, in the limit as $ka \to \infty$, can be evaluated by an integral over polar angle θ instead of the modal summation in Eq. (18).

B. Sound power radiation between polar angles θ and $\theta + \delta\theta$

Following Eq. (12), the expected value for the far-field sound power $E\{\delta W_f(\theta)\}$ radiated between angles θ and $\theta + \delta\theta$ is given by

$$E\{\delta W_f(\theta)\} = \frac{4\pi R^2}{\rho_0 c_0}\overline{p_f^2}(R, \theta)F(\theta)\sin\theta\delta\theta. \tag{24}$$

C. Relation between far-field power and in-duct power

For the case where the flow is uniform everywhere, and assuming that no energy is lost at the open end of the duct or back-reflected, the power radiated between the range of angles θ and $\theta + \delta\theta$ is equal to the power transported between this range of angles inside the duct; i.e.,

$$\delta W_f(\theta) = \delta W(\theta). \tag{25}$$

This is a good approximation for multimode sound propagation at high ka since only comparatively few modes are near cut-off and hence are significantly reflected back into the duct.[13] These modes radiate most strongly at angles close to 90°, and therefore the analysis is expected to be least accurate for radiation angles close to 90° to the duct axis.

D. Multimode far-field directivity in the high-ka limit

Equating the expression for in-duct sound power (23) to the expression for radiated sound power (24), and using Eqs. (13) and (20) for F and α, give an explicit expression for the mean square pressure as

$$\overline{p_f^2}(R, \theta) = \frac{1}{2}\left(\frac{a}{R}\right)^2\left(\frac{1}{2}ka\right)^2 \frac{\cos^2\theta}{(1 - M^2 \sin^2 \theta)^2} E\{|A_{mn}(\alpha(\theta))|^2\}. \tag{26}$$

Noting Eqs. (10a)–(10c) for $E\{|A_{mn}|^2\}$ the mean square pressures for the three source distributions are given by

$$\text{(a)}\quad \overline{p_f^2}(R, \theta) = \frac{1}{2}\left(\frac{a}{R}\right)^2 (\rho_0 c_0)^2 \frac{\overline{Q_s^2}}{2}\left(\frac{1}{2}ka/\beta\right)^2 \times \frac{(\sqrt{1 - M^2 \sin^2 \theta} - M\cos\theta)^2}{\beta^2(1 - M^2 \sin^2 \theta)^2}, \tag{27a}$$

$$\text{(b)}\quad \overline{p_f^2}(R, \theta) = \frac{1}{2}\left(\frac{a}{R}\right)^2 \frac{\overline{F_s^2}}{2}\left(\frac{1}{2}ka/\beta\right)^2 \times \frac{(M\sqrt{1 - M^2 \sin^2 \theta} - \cos\theta)^2}{\beta^2(1 - M^2 \sin^2 \theta)^2}, \tag{27b}$$

$$\text{(c)}\quad \overline{p_f^2}(R, \theta) = \frac{1}{2}\left(\frac{a}{R}\right)^2 \left(\frac{2\rho_0 c_0 W_0}{S}\right)\left(\frac{1}{2}ka/\beta\right)^2 \times \frac{(\sqrt{1 - M^2 \sin^2 \theta} - M\cos\theta)^2 \cos\theta}{\beta^2(1 - M^2 \sin^2 \theta)^{5/2}}. \tag{27c}$$

E. Multimode sound power in the high-ka limit

Now utilizing the expression for generalized directivity given by Eq. (26), the radiated sound power defined by Eq. (12) is now evaluated. Equating the radiated sound power to the in-duct transmitted power, the expected value of the source power is obtained by integrating the elementary sound power contributions $E\{\delta W(\theta)\}$ given by Eq. (23) between $\theta = 0$ and $\pi/2$. Thus, as $ka \to \infty$, contributions to the sound power from angles between $\pi/2$ and π are neglected (rear arc), and the expected value of the source power is given by

$$E\{W\} = \frac{S}{2\rho_0 c_0}\left(\frac{ka}{2}\right)^2 \int_0^{\pi/2} \frac{\sin 2\theta}{(1 - M^2 \sin^2 \theta)^2} \times \frac{\beta^4 \alpha(\theta)}{(1 - \alpha(\theta)M)^2} E\{|A_{mn}(\alpha(\theta))|^2\}\mathrm{d}\theta. \tag{28}$$

Substituting Eqs. (10a)–(10c) for $E\{|A_{mn}|^2\}$ the integration over θ can be determined analytically for the three source distributions, which gives the following expressions for the sound power in the high-ka limit:

$$\text{(a)}\quad E\{W\} = \frac{\rho_0 c_0 S \overline{Q_s^2}}{2}\left(\frac{1}{2}ka/\beta\right)^2, \tag{29a}$$

$$\text{(b)}\quad E\{W\} = \frac{S\overline{F_s^2}}{2\rho_0 c_0}\left(\frac{1}{2}ka/\beta\right)^2 \times \frac{2\beta^2 \ln(1 - M) + 2M + M^2 - M^3 - M^4}{M^3}, \tag{29b}$$

$$\text{(c)}\quad E\{W\} = W_0\left(\tfrac{1}{2}ka/\beta\right)^2. \tag{29c}$$

Noting from Rice[15] that $N = (\frac{1}{2}ka/\beta)^2$ is the high-ka asymptotic expression for the total number of propagating modes in the duct, the remaining factors represent the average sound power per mode.

Equation (29) can be used to compute the convective amplification factor $E\{W\}/E\{W|_{M=0}\}$, which is plotted in Fig. 4 versus Mach number M for the three source models under investigation. The figure shows that the amplification factor is identical for the source models having a uniform distribution of incoherent monopoles and equal power per mode. In these cases, the amplification factor is symmetrical with respect to $M=0$, and the sound power increases identically with Mach number irrespective of the flow direction. However, the amplification factor for the uniform distribution of incoherent axial dipoles is not symmetric about $M=0$, and reaches a minimum value of about 0.7 at $M=0.4$.

F. Non-dimensional directivity factor *Q* in the high-*ka* limit

Substituting the analytical expressions of Eqs. (26) and (28) into the definition of $Q(ka,\theta)$ given by Eq. (11) leads to

$$Q(ka,\theta)=\frac{4E\{|A_{mn}(\alpha(\theta))|^2\}\cos^2\theta/(1-M^2\sin^2\theta)^2}{\beta^4\int_0^{\pi/2}\alpha(\theta)E\{|A_{mn}(\alpha(\theta))|^2\}\sin 2\theta/[(1-M^2\cos^2\theta)^2(1-\alpha(\theta)M)^2]\mathrm{d}\theta}. \tag{30}$$

In the high-frequency limit $ka\to\infty$, the expression for $Q(ka,\theta)$ can be evaluated analytically for each of the three source models under investigation, i.e., for the following special cases: (a) a uniform distribution of incoherent monopoles, (b) a uniform distribution of incoherent axial dipoles, and (c) equal power per mode. The results are

$$\text{(a)}\quad Q=2\frac{(\sqrt{1-M^2\sin^2\theta}-M\cos\theta)^2}{\beta^2(1-M^2\sin^2\theta)^2}, \tag{31a}$$

$$\text{(b)}\quad Q=\frac{2}{\beta^2}\frac{M^3}{2M+M^2-M^3-M^4+2\beta^2\ln(1-M)}\times\frac{(M\sqrt{1-M^2\sin^2\theta}-\cos\theta)^2}{(1-M^2\sin^2\theta)^2}, \tag{31b}$$

$$\text{(c)}\quad Q=4\frac{(\sqrt{1-M^2\sin^2\theta}-M\cos\theta)^2}{\beta^2(1-M^2\sin^2\theta)^{5/2}}\cos\theta. \tag{31c}$$

Note that these high-ka results are valid for all subsonic Mach numbers $-1<M<1$, i.e., independent of flow direction.

At low Mach numbers, to leading order in M, the expressions for Q are approximately

$$\text{(a)}\quad Q\sim 2-4M\cos\theta, \tag{32a}$$

$$\text{(b)}\quad Q\sim 6\cos^2\theta+3M(3\cos^2\theta-4\cos\theta), \tag{32b}$$

$$\text{(c)}\quad Q\sim 4\cos\theta-8M\cos\theta. \tag{32c}$$

Equations (32a)–(32c) suggest that the effect of flow on the directivity functions is most pronounced on axis, $\theta=0°$, in the direction of flow. Note that as $M\to 0$,

$$\text{(a)}\ Q\to 2,\quad \text{(b)}\ Q\to 6\cos^2\theta,\quad \text{(c)}\ Q\to 4\cos\theta, \tag{33}$$

which are the directivity factors derived previously by Joseph and Morfey[1] for zero-flow.

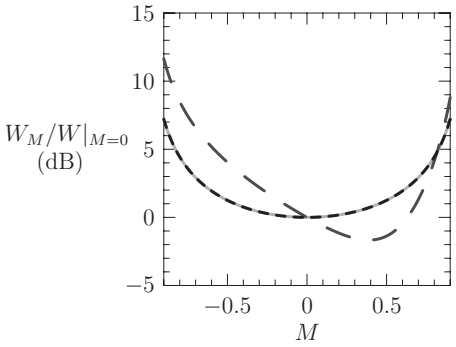

FIG. 4. In-duct power with uniform flow normalized by the power in the absence of flow versus Mach number. Results are shown for the source models: (a) a uniform distribution of incoherent monopoles (solid line), (b) a uniform distribution of incoherent axial dipoles (long-dashed line), and (c) equal power per mode (short-dashed line).

V. RESULTS

The directivity function $Q(ka,\theta)$ is plotted in Figs. 5–7 versus polar angle θ at $ka=50$, for a uniform distribution of incoherent monopoles, a uniform distribution of incoherent axial dipoles, and equal power per mode, respectively. In each figure are plotted the results at Mach numbers of $M=-0.9$, -0.3, 0, 0.3, and 0.9. In each polar plot the solid line shows the exact directivity function and the dashed line shows the high-frequency asymptotic solutions given by Eqs. (31a)–(31c), which are valid in the forward arc. Note that for the exact results the modal radiation transfer function H_{mn} used here has been computed from the transfer function in the absence of flow H^0_{mn}, given by Homicz and Lordi,[2] using either Eq. (7) or Eq. (8) depending on the sign of M, whereas the asymptotic solutions of Eqs. (31a)–(31c) are valid for all M. The agreement between the exact and high-frequency asymptotic solution is excellent up to about 80°.

For a uniform distribution of incoherent monopoles, the directivity is omnidirectional in the forward arc for $M=0$ [Fig. 5(c)]. For $M<0$, as the flow speed increases, Q increases approximately uniformly over the forward arc [Figs. 5(a) and 5(b)]. Different behavior is observed for $M>0$. In this case, as the flow speed increases, Q decreases at polar angles close to the duct axis and increases at angles further away from the duct axis [Figs. 5(d) and 5(e)].

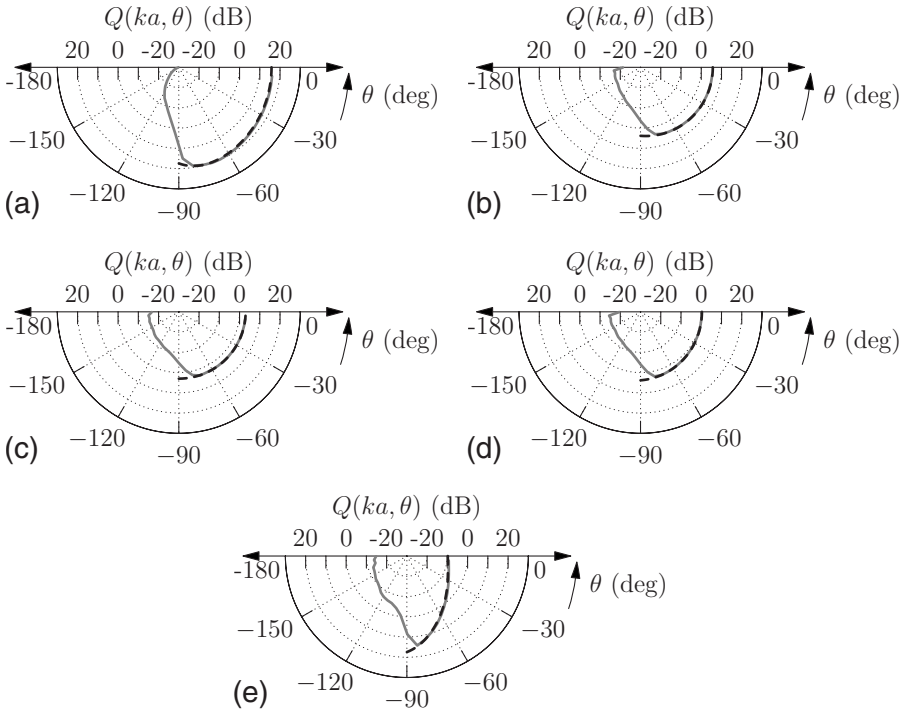

FIG. 5. [(a)–(e)] Multimode directivity function $Q(ka,\theta)$ for sound radiated from a circular duct with uniform flow. The source is a uniform distribution of incoherent monopoles. Results are shown for $ka=50$ and for five different values of Mach number M. The solid line represents the exact numerical solution given by Eq. (11) (see Sec. III). The dashed line represents the high-frequency asymptotic solution given by Eq. (31a).

For a uniform distribution of incoherent axial dipoles, the radiation pattern exhibits small deviations from omnidirectional behavior over the forward arc for $M=0$ [Fig. 6(c)]. However, for $M<0$, as the flow speed increases, the directivity pattern tends to become more uniform in the forward arc [Figs. 6(a) and 6(b)]. By contrast, for $M>0$, the directivity drops to zero at certain angles, and radiates more efficiently away from the duct axis as the flow speed increases [Figs. 6(d) and 6(e)]. From Eq. (31b), the angular position of the nulls in the directivity pattern is given by

$$\cos\,\theta_0 = \frac{M}{\sqrt{1-M^2}}. \tag{34}$$

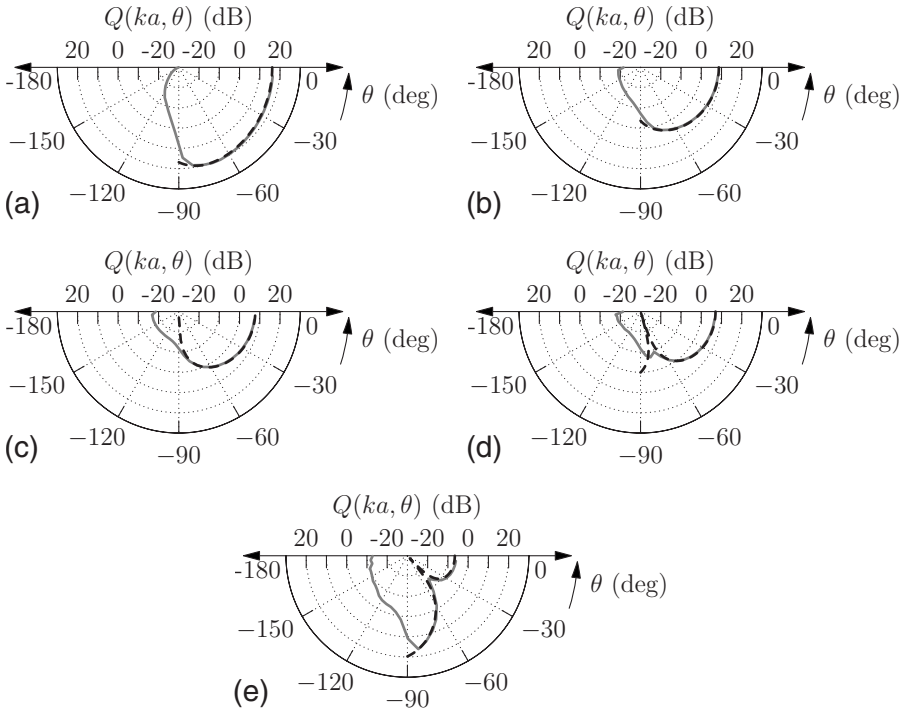

FIG. 6. [(a)–(e)] Multimode directivity function $Q(ka,\theta)$ for sound radiated from a circular duct with uniform flow. The source is a uniform distribution of incoherent axial dipoles. Results are shown for $ka=50$ and for five different values of Mach number M. The solid line represents the exact numerical solution given by Eq. (11) (see Sec. III). The dashed line represents the high-frequency asymptotic solution given by Eq. (31b).

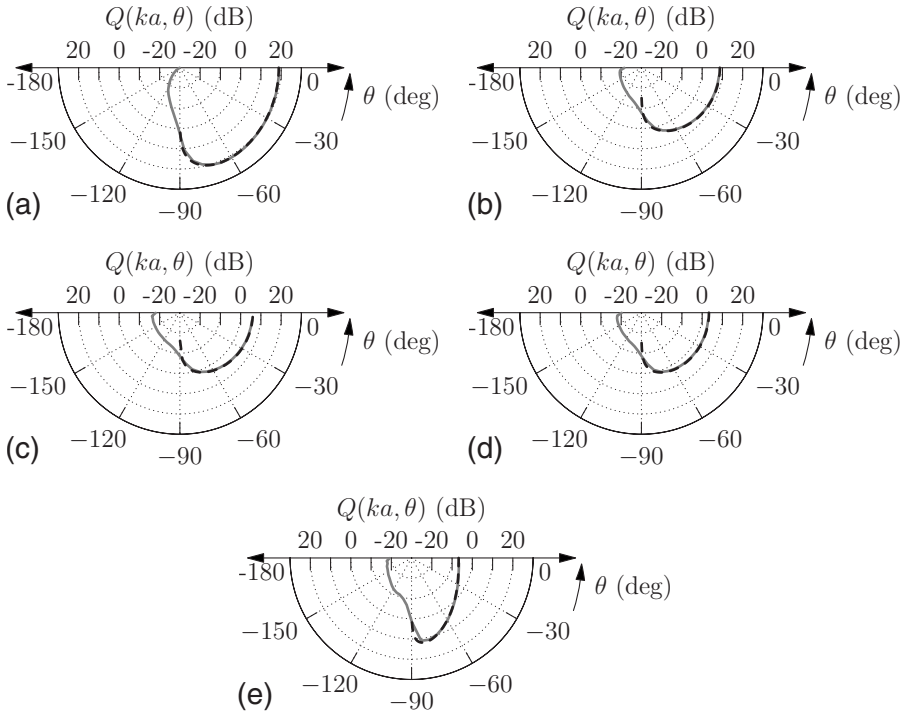

FIG. 7. [(a)–(e)] Multimode directivity function $Q(ka,\theta)$ for sound radiated from a circular duct with uniform flow. The source is equal power per mode. Results are shown for $ka=50$ and for five different values of Mach number M. The solid line represents the exact numerical solution given by Eq. (11) (see Sec. III). The dashed line represents the high-frequency asymptotic solution given by Eq. (31c).

From Eq. (10b) for the mode amplitude distribution due to axial dipoles, this angle corresponds to the modal propagation angle θ_0 at which $E\{|A_{mn}(\alpha(\theta_0))|^2\}=0$. This may be shown to be at the angle at which the modal group velocity is zero.

Finally, for equal power per mode, the behavior is similar to that for a uniform distribution of incoherent monopoles (Fig. 7).

VI. CONCLUSIONS

In this paper, the directivity function of multimode sound radiation from an unflanged, semi-infinite circular duct with uniform flow is investigated. Both inlet ($M<0$) and exhaust ($M>0$) cases are examined. This problem is of importance in the understanding of, for example, the radiation of fan broadband noise from aero-engine ducts. The behavior of the multimode radiation is considered for a general family of mode amplitude distribution function. Special cases are incoherent monopoles or axial dipoles uniformly distributed over the duct cross section, and the case of equal power per mode. A non-dimensional directivity function $Q(ka,\theta)$ is defined, normalized with respect to the total radiated acoustic power. Analytic expressions for Q are derived for these three source models that are valid in the high-frequency limit and in the forward arc. The dependence on the radiation polar angle θ and flow Mach number is revealed explicitly. The presence of a uniform mean flow in a duct has been demonstrated, through the mechanism of convective amplification, to alter the total radiated sound power compared with when flow is absent. The paper has shown that the variation in sound power radiation with M is identical for the mode distributions of "equal energy per mode" and a distribution of incoherent monopoles. Increases of less than 3 dB are predicted for flow speeds of $M<0.5$ for these two source models. However, an incoherent distribution of axial dipole sources has been shown to radiate less sound power for exhaust ducts for flow speed $M<0.5$ but radiate more sound power at higher flow speeds compared with when flow is absent. The effect of flow has been found to produce significant distortions of the far-field directivity patterns. Of the three mode distributions models investigated in detail in this paper the directivity patterns due to axial dipole sources are predicted to be most sensitive to flow. In the exhaust duct, the presence of flow has been shown to introduce an additional null in the directivity pattern corresponding to the main radiation lobe of the modes of zero group velocity. In general, however, the paper has shown that effects of flow may be neglected for flow Mach number of less than 100 m s^{-1} ($M<0.3$).

ACKNOWLEDGMENTS

The authors wish to thank Professor R. J. Astley (ISVR), and one of the referees, for their guidance regarding the use of the Lorentz transform to derive Eqs. (7) and (8).

APPENDIX: DERIVATION OF $\delta N(\theta)$

In this appendix an expression for the number of modes in a rigid-walled circular duct with propagation angles between θ and $\theta+\delta\theta$, in the high-frequency limit $ka\to\infty$, is derived. The duct is assumed to contain a uniform mean flow with Mach number M. The derivation makes use of previous work by Rice[15] on the total number of cut-on modes with

flow. Rice's result is expressed in terms of the cut-off ratio ξ, which is related to the cut-on ratio α of Eq. (3) by

$$\alpha = \sqrt{1 - \xi^{-2}}, \tag{A1}$$

and is in the range $\xi \geq 1$ for the propagating modes. Note that in this appendix we follow Rice's nomenclature, so the analysis is in terms of cut-off ratio ξ. Following Rice,[15] the total number of cut-on modes $N(\xi)$ having a cut-off ratio below a particular value ξ is given by

$$N(\xi) = \frac{\left(\frac{1}{2}ka\right)^2}{\xi^2}. \tag{A2}$$

Note that $(\frac{1}{2}ka/\beta)^2$ is the high-ka asymptotic expression for the total number of propagating modes in the duct.

Differentiating Eq. (A2) yields the following equation for the number of modes $\delta N(\xi)$ with cut-off ratio between ξ and $\xi + \delta\xi$, where $\delta\xi$ is small:

$$\delta N(\xi) = \frac{dN(\xi)}{d\xi}\delta\xi = -2\frac{\left(\frac{1}{2}ka\right)^2}{\xi^3}\delta\xi. \tag{A3}$$

The cut-off ratio may be related to the modal propagation angle using Eq. (19) first derived by Rice *et al.*,[14]

$$\cos\theta = \frac{\alpha\beta}{\sqrt{1 - M^2\alpha^2}}. \tag{A4}$$

The number of modes $\delta N(\theta)$ with propagation angles between θ and $\theta + \delta\theta$ may therefore be obtained by substituting Eqs. (A4) and (A1) into Eq. (A3) and noting that $\delta\xi = (d\xi/d\alpha)(d\alpha/d\theta)\delta\theta$, to give

$$\delta N(\theta) = \frac{\left(\frac{1}{2}ka\right)^2 \sin 2\theta}{(1 - M^2\sin^2\theta)^2}\delta\theta. \tag{A5}$$

[1] P. Joseph and C. L. Morfey, "Multimodal radiation from an unflanged, semi-infinite circular duct," J. Acoust. Soc. Am. **105**, 2590–2600 (1999).
[2] G. F. Homicz and J. A. Lordi, "A note on the radiative directivity patterns of duct acoustic modes," J. Sound Vib. **41**, 283–290 (1975).
[3] E. J. Rice, "Multimodal far-field acoustic radiation pattern," AIAA J. **16**, 906–911 (1978).
[4] R. M. Munt, "The interaction of sound with a subsonic jet issuing from a semi-infinite cylindrical pipe," J. Sound Vib. **83**, 609–640 (1977).
[5] R. M. Munt, "Acoustic transmission properties of a jet pipe with subsonic jet flow: I. The cold jet reflection coefficient," J. Sound Vib. **142**, 413–436 (1990).
[6] S. W. Rienstra, "Sound radiated from annular duct in flow," J. Sound Vib. **94**, 267–288 (1984).
[7] G. Gabard and R. J. Astley, "Theoretical model for sound radiation from annular jet pipes: Far- and near-field solutions," J. Fluid Mech. **549**, 315–341 (2006).
[8] D. W. Bechert, "Sound-absorption caused by vorticity shedding, demonstrated with a jet flow," J. Sound Vib. **70**, 389–405 (1980).
[9] Rice's cut-off ratio ξ is uniquely related to our cut-on ratio α; see the Appendix, Eq. (A1).
[10] J. M. Tyler and T. G. Sofrin, "Axial flow compressor noise studies," SAE Trans. **70**, 309–332 (1962).
[11] C. J. Chapman, "Similarity variables for sound radiation in a uniform flow," J. Sound Vib. **233**, 157–164 (2000).
[12] P. Joseph, C. L. Morfey, and C. R. Lowis, "Multi-mode sound transmission in ducts with flow," J. Sound Vib. **264**, 523–544 (2003).
[13] C. L. Morfey, "Sound transmission and generation in ducts with flow," J. Sound Vib. **14**, 37–55 (1971).
[14] E. J. Rice, M. F. Heidmann, and T. G. Sofrin, "Modal propagation angles in a cylindrical duct with flow and their relation to sound radiation," presented at the 17th Aerospace Sciences Meeting, New Orleans, LA, 15–17 January (1979), AIAA Paper No. 79-0183.
[15] E. J. Rice, "Modal density function and number of propagating modes in ducts," J. Acoust. Soc. Am. **60**, S112 (1976).

Effects of upper ocean sound-speed structure on deep acoustic shadow-zone arrivals at 500- and 1000-km range

Lora J. Van Uffelen,[a] Peter F. Worcester, Matthew A. Dzieciuch, and Daniel L. Rudnick
Scripps Institution of Oceanography, University of California at San Diego, La Jolla, California 92093

John A. Colosi
Naval Postgraduate School, 833 Dyer Road, Monterey, California 93943

(Received 16 September 2009; accepted 21 December 2009)

Deep acoustic shadow-zone arrivals observed in the late 1990s in the North Pacific Ocean reveal significant acoustic energy penetrating the geometric shadow. Comparisons of acoustic data obtained from vertical line arrays deployed in conjunction with 250-Hz acoustic sources at ranges of 500 and 1000 km from June to November 2004 in the North Pacific, with simulations incorporating scattering consistent with the Garrett–Munk internal-wave spectrum, are able to describe both the energy contained in and vertical extent of deep shadow-zone arrivals. Incoherent monthly averages of acoustic timefronts indicate that lower cusps associated with acoustic rays with shallow upper turning points (UTPs), where sound-speed structure is most variable and seasonally dependent, deepen from June to October as the summer thermocline develops. Surface-reflected rays, or those with near-surface UTPs, exhibit less scattering due to internal waves than in later months when the UTP deepens. Data collected in November exhibit dramatically more vertical extension than previous months. The depth to which timefronts extend is a complex combination of deterministic changes in the depths of the lower cusps as the range-average profiles evolve with seasonal change and of the amount of scattering, which depends on the mean vertical gradients at the depths of the UTPs. © *2010 Acoustical Society of America.* [DOI: 10.1121/1.3292948]

PACS number(s): 43.30.Ft, 43.30.Re [NPC] Pages: 2169–2181

I. INTRODUCTION

A long-range acoustic transmission experiment performed in the North Pacific Ocean from June to November 2004 confirmed the presence of deep shadow-zone arrivals. These stable, resolved acoustic arrivals 500–1000 m below predicted acoustic timefronts were first observed in the North Pacific in the 1990s (Dushaw *et al.*, 1999) in transmissions from a broadband 75-Hz source on Pioneer Seamount, off the coast of central California, to bottom-mounted receivers at megameter ranges. This penetration is much larger than predicted by diffraction theory, and all of the shadow-zone arrivals occurred at the times of cusps (caustics) in the predicted timefronts. The arrivals were identified on the receivers, but the horizontal orientation of the arrays did not capture the vertical structure of the extensions.

The 2004 Spice Experiment (SPICEX) incorporated two extensive vertical line arrays (VLAs) in close proximity, designed to elucidate the vertical structure of these arrivals. Acoustic receptions from 250-Hz sources moored near the sound channel axis (750 m) at ranges of 500 and 1000 km display the well-studied "accordion" pattern consisting of well-defined and identifiable early arrivals and a highly scattered, near-axial finale. The early arrivals with well-defined lower cusps are from high-angle rays that sample the full water column, including the highly variable upper ocean. These cusps, analogous to those observed on the horizontal arrays in the 1990s, were shown to extend downward well into the geometric shadow zone (Van Uffelen *et al.*, 2009). These extensions were consistently observed well below the depths of the caustics expected from simulations based upon a range-independent sound-speed profile derived from environmental measurements collected at the time of the experimental deployment (Fig. 1).

Since travel time is the primary observable of interest in acoustic tomography experiments, intensities of acoustic data have received little attention. In Van Uffelen *et al.* (2009), the acoustic data were carefully calibrated, taking account of signal processing gains, for direct comparison in units of absolute intensity to parabolic equation simulations incorporating details of the source spectra. Parabolic equation simulations incorporating sound-speed perturbations consistent with the Garrett–Munk (GM) internal-wave spectrum at full strength show good agreement with measurements both in intensity and depth of shadow-zone arrivals. The intensity and arrival characteristics of the internal-wave simulations also appropriately describe the intensity of the early geometric arrivals as well as the scattering of the near-axial finale. This work focused on a single daily average of receptions (six transmissions per source) on yearday 167, which coincided with the collection of oceanic temperature and salinity data used to determine the sound-speed environment for the propagation simulations.

Here, incoherent monthly averages of acoustic timefronts from June to November 2004 provide a better statisti-

[a]Author to whom correspondence should be addressed. Electronic mail: lvanuffe@ucsd.edu

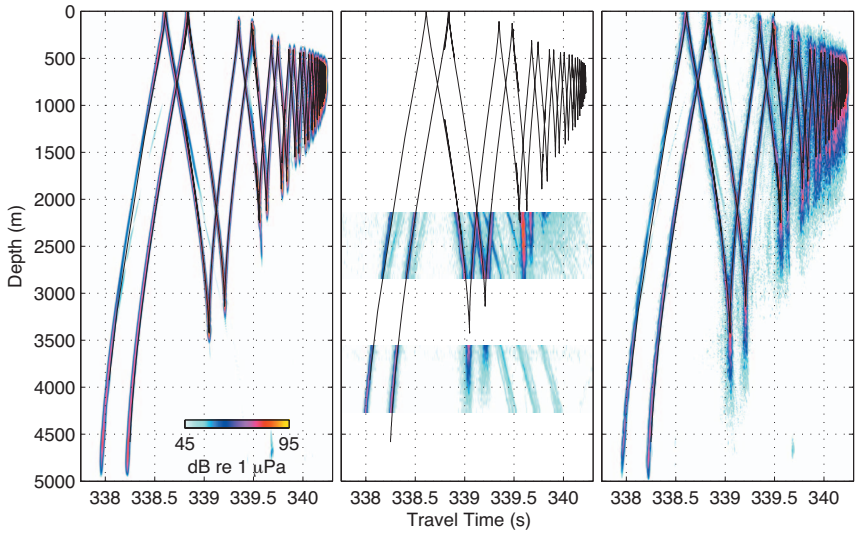

FIG. 1. Acoustic ray propagation simulation from an axial source at 500-km range to the DVLA overlaid on parabolic equation simulation for a range-independent profile (left), a profile including scattering consistent with the Garrett–Munk internal-wave energy spectrum (right), and an incoherent average of acoustic receptions received on the DVLA in the month of June 2004 (middle). The incoherent average of the measured receptions has been aligned with the predicted timefront by construction, as described in Sec. V A. The measured travel times do not agree with the predicted travel times as closely as the figure might seem to suggest, in part because of imperfect knowledge of the sound-speed field between the source and receiver and in part because of the error at high pressures in the equation used to compute sound speed from temperature and salinity (Dushaw *et al.*, 1993). Three steep arrivals corresponding to rays that reflect from both the sea surface and seafloor are clearly evident in the receptions between 339 and 340 s. These surface-reflected, bottom-reflected arrivals have intensities as large as 65 dB re 1 μPa and can complicate the analysis of the purely refracted arrivals when the two overlap, but they will not otherwise be studied further here.

cal characterization of the extension of the arrivals beyond the un-scattered caustic depths as well as an indication of how the depths of these cusps vary with time and with a changing upper ocean environment. The time variation in the scattering in the cusps is investigated quantitatively with respect to energy content in the lower cusp arrival as a function of depth.

The SPICEX is described in Sec. II. Section III presents the environmental data acquired during the experiment as well as the sound-speed and buoyancy-frequency profiles derived from the collected data. The lower cusps are examined in the absence of internal-wave scattering using ray tracing and parabolic equation simulations in Sec. IV, and the scattered shadow-zone extensions are presented in Sec. V and discussed in Sec. VI.

II. EXPERIMENT

Each of the two source moorings deployed during SPICEX supported two broadband acoustic sources. Hydroacoustics, Inc., Henrietta, NY, HLF-5 sources with a center frequency of 250 Hz (Munk *et al.*, 1995) were located at about 750-m depth, approximately on the sound channel axis. Webb Research Corporation (WRC) swept-frequency sources with a center frequency of 275 Hz (Morozov and Webb, 2003, 2007; Webb *et al.*, 2002) were located at about 3000-m depth, slightly above the estimated surface conjugate depth. Exact source depths are indicated in Fig. 2. Only results from the HLF-5 axial source transmissions are reported here.

The source moorings were approximately 500 km (S1) and 1000 km (S2) distant from a pair of VLA receiver moorings deployed approximately 5 km apart. Each VLA was constructed using quasi-independent subarrays of 20 hydrophones (High Tech, Inc., Gulfport, MS, HTI-90-U) at 35-m spacing and an overall length of 700 m (ATOC Instrumentation Group, 1995). One VLA receiver, referred to as the shallow VLA (SVLA), spanned the sound channel axis. It consisted of two subarrays, with a total of 40 hydrophones over the depth range 375.7–1739.3 m. The second VLA receiver, referred to as the deep VLA (DVLA), was designed to span the surface conjugate depth. It consisted of three subarrays. Unfortunately, the center subarray failed, leaving an upper subarray of 20 hydrophones over the depth range 2153.1–2819.6 m and a lower subarray of 20 hydrophones over the depth range 3575.3–4249.5 m. Because this work is focused on deep arrivals, only data from the DVLA are presented here.

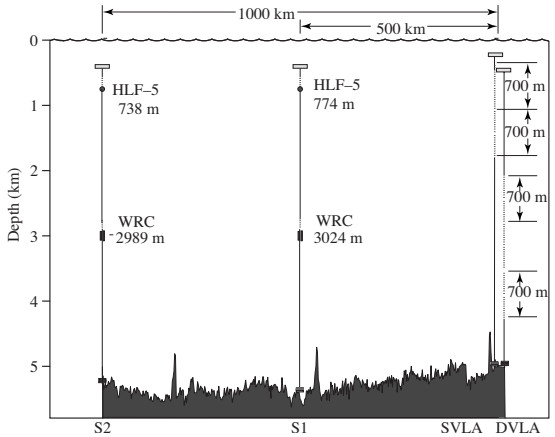

FIG. 2. SPICEX cross-sectional geometry overlaid on measured multibeam bathymetric data. Positions of SVLA and DVLA are not to scale due to their close proximity. [Reprinted from Van Uffelen *et al.* (2009). J. Acoust. Soc. Am. **125**, 3569–3588. Copyright 2009, Acoustical Society of America.]

TABLE I. SPICEX mooring locations and water depths.

Mooring	Latitude	Longitude	Depth
DVLA	33.418 92°N	222.317 53°E	5045
SVLA	33.418 40°N	222.259 07°E	5005
S1	34.267 22°N	216.982 92°E	5500
S2	34.889 12°N	211.591 97°E	5475

The positions of the sources and the positions and shapes of the VLAs were measured once an hour throughout the deployment by long-baseline acoustic navigation systems. The source and receiver positions were determined to within a few meters using Global Positioning System (GPS) navigation (Table I). The acoustic paths were nearly colinear. The source and VLA moorings were all deployed at approximately the same latitude in order to provide nearly zonal acoustic paths, with relatively range-independent sound-speed profiles. A detailed multibeam bathymetric survey was performed at each of the mooring sites prior to deployment, and bathymetric data were collected along the acoustic path while the ship was in transit between mooring deployment sites.

The hydrophone signals were amplified, bandpass filtered, and sampled at a 1000-Hz rate using 16-bit analog-to-digital converters. Large time-bandwidth signals and pulse-compression techniques were used to improve the signal-to-noise ratio of the receptions. The two near-axial HLF-5 acoustic sources simultaneously transmitted 11 periods of a 1023-digit phase-coded m-sequence with a carrier frequency of 250 Hz (Munk *et al.*, 1995). Each digit contained three cycles of the carrier ($Q=3$). Each digit was then 12.0 ms in duration, each sequence period was 12.276 s long, and the transmission lasted for 135.0360 s. Ten out of 11 periods, beginning at the nominal arrival time of the middle of the first sequence, were recorded and coherently processed. The source level was calibrated at the U.S. Navy Seneca Lake Sonar Test Facility to be 192 dB re 1 μPa at 1 m.

This is an abbreviated description of the SPICEX. More extensive experimental details are provided in Van Uffelen *et al.* (2009).

III. ENVIRONMENTAL DATA

Deep conductivity-temperature-depth (CTD) measurements were made at each mooring location at the time of deployment. During the Long Range Ocean Acoustic Propagation EXperiment (LOAPEX) cruise conducted in September of the same year (Mercer *et al.*, 2009), full-ocean depth CTD measurements were obtained at each of the source mooring locations, and a CTD cast down to 2300-m depth was performed at a location on the acoustic propagation path approximately 50 km from the VLA. Upper ocean conductivity and temperature measurements were also collected between the mooring sites using an underway CTD (UCTD) (Rudnick and Klinke, 2007). Ninety-six UCTD casts were obtained along the 1000-km propagation path between S2 and the VLAs in June during the SPICEX deployment, and 72 casts were obtained along approximately the same path in September during the LOAPEX cruise, sampling the upper approximately 400 m of the water column. In addition, Seabird Micro-CAT (Conductivity And Temperature) sensors were affixed to the SVLA mooring to collect environmental data in the upper ocean throughout the duration of the experiment.

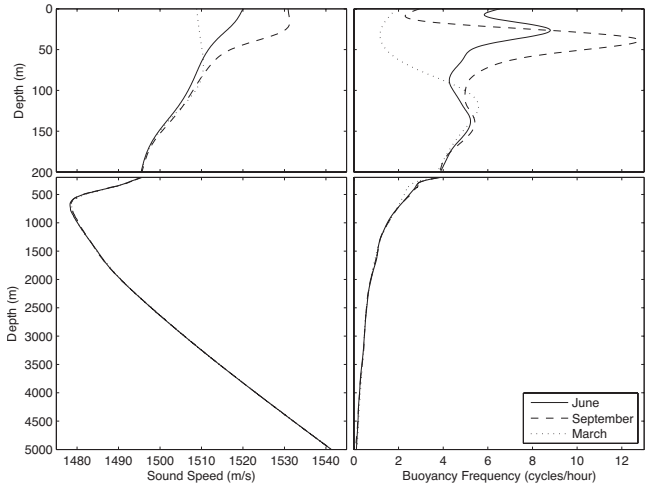

FIG. 3. Sound-speed profile (left) and buoyancy-frequency profile (right) constructed from SPICEX temperature and salinity data for June 2004, from LOAPEX data for September 2004, and from SeaSoar data in March 2005. The top (bottom) panels show the profiles above (below) 200 m.

A. June and September profiles

Range-independent temperature and salinity profiles were constructed from the UCTD data in the upper ocean and the deep CTD casts in the deep ocean. These range-independent profiles are averages of range-dependent fields constructed from the UCTD and CTD data (Van Uffelen *et al.*, 2009).

Range-independent sound-speed profiles for June and September were computed from the resulting range-independent temperature and salinity profiles using the sound-speed equation of Del Grosso (1974) (Fig. 3). The sound-speed profiles were smoothed using a cubic spline to mitigate erratic behavior exhibited by steep-angle acoustic rays propagated through a discontinuous sound-speed environment. The resulting June profile exhibits virtually no mixed layer, whereas the September profile exhibits a mixed layer approximately 20 m thick.

Similarly, range-independent buoyancy-frequency profiles were computed from the range-independent temperature and salinity profiles and subsequently smoothed using a cubic spline (Fig. 3).

B. Internal waves

Simulated internal-wave-induced sound-speed fluctuations were added to the range-average sound-speed profile to generate stochastic realizations of range-dependent sound-speed fields that include internal waves. The simulated fields were generated to be consistent with the empirical GM spectral model (Garrett and Munk, 1979), using the method of Colosi and Brown (1998).

These perturbations to the sound-speed profile, δc, are due to vertical displacements of a fluid parcel ζ,

TABLE II. Internal-wave parameters for June and September profiles.

Parameter	Description	June	September
B	Thermocline depth scale	1269 m	1198 m
N_0	Ref. buoyancy frequency	4.06 cph	4.38 cph
E	Ref. internal-wave energy	6.3×10^{-5}	6.3×10^{-5}
ω_i	Inertial frequency	8.18×10^{-5} s^{-1}	8.18×10^{-5} s^{-1}
j^*	Empirical constant	3	3
$j_{\max}$	Number of vertical modes	100	100
Δx	Range step size	0.2 km	0.2 km

$$\delta c = \left(\frac{\partial c}{\partial z}\right)_{\text{pot}} \zeta, \tag{1}$$

where $(\partial c/\partial z)_{\text{pot}}$ is the potential sound-speed gradient. The GM spectrum of internal-wave vertical displacement ζ as a function of range x and depth z for a frozen vertical slice is

$$\zeta(x,z) = \text{Re}\left[\frac{2B}{\pi}\left(\frac{E}{M}\right)^{1/2}\left(\frac{N_0}{N(z)}\right)^{1/2}(\Delta k_x)^{1/2}\cdots \times\sum_j \frac{\sin(j\pi\zeta(z))}{(j^2+j_*^2)^{1/2}}\sum_{k_x}(I(j,k_x))^{1/2}G_j(k_x)e^{ik_x x}\right], \tag{2}$$

where

$$\zeta(z) = \frac{1}{N_0 B}\int_{-h}^{z} N(z')dz', \tag{3}$$

$$I(j,k_x) = \frac{k_j}{k_x^2+k_j^2} + \frac{1}{2}\frac{k_x^2}{(k_x^2+k_j^2)^{3/2}}\ln\left(\frac{\sqrt{k_x^2+k_j^2}+k_j}{\sqrt{k_x^2+k_j^2}-k_j}\right), \tag{4}$$

$$M = \sum_{j=1}^{\infty}(j^2+j_*^2)^{-1}, \tag{5}$$

and

$$k_j = \pi\omega_i j/N_0 B. \tag{6}$$

In these simulations G_j is a complex Gaussian random variable. The values of the relevant parameters are given in Table II. The range-independent buoyancy-frequency profiles, $N(z)$, were used to construct the internal-wave fields (Fig. 3).

Figure 4 shows the rms sound-speed fluctuation due to these stochastic internal-wave perturbations. Ten realizations of the sound-speed perturbation fields were generated and subsampled at 10-km intervals, resulting in approximately 1000 quasi-independent profiles.

The Micro-CAT sensors on the SVLA mooring measured pressure as well as temperature and salinity. Sound speed was calculated from these data using the Del Grosso sound-speed equation. The instruments were deployed from June 2004 to June 2005 and collected data throughout the deployment. The rms sound-speed fluctuations presented in Fig. 4 are for the year-long deployment.

Internal waves are observed to occur from inertial to buoyancy frequencies. The mean sound speed was removed, and the sound-speed perturbation data were high-pass filtered to suppress frequencies below the inertial frequency. The

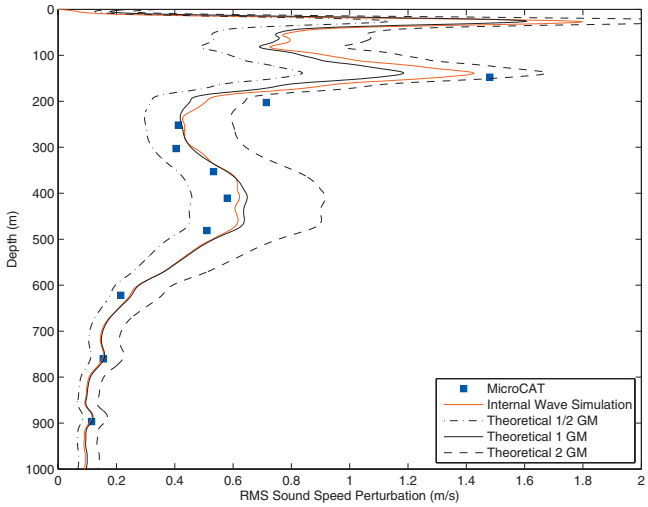

FIG. 4. Rms sound-speed perturbation based on data from Micro-CAT sensors on the VLA compared with rms sound-speed perturbations generated for 1-GM stochastic internal-wave simulations. Calculated rms sound-speed perturbations based on the theoretical variance of the Garrett–Munk spectrum for energy levels of 1/2 GM, 1 GM, and 2 GM are also included.

Micro-CAT sensors were sampled once every 7 min, with a Nyquist frequency of 4.3 samples/hour. The Nyquist frequency exceeds the buoyancy frequency at depths below approximately 180 m (Fig. 3), but data from the instrument located at 147 m may be undersampled.

The theoretical variance of the internal-wave spectrum is given by

$$\langle\zeta^2\rangle = \frac{1/2B^2EN_0}{N(z)}. \tag{7}$$

The square root of $\langle\zeta^2\rangle$ is multiplied by the smoothed potential sound-speed gradient for direct comparison to the rms sound-speed perturbations of the stochastic internal-wave realizations and the Micro-CAT data in Fig. 4. The result is scaled for 1/2-GM, 1-GM, and 2-GM energy levels. The 1-GM energy level is a good fit for the sensors below 250 m. The upper two sensors, however, display a higher variance, which suggests a higher internal-wave strength, closer to the 2-GM level.

The displacement spectra obtained from the Micro-CAT temperature data also indicate an internal-wave level of between 1/2 and 2 GM. The temperature data were high-pass filtered for frequencies above the inertial frequency prior to calculating the power spectral density and were multiplied by the buoyancy frequency for normalization. The displacement spectra were obtained from the temperature spectra using the relation

$$\delta T = \left(\frac{\partial T}{\partial z}\right)_{\text{pot}} \zeta. \tag{8}$$

The potential temperature gradient, $(\partial T/\partial z)_{\text{pot}}$, was smoothed with a cubic spline.

The vertical displacement spectra of the Micro-CAT data are compared with the theoretical GM vertical displacement spectra (Fig. 5) defined from inertial to buoyancy frequencies ω:

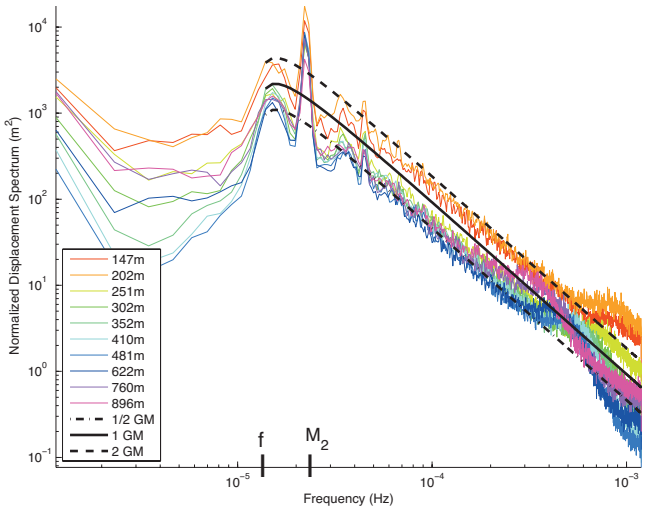

FIG. 5. Vertical displacement spectrum scaled by buoyancy frequency for the ten Micro-CAT sensors on the SVLA compared with the Garrett–Munk displacement spectra scaled for energy levels of 1/2 GM, 1 GM, and 2 GM. The inertial frequency $f=\omega_i/2\pi$ and M_2 tidal frequency are indicated.

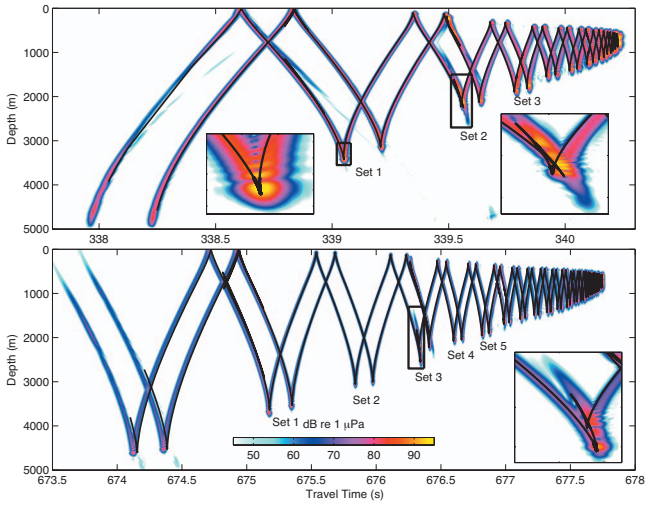

FIG. 6. Acoustic ray timefronts propagated through a range-independent June sound-speed profile overlaid on range-independent parabolic equation simulations for the 500-km (top) and 1000-km (bottom) propagation paths. Sets of cusps captured by the DVLA are labeled. Magnified insets depict a typical cusp (top left) and two atypical cusps (top and bottom right). The atypical cusps will not otherwise be considered here.

$$F_\zeta(\omega)=\frac{2EB^2N_0\omega_i(\omega^2-\omega_i^2)^{1/2}}{N\omega^3\pi}. \tag{9}$$

The spectrum drops off below the inertial frequency due to the high-pass filtering, but increases again at very low frequencies, presumably due to mesoscale variability. A strong semidiurnal tidal signal is also evident.

The shallowest two sensors again indicate an internal-wave strength of approximately 2 GM. Deeper sensors, which are located near the sound channel axis, are more consistent with 1/2 GM, so an energy level of 1/2 GM may be appropriate for looking at scattering in the axial finale. Overall, a level of 1 GM is the best fit for the data. All subsequent simulations in this paper that incorporate internal-wave-induced scattering will therefore use sound-speed perturbations consistent with an energy level of 1 GM.

IV. UNSCATTERED ARRIVALS

The lower cusps of acoustic timefront predictions propagated through a sound-speed environment in the absence of internal waves define the upper limit of acoustic shadow zones. The deep arrivals observed in SPICEX penetrate the acoustic shadow by 500–800 m (Van Uffelen *et al.*, 2009); however, the precise extent of these extensions is dependent upon the upper limit of the shadow zones, i.e., the lower cusps of the unscattered arrivals, which is determined by the structure of the sound-speed profile.

Acoustic ray predictions and broadband parabolic equation (PE) simulations utilizing the smooth, range-independent sound-speed profile described in Sec. III were performed to obtain unscattered timefronts. The earth-flattening transformation was applied to the sound-speed fields to account for the curvature of the earth along the acoustic path.

Broadband acoustic timefront arrival patterns were calculated using the split-step Padé solution to the parabolic equation (Collins, 1993, 1989). The PE simulations include diffractive effects. The PE simulations employed a grid spacing of 200 m in the horizontal and 0.5 m in the vertical. Six Padé coefficients were retained. An absorbent bottom was included with an attenuation coefficient of 5 dB/λ.

The solutions were modified to include the frequency-dependent transmission loss due to volume attenuation (Fisher and Simmons, 1977):

$$\alpha(f)=0.79A\frac{f^2}{0.8^2+f^2}+36\frac{f^2}{5000+f^2}\text{dB/km}, \tag{10}$$

where the frequency f is in kilohertz and $A=0.055$ for the North Pacific Ocean (Lovett, 1980). At 250 Hz, the volume attenuation is 0.0043 dB/km.

The resulting timefronts were converted into units of acoustic intensity, as described in Van Uffelen *et al.* (2009). Figure 6 presents the resulting range-independent timefronts for the 500-km and 1000-km propagation paths utilizing the June range-independent sound-speed profile. The three sets of lower cusps on the 500-km propagation path and five sets of lower cusps on the 1000-km path that were captured by the hydrophones on the DVLA are labeled.

The structure of a caustic with respect to depth can be described by the Airy function (Brekhovskikh and Lysanov, 2003) and is observable in the first cusp in set 1 of the 500-km propagation path (Fig. 6, inset), where the diffraction pattern of intensity peaks culminates at the caustic before decaying with depth. The lower cusp in the ray prediction, which overlies the PE prediction in Fig. 6, closely coincides with the peak of the Airy function.

One hundred rays per degree were traced from −16° to 16° from the horizontal for both the 500-km and 1000-km propagation paths. In the vicinity of the lower cusps, 1000 rays per degree were traced for better resolution. Rays displaying erratic behavior due to interactions with bathymetry were discarded in the ray traces.

TABLE III. Depths of lower cusps and corresponding upper turning points for 500- and 1000-km timefronts for rays propagated through range-independent June and September sound-speed profiles.

Cusp	z_{cusp} (m) June	z_{cusp} (m) Sept.	Difference (m)	UTP (m) June	UTP (m) Sept.
		500-km timefront			
1a	3423	3609	186	33	47
1b	3138	3263	125	76	76
2a	2218	2399	181	237	147
2b	2120	2115	−5	277	285
3a	1889	1948	59	347	346
3b	1807	1841	34	372	358
		1000-km timefront			
1a	3633	3868	235	19	41
1b	3528	3795	267	28	44
2a	3051	3103	52	94	97
2b	2997	3044	47	103	105
3a	2549	2682	133	148	144
3b	2221	2259	38	236	147
4a	2076	2097	21	296	294
4b	2047	2073	26	307	304
5a	1950	1985	35	339	351
5b	1898	1955	57	336	345

The depths of the ray cusps z_{cusp} are tabulated in Table III for both the June and September profiles. With the exception of the second cusp of set 2 (cusp 2b) on the 500-km propagation path, all of the cusps exhibit deepening, ranging from 21 to 267 m, for the September profile when compared with the June profile. This deepening is a result of the shape of the sound-speed profile and is evident in both the ray and PE simulated timefronts.

The upper turning points (UTPs) of the rays are also given for the deepest ray on each cusp. The upper turning points do not change much from June to September with the notable exceptions cusp 2a on the 500-km timefront and cusp 3b on the 1000-km timefront, which are approximately 90 m shallower in September than they are in June.

Neither of the cusps in set 2 on the 500-km propagation path display the classic fold caustic structure, but instead display an interesting triplication, which is linked to zeros of the α parameter (Brown, 1986a, 1986b; Brown and Tappert, 1987). Set 3 on the 1000-km propagation path also has a complicated arrival structure. The first cusps in set 2 of the 500-km timefront and set 3 of the 1000-km timefront are magnified in the insets of Fig. 6. The corresponding PE predictions also do not display the neat Airy-function decay typical of the simpler cusp structure. Due to their complexity, set 2 on the 500-km timefront and set 3 on the 1000-km timefront will not be considered further here.

V. DEEP SHADOW-ZONE ARRIVALS

A. Measurements

The intensities of the measured receptions were calculated using the measured hydrophone sensitivity (−168 dB re 1 V/μPa) and the DVLA system gain, taking account of the signal processing gains achieved using the large time-bandwidth signals with the assumption that the received signals are coherent over the duration of the transmission. Idealized *m*-sequence signals were generated to emulate the signal transmitted by the HLF-5 source and subsequently processed using the same signal processing as used for the acoustic data to experimentally determine the gain resulting from the processing algorithms. This processing gain was removed from the signal to calculate the intensity in the absence of pulse compression.

TABLE IV. Number of usable acoustic receptions recorded by the upper and lower segments of the DVLA for the 500- and 1000-km axial source transmissions for June–November 2004.

Month	500-km range Upper	500-km range Lower	1000-km range Upper	1000-km range Lower
June	9	22	10	22
July	22	44	20	45
August	20	46	19	44
September	19	35	19	36
October	22	41	24	43
November	18	38	16	37

Table IV summarizes the number of receptions recorded by the DVLA during the experiment. The disks from the AVATOC acoustic recording package for the upper segment of the DVLA were compromised during the mooring recovery, so the upper segment of the DVLA contains approximately half the number of data files as the lower DVLA. Receptions with background noise levels greater than 60 dB were discarded.

Monthly incoherent averages of intensity timefronts for the 500-km and 1000-km propagation paths were constructed using all receptions in a given month (Fig. 7).

The receptions for the month of June were time-aligned to sharpen the incoherent time-front average. The data were time-shifted by the offset of the maximum value of the cross-correlation of the acoustic arrival at each hydrophone with the clean, range-independent predicted arrival at the same depth. Similarly, the peaks in September were time-aligned with the peaks of the range-independent September profile.

Energy calculations presented in Sec. V B are not affected by this alignment due to the integrative nature of the calculation.

The branches of the acoustic timefronts shift slightly in travel time due to the evolving structure of the sound-speed profile with the seasonal change. Because this change occurs gradually, a single daily average from early July was first time-aligned with the June monthly average, and the rest of the July data receptions were aligned with the daily average, effectively shifting the entire monthly timefront to align with the June monthly timefront.

Similarly, the August, October, and November timefronts were aligned with the September timefront. The cusps for June and July therefore have different arrival times than the remaining months because they are aligned with a different simulated timefront. The travel times shown on the axes of the timefronts are not the absolute travel times recorded in

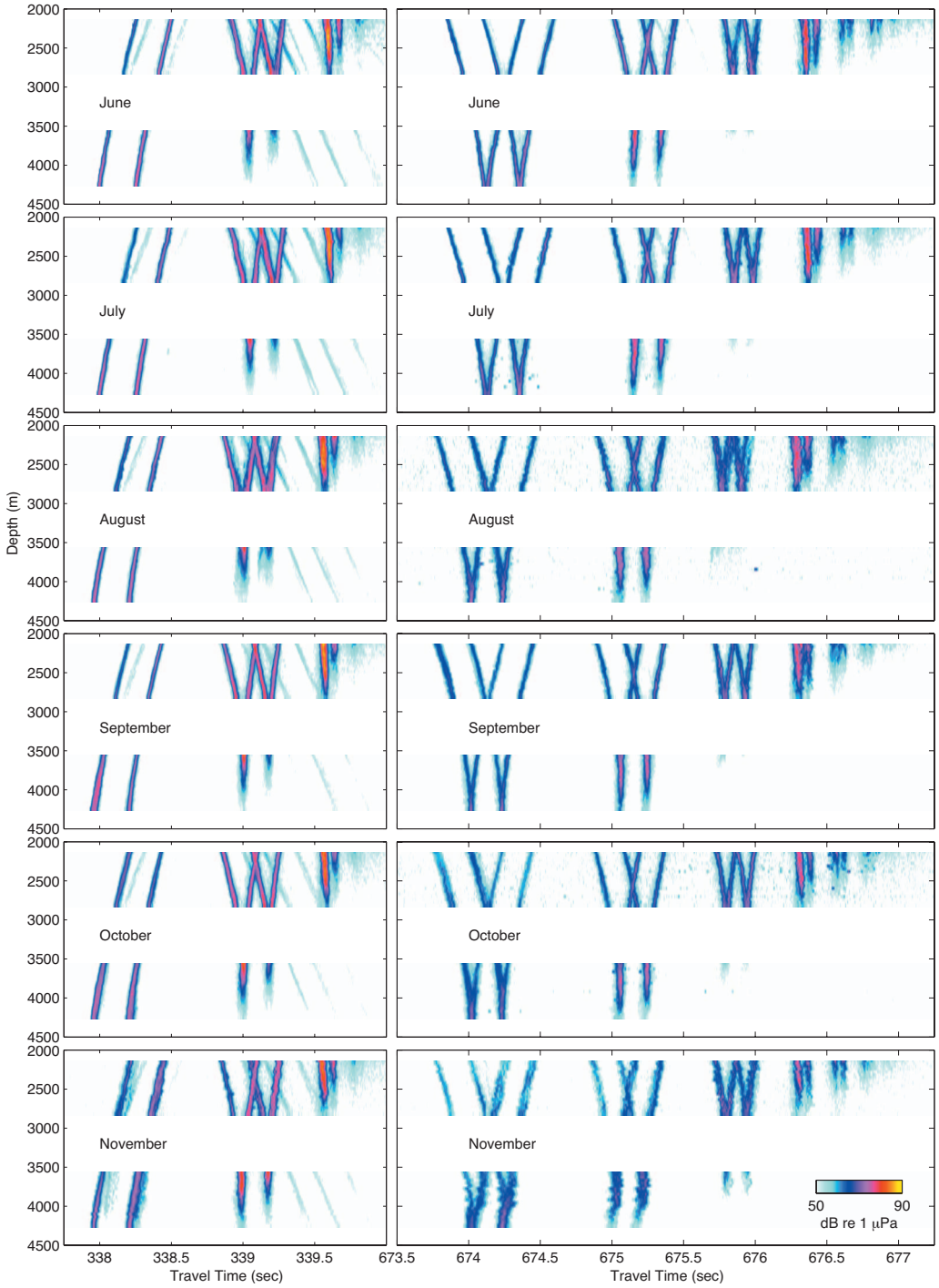

FIG. 7. Monthly incoherent averages of measured acoustic intensities (dB re 1 μPa) as a function of travel time and hydrophone depth for receptions from an axial source at 500-km (left) and 1000-km (right) ranges.

the acoustic data receptions, but are aligned with the travel time of propagation simulations through a smooth range-independent environment, and are used here for reference only.

Subtle changes in the acoustic timefronts become important when aligning peaks, but changes in travel time of a few milliseconds are difficult to discern on the time scale of Fig. 7. The June and September averaged timefronts are quite sharp because they most closely correspond with the environmental data that formed the basis of the range-independent PE simulations with which they were aligned. The timefront for November is less sharp due to a broadening of the peak of the cross-correlation function. November is the farthest removed from the times when the environmental data were collected, and the changing upper ocean structure affects the shape of the timefront. A perceptible development in the timefront structure is a broadening, sometimes nearly splitting, of the leading branches of the timefront of the 500-km propagation path (Fig. 7).

The most obvious differences in the timefronts from month to month are the vertical extensions of the lower cusps, i.e., the shadow-zone arrivals. The top panel of Fig. 8

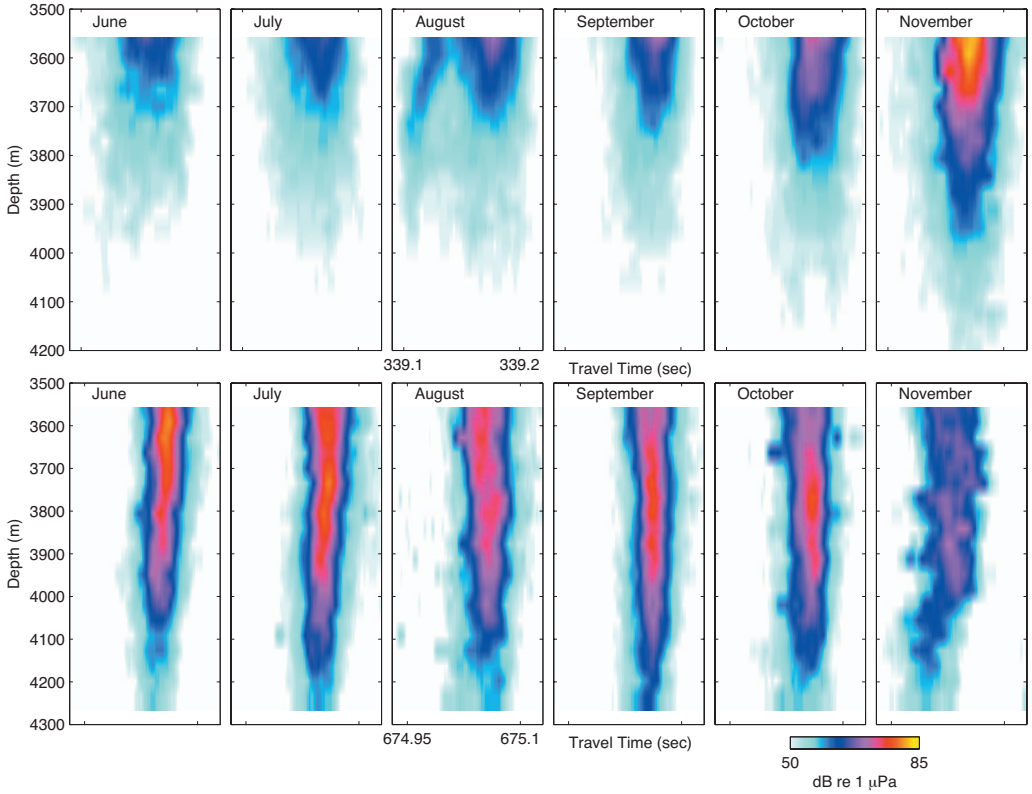

FIG. 8. Monthly incoherent averages of measured acoustic intensities (dB re 1 μPa) as a function of travel time and hydrophone depth for the second cusp of set 1 on the 500-km timefronts (top) and the first cusp of set 1 on the 1000-km timefronts (bottom) presented in Fig. 7.

is a magnification of the arrival of cusp 1b on the lower segment of the DVLA on the 500-km timefront. The depth of the scattering increases with each month and displays dramatic deepening in the month of November.

The cusps in set 3 of the 1000-km timefront also show significant deepening from June to September. The lower limit of these cusps is barely captured by the lower segment of the DVLA just prior to 676 s for most of the transmission period, but in November the cusps are unmistakable (Fig. 7).

B. Energies

Twenty Monte-Carlo realizations of broadband PE simulations incorporating sound-speed fluctuations consistent with the Garrett–Munk internal-wave energy spectrum at full strength were incoherently averaged in intensity for comparison with range-independent PE predictions (not shown). The internal-wave-scattered arrivals do not display an intense Airy-function peak at the caustic, but decay more gradually as the energy is scattered downward, primarily along the timefront, similar to the behavior of the lower cusps of received timefronts (Beron-Vera and Brown, 2004; Flatté and Colosi, 2008; Godin, 2007; Virovlyansky, 2003).

A quantitative measure of the vertical extent of the arrivals is the energy contained in the arrival at a particular depth. Figure 9 displays a measure of the energy in the cusp as it extends into the acoustic shadow. The energy E is calculated by integrating the intensity I of a peak in a specified time window T:

$$E = \int_T I dt. \tag{11}$$

The hydrophone noise level was determined by calculating the energy in a time window where there was no acoustic arrival. The noise levels for all of the monthly averages are between 41 and 48 dB re 1 μPa^2 s and generally seem to be higher for the later months, which may correspond with increasing noise due to winter storms.

The peak of the Airy function is evident in the energy of the range-independent simulations for both the June and September profiles, below which the energy quickly decays. The peak of the Airy function roughly coincides with the depth of the cusp of the deterministic ray arrivals (Fig. 6). The internal-wave simulations do not exhibit the same intense peak but have a scattered structure which decays more slowly and extends well below the peak of the Airy function of the range-independent arrival.

The top left panel of Fig. 9 shows the energy content of cusp 1a of the 500-km timefront. The energy level increases with time until November throughout the depth range captured by the DVLA. In November, a peak is evident in the profile at a depth of approximately 3800 m. This peak is approximately 400 m below the peak of the Airy function for the June profile and approximately 200 m below the peak in the Airy function for the September profile. The energy content for earlier months all falls between the energy levels predicted for the June and September internal-wave-scattered profiles.

Similar behavior is evidenced in the energy profile of the

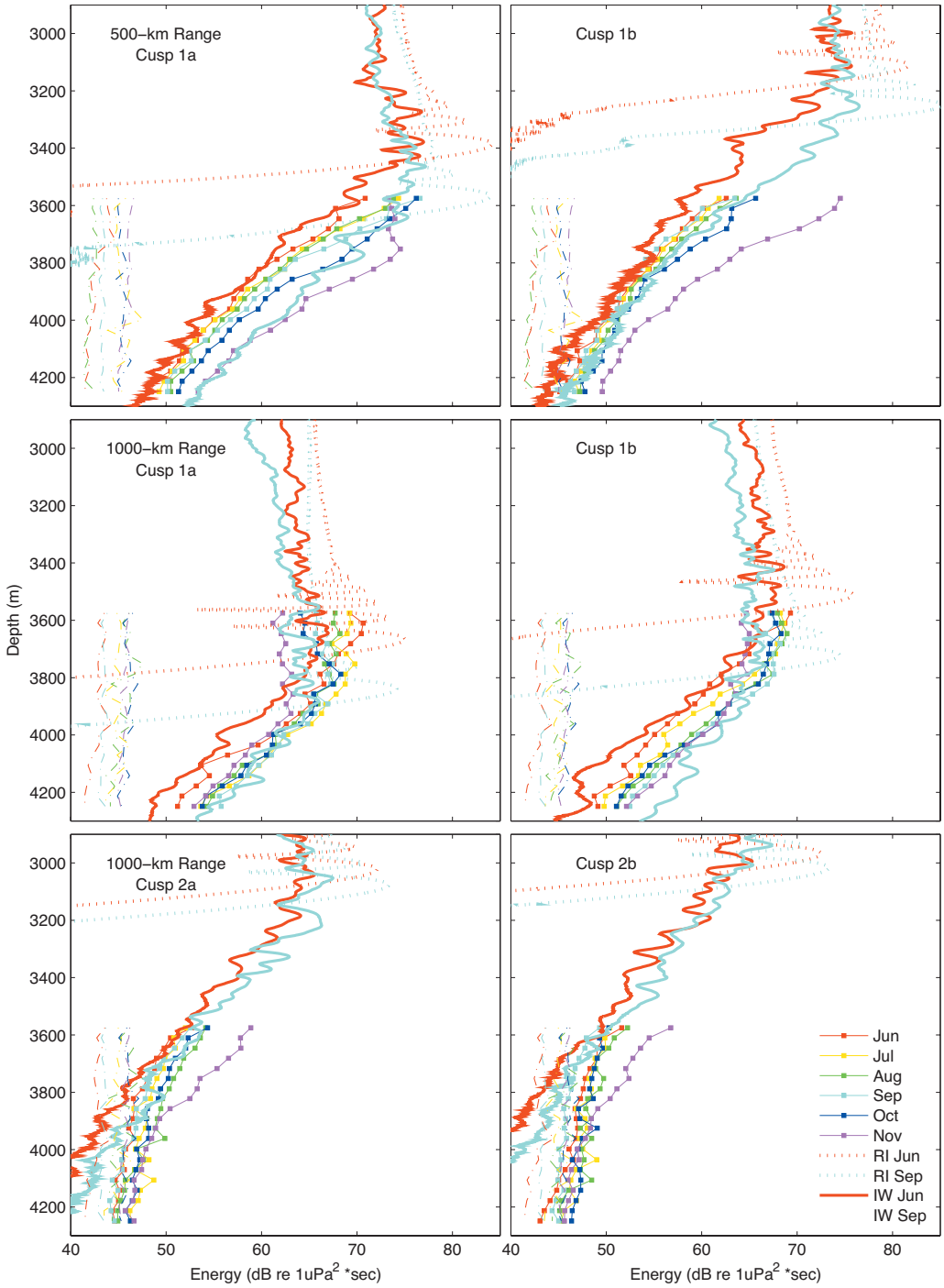

FIG. 9. Energy in the first (left) and second (right) cusps in set 1 on the 500-km timefront (top), set 1 on the 1000-km timefront (middle), and set 2 on the 1000-km timefront (bottom). Hydrophone data are shown for June–November for the 20 phones on the lower segment of the DVLA. Noise levels for each month are depicted by dash-dot lines colored to correspond with the acoustic data. Energy calculated for range-independent and internal-wave PE simulations for both June and September profiles is included.

second cusp in the set shown on the top right panel of Fig. 9. A dramatic increase in energy for the month of November is evident, which is consistent with the progression exhibited in Fig. 8. The energy contents for the previous months again lie between the predictions for the June and September internal-wave simulations. The ray traces also predict a deepening of the cusp by 186 m from June to September in the absence of internal-wave scattering. The timefront does not achieve this deepening by September, but far exceeds it by November (Fig. 8).

Both cusps in set 2 on the 1000-km timefront exhibit the same dramatic increase in energy in the month of November (Fig. 9, bottom). This dramatic increase is noticeable in the timefront plot shown in Fig. 7 and shows scattering as far as 700-m below the peak of the range-independent predictions. The early months again concur with the internal-wave-scattered predictions until they approach the noise level.

The rays associated with these two sets of cusps have shallow upper turning points, ranging from 33 to 103 m for June and from 47 to 105 m for September (Table III). These

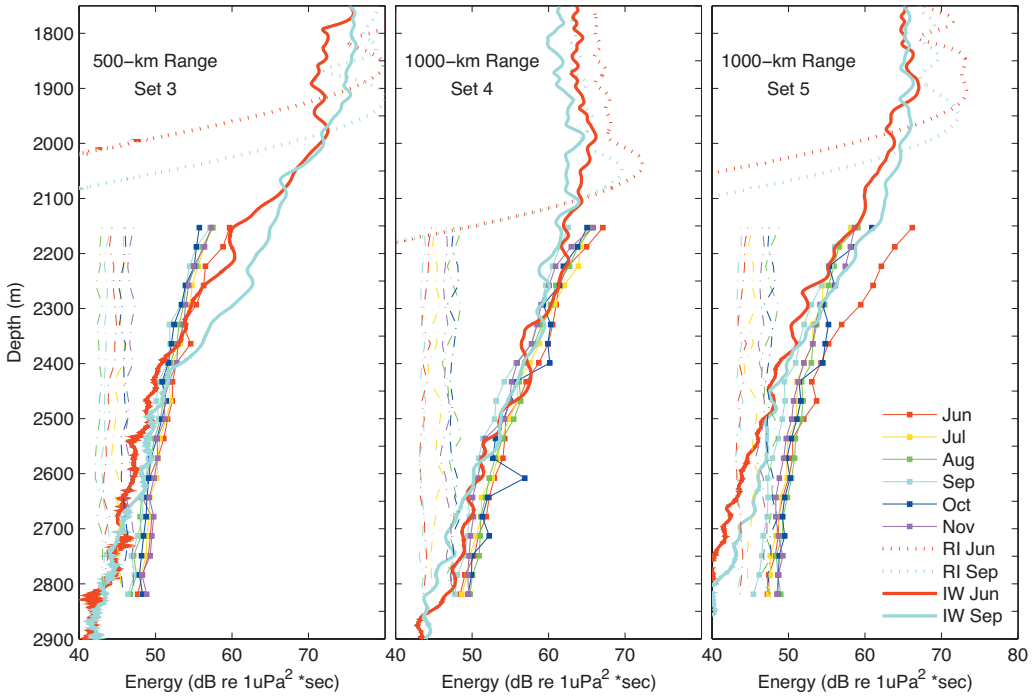

FIG. 10. Energy in the pairs of cusps in set 3 on the 500-km timefront and sets 4 and 5 on the 1000-km path. Due to extensive scattering, energy was calculated for a time window containing both cusps. Hydrophone data are shown for June–November for the 20 phones on the upper segment of the DVLA. Noise levels for each month are depicted by dash-dot lines colored to correspond with the acoustic data. Energy calculated for range-independent and internal-wave PE simulations for both June and September profiles is included.

relatively steep rays are highly sensitive to variable sound-speed structure in the upper ocean. The upper turning points are also very near the peak of the buoyancy-frequency profile, where there is increased internal-wave activity.

The progression of the first cusp in set 1 of the 1000-km timefront is pictured in the lower panels of Fig. 8. The sharp peak exhibited in June is not as prominent in later months. The arrivals in November are noticeably more scattered, although this is partly due to the imperfect alignment resulting from the changing timefront, as described in Sec. V A.

Both cusps in this set, with upper turning points of 19–28 m in June and 41–44 m in September, seem to display very different characteristics from those demonstrated by the cusps in set 2 of the 1000-km timefront and set 1 of the 500-km timefront (Fig. 9). The first June cusp displays the highest energy content in the upper phones, and the energy level progressively decreases in subsequent months. The second cusp in the set behaves similarly, although the effect is less striking. The monthly progression is not consistent for the deeper phones. In each of these cases, although June has the highest energy at the upper phones, it has the lowest energy at the deepest phones. Internal-wave simulations for the June profile also contain more energy than for the September profile in the depth range of the upper phones, but contain less energy than the September profile at the depths of the lower phones.

This rapid decay with depth is more consistent with less scattered cusp arrivals. The average energy for the lowest 20 phones for the first cusp is 65.7 dB for June and 61.0 dB for November. For the second cusp, the average energy is 62.6 dB for June and 62.2 dB for November. For comparison, the average energy for the lowest 20 phones in November for the first and second cusps in set 1 of the 500-km timefront, which demonstrated significant deepening, exceed the June average energy by 7.0 and 11.4 dB, respectively.

The upper turning points for this set of arrivals are shallower than set 1 of the 500-km timefront and set 2 of the 1000-km timefront. In June, the upper turning point is just 19 m from the sea surface. The June rays likely demonstrate less scattering by internal-wave fluctuations because they turn very near the sea surface, where internal-wave sound-speed perturbations approach zero (Fig. 3). Conversely, in November the rays are likely refracting off the base of the remnant summer thermocline, rather than becoming surface-reflected, giving the slower decay in energy with depth that is observed.

Neither set 3 of the 500-km timefront nor set 4 or 5 of the 1000-km timefront is predicted to be captured by the DVLA, but distinct arrivals seen several hundred meters below the range-independent cusps are consistent with internal-wave predictions (Fig. 10). Because the arrivals are diffuse, the two cusps cannot be separated in travel time and are therefore combined in the energy calculation. Other than a particularly strong June arrival in set 5 of the 1000-km timefront, there does not seem to be much difference in energy content for the different months, although these are not intense arrivals at the depths captured by the DVLA. These cusps all have upper turning points of approximately 300 m or deeper (Table III) and are less affected by the change in season than cusps with upper turning points higher in the water column.

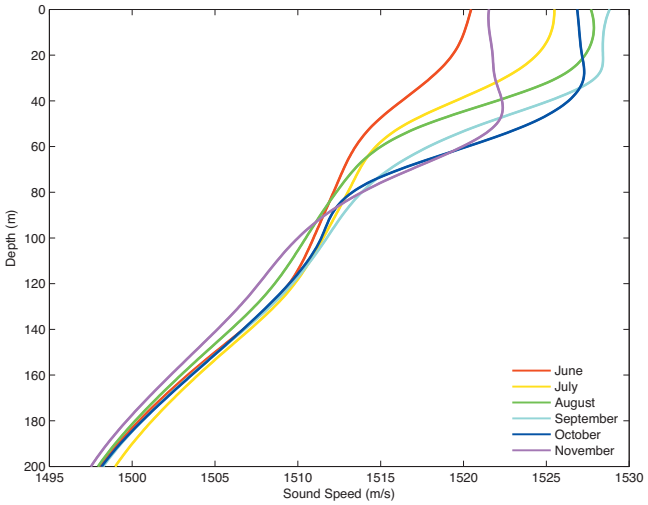

FIG. 11. Historical monthly sound-speed profiles for June–November from the World Ocean Atlas Database (2005).

VI. DISCUSSION

Mixed layers in the ocean form when summer winds mix warm surface waters downward, resulting in a layer of uniform temperature and salinity at the surface. This layer is thinnest in the early summer and thickens with sea-surface warming throughout the summer months. This warming also produces a steep temperature gradient, known as a summer thermocline. The development of the summer thermocline is exemplified in changes in the sound-speed profiles from June to September in Fig. 3. The summer thermocline subsides with winter cooling as the heat content of the warm surface waters is distributed to greater depths.

Figure 8 illustrates the deepening of lower cusps as winter approaches, indicating that the changes in the upper ocean sound-speed structure, i.e., the development and subsequent abatement of the summer thermocline, impact the depth of arrivals for cusps whose corresponding acoustic rays have shallow upper turning points. This figure indicates that seasonal changes are just beginning to affect the shadow-zone arrivals in November.

Although measured oceanic environmental data are not available in the month of November, historical sound-speed profiles give insight into what is likely happening in the upper ocean. The development of the summer thermocline due to surface warming is evident from June to September (Fig. 11). In October, the surface is beginning to cool and heat is mixed downward, but the effect is much more dramatic in November.

Acoustic ray propagation simulations through the historical November profile for cusp 1a on the 500-km timefront suggest that the depths of the UTP and of the lower cusp are only slightly greater in November than in September (Tables III and V). Acoustic rays are most sensitive to scattering when they approach the horizontal (Flatté *et al.*, 1979); therefore, rays with upper turning depths near the peak of the buoyancy frequency, where the internal-wave induced sound-speed fluctuations are most pronounced, are expected to be more sensitive to internal-wave scattering and display more deepening due to internal-wave interactions.

TABLE V. Depths of lower cusps and corresponding upper turning points for selected sets of cusps on the 500- and 1000-km timefronts for rays propagated through a historical November sound-speed profile.

Cusp	z_{cusp} (m)	UTP (m)
	500-km timefront	
1a	3658	58
1b	3471	67
	1000-km timefront	
1a	3715	50
1b	3738	53
2a	3140	89
2b	3002	105

The slightly higher energy level in November in Fig. 9 (top left panel) is therefore likely primarily due to increased scattering of rays turning near the base of the somewhat sharper November thermocline. This is also likely the case for cusps 2a and 2b on the 1000-km timefront, as the depths of the cusps and the UTPs are about the same from June to November.

Historical data suggest that the depth of cusp 1b on the 500-km timefront deepens significantly from June to September to November. The substantially higher energy levels in November in Fig. 8 (upper panel) and Fig. 9 (top right panel) are therefore likely in large part due to the increased depth of the cusp for the deterministic rays in the range-average profile, although there could also be some contribution from increased scattering of rays turning near the base of the November thermocline. This is the most dramatic change observed in the data.

According to historical data predictions, the depths of cusp 1a and 1b on the 1000-km timefront are about the same in November as in September, but deeper than in June. Although the energy levels in November in Fig. 9 (middle) are more-or-less comparable to those in earlier months, they decrease more slowly with depth in November than in June (the energy levels actually cross), likely due to less scattering of rays turning near or at the surface in June and increased scattering of rays turning near the base of the somewhat sharper thermocline in November. One expects surface-reflected rays to have less internal-wave-induced scattering.

Although acoustic transmissions terminated in November, temperature and salinity measurements down to approximately 400-m depth were acquired along the acoustic path using a SeaSoar during late March 2005, allowing simulations to be done for this oceanographically different time period. A March profile was constructed in a way similar to the construction of the June and September profiles (Sec. III A), except that climatological temperature and salinity data from the World Ocean Atlas database (2005) were used for the deep ocean (Levitus, 1982). The resulting sound-speed profile shows that the summer thermocline has subsided, and the mixed-layer base has deepened to approximately 100 m (Fig. 3).

Range-independent acoustic ray predictions indicate that the cusp 1b on the 500-km timefront has an upper turning

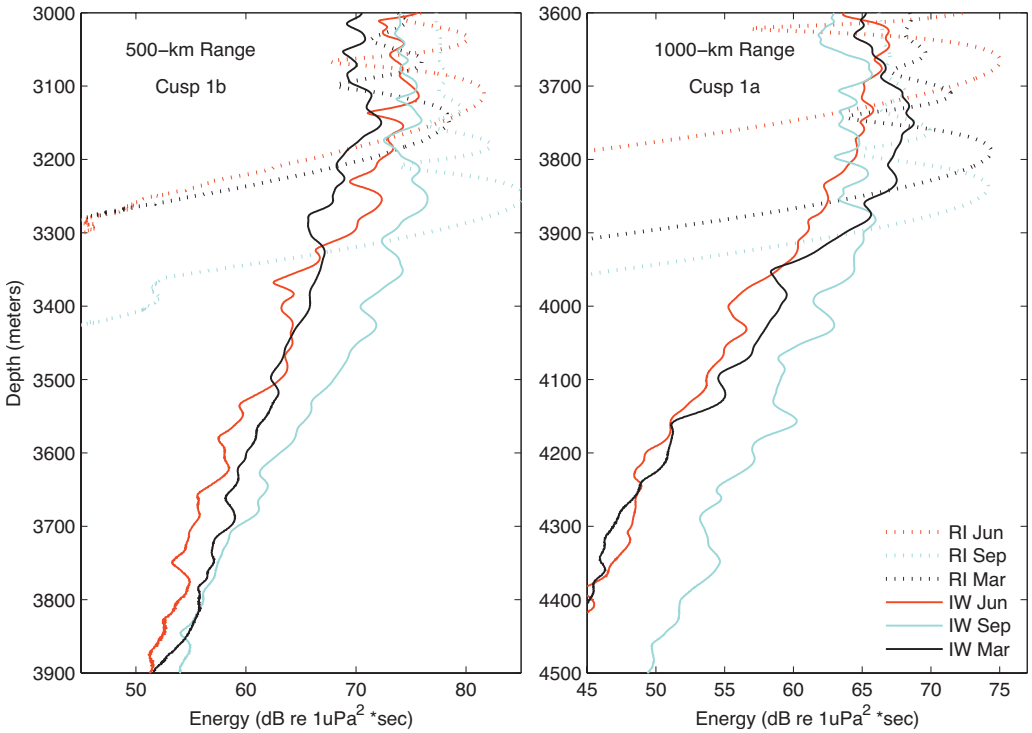

FIG. 12. Energy in cusp 1b from the 500-km timefront (left) and cusp 1a from the 1000-km timefront (right) from range-independent and internal-wave PE simulations for June, September, and March profiles.

point of 88 m in March, slightly deeper than in June and September, and very close to the base of the mixed layer, where internal-wave activity is increased. The heightened internal-wave activity is apparent in the scattering of the cusp indicated by the slow decay of energy with depth (Fig. 12, left panel).

In contrast, cusp 1a on the 1000-km timefront decays more quickly in March than in both June and September, demonstrating less scattering (Fig. 12, right panel). Analysis of the turning points of the unscattered acoustic rays indicates that the rays associated with this cusp have becomes surface-reflected, rather than refracted, for the March profile due to the decrease in the sound-speed gradient in the upper ocean. Since acoustic rays are most susceptible to internal-wave scattering while they are turning, i.e., near horizontal, rays which reflect off the sea surface are not expected to be as affected by internal-wave activity.

VII. CONCLUSIONS

Parabolic equation simulations incorporating sound-speed fluctuations consistent with the Garrett–Munk internal-wave spectrum at full strength appropriately describe the scattering into the acoustic shadow for data collected during SPICEX during months for which environmental data are available.

The relationship between time of year and shadow-zone extension is not direct. Shadow-zone arrivals refer to energy that arrives below the cusps of unscattered arrivals, so the depth at which an arrival is considered a shadow-zone arrival can change dramatically based on the shape of the sound-speed profile. The depth to which the timefronts extend as the seasons change is a complex combination of deterministic changes in the depths of the lower cusps as the range-average profiles evolve and of the amount of scattering, which depends on the depths of the UTPs and the mean vertical gradients at those depths. The most dramatic changes observed occur in November, as winter is beginning. Only historical environmental data are available for November, however, so the detailed conclusions are somewhat tentative.

Distinct arrivals are observable well below the deterministic unscattered cusps for all sets of lower cusps captured by the DVLA and considered here. As expected, the energy profile of cusps resulting from lower-angle rays with UTPs of approximately 300 m or deeper exhibits less seasonal dependence than those with UTPs in the upper ocean.

ACKNOWLEDGMENTS

The SPICEX data set which formed the basis of this paper is a product of the hard work of many individuals. The authors would especially like to thank D. Horwitt, L. Green, J. Kemp, M. Norenberg, and K. Wage. The experiment was funded by the Office of Naval Research Grant No. N00014-03-1-0182. L. J. Van Uffelen was also supported by the Office of Naval Research Graduate Traineeship Award No. N00014-07-1-0270.

ATOC Instrumentation Group (**1995**). "Instrumentation for the acoustic thermometry of ocean climate (ATOC) prototype pacific ocean network," in Oceans '95 MTS/IEEE Conference Proceedings, San Diego, CA, Vol. **3**, pp. 1483–1500.

Beron-Vera, F., and Brown, M. (**2004**). "Travel time stability in weakly range-dependent sound channels," J. Acoust. Soc. Am. **115**, 1068–1077.

Brekhovskikh, L., and Lysanov, Y. (**2003**). *Fundamentals of Ocean Acoustics*, 3rd ed. (Springer-Verlag, Berlin).

Brown, M. G. (**1986a**). "The transient wave fields in the vicinity of cuspoid caustics," J. Acoust. Soc. Am. **79**, 2385–1401.

Brown, M. G. (**1986b**). "The transient wave fields in the vicinity of the elliptic, hyperbolic and parabolic umbilic caustics," J. Acoust. Soc. Am. **79**, 1367–1384.
Brown, M. G., and Tappert, F. D. (**1987**). "Catastrophe theory, caustics and traveltime diagrams in seismology," Geophys. J. R. Astron. Soc. **88**, 217–229.
Collins, M. (**1993**). "A split-step Padé solution for the parabolic equation method," J. Acoust. Soc. Am. **93**, 1736–1742.
Collins, M. D. (**1989**). "A higher-order parabolic equation for wave propagation in an ocean overlying an elastic bottom," J. Acoust. Soc. Am. **86**, 1459–1464.
Colosi, J. A., and Brown, M. G. (**1998**). "Efficient numerical simulation of stochastic internal wave induced sound speed perturbation fields," J. Acoust. Soc. Am. **103**, 2232–2235.
Del Grosso, V. A. (**1974**). "New equation for the speed of sound in natural waters," J. Acoust. Soc. Am. **56**, 1084–1091.
Dushaw, B. D., Howe, B. M., Mercer, J. A., Spindel, R. C., and the ATOC Group (**1999**). "Multimegameter-range acoustic data obtained by bottom-mounted hydrophone arrays for measurement of ocean temperature," IEEE J. Ocean. Eng. **24**, 202–214.
Dushaw, B. D., Worcester, P. F., and Cornuelle, B. D. (**1993**). "On equations for the speed of sound in seawater," J. Acoust. Soc. Am. **93**, 255–275.
Fisher, F., and Simmons, V. P. (**1977**). "Sound absorption in sea water," J. Acoust. Soc. Am. **62**, 558–564.
Flatté, S., and Colosi, J. (**2008**). "Anisotropy of the wavefront distortion for acoustic pulse propagation through ocean sound-speed fluctuations: A ray perspective," IEEE J. Ocean. Eng. **33**, 477–488.
Flatté, S. M., Dashen, R., Munk, W. H., Watson, K. M., and Zachariasen, F. (**1979**). *Sound Transmission Through a Fluctuating Ocean* (Cambridge University Press, New York).
Garrett, C., and Munk, W. (**1979**). "Internal waves in the ocean," Annu. Rev. Fluid Mech. **11**, 339–369.
Godin, O. (**2007**). "Restless rays, steady wave fronts," J. Acoust. Soc. Am. **122**, 3353–336.
Levitus, S. (**1982**). "Climatological atlas of the world ocean," NOAA Professional Paper No. 191.
Lovett, J. (**1980**). "Geographic variation of low-frequency sound absorption in the Atlantic, Indian, and Pacific Oceans," J. Acoust. Soc. Am. **67**, 338–340.
Mercer, J. A., Colosi, J. A., Howe, B. M., Dzieciuch, M. A., Stephen, R., and Worcester, P. F. (**2009**). "LOAPEX: The long-range ocean acoustic propagation experiment," IEEE J. Ocean. Eng. **34**, 1–11.
Morozov, A., and Webb, D. (**2003**). "A sound projector for acoustic tomography and global ocean monitoring," IEEE J. Ocean. Eng. **28**, 174–185.
Morozov, A., and Webb, D. (**2007**). "Underwater tunable organ-pipe sound source," J. Acoust. Soc. Am. **122**, 777–785.
Munk, W., Worcester, P., and Wunsch, C. (**1995**). *Ocean Acoustic Tomography* (Cambridge University Press, Cambridge).
Rudnick, D. L., and Klinke, J. (**2007**). "The underway conductivity-temperature-depth instrument," J. Atmos. Ocean. Technol. **24**, 1910–1923.
Van Uffelen, L. J., Worcester, P. F., Dzieciuch, M. A., and Rudnick, D. L. (**2009**). "The vertical structure of shadow zone arrivals at long range in the ocean," J. Acoust. Soc. Am. **125**, 3569–3588.
Virovlyansky, A. (**2003**). "Ray travel times at long ranges in acoustic waveguides," J. Acoust. Soc. Am. **113**, 2523–2532.
Webb, D., Morozov, A., and Ensign, T. (**2002**). "A new approach to low frequency wideband projector design," in Oceans MTS/IEEE Conference Proceedings, Biloxi, MS, pp. 2342–2349.

Estimation of seismic velocities of upper oceanic crust from ocean bottom reflection loss data

Hefeng Dong[a)]
Department of Electronics and Telecommunications, Norwegian University of Science and Technology, NO-7491 Trondheim, Norway

N. Ross Chapman
School of Earth and Ocean Sciences, University of Victoria, Victoria, British Columbia V8W 3P6, Canada

David E. Hannay
JASCO Research Ltd., Suite 2101, 4464 Markham Street, Victoria, British Columbia V8Z 7X8, Canada

Stan E. Dosso
School of Earth and Ocean Sciences, University of Victoria, Victoria, British Columbia V8W 3P6, Canada

(Received 18 June 2009; revised 11 January 2010; accepted 18 January 2010)

This paper describes a Bayesian inversion of acoustic reflection loss versus angle measurements to estimate the compressional and shear wave velocities in young uppermost oceanic crust, Layer 2A. The data were obtained in an experiment on the thinly sedimented western flank of the Endeavor segment of the Juan de Fuca Ridge, using a towed horizontal hydrophone array and small explosive charges as sound sources. Measurements were made at three sites at increasing distance from the ridge spreading center to determine the effect of age of the crust on seismic velocities. The inversion used reflection loss data in a 1/3-octave band centered at 16 Hz. The compressional and shear wave velocities of the basalt were highly sensitive parameters in the inversion. The compressional wave velocity increased from 2547 ± 30 to 2710 ± 18 m/s over an age span of 1.4 million years (Ma) from the spreading center, an increase of $4.5 \pm 1.0\%$/Ma. The basalt shear wave velocity increased by nearly a factor of 2, from ~725 to 1320 m/s over the same age span. These results show a decreasing trend of Poisson's ratio with age, from a value of 0.46 at the youngest site closest to the ridge axis. © *2010 Acoustical Society of America.* [DOI: 10.1121/1.3311822]

PACS number(s): 43.30.Pc, 43.60.Pt [RAS] Pages: 2182–2192

I. INTRODUCTION

Oceanic crust generated by magmatic processes at midocean ridges gradually moves away from the ridge spreading centers over many millions of years (Ma). An increase in seismic velocity associated with the geological age of the basalt in the uppermost layer of oceanic crust, Layer 2A, was first inferred by Houtz and Ewing[1] based on analysis of sonobuoy refraction data from various sites worldwide. They concluded from the available data at the time that the seismic velocities in Layer 2A increased from ~3.3 km/s at the ridge crest spreading centers to values characteristic of mature basalt crust, >4.0 km/s, on the ridge flanks.

The increase in velocity is generally attributed to low temperature alteration of the physical properties of the crustal basalt associated with passive hydrothermal circulation within the ridge crest and flanks.[1–3] In this model, minerals are precipitated in the cracks and voids of the young basalt as the water circulates over time. The hydrothermal alteration and deposition process is temperature dependent and is strongly affected by the overlying sediment cover which can insulate the crust from the ocean water, thus increasing the temperature in the crust and accelerating the rate of alteration.[3,4] Consequently, the rate of aging is not uniform worldwide but is dependent on the ridge flank environment at each site.

Since the initial report by Houtz and Ewing, there have been several experiments to measure seismic velocities at midocean ridges, e.g., Refs. 5–9. Recently, measurements have also been made in transects from and across the ridge crests to document the rate of increase in seismic velocity with crustal age at a very fast spreading ridge, the East Pacific Rise,[10] and at the northern segments of an intermediate spreading ridge, the Juan de Fuca Ridge.[11] These experiments used established seismic techniques and inversions based on travel time analysis of data from ocean bottom hydrophones,[10] and multichannel seismic data[11] to determine profiles of the seismic velocity with depth in Layers 2A and 2B. Measurements of the basalt shear wave velocity have also been reported from experiments with ocean bottom hydrophones to detect interface waves generated at a ridge crest.[12] In addition to the seismic experiments, measurements of the velocities of ocean crust of all ages have been obtained from logging data, vertical seismic profiles, and by analysis of cores from various drilling operations of the ocean drilling projects: Deep Sea Drilling Project, Ocean Drilling Project, and Integrated Ocean Drilling Project (see, for instance, Ref. 13).

[a)]Author to whom correspondence should be addressed. Electronic mail: hefeng@iet.ntnu.no

 0001-4966/2010/127(4)/2182/11/$25.00

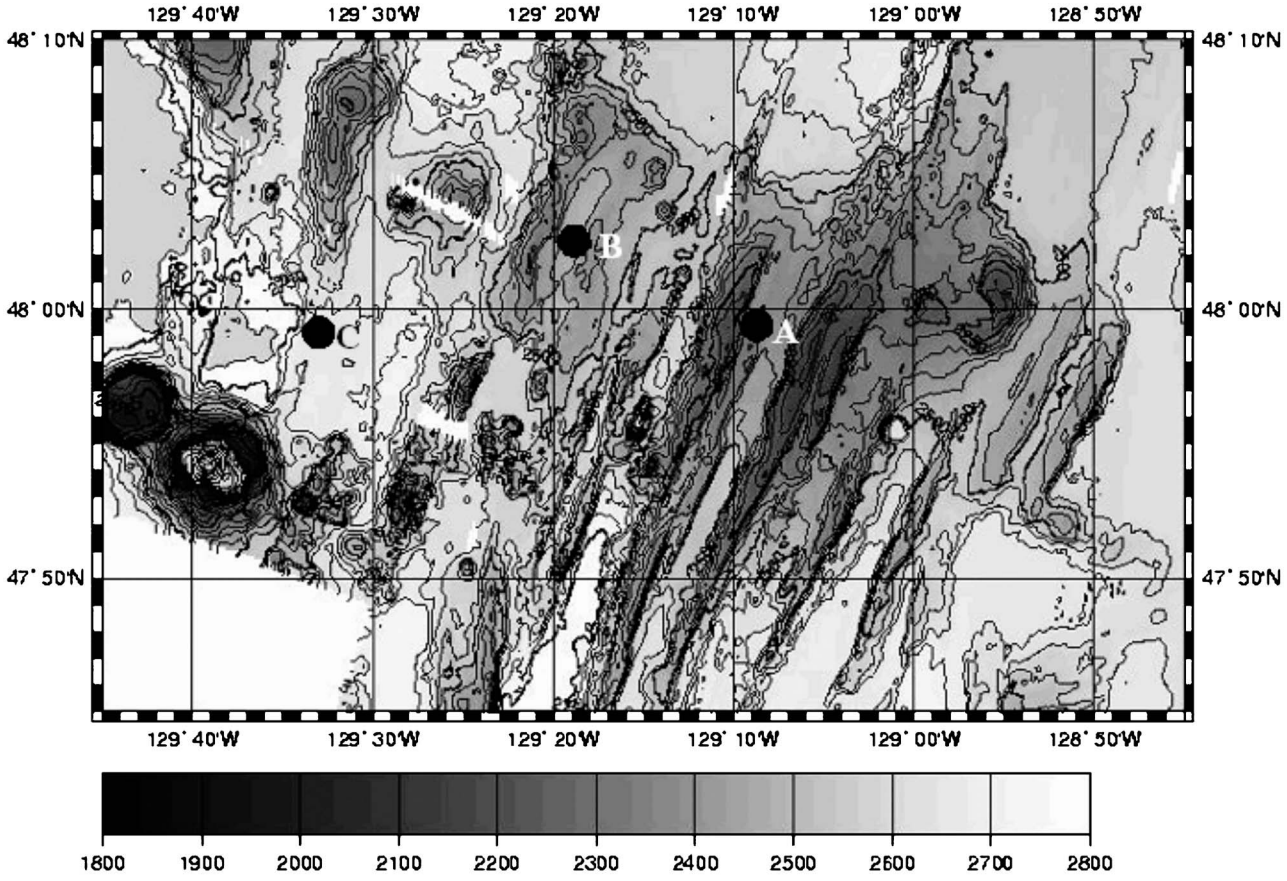

FIG. 1. Experimental locations for Sites A–C.

This paper describes a different technique for estimating seismic velocities and reports measurements from a transect on the western flank of the Endeavor segment of the Juan de Fuca ridge. The method is based on measurements of the ocean bottom reflection loss versus grazing angle, using small explosive charges as sound sources. The basic technique has been widely used in underwater acoustics to measure acoustic propagation loss and to characterize the ocean bottom in terms of geoacoustic profiles. Diachok *et al.*[14] described an application of the technique for inferring seismic velocities of the upper crust in the Rivera Ocean Seismic Experiment. In the present work, we adapt the method for use with a towed horizontal hydrophone line array.

The experiments were carried out in July 1991 and initial results were reported previously for the measurements of velocity at the ridge crest[15] and for a comparison with seismic velocities on the eastern flank of the ridge.[16] Here, we apply a Bayesian inversion technique to estimate the seismic velocities in Layer 2A from the reflection loss versus angle data at sites of increasing crustal age from ~0.1 to 1.5 Ma. In comparison with the results from the seismic experiments, our values for the compressional wave velocity are characteristic of the uppermost crustal material within a wavelength of the sea floor, and thus provide constraints for the velocity in the surface low velocity layer of Layer 2A. Moreover, the reflection loss method also provides an estimate of the associated shear wave velocity, and the Bayesian analysis provides realistic uncertainty measures for both velocities. Our results for the compressional wave velocity indicate an increase from ~2500 m/s at the ridge crest to ~2700 m/s at a distance of about 32 km from the spreading center, and the rate of increase is consistent with the result reported in Ref. 11. Of greater interest, the estimated shear wave velocity increases by roughly a factor of 2 over the same span of crustal ages.

In the remainder of this paper, we describe the experiment in Sec. II, and then discuss the inversion technique and the interpretation of reflection loss versus angle data. The results are then presented and discussed.

II. EXPERIMENTS

The acoustic reflection experiments were carried out along tracks at three sites west of the Endeavor segment of the Juan de Fuca Ridge (Fig. 1). The ridge axis at the spreading center is aligned NNE, approximately 23°, and the general topography west of the ridge in the Endeavor segment consists of a series of valleys and smaller ridges aligned parallel to the main axis. The sea floor is thinly sedimented, with sediments gradually increasing in thickness from a few meters near the ridge crest to values around 30–35 m out to distances of 35–40 km from the spreading center. However, the rate of increase is not uniform with distance from the spreading center, and there may be local pockets of thicker deposits. Estimates of the sediment thickness were obtained from analysis of single hydrophone data for the close range

TABLE I. Experimental site locations and environmental description.

Site	Latitude (N)	Longitude (W)	Water depth (m)	Age (Ma)	Sediment thickness (m)
A	47° 59.5′	129° 09′	2250	0.1	<10
B	48° 03′	129° 19′	2440	0.7	17–21
C	47° 59′	129° 33′	2640	1.5	21–23

shots at each site and from shots deployed from the array ship at the beginning of each track. The ranges of values from these data are listed in Table I. The experimental sites were located in the valleys between the ridges: Site A in the first valley 3 km west of the ridge crest at a depth of ~2250 m, Site B in the next valley approximately 18 km west of the crest at a depth of ~2440 m, and Site C in the third valley approximately 32 km west of the crest at a depth of ~2640 m. The locations and environmental data for the sites are listed in Table I.

Layer 2A has been mapped on each side of the ridge crest spreading center in the Endeavor segment in several reflection and refraction surveys.[4,7,11] On the thinly sedimented western flank, the compressional wave velocity increases gradually by about 24% from ~2500 m/s over an age span of ~5 Ma (corresponding to distances of ~120 km from the ridge crest).[11] By contrast, the eastern flank is thickly sedimented with terrigeneous material that fills the Cascadia Basin, with significant cover within 20 km of the ridge crest. Layer 2A velocity increases abruptly at this relatively close distance to the spreading center (corresponding to an age of ~0.6 Ma) and increases more rapidly to values characteristic of mature crustal basalt over an age span of about 5 Ma (an increase in velocity of 60%). This rapid rate of change is attributed to the effect of the thick sediment cover in closing the crust to hydrothermal circulation.[4] The depth to the Layer 2A/2B boundary varies from about 400 m on the western flank to ~200 m on the eastern flank.[11]

The ocean bottom reflectivity data reported in this paper were obtained in an experiment with two ships, using small explosive charges as sound sources. One ship, USNS DeSteiger, deployed 0.8 kg signal underwater sound (SUS) charges at nominal depths of 190 m on tracks that opened range from the receiving ship, CFAV Endeavor. The shot signals were received on the Canadian ocean acoustic measurement system (COAMS) horizontal line array that was towed at a depth of ~250 m by CFAV Endeavor. The array aperture was 1524 m with 40 hydrophone channels that were equispaced at 38.1 m. Array shape was monitored by six depth sensors at intervals of 310 m along the array, and the orientation and straightness were monitored by compass sensors at the array ends and mid point.

The ship tracks were designed so that the propagation paths of the shot signals were nearly broadside to the array and perpendicular to the ridge axis for all the shot deployments. The shooting ship opened range to a distance of about 35 km from the array ship on a course at a bearing of 65° to the array ship's course, as shown in Fig. 2. The courses and ship speeds were set so that the track of the midpoints between the two ships was aligned parallel to the direction of the ridge axis, about 23°. Ship positions were determined from global positioning system data that were collected on each ship.

The broadband shot signals received at the array were digitized at 700 samples/s and processed by a time delay beamformer to obtain the array responses in 37 beams from −30° to 30° centered at the broadside direction. The beam data were then filtered in 1/3-octave frequency bands with center frequencies from 16–125 Hz to obtain the beam responses versus time for the shot signals. The array processing provided spatial and temporal separation of the direct path and first bottom reflection signals into separate beams for ranges out to ~25 km. In addition, random signals from scattering centers on the sea floor were spatially filtered from the beams containing the specular bottom reflection path signals from the shots. Significant scattering in nonspecular paths was observed in the array data at higher frequencies at each site, but the impact of this effect was considerably reduced by using the specular beam for the 16 Hz band in this work.

Bottom reflection losses (BLs) (in decibels) for the first bottom reflection signals were determined from the specular beam data for the 1/3-octave band centered at 16 Hz according to

$$\mathrm{BL}(\theta) = H_m(\theta) - H_c, \tag{1}$$

where $H_m(\theta)$ is the measured propagation loss of the first bottom reflection at grazing angle θ, and H_c is the calculated loss, using ray theory and assuming perfect reflection at the sea floor. The measured losses were determined from the received energy level, $\mathrm{RL}(\theta)$, in the specular beam, using known values of the source levels (SLs) of the explosive charges,[17]

$$H_m(\theta) = \mathrm{SL} - \mathrm{RL}(\theta). \tag{2}$$

The charge weight of SUS charges varies less than 10% of the nominal value, but the SL in low frequency third octave

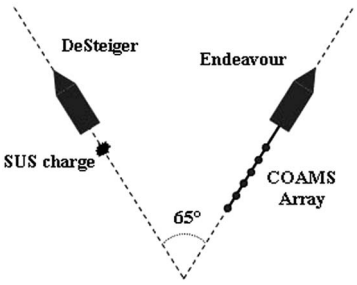

FIG. 2. Experimental geometry for the tracks of the two ships.

bands can vary appreciably from shot to shot depending on the explosion depth. In this analysis, the SL was corrected for the actual depth of each shot. Shot depths were determined from the bubble pulse periods, which were determined from the cepstrum of the received signals.[17]

Since the measured loss in the specular beam included the contributions from the four multipath components of the first bottom interaction, the calculated loss accounted for the coherent summation of these paths. The phases relative to the first component were derived from the experimental geometry. The array shape was also taken into account in determining the beam responses for each shot, using the data from the depth and compass monitoring sensors.

In this experiment, BL was obtained for a span of sea floor grazing angles from 80° at close range to ~10° at ranges of 25 km. The grazing angles were determined by ray tracing using the ship navigation data and water column sound speed profiles that were measured at each site. The sound speed profile was downward refracting for the source depths of around 190 m, so there was a distinct first bottom reflection for all the shots out the greatest range along the tracks. Reflection coefficients, $V(\theta)$, are related to the bottom loss for each grazing angle by

$$V(\theta) = 10^{-\mathrm{BL}(\theta)/20}. \tag{3}$$

Although the reflection points on the sea floor were different for each grazing angle in this experiment, the ship tracks were designed so that the locus of the reflection points followed a track parallel to the ridge axis, for which the age of the underlying crustal basalt was assumed to be constant. Thus, the reflection coefficient data from each site provide information about the geoacoustic properties of basalt at a well defined age.

III. INVERSION OF REFLECTION COEFFICIENT VS. ANGLE DATA

A. Inversion method

In this work, the reflection coefficient versus angle data $\mathbf{d}$ is inverted using a Bayesian approach to estimate properties of the posterior probability distribution for geoacoustic parameter model $\mathbf{m}$.[18,19] According to Bayes' rule, the posterior probability density (PPD), $\mathrm{P}(\mathbf{m}|\mathbf{d})$, can be expressed as

$$\mathrm{P}(\mathbf{m}|\mathbf{d})\mathrm{P}(\mathbf{d}) = \mathrm{P}(\mathbf{d}|\mathbf{m})\mathrm{P}(\mathbf{m}), \tag{4}$$

where $\mathrm{P}(\mathbf{m})$ represents prior information about the geoacoustic model. For measured (fixed) data $\mathbf{d}$, $\mathrm{P}(\mathbf{d}|\mathbf{m})$ is interpreted as the likelihood function, which can generally be expressed in the form $\mathrm{P}(\mathbf{d}|\mathbf{m}) \propto \exp[-E(\mathbf{m})]$, where E represents the data misfit function and $\mathrm{P}(\mathbf{d})$ is a constant. Equation (4) then can be written as

$$\mathrm{P}(\mathbf{m}|\mathbf{d}) = \frac{\exp(-\phi(\mathbf{m}))}{\int \exp(-\phi(\mathbf{m}'))d\mathbf{m}'}, \tag{5}$$

where $\phi(\mathbf{m}) = E(m) - \log_e \mathrm{P}(\mathbf{m})$ is the generalized misfit and the domain of integration spans the parameter space. The multidimensional PPD is interpreted in terms of properties defining parameter estimates and uncertainties, such as the maximum a *posteriori* (MAP) estimate $\hat{\mathbf{m}}$, the mean model $\overline{\mathbf{m}}$, the covariance $\boldsymbol{C}$ about the mean model, and marginal probability distributions $\mathrm{P}(m_i|\mathbf{d})$, defined as

$$\hat{\mathbf{m}} = \mathrm{Arg}_{\max}\{\mathrm{P}(\mathbf{m}|\mathbf{d})\}, \tag{6}$$

$$\overline{\mathbf{m}} = \int \mathbf{m}'\mathrm{P}(\mathbf{m}'|\mathbf{d})\mathbf{d}\mathbf{m}', \tag{7}$$

$$\mathbf{C} = \int (\mathbf{m}'-\overline{\mathbf{m}})(\mathbf{m}'-\overline{\mathbf{m}})^T\mathrm{P}(\mathbf{m}'|\mathbf{d})\mathbf{d}\mathbf{m}', \tag{8}$$

$$\mathrm{P}(m_i|\mathbf{d}) = \int \delta(m_i'-m_i)\mathrm{P}(\mathbf{m}'|\mathbf{d})\mathbf{d}\mathbf{m}', \tag{9}$$

where δ is the Dirac delta function and the domain of integration spans the parameter space. Parameter correlations are quantified by normalizing the covariance matrix to produce the correlation matrix

$$R_{ij} = \frac{C_{ij}}{\sqrt{C_{ii}C_{jj}}}. \tag{10}$$

Matrix elements R_{ij} are within $[-1,+1]$, with a value of +1, indicating perfect correlation between m_i and m_j. Parameter uncertainties can also be quantified in terms of credibility intervals, such as the β% highest-probability density credibility interval, representing the interval of minimum width containing β% of the area of the marginal distribution. For nonlinear problems, analytical solutions to Eqs. (6)–(9) do not exist, and precise solutions require numerical approaches. In this work MAP estimation, Eq. (6), was carried out by minimizing the generalized misfit using a hybrid optimization algorithm, adaptive simplex simulated annealing (ASSA).[20] PPD integration, Eqs. (7)–(9), was carried out using Metropolis–Hastings sampling in a principal-component parameter space.[18,19]

Assuming that the data errors (measurement error plus theory error) are independent, Gaussian-distributed random processes, the likelihood function is given by

$$L(\mathbf{m}) = \frac{1}{(2\pi)^{N/2}\prod_{i=1}^{N}\sigma_i}\exp\left\{-\sum_{i=1}^{N}\frac{[d_i - d_i(\mathbf{m})]^2}{2\sigma_i^2}\right\}, \tag{11}$$

where $\mathbf{d}$ is the vector of N measured data, $\mathbf{d}(\mathbf{m})$ is a vector of N modeled data, and σ_i represents the standard deviation for data d_i. The data misfit can be expressed by

$$E(\mathbf{m}) = \sum_{i=1}^{N}\frac{[d_i - d_i(\mathbf{m})]^2}{2\sigma_i^2}. \tag{12}$$

B. Reflection coefficient inversion

In this experiment, the sound reflected from the ocean bottom carries information about the interaction with a system of interfaces, including the basalt crust and the overlying sediment. However, we begin the discussion of the interpretation of the reflection loss data by considering the reflectiv-

ity for the more simple case of an elastic half-space. The reflection coefficient for a homogeneous elastic solid seabed is given by[21]

$$V_{01} = \frac{Z_1 \cos^2(2\gamma_1) + Z_t \sin^2(2\gamma_1) - Z_0}{Z_1 \cos^2(2\gamma_1) + Z_t \sin^2(2\gamma_1) + Z_0}, \tag{13}$$

where $Z_0 = \rho_0 c_0 / \sin\theta_0$, $Z_1 = \rho_1 c_1 / \sin\theta_1$, and $Z_t = \rho_1 b_1 / \sin\gamma_1$ are the impedances for the compressional wave in the water, and the compressional and shear waves in the seabed, respectively; c_0 is the sound speed in the water; c_1 and b_1 are the seabed compressional and shear wave velocities, respectively; ρ_0 and ρ_1 are the densities for the water and seabed; and θ_0, θ_1, and γ_1 are the grazing angles of incidence and transmission for compressional and shear waves, respectively. The compressional and shear wave attenuations are introduced by substituting complex wave velocities into Eq. (13),

$$c_1' = c_1\left(1 + i\frac{\alpha_{p1}}{40\pi \log_{10} e}\right), \tag{14}$$

$$b_1' = b_1\left(1 + i\frac{\alpha_{s1}}{40\pi \log_{10} e}\right), \tag{15}$$

where α_{p1} and α_{s1} are the compressional and shear wave attenuation coefficients, respectively, in terms of dB/λ (λ is wavelength). The reflection coefficient for the more complicated case of a multilayered ocean bottom can be expressed recursively in terms of impedances for the layered structure, following Brekhovskikh[21] for layered elastic media.

The analysis of the half-space seabed shows that the reflection coefficient depends on the impedance contrasts at the interface and the grazing angle of the incident wave. For reflection from a high sound velocity interface such as basalt, the most significant features of the reflection coefficient versus angle data are the peaks at the compressional and shear wave critical angles (if the shear wave velocity is greater than the sound speed in the water). At very high grazing angles (i.e., near normal incidence), the reflection coefficient is effectively constant and depends primarily on the acoustic impedance contrast. Since excitation of shear waves is weak at these angles, the data are sensitive to the density contrast. If the shear wave velocity is less than the water sound speed, information about the shear parameters is contained in the magnitude and shape of the reflection coefficient at angles less than the compressional wave critical angle.

The simple interpretation above is based on the reflection from a single interface and applies to the simple half-space geoacoustic model in Eq. (13). However, the experimental sites west of the Juan de Fuca ridge are sedimented and the reflected signal interacts with a system of layers. Intuitively, it would be expected that the presence of a thick sediment layer would have to be taken into account for interpreting the acoustic reflectivity, but a thin layer can also cause significant modifications to the simple half-space interpretation. Hovem[22] showed that the sediment layer generates Stoneley waves at the sediment basalt interface for certain frequencies and low grazing angles. Also for sufficiently thin elastic solid sediment layers, a resonance condition occurs due to the conversion of compressional to shear waves at the sediment basalt interface.[23] This effect has been shown to cause variations of several decibels in the reflection loss at low grazing angles.[24] These resonance effects complicate the interpretation of the experimental data, and it is important to account for them in modeling the reflection loss in the inversion.

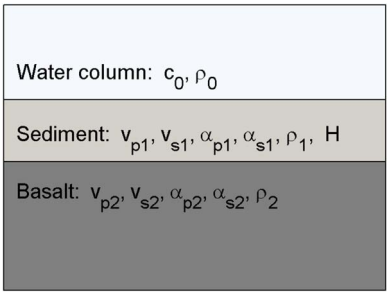

FIG. 3. (Color online) Single-layer geoacoustic model of the ocean bottom.

In order to demonstrate the effect of the overlying sediment on the reflection coefficient inversion, a synthetic environment was developed based on a simple thin sediment layer geoacoustic model (single-layer model). The model was parametrized by the compressional and shear wave velocities and attenuations, the densities of the sediment and basalt, and the thickness of the sediment layer, as shown in Fig. 3. The parameter values are typical of clayey silt or silty clay overlying young basalt, and are listed in Table II. The water layer was given a compressional wave speed of 1500 m/s and density of 1.03 g/cm^3. Reflection coefficient data were generated for this model at a frequency of 16 Hz to simulate experimental conditions.

A previous study of the sensitivity of the reflection coefficient to the model parameters of the single-layer geoacoustic model indicated that the most sensitive parameters were the compressional and shear wave velocities of the basalt, and the shear wave velocity of the sediment.[25] Here we use a different approach to show the effect of the sediment layer on the inversion. Uncorrelated zero-mean random Gaussian noise with standard deviation of 0.05 was added to the data, and then the simulated data were inverted by the optimization code, ASSA, to compare the behavior of two different geoacoustic models: a half-space model that used

TABLE II. Model parameters for the synthetic case.

Medium	Thickness (m)	v_p (m/s)	v_s (m/s)	α_p (dB/λ)	α_s (dB/λ)	ρ (g/cm^3)
Sediment	3.5–32	1530	210	0.3	1.8	1.55
Basalt	∞	2650	1100	0.1	0.5	2.50

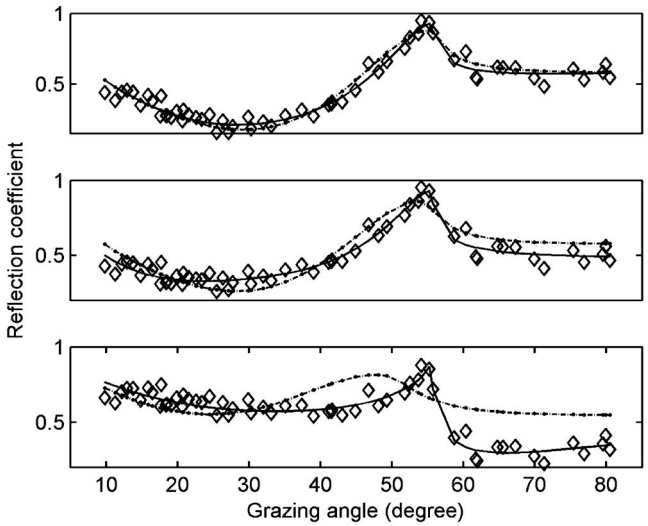

FIG. 4. Fits to synthetic data (diamonds) for the inversions with different sediment thicknesses: 3.5 m (top panel), 11.5 m (middle panel), and 32 m (bottom panel). The black solid curve is generated by the single-layer model and the dashed curve is generated by the half-space model.

the same values for the basalt shown in Table II; and then the single-layer model.

Figure 4 shows the fits to the synthetic data generated from the MAP estimates obtained from ASSA for the two models. The sediment thickness varies from 3.5 m (top panel), 11.5 m, (middle panel) to 32 m (bottom panel).

The figure indicates that for thin sediment layers, ~10 m (top and middle panels), the modeled reflection curves generated by the half-space model approximately predict the peak at the compressional wave critical angle of the basalt, 55.5°. But at other grazing angles the model fits are very poor. For thicker sediment layers, >20 m (bottom panel), the half-space model does not fit the data at all, except at very low grazing angles. Overall, the single-layer model clearly produces better fits to the data. This is in part expected due to the greater number of parameters in the model. However, we conclude from the synthetic data study that the single-layer model provides a better description of the physics of the reflection from the thin-layer/basalt system.

IV. INVERSION OF EXPERIMENTAL DATA

A. Inversion results

The data from Sites A–C on the western flank of the Endeavor segment were inverted using the Bayesian approach. The single sediment layer over a basalt half-space was used to model the upper crust environment. The constant sound velocity assumption for the basalt is consistent with the surface low velocity layer model[9,12] for the uppermost portion of Layer 2A, for which the velocity gradient is very small. This is a reasonable geoacoustic model for our analysis, since the reflection loss data in this experiment are primarily sensitive to the crustal material within a wavelength (~100 to 200 m) of the sea floor. If a small gradient of velocity does exist, our estimated values can be interpreted in terms of the average values over the layer.

The prior information applied in the inversion consisted of uniform distributions for each parameter within the bounds that are listed in Table III for the 11 model parameters. The bounds were chosen to be wide enough to allow the data to determine the solution in the inversion process, but to limit the estimates to physically reasonable values. The reflection coefficients were calculated for a third octave band centered at 16 Hz for each model that was tested in the inversion. The average was taken over 11 frequencies in the band.

At each site the data errors were assumed to be uncorrelated Gaussian distributed with nonidentical standard deviations. The analysis of the data error residuals indicated that the angle dependence of the data errors for Site A was strong, so two standard deviations were used: $\sigma_A=0.0545$, 0.0286 for data from grazing angles 28.6°–48.3° and 49.2°–65.2°, respectively. However, the angle dependence of the data errors for Sites B and C was not significant, so only one standard deviation for each site was used in the inversion: $\sigma_B=0.059$ and $\sigma_C=0.027$.

Figure 5 shows calculations of the reflection coefficient versus grazing angle based on the MAP estimates from the inversions for Sites A (upper panel), B (middle panel), and C (lower panel). The peak in each curve corresponds to the critical angle of the compressional wave in the basalt for each site. There is no similar peak for a shear wave critical angle at lower grazing angles, so the shear wave velocities are less than the water sound speed. The modeled data generally follow the features in the measured data very well.

The one-dimensional (1D) marginal probability distributions of the Bayesian inversion for Site A are shown in Fig. 6. The dashed and solid vertical lines show the MAP and mean estimates, respectively. The results in Fig. 6 indicate that the sediment thickness (H), basalt compressional wave velocity (v_{p2}), and shear wave velocity (v_{s2}) are the most sensitive parameters and are well estimated, as indicated by the narrow distributions within their prior bounds. The MAP

TABLE III. Model parameters and search bounds in the inversion. Note that some of the parameter bounds are adjusted in different data sites.

Medium	Bound	Thickness (m)	v_p (m/s)	v_s (m/s)	α_p (dB/λ)	α_s (dB/λ)	ρ (g/cm^3)
Sediment	Lower	0	1500	100	0.0	0.0	1.0
	Upper	50	1700	500	3.0	3.0	2.0
Basalt	Lower	···	2200	100	0.0	0.0	2.0
	Upper	···	3000	1500	3.0	3.0	3.0

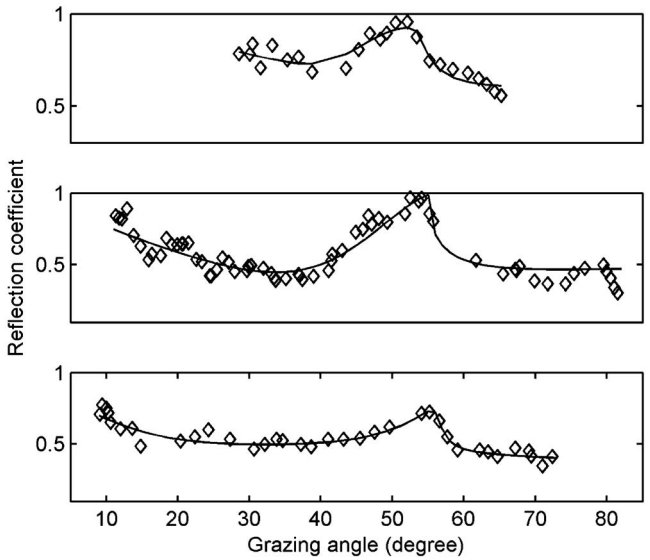

FIG. 5. Reflection coefficient magnitude versus grazing angle (diamonds) for the 16 Hz band at Sites A–C (top to bottom panels). Solid curves are calculated using the MAP estimates for each site.

and mean estimates for these sensitive parameters are similar. The basalt compressional wave attenuation (α_{p2}) shows some sensitivity. In comparison, the marginal distributions for all the other parameters are relatively flat, indicating that these parameters are insensitive and there is very little information about them in the reflection loss data.

Figures 7 and 8 show the same marginal probability distributions for Sites B and C. The three sensitive parameters, H, v_{p2}, and v_{s2}, are very well estimated, as for Site A, and the MAP and mean estimates for these parameters are again closely consistent. Notably, the sediment shear wave velocity (v_{s1}) is also well estimated for these sites. This result is consistent with expectations from the thin-layer model because the reflectivity at 16 Hz involves a constructive interference between the compressional wave and a converted shear wave reflected from the basalt. The converted wave is due to a shear wave generated at the basalt interface that propagates up and down in the sediment and generates a

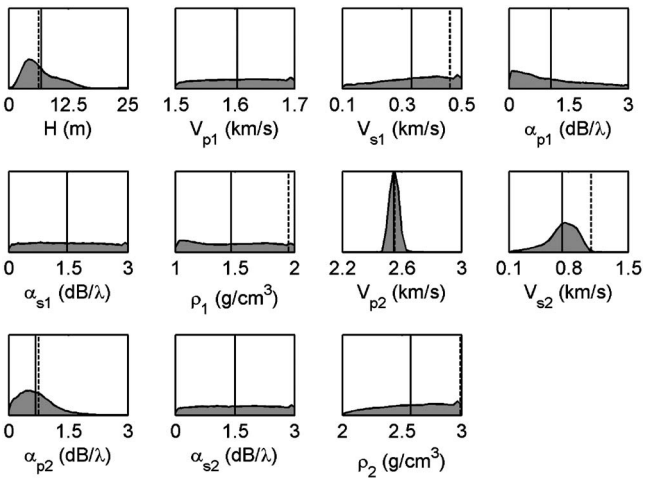

FIG. 6. Marginal probability distributions for Site A. Dashed and solid lines show the MAP and mean estimates, respectively.

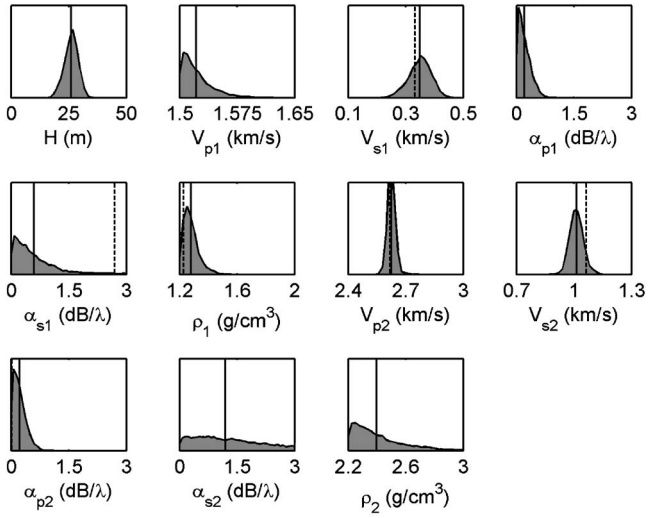

FIG. 7. Marginal probability distributions for Site B. Dashed and solid lines show the MAP and mean estimates, respectively.

converted compressional wave that reflects from the basalt, as described in Ref. 23. The basalt compressional wave attenuation (α_{p2}) shows some sensitivity at the two sites, as for Site A. The distributions for some of the parameters from the inversion for Site B cluster around the lower bounds, but the values of these insensitive parameters do not significantly affect the calculated loss.

The mean estimates and standard deviations for the sensitive model parameters at Sites A–C are listed in Table IV. The standard deviations were derived from the 1D marginal distributions for the model parameters. These distributions represent the information about the parameters obtained from the inversions, and are used to define quantitative measures of the uncertainties in this work. Compared with Table I, the estimated values of sediment thickness at the three sites are consistent with the range of values obtained from the measurements made from shots deployed from the array ship and analysis of the single hydrophone data for the short range shots in each track.

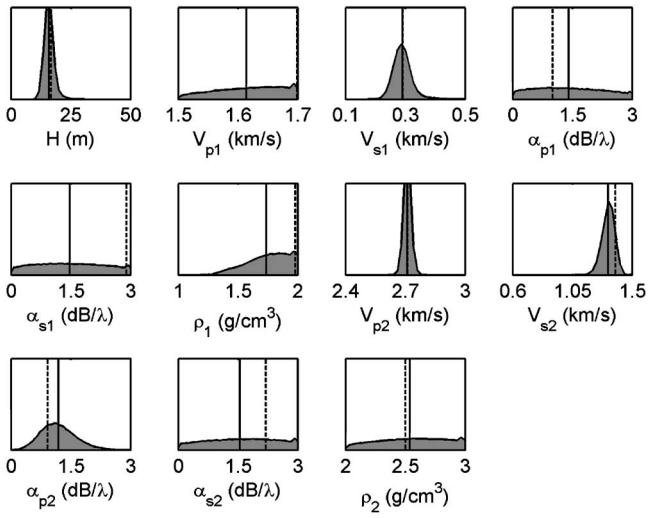

FIG. 8. Marginal probability distributions for Site C. Dashed and solid lines show the MAP and mean estimates, respectively.

TABLE IV. Mean estimates and standard deviations for the sensitive model parameters at Sites A–C.

Data site	Sediment thickness (m)	Basalt v_p (m/s)	Basalt v_s (m/s)
A	6.9 ± 3.8	2547 ± 30	725 ± 178
B	26 ± 2.9	2626 ± 20	1014 ± 35
C	17 ± 2.0	2710 ± 18	1320 ± 46

B. Model parameter correlations

The Bayesian inversion provides additional information about the relationships between model parameters in terms of interparameter correlations and joint marginal probability distributions. Figures 9–11 show the correlation matrices, defined in Eq. (10), for the relationships between the parameter pairs from the inversions at Sites A–C, respectively. The figures indicate positive correlation between the sediment layer thickness (H) and the shear wave velocity (v_{s1}) in the sediment, which is very strong for Sites B and C. This is related to the resonance from a thin sediment layer as discussed in Ref. 23. The correlation is also shown in Fig. 12 in the joint marginal distributions for the two parameters. The panels display the possible combinations of H and v_{s1} that generate converted shear wave resonances in the reflectivity.

C. Discussion of the results

The compressional wave velocities derived from the reflection loss experiment can be compared to other results from seismic experiments at various young crust sites. The most relevant comparison is with the seismic transect of Nedimovic *et al.*[11] for the western part of the transect across the Endeavor segment. The velocities obtained from the reflection loss data agree closely with the values inferred from the travel time analysis of the seismic data,[11] as shown in the upper left panel of Fig. 13. The solid lines in the figure indicate roughly the maximum and minimum values obtained from the seismic data along the transect. Our results

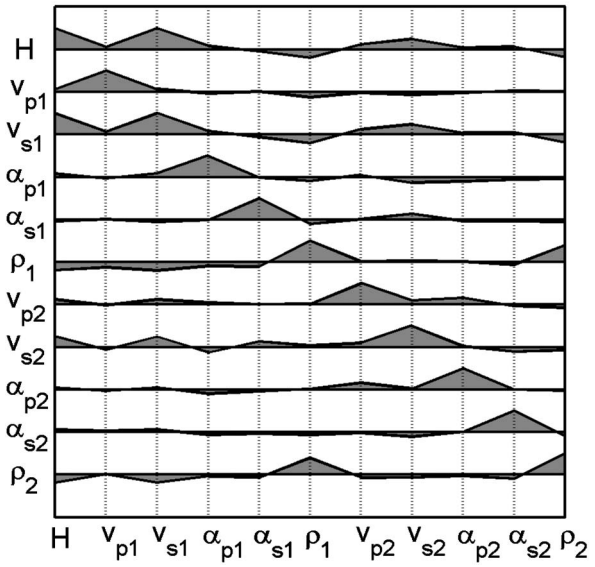

FIG. 10. Correlation matrices plotted by rows for inversion of data Site B.

are also consistent with the value inferred for the surface low velocity layer at ages <0.5 Ma (~ 2600 m/s) by Christeson *et al.*[26] from seismic experiments at the East Pacific Rise, 9°–10° N. Somewhat lower values of about 2200 m/s have been reported from experiments with ocean bottom seismometers by Sohn *et al.*[12] for the spreading center at 9° 50′ N and by McDonald *et al.*[27] from similar experiments at the Northern Cleft segment of the Juan de Fuca ridge at 45° N. However, these results are characteristic of near zero age crust at specific sites on the ridge axes. Harding *et al.*[5] and Vera *et al.*[6] reported values between 2200–2600 m/s for the first 100–200 m of Layer 2A from expanding spread geometry seismic experiments at 13° N and 9° N at the East Pacific Rise, respectively.

Our results for the compressional wave velocity in Layer 2A show a systematic increase in velocity with geological age of the basalt. This result is consistent with the results reported by Nedimovic *et al.*[11] for the western part of the

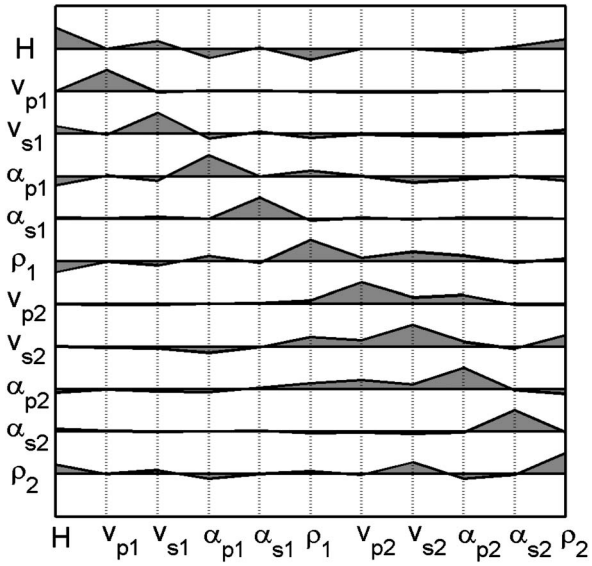

FIG. 9. Correlation matrices plotted by rows for inversion of data Site A.

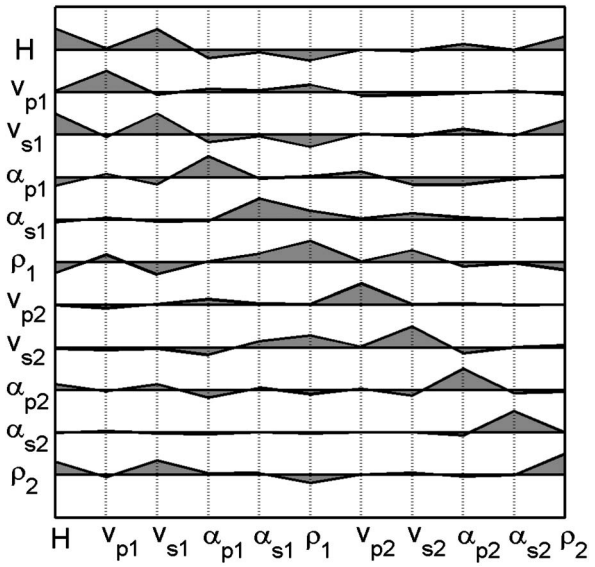

FIG. 11. Correlation matrices plotted by rows for inversion of data Site C.

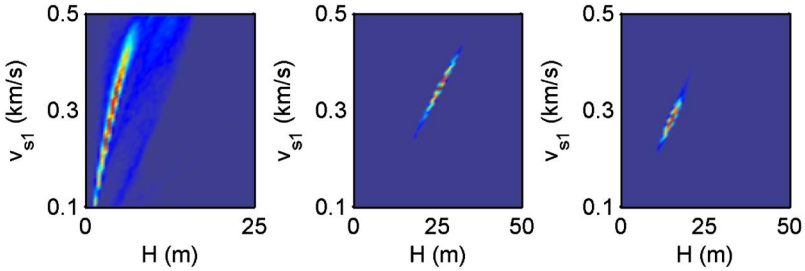

FIG. 12. (Color online) Joint marginal distributions of the sediment layer thickness and the shear wave velocity in the sediment from the inversion of data Sites A (leftmost panel), B (middle panel), and C (rightmost panel).

transect across the Endeavor segment, where they observed an increase of 24% in the seismic velocity in the upper portion of Layer 2A over an age span of 5 Ma from the ridge crest, or 4.8%/Ma. Our results indicate an increase of 6.3% over 1.4 Ma or ~4.5% per Ma, as shown in the lower left panel of Fig. 13. The distribution for the age increase was derived by computing all possible increases according to the marginal distributions for the velocities at Sites A and C. Consequently, our results support the general conclusion drawn by Nedimovic *et al.*[11] that the crustal aging rate on the western flank of the Endeavor segment, where the crustal basalt is thinly sedimented and open to hydrothermal circulation, is relatively slow. However, it is worth noting that both experiments were sensitive to the velocity in a direction perpendicular to the main ridge axis, i.e., across strike. There is no information in these studies about anisotropy in the velocity.

The reflection loss data provide additional information about the shear wave velocity and its variation with geological age. The inversions indicate that the shear wave velocity increases by about a factor of 2, from ~700 m/s at Site A to ~1300 m/s at Site C, as displayed in the upper right panel of Fig. 13. The error bars on the data are the 95% credibility limits that are derived from the marginal densities in the Bayesian inversion, which represent the probabilities of possible shear wave values. The low value at the youngest site is

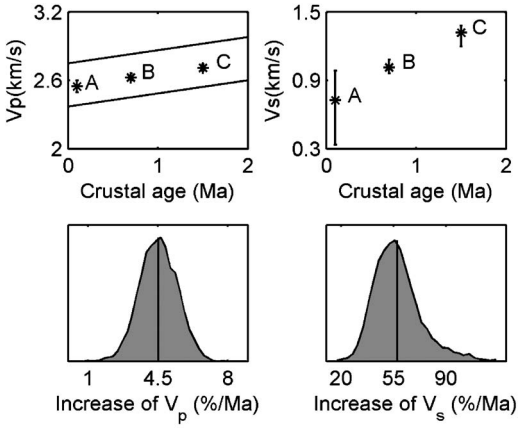

FIG. 13. Upper left panel: the mean compressional wave velocities (stars) of Layer 2A as function of age with error bars indicating the 95% credibility intervals for Sites A–C, and the solid lines indicate the range of values obtained from the seismic experiments of Nedimovic *et al.*;[11] upper right panel: the mean shear wave velocities (stars) of Layer 2A as function of age with error bars indicating the 95% credibility intervals for Sites A–C; bottom left panel: the distribution of percent increase in compressional wave velocity; bottom right panel: distribution of percent increase in shear wave velocity.

consistent with the results obtained by Sohn *et al.*,[12] who reported values between 300 and 500 m/s for near zero age crust from their experiments with interface waves at the East Pacific Rise. Christeson *et al.*[26] also reported low values between 450 and 900 m/s for the shear velocity in the surface low velocity layer from travel time analysis of ocean bottom seismometer data in the same region. Our results indicate a significant increase of around 60% per Ma for the shear wave velocity, as shown in the lower right panel of Fig. 13. Combining the results for the velocities, Poisson's ratio is very large, 0.46 at the youngest age crust where the sediment cover is thinnest, and decreases to 0.34 at the older sites where the sediment layer thickens. These results provide information for constraining models of the porosity in the uppermost crust.

The conclusion from many studies is that the velocity in the upper crust depends on the porosity of the basalt material. Moreover, Swift *et al.*[13] asserted from their study of data from the Integrated Ocean Drilling Program Expedition 309 that the correlations between velocity and porosity are valid over spatial scales from centimeters to seismic lengths. Wilkens and others[2,28] modeled the porosity in terms of a distribution of cracks of different sizes. The general results are well established: the presence of cracks decreases both the compressional and shear wave velocities differently; thin cracks tend to increase Poission's ratio, whereas thick cracks decrease Poisson's ratio. Over time, the cracks will be filled by various deposition processes. Our results for the shear wave velocity versus age provide new constraints for modeling the porosity in the surface low velocity layer. The very large value of Poisson's ratio at the youngest site suggests that thin cracks mostly remain open. At the older sites where the sediment cover is thicker, the decrease in Poisson's ratio suggests that the thin cracks are being filled, but the thicker cracks remain open. The theoretical results of Berge *et al.*[28] that predict porosities of between 25% and 30% for 0.1 Ma crust also predict shear wave velocities that are much larger (almost a factor of 2) than our estimated value for crust of similar age at Site A. Based on the estimates from the reflection loss inversions, it is likely that the basalt porosity at the site is higher than their predictions. Our results also suggest that the porosity decreases over the span of ages out to 1.4 Ma. This is perhaps related to the thicker sediment layer at the older sites.

A general characteristic of young crust is significant lateral variability of the physical properties and the surface roughness over very small spatial scales.[29] We comment here on the impact of these issues on the results of the reflection

loss inversions. Although we have assumed that the crustal age is constant at each site, there could be variations in the material properties along the track of the experiment. Our experimental design included some intrinsic averaging of different conditions along the track: the reflection point at the sea floor was different for each shot, and the data were averaged over angles using a three-point running average. Considering the reflection loss data shown in Fig. 5, the average behavior appears qualitatively consistent with the assumption of a homogeneous ocean bottom. The marginal densities for the sensitive parameters at Sites B and C (Figs. 7 and 8) support this observation, since the distributions are very narrow. However, the relatively wider distributions for the same parameters at Site A (Fig. 6) suggest that there could be more significant variability along the track at that site.

In addition to the physical effect of the shear wave resonances, scattering from the crustal basalt can affect the reflectivity measured in this experiment and contribute to the variability in the reflection loss data. Assuming that the rms roughness, s, of the interface is small, the magnitude of the scattering loss, L, at grazing angle θ can be modeled for a Gaussian randomly rough surface by the Eckart scattering relationship:[30]

$$L = -20 \log[\exp(-2g^2)], \tag{16}$$

where $g = sk \sin(\theta)$ and $k = 2\pi/\lambda$. In the experiment, the impact of scattering was minimized by spatial filtering the data in the specular beam of the array, and using the low frequency 1/3-octave band at 16 Hz. Since no other attempt was made to correct for scattering loss, it is clear from Eq. (16) that the effect is greatest at large grazing angles. At these angles, the reflection coefficient is most sensitive to the acoustic impedance contrast, so it is likely that scattering has the greatest impact on the estimate of the density. However, since the estimates of the basalt compressional and shear wave velocities are sensitive to features of the reflection loss at much lower angles, these parameters are not significantly affected.

V. SUMMARY

This paper described an experimental technique for estimating compressional and shear wave velocities in upper oceanic crust, based on inversion of reflection loss versus angle data. A Bayesian inversion was used to determine parameter values and their associated uncertainties. The method was applied to data from three sites on the thinly sedimented western flank of the Endeavor segment of the Juan de Fuca Ridge to determine the effect of crustal age on the seismic velocities in the surface low velocity layer of Layer 2A. The underlying basalt material is geologically young at these sites. The inversion generated well defined estimates for the compressional and shear wave velocities of the basalt and the sediment thickness at the three sites. The compressional wave velocity increased from 2547 ± 30 to 2710 ± 18 m/s over an age span of 1.4 Ma, corresponding to an increase in the velocity of $4.5 \pm 1.0\%$/Ma. The values estimated from the reflection loss inversion and the rate of increase with geological age were in good agreement with results from a conventional multichannel seismic survey along a parallel track over the ridge.[11] The reflection loss inversion also provided estimates of the shear wave velocity. The shear wave velocity increased by about a factor of 2, from ~700 m/s at the youngest site to ~1320 m/s at the oldest site. The corresponding value of Poisson's ratio is very large, 0.46 ± 0.02 for the youngest site. The results of this experiment suggest that the porosity is likely higher than 25–30%, and at the very least they provide new constraints for models of the porosity in the uppermost crust.

ACKNOWLEDGMENTS

H.D. would like to thank Dr. Michael J. Wilmut and Dr. Yong-min Jiang at the University of Victoria for helpful discussions during this work. N.R.C. acknowledges discussions with Orest Diachok, Ron Dicus, and John Wolf, then at the Naval Research Laboratory (NRL), in planning the reflection loss experiments, which were part of the Pacific Echo series of experiments carried out in collaboration between NRL and the Defense Research Establishment Pacific, 1986–1992. This work was partly done during H.D.'s sabbatical at the University of Victoria and partly supported by the Research Council of Norway under grant no. 186923/I30.

[1] R. Houtz and J. Ewing, "Upper crustal structure as a function of plate age," J. Geophys. Res. **81**, 2490–2498 (1976).
[2] R. H. Wilkens, G. J. Fryer, and J. Karstens, "Evolution of porosity and seismic ratios of upper oceanic crust: Importance of aspect ratios," J. Geophys. Res. **96**, 17981–17995 (1991).
[3] R. S. Jacobson, "Impact of crustal evolution on changes of the seismic properties of the uppermost ocean crust," Rev. Geophys. **30**, 23–42 (1992).
[4] K. M. M. Rohr, "Increase of seismic velocities in upper oceanic crust and hydrothermal circulation in the Juan de Fuca plate," Geophys. Res. Lett. **21**, 2163–2166 (1994).
[5] A. J. Harding, J. A. Orcutt, M. E. Kappus, E. E. Vera, J. C. Mutter, J. C. Buhl, R. S. Detrick, and T. M. Brocher, "Structure of young oceanic crust at 13°N on the East Pacific Rise from expanding spread profiles," J. Geophys. Res. **94**, 12163–12196 (1989).
[6] E. E. Vera, J. C. Mutter, P. Buhl, J. A. Orcutt, A. J. Harding, M. E. Kappus, R. S. Detrick, and T. M. Brocher, "Seismic imaging of oceanic layer 2A between 9° 30′ N and 10°N on the east Pacific Rise from two-ship wide-aperture profiles," J. Geophys. Res. **95**, 15529–15556 (1990).
[7] C. F. Cudrak and R. M. Clowes, "Crustal structure of Endeavour ridge segment, Juan de Fuca Ridge, from a detailed seismic refraction survey," J. Geophys. Res. **98**, 6329–6349 (1993).
[8] E. E. Vera and J. B. Diebold, "Seismic imaging of oceanic layer 2A between 9° 30′ N and 10°N on the East Pacific Rise from two-ship wide-aperture profiles," J. Geophys. Res. **99**, 3031–3041 (1994).
[9] G. L. Christeson, G. M. Purdy, and G. J. Fryer, "Seismic constraints on shallow crustal emplacement processes at the fast spreading East Pacific Rise," J. Geophys. Res. **99**, 17957–17973 (1994).
[10] I. Grevemeyer and W. Wiegel, "Increase of seismic velocities in upper oceanic crust: The superfast spreading East pacific Rise at 14° 14′ S," Geophys. Res. Lett. **24**, 217–220 (1997).
[11] M. R. Nedimović, S. M. Carbotte, J. B. Diebold, A. J. Harding, J. P. Canales, and G. M. Kent, "Upper crustal evolution across the Juan de Fuca ridge flanks," Geochem., Geophys., Geosyst. **9**, Q09006 (2008).
[12] R. A. Sohn, S. C. Webb, and J. A. Hildebrand, "Fine scale seismic structure of the shallow volcanic crust on the east Pacific Rise at 9° 50′ N," J. Geophys. Res. **109**, B12104 (2004).
[13] S. Swift, M. Reichow, A. Tikhu, M. Tominaga, and L. Gilbert, "Velocity structure of upper ocean crust at Ocean Drilling Program site 1256," Geochem., Geophys., Geosyst. **9**, Q12015 (2008).
[14] O. I. Diachok, R. L. Dicus, and S. C. Wales, "Elements of a geoacoustic model of the upper crust," J. Acoust. Soc. Am. **75**, 324–334 (1984).
[15] N. R. Chapman, D. E. Hannay, and K. M. M. Rohr, "Inversion of reflection loss versus angle data for elastic ocean bottom environments," in

Proceedings of the 3rd European Conference on Underwater Acoustics, edited by J. Papadakis (1996), pp. 613–618.
[16]K. M. M. Rohr and N. R. Chapman, "Evolution of uppermost oceanic crust: The Juan de Fuca Plate," American Geophysical Union, 1994 fall meeting, Eos Trans. AGU, Vol. 75, Fall Meet. Suppl., Abstract O12A-18 (1994).
[17]N. R. Chapman, "Source level of shallow explosive charges," J. Acoust. Soc. Am. **84**, 697–702 (1988).
[18]S. E. Dosso, "Quantifying uncertainties in geoacoustic inversion I: A fast Gibbs sampler approach," J. Acoust. Soc. Am. **111**, 129–142 (2002).
[19]S. E. Dosso and C. W. Holland, "Geoacoustic uncertainties from viscoelastic inversion of seabed reflection data," IEEE J. Ocean. Eng. **31**, 657–671 (2006).
[20]S. E. Dosso, M. J. Wilmut, and A.-L. S. Lapinski, "An adaptive-hybrid algorithm for geoacoustic inversion," IEEE J. Ocean. Eng. **26**, 324–336 (2001).
[21]L. M. Brekhovskikh, *Waves in Layered Media*, 2nd ed. (Academic, New York, 1980), pp. 1–59.
[22]J. M. Hovem and Å. Kristensen, "Reflection loss at a bottom with a fluid sediment layer over a hard solid half-space," J. Acoust. Soc. Am. **92**, 335–340 (1992).
[23]N. R. Chapman and D. M. F. Chapman, "A coherent ray model of plane-wave reflection from a thin sediment layer," J. Acoust. Soc. Am. **94**, 2731–2738 (1993).
[24]S. J. Hughes, D. M. F. Chapman, and N. R. Chapman, "The effect of shear wave attenuation on acoustic bottom loss resonance in marine sediments," in *Shear Waves in Marine Sediments*, edited by J. Hovem (Kluwer Academic, Dordrecht, 1991), pp. 439–446.
[25]D. E. Hannay and N. R. Chapman, "Inversion of geoacoustic profiles in thin-sediment environment from ocean bottom reflection loss data," Oceans 93 (1993), Vol. **III**, pp. 381–386.
[26]G. I. Christeson, P. R. Shaw, and J. D. Garmany, "Shear and compressional wave structure of the East Pacific Rise, 9°-10° N," J. Geophys. Res. **102**, 7821–7835 (1997).
[27]M. A. McDonald, S. C. Webb, J. A. Hildebrand, B. D. Cornuelle, and C. G. Fox, "Seismic structure and anisotropy of the Juan de Fuca Ridge at 45° N," J. Geophys. Res. **99**, 4857–4873 (1994).
[28]P. A. Berge, G. J. Fryer, and R. H. Wilkens, "Velocity-porosity relationships in upper oceanic crust: Theoretical considerations," J. Geophys. Res. **97** (B11), 15239–15254 (1992).
[29]R. A. Stephen, "Lateral heterogeneity in the upper oceanic crust at Deep Sea Drilling Project Hole 504," J. Geophys. Res. **93**, 6571–6584 (1988).
[30]C. S. Clay and H. Medwin, *Fundamentals of Acoustical Oceanography* (Academic, New York, 1998).

Adaptive passive fathometer processing

Martin Siderius
Department of Electrical and Computer Engineering, Portland State University, Portland, Oregon 97201

Heechun Song, Peter Gerstoft, and William S. Hodgkiss
Marine Physical Laboratory, Scripps Institution of Oceanography, La Jolla, California 92093-0238

Paul Hursky
HLS Research Inc., 3366 North Torrey Pines Court, Suite 310, La Jolla, California 92037

Chris Harrison
NATO Undersea Research Centre, Viale San Bartolomeo, 400, 19126 La Spezia, Italy

(Received 13 October 2009; revised 7 January 2010; accepted 8 January 2010)

Recently, a technique has been developed to image seabed layers using the ocean ambient noise field as the sound source. This so called passive fathometer technique exploits the naturally occurring acoustic sounds generated on the sea-surface, primarily from breaking waves. The method is based on the cross-correlation of noise from the ocean surface with its echo from the seabed, which recovers travel times to significant seabed reflectors. To limit averaging time and make this practical, beamforming is used with a vertical array of hydrophones to reduce interference from horizontally propagating noise. The initial development used conventional beamforming, but significant improvements have been realized using adaptive techniques. In this paper, adaptive methods for this process are described and applied to several data sets to demonstrate improvements possible as compared to conventional processing.
 [DOI: 10.1121/1.3303985]

PACS number(s): 43.30.Wi, 43.30.Pc, 43.30.Gv, 43.30.Nb [AIT] Pages: 2193–2200

I. INTRODUCTION

In sonar terminology, passive systems listen only while active systems transmit a signal and then receive and process the echoes. The echoes contain information about objects such as their distance and size. This is the basis for echolocation used by bats to hunt for insects in the dark. In the ocean, active sonars use sound projectors to transmit a signal. Recent work has shown that acoustic noise such as that from breaking waves can be used as a coherent sound source for "active" sonar processing.[1] Using noise this way, the sonar itself is passive but active sonar processing methods can be exploited. Previous noise processing methods have used noise intensity to estimate seabed layering[2,3] or seabed geoacoustic properties;[4,5] however, coherent noise processing differs since absolute depths of the seabed and sub-bottom layers are recovered. This coherent technique has been referred to as passive fathometer processing.[1] Since that initial passive fathometer work, theoretical expressions to show the dependency on factors such as averaging time, beam size, and the effects of measurements taken over a rough seabed were developed[6] and effects of sea-surface conditions on passive fathometry have been studied.[7]

A mathematical description of the processing in time and frequency was given in Ref. 8 where the adaptive passive fathometer was introduced. The sign of the adaptive reflection sequence has also been discussed.[9,10] The purpose of this article is to describe how adaptive processing can be applied to passive fathometer techniques and to demonstrate the advantages with several data sets.

Noise based sonar has several practical advantages: (1) There has been significant objection in recent years to man-made sounds in the ocean from either sound projectors or explosive sources. The effect of these sounds is difficult to quantify but in extreme cases has been implicated in marine mammals stranding themselves.[11] In less extreme situations, the sounds may cause behavior changes in marine life and this might be significant especially when this occurs in protected areas or around endangered species. (2) Using noise instead of a projector can greatly simplify the measurements. This is especially true when separations between the sound source and receiver are needed (e.g., to obtain different reflection angles off the seabed). Further, noise is usually very broadband and obtaining a sound source with as much bandwidth can be challenging. (3) Using ambient noise, and thus not having to expend battery power using an active transmitter, is especially attractive in autonomous systems, since this will significantly extend their missions, which in this instance will increase the area being mapped out.

The basis for the passive fathometer is the cross-correlation between the surface noise generated by breaking waves, and the echo return from the seabed. Except at lower frequencies dominated by shipping, breaking waves commonly are the predominant source of ambient noise. It is important to note that the passive fathometer processing is coherent, which is essential to preserve the travel times to the seabed and layers beneath. Coherent processing of noise signals dates back several years. Rickett and Claerbout[12] investigated this for seismic signals, and Weaver and Lobkis[13,14] explored applications in ultrasonics. For ocean acoustics, a

coherent arrival structure was obtained using horizontally separated noise measurements.[15–17] A theoretical framework for recovering Green's functions between point receptions of ocean noise has also been developed.[18–20] One of the differences between the passive fathometer applications and previous work is the use of beamforming to focus the received energy on the useful noise and reduce interference from unwanted noise sources. This has the effect of improving the estimates for seabed layering while reducing the needed averaging time.

This paper is organized as follows: Section II describes the processing methods. The conventional beamforming approach is described here for completeness, and is presented in a slightly more compact way than previously.[1] In addition, the adaptive methods are described that includes a description of the white noise gain constraint beamformer. Section III gives several examples with different hydrophone arrays, locations, and for both stationary and moving arrays.

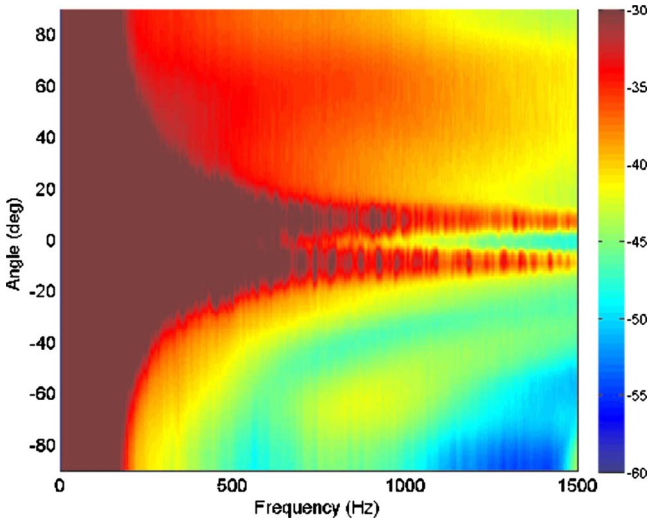

FIG. 1. (Color online) Conventional beamforming applied to 3 min of ocean noise data from the MAPEX2000bis experiment.

II. PROCESSING METHODS

The cross-correlation between the noise from the ocean surface and its echo from the seabed produces a time trace with peaks representing the water-sediment interface as well as sub-bottom layers. One of the key differences between typical noise correlation and the passive fathometer method is the use of a vertical hydrophone array. The array is used to emphasize the noise directly above rather than from horizontal directions. The details of the conventional passive fathometer are described in Sec. II A, and the extension for adaptive processing follows in Sec. II B.

A. Conventional passive fathometer

In the original formulation, conventional beamforming was used and a brief summary is given here. The hydrophone data for each channel at angular frequency ω are written as a column vector $\mathbf{p}=[p_1,p_2,\ldots,p_M]$ for the M hydrophones. Each entry is determined through a Fourier transform [implemented using the fast Fourier transform (FFT)] of an ambient noise time series measured on each channel, $p_m(\omega)=\mathcal{F}\{p_m(t)\}$. The number of sample points in the FFT processing will be referred to as the snapshot size (the snapshot size may equivalently be expressed in seconds by dividing the number of sample points by the sampling frequency).

With conventional beamforming, the weight for the mth hydrophone steered at angle θ for plane waves arriving at grazing angle θ between the hydrophones separated by distance d is written as

$$w_m = e^{-imkd\sin\theta}. \tag{1}$$

The array is referenced to the shallowest hydrophone, which is element $m=0$. The wavenumber is $k=\omega/c$ and c is the sound speed in the water (around 1500 m/s).

Writing the steering weights as a column vector, $\mathbf{w}=[w_0,w_1,\ldots,w_{M-1}]$, the beam $b(\theta)$ is written as

$$b(\theta)=\mathbf{w}^{\dagger}\mathbf{p}, \tag{2}$$

where † represents the conjugate transpose operation. The conventional instantaneous beam power for a given direction θ is computed by the following:

$$B(\theta)=\mathbf{w}^{\dagger}\mathbf{p}(\mathbf{w}^{\dagger}\mathbf{p})^{\dagger}=\mathbf{w}^{\dagger}\mathbf{p}\mathbf{p}^{\dagger}\mathbf{w}=\mathbf{w}^{\dagger}\mathbf{K}\mathbf{w}, \tag{3}$$

where the single snapshot cross-spectral density matrix (CSDM) $\mathbf{K}$ is identified as $\mathbf{p}\mathbf{p}^{\dagger}$. Forming the CSDM allows for multiple snapshots to be averaged before beamforming.

An example of conventional beamforming ocean noise can be illustrated using data from the MAPEX2000bis experiment[5,21] (see Fig. 1). These data were collected by the NATO Undersea Research Centre in the Strait of Sicily between Italy and Malta in November 2000 and analyzed in Refs. 2, 8, and 21. The array had 64 hydrophones of different separations and, here, the 0.5 m equally spaced 32 hydrophones of the array were used for analysis. The array was positioned in about 130 m water depth and moored to the bottom. 3 min of data were averaged to form the CSDM used for beamforming. Figure 1 shows the beamformed output normalized for a maximum of 0 dB (note that the color scaling is from −60 to −30 dB so that all values greater than −30 dB appear in color as the −30 dB value). The positive angles correspond to the beams steered toward the surface (up-looking beams), which capture signals traveling downward from the surface. The negative angles are beams steered down toward the seabed (down-looking beams) and capture signals traveling upward from the seabed. In Fig. 1, the higher intensity noise is evident on the up-looking beams since the down-looking beams see the surface through a seabed reflection and therefore experience losses. Also note the high intensity noise coming from near horizontal. These data consist of a variety of noise sources including breaking waves and distant shipping.

For passive fathometer processing, the interest is in correlating the up-looking beam with the down-looking beam rather than forming the beam power at each grazing angle. To steer an up-looking beam directly upward toward the sur-

face, $\theta=+90°$, and to steer directly toward the seabed, $\theta=-90°$. The steering weights are $w_m=e^{\mp(imkd)}$ and the up-looking weight will be denoted $\mathbf{w}_+$ and the down-looking as $\mathbf{w}_-$. Therefore,

$$b_{\mathrm{up}}=\mathbf{w}_+^{\dagger}\mathbf{p}, \tag{4}$$

and the downward beam

$$b_{\mathrm{dn}}=\mathbf{w}_-^{\dagger}\mathbf{p}. \tag{5}$$

Expressed in the frequency domain, the correlation of these two beams is

$$C=(\mathbf{w}_-^{\dagger}\mathbf{p})(\mathbf{w}_+^{\dagger}\mathbf{p})^{\dagger}=\mathbf{w}_-^{\dagger}\mathbf{p}\mathbf{p}^{\dagger}\mathbf{w}_+=\mathbf{w}_-^{\dagger}\mathbf{K}\mathbf{w}_+. \tag{6}$$

But, for conventional processing, the down-looking beam is just the conjugate of the up-looking beam $\mathbf{w}_-=\mathbf{w}_+^*$. The conventional beamforming correlation then can be written simply using $\mathbf{w}=\mathbf{w}_-$ as follows:

$$C=\mathbf{w}^{\dagger}\mathbf{K}\mathbf{w}^*. \tag{7}$$

The conventional passive fathometer in Eq. (7) differs only from the conventional beamformer output given by Eq. (3) in that the $\mathbf{w}$ to right is conjugated. As a result, B is positive real and C is a complex number. The corresponding phase of C contains the information on the reflection arrival times. As with conventional beamforming, the CSDM given in Eq. (7) can be formed over as many snapshots of data $\mathbf{p}$ as needed to obtain the desired averaging. Averaging time may vary depending on factors such as array motion, noise level, and number of elements in the array.

B. Adaptive passive fathometer

As evident in Fig. 1, there is significant noise intensity at grazing angles near horizontal. This high intensity noise away from the +90° and −90° directions (i.e., away from endfire) degrade the passive fathometer output due to leakage through sidelobes. Sidelobe leakage is a common problem in beamforming and one of the mitigation strategies is to use adaptive methods such as minimum variance distortionless response (MVDR).[22,23] To adaptively beamform using MVDR, the steering weights $\tilde{\mathbf{w}}$ are computed according to

$$\tilde{\mathbf{w}}=\frac{\mathbf{K}^{-1}\mathbf{w}}{\mathbf{w}^{\dagger}\mathbf{K}^{-1}\mathbf{w}}. \tag{8}$$

Using Eq. (7) and continuing to assume $\tilde{\mathbf{w}}_-=\tilde{\mathbf{w}}_+^*$, the MVDR correlation at frequency ω is

$$C_A=\tilde{\mathbf{w}}^{\dagger}\mathbf{K}\tilde{\mathbf{w}}^*. \tag{9}$$

Note that for the typical application of MVDR beamforming (as opposed to cross-correlating beams), the beamformer output can be written as was done in Eq. (3) but with adaptive weights

$$B_A(\theta)=\tilde{\mathbf{w}}^{\dagger}\mathbf{K}\tilde{\mathbf{w}}. \tag{10}$$

And, using Eq. (8), the beamformer output reduces to a much simpler expression that uses the conventional weights

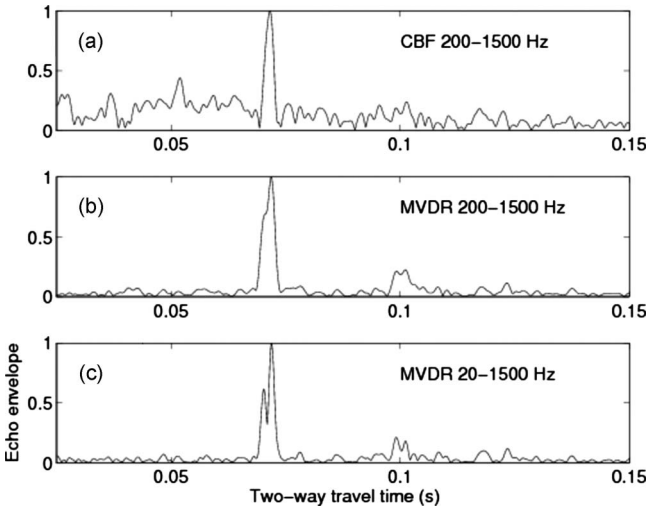

FIG. 2. Example of conventional beamforming (a) and adaptive (MVDR) beamforming (b) on the same cross-spectral density matrix of data. The envelope of $c(t)$ is shown using a 200–1500 Hz band. Panel (c) shows MVDR results in the 20–1500 Hz band.

$$B_A(\theta)=\left[\frac{\mathbf{K}^{-1}\mathbf{w}}{\mathbf{w}^{\dagger}\mathbf{K}^{-1}\mathbf{w}}\right]^{\dagger}\mathbf{K}\left[\frac{\mathbf{K}^{-1}\mathbf{w}}{\mathbf{w}^{\dagger}\mathbf{K}^{-1}\mathbf{w}}\right]=(\mathbf{w}^{\dagger}\mathbf{K}^{-1}\mathbf{w})^{-1}. \tag{11}$$

MVDR is sometimes implemented with this expression since it is less computationally involved than Eqs. (8) and (10).

For adaptive processing, the weights for up- and down-looking beams are not necessarily conjugates of each other (i.e., $\tilde{\mathbf{w}}_-\neq\tilde{\mathbf{w}}_+^*$), and the correct expression for the correlation is

$$C_A=\tilde{\mathbf{w}}_-^{\dagger}\mathbf{K}\tilde{\mathbf{w}}_+. \tag{12}$$

For implementation, we derive the up- and down-looking beam adaptive weights separately using Eq. (8) and then compute the correlation using Eq. (12). The time-series passive fathometer response is simply the inverse Fourier transform of C or $c(t)=\mathcal{F}^{-1}\{C(\omega)\}$ (or the inverse Fourier transform of C_A). For a one-dimensional (1D) medium with a single point source Green's function is proportional to the noise cross-correlation $c(t)$.[8] This model resembles the main wave propagation for the fathometer and thus the reflection response is proportional to $c(t)$. It should be mentioned that the adaptive processing introduces a negative sign on the main reflections although this is not important here where only the envelope of $c(t)$ is considered. Recently the sign anomaly was explained mathematically under simplifying assumptions.[9]

An example of the difference between conventional and MVDR adaptive beamforming is shown in Fig. 2. Both results use the same CSDM averaged over 3 min (same CSDM as used in Fig. 1). The envelope of the time domain expression $c(t)$ is shown in panel (a) for conventional beamforming in the band 200–1500 Hz processed using Eq. (6). Panel (b) shows the MVDR results in the same band using Eq. (9). Panel (c) of Fig. 2 shows MVDR over a larger bandwidth of 20–1500 Hz. The MVDR better rejects the horizontal noise (see Sec. III B) and therefore it is possible to include lower frequencies, which penetrate farther into the seabed, and with the increased bandwidth better time resolution is possible.

C. White noise gain constraint

Since MVDR processing involves inverting the CSDM, problems can occur when the matrix is less than full rank. To stabilize the inversion, the MVDR weights are recast with diagonal loading

$$\tilde{\mathbf{w}} = \frac{[\mathbf{K} + \epsilon\mathbf{I}]^{-1}\mathbf{w}}{\mathbf{w}^{\dagger}[\mathbf{K} + \epsilon\mathbf{I}]^{-1}\mathbf{w}}, \tag{13}$$

where $\mathbf{I}$ is the identity matrix and the ϵ parameter is the adjustable diagonal loading strength. The diagonal loading is equivalent to adding white noise with its power depending on the strength parameter ϵ.[24]

In cases considered here, the array is either stationary or slowly drifting, and there is no snapshot deficiency. However, the MVDR processor is also known to be sensitive to mismatch. For example, this mismatch can come in the form of environmental factors (such as non-plane-wave propagation) or the actual array shape being different from the assumed shape. The white noise gain constraint beamformer[25] adjusts ϵ for each angle to provide robustness to the adaptive processor, which is constrained by the value selected for the white noise gain constraint δ^2 such that

$$\delta^2 \leq G_w \leq M, \tag{14}$$

where the white noise gain G_w is defined by

$$G_w = |\tilde{\mathbf{w}}^{\dagger}\tilde{\mathbf{w}}|^{-1}, \tag{15}$$

and M is the number of hydrophones. The white noise gain constraint beamformer can be tuned to be pure MVDR ($\epsilon = 0$), pure conventional ($\epsilon = \infty$), or somewhere in between, according to the value selected for δ^2. Algorithmically, for any given angle, the diagonal loading ϵ is increased until constraint equation (14) is satisfied. Unfortunately, the relationship between ϵ and δ^2 is not simple except that the upper limit of $\delta^2 = M$ corresponds to pure conventional ($\epsilon = \infty$). In typical sonar processing (e.g., detecting weak targets), a normalized δ^2, defined by $\mathrm{WNC} = 10\log(\delta^2/M)$ dB, is set to -2 or -3 dB.[24] However, for passive fathometer processing, the WNC value is set to -10 dB, as will be presented in Sec. III.

III. RESULTS

The previous example for the MAPEX2000bis experiment shown in Fig. 2 illustrated the benefits of adaptive over conventional beamforming. The adaptive approach has better time resolution, better "signal-to-noise" ratio, and shows sub-bottom layers that are not evident in the conventional results. But, are these resolved layers in the adaptive processing real? In the next sections different arrays are used along with seismic profile data to build the case for the adaptive results being correct and a significant improvement over the conventional processing. In Sec. III A, the MAPEX2000bis example along with an additional data set are presented. In each case a different array is used but both are stationary (i.e., moored). The fixed geometry simplifies the analysis and also demonstrates performance improvements using adaptive methods in different frequency bands and with different arrays. To map a seabed, the array will be moving and two cases using drifting arrays are given in Secs. III B and III C.

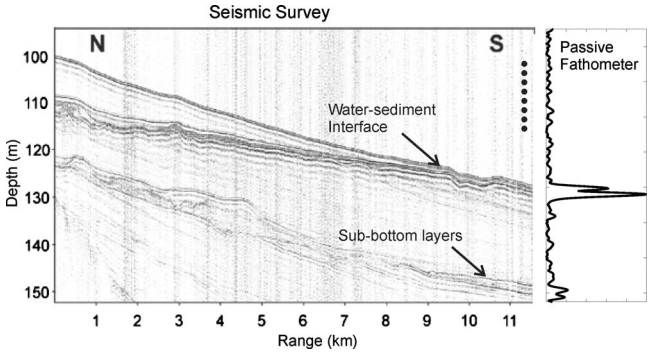

FIG. 3. Left side shows the sub-bottom profile for the MAPEX2000bis site (sub-bottom profile from Ref. 26) along with the adaptive passive fathometer result shown on the right. The approximate position of the vertical array is indicated by the vertical dots in the sub-bottom profile.

A. Adaptive vs conventional processing with fixed arrays

Figure 3 shows the passive fathometer time trace (far right of figure) along with a corresponding seismic profile taken in the same location. The fixed array was located at the south end of the seismic track; the approximate array location is indicated in the figure near range 11 km and is denoted using black vertical dots. The passive fathometer time trace gives an indication of some interfering layers near the water-sediment interface, which is consistent with the joining of two layers in the seismic profile. Also, the passive fathometer shows two sub-bottom layers approximately 20 m below the water-sediment interface. Recall that in Fig. 2 the conventional processing did not resolve layers near the water-sediment interface and the deeper layers are not identifiable.

The next data set considered is from Dabob Bay in Washington; see Fig. 4. This is a well protected area with the middle of the Bay approximately 180–200 m deep. The array

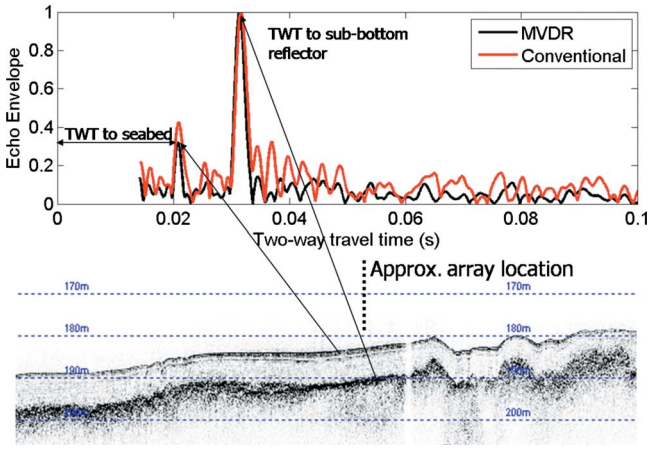

FIG. 4. (Color online) Adaptive passive fathometer result for Dabob Bay experiment. Top panel shows the passive fathometer response (conventional and MVDR adaptive processing). Lower panel shows the sub-bottom profile and the approximate array location. Note the correspondence between the layers in the two plots as well as the improvement in the response using MVDR.

used here had 16 hydrophones at 0.5 m spacing with first phone at 15 m off the seafloor. The frequency band used for the MVDR processing was 50–1500 Hz. After the experiment a sub-bottom profile was taken using the Knudsen 320B system on the R/V New Horizon. The water depth was about 185 m. The short two way travel time (TWT) from the array to the seabed (about 0.02 s) is because the array was moored close to the seabed (about 7.5 m from the bottom hydrophone to the seabed). The passive fathometer return shows a relatively weak arrival at the water-seabed interface at about 0.02 s TWT with a much stronger return at around 0.03 s. This stronger second return suggests a higher impedance contrast for the second interface. This also is suggested in the sub-bottom profile. For comparison, the conventional processing result is also superimposed in Fig. 4, exhibiting higher noise levels especially just past the second peak (0.03 s).

B. Adaptive vs conventional processing with drifting arrays: Boundary 2003

The next experimental example is from a drifting array during the NURC's Boundary 2003 experiment. These experiments were originally set up to test out a different technique (spectral factorization) for investigating layer echoes[2,3] and also bottom reflection properties.[5] The first part of this track was processed previously using the conventional passive fathometer approach.[1] The drifting array has 32 hydrophones spaced at 0.18 m (design frequency of 4.2 kHz). The depth of the reference hydrophone was approximately 73.5 m. The wind varied during the experiment but was, on average, about 15 kn. In this case, the moving array limits the number of snapshots that can be taken per time trace and, here, snapshots were averaged over 90 s to form the CSDM. The adaptive processing parameters for these data were as follows: frequency band 50–4000 Hz, snapshot size T_{snap} = 1.4 s, and total averaging time T_{ave} = 90 s. For the conventional processing the same parameters were used. However, the frequency band was reduced to 200–4000 Hz because of significant shipping noise below 200 Hz that cannot be suppressed using the conventional approach.

Results for the Boundary 2003 track using conventional passive fathometer processing are shown in Fig. 5(a). The record number corresponds to a passive fathometer time trace with 90 s of noise averaging time. Therefore each record number (horizontal axis) also equates to range as the array drifted over time. The vertical axis is depth in meters converted from the two way travel times using sound speed of 1500 m/s. Passive MVDR fathometer results are shown in Fig. 5(b). Comparing the conventional processing results [Fig. 5(a)] and adaptive processing [Fig. 5(b)], there are several sub-bottom reflectors that agree with each other. However, the overall image for the conventional processing is less clear than for the adaptive processing. After the drifting array was recovered, a Uniboom (active sonar with towed array) system was used to measure the sub-bottom properties along the same track as the array drifted.[3] It was only possible to approximately capture the array drift track in the survey and the results are shown in Fig. 5(c). In Fig. 5(c) the horizontal axis is the ping number that equates to range since

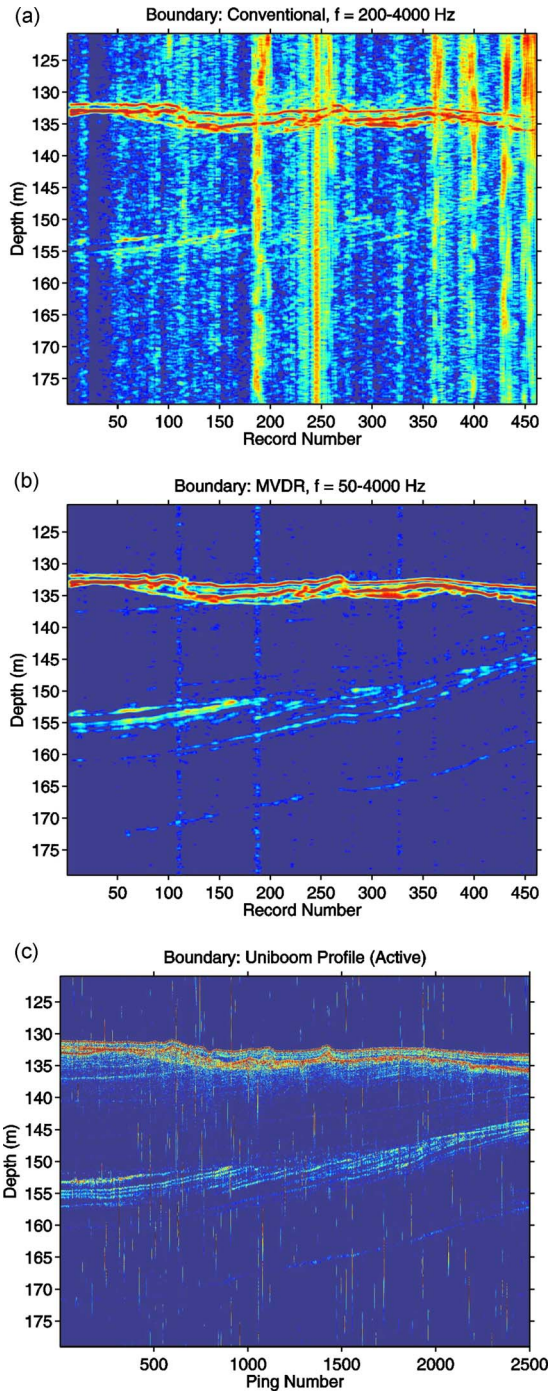

FIG. 5. (Color online) (a) Conventional (200–4000 Hz) and (b) MVDR (50–4000 Hz) passive fathometer results for Boundary 2003 drifting array data. Horizontal axis is the record number that corresponds to range as the array drifted (20 dB dynamic color scale). Panel (c) shows the results from data collected using a Uniboom active seismic system along approximately the same track as the array drift. Ping number on the horizontal axis in (c) corresponds to range along the track (20 dB dynamic color scale).

each ping corresponds to individual transmissions from the Uniboom system as it was towed over the track. Although unlikely that the exact same track was measured with the passive fathometer and the seismic survey, there are several features in the sub-bottom that agree with both the conventional and adaptive results. However, the adaptive passive fathometer results [in Fig. 5(b)] produces an image that is

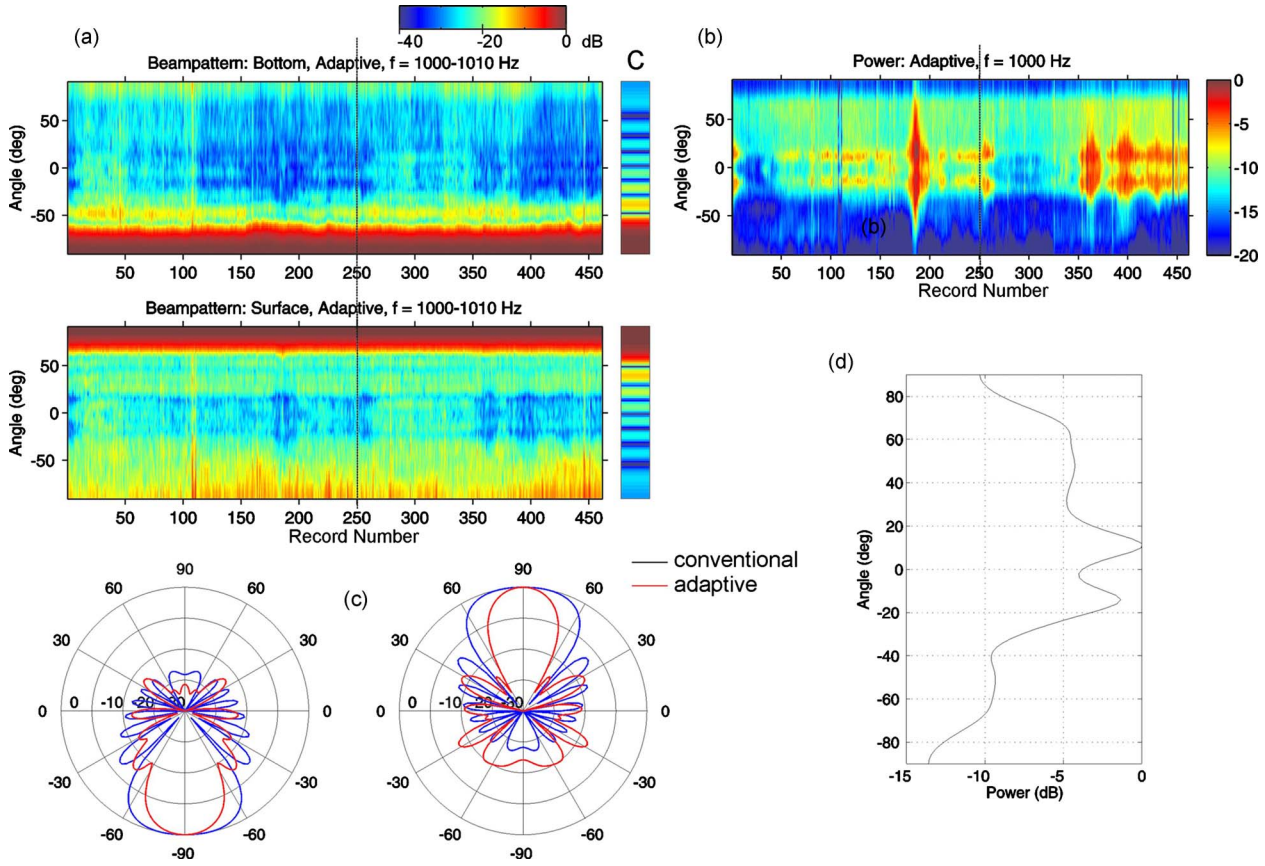

FIG. 6. (Color online) Data from Boundary 2003 in the 1000–1010 Hz band. (a) Down-looking (top panel) and up-looking (bottom panel) beampatterns for the adaptive processing as a function of record number as the array drifts. Conventional beampatterns are constant and are shown as the small vertical bars on the right (labeled C). (b) Beam power output for adaptive processing. As in Fig. 1, the high intensity noise is observed on the up-looking beams. There is strong horizontal energy, which is likely due to distant shipping to be suppressed. (c) Adaptive and conventional polar beampatterns for the down-and up-looking beams used in the passive fathometer for record number 250. (d) A sample slice of the beam power is shown for record number 250.

much more similar to the Uniboom image [in Fig. 5(c)] than does the conventional processing image [in Fig. 5(a)].

This Boundary 2003 data are further analyzed to understand the improvements provided using adaptive processing. In Fig. 6, a beampattern analysis is shown for the 1000–1010 Hz band. In Fig. 6(a), the beampatterns are shown for the adaptive processing as a function of record number as the array drifts. The horizontal axis is the record number that corresponds to range as the array drifts, and the vertical axis is the grazing angle. The top panel in Fig. 6(a) is the down-looking beampattern and the bottom panel is up-looking beampattern, which is quite distinct from the top panel. Recall that only directly up and down steering directions ($\theta = \pm 90°$) are used. Note the regions near horizontal grazing angle in both panels of Fig. 6(a) that are 30–40 dB down where the adaptive processor tries to null the beamform response. In addition, the top panel in Fig. 6(a) suppresses the high intensity beams above horizontal (traveling downward). Anything not coming from straight up or straight down is treated as interference so improvement is achieved by suppressing the interference. Shown in Fig. 6(a) on the far right (small vertical bars) is the conventional beampatterns for comparison. Contrary to adaptive processing where the beampatterns change with time the conventional beampatterns is fixed so only a single plot is needed. Note that the sinc-like pattern for conventional beamforming has much less suppression of the interferers near horizontal.

In Fig. 6(b) the beam power output for adaptive processing is shown along the track as the array drifts. This plot shows the actual beamformed power for all angles (not just the straight up- and down-looking beams). As in Fig. 1, the high intensity noise is observed on the up-looking beams. There also is strong horizontal energy, which is likely due to distant shipping. Not surprisingly, the adaptive beampatterns in Fig. 6(a) show deep nulls around the horizontal. In particular, the event near record number 180 shows a strong interferer, which is being effectively suppressed in Fig. 6(a).

In Fig. 6(c), the adaptive and conventional beampatterns are shown in polar coordinates for the up- and down-looking beams used in the passive fathometer. The conventional beampatterns do not change over time as the data change; however, the adaptive beampatterns are modified depending on the data. Shown in Fig. 6(c) are the adaptive beampatterns for record number 250 along with the conventional beampatterns. The adaptive beampatterns display a sidelobe structure that is quite different from the conventional ones. In particular, note the narrower beams in the $\pm 90°$ directions shown. Also note the differences in the sidelobe structure where the adaptive beams are adjusting to noise coming from direc-

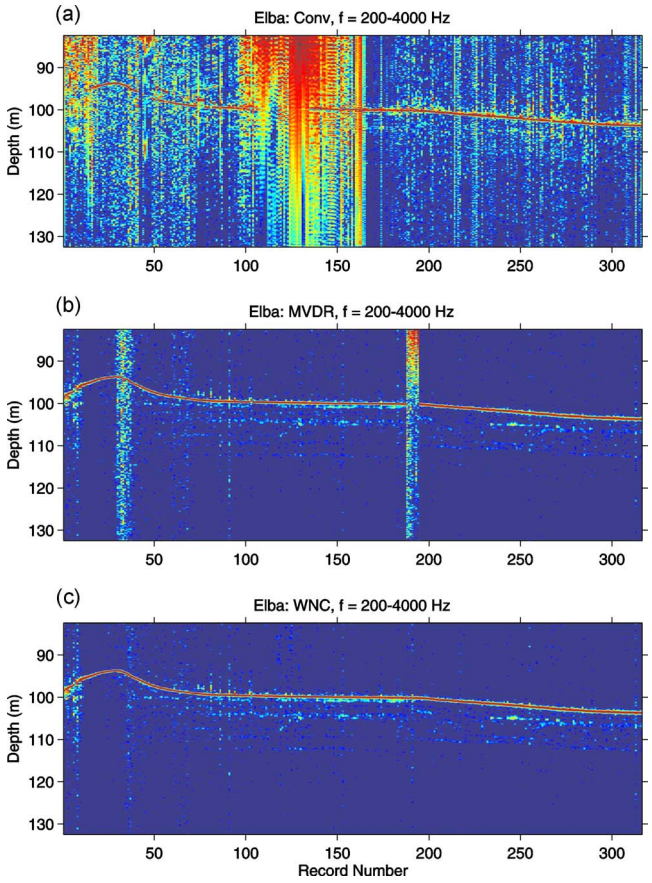

FIG. 7. (Color online) Passive fathometer results from Elba drift: (a) Conventional beamforming, (b) MVDR, and (c) white noise gain constraint beamformer with WNC=−10 dB (20 dB dynamic color scale).

tions other than ±90°. Similarly in Fig. 6(d), a sample slice of the beam power shown in Fig. 6(b) is shown for record number 250.

C. Adaptive vs conventional processing with drifting arrays: Elba

The ElbaEx data were collected between the islands of Elba and Capraia in the Mediterranean Sea in October 2003. The same array as for Boundary 2003 was used with the depth of the reference hydrophone at approximately 73.5 m. Processing parameters used for the Elba data were similar to those for the Boundary data. The frequency band was 200–4000 Hz, snapshot size T_{snap}=0.34 s, and total averaging time T_{ave}=44 s (i.e., the record length). Unfortunately, there were no corresponding seismic data for this drift event. However, it is instructive to compare the conventional and adaptive outputs since the continuity of data along the track provides some measure of the quality of the two results. Shown in Fig. 7 are the results from all three processing types discussed: (a) shows the conventional beamforming passive fathometer, (b) is the straight MVDR, and (c) uses the white noise gain constraint beamformer with WNC=−10 dB. There are regions in (a) that are significantly contaminated in the response and these may be due to local interference effects. While the MVDR (b) is much improved over the conventional approach (a), there still are regions of data contamination. The best results are achieved from the white noise gain constraint beamformer, Fig. 7(c).

IV. CONCLUSION

The passive fathometer processing is a recently developed technique to extract bathymetry and seabed layering information using measurements of ocean ambient noise. This method originally used conventional processing, and the extension to adaptive processing is presented here along with results from several experiments. These experiments used different arrays, and both moored and drifting arrays were used. In all cases, the adaptive results show significant improvements compared to the original conventional results. Adaptive methods allow a larger bandwidth to be included, which gives better time resolution. Further, adaptive methods suppress the horizontal sound that interferes with the surface noise, and this allows weaker sub-bottom layers to be better resolved as compared with conventional processing.

ACKNOWLEDGMENTS

We would like to gratefully acknowledge support for this research by the Office of Naval Research Ocean Acoustics Program. We also would also like to acknowledge the NURC for providing the MAPEX2000bis, Boundary 2003, and ElbaEx data. We would like to thank Peter Nielsen, Mark Stevenson, Finn Jensen, Charles Holland, and Michael Porter for their collaboration on these experiments and data sets, and Keyko McDonald and Brian Granger from SPAWAR for providing the Dabob Bay data.

[1]M. Siderius, C. H. Harrison, and M. B. Porter, "A passive fathometer technique for imaging seabed layering using ambient noise," J. Acoust. Soc. Am. **120**, 1315–1323 (2006).
[2]C. H. Harrison, "Sub-bottom profiling using ocean ambient noise," J. Acoust. Soc. Am. **115**, 1505–1515 (2004).
[3]C. H. Harrison, "Performance and limitations of spectral factorization for ambient noise sub-bottom profiling," J. Acoust. Soc. Am. **118**, 2913–2923 (2005).
[4]M. J. Buckingham and S. A. S. Jones, "A new shallow-ocean technique for determining the critical angle of the seabed from the vertical directionality of the ambient noise in the water column," J. Acoust. Soc. Am. **81**, 938–946 (1987).
[5]C. H. Harrison and D. G. Simons, "Geoacoustic inversion of ambient noise: A simple method," J. Acoust. Soc. Am. **112**, 1377–1389 (2002).
[6]C. H. Harrison and M. Siderius, "Bottom profiling by correlating beam-steered noise sequences," J. Acoust. Soc. Am. **123**, 1282–1296 (2008).
[7]S. L. Means and M. Siderius, "Effects of sea-surface conditions on passive fathometry and bottom characterization," J. Acoust. Soc. Am. **126**, 2234–2241 (2009).
[8]P. Gerstoft, W. S. Hodgkiss, M. Siderius, C.-F. Huang, and C. H. Harrison, "Passive fathometer processing," J. Acoust. Soc. Am. **123**, 1297–1305 (2008).
[9]C. H. Harrison, "Anomalous signed passive fathometer impulse response when using adaptive beam forming," J. Acoust. Soc. Am. **125**, 3511–3513 (2009).
[10]J. Traer, P. Gerstoft, H. Song, and W. S. Hodgkiss, "On the sign of the adaptive passive fathometer impulse response," J. Acoust. Soc. Am. **126**, 1657–1658 (2009).
[11]A. Frantzis, "Does acoustic testing strand whales?," Nature (London) **392**, 29 (1998).
[12]J. Rickett and J. Claerbout, "Acoustic daylight imaging via spectral factorization: Helioseismology and reservoir monitoring," The Leading Edge **18**, 957–960 (1999).
[13]R. L. Weaver and O. I. Lobkis, "Ultrasonics without a source: Thermal

fluctuation correlations at MHz frequencies," Phys. Rev. Lett. **87**, 134301–134304 (2001).
[14]O. I. Lobkis and R. L. Weaver, "On the emergence of the Green's function in the correlations of a diffuse field," J. Acoust. Soc. Am. **110**, 3011–3017 (2001).
[15]P. Roux, W. A. Kuperman, and the NPAL Group, "Extracting coherent wave fronts from acoustic ambient noise in the ocean," J. Acoust. Soc. Am. **116**, 1995–2003 (2004).
[16]P. Roux, K. G. Sabra, and W. A. Kuperman, "Ambient noise cross correlation in free space: Theoretical approach," J. Acoust. Soc. Am. **117**, 79–83 (2005).
[17]L. A. Brooks and P. Gerstoft, "Green's function approximation from cross-correlations of 20–100 Hz noise during a tropical storm," J. Acoust. Soc. Am. **125**, 723–734 (2009).
[18]K. G. Sabra, P. Roux, and W. A. Kuperman, "Arrival-time structure of the time-averaged ambient noise cross-correlation function in an oceanic waveguide," J. Acoust. Soc. Am. **117**, 164–174 (2005).
[19]K. G. Sabra, P. Roux, and W. A. Kuperman, "Emergence rate of the time-domain Green's function from the ambient noise cross-correlation function," J. Acoust. Soc. Am. **118**, 3524–3530 (2005).
[20]O. A. Godin, "Recovering the acoustic Green's function from ambient noise cross correlation in an inhomogeneous moving medium," Phys. Rev. Lett. **97**, 054301 (2006).
[21]M. Siderius, P. L. Nielsen, and P. Gerstoft, "Range-dependent seabed characterization by inversion of acoustic data from a towed receiver array," J. Acoust. Soc. Am. **112**, 1523–1535 (2002).
[22]H. L. Van Trees, *Detection, Estimation, and Modulation Theory: Part IV: Optimum Array Processing* (Wiley, New York, 2002).
[23]W. S. Burdic, *Underwater Acoustic System Analysis* (Prentice-Hall, Englewood Cliffs, NJ, 1984).
[24]H. C. Song, W. A. Kuperman, W. S. Hodgkiss, P. Gerstoft, and J. S. Kim, "Null broadening with snapshot-deficient covariance matrices in passive sonar," IEEE J. Ocean. Eng. **28**, 250–261 (2003).
[25]H. Cox, R. M. Zeskind, and M. M. Owen, "Robust adaptive beamforming," IEEE Trans. Acoust., Speech, Signal Process. **35**, 1365–1376 (1987).
[26]C. W. Holland, "Coupled scattering and reflection measurements in shallow water," IEEE J. Ocean. Eng. **27**, 454–470 (2002).

Models for wave propagation in two-dimensional random composites: A comparative study

Jin-Yeon Kim[a)]
School of Civil and Environmental Engineering, Georgia Institute of Technology, Atlanta, Georgia 30332-0355

(Received 27 May 2009; revised 7 January 2010; accepted 8 January 2010)

This paper provides a set of benchmark results on existing theoretical models for wave propagation in two-dimensional composite materials. This comparative study is motivated to investigate the reason why results from an accurate ultrasonic measurement often significantly contradict theoretical predictions. Eight different models are evaluated with their numerically calculated effective wave speeds and coherent attenuations. For computational simplicity, the problem of horizontal shear wave propagation in an elastic matrix containing parallel circular cylinders is considered. Numerical calculations are conducted for different composites in wide ranges of material properties, volume concentration, and frequency. Some of the numerical results are compared with experimental data. Judgments are made based on fundamental theoretical and physical criteria as well as relative agreements in the numerical results, and then possible causes of failures are discussed. The effect of microstructure, potentially as a major source of the observed disagreements between models, is also discussed.
 [DOI: 10.1121/1.3308408]

PACS number(s): 43.35.Cg, 43.20.Jr, 43.20.Fn, 43.20.Bi [JAT] Pages: 2201–2209

I. INTRODUCTION

For last several decades, authors in theoretical physics, applied mathematics, and engineering have proposed numerous models for multiple scattering and propagation of waves in random inhomogeneous media. Reviews on the models and their mathematical backgrounds can be found in Refs. 1–3. In spite of the abundance in literature, comprehensive exposure of the subject to engineering investigators is severely limited, possibly due to the complex physical processes involved in the multiple-scattering phenomenon and accordingly difficult mathematical treatments. While every model proves its validity through a comparison with some experimental data or with the classical theories of Foldy,[4] Lax,[5] or Waterman and Truell,[6] significant disagreements between experimental and theoretical results are often encountered. In most cases, experimental errors are blamed to be responsible for the disagreements. Meanwhile, it is also found that there are little agreements between different theoretical models. These pose a need of a large scale comparative evaluation study on the existing models. However, due to the mathematical complexity in the theories, an analytical study on the validity range of a model is a challenging task. The major difficulty in such an evaluation study is the lack of an exact reference solution, either from an analysis or an experiment. A numerical approach such as the Monte Carlo simulation[7,8] and the semianalytical technique[9] may be used. However, these numerical simulations are, by nature, limited to simple cases. On the other hand, experiments often suffer from the multiple-scattering noise that causes troubles identifying coherent signals. For these reasons, few works on the evaluation of multiple-scattering models have been reported so far.

Anson and Chiver[10] examined 12 different theoretical models for their wave speeds in the long wavelength limit and broadly concluded that except for four models that failed to satisfy test conditions considered, all of the remaining models are in a qualitative agreement with the experimental results. In their study, comparisons were made only for wave speeds, mainly in the long wavelength limit. Romack and Weaver[7] conducted Monte Carlo simulations for one- and two-dimensional wave propagations in a random lattice composed of a large number of simple oscillators and concluded that the multiple scattering is considered in the same degree of accuracy both in the quasicrystalline approximation (QCA) and the coherent potential approximation (CPA). The Monte Carlo simulations for multiple scattering of electromagnetic waves have been performed to compare the QCA and the combined QCA-CPA methods.[8] Berryman[11] examined three single scattering approximations—the average *T*-operator approximation, the CPA, and the differential effective medium, for the coefficients in the Biot's poroelasticity equations. Martin[1] theoretically compared several multiple scattering models.

In this paper, a comparative study is conducted for eight existing models for predicting the dynamic effective properties (the effective wave speed and coherent attenuation) of two-dimensional random composites. Models considered include the models of Waterman and Truell,[6] Lloyd and Berry,[12] Varadan *et al.*,[13] Kanaun and Levin,[14] Sabina and Willis,[15] Kim,[16] Beltzer and Brauner,[17] and Yang and Mal.[18] A brief review with comments is given for each model. The models are tested for weak scattering, quasistatic wave speed, and low frequency attenuation. The effects of micro-

[a)]Author to whom correspondence should be addressed. Electronic mail: jinyeon.kim@me.gatech.edu

structure on the wave speed are also considered. For composites having quite different dynamic characteristics, the calculated wave speeds and attenuation factors are compared for high fiber volume concentrations and in a wide frequency range. The judgments are based on some pertinent theoretical and physical criteria. When a sound physical criterion is not available, relative coincidence among the calculated results is used; however, no generalization is made beyond the test conditions.

II. MODELS

A. Multiple-scattering theories

Foldy[4] and Lax[5] developed a probabilistic theory for multiple scattering of waves by randomly distributed point scatterers in which the scattered field is ensemble averaged with the probability distributions for their absolute and relative positions. These configuration averages result in an infinite hierarchy of integral equations in which the average scattered field with n scatterers fixed is expressed in terms of the average scattered field with $n+1$ scatterers fixed. To truncate the hierarchy, Foldy[4] assumed that the average exciting field near a fixed scatterer is approximately equal to the average total field near that scatterer; thus, the first-order single scattering is considered. Lax[5] proposed the QCA in which the average exciting field with two scatterers fixed is approximately equal to the average exciting field with one scatterer fixed. Since the total scattering field is described as a collection of singly and doubly scattered fields in this approximation, the probability distribution for the relative positions of two scatterers, that is, the pair-correlation function (PCF) suffices in the analysis. The QCA has been widely used in the analyses of finite-size scatterer systems.

Many authors attempted to extend the theory of Foldy and Lax to the case in which scatterers are finite sized and thus spatial correlations among the scatterers are important. Waterman and Truell[6] obtained a formula for the effective wavenumber for three-dimensional finite-sized scatterers using the Foldy's approximation and therefore, ignoring the correlation between scatterers. A two-dimensional version of the Waterman–Truell formula is

$$k_e^2 = k_1^2 - 4in_o f(0) - \frac{4n_o^2}{k_1^2}[f^2(0) - f^2(\pi)], \tag{1}$$

where k_1 and k_e are the wavenumbers associated with the wave speeds in the matrix and the effective medium, i is the imaginary unit, n_o is the number of scatterers in the unit area, and $f(\theta)$ is the directional scattering amplitude; $f(0)$ and $f(\pi)$ are the forward and backward scattering amplitudes. In their almost forgotten paper, Lloyd and Berry[12] pointed out that the second-order term (n_o^2) in the Waterman–Truell formula is incorrect and proposed a corrected one for three-dimensional problems. Recently, Linton and Martin[19] confirmed the Lloyd–Berry formula and also derived the formula for two dimensions,

$$k_e^2 = k_1^2 - 4in_o f(0) + \frac{8n_o^2}{\pi k_1^2}\int_0^{\pi} \cot(\theta/2)\frac{d}{d\theta}[f(\theta)]^2 d\theta. \tag{2}$$

These two formulas are extensions of Foldy's formula $k_e^2 = k_1^2 - 4in_o f(0)$ to finite-sized scatterers. Fikioris and Waterman,[20] starting from the earlier work,[6] made the so-called hole corrections in which the volume around the fixed scatterer where other scatterers cannot reside is excluded from the integral for average excitation field. This meets the requirement of the impenetrability between scatterers but it is valid at a low concentration of small scatterers.

Bose and Mal,[21] using the wave function expansion technique, derived an integral for averaged wave field with two scatterers fixed and then applied the Lax's QCA and extinction theorem[5] to obtain a secular (or dispersion) equation for the unknown effective wavenumber,

$$|\delta_{\mathrm{nm}} - 8v_2 T_m F_{n-m}| = 0, \quad \text{for} \quad m,\ n \in \{-\infty, \infty\}, \tag{3}$$

where δ_{nm} is the Kronecker delta and v_2 is the fiber volume concentration,

$$T_m = \frac{\mu_2 k_2 J_m'(k_2 a) J_m(k_1 a) - \mu_1 k_1 J_m'(k_1 a) J_m(k_2 a)}{\mu_1 k_1 J_m(k_2 a) H_m'(k_1 a) - \mu_2 k_2 J_m'(k_2 a) H_m(k_1 a)}, \tag{4}$$

$$F_n = \frac{k_1 J_n(2k_e a) H_n'(2k_1 a) - k_e J_n'(2k_e a) H_n(2k_1 a)}{2a(k_1^2 - k_e^2)} + \int_1^{\infty} (g(x) - 1) H_n(2k_1 a x) J_n(2k_e a x) x dx. \tag{5}$$

In Eq. (4), μ_1 and μ_2 are the shear moduli of the matrix and the fiber, respectively, a is the fiber radius, k_2 is the wavenumber associated with the wave speed in the fiber, $J_n(z)$ is the Bessel function of order n, and $H_n(z)$ is the first kind Hankel function of order n. $g(x)$ in Eq. (5) is the PCF for impenetrable scatterers (hard disks).[22] Bose and Mal assumed an exponentially decaying PCF, while Varadan *et al.*[13] used an exact PCF to improve the accuracy of the QCA at high frequencies and high volume concentrations. The exact PCFs can be obtained from the Monte Carlo simulation.[3,22,23] In this theoretical context, the Bose and Mal formulation with the exact PCF, that is, the method of Varadan *et al.*,[13] appears to be most accurate.

B. Effective medium theories

The effective medium theories are commonly based on the following hypothesis:[1,24] Every inclusion in the composite behaves as an isolated inclusion embedded in a homogeneous medium with the effective properties of the composite. The field that acts on this inclusion is a plane wave propagating in the effective medium. While this hypothesis is hard to justify theoretically, it offers a simple way to calculate the effective properties; it reduces the original multiple-scattering problem defined in the host medium to a single scattering problem defined in the effective medium. These theories have been often very successful in many occasions.[24–26]

A few variants of the effective medium theory exist, in which the roles of the host medium and inclusions are treated

in different ways. A simplest one is to embed both the matrix and inclusions in the effective medium having yet-unknown properties (self-consistent embedding) and then apply the self-consistency condition that the ensemble average of the total scattering vanishes in the effective medium. The average total scattering field is approximated as the average of the single scattering fields of the inclusion and matrix weighted by their volume concentrations. The conditions for the effective medium (the effective density ρ_e and the effective shear modulus μ_e) of a two-dimensional composite medium are obtained,[16,27]

$$\sum_{p=1,2} v_p(\rho_e - \rho_p)\langle \Lambda_\rho^p \rangle_{\Omega_p} = 0, \tag{6}$$

$$\sum_{p=1,2} v_p(\mu_e - \mu_p) i\mathbf{k}_e \cdot \langle \mathbf{\Lambda}_\mu^p \rangle_{\Omega_p} = 0. \tag{7}$$

where Ω_p is the representative volume element of the pth kind of material, $\langle\ \rangle_{\Omega_p}$ denotes the volume average of a physical quantity over Ω_p, and

$$\langle \Lambda_\rho \rangle_{\Omega_p} = \frac{1}{\Omega_p} \int_{\Omega_p} u(\mathbf{r}) e^{-i\mathbf{k}_e \cdot \mathbf{r}} d\Omega, \tag{8}$$

$$\langle \mathbf{\Lambda}_\mu \rangle_{\Omega_p} = \frac{1}{\Omega_p} \int_{\Omega_p} \nabla u(\mathbf{r}) e^{-i\mathbf{k}_e \cdot \mathbf{r}} d\Omega. \tag{9}$$

Note that adding Eqs. (6) and (7) yields

$$\sum_{p=1,2} v_p \langle \bar{f}_p(0) \rangle_{\Omega_p} = 0, \tag{10}$$

where the overbar means that the forward scattering amplitudes are obtained in the effective medium. Equation (10) gives the physical notion that the effective medium in this theory is defined such that the average forward scattering amplitudes in the effective medium vanishes, that is, a medium in which there is no scattering of the mean field by the constituents, which fulfills the presumed self-consistency. This approach is analogous to the CPA in the solid-state physics,[28] and has been used also in the electromagnetic wave propagation problems.[29] Berge *et al.*[26] and Berryman[30] used a similar approach for quasistatic properties of three-dimensional composites. Note that Eqs. (6) and (7) are in the symmetric form, indicating that this model treats the matrix and the fibers equally and thus assumes implicitly a microstructure in which the roles of the matrix and the fibers are not distinguishable (an aggregate or granular structure[31]). Authors have criticized that the roles of the matrix and inclusions should be treated differently. Various aspects of this issue have been discussed.[27]

Another effective medium model is the scheme proposed by Kanaun and Levin.[14,32] In this scheme, the average field inside the inclusions is first estimated by solving the scattering problem for a single inclusion in the effective medium and then the inclusions having the average field are embedded in the original host medium and the scattered field by these inclusions is averaged. Finally, the self-consistent condition that the effective field is the plane wave propagating in the effective medium is applied to obtain the following equations for the effective shear modulus and density:

$$\rho_e = \rho_1 + v_2(\rho_2 - \rho_1)\langle \Lambda_\rho \rangle_{\Omega_2}, \tag{11}$$

$$\mu_e = \mu_1 - v_2(\mu_2 - \mu_1) i\mathbf{k}_e \cdot \langle \mathbf{\Lambda}_\mu \rangle_{\Omega_2} / k_e^2. \tag{12}$$

Note that this model is a dynamic generalization of the static self-consistent theory of Hill and Budiansky.[33] Kanaun and Levin also showed that these equations are reduced to the two-dimensional version of Sabina and Willis' self-consistent equations[15] under an appropriate approximation to the field inside the inclusion:

$$\rho_e = \rho_1 + v_2 h^2(k_e)(\rho_2 - \rho_1)[1 + \bar{M}_t(\rho_2 - \rho_e)]^{-1}, \tag{13}$$

$$\mu_e = \mu_1 + v_2 h^2(k_e)(\mu_2 - \mu_1)[1 + \bar{S}_x(\mu_2 - \mu_e)]^{-1}, \tag{14}$$

where $h(k_e) = 2J_1(k_e a)/k_e a$, $\bar{S}_x = i\pi H_1(k_e a) J_1(k_e a)/2\mu_e$, and $\bar{M}_t = (1 - i\pi H_1(k_e a) J_1(k_e a))/\rho_e$, which are the average of the effective wave over the inclusion and the average convolution operators,[16] respectively.

C. Dynamic generalized self-consistent model

A dynamic generalization of the generalized self-consistent model for the static effective properties[34] has been set out by Yang and Mal.[18] As in the static version, a concentric cylindrical fiber embedded in an infinite medium possessing unknown effective properties is considered. The ratio between two radii in the concentric cylinder is determined by the volume concentrations of constituents. The model uses the self-consistency that the incident wave propagating in the effective medium is equal to the effective wave field. This self-consistency is implemented in the dispersion relation of Waterman and Truell[6] [Eq. (1)],

$$\bar{f}(0) - \frac{in_o}{k_e^2}[\bar{f}^2(0) - \bar{f}^2(\pi)] = 0. \tag{15}$$

It has been shown[35] that this condition is equivalent to

$$\bar{f}(0) = 0, \tag{16}$$

which means that the forward scattering amplitude vanishes when the unknown surrounding medium has the effective properties. This condition is similar to Eq. (10) and is found in many other effective medium theories. With Eq. (16) and the effective static density $\rho_e = v_1\rho_1 + v_2\rho_2$, the effective wavenumber is calculated. This model has attracted significant attention for the success of its static counterpart.

D. Differential approach

Beltzer and Brauner[17] proposed an incremental realization of the effective medium concept in a way similar to the differential effective medium theory for the effective static moduli.[36] Since it is difficult to derive a set of differential equations for dynamic moduli and density, the method instead numerically implements the homogenization process.

TABLE I. Summary on the models.

Model	Assumption/microstructure	Abbreviation	Equation(s)	Symbol
Waterman and Truell	Point scatterers	WT2	(1)	Red dash dot
Lloyd and Berry	Point scatterers	LB2	(2)	Dash dot
Varadan, Varadan and Ma	QCA, isolated scatterers	VVM	(3)–(5)	Circle line
Kim	Aggregated (granular)	KM	(6) and (7)	Solid line
Kanaun and Levin	Aggregated (granular)	KL	(11) and (12)	Red solid line
Sabina and Willis	Constant fields in scatterers Aggregated (granular)	SW2	(13) and (14)	Blue dotted line
Yang and Mal	Isolated scatterers (three-phase model), constant density	YM	(16)	Blue dashed line
Beltzer and Brauner	Isolated scatterers	BB	(17) and (18)	Triangle-line

The attenuation is calculated from the single scattering by a newly added small amount of inclusions in the medium homogenized in the previous step:

$$\alpha(\nu_2 + \Delta\nu_2) = \alpha(\nu_2) + \frac{\Delta\nu_2}{2\Omega_2}\bar{\gamma}^{\text{ext}}, \tag{17}$$

where Δv_2 is the increment of volume concentration, Ω_2 is the volume of the single inclusion, and $\bar{\gamma}^{\text{ext}}$ is the extinction cross section of the fiber in the energy-absorbing medium.[37] The current step is completed by calculating the frequency-dependent wave speed using the Kramers–Kronig relation:[17]

$$\frac{1}{c(\omega)} - \frac{1}{c(0)} = \frac{2\omega^2}{\pi} P \int_0^\infty \frac{\alpha(\varpi)}{\varpi^2(\varpi^2 - \omega^2)} d\varpi, \tag{18}$$

where $c(0)$ is the wave speed at $\omega=0$ and the integral is a principal value integral. Note that since this model does not yield $c(0)$, one should specify it as an input parameter. In the numerical calculations, $c(0)$ is calculated with Hashin and Rosen's[38] effective shear modulus which corresponds to the lower bound. Note that the differential scheme assumes an isolated microstructure.[36]

Finally, it should be noted that all these theories are approximate and this fact may be one fundamental reason for discrepancies among them which are shown in Sec. III.

III. RESULTS AND DISCUSSION

Table I summarizes assumptions and microstructures, abbreviations, equations used in computations, and symbols in figures. Numerical calculations are performed for two-phase composites having much different combinations of constituent properties. The mechanical properties of constituent materials are listed in Table II and characteristics of the composites are in Table III. The effective wave speed and coherent wave attenuation are calculated for frequencies up to $k_1a=3.5$ and for volume concentrations up to 47%. While any of these theories has been proven to be applicable at a frequency above $k_1a=1$, there are many cases in which these theories successfully predict wave speeds and attenuations at high frequencies (e.g., Ref. 26). Therefore, it will be interesting to see how these models are compared in the high frequency region. In this study, the maximum frequency range is where the wavelength is comparable to the size (diameter) of the inclusions. At higher frequencies where the wavelength is much shorter than the size of scatters, the wave speed and attenuation reach their geometric optics limits that are constant values. The coherent dynamic response of composites at such high frequencies is negligible due to the high attenuation and thus is not experimentally measurable, thereby losing its practical meaning.

The directional scattering amplitude in Eqs. (1) and (2) is calculated $f(\theta)=2T_0+\Sigma_{m=1}^{\infty}T_m\cos(m\theta)$, and the effective wave speed and attenuation are obtained directly from the effective wave number. The determinant in Eq. (3) is truncated to a finite order (increasing with frequency) and the roots (the effective wave numbers) of the complex nonlinear equation are searched numerically. Equations (6) and (7) are a system of nonlinear equations for complex effective density and shear modulus. The multidimensional Newton–Raphson method is used to calculate these parameters. The same procedure is used for computations of Eqs. (11) and (12) and Eqs. (13) and (14). Equation (16) is solved using two dimensional (real and imaginary parts of k_e) Newton–Raphson method. Equations (17) and (18) are calculated incrementally with a small Δv_2. The extinction cross section is calculated using the method of Kim,[37] and then the integral is evaluated using the Simpson rule with a high frequency limit ($k_1a=20$) above which the integrand is assumed to be

TABLE II. Elastic properties of constituents.

Materials	Density (kg/m^3)	Shear modulus (GPa)	Phase velocity (m/s)
Aluminum	2720	38.7	3772
Steel	7800	80.9	3220
Graphite	1310	21.0	4004
Titanium	4510	41.4	3030
SiC (SCS-6)	3200	182.0	7542
Epoxy	1260	$1.98-0.06i$	1254

TABLE III. Characteristics of composites.

Composites	ρ_2/ρ_1	μ_2/μ_1	Remarks
Steel/aluminum	2.9	2.1	$\rho_2>\rho_1$, $\mu_2>\mu_1$
Graphite/aluminum	0.48	0.54	$\rho_2<\rho_1$, $\mu_2<\mu_1$
SiC/titanium	0.71	4.4	$\rho_2<\rho_1$, $\mu_2>\mu_1$
Graphite/epoxy[a]	1.04	10.6	$\rho_2\approx\rho_1$, $\mu_2\gg\mu_1$

[a]Real part of the shear modulus of epoxy is used.

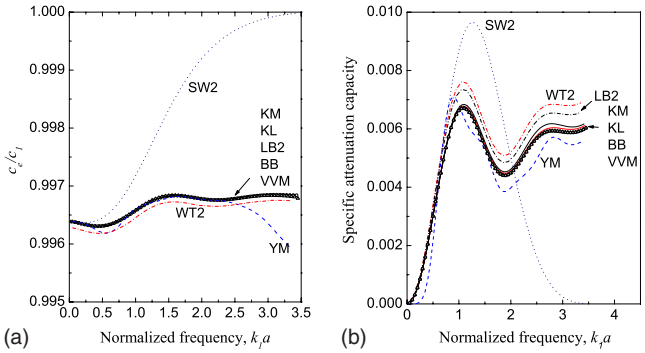

FIG. 1. (Color online) Effective wave speed (a) and coherent attenuation (b) for weak scattering.

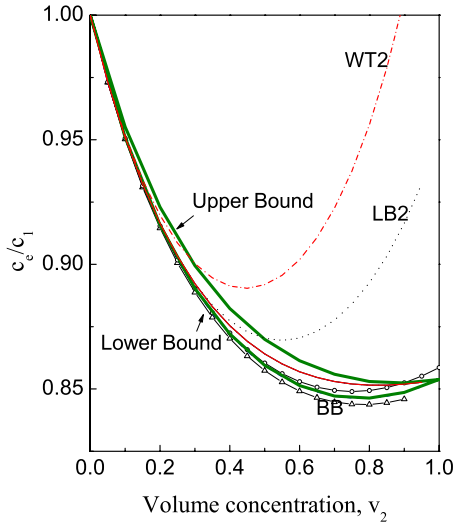

FIG. 2. (Color online) Upper and lower bounds of the effective wave speed in steel/aluminum composite compared with those from different models.

constant. All computations were validated by comparing with those numerical results presented in the original papers. The numerical calculations are performed within the accuracy of the double precision floating point.

A. Weak scattering

When the scattering of each fiber is weak and the fiber volume concentration is low, the multiple-scattering effect will be small. The condition for the weak scattering is that the properties of constituents are similar, that is, $\rho_2/\rho_1 \sim 1$ and $\mu_2/\mu_1 \sim 1$. Then, the total scattering field can be approximated as the sum of the single scattering field from every scatterer (the single scattering approximation). In this weak scattering limit, one may expect that all of these different multiple-scattering models would yield a single coincident result. This criterion will examine the soundness of fundamental assumptions in each model and the model's capability of predicting the multiple-scattering effect in more complicated cases. A model which is incapable of correctly predicting this weak multiple-scattering effect would not predict correctly or even approximately a stronger multiple-scattering effect. Therefore, the weak scattering problem can be a good benchmark problem.

Figure 1 shows the normalized wave speeds (c_e/c_1) and the normalized attenuation coefficients (the specific attenuation capacity, $4\pi\,\mathrm{Im}[k_e]/\mathrm{Re}[k_e]$) versus the normalized frequency (k_1a), predicted by the different models. The material properties are assumed $\rho_2/\rho_1=1.2$ and $\mu_2/\mu_1=1.1$ and the fiber volume concentration is 0.07. The wave speeds from five models coincide strikingly well [Fig. 1(a)]—a definitive indication that this coincident wave speed is the true effective wave speed at least for this weak scattering case and for this particular composite. The SW2, YM, and WT2 models visibly deviate from the true wave speed. These models may attribute their failures to different causes. The SW2 model assumes a constant field inside the scatterer, which makes the effective wave speed to approach the wave speed in the matrix and the attenuation to vanish ($c_e \to c_1$ and $\mathrm{Im}[k_e] \to 0$). As pointed out earlier by Lloyd and Berry[12] and readdressed recently by Linton and Martin,[19] the second-order terms in the dispersion relation of WT2 model is incorrect, which would lead to this inaccuracy. This fact implies an important conclusion that a model that is built based on the Waterman and Truell model will suffer from the same problem either in an explicit or implicit manner. The three-phase geometry in the YM model introduces excessive fluctuations in the dispersion curve and also in the attenuation shown below as the result of spurious wave motions in the annulus that represents the matrix phase (the structure effect), which obviously disappears in the static limit where wavelength is greater than any of the geometric parameters.

Figure 1(b) shows that four models predict very close attenuations, even though the agreement is not as good as in the wave speed. Consistently as in the wave speed, the SW2, YM, and WT2 models show attenuations more or less different from the attenuation agreed by the other four. The attenuation by the LB2 model is closer to the agreed one, demonstrating that the model is correct under the assumption of uncorrelated scatterers.

B. Wave speed in long wavelength limit

Figure 2 shows the wave speeds in a steel/aluminum composite in the low frequency limit ($k_1a=0.05$), predicted by different models. The thick lines are the upper and lower bounds of the effective wave speed. These are calculated with the average static density $\rho_e=\rho_1(1-v_2)+\rho_2 v_2$ and the variational bounds for the axial shear modulus of Hashin.[38] While the bound solution is not unique, Hashin's variational bounds are tight and have a clear physical meaning. The interpretation of these bounds is closely related to the role of constituents: when a stiffer phase forms a more continuous phase, the effective stiffness will be close to the upper bound, and vice versa. While the assembly of impenetrable circular disks has its full packing limit at the volume concentration 0.785, numerical calculations are shown up to 1. It is interesting to note that the models for point scatters (WT2 and LB2) may be used to predict the wave speed at a high volume concentration, for example, up to 0.5 for LB2. In other words, the size and shape (e.g., noncircularity) of scatterers are unimportant for the volume concentration below 0.5 in the quasistatic limit. All other models for finite-sized scatterer fall in the upper and lower bounds. The YM, BB,

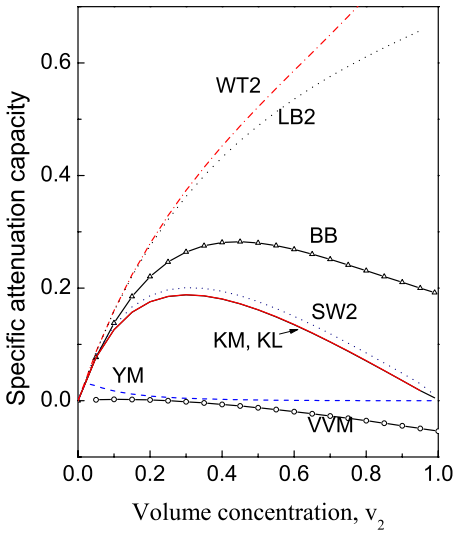

FIG. 3. (Color online) Low frequency attenuation versus the fiber volume fraction for steel/aluminum composite predicted with different models.

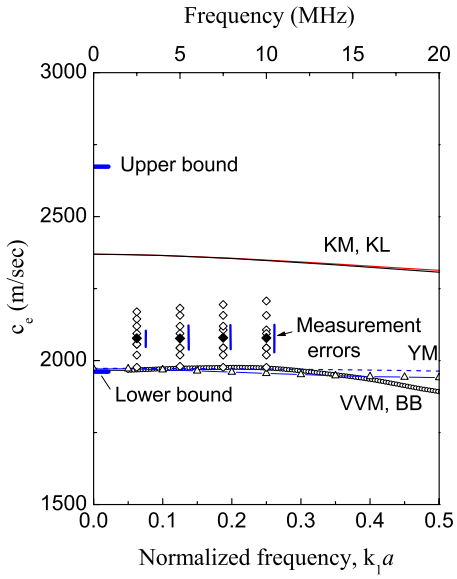

FIG. 4. (Color online) Effective wave speeds from an experiment and the models for graphite/epoxy composite with a fiber volume fraction 52%. Open rhombuses are the measurement results for seven points and the solid one is the average of all 28 measurements. Bars next to rhombuses represent the ranges of experimental errors.

and VVM models predict the wave speed coincident with the lower bound, while wave speeds by the effective medium models (KM and KL) are close to the lower bound at low volume concentrations and to the upper bound at higher volume concentrations. The small departure of the BB model at high volume concentrations is possibly due to numerical errors (the volume increment may have been coarse).

C. Low frequency attenuation

Figure 3 shows the attenuation in the steel/aluminum composite versus the volume concentration calculated at frequency $k_1a=0.2$. Many interesting facts are observed.

At this frequency, the wavelength is about 15 times larger than the diameter of scatterers. So, the propagating wave interacts with a few scatterers at the same time and sees the average response of the matrix-scatterer assemblage. In this low frequency range, the coherent attenuation of propagating waves will be simply proportional to the degree of disorder or the spatial randomness. In view of the microstructure of a two-phase mixture, the spatial fluctuation in material properties will be maximum at a volume concentration around $v_2=0.5$, where the attenuation is accordingly expected to be maximum. Another consequence is the endpoint constraint that the coherent attenuation should vanish at $v_2=0$ and 1.0 where no macroscopic randomness exists. It is seen that only the effective medium models (SW2, KM, and KL) satisfy this constraint. The iterative homogenization process of building up the effective properties in the BB model does not exactly satisfy the constraint at $v_2=1.0$.

The VVM model predicts negative attenuations in the entire range of frequency, violating the passivity requirement—the material as a passive linear system. This is a quite surprising result since it is expected[7] that QCA would give the same level of accuracy as CPA (the effective medium model). Moreover, the exact PCF is used to overcome this defect in the model without the exact one. The YM model produces small attenuation that decreases with volume concentration. This is the result of the geometric requirement for constructing the three-phase-model (again the structure effect). The outer radius of the concentric circle is determined by $v_1=(r_2/r_1)^2$. For a given size of the fiber (r_2), r_1 should decrease with the increase in volume concentration. Since the scattered power in the low frequency region is proportional to the fourth power of the scatterer size, the model predicts more incident power scatters at a low volume concentration than at a higher volume concentration. The SW2, WT2, and LB2 models will not be further examined hereafter.

D. Effects of microstructure

Figure 4 shows calculated and measured wave speeds in a unidirectional graphite/epoxy composite with a fiber volume concentration 53% and a fiber diameter 6 μm. For conducting ultrasonic measurements at different frequencies (2.5, 5.0, 7.5, and 10 MHz), composite plates with various thicknesses (2.5–8 mm) were prepared. The pulse-echo method using a single narrow band shear wave contact transducer with a radius of 3.2 mm was employed in which axially polarized shear wave pulses propagate in the direction perpendicular to the fiber axis. Both the pulse overlap[39] and phase spectrum[40] techniques were used to accurately determine the wave speed from measured ultrasonic signals.

Microscopic study revealed that the arrangement of fibers varied from one location to the other. Among numerously different fiber arrangements, three distinctive were observed: First, most of fibers are isolated each other [Fig. 5(a)]; second, fibers are locally agglomerated forming several clusters of fibers [Fig. 5(b)]; third, the fibers are in contact, forming long chains and some chains are bridging across the sample thickness [Fig. 5(c)]. To study the effects of the microstructure on the wave speed, the measurements were performed at 28 different locations on the same plate

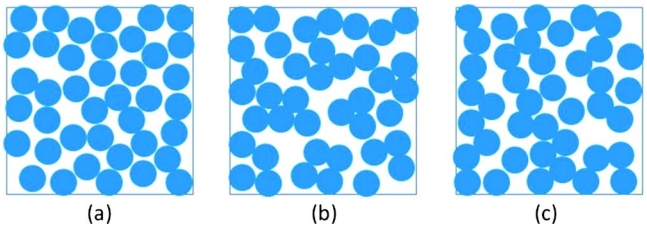

FIG. 5. (Color online) Schematics of three distinctive microstructures: isolated microstructure (a), locally agglomerated microstructure (b), and aggregate (granular) microstructure (c).

and repeated about ten times at each location. The measured wave speeds were then averaged. Note that no data were discarded or selected as they were apart from or close to predetermined theoretical results.

In Fig. 4, open rhombuses are the wave speeds for seven representative locations (out of 28). Note that each open rhombus represents an average of ten wave speeds for one location and also that all 28 wave speeds fall in the range covered by the seven; only seven are shown for a better presentation. The absolute measurement error range for each frequency (and plate thickness) is calculated by averaging error ranges of all 28 locations and is indicated in Fig. 4 with a vertical bar next to the solid rhombus that represents the average of 28 wave speeds. It is seen that the variability range of the wave speed about 200 m/s is not from the measurement error, which is about 100 m/s, but it is thought to be due to the local variation in the microstructure. Calculated lower (1961 m/s) and upper (2673 m/s) bound wave speeds are also shown. As mentioned earlier, the VVM and YM models predict the lower bound while the effective medium models (KM and KL) predict a wave speed in the middle between the lower and upper bounds. In general, the measured wave speeds are closer to the lower bound, indicating that fibers in these composite samples are mostly isolated in the matrix. At the location where the wave speed is high, fibers are possibly more in contact with each other so that they form many channels of fiber clusters along the wave propagation direction [Fig. 5(c)]. A direct comparison between the ultrasonic result and the microstructure analysis was quite difficult because the ultrasonic waves cover a finite area while microscopy can be done for only few cross sections in that area. However, a few good correlations were observed that the wave speed is faster in the section with more contacting fibers. This is somewhat analogous to the critical phenomenon of the insulator-conductor transition in electrical properties of this composite,[41] while the transition in the elastic property is very small. This experimental result demonstrates that the overall properties of a composite are sensitive to the microstructural arrangement of constituents. Therefore, a blind comparison between experimental and theoretical results ignoring the composite's microstructure can lead to a meaningless conclusion. Berge *et al.*[26] showed that the self-consistent theory (effective medium model) best predicts the ultrasonic speeds in the artificial sandstone samples. They interpreted that the assumed microstructure in the self-consistent theory is compatible with the actual microstructure of the sample materials.

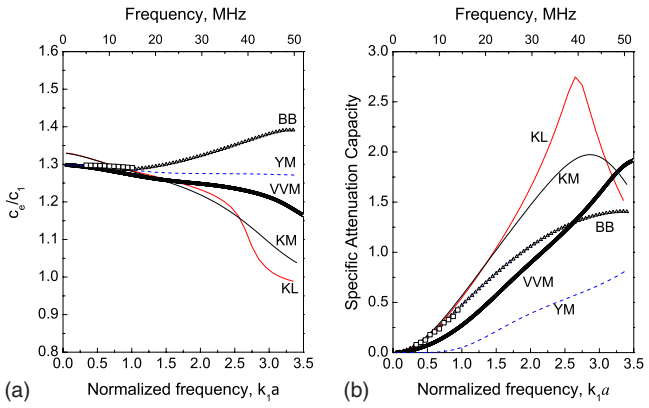

FIG. 6. (Color online) Effective wave speed (a) and coherent attenuation (b) versus frequency for SiC/titanium composite for v_2=0.33. Open squares are experimental data.

E. Behaviors at finite frequencies and high volume concentrations

Four composites having different combinations of constituent materials (see Table III) are used in the numerical calculations. In Fig. 6, the wave speed and attenuation calculated for a SiC/Ti composite having a fiber volume concentration 0.33 are plotted together with experimental data (open squares) in 5–15 MHz (k_1a=0.35–1.05). The experimental wave speed in this frequency range is nearly constant (3924 m/s). This is close to the lower bound static wave speed as a result that fibers in this composite are well isolated each other (see, for example, the micrograph in Ref. 42). So, the YM, BB, and VVM models predict wave speeds close to the experimental results, while the effective medium models (KM and KL) are not suitable to this microstructure. The attenuation from the experiment agrees well with the BB model. The numerical predictions exhibit increasing discrepancies among the models with the increase in frequency ($k_1a>1$), possibly due to the different microstructures assumed in these models. Very similar trends both in the wave speed and attenuation were seen in the computation results for a graphite/epoxy composite with a volume concentration 0.3, which are not presented here.

Figure 7 shows the numerical results for a steel/aluminum composite having a fiber volume concentration of 0.27. A qualitative agreement both in the wave speed and attenuation is seen with an exception that the YM model

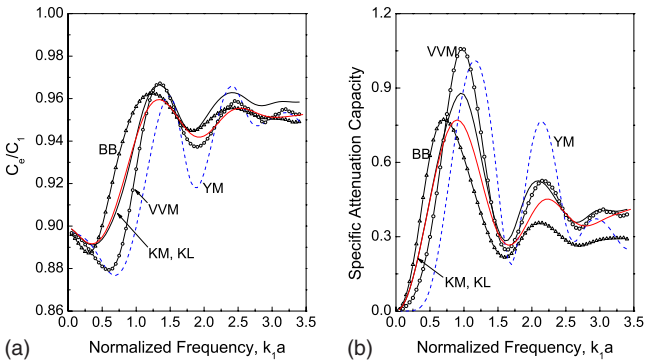

FIG. 7. (Color online) Effective wave speed (a) and coherent attenuation (b) versus frequency for steel/aluminum composite for v_2=0.27.

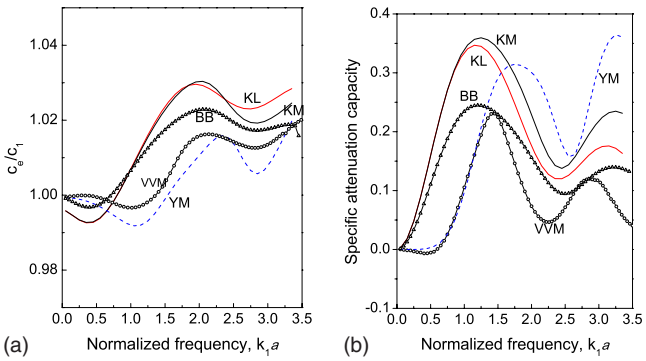

FIG. 8. (Color online) Effective wave speed (a) and coherent attenuation (b) versus frequency for graphite/aluminum composite for $v_2=0.47$.

exhibits excessive undulation. The wave speed and attenuation in this composite converge quickly to their geometric optics limits after the wave speed rises rapidly and the attenuation reaches a peak at the low frequency where the rigid-body resonance of particles occurs. This is a common characteristic of composites with heavy inclusions,[26,43] which determines the shape of the dispersion and attenuation. It is thought that the relative good agreement comes from this strong characteristic of the single fiber scattering that dominates over the multiple-scattering effect at this volume concentration.

The wave speed and attenuation in a graphite/aluminum composite having a fiber volume concentration of 0.47 are shown in Fig. 8. This material exhibits a weak dispersion and oscillatory attenuation. Near zero (YM model) and negative (VVM model) attenuations are seen in $k_1a<0.75$.

IV. CONCLUSIONS

Many interesting facts are found in this study. First of all, the results for the weak scattering critically compare the soundness of fundamental assumptions in the models considered. Whenever the point scattering approximation is relevant, the LT2 model is more accurate than the WT2 model. This needs to be emphasized because many authors take the WT2 model as a reference for validating their results and also attempt to extend the model to more general cases. The layered three-phase geometry in the YM model produces undesirable structure effects in the finite frequency regime. The approximate consideration of the double scattering through the QCA using the exact PCF appears to be not accurate enough when the constituent densities differ by more than two times. The two effective medium models (KM and KL), possibly due to the common hypothesis and the similar self-consistency condition, predict values close to each other, and do not exhibit an apparent failure in all cases considered. The assumed granular microstructure enables these models to adapt to geometrically more complex microstructures such as clustered fibers and aggregated mixture of phases. Since the overall properties are sensitive to the composite's microstructure, the microstructure should first be investigated before choosing a model for comparing experimental results. In all cases considered, the disagreement in attenuation is more pronounced than in wave speed. Recalling that the attenuation is more sensitive to the composite's microstructure, the disagreements should be, to a large degree, due to the different microstructures assumed in these different models. While the subject of the wave propagation in inhomogeneous media has long been investigated, the present evaluation study reveals numerous fundamental questions to be answered. The indirect method such as the effective medium theory might be a choice for further studies on this subject.[1]

[1] P. A. Martin, *Multiple Scattering: Interaction of Time-Harmonic Waves with N Obstacles* (Cambridge University Press, Cambridge, 2006).
[2] A. Ishimaru, *Wave Propagation and Scattering in Random Media* (Academic, New York, 1978).
[3] L. Tsang, J. A. Kong, K.-H. Ding, and C.-O. Ao, *Scattering of Electromagnetic Waves* (Wiley, New York, 2001).
[4] L. L. Foldy, "The multiple scattering of waves," Phys. Rev. **67**, 107–119 (1945).
[5] M. Lax, "The effective field in dense systems," Phys. Rev. **85**, 621–629 (1952).
[6] P. C. Waterman and R. Truell, "Multiple scattering of waves," J. Math. Phys. **2**, 512–537 (1961).
[7] G. M. Romack and R. L. Weaver, "Monte Carlo studies of multiple scattering of waves in one-dimensional random media," J. Acoust. Soc. Am. **87**, 487–494 (1990); "Monte Carlo studies of multiple scattering of waves in two-dimensional random media," J. Acoust. Soc. Am. **94**, 506–513 (1993).
[8] L. M. Zurk, L. Tsang, K. H. Ding, and D. P. Winebrenner, "Monte Carlo simulations of the extinction rate of densely packed spheres with clustered and nonclustered geometries," J. Opt. Soc. Am. A **12**, 1772–1778 (1995); L. Tsang, C. E. Mandt, and K. H. Ding, "Monte Carlo simulations of the extinction rate of dense media with randomly distributed dielectric spheres based on solution of Maxwell's equation," Opt. Lett. **17**, 314–316 (1992).
[9] S. Biwa, S. Yamamoto, F. Kobayashi, and N. Ohno, "Computational multiple scattering analysis for shear wave propagation in unidirectional composites," Int. J. Solids Struct. **41**, 435–457 (2004).
[10] L. W. Anson and R. C. Chivers, "Ultrasonic velocity in suspensions of solid in solids—A comparison of theory and experiment," J. Phys. D **26**, 1566–1575 (1993).
[11] J. G. Berryman, "Single-scattering approximations for coefficients in Biot's equations of poroelasticity," J. Acoust. Soc. Am. **91**, 551–571 (1992).
[12] P. Lloyd and M. V. Berry, "Wave propagation through an assembly of spheres. IV. Relations between different multiple-scattering theories," Proc. Phys. Soc. **91**, 678–688 (1967).
[13] V. K. Varadan, V. V. Varadan, and Y. Ma, "Multiple scattering of elastic waves by cylinders of arbitrary cross section. II. Pair-correlated cylinders," J. Acoust. Soc. Am. **78**, 1874–1878 (1985).
[14] S. K. Kanaun and V. M. Levin, "Effective medium method in the problem of axial elastic shear wave propagation through fiber composites," Int. J. Solids Struct. **40**, 4859–4878 (2003).
[15] F. J. Sabina and J. R. Willis, "A simple self-consistent analysis of wave propagation in particulate composites," Wave Motion **10**, 127–142 (1988).
[16] J.-Y. Kim, "Dynamic self-consistent analysis for elastic wave propagation in fiber reinforced composites," J. Acoust. Soc. Am. **100**, 2002–2010 (1996).
[17] A. I. Beltzer and N. Brauner, "The effective dynamic response of random composites by a causal differential method," Mech. Mater. **6**, 337–345 (1987).
[18] R.-B. Yang and A. K. Mal, "Multiple scattering of elastic waves in a fiber-reinforced composite," J. Mech. Phys. Solids **42**, 1945–1968 (1994).
[19] C. M. Linton and P. A. Martin, "Multiple scattering by random configurations of circular cylinders: Second-order corrections for the effective wavenumber," J. Acoust. Soc. Am. **117**, 3413–3423 (2005); C. M. Linton and P. A. Martin, "Multiple scattering by multiple spheres: A new proof of the Lloyd-Berry formula for the effective wavenumber," SIAM J. Appl. Math. **66**, 1649–1668 (2006).
[20] J. G. Fikioris and P. C. Waterman, "Multiple scattering of waves. II. Hole corrections in the scalar case," J. Math. Phys. **5**, 1413–1420 (1964).
[21] S. K. Bose and A. K. Mal, "Longitudinal shear waves in a fiber-reinforced composite," Int. J. Solids Struct. **9**, 1075–1085 (1973).
[22] D. Chandler, *Introduction to Modern Statistical Mechanics* (Oxford University Press, New York, 1987).
[23] J.-Y. Kim, J.-G. Ih, and B.-H. Lee, "Dispersive wave propagation in the viscoelastic matrix reinforced by elastic fibers," J. Acoust. Soc. Am. **95**,

1213–1222 (1994).
[24]J.-Y. Kim, J.-G. Ih, and B.-H. Lee, "Dispersion of elastic waves in random particulate composites," J. Acoust. Soc. Am. **97**, 1380–1388 (1995).
[25]T. C. Choy, *Effective Medium Theory: Principles and Applications* (Oxford University Press, New York, 2000).
[26]P. A. Berge, B. P. Bonner, and J. G. Berryman, "Ultrasonic velocity-porosity relationships for sandstone analogs made from fused glass beads," Geophysics **60**, 108–119 (1995); P. A. Berge, J. G. Berryman, and B. P. Bonner, "Influence of microstructure on rock elastic properties," Geophys. Res. Lett. **20**, 2619–2622 (1993).
[27]J.-Y. Kim, "Effective medium theories for two-dimensional random composites," J. Mech. Mater. Struct. In press (2010).
[28]P. Soven, "Coherent-potential model of substitutional disordered alloys," Phys. Rev. **156**, 809–813 (1965); B. Velický, S. Kirkpatrick, and H. Ehrenreich, "Single-site approximations in the electronic theory of simple binary alloys," *ibid.* **175**, 747–766 (1968).
[29]G. A. Niklasson, C. G. Granqvist, and O. Hunderi, "Effective medium models for the optical properties of inhomogeneous materials," Appl. Opt. **20**, 26–30 (1981); D. Stroud and F. P. Pan, "Self-consistent approach to electromagnetic wave propagation in composite media: Application to model granular metals," Phys. Rev. B **17**, 1602–1610 (1978).
[30]J. G. Berryman, "Theory of elastic properties of composite materials," Appl. Phys. Lett. **35**, 856–858 (1979); "Long-wavelength propagation in composite elastic media I. Spherical inclusions," J. Acoust. Soc. Am. **68**, 1809–1819 (1980).
[31]F. Yonezawa and M. H. Cohen, "Granular effective medium approximation," J. Appl. Phys. **54**, 2895–2899 (1983); G. W. Milton, "The coherent potential approximation is a realizable effective medium scheme," Commun. Math. Phys. **99**, 463–500 (1985).
[32]S. K. Kanaun, V. M. Levin, and F. J. Sabina, "Propagation of elastic waves in composites with random set of spherical inclusions (effective medium approach)," Wave Motion **40**, 69–88 (2004).
[33]R. Hill, "A self-consistent mechanics of composite materials," J. Mech. Phys. Solids **13**, 213–222 (1965); B. Budiansky, "On the elastic moduli of some heterogeneous materials," *ibid.* **13**, 223–227 (1965).
[34]R. M. Christensen and K. H. Lo, "Solutions for effective shear properties in three phase sphere and cylinder models," J. Mech. Phys. Solids **27**, 315–330 (1979).
[35]J.-Y. Kim, "On the generalized self-consistent model for elastic wave propagation in composite materials," Int. J. Solids Struct. **41**, 4349–4360 (2004).
[36]A. N. Norris, "A differential scheme for the effective moduli of composites," Mech. Mater. **4**, 1–16 (1985); M. Avellaneda, "Iterative homogenization, differential effective medium theory and applications," Commun. Pure Appl. Math. **40**, 527–554 (1987).
[37]J.-Y. Kim, "Extinction of elastic wave energy due to scattering in a viscoelastic medium," Int. J. Solids Struct. **40**, 4319–4329 (2003); J.-Y. Kim, "Extinction and propagation of elastic waves in inhomogeneous materials," Mech. Mater. **35**, 877–884 (2003).
[38]Z. Hashin, "Theory of fiber reinforced materials," NASA Report No. CR-1974, National Aeronautics and Space Administration, Washington, DC, 1974.
[39]H. L. McSkimin, "Pulse superposition method for measuring ultrasonic velocity in solids," J. Acoust. Soc. Am. **33**, 12–23 (1961).
[40]W. Sachse and Y.-H. Pao, "On the determination of phase and group velocities of dispersive waves in solids," J. Appl. Phys. **49**, 4320–4327 (1978).
[41]B. E. Springett, "Effective medium theory for the ac behavior of random system," Phys. Rev. Lett. **31**, 1463–1465 (1973).
[42]W. Huang and S. I. Rokhlin, "Frequency dependences of ultrasonic wave velocity and attenuation in fiber composites. Theory and Experiments," in *Review of Progress in Quantitative Nondestructive Evaluation*, edited by D. O. Thompson and D. E. Chimenti (Plenum, New York, 1995), Vol. **14**. pp. 1233–1240.
[43]F. C. Moon and C. C. Mow, "Wave propagation in a composite material containing dispersed rigid spherical inclusions," Rand Corp. Report No. RM-6139-PR, Rand Corporation, Santa Monica, CA, 1979.

Phase and group velocity measurement of ultrasonic guided wavetrains in plates by pulsed TV holography

X. Luís Deán-Ben, Cristina Trillo, Ángel F. Doval, and José L. Fernández
Departamento de Física Aplicada, Universidade de Vigo, E. T. S. Enxeñeiros Industriais, Campus Universitario, E36310 Vigo, Spain

(Received 29 September 2009; revised 22 January 2010; accepted 26 January 2010)

A method for the measurement of the phase and group velocities of guided acoustic waves is presented. For this purpose, a unique capability of a self-developed double-pulsed TV holography system to create movies of the propagation of guided acoustic wavetrains is used. Thereby, the experimental visualization of the evolution of Lamb and Rayleigh wavetrains in aluminum plates is shown, including several movies that illustrate different dispersive behaviors. Each movie shows the propagation of a narrowband wavetrain with a central frequency in the order of 1 MHz that consists of a carrier moving with the phase velocity, modulated by an envelope moving with the group velocity. Each snapshot is a two-dimensional map of the instantaneous out-of-plane displacement field of the surface points of the plate, with amplitudes in the order of several nanometers, acquired with the double-pulsed TV holography system. Then, by repeating the acquisition with successively increasing delays between the generation and detection instants, a sequence of maps is obtained from which a movie is composed. The phase and group velocities of the waves are accurately measured from the movies, yielding values that match well with the reference values for the same plates obtained from independent measurements.
 [DOI: 10.1121/1.3327795]

PACS number(s): 43.35.Cg, 43.35.Pt, 43.35.Sx [TDM] Pages: 2210–2219

I. INTRODUCTION

The behavior of waves propagating in dispersive media has been extensively studied.[1] Under time-harmonic variation, the wave has neither beginning nor end, and so the propagation velocity of the motion can only be associated with the phase velocity, i.e., the velocity of a point that successively occupies positions of a given value of the phase. In practice, the phase velocity at a given frequency f corresponds approximately to the velocity of the carrier wave of a finite-length narrowband wavetrain having such central frequency and modulated in amplitude by a certain envelope. Nevertheless, the movement of the envelope cannot be described with the phase velocity but with the group velocity instead, which is associated with the propagation of energy in conservative media.[2] In non-dispersive waves, the phase velocity is the same, regardless of the frequency, and phase and group velocities are equal, so the envelope and the carrier inside it move at the same speed. On the contrary, in dispersive waves, the carrier moves faster or slower than the envelope.

Lamb waves are a well-known kind of dispersive acoustic waves that propagate in plates with stress-free boundaries.[3] They are multimode in nature and the phase and group velocities of each mode depend, for a given frequency, on the elastic constants of the plate material, so that the measurement of these velocities can be a useful means to determine such elastic properties.[4] On the other hand, Rayleigh waves correspond to guided acoustic waves in the surface of plates with infinite depth, and can be regarded as a specific kind of Lamb waves.

Many techniques have been reported for the measurement of the phase and group velocities of Lamb waves as a function of frequency. The usual procedure is based on the recording of the time evolution of the wave at different points of the plate surface by means of a point-wise method (piezoelectric transducer, electromagnetic acoustic transducer, point-wise interferometer, etc.). Thereby, if the distance between the measurement points is known, the group velocity c_g of a single mode can easily be measured from the time-of-flight of the wavetrain.[5] Even if the wave consists of several modes, it is possible to perform the measurement, provided that the distance traveled by the wavetrain is long enough to prevent the overlapping of the peaks corresponding to the different modes in the envelope of the signal.[6] A good accuracy in the measurement of the time-of-flight is also obtained by using frequency-chirped sources and applying correlation techniques to the signal.[7,8] Another commonly employed procedure is based on the use of time-frequency distributions for the measurement points,[9] which yield the frequency content of the signal as a function of time, in a way that the arrival time of the wavetrain for a given mode and frequency is determined from the corresponding peak in the distribution. Examples of time-frequency distributions that have been utilized for this purpose are the wavelet transform,[10] the short-time Fourier transform,[11] and a variant of the Wigner distribution.[12]

The phase velocity c_p can be determined by analyzing the variation in the phase with respect to the propagating distance. However, from a point-wise measurement, the phase can only be calculated modulo 2π, so, in order to calculate the actual phase difference between two points, the number of wavelengths in between must be either known or

determined by using an alternative method. To avoid this problem, the distance between the measuring points is typically chosen to be less than half the wavelength of the Lamb mode for the frequency of interest. The phase of each spectral component of a broadband wavetrain at a certain surface point is usually calculated from the Fourier transform of the temporal signal.[13,14] On the other hand, when dealing with narrowband signals, although using Fourier transforming is also valid, the phase difference between two points can also be measured by tracking the position of a certain point of the signal (e.g., a zero-cross point)[5] or by cross-correlating the signals at different locations.[15] Another procedure that is commonly employed to calculate phase velocities is based on the calculation of the frequency spectrum of the wave, i.e., a representation of the circular frequency ω as a function of the wavenumber k_1. For this purpose, the time evolution of the wavetrain is recorded at several points, separated by a small distance, and the spectrum is calculated by the two-dimensional (2D) Fourier transform of this spatio-temporal data set.[16,17] The measurement of the wavelength λ_1 of narrowband waves is another option to determine the phase velocity, as it is well-known that $c_p=\lambda_1 f$. The value of the wavelength can be precisely obtained from the 2D surface displacements maps yielded by full-field techniques,[4,18] although it is also possible to use a set of point-wise measurements in the case of standing waves.[19,20] Other methods exist to measure the phase velocity of guided acoustic waves. They range from acoustic microscopy techniques[21,22] to the study of the diffraction patterns yielded by the scattered light reflected from the plate surface[23] or by the light that traverses a liquid load medium, in which a leaky Lamb wave radiates energy.[24] Finally, a different approach consists in measuring the central frequency of the wavetrain when the phase velocity is known, due to constraints imposed by the acoustic source.[25,26]

It is important to take into account that phase and group velocities are not uncorrelated, but each one depends on the variations of the other with respect to frequency. If we represent ω as a function of k_1, the phase velocity is calculated as $c_p=\omega/k_1$, and the group velocity as $c_g=d\omega/dk_1$. Therefore, the group velocity can be calculated from the phase velocity,[27] provided that the spectrum is known, and it is also possible to calculate the phase velocity from the group velocity, but integration is required, and hence, the knowledge of the integration constant, that is, the phase velocity at a certain frequency must be determined by other means.[8]

The availability of a self-developed double-pulsed TV holography (TVH) system, which is capable to measure the time history of the wave-induced surface displacement field with high resolution,[28] allows to perform a different approach to measure the phase and group velocities of guided acoustic wavetrains in plates. A movie corresponding to the propagation of a Rayleigh or Lamb wavetrain is composed from a sequence of 2D maps of the instantaneous out-of-plane acoustic displacement field, obtained with our TVH system under repeatability conditions. The amplitude of these wavetrains is in the order of a few nanometers, and their frequency is in the order of 1 MHz. As we restricted the experiments to narrowband wavetrains, their propagation can be described in terms of a carrier wave, modulated by an envelope that does not change in shape. Then, the measurement of the group and phase velocities is performed by tracking the positions of the envelope peak and of a point with constant phase, respectively, in the sequence of maps. Although the principle of operation is well-known and quite direct, the small displacement amplitudes and high frequencies of the ultrasonic waves under study impose serious difficulties to obtain instantaneous displacement fields, so the presented snapshots and videos provide material of potential interest for the Acoustics community. On the other hand, this procedure presents several advantages that are discussed in the last two sections of the paper. It is well-known that Lamb waves present different dispersion behaviors, depending on mode and frequency, i.e., the phase velocity can be equal, larger, or smaller than the group velocity. In order to exhibit these three cases, several wavetrains (corresponding to two Lamb modes and to a Rayleigh wave) were measured in aluminum plates with different thicknesses.

II. DISPERSION OF LAMB WAVES

Lamb waves arise in plates having stress-free boundaries as a consequence of the superposition of longitudinal and vertically polarized shear waves successively reflected in the boundaries. There exist infinite dispersive modes, so that a Lamb wave with time-harmonic variation induces a distribution of stress and strain that depends on mode and frequency, according to a wave equation. For example, the out-of-plane displacement field of the surface points, due to a single-mode time-harmonic Lamb wave propagating along the direction x_1, is given by

$$u_3(x_1,t) = \mathrm{Re}[\hat{u}_3(x_1,t)] = \mathrm{Re}\{\hat{u}_{30}\exp[j(k_{10}x_1 - \omega_0 t)]\}, \quad (1)$$

where $\hat{u}_{30}$ is a complex constant, k_{10} is the wavenumber, and $\omega_0=2\pi f_0$ is the circular frequency. The relation between frequency and wavenumber in an isotropic plate of thickness $2h$ stems from the elasticity equations considering time-harmonic dependence and the constraints imposed by the plate. It is well-known that, for isotropic materials, Lamb waves can be classified into two different types, namely, symmetric and antisymmetric modes, depending on the distribution of the particle motion with respect to the mean plane of the plate. The condition that a symmetric (S) or antisymmetric (A) Lamb mode must fulfill is given in Eq. (2) in adimensional form[29]

$$F_A^S = \frac{\tan[(\pi/2)\sqrt{\gamma^2\chi^2-\xi^2}]}{\tan[(\pi/2)\sqrt{\gamma^2-\xi^2}]} + \left[\frac{4\xi^2\sqrt{\gamma^2\chi^2-\xi^2}\sqrt{\gamma^2-\xi^2}}{(2\xi^2-\gamma^2\chi^2)^2}\right]^{\pm 1} = 0, \quad (2)$$

where $\xi=2hk_1/\pi$ is the normalized wavenumber, $\gamma=2h\omega/\pi c_L$ is the normalized frequency, and $\chi=c_L/c_T$ is the velocity ratio. These constants are given as a function of the wavenumber k_1, the circular frequency ω, and the phase velocities of the longitudinal and shear waves inside the plate material (c_L and c_T, respectively).

If, instead of a monochromatic wave, there is a wavetrain with an arbitrary number of cycles, it is useful to consider the temporal spectrum of the excitation signal, and so, recalling the principle of superposition valid for linear Elasticity, the wavetrain is determined by[29]

$$\hat{u}_3(x_1,t) = \frac{1}{\sqrt{2\pi}}\int_{-\infty}^{+\infty} \tilde{\hat{u}}_{30}(\omega)\exp\{j[k_1(\omega)x_1 - \omega t]\}d\omega, \quad (3)$$

where $\tilde{\hat{u}}_{30}(\omega)$ is the amplitude spectral density calculated as the Fourier transform of $\hat{u}_3(x_1,t)$ at $x_1=0$, and the relation $k_1(\omega)$ between wavenumber and circular frequency stems from the nature of the wave. When the burst is narrowband, a proper description of its temporal evolution can be done by means of the product of an envelope and a carrier that oscillates at a central frequency. The shape of the envelope depends, of course, on the wave generator characteristics. In our case (bursts a few cycles long), as we will see in Sec. IV, a good approximation is a Gaussian curve so that the complex out-of-plane displacement at $x_1=0$ is given by

$$\hat{u}_3(0,t) \equiv \hat{u}_{30}(t) = u_{30}\exp\left(\frac{-t^2}{2\tau^2}\right)\exp(-j\omega_0 t), \quad (4)$$

where u_{30} is a constant, ω_0 is the carrier circular frequency, and τ is related to the length of the burst. The frequency spectrum of this function is

$$\tilde{\hat{u}}_{30}(\omega) = u_{30}\tau\exp\left[-\frac{(\omega-\omega_0)^2\tau^2}{2}\right]. \quad (5)$$

Therefore, provided that the relation between the wavenumber and the circular frequency is known, the spatio-temporal evolution of this Gaussian wavetrain can be evaluated. Such relation is calculated numerically from Eq. (2) and cannot be analytically expressed, but an approximation of the curve $k_1(\omega)$ by a Taylor polynomial around the carrier frequency is done. A first order approximation suffices in our case since the bandwidth of the wavegroups is rather narrow, and the second derivative of the curves $k_1(\omega)$ is small for all the frequencies and modes, i.e., we neglect the group velocity dispersion (GVD)

$$k_1(\omega) \approx k_{10} + (\omega-\omega_0)k'_{10}, \quad (6)$$

where $k_{10}=k_1(\omega_0)$ and $k'_{10}=dk_1/d\omega|_{\omega_0}$. Then, from Eqs. (3), (5), and (6)

$$\hat{u}_3(x_1,t) = \underbrace{u_{30}\exp\left[-\frac{(t-k'_{10}x_1)^2}{2\tau^2}\right]}_{\text{envelope}}\underbrace{\exp[j(k_{10}x_1-\omega_0 t)]}_{\text{carrier}} \quad (7)$$

Equation (7) corresponds to the well-known propagation of a carrier with the phase velocity $c_p=\omega_0/k_{10}$ inside an envelope, moving with the group velocity $c_g=1/k'_{10}$ that does not change in shape. When both velocities are equal, the wave is non-dispersive and no relative motion between the envelope and the carrier occurs. On the other hand, when they are different, the waves seem to originate at one edge of the wavetrain, travel to the opposite one and disappear. The phase and group velocities of the *A*0 and *S*0 Lamb modes, calculated from Eq. (2) for an aluminum plate, are represented in adimensional form in Fig. 1, as a function of the frequency-thickness product.

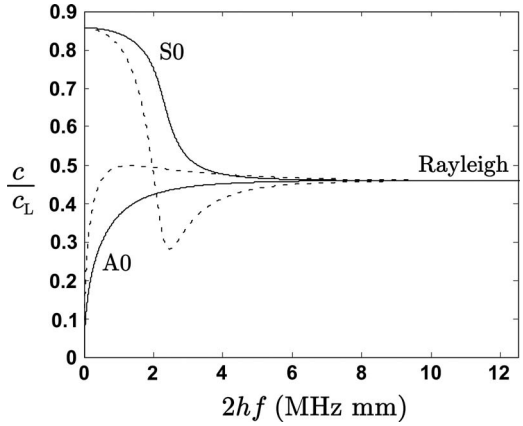

FIG. 1. Phase and group velocities of the *A*0 and *S*0 Lamb modes as a function of the frequency-thickness product for an aluminum plate having $c_L=6330$ m/s and $c_T=3117$ m/s. The continuous lines represent the phase velocity and the dashed lines stand for the group velocity. The four curves converge to the phase and group velocity of the non-dispersive Rayleigh wave.

The *A*0 and *S*0 modes tend to be non-dispersive for high values of the frequency-thickness product. As a matter of fact, the superposition of the *A*0 and *S*0 Lamb modes tends to the well-known Rayleigh wave if both modes have the same amplitude, and the thickness of the plate is much larger than the wavelength of the modes (Fig. 1). Rayleigh waves are non-dispersive, so $k'_{10}=k_{10}/\omega_0$, being the phase or group velocity c_R, given as a function of the bulk wave velocities of the sample material as[29]

$$F_R = \left(\frac{c_R}{c_T}\right)^6 - 8\left(\frac{c_R}{c_T}\right)^4 + \left[24 - 16\left(\frac{c_T}{c_L}\right)^2\right]\left(\frac{c_R}{c_T}\right)^2 - 16\left[1-\left(\frac{c_T}{c_L}\right)^2\right] = 0. \quad (8)$$

III. MATERIALS AND METHODS

A. Test plates

The proposed method was tested in aluminum plates (alloy denomination EN AW-2017A-T4) with thicknesses in the range of the millimeters. The plates rest on a horizontal board covered in velvet fabric so that the constraints at the surface are minimized. The transversal dimensions of the plate (200×500 mm^2) are large enough to prevent the interaction of the Lamb wave with its edges for the limited width of the wavefronts and the short propagation times that we used in our experiments.

The elastic constants of the plates were measured by means of a procedure described in Ref. 4 with an uncertainty lower than 1%, so the theoretical phase and group velocities for the frequencies and the modes used in the experiments can be calculated with a good accuracy and are displayed in Table I.

TABLE I. Experimental values of the phase and group velocities measured from the movies for the four modes considered in the experiment. The reference values of the theoretical phase and group velocities are also displayed.

				Experimental values		Reference values	
Mode	$2h$ (mm)	f (MHz)	$2hf$ (MHz mm)	c_p (m/s)	c_g (m/s)	c_p (m/s)	c_g (m/s)
Rayleigh	30.0	1.000	30.00	2995	2987	3000	3000
*A*0	1.97	0.741	1.460	2502	3151	2527	3163
*S*0	1.51	0.909	1.373	5243	4759	5243	4750
*S*0	2.98	0.870	2.593	3714	1843	3688	1832

B. Wave generation system

The classical wedge method[3] was employed to generate the guided acoustic waves. Basically, the wedge couples to the plate the longitudinal wave emitted by a resonant piezoelectric element, creating a stress profile at the plate surface that acts as a guided wave source. This method presents the drawbacks associated with its contact nature (liquid couplants, flatness of the plate surface, controlled pressure, and position of the wedge), but on the other hand, it allows a fine control of the wavetrain shape.

The layout of the experimental wave generation system is shown in Fig. 2. The modes excited with this method are predominantly those whose phase velocity is close to the phase velocity imposed by the wedge, which is given by[3]

$$c_p = \frac{c_w}{\sin\theta}, \tag{9}$$

where c_w is the phase velocity of the longitudinal bulk wave inside the wedge and θ is the angle between the direction of propagation of this wave and the normal to the plate.

The plastic wedges used in our experiments have been machined on poly(methyl methacrylate) with $c_w = 2700$ m/s, and have a width of 40 mm.

Narrowband bursts of 5 and 10 cycles in length were used to excite the piezoelectric in order to generate the wavetrains. The wedge angle was selected to match the phase velocity of the desired mode at the central frequency of the burst imposed by the driving electronics.

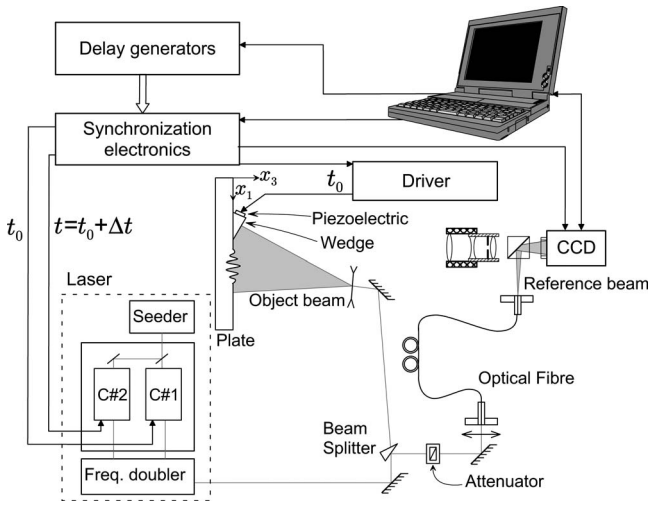

FIG. 2. Layout of the experimental system.

C. Measurement of the acoustic field

The detection was performed with a self-developed double-pulsed TVH system described in Ref. 30, and whose layout is depicted in Fig. 2. With each laser pulse, a correlogram is formed as the interference of a reference beam and an object beam backscattered by the plate surface. Both correlograms are recorded in separate frames of a CCD camera, and a processing procedure based on the spatial Fourier transform is applied, which renders a 2D map of the instantaneous optical phase-change that is proportional to the out-of-plane component of the displacement of the surface points.[31]

The instant t_0 of emission of the first laser pulse coincides with the beginning of the excitation burst of the piezoelectric, so that there is no acoustic wave in the field of view (null displacement of the surface points) when the first correlogram is recorded. The second laser pulse is delayed Δt with respect to the first one, so the instantaneous optical phase-change map can be described as

$$\Delta\Phi(\mathbf{x},t) = \frac{4\pi}{\lambda} u_3(\mathbf{x},t), \tag{10}$$

where λ is the wavelength of the laser. $t=t_0+\Delta t$ is the instant when the second laser pulse is emitted (see Fig. 2) and $\mathbf{x}=(x_1,x_2)$ is a generic point of the plate surface. Figure 3(a) displays the optical phase-change map corresponding to a *S*0 Lamb mode.

D. Visualization of the propagation of the wavetrains

The excitation burst of the piezoelectric is synchronized with the laser pulses in such a way that it is possible to accurately control the measurement instant. Therefore, under repeatability conditions, a set of N maps $\Delta\Phi_i(\mathbf{x},t_i)$ with $i=1,2,\ldots,N$ are successively recorded with increasing delays between excitation and detection. These maps can be used as snapshots to build a movie that allows to visualize the propagation of the wavetrain.[28]

A second processing procedure, based on the fast Fourier transform (FFT), is applied to the optical phase-change maps to evaluate the complex amplitude of the wave. It can be applied to each individual map by utilizing the 2D FFT[31] or, as we did in the present work, to the whole set of maps by

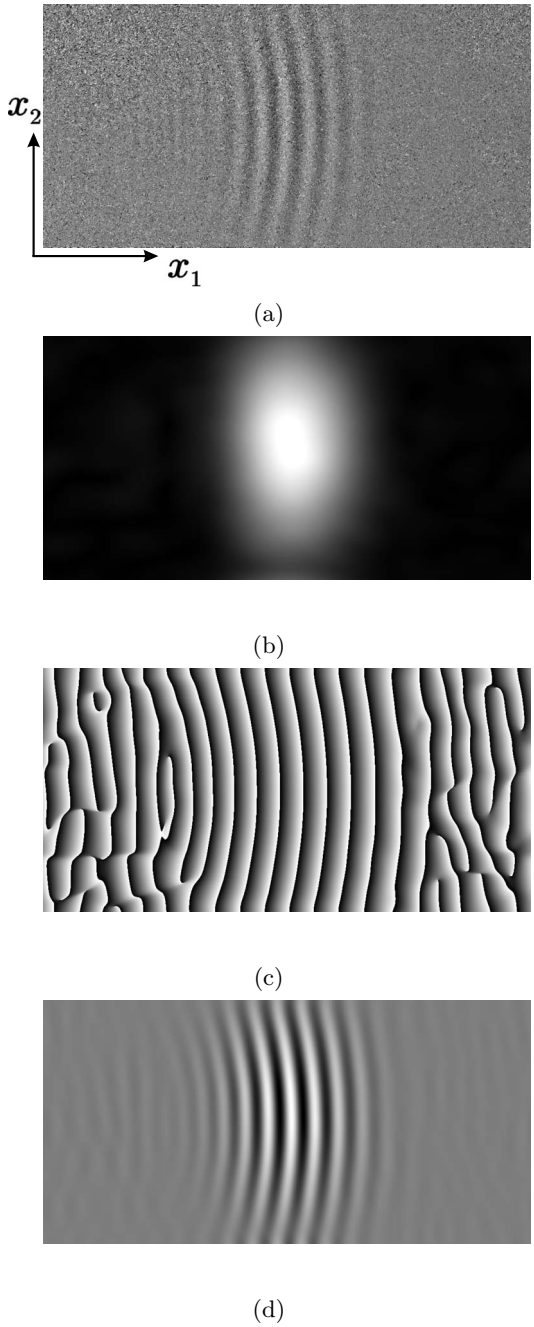

FIG. 3. Maps corresponding to the out-of-plane displacement field of the surface points of a plate 1.51 mm thick produced by a *S*0 wavetrain, consisting of 5 temporal cycles with a central frequency of 0.909 MHz at a given instant t_i. (a) Instantaneous optical phase-change $\Delta\Phi_i(\mathbf{x},t_i)$, which is proportional to the instantaneous out-of-plane displacement. (b) Modulus of the instantaneous complex optical phase-change mod$[\Delta\hat{\Phi}_i(\mathbf{x},t_i)]$, which is proportional to the instantaneous acoustic amplitude. (c) Phase of the instantaneous complex optical phase-change arg$[\Delta\hat{\Phi}_i(\mathbf{x},t_i)]$, which is equal to the instantaneous acoustic phase. (d) Instantaneous filtered optical phase-change $\Delta\Phi_i^{\mathrm{F}}(\mathbf{x},t_i)$. The actual size of the field of view is 120×60 mm^2

means of the spatiotemporal three-dimensional (3D) FFT,[32] rendering in both cases a set of complex optical phase-change maps $\Delta\hat{\Phi}_i(\mathbf{x},t_i)$, with $i=1,2,\ldots,N$. Each of these maps is proportional to the complex instantaneous out-of-plane acoustic displacement $\hat{u}_3(\mathbf{x},t_i)$, i.e.,

$$\Delta\hat{\Phi}_i(\mathbf{x},t_i)=\frac{2\pi}{\lambda}\hat{u}_3(\mathbf{x},t_i). \tag{11}$$

The modulus of $\Delta\hat{\Phi}_i(\mathbf{x},t_i)$, depicted in Fig. 3(b), is proportional to the acoustic amplitude mod$[\hat{u}_3(\mathbf{x},t_i)]$, and its argument, depicted in Fig. 3(c), is equal to the acoustic phase arg$[\hat{u}_3(\mathbf{x},t_i)]$ for the points within the wavetrain. In the procedure, to obtain $\Delta\hat{\Phi}_i(\mathbf{x},t_i)$, a bandpass filter is applied in the frequency domain to isolate the spatio-temporal frequencies corresponding to the guided acoustic wave.[32] For this reason, the phase in Fig. 3(c) shows vertical stripes with a spatial period similar to the wavelength of such acoustic wave throughout the map. However, for the region outside the wavetrain (points with practically null amplitude), the value of arg$[\Delta\hat{\Phi}_i(\mathbf{x},t_i)]$ is dominated by the noise, being meaningless. The so called acoustic amplitude and acoustic phase maps of Figs. 3(b) and 3(c), respectively, allow not only to assess the behavior of the wavetrain, but also, as detailed below, permit to perform an accurate measurement of the phase and group velocities. By taking the real part of $\Delta\hat{\Phi}_i(\mathbf{x},t_i)$, the instantaneous filtered optical phase-change $\Delta\Phi_i^{\mathrm{F}}(\mathbf{x},t_i)$ is computed, as depicted in Fig. 3(d). This map is also proportional to the instantaneous out-of-plane displacement field of the surface points $u_3(\mathbf{x},t_i)$, but with less noise than the original optical phase-change map of Fig. 3(a). Typical values of the noise in the filtered displacement are below 1 nm,[28] as can be seen in the profile of Fig. 4(a), in which the ripples outside the pulse are well below 1 nm.

E. Measurement of the group velocity

In order to measure the group velocity, we assume that it is constant throughout the inspected area of the plate and that the envelope of the wavetrain is Gaussian. The procedure that we used to measure the group velocity of guided acoustic wavetrains consists of the measurement of the velocity of the peak of the envelope. The 2D shape of the envelope is shown in the acoustic amplitude map [Fig. 3(b)], so from this map, its horizontal and vertical center can be located in a way that both components of the group velocity can be calculated, thus avoiding the cosine type error in the case that the velocity direction is different from the horizontal one. Also, the evolution of the shape of the envelope can be observed, and then it is possible to study phenomena related to the propagation of the wavetrain such as the broadening of the envelope due to GVD or the changes in the angular aperture of the beam. All these are specific advantages of the present method, rarely encountered in alternative methods.

In the wavetrains recorded in the experiments, there is no significant GVD, and the propagation direction is horizontal (the cosine type error is negligible), so the calculation of the group velocity is performed by considering solely the horizontal coordinate x_1. Figure 4(a) shows a profile along the horizontal pixel row of the 2D map of Fig. 3(d), $\Delta\Phi_i^{\mathrm{F}}(x_1,t_i)$, corresponding to a value of the vertical coordinate x_2 [defined in Fig. 3(a)] for which the acoustic amplitude depicted in Fig. 3(b) takes the maximum value. The horizontal profile of the acoustic amplitude for the same value of x_2 is also depicted in Fig. 4(a) (dashed line). The peak of the envelope is obtained as the center of the Gaussian curve that best fits the profile of the acoustic amplitude. Such Gaussian curve is shown in Fig. 4(a) (continuous line).

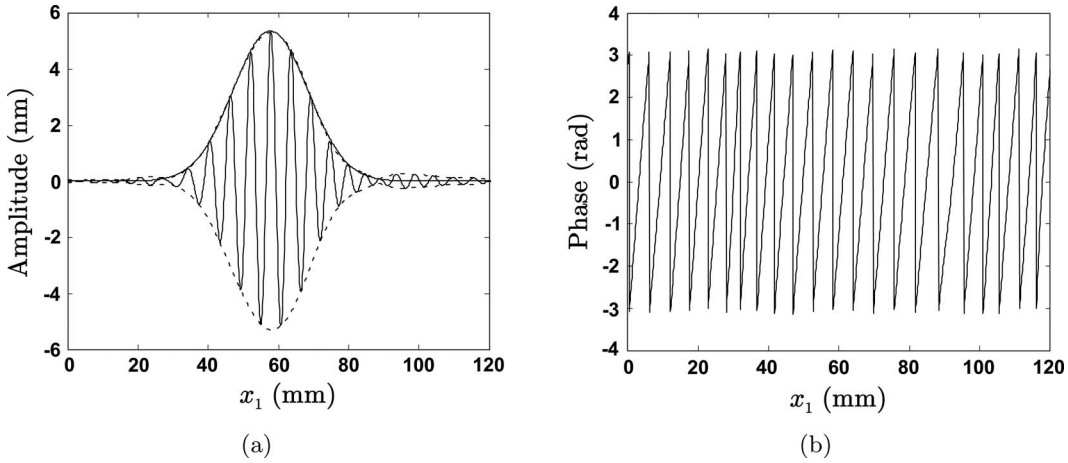

FIG. 4. Profiles of the maps of Fig. 3 along the horizontal pixel row corresponding to the vertical coordinate x_2 in which the acoustic amplitude is maximum. (a) Profile of Fig. 3(d) (continuous line) along with the envelope (dashed line), which is obtained from Fig. 3(b). The Gaussian curve that best fits the envelope is also shown (continuous line). (b) Profile of Fig. 3(c).

The fitting of the Gaussian curve is very good, so the hypothesis of Gaussian-shape envelope can be assumed for the central horizontal profile of the wavetrain, i.e., $\hat{u}_3(\mathbf{x},t_i)$ is approximately given by Eq. (7) in this region.

The group velocity c_g is measured by tracking the position of the maximum of the successive fitted Gaussian curves. The straight line corresponding to the least square fitting of the set of experimental points, which represents the position of the maximum against time, is calculated, and the group velocity is obtained as the slope of this line.

F. Measurement of the phase velocity

In order to measure the phase velocity, we assume that it is constant throughout the inspected area of the plate, and that the propagating direction is given by the gradient of the acoustic phase, i.e., it is normal to the wavefront. The procedure that we used to measure the phase velocity of guided acoustic wavetrains consists in measuring the velocity of a point with a given value of the acoustic phase. The 2D distribution of the acoustic phase is shown in the acoustic phase map [Fig. 3(c)]. From a certain acoustic phase map, the set of points having a given value of the acoustic phase can be located, so that the curvature of the wavetrain is determined. Then, from the next map, a set of points with the same value of the phase can be located, in a way that the vertical and horizontal displacement of points with a given value of the phase can be obtained, considering that their movement is normal to the wavefront. Therefore, both components of the phase velocity can be measured from the set of acoustic phase maps.

In the recorded wavetrains, the curvature of the wavetrain is negligible, and furthermore, in the region close to the central horizontal profile, the wavefront can be assumed to be normal to the horizontal direction x_1, so that in this region, we assume that the propagation takes place along x_1. Therefore, the calculation of the phase velocity is performed by considering solely the horizontal profile of the acoustic phase corresponding to the same coordinate x_2 for which the group velocity is calculated. The horizontal profile of the acoustic phase for this value of x_2 is taken from the acoustic phase map of Fig. 3(c) and is depicted in Fig. 4(b).

The phase velocity c_p is measured by tracking in the successive acoustic phase profiles, the position of a point where a transition from $-\pi$ to π exists. The straight line corresponding to the least square fitting of the set of experimental points is calculated, in a way that the value of the phase velocity is obtained as the slope of this line.

IV. EXPERIMENTAL RESULTS

The experimental results for the modes reported in Table I are shown in Fig. 5 and in the video files.[33] Figure 5 displays the 2D maps of the instantaneous filtered optical phase-change, showing three different instants of propagation for each mode considered in the experiment. On the other hand, four maps corresponding to the same mode are shown in each video file, namely, the same maps depicted in Fig. 3. In Fig. 5 the positions of the peak of the envelope and of a point with a given value of the phase are respectively marked by a dot and a cross. In the movies, they are replaced by a red dot and a blue dot, respectively.

The positions of the points marked in the movies are represented against time in Fig. 6 for the modes considered in the experiment, where the dots stand for the peak of the envelope and the crosses represent points in which a transition in the phase between $-\pi$ to π takes place and are close to the center of the wavetrain (within the region in which the amplitude is larger than half its maximum value). Then, the phase and group velocities are calculated as the slopes of the straight lines that best fit the dots and the crosses, respectively.

Four different modes were selected in the experiment in order to illustrate the different dispersion behavior that Lamb and Rayleigh waves present. The values of the measured phase and group velocities for the four modes obtained from the experiments are displayed in Table I, together with the reference ones, calculated as stated in Sec.III A.

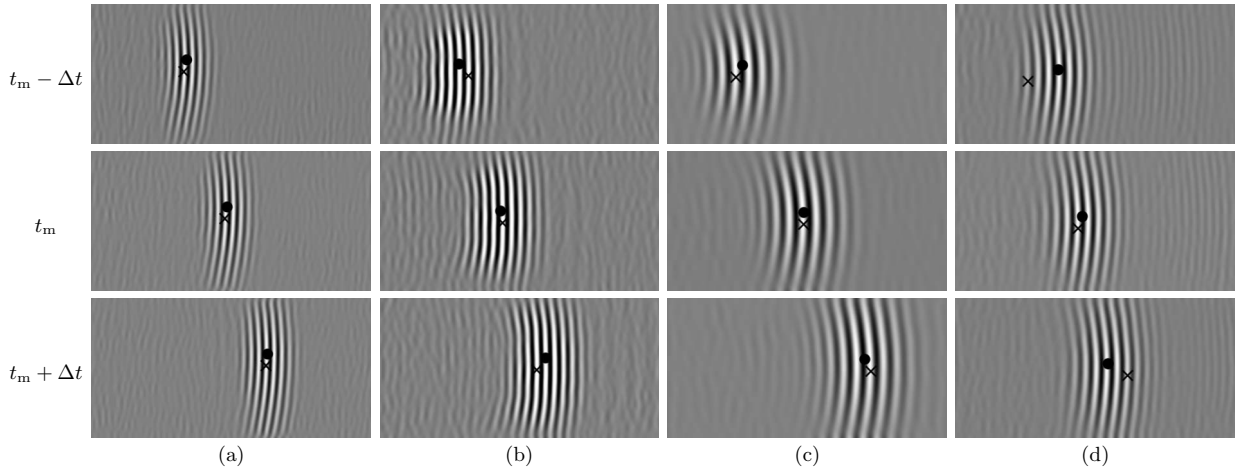

FIG. 5. Maps of the instantaneous filtered optical phase-change $\Delta\Phi_i^F(\mathbf{x},t_i)$, corresponding to four wavetrains showing different dispersive behaviors. The maps show three different instants of propagation around an arbitrary time instant t_m. The dot marks the envelope peak, while the cross marks a point with a given value of the phase. (a) Rayleigh wavetrain in an aluminum slab 30.0 mm thick, consisting of 5 temporal cycles with a central frequency of 1.000 MHz. The actual size of the field of view is 111×55 mm^2 and $\Delta t=5.4$ μs. (b) *A*0 wavetrain in an aluminum plate 1.97 mm thick, consisting of 5 temporal cycles with a central frequency of 0.714 MHz. The actual size of the field of view is 111×55 mm^2 and $\Delta t=5.4$ μs. (c) *S*0 wavetrain in an aluminum plate 1.51 mm thick, consisting of 5 temporal cycles with a central frequency of 0.909 MHz. The actual size of the field of view is 120×60 mm^2 and $\Delta t=5.5$ μs. (d) *S*0 wavetrain in an aluminum plate 2.98 mm thick, consisting of 10 temporal cycles with a central frequency of 0.870 MHz. The actual size of the field of view is 115×57 mm^2 and $\Delta t=5.5$ μs.

A. Non-dispersive wave, $c_p=c_g$

The Rayleigh wave was used as an example of a non-dispersive wave, for which the phase velocity is equal to the group velocity.

We used a burst of 5 temporal cycles with a central frequency of 1.000 MHz to generate a Rayleigh wavetrain in an aluminum slab 30.0 mm thick, by means of a wedge with $\theta=65°$. The separation between two consecutive maps is 200 ns. Figure 5(a) displays the instantaneous filtered optical phase-change map for three different instants delayed by $\Delta t=5.4$ μs. No relative motion between the envelope peak and the point of constant phase is detected, which means that, as expected, the phase and group velocities have the same value.

B. Dispersive wave with $c_p<c_g$

The *A*0 mode is the only mode in which the group velocity is larger than the phase velocity throughout the whole frequency range, converging to the non-dispersive Rayleigh wave for high frequencies (Fig. 1).

A wavetrain consisting of 5 temporal cycles with a central frequency of 0.714 MHz was generated in an aluminum plate 1.97 mm thick, by means of a wedge with $\theta=68°$. The separation between two consecutive maps is 200 ns. Figure 5(b) displays the instantaneous filtered optical phase-change map for three different instants delayed by $\Delta t=5.4$ μs. It is clearly noticeable that the carrier wave inside the wavetrain moves slower than the envelope, so that ripples seem to appear at the front edge of the wavetrain, and propagate backward inside it.

C. Dispersive wave with $c_p>c_g$

For the *S*0 mode, the phase velocity is larger than the group velocity throughout the whole frequency range. For low frequencies, both velocities are very similar, and commonly, the waves are approximated as non-dispersive. However, as the frequency is increased, the mode presents a more dispersive region and eventually converges to the non-dispersive Rayleigh wave.

A wavetrain corresponding to the low dispersion region is shown in Fig. 5(c), it was generated by means of a wedge with $\theta=31°$ in an aluminum plate 1.51 mm thick, by using a burst of 5 temporal cycles having a central frequency of 0.909 MHz. The separation between two consecutive maps is 275 ns. The three snapshots of Fig. 5(c) are delayed by $\Delta t=5.5$ μs, in a way that a slight difference between the phase and group velocities is detected that fits well with the theoretical prediction.

Another wavetrain was excited in an aluminum plate 2.98 mm thick with a burst that is 10 temporal cycles long and a central frequency of 0.870 MHz, by utilizing a wedge with $\theta=45°$. The separation between two consecutive maps is 275 ns. It corresponds to the most dispersive region of mode *S*0, so that, as it is noticed in the three snapshots of Fig. 5(d) (delayed by $\Delta t=5.5$ μs), the phase velocity is clearly larger than the group velocity, i.e., the carrier appears to originate at the trailing edge of the wavetrain and rapidly propagate forward.

V. DISCUSSION

The presented 2D movies allow to visualize experimentally the displacement fields of guided acoustic wavetrains with amplitudes in the order of several nanometers and frequencies in the order of 1 MHz. Several phenomena related to the propagation of the wavetrains can be evaluated with the set of maps that compose the movies. In this paper, we measured the group and phase velocities of narrowband wavetrains as the velocities of the envelope and the carrier inside it, respectively. Furthermore, the attenuation of the wavetrain can be observed in the acoustic amplitude maps.

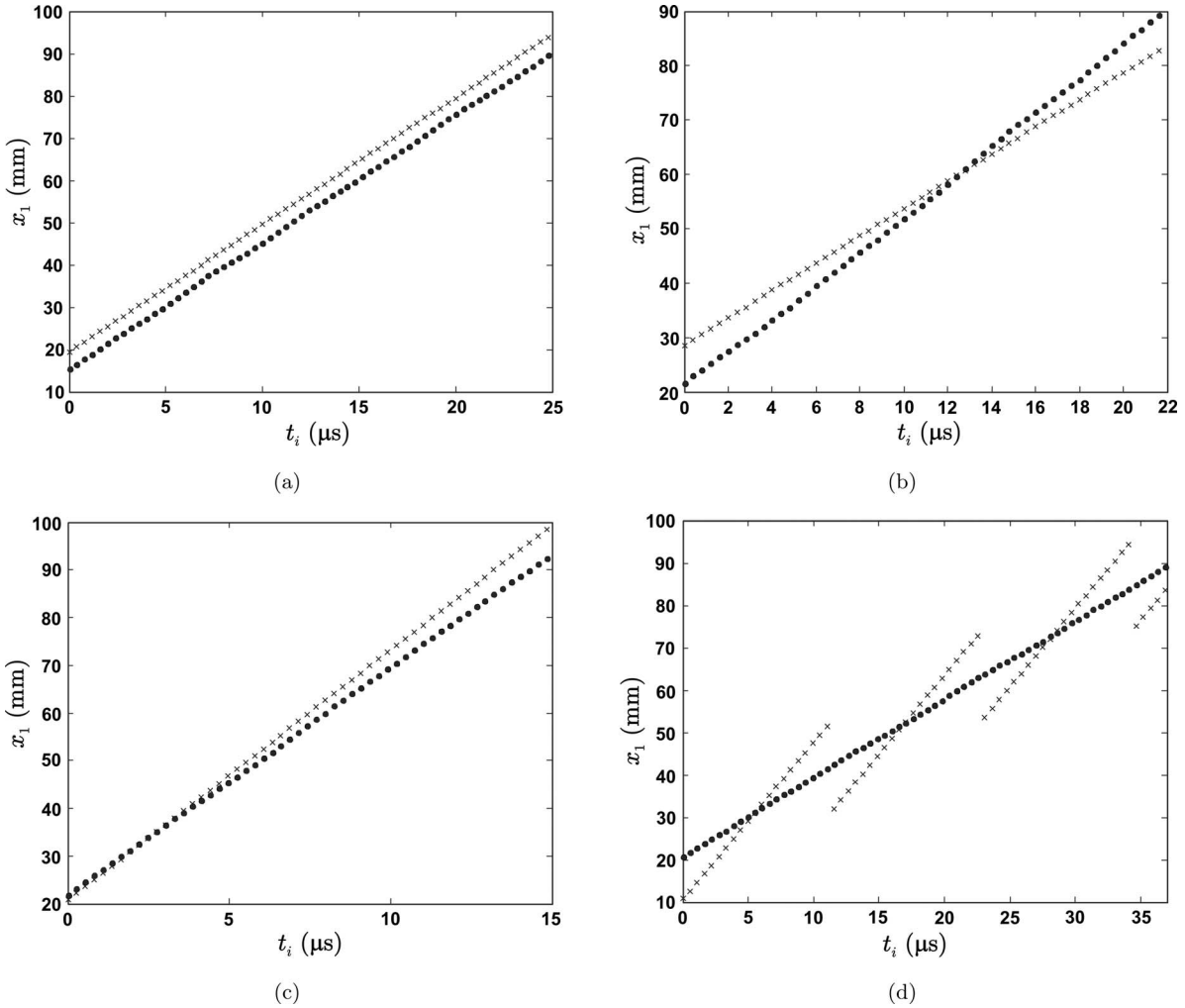

FIG. 6. Measured positions of the envelope peak (dots) and of a point with a given value of the phase (crosses) vs. time. The envelope peak is taken at the center of the Gaussian curve that best fits the envelope in a horizontal pixel row, as shown in Fig. 4(a). The constant phase point is taken in the same row, in particular, we consider a point where a transition in the phase between $-\pi$ and π takes place, and is located within the region in which the amplitude is larger than half its maximum value. (a) Rayleigh wavetrain in Fig. 5(a). (b) $A0$ wavetrain in Fig. 5(b). (c) $S0$ wavetrain in Fig. 5(c). (d) $S0$ wavetrain in Fig. 5(d). For the sake of clarity, in (a), the points of a given value of the phase are vertically shifted 5 mm, and in (a), (b), and (d), only one out of two consecutive points is represented [all the points are represented in (c) as the number of maps in the corresponding sequence is much lower than in the other cases].

In our case, it is mainly due to the angular spread of the wavetrain (geometric attenuation) and, for the short propagation distances employed, it is not relevant. The curvature of the wavefront can also be observed and measured. Another interesting phenomenon that can be observed with our technique is the broadening of the wavetrain that takes place when the frequency band is relatively broad, in which case, the GVD becomes significant and the model of a carrier wave propagating inside an envelope that does not change in shape is not applicable. In fact, the phase and group velocities of guided acoustic waves can be measured with the presented method, regardless of their values, as long as the GVD is negligible. This effect does not appear in the waves studied in this work, due to their narrowband character.

Although the calculation of the phase and group velocities was performed in our case by solely considering the horizontal profiles of the maps, it is important to take into account that the measurement of the variation in the acoustic displacement field in a 2D area allows to calculate the direction of propagation of the wavetrain, which remains unknown when measuring the wavetrains by pointwise methods. Furthermore, we were able to check by means of the maps that there is no significant broadening of the wavetrain, curvature of the wavefront, and angular spread.

The presented method to measure the phase and group velocities of guided acoustic waves has limitations with respect to the following.

- The acoustic frequency. There is an upper limit due to the need of freezing the observed displacement field, for which the laser pulse duration must be small, compared to the acoustic period. The employed equipment, with a laser pulse duration around 20 ns, can measure waves with frequencies up to several MHz.
- The measurable acoustic displacement. There is a lower limit due to the noise of the measured maps and limitations of the measuring process (dynamic range of the sensor, discretization densities, total number of spatial and temporal samples, etc.). The noise floor of our system is typically below 1 nm and the minimum measurable acoustic displacements are in the order of several nm.
- The direction of the displacements of the surface points.

Our TVH interferometer is configured for out-of-plane sensitivity because it allows employing a smooth reference beam, achieving a high signal-to-noise ratio. However, it is well-known that there are TVH configurations with in-plane sensitivity,[34] which are able to measure the displacement in a particular direction in the (x_1, x_2) plane. Although we have not yet explored this possibility in our system, it is an attractive possibility for future work.

VI. CONCLUSIONS

A method to visualize the dispersive behavior of guided acoustic waves in plates, as well as to measure their phase and group velocities, was presented. The method is based on recording a set of full-field displacement maps of the plate surface by means of a double-pulsed TV holography system, and composing a movie with them. To test the method, several Rayleigh and Lamb narrowband wavetrains, generated in aluminum plates by means of the wedge method, were recorded and analyzed.

The movies, included in the on-line version of the journal, serve to illustrate the behavior of the wavetrains. In particular, it is possible to visualize the relative motion between the envelope, which moves at the group velocity, and the carrier, which moves at the phase velocity. The Rayleigh wave and the $A0$ and $S0$ Lamb modes were chosen in the experiment to illustrate the behavior of wavetrains with a group velocity equal, larger, or smaller than the phase velocity, respectively.

To measure the phase and group velocities, the sequence of maps is processed by means of the spatiotemporal 3D fast Fourier transform, so that we obtain a set of complex maps whose modulus and argument stand for the instantaneous acoustic amplitude and phase. Then, the group velocity is measured by tracking the position of the peak of the envelope and the phase velocity is obtained by tracking the position of a point with a given value of the phase. The resulting values of the phase and group velocities match well with the reference values for the same plates obtained from independent measurements.

ACKNOWLEDGMENTS

This work was co-funded by the Spanish Ministerio de Educación y Ciencia and by the European Comission (ERDF) in the context of the Plan Nacional de $I+D+i$ (Project No. DPI2005-09203-C03-01) and by the Dirección Xeral de Investigación, Desenvolvemento e Innovación da Xunta de Galicia in the context of the Plan Galego de IDIT (Project No. INCITE08PXIB303252PR). Supplementary cofunding from the Universidade de Vigo (Project No. I608122F64102) is also acknowledged.

[1] L. Brillouin, *Wave Propagation and Group Velocity* (Academic, New York, 1960).
[2] M. A. Biot, "General theorems on the equivalence of group velocity and energy transport," Phys. Rev. **105**, 1129–1137 (1957).
[3] I. A. Viktorov, *Rayleigh and Lamb Waves* (Plenum, New York, 1967).
[4] J. L. Deán, C. Trillo, A. F. Doval, and J. L. Fernández, "Determination of thickness and elastic constants of aluminum plates from full-field wavelength measurements of single-mode narrowband Lamb waves," J. Acoust. Soc. Am. **124**, 1477–1489 (2008).
[5] K. Kobayashi, "Relationship between speed of Lamb wave and measurement error on distance," Jpn. J. Appl. Phys. **33**, 3115–3120 (1994).
[6] C. W. Chan and P. Cawley, "Lamb waves in highly attenuative plastic plates," J. Acoust. Soc. Am. **104**, 874–881 (1998).
[7] T. W. Murray, K. C. Baldwin, and J. W. Wagner, "Laser ultrasonic chirp sources for low damage and high detectability without loss of temporal resolution," J. Acoust. Soc. Am. **102**, 2742–2746 (1997).
[8] J. D. N. Cheeke, X. Li, and Z. Wang, "Observation of flexural Lamb waves ($A0$ mode) on water-filled cylindrical shells," J. Acoust. Soc. Am. **104**, 3678–3680 (1998).
[9] M. Niethammer, L. J. Jacobs, J. Qu, and J. Jarzynski, "Time-frequency representations of Lamb waves," J. Acoust. Soc. Am. **109**, 1841–1847 (2001).
[10] Y. Hayashi, S. Ogawa, H. Cho, and M. Takemoto, "Non-contact estimation of thickness and elastic properties of metallic foils by the wavelet transform of laser-generated Lamb waves," NDT Int. **32**, 21–27 (1999).
[11] H. Kwun and K. A. Bartels, "Experimental observation of elastic-wave dispersion in bounded solids of various configurations," J. Acoust. Soc. Am. **99**, 962–968 (1996).
[12] W. H. Prosser, M. D. Seale, and B. T. Smith, "Time-frequency analysis of the dispersion of Lamb modes," J. Acoust. Soc. Am. **105**, 2669–2676 (1999).
[13] A. Neubrand and P. Hess, "Laser generation and detection of surface acoustic waves: Elastic properties of surface layers," J. Acoust. Soc. Am. **71**, 227–238 (1992).
[14] A. S. Murfin and R. J. Dewhurst, "Estimation of wall thinning in mild steel using laser ultrasound Lamb waves and a non-steady-state photo-EMF detector," Ultrasonics **40**, 777–781 (2002).
[15] M. G. Somekh, M. Liu, H. P. Ho, and C. W. See, "An accurate non-contacting laser based system for surface wave velocity measurement," Meas. Sci. Technol. **6**, 1329–1337 (1995).
[16] D. Alleyne and P. Cawley, "A two-dimensional Fourier transform method for the measurement of propagating multimode signals," J. Acoust. Soc. Am. **89**, 1159–1168 (1991).
[17] Y. Shi, S.-C. Wooh, and M. Orwat, "Laser-ultrasonic generation of Lamb waves in the reaction force range," Ultrasonics **41**, 623–633 (2003).
[18] K. L. Telschow and V. A. Deason, "Imaging anisotropic elastic properties of an orthotropic paper sheet using photorefractive dynamic holography," Ultrasonics **40**, 1025–1035 (2002).
[19] T. Makkonen, T. Pensala, J. Vartiainen, J. V. Knuuttila, J. Kaitila, and M. M. Salomaa, "Estimating materials parameters in thin-film BAW resonators using measured dispersion curves," IEEE Trans. Ultrason. Ferroelectr. Freq. Control **51**, 42–51 (2004).
[20] L. Boeckx, P. Leclaire, P. Khurana, C. Glorieux, W. Lauriks, and J. F. Allard, "Guided elastic waves in porous materials saturated by air under Lamb conditions," J. Appl. Phys. **97**, 094911 (2005).
[21] M. Lematre, Y. Benmehrez, G. Bourse, J. W. Xu, and M. Ourak, "Determination of elastic parameters in isotropic plates by using acoustic microscopy measurements and an optimization method," NDT Int. **35**, 493–502 (2002).
[22] Y.-C. Lee and S.-W. Cheng, "Measuring Lamb wave dispersion curves of a bi-layered plate and its application on material characterization of coating," IEEE Trans. Ultrason. Ferroelectr. Freq. Control **48**, 830–837 (2001).
[23] D. C. Auth and W. G. Mayer, "Scattering of light reflected from acoustic surface waves in isotropic solids," J. Appl. Phys. **38**, 5138–5140 (1967).
[24] M. Ohki, M. Inoue, and K. Toda, "Measurement of leaky Lamb wave velocity using Raman–Nath diffraction," Jpn. J. Appl. Phys. **36**, 3171–3175 (1997).
[25] Y. H. Kim, S.-J. Song, S.-D. Kwon, Y.-M. Cheong, and H.-K. Jung, "Determination of ultrasonic wave velocities and phase velocity dispersion curves of an Inconel 600 plate using resonant ultrasound spectroscopy and leaky Lamb waves," Ultrasonics **42**, 551–555 (2004).
[26] X. Chen and M. Wan, "Parameter measurement of the cylindrically curved thin layer using low-frequency circumferential Lamb waves," Ultrasonics **43**, 357–364 (2005).
[27] M. Murase, K. Kawashima, and O. Yoshida, "Group velocity measurement of various Lamb waves with two-beam laser interferometer," Jpn. J. Appl. Phys. **40**, 3595–3598 (2001).
[28] J. L. Fernández, A. F. Doval, C. Trillo, J. L. Deán, and J. C. López, "Video ultrasonics by pulsed TV holography: A new capability for non-destructive testing of shell structures," Int. J. Optomechatronics **1**, 122–153 (2007).
[29] K. F. Graff, *Wave Motion in Elastic Solids* (Dover, New York, 1975).
[30] C. Trillo, D. Cernadas, A. F. Doval, C. López, B. V. Dorrío, and J. L. Fernández, "Detection of transient surface acoustic waves of nanometric

amplitude with double-pulsed TV holography," Appl. Opt. **42**, 1228–1235 (2003).
[31]C. Trillo, A. F. Doval, D. Cernadas, O. López, J. C. López, B. V. Dorrío, J. L. Fernández, and M. Pérez-Amor, "Measurement of the complex amplitude of transient surface acoustic waves using double-pulsed TV holography and a two-stage spatial Fourier transform method," Meas. Sci. Technol. **14**, 2127–2134 (2003).
[32]C. Trillo and A. F. Doval, "Spatiotemporal Fourier transform method for the measurement of narrowband ultrasonic surface acoustic waves with TV holography," Proc. SPIE, **6341**, 63410M (2006).
[33]See supplementary material at http://dx.doi.org/10.1121/1.3327795 Document No. E-JASMAN-127-035004 for downloadable files containing the four video files showing the wavetrain propagation for each mode considered in the experiment. For more information, see http://www.aip.org/pubservs/epaps.html.
[34]A. F. Doval, "A systematic approach to TV holography," Meas. Sci. Technol. **11**, R1–R36 (2000).

Shear horizontal guided wave modes to infer the shear stiffness of adhesive bond layers

Bénédicte Le Crom[a] and Michel Castaings
Laboratoire de Mécanique Physique, Université de Bordeaux, UMR CNRS 5469, 351 cours de la Libération, 33400 Talence, France

(Received 3 December 2009; revised 13 January 2010; accepted 15 January 2010)

This paper presents a non-destructive, ultrasonic technique to evaluate the quality of bonds between substrates. Shear-horizontally polarized (SH) wave modes are investigated to infer the shear stiffness of bonds, which is necessarily linked to the shear resistance that is a critical parameter for bonded structures. Numerical simulations are run for selecting the most appropriate SH wave modes, i.e., with higher sensitivity to the bond than to other components, and experiments are made for generating-detecting pre-selected SH wave modes and for measuring their phase velocities. An inverse problem is finally solved, consisting of the evaluation of the shear stiffness *modulus* of a bond layer at different curing times between a metallic plate and a composite patch, such assembly being investigated in the context of repair of aeronautical structures.
 [DOI: 10.1121/1.3309441]

PACS number(s): 43.35.Cg, 43.35.Zc [YHB] Pages: 2220–2230

I. INTRODUCTION

Bonded joints are often submitted to shearing loads, and breaking when occurring is often in the shearing mode, so designers are trying to make bonds so that they resist well to shearing. Shear resistance is then a critical parameter for adhesive bonds, and its non-destructive evaluation is of interest, especially in the aeronautic or aerospace context for safety reasons. For instance, the problem, which is investigated in this paper, concerns the repair of aeronautical metallic structures with adhesively bonded composite patches. The evaluation of the bond quality is of great importance, and especially of its shear resistance since thin patches bonded on large metallic surfaces are likely to be loaded in the shearing mode.

Thermography, reflective fringe pattern techniques, or standard ultrasonic techniques have shown to be useful for detecting local disbonds or lack of glue in bonds,[1–6] but since such severe defects may be routinely avoided with high-performance bonding processes, the need in bond testing is nowadays more oriented toward the characterization of the bond quality. This means that quantitative estimation of some physical properties of the bonds is required. Evidently, cohesive properties of the adhesive layer are of interest not only to check the curing state after the bonding is realized, but also to monitor eventual changes during the life of the bond. Imperfections in adhesive joints can often be confined to a very thin layer in the form of an interphase separating the joining materials.[7] The evaluation of adhesive interfacial properties is then also of interest. Even more, the need of correlating these estimated properties to the resistance of the bond to mechanical loads is clearly expressed by industrial partners. Moreover, no or little contact is often allowed for *in-situ* testing, and remote access to the tested bond line is sometimes required.

Ultrasonic guided waves can be good candidates for testing the cohesive properties of joints or the adhesion at each interface between the joint and the substrates, as they will integrate the bond properties while propagating along it. The through-thickness distribution of the stress and power-flow produced by a guided wave mode will determine its sensitivity to the various components or zones across the assembly.[8–10] These quantities must therefore be carefully examined during the mode selection process. Shear-horizontally polarized (SH) guided waves are particularly interesting because they are sensitive to the shear stiffness of the bond,[11] which is necessarily linked to its shear resistance that is a critical parameter for adhesive joints, as explained before. Moreover, guided waves are well known to propagate along long distances, so they can often be generated and/or detected remotely, thus being suitable for those of the *in-situ* testing involving this requirement.

In this paper, a one-dimensional semi-analytical finite element (SAFE) model is firstly used for predicting the dispersion curves and mode shapes of SH guided waves propagating along multi-layered plates made of anisotropic and viscoelastic materials. A specific spring model is implemented in this SAFE method to simulate variable boundary conditions at the interface between two layers. This tool is then used for modeling the propagation of the three low-order wave modes SH_0, SH_1, and SH_2, along a three-layered medium made of a composite patch, an adhesive layer, and an aluminum plate, the aluminum/adhesive interface being supposed to be the weak interface modeled by the spring boundary conditions. Numerical simulations are made to select modes, which sensitivity is higher to the bond layer and/or to the interface between this bond and the metallic plate than to the metallic plate or composite patch. A laser-based technique is finally set up for detecting SH guided wave modes, which are launched using a standard ultrasonic

[a]Author to whom correspondence should be addressed. Electronic mail: b.lecrom@lmp.u-bordeaux1.fr

TABLE I. Density (±3%), thickness (±5% for the substrates and ±15% for the adhesive), and viscoelastic properties of the materials used in the study with measurement errors of about ±5% for the elastic moduli of aluminum, and ±10% and ±15% for the real and imaginary parts, respectively, of the viscoelastic moduli of the other materials.

	Aluminum	Adhesive	Carbon epoxy
Density (g/cm^3)	2.67	1.05	1.58
Thickness (mm)	3	0.1	1.2
C_{11} (GPa)	103	5.6+0.5*I*	74.0+4*I*
C_{22} (GPa)	107	5.6+0.5*I*	15.5+0.4*I*
C_{33} (GPa)	107	5.6+0.5*I*	74.0+4*I*
C_{12} (GPa)	54	4.5+0.4*I*	7.6+0.2*I*
C_{13} (GPa)	54	4.5+0.4*I*	12+0.3*I*
C_{66} (GPa)	26	0.5+0.05*I*	4.6+0.1*I*
C_{55} (GPa)	26	0.5+0.05*I*	6.6+0.1*I*
C_{44} (GPa)	25	0.5+0.05*I*	4.5+0.1*I*
C_{23} (GPa)	54	4.5+0.4*I*	7.6+0.2*I*

piezoelectric transducer (PZT). This technique is first validated by successfully comparing the measured and predicted phase velocities for an aluminum plate sample and for a composite plate sample. Then it is used to measure velocities of SH-like modes for an aluminum/adhesive/patch assembly with different levels in the bond quality. A shear stiffness value corresponding to each of these levels is finally evaluated by comparing the measured and predicted velocities (inverse problem). The use of guided SH modes is shown to allow remote access to the tested bond, and laser-based detection reduces contact with the tested specimen, as demanded by the industrial partner.

II. MATERIALS

In this study, the structure of interest is made of three different material components: one elastic isotropic aluminum plate, one viscoelastic isotropic adhesive layer, and one viscoelastic orthotropic composite patch. The aluminum plate is 3 mm thick, and its elastic constants have been inferred using a well-established ultrasonic technique, based on the measurement of the phase velocities of bulk longitudinal or shear waves propagating through the plate immersed in water.[12] The sample was insonified by two 25-mm-diameter, circular transducers (Ultran WS100-5) in the frequency range 2.5–6.8 MHz. Time of flights (and so velocities) have been measured for angles of the incident plane wave running from 0° to 30°, every 1°. This set of measurements was then used as input data for solving the inverse problem leading to the stiffness *moduli* supplied in Table I.

The composite patch is made of eight carbon epoxy plies with a $[0°/90°]_{2s}$ stacking sequence. It is 1.2 mm thick and its viscoelastic moduli have been measured using an immersion technique slightly different than that mentioned above, and makes the characterization of thin samples possible.[13,14] This is based on the ultrasonic plane-wave transmission of fluid-immersed plates, and allows the measurement of complex viscoelasticity moduli for anisotropic materials, the real parts representing the elasticity of the material and the imaginary parts its damping. The sample was insonified by two rectangular transducers (Imasonic 3258 A101), with 100×40 mm^2 long sides in the frequency range 0.2–0.9 MHz, and the results are presented in Table I. A 5 mm thick composite sample made of the same material as the 1.2 mm thick one is also used for testing the generation, propagation, and detection of SH guided wave modes as explained further.

Finally the adhesive is a two-component epoxy adhesive: a premium resin Araldite GY-784 and an Aradur 125 curing agent. To establish an initial set of the adhesive viscoelasticity, a specific assembly has been realized. This was made of two glass plates with very well-known mechanical properties, bonded together using the studied adhesive. The sample has been sealed, immersed into water, and its characterization has been realized using the ultrasonic plane-wave transmission technique mentioned above for the patch characterization. The rectangular transducers Imasonic 3258 A101 previously used for the patch were also employed here. The inverse problem, consisting of optimizing complex viscoelastic moduli of one unknown material layer among other layers of well-known properties, has been solved earlier and published in Ref. 14. In the actual case, the unknown layer is the adhesive and the well-known layers are both glass plates. The interest in using two glass plates is that glass is perfectly uniform, isotropic, elastic, and also transparent so allowing easy control of any unwanted air bubble in the bond layer. Results for the adhesive characterization are presented in Table I. This immersion technique obviously does not satisfy any of the *in-situ* requirements; however, it provides necessary data for running numerical models that will further allow setting up guided-wave-based techniques, which are more suitable for industrial applications, since these can be generated-detected using, for example, dry-contact PZT elements or air-coupled transducers, and eventually make single-sided access possible.

For the characterization results supplied in Table I, errors of about ±5% for the aluminum stiffness, and ±10% and ±15% for the real (stiffness) and imaginary (viscoelasticity) parts, respectively, of the composite or adhesive moduli have been obtained. These intervals of confidence will be further taken into account for numerically predicting the sensitivity of the SH wave modes to the material properties. More specifically, the purpose will consist of finding modes with higher sensitivity to changes in the bond quality than to fluctuations of the aluminum or patch properties. Possible changes of about ±3% in the densities of any of the materials will be considered in these numerical predictions of the SH wave modes' behavior. Effects of changes in the thicknesses will also be numerically investigated: ±5% changes in the composite or aluminum thicknesses, and ±15% changes in that of the bond layer.

III. THE 1D SAFE MODEL

A. Principle and equations

A SAFE model is used to calculate the dispersion curves and mode shapes of the SH wave modes that may propagate along the waveguide made of the aluminum plate, adhesive bond, and composite patch. This SAFE method is particularly convenient for modeling wave propagation along guides of arbitrary cross-section, whether these are made of

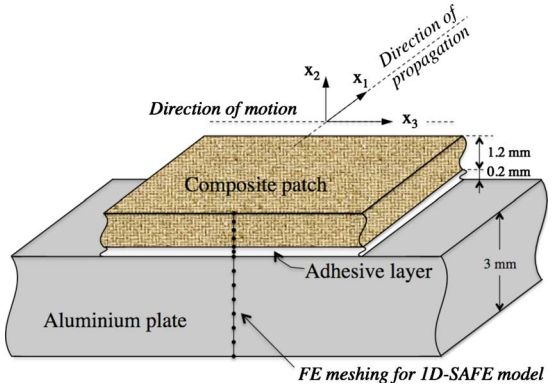

FIG. 1. (Color online) Three-dimensional (3D) schematic of aluminum plate/bond line/composite patch structure, with 1D SAFE meshing shown as series of dots through thickness.

one or several isotropic or anisotropic, elastic or viscoelastic materials.[15–19] This consists of solving an eigen-value equation of motion, the solutions of which are couples of the type (f,k), where f is the frequency and k is the complex wave-number of the wave mode. Each solution enables arbitrary definitions of the mode shape in the cross-section of the waveguide, together with a harmonic description along the propagation direction. All types of propagating or evanescent modes are usually in the set of the solutions. If the guide section has uniform geometrical and mechanical properties along the transverse-to-thickness direction (case of a plate-like guide, for instance), then Lamb and SH-like guided waves constitute the set of solutions. In the actual study, the eigen-value equation of motion is restricted to modeling SH-like guided wave modes only; i.e., displacement components in the direction of propagation and normally to the plate, as well as corresponding strains, are not permitted by this equation. This allows significantly speeding up its resolution, and also removing all unwanted Lamb-type solutions, which are not of interest in this study, thus simplifying the post-processing of the set of solutions. Moreover, the model takes into account the viscoelasticity of both the adhesive and composite components, as well as the orthotropy of the composite patch. Finally, the adhesion at the interface between the aluminum plate and the adhesive layer is implemented by using a shear-spring model.

The waveguide is then made of a 3 mm thick aluminum plate, a 0.2 mm thick adhesive layer, and a 1.2 mm thick composite patch. As illustrated in Fig. 1, these three components are supposed to be of infinite extent along the x_3 direction, which is parallel to the surfaces of the guide and normal to the direction of propagation, i.e., to x_1. In these conditions a 1D SAFE model can be defined so that three aligned cross-section lines only constitute the FE meshed domain, each of these corresponding to one of the three materials. The displacement vector of a harmonic shear horizontal guided wave propagating along the x_1 axis and polarized along the x_3 axis is then considered as

$$\boldsymbol{U}(x_1,x_2,x_3,t) = \begin{pmatrix} 0 \\ 0 \\ \tilde{u}_3(x_2)e^{I(\omega t - kx_1)} \end{pmatrix}, \quad I^2 = -1, \tag{1}$$

where $\omega = 2\pi f$ is the angular frequency, f being the frequency, t is the time variable, and k is the wave-number. In this case, considering that the only non-zero displacement component $\tilde{u}_3 e^{I(\omega t - kx_1)}$ is uniform along the x_3 direction, the equation of dynamic equilibrium in the frequency domain and for anisotropic materials can be expressed as follows:

$$C_{44}\frac{\partial^2 \tilde{u}_3}{\partial x_2^2} - k^2 C_{55}\tilde{u}_3 + \rho\omega^2\tilde{u}_3 = 0 \quad \text{in a domain } \Omega, \tag{2}$$

where C_{55} and C_{44} are moduli representative of the mechanical properties of the material of interest, defined in the coordinate axis shown in Fig. 1. These can be either real or complex, depending on whether the material is elastic or viscoelastic, respectively.

The expression of the stress vector $\boldsymbol{T} = \boldsymbol{\sigma}\cdot\boldsymbol{n}$, where $\boldsymbol{n}$ is a unit vector outward to a domain Ω and normal to its boundary, is

$$\begin{pmatrix} T_1 \\ T_2 \\ T_3 \end{pmatrix} = \begin{pmatrix} 0 & 0 & \sigma_{13} \\ 0 & 0 & \sigma_{23} \\ \sigma_{13} & \sigma_{23} & 0 \end{pmatrix} \cdot \begin{pmatrix} n_1 \\ n_2 \\ n_3 \end{pmatrix} = \begin{pmatrix} \sigma_{13}n_3 \\ \sigma_{23}n_3 \\ \sigma_{13}n_1 + \sigma_{23}n_2 \end{pmatrix}. \tag{3}$$

At the outer or internal surfaces of the stacking, the unit outward vector is defined along the x_2 direction so the stress vector is reduced to only one non-zero component, the third one

$$T_3 = \sigma_{23}n_2 = C_{44}\frac{\partial \tilde{u}_3}{\partial x_2}n_2, \tag{4}$$

where n_2 is the second component of $\boldsymbol{n}$ and is equal to ± 1.

The outer boundaries of the system, i.e., the surfaces of the three-layered plate, are free of stress, so T_3 is equal to zero. At the inner interface between the composite patch and the adhesive layer, the boundary conditions are defined to satisfy the continuity of displacements in the x_3 direction and also of stresses T_3. At the inner interface between the adhesive bond and the aluminum plate, the boundary conditions are defined so that the stress T_3 is continuous, but there might be a jump of displacements in the x_3 direction. A shear-spring model is defined below to ensure these boundary conditions. It allows modeling the effect of bad adhesion at this known-to-be-critical interface on the propagation of SH-like wave modes.

$$T_3 = k_T \Delta\tilde{u}_3 \quad \text{at adhesive/aluminum interface}, \tag{5}$$

where k_T represents a uniform density of shear springs $(\mathrm{N/m^3})$ along the adhesive/aluminum interface, and $\Delta\tilde{u}_3 = \tilde{u}_3^{\text{adhesive}} - \tilde{u}_3^{\text{aluminum}}$ is the displacement jump between the adhesive and the aluminum, the sign of the difference depending on the material this jump is considered from. As shown in previous publication,[20] such an interface could also be modeled as a very thin material layer with a thickness $h_{\text{interface}}$, a mass density, and an elastic shear *modulus*

$C_{44}^{\text{interface}} = k_T h_{\text{interface}}$. Such a model would involve no specific implementation in the SAFE model since this is classically made for modeling wave propagation along material layers; however, it would be much more demanding in terms of number of degrees of freedom because of the very small finite element mesh elements that would require the thin interface layer, including serious consequences on the size of the remaining elements of the model for ensuring displacements and stresses' continuity over the various domains.[21]

B. FE-based commercial software

The used commercially available finite element code[22] is particularly suitable for implementing such specific models. In this paper, it is used for solving eigen-value equation (2) for the three domains (aluminum, adhesive, and composite) joined together, and satisfying the various boundary conditions previously mentioned, i.e., stress-free outer surfaces and stress continuity with or without jump in displacements at inner interfaces. The solution is a set of real, imaginary, or complex wave-numbers k, obtained for one angular frequency ω chosen within a frequency range of interest. Each wave-number corresponds to one possible shear horizontal guided mode that can exist in the three-layered waveguide. By solving this problem at different frequencies, and by classifying properly the solutions, the dispersion curves of the SH waves can be plotted. For each solution (ω,k), the mode shape is obtained from the eigen-vector, which allows plotting various components versus the through-thickness position x_2, like for instance displacements $\tilde{u}_3(x_2)$, stresses $\sigma_{23}(x_2)$ and $\sigma_{13}(x_2)$, or the Poynting vector $\boldsymbol{P}(x_2) = -\frac{1}{2}\mathrm{Re}(\boldsymbol{\sigma}:\mathbf{v}^*)$, which represents the time-average power-flow carried by the mode.[23] These may be particularly useful for understanding the sensitivity of modes to the bond quality, as it will be shown further.

In this commercial software, the formalism for eigenvalue problems has the following expression for general anisotropic materials:

$$\nabla \cdot (c\,\nabla \boldsymbol{U} + \alpha \boldsymbol{U} - \gamma) - a\boldsymbol{U} - \beta \cdot \nabla \boldsymbol{U} + d_a \lambda \boldsymbol{U} - e_a \lambda^2 \boldsymbol{U} = 0 \quad \text{in the domain } \Omega, \tag{6}$$

$$\boldsymbol{n} \cdot (c\,\nabla \boldsymbol{U} + \alpha \boldsymbol{U} - \gamma) + q\boldsymbol{U} = g \quad \text{on the boudaries } \partial\Omega, \tag{7}$$

where c, α, γ, a, β, d_a, e_a, q, and g may be scalar, vector, or matrix coefficients with no particular physical meaning, $\boldsymbol{U}$ represents the displacement vector, and λ is the searched eigen-value. The first equation corresponds to the equation of dynamic equilibrium and the second one to a Neumann boundary condition. Finally if Eqs. (6) and (7) are compared to Eqs. (2) and (4), respectively, then the various above coefficients can be set to

$$\alpha = \beta = d_a = \gamma = q = 0,$$

$$c = C_{44}, \quad e_a = C_{55}, \quad a = -\rho\omega^2, \quad \text{and} \quad g = T_3. \tag{8}$$

C. Geometry and meshing

The assembly structure is made of components having quite different thicknesses, e.g., up to 15 in ratio between the aluminum and the adhesive thicknesses, and even up to 300 in ratio between the aluminum and the interface thicknesses, if the interface is modeled as a 10 μm thick layer for validation purposes of the shear-spring model. Such high ratios between thicknesses of different domains cause strong irregularities in the size of the FE mesh elements running all through the model. For instance, if one considers that a minimum number of four quadratic (second order) linear elements are needed across each layer for describing properly the mode shapes, then elements with 2.5 or 50 μm lengths are required across the interface or adhesive layers, respectively, while elements with 0.75 mm length are required across the aluminum layer. However, considering that the size of FE elements should not vary too rapidly across the domain to avoid scattering or distortion phenomena in the ultrasonic propagation,[21] the need of very small elements within thin layers has then a direct and severe consequence on the whole number of degrees of freedom of the model, thus justifying the interest of the spring model that gets rid of the 10 μm thick interface layer. Indeed, if a minimum of four quadratic elements are used across each layer, then the four-layer model is a 273 degree-of-freedom model, while the three-layer model obtained by replacing the 10 μm thick interface layer with a spring interface model has 138 degrees of freedom only, which means a 49% improvement in term of degrees of freedom. The dispersion curves calculated with both SAFE models have less than 1% difference, and they perfectly agree (less than 2% difference) with curves predicted by the more classical surface impedance matrix method,[14] which has been widely validated in the past. The interest of the SAFE model in comparison to classical methods such as the surface impedance matrix method or other matrix-based methods is that it allows easy implementation of the spring model to simulate variable adhesion at one interface of the medium, for example. Also, FE-based models are well known for being convenient for varying the material mechanical properties with space, or for simulating local defects, so this could be investigated in further studies with the SAFE model.

IV. NUMERICAL INVESTIGATION OF SH WAVES' SENSITIVITY TO MATERIAL PROPERTIES OF ASSEMBLY

The purpose of this preliminary numerical study is to establish frequency ranges within which properties of any of the three materials may cause trouble to the use of SH-like modes for quantifying the quality of the adhesive bond, i.e., its adhesive or cohesive properties. As mentioned in Sec. II, the densities and thicknesses of the different materials are measured with accuracies of about $\pm 3\%$ and $\pm 5\%$, respectively, except for the adhesive layer the thickness of which is estimated with $\pm 15\%$ accuracy. The stiffness of the substrates is measured with accuracies of about $\pm 5\%$ for the aluminum and $\pm 10\%$ for the composite. Numerical investigations are then realized to quantify the effect of changes in

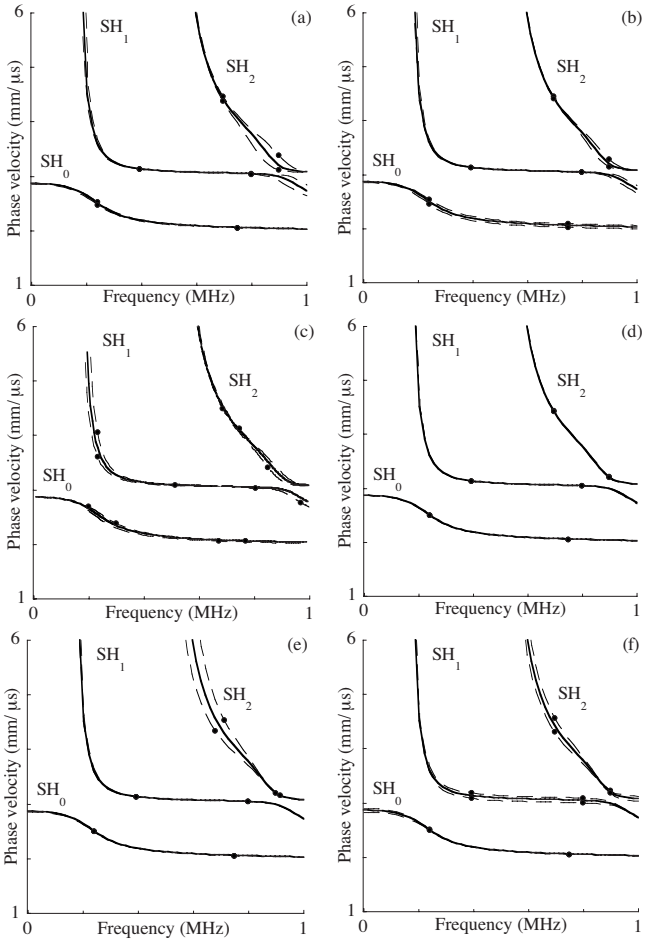

FIG. 2. Numerical predictions of SH_0, SH_1, and SH_2 phase velocity sensitivity to either $\pm p\%$ changes in thickness (left column) or $\pm 3\%$ changes in density (right column) of [(a) and (b)] composite patch ($p=5$), [(c) and (d)] adhesive bond ($p=15$), and [(e) and (f)] aluminum ($p=5$); (—) are results for nominal properties (central values of data measured in Sec. II) and (—●—) for modified properties.

these parameters, within the intervals of confidence of their measurements, on the phase velocities of the SH_0, SH_1, and SH_2 modes propagating along the three-layered assembly, in the frequency range 0.01–1 MHz. The errors on the imaginary parts of the moduli are not investigated in this paper, since these have been checked to have no or negligible effects of the velocities of guided wave modes.

A. Sensitivity to densities and thicknesses

Non-surprisingly, $\pm 3\%$ changes in the density of any of the three materials do not induce significant changes either in the phase velocities ($\leq 1.5\%$) or in the frequencies cut-off ($\leq 4\%$) of the guided SH modes [Figs. 2(b), 2(d), and 2(f)]. Similarly, $\pm 15\%$ changes in the thickness of the bond line have little effects on the dispersion curves [Fig. 2(c)]. But, as shown in Fig. 2(a), a particular attention should be paid to the thickness of the composite patch if the SH_2-like mode is selected between 0.7 and 1 MHz to quantify the quality of the adhesive. Indeed, $\pm 5\%$ changes in this parameter induce up to 15% changes in the phase velocity of this mode. Similarly, the accurate knowledge of the aluminum plate thickness is of importance if the SH_2-like mode is used at frequencies close to its cut-off to evaluate the adhesive quality. Indeed, as shown in Fig. 2(e), $\pm 5\%$ changes in the aluminum thickness cause up to 10% changes in the cut-off frequency of the SH_2-like mode. In the context of using SH-like modes for quantifying the cohesive or adhesive properties of the bond layer placed between a 3 mm thick aluminum plate and a 1.2 mm thick carbon epoxy patch, it is therefore recommended to avoid the use of the second order mode (SH_2).

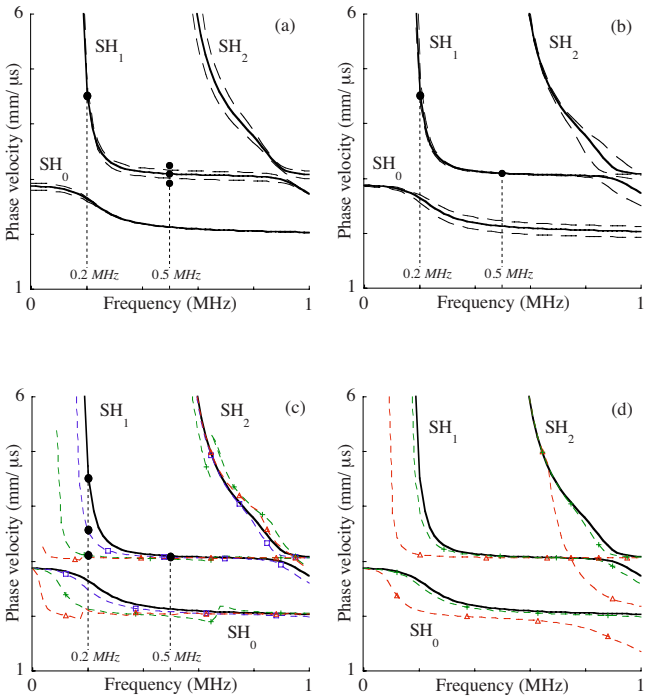

FIG. 3. (Color online) Numerical predictions of SH_0, SH_1, and SH_2 phase velocity sensitivity to (a) $\pm 5\%$ changes in C_{44} (and $C_{55}=C_{44}$) of aluminum, (b) $\pm 10\%$ changes in C_{44} and C_{55} of composite patch, (c) -40% (–□–) or -85% (–+–) or -99% (–△–) drop in C_{44} of adhesive layer, and (d) -85% (–+–) or -99% (–△–) drop in k_T of interface between aluminum and adhesive; (—) are results for nominal properties (central values of data measured in II) and various dashes are for modified properties.

B. Sensitivity to shear properties of substrates, adhesive, and interface

In the same way, taking into account the $\pm 5\%$ or $\pm 10\%$ errors related to the stiffness measurements of the aluminum or composite patch, respectively, allows showing that the SH_2-like mode is pretty sensitive to the properties of the assembled media. Indeed, as shown in Figs. 3(a) and 3(b), the phase velocity of this mode is quite modified when varying the aluminum or composite shear moduli by $\pm 5\%$ or $\pm 10\%$, respectively. Figures 3(c) and 3(d) show that up to 85% decay in the value of either the Coulomb modulus C_{44} of the adhesive or the shear stiffness k_T of the interface between the adhesive and the aluminum would cause less or similar amount of changes in the dispersion curve of this SH_2-like mode, than the aluminum or patch stiffness do, provided that these later do not change beyond the intervals of confidence of their measurements. This confirms the conclusion of Sec. IV A, that the SH_2-like mode should be avoided for testing the bond quality of the assembly considered in this study.

Similarly, at some frequencies, the SH_0- and SH_1-like modes are more sensitive to either the aluminum or patch properties than to the adhesive layer or to its adhesion with the aluminum, except if this later is set equal to 1% of its nominal value, such extremely low value corresponding to almost no adhesion at all. This is true for frequencies greater than the frequency cut-off of SH_1, which is therefore a frequency region to be avoided if any of SH_0- and SH_1-like modes is intended for testing the bond quality of the actual structure. In the low frequency regime, i.e., for frequencies below or around the SH_1 cut-off (≈0.2 MHz for the assembly considered in this study), both SH_0- and SH_1-like modes are more sensitive to the cohesive property C_{44} of the bond layer than to the aluminum or patch stiffness, or also to their thicknesses or densities. Indeed, the comparison between Figs. 3(a)–3(c) and 2 indicates that accurate measurements of the phase velocities of SH_0- and SH_1-like modes below and around the SH_1 cut-off should allow detecting about 40% (and even down to 30% according to simulations not all shown here) or more degradation in the shear (Coulomb) modulus of the adhesive layer. Regarding the adhesion between the adhesive layer and the aluminum, Fig. 3(d) and its comparison with Figs. 3(a), 3(b), and 2 show that the SH_1-like mode may detect from about 85% degradation in this adhesion, if its phase velocity is very accurately measured around its cut-off. However, the sensitivity of this mode to the cohesive shear property of the adhesive layer is much larger than that to the interface shear stiffness, as seen by comparing Figs. 3(c) and 3(d) together. Therefore, any uncertainty in the cohesive property of the bond may prevent inferring the interface stiffness, but the reverse is not true. Consequently, accurate measurements of the phase velocity of the SH_1-like mode, around its cut-off, should provide a reasonably correct estimation of the shear modulus of the bond only, whether the adhesion between this bond and the aluminum layer is of good or average quality.

In Figs. 3(c) and 3(d), parts of the dispersion curves plotted for 99% degradation of either the adhesive layer or the adhesion between this layer and the aluminum, respectively, tend toward those of the single aluminum or composite plates, or of the composite/adhesive bi-layer. Such solutions are sensible since 99% degradation in either the adhesive bond or adhesive/aluminum interface corresponds to almost total mechanical disconnection between the materials. The sensitivity of ultrasonic wave modes to such level of degradation may be interesting for detecting large disbonds that could be present in a large structure, this latest still looking fine if, for example, 80% of the bonded area is good.

The low frequency regime identified as the domain of highest sensitivity of the SH_0 and SH_1 modes to the bond line is a bit unconventional and surprising, since ultrasounds usually should have small wavelengths to detect small defects or to be sensitive to small regions lost in large media. In order to understand this phenomenon, the distributions of displacements, stresses, and power-flow across the thickness of the assembly have been plotted and analyzed at various frequencies. As examples, Figs. 4 and 5 show displacements u_3 and stresses σ_{23} and σ_{13} produced by the SH_1-like mode at

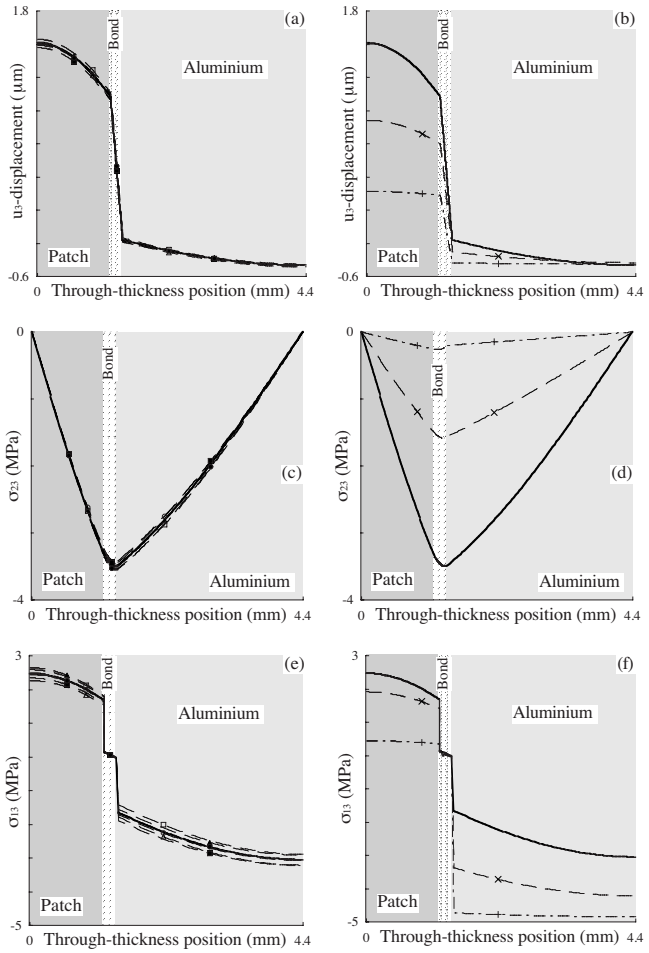

FIG. 4. Numerical predictions of power-normalized [(a) and (b)] u_3 displacement, [(c) and (d)] σ_{23} stress, and [(e) and (f)] σ_{13} stress versus through-thickness position, for changes in material moduli C_{44} and/or C_{55}; (—) are results for central values of data measured in II, left column is for changes in aluminum or patch properties: +5% (—■ —) or −5% (—□—) of aluminum C_{44} and $C_{55}=C_{44}$, +10% (—▲—) or −10% (—△—) of patch C_{44}, +10% (—●—) or −10% (—○—) of patch C_{55}, and right column is for changes in adhesive properties: −40% (—×—) or −85% (—+—) of adhesive C_{44} and $C_{55}=C_{44}$ modes is SH_1 at 0.2 MHz.

0.2 and 0.5 MHz, respectively. These operating points are shown by dots in Fig. 3, and have been chosen so that they correspond to two extreme cases of higher or lower sensitivity to the adhesive than to the aluminum and composite. The mode shapes have been calculated first using the nominal values of the measured material properties as input data, i.e., central values of data given in Table I, and then by alternatively varying these data. The aluminum C_{44} (or $C_{55}=C_{44}$) has been changed within the ±5% interval of confidence related to characterization measurement errors, the composite C_{44} and then C_{55} have been changed within the ±10% interval of confidence, and the C_{44} (or $C_{55}=C_{44}$) for the adhesive layer has been decreased by 40% and then 85% of its nominal value, in agreement with previous changes imposed when plotting the dispersion curves (Fig. 3). Figure 4 indicates that both 40% and 85% decays in the adhesive shear modulus produce much more changes in the mode shape of the SH_1-like mode around 0.2 MHz than any of the ±5% or ±10% variability in the aluminum or composite components. This can explain why the phase velocity of this mode

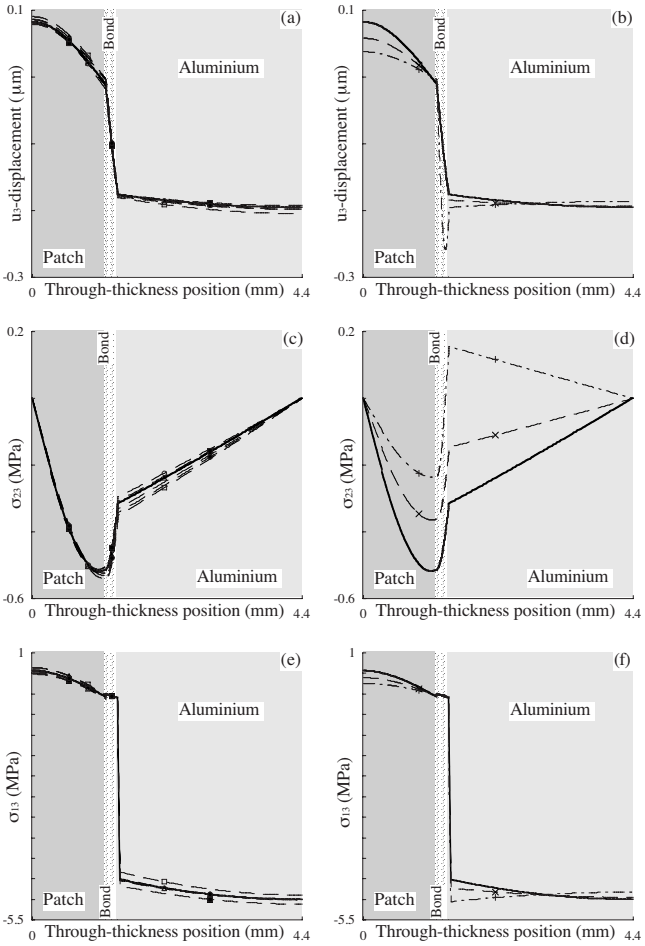

FIG. 5. Same as Fig. 4 but mode is SH_1 at 0.5 MHz.

is more sensitive to the bond layer stiffness than to the aluminum or composite ones, around its cut-off (0.2 MHz is in the vicinity of this cut-off). Similar observation has been made for the SH_0-like mode in the low frequency regime below 0.2 MHz, thus also explaining higher sensitivity of the phase velocity of this mode to the bond layer shear elasticity than to the aluminum or composite ones.

Figure 5 corresponds to a frequency equal to 0.5 MHz at which the SH_1-like mode is roughly as sensitive to the bond shear property as to the aluminum or composite ones. Figure 5(d) shows that σ_{23} is much more sensitive to the adhesive than to any of both assembled materials, but careful attention to the scale of this graph shows that the order of magnitude of this stress component is much smaller (about a tenth) than that of σ_{13} [Fig. 5(f)], so σ_{23} is not enough to render the SH_1-like mode more sensitive to the bond layer than to the aluminum or composite. It is very interesting to note that even up to 85% decay in the shear modulus of the adhesive layer does not cause more changes in the SH_1-like mode shape, at 0.5 MHz, than $\pm 5\%$ or $\pm 10\%$ variability in the shear properties of the aluminum or composite components. This can justify why the phase velocity of this mode is so sensitive-less around 0.5 MHz when changing the bond properties, as shown in Fig. 3.

Now the low frequency domain together with the SH_1-like mode cut-off region have been identified as the ranges of highest sensitivity, it is interesting to proceed to

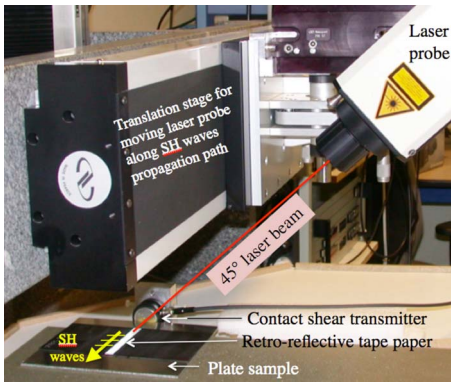

FIG. 6. (Color online) Photo of experimental setup used for launching-detecting SH guided wave modes and for measuring their phase velocities.

experimental measurements, and to check whether measured phase velocities of the SH_0-like and SH_1-like modes can confirm the numerical predictions, at least for validation cases.

V. EXPERIMENTS

A. Setup

The experimental setup is shown in Fig. 6. A 25-mm-diameter, circular PZT transducer (Panametrics V152) is placed into contact with the edge of a plate sample, and coupled using honey. This element is a shear transducer oriented so that it produces horizontal motion, which is suitable for launching SH modes guided along the sample. The excitation signal is a Hanning windowed toneburst with number of cycles and center frequency chosen in order to launch wave modes within a specific frequency range, which depends on the sample to be tested. These will be specified for the various cases presented below. An arbitrary function generator (Agilent 33120A) and a power amplifier (Ritec GA 2500A) are used to produce the desired excitation, with an amplitude of about 400 V peak-to-peak, such high level being necessary for improving the signal-to-noise ratio of the measured waveforms. The end access and use of honey as a couplant are not of practical interest for industrial applications, and the use of electromagnetic acoustic transducers (EMATs), for instance, for launching the SH wave mode may offer a more practical alternative solution.

The displacements produced by the SH guided waves are measured using a Polytec Doppler velocimeter of 0.005 m s^{-1}/V in sensitivity. Only the x_3-component of the displacement is to be measured since this is either the only non-zero component (standard SH waves) or the dominant one, for instance, in the case of SH-like waves propagating along non-principal directions of anisotropic materials for which some motion in the way of the propagation, i.e., along x_1, also exists.[24] To pick up this horizontal u_3 displacement, the laser probe should be tilted at grazing incidences, but for obvious practical reasons it is difficult to produce an angle greater than 60°. The probe is therefore oriented at 45°, an angle which ensures sufficient high level of the detected u_3 displacements (in fact, $u_3 \times \cos 45°$ is detected), as well as good stability of the apparatus when being moved along the path of propagation for proceeding to phase velocities' mea-

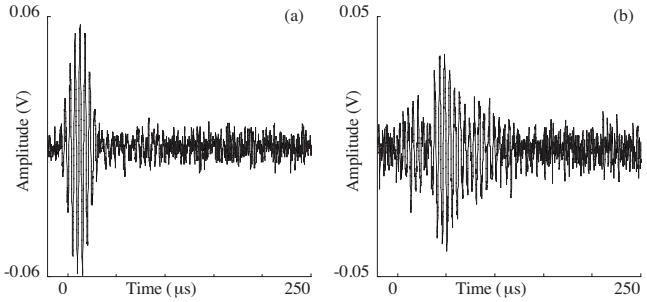

FIG. 7. Real-time signals (particle velocity in V/μs) measured on top of a 5 mm thick carbon epoxy plate using the 45° angled laser probe at distances of (a) 50 and (b) 80 mm away from the contact PZT transmitter shown in Fig. 6.

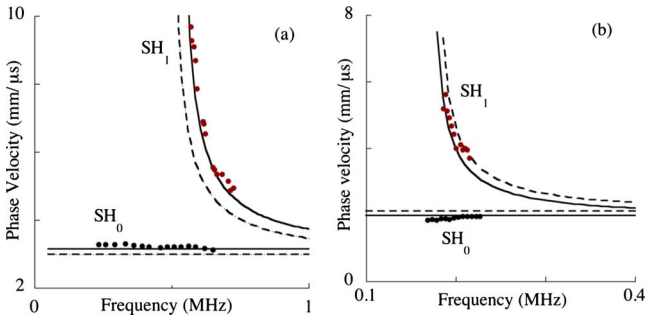

FIG. 8. (Color online) Phase velocities of SH_0 and SH_1 modes along (a) 3 mm thick aluminum plate and (b) 5 mm carbon epoxy plate; numerical predictions (1D SAFE model) with non-optimized (- - -) and with optimized (—) C_{44} and C_{55}, and experimental data (●).

surements. In order to retro-reflect the optical beam of the laser probe back to its 45° incidence, a specific retro-diffusive taper is bonded on the top of the plate sample, along the propagation path. Note that the 45° laser probe is equally sensitive to in- and out-of-plane displacements, but since the propagating SH-like modes produce in-plane displacements only, then these are very well detected.

Figure 7 shows typical real-time (no averaging) waveforms measured on a 5 mm thick carbon epoxy plate at two distances equal to 50 and 80 mm, remote from the PZT transmitter. The signal-to-noise ratio is good enough to identify the guided modes in these measured waveforms. Of course, filtering and averaging are applied to such data in order to reduce the noise and to allow optimum signal processing.

The laser probe is then moved away along the propagation path using a motorized translation stage, and over a distance of about once or twice the expected maximum wavelength (λ_{max}), with steps equal to about a quarter of the expected smallest wavelength (λ_{min}), in the whole frequency range. A two-dimensional fast Fourier transform (2D-FFT) is then applied to the series of measured waveforms to quantify the phase velocities of each mode propagating in the tested sample.[25] These experimental phase velocities can finally be compared to numerical predictions for validation purposes or for characterizing the bond quality. For this latest goal, an inverse problem is solved consisting of adjusting the value of the shear modulus C_{44} of the adhesive layer so that best fitting is obtained between the experimental and theoretical velocities.

B. Validation cases

To validate the laser-based technique, phase velocities are measured for both fundamental SH modes propagating along a free aluminum plate. In this case, the excitation is a 4-cycle toneburst with 0.45 MHz center frequency, so that the frequency range is 0.2–0.7 MHz, down to −20 dB. Sixty-four signals are captured every 0.8 mm ($\approx\lambda_{min}/4$) over 51.2 mm ($\approx\lambda_{max}$) of propagation length. Experimental results are presented by dots in Fig. 8(a), and compared to numerical predictions made (1) with data supplied in Table I (dashed lines) and (2) with slightly optimized C_{44} and C_{55} moduli of the aluminum (plain lines). The slight adjustment of these quantities from their initial values given in Table I to 26.5 and 27.5 GPa, respectively, allows obtaining very good correlation between the experimental and numerical phase velocities. This new estimation of both C_{44} and C_{55} moduli is very close to the initial one made with the immersion technique, if the ±5% measurement errors due to each technique are considered.

The phase velocities of both SH_0 and SH_1 modes are also measured for a free 5 mm thick composite plate. In this case, the excitation is a 5-cycle toneburst with 0.2 MHz center frequency, so that the frequency range is 0.12–0.26 MHz, down to −15 dB. Forty-six signals are captured every 1.5 mm ($\approx\lambda_{min}/4$) over 69 mm ($\approx 2\times\lambda_{max}$) of propagation length. Figure 8(b) compares the experimental phase velocities (dots) with those calculated (1) with data supplied in Table I (dashed lines) and (2) with slightly optimized C_{44} and C_{55} moduli of the composite (plain lines). When optimized, these quantities are shown to be equal to $4.75\times(1+I\ 3\%)$ and $6.2\times(1+I\ 3\%)$ GPa, respectively, with an accuracy of about ±5%. These values confirm those previously obtained and presented in Table I (less than 5% difference). Indeed, as seen in Fig. 8(b), both sets of predictions made using either the initial or optimized moduli are very close to each other.

C. Inferring shear stiffness of bond

The experimental setup has then been tested for an assembly made of a 1.2 mm thick composite patch coupled to a 3 mm thick aluminum plate by a 0.1 ± 0.05 mm thick adhesive bond line having a particularly slow curing process. This approach represents a useful and easy way to monitor changes in the ultrasonic wave propagation for various states of the bonding agent. The incident wave is the SH_0 mode launched from the PZT transmitter along the aluminum plate, as shown in Fig. 6. This propagates along the free aluminum plate before reaching the area where the patch is deposited. Then it propagates along the aluminum/bond/patch region over a 100 mm long path, which corresponds to the width of the square patch sample. In this region, mode conversion occurs and modes corresponding to the three-layered system are produced. Then, past the patch, these modes will be converted back to the SH_0 mode along the aluminum plate. No SH_1 mode is produced along the single-aluminum regions because the frequencies in these experiments do not exceed 0.4 MHz, which is below the frequency cut-off of the SH_1 mode in the 3 mm thick aluminum plate. In fact, the excita-

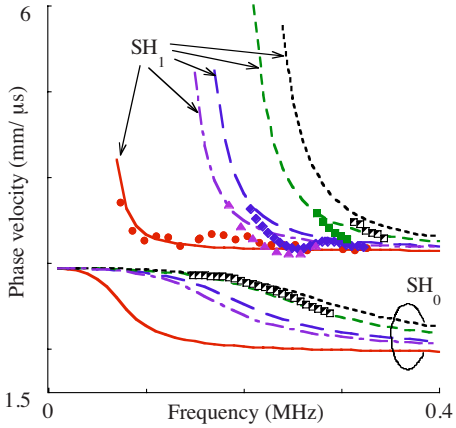

FIG. 9. (Color online) Phase velocities of SH_0 and/or SH_1 modes along 3 mm aluminum plate/0.1 mm adhesive bond/1.2 mm carbon epoxy patch assembly; numerical predictions with optimized C_{44} of adhesive (lines) and experiments (symbols) made at different curing times of adhesive: 45 min (—, ●), 4 h (— – —, ▲), 8 h and 30 min (— —, ◆), 35 h (— —, ■), and infinite time (- - -, ◩).

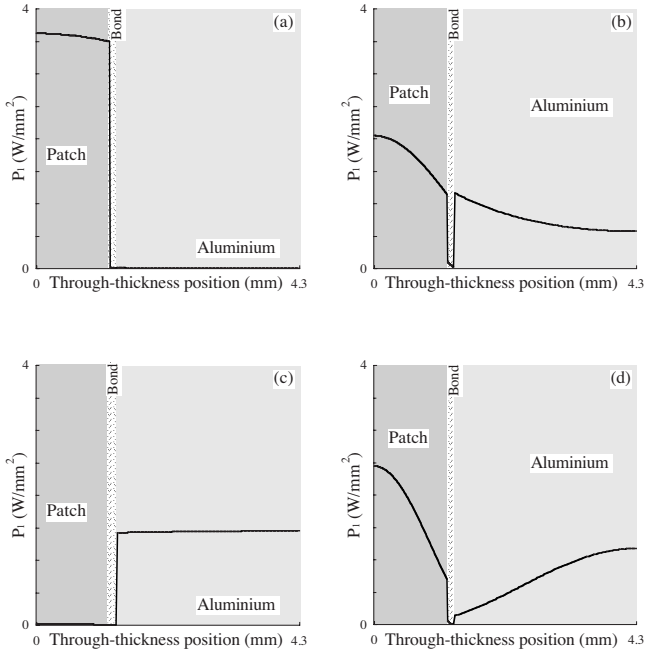

FIG. 10. In-plane power-flow distributions through the aluminum/adhesive/composite assembly for (left column) weak adhesive, i.e., C_{44} corresponds to time 45 min curing process, and for (right column) strong adhesive, i.e., C_{44} corresponds to time few days curing process; top and bottom plots are for SH_0- and SH_1-like modes, respectively, at 0.25 MHz.

tion this time is a 5-cycle toneburst with 0.25 MHz center frequency, so that the frequency range is 0.15–0.35 MHz, down to −15 dB.

Modes produced along the three-layered system are monitored by picking up u_3 displacements at the surface of the composite patch, using the laser probe oriented at 45° and retro-reflective taper placed on the patch, as previously explained. The probe is moved along an 80 mm long propagation path, and temporal signals are stored every 0.8 mm. As previously explained, a 2D-FFT transform is applied to the series of measured waveforms to quantify the phase velocities of each mode propagating along the tested three-layered specimen. Figure 9 shows results obtained at five different times during the curing process of the adhesive: 45 min, 4 h, 8 h and 30 min, 35 h, and finally few days after the bonding is realized. At the very beginning, the adhesive is extremely viscous, and then becomes gradually stiffer and less viscous with time. Measured phase velocities (various symbols) are compared to those predicted (various lines) after C_{44} modulus of the adhesive is optimized (and so $C_{55}=C_{44}$ since the adhesive is supposed to be isotropic). This process consists, in fact, of solving an inverse problem, the purpose of which is to non-destructively characterize the shear stiffness of the bond line. Numerical values obtained for the C_{44} of the adhesive, at the various times, are summarized in Table II. Real quantities have been obtained from this inversion process although C_{44} should be a complex quantity, its imaginary part representing the viscosity of the epoxy-based adhesive. This imaginary component is weakly connected to phase velocities of the SH modes, so no information about it is obtained when measuring these velocities, thus preventing its estimation. However, the initial characterization of this adhesive placed between two glass plates has revealed imaginary parts equal to about 10% of the real parts (Table I). This seems to be a standard estimation for imaginary parts of viscoelastic moduli for epoxy-like materials,[14,26] so it could reasonably be used if complex moduli of the adhesive layer are required.

It is interesting to note that while the SH_0 mode is launched from the PZT transmitter in the aluminum component, only the SH_1-like mode is measured along the aluminum/adhesive/composite assembly for all states of the adhesive, except when this is fully cured. In fact, no or extremely little SH_0-like mode is detected for the first 35 h in the frequency–wave-number diagram plotted from the measured signals, while clear SH_1-like mode is seen, and this is the reverse after the bond has finished curing. This is a very interesting phenomenon, which may be useful for detecting little weaknesses in shear properties of adhesive bonds due to either bad curing or to small degradation occurring in time. This mode conversion phenomenon can be explained in Fig. 10, which displays in-plane power-flow distributions through the aluminum/adhesive/composite assembly, for two extreme states of the adhesive. The first state corresponds to time 45 min right after beginning of the curing process, and the second one to few days after it. In these power-flow calculations, the C_{44} modulus of the bond is set equal to the corresponding optimized value given in Table II, i.e., to 0.02 GPa for the weak state and 0.53 GPa for the strong state, respec-

TABLE II. Optimized real parts of C_{44} of the adhesive joint obtained from the SH phase velocities measured during the curing of an aluminum/adhesive/carbon epoxy assembly.

Curing time	45 min	4 h	8 h and 30 min	35 h	Few days
Optimized C_{44} (GPa)	0.02	0.13	0.18	0.35	0.53

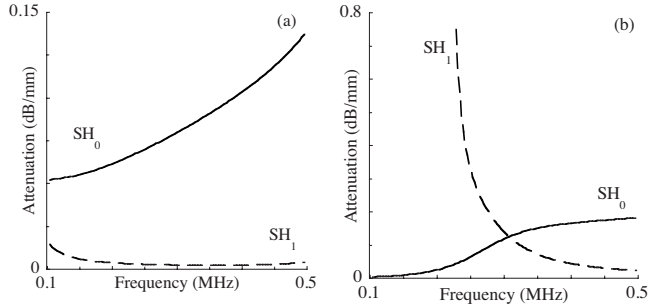

FIG. 11. Predicted attenuation versus frequency for SH_0- and SH_1-like modes propagating along aluminum/adhesive/composite assembly for (a) weak and (b) strong adhesives.

tively. Moreover, according to the explanation given in the previous paragraph, an imaginary part equal to 10% of the real part was added to C_{44} to model the viscosity of the adhesive. Also, the frequency was chosen so that both SH_0- and SH_1-like modes may coexist in the assembly, i.e., equal to 0.2 and 0.3 MHz for the weak and strong states of the adhesive, respectively. Figures 10(a) and 10(c) show that the SH_0-like mode produces no power-flow across the aluminum if the bond is weak (adhesive not cured), while the SH_1-like mode does. This explains why the SH_0 mode incident from the aluminum plate is not coupled to the SH_0-like mode but is coupled to the SH_1 one, in the three-layered region, and so does excite this later only. Figures 10(b) and 10(d) show that both SH_0- and SH_1-like modes produce power-flow across the aluminum if the adhesive is well cured. In this case, the SH_0 mode incident from the aluminum plate should be coupled to both of these modes in the three-layered region. However, as shown in Fig. 11(b), which corresponds to the situation of a well-cured adhesive, the SH_1-like mode has a huge attenuation below 0.25 MHz (>4 dB/cm), which is going down and getting very close to 0 dB/cm as the frequency increases, while the attenuation of the SH_0-like mode is very small below 0.25 MHz, and slowly increases with frequency until it reaches a plateau of about 2 dB/cm maximum. This contributes to the detection of the SH_0-like mode when the bond is of good quality, and to the non-detection of the SH_1-like mode, at least for the lowest frequencies of the frequency range of investigation, which is especially what is shown in Fig. 9. The close-to-zero power-flow in the composite component for the SH_1-like mode propagating with a weak bond [Fig. 10(c)] does not mean that this mode cannot be detected at the surface of the composite. The u_3-displacement component should be considered to estimate whether this mode can be detected or not, and such component is shown to be quite large or at least different than zero, in Fig. 4(b), for example, for various states of the adhesive. In the case of uncured adhesive, as seen in Fig. 11(a), the attenuation is extremely small for the SH_1-like mode, but not for the SH_0-like mode, all over the frequency range of investigation. This also contributes to detecting SH_1 only for cases of weak bonds, and this also is particularly well shown in Fig. 9.

The second interesting result to note in Fig. 9 is the gradual change in the position of the SH_1-like mode cut-off as the adhesive cures. The measured phase velocities for the SH_1-like mode indicate that its frequency cut-off continuously increases from about less than 0.1 MHz to about 0.28 MHz, as the adhesive cures. Such result is very complementary to the previous one, which has shown to make it possible the detection of small degradation in the adhesive shear stiffness, since it will allow different levels of a bad adhesive to be distinguished with each other and eventually the corresponding shear modulus to be inferred, as this has been done in this paper (see Table II).

VI. CONCLUSIONS

The three low-order shear-horizontally polarized guided wave modes have been considered to quantitatively characterize the shear properties of an adhesive bond layer between an aluminum plate and a carbon epoxy composite patch. Numerical predictions have been made using a one-dimensional SAFE model, with specifically implemented shear-spring boundary conditions to consider variable adhesion at the interface between the bond layer and the metallic plate. Phase velocity dispersion curves have been plotted for various states of the bond (cohesive or adhesive properties) and also considering the material variability of either the aluminum or composite components. No SH-like mode has been shown to have phase velocities more sensitive to the shear stiffness of the interface between the bond and the metallic plate, than to any of the shear moduli of the aluminum or composite media. This indicates that phase velocities of any of the three low-order modes should not be used to monitor changes in the adhesion at this interface. The SH_2-like mode has shown to be unsuitable for testing the cohesive properties of the bond because of its high sensitivity to other components (aluminum and composite) or parameters (thickness). However, both SH_0- and SH_1-like modes have revealed higher sensitivities to about 40% and 30% changes, respectively, in the cohesive shear property (shear modulus) of the adhesive layer than in small changes (10% or less) in either the aluminum or composite shear moduli. This phenomenon was particularly visible in the low frequency regime, around or below the SH_1-like mode frequency cut-off, and has been explained by mode shapes plotted at different frequencies.

A laser-based technique has been set up for detecting SH guided wave modes launched by a PZT contact shear transducer. After its validation, this experimental process has been used to measure velocities of SH-like modes propagating along an aluminum/adhesive/patch zone, the incident mode being the pure SH_0 mode produced along the aluminum component, which was much larger than the patch. The adhesive has been selected to have a particularly slow curing process, thus providing an easy way to gradually increase the bond quality over several hours. Phase velocities have then been measured at various times running from right after the bonding was realized to few days after that, to ensure the adhesive curing was finished. Strong mode conversion from the incident SH_0 mode in the aluminum to the SH_1-like mode in the three-layered zone has been clearly observed at all times before the adhesive curing was complete, and no or negligible-in-amplitude SH_0-like mode was detected. Then, after the curing was over, no or very little SH_1-like mode was

detected and strong SH_0-like mode was measured along the assembly. The detection of the SH_1-like mode while the adhesive is not properly cured indicates that this mode conversion phenomenon may be used to monitor changes, due to aging, for example, in initially well-made adhesive bonds. This observed mode conversion phenomenon has been explained by analyzing the through-thickness power-flow together with the attenuation calculated for two extreme levels of the bond quality corresponding to beginning and ending states of the curing process, respectively. The strong sensitivity to the bond of the SH_1-like mode phase velocity, close to its frequency cut-off, allowed the shear moduli of the adhesive layer to be successfully inferred by comparing velocities measured at the various curing times to those predicted using the SAFE model. All these results demonstrate a strong potential of the low-order SH_0- and SH_1-like guided modes to quantify the shear stiffness of adhesive bond layers.

ACKNOWLEDGMENTS

This work was supported by French *Direction Générale des Armées* (DGA). The authors thank the *Centre d'Essais Aéronautiques de Toulouse, France* (CEAT) for providing the composite samples.

[1]M. Genest, M. Martinez, N. Mrad, G. Renaud, and A. Fahr, "Pulsed thermography for nondestructive evaluation and damage growth monitoring of bonded repairs," Compos. Struct. **88**, 112–120 (2009).
[2]ASTM E2582-07, "Standard practice for infrared flash thermography of composite panels and repair patches used in aerospace applications."
[3]F. W. Y. Chan and T. W. Yeung, "Non-destructive evaluation of adhesive bonding using reflective fringe pattern technique," J. Nondestruct. Eval. **27**, 105–114 (2008).
[4]C. J. Brotherhood, B. W. Drinkwater, and S. Dixon, "The detectability of kissing bonds in adhesive joints using ultrasonic techniques," Ultrasonics **41**, 521–529 (2003).
[5]A. M. Robinson, B. W. Drinkwater, and J. Allin, "Dry-coupled low-frequency ultrasonic wheel probes: Application to adhesive bond inspection," NDT & E Int. **36**, 27–36 (2003).
[6]K. Vine, P. Cawley, and A. J. Kinloch, "Comparison of normal and oblique incidence ultrasonic measurements for the detection of environmental degradation of adhesive joints," NDT & E Int. **35**, 241–253 (2002).
[7]A. Baltazar, L. Wang, B. Xie, and S. I. Rokhlin, "Inverse ultrasonic determination of imperfect interfaces and bulk properties of a layer between two solids," J. Acoust. Soc. Am. **114**, 1424–1434 (2003).
[8]M. J. S. Lowe, R. E. Challis, and C. W. Chan, "The transmission of Lamb waves across adhesively bonded lap joints," J. Acoust. Soc. Am. **107**, 1333–1345 (2000).
[9]K. Maslov and T. Kundu, "Selection of Lamb modes for detecting internal defects in composite laminates," Ultrasonics **35**, 141–150 (1997).
[10]J. Laperre and W. Thys, "Experimental and theoretical study of Lamb wave dispersion in aluminum/polymer bilayers," J. Acoust. Soc. Am. **94**, 268–278 (1993).
[11]C. H. Yew, "Using ultrasonic SH waves to estimate the quality of adhesive bonds: A preliminary study," J. Acoust. Soc. Am. **76**, 525–531 (1984).
[12]B. Hosten, "Heterogeneous structure of modes and Kramers–Kronig relationship in anisotropic viscoelastic materials," J. Acoust. Soc. Am. **104**, 1382–1388 (1998).
[13]M. Castaings, B. Hosten, and T. Kundu, "Inversion of ultrasonic plane-wave transmission data in composite plates to infer viscoelastic material properties," NDT & E Int. **33**, 377–392 (2000).
[14]M. Bruneau and C. Potel, *Materials and Acoustics Handbook* (ISTE-WILEY, London, 2009).
[15]I. Bartoli, A. Marzani, F. Lanza di Scalea, and E. Viola, "Modeling wave propagation in damped waveguides of arbitrary cross-section," J. Sound Vib. **295**, 685–707 (2006).
[16]D. Roy Mahapatra and S. Gopalakishnan, "A spectral finite element model for analysis of axial-flexural-shear coupled wave propagation in laminate composite beams," Compos. Struct. **59**, 67–88 (2003).
[17]M. V. Predoi, M. Castaings, B. Hosten, and C. Bacon, "Wave propagation along transversely periodic structures," J. Acoust. Soc. Am. **121**, 1935–1944 (2007).
[18]B. R. Mace, D. Duhamel, M. J. Brennan, and L. Hinke, "Finite element prediction of wave motion in structural waveguides," J. Acoust. Soc. Am. **117**, 2835–2843 (2005).
[19]M. Castaings and M. J. S. Lowe, "Finite element model for wave guided along solid system of arbitrary section coupled to infinite solid media," J. Acoust. Soc. Am. **123**, 696–708 (2008).
[20]B. Hosten and M. Castaings, "Finite elements methods for modeling the guided waves propagation in structures with weak interfaces," J. Acoust. Soc. Am. **117**, 1108–1113 (2005).
[21]M. Drozdz, "Efficient finite element modelling of ultrasound waves in elastic media," Ph.D. thesis, Mechanical Engineering, Imperial College, London, 2008.
[22]COMSOL, "User's guide and introduction," Version 3.5 by COMSOL AB 2005, http://www.comsol.com/ (Last viewed 10/3/2009).
[23]B. A. Auld, *Acoustic Fields and Waves in Solids* (Robert E Krieger, Malabar, FL, 1990).
[24]M. Castaings and B. Hosten, "Lamb and SH waves generated and detected by air-coupled ultrasonic transducers in composite material plates," NDT & E Int. **34**, 249–258 (2001).
[25]D. Alleyne and P. Cawley, "A two-dimensional Fourier transform method for the measurement of propagating multimode signals," J. Acoust. Soc. Am. **89**, 1159–1168 (1991).
[26]B. Hosten and M. Castaings, "Comments on the ultrasonic estimation of the viscoelastic properties of anisotropic materials," Composites, Part A **39**, 1054–1058 (2008).

Detecting cavitation in mercury exposed to a high-energy pulsed proton beam

Nicholas J. Manzi,[a] Parag V. Chitnis, R. Glynn Holt, Ronald A. Roy, and Robin O. Cleveland
Department of Mechanical Engineering, Boston University, 110 Cummington Street, Boston, Massachusetts 02215

Bernie Riemer and Mark Wendel
Spallation Neutron Source, Oak Ridge National Laboratory, Oak Ridge, Tennessee 37831

(Received 5 October 2009; revised 8 February 2010; accepted 10 February 2010)

The Oak Ridge National Laboratory Spallation Neutron Source employs a high-energy pulsed proton beam incident on a mercury target to generate short bursts of neutrons. Absorption of the proton beam produces rapid heating of the mercury, resulting in the formation of acoustic shock waves and the nucleation of cavitation bubbles. The subsequent collapse of these cavitation bubbles promote erosion of the steel target walls. Preliminary measurements using two passive cavitation detectors (megahertz-frequency focused and unfocused piezoelectric transducers) installed in a mercury test target to monitor cavitation generated by proton beams with charges ranging from 0.041 to 4.1 μC will be reported on. Cavitation was initially detected for a beam charge of 0.082 μC by the presence of an acoustic emission approximately 250 μs after arrival of the incident proton beam. This emission was consistent with an inertial cavitation collapse of a bubble with an estimated maximum bubble radius of 0.19 mm, based on collapse time. The peak pressure in the mercury for the initiation of cavitation was predicted to be 0.6 MPa. For a beam charge of 0.41 μC and higher, the lifetimes of the bubbles exceeded the reverberation time of the chamber ($\sim$300 μs), and distinct windows of cavitation activity were detected, a phenomenon that likely resulted from the interaction of the reverberation in the chamber and the cavitation bubbles.
 [DOI: 10.1121/1.3353095]

PACS number(s): 43.35.Ei, 43.20.Ye [DLM] Pages: 2231–2239

I. INTRODUCTION

The Spallation Neutron Source (SNS) is an accelerator-based pulsed neutron source located at the Oak Ridge National Laboratory (ORNL). Currently the SNS is the most intense pulsed neutron beam in the world and is used for scientific research and industrial development.[1] A proton beam is fired at rate of 60 Hz into a mercury target. The proton beam is absorbed in a series of collisions (spallation reaction) that release a burst of neutrons and generate heat within the interaction volume. The microsecond time-scale rise in temperature results in an intense acoustic wave propagating throughout the mercury chamber. The expectation is that the amplitude and duration of the tensile portion of the wave are sufficient to produce cavitation bubbles in the mercury. The inertial collapse of bubbles and/or bubble clouds in close proximity to the inner walls of the target vessel may result in mercury jets that impact the boundary,[2–5] leading to erosion and a reduced service lifetime of the vessel.[6]

The walls of the target vessel in the SNS are made of stainless steel. The photograph in Fig. 1 shows a specimen of the steel wall extracted from the first SNS target module. This specimen is from an interior vessel wall layer that separates the main mercury flow volume from a channel flow that is dedicated to cooling the vessel where the proton beam enters the target. The damaged wall is not a containment boundary but the extent of damage is significant especially considering the limited beam power this first target experienced. This target was removed in July 2009 after more than 3000 MW h of operation. However, more than a third of the hours were below 100 kW and less than 6% was above 700 kW. At maturity the SNS is designed to operate at 1.4 MW (24 μC charge) although upgrades may allow for even higher power. Aggressive cavitation damage threatens to limit the lifetime and power capacity of the target. A research and development program to develop technologies to mitigate such damage has been underway since 2001, under which the experiments reported in this paper were carried out.

One parameter of interest in assessing the damage potential of cavitation in the SNS is the threshold proton beam energy on target for which the onset of cavitation in mercury occurs. Attempts to externally monitor and characterize cavitation activity have been carried out using a laser Doppler vibrometer (LDV) to measure the vibration induced in the mercury chamber walls by the collapsing bubble clouds. The relationship between the acoustic vibration induced by the impact of the collapsing bubbles and the subsequent pitting damage was used to quantify cavitation-induced damage on the wall.[7] A threshold for the onset of cavitation activity in mercury was not reported in this reference.

[a]Author to whom correspondence should be addressed. Electronic mail: nmanzi@bu.edu

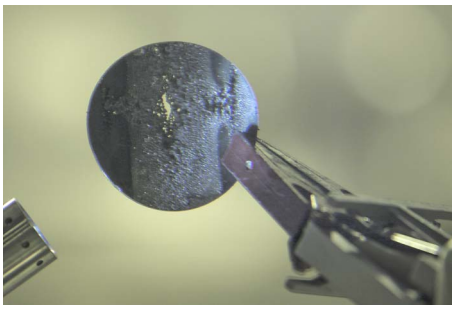

FIG. 1. (Color online) Picture of a specimen extracted from the first SNS target module. This specimen (diameter ~60 mm; original thickness 3 mm) is from an interior vessel wall layer that separates the main mercury flow volume from a channel flow that is dedicated to cooling the vessel where the proton beam enters the target.

It is well documented in water that collapsing cavitation bubbles and clouds produce a distinguishable characteristic acoustic emission upon collapse.[8–11] The goal here was to assess the feasibility of monitoring this acoustic emission to determine a threshold proton beam energy where cavitation first occurs. Megahertz-frequency acoustic transducers immersed in mercury were employed as passive cavitation detectors (PCDs) to record acoustic activity produced within mercury by the collapsing cavitation bubbles.

II. EXPERIMENTAL SETUP

A. Mercury target and PCD alignment

The test target was approximately rectangular in shape with walls made of 4.8-mm-thick 316L stainless steel. The inner dimensions were $203.2 \times 142.9 \times 41.3$ mm^3: A schematic of the target can be seen in Fig. 2. The back wall of the chamber was fitted with two ultrasonic transducers, which were mounted off the axis of the incident proton beam in order to reduce direct radiation exposure to the transducers. The transducers were angled at 11° so that their acoustic axes

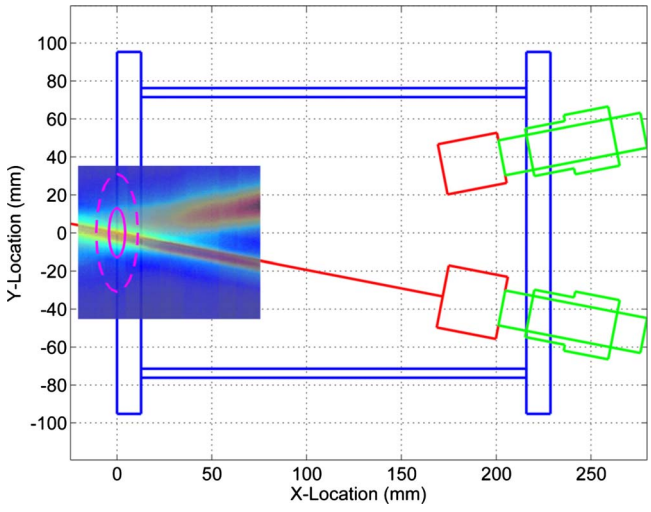

FIG. 2. (Color online) Plan view schematic of the mercury target. The incoming proton beam profiles are shown by the solid ellipse with the width in the *Y*-axis and the height, which is out of the page shown in the *X*-axis. The dashed ellipse shows the large beam profile. The predicted sensing regions for the focused and unfocused transducers are portrayed by the color maps.

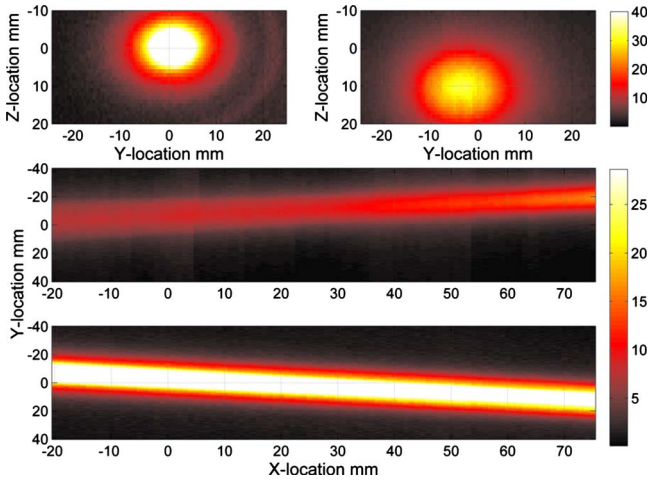

FIG. 3. (Color online) (Top) *Y-Z* scan in the plane of the incident proton beam for the unfocused 1 MHz focused 2.25 MHz transducers. (Bottom) *X-Y* scan of the unfocused 1 MHz and focused 2.25 MHz transducers.

crossed where the proton beam entered the chamber. The two transducers employed were a 2.25 MHz, 25.4 mm diameter, 200 mm spherically focused transducer (model V304, Olympus-NDT, Waltham, MA), and a 1 MHz, 19.05 mm diameter, unfocused transducer (model V314, Olympus-NDT, Waltham, MA). The predicted acoustic fields for the two transducers are also shown in Fig. 2, with the unfocused field calculated using a semi-analytical expression[12] and the focused source by means of an angular spectrum calculation. Piezoelectric transducers typically act as reciprocal devices,[13] and therefore field patterns shown in Fig. 2 also correspond to the regions that the transducers are sensitive to when they are used as receivers. The unfocused transducer was chosen to allow cavitation to be detected over a relatively broad region and the focused transducer was chosen to provide a more sensitive response, albeit for a smaller region.

Prior to immersion in mercury the transducers were mounted into the stainless steel wall and their acoustic fields characterized in water. We note that the sound speed in mercury (~1450 m/s) is close to that of water (~1500 m/s) and therefore the measured spatial acoustic field should be close to that in mercury (the difference in density is only a multiplicative factor). Figure 3 shows results obtained by scanning a broadband point source 175 mm away from the front face of the transducer in the *Y-Z* plane. As seen in Fig. 3 the alignment of the transducers' beam axes in the *Z*-axis was approximately 10 mm off. This suggests a 2°–3° offset in the welded mounting holes used to secure the PCDs. This misalignment was not ideal, but as seen in Fig. 2 the acoustic sensing region of both transducers still coincides with the expected location of the incoming proton beam.

Scans in the *X-Y* plane were also conducted to check the axial sensitivity of the transducers. As expected the unfocused transducer has a larger diameter beam width, ≈20 mm, than the focused transducer ≈6 mm. On the other hand the tighter beam of the focused transducer resulted in great sensitivity at $X=0$, the location where cavitation is anticipated to be most prevalent. The measured beams were well aligned in the *Y*-axis and also in good agreement with the

predicted profiles shown in Fig. 2. The sensitive regions also extend along the length of the chamber and so cavitation activity will also be detected away from the wall.

The PCD transducer configuration was tested by monitoring cavitation activity produced by a shock wave lithotripter in water.[9,14–16] The PCDs were mounted in the plate and placed 175 mm away from the focus of the lithotripter (same distance as in the mercury tests). In this test 50 m long Bayonet Neill-Concelman (BNC) coaxial cables were employed to mimic the long cable path in the proton beam tests as the electromagnetic pulse generated by the proton beam can adversely affect nearby electronic equipment. Cavitation signals were detected by both PCDs with no spurious signal or noise artifacts induced by the use of 50 m cables. In one set of mercury experiments the signal level was determined to be too low and an active filter (model 3944, Krohn-Hite, Brockton, MA) with a 10 kHz high pass filter and 20 dB input gain was placed in a shielded enclosure close to the test target and drove the BNC cable. The data from both PCDs were collected by a digital oscilloscope (LeCroy Waverunner LT344, 8 bits, 500 Msample/s).

B. Pulsed proton beam facility

The Los Alamos Neutron Science Center (LANSCE) at the Los Alamos National Laboratory (LANL) provided the pulsed proton beam used in the experiment. In the LANSCE facility, a linear accelerator accelerates protons to approximately 84% of the speed of light (800 MeV). The proton beam was varied from 1% of full beam charge (0.041 μC) to 100% of full beam charge (4.1 μC). A total of 86 shots were fired over a 2-h time period with at least 30 s in between each shot. The duration of the proton pulse was 0.3 μs. The spatial distribution of the beam is elliptical with 3:1 $X:Y$ aspect ratio and for the bulk of the experiments reported here a beam of 21×7 mm^2 half-width half-height was employed. A full charge of 4.1 μC results in 26×10^{12} protons with a corresponding flux of 28×10^9 protons/mm^2 per pulse. Even though the charge is less than in the SNS at 1.4 MW on a per pulse basis the 4.1 μC charge is equivalent to the SNS running at 2.1 MW because in the SNS the protons are spread over a larger area. Based on nuclear calculations the absorption of the proton beam by mercury should result in a peak pressure of 35 MPa in the mercury.[17] To first order the peak pressure scales linearly with proton flux, that is, at 10% charge (0.41 μC) the peak pressure in the mercury will be 3.5 MPa. Over the duration of the experiment the temperature of the mercury increased by 7.6 K. The primary objective of the proton beam study was to assess damage to the steel chamber,[6] and the PCD experiments reported here were subsequently added to the test plan. The digital oscilloscope used to acquire the PCD signals was triggered by a synchronization pulse provided by LANSCE. This trigger was generated by a sensor that detected the proton beam nanoseconds prior to hitting the mercury target and defines time $t=0$ for all waveforms shown below.

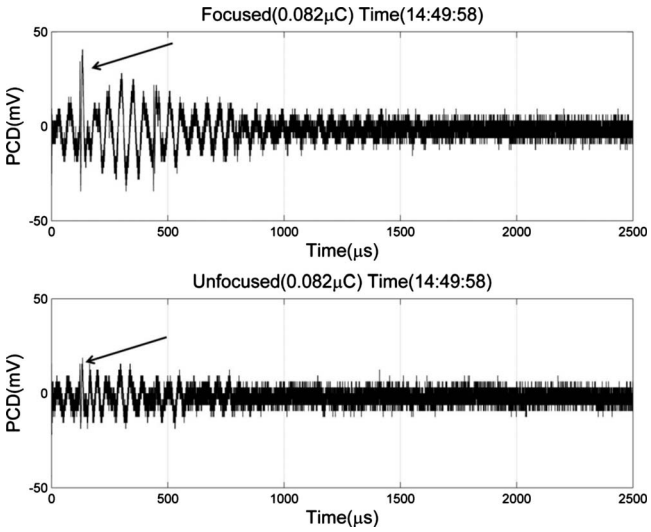

FIG. 4. (Top) Unfiltered signal obtained by the focused transducer for a beam charge of 0.082 μC (2%). (Bottom) Unfiltered signal obtained by the unfocused transducer for a beam charge of 0.082 μC (2%).

III. RESULTS AND DISCUSSION

Examples of the raw waveforms recorded from both PCDs for a beam charge of 2% (0.082 μC) are shown in Fig. 4. The transducers were located 178.5 mm from the entrance of the proton beam and therefore (based on the 1450 m/s sound speed in mercury) the first arrival associated with acoustic activity where the proton beam enters the mercury will be at 124 μs. It is expected that the dominant acoustic signals from the thermo-elastic response of the mercury and the dominant cavitation activity will originate close to where the proton beam enters. Signals prior to 124 μs can most likely be attributed to acoustic waves generated by the proton pulse elsewhere in the fluid and electronic noise. In the raw data shown in Fig. 4, a low frequency signal ($\approx$20 kHz) was observed prior to the expected 124 μs arrival time. The amplitude of this low frequency signal nearly doubled when the beam charge was increased to 5%. The low frequency signal became less prevalent with a continuing increase in the beam energy, but was nonetheless still a substantial part of the signal. Simulations of the acoustic field in the chamber (data not shown) indicated that the $\approx$20 kHz signal could be attributed to reverberation in the vertical axis of the chamber; the height of 41.3 mm has a propagation time of 60 μs. We note that this signal is 50 times lower than the center frequency of the PCDs and thus has already been reduced by the transfer function of the transducers. Given that emissions associated with cavitation are generally high frequency signals ($\geq$100 kHz) a digital high pass filter (fourth order, Butterworth filter with a 100 kHz cut off frequency) was applied to the received data in order to further attenuate these low frequency signals.

Figure 5 shows digitally high passed filtered waveforms collected by the focused and unfocused transducers for beam charges ranging from 1% (0.041 μC) to 100% (4.1 μC). In the waveforms recorded by the focused transducer, for 1%, 2%, and 5% beam charges, there are signals around 124 and 440 μs that appear above the noise. The unfocused transducer also picked up weak signals at 124 and 440 μs with

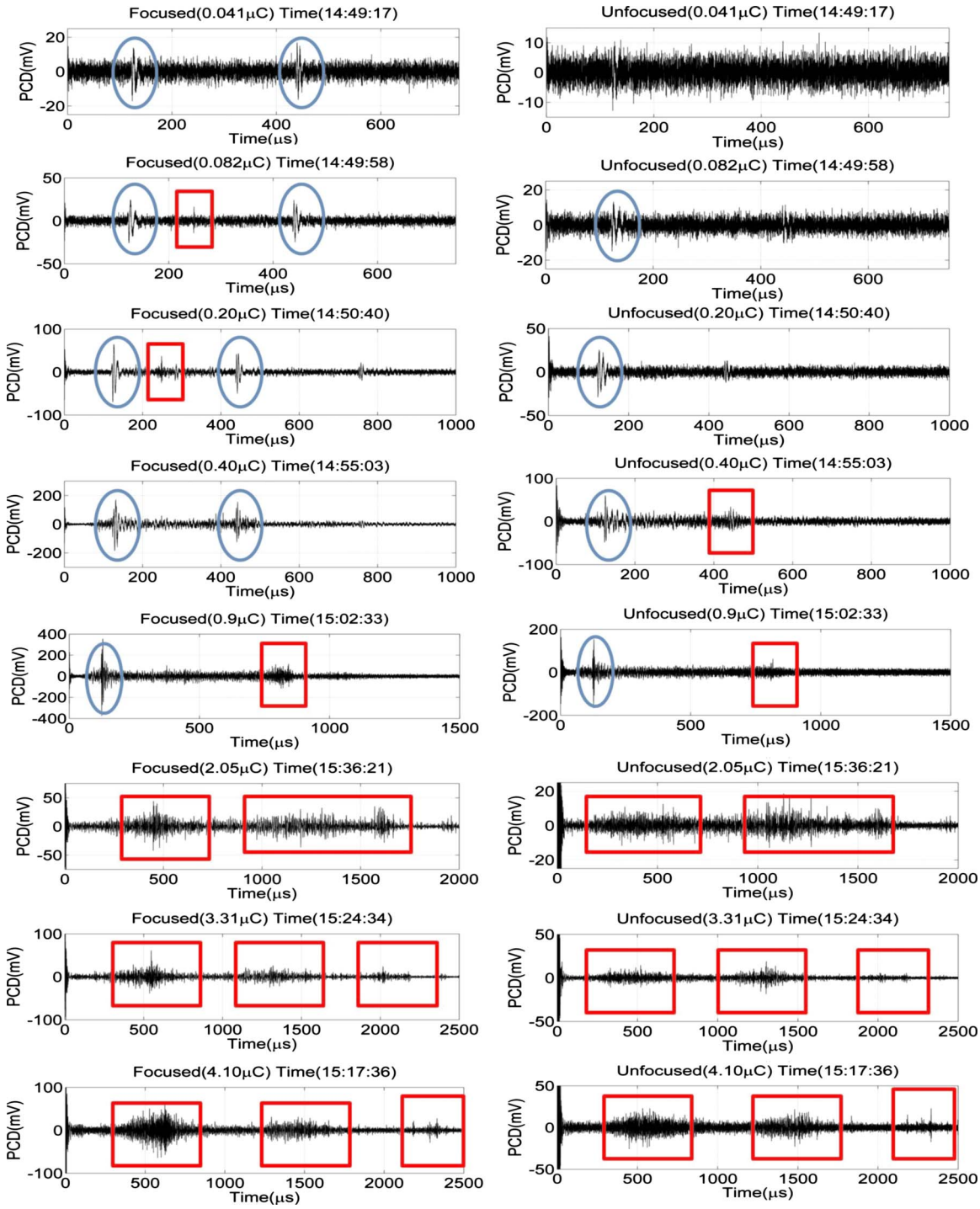

FIG. 5. (Color online) Filtered signals obtained by the focused transducer (left column) and the unfocused transducer (right column) for beam charges of 0.041, 0.082, 0.20, 0.40, 0.90, 2.05, 3.31, and 4.10 μC. Ellipses represent acoustic signals and squares represent cavitation signals. Note that the temporal scale increases as charge increases from 0.4 to 2.05 μC.

the amplitude of this signal approximately half the amplitude produced by the focused transducer. The signal at 124 μs corresponds to the first arrival of the initial pressure wave created by rapid heating of the mercury at the entry point of the proton beam (path length approximately 178 mm), and it what follows it will be referred to as the "direct wave." The signal at 440 μs is caused by a wave that reflects off the back wall, then the front wall, and propagates to the transducer (total path length of about 628 mm); this will be referred to as the "reverberation wave." These two signatures are not associated with cavitation activity and will be identified by circles on the figures.

A. Cavitation threshold

For a beam charge of 1% there was no evidence of cavitation in either PCD trace. As the proton beam charge was increased to 2% (0.082 μC) the amplitude of the direct

wave doubled consistent with the expected linear relationship between beam charge and acoustic generation. Evidence of a very weak cavitation emission is present in the focused transducer data at approximately 240 μs; however, this signal was not detected by the unfocused PCD.

For a beam charge of 5% (0.205 μC) the increase in the amplitude of the direct wave remained consistent with a linear pressure-charge relationship. The focused transducer showed the emergence of two distinct cavitation-related signals: one at 240 μs and the other at approximately 290 μs. These are consistent with the collapse of a cavitation bubble or bubble cloud near the wall where the proton beam was incident. The cavitation event was characterized by a characteristic time $t_c \approx 115$ μs, which is the time between the direct wave (that initiates the cavitation) and the acoustic emission from the bubble collapse.[10] The rebound time $t_r \approx 50$ μs is the time between the acoustic emission from the initial bubble collapse and the second emission from the bubble presumably as a result of a rebound.[11] Again, the cavitation signals were not observed above the noise floor of the unfocused PCD. The focused PCD provides greater sensitivity to cavitation activity and the presence of the cavitation signals indicates that the bubble activity was in or near the sensing volume of the focused PCD. In what follows all transient signals that do not correspond to the direct and reverberation waves will be classified as cavitation signals and in the figures they will be identified by a rectangle.

For a beam charge of 10% (0.41 μC) the arrival of the direct wave was still clearly visible at 124 μs. However, the rest of the waveform has now changed qualitatively. The expected reverberation wave, which should arrive at 440 μs, is not distinguishable from a sequence of signals that arrive over the time period of 375–500 μs. The spikes appear to grow in amplitude and peak at around 450 μs and then rapidly decay such that after 500 μs the signal is barely detectable. The same signal structure was observed in both the focused and unfocused PCDs. We propose that at this beam charge a cloud of cavitation is generated that extends from the entrance window into the bulk of the mercury. These cavitation bubbles are driven hard enough that they have a lifetime greater than the reverberation time of the chamber. As the reverberation wave returns to the front wall it scatters off and/or collapses the cavitation bubbles along its path, which result in the sequence of arrivals observed in the figure with the peak occurring when the reverberation wave interacts with the largest bubbles near the entrance window.

At the next increase in beam charge (20% or 0.90 μC), the focused transducer was still able to pick up the direct wave at 124 μs. The cavitation activity now extended over a time frame that started almost immediately after the incident pulse arrival and grew with time, reaching a peak at 800 μs and then quickly concluding by 900 μs, with the hint of a rebound signature at 1100 μs. There is significant "noise" after the emission at 900 μs suggesting that bubbles remained active for a long time either oscillating and continuing to radiate sound or scattering reverberation waves. The unfocused transducer showed similar behavior but with the direct wave and collapse emission appearing less distinct. These data suggest that cavitation activity is now occurring through much of the mercury. The bubbles further from the window are not driven as hard resulting in a shorter collapse time and a less energetic collapse. In addition, these events are closer to the transducer and therefore will arrive sooner. The cavitation near the window is likely driven the hardest and therefore has the longest time scale, most energetic collapse, and due to the propagation distance will arrive the latest. This is consistent with the strong collapses seen around 800–900 μs. The absence of minor peaks for the unfocused transducer may have been because it was sensitive to a much larger region of space and the emissions from the various bubbles did not arrive in phase.

At a beam charge of 50% (2.05 μC) the direct wave at 124 μs was detectable on both transducers. The focused transducer showed emission activity from 250 to 600 μs with a peak around 440 μs, the time of flight corresponding to the reverberation wave in a bubble free fluid, and may be due to scattering of the reverberation wave from bubbles near the window or acoustic emissions from bubbles that are driven to collapse by the reverberation wave. The cavitation emissions showed a second distinct peak at 1600 μs after which activity decayed.

At a beam charge of 80% (3.31 μC) no clear direct wave was identifiable but this may be related to the apparent loss of sensitivity of the transducer, as will be described in Sec. III C. The PCDs now recorded three "time windows" of cavitation activity. The first window at 550 μs does not correspond to the travel time of the reverberated wave; however, the pulse propagated through a two-phase mercury mixture. We speculate that the presence of bubbles in the bulk of the mercury reduced the effective sound speed thus delaying the arrival of the reverberation wave. The second "time window of activity" occurred between 1100 and 1600 μs similar to the second peak at 50%. A third distinct event occurred at 2100 μs suggestive of a rebound.

For proton beam charge of 4.10 μC (100%) again three windows of cavitation activity were observed. The first window occurred from 400 to 750 μs with distinct acoustic activity around 600 μs. This is an additional 100 μs later than at 80% beam charge and suggests that the propagation speed of the echo signal may have been further slowed by the presence of bubbles in the mercury. The second distinct "time window" occurred from 1250 to 1600 μs. A third time window of cavitation signal occurred around 2250 μs. These windows of cavitation activity were also present in the unfocused signal.

B. Rayleigh collapse

For the lower beam charges of 0.082 and 0.205μC the PCD recorded the characteristic double bang signature of inertial cavitation with a $t_C = 120$ μs. This behavior is indicative of single bubble activity or perhaps a coherent cloud at the surface of the wall. If we assume that the emissions are due to a single bubble and further assume that a bubble spends half of this time in a growth phase and half in a collapse phase then t_C will be twice the Rayleigh collapse time of a cavity.[11,18] The maximum radius of the bubble can then be estimated from the Rayleigh collapse time

$$R_{\max} = \frac{t_C}{1.83}\sqrt{\frac{P_0}{\rho_0}},$$

where P_0 and ρ_0 are the ambient pressure and density of the mercury. In these experiments the mercury was slightly overpressured and P_0=112 kPa in which case the relationship becomes $R_{\max}$=1.6 m/s·t_C and the measured time of 120 μs corresponds to a maximum radius of 0.19 mm. For beam charges of 0.41 μC and higher the double bang signature was lost and instead there were distinct windows of extended cavitation activity. We speculate that for the higher beam charges the collapse time of the cavitation increased such that it was longer than the reverberation time of the chamber. Based on the reverberation time of the chamber the Rayleigh collapse formula predicts that cavitation bubbles grew to a radius greater than 0.5 mm. It is also likely that at the higher beam charges a cloud of cavitation exists in the mercury. Therefore, when the reverberation wave reflected off the back wall it propagated through the bubbles before they had collapsed inertially. Instead the bubbles were driven to collapse by the reflected acoustic pulse.

C. Transducer status

In the course of the experiments, an apparent reduction in the sensitivity of the transducers was observed. This was assessed by monitoring the amplitude of the direct wave during the tests. The pressure amplitude of the direct wave should be linearly proportional to the proton flux and therefore the direct wave amplitude divided by the beam charge should remain constant throughout the experiments. Figure 6 shows the direct wave amplitude normalized by the beam charge as a function of time (top) and the beam charge as a function of time (bottom). Also shown is the amplitude of the noise normalized by the beam charge.

For the first 18 min both the normalized direct wave and the normalized noise remain reasonably constant. At 18 min, when a beam charge of 50% (2.05 μC) was employed, the direct wave amplitude dropped to that of the noise floor. As the beam charge was increased to 4.10 μC both normalized levels dropped reaching a minimum at about 35 min—associated with the last proton beam at 4.10 μC. In particular, the normalized direct wave amplitude was about 400 times less than the value at 0 min. From 35 to 65 min the beam charge was stepped down to 0.41 μC and the normalized levels started to increase. However, at 65 min, neither the direct wave nor noise level has recovered to their initial values. The data suggest a transient change in the signal levels detected by the PCDs for the higher beam charge.

In order to estimate the performance of the transducers, the response was assessed before, during, and after radiation exposure by transmitting a broadband pulse with the unfocused transducer and sensing the reflection from the window with the focused transducer. This yielded information regarding the combined response of both transducers (plus the reflectivity of the window) rather than the response of an individual transducer. The unfocused transducer was excited with a pulser-receiver [model 5072PR, Panametrics (now Olympus-NDT), Waltham, MA]. Figure 7 shows the evolution of the combined response (temporal and spectral). Prior to exposure to proton beam pulses, the received signal was 400 mV_{pp} and the spectrum contained two distinct peaks at 0.75 and 1.75 MHz. A measurement taken midway in the beam experiments (at a time just after 65 min on Fig. 6, which corresponded to approximately 50 beam pulses) showed a dramatic change in the temporal and spectral responses to the reflected wave. The amplitude dropped by nearly a factor of 50 to about 8 mV_{pp}, and the two peaks at 0.75 and 1.75 MHz are no longer present in the spectrum. The change in amplitude is consistent with the change in the normalized direct wave shown in Fig. 6.

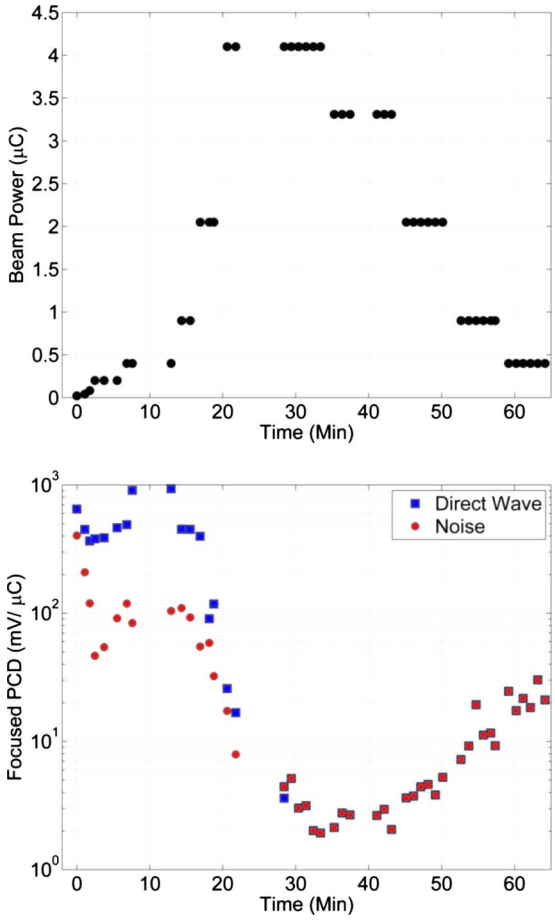

FIG. 6. (Color online) (Top) Response, normalized to beam power, of the focused PCD prior to the arrival of the direct wave (squares) and the subsequent noise floor (circles) of that response as a function of time. (Bottom) Beam charge in microcoloumb as a function of time.

Waveforms taken immediately following the completion of beam exposure show a shape similar to that taken midway through beam exposure; however, the waveforms did show an increase in the signal level to about 70 mV_{pp}, and the spectral signal around 1 MHz is beginning to recover. The transducer's response recovered to near pre-exposure levels (approximately 325 mV_{pp}) 20 h after beam exposure, and was comparable to the pre-beam exposure temporal and spectral responses. It is possible that the proton beam induced a transient change in the piezoelectric efficiency of the transducers, although we would anticipate that in this scenario a permanent depolarization would occur. Another ex-

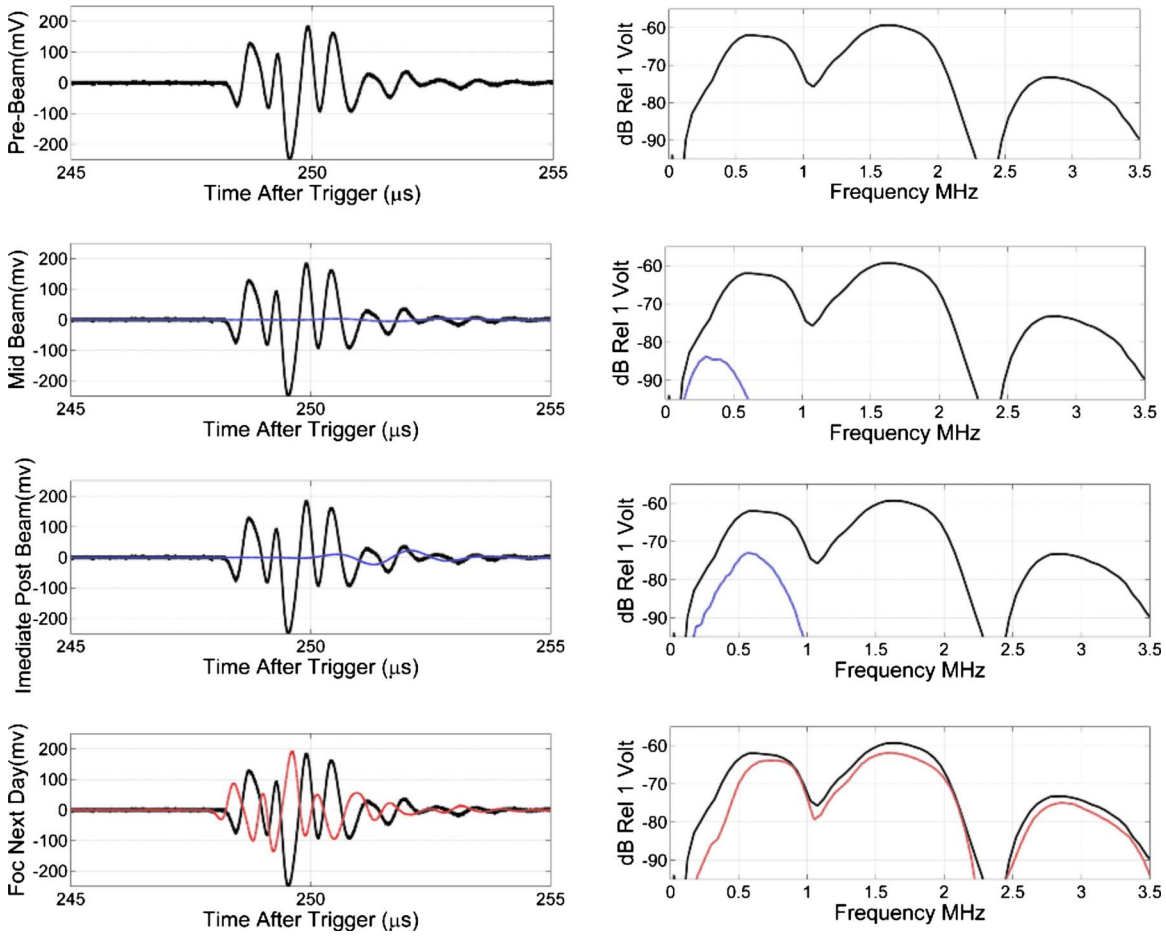

FIG. 7. (Color online) Response of the PCDs prior to, midway through, immediately following, and 1 day after proton beam exposure. (Left) Temporal response measured by pulsing with the unfocused transducer and listening to reflected wave off the front window of the mercury chamber with the focused transducer. (Right) The associated amplitude spectra. For the later responses the initial response is also shown as a solid line.

planation is that the increases in temperature of the bulk fluid may have contributed to the changes. However, only a 7 K increase in temperature was recorded and this certainly did not affect the sound speed as can be ascertained from the arrival times in Fig. 7. Also the temperature hypothesis is not consistent with the initial recovery seen at the end of the experiments as the temperature should have still be increasing.

A more likely explanation for the change is the presence of bubbles, which attenuated the acoustic wave. The absence of a temporal shift in the arrival time of the pulses suggests that it was probably not due to bubbles in the bulk. Therefore we speculate that the reduction in sensitivity was due to the accumulation of stable bubbles on the face of the transducer. Mercury does not readily wet most solid surfaces (typical contact angles between 130° and 140°) and further our experience indicates that mercury tends to push out particulates and impurities and deposit them on the surfaces of the chamber. Cavitation bubbles formed close to the transducers at high beam charges may have migrated to the surface and remained there—perhaps partially stabilized by the impurities that had been ejected by the mercury. Such a bubble wall would serve to acoustically isolate the sensor. The mercury was slightly overpressured with helium gas and so there was gas in the mercury, which could have diffused into bubbles during cavitation activity. This gas would diffuse back into the mercury in the quiet times between proton pulses. We speculate that as the beam charge was increased the amount of gas driven into the bubbles increased and the bubbles grew to a large enough size or number density that they shielded the PCDs. As the beam charge was reduced the cavitation activity also reduced and so less gas was driven into the bubble and the bubbles shrunk during the quiet periods—this would be consistent with the slow recovery observed in Fig. 6 toward the end of the experiments.

Figure 8 shows PCD measurements after the change in sensitivity of the transducers for a beam charge of 50%. In comparison to the waveforms shown in Fig. 5 for 50% beam charge it can be seen that the direct wave is no longer detected but three distinct windows of cavitation activity are observed. The first at 450 μs is consistent with the emissions shown in Fig. 5. The second at 1600 μs is about 100 μs later than seen in Fig. 5. A third out-lying distinct cavitation signal also occurred at 1950 μs, which was not detected in the earlier data. These three windows of cavitation activity are also present in the unfocused signal. These later signals also show an apparent reduction in "noise" signal between the emissions.

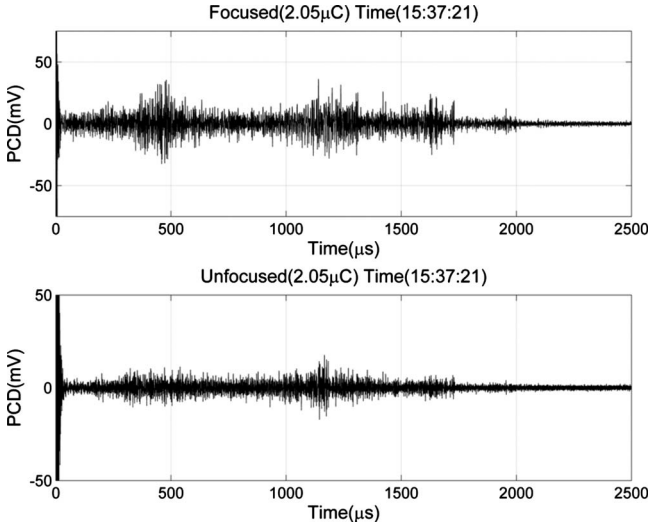

FIG. 8. PCD measurements after the change in sensitivity of the transducers for a beam charge of 2.05 μC (50%).

D. Beam shape study

The previous experiments all employed an elliptical incident beam profile that had a nominal half-width of 21 mm and a half-height of 7 mm. In order to assess the effect of the spatial profile of the proton beam on cavitation activity, full beam charge experiments were conducted with a small (15×5 mm^2) and a large beam (30×11 mm^2). To account for the reduction in sensitivity of both PCDs signals from each transducer were amplified with 20 dB gain and filtered at 10 kHz high pass. The digitized signals were then passed through the 100 kHz digital high pass filter described previously. Figure 9 shows representative waveforms taken for the small and large beams.

For the small beam the PCD waveforms look remarkably similar to those for the nominal (medium) beam size in Fig. 5. There are windows of cavitation activity from 400–700 and 1250–1600 μs, which are temporally and morphologically similar to what was observed for the regular beam. It is not possible to conclude whether cavitation fields generated by the small and medium beams are significantly different.

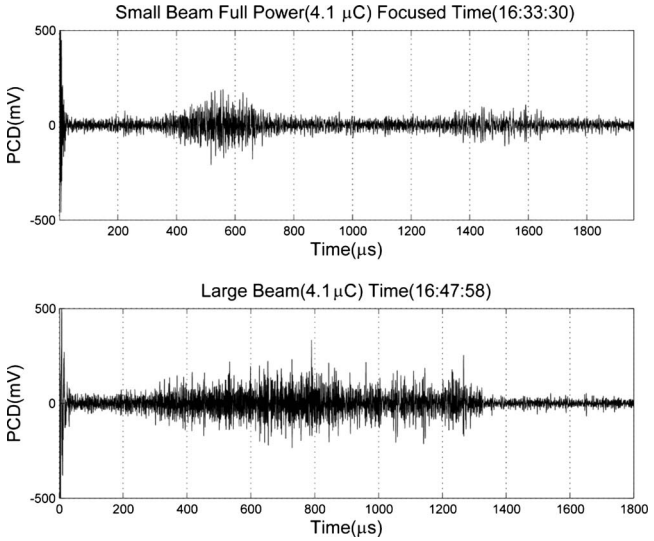

FIG. 9. Representative waveforms obtained for different beam sizes at full charge 4.1 μC. (Top) Smaller beam size (15 mm half-width $\times 5$ mm half-height). (Bottom) Larger beam size (30 mm half-width $\times 11$ mm half-height).

In contrast, the waveforms for the large beam showed a distinct change in the cavitation signature. There was no longer the presence of two distinct time windows of cavitation. Instead there was one window of activity, which began slightly earlier ($\approx$300 μs) and remained present until an abrupt transition at approximately 1300 μs. This single episode of cavitation suggests that the large beam produced a cavitation cloud of larger spatial extent that interfered so strongly with the acoustic reverberation that the cavitation patterns seen for the medium and small beams did not occur here.

IV. CONCLUSIONS

We have demonstrated that both focused and unfocused megahertz-frequency immersion transducers, acting as passive cavitation detectors, are able to identify acoustic emissions from cavitation induced by the rapid absorption of a pulsed proton beam in mercury. The focused PCD proved more sensitive and was able to detect cavitation signals for a beam charge as low as 0.082 μC. Calculations predict a pressure amplitude of 0.6 MPa in the mercury at this charge and this is therefore an estimate of the cavitation threshold in mercury.

PCD measurements taken for a proton beam with a reduced beam size resulted in cavitation signatures similar to the normal-sized beam. However, for a wider proton beam, cavitation signals were only received over one time window indicating that the proton beam energy produced a cavitation field with different spatial and temporal characteristics. Despite exposure to an intense proton beam the two transducers remained operational throughout the process. However, the overall sensitivity and high frequency response of both detectors did decay during exposure. The effect proved transient, as the response recovered the following day, and we speculate that it was due to the buildup of bubbles on the transducer surface.

These results demonstrate that proton beam induced cavitation can be detected in mercury using PCDs. By using a focused detector, one can achieve resolution in both space and time. For low beam powers the cavitation signatures were similar to the double bang emissions expected from inertial cavitation. As the beam power increased it appeared that reverberation in the chamber interacted with the cavitation field to result in more complex cavitation activity with cavitation collapses throughout the mercury. The results suggest that PCDs could be incorporated into the SNS mercury target in order to monitor cavitation activity during operation.

ACKNOWLEDGMENTS

This work was supported by the ORNL Spallation Neutron Source, which is managed by University of Tennessee (UT)-Battelle, LLC, under Contract No. DE-AC05-

00OR22725 for the U.S. Department of Energy. The authors would like to thank the LANL and ORNL staffs, in particular, David Felde (ORNL), for technical help with the experiments. This work has benefited from the use of the Los Alamos Neutron Science Center at the Los Alamos National Laboratory, a facility funded by the U.S. Department of Energy.

[1]http://neutrons.ornl.gov/aboutsns/aboutsns.shtml (Last viewed 2/8/2010).
[2]T. Benjamin and A. Ellis, "The collapse of cavitation bubbles and the pressure thereby produced against solid boundaries," Philos. Trans. R. Soc. London, Ser. A **260**, 221–240 (1966).
[3]J. Blake and D. Gibson, "Growth and collapse of a vapor cavity near a free surface," J. Fluid Mech. **111**, 123–140 (1981).
[4]J. Blake and D. Gibson, "Cavitation bubbles near boundaries," Annu. Rev. Fluid Mech. **19**, 99–123 (1987).
[5]T. Leighton, *The Acoustic Bubble* (Academic, Boston, MA, 1997), pp. 531–545.
[6]J. Haines, B. Riemer, D. Felde, J. Hunn, S. Pawel, and C. Tsai, "Summary of cavitation erosion investigations for the SNS mercury target," J. Nucl. Mater. **343**, 58–69 (2005).
[7]M. Futakawa, H. Kogawa, S. Hasegawa, Y. Ikeda, B. Riemer, M. Wendel, J. Haines, G. Bauer, T. Naoe, N. Tanaka, K. Okita, A. Fijiwara, and Y. Matsumoto, "Cavitation erosion by proton beam bombarding mercury target for spallation neutron source," Sixth International Symposium on Cavitation, Wageningen, The Netherlands (2006).
[8]A. Vogel and W. Lauterborn, "Acoustic transient generation by laser-produced cavitation bubbles near solid boundaries," J. Acoust. Soc. Am. **84**, 719–731 (1988).
[9]A. Coleman, J. Saunders, L. Crum, and M. Dyson, "Acoustic cavitation generated by an extra corporeal shock wave lithotripter," Ultrasound Med. Biol. **13**, 69–76 (1987).
[10]A. Coleman, M. Choi, J. Saunders, and T. Leighton, "Acoustic emission and sonoluminescence due to cavitation at the beam focus of an electro hydraulic shock wave lithotripter," Ultrasound Med. Biol. **18**, 267–281 (1992).
[11]R. Cleveland, O. Sapozhnikov, M. Bailey, and L. Crum, "A dual passive cavitation detector for localized detection of lithotripsy-induced cavitation in vitro," J. Acoust. Soc. Am. **107**, 1745–1758 (2000).
[12]D. Hutchins, H. Mair, P. Puhach, and A. Osei, "Continuous-wave pressure fields of ultrasonic transducers," J. Acoust. Soc. Am. **80**, 1–12 (1986).
[13]M. Willatzen, "Ultrasound transducer modeling—General theory and applications to ultrasound reciprocal systems," IEEE Trans. Ultrason. Ferroelectr. Freq. Control **48**, 100–12 (2001).
[14]L. Crum, "Cavitation micro-jets as a contributory mechanism for renal calculi disintegration in ESWL," J. Urol. (Baltimore) **140**, 1587–1590 (1988).
[15]G. Delacrétaz, K. Rink, G. Pittomvils, J. P. Lafaut, H. Vandeursen, and R. Boving, "Importance of the implosion of ESWL-induced cavitation bubbles," Ultrasound Med. Biol. **21**, 97–103 (1995).
[16]Y. Pishchalnikov, O. Sapozhnikov, M. Bailey, J. Williams, Jr., R. Cleveland, T. Colonius, L. Crum, A. Evan, and J. McAteer, "Cavitation bubble cluster activity in the breakage of kidney stones by lithotripter shock waves," J. Endourol **17**, 435–446 (2003).
[17]B. Riemer, "Benchmarking dynamic strain predictions of pulsed mercury spallation target vessels," J. Nucl. Mater. **343**, 81–91 (2005).
[18]P. Chitnis and R. Cleveland, "Quantitative measurements of acoustic emissions from cavitation at the surface of a stone in response to a lithotripter shock wave," J. Acoust. Soc. Am. **119**, 1929–1932 (2006).

On wavemodes at the interface of a fluid and a fluid-saturated poroelastic solid

K. N. van Dalen,[a] G. G. Drijkoningen, and D. M. J. Smeulders
Department of Geotechnology, Faculty of Civil Engineering and Geosciences, Delft University of Technology, Stevinweg 1, 2628 CN Delft, The Netherlands

(Received 21 April 2009; revised 12 January 2010; accepted 12 January 2010)

Pseudo interface waves can exist at the interface of a fluid and a fluid-saturated poroelastic solid. These waves are typically related to the pseudo-Rayleigh pole and the pseudo-Stoneley pole in the complex slowness plane. It is found that each of these two poles can contribute (as a residue) to a full transient wave motion when the corresponding Fourier integral is computed on the principal Riemann sheet. This contradicts the generally accepted explanation that a pseudo interface wave originates from a pole on a nonprincipal Riemann sheet. It is also shown that part of the physical properties of a pseudo interface wave can be captured by loop integrals along the branch cuts in the complex slowness plane. Moreover, it is observed that the pseudo-Stoneley pole is not always present on the principal Riemann sheet depending also on frequency rather than on the contrast in material parameters only. Finally, it is shown that two additional zeroes of the poroelastic Stoneley dispersion equation, which are comparable with the $\bar{P}$-poles known in nonporous elastic solids, do have physical significance due to their residue contributions to a full point-force response.
 [DOI: 10.1121/1.3308473]

PACS number(s): 43.35.Pt, 43.20.Jr, 43.20.Gp, 43.20.Bi [JM] Pages: 2240–2251

I. INTRODUCTION

Interface waves such as Rayleigh and Stoneley waves are often used to investigate materials. One can think of applications in ultrasonic testing of structures, borehole logging in geotechnical and reservoir engineering, and surface seismics in geophysics, see, e.g., Refs. 1–4. In the case of porous materials, interface waves carry information on elastic properties but also on properties such as porosity, permeability, and fluid mobility.[1] Rosenbaum[5] found that, compared to all other surface and body wavemodes, the Stoneley-type wave that travels along the open-pore interface of a fluid and a porous medium, carries the best measure of permeability.

Several theoretical studies were performed on interface waves that propagate along the boundary of a porous medium. These studies were carried out in the context of Biot's theory for wave propagation in fluid-saturated poroelastic solids. Deresiewicz[6] showed the existence of a Rayleigh-type wave that propagates along the free surface of a poroelastic half-space and analyzed the frequency-dependent phase velocity and attenuation.

For a fluid/poroelastic-medium configuration, Rosenbaum[5] predicted the existence of the pseudo-Rayleigh (*pR*) and the pseudo-Stoneley (*pSt*) wave. The latter was explicitly named as such by Feng and Johnson,[7,8] since a pseudo interface wave has part of its energy leaking into slower bulk modes as it propagates along the interface. Feng and Johnson[7] also showed the existence of another interface wavemode, the nonleaky true interface wave. It was found that the existence of this wave depends on whether or not the pores are open for pore fluid to flow across the interface. Feng and Johnson[8] derived Green's functions (impulse responses) for high-frequency Biot theory that confirmed the existence of the three different waves.

Experimental evidence was found for all three types of interface wavemodes, see, e.g., Refs. 9–11.

Feng and Johnson[7] argued that other zeroes of the poroelastic Stoneley dispersion equation have no physical significance as pseudo interface modes. The corresponding propagation velocities would be larger than that of shear waves, which is not realistic.

In order to obtain the characteristics of the interface wavemodes, Feng and Johnson[7] used the zeroes of the nonviscid poroelastic Stoneley dispersion equation in the complex plane to obtain the propagation velocities and attenuations. Gubaidullin *et al.*[12] went a step further and analyzed the frequency dependence of the interface wavemodes by incorporating the viscous loss mechanism of Johnson *et al.*[13] They also used the zeroes of the dispersion equation to derive the characteristics of the interface waves. The same approach was adopted by Edelman and Wilmanski,[14] Albers,[15] and Markov.[16] In most of the papers, specific restrictions for the involved square roots (i.e., their Riemann sheets) are given.

The generally accepted explanation for a pseudo interface wave is that it originates from a zero that forms a pole singularity on another Riemann sheet than the so-called "principal" sheet. It affects the behavior of the integrand on the principal Riemann sheet by causing a local maximum in the integrand.[17] In case the pole lies close to the real axis, it might have a contribution to the Green's function.

In a series of publications, Allard *et al.*[11,18,19] studied the propagation of interface waves along the boundaries of poroelastic and nonporous elastic media. In the case of an air/air-saturated poroelastic-solid configuration, they found that

[a]Author to whom correspondence should be addressed. Electronic mail: k.n.vandalen@tudelft.nl

 0001-4966/2010/127(4)/2240/12/$25.00

taking the residue of the pseudo-Rayleigh pole is sufficient to describe the entire pseudo-Rayleigh waveform.[19] For the water/water-saturated poroelastic-solid configuration, they found that the pseudo-Stoneley pole residue describes the entire waveform of the pseudo-Stoneley wave.[11] However, for the water/elastic-solid configuration, they found that the pseudo-Rayleigh waveform is strongly affected by the loop integrals along the branch cuts.

In summary, taking just the location of the zeroes of the dispersion equation rather than computing the full transient response is a very fast way to predict the kinematic properties of pseudo interface waves, but the question arises if these predictions are always complete.

Therefore, in this paper we analyze the three-dimensional transient wave propagation due to a point force applied at the interface of a fluid and a fluid-saturated poroelastic solid. The aims are as follows.

(1) To investigate if a zero of the poroelastic Stoneley dispersion equation indeed yields the pertinent physical properties of the corresponding pseudo interface wavemode. This is done by quantitative comparison between the residues of specific poles and the full transient response.
(2) To verify if a pseudo interface wave indeed necessarily originates from a pole on a nonprincipal Riemann sheet.
(3) To verify the physical significance of additional zeroes of the poroelastic Stoneley dispersion equation that are not related to pseudo interface waves.[7]

The paper is organized as follows. In Sec. II, we present the model to analyze the fluid/poroelastic-medium configuration. Subsequently, in Sec. III, the derivation of Green's function is summarized. The implementation of the numerical integration is discussed in Sec. IV. We discuss the results in Sec. V. The conclusions are given in Sec. VI.

II. MODEL

To study the transient wave propagation in a fluid/poroelastic-medium configuration, we consider a configuration that consists of a fluid half-space on top of a fluid-saturated poroelastic half-space. A vertical point force $F(t)$ is applied at the interface [see Fig. 1(a); Fig. 1(b) is referred to later]. Both half-spaces are considered to be homogeneous and isotropic. The configuration is similar to the one applied by Gubaidullin *et al.*[12] but extended to three dimensions.

The behavior in the lower half-space ($x_3>0$) is governed by the well-known Biot equations of motion for a fluid-saturated poroelastic solid that were extensively discussed in this journal, see, e.g., Refs. 20 and 21. Following Biot's theory, we assume that for long wavelength disturbances with respect to the characteristic pore scale, average local displacements can be defined for the solid (frame) $\mathbf{u}(\mathbf{x},t)=(u_1,u_2,u_3)^T$ and the fluid $\mathbf{U}(\mathbf{x},t)=(U_1,U_2,U_3)^T$. Considering a cube of unit size of bulk material (porosity ϕ), the forces per unit bulk area applied to that part of the cube faces occupied by the solid are denoted by τ_{ij}. They are constituted by both fluid pressure p_f and intergranular stresses σ_{ij} according to

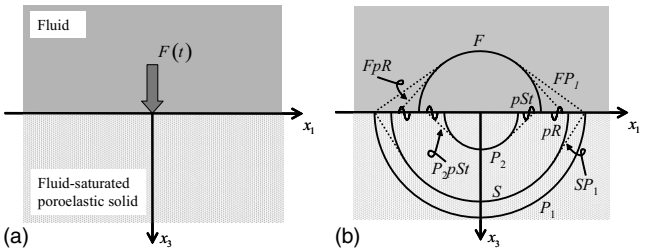

FIG. 1. (a) Point force $F(t)$ applied at the interface of a fluid-saturated poroelastic half-space and a fluid half-space. Both half-spaces are homogeneous and isotropic. (b) Schematic snapshot of the full response with separate arrivals: fast compressional (P_1) wave, slow compressional (P_2) wave, shear (S) wave, fluid (F) wave, pseudo-Rayleigh (pR) wave, and pseudo-Stoneley (pSt) wave. The double-mode symbols (e.g., SP_1) indicate lateral waves ($\cdots$). The first symbol denotes the wavemode of the specific arrival; the second denotes the one from which it is radiated. Here, the F-wave velocity is assumed higher than the P_2-wave velocity. For clarity, we omitted the following arrivals: FS, P_2P_1, P_2S, P_2pR, and P_2F.

$$\tau_{ij} = -\sigma_{ij} - (1-\phi)p_f\delta_{ij}, \tag{1}$$

where δ_{ij} is the Kronecker delta. The total normal tension force per unit bulk area applied to the fluid faces of the unit cube, denoted by τ, is constituted by p_f only,

$$\tau = -\phi p_f. \tag{2}$$

Here, σ_{ij} and p_f are defined positive in compression and, consequently, τ_{ij} and τ are positive in tension, see also Ref. 12. In the case of isotropic materials, the stress-strain relations for the solid and the fluid can be written as

$$\tau_{ij} = G(\partial_i u_j + \partial_j u_i) + A\partial_k u_k \delta_{ij} + Q\partial_k U_k \delta_{ij}, \tag{3}$$

$$\tau = Q\partial_k u_k + R\partial_k U_k, \tag{4}$$

where Einstein's summation convention for repeated indices is applied, and $\partial_j = \partial/\partial x_j$. A, Q, and R are generalized elastic constants that can be related via Gedanken experiments to porosity, grain bulk modulus K_s, fluid bulk modulus K_f, bulk modulus of porous drained frame K_b, and shear modulus G of both drained frame and total composite.[22,23] The physical background of Eqs. (3) and (4) is discussed in more detail in Ref. 20.

The equations of motion are found from combination of momentum conservation and the stress-strain relations, Eqs. (3) and (4), and can be written as[20,21]

$$\rho_{11}\partial_t^2\mathbf{u} + \rho_{12}\partial_t^2\mathbf{U} + b * \partial_t(\mathbf{u}-\mathbf{U}) = P\nabla\nabla\cdot\mathbf{u} - G\nabla\times\nabla\times\mathbf{u} + Q\nabla\nabla\cdot\mathbf{U}, \tag{5}$$

$$\rho_{12}\partial_t^2\mathbf{u} + \rho_{22}\partial_t^2\mathbf{U} - b * \partial_t(\mathbf{u}-\mathbf{U}) = Q\nabla\nabla\cdot\mathbf{u} + R\nabla\nabla\cdot\mathbf{U}, \tag{6}$$

where the asterisk denotes convolution, $P=A+2G$, and the effective densities are defined as

$$\rho_{11} = (1-\phi)\rho_s - \rho_{12},$$

$$\rho_{22} = \phi\rho_f - \rho_{12},$$

$$\rho_{12} = -(\alpha_\infty - 1)\phi\rho_f, \tag{7}$$

where the tortuosity $\alpha_\infty \geq 1$, and hence $\rho_{12} \leq 0$. Solid and fluid densities are denoted as ρ_s and ρ_f, respectively. The

linear time-convolution operator b was formulated in the frequency domain as the viscous correction factor by Johnson *et al.*,[13] according to

$$\hat{b}(\omega) = b_0\left(1 + \tfrac{1}{2}iM\omega/\omega_c\right)^{1/2}, \tag{8}$$

where the viscous damping factor $b_0 = \phi^2\eta/k_0$. Here, the dynamic fluid viscosity is denoted by η and k_0 represents the zero-frequency Darcy permeability. The shape factor M is usually taken equal to 1.[24] The rollover frequency, which represents the transition from low-frequency viscosity-dominated to high-frequency intertia-dominated behavior, is defined as $\omega_c = \eta\phi/(\alpha_\infty\rho_f k_0)$.

The behavior of the upper (fluid) half-space ($x_3 < 0$) is governed by the acoustic wave equation

$$\rho_F\partial_t^2 p_F = K_F\nabla^2 p_F, \tag{9}$$

where K_F and ρ_F denote the bulk modulus and density of the fluid, respectively, and p_F denotes the fluid pressure.

We assume that the behavior at the interface is governed by conventional open-pore conditions, i.e., by continuity of volume flux and fluid pressure, and vanishing intergranular vertical and shear stresses. The force is applied to the solid. The open-pore boundary is a realistic choice to model the fluid/poroelastic-medium interface,[1] and a limiting case of the situation where a finite surface flow impedance is considered, see e.g., Refs. 12, 25, and 26. It implies that the true interface wave is absent in the response.[7,8] Hence, in the limit of $x_3 \to 0$, the following conditions should be satisfied

$$(1-\phi)u_3 + \phi U_3 - U_{F,3} = 0, \tag{10}$$

$$p_f - p_F = 0, \tag{11}$$

$$\sigma_{13} = 0, \tag{12}$$

$$\sigma_{23} = 0, \tag{13}$$

$$\sigma_{33} = F(t)\delta(x_1)\delta(x_2), \tag{14}$$

where $\delta(\cdots)$ denotes the Dirac delta function, and $U_{F,3}$ denotes the vertical particle displacement in the upper half-space. The fact that the intergranular stress σ_{33} is zero does not imply that the total solid stress τ_{33} vanishes, see Eq. (1).

The medium is considered to be at rest at $t \le 0$. At infinite distance from the source, the motions are bounded.

III. GREEN'S FUNCTIONS

In this section, we summarize the derivation of the Green's functions (impulse responses) as described by the solution to the set of governing equations, Eqs. (5), (6), and (9)–(14). The main part of the derivation is given in Appendices A and B and we refer to them where necessary.

In order to analyze the response in the plane-wave domain, the Fourier transform is applied over time according to

$$\hat{\mathbf{u}}(\mathbf{x},\omega) = \int_{-\infty}^{\infty}\mathbf{u}(\mathbf{x},t)\exp(-i\omega t)dt, \tag{15}$$

where ω denotes radial frequency. It is assumed that $\mathbf{u}(\mathbf{x},t)$ is real valued and hence, it is sufficient to consider $\omega \ge 0$. Following Aki and Richards,[4] the Fourier transform over horizontal spatial coordinates can be defined as

$$\tilde{\mathbf{u}}(\mathbf{p},x_3,\omega) = \int_{-\infty}^{\infty}\int_{-\infty}^{\infty}\hat{\mathbf{u}}(\mathbf{x},\omega)\exp(i\omega\mathbf{p}\cdot\mathbf{r})dx_1dx_2, \tag{16}$$

where $\mathbf{p} = (p_1,p_2)^T$ is the horizontal slowness vector and $\mathbf{r} = (x_1,x_2)^T$ is the horizontal space vector. The transforms are applied similarly to the other field quantities. The hat refers to the $(\mathbf{x},\omega)$-domain and the tilde to the $(\mathbf{p},x_3,\omega)$-domain.

The response in the $(\mathbf{p},x_3,\omega)$-domain is described by the physical quantities $\tilde{u}_i$ and $\tilde{p}_f$ in the lower half-space, collected in the vector $\tilde{\mathbf{w}} = (\tilde{u}_1,\tilde{u}_2,\tilde{u}_3,-\phi\tilde{p}_f)^T$, and by $\tilde{p}_F$ in the upper half-space, see Eqs. (A1), (A4), and (A6). The expressions for the response are obtained using Helmholtz decomposition of the equations of motion and substitution of the general solutions into the boundary conditions. This gives a set of equations that is solved analytically (see Appendix A).

The response can be written in terms of Green's functions according to

$$\tilde{\mathbf{w}} = \tilde{\mathbf{g}}^+\hat{F} = \frac{\tilde{\mathbf{n}}^+}{\Delta_{St}}\hat{F}, \tag{17}$$

$$\tilde{p}_F = \tilde{g}^-\hat{F} = \frac{\tilde{n}^-}{\Delta_{St}}\hat{F}, \tag{18}$$

where $\tilde{\mathbf{g}}^+$ and $\tilde{g}^-$ are the Green's functions in the lower and upper media, respectively, $\tilde{\mathbf{n}}^+$ and $\tilde{n}^-$ are the corresponding numerators, and $\hat{F}$ is the Fourier transform of the force signature. From Eqs. (A1), (A4), and (A6), it follows that $\tilde{\mathbf{g}}^+$ consists of a superposition of all possible body modes: the fast (P_1) and slow (P_2) compressional waves, and the vertically polarized shear (SV) wave. The horizontally polarized shear (SH) mode is not excited by the vertical force. The Green's function $\tilde{g}^-$ only contains the fluid (F) compressional mode. Both Green's functions have the "poroelastic Stoneley-wave denominator" $\Delta_{St} = \Delta_{St}(p,\omega)$ that is associated with interface waves along the fluid/poroelastic-medium interface, which is very similar to the "Scholte-wave denominator" for a fluid/elastic-solid interface.[27] Here, $p = (p_1^2 + p_2^2)^{1/2}$ denotes the magnitude of the horizontal slowness.

The body-wave slownesses s_j, $j = \{P_1,P_2,F,S\}$, are defined in Appendix A (Table III). The corresponding vertical slownesses are defined as $q_j = (s_j^2 - p^2)^{1/2}$, where $\mathrm{Im}(q_j) \le 0$ due to Sommerfeld's radiation condition.

To find the Green's functions in the $(\mathbf{x},\omega)$-domain, the inverse Fourier transform is applied according to

$$\hat{\mathbf{g}}^+ = \frac{\omega^2}{(2\pi)^2}\int_{-\infty}^{\infty}\int_{-\infty}^{\infty}\frac{\tilde{\mathbf{n}}^+(\mathbf{p},x_3,\omega)}{\Delta_{St}}\exp(-i\omega\mathbf{p}\cdot\mathbf{r})dp_1dp_2, \tag{19}$$

where $\omega \ge 0$. We only show the derivation of $\hat{\mathbf{g}}^+$, but the expressions for $\hat{g}^-$ are obtained by simply replacing $\tilde{\mathbf{n}}^+$ by $\tilde{n}^-$. When cylindrical coordinates are introduced, Eq. (19) can be written as

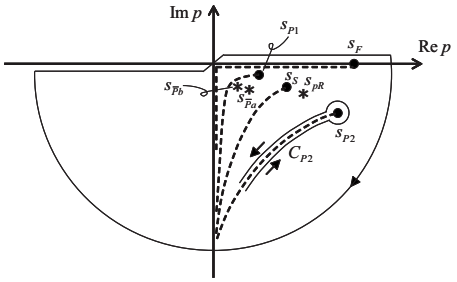

FIG. 2. Complex p-plane with (– –) branch cuts, (•) branch points s_j, $j=\{P_1,P_2,F,S\}$, and (∗) poles s_{pR} (pseudo-Rayleigh), $s_{\bar{P}a}$ and $s_{\bar{P}b}$ (additional), for the calculation of the Green's functions for Bentheimer/air configuration 2 (see Table I). The branch points are formed by the body-wave slownesses specified in Appendix A (Table III). The hyperbolic branch cuts are described by $\mathrm{Im}(q_j)=0$. Poles are zeroes of the poroelastic Stoneley denominator, see Eq. (21). Only part of the closed integration contour (–) is displayed: real axis, arc in lower half-plane, and loop C_{P2} along the q_{P2}-branch cut. The direction of integration is indicated.

$$\hat{\mathbf{g}}^+ = \frac{\omega^2}{4\pi}\int_{-\infty}^{\infty} \frac{\tilde{\mathbf{n}}^+(p,\partial_\alpha,x_3,\omega)}{\Delta_{St}} H_0^{(2)}(\omega p r) p dp, \tag{20}$$

where $r=(x_1^2+x_2^2)^{1/2}$ and in which the horizontal derivatives ∂_α, $\alpha=\{1,2\}$, are applied to the Hankel function $H_0^{(2)}(\cdots)$, see Eqs. (B3) and (B4) (Appendix B).

Now we change the real-axis integral into a contour integral in the complex p-plane. The idea is that by integration in the complex plane, contributions from loop integrals and from pole residues can be distinguished. We choose branch cuts along the hyperbolic lines[3] $\mathrm{Im}(q_j)=0$. In this way $\mathrm{Im}(q_j)\leq 0 \ \forall \ p$, which ensures the decay of the exponential terms $\exp(\mp i\omega q_j x_3)$ for large p [see Eqs. (A1) and (A4)]. The branch cuts depart from the branch points associated with the body-wave slownesses s_j, as shown in Fig. 2. The q_F-branch cut reduces to the imaginary axis and part of the real axis since the slowness of the fluid wave (s_F) is real.

The current branch cuts are referred to as the "fundamental" branch cuts.[28] The corresponding Riemann sheet is referred to as the principal Riemann sheet[17] or the "physical" Riemann sheet.[4]

In Fig. 2 the closed contour is also displayed. It is formed by the entire real axis, the loops along the branch cuts and around the branch points, and an arc of infinite radius in the lower half-plane. For $\mathrm{Re}(p)\leq 0$, the horizontal part of the contour lies just below the axis due to the presence of a branch cut of the Hankel function at the negative real axis.[29]

Applying Cauchy's residue theorem,[30] we obtain

$$\hat{\mathbf{g}}^+ = \int_{-\infty}^{\infty} \tilde{\mathbf{f}}^+ dp = -2\pi i \sum_m \mathrm{Res}_{p=s_m} \tilde{\mathbf{f}}^+ - \sum_j \int_{C_j} \tilde{\mathbf{f}}^+ dp,$$

$$\tilde{\mathbf{f}}^+ = \frac{\omega^2}{4\pi} \frac{\tilde{\mathbf{n}}^+(p,\partial_\alpha,x_3,\omega)}{\Delta_{St}} H_0^{(2)}(\omega p r) p, \tag{21}$$

where every s_m denotes a first-order pole of the integrand inside the integration contour and every C_j denotes a loop along the specific branch cut. In Eq. (21), the contribution of the arc vanishes because of Jordan's lemma.[31] The contributions around the branch points are also zero.

The poles s_m result from zeroes of the poroelastic Stoneley dispersion equation ($\Delta_{St}=0$) on the principal Riemann sheet. The number of poles N present inside contour C is determined by applying the principle of the argument to the Stoneley equation[30]

$$N = \frac{1}{2\pi i}\oint_C \frac{\partial_p \Delta_{St}}{\Delta_{St}} dp. \tag{22}$$

The residue of the integrand at a first-order pole is given as

$$\mathrm{Res}_{p=s_m} \tilde{\mathbf{f}}^+ = \left[\frac{\omega^2}{4\pi} \frac{\tilde{\mathbf{n}}^+(p,\partial_\alpha,x_3,\omega)}{\partial_p \Delta_{St}} H_0^{(2)}(\omega p r) p \right]_{p=s_m}. \tag{23}$$

IV. NUMERICAL IMPLEMENTATION

To perform the integration along the hyperbolic branch cuts, we choose $p_i=\mathrm{Im}(p)$ as the variable of integration according to

$$\int_{C_j} \tilde{\mathbf{f}}^+ \frac{\partial p}{\partial p_i} dp_i, \tag{24}$$

where

$$p = \frac{\mathrm{Re}(s_j)\mathrm{Im}(s_j)}{p_i} + i p_i, \quad \frac{\partial p}{\partial p_i} = -\frac{\mathrm{Re}(s_j)\mathrm{Im}(s_j)}{p_i^2} + i. \tag{25}$$

For the q_F-branch cut, the integration path is the imaginary axis and part of the real axis, which follows from Eq. (25) for vanishing imaginary part of the slowness $\mathrm{Im}(s_F)\uparrow 0$ (Fig. 2). Along the cut of q_j, at the left side $\mathrm{Re}(q_j)>0$ and at the right side $\mathrm{Re}(q_j)<0$. At the specific cut $\mathrm{Im}(q_j)=0$ and everywhere else $\mathrm{Im}(q_j)<0$.

The numerical integration is performed using an adaptive eight-point Legendre–Gauss algorithm,[29,32] which can handle integrable singularities such as branch points.

For the numerical implementation of the principle of the argument, we apply Eq. (22) separately for the areas between the various parts of the integration contour (branch cuts, real axis, and arc, see Fig. 2) to find out where the poles can be expected. Subsequently, the pole locations are found numerically by minimizing the left-hand side of equation $|\Delta_{St}|=0$. Since it contains local minima and branch-cut discontinuities, it is important to choose a proper starting value. This requires some manual iteration. The accuracy, as expressed by $|\Delta_{St}(p=s_m)|/|\Delta_{St}(p=0)|$, is typically $O(10^{-10})$. Here s_m denotes the numerical value of the pole location.

V. NUMERICAL RESULTS AND DISCUSSION

In this section, we investigate the transient responses for four different fluid/poroelastic-medium configurations (see Table I). In the first three configurations, water-saturated Bentheimer sandstone (see Table II) is used as porous medium. The upper half-space is subsequently filled with water, air, or a light fluid. In the fourth configuration, which is the one of Feng and Johnson,[7,8] the porous medium is formed by water-saturated fused glass beads, while the upper half-space is filled with water.

For every configuration, we will show the vertical component of particle velocity v_3 and the fluid pressure p_f for an

TABLE I. Various configurations for which the transient response is calculated. The type of sandstone is Bentheimer. For fused glass beads, the bulk modulus of the drained matrix is chosen as $K_b=10$ GPa and the permeability is chosen as $k_0=10^{-11}$ m^2. The upper half-space is filled with either water ($K_F=K_f$, $\rho_F=\rho_f$), or air ($K_F=1.42\times10^2$ kPa, $\rho_F=1.25$ kg m^{-3}), or a light fluid ($K_F=K_f/10$, $\rho_F=\rho_f/8$). For every configuration, the poles present on the principal Riemann sheet are indicated: pseudo-Stoneley (pSt), pseudo-Rayleigh (pR), and two additional ($\bar{P}_a,\bar{P}_b$) poles.

	Porous solid	Saturating fluid	Upper half-space	Poles
1	Sandstone	Water	Water	pSt
2	Sandstone	Water	Air	$\bar{P}_a,\bar{P}_b$,[a] pR
3	Sandstone	Water	Light fluid	pR, pSt [a]
4	Fused glass beads	Water	Water	pSt [a]

[a]Its residue is not shown.

observation point at the interface $x_3=0$ at offset $r=x_1=0.1$ m. Fluid pressure is related to dilatation only [see Eq. (4)] and hence, v_3 and p_f contain different information. Also, the comparison between the full response and a pole residue can be different in v_3 and p_f, as will be shown.

The point force has Ricker signature,[33]

$$F(t)=F_{\max}\left(\tfrac{1}{2}\omega_0^2\bar{t}^2-1\right)\exp\left(-\tfrac{1}{4}\omega_0^2\bar{t}^2\right), \tag{26}$$

where $\bar{t}=t-t_s$, $\omega_0=2\pi f_0$, and center frequency $f_0=500$ kHz (see Fig. 3). The magnitude $F_{\max}=1$ N and time shift $t_s=5$ μs. We perform the integration for the frequency range $0<f\leq2$ MHz. The full response is obtained by multiplication of the spectra of the Green's functions and the source [see Eqs. (17) and (18)], and using a standard fast Fourier transform algorithm.

A. Residue contribution vs full response

First, we address the relation between a pole and a pseudo interface wave, as raised in point (1) in the Introduction (Sec. I). For configurations 1–3, the full transient responses and separate pole residues [see Eq. (21)] are displayed in Figs. 3–5. We identified the different arrivals in the full responses using the propagation velocities as obtained from the modal slownesses. Head waves are identified geometrically using the pertaining modal velocities and are indicated with double-mode symbols [e.g., SP_1: the shear (S) wave radiated by the fast (P_1) compressional wave]. For the sake of clarity, a schematic snapshot of the full response with the different arrivals is shown in Fig. 1(b).

TABLE II. Material parameters as used for water-saturated Bentheimer sandstone (Ref. 34). The bulk modulus of the matrix K_b is found according to $K_b=K_p-\frac{4}{3}G$.

Solid (frame) density ρ_s	2630 kg m^{-3}
Fluid density ρ_f	1000 kg m^{-3}
Tortuosity α_∞	2.4
Porosity ϕ	0.23
Permeability k_0	3.7 μm^2
Dynamic fluid viscosity η	0.001 Pa s
Shear modulus G	6.8 GPa
Constrained modulus K_p	14 GPa
Grain bulk modulus K_s	36.5 GPa
Fluid bulk modulus K_f	2.22 GPa

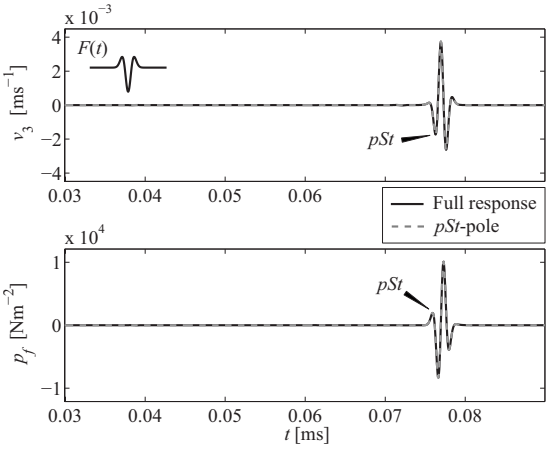

FIG. 3. Full response and pSt-pole residue at $x_2=x_3=0$ and offset $x_1=0.10$ m for Bentheimer/water configuration 1. The pSt-pole residue coincides with the pSt-waveform in the full response. Other wavemodes are too weak to be observed in this figure. The source signature $F(t)$ is also displayed.

We first note that the P_1-wave is present quite strongly in v_3 although this component is perpendicular to the direction of propagation of this longitudinal wave (Figs. 4 and 5). This is due to the contraction in vertical direction that can easily take place at the air/sandstone or light-fluid/sandstone interface. Remarkably, there is an arrival present in p_f at the S-wave arrival time (Figs. 4 and 5). This is not an S-wavefront but radiated slow compressional (P_2) and fluid (F) head waves, see Fig. 1(b).

Now, we focus on the comparison of interface waves in the full responses and corresponding pole residues. The pole(s) that are present on the principal Riemann sheet contributing a residue are given in Table I, for each configuration separately. We found the pseudo-Stoneley (pSt), the pseudo-Rayleigh (pR), and two additional ($\bar{P}_a,\bar{P}_b$) poles. The latter ones are discussed in Sec. V C.

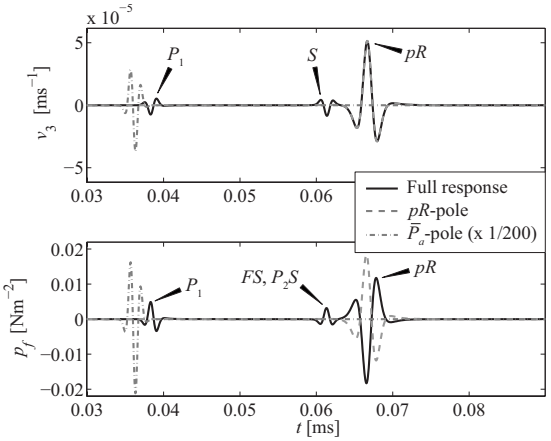

FIG. 4. Full response and residues of pR-pole and $\bar{P}_a$-pole at $x_2=x_3=0$ and offset $x_1=0.10$ m for Bentheimer/air configuration 2. The $\bar{P}_a$-pole residue has been scaled down by a factor 200 to make it entirely visible. The pR-pole residue coincides with the pR-waveform in the full response of v_3. The double-mode symbols are explained in Fig. 1(b).

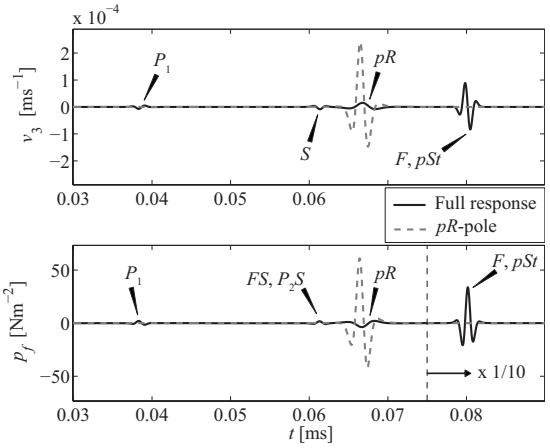

FIG. 5. Full response and pR-pole residue at $x_2=x_3=0$ and offset $x_1=0.10$ m for Bentheimer/light-fluid configuration 3. From the dashed vertical line onwards, the response p_f has been scaled down by a factor 10 to make it entirely visible. The double-mode symbols are explained in Fig. 1(b).

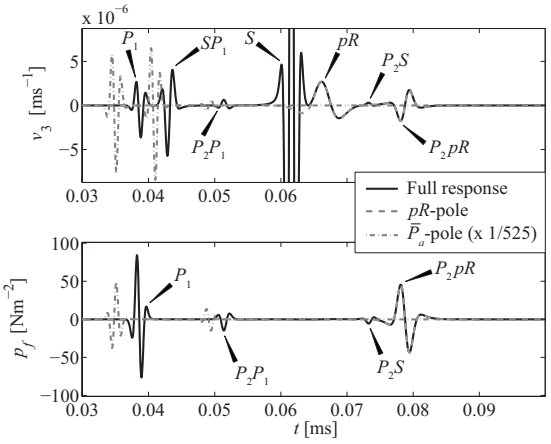

FIG. 7. Full response and residues of pR-pole and $\bar{P}_a$-pole at $x_2=0$, $x_3=0.01$ m, and offset $x_1=0.10$ m for Bentheimer/air configuration 2. The pR-pole residue coincides with the pR- and the P_2pR-waveforms in the full response. The $\bar{P}_a$-pole residue has been scaled down by a factor 525 to make it entirely visible. The double-mode symbols are explained in Fig. 1(b).

For configuration 1 (water as upper fluid), only the pSt-pole is found on the principal Riemann sheet. From Fig. 3, we observe that its residue yields the entire pSt-waveform. For configuration 2 (air as upper fluid), the pR-pole is found on the principal Riemann sheet. From Fig. 4, it is observed that its residue coincides with the pR-waveform in the full response of v_3 (actually, the difference is nonzero but too small to be observed). However, it does not coincide with that in the full response of p_f. Its contribution is opposite, which means that the loop integrals along the branch cuts also contribute to the pseudo interface waveform. This was also found by Allard *et al.*[11] It implies that part of the pertinent physical properties of the pseudo interface wave is captured by the loop integrals.

This is more pronounced for configuration 3 (light upper fluid), as shown in Fig. 5, in which both the pR-pole and the pSt-pole are found on the principal Riemann sheet. In both components (v_3 and p_f), the pR-pole residue does not coincide with the pR-waveform in the full response. The pSt-pole residue is not displayed separately because the pSt-wave strongly interferes with the F-wave.

To investigate how the residues and the interface waveforms in the full responses compare for an observation point that lies off the interface, we calculated the responses for configurations 1 to 3 at $x_3=0.01$ m and offset $r=x_1=0.1$ m. The corresponding results are displayed in Figs. 6–8. Compared to the previous responses at $x_3=0$, various head waves can now be distinguished as separate arrivals, generated by the body wavefronts that propagate along the interface, cf. Fig. 1(b). From Figs. 6–8, we also observe that the residues now yield two waveforms in the full responses. The first one (pR or pSt) is the waveform of the specific interface wave itself, while the second (P_2pR or P_2pSt) corresponds to the P_2-mode that is radiated by the propagating pseudo interface wave. For configurations 1 (water as upper fluid, Fig. 6) and 2 (air as upper fluid, Fig. 7), it is observed that both waveforms are now captured entirely by the residue of the corresponding pole. For configuration 3 (light upper fluid, Fig. 8), this is not the case, as for $x_3=0$.

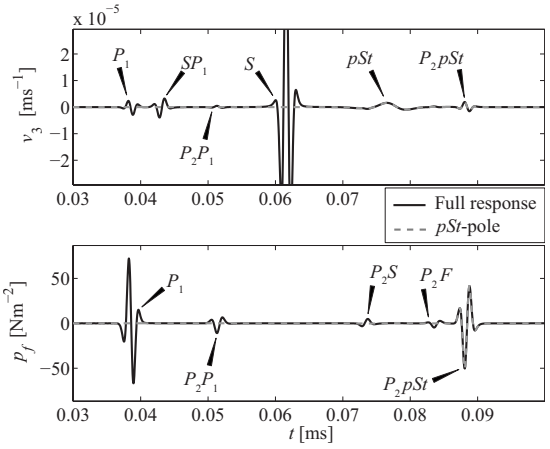

FIG. 6. Full response and pSt-pole residue at $x_2=0$, $x_3=0.01$ m, and offset $x_1=0.10$ m for Bentheimer/water configuration 1. The pSt-pole residue coincides with the pSt- and P_2pSt-waveforms in the full response. The double-mode symbols are explained in Fig. 1(b).

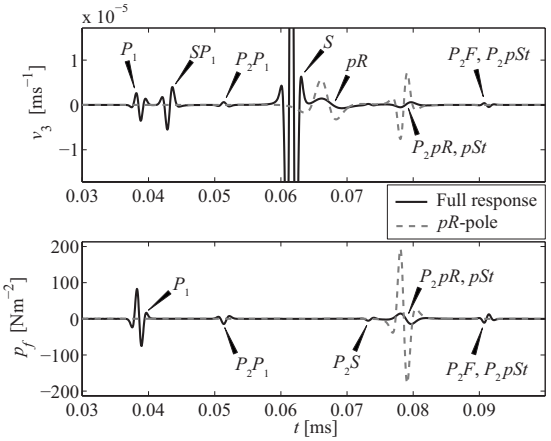

FIG. 8. Full response and pR-pole residue at $x_2=0$, $x_3=0.01$ m, and offset $x_1=0.10$ m for Bentheimer/light-fluid configuration 3. The double-mode symbols are explained in Fig. 1(b).

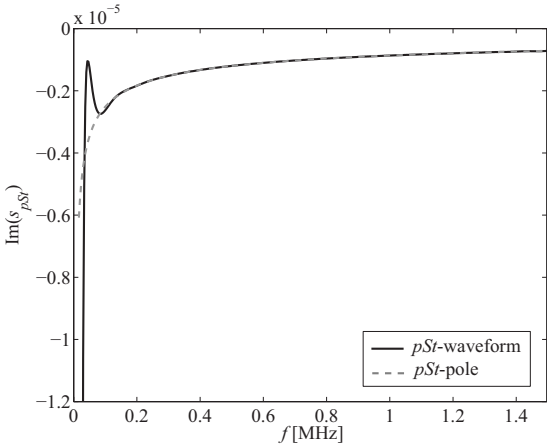

FIG. 9. True attenuation, defined as $\mathrm{Im}(s_{pSt}^{\mathrm{tr}})$, retrieved from windowed *pSt*-waveforms for Bentheimer/water configuration 1, at $x_2=x_3=0$ and fromoffsets $x_1=0.24-0.26$ m. The attenuation $\mathrm{Im}(s_{pSt})$ obtained from the corresponding pole residue is also displayed.

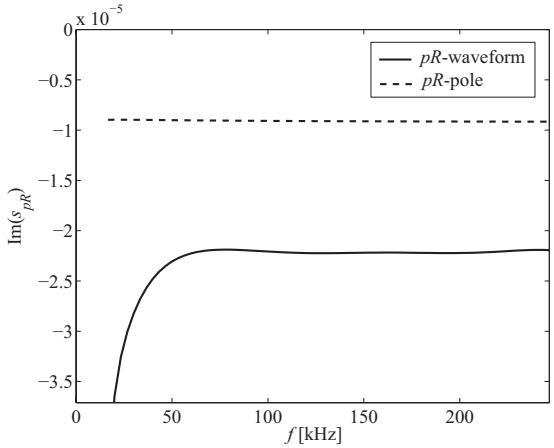

FIG. 10. True attenuation, defined as $\mathrm{Im}(s_{pR}^{\mathrm{tr}})$, retrieved from windowed *pR*-waveforms for Bentheimer/light-fluid configuration 3, at $x_2=x_3=0$ and from offsets $x_1=0.24-0.26$ m. The attenuation $\mathrm{Im}(s_{pR})$ obtained from the corresponding pole is also displayed.

In addition to the observations on responses with entire waveforms, we give attention to the characteristics of a pseudo interface wave. With regard to the propagation velocity, we observe that it is predicted properly by the residue of the corresponding pole for all presented numerical results. Concerning the attenuation, it was proposed by van der Hijden[17] to quantify the true attenuation of a pseudo interface wave based on the full transient response. This is also done by Rosenbaum,[5] but he only showed the decay of the total waveform, which would result in one value for the attenuation. This is quite restrictive and therefore we use the following method to retrieve the frequency-dependent attenuation from a windowed pseudo interface waveform in the full response. Here, attenuation is defined by $\mathrm{Im}(s_m^{\mathrm{tr}})$, where s_m^{tr} represents the true wave slowness and $m=\{pR,pSt\}$. As a starting point, we consider the pseudo interface wave in the far field where it does not interfere with other wavemodes, and we assume that it is described by

$$\hat{v}_{m,3}(r) \propto r^{-1/2} \exp(-i\omega s_m^{\mathrm{tr}} r), \tag{27}$$

which is found from the asymptotic behavior of the Hankel function.[29] The imaginary part of the wave slowness can be retrieved by comparing the amplitude spectra of the windowed waveform $|\hat{v}_{m,3}(r)|$ at two different observation points $r=r_a$ and $r=r_b$, according to

$$\mathrm{Im}(s_m^{\mathrm{tr}}(f)) = \frac{1}{2\pi f(r_b-r_a)} \ln\left(\frac{r_b^{1/2}|\hat{v}_{m,3}(r_b)|}{r_a^{1/2}|\hat{v}_{m,3}(r_a)|}\right). \tag{28}$$

For configurations 1 (water as upper fluid) and 3 (light upper fluid), the attenuations are displayed in Figs. 9 and 10, respectively, together with the corresponding predictions obtained from the poles $p=s_m$. The limited frequency range is due to the limited bandwidth of the retrieved spectra. For configuration 1 (water as upper fluid), we observe that the attenuation is described very well by the *pSt*-pole, except for the low frequencies where the far-field approximation of the Hankel function in Eq. (27) is not valid. For configuration 3 (light upper fluid), however, the true attenuation of the *pR*-wave is much greater than the value obtained from the *pR*-pole residue. Obviously, the loop integrals along the branch cuts cannot only affect the waveform but also the spatial decay of a pseudo interface wave.

Sometimes, a residue of a pole is (implicitly) considered to represent the corresponding interface-wave part of the spectrum of the Green's function (see e.g., Refs. 7, 12, and 14–16), while the loop integrals are considered to constitute the part related to body waves and head waves (if present). This can be true but we emphasize that the choice of branch cuts is not unique. Therefore, the integration can be performed on another physically allowed Riemann sheet, i.e., a Riemann sheet that also meets the requirement of $\mathrm{Im}(q_j) \leq 0$ for real p,[2,4] which is the original path of integration [see Eq. (20)]. This was done by Allard *et al.*[11] and Tsang,[35] and clarified by Harris and Achenbach.[36] Then, the construction of the $(\mathbf{x},\omega)$-domain Green's function is different as other poles have to be taken into account and different loop integrals are to be evaluated. Therefore, it might very well be that (part of) the pertinent physical properties of a true or pseudo interface wave are captured by the integrals along the closed contour, rather than by the residue of a specific pole (alone).

From the current observations, we conclude that a residue of a pole on the principal Riemann sheet does not necessarily yield all the pertinent physical properties of the corresponding pseudo interface wave.

B. Presence of *pR*-pole and *pSt*-pole on Riemann sheets

Now we address the issue concerning the origin of a pseudo interface wave, as raised in point (2) of the Introduction (Sec. I). In the computations in Sec. V A, we already found that a pole related to a pseudo interface wave can be located on the principal Riemann sheet and, obviously, contribute a residue to the full response (see Table I). This contradicts the conventional explanation that a pseudo interface wave originates from a pole on a different Riemann sheet and is accounted for only by the loop integrals along branch cuts by causing a local maximum in the integrand. Allard *et*

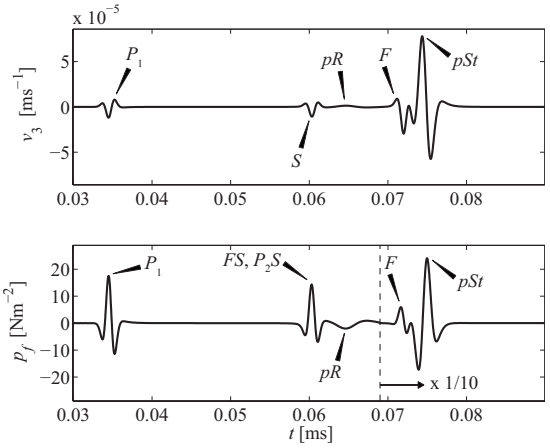

FIG. 11. Full response at $x_2=x_3=0$ and offset $x_1=0.10$ m for fused glassbeads/water configuration 4. From the dashed vertical line onwards, the response p_f has been scaled down by a factor 10 to make it entirely visible. The double-mode symbols are explained in Fig. 1(b).

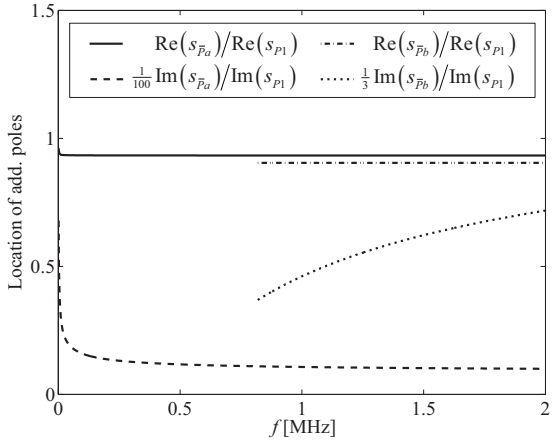

FIG. 13. The location of the additional poles $p=s_{\bar{P}a}$ and $p=s_{\bar{P}b}$ in the complex p-plane with respect to the P_1-wave slowness s_{P1}. The $\bar{P}_b$-pole is only present on the principal Riemann sheet for limited frequency range 818.75 kHz$\leq f\leq$2 MHz.

al.[11] already found this contradiction, but they did not refer to this as such because their concern was to determine whether or not a pole is related to a separate arrival in the full response.

Surprisingly, in case of fused glass beads saturated with water and covered with water (configuration 4, Fig. 11) the *pSt*-pole is present on the principal Riemann sheet only for a limited frequency range. In Fig. 12, the position of the pole in the complex plane is given, as expressed by $\mathrm{Im}(s_{pSt})$. Also the position of the q_{P2}-branch cut is displayed, as expressed by its imaginary part at $\mathrm{Re}(p)=\mathrm{Re}(s_{pSt})$. As frequency increases, the *pSt*-pole moves toward the branch cut and as soon as it reaches the cut, it vanishes from the sheet. The pole is not present on the principal sheet for 310 kHz$<f\leq$2 MHz. Therefore, the residue of the *pSt*-pole is not shown in Fig. 11. For the material properties used by Gubaidullin *et al.*,[12] exactly the same situation occurs, although the transition takes place at a different frequency. Obviously, the presence of a pole on a certain Riemann sheet is not only a matter of the contrast in material parameters of the half-spaces[37] but can also depend on frequency in case of viscous poroelastic media.

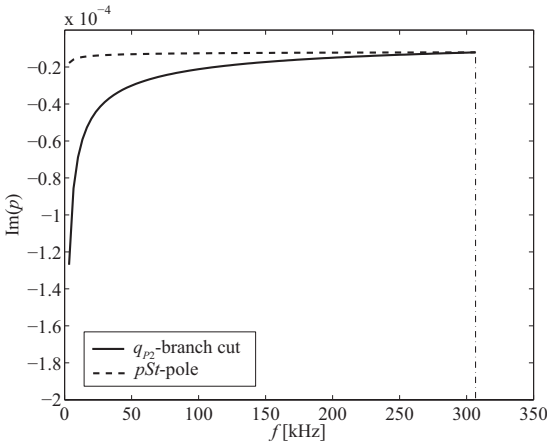

FIG. 12. The location of the *pSt*-pole in the complex p-plane, as expressed by $\mathrm{Im}(p)=\mathrm{Im}(s_{pSt})$, with respect to the location of the q_{P2}-branch cut at $p=\mathrm{Re}(s_{pSt})$, as expressed by $\mathrm{Im}(p)=\mathrm{Re}(s_{P2})\mathrm{Im}(s_{P2})/\mathrm{Re}(s_{pSt})$, for fused glass beads/water configuration 4. The (–·) line indicates the frequency at the intersection.

The behavior of the *pSt*-pole illustrates both the nonconventional and the conventional explanation about the origin of a pseudo interface wave. The pole does contribute a residue over a certain frequency range and not outside that specific range. For the *pR*-wave present in the full response of configuration 4 (Fig. 11), only the conventional explanation holds as the *pR*-pole is not found on the principal Riemann sheet and the entire waveform is captured by the loop integrals.

C. Physical significance of additional poles

Finally, we give attention to the physical significance of two additional zeroes of the poroelastic Stoneley dispersion equation ($\Delta_{St}=0$) as raised in point (3) of the Introduction (Sec. I). In configuration 2 (air as upper fluid), these zeroes show up as poles on the principal Riemann sheet at $p=s_{\bar{P}a}$ and $p=s_{\bar{P}b}$. They are located to the left of the fast compressional-wave slowness $[\mathrm{Re}(s_{\bar{P}a,\bar{P}b})<\mathrm{Re}(s_{P1})]$ close to the q_{P1}-branch cut (see Fig. 2; $p=s_{\bar{P}a}$ signifies the pole that lies the closest to $p=s_{P1}$). The additional $(\bar{P}_a,\bar{P}_b)$ poles are comparable with the so-called $\bar{P}$-poles that occur in nonporous elastic solids with an interface, as described by Gilbert and Laster[38] and Aki and Richards.[4] The scaled real and imaginary parts of the poles are displayed in Fig. 13. The $\bar{P}_b$-pole is only present on the principal Riemann sheet for limited frequency range 818.75 kHz$\leq f\leq$2 MHz.

Allard *et al.*[18] also found one of the poles and refer to it as an improper surface mode. Feng and Johnson[7] stated that poles located to the left of shear-wave branch point $[\mathrm{Re}(p)<\mathrm{Re}(s_S)]$ have lost all physical significance as pseudo interface modes. In the latter paper, the authors consider pseudo interface modes in the conventional way. In their configuration, the additional poles might indeed lie on a different Riemann sheet, but we find that they can also show up on the principal Riemann sheet. From Fig. 4 we observe that the $\bar{P}_a$-pole has a substantial residue contribution to the full re-

sponse, although it does not correspond to an interface wavemode ($\bar{P}_b$-pole similarly). Any pole that contributes to the full response should be considered as physically significant.

Gilbert and Laster[38] and Aki and Richards[4] related the $\bar{P}$-poles in elastic solids to a separate arrival. Van der Hijden,[17] however, stated that the concept of a separate pulse should be dismissed because it is just a peculiar tail to the compressional head-wave arrival. Harris and Achenbach[36] confirmed this by stating that the poles yield features of the lateral waves. The observations in the current computations for poroelastic media also confirm this. From Fig. 7, we observe that the $\bar{P}_a$-pole contributes to the head waves generated by the P_1-wavefront. It also contributes to the P_1-wavefront itself because it yields a strong pulse that arrives even earlier (Figs. 4 and 7), which is obviously explained by the pole lying to the left of the compressional-wave slowness. The same is true for the $\bar{P}_b$-pole. The early-arriving parts are not present in the full responses and hence, the P_1-waveform is constituted by both the residues of the $\bar{P}$-poles and the loop integrals along the branch cuts. The fact that a pole contributes to the P_1-waveform illustrates that it lies in the vicinity of the saddle point of the body wave, as used in asymptotic ray theory.[35,39]

There is one remarkable difference between the $\bar{P}$-poles in elastic and the ones in poroelastic media. In former, the poles never show up on the principal Riemann sheet[4] while this is possible for the latter. A similarity lies in the fact that in elastic solids (with rather small values of Poisson's ratio), the poles lie also to the left of the compressional-wave slowness.[35]

VI. CONCLUSIONS

In this paper, we analyze the three-dimensional transient response of a fluid/poroelastic-medium configuration that is subjected to a vertical point force at the interface. For different materials, we quantitatively compare the full transient response with the residue contributions of pole singularities present on the so-called principal or physical Riemann sheet of integration. The poles are formed by zeroes of the poroelastic Stoneley dispersion equation, i.e., the pseudo-Stoneley *(pSt)* and the pseudo-Rayleigh *(pR)* poles.

We find that the residues of these poles do not necessarily contain all pertinent physical properties of the corresponding pseudo interface waves. Part of them can be captured by the loop integrals along the branch cuts. Therefore, it can be erroneous to use only the location of a zero of the Stoneley dispersion equation on the principal Riemann sheet, to predict the entire waveform, the propagation velocity, and attenuation of the corresponding pseudo interface wave.

According to the generally accepted explanation about the origin of a pseudo interface wave, it originates from a pole that lies on a nonprincipal Riemann sheet. The influence of the pole is only indirect in the sense that it causes a local maximum in the integrand of the Green's function when its location is close to the real axis. We find, however, that this conventional explanation is not necessarily confirmed in the context of Biot's theory for poroelasticity. The poles can show up on the principal Riemann sheet. For the *pSt*-pole, we even show that its presence on the principal Riemann sheet is not only determined by the contrast in the material properties, but also by frequency.

Finally, we find that two additional zeroes of the poroelastic Stoneley dispersion equation do have physical significance due to their residue contributions to the fast compressional wavefront and to the head waves that are radiated by this wavefront. In the literature the additional poles are, however, referred to as nonphysical because they are not related to pseudo interface waves. The poles are comparable with the $\bar{P}$-poles known in nonporous elastic solids, Refs. 38 and 4. Depending on the specific material parameters and frequency, they can be present on the principal Riemann sheet or on another one.

TABLE III. Symbols used in Appendix A The various indices are defined as $j=\{P_1,P_2,F,S\}$, $k=\{P_1,P_2\}$, and $\ell=\{P_1,P_2,S\}$. Behind a number of definitions, references are displayed where the specific expressions originate from.

$\hat{\rho}_{11}$	=	$\rho_{11}-i\hat{b}/\omega$	Ref. 23
$\hat{\rho}_{22}$	=	$\rho_{22}-i\hat{b}/\omega$	Ref. 23
$\hat{\rho}_{12}$	=	$\rho_{12}+i\hat{b}/\omega$	Ref. 23
d_0	=	$\hat{\rho}_{11}\hat{\rho}_{22}-\hat{\rho}_{12}^2$	Ref. 23
d_1	=	$-(R\hat{\rho}_{11}+P\hat{\rho}_{22}-2Q\hat{\rho}_{12})$	Ref. 23
d_2	=	$PR-Q^2$	Ref. 23
s_k^2	=	$(-d_1\mp(d_1^2-4d_0d_2)^{1/2})/(2d_2)$, $\mathrm{Im}(s_k)\leq 0$	Ref. 23
s_S^2	=	$d_0/(G\hat{\rho}_{22})$, $\mathrm{Im}(s_S)\leq 0$	Ref. 23
s_F^2	=	ρ_F/K_F	
p	=	$(p_1^2+p_2^2)^{1/2}\geq 0$	
q_j	=	$(s_j^2-p^2)^{1/2}$, $\mathrm{Im}(q_j)\leq 0$	
$\hat{\beta}_k$	=	$-(\hat{\rho}_{11}-Ps_k^2)/(\hat{\rho}_{12}-Qs_k^2)$	Ref. 23
$\hat{\beta}_S$	=	$-\hat{\rho}_{12}/\hat{\rho}_{22}$	Ref. 23
A'	=	$A-(1-\phi)Q/\phi$	Ref. 12
Q'	=	$Q-(1-\phi)R/\phi$	Ref. 12
H_k	=	$Q+R\hat{\beta}_k$	Ref. 12
K_k	=	$A'+Q'\hat{\beta}_k+2G$	Ref. 12
ϕ_ℓ	=	$1-\phi+\phi\hat{\beta}_\ell$	Ref. 12
Δ_1	=	$s_{P2}^2H_{P2}-s_{P1}^2H_{P1}$	
Δ_2	=	$q_{P1}s_{P2}^2H_{P2}-q_{P2}s_{P1}^2H_{P1}$	
Δ_3	=	$-4p^4\phi\hat{\rho}_{22}^{-1}(q_{P1}s_{P1}^2H_{P1}-q_{P2}s_{P2}^2H_{P2})+4p^2q_Sq_{P1}q_{P2}\phi\hat{\rho}_{22}^{-1}\Delta_1$ $+2p^2s_S^2(q_{P1}(\phi_{P1}+\phi d_2^{-1}H_{P1}K_{P2})-q_{P2}(\phi_{P2}+\phi d_2^{-1}H_{P2}K_{P1}))$ $-s_S^2G^{-1}(q_{P1}\phi_{P1}s_{P2}^2K_{P2}-q_{P2}\phi_{P2}s_{P1}^2K_{P1})$	

ACKNOWLEDGMENTS

This research is supported by The Netherlands Research Centre for Integrated Solid Earth Sciences (ISES). The authors are also grateful to E. C. Slob and A. V. Metrikine for the valuable discussions, and to B. Rossen for textual remarks and suggestions.

APPENDIX A: TRANSFORM-DOMAIN RESPONSE

In this Appendix, we derive the $(\mathbf{p},x_3,\omega)$-domain solution to Eqs. (5), (6), and (9)–(14). Many of the involved symbols are explained in Table III.

The general solution to the acoustic wave equation [Eq. (9)] in the $(\mathbf{p},x_3,\omega)$-domain can be readily found by applying the Fourier transform [Eqs. (15) and (16)] and solving the obtained ordinary differential equation. The result is

$$\tilde{p}_F = i\omega\rho_F \tilde{A}_F \exp(+i\omega q_F x_3), \quad x_3 < 0, \tag{A1}$$

where $\tilde{A}_F$ is the complex plain-wave amplitude of the fluid (F) wave and $q_F=(s_F^2-p^2)^{1/2}$ is the vertical slowness. It contains the wave slowness s_F and the magnitude of the horizontal slowness p that are defined in Table III.

The general solution to the Biot equations [Eqs. (5) and (6)] can be derived by applying Helmholtz decomposition in the $(\mathbf{x},\omega)$-domain to these equations, according to[12,23]

$$\hat{\mathbf{u}} = \nabla\hat{\varphi}_{P1} + \nabla\hat{\varphi}_{P2} + \nabla\times\hat{\boldsymbol{\psi}}, \tag{A2}$$

$$\hat{\mathbf{U}} = \hat{\beta}_{P1}\nabla\hat{\varphi}_{P1} + \hat{\beta}_{P2}\nabla\hat{\varphi}_{P2} + \hat{\beta}_S\nabla\times\hat{\boldsymbol{\psi}}, \tag{A3}$$

where $\hat{\varphi}_{P1}$ and $\hat{\varphi}_{P2}$ denote the scalar potentials for the fast (P_1) and slow (P_2) compressional waves, respectively, and $\hat{\boldsymbol{\psi}}$ denotes the shear-wave (S) vector potential. $\hat{\beta}_{P1}$, $\hat{\beta}_{P2}$, and $\hat{\beta}_S$ are the well-known fluid-solid (frame) amplitude ratios[23] for the separate body wavemodes (Table III).

Applying the Helmholtz decomposition, the governing equations are decoupled and once the spatial Fourier transform [Eq. (16)] is applied, the decoupled equations turn into ordinary differential equations for $\tilde{\varphi}_{P1}$ and $\tilde{\varphi}_{P2}$, and $\tilde{\boldsymbol{\psi}}$ that can be solved separately. The general solution for the displacements is obtained by adding the separate contributions according to Eqs. (A2) and (A3). When the shear-wave term is split into a vertically polarized (SV) and a horizontally polarized (SH) part, the result for the wave vector $\tilde{\mathbf{w}}=(\tilde{u}_1,\tilde{u}_2,\tilde{u}_3,-\phi\tilde{p}_f)^T$ can be written as

$$\tilde{\mathbf{w}} = \begin{bmatrix} p_1 & p_1 & q_S\dfrac{p_1}{p} & s_S^2\dfrac{p_2}{p^2} \\ p_2 & p_2 & q_S\dfrac{p_2}{p} & -s_S^2\dfrac{p_1}{p^2} \\ q_{P1} & q_{P2} & -p & 0 \\ -i\omega s_{P1}^2 H_{P1} & -i\omega s_{P2}^2 H_{P2} & 0 & 0 \end{bmatrix} \times \begin{bmatrix} \tilde{A}_{P1}\exp(-i\omega q_{P1}x_3) \\ \tilde{A}_{P2}\exp(-i\omega q_{P2}x_3) \\ \tilde{A}_{SV}\exp(-i\omega q_S x_3) \\ \tilde{A}_{SH}\exp(-i\omega q_S x_3) \end{bmatrix}, \quad x_3 > 0. \tag{A4}$$

Next to the solid displacements $\tilde{\mathbf{u}}$, the wave vector $\tilde{\mathbf{w}}$ contains the fluid pressure $\tilde{p}_f$ rather then the fluid displacements $\tilde{\mathbf{U}}$ because the four components of $\tilde{\mathbf{w}}$ describe the wave field totally: there are only four independent variables, see Ref. 40. In Eq. (A4), $\tilde{A}_{P1}$, $\tilde{A}_{P2}$, $\tilde{A}_{SV}$, and $\tilde{A}_{SH}$ denote the complex plain-wave amplitudes of the corresponding body wavemodes. In Table III, the vertical slownesses q_{P1}, q_{P2}, and q_S are defined (together with q_F), as well as the fluid compressibility terms H_{P1} and H_{P2}.

The body-wave slownesses have $\mathrm{Im}(s_j)\leq 0$ and Sommerfeld's radiation condition requires that $\mathrm{Im}(q_j)\leq 0$ for all body modes, $j=\{P_1,P_2,F,S\}$.

The complex plane-wave amplitudes are determined by the boundary conditions at the interface $x_3=0$. Applying the transforms [Eqs. (15) and (16)] to the boundary conditions [Eqs. (10)–(14)] and substituting the wave fields [Eqs. (A1) and (A4)], the following set of equations is obtained

$$\begin{bmatrix} 2Gp^2-s_{P1}^2K_{P1} & 2Gp^2-s_{P2}^2K_{P2} & 0 & 2Gpq_S & 0 \\ s_{P1}^2H_{P1} & s_{P2}^2H_{P2} & -\phi\rho_F & 0 & 0 \\ q_{P1}\phi_{P1} & q_{P2}\phi_{P2} & q_F & -p\phi_S & 0 \\ 2pq_{P1} & 2pq_{P2} & 0 & s_S^2-2p^2 & +\dfrac{p_2}{p_1 p}q_S s_S^2 \\ 2pq_{P1} & 2pq_{P2} & 0 & s_S^2-2p^2 & -\dfrac{p_1}{p_2 p}q_S s_S^2 \end{bmatrix} \times \begin{bmatrix} \tilde{A}_{P1} \\ \tilde{A}_{P2} \\ \tilde{A}_F \\ \tilde{A}_{SV} \\ \tilde{A}_{SH} \end{bmatrix} = \begin{bmatrix} \dfrac{\hat{F}}{i\omega} \\ 0 \\ 0 \\ 0 \\ 0 \end{bmatrix}, \tag{A5}$$

which is similar to that in Ref. 12, but extended to three dimensions. The constrained moduli K_{P1} and K_{P2} are defined in Table III. The solution is calculated analytically using MAPLE©:

$$\begin{aligned} \tilde{A}_{P1} &= \frac{-\hat{F}}{i\omega G\Delta_1\Delta_{St}}(\phi\rho_F q_{P2}(s_S^2\phi_{P2}-2p^2\phi\hat{\rho}_{22}^{-1}s_{P2}^2H_{P2}) \\ &\quad + q_F(s_S^2-2p^2)s_{P2}^2H_{P2}), \\ \tilde{A}_{P2} &= \frac{\hat{F}}{i\omega G\Delta_1\Delta_{St}}(\phi\rho_F q_{P1}(s_S^2\phi_{P1}-2p^2\phi\hat{\rho}_{22}^{-1}s_{P1}^2H_{P1}) \\ &\quad + q_F(s_S^2-2p^2)s_{P1}^2H_{P1}), \\ \tilde{A}_F &= \frac{\hat{F}}{i\omega G\Delta_1\Delta_{St}}((q_{P1}\phi_{P1}s_{P2}^2H_{P2}-q_{P2}\phi_{P2}s_{P1}^2H_{P1}) \\ &\quad \times(s_S^2-2p^2)+2p^2\Delta_2\phi_S), \\ \tilde{A}_{SV} &= \frac{2p\hat{F}}{i\omega G\Delta_1\Delta_{St}}(\phi^2\rho_F\hat{\rho}_{22}^{-1}q_{P1}q_{P2}\Delta_1+q_F\Delta_2), \end{aligned} \tag{A6}$$

and $\tilde{A}_{SH}=0$. Here, the "poroelastic Stoneley-wave denominator" (see Sec. III) is defined as

$$\Delta_{St} = q_F\Delta_R + \phi\rho_F\Delta_3/\Delta_1, \tag{A7}$$

which is associated with interface waves along the fluid/poroelastic-medium interface. It is very similar to the "Scholte-wave denominator" for a fluid/elastic-solid interface,[27] and equivalent to the one as given by Denneman *et al.*[41] It contains the "poroelastic Rayleigh-wave denominator" that is associated with interface waves along a vacuum/poroelastic-medium interface

$$\Delta_R = (s_S^2-2p^2)^2 + 4p^2q_S\Delta_2/\Delta_1, \tag{A8}$$

which is very similar to the one for a vacuum/elastic-solid interface.[4,31]

Now the plain-wave amplitudes are known, the $(\mathbf{p},x_3,\omega)$-domain solution to Eqs. (5), (6), and (9)–(14) is determined and given by Eqs. (A1) and (A4).

APPENDIX B: INVERSE FOURIER INTEGRAL

In this Appendix, we show how Eq. (19) can be written in terms of a single integral according to Eq. (20), following Ref. 4. Transforming Eq. (19) to cylindrical coordinates according to $p_1=p\cos\varphi$, $p_2=p\sin\varphi$, and $x_1=r\cos\vartheta$, $x_2=r\sin\vartheta$, where $r=(x_1^2+x_2^2)^{1/2}$, it can be written as

$$\hat{\mathbf{g}}^+=\frac{\omega^2}{(2\pi)^2}\int_0^\infty\int_0^{2\pi}\frac{\tilde{\mathbf{n}}^+(p,\varphi,x_3,\omega)}{\Delta_{St}}\times\exp(-i\omega pr\cos(\varphi-\vartheta))pd\varphi dp. \tag{B1}$$

The φ-dependence of $\tilde{\mathbf{n}}^+$ can be replaced by (horizontal) partial-derivative operators ∂_α, $\alpha=\{1,2\}$, since the factors p_α that appear in $\tilde{\mathbf{n}}^+$ [see Eqs. (A4) and (17)] correspond to horizontal derivatives $(-i\omega p_\alpha\leftrightarrow\partial_\alpha)$ in the $(\mathbf{x},\omega)$-domain. Therefore, $\tilde{\mathbf{n}}^+(p,\varphi,x_3,\omega)$ is defined such that it contains the appropriate derivative operators according to

$$\begin{aligned}\hat{\mathbf{g}}^+&=\frac{\omega^2}{(2\pi)^2}\int_0^\infty\frac{\tilde{\mathbf{n}}^+(p,\partial_\alpha,x_3,\omega)}{\Delta_{St}}\times\int_0^{2\pi}\exp(-i\omega pr\cos(\varphi-\vartheta))d\varphi pdp\\&=\frac{\omega^2}{2\pi}\int_0^\infty\frac{\tilde{\mathbf{n}}^+(p,\partial_\alpha,x_3,\omega)}{\Delta_{St}}J_0(\omega pr)pdp,\end{aligned} \tag{B2}$$

where we used the integral representation of the zeroth-order Bessel function $J_0(\cdots)$, see Ref. 42. The Bessel function is replaced by the sum of two zeroth-order Hankel functions of the first and second kinds,[42] i.e., $J_0(z)=\frac{1}{2}(H_0^{(1)}(z)+H_0^{(2)}(z))$. Using the equality $H_0^{(1)}(z)=-H_0^{(2)}(-z)$ and the evenness of the $(\mathbf{p},x_3,\omega)$-domain Green's functions in p, Eq. (B2) can be written as

$$\hat{\mathbf{g}}^+=\frac{\omega^2}{4\pi}\int_{-\infty}^\infty\frac{\tilde{\mathbf{n}}^+(p,\partial_\alpha,x_3,\omega)}{\Delta_{St}}H_0^{(2)}(\omega pr)pdp, \tag{B3}$$

where the horizontal derivatives are applied to the Hankel function before the integration is performed, according to

$$\partial_\alpha H_0^{(2)}(\omega pr)=-\omega p\frac{x_\alpha}{r}H_1^{(2)}(\omega pr). \tag{B4}$$

[1] D. R. Burns, "Acoustic waveform logs and the in-situ measurement of permeability—A review," in *Geophysical Applications for Geotechnical Investigations*, edited by F. L. Paillet and W. T. Saunders (ASTM, Philadelphia, 1990).
[2] I. A. Viktorov, *Rayleigh and Lamb Waves: Physical Theory and Applications* (Plenum, New York, 1967).
[3] W. M. Ewing, W. S. Jardetzky, and F. Press, *Elastic Waves in Layered Media* (McGraw-Hill, New York, 1957).
[4] K. Aki and P. G. Richards, *Quantitative Seismology* (Freeman and Co., New York, 1980).
[5] J. H. Rosenbaum, "Synthetic microseismograms: Logging in porous formations," Geophysics **39**, 14–32 (1974).
[6] H. Deresiewicz, "The effect of boundaries on wave propagation in a liquid-filled porous solid: IV. Surface waves in a half-space," Bull. Seismol. Soc. Am. **52**, 627–638 (1962).
[7] S. Feng and D. L. Johnson, "High-frequency acoustic properties of a fluid/porous solid interface. I. New surface mode," J. Acoust. Soc. Am. **74**, 906–914 (1983).
[8] S. Feng and D. L. Johnson, "High-frequency acoustic properties of a fluid/porous solid interface. II. The 2D reflection Green's function," J. Acoust. Soc. Am. **74**, 915–924 (1983).
[9] M. J. Mayes, P. B. Nagy, L. Adler, B. P. Bonner, and R. Streit, "Excitation of surface waves of different modes at fluid-porous solid interface," J. Acoust. Soc. Am. **79**, 249–252 (1986).
[10] L. Adler and P. B. Nagy, "Measurements of acoustic surface waves on fluid-filled porous rocks," J. Geophys. Res. **99**, (B9), 17863–17869 (1994).
[11] J. F. Allard, M. Henry, C. Glorieux, W. Lauriks, and S. Petillon, "Laser-induced surface modes at water-elastic and poroelastic interfaces," J. Appl. Phys. **95**, 528–535 (2004).
[12] A. A. Gubaidullin, O. Y. Kuchugurina, D. M. J. Smeulders, and C. J. Wisse, "Frequency-dependent acoustic properties of a fluid/porous solid interface," J. Acoust. Soc. Am. **116**, 1474–1480 (2004).
[13] D. L. Johnson, J. Koplik, and R. Dashen, "Theory of dynamic permeability and tortuosity in fluid-saturated porous-media," J. Fluid Mech. **176**, 379–402 (1987).
[14] I. Edelman and K. Wilmanski, "Asymptotic analysis of surface waves at vacuum/porous medium and liquid/porous medium interfaces," Continuum Mech. Thermodyn. **14**, 25–44 (2002).
[15] B. Albers, "Monochromatic surface waves at the interface between poroelastic and fluid half-spaces," Proc. R. Soc. London, Ser. A **462**, 701–723 (2006).
[16] M. G. Markov, "Low-frequency Stoneley wave propagation at the interface of two porous half-spaces," Geophys. J. Int. **177**, 603–608 (2009).
[17] J. H. M. T. van der Hijden, "Quantitative analysis of the pseudo-Rayleigh phenomenon," J. Acoust. Soc. Am. **75**, 1041–1047 (1984).
[18] J. F. Allard, G. Jansens, G. Vermeir, and W. Lauriks, "Frame-borne surface waves in air-saturated porous media," J. Acoust. Soc. Am. **111**, 690–696 (2002).
[19] J. F. Allard, M. Henry, C. Glorieux, S. Petillon, and W. Lauriks, "Laser-induced surface modes at an air-porous medium interface," J. Appl. Phys. **93**, 1298–1304 (2003).
[20] M. A. Biot, "Theory of propagation of elastic waves in a fluid-saturated porous solid. I. Low-frequency range," J. Acoust. Soc. Am. **28**, 168–178 (1956).
[21] M. A. Biot, "Theory of propagation of elastic waves in a fluid-saturated porous solid. II. Higher frequency range," J. Acoust. Soc. Am. **28**, 179–191 (1956).
[22] M. A. Biot and D. G. Willis, "The elastic coefficients of the theory of consolidation," J. Appl. Mech. **24**, 594–601 (1957).
[23] J. F. Allard, *Propagation of Sound in Porous Media: Modelling of Sound Absorbing Materials* (Elsevier Applied Science, London, 1993).
[24] D. M. J. Smeulders, R. L. G. M. Eggels, and M. E. H. van Dongen, "Dynamic permeability: Reformulation of theory and new experimental and numerical data," J. Fluid Mech. **245**, 211–227 (1992).
[25] H. Deresiewicz and R. Skalak, "On uniqueness in dynamic poroelasticity," Bull. Seismol. Soc. Am. **53**, 783–788 (1963).
[26] B. Gurevich and M. Schoenberg, "Interface conditions for Biot's equations of poroelasticity," J. Acoust. Soc. Am. **105**, 2585–2589 (1999).
[27] A. T. de Hoop and J. H. M. T. van der Hijden, "Generation of acoustic waves by an impulsive line source in a fluid-solid configuration with a plane boundary," J. Acoust. Soc. Am. **74**, 333–342 (1983).
[28] K. Attenborough, S. I. Hayek, and J. M. Lawther, "Propagation of sound above a porous half-space," J. Acoust. Soc. Am. **68**, 1493–1501 (1980).
[29] M. Abramowitz and I. A. Stegun, *Handbook of Mathematical Functions* (Dover, New York, 1972).
[30] B. A. Fuchs, B. V. Shabat, and J. Berry, *Functions of a Complex Variable and Some of Their Applications* (Pergamon, Oxford, 1964).
[31] J. D. Achenbach, *Wave Propagation in Elastic Solids* (North-Holland, Amsterdam, 1973).
[32] P. J. Davies and P. Rabinowitz, *Methods of Numerical Integration* (Academic, New York, 1975).
[33] N. Ricker, "Wavelet contraction, wavelet expansion, and the control of seismic resolution," Geophysics **18**, 769–792 (1953).
[34] C. J. Wisse, "On frequency dependence of acoustic waves in porous cylinders," Ph.D. thesis, Delft University of Technology, The Netherlands (1999).
[35] L. Tsang, "Time-harmonic solution of the elastic head wave problem incorporating the influence of Rayleigh poles," J. Acoust. Soc. Am. **63**, 1302–1309 (1978).

[36]J. G. Harris and J. D. Achenbach, "Comment on 'On the complex conjugate roots of the Rayleigh equation: The leaky surface wave'," J. Acoust. Soc. Am. **112**, 1747–1748 (2002).
[37]J. G. Scholte, "The range of existence of Rayleigh and Stoneley waves," Mon. Not. R. Astron. Soc. **5**, 120–126 (1947).
[38]F. Gilbert and S. J. Laster, "Excitation and propagation of pulses on an interface," Bull. Seismol. Soc. Am. **52**, 299–319 (1962).
[39]B. L. van der Waerden, "On the method of saddle points," Appl. Sci. Res., Sect. B **2**, 33–45 (1952).
[40]G. Bonnet, "Basic singular solutions for a poroelastic medium in the dynamic range," J. Acoust. Soc. Am. **82**, 1758–1762 (1987).
[41]A. I. M. Denneman, G. G. Drijkoningen, D. M. J. Smeulders, and K. Wapenaar, "Reflection and transmission of waves at a fluid/porous-medium interface," Geophysics **67**, 282–291 (2002).
[42]I. S. Gradshteyn and I. M. Ryzhik, *Table of Integrals, Series and Products* (Academic, London, 1980).

An acoustic microscopy technique to assess particle size and distribution following needle-free injection

Jamie Condliffe[a] and Heiko A. Schiffter
Institute of Biomedical Engineering, University of Oxford, Oxford OX3 7DQ, United Kingdom

Robin O. Cleveland
Department of Mechanical Engineering, Boston University, Boston, Massachusetts 02215

Constantin-C. Coussios
Institute of Biomedical Engineering, University of Oxford, Oxford OX3 7DQ, United Kingdom

(Received 5 June 2009; revised 20 January 2010; accepted 20 January 2010)

Needle-free injection is a novel technique for transdermal drug and vaccine delivery, the efficacy of which depends on the number density and mean penetration depth of particles beneath the skin. To date, these parameters have been assessed optically, which is time-consuming and unsuitable for use *in vivo*. The present work describes the development of a scanning acoustic microscopy technique to map and size particle distributions following injection. Drug particles were modeled using a polydisperse distribution of polystyrene spheres, mean diameter 30.0 μm, and standard deviation 16.7 μm, injected into agar-based tissue-mimicking material, and later, as polydisperse stainless steel spheres, mean diameter 46.0 μm, and standard deviation 13.0 μm, injected both into agar and into porcine skin. A focused broadband immersion transducer (10–75 MHz), driven in pulse-echo mode, was scanned over the surface of the injected samples. Recorded echo signals were post-processed to deduce particle penetration depth (30–300 μm). Furthermore, post-injection size distribution of the spheres was calculated using a novel, automated spectral analysis technique. Experimental results were validated optically and found to predict penetration depth and particle size accurately. The availability of simultaneous particle penetration depth and particle size information makes it possible for the first time to optimize particle design for specific drug delivery applications. © *2010 Acoustical Society of America.* [DOI: 10.1121/1.3314252]

PACS number(s): 43.35.Sx, 43.40.Fz [YHB] Pages: 2252–2261

I. INTRODUCTION

Needle-free particle injection is a technique, which allows pain-free, transdermal delivery of drugs and vaccines.[1] Typically, devices employ a high-speed gas flow, caused by rupturing a pressurized gas canister held at 60 bars, in which particles are entrained. The gas flow, with an exit velocity in the region of Mach 0.8–1.0, is aimed at the skin, and the particles penetrate to depths of hundreds of microns.[2]

Previous work has suggested that, based on calculations using momentum and size, particles penetrate to depths proportional to the product of their density, radius, and velocity.[3] Though no experimental evidence is available, which confirms this hypothesis, it is believed that larger particles penetrate deeper into a target than smaller ones. Work has previously been conducted using monodisperse polystyrene particles, of diameter 48.0 ± 3.8 μm and density of 1050 kg/m^3 (Thermo Fisher Scientific), which were fired into agar targets. The penetration depth of these particles was subsequently measured by slicing the sample and analyzing sections using optical microscopy (see Fig. 1).[4] It has been shown that 48.0 μm polystyrene particles penetrate 3% agar to an average depth of around 300 μm over a surface, or injection "footprint," which is approximately circular with a diameter of 10 mm.[4]

As optical microscopy is time-consuming and inherently invasive, it would be desirable to develop an automated, noninvasive method of measuring particle penetration depth and size in order to assess the efficacy of the injection device, or to assess other forms of subcutaneous dosage administration. Previous work by the authors has shown that ultrasonic imaging techniques show great promise in identifying particles beneath a surface, with work at 15 MHz providing accurate estimations of relative particle number density within a tissue-mimicking material.[4] Furthermore, it has been suggested that frequency domain analysis could provide a means of measuring particle size, though such a technique has never been applied to the case of polydisperse size distributions, nor automated[5] and compared directly to optical measurements in order to assess its accuracy. For these reasons, this study considers the development of an acoustic microscopy technique—over technologies such as optical coherence tomography[6]—which can be used to assess the size distribution and penetration depth of particles injected using needle-free injection. Unlike previous works, this study considers polydisperse particle distributions, injected into both agar and skin targets.

Though the acoustic scattering from particles in agar has been considered previously,[5,7] to the best knowledge of the

[a]Author to whom correspondence should be addressed. Electronic email: jamie.condliffe@gmail.com

 0001-4966/2010/127(4)/2252/10/$25.00

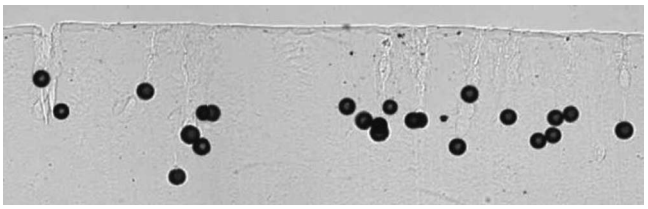

FIG. 1. Image of a typical lateral agar slice, containing 48.0 μm polystyrene particles, captured using a Nikon CCD-equipped microscope.

authors, the present work represents the first attempt to develop an acoustic microscopy technique to image particles embedded within skin, following transdermal delivery. Furthermore, this work develops a novel means of noninvasively measuring the size of polydisperse particles surrounded by both inviscid and visco-elastic media. The overall objective is to develop a microscopy technique to measure particle size and penetration depth in agar and skin simultaneously, that can be exploited to optimize particles and devices for a broad range of drug and vaccine delivery applications.

II. THEORY

A. Scattering from an elastic sphere

The acoustic microscopy technique presented here relies on the ability to relate the acoustic signal backscattered by particles embedded in agar or skin samples to the electrical signal received by the interrogating transducer. The scattered wave varies depending on the acoustic properties of the surrounding medium and the scatterer, the frequency of the incident sound, and the size and shape of the scatterer. In general, the surrounding medium and scatterer will support both compressional and shear waves. To simplify the theoretical discussion, the case of a particle surrounded by agar is first considered. Agar has a shear modulus G of 100 kPa, assumed to be negligible compared to the bulk modulus K of 2.25 GPa.[8,9] In what follows, therefore, theoretical modeling is shown, which assumes that a particle is surrounded by agar, treated as an inviscid compressible fluid. This theory is developed into a means of assessing particle size in later sections.

The particles considered here are made of polystyrene and stainless steel. Polystyrene spheres have a density of 1050 kg/m^3, bulk modulus of 5.8 GPa, shear modulus of 1.27 GPa, and Poisson's ratio ν of 0.34; stainless steel particles have a density of 8000 kg/m^3, bulk modulus of 193 GPa, shear modulus of 82 GPa, and Poisson's ratio of 0.30. The surrounding medium is assumed to be a 3% agar gel, with density of 1030 kg/m^3, bulk modulus of 2.25 GPa, and shear modulus of 100 kPa.

An exact solution for scattering of sound by an elastic sphere in an inviscid fluid was developed by Faran.[10] This solution is implemented here to model the response of the particles in agar to an incident ultrasound pulse. Figure 2 shows the theoretical variation in differential backscattering cross-section—backscattered power per unit incident intensity—with frequency for a 48.0 μm polystyrene sphere in agar. Also plotted in Fig. 2 is the experimentally acquired

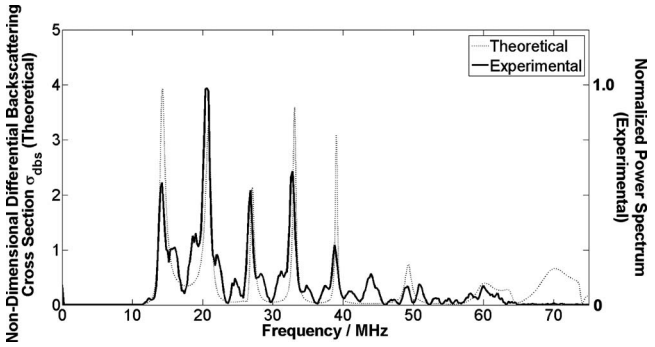

FIG. 2. Plot showing variation in differential back scatter, σ_{dbs}, with frequency for a polystyrene particle, diameter 48.0 μm, surrounded by agar, as predicted by the Faran model (dashed). Shown for comparison is the experimentally measured frequency response of a particle of the same size, acquired using a 10–75 MHz transducer (black). The experimental result is not corrected for the frequency response of the transducer.

frequency response of a single, isolated particle known to be of diameter 48.0 μm, measured using the 10–75 MHz transducer described in Sec. III B, which has been normalized to match the peak amplitude at 20 MHz. It can be seen that the two results are in close agreement, with the theoretical model correctly predicting the sharp resonances of the particle. Similar agreement (data not shown) was obtained for the case of a stainless steel sphere surrounded by agar—a second particle type that will be used in subsequent studies.

B. Spectral method for particle sizing

In Fig. 2, it can be seen that the 48 μm sphere has five distinct resonance peaks below 50 MHz, and the spacing between these peaks is 6.2 MHz. For small values of the non-dimensional size parameter ka, where k is the wavenumber and a is the particle radius, it is found that the spacing between the resonance peaks is inversely proportional to the particle diameter. For the particular case of a 48.0 μm polystyrene sphere in agar, this is no longer true above 60 MHz, where the simple, low-order elastic resonances of the particle become confounded with higher-order modes of oscillation. However, over the frequency range containing the strong resonances, the spectral peak spacing can be directly correlated with particle diameter, as illustrated in Fig. 3. The values for inter-peak spacing in Fig. 3 were determined from the Faran solution, which was evaluated for polystyrene and

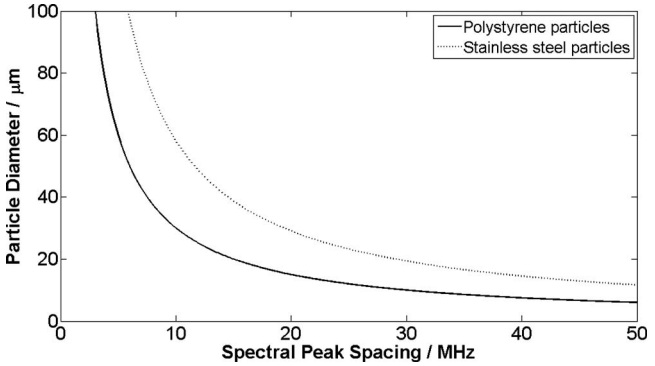

FIG. 3. A plot showing variation in particle size with inter-peak spacing in frequency response.

stainless steel particles of size 1–100 μm. The resonances were detected using a peak finding algorithm, and their spacing was recorded. The relationship shown in Fig. 3 provides a means of non-invasive, real-time particle sizing, under certain assumptions, which are discussed in Sec. III E 1.

C. Multiple scattering

The particle sizing concept described in Sec. II B can only be applied to an experimental situation involving multiple scatterers if it can be assumed that individual scatterers do not interact. The multiple scattering criterion developed by Waterman and Truell[11] states that the single scattering approximation holds when

$$\frac{n\sigma_s}{k_0} \ll 1, \tag{1}$$

where σ_s is the total scattering cross-section of the object, n is the number of scatterers per unit volume, and k_0 is the wave number in the surrounding medium. In the current work, this parameter is of the order of 0.2, even for the highest payload conditions of both polystyrene and stainless steel particles, assuming frequencies in the range 10–75 MHz. It may therefore be assumed that the single scattering approximation holds.

III. MATERIALS AND METHODS

A. Needle-free injection apparatus

The experimental needle-free particle injection system shown in Fig. 4 was used. Particles were weighed using a microbalance (MT 5, Mettler-Toledo, U.K.) and inserted into a disposable cartridge, which fits into the main body of the needle-free device. The number density of particles was chosen to reflect that typically injected in a clinical setting. The particles were fired at the sample from a height of 10 mm above the surface with the "gun" mounted on a specially designed delivery console to ensure that the direction of injection was orthogonal to the target surface.

Two targets were used during this work. The first was a 3%, by mass, agar gel, which has been previously shown to provide a good experimental model for needle-free injection.[4] In terms of acoustic properties, a 3% agar gel has a density of 1030 kg/m^3 and sound speed of 1540 m/s.[8] These values compare favorably with the acoustic properties of human skin, which has a density of approximately 1000 kg/m^3 and a sound speed of 1480 m/s.[12–14] The tissue-mimicking agar material was manufactured in the laboratory by combining agar powder with water, which was heated (~80 °C) while stirring, and then degassed under a vacuum (~50 kPa). The resulting molten agar was injected into specially designed molds, and refrigerated for at least 3 h to ensure complete solidification prior to injection of particles.

The second target was excised porcine tissue, which is similar histomechanically and biomechanically to that of humans,[15] and is also of a similar thickness.[16] Pig skin exhibits a sound speed that is slightly higher than that of human skin, at around 1720 m/s.[13] Samples were taken from the inguinal region (inner thigh) and dorsal pinna (back of the ear) of an English white pig. The skin was marked before removal from the body, and its dimensions were noted so that the skin could be tensioned, to restore its dimensions before retrieval during experimentation, providing continuity between the *in vivo* and *ex vivo* cases. Experiments were conducted in the shortest time possible, following harvest from the pig, and in all cases, experiments were performed within 3 days. The skin was at all times stored at a constant temperature of 4 °C.

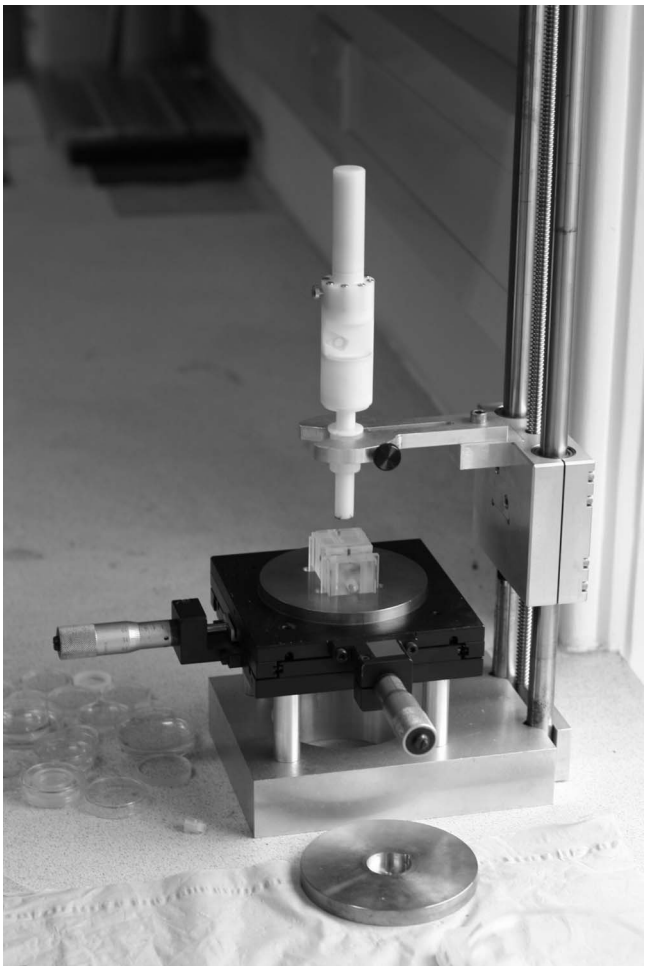

FIG. 4. Needle-free injection system mounted on a delivery console, which enables accurate positioning of the phantom and orthogonal injection of particles.

Monodisperse polystyrene particles of diameter 48.0 μm and density 1050 kg/m^3 have been used in previous works to model drug and vaccine particles.[4] However, the use of monodisperse particle distributions undoubtedly constitutes an over-simplification of the polydisperse particles, which are injected in a clinical context. The work presented here therefore uses polydisperse polystyrene particles, mean diameter of 30.0 μm, and standard deviation of 16.7 μm, and stainless steel particles, mean diameter of 46.0 μm, and standard deviation of 13.0 μm (Thermo Fisher Scientific). The polystyrene spheres are able to penetrate human skin, but we found that these were not able to penetrate deep enough into porcine skin. Therefore, stainless steel particles were chosen for the experiments in the porcine skin because their higher density allowed them to penetrate

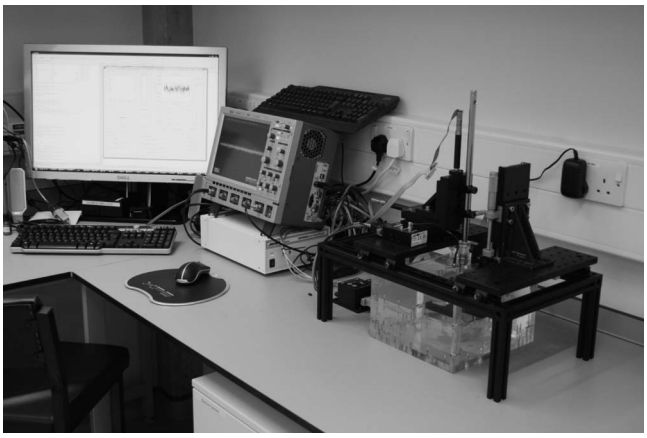

FIG. 5. General layout of the scanning acoustic microscope, showing the automated positioning system and support frame (Thorlabs), acoustic tank, pulser-receiver (DPR500, JSR Ultrasonics), and the digital oscilloscope (Wavesurfer 104MXi, LeCroy) used for data acquisition.

to depths more relevant to the clinical application. We note that this does not affect signal to noise ratio, with the scattering cross-section of 46 μm stainless steel spheres being of the same order as that of 30 μm polystyrene spheres over the frequency range investigated here. It should be noted that all references to size distributions hereafter refer to number distributions and not to volume distributions.

B. Scanning acoustic microscopy apparatus

Following injection, targets were exposed to ultrasound using the scanning acoustic microscopy (SAM) set-up pictured in Fig. 5. The basic premise of the experimental layout was that the sample, with embedded particles, was held in a fixed position inside the ultrasound tank while planar scans, parallel to its surface, were performed using an ultrasound transducer.

The sample was mounted on a goniometer stage (GN1/M, Thorlabs) with its free surface facing upwards inside a custom-built water tank, which contained filtered, degassed, and deionized water maintained at a temperature of 20 °C. A 10–75 MHz, spherically focused PVDF transducer (PI175–1-R0.50, S/N: 200411, Olympus NDT) was mounted above the sample holder on a software-controlled, three-dimensional motorized positioning system of sub-micron precision (Z825 and TST001, Thorlabs). The transducer was mounted with its acoustic axis normal to the sample surface and driven in pulse-echo mode using a high frequency pulser-receiver (DPR500, JSR Ultrasonics). The waveform received by the pulser-receiver was recorded by a digital oscilloscope (1 GHz bandwidth, 8-bit, Wavesurfer 104Mxi, LeCroy), and transferred to a PC (XPS, Dell) via TCP/IP for storage and further processing.

C. Transducer characterization

According to O'Neil's theoretical model for focused radiators,[17] the focal point of the transducer used in the present study is 13.2 mm from the face of the transducer when calculated at a frequency of 75 MHz. The focal zone depth, defined as the distance between the −6 dB points for pulse-echo response, is 6 mm, and the beam diameter is 120 μm at the −6 dB points.

The implication of these calculations is twofold. Axially, the focal zone depth of the transducer is such that the pressure amplitude of the ultrasound wave received by the embedded particles can effectively be assumed to be constant over penetration depths of hundreds of microns. The beam diameter further determines the scanning step size required to achieve complete characterization of the sample.

D. Sample alignment and data acquisition

Following mounting of the sample in the water tank, the transducer was moved axially until its focus coincided with the water-sample interface. The goniometer, on which the sample holder was mounted, was then adjusted to ensure that the surface of the sample was perpendicular to the transducer axis. Performing this alignment at several points across the sample surface ensured that the water-sample interface was normal to the transducer axis, and was always coincident with the transducer focus.

Motion control, pulser-receiver settings, and data acquisition from the oscilloscope were controlled using a custom-built graphical user interface developed in MATLAB (Mathworks). The excitation pulse settings were set so as to keep the pulse length short, to improve axial resolution, while also maintaining high signal-to-noise ratio (SNR). Parameters of 330 V driving voltage, 25 Ω damping, and "high" energy produced an ultrasound pulse duration of 20 ns, equivalent to a spatial pulse length of 30 μm, which was generated with a pulse repetition frequency of 20 kHz.

Once alignment was achieved, the transducer was moved transversely so that its focus approximately coincided with the center of the needle-free injection site. A scan was launched in a plane parallel to the sample surface, henceforth referred to as the *XY* plane. Based on the transducer characterization, a transverse step size of 100 μm was chosen. At each *XY* position, 50 consecutive traces were averaged on the oscilloscope to enhance SNR before transferring the data to the PC.

E. Post-processing

A typical raw trace, taken from an experiment using polystyrene particles in agar, is shown at the top of Fig. 6. Two features are readily discerned. At 17.6 μs, the discontinuity in acoustic impedance between the water and the agar surface causes a reflection of the incident ultrasound pulse. The second feature, starting at 18 μs, consists of a multiple set of pulses, which corresponds to scattering from a single particle in the agar. Traces taken from experiments performed in skin are extremely similar, though there is an appreciable increase in signal noise present. Post-processing of these raw time traces is required to quantify particle properties and particle position beneath the target surface.

The distinctive features of these waveforms can be used to extract parameters of interest: Signal amplitude and time of flight can yield an estimate of penetration depth, while frequency domain analysis can be used to predict particle

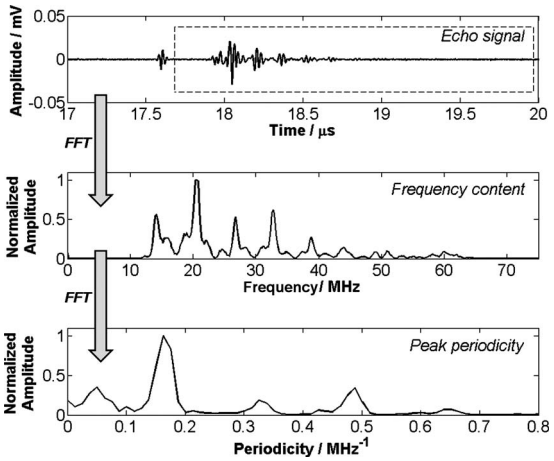

FIG. 6. A typical, averaged, received echo signal from a polystyrene particle in agar (top), with returns from the water-sample interface, and the polystyrene spheres are clearly visible. The dashed box represents the gated signal, which is used in the spectral analysis explained in the text. Below this is the corresponding frequency content of the signal, determined by taking a Fourier transform of the gated echo signal (middle). Finally, the periodicity of the resonance peaks is obtained by taking a Fourier transform of the amplitude spectrum (bottom).

size. The following two post-processing algorithms were developed to analyze the raw data; the first uses a novel means of frequency domain analysis to measure post-injection particle size non-invasively, while the second uses thresholding and analysis of B-mode images to measure particle penetration depth.

1. Measuring particle size

As illustrated in Fig. 3, the inter-peak spacing of the sharp resonances in the frequency response are unique for a given particle size. To measure the size of the particles from the echo data, an algorithm has been developed, which determines the periodicity of resonances in the frequency domain and matches this to the most probable particle size. First, the reflection from the water-sample interface is gated out, leaving just the signal present as a result of scattering from the particles. This is shown in the top plot in Fig. 6, which shows an echo signal from a 48.0 ± 3.8 μm particle. The dashed box represents the gated signal that is used. The Fourier transform of this part of the signal is taken, providing the frequency spectrum of the signal due to scattering, as is shown in the middle plot of Fig. 6. Finally, the periodicity of the peaks in this spectrum is calculated by evaluating the Fourier transform of the amplitude spectrum in the range 1–100 MHz, providing a plot of peak periodicity, as shown at the bottom of Fig. 6.

A sharp peak is apparent in this plot, whose position corresponds to the periodicity of the peaks due to scattering in the frequency domain. The peak periodicity, of units MHz^{-1}, is the inverse of the peak spacing. Here, the peak occurs at 0.163 MHz^{-1}, corresponding to a peak spacing of 6.16 MHz. This value can be used to asses particle size using the curve presented in Fig. 3. In the illustrated case, the algorithm would predict that the particle has diameter 49 μm. This procedure is undertaken across the footprint to identify a particle size for each XY point. This algorithm is reliable for the cases where (i) there is one particle of any size in the focal zone of the transducer, and (ii) where there are multiple particles in the focal zone of the same size. For cases where this is not true, it is assumed that multiple particles in the focal region are of the same size. However, optical examination of the injection footprints in several samples reveals that over 90% of the data points will contain only one particle, which implies that sizing errors introduced by signals attributable to multiple particles in a single time trace should be relatively small over the entire injection footprint.

2. Measuring particle penetration depth

The magnitude of the analytic signal (described interchangeably from here on as the "envelope"), generated using the Hilbert transform, is commonly used in medical ultrasound imaging systems to create B-mode images.[18] The B-mode image shown at the top of Fig. 7 was created using this technique. The magnitudes of the analytic signals from each RF line, across a particular line of constant x or y, were calculated, and "stacked" next to each other in a two-dimensional matrix. The magnitudes of each element of the matrix were then converted to a log-compressed greyscale. The resulting images, shown for the case of skin in Fig. 7 (top), clearly show the surface of the sample and the particles lying beneath.

To measure penetration depth, successive B-mode images taken from the footprint were considered separately. Thresholding and image analysis were used to correctly identify particles below the surface, and filtering of object properties allowed the effects of artifacts from skin to be ignored. In each case, the surface of the sample was identified using thresholding. The first return from the agar interface was roughly located along each A-line in the B-mode image using thresholding, whereby the first occurrence of the signal, being greater than five times the amplitude of the noise floor, was sought. The noise floor was calculated as the mean value of the first 1 μs of the envelope signal, which is a part of the signal originating from before the surface of the sample. Upon locating the first occurrence of the signal being above this threshold, the local maximum along the A-line, within 20 ns of the first occurrence, was sought, and the interface between water and sample was defined to be half of an acoustic pulse length prior to this maximum. This was used to define the sample surface across each B-mode image.

In the current case, the scattered power from the particle was greater in magnitude than that reflected by the surface. In fact, this was true over the range of size and particle types used throughout this work. By assessing the return from the agar surface, at a position away from the injection footprint, it was possible to calculate an average return from the surface. A threshold was then set, at 1.5 times the average surface reflection amplitude, above which a peak was assumed to occur due to the possible presence of a particle. This threshold was used to create a binary image. Pixels with a value lower than the threshold were assigned a value of zero, while those greater than the threshold were assigned a value

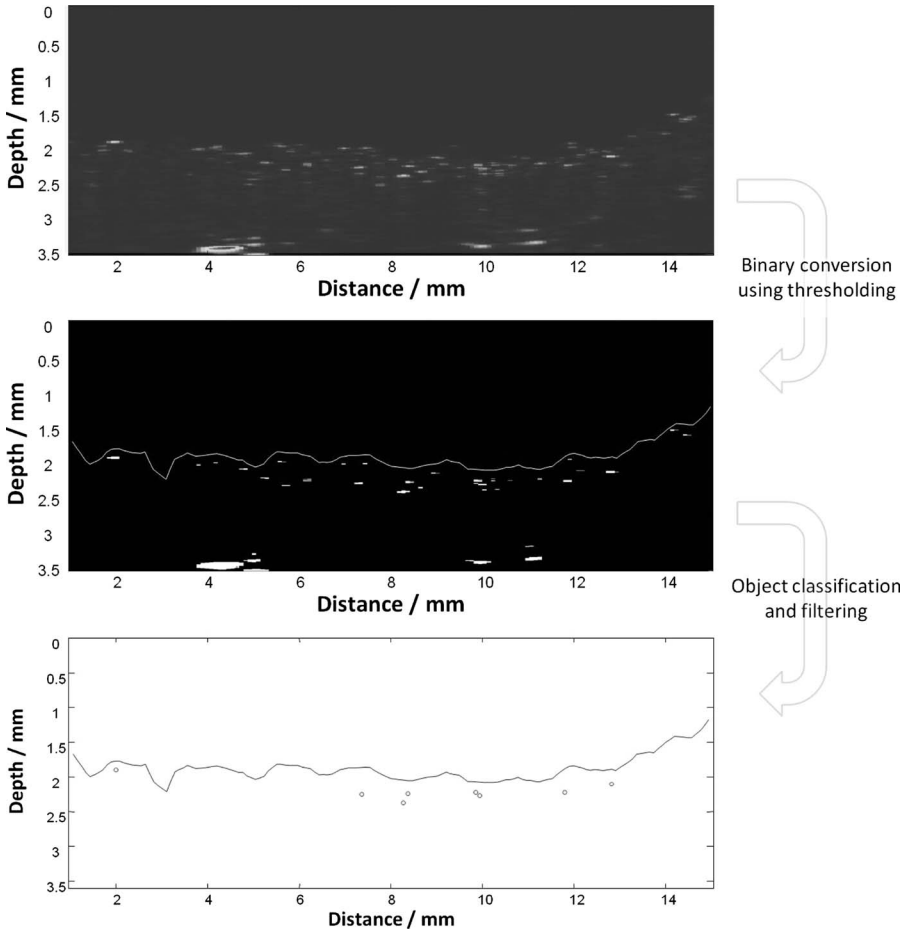

FIG. 7. Schematic explaining algorithm used to determine penetration depth in skin. A B-mode image (top) is converted to a binary image (middle) using thresholding. The skin surface is shown in white for reference. The binary image's "objects" are then sized and classified either as particles or as non-particles. This image allows a plot (bottom) of the skin surface and particles (circles) to the created.

of unity. The resulting black and white image is shown in the second sub-plot of Fig. 7, which includes the superposition of the skin surface.

At this point, the spatial characteristics of the objects identifiable on the binary image were analyzed to extract the area, minimum axis length $l_{\min}$, major axis length l_{maj}, and perimeter, where all values were measured in pixels. We observed that particles appeared circular in the B-mode images. As a result, in order for a shape to be identified as a particle, it had to be sufficiently "round" [i.e., have a ratio of $l_{\mathrm{maj}}/l_{\min}$ close to unity and a perimeter approximately given by $\pi(l_{\mathrm{maj}}+l_{\min})$] and have a pixel area within a certain range. Objects, which were sufficiently small, large, or strangely shaped, were excluded, and those of the correct size and shape were included. This process allowed artifacts due to hair follicles, sweat glands, and other skin sub-structures to be ignored in the analysis. Those objects, which were included, had their centroids defined as the particle center, and a penetration depth calculated using the speed of sound in skin and the time delay from the sample surface to the aforementioned centroid. For illustrative purposes, those objects determined to be particles are plotted at the bottom of Fig. 7 as circles, and beneath the skin surface, plotted as a line. Each value of penetration depth was recorded and tagged with the *XY* position at which it was measured.

F. Validation

Penetration depth measurements were validated using optical microscopy. Following completion of the acoustic scan, the sample was removed from the tank and was sectioned. Previous work has introduced a variety of optical imaging techniques to evaluate particle penetration depths.[4] Agar was sectioned in the laboratory perpendicular to its surface, in the *XZ* plane, using a specially produced "guillotine" that resulted in slices of around 200 μm in thickness. The sections were then photographed using a microscope with a CCD-camera (ECLIPSE Ti, Nikon), providing images such as that in Fig. 1. An algorithm developed in MATLAB allowed the upper surface of the gel to be detected and the distance from this surface to the centroid of each particle to be measured. A calibration image from the microscope was then used to convert measurements in pixels to an actual penetration depth that can be directly compared with acoustic measurements.

For the case of tissue, the sample was fixed in a solution of saline buffered 10% formalin, and histology subsequently performed at the Northwick Park Institute for Medical Research (U.K.). The samples were cut to provide transverse slices, sectioned perpendicular to their surface in the *XZ* plane, and stained with hematoxylin and eosin. Images of the slides were captured using the CCD-camera equipped microscope, and depth measurements were performed using image analysis software (NIS-Elements, Nikon).

All particle size measurements were validated using laser-light diffraction. Measurements were performed using a Mastersizer S (Malvern Instruments), fitted with a 300RF lens and backscatter detector, within a small volume sample dispersion unit. This provided accurate distributions of par-

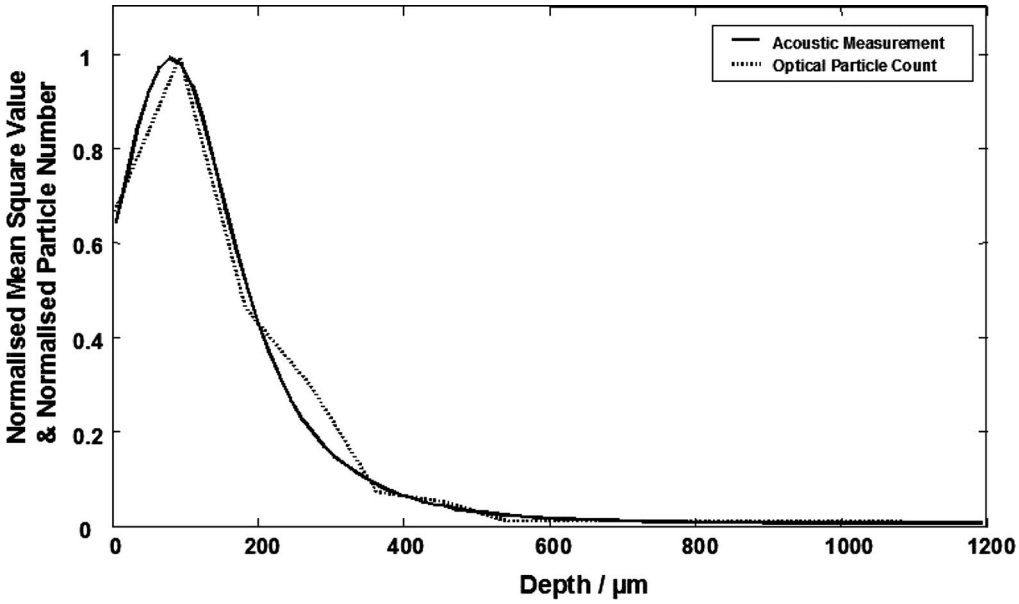

FIG. 8. Comparison between acoustical and optical estimates of particle penetration depth of polydisperse polystyrene particles, mean diameter 30 μm, in agar.

ticles size. Optical microscopy and laser-light diffraction were considered to be the "gold standard" for the purposes of validation of the acoustic technique.

IV. RESULTS AND DISCUSSION

Samples of 3% agar were prepared, and differing payloads of polydisperse polystyrene and stainless steel particles were embedded into each using the experimental needle-free injection device. Porcine tissue samples were also prepared and injected with polydisperse stainless steel particles. Each sample was individually analyzed using the SAM apparatus, in conjunction with the two aforementioned algorithms for measuring penetration depth and estimating particle size, before being sliced and analyzed optically.

A. Penetration depth

Use of the post-processing algorithm described in Section III E 2 can be used to evaluate the distribution of penetration depth in the sample. Figure 8 shows a plot of the distribution of penetration depths for the case of a 350 μg payload of polydisperse polystyrene particles, mean diameter of 30 μm, injected into agar. Alongside values computed from the acoustic data, the reader may observe results acquired from the optical validation, normalized in the same way. It can be seen that the modal penetration depth, represented graphically as the peak of the curve, is accurately measured by the acoustic technique. Furthermore, computation of the mean penetration depth, measured to be 173 μm acoustically and 184 μm optically, and standard deviation, measured to be 105 μm acoustically and 103 μm optically, are in good agreement.

For the sake of brevity, the mean and standard deviation of penetration depth was calculated and recorded for each experiment, which was performed, providing values for ten data sets in total: three corresponding to polydisperse polystyrene particles in agar, three to polydisperse stainless steel particles in agar, and four to polydisperse stainless steel particles in skin. Similar values were calculated from the optical analysis for comparison. Figure 9 (top) shows a scatter plot of mean penetration depth of particles, measured acoustically and optically. It can be seen that there exists strong correlation between the two, with correlation coefficient of $R=0.9866$. Alongside this strong value of correlation coefficient, the data exhibits an extremely small p-value (calculated by transforming the R value into a paired, two-tailed t-statistic) at $p=1.3944\times10^{-7}$. Therefore, the results exhibit strong correlation, which is also statistically significant, satisfying a 99.99% confidence interval. The mean penetration is therefore accurately represented by the acoustic technique.

Figure 9 (bottom) shows a similar scatter plot for the standard deviation of penetration, measured both acoustically and optically. Relatively strong correlation is once again observed, with a correlation coefficient of $R=0.9335$, which is again shown to be statistically significant, with a p-value of $p=7.8756\times10^{-5}$. The standard deviations seem to vary rather more than the mean penetration depth, and it is hypothesized that this is due to slight disruption of the particles during optical validation. As the cutting blade is passed through a sample, particles, especially in the case of those made of stainless steel, are dislodged, and as a result, there is a tendency for increased variation between the two measurements. Regardless, these results suggest that the acoustic technique is capable of accurately representing the mean penetration depth, and provides a good indication of the standard deviation.

B. Particle size

Post-processing of the acoustic microscopy data using the novel algorithm described in Section III E 1 provides estimates of particle size at every point across the acoustic scan. The same algorithm developed in agar was employed to estimate particle size in skin. Shown in Fig. 10 (top) is a

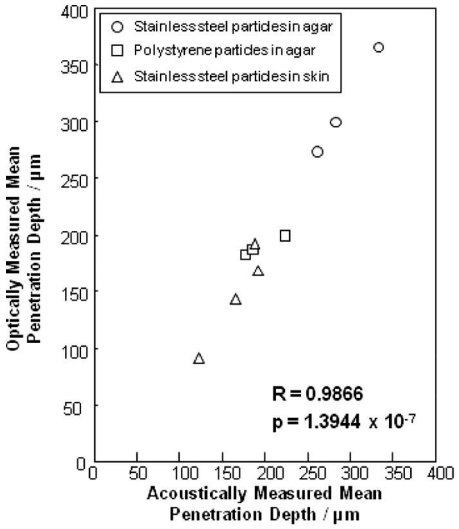

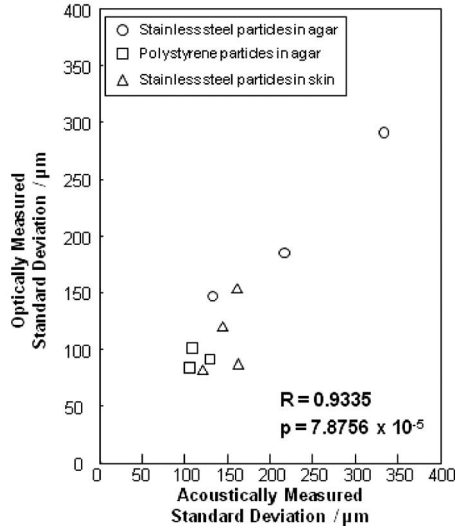

FIG. 9. Scatter plots for mean (top) and standard deviation (bottom) of penetration depth data, for polystyrene and stainless steel particles injected in agar, and for stainless steel particles injected in skin, as measured acoustically and optically. Values of correlation coefficient R and significance p-value are included.

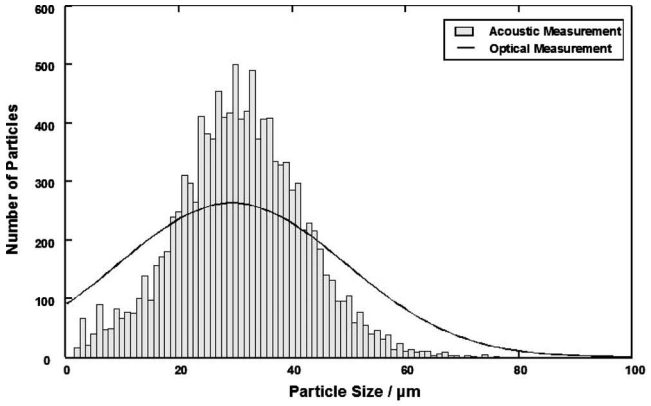

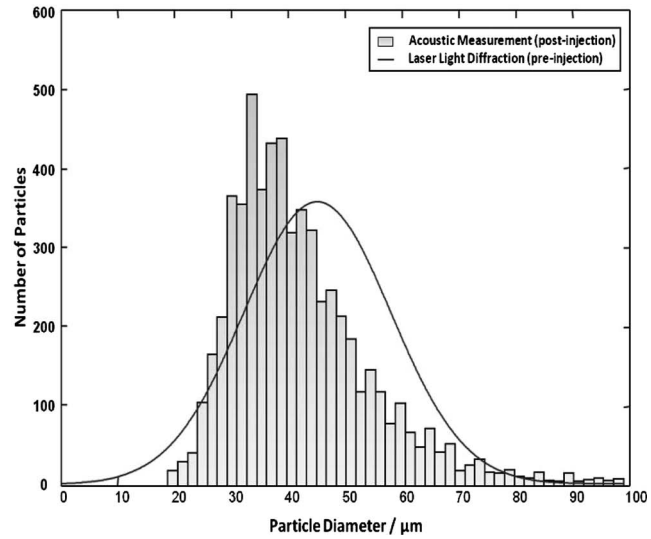

FIG. 10. Distribution of particle sizes, as predicted by the acoustical technique following injection (gray histogram) and optical method prior to injection (black line), for the case of polydisperse polystyrene particles in agar (top) and polydisperse stainless steel particles in skin (bottom). The optically generated curves are normalized to have the same integral over the plotted range as the histogram.

histogram representing particle size distribution measured acoustically for the case of a 350 μg payload of polydisperse polystyrene particles injected into agar. The overlaid black curve represents the particle size distribution measured, pre-injection, using laser-light diffraction techniques, and is normalized such that the integral under the curve is equal to that of the histogram. It can be seen that the mean particle size of 30.0 μm is accurately measured by the acoustic technique, though the standard deviation of the distribution, at 13.4 μm, is smaller than that measured using light diffraction, at 16.7 μm. The lack of smaller particles in the distribution may be due to the inability of such particles to penetrate the agar surface; previous experiments have tended to suggest that smaller particles penetrate less effectively, so that very small particles may not penetrate the sample at all. Prior evidence also suggests that larger particles may deform on impact with the target, meaning that they are effectively converted into smaller particles post-injection. This was confirmed by melting an agar sample post-injection and performing laser-light diffraction measurements using the remaining particles, showing a similar decrease in the number of large particles present. This could, therefore, account for the acoustically measured decrease in the number of particles in the larger size range.

Figure 10 (bottom) shows a typical acoustically measured size distribution of polydisperse stainless steel particles in skin (histogram), alongside the size distribution of the same particles measured pre-injection using laser-light-diffraction (solid line). It can be observed that, though the modal size (i.e., the size exhibited by most particles; the peak of the distribution) of the acoustically measured distribution is different to that measured pre-injection, the mean at 43 μm, and standard deviation at 16 μm, are extremely similar to those measured using laser-light diffraction. These observations suggest that the particle sizing technique is, to some extent, affected by the change in surrounding medium from agar to skin. It is worth noting that the sizing technique assumed that the particle, which was being sized, was surrounded by an inviscid fluid. The algorithm could be adapted to compensate for the visco-elastic effects of the surrounding

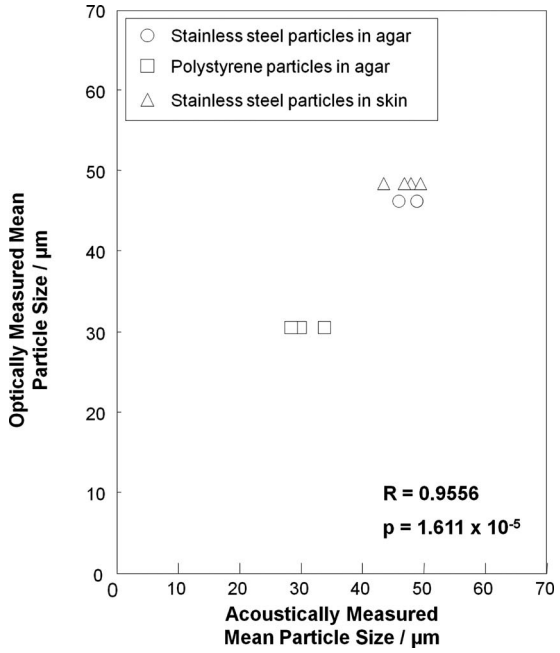

FIG. 11. Scatter plot of mean particle diameter, for polystyrene and stainless steel particles injected in agar, and for stainless steel particles injected in skin, as measured acoustically and optically. Values of correlation coefficient R and significance p-value are included.

medium, but as the properties of skin vary so much with depth, site, and age,[13] assigning correct elastic parameters to the model will likely be extremely difficult. The results achieved with the inviscid model were deemed accurate enough, and the algorithm was used throughout this work to measure particle size.

The mean particle size measured acoustically was recorded for each experiment performed, providing data across all ten experiments. The acoustically measured penetration depth is plotted against the mean particle size measured using laser-light diffraction, and this is shown in Fig. 11. It can be seen that there is strong correlation between the acoustic and optic measurements, with a value of correlation coefficient $R=0.9556$. This may also be shown to be statistically significant, with a p-value of 1.611×10^{-5}, which satisfies a 99.99% confidence interval. The acoustic technique therefore provides a way of measuring particle size, following needle-free injection, non-invasively, in both agar and skin. This has never been achieved in the past, and provides a useful new tool for the developers of needle-free injection. The ability to size and localize particles using a single modality, scanning acoustic microscopy, offers a unique opportunity for the first time to correlate particle size with penetration depth. This is explored in Sec. IV C.

C. Correlating penetration depth and particle size

It has been hypothesized in previous works that larger particles will penetrate samples to greater depths due to their greater momentum.[3] The data presented above makes it possible to correlate penetration depth and particle size, as for every position, where a penetration depth was measured, a particle size has been calculated. The use of a bubble plot—a two-dimensional scatter plot where a third variable is represented by the size of the points—allows analysis of correlation between particle size and penetration depth, while also providing an insight into where small and large numbers of points lie. Shown in Fig. 12 are bubble plots from typical experiments performed using polydisperse particles in both agar and skin during this research: polydisperse polystyrene in agar (top), and stainless steel in agar (middle) and skin (bottom). The circle diameter on the bubble plot is directly proportional to the number of particles present at a particular size and depth, and each circle is centered at the mean particle size and penetration depth of its constituent points. Data was binned along the particle size axis.

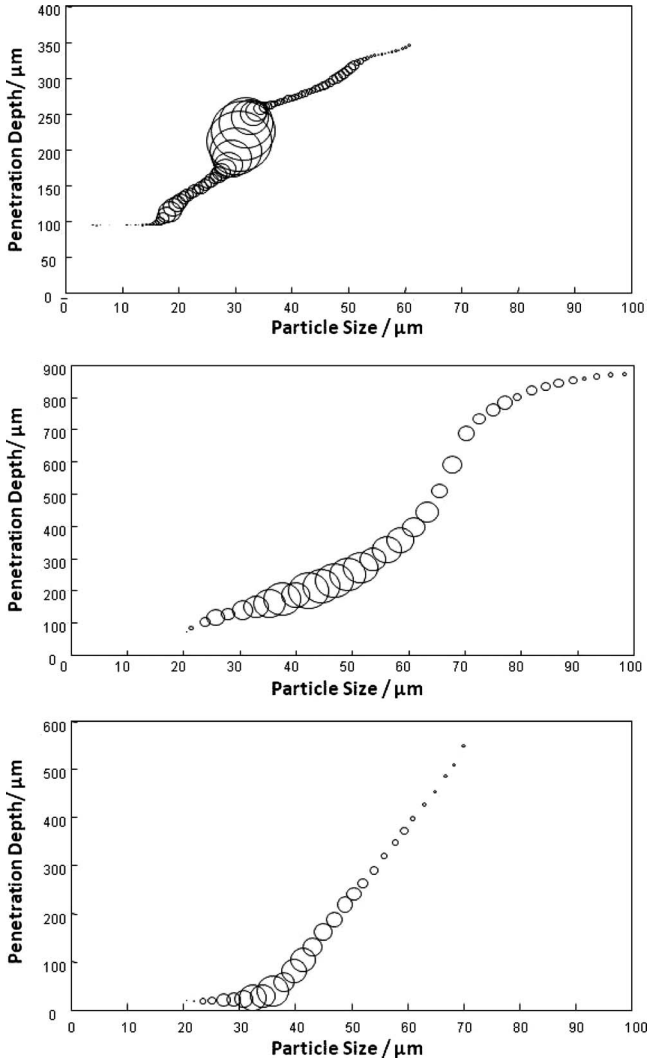

FIG. 12. Variation in penetration depth with particle size, both measured acoustically, for polydisperse polystyrene particles in agar (top), and stainless steel particles in agar (middle) and skin (bottom). Circle diameter is directly proportional to number of particles, and each circle is centered at the mean particle size and penetration depth of its constituent points. Data was binned along the particle size axis.

It is immediately obvious in each case that there is a strong trend for large particles to penetrate to greater depths than smaller ones, as predicted by previous works. However, it can be seen that, though it is clear that penetration depth increases monotonically with increasing particle size, the linear relationship predicted by previous works is less obvious.[2,3] This further emphasizes the potential usefulness

of the acoustic technique in establishing the relationship between particle size and penetration depths for particular particle types in different media. The data in Fig. 12 can be acquired non-invasively and in a relatively short time using the novel acoustic technique presented here, and such results have not been acquired in the past. The value of this data for the development of transdermal drug and vaccine delivery modalities should not be underestimated: From a single experiment using a range of particle sizes, it becomes possible to choose the right particle size range for a particular application.

V. CONCLUSIONS AND FUTURE WORK

An innovative acoustic microscopy technique, which is capable of measuring penetration depth and particle size, simultaneously following needle-free injection, has been developed. Acoustic measurements of particle penetration depth are in strong agreement with those measured using optical microscopy, in both agar and porcine skin. In fact, there exists a strong, statistically significant, correlation between mean and standard deviation of particle depth measured acoustically and optically. The novel, automated particle sizing algorithm presented here has also been shown to provide an accurate measurement of post-injection particle diameter. Once more, strong correlation exists between particle diameter measurements performed acoustically and using laser-light diffraction. The unique opportunity to compare size and penetration depth showed that the two are strongly correlated, with larger particles penetrating the sample to greater depths. Scanning acoustic microscopy could provide a viable means of non-invasively optimizing particle size and properties to achieve specific penetration depths for particular transdermal drug and vaccine delivery applications.

The sizing techniques presented here offer the most interesting opportunities for future development. The obvious extension is to develop the technique to assess changing particle size, as real drug-loaded particles tend to dissolve over time. Furthermore, though the technique has been shown to be of use in assessing the efficacy of needle-free injection, it is suggested that it could also be utilized in analyzing many other solid dosage forms administered to the skin, such as implants. It is hoped that the acoustic technique developed as part of the present work will act as a springboard, and a common denominator, in several future studies of particle behavior in skin.

ACKNOWLEDGMENTS

The authors would like to thank Dr. Manish Arora and Jamie Collin from the Biomedical Ultrasound and Biotherapy Laboratory at the University of Oxford, for their advice and support; James Fisk and Roger Lewis for their help in manufacturing a wide array of essential experimental components; Prof. Ronald A. Roy for his assistance during preliminary experimentation at Boston University; and Tahera Ansari at the Northwick Park Institute of Surgical Research (U.K.) for her assistance with histology of injected skin samples. Funding and support from the U.K.'s Engineering and Physical Sciences Research Council, Particle Therapeutics Ltd. and the Royal Society's Paul Instrument Fund are also gratefully acknowledged. Finally, R.O.C. acknowledges support from CenSSIS, the Gordon Center for Subsurface Sensing and Imaging Systems, under the Engineering Research Centers Program of the National Science Foundation (Grant No. EEC-9986821).

[1]M. Kendall, "Engineering of needle-free physical methods to target epidermal cells for DNA vaccination," Vaccine **24**, 4651–4656 (2006).
[2]T. Burkoth, B. Bellhouse, G. Hawson, D. Longridge, A. Muddle, and D. Sarphie, "Transdermal and transmucosal powdered drug delivery," Crit. Rev. Ther. Drug Carrier Syst. **16**, 331–384 (1999).
[3]T. Mitchell, "The ballistics of micro-particles into the mucosa and skin," Ph.D. thesis, Department of Engineering Science, Oxford University, United Kingdom (2002).
[4]J. Condliffe, J. Collin, F. Carter, G. Costigan, and C.-C. Coussios, "Development of an acoustic microscopy technique to assess particle distribution following needle-free injection," Proceedings of the Institute of Acoustics, Vol. **28**, Pt. 1 (2006).
[5]R. Baddour, M. Sherar, J. Hunt, G. Czarnota, and M. Kolios, "High-frequency ultrasound scattering from microspheres and single cells," J. Acoust. Soc. Am. **117**, 934–943 (2005).
[6]A. Fercher, C. Hitzenberger, W. Drexler, G. Kamp, and H. Sattmann, "In vivo optical coherence tomography," Am. J. Ophthalmol. **116**, 113–114 (1993).
[7]S. Bridal, K. Wallace, R. Trousil, S. Wickline, and J. Millern, "Frequency dependence of acoustic backscatter from 5 to 65 MHz of polystyrene beads in agarose," J. Acoust. Soc. Am. **100**, 1841–1848 (1996).
[8]M. Burlew, E. Masden, J. Zagzebski, R. Banjavic, and S. Sum, "A new ultrasound tissue-equivalent material," Radiology **134**, 517–520 (1990).
[9]M. A. LeRoux, F. Guilak, and L. A. Setton, "Compressive and shear properties of alginate gel: Effects of sodium ions and alginate concentration," J. Biomed. Mater. Res. **47**, 46–53 (1999).
[10]J. Faran, "Sound scattering by solid cylinders and spheres," J. Acoust. Soc. Am. **23**, 405–418 (1951).
[11]P. C. Waterman and R. Truell, "Multiple scattering of waves," J. Math. Phys. **2**, 512–537 (1961).
[12]S. A. Goss, R. L. Johnston, and F. Dunn, "Comprehensive compilation of empirical ultrasonic properties of mammalian tissues," J. Acoust. Soc. Am. **64**, 423–457 (1978).
[13]F. Duck, *Physical Properties of Tissue: A Comprehensive Reference Book* (Academic, New York, 1990).
[14]M. Anderson and G. Trahey, "The direct estimation of sound speed using pulse echo ultrasound," J. Acoust. Soc. Am. **104**, 3099–3106 (1998).
[15]N. A. Monteiro-Riviere, D. G. Bristol, T. O. Manning, R. A. Rogers, and J. E. Riviere, "Interspecies and interregional analysis of the comparative histologic thickness and laser Doppler blood flow measurements at five cutaneous sites in nine species," J. Invest. Dermatol. **95**, 582–586 (1990).
[16]R. Bronaugh, R. Stewart, and E. Congdon, "Methods for in vitro percutaneous absorption studies II—Animal models for human skin," Toxicol. Appl. Pharmacol. **62**, 481–488 (1982).
[17]H. T. O'Neil, "Theory of focusing radiators," J. Acoust. Soc. Am. **21**, 516–526 (1949).
[18]M. Anderson and G. Trahey, *A Seminar on k-Space Applied to Medical Ultrasound* (Department of Biomedical Engineering, Duke University, Durham, North Carolina, 2006) (dukemil.bme.duke.edu/Ultrasound/k-space/bme265.pdf).

Sound radiation from a resilient spherical cap on a rigid sphere

Ronald M. Aarts[a] and Augustus J. E. M. Janssen
Philips Research Europe, HTC 36 (WO-02), NL-5656AE Eindhoven, The Netherlands

(Received 25 June 2009; revised 7 January 2010; accepted 7 January 2010)

It has been argued that the sound radiation of a loudspeaker is modeled realistically by assuming the loudspeaker cabinet to be a rigid sphere with a resilient spherical cap. Series expansions, valid in the whole space outside the sphere, for the pressure due to a harmonically excited cap with an axially symmetric velocity distribution are presented. The velocity profile is expanded in functions orthogonal on the cap, rather than on the whole sphere. As a result, only a few expansion coefficients are sufficient to accurately describe the velocity profile. An adaptation of the standard solution of the Helmholtz equation to this particular parametrization is required. This is achieved by using recent results on argument scaling of orthogonal (Zernike) polynomials. The approach is illustrated by calculating the pressure due to certain velocity profiles that vanish at the rim of the cap to a desired degree. The associated inverse problem, in which the velocity profile is estimated from pressure measurements around the sphere, is also feasible as the number of expansion coefficients to be estimated is limited. This is demonstrated with a simulation.
 [DOI: 10.1121/1.3303978]

PACS number(s): 43.38.Ar, 43.20.Bi, 43.20.Px, 43.40.At [AJZ] Pages: 2262–2273

I. INTRODUCTION

The sound radiation of a loudspeaker is quite often modeled by assuming the loudspeaker cabinet to be a rigid infinite baffle around a circularly symmetric membrane. Given a velocity distribution on the membrane, the pressure in front of the baffle due to a harmonic excitation is then described by the Rayleigh integral[1] or by King's integral.[2] These integrals have given rise to an impressive arsenal of analytic results and numerical methods for the pressure and other acoustical quantities in journal papers[3–17] and textbooks.[18–24] The results thus obtained are in good correspondence with what one finds, numerically or otherwise, when the loudspeaker is modeled as being a finite-extent boxlike cabinet with a circular, vibrating membrane. Here, one should limit attention to the region in front of the loudspeaker and not too far from the axis through the middle of and perpendicular to the membrane. The validity of the infinite baffle model becomes questionable, or even nonsensical, on the side region or behind the loudspeaker[22] (p. 181). An alternative model, with potential for more adequately dealing with the latter regions, assumes the loudspeaker to be a rigid sphere equipped with a membrane in a spherical cap of the sphere. It has been argued by Morse and Ingard[20] (Sec. 7.2) that using the sphere as a simplified model of a loudspeaker, whose cabinet has roughly the same width, height, and depth, produces comparable acoustical results as the true loudspeaker (also see Fig. 2 of the present paper). An application for the cap model is that it can be used to predict the polar behavior of a loudspeaker cabinet. Modeling the loudspeaker as a resilient spherical cap on a rigid sphere would have the attractive feature that the solution of the Helmholtz equation for the pressure is feasible as a series involving the spherical harmonics and spherical Hankel functions, see Ref. 18 (Chap. 11.3), Ref. 19 (Chap. III, Sec. VI), Ref. 20 (Chap. 7), and Ref. 21 (Chaps. 19–20), and expansion coefficients to be determined from the boundary condition at the sphere (including the resilient cap).

In the present paper, the velocity profile is assumed to be axially symmetric but otherwise general. It was shown by Frankort[25] that this is a realistic assumption for loudspeakers, because their cones mainly vibrate in a radially symmetric fashion. These loudspeaker velocity profiles can be parameterized conveniently and efficiently in terms of expansion coefficients relative to functions orthogonal on the cap. The orthogonal functions used are the Zernike terms $R^0_{2\ell}$ as it occurred in Refs. 16 and 17 for the case of a resilient circular radiator in an infinite baffle, to which an appropriate variable transformation is applied, so as to account for the geometry of the cap. A formula will be developed that expresses the required coefficients in the standard solution of the Helmholtz equation in terms of the Zernike expansion coefficients of the velocity profile on the cap. This then gives rise to a formula, explicitly in terms of these Zernike coefficients for the pressure at any point on and outside the sphere. As examples of the resulting forward computation scheme, profiles of the Stenzel type (certain type of smooth functions of the elevation angle that vanish at the rim of the cap to any desired degree) are considered. The corresponding inverse problem, in which the expansion coefficients of the unknown profile are estimated from the measured pressure that the profile gives rise to, is also feasible. This is largely due to the fact that the expansion terms are orthogonal and complete so that for smooth velocity profiles only a few coefficients are required. Thus, for such velocity profiles, the profile can be readily estimated from pressure measurements around the sphere.

In Refs. 16 and 17, a similar approach has been used for radiation from a circular radiator in an infinite baffle. A spe-

[a]Author to whom correspondence should be addressed. Electronic mail: ronald.m.aarts@philips.com

cial Zernike expansion of the exponential factor occurring in the Rayleigh integral for the pressure yields in Ref. 16 an explicit formula for the on-axis pressure in terms of the Zernike coefficients of the velocity profile on the radiator. This formula is used for forward computation of the on-axis pressure, as well as for solving the inverse problem of estimating the velocity profile through its Zernike coefficients from measured on-axis pressure data. Furthermore, the zeroth order Hankel transform of the Zernike terms have a particular simple form in terms of Bessel functions of the first kind. In Ref. 16, this is used to express the far-field pressure explicitly in terms of the Zernike coefficients of the velocity profile on the radiator. In Ref. 17, a similar thing is done, via King's integral expression for the pressure, to find series expansions for acoustical quantities such as the pressure at the edge of the radiator, the radiator force on the radiator, the radiated power, and the directivity.

The results and methods in the present paper differ from those in the previous literature[18–21] and from those in Refs. 16 and 17 in the following manner. In Refs. 18–21, the attention is restricted to the case of a velocity profile with constant radial or axial component. In this paper, general axially symmetric profiles are allowed. Next, the pressure in the whole space in and outside the sphere (and not just on the axis or in the far field) is computed. This naturally gives rise to expressions for the on-axis and for the far-field pressure, as in Ref. 16, and to expressions for the acoustical quantities, as considered in Ref. 17, for the case of radiation from a spherical cap on a spherical baffle. Due to the different geometry than the one used in Refs. 16 and 17, a variable transformation is required to pass from orthogonal functions on the disk to orthogonal functions on the cap. Furthermore, the expansion coefficients required in the solution of the Helmholtz equation must be expressed in terms of the expansion coefficients of the velocity profile on the cap. This is achieved here by using a recent explicit result[26,27] on variable-scaling of Zernike terms, a result that has not been used previously in the acoustical setting.

The results in this paper are of a (semi)analytical nature, which distinguish these from the ones obtained by more numerically oriented method, such as in Refs. 28 and 29. In Ref. 28, a boundary element method (BEM) is used to predict acoustical radiation from axisymmetric surfaces with arbitrary boundary conditions, and in Ref. 29, near-field acoustical holography (NAH) is used to characterize acoustical radiators from near-field pressure data. While these methods are powerful tools for the forward and inverse problem, the analytic approach with a simplified model can yield additional insights as to the role of the various parameters and expansion coefficients. In particular, in the forward method, the influence on the pressure and related quantities of a particular Zernike term in the expansion of the velocity profile is reflected directly in terms of the involved expansion coefficient, of which, quite often, only a few are needed. Furthermore, the inverse method can also be used for design purposes, in which one has to match a desired, rather than a measured, pressure distribution in the field.

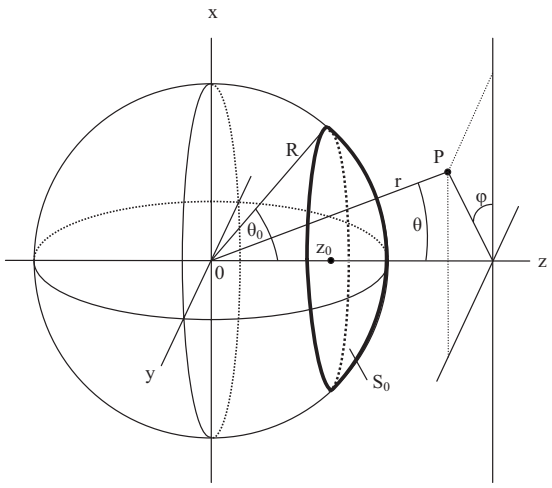

FIG. 1. Geometry and notations. The area outlined with the thick curves is the cap denoted by S_0.

II. BASIC FORMULAS AND OVERVIEW

Assume a general velocity profile $V(\theta,\varphi)$ on a spherical cap, given in spherical coordinates as

$$S_0 = \{(r,\theta,\varphi)|r = R,\ 0 \le \theta \le \theta_0,\ 0 \le \varphi \le 2\pi\}, \tag{1}$$

with R the radius of the sphere with center at the origin and θ_0 the angle between the z-axis (elevation angle $\theta=0$) and any line passing through the origin and a point on the rim of the cap. See Fig. 1 for the geometry and the notations used in this paper. Thus, it is assumed that V vanishes outside S_0. Furthermore, in loudspeaker applications, the cap moves parallel to the z-axis, and so $V(\theta,\varphi)$ will be identified with its z-component, and has normal component

$$W(\theta,\varphi) = V(\theta,\varphi)\cos\ \theta. \tag{2}$$

The average of this normal component over the cap,

$$\frac{1}{A_{S_0}}\int\int_{S_0} W(\theta,\varphi)\sin\ \theta d\theta d\varphi, \tag{3}$$

is denoted by w_0, where A_{S_0} is the area of the cap, see Eq. (10). Then the time-independent part $p(r,\theta,\varphi)$ of the pressure due to a harmonic excitation of the membrane is given by

$$p(r,\theta,\varphi) = -i\rho_0 c\sum_{n=-\infty}^{\infty}\sum_{m=-n}^{n} W_{mn}P_n^{|m|}(\cos\ \theta)\frac{h_n^{(2)}(kr)}{h_n^{(2)\prime}(kR)}e^{im\varphi}, \tag{4}$$

see Ref. 20 (Chap. 7) or Ref. 21 (Chap. 19, Helmholtz equation with spherical boundary conditions). Here, ρ_0 is the density of the medium, c is the speed of sound in the medium, $k=\omega/c$ is the wave number, and ω is the radial frequency of the applied excitation, and $r \ge R$, $0 \le \theta \le \pi$, $0 \le \varphi \le 2\pi$. Furthermore, $P_n^{|m|}(\cos\ \theta)e^{im\varphi}$ is the spherical harmonic Y_n^m in exponential notation [compare with Ref. 20 (Sec. 7.2), where sine-cosine notation has been used], $h_n^{(2)}$ is the spherical Hankel function, see Ref. 30 (Chap. 10), of order n, and W_{mn} are the expansion coefficients of $W(\theta,\varphi)$, $0 \le \theta \le \pi$, $0 \le \varphi \le 2\pi$, relative to the basis $Y_n^m(\theta,\varphi)$. Thus,

$$W_{mn} = \frac{n+1/2}{2\pi}\frac{(n-|m|)!}{(n+|m|)!}\int_0^{\pi}\int_0^{2\pi} W(\theta,\varphi)P_n^{|m|}(\cos\,\theta) \times e^{-im\varphi}\sin\,\theta d\theta d\varphi, \tag{5}$$

where it should be observed that the integration over θ in Eq. (5) is in effect only over $0 \le \theta \le \theta_0$ since V vanishes outside S_0.

In the case of axially symmetric velocity profiles V and W, written as $V(\theta)$ and $W(\theta)$, Eqs. (4) and (5) become independent on φ and is simplified to

$$p(r,\theta,\varphi) = -i\rho_0 c\sum_{n=0}^{\infty} W_n P_n(\cos\,\theta)\frac{h_n^{(2)}(kr)}{h_n^{(2)\prime}(kR)} \tag{6}$$

and

$$W_n = (n+1/2)\int_0^{\pi} W(\theta)P_n(\cos\,\theta)\sin\,\theta d\theta, \tag{7}$$

respectively, with P_n as the Legendre polynomial of degree n. The integration in Eq. (7) is actually over $0 \le \theta \le \theta_0$. Since loudspeakers mainly vibrate in a radially symmetric fashion, almost all attention in this paper is limited to axially symmetric velocity profiles V and W. In Sec. VI, the generalization to nonaxial symmetric profiles is briefly considered.

The case that W is constant w_0 on the cap S_0 has been treated in Ref. 19 (Part III, Sec. VI), Ref. 20 (p. 343), and Ref. 21 (Sec. 20.5), with the result that

$$W_n = \tfrac{1}{2}w_0(P_{n-1}(\cos\,\theta_0) - P_{n+1}(\cos\,\theta_0)). \tag{8}$$

The pressure p is then obtained by inserting W_n into Eq. (6). Similarly, the case that V is constant v_0 on S_0 has been treated by Ref. 21 (Sec. 20.6), with the result that

$$W_n = \frac{1}{2}v_0\left\{\frac{n+1}{2n+3}(P_n(\cos\,\theta_0) - P_{n+2}(\cos\,\theta_0)) + \frac{n}{2n-1}(P_{n-2}(\cos\,\theta_0) - P_n(\cos\,\theta_0))\right\}. \tag{9}$$

In Eqs. (8) and (9) the definition $P_{-n-1}=P_n$, $n=0,1,\ldots$, has been used to deal with the case $n=0$ in Eq. (8) and the cases $n=0,1$ in Eq. (9). In Fig. 2, the resemblance is shown between the polar plots of: a real driver in a rectangular cabinet [Fig. 2(a)], a rigid piston in an infinite baffle [Fig. 2(b)], and a rigid spherical cap in a rigid sphere [Fig. 2(c)] using Eqs. (6) and (9). The driver (Vifa MG10SD09-08, $a=3.2$ cm) was mounted in a square side of a rectangular cabinet with dimensions $13\times13\times18.6$ cm^3 and measured on a turning table in an anechoic room at 1 m distance. Figure 2 clearly shows that the resemblance between polar plots of the measured loudspeaker [Fig. 2(a)] and those of the sphere model [Fig. 2(c)] is much better than the often used infinite baffle model [Fig. 2(b)]. In particular, at low frequencies, the (solid) curve in Fig. 2(b) is independent of the angle, which is not the case for Figs. 2(a) and 2(c). At higher frequencies, the overall shape and, in particular, the notches of Fig. 2(b), does not exhibit the resemblance such as between Figs. 2(a) and 2(c). Finally, for angles between 90° and 270° the infinite baffle model [Fig. 2(b)] is nonsensical. The area of the spherical cap is equal to

$$A_{S_0} = 4\pi R^2\,\sin^2(\theta_0/2). \tag{10}$$

If this area is chosen to be equal to the area of the flat piston, there follows for the piston radius

$$a = 2R\,\sin(\theta_0/2). \tag{11}$$

The parameters used for Fig. 2, $a=3.2$ cm, $\theta_0=\pi/8$, $R=8.2$ cm, are such that—using Eq. (11)—the area of the piston and the cap are equal. The radius R of the sphere is such that the sphere and cabinet have comparable volumes, 2.3 and 3.1 l, respectively. If R is such that the sphere volume is the same as that of the cabinet, and θ_0, such that the area of the piston and the cap are equal, one gets $R=9.0873$ cm and $\theta_0=0.353\,99$ rad ($\approx 20°$). The corresponding polar plot—Fig. 2(d)—is very similar to Fig. 2(c); the deviations are about 1 dB or less. Apparently, the actual value of the volume is of modest influence.

It should be noted that the W_n in Eqs. (8) and (9) have slow decay, roughly like $n^{-1/2}$ [see Eq. (B5) in Appendix B], and this shows that the representation of W through its Legendre coefficients is highly inefficient. While slow decay of W_n in Eq. (6) is not necessarily a problem for the forward problem [where the pressure p is computed from W using Eqs. (6) and (7)], it certainly is for the inverse problem. In the inverse problem, one aims at estimating the velocity profile W (or V) from pressure measurements around the sphere. This can be done, in principle, by adopting a matching approach in Eq. (6), in which the W_n are optimized with respect to match of the measured pressure p and the theoretical expression for p in Eq. (6) involving the W_n. Already for the simplest case that W is constant, it is seen from the slow decay of the W_n and the slow decay of $P_n(\cos\,\theta)$ that a very large number of terms are required in the Legendre series $W(\theta)=\Sigma_{n=0}^{\infty}W_nP_n(\cos\,\theta)$.

In this paper, a more efficient representation of W is employed. This representation uses orthogonal functions on the cap that are derived from Zernike terms

$$R_{2\ell}^0(\rho) = P_\ell(2\rho^2-1), \quad 0\le\rho\le1, \quad \ell=0,1,\ldots \tag{12}$$

that were also used in Refs. 16 and 17. These Zernike terms arise uniquely when the set of radially symmetric functions $\rho^{2j}=(x^2+y^2)^j$, $j=0,1,\ldots$, on the unit disk $x^2+y^2\le1$ are orthogonalized with respect to the inner product

$$\int\int_{x^2+y^2\le1} A(x,y)B^*(x,y)dxdy \tag{13}$$

for functions A and B on the unit disk [also see Eq. (27) and the text below Eq. (27)]. Thus,

$$\frac{1}{\pi}\int\int_{x^2+y^2\le1} R_{2\ell}^0((x^2+y^2)^{1/2})R_{2k}^0((x^2+y^2)^{1/2})dxdy = 2\int_0^1 R_{2\ell}^0(\rho)R_{2k}^0(\rho)\rho d\rho = \frac{\delta_{\ell k}}{2\ell+1}. \tag{14}$$

Because of the geometry of the spherical cap, a variable transformation is required to pass from orthogonal function

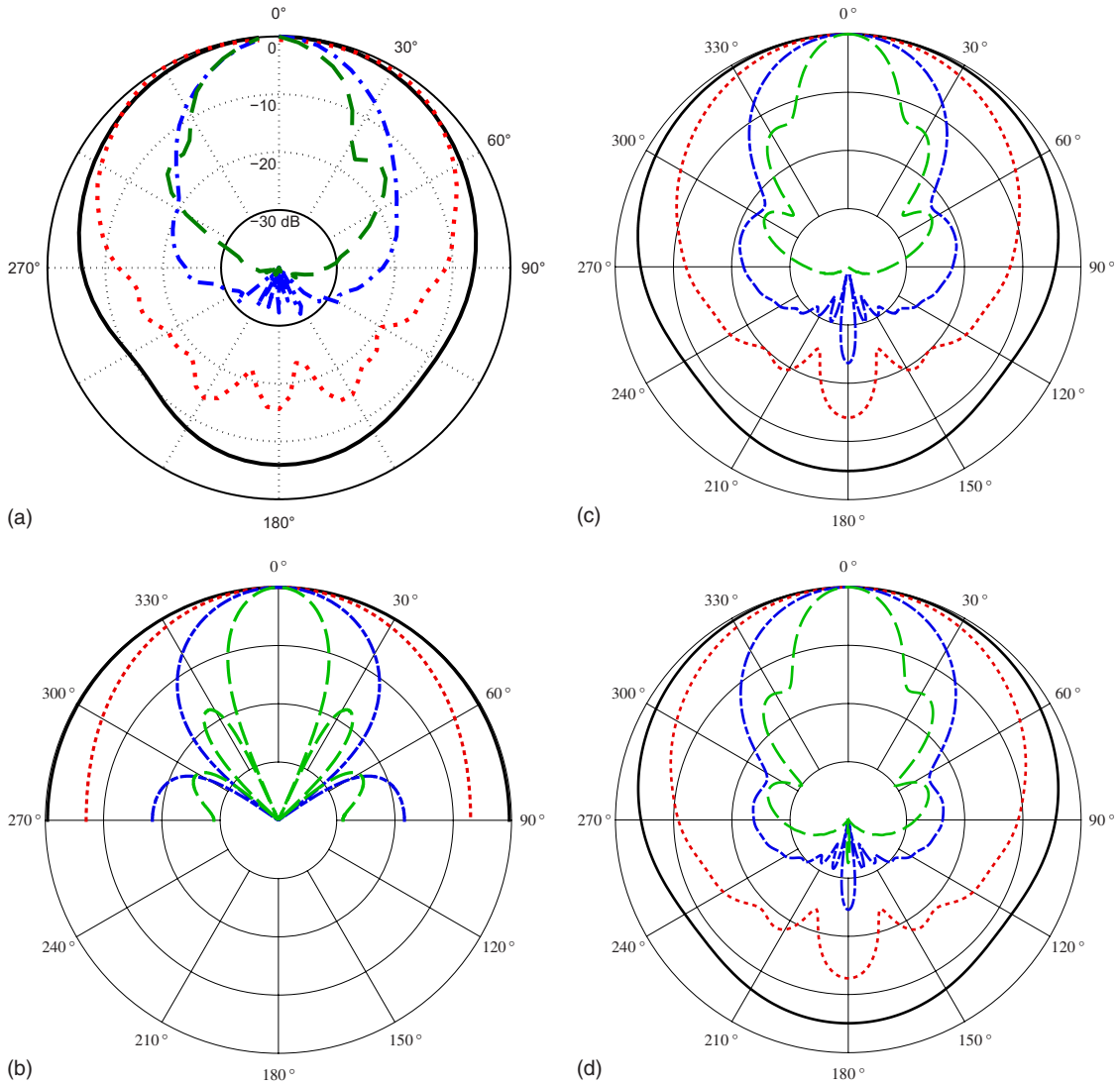

FIG. 2. (Color online) Polar plots of the SPL (10 dB/div), $f=1$ kHz (solid curve), 4 kHz (dotted curve), 8 kHz (dashed-dotted curve), and 16 kHz (dashed curve), corresponding for $c=340$ m/s and $a=3.2$ cm to ka values: 0.591, 2.365, 4.731, 9.462. (a) Loudspeaker (radius $a=3.2$ cm, measuring distance $r=1$ m) in rectangular cabinet. (b) Rigid piston ($a=3.2$ cm) in infinite baffle. (c) Rigid spherical cap (aperture $\theta_0=\pi/8$, sphere radius $R=8.2$ cm, $r=1$ m) using Eqs. (6) and (9). The parameters a, R, and θ_0 are such that—using Eq. (11)—the area of the piston and the cap are equal. (d) Same as (c) but with a sphere volume equal to that of the cabinet, and $R=9.0873$ cm and $\theta_0=0.353\,99$ rad. All curves are normalized, such that the SPL is 0 dB at $\theta=0$.

$R_{2\ell}^0$ on the disk to orthogonal functions on the cap. This is achieved by setting

$$C_{2\ell}^0(\theta)=R_{2\ell}^0\left(\frac{\sin\frac{1}{2}\theta}{\sin\frac{1}{2}\theta_0}\right),\quad 0\le\theta\le\theta_0 \tag{15}$$

for $\ell=0,1,\ldots$, see Appendix A. With

$$\theta=2\arcsin(s_0\rho),\quad s_0=\sin\tfrac{1}{2}\theta_0, \tag{16}$$

the inverse of the variable transformation used in Eq. (15), it holds by completeness and orthogonality of the Zernike terms that

$$W(2\arcsin(s_0\rho))=w_0\sum_{\ell=0}^{\infty}u_\ell R_{2\ell}^0(\rho),\quad 0\le\rho\le 1, \tag{17}$$

where the expansion coefficients w_0u_ℓ are given by

$$w_0u_\ell=2(2\ell+1)\int_0^1 W(2\arcsin(s_0\rho))R_{2\ell}^0(\rho)\rho d\rho. \tag{18}$$

It is this parametrization of W in terms of the expansion coefficients u_ℓ that will be preferred in the sequel. This parametrization is obtained by "warping" W according to Eq. (16) and expanding the resulting warped function as in Eqs. (17) and (18), with s_0 given in Eq. (16).

The efficiency of the representation in Eq. (17) is apparent from the fact that a smooth profile W requires only a limited number terms with coefficients u_ℓ of relatively small amplitude in Eq. (17) to yield an accurate approximation of $W(2\arcsin(s_0\rho))$. For instance, the constant profile $W=w_0$ on S_0 is represented exactly by only one such term, $w_0R_0^0(\rho)$, in the expansion in Eq. (17), and the profile $W=v_0\cos\theta$, corresponding to the case that V is constant v_0 on S_0, is represented exactly by two terms $v_0[(1-s_0^2)R_0^0(\rho)-s_0^2R_2^0(\rho)]$. More complicated examples arise when V or W is a multiple of the

Stenzel profile

$$(n+1)\left(\frac{\cos\theta-\cos\theta_0}{1-\cos\theta_0}\right)^n, \tag{19}$$

and these require $n+1$ terms in the representation in Eq. (17). These profiles vanish at the rim of S_0 to degree n and are considered in Secs. V and VI to illustrate the methods developed in this paper.

In Sec. III, it will be shown that the expansion in Eq. (17) gives rise to the formula

$$W_n=(-1)^n s_0 w_0 \sum_{\ell=0}^{n}(R_{2n+1}^{2\ell+1}(s_0)-R_{2n-1}^{2\ell+1}(s_0))u_\ell, \tag{20}$$

expressing the coefficients W_n required in Eq. (6) for the pressure in terms of the expansion coefficients u_ℓ in Eq. (17). From this a series expansion for the pressure p in the whole space $r\geq R$, $\theta\in[0,\pi]$, and $\varphi\in[0,2\pi]$ follows as

$$p(r,\theta,\varphi)=-i\rho_0 c w_0\sum_{\ell=0}^{\infty}u_\ell S_\ell(r,\theta), \tag{21}$$

where

$$S_\ell(r,\theta)=\sum_{n=\ell}^{\infty}(-1)^n s_0(R_{2n+1}^{2\ell+1}(s_0)-R_{2n-1}^{2\ell+1}(s_0))P_n(\cos\theta)\frac{h_n^{(2)}(kr)}{h_n^{(2)\prime}(kR)}. \tag{22}$$

In Eqs. (20), (22)

$$R_n^m(\rho)=\rho^m P_{(n-m)/2}^{(0,m)}(2\rho^2-1), \tag{23}$$

for integer $n,m\geq 0$ with $n-m$ even and ≥ 0 ($R_n^m\equiv 0$ otherwise) with $P_k^{(\alpha,\beta)}(x)$ the general Jacobi polynomial.[30] The functions

$$A_{nm}(x,y)=R_n^{|m|}(\rho)e^{im\alpha},\quad x=\rho\cos\alpha,\quad y=\rho\sin\alpha \tag{24}$$

are known in optics[31,32] as the circle polynomials of Zernike and they have been introduced recently in acoustics as well.[16,17] They have been shown by Bhatia and Wolf[31] to arise uniquely as orthogonal functions, see Eq. (13), that satisfy form invariance under rotations of the unit disk.

The main result in Eqs. (20)–(23) provides the generalization of the forward computation scheme in Eqs. (6), (8), and (9) to general axially symmetric velocity profiles W. Furthermore, it provides the basis for the inverse problem, in which the expansion coefficients u_ℓ are estimated from measured pressure data around the sphere by adopting a best match approach in Eq. (21). From these estimated coefficients, an estimate of W can be made on basis of Eq. (17).

In Sec. IV, the forward computation scheme embodied by Eqs. (21)–(23) is discussed in some detail. It is shown how the results in Eqs. (8) and (9) arise for the two special cases considered there, and the matter of convergence of the series in Eq. (22) and some computational issues are addressed. In Sec. V, the forward method is exemplified for the case that V or W is a Stenzel-type profile, see Eq. (19). In Sec. VI, the inverse method is illustrated in simulation. In Sec. VII, the extension of the methodology to nonaxial symmetric profiles is briefly discussed. In Sec. VIII, the results of this paper are discussed, applications of these to audio engineering phenomena and quantities are considered, and some issues for future investigations are mentioned. The conclusions are presented in Sec. IX. Finally, in Appendix A, the orthogonality of the functions $C_{2\ell}^0$ in Eq. (15) is established, in Appendix B, the asymptotics of the terms in the series for S_ℓ in Eq. (22) as $n\to\infty$ is given, which is required for the convergence matter in Sec. IV, and in Appendix C, the R_n^m are given in the form of a discrete cosine transform, which allows fast and reliable computation of the Zernike terms of large degree.

III. DERIVATION OF THE MAIN RESULT

In this section, the main result of Eqs. (20)–(23) on the coefficients W_n required in the solution of the Helmholtz equation and the pressure p due to an axially symmetric, radial velocity component $W(\theta)$ vanishing outside the spherical cap S_0 is proved. Our initial aim is to show Eq. (28) that expresses W_n in terms of $W(\theta)$, warped according to Eqs. (16) and (17), and the scaled Zernike terms $R_{2n}^0(s_0\rho)$. Then a result from the scaling theory of Zernike terms is used to establish Eq. (20) and, subsequently, Eqs. (22) and (23). Thus, from Eq. (7) and the substitutions $\mu=\cos\theta$, $\mu=2y^2-1$, it follows that

$$\begin{aligned}W_n&=(n+1/2)\int_0^{\theta_0}W(\theta)P_n(\cos\theta)\sin\theta d\theta\\&=4(n+1/2)\int_{\cos 1/2\theta_0}^{1}W(\arccos(2y^2-1))\\&\quad\times P_n(2y^2-1)ydy.\end{aligned} \tag{25}$$

Next, the substitution $y=\sqrt{1-x^2}$ is made, and it is used that

$$P_n(-z)=(-1)^n P_n(z),\quad \arccos(1-2x^2)=2\arcsin x. \tag{26}$$

This gives

$$W_n=2(2n+1)(-1)^n\int_0^{s_0}W(2\arcsin x)P_n(2x^2-1)xdx, \tag{27}$$

where $s_0=\sin\frac{1}{2}\theta_0$ as in Eq. (16). Next, the definition $R_{2n}^0(x)=P_n(2x^2-1)$, see Eq. (12), is used, the substitution $x=s_0\rho$ with $0\leq\rho\leq 1$ is made, and it follows that

$$W_n=2(2n+1)(-1)^n s_0^2\int_0^1 W(2\arcsin(s_0\rho))R_{2n}^0(s_0\rho)\rho d\rho. \tag{28}$$

Now there is the following general result[26,27] on argument scaling of the polynomials R_s^r, see Eq. (23):

$$R_s^r(\epsilon\rho)=\sum_t\frac{t+1}{s+1}\frac{1}{\epsilon}(R_{s+1}^{t+1}(\epsilon)-R_{s-1}^{t+1}(\epsilon))R_t^r(\rho). \tag{29}$$

Here, r and s are integers ≥ 0 with $s-r$ even and ≥ 0 (recall that $R_n^m=0$ when $n<m$) and t in the summation in Eq. (29)

assumes the values $r, r+2, \ldots, s$; ϵ and ρ are arbitrary ≥ 0. Using this result with

$$r=0, \quad s=2n, \quad \epsilon=s_0, \quad \rho=\rho \tag{30}$$

in Eq. (28), together with Eq. (18), it follows that

$$W_n=(-1)^n s_0 w_0 \sum_{\ell=0}^{n} (R_{2n+1}^{2\ell+1}(s_0)-R_{2n-1}^{2\ell+1}(s_0))u_\ell. \tag{31}$$

This is Eq. (20). Then Eq. (21) for p, with S_ℓ given by Eq. (22), follows upon inserting the result of Eq. (31) for W_n into Eq. (6) and interchanging the summations over n and ℓ.

IV. DISCUSSION OF THE MAIN RESULT

In this section, the main result in Eqs. (20)–(23) is discussed in some detail. It is shown how the special cases of constant W or constant V on the cap arise, see Eqs. (6)–(9). Furthermore, the order of magnitude of the terms in the series for S_ℓ in Eqs. (22) as $n \to \infty$ is indicated. The latter analysis shows that, especially when r is not large compared to R, many terms of n are required. In Sec. IV C, it is proposed to compute (high-degree) Zernike polynomials by employing their representation in Eq. (23), in terms of Jacobi polynomials, where the latter are computed using MATHEMATICA. An alternative method, based on an expression for $R_n^m(\rho)$, using the discrete cosine transform, is presented in Appendix C.

A. Special case $W=w_0$ on S_0

The result in Eq. (8) for the special case that W is constant w_0 on S_0 does not immediately follow from Eq. (20). As already noted, $u_0=1$, $u_1=u_2=\cdots=0$ in this case. Due to the various recurrence relations[30] that exist for the Jacobi polynomials, the result in Eq. (20) can be brought into a variety of different forms. As one of these, there holds for $n=1,2,\cdots$

$$2s_0(R_{2n+1}^1(s_0)-R_{2n-1}^1(s_0))= R_{2n+2}^0(s_0)-R_{2n-2}^0(s_0)), \tag{32}$$

and Eq. (8) for W_n follows using that, see Eq. (12),

$$\begin{aligned} R_{2k}^0(s_0) &= P_k\left(2\sin^2\tfrac{1}{2}\theta_0-1\right) \\ &= P_k(-\cos\theta) \\ &= (-1)^k P_k(\cos\theta). \end{aligned} \tag{33}$$

In principle, recursion techniques can also be used to establish the result in Eq. (9) for W_n, in the case that V is constant v_0 on S_0.

B. Special case W is a simple source on S_0

If the polar cap aperture θ_0 is decreasing, in the limit, the cap will act as a simple source. Using Eqs. (21)–(23) and by proper normalization by the cap area A_{S_0}, using Eq. (10), and the definition of w_0 by Eq. (3), there holds

$$p(r,\theta,\varphi)=-i\rho_0 c w_0 \sum_{n=0}^{\infty} (2n+1)P_n(\cos\theta)\frac{h_n^{(2)}(kr)}{h_n^{(2)\prime}(kR)}. \tag{34}$$

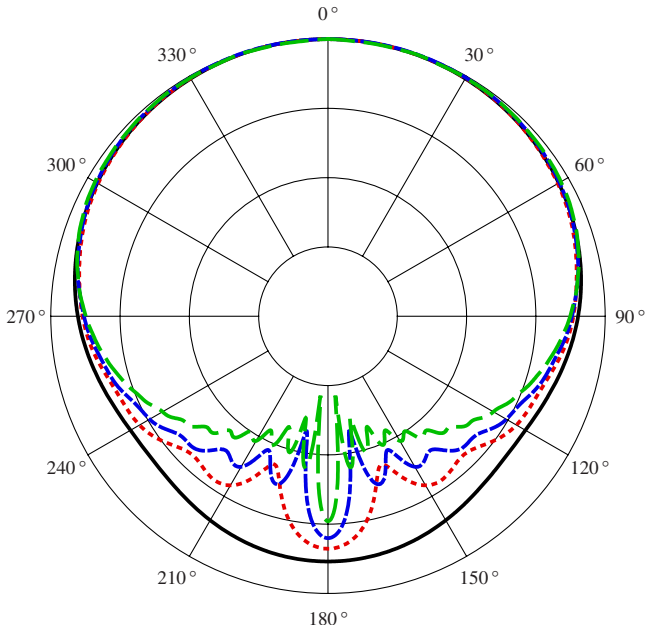

FIG. 3. (Color online) Polar plots of the SPL (10 dB/div) of a simple source on a sphere of radius $R=0.082$ m. Frequency $f=1$ kHz (solid curve), 4 kHz (dotted curve), 8 kHz (dashed-dotted curve), and 16 kHz (dashed curve), at distance $r=1$ m, using Eqs. (34). All curves are normalized, such that the SPL is 0 dB at $\theta=0$.

In Fig. 3, the corresponding polar plot is illustrated, where the same sphere radius and frequencies are used as in Fig. 2(c).

C. Convergence analysis of the series S_ℓ and computational aspects

As already said, for smooth velocity profiles W, only a limited number of coefficients u_ℓ in the expansion in Eq. (17) have to be considered. In Appendix B, it is shown that the terms

$$s_0(R_{2n+1}^{2\ell+1}(s_0)-R_{2n-1}^{2\ell+1}(s_0))P_n(\cos\theta)\frac{h_n^{(2)}(kr)}{h_n^{(2)\prime}(kR)} \tag{35}$$

in the series defining S_ℓ in Eq. (22) are of the order of magnitude

$$\frac{kR}{(n+1)^{3/2}}\left(\frac{R}{r}\right)^{n+1} \quad \text{and} \quad \frac{kR}{(n+1)^2}\left(\frac{R}{r}\right)^{n+1}, \tag{36}$$

respectively, when θ is near 0 or π and away from 0 and π, respectively. Here, it is assumed that θ_0 is not close to 0 or π. The estimate of the order of magnitude is accurate when ℓ is fixed and n exceeds $\frac{1}{4}(kr)^2$. It then follows from the analysis in Ref. 33 (Sec. V) that the truncation error after the Nth term in the series of Eq. (22) for S_ℓ has order of magnitude $kN^{-1/2}(R/r)^N$ and $kN^{-1}(R/r)^N$, respectively, for the corresponding θ-ranges. Hence, when r is allowed to approach R, a relatively large number of terms is required in the series for S_ℓ.

Implementation of Eqs. (21) and (22) requires computation of the quantity in Eq. (35), normally for low or moderate values of ℓ and possibly for large values of n. These computations have been done for the present paper in MATH-

EMATICA. The Zernike polynomials and Legendre polynomials occurring in Eqs. (35) can be expressed in terms of Jacobi polynomials $P_j^{(\alpha,\beta)}$, see Eqs. (12) and (23), and MATHEMATICA computes these polynomials, virtually without any restrictions to the values of the parameters α and β or to the degree j, provided that a sufficient precision has been set. If this is not applicable, then the method discussed in Appendix C might be useful because Eq. (C2) is very robust against precision problems. Next, $h_n^{(2)}(kr)$ and $h_n^{(2)\prime}(kR)$ must be computed. Now $h_n^{(2)\prime}$ can be expressed in terms of $h_n^{(2)}$, $h_{n\pm1}^{(2)}$, see Ref. 30, Eqs. 10.1.19–10.1.19.22, and the evaluation of the $h^{(2)}$-functions can be done in MATHEMATICA, virtually without any restriction to the order j and argument z of $h_j^{(2)}(z)$. Finally, $h_n^{(2)\prime}(kR)$ occurs in the numerator in Eq. (35), and for this it should be checked that $h_n^{(2)\prime}$ has no real zeros. By Ref. 30, Eq. 10.1.6,

$$W\{j_n(z),y_n(z)\} = j_n(z)y_n'(z) - j_n'(z)y_n(z) = \frac{1}{z^2} \tag{37}$$

and by Ref. 30, Subsec. 10.1.1,

$$h_n^{(2)\prime}(z) = j_n'(z) - iy_n'(z), \tag{38}$$

in which $j_n'(z)$ and $y_n'(z)$ are real for real z. Hence,

$$|h_n^{(2)\prime}(z)|^2 = |j_n'(z)|^2 + |y_n'(z)|^2 \geq \frac{1}{|z|^4(|j_n(z)|^2 + |y_n(z)|^2)}, \tag{39}$$

showing that $h_n^{(2)\prime}(z)$ is bounded away from 0.

V. STENZEL-TYPE PROFILES AND FORWARD COMPUTATION

Consider the profile

$$V^{(K)}(\theta) = v_0^{(K)}(K+1)\left(\frac{\cos\theta - \cos\theta_0}{1-\cos\theta_0}\right)^K, \quad 0 \leq \theta \leq \theta_0, \tag{40}$$

with $V^{(K)}(\theta)=0$ for $\theta_0 < \theta \leq \pi$ (as usual), $K=0,1,\ldots$. Then a simple computation shows that

$$V^{(K)}(2\arcsin(s_0\rho)) = v_0^{(K)}(K+1)(1-\rho^2)^K, \quad 0 \leq \rho \leq 1. \tag{41}$$

The right-hand side of Eq. (41) is the Stenzel profile, considered extensively in Ref. 16. Thus,

$$V^{(K)}(2\arcsin(s_0\rho)) = v_0^{(K)}\sum_{\ell=0}^{K} q_\ell^{(K)} R_{2\ell}^0(\rho), \quad 0 \leq \rho \leq 1, \tag{42}$$

where

$$q_\ell^{(K)} = (K+1)(-1)^\ell \frac{2\ell+1}{\ell+1}\frac{\binom{K}{\ell}}{\binom{K+\ell+1}{K}},$$

$$\ell = 0,1,\ldots,K. \tag{43}$$

From

$$W^{(K)}(\theta) = V^{(K)}(\theta)\cos\theta = \frac{K+1}{K+2}(1-\cos\theta_0)V^{(K+1)}(\theta) + (\cos\theta_0)V^{(K)}(\theta), \tag{44}$$

it follows that

$$W^{(K)}(2\arcsin(s_0\rho)) = w_0^{(K)}\sum_{\ell=0}^{K+1} u_\ell^{(K)} R_{2\ell}^0(\rho), \quad 0 \leq \rho \leq 1, \tag{45}$$

where

$$w_0^{(K)} = \frac{K+1+\cos\theta_0}{K+2} v_0^{(K)}, \tag{46}$$

and, for $\ell=0,1,\ldots,K+1$,

$$u_\ell^{(K)} = \frac{v_0^{(K)}}{w_0^{(K)}}\left[\frac{K+1}{K+2}(1-\cos\theta_0)q_\ell^{(K+1)} + (\cos\theta_0)q_\ell^{(K)}\right]. \tag{47}$$

Thus, one can compute the pressure using the formulas in Eqs. (21)–(23) with $u_\ell = u_\ell^{(K)}$.

In Fig. 4, polar plots are displayed of the sound pressure level (SPL) (10 dB/div) of a spherical cap ($\theta_0=\pi/8$, $R=8.2$ cm, $r=1$ m) with various Stenzel velocity profiles, $K=0$ (solid curve), $K=1$ (dotted curve), $K=2$ (dashed-dotted curve), and $K=3$ (dashed curve): (a) $f=4$ kHz and (b) $f=8$ kHz. It appears that the difference between the various velocity profiles are more pronounced at higher frequencies. Also, the cap becomes less directive for higher K values because in the limit $K\to\infty$, it would behave like a simple source on a sphere. Furthermore, it appears that the solid curves ($K=0$) for (a) $f=4$ kHz and (b) $f=8$ kHz are the same as the dotted and dashed-dotted curves, respectively, in Fig. 2(c), while different formulas were involved.

VI. INVERSE PROBLEM

Equations (21)–(23) show how to compute the pressure in the space $r \geq R$ due to a harmonically excited (wave number k) membrane on the spherical cap $0 \leq \theta \leq \theta_0$ with a known radial component W of a velocity profile. In the reverse direction, Eqs. (21)–(23) can serve as the basis for a method for estimating W from measurements of the pressure p in the space $r \geq R$ that W gives rise to. Such a profile W can usually be estimated accurately by a limited number of expansion coefficients u_ℓ in Eq. (17), and these can be estimated by taking a matching approach in Eq. (22), in which the u_ℓ are chosen, such that they optimize the match between the measured pressure and the theoretical expression involving the u_ℓ at the right-hand side of Eq. (22). Given measurements, see Fig. 1,

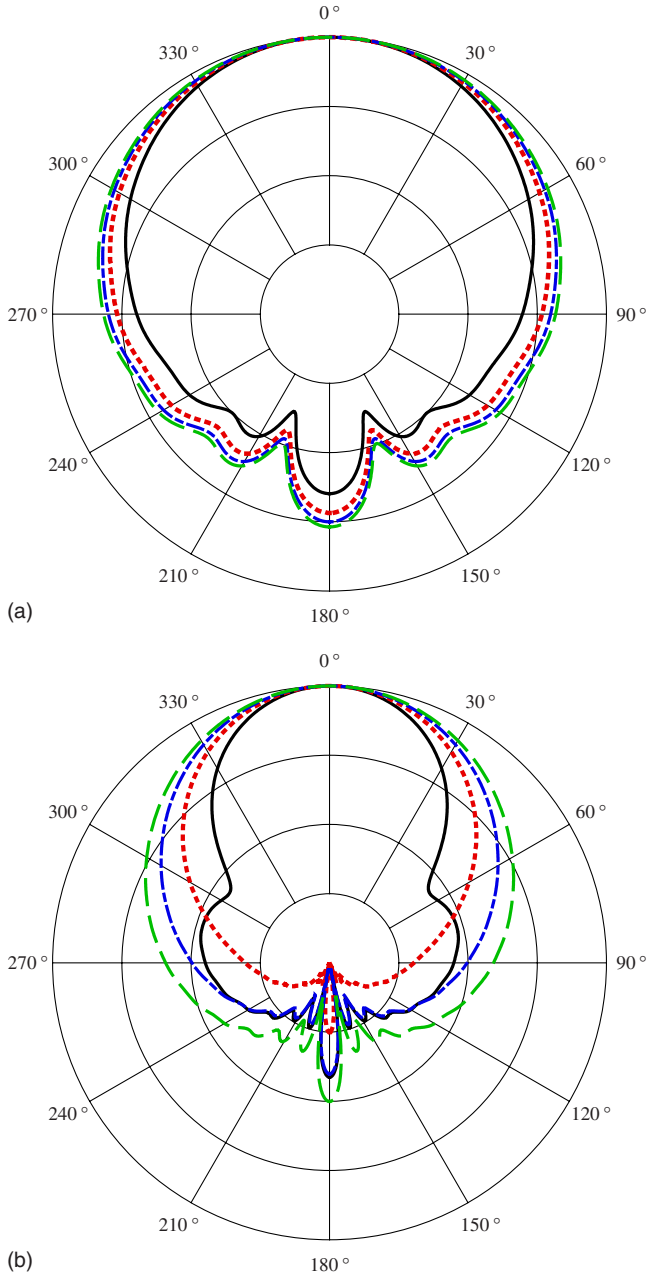

FIG. 4. (Color online) Polar plots of the SPL (10 dB/div) of a spherical cap ($\theta_0=\pi/8$, $R=8.2$ cm, $r=1$ m) with various Stenzel velocity profiles, $K=0$ (solid curve), $K=1$ (dotted curve), $K=2$ (dashed-dotted curve), and $K=3$ (dashed curve). (a) $f=4$ kHz, (b) $f=8$ kHz. All curves are normalized, such that the SPL is 0 dB at $\theta=0$.

$$\hat{p}_j=\hat{p}_j(P_j), \quad P_j=r_j(\cos\varphi_j\sin\theta_j,\sin\varphi_j\sin\theta_j,\cos\theta_j), \tag{48}$$

where $j=0,1,\ldots,J$, the numbers d_ℓ, $\ell=0,1,\ldots,L$, are chosen, such that

$$\sum_{j=0}^{J}\left|\hat{p}_j-\sum_{\ell=0}^{L}d_\ell S_\ell(r_j,\theta_j)\right|^2\sin\theta_j \tag{49}$$

is minimal. The solution of this minimization problem can be obtained by using "Solve" of MATHEMATICA or by other means. Then w_0, u_ℓ, $\ell=0,1,\ldots,L$ are estimated by setting

$$d_0=-i\rho_0 c w_0, \quad u_\ell=d_\ell/d_0, \quad \ell=0,1,\ldots,L. \tag{50}$$

There are various questions that arise in connection with the above optimization problem, such as number and choice of the measurement points P_j, choice of L, condition of the linear systems that occur, influence of noise and of systematic errors (such as incorrect setting of R and/or θ_0), etc. It is out of the scope of the present paper to address any of these issues in detail. Instead, just one simulation example is given.

VII. SIMULATION EXAMPLE

Take $R=8.2$ cm, $\theta_0=\pi/4$, $k=\omega/c=2\pi f/c$ with $c=340$ m/s, $f=4$ kHz, so that $kR=6$. The measurement points $P_j(r_j,\theta_j,\varphi_j)$ are taken in the form

$$R2^{j_1/J_1}=r(j_1), \quad \frac{\pi\left(j_2-\frac{1}{2}\right)}{J_2}=\theta(j_2),$$

$$\frac{2\pi\left(j_3-\frac{1}{2}\right)}{J_3}=\varphi(j_3), \tag{51}$$

with $j_1=1,\ldots,J_1=4$, $j_2=1,\ldots,J_2=6$, $j_3=1,\ldots,J_3=6$. Such set of measurement points yields a convenient implementation of the solution of the optimization problem, but does not need to be optimal in any other respect (matters as optimal choice of the measurement points are outside the scope of this paper). The profile W is chosen to be

$$W^{(K)}(\theta)=V^{(K)}(\theta)\cos\theta, \quad 0\le\theta\le\theta_0, \tag{52}$$

where $V^{(K)}(\theta)$ is the Kth Stenzel-type profile as in Sec. V [see Eqs. (40) and (44)], and $K=2$. We require for this example $v_0=v_0^{(K)}=1$ m/s and by Eqs. (46) and (47), we get, respectively, $w_0=w_0^{(K)}$ and

$$u_\ell^{(K)}=\frac{K+2}{K+1+\cos\theta_0}\left[\frac{K+1}{K+2}(1-\cos\theta_0)q_\ell^{(K+1)}+(\cos\theta_0)q_\ell^{(K)}\right]. \tag{53}$$

Using $q_\ell^{(K+1)}$, $q_\ell^{(K)}$ given by Eq. (43), the pressure p is computed in accordance with Eq. (21) with $u_\ell=u_\ell^{(K)}$. Measurements $\hat{p}_j$ are obtained in simulation by adding complex white noise (by adding scaled random numbers by MATHEMATICA's "RandomComplex[−1−I, 1+I, Length[p]]," where the scaling is such that the signal to noise ratio becomes 40 dB) to the computed $p(P_j)$. The nonzero coefficients of $W^{(K)}$ are estimated by taking $L=K+1$ in the optimization problem, and this yields estimates $\hat{w}_0,\hat{u}_0,\ldots,\hat{u}_{K+1}$ of $w_0,u_0,\ldots,u_{K+1}$. Figure 5 shows the input profile $W^{(K)}$ of Eq. (52) using Eq. (40) directly (solid curve), together with the reconstructed profiles

$$\hat{W}^{(K)}(\theta)=\hat{w}_0^{(K)}\sum_{\ell=0}^{K+1}\hat{u}_\ell R_{2\ell}^0\left(\frac{\sin\frac{1}{2}\theta}{\sin\frac{1}{2}\theta_0}\right), \quad 0\le\theta\le\theta_0, \tag{54}$$

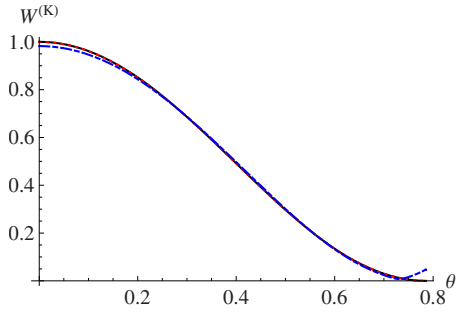

FIG. 5. (Color online) Input profile $W^{(K)}/(K+1)$ ($K=2$ and $\theta_0=\pi/4$) of Eq. (52) using Eq. (40) directly (solid curve) together with the reconstructed profiles $\hat{W}^{(K)}$ without noise (dotted curve) and with noise added to the pressure points $\hat{p}_j$ (dashed-dotted curve). The (noiseless) reconstructed profile (dotted curve) coincides with the input profile (solid curve).

without noise (dotted curve) and with noise (dashed-dotted curve) added to the pressure points $\hat{p}_j$. The recovered $\hat{u}_\ell$ are computed by solving Eq. (49), and using Eqs. (50) and (45), and s_0 from Eq. (16). Figure 5 shows that the (noiseless) reconstructed profile (dotted curve) coincides with the input profile (solid curve), and that the recovered profile using the noisy pressure points (dashed-dotted curve) is very similar to the other two curves. The method appears to be robust for noise contamination. Figure 6 shows the pressure points at various angles and distances vs. index i, using Eq. (51) and $i=j_3+(j_2-1)J_3+(j_1-1)J_2J_3$, with the pressure points $|p_i|$ without noise (filled circles), pressure points $|\hat{p}_i|$ with noise (squares), and recovered pressure points (45° rotated squares). Note that the noiseless and recovered pressure points are nearly coincident, which again shows that the method appears to be robust for noise contamination. Figure 7 shows the corresponding polar plot of the velocity profile of Fig. 5. The solid curve in Fig. 7 is for the near field ($r=0.0975$ m), and the dotted curve is for the far field ($r=1$ m).

VIII. EXTENSION TO NONAXIALLY SYMMETRIC PROFILES

Loudspeaker membranes vibrate mainly in a radially symmetric fashion, in particular, at low frequencies. At higher frequencies, break-up behavior can occur, and then it may be necessary to consider nonradially symmetric profiles. In the present context, where a loudspeaker is modeled as consisting of a rigid spherical cabinet with a resilient spherical cap, this requires consideration of nonaxially symmetric velocity profiles $V(\theta,\varphi)$ and $W(\theta,\varphi)$ on S_0. Thus, the general formula in Eq. (5) has to be considered now. The methodology of this paper is extended to this situation by considering the expansion on the disk $0\le\rho\le 1$, $0\le\varphi\le 2\pi$,

$$W(2\arcsin(s_0\rho,\varphi)) = w_0\sum_{m=-\infty}^{\infty}\sum_{s=0}^{\infty} a_{|m|+2s}^{|m|} R_{|m|+2s}^{|m|}(\rho)e^{im\varphi}, \tag{55}$$

with the general polynomials $R_n^m(\rho)$ given by Eq. (23). This then leads to a series expansion for the pressure p of the form

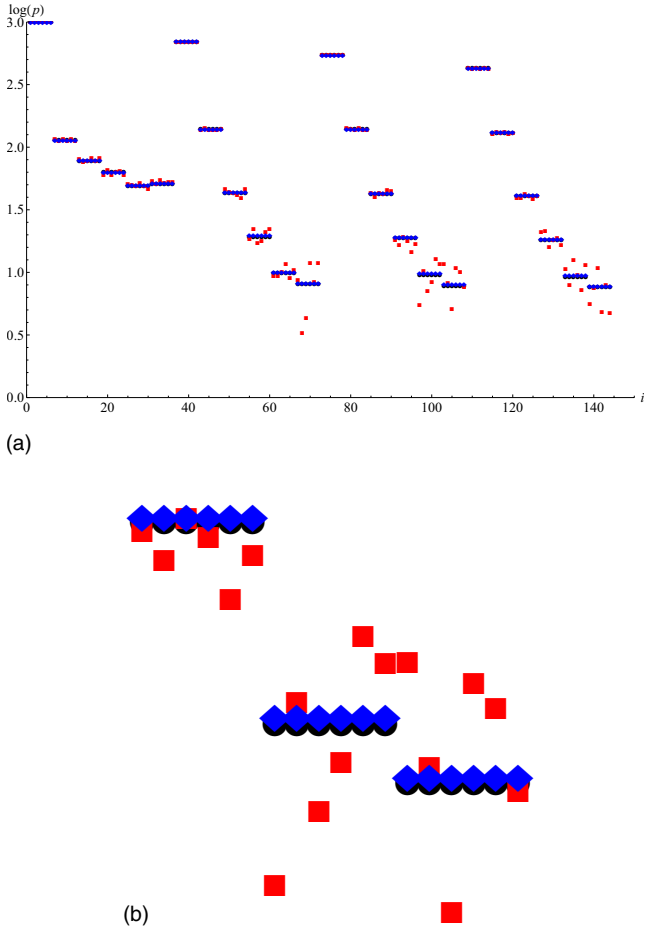

FIG. 6. (Color online) (a) Pressure points at various angles and distances vs. index i, using Eq. (51) and $i=j_3+(j_2-1)J_3+(j_1-1)J_2J_3$, with the pressure points $|p_i|$ without noise (filled circles), pressure points $|\hat{p}_i|$ with noise (squares), and recovered pressure points (45° rotated squares). The noiseless and recovered pressure points are nearly coincident. (b) Enlarged portion of (a) from $90\le i\le 110$, and $0.6\le\log(|p|)\le 1.3$.

$$p(r,\theta,\varphi) = -i\rho c w_0\sum_{m=-\infty}^{\infty}\sum_{s=0}^{\infty} a_{|m|+2s}^{|m|} T_{ms}(r,\theta,\varphi), \tag{56}$$

where

$$T_{ms}(r,\theta,\varphi) = \sum_{n=|m|}^{\infty} Q_{mns} P_n^{|m|}(\cos\theta)\frac{h_n^{(2)}(kr)}{h_n^{(2)\prime}(kR)}, \tag{57}$$

and where the quantities Q_{mns} are to be discussed below. The formula in Eq. (56) can be used for forward computation, when the profile W and its expansion coefficients $a_{|m|+2s}^m$ are known, as well as for solving the inverse problem, in which the profile W is estimated via its expansion coefficients from measured pressure data around the sphere $r=R$.

The Q_{mns} in Eq. (57) are obtained by inserting the expansion in Eq. (55) into the integral expression in Eq. (5) for W_{mn}. Upon integration over φ, this yields

$$Q_{mns} = 4(n+1/2)s_0^2\frac{(n-|m|)!}{(n+|m|)!}J_{ns}^{|m|}, \tag{58}$$

where

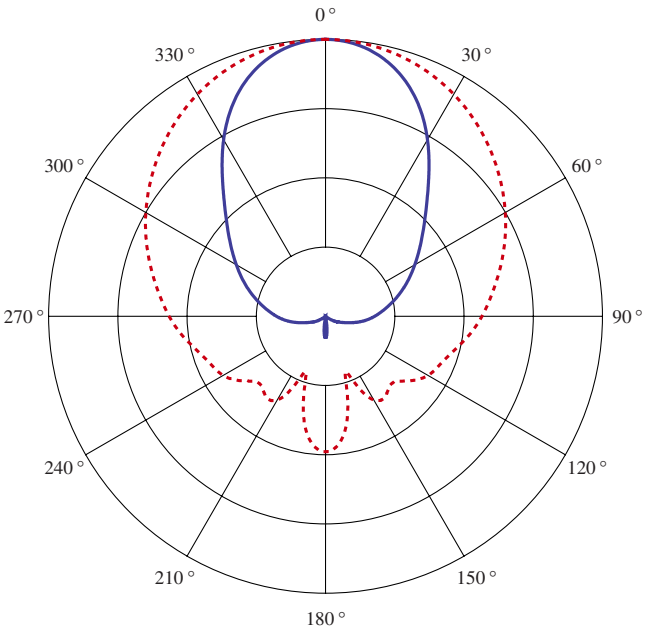

FIG. 7. (Color online) Polar plots (10 dB/div) in the near field (solid curve, $r=0.0975$ m) and in the far field (dotted curve, $r=1$ m), corresponding to the parameters of the simulation example and the velocity profile of Fig. 5. All curves are normalized, such that the SPL is 0 dB at $\theta=0$.

$$J_{ns}^{|m|} = \int_0^1 P_n^{|m|}(1-2s_0^2\rho^2)R_{|m|+2s}^{|m|}(\rho)\rho d\rho. \tag{59}$$

The evaluation of the J-integrals is still feasible in semi-analytic form using the general scaling result in Eq. (29), but is quite a bit more complicated than in the case that $m=0$. This is due to the fact that $P_n^m(1-2x^2)$ is given by the complicated expression

$$P_n^m(1-2x^2) = \frac{(n+m)!}{n!}x^m(1-x^2)^{m/2}P_{n-m}^{(m,m)}(1-2x^2), \tag{60}$$

with $P_j^{(\alpha,\beta)}$ as the general Jacobi polynomials. Therefore, the evaluation of the $J_{ns}^{|m|}$ as $R_{|m|+2s}^{|m|}$-coefficients of the function $P_n^{|m|}(1-2s_0^2\rho^2)$ requires dedicated results from the theory of polynomial expansions. This is outside the scope of the present paper.

IX. DISCUSSION AND OUTLOOK

In this paper, the foundation is laid for a method to perform forward and inverse sound pressure computations for a spherical cap on an otherwise rigid sphere with a non-uniform velocity profile. This method naturally applies to spherically shaped loudspeakers, but it appears that even nonspherical loudspeakers with a cone shaped driver have polar responses that resemble quite well the polar responses produced by the spherical model for frequencies from low frequencies to well over 10 kHz. Thus, the spherical model can be used more generally to predict loudspeaker behavior and for loudspeaker design purposes. In the forward problem, the velocity profile is assumed to be known and the sound pressure is expressed in the whole space on and outside the sphere as a series involving the special functions S_ℓ, of Eq. (22), with coefficients u_ℓ as the expansion coefficients of the velocity profile warped as in Eqs. (16) and (17). This yields a versatile tool, both for the forward problem of computing p from the velocity profile and for the inverse problem. In the inverse problem, the velocity profile is unknown and is estimated in terms of Zernike expansion coefficients from pressure data measured around the sphere by adopting a matching approach, based on the series solution just mentioned for the pressure. Well-behaved velocity profiles are already adequately represented by only a few terms of their Zernike expansion. Therefore, the Zernike series approach is convenient for both the forward problems and the inverse problem.

The inverse procedure has not been fully worked out in the present paper due to a variety of practical issues that need to be addressed. Among these practical issues are

- choice of the measurement points,
- condition of the linear systems that arise,
- influence of wave number k, radius R, and aperture angle $2\theta_0$,
- influence of noise,
- influence of misalignment of the measurement points, for instance, due to wrong choice of origin,
- influence of inclination of the axis, and
- incorrect setting of the radius of the radiator.

While various combinations of these issues should also be considered. The authors intend to work out the method for the loudspeaker assessment with attention for the above mentioned points.

In the present paper, we have considered only the pressure in the field. However, having the required field point pressure in analytical form, various acoustical quantities become available in an analytical form. In investigations that are carried out presently, a remarkable resemblance is seen between measured quantities—such as baffle-step response, sound power, directivity, and acoustic center—from the loudspeaker of Fig. 2(a) and the corresponding quantities computed using the spherical model.

There are presently available numerical methods that can be used both for the forward problem, for instance, BEMs,[28] and for the inverse problem, for instance, NAH.[29] These methods can be deployed in case of general geometries and yield the pressure with arbitrary accuracy. However, for a general understanding and to get a feeling for the influence of the various parameters on both the pressure and associated quantities, the availability of a simple analytic, in certain respects adequate model, as the one that we have here, is of complementary value.

X. CONCLUSIONS

Appropriately warped Legendre polynomials provide an efficient and robust method to describe velocity profiles of a resilient spherical cap on a rigid sphere. Only a few coefficients are necessary to approximate various velocity profiles, in particular, Stenzel profiles. The polar plot of a rigid spherical cap on a rigid sphere is already quite similar to that of a real loudspeaker, and is useful in the full 4π-field. The

spherical cap model yields polar plots that exhibit good full range similarity with the polar plots from real loudspeakers. It thus outperforms the more conventional model, in which the loudspeaker is modeled as a rigid piston in an infinite baffle. The cap model can be used to predict the polar behavior of a loudspeaker cabinet. The presented method enables one to solve the inverse problem of calculating the actual velocity profile of the cap radiator using (measured) on- and off-axis sound pressure data. This computed velocity profile allows the extrapolation to far-field loudspeaker pressure data, including off-axis behavior.

ACKNOWLEDGMENTS

The authors wish to thank Okke Ouweltjes for assisting in the loudspeaker measurements and making the plot for Fig. 2(a), and Prof. Fred Simons for providing pertinent assistance in programming MATHEMATICA, in particular, to make Fig. 5.

APPENDIX A: ORTHOGONALITY OF $C^0_{2\ell}$

From the definition in Eq. (15) and orthogonality of the $R^0_{2\ell}$, as in Eq. (14), it follows that

$$\int_0^{\theta_0} C^0_{2\ell}(\theta)C^0_{2k}(\theta)\sin\theta d\theta = 4\int_0^{\theta_0} R^0_{2\ell}\left(\frac{\sin\frac{1}{2}\theta}{\sin\frac{1}{2}\theta_0}\right)R^0_{2k}\left(\frac{\sin\frac{1}{2}\theta}{\sin\frac{1}{2}\theta_0}\right) \times\sin\frac{1}{2}\theta d\left(\sin\frac{1}{2}\theta\right) = \frac{2\delta_{\ell k}}{2\ell+1}s_0^2. \tag{A1}$$

Here, $s_0=\sin\frac{1}{2}\theta_0$, as in Eq. (16), and the substitution $\rho=s_0^{-1}\sin\frac{1}{2}\theta$ has been used so that Eq. (14) can be applied.

APPENDIX B: LARGE n BEHAVIOR OF THE TERMS IN EQ. (36)

The large-n behavior of the terms in Eq. (35) is determined by the large-n behavior of the three factors

$$s_0(R^{2\ell+1}_{2n+1}(s_0)-R^{2\ell+1}_{2n-1}(s_0)),\quad P_n(\cos\theta),\quad \frac{h^{(2)}_n(kr)}{h^{(2)\prime}_n(kR)}. \tag{B1}$$

Here, $s_0=\sin\frac{1}{2}\theta_0$, $r\geq R$, and ℓ is assumed to be fixed.

It follows from the definition of R^m_n in Eq. (23) and Ref. 34 (Thm. 8.21.12) that

$$s_0(R^{2\ell+1}_{2n+1}(s_0)-R^{2\ell+1}_{2n-1}(s_0)) = (-1)^{n-\ell}\left(\tfrac{1}{2}\theta_0\tan\tfrac{1}{2}\theta_0\right)^{1/2}, \{\delta_{n+1}J_{2\ell+1}((n+1)\theta_0)+\delta_n J_{2\ell+1}(n\theta)\}, \tag{B2}$$

with absolute error of the order $\theta_0^{1/2}n^{-3/2}$. Here, $J_{2\ell+1}$ is the Bessel function of the first kind and of order $2\ell+1$, and $0\leq\delta_n,\delta_{n+1}\leq 1$. It is assumed here that $\theta_0\in(0,\pi)$ is not close to π. When θ_0 is also not close to 0, it follows from the asymptotics of $J_{2\ell+1}(z)$ as $z\to\infty$, see Ref. 30 (Chap. 9) that

$$s_0(R^{2\ell+1}_{2n+1}(s_0)-R^{2\ell+1}_{2n-1}(s_0)) = O\left(\frac{1}{\sqrt{n+1}}\right) \tag{B3}$$

as $n\to\infty$, with constant implied by the O-symbol of order unity.

Next, by Ref. 34 (Thm. 8.21.6),

$$P_n(\cos\theta) = \left(\frac{\theta}{\sin\theta}\right)^{1/2}J_0((n+1/2)\theta), \tag{B4}$$

as $n\to\infty$, with absolute error of the order $\theta^{1/2}n^{-3/2}$. Here, $\theta\in(0,\pi)$ is not close to π. Using that $P_n(\cos(\pi-\theta))=(-1)^nP_n(\cos\theta)$, it is concluded from $|J_0(z)|\leq 1$ and the asymptotics of $J_0(z)$ as $z\to\infty$, see Ref. 30 (Chap. 9), that

$$P_n(\cos\theta)=O(1)\quad\text{and}\quad O\left(\frac{1}{\sqrt{n+1}}\right), \tag{B5}$$

as $n\to\infty$, and where $\theta\in[0,\pi]$ is arbitrary and $\theta\in(0,\pi)$ is away from 0 and π, respectively. The constants implied by the O-symbols in Eq. (B5) are of the order unity. Finally, from Ref. 30 (Chap. 10),

$$h^{(2)}_n(z) = i\frac{1\cdot 3\cdots(2n-1)}{z^{n+1}},$$

$$h^{(2)\prime}_n(z) = -(n+1)i\frac{1\cdot 3\cdots(2n-1)}{z^{n+2}} \tag{B6}$$

as $n\to\infty$, with relative errors of the order $z^2/4n$. Thus,

$$\frac{h^{(2)}_n(kr)}{h^{(2)\prime}_n(kR)} = \frac{-kR}{n+1}\left(\frac{R}{r}\right)^{n+1}, \tag{B7}$$

as $n\to\infty$, with relative error of the order $(kr)^2/4n$ when $r\geq R$.

From Eqs. (B3), (B5), and (B7), the claims on the order of magnitude of the terms in Eq. (35) for large n and fixed ℓ follow.

APPENDIX C: COMPUTATION OF R^m_n WITH LARGE n

The $R^m_n(\rho)$ are polynomials in ρ of degree n, given explicitly as

$$R^m_n(\rho) = \sum_{s=0}^{p}\binom{n-s}{p}\binom{p}{s}(-1)^s\rho^{n-2s}, \tag{C1}$$

where $p=\frac{1}{2}(n-m)$. This explicit form is for some software awkward to use in computations for large n: when $m=0$, $n=40$, loss-of-digits occurs in 15 decimal places. For $m=0,1,\ldots$ fixed, and $M=0,1,\ldots$ fixed, the R^m_n can be computed for $n=m,m+2,\ldots,m+2M$ in the form of a discrete cosine transform as[35]

$$R^m_n(\rho) = \frac{1}{N}\sum_{k=0}^{N-1}U_n\left(\rho\cos\frac{2\pi k}{N}\right)\cos\frac{2\pi mk}{N},\quad 0\leq\rho\leq 1, \tag{C2}$$

where U_n is the Chebyshev polynomial of degree n and of the second kind, and N is any integer $>2(m+M)$.

[1]J. W. S. Rayleigh, *The Theory of Sound* (Dover, New York, 1896), Vol. **2**.
[2]L. V. King, "On the acoustic radiation field of the piezo-electric oscillator and the effect of viscosity on transmission," Can. J. Res. **11**, 135–155 (1934).
[3]M. Greenspan, "Piston radiator: Some extensions of the theory," J. Acoust. Soc. Am. **65**, 608–621 (1979).
[4]G. R. Harris, "Review of transient field theory for a baffled planar piston," J. Acoust. Soc. Am. **70**, 10–20 (1981).
[5]R. New, R. I. Becker, and P. Wilhelmij, "A limiting form for the nearfield of the baffled piston," J. Acoust. Soc. Am. **70**, 1518–1526 (1981).
[6]T. Hasegawa, N. Inoue, and K. Matsuzawa, "A new rigorous expansion for the velocity potential of a circular piston source," J. Acoust. Soc. Am. **74**, 1044–1047 (1983).
[7]D. A. Hutchins, H. D. Mair, P. A. Puhach, and A. J. Osei, "Continuous-wave pressure fields of ultrasonic transducers," J. Acoust. Soc. Am. **80**, 1–12 (1986).
[8]R. C. Wittmann and A. D. Yaghjian, "Spherical-wave expansions of piston-radiator fields," J. Acoust. Soc. Am. **90**, 1647–1655 (1991).
[9]T. Hélie and X. Rodet, "Radiation of a pulsating portion of a sphere: Application to horn radiation," Acta. Acust. Acust. **89**, 565–577 (2003).
[10]R. M. Aarts and A. J. E. M. Janssen, "Approximation of the Struve function $\mathbf{H}_1$ occurring in impedance calculations," J. Acoust. Soc. Am. **113**, 2635–2637 (2003).
[11]R. J. McGough, T. V. Samulski, and J. F. Kelly, "An efficient grid sectoring method for calculations of the near-field pressure generated by a circular piston," J. Acoust. Soc. Am. **115**, 1942–1954 (2004).
[12]T. D. Mast and F. Yu, "Simplified expansions for radiation from a baffled circular piston," J. Acoust. Soc. Am. **118**, 3457–3464 (2005).
[13]T. J. Mellow, "On the sound field of a resilient disk in an infinite baffle," J. Acoust. Soc. Am. **120**, 90–101 (2006).
[14]J. F. Kelly and R. J. McGough, "An annular superposition integral for axisymmetric radiators," J. Acoust. Soc. Am. **121**, 759–765 (2007).
[15]X. Zeng and R. J. McGough, "Evaluation of the angular spectrum approach for simulations of near-field pressures," J. Acoust. Soc. Am. **123**, 68–76 (2008).
[16]R. M. Aarts and A. J. E. M. Janssen, "On-axis and far-field sound radiation from resilient flat and dome-shaped radiators," J. Acoust. Soc. Am. **125**, 1444–1455 (2009).
[17]R. M. Aarts and A. J. E. M. Janssen, "Sound radiation quantities arising from a resilient circular radiator," J. Acoust. Soc. Am. **126**, 1776–1787 (2009).
[18]P. M. Morse and H. Feshbach, *Methods of Theoretical Physics* (McGraw-Hill, New York, 1953).
[19]H. Stenzel and O. Brosze, *Guide to Computation of Sound Phenomena (Leitfaden zur Berechnung von Schallvorgängen)*, 2nd ed. (Springer-Verlag, Berlin, 1958).
[20]P. M. Morse and K. U. Ingard, *Theoretical Acoustics* (McGraw-Hill, New York, 1968).
[21]E. Skudrzyk, *The Foundations of Acoustics* (Springer-Verlag, New York, 1971).
[22]L. E. Kinsler, A. R. Frey, A. B. Coppens, and J. V. Sanders, *Fundamentals of Acoustics* (Wiley, New York, 1982).
[23]A. D. Pierce, *Acoustics, An Introduction to Its Physical Principles and Applications* (Acoustical Society of America through the American Institute of Physics, New York, 1989).
[24]D. T. Blackstock, *Fundamentals of Physical Acoustics* (Wiley, New York, 2000).
[25]F. J. M. Frankort, "Vibration and sound radiation of loudspeaker cones," Ph.D. thesis, Delft University of Technology, Netherlands (1975).
[26]A. J. E. M. Janssen and P. Dirksen, "Concise formula for the Zernike coefficients of scaled pupils," J. Microlithogr., Microfabr., Microsyst. **5**, 030501 (2006).
[27]A. J. E. M. Janssen, S. van Haver, P. Dirksen, and J. J. M. Braat, "Zernike representation and Strehl ratio of optical systems with variable numerical aperture," J. Mod. Opt. **55**, 1127–1157 (2008).
[28]L. Wright, S. P. Robinson, and V. F. Humphrey, "Prediction of acoustic radiation from axisymmetric surfaces with arbitrary boundary conditions using the boundary element method on a distributed computing system," J. Acoust. Soc. Am. **125**, 1374–1383 (2009).
[29]M. J. Crocker, "Use of near-field acoustical holography in noise and vibration measurements," *Handbook of Noise and Vibration Control* edited by E. G. Williams (Wiley, New York, 2007), Chap. 50.
[30]M. Abramowitz and I. A. Stegun, *Handbook of Mathematical Functions* (Dover, New York, 1972).
[31]A. B. Bhatia and E. Wolf, "On the circle polynomials of Zernike and related orthogonal sets," Proc. Cambridge Philos. Soc. **50**, 40–48 (1954).
[32]M. Born and E. Wolf, *Principles of Optics*, 7th ed. (Cambridge University Press, Cambridge, England, 2002), Chap. 9.
[33]A. J. E. M. Janssen and J. S. H. van Leeuwaarden, "Relaxation time for the discrete D/G/1 queue," Queueing Syst. **50**, 53–80 (2005).
[34]G. Szegö, *Orthogonal Polynomials*, 4th ed. (AMS, Providence, RI, 1939).
[35]A. J. E. M. Janssen and P. Dirksen, "Computing Zernike polynomials of arbitrary degree using the discrete Fourier transform," J. Eur. Opt. Soc. Rapid Publ. **2**, 07012 (2007).

Experimental modeling and design optimization of push-pull electret loudspeakers

Mingsian R. Bai[a] and Chun-Jen Wang
Department of Mechanical Engineering, National Chiao-Tung University, 1001 Ta-Hsueh Road, Hsin-Chu 300, Taiwan

Dar-Ming Chiang and Shu-Ru Lin
Taiwan Electrets Electronics Co., Ltd., 7F-3, 9, Prosperity 1st Road, Hsinchu Science Park, Hsinchu City 30078, Taiwan

(Received 9 August 2009; revised 4 December 2009; accepted 3 February 2010)

A fully experimental modeling technique and a design optimization procedure are presented in this paper for push-pull electret loudspeakers. Conventional electrical impedance-based parameter identification methods are not completely applicable to electret speakers due to the extremely weak electromechanical coupling. This prompts the development of an experimental technique for identifying the electroacoustic parameters of the electret speakers. Mechanical parameters are identified from the membrane velocity measured using a laser vibrometer. The voltage-force conversion factor and the motional impedance are estimated, with the aid of a test-box method. This experimentally identified model serves as the simulation platform for predicting the response of the electret loudspeaker and optimizing the design. Optimal parameters are calculated by using the simulated annealing (SA) algorithm to fulfill various design goals and constraints. Either the comprehensive search for various parameters or the simple search for the optimal gap distance can be conducted by this SA procedure. The results reveal that the optimized design has effectively enhanced the performance of the electret loudspeaker.
 [DOI: 10.1121/1.3337224]

PACS number(s): 43.38.Bs, 43.38.Ja, 43.40.Dx [AJZ] Pages: 2274–2281

I. INTRODUCTION

Electret loudspeakers are the electrostatic loudspeakers with precharged membranes. Electret loudspeakers offer advantages of compactness, light weight, excellent mid- and high frequency reproductions, high electroacoustic efficiency, waiver of externally bias circuit, etc.[1] Due to these characteristics, the loudspeakers have promise in the application to consumer electronics.

Electret configuration will result in slightly different forms of voltage-force sensitivity and the associated nonlinearity from those of conventional push-pull electrostatic loudspeakers. Nevertheless, one may equate the electret electrostatic speaker with an external polarizing voltage. On the surface, the two kinds of loudspeaker look alike. Their equivalent electrical circuits are the same and the analyses of their mechanical and acoustical parameters are identical. However, where they differ is in the electromechanical force conversion. A non-electret electrostatic has an external polarizing voltage supply, which creates a monopole charge on the membrane. For an electret speaker this is difficult to achieve because, in the absence of a supply, a monopole charge is relatively unstable over time. Hence, electret speakers typically use membranes with conductive coatings, which carry an induced charge of opposite polarity (dipoles) to that of the membrane. This makes the analysis somewhat more complicated. It turns out that the two kinds of loudspeaker are equivalent but not the same. In the case of the dipole electret, it is like applying a polarizing voltage of an equivalent non-electret speaker across the conductive coating and a virtual electrode somewhere in the middle of the membrane, where this virtual electrode contains all the membrane charge in a concentrated layer. The electrical input capacitance of an electret speaker is also different from that of a non-electret type due to the presence of the electret membrane, although the contribution this makes depends on the size of the air gap.[2,3]

Electret materials have been studied by several researchers. Lekkala and Paajanen[4] introduced a new electret material, electromechanical film (EMFi), at the turn of the century. Not before long, EMFi was applied to microphones, actuators, and even loudspeaker panels.[5] Cao *et al.*[6] discussed the relationship between the microstructures and the properties of the electret material, where the electret properties of the porous polytetrafluoroethylene (PTFE) were studied. It is found that the porous dielectrics can be good electret materials. Recently, Chiang *et al.*[7] proposed the nanoporous Teflon-fluorinated ethylene propylene film that allows for higher charge density stored in the film with improved stability. The nanoporous electret material was applied to flexible electrostatic loudspeakers.[8] Their electret diaphragms are made of fluoro-polymer with nano-meso-micro-pores precharged by the corona method.

It was not until recently that Mellow and Kärkkäinen[3,9] conducted a rigorous theoretical analysis of electret loud-

[a]Author to whom correspondence should be addressed. Electronic mail: msbai@mail.nctu.edu.tw

speakers. Transducers with single-ended and push-pull constructions are investigated in terms of the static force acting on the diaphragm and the stored charge density. Bai *et al.*[10] suggested a hybrid modeling approach combining experimental measurement and finite-element-analysis (FEA) for a single-ended electret loudspeaker. Experimental verification reported in the work revealed that the single-ended loudspeaker suffered from high nonlinear distortion problems.

This paper aims at three purposes. First, electret loudspeakers in push-pull construction are proposed in order to reduce the nonlinear distortions encountered in the single-ended device. Second, a more accurate fully experimental modeling technique is suggested to estimate the lumped parameters of the equivalent circuits without resorting to FEA. Because the coupling between the electrical and mechanical systems is extremely weak, the parameters of the mechanical system are unidentifiable using the electrical impedance measurement.[11–13] To overcome the difficulty, a test-box approach in conjunction with laser measurement is taken in this paper. Third, on the basis of the preceding simulation model, an optimization procedure using simulated annealing (SA) algorithm[14–16] is developed, aiming at optimizing design parameters of electret loudspeakers to maximize the sound pressure level (SPL) output and the bandwidth as well.

II. EXPERIMENTAL MODELING OF ELECTRET LOUDSPEAKERS

A. Operating principles

A sample of a 493×129 mm^2 electret loudspeaker is shown in Fig. 1(a). In its push-pull construction, the loudspeaker comprises a charged flexible membrane and two perforated rigid back plates with 52.1% perforation ratio. The membrane is made of fluoro-polymer, which contains nanopores to enhance the charge stability and density.[8] The membrane is placed at the center between two electrode plates spaced by 2.4 mm, as shown in Fig. 1(b). The construction is also referred to as the push-pull configuration with a fully floating membrane by Mellow and Kärkkäinen.[3] The membrane is divided into six equal partitions (242×37 mm^2) by stainless steel spacers.

Due to high input impedance of the electret loudspeaker, a transformer is used for impedance matching and e_{spk} is the output voltage of the transformer. The turn ratio is 138. The net force f acting on the membrane can be estimated by[3]

$$f=\frac{\varepsilon_r\varepsilon_{r1}hS_D\sigma_m}{2(\varepsilon_r d+\varepsilon_{r1}h)^2}e_{\mathrm{spk}}+\frac{\varepsilon_r\varepsilon_{r1}h^2S_D\sigma_m^2}{2\varepsilon_0(\varepsilon_r d+\varepsilon_{r1}h)^3}\delta=\phi e_{\mathrm{spk}}+\kappa\delta, \tag{1}$$

where ε_r and ε_{r1} are the relative permittivities of the membrane and the medium at the gap, respectively, ε_0 is the vacuum permittivity, h is one-half of the thickness of the membrane, S_D is the area of membrane, σ_m is the surface charge density of the membrane, d is the gap between the membrane and the electrode plate, and δ is the displacement of the membrane. The first term of Eq. (1) is due to the input voltage, whereas the second term is due to the negative stiffness resulting from the membrane attractions. The voltage-force conversion factor ϕ and the negative stiffness κ can be written as[3]

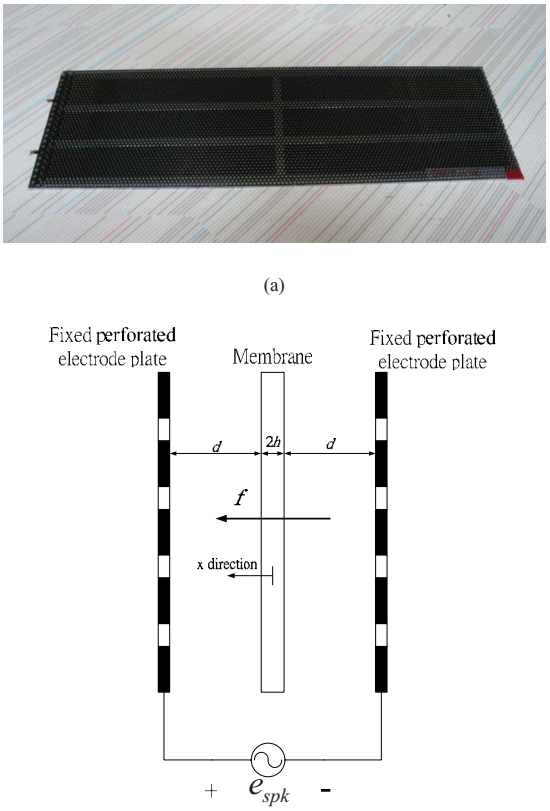

(a)

(b)

FIG. 1. (Color online) The push-pull electret loudspeaker. (a) Photo. (b) The schematic of the loudspeaker construction.

$$\phi=\frac{K_1}{d^2},\quad d\gg\frac{\varepsilon_{r1}h}{\varepsilon_r} \tag{2}$$

with $K_1=\varepsilon_{r1}hS_D\sigma_m/2\varepsilon_r$, and

$$\kappa=\frac{K_2}{d^3},\quad d\gg\frac{\varepsilon_{r1}h}{\varepsilon_r} \tag{3}$$

with $K_2=\varepsilon_{r1}h^2S_D\sigma_m^2/2\varepsilon_0\varepsilon_r^2$.

B. Analogous circuits

The electret loudspeaker can be modeled with the analogous circuit, as shown in Fig. 2(a). The mechanical impedance and the radiation impedance are identified as a lumped sum in the parameter identification procedure. That is, the radiation impedance has been taken into account in the modeling. In the electrical domain, the circuit is modeled with the Thévenin equivalent circuit, where e_{in} is the voltage source of the transformer input, i is the current, and R_E and L_E are the electric resistance and inductance of the transformer. C_E is the static capacitance when the membrane is blocked. In the mechanical domain, Z_M represents the open-circuit mechanical impedance and u is the membrane velocity. In the acoustical domain, Z_A represents the acoustical impedance.

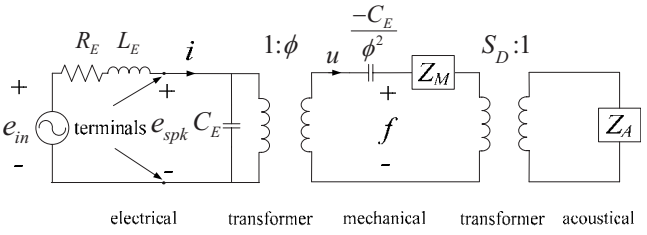

(a)

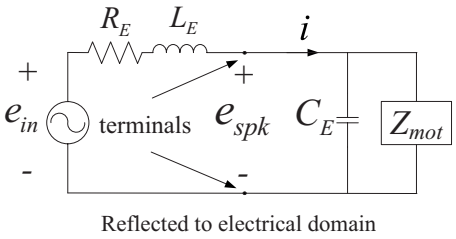

(b)

FIG. 2. The electroacoustic analogous circuits of the push-pull electret loudspeaker. (a) Electrical, mechanical, and acoustics systems. (b) Combined circuit referred to the electrical system.

Figure 2(b) shows the combined circuit as the mechanical and acoustical systems are reflected to the electrical system, where the motional impedance Z_{mot} is defined as

$$Z_{\text{mot}} = \frac{Z_{ms} + S_D^2 Z_A}{\phi^2}, \tag{4}$$

$$Z_{ms} = Z_M - \left(j\omega \frac{C_E}{\phi^2}\right)^{-1}, \tag{5}$$

where Z_{ms} is the short-circuit mechanical impedance and ω is the angular frequency. To measure the electrical impedance, we need an experimental arrangement, as shown in Fig. 3(a). The input voltage from the signal generator e_g is 1.5 V and the current-sampling resistor R is 100 Ω. The electrical impedance of the loudspeaker is given by

$$Z_{\text{spk}} = \frac{e_g G_1 G_2 - e_R}{e_R} R, \tag{6}$$

where G_1 and G_2 denote the effective gains of the amplifier and the transformer, respectively, and e_R is the voltage drop across the resistor R. The thus measured electrical impedance of Fig. 3(b) resembles that of a capacitance due to weak electromechanical coupling[10]

$$|Z_E| = (\omega C_E)^{-1}. \tag{7}$$

It follows that only the static capacitance C_E can be extracted from the electrical impedance measurement

$$C_E = (\omega |Z_E|)^{-1}. \tag{8}$$

For the sample in Fig. 1, the C_E was found to be 1.86 nF.

C. Parameter identification

In Fig. 2(b), as the inductance L_E of the transformer output end is connected to the electret loudspeaker, which behaves like a capacitance due to the aforementioned weak

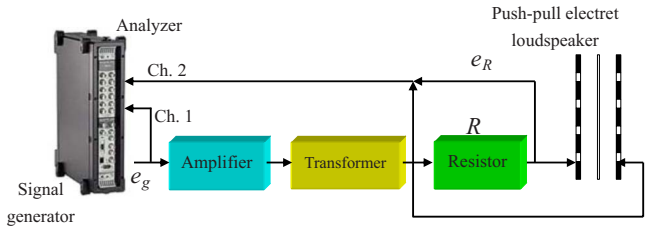

(a)

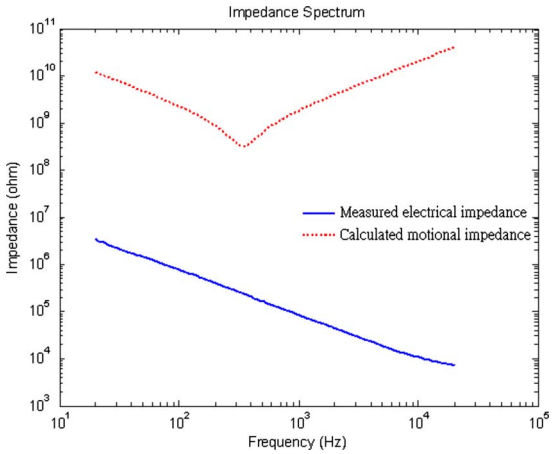

(b)

FIG. 3. (Color online) The electrical impedance measurement of the push-pull electret loudspeaker. (a) Experimental arrangement. (b) The electrical impedance versus the motional impedance.

coupling, the combined electrical system becomes a second-order low-pass system. Figure 4 shows the frequency response of the unloaded transformer, which is nearly constant throughout the range 20–20 kHz. As the electret loudspeaker is connected to the transformer, the frequency response becomes a low-pass function with cutoff frequency ω_{E0} =8736.4 Hz as follows:

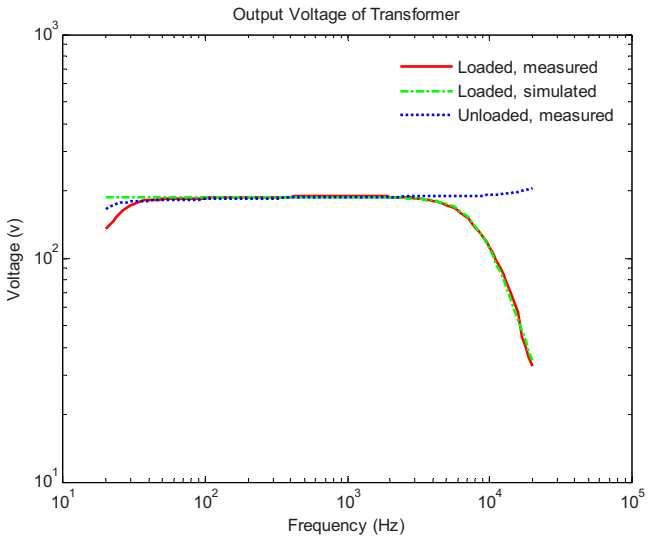

FIG. 4. (Color online) The comparison of the measured and simulated output voltage responses of the loaded and unloaded transformers.

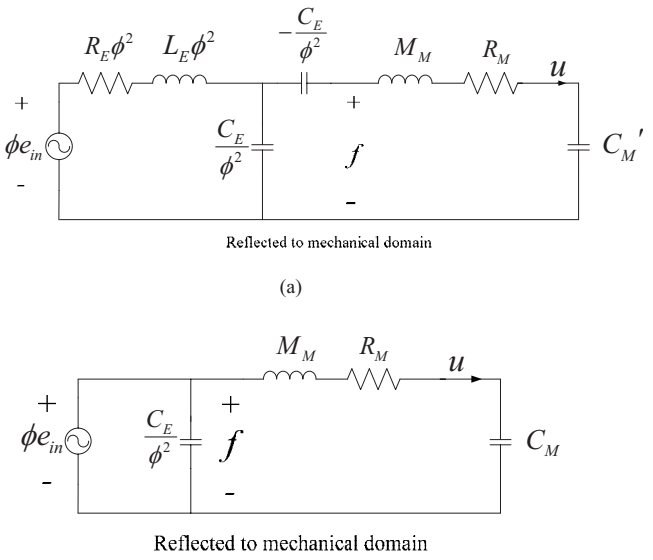

FIG. 5. The electroacoustic analogous circuits of the push-pull electret loudspeaker. (a) Combined circuit referred to the mechanical system. (b) The weakly coupled approximation.

$$e_{\text{spk}}(s) = H(s)e_{\text{in}}(s) = \frac{1}{C_E L_E s^2 + C_E R_E s + 1} e_{\text{in}}(s)$$

$$= \frac{1}{\left(\frac{s}{\omega_{E0}}\right)^2 + \frac{1}{Q_E}\frac{s}{\omega_{E0}} + 1} e_{\text{in}}(s), \tag{9}$$

where $H(s)$ is the transfer function between e_{spk} and e_{in}, Q_E is the quality factor, and $s=j\omega$ is the Laplace variable. The effective inductance and resistance at the output end of the transformer can be calculated by

$$L_E = (\omega_{E0}^2 C_E)^{-1}, \tag{10}$$

$$R_E = (Q_E \omega_{E0} C_E)^{-1}. \tag{11}$$

At the resonance frequency, the real part of the transfer function in Eq. (9) is zero. It follows that the quality factor can be calculated by

$$|H(j\omega_{E0})| = |-jQ_E| = Q_E. \tag{12}$$

For the sample in Fig. 1, the quality factor Q_E=0.6845, the inductance L_E=0.178 H, and the resistance R_E=14.3 kΩ, respectively. In Fig. 4, the measurement (solid line) and the simulation (dashed-dotted line) of e_{spk} are in good agreement. The cutoff frequency is measured according to the phase switching principle.

As mentioned previously, the mechanical parameters are unidentifiable with the electrical impedance measurement. We need to devise a method based on direct mechanical measurement. To this end, the electrical and acoustical systems are reflected to the mechanical system, as shown in Fig. 5(a). For simplicity, we approximate the combined acoustical impedance and the mechanical impedance to be a second-order system. The lumped parameters R_M, M_M, and C_M' denote the resistance, the mass, and the compliance, respectively, of the combined impedance.

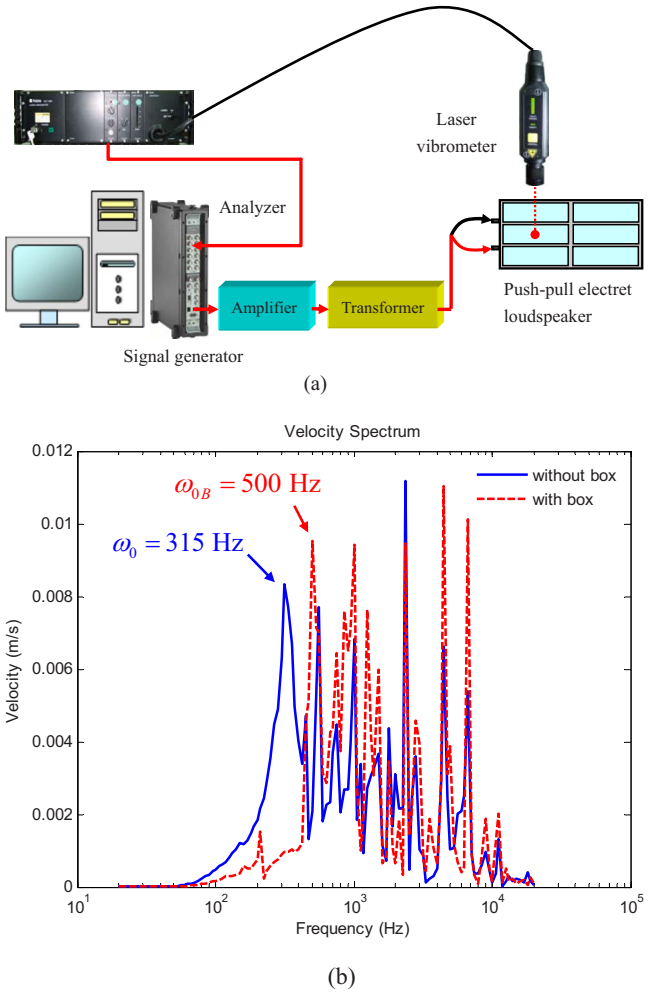

FIG. 6. (Color online) The membrane velocity measurement of the push-pull electret loudspeaker. (a) Experimental arrangement. (b) The comparison of the velocity responses of the loudspeaker, with and without the test box.

Due to weak coupling ($\phi \approx 0$), $R_E\phi^2$ and $L_E\phi^2$ can be neglected, leading to the simplified circuit of Fig. 5(b). Solving the circuit yields the expression of the membrane velocity u as follows:

$$u = \frac{C_M s}{M_M C_M s^2 + R_M C_M s + 1} \phi e_{\text{in}}$$

$$= \frac{1}{R_M} \frac{\frac{1}{Q_u}\left(\frac{s}{\omega_0}\right)}{\left(\frac{s}{\omega_0}\right)^2 + \frac{1}{Q_u}\left(\frac{s}{\omega_0}\right) + 1} \phi e_{\text{in}}, \tag{13}$$

where the compliance C_M is the series combination of C_M' and the negative compliance $-C_E/\phi^2$, ω_0 is the fundamental resonance frequency, and Q_u is the quality factor. The membrane velocity can be measured by a laser vibrometer, as shown in Fig. 6(a). In the following, we concentrate on only the fundamental mode and ignore higher-order modes. From the velocity measurement, the fundamental resonance frequency ω_0 can be located and the quality factor corresponding to the fundamental resonance can be estimated as follows:

$$Q_u = \frac{\omega_0}{\omega_2 - \omega_1}, \tag{14}$$

where the ω_2 and ω_1 are -3 dB points in the velocity response.

Given the $\omega_0 = 1/\sqrt{M_M C_M}$, it is impossible to determine the respective values of the compliance C_M and the mass M_M based on one measurement. To overcome the difficulty, a test-box method with volume 5.51 l is employed to obtain another velocity measurement. The result of the membrane velocity measurement is shown in Fig. 6(b). The fundamental resonance frequency is increased from 315 to 500 Hz due to the acoustical compliance of the test box. The additive acoustical compliance C_{AB} and the additive mechanical compliance ΔC_M due to the test box can be calculated as

$$C_{AB} = \frac{V_{\text{box}}}{\rho c^2}, \tag{15}$$

$$\Delta C_M = \frac{C_{AB}}{S_D^2}, \tag{16}$$

where V_{box} is the volume of the test box, ρ is the density of air, and c is the velocity of sound. Thus, based on these two membrane velocity measurements, the mechanical parameters can be determined as

$$C_M = \left[\left(\frac{\omega_{0B}}{\omega_0}\right)^2 - 1\right]\Delta C_M, \tag{17}$$

$$M_M = (\omega_0{}^2 C_M)^{-1}, \tag{18}$$

$$R_M = (\omega_0 Q_u C_M)^{-1}, \tag{19}$$

$$C_M' = \frac{C_M\left(\frac{C_E}{\phi^2}\right)}{C_M + \frac{C_E}{\phi^2}}, \tag{20}$$

where ω_{0B} is the fundamental resonance frequency of the velocity response when loaded with the test box and ΔC_M is the additive mechanical compliance due to the test box. Finally, the voltage-force conversion factor ϕ can be determined by letting $\omega = \omega_0$ in Eq. (13) as follows:

$$\phi = \frac{R_M u(\omega_0)}{e_{\text{in}}}, \tag{21}$$

where $u(\omega_0)$ is the peak magnitude of the membrane velocity response at the fundamental resonance frequency. Using the formula, ϕ is found to be 1.88×10^{-4} for the sample in Fig. 1.

D. Numerical and experimental investigations

Experiments were conducted to validate the preceding model of the electret loudspeaker. The experimental arrangement for measuring the on-axis SPL is shown in Fig. 7(a). According to the standard AES2-1984 (r2003),[17] a 2475 $\times$ 2025 mm^2 baffle is used in the measurement. The 132.6 Vrms swept-sine signal is used to drive the loudspeaker in the frequency range 20–20 kHz. The microphone is positioned 1 m away from the loudspeaker.

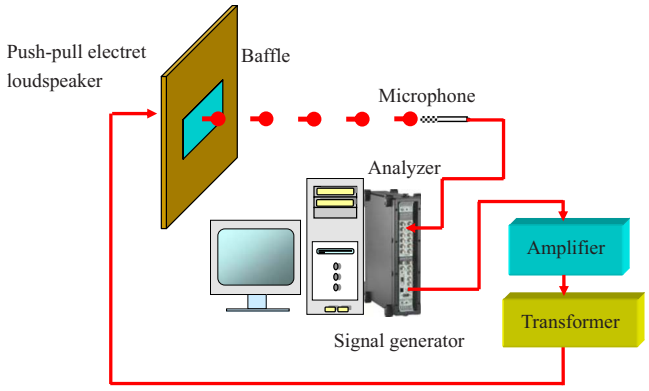

(a)

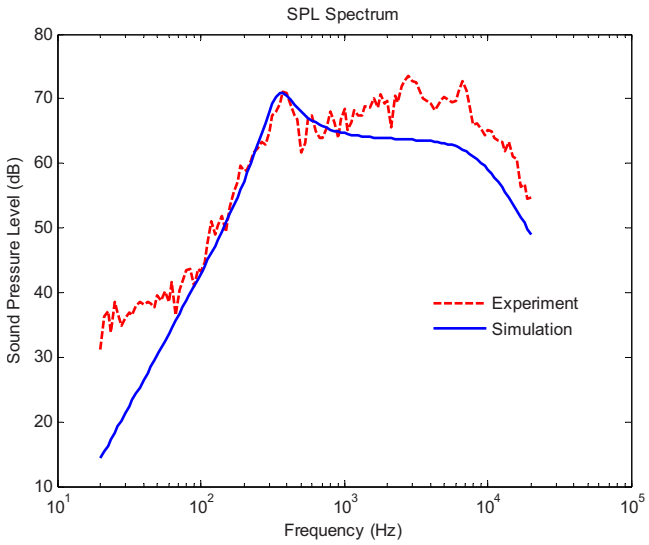

(b)

FIG. 7. (Color online) The on-axis SPL measurement of the push-pull electret loudspeaker. (a) Experimental arrangement. (b) The comparison of the measured and the simulated on-axis SPL responses.

Figure 7(b) compares the on-axis SPL responses obtained using the simulation and the measurement. The simulated response (solid line) is in good agreement with the measured response (dashed line), albeit discrepancies are seen at high frequencies due to un-modeled flexural modes of membrane. It should be borne in mind that, in the preceding model, only the fundamental mode is modeled in the analogous circuit and high-order modes are neglected.

It can also be observed from Fig. 7(b) that the SPL response starts to roll off at approximately 8 kHz due to the inductance of the transformer as predicted. Furthermore, in Fig. 3(b), the motional impedance obtained using the model is much greater than the electrical impedance, rendering the former an open circuit in Fig. 2(b). This is the evidence of weak coupling.

For assessing the nonlinear distortion of the electret loudspeaker, total harmonic distortion (THD) is calculated from the measured on-axis SPL response.[18] In Fig. 8, the

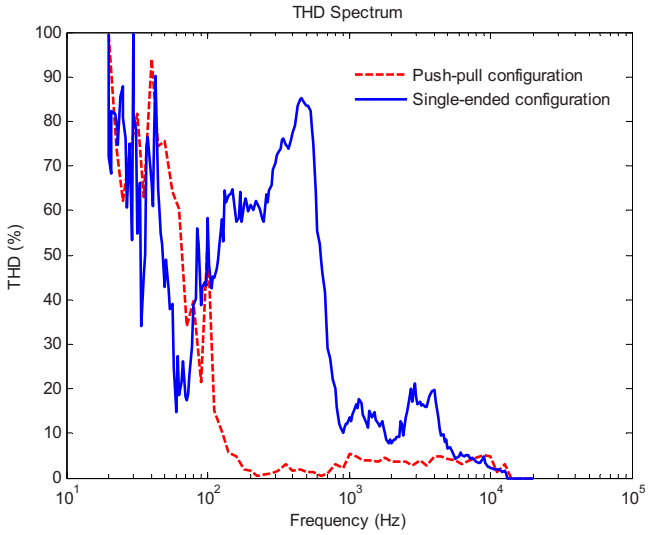

FIG. 8. (Color online) The comparison of the measured THD of the electret loudspeaker between the push-pull and the single-ended configurations.

measured THD of the electret loudspeaker in push-pull construction is compared with that of the single-ended construction, which was investigated by Bai *et al.*[10] The average THD of the push-pull configuration is below 6% in the range 140–20 kHz, while the THD of the single-ended configuration can reach as high as 17%. Evidently, the push-pull configuration has effectively addressed the nonlinearity problem of the single-ended configuration.

III. PARAMETER OPTIMIZATION OF ELECTRET LOUDSPEAKERS

The preceding model of electret loudspeaker serves as a useful simulation platform for optimizing the loudspeaker parameters. In the following, a procedure based on the simulated annealing (SA) algorithm[14–16] is exploited for the design optimization.

A. The SA algorithm

The SA algorithm is a generic probabilistic meta-algorithm for the global optimization problem, namely, locating a good approximation to the global optimum of a given function in a large search space. The major advantage of the SA is the ability to avoid becoming trapped in the local minima. In the SA method, each state in the search space is analogous to the thermal state of the material annealing process. The objective function G is analogous to the energy of the system in that state. The purpose of the search is to bring the system from the initial state to a randomly generated state with the minimum objective function. An improve state is accepted in two conditions. If the objective function is decreased, the new state is always accepted. If the objective function is increased and the following inequality holds, the new state will be accepted:[16]

$$P = \exp\left(-\frac{\Delta G}{T}\right) > \gamma, \tag{22}$$

where P is the acceptance probability function, ΔG is the difference of objective function between the current and the previous states, T is the current system temperature, and γ is a random number, which is generated in the interval (0,1). In the high temperature T, there is high probability P to accept a new state that is "worse" than the present one. This mechanism prevents the search from being trapped in a local minimum. As the annealing process goes on and T decreases, the probability P becomes increasingly small until the system converges to a stable solution. The annealing process begins at the initial temperature T_i and proceeds with temperature that is decreased in steps according to

$$T_{k+1} = \alpha T_k, \tag{23}$$

where $0 < \alpha < 1$ is a annealing coefficient. The SA algorithm is terminated at the preset final temperature T_f. In the electret loudspeaker optimization, we choose $T_i = 1000$, $T_f = 1 \times 10^{-9}$, and $\alpha = 0.95$. Next, two design optimization problems will be examined. The first problem concentrates on only optimizing the gap distance d between the membrane and the electrode plate, whereas the second problem attempts to optimize four design parameters: the gap distance d, the compliance C'_M, the mass M_M, and the resistance R_M.

B. Optimizing the gap distance

In the section, only the gap distance that is easiest to alter in making a mockup will be optimized. If all other conditions remain unchanged, the net attraction force acting on the membrane and hence the SPL output will increase as the gap is decreased. However, the gap cannot be reduced indefinitely, or else, stick-up condition of the membrane and the electrode plates can occur. Another issue is that the upper roll-off frequency will also become lower (because of the increased static capacitance) as the gap is decreased.

As we keep decreasing the gap to increase the attraction force until the displacement of the membrane equals the gap distance, we call this distance the critical gap distance. Only dynamic distance needs to be concerned since, at the quiescent state, the static attraction forces due to resident charges in the membrane are balanced with the push-pull construction. Membrane displacement can be obtained by integrating the velocity expression in Eq. (13) as follows:

$$\delta = \frac{u}{s} = \frac{K_1}{R_M Q_u \omega_0} \frac{1}{\left(\frac{s}{\omega_0}\right)^2 + \frac{1}{Q_u}\left(\frac{s}{\omega_0}\right) + 1} \frac{e_{\text{in}}}{d^2}, \tag{24}$$

where $\phi = K_1/d^2$ in Eq. (2) has been invoked. The collision condition occurs when the peak value of the displacement $|\delta|_{\max}$ is equal to the gap distance d. This gives the critical gap distance

$$d^* = \left\{ \frac{K_1}{R_M Q_u \omega_0} \frac{Q_u^2}{\sqrt{Q_u^2 - 0.25}} |e_{\text{in}}| \right\}^{1/3}. \tag{25}$$

In the experiment, the driving signal is a 132.6 Vrms swept sine. That corresponds to a critical gap distance 0.19 mm, which also represents an upper bound of displacement for the following optimization. Figure 9(a) compares the SPL responses for various gap distances (including the critical gap). Clearly, the SPL is increased if the gap distance is decreased.

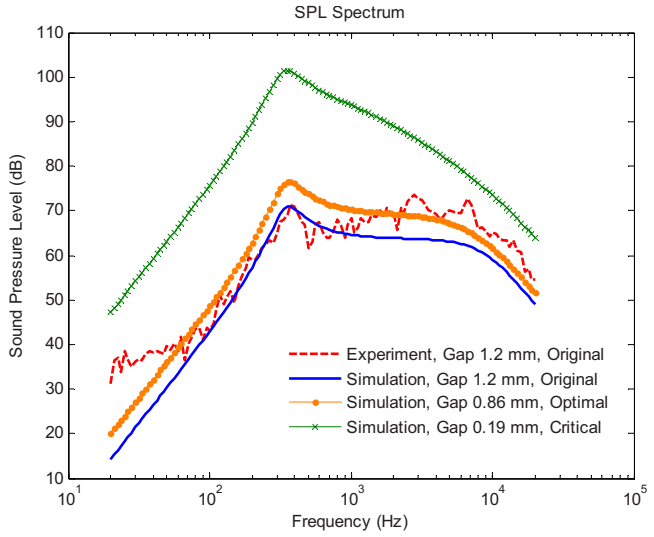

(a)

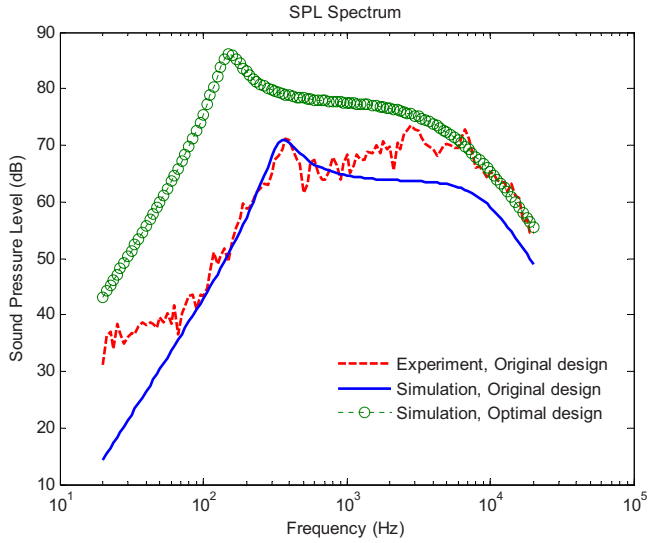

(b)

FIG. 9. (Color online) The comparison of the on-axis SPL responses between the original and the optimal designs. (a) Results of optimizing only the gap distance. (b) Results of optimizing four parameters including the gap distance, the resistance, the mass, and the compliance.

However, this comes at the expense of decreased bandwidth due to increased static capacitance.

In order to find a compromise solution between the original design and the design with the critical gap, the SA algorithm is employed alongside the preceding simulation model for finding the optimal gap distance. Two goals are set up for the design optimization. It is hoped that the SPL in the range 800–5 kHz is maximized while maximizing the upper roll-off frequency, i.e.,

$$G_1 = \sqrt{\frac{1}{N}\sum_{n=1}^{N} (\mathrm{SPL}_{\mathrm{new}}(n))^2}, \quad f(n) \in [800\ \mathrm{Hz}, 5\ \mathrm{kHz}],$$
$$n = 1, \ldots, N, \tag{26}$$

TABLE I. Parameters of the optimized design versus the original nonoptimized design.

	R_M (N s/m)	C'_M (m/N)	M_M (kg)	Gap (mm)
Original (1)	3.47	1.95×10^{-5}	1.17×10^{-2}	1.2
Optimal (2)	4.0	1.03×10^{-4}	1.1×10^{-2}	0.55
(2)/(1)%	115.44	528.21	94.83	45.83

$$G_2 = f_{\mathrm{uc}}, \tag{27}$$

where $\mathrm{SPL}_{\mathrm{new}}$ is the current SPL response, n is the frequency index in the range 800–5 kHz, and f_{uc} is the upper -3 dB cutoff frequency of $\mathrm{SPL}_{\mathrm{new}}$. The compound objective function G_{TG} can be written as

$$G_{TG} = \frac{1}{G_1} + w \times \frac{1}{G_2}, \tag{28}$$

where w is a weighting constant ($w=0.23$ in the simulation). In addition, the design variable (gap distance) and the associated constraints are given in the following inequalities:

$$0.4\ \mathrm{mm} < d < 2.0\ \mathrm{mm},$$
$$|\delta|_{\max}(\mathrm{mm}) < d(\mathrm{mm}). \tag{29}$$

With the SA procedure, the optimal gap distance is found to be 0.86 mm, which enhances the average SPL by approximately 5 dB, as shown in Fig. 9(a).

C. Optimizing multi-parameters

In the section, we shall extend the preceding one-parameter optimization to more comprehensive optimization for four parameters: the gap distance, the resistance R_M, the mass M_M, and the compliance C'_M. Apart from the level and the upper cutoff design goals, a third goal of the lower cutoff is added to the objective function

$$G_3 = f_{\mathrm{lc}}, \tag{30}$$

where f_{lc} denotes the lower -3 dB cutoff frequency of $\mathrm{SPL}_{\mathrm{new}}$. The compound objective function G_{TM} reads

$$G_{TM} = w_1 \times \frac{1}{G_1} + w_2 \times \frac{1}{G_2} + G_3, \tag{31}$$

where the weights $w_1=2400$ and $w_2=150\,000$ in the simulation. The design variables and the associated constraints are given in the following inequalities:

$$0.698\ \mathrm{N\ s/m} \le R_M \le 69.8\ \mathrm{N\ s/m},$$
$$1.4\times10^{-3}\ \mathrm{kg} \le M_M \le 1.43\times10^{-1}\ \mathrm{kg},$$
$$1.95\times10^{-6}\ \mathrm{m/N} \le C'_M \le 1.95\times10^{-4}\ \mathrm{m/N},$$
$$0.4\ \mathrm{mm} \le d \le 2.0\ \mathrm{mm},$$
$$|\delta|_{\max}(\mathrm{mm}) < d(\mathrm{mm}). \tag{32}$$

The results of optimization using the SA algorithm are summarized in Table I. The design with optimized parameters is

simulated in Fig. 9(b). The lower cutoff frequency of the optimal design (circled mark) has been decreased from 315 Hz of the original design to 150 Hz as the mechanical compliance is increased by 528%. The average SPL is enhanced by about 12 dB as the gap is decreased to 0.55 mm.

IV. CONCLUSIONS

A fully experimental modeling technique and an optimization procedure have been developed in this work for push-pull electret loudspeakers. The experimental modeling technique relies on not only the electrical impedance measurement but also the membrane velocity measured by using a laser vibrometer. With the aid of a test box, the voltage-force conversion factor and characteristics of motional impedance can be identified from the membrane velocity. One of the most important contributions of the present work is that it verifies the theory and proves the linearity of the transduction. The experimentally identified model serves as the simulation platform for optimizing the design parameters of the electret loudspeaker. The SA algorithm was exploited to find the parameters that yield optimal level-bandwidth performance. Either only the gap distance or the comprehensive search for various parameters can be optimized by using the SA procedure. The results reveal that the optimized design has effectively enhanced the performance of the electret loudspeaker, as compared to the original design. In addition, a high-quality audio transformer with wider bandwidth may further enhance the performance and ease the optimization limitations. The search of such transformers is included in the list of action items of future work.

ACKNOWLEDGMENTS

The work was supported by the National Science Council of Taiwan, under Project No. NSC 95-2221-E-009-009-MY2. Special thanks also go to the Material and Chemical Research Laboratories, Industrial Technology Research Institute (ITRI) in Taiwan.

[1]P. J. Baxandall, "Electrostatic loudspeakers," in *Loudspeaker and Headphone Handbook*, 3rd ed., edited by J. Borwick (Focal, Oxford, 2001).
[2]F. V. Hunt, *Electroacoustics: The Analysis of Transduction, and Its Historical Background* (American Institute of Physics, Melville, NY, 1982).
[3]T. Mellow and L. Kärkkäinen, "On the forces in single-ended and push-pull electret transducers," J. Acoust. Soc. Am. **124**, 1497–1504 (2008).
[4]J. Lekkala and M. Paajanen, "EMFi—New electret material for sensors and actuators," IEEE Tenth International Symposium on Electrets, Athens, Greece (1999).
[5]M. Paajanen, J. Lekkala, and K. Kirjavainen, "Electromechanical film (EMFi)—A new multipurpose electret material," Sens. Actuators, A **84**, 95–102 (2000).
[6]Y. Cao, Z. Xia, Q. Lin, J. Shen, L. Chen, and B. Zhou, "Study of porous dielectrics as electret materials," IEEE Trans. Dielectr. Electr. Insul. **5**, 58–62 (1998).
[7]D. M. Chiang, W. L. Liu, J. L. Chen, and R. Susuki, "PALS and SPM/EFM investigation of charged nanoporous electret films," Chem. Phys. Lett. **412**, 50–54 (2005).
[8]D. M. Chiang and J. L. Chen, "A novel flexible loudspeaker driven by an electret diaphragm," AES 121st Convention, San Francisco, CA (2006).
[9]T. Mellow and L. Kärkkäinen, "On the sound field of a circular membrane in free space and an infinite baffle," J. Acoust. Soc. Am. **120**, 2460–2477 (2006).
[10]M. R. Bai, R. L. Chen, and C. J. Wang, "Electroacoustic analysis of an electret loudspeaker using combined finite-element and lumped-parameter models," J. Acoust. Soc. Am. **125**, 3632–3640 (2009).
[11]H. Olson, *Acoustical Engineering* (Van Nostrand, New York, 1957), reprinted by Professional Audio Journals (Philadelphia, PA, 1991).
[12]L. L. Beranek, *Acoustics* (Acoustical Society of America, Melville, NY, 1996).
[13]W. M. Leach, Jr., *Introduction to Electroacoustics and Audio Amplifier Design* (Kendall-Hunt, Dubuque, IA, 2003).
[14]N. Metropolis, A. W. Rosenbluth, M. N. Rosenbluth, A. H. Teller, and E. Teller, "Equations of state calculations by fast computing machines," J. Chem. Phys. **21**, 1087–1092 (1953).
[15]*Quantum Annealing and Related Optimization Methods*, edited by A. Das and B. K. Chakrabarti (Springer, Heidelberg, 2005).
[16]J. de Vicente, J. Lanchares, and R. Hermida, "Placement by thermodynamic simulated annealing," Phys. Lett. A **317**, 415–423 (2003).
[17]Audio Engineering Society Inc., AES Recommended Practice Specification of Loudspeaker Components Used in Professional Audio and Sound Reinforcement, AES2-1984, NY (2003).
[18]M. R. Bai and R. L. Chen, "Optimal design of loudspeaker systems based on sequential quadratic programming (SQP)," J. Audio Eng. Soc. **55**, 44–54 (2007).

Influence of an oscillating circuit on the radiation of transient acoustic waves by an electroelastic cylinder

A. E. Babaev
Department of Theory of Vibrations, Institute of Mechanics, National Academy of Sciences of Ukraine, 3 Nesterova Strasse, Kyiv 03057, Ukraine

A. A. Babaev
Department of Applied Mechanics, Economy and Transport Technology, Kyiv University, 19 Lukashevicha Strasse, Kyiv 03049, Ukraine

I. V. Yanchevskiy[a)]
Department of Machine Elements, Kharkiv National Automobile and Highway University, 25 Petrovskogo Strasse, Kharkiv 61002, Ukraine

(Received 15 June 2009; revised 16 December 2009; accepted 18 December 2009)

The problem of nonstationary wave radiation in an infinitely long thick-wall piezoelectric cylinder in fluid medium is considered. The influence of an oscillating circuit with lumped parameters on characteristics of transient process is taken into consideration. Problem formulation is executed within the forced electrostatic theory, acoustic approximations, and quasistatic theory for electric circuit. The solution method is based on the integral Laplace transform in time. This allows analytically reducing the problem to solving a system of Volterra integral equations with retarded arguments. The numerical results of calculations are presented and analyzed.
 [DOI: 10.1121/1.3291035]

PACS number(s): 43.38.Fx, 43.38.Pf [AJZ] Pages: 2282–2289

I. INTRODUCTION

The widespread use of piezoelectric energy transducers drives the intensive development of electroelasticity and hydroelectroelasticity theories. The majority of studies consider periodical processes in electroelastic bodies and hydroelectroelastic systems. Recent publications on this subject are those of Refs. 1–3. The functional capacities of ultrasonic devices having piezoelectric energy transducers can be significantly expanded when they function in impulse conditions. This is the underpinning of the significant interest in hydroelectroelasticity problems in the nonstationary statement. The studies in this problem to date have been summarized in the monograph[4] and the review paper.[5] The publications of Refs. 6–11 should be also mentioned as recent publications on bounded electroelasticity. Most modern studies assume that piezoelectric radiator excitation occurs due to a set potential difference on its electroconductive coating. In real conditions, electromechanical transducers interact with media and are connected to generators by conducting lines. The latter can be represented by linear electrical circuits with point parameters. These circuits have inductances, capacitances, and resistances (oscillating circuits) or distributed parameters (cables). As a result, the radiator is driven by an electric pulse differing from the input one. Several published papers[12–14] have studied the influence of the cable on the functioning of the thin-wall spherical and cylindrical radiators excited in nonstationary conditions. These studies were conducted within the framework of the theory of thin-wall electroelastic shells[15] based on the Kirchhoff–Love hypotheses. Note that the application of this model does not make it impossible to consider the wave fields in the piezoelectric transducer. This paper formulates the problem of waves radiated by a thick-wall electroelastic cylinder immersed in fluid and connected to the generator. The latter generates nonstationary electric pulses in a conducting line with point parameters. An effective method for solving the problem with account of transient processes in the system is also offered.

II. MATHEMATICAL MODELS

This paper is a study of a hydroelectroelastic system. It consists of an infinitely long thick-wall radially polarized cylindrical piezoelectric transducer in an infinite fluid medium (Fig. 1). The inside of the cylinder is assumed to be vacuum. Piezoelectric material of the cylinder is in tetragonal crystal system. The transducer is completely coated with an electroconducting substance and connected to a source of nonstationary electric pulses with a conducting line. The line consists of a series-connected inductance, capacitance, and resistance (a series oscillatory circuit). Such a conducting line with point parameters does not minimize the universal nature of the offered solution method. The fluid is assumed to be an ideal compressible medium and its perturbation is considered using the acoustic theory. The equations of the linear theory of electroelasticity[15] are applied to describe electromechanical fields in a cylindrical radiator. The processes in the conducting line are considered as quasistationary (i.e., instantaneous values of electrical quantities described by the Kirchhoff law).

[a)]Author to whom correspondence should be addressed. Electronic mail: yanchevsky@khadi.kharkov.ua

 0001-4966/2010/127(4)/2282/8/$25.00

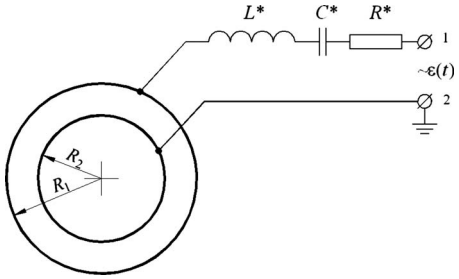

FIG. 1. Schematic diagram of an electroelastic cylindrical radiator with an oscillating circuit.

The radial coordinate is designated as r, time as t, the geometric and physical characteristics of the electroelastic cylinder as R_1 and R_2 (external and internal radii); γ is density; C_{33}^E, C_{13}^E, C_{11}^E, and C_{12}^E are elasticity modules; e_{33} and e_{31} are piezomodules; d_{33} is piezoelectric constant; and ε_{33}^S is dielectric permittivity. The parameters of the acoustic media are designated as ρ (density) and c (sonic velocity). The parameters of the oscillating contour are L^* (inductance), C^* (capacitance), and R^* (resistance).

At the initial moment of time ($t=0$), the investigated system is excited by an electric pulse at the input terminals of the conducting line. The pulse shape is described by the function $\varepsilon(t)H(t)$ [where $H(t)$ is the Heaviside function].

The quantities that characterize the transient processes in the piezoelectric transducer are unknown: u_r is radial component of the displacement vector; σ_{rr} is normal stress in the radial direction; E_r, D_r, and Ψ are intensity, electric displacement, and potential of the electrical field; and U_p is voltage drop, occurring when the electric current flows through the electrode surfaces of the cylinder. In the acoustic medium: V_r is radial velocity of its particles; p is pressure; φ is wave potential, and in the conducting circuit: U_{L^*}, U_{C^*}, and U_{R^*} are voltage drops across the inductance, capacitance, and resistance, and I is electric current in these elements.

Then we apply dimensionless parameters, according to which the quantities u_r, r, R_1, and R_2 are divided by R_1; p and σ_{rr} are divided by ρc^2; E_r is divided by $1/d_{33}$; D_r is divided by $\varepsilon_{33}^S/d_{33}$; Ψ, U_p, U_{L^*}, U_{C^*}, and U_{R^*} are divided by R_1/d_{33}; I is divided by $c\varepsilon_{33}^s R_1/d_{33}$; V_r is divided by c; φ is divided by cR_1; and t is divided by R_1/c.

With all the above assumptions, we apply the following initial system of equations describing the transducer motion:

$$\frac{\partial^2 u_r}{\partial r^2}+\frac{1}{r}\frac{\partial u_r}{\partial r}-a_1\frac{u_r}{r^2}-a_2\frac{\partial E_r}{\partial r}-a_3\frac{1}{r}E_r=a_4\frac{\partial^2 u_r}{\partial t^2}, \tag{1}$$

forced electrostatics,

$$\frac{\partial}{\partial r}(rE_r)=-a_5\frac{\partial u_r}{\partial r}-a_6\frac{\partial}{\partial r}\left(r\frac{\partial u_r}{\partial r}\right), \tag{2}$$

$$E_r=-\frac{\partial \Psi}{\partial r}, \tag{3}$$

and the dependences

$$\sigma_{rr}=a_7\frac{\partial u_r}{\partial r}+a_8\frac{\partial u_r}{\partial r}-a_9E_r, \tag{4}$$

$$D_r=E_r+a_5\frac{u_r}{r}+a_6\frac{\partial u_r}{\partial r}, \tag{5}$$

for the electroelastic cylinder.[15] Here, $a_1=C_{11}^E/C_{33}^E$, $a_2=e_{33}/C_{33}^E d_{33}$, $a_3=(e_{33}-e_{31})/C_{33}^E d_{33}$, $a_4=\gamma c^2/C_{33}^E$, $a_5=e_{31}d_{33}/\varepsilon_{33}^s$, $a_6=e_{33}d_{33}/\varepsilon_{33}^s$, $a_7=C_{33}^E/\rho c^2$, $a_8=C_{13}^E/\rho c^2$, and $a_9=e_{33}/d_{33}\rho c^2$.

The wave equation of the perturbation motion potential of the acoustic media φ is

$$\frac{\partial^2 \varphi}{\partial r^2}+\frac{1}{r}\frac{\partial \varphi}{\partial r}=\frac{\partial^2 \varphi}{\partial t^2}. \tag{6}$$

Using this equation, the radial velocity of its particles V_r and pressure p are

$$V_r=\frac{\partial \varphi}{\partial r}, \quad p=\frac{\partial \varphi}{\partial t}. \tag{7}$$

The equation that demonstrates the accuracy of the Kirchhoff law for electric current in the series oscillating circuit and the piezoelectric transducer is

$$U_p+U_{L^*}+U_{C^*}+U_{R^*}=\varepsilon(t)H(t), \tag{8}$$

where

$$U_p=\Psi|_{r=R_1}-\Psi|_{r=R_2}, \quad U_{L^*}=\lambda_L\frac{dI}{dt}, \quad \frac{dU_{C^*}}{dt}=\lambda_C I, \quad U_{R^*}=\lambda_R I, \tag{9}$$

$\lambda_L=L^*(c^2\varepsilon_{33}^S/R_1)$, $\lambda_C=\varepsilon_{33}^S R_1/C^*$, and $\lambda_R=R^*c\varepsilon_{33}^S$ are constants.

It is assumed that the joint motion of the cylinder and the external acoustic medium on the contact boundary ($r=R_1$) excludes any interruptions and that the inner surface ($r=R_2$) has no load:

$$V_r|_{r=R_1}=\left.\frac{\partial u_r}{\partial t}\right|_{r=R_1}, \quad \sigma_{rr}|_{r=R_1}=-p|_{r=R_1}, \quad \sigma_{rr}|_{r=R_2}=0. \tag{10}$$

The particles in the acoustic media, which are infinitely far from the radiator, retain their unperturbed state.

Equal values of electric currents in the conducting line and the piezoelectric radiator are described by the equation

$$\left.\frac{dD_r}{dt}\right|_{r=R_1}=-\frac{I}{2\pi R_1}. \tag{11}$$

The initial conditions are assumed to be zero.

III. SOLUTION METHOD

The problem is solved using the operational method. The integral Laplace transform in time is applied to the initial equations and boundary conditions (1)–(11). This serves to satisfy zero initial conditions.

Integration of transformed equation (2) yields the following expression for electric field strength E_r^L:

$$E_r^L=-a_5\frac{u_r^L}{r}-a_6\frac{du_r^L}{dr}+\frac{1}{rs}C^L(s). \tag{12}$$

Index L designates respective transformants, s is parameter of transformation, and $C^L(s)$ is unknown function of s.

Substitution of formula (12) into Laplace-transformed equation: (1) gives an equation with respect to a single unknown $u_r^L(s,r)$

$$\frac{d^2u_r^L}{dr^2}+\frac{1}{r}\frac{du_r^L}{dr}-\left(\frac{\nu^2}{r^2}+\lambda^2 s^2\right)u_r^L=\beta\frac{1}{sr^2}C^L(s), \tag{13}$$

where $\nu=\sqrt{(C_{11}^E\varepsilon_{33}^s+e_{31}^2)/(C_{33}^E\varepsilon_{33}^s+e_{33}^2)}$, $\lambda=\sqrt{\gamma c^2\varepsilon_{33}^s/(C_{33}^E\varepsilon_{33}^s+e_{33}^2)}$, and $\beta=-e_{31}\varepsilon_{33}^s/(C_{33}^E\varepsilon_{33}^s+e_{33}^2)d_{33}$.

The general solution of Eq. (13) is obtained using the method of variation of constants,

$$\begin{aligned}u_r^L=C^L(s)\frac{1}{s}\{&A^L(s)e^{-s\lambda(R_1-r)}f_{0\nu}^L(s,\lambda r)\\&+B^L(s)e^{-s\lambda(r-R_2)}g_{0\nu}^L(s,\lambda r)-\beta[f_{0\nu}^L(s,\lambda r)W^L(s,r)\\&+g_{0\nu}^L(s,\lambda r)V^L(s,r)]\},\end{aligned} \tag{14}$$

where $A^L(s)$, $B^L(s)$, and $C^L(s)$ are unknown functions of parameter s,

$$f_{m\nu}^L(s,\lambda r)=\frac{1}{s^m}e^{-s\lambda r}I_\nu(s\lambda r),\quad g_{m\nu}^L(s,\lambda r)=\frac{1}{s^m}e^{s\lambda r}K_\nu(s\lambda r),$$

$$V^L(s,r)=\int_{R_2}^{r}e^{-s\lambda r}\frac{1}{x}I_\nu(s\lambda x)dx,$$

$$W^L(s,r)=\int_{r}^{R_1}e^{s\lambda r}\frac{1}{x}K_\nu(s\lambda x)dx, \tag{15}$$

where I_ν and K_ν are modified Bessel functions of the first and the second kinds.

After integrating the Laplace-transformed wave equation (6), we obtain the following expression for potential φ^L:

$$\varphi^L=C^L(s)\frac{1}{s}D^L(s)e^{s(r-R_1)}g_{00}^L(s,r). \tag{16}$$

Functions $A^L(s)$, $B^L(s)$, $C^L(s)$, and $D^L(s)$ will be found after satisfying the boundary conditions. Formula (16) takes into account the attenuation of perturbations in infinity points.

Based on the general solutions (14) and (16), and dependencies (4) and (7), unknown values σ_{rr}^L, V_r^L, and p^L can be represented as

$$\begin{aligned}\sigma_{rr}^L=C^L(s)\Big\{&A^L(s)e^{-s\lambda(R_1-r)}F^L(s,r)\\&+B^L(s)e^{-s\lambda(r-R_2)}G^L(s,r)-\beta F^L(s,r)W^L(s,r)\\&-\beta G^L(s,r)V^L(s,r)-\mu\frac{1}{rs}\Big\}.\end{aligned} \tag{17}$$

$$V_r^L=-C^L(s)[D^L(s)e^{-s(r-R_1)}g_{01}^L(s,r)].$$

$$p^L=-C^L(s)[D^L(s)e^{-s(r-R_1)}g_{00}^L(s,r)]. \tag{18}$$

In formulas (17) and (18), the following designations have been accepted:

$$F^L(s,r)=\xi f_{0\nu+1}^L(s,\lambda r)+\varsigma\frac{1}{r}f_{1\nu}^L(s,\lambda r),$$

$$G^L(s,r)=-\xi g_{0\nu+1}^L(s,\lambda r)+\varsigma\frac{1}{r}g_{1\nu}^L(s,\lambda r), \tag{19}$$

where

$$\xi=\frac{C_{33}^E\varepsilon_{33}^s+e_{33}^2}{\rho c^2\varepsilon_{33}^s}\lambda,\quad \varsigma=\frac{C_{33}^E\varepsilon_{33}^s+e_{33}^2}{\rho c^2\varepsilon_{33}^s}\nu+\frac{C_{13}^E\varepsilon_{33}^s+e_{33}e_{31}}{\rho c^2\varepsilon_{33}^s},\quad \mu=\frac{e_{33}}{\rho c^2 d_{33}}.$$

According to Eqs. (3) and (12), potential Ψ^L is expressed by the displacements of u_r^L as

$$\begin{aligned}\Psi^L(s,r)=a_6[u_r^L(s,r)-u_r^L(s,R_2)]+a_5\int_{R_2}^{r}\frac{u_r^L(s,x)}{x}dx\\-C^L(s)\frac{1}{s}\ln\frac{r}{R_2}+\Psi^L(s,R_2).\end{aligned} \tag{20}$$

Taking into account formulas (9), (14), and (20), the voltage drop across the electroelastic cylinder U_p^L is

$$U_p^L=C^L(s)\frac{1}{s}\left[\Phi^L(s)-\ln\frac{R_1}{R_2}\right], \tag{21}$$

where

$$\begin{aligned}\Phi^L(s)=&A^L(s)[a_6f_{0\nu}^L(s,\lambda R_1)+a_5V^L(s,R_1)]\\&+B^L(s)[-a_6g_{0\nu}^L(s,\lambda R_2)+a_5W^L(s,R_2)]\\&+a_6[-A^L(s)f_{0\nu}^L(s,\lambda R_2)+B^L(s)g_{0\nu}^L(s,\lambda R_1)]\\&\times e^{-s\lambda(R_1-R_2)}+\beta a_6[-g_{0\nu}^L(s,\lambda R_1)V^L(s,R_1)\\&+f_{0\nu}^L(s,\lambda R_2)W^L(s,R_2)]-a_5\beta Z^L(s),\end{aligned} \tag{22}$$

$$\begin{aligned}Z^L(s)=&\int_{R_2}^{R_1}\frac{1}{x}I_\nu(s\lambda x)\int_{x}^{R_1}\frac{1}{y}K_\nu(s\lambda y)dydx\\&+\int_{R_2}^{R_1}\frac{1}{x}K_\nu(s\lambda x)\int_{R_2}^{x}\frac{1}{y}I_\nu(s\lambda y)dydx.\end{aligned} \tag{23}$$

Proceeding from Eqs. (3), (5), (11), and (20), the electric current I^L in the conducting circuit and the piezoelectric transducer can be expressed by unknown functions $C^L(s)$ in the space of representations:

$$I^L=-\frac{2\pi}{R_1}C^L(s), \tag{24}$$

allowing to present voltages $U_{L^*}^L$, $U_{C^*}^L$, and $U_{R^*}^L$ as

$$U_{L^*}^L=b_1sC^L(s),\quad U_{C^*}^L=b_2\frac{1}{s}C^L(s),\quad U_{R^*}^L=b_3C^L(s), \tag{25}$$

where b_1, b_2, and b_3 are constants: $b_1=(-2\pi/R_1)\lambda_L$, $b_2=(-2\pi/R_1)\lambda_C$, $b_3=(-2\pi/R_1)\lambda_R$.

Subsequently, by substituting formulas (14), (16), (21), and (25) into Laplace-transformed conditions (10) and (8),

we obtain a system of three algebraic equations for unknown values $A^L(s)$, $B^L(s)$, and $D^L(s)$, and an equation for $C^L(s)$,

$$A^L(s)F^L(s,R_1) - D^L(s)g_{00}^L(s,R_1) = X_1^L(s) - B^L(s)e^{-s\lambda(R_1-R_2)}G^L(s,R_1),$$

$$A^L(s)f_{0\nu}^L(s,\lambda R_1) + D^L(s)g_{01}^L(s,R_1) = X_2^L(s) - B^L(s)e^{-s\lambda(R_1-R_2)}g_{0\nu}^L(s,\lambda R_1),$$

$$B^L(s)G^L(s,R_2) = Y_1^L(s) - A^L(s)e^{-s\lambda(R_1-R_2)}F^L(s,R_2). \quad (26)$$

$$b_1C^L(s) + C^L(s)\Omega^L(s) = \frac{1}{s}\varepsilon^L(s). \quad (27)$$

Functions F^L, G^L, $f_{0\nu}^L$, $g_{0\nu}^L$, g_{00}^L, and g_{01}^L have been described earlier [formulas (15) and (19)], and functions X_1^L, X_2^L, Y_1^L, and Ω^L have the form

$$X^L(s) = \beta G^L(s,R_1)V^L(s,R_1) + \frac{\mu}{R_1}\frac{1}{s},$$

$$X_2^L(s) = \beta g_{0\nu}^L(s,\lambda R_1)V^L(s,R_1),$$

$$Y_1^L(s) = \beta F^L(s,R_2)W^L(s,R_2) + \frac{\mu}{R_2}\frac{1}{s},$$

$$\Omega^L(s) = \frac{1}{s^2}\Phi^L(s) - \frac{1}{s^2}\ln\frac{R_1}{R_2} + b_3\frac{1}{s} + b_2\frac{1}{s^2}. \quad (28)$$

The formulas obtained by solving Eqs. (26) and (27) will be so involved that the subsequent Laplace inversion of the sought for quantities, intended to verify the results obtained, appears to be challenging. According to the solution method elaborated here, an exact inversion of Eqs. (26) and (27) occurs, the boundary conditions being satisfied in the space of the originals. As a result, the problem is reduced to solving a system of integral Volterra equations with retarded arguments to find unknown values $A(t)$, $B(t)$, and $D(t)$,

$$\int_0^t A(\tau)F(t-\tau,R_1)d\tau - \int_0^t D(\tau)g_{00}(t-\tau,R_1)d\tau = X_1(t) - \int_0^{t-\lambda(R_1-R_2)} B(\tau)G(t-\lambda(R_1-R_2)-\tau,R_1)d\tau,$$

$$\int_0^t A(\tau)f_{0\nu}(t-\tau,\lambda R_1)d\tau - \int_0^t D(\tau)g_{01}(t-\tau,R_1)d\tau = X_2(t) - \int_0^{t-\lambda(R_1-R_2)} B(\tau)g_{0\nu}(t-\lambda(R_1-R_2) - \tau,\lambda R_1)d\tau,$$

$$\int_0^t B(\tau)G(t-\tau,R_2)d\tau = Y_1(t) - \int_0^{t-\lambda(R_1-R_2)} A(\tau)F(t-\lambda(R_1-R_2)-\tau,R_2)d\tau, \quad (29)$$

and an equation for finding the unknown value $C(t)$,

$$b_1C(t) + \int_0^t C(\tau)\Omega(t-\tau)d\tau = \int_0^t \varepsilon(\tau)d\tau. \quad (30)$$

The originals $g_{0\nu}(t,z)$, $g_{1\nu}(t,z)$, $f_{0\nu}(t,z)$, and $f_{1\nu}(t,z)$ were taken from operational calculus tables.[16] These formulas are presented in Appendix A. Functions $V(t,z)$ and $W(t,z)$ are derived using these formulas. Formulas for $V(t,z)$ and $W(t,z)$, derived by calculating spatial value integrals (15) in the space of original, are given in Appendix B.

The kernel $F(t,z)$ is a linear combination of functions $f_{0\nu+1}(t,z)$ and $f_{1\nu}(t,z)$, $G(t,z)$-$g_{0\nu+1}(t,z)$, and $g_{1\nu}(t,z)$ (19). The original $X_1(t)$, $X_2(t)$, and $Y(t)$ are obtained as integrals

$$X_1(t) = \beta\int_0^t G(t-\tau,R_1)V(\tau,R_1)d\tau + \frac{\mu}{R_1},$$

$$X_2(t) = \beta\int_0^t g_{0\nu}(t-\tau,\lambda R_1)V(\tau,R_1)d\tau,$$

$$Y_1(t) = \beta\int_0^t F(t-\tau,R_2)W(\tau,R_2)d\tau + \frac{\mu}{R_2}. \quad (31)$$

The system of integral equations (29) was solved using the quadratic formulas method. The time interval was divided into segments. For each one, numerical integration was applied (by using the mean-value theorem). In so doing, the sought for values of $A(t)$, $B(t)$, and $D(t)$ were found stepwise in time. Note that the shift in the arguments of the unknown components in the right-hand parts of Eq. (31) allowed satisfying boundary conditions ($r=R_1$ and $r=R_2$) independently at any moment in time. Thus, when $t<\lambda(R_1-R_2)$, integrals with retarded arguments are equal to zero. The values of $A(t)$ and $D(t)$ were obtained from the first two equations of system (31), and value $B(t)$ was found from the third one. These results take into account the time shift used. They have been applied in calculations related to a later stage of the transient process [$t>\lambda(R_1-R_2)$].

As soon as $A(t)$, $B(t)$, and $D(t)$ have been determined, integral equation (29) is solved. To determine its kernel $\Omega(t)$, the original of function $Z^L(s)$ was created. In so doing, the function was differentiated with respect to s to find the primitives of double integrals (23). Having analytically inverted the equation obtained, we can also express $Z(t)$ as

$$Z(t) = -\frac{2}{t}\left[\int_0^t g_{1\nu}(\tau,\lambda R_1)V(t-\tau,R_1)d\tau - \int_0^t f_{1\nu}(\tau,\lambda R_2)W(t-\tau,R_2)d\tau\right]. \quad (32)$$

Using the values $A(t)$ and $B(t)$ obtained by solving system (29), and by applying formula (32), the integrals in representation $\Phi(t)$ were numerically calculated using quadrature formulas,

$$\Phi(t) = \int_0^t A(\tau)[a_6 f_{0\nu}(t-\tau,\lambda R_1) - a_5 V(t-\tau,R_1)d\tau] + \int_0^t B(\tau)[-a_6 g_{0\nu}(t-\tau,\lambda R_2) + a_5 W(t-\tau,R_2)]d\tau + a_6 \int_0^{t-\lambda(R_1-R_2)} [-A(\tau)f_{0\nu}(t-\tau-\lambda(R_1 - R_2),\lambda R_2) + B(\tau)g_{0\nu}(t-\tau-\lambda(R_1-R_2),\lambda R_1)]d\tau + \beta a_6 \left[-\int_0^t g_{0\nu}(\tau,\lambda R_1)V(t-\tau,R_1)d\tau + \int_0^t f_{0\nu}(\tau,\lambda R_2)W(t-\tau,R_2)d\tau \right] - a_5\beta Z(t). \quad (33)$$

Hence, the sought for original of function $\Omega^L(s)$ can be written down as

$$\Omega(t) = \int_0^t (t-\tau)\Phi(\tau)d\tau - t\left[\ln\frac{R_1}{R_2} + b_2\right] + b_3. \quad (34)$$

The quadrature formulas method was also used for solving integral equation (30). Having obtained the values of $A(t)$, $B(t)$, $D(t)$, and $C(t)$, it is easy to calculate the physical characteristics of the transient process under investigation. A formula for calculating radial stresses σ_{rr} (17) is given below:

$$\sigma_{rr}(t,r) = \int_0^t C(\tau)N(t-\tau,r)d\tau, \quad (35)$$

where

$$N(t,r) = \int_0^{t-\lambda(R_1-r)} [A(\tau)F(t-\lambda(R_1-r)-\tau,r) + a_5 W(t-\tau,R_2)]d\tau + \int_0^{t-\lambda(r-R_2)} B(\tau)G(t-\lambda(r-R_2)-\tau,r)d\tau - \beta\int_0^t [F(\tau,r)W(t-\tau,r) + G(\tau,r)V(t-\tau,r)]d\tau - \frac{\mu}{r}.$$

The displacement $u_r(t,r)$, the potential difference $U_p(t)$, the pressure in the acoustic media $p(t,r)$, and other values were determined likewise.

IV. NUMERICAL RESULTS

Calculations were based on the following physical parameters of the piezoelectric cylindrical transducer of dimensionless thickness $R_1-R_2=0.2(R_1=1)$: $C_{11}^E=15.1\times10^{10}$ N/m^2, $C_{13}^E=8.0\times10^{10}$ N/m^2, $C_{33}^E=13.6\times10^{10}$ N/m^2, $\gamma=7.21\times10^3$ kg/m^3, $e_{31}=-7.9$ C/m^2, $e_{33}=17.7$ C/m^2, $d_{33}=2.86\times10^{-10}$ C/N, $\varepsilon_{33}^s=1.280\varepsilon_0$, where $\varepsilon_0=8.84\times10^{-12}$ F/m is the dielectric permittivity of vacuum [these parameters correspond to the characteristics of material TsTBS-3 (Ref. 17)] and the acoustic medium: $c=1.5\times10^3$ m/s and $\rho=10^3$ kg/m^3 (water). The calculation accuracy was controlled by varying the time interval Δt steps. Thus, the difference of the extreme values of the required physical characteristics of the transient process, when $\Delta t=1/500$ and $\Delta t=1/1000$, did not exceed 1%.

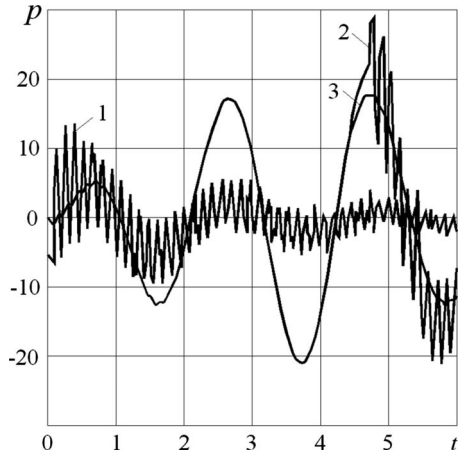

FIG. 2. Hydrodynamic pressure p on the cylindrical radiator surface $r=R_1$, where $\omega_0=3$; $\lambda_L=\lambda_C=\lambda_R=0$ (the oscillating radiator is absent), $\varepsilon(t)=1$ (Curve 1), $\varepsilon(t)=\sin(\omega_0 t)H(T_0-t)$, $T_0=4.7$ (Curve 2), and $T_0=4.2$ (Curve 3).

Curves in Fig. 2 are pressures $p|_{r=R_1}$ when the cylinder is actuated by electric signal of step electric impulse $\varepsilon(t)=H(t)$ (curve 1) and by electric signal of sinusoidal form $\varepsilon(t)=\sin(\omega_0 t)\cdot H(T_0-t)$, where $H(t)$ is the Heaviside function, T_0 is impulse duration, and $\omega_0=3$ corresponds to the radiator oscillating frequency. Thus for the second case during time space $0<t<T_0$, amplitude of the pressure on outsides cylinder surfaces increases. After stopping actuating of the cylinder by the external signal ($t>T_0$), amplitude decreases. Figures 3 and 4 illustrate the results of calculations $u_r|_{r=R_1}$ and $p|_{r=R_1}$, obtained when the potential difference $\varepsilon(t)=1$ was set across the input terminals of the conducting circuit that includes inductance ($\lambda_C=0$ and $\lambda_R=0$). Note that the radiator has the form of a cylindrical capacitor. Its dimensionless static (in the nondeformed state) capacitance is C_{st}

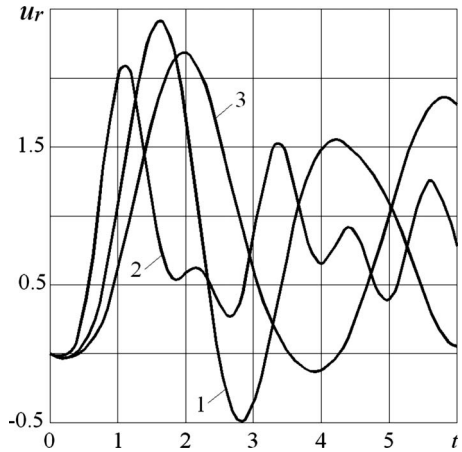

FIG. 3. Displacement u_r of the cylindrical radiator surface $r=R_1$, where $\varepsilon(t)=1$, $\lambda_C=\lambda_R=0$, and $\lambda_L=0.001$ (Curve 1), $\lambda_L=0.004$ (Curve 2), and $\lambda_L=0.008$ (Curve 3).

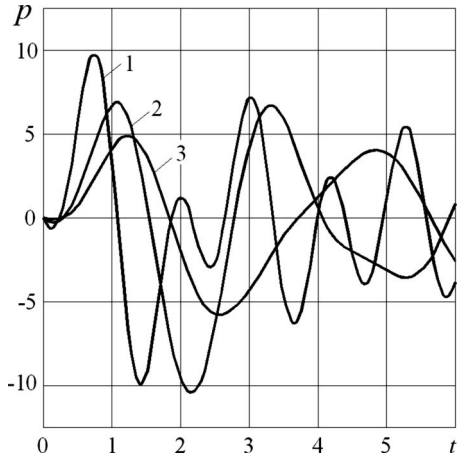

FIG. 4. Hydrodynamic pressure p on the cylindrical radiator surface $r=R_1$, where $\varepsilon(t)=1$, $\lambda_C=\lambda_R=0$, and $\lambda_L=0.001$ (Curve 1), $\lambda_L=0.004$ (Curve 2), and $\lambda_L=0.008$ (Curve 3).

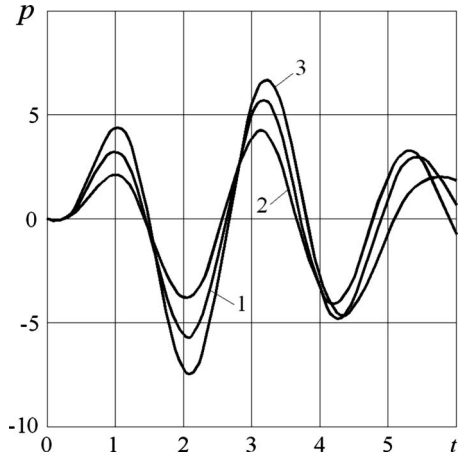

FIG. 6. Hydrodynamic pressure p on the cylindrical radiator surface ($r=R_1$), where $\varepsilon(t)=1$, $\lambda_R=0$ and $\lambda_C=0.035$, $\lambda_L=0.008$ (Curve 1), $\lambda_C=0.07$, $\lambda_L=0.012$ (Curve 2), and $\lambda_C=0.0175$, $\lambda_L=0.006$ (Curve 3).

$=2\pi/\ln(R_1/R_2)$. That is why the value of dimensionless inductance L^* was selected from the condition $1/\sqrt{L^*C_{\text{st}}}=\omega_0$. When this condition ($\lambda_L=0.004$ when the electric current amplitude reaches its maximum) is satisfied, the resonance frequency of the series circuit including capacitance C_{st} and inductance L^* coincides with the frequency ω_0. Figure 5 is the potential difference between the cylinder electrodes vs time dependence for this case. The diagrams above present the results of calculations for $\lambda_L=0.004$ (Curve 1) and also, for comparison, when $\lambda_L=0.001$ (Curve 2) and $\lambda_L=0.008$ (Curve 3). Figure 6 shows the time behavior of $p|_{r=R_1}$ when the conducting circuit has a capacitance and an inductance ($\lambda_R=0$) with the following initial parameters: $\lambda_C=1/C_{\text{st}}=0.035$ ($C^*=C_{\text{st}}$), $\lambda_L=0.008$ (Curve 1); $\lambda_C=2/C_{\text{st}}=0.07$, $\lambda_L=0.012$ (Curve 2) and $\lambda_C=1/(2C_{\text{st}})=0.0175$, $\lambda_L=0.006$ (Curve 3); $\varepsilon(t)=1$. Parameter λ_L was found on the condition that the resonance frequency of the oscillating circuit equals ω_0. Figure 7 shows the pressure $p|_{r=R_1}$ for the case of the input sinusoidal electric impulse $[\varepsilon(t)=\sin(\omega_0 t)H(T_0-t)]$. The parameters of the oscillation circuit ($\lambda_R=0$) were chosen as follows: $\lambda_C=0.035$ and $\lambda_L=0.008$ for Curve 1 ($T_0=4.7$) and Curve 2 ($T_0=4.2$); $\lambda_C=0.07$ and $\lambda_L=0.012$ for Curve 3 ($T_0=4.7$) and Curve 4 ($T_0=4.2$); $\lambda_C=0.0175$ and $\lambda_L=0.006$ for Curve 5 ($T_0=4.7$) and Curve 6 ($T_0=4.2$). Considering that resistor R^* affects only the amplitudes of the design volumes, this element was not taken into account ($\lambda_R=0$).

The calculations have demonstrated that when a step electric impulse is applied to the conducting coatings of the cylinder, the abrupt change in the potential difference across the electrodes excites elastic waves with large gradients. These waves are iteratively reflected from the boundary surfaces ($r=R_1$ and $r=R_2$) (Fig. 2, Curve 1). A similar phenomenon occurs after the sinusoidal impulse termination with the $T_0=4.7$ length (Curve 2). In this case the potential difference $\varepsilon(t)$ at the moment of time $t=4.7$ changes abruptly from 1 to 0. For $T_0=4.2$ $\varepsilon(t)|_{t=T_0}=0$ and there are no sharp increases in pressure $p|_{r=R_1}$ for $t>T_0$ (Fig. 2, Curve 3). These results show that choice of the electrical signal duration can appreciably influence on variation in time radiated by cylinder acoustic waves. The conducting circuit with an inductance (Fig. 5) significantly alters the form of the electric impulse

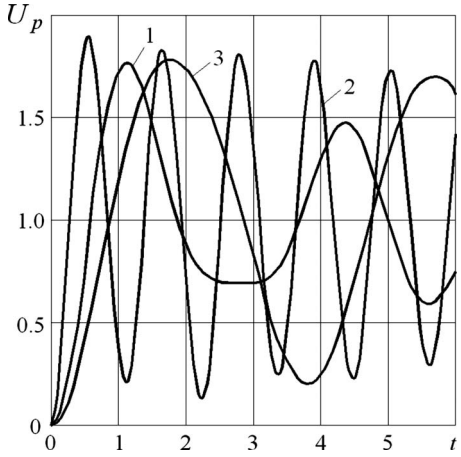

FIG. 5. Potential difference across the electrodes of the cylindrical radiator, where $\varepsilon(t)=1$, $\lambda_C=\lambda_R=0$, and $\lambda_L=0.001$ (Curve 1), $\lambda_L=0.004$ (Curve 2), and $\lambda_L=0.008$ (Curve 3).

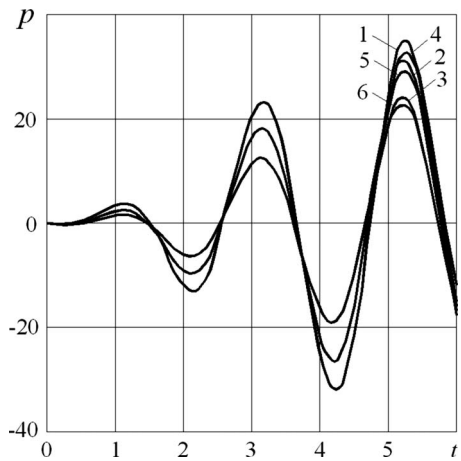

FIG. 7. Hydrodynamic pressure p on the cylindrical radiator surface ($r=R_1$), where $\varepsilon(t)=\sin(\omega_0 t)H(T_0-t)$, $\omega_0=3$, $\lambda_R=0$, and $\lambda_C=0.035$, $\lambda_L=0.008$, $T_0=4.7$ (Curve 1); $\lambda_C=0.035$, $\lambda_L=0.008$, $T_0=4.2$ (Curve 2); $\lambda_C=0.07$, $\lambda_L=0.012$, $T_0=4.7$ (Curve 3); $\lambda_C=0.07$, $\lambda_L=0.012$, $T_0=4.2$ (Curve 4); $\lambda_C=0.0175$, $\lambda_L=0.006$, $T_0=4.7$ (Curve 5); $\lambda_C=0.0175$, $\lambda_L=0.006$, $T_0=4.2$ (Curve 6).

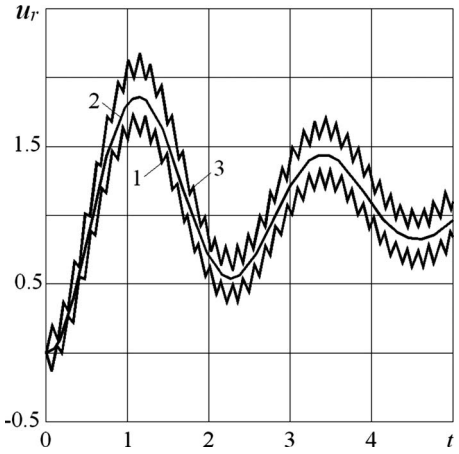

FIG. 8. Radial displacements u_r in points $r=R_1$ (Curve 1), $r=R_2$ (Curve 3), and $r=(R_1+R_2)/2$ (Curve 2) to result verification.

between the electrodes of the transducer as compared to the initial one $\varepsilon(t)=1$. This results in actual elimination of high-frequency oscillations u_r and in sharp changes of p (Figs. 3 and 4). The time dependence of displacements and pressures has an oscillating nature characterized by a relatively low frequency that rises with increasing parameter λ_L. If the parameters of the oscillating circuit with a capacitance and inductance are chosen so that its resonance frequency with account of the static capacitance of the electroelastic cylinder is equal to ω_0, by varying λ_L and λ_C, the pressure amplitudes in the emitted wave may be changed, when $\varepsilon(t)=1$ (Fig. 6) and when $\varepsilon(t)=\sin(\omega_0 t)H(T_0-t)$ (Fig. 7). After termination of the impulse with the duration $T_0=4.7$, when function $\varepsilon(t)$ has a step and $T_0=4.2$, when it is absent, the curves $p|_{r=R_1}$ differ insignificantly (Fig. 7). In summary, note that the solution method developed is applicable when the cylindrical piezoelectric converter is connected to a source of electric impulses with a parallel oscillating circuit and also when the elements of a wire line are extended. Besides, this method allows for calculations with an electric impulse of practically any shape.

To estimate the reliability of results, a comparison of the radial displacements u_r has been executed. Values of u_r were calculated by the method presented in the manuscript and the finite element analysis realized in complex ANSYS. Results of specified calculations practically coincide and they are shown in Fig. 8 where Curve 1 designates function u_r in point $r=R_1$, Curve 3 designates u_r in point R_2, and Curve 2 designates in $(R_1+R_2)/2$, in case of the cylinder loading by a step electric impulse $\varepsilon(t)=H(t)$ and oscillating circuit absence.

APPENDIX A: THE ORIGINALS OF FUNCTIONS g_*^L AND f_*^L

$$g_{0\nu}(t,z)=\frac{\mathrm{ch}(\nu\,\mathrm{arcch}((t+z)/z))}{z\sqrt{((t+z)/z)^2-1}},$$

$$g_{1\nu}(t,z)=\frac{1}{\nu}\mathrm{sh}\left(\nu\,\mathrm{arcch}\frac{t+z}{z}\right),$$

$$f_{0\nu}(t,z)=\frac{\cos(\nu\arccos((z-t)/z))}{\pi z\sqrt{1-((z-t)/z)^2}}H(2z-t)-\frac{\sin(\nu\pi)}{\pi}\frac{e^{-\nu\,\mathrm{arcch}(t-z)/z}}{z\sqrt{((t-z)/z)^2-1}}H(t-2z),$$

$$f_{1\nu}(t,z)=\frac{\sin(\nu\arccos((z-t)/z))}{\nu\pi}H(2z-t)+\frac{\sin(\nu\pi)}{\nu\pi}e^{-\nu\,\mathrm{arcch}(t-z)/z}H(t-2z).$$

APPENDIX B: THE ORIGINALS OF FUNCTIONS V^L AND W^L

$$V(t,z)=\frac{\sin\left(\nu\arccos\frac{z-t}{z}\right)}{\nu\pi(z-t)}H(z-\lambda R_2-t)+\frac{\sin\left(\nu\arccos\frac{z-t}{z}\right)-\sin\left(\nu\arccos\frac{z-t}{\lambda R_2}\right)}{\nu\pi(z-t)}\times H(t-z+\lambda R_2)H(z+\lambda R_2-t)+\left[\frac{\sin(\nu\arccos(z-t)/z)}{\nu\pi(z-t)}+\frac{\sin(\nu\pi)}{\nu\pi}\frac{e^{-\nu\,\mathrm{arcch}(t-z)/\lambda R_2}}{t-z}\right]H(t-z-\lambda R_2)H(2z-t)+\frac{\sin(\nu\pi)}{\nu\pi}\frac{e^{-\nu\,\mathrm{arcch}(t-z)/\lambda R_2}-e^{-\nu\,\mathrm{arcch}(t-z)/z}}{t-z}H(t-2z),$$

$$V(t,z)|_{t=z}=\frac{\cos(\nu\pi/2)}{\pi}\frac{z-\lambda R_2}{z\lambda R_2},$$

$$W(t,z)=\frac{sh\left(\nu\,\mathrm{arcch}\frac{t+z}{z}\right)}{\nu(t+z)}H(\lambda R_1-z-t)+\frac{sh\left(\nu\,\mathrm{arcch}\frac{t+z}{z}\right)-sh\left(\nu\,\mathrm{arcch}\frac{t+z}{\lambda R_1}\right)}{\nu(t+z)}H(t-\lambda R_1+z).$$

[1] T. Oishi, B. Aronov, and D. Browna, "Broadband multimode baffled piezoelectric cylindrical shell transducers," J. Acoust. Soc. Am. **121**, 3465–3471 (2007).

[2] M. Lematre, G. Feuillard, E. Clezio, and M. Lethiecq, "Modeling of the influence of a prestress gradient on guided wave propagation in piezoelectric structures," J. Acoust. Soc. Am. **120**, 1964–1975 (2006).

[3] I. Kirichok and T. Karnaukhova, "Resonant vibration and dissipative heating of an infinite-piezoceramic cylinder," Int. Appl. Mech. **41**, 309–314 (2005).

[4] A. Babaev, *Transient Waves in Continuums with a System of Reflecting Surfaces* (Naukova Dumka, Kyiv, 1990).

[5] A. Guz, V. Kubenko, and A. Babaev, "Dynamics of the system of shells interacting with a liquid," Int. Appl. Mech. **38**, 260–301 (2002).

[6] N. Shul'ga and L. Grigorieva, "Method of characteristics in analysis of the propagation of electroelastic thickness oscillations in a piezoceramic layer under electric excitation," Int. Appl. Mech. **44**, 1093–1097 (2008).

[7]N. Shul'ga and L. Grigorieva, "Propagation of two-dimensional nonstationary vibrations in an electrically excited piezoceramic prismatic body," Int. Appl. Mech. **44**, 1258–1264 (2008).
[8]H. Ding, H. Wang, and P. Hou, "The transient responses of piezoelectric hollow cylinders for axisymmetric plane strain problems," Int. J. Solids Struct. **40**, 105–123 (2003).
[9]H. Wang, H. Ding, and Y. Chen, "Dynamic solution of a multilayered orthotropic piezoelectric hollow cylinder for axisymmetric plane strain problems," Int. J. Solids Struct. **42**, 85–102 (2005).
[10]A. Babaev, V. Savin, and A. Leiko, "Transient interaction of parallel thin-wall cylindrical piezoelectric ceramic radiators," J. Acoust. Soc. Am. **108**, 157–166 (2000).
[11]A. Babaev and L. Dokuchaeva, "Emission of nonstationary waves by the spherical piezo-converter filled with viscous and surrounded by ideal compressible liquids," Int. Appl. Mech. **38**, 477–484 (2002).
[12]V. Kubenko and A. Babaev, "Influence of a cable line on the transient operation of a piezoelectric transmitter," Int. Appl. Mech. **33**, 888–894 (1997).
[13]A. Babaev, "Excitation of a spherical piezoemitter which generates nonsteady electric signals with allowance for processes in the cable channel," Int. Appl. Mech. **35**, 145–151 (1999).
[14]A. Babaev, "Nonsteady operating conditions of a multimode cylindrical radiator, taking account of processes in the cable channel," Int. Appl. Mech. **35**, 784–793 (1999).
[15]V. Grinchenko, A. Ulitko, and N. Shul'ga, *Electroelasticity*, Mechanics of Coupled Fields in Structural Elements (Naukova Dumka, Kyiv, 1989).
[16]V. Ditkin and A. Prudnikov, *Handbook on Operational Calculus* (Vysshaya Shkola, Moscow, 1965).
[17]*Piezoelectric Ceramic Transducer*, edited by S. Pugachov (Sudostroenie, Leningrad, 1984).

Radiation impedance of condenser microphones and their diffuse-field responses[a)]

Salvador Barrera-Figueroa[b)] and Knud Rasmussen
Danish Fundamental Metrology, Danish Primary Laboratory of Acoustics, Matematiktorvet 307, 2800 Kongens Lyngby, Denmark

Finn Jacobsen
Acoustic Technology, Department of Electrical Engineering, Technical University of Denmark, Ørsteds Plads 352, 2800 Kongens Lyngby, Denmark

(Received 3 August 2009; revised 8 February 2010; accepted 9 February 2010)

The relation between the diffuse-field response and the radiation impedance of a microphone has been investigated. Such a relation can be derived from classical theory. The practical measurement of the radiation impedance requires (a) measuring the volume velocity of the membrane of the microphone and (b) measuring the pressure on the membrane of the microphone. The first measurement is carried out by means of laser vibrometry. The second measurement cannot be implemented in practice. However, the pressure on the membrane can be calculated numerically by means of the boundary element method. In this way, a hybrid estimate of the radiation impedance is obtained. The resulting estimate of the diffuse-field response is compared with experimental estimates of the diffuse-field response determined using reciprocity and the random-incidence method. The different estimates are in good agreement at frequencies below the resonance frequency of the microphone. Although the method may not be of great practical utility, it provides a useful validation of the estimates obtained by other means.
 [DOI: 10.1121/1.3353093]

PACS number(s): 43.38.Kb, 43.58.Bh, 43.58.Vb [AJZ] Pages: 2290–2294

I. INTRODUCTION

Measurement microphones are used in a diversity of acoustic environments: in couplers where uniform acoustic pressure prevails, in open spaces with nearly free-field conditions, and in rooms where nearly diffuse-field conditions occur. Typically, a microphone is calibrated under uniform pressure conditions either using a primary method such as reciprocity or by a secondary method such as comparison calibration or calibration with an electrostatic actuator. The free-field or diffuse-field sensitivity is determined with the aid of a correction that is typical for the type of microphone in question. More rarely a microphone is calibrated under free-field or diffuse-field conditions either using primary or secondary techniques.

Whereas pressure and free-field calibration are more or less well-established techniques at primary and secondary levels,[1] and a good deal of scientific development has been focused on such techniques, diffuse-field calibration on the other hand is a less frequently visited area. Diestel[2] established the fundamentals of diffuse-field reciprocity calibration. Nakajima[3] used the same fundamentals in a realization of the technique in a small reverberation room filled with nitrogen. More recently, Bietz and Vorländer[4] studied the possibility of performing simultaneous free-field and diffuse-field calibration using a time-selective technique. Barrera-Figueroa *et al.*[5] made some observations about the accuracy of the reciprocity estimate in a diffuse field due to the statistical characteristics of the sound field in a reverberant room.

Diffuse-field reciprocity calibration is a primary method that may not be suitable for all types of microphones. Secondary methods for determining the diffuse-field sensitivity have been also developed. The most widespread of these is the random-incidence technique. This is a relative or secondary method that can be applied to microphones and other devices such as sound level meters.[6–8] It is worth noting that the random-incidence response (also in general, free-field, and diffuse-field responses) can be determined relative to the true pressure response[6,7] or to the electrostatic actuator response.[8]

Shaw[9] suggested an alternative formulation based on the concept of radiation resistance. So far, no one has reported the use of this relation for determining the diffuse-field sensitivity of measurement microphones, probably because of the practical difficulties in measuring the velocity of the membrane of the microphone and the pressure on the surface of the membrane. However, it has recently been reported that it is possible to measure the velocity distribution of the microphone membrane with good accuracy and to use these measurements as boundary conditions in numerical calculations for determining microphone parameters, such as pressure response and acoustic centers. Although the underlying assumptions, mainly the need of having a reciprocal microphone with an exposed membrane, might limit the applica-

[a)]Portions of this paper were presented in "On the relation between the radiation impedance and the diffuse-field response of measurement microphones," Proceedings of the Inter-Noise 2008, Shanghai, China, October 2008.

[b)]Author to whom correspondence should be addressed. Electronic mail: sbf@dfm.dtu.dk

 0001-4966/2010/127(4)/2290/5/$25.00

tion of such a technique, its study is an interesting way of validating the other well-established techniques.[10,11]

In this paper, a relation between the diffuse-field response and the radiation resistance of a measurement microphone is derived. A hybrid numerical and experimental method is used to determine the radiation impedance from measurements of the velocity of the membrane of a condenser microphone by using it as a boundary condition in a formulation of the boundary element method (BEM). The results of the hybrid method are compared with the results from free-field reciprocity calibration and random-incidence measurements.

II. RELATION BETWEEN RADIATION IMPEDANCE AND DIFFUSE-FIELD RESPONSE

The diffuse-field response of a microphone is related to the sound power it emits when it is acting as a source. Diestel[2] defined such a relation between the power, P, and the diffuse-field sensitivity. Diestel considered the sound power radiated to a solid angle element by a reciprocal transducer acting as a source in a free field. He obtained a differential expression of the free-field response of the transducer to a wave coming in the direction of the solid angle element by combining the expressions of the sound power and the reciprocity parameter in a free field. Diestel then determined the squared diffuse-field response by integrating the square of the free-field response to sound waves coming from all directions (random-incidence). From Diestel's expression, one can obtain

$$P = (4\pi)\left(\frac{\rho f}{2}\right)^2\left(\frac{|i|^2/2}{\rho c}\right)M_d^2, \tag{1}$$

where M_d is the diffuse-field sensitivity, ρ is the density of air, f is the frequency, c is the speed of sound, and i is the complex current flowing through the terminals of the microphone.

If the microphone can be assumed to radiate sound like a monopole with a volume velocity q, then the sound power emitted by the microphone is[12]

$$P = \tfrac{1}{2}|q|^2\ \mathrm{Re}\{Z_{\mathrm{rad}}\}, \tag{2}$$

where the acoustic radiation impedance Z_{rad} is the ratio of the (complex) sound pressure averaged over the surface of the membrane of the microphone, S, to the volume velocity,

$$Z_{\mathrm{rad}} = \left(\frac{p_{\mathrm{av}}}{q}\right). \tag{3}$$

Note, however, that Eq. (2) is only valid if the pressure does not vary too much over the membrane, and this is probably only the case if all parts of the membrane essentially move in phase. Combining Eqs. (1) and (2), one obtains

$$M_d^2 = \frac{|q|^2}{|i|^2}\frac{c}{\pi\rho f^2}\mathrm{Re}\{Z_{\mathrm{rad}}\}. \tag{4}$$

Furthermore, recalling that the pressure sensitivity is defined as $M_p = -q/i$,[1,12] Eq. (4) can be rewritten as

$$\frac{M_d^2}{M_p^2} = \frac{c}{\pi\rho f^2 S}\mathrm{Re}\{Z_{\mathrm{rad}}\}. \tag{5}$$

The expression on the left-hand side of Eq. (5) is the diffuse-field factor. In logarithmic form, it is known as the diffuse-field correction:

$$C_d = 10\log_{10}\left(\frac{|M_d|^2}{|M_p|^2}\right). \tag{6}$$

The diffuse-field correction determined using the radiation resistance in combination with the pressure sensitivity can be compared with other methods, such as diffuse-field reciprocity and random-incidence calibration. Equation (5) is very similar to an expression determined by Shaw.[9]

At high frequencies there may be a phase lag between the velocity at the center of the membrane and near the rim corresponding to wave motion in the membrane.[11] Under such conditions, the pressure may vary significantly in amplitude and phase over the membrane, and then the validity of Eq. (2) is no longer obvious.

III. HYBRID NUMERICAL EXPERIMENTAL METHOD

In order to determine the radiation impedance of the microphone, a hybrid numerical and experimental method is introduced. The method is based on the use of the measured velocity of the membrane of the microphone in numerical calculations of the sound field. A more detailed description of the method, the experimental setup, and examples of its application can be found in Ref. 11. The method consists of three steps: (a) the velocity of the membrane of a microphone is measured using a laser vibrometer, (b) this measured velocity is used in a BEM model of a microphone as a boundary condition on the membrane of the microphone, and (c) the calculated sound field is used to determine the pressure distribution on the membrane of the microphone; other parameters such as the directivity index and the acoustic center of the microphone can also be obtained using the calculated sound field.[11]

A. Experimental setup

Some experiments have been carried out. The velocity of the membrane of a microphone was measured using a laser vibrometer Polytech type PDV-100. The microphone membrane was excited using a reciprocity apparatus Brüel & Kjær type 5998. The voltage on the terminals of the reference impedance on the transmitter unit Brüel & Kjær type ZE0796 and the output of the vibrometer were measured using a Brüel & Kjær "PULSE" analyzer. Figure 1 shows a block diagram of the measurement setup.

The signal used for exciting the microphone was pseudorandom noise with a bandwidth of 25.6 kHz and 6400 spectral lines. The laser vibrometer can measure up to a frequency of 24 kHz. Only 1 in. and $\frac{1}{2}$ in. Laboratory Standard microphones (LS1 and LS2, respectively) were examined.

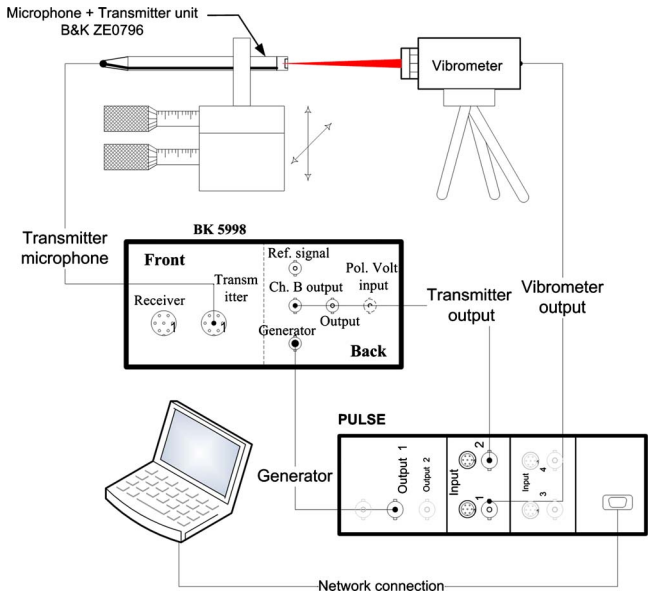

FIG. 1. (Color online) Block diagram of the measurement system.

B. BEM modeling

In the numerical modeling, the semi-infinite rod where the microphone is mounted was approximated by a cylindrical rod with a length of 60 cm with a hemispherical back-end. This will introduce a small disturbance in the simulated results because of reflections from the back of the rod. However, because of the length of the rod, they are expected to have small amplitude. The frequency range used in the calculations was from 1 to 20 kHz for LS1 microphones and from 2 to 21 kHz for LS2 microphones. The sizes of the smallest element in the axisymmetric mesh is 2.5 and 1.5 mm for LS1 and LS2 microphones, respectively. Thus, there were at least six elements per wavelength at the highest frequency.

In order to avoid the nonuniqueness problem, a random CHIEF point has been added in the interior of the geometry as described in Ref. 13, and the calculation has been checked by determining the condition numbers of the BEM matrices and by repeating calculations with small frequency shifts.[14]

In the problem at hand, the microphone acts as a sound source; thus, the radiation problem was solved by assigning the complex velocity measured with the vibrometer to the membrane of the microphone.

IV. DISCUSSION OF RESULTS

A. Movement of the membrane

Figures 2 and 3 show the velocity of the membrane of LS1 and LS2 microphones at different frequencies. It can be seen that in the two cases, the movement of the membrane below the resonance frequency follows the usual assumption, that is, the movement is parabolic. However, at frequencies above the resonance, the interaction between membrane, back-cavity, and air film between membrane and back-plate makes the membrane move in very particular shapes, different from any simple theoretical assumption.

It can also be observed that there is a phase lag at the center of the membrane with respect to the outer portions of the membrane and that the delay increases with the frequency. Thus, the membrane does not move uniformly back and forth in the whole frequency range, and this might have an effect on the determination of the radiation resistance of the microphone. However, it is only at very high frequencies for LS1 microphones (compared with their resonance fre-

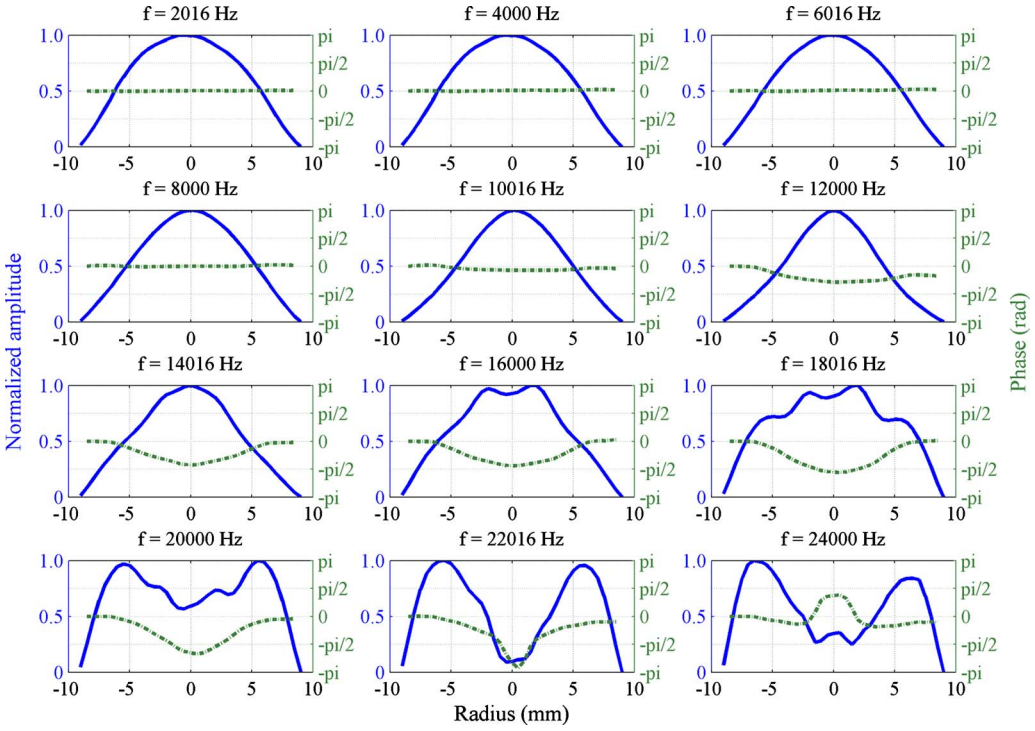

FIG. 2. (Color online) Normalized amplitude and phase of the velocity of the membrane of an LS1 microphone at several frequencies. Solid line: normalized amplitude; dash-dotted line: phase.

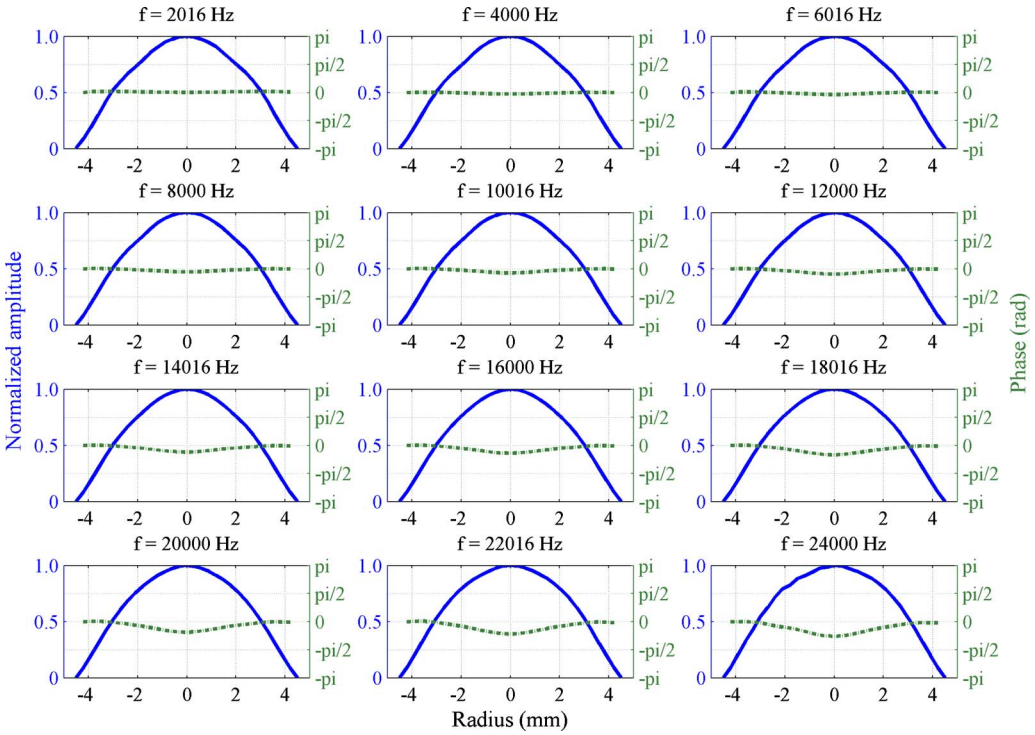

FIG. 3. (Color online) Normalized amplitude and phase of the velocity of the membrane of an LS2 microphone at several frequencies. Solid line: normalized amplitude; dash-dotted line: phase.

quency) that the phase lag becomes significantly large, introducing a clear wave movement on the membrane of the microphone. In the case of LS2 microphones, the wave motion is also present, but it can be regarded as negligible. This is because the upper frequency limit of the measurements is not sufficiently high compared with the resonance frequency of the microphone.

B. Radiation impedance and diffuse-field response of a microphone

Figures 4 and 5 show the diffuse-field correction of LS1 and LS2 microphones, respectively, determined using different methods: diffuse-field reciprocity, random incidence, and radiation impedance. In the last mentioned case, the correction was calculated using the radiation impedance determined using the measured velocity of the membrane of the microphone in the axisymmetric BEM formulation. The figures also show the difference between the individual estimates and an average of the three estimates.

Results of the diffuse-field sensitivity determined using reciprocity are only presented from 2 kHz for LS1 and LS2 microphones. The diffuse-field results at frequencies below 2 kHz for LS1 and below 3 kHz for LS2 microphones cannot be trusted. The estimate presents large deviations due to the time-selective procedure applied for separating the free-field and diffuse responses, and more specifically because of the roll-off frequencies of the passband filter used in the time-selective procedure. Details can be found in Ref. 5. Similarly, results of the random-incidence correction are only presented from 1 kHz for LS1 microphones and from 2 kHz for LS2 microphones. In this case, the values of the random-incidence correction are not reliable because of the application of the time-selective procedure described in Ref. 7. For the sake of clarity, the graph showing the difference between estimates for LS1 microphones shows only values above 2 kHz and 3 kHz for LS2 microphones.

It can be seen that the diffuse-field correction of LS1 microphones determined using the radiation resistance at low

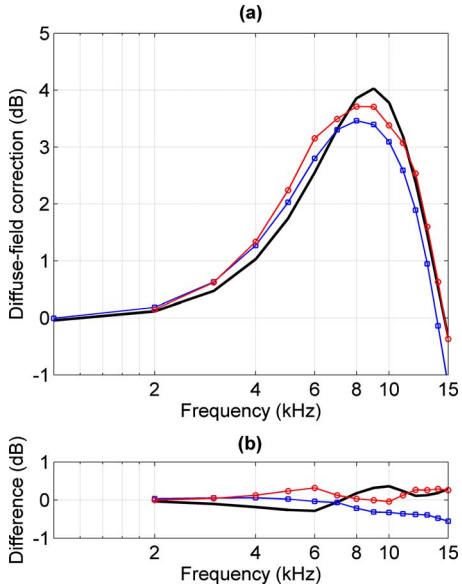

FIG. 4. (Color online) Diffuse-field correction for LS1 microphones: (a) modulus of the correction determined using different techniques and (b) difference between the individual estimates and the average of the three different techniques. In both graphs, the thick solid line is the diffuse-field correction determined from the radiation resistance, the line with circular markers is the diffuse-field correction determined using reciprocity from Ref. 5, and the line with square markers is the random-incidence correction from Ref. 7.

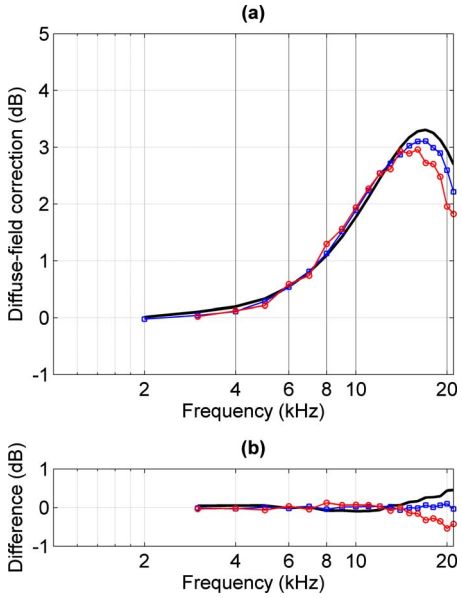

FIG. 5. (Color online) Diffuse-field correction for LS2 microphones: (a) modulus of the correction determined using different techniques and (b) difference between the individual estimates and the average of the three different techniques. In both graphs, the thick solid line is the diffuse-field correction determined from the radiation resistance, the line with circular markers is the diffuse-field correction determined using reciprocity from Ref. 5, and the line with square markers is the random-incidence correction from Ref. 7.

and midfrequencies (up to 7 kHz) is in reasonable agreement with the estimates obtained using the reciprocity and random-incidence techniques; the average difference between estimates is within 0.2 dB. Around the resonance frequency of the microphone (between 7 and 10 kHz), this agreement degrades. Above 10 kHz the agreement seems to improve again. The diffuse-field correction for LS1 microphones shown in Fig. 4 is not reliable above 15 kHz because the pressure sensitivity determined by reciprocity has reached its limits of applicability.

The behavior of the diffuse-field correction of LS2 microphones is very similar to the LS1 correction. At midfrequencies and up to 15 kHz, the agreement between the different estimates is good; the average difference between estimates is better than 0.1 dB. Above 15 kHz the agreement degrades, and the average difference takes values up to 0.5 dB.

The agreement between estimates at midfrequencies is much better for LS2 microphones than for LS1 microphones. A possible explanation for this behavior is that the assumption made in deriving Eq. (2), that either the velocity of the membrane or the sound pressure on the membrane do not vary too much over the surface of the membrane, is satisfied to a larger extent for LS2 than for LS1 microphones, because the surface of the membrane is larger and more compliant in the latter case. This gives rise to larger phase differences between the center of the membrane and the portions closer to the rim. There is no apparent reason why the diffuse-field response determined from the radiation impedance differs from the reciprocity and random-incidence estimates.

V. CONCLUSIONS

A relation between the radiation impedance and the diffuse-field response of a transducer has been derived. The validity of this relation is limited to sources with real-valued surface velocities.

The diffuse-field correction has been determined from the derived relation making use of a hybrid experimental-numerical method. The velocity of the membrane of LS1 and LS2 microphones has been measured with a laser vibrometer. This measured velocity was used in a BEM formulation for determining the radiation impedance. The results of the hybrid method are in good agreement with other realizations of the diffuse-field correction, namely, diffuse-field reciprocity and random-incidence measurements. Thus, this method can be used as a validation of the traditional methods.

Furthermore the hybrid method can also provide more reliable values of the diffuse-field correction at low frequencies where the traditional methods fail.

ACKNOWLEDGMENT

This project was carried out with the support of the Danish Agency for Science and Technology (FTP).

[1]International Standard IEC 61094 Parts 1–7 (International Electrotechnical Commission, Geneva, Switzerland).
[2]H. G. Diestel, "Reciprocity calibration of microphones in a diffuse sound field," J. Acoust. Soc. Am. **33**, 514–518 (1961).
[3]T. Nakajima, "Reciprocity calibration of laboratory standard microphones in a diffuse sound field," Researches of the Electrotechnical Laboratory **706**, 1–87 (1970) (in Japanese).
[4]M. Vorländer and H. Bietz, "Novel broad-band reciprocity technique for simultaneous free-field and diffuse-field microphone calibration," Acustica **80**, 365–377 (1994).
[5]S. Barrera-Figueroa, K. Rasmussen, and F. Jacobsen, "A note on determination of the diffuse-field sensitivity of microphones using the reciprocity technique," J. Acoust. Soc. Am. **124**, 1505–1512 (2008).
[6]"International Standard IEC 61183, Electroacoustics — Random-incidence and diffuse-field calibration of sound level meters (International Electrotechnical commission, Geneva, Switzerland, 1994)."
[7]S. Barrera-Figueroa, K. Rasmussen, and F. Jacobsen, "On experimental determination of the random-incidence response," J. Acoust. Soc. Am. **121**, 2628–2636 (2007).
[8]J. Gramtorp and E. Frederiksen, "Measurement of microphone random-incidence and pressure-field responses and determination of their uncertainties," Brüel & Kjær Technical Review **1**, 36–39 (2001).
[9]E. A. G. Shaw, "Diffuse field response, receiver impedance, and the acoustical reciprocity principle," J. Acoust. Soc. Am. **84**, 2284–2287 (1988).
[10]G. Behler and M. Vorländer, "Reciprocal measurements on condenser microphones for quality control and absolute calibration," Acta. Acust. Acust. **90**, 152–160 (2004).
[11]S. Barrera-Figueroa, F. Jacobsen, and K. Rasmussen, "Hybrid method for determining the parameters of condenser microphones from measured membrane velocities and numerical calculations," J. Acoust. Soc. Am. **126**, 1788–1795 (2009).
[12]A. D. Pierce, *Acoustics: An Introduction to Its Physical Principles and Applications* (Acoustical Society of America, Melville, NY, 1989).
[13]H. A. Schenck, "Improved integral formulation for acoustic radiation problems," J. Acoust. Soc. Am. **44**, 41–58 (1968).
[14]P. M. Juhl, F. Jacobsen, V. Cutanda, and S. Quiros-Alpera, "On the non-uniqueness problem in a 2-D half-space BEM formulation," in Proceedings of the 9th International Congress on Sound and Vibration, Orlando, FL (2002).

A generalization of the membrane-plate analogy to non-homogeneous polygonal domains consisting of homogeneous subdomains

Carlos P. Filipich
CIMTA, Universidad Tecnológica Nacional (FRBB) and Department of Engineering, Universidad Nacional del Sur, Alem 1253, 8000 Bahía Blanca, Argentina

Marta B. Rosales[a)]
Department of Engineering, Universidad Nacional del Sur and CONICET, Alem 1253, 8000 Bahía Blanca, Argentina

(Received 14 August 2009; revised 4 December 2009; accepted 3 February 2010)

The well-known membrane-plate analogy that relates the natural frequencies when dealing with polygonal homogeneous domains is herein extended to non-homogeneous systems comprised of homogeneous subdomains. The analogy is generalized and demonstrated and it is shown that certain restrictions among the frequency parameters of the membranes and plates arise. Several examples of membranes and plates with interfaces separating areas with different material properties are numerically solved with different approaches. The subdomains are separated by straight, curved, and closed line interfaces. It is shown that the analogy is verified provided that the restrictions are satisfied. The analogy is first demonstrated and presented as a practical methodology to find the natural frequencies of membranes knowing the corresponding ones of the plates or vice versa. Second, the plate and membrane vibration problems, governed by the bi-Laplacian and Laplacian differential operators, respectively, can be solved without distinction, though under certain conditions, i.e., solve one of them and deduce the other using the analogy. Various numerical examples validate the analogy. © *2010 Acoustical Society of America.* [DOI: 10.1121/1.3337222]

PACS number(s): 43.40.Dx [JAT] Pages: 2295–2300

I. INTRODUCTION

The *membrane-plate analogy* is known[1] for the problem of natural vibrations between simply supported plane plates and fixed membranes in homogeneous polygonal domains. Regarding the origin of the analogy, Timoshenko and Woinowsky-Krieger[2] referenced an earlier work of Marcus.[3] Also Conway and Farham[4] are frequently cited for his work on the vibration problem. On the other hand, the non-homogeneous membranes have received the attention of researches.[5–7] However, the above-mentioned analogy may be lost when some complexities are present, and extensions to it have been addressed by several authors, such as compression buckling, hygrothermal buckling, and vibration of sandwich plates,[8] laminated plates,[9] shallow shells,[10] intermediate partial supports,[11] or, as is the topic of this study, the consideration of non-homogeneous domains made of homogeneous subdomains.[12] Here, the original idea is extended to non-homogeneous domains (distributed in homogeneous regions). In particular, polygonal domains with various interfaces are tackled. Despite that the study deals with a theoretical demonstration, it also proposes a methodology of practical interest for non-homogeneous domains. Let us assume constant thickness h_0 (the dimension in the z direction) and accept that T_0 (force per unit of length) when used in the Helmholtz equation is uniform and the same for all the regions. That is, each region is made of a homogeneous material but, in general, with the following physical characteristics varying from region to region, i.e., mass density $\rho_j = \rho_0 r_j$, Young's modulus $E_j = E_0 e_j$, and Poisson's ratio $\nu_j = \nu_0 n_j$, where ρ_0, E_0, and ν_0 are arbitrary reference constants and ρ_j, E_j, and ν_j are constant within each region. A schematic drawing of a rectangular domain with one interface (two regions, I and II) is shown in Fig. 1, though obviously the number is arbitrary. The most general analogy that will be found in what follows includes, as a particular case, the classical one (homogeneous materials) and will yield the restrictions to be satisfied in order for the new analogy to be valid.

In short, the analogy object of the present study is within the following definition: The aim is to find a relationship among the mode shapes of the membrane v_j and plate w_j, where j denotes one of the homogeneous domains.

$$v_j = G_j(w_j), \tag{1}$$

in such way that some condition among the non-dimensional frequency parameters Ω of both systems (subscripts m and p stand for membrane and plate, respectively)

$$\Omega_p = g(\Omega_m) \tag{2}$$

exists. It can be shown below that one is led to additional restrictions that will be only verified for homogeneous domains. This approach is not shown herein for the sake of brevity. Alternatively, a more general expression will be proposed,

a)Author to whom correspondence should be addressed. Electronic mail: mrosales@criba.edu.ar

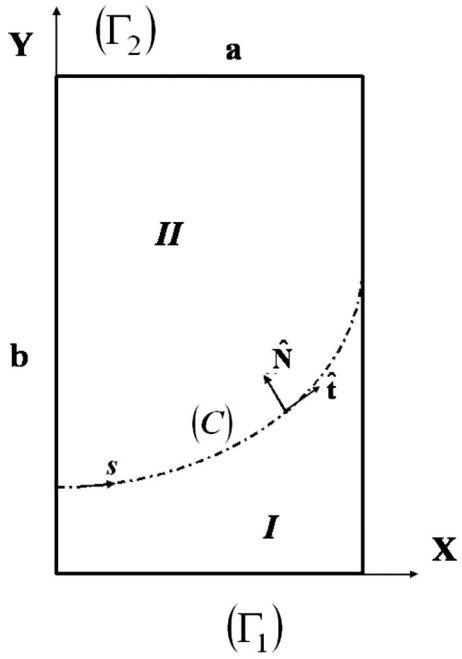

FIG. 1. Membrane configuration for the particular case of two regions.

$$v_j = \alpha_j \nabla^2 w_j + \beta_j w_j, \tag{3}$$

in which the constants α_j and β_j will be found provided that the boundary conditions (BCs) and the continuity conditions (CCs) are satisfied for membranes and find any $\Omega_p = g(\Omega_m)$. At the end, we will find the following relationship between membrane and plate non-dimensional frequency parameters:

$$\Omega_p = K\Omega_m^2, \tag{4}$$

in which K is a constant value that is found with the material properties involved in the problem.

Although not included, the analogy is also valid for the plate buckling of plates with uniform plane load.

II. GOVERNING EQUATIONS

The governing equation of the elastic, homogeneous, isotropic, vibrating plate (Germain–Lagrange)[2,13] with constant thickness h_0 in z direction is

$$\nabla^2(\nabla^2 w_j) - \Omega_p^2 f_j^2 w_j = 0, \tag{5}$$

where $w_j = w_j(X,Y)$ is the plate mode shape for each j region that should satisfy the BCs and the CCs at the interface. In what follows, and without loss of generality, it will be assumed that $j = \mathrm{I}, \mathrm{II}$. The adopted plate frequency parameter is

$$\Omega_p \equiv \sqrt{\frac{\rho_0 h_0}{D_0}}\omega_p a^2, \tag{6}$$

where ω_p are the circular natural frequencies of the whole plate, a is an arbitrary reference length, and the flexural rigidity D_0 writes

$$D_0 \equiv \frac{E_0 h_0^3}{12(1-\nu_0^2)} \tag{7}$$

and

$$f_j^2 \equiv \frac{r_j(1-\nu_0^2 n_j^2)}{e_j(1-\nu_0^2)}. \tag{8}$$

In turn, the differential equations governing the natural vibration of a homogeneous membrane of constant thickness h_0 under a constant force per unit of length T_0 (Helmholtz equation[14]) is

$$\nabla^2 v_j + \Omega_m^2 r_j v_j = 0, \tag{9}$$

where $v_j = v_j(X,Y)$ denotes the membrane mode shape of each region, which should satisfy the BCs on the boundaries and the CCs at the interface, and where the adopted membrane frequency parameter is

$$\Omega_m = \sqrt{\frac{\rho_0 h_0}{T_0}}\omega_m a, \tag{10}$$

where ω_m are the successive circular natural frequencies of the whole membrane. It is accepted, for the sake of simplicity, that both plates and membranes have the same mass distribution.

In this problem, the BCs are considered simply supported for the plate and fixed for the membrane. That is, with $j = \mathrm{I}, \mathrm{II}$ (see Fig. 1),

$$w_j(0,y) = w_j(a,y) = 0, \tag{11a}$$

$$\frac{\partial^2 w_j}{\partial x^2}(0,y) = \frac{\partial^2 w_j}{\partial x^2}(a,y) = 0, \tag{11b}$$

$$w_{\mathrm{I}}(x,0) = w_{\mathrm{II}}(x,b) = 0, \tag{11c}$$

$$\frac{\partial^2 w_{\mathrm{I}}}{\partial y^2}(x,0) = \frac{\partial^2 w_{\mathrm{II}}}{\partial y^2}(x,b) = 0. \tag{11d}$$

It is important to observe that, from BC (11), the following consequences yield

$$\nabla^2 w_j(0,y) = \nabla^2 w_j(a,y) = 0, \tag{12a}$$

$$\nabla^2 w_{\mathrm{I}}(x,0) = \nabla^2 w_{\mathrm{II}}(x,b) = 0. \tag{12b}$$

Equations (12a) and (12b) are derived from Eq. (11b). In turn, Eq. (12b) comes from Eq. (11d). Also

$$v_j(0,y) = v_j(a,y) = 0, \tag{13a}$$

$$v_{\mathrm{I}}(x,0) = v_{\mathrm{II}}(x,b) = 0. \tag{13b}$$

Now, with respect to the CCs that should hold over the interface, it is true that plates require two geometric (or essential) conditions to be fulfilled. They are related with the function w and the slope in the normal sense, $\partial w/\partial N$, and two force (or natural) conditions (bending moment M_N and the shear force V_N in the Nz plane). In the membrane case, two geometric conditions are to be imposed: function and slope in the normal direction.

A. Continuity condition for plane plates over interface $\mathcal{C}$ (Fig. 1)

The interface $\mathcal{C}$ limits the regions with different material properties. Let us recall[2,13] that a bending force M_N over an interface curve writes

$$M_N = -D\left[\nabla^2 w + (\nu - 1)\frac{\partial^2 w}{\partial t^2}\right], \tag{14}$$

and the total shear force V_N in the area element with normal N, parallel to z, is

$$V_N = -D\left[\frac{\partial}{\partial N}(\nabla^2 w) + (1-\nu)\frac{\partial^3 w}{\partial N\,\partial t^2}\right], \tag{15}$$

where

$$\nabla^2 w = \frac{\partial^2 w}{\partial x^2} + \frac{\partial^2 w}{\partial y^2} = \frac{\partial^2 w}{\partial N^2} + \frac{\partial^2 w}{\partial t^2}, \tag{16}$$

in which $\partial(\cdot)/\partial N$ and $\partial(\cdot)/\partial t$ are directional derivatives. The bending stiffness D in Eqs. (14) and (15) is, for each region of the plate,

$$D_j = \frac{E_j h_0^3}{12(1-\nu_j^2)} = \frac{r_j}{f_j^2} D_0. \tag{17}$$

Then, the four CCs over the interface are given as follows.

- Function:

$$(w_{\mathrm{I}})_{(\mathcal{C})} = (w_{\mathrm{II}})_{(\mathcal{C})} (\equiv w^*). \tag{18a}$$

- Slope with respect to normal direction:

$$\left(\frac{\partial w_{\mathrm{I}}}{\partial N}\right)_{(\mathcal{C})} = \left(\frac{\partial w_{\mathrm{II}}}{\partial N}\right)_{(\mathcal{C})} \left(\equiv \frac{\partial w^*}{\partial N}\right). \tag{18b}$$

- Bending moment:

$$(D_{\mathrm{I}}\nabla^2 w_{\mathrm{I}})_{(\mathcal{C})} - (D_{\mathrm{II}}\nabla^2 w_{\mathrm{II}})_{(\mathcal{C})} = -[D_{\mathrm{I}}(\nu_{\mathrm{I}} - 1) - D_{\mathrm{II}}(\nu_{\mathrm{II}} - 1)]\frac{\partial^2 w^*}{\partial t^2}. \tag{18c}$$

- Shear in plane tz:

$$\left(D_{\mathrm{I}}\frac{\partial(\nabla^2 w_{\mathrm{I}})}{\partial N}\right)_{(\mathcal{C})} - \left(D_{\mathrm{II}}\frac{\partial(\nabla^2 w_{\mathrm{II}})}{\partial N}\right)_{(\mathcal{C})} = -[D_{\mathrm{I}}(1-\nu_{\mathrm{I}}) - D_{\mathrm{II}}(1-\nu_{\mathrm{II}})]\frac{\partial^3 w^*}{\partial N\,\partial t^2}. \tag{18d}$$

The definitions using $w^* = w^*(s)$ and its derivatives are just a simplifying notation.

B. Continuity condition for membranes over $\mathcal{C}$

The CCs and its consequences over the interface write the following.

- Function:

$$(v_{\mathrm{I}})_{(\mathcal{C})} = (v_{\mathrm{II}})_{(\mathcal{C})}. \tag{19a}$$

- Slope along N:

$$\left(\frac{\partial v_{\mathrm{I}}}{\partial N}\right)_{(\mathcal{C})} = \left(\frac{\partial v_{\mathrm{II}}}{\partial N}\right)_{(\mathcal{C})}. \tag{19b}$$

III. STATEMENT OF AN ANALOGY

In what follows the analogy proposed in the Introduction is stated and demonstrated. As mentioned before, the analogy that is object of the present study is within the following definition (that includes the well-known analogy valid for homogeneous polygonal domains as a particular case): Find a relationship among the membrane and plate mode shapes

$$v_j = G_j(w_j), \tag{20}$$

in such way that some condition among the frequencies of both systems

$$\Omega_p = g(\Omega_m) \tag{21}$$

exists. A second approach (inversely to the first one) would perhaps be possible; that is, the proposition of a functional relationship among frequencies and then, the derivation of the link between the mode shapes. Here the first approach is followed.

In order to start the search, let us rewrite Eq. (5) in the following format (recall that each f_j is constant):

$$\nabla^2(\nabla^2 w_j - \Omega_p f_j w_j) + \Omega_p f_j(\nabla^2 w_j - \Omega_p f_j w_j) = 0. \tag{22}$$

By simple observation $G_j(\cdot)$ [from Eq. (20)] may be selected as

$$v_j = G_j(w_j) \equiv \nabla^2 w_j - \Omega_p f_j w_j. \tag{23}$$

This is no more that the classical relationship extended to non-homogeneous domains. To start with a proposition similar to the classical analogy was the motivation of the present approach. It was be shown (not included herein) that it conduces to additional restrictions that will only be verified for homogeneous domains. Thus a more general expression will have to be used,

$$v_j = \alpha_j \nabla^2 w_j + \beta_j w_j, \tag{24}$$

in which the constants α_j and β_j will be found provided that the BCs and CCs are satisfied for membranes and find any $\Omega_p = g(\Omega_m)$. Particularly, if $\alpha_j = 1$ and $\beta_j = -\Omega_p f_j$, we obtain Eq. (23). Equation (23) would lead to the conclusion that it is only verified by homogenous domain cases. The need of a more complex relationship among the membrane and plate mode shapes [Eq. (24)] becomes apparent (Sec. III A).

A. Generalization of the analogy

A more general $G_j(w_j)$ is introduced in Eq. (24); i.e., $v_j = \alpha_j \nabla^2 w_j + \beta_j w_j$. The constants α_j and β_j will be found satisfying the BCs and CCs for membranes and with the aim of finding any $\Omega_p = g(\Omega_m)$. With relationship (24) and Eq. (5), Eq. (9) yields

$$(\beta_j + \alpha_j \Omega_m^2 r_j)\nabla^2 w_j + (\alpha_j \Omega_p^2 f_j^2 + \beta_j \Omega_m^2 r_j) w_j = 0. \tag{25}$$

These Helmholtz equations for each plate mode shape w_j are not—in general—satisfied. The only simultaneous conditions to identically verify Eq. (25) are

$$\beta_j + \alpha_j \Omega_m^2 r_j = 0, \tag{26a}$$

$$\alpha_j \Omega_p^2 f_j^2 + \beta_j \Omega_m^2 r_j = 0, \tag{26b}$$

from which and for each j the following results:

$$\beta_j = -\alpha_j \Omega_m^2 r_j, \tag{27a}$$

$$\Rightarrow \alpha_j (\Omega_p^2 f_j^2 - \Omega_m^4 r_j^2) = 0. \tag{27b}$$

In order for Eq. (27b) to be satisfied, it only remains that [if $\alpha_j=0$ due to Eq. (27a) $\Rightarrow \beta_j=0 \Rightarrow$ and due to Eq. (24) $v_j \equiv 0$]

$$\alpha_j \neq 0, \tag{28a}$$

$$\Omega_p = \Omega_m^2 \frac{r_j}{f_j}, \tag{28b}$$

since Ω_p, Ω_m, r_j, and f_j are essentially positive. As before, we find a possible function $g(\cdot)$, but a first additional restriction should be verified as

$$r_I f_{II} = r_{II} f_I \Rightarrow \frac{r}{f} = \text{const}, \tag{29}$$

in order for the frequencies to be region independent. Then, the frequencies relationship may be written as

$$\Omega_p = \Omega_m^2 \frac{r_I}{f_I} = \Omega_m^2 \frac{r_{II}}{f_{II}} = \Omega_m^2 \frac{r}{f}. \tag{30}$$

In this case the α_j's remain free and Eq. (24) with Eq. (27a) may be written as follows:

$$v_j = G_j(w_j) = \alpha_j (\nabla^2 w_j - \Omega_m^2 r_j w_j). \tag{31}$$

Let us now impose for $v_j=G_j(w_j)$ the BCs and the CCs for the membrane [taking also into account the plate BCs—recall Eqs. (11a), (11b), (12a), and (12b)]. First, we will analyze the CCs. Making use of Eq. (31) we impose Eqs. (19a) and (19b), taking into account Eq. (18a) and their consequences,

$$(\alpha_I \nabla^2 w_I)_{(C)} - (\alpha_{II} \nabla^2 w_{II})_{(C)} = \Omega_m^2 (\alpha_I r_I - \alpha_{II} r_{II}) w^*, \tag{32a}$$

$$\left(\alpha_I \frac{\partial \nabla^2 w_I}{\partial N}\right)_{(C)} - \left(\alpha_{II} \frac{\partial \nabla^2 w_{II}}{\partial N}\right)_{(C)} = \Omega_m^2 (\alpha_I r_I - \alpha_{II} r_{II}) \frac{\partial w^*}{\partial N}. \tag{32b}$$

After comparing Eq. (32) with Eqs. (18c) and (18d), the following restrictions are mandatory. They avoid incoherences and, on the other hand, lead to the simpler and most direct conditions.

$$\alpha_I r_I - \alpha_{II} r_{II} = 0, \tag{33a}$$

$$\alpha_j = C D_j, \tag{33b}$$

$$D_I (1 - \nu_I) - D_{II} (1 - \nu_{II}) = 0, \tag{33c}$$

where C is an arbitrary constant. These restrictions must be added to Eq. (29). However, and due to Eq. (33b), it may be deduced that Eq. (33a) is equivalent to Eq. (29). In effect the use of Eqs. (17) and (33b) leads us to this conclusion. On the other hand after taking into account Eq. (33a), Eq. (33c) may be written as

$$r_{II}(1 - \nu_I) = r_I (1 - \nu_{II}) \Rightarrow \frac{r}{1 - \nu} = \text{const}. \tag{34}$$

Moreover, with this relationship and Eq. (29) and recalling Eq. (8), the following result is found:

$$e_{II}(1 + \nu_I) = e_I (1 + \nu_{II}). \tag{35}$$

Then, if, for instance, we choose

$$r_{II} = k r_I (\Rightarrow f_{II} = k f_I), \tag{36}$$

k should be real and positive for real materials. Equation (34) automatically defines the following relationship:

$$(1 - \nu_{II}) = k (1 - \nu_I). \tag{37}$$

There are infinite possibilities of choosing the ν_j's (and not necessarily between 0 and 0.5, as is required in lineal elasticity). Furthermore, due to Eq. (35), a relation among the e_j is obtained.

$$e_{II} = \frac{2 - k(1 - \nu_I)}{(1 + \nu_I)} e_I. \tag{38}$$

Summing up, the present proposition (24) consisted in linking each membrane mode shape v_j as a linear combination of the plate mode shape and its Laplacian for each region. With this proposition, an analogy for non-homogeneous domains composed of homogeneous subdomains is found, with restrictions [Eqs. (29) and (34)]. This analogy works in the following way: *One* real or fictitious system is solved in order to find frequencies and mode shapes of *other* real system.

Obviously, the above presented analogy includes the classical one, i.e., when $r_I=r_{II}$, $f_I=f_{II}$, and $\nu_I=\nu_{II}$ (i.e., $\alpha_j=1$).

The analogy is valid for all orders of frequencies and for an arbitrary number of regions. Successive relationships such as Eqs. (29) and (34) must be employed for each region when more than two regions are present. At present, the authors cannot assert the uniqueness of an analogy of this type; i.e., no guarantee can be provided that other analogies do not exist.

IV. EXAMPLES

In this section various numerical examples illustrate the analogy between plates and membranes with non-homogeneous domains with homogeneous subdomains. The necessary conditions have to be fulfilled in each case. Some cases are two-way statements but others are only in one way; i.e., a fictitious plate serves to find the natural frequencies of a real membrane (see example 1c below). Figure 2 shows the five different solved configurations: a rectangular/square plate/membrane with two regions separated by either a straight line parallel to one of the boundaries, an inclined straight line, a curved line, and a closed line (i.e., a closed region inside another one). Finally a non-rectangular domain was studied: a triangular plate/membrane with three regions separated by lines parallel to one side.

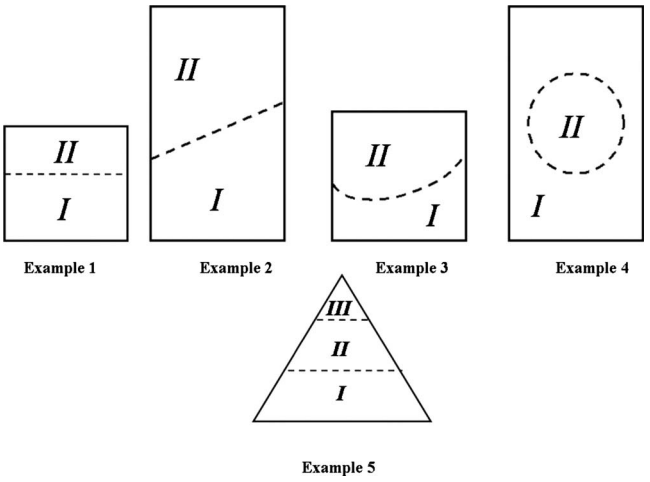

FIG. 2. Numerical examples. Schemes of the non-homogeneous domains.

The first group of numerical examples deals with a square shaped membrane/plate with two regions separated by a straight line parallel to one side. If X and Y are the axes located at the left inferior corner, the line is $Y=0.6a$, in which $0 \leq X \leq a$, $a=1$ (side of the square). Three different illustrations are presented in this case (examples 1a, 1b, and 1c). In all cases, the reference properties are $\nu_0=0.3$, E_0, and ρ_0, and the parameter values are depicted in Table I. As can be observed, conditions (29) and (34) are verified. The plate frequencies were found with the finite element software ALGOR (Ref. 15) for cases 1a and 1b. The well-known Levy solution[2] was employed to solve the vibration plate problem for case 1c and the membrane frequencies were found solving Eq. (9) with FLEXPDE.[16] The frequencies of the plates and the membranes were numerically found and compared in Table II. The error was calculated in all the examples with the following expression:

$$\epsilon\% = 100\left[\frac{r\Omega_m^2}{f\Omega_p} - 1\right]. \tag{39}$$

The following three examples deal with rectangular or square shapes with other interfaces. First a rectangular membrane/plate with two regions separated by an inclined straight line ($Y=0.3X+0.7$) is addressed (axes X and Y are located at the left inferior corner) (example 2). The sides of the rectangle are $a=1$ (X direction) and $b=1.8$ (Y direction). In this case $\nu_0=0.5$, $r_{\mathrm{I}}=1$, $e_{\mathrm{I}}=1$, $n_{\mathrm{I}}=1$, $r_{\mathrm{II}}=2$, $e_{\mathrm{II}}=2/3$, $n_{\mathrm{II}}=0$, $f_{\mathrm{I}}=1$, $f_{\mathrm{II}}=2$, and $\Omega_m^2/\Omega_p=f/r=1$. The membrane frequencies Ω_m were found using a trigonometric series approach as reported in a previous paper by the authors.[12] The plate frequencies Ω_p were found with ALGOR.[15] Next, the case of two regions separated by a curved interface $Y=0.8X^2-0.5X+0.4$ was tackled (the same data hold for the other properties) (example 3). In the membrane case, Eq. (9) was solved straightforwardly with FLEXPDE.[16] The plate frequencies were found also with FLEXPDE after rewriting Eq. (5) into two coupled membrane equations and the appropriate boundary conditions. This is necessary since this finite element software handles up to second order differential equations. A rectangular membrane/plate ($a=1$, $b=1.8$) with a region limited by a closed curve (a centered circumference of radius $R=0.4$) (example 4) was studied. Again both membrane and plates were solved with FLEXPDE. Table III contains the numerical values of the first three natural frequencies for the three cases.

TABLE I. Example 1. Data: parameters r_j, e_j, and n_j, and calculated values of f_j ($j=1,2$).

Parameter	1a	1b	1c
r_{I}	1	0.6	1
r_{II}	2	1	2
e_{I}	1	1.3	1
e_{II}	2/3	1	0.461 5
n_{I}	5/3	1.619 03	1
n_{II}	0	0.476 2	−1.333
f_{I}	0.907 841	0.622 52	1
f_{II}	1.815 682	1.037 53	2
$\Omega_m^2/\Omega_p=f/r$	0.907 841	1.037 53	1

TABLE II. Example 1. First four natural frequencies for a square domain with a linear interface parallel to one side. Membrane equation (9) was solved with FLEXPDE (Ref. 16) and plate equation (5) was solved with ALGOR (Ref. 15) for cases 1a and 1b. Plate of case 1c was tackled with Levy solution. The error is computed with Eq. (39).

Example	Order of frequency	Membrane Ω_m^2	Plate Ω_p	Error $\epsilon\%$
1a	1	14.2537	15.7044	−0.024
	2	33.0705	36.4348	−0.019
	3	36.7375	40.4691	−0.005
	4	61.1121	67.3298	−0.020
1b	1	26.4785	25.5251	−0.017
	2	63.2931	61.0124	−0.014
	3	65.5396	63.1734	−0.007
	4	108.3759	104.4600	−0.004
1c	1	14.2537	14.2563	−0.018
	2	33.0705	33.0713	−0.002
	3	36.7375	36.7373	0.0005
	4	61.1121	61.1080	0.006

TABLE III. Examples 2–4. First three natural frequencies for the membranes (example 2—see Ref. 12—and examples 2 and 3 with FLEXPDE, see Ref. 16) and plates [example 2 with ALGOR (Ref. 15) and examples 3 and 4 with FLEXPDE]. The error was computed with Eq. (39).

Example	Order of frequency	Membrane Ω_m^2	Plate Ω_p	Error $\epsilon\%$
2	1	7.6618	7.6662	−0.06
	2	15.728	15.737	−0.06
	3	23.473	23.502	−0.12
3	1	11.133	11.141	−0.072
	2	27.649	27.660	−0.040
	3	31.751	31.787	−0.113
4	1	7.5006	7.5037	−0.040
	2	16.132	16.126	−0.037
	3	25.185	25.248	−0.249

TABLE IV. Example 5. First five natural frequencies for a triangular membrane/plate with three regions. The error is computed with Eq. (39).

Order of frequency	Membrane Ω_m^2	Membrane $\times r/f$ $\Omega_m^2 r/f$	Plate Ω_p	Error $\epsilon\%$
1	33.301 90	42.621 23	42.621 23	0
2	73.470 89	94.031 26	94.031 25	0
3	89.789 84	114.917 0	114.916 9	0
4	117.985 2	151.002 6	150.994 8	0.005
5	153.384 8	196.308 6	196.278 7	−0.015

Finally, example 5 deals with an equilateral triangular domain with three regions, as is shown in Fig. 2. The data for this case are $\rho_0=1$, $E_0=1$, $\nu_0=0.3$, $r_1=1$, $r_2=2$, $r_3=3$, $e_1=1$, $e_2=0.8$, $e_3=0.6$, $n_1=0.2$, $n_2=0.1$, and $n_3=0$. Consequently $r_j/f_j=r/f=\Omega_p/\Omega_m^2=1.2798$. The results are reported in Table IV. Both membrane and plates were solved using FLEXPDE.[16]

As can be observed, errors are negligible. They are within the numerical inevitable errors that are involved in both the finite element calculations, as well as the other analytical approaches. Recall that the analogy is theoretically correct.

V. CONCLUSIONS

An analogy between membranes and simply supported plates for non-homogeneous domains comprised of homogeneous subdomains has been presented. It is verified within polygonal domains. Concretely, the analogy is derived from Eq. (24) that relates each membrane mode shape v as a linear combination of the plate mode shape w and its Laplacian. With this proposition, some restrictions arise [Eqs. (29) and (34)]. Several examples illustrate its validity provided that the required restrictions are satisfied. Through the demonstrated analogy, the plate and membrane vibration problems governed by the bi-Laplacian and Laplacian differential operators, respectively, can be solved without distinction, under certain conditions, i.e., solve one of them and deduce the other using the relationship. Obviously, the analogy includes the classic one when the whole domain is homogeneous.

ACKNOWLEDGMENTS

The authors wish to acknowledge the financial support of Universidad Nacional del Sur (SGCyT) and CONICET, both Argentine institutions.

[1]R. Blevins, *Formulas for Natural Frequency and Mode Shape* (Van Nostrand Reinhold, New York, 1979).
[2]S. Timoshenko and S. Woinowsky-Krieger, *Theory of Plates and Shells* (McGraw-Hill, New York, 1959).
[3]H. Marcus, *Die Theorie Elastischer Gewebe* (Springer-Verlag, Berlin, 1932).
[4]H. Conway and K. Farnham, "The free flexural vibrations of triangular, rhombic and parallelogram plates and some analogies," Int. J. Mech. Sci. **7**, 811–816 (1965).
[5]C. Wang, "Some exact solutions of the vibration of non-homogeneous membranes," J. Sound Vib. **210**, 555–558 (1998).
[6]S. Kang and J. Lee, "Free vibration analysis of composite rectangular membranes with an oblique interface," J. Sound Vib. **251**, 505–517 (2002).
[7]P. Amore, "A new method for studying the vibration of non-homogeneous membranes," J. Sound Vib. **321**, 104–114 (2009).
[8]Z. Cheng and S. Kitipornchai, "Membrane analogy of buckling and vibration of inhomogeneous plates," J. Eng. Mech. **125**, 1293–1297 (1999).
[9]Z. Cheng and R. Batra, "Exact correspondence between eigenvalues of membranes and functionally graded simply supported polygonal plates," J. Sound Vib. **229**, 879–895 (2000).
[10]J. Reddy and Z. Cheng, "Frequency correspondence between membranes and functionally graded spherical shallow shells of polygonal planform," Int. J. Mech. Sci. **44**, 967–985 (2002).
[11]C. Filipich and E. Bambill, "Natural frequencies of rectangular membranes with partial intermediate supports," J. Sound Vib. **310**, 21–37 (2008).
[12]C. Filipich and M. Rosales, "Vibration of non-homogeneous rectangular membranes with arbitrary interfaces," J. Sound Vib. **305**, 582–595 (2007).
[13]A. Leissa, *Vibration of Plates (NASA SP-160)* (US Government Printing Office, Washington, DC, 1969).
[14]R. Courant and D. Hilbert, *Methods of Mathematical Physics* (Interscience, New York, 1953).
[15]Autodesk Inc., ALGOR finite element analysis system V23 (2007).
[16]PDE Solutions Inc., FLEXPDE V6 reference manual (2009).

A field study of the exposure-annoyance relationship of military shooting noise

Mark Brink[a)]
D-MTEC Public and Organizational Health, ETH Zurich, CH-8092 Zurich, Switzerland

Jean-Marc Wunderli
Laboratory of Acoustics, Empa Swiss Federal Laboratories for Materials Testing and Research, CH-8600 Duebendorf, Switzerland

(Received 20 April 2009; revised 15 December 2009; accepted 6 February 2010)

This article reports a field study on noise annoyance from military shooting with small, midsize, and heavy weapons that was carried out among 1002 residents living near eight different training grounds of the Swiss army. The goal of the study was to derive the exposure-annoyance relationship for military shooting noise in communities in the vicinity of average military training grounds. Annoyance was determined in a telephone survey by means of the 5-point verbal and 11-point numerical annoyance scale recommended by the International Commission on Biological Effects of Noise. Exposure was calculated using acoustical source models of weapons and numbers of shots fired, as recorded by the army. Annoyance predictor variables investigated were L_{AE}, L_{CE}, $L_{CE}-L_{AE}$, number of shots above threshold, as well as individual moderators. Exposure-annoyance relationships were modeled by means of linear and logistic regression analyses. The sound exposure level L_E of shooting noise better explained variations in annoyance than other operational and/or acoustical predictors. Annoyance on the 5-point scale was more closely related to noise exposure than expressed on the 11-point scale. The inclusion of the C-A frequency weighting difference as a second explaining variable, as suggested earlier, did not substantially enhance the predictability of high annoyance. © *2010 Acoustical Society of America.* [DOI: 10.1121/1.3337234]

PACS number(s): 43.50.Qp, 43.50.Pn, 43.50.Sr [BSF] Pages: 2301–2311

I. INTRODUCTION

A. Study rationale

Exposure-response relationships are commonly used to assess the annoyance impact of many kinds of traffic or industrial noise. In their most common form, they relate noise exposure to the percentage of highly annoyed persons (%HA). As military shooting noise (as a result of military training activities in times of peace) is less of a problem for the majority of the population, there exist only a few field studies in the literature that investigated its effects. Hence the impact of military shooting noise from training grounds of armies is far less well understood than effects of other noise sources. The goals of the current study were thus the establishment of a statistical model that explains variation of community annoyance by operational and acoustical descriptors of military shooting activity and to provide an exposure-effect function for high annoyance (%HA) among residents in the vicinity of typical military training grounds in Switzerland.

Despite a relatively large body of literature, which mostly pertains to laboratory studies (Meloni and Rosenheck, 1995; Schomer *et al.*, 1994; Vos, 2001, 2003; Vos and Geurtsen, 2003), there have only few exposure-effect functions for (military) shooting noise been published so far (e.g., in Schomer, 1985). In the real-world situation, people use adaptive mechanisms that try to ignore noise as much as possible, whereas in a laboratory setting they do the opposite and inevitably concentrate on the noise. This provides a strong rationale to investigate shooting noise effects in the field, at the homes of the affected population.

The current study was carried out in Switzerland, where one can find several multipurpose training grounds where military shooting activity comprises small, middle, and heavy weapon shooting in one and the same place, and, because plain space is very scant, often in close vicinity to inhabited areas. This specific geographic situation therefore appears to be well suited to investigate military shooting noise annoyance by means of a field study. At this point, the notion is relevant that this study is not primarily about the effects of large army weapons such as tanks or artillery, since the number of rounds of such types of weapons each year is considerably lower than from small caliber arms.

B. Shooting noise descriptors and exposure-effect relationships

While exposure assessment following the equal energy principle has been adopted for the most distinctive noise sources, at least pertaining to annoyance as dependent variable, no commonly accepted noise descriptor for assessing community annoyance to shooting noise has successfully established itself to date. Of the few field studies on community annoyance due to weapon noise at hand (Buchta and Vos, 1998; Bullen and Hede, 1982; Fidell *et al.*, 1983; Levein and Ahrlin, 1988; Rylander and Lundquist, 1996;

a)Author to whom correspondence should be addressed. Electronic mail: brink@ethz.ch

Schomer, 1985; Schomer *et al.*, 1994; Sorensen and Magnusson, 1979), only few exposure-effect functions explaining annoyance due to a mixture of different kinds of army weapons emerged.

In the literature, noise descriptors that were identified to yield the highest degrees of explained variance of annoyance from impulsive sounds vary from accumulated peak level (Bullen *et al.*, 1991), maximum sound pressure level (Levein and Ahrlin, 1988), A-weighted FAST maximum sound pressure level (Sorensen and Magnusson, 1979), number of shots above a C-weighted threshold level (Rylander and Lundquist, 1996), C-weighted average day-night level L_{CDN} (Schomer, 1985), and Schomer's (Schomer, 1994) "new descriptor for high-energy impulsive sounds" (Buchta and Vos, 1998), the L_{Aeq}, to even surrogate measurements of ground vibration in the case of blast noise from surface mines (Fidell *et al.*, 1983). Most of these studies investigated the noise effect from particular source (weapon) types, either from, e.g., rifle shooting ranges or from large weapon training facilities. Shooting with firearms on multipurpose training grounds with different combinations of small to very large caliber weapons creates a complex blend of different sounds. It therefore appears that the construction of an all-purpose exposure-effect curve regarding military shooting noise is much more difficult than for other more uniform noise types. Depending on the predominant weapon type used, one or the other noise descriptor probably better predicts community annoyance. For example, noise annoyance from large weapons which also elicit rattle and vibrations might better be predicted using a C-weighted measure than an A-weighted measure. The question which predictor best accounts for the variation of military shooting noise annoyance *in general*, that means for any kind and combination of weapons, cannot easily be answered.

C. Frequency weighting

The question of the choice of frequency weighting to best predict impulsive or weapon noise annoyance respectively has received considerable attention in the literature. Insights into the relationship between shots of weapons and annoyance, especially with regard to impulse correction and frequency weighting have been collected in a series of laboratory studies (Meloni and Rosenheck, 1995; Schomer and Wagner, 1995; Schomer *et al.*, 1994; Vos, 1990, 2001). The use of the A-weighting is widespread in the evaluation of gunfire noise from small arms, usually including a penalty correction of between 5 and 12 dB for the added annoyance of impulsive sounds (Buchta, 1990; Vos, 1990). However, for the assessment of large caliber or high-energy weapon noise, the C weighting and the measure L_{CE} (or L_{CDN}) have been suggested in the past (Schomer, 1986) or are recommended in ISO 1996-1 (International Standards Organisation, 2003). The assessment methodology applied in many European countries uses $L_{AF,max}$ (Germany, Switzerland) or $L_{AI,max}$ (Austria, Finland, Denmark, Norway, and Sweden) for small arms, and C-weighted measures such as L_{CE} (Finland, Norway, Sweden) and L_{Ceq} (Germany, The Netherlands, and Denmark) for large weapons.

For the whole set of impulse sound types produced by various firearms ranging in caliber from 7.62 to 155 mm, the annoyance rating in the laboratory study of Vos (2001) was almost entirely determined by the "outdoor" L_{AE} of the impulses, as long as the artificial laboratory situation reflected a scenario with open windows. Similar results were reported by Meloni and Rosenheck (1995) who found that if shooting noise is predominantly heard through open windows, the A-weighted sound exposure level is appropriate for predicting annoyance.

Vos (2001) suggested to include the difference between the C- and A-weighted levels as a second annoyance predictor alongside the A-weighted level as principal predictor (Vos, 2001). Because the addition of the C-weighted level in the regression equations in most instances only very slightly increased the explained variance of the exposure-effect relationship, it remains arguable, whether the additional effort of C-weighted measurements and/or calculations is justified, particularly for the assessment of the "outside situation," as Vos (2001, 2003) demonstrated in his laboratory studies. It is therefore desirable to empirically test the advantage of the incorporation of C-weighted measurements not only in the laboratory but also within the scope of community reaction surveys in the field, such as the present one.

II. METHODS

A. Sampling procedure

Depending on the site-specific combinations of weapons/ammunition used, average distances of dwellings from the shooting ground, the degree of visibility of army activities in the surrounding neighborhood, involvement with the army (e.g., as employee), and many other factors, one would expect exposure-effect relationships for annoyance to show a rather wide variation. As the primary goal of the study was collecting data for constructing an exposure-effect relationship, a representative amount of residents near the eight largest training grounds of the Swiss army, that were located sufficiently close to inhabited areas to potentially evoke annoyance reactions from noise, were sampled. The corresponding sites were the army training grounds of Bière, Thun, Wangen an der Aaare, Gehren-Erlinsbach, Krähtal-Riniken, Walenstadt, Herisau-Gossau, and Chur. At each of these eight sites, the exposure contours from preliminary exposure calculations (that did not account for elevation above ground and shielding effects from neighboring buildings) were used to assign exposure values to building addresses using a GIS system provided by the Swiss statistics office. The exposure was calculated as the yearly sound exposure level L_{AE}, i.e., the total acoustic energy resulting from shooting activity during an entire year. At each of the eight sites, the primary sampling area was defined as the area that was enclosed by the 104 dB L_{AE} exposure contour. Each address was then assigned an exposure stratum (104–107, 107–110, 110–113, 113–116, 116–119, 119–122, 122–125, 125–128, and >128 dB). Over all eight sites, a total of 5901 building addresses within the 104 dB(A) contour were identified. These addresses were aligned with a commercial address database to yield all available landline telephone numbers of

households. 5851 individual telephone numbers were identified. The telephone numbers were stored together with their exposure level category and served as the primary sample. The survey was carried out by computer assisted telephone interviews (CATIs). Within each household, one person over 16 years of age was selected using a modified Troldahl–Carter method (Troldahl and Carter, 1964). The CATI software was configured to try to sample equal amounts of subjects in the different exposure strata, as far as possible. 5851 individual numbers were called. A total of 1002 interviews could be realized. 2137 calls were either never answered or were not valid due to technical reasons (e.g., a FAX device at the other end of the line). Of the 3714 remaining calls that resulted in a voice contact, the following statistics apply: Valid interviews conducted: 27%; interview scheduled, but did not take place for unknown reasons: 8%; communication or language problems make interview impossible: 4%; no target person living in household: 2%; person called refused interview: 59%.

B. Telephone interviews

Interviews lasted about 15–20 min and took place during the evening hours of September, October, and November 2007. The schedule moved gradually from questions about the satisfaction with the immediate environment to the topic of military shooting noise. The true aim of the survey was disclosed to all interviewees only after the interview was finished and they were given the opportunity to withdraw, an option no one exercised.

For the interviews, a questionnaire was used that first asked about various criteria of living quality of the interviewee, among them, noise exposure and annoyance from different sources (five-point verbal scale, including military shooting noise). These were asked in random order of the sources, followed by the items of the short form of the "Lärmempfindlichkeitsfragebogen" (LEFK; English: "Noise sensitivity questionnaire") by Zimmer and Ellermeier (1998) to assess noise sensitivity. In the middle of the interview, the main block about military shooting noise exposure and annoyance was placed. This main block of questions included the German version of the 11-point annoyance scale from 0 to 10 recommended by the International Commission on Biological Effects of Noise (ICBEN) that were published by Fields *et al.* (2001), a question about strategies to cope with the noise, and three items about the respondent's attitude toward the army (these items were "Switzerland does need an army," "The Swiss army sufficiently cares for the environment," and "Military shooting noise is a necessary evil") that had do be answered on a 1 to 5 scale with the end points "totally agree" and "totally disagree."

C. Exposure assessment

After the selection of the eight study sites and the collection of the survey data, the relevant source data for the final (high detail) noise exposure calculations were collected from army officials that were in command of the respective training grounds. Their task basically encompassed the reporting of the weapons and ammunitions used, the corresponding number of shots and shooting days, as well as the distribution of shots fired between day and evening (night shootings were very rare). Each weapon/ammunition combination was assigned one of the following categories: small caliber (<10 mm, e.g., assault rifles), middle caliber (10–100 mm, e.g., antiaircraft guns), large caliber (>=100 mm, e.g., large tank cannons), grenades and explosive charges, mortars, and practice ammunition.

For all receiver points in the survey, the exposure from every emplacement/weapon/ammunition combination of the respective study site was calculated using the "WL04" source and propagation model developed by the Swiss Federal Laboratories for Materials Testing and Research (Empa). This model delivers exposure spectra in octave bands from 31.5 Hz to 4 kHz of direct and reflected sounds as well as for each source and receiver combination and for up to 16 distinct weather conditions that were derived for each study site based on long-term weather statistics (the 16 Hz octave band was omitted as it does not relevantly contribute to the total exposure, even for large weapons). The model accounts for three types of sound sources: muzzle blasts, sonic booms, and detonations. Receiver points were set on the facade of the building aiming at the shooting ground. The height of the receiver points was set to 1.8 m for detached houses and ground floor apartments. For each additional floor, the height was increased by 2.6 m. Exposure calculations were performed separately for the years 2004, 2005, and 2006 and separately for daytime and evening shootings. Shootings in the night past 23:00 h were extremely rare, as were shootings during weekends.

The total yearly exposure levels were calculated as the sum of the energetic products of each emplacement/weapon/ammunition sound exposure level with their corresponding number of shots fired in the respective year.

As the timely distribution of the intensity of shooting often varies considerably across a year, a (daily) average exposure value, e.g., a 12 h L_{eq} or a 24 h L_{eq}, does not in most cases reflect a meaningful description of the noise exposure residents are affected with. Dose values in this article are therefore simply given as L_E values, representing the total (integrated) energy of shooting noise exposure in a year (or as the average over 3 years). A corresponding energy equivalent continuous level over a particular time period can be obtained by transforming the given L_E value, e.g., using

$$L_{eq} = L_E - 10\log(N_{SD} \times N_{HD} \times 3600), \quad (1)$$

where L_{eq} is equivalent sound level for a particular number of hours of a particular number of days (within a year), N_{SD} is number of days in a year when shootings/trainings take place, N_{HD} is number of hours per day for which the average sound level should be calculated (e.g., 12). For example, the average daily 12 h L_{eq} would thus be $L_E - 10\log(365 \times 12 \times 3600)$.

III. RESULTS

A. Sample description

A total of 460 male (46%) and 542 female (54%) participants constituted the sample of 1002 residents. Shooting

TABLE I. Number of interviews conducted at each study site and per exposure category.

Study site	90–95 dB [L_{AE}]	95–100 dB [L_{AE}]	100–105 dB [L_{AE}]	105–110 dB [L_{AE}]	110–115 dB [L_{AE}]	115–120 dB [L_{AE}]	120–125 dB [L_{AE}]	125–130 dB [L_{AE}]
Bière	14	21	50	42	51	42	10	
Chur	1	15	62	56	23	2		
Gehren-Erlinsbach		2	6	11	8	2		
Herisau-Gossau		11	25	20	7		1	2
Krähtal-Riniken	1	5	25	16	10	1		
Thun		7	27	59	92	52	34	8
Wangen an der Aare		15	10	8	12	3		
Walenstadt		25	28	46	34			
Total	16	101	233	258	237	102	45	10
Percent	1.60	10.08	23.25	25.75	23.65	10.18	4.49	1.00

noise exposure was calculated for 918 distinct receiver points. For a small number of the receiver points, more than one respondent were interviewed (e.g., more than one family member living in the same apartment). 232 interviews were made in the French speaking part of Switzerland. Respondents were in the age range from 16 to 94 years. The average age of the respondents was 50 years. The age class distribution was as follows (in parentheses are the percentages of the population older than 16): between 16 and 20 years: 5% (5%); 20–40: 25% (34%); 40–60: 37% (34%); and older than 60 years: 33% (26%).

The respondents experienced yearly military shooting noise exposure levels at their homes between 92 and 130 dB L_{AE} or 98 and 141 dB L_{CE}, respectively. Unlike the (quite simple) preliminary calculations that were used for sample stratification and definition of the address sampling areas, the definitive exposure calculation for each respondent accounted for the elevation above ground and shielding effects from other buildings; thus yearly L_{AE} levels down to 92 dB were reached in the sample. Table I shows the distribution of the number of telephone interviews that were realized per L_{AE} exposure level category (as 3 year energetic average) and study site.

Table II shows the yearly average number of shots as well as the number of shots above the 50, 60, 70, and 80 dB L_{AE} thresholds per weapon type, as experienced at the 918 receiver points in the sample. The figures given in the last four columns represent the average number of shots above the respective threshold, which is defined as the average A-weighted sound exposure level of one *individual* shot of a distinct source (more clearly the emplacement/weapon/ammunition combination) at the receiver points within the study sample, as the average of the 3 years 2004, 2005, and 2006.

The average shooting activity per year was about the same for all 3 years and no substantial changes have occurred at any of the eight grounds between 2004 and 2006.

B. Annoyance ratings and exposure metrics

In light of the different approaches to define *high annoyance* and for reasons of comparability, *both* ICBEN scales to assess (high) annoyance in the respondent (Fields *et al.*, 2001) were part of the interview. Concerning the five-point verbal scale, ICBEN's recommendation is to use the upper two categories (the verbal marks "very" and "extremely") as indicators of high annoyance. This corresponds to a cutoff point at 60% of the scale. No recommendation is given for the 11-point scale, but according to common practice, the upper three points on the numerical scale (8, 9, 10) define the presence of "high annoyance" in the respondent. In this case, the cutoff lies at 72.7% (see Schultz, 1978). In total, on the 11-point numerical scale, 170 of 1002 respondents qualified as *highly annoyed*, on the 5-point scale 241 of 1002.

The annoyance questions were asked in the following order: the first time during the interview using the 5-point verbal scale with the marks "not at all," "slightly," "moderately," "very," and "extremely" within a block of noise annoyance questions for different noise sources, and the second time later during the interview using the 11-point numerical scale. For all further quantitative analyses, the verbal answer alternatives of the five-point scale have been transformed to numerical values 1–5 and treated as continuous.

TABLE II. Number of shots and number of shots above threshold at the 918 receiver points in the sample (all values represent the yearly average over the years 2004, 2005, and 2006).

Type of weapon/ammunition	No. of shots during day	No. of shots during evening	No. of shots $>L_{AE}$=50 dB	No. of shots $>L_{AE}$=60 dB	No. of shots $>L_{AE}$=70 dB	No. of shots $>L_{AE}$=80 dB
Large caliber	5 088	179	2 119	1 701	834	207
Middle caliber	336 351	11 808	38 141	18 954	17 194	14 699
Small caliber	8 554 533	532 128	303 277	179 902	73 783	0
Practice ammunition	32 650	4 862	0	0	0	0
Grenades/explosive charges	17 163	1 065	2 356	1 712	816	471
Mortars	6 443	583	1 514	1 271	1 266	737

TABLE III. Mean annoyance and percent highly annoyed (%HA) for different degrees of exposure. The categories are defined based on the L_{AE} metric, the average exposure values $\varnothing$-L_{AE} and $\varnothing$-L_{CE} pertain to the arithmetic average of all cases within the category boundaries. *N* refers to the number of cases in each exposure level category.

Level category (range of L_{AE} values)	Scale	Mean annoyance	CI −95%	CI +95%	St. dev.	%HA
90–95 (N=16)	11-point [0,…,10]	3.38	2.12	4.63	2.36	6.25
$\varnothing$-L_{AE}=93.64	5-point [1,…,5]	1.81	1.46	2.16	0.66	0.00
$\varnothing$-L_{CE}=114.87						
95–100 (N=101)	11-point [0,…,10]	2.83	2.27	3.40	2.86	7.92
$\varnothing$-L_{AE}=98.07	5-point [1,…,5]	2.10	1.89	2.31	1.05	7.92
$\varnothing$-L_{CE}=111.50						
100–105 (N=233)	11-point [0,…,10]	3.83	3.47	4.19	2.77	10.73
$\varnothing$-L_{AE}=102.67	5-point [1,…,5]	2.41	2.26	2.55	1.12	15.45
$\varnothing$-L_{CE}=116.37						
105–110 (N=258)	11-point [0,…,10]	4.14	3.77	4.51	3.00	16.28
$\varnothing$-L_{AE}=107.53	5-point [1,…,5]	2.53	2.38	2.68	1.20	23.26
$\varnothing$-L_{CE}=119.66						
110–115 (N=237)	11-point [0,…,10]	4.65	4.26	5.03	3.03	22.78
$\varnothing$-L_{AE}=112.30	5-point [1,…,5]	2.97	2.82	3.13	1.24	32.07
$\varnothing$-L_{CE}=123.77						
115–120 (N=102)	11-point [0,…10]	5.35	4.78	5.92	2.91	28.43
$\varnothing$-L_{AE}=117.32	5-point [1,…,5]	3.41	3.18	3.65	1.20	43.14
$\varnothing$-L_{CE}=129.21						
120–125 (N=45)	11-point [0,…,10]	5.09	4.30	5.88	2.63	22.22
$\varnothing$-L_{AE}=122.21	5-point [1,…,5]	3.11	2.78	3.44	1.09	35.56
$\varnothing$-L_{CE}=131.40						
125–130 (N=10)	11-point [0…10]	3.90	1.68	6.12	3.11	10.00
$\varnothing$-L_{AE}=127.74	5-point [1,…,5]	2.60	2.00	3.20	0.84	10.00
$\varnothing$-L_{CE}=134.09						

Using linear regression models, it was first assessed which exposure metrics appear to be the best predictors of annoyance. The following potential predictors were investigated: Total energetic and arithmetic average (over 3 years) sound exposure levels (L_{AE} and L_{CE}), energetic and arithmetic average sound exposure level (L_{AE} and L_{CE}) during day and during evenings, energetic average sound exposure level (L_{AE} and L_{CE}) of small caliber shots and of large caliber shots, total number of small caliber shots over 50 dB L_{AE}, and total number of large caliber shots over 98 dB L_{CE}. From these preliminary analyses, it became evident that the basic energetic dose measures L_{AE} and L_{CE} are the best predictors for shooting noise annoyance. Table III tabulates the mean annoyance rating per exposure level category as well as the percentage of highly annoyed persons (%HA) in each category, according to the "standard" cutoff points (5-point: 60%; 11-point: 72.7%) on the scales.

Annoyance is an increasing function of the sound exposure level up to the exposure level category of 115–120 dB L_{AE}. Contrary to expectation, within the higher level categories (120–125 and 125–130 dB L_{AE}), mean annoyance as well as the percentage of highly annoyed persons (%HA) drop to a level close to the level reported by respondents that are 15 or even 20 dB less exposed. This could be explained by some types of self-selection process being at work insofar as people not being annoyed by military shooting noise are over-represented in areas close to military shooting grounds, maybe because they are less sensitive to noise and/or have a more positive attitude toward the army, e.g., because they are army employees that live in the vicinity of their employer. This explanation appears feasible since (a) noise sensitivity (as measured by the LEFK) is a significant negative predictor of the exposure, as expressed in the L_{AE} in linear regression analysis [β=−0.11, $t(1000)$=−2.33, p=0.02]; (b) annoyance, as measured using the five-point verbal scale, and attitude toward the army (an index value between 1 and 5 with higher values denominating a more positive attitude, derived from items of the questionnaire, see Sec. II B) is negatively correlated within the sample [r=−0.28; $p<0.0001$]. (b) Furthermore, in general linear modeling of annoyance (five-point verbal scale), both L_{AE} and attitude independently predict annoyance [L_{AE}: $F(1)$=94.23, $p<0.0001$; attitude: $F(1)$=89.64, $p<0.0001$], whereas attitude is negatively related to annoyance in this model.

The annoyance ratings showed considerable variability as can bee estimated from the confidence intervals reported in Table III. Linear regression results of the individual data (not the grouped data) for the 11-point numerical scale yielded R^2 values of less than 0.05, and the 5-point verbal scale yielded an adjusted R^2 value of 0.08 for both L_{AE} and L_{CE} as predictor. While with transportation noise, on the individual level, R^2 values between 0.1 and 0.2 are common, the marginal relationship found with military shooting noise is no surprise, assuming that individual moderators more strongly influence the annoyance rating than would be the case with transportation noise.

TABLE IV. Logistic regression analysis results of P_{HA} explained by L_{AE} and individual moderators. Noise sensitivity was assessed using the LEFK questionnaire and is expressed on a scale from 0 to 27. Attitude toward the army is expressed on a scale from 1 to 5.

Dependent	Parameter	Coefficient (B)	Standard error	Wald stat.	p
P_{HA} (five-point, cutoff 60%)	Intercept	−10.12	1.36	55.81	<0.0001
	L_{AE}	0.09	0.01	52.81	<0.0001
	Noise sensitivity	0.08	0.02	20.75	<0.0001
	Attitude toward army	−0.45	0.07	46.31	<0.0001
	McKelvey and Zavoina R^2: 0.45				

C. Exposure-effect relationships for L_{AE} and L_{CE} as principal predictors

The derivation of a fitting function in order to formalize an exposure-effect relationship requires practical- as well as theory-based choices about the functional form with which the observed exposure-effect relationship can be represented in a pertinent and useful way. Since the relevant effect in the current study—being highly annoyed or not—is binary by nature, the logistic form is preferable. To predict the proportion of highly annoyed persons at any given L_E level, a sound statistical model must prevent of predicting values that are theoretically inadmissible; the statistical analysis must therefore account for the binomial nature of the distribution of the dependent variable. This is achieved with logistic regression analysis. Logistic regression analyses on the probability of high annoyance (P_{HA}) using the L_{AE} and L_{CE} predictor were calculated with the SAS STAT system (SAS VERSION 9, SAS Institute, Cary, NC). To roughly assess the degree of explained variance in the model building process, the pseudo-R^2 statistic according to McKelvey and Zavoina (1975) was calculated.

First, it was assessed which nonacoustic factors exert influence on the probability of high annoyance P_{HA} (on the five-point verbal scale). The language in which the interview was conducted (French or German) did not have a significant effect on the reported annoyance. Also, no significant effect of gender on annoyance could be found in a range of models. There could be found an influence of age in a few models though, insofar as elderly persons were less annoyed than younger. No effect was found with the duration of living near the shooting ground, nor did house owner's annoyance significantly differ from the annoyance of tenants. The best logistic model comprised the predictors L_{AE}, attitude toward the army and noise sensitivity (as measured by the LEFK). To permit the readers to gauge the relative impact of these variables in a composite model, the corresponding parameter estimates are given in Table IV.

Since individual moderators of noise annoyance cannot be accounted for within the scope of noise legislation and abatement policy, and also because no other operational characteristics of shooting appeared to be relevant in their influence on annoyance, here, a set of logistic models is proposed which solely rely on either the L_{AE} or L_{CE} dose measure as main predictor. In the following analyses, to simplify matters, only the L_{AE} metric is further used. However, the L_{CE} metric would almost equally well serve the same purpose.

The two types of annoyance scales and their most common cutoff points for the "HA" definition did not lead to congruent exposure-effect curves (see Fig. 1). This points to the fact that the numerical and the verbal scales and their most commonly used cutoff points for the HA definition obviously do not measure the same thing. There have been successful attempts to attain congruent curves in other studies (e.g., Schreckenberg and Meis, 2006) by statistically raising the cutoff point of the five-point scale to 72% by weighting the response category "very" on the five-point scale as proposed by Miedema and Vos (1998). A similar attempt was not very successful with the current data. The weighted curve (which corresponds to a cutoff point at 72%) from the 5-point scale is displaced by about 10 dB, but has a more steep characteristic than the dose-response curve based on the 11-point scale. The parameters of the corresponding weighted logistic regression are tabulated in the last rows in Table V.

Although the issue of noncongruent exposure-effect curves from scales that are both designed to assess high annoyance is important for noise effects research and for noise policy in general, the discrepancy of the measurement result with military shooting noise cannot be investigated any further within the scope of the present article. The question about which of the three displayed curves better serves policy purposes will be discussed in Sec. IV.

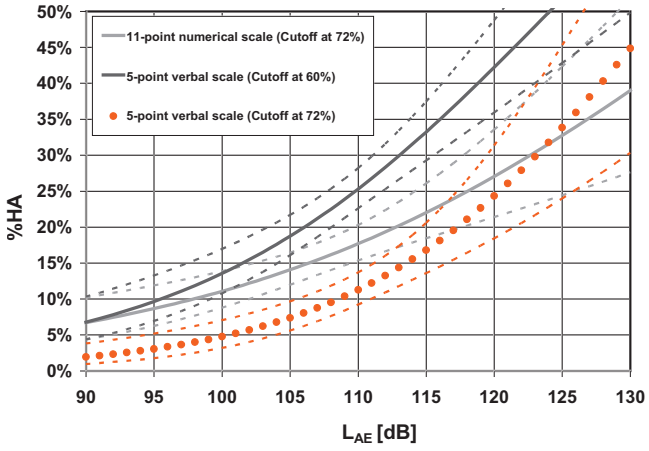

FIG. 1. Logistic dose-response curves and 95% confidence intervals for three different methods of defining the percentage of highly annoyed persons in the current sample. The curve based on the 5-point verbal scale that uses a cutoff point of 72% was generated by weighting the cases, where the respondent chose the "very" modifier on the scale, with 0.4 in the logistic regression analysis.

TABLE V. Results of the logistic regression analyses of P_{HA} with L_{AE} or L_{CE} as only predictor.

Predictor	Dependent	Parameter	Coefficient (B)	Standard error	Wald stat.	p
L_{AE}	P_{HA} (11-point scale)	Constant	−7.53	1.34	31.74	<0.0001
		L_{AE}	0.05	0.01	20.15	<0.0001
		McKelvey and Zavoina R^2: 0.11				
L_{AE}	P_{HA} (5-point scale)	Constant	−9.54	1.23	60.49	<0.0001
		L_{AE}	0.08	0.01	47.68	<0.0001
		McKelvey and Zavoina R^2: 0.23				
L_{AE}	P_{HA} (5-point scale, cutoff at 72%)	Constant	−12.28	1.78	47.83	<0.0001
		L_{AE}	0.09	0.02	34.00	<0.0001
		McKelvey and Zavoina R^2: 0.28				
L_{CE}	P_{HA} (11-point scale)	Constant	−7.88	1.50	27.72	<0.0001
		L_{CE}	0.05	0.01	17.96	<0.0001
		McKelvey and Zavoina R^2: 0.11				
L_{CE}	P_{HA} (5-point scale)	Constant	−9.67	1.36	50.43	<0.0001
		L_{CE}	0.07	0.01	39.79	<0.0001
		McKelvey and Zavoina R^2: 0.20				
L_{CE}	P_{HA} (5-point scale, cutoff at 72%)	Constant	−14.96	2.06	52.60	<0.0001
		L_{CE}	0.10	0.02	40.14	<0.0001
		McKelvey and Zavoina R^2: 0.35				

The confidence intervals of the functions in Fig. 1 and the standard errors reported in Table V pertain to the uncertainty of the annoyance measurement in the sample, not the uncertainty of noise exposure calculations. Therefore, the true confidence boundaries are most probably wider. The extended uncertainty of the exposure-effect relationship was not calculated since the nonconsideration of acoustic measurement uncertainty is a shortcoming of almost all annoyance studies of this kind, and accounting for acoustic uncertainty would possibly compromise the comparability of the confidence intervals in this study with the ones from other studies.

D. Accounting for low frequency components in L_{AE} based linear and binary logistic regression models

The sound exposure spectra of large caliber weapons, such as tank cannons, are dominated by the energy in the low frequency bands. For this kind of shooting events, C-weighted measures might better predict annoyance. In the literature, e.g., in Vos, 2001, there have been discussed models which account for both A-weighted and C-weighted properties of shooting sounds. The aim of such kind of modeling is to arrive at one single rating procedure for both small- and medium-large weapon sounds. The following analyses were performed to test the benefits of the inclusion of C-weighted measures in the prediction of (high) annoyance. It must be noted that the proportion of heavy weapon shooting events, which react much stronger to C-weighted measurements, is relatively small in the current sample. Thus the following analyses do not necessarily reflect a situation with considerably more intense heavy weapons shooting activity.

1. Linear models

The degree of annoyance, as measured with the 11- and 5-point scales, was modeled with linear regression analysis (GLM Module of STATISTICA 7, Stat Soft Inc., Tulsa, OK) with the two predictors L_{AE} and the difference between the C-weighted and the A-weighted levels ($L_{CE}-L_{AE}$), as has been suggested by Vos (2001). The inclusion of this second predictor is based on the idea that for large weapons with considerable low frequency content, the A-weighted level alone does not sufficiently account for the variation in annoyance. The results are presented in Table VI.

Both predictors, L_{AE} and ($L_{CE}-L_{AE}$), account for the variance in annoyance. The inclusion of ($L_{CE}-L_{AE}$) as a second predictor slightly improved the explained variance (R^2 adjusted) of both the models by about 0.01 points. Also, as can be learned from Table VI, answers on the 5-point verbal scale better predicted the annoyance rating than did the 11-point numerical scale.

It must be noted that ($L_{CE}-L_{AE}$) is strongly dependent on weapon type. With small arms, the difference is near 0 dB, and increases with increasing caliber, as the low frequency energy becomes more and more determining. In the current sample, the arithmetic average C-A level differences at the receiver points for the different weapon categories were as follows (rounded to full numbers): large caliber: 19 dB; middle caliber: 10 dB; small caliber: 3 dB; practice ammunition: 5 dB; grenades/explosive charges: 16 dB; mortars: 16 dB.

Albeit the most important components determining annoyance due to military shooting noise most probably are outside the acoustic domain (but rather considering individual moderators such as noise sensitivity and attitude to-

TABLE VI. Results of the linear regression analyses on the annoyance rating with L_{AE} and $(L_{CE}-L_{AE})$ as predictors.

Dependent	Parameter	B	Beta	F	df	p	Whole model statistics
Annoyance rating (11-point scale)	Intercept	−7.36		21.06	1	0.0001	
	L_{AE}	0.10	0.23	50.89	1	<0.0001	R^2 adj.=0.05; $F(2)=26.08$, $p<0.0001$
	$(L_{CE}-L_{AE})$	0.07	0.10	10.42	1	0.0013	
Annoyance rating (5-point scale)	Intercept	−3.70		33.01	1	<0.0001	
	L_{AE}	0.06	0.03	101.15	1	<0.0001	R^2 adj.=0.09; $F(2)=50.59$, $p<0.0001$
	$(L_{CE}-L_{AE})$	0.02	0.03	8.11	1	0.0045	

ward the army, see Sec. III C), the results at hand confirm the predictive value of incorporating the difference between C- and A-weighted measurements. However, in light of the comparatively small effect of acoustic predictors anyway, the additional variance explanation appears negligible.

2. Binary logistic models

Two binary logistic models that predict the probability of high annoyance (P_{HA}) with L_{AE} and $(L_{CE}-L_{AE})$ as independent variables were estimated using the procedure LOGISTIC of SAS. The results are presented in Table VII.

In contrast to linear modeling of the annoyance rating (see Table VI), the inclusion of $(L_{CE}-L_{AE})$ in the binary logistic models did not significantly contribute to the prediction of the probability of high annoyance (P_{HA}). It therefore appears not necessary to implement C-weighted measurements or a difference between the C- and A-weighted levels in the modeling of exposure-effect functions.

IV. DISCUSSION

As military shooting noise resulting from training activities in times of peace is less of a problem for the majority of the population, there are relatively few reports about such noise effects to be found and hence the impact of military shooting noise from training grounds of armies is far less well understood than effects of traffic or industrial noise. The current research therefore investigated shooting noise annoyance of residents in communities near eight large military training grounds by means of a field study. In the following, the study design and main findings are briefly discussed.

A. Study design and response rate

The chosen *study procedure* basically adopted a protocol that is standard practice in so called "socioacoustic surveys" where in the first stage, study sites with relevant noise exposure are identified, and then a stratified sample of residents is drawn, which then are finally interviewed. In contrast to laboratory studies—which somehow reflect the "traditional" form of investigating shooting noise annoyance—in field studies control over the noise emitting factors is limited. Limited control can—as in the current case—lead to certain imbalances. For example, the number of large caliber weapon rounds in the current sample is considerably smaller than for other weapon types, thus the results may not be applied to grounds with predominantly large weapon shooting activity. A perfectly balanced study would probably better allow making inferences as to the annoying potential of such weapons and concerning the differences in annoyance between small and large weapons. However, perfectly balanced field studies of noise exposure and annoyance are in many cases unaccomplishable, as different types of noise events from a particular noise emitting installation are not necessarily equally distributed (e.g., there are usually less heavy airplanes than light ones at airports and one almost always finds more passenger cars than trucks on roads). The current study aimed at elucidating the exposure-effect relationship as shooting is experienced in a real setting, and this includes also that the proportions of different weapons account for the overall "sound impression" in a representative manner.

The *response rate* of 27% in the CATI interviews was relatively small, but not really uncommon. A lot of studies that require (notably unpaid) people to respond by complet-

TABLE VII. Results of the logistic regression analyses on P_{HA} with L_{AE} and $(L_{CE}-L_{AE})$ as predictors.

Dependent	Parameter	Coefficient (B)	Standard error	Wald stat.	p
P_{HA} (11-point scale)	Intercept	−8.30	1.51	30.34	<0.0001
	L_{AE}	0.06	0.01	21.23	<0.0001
	$(L_{CE}-L_{AE})$	0.02	0.02	1.27	0.2592
	McKelvey and Zavoina R^2:0.14				
P_{HA} (5-point scale)	Intercept	−10.36	1.38	56.79	<0.0001
	L_{AE}	0.08	0.01	48.65	<0.0001
	$(L_{CE}-L_{AE})$	0.02	0.02	1.84	0.1753
	McKelvey and Zavoina R^2:0.22				

ing a questionnaire face the growing threat of nonresponse. Response rates to household telephone surveys are diminishing because of changes in telecommunications, marketing, and culture (O'Toole *et al.*, 2008). Evidence is most compelling from long-term trend surveys that have been repeated over many years. One possible explanation might be that people are getting more and more reluctant to take part in telephone surveys, especially because "phone spam" is increasing. Many callees perhaps reflexively refused to talk to the interviewers on the telephone, wrongly assuming that the caller has some commercial interests.

B. Exposure-annoyance relationship

Establishing the criteria for rating weapon noise has proven to be a quite difficult task as annoyance ratings from residents were strongly influenced by nonacoustic, but quite powerful moderating factors such as the attitude toward the army and the individual noise sensitivity (see Table IV). The results show that an energy type of model such as one based on L_{AE} or L_{CE} is the best available descriptor for community response to shooting with military weapons—a finding which is in line with previous research (Schomer, 1985). However, the relationship between the reactions of the respondents and exposure was not very strong for any exposure measure. The weak exposure-annoyance link was expected and is quite in line with previous attempts of deriving exposure-effect relationships of shooting noise annoyance in field studies (e.g., Bullen *et al.*, 1991).

In light of the fact that only a few field studies on community reactions to military noise have been carried out so far, and many of these did not report a statistically modeled exposure-effect function at all, any attempt to compare the current findings with previous research is difficult. The only study that allows a more or less direct comparison with the current one was the one from Buchta and Vos (1998). They conducted a field study on annoyance from artillery firing and found 25% HA at a L_{CDN} of about 57 dB. Since in the current case, night and evening shootings are very rare, the L_{DN} is practically equal to the $L_{eq,24\ h}$. The L_{CDN} level of 57 dB roughly corresponds to a yearly L_{CE} level of 132 dB. In Fig. 1 one can find 25% HA (using the 11-point scale and cutoff point at 72 %) at an L_{CE} of about 131 dB. The two field studies thus appear to correspond quite well.

C. Annoyance scales and cutoff points

Schultz (1978) already observed that the largest uncertainties in deriving his influential dose-effect curve were associated with the judgment as to which respondents are counted as highly annoyed. Obviously, this is a statement that still holds. When applying the most commonly used cutoff points (60% and 72.7%) on both the verbal and numerical annoyance scales suggested by ICBEN (Fields *et al.*, 2001), the two resulting logistic curves are non-congruent and predict different amounts of highly annoyed persons (%HA), especially within higher exposure level categories. The data also demonstrate that statistically aligning the cutoff points of both scales using the weighting method described by Miedema and Vos (1998) might not necessarily be a sound basis for comparing the two scales.

However, the observation that the %HA predictions from the two scales do not match and the ratings on the five-point scale are higher might also be the result of an order effect and not necessarily an effect of the underlying scale: The annoyance question using the five-point verbal scale was asked first and early in the interview, after a few non-noise related questions were asked. On the contrary, the 11-point numerical scale was presented after the interview dealt with several noise related questions. The cognitive occupation with the noise topic could have lead to a relativization of the noise annoyance issue and may prevent the respondents to give extreme answers.

The results strongly suggest that the 5-point scale better explains variance, at least for shooting noise annoyance, than the 11-point scale. The explained variance of the 5-point scale is even a bit higher when applying a cutoff point at 72% instead of 60% (see Table V).

D. Frequency weighting

The observations made in previous laboratory studies (e.g., Vos, 2001), that explained variability of annoyance (slightly) rises when including the difference between the C- and A-weighted levels as an additional predictor, could be confirmed in linear regression analyses. However, the additional variance explanation through incorporation of the $L_{CE}-L_{AE}$ difference was rather small and disappeared within the scope of binary logistic modeling of the probability of high annoyance. The $L_{CE}-L_{AE}$ predictor does not seem to offer a specific benefit that would warrant the effort of additional calculation or measurement of C-weighted exposure levels.

In the present study, L_{AE} and L_{CE} equally well (or bad) predict annoyance and both descriptors can basically be used interchangeably as main predictor. The use of C-weighting has some advantages when it comes to measurement instead of calculation, but only at relatively high exposure levels. This advantage is again outweighed by the high sensitivity of C-weighted measurements to wind noises. The use of L_{AE} (or alternatively L_{CE}) as the sole predictor of high annoyance in most cases captures as much variation as is appropriately derivable from operational and acoustical data, at least in the vicinity of military shooting grounds where shooting takes place predominantly with small- and midsized caliber weapons. As the $L_{CE}-L_{AE}$ difference becomes larger with larger calibers, the incorporation of C-weighted measurements might lead to a better prediction of annoyance at grounds with more heavy weapon shooting activities and/or considerably higher levels of exposure, or in countries with usually more permeable building envelopes.

In the literature of noise effects from military weapons, the presence of vibrations and rattle is reported to be the strongest adverse impulsive noise factor, and that a C-weighted measure is the best available standard weighting for including those spectral bands responsible for building rattle (Schomer, 1985). Although quite a few respondents in

the current sample reported to be particularly annoyed by rattle (Brink *et al.*, 2008), rattle appears as not being that important factor in Switzerland as it possibly is in other countries with less rigorous construction standards for detached houses, e.g., in the United States.

E. Policy recommendations

It appears that exposure itself is only a moderate determinant of people's propensity for shooting noise annoyance. The current results suggest studies of community noise annoyance to basically keep with the five-point verbal scale since it features a larger degree of explained variance of annoyance.

The curve(s) based on the five-point scale and employing a cutoff point at 60% of the scale length can be expressed as second order polynomial with sufficient accuracy in the relevant exposure range with P_{HA} expressing the fraction of highly annoyed persons for a given L_{AE} or L_{CE} value, as follows:

$$\text{Using } L_{AE}: P_{HA} = 1.404329 - 0.034881 \times L_{AE} + 0.000222 \times {L_{AE}}^2.$$

$$\text{Using } L_{CE}: P_{HA} = 1.696684 - 0.036492 \times L_{CE} + 0.000202 \times {L_{CE}}^2 \quad (2)$$

These curves represent military shooting noise annoyance which predominantly occurs with (1) most of the shootings taking place during day, (2) a fraction of about 5%–10% of the shootings taking place during the evening hours, and (3) no shootings during the core night hours. Furthermore, the curve rather represents an exposure situation with a considerable portion of small caliber shots (see Table II). With the advent of more sophisticated training simulators for mainly heavy weapon systems (e.g., for tanks), which will more and more replace the training with real weapons, large caliber weapon noise will most probably be less of a problem in the future. The proposed exposure-effect relationship for small caliber dominated shooting activity appears to be well suited to forecast shooting noise annoyance in the Swiss population—e.g., for regulatory purposes—and is possibly also applicable to similar shooting grounds in other European countries. It might be applied to military installations on the continental United States only with reservation, as (primarily) spatial and climatic conditions as well as cultural peculiarities such as construction standards for buildings considerably differ between the two countries.

ACKNOWLEDGMENTS

This study was funded by the Swiss Federal Office for the Environment to which we are very grateful. We thank the Swiss Federal Statistical Office for their collaboration with address sampling and IHA GfK for carrying out the telephone interviews for us. We also thank the Swiss Army for providing operational data in order to make the exposure calculations. We wish to express our gratitude to Rainer Guski and Christian Maschke for commenting an early version of the manuscript as well as to Hans Boegli and Kurt Heutschi for other helpful contributions. Finally, M.B. would like to acknowledge the valuable discussions, in particular, with Joos Vos, but also with Jim Fields and Dick Botteldooren about several aspects of this study during the 9th ICBEN Conference at Foxwoods, CT in 2008.

Brink, M., Wunderli, J.-M., and Boegli, H. (**2008**). "Community response to military shooting noise immissions—Preliminary results," paper presented at the 9th International Congress on Noise as a Public Health Problem (ICBEN), Foxwoods, CT.

Buchta, E. (**1990**). "A field survey on annoyance caused by sounds from small firearms," J. Acoust. Soc. Am. **88**, 1459–1467.

Buchta, E., and Vos, J. (**1998**). "A field survey on the annoyance caused by sounds from large firearms and road traffic," J. Acoust. Soc. Am. **104**, 2890–2902.

Bullen, R. B., and Hede, A. J. (**1982**). "Assessment of community noise exposure from rifle shooting," J. Sound Vib. **82**, 29–37.

Bullen, R. B., Hede, A. J., and Job, R. F. S. (**1991**). "Community reaction to noise from an artillery range," Noise Control Eng. J. **37**, 115–128.

Fidell, S., Horonjeff, R., Schultz, T., and Teffeteller, S. (**1983**). "Community response to blasting," J. Acoust. Soc. Am. **74**, 888–893.

Fields, J. M., De Jong, R. G., Gjestland, T., Flindell, I. H., Job, R. F. S., Kurra, S., Lercher, P., Vallet, M., Yano, T., Guski, R., Felscher-Suhr, U., and Schumer, R. (**2001**). "Standardized general-purpose noise reaction questions for community noise surveys: Research and a recommendation," J. Sound Vib. **242**, 641–679.

International Standards Organisation (**2003**). ISO 1996-1:2003 (Acoustics—Description, measurement and assessment of environmental noise Part 1).

Levein, B., and Ahrlin, U. (**1988**). "Annoyance caused by shooting range noise," J. Sound Vib. **127**, 589–592.

McKelvey, R. D., and Zavoina, W. (**1975**). "Statistical model for the analysis of ordinal level dependent variables," J. Math. Sociol. **4**, 103–120.

Meloni, T., and Rosenheck, A. (**1995**). "Choice of frequency-weighting for the evaluation of weapon noise," J. Acoust. Soc. Am. **97**, 3636–3641.

Miedema, H., and Vos, H. (**1998**). "Exposure-response relationships for transportation noise," J. Acoust. Soc. Am. **104**, 3432–3445.

O'Toole, J., Sinclair, M., and Leder, K. (**2008**). "Maximising response rates in household telephone surveys," BMC Med. Res. Methodol. **8**, 71.

Rylander, R., and Lundquist, B. (**1996**). "Annoyance caused by noise from heavy weapon shooting ranges," J. Sound Vib. **192**, 199–206.

Schomer, P. D. (**1985**). "Assessment of community response to impulsive noise," J. Acoust. Soc. Am. **77**, 520–535.

Schomer, P. D. (**1986**). "High-energy impulsive noise assessment," J. Acoust. Soc. Am. **79**, 182–186.

Schomer, P. D. (**1994**). "New descriptor for high-energy impulsive sounds," Noise Control Eng. J. **42**, 179–191.

Schomer, P. D., and Wagner, L. R. (**1995**). "Human and community response to military sounds. 2. Results from field-laboratory tests of sounds of small arms, 25-mm cannons, helicopters, and blasts," Noise Control Eng. J. **43**, 1–14.

Schomer, P. D., Wagner, L. R., Benson, L. J., Buchta, E., Hirsch, K. W., and Krahe, D. (**1994**). "Human and community response to military sounds-results from field-laboratory tests of small-arms, tracked-vehicle, and blast sounds," Noise Control Eng. J. **42**, 71–84.

Schreckenberg, D., and Meis, M. (**2006**). "Belästigung durch Fluglärm im Umfeld des Frankfurter Flughafens [Endbericht; Langfassung] (Effects of aircraft noise on noise annoyance around frankfurt airport [unabridged final report])," available at http://www.dialogforum-flughafen.de/fileadmin/PDF/Presse/Belaestigungsstudie_Langfassung.pdf (Last viewed 4/20/09).

Schultz, T. J. (**1978**). "Synthesis of social surveys on noise annoyance," J. Acoust. Soc. Am. **64**, 377–405.

Sorensen, S., and Magnusson, J. (**1979**). "Annoyance caused by noise from shooting ranges," J. Sound Vib. **62**, 437–442.

Troldahl, V. C., and Carter, R. E. (**1964**). "Random selection of respondents within households in phone surveys," J. Mark. Res. **1**, 71–76.

Vos, J. (**1990**). "On the level-dependent penalty for impulse sound," J. Acoust. Soc. Am. **88**, 883–893.

Vos, J. (**2001**). "On the annoyance caused by impulse sounds produced by small, medium-large, and large firearms," J. Acoust. Soc. Am. **109**, 244–253.

Vos, J. (**2003**). "A- and C-weighted sound levels as predictors of the annoy-

ance caused by shooting sounds, for various facade attenuation types," J. Acoust. Soc. Am. **113**, 336–347.
Vos, J., and Geurtsen, F. W. (**2003**). "On the assessment of shooting sounds: loudness-level weightings versus A- and C-weighted sound exposure levels (L)," J. Acoust. Soc. Am. **114**, 1729–1732.
Zimmer, K., and Ellermeier, W. (**1998**). "Ein Kurzfragebogen zur Erfassung der Lärmempfindlichkeit (A short questionnaire to measure noise sensitivity)," Umweltpsychologie **2**, 54–63.

One-dimensional transport equation models for sound energy propagation in long spaces: Theory

Yun Jing[a)]
Graduate Program of Architectural Acoustics, Rensselaer Polytechnic Institute, Troy, New York 12180

Edward W. Larsen
Department of Nuclear Engineering and Radiological Sciences, University of Michigan, Ann Arbor, Michigan 48109

Ning Xiang
Graduate Program of Architectural Acoustics, Rensselaer Polytechnic Institute, Troy, New York 12180

(Received 15 July 2009; revised 4 January 2010; accepted 5 January 2010)

In this paper, a three-dimensional transport equation model is developed to describe the sound energy propagation in a long space. Then this model is reduced to a one-dimensional model by approximating the solution using the method of weighted residuals. The one-dimensional transport equation model directly describes the sound energy propagation in the "long" dimension and deals with the sound energy in the "short" dimensions by prescribed functions. Also, the one-dimensional model consists of a coupled set of N transport equations. Only $N=1$ and $N=2$ are discussed in this paper. For larger N, although the accuracy could be improved, the calculation time is expected to significantly increase, which diminishes the advantage of the model in terms of its computational efficiency. © *2010 Acoustical Society of America.* [DOI: 10.1121/1.3298936]

PACS number(s): 43.55.Br, 43.55.Ka [EJS] Pages: 2312–2322

I. INTRODUCTION

Long spaces, in which one dimension is much larger than the other two, are of particular interest in room acoustics, as they usually take place in tunnels, underground stations, corridors, and some factories. Speech intelligibility and noise evaluation in these public places are critically important[1] and sometimes need to be predicted before construction.

The classical statistical theory, e.g., the Sabine equation, is not applicable in these situations because the sound field is highly nonuniform.[1,2] Other approaches, which fall into the category of the geometrical acoustic model, have recently been studied intensively, including the image source method,[3–5] the ray-tracing based method,[6,7] radiosity,[3,8,9] the diffusion equation model,[10–13] and the rendering equation model.[14] The image source method fails to include diffuse reflections, which have been found to be crucial when studying the steady-state and transient sound fields in long enclosures.[15] In contrast, the diffusion equation and original radiosity methods only take diffuse reflection into account. Although empirical modifications[16] have been applied to the diffusion equation method to model specular reflections, the model itself is inherently only suitable for low absorptive surfaces. The radiosity method can be modified to treat partially diffusely reflecting surfaces by combining the extended radiosity and mirror-image methods.[17] The ray-tracing based method is able to consider specular and diffuse reflections, but it is time-consuming due to its use of the Monte Carlo method. More recently Polles *et al.*[18,19] touched upon the transport theory in the context of urban streets. However, they did not formulate explicit solutions of the transport equations in their modeling effort rather than resort to asymptotic solutions in the form of diffusion equations.

The purpose of this work is to introduce a family of versatile one-dimensional transport equation models, which can simulate specular and diffuse reflections, air dissipations, scattering objects inside the enclosures, and different source types, as well as source directivities. These one-dimensional transport equations are (i) derived from a fundamental three-dimensional transport equation for sound propagation in enclosures and (ii) less computationally expensive than directly solving the three-dimensional transport equation since the number of independent spatial variables is reduced from 3 to 1.

All the theoretical considerations are presented in Sec. II. Although the mathematics is based on previous work in neutral particle transport,[20–22] differences are brought in by introducing several acoustic concepts. Specifically, different types of acoustic sources, boundary conditions at the two ends of a long space, and the specular reflections on side walls for a so-called two-group model are introduced for the first time in architectural acoustics.

This paper is structured as follows: first, Sec. II A presents the exact three-dimensional transport equation with corresponding boundary conditions. Then the method of weighted residuals is utilized to approximate the three-dimensional transport equation and simplify it to a coupled system of one-dimensional transport equations. Section II B discusses the details of the two simplest models, one having one one-dimensional transport equation, and the other having two coupled one-dimensional transport equations. The latter is shown through a simple test to be more accurate. Section

[a)]Author to whom correspondence should be addressed. Electronic mail: jingy@bwh.harvard.edu

 0001-4966/2010/127(4)/2312/11/$25.00

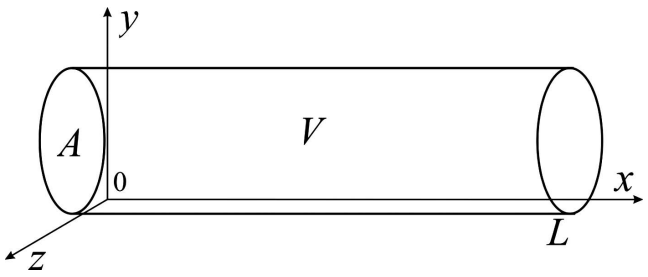

FIG. 1. Three-dimensional geometry of a long space.

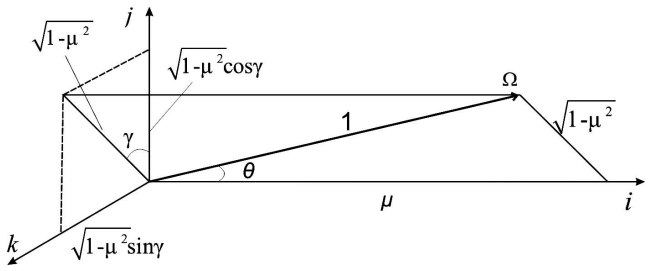

FIG. 2. Notations relevant to the transport equation.

II C also discusses the possibilities of modeling different sound sources and scattering objects inside the room. These would extend the application of the theory to a wider range of problems.

II. TRANSPORT EQUATION MODELS

In the geometrical acoustic model for room-acoustic predictions, the concept of sound waves is replaced by the notion of sound rays (or phonons[23]), which significantly reduces the difficulty of directly solving acoustic wave equations. The geometrical acoustic model is an energy-based method, which ignores complex wave phenomena including interference and diffraction. Sound is considered as rays propagating in straight lines with a certain amount of energy. This assumption is considered to be valid in the broad-band high frequency range, where the acoustic wavelength is much smaller than the room dimensions.

Under this circumstance, the sound energy can be described by the concept of a particle distribution function[19] $\psi(\boldsymbol{r},\boldsymbol{\Omega},t)$, where $\boldsymbol{r}$ is the position variable, $\boldsymbol{\Omega}$ is the angular variable, and t is time. More details of these variables are provided in Sec. II A. This particle distribution function can also be termed the sound energy angular flux, which is analogous to the term in neutral particle transport.

A. Three-dimensional transport equation model

This work considers a physical system consisting of a convex area A in the y,z-plane, extended in a "tubelike" or "ductlike" manner into the x-direction, creating a three-dimensional volume V (Fig. 1).

Assuming that V is "long and slender," implying that if the length L of the duct is finite, then

$$\frac{\sqrt{A}}{L} \ll 1. \tag{1}$$

Considering sound particle transport within the elongated volume V, in which the particle can be reflected specularly or diffusely (Lambert reflection) off the walls, the time-dependent transport equation is[19]

$$\frac{1}{c}\frac{\partial\psi}{\partial t}(\boldsymbol{r},\boldsymbol{\Omega},t) + \boldsymbol{\Omega}\cdot\nabla\psi(\boldsymbol{r},\boldsymbol{\Omega},t) + M\psi(\boldsymbol{r},\boldsymbol{\Omega},t) = \frac{Q(\boldsymbol{r},t)}{4\pi},$$
$$0 < x < L \quad (y,z) \in A, \tag{2}$$

where ψ is the sound angular flux (W m^{-2} sr^{-1}), c is the speed of sound (m s^{-1}), Q is an isotropic sound source term (W m^{-3}), $\boldsymbol{\Omega}$ is the unit vector in direction of particle propagation, and M is the atmospheric attenuation constant (m^{-1}). The boundary condition for the long side walls is

$$\psi(\boldsymbol{r},\boldsymbol{\Omega},t) = R\left[(1-s)\psi(\boldsymbol{r},\hat{\boldsymbol{\Omega}},t) + \frac{s}{\pi}\int_{\boldsymbol{\Omega}'\cdot\boldsymbol{n}>0} \boldsymbol{\Omega}'\cdot\boldsymbol{n}\,\psi(\boldsymbol{r},\boldsymbol{\Omega}',t)d\Omega'\right],$$
$$0 < x < L \ , \ (y,z) \in \partial A, \ \boldsymbol{\Omega}\cdot\boldsymbol{n} < 0, \tag{3}$$

where R is the energy reflection coefficient ($R=1-\alpha$, where α is the absorption coefficient), s is the scattering coefficient, and $\boldsymbol{n}$ is the unit outer normal vector. The first term on the right side of Eq. (3) represents specular reflection, and the second (integral) term describes diffuse reflection. These terms are explained in more detail below. For simplicity in the following, all the walls have the same reflection and scattering coefficients. In addition, it is possible to include sound transmissions from adjacent rooms by adding an external source term.[24] However, this is beyond the scope of this work and will not be discussed further.

To explain the notation in these equations (Fig. 2), let $\boldsymbol{i}$, $\boldsymbol{j}$, and $\boldsymbol{k}$ denote the unit vector in the direction of the positive x-, y-, and z-axes, respectively, then the position variable (vector):

$$\boldsymbol{r} = (\vec{x},\vec{y},\vec{z}) = x\boldsymbol{i} + y\boldsymbol{j} + z\boldsymbol{k}. \tag{4}$$

Also, the unit vector in direction of flight

$$\boldsymbol{\Omega} = (\mu, \sqrt{1-\mu^2}\cos\,\gamma, \sqrt{1-\mu^2}\sin\,\gamma), \tag{5}$$

where

$$\mu = \cos\,\theta = \text{polar cosine}, \tag{6a}$$

$$\theta = \sphericalangle \text{ between } \boldsymbol{\Omega} \text{ and } \boldsymbol{i},$$

$$\gamma = \sphericalangle \text{ between the projection of } \boldsymbol{\Omega} \text{ onto the } \boldsymbol{j},\boldsymbol{k}\text{-plane and } \boldsymbol{j} = \text{azimuthal angle}. \tag{6b}$$

Equation (5) can be written as

$$\boldsymbol{\Omega} = \mu\,\boldsymbol{i} + \sqrt{1-\mu^2}\boldsymbol{\phi}, \tag{7}$$

where $\boldsymbol{\phi}$ is the unit vector

$$\boldsymbol{\phi} = \cos\,\gamma\boldsymbol{j} + \sin\,\gamma\boldsymbol{k}. \tag{8}$$

All the notations in Eq. (2) have now been defined.

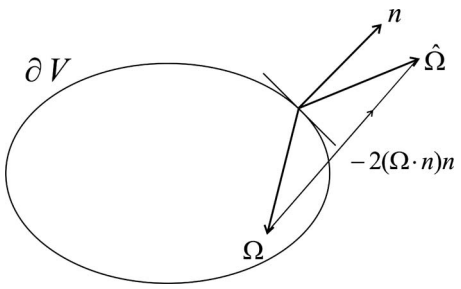

FIG. 3. Notations relevant to the specular reflection.

In Eq. (3), $\hat{\mathbf{\Omega}}$ is the "specular reflection" of the incident direction vector $\mathbf{\Omega}$ across the tangent plane at a point $\boldsymbol{r}$ on the boundary of V (Fig. 3), i.e.,

$$\hat{\mathbf{\Omega}} = \mathbf{\Omega} - 2(\mathbf{\Omega}\cdot\boldsymbol{n})\boldsymbol{n}. \tag{9}$$

Since $\boldsymbol{n}$ lies in the $\boldsymbol{j},\boldsymbol{k}$ plane, $\boldsymbol{n}\cdot\boldsymbol{i}=0$. Equation (9) yields

$$\hat{\mu} = \hat{\mathbf{\Omega}}\cdot\boldsymbol{i} = \mathbf{\Omega}\cdot\boldsymbol{i} = \mu, \tag{10}$$

and hence $\hat{\mu}=\mu$. When a particle specularly reflects, its μ-value does not change, but its γ-value does change. Equation (9) also implies that

$$\hat{\mathbf{\Omega}}\cdot\boldsymbol{n} = \mathbf{\Omega}\cdot\boldsymbol{n} - 2(\mathbf{\Omega}\cdot\boldsymbol{n}) = -\mathbf{\Omega}\cdot\boldsymbol{n}. \tag{11}$$

Thus, the projection of $\hat{\mathbf{\Omega}}$ onto $\boldsymbol{n}$ is positive, while the projection of $\mathbf{\Omega}$ onto $\boldsymbol{n}$ is negative and has the same magnitude.

In Eq. (3), $\mathbf{\Omega}'$ is a variable of integration that describes all the unit vectors in the outgoing directions. The integral term and the constant $1/\pi$ manifest that the reflected angular flux is uniform in all incoming directions (Lambert's law).[19] Furthermore, the constant s satisfies $0\le s\le 1$, and s represents the probability that when a particle scatters off the wall, it scatters diffusely, $(1-s)$ represents the probability that when a particle scatters off the wall, it scatters specularly.

Moreover, an operation on both sides of Eq. (3) by

$$\int_{\mathbf{\Omega}\cdot\boldsymbol{n}<0} |\mathbf{\Omega}\cdot\boldsymbol{n}|(\cdot)\,d\Omega \tag{12}$$

yields

$$\begin{aligned}\int_{\mathbf{\Omega}\cdot\boldsymbol{n}<0} |\mathbf{\Omega}\cdot\boldsymbol{n}|\psi(\boldsymbol{r},\mathbf{\Omega},t)\,d\Omega &= R\left[(1-s)\int_{\mathbf{\Omega}\cdot\boldsymbol{n}<0} |\mathbf{\Omega}\cdot\boldsymbol{n}|\psi(\boldsymbol{r},\hat{\mathbf{\Omega}},t)\,d\Omega\right.\\ &\left.+\frac{s}{\pi}\left(\int_{\mathbf{\Omega}\cdot\boldsymbol{n}<0} |\mathbf{\Omega}\cdot\boldsymbol{n}|\,d\Omega\right)\int_{\mathbf{\Omega}'\cdot\boldsymbol{n}>0} \mathbf{\Omega}'\cdot\boldsymbol{n}\psi\,d\Omega'\right].\end{aligned} \tag{13}$$

However,

$$\frac{1}{\pi}\int_{\mathbf{\Omega}\cdot\boldsymbol{n}<0} |\mathbf{\Omega}\cdot\boldsymbol{n}|\,d\Omega = \frac{1}{\pi}\int_0^{2\pi}\int_{-1}^{0} \mu\,d\mu\,d\gamma = 1. \tag{14}$$

Also, Eq. (11) and $d\hat{\Omega}=d\Omega$ yield

$$\int_{\mathbf{\Omega}\cdot\boldsymbol{n}<0} |\mathbf{\Omega}\cdot\boldsymbol{n}|\psi(\boldsymbol{r},\hat{\mathbf{\Omega}},t)\,d\Omega = \int_{\mathbf{\Omega}\cdot\boldsymbol{n}>0} \mathbf{\Omega}\cdot\boldsymbol{n}\psi(\boldsymbol{r},\mathbf{\Omega},t)\,d\Omega. \tag{15}$$

Thus, Eq. (13) becomes

$$\int_{\mathbf{\Omega}\cdot\boldsymbol{n}<0} |\mathbf{\Omega}\cdot\boldsymbol{n}|\psi(\boldsymbol{r},\mathbf{\Omega},t)\,d\Omega = R\int_{\mathbf{\Omega}\cdot\boldsymbol{n}>0} \mathbf{\Omega}\cdot\boldsymbol{n}\psi(\boldsymbol{r},\mathbf{\Omega},t)\,d\Omega, \tag{16}$$

implying that the rate per unit area, at which particles are reflected off the wall at $\mathbf{r}\in\partial V$, equals R times the rate per unit area, at which particles are incident on the wall at $\mathbf{r}\in\partial V$. Therefore, $0\le R\le 1$ and R represents the probability that when a particle strikes the wall it will be reflected (specularly or diffusely). This completes the interpretation of the terms in Eqs. (2) and (3).

Finally, for the boundary conditions of the two ends of the volume V, consider two models. The first model only takes specular reflections into account and is simply written as

$$\psi(0,y,z,\gamma,\mu,t) = R'\psi(0,y,z,\gamma,-\mu,t), \quad 0<\mu\le 1, \tag{17a}$$

$$\psi(L,y,z,\gamma,\mu,t) = R''\psi(L,y,z,\gamma,-\mu,t), \quad -1\le\mu<0, \tag{17b}$$

where R' and R'' are the reflection coefficients of the two ends, respectively.

For purely diffusely reflecting boundaries, according to Eq. (3),

$$\psi(\boldsymbol{r},\mathbf{\Omega},t) = \frac{R'(\text{or } R'')}{\pi}\int_{\mathbf{\Omega}'\cdot\boldsymbol{n}>0} \mathbf{\Omega}'\cdot\boldsymbol{n}\psi(\boldsymbol{r},\mathbf{\Omega}',t)\,d\mathbf{\Omega}', \quad \mathbf{\Omega}\cdot\boldsymbol{n}<0, \tag{18}$$

which leads to

$$\begin{aligned}&\psi(0,y,z,\gamma,\mu,t)\\ &= \frac{R'}{\pi}\int_{\gamma'=0}^{2\pi}\int_{\mu'=-1}^{0}(-\mu')\psi(0,y,z,\gamma',\mu',t)\,d\mu'\,d\gamma',\\ &\quad 0<\mu\le 1,\end{aligned} \tag{19a}$$

$$\begin{aligned}&\psi(L,y,z,\gamma,\mu,t)\\ &= \frac{R''}{\pi}\int_{\gamma'=0}^{2\pi}\int_{\mu'=0}^{1}\mu'\psi(L,y,z,\gamma',\mu',t)\,d\mu'\,d\gamma',\\ &\quad -1\le\mu<0.\end{aligned} \tag{19b}$$

For partially diffusely reflecting boundary condition, a linear combination of the above two is utilized.

B. One-dimensional transport approximation

To proceed, define

$$A' = \int\int_A dydz = \text{cross-sectional area of } A,$$

$$L' = \int_{\partial A} ds' = \text{circumference of } A, \tag{20}$$

where ds' denotes an increment of arc length.

Combine Eqs. (2) and (7) to get

$$\frac{1}{c}\frac{\partial \psi}{\partial t}(\boldsymbol{r},\boldsymbol{\Omega},t) + \mu\frac{\partial \psi}{\partial x}(\boldsymbol{r},\boldsymbol{\Omega},t) + \sqrt{1-\mu^2}\boldsymbol{\phi}\cdot\nabla\psi(\boldsymbol{r},\boldsymbol{\Omega},t) + M\psi(\boldsymbol{r},\boldsymbol{\Omega},t) = \frac{Q(\boldsymbol{r},t)}{4\pi}. \tag{21}$$

Intuitively, a very simple way to arrive at a one-dimensional transport equation is to disregard the y, z-dependency of the distribution function ψ by setting the third term in Eq. (21) to zero. However, this would not give a correct one-dimensional transport equation. As shown below, keeping the third term in Eq. (21) is imperative when integrating Eq. (21) and the boundary condition, i.e., Eq. (3).

An approximation of ψ by the method of weighted residuals is then introduced as

$$\psi(\boldsymbol{r},\mu,\gamma,t) \approx \sum_{j=1}^{N} \alpha_j(y,z,\gamma)\psi_j(x,\mu,t), \tag{22}$$

where α_j are specified basis functions and ψ_j are unknown expansion functions. The criterion for selecting the basis functions is that: In a long space, it is reasonable to assume that the sound field is strongly dependent on the long dimension (x-axis) and weakly dependent on the lateral coordinates (y- and z-axes). In other words, it is expected that the sound field varies significantly along the long dimension but insignificantly across the cross section. Similarly, it is assumed that the angle dependence of sound angular flux on μ is much stronger than on γ. Therefore, it is decided to separate y, z, and γ from x and μ by using the basis functions, which are predefined. In this way, the original equation discards the y, z, and γ dependences and is only x and μ dependent.

Substituting the approximation of ψ generates an error or a residual, which is required to be orthogonal to certain weight functions, $\beta_i(y,z,\gamma)$ $(1 \le i \le N)$. Equivalently, the method of weighted residuals forces the residual to zero in an average way over a certain domain, which leads to minimum error.

To explicitly show this and determine the equations for the ψ_j, an operation on both sides of Eq. (21) by $\int\int_A \int_{\gamma=0}^{2\pi} \beta_j(\cdot)d\gamma dydz$ and an operation on both sides of Eq. (3) by $\int_{\partial A}\int_{\boldsymbol{\phi}\cdot\boldsymbol{n}<0}\beta_j(\cdot)d\gamma ds$ yield

$$\int\int_A \int_{\gamma=0}^{2\pi} \beta_j\left[\frac{1}{c}\frac{\partial\psi}{\partial t} + \mu\frac{\partial\psi}{\partial x} + \sqrt{1-\mu^2}\boldsymbol{\phi}\cdot\nabla\psi + M\psi - \frac{Q(\boldsymbol{r},t)}{4\pi}\right]d\gamma dydz = 0, \tag{23}$$

$$\int_{\partial A}\int_{\boldsymbol{\phi}\cdot\boldsymbol{n}<0}\beta_j\left\{\psi - R\left[(1-s)\psi + \frac{s}{\pi}\int_{\boldsymbol{\Omega}'\cdot\boldsymbol{n}>0}\boldsymbol{\Omega}'\cdot\boldsymbol{n}\psi d\Omega'\right]\right\}d\gamma ds' = 0. \tag{24}$$

In addition, α_j and β_i are assumed to satisfy

$$\frac{1}{2\pi A'}\int_A\int_0^{2\pi}\alpha_j\beta_i d\gamma dydz = \delta_{ij}, \quad 1 \le i, \quad j \le N, \tag{25}$$

where δ_{ij} is the Kronecker delta. Equations (22) and (25) imply that

$$\psi_i = \frac{1}{2\pi A'}\int_A\int_0^{2\pi}\beta_i\psi d\gamma dydz, \quad 1 \le i \le N. \tag{26}$$

For a point source at $\boldsymbol{r}_0=(x_0,y_0,z_0)$, i.e., $Q(\boldsymbol{r},t) = Q(t)\delta(x-x_0)\delta(y-y_0)\delta(z-z_0)$, apply the divergence theorem to Eq. (23), then use Eq. (24), and finally arrive at the following set of N transport equations (see Appendix for details):

$$\frac{1}{c}\frac{\partial\psi_i}{\partial t} + \mu\frac{\partial\psi_i}{\partial x} + M\psi_i + \sqrt{1-\mu^2}\sum_{j=1}^{N}a_{ij}\psi_j = \frac{2Rs}{\pi}\sqrt{1-\mu^2}\sum_{j=1}^{N}b_{ij}\int_{-1}^{1}\sqrt{1-\mu'^2}\psi_j(\mu')d\mu' + Q_i, \tag{27}$$

where the derivation of a_{ij} and b_{ij} can be found in the Appendix. For example,

$$a_{ij} = \frac{1-R(1-s)}{2\pi A'}\left[\int_{\partial A}\int_{\boldsymbol{\phi}\cdot\boldsymbol{n}>0}\boldsymbol{\phi}\cdot\boldsymbol{n}\beta_i\alpha_j d\gamma ds'\right], \quad i = 1 \tag{28}$$

$$b_{ij} = \frac{1}{4\pi A'}\int_{\partial A}\left(\int_{\boldsymbol{\phi}\cdot\boldsymbol{n}<0}|\boldsymbol{\phi}\cdot\boldsymbol{n}|\beta_i d\gamma\right)\times\left(\int_{\boldsymbol{\phi}\cdot\boldsymbol{n}>0}\boldsymbol{\phi}\cdot\boldsymbol{n}\alpha_j d\gamma\right)ds' \quad \text{for } 1 \le i \le 2, \tag{29}$$

and

$$Q_i = \frac{1}{2\pi A'}\int_A\int_0^{2\pi}\beta_i\frac{Q(t)\delta(\boldsymbol{r}-\boldsymbol{r}_0)}{4\pi}d\gamma dydz. \tag{30}$$

In addition, substitution of Eqs. (17a) and (17b) into Eq. (26) yields the purely specular boundary condition for the two ends as

$$\psi_i(0,\mu,t) = R'\psi_i(0,-\mu,t), \quad 0 < \mu \le 1, \tag{31a}$$

$$\psi_i(L,\mu,t) = R''\psi_i(L,-\mu,t), \quad -1 \le \mu < 0. \tag{31b}$$

Similarly, for diffuse reflection,

$$\psi_i(0,\mu,t) = \frac{R'}{\pi}\times\frac{1}{2\pi A'}\int_A\int_0^{2\pi}\beta_i\left[\int_0^{2\pi}\int_{-1}^{0}(-\mu')\times\psi(0,y,z,\mu',\gamma',t)d\mu' d\gamma'\right]d\gamma dydz, \quad 0 < \mu \le 1, \tag{32a}$$

$$\psi_i(L,\mu,t) = \frac{R''}{\pi} \times \frac{1}{2\pi A'} \int_A \int_0^{2\pi} \beta_i \left[\int_0^{2\pi} \int_0^1 \mu' \psi(0,y,z, \mu',\gamma',t) d\mu' d\gamma' \right] d\gamma dy dz, \quad -1 \le \mu < 0, \tag{32b}$$

Now the exact three-dimensional equations, i.e., Eqs. (2) and (3), have been reduced to a coupled set of N one-dimensional transport equations, in the expectation that the resulting computation will be less cumbersome. In this set of equations, α_j and β_i have to be specified. Large N should increase the computational load but should also reduce the error of the approximation. Thus, the choice of N, the number of transport equations in the approximate one-dimensional model, is a compromise between computational effort and accuracy. This study only considers $N=1$ and 2, which are treated in detail below.

1. One-group model ($N=1$)

This subsection begins with the choice of the basis functions and weight functions. There are different ways to select these functions, for example, the collocation method (the weight functions are chosen to be Dirac delta functions), the least-squares method (which uses derivatives of the residual itself as weight functions), and the Galerkin method.[25] The Galerkin method is preferred because it has already been shown to be accurate for this specific transport equation model.[22] In the Galerkin method, the weight functions are chosen to be identical to the basis functions, and for $N=1$

$$\alpha_1(y,z,\gamma,t) = \beta_1(y,z,\gamma,t) = 1. \tag{33}$$

The constant of 1 is a convenient choice suggested in previous work.[22] Thus

$$\psi(\boldsymbol{r},\mu,\gamma,t) \approx \psi_1(x,\mu,t). \tag{34}$$

Based on this equation, the three-dimensional transport equation is reduced to a truly "one-dimensional model" since the y and z coordinates disappear. It indicates that the y, z, and γ-dependences of ψ are weak; i.e., the energy is almost uniform in the y-z plane and over the γ angle. This is expected to be a good approximation when the absorption on the boundary is weak and the long space is sufficiently narrow. The theoretical demonstration of this statement has been given in Ref. 22, which is conveyed in a rather mathematical way. It might be more illustrating to explain this from the acoustic point of view: if the absorption on the side walls are strong, the variation in the sound energy across the cross section will be significant, which has been shown in previous literatures, e.g., Ref. 12. This implies that the sound energy is no more weakly y- and z-dependent, which violates the assumption of the one-group model. It has also been theoretically proved that this approximation is valid if the receiver is sufficiently far away from the ends of the long space.[22] Substitution of Eq. (33) into Eqs. (28) and (29) yields

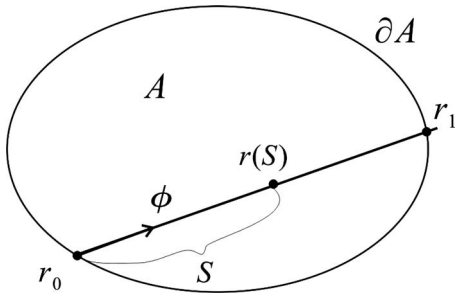

FIG. 4. Notations relevant to function D.

$$a_{11} = [1 - R(1-s)] \frac{L'}{\pi A'}, \quad b_{11} = \frac{L'}{\pi A'}. \tag{35}$$

The one-dimensional transport equation model for $N=1$ is then

$$\frac{1}{c}\frac{\partial \psi_1}{\partial t} + \mu \frac{\partial \psi_1}{\partial x} + \left[M + \sqrt{1-\mu^2} \frac{1-R(1-s)}{\lambda} \right] \psi_1 = \frac{2Rs}{\lambda \pi} \sqrt{1-\mu^2} \int_{-1}^{1} \sqrt{1-\mu'^2} \psi_1(\mu') d\mu', \tag{36}$$

where

$$\lambda = \frac{\pi A'}{L'}. \tag{37}$$

The specular boundary conditions for the two ends are

$$\psi_1(0,\mu,t) = R' \psi_1(0,-\mu,t), \quad 0 < \mu \le 1, \tag{38a}$$

$$\psi_1(L,\mu,t) = R'' \psi_1(L,-\mu,t), \quad -1 \le \mu < 0. \tag{38b}$$

Also, the diffuse boundary conditions are

$$\psi_1(0,\mu,t) = 2R' \int_{-1}^{0} (-\mu') \psi_1(0,\mu',t) d\mu', \quad 0 < \mu \le 1, \tag{39a}$$

$$\psi_1(L,\mu,t) = 2R'' \int_0^1 \mu' \psi_1(L,\mu',t) d\mu', \quad -1 \le \mu < 0. \tag{39b}$$

This one-group one-dimensional transport equation is the same for two different structures having the same ratio of A' to L'.

To explain the physical interpretation of the constant λ in Eq. (37), a function $D(y,z,\boldsymbol{\phi})$ is defined as the distance from a point (x,y,z) in the interior of the volume to the inner wall in the direction $-\boldsymbol{\phi}$ so that

$$\boldsymbol{\phi} \cdot \nabla D(y,z,\boldsymbol{\phi}) = 1 \quad (y,z) \in A, \tag{40a}$$

$$D(y,z,\boldsymbol{\phi}) = 0 \quad (y,z) \in \partial A, \quad \boldsymbol{\phi} \cdot \boldsymbol{n} < 0, \tag{40b}$$

where $\boldsymbol{n}$ is the unit outer normal vector. If $\boldsymbol{r}_0 = (x,y,z) \in \partial A$ and $\boldsymbol{\phi} \cdot \boldsymbol{n} < 0$ (i.e., $\boldsymbol{\phi}$ points into A), then on the line $\boldsymbol{r}(S) = \boldsymbol{r}_0 + S\boldsymbol{\Omega}$, Eq. (40) yields $D[\boldsymbol{r}(S), \boldsymbol{\phi}] = S$ (Fig. 4).

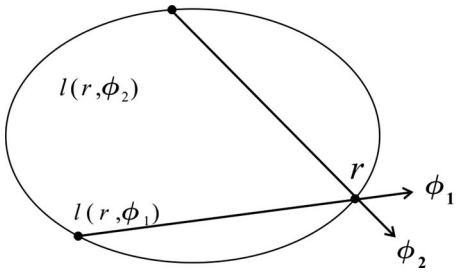

FIG. 5. Notations relevant to function l.

At the point $\boldsymbol{r}_1 \in \partial A$, where the line "exits" A, $D(\boldsymbol{r}_1, \boldsymbol{\phi}) = |\boldsymbol{r}_1 - \boldsymbol{r}_0|$ = distance through A in the direction $\boldsymbol{\phi} \equiv l(\boldsymbol{r}_1, \boldsymbol{\phi})$ (Fig. 5).

Now an operation on both sides of Eq. (40a) by $\int_A \int_{\gamma=0}^{2\pi} (\cdot) d\gamma dy dz$ yields

$$
\begin{aligned}
2\pi A &= \int_A \int_{\gamma=0}^{2\pi} \boldsymbol{\phi} \cdot \nabla D d\gamma dx dy \\
&= \int_{\gamma=0}^{2\pi} \left(\int_{\partial A} \boldsymbol{n} \cdot \boldsymbol{\phi} D ds' \right) d\gamma \\
&= \int_{\partial A} \left(\int_{\boldsymbol{\phi}\cdot\boldsymbol{n}>0} \boldsymbol{n} \cdot \boldsymbol{\phi} D d\gamma \right) ds' \\
&= \int_{\partial A} \int_{\boldsymbol{\phi}\cdot\boldsymbol{n}>0} \boldsymbol{n} \cdot \boldsymbol{\phi} l(\boldsymbol{r}, \boldsymbol{\phi}) d\gamma ds'. \qquad (41)
\end{aligned}
$$

But also,

$$
\int_{\partial A} \left(\int_{\boldsymbol{\phi}\cdot\boldsymbol{n}>0} \boldsymbol{\phi} \cdot \boldsymbol{n} d\gamma \right) ds' = \int_{\partial A} 2 ds' = 2L'. \qquad (42)
$$

Hence, λ has the geometrical interpretation:

$$
\lambda = \langle l \rangle = \frac{\int_{\partial A} \int_{\boldsymbol{\phi}\cdot\boldsymbol{n}>0} \boldsymbol{n} \cdot \boldsymbol{\phi} l(\boldsymbol{r}, \boldsymbol{\phi}) d\gamma ds'}{\int_{\partial A} \int_{\boldsymbol{\phi}\cdot\boldsymbol{n}>0} \boldsymbol{n} \cdot \boldsymbol{\phi} d\gamma ds'} = \frac{\pi A'}{L'}, \qquad (43)
$$

which is the classical diffuse mean free path length for two dimensions,[26] or mean chord length[27] across A. This completes the discussion of the one-group transport equation model.

2. Two-group model ($N=2$)

The choice of the basis functions and weight functions for the two-group model ($N=2$) is based on a linear combination of the constant function 1, and $D(y,z,\gamma)$, defined in Sec. II B 1 to be the distance from a point (x,y,z) in the interior of the volume to the inner wall in the direction $-\boldsymbol{\phi}$. They are expressed explicitly as

$$
\alpha_1(y,z,\gamma,t) = \beta_1(y,z,\gamma,t) = 1, \qquad (44)
$$

$$
\alpha_2(y,z,\gamma,t) = \beta_2(y,z,\gamma,t) = u[D(y,z,\boldsymbol{\phi}) - v], \qquad (45)
$$

where

$$
u = \left\{ \frac{1}{2\pi A'} \int_A \int_0^{2\pi} [D(y,z,\boldsymbol{\phi}) - v]^2 d\gamma dy dz \right\}^{-1/2}, \qquad (46)
$$

$$
v = \frac{1}{2\pi A'} \int_A \int_0^{2\pi} D(y,z,\boldsymbol{\phi}) d\gamma dy dz, \qquad (47)
$$

or in the form of curve integral:

$$
u = \left[\frac{1}{6\pi A'} \int_{\partial A} \int_0^{2\pi} \boldsymbol{\phi} \cdot \boldsymbol{n} (D - v)^3 d\gamma ds' \right]^{-1/2}, \qquad (48)
$$

$$
v = \frac{1}{4\pi A'} \int_{\partial A} \int_{\boldsymbol{\phi}\cdot\boldsymbol{n}>0} \boldsymbol{\phi} \cdot \boldsymbol{n} D^2 d\gamma ds', \qquad (49)
$$

which can be obtained using the divergence theorem (Gauss's theorem) and the identity[22]

$$
D = (\boldsymbol{\phi} \cdot \nabla D^2)/2. \qquad (50)
$$

To show how to derive the matrices a_{ij} and b_{ij}, using a_{12} as an example:

$$
\begin{aligned}
a_{12} &= \frac{1 - R(1-s)}{2\pi A'} \int_{\partial A} \int_{\boldsymbol{\phi}\cdot\boldsymbol{n}>0} \boldsymbol{\phi} \cdot \boldsymbol{n} u (D - v) d\gamma ds' \\
&= \frac{1 - R(1-s)}{2\pi A'} u \left(\int_{\partial A} \int_0^{2\pi} \boldsymbol{\phi} \cdot \boldsymbol{n} D d\gamma ds' \right. \\
&\quad \left. - \int_{\partial A} \int_{\boldsymbol{\phi}\cdot\boldsymbol{n}>0} \boldsymbol{\phi} \cdot \boldsymbol{n} d\gamma ds' \right) \\
&= \frac{1 - R(1-s)}{2\pi A'} u \left(\int_A \int_0^{2\pi} \boldsymbol{\phi} \cdot \nabla D d\gamma dy dz - v 2L' \right) \\
&= [1 - R(1-s)] \left(u - uv \frac{L'}{\pi A'} \right). \qquad (51)
\end{aligned}
$$

In similar fashion, other matrix elements can be derived. Omitting the lengthy algebra, the final results of the matrices a_{ij} and b_{ij} can be expressed as

$$
\begin{aligned}
a_{11} &= [1 - R(1-s)] \frac{L'}{\pi A'}, \\
a_{12} &= [1 - R(1-s)] \left(u - uv \frac{L'}{\pi A'} \right), \\
a_{21} &= [R(1-s) - 1] \frac{uvL'}{\pi A'}, \\
a_{22} &= \frac{u^2 v^2 L'}{\pi A'} + R(1-s) uv \left(u - \frac{uvL'}{\pi A'} \right), \qquad (52)
\end{aligned}
$$

$$
b_{ij} = \begin{bmatrix} L'/(\pi A') & u - uvL'/(\pi A') \\ -uvL'/(\pi A') & -uv[u - uvL'/(\pi A')] \end{bmatrix}. \qquad (53)
$$

The specular boundary conditions on the two ends are

$$
\psi_1(0, \mu, t) = R' \psi_1(0, -\mu, t), \quad 0 < \mu \le 1, \qquad (54a)
$$

$$\psi_1(L,\mu,t) = R''\psi_1(L,-\mu,t), \quad -1 \le \mu < 0, \tag{54b}$$

$$\psi_2(0,\mu,t) = R'\psi_2(0,-\mu,t), \quad 0 < \mu \le 1, \tag{54c}$$

$$\psi_2(L,\mu,t) = R''\psi_2(L,-\mu,t), \quad -1 \le \mu < 0. \tag{54d}$$

The diffuse boundary conditions are given by

$$\psi_1(0,\mu,t) = 2R'\int_{-1}^{0}(-\mu')\psi_1(0,\mu',t)d\mu', \quad 0 < \mu \le 1, \tag{55a}$$

$$\psi_1(L,\mu,t) = 2R''\int_{0}^{1}\mu'\psi_1(0,\mu',t)d\mu', \quad -1 \le \mu < 0, \tag{55b}$$

$$\psi_2(0,\mu,t) = \frac{R'u^2}{2\pi^2A'}\left[\int_A\left(\int_0^{2\pi}Dd\gamma\right)^2 dydz - 4\pi^2v^2A'\right] \times \int_{-1}^{0} -\mu'\psi_2(0,\mu',t)d\mu', \quad 0 < \mu \le 1, \tag{55c}$$

$$\psi_2(L,\mu,t) = \frac{R''u^2}{2\pi^2A'}\left[\int_A\left(\int_0^{2\pi}Dd\gamma\right)^2 dydz - 4\pi^2v^2A'\right] \times \int_{0}^{1}\mu'\psi_2(0,\mu',t)d\mu', \quad -1 \le \mu < 0, \tag{55d}$$

where for a long space with circular cross section A, u, and v are given analytically as

$$u = 3\pi(9\pi^2 - 64)^{-1/2}/\rho' \quad \text{and} \quad v = 8\rho'/(3\pi), \tag{56}$$

with ρ' being the radius of the circle. a_{ij} and b_{ij} are then immediately known by employing Eqs. (52) and (53). For noncircular geometries, u and v can either be analytically or numerically derived. For instance, implementing Eqs. (48) and (49) for a square of width of d yields

$$u \approx 3.25/d \quad \text{and} \quad v \approx 0.47d. \tag{57}$$

Comparing the one-group and two-group models, the latter has an additional transport equation, which increases its complexity. However, the accuracy should also be increased, since the energy is not assumed to be uniform in the y-z plane or over the γ angle as the one-group model does. While the one-group model is legitimate when absorption is weak, the two-group model should be valid for a wider range of absorption coefficients. In addition, the function D distinguishes different types of cross-sectional geometry by generating different u and v, and it brings back the coordinates y, z, and γ. Thus the two-group model allows the consideration of the positions of both a receiver and source in the y-z plane.

Next, consider a simple numerical example to compare the accuracy of the one-group and two-group models. Assuming a semi-infinite circular duct with a radius of 1 m, and having all the surfaces perfectly absorbing, the sound energy decay along the long dimension is investigated when an omnidirectional point source is located at the center of the origin ($x=y=z=0$). This problem is equivalent to the sound propagation from a point source to a free space, where the sound field can be analytically solved. Therefore, we can use the exact analytic solution as the benchmark.

By assigning the reflection coefficient R and the attenuation coefficient M to zero in the one-group model, the analytic solution can be obtained as

$$\psi_1(x,\mu) = \frac{Q}{4\pi A'\mu}\exp\left(-x\frac{\sqrt{1-\mu^2}}{\lambda\mu}\right), \tag{58}$$

where Q is the sound source power, and the time t is discarded since the steady-state solution is of concern in this case. For the two-group model, a numerical solution is obtained. A follow-up paper[28] will report on details of the numerical implementations.

So far only the angular flux ψ has been discussed. However, in room acoustics, the sound energy or the sound pressure level is most frequently focused. Knowing the angular flux ψ, the sound pressure level can be written as[29]

$$L_p(\boldsymbol{r}) = 10\log\left[\frac{I(\boldsymbol{r})\rho c}{P_{\text{ref}}^2}\right], \tag{59}$$

where

$$I = \int_0^{2\pi}\int_{-1}^{1}\psi d\mu d\gamma \tag{60}$$

is the magnitude of sound intensity, ρ is the air density, and $P_{\text{ref}}=2\times10^{-5}$ Pa is the pressure reference. Thus, the intensity is an integral of the angular flux over all the angles. While the Monte Carlo simulation normally only provides the sound energy, which is angularly independent, the transport equation model provides more detailed angular information through the angular flux ψ.

By numerically implementing Eq. (60) for the solutions of the one-group and two-group models, the sound intensities along the long dimension can be obtained and are plotted in Fig. 6. These solutions are normalized at a distance of 1 m to the source. The exact solution $\psi(\boldsymbol{r},\boldsymbol{\Omega})$ of Eq. (2) with $\partial\psi/\partial t=0$, $M=0$, and $Q(\boldsymbol{r})=Q\delta(\boldsymbol{r})$ satisfies

$$\int_0^{2\pi}\int_{-1}^{1}\psi(\boldsymbol{r},\boldsymbol{\Omega})d\mu d\gamma = \frac{Q}{4\pi r^2}, \tag{61}$$

where $r=\sqrt{x^2+y^2+z^2}$ is the distance from the source. Figure 6 illustrates this result, which is normalized at $x=1$, as a benchmark. Figure 6(a) indicates that the two-group solution decays at a faster and more accurate rate than the one-group solution. It seems plausible that the one-group model is not such a bad match to the analytic solution at a long distance. However, Fig. 6(b), illustrating the sound intensity on a logarithmic scale, indicates that the one-group model becomes even worse at a long distance. Therefore, the one-group model is not able to accurately predict the sound field in this open-space case. This is because, as demonstrated in Sec. II B 1, the one-group model will fail when the absorption on

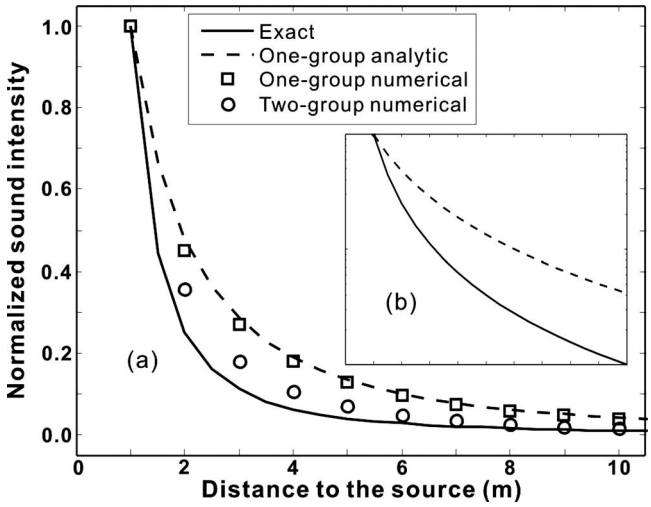

FIG. 6. Comparison of the sound intensity decay along the long dimension of a circular duct between the one-group model and the two-group model in a free space scenario. The analytic solution ($1/r^2$ law) is used as a benchmark. (a) The sound intensity is plotted on a linear scale. (b) The sound intensity is plotted on a logarithmic scale: only the exact solution and the analytic one-group model solution are presented.

the wall is strong (as in this case, where the absorption coefficient is 1.0). Additional simulations show that the numerical results of both one- and two-group models converge to the analytic solution when narrowing the duct.

Indeed, the sound propagation in a free space is somehow an unrealistic case. It is expected that the result would be totally different if the tube wall had been given a reflection coefficient close to 1, especially for the one-group model which is validated when the reflection is strong. However, the purpose of this example is only to demonstrate that the two-group model is more accurate than the one-group model. And the reason for choosing this simple example is that the analytic solutions of the one-group model as well as the three-dimensional exact equation can be easily found. More complicated cases (reflection coefficient being nonzero) require sophisticated numerical methods for both one- and two-group models, which will be detailed in a follow-up paper.[28]

C. Other considerations

1. Sources

This subsection briefly discusses the possibility of taking into account different types of sound sources and source directivity. This demonstrates the flexibility of the present model.

So far, only the omnidirectional point source has been considered. According to Eq. (30) and the definition of the Dirac delta function, for the two-group model,

$$Q_1 = \frac{Q(t)}{4\pi A'}\delta(x-x_0), \tag{62a}$$

$$Q_2 = \frac{Q(t)}{8\pi^2 A'}\delta(x-x_0)\times\int_0^{2\pi} u[D(y_0,z_0,\boldsymbol{\phi})-v]d\gamma. \tag{62b}$$

For a point source at $\boldsymbol{r}_0$ with directivity, the source term in Eq. (2) is written as $Q(\gamma,\mu,t)\delta(\boldsymbol{r}-\boldsymbol{r}_0)$ instead, and similarly

$$Q_1 = \frac{1}{2\pi A'}\delta(x-x_0)\int_0^{2\pi} Q(\gamma,\mu,t)d\gamma, \tag{63a}$$

$$Q_2 = \frac{1}{2\pi A'}\delta(x-x_0)\int_0^{2\pi} u[D(y_0,z_0,\boldsymbol{\phi})-v]Q(\gamma,\mu,t)d\gamma. \tag{63b}$$

Besides the point source, which is the most effective source in room-acoustic simulations, line sources and plane sources can also be treated by the one-dimensional transport equation model. For a line source at $x=x_0$, $y=y_0$, which spans from z_0 to z_1, the source term is written as $Q(\gamma,\mu,t)\delta(x-x_0)\delta(y-y_0)\chi_{[z_0,z_1]}(z)$, where χ is the indicator function,

$$\chi_{[B]}(x)=1 \quad \text{if } x\in B,$$

$$\chi_{[B]}(x)=0 \quad \text{if } x\notin B. \tag{64}$$

Q_i immediately becomes

$$Q_1 = \frac{1}{2\pi A'}\delta(x-x_0)(z_1-z_0)\int_0^{2\pi} Q(\gamma,\mu,t)d\gamma, \tag{65a}$$

$$Q_2 = \frac{1}{2\pi A'}\delta(x-x_0)\times\int_0^{2\pi} Q(\gamma,\mu,t)\int_{z_0}^{z_1} u[D(y_0,z,\boldsymbol{\phi})-v]dzd\gamma. \tag{65b}$$

In the same fashion, the source term for a plane source at $x=x_0$ is $Q(\gamma,\mu,t)\delta(x-x_0)$. Q_i are written as

$$Q_1 = \frac{1}{2\pi}\delta(x-x_0)\int_0^{2\pi} Q(\gamma,\mu,t)d\gamma, \tag{66a}$$

$$Q_2 = \frac{1}{2\pi A'}\delta(x-x_0)\times\int_0^{2\pi} Q(\gamma,\mu,t)\int_A u[D(y,z,\boldsymbol{\phi})-v]dydzd\gamma. \tag{66b}$$

For one-group model, only Q_1 is needed.

2. Furnished rooms

In furnished rooms (sometimes also called fitted rooms[30]), the interior contains noticeable objects (fittings), e.g., machines, chairs, and desks. Some factories, classrooms, and offices are studied as furnished rooms. In these cases, the theory for empty rooms no longer holds—the fittings inside the room need to be considered. In general, the sound field in a furnished room is complex due to different locations, absorption, and scattering coefficients of objects inside the room. Our goal is to model a simple case where the objects inside the room have more or less the same absorption and scattering coefficients, and the positions of

these scattering objects can be statistically described by the mean free path between them, which can be obtained by a best-fit approach.[31] To further simplify the problem, the scattering of the sound by the fittings is modeled as a uniform isotropic scattering. For furnished rooms, the three-dimensional transport equation is

$$\frac{1}{c}\frac{\partial \psi}{\partial t}(\boldsymbol{r},\boldsymbol{\Omega},t)+\boldsymbol{\Omega}\cdot\boldsymbol{\nabla}\psi(\boldsymbol{r},\boldsymbol{\Omega},t)+(M+\sigma_T)\psi(\boldsymbol{r},\boldsymbol{\Omega},t)$$
$$=\frac{\sigma_S}{4\pi}\int_{4\pi}\psi(\boldsymbol{r},\boldsymbol{\Omega}',t)d\Omega'+\frac{Q(\boldsymbol{r},t)}{4\pi},$$
$$0<x<L,\quad (y,z)\in A, \tag{67}$$

where $\sigma_T=\sigma_S+\sigma_A$, and σ_S and σ_A are the so-called scattering and absorption coefficients for the fittings, respectively. It can be shown that[13]

$$\sigma_T=\frac{1}{\lambda'}, \tag{68a}$$

$$\sigma_A=\frac{-\ln(1-\alpha_f)}{\lambda'}, \tag{68b}$$

where λ' is the mean free path between the scattering objects in the room, and α_f is the sound energy absorption coefficient of the fittings. A similar equation is documented in Ref. 32, with the absorption term being

$$\sigma_A=\frac{\alpha_f}{\lambda'}. \tag{69}$$

This difference has been explained in Refs. 13 and 33.

Repeating the same analysis for the empty room case, the one-dimensional transport equation model for the furnished rooms can be obtained. For example, the one-group model is written as

$$\frac{1}{c}\frac{\partial \psi_1}{\partial t}+\mu\frac{\partial \psi_1}{\partial x}+(M+\sigma_T)\psi_1+\sqrt{1-\mu^2}a_{11}\psi_1$$
$$=\frac{\sigma_S}{2}\int_{-1}^{1}\psi_1(\mu')d\mu'+\frac{2sR}{\pi}\sqrt{1-\mu^2}b_{11}$$
$$\times\int_{-1}^{1}\sqrt{1-\mu'^2}\psi_1(\mu')d\mu'+Q_1. \tag{70}$$

III. CONCLUSIONS

This paper proposes a set of coupled one-dimensional transport equations, which are derived from the exact three-dimensional transport equation, to predict the steady-state and time-dependent sound fields in elongated spaces.

The aim of this work is to develop an efficient mathematical model for predicting long room acoustics by concentrating on the long dimension and "eliminating" the other two dimensions. It is hoped that, by using this one-dimensional model, the calculation load can be significantly lessened with little loss of accuracy.

The "journey" from the three-dimensional transport equation to the one-dimensional transport equations lies in the method of weighted residuals, by which the sound angular flux is essentially divided into two parts. One is the sound energy propagation in the long dimension, while the other is a set of predetermined basis functions of cross-sectional parameters.

The one-dimensional one- and two-group transport equation models developed in this paper have simple formats. They differ from each other by having one one-dimensional transport equation and two one-dimensional transport equations, respectively. The one-group transport equation model essentially assumes that the energy flux has weak dependence on the cross-sectional spatial and angular variables. Therefore, it is likely to be suitable only for cases where a light-damping condition is satisfied. The two-group transport equation model improves the accuracy of the one-group model by taking the dependence on the cross-sectional variables into account. However, the two-group model is more complex. A simple numerical example has been carried out for sound propagation from an omnidirectional source to a free space. The result suggests that the two-group model is indeed more accurate.

This paper has shown that the one-dimensional models are able to simulate different types of sources, with various directivities. Fittings in the room can also be modeled as interior scattering objects. Thus, the one-dimensional models are applicable for modeling empty rooms and fitted rooms.

ACKNOWLEDGMENTS

The authors would like to thank Professor H. Kuttruff, Professor M. M. R. Williams, and Professor Roberto D. M. Garcia for helpful discussions.

APPENDIX: DERIVATION OF THE ONE–DIMENSIONAL TRANSPORT EQUATION MODEL

This appendix elaborates on the derivation of the one-dimensional transport equation model, i.e., Eq. (27). Applying Eq. (22) to Eq. (23) first, using the identity

$$\beta_i\boldsymbol{\phi}\cdot\boldsymbol{\nabla}\psi=\boldsymbol{\phi}\cdot\boldsymbol{\nabla}(\beta_i\psi)-\psi\boldsymbol{\phi}\cdot\boldsymbol{\nabla}\beta_i$$
$$=\boldsymbol{\nabla}\cdot(\beta_i\psi\boldsymbol{\phi})-\beta_i\psi\boldsymbol{\nabla}\cdot\boldsymbol{\phi}-\psi\boldsymbol{\phi}\cdot\boldsymbol{\nabla}\beta_i \tag{A1}$$

and the divergence theorem to Eq. (23), yields

$$F_i=-\frac{\sqrt{1-\mu^2}}{2\pi A'}\left(\int_{\partial A}\int_0^{2\pi}\boldsymbol{\phi}\cdot\boldsymbol{n}\beta_i\psi d\gamma ds'\right.$$
$$\left.-\int_A\int_0^{2\pi}\psi\boldsymbol{\phi}\cdot\boldsymbol{\nabla}\beta_i d\gamma dydz\right), \tag{A2}$$

where

$$F_i=\frac{1}{c}\frac{\partial \psi_i}{\partial t}+\mu\frac{\partial \psi_i}{\partial x}+M\psi_i-Q_i. \tag{A3}$$

By splitting the integral over γ into two parts: $\boldsymbol{\phi}\cdot\boldsymbol{n}<0$ and $\boldsymbol{\phi}\cdot\boldsymbol{n}>0$, substitution of Eq. (3) into Eq. (A2) yields

$$F_i = -\frac{\sqrt{1-\mu^2}}{2\pi A'}\left\{\int_{\partial A}\int_{\boldsymbol{\phi}\cdot\boldsymbol{n}>0}\boldsymbol{\phi}\cdot\boldsymbol{n}\beta_i\psi d\gamma ds' + \int_{\partial A}\int_{\boldsymbol{\phi}\cdot\boldsymbol{n}<0}\boldsymbol{\phi}\cdot\boldsymbol{n}\beta_i R\left[(1-s)\psi(\hat{\boldsymbol{\Omega}}) + \frac{s}{\pi}\int_{\boldsymbol{\Omega}'\cdot\boldsymbol{n}>0}\boldsymbol{\Omega}'\cdot\boldsymbol{n}\psi(\boldsymbol{\Omega}')d\Omega'\right]d\gamma ds' - \int_A\int_0^{2\pi}\psi\boldsymbol{\phi}\cdot\nabla\beta_i d\gamma dy dz\right\}. \quad (A4)$$

From Eqs. (10), (11), and (40b),

$$\int_{\boldsymbol{\phi}\cdot\boldsymbol{n}<0}\boldsymbol{\phi}\cdot\boldsymbol{n}\psi(\hat{\boldsymbol{\Omega}})d\gamma = -\int_{\hat{\boldsymbol{\phi}}\cdot\boldsymbol{n}>0}\hat{\boldsymbol{\phi}}\cdot\boldsymbol{n}\psi(\hat{\boldsymbol{\Omega}})d\hat{\gamma} = -\int_{\boldsymbol{\phi}\cdot\boldsymbol{n}>0}\boldsymbol{\phi}\cdot\boldsymbol{n}\psi(\boldsymbol{\Omega})d\gamma, \quad (A5)$$

and

$$\int_{\boldsymbol{\phi}\cdot\boldsymbol{n}<0}\boldsymbol{\phi}\cdot\boldsymbol{n}u(D-v)\psi(\hat{\boldsymbol{\Omega}})d\gamma = 0 - uv\int_{\boldsymbol{\phi}\cdot\boldsymbol{n}<0}\boldsymbol{\phi}\cdot\boldsymbol{n}\psi(\hat{\boldsymbol{\Omega}})d\gamma = uv\int_{\boldsymbol{\phi}\cdot\boldsymbol{n}>0}\boldsymbol{\phi}\cdot\boldsymbol{n}\psi(\boldsymbol{\Omega})d\gamma. \quad (A6)$$

Substitution of Eqs. (44), (45), (A5), and (A6) into Eq. (A4) yields

$$F_1 = -\frac{\sqrt{1-\mu^2}}{2\pi A'}\left\{[1-R(1-s)]\int_{\partial A}\int_{\boldsymbol{\phi}\cdot\boldsymbol{n}>0}\boldsymbol{\phi}\cdot\boldsymbol{n}\psi d\gamma ds' + \frac{Rs}{\pi}\int_{\partial A}\int_{\boldsymbol{\phi}\cdot\boldsymbol{n}<0}\boldsymbol{\phi}\cdot\boldsymbol{n}\int_{\boldsymbol{\Omega}'\cdot\boldsymbol{n}>0}\boldsymbol{\Omega}'\cdot\boldsymbol{n}\psi(\boldsymbol{\Omega}')d\Omega' d\gamma ds'\right\} \quad (A7)$$

and

$$F_2 = -\frac{\sqrt{1-\mu^2}}{2\pi A'}\left[\int_{\partial A}\int_{\boldsymbol{\phi}\cdot\boldsymbol{n}>0}\boldsymbol{\phi}\cdot\boldsymbol{n}\beta_2\psi d\gamma ds' + R(1-s)uv \times\int_{\partial A}\int_{\boldsymbol{\phi}\cdot\boldsymbol{n}>0}\boldsymbol{\phi}\cdot\boldsymbol{n}\psi d\gamma ds' + \frac{Rs}{\pi}\int_{\partial A}\int_{\boldsymbol{\phi}\cdot\boldsymbol{n}<0}\boldsymbol{\phi}\cdot\boldsymbol{n}\beta_2 \times\int_{\boldsymbol{\Omega}'\cdot\boldsymbol{n}>0}\boldsymbol{\Omega}'\cdot\boldsymbol{n}\psi(\boldsymbol{\Omega}')d\Omega' d\gamma ds' - \int_A\int_0^{2\pi}\psi\boldsymbol{\phi}\cdot\nabla\beta_2 d\gamma dy dz\right]. \quad (A8)$$

For F_i where $i>2$, similar equations can be derived if α_i and β_i are known. This is, however, not discussed here.

Moreover, by recognizing that

$$\int_{\boldsymbol{\Omega}'\cdot\boldsymbol{n}>0}(\boldsymbol{\Omega}'\cdot\boldsymbol{n})(\cdot)d\Omega' = \int_{\boldsymbol{\phi}'\cdot\boldsymbol{n}>0}\boldsymbol{\phi}'\cdot\boldsymbol{n}\int_{-1}^{1}\sqrt{1-\mu'^2}(\cdot)d\mu' d\gamma' \quad (A9)$$

and employing Eq. (22),

$$\int_{\boldsymbol{\phi}\cdot\boldsymbol{n}<0}\boldsymbol{\phi}\cdot\boldsymbol{n}\beta_i\left[\int_{\boldsymbol{\Omega}'\cdot\boldsymbol{n}>0}\boldsymbol{\Omega}'\cdot\boldsymbol{n}\psi(\boldsymbol{\Omega}')d\Omega'\right]d\gamma = \int_{\boldsymbol{\phi}\cdot\boldsymbol{n}<0}\boldsymbol{\phi}\cdot\boldsymbol{n}\beta_i \times\left[\int_{\boldsymbol{\phi}'\cdot\boldsymbol{n}>0}\boldsymbol{\phi}'\cdot\boldsymbol{n}\left(\int_{-1}^{1}\sqrt{1-\mu'^2}\psi d\mu'\right)d\gamma'\right]d\gamma = -\sum_{j=1}^{N}\left(\int_{-1}^{1}\sqrt{1-\mu'^2}\psi_j d\mu'\int_{\boldsymbol{\phi}\cdot\boldsymbol{n}<0}|\boldsymbol{\phi}\cdot\boldsymbol{n}|\beta_i d\gamma \times\int_{\boldsymbol{\phi}\cdot\boldsymbol{n}>0}\boldsymbol{\phi}\cdot\boldsymbol{n}\alpha_j d\gamma\right). \quad (A10)$$

Substituting Eq. (A10) into Eqs. (A7) and (A8), the one-dimensional transport model, Eq. (27), is finally obtained.

[1] J. Kang, *Acoustics in Long Spaces: Theory and Design Guide* (Thomas Thelford, London, 2002).
[2] H. Kuttruff, *Room Acoustics*, 4th ed. (Spon, New York, 2000).
[3] H. Kuttruff, "Stationare schallausbreitung in langraumen (Steady-state sound transmission in elongated enclosures)," Acustica **69**, 53–62 (1989).
[4] J. Kang, "Reverberation in rectangular long enclosures with geometrically reflecting boundaries," Acust. Acta Acust. **82**, 509–516 (1996).
[5] K. M. Li and K. K. Lu, "Propagation of sound in long enclosures," J. Acoust. Soc. Am. **116**, 2759–2770 (2004).
[6] A. M. Ondet and J. L. Barbry, "Modeling of sound propagation in fitted workshops using ray tracing," J. Acoust. Soc. Am. **85**, 787–796 (1989).
[7] L. Yang and B. M. Shield, "The prediction of speech intelligibility in underground stations of rectangular cross section," J. Acoust. Soc. Am. **109**, 266–273 (2001).
[8] M. M. Carroll and C. F. Chien, "Decay of reverberant sound in a spherical enclosure," J. Acoust. Soc. Am. **62**, 1442–1446 (1977).
[9] J. Kang, "Reverberation in rectangular long enclosures with diffusely reflecting boundaries," Acust. Acta Acust. **88**, 77–87 (2002).
[10] J. Picaut, L. Simon, and J. D. Polack, "A mathematical model of diffuse sound field based on a diffusion equation," Acust. Acta Acust. **83**, 614621 (1997).
[11] V. Valeau, J. Picaut, and M. Hodgson, "On the use of a diffusion equation for room-acoustic prediction," J. Acoust. Soc. Am. **119**, 1504–1513 (2006).
[12] Y. Jing and N. Xiang, "A modified diffusion equation for room-acoustic predication," J. Acoust. Soc. Am. **121**, 3284–3287 (2007).
[13] Y. Jing and N. Xiang, "On boundary conditions for the diffusion equation in room-acoustic prediction: Theory, simulations, and experiments," J. Acoust. Soc. Am. **123**, 145–153 (2008).
[14] S. Siltanen, T. Lokki, S. Kiminki, and L. Savioja, "The room acoustic rendering equation," J. Acoust. Soc. Am. **122**, 1624–1635 (2007).
[15] M. Hodgson, "Evidence of diffuse surface reflections in rooms," J. Acoust. Soc. Am. **89**, 765–771 (1991).
[16] C. Foy, V. Valeau, A. Billon, J. Picaut, and A. Sakout, "An empirical diffusion model for acoustic prediction in rooms with mixed diffuse and specular reflections," Acust. Acta Acust. **95**, 97–105 (2009).
[17] N. Korany, J. Blauert, and O. A. Alim, "Acoustic simulation of rooms with boundaries of partially specular reflectivity," Appl. Acoust. **62**, 875–887 (2001).
[18] T. Le Pollès, J. Picaut, M. Bérengier, and C. Bardos, "Sound field modeling in a street canyon with partially diffusely reflecting boundaries by the transport theory," J. Acoust. Soc. Am. **116**, 2969–2983 (2004).

[19]T. Le Pollès, J. Picaut, S. Colle, M. Bérengier, and C. Bardos, "Sound-field modeling in architectural acoustics by a transport theory: Application to street canyons," Phys. Rev. E **72**, 046609 (2005).
[20]A. K. Prinja and G. C. Ponraning, "A statistical model for transport in a vacuum," Transp. Theory Stat. Phys. **13**, 567–598 (1984).
[21]E. W. Larsen, "A one-dimensional model for three-dimensional transport in a pipe," Transp. Theory Stat. Phys. **13**, 599–614 (1984).
[22]E. W. Larsen, F. Malvagi, and G. C. Pomraning, "One-dimensional models for neutral particle transport in ducts," Nucl. Sci. Eng. **93**, 13–30 (1986).
[23]W. B. Joyce, "Classical-particle description of photons and phonons," Phys. Rev. D **9**, 3234–3256 (1974).
[24]A. Billon, C. Foy, J. Picaut, V. Valeau, and A. Sakout, "Modeling the sound transmission between rooms coupled through partition alls by using a diffusion model," J. Acoust. Soc. Am. **123**, 4261–4271 (2008).
[25]H. Grandin, *Fundamentals of the Finite Element Method* (Waveland Press, Inc., Prospect Heights, IL, 1991).
[26]P. S. Krämer, "Mean free path length for radiating point source in specular reflecting enclosures," Acust. Acta Acust. **83**, 629–634 (1997).
[27]W. J. M. de Kruijf and J. L. Kloosterman, "On the average chord length in reactor physics," Ann. Nucl. Energy **30**, 549–553 (2003).
[28]Y. Jing and N. Xiang, "One-dimensional transport equation models for sound energy propagation in long spaces: Simulations and experiments," J. Acoust. Soc. Am. **127**, 2323–2331 (2010).
[29]A. D. Pierce, *Acoustics: An Introduction to Its Physical Principles and Applications* (Acoustical Society of America, New York, 1981).
[30]V. Valeau, M. Hodgson, and J. Picaut, "A diffusion-based analogy for the prediction of sound fields in fitted rooms," Acust. Acta Acust. **93**, 94–105 (2007).
[31]M. Hodgson, "Effective densities and absorption coefficients of fittings in industrial work-rooms," Acust. Acta Acust. **85**, 108–112 (1999).
[32]H. Kuttruff, "A mathematical model for noise propagation between buildings," J. Sound Vib. **85**, 115–128 (1982).
[33]U. J. Kurze, "Scattering of sound in industrial spaces," J. Sound Vib. **98**, 349–364 (1985).

One-dimensional transport equation models for sound energy propagation in long spaces: Simulations and experiments

Yun Jing[a] and Ning Xiang
Graduate Program in Architectural Acoustics, School of Architecture, Rensselaer Polytechnic Institute, Troy, New York 12180

(Received 8 September 2009; revised 5 January 2010; accepted 7 January 2010)

In this paper, the accuracy and efficiency of the previously discussed one-dimensional transport equation models [Y. Jing *et al.*, J. Acoust. Soc. Am. **127**, 2312–2322 (2010)] are examined both numerically and experimentally. The finite element method is employed to solve the equations. Artificial diffusion is applied in the numerical implementation to suppress oscillations of the solution. The transport equation models are then compared with the ray-tracing based method for different scenarios. In general, they are in good agreement, and the transport equation models are substantially less time consuming. In addition, the two-group model is found to yield more accurate results than the one-group model for the tested cases. Lastly, acoustic experimental results obtained from a 1:10 long room scale-model are used to verify the transport equation models. The results suggest that the transport equation models are able to accurately model the sound field in a long space. © *2010 Acoustical Society of America.* [DOI: 10.1121/1.3303981]

PACS number(s): 43.55.Br, 43.55.Ka [EJS] Pages: 2323–2331

I. INTRODUCTION

This paper verifies the one-dimensional transport equation models in long spaces[1] using both numerical simulations and acoustical experimental results. A companion paper has presented theoretical formulations of a subset of one-dimensional transport equation models for acoustic prediction in long spaces. These models drastically simplify the three-dimensional exact model by reducing five variables to two (three in space, two in angle); thus, they are expected to be less time consuming in comparison with ray-tracing based methods[2] or radiosity based methods[3] when implemented numerically. On the other hand, a simple example of a sound field in free space has demonstrated that these models are fairly good approximations to the exact model.[1] Particularly, since the diffusion equation can be derived as the asymptotic approximation of the transport equation in certain cases,[4,5] the transport equation method will perform significantly better than the diffusion equation model[4,6–9] recently applied in room-acoustics. For example, the transport equation takes the direct sound field into account while the diffusion equation fails to do so; therefore, the diffusion equation is only valid in the late time.[10] The diffusion equation is inherently unsuitable for problems where the absorption involved is high,[11] while the transport equation is much less restricted to this condition. The diffusion equation model assumes diffusely reflecting surface in the enclosure under investigation while the transport equation can handle explicitly partial specular and partial scattering reflections. In addition, solving the present one-dimensional transport equation does not necessarily take much longer time than solving the three-dimensional diffusion equation. This follow-up paper focuses on solving both the one- and two-group transport equation models numerically for different long spaces and compares the results with those obtained with a ray-tracing based method as well as experimental results obtained from a long room scale-model.

This paper is structured as follows: Sec. II briefly revisits the one-dimensional transport equation models for room-acoustic prediction in long spaces and then introduces solution methods used in solving the equations. Section III discusses simulation results obtained using the transport equation models in comparison with the ray-tracing based method. Section IV describes the scale-model experiments and compares the acoustical measurement results with those obtained using the two-group transport equation model. Section V concludes the paper.

II. ONE-DIMENSIONAL TRANSPORT EQUATION MODELS

A. Governing equations

This section briefly reviews the one-dimensional transport equation models for sound propagation in a long enclosure.

Based on the concept of geometrical acoustics, the sound angular flux $\psi(\mathbf{r},\mathbf{\Omega},t)$ everywhere in a long space [with $\mathbf{r}=(x,y,z)$ and x being the longest dimension ranging from 0 to L] is shown to be the solution of a three-dimensional transport equation

$$\frac{1}{c}\frac{\partial\psi}{\partial t}(\mathbf{r},\mathbf{\Omega},t)+\mathbf{\Omega}\cdot\nabla\psi(\mathbf{r},\mathbf{\Omega},t)+M\psi(\mathbf{r},\mathbf{\Omega},t)=\frac{Q(\mathbf{r},t)}{4\pi},\quad 0<x<L\quad (y,z)\in A, \tag{1}$$

with appropriate boundary conditions, where $\mathbf{\Omega}$ is the unit vector in direction of flight, c is the speed of sound, M is the

[a]Author to whom correspondence should be addressed. Electronic mail: jingy@bwh.harvard.edu

atmospheric attenuation constant, Q is a source term, t is the time, and A is the cross section of the long space.

This radiative transport equation has the same form as the one used in the geometrical optic model.[12] Both models assume that waves behave as particles: phonon and photon. The direct solution of this transport equation is the angular flux (sometimes called radiance), which can immediately lead to the sound intensity and sound pressure by applying an integral over all the angles. Mathematically, a similar radiative transport equation can be derived from the wave equation in the high frequency regime by using the Wigner distribution.[13–15] The solution of this transport equation is an energy density in the phase space whose average over wavenumbers provides the spatial distribution of the energy density. However, this model is more mathematically complicated and less understood in room-acoustic community, which has not adopted it for use in room-acoustic predictions.

Using the method of weighted residuals (Galerkin), the angular flux ψ can be approximated by[16]

$$\psi(x,y,z,\mu,\gamma,t) \approx \sum_{j=1}^{N} \alpha_j(y,z,\gamma)\psi_j(x,\mu,t), \tag{2}$$

where α_j are prescribed basis functions, ψ_j are unknown expansion functions, μ and γ are angular variables, and the three-dimensional exact transport equation can be reduced to a coupled set of one-dimensional transport equations. Keeping the first or the first two one-dimensional transport equations leads to the so-called one- and two-group models, respectively. For an omnidirectional point source at (x_0,y_0,z_0), the one-dimensional transport equation model is written as

$$\frac{1}{c}\frac{\partial \psi_i}{\partial t} + \mu\frac{\partial \psi_i}{\partial x} + M\psi_i + \sqrt{1-\mu^2}\sum_{j=1}^{N} a_{ij}\psi_j = \frac{2Rs}{\pi}\sqrt{1-\mu^2}\sum_{j=1}^{N} b_{ij}\int_{-1}^{1}\sqrt{1-\mu'^2}\psi_j(\mu')d\mu' + Q_i, \tag{3}$$

where $N(\text{or } i)=1,2$ for one- and two-groups models, respectively, R is the average energy reflection coefficient, s is the average scattering coefficient,[17] which expresses the energy fraction between nonspecualr and specular reflections, and a_{ij} and b_{ij} are predefined functions associated with the basis functions

$$a_{11} = [1-R(1-s)]\frac{L'}{\pi A'},$$

$$a_{12} = [1-R(1-s)]\left(u - uv\frac{L'}{\pi A'}\right),$$

$$a_{21} = [R(1-s)-1]\frac{uvL'}{\pi A'},$$

$$a_{22} = \frac{u^2v^2L'}{\pi A'} + R(1-s)uv\left(u - \frac{uvL'}{\pi A'}\right), \tag{4}$$

$$b_{ij} = \begin{bmatrix} L'/(\pi A') & u - uvL'/(\pi A') \\ -uvL'/(\pi A') & -uv[u - uvL'/(\pi A')] \end{bmatrix}. \tag{5}$$

Here A' is the area of the cross section, which can be arbitrarily convex (circular, rectangular, etc.), L' is the circumference of the cross section, and u and v are both constants:

$$u = \left[\frac{1}{6\pi A'}\int_{\partial A}\int_{0}^{2\pi} \phi\cdot\mathbf{n}(D-v)^3 d\gamma ds'\right]^{-1/2}, \tag{6}$$

$$v = \frac{1}{4\pi A'}\int_{\partial A}\int_{\phi\cdot\mathbf{n}>0} \phi\cdot\mathbf{n}D^2 d\gamma ds', \tag{7}$$

where ds' denotes an increment of arc length. In this study, only square cross-section is considered as it is representative in room-acoustics. A square with a width of d gives that

$$u \approx 3.25/d, \quad v \approx 0.47d. \tag{8}$$

Lastly, the first two terms of the source functions Q_i are formulated as

$$Q_1 = \frac{Q(t)}{4\pi A'}\delta(x-x_0), \tag{9a}$$

$$Q_2 = \frac{Q(t)}{8\pi^2 A'}\delta(x-x_0)\times\int_0^{2\pi} u[D(y_0,z_0,\phi)-v]d\gamma, \tag{9b}$$

where $Q(t)$ is the sound source power, δ is the Dirac function, and $D(y,z,\phi)$ is the distance from an interior point (x,y,z) to the boundary along the direction $-\phi$ (where ϕ is the corresponding flight direction of γ).

Two types of boundary conditions for the opposing ends of the long enclosure are proposed to take the absorption into account, when the reflections are either diffuse or specular. The specularly reflecting boundary condition is

$$\psi_1(0,\mu,t) = R'\psi_1(0,-\mu,t), \quad 0<\mu\le 1, \tag{10a}$$

$$\psi_1(L,\mu,t) = R''\psi_1(L,-\mu,t), \quad -1\le\mu<0, \tag{10b}$$

$$\psi_2(0,\mu,t) = R'\psi_2(0,-\mu,t), \quad 0<\mu\le 1, \tag{10c}$$

$$\psi_2(L,\mu,t) = R''\psi_2(L,-\mu,t), \quad -1\le\mu<0, \tag{10d}$$

where R' and R'' are the reflection coefficients of the two ends, respectively.

The diffusely reflecting boundary conditions as follows:

$$\psi_1(0,\mu,t) = 2R'\int_{-1}^{0}(-\mu')\psi_1(0,\mu',t)d\mu', \quad 0<\mu\le 1, \tag{11a}$$

$$\psi_1(L,\mu,t) = 2R''\int_{0}^{1}\mu'\psi_1(0,\mu',t)d\mu', \quad -1\le\mu<0, \tag{11b}$$

$$\psi_2(0,\mu,t) = \frac{R'u^2}{2\pi^2 A'}\left[\int_A \left(\int_0^{2\pi} D d\gamma\right)^2 dydz - 4\pi^2 v^2 A'\right] \times \int_{-1}^{0} -\mu' \psi_2(0,\mu',t) d\mu', \quad 0 < \mu \le 1, \tag{11c}$$

$$\psi_2(L,\mu,t) = \frac{R''u^2}{2\pi^2 A'}\left[\int_A \left(\int_0^{2\pi} D d\gamma\right)^2 dydz - 4\pi^2 v^2 A'\right] \times \int_{0}^{1} \mu' \psi_2(0,\mu',t) d\mu', \quad -1 \le \mu < 0. \tag{11d}$$

Note for the diffusely reflecting boundary condition since

$$\frac{R'u^2}{2\pi^2 A'}\left[\int_A \left(\int_0^{2\pi} D d\gamma\right)^2 dydz - 4\pi^2 v^2 A'\right] \tag{12}$$

is usually very small, the present numerical simulations assume it to be zero. Therefore, Eqs. (11c) and (11d) become

$$\psi_2(0,\mu,t) \approx 0, \quad 0 < \mu \le 1, \tag{13a}$$

$$\psi_2(L,\mu,t) \approx 0, \quad -1 \le \mu < 0. \tag{13b}$$

A linear combination of these two boundary condition types in terms of the absorption and scattering coefficients can be used for partially diffuse reflection. However, for simplification, this study only considers purely specular or diffuse reflections.

The sound pressure level is of the most concern and can be written as

$$L_p(x,y,z,t) = 10 \log\left(\frac{I(x,y,z,t)\rho c}{P_{\text{ref}}^2}\right), \tag{14}$$

where

$$I(x,y,z,t) = \int_0^{2\pi}\int_{-1}^{1} \psi d\mu d\gamma \tag{15}$$

is the magnitude of the sound intensity, ρ is the air density, and $P_{\text{ref}}=2\times10^{-5}$ Pa is the pressure reference.

The transport equation models described above will be most accurate when the enclosure considered is sufficiently long (or narrow), as the unknown functions $\psi_j(x,\mu,t)$ imply that the sound energy flux is weakly dependent on y, z, and γ. The limits of aspect ratios (correlated dimensions) where this theory can be applied should be determined on a case-by-case basis in light of the desirable accuracy. However, in this study, the ratio between the length and width (or height) is always larger than 8, and good accuracy has been obtained.

B. Solution method

The one-dimensional transport equation model, which consists of integropartial differential equations, can be solved through the discrete ordinate method.[16] This study utilizes a finite element modeling software to generate the mesh in the domain using the Galerkin method and solve the equations. The spatial x and angular μ variables are discretized (see Fig. 1). Lagrange-quadratic and Lagrange-linear elements are used (basis functions in the finite element implementation are either linear or quadratic on each mesh interval). Their suitability will be discussed. The mesh condition can be found in the convergence study (Sec. III).

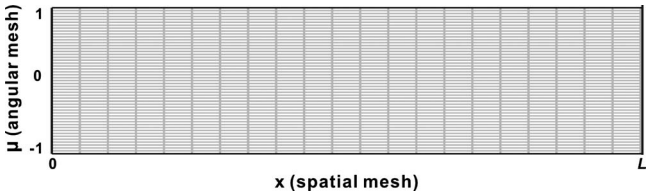

FIG. 1. Meshes for the finite element modeling in the spatial and angular domains.

When solving the steady-state transport equation numerically, artificial oscillations arise, primarily due to two reasons: (1) the equation is convection dominated and (2) the point source term in Eq. (3) introduces a discontinuity/singularity, which cannot be well resolved by the mesh. This will cause an initial disturbance that propagates through the computational domain. Refining the mesh resolution does not reduce the numerical oscillations since the discontinuity still exists and there is no diffusion term in the equation. Also it will be overly demanding of computing resources. Therefore, the anisotropic diffusion technology[18–20] is employed to suppress the oscillations and guarantee reasonable calculation time. The following simple example will briefly explain this. For more information, the reader is referred to Refs. 18–20. Assuming a convection-diffusion transport equation (a parabolic partial differential equation),

$$\frac{\partial u'}{\partial t} + \varepsilon \nabla u' = \nabla(\tau \nabla u'). \tag{16}$$

The Péclet number (Pe)[18–20] is defined as a function of the diffusion coefficient τ, convection function ε, and the mesh element size h,

$$\text{Pe} = \frac{\|\varepsilon\| h}{2\tau}. \tag{17}$$

Since the finite element discretization method used is the Galerkin method, solving such a transport equation becomes unstable when the Péclet number (Pe) is larger than 1. Notice that, in the acoustic transport equation [Eq. (3)], there is no diffusion term, implying that the Péclet number is always larger than 1.

By adding an artificial diffusion term τ_{art}, it is possible to make the Péclet number smaller than 1. The convection term ε is a vector, and anisotropic artificial diffusion adds diffusion only in the direction of the streamline. That is, there is no diffusion added in the direction orthogonal to ε. We now have

$$\tau_{\text{art}} = \frac{\varrho h \varepsilon_i \varepsilon_j}{\|\varepsilon\|}, \quad \text{Pe} = \frac{\|\varepsilon\| h}{2(\tau + \tau_{\text{art}})}, \tag{18}$$

where ϱ is a constant and ε_i and ε_j are components of ε. In this way, the Péclet number measured in the streamline di-

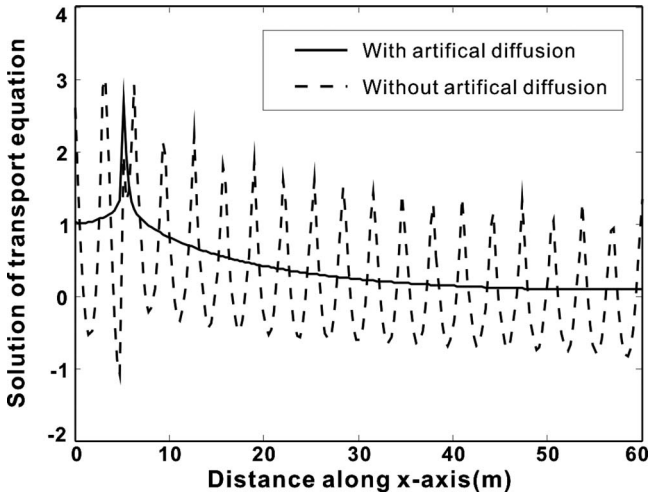

FIG. 2. Comparison of the solution ψ_1 with and without the artificial diffusion.

rection does not exceed 1, given that the constant ϱ is carefully chosen. In the present acoustic transport equation $\varepsilon = [\mu; 0]$ (no derivative in the μ-direction), and ϱ is chosen as 0.25. Therefore, to each coupled transport equation, a diffusion term

$$\frac{\varrho h \mu^2}{\|\varepsilon\|} \frac{\partial^2 \psi_i}{\partial x^2} \tag{19}$$

is added. Figure 2 shows the comparison between the results with and without artificial diffusion. The artificial diffusion indeed significantly reduces the numerical oscillations. Section III A 1 will discuss the validity of the solution.

When solving the time-dependent transport equation, the interpolating polynomial used in the time-stepping method is the second-order backward differentiation formula.[21] Introducing anisotropic diffusion to suppress oscillations turns out to produce noticeable numerical damping. Therefore, the initial condition should be defined so that it is continuous across the spatial domain, in order to minimize numerical oscillations. An initial condition is used with the Gaussian form

$$\psi(x,y,z,\mu,\gamma,0) = \delta(y-y_0)\,\delta(z-z_0)e^{-((x-x_0)^2/c_0)}, \tag{20}$$

where c_0 controls the width of the Gaussian distribution. Although c_0 should be a frequency dependent parameter, it is chosen as 1.0 in this study for simplicity. It is also found that for smaller c_0, the mesh needs to be denser for obtaining stable numerical results.

Note that in the present model, a single calculation throughout the domain generates the solution at all locations in the volume, which is fundamentally different from the ray-tracing based method where receiver location(s) usually need to be prescribed.

III. NUMERICAL RESULTS

A. Steady-state case

1. Verifications

This section discusses verifications of the present solution method. Same as in Ref. 16, where the study is about neutral particle transport, a circular duct with radius 1 m and length 50 m is tested. The boundaries are all diffusely reflecting. Sound particles enter the duct through one end ($x=0$) of the duct in an isotropic way and leave the duct through the other end which is completely open. The reflection probability at $x=0$ is defined as[16]

$$\hat{R} = \frac{\int_0^1 \mu\psi_1(0,-\mu)d\mu}{\int_0^1 \mu\psi_1(0,\mu)d\mu}. \tag{21}$$

The one-dimensional transport equations for steady-state are solved where the time t is neglected. Numerical results given are from a mesh resolution of 100 angular points and 200 spatial points. Calculation time is around 10 s for the one-group model and 40 s for the two-group model on a current laptop personal computer. The present results are compared with the results from Ref. 16 in Table I, showing good agreements.

TABLE I. Comparison between the present numerical results with the ones in Ref. 16: The probability of reflection for a circular duct with isotropic incidence.

α	$N=1$	$N=1$ [a]	Reflection probability $N=2$	$N=2$ [a]
0.1	0.018	0.018	0.0255	0.0256
0.2	0.038	0.038	0.0539	0.0541
0.3	0.062	0.061	0.0859	0.0862
0.4	0.089	0.089	0.1225	0.1229
0.5	0.123	0.122	0.1652	0.1656
0.6	0.164	0.164	0.2165	0.2170
0.7	0.219	0.218	0.2808	0.2814
0.8	0.296	0.295	0.3671	0.3677
0.9	0.423	0.423	0.5008	0.5014
0.99	0.751	0.751	0.8024	0.8027

[a]From Ref. 16.

2. Convergence study

The goal of this section is to first study the convergence condition when numerically solving the steady-state one-dimensional transport equation models and then to briefly compare the transport equation models with the ray-tracing based method, i.e., the solution of the three-dimensional transport equation. This section only discusses the two-group model since it is expected to be more accurate based on the previous discussion.[1] For steady-state transport equation models, the time variable t is simply discarded. An imaginary long room with dimensions $80\times4\times4$ m^3 is studied. The scattering coefficient is 0.8. The two ends are considered to be specularly reflecting. The absorption coefficient for all surfaces is 0.5. An omnidirectional source is located at (40, 2, 2) m with a sound power of 0.01 W. Here, numerical simulations only involve Lagrange-quadratic elements and observe the sound pressure level at position (60, 2, 2) m for different mesh resolutions. Note that the solution given by the ray-tracing method is 68.3 dB, and the calculation time is more than 5 min for obtaining well converged results. Table II lists the numerical results and suggests that the result in-

TABLE II. Sound pressure level prediction with varying mesh resolutions for a long room.

Spatial point number	Angular point number	Sound pressure level (dB)	Calculation time (s)
50	20	68.38	1
50	50	68.55	4
50	100	68.62	9
100	20	68.20	3
100	50	68.37	8
100	100	68.44	17
200	20	68.11	6
200	50	68.29	15
200	100	68.36	35
400	20	68.07	9
400	50	68.24	31
400	100	68.32	72

deed converges to a finite value as either the spatial or angular resolution increases. In addition, the difference between each prediction is within a tolerable range, which indicates that for predicting sound pressure level, a coarse mesh can be used for solving the one-dimensional two-group transport equation model. The most accurate result (68.32 dB) naturally occurs using the finest mesh. This agrees well with the ray-tracing result.

3. Comparison with ray-tracing simulations

This section compares numerical results from the present transport equation model with the ones from the ray-tracing based method implemented by a commercially available software CATT-acoustics®, for two representative scenarios. A long room with dimensions $60\times6\times6$ m^3 is modeled. An omnidirectional sound source is located at (5, 3, 3) m with sound power of 0.01 W. The receivers are along the line $y=z=3$ m. For the first case, the absorption coefficient is uniform and is 0.05, while in the second case, it is 0.5. The scattering coefficient for all side walls in the first case is 0.9 and 1.0 in the second case. The two end walls are diffusely reflecting. The number of rays for each ray-tracing is 500 000. The truncation time is long enough so that the sound energy decays to a negligible amount. When solving the transport equation, 10 000 mesh elements are constructed. Figures 3 and 4 show the sound pressure level distribution along the x-axis across the center of the long room. The following observations are worth discussing.

(1) For both examples, the two-group model agrees fairly well with the ray-tracing simulation, while the one-group model agrees less well, especially when the receivers are far away from the source, and the absorption involved is high. This observation is consistent with the conclusion in Larsen's paper.[16]
(2) For low absorption case, the maximum deviation of the one-group model from the ray-tracing simulation is around 2.0 dB, which is still acceptable. This suggests that, for stationary sound field predictions in weakly damping long rooms, both one- and two-group models can be employed. Particularly, if the sound field far away from the source is not of major concern, the one-group model works reasonably well.
(3) In Fig. 4, all the three curves show that the sound pressure level increases slightly when the receiver approaches the end ($x=60$ m). This important characteristic, however, cannot be captured by the diffusion equation model,[22] because the diffusion equation model is not accurate near the boundary.[11]

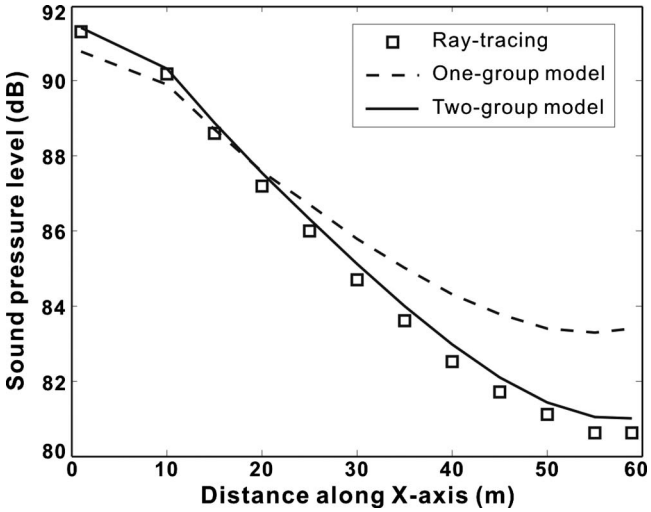

FIG. 3. Comparisons of sound pressure level distributions for a long room ($60\times6\times6$ m^3, uniform absorption coefficient of 0.05, scattering coefficient of 0.9, two end walls are diffusely reflecting) among ray-tracing simulations: one- and two-group models.

B. Time-dependent case

1. Convergence study

This section studies the convergence condition for the time-dependent case in terms of the reverberation time (RT) and early decay time (EDT), again for the two-group model. Compared with the steady-state case, one additional variable, i.e., time t, needs to be counted. The choice of the time step

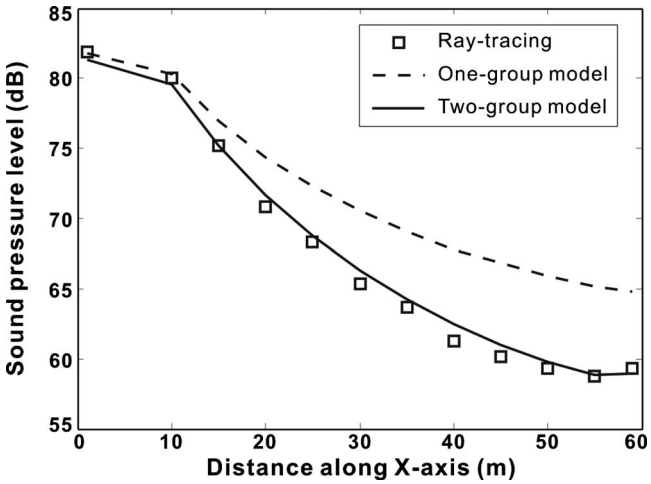

FIG. 4. Comparisons of sound pressure level distributions for a long room ($60\times6\times6$ m^3, uniform absorption coefficient of 0.5, scattering coefficient of 1.0 for all the walls) among ray-tracing simulations: one- and two-group models.

determines the accuracy of the solution and the calculation time, and therefore needs to be carefully examined. For results summarized here, the total number of mesh elements is changed, i.e., the product of both distance and angular point numbers, rather than both distance and angular mesh sizes being varied independently. Two types of mesh elements are considered: quadratic and linear. As anticipated, the former requires longer calculation time. The decay time parameters are found by exciting an impulse in the room using Eq. (20), solving for the sound intensity impulse response from the transport model, and using Schroeder integration[23] to compute for the sound intensity decay function. For calculating the reverberation time, the normalized decay level interval of -5 to -35 dB is used, and for early decay time, from 0 to -10 dB.[24]

The long room model has the same geometry, with dimensions $80\times4\times4$ m^3, as that for the steady-state convergence investigation, the source is also the same, the receiver is located at (20, 2, 2) m, the scattering coefficient for the side walls is 0.8, and the absorption coefficient for all walls is 0.4. For a narrow long room, if the two ends are specularly reflecting and strongly reflective, a randomized ray that happens to shoot exactly perpendicular to the end walls will continue to bounce back and forth between the end walls and create flutter echoes, which makes the energy decay curve irregular/nonexponential. In addition, relatively strong numerical damping has been found for the sound traveling in the direction perpendicular to the end walls ($\mu=\pm1$). Therefore, in the time-dependent case, only diffusely reflecting ends are included in the discussions. The total calculated time length for the transport equation model is 0.8 s, which is much longer than the expected reverberation time. The simulation results given by ray-tracing are 0.38 and 0.35 s for reverberation and early decay times, respectively. The calculation by ray-tracing takes more than 15 min. Figure 5 shows the energy impulse response, energy-time curve, and Schroeder integration curve at the receiver position. The transport equation model simulates the direct sound properly as the energy peak shown approximately at 0.06 s (the time the sound particles take to travel from $x=40$ to 20 m). Table III lists all the results. The first three results are produced with quadratic elements only because linear elements are extremely inaccurate for these three cases. Linear elements are actually also inaccurate for the next three cases, but we keep the results to demonstrate the required element number for linear elements. Table III, along with other related calculations, shows that using a fairly coarse spatial mesh and time step can produce accurate results for both reverberation and early decay times. Linear elements take less time than quadratic elements, and results from the former are reasonably accurate for sufficiently many mesh elements. The key point is that solving the transport equation model produces accurate results in much less time than ray-tracing and the solution at all mesh points throughout the space under investigation is achieved within one calculation run.

2. Comparison with ray-tracing simulations

This section compares numerical results from the present transport equation model with the ray-tracing results for two representative scenarios. A long room with dimension $40\times4\times4$ m^3 is modeled. The source is omnidirectional and is located at (10, 2, 2) m. The receivers are along the line $y=z=2$ m. In the first example, the absorption coefficient 0.2 is assigned uniformly. The scattering coefficient for all the side walls is 0.7. The two end walls are diffusely reflecting, i.e., $s=1.0$. The number of rays is 500 000 for the ray-tracing implementation. 8000 quadratic elements are generated when solving the transport equation. The time step is 0.001 s. Figure 6 shows the reverberation and early decay time trends along the x-axis. The two-group transport model agrees very well with the ray-tracing results, while the one-group model shows noticeable discrepancies with the ray-tracing results for reverberation times. All the models are able to show that reverberation time increases slowly while early decay time increases quickly.[7]

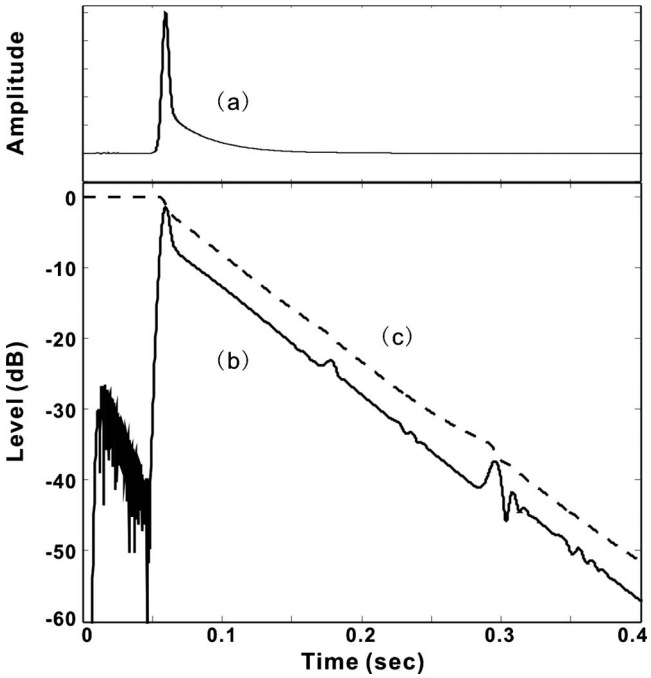

FIG. 5. Time-dependent simulation result: (a) energy decay curve in a long room; (b) logarithmic energy decay; and (c) Schroeder integration curve.

In the second example, the absorption coefficients are 0.4 for the side walls and 0.01 for the two end walls. The scattering coefficient is reduced to 0.5. Figure 7 shows the reverberation and early decay time results. Note that the one-group model is not included in this comparison. The discrepancy between the ray-tracing results and transport equation model results is still sufficiently small. These two cases suggest that the transport equation model, especially the two-group model, is fully capable of predicting sound energy decays in a long space. At least the accuracy of the present model is on the same level as a commercial acoustic prediction software.

IV. EXPERIMENTAL RESULTS

A. Experimental setup

A long room tenth scale-model is built to further assess the accuracy of the transport equation model. The reasons for

TABLE III. Reverberation time and early decay time predictions with varying mesh resolutions and time steps for a long room.

Element No.	Element type	Time step (s)	RT (s)	EDT (s)	Calculation time (s)
1000	Quadratic	0.002	0.404	0.419	19
1000	Quadratic	0.001	0.406	0.419	30
1000	Quadratic	0.0005	0.406	0.418	53
2000	Quadratic	0.002	0.401	0.376	38
2000	Linear	0.002	0.002	0.013	6
2000	Quadratic	0.001	0.402	0.379	61
2000	Linear	0.001	0.001	0.019	18
2000	Quadratic	0.0005	0.403	0.380	105
2000	Linear	0.0005	0.001	0.019	18
5000	Quadratic	0.002	0.401	0.360	99
5000	Linear	0.002	0.391	0.374	17
5000	Quadratic	0.001	0.404	0.362	166
5000	Linear	0.001	0.387	0.376	29
5000	Quadratic	0.0005	0.404	0.360	273
5000	Linear	0.0005	0.387	0.377	52

choosing physical scale modeling are its versatility and easy access.[10,25] The dimensions of the scale-model are $2.4 \times 0.24 \times 0.24$ m^3, which corresponds to $24 \times 2.4 \times 2.4$ m^3 for real size. This scale-model is built of $\frac{3}{8}$ in.-thick hard plywood. The wall surfaces are relatively smooth, only featured with small scale roughness (<0.2 cm in depth). Figure 8 shows a photograph of the scale-model with the top and two ends open. A miniature dodecahedron loudspeaker system used as the sound source is located at (6.1, 1.2, 1.2) m [see Fig. 9(a)]. It is reasonably omnidirectional up to 32 kHz. A $\frac{1}{4}$ in. microphone is used as the receiver to measure the room impulse responses excited by maximal-length sequences of $2^{18}-1$, averaged over ten repetitions. The microphone is moved along the centerline of the scale-model throughout the measurements. Fourteen measurements are conducted with an equidistant separation along the x-axis and are repeated five times to show the repeatability/uncertainty of the experiment. Measurements of the sound field close to the source are avoided since the source directivity has a greater impact on the near field. Neither nitrogen nor air drying is used to compensate for the air attenuation, as the air attenuation can be included in the transport equation model (see Sec. IV B), and the purpose of this measurement is only to verify the present model rather than to model an existing space. (The following discussion will only use real-sized dimensions.)

B. Experimental verifications of the transport equation model

This section aims to verify the transport equation model by comparing the experimental results with the simulation results. As the geometrical-acoustic model works only properly in a high frequency broad-band range, the results at 1–2

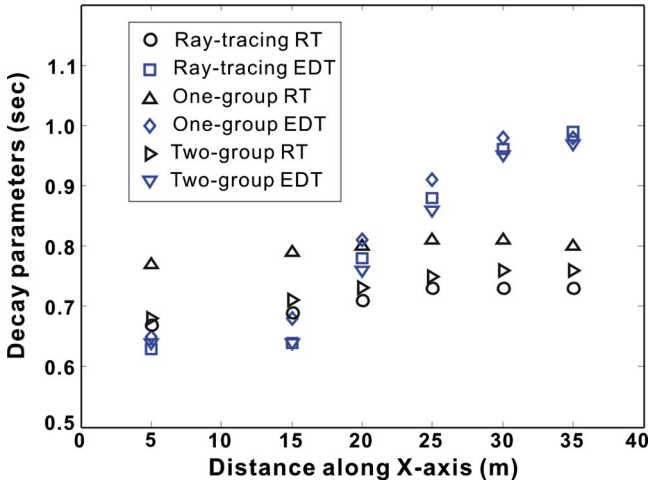

FIG. 6. (Color online) Comparisons of reverberation time and early decay time distributions for a long room ($40 \times 4 \times 4$ m^3, uniform absorption coefficient of 0.2, scattering coefficient of 0.7) among ray-tracing simulations: one- and two-group models.

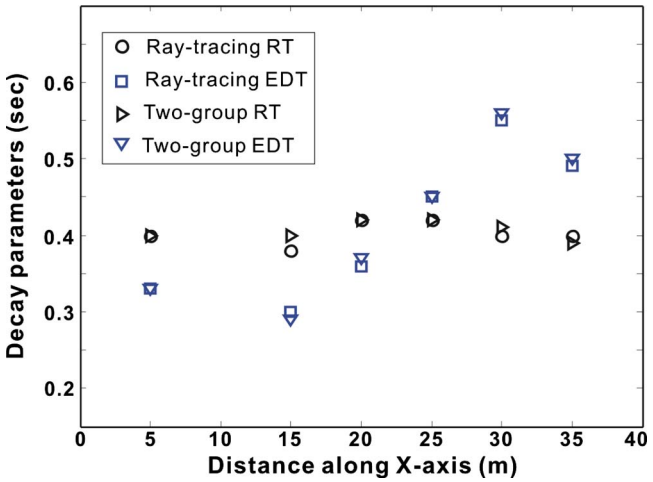

FIG. 7. (Color online) Comparisons of reverberation time and early decay time distributions for a long room ($40 \times 4 \times 4$ m^3, absorption coefficient of 0.4 for the side walls and 0.01 for the end walls, scattering coefficient of 0.5) between ray-tracing simulations and the two-group model.

FIG. 8. (Color online) Photograph of the long room tenth scale-model with the top and two ends open. Bottom left shows the miniature dodecahedron loudspeaker.

kHz octave broadband are chosen for comparison. In lower frequency bands, wave phenomena, e.g., standing waves, are observed, which cannot be modeled by the transport equation model. In the frequency range of interest (1–2 kHz), the absorption coefficient is estimated to be 0.15. The scattering coefficient is difficult to estimate but is expected to be low (as mentioned above, the wall surface is relatively smooth). An average air attenuation constant of 0.00391 Np/m is used for 10–20 kHz for the tenth-scale factor[26] (temperature of 20 °C and humidity of 50%).

This section only considers the two-group model. The reflections at the two ends are set to be completely diffused. Since two ends of the scale-model are relatively smooth, this will introduce a source of error; however, it is expected to be insignificant because the two ends are small compared with the side walls. For both steady-state and time-dependent cases, two simulations with scattering coefficients of 0.1 and 0.3, respectively, are carried out.

Figure 9(b) shows the comparison of sound pressure level distributions. The transport equation model with scattering coefficient of 0.3 agrees well with the experimental results. Most of results show small deviations (<1 dB). The transport equation model with scattering coefficient of 0.1 matches the experimental results less well but the disparity is still tolerable. This implies that the scattering coefficient is indeed low. To further confirm this, the simulated and measured reverberation times will be compared. Figure 10(a) presents a segment of the room impulse responses recorded 4.6 m from the source. Figure 10(b) illustrates the Schroeder curves given by experimental measurement in comparison with the transport equation model with scattering coefficients of 0.1 and 0.3.

Figure 11 shows a detailed comparison of the reverberation time prediction. Both simulation curves agree well with the measurement. Together with the sound pressure level distribution results, it appears that the scattering coefficient is likely to be between 0.1 and 0.3. So far, the experimental comparisons have demonstrated the validity of the one-dimensional transport equation model for a long space.

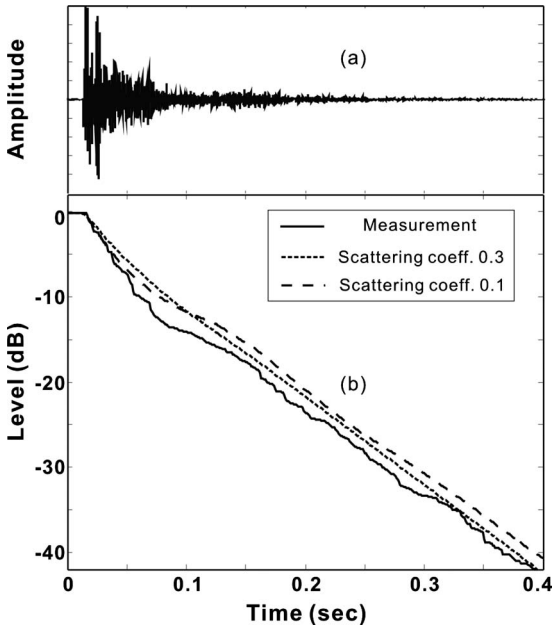

FIG. 10. Comparison between simulated and experimental results in a long room tenth scale-model: (a) segment of a room impulse response measured in a 1:10 long room scale-model; (b) comparison of the Schroeder curve between experiment and simulation. For simulated results, two scattering coefficients of 0.1 and 0.3 are used.

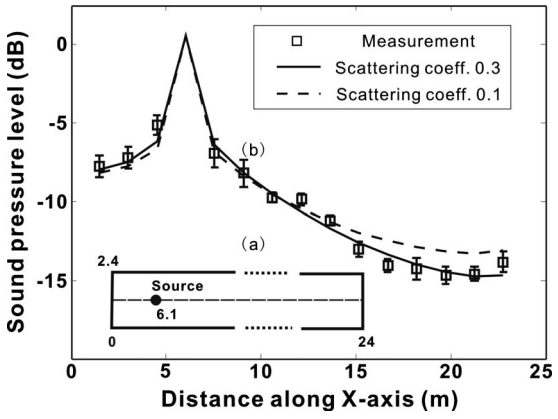

FIG. 9. Comparison between simulated and experimental results in a long room tenth scale-model: (a) top-view of a 1:10 long room scale-model; (b) comparison of sound pressure level distribution between simulated and experimental results. For simulated results, two scattering coefficients of 0.1 and 0.3 are used. The experimental results with error bars are evaluated from five sequentially repetitive measurements.

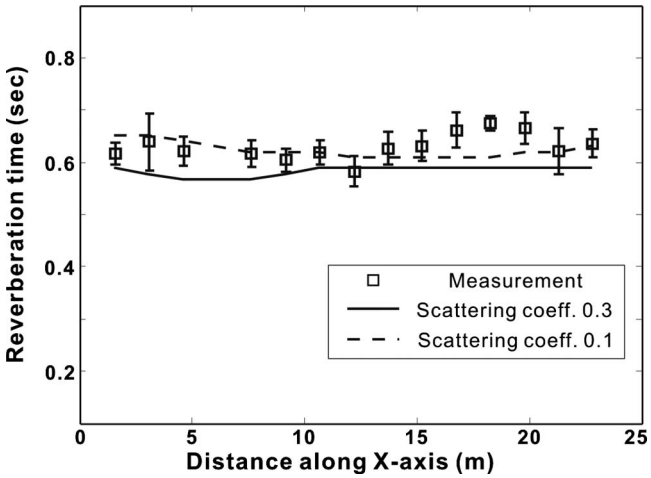

FIG. 11. Comparison of reverberation time between simulated and experimental results in a 1:10 long room scale-model. For simulated results, two scattering coefficients of 0.1 and 0.3 are used. The experimental results with error bars are evaluated from five sequentially repetitive measurements.

V. CONCLUSIONS

This paper has discussed numerical results for a long space room-acoustic model based on one-dimensional transport equations. The transport equation models explicitly handle partial specular, partial scattering, tolerate high overall absorption, and contain direct sound and early reflection portions of sound propagation. Comparisons between the transport equation model and the ray-tracing approach indicate that the solutions given by the one-dimensional transport equation model well approximate the three-dimensional exact solution. Particularly, the two-group model can work properly in a wide range of scenarios. In addition, numerically solving the transport equation models is significantly less time consuming than the ray-tracing approach. Note that the current solution method for the transport equation models is not specifically optimized; therefore, it is possible to speed up the simulation by using advanced technologies.[27] Finally, experimental results from a long room scale-model further validate the transport equation model.

Within the scope of this work, only empty rooms and omnidirectional sound sources are considered. However, these transport equation models can also take interior scattering objects and source directivity into account. These transport equation models can be extended to simulate side walls with nonuniform absorption or scattering coefficients, which makes the model more flexible. This study points out that the transport equation model is more accurate than the diffusion equation model, e.g., near a boundary. Detailed comparisons between the transport and diffusion equation models, which will clarify the relationship of these two models, are also attractive. These issues are expected to be addressed in future work.

ACKNOWLEDGMENTS

The authors would like to thank Professor E. Larson, Professor H. Kuttruff, Profesor W. Siegmann, and Professor J. Wei for their helpful discussions. The authors would also like to thank Mr. Joon Hee Lee and Mr. Gino Pellicano for their assistance in collecting experimental results, and Mr. Robert Bocala and Dr. Phillip Jason White for their critical reviews of the manuscript.

[1]Y. Jing, E. W. Larsen, and N. Xiang, "One-dimensional transport equation models for sound energy propagation in long spaces: Theory," J. Acoust. Soc. Am. **127**, 2312–2322 (2010).
[2]M. Vorländer, "Simulation of the transient and steady-state sound propagation in rooms using a new combined ray-tracing/image-source algorithm," J. Acoust. Soc. Am. **86**, 172–178 (1989).
[3]E. Nosal, M. Hodgson, and I. Ashdown, "Improved algorithms and methods for room sound-field prediction by acoustical radiosity in arbitrary polyhedral rooms," J. Acoust. Soc. Am. **116**, 970–980 (2004).
[4]T. Le Pollès, J. Picaut, M. Bérengier, and C. Bardos, "Sound field modeling in a street canyon with partially diffusely reflecting boundaries by the transport theory," J. Acoust. Soc. Am. **116**, 2969–2983 (2004).
[5]T. Le Pollès, J. Picaut, S. Colle, M. Bérengier, and C. Bardos, "Sound-field modeling in architectural acoustics by a transport theory: Application to street canyons," Phys. Rev. E **72**, 046609 (2005).
[6]J. Picaut, L. Simon, and J. D. Ploack, "A mathematical model of diffuse sound field based on a diffusion equation," Acust. Acta Acust. **83**, 614–621 (1997).
[7]V. Valeau, J. Picaut, and M. Hodgson, "On the use of a diffusion equation for room-acoustic prediction," J. Acoust. Soc. Am. **119**, 1504–1513 (2006).
[8]Y. Jing and N. Xiang, "A modified diffusion equation for room-acoustic predication," J. Acoust. Soc. Am. **121**, 3284–3287 (2007).
[9]Y. Jing and N. Xiang, "On boundary conditions for the diffusion equation in room-acoustic prediction: Theory, simulations, and experiments," J. Acoust. Soc. Am. **123**, 145–153 (2008).
[10]N. Xiang, Y. Jing, and A. Bockman, "Investigation of acoustically coupled enclosures using a diffusion-equation model," J. Acoust. Soc. Am. **126**, 1187–1198 (2009).
[11]P. M. Morse and H. Feshbach, *Methods of Theoretical Physics* (McGraw-Hill, New York, 1953).
[12]A. D. Klose and E. W. Larsen, "Light transport in biological tissue based on the simplified spherical harmonics equations," J. Comput. Phys. **220**, 441–470 (2006).
[13]L. Ryzhik, G. Papanicolaou, and J. B. Keller, "Transport equations for elastic and other waves in random media," Wave Motion **24**, 327–370 (1996).
[14]G. Bal and O. Pinaud, "Accuracy of transport models for waves in random media," Wave Motion **43**, 561–578 (2006).
[15]O. Runborg, "Mathematical models and numerical methods for high frequency waves," Comm. Comp. Phys. **2**, 827–880 (2007).
[16]E. W. Larsen, F. Malvagi, and G. C. Pomraning, "One-dimensional models for neutral particle transport in ducts," Nucl. Sci. Eng. **93**, 13–30 (1986).
[17]M. Vorländer and E. Mommertz, "Definition and measurement of random-incidence scattering coefficients," Appl. Acoust. **60**, 187–199 (2000).
[18]O. C. Zienkiewicz, R. L. Taylor, and P. Nithiarasu, *The Finite Element Method for Fluid Dynamics*, 6th ed. (Elsevier, New York, 2005).
[19]C. Johnson, "Numerical solution of partial differential equations by the finite element method," Acta Applicandae Mathematicae. **18**,184–186 (1987) .
[20]R. Codina, "Comparison of some finite element methods for solving the diffusion-convection-reaction equation," Comput. Methods Appl. Mech. Eng. **156**, 185–210 (1998).
[21]L. F. Shampine, *Numerical Solution of Ordinary Differential Equations* (Chapman and Hall, London, 1994).
[22]J. Picaut, L. Simon, and J. D. Ploack, "Sound field in long rooms with diffusely reflecting boundaries," Appl. Acoust. **56**, 217–240 (1999).
[23]M. R. Schroeder, "New method of measuring reverberation time," J. Acoust. Soc. Am. **37**, 409–412 (1965).
[24]ISO-3382, "Acoustics measurement of room acoustic parameters" (2008).
[25]N. Xiang and J. Blauert, "Binaural scale modeling for auralisation and prediction of acoustics in auditoria," Appl. Acoust. **38**, 267–290 (1993).
[26]ISO-9613, "Acoustics attenuation of sound during propagation outdoors, Part 1: Calculation of the absorption of sound by the atmosphere" (1993).
[27]R. D. M. Garcia and S. Ono, "Improved discrete ordinates calculations for an approximate model of neutral particle transport in ducts," Nucl. Sci. Eng. **133**, 40–54 (1999).

Statistical properties of kinetic and total energy densities in reverberant spaces[a)]

Finn Jacobsen[b)]
Department of Electrical Engineering, Acoustic Technology, Technical University of Denmark, Building 352, DK-2800 Kongens Lyngby, Denmark

Alfonso Rodríguez Molares
E.T.S.E. Telecomunicación, Universidade de Vigo, Campus Lagoas-Marcosende, E-36310 Vigo, Spain

(Received 16 July 2009; revised 7 January 2010; accepted 8 January 2010)

Many acoustical measurements, e.g., measurement of sound power and transmission loss, rely on determining the total sound energy in a reverberation room. The total energy is usually approximated by measuring the mean-square pressure (i.e., the potential energy density) at a number of discrete positions. The idea of measuring the total energy density instead of the potential energy density on the assumption that the former quantity varies less with position than the latter goes back to the 1930s. However, the phenomenon was not analyzed until the late 1970s and then only for the region of high modal overlap, and this analysis has never been published. Moreover, until fairly recently, measurement of the total sound energy density required an elaborate experimental arrangement based on finite-difference approximations using at least four amplitude and phase matched pressure microphones. With the advent of a three-dimensional particle velocity transducer, it has become somewhat easier to measure total rather than only potential energy density in a sound field. This paper examines the ensemble statistics of kinetic and total sound energy densities in reverberant enclosures theoretically, experimentally, and numerically.
 [DOI: 10.1121/1.3304158]

PACS number(s): 43.55.Cs, 43.58.Bh [AJZ] Pages: 2332–2337

I. INTRODUCTION

Many acoustical measurements rely on determining the sound energy in an enclosure. Examples include standardized measurements of sound power and transmission loss in reverberation rooms. The total sound energy is usually estimated by measuring the mean-square pressure (that is, the potential energy density) either at a number of discrete positions or using a moving microphone, and much effort has been spent on developing efficient averaging procedures.[1,2] The idea of measuring the total energy density rather than the potential energy density on the assumption that the former quantity varies less with position than the latter goes back to the 1930s and has occasionally been discussed in the literature.[3,4] In the late 1970s the phenomenon was analyzed using a stochastic interference model of a diffuse sound field,[5] and in the late 1980s the matter was examined experimentally for the first time.[6] However, until recently measurement of the total sound energy density has required an elaborate arrangement based on finite-difference approximations using at least four pressure microphones.[6–9] The microphones should be amplitude and phase matched very well, and the signal-to-noise ratio is poor because the finite-difference signals should be time integrated,[10] which is perhaps one of the reasons why the method has not been used much in practice. With the advent of a three-dimensional particle velocity transducer, "Microflown,"[11] it has become somewhat easier to measure kinetic and total rather than only potential energy density in a sound field, as demonstrated a few years ago.[12]

A recent investigation examined the ensemble statistics of the sound power emitted by a monopole in reverberant surroundings using Waterhouse's random wave theory[13] extended to the region of low modal overlap.[14] Another recent investigation used the same model to examine the ensemble statistics of potential energy density.[15] The purpose of the present study is to examine the ensemble statistics of kinetic and total sound energy densities in reverberant spaces theoretically, experimentally, and numerically.

II. THE RANDOM WAVE THEORY

A. The region of high modal overlap

The starting point of this investigation is a stochastic pure-tone diffuse-field interference model of the sound field in a reverberation room originally developed by Waterhouse.[13] This model describes the sound field as a sum of plane waves arriving with random phase angles from random directions,

[a)]Portions of this work were presented in "Measurement of total sound energy in an enclosure at low frequencies," Proceedings of Acoustics '08, Paris, France, July 2008, pp. 3249–3254, and "The uncertainty of pure tone measurements in reverberation rooms below the Schroeder frequency," Proceedings of Sixteenth International Congress on Sound and Vibration, Krakow, Poland, July 2009.

[b)]Author to whom correspondence should be addressed. Electronic mail: fja@elektro.dtu.dk

$$p(\mathbf{r}) = \lim_{N\to\infty} \frac{1}{\sqrt{N}} \sum_{n=1}^{N} A_n e^{j(\omega t - \mathbf{k}_n \cdot \mathbf{r})}, \tag{1}$$

where $p(\mathbf{r})$ is the sound pressure at position $\mathbf{r}$, A_n is a complex random amplitude the phase angle of which is uniformly distributed between 0 and 2π, and $\mathbf{k}_n$ is a random wave number vector with a uniform distribution over all directions. The corresponding particle velocity components in three perpendicular directions can be written as

$$u_x(\mathbf{r}) = \lim_{N\to\infty} \frac{1}{\sqrt{N}} \sum_{n=1}^{N} \frac{A_n \sin\theta_n \cos\varphi_n}{\rho c} e^{j(\omega t - \mathbf{k}_n \cdot \mathbf{r})}, \tag{2a}$$

$$u_y(\mathbf{r}) = \lim_{N\to\infty} \frac{1}{\sqrt{N}} \sum_{n=1}^{N} \frac{A_n \sin\theta_n \sin\varphi_n}{\rho c} e^{j(\omega t - \mathbf{k}_n \cdot \mathbf{r})}, \tag{2b}$$

$$u_z(\mathbf{r}) = \lim_{N\to\infty} \frac{1}{\sqrt{N}} \sum_{n=1}^{N} \frac{A_n \cos\theta_n}{\rho c} e^{j(\omega t - \mathbf{k}_n \cdot \mathbf{r})}, \tag{2c}$$

where φ_n and θ_n are the azimuth and polar angles defining the wave number vector of the nth wave, and ρc is the characteristic impedance of air.[5] Each set of random amplitudes and wave number vectors corresponds to an outcome of a stochastic process, and above the Schroeder frequency there is no difference between the statistics with respect to position and the full ensemble statistics.[5,14] It is easy to show that the mean-square values of the pressure and each component of the particle velocity can be expressed as a sum of two independent squared Gaussian variables (random sums) with zero mean.[5,13] Thus, the mean-square pressure as well as the mean-square value of any individual component of the particle velocity have a chi-square distribution with two degrees of freedom (also known as the exponential distribution),[13,16] from which it follows that their relative (normalized) ensemble variance is 1. (The relative variance of a stochastic variable X, $\varepsilon^2\{X\}$, is the squared ratio of its standard deviation $\sigma\{X\}$ to its expected value $E\{X\}$.) Moreover, these four random variables can be shown to be statistically independent.[5] This combined with the fact that the variance of a sum of independent random variables equals the sum of their variances[16] leads to the conclusion that the relative variance of the kinetic energy density is

$$\varepsilon^2\{w_{\text{kin}}\} = \frac{\sigma^2\{w_{\text{kin},x} + w_{\text{kin},y} + w_{\text{kin},z}\}}{(E\{w_{\text{kin},x} + w_{\text{kin},y} + w_{\text{kin},z}\})^2} = \frac{3\sigma^2\{w_{\text{kin},x}\}}{9E^2\{w_{\text{kin},x}\}} = \frac{1}{3}, \tag{3}$$

where $w_{\text{kin},x}$, $w_{\text{kin},y}$, and $w_{\text{kin},z}$ are the kinetic densities corresponding to the particle velocity components associated with the x-, y-, and z-directions. Since the ensemble average of the potential energy density must equal the ensemble average of the kinetic energy density, the relative variance of the total energy density becomes

$$\varepsilon^2\{w_{\text{tot}}\} = \frac{\sigma^2\{w_{\text{pot}} + w_{\text{kin}}\}}{(E\{w_{\text{pot}} + w_{\text{kin}}\})^2} = \frac{\sigma^2\{w_{\text{pot}}\} + \sigma^2\{w_{\text{kin}}\}}{4E^2\{w_{\text{pot}}\}} = \frac{1 + \frac{1}{3}}{4} = \frac{1}{3}. \tag{4}$$

To summarize, in the region of high modal overlap, measuring the kinetic sound energy density at one position in a reverberation room gives the same statistical information as measuring the potential energy density at three statistically independent positions. No further gain is obtained by measuring the total energy density. These results have been validated experimentally[6] and, more recently, also confirmed by a numerical implementation of the Green's function in a room.[12]

B. The region below the Schroeder frequency

When the modal overlap cannot be assumed to be high, the source that generates the sound field can no longer be assumed to emit its free field sound power.[14] The reason is that the radiation impedance is affected by the random reverberant part of the sound field, which moreover is increased at the source position because of coherent backscattering or "weak Anderson localization" as predicted by Weaver and Burkhardt.[17] Besides, one can no longer expect the same statistics with respect to position as would be found in an ensemble of rooms.[14,15] The resulting relative ensemble variance of the sound power emitted by a monopole has been found, based on Eq. (1), to be

$$\varepsilon^2\{P_a\} = \frac{2}{M_s}, \tag{5}$$

where M_s is the statistical modal overlap of the room.[14] This quantity is the product of the modal density and the statistical modal bandwidth) and can be written as

$$M_s = \frac{12\pi \ln(10) V f^2}{T_{60} c^3} = \frac{\pi A f^2}{2c^2}, \tag{6}$$

where V is the volume of the room, T_{60} is its reverberation time, A is the total absorption area of the room, f is the frequency, and c is the speed of sound. A very different modal model based on an assumption of the modal frequencies being distributed according to the random matrix theory of Gaussian orthogonal ensembles leads to almost the same expression.[18]

Since the average of the squared amplitudes of the waves that compose the sound field at any frequency and in any room is proportional to the sound power emitted by the source that generates the sound field, it follows that one may expect additional ensemble variations in the kinetic and total energy densities when the modal overlap is low. Such additional variations, reflected in an increase in the relative ensemble variance, have recently been demonstrated for potential energy density.[15] Moreover, because these additional variations affect the pressure and the three perpendicular particle velocity components in the same way, these components

can no longer be assumed to be statistically independent, nor can kinetic and potential energy densities be expected to be statistically independent.

One can model the phenomenon by multiplying each of the original independent exponentially distributed variables in Eqs. (3) and (4) by another random variable that represents the relative variations in the emitted sound power,

$$1 + W = \frac{P_a}{E\{P_a\}}. \tag{7}$$

The new variable W is normally distributed and has zero mean and a variance given by Eq. (5). It is statistically independent of the other quantities because the variations in the sound power depends only on the reverberant part of the sound pressure at the source position.[14] The relative ensemble variance of the mean-square particle velocity component in an arbitrary direction now becomes

$$\begin{aligned}\varepsilon^2\{w'_{\mathrm{kin},x}\} &= \frac{E\{w_{\mathrm{kin},x}^2(1+W)^2\}}{(E\{w_{\mathrm{kin},x}(1+W)\})^2} - 1 \\ &= \frac{E\{w_{\mathrm{kin},x}^2\}E\{(1+W)^2\}}{E^2\{w_{\mathrm{kin},x}\}E^2\{1+W\}} - 1 \\ &= \frac{2E^2\{w_{\mathrm{kin},x}\}E\{(1+W)^2\}}{E^2\{w_{\mathrm{kin},x}\}E^2\{1+W\}} - 1 \\ &= 2(1+E\{W^2\}) - 1 = 2\left(1+\frac{2}{M_s}\right) - 1 = 1 + \frac{4}{M_s}, \end{aligned} \tag{8}$$

where $w'_{\mathrm{kin},x}$ is the modified kinetic energy density associated with the x-direction. [The first step in Eq. (8) follows from the general relation $\varepsilon^2\{X\}=E\{X^2\}/E^2\{X\}-1$, the second step follows because the variables are statistically independent, and the third step follows from the fact that the relative variance of $w_{\mathrm{kin},x}$ is unity.] This expression is identical with the relative ensemble variance of potential energy density,[15]

$$\varepsilon^2\{w'_{\mathrm{pot}}\} = 1 + \frac{4}{M_s}. \tag{9}$$

(The modal model mentioned above leads to a very similar expression.[18]) In the same way, Eq. (3) becomes

$$\begin{aligned}\varepsilon^2\{w'_{\mathrm{kin}}\} &= \frac{E\{(w_{\mathrm{kin},x}+w_{\mathrm{kin},y}+w_{\mathrm{kin},z})^2(1+W)^2\}}{(E\{(w_{\mathrm{kin},x}+w_{\mathrm{kin},y}+w_{\mathrm{kin},z})(1+W)\})^2} - 1 \\ &= \frac{E\{(w_{\mathrm{kin},x}+w_{\mathrm{kin},y}+w_{\mathrm{kin},z})^2\}E\{(1+W)^2\}}{(3E\{w_{\mathrm{kin},x}\})^2E^2\{(1+W)\}} - 1 \\ &= \frac{3E\{w_{\mathrm{kin},x}^2\}+6E^2\{w_{\mathrm{kin},x}\}}{9E^2\{w_{\mathrm{kin},x}\}}(1+E\{W^2\}) - 1 \\ &= \frac{12E^2\{w_{\mathrm{kin},x}\}}{9E^2\{w_{\mathrm{kin},x}\}}\left(1+\frac{2}{M_s}\right) - 1 = \frac{1}{3} + \frac{8}{3M_s}, \end{aligned} \tag{10}$$

where w'_{kin} is the modified kinetic energy density.

It is apparent that the relative variance of the modified kinetic energy density is not simply one-third of the relative variance of a single component, given by Eq. (8); it is somewhat larger. The explanation is that the modified components are no longer independent. An alternative derivation of Eq. (10) could be based on the covariance between the three modified components of the kinetic energy density.

Note that

$$\frac{\varepsilon^2\{w'_{\mathrm{pot}}\}}{\varepsilon^2\{w'_{\mathrm{kin}}\}} = \frac{1+\frac{4}{M_s}}{\frac{1}{3}+\frac{8}{3M_s}} = 3\frac{1+\frac{4}{M_s}}{1+\frac{8}{M_s}} \to \begin{cases} 3 & \text{for} \quad M_s \to \infty \\ \frac{3}{2} & \text{for} \quad M_s \to 0, \end{cases} \tag{11}$$

which shows that the statistical advantage of determining kinetic rather than potential energy density is halved at low modal overlap because of the correlation between the three particle velocity components due to the varying sound power.

Equation (4) can be modified in the same manner,

$$\begin{aligned}\varepsilon^2\{w'_{\mathrm{tot}}\} &= \frac{E\{(w_{\mathrm{kin},x}+w_{\mathrm{kin},y}+w_{\mathrm{kin},z}+w_{\mathrm{pot}})^2(1+W)^2\}}{(E\{(w_{\mathrm{kin},x}+w_{\mathrm{kin},y}+w_{\mathrm{kin},z}+w_{\mathrm{pot}})(1+W)\})^2} - 1 \\ &= \frac{3E\{w_{\mathrm{kin},x}^2\}+6E^2\{w_{\mathrm{kin},x}\}+E\{w_{\mathrm{pot}}^2\}+6E\{w_{\mathrm{pot}}\}E\{w_{\mathrm{kin},x}\}}{4E^2\{w_{\mathrm{pot}}\}}(1+E\{W^2\}) - 1 \\ &= \frac{12E^2\{w_{\mathrm{kin},x}\}+2E^2\{w_{\mathrm{pot}}\}+6E\{w_{\mathrm{pot}}\}E\{w_{\mathrm{kin},x}\}}{4E^2\{w_{\mathrm{pot}}\}}\left(1+\frac{2}{M_s}\right) - 1 \\ &= \frac{\frac{12}{9}+2+\frac{6}{3}}{4}\left(1+\frac{2}{M_s}\right) - 1 = \frac{1}{3}+\frac{8}{3M_s}. \end{aligned} \tag{12}$$

Apparently, there is no statistical advantage in measuring total rather than kinetic energy density in the region of low modal overlap either.

To summarize, the stochastic model derived in the foregoing is based on the fundamental assumption that Eq. (1) is also valid in the region of low modal overlap, although there

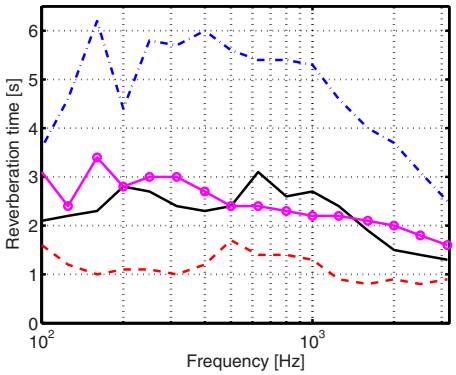

FIG. 1. (Color online) Reverberation time of the test rooms. Solid line: small lightly damped room; dashed line: small damped room; dash-dotted line: large reverberation room; line with circle markers: large damped reverberation room.

are additional variations in the random set of squared wave amplitudes, $|A_n|^2$, caused by the variations in the sound power emitted by the source. It is worth noting that in this frequency range the spatial statistics in any room depend strongly on whether the frequency is coinciding with a modal frequency or not. Equations (5), (8)–(10), and (12) express the relative variances associated with an ensemble of rooms with slightly different dimensions but the same modal overlap.

III. EXPERIMENTAL RESULTS

Some experiments have been carried out in various rooms at the Technical University of Denmark in order to validate the foregoing stochastic considerations: a small (40 m^3) lightly damped room, the same room with extra absorption, a large (245 m^3) reverberation room, and the same large room with added absorption. The reverberation times of the four rooms are shown in Fig. 1. The corresponding Schroeder frequencies are 500, 330, 310, and 200 Hz, respectively. All rooms are essentially rectangular although there are large stationary diffusers in the reverberation room.

The rooms were driven with a Brüel & Kjær (B&K) "OmniSource" (a loudspeaker) fitted with a B&K "Volume velocity adapter," a device with two matched quarter-inch microphones for measuring the output volume velocity and sound power. Kinetic, potential, and total energy densities were measured at a number of positions using an "Ultimate sound probe" (USP), a three-dimensional pressure-velocity probe produced by Microflown (Zevenaar, The Netherlands). The three particle velocity channels were calibrated as described in Ref. 19. The frequency responses between the volume velocity of the source and the sound pressure and three perpendicular components of the particle velocity were measured with a B&K "PULSE" analyzer using pseudorandom noise (6400 spectral lines) synchronized to the analysis in the frequency range up to 3.2 kHz. The experimental technique

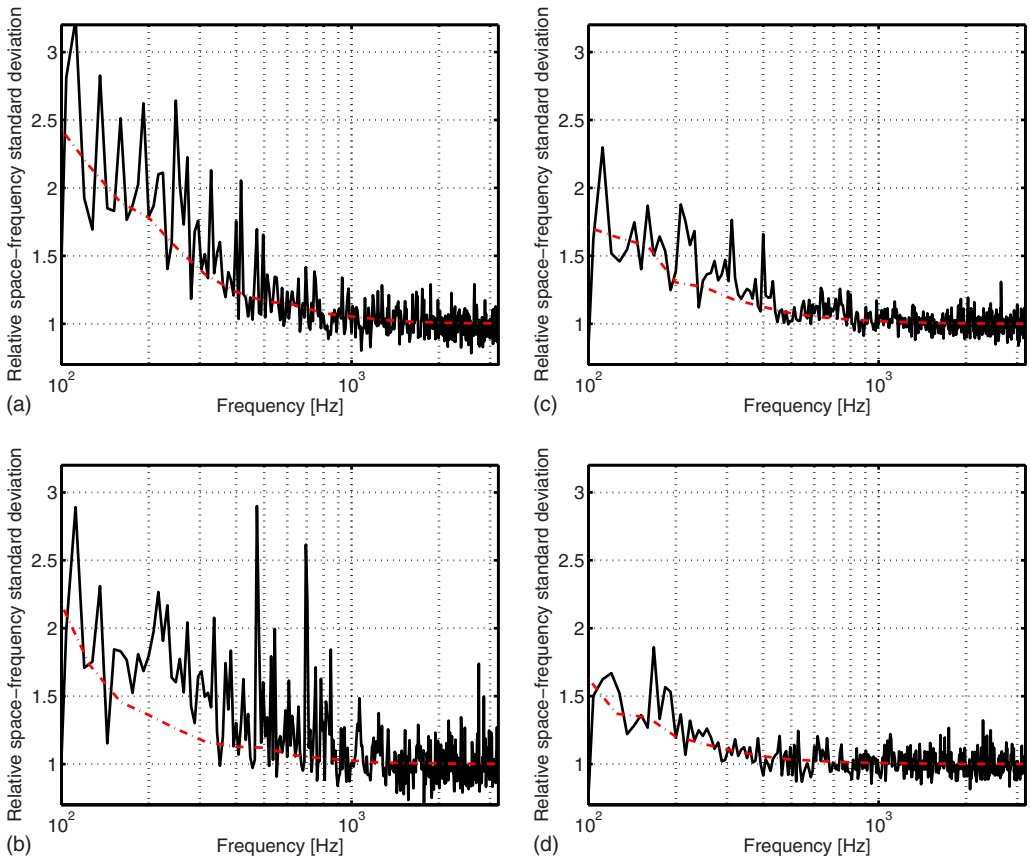

FIG. 2. (Color online) Relative space-frequency standard deviation of the mean-square value of one component of the particle velocity in (a) a small lightly damped room, (b) a small damped room, (c) a large reverberation room, and (d) a large damped reverberation room. Solid line: measured standard deviation; dash-dotted line: theory [Eq. (8)].

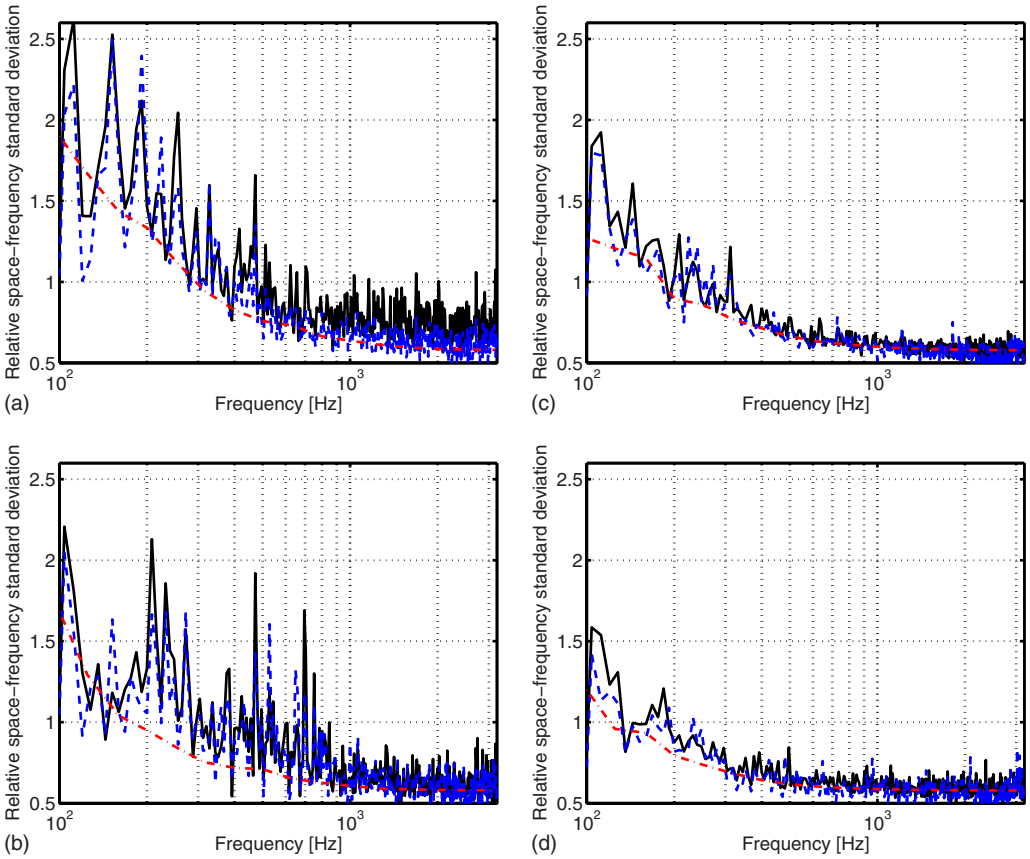

FIG. 3. (Color online) Relative space-frequency standard deviation of kinetic and total energy densities in (a) a small lightly damped room, (b) a small damped room, (c) a large reverberation room, and (d) a large damped reverberation room. Solid line: measured standard deviation of kinetic energy density; dashed line: measured standard deviation of total energy density; dash-dotted line: theory [Eqs. (10) and (12)].

has been described in detail in Ref. 14. Obviously one cannot measure in an ensemble of rooms, so in order to approach the full variation associated with ensemble statistics, both source and receiver positions were varied. In the postprocessing of the results, obtained at 25 pairs of positions, additional variations over 8 Hz bands (16 adjacent frequency bins) were also taken into account to produce space-frequency variations, which can be expected to approximate the ensemble variations.[14]

Figure 2 compares the measured relative space-frequency standard deviation of a single mean-square particle velocity component in an arbitrary direction with the predicted value calculated using Eq. (8). It is apparent that the results fluctuate significantly with frequency, but there is nevertheless fairly good agreement, confirming that a single mean-square particle velocity component exhibits the same statistics as the mean-square pressure. At high modal overlap the relative standard deviation approaches unity, but there is a large increase at low modal overlap. The agreement between measurements and predictions is better for the large room than for the small room, and for some reason Eq. (8) seems to underestimate the variations observed in the small damped room below the Schroeder frequency [Fig. 2(b)].

Figure 3 compares the relative space-frequency standard deviation of kinetic and total energy densities with the theory given by the identical expressions (10) and (12). The agreement is fairly good, confirming that the relative standard deviation of both quantities approaches $1/\sqrt{3} \simeq 0.58$ at high modal overlap and takes higher values at low modal overlap, although not as high values as the standard deviation of a single mean-square particle velocity component. In some cases the theory seems to underestimate the experimental results below the Schroeder frequency, though, but all data certainly confirm that the kinetic energy density exhibits the same statistics as the total energy density.

There is no obvious explanation for the tendency to underestimation observed in Fig. 2(b). The measurements presented in Fig. 3 are more difficult since they rely on accurate calibration of the three channels of the particle velocity transducer. Inaccurate calibration of the three channels of the particle velocity transducer may have emphasized one channel; this would tend to increase the experimental variance.

IV. NUMERICAL RESULTS

The full ensemble standard deviation is rather difficult to measure, but it can be estimated with a numerical model. A finite element model of 25 different rooms, constructed using the commercial software packet ACTRAN, was used in this investigation. The rooms were rectangular, and their dimensions were chosen as uniformly distributed random variables varying between 2 and 6 m. The source positions were placed randomly, but they were at least 0.4 m away from any wall. The calculations were carried out from 200 to 300 Hz with a frequency step of 2 Hz. The element size was chosen so as to provide a low numerical pollution in the examined

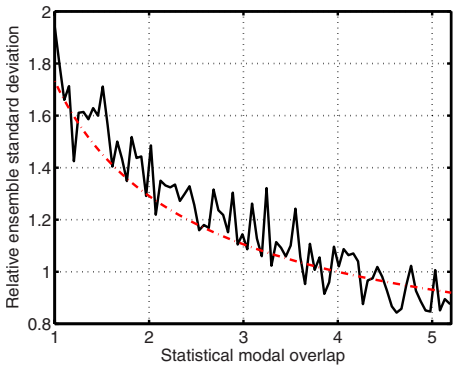

FIG. 4. (Color online) Relative ensemble standard deviation of kinetic energy density. Solid line: finite element calculations; dash-dotted line: theory [Eq. (10)].

frequency range. The mean-square values of the particle velocity vector were calculated at 50 000 randomly chosen nodal points of the mesh. Nodes closer than 0.4 m away from the walls or closer than 1 m from the source were not used. In order to determine the relative ensemble standard deviation as a function of the modal overlap, the data were sorted into appropriate modal overlap intervals. A similar technique was used recently in Refs. 14 and 15.

Figure 4 shows the results. There is excellent agreement, confirming the validity of Eq. (10) and indeed of the probabilistic approach described in Sec. II. Finally Fig. 5 compares the ratio of the relative variance of potential energy density to the relative variance of kinetic energy density with the theoretical ratio given by Eq. (11). There is very good agreement.

V. CONCLUSION

Waterhouse's simple free-wave theory has been extended to the region of low modal overlap and used for determining the relative ensemble variance of kinetic and total energy densities in reverberation rooms, and the predictions have been confirmed by experimental and numerical results. At high modal overlap, the relative variance of both quantities approaches one-third, and it is statistically three times more efficient to measure kinetic or total energy density than to measure potential energy density. At lower modal overlap, there is an increase in the relative variance of both kinetic and total energy densities that is inversely proportional to the modal overlap, that is, proportional to the ratio of the reverberation time to the room volume and inversely proportional to the square of the frequency. In this frequency range, the statistical advantage of measuring kinetic or total energy density is reduced, and ultimately halved, because the different components of the particle velocity are no longer statistically independent.

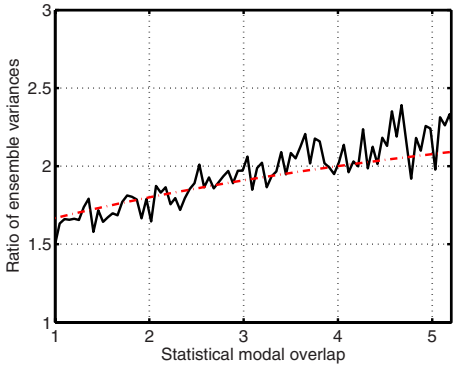

FIG. 5. (Color online) Ratio of relative variance of potential energy density to relative variance of kinetic energy density. Solid line: finite element calculations; dash-dotted line: theory [Eq. (11)].

ACKNOWLEDGMENTS

The authors would like to thank Microflown for lending us a "USP" pressure-velocity transducer. F.J. would like to thank John Davy for suggesting approximating the ensemble variance by the space-frequency variance in the experiments.

[1]R. V. Waterhouse and D. Lubman, "Discrete versus continuous space averaging in a reverberant sound field," J. Acoust. Soc. Am. **48**, 1–5 (1970).
[2]D. Lubman, R. V. Waterhouse, and C. Chien, "Effectiveness of continuous averaging in a diffuse sound field," J. Acoust. Soc. Am. **53**, 650–659 (1973).
[3]I. Wolff and F. Massa, "Direct measurement of sound energy density and sound energy flux in a complex sound field," J. Acoust. Soc. Am. **3**, 317–318 (1932).
[4]R. K. Cook and P. A. Schade, "New method for measurement of the total energy density of sound waves," in Proceedings of the Inter-Noise 74, Washington, DC (1974), pp. 101–106.
[5]F. Jacobsen, "The diffuse sound field," Ph.D. thesis, Technical University of Denmark, Kongens Lyngby, Denmark (1979).
[6]J. A. Moryl and E. L. Hixson, "A total acoustic energy density sensor with applications to energy density measurement in a reverberation room," in Proceedings of the Inter-Noise 87, Beijing, China (1987), pp. 1195–1198.
[7]J. W. Parkins, S. D. Sommerfeldt, and J. Tichy, "Error analysis of a practical energy density sensor," J. Acoust. Soc. Am. **108**, 211–222 (2000).
[8]B. S. Cazzolato and J. Ghan, "Frequency domain expressions for the estimation of time-averaged acoustic energy density," J. Acoust. Soc. Am. **117**, 3750–3756 (2005).
[9]J.-C. Pascal and J.-F. Li, "A systematic method to obtain 3D finite difference formulations for acoustic intensity and other energy quantities," J. Sound Vib. **310**, 1093–1111 (2008).
[10]F. Jacobsen, "A note on finite difference estimation of acoustic particle velocity," J. Sound Vib. **256**, 849–859 (2002).
[11]D. R. Yntema, W. F. Druyvesteyn, and M. Elwenspoek, "A four particle velocity sensor device," J. Acoust. Soc. Am. **119**, 943–951 (2006).
[12]D. B. Nutter, T. W. Leishman, S. D. Sommerfeldt, and J. D. Blotter, "Measurement of sound power and absorption in reverberation chambers using energy density," J. Acoust. Soc. Am. **121**, 2700–2710 (2007).
[13]R. V. Waterhouse, "Statistical properties of reverberant sound fields," J. Acoust. Soc. Am. **43**, 1436–1444 (1968).
[14]F. Jacobsen and A. Rodríguez Molares, "Sound power emitted by a pure-tone source in a reverberation room," J. Acoust. Soc. Am. **126**, 676–684 (2009).
[15]F. Jacobsen and A. Rodríguez Molares, "The ensemble variance of pure-tone measurements in reverberation rooms," J. Acoust. Soc. Am. **127**, 233–237 (2010).
[16]A. Papoulis and S. U. Pillai, *Probability, Random Variables, and Stochastic Processes*, 4th ed. (McGraw-Hill, New York, 1991).
[17]R. L. Weaver and J. Burkhardt, "Weak Anderson localization and enhanced backscatter in reverberation rooms and quantum dots," J. Acoust. Soc. Am. **96**, 3186–3190 (1994).
[18]J. L. Davy, "The variance of the discrete frequency transmission function of a reverberation room," J. Acoust. Soc. Am. **126**, 1199–1206 (2009).
[19]F. Jacobsen and V. Jaud, "A note on the calibration of pressure-velocity sound intensity probes," J. Acoust. Soc. Am. **120**, 830–837 (2006).

Design and performance evaluation of a broadband three dimensional acoustic intensity measuring system

Khalid H. Miah[a] and Elmer L. Hixon
Department of Electrical and Computer Engineering, The University of Texas at Austin, Austin, Texas 78712

(Received 18 November 2008; revised 22 January 2010; accepted 25 January 2010)

A seven-microphone three dimensional (3D) intensity measuring system has been developed and evaluated for performance for a broad frequency band (200 Hz–6.5 kHz). Six microphones are arranged in a concentric array with one microphone at the center of the probe. The screw adjustable center microphone is the probe reference microphone, and is used for calibrations of the other microphones in the probe. This probe addresses limitations of the traditional two-microphone system in measuring acoustical properties in a 3D space from the one dimensional measurements. This probe also eliminates the need of spacers used in the existing 3D probes for broadband measurements. Diffraction and reflection effects on calibrations due to presence of the microphones and the probe supporting structure are negligible. This seven-microphone probe provided better results in the intensity measurements for the wide frequency band than that of a similar four-microphone array probe. © *2010 Acoustical Society of America.* [DOI: 10.1121/1.3327508]

PACS number(s): 43.58.Fm, 43.60.Fg [AJZ] Pages: 2338–2346

I. INTRODUCTION

Precise measurement of different acoustical quantities in different spatial environment has been the key in improving the sound-quality and in reducing acoustical noise from various sources. Sound intensity is one of the quantities defined as the rate of energy flow at a point in space through a unit area. In the SI (International System of Units), the unit of intensity is W/m^2. By definition, the instantaneous sound intensity is the product of the instantaneous acoustic pressure and the instantaneous particle velocity.[1] So, a sound intensity measuring device needs to incorporate transducers to measure both the pressure and the particle velocity. Since the particle velocity can be calculated from the difference of sound pressures between the two adjacent microphones, a pressure transducer such as microphone can be used in the intensity probe. Many sound intensity devices use two identical microphones in a face-to-face configuration.[2] However, the two-microphone design has three inherent problems, described by Nagata *et al.*:[3] (1) Measurement errors due to the phase mismatch increase with the decreased frequencies, (2) any misalignment between the two microphone axes can cause measurement error since a pressure gradient between the two microphones is used to calculate the particle velocity, and (3) the directional characteristics of a two-microphone system limit multi-dimensional vector measurements at high frequencies.[4]

The two-microphone system works well for the one dimensional measurements but requires scanning around the entire enclosed surface to cover sound fields in a three dimensional (3D) space. This need of an extra piece of equipment gives rise to the three dimensional vector intensity sensors. Several three dimensional intensity probes have been proposed in the past decades addressing those three concerns in their different ways. They all vary in their geometrical configurations and the use of different types of microphones, focused on particular applications. One of these configurations is the four-microphone tetrahedral configurations proposed by Moryl and Hixson[5] and then commercially manufactured by a Japanese company, Ono Sokki.[6] This four-microphone tetrahedral configuration uses a center microphone as the reference microphone, and forms three pairs with the three orthogonal microphones. Two different six-microphone face-to-face configuration intensity probes were introduced by Brüel & Kjaer and GRAS,[2] but their applications were very limited. The performance of these two similar probes were severely affected by reflection and diffraction around the microphones, and their supporting structures. Both the six-microphone and the four-microphone configurations use three pairs of closely spaced microphones to calculate the particle velocity vectors. The differences between these two configurations lie in the probe center pressure estimation, and in microphone orientations within the probe. The six-microphone configuration uses a finite-sum method to estimate the center pressure while the four-microphone configuration uses the direct pressure measurements from the center microphone. The four-microphone tetrahedral probe has side-by-side microphone orientation while the two six-microphone probes have face-to-face microphone orientation.[7,8]

Microphone size, effective spacing, and orientation within the probe have significant impact on the intensity measurements and on subsequent applications in source localization. Sound fields around microphones in the probe can distort measurements due to effects of diffraction and reflection around the sensor elements and their supporting structures, especially for closely spaced microphones with a large overall dimension. Microphone spacing also affects the finite-difference error approximation, especially at the low

[a]Author to whom correspondence should be addressed. Electronic mail: miah@mail.utexas.edu

 0001-4966/2010/127(4)/2338/9/$25.00

frequencies where the acoustic wavelength is large compared to the microphone spacing. Another four-microphone configuration similar to Moryl and Hixson,[5] proposed by Schumacher[9] for acoustic energy density and intensity measurements, uses microphones arranged in an orthogonal array with one microphone at the center of the coordinate system. For that design, the spacing between the microphones are fixed. This configuration works well for a particular frequency band (200 Hz–3.5 kHz), but cannot be used to cover a wide frequency band (200 Hz–6.5 kHz) without physically modifying the spacing between the microphones. The other (four- and six-microphone) configurations mentioned above also need spacing adjustment for measurements involving sound field of wide frequency band. Most of these configurations have face-to-face microphone orientation, which is not suitable for source localization without any external rotating device. Also, reflection and diffraction around the microphones, and the supporting structures can add significant distortions in the measurements.

In this paper, a seven-element three dimensional intensity probe with omnidirectional microphone arranged in a two-concentric orthogonal array is discussed and demonstrated. The two orthogonal arrays are for the high-frequency (1.0–6.5 kHz) and low-frequency (200 Hz–1.0 kHz) measurements without the need of any spacing adjustment between the microphones. The outer-array is for the low-frequency and the inner-array is for the high-frequency measurements. Microphones of small dimensions were used in a side-by-side configuration to reduce adverse effect due to diffraction and reflection. A movable center microphone is used for the calibration and as the reference microphone of the probe. Simultaneous microphone calibration technique in the anechoic room, and quantitative analysis of effects of reflection and diffraction due to the presence of the microphone and its supporting structures are also discussed in this paper. This analysis can be an effective tool in improving the performance and accuracy of the probe.

Total intensity is calculated and compared with the high-frequency and low-frequency components to show improvements in the measurement accuracy. This intensity probe can also be used to locate sound sources of different frequencies as an application of the system. The initial design of the proposed intensity measuring system is first presented by authors of this article in an abstract published in the Acoustical Society of America (ASA) conference proceedings.[10]

In Sec. II, we present design of the intensity measuring system, and discuss inherent systematic errors associated with this design. In Sec. III, microphone calibration technique, and a quantitative analysis of reflection and diffraction effects due to the probe supporting structures are discussed. Section IV discusses theory and operating principles of the probe. In Sec. V, the probe performance in terms of intensity measurements and directivity patterns is discussed. Section VI ends the paper with a brief conclusion.

II. DESIGN OF THE INTENSITY PROBE

The acoustic intensity measuring system discussed in this paper is developed in the Acoustics Research Laboratory at the University of Texas at Austin. This system has three components: the microphone array with interface analog circuits, data acquisition device, and a personal computer with custom signal processing software.

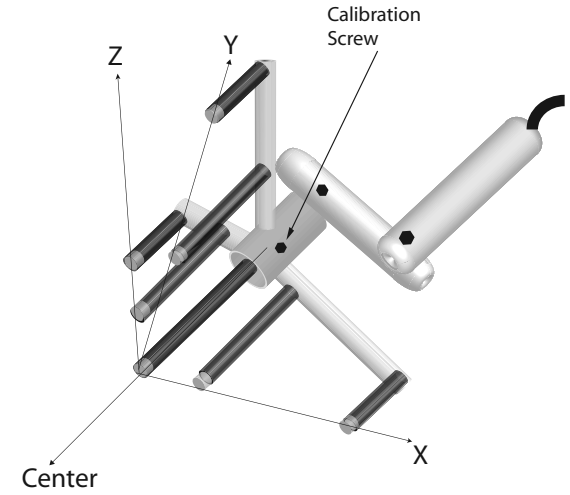

FIG. 1. Seven microphones are arranged in a two-concentric array along the three axes with a screw adjustable reference microphone at the origin of the coordinate system.

A. Microphone spacing

The three dimensional intensity probe developed in this paper consists of seven microphones in a side-by-side configuration. Six microphones are arranged in a two-concentric array with one microphone located at the center of the probe (Figs. 1 and 2). The center microphone is used as the reference microphone of the system. The inner-array is for the high-frequency (1.0–6.5 kHz), with an effective spacing between the reference and each of the three microphones,

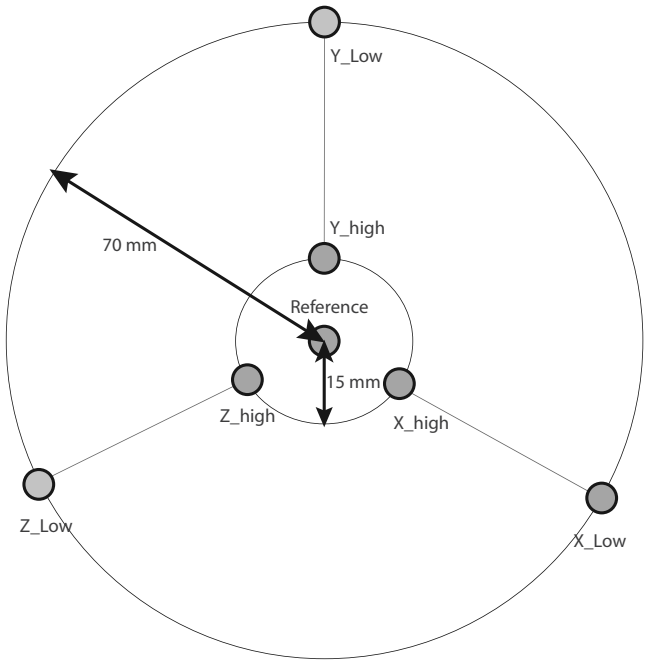

FIG. 2. A schematic of the horizontal spacing of the seven-microphone two-concentric array of the probe.

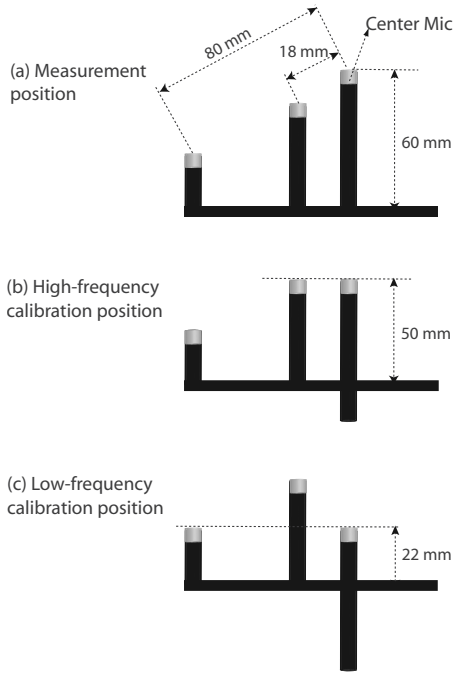

FIG. 3. Microphone spacing with an adjustable center microphone in the measured, high- and low-frequency calibration positions.

which is 18 mm. The outer-array is for the low-frequency (200 Hz–1.0 kHz) measurements, with an effective spacing between the reference microphone and each of the three microphones, which is 80 mm. The "effective" spacing is defined as the center-to-center distance between the two microphones. The reference microphone can be moved either in the forward or in the backward direction along the probe axis by adjusting a screw. Microphone effective distances were selected to keep the finite-difference approximation error and the phase mismatch error to a minimum. The center reference microphone can be adjusted to any of the three different positions: measurement, low-frequency calibration, and high-frequency calibration (Fig. 3). The purpose of the center reference microphone adjustment for different calibration positions is to place all the microphones of each array on a plane, for the calibration in an anechoic chamber.

B. Inherent systematic errors

The spacing between a surrounding microphone and the center microphone has great impact on both the high-frequency and low-frequency measurement errors. The finite-difference approximation error at high frequencies, and the phase mismatch error at low frequencies are greatly affected by the microphone spacing.

The finite-difference approximation error affects both the mean pressure and the particle velocity calculations. Thus, it affects the overall intensity measurement and subsequent acoustic parameter estimations. This error originates from the pressure estimation at the midpoint between the two microphones. In this estimation, the midpoint pressure is the average value of pressures measured at each microphone in a two-microphone pair. Another error of the finite-difference approximation is from the estimation of the pressure gradient at the midpoint of a two-microphone pair as the slope of pressures across the two microphones.

Another potential error that was considered while selecting the microphone spacing for each array is the phase mismatch between the microphones in the probe. The microphones in each array were placed in an equal distance from the center (origin) microphone. Ideally, if these microphones are subject to a plane wave, then the phase differences among the microphones would be zero. From a measurement standpoint, these phase differences are rarely zero, and can be termed as phase mismatch among the microphones. This phase mismatch error has adverse effects in low frequencies where the signal wavelength is very large compared to the spacing between the two microphones. If the spacing between the microphones is very small, then the physical phase difference (due to the physical separation of the microphones from each other) could be masked by the phase mismatch error introduced by the instrumentation. Now, the phase error (decibel) in the probe can be related to the phase mismatch in the microphones due to their spacing by the following equation:[2]

$$e_\theta = 10 \log_{10}\left(1 + \frac{\Delta\alpha}{\Delta\phi}\right), \tag{1}$$

where $\Delta\alpha$ is the phase mismatch introduced by the instrumentation, and $\Delta\phi$ is the actual physical phase difference due to the physical separation of the two microphones. It can be seen in the above equation that if the physical phase difference is small compared to the instrumentation phase mismatch then the probe error will be large. So, to keep this error small for a fixed instrumentation, the physical phase difference needs to be large. The large physical phase difference can be achieved by increasing the spacing between the microphones. So, to keep the probe error due to the phase mismatch at a minimum, a large microphone spacing is preferred. Now, it is to be remembered that as the microphone spacing becomes large, so thus the finite-difference approximation error.

In the intensity probe developed in this paper, the effective distance between the two microphones was selected to be 18 and 80 mm for the inner- and the outer-array, respectively. Since a small spacing between the two microphones causes a large phase mismatch error, and a large spacing causes a big finite-difference approximation error at high frequencies, there was a trade-off in selecting the microphone spacing to keep both of the errors at a minimum. The probe error related to the sensor spacing is shown in Fig. 4. It can be seen in the probe error vs frequency plot that the outer low-frequency array spacing has an error of about −2.0 dB at 1000 Hz, while the inner high-frequency array has an error of about −4.0 dB at 6.5 kHz.

C. Microphone orientation and data acquisition

A side-by-side microphone configuration was chosen to minimize diffraction and reflection around the supporting structures. Each microphone of the probe is an omnidirectional condenser microphone (Panasonic, Japan; model,

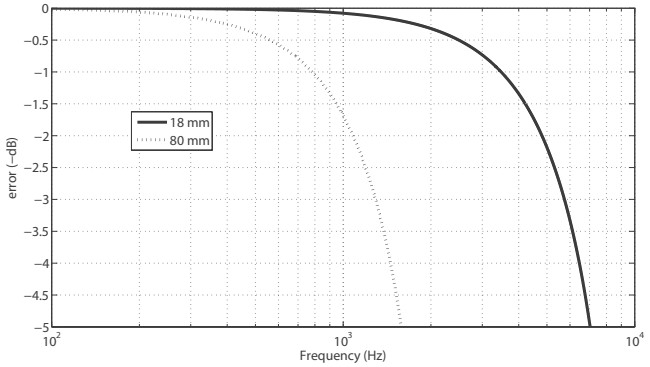

FIG. 4. Probe error due to the finite-difference approximation dependent on the microphone spacing within the array.

WM-61A) with a sensitivity of −30 dB in the standard operating voltage (9.0 V) with the load impedance, 10.0 kΩ. Each microphone has the diameter of 6.0 mm and height of 3.4 mm. The magnitude of the frequency response of each of these microphones is nearly flat (±2 dB) for frequencies from 50 Hz to 7.0 kHz.

An eight-channel analog input data acquisition device (model: PCI-4472 manufactured by the National Instrument Inc., USA) was used to acquire microphone signals for subsequent calculations of the intensity and other acoustic parameters. The simultaneous signal acquisition from all the seven microphones using a single DAQ (Data Acquisition Device) prevented any potential time-delay mismatch among the channels. The sampling rate for the acquisition was chosen to be 16 kHz considering the upper limit of the target bandwidth (200 Hz–6.5 kHz).

III. MICROPHONE CALIBRATION TECHNIQUES

In this section, the center (origin) microphone was first calibrated using a standard reference microphone. Once the center microphone was calibrated, it is used as the reference microphone to simultaneously calibrate the three microphones of each array, separately. In the anechoic chamber, a point source radiates spherical waves. If the distance of the probe is far enough from the sound source, then the microphones of probe would experience a plane wave. This plane wave justification in the anechoic chamber is discussed in the Appendix.

A. The center (origin) microphone calibration

The center (origin) microphone was calibrated using a calibrated standard reference microphone in the anechoic chamber. In this measurement, a 1 kHz sine wave of 84 dB re 20 μPa was used as the excitation signal. First, the standard reference microphone was placed in the anechoic chamber without the intensity probe. The sound pressure level (SPL) in decibel was recorded using a sound level meter. Then the intensity probe was placed inside the anechoic chamber. The center microphone was placed exactly at the same position as the standard reference microphone. The measured SPL of the center microphone was then adjusted to the SPL of the standard reference microphone. Then the frequency response of the center microphone was calculated for the frequency range 200 Hz–7.0 kHz. Before the center microphone frequency response measurements, the frequency response of the two different sizes (3 and 6 in.) loudspeakers was calculated as a precaution, and was checked for any diffraction effects of the loudspeaker housing on the measurements. The diffraction and reflection effects on the loudspeaker frequency response were random. It is to be noted that both the small and the large loudspeakers were covered with sound absorbing material (fiber glass) to minimize any potential effect due to diffraction around the loudspeaker housing. The frequency response of the center (origin) microphone was nearly flat (±0.5 dB) for the frequency range 200 Hz–7.0 kHz. This frequency response is used to compare any diffraction and reflection effect of the probe microphones, and the supporting structures.

B. The surrounding microphones calibration

The already calibrated center (origin) microphone is then used in calibrating the other microphones of the probe. All (three) microphones of the inner- (or outer-) array were placed in the same plane as the center microphone. In this configuration, each microphone of the array should experience the same sound pressure amplitude, and have zero phase difference between the microphones considering the microphones plane is perpendicular to the incoming plane wave direction. Thus, the three microphones of the probe can be calibrated simultaneously using the origin microphone. The other array of the probe was then calibrated similarly. As for measurements, 1 kHz sine wave of 84 dB re 20 μPa measured by the center (origin) microphone was used as the sound source. Then, the measured SPLs from the three microphones (inner-array or outer-array) were adjusted to the center microphone SPL. Then a broadband random noise was used to calibrate the frequency response of the surrounding microphones of each of the two arrays. The magnitude and phase responses of the center microphone were used as the reference values to calibrate the other microphone of the probe. Thus, each microphone of the probe was calibrated using the already calibrated center (origin) microphone. In the calibration procedure, even though the SPL for each microphone was adjusted with the SPL of the center microphone using a 1.0 kHz sine wave, the sensitivity plots over the frequency range of each array show a very small deviation in SPL at 1.0 kHz among the microphone due to random diffraction and reflection effects around the microphones and the supporting structure. The effect of reflection and diffraction around the microphone and its supporting structure is analyzed in Sec. III C.

The calibrated microphones of the inner-array have an overall sensitivity offset of ±0.3 dB for the frequency range 200 Hz–6.5 kHz. The overall phase offset for the same array is about ±0.6°. The calibrated microphones of the outer- (low-frequency) array have an overall sensitivity offset of ±1.0 dB for the frequency range 200 Hz–6.5 kHz. The overall phase offset for the same array is about ±1.1°. For the low-frequency array, the useful frequency range is from 200 Hz to 1.0 kHz. For the high-frequency array, the useful fre-

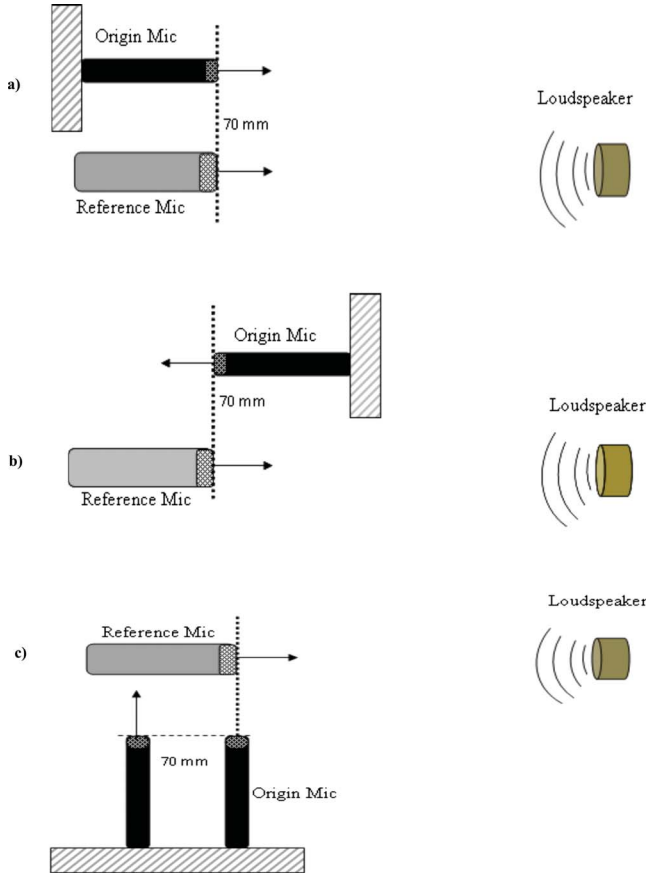

FIG. 5. (Color online) (a) The probe is placed in the same plane as the standard reference microphone and facing directly to the loudspeaker, (b) the probe is facing directly opposite to the loudspeaker, and (c) the probe is facing perpendicular to the standard reference microphone.

quency range is from 1.0 to 6.5 kHz. So, the sensitivity and phase offsets outside their respective ranges were not considered for the measurements.

C. Reflection and diffraction analyses

To understand and to quantify diffraction and reflection effects on the center (origin) microphone due to the presence of the standard reference microphone and the probe structure, the probe was placed in the three different positions around the standard reference microphone in the anechoic chamber. First, the low-frequency array microphone of the probe was placed in the same plane as the standard reference microphone along the perimeter of the array. In this setup, the microphones were facing directly the sound source where the probe structure can cause reflections. Second, the probe position was reversed and was facing the standard reference microphone where the probe structure can cause diffractions. Third, the probe origin microphone was placed in the same plane as the standard reference microphone but was facing perpendicular to the reference microphone axis (Fig. 5).

The frequency response plots of the center (origin) microphone in Fig. 6 show the diffraction and reflection effects due to the presence of the probe structure. The overall pattern of the deviation from the response without the probe is somewhat random, but varied ±0.5 dB over the target frequency band. The presence of the standard reference microphone at different locations in relation to the probe did not make any coherent impact on the center (origin) microphone frequency response.

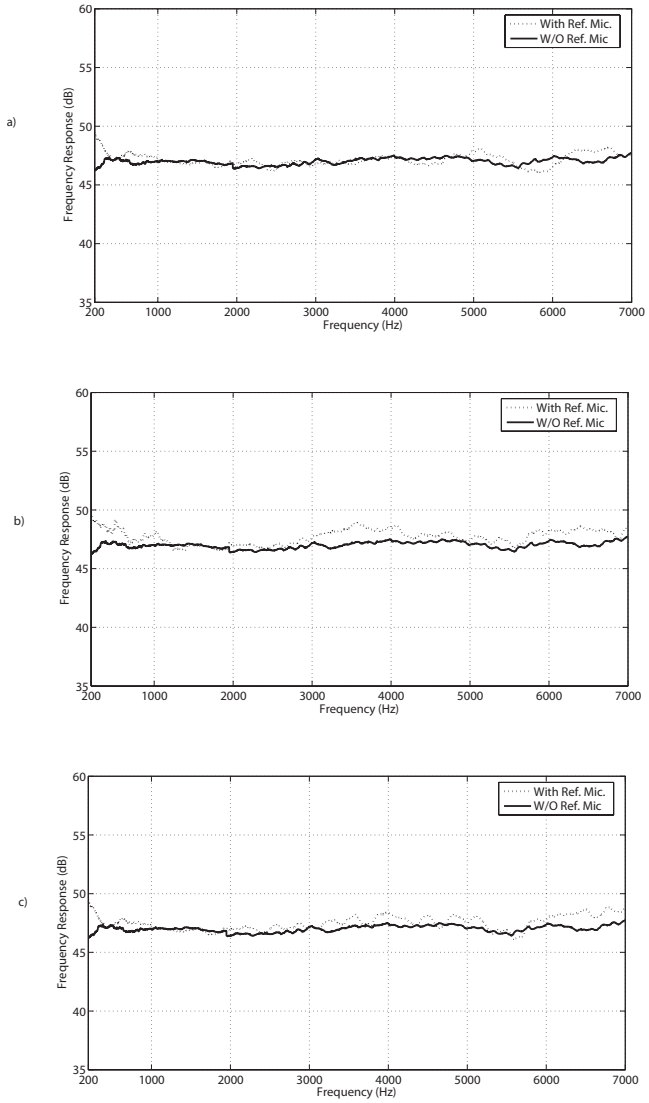

FIG. 6. (Color online) Frequency response (in dB re 20 μPa) of the center microphone is compared with that of the reference microphone: (a) The probe is placed in the same plane as the standard reference microphone and facing directly to the loudspeaker, (b) the probe is facing directly opposite to the loudspeaker, and (c) the probe is facing perpendicular to the standard reference microphone.

IV. TECHNIQUES AND OPERATING PRINCIPLES

Measuring acoustic intensity in the frequency domain requires the knowledge of pressure amplitudes and their phase relations between the two microphones. Based on Refs. 11, 4, and 12, the expression for the acoustic intensity for the two closely spaced microphones in any given direction is given by

$$I(f) = \frac{\mathrm{Im}(D_{12})}{2\rho\Delta r\omega}, \tag{2}$$

where the angular frequency $\omega = 2\pi f$, f is the frequency. The cross-spectral density $D_{12} = P_1(f)P_2^*(f)$, where $P_1(f)$ and $P_2(f)$ are the Fourier transforms of the two time domain

pressure signals sensed by the two microphones (the center microphone and one of the microphones along the axis of the coordinate system), ρ is the density of the air, and Δr is the effective distance between the two sensing microphones. * in the above equation denotes complex conjugate and can be shown that $P_1(f)P_2^*(f)=[P_2(f)P_1^*(f)]^*$. Now, the equations for x, y, and z components of the intensity for the inner- and outer-arrays can be written as

$$I_{lx}(f) = \frac{\mathrm{Im}(P_o(f)P_{lx}^*(f))}{2\rho\Delta r_l\omega}, \tag{3}$$

$$I_{ly}(f) = \frac{\mathrm{Im}(P_o(f)P_{ly}^*(f))}{2\rho\Delta r_l\omega}, \tag{4}$$

$$I_{lz}(f) = \frac{\mathrm{Im}(P_o(f)P_{lz}^*(f))}{2\rho\Delta r_l\omega}, \tag{5}$$

$$I_{hx}(f) = \frac{\mathrm{Im}(P_o(f)P_{hx}^*(f))}{2\rho\Delta r_h\omega}, \tag{6}$$

$$I_{hy}(f) = \frac{\mathrm{Im}(P_o(f)P_{hy}^*(f))}{2\rho\Delta r_h\omega}, \tag{7}$$

$$I_{hz}(f) = \frac{\mathrm{Im}(P_o(f)P_{hz}^*(f))}{2\rho\Delta r_h\omega}, \tag{8}$$

where Δr_l and Δr_h are the effective microphone spacing between the two microphones in the outer- and inner-arrays, respectively. Now, the low- and high-frequency components of the intensity for each orthogonal axis are combined to form the overall intensity components for frequencies from 200 Hz to 6.5 kHz. For the low-frequency components, the frequency range is 200 Hz–1.0 kHz. For the high-frequency components, the frequency range is 1.0–6.5 kHz. The following expression summarized overall intensity in all three axes:

$$I_{x,y,z}(f)\begin{cases} \dfrac{\mathrm{Im}(P_o(f)P_{lx,ly,lz}^*(f))}{2\rho\Delta r_l\omega} & \text{for } f = 200 \text{ Hz to } fl - df \\ \dfrac{\mathrm{Im}(P_o(f)P_{hx,hy,hz}^*(f))}{2\rho\Delta r_h\omega} & \text{for } f = fl + df \text{ to } 6500 \text{ Hz} \\ \dfrac{1}{2}\left(\dfrac{\mathrm{Im}(P_o(f)P_{lx,ly,lz}^*(f))}{2\rho\Delta r_l\omega} + \dfrac{\mathrm{Im}(P_o(f)P_{hx,hy,hz}^*(f))}{2\rho\Delta r_h\omega}\right) & \text{for } fl - df < f < fl + df, \end{cases} \tag{9}$$

where $I_{x,y,z}(f)$, $I_{lx,ly,lz}(f)$, and $I_{hx,hy,hz}(f)$ are the overall, low- and high-frequency components, respectively, along the x, y, and z axes of the coordinate system. fl is the high end of the low-frequency range, while df is the length of frequency band over which averaging is done to smooth out transition between high-frequency and low-frequency components of the intensity level. In the above, cross-correlations between sound pressures of the two microphones (the center and along an axis) were used to calculate the sound intensity. Then the individual intensity vector components along the three axes were combined to form the total intensity. The total sound intensity at the probe center can be calculated from the surrounding microphone pressures using Eq. (2).

V. PROBE PERFORMANCE IN THE INTENSITY MEASUREMENTS

In this section, the overall probe intensity as a function of frequency is calculated and compared with each of the two arrays of the two-concentric array probe. The intensity from the origin microphone was calculated using the mean-squared pressure and was used as the reference intensity. The measurements were done in the anechoic chamber using a loudspeaker as the source. A broadband (200 Hz–7.0 kHz) noise signal was used as the excitation source. In Fig. 7, the inner-array, the outer-array, and the overall probe intensity were compared with the intensity measured from the origin (reference) microphone. The maximum deviation from the reference microphone intensity was ±1.5 dB over the frequency range 200 Hz–6.5 kHz. The overall probe intensity was calculated by combining the low-frequency components (200 Hz–1.0 kHz) of the outer-array, and the high-frequency components (1.0–6.5 kHz) of the inner-array. The ±1 dB random oscillations resulted from diffraction around the loudspeaker enclosure.

The seven-microphone intensity probe developed in this paper was compared with one type of four-microphone configuration,[6] and two types of six-microphone configurations.[2] Cazzolato and Hansen[8] showed that for the plane wave conditions, the four-microphone configuration intensity probe works better than the six-microphone configurations in terms of bias errors arising from the finite-difference approximation error, the phase mismatch error, and the spatial error. In terms of intensity measurements, our probe outperformed the four-microphone probe developed by Suzuki *et al.*[6,13] in the frequency band of 200 Hz–6.5 kHz. Even though Suzuki *et al.* might have anticipated the relationship between the microphone spacing and the performance in different frequency bands, the upper limit of the probe developed in their paper[6] is limited to only 4 kHz.

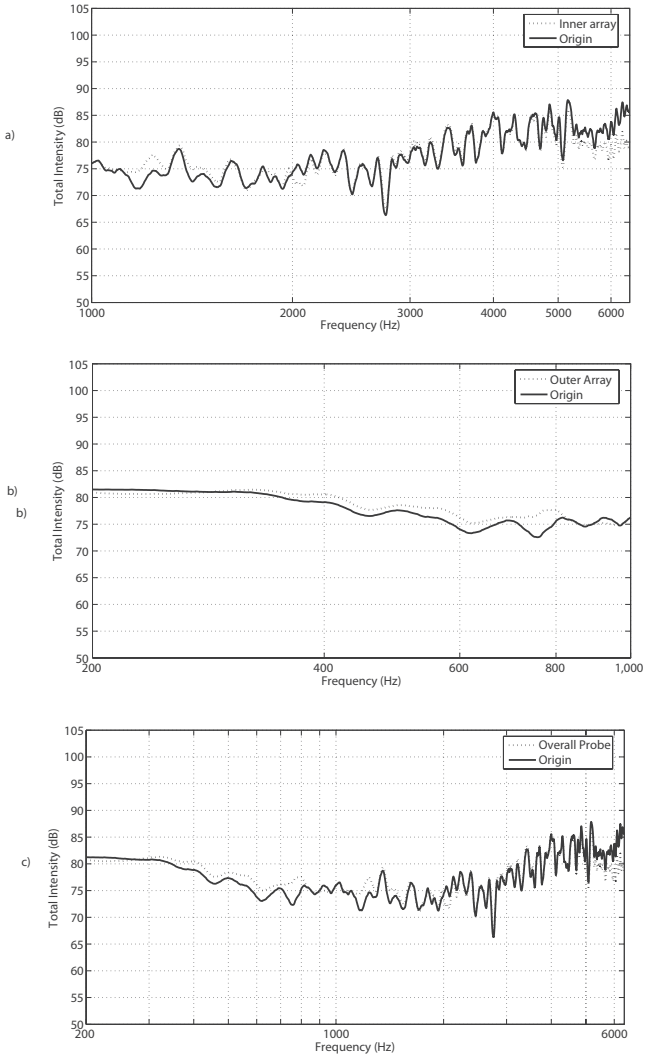

FIG. 7. Total intensity plots of the loudspeaker from the origin microphone and from the (a) inner-array, (b) outer-array, and (c) overall probe (unit: dB re 20 μPa).

Also, Suzuki *et al.*'s[6] paper briefly discussed the topic of adverse effects due to diffraction and reflection without a specific measurement technique and a concrete analysis.

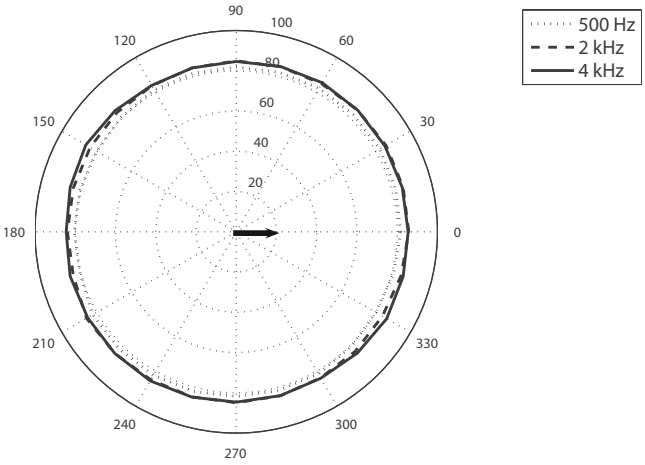

FIG. 8. Directivity patterns of the overall probe intensity (decibel) along the reference *X*-*Y* plane.

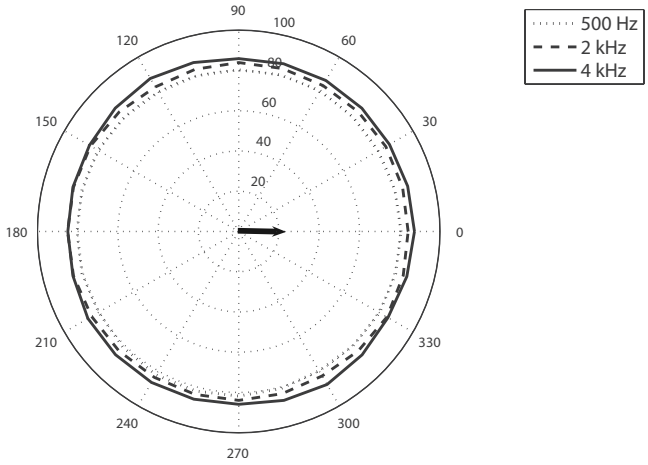

FIG. 9. Directivity patterns of the overall probe intensity (decibel) along the reference *Y*-*Z* plane.

Also, the plane wave approximation of the spherical waves just 1 m from the source in the anechoic chamber is questionable considering disturbances due to strong near-field effects at the probe. In this paper, measurements were made 2 m from the source in the anechoic chamber to minimize any potential near-field effect.

A. Directivity patterns of the probe

To understand the directional characteristic of the probe, the intensity levels were calculated at each plane. Three different (500 Hz, 2 kHz, and 4 kHz) single tone sine waves were used as the excitation signal for these measurements. To measure intensity in the *X*-*Y* plane, the *z*-axis of the probe was first aligned along the center of the sound source (loudspeaker). Then the probe was rotated around the *z*-axis 360° to cover the entire plane. Measurements in the other two planes were made similarly. Polar plots of the directivity patterns are shown in Figs. 8–10. Difference in the intensity level among different frequencies was ±3 dB. The arrow in Figs. 8–10 indicates the source direction. Variation in the

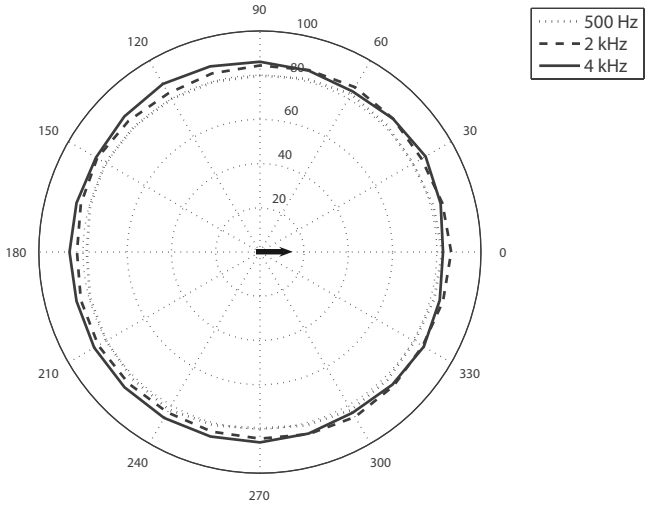

FIG. 10. Directivity patterns of the overall probe intensity (decibel) along the reference *Z*-*X* plane.

intensity measurements when the probe was facing opposite the sound was about ±1.5 dB compared to the probe facing the sound source directly.

This variation can be attributed to the diffraction effect around the microphones, and the supporting structures.

VI. CONCLUSIONS

The main motivation of this paper was to develop an acoustical probe system to measure intensity vectors in a 3D space. This probe addresses limitations of the two-microphone system in measuring the intensity in a 3D space from the one dimensional measurements. The probe eliminates the need of an extra piece of equipment (rotating device) unlike a two-microphone system. The two-concentric array in the probe has advantage in the intensity measurements in a wide frequency range (200 Hz–6.5 kHz) compared to a somewhat similar four-microphone configuration and two types of six-microphone configuration 3D intensity probes. This probe increases the measurement bandwidth in comparison with the other 3D acoustic probes by combining the two different arrays in the same system. This newly developed probe does not need any spacing adjustment during measurements. Diffraction and reflection effects on the microphone calibration and on subsequent measurements were analyzed in the anechoic room environment. Directivity patterns of the probe confirm overall uniformity in 3D measurements with a reasonable tolerance. Since the pressure and particle velocity can be measured using this probe, other acoustical quantities such as the total energy density, impedance, and sound power can also be determined using similar measurements. Source localization in an office or in an enclosed environment is one of the applications where this probe can be used, considering its nearly uniform directivity patterns in a 3D space.

ACKNOWLEDGMENT

The authors would like to thank Dr. Michael Becker for being instrumental in the completion of the research activities toward this paper.

APPENDIX: PLANE WAVE JUSTIFICATION OF THE SPHERICAL WAVES

If the center of the probe and the center of the sound source are both in the same axis, and the distance from the center microphone to any of the surrounding microphones is small, then the arc of the spherical wave between the center and a surrounding microphone can be considered close to a straight line. The straight line approximation is illustrated in Fig. 11. In the schematic (Fig. 11), r is the distance from the loudspeaker to the outer-array microphone, R is the distance from the loudspeaker center to the center (origin) microphone, d is the effective distance between the center of the origin and one of the microphones in the array, and is perpendicular to the R, and Δr is the distance from the center of the surrounding microphone to the crossing point between the arc and the hypotenuse. The r forms the hypotenuse of the right triangle formed by d, R, and r. So, for a given R and d, the r can be calculated as

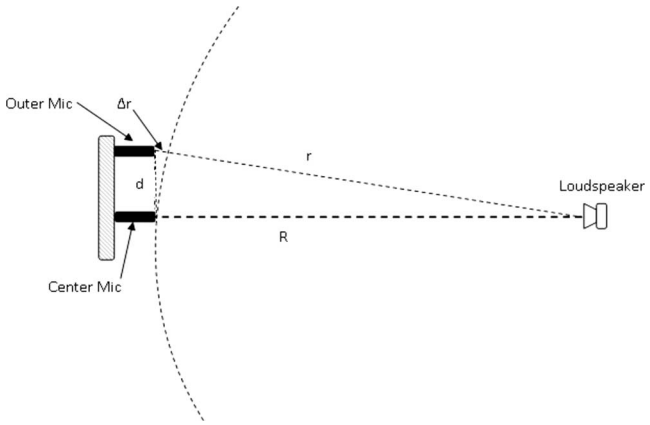

FIG. 11. A schematic of the plane wave justification of a spherical progressive wave.

$$r = \sqrt{d^2 + R^2}, \tag{A1}$$

$$\Delta r = \sqrt{d^2 + R^2} - R. \tag{A2}$$

Now, using the binomial expansion, Δr can be approximated as

$$\Delta r \approx \frac{d^2}{2R}. \tag{A3}$$

Now, knowing R, given d, the effect of the plane wave assumption on the amplitude deviation can be calculated as

$$E_{|p|} \approx \frac{1}{1 + \dfrac{d^2}{2R^2}}, \tag{A4}$$

$$(E_{|p|})_{\mathrm{dB}} \approx -20 \log_{10}\left(1 + \frac{d^2}{2R^2}\right). \tag{A5}$$

Similarly, the phase deviation (in degree) due to the plane wave approximation can be calculated as

$$E_{\angle p} \approx \frac{\Delta r}{\lambda} * 2\pi, \tag{A6}$$

where λ is the signal wavelength. Now, for the measurements in the anechoic chamber, the distance between the source and the center (origin) microphone $R=2$ m, and the distance between the center and the surrounding microphone $d=70$ mm for the outer- (low-frequency) array and 15 mm for the inner- (high-frequency) array, respectively. Based on these parameters, the amplitude deviations at the inner-array microphones are calculated to be 0.0002 dB, and 0.005 dB for the outer-array. Now the effect of the plane wave justification on the phase deviation at 1 kHz is 1.2° at the outer-array microphone, and at 6.5 kHz the phase deviation is 0.38°. These deviations are small and were neglected for subsequent measurements.

[1]M. Moser, *Engineering Acoustics—An Introduction to Noise Control*, 2nd ed. (Springer, Berlin, 2004).
[2]F. J. Fahy, *Sound Intensity*, 2nd ed. (E FN SPON, London, 1995).
[3]S. Nagata, K. Furihata, T. Wada, D. K. Asano, and T. Yanagisawa, "A three-dimensional sound intensity measurement system for sound source

identification and sound power determination by ln models," J. Acoust. Soc. Am. **118**, 3691–3705 (2005).
[4]F. J. Fahy, "Measurement of acoustic intensity using the cross-spectral density of two microphone signals," J. Acoust. Soc. Am. **62**, 1057–1059 (1977).
[5]J. A. Moryl and E. L. Hixson, "A total acoustic energy density sensor with applications to energy density measurement in a reverberation room," Proceedings of the Inter-Noise 87 (1987), pp. 1195–1198.
[6]H. Suzuki, S. Oguro, M. Anzai, and T. Ono, "Performance evaluation of a three dimensional intensity probe," J. Acoust. Soc. Jpn. (E) **16**, 233–238 (1995).
[7]G. Rasmussen, "Measurements of vector fields," Proceedings of the 2nd International Congress on Acoustic Intensity (1985), pp. 53–58.
[8]B. S. Cazzolato and C. H. Hansen, "Errors arising from three-dimensional acoustic energy density sensing in one-dimensional sound fields," J. Sound Vib. **236**, 375–400 (2000).
[9]M. Schumacher, "A transducer and processing system for acoustic energy density measurements," Master's thesis, University of Texas at Austin, Austin, TX (1984).
[10]K. H. Miah and E. L. Hixson, "Three-dimensional microphone array intensity vector sensors for measurement of various acoustical properties in different spatial environment (A)," J. Acoust. Soc. Am. **120**, 3178 (2006).
[11]J. Y. Chung, "Cross-spectral method of measuring acoustic intensity without error caused by instrument phase mismatch," J. Acoust. Soc. Am. **64**, 1613–1616 (1978).
[12]G. Krishnappa, "Cross-spectral method of measuring acoustic intensity by correcting phase and gain mismatch errors by microphone calibration," J. Acoust. Soc. Am. **69**, 307–310 (1981).
[13]H. Suzuki, S. Oguro, and T. Ono, "A sensitivity correction method for a three-dimensional sound intensity probe," J. Acoust. Soc. Jpn. (E) **21**, 259–265 (2000).

Insights into head-related transfer function: Spatial dimensionality and continuous representation

Wen Zhang,[a] Thushara D. Abhayapala, and Rodney A. Kennedy
Department of Information Engineering, Research School of Information Sciences and Engineering, College of Engineering and Computer Science, The Australian National University, Canberra ACT 0200, Australia

Ramani Duraiswami
Perceptual Interfaces and Reality Laboratory, Institute for Advanced Computer Studies, University of Maryland, College Park, Maryland 20742

(Received 12 October 2009; revised 27 January 2010; accepted 1 February 2010)

This paper studies head-related transfer function (HRTF) sampling and synthesis in a three-dimensional auditory scene based on a general modal decomposition of the HRTF in all frequency-range-angle domains. The main finding is that the HRTF decomposition with the derived spatial basis function modes can be well approximated by a finite number, which is defined as the spatial dimensionality of the HRTF. The dimensionality determines the minimum number of parameters to represent the HRTF corresponding to all directions and also the required spatial resolution in HRTF measurement. The general model is further developed to a continuous HRTF representation, in which the normalized spatial modes can achieve HRTF near-field and far-field representations in one formulation. The remaining HRTF spectral components are compactly represented using a Fourier spherical Bessel series, where the aim is to generate the HRTF with much higher spectral resolution in fewer parameters from typical measurements, which usually have limited spectral resolution constrained by sampling conditions. A low-computation algorithm is developed to obtain the model coefficients from the existing measurements. The HRTF synthesis using the proposed model is validated by three sets of data: (i) synthetic HRTFs from the spherical head model, (ii) the MIT KEMAR (Knowles Electronics Mannequin for Acoustics Research) data, and (iii) 45-subject CIPIC HRTF measurements.
 [DOI: 10.1121/1.3336399]

PACS number(s): 43.60.Ac, 43.60.Uv, 43.66.Pn [EJS] Pages: 2347–2357

I. INTRODUCTION

A. Motivation and background

People hear sound in three dimensions and the perception of the spatial aspects of sound has been essential to people's lives. Multiple cues are involved for the spatial localization[1] including the amplitude and the time arrival of the sound at each ear and, most importantly, the spectrum of the sound, which is modified by the interaction between the sound wave and a person's body (the torso, head, and external pinna shape). The head-related transfer function (HRTF),[2] an acoustic transfer function from the sound source to a listener's eardrums, contains all the listening cues used by the hearing mechanism for decoding spatial information encoded in binaural signals. The HRTF changes with direction from which sound arrives to the listener, and any sound source can be realistically located by filtering sound with the HRTF corresponding to the desired location and presenting the resulting binaural signals to the subject using two playback channels achieved typically by a pair of headphones.[3]

Nowadays, in practice, hundreds of measured HRTFs from all directions surrounding a subject (person or dummy head) are fully recorded and have always been directly applied to study the transformation characteristics of the external ear and to synthesize virtual reality over headphones.[2,4,5] Two major problems with the direct use of measured HRTFs are that first it is impossible to simulate every conceivable direction and create source movement (panning) smoothly through the space given the HRTF measurements are discrete by necessity, and second there is no standard HRTF spatial sampling theory to make HRTF measurement practical for commercial applications.

One common approach toward the goal to study the HRTF is to model the HRTF or head-related impulse response (HRIR) by a reduced number of parameters and to make the processing more effective by operating in this parametric domain. In the case of discrete data and sets of measurements corresponding to different human subjects, many techniques have been proposed for HRTF modeling. The filter bank models[3,6] could achieve accurate reconstruction of the original HRTF measurements, but the expansion weights in the model are coupled with both angle and frequency variables, which limits the usefulness of the model for HRTF analysis. Statistical methods have been used to analyze the HRTF in an effort to reduce the redundancy (correlation) of a data set. One important study is principal component analysis (PCA).[7,8] However, the facts are that this PCA represen-

[a]Author to whom correspondence should be addressed. Electronic mail: wen.zhang@anu.edu.au

tation is not continuous and the basis vectors may change for each individual. Both filter bank models and statistical models such as PCA only allow the synthesis of the measured HRTF samples. Interpolation is still required[9–11] between the discrete measurement positions.

HRTFs have also been represented as a weighted sum of spherical harmonics in three dimensions,[12] and as a series of multipoles based on the reciprocity principle.[13] The spherical harmonics, a complete orthogonal basis function on the two-sphere, provide a natural continuous representation in the angular domain. Therefore, it leads to a straightforward solution to the problem of HRTF interpolation in elevation and azimuth. In both models, the expansion weights are functions of frequency; analyzing these components can provide a new means to study the scattering behavior of the human body.

B. Contributions and organization

In the previous work,[14] we studied horizontal plane HRTF representation. Here we extended our work to three-dimensional auditory scene. Three main contributions of this paper are summarized below.

In Sec. II, we use the acoustic reciprocity principle and modal expansion of the wave equation solution to develop a general HRTF representation in all frequency-range-angle domains. We show that the HRTF decomposition with the derived spatial basis function *modes* can be truncated to a finite number and still with relative high accuracy. This means that the HRTF is essentially a mode-limited function; a finite number of spatial modes (named the *dimensionality*) can represent the HRTF corresponding to all directions. The value of dimensionality also determines the required spatial resolution in HRTF measurement.

In Sec. III, we further develop the general HRTF model to a continuous representation. We apply *normalized spatial modes* to achieve near-field and far-field HRTF representations in one formulation, which provides a way to obtain the range dependence of the HRTF from measurements conducted at only a single range. We study the radially invariant HRTF spectral components and find that the HRTF spectrum has an underlying pattern similar to the spherical Bessel functions. We use an orthogonal property of the Bessel functions to form frequency basis functions, Fourier spherical Bessel (FSB) series, to model the HRTF spectral components. Besides achieving much higher spectral resolution, this series representation can has far few parameters compared to the measurements for a more efficient HRTF representation.

The practical model implementation issues are discussed in Sec. IV. A low-computation algorithm is proposed to calculate the model coefficients from discrete measurements. The proposed method separates the HRTF azimuth and elevation sampling effects, from which we have the following observations: (i) The HRTF measurements that are coarsely sampled in elevation can still be reconstructed with reasonable accuracy and (ii) as for the azimuth, we need finer azimuthal sampling on the elevations closer to the equator but less azimuthal sampling points closer to the pole.

Section V validates the developed HRTF sampling theory and the proposed HRTF continuous representation by decomposing the experimentally measured[15,16] (or analytically simulated[17]) HRTFs on a single sphere and synthesizing HRTFs at any frequency for an arbitrary spatial location to check both reconstruction and interpolation performances.

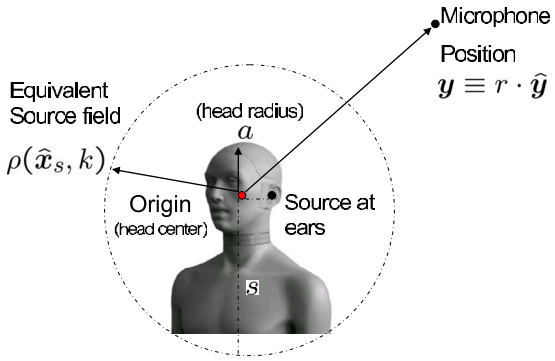

FIG. 1. (Color online) Geometry of HRTF measurement based on the reciprocity principle.

II. MODAL ANALYSIS OF HRTF

HRTFs are usually obtained by emitting a signal from a loudspeaker at different positions in space and recording it at a microphone in the listener's ear. At the physical level, the HRTF is characterized by the classical wave equation subject to boundary conditions. The general solution to the wave equation can be obtained by separation of variables (frequency, range, azimuth, and elevation angles). Thus, in principle, we can use the wave equation solution to expand the HRTF with separable basis functions.

A. Theoretical development

When sound propagates from the source to the listener, the received sound at the listener's ear is transformed by the structure and shape of the listener's body. We seek a representation of the sound pressure at the listener's ear (left or right), where two sources should be taken into account: one is the original acoustic source from the speaker and the other is the secondary source due to the scattering of human body. It is a complicated problem to apply the wave equation in this configuration because the receiver, the listener's ear, is within the scatterer region of human body. The *principle of reciprocity*[18] can be used to remove this difficulty and to develop a general representation of the HRTF.[13]

To apply the principle of reciprocity to the HRTF analysis, we assume that the original acoustic source is located at the listener's ear and microphones are some distance away (Fig. 1). Here, we consider all the scattering sources of human body as the secondary level sources with the original sources at the listener's ear together constituting the source field. From Huygens' principle,[19] the sum of the waves from all the sources (including both original and secondary sources) to any point beyond the scatterers (the human body) can be calculated by integration or numerical modeling. To exactly model the effect of the source field, we develop an *equivalent source field* on a sphere of radius s with origin at the head center, as shown in Fig. 1, where the sphere should

be large enough to enclose all the sources. Note that the reason we choose the sphere to include all the sources is because we can use a specific set of orthogonal series, spherical harmonics, to represent the source field; for example, we write the equivalent source field as a function of angular position and wavenumber; i.e.,

$$\rho(\hat{\boldsymbol{x}}_s,k)=\sum_{n=0}^{\infty}\sum_{m=-n}^{n}\alpha_n^m(k)Y_n^m(\hat{\boldsymbol{x}}_s), \tag{1}$$

where $\hat{\boldsymbol{x}}_s$ is a unit vector (or a set of 2D angles, elevation and azimuth $\{\theta_s,\phi_s\}$) pointing into the equivalent source direction and $\boldsymbol{x}_s\equiv s\cdot\hat{\boldsymbol{x}}_s$ defines the equivalent source position. The wavenumber is defined as $k=2\pi f/c$, where f is frequency and c is the speed of sound propagation. $Y_n^m(\hat{\boldsymbol{x}}_s)$ are the spherical harmonics characterized by two indices, degree n and order m,

$$Y_n^m(\hat{\boldsymbol{x}}_s)\triangleq\sqrt{\frac{2n+1}{4\pi}\frac{(n-|m|)!}{(n+|m|)!}}P_n^{|m|}(\cos\,\theta_s)e^{im\phi_s}. \tag{2}$$

$\alpha_n^m(k)$ are the spherical harmonic coefficients of the equivalent source field at wavenumber k and obtained from

$$\alpha_n^m(k)=\int_{\mathbb{S}^2}\rho(\hat{\boldsymbol{x}}_s,k)\overline{Y_n^m(\hat{\boldsymbol{x}}_s)}d\varrho(\hat{\boldsymbol{x}}_s) \tag{3}$$

on the two-sphere $\mathbb{S}^2$, where $\overline{(\cdot)}$ stands for the complex conjugate and $\int_{\mathbb{S}^2}d\varrho(\hat{\boldsymbol{x}}_s)=\int_0^{2\pi}\int_0^{\pi}\sin\,\theta_s d\theta_s d\phi_s$. We can see that the $\alpha_n^m(k)$ carry information about the original source and also the human body scattering behavior. Then the received signal at $\boldsymbol{y}\equiv r\cdot\hat{\boldsymbol{y}}$ (the HRTF corresponding to that position) can be written in terms of the equivalent source field as

$$\hat{H}(\boldsymbol{y},k)=\int_{\mathbb{S}^2}\rho(\hat{\boldsymbol{x}}_s,k)\frac{e^{ik\|\boldsymbol{x}_s-\boldsymbol{y}\|}}{4\pi\|\boldsymbol{x}_s-\boldsymbol{y}\|}d\varrho(\hat{\boldsymbol{x}}_s),\quad r>s, \tag{4}$$

where r is the distance between the head center (origin or source center) and the receiver position and $\hat{\boldsymbol{y}}$ is the direction of the receiver. The integral is over the sphere to account for all sources. Using the Jacobi–Anger expansion,[19] we have

$$\frac{e^{ik\|\boldsymbol{x}_s-\boldsymbol{y}\|}}{4\pi\|\boldsymbol{x}_s-\boldsymbol{y}\|}=ik\sum_{n=0}^{\infty}\sum_{m=-n}^{n}j_n(ks)h_n^{(1)}(kr)\overline{Y_n^m(\hat{\boldsymbol{x}}_s)}Y_n^m(\hat{\boldsymbol{y}}),\quad r>s, \tag{5}$$

where $j_n(\cdot)$ is the spherical Bessel function and $h_n^{(1)}(\cdot)$ is the spherical Hankel function of the first kind. By substituting Eq. (5) into Eq. (4), we can expand the HRTF at position $\boldsymbol{y}$ as

$$\hat{H}(r,\hat{\boldsymbol{y}},k)=\sum_{n=0}^{\infty}\sum_{m=-n}^{n}\hat{\beta}_n^m(k)h_n^{(1)}(kr)Y_n^m(\hat{\boldsymbol{y}}), \tag{6}$$

where

$$\hat{\beta}_n^m(k)=4\pi ik\alpha_n^m(k)j_n(ks). \tag{7}$$

In Eq. (6), the HRTF dependence on each variable (frequency, range, and 2D angle) is represented by separable basis functions. The spatial modes, i.e.,

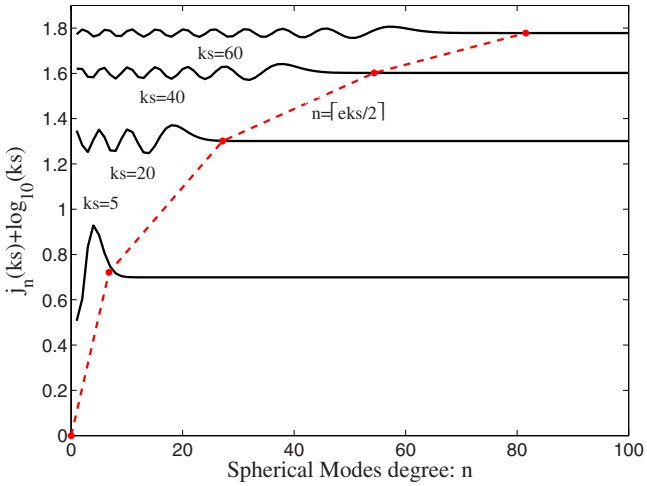

FIG. 2. (Color online) Dependence of the spherical Bessel function $j_n(ks)$ vs degree n at different ks shown on the vertically shifted curves.

$$h_n^{(1)}(kr)Y_n^m(\hat{\boldsymbol{y}}), \tag{8}$$

account for the HRTF spatial variations and $\hat{\beta}_n^m(k)$ are the modal decomposed HRTF spectral components.

B. Dimensionality of HRTF as a mode-limited function

In this section, we show that the HRTF decomposition in Eq. (6) can be well approximated by choosing a sufficiently large truncation order N, viz.,

$$\hat{H}(r,\hat{\boldsymbol{y}},k)\cong\sum_{n=0}^{N}\sum_{m=-n}^{n}\hat{\beta}_n^m(k)h_n^{(1)}(kr)Y_n^m(\hat{\boldsymbol{y}}), \tag{9}$$

which indicates that the HRTF is essentially a mode-limited function.[20] The required number $(N+1)^2$ of spatial modes (8) to represent the HRTF spatial variations should be determined by a typical size of human head/torso and by bounds on the spherical Bessel function $j_n(ks)$, which decides the upper limit of $\hat{\beta}_n^m(k)$ in Eq. (6) [because first, both the source field coefficients $\alpha_n^m(k)$ and the spherical harmonics $Y_n^m(\cdot)$ are bounded functions; second, the spherical Hankel function $h_n^{(1)}(kr)$ has a weaker impact than the same order of the spherical Bessel function $j_n(ks)$ (Ref. 21)]. We define this number of spatial modes as the spatial dimensionality of the HRTF.

Figure 2 illustrates typical dependence of the spherical Bessel function on the degree n for various values of ks. It is clearly seen that there are two distinct regions separated by value[22,23]

$$N=\lceil eks/2\rceil. \tag{10}$$

For $n<\lceil eks/2\rceil$, the spherical Bessel functions oscillate and there is no decay in the amplitude for growing n. However, when $n\geq\lceil eks/2\rceil$, the functions monotonically decay to zero with growing n, and the decay is very fast. Therefore, we only need to include all spatial modes lower than the order of $N=\lceil eks/2\rceil$ for HRTF spatial representation. This yields the spatial dimensionality of the HRTF, or the required number of weights $\{\hat{\beta}_n^m(k)\}$ that can represent HRTFs corresponding to all directions; i.e.,

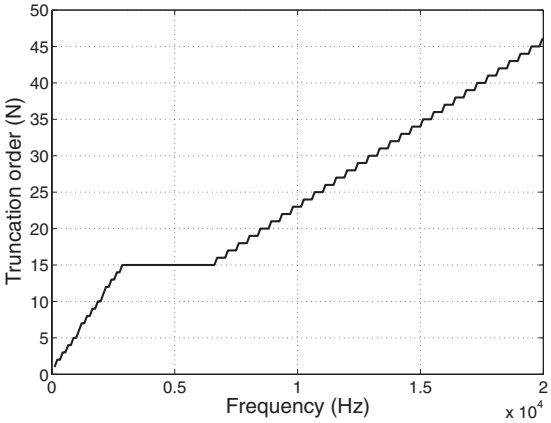

FIG. 3. Calculated the required truncation order N for the HRTF representation as a function of frequency.

$$\mathrm{DIM}(H) = (N+1)^2 = (\lceil eks/2 \rceil + 1)^2. \tag{11}$$

In order to obtain the required number of weights, Eq. (11) also defines the least number of the HRTF samples in the space. The dimensionality depends on the wavenumber k and the radius of the equivalent source field s, and we have the following comments.

(1) The dimensionality increases with wavenumber/frequency. This is because for a fixed size region of sphere, the low frequency HRTF requires fewer spatial modes since the waves are spatially varying more slowly; for increasing frequency, we need more spatial modes as the smaller wavelength indicates faster changes in the space.

(2) The value of s relates to the typical size of human head/torso. For example, for the spherical head, the value of s is simply the radius of the head (0.09 m). While for the Knowles Electronics Mannequin for Acoustics Research (KEMAR) or human subjects, we need to enlarge the radius of the equivalent source field to include the main torso effect, i.e., the shoulder reflection. However, the torso only contributes to the HRTF at frequencies below 3 kHz. For frequencies above 3 kHz, it is the pinna effect that allows the perception of elevation effects.[24,25] So we propose to set two separate values of the equivalent source field radius for two ranges of frequency, that is,

$$s = \begin{cases} 0.20 \text{ m} & \text{for } f \le 3 \text{ kHz} \\ 0.09 \text{ m} & \text{for } f > 3 \text{ kHz}. \end{cases} \tag{12}$$

(3) Figure 3 plots the calculated truncation order N required for HRTF representation (9) as a function of frequency (note that an interpolation function on the truncation order derived from the two equivalent source field radii is applied; the value of N in the frequency range of [3, 6] kHz is decided by the maximum value at $f=3$ kHz after which the source field radius reduces to 0.09 m). In the case for a given frequency range, such as the audible frequency range (200 Hz—20 kHz), the maximum number of the discrete frequency points included in the frequency range determines the least number of measurements. For example, 20 kHz bandwidth has the highest truncation order $N=46$ and requires at least 2209 HRTF measurements in the space.

III. HRTF CONTINUOUS REPRESENTATION

In this section, we further develop general representation (9) into a continuous HRTF model, which can (i) link near-field and far-field HRTFs directly, and (ii) parametrize the spectral components by a set of basis functions.

A. Normalized modes for HRTF spatial representation

The spatial modes in Eq. (6) cannot directly represent far-field HRTFs because the radial term tends to zero, viz.,

$$h_n^{(1)}(kr) \sim (-i)^{(n+1)} \frac{e^{ikr}}{kr} \to 0 \quad \text{as} \quad r \to \infty. \tag{13}$$

It is desirable to normalize the spherical Hankel function; i.e.,

$$R_n(kr) \triangleq i^{(n+1)} kr e^{-ikr} h_n^{(1)}(kr), \tag{14}$$

so that we can achieve both near-field HRTF and far-field HRTF representations in one formulation. As demonstrated later in this section, we will show that this definition is consistent with the analytical spherical HRTF model.

Referring to Eq. (9), the modified HRTF representation with the normalization is then

$$H(r,\hat{\mathbf{y}},k) = \sum_{n=0}^{N} \sum_{m=-n}^{n} \beta_n^m(k) R_n(kr) Y_n^m(\hat{\mathbf{y}}), \tag{15}$$

noting that $\lim_{r\to\infty} R_n(kr)=1, \quad \forall n$, when $r\to\infty$, we have the normalized far-field representation

$$H(\hat{\mathbf{y}},k) = \sum_{n=0}^{N} \sum_{m=-n}^{n} \beta_n^m(k) Y_n^m(\hat{\mathbf{y}}). \tag{16}$$

Equations (15) and (16) show that the HRTF spectral components $\beta_n^m(k)$ are radially invariant and can be obtained from the spherical harmonic transform of the measurements at a single radius; i.e.,

$$\beta_n^m(k) = \begin{cases} \dfrac{1}{R_n(kr)} \displaystyle\int_{S^2} H(r,\hat{\mathbf{y}},k) \overline{Y_n^m(\hat{\mathbf{y}})} d\varrho(\hat{\mathbf{y}}) & \text{near-field} \\ \displaystyle\int_{S^2} H(\hat{\mathbf{y}},k) \overline{Y_n^m(\hat{\mathbf{y}})} d\varrho(\hat{\mathbf{y}}) & \text{far-field}, \end{cases} \tag{17}$$

and later used for HRTF reconstruction at any spatial point. In addition, from Eq. (7), we have

$$\beta_n^m(k) = \frac{\hat{\beta}_n^m(k)}{i^{(n+1)} kr e^{-ikr}} = \frac{4\pi \alpha_n^m(k) j_n(ks)}{i^n r e^{-ikr}}. \tag{18}$$

Example of spherical head model. We use the spherical head model[17] as an example to solve the HRTF spectral components, in which the HRTFs are represented as

$$\varphi_H(r,\Theta,k) = \frac{-r}{ka^2} e^{-ikr} \sum_{n=0}^{\infty} (2n+1) P_n(\cos\Theta) \frac{h_n^{(1)}(kr)}{h_n'^{(1)}(ka)}, \quad r > a, \tag{19}$$

where a is the spherical head radius, Θ is the angle of incidence (the angle between the ray from the center of the sphere to the source, $\hat{\boldsymbol{y}}$, and the ray to the measurement point on the surface of the sphere, $\hat{\boldsymbol{\vartheta}}_{\text{ear}}$), $P_n(\cdot)$ is the Legendre function of degree n, and $h_n^{(1)}(\cdot)$ and $h_n'^{(1)}(\cdot)$ are the spherical Hankel function of the first kind and its derivative. Applying the addition theorem,[19] we have

$$P_n(\cos\Theta) = \frac{4\pi}{2n+1} \sum_{m=-n}^{n} Y_n^m(\hat{\boldsymbol{y}}) \overline{Y_n^m(\hat{\boldsymbol{\vartheta}}_{\text{ear}})}. \tag{20}$$

Then we can expand the spherical head model HRTF with the normalized modes, where the spectral components are

$$\beta_n^m(k) = \frac{4\pi \overline{Y_n^m(\hat{\boldsymbol{\vartheta}}_{\text{ear}})}}{i^n} \left(j_n(ka) - j_n'(ka) \frac{h_n^{(1)}(ka)}{h_n'^{(1)}(ka)} \right). \tag{21}$$

B. Fourier spherical Bessel series for HRTF spectral representation

The goal of seeking an efficient continuous HRTF spectral representation is to determine the spectrum of the HRTF with higher spectral resolution and fewer parameters from a finite number of measurements, which usually have limited spectral resolution constrained by the sampling rate and number of samples (or the record time).

The $\beta_n^m(k)$ exhibit an underlying pattern similar to the spherical Bessel functions [implicitly shown in Eq. (18)].[26] An example is the spectral components of the spherical head HRTF, Eq. (21), in which the first component represents the incident wavefield and the second term is the scattered field. Both terms show the similar structures to the spherical Bessel functions, so we can observe the strong correlation between the HRTF spectral components and spherical Bessel functions in Fig. 4.

Figure 5 shows the energy spread of the HRTF spectrum over the spatial modes (n,m) and wavenumber k, which has a significant triangular null region and has been described as the butterfly shape of the HRTF spectrum[14,27] for the horizontal plane HRTF. The explanation for this special shape of the spectrum is because the HRTF dimensionality increases linearly with frequency, as shown in Sec. II B. At low frequencies, only low order spatial modes are signification and the high spatial modes have very small contributions; at higher frequencies, the higher order spatial modes become significant. Therefore, most of $\beta_n^m(k)$ energy is present in a triangular shaped region and, outside this region, the energy is greatly reduced.

In Fig. 4, the resemblance between the patterns of $\beta_n^m(k)$ and the spherical Bessel functions of the same degree indicates that the HRTF spectrum can be compactly represented by the spherical Bessel functions. Here, we apply the FSB series for the representation of the HRTF spectral components. The FSB series[28] (derived from the Fourier Bessel series used for the horizontal plane HRTF spectral representation[14]) are orthogonal basis functions on the interval (0,1) as follows:

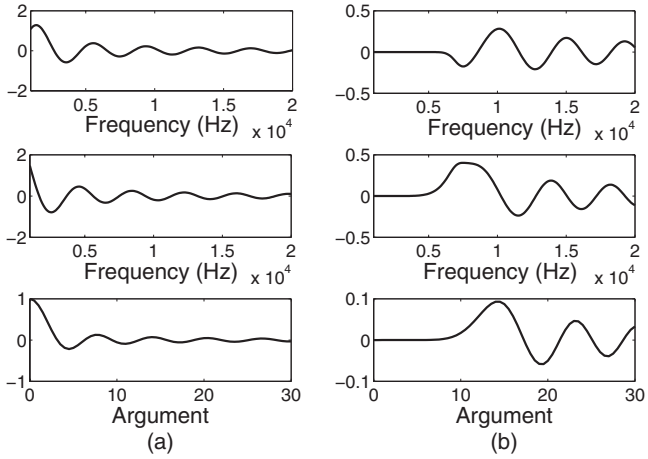

FIG. 4. Examples to demonstrate the structural similarities between the HRTF spectral components $\beta_n^m(k)$ and the spherical Bessel functions of the first kind. Top plots and middle plots are the real and imaginary parts of $\beta_n^m(k)$ with (a) $n=0,m=0$ and (b) $n=12,m=0$; and the bottom plots are the spherical Bessel functions $j_n(\cdot)$ at the corresponding degrees $n=0$ and $n=12$ against arguments from 0 to 30.

$$\int_0^1 x^2 j_n(xZ_\ell^{(n)}) j_n(xZ_h^{(n)}) dx = \frac{1}{2} \delta_{\ell,h} (j_{n+1}(Z_\ell^{(n)}))^2, \tag{22}$$

where $Z_\ell^{(n)}$ and $Z_h^{(n)}$ are the positive roots of the $j_n(\cdot)$, and $\delta_{\ell,h}$ is the Dirac delta function. The derived HRTF spectral component representation is

$$\beta_n^m(k) = \sum_{\ell=1}^{\infty} A_{n;\ell}^m j_n\left(\frac{Z_\ell^{(n)}}{k_{\max}} k \right), \tag{23}$$

where from Eq. (22)

$$A_{n;\ell}^m = \frac{2}{k_{\max}^3 j_{n+1}^2(Z_\ell^{(n)})} \int_0^{k_{\max}} k^2 \beta_n^m(k) j_n\left(\frac{Z_\ell^{(n)}}{k_{\max}} k \right) dk. \tag{24}$$

$k_{\max}$ is the maximum wavenumber of a HRTF data set being modeled. In Eq. (23), the HRTF spectral components are decomposed as a linear combination of FSB series. Given

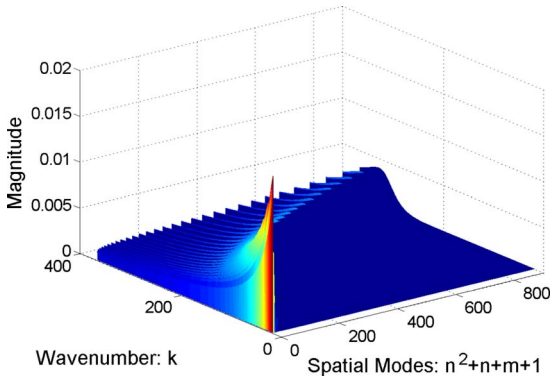

FIG. 5. (Color online) Magnitude of the HRTF spectral components over spatial modes and wavenumber for the spherical head case. The spatial mode of degree n and order m corresponds to number of $n^2+n+m+1$ on x-axis.

the FSB series expansion is convergent, Eq. (23) can be truncated as

$$\beta_n^m(k) \cong \sum_{\ell=1}^{L} A_{n;\ell}^m j_n\left(\frac{Z_\ell^{(n)}}{k_{\max}}k\right), \tag{25}$$

where by choosing L sufficiently large the contribution of the neglected higher order FSB terms can be made sufficiently small. Section IV gives a practical way to determine L.

Besides compact representation, the continuous FSB series can achieve HRTF spectral reconstruction at any frequency value (not necessity of measured frequencies) and therefore provide a way for generating HRTFs at higher spectral resolutions than the measurements.

C. Proposed continuous HRTF model

In summary, the above development leads to the HRTF functional model written as

$$H(r,\hat{\mathbf{y}},k) = \sum_{n=0}^{N}\sum_{m=-n}^{n}\sum_{\ell=1}^{L} A_{n;\ell}^m j_n\left(\frac{Z_\ell^{(n)}}{k_{\max}}k\right) R_n(kr) Y_n^m(\hat{\mathbf{y}}), \tag{26}$$

which can transform any HRTF data set to a set of coefficients $\{A_{n;\ell}^m\}$ of cardinality $(N+1)^2 \times L$. This HRTF representation exhibits three significant advantages.

- First, the representation has well studied closed form orthogonal basis functions, which can make the HRTF approximation easily implemented and model parameters $A_{n;\ell}^m$ simply computed using Eqs. (17) and (24). A low-computation algorithm is developed in Sec. IV given finite discrete measured HRTFs.
- Second, using continuous basis functions, the proposed model is powerful for the computation of the HRTF at any frequency point for an arbitrary direction from a given set of measurements at a fixed radius.
- Third, the basis functions are independent of the data. As the basis is same for all subjects, the model coefficients $A_{n;\ell}^m$ carry all information about the individuality. Thus, the model has capability to represent the individualized HRTF by assigning a subject specific set of parameters to the model.

IV. IMPLEMENTATION ANALYSIS

In this section, we investigate the modal decomposition of the discrete measured HRTFs using the proposed functional model (26). A practical method to solve integral equations (17) and (24) given the typical HRTF measurement setup is introduced in the following.

A. Typical HRTF measurement setup

Typically HRTFs are measured from humans or mannequins for both left and right ears at a fixed radius from the head center. Thus, the source location is specified by a 2D angle, elevation θ, and azimuth ϕ (denoted as a unit vector $\hat{\mathbf{y}}$ in our previous analysis). The elevation angle θ from top to bottom is defined as changing from 0° to 180°; and the azimuth ϕ is counterclockwise rotating from 0° to 360°, where 0° and 180° are the direct front and back directions and 90° and 270° are defined as the left and right sides (note that this definition is in accordance with the right hand coordinate system and may be different from others).

It is commonly believed that the HRTF should be sampled uniformly on the sphere; however, arranging points evenly on the sphere is a complicated mathematical problem. Two most used strategies for HRTF measurement are equidistance in the azimuth arc[15] and equiangular.[16] In the former one, the sampling points are distributed equally in the azimuth arc at all elevations, resulting in a decline of azimuth resolution toward the pole of the sphere. While the latter one applies the equal angular interval along both elevation and azimuth and samples the sphere with very high spatial resolution. These two sampling arrangements are compared in Sec. V using the proposed modal decomposition method, which helps us to thoroughly investigate the azimuth and the elevation sampling effects.

B. Practical modal decomposition method

The proposed modal decomposition method is a two-step procedure corresponding to approximating the two integral equations (17) and (24) given the discrete measured HRTFs.

1. Estimating HRTF spectral components

The HRTF spectral components are obtained from the spherical harmonic transform of the measurements on a single sphere, as shown in Eq. (17). We rewrite the spherical harmonic transform in elevation and azimuth, given $\hat{\mathbf{y}} = \{\theta, \phi\}$, as

$$\beta_n^m(k) = \int_{-\pi}^{\pi}\int_{0}^{\pi} H(\theta,\phi,k)\overline{Y_n^m(\theta,\phi)}\sin\theta d\theta d\phi. \tag{27}$$

Note here we only consider extracting $\beta_n^m(k)$ from far-field HRTFs; same procedure can be applied to near-field measurements with an additional step of dividing the normalized spherical Hankel function.

Let $H(\theta_q,\phi_v,k)$ be the HRTFs measured at several elevations θ_q, $q=1,\ldots,Q$, and several different/same azimuths ϕ_v, $v=1,\ldots,V_q$, at each elevation. We write the far-field measured HRTF decomposition with spherical harmonics (16) as

$$H(\theta_q,\phi_v,k) = \sum_{n=0}^{N}\sum_{m=-n}^{n} \beta_n^m(k) Y_n^m(\theta_p,\phi_v), \tag{28}$$

where the spherical harmonics $Y_n^m(\cdot)$ are defined in terms of the associated Legendre function $P_n^{|m|}(\cdot)$ and the exponential function, as shown in Eq. (2). We use Eq. (2) to express Eq. (28) in terms of the normalized Legendre function $\mathcal{P}_n^{|m|}(\cdot)$ and the normalized exponential function $E_m(\cdot)$ as

$$H(\theta_q,\phi_v,k) = \sum_{n=0}^{N}\sum_{m=-n}^{n} \beta_n^m(k)\mathcal{P}_n^{|m|}(\cos\theta_q)E_m(\phi_v), \tag{29}$$

where $E_m(\phi_v) \triangleq (1/\sqrt{2\pi})e^{im\phi_v}$ and

$$\mathcal{P}_n^{|m|}(\cos\theta_q) \triangleq \sqrt{\frac{2n+1}{2}\frac{(n-|m|)!}{(n+|m|)!}}P_n^{|m|}(\cos\theta_q). \tag{30}$$

Azimuth harmonics. At each elevation with the use of the orthogonality of the exponential functions over circle, we get an *azimuth harmonics*

$$a_m(\theta_q,k)=\sum_{n=|m|}^{N}\beta_n^m(k)\mathcal{P}_n^{|m|}(\cos\theta_q); \tag{31}$$

while given V_q azimuth samplings at each elevation θ_q, we have

$$a_m(\theta_q,k)\approx\Delta\phi_v\sum_{v=1}^{V_q}H(\theta_q,\phi_v,k)E_{-m}(\phi_v),$$

$$|m|\le\lfloor(V_q-1)/2\rfloor, \tag{32}$$

where $\Delta\phi_v$ is the azimuth sampling interval in radians. The azimuthal HRTFs of V_q samples contain at most V_q expansion components, which means we can estimate $a_m(\theta_q,k)$ for $|m|\le\lfloor(V_q-1)/2\rfloor$. However, if the sampling is non-uniform, we should emphasize that approximation (32) is determined by the maximum sampling interval; only the coefficients of $|m|\le\lfloor(2\pi/\Delta\phi_v^{\max}-1)/2\rfloor$ can be accurately solved.

Least-squares fitting. By writing Eq. (31) for a specific order of m for all measured elevations, we can now form a system of simultaneous equations given by

$$\mathbf{P}_m\mathbf{b}_m=\mathbf{a}_m,\quad m=-N,\ldots,N, \tag{33}$$

where the matrix $\mathbf{P}_m$ and the vector $\mathbf{b}_m$ are in the following forms:

$$\mathbf{P}_m=\begin{bmatrix}\mathcal{P}_{|m|}^{|m|}(\cos\theta_1) & \cdots & \mathcal{P}_N^{|m|}(\cos\theta_1)\\ \vdots & \ddots & \vdots\\ \mathcal{P}_{|m|}^{|m|}(\cos\theta_Q) & \cdots & \mathcal{P}_N^{|m|}(\cos\theta_Q)\end{bmatrix}, \tag{34}$$

$$\mathbf{b}_m=[\beta_{|m|}^m(k),\beta_{|m|+1}^m(k),\ldots,\beta_N^m(k)]^T, \tag{35}$$

and

$$\mathbf{a}_m=[a_m(\theta_1,k),a_m(\theta_2,k),\ldots,a_m(\theta_Q,k)]^T. \tag{36}$$

The HRTF spectral components $\beta_n^m(k)$ can be calculated by solving these linear equations described by Eq. (33) for each order m. Since there will be noise in the HRTF measurement, it is necessary to solve Eq. (33) in the least-squares sense by minimizing the mean squared error $\|\mathbf{P}_m\mathbf{b}_m-\mathbf{a}_m\|^2$. Another issue in the HRTF measurement is that no samplings are made for lower elevations (i.e., $\theta\ge140°$) because of the strong distortions from the ground and measurement apparatus. To avoid the enlargement of the unmeasured HRTFs, we need to regularize the solution (the power in the $\|\mathbf{b}_m\|^2$ may be included as a constraint). The minimum norm least-squares solution is denoted by

$$\mathbf{b}_m^+=\mathbf{P}_m^+\mathbf{a}_m, \tag{37}$$

where $\mathbf{P}_m^+$ is the general inverse of $\mathbf{P}_m$.[29] Given the size of $\mathbf{P}_m$ is $Q\times(N-|m|+1)$, there are two cases of interest and the Tikhonov regularized solutions are given explicitly by

$$\mathbf{P}_m^+=[\mathbf{P}_m^T\mathbf{P}_m+\lambda\mathbf{I}]^{-1}\mathbf{P}_m^T,\quad Q\ge(N-|m|+1), \tag{38}$$

$$\mathbf{P}_m^+=\mathbf{P}_m^T[\mathbf{P}_m\mathbf{P}_m^T+\lambda\mathbf{I}]^{-1},\quad Q<(N-|m|+1), \tag{39}$$

where λ is the regularization control parameter and $\mathbf{I}$ is the identity matrix. A systematic approach to evaluate λ for a meaningful result is given in the work.[30] In our experiment, we set a small value of $\lambda=10^{-5}$, which was seen to achieve reasonable reconstruction and interpolation quality.

Insights into spatial sampling. The main contribution of this low-computation algorithm is based on factorization of the spherical harmonics, which helps to separate the azimuth and the elevation sampling effects. We have the following comments regarding on the HRTF spatial sampling.

(1) In theory, it is necessary to set Eq. (33) as an overdetermined system; i.e., the number of elevation samples should be greater than $(N+1)$, so that the least-squares solutions are valid. However, with the use of the regularization technique, we can loosen this condition. Our experiment results show the HRTF measurements that are coarsely sampled in elevation (given the total number of samples greater than the dimensionality) can still be reconstructed with reasonable accuracy.
(2) For smaller elevations (θ toward the pole), the associated Legendre functions $P_n^{|m|}(\cos\theta)$ have values close to zero for higher m; i.e., $P_n^{|m|}(\cos 0)=0$, for $m\ne0$.[31] This means as elevation increases from the pole toward the equator, higher order m of coefficients begin to appear. Thus, in principle, we need less dense azimuth sampling closer to the pole and more azimuth sampling points on the elevations closer to the equator. This shows that the sampling of equidistance in the azimuth arc is appropriate for the HRTF measurement, which we will further corroborate using the real data validation.

2. Calculating model coefficients

From the estimated HRTF spectral components $\beta_n^m(k)$, the model coefficient $A_{n;\ell}^m$ is obtained by using the left Riemann sum to approximate integral (24). The most important issue is to determine the truncation order L. We define the relative power of the ℓth order FSB series term against the total power as

$$\eta_\ell=\frac{|A_{n;\ell}^m|^2}{\sum_{\ell=1}^{\infty}|A_{n;\ell}^m|^2},\quad \ell=1,2,\ldots. \tag{40}$$

In Eq. (40), the denominator is an infinite sum over model coefficients. Since only HRTFs at discrete frequencies are obtained by measurements, we evaluate the contribution of the FSB series over the maximum order L_f (the number of HRTF frequency samples); and the relative power ratio is defined as

$$\eta=\frac{\sum_{\ell=1}^{L}|A_{n;\ell}^m|^2}{\sum_{\ell=1}^{L_f}|A_{n;\ell}^m|^2}. \tag{41}$$

TABLE I. MIT KEMAR data measurement steps (angles in degrees).

Elevation (θ)	Azimuth resolution (ϕ)	No. of azimuthal measurements
70–110	5.00	72
60 and 120	6.00	60
50 and 130	6.43	56
40	8.00	45
30	10.00	36
20	15.00	24
10	30.00	12
0	⋯	1

Then for each HRTF spectral component $\beta_n^m(k)$, calculate η for $L=1,2,\ldots,L_f$ and when η reaches a power threshold (such as 0.9), L is chosen as the truncation order above which the contribution of higher order FSB series is negligible.

V. SIMULATION RESULTS

A. HRTF database

Three sets of HRTF database are used.

(1) *Analytically simulated HRTF from the spherical head model.*[17] The HRTF for an ideal rigid sphere is defined as the pressure on the sphere at the defined ear position divided by the pressure that would exist at the sphere center in the absence of the sphere. The synthetic data are without noise influence and provide reliable reference to check the proposed sampling theory and the continuous model performance.

(2) *The HRTF database for KEMAR from the MIT media laboratory.*[15] KEMAR is designed according to the mean anatomical size of the population; thus results from KEMAR HRTF represent the mean performance. The measurements are the head-related impulse responses in the time domain at 44.1 kHz sampling rate and each response is 512 samples long, from which a 512-tap HRTF can be obtained by the discrete-time Fourier transform. The speakers were at a distance of 1.4 m away from the head center. The HRIRs (or HRTFs) were sampled in the equidistance in the azimuth arc, where the measurements are available for elevation steps of 10° ranging from 0° (north pole) to 130° (40° underneath the horizontal plane) and for full azimuth cover but have a decline of azimuthal resolution toward the pole, as shown in Table I.

(3) *HRTF database of human subjects from CIPIC interface laboratory.*[16] The HRIR measurements performed at CIPIC include 45 subjects. A 200 samples long pseudo-random signal generated by the snapshot system (sampling frequency is 44.1 kHz) is used as the test signal. For each subject, the HRTFs are measured at 1250 points on the sphere of 1 m away from the listener. The elevation varies uniformly from 0° to 135° in the step of 5.625°; and there are 50 azimuth samples at each elevation but not uniformly sampled; i.e., $\phi=[0:5:45, 55,65,80,100,115,125,135:5:225,235,245,260,280, 295,305,315:5:355]°$. The samplings are more dense near the median plane but very coarse near the ear where the azimuth varies in the step of 20°.

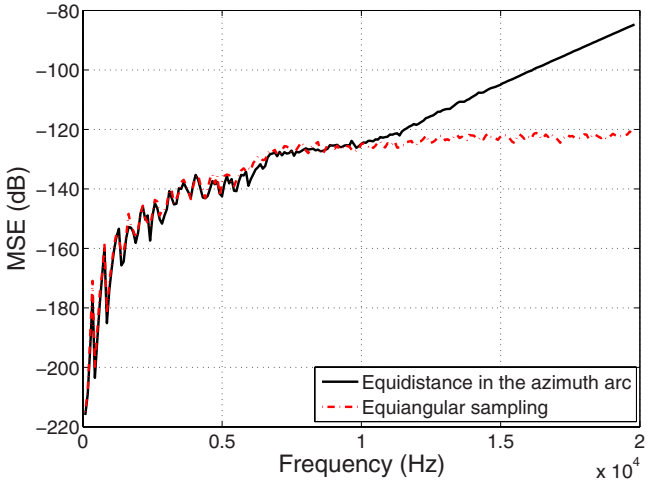

FIG. 6. (Color online) Synthetic HRTF reconstruction error performance for the audible frequency range of [0.2, 20] kHz.

B. Results for dimensionality and analysis

Simulations are run on some audible frequency range for each HRTF database, where the total number of spatial samples determines the maximum frequency point that can be reconstructed with high accuracy. The relative mean square error (MSE) over all M angles (including both azimuth and elevation) at each frequency is used as the error metric

$$\varepsilon(f)=\frac{\sum_{j=1}^{M}|H(f,\hat{\mathbf{y}}_j)-\tilde{H}(f,\hat{\mathbf{y}}_j)|^2}{\sum_{j=1}^{M}|H(f,\hat{\mathbf{y}}_j)|^2}, \tag{42}$$

where $H(f,\hat{\mathbf{y}}_j)$ and $\tilde{H}(f,\hat{\mathbf{y}}_j)$ are the original and the reconstructed HRTFs, respectively.

Figure 6 plots the synthetic HRTF reconstruction performance for the whole audible frequency range up to 20 kHz. The analytically simulated HRTFs are generated at 1.0 m away from the head center on a sphere according to the equidistance in the azimuth arc sampling (2640 samples) and the equiangular sampling (4371 samples); both satisfy the required dimensionality (2209 samples) for reconstruction up to 20 kHz. We can see that the maximum reconstruction error is at the highest frequency. This shows that more than dimensionality large number of measurements can fit the low frequency data very well. Both equiangular and equidistance samplings have very small reconstruction errors; but the equiangular method needs much more samples and its biggest failure is that the sampling points near the pole are dense, small, and can be very distorted when measurements in this region are contaminated by noise.

We next investigate the dimensionality results of the HRTF measurements on KEMAR mannequin and human subjects. Figure 7 shows that both data set reconstruction

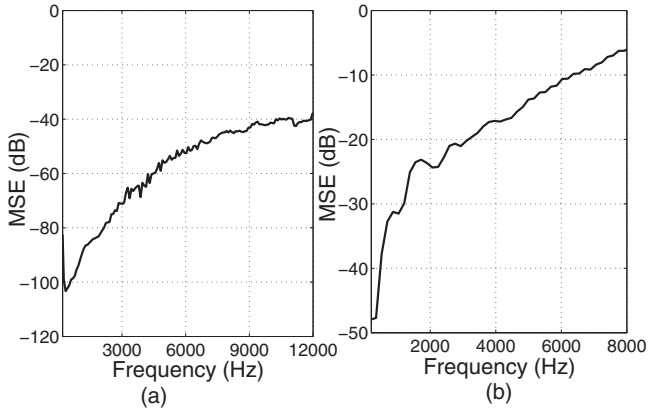

FIG. 7. HRTF measurement reconstruction error performances. (a) MIT KEMAR mannequin measurements of frequency range [0.2, 12] kHz. (b) HRTFs of CIPIC subject 3 of frequency range [0.2, 8] kHz.

errors are larger than that of the theoretical model due to the possibility of noise contamination at some measurements. This is especially more likely to occur for human subjects where the movement of the subject in the measurements can lead to inconsistency in the measured response. Thus, we can see that the reconstruction of KEMAR HRTFs is more accurate than that of the human subject data. In addition, both data sets have very similar error pattern.

As introduced in Sec. V A, the MIT KEMAR measurements are equidistance sampled, which has 72 azimuth samples on the horizontal plane and less azimuth samplings for the elevations toward the pole. In total there are 710 spatial samples on the sphere, which means we can solve the spatial mode decomposition up to $N=25$ corresponding to the frequency about 12 kHz according to Eq. (11). In Fig. 7(a), the MIT data reconstruction shows a reasonable match to the original data in the frequency range of [0.2, 12] kHz with maximum error less than −40 dB.

The CIPIC data have finer elevation samplings but are not uniformly sampled in azimuth. Even though the CIPIC measurements are sampled at a much higher spatial resolution (1250 samples on sphere), it has even larger errors [Fig. 7(b)] compared to MIT measurements. This is due to the possible large measurement variations and the coarse azimuthal sampling (50 not uniformly azimuths at each elevation). Very large azimuthal interval of 20° at both ear sides determines that the model coefficients can only be solved accurately for low order N. This is corroborated in Fig. 7(b), where the CIPIC data reconstruction errors are less than −17 dB for $f \leq 4$ kHz and increase to large values for higher frequencies.

In summary, the simulation results prove that the proposed dimensionality (11) determines the required number of spatial samples in the HRTF measurement. Only when the number of measurements is larger than the required dimensionality for a given frequency range (or a particular frequency point), reasonable reconstruction with high accuracy can be achieved. As for the HRTF measurement, equidistance in the azimuth arc is appropriate; with the use of the regularization technique, the spatial sampling for elevations

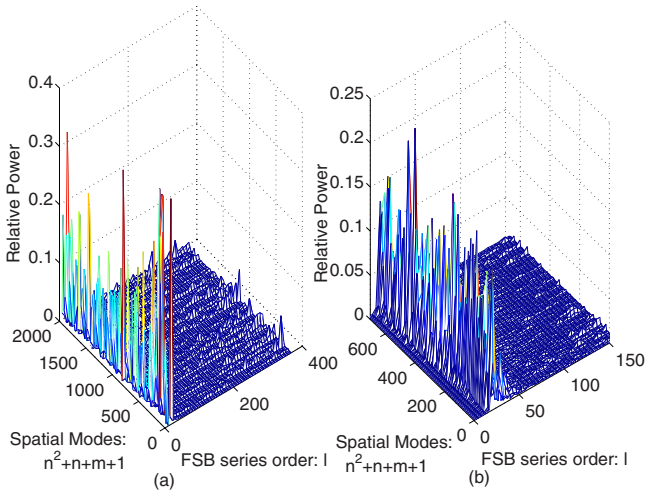

FIG. 8. (Color online) The relative power distribution of the FSB series components for the HRTF spectral representation. (a) Analytically simulated HRTFs from the spherical head model and (b) MIT KEMAR mannequin left ear HRTFs. For all spatial modes, the relative contribution of lower order FSB series is significant.

can be coarse while the sampling along the azimuth should be finer (especially for the measurements close to the equator).

C. Continuous model performance

1. HRTF reconstruction results

Figure 8 shows how the relative power distribution of each FSB series coefficient varies with the spatial modes. We can clearly see that for all spatial modes, the relative contribution of lower order FSB series is significant, which corresponds to the smooth HRTF spectral variations. It also proves that using the relative power ratio as the criterion to choose the truncation order of the FSB series expansion is appropriate. We suggest the truncation order of the FSB series expansion based on the power criterion of 0.9. Table II summarizes the number of FSB series and the number of spatial modes (i.e., the dimensionality results given in Sec. V B) for the three sets of HRTF database representation for a given frequency range. Note that we only validate the CIPIC data at low frequencies here because its spectral components are accurately solved up to 4 kHz, as stated in Sec. V B. It can be seen that the number of FSB series for the HRTF spectral representation increases with frequency; in addition, the human subjects' HRTF needs more basis functions to emulate.

TABLE II. Summary of the number of spatial modes and the number of FSB series for the three sets of HRTF database.

	Given frequency range (kHz)	No. of spatial modes	No. of FSB series	Average MSE (dB)
Synthetic HRTF	[0.2, 20]	$47^2=2209$	85	−78.7
KEMAR HRTF	[0.2, 12]	$26^2=676$	67	−28.6
Subject HRTF	[0.2, 4]	$16^2=256$	16	−8.6

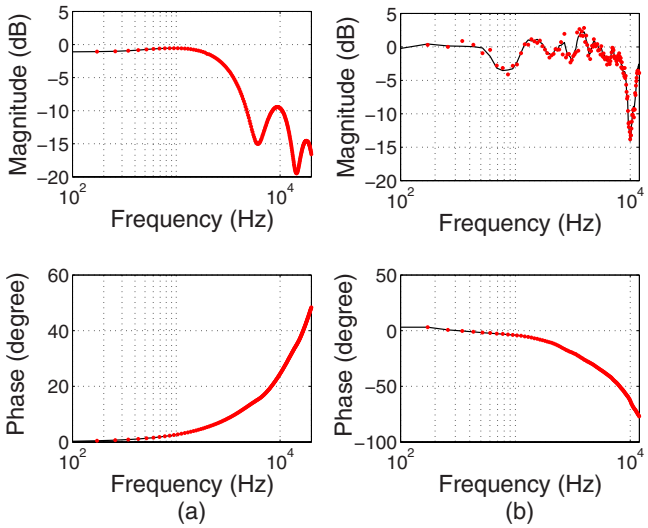

FIG. 9. (Color online) Examples of analytical simulated and measured HRTF reconstruction using the proposed continuous model. (a) Analytical simulated HRTFs at elevation 90° and azimuth of 80° (−85.3 dB error) and (b) left ear MIT KEMAR data at elevation 60° and azimuth of 0° (−41.5 dB error). Original: dotted line (·) and reconstruction: solid line (–).

Figure 9 plots the original and reconstructed HRTF magnitude and phase for synthetic HRTF (θ=90°, ϕ=80°) and KEMAR left ear measurements (θ=60°, ϕ=0°). The reconstruction errors for both data sets are shown in Table II. It is clear that the reconstructed responses closely match the synthetic and the KEMAR responses in both cases. We also use CIPIC subject measurements to check the model performance. The emulation error of subjects' HRTF tends to be a larger value (average MSE around −8.6 dB), which demonstrates that human subjects are harder to model than the spherical head and the KEMAR mannequin.

2. HRTF interpolation and range extrapolation

We further investigate the HRTF interpolation and range extrapolation performances using the proposed continuous model. The MIT KEMAR data are measured at the sampling frequency of 44.1 kHz with 512 samples for each measurement. Figure 10 plots the polar response magnitudes for data

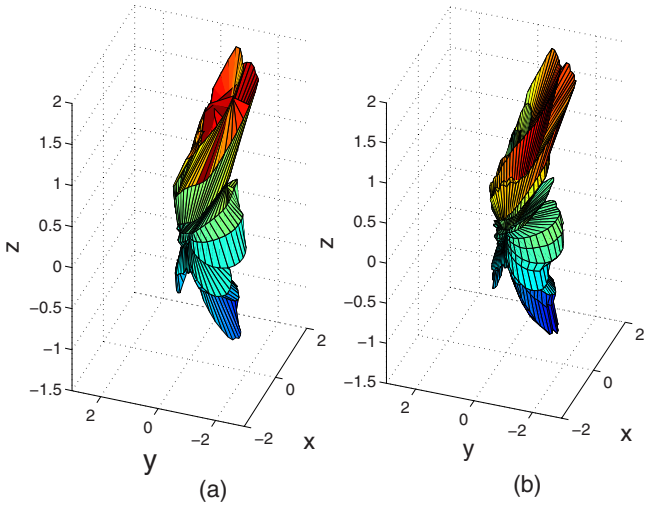

FIG. 10. (Color online) MIT left ear HRTF polar response at 8 kHz: (a) original data and (b) synthesized response over the sphere.

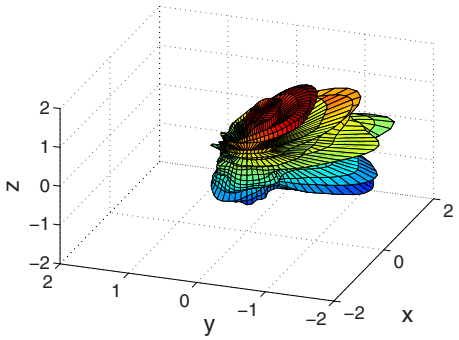

FIG. 11. (Color online) MIT left ear HRTF polar response at 4.15 kHz, which is not measured but interpolated by applying the modal decomposed coefficients to the continuous spectral modeling basis functions, FBS series.

at 8 kHz, where the synthesized polar responses (generated at much higher spatial resolutions of $\Delta\theta$=5° and $\Delta\phi$=5° at each elevation) are smooth forms of the original data and the match is reasonably accurate. In addition, the polar response at not measured frequency (f=4.15 kHz) is interpolated by applying the decomposed model coefficients to the continuous HRTF model, as shown in Fig. 11. We can see that the proposed continuous FSB series can achieve reasonable HRTF spectrum interpolation.

In Fig. 12, the plots on the left are the magnitudes of the analytical HRTFs at different ranges on the horizontal plane, compared to the range extrapolation results from the proposed model on the right. We observe that the reconstruction is perfect with average approximation error around 0.52% (−45 dB).

3. Discussion

We summarize the performance of the proposed continuous model in the following three aspects. First, the proposed continuous functional HRTF model provides accurate reconstruction to the experimental measurements. The interpolated results are also reasonable emulations. Second, as given in Table II, each of the individualized HRTF data set is trans-

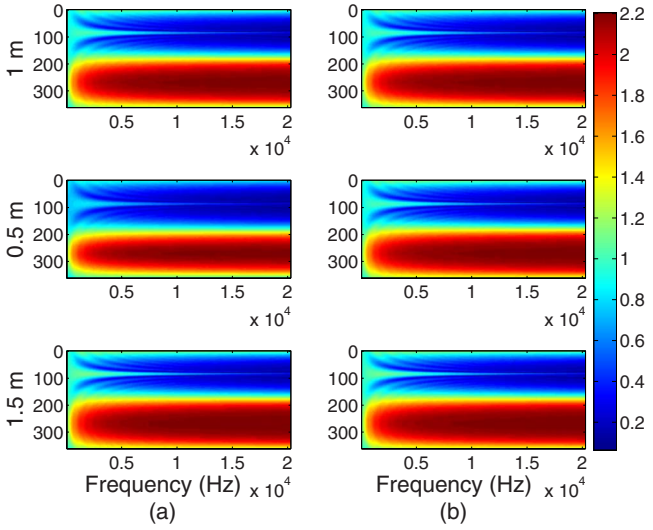

FIG. 12. (Color online) Analytically simulated HRTFs at r=1.0 m (top plots) and the extrapolated HRTFs at r=0.5 and r=1.5 m (b) compared to the reference (a). The horizontal axis is frequency and the vertical axis is azimuth from [0°, 360°).

formed to a set of coefficients. This coefficient set is much smaller in size compared to the original HRTF database. For example, for frequency range of [0.2, 12] kHz, original MIT databases have 81 920 sample points (710 directions and 160 frequency samples for each position); now the transformed coefficient just has 45 292 entries ($N=25$, $\ell=67$). The data that need to be saved have been reduced by nearly 45%. Compared to the statistical PCA model,[8] which is truly the optimal low-dimensional description for the HRTF data set, the disadvantage of our model using more basis functions is countered by the universality (data independent and measurement grid independence of the basis) and the continuous nature of the basis functions (eliminating the need for interpolation). Third, the proposed model can be regarded as noise discriminated as the basis functions we choose have structural similarities to the HRTF being analyzed. Thus, the unwanted components (noise or distortion) will not be represented with the same accuracy as the signal interested. For example, the noise components of high spatial bandwidth ($n>N$) are removed and the noise with frequency components outside the triangular shaped region will be significantly reduced.

VI. CONCLUSION

A general HRTF representation in all frequency-range-angle domains was developed in this paper. The HRTF spatial dimensionality is defined as the required number of spatial modes to represent HRTFs corresponding to all directions. A continuous functional model can represent the HRTF in both spatial and spectral domains. The model is powerful for the computation of the HRTF at any arbitrary position in space and at any frequency point from a given set of measurements at a fixed distance. A practical method was developed to obtain the model coefficients. We observed good HRTF spatial and spectral components' reconstruction and interpolation results from both analytical solutions and measurement data. We also need to state that the current approach is dealing with the representation of empirical measurements at the technical level. Psychoacoustic validation has to be performed in the future to confirm the error bounds and the truncation orders given in the paper.

[1]L. Rayleigh, "On our perception of sound direction," Philos. Mag. **13**, 214–232 (1907).

[2]J. Blauert, *Spatial Hearing-Revised Edition: The Psychophysics of Human Sound Localization* (MIT, Cambridge, MA, 1996).

[3]F. L. Wightman and D. J. Kistler, "Headphone simulation of free-field listening I: Stimulus synthesis II: Psychophysical validation," J. Acoust. Soc. Am. **85**, 858–878 (1989).

[4]J. Braasch and K. Hartung, "Localization of distracted sound sources: Determining the role of binaural cues using unilaterally attenuated and interaurally uncorrelated signals (A)," J. Acoust. Soc. Am. **105**, 1151 (1999).

[5]S. Carlile, "The auditory periphery of the ferret. I: Directional response properties and the pattern of interaural level differences," J. Acoust. Soc. Am. **88**, 2180–2195 (1990).

[6]A. Kulkarni and H. S. Colburn, "Infinite-impulse-response models of the head-related transfer function," J. Acoust. Soc. Am. **115**, 1714–1728 (2004).

[7]W. L. Martens, "Principal components analysis and resynthesis of spectral cues to perceived direction," in Proceedings of the 1987 International Computer Music Conference (1987), pp. 274–281.

[8]D. J. Kistler and F. L. Wightman, "A model of head-related transfer functions based on principal components analysis and minimum-phase reconstruction," J. Acoust. Soc. Am. **91**, 1637–1647 (1992).

[9]K. Hartung, J. Braasch, and S. J. Sterbing, "Comparison of different methods for the interpolation of head-related transfer functions," in Proceedings of the 16th Audio Engineering Society International Conference: Spatial Sound Reproduction (1999), pp. 319–329.

[10]S. Carlile, C. Jin, and V. V. Raad, "Continuous virtual auditory space using HRTF interpolation: Acoustic and psychophysical errors," in Proceedings of the IEEE 2000 International Symposium on Multimedia Information Processing (2000), pp. 220–223.

[11]M. Matsumoto, S. Yamanaka, M. Tohyama, and H. Nomura, "Effect of arrival time correction on the accuracy of binaural impulse response interpolation," J. Audio Eng. Soc. **52**, 56–61 (2004).

[12]M. J. Evans, J. A. S. Angus, and A. I. Tew, "Analyzing head-related transfer function measurements using surface spherical harmonics," J. Acoust. Soc. Am. **104**, 2400–2411 (1998).

[13]R. Duraiswami, D. N. Zotkin, and N. A. Gumerov, "Interpolation and range extrapolation of HRTFs," in Proceedings of the IEEE International Conference on Acoustics, Speech, and Signal Processing, ICASSP 2004 (2004), Vol. **IV**, pp. 45–48.

[14]W. Zhang, R. A. Kennedy, and T. D. Abhayapala, "Efficient continuous HRTF model using data independent basis functions: Experimentally guided approach," IEEE Trans. Audio, Speech, Lang. Process. **17**, 819–829 (2009).

[15]W. G. Gardner and K. D. Martin, "HRTF measurements of a KEMAR," J. Acoust. Soc. Am. **97**, 3907–3908 (1995).

[16]V. R. Algazi, R. O. Duda, D. M. Thompson, and C. Avendano, "The CIPIC HRTF database," in Proceedings of the 2001 IEEE Workshop on Applications of Signal Processing to Audio and Acoustics (2001), pp. 99–102.

[17]R. O. Duda and W. L. Martens, "Range dependence of the response of a spherical head model," J. Acoust. Soc. Am. **104**, 3048–3058 (1998).

[18]P. M. Morse and K. U. Ingard, *Theoretical Acoustics* (Princeton University Press, Princeton, NJ, 1987).

[19]D. Colton and R. Kress, *Inverse Acoustic and Electromagnetic Scattering Theory* (Springer, New York, 1998).

[20]F. J. Simons, F. A. Dahlen, and M. A. Wieczorek, "Spatiospectral concentration on a sphere," SIAM Rev. **48**, 504–536 (2006).

[21]N. A. Gumerov and R. Duraiswami, *Fast Multipole Methods for the Helmholtz Equation in Three Dimensions* (Elsevier, Oxford, 2005).

[22]R. A. Kennedy, P. Sadeghi, T. D. Abhayapala, and H. M. Jones, "Intrinsic limits of dimensionality and richness in random multipath fields," IEEE Trans. Signal Process. **55**, 2542–2556 (2007).

[23]T. D. Abhayapala, T. S. Pollock, and R. A. Kennedy, "Characterization of 3D spatial wireless channels," in Proceedings of the IEEE 58th Vehicular Technology Conference, VTC 2003-Fall (2003), Vol. **1**, pp. 123–127.

[24]V. R. Algazi, C. Avendano, and R. O. Duda, "Elevation localization and head-related transfer function analysis at low frequencies," J. Acoust. Soc. Am. **109**, 1110–1122 (2001).

[25]E. A. G. Shaw, "Acoustical features of the human external ear," in *Binaural and Spatial Hearing in Real and Virtual Environments*, edited by R. H. Gilkey and T. R. Anderson (Erlbaum, Mahwah, NJ, 1997), pp. 25–47.

[26]W. Zhang, T. D. Abhayapala, R. A. Kennedy, and R. Duraiswami, "Modal expansion of HRTFs: Continuous representation in frequency-range-angle," in Proceedings of the IEEE International Conference on Acoustics, Speech, and Signal Processing, ICASSP 2009 (2009), pp. 285–288.

[27]T. Ajdler, C. Faller, L. Sbaiz, and M. Vetterli, "Sound field analysis along a circle and its applications to HRTFs interpolation," J. Audio Eng. Soc. **56**, 156–175 (2008).

[28]T. D. Abhayapala, "Generalized framework for spherical microphone arrays: Spatial and frequency decomposition," in Proceedings of the IEEE International Conference on Acoustics, Speech, and Signal Processing, ICASSP 2008 (2008), pp. 5268–5271.

[29]C. R. Rao and S. K. Mitra, *Generalized Inverse of Matrices and Applications* (Wiley, New York, 1972).

[30]D. N. Zotkin, R. Duraiswami, and N. A. Gumerov, "Regularized HRTF fitting using spherical harmonics," in Proceedings of the 2009 IEEE Workshop on Applications of Signal Processing to Audio and Acoustics (2009), pp. 257–260.

[31]T. D. Abhayapala and A. Gupta, "Alternatives to spherical microphone arrays: Hybrid geometries," in Proceedings of the IEEE International Conference on Acoustics, Speech, and Signal Processing, ICASSP 2009 (2009), pp. 81–84.

A simple and effective noise whitening method for underwater acoustic orthogonal frequency division multiplexing

Christian R. Berger[a)]
Department of Electrical and Computer Engineering, Carnegie Mellon University, 5000 Forbes Avenue HH D201, Pittsburgh, Pennsylvania 15213

Weian Chen, Shengli Zhou, and Jie Huang
Department of Electrical and Computer Engineering, University of Connecticut, 371 Fairfield Road Unit 2157, Storrs, Connecticut 06269

(Received 12 November 2009; revised 14 January 2010; accepted 15 January 2010)

Underwater acoustic orthogonal frequency division multiplexing (OFDM) enables simple frequency domain equalization, but its performance is often limited by intercarrier interference (ICI) that is induced by channel variation, in addition to the ambient noise. As the signal itself, the variance of the ICI is frequency dependent as (i) the transmitter often has a nonideal transmit voltage response (TVR) and (ii) underwater acoustic propagation introduces frequency dependent attenuation. In this paper, a simple method to account for the frequency dependent spectrum of the ICI plus noise is proposed. Specifically, the power spectrum of the ICI plus noise is approximated using a low-order polynomial in the log domain, by fitting the measurements on the null subcarriers embedded in each OFDM symbol. Prewhitening is then applied to each OFDM symbol before channel estimation and data demodulation. The proposed method is tested using experimental data collected from the SPACE08 and RACE08 experiments, where signals with and without transmitter precompensation are compared side by side in the former. Impressive performance gains are found whenever the signal is significantly colored. This is the case when either the TVR is not compensated or the transmission distance and bandwidth are large.
 [DOI: 10.1121/1.3309452]

PACS number(s): 43.60.Dh, 43.60.Cg, 43.60.Ek [EJS] Pages: 2358–2367

I. INTRODUCTION

Underwater acoustic (UWA) channels are wideband in nature due to the large bandwidth to carrier frequency ratio. Frequency dependency is one unique feature that distinguishes wideband from narrowband channels. Specifically, for underwater acoustic communication systems, the following facts are well known.

- The acoustic transducer has a nonflat transmit voltage response (TVR), as perfect circuit matching to the amplifier is difficult to achieve across the whole signal band.
- Signal attenuation depends on both the distance and the frequency.[1–3] In general, high frequency acoustic signals are absorbed more than low frequency signals.
- The spectrum of the ambient noise is not white.[1–3]

While the effect of a nonideal TVR and the frequency dependent attenuation on the signal can be subsumed into a composite channel frequency response, operation in colored noise has rarely been considered in practical receiver designs.

Multicarrier modulation in the form of orthogonal frequency division multiplexing (OFDM) has been extensively investigated recently.[4–15] One limiting factor for OFDM is intercarrier interference (ICI) that is caused by Doppler effects. A resampling operation can significantly reduce the level of ICI,[7,16] but some ICI will be unavoidable, due to the fact that different paths could have different Doppler scaling factors.[17,18] We, in this paper, consider a block-by-block receiver,[6,7] which treats the residual ICI on each subcarrier as additive noise. As ICI originates from many neighboring subcarriers, the common approximation as Gaussian noise is often justified; the ICI power will depend on the average signal power of the neighboring subcarriers. Considering this together with the previously stated facts, we can expect that the ICI power will vary significantly across the signal bandwidth due to the colored signal spectrum.

We in this work aim to improve the system performance by accounting for the frequency dependent spectrum of the ICI plus noise. In a block-by-block receiver, the channel frequency response is estimated by inserting known pilot subcarriers at even intervals between the data subcarriers, and then the complete channel frequency response is attained by interpolating across the observations.[6,7] We propose to apply a similar principle to estimate the ICI plus noise spectrum.

- The block-by-block design includes evenly spaced null subcarriers in every OFDM symbol[6,7] that can be used to observe the ICI plus noise power.
- The ICI plus noise spectrum is estimated via interpolation techniques; we choose to approximate the spectrum as a low-order polynomial in logarithmic scale.
- The receiver prewhitens the current OFDM symbol before channel estimation and data demodulation.

[a)]Author to whom correspondence should be addressed. Electronic mail: crberger@ece.cmu.edu

Note that the prewhitening is accomplished by simple scalar multiplication, as we only have to scale each subcarrier to achieve unit noise power. Also note that commonly used symbol demodulation schemes do not depend on the noise power, so bit error performance without error correcting coding will not be improved. The main achievement here is a statistically more accurate description of the reliability of the observations that is vital to any error correction algorithm.

We test the proposed method using data recorded from the SPACE08 experiment, which was conducted off the coast of Martha's Vineyard, MA, during October 2008 and the RACE08 experiment, held at Narragansett Bay, RI, March 2008.

For the SPACE08 experiment, we conduct side-by-side performance comparisons on two sets of signals, where one signal set applies a digital filter to compensate the nonideal TVR, and the other does not. We also consider various transmission distances (at 60, 200, and 1000 m) to evaluate the effect of frequency dependent attenuation. We have the following observations for the SPACE08 experiment.

- For a 10 kHz bandwidth, the nonideal TVR decreases about 15 dB between the lower and higher bandwidth edges in a roughly monotonic fashion. If a precompensation filter is applied, the output signal is approximately white.
- At a carrier frequency of 13 kHz and 1000 m transmission distance, we observe a frequency dependent attenuation within the 10 kHz bandwidth of about 8 dB; at the shorter distances, the frequency dependent attenuation is roughly negligible.
- The observed noise plus ICI spectrum largely follows the signal spectrum; this indicates that the receiver operates in an ICI-limited scenario.
- Applying a first-order polynomial (a straight line) in logarithmic scale to approximate the noise plus ICI spectrum, significant performance improvements can be observed for any uncompensated transmission and compensated transmission at 1000 m distance.

On the contrary in the RACE08 experiment, only small performance improvement can be achieved, even though no TVR precompensation filter is available and we consider significant transmission distances of 400 and 1000 m. We attribute this to the following reasons: (i) the TVR varies by less than 6 dB across the spectrum, (ii) the signal bandwidth is only 5 kHz, and (iii) the level of ICI is lower due to the more sheltered bay environment.

Overall we feel that our experimental findings closely match our reasoning and that our suggested approach of noise whitening will lead to significant performance improvement in case of a significantly nonflat TVR or frequency dependent attenuation in conjunction with a Doppler rich environment, for multicarrier transmission.

The rest of this paper is organized as follows. Section II describes the system model and Sec. III presents the proposed noise whitening method. Performance evaluation is carried out in Secs. IV and V based on experimental data and concluding remarks are collected in Sec. VI.

II. SYSTEM MODEL

When describing the system model, we highlight the frequency dependency at the transmitter, the channel, and the receiver.

A. Transmitter voltage response

We consider zero-padded (ZP) OFDM.[4–7] Let T denote the signal duration and T_g the zero padding interval, leading to a total OFDM symbol duration of $T'=T+T_g$. The subcarriers are located at frequencies

$$f_k = f_c + k/T, \quad k = -K/2, \ldots, K/2-1, \tag{1}$$

where f_c is the center frequency, and K is the total number of subcarriers. The subcarrier spacing is $1/T$ and the bandwidth is $B=K/T$.

Define $\mathcal{S}_A$ and $\mathcal{S}_N$ as the nonoverlapping sets of active and null subcarriers, respectively, that satisfy $\mathcal{S}_A \cup \mathcal{S}_N = \{-K/2, \ldots, K/2-1\}$. Let $s[k]$ denote the symbol to be transmitted on the kth subcarrier. One OFDM symbol in passband is

$$\tilde{s}(t) = 2\,\mathrm{Re}\left\{ \sum_{k\in\mathcal{S}_A} s[k] e^{j2\pi f_k t} g(t) \right\}, \quad t \in [0, T'], \tag{2}$$

where $g(t)$ is the pulse shaping filter. In ZP-OFDM with rectangular pulse shaping, we have

$$g(t) = \begin{cases} 1, & t \in [0, T] \\ 0 & \text{otherwise}. \end{cases} \tag{3}$$

Other pulse shaping filters such as raised cosine filters can be considered as well. The Fourier transform of $\tilde{s}(t)$ is

$$\tilde{S}(f) = \sum_{k\in\mathcal{S}_A} s[k] G(f - f_k), \tag{4}$$

for all positive frequencies $f>0$; we ignore the negative frequency part in our presentation because for any real signal $\tilde{S}(-f)=\tilde{S}^*(f)$. $G(f)$ is the Fourier transform of $g(t)$. For $g(t)$ in Eq. (3), we have

$$G(f) = \frac{\sin(\pi f T)}{\pi f T} e^{-j\pi f T}. \tag{5}$$

The hallmark of OFDM is that the pulse shaping filters are orthogonal at the frequencies f_k, i.e., if we evaluate the waveform at frequency $f_m=f_c+m/T$, we retrieve symbol $s[m]$,

$$\tilde{S}(f_m) = \sum_{k\in\mathcal{S}_A} s[k] G\left(\frac{m-k}{T}\right) = s[m]. \tag{6}$$

Define $V(f)$ as the transmitter voltage response (TVR). $V(f)$ is not a constant due to imperfect circuit matching to the transducer across the whole signal band. In practice, a precompensation filter could be applied to render $V(f)$ to be close to a constant. Due to a nonideal TVR, the signal $x(t)$ emitted from the transmitter has a Fourier transform of

$$X(f) = V(f)\tilde{S}(f) = V(f)\sum_{k\in\mathcal{S}_A} s[k]G(f-f_k). \tag{7}$$

Therefore, frequency dependent attenuation occurs already before the signal enters the water medium.

B. Frequency dependent propagation and noise

First, consider a static UWA channel. One can represent the multipath channel in the time domain as

$$h(\tau) = \sum_{p=1}^{N_p} A_p \gamma_p(\tau-\tau_p), \tag{8}$$

and in the frequency domain as

$$H(f) = \sum_{p=1}^{N_p} A_p e^{-j2\pi f\tau_p}\Gamma_p(f), \tag{9}$$

where N_p is the number of paths, A_p is the path amplitude for the pth path, $\Gamma_p(f)$ is the frequency dependent attenuation pattern for the pth path, and $\gamma_p(t)$ is the inverse Fourier transform of $\Gamma_p(f)$. Detailed discussions and illustrations of $\Gamma_p(f)$ and $\gamma_p(t)$ can be found in the literature.[2,3]

Given this channel model, at the receiver we will observe the following waveform:

$$y(t) = x(t) * h(\tau) + n(t), \tag{10}$$

where $n(t)$ stands for the ambient noise, which may have a colored spectrum. In frequency this is simply

$$Y(f) = H(f)X(f) + N(f), \tag{11}$$

which is why OFDM was specifically designed for such linear time-invariant (LTI) systems, as the orthogonality is not impaired. Evaluating at a frequency f_m, we get simply

$$Y(f_m) = \underbrace{H(f_m)V(f_m)}_{\text{composite channel}} s[m] + N(f_m), \tag{12}$$

where $N(f)$ is the Fourier transform of $n(t)$.

Now consider a time-varying channel. Within each OFDM symbol, we assume that A_p remains constant, and that the delay on the pth path can be approximated by

$$\tau_p(t) = \tau_p - a_p t, \tag{13}$$

where a_p is the Doppler scale factor on the pth path.[8] The time-varying channel within one OFDM symbol can then be described by

$$h(\tau;t) = \sum_{p=1}^{N_p} A_p \gamma_p(\tau-\tau_p(t)) \tag{14}$$

with $\tau_p(t)$ defined in Eq. (13).

Passing through the time-varying channel in Eq. (14), the received signal in the passband is

$$\begin{aligned} y(t) &= x(t) * h(\tau;t) + n(t) \\ &= \sum_{p=1}^{N_p} A_p \int x(\tau)\gamma_p((1+a_p)t-\tau-\tau_p)d\tau + n(t). \end{aligned} \tag{15}$$

The Fourier transform of $y(t)$ is

$$\begin{aligned} Y(f) = \sum_{p=1}^{N_p} \frac{A_p}{1+a_p} e^{-j2\pi[f/(1+a_p)]\tau_p}\Gamma_p\left(\frac{f}{1+a_p}\right)X\left(\frac{f}{1+a_p}\right) \\ + N(f). \end{aligned} \tag{16}$$

C. Receiver intercarrier interference

For simplicity, assume that no resampling operation is necessary. The receiver will shift the passband signal to baseband, compensate the Doppler shift by multiplying $e^{-j2\pi\epsilon t}$ to the baseband signal, and then perform the FFT[19] operation.[6] The FFT output z_m at the mth subcarrier is simply

$$z_m = Y(f_m+\epsilon), \quad m = -K/2, \ldots, K/2-1. \tag{17}$$

Substituting Eqs. (16) and (7) into Eq. (17), we obtain Eq. (18). Doppler shift compensation is motivated by simplifying assumptions, including a single dominant Doppler effect $a_p \approx a$, and no wideband effect $af_m \approx af_c$. If these assumptions were correct, a choice of $\epsilon = af_c$ would eliminate the ICI. These assumptions are far from correct in UWA OFDM, but using a simple grid search some choices of ϵ have been shown to still reduce the amount of ICI.[6,7]

Assume that (i) $\Gamma_p(f)$ is the same for all paths, i.e., $\Gamma_p(f)=\Gamma(f)$, (ii) $V(f)$ and $\Gamma(f)$ are smooth, and (iii) $a_p \ll 1$, $\epsilon \ll f_m$. We can then approximate z_m in Eq. (18) by the expression in Eq. (19).

$$\begin{aligned} z_m = &\underbrace{\left[\sum_{p=1}^{N_p} \frac{A_p}{1+a_p} e^{-j2\pi[(f_m+\epsilon)/(1+a_p)]\tau_p}\Gamma_p\left(\frac{f_m+\epsilon}{1+a_p}\right)V\left(\frac{f_m+\epsilon}{1+a_p}\right)G\left(\frac{\epsilon-a_p f_m}{1+a_p}\right)\right]s[m]}_{\text{desired signal}} \\ &+ \underbrace{\left[\sum_{p=1}^{N_p} \frac{A_p}{1+a_p} e^{-j2\pi[(f_m+\epsilon)/(1+a_p)]\tau_p}\Gamma_p\left(\frac{f_m+\epsilon}{1+a_p}\right)V\left(\frac{f_m+\epsilon}{1+a_p}\right)\sum_{k\in\mathcal{S}_A,k\neq m} G\left(f_m-f_k+\frac{\epsilon-a_p f_m}{1+a_p}\right)s[k]\right]}_{\text{inter-carrier-interference}} \\ &+ \underbrace{N(f_m+\epsilon)}_{\text{additive noise}}. \end{aligned} \tag{18}$$

$$z_m \approx \underbrace{\Gamma(f_m)V(f_m)\left[\sum_{p=1}^{N_p}\frac{A_p}{1+a_p}e^{-j2\pi[(f_m+\epsilon)/(1+a_p)]\tau_p}G\left(\frac{\epsilon-a_pf_m}{1+a_p}\right)\right]s[m]}_{\text{desired signal}}$$

$$+\underbrace{\Gamma(f_m)V(f_m)\left[\sum_{p=1}^{N_p}\frac{A_p}{1+a_p}e^{-j2\pi[(f_m+\epsilon)/(1+a_p)]\tau_p}\sum_{k\in\mathcal{S}_A,k\neq m}G\left(f_m-f_k+\frac{\epsilon-a_pf_m}{1+a_p}\right)s[k]\right]}_{\text{inter-carrier-interference}}$$

$$+\underbrace{N(f_m+\epsilon)}_{\text{additive noise}}. \tag{19}$$

Clearly, the signal power is frequency dependent, and so is the ICI. In fact, the ICI spectrum follows a similar frequency dependency pattern as the desired signal.

In short, the ICI plus noise at the FFT output is nonwhite. A receiver that ignores this fact might incur considerable performance loss.

III. THE PROPOSED NOISE-WHITENING APPROACH

The receiver treats both the ICI term and the noise term in Eq. (18) as the effective additive Gaussian noise.[6,7] It operates assuming a LTI channel model as in Eq. (12):

$$z_m = H_m s[m] + v_m, \tag{20}$$

where H_m is the frequency response on the mth subcarrier of the composite channel that includes the TVR and the frequency dependent propagation effects, and v_m incorporates both the additive noise and the ICI. In previous work, v_m was assumed to be white.[6,7]

A fraction of the data symbols $s[k]$, $k \in \mathcal{S}_P \subset \mathcal{S}_A$ are pilot symbols, which are used to estimate the channel's frequency response H_m. Once the channel estimate is available, one-tap data demodulation is done per subcarrier.

Comparing Eq. (20) with Eq. (19), we notice that the receiver will simply include effects such as the nonideal TVR or frequency dependent attenuation into the estimated channel's frequency response. Therefore, the receiver will accurately determine the effective signal power on each subcarrier, but the effect on the noise and ICI spectrum is neglected.

A. Estimating the ICI-plus-noise spectrum

In this paper, we propose a simple method to estimate the variance $\Phi_{vv}[m]=E\{|v_m|^2\}$ of the ICI-plus-noise across all subcarriers. We assume that the spectrum is generally smooth, and can be approximated by a Qth-order polynomial in the logarithmic scale. Specifically, we assume

$$\Phi_{vv}[m] = 10^{\mathcal{P}_Q(m)/10} \tag{21}$$

in the linear domain or

$$10\log_{10}(\Phi_{vv}[m]) = \mathcal{P}_Q(m) = \sum_{q=0}^{Q} p_q m^q \tag{22}$$

in the log domain, where $m=-K/2,\ldots,K/2-1$. The parameter p_0 represents the noise variance at the center frequency. The white noise model is included as a special case with $Q=0$ and $p_0=10\log_{10}(N_0)$.

To estimate the model parameters, we use the measurements on the null subcarriers, which are inserted for each OFDM symbol for Doppler shift compensation.[6,7] We here propose two methods.

1. Linear regression in log domain

A simple linear regression (LR) model in the log domain can be formulated as

$$\{\mathcal{P}_Q\}_{\text{LR}} = \arg\min_{\{p_q\}} \sum_{m\in\mathcal{S}_N}\left|10\log_{10}|z_m|^2 - \sum_{q=0}^{Q} p_q m^q\right|^2. \tag{23}$$

This method is of very low complexity. However, fitting in the log domain tends to lead to a negative bias on p_0 (i.e., underestimating the noise variance), as small values are amplified in the log domain. A simple remedy is to apply some smoothing on the observations $|z_m|^2$ before transforming to the log domain.

2. ML variance estimator

By the central limit theorem, v_m can be viewed to have a Gaussian distribution. Hence, $|v_m|^2$ is exponentially distributed. The maximum likelihood (ML) solution for the model parameters can be formulated as

$$\{\mathcal{P}_Q\}_{\text{ML}} = \arg\max_{\{p_q\}} \sum_{m\in\mathcal{S}_N} -\left[\ln(10^{\mathcal{P}_Q(m)/10}) + \frac{|z_m|^2}{10^{\mathcal{P}_Q(m)/10}}\right]. \tag{24}$$

For any larger Q, the complexity of an exhaustive search quickly becomes prohibitive. We only consider the ML approach for the two-dimensional problem, $Q=1$. Furthermore to keep the complexity low, a multigrid search can be applied or a final solution can be improved via simple interpolation techniques.

B. Whitening in the frequency domain

Once the variance of the ICI-plus-noise has been estimated, the data can be easily whitened as

$$\tilde{z}_m = \frac{z_m}{\sqrt{\hat{\Phi}_{vv}[m]}} = \tilde{H}_m s[m] + \tilde{v}_m. \tag{25}$$

Channel estimation and data demodulation can then be performed on $\tilde{z}_m$, where $m \in \mathcal{S}_A$. We would like to point out that the main benefit of this approach is in generating a more accurate statistical description of the observations that can be used to generate *soft* inputs to an error correcting algorithm, such as the VITERBI algorithm for convolutional codes,[20] the sum-product algorithm for low density parity check (LDPC) codes, or in our case the min-sum algorithm[21] for LDPC codes.

IV. SPACE08 EXPERIMENT

A. Overview and experiment setup

We now focus on experimental data from the SPACE08 experiment, which was held off the coast of Martha's Vineyard, MA, during October 2008. We will consider three receivers used in the experiment, where receiver S1 was at 60 m from the transmitter, receiver S3 was at 200 m, and receiver S5 was at 1000 m. Each receiver has multiple phones, which can be combined to increase effective signal-to-noise ratio (SNR). An additional receiver S0 was positioned at 1 m from the transmitter.

To compensate the nonideal TVR of the acoustic transducer used in this experiment, a compensation filter was available. We will first focus on Julian date 292 of the experiment, as for this day both signals using the compensation filter and signals without the filter were transmitted. Also we will focus on linear approximation in the logarithmic domain ($Q=1$).[22] Afterward we will consider a larger set of SPACE08 data, where only compensated data were transmitted, and higher order polynomial fitting ($Q>1$).

The transmission bandwidth is between 8 and 18 kHz. The estimated signal spectrum for both the uncompensated and compensated signals at receiver S0 are shown Fig. 1, from which we can infer the approximate TVR. Precompensation can reduce the signal power variation across the signal band. However, it leads to a smaller power output in our setting, as the peak-to-average-power control[21] has been applied on the uncompensated signals only; the precompensation filter was not considered during the signal design phase.

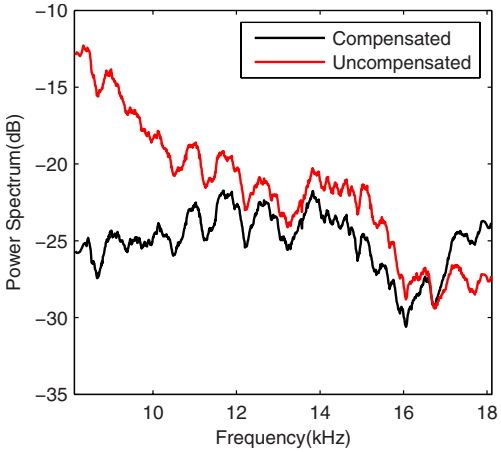

FIG. 1. (Color online) Measured signal spectrum at the receiver S0, from which we can infer the transmit voltage response. The output power can vary by up to 15 dB across the used frequency band if the TVR is not compensated.

B. Julian date 292

Observing the uncompensated approximate TVR, we see that a first-order approximation ($Q=1$) will capture the main trend. This is not the case for the compensated signal (a first-order approximation will not reflect details as the reduced output power around 16 kHz; see Fig. 1); we will come back to this later when we consider more general polynomial approximation ($Q>1$). We will next try to quantify the effects caused by the frequency dependent attenuation due to propagation in the water medium.

To estimate the signal power spectrum, we use the FFT outputs on data and pilot subcarriers and evaluate $E[|z_m|^2]$, $m \in \mathcal{S}_A$, where the expectation is carried out by averaging over a large number of received OFDM symbols (a few hundreds). We evaluate this average using received data spread over the day in the hope that due to time variation the channel effects can be averaged out, and hence the systematic effects such as the nonideal TVR and frequency dependent attenuation can be seen.

Figure 2 plots the estimated signal spectrum after varying transmission distances. It is immediately obvious that the signal attenuates with increasing distance, but the frequency

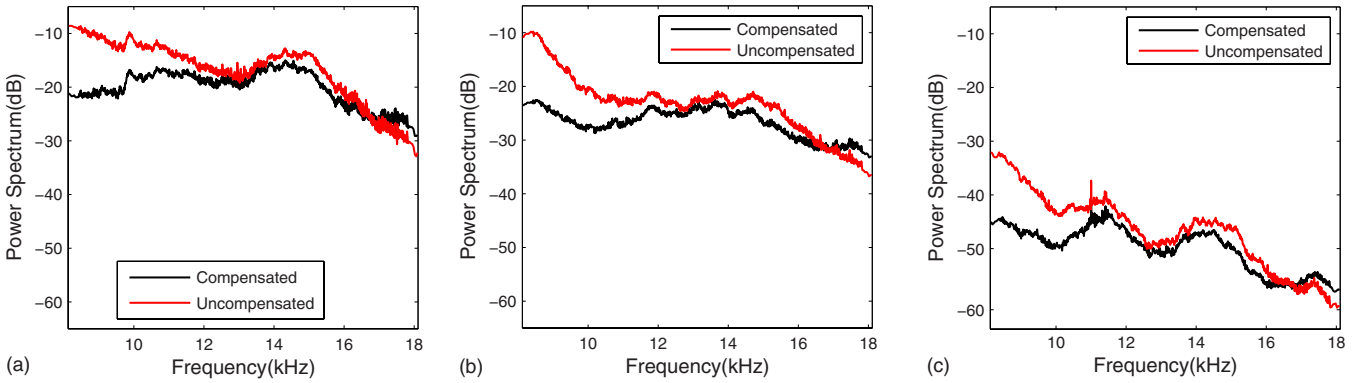

FIG. 2. (Color online) Experimentally measured signal spectrum at three receivers, Julian date 292. (a) S1 (60 m), (b) S3 (200 m), and (c) S5 (1000 m).

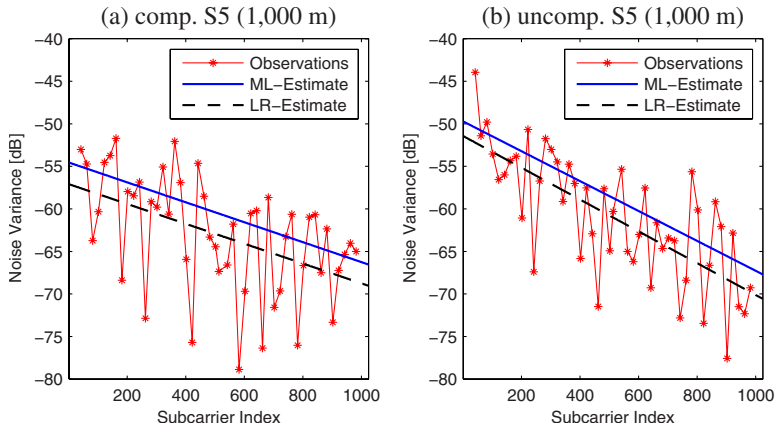

FIG. 3. (Color online) Example of a first-order noise PSD estimate for Julian date 292; the uncompensated signal is more significantly colored and the linear regression in log domain leads to a negative bias.

dependence at short distances is mainly caused by the TVR. At receivers S1 and S3, we notice that the compensated signal is approximately white, varying by at most 10 dB across the spectrum. In sharp contrast the uncompensated signal varies by easily 20 dB. The difference matches our estimate of the nonideal TVR in Fig. 1. The uncompensated signal has always higher signal power, especially at the lower end of the signal bandwidth. For the receiver S5, at a distance of 1000 m, the spectrum of the compensated and uncompensated signals have similar overall shapes, which we attribute to the frequency dependent attenuation.

We would like to point out that using empirical formulas,[2,3] the frequency dependent signal absorption is typically assumed to be less than 3 dB at the considered 10 kHz bandwidth and 1 km distance. Our observations for this particular shallow water experiment lead to a frequency dependent attenuation of about 8 dB across the frequency band, which does not agree very well to the empirical formulas.

1. Estimates of noise spectrum

We estimate the ICI-plus-noise spectrum using the proposed linear regression and ML approaches on Julian date 292. An example plot is shown in Fig. 3, where for the two-dimensional problem the ML approach can be easily afforded. Comparing to Fig. 2(c), we notice that the noise spectrum closely follows the signal spectrum, indicating that the effective noise level is largely caused by the ICI. Comparing the simple linear regression with the ML estimates in Fig. 3, we find that the linear regression shows approximately a -3 dB bias as predicted. However, the estimates of the slope closely match the ML estimate

To have a systematic comparison, we focus on the slope parameter p_1. We plot histograms for both the compensated and uncompensated signals in Fig. 4, sorted by transmitter-receiver distance. We observe that the compensated signals at the two closer receivers S1 and S3 have an average slope of $p_1=0$, while the uncompensated signals have a significant slope leading to a total difference between the bandwidth edges of $Kp_1 \approx 12$ dB. Although the ambient noise should be the same for either signal, the ICI will follow the signal spectrum—in case of the uncompensated signal leading to a significantly colored noise plus ICI spectrum. This again points toward the fact that at a close distance from the transmitter, the ICI is dominating the ambient noise. At receiver S5, both signal spectra are increasingly affected by the frequency dependent attenuation, leading to a colored ICI spectrum. Still, the slope of the uncompensated signals is always about 6 dB more pronounced than that of the compensated signals.

2. BLER performance

We look at receiver performance in terms of block-error rate (BLER). Each OFDM symbol $K=1024$ subcarriers, consisting of $|\mathcal{S}_N|=96$ null subcarriers and $|\mathcal{S}_P|=256$ pilot sub-

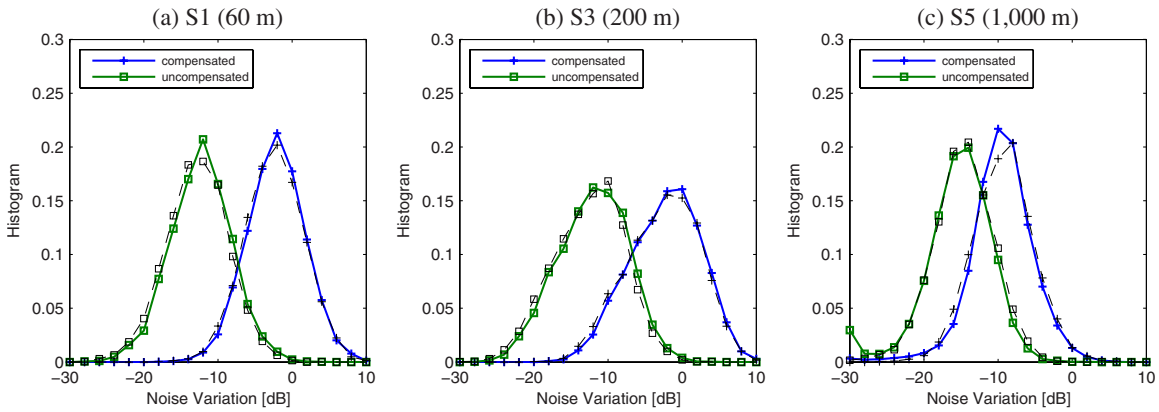

FIG. 4. (Color online) Histogram of the estimates of the slope parameter p_1; full lines are ML estimates and dashed lines are based on linear regression.

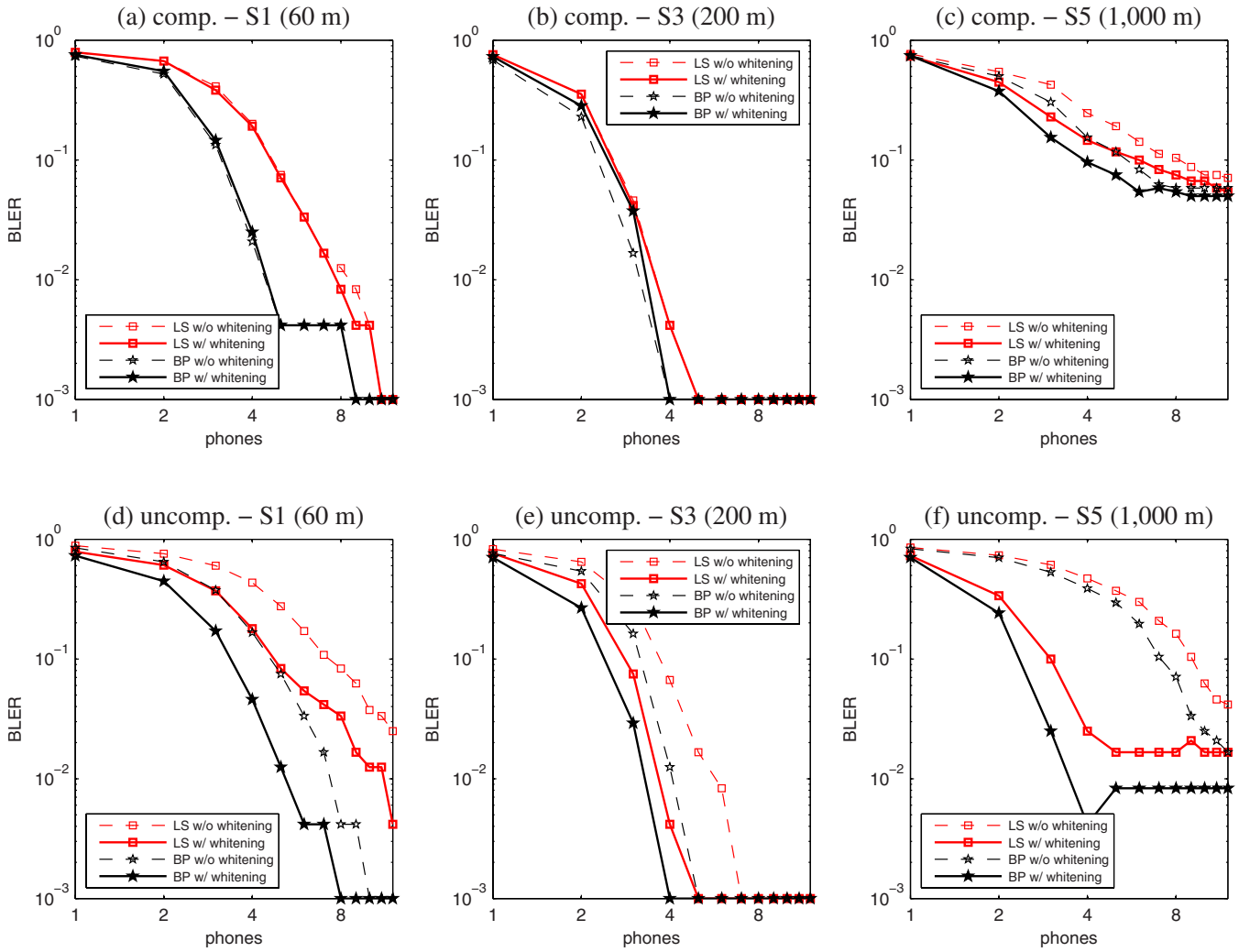

FIG. 5. (Color online) Performance comparison for compensated and uncompensated signals on Julian date 292 in the SPACE08 experiment, 16 QAM.

carriers, leaving $|\mathcal{S}_A|-|\mathcal{S}_P|=672$ for data transmission. We consider 16-point quadrature amplitude modulation (QAM) and a rate 1/2 nonbinary LDPC code.[21] The symbol duration is $T=104.86$ ms, the guard time is $T_g=24.6$ ms, leading to a bandwidth of $B=K/T=9.77$ kHz. This leads to the following spectral efficiency and data rate:

$$\alpha = \frac{T}{T+T_g}\frac{672}{1024}\frac{1}{2}\log_2(16) = 1.06 \text{ bits/s Hz}, \tag{26}$$

$$R = \alpha B = 10.4 \text{ kbytes/s}. \tag{27}$$

Two types of channel estimators are used: least squares[6] (LS) and basis pursuit[8] (BP).

It is important to note that the min-sum channel decoder used for nonbinary LDPC codes[21] does not require a noise variance estimate. Although the linear regression method in Eq. (23) does not give a reliable estimate on the absolute noise level p_0, it leads to the same BLER performance as the ML method in Eq. (24), as both can estimate the slope p_1 well and prewhiten the signals in the same fashion; different scalings on the signals do not affect the decoding performance.

The BLER results are plotted in Fig. 5. We notice that at receivers S1 and S3—for the compensated signal—the performance assuming white noise is basically identical to that using the ML noise estimates. This is in sharp contrast to the uncompensated signal, which suffers significant performance degradation when not accounting for the colored noise.

At the farthest receiver, S5, both signals show improved performance when using the colored noise model. This matches the observation that also the compensated signal has significant noise variation at S5 [see Fig. 4(c)]. Furthermore, the uncompensated signals outperform the compensated signals significantly after addressing the colored noise correctly, due to higher transmit power.

C. Compensated transmission and higher order fitting

Following the logic of the previous discussion, the impact of noise whitening depends on the TVR shape of the acoustic transducer and the frequency dependent attenuation that increases with distance. Therefore at the farthest receiver S5 (1000 m), the effect should have been clearly visible, also for the compensated signals. Since the performance was weak overall at receiver S5 on Julian date 292, we now consider other days of the experiment, although only compensated signals were transmitted.

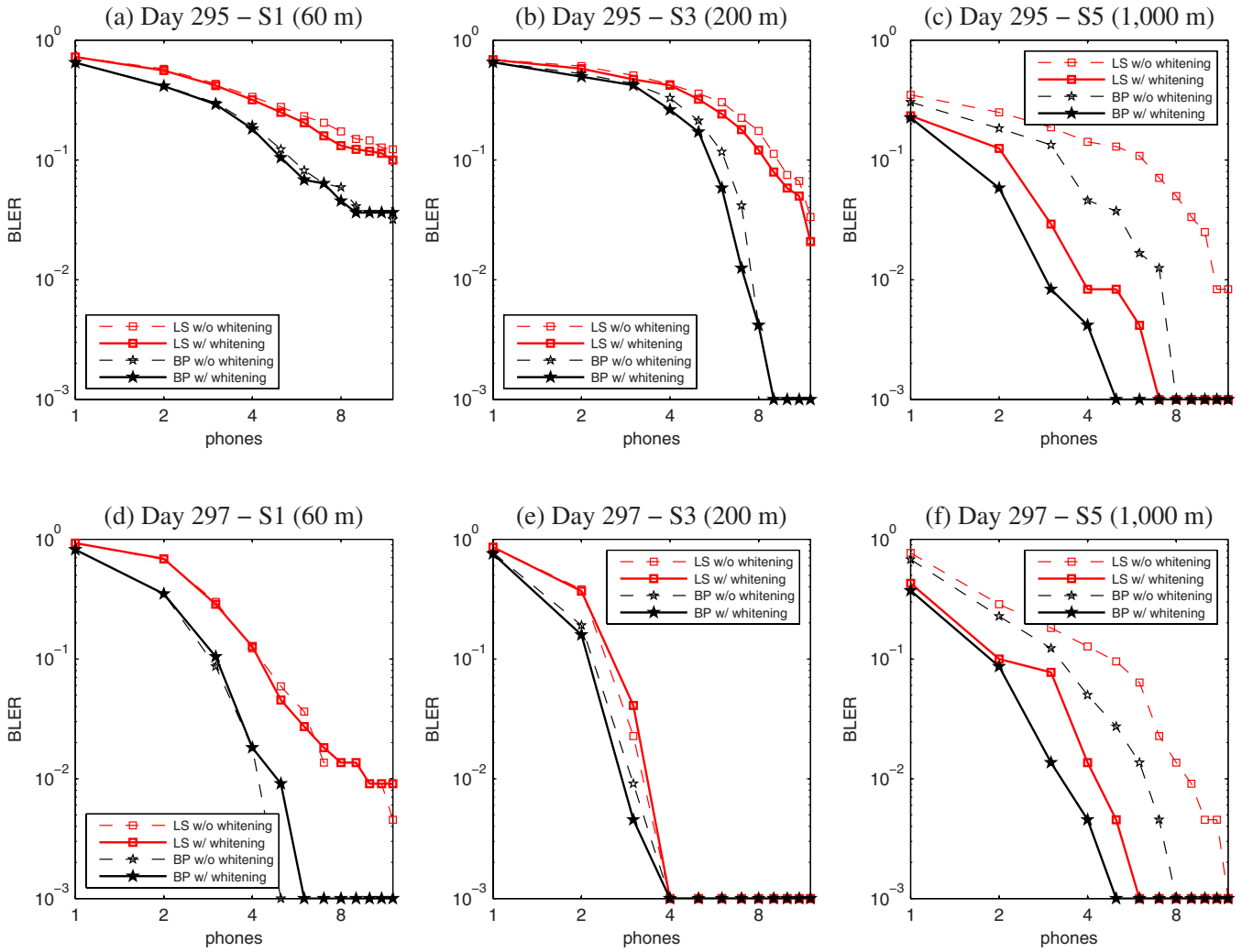

FIG. 6. (Color online) Performance comparison for compensated signals on Julian dates 295 and 297 in the SPACE08 experiment, 16 QAM.

In Fig. 6 we show performance results for compensated signals on Julian dates 295 and 297, which have quite different environmental conditions compared to Julian date 292. While previously the performance at receiver S5 was always the worst, in these data sets this receiver has quite reasonable performance. This allows us to observe significant performance improvement when applying noise whitening. Matching our previous discussion, the performance at the shorter distances (S1 and S3) is largely unaffected by the noise whitening.

We next consider more general polynomial fitting of the noise ($Q>1$). Considering Fig. 1, we notice that the compensated signal is not exactly white, showing a drop of over 6 dB around 16 kHz. Also the performance with whitening based on linear approximation in the logarithmic domain ($Q=1$) was sometimes worse than without noise whitening at receiver S1 (particularly on Julian dates 292 and 297). We therefore apply a polynomial approximation of order $Q=5$, see Fig. 7. Although the improvement is small, using a fifth order polynomial, the performance with whitening is never worse than without whitening. This is also true for receivers S3 and S5, but in these cases the simple straight-line approximation ($Q=1$) delivers often the best performance. Generally it is not obvious which order polynomial will deliver the best performance and no clear trend could be observed. Nonetheless, for significantly colored signals, any polynomial fitting ($Q<8$) outperforms a receiver without prewhitening.

V. RACE08 EXPERIMENT

We now briefly discuss some results of the RACE08 experiment, where no compensation filter for the TVR was supplied. The RACE08 experiment was held in the Narragansett Bay, RI, March 2008. The water depth in the area ranges from 9 to about 14 m. The primary source of an ITC1007 transducer for acoustic transmissions was located approximately 4 m above the bottom. We consider two of the receive arrays, S3 and S6, which were deployed at 400 and 1000 m from the transmitter, respectively.

The OFDM parameters are similar to the SPACE08 experiment, but the bandwidth is reduced to half $B=4.88$ kHz, which leads to a doubling of the symbol duration $T=209.72$ ms. The guard interval is 25 ms; assuming 64-QAM this leads to a spectral efficiency and data rate of

$$\alpha = \frac{T}{T+T_g}\frac{672}{1024}\frac{1}{2}\log_2(64) = 1.76 \text{ bits/s Hz}, \tag{28}$$

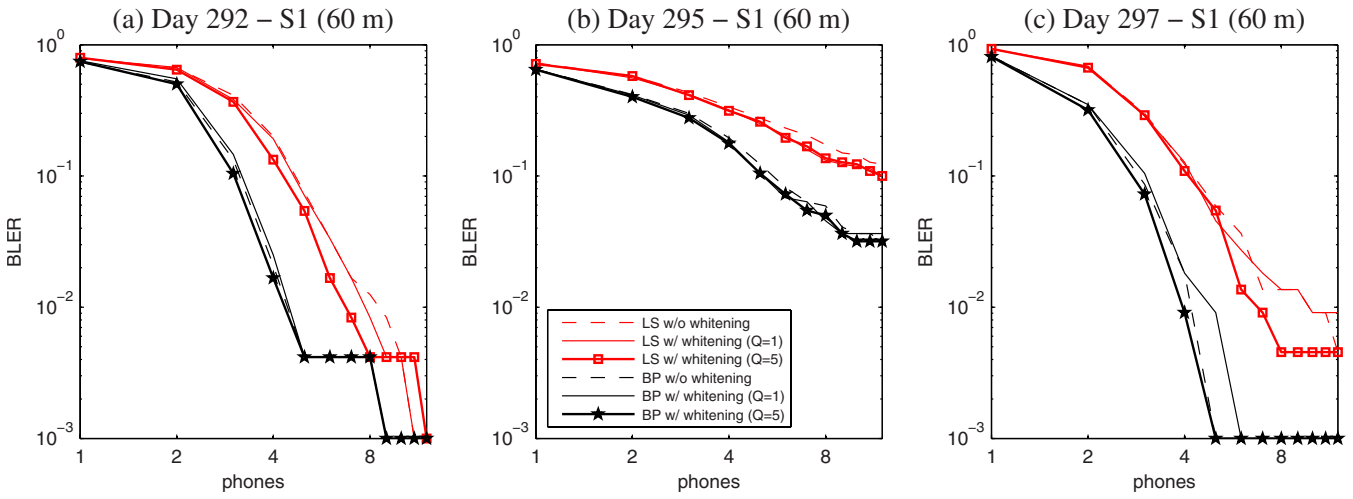

FIG. 7. (Color online) Using higher order polynomial approximation ($Q=5$), some performance gains can be seen for compensated signals at receiver S1 (60 m); SPACE08 experiment, 16 QAM.

$$R = \alpha B = 8.6 \text{ kbytes/s}. \quad (29)$$

We include example plots in Fig. 8. The TVR shape seems nonmonotonic, probably caused by the circuits being matched to the center frequency. In any case, this makes first-order polynomials ineffective. We therefore resort to fourth-order polynomials to approximate the noise PSD. The coefficients were determined via linear regression in the log domain, as exhaustive search for the ML solution now entails high complexity.

Although the shape of the TVR is somewhat more complex, the total variation is only about 6 dB—significantly less than in the SPACE08 experiment. Also the frequency dependent attenuation is less pronounced, as at the same distance, the total bandwidth (and therefore variation) is only half of that in the SPACE08 experiment.

The BLER performance is shown in Fig. 9, where we focus only on 64-QAM, as in the bay area the overall performance was usually better compared to the SPACE08 experiment. Although some improvement can be observed, the level is significantly less than in the SPACE08 experiment.

VI. CONCLUSION

We proposed a simple method to prewhiten the residual ICI plus the ambient noise for a block-by-block OFDM receiver, where the noise spectrum is estimated based on observations on the null subcarriers. Based on experimental data, we found the following.

- The signal spectrum can be significantly colored due to nonideal transmit amplifier and/or frequency dependent attenuation that increases with distance and signal bandwidth.
- OFDM receivers often operate in an ICI-limited environment due to the significant Doppler effects; the noise plus ICI spectrum will then largely follow the signal spectrum as it is dominated by ICI.
- Significant performance gains can be realized by applying simple prewhitening before channel estimation and data modulation, where the noise plus ICI spectrum is estimated using interpolation based on a low-order polynomial approximation in logarithmic domain.

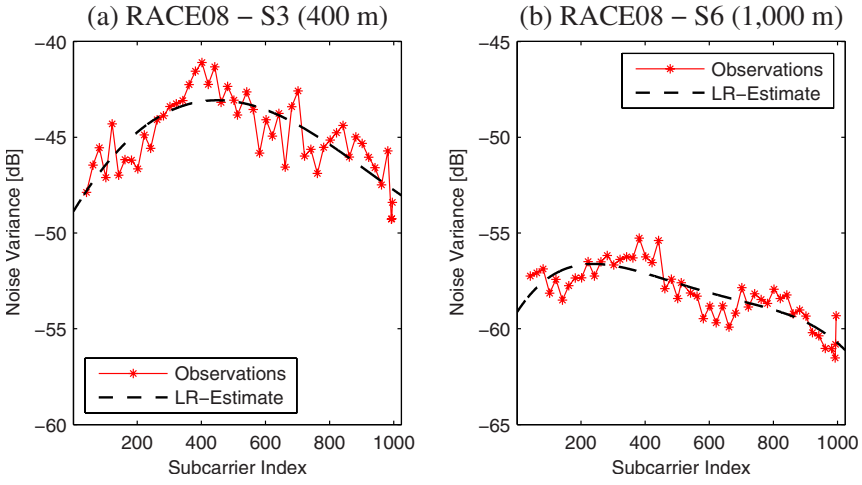

FIG. 8. (Color online) Example of a fourth-order noise PSD estimate for Julian date 081; the nonmonotonic shape makes first-order fitting ineffective.

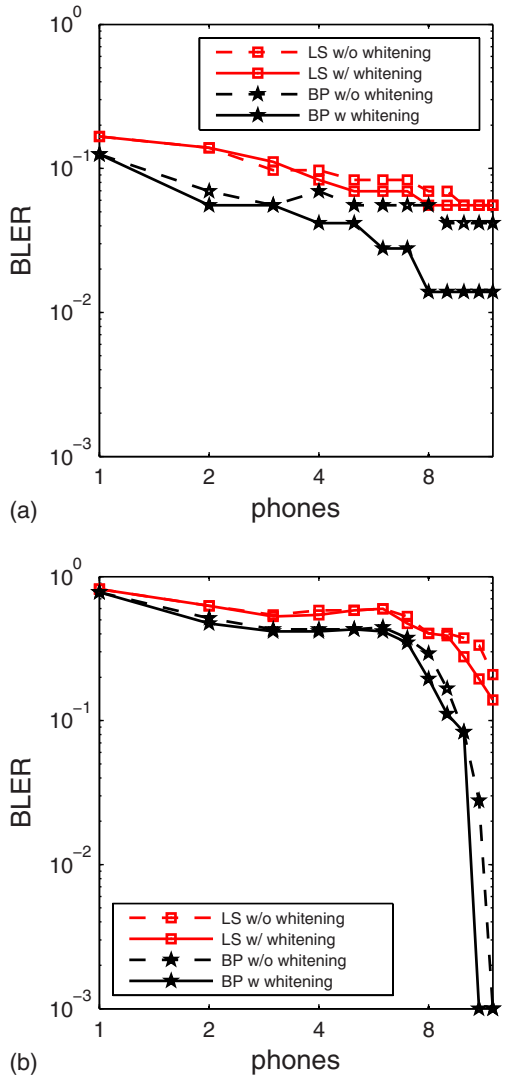

FIG. 9. (Color online) Performance comparison for uncompensated signals in the RACE08 experiment Julian date 081, using a $Q=4$ polynomial, 64 QAM. (a) S3 (400 m) and (b) S6 (1000 m).

In future work, we would like to investigate the noise whitening effect on OFDM receivers that explicitly deal with ICI, e.g., those reported recently in Refs. 8, 9, and 15.

ACKNOWLEDGMENTS

This work is supported by the NSF Grant No. CNS-0721834 and the ONR Grant Nos. N00014-07-1-0805 (YIP) and N00014-09-1-0704 (PECASE). The authors would like to thank Dr. James C. Preisig and his team for conducting the SPACE08 and RACE08 experiments.

[1]D. B. Kilfoyle and A. B. Baggeroer, "The state of the art in underwater acoustic telemetry," IEEE J. Ocean. Eng. **25**, 4–27 (2000).
[2]M. Stojanovic, "On the relationship between capacity and distance in an underwater acoustic channel," in Proceedings of the ACM International Workshop on Underwater Networks (WUWNet), Los Angeles, CA (2006).
[3]M. Stojanovic and J. Preisig, "Underwater acoustic communication channels: Propagation models and statistical characterization," IEEE Commun. Mag. **47**, 84–89 (2009).
[4]M. Stojanovic, "Low complexity OFDM detector for underwater channels," in Proceedings of the MTS/IEEE OCEANS Conference, Boston, MA (2006).
[5]M. Stojanovic, "High rate acoustic communications based on orthogonal frequency division multiplexing (A)," J. Acoust. Soc. Am. **123**, 3891 (2008).
[6]B. Li, S. Zhou, M. Stojanovic, L. Freitag, and P. Willett, "Multicarrier communication over underwater acoustic channels with nonuniform Doppler shifts," IEEE J. Ocean. Eng. **33**, 198–209 (2008).
[7]S. Mason, C. R. Berger, S. Zhou, and P. Willett, "Detection, synchronization, and Doppler scale estimation with multicarrier waveforms in underwater acoustic communication," IEEE J. Sel. Areas Commun. **26**, 1638–1649 (2008).
[8]C. R. Berger, S. Zhou, J. Preisig, and P. Willett, "Sparse channel estimation for multicarrier underwater acoustic communication: From subspace methods to compressed sensing," in Proceedings of the MTS/IEEE OCEANS Conference, Bremen, Germany (2009).
[9]S. Mason, C. R. Berger, S. Zhou, K. Ball, L. Freitag, and P. Willett, "Receiver comparisons on an OFDM design for Doppler spread channels," in Proceedings of the MTS/IEEE OCEANS Conference, Bremen, Germany (2009).
[10]F. Qu and L. Yang, "Basis expansion model for underwater acoustic channels?," in Proceedings of the MTS/IEEE OCEANS Conference, Quèbec City, Quebec (2008).
[11]T. Kang and R. A. Iltis, "Iterative carrier frequency offset and channel estimation for underwater acoustic OFDM systems," IEEE J. Sel. Areas Commun. **26**, 1650–1661 (2008).
[12]G. Leus and P. A. van Walree, "Multiband OFDM for covert acoustic communications," IEEE J. Sel. Areas Commun. **26**, 1662–1673 (2008).
[13]S.-J. Hwang and P. Schniter, "Efficient multicarrier communication for highly spread underwater acoustic channels," IEEE J. Sel. Areas Commun. **26**, 1674–1683 (2008).
[14]Y. Emre, V. Kandasamy, T. M. Duman, P. Hursky, and S. Roy, "Multiinput multioutput OFDM for shallow-water UWA communications (A)," J. Acoust. Soc. Am. **123**, 3891 (2008).
[15]K. Tu, D. Fertonani, T. M. Duman, and P. Hursky, "Mitigation of intercarrier interference in OFDM systems over underwater acoustic channels," in Proceedings of the MTS/IEEE OCEANS Conference, Bremen, Germany (2009).
[16]B. S. Sharif, J. Neasham, O. R. Hinton, and A. E. Adams, "A computationally efficient Doppler compensation system for underwater acoustic communications," IEEE J. Ocean. Eng. **25**, 52–61 (2000).
[17]J. C. Preisig and G. B. Deane, "Surface wave focusing and acoustic communications in the surf zone," J. Acoust. Soc. Am. **116**, 2067–2080 (2004).
[18]M. Siderius, M. B. Porter, P. Hursky, and V. McDonald, "Modeling Doppler effects for acoustic communications (A)," J. Acoust. Soc. Am. **119**, 3397 (2006).
[19]The mathematical operation applied is a discrete Fourier transform (DFT), while the term fast Fourier transform (FFT) refers to its efficient implementation. In practice these terms are often used interchangeably.
[20]J. G. Proakis, *Digital Communications*, 4th ed. (McGraw-Hill, New York, 2001).
[21]J. Huang, S. Zhou, and P. Willett, "Nonbinary LDPC coding for multicarrier underwater acoustic communication," IEEE J. Sel. Areas Commun. **26**, 1684–1696 (2008).
[22]C. R. Berger, S. Zhou, W. Chen, and J. Huang, "A simple and effective noise whitening method for underwater acoustic OFDM," in Proceedings of the MTS/IEEE OCEANS Conference, Biloxi, MS (2009).

Adaptive phase calibration of a microphone array for acoustic holography

Paul D. Teal[a)]
Victoria University of Wellington, P.O. Box 600, Wellington 6140, New Zealand

Mark A. Poletti
Industrial Research Ltd, P.O. Box 31-310, Lower Hutt 5040, New Zealand

(Received 17 August 2009; revised 27 January 2010; accepted 1 February 2010)

Previous work has indicated that a limitation on the performance of a circular microphone array for holographic sound field recording at low frequencies is phase mismatch between the microphones in the array. At low frequencies these variations become more significant than at mid-range and high frequencies because the high order phase mode responses at low frequencies are lower in amplitude. This paper demonstrates the feasibility of a "self-calibration" method. The basis of the calibration is to estimate the location of one or more wide-band sources using mid-range frequencies and to use this source location information to perform correction to the array at low frequencies. In its simplest form the calibration must be performed in an anechoic environment, since multipath effects at widely differing frequencies are uncorrelated. The approach is first demonstrated in such an environment using recordings from an array of high quality microphones. The technique is then extended to an adaptive calibration that can be used in an environment that is somewhat reverberant. The validity of the adaptive approach is demonstrated using recordings from an array of inexpensive microphones. © *2010 Acoustical Society of America.* [DOI: 10.1121/1.3336401]

PACS number(s): 43.60.Fg, 43.38.Kb, 43.60.Sx [EJS] Pages: 2368–2376

I. INTRODUCTION

Microphone arrays offer the possibility of sampling a sound field over a region in such a way that the field in that region, rather than the sound at just a single point, can be reconstructed.[1,2] A limiting factor on the accuracy with which a microphone array can record a sound field is mismatch between the microphone elements in the array. The following introduction explains why this is so, and hence motivates the solution elaborated in the remainder of the paper.

Most methods of storage and subsequent reconstruction of the sound field information involve transforming the microphone data into spherical or circular harmonics. In this paper we focus particularly on circular microphone arrays, which are particularly suited to recording of two-dimensional sound fields, as they allow recording of the horizontal spherical harmonics with fewer microphones than are required for a three-dimensional array.[3] For simplicity we ignore the vertical directivity required to attenuate higher order elevational modes. Since we are dealing with horizontal circular arrays, the elevation of all microphones and sources is assumed to be $\theta=\pi/2$, and the elevation dependence is suppressed in the notation. The techniques described can be extended to three-dimensional arrays.

We denote by $z_n(k,\phi_i)$ the response of microphone element n (in an array having N elements) to a plane wave of wave number k with angle of arrival ϕ_i from the front of that microphone element. Since this response is periodic, it can be expressed in terms of a Fourier series decomposition

$$z_n(k,\phi_i)=\sum_{q=-\infty}^{\infty} a_n(k,q)e^{-jq\phi_i}, \tag{1}$$

with coefficients given by

$$a_n(k,q)=\frac{1}{2\pi}\int_0^{2\pi} z_n(k,\phi_i)e^{jq\phi_i}d\phi_i. \tag{2}$$

Previous work[4] has shown that the pressure field near the array can be described in terms of a periodic far-field source distribution $S(k,\phi)$ and that this also can be conveniently expressed in terms of its complex Fourier coefficients, which have been termed *phase modes*.[5]

The mth mode, being the response to a plane wave from azimuth angle ϕ_i, is

$$r_m(k,\phi_i)=\frac{1}{N}\sum_{n=0}^{N-1} z_n(k,\phi_i-\phi_n)e^{-jm\phi_n}. \tag{3}$$

If all the microphone elements are identical, then $a_n(k,q)=a(k,q)$, and so the mth mode response becomes

$$\begin{aligned} r_m(k,\phi_i)&=\frac{1}{N}\sum_{n=0}^{N-1}\sum_{q=-\infty}^{\infty} a(k,q)e^{-jq(\phi_i-\phi_n)}e^{-jm\phi_n}\\ &=\sum_{q=-\infty}^{\infty} a(k,q)e^{-jq\phi_i}\left[\frac{1}{N}\sum_{n=0}^{N-1} e^{j(q-m)\phi_n}\right]\\ &=\sum_{l=-\infty}^{\infty} a(k,m-lN)e^{-j(m-lN)\phi_i}. \end{aligned} \tag{4}$$

The last line follows from the fact that the microphone elements are equally spaced ($\phi_n=2\pi n/N$) and so the term in square brackets is equal to 1 for $q=m-lN$ for any integer l, and is zero otherwise. If $a(k,m-lN)$ is small for any values

[a)]Author to whom correspondence should be addressed. Electronic mail: paul.teal@vuw.ac.nz

 0001-4966/2010/127(4)/2368/9/$25.00

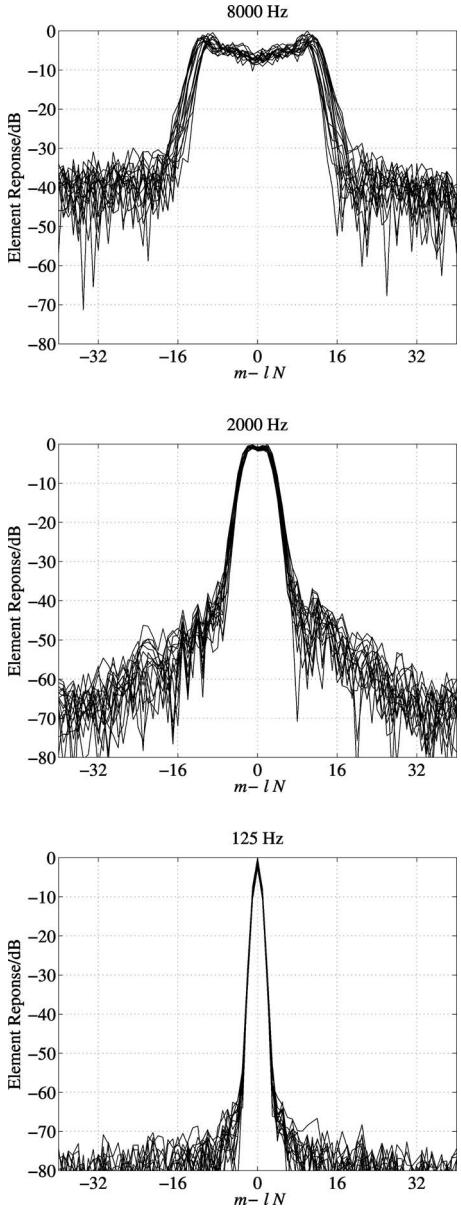

FIG. 1. Normalized Fourier transforms of the complex responses at 8 kHz (top), 2 kHz (middle), and 125 Hz (bottom).

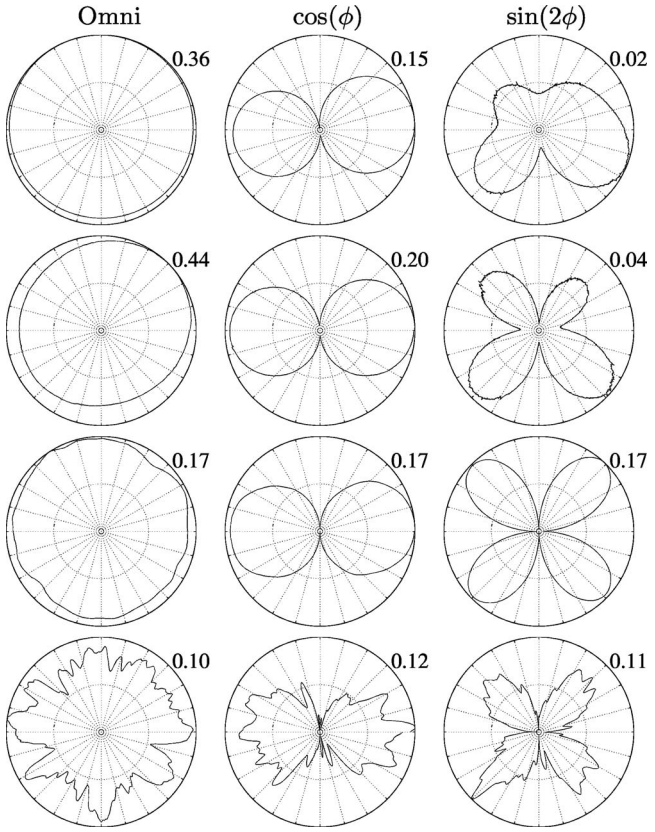

FIG. 2. Example raw polar responses for an open microphone array: 125 Hz (top row), 250 Hz (second row), 2 kHz (third row), and 8 kHz (bottom row). The maximum amplitude is the number at the top right of each response plot.

of l other than zero, we then obtain the important result that the low order polar responses of the array are *independent* of the polar responses of the individual microphones. For most microphone patterns this will be true below some frequency. Beyond this frequency, we say that aliasing has occurred. The complex value $a(k,0)$ will in general vary depending on the frequency, and so equalization across frequency will be required.

The number of modes we are able to accurately estimate from the measured data is an important measure of the effectiveness of the array for holographic sound field recording. For element independence as described in Eq. (4) we wish the approximation $a(k,m-lN) \ll a(k,0)$ to be true for as large a value of m as possible. However, to record high order modes, we have the conflicting requirement that $a(k,m)$ must be large for as large a value of m as possible.

Two microphone arrays were constructed as part of this work, and their details are described in Sec. IV. The complex responses of the arrays were measured as the array was rotated through 360°. The magnitude of the Fourier coefficients $a_n(k,q)$ for a 16 element array is shown in Fig. 1. The figure clearly illustrates the conflicting requirements. At high frequencies (e.g., 8000 Hz), the response is not small for $m-lN=\pm 16$. This results in aliasing for all modes. At low frequencies (e.g., 125 Hz) the response is small for $m-lN=\pm 16$, and so the zeroth order mode ($m=0$) can be reliably constructed. However, for first order terms ($m-lN=\pm 1$), the response is also quite small; −7 dB compared to the zeroth order. The second order term is smaller still at −30 dB, and so higher order modes are considerably attenuated compared to those at mid-range frequencies. At mid-band frequencies, the response is quite large in amplitude for $|m-lN| \leq 3$, but very small for $|m-lN| \geq 16$, and so modes up to second or third order can be accurately measured.

Examples of omnidirectional, first order and second order responses from the same measurements are shown in Fig. 2. Note that for the purpose of illustration in this paper, we show plots of real quantities: Half of the sum of the modes for $m=\pm 1$ creates a term labeled $\cos(\phi)$, and the difference between the modes for $m=\pm 2$ (divided by $2j$) creates a term labeled $\sin(2\phi)$. If the microphones were indeed identical then these terms would be real, though in practice there is a small imaginary component, which is not shown.

The aliasing at high frequencies is very apparent in Fig. 2. Unfortunately there is little that can be done about this short of increasing the number of microphones (at additional

cost) or decreasing the radius of the array (resulting to reduced signal to noise ratio at low frequency). The possibility of cost effectively increasing the number of microphones is discussed in Sec. IV A.

Figure 2 also shows the very low amplitude and the distortion of the second order response at low frequencies. Here some improvements may be possible. A fundamental observation for this paper is that this distortion is caused by differences in the phase response between the elements of the array.[4] These differences become more significant at low frequencies since the high order modes at low frequencies are small amplitude signals found from the phased combination of equal amplitude microphone signals.

The conjecture motivating the research described in this paper is that the inter-element variation in low frequency responses may be estimated from certain signals. In this way the microphone array can "self-calibrate." In particular, the idea is to estimate the direction of arrival of a source or sources at mid-range frequencies, where the phase difference is not so significant. If the sources are also generating signals at low frequencies, the location information can then be used to estimate the phase difference to each of the microphones, and hence the phase error can be calculated.

In Sec. II a simple criterion is presented for measuring the success of the proposed calibration scheme. Section III is a discussion of a suitable model for each microphone element of the array. Estimating the parameters of this model allows calibration to be performed. Section IV describes the design of the two microphone arrays that were constructed to collect data to evaluate the techniques and the measurement procedure. In Sec. V the method of self-calibration is presented and shown to improve the array response. It is then extended to the situation where the calibration must be performed in a reverberant environment.

II. MODE ERROR CRITERION

The polar plots shown in Fig. 2 illustrate the problem in generating second order modes at low frequencies. However, for purposes of comparison, it is desirable to have an objective measure of the error. The measure used here is a simple squared error comparison with the ideal mode response. The ideal phase mode response can be factored in the form[4]

$$r_m(k,\phi_i) = \beta_m(k)e^{-jm\phi_i}. \tag{5}$$

If we have measurements $r_m(\phi_i)$ of this response at a discrete set of angles ϕ_i, then the total normalized error is given by

$$\sum_{i=1}^{N} \left| e^{jm\phi_i} - \frac{r_m(\phi_i)}{\beta_m} \right|^2. \tag{6}$$

For the purposes of providing an error measure, we are free to choose a value of the amplitude β_m that minimizes this error. (This ignores frequency continuity, which will become important when equalization of the responses across frequency is performed, but at present we are only concerned with phase correction at individual frequencies.) We therefore equate to zero the derivative of this expression with respect to the complex conjugate β_m^* of β_m, and choose

$$\beta_m = \frac{\sum_{i=1}^{N} r_m(\phi_i) r_m^*(\phi_i)}{\sum_{i=1}^{N} e^{-jm\phi_i} r_m^*(\phi_i)}. \tag{7}$$

This value of β_m can then be used in Eq. (6) to obtain the error measure. We use this in the remainder of this paper to evaluate the effectiveness of the proposed calibration schemes.

III. MICROPHONE MODEL

Implicit in the concept of calibration of the microphone array in this paper is the notion that there are some small number of parameters (ideally one parameter), which characterize each element of the array. To derive a calibration method, we thus need a model for the elements. The model should be capable of being decomposed into two components:

(1) the parameter or parameters required for calibration, which encapsulate the differences between the elements; and
(2) the complex response of the element as a function of arrival angle, after the simple parametrization of component 1 has been removed; ideally there should be very little variation in this for an entire batch of microphone elements.

Some effort was put into producing an electrical equivalent model of each element based on physical considerations. The idea behind this approach is that the differences between each element must ultimately arise from some physical difference in their construction or arrangement. Some useful references for development of these models are available.[6–9] However, if the elements are active, having a field effect transistor (FET) amplifier stage, element differences may also be due to the electronics. For this paper it was decided to use an empirical model for the elements.

Section III A presents the choice of the calibration parameter and Sec. III B presents the remaining part of the model that is assumed to be common to microphone elements after the calibration parameter has been removed.

A. Element differences for calibration

The complex polar responses for each of the 16 elements are overlaid in Fig. 3. The responses at low frequencies, where we most wish to correct for differences, suggest that a simple rotation (multiplication by a complex factor of unitary magnitude) is all that is necessary to compensate for microphone differences. A complex scaling, which includes an amplitude scaling as well as a rotation, may achieve better alignment, but at the cost of an additional real parameter to estimate.

We first investigate whether this model can be used to obtain better first and second order harmonics at low frequencies, in the situation where all of the response information is available.

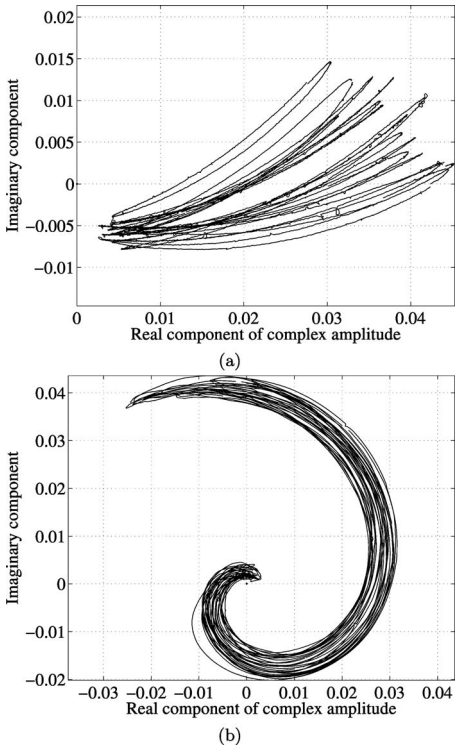

FIG. 3. Overlaid raw complex polar responses for 16 microphone elements at 125 Hz (a) and at 2 kHz (b).

Suppose then that we have two complex vectors $\mathbf{x}$ and $\mathbf{y}$, representing, respectively, the measured response and an ideal response. We wish to find a complex scaling a so that $a\mathbf{x}$ and $\mathbf{y}$ are closest in some sense. For simplicity we again choose for our alignment metric the sum of the squared error between the two vectors, or

$$\eta_n = \|a_n \mathbf{x}_n - \mathbf{y}\|^2. \tag{8}$$

Equating the derivative with respect to a_n^* to zero, we obtain

$$a_n = \frac{\mathbf{x}_n^H \mathbf{y}}{\mathbf{x}_n^H \mathbf{x}_n}. \tag{9}$$

If we instead use a strict rotation, $e^{j\theta_n}$ with no scale adjustment, and equate the derivative with respect to θ_n to zero, we obtain

$$e^{j\theta_n} = \frac{\mathbf{x}_n^H \mathbf{y}}{\|\mathbf{x}_n^H \mathbf{y}\|}. \tag{10}$$

Continuing with a squared loss metric, we may wish to find a "central" vector $\mathbf{y}$, which produces the lowest total loss summed over all of the N elements of the array, or

$$\eta = \sum_{n=1}^{N} \eta_n = \sum_{n=1}^{N} \|\mathbf{y} - \mathbf{x}_n a_n\|^2. \tag{11}$$

Taking the derivative with respect to $\mathbf{y}$ we obtain

$$\mathbf{y} = \frac{1}{N} \sum_{n=1}^{N} \mathbf{x}_n a_n \tag{12}$$

or

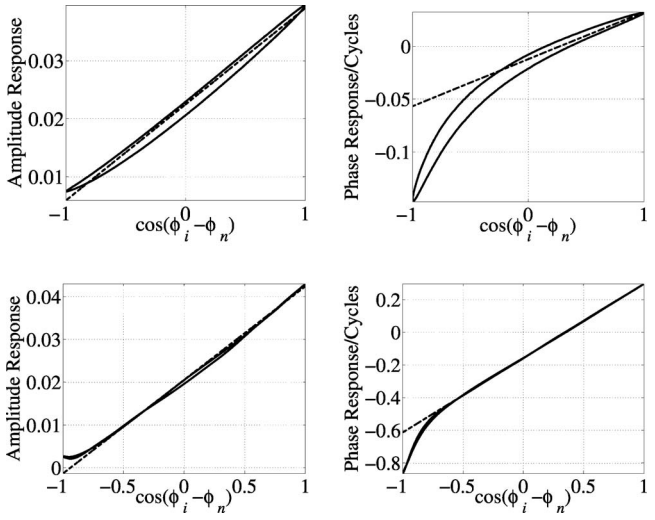

FIG. 4. The mean amplitude and phase responses for 125 Hz (top row) and 2 kHz (bottom row), each presented as the solid curve as a function of $\cos(\phi_i - \phi_n)$. In each case a weighted linear fit is shown by the dashed line.

$$\mathbf{y} = \frac{1}{N} \sum_{n=1}^{N} \mathbf{x}_n e^{j\theta_n}. \tag{13}$$

Iteration between Eqs. (9) and (12), or between Eqs. (10) and (13) rapidly converges to a self-consistent solution. If scaling is allowed, then the vector of a_n must be scaled at each iteration

$$\mathbf{a} \leftarrow \mathbf{a} \frac{\sqrt{N}}{\|\mathbf{a}\|}. \tag{14}$$

This is to prevent the iterative process from minimizing the squared error by simply making the scaling factor smaller at every stage.

This computation is not self-calibration as intended in this paper, but provides a justification for the model used. The resulting improvement in the calculation of modes is presented in Sec. III C.

B. Single element model

Figure 4 shows the amplitude and phase response of the microphones presented as functions of $\cos(\phi_i - \phi_n)$. (These are actually the averaged responses for several elements after alignment as discussed in Sec. III A.) Both the magnitude and phase appear to be approximately linear functions of $\cos(\phi_i - \phi_n)$. A least-squares fit is shown as the line in each case. The error minimization for this line was weighted so that values for which the amplitude is small contributed smaller error. Linearity of both amplitude and phase with $\cos(\phi_i - \phi_n)$ is suggested by the first order microphone model,[4] which gives the complex response [for waves of elevation $(\theta = \pi/2)$] as

$$z_m(k, \phi_i - \phi_n) = [\alpha + (1 - \alpha)\cos(\phi_i - \phi_n)] \times \exp[jkR\cos(\phi_i - \phi_n)], \tag{15}$$

where α is $\frac{1}{2}$ for an ideal cardioid, and R is the radius of the array. This equation is not applicable to the case of a baffled array, but empirically it was found that the approximate lin-

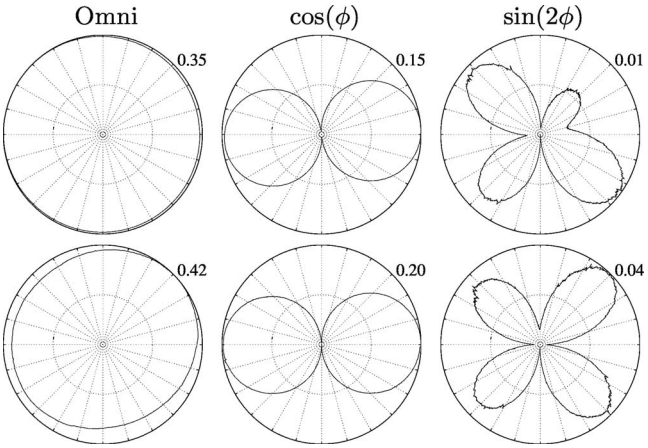

FIG. 5. Example polar responses from measured microphone data corrected via a phase rotation: 125 Hz (top row) and 250 Hz (bottom row). The maximum amplitude is the number in the top right of each response plot. This should be compared to the upper half of Fig. 2.

earity applies for both arrays used in the experiments. At low frequencies a linear approximation for the phase is evidently not such a good approximation. There is also a loop in the response, indicating some asymmetry in the array construction. Correcting this is beyond the scope of this paper. What is more significant, and is relatively easy to incorporate into the model, is the fact that at low frequencies, the phase difference between microphones separated by 180° is greater than kR.

This is consistent with the effects of baffling at low frequencies, where it is known, for example, that the phase difference around a sphere is larger than predicted by the free-field case[10] by a factor of 1.5 and for a cylinder is greater by a factor of 2.

For an array embedded in an acoustically hard cylinder of radius R, aligned on the z axis, the pressure around the cylinder (at azimuthal angle ϕ) for a vertical plane wave (independent of z) incident from angle ϕ_i is

$$p(R,\phi) = \frac{2i}{\pi kR}\sum_{m=-\infty}^{\infty}\frac{(-j)^m}{H'_m(kR)}e^{jm(\phi-\phi_i)}. \tag{16}$$

At low frequencies, only the low order terms are significant.

TABLE I. Error for each of several modes for raw data, and data with an optimal rotation (with or without scaling) applied to each element. The last two rows are the result for a complex rotation estimated from a calibration signal.

	f (Hz)	Omni	$\cos(\phi)$	$\sin(\phi)$	$\cos(2\phi)$	$\sin(2\phi)$
Raw	125	0.028	0.081	0.106	0.447	0.593
	250	0.096	0.065	0.059	0.159	0.259
Rotate	125	0.029	0.083	0.076	0.303	0.485
	250	0.072	0.054	0.042	0.141	0.157
Rotate and scale	125	0.018	0.057	0.049	0.236	0.276
	250	0.065	0.027	0.045	0.141	0.112
Self-calibration	125	0.025	0.055	0.063	0.376	0.250
	250	0.070	0.045	0.057	0.127	0.090

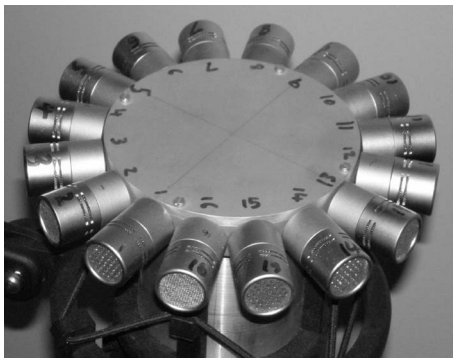

FIG. 6. The cardioid open array.

Applying the low frequency approximation of the Hankel derivative to the $m=-1,0,1$ terms yields

$$p(R,\phi) \approx 1 - j2kR\cos(\phi-\phi_i). \tag{17}$$

This compares with the phase due to a free-field plane wave

$$p(R,\phi) = e^{-jKR\cos(\phi-\phi_i)} \approx 1 - jkR\cos(\phi-\phi_i). \tag{18}$$

Hence the phase shift with the cylinder is two times that of the free field at low frequencies.

It is simple to incorporate this effect into our single element model by using a "virtual" radius, which is a function of frequency, rather than the true radius, or (as in Sec. V B) to use an anechoically measured response of one of the microphones.

C. Element difference model verification

For the arrays described in Sec. IV, the approach of applying a rotation to each of the measured complex responses of the array elements was performed as described in Sec. III A. Even though the algorithm for applying the rotation was not specifically optimized for minimizing the error for any particular mode, a reduction in the error is apparent. This is shown by comparing Fig. 5 with the upper half of Fig. 2.

The errors for the modes, using the measure discussed in Sec. II for both rotation and complex scaling, are shown in Table I. It is apparent that the error, particularly for the second order modes, can be reduced using this simple phase calibration approach.

IV. MEASUREMENTS

A. Array design

The calibration procedures proposed in this paper were trialed using two different microphones arrays, as shown in Figs. 6 and 7. The motivation for the design of each is briefly explained as follows.

It has been shown[3,11] that equalization of the mth mode for an array radius of R is not possible using omnidirectional microphones for frequencies at which kR coincides with zeros of the Bessel function $J_m(kR)$. Several methods have been proposed for overcoming this problem. One is to use first order microphones facing radially outwards,[11] and a second is to use a solid cylinder containing flush mounted pressure microphones.[12] The two arrays presented in this paper use these two methods. The first was constructed using 16

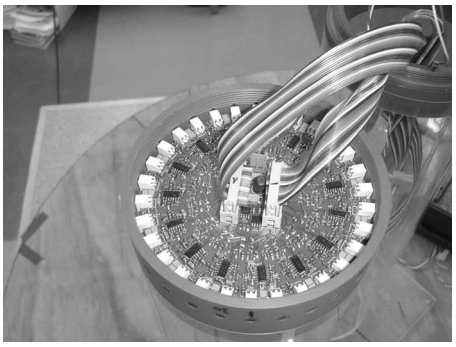

FIG. 7. The flush mounted baffled microphone array.

Rode NT cardioid elements, and is shown in Fig. 6. This approximates an open array but there is a baffle present, which produces some variation from the ideal open array. At 2 kHz, the array radius can be estimated from the phase gradient as 77.5 mm, which is very close to the physical radius of 77.8 mm. At 125 Hz, however, the phase gradient corresponding to the least-squares line shown in Fig. 4 leads to an estimated radius of 116 mm.

The second array used 30 electret condenser microphones, flush mounted halfway along a Perspex cylinder of 134 mm diameter and 1 m height. This baffled array is shown partly assembled in Fig. 7. It has been shown[3] that a considerable improvement in signal to noise ratio is obtained by using a large number of microphones. Closely spaced microphones also increase the upper frequency limit above which aliasing occurs. The problem with a large number of microphones is of course the cost of the microphones and recording equipment. Part of the motivation for construction of the second array described in this paper was to verify the operation of the array using very cost effective components. Lower cost microphones typically show more variation between individual elements, and hence a calibration procedure becomes more necessary.

The second array was designed with cost saving in mind. It was constructed using 30 inexpensive MB6022APC-0 electret condenser microphones. Each of these was followed by a filter and amplifier based on a TLV2464 operational amplifier, and the results were sampled and multiplexed using two analog switches (ADG732) before analog to digital conversion. The cost saving resulting from multiplexing is that only 2 analog to digital converters are required for all 30 channels. The sampling rate for each channel was 42 666 Hz. The multiplexing necessarily involves time differences (in this case in steps of 1/15 of the sample period) between the sampling instants of the channels, so sample simultaneity was restored in subsequent multirate processing.

The differences between elements for this array of electret microphones are due not only to mechanical manufacturing variations but also to electrical differences between the FET impedance buffers. The element differences are very obvious in Fig. 8. For these microphones there are considerable differences in the amplitudes as well as the phases, so we here model the differences using

$$z_n(k,\phi) = z(k,\phi)c_n(k), \tag{19}$$

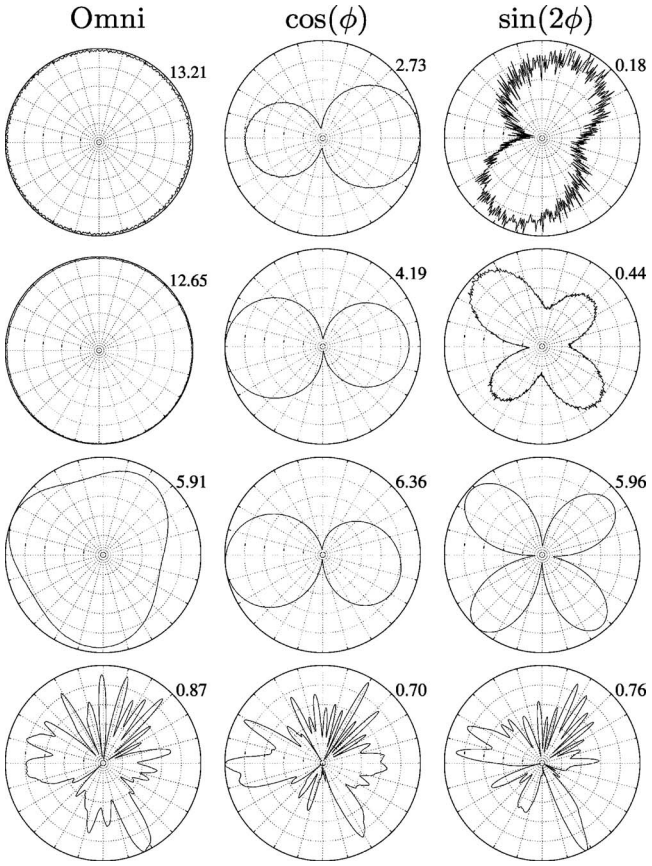

FIG. 8. Overlaid raw complex polar responses for 30 microphone elements at 2 kHz.

where $z(k,\phi)$ is the response of any one of microphones, and $c_n(k)$ is a frequency dependent complex calibration factor for each microphone.

Though it is not the subject of this paper, we note in passing that low quality microphones will usually have large variation with frequency, and this will be reflected in the variation of the calibration value $c_n(k)$ with frequency. This means that, though low quality microphones offer more scope for improvement using a calibration technique, a larger number of taps will be required for an equalizing filter to compensate for the frequency variation.

B. Data collection

Both arrays were mounted on a rotator and rotated through 360° in 0.5° steps. The impulse response from a loudspeaker to each microphone at each position was measured both in an anechoic chamber and in various configurations in a laboratory having $T_{60} \approx 0.70$ s. It was found that there were some minor issues caused by misalignment of the rotation axis and the microphone array axis, and allowance was made for these; the details, however, are not within the scope of this paper.

Example omnidirectional, first order and second order responses for the open array are shown in Fig. 2, and for the baffled array in Fig. 9. As we would expect, the plots for the array of lower quality microphones of Fig. 9 are considerably more distorted than those for the array of higher quality microphones in Fig. 2. The aliasing at high frequencies is

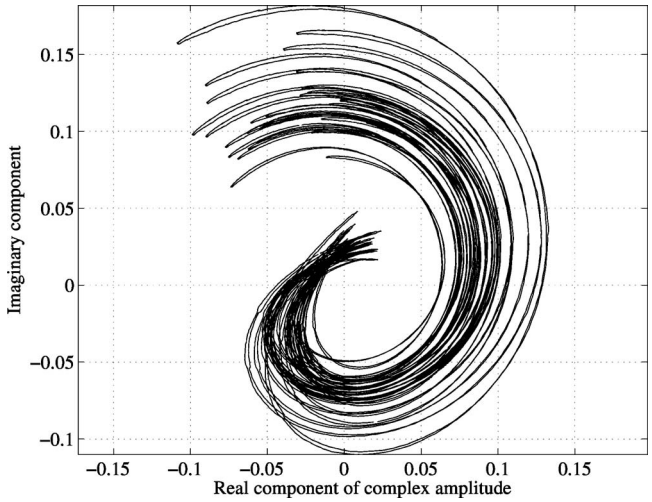

FIG. 9. Example raw polar responses from the second microphone array: 125 Hz (top row), 250 Hz (second row), 2 kHz (third row), and 16 kHz (bottom row). The maximum amplitude is the number at the top right of each response plot.

very apparent for all modes, as well as the distortion of the second order responses at low frequencies.

C. Beamforming

The approaches to be proposed in Sec. V require beamforming at mid-band frequencies to locate the position of the source. For an open array, the required beamformer is simply based on the difference of time of arrival caused by the geometry of the array. For a "closed" array, the microphones are all embedded in a cylindrical baffle, so the beamforming must take into account diffraction around the cylinder. This can be calculated analytically, since the diffraction around a cylinder is well understood. Alternatively the measured anechoic responses of one of the microphones can be used. The response of each microphone will of course be different for different microphones and for different frequencies, but the variation with azimuth angle we can expect to be independent of the particular element used. If the array were to be mass produced, this measurement would only need to be performed once.

V. SELF-CALIBRATION

A. Calibration using a single source

The idea of estimating a source location using mid-band frequencies, and using this location information to calibrate at low frequencies, was first implemented on a one-shot basis; i.e., one source location was estimated, and the improvement resulting from the calibration quantified.

A maximum likelihood beamforming method,[13] assuming error caused by additive white normal noise, was used at 2 kHz to estimate the location of a single source

$$\hat{\phi} = \max_{\phi} |\mathbf{x}(k)\mathbf{z}^H(k,\phi)|, \tag{20}$$

where $\mathbf{x}(k) = (x_1(k), \ldots, x_N(k))^T$ is the measured response for wave number k to the source, and $\mathbf{z}(k,\phi) = (z_1(k,\phi), \ldots, z_N(k,\phi))^T$ is the expected response to a source at azimuth ϕ from an array of identical elements as discussed in Sec. III B. Consistent with the effect discussed in Sec. III B it was found that using the true radius of the array did not necessarily minimize the error variance. The measured response of the source at a *different*, lower wave number k was then divided by the ideal model response to obtain a complex calibration factor for each of the N microphone elements.

$$c_n(k) = \frac{x_n(k)}{z(k,\hat{\phi})}, \tag{21}$$

where $x_n(k)$ is the measured response of element n, and the amplitude of $c_n(k)$ may be forced to unity or retained, as discussed in Sec. III A.

The error obtained with these calibrations was found to depend on the actual location of the source, but one example is shown in the last two lines of Table I. The error can be seen to be comparable to that obtained for the "omniscient" calibration of Sec. III C.

Attempts to further improve the calibration using a second source were not found to be successful. Consideration of this problem leads to the development of the adaptive approach discussed in Sec. V B.

B. Calibration using multiple sources

We now attempt to improve the calibration by repeating the procedure for different source angles and in different environments. The direction of arrival estimate used is the same as Eq. (20), with the notation now including the possibility of the source having different true locations for different time indices, indicated by the superscript $^{(t)}$ as follows:

$$\hat{\phi} = \max_{\phi} |\mathbf{x}(k,\phi^{(t)})\mathbf{z}^H(k,\phi)|, \tag{22}$$

where $\mathbf{x}(k,\phi^{(t)})$ is the measured response for wave number k to the source that at time index t is located at azimuth $\phi^{(t)}$.

The calibration is basically the same as Eq. (21) as follows:

$$c_n(k) = \frac{x_n(k,\phi^{(t)})}{z(k,\hat{\phi})}, \tag{23}$$

where $x_n(k,\phi^{(t)})$ is the measured response of element n at time instant t. As expected, this resulted in an improvement in the response. However, this calibration technique requires careful measurement in an anechoic chamber for every set of microphone elements. We would like the array to self-calibrate in a real environment.

Using the earlier method on data acquired in a reverberant environment results in only very slight changes in the quality of the response, and this change is not always an improvement. This is because in a diffuse scattering environment, the apparent directions of arrival are uncorrelated for any pair of frequencies separated by more than the correlation bandwidth.[14]

C. Adaptive calibration

In order to provide a calibration scheme that will work in a real environment, we adopted an adaptive approach, represented by the equation

$$c_n^{(t+1)}(k) = \lambda \frac{x_n(k,\phi^{(t)})}{z^{(t)}(k,\phi)} + (1-\lambda)c_n^{(t)}(k), \tag{24}$$

where λ is the learning rate. At each stage the vector of calibration factors $\mathbf{c}^{(t+1)}(k) = (c_1^{(t+1)}(k), \ldots, c_N^{(t+1)}(k))^T$ was divided by its norm. This is not essential to the process, but prevents the overall scaling from changing arbitrarily if no actual improvement is being achieved.

If this approach is used over several different scattering scenarios, an improvement is often seen, but the results do not improve consistently.

It was found that this inconsistency was due to errors in the direction of arrival estimate $\hat{\phi}$. This suggested that the calibration should be performed at all frequencies, and that the calibration information obtained so far should be used to improve the location estimation process. This can be represented as

$$z_n^{(t+1)}(k,\phi) = z(k,\phi)c_n^{(t)}(k). \tag{25}$$

The adaptive process then consists of iteration between Eqs. (22), (24), and (25), using the latest calibration information to improve the angle of arrival estimation in the next calibration environment.

For the approach to work best, each iteration involves both beamforming and calibrating at several different frequencies. The direction of arrival estimate $\hat{\phi}$ in this case is the value minimizing the sum of the squared errors of the beamformers at each of the separate frequencies. Other wideband beamforming techniques are known of course, but this method was found to be simple and effective. The algorithm is summarized in Algorithm 1.

Algorithm 1. Adaptive microphone array calibration algorithm.

Initialize learning rate λ.

Calculate or measure anechoic response of single element $z(k,\phi)$ to plane wave at wave number k and angle of arrival ϕ.

Initialize relative importance weights w_k for each frequency in direction of arrival estimation.

for $t>0$ do

  for k do

    Normalize calibration coefficients: $\mathbf{c}(k) = \mathbf{c}_k / \|\mathbf{c}(k)\|$

  Obtain sound from source in a new environment, and transform to the frequency domain $\mathbf{x}(k,\phi)$.

  for k do

    Calculate array response using Eq. (25)
    $z_n^{(t+1)}(k,\phi) = z(k,\phi)c_n^{(t)}(k)$

  Estimate azimuth based on weighted metric:
  $\hat{\phi} = \max_\phi \Sigma_k w_k |\mathbf{x}(k,\phi^{(t)})(\mathbf{z}^{(t)}(k,\phi))^H|^2$

  for k do

    Update calibration coefficients using Eq. (24) as follows: $c_n^{(t+1)}(k) = \lambda x_n(k,\phi^{(t)})/z^{(t)}(k,\phi) + (1-\lambda)c_n^{(t)}(k)$

It was found that the robustness of the method to reverberation depends on the number of frequencies used. For 85 semi-tone spaced frequencies from 125 to 16 000 Hz, it was found that this approach is effective for direct to reverberant ratios of about 10 dB, although the results are best for ratios of 15 dB and greater. This can only be regarded as mildly reverberant at best but does demonstrate that calibration is possible without a completely anechoic environment.

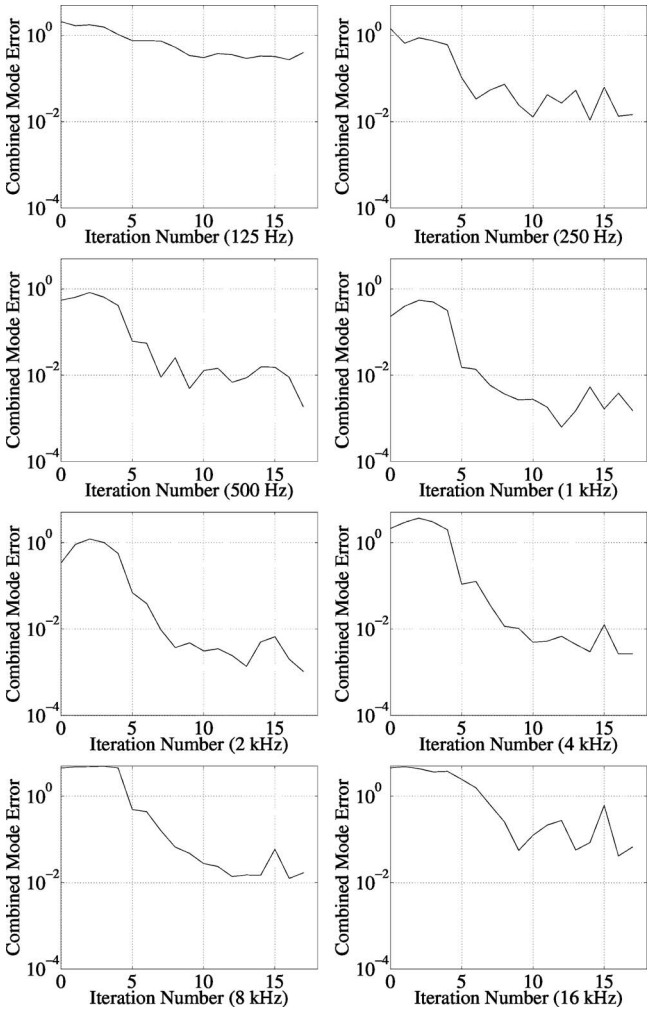

FIG. 10. Convergence results for the proposed adaptive calibration algorithm for eight different frequencies.

The reverberation interferes with the calibration in two ways: First it decreases the accuracy of the source localization, and second it causes spurious values in the calibration coefficients. It was found that eliminating one but not both of these sources of error does not ensure calibration accuracy. In particular, more sophisticated methods of localization are known to exist,[15–18] which are specifically designed for robustness to reverberation. These could be used to solve for the first of these difficulties. Applying the *principles* of these techniques to solve the second of these difficulties may be effective, but is not trivial, and is the subject of future research.

The method does of course rely on adaptation over several different scattering scenarios. However, it was found that the convergence is fast and reliable enough that only a few different scattering environments are required, provided several slightly different microphone positions and orientations are available.

Convergence results are shown in Fig. 10. The error in

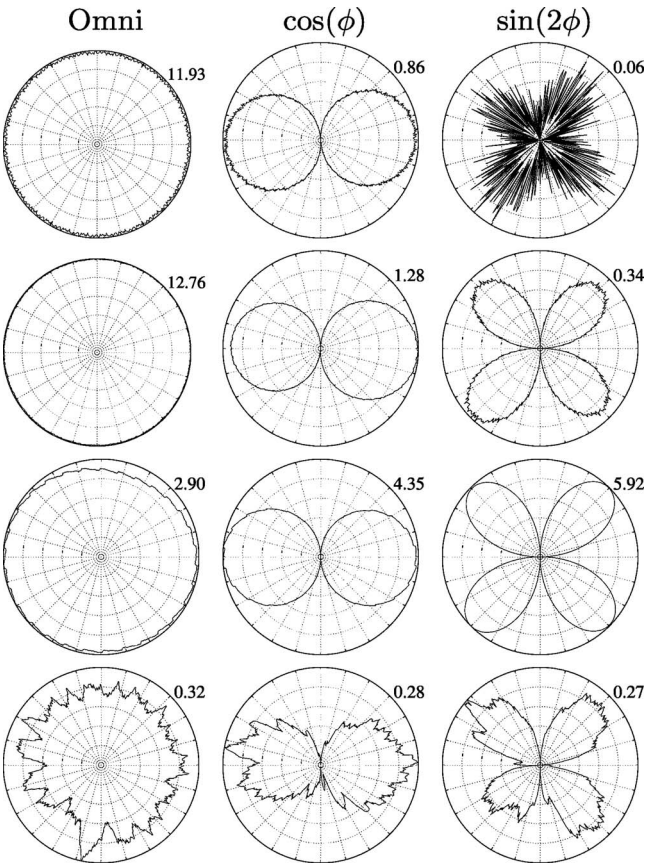

FIG. 11. Example polar responses after adaption: 125 Hz (top row), 250 Hz (second row), 2 kHz (third row), and 16 kHz (bottom row). These should be compared with the responses of Fig. 9.

each case is a combination of the squared error for the modes $m=-2,-1,0,1,2$. The learning rate for these experiments was $\lambda=0.9$. If there is less certainty that there was a dominant broadband source in the calibration environment, then this learning rate should be reduced.

Some example mode plots are shown in Fig. 11. As we would expect, the response is still not ideal at very low and at very high frequencies, but is still a vast improvement over the raw responses shown in Fig. 9. The error "floor" at low and high frequencies compared to mid-band frequencies is also apparent in Fig. 10. At 125 Hz the poor signal to noise ratio performance of the microphones is apparent, and element mismatch is no longer the limiting factor.

VI. CONCLUSION

It has been shown that estimation of the second order and higher modes of a sound field using a microphone array is difficult at low frequencies. This is primarily because the magnitude of the modes is very small. This results in any variations in the element properties becoming very significant. It has been further shown that these variations can be simply accounted for by a complex scaling, and in this way the usable low frequency range of the array can be extended. The scaling can be estimated from actual measured signals, provided that the direction of arrival information derived at mid-range frequencies can be applied to low frequencies.

The inter-element variations that cause the difficulty are particularly significant for low cost microphone elements, which typically have large manufacturing variation. In this paper we have shown that an adaptive algorithm can significantly reduce the effects of these inter-element variations. This adaptive algorithm needs to be initialized with accurate information on the angular response of a single element. The algorithm can then determine the complex gain of each microphone element. In order for the self-calibration to operate, the array must be presented with a number of different scattering environments. Convergence is fairly rapid, and the technique can be used in the presence of mild levels of reverberation.

[1]G. Weinreich and E. Arnold, "Method for measuring acoustic radiation fields," J. Acoust. Soc. Am. **68**, 404–411 (1980).
[2]T. Abhayapala and D. Ward, "Theory and design of high order sound field microphones using spherical microphone arrays," in Proceedings of the IEEE ICASSP, Orlando, FL (2002), pp. 1949–1952.
[3]M. Poletti, "A unified theory of horizontal holographic sound systems," J. Audio Eng. Soc. **48**, 1155–1182 (2000).
[4]M. Poletti, "Effect of noise and transducer variability on the performance of circular microphone arrays," J. Audio Eng. Soc. **53**, 371–384 (2005).
[5]A. Rudge, K. Milne, A. Oliver, and P. Knight, *The Handbook of Antenna Design* (Peter Peregrinus, London, UK, 1983).
[6]H. Olson, *Elements of Acoustical Engineering* (D. Van Nostrand, New York, 1940).
[7]L. Beranek, *Acoustics* (Acoustical Society of America, Melville, NY, 1993).
[8]S. Peus, "Modern acoustic and electronic design of studio condenser microphones," in Audio Engineering Society Convention, Berlin (2004), p. 6131.
[9]R. S. Grinnip III, "Advanced simulation of a condensor microphone capsule," J. Audio Eng. Soc. **54**, 157–166 (2006).
[10]G. Kuhn, "Model for the interaural time differences in the azimuthal plane," J. Acoust. Soc. Am. **62**, 157–167 (1977).
[11]M. Poletti, "Three-dimensional surround sound systems based on spherical harmonics," J. Audio Eng. Soc. **53**, 1004–1025 (2005).
[12]Meyer, J., and Elko, G., "Spherical microphone arrays for 3D sound recording," in *Audio Signal Processing for Next-Generation Multimedia Communication Systems*, edited by Y. A. Huang and J. Benesty (Kluwer Academic, Boston, MA, 2004).
[13]H. van Trees, *Optimum Array Processing (Detection, Estimation, and Modulation Theory, Part IV)* (Wiley, New York, 2002).
[14]M. R. Schroeder, "Frequency-correlation functions of frequency response in rooms," J. Acoust. Soc. Am. **34**, 1819–1823 (1962).
[15]C. Knapp and G. Carter, "The generalized correlation method for estimation of time delay," IEEE Trans. Acoust. Speech Signal Process. **24**, 320–327 (1976).
[16]Y. Huang, J. Benesty, and G. W. Elko, "Adaptive eigenvalue decomposition algorithm for realtime acoustic source localization system," in Proceedings of the IEEE Conference on Acoustics, Speech and Signal Processing (1999), Vol. **2**, pp. 937–940.
[17]J. Benesty, "Adaptive eigenvalue decomposition algorithm for passive acoustic source localization," J. Acoust. Soc. Am. **107**, 384–391 (2000).
[18]Y. A. Huang and J. Benesty, "Adaptive multichannel time delay estimation based on blind system identification for acoustic source localization," in *Adaptive Signal Processing—Applications to Real-World Problems*, edited by J. Benesty and Y. A. Huang (Springer, Berlin, 2003), Chap. 8, pp. 227–248.

An analytical comparison of ultrasonic array imaging algorithms

Alexander Velichko[a] and Paul D. Wilcox
Department of Mechanical Engineering, University of Bristol, Bristol BS8 1TR, United Kingdom

(Received 5 March 2009; revised 11 January 2010; accepted 11 January 2010)

In the paper different techniques for post-processing data from an ultrasonic transducer array are considered. First, a mathematical model of the transmit-receive array data is developed. Then based on this model three imaging methods are formulated: the total focusing method, the wavenumber algorithm, and the back-propagation method. Although these methods are conceptually different and use different approximations they can all be expressed in the form of a linear superposition of transmit-receive signals in the frequency domain with some focusing coefficients. The equivalent coefficients for each processing algorithm are derived, and difference between approaches is discussed. It is shown that in the general case the most appropriate imaging method is the back-propagation method, which is based on the back-propagation of the angular spectrum of transmit-receive signals. The relative performance of the imaging methods is illustrated using simulated and experimental data. © *2010 Acoustical Society of America.*
[DOI: 10.1121/1.3308470]

PACS number(s): 43.60.Fg, 43.60.Uv, 43.20.Bi, 43.35.Zc [TDM] Pages: 2377–2384

I. INTRODUCTION

Ultrasonic arrays are now widely used in many areas of nondestructive evaluation (NDE).[1] One of the possible modes of operation of such an array is to collect time-domain signals from each transmitter-receiver combination. Any imaging algorithm can then be applied in post-processing in order to localize defects in the test object.

In recent years several methods for processing ultrasonic array data have been developed. It is possible to distinguish between three techniques: the total focusing method (TFM),[2] the inverse wave field extrapolation,[3] and the wavenumber algorithms.[4] Although these methods are conceptually different, use different approximations, and have different implementations, for the modeling and experimental examples considered they all exhibit similar performance in terms of resolution. Therefore, from the practical point of view, it is unclear which method in which situation is better.

The objective of this paper is to present a theoretical comparison between the different imaging techniques for the processing of the full transmit-receive array data. In the first part of the paper a general mathematical model of the ultrasonic array data is developed. Then based on this model the different imaging methods are considered. Any linear imaging method with respect to the array data can be represented as a linear superposition of transmit-receive signals in the frequency domain with some focusing coefficients. The equivalent coefficients for each processing algorithm are derived and the difference between approaches in terms of resolution and signal-to-noise ratio is investigated. In addition, the computational performance of the imaging methods is considered and the preferred numerical implementation method in two-dimensional (2D) and three-dimensional (3D) cases is discussed.

[a]Author to whom correspondence should be addressed. Electronic mail: a.velichko@bristol.ac.uk

II. MATHEMATICAL MODEL OF ULTRASONIC ARRAY DATA

Any time-domain signal $u(t)$ can be expressed as a linear superposition of its spectral components $u(\omega)$ as follows:

$$u(t) = \frac{1}{2\pi}\int u(\omega)e^{i\omega t}d\omega. \tag{1}$$

Therefore in this section only time-harmonic wave fields are considered and the factor $\exp(i\omega t)$ is omitted.

To simplify the notation a 2D elastic isotropic half-space is considered. However, the extension to the 3D model is straightforward and results in Sec. IV are given for both 2D and 3D cases. The Cartesian coordinate axes (x,z) are defined with the z axis normal to the surface of the half-space. A transmitter element is modeled by a time-harmonic load $\mathbf{q}$ applied to the free surface $z=0$ in a contact area with its center at $x=x_T$. The system is illustrated schematically in Fig. 1.

In this paper only longitudinal waves are considered. In this case the scalar potential ϕ can be used instead of the displacement vector $\mathbf{u}$, so $\mathbf{u}=\nabla\phi$. Using the integral transform method[5] and taking the part of the solution associated with the longitudinal wave, the resulting time-harmonic potential field ϕ_T can be written in the form

$$\phi_T(\mathbf{r}) = \frac{1}{2\pi}\int \Phi_T(k_{x(T)})e^{-i\mathbf{k}_{(T)}\cdot(\mathbf{r}-\mathbf{r}_{(T)})}dk_{x(T)}, \tag{2}$$

where $\mathbf{k}_{(T)}=\{k_{x(T)},k_{z(T)}\}^T$ is the wave vector, k is the wavenumber, and $k_{z(T)}=\sqrt{k^2-k_{x(T)}^2}$. The branch of the function $k_{z(T)}$ in the complex $k_{x(T)}$ domain is chosen by the condition[5] $\mathrm{Re}\, k_{z(T)}\geq 0$, $\mathrm{Im}\, k_{z(T)}\leq 0$, $\omega>0$. The function $\Phi_T(\mathbf{k}_{x(T)})$ is the

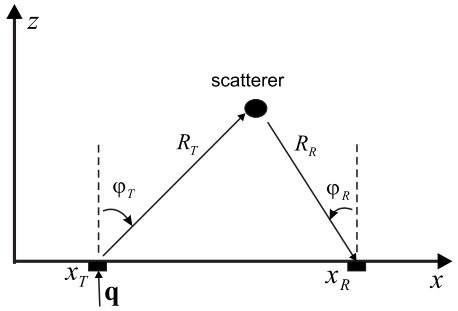

FIG. 1. System geometry.

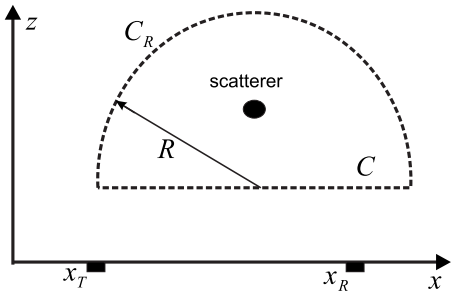

FIG. 2. A contour C enclosing a scatterer region for application of Auld's formula 8.

angular spectrum of the excited field and $\mathbf{r}=\{x,z\}^T$, $\mathbf{r}_{(T)}=\{x_T,0\}^T$.

In the far-field of the transmitter element $k|\mathbf{r}-\mathbf{r}_{(T)}|\gg 1$ integral (2) can be calculated using the stationary phase method. The local polar coordinate system R_T, φ_T is defined with its origin at the center of the transmitter element, as illustrated in Fig. 1. The resulting far-field expression for the displacements $\mathbf{u}_T$ is given by

$$\mathbf{u}_T=\mathbf{e}_{R(T)}f_T(\varphi_T)\sqrt{\frac{\lambda}{R_T}}e^{-ikR_T},\quad \mathbf{e}_{R(T)}=\{\sin\varphi_T,\cos\varphi_T\}^T, \tag{3}$$

where $\lambda=2\pi/k$ is the wavelength, and the directivity function of the transmitter element f_T has the form

$$f_T(\varphi_T)=\frac{e^{-i\pi/4}}{2\pi}k^2\cos(\varphi_T)\Phi_T(k\sin\varphi_T). \tag{4}$$

In the particular case of a unit line load normal to the surface, $\mathbf{q}=\{0,1\}^T\delta(\mathbf{r}-\mathbf{r}_T)$, the function Φ_T is given by[5]

$$\Phi_T(k_x)=i\frac{k_S^2-2k_x^2}{\mu((k_S^2-2k_x^2)^2+4k_x^2k_zk_{S,z})}, \tag{5}$$

where μ is the shear Lame elastic constant, k_S is the wavenumber of the shear wave, and $k_{S,z}=\sqrt{k_S^2-k_x^2}$. In this case formula (4) for the directivity function agrees with the result obtained by Miller and Pursey.[6]

The wave field from any transmitter element propagates into the material and interacts with the scatterers. Each scatterer acts as a secondary source and generates a scattered wave field. This secondary source can be modeled by a distribution of bulk forces, which are applied in the area occupied by the scatterer.

It is assumed that the scatterer is located in the half-space $z\geq z_{\min}>0$ and occupies the vicinity of the point $\mathbf{r}_0=\{x_0,z_0\}^T$. Let the wave incident on a scatterer be a plane wave $\exp(-i\mathbf{k}_{(T)}(\mathbf{r}-\mathbf{r}_0))$. The response of the scatterer is described by the force distribution $f(\mathbf{k}_{(T)},\mathbf{r}-\mathbf{r}_0)$. Then the scattered wave field is given by the convolution of Green's function with the function f. Using the integral representation of Green's function,[7] the scattered wave field in the region $z\leq z_{\min}$ can be written as

$$\phi_{\rm sc}(k_{x(T)},\mathbf{r})=\frac{1}{2\pi}\int k_{z(R)}^{-1}\Phi_{\rm sc}(k_{x(T)},k_{x(R)})e^{-i\mathbf{k}_{(R)}\cdot(\mathbf{r}-\mathbf{r}_0)}dk_{x(R)}, \tag{6}$$

where $\mathbf{k}_{(R)}=\{k_{x(R)},-k_{z(R)}\}^T$ is the wave vector, $k_{z(R)}=\sqrt{k^2-k_{x(R)}^2}$, and the function $\Phi_{\rm sc}(k_{x(T)},k_{x(R)})$ is given by

$$\Phi_{\rm sc}(k_{x(T)},k_{x(R)})=-\frac{i}{2}\int f(\mathbf{k}_{(T)},\mathbf{r}')e^{i\mathbf{k}_{(R)}\cdot\mathbf{r}'}d\mathbf{r}'. \tag{7}$$

The scattered wave propagates back and is detected by the transducer element located at the point $\mathbf{r}_{(R)}=\{x_R,0\}$. The action of the transducer as a receiver can be defined using the electromechanical reciprocity argument of Auld.[7–9] Therefore, the signal $g(\omega,x_T,x_R)$ measured by the receiver element at $\mathbf{r}_{(R)}$ when the element at $\mathbf{r}_{(T)}$ is the transmitter can be written in the form

$$g(\omega,x_T,x_R)=\frac{i\omega}{4P}\int_C(\mathbf{t}_{1n}\cdot\mathbf{u}_2-\mathbf{t}_{2n}\cdot\mathbf{u}_1)dS, \tag{8}$$

where C is an arbitrary contour enclosing the scatterer, $\mathbf{u}$ is the displacement vector, $\mathbf{t}_n$ is the normal stress on the contour C, and P is some quantity, which is proportional to the squared amplitude of the electrical signal in the transmitter.[9] Index 1 refers to the wave field generated by the transmitter element when the scatterer is present and index 2 refers to the wave field generated by the receiver element when the scatterer is absent. For the geometry considered it is convenient to choose the contour C, as shown in Fig. 2. In this case the integral along the semicircle C_R vanishes as $R\to\infty$, and the measured signal can be written as

$$g(\omega,x_T,x_R)=\frac{1}{4\pi^2}\int\int G(\omega,k_{x(T)},k_{x(R)})\times e^{-i(k_{x(T)}x_T+k_{x(R)}x_R)}dk_{x(T)}dk_{x(R)}, \tag{9}$$

or alternatively in the $(k_{x(T)},k_{x(R)})$ domain as

$$G(\omega,k_{x(T)},k_{x(R)})=k^4\Phi_0(\omega)\Phi_T(-k_{x(T)})\times\Phi_{\rm sc}(-k_{x(T)},k_{x(R)})\Phi_T(-k_{x(R)})\times e^{i(k_{x(T)}+k_{x(R)})x_0}e^{-i(k_{z(T)}+k_{z(R)})z_0}, \tag{10}$$

where $\Phi_0(\omega)=-i\rho v^3U_0(\omega)/(2P)$, ρ is the material density, v is the longitudinal wave speed, and $U_0(\omega)$ is the frequency spectrum of the transmitted signal.

III. PROCESSING METHODS

Any method of processing array data can be considered as an operator that transforms the transmit-receive array data set $g(t,x_T,x_R)$ into a new data set $I(x,z)$ usually called an image.

Note that recently non-linear imaging methods with regard to the data such as the decomposition of the time reversal operator (DORT),[10] MUSIC,[11,12] and linear sampling method[13] have been developed. The DORT and MUSIC are eigenvalue approaches and the linear sampling method provides a solution to the inverse problem of reconstructing the shape of a scatterer from knowledge of the far-field reflection pattern. They are not considered in this paper. Here, three different imaging algorithms corresponding to a linear operator are investigated.

A. Wavenumber method

Formula (7) for the reflected wave field represents the superposition of responses from point sources distributed within the scatterer with amplitudes $f(\mathbf{k}_{(T)},\mathbf{r})$. If the effect of the scatterers on the incident wave field is small then the Born approximation can be applied. This means that the amplitude of each point source is proportional to the amplitude of the incident wave at the location of that point. If in addition each point scatterer is omnidirectional with respect to the incident wave, then the function f can be written as

$$f(\mathbf{k}_{(T)},\mathbf{r}) = c_1(\omega) f_1(\mathbf{r}+\mathbf{r}_0) e^{-i\mathbf{k}_{(T)}\cdot\mathbf{r}}, \tag{11}$$

where $c_1(\omega)$ is the constant of proportionality, the point $\mathbf{r}_0$ is the nominal center of the scatterer, and the function $f_1(\mathbf{r})$ is the object function of a scatterer, which describes the scatterer distribution. So, in this case, the imaging can be considered as an inverse problem of reconstructing the object function $f_1(\mathbf{r})$ from the array data.

Substituting expression (11) into formula (7) and evaluating the spatial integral yield the following expression:

$$\Phi_{\mathrm{sc}}(k_{x(T)},k_{x(R)}) = c_2 F_1(\mathbf{k}_{(R)}-\mathbf{k}_{(T)}) e^{i(\mathbf{k}_{(T)}-\mathbf{k}_{(R)})\cdot\mathbf{r}_0}, \tag{12}$$

where $c_2=-ic_1(\omega)/2$ and F_1 is the 2D spatial Fourier transform of the function f_1.

For further calculations it is assumed that the constant c_2 is equal to unity. Expression (10) for the measured signal also contains the characteristics of the transmitted signal Φ_0 and the beampattern of the transducer element Φ_T. However, these effects can be compensated for in a pre-processing step, as shown in Ref. 4. Therefore, below it is assumed that the function $\Phi_0=1$ and the array elements are omnidirectional. If the directivity function of transducer is equal to unity, then from Eq. (4) it follows that the transducer angular spectrum $\Phi_T(k_{x(T)})=2\pi e^{i\pi/4}(kk_{z(T)})^{-1}$. Using formulas (12) and (10) the Fourier domain array data $G(\omega,k_{x(T)},k_{x(R)})$ can now be written as

$$G(\omega,k_{x(T)},k_{x(R)}) = 4\pi^2 ik^2 \frac{F_1(k_x,-k_z)}{k_{z(T)}k_{z(R)}}, \tag{13}$$

where $k_x=k_{x(T)}+k_{x(R)}, k_z=k_{z(T)}+k_{z(R)}$.

Relationship (13) between the array data and the object function agrees with the results that have been obtained earlier for a 2D medium[4] and a 3D medium.[14] From Eq. (13) it can be seen that there is significant redundancy in the array data. Indeed, the object function can be fully reconstructed by using only diagonal data, $k_{x(T)}=k_{x(R)}=k_x/2$, in the Fourier $(\omega,k_{x(T)},k_{x(R)})$ domain and applying the 2D inverse Fourier transform with respect to the variables k_x and k_z to the function $-ik_z^2 G(\omega,k_x/2,k_x/2)/(16\pi^2k^2)$ as follows:

$$f_1(x,z) = \frac{-i}{(8\pi^2)^2}\int\int G\left(\omega,\frac{k_x}{2},\frac{k_x}{2}\right)\frac{k_z^2}{k^2}e^{-i(k_x x-k_z z)}dk_x dk_z. \tag{14}$$

However, it should be stressed that this data redundancy is caused by the approximate model of scatterer (11) only. In this case each point (k_x,k_z) corresponds to some curve $l(k_x,k_z)$ in the $(\omega,k_{x(T)},k_{x(R)})$ domain. In practice the effect of noise and side lobes can be reduced by additional averaging of the array data over the curve l. If the variable $k_{x(T)}$ is chosen as a parameter of the curve l then the resulting image can be written in the form[4]

$$I(x,z) = \frac{-i}{(4\pi^2)^2}\int\int\int G(\omega,k_{x(T)},k_{x(R)})\frac{k_{z(T)}k_{z(R)}}{k^2} \times N(k_{x(T)},k_x,k_z)e^{-i(k_x x-k_z z)}dk_{x(T)}dk_x dk_z, \tag{15}$$

where $N=N_0(k_x,k_z)dl/dk_{x(T)}$. The coefficient N_0 is the normalization factor and can be taken in the form $N_0=\lim_{L\to+\infty}\int_{-L}^{L}dl_0(\int_{-L}^{L}dl)^{-1}$, where l_0 is the reference curve corresponding to some point (k_{x0},k_{z0}). Note, that formula (14) can be obtained from Eq. (15) by taking $N=\delta(k_{x(T)}-k_{x(R)})$.

B. Total focusing method

The wavenumber imaging method is based on approximate model (11) of the scatterer. This model can be justified for the scattering from an elastic inclusion with properties that only slightly differ from the host material and which is located in the far-field of the array.[7,14] However, approximation (11) is quite restrictive and is not valid, for example, in the case of a cracklike defect. Therefore, if the distribution of the scatterers is described by a general function $\mathbf{f}(\mathbf{k}_T,\mathbf{r})$ then a different imaging procedure is needed. One of the possible ways to construct an image is by back-propagation of the detected wave field, and this is the basis of the TFM (Ref. 2) and the back-propagation method.

In the TFM the back-propagation is the mapping of the signal $g(t)$ to a function of propagation distance r by the relationship $r=vt$. For the transmit-receive signal $g(t,x_T,x_R)$ the propagation distance is equal to the sum of the distances between the transmitter and receive positions and the imaging point R_T+R_R. Then as an approximation to the back-propagation image the sum of the individually back-propagated transmit-receive signals can be taken as

$$I(x,z) = \int\int g\left(\frac{R_T+R_R}{v},x_T,x_R\right)dx_T dx_R. \tag{16}$$

C. Back-propagation method

An alternative to the TFM is to back-propagate the angular spectrum. From expressions (9) and (10) for the array data it is seen that the angular spectrum $E(\omega,k_{x(T)},k_{x(R)},z)$ of the transmit-receive array data at the depth z is given by

$$E(\omega,k_{x(T)},k_{x(R)},z)=G(\omega,k_{x(T)},k_{x(R)})e^{ik_z z}, \tag{17}$$

where $G(\omega,k_{x(T)},k_{x(R)})$ is the angular spectrum at $z=0$. Note that because $k_z=k_{z(T)}+k_{z(R)}$ this equation can be considered as two consecutive back-propagations in transmission and reception. Then the time-domain signal $e(t,x_T,x_R,z)$ measured by the receiver element located at $\{x_R,z\}$ when the transmitter element located at $\{x_T,z\}$ is activated can be written as

$$e(t,x_T,x_R,z)=\frac{1}{8\pi^3}\int\int\int E(\omega,k_{x(T)},k_{x(R)},z) \times e^{i(\omega t-k_{x(T)}x_T-k_{x(R)}x_R)}dk_{x(T)}dk_{x(R)}d\omega. \tag{18}$$

In order to estimate the location of the scatterers the back-propagated array data corresponding to $x_T=x_R$ are considered. At the moment of time t the signal $e(t,x,x,z)$ is localized in the vicinity of the points (x,z) such that the time required for the wave propagation from the point (x,z) to the scatterer location and back is equal to t. Therefore, at the moment of time $t=0$, the data $e(t,x,x,z)$ are nonzero only in the vicinity of the areas occupied by the scatterers, and to form an image $I(x,z)$ the function $e(0,x,x,z)$ can be taken. From formula (18) it follows that

$$I(x,z)=\frac{1}{8\pi^3}\int\int\int G(\omega,k_{x(T)},k_{x(R)}) \times e^{-i(k_x x-k_z z)}dk_{x(T)}dk_{x(R)}d\omega. \tag{19}$$

IV. THEORETICAL COMPARISON OF IMAGING METHODS

In Sec. III the wavenumber, the TFM, and the back-propagation imaging methods for the processing of the full matrix of transmit-receive array data have been described. These methods are conceptually different, use different approximations, and have different expressions for the image construction. However, in order to compare the image quality provided by the different imaging techniques, it is instructive to express them in a similar form.

If the imaging operator is linear then the relationship between image and array data for an ideal array with continuous element locations can be written in the form

$$L[g(t,\mathbf{r}_{(T)},\mathbf{r}_{(R)})]=\frac{1}{2\pi}\int\int\int s(\omega,x_T,x_R,x,z) \times g(\omega,x_T,x_R)d\omega dx_T dx_R, \tag{20}$$

where the function s represents focusing coefficients. Therefore, different linear processing methods can be compared in terms of the focusing coefficients s. In this section the equivalent coefficients for each processing algorithm are derived.

Using the change in variables $(k_x,k_z)\rightarrow(k_{x(R)},\omega)$ integral (15) for the wavenumber method can be rewritten in the form of Eq. (20) in (x_T,x_R,ω) variables with the following focusing coefficients s_{wn}:

$$s_{wn}=\frac{-i}{8\pi^3\omega}\int\int k_z N(\omega,k_{x(T)},k_{x(R)}) \times e^{i(k_{x(T)}(x_T-x)+k_{x(R)}(x_R-x))}e^{ik_z z}dk_{x(T)}dk_{x(R)}. \tag{21}$$

Using representation (1) of the time-domain signal, Eq. (16) for the TFM can be expressed in form (22) with the focusing coefficients s_{tfm} as follows:

$$s_{tfm}(\omega,x_T,x_R,x,z)=e^{ik(R_T+R_R)}. \tag{22}$$

For the back-propagation method the corresponding focusing coefficients s_{bp} are given by

$$s_{bp}(\omega,x_T,x_R,x,z)=\frac{1}{4\pi^2}\int e^{ik_{x(T)}(x_T-x)}e^{ik_{z(T)}z}dk_{x(T)} \times\int e^{ik_{x(R)}(x_R-x)}e^{ik_{z(R)}z}dk_{x(R)}. \tag{23}$$

Note that the integrals in this formula can be evaluated explicitly as

$$s_{bp}=\frac{\partial}{\partial z}E(kR_T)\frac{\partial}{\partial z}E(kR_R), \tag{24}$$

where the function E is given by $E=iH_0^{(1)}(kr)/2$ in 2D case and $E=\exp(ikr)/(2\pi r)$ in 3D case.

In practical testing ultrasonic arrays are operated at frequencies of several megahertz, which correspond to wavelengths of order 1 mm. The typical array element size is about 0.5 mm and the inspection area is usually situated at the distance of several centimeters from the array. Therefore, the array elements can be considered as point sources and the inspection area is in the far-field of the individual array elements. In this case the far-field approximation for focusing coefficients (21) and (24) can be taken as

$$s_{wn,bp}=-c\frac{k}{2\pi}f_{wn,bp}s_{tfm}, \tag{25}$$

where s_{tfm} is the phase-addition term given by formula (22), and the functions f_{wn} and f_{bp} are given by

$$f_{wn}=\frac{\cos\varphi_T\cos\varphi_R(\cos\varphi_T+\cos\varphi_R)}{2\pi v(R_T R_R)^n}, \tag{26}$$

$$f_{bp}=i\frac{\cos\varphi_T\cos\varphi_R}{(R_T R_R)^n}. \tag{27}$$

In these expressions the parameters $c=1$, $n=1/2$ in the 2D case and $c=-ik/(2\pi)$, $n=1$ in the 3D case; v is the wave speed. Note that in formula (26) for the wavenumber method it is assumed that $N=1$. In principle, the coefficient N as a function of frequency ω and the angles φ_T and φ_R can be computed numerically. However, this provides just a marginal improvement in the image quality and can be omitted.

For the wavenumber method without averaging the image is given by formula (14), and the corresponding focusing coefficients can be written as

$$s = c\frac{k}{8\pi^2 v}\frac{z^2}{R^n}e^{ikR}, \quad R = \sqrt{\left(\frac{x_T + x_R}{2} - x\right)^2 + z^2}, \tag{28}$$

where $c = -\exp(i\pi/4)(2\pi)^{-1/2}$, $n = 1/2$ in 2D case and $c = 1$, $n = 1$ in 3D case.

Note that in the 2D case the imaging method based on expression (20) with the far-field approximation to the back-propagation focusing coefficients (25) and (27) has been recently considered and called the inverse wave field extrapolation (IWEX) method.[3]

Expression (25) shows that apart from the scale factors the wavenumber algorithm and back-propagation method differ from the TFM only by the weighting coefficients f_{wn} and f_{bp}. These functions depend only on transmitter and receiver positions and the imaging point and can be considered as a frequency independent spatial filter. Because of this filter the wavenumber and the back-propagation methods generally provide lower side lobes in the image than the TFM. However, as will be demonstrated in Sec. VII, the actual improvement in the signal to coherent noise ratio given by the wavenumber and back-propagation methods relative to the TFM depends on the position of the scatterer relative to the array and its scattering behavior.

V. COMPUTATIONAL ANALYSIS

In practice an important property of an imaging algorithm is its computational efficiency. In this section the numerical implementation of the different imaging techniques and their computational performance are discussed.

As has been shown in Sec. IV, different imaging algorithms can be expressed in the form of a linear superposition of transmit-receive signals in the frequency domain with some focusing coefficients. Formula (20) leads to the TFM type implementation of the imaging methods and is ideally suited for parallel processing. Additionally, TFM type processing (20) can be performed while data acquisition is still in progress.

On the other hand, the wavenumber method operates in the Fourier domain, which naturally leads to its implementation using the fast Fourier transform algorithm.[4] This makes the wavenumber method in general computationally more efficient than the TFM. As has been shown in Ref. 4 for large data sets the computational cost of the wavenumber method is N times less than the computational cost of the TFM, where N is the number of array elements.

It can be shown that the back-propagation method can also be implemented in the Fourier domain. The back-propagation image given by expression (19) can be written in operator form as

$$I(x,z) = b(z,x,x), \tag{29}$$

where the function b is given by

$$b(z,x_T,x_R) = B[g(t,x_T,x_R)], \quad B = F^{-1}_{k_{x(T)}k_{x(R)}} H F_{x_T x_R}. \tag{30}$$

Here B is the back-propagation operator, symbols F and F^{-1} denote direct and inverse Fourier transforms, and H is the back-propagation of angular spectrum operator, which in the temporal frequency domain is defined by expression (17).

The Fourier operator $F_{x_T x_R}$ transfers the array time-domain data $g(t,x_T,x_R)$ into the angular spectrum $G(t,k_{x(T)},k_{x(R)})$. The back-propagation of angular spectrum operator H converts the time data $G(t,k_{x(T)},k_{x(R)})$ into a function of propagation distance $h(z,k_{x(T)},k_{x(R)})$, and can be written in the form

$$h(z,k_{x(T)},k_{x(R)}) \equiv H[G(t,k_{x(T)},k_{x(R)})] = \frac{1}{2\pi}\int G(\omega,k_{x(T)},k_{x(R)})e^{ik_z z}d\omega. \tag{31}$$

Expression (10) shows that each time trace $G(t,k_{x(T)},k_{x(R)})$ represents a one-dimensional (1D) wave propagating in the z direction with the wavenumber $k_z = k_{z(T)} + k_{z(R)}$. If $k_{x(T)} \neq 0$ or $k_{x(R)} \neq 0$ this wave is dispersive and the back-propagation of angular spectrum (31) is equivalent to the dispersion compensation method.[15] Note that the wavenumber k_z non-linearly depends on the frequency ω, and direct calculation using formula (31) is very time consuming. However, if the integration variable is changed from ω to k_z, then integral (31) can be written in the form of a Fourier transform as[15]

$$h(z,k_{x(T)},k_{x(R)}) = \frac{1}{2\pi}\int G(\omega(k_z),k_{x(T)},k_{x(R)})v_z e^{ik_z z}dk_z, \tag{32}$$

where $v_z = (dk_z/d\omega)^{-1}$ is the group velocity.

Therefore, the back-propagation operator B can be represented as a series of Fourier transforms and has the same advantages in terms of computational performance as the wavenumber algorithm. However, the Fourier domain implementation requires simultaneous processing of the full matrix of array data, which results in a heavy memory load compared with the TFM. Moreover, if a scatterer is located outside the array aperture, then additional coherent noise appears in the image because of the aliasing effect. To avoid this the original array aperture data must be padded with zeros in order to perform its Fourier transform with more x_T, x_R-positions. Consequently, the number of sampling points in the Fourier domain is generally greater than the number of array elements.

Consider first 2D imaging using 1D array. In practical testing the total number of sampling points in the x-domain (i.e., the number of array elements and the number of padded zeros) is typically of order of $N \cong 10^2$. Therefore, the number of sampling points in the Fourier $(k_{x(T)},k_{x(R)})$ domain is $N^2 \cong 10^4$. Consider now 3D imaging using 2D array. It is assumed that the array is located in the (x,y)-plane. To cover the imaging area of the same aperture as for the 1D array the number of sampling points in the (x,y)-domain is N^2 and the number of sampling points in the four-dimensional (4D) Fourier $(k_{x(T)},k_{y(T)},k_{x(R)},k_{y(R)})$ domain is $N^4 \cong 10^8$. There-

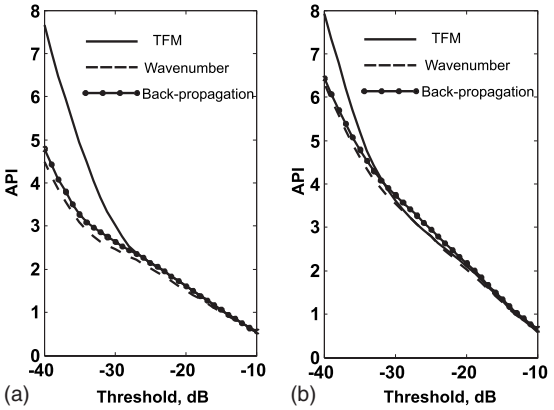

FIG. 3. Dependence of the array performance indicator on the threshold level for the point scatterers with x-coordinates corresponding to the (a) center of the array and (b) end of the array.

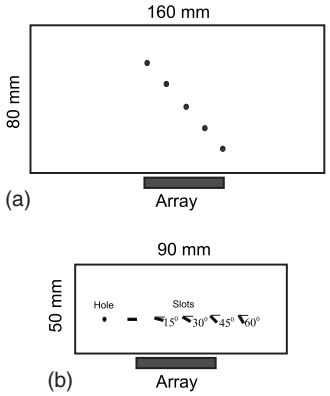

FIG. 4. Schematics of experimental samples. (a) Sample 1 with five side-drilled holes of 1 mm diameter, and (b) sample 2 with 1-mm-diameter hole and five through-thickness slots of 1 mm length at various orientations.

fore, for 2D arrays, the computer memory requirements make the Fourier domain implementation of the imaging algorithms impractical. In this case the TFM type implementation based on expression (20) with the equivalent focusing coefficients is preferable.

VI. MODELING EXAMPLES

In this section the performances of the wavenumber, TFM, and back-propagation imaging algorithms are compared in terms of their image resolution. The image resolution can be quantified by the array performance indicator[2] (API), which is defined in two dimensions as

$$P = \frac{A}{\lambda^2}, \tag{33}$$

where A is the area over which the amplitude of the point-spread function (i.e., the image of an omnidirectional point scatterer) is greater than some threshold below its maximum value, and λ is the wavelength at the center frequency. Therefore, the function P depends on the imaging point and the threshold value.

The specifications of a commercial 64-element array (manufactured by Imasonic, Besançon, France) were used for the modeling. The array has an element pitch of $\Delta x = 0.63$ mm and a total length of $L = 40$ mm. The simulated specimen was mild steel with a longitudinal wave velocity of 5900 m/s. The directivity function of the array elements was modeled using formulas (4) and (5). The transmitted signal was a Hanning windowed toneburst with a center frequency of 5 MHz.

The API maps corresponding to a -20 dB threshold for the TFM and the wavenumber algorithm were calculated in Ref. 4. It has been shown[4] that the wavenumber algorithm provides a marginally better point-spread function than the TFM. In this paper the API as a function of the threshold value is investigated.

Figure 3 shows the dependence of the API for different imaging algorithms on the threshold value for two different point omnidirectional scatterers located at the same depth $z = 20$ mm from the array. The x-coordinate was taken equal to the center of the array ($x_0 = 0$) for the first scatterer and the end of the array ($x_0 = L/2$) for the second scatterer. It is seen that the wavenumber algorithm and back-propagation method have approximately the same API for all threshold values. Moreover, all three imaging methods provide very similar resolution for threshold values greater than -26 dB for the first scatterer and for threshold values greater than -32 dB for the second scatterer. For lower thresholds the API corresponding to the TFM increases much faster than APIs for the wavenumber and back-propagation methods. For example, at -40 dB threshold, the resolution of the wavenumber and back-propagation methods is about 1.7 times better than the resolution of TFM for the scatterer in the middle of the array and about 1.2 times better for the scatterer at the end of the array. Note that in both cases the wavenumber algorithm has slightly better resolution. This is expected since the scatterers are omnidirectional and this assumption is implied in the wavenumber algorithm.

VII. EXPERIMENTAL EXAMPLES

In order to illustrate the performance of different imaging methods two experiments were set up. The 64-element Imasonic array with 5-MHz center frequency described above was used for imaging in all the experiments.

The first experiment was performed on a mild steel block with dimensions $160 \times 80 \times 20$ mm^3. The velocity of the bulk longitudinal wave is approximately 5900 m/s, so the element pitch is $0.53\lambda_0$, where $\lambda_0 = 1.18$ mm is the wavelength at the center frequency. Five circular holes with 1 mm diameter were drilled through the side of the specimen, as schematically illustrated in Fig. 4(a).

The TFM image is shown in Fig. 5(a), and the image obtained by the back-propagation method is shown in Fig. 5(b). The images obtained by the wavenumber algorithm have approximately the same signal-to-noise ratio and resolution as the back-propagation images and, therefore, are not shown. Note that all processing was performed using positive frequencies only and then the absolute value of the image function was taken. This is equivalent to the extraction of the envelope of the image.

For this example the Nyquist frequency is about 10 MHz and the element pitch is equal to the half wavelength at the center frequency of 5 MHz. Therefore, at frequencies greater

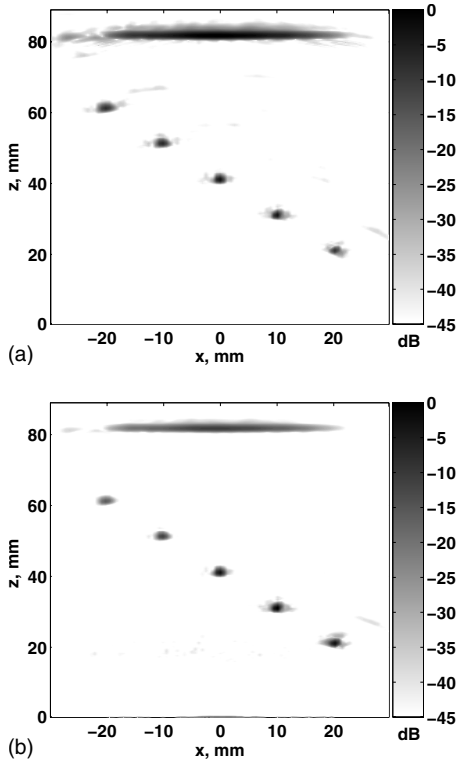

FIG. 5. Results from sample 1 processed with (a) TFM and (b) back-propagation method.

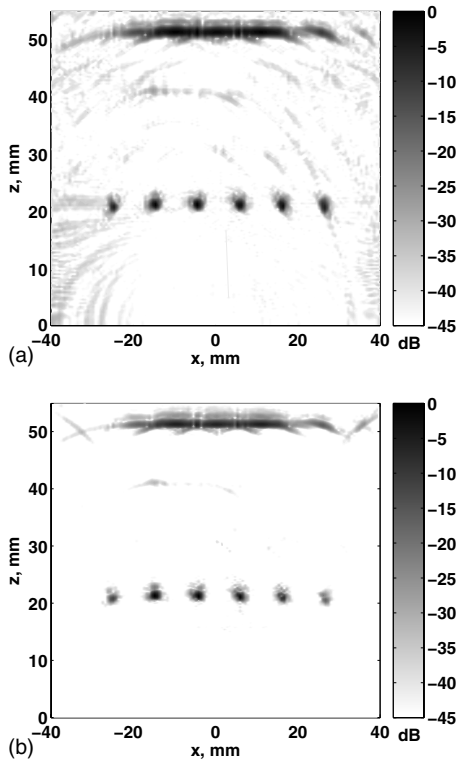

FIG. 6. Results from sample 2 processed with (a) TFM and (b) back-propagation method.

than the center frequency, the Nyquist criterion is not satisfied and grating lobes should appear in the image. However, it can be seen that all methods give similar signal-to-noise ratio of about 45 dB, which can be explained by the scattering behavior of the scatterers. In this case the scattered energy is contained mainly in the non-wrapped part of the wavenumber spectra and, hence, the amplitude of the grating lobes is below −45 dB for all imaging methods. Therefore, in this situation, the wavenumber and back-propagation methods have no improvement over the TFM in terms of the signal-to-noise ratio. However, as has been predicted, there is some improvement in the resolution. For example, the −40 dB API of the scatterer located in the middle of the array is 8.5 for the TFM and 7 and 6.5 for the asymptotic back-propagation and asymptotic wavenumber methods, respectively.

The second experiment was performed on an aluminum block with dimensions $90\times50\times20$ mm^3. The velocity of the bulk longitudinal wave is approximately 6400 m/s, so the element pitch is half of the wavelength at the center frequency. Six reflectors were machined into sample, as schematically shown in Fig. 4(b). The first reflector is a 1-mm-diameter through-thickness hole and the other reflectors are through-thickness slots at various orientations. A detailed description of the experimental setup and parameters of the reflectors can be found in Ref. 16.

The results of processing the data using the TFM and the back-propagation method are shown in Fig. 6. It is seen that the back-propagation method provides a signal-to-noise ratio of about 45 dB. However, for this configuration of the array and scatterers, grating lobes appear in the TFM image at about −35 dB. Therefore, in this case, the wavenumber and back-propagation methods could be regarded as an improvement over the TFM. The main effect here is given by the spatial filters f_{wn} and f_{bp} [formulas (26) and (27)] compared to the TFM coefficients that have equal amplitudes. Note that these filters also reduce the amplitude of the scatterers on the image located at large angles φ_T and φ_R. For example, the amplitudes of the first and the sixth scatterer on the back-propagation image are smaller than the amplitudes of the same scatterers on the TFM image.

VIII. CONCLUSION

A general mathematical model of the ultrasonic transmit-receive array data has been developed. Such a model provides a unified basis for the post-processing of array data in order to obtain an image. Different imaging algorithms have been expressed in the form of a linear superposition of transmit-receive signals in the frequency domain with some focusing coefficients. The equivalent coefficients for each processing algorithm have been derived and the difference between approaches has been discussed. In the general case the most appropriate imaging method is the back-propagation method, which is based on the back-propagation of the angular spectrum of transmit-receive signal. In a similar manner to the wavenumber algorithm,[4] the back-propagation method can be efficiently implemented using Fourier transforms, which provide superior computational performance. On the other hand, TFM type formula (20) is ideally suited for parallel processing. Also the Fourier domain implementation has a heavy computer memory load

compared with the TFM, which makes it impractical for 3D imaging with 2D arrays. In this case the TFM type implementation is more preferable.

[1]B. W. Drinkwater and P. D. Wilcox, "Ultrasonic arrays for non-destructive evaluation: A review," NDT & E Int. **39**, 525–541 (2006).

[2]C. Holmes, B. Drinkwater, and P. Wilcox, "Post-processing of the full matrix of ultrasonic transmit-receive array data for non-destructive evaluation," NDT & E Int. **38**, 701–711 (2005).

[3]N. Pörtzgen, D. Gisolf, and G. Blacquiére, "Inverse wave field extrapolation: A different NDI approach to imaging defects," IEEE Trans. Ultrason. Ferroelectr. Freq. Control **54**, 118–127 (2007).

[4]A. J. Hunter, B. W. Drinkwater, and P. D. Wilcox, "The wavenumber algorithm for full-matrix imaging using an ultrasonic array," IEEE Trans. Ultrason. Ferroelectr. Freq. Control **55**, 2450–2462 (2008).

[5]E. Glushkov, N. Glushkova, A. Ekhlakov, and E. Shapar, "An analytically based computer model for surface measurements in ultrasonic crack detection," Wave Motion **43**, 458–473 (2006).

[6]G. F. Miller and H. Pursey, "The field and radiation impedance of mechanical radiators on the free surface of a semi-infinite isotropic solid," Proc. R. Soc. London, Ser. A **223**, 521–541 (1954).

[7]L. W. Schmerr, *Fundamentals of Ultrasonic Nondestructive Evaluation* (Plenum, New York, 1998).

[8]A. Boström and H. Wirdelius, "Ultrasonic probe modeling and nondestructive crack detection," J. Acoust. Soc. Am. **97**, 2836–2848 (1995).

[9]B. A. Auld, "General electromechanical reciprocity relations applied to the calculation of elastic wave scattering coefficients," Wave Motion **1**, 3–10 (1979).

[10]E. Kerbrat, C. Prada, D. Cassereau, and M. Fink, "Ultrasonic nondestructive testing of scattering media using the decomposition of the time-reversal operator," IEEE Trans. Ultrason. Ferroelectr. Freq. Control **49**, 1103–1113 (2002).

[11]S. K. Lehman and A. J. Devaney, "Transmission mode time-reversal super-resolution imaging," J. Acoust. Soc. Am. **113**, 2742–2753 (2003).

[12]E. A. Marengo, F. K. Gruber, and F. Simonetti, "Time-reversal music imaging of extended targets," IEEE Trans. Image Process. **16**, 1967–1984 (2007).

[13]D. Colton, J. Coyle, and P. Monk, "Recent developments in inverse acoustic scattering theory," SIAM Rev. **42**, 369–414 (2000).

[14]R. Y. Chiao and L. J. Thomas, "Analytic evaluation of sampled aperture ultrasonic imaging techniques for NDE," IEEE Trans. Ultrason. Ferroelectr. Freq. Control **41**, 484–493 (1994).

[15]P. D. Wilcox, "A rapid signal processing technique to remove the effect of dispersion from guided wave signals," IEEE Trans. Ultrason. Ferroelectr. Freq. Control **50**, 419–427 (2003).

[16]P. D. Wilcox, C. Holmes, and B. W. Drinkwater, "Advanced reflector characterization with ultrasonic phased arrays in NDE applications," IEEE Trans. Ultrason. Ferroelectr. Freq. Control **54**, 1541–1550 (2007).

Physically constrained maximum likelihood mode filtering

Joseph C. Papp,[a] James C. Preisig, and Andrey K. Morozov
Woods Hole Oceanographic Institution, MS 44, Woods Hole, Massachusetts 02543

(Received 28 September 2009; revised 24 January 2010; accepted 27 January 2010)

Mode filtering is most commonly implemented using the sampled mode shapes or pseudoinverse algorithms. Buck *et al.* [J. Acoust. Soc. Am. **103**, 1813–1824 (1998)] placed these techniques in the context of a broader maximum *a posteriori* (MAP) framework. However, the MAP algorithm requires that the signal and noise statistics be known *a priori*. Adaptive array processing algorithms are candidates for improving performance without the need for *a priori* signal and noise statistics. A variant of the physically constrained, maximum likelihood (PCML) algorithm [A. L. Kraay and A. B. Baggeroer, IEEE Trans. Signal Process. **55**, 4048–4063 (2007)] is developed for mode filtering that achieves the same performance as the MAP mode filter yet does not need *a priori* knowledge of the signal and noise statistics. The central innovation of this adaptive mode filter is that the received signal's sample covariance matrix, as estimated by the algorithm, is constrained to be that which can be physically realized given a modal propagation model and an appropriate noise model. Shallow water simulation results are presented showing the benefit of using the PCML method in adaptive mode filtering. © *2010 Acoustical Society of America.*
[DOI: 10.1121/1.3327799]

PACS number(s): 43.60.Mn [EJS] Pages: 2385–2391

I. INTRODUCTION

Buck *et al.*[1] presented a unified framework for mode filtering using a model of the underwater environment containing propagating modes plus noise. Nonadaptive linear mode filters such as the sampled mode shapes and pseudoinverse filters were analyzed and the MAP filter was presented to make use of signal and noise statistics and showed a significant performance improvement. However, the statistics are required to be known *a priori*. This paper proposes an adaptive mode filter based on the minimum power distortionless response (MPDR) beamformer that uses pressure field statistics estimated from the data. However, in a nonstationary environment there are often an insufficient number of snapshots available to accurately estimate the required statistics. Kraay[2] presented a physically constrained, maximum likelihood (PCML) method for using knowledge of the spatial environment to estimate the statistics using fewer snapshots. This paper adapts the PCML method to the underwater mode estimation problem using adaptive mode filters based on the MPDR and MAP frameworks.

The remaining sections of the introduction introduce the signal and noise model used in this paper and describe several established mode filtering techniques—the sampled mode shapes, pseudoinverse, diagonally weighted pseudoinverse, reduced rank pseudoinverse, and maximum *a posteriori* (MAP) mode filters. Section II describes the MPDR mode filter and a diagonal weighting technique to address the snapshot deficiency problem. Section III outlines the PCML algorithm developed by Kraay for a spatial beamformer. Section IV describes the adaptation of the PCML algorithm for the mode estimation problem. Lastly, Sec. V presents the performance of the various mode filters in a shallow water simulation and Sec. VI summarizes the main conclusions of this paper.

A. Modes as basis functions

Modes are physically motivated, orthogonal basis functions for the vertical sound field. They are derived from solutions to the wave equation and are dependent on frequency and environmental conditions, such as water depth, temperature, salinity, and bottom properties.[3] Equation (1) shows the pressure field as a sum of modes, where $\mathbf{p}(z,f)$ is the complex acoustic pressure at frequency f and depth z, d_m is the mode coefficient of the m^{th} mode, and $\boldsymbol{\psi}_m(z,f)$ is the mth mode shape as a function of depth and frequency,

$$p(z,f) = \sum_m d_m(f)\psi_m(z,f). \tag{1}$$

B. Signal and noise model used

Equation (2) shows the signal model used to represent the sound pressure field,

$$\begin{bmatrix} p(z_1) \\ \vdots \\ p(z_N) \end{bmatrix} = \begin{bmatrix} \psi_1(z_1) & \cdots & \psi_M(z_1) \\ \vdots & \ddots & \vdots \\ \psi_1(z_N) & \cdots & \psi_M(z_N) \end{bmatrix} \begin{bmatrix} d_1 \\ \vdots \\ d_M \end{bmatrix} + \begin{bmatrix} n(z_1) \\ \vdots \\ n(z_N) \end{bmatrix}, \tag{2}$$

where $n(z)$ is the noise received by the sensor at depth z. The functional dependence of all quantities on frequency has been dropped for notational convenience. In this paper, the mode shapes, $\boldsymbol{\psi}$, are assumed known *a priori* and the goal is to estimate the complex mode coefficients d given measurements of the pressure field $\mathbf{p}$. Written in vector notation, the above equation becomes

[a]Author to whom correspondence should be addressed. Electronic mail: jcpapp@mit.edu

$$\mathbf{p} = \boldsymbol{\psi}\mathbf{d} + \mathbf{n}, \tag{3}$$

where $\boldsymbol{\psi}$ is the matrix of sampled mode shapes at a particular frequency

$$\boldsymbol{\psi} = \begin{bmatrix} \psi_1(z_1) & \cdots & \psi_M(z_1) \\ \vdots & \ddots & \vdots \\ \psi_1(z_N) & \cdots & \psi_M(z_N) \end{bmatrix}, \tag{4}$$

and $\mathbf{d}$ is a vector of complex-valued mode amplitudes and is assumed to be zero mean. A spatially white (SW) noise model is used in this paper. The SW noise model assumes the noise is complex valued and zero mean, with the noise at each hydrophone uncorrelated with noise at all of the other hydrophones. Assuming that the noise has save variance at each sensor, the covariance matrix for this type of noise is

$$\mathbf{R_n} = \sigma^2\mathbf{I}. \tag{5}$$

Often noise is contained in the propagating modes as well, and this type of noise is described by the Kuperman–Ingenito model.[4] The goal of mode filtering, however, is to simply estimate the coefficients of the received energy in each mode and not to distinguish between signal and noise contained in the modes. Determining what part of the mode amplitude is from signal and what part is from noise is an application specific problem. Therefore, only spatially white noise will be considered in this paper.

C. Established mode filtering techniques

This section outlines several established mode filtering techniques. Mode filters estimate the complex-valued amplitude of a particular mode at a particular frequency given the measured vertical pressure field and knowledge of the mode shapes. Further information about the mode filtering techniques can be found in Ref. 1. Equation (6) expresses the estimated mode amplitudes as a function of the vertical pressure field and a linear mode filter, $\mathbf{H}$.

$$\hat{\mathbf{d}} = \mathbf{H}\mathbf{p}. \tag{6}$$

The remaining part of this subsection lists several choices for $\mathbf{H}$ that can be used in estimating the mode amplitudes.

(a) Sampled mode shape (SMS) mode filter.

$$\mathbf{H}_{\mathrm{SMS}} = \begin{bmatrix} \psi_1(z_1) & \cdots & \psi_1(z_N) \\ \vdots & \ddots & \vdots \\ \psi_M(z_1) & \cdots & \psi_M(z_N) \end{bmatrix} = \boldsymbol{\psi}^H. \tag{7}$$

(b) Pseudoinverse (PI) mode filter.

$$\mathbf{H}_{PI} = (\boldsymbol{\psi}^H\boldsymbol{\psi})^{-1}\boldsymbol{\psi}^H. \tag{8}$$

(c) Diagonal weighting on pseudoinverse mode filter.

$$\mathbf{H}_{\mathrm{DW}} = (\boldsymbol{\psi}^H\boldsymbol{\psi} + \beta\mathbf{I})^{-1}\boldsymbol{\psi}^H, \tag{9}$$

where β is real valued and greater than zero.

(d) Reduced rank pseudoinverse mode filter. Let the singular value decomposition of $\boldsymbol{\psi}$ be

$$\boldsymbol{\psi} = \mathbf{U}\mathbf{S}\mathbf{V}^T, \tag{10}$$

where $\mathbf{S}$ is a diagonal matrix consisting of the singular values of $\boldsymbol{\psi}$, and $\mathbf{U}$ and $\mathbf{V}$ are orthogonal matrices representing the eigenvectors of $\boldsymbol{\psi}\boldsymbol{\psi}^T$ and $\boldsymbol{\psi}^T\boldsymbol{\psi}$, respectively. The reduced rank pseudoinverse mode filter can be written as

$$\mathbf{H}_{RR} = \boldsymbol{\psi}^+ = \mathbf{V}\mathbf{S}^+\mathbf{U}^T, \tag{11}$$

where $\mathbf{S}^+$ is the pseudoinverse of the diagonal matrix $\mathbf{S}$, where the inverses of diagonal elements less than some threshold (1/100 of the maximum diagonal value for this paper) are set to zero.[5]

(e) MAP mode filter.

$$\mathbf{H}_{\mathrm{MAP}} = (\mathbf{R_d}^{-1} + \boldsymbol{\psi}^H\mathbf{R_n}^{-1}\boldsymbol{\psi})^{-1}\boldsymbol{\psi}^H\mathbf{R_n}^{-1}, \tag{12}$$

where $\mathbf{R_d}$ is the covariance matrix of the mode coefficients and $\mathbf{R_n}$ is the noise covariance matrix. This assumes that the mode amplitude coefficients and noise are jointly Gaussian random variables and that the mode amplitude coefficients are independent of the noise.

II. MINIMUM POWER DISTORTIONLESS RESPONSE MODE FILTER

The MPDR mode filter minimizes the filter output power subject to the constraint that the desired mode is passed with a gain equal to 1. It is based on the MPDR beamformer used in spatial array processing, with a substitution of the mode shape vector in place of the spatial steering vector.[6–8] The goal is to minimize contributions from interfering signals and noise while preserving the signal propagating in the desired mode. Let the received vertical pressure field be $\mathbf{p}$ and the desired mode be n. $\mathbf{w}_n$ is the weight vector that filters for mode n, with the output of the mode filter being $\mathbf{w}_n^H\mathbf{p}$. The MPDR filter is defined by the following constrained optimization problem:

$$\begin{aligned} \mathbf{w}_n &= \arg\min_{\mathbf{w}_n} \mathrm{E}[|\mathbf{w}_n^H\mathbf{p}|^2] \\ &= \arg\min_{\mathbf{w}_n} \mathbf{w}_n^H\mathbf{R_p}\mathbf{w}_n \quad \text{such that} \quad \mathbf{w}_n^H\boldsymbol{\psi}_n = 1. \end{aligned} \tag{13}$$

The solution is given by[9,10]

$$\mathbf{w}_n = \frac{\mathbf{R_p}^{-1}\boldsymbol{\psi}_n}{\boldsymbol{\psi}_n^H\mathbf{R_p}^{-1}\boldsymbol{\psi}_n}, \tag{14}$$

where $\mathbf{R_p}$ is the covariance matrix of the vertical pressure field at a particular frequency. In practice, $\mathbf{R_p}$ is not known *a priori* and must be estimated from the received data. The sample covariance matrix is one option for estimating $\mathbf{R_p}$, but it requires a large number of snapshots to accurately estimate the matrix. The linear mode filter $\mathbf{H}$ that estimates all the modes together is formed by combining the weights for each mode:

$$\mathbf{H}_{\mathrm{MPDR}} = \begin{bmatrix} \mathbf{w}_1^H \\ \mathbf{w}_2^H \\ \vdots \\ \mathbf{w}_M^H \end{bmatrix}. \tag{15}$$

The sample covariance matrix, $\hat{\mathbf{R}}_{\mathrm{data}}$, defined as

$$\hat{\mathbf{R}}_{\mathrm{data}} = \frac{1}{L} \sum_{l=1,\ldots,L} \mathbf{X}_l(\omega)\mathbf{X}_l(\omega)^H \tag{16}$$

is often used as the estimate of $\mathbf{R}_{\mathbf{p}}$, where $\mathbf{X}_l(\omega)$ is the array snapshot vector at frequency ω.[6] This matrix is the unconstrained maximum likelihood estimate of the covariance matrix.[11] $\hat{\mathbf{R}}_{\mathrm{data}}$ is a good approximation of the true matrix only when a large number of snapshots are used. An inadequate number of snapshots results in poor adaptive algorithm performance.[6,12]

A diagonal weighting technique may be used on the sample covariance matrix to compensate for an inadequate number of snapshots and improve filter performance, similar to the diagonally weighted PI filter.[6,13] When the weighting factor, β, increases by a large amount, $\hat{\mathbf{R}}_{\mathrm{DW}}$ becomes proportional to the identity matrix and the diagonally weighted MPDR filter becomes the same as the SMS filter.

$$\hat{\mathbf{R}}_{\mathrm{DW}} = \hat{\mathbf{R}}_{\mathrm{data}} + \beta\mathbf{I}. \tag{17}$$

III. PCML METHOD

This section describes a physically constrained, maximum likelihood method for estimating the spatial covariance matrix used in adaptive filters. This method was proposed by Kraay in 2003.[2] The goal of the PCML method is to improve adaptive array processing methods under snapshot-deficient conditions. The algorithm determines the maximum likelihood estimate of the spatial covariance matrix subject to known physical constraints. The physical constraints come from our knowledge that the received signal is composed of a propagating component plus spatially white sensor noise. As a result of the physical constraints, fewer snapshots are required to obtain an accurate estimate of the spatial covariance matrix.

A. PCML covariance matrix estimate

The signal snapshots are modeled as series of independent, identically distributed (i.i.d.) zero-mean complex Gaussian random vectors (CGRVs). The joint probability density function of L such snapshots is[14]

$$p(\mathbf{X}_l, \ldots, \mathbf{X}_L) = \prod_{l=1,\ldots,L} \frac{1}{\pi^N |\mathbf{R}|} e^{-\mathbf{X}_l^H \mathbf{R}^{-1} \mathbf{X}_l}, \tag{18}$$

where $\mathbf{R}$ is the covariance matrix of those snapshots and N is the number of elements in each vector $\mathbf{X}$. The ML estimate of this covariance matrix given the received snapshots is

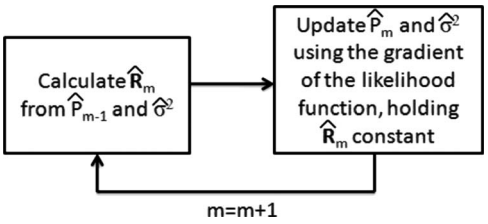

FIG. 1. Iteration used in the PCML algorithm to find the constrained maximum likelihood spatial covariance matrix estimate.

$$\begin{aligned}
\hat{\mathbf{R}}_{\mathrm{ML}} &= \arg\max_{\mathbf{R}} p(\mathbf{X}_1, \ldots, \mathbf{X}_L) \\
&= \arg\max_{\mathbf{R}} \prod_{l=1\ldots L} \frac{1}{\pi^N |\mathbf{R}|} e^{-\mathbf{X}_l^H \mathbf{R}^{-1} \mathbf{X}_l} \\
&= \arg\max_{\mathbf{R}} \pi^{-NL} |\mathbf{R}|^{-L} e^{-\Sigma_{l=1\ldots L} \mathbf{X}_l^H \mathbf{R}^{-1} \mathbf{X}_l} \\
&= \arg\max_{\mathbf{R}} -\log|\mathbf{R}| - \frac{1}{L} \sum_{l=1,\ldots,L} \mathrm{Tr}(\mathbf{X}_l^H \mathbf{R}^{-1} \mathbf{X}_l) \\
&= \arg\max_{\mathbf{R}} -\log|\mathbf{R}| - \mathrm{Tr}\left(\frac{1}{L} \sum_{l=1,\ldots,L} \mathbf{R}^{-1} \mathbf{X}_l \mathbf{X}_l^H \right) \\
&= \arg\max_{\mathbf{R}} -\log|\mathbf{R}| - \mathrm{Tr}(\mathbf{R}^{-1} \hat{\mathbf{R}}_{\mathrm{data}}),
\end{aligned} \tag{19}$$

where $L(\mathbf{R}, \hat{\mathbf{R}}_{\mathrm{data}}) = -\log|\mathbf{R}| - \mathrm{Tr}(\mathbf{R}^{-1}\hat{\mathbf{R}}_{\mathrm{data}})$ is the log-likelihood function. There is no closed form solution for the $\mathbf{R}$ that maximizes this log-likelihood function when the physical constraint of Eq. (20) is imposed. It is, however, possible to use derivatives of the likelihood function in an iterative approach to finding the constrained ML estimate. Kraay[2] derived this method for a spatial beamformer. The covariance matrix is separated into its propagating component plus spatially white sensor noise,

$$[\mathbf{R}]_{ij} = \sigma^2 \delta_{ij} + \frac{1}{(2\pi)^3} \int_{\Omega(\mathbf{k})} P(\omega, \mathbf{k}) [\mathbf{v}(\mathbf{k})]_i [\mathbf{v}^{\mathbf{H}}(\mathbf{k})]_j d\mathbf{k}, \tag{20}$$

where $[\mathbf{v}(\mathbf{k})]_n = e^{-j\mathbf{k}^T \mathbf{p}_n}$ is the nth element of the array manifold vector, $\mathbf{p}_n$ is the location of the nth array element, $\mathbf{k}$ is the spatial wavenumber vector, and $P(\omega, \mathbf{k})$ is the frequency wavenumber power spectrum. $\Omega(\mathbf{k})$ is the region of support of the wavenumber field imposed by the wave equation, $\|\mathbf{k}\| = 2\pi/\lambda = \omega/c$.

B. Iteration structure

The PCML algorithm iterates between estimating $\mathbf{R}$ given current estimates of $P(\omega, \mathbf{k})$ and σ^2 and using the gradient of the likelihood function with respect to $P(\omega, \mathbf{k})$ and σ^2 to update $\hat{P}_m(\omega, \mathbf{k})$ and $\hat{\sigma}_m^2$, where the subscript m denotes the estimate of the quantity at the mth iteration. The structure is shown in Fig. 1 and is discussed in detail in Secs. III C and III E.

C. Initialization

The PCML algorithm initializes its estimate of the covariance matrix with the sample covariance matrix, $\hat{\mathbf{R}}_0 = \hat{\mathbf{R}}_{\text{data}}$. The initial frequency wavenumber spectral estimate, $P(\omega, \mathbf{k})$, is estimated using the MPDR estimator,[8]

$$\hat{P}_0(\omega, \mathbf{k}_n) = \mathbf{w}_{\text{MPDR}}^H(\mathbf{k}_n)\hat{\mathbf{R}}_{\text{data}}\mathbf{w}_{\text{MPDR}}(\mathbf{k}_n) = \frac{1}{\mathbf{v}^H(\mathbf{k}_n)\hat{\mathbf{R}}_{\text{data}}^{-1}\mathbf{v}(\mathbf{k}_n)}. \tag{21}$$

The white noise power estimate is initialized as one-tenth the average diagonal value of $\hat{\mathbf{R}}_{\text{data}}$ since it is physically restricted to lie between zero and the smallest diagonal value of $\hat{\mathbf{R}}_{\text{data}}$.

$$\hat{\sigma}_0^2 = \frac{1}{10N}\text{Tr}(\hat{\mathbf{R}}_{\text{data}}). \tag{22}$$

D. Covariance matrix update

The first iterative step is to obtain a new estimate of the covariance matrix. This is done by inverse Fourier transforming the frequency wavenumber spectrum with respect to the wavenumber vector $\mathbf{k}$.

$$[\hat{\mathbf{R}}_m]_{ij} = [\mathcal{F}^{-1}(\hat{P}_{m-1}(\omega, \mathbf{k}) + \hat{\sigma}_{m-1}^2)]_{i,j} = \hat{\sigma}_{m-1}^2\delta_{ij} + \frac{1}{(2\pi)^3}\int_{\Omega(\mathbf{k})} \hat{P}_{m-1}(\omega, \mathbf{k})e^{-j\mathbf{k}^T(\mathbf{p}_i - \mathbf{p}_j)}d\mathbf{k}, \tag{23}$$

where $\hat{P}_{m-1}(\omega, \mathbf{k})$ is the estimate of the power at frequency ω coming from the direction specified by $\mathbf{k}$ at iteration $m-1$. Since $\hat{P}_m$ can only be calculated at discrete points, a covariance matrix taper is used to smooth the estimates of propagating energy around the discrete spatial plane wave samples. Each sample, $\hat{P}_{m-1}(\omega, \mathbf{k})$, is approximated as a weighted, shifted window in $\mathbf{k}$-space,

$$\hat{P}_{m-1}(\omega, \mathbf{k}) = \sum_n [\hat{P}_{m-1}(\omega, \mathbf{k}_n)W(\mathbf{k} - \mathbf{k}_n)], \tag{24}$$

where $\mathbf{k}_n$ is the nth sample of $\mathbf{k}$ at which the frequency wavenumber spectrum is calculated. The integral in Eq. (23) then becomes a summation,

$$[\hat{\mathbf{R}}_m]_{ij} = \hat{\sigma}_{m-1}^2\delta_{ij} + \left(\sum_n \hat{P}_{m-1}(\omega, \mathbf{k}_n)e^{-j\mathbf{k}_n^T(\mathbf{p}_i - \mathbf{p}_j)}\right)\mathbf{W}_{ij}, \tag{25}$$

where $\mathbf{W}_{ij}$ is the inverse Fourier transform of the covariance matrix taper.[15,16] The taper primarily used by Kraay was a uniform window given by[13]

$$W(\mathbf{u}) = W(u_x, u_y) = \begin{cases} 1 & \text{for } |u_x| < \Delta u/2 \quad \text{and} \quad |u_y| < \Delta u/2 \\ 0 & \text{otherwise,} \end{cases} \tag{26}$$

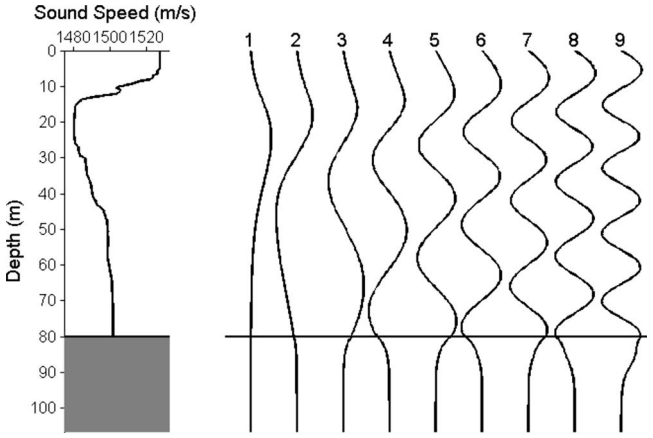

FIG. 2. Shallow water sound speed profile and mode shapes at 200 Hz.

where $\mathbf{u}$ is the wavenumber vector, normalized by $2\pi/\lambda$, and Δu is the wavenumber grid spacing. The inverse Fourier transform of this window is

$$\mathbf{W}_{i,j} = \int W(\mathbf{u})e^{+j(2\pi/\lambda)\mathbf{u}^T(\mathbf{p}_i - \mathbf{p}_j)}d\mathbf{u} = \Delta u\ \text{sinc}\left(\frac{2\pi}{\lambda}\frac{\Delta u}{2}(p_{i,x} - p_{j,x})\right)\Delta u\ \text{sinc} \times \left(\frac{2\pi}{\lambda}\frac{\Delta u}{2}(p_{i,y} - p_{j,y})\right). \tag{27}$$

E. Power spectrum and noise power updates

The power spectral density estimates of the power in each mode are updated using the gradient of the likelihood function [Eq. (19)] with respect to the power estimates.

The gradient with respect to the power at a given wavenumber is given by

$$\frac{\partial L(\hat{\mathbf{R}}_m, \hat{\mathbf{R}}_{\text{data}})}{\partial \hat{P}_m(\omega, \mathbf{k}_n)} = -\mathbf{v}^H(\mathbf{k}_n)\hat{\mathbf{R}}_m^{-1}\mathbf{v}(\mathbf{k}_n) + \mathbf{v}^H(\mathbf{k}_n)\hat{\mathbf{R}}_m^{-1}\hat{\mathbf{R}}_{\text{data}}\hat{\mathbf{R}}_m^{-1}\mathbf{v}(\mathbf{k}_n) \tag{28}$$

and the gradient with respect to the white noise power is given by

$$\frac{\partial L(\hat{\mathbf{R}}_m, \hat{\mathbf{R}}_{\text{data}})}{\partial \hat{\sigma}_m^2} = \text{Tr}((\hat{\mathbf{R}}_m^{-1}\hat{\mathbf{R}}_{\text{data}} - \mathbf{I})\hat{\mathbf{R}}_m^{-1}). \tag{29}$$

The second order gradient can be used to verify that a maximum of the likelihood function is reached and not a minimum. The multiplicative update proposed by Kraay provides a convenient mapping between the gradients of the likelihood function and a multiplicative scaling factor. The update is chosen such that when the gradient of the likelihood function is zero, the power estimates remain unchanged. The scale factor increases monotonically for a positive gradient and decreases monotonically for a negative gradient.

$$\hat{P}_m(\omega,\mathbf{k}_n)=\begin{cases}\hat{P}_{m-1}(\omega,\mathbf{k}_n)\left[\dfrac{A-1}{e^{\pi/2}-1}(e^{\arctan(\alpha\partial L/(\partial\hat{P}_{m-1}(\omega,\mathbf{k}_n)))}-1)+1\right], & \dfrac{\partial L}{\partial\hat{P}_{m-1}}>0\\ \hat{P}_{m-1}(\omega,\mathbf{k}_n)\left[\dfrac{B-1}{e^{-\pi/2}-1}(e^{\arctan(\beta\partial L/(\partial\hat{P}_{m-1}(\omega,\mathbf{k}_n)))}-1)+1\right] & \text{otherwise,}\end{cases} \tag{30}$$

where A and B are the scale's upper and lower limits, and α and β are parameters that control how quickly the algorithm steps as a function of the gradient. For the white noise power update, Kraay used an additive form since it offered better stability in her environment.

$$\hat{\sigma}_m^2=\hat{\sigma}_{m-1}^2+10^{-4}\frac{\partial L}{\partial\hat{\sigma}_{m-1}^2}\Big/\left|\frac{\partial^2 L}{(\partial\hat{\sigma}_{m-1}^2)^2}\right|. \tag{31}$$

The PCML algorithm iterates for a number of iterations until the covariance matrix estimate has converged to its most likely value. The PCML frequency wavenumber spectrum estimates are the values of $\hat{P}_m(\omega,\mathbf{k})$ at the final iteration of the algorithm. The likelihood function can be calculated at each iteration to provide an indication of whether the algorithm has converged, and a stopping condition can be formed based on this. Kraay chose to run the algorithm for 50 iterations.

IV. PCML ALGORITHM APPLIED TO MODES

This section describes the application of Kraay's PCML algorithm to the problem of estimating complex-valued mode amplitudes. For the underwater environment model of Eq. (1), the covariance matrix of the acoustic pressure field can be decomposed into a propagating modal component plus spatially white sensor noise. In this case, there are a discrete number of propagating modes to sum instead of an infinite number of spatial plane waves to integrate over, so no covariance matrix taper is necessary. Thus Eqs. (23) and (25) become

$$\hat{\mathbf{R}}=\hat{\sigma}^2\mathbf{I}+\sum_{n=1,\ldots,M}\hat{P}(\omega,\boldsymbol{\psi}_n)\boldsymbol{\psi}_n\boldsymbol{\psi}_n^H. \tag{32}$$

The second change is that instead of steering the beamformer to a spatial direction, it is steered to a particular mode. The array steering vector, $\mathbf{v}(\mathbf{k})$, becomes

$$\mathbf{v}(\mathbf{k}_n)=\boldsymbol{\psi}_n. \tag{33}$$

With these modifications, the PCML algorithm developed by Kraay can be applied to determine the maximum likelihood estimate of the covariance matrix given the physical constraint. With each iteration, the PCML algorithm generates an estimate of the power in each mode and the power of the spatially white noise. These estimates are used to generate an estimate of the covariance matrix using Eq. (32). Once the PCML algorithm has converged, the PCML-MPDR filter uses the estimate of the covariance matrix at the final iteration of the PCML algorithm in the MPDR filter, Eqs. (14) and (15). The PCML-MAP filter implements a MAP mode filter using the estimates of the signal and noise statistics from the final iteration of the PCML algorithm. That is, the filter assumes that the mode amplitude coefficients are uncorrelated, and the noise is spatially white and calculates

$$\mathbf{R_d}=\begin{bmatrix}\hat{P}(\omega,\boldsymbol{\psi}_1)^2 & 0 & \cdots & 0\\ 0 & \hat{P}(\omega,\boldsymbol{\psi}_2)^2 & \ddots & \vdots\\ \vdots & \vdots & \ddots & 0\\ 0 & \ldots & 0 & \hat{P}(\omega,\boldsymbol{\psi}_M)^2\end{bmatrix} \tag{34}$$

and

$$\mathbf{R_n}=\hat{\sigma}^2\mathbf{I} \tag{35}$$

in Eq. (12), using $\hat{P}$ and $\hat{\sigma}^2$ from the final PCML iteration.

V. PERFORMANCE AND ANALYSIS

A. Simulation setup

This section describes the setup of the shallow water simulation. The mode coefficient vector, $\mathbf{d}$, is modeled as a zero-mean complex Gaussian random vector. The noise is modeled as spatially white. The real and imaginary parts of $\mathbf{d}$ and $\mathbf{n}$ are i.i.d. and Gaussian, and therefore their covariance matrices are real valued.[14] The simulation is similar to the one described by Buck *et al.*[1] for a shallow water environment. The simulated environment had typical shallow water sound speed profile and bottom properties and was 80 m deep. Figure 2 shows the sound speed profile and the corresponding mode shapes at a frequency of 200 Hz.

A vertical array of 20 equally spaced hydrophones was used. The location of the bottom hydrophone was fixed at 79 m depth and the depth of the top hydrophone was varied from the water surface to a depth of 40 m (half the water column). This gradually reduced the fraction of the water column that was spanned by the array. For each aperture, 500 trials were run using independent realizations of the mode coefficients and noise vector. Linear mode filters were applied to the simulated pressure field to obtain an estimate of the mode amplitudes. The error criteria are the sample mean squared errors, $\|\hat{\mathbf{d}}-\mathbf{d}\|^2$, between the estimate of the complex mode amplitudes and their actual values over the 500 trials. The total mode energy is included in the plots for reference and represents the error that would result from estimating each mode to have zero amplitude. The mode coefficients, $\mathbf{d}$, were assumed to be an i.i.d., zero-mean, CGRV. Except where stated otherwise, 25 snapshots were used to initialize the sample covariance matrix for the PCML algorithms and for the MPDR filter.

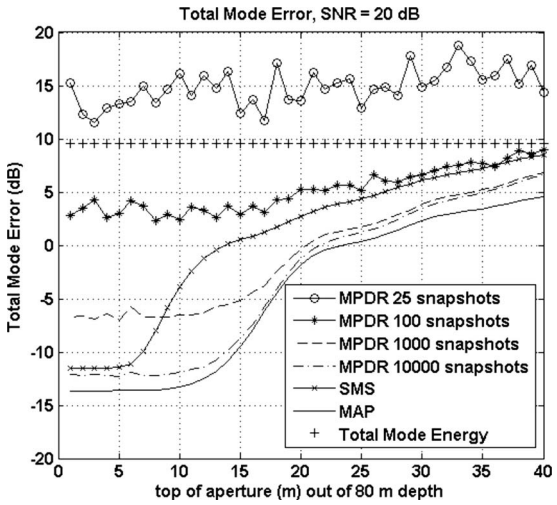

FIG. 3. Comparison of the performance of the MPDR mode filters as the number of snapshots used in the sample covariance matrix is varied. The SMS and MAP filter performances and the total mode energy are included for reference.

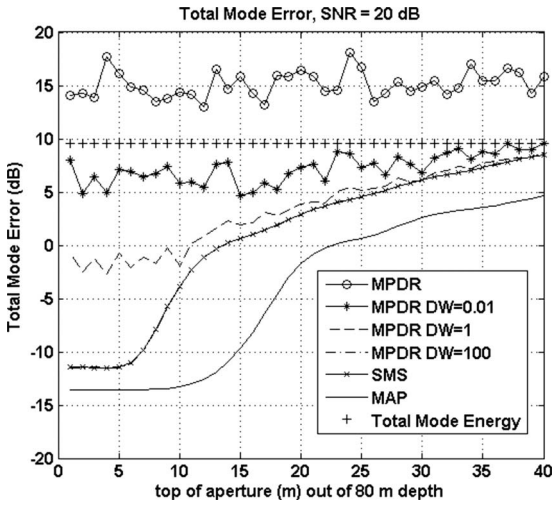

FIG. 5. Comparison of the performance of the diagonally weighted MPDR filter as the weighting factor is varied, using 25 snapshots to generate the sample covariance matrix in the MPDR filters. The SMS and MAP filter performances and the total mode energy are included for reference. With a diagonal weighting of 100, the MPDR curve falls on top of the SMS curve.

B. Simulation results

Figure 3 shows the performance of the MPDR filter using the sample covariance matrix as the number of snapshots is varied. As was discussed in Sec. II, thousands of snapshots are required for the covariance matrix to converge to its final value. When sufficient snapshots are used, the MPDR filter's performance matches that of the MAP filter for a full spanning array, but is a few dB worse than the MAP filter when the array span is reduced.

Figure 4 shows the effect of changing the loading parameter on the diagonally weighted PI filter. With only small amounts of weighting, the filter still suffers from sensitivity to white noise as the span of the array is reduced. With large amounts of weighting, the filter performs poorly, as the amplitude of the mode estimates approaches zero. Only when the correct weighting is applied is the filter able to perform the same as the MAP filter.

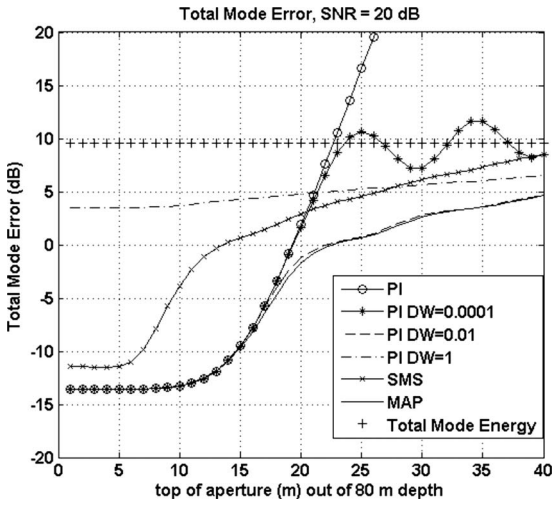

FIG. 4. Comparison of the performance of the diagonally weighted PI filter as the weighting factor is varied. The SMS and MAP filter performances and the total mode energy are included for reference.

Figure 5 shows the effect of changing the loading parameter on the diagonally weighted MPDR filter. The filter converges on the SMS filter as the weighting is increased; however, it is unable to perform better than SMS.

Figure 6 shows the simulation results for the PCML-MAP, PCML-MPDR, and reduced rank PI filters. With only 25 snapshots, the PCML-MPDR filter is able to do as well as the unconstrained MPDR filter using 10 000 snapshots. Furthermore, the PCML-MAP filter performs as well as the MAP filter that has full knowledge of the signal and noise statistics. The sawtooth pattern in the reduced rank PI filter is a result of the changing number of singular values used in the pseudoinversion as the condition number of $\boldsymbol{\psi}$ changes. As the condition number worsens, singular values are dropped one at a time resulting in the observed pattern.

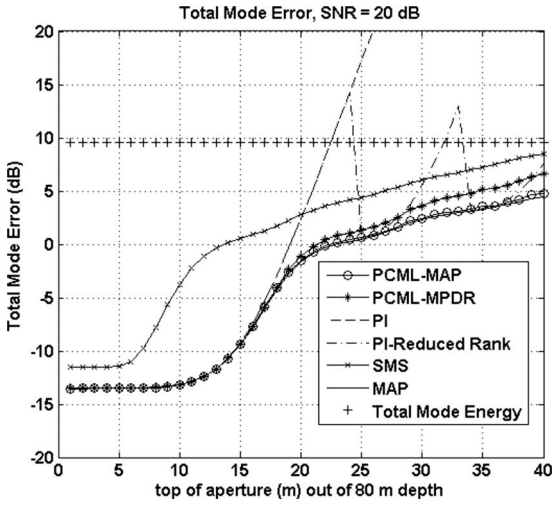

FIG. 6. Comparison of the performance of the PCML-MAP, PCML-MPDR, PI, and reduced rank PI filters. The SMS and MAP filter performances and the total mode energy are included for reference. The PCML algorithms were initialized with 25 data snapshots.

VI. CONCLUSIONS

The MPDR filter using the sample covariance matrix requires a large number of snapshots in order to estimate the received signal covariance matrix, $\mathbf{R_p}$, with accuracy sufficient for the algorithm to yield satisfactory results. While diagonal loading of the sample covariance matrix can compensate for an insufficient number of snapshots, the performance of the diagonally loaded PI and MPDR algorithms is sensitive to the choice of the loading parameter. This sensitivity is undesirable in real world applications.

The PCML algorithm uses physical constraints to estimate $\mathbf{R_p}$ and the second order statistics of the mode amplitudes and noise. When the resulting $\mathbf{R_p}$ is then used in a MPDR mode filter, it is found that the snapshot requirement can be reduced by over two orders of magnitude without sacrificing the resulting algorithm performance. Furthermore, using the same number of snapshots as used for the PCML-MPDR algorithm, the estimated second order signal and noise statistics can be used in the MAP mode filter and achieve the same performance as the MAP mode filter that has *a priori* knowledge of these statistics.

ACKNOWLEDGMENTS

This paper is based on a thesis submitted in partial fulfillment of the requirements of the degree of Master of Science in the Department of Electrical Engineering and Computer Science at the Massachusetts Institute of Technology and Woods Hole Oceanographic Institution in September, 2009. This work was supported by the Office of Naval Research through ONR Grant Nos. N00014-05-10085 and N00014-06-10788 and through the WHOI Academic Programs Office.

[1]J. R. Buck, J. C. Preisig, and K. E. Wage, "A unified framework for mode filtering and the maximum a posteriori mode filter," J. Acoust. Soc. Am. **103**, 1813–1824 (1998).
[2]A. L. Kraay, "Physically constrained maximum-likelihood method for snapshot-deficient adaptive array processing," Master Thesis, Massachusetts Institute of Technology, Cambridge, MA (2003).
[3]F. B. Jensen, W. A. Kuperman, M. B. Porter, and H. Schmidt, *Computational Ocean Acoustics* (Springer-Verlag, New York, 2000).
[4]W. A. Kuperman and F. Ingenito, "Spatial correlation of surface generated noise in a stratified ocean," J. Acoust. Soc. Am. **67**, 1988–1996 (1980).
[5]G. Strang, *Linear Algebra and Its Applications*, 4th ed. (Thompson Brooks/Cole, Belmont, CA, 2006).
[6]H. L. VanTrees, *Optimum Array* (Wiley-Interscience, New York, 2002), Part IV.
[7]B. D. Vanveen and K. Buckley, "Beamforming: A versatile approach to spatial filtering," IEEE ASSP Magazine (1988).
[8]J. Capon, "High-resolution frequency-wavenumber spectrum analysis," Proc. IEEE **57**, 1408–1418 (1969).
[9]O. L. Frost, "An algorithm for linearly constrained adaptive array processing," Proc. IEEE **60**, 926–935 (1972).
[10]D. H. Brandwood, "A complex gradient operator and its application in adaptive array theory," IEE Proc. F, Commun. Radar Signal Process. **130**, 11–16 (1983).
[11]J. R. Guerci, *Space-Time Adaptive Processing for Radar* (Artech House, Inc., Norwood, MA, 2003).
[12]A. B. Baggeroer and H. Cox, "Passive sonar limits upon nulling multiple moving ships with large aperture arrays," Conference Record of the 33rd Asilomar Conference on Signals, Systems, Computers (1999), Vol. **1**, pp. 103–108.
[13]A. L. Kraay and A. B. Baggeroer, "A physically constrained maximum-likelihood method for snapshot-deficient adaptive array processing," IEEE Trans. Signal Process. **55**, 4048–4063 (2007).
[14]D. Tse and P. Viswanath, *Fundamentals of Wireless Communication* (Cambridge University Press, New York, 2005).
[15]J. R. Guerci, "Theory and application of covariance matrix tapers for robust adaptive beamforming," IEEE Trans. Signal Process. **47**, 977–985 (1999).
[16]F. J. Harris, "On the use of windows for harmonic analysis with the discrete Fourier transform," Proc. IEEE **66**, 51–83 (1978).

Multiple signal classification method for detecting point-like scatterers embedded in an inhomogeneous background medium

Xudong Chen
Department of Electrical and Computer Engineering, National University of Singapore, Singapore 117576, Singapore

(Received 15 September 2009; revised 5 January 2010; accepted 7 January 2010)

The multiple signal classification (MUSIC) type method has been widely used to detect point-like scatterers embedded in a homogeneous background medium. This paper extends the MUSIC-type method to the detection of point-like scatterers that are embedded in an inhomogeneous background. Although the background Green's function at each test point is not directly available in inhomogeneous background scenario, this paper proposes an approach, based on the finite element method, to simultaneously obtain the Green's function at all test points. Numerical simulations illustrate the efficacy of the proposed theory and algorithm presented in this paper, and some interesting observations, which are absent in homogeneous background scenario, are highlighted and discussed. © *2010 Acoustical Society of America.* [DOI: 10.1121/1.3303984]

PACS number(s): 43.60.Pt, 43.60.Tj [EJS] Pages: 2392–2397

I. INTRODUCTION

The time-reversal multiple signal classification (MUSIC) method has been widely used to detect point-like scatterers using either acoustic or electromagnetic waves.[1–4] Some references simply refer to it as the MUSIC method.[5–7] In this paper, we refer to the method as the MUSIC-type method.[8] The MUSIC method was first developed in the signal processing community to determine the direction of arrival (DOA),[9] and later was extended to locate point-like scatterers.[1] Reference 5 provides a good link between the MUSIC method and the DORT (Ref. 10) method (the French acronym of "decomposition of the time reversal operator") by interpreting the DORT operator as a covariance matrix. To the best of the author's knowledge, MUSIC-type method developed so far is mainly for scattering problems with homogeneous background medium, or at most half-space background medium, where the closed-form expression of the corresponding Green's function is available. We refer to this scenario as the homogeneous scenario. In comparison, in the inhomogeneous scenario, where the background medium is inhomogeneous and the corresponding Green's function does not have a closed-form expression, the MUSIC method has not been reported so far. One of main obstacles for the development of the MUSIC-type algorithm for inhomogeneous scenario is the numerical calculation of the Green's function in inhomogeneous background. In order to obtain a pixel in the MUSIC pseudospectrum, one has to solve once the forward numerical problem in which a point source is placed at the test point.

This paper extends the MUSIC-type method to the detection of point-like scatterers that are embedded in an inhomogeneous background medium. Although the background Green's function at each test point is not directly available in inhomogeneous scenario, the proposed MUSIC-type algorithm uses the finite element method (FEM) to simultaneously obtain the background Green's function at all test points. It is worth mentioning an interesting observation that is absent in the homogeneous scenario. In homogeneous scenario, one point-like scatterer corresponds to one singular value of the multistatic response (MSR) matrix. It is worth highlighting that this claim applies to the case of a small amount of scatterers, as discussed in Refs. 1–6, 8, and 10, and the case of densely distributed random scatterers, as discussed in Refs. 11 and 12, is beyond the scope of this paper. In comparison, in the proposed MUSIC-type algorithm for inhomogeneous scenario, due to the discretization nature of the numerical algorithm, one point-like scatterer corresponds to more than one singular value. For example, when one point-like scatterer is modeled as a square element in the FEM modeling, one scatterer corresponds to four singular values. The reason for this is discussed in the paper. Numerical simulations illustrate the efficacy of the proposed theory and algorithm. In conclusion, the proposed algorithm in this paper greatly generalizes the applicability of MUSIC-type method.

II. FORWARD PROBLEM SOLVER

Consider a two-dimensional acoustic or electromagnetic (transverse magnetic) scattering problem, in which the field satisfies the scalar Helmholtz equation. Some *a priori* known objects are distributed in an otherwise homogeneous background medium the wave number of which is k_0. The known objects and the otherwise homogeneous background are referred to as the known inhomogeneous background, and the distribution of the wave number of it is denoted as $k_b(\mathbf{r})$, where $\mathbf{r}=(x,y)$ represents the spacial dependence. A total number of M small but finite scatterers are embedded in the known inhomogeneous background. The dimensions of these scatterers are much smaller than the wavelength so that they can be referred to as point-like scatterers. The positions of point-like scatterers are given by $\mathbf{r}_m^s$, $m=1,2,\ldots,M$. The distribution of wave number of the scattering system, including

 0001-4966/2010/127(4)/2392/6/$25.00

point-like scatterers and known inhomogeneous background, is denoted as $k(\mathbf{r})$. In the inverse scattering problem, to locate the positions of point-like scatterers, the test domain is successively illuminated by a number of incident waves and the scattered waves are measured at an array of receivers. A total number of N_t transmitters are located at $\mathbf{r}_i^t$, $i=1,2,\ldots,N_t$, and a total number of N_r receivers are located at $\mathbf{r}_j^r$, $j=1,2,\ldots,N_r$. The forward scattering problem for the inhomogeneous scenario is solved by the FEM method in this paper. The FEM is a widely used computational method, and there is abundance of references on it, for example, Refs. 13 and 14. This section details on the FEM implementation.

The domain of interest D has a closed boundary ∂D, the outward normal direction of which is denoted $\hat{\mathbf{n}}$. Transmitters and receivers are located outside of D, and the medium outside of D is homogeneous. For later convenience, the relative refractive index is introduced as $n(\mathbf{r})=k(\mathbf{r})/k_0$. The relative refractive index of the known inhomogeneous background medium is denoted as $n_b(\mathbf{r})$. In D, the total field $u(\mathbf{r})$ satisfies the Helmholtz equation

$$[\nabla^2 + k_0^2 n^2(\mathbf{r})]u(\mathbf{r}) = 0. \tag{1}$$

It can be converted to the "weak" form by multiplying both sides with a testing function $T(\mathbf{r})$ and performing an integral over D,

$$\int\int_D (\nabla T(\mathbf{r})\cdot\nabla u(\mathbf{r}) - k_0^2 n^2(\mathbf{r})T(\mathbf{r})u(\mathbf{r}))ds = \oint_{\partial D} T(\mathbf{r})\frac{\partial u(\mathbf{r}(t))}{\partial n(t)}dt, \tag{2}$$

where $\partial u/\partial n$ means the derivative in the normal direction of the boundary ∂D. In the exterior of ∂D, the total field is the sum of the incident wave $u^i(\mathbf{r})$ and the scattered wave $u^s(\mathbf{r})$, and the latter can be formulated by the Green's theorem,

$$u^s(\mathbf{r}) = \oint_{\partial D}\left[-\frac{\partial u(\mathbf{r}'(t'))}{\partial n(t')}G(\mathbf{r},\mathbf{r}'(t')) + u(\mathbf{r}'(t'))\frac{\partial G(\mathbf{r},\mathbf{r}'(t'))}{\partial n(t')}\right]dt'. \tag{3}$$

At the boundary ∂D, the incident field and the total field satisfy the following equation:

$$u(\mathbf{r}(t)) + \oint_{\partial D}\left[\frac{\partial u(\mathbf{r}'(t'))}{\partial n(t')}G(\mathbf{r}(t),\mathbf{r}'(t')) - u(\mathbf{r}'(t'))\frac{\partial G(\mathbf{r}(t),\mathbf{r}'(t'))}{\partial n(t')}\right]dt' = u^i(\mathbf{r}(t)), \tag{4}$$

where t is a parametric variable along ∂D. Once the total field on the boundary and its normal derivative are obtained from Eqs. (2) and (4), the scattered field is subsequently obtained from Eq. (3). In this paper, the FEM is used to solve for the total field on the boundary and its normal derivative, as well as the total field in the interior of D.

In this paper, the domain D is discretized into rectangular-cell meshes. The number of interior nodes is denoted as N_{int} and the number of nodes located on the boundary ∂D is denoted as N_{bou}. The mesh size is so small such that the refractive index is treated as a constant n_n within the nth mesh. The interior total field is expanded in basis functions

$$u(\mathbf{r}) \cong \sum_{n=1}^{N_{\text{int}}} u_n^{\text{int}} B_n(\mathbf{r}) + \sum_{n=N_{\text{int}}+1}^{N_{\text{int}}+N_{\text{bou}}} u_n^{\text{bou}} B_n(\mathbf{r}), \tag{5}$$

where $B_n(\mathbf{r})$ denotes the basis function centered at node n, and u_n^{int} and u_n^{bou} represent the value of total field at that node. Following Ref. 14, this paper adopts the bilinear basis function for rectangular cells. The total field at the boundary ∂D is automatically given by

$$u(\mathbf{r}(t)) \cong \sum_{n=N_{\text{int}}+1}^{N_{\text{int}}+N_{\text{bou}}} u_n^{\text{bou}} B_n(t), \tag{6}$$

where $B_n(t)$ is the projection of $B_n(\mathbf{r})$ onto the boundary.

The notation $J^{\text{bou}}(t)$ is introduced as a shorthand for $\partial u(\mathbf{r}(t))/\partial n(t)$ and it is interpreted as the equivalent surface source. The $J^{\text{bou}}(t)$ can also be expanded in basis functions as

$$J^{\text{bou}}(t) \cong \sum_{n=1}^{N_{\text{bou}}} J_n^{\text{bou}} \tilde{B}_n(t), \tag{7}$$

where $\tilde{B}_n(t)$ denotes the basis function for the equivalent boundary source and it is chosen as the piecewise-constant function. For a boundary point with parameter t that is located in the nth boundary line element, the value of $J^{\text{bou}}(t)$ is given by J_n^{bou}.

If Eqs. (5) and (7) are substituted into Eq. (2), a total number of $N_{\text{int}}+N_{\text{bou}}$ linearly independent equations can be generated using the basis functions as testing functions,

$$T(\mathbf{r}) = B_n(\mathbf{r}), \quad n = 1,2,\ldots,N_{\text{int}}+N_{\text{bou}}. \tag{8}$$

This method is the well known Galerkin FEM. The resulting matrix equation has the form

$$\begin{bmatrix} \bar{\bar{X}}^{\text{int}} & \bar{\bar{X}}^{\text{cros,A}} \\ \bar{\bar{X}}^{\text{cros,B}} & \bar{\bar{X}}^{\text{bou}} \end{bmatrix} \cdot \begin{bmatrix} \bar{u}^{\text{int}} \\ \bar{u}^{\text{bou}} \end{bmatrix} = \begin{bmatrix} \bar{0} \\ \bar{\bar{Y}}\cdot\bar{J}^{\text{bou}} \end{bmatrix}, \tag{9}$$

where $\bar{\bar{X}}^{\text{int}}$, $\bar{\bar{X}}^{\text{cros,A}}$, $\bar{\bar{X}}^{\text{cros,B}}$, and $\bar{\bar{X}}^{\text{bou}}$ have the common form

$$\bar{\bar{X}}_{mn} = \int\int_D \nabla B_m\cdot\nabla B_n - k_0^2 n^2 B_m B_n ds, \tag{10}$$

and the entries of $\bar{\bar{Y}}$ are given by

$$\bar{\bar{Y}}_{mn} = \oint_{\partial D} B_m \tilde{B}_n. \tag{11}$$

If Eqs. (6) and (7) are substituted into Eq. (4) and in the meanwhile testing functions are chosen as the Dirac delta function located in the center of each line element around the boundary ∂D, a total number of N_{bou} linearly independent equations are generated, which are expressed in matrix form as

$$\bar{\bar{L}} \cdot \bar{u}^{\text{bou}} + \bar{\bar{M}} \cdot \bar{J}^{\text{bou}} = \bar{u}^{\text{i}}, \tag{12}$$

where the matrices $\bar{\bar{L}}$ and $\bar{\bar{M}}$ are calculated as integrals over the line element of the boundary ∂D, the detail of which can be found in Ref. 14. The unknowns $\bar{u}^{\text{int}}$, $\bar{u}^{\text{bou}}$, and $\bar{J}^{\text{bou}}$ can be solved from the linear equation system equations (9) and (12). Then the scattered fields at all receivers can be obtained from Eq. (3) and can be written in an N_r-dimensional vector,

$$\bar{u}^{s} = -\bar{\bar{L}}_s \cdot \bar{u}^{\text{bou}} - \bar{\bar{M}}_s \cdot \bar{J}^{\text{bou}}, \tag{13}$$

where $\bar{\bar{L}}_s$ and $\bar{\bar{M}}_s$ are similar to $\bar{\bar{L}}$ and $\bar{\bar{M}}$, respectively, with only minor differences.

The above FEM formulation has been validated numerically. For serval scattering configurations, the scattered fields calculated by the FEM method agree well with those obtained by the method of moment[14] and the coupled dipole method,[15] and the difference between them is negligibly small.

III. MUSIC-TYPE ALGORITHM

For each incidence, the scattered fields received at all receivers are written in an N_r-dimensional vector. For all N_t incidences, a scattering matrix $\bar{\bar{K}}$ of dimension $N_r \times N_t$ is generated, called the MSR matrix. The singular value decomposition (SVD) of $\bar{\bar{K}}$ is given by $\bar{\bar{K}} = \Sigma \sigma_p \bar{u}_p \bar{v}_p^H$, where the superscript H denotes Hermitian. The subspace spanned by the left singular vectors ($\bar{u}_p$, with $\sigma_p > 0$) corresponding to positive singular values is orthogonally complementary to the subspace spanned by the left singular vectors ($\bar{u}_p$, with $\sigma_p = 0$) corresponding to vanishing singular values. These two subspaces are referred to as the signal subspace and noise subspace, respectively. For point-like scatterers, the signal subspace is the same as the subspace spanned by the background Green's function vectors evaluated at point-like scatterers, $\bar{g}_b(\mathbf{r}) = [G_b(\mathbf{r}_1^r, \mathbf{r}), G_b(\mathbf{r}_2^r, \mathbf{r}), \ldots, G_b(\mathbf{r}_{N_r}^r, \mathbf{r})]^{\top}$, for $\mathbf{r} = \mathbf{r}_1, \mathbf{r}_2, \ldots, \mathbf{r}_M$, where G_b denotes background Green's function and the superscript $\top$ denotes transpose operator.

MUSIC method locates point-like scatterers by identifying the (ideally infinitely large) peaks of the pseudospectrum,

$$\Phi(\mathbf{r}) = \left[\sum_{\sigma_p = 0} |\bar{u}_p^H \bar{g}_b(\mathbf{r})|^2 \right]^{-1}. \tag{14}$$

For homogeneous medium background, the background Green's function is available in closed form. However, for inhomogeneous medium background, the closed form background Green's function is not available. If the background Green's function vector $\bar{g}_b(\mathbf{r})$ is numerically calculated by solving a forward problem for every test point $\mathbf{r}$ of the domain D, the computational burden is prohibitively high. This paper proposes a method to simultaneously obtain the background Green's function vectors for all test points.

To proceed, the total field in the known inhomogeneous medium background $u_b(\mathbf{r})$, i.e., in the absence of point-like scatterers, also satisfies the Helmholtz equation,

$$[\nabla^2 + k_0^2 n_b^2(\mathbf{r})] u_b(\mathbf{r}) = 0. \tag{15}$$

The combination of Eqs. (15) and (1) yields

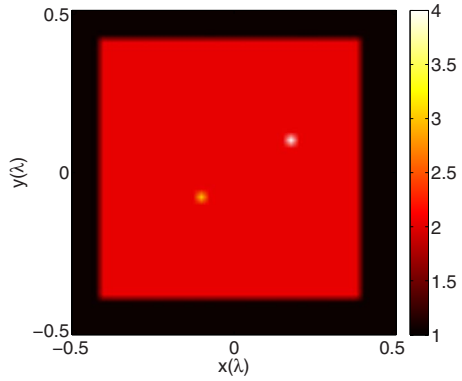

FIG. 1. (Color online) The exact configuration of the inhomogeneous background and point-like scatterers. The inhomogeneous background is a square of side length 0.8λ. The color bar represents the value of the square of relative refractive index, i.e., n^2.

$$[\nabla^2 + k_0^2 n_b^2(\mathbf{r})](u(\mathbf{r}) - u_b(\mathbf{r})) = -k_0^2 [n^2(\mathbf{r}) - n_b^2(\mathbf{r})] u(\mathbf{r}). \tag{16}$$

The right hand side is interpreted as the induced source, which is also called secondary source or contrast source.[16] The right hand side is written in shorthand as $-J^{\text{con}}(\mathbf{r})$, and the contrast field $u(\mathbf{r}) - u_b(\mathbf{r})$ is denoted as $u_c(\mathbf{r})$. It is easy to see that scattered contrast field can be understood as the reradiated field by the contrast source. The application of Galerkin FEM, as done in Sec. II, to Eq. (16) yields a linear equation system

$$\begin{bmatrix} \bar{\bar{X}}_b^{\text{int}} & \bar{\bar{X}}_b^{\text{cros},A} \\ \bar{\bar{X}}_b^{\text{cros},B} & \bar{\bar{X}}_b^{\text{bou}} \end{bmatrix} \cdot \begin{bmatrix} \bar{u}_c^{\text{int}} \\ \bar{u}_c^{\text{bou}} \end{bmatrix} = \begin{bmatrix} \bar{\bar{Z}}^{\text{int}} & \bar{\bar{Z}}^{\text{cros},A} \\ \bar{\bar{Z}}^{\text{cros},B} & \bar{\bar{Z}}^{\text{bou}} \end{bmatrix} \cdot \bar{J}^{\text{con}} + \begin{bmatrix} \bar{0} \\ \bar{\bar{Y}} \cdot \bar{J}_c^{\text{bou}} \end{bmatrix}, \tag{17}$$

where $\bar{\bar{X}}_b^{\text{int}}$, $\bar{\bar{X}}_b^{\text{cros},A}$, $\bar{\bar{X}}_b^{\text{cros},B}$, and $\bar{\bar{X}}_b^{\text{bou}}$ are defined as the inhomogeneous background (in absence of point-like scatterers) counterpart of Eq. (10), and $\bar{\bar{Z}}^{\text{int}}$, $\bar{\bar{Z}}^{\text{cros},A}$, $\bar{\bar{Z}}^{\text{cros},B}$, and $\bar{\bar{Z}}^{\text{bou}}$ have the common form as $\bar{\bar{Z}}_{mn} = \int\int_D B_m B_n ds$. Since there is no contrast in incident field, the linear equation system generated at the boundary, Eq. (12), becomes

$$\bar{\bar{L}} \cdot \bar{u}_c^{\text{bou}} + \bar{\bar{M}} \cdot \bar{J}_c^{\text{bou}} = 0. \tag{18}$$

The substitution of Eq. (18) into Eq. (17) yields

$$\begin{bmatrix} \bar{\bar{X}}_b^{\text{int}} & \bar{\bar{X}}_b^{\text{cros},A} \\ \bar{\bar{X}}_b^{\text{cros},B} & \bar{\bar{X}}_b^{\text{bou}} + \bar{\bar{Y}} \cdot \bar{\bar{M}}^{-1} \cdot \bar{\bar{L}} \end{bmatrix} \cdot \begin{bmatrix} \bar{u}_c^{\text{int}} \\ \bar{u}_c^{\text{bou}} \end{bmatrix} = \begin{bmatrix} \bar{\bar{Z}}^{\text{int}} & \bar{\bar{Z}}^{\text{cros},A} \\ \bar{\bar{Z}}^{\text{cros},B} & \bar{\bar{Z}}^{\text{bou}} \end{bmatrix} \cdot \bar{J}^{\text{con}}. \tag{19}$$

For convenience, the matrices on the left and right hand sides can be denoted as $\bar{\bar{A}}$ and $\bar{\bar{B}}$, respectively. Furthermore, define the matrix $\bar{\bar{P}}$, which picks up the boundary nodes out of all nodes, as $[\bar{\bar{0}}_{N_{\text{bou}} \times N_{\text{int}}}, \bar{\bar{I}}_{N_{\text{bou}} \times N_{\text{bou}}}]$, where $\bar{\bar{I}}$ denotes identity matrix. Thus, the contrast field at the boundary is obtained from Eq. (19),

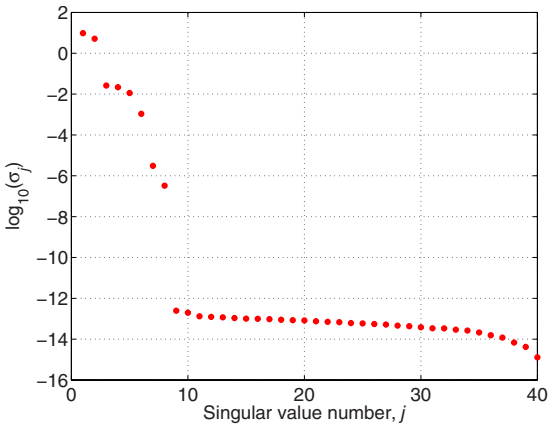

FIG. 2. (Color online) Singular values of the contrast multistatic response matrix in the absence of noise in the first numerical example.

$$\bar{u}_c^{\text{bou}} = \bar{\bar{P}} \cdot \bar{\bar{A}}^{-1} \cdot \bar{\bar{B}} \cdot \bar{J}^{\text{con}}. \tag{20}$$

Finally, the scattered contrast field is obtained from Eq. (13), after the substitution of Eqs. (18) and (20),

$$\bar{u}_c^{\text{sca}} = (-\bar{\bar{L}}_s + \bar{\bar{M}}_s \cdot \bar{\bar{M}}^{-1} \cdot \bar{\bar{L}}) \cdot \bar{\bar{P}} \cdot \bar{\bar{A}}^{-1} \cdot \bar{\bar{B}} \cdot \bar{J}^{\text{con}}, \tag{21}$$

which is written in a compact form as $\bar{u}_c^{\text{sca}} = \bar{\bar{W}} \cdot \bar{J}^{\text{con}}$. It is obvious that the columns of $\bar{\bar{W}}$ are the background Green's function vectors $\bar{g}_b(\mathbf{r})$ evaluated at all nodes.

Define the background MSR matrix $\bar{\bar{K}}_b$ as the background (in absence of point-like scatterers) counterpart of $\bar{\bar{K}}$. Subsequently, the contrast multistatic response matrix is denoted as $\bar{\bar{K}}_c = \bar{\bar{K}} - \bar{\bar{K}}_b$. After the SVD of $\bar{\bar{K}}_c$, the pseudospectrum is obtained from Eq. (14). For inhomogeneous background scattering problem, Eq. (21) shows that the background Green's function vectors for all nodes are simultaneously obtained, which results in a fast generation of the pseudospectrum.

IV. NUMERICAL SIMULATION

To test the performance of the proposal MUSIC method, this section considers two numerical examples. In both numerical examples, the domain of interest D is a square of side length λ, where $\lambda = 2\pi/k_0$ denotes the wavelength, and D is discretized into 40×40 square elements. The numbers of transmitters and receivers are both 40, and they are uniformly distributed on a circle of radius 3λ.

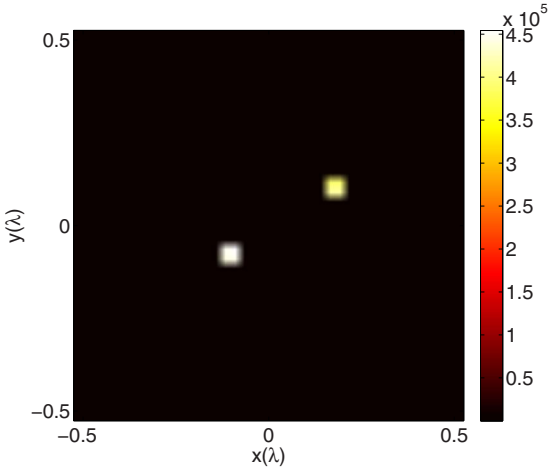

FIG. 3. (Color online) MUSIC pseudospectrum of the first numerical example (in the absence of noise).

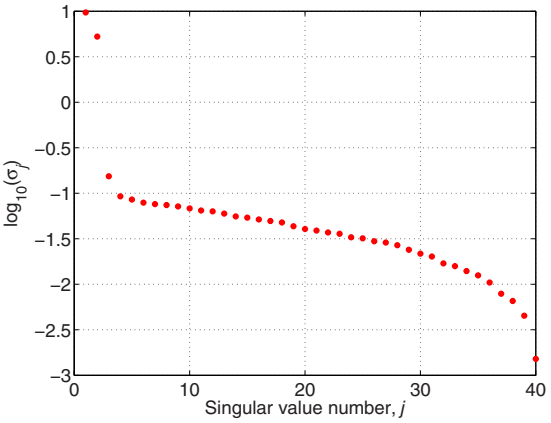

FIG. 4. (Color online) Singular values of the contrast multistatic response matrix in the presence of 20 dB additive white Gaussian noise in the first numerical example.

In the first numerical example, the inhomogeneous background medium is a square of side length 0.8λ centered at the origin, and its relative refractive index is $\sqrt{2}$, as shown in Fig. 1. Two point-like scatterers are located at $(-0.1\lambda, -0.1\lambda)$ and $(0.2\lambda, 0.1\lambda)$, and their relative refractive indices are $\sqrt{3}$ and 2, respectively. In the absence of noise, the singular values of the contrast MSR matrix are plotted in Fig. 2. Unlike the homogeneous background scenario where the number of dominant singular values is equal to the number of point-like scatterers, Fig. 2 illustrates that, in inhomogeneous background scenario, there are eight dominant singular values for two point-like scatterers. The reason for this interesting observation lies in the FEM implementation of the forward scattering problem. Each point-like scatterer is represented by a square element, and the contrast source is distributed in this square element. Since the contrast source within the square element is represented by the bilinear interpolation of the contrast sources at four corner nodes, each scatterer corresponds to four singular values. Treating the first eight left singular vectors as the basis of the signal subspace and the rest as the basis of the noise subspace, the

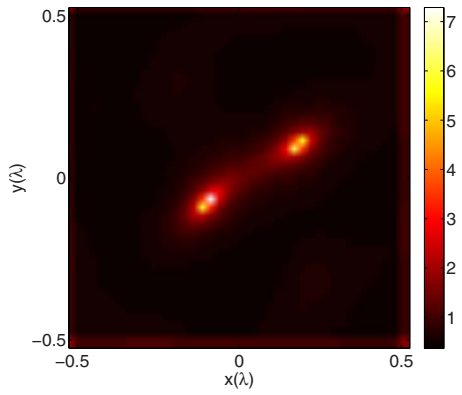

FIG. 5. (Color online) MUSIC pseudospectrum of the first numerical example (in the presence of 20 dB additive white Gaussian noise).

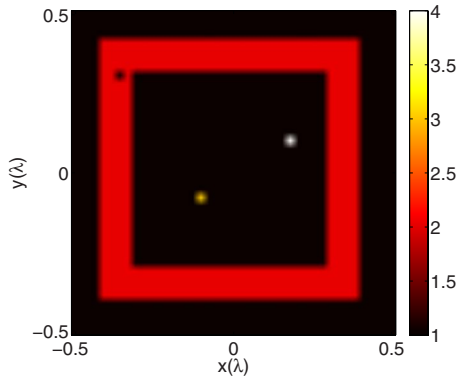

FIG. 6. (Color online) The exact configuration of the inhomogeneous background and point-like scatterers. The inhomogeneous background is a closed wall of outer side length 0.8λ and inner side length 0.6λ. The color bar represents the value of the square of relative refractive index, i.e., n^2.

MUSIC pseudospectrum is given by Fig. 3. Both scatterers are correctly located, except that the sizes of the peaks in the pseudospectrum are four times of the actual sizes of scatterers due to the aforementioned reason. Next, 20 dB additive white Gaussian noise is added to the contrast MSR matrix, and the singular values of the noise-contaminated $\bar{\bar{K}}_c$ is shown in Fig. 4, which illustrates that only two singular values are dominant. This fact is expected since four corner nodes of a square element are so close to each other that the Gaussian noise blurs the distinction of contributions of four corner nodes to the scattered contrast field. Treating the first two left singular vectors as the basis of the signal subspace and the rest as the basis of the noise subspace, the MUSIC pseudospectrum is given by Fig. 5, which shows that both scatterers are correctly located.

In the second numerical example, the inhomogeneous background medium, as shown in Fig. 6, is a square wall, with the outer side length 0.8λ and inner side length 0.6λ, and its relative refractive index is $\sqrt{2}$. Three point-like scatterers are located in the domain of interest. The first two scatterers are the same as those in the first numerical example. The third one is located at $(-0.35\lambda,\ 0.3\lambda)$, and its relative refractive index is 1. It is easy to see that the third scatterer is a bubble inside the wall. In the absence of noise, the singular values of the contrast MSR matrix are plotted in

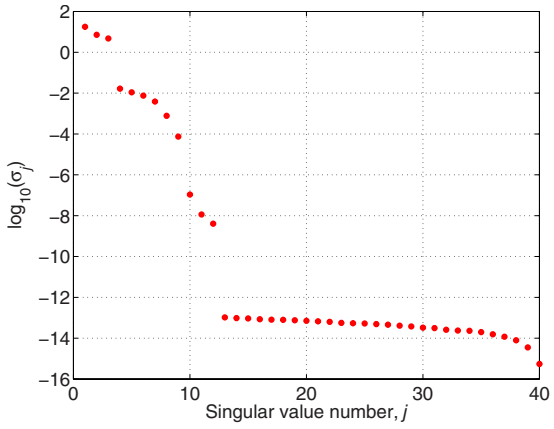

FIG. 7. (Color online) Singular values of the contrast multistatic response matrix in the absence of noise in the second numerical example.

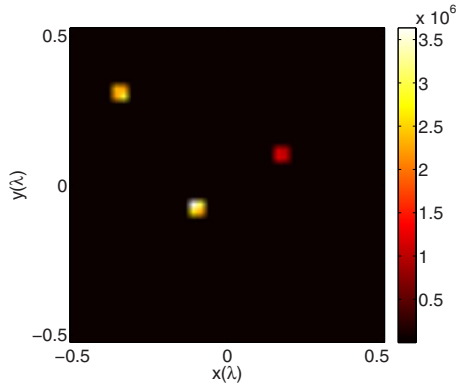

FIG. 8. (Color online) MUSIC pseudospectrum of the second numerical example (in the absence of noise).

Fig. 7, which illustrates 12 dominant singular values. This observation agrees with the aforementioned explanation that each scatterer corresponds to four singular values. Treating the first 12 left singular vectors as the basis of the signal subspace and the rest as the basis of the noise subspace, the MUSIC pseudospectrum is given by Fig. 8. All three scatterers are correctly located. Next, 10 dB additive white Gaussian noise is added to $\bar{\bar{K}}_c$, the singular values of which are shown in Fig. 9, where three singular values are dominant. This observation also agrees with the aforementioned reasons. Treating the first three left singular vectors as the basis of the signal subspace, the MUSIC pseudospectrum is given by Fig. 10, which shows that all three scatterers are correctly located.

V. DISCUSSION AND CONCLUSION

In the proposed FEM implementation, the finite element is chosen to be square element because of ease of generation and visualization, which is greatly desirable in inverse problems. During the implementation of the MUSIC-type method proposed in Sec. III, the inverse operators appearing in Eqs. (20) and (21) are only symbolic, and in practice, there is no need to obtain the explicit inverse of a matrix. For example, in MATLAB software, the matrix left division is used to solve a linear equation. Although the proposed MUSIC-type

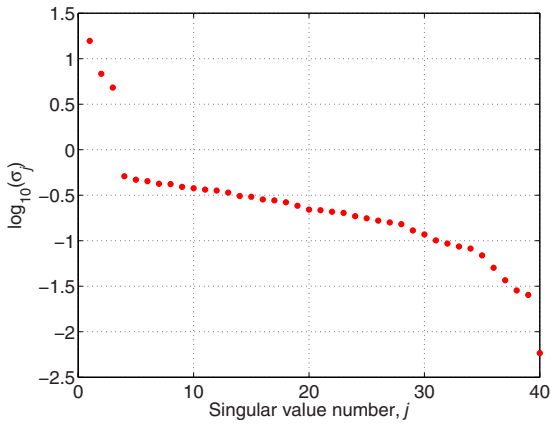

FIG. 9. (Color online) Singular values of the contrast multistatic response matrix in the presence of 10 dB additive white Gaussian noise in the second numerical example.

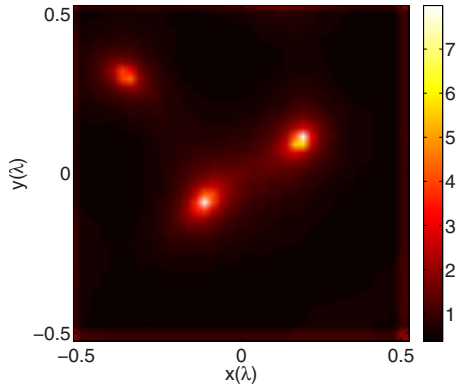

FIG. 10. (Color online) MUSIC pseudospectrum of the second numerical example (in the presence of 10 dB additive white Gaussian noise).

method is for detection of point-like scatterers, it can also be applied to determine the approximate geometric shapes of large scatterers. The homogeneous counterpart of this work has been done in Ref. 17. For inhomogeneous scenario, this research work will be investigated in the future study and will be published somewhere.

This paper extends the MUSIC-type method to the detection of point-like scatterers that are embedded in an inhomogeneous background, thus greatly generalizing the applicability of MUSIC-type method. Although the background Green's function at each test point is not directly available in inhomogeneous scenario, the proposed MUSIC-type algorithm uses the finite element method to simultaneously obtain the background Green's function at all test points. An interesting fact, which is absent in homogeneous scenario, is observed that one point-like scatterer corresponds to four singular values if a point-like scatterer is modeled as a square element in the finite element modeling. This is due to the fact that the contrast source within the square element is represented by the bilinear interpolation of the contrast sources at four corner nodes of the square elements. It is stressed that this is due to the discretization nature of the numerical algorithm instead of the inhomogeneous nature of the background. Numerical simulations in both noise free and noisy cases illustrate the efficacy of the proposed theory and algorithm.

ACKNOWLEDGMENT

The author acknowledges the financial support from the U.S. Department of the Air Force AOARD R&D Grant No. 094130.

[1] A. J. Devaney, "Super-resolution processing of multi-static data using time-reversal and MUSIC," available at http://www.ece.neu.edu/faculty/devaney/ajd/preprints.htm (Last viewed 1/5/2010).
[2] A. J. Devaney, E. A. Marengo, and F. K. Gruber, "Time-reversal-based imaging and inverse scattering of multiply scattering point targets," J. Acoust. Soc. Am. **118**, 3129–3138 (2005).
[3] E. A. Marengo and F. K. Gruber, "Noniterative analytical formula for inverse scattering of multiply scattering point targets," J. Acoust. Soc. Am. **120**, 3782–3788 (2006).
[4] E. A. Marengo and F. K. Gruber, "Subspace-based localization and inverse scattering of multiply scattering point targets," EURASIP Journal on Advances in Signal Processing **2007**, 17342 (2007).
[5] C. Prada and J. L. Thomas, "Experimental subwavelength localization of scatterers by decomposition of the time reversal operator interpreted as a covariance matrix," J. Acoust. Soc. Am. **114**, 235–243 (2003).
[6] Y. Zhong and X. Chen, "MUSIC imaging and electromagnetic inverse scattering of multiply scattering small anisotropic spheres," IEEE Trans. Antennas Propag. **55**, 3542–3549 (2007).
[7] A. Kirsch, "The MUSIC-algorithm and the factorization method in inverse scattering theory for inhomogeneous media," Inverse Probl. **18**, 1025–1040 (2002).
[8] E. Iakovleva, S. Gdoura, D. Lesselier, and G. Perrusson, "Multistatic response matrix of a 3-D inclusion in half space and MUSIC imaging," IEEE Trans. Antennas Propag. **55**, 2598–2609 (2007).
[9] R. O. Schmidt, "Multiple emitter location and signal parameter estimation," IEEE Trans. Antennas Propag. **34**, 276–280 (1986).
[10] C. Prada and M. Fink, "Eigenmodes of the time-reversal operator: A solution to selective focusing in multiple-target media," Wave Motion **20**, 151–163 (1994).
[11] T. Varslot, H. Krogstad, E. Mo, and B. A. Angelsen, "Eigenfunction analysis of stochastic backscatter for characterization of acoustic aberration in medical ultrasound imaging," J. Acoust. Soc. Am. **115**, 3068–3076 (2004).
[12] A. J. Devaney and M. Dennison, "Inverse scattering in inhomogeneous background media," Inverse Probl. **19**, 855–870 (2003).
[13] S. C. Brenner and L. R. Scott, *The Mathematical Theory of Finite Element Methods* (Springer, New York, 2008).
[14] A. F. Peterson, S. L. Ray, and R. Mittra, *Computational Methods for Electromagnetics* (IEEE, New York, 1998).
[15] A. Lakhtakia, "Strong and weak forms of the method of moments and the coupled dipole method for scattering of time-harmonic electromagnetic fields," Int. J. Mod. Phys. C **3**, 583–603 (1992).
[16] P. M. van den Berg, A. L. van Broekhoven, and A. Abubakar, "Extended contrast source inversion," Inverse Probl. **15**, 1325–1344 (1999).
[17] E. A. Marengo, F. K. Gruber, and F. Simonetti, "Time-reversal MUSIC imaging of extended targets," IEEE Trans. Image Process. **16**, 1967–1984 (2007).

Coherent reflection without traveling waves: On the origin of long-latency otoacoustic emissions in lizards

Christopher Bergevin
Department of Mathematics, University of Arizona, Tucson, Arizona 85705

Christopher A. Shera
Eaton-Peabody Laboratory of Auditory Physiology, Massachusetts Eye and Ear Infirmary, 243 Charles Street, Boston, Massachusetts 02114 and Department of Otology and Laryngology, Harvard Medical School, Boston, Massachusetts, 02115

(Received 13 July 2009; revised 6 January 2010; accepted 7 January 2010)

Lizard ears produce otoacoustic emissions with characteristics often strikingly reminiscent of those measured in mammals. The similarity of their emissions is surprising, given that lizards and mammals manifest major differences in aspects of inner ear morphology and function believed to be relevant to emission generation. For example, lizards such as the gecko evidently lack traveling waves along their basilar membrane. Despite the absence of traveling waves, the phase-gradient delays of gecko stimulus-frequency otoacoustic emissions (SFOAEs) are comparable to those measured in many mammals. This paper describes a model of emission generation inspired by the gecko inner ear. The model consists of an array of coupled harmonic oscillators whose effective damping manifests a small degree of irregularity. Model delays increase with the assumed sharpness of tuning, reflecting the build-up time associated with mechanical resonance. When tuning bandwidths are chosen to match those of gecko auditory-nerve fibers, the model reproduces the major features of gecko SFOAEs, including their spectral structure and the magnitude and frequency dependence of their phase-gradient delays. The same model with appropriately modified parameters reproduces the features of SFOAEs in alligator lizards. Analysis of the model demonstrates that the basic mechanisms operating in the model are similar to those of the coherent-reflection model developed to describe mammalian emissions. These results support the notion that SFOAE delays provide a noninvasive measure of the sharpness of cochlear tuning.
 [DOI: 10.1121/1.3303977]

PACS number(s): 43.64.Bt, 43.64.Jb, 43.64.Kc [ADP] Pages: 2398–2409

I. INTRODUCTION

Sounds evoked from the ear, known as otoacoustic emissions (OAEs), provide a noninvasive window on the mechanics of hearing. In mammalian ears, two broad classes of OAE generation mechanisms—so-called "wave-fixed" and "place-fixed"—have been identified on the basis of emission phase-versus-frequency functions (Kemp and Brown, 1983; Shera and Guinan, 1999). The characteristics of place-fixed emissions—those with rapidly rotating phases or, equivalently, long phase-gradient delays—appear well described by the coherent-reflection model (Zweig and Shera, 1995; Talmadge *et al.*, 2000; Shera *et al.*, 2005). In this model, the emissions arise when pressure-difference waves traveling within the cochlear duct encounter intrinsic micromechanical irregularities in the organ of Corti. According to the cochlear model equations, mechanical irregularities give rise to a reverse energy flow through a process analogous to the scattering of waves by perturbations in the impedance of the medium (e.g., the scattering of light within a medium of variable refractive index). Place-fixed OAEs are therefore also known as "reflection-source" otoacoustic emissions.

Although the coherent-reflection model was developed to account for mammalian place-fixed OAEs, recent work shows that a similar place- versus wave-fixed distinction among OAE mechanisms also pertains in certain non-mammalian vertebrates such as the chicken and the gecko (Bergevin *et al.*, 2008). The existence in lizards of OAEs with steep phase gradients and other characteristics of mammalian reflection-source OAEs presents a serious challenge. Although lizard ears evidently produce OAEs with spectral levels and phase gradients comparable to those found in many mammals (Bergevin *et al.*, 2008), important aspects of their inner ear morphology and physiology are rather different. Most significantly for models of emission generation, lizards evidently lack a clear analog of the mammalian traveling wave (e.g., Peake and Ling, 1980; Manley, 1990), and their tonotopy is thought to arise micromechanically at the level of the hair-cell bundle (Manley *et al.*, 1999; Aranyosi and Freeman, 2004). Despite these major functional differences between the inner ears of mammals and lizards, the striking similarities in their emission characteristics suggest that the underlying mechanisms of OAE generation are somehow equivalent (e.g., Köppl, 1995).

The following conundrum thus arises: If the coherent-reflection model applies in mammals, how can similar mechanisms be operating in the lizard, where there are no waves to be reflected? Alternatively, might some other as yet unidentified generation mechanism be operating in both cases? At a minimum, any candidate model must account for the long phase-gradient delays found in both mammalian and

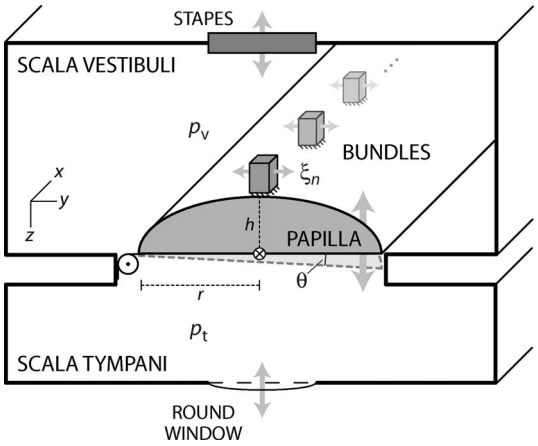

FIG. 1. Schematic cross-section of the model showing two chambers filled with incompressible fluid and separated by a rigid partition (papilla) attached to the left-hand wall by a stiff, lossy hinge (⊙). An array of masses (bundles, $n=1,\ldots,N$) sits atop the papilla, each coupled to the papilla through an elastic element. The bundles are arranged longitudinally, parallel to the x-axis. Vibration of the stapes induces a papilla rotation through the angle θ with the horizontal, which is taken parallel to the y-axis. In the small-angle limit, rotation of the papilla has two important effects: It moves the center of the basilar membrane (⊗) vertically (i.e., parallel to the z-axis) by an amount $\xi_z \cong r\theta$, where $2r$ is the papilla width, and it drags the bundles horizontally through the fluid. The total horizontal displacement of bundle n is denoted ξ_n. The elastic force on each bundle is taken proportional to its displacement relative to the top surface of the papilla (i.e., to $\xi_n - \xi_y$, where $\xi_y \cong h\theta$ is the papilla displacement just below the bundle and h is the papilla height). Bundle motion is damped by viscous losses in the fluid. The resonant frequencies and quality factors of the bundle oscillators are taken to vary systematically along the papilla.

non-mammalian ears (typically 1–10 ms or longer, depending on stimulus frequency and intensity). These substantial delays are not due to middle-ear transmission, whose contribution amounts to only several tens of microseconds (e.g., Guinan and Peake, 1967; Rosowski *et al.*, 1985; Manley *et al.*, 1988). Inner-ear dimensions may play a role but can hardly be invoked to explain why geckos (whose basilar papilla measures 1.5–2 mm in length) have phase-gradient delays similar to those of cats (whose basilar membrane is some 15 times longer). Thus, although delays associated with wave propagation presumably contribute in mammals, the origin of the long delays in non-mammals, especially those lacking basilar-membrane (BM) traveling waves (or, as in amphibians, a flexible BM altogether), remains unclear.

In this paper, we address questions raised by the existence of long-latency reflection-source OAEs in lizard. In particular, we develop a simplified model inspired by the lizard inner ear to determine whether the basic principles and predictions of coherent-reflection theory might somehow apply even in the absence of traveling waves. In the process, we test the conjecture (Shera, 2003; Shera and Guinan, 2008) that the generation of realistic reflection-source OAEs requires nothing more than a slightly irregular array of tuned mechanical resonators.

II. A MODEL INSPIRED BY THE GECKO INNER EAR

To explore possible mechanisms of OAE generation, we adopt a highly simplified model inspired by the functional anatomy of the gecko inner ear (see Fig. 1). Detailed descriptions of the anatomy and physiology of the gecko ear are available elsewhere (e.g., Wever, 1978; Köppl and Authier, 1995; Manley *et al.*, 1999; Bergevin *et al.*, 2008). Briefly, the gecko inner ear consists of 1000–2000 hair cells sitting atop the relatively rigid basilar papilla. Although gecko hair cells lack the somatic motility characteristic of mammalian outer hair cells (Köppl *et al.*, 2004), they presumably manifest mechanisms of active amplification within their bundles. Whereas the low-frequency portion of the papilla is covered by a continuous tectorial membrane, the hair cells sensitive to frequencies above ~1 kHz are covered by discrete sections of tectorium (sallets), which couple small groups of hair cells together into a single radial row (Wever, 1978). Although gecko ears apparently lack analogs of BM traveling waves (Manley *et al.*, 1999), they produce robust otoacoustic emissions (Manley *et al.*, 1996; Bergevin *et al.*, 2008) and have auditory-nerve fiber (ANF) responses with thresholds and frequency tuning comparable to many mammals (Eatock *et al.*, 1981; Sams-Dodd and Capranica, 1994; Manley *et al.*, 1999).

Since our purpose here is to explore the origin of long-latency OAEs in a mechanical system without basilar-membrane traveling waves, we simplify the analysis by boiling the many exquisite details of gecko functional anatomy down to a few idealized mechanical elements. Taken together, these elements provide perhaps the simplest realization of a mechanically tuned inner ear. Although the physical framework we adopt was inspired by the gecko—and appears isomorphic to other, more physically and biologically realistic models of the lizard inner ear (e.g., Weiss *et al.*, 1985; Authier and Manley, 1995)—we make no attempt to faithfully represent the complex inner ear morphology or mechanics of any particular species. Although our model is therefore an abstract representation of lizard functional anatomy, it is not unphysical. The hydromechanical system we describe could, in principle, be built and experimented upon in the laboratory.

Figure 1 shows a schematic of the model, which consists of two rigid-walled cavities (the scala vestibuli and tympani) filled with incompressible fluid and separated by a rigid partition (papilla). Tuned mechanical elements representing hair bundles (or groups of hair bundles coupled by sallets) sit atop the papilla. The pressures in the two scalae (p_v and p_t) are driven by the motions of the stapes and round window, and are presumed uniform throughout their respective cavities. The papilla and the hair cells on its surface are represented as linear, passive resonators (e.g., Authier and Manley, 1995; Aranyosi and Freeman, 2004). The hair-cell resonators (hereafter referred to as "bundles") are elastically coupled to the movement of the papilla. Much like the papilla in the alligator lizard (Frishkopf and DeRosier, 1983; Holton and Hudspeth, 1983), the model papilla rotates about a longitudinal axis. For simplicity, we locate the axis of rotation along one edge of the papilla, parallel to the x-axis. For small-angle motions,[1] rotation about this axis can be regarded as the superposition of a bulk translational motion and a pure rotation about the center of the basilar membrane (⊗ in Fig. 1). The translational motion of the papilla produces a net vertical fluid displacement that couples to the

motion of the stapes, and the rotational motion stimulates the bundles by dragging them horizontally through the fluid. Analogues of these two coupled modes of motion have been observed in the alligator lizard (Aranyosi and Freeman, 2005).

A. Motion of the papilla and the bundles

The model papilla rotates as a rigid body driven both by the pressure difference across its surface and by forces from the bundles. Although the spatial arrangement of the bundles is not important in the model (due to the rigidity of the papilla), we facilitate bookkeeping by assuming that the bundles are uniformly distributed along the papilla and are numbered in order of increasing distance from the apical end. Summing the forces on the papilla, including those from each of the N bundles, and applying Newton's second law yields

$$I\ddot{\theta} + R\dot{\theta} + K\theta + h\sum_{n=1}^{N} k_n(\xi_y - \xi_n) \cong rA(p_v - p_t), \tag{1}$$

where diacritical dots represent time derivatives. In this equation, the clockwise angular displacement of the papilla about its "hinge" at the left edge is denoted θ; the symbols I, R, and K represent the corresponding rotational mass (moment of inertia), damping, and stiffness of the papilla. The papilla has length L in the x direction, width $2r$ in the y direction, and height h in the z direction. Each of the N bundles acts through an elastic element (stiffness k_n) to produce a torque proportional to its horizontal displacement (ξ_n) relative to that of the top of the papilla (ξ_y). The effective moment arm is the papilla height h; in the small-angle limit, $\xi_y \cong h\theta$. The quantity $rA(p_v - p_t)$ on the right represents the torque arising from the trans-papilla pressure. The moment arm r is the papilla half-width, and A is the effective area of the papilla in the xy-plane ($A \cong 2rL$). Note that vertical (or transverse) displacements of the papilla are defined as positive toward scala tympani (i.e., in the direction produced by stapes displacements *into* the inner ear).

Each bundle is a miniature harmonic oscillator driven by the elastic element that couples it to the horizontal motion (ξ_y) of the top of the papilla:

$$m_n\ddot{\xi}_n + r_n\dot{\xi}_n + k_n(\xi_n - \xi_y) = 0. \tag{2}$$

The effective mass of each bundle is denoted m_n. The damping force (proportional to r_n) is taken to be dominated by the viscous drag of the bundle as it moves back and forth through the fluid (assumed stationary in the horizontal direction). Exploiting the assumed linearity, we adopt harmonic time dependence and represent dynamical variables by Fourier coefficients (uppercase) at angular frequency $\omega = 2\pi f$ [i.e., $\xi_y(t) = \Xi_y(\omega)e^{i\omega t}$]. Equation (2) then simplifies to

$$\Xi_n = \frac{\Xi_y}{1 - \beta_n^2 + i\beta_n/Q_n}, \tag{3}$$

where β_n is normalized frequency (i.e., $\beta_n \equiv f/\mathrm{CF}_n$, with $\mathrm{CF}_n \equiv \sqrt{k_n/m_n}/2\pi$ representing the resonant frequency of bundle n) and Q_n is the quality factor of the resonance ($Q_n \equiv \sqrt{m_n k_n}/r_n$).

Equation (3) for the bundle response is consistent with previous studies in lizards (e.g., Weiss and Leong, 1985; Authier and Manley, 1995), which have found that the "micromechanical transfer function" (Ξ_n/Ξ_y) is well approximated by a second-order system. Combining Eqs. (1) and (3) and using the small-angle approximation ($\Theta \cong \Xi_y/h$) yields

$$\Xi_y\left[(i\omega)^2 I + i\omega R + K + h^2\sum_{n=1}^{N} k_n\frac{-\beta_n^2 + i\beta_n/Q_n}{1 - \beta_n^2 + i\beta_n/Q_n}\right] = rhA(P_v - P_t), \tag{4}$$

an equation that relates the horizontal displacement of the papilla beneath the bundle to the driving pressure force.

B. Coupling to the middle ear

The inner ear couples to the middle ear, and thereby to the external acoustic environment, through the motions of the oval and round windows. Conservation of mass requires that the volume velocity of the papilla equal that of the oval window,

$$i\omega A\Xi_z = U_{ow}, \tag{5}$$

where U_{ow} is the volume velocity of the oval window (stapes) and $\Xi_z \cong r\Theta$ is the mean vertical displacement of the papilla. Because of fluid incompressibility, the volume velocities of the oval and round windows are equal in magnitude but opposite in phase.

The mechanics of the papilla and its bundles can be represented by an acoustic impedance, defined as $Z_{ie} = (P_v - P_t)/U_{ow}$, where the subscript stands for "inner ear."[2] Solving for Z_{ie} using Eqs. (4) and (5) yields

$$Z_{ie} \cong Z_p + \frac{1}{i\omega}\left(\frac{h}{rA}\right)^2\sum_{n=1}^{N} k_n\frac{-\beta_n^2 + i\beta_n/Q_n}{1 - \beta_n^2 + i\beta_n/Q_n}, \tag{6}$$

where $Z_p = (K_p/i\omega)\ (1 - \beta_p^2 + i\beta_p/Q_p)/A^2$ is the acoustic impedance of the papilla expressed in terms of its effective stiffness ($K_p = K/r^2$), normalized resonant frequency (β_p), and quality factor (Q_p). The summation over n implies that every bundle affects the impedance of the inner ear, and is thereby coupled to the middle and external ears. Equation (6) indicates that when tuning is sufficiently sharp any given bundle contributes maximally to the impedance Z_{ie} near the bundle's resonant frequency ($\beta_n \cong 1$).

C. Bundle irregularity

Anatomical studies in tokay geckos and other lizards find spatial irregularities throughout the inner ear, including the width and thickness of the papilla, the number of hair cells in a given radial cross-section, and the heights of the hair bundles (e.g., Miller, 1973; Wever, 1978; Köppl and Authier, 1995). We parametrize these and other variations not so apparent in the anatomy by assuming that the mechanical properties of the bundles vary somewhat irregularly from row to row. A similar approach has been used to model the generation of reflection-source OAEs in the mammalian

TABLE I. Parameter values used to compute model SFOAEs in gecko and alligator lizard. Values for alligator lizard (see Sec. V B) are listed only when they differ from gecko.

		Gecko	Alligator lizard
Papilla length	L	1.7 mm[a]	0.3 mm[b–d]
Papilla area	A	0.15 mm^2 [c]	0.04 mm^2 [c]
Papilla resonant frequency	f_p	1.5 kHz[e]	2 kHz[f]
Papilla quality factor	Q_p	2[e]	0.5[f]
Papilla volume compliance	C_p	0.57×10^{-6} mm^3/Pa [g]	
Papilla stiffness	K_p	A^2/C_p	
Papilla aspect ratio	h/r	1.0[c,h]	1.0[j]
No. of bundles (rows)	N	250[h]	130[b–d]
Maximum bundle CF	CF_{max}	5 kHz[a]	6 kHz[b,j]
Tonotopic map space constant	ℓ	0.5 mm[a]	0.16 mm[b–d]
Bundle $Q_{10\ dB}$ (at 1 kHz)	$Q_{10\ dB}$	2.3[a]	1.1[b]
$Q_{10\ dB}$ power-law exponent		0.35[a]	0.55[b]
Bundle stiffness	k_n	K_p/N	
Irregularity size	rms(ϵ_n)	0.03 (or 3%)	
Round-trip middle-ear gain	G_{me}	0.25[g]	
Stimulus pressure	P	20 dB SPL[k]	

[a]Manley *et al.* (1999).
[b]Weiss *et al.* (1976).
[c]Wever (1978).
[d]Manley (1990).
[e]Chiappe (2006).
[f]Peake and Ling (1980).
[g]Rosowski *et al.* (1985).
[h]Köppl and Authier (1995).
[i]Mulroy(1974).
[j]Inferred from SFOAE magnitudes, which fall off above about 6 kHz in alligator lizard.
[k]Bergevin *et al.* (2008).

cochlea (Shera and Zweig, 1993; Zweig and Shera, 1995) and the production of spontaneous OAEs in the bobtail lizard (Vilfan and Duke, 2008). Specifically, we take the quality factors Q_n that characterize the tuning of the bundles to manifest small fractional deviations ϵ_n about some mean value that varies with location along the papilla. Thus, $\tilde{Q}_n = Q_n(1-\epsilon_n)$, where Q_n varies smoothly with n and we have used the diacritical tilde to indicate the presence of mechanical irregularity. Although we have placed the effective mechanical irregularity in the bundle damping, based on the physical expectation that irregularities in this parameter will dominate near resonance, locating the irregularity in other mechanical properties of the bundle gives similar results.

D. Impedance and pressure changes

The effects of bundle irregularity on the impedance of the inner ear (now denoted $\tilde{Z}_{ie}$) can be quantified by computing the difference $\Delta Z=\tilde{Z}_{ie}-Z_{ie}$, where Z_{ie} is the impedance of the corresponding "smooth" model ($\epsilon_n=0$). Equation (6) implies that to first order in the irregularity ϵ_n,

$$\Delta Z \cong \frac{1}{\omega A^2}\sum_{n=1}^{N}\frac{\epsilon_n k_n \beta_n/Q_n}{(1-\beta_n^2+i\beta_n/Q_n)^2}. \tag{7}$$

When transmitted through the middle ear, the impedance change ΔZ produces a change ΔP in the calibrated ear-canal pressure P. When the fractional changes $\Delta Z/Z_{ie}$ and $\Delta P/P$ are both small (as they are here), the two are proportional. To first order, the pressure change therefore has the form

$$\Delta P \cong G_{me}(\Delta Z/Z_{ie})P, \tag{8}$$

where G_{me} is the "proportionality constant." Physically, G_{me} depends on both the acoustics of the stimulus source and the combined effects of forward and reverse middle-ear transmission. At any given frequency, the value of G_{me} can be found from explicit models of the transducer and middle ear (e.g., Rosowski *et al.*, 1985) or, more generally, by representing the transducer by its Thevenin equivalent, and the middle ear as an acousto-mechanical two-port network characterized by a transfer matrix (e.g., Shera and Zweig, 1992; Puria, 2003; Songer and Rosowski, 2007).[3]

The pressure change ΔP given by Eq. (8) is the stimulus-frequency otoacoustic emission (SFOAE) produced by the model. As we demonstrate below, this computational definition of the SFOAE extracts what amounts to a delayed component from the total ear-canal pressure. In actual SFOAE measurements, the delayed component can be obtained using a variety of methods (e.g., by exploiting mechanical nonlinearity or by using signal-processing techniques to smooth the measured frequency response), all of which yield equivalent results, at least in humans (Kalluri and Shera, 2007).

E. Parameter values

Although the model simplifies the morphology of the gecko inner ear, we have chosen parameter values with an eye toward capturing some of the relevant physiology. Most important to the questions explored here are the parameters that characterize the frequency tuning of the bundles. On the supposition that peripheral tuning is predominantly mechanical in origin, we have selected the parameters of bundle tuning to match neurophysiological estimates of ANF tuning in the tokay gecko *(Gekko gecko).* Table I summarizes all parameters.

We assume that the $N\sim250$ bundles are spaced uniformly along the papilla, with spacing $\Delta x=L/N$, where L is

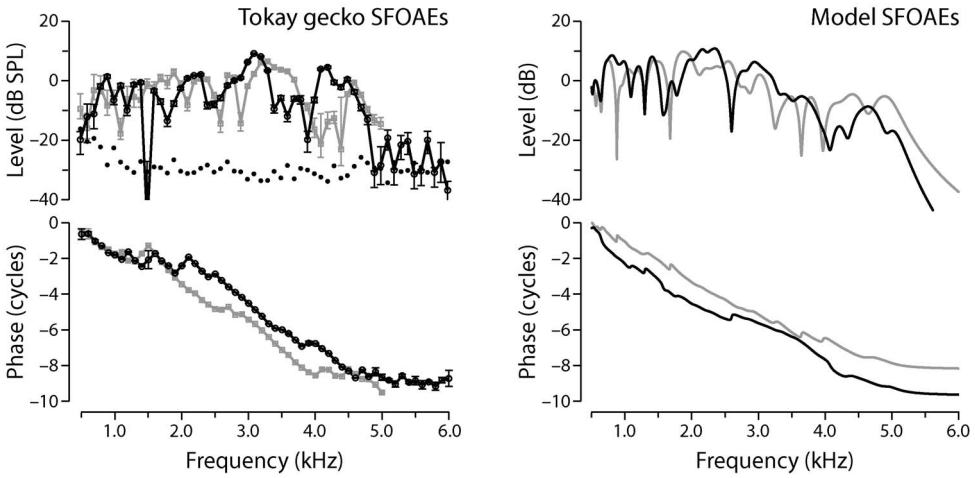

FIG. 2. Measured and model stimulus-frequency OAEs. Panel A: Representative SFOAEs at probe levels of 20 dB SPL in the tokay gecko (*G. gecko*) from the study of Bergevin *et al.* (2008). Black and gray lines show data from two different geckos. Error bars on the data points give the standard error of the mean (35 measurements at each frequency in each gecko). The dotted line shows the acoustic noise floor. Panel B: Simulated SFOAEs ΔP computed from Eq. (8) using random micromechanical irregularities and the parameter values given in Table I. The emission magnitudes have been scaled up by 45 dB to approximate those of the measurements (see text). Black and gray lines show model results for two different "ears" (i.e., different irregularity patterns).

the length of the papilla ($L \cong 1.7$ mm giving $\Delta x \cong 7$ μm). In accord with ANF tracing experiments (Manley *et al.*, 1999), which determine the characteristics of ANF tuning as a function of location along the papilla, we take the bundle resonant frequencies to vary exponentially with position. More precisely, $\mathrm{CF}_n = \mathrm{CF}_{\max} e^{-x_n/\ell}$, where $\mathrm{CF}_{\max} = 5$ kHz, $x_n = (n-1)\Delta x$, and the distance $\ell \cong 0.5$ mm is the space constant of the tonotopic map (Manley *et al.*, 1999).[4] Note that x is the distance from the *apical* end of the papilla; the gecko's tonotopic map is reversed and fibers tuned to low frequencies innervate the basal end (Manley *et al.*, 1999). The quality factors Q_n of the bundle resonators are assumed to vary with CF as $Q_n = 3Q_{10\ \mathrm{dB}}(\mathrm{CF}_n)$, where $Q_{10\ \mathrm{dB}}(\mathrm{CF}) = 2.3(\mathrm{CF/kHz})^{0.35}$ is a power-law fit to tokay gecko ANF tuning data (Manley *et al.*, 1999). For internal consistency, we use tuning data from the same study that determined the tonotopic map (Manley *et al.*, 1999). The factor of 3 that converts physiological $Q_{10\ \mathrm{dB}}$ values to equivalent Q_n values is an approximation valid for second-order filters (e.g., Hartmann, 1998).

Although most of the other model parameters have little impact on our basic results—they primarily affect overall OAE amplitude, which we make no attempt to match due to the absence of active bundle amplification in the model—several do warrant mention. We used the papilla volume compliance reported in alligator lizard (Rosowski *et al.*, 1985) to determine the stiffness K_p. We then arbitrarily set the stiffness of the individual bundles to the value $k_n = K_\mathrm{p}/N$, independent of n.[5] Taking the bundle stiffness proportional to that of the papilla, but scaled down by a factor of N, compensates for the summation over bundles and guarantees that the papilla and the bundles make similar order-of-magnitude contributions to the inner ear impedance Z_ie. If this rough equality of impedances were grossly violated, specifically if the net bundle impedance were much smaller than that of the papilla, then the bundles would have negligible effect on ear-canal pressure and could not generate appreciable OAEs. For simplicity, and because delays introduced by middle-ear transmission are small compared to OAE delays, we assumed a constant value of round-trip middle-ear pressure gain G_me. Our value of G_me is roughly consistent with that predicted by the model of Rosowski *et al.* (1985) in alligator lizard. Finally, the irregularities ϵ_n were assumed to vary randomly from bundle to bundle. In the numerical simulations, values of ϵ_n were obtained by sampling from a Gaussian distribution with zero-mean and standard deviation 0.03; thus, the rms fractional irregularity was 3%. This value was chosen for consistency with that used in models of mammalian SFOAEs (e.g., Talmadge *et al.*, 2000; Shera *et al.*, 2005); the amount of irregularity may well be substantially larger in lizards. Because mean emission amplitudes vary in direct proportion to the size of the irregularities, the value of ϵ_n makes a significant contribution to overall OAE levels.

III. COMPARISON WITH GECKO EMISSIONS

Figure 2 compares model simulations with representative SFOAEs measured in the tokay gecko (Bergevin *et al.*, 2008). Model results for two different "ears" were obtained by using different patterns of irregularities. Despite the simplicity of the model, the simulated SFOAEs are in strong qualitative agreement with the data. An exception, of course, is the overall emission magnitude. With our choice of parameters, OAE levels are some 45 dB smaller than the measurements; including active mechanisms and/or larger irregularities would presumably narrow that gap substantially. Both the measurements and the model manifest relatively broad spectral maxima, punctuated at irregular intervals by sharp notches. The model predicts that the spectral structure characteristic of a given measurement reflects the distinctive pattern of mechanical irregularity in that ear. At stimulus frequencies above the maximum CF represented along the papilla (~5 kHz), both measured and model SFOAE magnitudes fall off sharply. The patterns of phase variation across frequency are also strikingly similar. In both cases,

SFOAE phase rotates rapidly, accumulating a phase lag of 8–10 cycles over the operative 4.5 kHz span of the figure. Phase gradients vary with frequency but correspond, on average, to a delay of about 2 ms.

IV. THE ORIGIN OF THE EMISSION PHASE GRADIENT

To explore the origin of the rapidly rotating OAE phase predicted by the model, we derive an approximate analytic expression for the emission phase-gradient delay. In a nutshell, the derivation indicates that the rapid rotation of OAE phase originates in mechanical phase shifts (delays) associated with the frequency tuning of the bundles. Because of their frequency selectivity, the bundles take time to respond, and the resulting delays are reflected in SFOAE phase gradients. At any given frequency, the delay associated with mechanical filtering by the bundle increases with the sharpness of tuning. As a result, we find that the predicted emission delay (expressed in periods of the stimulus frequency) is proportional to the quality factor of the resonance [Eq. (14) below]. The derivation sketched below generally parallels analysis of the coherent-reflection model; further discussion and technical details can be found in previous publications (e.g., Zweig and Shera, 1995; Talmadge *et al.*, 2000; Shera and Guinan, 2008).

A. Analytic approximation for the delay

We begin the derivation by noting that the delay in the model arises predominantly from the factor ΔZ in Eq. (8); delays associated with the factors $G_{\rm me}$ and $Z_{\rm ie}$ are negligible. Approximating the finite array of resonators [Eq. (7) for ΔZ] by a continuum and converting the sum over bundles into an integral over position yields

$$\omega A^2 \Delta Z(\omega) \cong \int_0^L \frac{\epsilon k \beta/Q}{(1-\beta^2+i\beta/Q)^2} dx, \tag{9}$$

where k is the bundle stiffness per unit length and all quantities in the integrand are regarded as functions of position. To simplify the derivation without any significant effect on the outcome, we henceforth assume that k and Q are constant. Using the exponential tonotopic map to rewrite the spatial integral in terms of $\beta(x,f)=f/{\rm CF}(x)$ yields

$$\omega A^2 \Delta Z(\omega) \cong (\ell k/Q) \int_{\beta_0}^{\beta_L} \epsilon [T e^{i\phi}]^2 d\beta, \tag{10}$$

where $dx=\ell(d\beta/\beta)$, ℓ is the space constant of the map, $\beta_{\{0,L\}} \equiv f/{\rm CF}(\{0,L\})$, and $Te^{i\phi} \equiv 1/(1-\beta^2+i\beta/Q)$ is the transfer function of the harmonic oscillator [with magnitude $T(\beta)$ and phase $\phi(\beta)$].

Decomposing the irregularity function $\epsilon(x)$ into spatial-frequency components κ facilitates description of phase-cancellation effects between contributions to the emission arising from different spatial locations (Shera and Zweig, 1993; Zweig and Shera, 1995). Just as in the coherent-reflection model, not all spatial frequencies κ contribute equally to the emission. In particular, the integral in Eq. (10) is dominated by spatial frequencies in a relatively narrow range about an "optimal" value, denoted $\hat{\kappa}$. For irregularities arrayed at this special spatial frequency, contributions from adjacent bundles tend to combine coherently rather than cancel one another. To see this, and find the value of $\hat{\kappa}$, we consider the case of a single (unspecified) spatial frequency and take $\epsilon(x) \to 2\cos(\kappa x) = e^{i\kappa x} + e^{-i\kappa x}$. For $\kappa > 0$, it suffices to consider only the term $e^{i\kappa x}$,[6] which can be written in the form $e^{i\kappa\ell \ln(\beta/\beta_0)}$. The integral in Eq. (10) then becomes

$$e^{-i\kappa\ell \ln \beta_0} \int_{\beta_0}^{\beta_L} T^2(\beta) e^{i[\kappa\ell \ln \beta + 2\phi(\beta)]} d\beta. \tag{11}$$

When the oscillators are sharply tuned, the factor $T^2(\beta)$ is strongly peaked at some value $\hat{\beta}$ near $\beta \cong 1$. The spatial frequency that yields the dominant contribution to the emission can be found by applying the principle of stationary phase and requiring that the phase of the integrand be constant near its magnitude peak at $\hat{\beta}$. This yields

$$\frac{\partial}{\partial\beta}[\kappa\ell \ln \beta + 2\phi(\beta)]\big|_{\hat{\beta}} = 0 \Rightarrow \hat{\kappa} = -2\hat{\beta}\hat{\phi}'/\ell, \tag{12}$$

where $\hat{\phi}' = \partial\phi/\partial\beta|_{\hat{\beta}}$ is the slope of the transfer function phase at the magnitude peak.

To determine how the predicted emission phase varies with frequency, we exploit the "local scaling" manifest by the bundle responses in the model. Local scaling means that, at least near their magnitude peaks, the frequency responses depend on normalized frequency $\beta=f/{\rm CF}$, rather than on frequency and CF independently (Zweig, 1976). Local scaling applies in the model and also approximates the tip region of gecko ANF tuning curves (Manley *et al.*, 1999). As a consequence of local scaling, the value of the integral in Eq. (11) does not depend strongly on frequency except at frequencies close to the ends of the tonotopic map (indeed, if the papilla were infinite, the integral over β would evaluate to a constant, independent of frequency). Consequently, the frequency dependence of the phase is determined principally by the argument of the phasor $e^{-i\hat{\kappa}\ell \ln \beta_0}$ that multiplies the integral. The phase-gradient delay of ΔZ expressed in stimulus periods [succinctly expressed as $-d(\angle \Delta Z/2\pi)/d \ln f$] is therefore well approximated by the value $\hat{\kappa}\ell/2\pi$. Substituting the value of $\hat{\kappa}$ from Eq. (12) and using $\hat{\beta} \cong 1$ gives

$$N_{\rm SFOAE} \cong -2(\hat{\phi}'/2\pi), \tag{13}$$

where $N_{\rm SFOAE}$ is the emission delay in periods (the symbol N was chosen to denote the number of stimulus periods). Note that $-\hat{\phi}'/2\pi$ is just the peak phase-gradient delay of the harmonic oscillator transfer function expressed in periods of the characteristic frequency; $N_{\rm SFOAE}$ is twice this value.[7]

Computing $N_{\rm SFOAE}$ using the explicit form for $Te^{i\phi}$ employed in the model gives

$$N_{\rm SFOAE} \cong 2Q/\pi = 6Q_{10\ {\rm dB}}/\pi, \tag{14}$$

where we have evaluated ϕ' for the harmonic oscillator at resonance ($\hat{\beta} \cong 1$) using the excellent approximation $\phi'(\beta=1) \cong -2Q$. As discussed in Sec. II E, the factor of 3 relating Q and $Q_{10\ {\rm dB}}$ is valid for second-order filters. Although our derivation of Eq. (14) assumes, for simplicity, that Q is con-

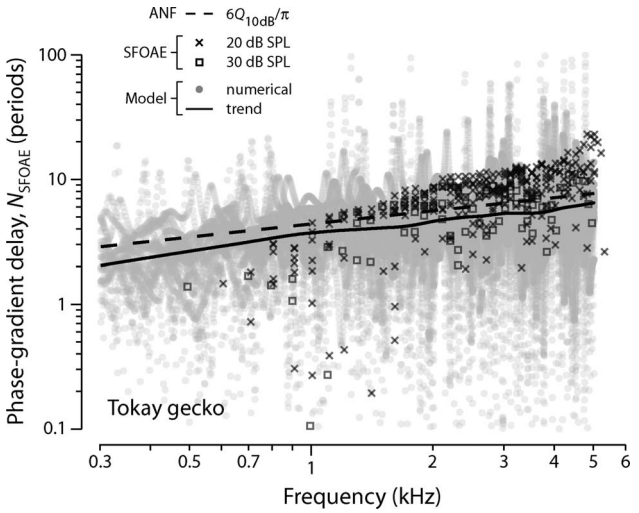

FIG. 3. Measured and model SFOAE phase-gradient delays N_{SFOAE} versus frequency. Delays are expressed in periods of the stimulus frequency. The symbols × and □ show delays measured in the tokay gecko at probe levels of 20 dB SPL (ten ears) and 30 dB SPL (three ears), respectively (Bergevin *et al.*, 2008). Data points whose corresponding SFOAE magnitudes fell within 10 dB of the noise floor are not shown. The gray dots show model N_{SFOAE} values obtained from numerical simulations of 25 different ears (i.e., irregularity patterns). The solid curve is a loess trend line (Cleveland, 1993) fit to the pooled model results. The dashed line gives the analytic approximation $6Q_{10\ \mathrm{dB}}/\pi$ [Eq. (14)], where $Q_{10\ \mathrm{dB}}(\mathrm{CF})$ is a power-law fit to ANF data (Manley *et al.*, 1999).

stant along the papilla, the result can be expected to hold so long as the change in Q over a distance corresponding to the bandwidth of the resonator remains small (i.e., so long as $|d \ln Q/d \ln \mathrm{CF}| \ll 1$). According to this analysis, the mean value of N_{SFOAE} at any given frequency is directly proportional to the quality factor of the bundle tuning at that frequency: the sharper the tuning (higher the $Q_{10\ \mathrm{dB}}$), the longer the delay in periods (larger the value of N_{SFOAE}).

B. Computational validation

Figure 3 shows model simulations that verify the approximate proportionality between N_{SFOAE} and $Q_{10\ \mathrm{dB}}$ predicted by Eq. (14). The dashed line in the figure is proportional to the empirical function $Q_{10\ \mathrm{dB}}(\mathrm{CF})$ used to determine the model value of Q_n at each CF $[Q_n = 3Q_{10\ \mathrm{dB}}(\mathrm{CF}_n)]$. Recall that $Q_{10\ \mathrm{dB}}(\mathrm{CF}) = 2.3(\mathrm{CF}/\mathrm{kHz})^{0.35}$ is a power-law fit to ANF measurements of the sharpness of tuning in the tokay gecko (Manley *et al.*, 1999). The gray dots and their trend (solid line) give the resulting model values of N_{SFOAE} versus frequency obtained from the phase-versus-frequency functions of simulated SFOAEs similar to those shown in Fig. 2. To improve the statistics, we computed and pooled the results for 25 different irregularity patterns (ears). Comparing the simulated SFOAE delays with the mean N_{SFOAE} values predicted by Eq. (14) shows that the analytic approximation $6Q_{10\ \mathrm{dB}}/\pi$ correctly predicts the trend of the model results. Although at any given frequency, the approximate formula $6Q_{10\ \mathrm{dB}}/\pi$ slightly overestimates the mean N_{SFOAE} value obtained from the model, it captures the slope of the variation across frequency almost exactly. A least-squares fit to the numerical values of N_{SFOAE} (gray dots) gives a power-law exponent of 0.355 ± 0.01, where the uncertainty represents the 95% confidence interval computed using bootstrap resampling.[8] The power-law exponent characterizing the relationship between SFOAE delay and frequency in the model is thus statistically indistinguishable from the value 0.35 used to set the quality factors of the bundle resonators (see Table I). Evidently, model variations in the value of $Q_{10\ \mathrm{dB}}$ along the length of the papilla produce corresponding changes in SFOAE delay, N_{SFOAE}.

Why does the analytic approximation [Eq. (14)] systematically overestimate the mean phase-gradient delay actually predicted by the model (compare the dashed and solid lines in Fig. 3)? By evaluating the phase-gradient delay $-\phi'/2\pi$ at the response peak ($\hat{\beta}$), the analytic formula assumes, in effect, that the entire emission originates at this point. In fact, however, the emission arises from a region about $\hat{\beta}$, whose effective spatial extent depends on such things as the sharpness of tuning. Because the value of ϕ' varies somewhat over the peak region [with $|\phi'(\beta)| \leq |\hat{\phi}'|$ for the harmonic oscillator], the phase-gradient delay of the actual emission is smaller than that estimated from the analytic approximation. Numerical simulations verify that the accuracy of the analytic approximation improves when the spatial region about $\hat{\beta}$ that contributes to the emission is artificially reduced by restricting the summation in Eq. (7) to bundles in the immediate vicinity of the peak.

C. Correlations between tuning and delay in the gecko

For comparison with the delays predicted by the model, Fig. 3 also plots values of N_{SFOAE} obtained from SFOAE measurements in the tokay gecko (Bergevin *et al.*, 2008). Measured values of N_{SFOAE} are shown at probe levels of 20 and 30 dB sound pressure level (SPL), roughly corresponding to the typical thresholds for the auditory-nerve fibers used to determine the dependence of $Q_{10\ \mathrm{dB}}$ on CF (Manley *et al.*, 1999). The delays are slightly shorter at the higher stimulus level, consistent with the trend observed in humans (e.g., Schairer *et al.*, 2006). Although our linear model does not explicitly capture this nonlinear effect, Eq. (14) reproduces the empirical trend when supplemented with the near ubiquitous observation that peripheral tuning broadens with increasing intensity.

The tokay SFOAE delays generally appear somewhat longer than those found in the model. Since the otoacoustic and neural measurements were made on different animals under different conditions, the discrepancy may reflect actual differences in the sharpness of tuning between the two groups. We note that tokay gecko ANF $Q_{10\ \mathrm{dB}}$ values vary somewhat across studies (e.g., Eatock *et al.*, 1981; Sams-Dodd and Capranica, 1994). At least in part, however, the discrepancy must reflect our choice to model the bundle resonators as harmonic oscillators, a form which is presumably too simple. Despite the model's underestimation of absolute SFOAE delay, the frequency dependence of the empirical trend is well described by an approximate proportionality between N_{SFOAE} and $Q_{10\ \mathrm{dB}}$, as predicted by Eq. (14).

Empirical evidence for the proportionality between tuning and delay predicted by the model is especially clear above 1–2 kHz. Although the data below 1 kHz are limited, they hint at possible deviations from the trend established at higher frequencies. In particular, SFOAE delays appear systematically shorter than those predicted by the model. Interestingly, a similar low-frequency deviation between measured SFOAE delays and those predicted by the coherent-reflection model appears in chinchilla (Shera and Guinan, 2003; Siegel *et al.*, 2005; Shera *et al.*, 2008), where it may stem from mixing between OAEs generated by multiple source mechanisms. Like mammals, geckos show evidence for both place- and wave-fixed generation mechanisms (Bergevin *et al.*, 2008); the present model describes only a place-fixed mechanism. In the gecko, possible correlates of the otoacoustic trend include a change in the morphology of the tectorial membrane near the 1 kHz location (Manley *et al.*, 1999), suggesting a change in the coupling between bundles. Another possible explanation for the discrepancy at low frequencies is that tuning in this region of the papilla may be primarily electrical in origin, rather than mechanical (Eatock *et al.*, 1991; Aranyosi, 2002). If so, the mechanisms of SFOAE generation at these frequencies may be quite different from those proposed here.

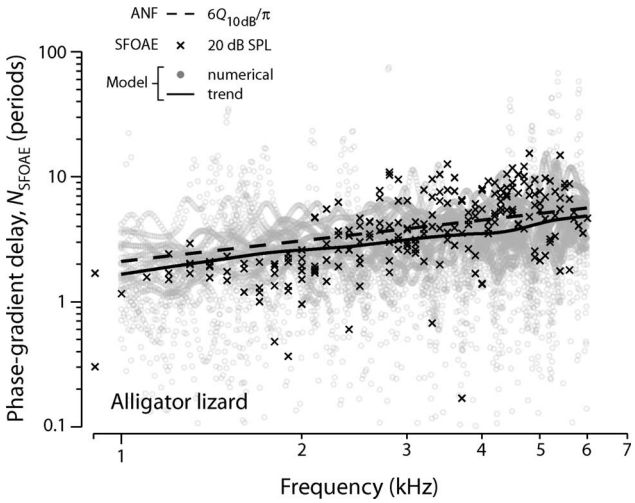

FIG. 4. Measured and model SFOAE phase-gradient delays N_{SFOAE} versus frequency in alligator lizard. The format is the same as Fig. 3. The symbol × shows delays in stimulus periods measured at a probe level of 20 dB SPL (six ears) using methods described elsewhere (Bergevin *et al.*, 2008). Data points within 10 dB of the noise floor are not shown. The gray dots show model N_{SFOAE} values obtained from numerical simulations of 25 different irregularity patterns. The solid curve is a loess trend line fit to the model results. The dashed line gives the analytic approximation $6Q_{10\ dB}/\pi$ [Eq. (14)], where $Q_{10\ dB}$(CF) is a power-law fit to ANF data (Weiss *et al.*, 1976). Data are taken the study of Bergevin *et al.* (2010).

V. DISCUSSION

This paper addresses the observation that so-called reflection-source OAEs with phase-gradient delays comparable to those found in many mammals can readily be measured in nonmammalian species that lack any clear analog of the mammalian traveling wave (Bergevin *et al.*, 2008). To keep the analysis tractable, we adopted a simplified model inspired by the functional anatomy of the gecko inner ear. Parameters were chosen to match the measured CF range and tuning of tokay gecko auditory-nerve fibers. The model described here thus serves to test the conjecture that realistic reflection-source OAEs can be produced by nothing more than a slightly irregular array of tuned oscillators (Shera, 2003; Shera and Guinan, 2008). Despite the simplicity of the assumptions—but consistent with the conjecture—the model produces SFOAEs with characteristics in qualitative and quantitative agreement (aside from a significant disparity in overall emission magnitude) with those measured in the tokay gecko. The unrealistically small emissions produced by the model result from the small coefficient of irregularity and the absence of any form of active amplification. In all other respects, however, the model reproduces the prominent features of tokay SFOAEs, including their overall spectral structure and the approximate value and frequency dependence of their phase-gradient delay.

A. Generality of the model results

The structure and assumptions of the present model are broadly consistent with the comprehensive model of Weiss *et al.* (1985), who developed a quantitative description of the entirety of the lizard auditory periphery, albeit for a species with free-standing stereocilia and minimal overlying tectorial membrane (the Southern alligator lizard, *Elgaria multicarinata*). Their model, summarized by mechanoelectric circuit analogs representing the various macro- and micromechanical stages (Rosowski *et al.*, 1985; Weiss and Leong, 1985), was carefully derived from biophysical considerations and a wealth of physiological data. Whenever possible we employed this more comprehensive model of the lizard auditory periphery to probe the validity of the simplifying assumptions made here. For example, we used their model of the lizard middle ear (Rosowski *et al.*, 1985) to validate our approximations regarding the round-trip middle-ear gain G_{me}. Most importantly, we note that the papilla and the hair bundles in the Weiss *et al.* (1985) model are represented, as they are here, by harmonic oscillators, that is, by second-order linear band-pass filters (Eatock *et al.*, 1991). Because of the isomorphism between these superficially distinct model representations of the lizard inner ear, we are confident that our principal conclusions regarding SFOAE generation (e.g., the origin of the rapidly rotating OAE phase and the approximate proportionality between N_{SFOAE} and $Q_{10\ dB}$) would survive if analogous OAE generation mechanisms were embedded in this more detailed and realistic model of the lizard ear.

B. Extension to the alligator lizard

The structural similarity between our model, inspired by the gecko and models of other lizard ears, suggests that the approach might provide a quantitative account of SFOAE phase gradients measured in other species. To test this conjecture, we adapted the model parameter values to approximate the features of the high-frequency region of the alligator lizard papilla, where the hair bundles are free-standing rather than grouped into sallets as in the gecko (see Table I). Figure 4 compares model results with measured SFOAE de-

lays in alligator lizard (Bergevin *et al.*, 2010). The overall agreement remains close; as predicted by the model, tuning and delay are strongly correlated. Note that both N_{SFOAE} and $Q_{10\ \mathrm{dB}}$ are somewhat smaller in the alligator lizard than in the gecko. Although the inner ears of the gecko and alligator lizard manifest major morphological differences—including the presence or absence of tectorial sallets, the overall length of the papilla, and the slope and orientation of the tonotopic map—our results suggest that the most important parameters for reproducing SFOAE delays are those controlling the sharpness of tuning with CF.

C. Robustness to changes in the bundle oscillators

Although we follow historical precedent and represent the hair bundles as harmonic oscillators, our main conclusions do not depend on this choice. For example, replacing the harmonic oscillators with gammatone filters[9] modifies quantitative details of the relationship between N_{SFOAE} and $Q_{10\ \mathrm{dB}}$, but leaves SFOAE characteristics nearly unchanged. Similarly, replacing the model's passive oscillators with active oscillators of the form derived from mammalian basilar-membrane data by Zweig (1991) complicates the analysis but does not affect our principal conclusions. The reason for the robustness of our results is not difficult to see: The analysis of the origin of the rapid rotation of SFOAE phase, culminating in Eq. (14) for N_{SFOAE}, depends in no essential way on the precise form of the underlying oscillators. We sought to emphasize the generality of the arguments following Eq. (10) by adopting the generic nomenclature $T(\beta)e^{i\phi(\beta)}$ for the oscillator response. Similar arguments would apply, and similar results would be obtained, no matter what the detailed functional form of the excitation pattern and associated mechanical phase shifts, so long as the response remains strongly peaked somewhere along the papilla and the principle of stationary phase can be applied. To underscore this point, note that Eq. (14) for N_{SFOAE} is *identical*—modulo the entropy of changes in notation—to equations derived using models of the mammalian cochlea [e.g., Eqs. (51)–(53) of Zweig and Shera (1995)], where excitation patterns take the form of basilar-membrane traveling waves.

D. Coherent reflection by any other name

The analysis presented in Sec. IV demonstrates that the mechanisms responsible for producing SFOAEs in the model are closely analogous to those of the coherent-reflection model. The only real difference is this: There are no basilar-membrane traveling waves. But the absence of traditional mammalian traveling waves in the gecko does not mean that there are no mechanical phase shifts between the responses of different bundles arrayed along the papilla. These mechanical phase shifts, and the fact that they couple back to the stapes via the papilla, come to play for the gecko the same role in the generation of reflection-source OAEs that traveling waves and their associated phase shifts play in the mammal.

Although the terminology of the coherent-reflection model derives from the mammalian case (Zweig and Shera, 1995), the basic mechanisms operating in the gecko model are fundamentally the same. In both models, the effects of intrinsic micromechanical irregularities couple back to the stapes, where they affect the impedance of the inner ear. In models of the mammalian cochlea, this coupling occurs via traveling pressure-difference waves. In the gecko model, the coupling between hair bundles and the stapes is mediated by the bulk motion of the papilla. In both models, contributions to the response at the stapes arise all along the partition, although the emission is usually dominated by contributions that arise near the peak of the mechanical response (the equations indicate that coupling to the stapes is strongest in this region).

Although the irregularities located within the peak region may be spatially "noisy" (i.e., the cell-to-cell variations in the mechanics may contain many different spatial-frequency components), their net contribution to the impedance is smoothed out by a filtering process whose analog in the mammal has been dubbed "coherent-reflection filtering" (Zweig and Shera, 1995). Filtering occurs because of phase-interference effects among contributions that arise from different locations within the peak region. The filtering process effectively eliminates contributions from all but a relatively narrow range of spatial frequencies (i.e., those near $\hat{\kappa}$). Contributions from spatial frequencies near $\hat{\kappa}$ combine coherently and can therefore sum up to a large value; all others effectively cancel one another out. This is why mechanically smooth cochleae do not produce appreciable reflection-source OAEs: The spatial variation of their mechanical properties does not contain significant spatial-frequency components near $\hat{\kappa}$.

Because of the filtering, the net effect of the irregularities is to produce quasiperiodic spectral oscillations in the impedance Z_{ie}. (If no filtering occurred, the impedance would be a noisy function of frequency, mirroring the noisy spatial pattern of irregularities.) Interpreted in the time domain, quasiperiodic spectral oscillations in the impedance represent the addition of a delayed component (i.e., an echo or emission) to the pressure measured in the ear canal. At any given frequency, the mean delay is determined by the value of the dominant spatial frequency $\hat{\kappa}$. As outlined in Sec. IV, stationary-phase analysis shows that $\hat{\kappa}$ is determined by the gradient of the response phase near the magnitude peak [Eq. (12)]. Filter theory indicates that this phase gradient is, in turn, proportional to the sharpness of tuning.

E. Invariance under spatial rearrangement of the bundles

Although our parameter values reflect the (reversed) exponential tonotopic organization of gecko hair cells (Manley *et al.*, 1999), the model requires no ordered array of CFs. Indeed, the model predictions are invariant under spatial permutation of the bundles. [Addition is commutative, and the expression for ΔZ in Eq. (7) is a discrete sum over independent bundles.] Unlike in the mammalian cochlea, where the basilar membrane participates in the tuning and the driving pressure forces are spatially nonuniform (e.g., Olson, 2001), in the lizard, the supporting structure (papilla) that couples the bundles to one another and to the stapes moves approximately as a rigid body; consequently, all places along the

papilla are created equal. In the model, the mechanical drive and response of any given bundle remain the same no matter where it may reside along the papilla and no matter who its neighbors happen to be. (Of course, the model simplifies the in-vivo physics; the actual papilla is not perfectly rigid and hydrodynamic coupling between adjacent salletal groups may sometimes be important.) Although concepts such as the "spatial pattern" or the "spatial-frequency content" of the irregularities are convenient for the analysis—and entirely appropriate in the tokay, where the tonotopy appears regular—they conceal the full generality of the model. What matters in the model is not the arrangement of the bundles or their irregularities with respect to *spatial position*, but their arrangement with respect to *characteristic frequency* (when the frequency-position map is smooth and monotonic, the two are simply related). Bundles are operationally "close" to one another if they have similar CFs, whether they reside in adjacent rows or at opposite ends of the papilla. The model therefore predicts that the principles of OAE generation operating in the normal lizard continue to apply even in some hypothetical mutant in which the regular exponential tonotopy of the papilla becomes radically, even randomly, reorganized during development.

F. Correlations between peripheral tuning and SFOAE delay

Independent of any model, the otoacoustic and neural data in Fig. 3 demonstrate an empirical correlation between measurements of N_{SFOAE} and $Q_{10\ \mathrm{dB}}$ in geckos. The covariation of SFOAE phase-gradient delay and the sharpness of tuning established here in geckos provides a reptilian analog of correlations previously demonstrated in mammals (Shera *et al.*, 2002; Shera and Guinan, 2003). Our model of SFOAE generation in the gecko accounts for this relationship [Eq. (14)], just as coherent-reflection theory accounts for it in the mammalian ear (Zweig and Shera, 1995).

The model predicts that species differences in the sharpness of tuning among lizards should correlate with differences in SFOAE delay. For example, Manley *et al.* (1996) report species differences between tokay and leopard geckos (*Gekko gecko* and *Eublepharis macularius*) in the relative bandwidths of suppression tuning curves obtained by measuring the response of SOAEs to external tones. As reviewed by Manley *et al.* (1996), the properties of SOAE suppression tuning curves generally match those obtained from neural measurements. The authors report that the values of $Q_{10\ \mathrm{dB}}$ in tokay geckos are generally larger than in leopard geckos by an average factor of 1.3–1.4. The biophysical origins of this species difference in the sharpness of gecko tuning are not known. But if the difference arises or is manifest mechanically, our model predicts that SFOAE phase-gradient delays should differ correspondingly [Eq. (14)]. We test this prediction in Fig. 5, which compares values of N_{SFOAE} measured in the two gecko species (Bergevin *et al.*, 2008). As predicted by the model, the emission data show that N_{SFOAE} is larger in tokay than in leopard geckos. Indeed, at frequencies above 2 kHz, where the SOAE suppression tuning curves were measured, the ratio of the SFOAE delays averages 1.4–1.5, in close agreement with reported ratios of tuning sharpness.

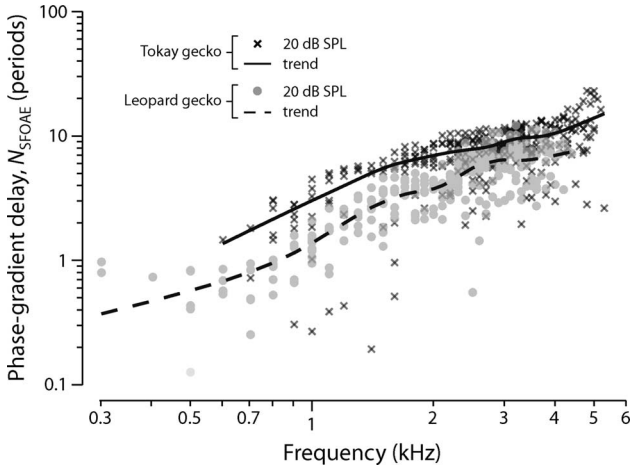

FIG. 5. SFOAE phase-gradient delays versus frequency in tokay and leopard geckos. The symbols × and ● show delays N_{SFOAE} (in periods) measured, respectively, in tokay (*G. gecko*, ten ears) and leopard geckos (*E. macularius,* 12 ears). The loess trend lines demonstrate that N_{SFOAE} values are generally larger in the tokay, consistent with the sharper tuning measured in this species (Manley *et al.*, 1996). Emission data are taken from the study of Bergevin *et al.* (2008). Probe levels were 20 dB SPL. Data points whose corresponding SFOAE magnitudes fell within 10 dB of the noise floor are not shown.

Extending these ideas to other lizards, we note that previous studies have suggested that an overlying tectorial membrane, when present, may somehow act to enhance the frequency selectivity of mechanical tuning (Manley *et al.*, 1988; Authier and Manley, 1995). If the presence of a tectorial membrane correlates with sharper tuning, then, all other things being equal (a significant caveat), our model predicts that SFOAE delays should generally be shorter in lizards that lack a tectorial covering over much of their papilla. If correlations between peripheral tuning and SFOAE delay hold more generally among vertebrates, then the frog may be an exception that tests the rule. At stimulus frequencies below 1–2 kHz (depending on species), frog SFOAE delays are significantly longer than those in geckos and many mammals (Meenderink and Narins, 2006; Bergevin *et al.*, 2008). Despite their longer OAE delays, frogs appear to have broader ANF tuning (Ronken, 1991). Reconciling these observations with the correlations between tuning and delay observed in other species requires additional mechanisms in the frog—perhaps traveling waves on the tectorial curtain of the amphibian papilla (Hillery and Narins, 1984)—that contribute significant mechanical delay without a corresponding effect on the sharpness of tuning.

Although traveling waves along both the basilar and tectorial membranes (Ghaffari *et al.*, 2007) also occur in mammals, the great bulk of the delay measured in mammalian cochlear mechanics and otoacoustic emissions appears well correlated with tuning (Shera *et al.*, 2007). To put it another way, signal-front delays constitute a relatively small fraction of the total mechanical delay (Temchin *et al.*, 2005), most of which is associated with "filter build-up." Unlike the waves that may propagate along the tectorial curtain in frogs, traveling waves in mammals propagate along and are influenced by the tuned structure itself. Since the mechanical response

builds up as the wave propagates, tuning and delay are inextricably linked in mammals, just as they appear to be in lizards.

ACKNOWLEDGMENTS

We thank Christine Köppl and Geoffrey Manley for providing us with the gecko auditory-nerve data. We also thank A. J. Aranyosi, Diek Duifhuis, John Guinan, Elizabeth Olson, and the anonymous reviewers for valuable comments and discussion. Our work was supported by the Howard Hughes Medical Institute (Grant No. 52003749), the National Science Foundation Division of Mathematical Sciences (Grant No. 0602173), and the NIDCD, National Institutes of Health (Grant No. R01 DC003687).

[1]Aranyosi and Freeman (2005) report papilla angular displacements in the alligator lizard of about 1° at sound levels of 120 dB SPL in the fluid (equivalent to 85–100 dB SPL at the eardrum). Thus, the small-angle approximation holds well, even at high sound levels; at the sound levels typically used to evoke SFOAEs (e.g., 20–40 dB SPL), the approximation is even better.

[2]Consistent with conventions in the mammalian literature, the stapes, annular ligament, and round window are here regarded as parts of the middle ear and are therefore not included in Z_{ie}.

[3]The round-trip pressure gain G_{me} has the value $G_{me}=T_{mef}T_{mer}/(1+Z_{ie}/Z_{out})$, where T_{mef} and T_{mer} are the forward and reverse middle-ear pressure transfer functions, and Z_{out} is the "output impedance" of the middle ear seen from the inner ear (cf. Shera, 2003).

[4]Extrapolating the exponential curve of Manley *et al.* (1999) for the tonotopic map all the way to the apical end of the papilla ($x=0$) gives a maximum CF of about 7.5 kHz. Because no ANF fibers with CFs greater than 5 kHz have been reported, and because OAE magnitudes fall off quite sharply above 5 kHz, we have adjusted the value of CF_{max} down to this value.

[5]Equation (7) indicates that varying the bundle stiffness with position changes mean OAE amplitudes systematically with frequency but has negligible effect on SFOAE phase and delay (so long as the model tuning is not unrealistically broad).

[6]As discussed elsewhere (Zweig and Shera, 1995), the term $e^{-i\kappa x}$ makes negligible contribution to the integral in Eq. (10). The reason, in a nutshell, is that the stationary-phase condition is never satisfied with $\kappa>0$, and the integral is therefore always small.

[7]Although perhaps reminiscent of the factor of 2 associated with the round-trip propagation of pressure-difference waves in the mammalian cochlea (Shera *et al.*, 2008), the numerical factor that relates the value of N_{SFOAE} to the peak phase-gradient delay of the bundle filter (here, a second-order, harmonic oscillator) depends on the type and order of the filter. It generalizes to a factor of $(m+1)/m$ for the mth-order gammatone filters.

[8]If the confidence intervals seem small given the apparent scatter in the data, note that whereas the visual impression of the figure is dominated by the outliers, the statistics are dominated by the large number of overlapping points close to the regression line.

[9]Gammatone filters, whose impulse response is the product of a sinusoid with the probability density function for a Gamma distribution (with shape parameter m), capture many of the linear features observed in mammalian ANF data (e.g., de Boer, 1975; Carney and Yin, 1988). Heuristically, the switch to gammatone filters is easily effected by changing Eq. (3) for the bundle displacement to read $\Xi_n=(Te^{i\phi})^m\Xi_p$, where $Te^{i\phi}$ is the transfer function of the harmonic oscillator [i.e., the case $m=1$; see Eq. (10)]. When approximate values of m and Q are determined by fitting ANF tuning curves, the model produces SFOAEs with essentially the same characteristics shown in Figs. 2 and 3. In the gammatone model, the approximate analytic relation between N_{SFOAE} and $Q_{10\ dB}$ generalizes to $N_{SFOAE}\cong(m+1)\sqrt{10^{1/m}-1}Q_{10\ dB}/\pi$, where we have used the formula $Q/Q_{10\ dB}=\sqrt{10^{1/m}-1}$ for the mth-order gammatone filter (Hartmann, 1998). Note that this equation reduces to Eq. (14) when $m=1$.

Aranyosi, A. J. (**2002**). "Measuring sound-induced motions of the alligator lizard cochlea," Ph.D. thesis, Massachusetts Institute of Technology, Cambridge, MA.

Aranyosi, A. J., and Freeman, D. M. (**2004**). "Sound-induced motions of individual cochlear hair bundles," Biophys. J. **87**, 3536–3546.

Aranyosi, A. J., and Freeman, D. M. (**2005**). "Two modes of motion of the alligator lizard cochlea: Measurements and model predictions," J. Acoust. Soc. Am. **118**, 1585–1592.

Authier, S., and Manley, G. A. (**1995**). "A model of frequency tuning in the basilar papilla of the tokay gecko, *Gekko gecko*," Hear. Res. **82**, 1–13.

Bergevin, C., Freeman, D. M., Saunders, J. C., and Shera, C. A. (**2008**). "Otoacoustic emissions in humans, birds, lizards, and frogs: Evidence for multiple generation mechanisms," J. Comp. Physiol. [A] **194**, 665–683.

Bergevin, C., Velenovsky, D., and Bonine, K. (**2010**). "Otoacoustic emission temperature dependence across the *Lacertilia*," Assoc. Res. Otolaryngol. Abstr. **33**, 150.

Carney, L. H., and Yin, T. C. (**1988**). "Temporal coding of resonances by low-frequency auditory nerve fibers: Single-fiber responses and a population model," J. Neurophysiol. **60**, 1653–1677.

Chiappe, E. (**2006**). "Functional differentiation of hair cells in a lizard papilla unveils a principle in the evolution of amniote cochleae," Ph.D. thesis, Rockefeller University, New York.

Cleveland, W. S. (**1993**). *Visualizing Data* (Hobart, Summit, NJ).

de Boer, E. (**1975**). "Synthetic whole-nerve action potentials for the cat," J. Acoust. Soc. Am. **58**, 1030–1045.

Eatock, R. A., Manley, G. A., and Pawson, L. (**1981**). "Auditory nerve fibre activity in the gecko. I. Implications for cochlear processing," J. Comp. Physiol. [A] **142**, 203–218.

Eatock, R. A., Weiss, T. F., and Otto, K. L. (**1991**). "Dependence of discharge rate on sound pressure level in cochlear nerve fibers of the alligator lizard: Implications for cochlear mechanisms," J. Neurophysiol. **65**, 1580–1597.

Frishkopf, L. S., and DeRosier, D. J. (**1983**). "Mechanical tuning of free-standing stereociliary bundles and frequency analysis in the alligator lizard cochlea," Hear. Res. **12**, 393–404.

Ghaffari, R., Aranyosi, A. J., and Freeman, D. M. (**2007**). "Longitudinally propagating traveling waves of the mammalian tectorial membrane," Proc. Natl. Acad. Sci. U.S.A. **104**, 16510–16515.

Guinan, J. J., and Peake, W. T. (**1967**). "Middle-ear characteristics of anesthetized cats," J. Acoust. Soc. Am. **41**, 1237–1261.

Hartmann, W. M. (**1998**). *Signals, Sound, and Sensation* (Springer, New York).

Hillery, C. M., and Narins, P. M. (**1984**). "Neurophysiological evidence for a traveling wave in the amphibian inner ear," Science **225**, 1037–1039.

Holton, T., and Hudspeth, A. J. (**1983**). "A micromechanical contribution to cochlear tuning and tonotopic organization," Science **222**, 508–510.

Kalluri, R., and Shera, C. A. (**2007**). "Comparing stimulus-frequency otoacoustic emissions measured by compression, suppression, and spectral smoothing," J. Acoust. Soc. Am. **122**, 3562–3575.

Kemp, D. T., and Brown, A. M. (**1983**). "An integrated view of cochlear mechanical nonlinearities observable from the ear canal," *Mechanics of Hearing*, edited by E. de Boer and M. A. Viergever, (Martinus Nijhoff, The Hague, The Netherlands), pp. 75–82.

Köppl, C. (**1995**). "Otoacoustic emissions as an indicator for active cochlear mechanics: A primitive property of vertebrate auditory organs," *Advances in Hearing Research*, edited by G. A. Manley, G. M. Klump, C. Köppl, H. Fastl, and H. Oeckinghaus, (World Scientific, Singapore), pp. 207–218.

Köppl, C., and Authier, S. (**1995**). "Quantitative anatomical basis for a model of micromechanical frequency tuning in the tokay gecko, *Gekko gecko*," Hear. Res. **82**, 14–25.

Köppl, C., Forge, A., and Manley, G. A. (**2004**). "Low density of membrane particles in auditory hair cells of lizards and birds suggests an absence of somatic motility," J. Comp. Neurol. **479**, 149–155.

Manley, G. A. (**1990**). *Peripheral Hearing Mechanisms in Reptiles and Birds* (Springer-Verlag, Berlin).

Manley, G. A., Gallo, L., and Köppl, C. (**1996**). "Spontaneous otoacoustic emissions in two gecko species, *Gekko gecko* and *Eublepharis macularius*," J. Acoust. Soc. Am. **99**, 1588–1603.

Manley, G. A., Köppl, C., and Sneary, M. (**1999**). "Reversed tonotopic map of the basilar papilla in *Gekko gecko*," Hear. Res. **131**, 107–116.

Manley, G. A., Yates, G. K., and Köppl, C. (**1988**). "Auditory peripheral tuning: Evidence for a simple resonance phenomenon in the lizard *Tiliqua*," Hear. Res. **33**, 181–189.

Meenderink, S. W., and Narins, P. M. (**2006**). "Stimulus frequency otoacoustic emissions in the Northern leopard frog, *Rana pipiens pipiens*: Implica-

tions for inner ear mechanics," Hear. Res. **220**, 67–75.
Miller, M. R. (**1973**). "A scanning electron microscope study of the papilla basilaris of *Gekko gecko*," Z. Zellforsch Mikrosk Anat. **136**, 307–328.
Mulroy, M. J. (**1974**). "Cochlear anatomy of the alligator lizard," Brain Behav. Evol. **10**, 69–87.
Olson, E. S. (**2001**). "Intracochlear pressure measurements related to cochlear tuning," J. Acoust. Soc. Am. **110**, 349–367.
Peake, W. T., and Ling, A. (**1980**). "Basilar-membrane motion in the alligator lizard: Its relation to tonotopic organization and frequency selectivity," J. Acoust. Soc. Am. **67**, 1736–1745.
Puria, S. (**2003**). "Measurements of human middle ear forward and reverse acoustics: Implications for otoacoustic emissions," J. Acoust. Soc. Am. **113**, 2773–2789.
Ronken, D. A. (**1991**). "Spike discharge properties that are related to the characteristic frequency of single units in the frog auditory nerve," J. Acoust. Soc. Am. **90**, 2428–2440.
Rosowski, J. J., Peake, W. T., Lynch, T. J., Leong, R., and Weiss, T. F. (**1985**). "A model for signal transmission in an ear having hair cells with free-standing stereocilia. II. Macromechanical stage," Hear. Res. **20**, 139–155.
Sams-Dodd, F., and Capranica, R. R. (**1994**). "Representation of acoustic signals in the eighth nerve of the Tokay gecko: I. Pure tones," Hear. Res. **76**, 16–30.
Schairer, K. S., Ellison, J. C., Fitzpatrick, D., and Keefe, D. H. (**2006**). "Use of stimulus-frequency otoacoustic emission latency and level to investigate cochlear mechanics in human ears," J. Acoust. Soc. Am. **120**, 901–914.
Shera, C. A. (**2003**). "Mammalian spontaneous otoacoustic emissions are amplitude-stabilized cochlear standing waves," J. Acoust. Soc. Am. **114**, 244–262.
Shera, C. A., and Guinan, J. J. (**1999**). "Evoked otoacoustic emissions arise by two fundamentally different mechanisms: A taxonomy for mammalian OAEs," J. Acoust. Soc. Am. **105**, 782–798.
Shera, C. A., and Guinan, J. J. (**2003**). "Stimulus-frequency-emission group delay: A test of coherent reflection filtering and a window on cochlear tuning," J. Acoust. Soc. Am. **113**, 2762–2772.
Shera, C. A., and Guinan, J. J. (**2008**). "Mechanisms of mammalian otoacoustic emission," *Active Processes and Otoacoustic Emissions*, edited by G. A. Manley, R. R. Fay, and A. N. Popper, (Springer, New York), pp. 305–342.
Shera, C. A., Guinan, J. J., and Oxenham, A. J. (**2002**). "Revised estimates of human cochlear tuning from otoacoustic and behavioral measurements," Proc. Natl. Acad. Sci. U.S.A. **99**, 3318–3323.
Shera, C. A., Guinan, J. J., and Oxenham, A. J. (**2007**). "Otoacoustic estimates of cochlear tuning: Validation in the chinchilla," Assoc. Res. Otolaryngol. Abstr. **30**, 519.
Shera, C. A., Tubis, A., and Talmadge, C. L. (**2005**). "Coherent reflection in a two-dimensional cochlea: Short-wave versus long-wave scattering in the generation of reflection-source otoacoustic emissions," J. Acoust. Soc. Am. **118**, 287–313.
Shera, C. A., Tubis, A., and Talmadge, C. L. (**2008**). "Testing coherent reflection in chinchilla: Auditory-nerve responses predict stimulus-frequency emissions," J. Acoust. Soc. Am. **124**, 381–395.
Shera, C. A., and Zweig, G. (**1992**). "Middle-ear phenomenology: The view from the three windows," J. Acoust. Soc. Am. **92**, 1356–1370.
Shera, C. A., and Zweig, G. (**1993**). "Order from chaos: Resolving the paradox of periodicity in evoked otoacoustic emission," *Biophysics of Hair Cell Sensory Systems*, edited by H. Duifhuis, J. W. Horst, P. van Dijk, and S. M. van Netten, (World Scientific, Singapore), pp. 54–63.
Siegel, J. H., Cerka, A. J., Recio-Spinoso, A., van Dijk, P., and Ruggero, M. A. (**2005**). "Delays of stimulus-frequency otoacoustic emissions and cochlear vibrations contradict the theory of coherent reflection filtering," J. Acoust. Soc. Am. **118**, 2434–2443.
Songer, J. E., and Rosowski, J. J. (**2007**). "Transmission matrix analysis of the chinchilla middle ear," J. Acoust. Soc. Am. **122**, 932–942.
Talmadge, C. L., Tubis, A., Long, G. R., and Tong, C. (**2000**). "Modeling the combined effects of basilar membrane nonlinearity and roughness on stimulus frequency otoacoustic emission fine structure," J. Acoust. Soc. Am. **108**, 2911–2932.
Temchin, A. N., Recio-Spinoso, A., van Dijk, P., and Ruggero, M. A. (**2005**). "Wiener kernels of chinchilla auditory-nerve fibers: Verification using responses to tones, clicks, and noise and comparison with basilar-membrane vibrations," J. Neurophysiol. **93**, 3635–3648.
Vilfan, A., and Duke, T. (**2008**). "Frequency clustering in spontaneous otoacoustic emissions from a lizard's ear," Biophys. J. **95**, 4622–4630.
Weiss, T. F., and Leong, R. (**1985**). "A model for signal transmission in an ear having hair cells with free-standing stereocilia. III. Micromechanical stage," Hear. Res. **20**, 157–174.
Weiss, T. F., Mulroy, M. J., Turner, R. G., and Pike, C. L. (**1976**). "Tuning of single fibers in the cochlear nerve of the alligator lizard: Relation to receptor morphology," Brain Res. **115**, 71–90.
Weiss, T. F., Peake, W. T., and Rosowski, J. J. (**1985**). "A model for signal transmission in an ear having hair cells with free-standing stereocilia. I. Empirical basis for model structure," Hear. Res. **20**, 131–138.
Wever, E. G. (**1978**). *The Reptile Ear* (Princeton University Press, Princeton, NJ).
Zweig, G. (**1976**). "Basilar membrane motion," *Cold Spring Harbor Symposia on Quantitative Biology* (Cold Spring Harbor Laboratory, Cold Spring Harbor, NY) Vol. **40**, pp. 619–633.
Zweig, G. (**1991**). "Finding the impedance of the organ of Corti," J. Acoust. Soc. Am. **89**, 1229–1254.
Zweig, G., and Shera, C. A. (**1995**). "The origin of periodicity in the spectrum of evoked otoacoustic emissions," J. Acoust. Soc. Am. **98**, 2018–2047.

High-frequency transient evoked otoacoustic emissions acquisition with auditory canal compensated clicks using swept-tone analysis

Christopher L. Bennett
Department of Biomedical Engineering, College of Engineering, University of Miami, 1251 Memorial Drive, 219A Coral Gables, Florida 33146

Özcan Özdamar[a)]
Department of Biomedical Engineering, College of Engineering, University of Miami, 1251 Memorial Drive, 219A Coral Gables, Florida 33146

(Received 1 September 2009; revised 2 December 2009; accepted 7 December 2009)

The meatus (auditory canal) plays a role in altering the waveform of incident sound, distorting time- and frequency-domain characteristics. Often in transient-evoked otoacoustic emission (TEOAE) recording protocols, a 75 μs click is utilized to elicit a click-evoked response. TEOAEs are recorded by a probe microphone placed in the meatus and last for about 20 ms. Time-domain ringing in the meatal response (MR) creates a stimulus artifact that lasts up to 5+ ms, obscuring early-latency TEOAEs. This research is motivated by the need for a real-time, ear and probe placement dependent method for minimizing the magnitude and phase distortions of the meatus. The MR is first obtained using swept-tone analysis, from which a compensated stimulus is created. Usage of a compensated click from normally hearing adult subjects show an improvement to the flatness of the magnitude response and linearization of the phase response. Furthermore, a reduction in effective duration of the MR is found, attenuating the meatal artifact for click stimuli. The high frequency TEOAE content found in the early latencies of the response that is typically obscured by the MR artifact is revealed with the use of a compensated click.
 [DOI: 10.1121/1.3279831]

PACS number(s): 43.64.Jb, 43.64.Ha, 43.64.Yp [BLM] Pages: 2410–2419

I. INTRODUCTION

Otoacoustic emissions (OAEs) were first discovered in 1978 by David Kemp and today are used clinically as a screening method for determining cochlear functioning (Kemp *et al.*, 1990; Kemp, 1978). The OAEs can be detected with a microphone placed in the ear canal to pick up the extremely low sound pressure levels (Probst *et al.*, 1991). Since diagnosis along increasing frequency bands is determined by these responses, it is desirable to recover the emissions that are uncorrupted and noise-free within a short acquisition period. For these reasons, often very short duration transients, such as clicks (generated by 75 μs rectangular electrical pulses), are used to stimulate the basilar membrane (BM) and evoke the transient evoked otoacoustic emissions (TEOAEs). Transients are generally broadband in nature (supplying roughly equal energy across all frequencies) and short in duration, so early-latency emissions can be collected.

TEOAEs evoked by impulsive stimuli, such as a click, are distorted by the transmission characteristics of the auditory canal and the middle ear. The response to a click signal shows frequency dispersion, mimicking the tonotopic organization of the cochlea. For this reason, there exists a strong relationship between the latency of TEOAE components and their frequencies. Typically early components consist of high-frequencies and late-latency components made up of low-frequencies (Tognola *et al.*, 1997; Notaro *et al.*, 2007).

Classically, OAEs were thought to arise from the electromotility of the outer hair cells, which amplify low intensity stimuli and increase frequency discrimination (Brownell *et al.*, 1985; Brundin *et al.*, 1989). More recently, however, the generation of OAEs is thought to arise from one or more mechanisms depending on the intensity of the stimulus. At low intensities, the response is dominated by a so-called reflection source, in which backscattering from cochlear irregularities (impedance boundaries and hair cell configuration) is the primary contributor (Shera and Guinan, 1999). Since these properties are not likely to change from moment to moment, the repeatability and reproducibility of TEOAE responses are very consistent and are therefore used clinically as a screening test for hearing loss. These tests are especially important for subjects whom cannot participate in subjective hearing tests, most notably newborns. At higher intensities, TEOAE generation mechanisms become harder to identify, whereby a wave-fixed distortion source contributes significantly to the composition of the TEOAE response (Sisto *et al.*, 2007; Withnell *et al.*, 2008). These distortion sources are found in the early-latency components and are therefore routinely removed by windowing. It becomes readily apparent that direct observation of these early-latency components is vital to the understanding of the generation mechanisms involved with TEOAEs.

[a)]Author to whom correspondence should be addressed. Electronic mail: oozdamar@miami.edu

However, a few caveats exist which obscure the TEOAE which are caused by distortions of the transducers and ear canal. One such distortion is the acoustical ringing of the meatus. If thought of as a single open-ended Helmholtz resonator 27 mm in length, the meatus will have a fundamental resonant frequency around 3 kHz. The acoustic ringing primarily occurs at this resonant frequency.

The acoustical ringing has two primary artifacts. In the frequency domain, first, a peak resonance is created with roll-off on either side, creating an unequal distribution of energy across frequency. This creates juxtaposition between the roughly equal energy distribution of the desired acoustical stimulus and the unequal energy distribution that actually reaches the tympanic membrane. Second, acoustic ringing causes a prolonged impulse response in the ear canal known as the meatal response (MR). An ideal click would be short in duration generating no oscillations afterwards. In reality, however, after the initial burst of energy, smaller pressure variations linger in the meatus for up to 6 ms. This creates a problem in the recovery of early-latency TEOAEs. Both of these artifacts negatively impact high-frequency OAEs; a high-frequency roll-off due to the resonant response of the meatus supplies less energy to high-frequencies, and the residual ringing in the meatus obscures the high-frequency OAEs, which are early-latency emissions.

A. Overview of current methods

In the past, several approaches have been attempted to eliminate or reduce the meatal response. These attempts can be grouped in three principle approaches: signal processing, physiology based manipulation, and acoustic reshaping. Signal processing techniques generally try to predict the MR using previous data. Sophisticated signal processing techniques such as wavelets (Yuwaraj and Kunov, 1995), linear prediction (Tujal and Souza, 2003), and independent component analysis (Liu *et al.*, 2004) have been used to predict and attenuate or eliminate MR in a few selected recordings. The effectiveness and efficacy of these preliminary methods, however, have yet to be verified in general populations by direct observation.

B. Physiology based methods

The well known physiological characteristics of OAEs offer two principle ways to eliminate or attenuate the MR in TEOAEs: masking and nonlinearities. Physiologic masking can suppress the OAEs by the introduction of another sound in the same (ipsilateral) or opposite (contralateral) ear, or both (binaural) ears (Wilson, 1980). If the OAEs are masked or suppressed by a simultaneous tone or noise, then the pure meatal response can be recorded (Arslan *et al.*, 2001; Tavartkiladze *et al.*, 1994). Generally an ipsilateral reproducible pseudo-random noise masker is presented simultaneously with the stimulus and a digital subtraction method is used to recover the MR-free TEOAEs by post-processing. At low stimulus levels such a technique revealed the existence of TEOAE components at latencies around 2.5–5.0 ms which were more linear than later components (Kruglov *et al.*, 1997). These components, however, were not found in all subjects and appeared to consist of lower frequencies than expected, probably due to MR contamination.

Compressive nonlinearity is a fundamental characteristic of OAEs and offers opportunities for online MR attenuation. The most commonly used technique for MR artifact reduction is the derived nonlinear response (DNLR) recovery method originally developed by Kemp and colleagues (Bray and Kemp, 1987; Kemp *et al.*, 1986). The term "nonlinear" is a slight misnomer, in that any type of stimulus input will cause compressive nonlinearity in the TEOAE response at a certain intensity level. DNLR averaging is so-named due to the exploitation of the nonlinear characteristics of TEOAEs that are evoked by high-intensity stimuli. In DNLR acquisition method, the polarity of the input stimuli is inverted, such that upon averaging, the artifacts associated with the meatal response are reduced. This technique uses three transient stimuli and a fourth stimulus of inverted polarity which has a relative magnitude of +9.5 dB (three times the amplitude) higher than the first three. The DNLR method depends on compressive nonlinearity and works better with moderate and high level stimuli. As such, the functional premise may not hold for low level stimuli, where the OAEs are nonsaturating. Furthermore, due to the subtraction, the signal to noise ratio (SNR) of the acquired response is reduced by 6 dB (Ravazzani and Grandori, 1993). In order to maintain a comparable SNR to the linear method, twice as many sweeps are needed.

Finally, a novel and patented technique known as double-evoked OAEs (2EOAE), which exploits the same nonlinear interactions as DNLR, was developed by Douglas Keefe at the Boys Town National Research Hospital (Keefe, 1998; Keefe and Ling, 1998). This method uses a two-source modality, whereby the first two stimuli are presented separately by two speakers and the third stimulus is a superposition of the first two by presenting two stimuli simultaneously. Upon subtraction, the 2EOAE results in an improved response since probe distortion is minimized. However, some of the same caveats that affect the DNLR technique also affect the 2EOAE technique; namely, since subtraction is used, more sweeps are needed to maintain SNR.

C. Acoustic waveshaping methods

In this approach the aim is to reduce the MR by presenting a special transient to the ear that will generate a more impulsive waveform in the ear canal than the rectangular click. Chertoff and colleagues used the recorded MR to model the ear canal transfer function with finite impulse response (FIR) pulses, band-limited from 256 to 10 512 Hz (Chertoff and Chen, 1996; Chertoff and Guruprasad, 1997). In these studies, FIR pulses were used to guarantee stability in frequency-domain division and to have a band-limited template. The computation procedure involves calculating the transfer function of the ear by dividing the recorded meatal response with the FIR pulses, then inverting and low-pass filtering the result.

However, the FIR pulse is not identical to a rectangular click that is used clinically. A FIR pulse necessarily contains ringing after the point of maximum energy. Since one of the

motivations of modifying a TEOAE stimulus is to reduce ringing, computing with a FIR pulse is not desirable since it will add ringing. To correct for this, Chertoff and Chen (1996) modified the computed click spectrum to have a roll-off, much like a rectangular pulse. Acoustic clicks were generated with this method, and TEOAEs were obtained. However, Chertoff and Guruprasad (1997) found that spectrally flattened stimuli actually reduced the overall TEOAE level and its reproducibility. This was attributed to the minimization of the 2–3 kHz spectral peak, which in turn reduced the saturation effect of the TEOAEs, which were acquired in DNLR mode.

Other previous studies have utilized a compensated click for the purposes of extending the high-frequency stimulation. The earliest such method was developed for the purposes of reducing ringing in auditory evoked responses (Van Campen *et al.*, 1994). In that study, supra-aural earphones, instead of inserts, were calibrated through complex frequency-domain division to produce tone-bursts and low-pass filtered dc pulses with reduced ringing. In another study, a compensated click was used for the purposes of studying the effects of click stimulus intermodulation distortion in evoking TEOAEs (Yates and Withnell, 1999). In that study, a high-pass filtered compensated click was used in guinea pigs. The MR was derived from a pseudo-random noise input, but the compensation technique was not elaborated upon. Furthermore, it is not known if the compensated click had reduced ringing, as the motivation was solely to deliver a spectrally flat stimulus.

Similar to the above acoustic waveshaping techniques, the present study aims to generate customized ear-dependent transient waveforms that will produce an acoustic impulse in the ear canal. Unlike the previous studies, the transfer function of the ear is obtained by using a swept-tone technique that distributes the concentrated energy of the rectangular input to an extended stimulation period. This method gives the impulse response of the meatus directly, and since no divisions are used in calculating the transfer function, computational errors and instability problems are avoided and more robust outcomes are produced.

II. THEORY AND COMPUTATIONAL METHODS

The objective is to design an equalization filter whose magnitude and phase responses will compensate that of any meatal response. Given a recorded ear response $h[n]$, the corresponding frequency-domain transfer function will be $H(\omega)$. Then some acoustic input $x[n]$ will be filtered by the meatus such that the recorded output, $y[n]$, will be

$$y[n] = x[n] * h[n] \Leftrightarrow Y(\omega) = X(\omega) \cdot H(\omega). \tag{1}$$

The objective is to find a linear time-invariant (LTI) filter that can be used to reshape the stimulus, resulting in $y[n]$ that is more like a desired acoustic click after being convolved with the auditory canal. In this study first a new approach, swept-tone analysis, will be introduced to find the transfer function of the ear. Then, this function will be used to find the compensation filter that will in turn generate the compensated click. The delivery of the compensated click to the ear canal will result in an impulsive acoustic input which will be similar to an ideal impulse function with reduced acoustic ringing.

A. Swept-tone analysis

A Hammerstein model, which consists of a weakly static nonlinear system followed by a dynamic linear system, can be used to represent the auditory canal. For this type of system, an exponentially frequency sweeping tone is used as an excitation signal (Farina, 2000; Muller and Massarani, 2001; Farina, 2007). The sinusoid $s[n]$, (swept-tone or sweep) is an increasing frequency modulated function of duration T with beginning and ending frequencies, ω_1 and ω_2. K and L are constants determining the scaling factor and the rate of change of the frequency, respectively.

$$s[n] = \sin(K \cdot (e^{n/L} - 1)),$$

$$K = \frac{T \cdot \omega_1}{\ln(\omega_2/\omega_1)} \quad L = \frac{T}{\ln(\omega_2/\omega_1)}. \tag{2}$$

An inverse sweep, $s^{-1}[n]$, is also generated, in which the sweep is time reversed with an exponentially decreasing amplitude envelope applied. The envelope whitens the signal by reducing the level −6 dB/octave. The subsequent convolution of $s[n]^* s^{-1}[n]$ under ideal conditions (large T and wideband ω) yields a Dirac delta function, $\delta[n]$. If $s[n]$ is used as an excitation signal, for example, in the meatus, the impulse response can then be obtained simply by convolving the measured output signal with the inverse sweep:

$$h[n] = s[n] * h[n] * s^{-1}[n]. \tag{3}$$

The sweep and inverse sweep can be derived in the frequency domain, $s[n] \Leftrightarrow S(\omega)$ and $s^{-1}[n] \Leftrightarrow S^{-1}(\omega)$, respectively. First the group delay, $\tau_g(\omega)$ is given as

$$\tau_g(\omega) = A + B \cdot \ln \omega,$$

$$A = \tau_g(\omega_1) - B \cdot \ln(\omega_2), \quad B = \frac{\tau_g(\omega_2) - \tau_g(\omega_1)}{\ln(\omega_2 - \omega_1)}. \tag{4}$$

Then the phase is related to the group delay by

$$\tau_g(\omega) = -\frac{d}{d\omega}\varphi(\omega) \tag{5}$$

Finally, the sweep and inverse sweep can be generated from the phase response, as calculated above, and assuming a flat magnitude response by the equations

$$s[n] = \mathcal{F}^{-1}\{S(\omega)\} = \mathcal{F}^{-1}\{e^{j\cdot\varphi(\omega)}\}, \tag{6}$$

$$s^{-1}[n] = \mathcal{F}^{-1}\{S^{-1}(\omega)\}. \tag{7}$$

The swept-tone method has many advantages over other impulse response extraction methods, such as the single input or the maximum-length sequence (MLS) methods (Thornton, 1993). First, for an equivalent number of sweeps, the excitation signal of a swept-tone stimulus is much longer, and so when compressed into an impulse, exhibits a much improved SNR. Second, in the swept-tone method, the distortion components of the system under test (in this case, the

meatus) are time-shifted away from the first-order or linear response. Therefore, $h[n]$ contains only the linear components. This is useful for subsequent inverse filtering to have nonlinear response (transducer or physiological) conveniently separated from linear response. Third, the MR obtained from a single input or MLS method using a rectangular pulse will contain inherent zero-notches in its frequency response, which is not conducive to inverse filtering. However, the swept-tone method, once time-compressed, results in a theoretical impulse response to the Dirac delta, and so does not contain any stimulus-related frequency-domain notches. Finally, the method for obtaining the transfer function is inherent in the swept-tone analysis, which produces the response from an idealized impulse. This is an improvement over conventional transfer-function measurements, which requires complex division of the output with the input, and can result in increased noise levels in bands outside the area of interest.

The above type of log-chirp is previously described by Keefe as a method to collect OAEs using the distortion-product paradigm, and "de-chirping" the result to obtain emissions reminiscent of those evoked by a transient (Keefe, 1998; Keefe and Ling, 1998). The chirp is defined in the frequency domain, beginning with a prescribed group delay that is a function of frequency, with some parameters controlling duration, and directionality. The constant-magnitude, logarithmic-group delay chirp is converted to the time-domain via inverse Discrete Fourier Transform (DFT). The de-chirped or time-compressed signal is obtained by using an all-pass filter with an inverted phase response. The convolution of the all-pass with the inverse all-pass yields an impulse.

B. Magnitude equalization

First, a magnitude equalization process is derived from the meatal impulse response obtained with the swept-tone technique. Very few epochs (on the order of 100) are needed to obtain the impulse response of the meatus. Magnitude equalization will dampen the main resonance of the meatus, which in turn shortens the duration of the impulse response. The equalization is applied to the stimulus, as a type of pre-emphasis, or compensation, which will flatten the magnitude response.

The solution is to create an inverse filter, $H^{-1}(\omega)$, that has peaks and notches that complement those of the meatal response, $H(\omega)$. However, certain elements of $H(\omega)$ may be very close to zero, particularly at the specification limits of the probe microphone, or generally very low- and very high-frequencies. If inverted, these elements will create extremely high values. For this reason, parametric band-limits were used to limit the inversion algorithm to the frequencies of interest. Typical TEOAE protocols define an analysis bandwidth of 0.8–4.0 kHz (Hatzopoulos *et al.*, 2003), but an extended upper limit is desired for this study, so a bandwidth of the decade spanning 0.8–8.0 kHz is used.

The quasi-inverse of $|H(\omega)|$ defined on $[0,\pi]$ is given as $|H'(\omega)|$ in the subset $[\omega_1,\omega_2]$ where ω_1,ω_2 are the upper and lower limits of the swept-sinusoid. Therefore, $|H'(\omega)|$ is defined piecewise as

$$|H'(\omega)| = \begin{cases} \dfrac{1}{|H(\omega)|}, & \omega \in [\omega_1,\omega_2] \\ 1, & \omega < \omega_1, \omega > \omega_2. \end{cases} \tag{8}$$

A transition region must be created to eliminate ringing in the time-domain at any created edge frequencies that arise from the piecemeal construction of the magnitude response. One of the stated objectives of this compensation method is to reduce ringing of the meatus; therefore, special attention must be given to the edge frequencies to eliminate the possibility of introducing new process-related ringing. Windowing is applied at the bands between baseline to ω_1 and between ω_2 to $\omega_2+\Delta\omega_2$, or some arbitrary higher frequency. A Hann window function was chosen to transition smoothly from the compensation region to the unity regions to eliminate time-domain edge frequency ringing.

C. Phase equalization

A transient signal should have constant group delay across all frequencies; this implies that the phase is linear. In the construction of the compensation filter, a compensation phase must be applied to linearize the phase of the meatal response. First, an ideal phase response must be computed which is given by a line connecting $H(\mathrm{dc})$ to $H(\pi)$. The phase is given by the argument of the complex variable H and will be denoted by $\angle H(\omega)$. Then the idealized phase as a function of ω is

$$\angle H_{\mathrm{ideal}}(\omega) = (\angle H(\pi) - \angle H(0)) \cdot \omega + \angle H(0). \tag{9}$$

If we let the phase at dc be equal to zero, then the ideal phase reduces to

$$\angle H_{\mathrm{ideal}}(\omega) = \angle H(\pi) \cdot \omega. \tag{10}$$

When a system of two LTI filters are in series, their phases sum linearly, so the phases of the compensation filter and the meatus should sum to our constructed idealized phase. So the phase of the compensation is the difference of the phase of the meatus and the idealized phase, whereby

$$\angle H'(\omega) = \angle H(\pi) \cdot \omega - \angle H(\omega). \tag{11}$$

D. Overall compensation filter

The compensation filter can now be constructed using the desired magnitude and phase responses, such that

$$h'[n] = \mathcal{F}^{-1}\{H'(\omega)\} = \mathcal{F}^{-1}\{|H'(\omega)| \cdot e^{j\cdot\angle H'(\omega)}\}. \tag{12}$$

The input click stimulus, or in this case a rectangular pulse denoted by $x[n]$, is filtered with the compensation filter, $h'[n]$, whereby the output is given as $y[n] = x[n]*h'[n]*h[n] \approx x[n]$. In other words, the stimulus in the ear canal with compensation filter is a close approximation to the actual desired stimulus than is the non-compensated stimulus. An overview of the compensation method is diagramed in Fig. 1.

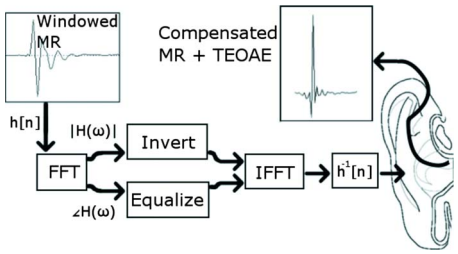

FIG. 1. (Color online) After obtaining the impulse response of the ear via the swept-tone technique, time windowing is performed to obtain the MR signal, $h[n]$. Frequency-domain inversion is performed by deriving the auditory canal compensation filter. The phase of $H^{-1}(\omega)$ is designed to sum with the phase of $H(\omega)$ to create a linear phase response (constant group delay). The magnitude of $H^{-1}(\omega)$ is designed such that the product with $H(\omega)$ is unity. The resulting time-domain transform yields the electrical stimulus, $h^{-1}[n]$.

III. MATERIALS AND EXPERIMENTAL METHODS

A. Subjects

Data were acquired from 12 ears of six young adult subjects (four male and two female) of ages ranging from 18 to 28, all in accordance with an IRB-approved protocol. All subjects had normal audiograms with thresholds better than 25 dB hearing level (HL) at frequencies 0.5, 1.0, 2.0, and 4.0 kHz, and bone-air gaps of less than 15 dB. For TEOAE acquisition, the subjects sat or lied down in an acoustically attenuated and electro-magnetically shielded environment. An Etymotic Research ER-10D OAE probe fitted with a rubber tip was inserted into the meatus to form an acoustic seal.

B. Equipment

The probe interfaced with a digital signal processor (Analog Devices ADSP-21369 Sharc EZ-Kit Lite) with an on-board ADC/DAC (AD1835: 24 bits, 48 kHz). The output of the DAC was calibrated to the sound source specifications of the ER-10D probe, in which a 1 V rms signal is equivalent to 86 dB sound pressure level (SPL). The ADC voltage levels were calibrated to pressure by taking into account the voltage range of the ADC and the sensitivity of the probe microphone. Further SNR and architecture specifications are described in Bennett and Özdamar, 2009.

C. Stimuli and response acquisition

For the standard click recordings, 75 μs clicks were used. The compensated stimuli were mean-adjusted to prevent unnecessary speaker excursion and digitally filtered forwards and backwards to prevent phase distortion using a four-pole Butterworth filter with cutoff frequencies of 0.8 and 8 kHz. The swept-tone stimulus used for acquiring the MR had beginning and end frequencies of 0.256 and 16.384 kHz, and were swept over 2400 samples. With a sampling rate of 48 kHz, the total duration of the swept-tone was 50 ms. A raised cosine window was applied to the first and last millisecond.

The compensated stimulus is expected to have complementary magnitude and phase characteristics to the transfer function of the auditory canal. The magnitude response of the compensated stimulus when multiplied with the magnitude response of the meatus created a flat spectrum, and the phase response of the compensated stimulus when summed with the phase of the meatus created a constant group delay. The phase response was unwrapped and detrended to emphasize the small fluctuations in the response, which can have a large impact on the group delay or the ringing of the time-domain response.

TEOAE responses were recorded at 86 dB peak sound pressure level (pSPL) or 400 mPa, down to 50 dB pSPL (6 mPa) in 6 dB steps. TEOAE recordings were obtained by synchronous mean averaging of 2000 sweeps. The averaging window was 25 ms, or 1200 samples at a 48 kHz sampling rate. The stimuli were presented to the subjects at a rate of 39.1 Hz in order to reduce the impact of electromagnetic interference through the process of averaging. Artifact rejection of 5 mPa (48 dB pSPL) was used during the time window of 5–25 ms post-stimulus onset.

D. Windowing criterion

An objective method for analyzing the duration of the MRs was selected in order to compare TEOAEs acquired via standard and compensated stimuli. The MPEG-7 standards delineate a specific temporal descriptor, which is intended to identify the effective duration of a transient (Peeters and Deruty, 2008). This measure first derives the temporal envelope estimation, $e[n]$, by the process of moving a selectable window across the calculated energy of the signal, given by

$$e[n] = \sqrt{\frac{1}{N}\sum_{i=n-N+1}^{n} h^2[i]}, \tag{13}$$

where $h[n]$ is the impulse response of the auditory canal, and N is the length of the averaging window and n is the discrete time index. The temporal envelope estimation is based on the short-time average energy, where the 1 ms window (N=48 at Fs=48 kHz) acts as a low-pass filter of the energy. The effective duration is the amount of time that the envelope is above a given threshold. A threshold of 0.75 mPa was chosen, so as not to exclude any TEOAEs and to choose a level low enough such that the MR will not obstruct the TEOAE response significantly.

E. Spectral flatness measure

In order to objectively compare the spectra of the standard click with the compensated click, a spectral flatness measure (SFM), adopted from the MPEG-7 standards of low level audio descriptors, was used (Hellmuth *et al.*, 2001). The spectral flatness is a scalar that is computed by the ratio of the geometric mean to the arithmetic mean of the spectrum of interest, and is given by

$$\mathrm{SFM} = \frac{\left(\prod_{k=k_1}^{k_2} H(k)\right)^{1/(k_2-k_1)}}{\frac{1}{(k_2-k_1)}\sum_{k=k_1}^{k_2} H(k)}, \tag{14}$$

where $H(k)$ is the value of the magnitude spectrum at bin index k, and specific indices k_1 and k_2 are the FFT bin loca-

tions of the upper and lower band limits ω_1 and ω_2. In this study, a 4096-point FFT was used, so ω_1 and ω_2 correspond to bins $k_1=44$ and $k_2=2796$. Using the SFM formula, tonal signals will have values closer to 0, and broadband signals will have values closer to 1.

F. Time-frequency analysis

The TEOAE responses were analyzed using the Morlet wavelets in order to observe the responses in the time-frequency domain. The wavelet transform allows for a relatively short signal to be decomposed into its elementary frequency constituents with good frequency and time resolution. The mother wavelet is scaled and shifted to the proper analysis frequency and latency, which in this study ranged from 0.8 to 8.0 kHz in 0.05 kHz steps from 0 to 20 ms post-stimulus onset. The Morlet wavelet, given by Eq. (15) below, is a complex Gaussian shaped function in both the time and frequency domains. It is also symmetric on the real and imaginary axes.

$$w(t,f_0)=\frac{e^{(-t^2/2\sigma_t^2)}e^{2j\pi f_0 t}}{\sqrt{\sigma_t\sqrt{\pi}}}. \tag{15}$$

Above, the mother wavelet, $w(t,f_0)$, is a function of the center frequency, f_0, and time, t, with σ_t representing the standard deviation of the signal in the time-domain.

Wavelet transformation is a useful post-processing tool to decompose TEOAE into its analysis contributing frequency components (Tognola *et al.*, 1997; Wit *et al.*, 1994). The point of maximal energy at a specific frequency is related to the latency of that component. Since the basilar membrane has a frequency-dependent topology from basal to apical end, a frequency-dependent TEOAE latency is expected as well as shown in the wavelet constructed time-frequency displays. In such analyses, however, the high-frequency early-latency components generally are obstructed by the extent of the meatal artifact.

G. Offline DNLR processing

Since recordings were taken in 6 dB steps, a modified offline DNLR technique was applied whereby two recordings from the same intensity were averaged with one inverted, higher-intensity (+6 dB) recording. Effective duration analysis was performed at each of the intensities: 80, 74, 68, 62, 56, and 50 dB pSPL. Spectral flatness cannot be analyzed on the DNLR response since the residue typically consists of probe or transducer distortions, which would not give an accurate representation of the spectral content within the auditory canal.

IV. RESULTS

Electrical and acoustical characteristics of the standard and compensated clicks are characterized as recorded from one subject (SUB01R) in Fig. 2. The rectangular click waveform displayed in the top row shows the expected slowly decreasing magnitude response with flat phase. The corresponding acoustic waveform plots in the second row display the acoustic ringing (the meatal response) resulting from the ear canal characteristics. The corresponding magnitude and phase plots show the expected magnitude gain around 3 kHz and the phase shifts at high-frequencies. The waveforms of the electrical compensated click, in the third row, show the complementary magnitude and phase characteristics to the plots shown in the second row. The electrical compensated click is comprised of several oscillations starting about 0.7 ms prior to the onset of the click and lasts about 2.7 ms. The resulting acoustic waveform of the compensated click is plotted in the fourth row (leftmost) and shows a more impulsive stimulus as expected. The magnitude response plot of the acoustic compensated click shows an improvement in the desired flatness (spectral flatness index for this case improved from 0.8819 to 0.9997), most notably in a boost to high-frequencies, and a smoothing of the low-frequency ripple (in-band ripple decreased in this case from 17.3 to 6.7 dB, a 10.6 dB reduction in ripple). Furthermore, the phase plot shows near zero phase characteristics, indicating a constant group delay.

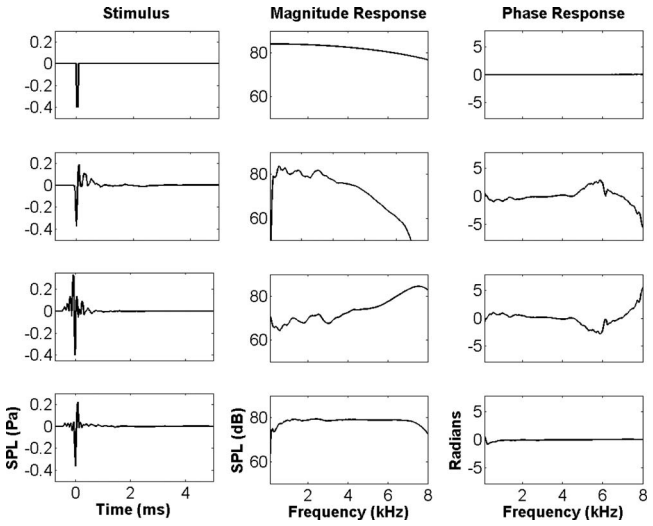

FIG. 2. Time and frequency characteristics of the signals of the OAE system: (left column) time-domain signals, (middle column) corresponding magnitude response and (right column) phase response. The top two rows show the 75 μs rectangular pulse electrical stimulus (first row) and corresponding acoustic response (second row) as recorded from the auditory canal. The bottom two rows show the electrical compensated stimulus (third row) and its acoustic compensated meatal response as recorded in the auditory canal (fourth row), respectively.

As expected the compensated stimuli varied from ear to ear, as each is unique to the individual transfer characteristics. However, some similarities among the stimuli existed; each stimulus contained 0.7 ms of pre-onset energy and 2.7 ms of post-onset energy for total stimulus duration of 3.4 ms. The equalization is performed on $h[n]$ that is normalized for digital processing to $[-1,1]$, the electrical compensated stimulus was then scaled to its proper output level to match the standard click in terms of dB pSPL as described by Burkard (1984). Alternative measurements of sound pressure level are peak to peak (ppSPL) and peak equivalent (peSPL), and the latter can be subdivided into baseline-to-peak or peak-to-peak peSPL. For a brief acoustic transient, the difference between ppSPL and peSPL is about 3.5 dB, which can be assumed as the margin of error in the intensity of the output level of the compensated click.

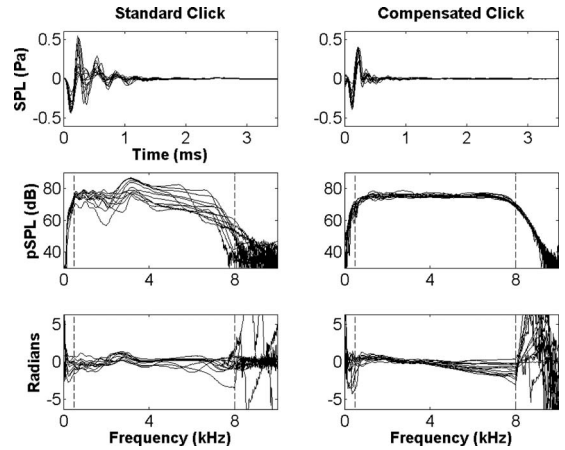

FIG. 3. The impulse response (top row), magnitude response (middle row), and phase response (bottom row) for a standard rectangular pulse (left column) and the ear canal compensated click (right column). The effective duration for the compensated click is much shorter, has a flatter magnitude response, and also displays a more linear phase response than its rectangular pulse counterpart.

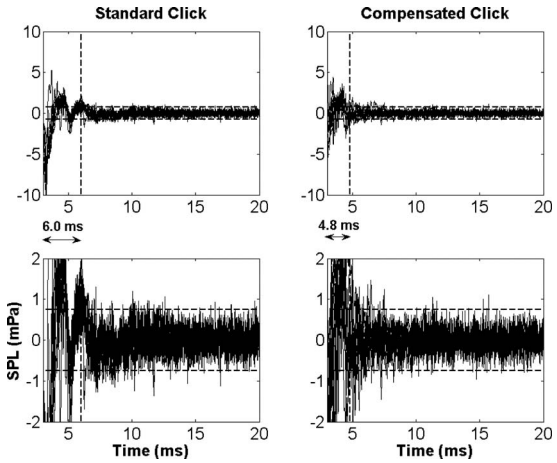

FIG. 4. Composite acoustic waveforms from all ears to 86 dB SPL stimulus showing the standard (left column) and compensated (right column) clicks from the time period of 3–20 ms. The bottom row shows *y*-axis zoomed version of the first row. The advantage of the compensated click becomes apparent at closer zoom intervals, whereby ringing in the time-domain is reduced by several milliseconds.

A collection of all of the individual ear canal responses recorded at 86 dB pSPL are shown in Fig. 3 in time and frequency-domain representations. The effective duration, as defined in Sec. III D, of the meatal responses are reduced at this intensity level by an average of 1.2 ms. Furthermore, as a result of the compensated click being represented as a true acoustic transient, the magnitude and phase responses are flattened between the bands of interest. The magnitude flatness, as measured by the spectral flatness index, improves on average from 0.7626 to 0.9918, which is close to a true acoustic transient, which has a theoretical spectral flatness index of 1.0. The flattening of the magnitude and phase response are merely the frequency-domain representations of shortening the impulse response of the acoustic stimulus. This is especially noticeable for the phase response, whose derivative directly gives the frequency-dependent group delay, such that a flatter phase response with no fluctuations will have a more constant group delay than a phase with many fluctuations.

When considering the removal of the meatal artifact, the ringing must be reduced to at least the level of TEOAEs, if not lower in order to classify the data as meaningful. So observation on a reduced pressure scale reveals how the compensated click truly reduces the meatal artifact across all ear canal recordings. Figure 4 shows the ear canal recordings at the highest-intensity recording (86 dB pSPL) for all subjects in both ears. The vertical axis is scaled for observation of the ringing at intensities near the windowing point. The window point is selected as the time at which the effective duration of the ear canal recording falls below 0.75 mPa. It is clear from Fig. 4 that the compensated click will have an effective duration that is shorter than the standard rectangular pulse. In fact, at 86 dB pSPL, the average effective duration for the standard click is 6.0 ms and for the compensated click is 4.8 ms.

The effective durations of MR for both standard and compensated clicks in linear and nonlinear mode are plotted for all intensities in Fig. 5. The horizontal axis indicates all of the intensity levels which were recorded, and the vertical axis indicates the effective duration, in ms, of the mean intersubject recordings. The effective duration is an indication of the duration of ringing in the ear canal recordings. As observed, in both linear and nonlinear modes the standard rectangular pulse click has a significantly longer effective duration than the compensated click for moderate to high-intensity stimuli. In linear mode, the smallest improvement is 0.22 ms at 50 dB pSPL and the greatest improvement is 1.5 ms at 68 dB pSPL. It is expected that lower intensities will have a smaller improvement in terms of ms, since there is inherently less ringing to begin with at lower intensities.

The use of the compensated click serves primarily to create an ideal acoustic click in the ear canal, of which the

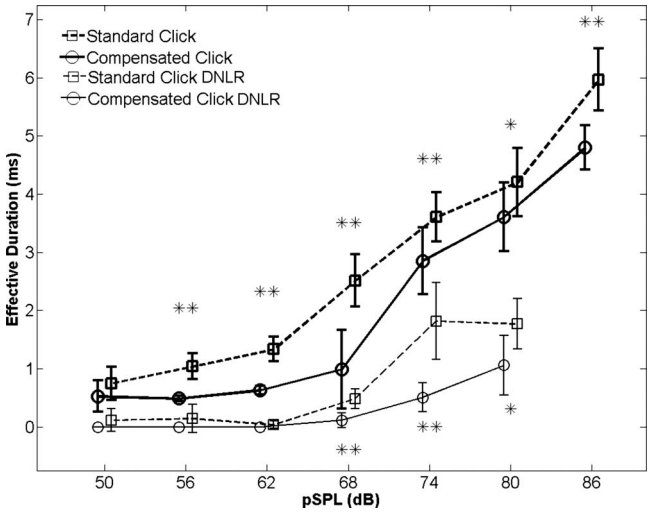

FIG. 5. The mean effective durations (±1 standard deviation) of the MR at each recorded intensity level for both the standard (dashed) and the compensated (solid) clicks are shown for linear acquisition (in bold) and for DNLR acquisition (in thin). An average of about 1 ms improvement is obtained by using an auditory canal compensated click. Significance ($*p<0.05$; $**p<0.01$) is found at moderate to high-intensity levels for both modalities, and even at low intensities for linear mode.

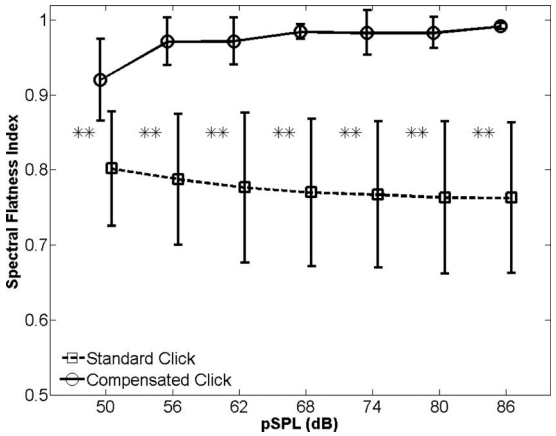

FIG. 6. The mean (±1 standard deviation) spectral flatness index plotted at each recorded intensity level for linear modality. The spectral flatness measure is a scalar from 0 (tonal) to 1 (broadband) indicating how flat the magnitude response is within a given band limit (0.8–8.0 kHz). Strong significance ($^{**}p<0.01$) is found at all click levels. Furthermore, the inter-subject variance is lower for the compensated click at all intensities.

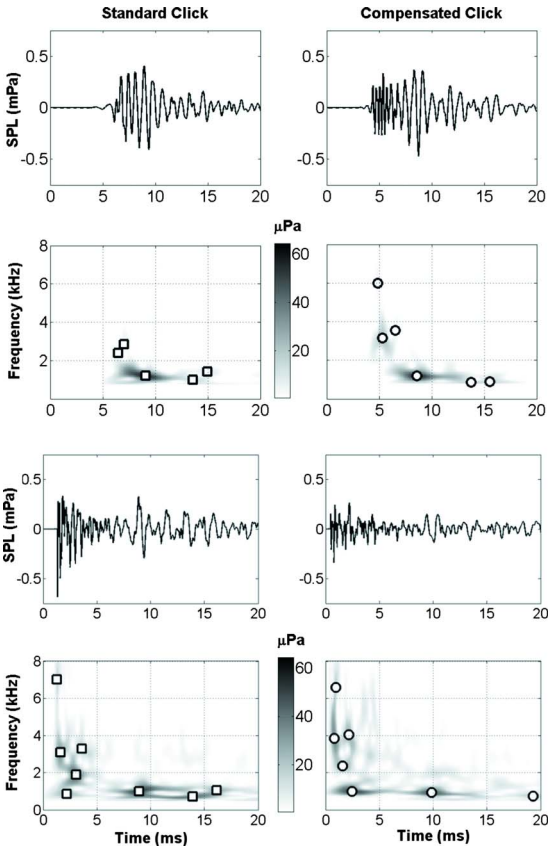

FIG. 7. (Color online) Standard and compensated click recordings are shown from one subject (SUB01R) for linear (top four panels) and nonlinear modalities (bottom four panels). The upper rows of each panel show the time-domain TEOAEs, and the lower rows show the corresponding time-frequency analysis using Morlet wavelets. An increase in high-frequency responses can be seen with the compensated click, due to more spectral energy provided to these frequencies. As well, a decrease in the effective duration of the acoustic click in both modalities is observed with the compensated click. Time-frequency peaks of the energy blobs are indicated with square (standard) and circle (compensated) markers.

two most salient features are a shortened impulse response and a flattened magnitude response. The impulse response was objectively determined using its effective duration as the modality of measurement, and similarly the magnitude response, or spectrum, is objectively determined with the use of a so-called spectral flatness measure, as described in Sec. III E. The spectral flatness measure is calculated from the values at each bin within the band of interest of the magnitude spectrum and is simply a ratio of the geometric mean to the arithmetic mean of these values. A scalar spectral flatness value nearer to 1 indicates a broadband spectrum and a value nearer to 0 indicates a tonal or resonant spectrum. As shown in Fig. 6, the compensated click has a significantly flatter spectrum ($p<0.01$) compared to a rectangular pulse click at all intensity levels. This indicates that, much like an ideal acoustic click, the compensated click has a magnitude response that is nearly flat, and 10%–15% more flat than the magnitude response from a standard click.

V. DISCUSSION

This study explores the improvements of using a compensated click which mimics an idealized acoustic click in the auditory canal. This is accomplished by acquiring the transfer function of the meatus via a swept-tone stimulus. From this transfer function, an inverse filter is created by equalizing both the magnitude and phase responses within the band limits of interest. The inverse filter is used to create the electrical stimulus, which when distorted by the meatus will produce an ideal acoustic click, meaning it will have a very short effective duration and will have a flat magnitude response.

Tests were done on 12 individual ears at multiple intensities from 50 to 86 dB pSPL in 6 dB steps with both the compensated click and a standard rectangular pulse click. Objective measures of the effective duration and the spectral flatness were determined by using low level audio descriptors from the MPEG-7 standard. It was found that use of the compensated click significantly reduces the effective duration of the ear canal MR. In turn, this reduces the meatal artifact, revealing early-latency TEOAEs, which are high-frequency emissions. In fact, at these early latencies, even a small shift of the windowing point toward the stimulus onset results in a large increase in the frequency acquisition. Many of the TEOAE time-frequency models use a power equation in the general form of $t=af^b$ whereby the TEOAE frequency, f, increases exponentially (according to constants, $b\approx-0.5$ and $a\approx10$) and with a large gradient near early-latency times, t. Furthermore, it was found that use of the compensated click significantly flattens the magnitude spectrum of the meatal response, presumably providing to the middle ear a more equal energy distribution in the TEOAE band of frequencies (0.8–8.0 kHz). Specifically, it was found that the compensated click removes a peak near 3 kHz (the Helmholtz resonant point of a 27 mm length cavity) and boosts the high-frequency roll-off.

The combination of revealing early-latency emissions while providing an increased output level to high-frequencies yields a TEOAE response that has an observably improved high-frequency response. Figure 7 (top panel) shows the recordings from a single ear at 86 dB pSPL using a standard

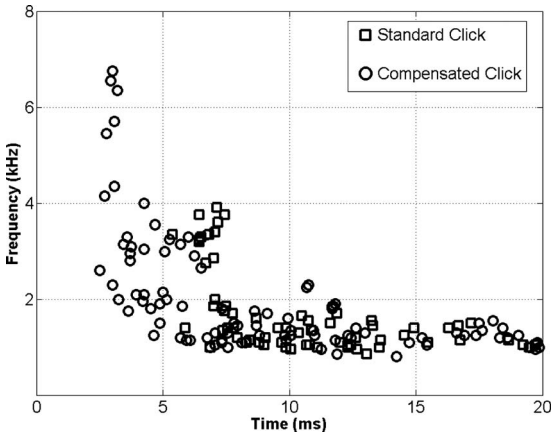

FIG. 8. The time-frequency peaks of the energy blobs obtained at 86 dB pSPL for all the ears using linear modality. All local maxima were found, and this number was reduced to only relevant peaks by applying a threshold (30 μPa). For high-intensity stimuli, the use of the compensated click (circles) reveals early-latency, high-frequency emissions better than a standard click (squares).

click and a compensated click, respectively. The window point was selected when the effective duration of the meatal response reached a threshold of 0.75 mPa. Time-frequency displays shown below the time plots reveal the concentrations of TEOAE energy for both types of clicks. Additionally, offline DNLR processing was performed using 80 and 86 dB pSPL recordings, shown in Fig. 7 (bottom panel). The compensated click has, in this specific case and on average, a shorter effective duration than a standard rectangular click even in nonlinear mode. Both linear and nonlinear modalities for the same subject show a reduction in effective duration, and in linear mode an increase in high-frequency responses can be observed. The reduction in the acoustic ringing exposes early-latency, high-frequency TEOAEs for the linear modality. In fact, this trend is seen generally across all of the subjects.

The time-frequency wavelet plots tend to reveal energy formed in blobs, which are groups of contiguous pixels with continuous frequency and time and mostly exhibiting an ellipsoid shape. The regional maxima for each of these blobs are determined for a neighborhood of at least eight connected pixels. Peaks below 30 μPa were removed from the blob peak analysis. A composite of all the blob peaks from all tested ears at 86 dB pSPL is shown in Fig. 8 for both click types. It can be seen that there is an improvement in high-frequency information using the compensated click. This suggests that the use of compensated clicks yields improved TEOAE information above the traditional upper band limit of 4.0 kHz.

As in the case in Fig. 7, it was generally seen that in linear mode, there was no significant change in low-frequency content of the TEOAE response, but in nonlinear mode a reduction in TEOAE response was found in the 1.0–3.0 kHz components. These results confirm those obtained by Chertoff and Guruprasad (1997) whom found a general reduction in TEOAE amplitudes when calibrated clicks were used. The Chertoff studies used the DNLR acquisition mode, which relies on the response heavily saturating at the high-intensity click. As the authors suggest, if the TEOAEs elicited from energy in the spectral peak drop out of saturation when the peak is reduced, then the reduction in response will be magnified due to the nature of nonlinear residual subtraction. As a confirmation of this hypothesis, in this study a similar reduction in nonlinear mode was found around the 1.0–3.0 kHz components.

Overall, the advantages of the compensated click described above may improve clinical OAE testing, especially in hearing screening. Time savings offered by the compensated click with the expanded information gained may reduce the number of false positives and reduce costs. In research, better modeling of TEOAEs can be achieved with spectrally compensated clicks. This could be especially important in animal models where high quality TEOAEs could not be obtained easily due to short durations and small amplitudes. Finally, insight into early-latency emissions may provide valuable information for TEOAE generation theories and time-frequency models, often used in research.

Arslan, R. B., Özdamar, Ö., and Ülgen, Y. (**2001**). "Digital subtraction method for transient evoked otoacoustic emissions recording with ipsilateral noise suppression: An application to stimulus artifact reduction," Audiology **40**, 55–62.

Bennett, C. L., and Özdamar, Ö. (**2009**). "High resolution system for improved transient-evoked otoacoustic emission acquisition," in Proceedings of the 31st Annual International Conference of IEEE Engineering in Medicine and Biology Society, Minneapolis, MN.

Bray, P., and Kemp, D. (**1987**). "An advanced cochlear echo technique suitable for infant screening," Br. J. Audiol. **21**, 191–204.

Brownell, W., Bader, C., Bertrand, D., and De Ribaupierre, Y. (**1985**). "Evoked mechanical responses of isolated cochlear outer hair cells," Science **227**, 194–196.

Brundin, L., Flock, A., and Canlon, B. (**1989**). "Sound-induced motility of isolated cochlear outer hair cells is frequency-specific," Nature (London) **342**, 814–816.

Burkard, R. (**1984**). "Sound pressure level measurement and spectral analysis of brief acoustic transients," Electroencephalogr Clin. Neurophysiol. Suppl. **57**, 83–91.

Chertoff, M. E., and Chen, J. (**1996**). "An in-situ calibration procedure for click stimuli," J. Am. Acad. Audiol **7**, 130–135.

Chertoff, M. E., and Guruprasad, S. N. (**1997**). "Application of a stimulus spectral calibration routine to click evoked otoacoustic emissions," J. Am. Acad. Audiol **8**, 333–341.

Farina, A. (**2000**). "Simultaneous measurement of impulse response and distortion with a swept-sine technique," in Proceedings of the 108th Convention of the Audio Engineering Society (Preprint 5093), Paris, France.

Farina, A. (**2007**). "Advancements in impulse response measurements by sine sweeps," in 122nd Audio Eng Soc Convention, Vienna, Austria.

Hatzopoulos, S., Petrucelli, J., Morlet, T., and Martini, A. (**2003**). "TEOAE recording protocols revised: Data from adult subjects," Int. J. Audiol. **42**, 339–347.

Hellmuth, O., Allamanche, E., Herre, J., Kastner, T., Cremer, M., and Hirsch, W. (**2001**). "Advanced audio identification using MPEG-7 content description," in 110th Audio Eng Soc Convention, New York, NY.

Keefe, D. H. (**1998**). "Double-evoked otoacoustic emissions. I. Measurement theory and nonlinear coherence," J. Acoust. Soc. Am. **103**, 3489–3498.

Keefe, D. H., and Ling, R. (**1998**). "Double-evoked otoacoustic emissions. II. Intermittent noise rejection, calibration and ear-canal measurements," J. Acoust. Soc. Am. **103**, 3499–3508.

Kemp, D. (**1978**). "Stimulated acoustic emissions from within the human auditory system," J. Acoust. Soc. Am. **64**, 1386–1391.

Kemp, D. T., Ryan, S., and Bray, P. (**1990**). "Otoacoustic emission analysis and interpretation for clinical purposes," in F. Grandori, G. Cianfrone and D. T. Kemp (eds.), *Cochlear Mechanisms and Otoacoustic Emissions*, Adv. Audiol. Vol. 7, Karger, Basel, pp. 77–98.

Kemp, D. T., Bray, P., Alexander, L., and Brown, A. M. (**1986**). "Acoustic emission cochleography—Practical aspects," Scand. Audiol. Suppl. **25**, 71–95.

Kruglov, A. V., Artamasov, S. V., Frolenkov, G. I., and Tavartkiladze, G. A. (**1997**). "Transient evoked otoacoustic emission with unexpectedly short latency," Acta Oto-Laryngol. **117**, 174–178.

Liu, J., Du, Y., Li, J., and Nie, K. (**2004**). "A new method for eliminating stimulus artifact in transient evoked otoacoustic emission using ICA," in Proceedings of the 5th International Conference on Independent Component Analysis and Blind Separation, Granada, Spain.

Muller, S., and Massarani, P. (**2001**). "Transfer-function measurement with sweeps," J. Audio Eng. Soc. **49**, 443–471.

Notaro, G., AlMaamury, A. M., Moleti, A., and Sisto, R. (**2007**). "Wavelet and matching pursuit estimates of the transient-evoked otoacoustic emission latency," J. Acoust. Soc. Am. **122**, 3576–3585.

Peeters, G. G., and Deruty, E. (**2008**). "Automatic morphological description of sounds," J. Acoust. Soc. Am. **123**, 3801.

Probst, R., Lonsbury-Martin, B. L., and Martin, G. K. (**1991**). "A review of otoacoustic emissions," J. Acoust. Soc. Am. **89**, 2027–2067.

Ravazzani, P., and Grandori, F. (**1993**). "Evoked otoacoustic emissions: Nonlinearities and response interpretation," IEEE Trans. Biomed. Eng. **40**, 500–504.

Shera, C. A., and Guinan, J. J., Jr. (**1999**). "Evoked otoacoustic emissions arise by two fundamentally different mechanisms: A taxonomy for mammalian OAEs," J. Acoust. Soc. Am. **105**, 782–798.

Sisto, R., Moleti, A., and Shera, C. A. (**2007**). "Cochlear reflectivity in transmission-line models and otoacoustic emission characteristic time delays," J. Acoust. Soc. Am. **122**, 3554–3561.

Tavartkiladze, G. A., Frolenkov, G. I., Kroglov, A. V., and Artamasov, S. V. (**1994**). "Ipsilateral suppression effects on transient evoked otoacoustic emission," Br. J. Audiol. **28**, 193–204.

Thornton, A. R. D. (**1993**). "High rate otoacoustic emissions," J. Acoust. Soc. Am. **94**, 132–136.

Tognola, G., Grandori, F., and Ravazzani, P. (**1997**). "Time-frequency distributions of click-evoked otoacoustic emissions," Hear. Res. **106**, 112–122.

Tujal, P. M., and Souza, M. N. (**2003**). "Stimulus artifact cancellation in click evoked otoacoustic emissions using linear prediction," in Proceedings of the 25th Annual International Conference of IEEE Engineering in Medicine and Biology Society, Cancun, Mexico.

Van Campen, L. E., Grantham, D. W., and Hall, J. W., III (**1994**). "Motivation and methods for manipulating acoustic ringing of earphones," Ear Hear. **15**, 461–466.

Wilson, J. P. (**1980**). "Evidence for a cochlear origin for acoustic re-emissions, threshold fine-structure and tonal tinnitus," Hear. Res. **2**, 233–252.

Wit, H. P., van Dijk, P., and Avan, P. (**1994**). "Wavelet analysis of real ear and synthesized click evoked otoacoustic emissions," Hear. Res. **73**, 141–147.

Withnell, R. H., Hazlewood, C., and Knowlton, A. (**2008**). "Reconciling the origin of the transient evoked ototacoustic emission in humans," J. Acoust. Soc. Am. **123**, 212–221.

Yates, G. K., and Withnell, R. H. (**1999**). "The role of intermodulation distortion in transient-evoked otoacoustic emissions," Hear. Res. **136**, 49–64.

Yuwaraj, M., and Kunov, H. (**1995**). "Wavelet based reduction of stimulus artifact in evoked otoacoustic emissions testing," in Proceedings of the 17th Annual International Conference of the IEEE Engineering in Medicine and Biology Society, Montreal, Canada.

Distortion product emissions from a cochlear model with nonlinear mechanoelectrical transduction in outer hair cells

Yi-Wen Liu and Stephen T. Neely
Boys Town National Research Hospital, 555 North 30th Street, Omaha, Nebraska 68131

(Received 10 November 2009; revised 4 February 2010; accepted 5 February 2010)

A model of cochlear mechanics is described in which force-producing outer hair cells (OHC) are embedded in a passive cochlear partition. The OHC mechanoelectrical transduction current is nonlinearly modulated by reticular-lamina (RL) motion, and the resulting change in OHC membrane voltage produces contraction between the RL and the basilar membrane (BM). Model parameters were chosen to produce a tonotopic map typical of a human cochlea. Time-domain simulations showed compressive BM displacement responses typical of mammalian cochleae. Distortion product (DP) otoacoustic emissions at $2f_1-f_2$ are plotted as isolevel contours against primary levels (L_1,L_2) for various primary frequencies f_1 and f_2 $(f_1<f_2)$. The L_1 at which the DP reaches its maximum level increases as L_2 increases, and the slope of the "optimal" linear path decreases as f_2/f_1 increases. When primary levels and f_2 are fixed, DP level is band passed against f_1. In the presence of a suppressor, DP level generally decreases as suppressor level increases and as suppressor frequency gets closer to f_2; however, there are exceptions. These results, being similar to data from human ears, suggest that the model could be used for testing hypotheses regarding DP generation and propagation in human cochleae.
 [DOI: 10.1121/1.3337233]

PACS number(s): 43.64.Kc, 43.64.Ld, 43.64.Jb [BLM] Pages: 2420–2432

I. INTRODUCTION

Nonlinear growth is characteristic of healthy mammalian cochleae (Rhode, 1971). Introducing nonlinearity to the damping coefficient of cochlear models (Kim *et al.*, 1973; Hall, 1974) enabled the simulation of distortion products (DPs) and other nonlinear responses. In several subsequent studies, the damping coefficient was allowed to be negative at low intensity so sounds were amplified in a frequency- and place-specific manner. As a result, model responses achieved high sensitivity and sharp tuning typical of mammalian hearing (Davis, 1983; Neely and Kim, 1983, 1986). Since then, understanding of the biophysical foundations for the putative "cochlear amplifier" has improved (see Dallos, 2008, for a review). Models proposed in recent years (Lu *et al.*, 2006; Ramamoorthy *et al.*, 2007; Liu and Neely, 2009; Rabbitt *et al.*, 2009) indicated that outer hair cells (OHCs) likely provide cycle-by-cycle amplification to cochlear traveling waves because of their capabilities to convert mechanical and electrical energy in both directions (Brownell *et al.*, 1985; Hudspeth, 1997). However, these newer results were obtained by linear analysis in the frequency domain; time-domain simulation of DP and other nonlinear responses from these models has not yet been reported.

The goals of the present study are (1) to construct a nonlinear cochlear model that incorporates recent findings in OHC biophysics and (2) to test the model's time-domain response to single and multitone stimuli for a broad range of stimulus conditions. Of particular interest is the simulation of distortion-product otoacoustic emissions (DPOAEs). First observed in late 1970s (Kemp, 1978; Kim *et al.*, 1980), DPOAEs have been measured for a wide range of stimulus frequencies and levels (e.g., Gaskill and Brown, 1990). Damage to the OHCs causes reduction of DPOAEs (Zurek *et al.*, 1982), confirming OHCs' contribution to cochlear nonlinearity. Computer simulation of DPOAE emerged in the 1990s. Using a variation of the Neely and Kim (1986) model, Kanis and de Boer (1993) calculated DP levels via a frequency-domain iterative quasilinear approach. Results suggested that the source of DP is distributed, and that DP travels backward to the middle ear via a slow transverse wave. A later revision of the Neely and Kim (1986) model included an explicit representation of the membrane potential in OHCs (Neely, 1993). Subsequently, simulation of DP was carried out using a time-domain approach (Neely and Stover, 1994); when the frequency of one primary tone (f_2) was fixed while the other $(f_1,f_1<f_2)$ was swept, DP level had a band-pass filtering characteristic similar to that observed in humans and rodents (Brown *et al.*, 1992). When the levels of the primaries were swept, the revised model also produced DPOAE input-output (I/O) functions typical of humans (Neely *et al.*, 2000). In the interim, theoretic treatment of DPOAE was conducted by Talmadge *et al.* (1998) using a frequency-domain, perturbative approach to explain fine structures and the band-pass filtering effect.

The present study is an extension to modeling efforts previously described in a few ways. First, the present model describes OHC biophysics in more detail (Liu and Neely, 2009), which makes it possible to place the nonlinearity specifically in the mechanoelectrical transduction (MET) channel of OHCs. The advantage of modeling OHCs biophysics is discussed in Sec. V. Second, DPOAEs for a wide range of primary levels and primary frequencies were simulated so

 0001-4966/2010/127(4)/2420/13/$25.00

TABLE I. Parameters for cochlear mechanics.

	Meaning (unit)	Base	Mid	Apex
	Organ of Corti mechanical parameters			
M	Mass in OHC load impedance (g)	2.8×10^{-8}	5.0×10^{-7}	2.8×10^{-5}
R	Resistance in OHC load impedance (g s^{-1})	9.4×10^{-4}	9.2×10^{-4}	2.7×10^{-3}
K	Stiffness in OHC load impedance (g s^{-2})	200	11	0.76
m	BM mass per unit area (g cm^{-2})	3.8×10^{-5}	2.8×10^{-4}	2.1×10^{-3}
r	BM resistance per unit area (g s^{-1} cm^{-2})	1.5	3.2	8.6
k	BM stiffness per unit area (g s^{-2} cm^{-2})	5.9×10^{5}	4.0×10^{4}	1.6×10^{3}
	Outer hair cell electromechanical properties			
α_d	MET's sensitivity to RL displacement (A/m)	1.6×10^{-3}	6.2×10^{-4}	2.0×10^{-4}
α_v	MET's sensitivity to RL velocity (C/m)	4.4×10^{-6}	1.8×10^{-6}	6.8×10^{-7}
$I_{\max}$	Maximum range of OHC receptor current (pA)	670	320	83
T	Piezoelectric transformer ratio (m/C)	2.4×10^{6}	2.4×10^{6}	2.4×10^{6}
G	Membrane conductance (nS)	91	51	33
C	Membrane capacitance (pF)	14	32	79
C_g	Gating capacitance (pF)	18	33	70
	Physical dimensions			
A	Cochlear cross-sectional area (cm^2)	6.3×10^{-2}	1.4×10^{-2}	3.1×10^{-3}
w	BM width (cm)	0.031	0.040	0.051
L	Length of cochlea (cm)	3.5		

results can be compared to data recently reported by Johnson *et al.* (2006). In addition, model responses to three-tone stimuli in a DP suppression paradigm are compared to data from normal-hearing humans (Rodríguez *et al.*, 2010).

It is noteworthy that, although DPOAE is a robust phenomenon routinely used for clinical purposes, there is still a debate regarding DP propagation. The existence of slow-traveling waves has been challenged (Nobili *et al.*, 2003), and transmission-line modeling efforts (e.g., Neely and Kim, 1983) have been criticized. Nobili *et al.* (2003) proposed that the motion of the stapes is coupled to the basilar membrane (BM) via fluid compressional waves. This theory found supports from a laser-scanning measurement of BM motion (Ren, 2004), which seems to suggest reverse propagation of DPs via compressional (fast) waves. However, the interpretation was based on the phase velocity of DP and its flaws have been noted (Shera *et al.*, 2007). By simultaneous measurements of DPOAE and intracochlear acoustic pressure, Dong and Olson (2008) found evidence for reverse-traveling waves in the phase response of DPOAE relative to the phase response of intracochlear DPs. As will be described in Sec. II, the macromechanical model for the present study is a transmission-line model. Therefore, results presented in this paper are based on the slow-traveling wave theory.

Besides DPs, a plethora of nonlinear phenomena has been observed in cochlear mechanics. Some of them have been reproduced in computational models, including level-dependent latency of transient responses (Neely, 1988), instantaneous-frequency glide in transient responses (Hubbard *et al.*, 2003), asymmetric onset and offset response time (Zhang *et al.*, 2009), and an in-depth investigation (Ku *et al.*, 2009) of spontaneous otoacoustic emissions (SOAEs). Transient responses are beyond the scope of this paper, while generation of SOAEs will be discussed in Sec. V.

The rest of this paper is organized as follows. Models for OHC biophysics, cochlear mechanics, and middle-ear mechanics are described in Sec. II. Parameter selection and methods for time-domain simulation are described in Sec. III. Model responses to single and multitone stimuli are reported in Sec. IV. Discussion is given in Sec. V, followed by conclusions in Sec. VI.

II. MODELS

Sections II A–II C describe the present model for cochlear mechanics, and Sec. II D describes a simple model for the mechanics of the middle ear. Cochlear and middle-ear parameters are listed in Table I and II, respectively.

A. Outer hair cells: Mechanoelectrical transduction

The receptor current that flows into an OHC is modulated by deflection of its hair bundle (HB). We previously proposed to model this as follows (Liu and Neely, 2009):

$$i_r = \alpha_v \dot{\xi}_r + \alpha_d \xi_r, \tag{1}$$

where i_r denotes the receptor current, and ξ_r and $\dot{\xi}_r$ denote the reticular-lamina (RL) displacement and velocity, respectively; tectorial-membrane motion is not considered explicitly in favor for simplicity here.[1] In the present study, Eq. (1) is generalized by introducing nonlinearity to it:

$$i_r = I(\alpha_v \dot{\xi}_r + \alpha_d \xi_r), \tag{2}$$

where $I(\cdot)$ denotes an arbitrary nonlinear function. For the present study, we defined $I(\cdot)$ as an antisymmetric function:

TABLE II. Parameters for middle-ear mechanics.

	Meaning (unit)	Value
	Maleus-incus-eardrum parameters	
A_m	Area of eardrum (cm^2)	0.5
M_m	Effective mass (g)	8.5×10^{-3}
R_m	Effective resistance (g s^{-1})	20
K_m	Effective stiffness (g s^{-2})	1.5×10^{5}
g_m	Maleus-incus lever ratio	0.7
	Incudo-stapedial joint	
R_i	Resistance (g s^{-1})	400
K_i	Stiffness (g s^{-2})	5.0×10^{6}
	Stapes parameters	
A_s	Area of stapes footplate (cm^2)	0.0625
M_s	Effective mass (g)	5.0×10^{-3}
R_s	Effective resistance (g s^{-1})	80
K_s	Effective stiffness (g s^{-2})	5.0×10^{5}
	Round-window parameters	
A_r	Area of round window (cm^2)	0.0625
M_r	Effective mass (g)	5.0×10^{-3}
R_r	Effective resistance (g s^{-1})	20
K_r	Effective stiffness (g s^{-2})	1.5×10^{5}

$$I(\eta) \triangleq I_{\max}\left(\frac{1}{1+\exp(-4\eta/I_{\max})}-\frac{1}{2}\right)=\frac{I_{\max}}{2}\tanh\frac{2\eta}{I_{\max}}, \tag{3}$$

where $\eta=\alpha_v\dot{\xi}_r+\alpha_d\xi_r$. Note that the full range of current output is $I_{\max}$, and the slope of $I(\cdot)$ is unity at the origin:

$$\left.\frac{\partial I}{\partial \eta}\right|_{\eta=0}=1.$$

Experiments have shown that the nonlinear function $I(\cdot)$ should be an asymmetric function because of rectification; i_r is larger when the HB is deflected toward the tallest row of stereocilia than i_r is negative when the HB is rarified (e.g., Corey and Hudspeth, 1983; Ricci *et al.*, 2005). Nevertheless, the nonlinearity given by Eq. (3) was suitable for this study because the main concern was to simulate DP at $2f_1-f_2$, which is an odd-order distortion.[2]

B. Outer hair cells: Electromotility

The present study adopts a one-dimensional (1D) piezoelectric OHC model that we previously proposed (Liu and Neely, 2009). The underlying assumptions of the model are summarized below. First, the receptor current i_r is the sum of capacitive, conductive, and gating components:

$$i_r=C\frac{dV}{dt}+GV+\frac{dQ}{dt}, \tag{4}$$

where C and G are the capacitance and the conductance of the plasmic membrane, respectively, V is the transmembrane potential, and Q is the charge accumulation that accompanies electromotility. Second, the OHC contraction displacement ξ_o is linearly proportional to Q,

$$\xi_o=TQ, \tag{5}$$

where T represents a piezoelectric constant. Finally, Q is a Boltzmann function of $\tilde{V}\triangleq V-Tf_{\mathrm{OHC}}$, where f_{OHC} is a contraction force generated by the OHC.

For the present study, the Boltzmann function $Q(\tilde{V})$ is linearized so the only source of nonlinearity is from the MET channel. Linearization of $Q(\tilde{V})$ is legitimate if $\tilde{V}$ is small in comparison to the voltage scale in the Boltzmann function—this appears to be the case at the stimulus levels of interest (SPL$\leq$100 dB, see Sec. V for further details). Therefore, Eq. (4) can be rewritten as

$$i_r=C\frac{dV}{dt}+GV+C_g\frac{d\tilde{V}}{dt}, \tag{6}$$

where $C_g\triangleq\partial Q/\partial\tilde{V}$ denotes a gating capacitance that is approximately constant in time.

In the present study, it is assumed that the OHC contracts and stretches against a simple mechanical load:[3]

$$f_{\mathrm{OHC}}=M\ddot{\xi}_o+R\dot{\xi}_o+K\xi_o, \tag{7}$$

where M, R, and K are the effective mass, resistance, and stiffness, respectively.

C. Cochlear macromechanics

The macromechanics of the cochlea are governed by Newton's laws and the principle of continuity. In a one-dimensional nonviscous model (Dallos, 1973), Newton's second law requires that

$$\partial_x P=-\frac{\rho}{A}\dot{U}, \tag{8}$$

where P denotes the pressure difference between two cochlear chambers (*scala vestibuli* and *scala tympani*), x denotes the longitudinal direction from base to apex, ρ denotes the effective fluid mass density, A denotes the cross-sectional area of the fluid chamber, and U denotes the volume velocity along the x-direction. The present study assumes that the fluid is incompressible, and the principle of continuity is represented by the following equation[4] (Neely and Liu, 2009):

$$\partial_x U=w\dot{\xi}_r, \tag{9}$$

where w is the width of cochlear partition. The displacement ξ_b of the BM, equal to the sum of ξ_r and ξ_o, is driven by the pressure P:

$$m\ddot{\xi}_b+r\dot{\xi}_b+k\xi_b=-P, \tag{10}$$

where m, r, and k are mass, resistance, and stiffness of BM per unit area.

The boundary condition at the apical end of the cochlea is

$$\partial_x P|_{x=L}=\frac{-\rho}{Am_h}P, \tag{11}$$

where $m_h=110$ g/cm^4 is an acoustic inductance which represents the mass of the fluid at the helicotrema [Puria and

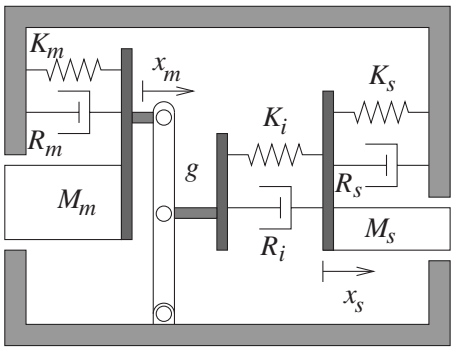

FIG. 1. Schematic diagram of middle-ear mechanics. Pressure and displacement are coupled between the ear canal (to the left) and the cochlear fluid (to the right). Subscript m denotes the malleus-incus-eardrum system, i denotes incudo-stapedial joint, and s denotes stapes.

Allen, 1991, Eq (11)]. The boundary condition at the basal end of the cochlea is

$$\partial_x P|_{x=0} = -\rho \dot{v}_s, \tag{12}$$

where v_s denotes the velocity of the stapes.

D. Modeling the middle ear

The present middle-ear model, adapted from Matthews (1983), is aimed to reproduce adequately the pressure magnitude transfer functions measured from human cadavers (e.g., Puria, 2003; Nakajima *et al.*, 2009) without pursuing other details in middle-ear mechanics. A schematic diagram of the middle ear is shown in Fig. 1. The malleus, the incus, and the eardrum are lumped into one system as suggested by Zwislocki (1962), while any motion on the eardrum that is not coupled to the ossicular chain is ignored. The malleus-incus-eardrum system is characterized by parameters $\{M_m, R_m, K_m\}$. The malleus-incus lever ratio is denoted as g ($g \leq 1$). The incudo-stapedial joint (ISJ) is characterized by parameters $\{R_i, K_i\}$. The stapes and its surrounding structures are represented by parameters $\{M_s, R_s, K_s\}$.

Given the diagram in Fig. 1, the *acoustic pressure*[5] P_{ED} at the eardrum and the cochlear fluid pressure P_{FL} at the stapes are coupled to each other via the following equations:

$$M_m \dot{v}_m = -K_m x_m - R_m v_m + g f_i + P_{\mathrm{ED}} A_e, \tag{13a}$$

$$(M_s + M_r)\dot{v}_s = -(K_s + K_r)x_s - (R_s + R_r)v_s - f_i - P_{\mathrm{FL}} A_s, \tag{13b}$$

where $f_i = K_i(x_s - g x_m) + R_i(v_s - g v_m)$ is the force transferred through the ISJ. In the preceding equations, A_e and A_s are effective areas of the eardrum and the stapes footplate, respectively; x_m and v_m, respectively, denote the displacement and velocity of the malleal system, and x_s and v_s denote the displacement and the velocity of the stapes, respectively. Also, in Eq. (13b), parameters $\{M_r, R_r, K_r\}$ represent the round window.[6] The present middle-ear model is similar to that of Talmadge *et al.* (1998) except for a nonrigid ISJ here. Middle-ear frequency responses are reported in Appendix A.

III. SIMULATION METHODS

A. Fine-tuning cochlear parameters

Table I shows the parameters used in the present cochlear model: the values listed are for the base ($x=0$), the longitudinal midpoint ($x=L/2$), and the apex ($x=L$). Parameter values intermediate to these three locations were determined by log-quadratic interpolation.[7] These values were carefully chosen to produce (1) tonotopic mapping typical of humans, (2) cochlear excitation profiles and frequency responses typical of mammals, and (3) nonlinear compression of BM motion typical of mammals. Approximation formulas were derived from frequency-domain analysis to facilitate the parameter-tuning process; more details are described in Appendix B. Parameter values listed in Table I are a result of this fine-tuning process. Then, these parameters were used in simulation of DP and DP suppression.

B. Delivering the stimulus

To simulate experimental conditions in a typical DPOAE measurement paradigm, we assumed that the stimulus is delivered as a force $f(t)$ that acts on a diaphragm, the diaphragm is latched on one end to a coupler inserted in the ear canal; at the other end of the coupler is the eardrum. Therefore, the dynamics of the diaphragm are described by the following equation:

$$M_d \dot{v}_d = f(t) - R_d v_d - K_d x_d - P_d A_d, \tag{14}$$

where v_d and x_d denote the velocity and the displacement of the diaphragm, respectively, P_d denotes the pressure in the enclosed space, and A_d is the area of the diaphragm. Two further assumptions about the coupler were made: first, the coupler is acoustically lossless; second, the physical dimension of the coupler is much smaller than the shortest wavelengths of interest. Therefore, P_d is approximately equal to the pressure P_{ED} at the eardrum in Eq. (13a), and the enclosed volume of air is acoustically compliant:

$$P_d = K_c(x_d A_d - x_m A_e). \tag{15}$$

Parameter values were as follows:[8] $K_c = 8.5 \times 10^5$ dyn/cm^5, $M_d = 5 \times 10^{-3}$ g, $R_d = 1.4 \times 10^3$ g/s, $K_d = 4 \times 10^8$ g/s^2, and $A_d = 0.75$ cm^2.

C. State-space formulation and numerical integration in time

To conduct a time-domain simulation, a minimal set of variables (displacements, velocities, currents, or voltages) were selected as *state variables* so their rates of change could be determined instantaneously given their present state and the stimulus. Then, the state variables were integrated numerically with respect to time.

The following variables were chosen as state variables: diaphragm variables $\{x_d, v_d\}$, middle-ear variables $\{x_m, v_m, x_s, v_s\}$, and cochlear variables including RL displacement $\xi_r(x)$, RL velocity $u_r(x)$, OHC contraction velocity $u_o(x)$, OHC membrane potential $V(x)$, and the gating charge $Q(x)$. With some algebra, Eqs. (5)–(7) and (10) can be rearranged as follows:

$$\dot{\xi}_r(x) = u_r, \tag{16a}$$

$$\dot{Q}(x) = T^{-1}u_o, \tag{16b}$$

$$\dot{u}_r(x) = \frac{Ru_o + KTQ}{M} - \frac{V - C_g^{-1}Q}{TM} - \frac{r(u_r + u_o) + k(\xi_r + TQ)}{m} - \frac{P(x)}{m}, \tag{16c}$$

$$\dot{u}_o(x) = -\frac{Ru_o + KTQ}{M} + \frac{V - C_g^{-1}Q}{TM}, \tag{16d}$$

$$\dot{V}(x) = \frac{1}{C}(i_r(u_r, \xi_r) - GV - T^{-1}u_o). \tag{16e}$$

In Eq. (16e), $i_r(u_r, \xi_r)$ is the nonlinear function defined in Sec. II A. Note that although $P(x)$ on the right hand side of Eq. (16c) is not a state variable, it could be solved instantaneously given the state variables. By combining Eqs. (8) and (9), the following approximation was derived,

$$\partial_x^2 P = -\frac{\rho}{A}\left(\partial_x\partial_t U - \partial_t U\frac{\partial_x A}{A}\right), \tag{17a}$$

$$\approx -\frac{\rho}{A}w\partial_t^2\xi_r. \tag{17b}$$

The second term on the right hand side of Eq. (17a) was neglected, assuming that $A^{-1}\partial_x A \approx 0$ (i.e., the taper of the area is small compared to its overall size). Combining Eqs. (17b) and (16c), we obtained the following relation between $P(x)$ and state variables:

$$\left(\partial_x^2 - \frac{\rho w}{mA}\right)P = l\big(u_r(x), u_o(x), \xi_r(x), Q(x), V(x)\big), \tag{18}$$

where $l(\cdot)$ denotes a linear combination. Then, Eq. (18) with boundary conditions described in Sec. II C was solved numerically by a finite-difference method with $N=700$ discrete cochlear segments. The computation load was $O(N)$.[9]

To summarize, the *state vector* consisted of 3500 cochlear variables and six other variables, and their rates of change were determined by Eqs. (13), (14), (16), and (18) given their present state and the stimulus $f(t)$. Let us denote the state vector as $\mathbf{x}(t)$, and its time derivative as $\mathbf{v}(\mathbf{x})$. State-space equations were numerically integrated with respect to time in steps of $\Delta t = 6.25$ μs. For each step in time t, $\mathbf{x}(t)$ was updated by a modified Sielecki method (Diependaal *et al.*, 1987) in two steps; first, $\mathbf{x}(t+\Delta t)$ was estimated by extrapolation:

$$\hat{\mathbf{x}} = \mathbf{x} + \Delta t \cdot \mathbf{v}(\mathbf{x}). \tag{19}$$

Then, $\mathbf{v}$ was re-evaluated at $\hat{\mathbf{x}}$, and the state variables were updated as follows:

$$\mathbf{x}(t + \Delta t) = \mathbf{x}(t) + \Delta t \cdot \frac{\mathbf{v}(\mathbf{x}(t)) + \mathbf{v}(\hat{\mathbf{x}})}{2}. \tag{20}$$

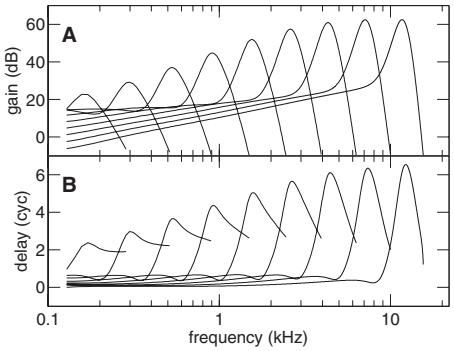

FIG. 2. Frequency responses at selected locations in the cochlea. Curves represent responses at nine different locations in equal distances: $x = \{0.9, 0.8, \ldots, 0.1\}$ times the length the cochlea, respectively. Characteristic frequency decreases as x increases (i.e., toward the apex). (A) RL-to-stapes displacement gain. (B) RL displacement group delay.

IV. RESPONSES TO STIMULI

A. Cochlear tuning and latency for low-level stimuli

To calculate cochlear tuning properties at low intensity, a wide-band (0.32–12 kHz) click was delivered to the diaphragm. The level of the click was set sufficiently low (peak-equivalent SPL $<$ 32 dB at the eardrum) so that the OHC receptor currents $i_r(t)$ were no more than 2.5% of $I_{\max}$ in Eq. (3) anytime and anywhere in the cochlea. The simulation ran for 70 ms, long enough for the traveling wave to reach the apical region of the cochlea.

In Fig. 2, the stapes-to-RL displacement gain and its group delay are plotted against frequency for nine different locations in the cochlea.[10] Characteristic frequency (CF) (i.e., frequency of maximum gain) decreases from base to apex. As shown in Fig. 2(A), the displacement gain at CF increases from 23 dB at the most apical location to 62 dB near the base. The group delay, when expressed in number of cycles, also reaches its maximum $N_{\max}$ near CF for every location.

By inspection, the responses in Fig. 2(A) are more sharply tuned at basal locations than apically. Further analyses show that the quality factor in terms of the *equivalent rectangular bandwidth*[11] (Q_{ERB}) increases from 1.8 to 9.9 from apex to base (Fig. 3, top panel). Between 0.5 and 10 kHz, the present values of Q_{ERB} are similar to those of cats and guinea pigs derived from auditory-nerve recordings (Shera *et al.*, 2002). The values are also similar to human Q_{ERB} values derived from DP suppression tuning data (Gorga *et al.*, 2008); however, they are smaller than the Q_{ERB} of humans derived from psychoacoustic experiments (Glasberg and Moore, 1990). Additionally, the model Q_{ERB} seems to flatten between 1 and 10 kHz, in agreement with older psychoacoustic findings but different from more recent data that suggest that (a) $Q_{\mathrm{ERB}} > 10$ for a wide range of frequencies, and (b) Q_{ERB} continues to increase at higher frequencies (Shera *et al.*, 2002).

The maximum group delay $N_{\max}$ for each location is plotted against CF in the bottom panel of Fig. 3, in comparison to cochlear latency estimated from stimulus-frequency otoacoustic emission (SFOAE) data across different species (Shera *et al.*, 2002). The model latency $N_{\max}$ is shorter than

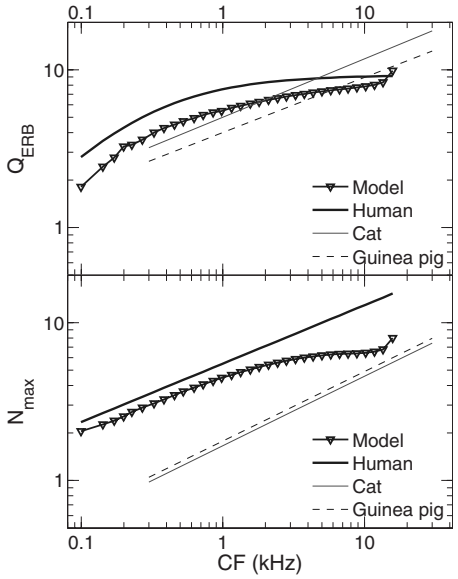

FIG. 3. Model Q_{ERB} (top panel) and latency N_{max} (bottom panel) plotted against characteristic frequency. Results are compared with curves derived from experimental data across three species. Human $Q_{ERB}=9.26CF/(CF+230\ Hz)$ is given by Glasberg and Moore (1990). Linear fits of human N_{max} and cat and guinea pig Q_{ERB} and N_{max} are given by Shera *et al.* (2002).

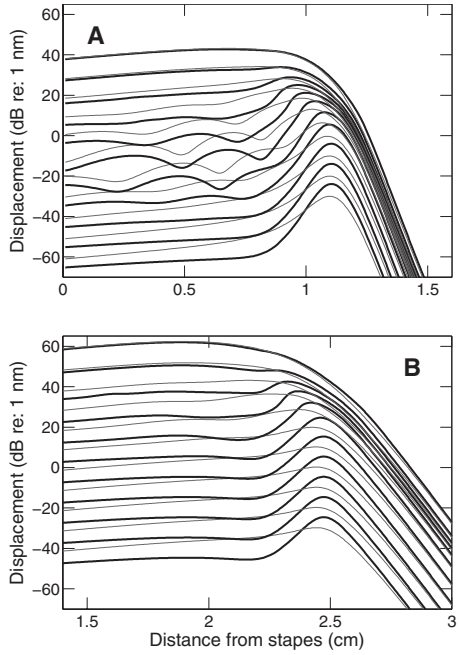

FIG. 4. Excitation patterns for pure-tone stimuli. BM displacement (thin lines) and RL displacement (thick lines) along the cochlea are plotted as the input level varies from 0 to 100 dB SPL in 10 dB steps. (A) Stimulus frequency $f_0=4$ kHz. (B) $f_0=500$ Hz.

that of human SFOAE forward latency but longer than that of cats and guinea pigs. Note that the model N_{max} also seem to flatten at above 1 kHz, a feature shared with the model Q_{ERB} but not observed in SFOAE data. The model latency, when expressed in absolute time, ranges from 7.0 ms at the 0.5 kHz place to 0.8 ms at the 8 kHz place. Compared to estimates of human cochlear forward latency based on auditory brainstem responses (Neely *et al.*, 1988; Harte *et al.*, 2009), the model latency is similar at 0.5 kHz but shorter at 8 kHz.

B. Compression of single tones

Figure 4 shows BM (thin lines) and RL (thick lines) magnitude responses to a single tone at two different frequencies for input levels L_0 from 0 to 100 dB sound pressure level (SPL) in 10 dB steps. The response plotted at every location is the magnitude of BM or RL displacement at the frequency of the stimulus f_0; harmonic distortions are omitted.

For each frequency, the magnitude response is compressed near its characteristic place (CP). For $f_0=4$ kHz, RL displacement at CP ($x=1.1$ cm) grows nearly linearly from $L_0=0$–30 dB (Fig. 5). When L_0 increases from 30 to 90 dB, the RL displacement at the CP increases only by an order of magnitude and the best place shifts toward the base (Rhode and Robles, 1974). For $f_0=500$ Hz, the response is nearly linear for $L_0\leq 40$ dB while the compression is more prominent for $L_0=50$–90 dB. The magnitude response is approximately linear near the base for $f_0=500$ Hz; the excitation pattern forms parallel lines for the first 2.0 cm from the stapes [Fig. 4(B)]. The near-linear growth at low intensity is consistent with recent experimental findings (Rhode, 2007, Fig. 1), in contrast to a cubic-root growth of amplitude predicted by "essential nonlinearity" (Eguíluz *et al.*, 2000) and Hopf bifurcation theory (Stoop and Kern, 2004). However, for $f_0=4$ kHz, this presumably linear growth is confounded by a standing-wave pattern that is prominent for $L_0=30$–70 dB. This standing-wave phenomenon indicates a reflection from the CP and was explained as a consequence of self-suppression of the forward-going waves for intermediate input levels (Kanis and de Boer, 1993, Fig. 2).

Compared to BM excitation patterns, the RL excitation patterns in Figs. 4(A) and 4(B) have higher tip-to-tail gains and are more sharply tuned. Since RL motion is more directly related to neural excitation, the present results suggest a distinction between tuning curves recorded from auditory nerves (e.g., Pfeiffer and Kim, 1975; van der Heijden and Joris, 2006) and BM tuning curves obtained by motion-sensing techniques (e.g., Rhode, 1971; Ruggero *et al.*, 1997).

Figure 5 shows the RL and BM displacements at CP as a function of stimulus level; their *rate of growth* (ROG), defined as the slope of the I/O function, is plotted in Fig. 6.

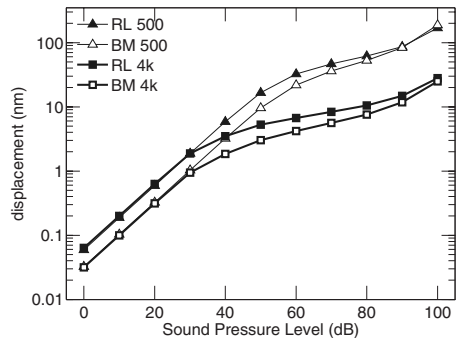

FIG. 5. Nonlinear growth of RL and BM displacements at CP, plotted against stimulus intensity. The stimulus is either a 4 kHz or a 500 Hz pure tone.

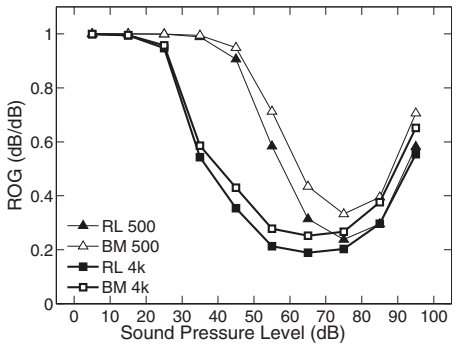

FIG. 6. RL and BM response rate of growth (ROG, see the text for definition), plotted against stimulus intensity.

As can be seen in Fig. 6, the response to 4 kHz stimuli is most compressive between 60 and 70 dB SPL, reaching a minimum ROG of 0.19 and 0.25 for RL and BM, respectively. The response to 500 Hz stimuli is linear for a more extended input range; the response is most compressive between 70 and 80 dB SPL, reaching minimum ROGs of 0.24 and 0.33 for RL and BM, respectively.

The model results for the 4 kHz stimuli have comparable ROG to BM vibration data from the 9 kHz place (Ruggero *et al.*, 1997, Fig. 3: ROG=0.2–0.5) and the 6 kHz place (Rhode, 2007, Fig. 3: ROG~0.3) in chinchilla cochleae. However, experimental results showed individual variability, and a more compressive BM response has also been reported (Rhode, 2007, Fig. 4: ROG~0.1).

C. Distortion-product otoacoustic emissions

To simulate DPOAE, the stimulus $f(t)$ was comprised of two tones at frequencies $\{f_1,f_2\}$ and levels $\{L_1,L_2\}$. The amplitude of the two tones was calibrated so that the SPL varied from 40 to 80 dB for L_1 and from 20 to 70 dB for L_2 in 2 dB steps, respectively. The range of L_2 is similar to that of a typical experiment on human subjects (e.g., Johnson *et al.*, 2006; Long *et al.*, 2009). A 5 ms cosine-square ramp was used for the onset of the stimulus. For each combination of $\{L_1,L_2\}$, the simulation ran for a sufficiently long time (more than the duration of the ramp plus 40 cycles of f_1) so that the DPOAE at the eardrum reached a steady level. Then, the magnitude L_d of DPOAE at $f_d=2f_1-f_2$ was calculated using discrete Fourier transform (DFT). The window length of DFT was set so that it contained minimal integer cycles of f_1 and f_2, respectively—for example, if f_2 is 4 kHz and $f_2/f_1=1.2$, the window length is 6 cycles of f_2, or 1.5 ms.

Results for 16 different conditions of primary frequencies $\{f_1,f_2\}$ are reported in Fig. 7: four f_2's (1, 2, 4, or 8 kHz) by four primary-frequency ratios ($f_2/f_1=1.4$, 1.3, 1.2, or 1.1). Each column represents a fixed f_2 and each row represents a fixed f_2/f_1. In each panel, isolevel contours for L_d as a function of L_1 and L_2 are plotted in 4 dB steps. Note that the contours are well rounded for $f_2/f_1=1.40$ across all f_2, and become more oblique and narrower as f_2/f_1 decreases. Therefore, for any fixed f_2 and L_2, the "optimal" L_1 that yields the highest DPOAE level has a tendency to decrease

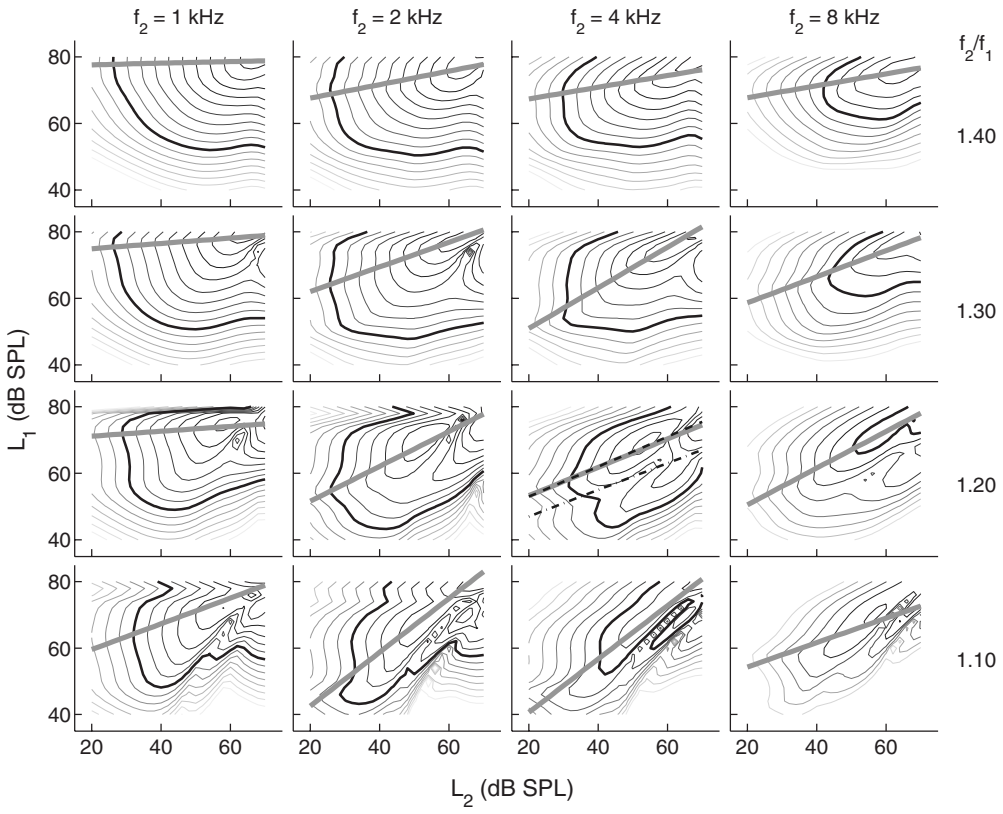

FIG. 7. DPOAE level L_d, plotted as a function of L_1 and L_2 for various combinations of $\{f_1,f_2\}$. Isolevel contours are plotted in 4 dB steps. As a reference, the contour corresponding to $L_d=0$ dB SPL is indicated with a thick black line. Otherwise, darker contours represent higher L_d. Only contours corresponding to $L_d>-30$ dB are shown. In each panel, the thick gray line represents linear regression of optimal L_1 as a function of L_2. Empirical optimal paths are shown on the panel for $f_2=4$ kHz and $f_2/f_1=1.20$ for comparison; dashed line was recommended by Neely *et al.* (2005), and dash-dotted line by Kummer *et al.* (1998).

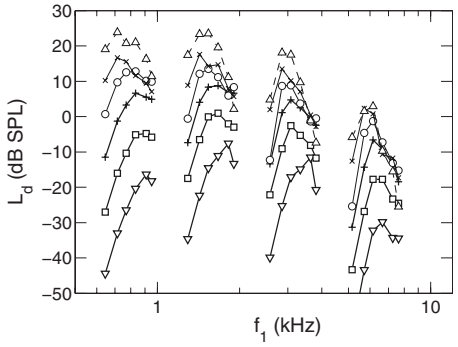

FIG. 8. DP filtering effects. DP level L_d is plotted against f_1 for a fixed f_2 =1, 2, 4, or 8 kHz. Curves marked with different symbols correspond to different L_2: ▽=20 (dB), □=30, +=40, ○=50, ×=60, and △=70, while $L_1=39+0.4L_2$.

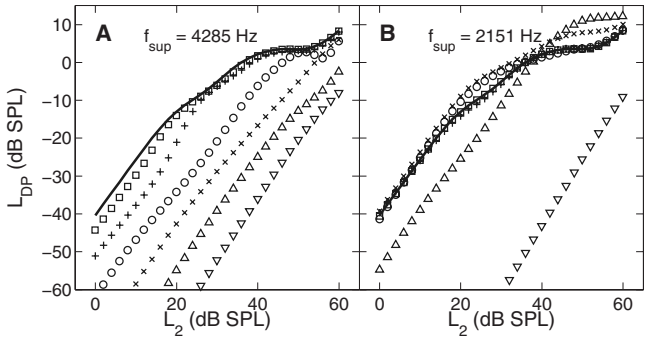

FIG. 9. Suppression of DPOAE by a third tone. Frequencies of the primary tones are: $f_2=4000$ Hz, and $f_1=f_2/1.22$. (A) "On-frequency" suppression, $f_{sup}\approx f_2$. (B) $f_{sup}\approx 0.5f_2$. In both panels, the solid line shows DP input-output (I/O) function with negligible suppression (suppressor level L_{sup} =0 dB). Symbols represent the I/O function for different L_{sup}: □=30, + =40, ○=50, ×=60, △=70, and ▽=80.

as f_2/f_1 decreases. This result agrees qualitatively with experimental data from normal-hearing humans (Johnson *et al.*, 2006). In each panel, the straight line shows a linear regression of optimal L_1 as a function of L_2. Among all linear paths shown in Fig. 7, the path for $f_2=4$ kHz and $f_2/f_1=1.20$ is $L_1=0.43L_2+45$, which comes closest to paths previously recommended. To obtain maximum DPOAE, Kummer *et al.* (1998) recommended the path of $L_1=0.4L_2+39$ and Neely *et al.* (2005) recommended $L_1=0.45L_2+44$.

Another way to visualize the DPOAE data is to plot L_d against primary frequencies. Following Kummer *et al.* (1998) recommendation, we set $L_1=0.4L_2+39$. DPOAE level L_d is plotted against f_1 for fixed $f_2=1$, 2, 4, or 8 kHz and fixed L_2 from 20 to 70 dB in 10 dB steps. In Fig. 8, each curve consists of six points corresponding to $f_2/f_1=1.55$, 1.4, 1.3, 1.2, 1.1, and 1.05, respectively. Results show that the optimal f_1 for each curve ranges from $f_2/1.4$ (e.g., for $f_2=1$ kHz, $L_2=60$ or 70 dB) to $f_2/1.1$ (e.g., for $f_2=2$ or 4 kHz, $L_2=20$ dB). Also, the optimal f_1 decreases as L_2 increases for $f_2=1$, 2, or 4 kHz.

Brown *et al.* (1992) reported human DPOAE at a fixed f_2 while f_1 was swept, so f_2/f_1 varied from 1.01 to 1.41. Primary levels were fixed at $L_2=40$ dB and $L_1=55$ dB. DP level was plotted against DP frequency f_d, and results showed a band-pass profile similar to Fig. 8 with a plateau of approximately 0.8 kHz wide and 5–10 dB (SPL) high. The peak level L_d for the $2f_1-f_2$ component occurred at an f_1 of approximately 3.3–3.4 kHz, which is higher than the best $f_1\approx 3.1$ kHz of the present model. This discrepancy will be discussed further in Sec. V.

D. Suppression of DPOAE

Model responses to three tones were tested in a DP suppression paradigm. The stimulus $f(t)$ consisted of two primary tones with $f_2/f_1=1.22$ and a suppressor tone at frequency f_{sup} and level L_{sup}. As L_2 varied, L_1 was set as recommended by Kummer *et al.* (1998): $L_1=0.4L_2+39$. The DP I/O function was measured in the same manner as described in Sec. IV C except that the window used for spectral analysis now contained minimal integer cycles of f_1, f_2, and f_{sup}.

Figure 9 shows DP I/O function for an "on-frequency" suppression condition [$f_{sup}\approx f_2$, Fig. 9(A)] and for f_{sup} at approximately one octave lower [Fig. 9(B)]. The thick line shows the DP I/O function when $L_{sup}=0$ dB SPL; at this suppressor level, any change of DP level due to the presence of the suppressor should be negligible. On-frequency suppression becomes prominent for $L_{sup}\geq 40$ dB SPL, and the I/O function generally shifts to the right as L_{sup} increases further. In contrast, the low-frequency suppressor does not cause L_d to reduce until $L_{sup}=70$ dB. Note that the low-frequency suppressor even causes L_d to increase for L_{sup} =50, 60, and 70 dB for different ranges of L_2. Possible reasons for this DPOAE increment induced by a low-frequency "suppressor" will be discussed in Sec. V.

The rightward shift of DP I/O function shown in Fig. 9 could be quantified by finding the input increment ΔL_2 necessary for the DP level L_d to reach a given level when the suppressor is present. In Fig. 10, ΔL_2 is plotted against L_{sup} for the on-frequency suppressor (filled symbols) and the low-frequency suppressor (open symbols) for L_d to reach −20 or −3 dB SPL. Results indicate that I/O curves begins to shift to the right ($\Delta L_2>0$) at a lower L_{sup} for $L_d=-20$ dB than for $L_d=-3$ dB; this is true for both the on-frequency and the

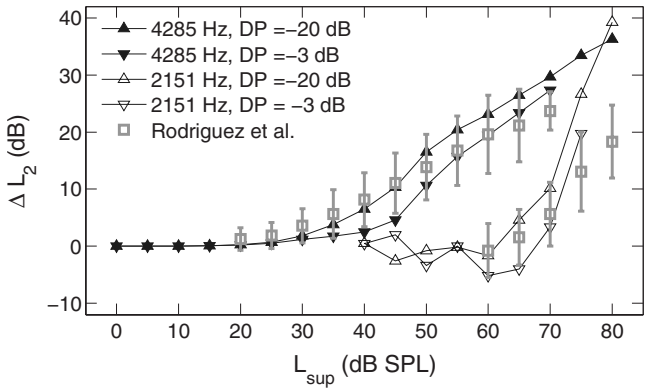

FIG. 10. DP input suppression. The increase ΔL_2 in input level required for DPOAE to reach a given level (−20 or −3 dB SPL) is plotted against suppressor level L_{sup}. Filled symbols represent the "on-frequency" suppression ($f_{sup}\approx f_2$). Open symbols represent f_{sup} at about one octave lower. Squares and error bars show means and standard deviations, respectively, of DP suppression data from normal-hearing humans (Rodríguez *et al.*, 2010).

low-frequency suppressors. The shift ΔL_2 produced by the present model is comparable to data from normal-hearing humans (Rodríguez *et al.*, 2010) for most of the lower L_{sup}'s. For the highest L_{sup} tested (70 dB for $f_{sup} \approx f_2$ and 75 or 80 dB for $f_{sup} \approx 0.5 f_2$), ΔL_2 produced by the model is at least one standard deviation higher than the mean in Rodríguez *et al.*'s data (in which ΔL_2 was measured with $L_d = -3$ dB SPL). This discrepancy will be discussed in Sec. V.

V. DISCUSSION

A. Cochlear tuning and parameter selection

Employing a frequency-domain analysis, we previously predicted that the present OHC model could provide amplification to the traveling waves in a frequency-selective manner (Liu and Neely, 2009) if parameters α_v (velocity sensitivity) and C_g (gating capacitance) are sufficiently large. During the parameter-selection process for the present study, we found that the tip-to-tail gain and the quality factor Q_{ERB} were both reduced when smaller values of α_v or C_g were used. In this sense, the present study serves as a time-domain confirmation of the frequency-domain analysis. Note that α_v and C_g represent different components of the "cochlear amplifier:" α_v represents the sensitivity of MET, which depends on the potential gradient across the apical membrane of the OHC; C_g depends on the density of motor molecules (*prestin*) on the OHC lateral membrane and is reduced when the cell is hyperpolarized (Santos-Sacchi, 1991). The present model makes it possible to investigate the relations between cochlear tuning properties and micromechanical parameters such as α_v and C_g. Simulation can be conducted to predict responses from cochleae with different types of OHC pathology. This might be of clinical interest and provides directions for future research.

In spite of the effort devoted to the parameter-selection process in order to make a tonotopic map typical of humans, the sharpness of tuning Q_{ERB} and the cochlear latency N_{max} produced by the present model (Fig. 3) fall below experimental values previously derived from human ears. Several other lines of evidence also suggest that the tuning of the present model is not as sharp as in human cochleae: first, the ratio f_2/f_1 that produces the highest DPOAE is higher in the present model than that obtained from normal-hearing human ears (Sec. IV C). This implies that the present model is not as sharply tuned as human cochleae because the cutoff frequency of the DP filter (Fig. 8) is an estimate of the bandwidth of cochlear responses. Second, in the present model, the low-frequency suppressor produces much more DPOAE suppression than empirically at high L_{sup} (Fig. 10). This indicates that the f_2 characteristic place in the present model has a larger response to low-frequency stimuli at high level than it does in human cochleae. Therefore, either the present model is less sharply tuned than human cochleae or its excitation pattern shifts toward the base excessively at high intensities. Further investigation is needed to explore these two possibilities.

The reduced sharpness of tuning may be a limitation of one-dimensional (long-wave) cochlear modeling. In a two-dimensional (2D) model, the real and imaginary parts of the wave propagation function, which are related to cochlear gain and cochlear latency respectively, are both greater than those predicted by a 1D model (Shera *et al.*, 2005). Kolston (2000) argued that it is necessary to model cochlear mechanics in three dimensions so as to match both the phase and the gain responses to experiment data. To increase the sharpness of tuning for the present 1D model, we could have set α_v or C_g to higher values. However, values higher than currently used might start to deviate from physical reality. Additionally, we found that higher α_v's resulted in spontaneous vibration in the cochlear partition, which could propagate from the cochlea as SOAE. The frequency of SOAE is hard to predict (Ku *et al.*, 2009), and its presence complicates spectral analysis since the present method assumed that the frequencies of all spectral components are of integer ratios. In the future, higher α_v values might be preferred to produce higher cochlear gain; an improved spectral-analysis method is also warranted.

B. Cochlear nonlinearities

In the present study, the gating capacitance of OHCs was linearized to confine the source of nonlinearity to MET of OHCs (see Sec. II B). Patuzzi (1996) argued that such simplification is legitimate at high frequencies because the response in OHC lateral-membrane potential is limited by membrane capacitance. However, at low frequencies and high intensities, Patuzzi (1996) stated that the membrane potential may change by tens of millivolts; in this case, the operating point shifts significantly, so the nonlinearity in OHC gating capacitance needs to be considered.

In light of Patuzzi's (1996) argument, we examined the maximum potential change elicited by acoustical stimuli in the present model. Results showed that the change in OHC membrane potential was indeed larger for low-frequency than for high-frequency stimuli, but was no more than 4.0 mV for single tones at 100 dB SPL at any frequency between 0.125 and 8 kHz. This amplitude was too small to have caused a significant shift in the OHC operating point. Though the model's findings deviated from Patuzzi's (1996) prediction, our attempt to linearize the dynamics of piezoelectrical membrane is justified as far as numerical simulation is concerned. Improving the representation of electrical properties of the OHC is an area for future work.

The present model reproduced, at least qualitatively, many features in nonlinear responses that are typical of humans and other mammals. We have argued that some discrepancies could be accounted for by increasing the sharpness of tuning throughout the cochlear model. Another discrepancy is in the absolute level of DPOAE; in Fig. 7, the DP level L_d reached >30 dB SPL for the highest L_1 and L_2 tested for $f_2 = 1$ or 2 kHz when $f_2/f_1 \geq 1.30$. In contrast, the mean of L_d across normal-hearing ears was never greater than 20 dB SPL as reported by Johnson *et al.* (2006). Nevertheless, the DP I/O function in Fig. 9(A) is similar to experimental data at $L_2 = 20-50$ dB SPL (Johnson *et al.*, 2006; Long *et al.*, 2009; Rodríguez *et al.*, 2010). While discrepancy of the absolute levels of DPOAE could be partially explained by transmission through the middle ear (see discussion in

Appendix A), discrepancy in the DP growth rate at high L_2 indicates that the nonlinearity in the present model is not sufficiently compressive.

Note that the DP level discrepancy becomes prominent at $L_2 \geq 50$ dB, at which the medial olivocochlear (MOC) efferent inhibition would be activated (Guinan, 2006). A recent study also showed that middle-ear muscle reflex (MEMR) was elicited by a 75 dB activator at 1 kHz in 25% of normal-hearing ears (Keefe *et al.*, 2010). It is possible that MOC efferents and MEMR both contribute to the suppression of DPOAE level when L_1 or L_2 is above their respective thresholds. Therefore, incorporating these negative feedback mechanisms to the present model may help reduce the excessive DPOAE it generates at high primary levels.

As stated previously, the one-dimensional treatment is known to affect tuning. Because tuning is related to compression in a nonlinear model, the absence of close quantitative agreement with experimental data could also be related to the simplified dimensionality of the present model.

C. Negative suppression

The *negative suppression* shown in Figs. 9(B) and 10 remains puzzling. It occurred only for a certain input range (50–70 dB). In fact, negative suppression of DPOAE has been observed empirically; for instance, the mean input suppression ΔL_2 in Rodríguez *et al.* (2010) is -0.8 dB at $L_{sup} = 60$ dB for the low-frequency suppressor. To explain Rodríguez *et al.*'s (2010) data, one can assume that the DP wavelets from the f_2 characteristic place and those reflected coherently (Zweig and Shera, 1995) from the DP place interfere destructively at the stapes. When a low-frequency suppressor is presented at an intermediate level, it reduces the wavelets that originate from the DP place and releases DPOAE from wave cancellation. This causes the DPOAE level to increase.

An alternative explanation for negative suppression is that the suppressor causes DP to be reflected from its characteristic place in a nonlinear fashion, much similar to the reflection observed in Fig. 4 and by Kanis and de Boer (1993). If the reflected wavelets interfere with the wavelets from the f_2 place *constructively*, there would be an increase in the level of DPOAE. In theory, waves are scattered wherever there is an impedance mismatch. If saturation nonlinearity causes the propagation-gain function to reduce locally at a high intensity, the wavenumber function should also be altered due to causality (Shera, 2007). Similarly, it may be possible to investigate how characteristic impedance is altered locally and waves scattered nonlinearly, perhaps using a quasilinear approach (Kanis and de Boer, 1993; Talmadge *et al.*, 1998). In the future, a time-domain model such as presented in this paper can serve as a numerical test bench for theories developed in this direction.

VI. CONCLUSIONS

Simulation of DPOAE at frequency $2f_1 - f_2$ can be achieved by introducing an antisymmetric nonlinearity to the MET channel of OHCs. The present nonlinear OHC models embedded in a one-dimensional transmission-line cochlear model collectively produce dynamic-range compression, broadening of excitation patterns, and shifting of excitation patterns toward the base, similar to responses observed in live mammalian cochleae. The model also produces DPOAE isolevel contour plots that vary with f_1 and f_2, DP band-pass filtering effects across three octaves of f_2, and a shift of DPOAE I/O functions due to suppression by a third tone. Several lines of evidence suggest that the present model is, however, less sharply tuned than human cochleae. The present results might be improved by setting a higher sensitivity of OHC receptor current with respect to RL velocity or by modeling mechanics of the cochlear fluid in two or three dimensions. Nevertheless, qualitative similarities between the present results and experimental data from normal-hearing ears suggest that the model may also be useful for studying other nonlinear responses in healthy cochleae. In addition, because of an explicit representation of OHC electromechanics, it is possible to alter parameters for the present model and simulate responses in ears with different types of OHC pathology. These provide directions for future research.

ACKNOWLEDGMENTS

We gratefully acknowledge two anonymous reviewers for providing valuable comments. We also thank Joyce Rodríguez and Emery Ku for giving critiques on previous versions of this manuscript. This study was supported by a grant from NIH-NIDCD (Grant No. R01-DC8318).

APPENDIX A: MIDDLE-EAR TRANSFER FUNCTIONS

Figure 11 shows middle-ear transfer functions in both the forward and the reverse direction. Results were obtained from a finite-difference, frequency-domain version of the present cochlear model. First, cochlear input impedance Z_c was calculated using a small-signal analysis (Puria and Allen, 1991), i.e., Eq. (1) was used instead of Eq. (2). Given Z_c, we drew an equivalent circuit for the middle-ear mechanics (Fig. 1) and derived the forward pressure transfer function S_{12}, defined as the acoustic pressure gain from the ear canal to the cochlear vestibule (Puria, 2003). To calculate transfer functions in the reverse direction, we assumed that the ear canal has an acoustic impedance of $\rho c/A$—ρ is the air density, c is the speed of sound, and A is the cross-sectional area of the ear canal; in other words, reflection of reverse-traveling sounds was ignored. The equivalent circuit was also used for calculation of the reverse pressure transfer function S_{21}, defined as the ratio of the ear canal pressure to the cochlear fluid pressure for reverse transmission. Finally, the reverse middle-ear impedance M_3, defined as the ratio of the vestibule pressure to the stapes volume velocity, was calculated. For comparison purposes, the symbols and definitions are borrowed from a previous study (Puria, 2003, Fig. 2).

The main discrepancy between the present results and human cadaver data is in the phase responses of pressure transfer functions. The phase accumulated to more than 300° for both S_{12} and S_{21} in Puria's (2003) data, and in one case more than 540° for S_{12} in Nakajima *et al.* (2009). This indicates a middle-ear latency, in the order of tens of μs (Dong

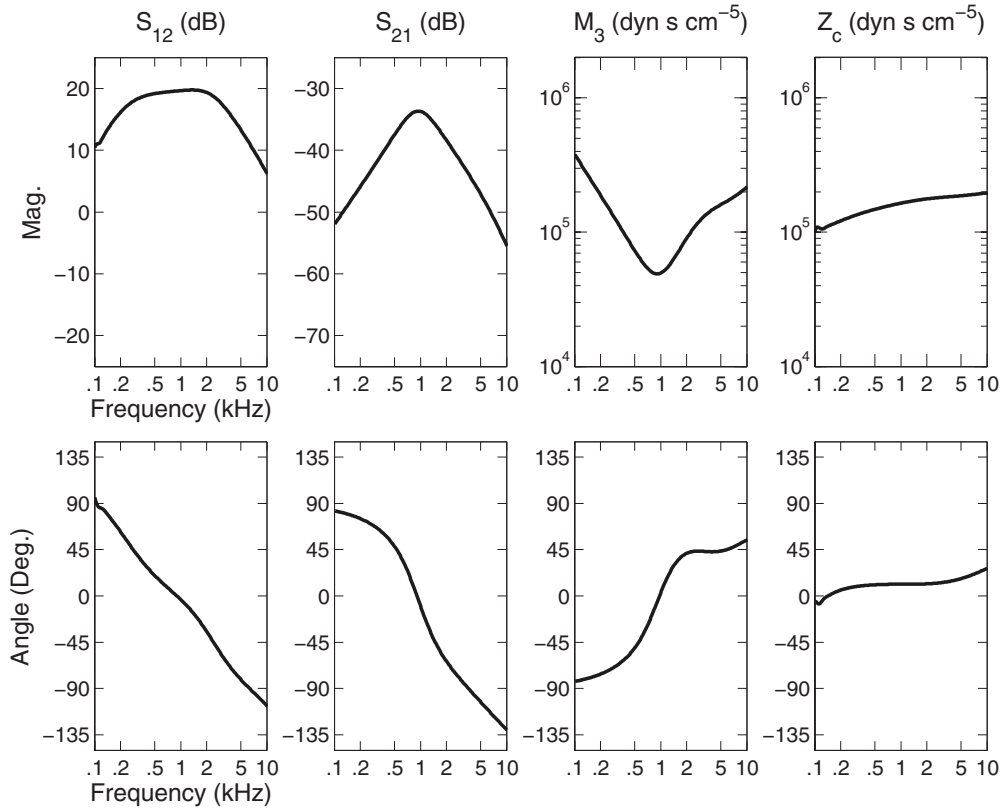

FIG. 11. Middle-ear transfer functions. Top panels show magnitude responses, and bottom panels show phase responses. From left to right, the four columns show forward pressure transfer function (S_{12}), reverse pressure transfer function (S_{21}), reverse middle-ear impedance (M_3), and the cochlear input impedance Z_c, respectively.

and Olson, 2006), that is not present in our model but has been attributed to tympanic membrane dynamics (Puria and Allen, 1998).

Compared to measurements from human cadavers (Puria, 2003; Nakajima *et al.*, 2009), the magnitude plateau in S_{12} is about the same height (10–20 dB gain). The width of the plateau is similar to Nakajima *et al.* (2009) (their Fig. 6) but appears wider than in Puria's data (his Fig. 2); the present S_{12} is as much as 10–15 dB higher at frequencies below 500 Hz and above 4 kHz. The magnitude of S_{21} are similar to Puria's (2003) result, peaking at around 1 kHz and rolls off approximately to -50 and -60 dB at 0.1 and 10 kHz, respectively. However, the maximum $|S_{21}|$ is smaller than Puria's (2003) but more similar to results from live gerbils (Dong and Olson, 2006, Fig. 5).

The magnitude of S_{12} and S_{21} influences the level of DPOAE directly (Keefe and Abdala, 2007). If the middle-ear parameters are adjusted to reduce S_{12} and match Puria's (2003) data, it will require higher L_1 and L_2 to achieve the same levels of DP inside the cochlea. Consequently, we can expect the DP contours to shift toward the upper-right corner in Fig. 7, more so for f_2=4 or 8 kHz than for 1 and 2 kHz. However, S_{12} and S_{21} are interdependent due to reciprocity; reducing S_{12} tends to increase S_{21}. It remains to be studied how much the difference between model-predicted DPOAE levels and those measured from normal-hearing humans (Johnson *et al.*, 2006, Fig. 1) can be resolved by jointly adjusting S_{12} and S_{21}.

APPENDIX B: METHODS FOR ADJUSTING THE COCHLEAR PARAMETERS

For a stimulus at sufficiently low intensity, the response at any given location in the cochlea can be characterized by three salient frequencies: a *shoulder frequency* f_{sh} above which the magnitude increases rapidly, a *pole frequency* f_p at which the response reaches its peak, and a *cutoff frequency* f_c at which the response starts to roll off. Based on the present assumptions on fluid coupling [Eq. (9)] and OHC electromechanics, these frequencies are approximately given by the following formulas:

$$2\pi f_{sh} = \sqrt{K_{eq}/M}, \tag{B1a}$$

$$2\pi f_p = \sqrt{(K_{eq} + \alpha_v/TC)/M}, \tag{B1b}$$

$$2\pi f_c = \sqrt{k/m}, \tag{B1c}$$

where $K_{eq}=K+(T^2C)^{-1}+(T^2C_g)^{-1}$. For negative damping to occur, it is necessary that $f_{sh}<f_p<f_c$ (Liu and Neely, 2009). Further, large capacitances C and C_g and high sensitivity α_v are preferred to achieve high amplification (Liu and Neely, 2009). All parameters listed in Table I were fine-tuned while maintaining that $f_p<f_c$ but maximizing α_v/TC so as to ensure a broad negative damping region. In Fig. 12, salient frequencies are compared against Greenwood's function (Greenwood, 1990) and the CF predicted by the present model. The model-predicted CF follows the pole frequency closely. Also, the CF does not deviate from Greenwood's

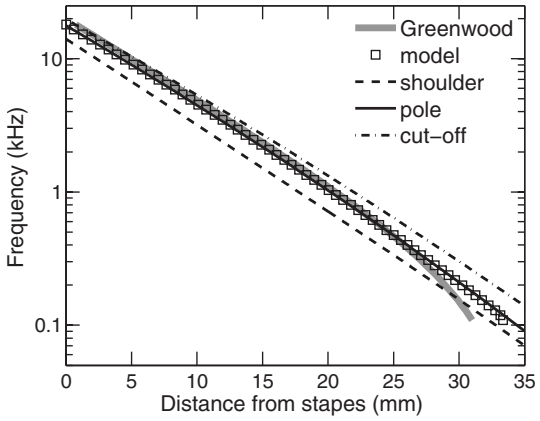

FIG. 12. Place-frequency functions. The shoulder frequency, the pole frequency, and the cutoff frequency were calculated as a function of distance from stapes. At selected places, the model-predicted CF is marked with a square. The Greenwood function was defined as $\mathrm{CF}(x)=F_0\cdot 2^{-x/l}-F_1$, where x is the distance from stapes, $l=5.0$ mm, $F_0=20$ kHz, and $F_1=0.165$ kHz.

function (Greenwood, 1990) by more than 10% except at the most apical 7 mm. The discrepancy there reflects the limitation of fitting the parameters spatially by log-quadratic interpolation (Sec. III A).

Finally, the parameter $I_{\max}$ which characterizes nonlinearity [see Eq. (3)] was adjusted to produce reasonable dynamic-range compression and DP I/O function. We found that a small $I_{\max}$ produces compression at low stimulus levels but limits the maximum DP level. Thus, $I_{\max}$ and middle-ear transfer functions S_{12} and S_{21} jointly affect the amount of DPOAEs produced by the present model.

[1]That is, any phase advance of i_r relative to ξ_r due to radial coupling between OHC hair bundles and the tectorial membrane was represented by the velocity-sensing parameter α_v [see Sec. VC of Liu and Neely (2009) for more discussion].

[2]Because Eq. (3) is antisymmetric, all the even-order terms vanish in its Taylor expansion around the origin. Consequently, even-order DPs vanish while odd-order products remain.

[3]In our previous study (Liu and Neely, 2009), an OHC was assumed to stretch against RL on one side, BM on the other side, and the stiffness of the OHC itself. We then argued that, because the stiffness of BM is much higher than that of RL, the impedance is approximately that of RL for the frequency range of interest. Therefore, the effective mass M and resistance R in Eq. (7) can be regarded as equivalent to the RL mass and resistance, whereas the effective stiffness K is equivalent to OHC stiffness plus RL stiffness in Liu and Neely (2009).

[4]Alternatively, Liu and Neely (2009) assumed that the volume velocity gradient couples to the velocity of both the RL and the BM; i.e., $\partial_x U=w(\dot{\xi}_r+\dot{\xi}_b)$. Empirically, Eq. (9) gives higher displacement gain in the cochlea.

[5]Hereafter, *acoustic pressure* is referred to as *pressure* for simplicity.

[6]Equation (13b) implicitly assumes that the displacement of the round window is equal to that of the stapes but in the opposite direction, and that the area of the round window is the same as the area of the stapes.

[7]Let q_0, q_1, and q_2 denote the value of a parameter q at the base, the midpoint, and the apex respectively. Then, $q(x)$ was calculated using the following formula: $q(x)=q_0\exp[ax(L-x)+bx]$, where $a=2\log(q_1^2/q_0q_2)/L^2$ and $b=\log(q_2/q_0)/L$.

[8]K_c corresponds to the acoustic compliance of enclosed air of 1.7 cm^3 at atmospheric pressure. Diaphragm parameters K_d, R_d, and M_d were chosen arbitrarily to produce a sufficiently flat response in the frequency range of interest. Note that the resonance frequency of the diaphragm, $\sqrt{K_d/M_d}/2\pi$, is above 40 kHz, and the Q-value ($\sqrt{K_dM_d}/R_d$) is about 1.0.

[9]Thus, the spatial resolution δ along the x-direction was 50 μm, and $\partial_x^2 P$ was approximated by $[P(x+\delta)-2P(x)+P(x-\delta)]/\delta^2$. So, Eq. (18) was solved by inverting a tridiagonal matrix via Gaussian elimination, which has a computation load of $O(N)$.

[10]To derive the gain and the group delay, the Fourier transform $X_r(x,f)$ of RL displacement $\xi_r(x,t)$ was calculated at every location x. Define a transfer function $T(x,f)=X_r(x,f)/X_s(f)$, where $X_s(f)$ is the Fourier transform of stapes displacement $x_s(t)$. The displacement gain plotted in Fig. 2(A) is $|T(x,f)|$ in dB, and the group delay plotted in Fig. 2(B) is defined as $N=-f\partial_f\phi$, where ϕ denotes the phase of $T(x,f)$.

[11]For an arbitrary tuning curve $T(f)$, its ERB is defined as $\Delta f=\int_0^\infty|T(f)|df/T_{\max}$, where $T_{\max}$ denotes the maximum of $|T(f)|$. Accordingly, Q_{ERB} is defined as $f_{\max}/\Delta f$, where $f_{\max}$ denotes the best frequency.

Brown, A. M., Gaskill, S. A., and Williams, D. M. (**1992**). "Mechanical filtering of sound in the inner ear," Proc. R. Soc. London, Ser. B **250**, 29–34.

Brownell, W. E., Bader, C. R., Bertrand, D., and de Ribaupierre, Y. (**1985**). "Evoked mechanical responses of isolated cochlear hair cells," Science **227**, 194–196.

Corey, D. P., and Hudspeth, A. J. (**1983**). "Kinetics of the receptor current in bullfrog saccular hair cells," J. Neurosci. **3**, 962–976.

Dallos, P. (**1973**). *The Auditory Periphery: Biophysics and Physiology* (Academic, New York).

Dallos, P. (**2008**). "Cochlear amplification, outer hair cells and prestin," Curr. Opin. Neurobiol. **18**, 370–376.

Davis, H. (**1983**). "An active process in cochlear mechanics," Hear. Res. **9**, 79–90.

Diependaal, R. J., Duifhuis, H., Hoogstraten, H. W., and Viergever, M. A. (**1987**). "Numerical methods for solving one-dimensional cochlear models in the time domain," J. Acoust. Soc. Am. **82**, 1655–1666.

Dong, W., and Olson, E. S. (**2006**). "Middle ear forward and reverse transmission in gerbil," J. Neurophysiol. **95**, 2951–2961.

Dong, W., and Olson, E. S. (**2008**). "Supporting evidence for reverse cochlear traveling waves," J. Acoust. Soc. Am. **123**, 222–240.

Eguíluz, V. M., Ospeck, M., Choe, Y., Hudspeth, A. J., and Magnasco, M. O. (**2000**). "Essential nonlinearities in hearing," Phys. Rev. Lett. **84**, 5232–5235.

Gaskill, S. A., and Brown, A. M. (**1990**). "The behaviour of the acoustic distortion product, 2f1-f2, from the human ear and its relation to auditory sensitivity," J. Acoust. Soc. Am. **88**, 821–839.

Glasberg, B. R., and Moore, B. C. J. (**1990**). "Derivation of auditory filter shapes from notched-noise data," Hear. Res. **47**, 103–138.

Gorga, M. P., Neely, S. T., Dierking, D. M., Kopun, J., Jolkowski, K., Groenenboom, K., Tan, H., and Stiegemann, B. (**2008**). "Low-frequency and high-frequency distortion product otoacoustic emission suppression in humans," J. Acoust. Soc. Am. **123**, 2172–2190.

Greenwood, D. D. (**1990**). "A cochlear frequency-position function for several species—29 years later," J. Acoust. Soc. Am. **87**, 2592–2605.

Guinan, J. J., Jr. (**2006**). "Olivocochlear efferents: Anatomy, physiology, function, and the measurement of efferent effects in humans," Ear Hear. **27**, 589–607.

Hall, J. L. (**1974**). "Two-tone distortion products in a nonlinear model of the basilar membrane," J. Acoust. Soc. Am. **56**, 1818–1828.

Harte, J. M., Pigasse, G., and Dau, T. (**2009**). "Comparison of cochlear delay estimates using otoacoustic emissions and auditory brainstem responses," J. Acoust. Soc. Am. **126**, 1291–1301.

Hubbard, A. E., Mountain, D. C., and Chen, F. (**2003**). "Time-domain responses from a nonlinear sandwich model of the cochlea," in *Biophysics of the Cochlea: From Molecules to Models*, edited by A. W. Gummer (World Scientific, Singapore), pp. 351–358.

Hudspeth, A. J. (**1997**). "Mechanical amplification of stimuli by hair cells," Curr. Opin. Neurobiol. **7**, 480–486.

Johnson, T. A., Neely, S. T., Garner, C. A., and Gorga, M. P. (**2006**). "Influence of primary-level and primary-frequency ratios on human distortion product otoacoustic emissions," J. Acoust. Soc. Am. **119**, 418–428.

Kanis, L. J., and de Boer, E. (**1993**). "Self-suppression in a locally active nonlinear model of the cochlea: A quasi-linear approach," J. Acoust. Soc. Am. **94**, 3199–3206.

Keefe, D. H., and Abdala, C. (**2007**). "Theory of forward and reverse middle-ear transmission applied to otoacoustic emissions in infant and adult ears," J. Acoust. Soc. Am. **121**, 978–993.

Keefe, D. H., Fitzpatrick, D., Liu, Y.-W., Sanford, C. A., and Gorga, M. P. (**2010**). "Wideband acoustic reflex test in a test battery to predict middle-ear dysfunction," Hear. Res. In press.

Kemp, D. T. (**1978**). "Stimulated acoustic emissions from within the human

auditory system," J. Acoust. Soc. Am. **64**, 1386–1391.
Kim, D. O., Molnar, C. E., and Mathews, J. W. (**1980**). "Cochlear mechanics: Nonlinear behavior in two-tone responses as reflected in cochlear-nerve-fibre responses and in ear canal sound pressure," J. Acoust. Soc. Am. **67**, 1704–1721.
Kim, D. O., Molnar, C. E., and Pfeiffer, R. R. (**1973**). "A system of nonlinear differential equations modeling basilar-membrane motion," J. Acoust. Soc. Am. **54**, 1517–1529.
Kolston, P. J. (**2000**). "The importance of phase data and model dimensionality to cochlear mechanics," Hear. Res. **145**, 25–36.
Ku, E. M., Elliott, S. J., and Lineton, B. (**2009**). "Limit cycle oscillations in a nonlinear state space model of the human cochlea," J. Acoust. Soc. Am. **126**, 739–750.
Kummer, P., Janssen, T., and Arnold, W. (**1998**). "The level and growth behavior of the 2f1-f2 distortion product otoacoustic emission and its relationship to auditory sensitivity in normal hearing and cochlear hearing loss," J. Acoust. Soc. Am. **103**, 3431–3444.
Liu, Y.-W., and Neely, S. T. (**2009**). "Outer hair cell electromechanical properties in a nonlinear piezoelectric model," J. Acoust. Soc. Am. **126**, 751–761.
Long, G. R., Jeung, C., and Talmadge, C. L. (**2009**). "Dependence of distortion-product otoacoustic emission components on primary-level ratio," in *Concepts and Challenges in the Biophysics of Hearing*, edited by N. P. Cooper and D. T. Kemp (World Scientific, Singapore), pp. 203–208.
Lu, T. K., Zhak, S., Dallos, P., and Sarpeshkar, R. (**2006**). "Fast cochlear amplification with slow outer hair cells," Hear. Res. **214**, 45–67.
Matthews, J. W. (**1983**). "Modeling reverse middle ear transmission of acoustic distortion signals," in *Mechanics of Hearing*, edited by E. de Boer and M. A. Viergever (Delft University Press, Delft), pp. 11–18.
Nakajima, H. H., Dong, W., Olson, E. S., Merchant, S. N., Ravicz, M., and Rosowski, J. J. (**2009**). "Differential intracochlear sound pressure measurements in normal human temporal bones," J. Assoc. Res. Otolaryngol. **10**, 23–36.
Neely, S. T. (**1988**). "Transient responses in an active, nonlinear model of cochlear mechanics," in *Basic Issues in Hearing*, edited by D. Duifuis, J. Horst, and H. Wit (Academic, New York).
Neely, S. T. (**1993**). "A model of cochlear mechanics with outer hair cell motility," J. Acoust. Soc. Am. **94**, 137–146.
Neely, S. T., Gorga, M. P., and Dorn, P. A. (**2000**). "Distortion product and loudness growth in an active, nonlinear model of cochlear mechanics," in *Recent Developments in Auditory Mechanics*, edited by H. Wada, T. Takasaka, K. Ikeda, K. Ohyama, and T. Koike (World-Scientific, Singapore), pp. 237–243.
Neely, S. T., Johnson, T. A., and Gorga, M. P. (**2005**). "Distortion-product otoacoustic emission measured with continuously varying stimulus level," J. Acoust. Soc. Am. **117**, 1248–1259.
Neely, S. T., and Kim, D. O. (**1983**). "An active cochlear model showing sharp tuning and high sensitivity," Hear. Res. **9**, 123–130.
Neely, S. T., and Kim, D. O. (**1986**). "A model for active elements in cochlear biomechanics," J. Acoust. Soc. Am. **79**, 1472–1480.
Neely, S. T., and Liu, Y.-W. (**2009**). "Retrograde propagation of cochlear distortion," in *Concepts and Challenges in the Biophysics of Hearing*, edited by N. P. Cooper and D. T. Kemp (World Scientific, Singapore), pp. 55–61.
Neely, S. T., Norton, S. J., Gorga, M. P., and Jesteadt, W. (**1988**). "Latency of auditory brain-stem responses and otoacoustic emissions using tone-burst stimuli," J. Acoust. Soc. Am. **83**, 652–656.
Neely, S. T., and Stover, L. J. (**1994**). "Otoacoustic emissions from a nonlinear, active model of cochlear mechanics," in *Biophysics of Hair Cell Sensory Systems*, edited by H. Duifhuis, J. W. Horst, P. van Dijk, and S. M. van Netten (World Scientific, Singapore), pp. 64–71.
Nobili, R., Vetešník, A., Turicchia, L., and Mammano, F. (**2003**). "Otoacoustic emissions from residual oscillations of the cochlear basilar membrane in a human ear model," J. Assoc. Res. Otolaryngol. **4**, 478–494.
Patuzzi, R. (**1996**). "Cochlear micromechanics and macromechanics," in *The Cochlea*, edited by P. Dallos, A. N. Popper, and R. R. Fay (Springer, New York), pp. 186–257.
Pfeiffer, R. R., and Kim, D. O. (**1975**). "Cochlear nerve fiber responses: Distribution along the cochlear partition," J. Acoust. Soc. Am. **58**, 867–869.
Puria, S. (**2003**). "Measurements of human middle ear forward and reverse acoustics: Implications for otoacoustic emissions," J. Acoust. Soc. Am. **113**, 2773–2789.
Puria, S., and Allen, J. B. (**1991**). "A parametric study of cochlear input impedance," J. Acoust. Soc. Am. **89**, 287–309.
Puria, S., and Allen, J. B. (**1998**). "Measurement and model of the cat middle ear: Evidence of tympanic membrane acoustic delay," J. Acoust. Soc. Am. **104**, 3463–3482.
Rabbitt, R. D., Clifford, S., Breneman, K. D., Farrell, B., and Brownell, W. E. (**2009**). "Power efficiency of outer hair cell somatic electromotility," PLOS Comput. Biol. **5**, e1000444.
Ramamoorthy, S., Deo, N. V., and Grosh, K. (**2007**). "A mechano-electro-acoustical model for the cochlea: Response to acoustic stimuli," J. Acoust. Soc. Am. **121**, 2758–2773.
Ren, T. (**2004**). "Reverse propagation of sound in the gerbil cochlea," Nat. Neurosci. **7**, 333–334.
Rhode, W. S. (**1971**). "Observations of the vibration of the basilar membrane in squirrel monkeys using the Mössbauer technique," J. Acoust. Soc. Am. **49**, 1218–1231.
Rhode, W. S. (**2007**). "Basilar membrane mechanics in the 6–9 kHz region of sensitive chinchilla cochleae," J. Acoust. Soc. Am. **121**, 2792–2804.
Rhode, W. S., and Robles, L. (**1974**). "Evidence from Mössbauer experiments for nonlinear vibration in the cochlea," J. Acoust. Soc. Am. **55**, 588–596.
Ricci, A. J., Kennedy, H. J., Crawford, A. C., and Fettiplace, R. (**2005**). "The transduction channel filter in auditory hair cells," J. Neurosci. **25**, 7831–7839.
Rodríguez, J., Neely, S. T., Patra, H., Kopun, J., Jesteadt, W., Tan, H., and Gorga, M. P. (**2010**). "The role of suppression in psychophysical tone-on-tone masking," J. Acoust. Soc. Am. **127**, 361–369.
Ruggero, M. A., Rich, N. C., and Robles, L. (**1997**). "Basilar-membrane responses to tones at the base of the chinchilla cochlea," J. Acoust. Soc. Am. **101**, 2151–2163.
Santos-Sacchi, J. (**1991**). "Reversible inhibition of voltage-dependent outer hair cell motility and capacitance," J. Neurosci. **11**, 3096–3110.
Shera, C. A. (**2007**). "Laser amplification with a twist: Traveling-wave propagation and gain functions from throughout the cochlea," J. Acoust. Soc. Am. **122**, 2738–2758.
Shera, C. A., Guinan, J. J., Jr., and Oxenham, A. J. (**2002**). "Revised estimates of human cochlear tuning from otoacoustic and behavioral measurements," Proc. Natl. Acad. Sci. U.S.A. **99**, 3318–3323.
Shera, C. A., Tubis, A., and Talmadge, C. L. (**2005**). "Coherent reflection in a two-dimensional cochlea: Short-wave versus long-wave scattering in the generation of reflection-source otoacoustic emissions," J. Acoust. Soc. Am. **118**, 287–313.
Shera, C. A., Tubis, A., Talmadge, C. L., de Boer, E., Fahey, P. F., and Guinan, J. J., Jr. (**2007**). "Allen-Fahey and related experiments support the predominance of cochlear slow-wave otoacoustic emissions," J. Acoust. Soc. Am. **121**, 1564–1575.
Stoop, R., and Kern, A. (**2004**). "Two-tone suppression and combination tone generation as computations performed by the Hopf cochlea," Phys. Rev. Lett. **93**, 268103.
Talmadge, C. L., Tubis, A., Long, G. R., and Piskorski, P. (**1998**). "Modeling otoacoustic emission and hearing threshold fine structures," J. Acoust. Soc. Am. **104**, 1517–1543.
van der Heijden, M., and Joris, P. X. (**2006**). "Panoramic measurements of the apex of the cochlea," J. Neurosci. **26**, 11462–11473.
Zhang, Y., Kim, C. K., Lee, K. J. B., and Park, Y. (**2009**). "A Brownian energy depot model of the basilar membrane oscillation with a braking mechanism," Eur. Phys. J. E **29**, 345–349.
Zurek, P. M., Clark, W. W., and Kim, D. O. (**1982**). "The behavior of acoustic distortion products in the ear canals of chinchillas with normal or damaged ears," J. Acoust. Soc. Am. **72**, 774–780.
Zweig, G., and Shera, C. A. (**1995**). "The origin of periodicity in the spectrum of evoked otoacoustic emissions," J. Acoust. Soc. Am. **98**, 2018–2047.
Zwislocki, J. (**1962**). "Analysis of the middle-ear function. Part I: Input impedance," J. Acoust. Soc. Am. **34**, 1514–1523.

The loudness of sounds whose spectra differ at the two ears

Brian R. Glasberg and Brian C. J. Moore[a)]
Department of Experimental Psychology, University of Cambridge, Downing Street, Cambridge CB2 3EB, England

(Received 10 September 2009; revised 20 January 2010; accepted 2 February 2010)

Moore and Glasberg [(2007). J. Acoust. Soc. Am. **121**, 1604–1612] developed a model for predicting the loudness of dichotic sounds. The model gave accurate predictions of data in the literature, except for an experiment of Zwicker and Zwicker [(1991). J. Acoust. Soc. Am. **89**, 756–764], in which sounds with non-overlapping spectra were presented to the two ears. The input signal was noise with the same intensity in each critical band (bark). This noise was filtered into 24 bands each 1 bark wide. The bands were then grouped into wider composite bands (consisting of 1, 2, 4, or 12 successive sub-bands) and each composite band was presented either to one ear or the other. Loudness estimates obtained using a scaling procedure decreased somewhat as the number of composite bands increased (and their width decreased), but the predictions of the model showed the opposite pattern. This experiment was similar to that of Zwicker and Zwicker, except that the widths of the bands were based on the ERB_N-number scale, and a loudness-matching procedure was used. The pattern of the results was consistent with the predictions of the model, showing an increase in loudness as the number of composite bands increased and their spacing decreased.
 [DOI: 10.1121/1.3336775]

PACS number(s): 43.66.Cb, 43.66.Pn, 43.66.Ba [MW] Pages: 2433–2440

I. INTRODUCTION

It is often assumed that the loudness evoked by presentation of a sound to both ears is a simple sum of the loudness (in sones) evoked by the sound at each ear separately (Fletcher and Munson, 1933; Hellman and Zwislocki, 1963). This assumption is incorporated in the ANSI (2007) standard for calculation of loudness, which is based on a loudness model developed in our laboratory (Moore *et al.*, 1997; Glasberg and Moore, 2006). If this assumption were correct, it would mean that (1) a diotically presented sound should be twice as loud as that same sound presented monaurally; and (2) for sound levels above about 40 dB sound pressure level (SPL), the level difference required for equal loudness of monaural and diotic sounds should be about 10 dB, since loudness roughly doubles for each 10-dB increase in sound level (Stevens, 1957; Hellman, 1976). In fact, most data suggest that the assumption of simple additivity of loudness across ears is not correct because (1) a diotically presented sound is less than twice as loud as that same sound presented monaurally, and is typically found to be about 1.5 times as loud (Scharf and Fishken, 1970; Zwicker and Zwicker, 1991; Marozeau *et al.*, 2006; Whilby *et al.*, 2006; Epstein and Florentine, 2009); and (2) for sound levels above 40 dB SPL, the level difference required for equal loudness of monaural and diotic sounds is about 5–7 dB (Whilby *et al.*, 2006; Edmonds and Culling, 2006, 2009); at lower levels the level difference is somewhat smaller (Whilby *et al.*, 2006; Gockel *et al.*, 2009). In addition, Scharf (1969) showed that the loudness of a narrowband sound presented to one ear could be reduced by presenting a narrowband sound of a different frequency to the opposite ear; the effect was broadly tuned, but disappeared when the two narrowband sounds were very widely separated in frequency. This effect cannot be explained by a simple summation of loudness across ears.

To model these effects, Moore and Glasberg (2007) used the concept of binaural inhibition (Gigerenzer and Strube, 1983; Lindemann, 1986; Breebaart *et al.*, 2001). The starting point was the model of Moore *et al.* (1997) with the modifications described by Glasberg and Moore (2006). The model has the following stages:

(a) A filter representing the transfer function from the sound source to the eardrum.
(b) A filter representing transfer through the middle ear.
(c) Calculation of an excitation pattern from the physical spectrum (Glasberg and Moore, 1990). The excitation pattern is calculated on an ERB_N-number scale, where ERB_N stands for the equivalent rectangular bandwidth of the auditory filter, as determined using young normally hearing listeners at moderate sound levels (Glasberg and Moore, 1990; Moore, 2003). The excitation level is calculated at intervals of $0.1ERB_N$.
(d) Transformation of the excitation pattern to a specific loudness pattern. Specific loudness is a kind of loudness density and has units sones/ERB_N. The transformation involves a compressive nonlinearity at medium to high levels, resembling the compression that occurs on the basilar membrane (Rhode, 1971; Sellick *et al.*, 1982; Robles and Ruggero, 2001).
(e) Summation of the specific loudness values over center frequency on an ERB_N-number scale, which gives the overall loudness for a given ear in sones.

Stages (a)–(e) are calculated separately for each ear.

[a)]Author to whom correspondence should be addressed. Electronic mail: bcjm@cam.ac.uk

To implement the concept of binaural inhibition, Moore and Glasberg (2007) assumed the following.

(1) There are inhibitory interactions between the two ears, such that a signal at the left ear inhibits (reduces) the loudness evoked by a signal at the right ear, and vice versa.
(2) The inhibitory interactions are relatively broadly tuned.

To implement the broad tuning of the inhibition, the specific loudness pattern at each ear was initially smeared or smoothed by convolution with a Gaussian weighting function (on an ERB_N-number scale). Gains characterizing the reduction in specific loudness in one ear produced by the signal in the other ear were derived from the relative values of the smoothed specific loudness patterns at the two ears, and applied to the original specific loudness values in each ear to give inhibited specific loudness values. The loudness for each ear was then calculated by summing the inhibited specific loudness values over center frequency on an ERB_N-number scale, and the overall binaural loudness was obtained by summing the (inhibited) loudness values across the two ears. For details, see Moore and Glasberg (2007).

The model makes the following predictions, all of which are consistent with the bulk of the experimental data.

(1) A diotically presented sound is about 1.5 times as loud as that same sound presented monaurally (regardless of the type of sound or the overall sound level).
(2) The level difference required for equal loudness of diotic and monaural sound varies with sound level. It is 5–7 dB at medium sound levels (depending on the type of sound), but smaller at low sound levels.
(3) The loudness of a sound presented to one ear can be reduced by presentation of a sound of different center frequency to the opposite ear.

Despite its general success in predicting data in the literature, the model failed to predict the pattern of results of experiment 2 of Zwicker and Zwicker (1991). That experiment is described next. Zwicker and Zwicker (1991) investigated the loudness of interaurally correlated noises presented via free-field equalized headphones, using a loudness-scaling paradigm. The starting point for generating the test signals was "uniformly exciting noise," with the same level in each critical band (Zwicker and Fastl, 1999) and with an overall level of 60 dB SPL. This noise was initially filtered into 24 bands, each one critical band (1 bark) wide (Zwicker and Fastl, 1999). These are referred to here as sub-bands. The sub-bands were then grouped into wider composite bands (consisting of 1, 2, 4, or 12 successive sub-bands) and each composite band was presented either to one ear or the other. For example, the sub-bands from 0 to 12 barks were presented to the left ear, and the sub-bands from 13 to 24 barks were presented to the right ear. Or, the sub-bands from 1–4, 9–12, and 17–20 barks were presented to the left ear and the sub-bands from 5–8, 13–16, and 21–24 barks were presented to the right ear. Thus, as the number of sub-bands making up each composite band decreased, the spacing and width of the composite bands decreased. Note that the overall level in each ear was 57 dB SPL (3 dB below the level of the unfiltered noise). The loudness of the dichotically presented sounds was judged (in separate blocks of trials) relative to either a monaural or a diotic standard consisting of all 24 bands, which was assigned 100 units of loudness.

The measured loudness decreased somewhat as the number of composite bands increased (see Table II in Moore and Glasberg, 2007). For example, the loudest stimulus was the one in which sub-bands from 0 to 12 Barks were presented to the left ear, and sub-bands from 13 to 24 barks were presented to the right ear, so there was only one broad composite band presented to each ear. However, the predictions of the model showed the opposite pattern. This might indicate a failing of the model. However, Moore and Glasberg (2007) pointed out that some aspects of the data appear strange. When all of the sub-bands (1–24) were presented monaurally, the predicted loudness (10.9 sones) was a factor of 1.5 smaller than when they were presented diotically (16.4 sones), and this was consistent with the loudness judgments obtained by Zwicker and Zwicker (1991). When sub-bands 1–12 were presented to one ear only, the predicted loudness was 5.7 sones, while when sub-bands 13–24 were presented to one ear only the predicted loudness was 5.8 sones. Since the smoothed specific loudness patterns evoked by sub-bands 1–12 and 13–24 overlap only moderately in frequency, the predicted loudness when sub-bands 1–12 were presented to one ear and sub-bands 13–24 were presented to the other ear (10.6 sones) was only slightly less than the sum of the monaural loudness for the two composite bands (5.7+5.8 =11.5). Also, the predicted loudness for dichotic presentation (10.6 sones) was similar to the predicted loudness for monaural presentation of sub-bands 1–24 (10.9 sones). These predictions all seem very reasonable. Yet, the loudness ratings obtained by Zwicker and Zwicker (1991) suggest that the loudness when sub-bands 1–12 were presented to one ear and sub-bands 13–24 were presented to the other ear was 20% greater than when all sub-bands were presented to one ear, with no signal at the other ear. It is difficult to understand why the loudness should be 20% greater in the former case when each of the two composite bands covers a wide frequency range and the bands do not overlap in frequency.

Because of these apparent anomalies in the data of Zwicker and Zwicker (1991), and because stimuli of the type used by Zwicker and Zwicker (1991) may provide an important test of the validity of the model of Moore and Glasberg (2007), we decided to conduct an experiment using stimuli similar to those of Zwicker and Zwicker (1991). Rather than using a loudness-scaling procedure, a loudness-matching procedure was used, in an attempt to reduce biases that can strongly influence the results of scaling procedures (Poulton, 1979). Although it is possible to design scaling experiments so as to minimize bias effects (Hellman and Zwislocki, 1961), the use of a standard stimulus with a reference loudness of 100 units in the experiments of Zwicker and Zwicker (1991) is likely to have led to biases.

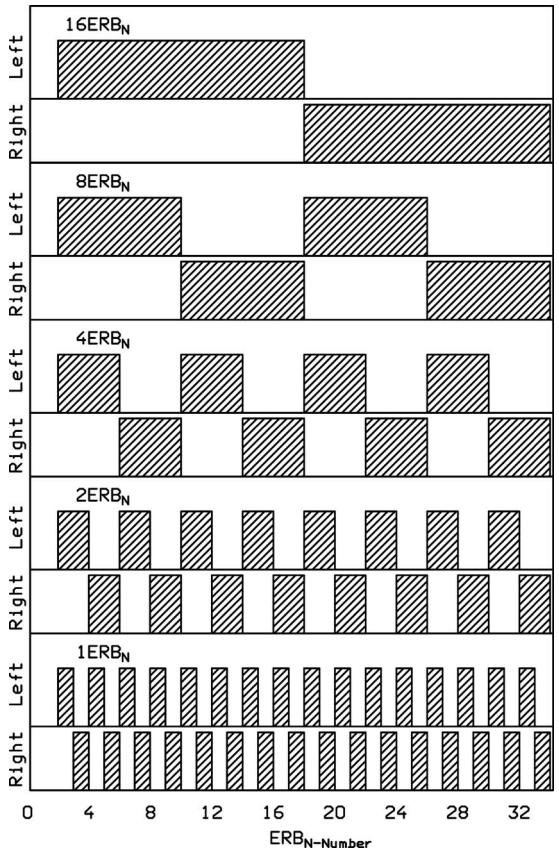

FIG. 1. Schematic illustration of the filters used to create the dichotic test stimuli. The input signal was noise with equal level per ERB_N. The condition labels ($16ERB_N$ to $1ERB_N$) correspond to the number of sub-bands in each composite band.

II. LOUDNESS MATCHING OF SOUNDS WITH DIFFERENT SPECTRA AT THE TWO EARS

A. Stimuli

All noise-band stimuli were derived from a broadband (50–8550 Hz) noise with equal energy in each 1-ERB_N-wide band. Note that this noise is not truly uniformly exciting, as it does not produce a flat excitation pattern after passing through the outer and middle ear. It is possible to produce a uniformly exciting noise by modifying the spectrum to allow for transmission through the outer and middle ear (Glasberg and Moore, 2000), but that was not done here, as we wanted to make the stimuli similar to those of Zwicker and Zwicker (1991). All sub-bands can be considered as "cut out" from this broadband noise. The test stimuli are illustrated schematically in Fig. 1. There were 32 1-ERB_N-wide sub-bands, extending from ERB_N-numbers 1.83 to 33.83. The reference sound contained all 32 bands and was presented either monaurally or diotically.

The dichotic test stimuli contained composite bands made up by combining the following sub-bands, going from top to bottom in the figure (the notation refers to the number of sub-bands within each composite band).

(1) $16ERB_N$. Sub-bands 1–16 were presented to the left ear and sub-bands 17–32 to the right ear. Hence, a single 16-ERB_N-wide composite band was presented to each ear.
(2) $8ERB_N$. Sub-bands 1–8 and 17–24 were presented to the left ear and sub-bands 9–16 and 25–32 to the right ear (two 8-ERB_N-wide composite bands to each ear).
(3) $4ERB_N$. Sub-bands 1–4, 9–12, 17–20, and 25–28 were presented to the left ear and sub-bands 5–8, 13–16, 21–24, and 29–32 to the right ear (four 4-ERB_N-wide composite bands to each ear).
(4) $2ERB_N$. Sub-bands 1–2, 5–6, 9–10, 13–14, 17–18, 21–22, 25–26, and 29–30 were presented to the left ear and sub-bands 3–4, 7–8, 11–12, 15–16, 19–20, 23–24, 27–28, and 31–32 to the right ear (eight 2-ERB_N-wide composite bands to each ear).
(5) $1ERB_N$. All odd-numbered sub-bands were presented to the left ear and all even-numbered sub-bands to the right ear (16 1-ERB_N-wide composite bands to each ear).

In all cases, matches were also made with the sounds switched between ears; e.g., for condition $16ERB_N$, sub-bands 1–16 were presented to the right ear and sub-bands 17–32 to the left. For the dichotic test stimuli, only the diotic reference sound was used for loudness matching.

In addition to conditions (1)–(5) above, loudness matches were made to the single-ear stimuli (e.g., sub-bands 1–16 or sub-bands 17–32). For convenience, these monaural stimuli are given the same labels, $16ERB_N$ to $1ERB_N$. Stimuli that included the lowest sub-band (band 1) are designated case "Lo," and stimuli that included the highest sub-band (band 32) are designated case "Hi." For these monaural test stimuli, loudness matches were made using both the monaural and diotic reference stimuli. When both the test and reference stimuli were monaural, they were presented to the same ear; both the left and right ears were used for each subject. Note that Zwicker and Zwicker (1991) did not include test stimuli comparable to our monaural test stimuli.

In one set of conditions, the level of the reference sound was fixed at 44 dB SPL/ERB_N and the test sound was varied in level to estimate the point of equal loudness. In another set of conditions, the level of the test sound was fixed at 44 dB SPL/ERB_N and the reference sound was varied in level to estimate the point of equal loudness. The test and reference sounds were alternated and the sequence continued indefinitely. Each sound lasted 500 ms, including 20-ms raised-cosine ramps. There was a 400-ms silent interval between the test and reference sounds, and a 600-ms interval between the reference and test sounds. Each sound was accompanied by a separate light. Pressing the button under one light caused the sound associated with that light to become relatively softer (either by decreasing its level or by increasing the level of the other sound), while pressing the button under the other light caused the sound associated with that light to become relatively softer.

Stimuli were digitally generated at a 50-kHz sampling rate, using an algorithm described by Singleton (1969). First the desired spectrum was calculated, assigning random phases to the frequency components. Components were spaced at 1-Hz intervals. Then, an inverse Fourier transform was used to produce a time-domain waveform. This allowed the generation of noise bands with very sharp spectral edges. The output waveform was generated using Tucker-Davis

Technologies (TDT) 16-bit DA1 digital-to-analog converters, and levels were controlled using TDT PA4 programmable attenuators. The spectra were checked using a Hewlett-Packard 35670A dual-channel dynamic signal analyzer. Stimuli were passed though a TDT HB6 headphone buffer and a Hatfield 2125 passive attenuator, and presented via Sennheiser HD580 headphones, which have approximately a diffuse-field response. Sound levels are specified as equivalent diffuse-field levels. The levels at the eardrum would be about 12 dB higher for frequencies around 3 kHz. Subjects were seated in a double-walled sound-attenuating chamber.

B. Method

To minimize biases, the starting level of the variable sound was randomly chosen from a 10-dB range centered around the mean of previous matching levels for that condition (Gabriel *et al.*, 1997). The range of starting levels for the first match for a given condition was based on pilot experiments. The subject pressed one button to increase the level of the variable sound, and another button to decrease the level of the variable sound, as described earlier. Subjects were instructed to adjust the variable sound using a bracketing procedure, so that it sounded alternately louder and softer than the fixed sound, and then to adjust the level until the loudness of the variable sound matched that of the fixed sound. They were asked to press a third button when they were satisfied with the match. The level of the variable sound was changed in 3-dB steps until two turnpoints (changes from increasing to decreasing level or vice versa) had occurred, and thereafter was changed in 1-dB steps. A match was not accepted until at least four turnpoints had occurred. Five matches were obtained for each condition for each subject, and the final matching level was taken as the mean of the five.

C. Subjects

Thirteen subjects with normal hearing were tested, seven with the test sound varied in level and six with the reference sound varied in level. However, one subject in the former case gave very erratic results, and these were discarded, leaving six subjects for each condition. All subjects had absolute thresholds better than 20 dB hearing level (HL) (ISO 389-8, 2004) for the audiometric frequencies from 250 to 8000 Hz. Subjects were given practice on a selection of conditions before testing proper started. Subjects were paid for their services.

III. RESULTS

The pattern of results was reasonably consistent across subjects, both when the reference sound was varied in level and when the test sound was varied in level to obtain a loudness match. In what follows, results are averaged across subjects within each group (reference varied or test varied). Also, results were similar when the case Lo stimuli were presented to the left and right ears, and when the case Hi stimuli were presented to the left and right ears. Results are also presented averaged across these two cases.

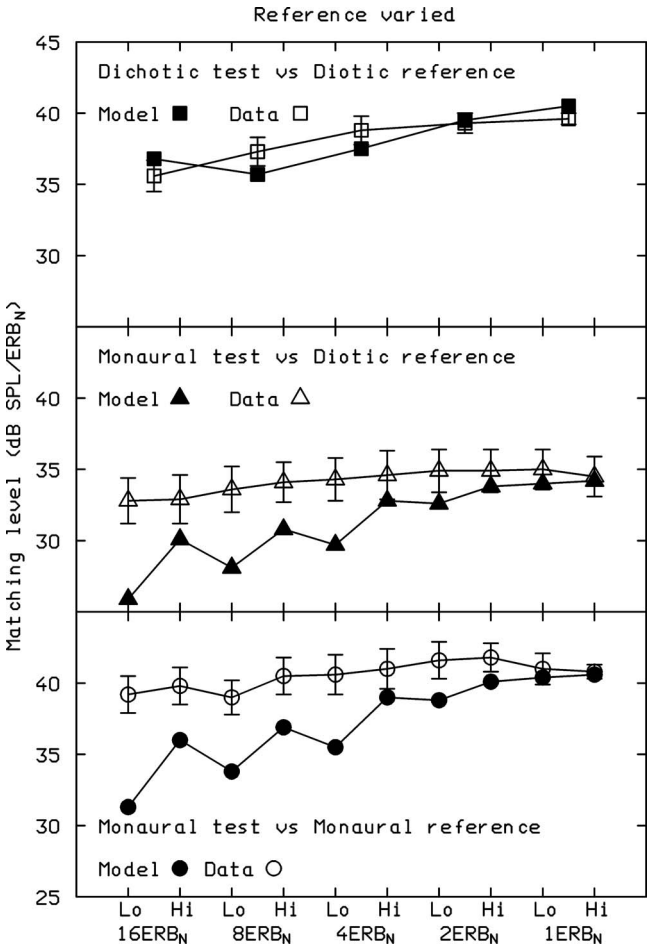

FIG. 2. Obtained loudness matches (open symbols) and matches predicted by the loudness model of Moore and Glasberg (2007) (filled symbols) for the set of conditions where the level of the reference sound was varied to determine a loudness match. The condition is indicated along the *x*-axis, and the level/ERB$_N$ of the reference sound is indicated on the *y*-axis. For the dichotic test stimuli, the data are plotted at a position between the positions for the corresponding Lo and Hi cases. The panels show, from top to bottom, data and predictions for the dichotic test stimuli with diotic reference, the monaural test stimuli with diotic reference, and the monaural test stimuli with monaural reference. Data are averaged across six subjects. Error bars show ±1 standard error.

A. Reference varied

The mean results for the set of conditions when the reference sound was varied in level to obtain a loudness match are shown in Fig. 2. The condition is indicated along the *x*-axis, and the level/ERB$_N$ of the reference sound that matched the loudness of the test sound is indicated on the *y*-axis. Error bars show ±1 standard error (SE) of the matches. Consider first the results when the test stimulus was dichotic, with different bands presented to the two ears (open squares, top panel), while the reference sound was diotic. The level at equal loudness tended to increase, indicating an increase in loudness of the test stimulus, as the number of composite bands increased and their width and spacing decreased (going from condition 16ERB$_N$ to 1ERB$_N$). The overall increase was about 4 dB.

Predictions of the loudness model of Moore and Glasberg (2007) were generated by first calculating the loudness of the test stimulus, and then adjusting the level of the ref-

erence stimulus until it led to the same calculated loudness. The predictions took into account the estimated response of the HD580 headphones at the eardrum, as measured using a KEMAR manikin (Burkhard and Sachs, 1975). The predictions for the case when the test sound was dichotic and the reference sound was diotic are shown by filled squares. The predictions correspond well with the data, and capture the general trend for the matching level to increase going from condition $16ERB_N$ to $1ERB_N$. The model predicted an increase of 3.7 dB, in good accord with the data. The largest difference between an obtained and predicted match was 1.6 dB.

Consider now the results for the monaural test stimuli. The matching levels of the reference were lower when the reference was presented diotically (open triangles, middle panel) than when it was presented monaurally (open circles, bottom panel), as expected. This effect is discussed in more detail later. The results showed only a slight increase in the matching level, of about 2 dB, going from condition $16ERB_N$ to $1ERB_N$. For conditions $16ERB_N$, $8ERB_N$, and $4ERB_N$, the predicted matching levels of the reference (filled triangles and circles) were well below the obtained levels. Surprisingly, the obtained matches were almost the same for the Lo and Hi cases, even for condition $16ERB_N$, when the test stimulus contained only the lower frequencies (up to 1336 Hz) for case Lo and only the higher frequencies (above 1336 Hz) for case Hi. The model predicts that, for conditions $16ERB_N$, $8ERB_N$, and $4ERB_N$, the loudness should be lower for case Lo than for case Hi, and so the loudness matches should show the same pattern. The predicted difference between case Lo and case Hi occurs because of the characteristics of the headphones (which boost frequencies around 3 kHz) and the characteristics of the middle ear (which attenuates frequencies below about 500 Hz).

A possible explanation for the discrepancy between the data and the predictions of the model for the monaural test stimuli is that, although subjects were asked to match the overall loudness of the test and reference stimuli, they had difficulty doing this because of the very different sound qualities of the two stimuli (Gabriel *et al.*, 1997). Indeed, several of the subjects complained of difficulty, especially in conditions $16ERB_N$ and $8ERB_N$. Subjects may have partly based their judgments on the loudness of the part of the spectrum that was common between the test and reference stimuli, rather than on the whole spectrum of the reference sound. For example, when the test stimulus contained sub-bands 1–16 (condition $16ERB_N$, case Lo), subjects may have matched the loudness of the low-frequency part of the spectrum of the reference sound with that of the test sound. This could account for the predicted matching level (based on the overall loudness of the reference) being well below the obtained level. It could also account for the finding that the loudness matches were similar for case Lo and for case Hi, even for conditions $16ERB_N$, $8ERB_N$, and $4ERB_N$.

To check on this idea, three normal-hearing subjects were asked to make a loudness match between cases Lo and Hi for condition $16ERB_N$. In other words, they were asked to match the loudness of a stimulus containing sub-bands 1–16 (condition $16ERB_N$, case Lo) with a stimulus containing sub-bands 17–32 (condition $16ERB_N$, case Hi). Subjects could not make a match based on the loudness of the part of the spectrum that was common between the two stimuli, since there was no common spectral region. The level of one stimulus was fixed at 44 dB SPL/ERB_N, while the level of the other stimulus was varied to achieve a loudness match, using the same procedure as described earlier. When the level of the case Lo stimulus was fixed at 44 dB SPL/ERB_N, the mean matching level of the case Hi stimulus was 37.2 dB SPL/ERB_N [standard deviation (SD)=1.9 dB]. The matching level predicted by the model was 38.7 dB SPL/ERB_N. When the level of the case Hi stimulus was fixed at 44 dB SPL/ERB_N, the mean matching level of the case Lo stimulus was 50.1 dB SPL/ERB_N (SD=1.7 dB). The matching level predicted by the model was 49.0 dB SPL/ERB_N. These results clearly show that, at equal levels, the case Lo stimulus was perceived as softer than the case Hi stimulus, by an amount that is reasonably consistent with the predictions of the model.

Returning to the data shown in Fig. 2, the discrepancy between the data and the predictions of the model for the monaural test stimuli became smaller going from condition $16ERB_N$ to $1ERB_N$. This is consistent with the explanation given above for the discrepancy between the results and predictions for conditions $16ERB_N$, $8ERB_N$, and $4ERB_N$. For the conditions where the composite bands were more finely spaced ($2ERB_N$ and $1ERB_N$), the test and reference stimuli sounded very similar in quality, and subjects reported that it was much easier to make a match. For condition $1ERB_N$, there was a very good correspondence between the data and the predictions of the model, for both the monaural and diotic references.

Another test of the model is the difference between the matching levels of the reference for a given monaural test stimulus when the reference was presented monaurally and when it was presented diotically. This gives an indirect measure of the level difference required for equal loudness between a monaural and a diotic reference stimulus; for brevity, this will be referred to as LDIFF. The measured values of LDIFF are plotted as open circles in the upper panel of Fig. 3. The mean value of LDIFF was 6.4 dB (SD=0.4 dB). The values of LDIFF predicted by the model are shown as filled circles. The mean LDIFF value predicted by the model was 6.0 dB (SD=0.3 dB). The correspondence between the data and predictions is very good. For both data and predictions, there is no clear trend for the LDIFF values to vary with the number of composite bands.

B. Test varied

The data obtained when the test stimuli were varied in level to determine a loudness match are shown in Fig. 4. The pattern of results is inverted relative to that obtained when the reference stimulus was varied. This is as expected; manipulations that increase the loudness of the test stimuli (going from condition $16ERB_N$ to $1ERB_N$) require a decrease in level of the test stimuli to match the loudness of the fixed reference stimulus. When the test stimulus was dichotic, and the reference stimulus was diotic (open squares, top panel),

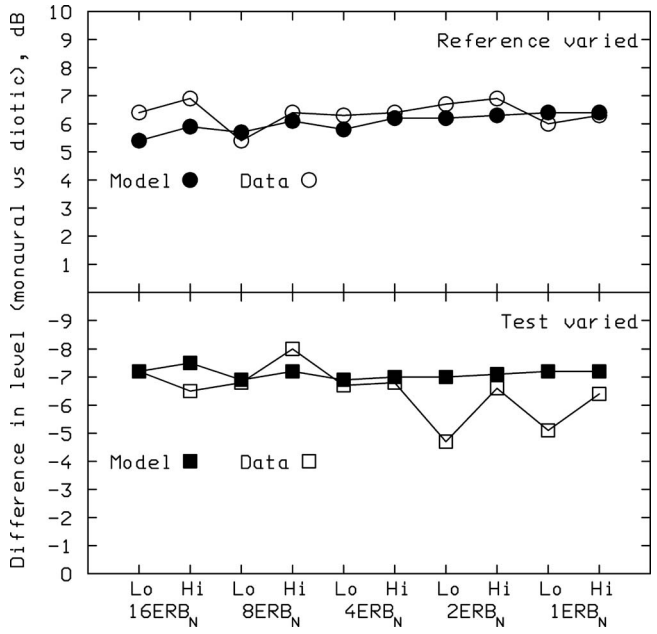

FIG. 3. The top panel shows values of LDIFF (the difference between the matching levels of the reference for a given monaural test stimulus when the reference was presented monaurally and when it was presented diotically) for the condition where the level of the test stimulus was fixed and the reference stimulus was varied in level. Open symbols show data and filled symbols show predictions of the model. The bottom panel shows corresponding results for the condition where the level of the reference stimulus was fixed and the test stimulus was varied in level.

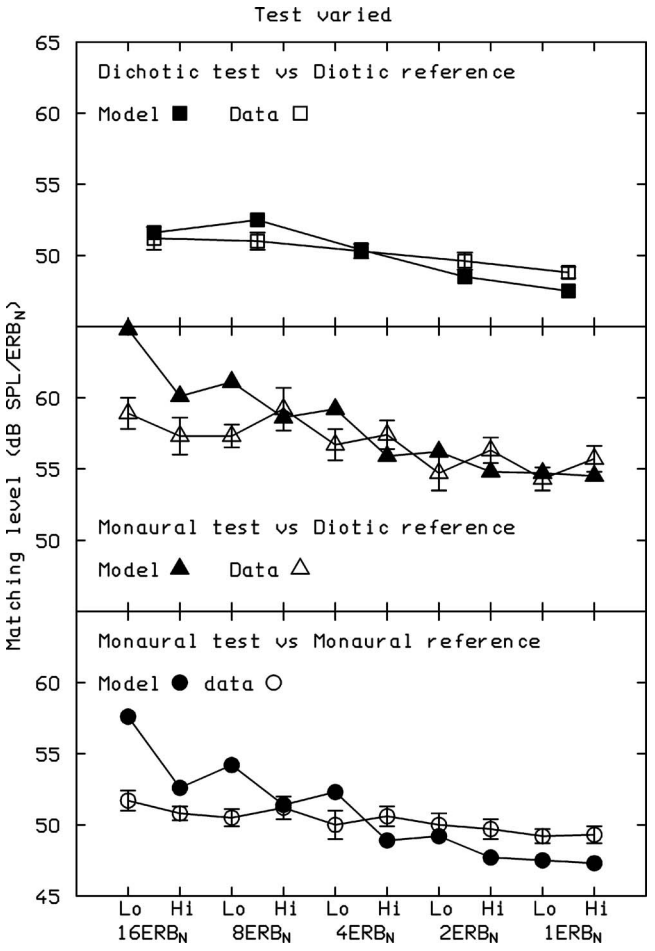

FIG. 4. As Fig. 2, but for the set of conditions where the level of the test sound was varied to determine a loudness match.

the level of the test stimulus at equal loudness tended to decrease as the number of composite bands increased (going from condition 16ERB$_N$ to 1ERB$_N$). The overall decrease was 2.4 dB. Predictions of the loudness model of Moore and Glasberg (2007) for this condition are shown by filled squares. These were generated by first calculating the loudness of the reference stimulus, and then adjusting the level of each test stimulus until it gave the same calculated loudness. There was a good correspondence between the data and predictions, although the model predicted a slightly larger overall decrease of 4.1 dB. The largest deviation between an obtained and predicted match was 1.5 dB.

As was the case when the reference stimulus was varied, the loudness matches for the monaural test stimuli (open circles for the monaural reference and open triangles for the diotic reference, middle and bottom panels) differ from the predictions of the model (filled circles and triangles, respectively), especially for conditions 16ERB$_N$ and 8ERB$_N$. These discrepancies can be explained in the same way as before; because of the very different qualities of the test and reference stimuli, subjects probably based their loudness matches partly on the spectral region that was common between the test and reference stimuli.

The difference between the matching levels of a given monaural test stimulus when the reference was presented monaurally and when it was presented diotically is related to the difference in loudness of the monaural and diotic references. The obtained differences are plotted as open squares in the lower panel of Fig. 3. The mean value was −6.5 dB (SD=0.9 dB). The differences predicted by the model are shown as filled squares. The mean difference predicted by the model was −7.1 dB (SD=0.2 dB). The correspondence between the data and predictions is very good.

IV. DISCUSSION

The pattern of results for the dichotic test stimuli, with non-overlapping spectra at the two ears, differed from that found for similar stimuli by Zwicker and Zwicker (1991); we found that loudness increased slightly as the composite bands became narrower and more finely spaced (going from condition 16ERB$_N$ to 1ERB$_N$), while Zwicker and Zwicker (1991) found that loudness decreased slightly. The reason for the discrepancy is not clear, although, as described in the Introduction, there were some anomalies in the data of Zwicker and Zwicker (1991). The pattern of results found here was in good correspondence with the predictions of the model of Moore and Glasberg (2007).

The model predicts that the loudness should also increase for the monaural test stimuli as the number of composite bands increases and they become narrower and more finely spaced. In fact, the predicted increase is larger for the monaural than for the dichotic test stimuli (see Figs. 2 and 4). The predicted increase for the monaural stimuli occurs because, when many finely spaced composite bands are used (as in conditions 2ERB$_N$ and 1ERB$_N$), there are only small

dips in the excitation pattern at frequencies corresponding to the spectral gaps between the bands, leading to an excitation pattern, and specific loudness pattern, that is not very different from that for the reference stimulus. In contrast, when a few wide composite bands are used (as in conditions $16ERB_N$ and $8ERB_N$), there are large dips in the excitation pattern at frequencies corresponding to the spectral gaps between bands, and this reduces the overall loudness. The increase in loudness going from condition $16ERB_N$ to $1ERB_N$ is predicted to be larger for the monaural than for the dichotic test stimuli, because for the latter the effects of binaural inhibition become progressively greater going from condition $16ERB_N$ to $1ERB_N$, as the excitation patterns at the two ears become more similar.

Unfortunately, the subjects appeared to have difficulty in matching the overall loudness of the monaural test stimuli to that of the reference stimulus, except when the composite bands in the test stimulus were relatively narrow and finely spaced. This difficulty probably arose from the fact that the test and reference stimuli had very different spectra (and excitation patterns), with only part of the spectrum in common. It appears that, for the monaural test stimuli, our subjects partly based their matches on the spectral region that was common to the test and reference stimuli, especially for conditions $16ERB_N$ and $8ERB_N$. One factor that may have contributed to this is the repeated alternation of the test and reference stimuli, which may have led to the formation of two perceptual streams (Bregman, 1990; Moore and Gockel, 2002); one stream would correspond to the test stimulus and the part of the reference stimulus whose spectrum overlapped with that of the reference stimulus. The other stream would correspond to the remaining part of the reference stimulus. Subjects may then have based their loudness matches mainly on the perceptual stream including the test stimulus. Previous work is consistent with the idea that loudness is determined after processes of perceptual organization have occurred (McAdams *et al.*, 1998).

Our suggestion that subjects partly based their matches on the spectral region that was common to the test and reference stimuli can account for the finding that the matches with the reference were almost the same for the Lo and Hi cases, for condition $16ERB_N$. When subjects made direct loudness matches between the stimuli for case Lo and case Hi in condition $16ERB_N$, the results clearly showed that the case Lo stimulus was softer, consistent with the predictions of the model.

Matches to the monaural test stimuli were made using both monaural and diotic reference stimuli. When the level of the test stimuli was fixed, the differences between matches for the two types of reference give an estimate of the level difference required for equal loudness of monaural and diotic reference stimuli, LDIFF. The mean value of LDIFF for the data was 6.4 dB, while the value predicted by the model was 6.0 dB, indicating very good agreement. The LDIFF value predicted by the model depends on the rate of growth of loudness with increasing level of the reference sound. The model predicts that a diotic sound is 1.5 times as loud as a monaural sound of the same level, so LDIFF corresponds to the level increase required to increase the loudness of the monaural reference stimulus by a factor of 1.5. The predicted loudness of the reference sound changes somewhat more slowly with increasing level than would be the case for a sinusoid or narrowband noise. For example, when the level/ERB_N of the monaural reference sound is increased from 40 to 50 dB SPL, the loudness is predicted to increase by a factor of 1.8 (from 9.3 to 16.7 sones), whereas the corresponding factor for a sinusoid or narrowband noise is about 2. The factor for the sinusoid depends partly on the spread of excitation that occurs with increasing level. For the reference sound used here, the excitation pattern is broad even at low levels, so there is little contribution to loudness of the spread of excitation with increasing level. Hence the predicted value of LDIFF is slightly greater for the reference sound used here than for a sinusoid or narrowband noise. This prediction is consistent with the data of Edmonds and Culling (2009). For $1\text{-}ERB_N$-wide monaural and diotic noises of various center frequencies, the average value of LDIFF was 5.3 dB. For noises of greater bandwidth, the average value of LDIFF was 5.8 dB. However, Edmonds and Culling (2009) also found an effect of the interaural correlation of the noise on loudness, an effect which cannot be accounted for by the current model, since the model is based only on the power spectrum of the sound.

We conclude that the model of Moore and Glasberg (2007) gives accurate predictions of loudness for sounds with non-overlapping spectra at the two ears. This, combined with earlier analyses indicating accurate predictions of loudness for stimuli with the same spectra (but differing levels) at the two ears, indicates that the model is likely to work well with more realistic binaural signals, where the spectra at the two ears are not identical but nevertheless overlap to a considerable degree. However, it should be noted that the model is only applicable to steady sounds. Epstein and Florentine (2009) recently presented evidence suggesting that binaural loudness summation is much less for speech than for steady tones. Also, binaural loudness summation was less when sounds were presented via a loudspeaker rather than via earphones. The extent to which these effects can be explained in terms of the time-varying nature of the sounds and/or differences in spectra across ears remains uncertain. The effects may partly reflect relatively high-level processes of loudness constancy, which are not taken into account in current loudness models. Loudness models for time-varying sounds have been developed (Zwicker, 1977; Glasberg and Moore, 2002; Chalupper and Fastl, 2002), but the published versions of these models do not implement any form of binaural inhibition of the type discussed in the present paper.

ACKNOWLEDGMENTS

This work was supported by the MRC (United Kingdom). We thank Myriam Guessoum for gathering some of the data reported here. We also thank Hedwig Gockel and two anonymous reviewers for helpful comments on an earlier version of this paper.

ANSI (**2007**). ANSI S3.4-2007. Procedure for the computation of loudness of steady sounds, American National Standards Institute, New York.
Breebaart, J., van de Par, S., and Kohlrausch, A. (**2001**). "Binaural process-

ing model based on contralateral inhibition. I. Model structure," J. Acoust. Soc. Am. **110**, 1074–1088.
Bregman, A. S. (**1990**). *Auditory Scene Analysis: The Perceptual Organization of Sound* (Bradford Books, MIT Press, Cambridge, MA).
Burkhard, M. D., and Sachs, R. M. (**1975**). "Anthropometric manikin for acoustic research," J. Acoust. Soc. Am. **58**, 214–222.
Chalupper, J., and Fastl, H. (**2002**). "Dynamic loudness model (DLM) for normal and hearing impaired listeners," Acta Acust. Acust. **88**, 378–386.
Edmonds, B. A., and Culling, J. F. (**2006**). "Interaural correlation and loudness (A)," J. Acoust. Soc. Am. **119**, 3235.
Edmonds, B. A., and Culling, J. F. (**2009**). "Interaural correlation and the binaural summation of loudness," J. Acoust. Soc. Am. **125**, 3865–3870.
Epstein, M., and Florentine, M. (**2009**). "Binaural loudness summation for speech and tones presented via earphones and loudspeakers," Ear Hear. **30**, 234–237.
Fletcher, H., and Munson, W. A. (**1933**). "Loudness, its definition, measurement and calculation," J. Acoust. Soc. Am. **5**, 82–108.
Gabriel, B., Kollmeier, B., and Mellert, V. (**1997**). "Influence of individual listener, measurement room and choice of test-tone levels on the shape of equal-loudness level contours," Acust. Acta Acust. **83**, 670–683.
Gigerenzer, G., and Strube, G. (**1983**). "Are there limits to binaural additivity of loudness?," J. Exp. Psychol. Hum. Percept. Perform. **9**, 126–136.
Glasberg, B. R., and Moore, B. C. J. (**1990**). "Derivation of auditory filter shapes from notched-noise data," Hear. Res. **47**, 103–138.
Glasberg, B. R., and Moore, B. C. J. (**2000**). "Frequency selectivity as a function of level and frequency measured with uniformly exciting notched noise," J. Acoust. Soc. Am. **108**, 2318–2328.
Glasberg, B. R., and Moore, B. C. J. (**2002**). "A model of loudness applicable to time-varying sounds," J. Audio Eng. Soc. **50**, 331–342.
Glasberg, B. R., and Moore, B. C. J. (**2006**). "Prediction of absolute thresholds and equal-loudness contours using a modified loudness model," J. Acoust. Soc. Am. **120**, 585–588.
Gockel, H. E., Carlyon, R. P., and Plack, C. J. (**2009**). "Pitch discrimination interference between binaural and monaural or diotic pitches," J. Acoust. Soc. Am. **126**, 281–290.
Hellman, R. P. (**1976**). "Growth of loudness at 1000 and 3000 Hz," J. Acoust. Soc. Am. **60**, 672–679.
Hellman, R. P., and Zwislocki, J. J. (**1961**). "Some factors affecting the estimation of loudness," J. Acoust. Soc. Am. **33**, 687–694.
Hellman, R. P., and Zwislocki, J. J. (**1963**). "Monaural loudness summation at 1000 cps and interaural summation," J. Acoust. Soc. Am. **35**, 856–865.
ISO 389-8 (**2004**). Acoustics—Reference zero for the calibration of audiometric equipment—Part 8: Reference equivalent threshold sound pressure levels for pure tones and circumaural earphones, International Organization for Standardization, Geneva.
Lindemann, W. (**1986**). "Extension of a binaural cross-correlation model by contralateral inhibition. I. Simulation of lateralization for stationary signals," J. Acoust. Soc. Am. **80**, 1608–1622.
Marozeau, J., Epstein, M., Florentine, M., and Daley, B. (**2006**). "A test of the binaural equal-loudness-ratio hypothesis for tones," J. Acoust. Soc. Am. **120**, 3870–3877.
McAdams, S., Botte, M. C., and Drake, C. (**1998**). "Auditory continuity and loudness computation," J. Acoust. Soc. Am. **103**, 1580–1591.
Moore, B. C. J. (**2003**). *An Introduction to the Psychology of Hearing*, 5th ed. (Academic, San Diego, CA).
Moore, B. C. J., and Glasberg, B. R. (**2007**). "Modeling binaural loudness," J. Acoust. Soc. Am. **121**, 1604–1612.
Moore, B. C. J., Glasberg, B. R., and Baer, T. (**1997**). "A model for the prediction of thresholds, loudness and partial loudness," J. Audio Eng. Soc. **45**, 224–240.
Moore, B. C. J., and Gockel, H. (**2002**). "Factors influencing sequential stream segregation," Acust. Acta Acust. **88**, 320–333.
Poulton, E. C. (**1979**). "Models for the biases in judging sensory magnitude," Psychol. Bull. **86**, 777–803.
Rhode, W. S. (**1971**). "Observations of the vibration of the basilar membrane in squirrel monkeys using the Mössbauer technique," J. Acoust. Soc. Am. **49**, 1218–1231.
Robles, L., and Ruggero, M. A. (**2001**). "Mechanics of the mammalian cochlea," Physiol. Rev. **81**, 1305–1352.
Scharf, B. (**1969**). "Dichotic summation of loudness," J. Acoust. Soc. Am. **45**, 1193–1205.
Scharf, B., and Fishken, D. (**1970**). "Binaural summation of loudness reconsidered," J. Exp. Psychol. **86**, 374–379.
Sellick, P. M., Patuzzi, R., and Johnstone, B. M. (**1982**). "Measurement of basilar membrane motion in the guinea pig using the Mössbauer technique," J. Acoust. Soc. Am. **72**, 131–141.
Singleton, R. C. (**1969**). "An algorithm for computing the mixed radix fast Fourier transform," IEEE Trans. Audio Electroacoust. **17**, 93–103.
Stevens, S. S. (**1957**). "On the psychophysical law," Psychol. Rev. **64**, 153–181.
Whilby, S., Florentine, M., Wagner, E., and Marozeau, J. (**2006**). "Monaural and binaural loudness of 5- and 200-ms tones in normal and impaired hearing," J. Acoust. Soc. Am. **119**, 3931–3939.
Zwicker, E. (**1977**). "Procedure for calculating loudness of temporally variable sounds," J. Acoust. Soc. Am. **62**, 675–682.
Zwicker, E., and Fastl, H. (**1999**). *Psychoacoustics—Facts and Models*, 2nd ed. (Springer-Verlag, Berlin).
Zwicker, E., and Zwicker, U. T. (**1991**). "Dependence of binaural loudness summation on interaural level differences, spectral distribution, and temporal distribution," J. Acoust. Soc. Am. **89**, 756–764.

Excitation-based and informational masking of a tonal signal in a four-tone masker[a)]

Lori J. Leibold[b)] and Jack J. Hitchens
Department of Allied Health Sciences, The University of North Carolina at Chapel Hill, Chapel Hill, North Carolina 27599

Emily Buss
Department of Otolaryngology/Head and Neck Surgery, The University of North Carolina at Chapel Hill, Chapel Hill, North Carolina 27599

Donna L. Neff
Boys Town National Research Hospital, Omaha, Nebraska 68131

(Received 22 July 2009; revised 31 December 2009; accepted 5 January 2010)

This study examined contributions of peripheral excitation and informational masking to the variability in masking effectiveness observed across samples of multi-tonal maskers. Detection thresholds were measured for a 1000-Hz signal presented simultaneously with each of 25, four-tone masker samples. Using a two-interval, forced-choice adaptive task, thresholds were measured with each sample fixed throughout trial blocks for ten listeners. Average thresholds differed by as much as 26 dB across samples. An excitation-based model of partial loudness [Moore, B. C. J. *et al.* (1997). J. Audio Eng. Soc. **45**, 224–237] was used to predict thresholds. These predictions accounted for a significant portion of variance in the data of several listeners, but no relation between the model and data was observed for many listeners. Moreover, substantial individual differences, on the order of 41 dB, were observed for some maskers. The largest individual differences were found for maskers predicted to produce minimal excitation-based masking. In subsequent conditions, one of five maskers was randomly presented in each interval. The difference in performance for samples with low versus high predicted thresholds was reduced in random compared to fixed conditions. These findings are consistent with a trading relation whereby informational masking is largest for conditions in which excitation-based masking is smallest.
 [DOI: 10.1121/1.3298588]

PACS number(s): 43.66.Dc, 43.66.Lj [CJP] Pages: 2441–2450

I. INTRODUCTION

Studies of simultaneous masking have shown large detrimental effects of masker-frequency uncertainty, often created by randomizing the frequency content of a multi-tonal masker each time it is presented (e.g., Watson *et al.*, 1975; Neff and Green, 1987; Kidd *et al.*, 1994; Oh and Lutfi, 1998; Alexander and Lutfi, 2004; Richards and Neff, 2004; Durlach *et al.*, 2005). For example, simultaneous-masking studies with fixed-frequency sinusoidal signals and random-frequency multi-tonal maskers have reported as much as 50 dB of masking for trained listeners (e.g., Neff and Green, 1987). The "informational" masking produced by varying the spectral content of the masker can be observed even when the frequency components that comprise the masker are restricted from falling within a presumed auditory filter centered on the signal. The use of a "protected region" centered on the signal frequency is intended to reduce the potential contributions of peripheral (i.e., energetic) masking. Thus, whereas energetic masking is believed to reflect interactions between the signal and masker at the auditory periphery, informational masking is believed to reflect interactions occurring within the central auditory system.

The processes underlying informational masking are incompletely understood and may well vary across stimuli, tasks, and listeners. One potential contributor to informational masking is a failure of sound source segregation (e.g., Bregman, 1990)—the process by which acoustic components are identified as coming from one or more sources. Evidence for this comes from reports of significant reductions in informational masking when cues that promote sound source segregation are introduced (e.g., Kidd *et al.*, 1994; Neff, 1995; Richards and Neff, 2004). Manipulations that decrease the similarity of the target relative to the masker can also yield substantial release from informational masking (e.g., Kidd *et al.*, 2002; Durlach *et al.*, 2003). Note that many cues believed to affect sound source segregation also influence target-masker similarity. Another related mechanism which likely contributes to informational masking is selective auditory attention—the ability to attend to a relevant target sound and ignore irrelevant, interfering sounds. Results from early studies of informational masking (e.g., Watson *et al.*, 1976; Spiegel *et al.*, 1981; Neff and Green, 1987) were interpreted as indicating that listeners were not able to attend only to information in the signal frequency region. Consistent with this explanation, Lutfi and colleagues (e.g., Lutfi, 1993; Lutfi

[a)] Portions of these results were presented to the 32nd MidWinter Meeting of the Association for Research in Otolaryngology in Baltimore, MD, February, 2009.

[b)] Author to whom correspondence should be addressed. Electronic mail: leibold@med.unc.edu

et al., 2003, Alexander and Lutfi, 2004) modeled informational masking in terms of the number and frequency range of auditory filters monitored when a listener is asked to detect a tonal signal at a fixed frequency in the presence of a random-frequency, multi-tonal masker. In that approach, data with little evidence of informational masking were modeled as resulting from a highly frequency-selective process, characterized in terms of a very narrow attentional filter. On the other hand, data with evidence of extensive informational masking were modeled as resulting from a combination of auditory filter outputs, characterized in terms of a wide attentional filter.

Interpreting effects of masker-frequency uncertainty is complicated by the observation of large within- and between-subjects variability in performance for multi-tonal masking conditions, even when the degree of masker-spectral uncertainty is modest (e.g., Neff and Callaghan, 1988; Neff and Dethlefs, 1995; Wright and Saberi, 1999; Alexander and Lutfi, 2004; Richards and Neff, 2004; Durlach *et al.*, 2005). Several studies have shown that thresholds in conditions with little or no masker-frequency uncertainty (e.g., masker samples fixed across intervals of each trial or across the entire block of trials) are often considerably higher than the absolute threshold for the signal in quiet (e.g., Neff and Callaghan, 1988; Neff and Dethlefs, 1995; Wright and Saberi, 1999; Alexander and Lutfi, 2004; Richards and Neff, 2004; Durlach *et al.*, 2005). Moreover, multi-tonal masker samples can differ widely in masking effectiveness when particular samples are selected at random from the pool of samples used for testing with minimal uncertainty (e.g., Neff and Callaghan, 1987; Wright and Saberi, 1999). For example, Wright and Saberi (1999) measured detection threshold for a 1000-Hz pure tone in the presence of a ten-tone masker; they found a range of more than 20 dB in average threshold across the ten masker samples tested. Differences in peripheral excitation patterns across the masker samples may be responsible for the substantial variability in masked threshold observed within a given subject.

In contrast to differences in performance within a listener, individual differences in susceptibility to informational masking appear to play a role in the substantial between-subjects variability in masked threshold observed for a fixed masker sample (e.g., Neff and Callaghan, 1987; Alexander and Lutfi, 2004; Durlach *et al.*, 2005). For example, Alexander and Lutfi (2004) reported thresholds ranging from 15- to 52 dB sound pressure level (SPL) across 16 normal-hearing listeners asked to detect a 2000-Hz pure tone in the presence of a ten-tone, fixed-frequency, simultaneous masker. Alexander and Lutfi (2004) noted that this variability in performance was inconsistent with expectations based on excitation-based masking and suggested that some listeners may have had difficulty perceptually segregating the signal from the masker even in the absence of stimulus uncertainty. Similarly, Durlach *et al.* (2005) reported average thresholds for a 1000-Hz signal ranging from 33 to 48 dB SPL across ten listeners in the presence of an eight-tone, fixed-frequency, simultaneous masker. Although individual differences do not in themselves indicate informational masking, the magnitude of these differences contrasts sharply with the well-established stability across listeners of thresholds in broadband noise and suggests non-peripheral contributions elevating thresholds for at least the poorer performers.

The current study examined the degree to which differences in both excitation-based and informational masking contribute to the differences in masking observed across multi-tonal masker samples and across listeners. In the first set of *Fixed* conditions, thresholds were measured for a 1000-Hz signal presented simultaneously with each of 25 different four-tone masker samples. The model of partial loudness from Moore *et al.* (1997) was used to estimate the contribution of peripheral, excitation-based masking to thresholds observed across masker samples. The relative contributions of excitation-based and informational masking to performance for conditions with high masker-spectral uncertainty were examined in a subsequent set of *Random* conditions, in which one of five masker samples was selected at random for each interval throughout a block of trials. Performance was compared across two random conditions: one in which the five masker samples were those with the smallest estimates of excitation-based masking, and one in which the five samples were those with the largest estimates of excitation-based masking.

II. METHOD

A. Listeners

Ten adults (19–37 years) with normal-hearing sensitivity participated in all conditions, including authors LL (L5) and JH (L121). All listeners had air-conduction thresholds less than 20 dB hearing level (HL) (re: ANSI, 2004) at octave frequencies from 250 to 8000 Hz and reported no known history of chronic ear disease. None of the listeners had more than 2 years of musical training, with the exception of author JH (L121) who is a trained musician.

All listeners had previously participated in similar psychoacoustic experiments using multi-tonal maskers. Although few studies have systematically examined training effects for these conditions, the available data suggest that some individual listeners may improve over time (Neff and Callaghan, 1988; Neff and Dethlefs, 1995). The rationale for including listeners with previous experience using similar multi-tonal maskers is that evidence of training effects appears to be limited to approximately the first 600 trials (Neff and Callaghan, 1988).

B. Stimuli and conditions

The signal was a 300-ms, 1000-Hz sinusoid, including 5-ms onset/offset ramps (raised cosine). Twenty-five masker samples were randomly generated prior to the experiment and stored to disk. The same 25 masker samples were used for all listeners. Maskers were multi-tonal complexes with four sinusoidal components, presented simultaneously with the signal (when present) for 300 ms. Masker frequencies were drawn randomly from a uniform distribution on a linear frequency scale with a range of 300–3000 Hz, excluding 920–1080 Hz. The frequency range from 920 to 1080 Hz extends beyond the equivalent rectangular bandwidth centered on 1000 Hz (Glasberg and Moore, 1990). Masker start-

TABLE I. Component frequencies (Hz) and predicted masked thresholds (dB SPL) for the 25 masker samples based on Moore *et al.* (1997), ordered from lowest to highest predicted threshold. The subscripts indicate samples used in the *RanLow* and *RanHigh* conditions.

Masker sample	Masker components (Hz)				Predicted threshold (dB SPL)
	Frequency 1	Frequency 2	Frequency 3	Frequency 4	
16_{low}	311	1758	2246	2805	6.3
11_{low}	447	1870	2276	2716	6.3
12_{low}	308	411	1638	2350	6.3
24_{low}	512	521	1914	2430	8.2
7_{low}	464	468	605	1443	12.8
9	585	659	1372	1973	19.9
17	491	627	1320	2737	19.4
6	314	719	1440	2067	23.1
20	309	372	726	1446	23.7
4	413	474	479	1205	25.3
3	772	2348	2478	2586	27.4
21	312	343	465	1159	29.4
14	505	1140	1311	1728	32.1
25	448	826	2094	2961	32.6
18	489	826	1447	2573	33.6
8	717	1177	2142	2173	34.1
22	364	677	830	854	37.6
2	835	1236	1858	1989	37.7
19	704	1128	1214	1279	38.1
10	704	1110	1513	2069	39.4
5_{high}	787	836	877	2564	39.4
23_{high}	396	847	903	1560	41.3
13_{high}	348	884	1148	2920	44.1
1_{high}	511	919	1213	2675	44.8
15_{high}	344	867	1109	1868	45.0

ing phases were drawn from a uniform distribution with a range of $0-2\pi$. Each masker tone was equal amplitude, and the four-tone complex was presented at an overall level of 60 dB SPL (54 dB SPL per component). Table I shows the four frequencies that comprised each masker sample. The column on the right-hand side lists the corresponding Moore *et al.* (1997) model threshold predictions.

Stimuli were digitally summed and played through a 24-bit digital-to-analog converter (Digital Audio Labs, Chanhassen, MN) at a sampling rate of 20 kHz. Stimuli were presented monaurally to the listener's left ear via Sennheiser HD-25 earphones. The presentation of stimuli was controlled by a computer using custom software.

In *Fixed* conditions, a single masker sample was used on every presentation throughout a block of trials. All 25 samples were tested in separate conditions without any masker randomization. In two *Random* conditions, the masker presented in each interval was randomly selected with replacement from a subset of five masker samples. In the *RanLow* condition, the five samples with the lowest predicted thresholds comprised the pool of randomly selected maskers. In the *RanHigh* condition, the five samples with the highest predicted thresholds were used. Masker samples used in the *RanLow* and *RanHigh* conditions are indicated by the subscripts "low" and "high" in Table I, respectively.

C. Procedure

Thresholds were measured using a two-interval, forced-choice adaptive procedure that estimated 70.7% correct on the psychometric function (Levitt, 1971). The signal occurred in either interval with equal *a priori* probability. Each trial consisted of two, 300-ms observation intervals separated by a 400-ms interstimulus interval. A 300-ms feedback interval followed the listener's response, visually indicating the interval that contained the signal. The starting level of the adaptive track was 10–15 dB above the expected threshold. The initial step size was 4 dB, followed by a step size of 2 dB after the second reversal. Testing continued until ten reversals were obtained, and threshold was computed as the average signal level at the last eight reversals.

Listeners were tested individually in a double-walled, sound-treated room (Industrial Acoustics, Bronx, NY) in 1-h sessions that included regular breaks. An average of seven sessions per listener was required to complete the conditions. Four threshold estimates were obtained for each listener and condition. Listeners completed testing for the *Fixed* conditions prior to data collection for the *Random* conditions. For both *Fixed* and *Random* conditions, a complete randomized set of conditions was tested before moving to the next repetition of the conditions. Conditions were independently randomized for each listener. Data reported include threshold averages and estimates of the standard error (SE) across the four replications per condition.

III. RESULTS

A. Predicted thresholds using the Moore *et al.* (1997) excitation-based model of partial loudness

Thresholds in quiet for the 1000-Hz signal ranged from −7 to 17 dB SPL across listeners (average=2.9). Threshold for the 1000-Hz tone in the presence of each of the 25 masker samples was predicted using an excitation-based model of partial loudness (Moore *et al.*, 1997). The Moore *et al.* (1997) model is based on loudness as a function of frequency, taking into account changes in spread of excitation with level. This model was selected to generate threshold predictions based on the power spectrum of each masker. In applying the model, predicted thresholds were obtained by finding the level at which the partial loudness of the signal component was equal to 2 phons. Several investigators have shown that predictions generated using this general approach provide a reasonable account of observed masked thresholds across a range of masking paradigms (Van Der Heijden and Kohlrausch, 1994; Jesteadt *et al.*, 2007). Note, however, that this approach assumes that the long term power spectrum is the sole determinant of threshold, and that the temporal properties of the stimulus play no role in detection. Although there are counterexamples to these assumptions in the literature (e.g., Zwicker, 1976; Green, 1988; Moore and Glasberg, 1987; Richards, 1992; Richards and Nekrich, 1993), the degree of agreement between predicted and observed thresholds for the different masker conditions provides a framework within which to examine the contribution of peripheral excitation to differences in observed threshold across masker samples.

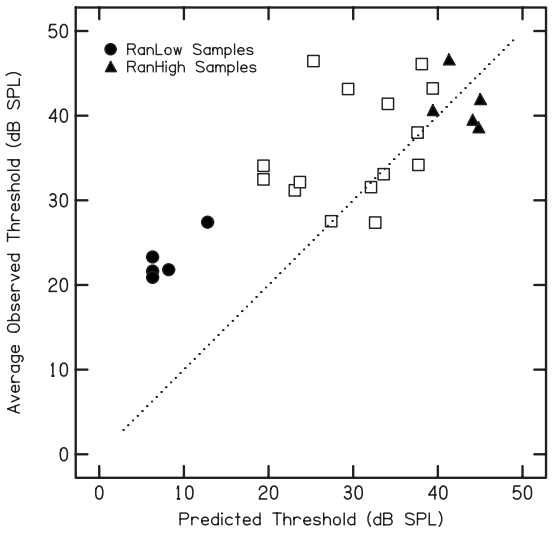

FIG. 1. Scatterplot of average observed threshold across listeners as a function of predicted threshold for the 25 masker samples. Filled symbols indicate data for samples used in the *RanLow* (circles) and *RanHigh* (triangles) conditions. Data on or near the dotted diagonal line indicate average observed thresholds that were well predicted by the model.

Thresholds predicted by the model for the 1000-Hz signal for the 25 masker samples are shown in Table I, rank ordered from lowest to highest predicted threshold. Despite the absence of masker components within 80 Hz of the signal frequency, predicted thresholds ranged from 6.3 to 45.0 dB SPL across masker samples. Predicted thresholds for *RanLow* maskers ranged from 6.3 to 12.8 dB SPL (mean =8.0), whereas predictions for *RanHigh* maskers ranged from 39.4 to 45.0 dB SPL (mean=42.9). Thus, the average difference in predicted threshold for *RanHigh* and *RanLow* conditions was approximately 35 dB. A relation between the proximity in frequency of the signal and neighboring masker tones is evident in Table I, with more masking for maskers with components closer to 1000 Hz.

B. Fixed conditions

Average masked thresholds across listeners for the 1000-Hz signal in the presence of each masker sample fixed across blocks are shown in Fig. 1, plotted as a function of predicted thresholds. Filled symbols indicate data for samples later used in the *RanLow* (circles) and *RanHigh* (triangles) conditions. Data on or near the dotted diagonal line indicate average observed thresholds that were well predicted by the model. Consistent with previous studies (e.g., Neff and Callaghan, 1987; Wright and Saberi, 1999), masker samples varied widely in masker effectiveness. Average masked thresholds ranged from 20.9 dB SPL (sample 11) to 46.6 dB SPL (sample 23), a range of approximately 26 dB. The preponderance of data above the dotted diagonal line in Fig. 1 indicates that threshold predictions based on excitation patterns often underestimated average observed thresholds. Nonetheless, there appears to be a relation between predicted and average observed thresholds.

Individual differences in the relationship between the predictions and the data were evident. Individual data for three listeners are shown in Fig. 2 to illustrate the range of results. No relation between the data and model predictions was found for L21 (R^2=0.19; $p>0.05$). In contrast, predicted thresholds for L121 accounted for half of the variance in observed thresholds (R^2=0.51; $p<0.01$). Finally, a strong relation between predicted and observed thresholds was observed for L99 (R^2=0.73; $p<0.01$).

Individual differences in masked threshold were more pronounced for some masker samples than for others. Figure 3 shows the difference between the observed and predicted thresholds for each masker sample and each listener, rank ordered by predicted threshold as in Table I. Data above the solid line indicate observed thresholds that were underpredicted by the model and data below the solid line indicate observed thresholds that were over-predicted by the model. Even without masker randomization, large individual differences in masked threshold were observed for many of the maskers, with thresholds spanning a range of up to 41 dB across listeners. Individual differences were most pronounced for samples predicted to produce little excitation-based masking. A Spearman's rank order correlation was computed to assess the relationship between predicted thresholds and the magnitude of individual differences, quantified as the standard deviation across threshold estimates. This correlation was −0.76 ($p<0.0001$), confirming that individual differences are greatest for masker samples with the lowest predicted thresholds. For example, the lowest predicted threshold (6.3 dB SPL) was found for masker samples 11, 12, and 16. Data-model differences as large as 35 dB were observed for these samples (L123). In contrast, the highest predicted threshold (45 dB SPL) was associated with

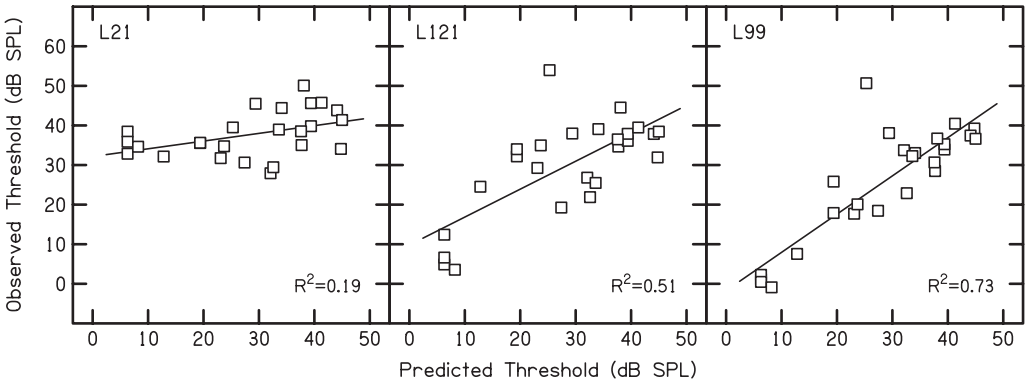

FIG. 2. Scatterplots of observed threshold as a function of predicted threshold for the 25 masker samples for three listeners (L21, L121, and L99). The solid line represents the best least-squares fit to all data points for each of the three listeners.

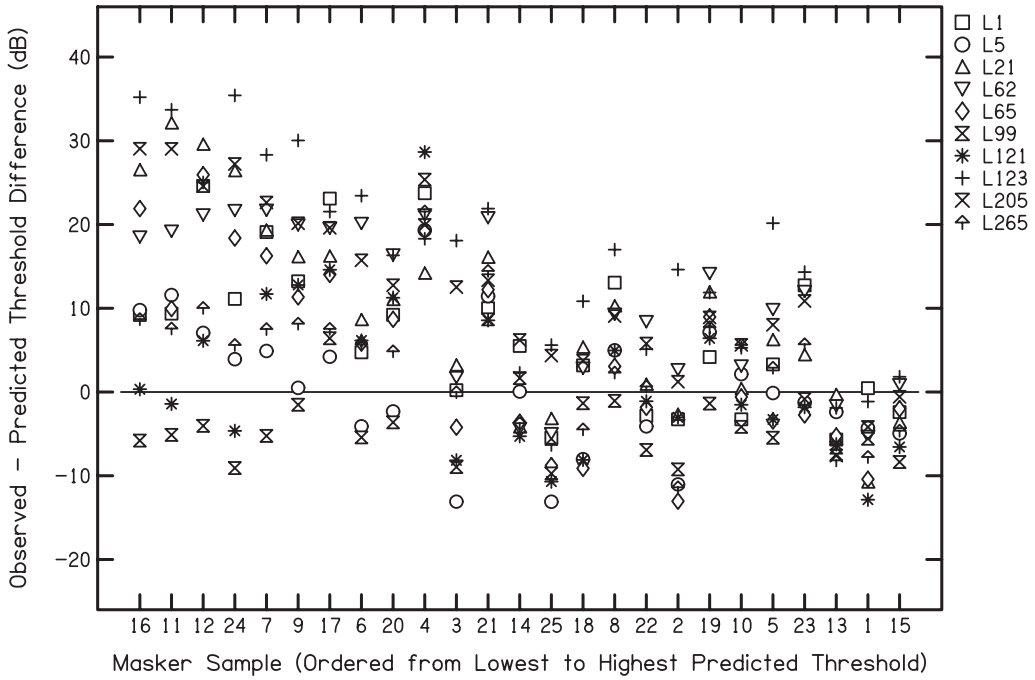

FIG. 3. Difference between observed and predicted thresholds as a function of masker sample for all listeners, ordered from lowest to highest predicted threshold. Data at or above the solid line indicate observed thresholds that were higher than the model predictions.

masker sample 15. The largest discrepancy between the data and model for any listener for this masker sample was −8 dB (L99).

Note that no evidence of significant practice effects was observed in the data. The average improvement in masked threshold across the first and fourth blocks of trials ranged from 0 to 6 dB across listeners (mean=2.5 dB). A within-subjects linear regression of threshold as a function of block number indicated no significant improvement in threshold with increasing block number [$F(1,99)=1.2$; $p=0.3$].

C. Random conditions

The effect of masker-frequency uncertainty was estimated by comparing thresholds obtained when each masker sample was presented alone for a block of trials to thresholds obtained when the masker samples were drawn randomly on each presentation from the pool of five samples within each block. Figure 4 presents individual masked thresholds and the average across listeners, with listeners ordered on the abscissa by thresholds in the *FixLow* condition. Open circles

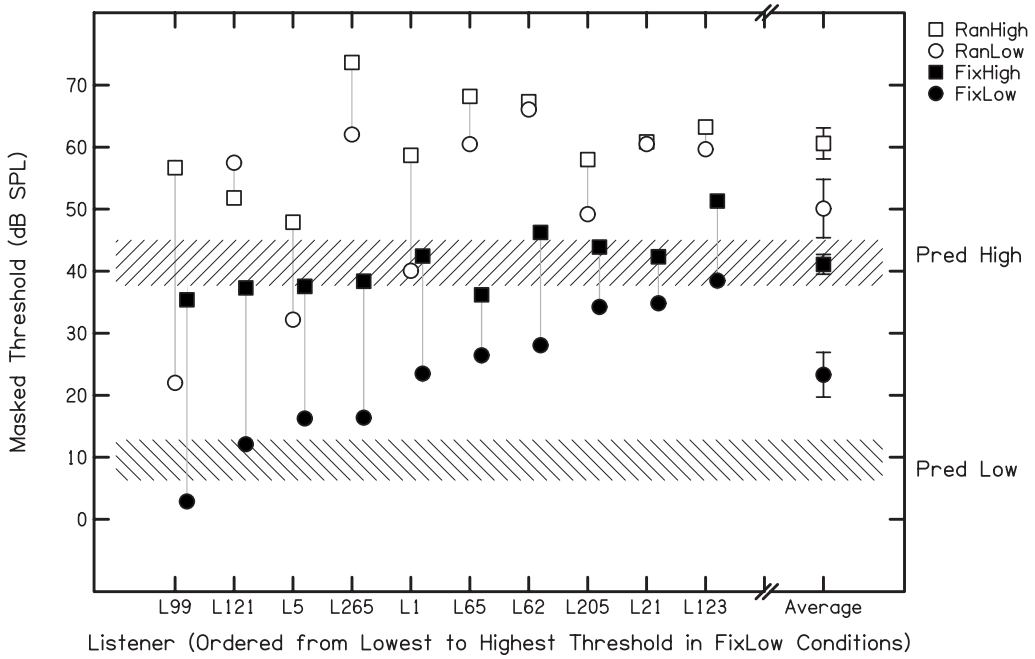

FIG. 4. Masked thresholds are plotted for individual listeners and for the average across listeners (with SEs) for *RanLow* (open circles) and *RanHigh* (open squares) conditions. Filled circles and squares show the average thresholds obtained in the fixed-presentation conditions across the five samples used for *RanLow* and *RanHigh*, respectively. The ranges of predicted thresholds for the five samples used for the *RanLow* and those for the *RanHigh* conditions are indicated with hatched shading.

and squares indicate *RanLow* and *RanHigh* conditions, respectively. Filled circles and squares indicate thresholds obtained in the associated fixed-presentation conditions. Error bars represent ±1 SE for the average data. The gray vertical lines emphasize the difference in threshold between conditions with low and high predicted thresholds for both random and fixed presentations. The ranges of masked thresholds predicted by the Moore *et al.* (1997) model for the five samples used for the *RanLow* samples and five *RanHigh* samples are shown by the hatched areas. Thus, the degree to which the data fall within these ranges provides an indication of whether or not the model provides a good account of observed thresholds.

Figure 4 clearly shows that the excitation-based model does not successfully predict the data for either random condition for any listener. Moreover, the estimated threshold for L121 in the *RanLow* condition is higher than in the *RanHigh* condition, offering the most serious violation of the model. Consistent with earlier reports (e.g., Neff and Callaghan, 1987; Wright and Saberi, 1999; Durlach *et al.*, 2005), however, masker-frequency uncertainty increased masked thresholds for all ten listeners. Thresholds were always higher for the *Random* conditions, even with only five samples randomly selected across presentations, than for the corresponding *Fixed* conditions. For data averaged across listeners, the threshold in the *RanLow* condition was 27.6 dB higher than the corresponding *FixLow* conditions (compare circles in Fig. 4). Similarly, the average threshold in the *RanHigh* condition was 19.5 dB higher than that for the *FixHigh* conditions (compare squares in Fig. 4). Note that for every listener the *RanLow* threshold was higher than the worst single *FixLow* threshold. Similarly, the *RanHigh* threshold was higher than the worst single *FixHigh* threshold. A two-way, repeated-measures analysis-of-variance, with two main factors of Uncertainty (random versus fixed) and Predicted Masking (low versus high), indicated a significant effect of Uncertainty [$F(1,9)=66.3$; $p<0.0001$]. The main effect of Predicted Masking was significant [$F(1,9)=25.8$; $p<0.01$], with higher observed thresholds for masker samples with high predicted thresholds compared to low predicted thresholds. The Uncertainty × Predicted Masking interaction was also significant [$F(1,9)=6.9$; $p<0.05$], indicating that the difference in performance for samples with low versus high predicted thresholds was smaller when masker samples were randomly interleaved on an interval-by-interval basis compared to fixed throughout a block of trials. That is, the extent to which listeners failed to achieve excitation-based threshold predictions was greatest when predicted thresholds were low.[1]

IV. DISCUSSION

A. Masking in the absence of masker-spectral uncertainty (*Fixed* conditions)

The present results demonstrated a wide range of thresholds across the 25 masker samples when the same masker sample was used on every presentation throughout trial blocks. Frequency components comprising the masker samples were excluded from falling within a 160-Hz region centered on the 1000-Hz signal. Nonetheless, average thresholds across listeners differed by as much as 26 dB across masker samples. As outlined in the Introduction, substantial differences in masked threshold across fixed-frequency multi-tonal masker samples have previously been reported in the literature (e.g., Neff and Callaghan, 1987; Wright and Saberi, 1999). The variability in masked thresholds observed in the present and earlier studies may reflect, in part, differences in peripheral excitation across masker samples. For example, sample 11 used in the current study was comprised of one tone more than an octave below the signal frequency (447 Hz) and three tones 800-Hz or more above the signal frequency (1870, 2276, and 2716 Hz). Both the predicted (6.3 dB SPL) and average observed (20.9 dB SPL) thresholds were lowest for this sample. In contrast, higher predicted (45 dB SPL) and average observed (41.9 dB SPL) thresholds were found for sample 15. Two of the four tones comprising this sample were close in frequency and flanked the 1000-Hz signal (867 and 1109 Hz).

Differences in predicted peripheral excitation across masker samples were systematically examined by computing thresholds for the 1000-Hz signal in the presence of each of the 25 samples using the excitation-pattern model of partial loudness proposed by Moore *et al.* (1997). Similar to observed thresholds, predicted thresholds differed widely across masker samples (range=6.3–45.0 dB SPL). Moreover, the model predicted a significant portion of the variance in the average observed thresholds for several listeners. These observations are inconsistent with the assumption that sparsely sampled multi-tonal maskers with a spectral gap centered on the signal frequency produce minimal energy-based masking. Instead, the variability in threshold across samples may reflect significant contributions from peripheral auditory processes.

It is difficult, however, to provide a complete account of listeners' thresholds in terms of differences in peripheral excitation patterns across the 25 masker samples. Average thresholds for some samples were not well predicted by the model. Whereas the model and data were in good agreement for samples with high predicted thresholds, the model tended to underestimate performance for samples with low predicted thresholds. This pattern of results suggests substantial contributions of informational masking for at least some fixed-frequency masker samples. In particular, informational masking appears to be largest for conditions in which effects of excitation-based masking are smallest.

The current results extend those of developmental studies showing remote-frequency masking under conditions of minimal stimulus uncertainty during infancy (Werner and Bargones, 1991; Leibold and Werner, 2006) and childhood (Leibold and Neff, 2007). For example, the presence of two, fixed-frequency tones remote from the signal frequency can produce significant amounts of informational masking of a 1000-Hz signal for infants and most children (Leibold and Werner, 2006; Leibold and Neff, 2007). Note also that several adults tested as control subjects in each of the developmental studies appeared to be susceptible to some degree of informational masking without masker-frequency uncertainty.

The presence of large individual differences, on the order of 40 dB for some masker samples, is also atypical of masking produced by peripheral mechanisms. Moreover, these individual differences do not appear to reflect listening strategies that can be improved with practice. Despite thousands of intervening trials, limited improvements in performance across listeners or across masker samples were observed between the first and fourth blocks of trials. The large individual differences and resistance to training suggest contributions of informational masking for at least the poorer performers (e.g., Neff and Dethlefs, 1995). Inconsistency across listeners in masking effectiveness for particular multi-tonal samples fixed across presentations has been noted in previous studies (Neff and Callaghan, 1987; Wright and Saberi, 1999; Alexander and Lutfi, 2004; Durlach *et al.*, 2005; Leibold and Neff, 2007). For example, Neff and Callaghan (1987) measured thresholds for a 1000-Hz tone in each of 50, ten-tone masker samples fixed across a block of trials. Maskers were then ranked in terms of effectiveness, and the top and bottom 10 selected in terms of amount of masking for each listener. There were four samples even at these extremes of the distributions that fell in the top category for one listener but the bottom for another.

The wide range of thresholds across listeners, most pronounced for samples with low predicted masking, suggests that listeners may have adopted different strategies to perform the detection task. Alternatively, all listeners may be pursuing the same strategy but with different degrees of success. A subset of listeners appeared limited in their ability to resolve the signal from the masker at the level of the auditory periphery. Observed thresholds for these listeners closely followed the model predictions. For example, L99 (see Fig. 2) used an effective strategy resulting in little evidence of informational masking for *Fixed* conditions. In contrast, other listeners appeared to adopt a non-optimal strategy for the detection task. These listeners showed relatively large discrepancies between the model and the data for some masker samples. For example, no relation between the model and data was found for L21. Observed thresholds exceeded predictions by as much as 30 dB for this listener (Fig. 2). As with the average data, differences between the model and data for L21 were largest for samples with low predicted thresholds.

Neff *et al.* (1993) suggested that the large range in performance across listeners with random-frequency multi-tonal maskers may be indicative of individual differences in the ability to listen "analytically." In the context of the current study, analytic listening refers to the extent to which listeners attended to the 1000-Hz target signal and ignored information at masker frequencies. Whereas listeners with little or no informational masking are described as analytic, listeners with substantial informational masking are described as holistic or synthetic listeners. Presumably, holistic listeners integrate information across frequency even though it is disadvantageous to do so. Several researchers have applied quantitative methods to evaluate these apparent individual differences in listening strategies with random-frequency maskers (e.g., Neff *et al.*, 1993; Lutfi, 1993; Richards *et al.*, 2002; Alexander and Lutfi, 2004; Durlach *et al.*, 2005). The most comprehensive model to date is the component-relative entropy (CoRE) model proposed by Lutfi (1993). Similar to models of energy detection, the CoRE model assumes that detection is based on the output of energy at the auditory filter centered on the signal frequency. The CoRE model differs from traditional energy-detection models, however, because it considers potential contributions from auditory filters that do not contain information about the presence of the signal. Using this model, Lutfi and colleagues observed a relation between amount of informational masking and both the number and frequency range of monitored filters (e.g., Lutfi, 1993; Alexander and Lutfi, 2004).

In a related approach, listeners' decision weights for the detection task are compared to weights of an ideal observer (e.g., Berg, 1989; Lutfi, 1995; Richards and Zhu, 1994). For detection of a fixed-frequency pure tone in the presence of a random-frequency masker, an ideal observer assigns weight exclusively to the output of auditory filters representing the signal. No weight is assigned to auditory filter outputs dominated by masker stimuli. Results from studies using this approach have shown that low-threshold listeners have weighting functions that more closely approximate those of an ideal listener, whereas high-threshold listeners assign significant weight to masker components (e.g., Alexander and Lutfi, 2004; Richards *et al.*, 2002). In addition, a significant negative relation between weighting efficiency and amount of informational masking has been observed (e.g., Alexander and Lutfi, 2004). These results are consistent with the idea that the individual differences in informational masking observed for random-frequency maskers reflect perceptual differences in analytic listening strategies.

Similar differences in the ability to listen analytically might be responsible for the wide range of thresholds observed across listeners for the current *Fixed* conditions. To examine individual listening strategies, an "attentional-filter" analysis was performed following the general approach described by Neff *et al.* (1993). Neff *et al.* (1993) compared thresholds for a 1000-Hz tone embedded in a random-frequency, multi-tonal masker while parametrically varying the width of the protected region around the 1000-Hz signal. Four of eight listeners showed substantial informational masking even for conditions with large spectral gaps in the maskers. In contrast, much smaller effects of masking were observed for the remaining four listeners across all conditions. Although notched-noise measures of auditory filter width (Patterson *et al.*, 1982) were similar across the two groups, high-threshold listeners had wider attentional filters and poorer estimates of processing efficiency compared to low-threshold listeners. That is, the listeners most susceptible to informational masking appeared to be unable to ignore the irrelevant masker energy.

Attentional filters were fitted to individual listeners' data in *Fixed* conditions following methods similar to those of Neff *et al.* (1993). The filter was defined as a two-parameter rounded-exponential (roex) model,

$$W(g) = (1 - r)(1 + pg)e^{-pg} + r,$$

where p defines the width of the filter, r is the dynamic range, and g is the frequency offset relative to the filter cen-

TABLE II. Results of fitting "attentional filters" with the roex model (see text) for individual listeners' data in *Fixed* conditions. Listeners are ordered based on lowest to highest mean threshold in the five *FixLow* conditions, as in Fig. 4.

Listener	p	r (dB)	K (dB)	VAC
L99	26.34	−49.19	−10.62	0.83
L121	16.73	−43.79	−14.19	0.63
L5	30.24	−36.91	−7.37	0.71
L265	19.98	−35.10	−10.80	0.73
L1	12.34	−51.72	−12.58	0.59
L65	6.81	−50.60	−20.50	0.34
L62	10.79	−31.66	−10.50	0.53
L205	11.30	−15.80	−10.82	0.55
L21	16.46	−14.27	−11.95	0.29
L123	9.80	−14.98	−7.21	0.27

ter frequency, defined as a ratio. An additional variable specifies the signal-to-noise ratio at the output of the filter that is associated with threshold. This value, described as efficiency (K), is assumed to be constant across frequency. In this analysis the spectra of the 25 masker samples were weighted in power by function W, and a separate least-squares fit was made to each individuals' *Fixed* masker thresholds. Resulting parameter estimates are reported in Table II, along with the percentage of variance accounted for by each fit. Data for each listener appear in a separate row, and listeners are ordered according to the averaged threshold in the five *FixLow* conditions, as in Fig. 4. There was a significant correlation between this rank ordering and estimates of both p and r ($p<0.05$), with better sensitivity being associated with narrower frequency resolution (larger values of p) and wider dynamic range (smaller values of r). There was a nonsignificant association between rank order based on sensitivity and K ($r=0.11$, $p=0.77$).

Contrary to the results for the subjects in Neff *et al.* (1993), these results on attentional filters indicate that individual differences for listeners in the present study can primarily be attributed to differential frequency selectivity rather than efficiency. What remains unclear, however, is to what extent these individual differences in filter width estimates reflect differences in frequency selectivity at peripheral or central levels within the auditory system. One interpretation of these results is that true individual differences in peripheral filtering are considerably larger than previously estimated using traditional notched-noise measures of auditory filter width (Patterson *et al.*, 1982). Alternatively, the magnitude of estimates for some listeners may suggest that these differences reflect "attentional" filtering at more central levels within the auditory system. Future studies are required to systematically examine the mechanisms responsible for these individual differences.

One approach that might be used to disentangle contributions of peripheral and central processes is to introduce an acoustic cue that has been shown to provide a substantial release from informational masking produced by random-frequency multi-tonal maskers and examine whether thresholds improve for listeners with relatively high thresholds in the *Fixed* conditions. We used this general approach to examine performance for one listener (L205) who exhibited relatively high thresholds for masker samples predicted to produce low levels of excitation-based masking. Following Neff (1995), a temporal cue believed to promote sound source segregation and reduce informational masking was provided. Masker duration was increased to 400 ms, resulting in a 100-ms masker fringe preceding the 300-ms signal; stimulus component starting phase was adjusted in the fringe conditions so that the 300-ms listening interval was identical in conditions with and without the preceding 100-ms fringe. If central, rather than peripheral, filtering underlies this listener's poor performance with masker samples predicted to produce minimal energetic masking, introducing this temporal fringe cue should produce large reductions in threshold. Thresholds were collected for L205 with the masker fringe for the five masker samples with the lowest predicted energetic masking (samples 16, 11, 12, 24, and 7), with conditions completed in random order. Mean threshold without fringe was 34.5 dB SPL (range=30.9–35.4 dB SPL), similar to *Fixed* thresholds for these maskers and this listener in the main experiment. In contrast, mean threshold with the temporal fringe was 15.2 dB SPL (range=10.9–23.3 dB SPL). Thus, temporal fringe reduced thresholds by 18.4 dB, consistent with a substantial effect of informational masking in the *Fixed* conditions for masker samples with low predicted thresholds in the main data set.

B. Effects of masker-spectral uncertainty (*Random* conditions)

Previous studies have established that randomizing masker spectra for multi-component maskers can produce substantial informational masking for many listeners (e.g., Neff and Dethlefs, 1995). The current observation that masked thresholds were elevated for *Random* relative to the corresponding *Fixed* conditions is in agreement with this earlier work. External stimulus uncertainty was not required, however, to produce informational masking for many listeners. Thresholds were higher for all listeners when one of five masker samples was randomly selected on each presentation (*Random* conditions) compared to thresholds for the same samples fixed on every presentation throughout trial blocks (*Fixed* conditions). Of particular interest, even listeners with little evidence of informational masking for *Fixed* conditions appeared to be susceptible to informational masking when masker-frequency uncertainty was introduced. For example, threshold for L99 was approximately 14-dB higher in the *RanLow* condition compared to this listener's highest threshold (sample 7) for the same samples presented in the *Fixed* conditions.

Differences in the stimuli used in the current and previous works limit comparisons of the effect of masker-frequency uncertainty across studies. Masker-frequency uncertainty is often produced by drawing component frequencies completely at random from a specified frequency range (e.g., Neff and Green, 1987). In the current *Random* conditions, the masker presented in each interval was randomly selected from a subset of five masker samples. Thus, listeners may have relied on their memory of the five

samples used for each *Random* condition and/or used a different decision strategy than if maskers had been drawn from a larger or completely random set. Data from Richards *et al.* (2002), however, suggest that listeners adopt consistent strategies for small and large sets of masker samples. Richards *et al.* (2002) examined measured detection thresholds for a 1000-Hz tone in the presence of a random-frequency, six-tone masker. The pool of masker samples was varied across conditions, resulting in masker set sizes ranging from 3 to 24. Performance was also assessed for a completely random masker set. The results were interpreted as showing that many listeners remembered individual masker samples, even when the set size was 24. However, there was no evidence that listeners changed their decision strategy as the masker set size was increased.

It is generally accepted that some portion of the masking produced by random-frequency multi-tonal maskers is informational in that it appears to arise from mechanisms other than those modeled by energy detection in peripheral auditory filters centered at the signal frequency. Effects of masker-frequency uncertainty appear to be greater, however, when samples with low compared to high predicted masking were randomly selected on each presentation. The mechanisms responsible for this apparent difference in the effect of masker-frequency uncertainty are not understood. One possible explanation is that strategies based on frequency-specific cues support the best sensitivity, though the success of these strategies differs across listeners and across masker samples. In cases where frequency-specific detection cues are not used effectively, listeners might rely on differences in overall loudness across the two intervals at higher signal levels, effectively placing an upper limit on thresholds. Note that a strategy based on overall loudness does not require perceptual segregation of the signal and masker.

C. Implications of the present results for understanding informational masking

The majority of results reported here are not unique to the current study. For example, a number of previous studies have compared performance across fixed- and random-frequency multi-tonal maskers (e.g., Neff and Callaghan, 1988; Neff and Dethlefs, 1995; Wright and Saberi, 1999; Alexander and Lutfi, 2004; Richards and Neff, 2004; Durlach *et al.*, 2005; Leibold and Neff, 2007). Similarly, previous investigations have provided estimates of the amount of energetic masking that might be expected for given multi-tonal masker samples (e.g., Lutfi, 1993; Durlach *et al.*, 2005) and the effects of energetic masking on magnitude of informational masking associated with stimulus frequency uncertainty (Neff *et al.*, 1993). The novel approach used in the current study was to examine contributions of peripheral excitation and informational masking to the variability in masking effectiveness in *Fixed* conditions observed across samples of multi-tonal maskers using a combination of these previously reported approaches.

A common metric for determining informational masking related to masker-frequency uncertainty is the difference in performance between conditions using random-frequency multi-tonal maskers and either quiet thresholds or thresholds in conditions using equal power, broadband-noise maskers. We have recently argued, however, that a multi-tonal masker sample should be used as a reference condition to estimate the contribution of masker-frequency variability to informational masking (Leibold and Werner, 2006; Leibold and Neff, 2007). In this approach, the fixed-frequency multi-tonal masker sample is matched to the random-frequency multi-tonal masker in as many aspects as possible except spectral variability, as in the minimal-uncertainty conditions first described by Watson *et al.* (1976). The present data indicate that estimates of informational masking based on comparison across fixed and random masker conditions depend critically on selecting conditions with comparable energetic masking. Data based on stimuli with low predicted thresholds would result in large estimates of variability-based masking, whereas stimuli with high predicted thresholds would result in small estimates of variability-based masking.

The observation of informational masking in the absence of stimulus uncertainty complicates efforts to define informational masking. Informational masking is often defined as masking that occurs in excess of energetic masking. As Kidd *et al.* (2008) stated, "…it would be helpful in attempting to quantify informational masking if there were a precise model of energetic masking that could accurately predict performance for a wide range of stimuli or a measurement procedure in which one could be certain that only energetic masking was present" (p. 145). The Moore *et al.* (1997) model provides a useful framework for conditions with simultaneous multi-tonal maskers, providing estimates of masked threshold based on excitation patterns (e.g., Jesteadt *et al.*, 2007). Applying this framework to the current data for *Fixed* conditions indicates contributions of both energetic and informational masking to the masking produced by four-tone masker samples for many listeners despite the absence of external stimulus uncertainty. In addition, the relatively close correspondence between threshold predictions and behavioral thresholds from the best-performing listener (L99) lends some credibility to this model of energetic masking for these stimuli. The current data are consistent with Durlach *et al.* (2003) who argued that stimulus variability is not required to produce informational masking, but that informational masking may also be determined by the degree of similarity between the signal and the masker.

V. SUMMARY AND CONCLUSIONS

Consistent with previous studies (e.g., Neff and Callaghan, 1987; Wright and Saberi, 1999), individual masker samples varied widely in masking effectiveness. Average thresholds in conditions in which particular samples were fixed across blocks differed by as much as 26 dB across masker samples.

There were marked individual differences in masked threshold, on the order of 40 dB for some fixed samples. Observed thresholds also differed substantially from predicted thresholds in some cases. This model-data discrepancy was most pronounced for samples with low predicted thresholds.

When masker samples were randomly selected on a trial-by-trial basis, the difference in performance for samples with low versus high predicted thresholds was reduced.

The mechanisms responsible for the individual differences in performance across listeners for specific masker samples require further investigation. Masking remains an operational definition with multiple contributing mechanisms even for stimuli and conditions in which sensitivity is often assumed to be limited by peripheral mechanisms. The current results are consistent with the view that informational masking can be affected by multiple factors, including stimulus uncertainty and availability of cues aiding sound segregation for signals and maskers.

ACKNOWLEDGMENTS

This work was supported by NIH NIDCD Grant Nos. R03 DC008389 and R01 DC007391. We thank Walt Jesteadt and Hongyang Tan for use of custom programs. Brian Glasberg and Brian Moore have generously made their software openly available.

[1]There was no difference in the basic form of the data or conclusions drawn when amount of masking was analyzed instead of masked thresholds.

Alexander, J. M., and Lutfi, R. A. (**2004**). "Informational masking in hearing-impaired and normal-hearing listeners: Sensation level and decision weights," J. Acoust. Soc. Am. **116**, 2234–2247.

ANSI (**2004**). ANSI S 3.6-2004, "American national standard specification for audiometers" (American National Standards Institute, New York).

Berg, B. G. (**1989**). "Analysis of weights in multiple observation tasks," J. Acoust. Soc. Am. **86**, 1743–1746.

Bregman, A. S. (**1990**). *Auditory Scene Analysis* (MIT Press, Cambridge, MA).

Durlach, N. I., Mason, C. R., Gallun, F. J., Shinn-Cunningham, B., Colburn, H. S., and Kidd, G., Jr. (**2005**). "Informational masking for simultaneous nonspeech stimuli: Psychometric functions for fixed and randomly mixed maskers," J. Acoust. Soc. Am. **118**, 2482–2497.

Durlach, N. I., Mason, C. R., Shinn-Cunningham, B. G., Arbogast, T. L., Colburn, H. S., and Kidd, G., Jr. (**2003**). "Informational masking: Counteracting the effects of stimulus uncertainty by decreasing target-masker similarity," J. Acoust. Soc. Am. **114**, 368–379.

Glasberg, B. R., and Moore, B. C. J. (**1990**). "Derivation of auditory filter shapes from notched-noise data," Hear. Res. **47**, 103–138.

Green, D. M. (**1988**). *Profile Analysis* (Oxford University Press, Oxford).

Jesteadt, W., Khaddam, S., Tan, H., and Leibold, L. J. (**2007**). *Prediction of Behavioral Thresholds Using a Model of Partial Loudness*, in Abstracts of the 30th Annual MidWinter Research Meeting of the Association for Research in Otolaryngology. Abstract No. 936.

Kidd, G., Jr., Mason, C. R., and Arbogast, T. L. (**2002**). "Similarity, uncertainty, and masking in the identification of nonspeech auditory patterns," J. Acoust. Soc. Am. **111**, 1367–1376.

Kidd, G., Jr., Mason, C. R., Deliwala, P. S., Woods, W. S., and Colburn, H. S. (**1994**). "Reducing informational masking by sound segregation," J. Acoust. Soc. Am. **95**, 3475–3480.

Kidd, G., Jr., Mason, C. R., Richards, V. M., Gallun, F. J., and Durlach, N. I. (**2008**). "Informational masking," in *Auditory Perception of Sound Sources*, edited by W. A. Yost, A. N. Popper, and R. R. Fay (Springer, New York), pp. 143–190.

Leibold, L. J., and Neff, D. L. (**2007**). "Effects of masker-spectral variability and masker fringes in children and adults," J. Acoust. Soc. Am. **121**, 3666–3676.

Leibold, L. J., and Werner, L. A. (**2006**). "Effect of masker-frequency variability on the detection performance of infants and adults," J. Acoust. Soc. Am. **119**, 3960–3970.

Levitt, H. (**1971**). "Transformed up-down methods in psychoacoustics," J. Acoust. Soc. Am. **49**, 467–477.

Lutfi, R. A. (**1993**). "A model of auditory pattern analysis based on component-relative-entropy," J. Acoust. Soc. Am. **94**, 748–758.

Lutfi, R. A. (**1995**). "Correlation coefficients and correlation ratios as estimates of observer weights in multiple-observation tasks," J. Acoust. Soc. Am. **97**, 1333–1334.

Lutfi, R. A., Kistler, D. J., Oh, E. L., Wightman, F. L., and Callahan, M. R. (**2003**). "One factor underlies individual differences in auditory informational masking within and across age groups," Percept. Psychophys. **65**, 396–406.

Moore, B. C. J., and Glasberg, B. R. (**1987**). "Factors affecting thresholds for sinusoidal signals in narrow-band maskers with fluctuating envelopes," J. Acoust. Soc. Am. **82**, 69–79.

Moore, B. C. J., Glasberg, B. R., and Baer, T. (**1997**). "A model for the prediction of thresholds, loudness, and partial loudness," J. Audio Eng. Soc. **45**, 224–237.

Neff, D. L. (**1995**). "Signal properties that reduce masking by simultaneous, random-frequency maskers," J. Acoust. Soc. Am. **98**, 1909–1920.

Neff, D. L., and Callaghan, B. P. (**1987**). "Psychometric functions for multicomponent maskers with spectral uncertainty," J. Acoust. Soc. Am. **81**, S53.

Neff, D. L., and Callaghan, B. P. (**1988**). "Effective properties of multicomponent simultaneous maskers under conditions of uncertainty," J. Acoust. Soc. Am. **83**, 1833–1838.

Neff, D. L., and Dethlefs, T. M. (**1995**). "Individual differences in simultaneous masking with random-frequency, multicomponent maskers," J. Acoust. Soc. Am. **98**, 125–134.

Neff, D. L., Dethlefs, T. M., and Jesteadt, W. (**1993**). "Informational masking for multicomponent maskers with spectral gaps," J. Acoust. Soc. Am. **94**, 3112–3126.

Neff, D. L., and Green, D. M. (**1987**). "Masking produced by spectral uncertainty with multicomponent maskers," Percept. Psychophys. **41**, 409–415.

Oh, E. L., and Lutfi, R. A. (**1998**). "Nonmonotonicity of informational masking," J. Acoust. Soc. Am. **104**, 3489–3499.

Patterson, R. D., Nimmo-Smith, I., Weber, D. L., and Milroy, R. (**1982**). "The deterioration of hearing with age: Frequency selectivity, the critical ration, the audiogram, and speech threshold," J. Acoust. Soc. Am. **72**, 1788–1803.

Richards, V. M. (**1992**). "The detectability of a tone added to narrow bands of equal-energy noise," J. Acoust. Soc. Am. **91**, 3424–3435.

Richards, V. M., and Neff, D. L. (**2004**). "Cuing effects for informational masking," J. Acoust. Soc. Am. **115**, 289–300.

Richards, V. M., and Nekrich, R. D. (**1993**). "The incorporation of level and level-invariant cues for the detection of a tone added to noise," J. Acoust. Soc. Am. **94**, 2560–2574.

Richards, V. M., Tang, Z., and Kidd, G. D., Jr. (**2002**). "Informational masking with small set sizes," J. Acoust. Soc. Am. **111**, 1359–1366.

Richards, V. M., and Zhu, S. (**1994**). "Relative estimates of combination weights, decision criteria, and internal noise based on correlation coefficients," J. Acoust. Soc. Am. **95**, 423–434.

Spiegel, M. F., Picardi, M. C., and Green, D. M. (**1981**). "Signal and masker uncertainty in intensity discrimination," J. Acoust. Soc. Am. **70**, 1015–1019.

Van Der Heijden, M., and Kohlrausch, A. (**1994**). "Using an excitation-pattern model to predict auditory masking," Hear. Res. **80**, 38–52.

Watson, C. S., Kelly, W. J., and Wroton, H. W. (**1976**). "Factors in the discrimination of tonal patterns. II. Selective attention and learning under various levels of stimulus uncertainty," J. Acoust. Soc. Am. **60**, 1176–1186.

Watson, C. S., Wroton, H. W., Kelly, W. J., and Benbassat, C. A. (**1975**). "Factors in the discrimination of tonal patterns. I. Component frequency, temporal position, and silent intervals," J. Acoust. Soc. Am. **57**, 1175–1185.

Werner, L. A., and Bargones, J. Y. (**1991**). "Sources of auditory masking in infants: Distraction effects," Percept. Psychophys. **50**, 405–412.

Wright, B. A., and Saberi, K. (**1999**). "Strategies used to detect auditory signals in small sets of random maskers," J. Acoust. Soc. Am. **105**, 1765–1775.

Zwicker, E. (**1976**). "Masking-period patterns of harmonic complex tones," J. Acoust. Soc. Am. **59**, 166–175.

The origin of binaural interaction in the modulation domain

Aleksander Sek, Brian R. Glasberg, and Brian C. J. Moore[a)]
Department of Experimental Psychology, University of Cambridge, Downing Street, Cambridge CB2 3EB, England

(Received 17 September 2008; revised 15 January 2010; accepted 26 January 2010)

The purpose of these experiments was to assess whether the detection of diotic 5 Hz "probe" modulation of a 4000 Hz sinusoidal carrier was influenced by binaural interaction of "masker" modulators presented separately to each ear and applied to the same carrier. A 50 Hz masker modulator was applied to one ear and the masker modulator applied to the other ear had a frequency of 55 or 27.5 Hz. The starting phase of the masker modulators was fixed, and the starting phase of the probe modulator was varied. For both pairs of masker modulators, the threshold for detecting the probe modulation varied slightly but significantly with probe starting phase. Further experiments measuring probe detectability as a function of probe modulation depth did not provide clear evidence to support the idea that the internal representations of the masker modulators interacted binaurally to produce a weak distortion component in the internal representation of the modulation at a 5 Hz frequency. Also, the obtained phase effects were not correctly predicted using a model based on short-term loudness fluctuations. © *2010 Acoustical Society of America.*
[DOI: 10.1121/1.3327798]

PACS number(s): 43.66.Dc, 43.66.Mk, 43.66.Nm, 43.66.Ba [RLF] Pages: 2451–2460

I. INTRODUCTION

Several recent models for the perception of amplitude modulation (AM) in sounds are based on the idea that the envelopes of the outputs of the (peripheral) auditory filters are fed to a second array of overlapping bandpass filters tuned to different envelope modulation frequencies (Kay, 1982; Martens, 1982; Dau *et al.*, 1997a, 1997b; Ewert and Dau, 2000; Ewert *et al.*, 2002; Verhey *et al.*, 2003). This set of filters is usually called a "modulation filter bank" (MFB). Psychoacoustical evidence consistent with the concept of a MFB has come from experiments involving detection of "probe" modulation in the presence of masker modulation; these experiments appear to show frequency selectivity in the modulation domain (Bacon and Grantham, 1989; Houtgast, 1989; Ewert *et al.*, 2002). Also, listeners appear to have some ability to "hear out" the sinusoidal components of a complex modulator, provided that the components are widely spaced in frequency (Sek and Moore, 2003, 2006). The present experiments are concerned with binaural interactions in the modulation domain, and specifically whether such interactions are influenced by modulation distortion products.

Several lines of evidence suggest that human listeners are sensitive to the interaural phase of the envelope of amplitude-modulated sounds for modulation frequencies up to several hundred hertz. First, sounds can be lateralized based on the interaural envelope delay, for envelope rates up to at least 400 Hz (Henning, 1974; Nuetzel and Hafter, 1981). Second, McFadden and Pasanen (1975) described an analog of binaural beats (Licklider *et al.*, 1950) in the modulation domain. They presented a high-frequency two-tone complex to each ear. Each complex produced beats at a rate equal to the frequency difference between the two tones. Subjects were required to distinguish between two stimuli. In one, the beat rate was the same at the two ears (e.g., 50 Hz). In the other, the beat rate was chosen to be slightly different in the two ears (e.g., 50 Hz in one ear and 51 Hz in the other). When the difference in beat rate between the two ears was relatively small (5 Hz or less), subjects performed well above chance on this task. Subjects reported hearing a fluctuation at a rate corresponding to the difference in beat rate between the two ears: 1 Hz in the example given above. The effect occurred at low levels, or in the presence of an intense low-pass noise, so combination tones cannot account for the effect. McFadden and Pasanen (1975) also found that the carrier frequencies in the two ears did not have to be very close. For example, sinewaves of 2000 and 2050 Hz in one ear and 3000 and 3051 Hz in the other led to a beat sensation with a 1 Hz rate. They concluded that "the auditory system is apparently able to extract envelope periodicities monaurally and compare their temporal relations binaurally, and this ability gives rise not only to time-based lateralization performance at high frequencies, but also to a binaural beat similar in many respects to that heard with low-frequency sinusoids."

Related experiments were reported by Bernstein and Trahiotis (1996). They presented two-tone complexes centered at 3500 Hz with a different beat rate at each ear. In one experiment, listeners were required to distinguish between rightward or leftward directions of intracranial movement produced by the binaural beat. The stimuli and experimental paradigm were designed so that such judgments would be made based on the dynamically varying, envelope-based interaural temporal disparities. Listeners were able to perform reasonably well on this task, at least for a very low interaural beat rate of 0.25 Hz; performance was close to chance for an interaural beat rate of 1 Hz. In a second experiment, listeners

[a)]Author to whom correspondence should be addressed. Electronic mail: bcjm@cam.ac.uk

were required only to distinguish between the presence or absence of an envelope-based binaural beat, as in the experiment of McFadden and Pasanen (1975). In this case, the results could be explained by assuming that listeners base their decisions on the presence or absence of dynamically varying interaural intensity disparities.

Other experiments have demonstrated directly that human listeners are sensitive to changes in the interaural phase of the envelopes of high-frequency carriers. For example, Grantham (1984) showed that subjects could discriminate an amplitude-modulated bandpass filtered noise in which the modulating sinusoid was interaurally in phase from the same AM noise in which the modulator was interaurally phase reversed. However, the modulation depth required for 71% discriminability did tend to increase as the modulation frequency was increased up to 50 Hz. In a related experiment, Thompson and Dau (2008) found that discrimination of interaural modulator phase was better for a 5000 Hz sinusoidal carrier than for narrowband-noise diotic carriers at the same center frequency. For all carriers, the task could be performed for modulation rates up to 128 Hz (the highest tested).

The present experiments were intended to assess whether some of the binaural interactions described above, especially envelope-based binaural beats, might be explained in terms of a distortion product in the modulation domain, produced at some point in the auditory system where the modulators at the two ears interact. The experiments were similar in design to experiments that have been conducted previously to examine the possible influence of "distortion" in the modulation domain for monaural stimuli, so we give next a brief overview of such experiments.

Moore *et al.* (1999) examined masking in the amplitude-modulation domain when the probe modulation frequency was remote from any spectral frequency in the masker modulation, but there was nevertheless a similarity between the temporal pattern of the masker modulation and the probe modulation. This was achieved by using a two-component modulator. The "beats" between these two components occurred at a rate that was equal to or close to the probe frequency. A similar method had been used earlier by Sheft and Yost (1997) to examine modulation detection interference. Moore *et al.* (1999) found that the threshold for detecting 5 Hz probe modulation was affected by the presence of a pair of masker modulators beating at a 5 Hz rate (40 and 45 Hz, 50 and 55 Hz, or 60 and 65 Hz). The threshold was dependent on the phase of the probe modulation relative to the beat cycle of the masker modulators. Moore *et al.* (1999) proposed an explanation for their results based on the idea that nonlinearities within the auditory system introduce distortion in the internal representation of the envelopes of the stimuli. This notion was initially suggested by Shofner *et al.* (1996) based on a study of neural responses in the cochlear nucleus to two-component modulators. In the case of two-component beating modulators, a weak component, corresponding to the simple difference component, would be introduced at the beat rate. Several other researchers have demonstrated modulation masking effects related to the beat rate of complex modulators (Verhey *et al.*, 2003; Sek and Moore, 2004; Füllgrabe *et al.*, 2005). The results have been explained in terms of distortion in the modulation domain (Sek and Moore, 2004; Füllgrabe *et al.*, 2005; Uchanski *et al.*, 2006), the combined effects of cochlear filtering and off-frequency listening (Füllgrabe *et al.*, 2005), the perception of slow fluctuations at the output of a modulation filter tuned to the "primary" modulator components (Uchanski *et al.*, 2006), or a mechanism that explicitly extracts the envelope of a complex modulator (Verhey *et al.*, 2003).

The present experiments were similar to the experiments described above, except that the masker modulator presented to each ear was a single sinewave. The 5 Hz probe modulation that the subject was asked to detect was presented diotically, but the masker modulator had a different frequency at the two ears, for example, 50 Hz in one ear and 55 Hz in the other ear. The threshold for detecting the probe modulation was measured as a function of the starting phase of the probe modulation. We reasoned that if a modulation distortion product at 5 Hz was generated following binaural interaction, then a phase effect should be found. This turned out to be the case. Further experiments were performed to assess more specifically whether the phase effect could be explained in terms of a distortion component in the internal representation of the modulation.

II. EXPERIMENT 1: 50 AND 55 Hz MODULATION MASKERS

A. Stimuli

The carrier was a 4000 Hz sinusoid with a level of 70 dB sound pressure level, presented to both ears. This relatively high carrier frequency was chosen so that the spectral sidebands produced by the modulation would not be resolved by the peripheral auditory filters. The probe modulation frequency was 5 Hz, and the probe modulator was applied to both ears, with the same phase at the two ears. A sinusoidal masker modulator with a frequency of 50 Hz was applied to the carrier in the left ear, and a sinusoidal masker modulator with a frequency of 55 Hz was applied to the right ear. The modulation index for each masker modulator was 0.33. The equation describing the *envelope* of the masker plus probe in the left ear, $E_L(t)$, is

$$E_L(t) = 1 + m_m \cos(2\pi f_{mL} t) + m_p \cos(2\pi f_p t + \varphi), \quad (1)$$

where m_m is the depth of the masker modulator (0.33), f_{mL} is the frequency of the masker modulator in the left ear (50 Hz), t is time, f_p is the frequency of the probe modulator (5 Hz), m_p is the probe modulation depth, and φ is the starting phase of the probe modulator. The starting phase of the masker modulator was fixed. The equation describing the envelope of the masker plus probe in the right ear, $E_R(t)$, is

$$E_R(t) = 1 + \ m_m \cos(2\pi f_{mR} t) + m_p \cos(2\pi f_p t + \varphi), \quad (2)$$

where f_{mR} is the frequency of the masker modulator in the right ear (55 Hz). Values of φ were 0°, 45°, 90°, 135°, 180°, 225°, 270°, and 315°. The left and right columns of Fig. 1 show the envelope (without dc component) of the masker alone (top), probe alone (middle), and masker plus probe (bottom) when φ=90°, for the left and right ears, respec-

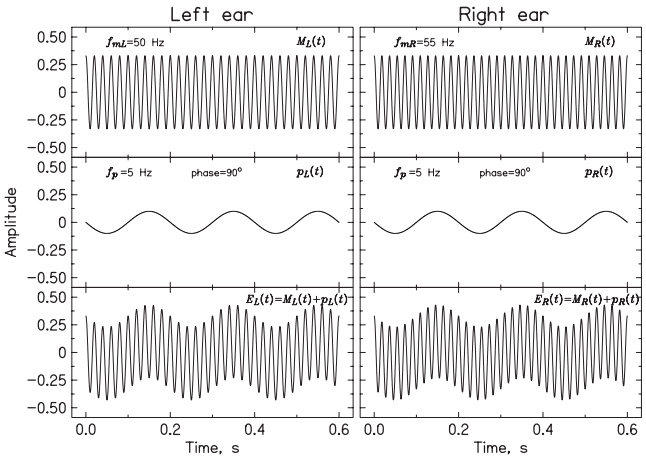

FIG. 1. Illustration of modulator waveforms (without dc component) presented to the left and right ears for a starting probe phase (as defined in Eqs. (1) and (2)) of 90°. The top panels show waveforms for the maskers alone [$M_L(t)$ and $M_R(t)$, for the left and right ears, respectively], the middle panels show waveforms for the probe alone [$P_L(t)$ and $P_R(t)$], and the bottom panels show the masker+probe waveforms [$E_L(t)$ and $E_R(t)$].

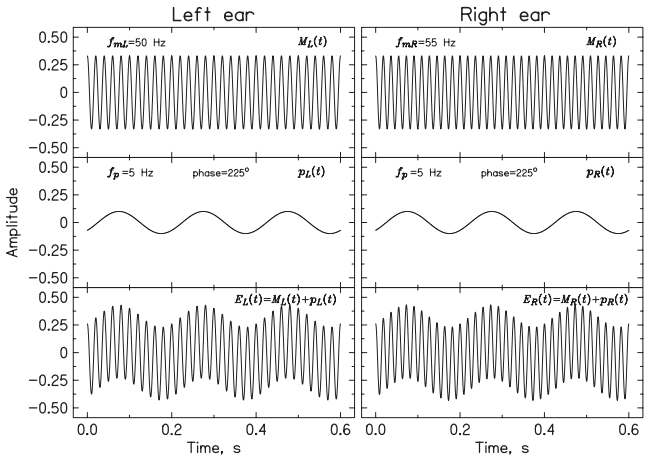

FIG. 2. As Fig. 1, but for a starting probe phase of 225°.

tively. Figure 2 shows corresponding envelopes for $\varphi = 225°$.

Thresholds for detecting the probe modulation were also measured for the probe alone, and for the probe in the presence of a 50 Hz masker modulator presented to the left ear only, with masker modulation depths of 0.33 and 0.5; the latter is comparable to the root-mean-square modulation depth that would be obtained if two modulation maskers were applied to the same ear, each with a modulation depth of 0.33. Note that the probe modulation was applied to both ears, even when the masker modulation was applied to one ear only.

On each trial, the carrier was presented in two bursts separated by a silent interval of 300 ms. Each burst had 20-ms raised-cosine rise and fall ramps, and an overall duration (including rise/fall times) of 1000 ms. The modulation was applied during the whole of the carrier, and the starting phase of the modulation was defined relative to the start of the carrier.

Stimuli were generated using a Tucker-Davis Technologies array processor (TDT-AP2) in a host PC and two channels of a 16 bit digital to analog converter (TDT-DD1) operating at a 50 kHz sampling rate. The stimuli were attenuated (TDT-PA4) and sent through an output amplifier (TDT-HB6) to Sennheiser HD580 headphones. Subjects were seated in a double-walled sound-attenuating chamber.

B. Procedure

Thresholds were measured using an adaptive two-interval forced-choice (2IFC) procedure, with a two-down one-up stepping rule that estimates the 70.7% correct point on the psychometric function. The masker modulation was present in both intervals of a trial, and the probe modulation was presented in either the first or the second interval, selected at random. The task of the subject was to indicate, by pressing one of two buttons, the interval containing the probe modulation. Feedback was provided by lights following each response. At the start of a run, the probe modulation depth, m, was chosen to be well above the threshold value. Following two correct responses, m was decreased, while following one incorrect response it was increased. The step size was 3.5 dB (in terms of 20 log m) until four reversals occurred, after which it was decreased to 2 dB and eight more reversals were obtained. The threshold for a given run was taken as the mean value of 20 log m at the last eight reversals. Each threshold reported here is based on the mean of four runs.

C. Subjects

Four subjects were tested, all of whom were paid for their services. All subjects had absolute thresholds less than 20 dB HL at all audiometric frequencies from 250 to 8000 Hz and had no history of hearing disorders. All had extensive previous experience in psychoacoustic tasks, including tasks similar to the one used here. They received 4 h of training on the task used here before data collection started.

D. Results

Figure 3 shows the individual results and the mean results across subjects (bottom left). The filled square indicates the threshold for detecting the probe modulation in the absence of masker modulation. The hexagon and the filled inverted triangle show the probe detection thresholds with 50 Hz masker modulation applied to the left ear only, with masker modulation depths of 0.33 and 0.5, respectively. The masker with the lower depth had almost no effect, as might be expected from the wide separation of the probe and masker frequencies in the modulation domain. The masker with the greater depth did produce a small amount of modulation masking, even though the probe in the right ear was presented without any modulation masker. This means that subjects could not listen only to the right ear stimulus, ignoring the masker modulation in the left ear.

The open squares in Fig. 3 show probe detection thresholds as a function of the starting phase of the probe modulator when the dichotic modulation masker was present, with the 50 Hz modulation presented to the left ear and the 55 Hz modulation presented to the right ear. The dichotic modulation masker produced only a small amount of masking. How-

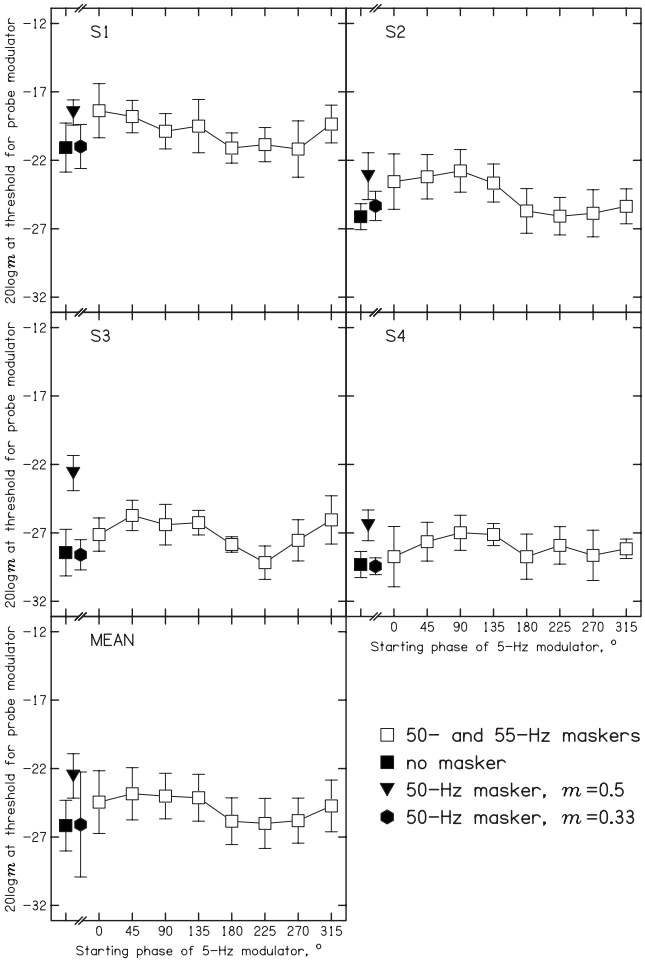

FIG. 3. Individual and mean results for experiment 1. The detection threshold for the probe modulation is plotted as a function of the starting phase of the probe modulator. For the individual results, error bars indicate ±1 standard deviation (SD) across repeated runs. For the mean results, error bars indicate ±1 SD across subjects. Filled symbols on the left of each panel show probe detection thresholds measured with no masker (squares), a 50 Hz masker with $m=0.5$ (inverted triangles), and a 50 Hz masker with $m=0.33$ (hexagons). In the last two cases, the masker modulator was applied to the left ear only.

ever, there was a distinct variation in the probe threshold with starting phase, and the pattern of variation was consistent across subjects. The probe threshold was highest when the starting phase was 45°–135° and was lowest when the starting phase was 180°–270°. A within-subjects analysis of variance (ANOVA) was conducted with factor probe starting phase. The effect of phase was significant: $F(7,21)=6.27$, $p<0.001$. These results suggest that the detection of the probe was influenced by interaction in the binaural system of the masker modulator presented to each ear.

III. EXPERIMENT 2: DETECTABILITY OF PROBE MODULATION AS A FUNCTION OF PROBE MODULATION DEPTH

A. Rationale

A possible explanation for the results presented above is that the masker modulators produced a weak 5 Hz distortion component in the modulation domain at a level in the auditory system where binaural interaction occurs. The probe detection threshold for a probe phase of about 90° might be relatively high because the probe is almost in opposite phase to the distortion component and is partially canceled. Conversely, for a probe phase of about 225°, the probe and distortion components might be in phase, and their addition would enhance detection of the probe. If this explanation is correct, then, for a probe with very small modulation depth, the detectability of the probe might actually become negative for a probe phase of 90°; in other words, subjects would hear the probe as being in the "wrong" interval of a forced-choice trial. This could happen because the probe and distortion component would almost cancel each other in the signal interval, but the distortion component would remain in the nonsignal interval. This idea was tested in experiment 2 by measuring the detectability of the probe as a function of probe modulation depth, using two starting phases of the probe which led to relatively high and low thresholds for detection of the probe modulation in experiment 1. One might expect that the phases leading to the highest and lowest thresholds would differ by 180°, so we could have chosen phases of 90° and 270°, or 45° and 225°. However, since we did not know which pair might give the most clear cut results, we decided to use the phases which led to the highest and lowest empirically measured thresholds, namely, 90° and 225°. A similar method has been used to check for the presence of a distortion component in the modulation domain produced by monaural interaction of masker modulator components (Sek and Moore, 2004; Füllgrabe *et al.*, 2005).

B. Method

Three of the subjects from experiment 1 took part (the fourth was no longer available). Because the putative distortion product in the modulation domain was likely to be very weak, we increased the modulation depth of each masker to 0.5 (compared to the value of 0.33 in experiment 1), so as to increase the likely magnitude of the distortion product. The timing of the stimuli was the same as for experiment 1. A 2IFC procedure was again used. However, instead of using an adaptive procedure, we measured the percent correct in blocks of 55 trials using a fixed probe modulation depth. Responses for the first five trials in each block were regarded as "warm up" and were discarded. At least four blocks of trials were run for each probe modulation depth. Pilot runs showed that the probe modulation depth needed to be very small to obtain negative detectability for the probe starting phase of 90°. This guided the choice of fixed probe modulation depths, which were −37, −40, −43, −46, and −48 dB (in terms of 20 log m_p). No feedback was given because it was anticipated that the probe might sometimes be heard in the wrong interval.

C. Results

The percent correct scores were converted to values of the detectability index, d' (Hacker and Ratcliff, 1979). The individual and mean values of d' are shown in Fig. 4. All of the d' values were close to zero, as would be expected given the very small probe modulation depths. Nevertheless, there was a consistent phase effect, d' values being higher for the

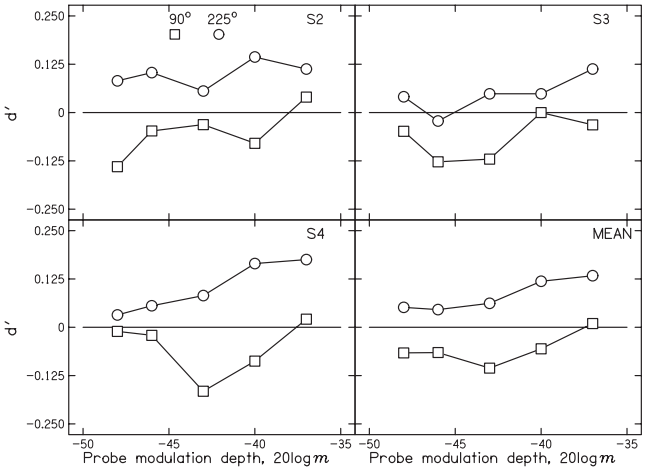

FIG. 4. Individual and mean results for experiment 2. The detectability of the probe modulation, d', is plotted as a function of the probe modulation depth for two starting phases of the probe, 90° and 225°.

probe phase of 225° than for the phase of 90°. Also, the values of d' for the probe phase of 90° tended to fall below zero, especially for modulation depths around −43 dB. A within-subjects ANOVA with factors probe phase and probe modulation depth gave a significant effect of phase, $F(1,2)=100.3$, $p=0.01$, and of modulation depth, $F(4,8)=5.21$, $p=0.023$. The interaction was not significant. However, given that we used only three subjects with 200 observations per subject per condition, the 95% confidence interval for the proportion correct values is about 0.04, which means that for a d' value to be significantly below zero it would have to be less than −0.14. None of the measured mean d' values fell below −0.14. Thus, subjects did not score significantly below chance for these very small modulation depths. The results do not provide clear support for the idea that there was a weak distortion component in the modulation domain, which partially or completely canceled the probe modulation for the probe phase of 90° and led to the subjects identifying the probe in the wrong interval.

IV. EXPERIMENT 3: 50- AND 27.5-Hz MODULATION MASKERS

A. Rationale

The stimuli in experiments 1 and 2 might be thought of as analogous to stimuli which lead to envelope distortion, but with the distortion produced following binaural interaction. The modulation distortion component corresponds to f_2-f_1, where f_1 and f_2 are the frequencies of the primary modulator components and $f_2 > f_1$. In experiments 3 and 4, we pursued the distortion analogy using as dichotic modulation maskers components with frequencies of 27.5 and 50 Hz. In other words, the experiments were similar to experiments 1 and 2, except that f_{mR}, the frequency of the masker modulator component in the right ear was 27.5 Hz, rather than 55 Hz. Modulators with frequencies of 50 and 27.5 Hz might interact in the binaural system to produce a modulation distortion component at 5 Hz, corresponding to $2f_2$-f_1.

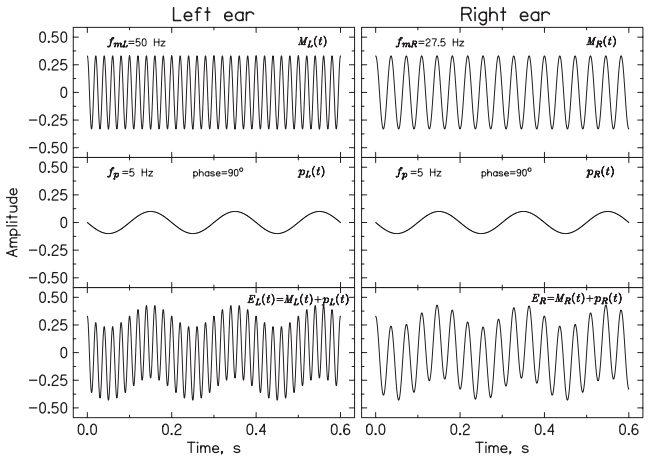

FIG. 5. As Fig. 1, but with the masker modulation frequency for the right ear set to 27.5 Hz.

B. Method

The subjects were the same as for experiment 1. The stimuli and method were also the same as for experiment 1, except that f_{mR}, the frequency of the modulator component applied to the carrier in the right ear, was 27.5 Hz, rather than 55 Hz. Figures 5 and 6 illustrate the modulator waveforms (without dc component) for probe starting phases of 90° and 225°, respectively.

C. Results

Figure 7 shows the individual and mean results. The filled square indicates the mean threshold for detecting the probe modulation in the absence of masker modulation. The hexagon and the filled inverted triangle show the probe detection thresholds with 27.5 Hz masker modulation applied to the left ear only, with masker modulation depths of 0.33 and 0.5, respectively. Overall, the masker with the lower depth had a slightly greater effect than found for the 50 Hz modulator in experiment 1, but, based on a t-test, this effect was not statistically significant ($p=0.86$). As expected, the

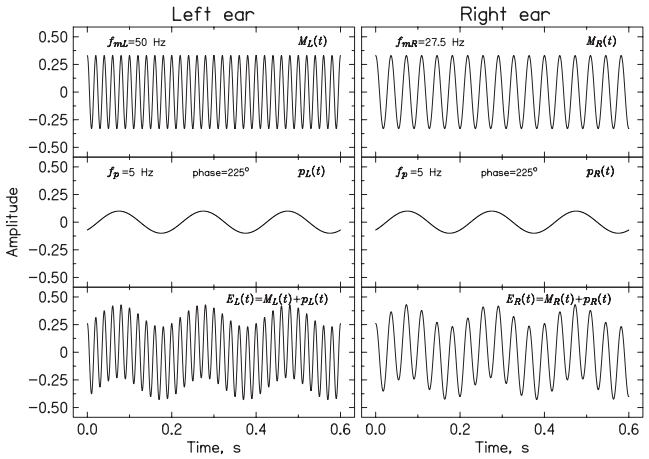

FIG. 6. As Fig. 2, but with the masker modulation frequency for the right ear set to 27.5 Hz.

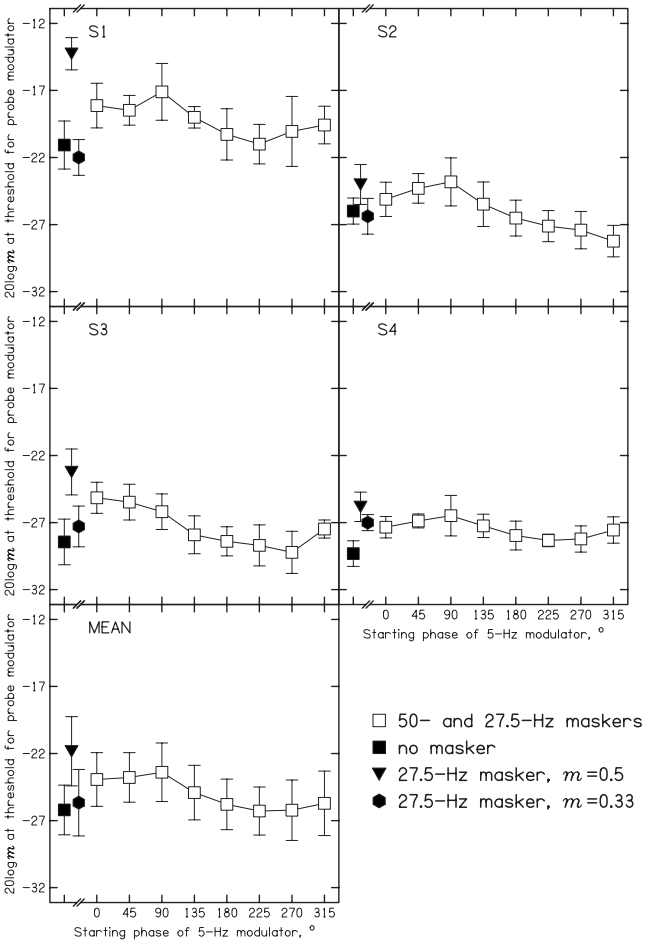

FIG. 7. As Fig. 3, but showing results for experiment 3, with the masker modulation frequency for the right ear set to 27.5 Hz.

masker with higher depth produced somewhat more modulation masking, but a t-test showed that this effect was also not statistically significant ($p=0.23$).

The open squares in Fig. 7 show probe detection thresholds as a function of the starting phase of the probe when the dichotic modulation masker was present: 50 Hz to the left ear and 27.5 Hz to the right ear. As in experiment 1, the dichotic modulation masker produced only a small amount of masking, but there was a distinct variation in the probe threshold with starting phase, and the pattern of variation was consistent across subjects. The probe threshold was highest when the starting phase was in the range 0°–90° and was lowest when the starting phase was in the range 180°–270°. A within-subjects ANOVA was conducted with factor probe starting phase. The effect of phase was significant: $F(7,21)=11.32$, $p<0.001$. These results suggest that the detection of the probe was influenced by interaction in the binaural system of the masker modulator presented to each ear.

V. EXPERIMENT 4: DETECTABILITY OF PROBE MODULATION AS A FUNCTION OF PROBE MODULATION DEPTH

A. Rationale

The rationale for this experiment was similar to that for experiment 2. If the masker modulators produced a weak 5 Hz distortion component in the modulation domain, the detectability of the probe might become negative at very low probe modulation depths for the probe phase that led to the highest threshold in experiment 3, which was 90°; subjects would hear the probe as being in the wrong interval of a forced-choice trial.

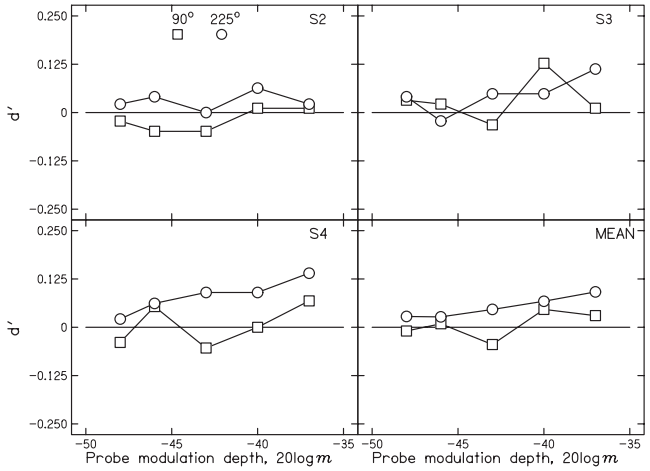

FIG. 8. As Fig. 4, but showing results for experiment 4, with the masker modulation frequency for the right ear set to 27.5 Hz.

B. Method

The subjects and procedure were the same as for experiment 2. The stimuli were also the same as for experiment 2, except that the masker modulator frequency in the right ear was 27.5 Hz.

C. Results

The individual and mean values of d' are shown in Fig. 8. All of the d' values are close to zero, as would be expected given the very small probe modulation depths. There appears to be a very small effect of probe phase for subjects S2 and S4, but not for S3. A within-subjects ANOVA showed no significant effect of probe modulation depth or probe starting phase, and no significant interaction. The d' values did not fall consistently below zero for the probe phase of 90°. Thus, these results do not support the idea that interaction of the masker modulators in the binaural system led to a distortion product in the modulation domain with frequency corresponding to $2f_2$-f_1.

VI. DISCUSSION

A possible confounding factor in our experiments is that the threshold for detecting 5 Hz probe modulation might depend on the starting phase of the modulation, independent of the characteristics of the maskers. Such sensitivity is possible when the modulator has a very low frequency, given that subjects appear to be sensitive to the starting phase of a single sinusoidal modulator when the modulation rate is below about 12 Hz (Dau, 1996; Sheft and Yost, 2007). However, it has been shown that psychometric functions for the detection of 5 Hz sinusoidal AM are not affected by the starting phase of the AM for a wide range of carrier frequen-

cies (Sek and Skrodzka, 1999). Therefore, we believe that the pattern of phase effects found in experiments 1–3 cannot be explained by a dependence of the (absolute) threshold for probe detection on the starting phase of the probe.

Our results appear to reflect an interaction in the binaural system of the stimuli presented to each ear. Consistent with this interpretation, for the stimuli of experiment 1 subjects reported hearing a weak fluctuation at a relatively low rate when listening to the masker modulators alone (the 50 Hz modulator in one ear and the 55 Hz modulator in the other ear). It was not clear to the subjects whether the fluctuation was in loudness or in spatial position. The reported fluctuation is comparable to that reported by McFadden and Pasanen (1975), as described in the Introduction.

The results of our experiment 1 are consistent with the idea that listeners are sensitive to dynamic variations in interaural time or intensity. The envelope periodicities of 50 Hz in the left ear and 55 Hz in the right would have given rise to fluctuations in interaural intensity at a 5 Hz rate. Also, the interaural time difference associated with the envelope would fluctuate at a 5 Hz rate. Both of these fluctuations might influence the detection of 5 Hz probe modulation. However, it is not obvious why the fluctuations would lead to an effect of relative modulator phase.

One possible explanation of our results is related to short-term fluctuations in loudness. The loudness of the masker may have fluctuated at a 5 Hz rate, owing to the fluctuating interaural level difference. The addition of the probe modulation might change the perceived amount of loudness fluctuation, and this might be the cue used to detect the probe modulation. To assess this possibility we used a model of loudness for time-varying sounds. The model was similar to that described by Glasberg and Moore (2002) but modified to incorporate the concept of binaural inhibition proposed by Moore and Glasberg (2007). The model described by Glasberg and Moore (2002) starts by calculating the "instantaneous loudness" from the short-term spectrum of the stimulus. This is an intervening variable, assumed not to be accessible to conscious perception. The instantaneous loudness is subjected to an initial stage of smoothing or averaging over time using a mechanism similar to an automatic gain control system, with an attack time and a release time. This gives the short-term loudness. The model also includes a second stage of averaging, using longer attack and release times, to give an estimate of the overall loudness impression of a fluctuating sound. However, here we considered only the output of the first stage of averaging, i.e., we assumed that only the short-term loudness estimate was relevant. In the version of the model used here, the instantaneous loudness was calculated separately for each ear, and then the instantaneous loudness was combined across ears using the method described by Moore and Glasberg (2007), so as to include the effect of binaural inhibition. Summation across ears prior to averaging meant that rapid fluctuations in amplitude were preserved at the point of binaural interaction. Then the binaural instantaneous loudness was smoothed as described above to give the short-term loudness as a function of time.

Figure 9 shows the output of the model for the case when the masker modulation had a frequency of 50 Hz in one ear and 55 Hz in the other. The solid line shows the short-term loudness level in phons for the masker alone, and the dashed line shows the short-term loudness when probe modulation with a starting phase of 0° was added; the probe modulation depth was equal to the mean measured threshold value for that probe starting phase. The curve for the masker alone shows a weak rapid fluctuation corresponding roughly to the mean of the two masker modulation frequencies and a slower fluctuation corresponding to the 5 Hz beat rate of the masker modulators. However, the amount of fluctuation is small in both cases. The small fluctuation at a 5 Hz rate is consistent with the subjective reports of the subjects. The addition of the probe modulation caused an increase in the amount of fluctuation at the 5 Hz rate which might have been used as a cue for detection of the probe.

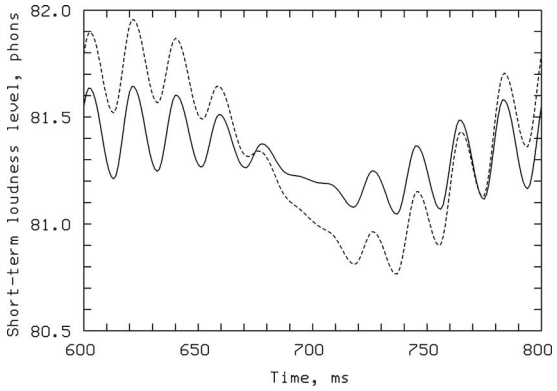

FIG. 9. Output of the loudness model described in the text, showing short-term loudness as a function of time. The solid line is for the masker modulator alone (50 Hz in one ear and 55 Hz in the other).

To assess whether the pattern of phase effects could be explained in terms of fluctuations in the short-term loudness, we used as a decision variable the difference in short-term loudness for the masker alone and the masker plus probe. For the example in Fig. 9, this corresponds to the difference between the solid and dashed curves on a point-by-point basis. We denote this difference $STL_{M\text{-}P}(t)$. We assumed that performance was related to the peak-to-valley difference of $STL_{M\text{-}P}(t)$. We initially used as input to the model the mean value of the probe modulation depth at threshold for each probe starting phase. Averaged across starting phases, the mean value of the peak-to-valley difference of $STL_{M\text{-}P}(t)$ was 0.61 phons. Then for each phase condition, we iteratively adjusted the probe modulation depth so that the obtained value of the peak-to-valley difference of $STL_{M\text{-}P}(t)$ was 0.61 phons. The probe modulation depth obtained in this way was taken as the predicted probe modulation depth at threshold.

The outcome is shown in Table I. The obtained thresholds differed by 2.3 dB across conditions, whereas the predicted thresholds differed by only 0.7 dB across conditions. Furthermore, the phase effects were not predicted correctly. The obtained threshold was highest for the probe starting phase of 45° and lowest for the phase of 225°, while the predicted threshold was highest for the phase of 0° and lowest for the phase of 135°. Predictions were generated using several other decision variables, but none led to correct pre-

TABLE I. Comparison of mean obtained probe modulation depths at threshold from experiment 1 (using masker modulators with frequencies of 50 and 55 Hz), with predictions derived using the loudness model described in the text. The data are the same as shown in Fig. 3.

Probe starting phase (deg)	Obtained threshold (dB)	Predicted threshold (dB)
0	−24.5	−24.4
45	−23.8	−24.8
90	−24.0	−25.0
135	−24.1	−25.1
180	−25.9	−24.8
225	−26.1	−24.9
270	−25.8	−24.9
315	−24.7	−24.8

dictions of the observed phase effects. Overall, it appears that the results cannot be adequately explained in terms of the short-term fluctuations in loudness predicted by the model. It should be noted that the model of Glasberg and Moore (2002) was designed to account for the loudness perception of time-varying monaural or diotic sounds, while the model of Moore and Glasberg (2007) was designed to account for the loudness perception of static diotic and dichotic sounds. It is possible that the model used here does not correctly account for the loudness of time-varying dichotic sounds and that a different model might give results that fit the data better. However, we tried several other versions of the model, including one in which the instantaneous loudness was simply summed across ears, and none of them predicted the phase effects correctly. Furthermore, it is difficult to think of any way in which the loudness model could be modified so as to predict the phase effects correctly.

Given that the results could not be predicted using the loudness models that we tried, it is worth considering again the idea that there might have been a weak "distortion component" in the modulation domain with a frequency corresponding to 5 Hz, even though our results did not provide clear evidence to support the existence of such a distortion component. Sek and Moore (2004) conducted an experiment similar to experiment 2, except that the 50 and 55 Hz masker modulators were presented to the same ear. They found negative d' values for some conditions. The minimum value of d' was about −0.43 and it occurred for a probe modulation depth of about −30 dB. Füllgrabe *et al.* (2005) used a white noise carrier and a second-order masker modulator (a "carrier" modulator with frequency of 64, 180, or 200 Hz, whose depth was sinusoidally varied at a 5 Hz rate). For the 64 Hz carrier modulation frequency, the minimum value of d' (≈−1) occurred for a probe modulation depth of about −23 dB. In contrast, in experiment 2 of the present paper, the minimum value of d' was −0.106, and it occurred for a probe modulation depth of about −43 dB. These comparisons suggest that, if there is a distortion component produced by binaural interaction, its effective level is much lower than that produced by monaural presentation of the masker modulators.

It is not clear how to explain the results of experiment 3. In that experiment, the envelope modulation rate was 50 Hz in one ear and 27.5 Hz in the other. A significant effect of the phase of the 5 Hz probe on detectability of the probe was found, but the results of experiment 4 did not provide support for the idea that there was a distortion component in the modulation domain corresponding to $2f_2$-f_1. Assuming that the time pattern of the modulators is preserved at the point of binaural interaction, it is relevant to consider the modulation waveform produced by summing the 50 and 27.5 Hz components. The result of this summation is illustrated in the top panel of Fig. 10. This waveform is reproduced in the middle panel of Fig. 10, which also shows the Hilbert envelope of the summed modulation (thick line) (The Hilbert envelope is used here merely as a convenient way of estimating the envelope). The Hilbert envelope is periodic, repeating 22.5 times per second, which corresponds to the difference in frequency between the two modulator components. Not surprisingly, the Hilbert envelope does not show any periodicity at a 5 Hz rate. However, the major peaks in the summed modulation are spaced at approximately 0.2 s, corresponding to the 5 Hz period of the probe modulation. This is illustrated in the bottom panel of Fig. 10, which shows the summed modulator waveform together with a 5 Hz sinewave which has been scaled so as to coincide approximately with the main peaks in the waveform. Thus, the temporal pattern of the summed modulator waveform includes temporal features occurring at a 5 Hz rate, even though the Hilbert envelope does not reveal these features.

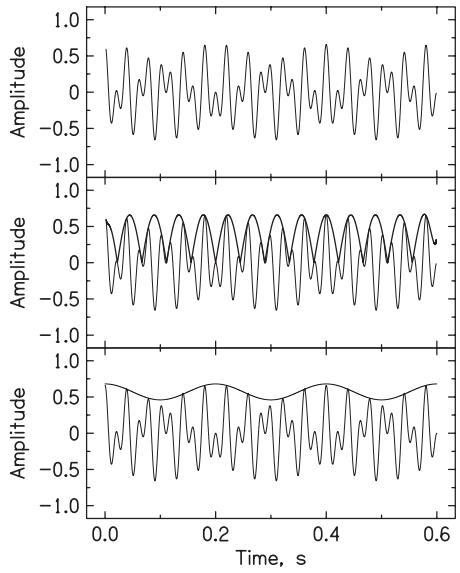

FIG. 10. The top panel shows the modulation waveform (without dc component) resulting from summing the 50 Hz and 27.5 Hz modulators, each with m=0.33. The middle panel reproduces that waveform and also shows the Hilbert envelope of the waveform as a thick line. The bottom panel shows the same waveform, together with a 5 Hz sinewave that has been scaled to coincide with the major peaks of the waveform.

Füllgrabe and Lorenzi (2005) investigated the perception of a noise carrier, amplitude modulated at frequency f_m, when the AM depth of this "carrier" modulation was itself sinusoidally modulated by a "second-order" modulator with a 5 Hz rate. They included conditions where f_m was an integer multiple of 5 Hz (so that the envelope was strictly periodic with a 5 Hz repetition period), and where f_m was shifted

in frequency, so as to create a more complex modulator (but where the Hilbert envelope of the modulation waveform was still periodic with a 5 Hz repetition period). The perceived envelope "beat" rate was estimated using a matching procedure. The results indicated that the perceived beat rate was influenced by the frequency shift, at least for $f_m < 20$ Hz. Füllgrabe and Lorenzi (2005) suggested that the perceived envelope beat rate is determined by the time intervals between major peaks in the first-order envelope and not by the repetition rate of the Hilbert envelope of the modulator or by a distortion component in the modulation domain. Something similar could be the case for our stimuli of experiment 3, except that the internal representations of the modulators presented separately to the two ears would have to be summed at a point in the auditory system where their temporal structure was preserved. The detection of the 5 Hz probe modulation could be influenced by its phase relative to the perceived beat in the complex modulator. For some phases, the probe might make the perceived beat more or less salient, while for other phases it might make the beat qualitatively different, for example, by doubling the apparent beat rate. When questioned about whether they could hear a relatively slow (5 Hz) beat when listening to the 50 Hz modulator in one ear and the 27.5 Hz modulator in the other ear, the reports of our subjects were mixed; two reported hearing such a beat and two did not.

VII. SUMMARY AND CONCLUSIONS

To assess the possible existence of distortion components in the modulation domain, produced following binaural interaction, the detection of diotic 5 Hz probe modulation of a 4000 Hz sinusoidal carrier was measured in the presence of two higher-frequency masker modulators, one presented to each ear. The following are the main results.

(1) When the masker modulator frequencies were 50 and 55 Hz, the probe modulation depth at threshold varied slightly but significantly with the starting phase of the probe. The probe threshold was highest when the starting phase was 45°–135° and was lowest when the starting phase was 180°–270°. The pattern of the phase effects could not be predicted based on short-term fluctuations in loudness at the output of a loudness model.
(2) When the masker modulator frequencies were 50 and 55 Hz, the detectability of the probe modulation, d', for very low probe modulation depths was lower when the probe starting phase was 90° than when it was 225°. For the 90° starting phase, d' was slightly but not significantly below zero for probe modulation depths close to −43 dB. The results indicate that if the internal representations of the 50 and 55 Hz masker modulators interacted binaurally to produce a weak distortion component in the internal representation of the modulation at a 5 Hz frequency, then that distortion component was very weak.
(3) When the masker modulator frequencies were 50 and 27.5 Hz, the probe modulation depth at threshold varied slightly but significantly with the starting phase of the probe. The probe threshold was highest when the starting phase was 0°–90° and was lowest when the starting phase was 180°–270°.
(4) When the masker modulator frequencies were 50 and 27.5 Hz, the detectability of the probe modulation, d', for very low probe modulation depths was not significantly different for probe starting phases of 90° and 225°. The value of d' did not fall significantly below zero. These results do not provide evidence for a 5 Hz distortion component in the internal representation of the modulation.

ACKNOWLEDGMENTS

This work was supported by the Wellcome Trust, Deafness Research UK and the Medical Research Council (UK). We thank Christian Füllgrabe, Christian Lorenzi, Richard Freyman, and two anonymous reviewers for helpful comments on an earlier version of this paper.

Bacon, S. P., and Grantham, D. W. (**1989**). "Modulation masking: Effects of modulation frequency, depth and phase," J. Acoust. Soc. Am. **85**, 2575–2580.
Bernstein, L. R., and Trahiotis, C. (**1996**). "Binaural beats at high frequencies: Listeners' use of envelope-based interaural temporal and intensive disparities," J. Acoust. Soc. Am. **99**, 1670–1679.
Dau, T. (**1996**). "Modeling auditory processing of amplitude modulation," Ph.D. thesis, University of Oldenburg, Germany.
Dau, T., Kollmeier, B., and Kohlrausch, A. (**1997a**). "Modeling auditory processing of amplitude modulation. I. Detection and masking with narrowband carriers," J. Acoust. Soc. Am. **102**, 2892–2905.
Dau, T., Kollmeier, B., and Kohlrausch, A. (**1997b**). "Modeling auditory processing of amplitude modulation. II. Spectral and temporal integration," J. Acoust. Soc. Am. **102**, 2906–2919.
Ewert, S. D., and Dau, T. (**2000**). "Characterizing frequency selectivity for envelope fluctuations," J. Acoust. Soc. Am. **108**, 1181–1196.
Ewert, S. D., Verhey, J. L., and Dau, T. (**2002**). "Spectro-temporal processing in the envelope-frequency domain," J. Acoust. Soc. Am. **112**, 2921–2931.
Füllgrabe, C., and Lorenzi, C. (**2005**). "Perception of the envelope-beat frequency of inharmonic complex temporal envelopes," J. Acoust. Soc. Am. **118**, 3757–3765.
Füllgrabe, C., Moore, B. C. J., Demany, L., Ewert, S. D., Sheft, S., and Lorenzi, C. (**2005**). "Modulation masking produced by second-order modulators," J. Acoust. Soc. Am. **117**, 2158–2168.
Glasberg, B. R., and Moore, B. C. J. (**2002**). "A model of loudness applicable to time-varying sounds," J. Audio Eng. Soc. **50**, 331–342.
Grantham, D. W. (**1984**). "Discrimination of dynamic interaural intensity differences," J. Acoust. Soc. Am. **76**, 71–76.
Hacker, M. J., and Ratcliff, R. (**1979**). "A revised table of d' for M-alternative forced choice," Percept. Psychophys. **26**, 168–170.
Henning, G. B. (**1974**). "Detectability of interaural delay in high-frequency complex waveforms," J. Acoust. Soc. Am. **55**, 84–90.
Houtgast, T. (**1989**). "Frequency selectivity in amplitude-modulation detection," J. Acoust. Soc. Am. **85**, 1676–1680.
Kay, R. H. (**1982**). "Hearing of modulation in sounds," Physiol. Rev. **62**, 894–975.
Licklider, J. C., Webster, J. C., and Hedlun, J. M. (**1950**). "On the frequency limits of binaural beats," J. Acoust. Soc. Am. **22**, 468–473.
Martens, J.-P. (**1982**). "A new theory for multi-tone masking," J. Acoust. Soc. Am. **72**, 397–405.
McFadden, D., and Pasanen, E. G. (**1975**). "Binaural beats at high frequencies," Science **190**, 394–396.
Moore, B. C. J., and Glasberg, B. R. (**2007**). "Modeling binaural loudness," J. Acoust. Soc. Am. **121**, 1604–1612.
Moore, B. C. J., Sek, A., and Glasberg, B. R. (**1999**). "Modulation masking produced by beating modulators," J. Acoust. Soc. Am. **106**, 908–918.
Nuetzel, J. M., and Hafter, E. R. (**1981**). "Lateralization of complex waveforms: Spectral effects," J. Acoust. Soc. Am. **69**, 1112–1118.
Sek, A., and Moore, B. C. J. (**2003**). "Testing the concept of a modulation

filter bank: The audibility of component modulation and detection of phase change in three-component modulators," J. Acoust. Soc. Am. **113**, 2801–2811.
Sek, A., and Moore, B. C. J. (**2004**). "Estimation of the level and phase of the simple distortion tone in the modulation domain," J. Acoust. Soc. Am. **116**, 3031–3037.
Sek, A., and Moore, B. C. J. (**2006**). "Perception of amplitude modulation by hearing-impaired listeners: The audibility of component modulation and detection of phase change in three-component modulators," J. Acoust. Soc. Am. **119**, 507–514.
Sek, A. P., and Skrodzka, E. B. (**1999**). "An influence of a modulating signal starting phase on the modulation detection," Arch. Acoust. **24**, 39–47.
Sheft, S., and Yost, W. A. (**1997**). "Modulation detection interference with two-component masker modulators," J. Acoust. Soc. Am. **102**, 1106–1112.
Sheft, S., and Yost, W. A. (**2007**). "Discrimination of starting phase with sinusoidal envelope modulation," J. Acoust. Soc. Am. **121**, EL84–89.
Shofner, W. D., Sheft, S., and Guzman, S. J. (**1996**). "Responses of ventral cochlear nucleus units in the chinchilla to amplitude modulation by low-frequency, two-tone complexes," J. Acoust. Soc. Am. **99**, 3592–3605.
Thompson, E. R., and Dau, T. (**2008**). "Binaural processing of modulated interaural level differences," J. Acoust. Soc. Am. **123**, 1017–1029.
Uchanski, R. M., Moore, B. C. J., and Glasberg, B. R. (**2006**). "The effect of modulation maskers on the detection of second-order amplitude modulation in the absence and presence of notched noise," J. Acoust. Soc. Am. **119**, 2937–2946.
Verhey, J. L., Ewert, S. D., and Dau, T. (**2003**). "Modulation masking produced by complex tone modulators," J. Acoust. Soc. Am. **114**, 2135–2146.

The effect of onset asynchrony on relative weights in profile analysis[a)]

Jinyu Qian[b)] and Virginia M. Richards[c)]
Department of Psychology, University of Pennsylvania, 3401 Walnut Street, Suite 302C, Philadelphia, Pennsylvania 19104

(Received 9 September 2009; revised 17 January 2010; accepted 20 January 2010)

Decision weights were estimated in a profile analysis task to determine whether onset asynchronies between the signal component and the nonsignal components encourage the segregation of the signal relative to the other components. The signal component onset was either synchronous or asynchronous with respect to the nonsignal components. In the asynchronous conditions, thresholds were higher and the decision weights were less efficient than in the synchronous conditions. These data are largely consistent with a segregation hypothesis: onset asynchrony encourages subjects to shift strategies from one of spectral shape discrimination toward one of intensity discrimination.
 [DOI: 10.1121/1.3314251]

PACS number(s): 43.66.Fe, 43.66.Ba [MW] Pages: 2461–2465

I. INTRODUCTION

Past research has shown that the ability to detect changes in spectral shape depends on the relative onsets of the components comprising the stimulus. Consider, for example, the detection of an increment to the level of the central component (signal component) of several equal-amplitude tones (nonsignal components). Thresholds increase when the onset of the signal components is changed from synchronous to asynchronous relative to the nonsignal components (Green and Dai, 1992; Hill and Bailey, 1997; Lentz *et al.*, 2004). One potential account for this result is the segregation hypothesis: the onset asynchrony between the signal and nonsignal components results in the segregation of the signal from the nonsignal components. Consequently, there is no longer a common reference system for the two segregated sounds, and thus level comparisons between the signal and nonsignal components are compromised. An implication of this hypothesis is that as the signal and nonsignal components become segregated, the subjects' decision strategy would shift from one associated with changes in spectral shape to one associated with changes in intensity at the signal frequency.

To provide an example, Hill and Bailey (1997) found that thresholds were higher when the signal component preceded the nonsignal components by 320 ms compared to when all components shared a common onset. To reduce the degree of segregation, they introduced two "captor tones," one higher and one lower in frequency than the signal frequency. The captor tones were turned on with the signal and were turned off when the nonsignal components were turned on. Thus the early portion of the signal could be grouped with the captor tones, freeing the latter portion of the signal component to be grouped with the nonsignal components. Consistent with this argument, the captor tones did result in lower thresholds relative to when there were no captor tones. Not all methods to promote the segregation of the signal component and thresholds in profile analysis, however, have succeeded. Hill and Bailey (2000) examined the effect of mistuning the signal component relative to the harmonically related nonsignal components. Those measures failed to indicate a change in threshold when the signal component was perceptually segregated from the nonsignal components.

The aim of the current study is to examine the effect of onset asynchrony on decision strategies in a profile analysis task. The subjects' task is to detect which of two sounds has an increment to the 1000 Hz component relative to the other equal-amplitude components. Decision strategies are revealed by estimating decision weights, or relative weights, for conditions in which the signal onset is either asynchronous or synchronous relative to the nonsignal components. Both 5- or 15-tone complexes are tested in different sets of conditions to investigate whether the effect of onset asynchrony on relative weights varies depending on the number of frequency components. In addition, the amount of asynchrony is varied in different conditions to reveal systematic changes in the results.

In each condition, relative weights for each frequency component and for the overall level are estimated (Berg and Green, 1990; Berg, 2004). For an ideal (linear) profile analysis observer, if the relative weight for the signal component is arbitrarily set to 1, the weight for the nonsignal components should be $-1/(n-1)$, where n is the total number of frequency components of the multitone complex (Berg and Green, 1990). Additionally, for an ideal profile-listening strategy, there should be no effect of level randomization (i.e., a weight of zero associated with overall level randomization). In contrast, a strict intensity discrimination decision strategy would not incorporate information from the nonsignal components and would show a strong effect of overall

[a)]Portions of this research were presented at the 31st MidWinter Meeting of Association for Research in Otolaryngology, Phoenix, AZ, 16–21 February 2008, Abstract 911.
[b)]Author to whom correspondence should be addressed. Electronic mail: qjyspace@yahoo.com
[c)]Present address: Department of Cognitive Sciences, University of California, 3151 Social Science Plaza, Irvine, CA, 92697.

level randomization. Overall, if subjects' detection strategies change from an across-frequency comparison strategy to an intensity discrimination strategy when an onset asynchrony is introduced, two related predictions can be made: (a) as the onset asynchrony increases, the relative weights associated with overall level randomization should increase, and (b) the weights associated with the nonsignal frequencies should approach zero. If, however, onset asynchrony does not influence decision strategies but affects processes such as the efficiency with which the subjects' decision rules are carried out (e.g., an overall increase in "internal noise"), no changes in the pattern of relative weights would be expected. To discriminate between these alternatives, in the current experiment subjects' efficiencies as well as decision weights are estimated (see Berg, 2004).

II. METHODS

A. Stimuli

The standard stimulus consisted of equal-amplitude tones equally spaced on a logarithmic frequency scale with frequencies ranging from 200 to 5000 Hz. In the target stimulus, a 1000 Hz tone was added in phase to the 1000 Hz signal component of the standard stimuli. The phase of each component was randomly chosen from a uniform distribution for each trial but fixed across two intervals. In order to derive relative weights for all components, independent level perturbations drawn from a standard normal distribution ($\mu = 0$ dB, $\sigma = 1$ dB) were added in phase to each component in each interval. On each presentation, the overall level of the stimulus was drawn at random from a uniform distribution ranging from 40 to 60 dB sound pressure level.

There were six conditions: the 5- or 15-tone simultaneous conditions, the 5- or 15-tone leading-100 conditions, and the 5- or 15-tone leading-300 conditions. In the first two conditions, the signal and nonsignal components had the same onset. In the last four leading conditions, the signal component started earlier than the nonsignal components by either 100 or 300 ms. The multitone stimuli in each condition had either 5 or 15 frequency components. All nonsignal components had the same onset and the same duration of 200 ms. All stimuli had 5 ms raised cosine rise/fall ramps at the stimulus onsets and offsets.

The stimuli were presented diotically over Sennheiser HD410 SL headphones with visual feedback following each of the subjects' responses. Subjects were tested in a double-walled sound-attenuated booth in a quiet room and the stimuli were generated by TDT system II hardware controlled by MATLAB software.

B. Subjects and procedure

Four young adults aged 20–31 with normal hearing (<15 dB hearing loss at frequencies of 250, 500, 1000, 2000, 4000, 6000, and 8000 Hz in both ears) served as subjects. A two-alternative forced-choice procedure with a 2-down 1-up adaptive rule was used to estimate the threshold corresponding to 71% correct responses (Levitt, 1971) or a d' of 0.77. Thresholds and relative weight estimates are based on 50 50-trial runs (a total of 2500 trials) for each condition. Subjects S1 and S2 ran the 5-tone simultaneous and the 5-tone leading-300 conditions in different orders, followed by the 15-tone simultaneous and the 15-tone leading-300 conditions in different orders, and then the 5- and 15-tone leading-100 conditions in different orders. Subjects S3 and S4 ran the three 15-tone conditions in different orders, followed by the three 5-tone conditions in different orders. All subjects had at least four hours of practice prior to data collection.

C. Relative weight estimation

1. Decision model

For each trial the decision variable (DV) was modeled as the difference between the weighted sums of the level of each frequency component in the first interval and in the second interval (Berg, 2004).[1] The specific weights assigned to different frequency components are the relative weights to be estimated. Theoretically, the sum of the relative weights for individual frequency components forms the weight for overall level randomization (Berg, 2004). However, to avoid the cumulative error of estimation, the weight for overall level randomization was estimated independently.

2. Relative weights

Logistic regression was applied to estimate relative weights (e.g., Alexander and Lutfi, 2004; Dye *et al.*, 2005) for the overall level randomization and each frequency component of the multitone stimuli. Using a MATLAB build-in function (glmfit), the relative weights and the standard errors of these weights were estimated from a predictor matrix and a response array. The predictor matrix included the differences in the overall level randomization between two intervals for every trial and the level differences for each frequency component between the two intervals excluding the differences in the overall level randomization. The response array consisted of the responses coded as zeros ("target in interval 2") or ones ("target in interval 1"). The relative weights were based on 2500 trials (50 sets of 50 trials) for each condition. Each set of relative weights was normalized so that the weight of the signal component was 1. The standard errors of the relative weights were normalized accordingly.

3. Measures of efficiency

Efficiency measures allow a comparison between the ideal and subjects' performance and between different subjects' performance. The ideal observer maximizes the d' based on the best linear decision model. Here, overall efficiency, η, is described as the product of two quantities: the weighting efficiency, η_W, and the noise efficiency, η_N. (Berg, 1990; Doherty and Lutfi, 1999; Berg, 2004). The weighting efficiency describes the efficiency of the subject's weighting strategy relative to the ideal weighting strategy. The noise efficiency describes the efficiency associated with processes other than the pattern of relative weights alone, such as peripheral and central internal noises. Following the notation of Berg (2004), the three efficiencies are defined as follows:

TABLE I. Individual and averaged thresholds (dB: signal level relative to the standard level) are shown. The standard errors of the mean are shown at the bottom row.

	Conditions					
	5-tone			15-tone		
Subjects	Sim	Lead-100	Lead-300	Sim	Lead-100	Lead-300
S1	−9.5	−6.7	−2.0	−14.8	−5.3	−1.3
S2	−6.1	1.4	0.6	−12.8	−4.0	0.1
S3	−11.0	−4.1	−1.8	−6.7	−2.0	0.3
S4	−12.0	−0.4	1.6	−13.1	−5.5	−2.7
AVG	−9.7	−2.4	−0.4	−11.8	−4.2	−0.9
SEM	1.3	1.8	0.9	1.8	0.8	0.7

$$\eta = \eta_W \times \eta_N = (d'_W/d')^2 \times (d'_{\text{obs}}/d'_W)^2, \quad (1)$$

where d' is the sensitivity index for an ideal observer, d'_W is the highest sensitivity index based on the estimated pattern of relative weights, and d'_{obs} is the subject's actual sensitivity index.

The d'_W calculation was based on the Eq. (2) below given by Berg and Green (1990) and Berg (2004).[3] For each subject this equation was applied using the signal level appropriate for the various conditions,

$$d'_W = \frac{\sqrt{2}\Delta_s}{\sqrt{\sum_{i=1}^{n} w_i^2\sigma^2 + w_L^2\sigma_L^2}}, \quad (2)$$

where Δ_s is the signal level increment in dB at the subjects' thresholds, w_i and w_L are the relative weights for the ith frequency component and the weight for overall level randomization, respectively. The variance of the level perturbations is given by σ^2 and σ_L^2 is the variance of overall level randomization. The number of frequency components is given by n.

The same equation was used to calculate the d', the sensitivity index for an ideal observer, except that the subjects' relative weights were replaced with the ideal relative weights in Eq. (2).

III. RESULTS AND DISCUSSION

A. Psychophysical results

Table I shows the thresholds (in dB signal re. standard) for the four subjects and the averaged data. In the simultaneous conditions, thresholds are lower for the 15-than the 5-tone condition, although the difference is only 2 dB. A two-way, within-subjects analysis of variance (ANOVA) showed no significant difference between the 5- and 15-tone conditions, and no significant interaction between the number of components and onset asynchrony. In contrast, the effect of onset asynchrony was significant [$F(2,6)=92$, $p<0.0005$]. These data are in accord with past results, except that in the current experiment the change in thresholds with number of components is somewhat smaller than in the past (Green and Dai, 1992; Hill and Bailey, 1997; Lentz *et al.*, 2004; Berg, 2004).

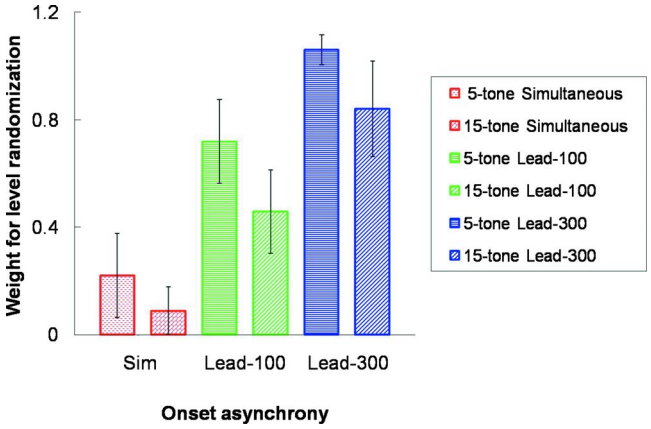

FIG. 1. (Color online) The values of relative weight for level randomization averaged across subjects. Each bar represents one condition and error bars indicate 1 standard error of the mean. For each onset asynchrony, the left and the right bars are for the 5-tone and 15-tone stimuli, respectively.

B. Subject's relative weights

Figure 1 shows the values of relative weights for level randomization averaged across subjects for the six conditions tested (from left to right: 5-tone and 15-tone simultaneous, 5-tone and 15-tone leading-100, and 5-tone and 15-tone leading-300). Error bars show the standard errors of the mean. The results for individual subjects are similar to the pattern of results shown in Fig. 1, with the exception that for S4 in the 15-tone condition the relative weights are approximately the same across the three levels of onset asynchrony. A two-way, within-subjects ANOVA indicated a significant effect of onset asynchrony [$F(2,6)=28.8$; $p<0.001$] but did not indicate a significant effect of number of components[4] nor a significant interaction between number of components and onset asynchrony. These results are consistent with the segregation argument, suggesting that the signal component may be perceptually segregated from the other components in the leading conditions and that the subjects may, at least partially, shift their strategies from the spectral shape discrimination in the simultaneous conditions to intensity discrimination in the leading conditions.

Normalized relative weights for all of the components are plotted as a function of frequency in Fig. 2(a) (5-tone conditions) and Fig. 2(b) (15-tone conditions). Each panel includes one subject's data from simultaneous (circles), leading-100 (diamonds) and leading-300 (squares) conditions. The standard errors of the estimated relative weights ranged from approximately 0.01 to 0.25 across subjects and conditions (not shown in Fig. 2).

According to the second prediction of the segregation hypothesis, one would expect the relative weights at the nonsignal frequencies to approach zero as the signal onset asynchrony increases. For 5-tone conditions shown in Fig. 2(a), nonsignal weights at frequencies lower than the signal frequency are negative for simultaneous (circles) conditions but approach zero for the leading-300 conditions (squares). However, the relative weights for components at frequencies higher than the signal frequency are approximately zero in all conditions.

For the 15-tone stimuli shown in Fig. 2(b), the nonsignal

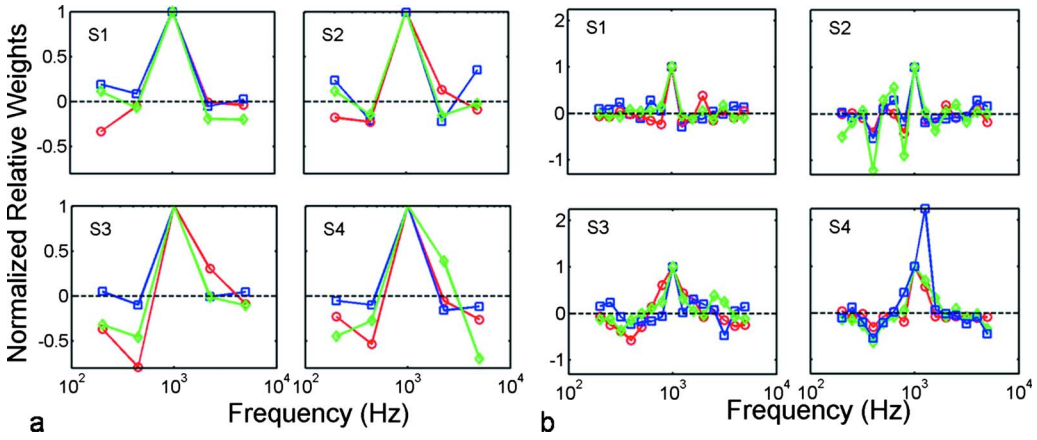

FIG. 2. (Color online) Relative weights plotted as a function of frequency are shown for each subject (panels) for the (a) 5-tone complex and (b) 15-tone complex stimuli. Values are plotted separately for the simultaneous (circles), leading-100 (diamonds), and leading-300 (squares) conditions.

weights are near zero and do not appear to systematically change as the asynchrony grows. This is not surprising—for the simultaneous conditions normalized ideal nonsignal weights are −1/4 for the 5-tone stimuli but −1/14 for the 15-tone stimuli.

In an effort to provide an overview of the change in relative weights with onset asynchrony, and because we had no *a priori* hypotheses regarding changes in the complex pattern of relative weights, for each of the three onset asynchronies (0, 100, and 300 ms), the relative weights were averaged across all nonsignal components. Then a within-subjects two-factor ANOVA was run on these averages to determine whether the nonsignal relative weights gravitate toward zero as the onset asynchrony increases. The results did not reveal a significant effect of number of components,[4] nor was the interaction between number of components and onset asynchrony significant. The main effect of onset asynchrony, however, was significant $[F(2,6)=55.3,\ p<0.001]$. For the 5-tone stimuli, the relative weights averaged across subjects and all nonsignal components were −0.17, −0.15, and 0.00 for the simultaneous, leading-100, and leading-300 conditions, respectively. As one would anticipate, for the 15-component conditions, the change was smaller: −0.05, −0.05, and 0.02 for the simultaneous, leading-100, and leading-300 conditions, respectively. Overall, these results are in accord with the argument that onset asynchrony makes across-frequency comparisons of level more difficult, leading to a shift in strategy.

To summarize, the relative weights are consistent with a segregation-based argument: as the signal onset asynchrony is increased, subjects shift from a spectral shape discrimination strategy toward an intensity discrimination strategy because across-frequency level comparison of the signal and nonsignal components becomes difficult. First, as the onset asynchrony increases, the relative weight associated with the overall level randomization increases. Second, as the signal onset asynchrony increases, the average of the relative weights of the nonsignal components approaches zero. Both of these factors suggest a shift from detecting differences in spectral shape toward detecting changes in intensity at the signal frequency.

C. Weighting efficiency and noise efficiency

The weighting and noise efficiencies, for the individual subjects and their averages, are listed in Tables II and III, respectively. Consistent with the pattern of relative weights described above, the weighting efficiencies fall dramatically as the onset asynchrony increases for both the 5-tone and 15-tone stimuli. The noise efficiencies grow somewhat as the onset asynchrony increases for the 5-tone stimuli but do not appear to change for the 15-tone stimuli. The results of within-subjects two-way ANOVAs are consistent with this observation. For the weighting efficiencies, the effect of onset asynchrony is significant $[F(2,6)=38,\ p<0.0001]$ but the number of components, and the interaction term, did not approach significance. For the noise efficiencies, neither main effect nor the interaction reached significance. The factor of onset asynchrony, did, however, approach significance $[F(2,6)=3.3,\ p\sim0.1]$. Overall, the effect of asynchrony on weighting efficiencies far exceeded the effect on noise efficiencies, suggesting that threshold elevations due to onset asynchrony reflect "inefficient" changes in decision strategies rather than increases in internal noise.

IV. SUMMARY AND CONCLUSIONS

Spectral shape discrimination deteriorates when an onset asynchrony is introduced between signal and nonsignal fre-

TABLE II. Individual and averaged weighting efficiencies are shown. The standard errors of the mean are shown at the bottom row.

	Conditions					
	5-tone			15-tone		
Subjects	Sim	Lead-100	Lead-300	Sim	Lead-100	Lead-300
S1	0.24	0.09	0.03	0.55	0.10	0.03
S2	0.11	0.03	0.02	0.43	0.25	0.03
S3	0.42	0.07	0.04	0.25	0.04	0.03
S4	0.58	0.17	0.03	0.48	0.14	0.11
AVG	0.34	0.09	0.03	0.43	0.13	0.05
SEM	0.10	0.03	0.00	0.06	0.04	0.02

TABLE III. Individual and averaged noise efficiencies are shown. The standard errors of the mean are shown at the bottom row.

	Conditions					
	5-tone			15-tone		
Subjects	Sim	Lead-100	Lead-300	Sim	Lead-100	Lead-300
S1	0.25	0.36	0.41	0.28	0.22	0.33
S2	0.28	0.29	0.38	0.23	0.07	0.31
S3	0.19	0.29	0.35	0.12	0.28	0.29
S4	0.17	0.07	0.24	0.22	0.17	0.13
AVG	0.22	0.25	0.35	0.21	0.19	0.27
SEM	0.03	0.06	0.04	0.03	0.04	0.05

quency components of the stimuli (Green and Dai, 1992; Hill and Bailey, 1997; Lentz *et al.*, 2004). It has been suggested that asynchrony leads to the perceptual segregation of the signal component relative to the nonsignal components, impairing the across-frequency comparison required for spectral shape discrimination.

Relative weights were derived to explore the effect of onset asynchrony on decision strategies in profile analysis. Across subjects and conditions, both thresholds and the relative weights for the overall level randomization increase with increases in onset asynchrony. Moreover, the average of the relative weights for the nonsignal components approach zero as the onset asynchrony increases. These features are consistent with expectations that increasing the onset asynchrony hinders across-frequency comparisons of level, forcing subjects to shift from a strategy of discriminating spectral shape toward a strategy of discriminating changes in level at the signal frequency (intensity discrimination). The measurement of subjects' noise efficiencies do not provide support for an alternative account—that thresholds increase with increases in onset asynchrony because the internal noise is effectively increased. Overall, the current results support the segregation hypothesis: as the onset asynchrony between the signal and the other components increases, thresholds deteriorate because subjects can no longer compare the levels of the signal component and the remaining components.

ACKNOWLEDGMENTS

We would like to thank the associate editor, Dr. Hedwig E. Gockel, and Dr. Robert A. Lutfi who provided valuable comments on early versions of the paper. This work was supported by Grant No. R01 DC002012 from the National Institutes of Health.

[1]The decision variable, DV, is defined as $DV=\Sigma_{i=1}^{n} w_i \Delta l_i$, where the w_i are the relative weights for ith frequency component, and the Δl_i are the level differences between the two intervals of the ith frequency component. Note that Δl_i is the sum of the overall level difference, ΔL, and the level difference excluding the overall level difference, Δp_i. Thus, the decision variable may be rewritten as $DV=\Sigma_{i=1}^{n} w_i(\Delta L+\Delta p_i)=\Delta L\Sigma_{i=1}^{n} w_i + \Sigma_{i=1}^{n} w_i \Delta p_i = \Delta L w_L + \Sigma_{i=1}^{n} w_i \Delta p_i$, where $w_L=\Sigma_{i=1}^{n} w_i$.

[3]The development of Eq. (2) assumed normally distributed level variation in addition to normally distributed perturbations. Here uniformly distributed level variation was tested. Simulations were also run to provide estimates of d'_w and subsequent values of efficiency (e.g., Qian and Richards, 2008). The results were not appreciably different from those obtained using Eq. (2).

[4]A main effect of the number of components, 5 vs. 15, provides little information because the relative weights (a) have been independently normalized and (b) are not assured to have the same scaled values prior to normalization. This factor is included in the ANOVA to allow for a test of an interaction.

Alexander, J. M., and Lutfi, R. A. (**2004**). "Informational masking in hearing-impaired and normal-hearing listeners: Sensation level and decision weights," J. Acoust. Soc. Am. **116**, 2234–2247.

Berg, B. G. (**1990**). "Observer efficiency and weights in a multiple observation task," J. Acoust. Soc. Am. **88**, 149–158.

Berg, B. G. (**2004**). "A molecular description of profile analysis: Decision weights and internal noise," J. Acoust. Soc. Am. **115**, 822–829.

Berg, B. G., and Green, D. M. (**1990**). "Spectral weights in profile listening," J. Acoust. Soc. Am. **88**, 758–766.

Doherty, K. A., and Lutfi, R. A. (**1999**). "Level discrimination of single tones in a multitone complex by normal-hearing and hearing-impaired listeners," J. Acoust. Soc. Am. **105**, 1831–1840.

Dye, R. H., Stellmack, M. A., and Jurcin, N. F. (**2005**). "Observer weighting strategies in interaural time-difference discrimination and monaural level discrimination for a multi-tone complex," J. Acoust. Soc. Am. **117**, 3079–3090.

Green, D. M., and Dai, H., (**1992**). "Temporal relations in profile comparisons," in *Auditory Physiology and Perception*, edited by Y. Cazals, L. Demany, and K. Horner, (Pergamon, Oxford), pp. 471–477.

Hill, N. I., and Bailey, P. J. (**1997**). "Profile analysis with an asynchronous target: Evidence for auditory grouping," J. Acoust. Soc. Am. **102**, 477–481.

Hill, N. I., and Bailey, P. J. (**2000**). "Profile analysis of harmonic complexes: Effects of mistuning the target," J. Acoust. Soc. Am. **107**, 2291–2294.

Lentz, J. J., Leek, M. R., and Molis, M. R. (**2004**). "The effect of onset asynchrony on profile analysis by normal-hearing and hearing-impaired listeners," J. Acoust. Soc. Am. **116**, 2289–2297.

Levitt, H. (**1971**). "Transformed up-down methods in psychoacoustics," J. Acoust. Soc. Am. **49**, 467–477.

Qian, J., and Richards, V. M. (**2008**). "Relative weights for frequency glide detection using narrowband noise," J. Acoust. Soc. Am. **123**, 2692–2700.

Combining information across frequency regions in fundamental frequency discrimination[a)]

Hedwig E. Gockel[b)] and Robert P. Carlyon
MRC Cognition and Brain Sciences Unit, 15 Chaucer Road, Cambridge CB2 7EF, United Kingdom

Christopher J. Plack
Division of Human Communication and Deafness, University of Manchester, Manchester M13 9PL, United Kingdom

(Received 2 September 2009; revised 28 January 2010; accepted 28 January 2010)

Sensitivity to fundamental frequency (F0) differences was measured for two complex tones, A and B, which had the same F0 but were filtered into two different frequency regions. Tones were presented either alone or together. A signal-detection analysis was used to predict effects of combining F0 information across frequency regions. For 400-ms tones containing only unresolved harmonics, the first experiment showed that performance (in terms of d') for the combined presentation was better than for the isolated tones but was not optimal (assuming independent channels and noises) and was independent of the relative timing of pulses in the envelopes of tones A and B (varied by changing the starting phase of components of tone B relative to those of tone A). The nonoptimal performance was shown not to be due to peripheral masking (experiment II), or to listeners paying attention mainly to one frequency region (experiment III), nor was it specific to conditions where all harmonics were unresolved (experiment IV). In contrast, optimal performance in F0 discrimination for combined presentation *was* observed for 50-ms tones (experiment V). The results may reflect the limited ability of the human auditory system to integrate information simultaneously in the time and the frequency domains.
 [DOI: 10.1121/1.3327811]

PACS number(s): 43.66.Hg, 43.66.Ba, 43.66.Fe [MW] Pages: 2466–2478

I. INTRODUCTION

In many everyday situations, listeners are required to estimate the fundamental frequency (F0) of periodic sounds, such as the voiced portions of speech. Such sounds are often broadband and sometimes contain several fairly discrete spectral peaks, indicating that the majority of information comes from fairly discrete spectral regions. Thus, it is important to understand the extent to which the auditory system can combine F0 information across spectral regions and the dependence of this ability on the physical parameters of the stimulus.

In recent years, several studies have reported an impairment in discrimination of F0 for two sequentially presented complex target tones due to the presence of another complex tone (the interferer) which was filtered into a spectral region remote from that of the target tones (Gockel *et al.*, 2004, 2005, 2009a, 2009b; Micheyl and Oxenham, 2007). This "pitch discrimination interference (PDI)" is strongest when target and interferer tones have similar F0s, but can be observed even for large F0 separations between the target and interferer (Gockel *et al.*, 2004). Its existence indicates that listeners are not able to optimally weight information across spectrally separated regions for the purpose of deriving the residue pitch of a target tone. It may impair the ability of the listener to process pitch when more than one sound is present.

A somewhat simpler paradigm concerns the ability of listeners to combine information on a single pitch. If across-frequency integration is the "default" mode of operation, especially when the complex tones in the two regions have similar F0s, then listeners might do well in this situation. For example, Kaernbach and Bering (2001) measured F0 discrimination for high-pass filtered harmonic complexes, and showed that performance improved as the high-pass cutoff frequency was lowered. However, in their experiment, it was not possible to determine whether this improvement was the result of across-frequency combination of information or simply due to the introduction of frequency regions where sensitivity was relatively high. The present study investigated the combination of information across frequency regions, using a paradigm that controlled for sensitivity in each individual spectral region.

The main objective of the present study was to investigate how well pitch information is combined across spectral regions when combination of information is advantageous for the task. Two complex tones, A and B, were filtered into two separate spectral regions. With one exception, which will be discussed later, tones A and B had identical F0s. F0 discrimination performance was measured for each of the tones presented alone and for the two presented together. The exact spectral (and other) parameters of tones A and B were chosen

[a)]Parts of this work were presented at the 155th meeting of the Acoustical Society of America, Paris, France, 29 June–4 July 2008 [J. Acoust. Soc. Am. **123**, 3563 (2008)].
[b)]Author to whom correspondence should be addressed. Electronic mail: hedwig.gockel@mrc-cbu.cam.ac.uk

 0001-4966/2010/127(4)/2466/13/$25.00

so as to give approximately equal d' values for discrimination of each of the tones when presented alone. This reduced the risk of performance in the combined case being dominated by performance for either A or B, and thus increased the chance of observing any effect of combination of information across spectral regions. The combination of F0 information across regions was measured in five experiments under various conditions.

Signal detection theory (Green and Swets, 1966) predicts that, if performance is mainly limited by independent internal peripheral noises[1] for each of the two complexes, and if information is combined optimally across the two regions, i.e., there is no central noise at the decision stage, then the d' value observed in the combined case, d'_c, should correspond to

$$d'_c = (d'^2_A + d'^2_B)^{0.5}, \quad (1)$$

where d'_A and d'_B are the d' values for discrimination of tones A and B, respectively, when presented alone.

If the internal peripheral noises that mainly limit performance were partly correlated across the two complexes, due to, for example, respiratory or circulatory processes, and if information is combined optimally across the two regions, then d'_c is given by

$$d'_c = [(d'^2_A + d'^2_B - 2 \cdot r \cdot d'_A \cdot d'_B)/(1 - r^2)]^{0.5}, \quad (2)$$

where r corresponds to the correlation between the two internal noises across the two complexes (with $r < 1$). Thus, by assuming a partial correlation between the peripheral noises affecting F0 discrimination for the two complexes, the predicted value for d'_c will be smaller than under the assumption of independent noises. Solving Eq. (2) for r gives

$$r = d'_A \cdot d'_B/d'^2_c - [(d'_A \cdot d'_B/d'^2_c)^2 - (d'^2_A + d'^2_B - d'^2_c)/d'^2_c]^{0.5}. \quad (3)$$

The derivation for Eq. (2) and the resulting solution for r are given in the Appendix. Here and throughout, the terms central and peripheral noises do not refer to anatomical structures but are used in the context of decision theory where peripheral noise refers to noise added before (rather than after) information has been combined across spectral regions.

If performance is mainly limited by a central noise that is common to A and B, occurring after information from A and B has been combined, and if information is combined optimally, then the d' value observed in the combined case should correspond to

$$d'_c = d'_A + d'_B. \quad (4)$$

It is conceivable that a large central noise limits performance for frequency discrimination. For example, Siebert (1970) argued that, in the case of frequency discrimination of pure tones, the information that is available in the auditory nerve is not used optimally at a later stage. This argument was based on his optimal observer calculations, which predicted much lower thresholds than observed. A study by Hafter *et al.* (1990) provides an example of additivity of d' values in auditory perception due to the combined presentation of two signals. Hafter *et al.* (1990) investigated how information arising from interaural level differences (ILDs) and interaural time differences (ITDs) is combined. Stimuli were bandpass filtered clicks (centered at 4 kHz) with various combinations of ILD and ITD. Performance was measured using a two-interval two-alternative forced choice (2I-2AFC) task, where in one randomly chosen interval, the interaural differences favored the left side, while in the other, they favored the right side; when both ILD and ITD were present, they always favored the same side. Subjects listened for the lateral movement of the images between the two intervals. The results showed that the d' values for the combined conditions (when an ILD and an ITD were present) were the sum of the individual d' values observed when only ILD or only ITD was present.

The second objective of the present study was to investigate whether, when tones A and B contained only harmonics which were unresolved by the peripheral auditory system, there was an effect of the relative timing of peaks (sometimes called pitch pulses) in the envelopes of tones A and B. Human listeners have been shown to be sensitive to asynchronies of pitch pulses [pitch pulse asynchrony (PPA)] in different frequency regions (Patterson, 1987; Summerfield and Assmann, 1991; Carlyon, 1994; Carlyon and Shackleton, 1994). Thus, it is conceivable that the size of the PPA affects performance for F0 discrimination in the combined condition. For example, envelope modulation which is in-phase across auditory filters (synchronization in time of envelope peaks in different auditory filters) might lead to a more salient temporal pitch than out-of-phase modulation. This assumption has been made e.g., by Laneau *et al.* (2006) in their development of a sound processing scheme that was designed to optimize pitch perception in cochlear implant (CI) listeners (see also Vandali *et al.*, 2005). As in most processing schemes, F0 information was conveyed by the envelope repetition rate applied to pulse trains on a number of electrodes, and Laneau *et al.* (2006) investigated the effects of enhancing the envelope modulation depth and of synchronizing the envelopes across electrodes. Although a modest improvement was observed, it is not clear whether this was due to the envelope enhancement or to the synchronization. The present study, using acoustic stimuli and normal-hearing listeners, provides a more direct measure of the effect of relative envelope phase on the integration of F0 information by keeping constant the envelope modulation depth within auditory channels tuned to the passband of the stimuli.

II. GENERAL METHOD AND PROCEDURE

In all experiments, a 2I-2AFC task was used. Subjects had to indicate which of the two intervals contained the sound with the higher F0 ("higher pitch"). Visual feedback was provided on whether their answer was right or wrong, except in experiment III. The method of constant stimuli was used, and performance was expressed in terms of d' (Macmillan and Creelman, 1991). For each subject, the exact characteristics of the tones were determined in preliminary experiments such that the d' values for F0 discrimination of

tones A and B when presented alone were approximately equal and ranged from 1.0 to 1.2. The details are described below for each experiment.

In experiments I–III and V, the overall root-mean-square (rms) level of tones A and B was 52 dB sound pressure level (SPL), irrespective of bandwidth. In experiment IV, the rms level of the tone in the low-frequency region was increased to 55 dB SPL, to make it approximately as loud as the tone in the midfrequency region. A continuous background of pink noise with a spectrum level of 15 dB (re 20 μPa) at 1 kHz was presented in all experiments. Its purpose was to mask possible distortion products and to prevent subjects from relying on possible within-channel cues arising from the interaction of components at the outputs of auditory filters having center frequencies midway between the two spectral regions, specifically in experiments I and V, where complex tones were separated in spectral region by one octave and consisted of unresolved harmonics (see below). Calculation of excitation patterns (following Moore *et al.*, 1997) for the pink noise and for the two complexes together (as used in experiments I and V) showed that the excitation level of the pink noise at the output of an auditory filter midway between the two regions was at least 5 dB above the excitation level of the primary components. While Gockel *et al.* (2002) showed that masked thresholds for complex tones in noise could be as low as −9.5 dB when the components were added in cosine phase and the F0 was low (62.5 Hz), the contribution from auditory filters with such a low signal to noise ratio toward F0 discrimination was expected to be negligible relative to the contribution of auditory filters centered on the passbands of the two regions. Furthermore, due to the presence of the pink noise, the sensation levels of the complex tones would be far below that required (about 50 dB SL) to produce an audible distortion product at the F0 (see Plomp, 1965).

In experiments I–IV, the duration of the stimuli was 400 ms, and in experiment V the duration was 50 ms. All durations included 20-ms raised-cosine onset and offset ramps. The silent interval between the two intervals within a trial was 500 ms.

Tones were generated and (in experiments I–III and V) bandpass filtered digitally in MATLAB (The MathWorks, Inc., Natick, MA). Bandpass filtering was achieved with a linear-phase finite impulse response (FIR) filter (order 16000) implemented in MATLAB with a flat passband and linear slopes on a logarithmic frequency scale of 48 dB/octave. Stimuli were played out using a 16-bit digital-to-analog converter (CED 1401 plus), with a mean sample rate of 40 kHz. The actual sample rate was varied between trials over the range ±10% (this produced a slight variation in F0, duration, and the filter cutoff frequencies). This was done to encourage subjects to compare the F0s of the stimuli across the two intervals within a trial and to discourage them from using a long-term memory representation of the pitches. Stimuli were passed through an antialiasing filter (Kemo 21C30) with a cutoff frequency of 14 kHz (slope of 96 dB/oct) and were presented using Sennheiser HD250 headphones.

Conditions were fixed in blocks of 105 trials. The first five trials were considered as "warm-up" trials and results from those were discarded. Conditions were run in counterbalanced order. The duration of each session was about 2 h, including rest times. Before data collection proper, subjects were trained until performance seemed stable. Including the preliminary experiments, aimed at finding stimulus parameters resulting in approximately equal d' values for tones A and B, typically about four to ten sessions were run for each subject in each experiment. Usually, the final d' value for each subject and condition was based on at least 500 trials.

Overall, eight subjects participated, one of whom was the first author. They ranged in age from 19–47 years, and their absolute thresholds at octave frequencies between 250 and 8000 Hz were within 15 dB of the ISO 389-8 (2004) standard. Six of them had some musical training.

III. EXPERIMENT I: MONAURAL UNRESOLVED TONE COMPLEXES

A. Rationale

It is generally believed that components in a harmonic complex tone are resolved up to about the eighth harmonic (Plomp, 1964; Plomp and Mimpen, 1968; Moore and Ohgushi, 1993; Shackleton and Carlyon, 1994; Bernstein and Oxenham, 2003). For harmonic complex tones containing only unresolved harmonics, pitch information is carried in the repetition rate of the envelope fluctuations and possibly, for intermediate harmonics (8th–13th), in the temporal fine structure (Moore *et al.*, 2006, but see Oxenham *et al.*, 2009). The main objective of the first experiment was to determine whether and how well F0 information is combined across frequency regions when the complex tones in both regions contain only unresolved harmonics (above the 13th), i.e., pitch information is only carried in the repetition rate of the envelope fluctuations, and are presented to the same ear. The second objective was to investigate whether the relative timing of the envelope peaks in the two frequency regions has an effect on F0 discrimination in the combined condition. It has previously been shown that listeners (i) can discriminate a stimulus with a PPA from a stimulus without a PPA (Carlyon, 1994), (ii) are moderately sensitive to the direction of the PPA across frequency regions (Gockel *et al.*, 2005), and (iii) can use PPA to discriminate the F0 of one tone complex in the presence of another tone complex with fixed F0 (Miyazono and Moore, 2009). Thus, it is conceivable that the relative timing of the pitch pulses of the two complex tones affects F0 discrimination performance. For example, the tones might sound more fused if the pitch pulses occur simultaneously in the two regions.

B. Stimuli and subjects

The 400-ms complex tones were presented monaurally to the left ear of each of six subjects. For three subjects, tone A was filtered from 1350–1650 Hz (mid region) and tone B was filtered from 3300–4200 Hz (high region). The nominal F0, which was identical for the two tones, was 75 Hz, and for both complexes components were added in sine phase. The difference in F0, ΔF0, between the complex tones in the two intervals of the 2AFC task was fixed at 3%, 4%, and 5% for subjects 1, 2, and 3, respectively. Preliminary experiments

showed that for these three subjects equal performance for the two tones, with d' values around 1.1, could be achieved with those parameters. For the other subjects, with the same parameters, sensitivity was greater for tone A than for tone B. For subjects 4, 5, and 6, the components in both complexes were added in alternating phase. This doubled the repetition rate in the stimulus envelope, thereby increasing the pitch by one octave (Shackleton and Carlyon, 1994), and increased sensitivity to F0 differences in the high frequency region relative to that in the mid region. For subjects 4 and 5, performance was about equal for the two tones, with nominal F0 and filter regions identical to those used for subjects 1–3. For these two subjects, ΔF0 was fixed at 1.5% and 4%. For the sixth subject, in order to obtain equal sensitivity for the two tones, the nominal F0 was increased to 90 Hz and the filter regions were adjusted to 1375–1875 Hz and 3900–5400 Hz. For this subject, ΔF0 was fixed at 3%.

In the combined condition, where tones A and B were presented simultaneously, to introduce a PPA, the envelope (but not the onset) of tone B was advanced relative to that of tone A by various amounts. To achieve this, the starting phase of the nth harmonic in tone B was shifted by $n \cdot \Delta\varphi$. The values of $\Delta\varphi$ were 0°, 90°, 180°, and 270°.

To prevent subjects from using differences in the shape of the waveform at onset between the two stimuli to be discriminated, the time point within each period at which the waveform was turned on was chosen at random for each presentation. Note that this did not affect the difference between the starting phases of components in the two frequency regions, i.e., ongoing differences between the peaks in the envelopes in the two regions were unaffected.

C. Results and discussion

In the combined condition, the mean d' values [and standard errors (SEs) across subjects] observed for the four values of $\Delta\varphi$ were 1.27 (0.07), 1.24 (0.06), 1.27 (0.7), and 1.22 (0.05) for $\Delta\varphi$ equal to 0°, 90°, 180°, and 270°, respectively. There was no significant difference between these d' values, as shown by the results of a repeated-measures one-way analysis of variance (ANOVA) performed on the individual d' values [$F(3,15)=0.86$, $p=0.47$].[2] Thus, the relative timing of the pulses in the two frequency regions did not significantly affect F0 discrimination when both tones were presented simultaneously, at least not for the values of $\Delta\varphi$ chosen here. Therefore, in what follows, the d' value shown for the combined condition is based on the percent correct values averaged across the four $\Delta\varphi$ conditions.

Figure 1 shows the mean d' values and the corresponding SEs across subjects for the conditions where tones A and B were presented individually (conditions "Mid" and "High," white bars), and simultaneously (condition "Combined," black bar), and the predicted d' value for the combined condition, assuming optimal combination of information across frequency regions and independent noises [Eq. (1), hatched bar]. In the rest of the paper, we focus on the predictions for d' derived from Eq. (1) [and correlation values derived from Eq. (3)], because the differences between predicted and observed d' values in the combined condition would be even larger for predictions based on Eq. (4). The predicted d' value was calculated first for each subject individually. The mean and the SE across subjects' individual predictions are shown.

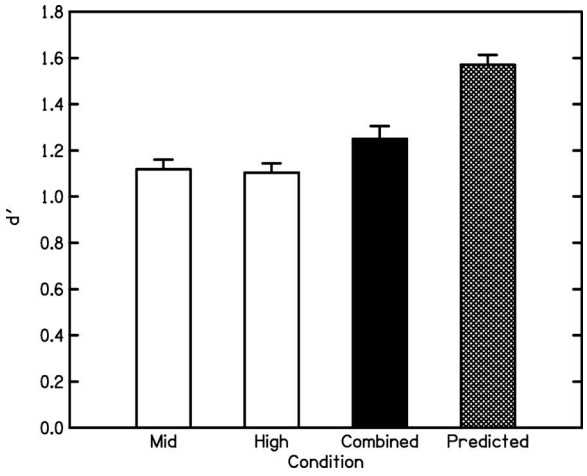

FIG. 1. Means and SEs of obtained d' values for experiment I, plus prediction, for F0-discrimination task. Stimuli were 400-ms complex tones filtered either into a mid spectral region (tone A) or a high spectral region (tone B) (white bars) or tones A and B combined (black bar). The prediction for the combined condition, assuming optimal combination of F0 information across the two frequency regions, is shown by the hatched bar. See text for details.

As intended, mean d' values for the individually presented tones were about 1.1 and were very similar for the two frequency regions. In the combined condition, the mean d' value was 1.25, which indicates a small improvement over individual presentation. A paired-sample t-test showed that the d' value in the combined condition was significantly larger than the higher of the two d' values observed for individual presentation [$t(5)=2.08$, $p<0.05$; one-tailed]. The predicted mean for the combined condition, assuming optimal combination of information and independent noises, was 1.57. The observed sensitivity in the combined condition was clearly below the prediction (by a factor of 0.79). A paired-sample t-test showed this difference to be highly significant [$t(5)=8.15$, $p<0.001$; two-tailed]. Assuming partial correlation between the two noises, the mean of the estimated r values was 0.64, with a SE (across subjects) of 0.09.

Overall, the results showed a small but significant improvement in F0 discrimination when tones A and B were presented simultaneously compared to when they were presented in isolation. This indicates that information can be combined across frequency regions. This effect was not dependent on the relative timing of the pitch pulses in the two regions and was markedly less than predicted assuming optimal combination of information and independent noises.

IV. EXPERIMENT II: MONAURAL AND DICHOTIC UNRESOLVED SPECTRALLY ADJACENT TONE COMPLEXES

A. Rationale

The objective of the second experiment was to investigate whether the nonoptimal combination of information across frequency regions (assuming independent noises) that

was observed in the first experiment could have been partly due to partial masking between the two stimuli, in spite of them being filtered into frequency regions separated by one octave and being presented at a low level in a pink background noise. The calculated excitation patterns for the stimuli in experiment I (see Sec. II) showed that the signal to noise ratio at auditory filters centered halfway between the two regions was below about −5 dB. Thus, the effect of partial masking on F0 discrimination for the combined condition was expected to be negligible. To investigate any remaining role of peripheral masking, here the frequency separation between the two spectral regions was reduced relative to that in experiment I. Tones A and B were presented either to opposite ears or to the same ear. If peripheral masking had a negative effect, performance would be expected to be better for dichotic than for monaural presentation of the two tones.

B. Stimuli and subjects

The same six subjects as in experiment I participated. Tone A, filtered into the mid region, had exactly the same parameters as in the first experiment. Tone B was filtered into a high region which was now adjacent to the mid region, rather than separated by an octave. Thus, the lower cut-off frequency (3-dB down point) of the high region was 1650 Hz for subjects 1–5 and 1875 Hz for subject 6. Following preliminary experiments, the upper cut-off frequency of the high region was fixed at 2250 Hz for subject 1, at 1950 Hz for subjects 2–4, at 2600 Hz for subject 5, and at 2100 Hz for subject 6. This was done to achieve approximately equal d' values for F0 discrimination of the two tones, for each subject. The values of ΔF0 used were the same as in experiment I, except for subject 3, for whom it was decreased from 5% to 4%, and for subject 6, for whom it was increased from 3% to 3.4%.

As experiment I showed no effect of PPA, here the value of $\Delta\varphi$ was fixed at 0°. In the monaural condition, both tones were presented to the left ear. In the dichotic condition, tones A and B were delivered to the left and to the right ears, respectively. Note that, in the dichotic condition, subjects reported perceiving a single sound source which was located at the center of the head, i.e., the two complex tones were fused, consistent with previous evidence (Broadbent and Ladefoged, 1957).

C. Results and discussion

Figure 2 shows the results of experiment II. As intended, the mean d' values for the individually presented complex tones were quite similar at 1.09 and about 1.17 for the mid- and the high regions, respectively (three white bars on the left-hand side). In the combined conditions (black bars), the mean d' values were 1.32 and 1.36 for monaural and dichotic presentations, respectively. Thus, as in the first experiment, F0 discrimination was somewhat better for combined than for individual presentation of the two tones. Paired-sample t-tests showed that, for both monaural and dichotic presentation, the d' values in the combined conditions were significantly larger than the higher of the two d' values ob-

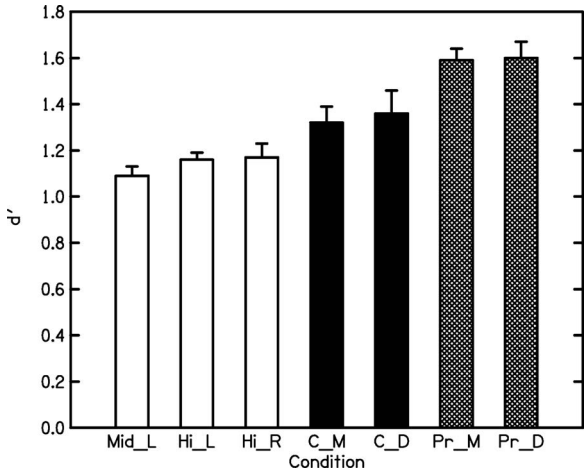

FIG. 2. Results and predictions for F0-discrimination task (experiment II). The mean obtained d' values and the corresponding SEs across subjects are shown by the five bars to the left and the predictions are shown by the two hatched bars to the right. The three white bars show performance in the conditions where each tone was presented individually: outer left—tone A, filtered into the mid region and presented to the left ear (Mid_L); second from the left—tone B, filtered into the high region and presented to the left ear (Hi_L); third from the left—tone B, filtered into the high region and presented to the right ear (Hi_R). The two black bars show performance in the conditions where the tones were combined: left—combined, monaural presentation (C_M); right—combined, dichotic presentation (C_D). The two hatched bars on the right-hand side show the predictions derived for the monaural combined condition (Pr_M) and for the dichotic combined condition (Pr_D), assuming optimal combination of information across frequency regions and independent noises. See text for details.

served for the corresponding individual presentations [monaural: $t(5)=2.47$, $p<0.05$; one-tailed; dichotic: $t(5)=2.19$, $p<0.05$; one-tailed]. In the combined conditions, performance was unaffected by whether the tones were presented monaurally or dichotically, and was clearly below the level(s) predicted, assuming independent noises and optimal combination of information across regions (by factors of 0.83 and 0.84 in the monaural and the binaural conditions, respectively). This was supported by the results of a repeated-measures two-way ANOVA, which used the obtained and the predicted d' values for monaural and dichotic presentations as input. There was a significant main effect of the factor observed vs predicted [$F(1,5)=15.08$, $p<0.05$], but no significant main effect of mode of presentation (monaural vs dichotic) nor interaction. Furthermore, an additional paired-sample t-test, calculated on the data for the dichotic condition only, showed that the d' values obtained in the combined condition were significantly smaller than the predicted d' values [following Eq. (1)] [$t(5)=3.2$, $p<0.05$; two-tailed]. Assuming partial correlation between the two noises, the mean of the estimated r values was 0.53, with a standard error of 0.13 [following Eq. (3)].

Overall, the results were quite similar to those observed for experiment I, where the two complexes were more spectrally separated. Furthermore, there was no effect of monaural vs dichotic presentation, and, for dichotic presentation, obtained performance in the combined condition was below optimal performance (assuming independent noises), similar to what has been observed for monaural presentation. The

results indicate that the nonoptimal combination of information [following Eq. (1)] was not caused by partial masking in the auditory periphery.

V. EXPERIMENT III: RELATIVE DOMINANCE

A. Rationale

The objective of the third experiment was to investigate whether the nonoptimal combination of F0 information across frequency regions (assuming independent noises) observed in experiments I and II could have been due to subjects mostly ignoring F0 information coming from one frequency region. For example, it could be that, in spite of equal performance for the individually presented tones, when both were presented together, the tone in the lower frequency region was dominant because it was closer to the usual dominance region (Ritsma, 1967; Moore *et al.*, 1985a; Dai, 2000).

To address this question, tones A and B were presented simultaneously, in both intervals of the 2AFC task. In each interval, tones A and B now had different F0s, rather than the same F0 as in the previous experiments. In one randomly chosen interval, the F0 of tone A (mid region) was increased above the nominal F0, while that of tone B (high region) was decreased below the nominal F0; this is called the interval with the "compressed signal." In contrast, the other interval contained the "stretched signal;" the F0 of the tone in the lower frequency region was decreased below the nominal F0, while that of the tone in the higher frequency region was increased above the nominal F0. Subjects still had to indicate which of the two intervals had the complex with the higher pitch. The idea was that if subjects attended to both regions, then the stretched and the compressed signal should be chosen about equally often. In contrast, if subjects listened mainly to a specific frequency region, then their pitch judgments should follow the change in F0 of the tone in that region, and thus, scores should markedly differ from 50%.

B. Stimuli and subjects

The same six subjects as in the first two experiments participated in experiment III. For each subject, tones A and B were filtered as in experiments I and II. Specifically, there were two filter conditions: the "far regions" condition, where the tones were filtered into two spectral regions separated by one octave (with filter parameters as in experiment I), and the "adjacent regions" condition, where the tones were filtered into two spectrally adjacent regions (with filter parameters as in experiment II). The nominal F0 and the phase relationship between components within each region were identical to those in the previous experiments, for each subject. In one randomly chosen interval, the F0 of tone A was lowered by $\Delta F0/2$ from the nominal F0, while the F0 of tone B was increased by $\Delta F0/2$, and in the other interval it was the other way round. The difference between the F0s of tones A and B within each interval could take two values for each subject: one was identical to the value of $\Delta F0$ with which this subject had been tested in experiment II (which resulted in a d' value of about 1.1 when this F0 difference occurred between the two intervals of a trial for each of tones A and B; condition "small $\Delta F0$") and the other was twice that size (condition "large $\Delta F0$"). Both tones were always presented monaurally and simultaneously. They were perceived as one sound source in the small $\Delta F0$ condition, but were perhaps somewhat less fused in the large $\Delta F0$ condition. In each of the four conditions, at least 1400 trials were collected for each subject.

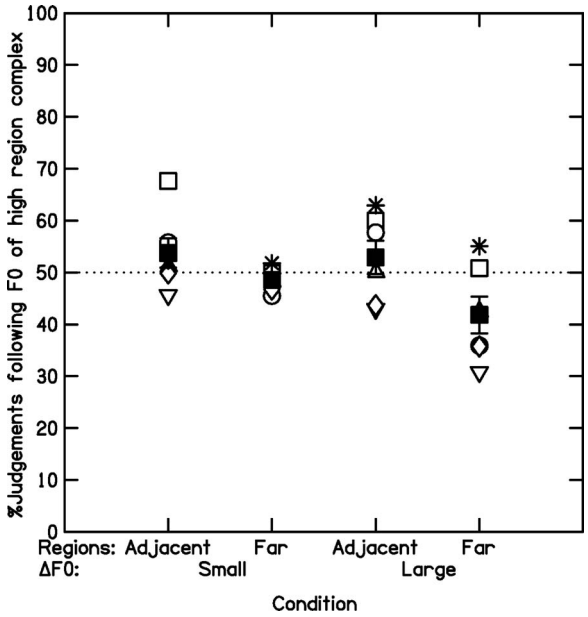

FIG. 3. Results for experiment III, showing the percentage of trials in which subjects judged the stretched signal (F0 of complex in high region increased; F0 of complex in mid region decreased) to be higher in pitch than the compressed signal (F0 of complex in high region decreased; F0 of complex in mid region increased). Empty symbols show the scores for six subjects. The solid squares (and error bars) show the mean score (and SEs) across subjects. See text for details.

C. Results and discussion

Figure 3 shows the percentage of trials in which subjects judged the stretched signal to be higher in pitch than the compressed signal, i.e., where their judgments followed the change in F0 of the complex filtered into the high region. The empty symbols show the individual results for each of the six subjects. The solid squares and error bars show the mean and SEs across subjects. For all conditions, the mean scores were around 50%, although scores in the far-region condition with the large $\Delta F0$ (far right) seem to be somewhat lower. The individual scores within conditions clearly do not follow a bimodal distribution. This is important because it indicates that the mean scores around 50% are not the result of half of the subjects only listening to one frequency region and the other half only listening to the other region.

A repeated-measures two-way ANOVA, with factors filter condition and $\Delta F0$, was calculated. The results showed a significant main effect of filter condition [$F(1,5) = 14.72$, $p < 0.05$]. Neither the main effect of size of $\Delta F0$ nor the interaction was significant. Therefore, within each filter condition, the mean was determined across the two $\Delta F0$ conditions. Two separate one-sample t-tests (one for each filter condition) showed that the mean percentages were

both not significantly different from 50% [adjacent region: $t(5)=1.09$, $p>0.05$; far region: $t(5)=2.07$, $p>0.05$; two-tailed for both filter conditions].

In an additional analysis, it was checked whether, across subjects, a somewhat larger deviation from a 50% score in the present experiment might be correlated with less optimal combination of information across frequency regions in experiment I or II. Spearman's rank correlation coefficients were calculated between the ratios of observed to predicted d' values obtained in experiments I and II, on the one hand, and the unsigned deviations from 50% scores observed in conditions with large ΔF0s and corresponding frequency region in the present experiment, on the other hand. A negative correlation between these two measures would indicate that the nonoptimal combination of information could have been due to subjects consistently listening more to (or giving more weight to) pitch information coming from one frequency region than from the other. The values of the correlation coefficients were (i) 0.086, for the correlation between the ratios of observed to predicted d' values obtained in experiment I and the unsigned deviations from 50% scores in the far-region large-ΔF0 condition; (ii) 0.886, for the correlation between the ratios of observed to predicted d' values obtained in experiment II in the monaural condition and the unsigned deviations from 50% scores in the adjacent-region large-ΔF0 condition; and (iii) 0.314, for the correlation between the ratios of observed to predicted d' values obtained in experiment II in the dichotic condition and the unsigned deviations from 50% scores in the adjacent-region large-ΔF0 condition. Only the second of these coefficients was (just) significant ($p<0.05$; two-tailed), but it actually had the opposite sign to that predicted, i.e., a somewhat larger deviation from the 50% score was correlated with somewhat more optimal combination of information across frequency regions.

In summary, the results indicate that subjects did not selectively and consistently listen to one specific frequency region. Thus, the nonoptimal combination of information across frequency regions [following Eq. (1)] observed in experiments I and II cannot be explained by the existence of a "dominant region" which leads subjects to ignore information from the other region. Note, however, that the data of the third experiment do not necessarily imply that the pitch of the stretched and compressed signals was perceived as equal and that, therefore, subjects responded randomly. This is because a similar pattern of results might be observed if subjects sometimes listened to one region and sometimes to the other.

VI. EXPERIMENT IV: RESOLVED TONE COMPLEXES

A. Rationale

The objective of the fourth experiment was to investigate whether the nonoptimal combination of F0 information across frequency regions (assuming independent noises) was specific to complex tones containing only unresolved harmonics. It could be that nonoptimal combination occurs only for pitches encoded solely by envelope information. To test this idea, complex tones containing at least some resolved harmonics were used as stimuli.

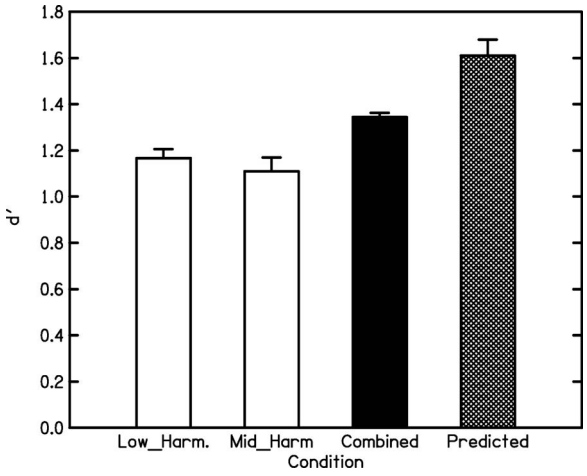

FIG. 4. Results for experiment IV. As Fig. 1, but for complex tones containing resolved harmonics.

B. Stimuli and subjects

Four subjects participated, three of whom also took part in the previous three experiments. Tone A consisted of harmonics 1–3 of a 400-ms harmonic complex tone with an F0 of 200 Hz, added in sine phase (condition "Low Harmonics"), for all subjects. Tone B contained higher harmonics of a 200-Hz F0 complex, also added in sine phase (condition "Mid Harmonics"). Which harmonics were present in tone B and the size of ΔF0 between the two intervals in the 2AFC F0-discrimination task were determined in a preliminary experiment individually for each subject, such that performance for tones A and B was approximately equal and that d' values were around 1.1–1.2. For two subjects, tone B consisted of harmonics 6–8 and ΔF0 was set to 0.4% and 0.32%, respectively. For the third and fourth subjects, tone B contained harmonics 7–9 and 6–9, and ΔF0 was fixed at 0.2% and 0.6%, respectively. The rms level of tone A was increased from 52 to 55 dB SPL, so that it was approximately as loud as tone B.

C. Results and discussion

Figure 4 shows the mean d' values and the corresponding SEs across subjects for the conditions where tones A and B were presented individually (conditions Low Harmonics and Mid Harmonics, white bars), and simultaneously (condition "Combined," black bar), and the predicted d' value for the combined condition, assuming optimal combination of information across frequency regions (hatched bar), following Eq. (1).

Mean d' values for the individually presented tones were quite similar at about 1.17 and 1.11 for the Low Harmonics and Mid Harmonics conditions, respectively. In the combined condition, the mean d' value was 1.34, again indicating a small improvement over individual presentation. A paired-sample t-test showed that the d' value for the combined condition was significantly larger than the higher of the two d' values observed for individual presentation [$t(3)=5.5$, $p<0.01$; one-tailed]. The predicted mean for the combined condition, assuming optimal combination of information [following Eq. (1)], was 1.61. As in the previous experi-

ments, the observed sensitivity in the combined condition was clearly below the prediction (by a factor of 0.84). A paired-sample t-test showed that this difference was significant [$t(3)=4.17$, $p<0.05$; two-tailed]. Assuming partial correlation between the two noises [following Eq. (2)], the mean of the estimated r values was 0.44, with a SE of 0.1. To assess whether performance in the combined condition was closer to optimal performance when the tone complexes contained resolved (experiment IV) rather than only unresolved harmonics (experiment I), an independent-sample t-test was calculated on the factors by which the observed combined performance was smaller than the predicted optimal performance for the six subjects in experiment I and the four subjects here. This t-test showed that the observed shortfalls from optimal performance (mean ratios of 0.79 and 0.84 in experiments I and IV, respectively) were not significantly different [$t(8)=1.15$, $p>0.05$; two-tailed].

To summarize, the results showed a significant improvement in F0 discrimination when the tones in the two frequency regions were presented simultaneously compared to when they were presented in isolation. However, this improvement was significantly smaller than predicted assuming optimal combination of information [following Eq. (1)], and was not significantly closer to optimal performance than observed in the previous experiments with tones containing only unresolved harmonics. This indicates that nonoptimal combination of information across frequency regions occurs for tones with both resolved and unresolved harmonics.

VII. EXPERIMENT V: SHORT DURATION

A. Rationale

In the previous experiments, the stimulus duration was always 400 ms. This duration was chosen so that the current results could be compared with previous findings on PDI, where F0 information seemed to be combined across regions, in spite of it being disadvantageous, and where the stimulus duration was also 400 ms.

The objective of experiment V was to investigate whether combination of F0 information across frequency regions would improve for shorter stimuli. One reason to suspect that signal duration might affect combination of F0 information across frequency comes from a study on signal detection by Houtgast (1987). He presented listeners with a compound stimulus that consisted of nine individual Gaussian-shaped tone pulses. Each tone pulse covered a well-defined and restricted region in time and frequency. All nine individual tone pulses had the same masked threshold when present in pink noise. Houtgast (1987) measured the masked threshold for the compound stimulus for various placements of the nine pulses in spectral region and time. He found that concentrating the signal energy in either time or frequency led to lower masked thresholds than spreading pulses over 100 ms and several critical bands. For short tone pulses, optimal combination of (energy) information across critical bands was observed when the peaks of all Gaussian envelopes coincided in time. Later studies confirmed the importance of very short signal duration (less than about 30 ms) for (near) optimal integration of energy across frequency regions for signal detection in a background noise (see van den Brink and Houtgast, 1988, 1990a, 1990b). While the current study is not concerned with signal detection in the sense of energy detection and integration, it is conceivable that pitch discrimination and integration of pitch relevant information from sounds that are clearly audible are limited in a similar way, i.e., subjects can either integrate over time or over frequency, but not both.

B. Stimuli and subjects

Four subjects participated. Of those four, two also took part in experiments I–III, one had participated in experiment IV and one was recruited new. Apart from the duration being shortened from 400 to 50 ms, the main stimulus parameters were identical to those for experiment I, i.e., tones A and B contained only unresolved harmonics, they were filtered into regions separated by one octave, and the starting phase of the nth harmonic in tone B was shifted by $n\cdot\Delta\varphi$, with values of $\Delta\varphi$ at 0°, 90°, 180°, and 270°. As in experiment I, the time point within each period at which the waveform was turned on was chosen at random for each presentation. This discouraged subjects from relying on onset differences and on differences in the duration between the first and last pulses in each interval. Different PPAs between the envelope peaks in the two frequency regions were tested again, just to check whether the absence of an effect would also be observed for the short stimulus duration.

For three subjects, tones A and B were filtered from 1350–1650 Hz (mid region) and 3300–4200 Hz (high region), respectively, and the nominal F0 was 75 Hz. For two of the three subjects, components in both complexes were added in sine phase and for the third one they were added in alternating phase. The values of ΔF0 were fixed at 12%, 14%, and 5.5% for subjects 1, 2, 3, respectively. Preliminary experiments showed that, for these three subjects, similar performance levels for tones A and B could be achieved with these parameters, with d' values around 1.1–1.2. For the fourth subject, in order to obtain equal sensitivity for the two tones, the nominal F0 was increased to 90 Hz, the filter regions were adjusted to 1375–1875 and 3900–5400 Hz, and components within each tone were added in alternating phase. For this subject, ΔF0 was fixed at 14%. This subject was not the same as the sixth subject in experiment I, who also was tested with a 90 Hz F0. Note that the values of ΔF0 required to achieve d' values around 1.1–1.2 are markedly larger than those in experiment I, where the duration of the stimulus was 400 rather than 50 ms. All tones were presented monaurally to the left ear of each subject.

C. Results and discussion

In the combined condition, the mean d' values (and SEs across subjects) observed for the four values of $\Delta\varphi$ were 1.63 (0.09), 1.58 (0.09), 1.57 (0.11), and 1.51 (0.11) for $\Delta\varphi$ equal to 0°, 90°, 180°, and 270°, respectively. There was no significant difference between these d' values, as shown by the results of a repeated-measures one-way ANOVA performed on the individual d' values [$F(3,9)=1.11$, $p=0.38$]. Thus, as in experiment I for the longer stimulus du-

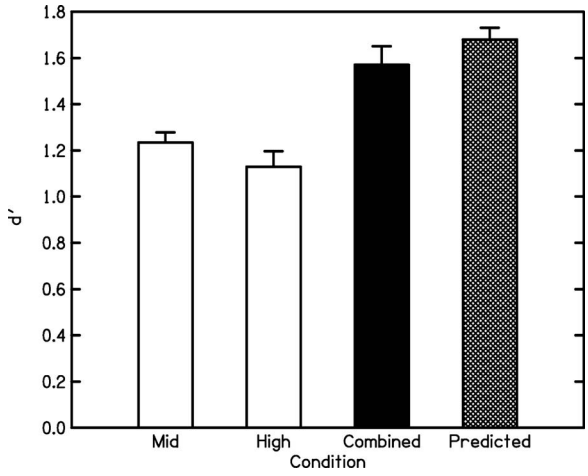

FIG. 5. Results for experiment V. As Fig. 1, but for tones with a duration of 50 ms.

ration, the relative timing of the pulses in the two frequency regions did not affect F0 discrimination significantly when both tones were presented simultaneously. Therefore, in what follows, the d' value for the combined condition is based on the percent correct values averaged across the four $\Delta\varphi$ values.

Figure 5 shows the results of experiment V. Mean d' values for the individually presented tones were quite similar at about 1.23 and 1.13 for the mid- and high region conditions, respectively (two white bars to the left). For the combined condition (black bar), the mean d' value was 1.57, indicating a clear improvement over individual presentation. A paired-sample t-test showed that the d' value for the combined condition was significantly larger than the higher of the two d' values for individual presentation [$t(3)=5.03$, $p<0.01$; one-tailed]. The predicted mean d' for the combined condition, assuming optimal combination of information and independent noises, was 1.68 (hatched bar on the right-hand side). The observed sensitivity in the combined condition was somewhat below the predicted value, but only by a factor of 0.93. This factor is clearly larger than those observed in the previous experiments (experiment I: 0.79; experiment II: 0.83, monaural and 0.84, binaural; experiment IV: 0.84). An independent-sample t-test was calculated on the factors by which the observed combined performance was smaller than the predicted optimal performance for the six subjects in experiment I and the four subjects here. The results showed that the ratio of observed to predicted d' values was significantly larger [$t(8)=3.88$, $p<0.01$; two-tailed] for the 50-ms than for the 400-ms stimuli. Furthermore, a paired-sample t-test showed that, for the short duration, the observed and the predicted d' values for the combined condition were not significantly different from each other [$t(3)=3.06$, $p>0.05$; two-tailed]. Assuming partial correlation between the two noises, the mean of the estimated r values was 0.16, with a standard error of 0.05.

To summarize, the results showed a clear improvement in F0 discrimination when the short tones A and B were presented simultaneously, compared to when they were presented in isolation. This improvement was significantly larger than that observed in experiment I, where similar but longer tone complexes were used. As for the longer duration tones, performance did not depend on PPA. Performance observed for the 50-ms duration was not significantly different from that predicted assuming (1) optimal combination of information across frequency regions and (2) independent internal noises for each of the two complexes as the main factor limiting performance. The difference in results for the long and short tones may indicate that, when subjects discriminate between the F0s of two clearly audible complex tones, they cannot simultaneously and optimally integrate pitch information over frequency *and* time. This limitation resembles that previously observed in signal-detection tasks (Houtgast, 1987; van den Brink and Houtgast, 1988, 1990a, 1990b).

VIII. GENERAL DISCUSSION

In the Introduction, we described a phenomenon—PDI—in which listeners are unable to selectively process F0 information in a specific frequency region (Gockel *et al.*, 2004; 2005, 2009a, 2009b; Micheyl and Oxenham, 2007). The present results showed that nonoptimal combination of F0 information [following Eq. (1)] occurs even in a paradigm where combination is advantageous, for the same stimulus duration as used in the PDI studies (400 ms). Thus, the nonoptimal performance previously reported in PDI studies is not restricted to situations that require assigning a zero weight to a particular frequency region.

Somewhat in contrast to the present results, Moore *et al.* (1984) observed optimal combination of information across frequency for long duration (420 ms) stimuli. In a 2I-2AFC task, they measured frequency difference limens (DLs) for individual harmonics within complex tones (in the presence of the remainder of the complex) and F0DLs for the periodicity (the residue pitch) of the whole complex. They found that the F0DLs were always smaller than the smallest of the DLs for the individual harmonics and that the former could be predicted from the latter, using a modified version of Goldstein's (1973) model in which no "central" noise was assumed. This indicated optimal combination of information about the frequencies of the harmonics within the complex for the purpose of deriving the residue pitch.

More recently, Gockel *et al.* (2007) investigated whether this also held for shorter stimulus durations. They used the same paradigm as Moore *et al.* (1984), and complex tones of 200-, 50-, and 16-ms durations. For the 200-ms duration, the pattern of results found by Gockel *et al.* (2007) was consistent with that observed by Moore *et al.* (1984). However, for the 50-ms duration, the predicted F0DLs were consistently *larger* than the obtained values. This was assumed to be due to difficulties in hearing out individual harmonics when the duration of the sound was short, leading to increased DLs for the individual harmonics within the complex and resulting in an underestimate of the precision with which the frequencies of the individual harmonics were represented at the input to the central pitch processor. For the 16-ms duration, the F0DLs predicted from the DLs for the individual harmonics were not significantly different from the observed F0DLs. While this seemed to indicate optimal combination of infor-

mation across frequencies, this interpretation was questioned by the results of a supplementary pitch-matching experiment. The pitch-matching experiment showed that the contribution of the upper-edge harmonic to the residue pitch of the complex was markedly smaller than would be predicted from its especially small FDL (relative to the FDLs observed for the other harmonics).

In summary, the studies by Moore *et al.* (1984) and Gockel *et al.* (2007) indicated that, for the purpose of deriving the residue of a complex tone, information about the frequencies of the individual harmonics seemed to be combined optimally for long tone durations, with "supra-optimal" combination for the 50-ms tones. This differs from the present study for combination of F0 information across frequency regions, which showed optimal combination for short complex tones but sub-optimal combination for long complex tones (assuming independent noises). We can think of two possible reasons for this. The first reason is related to the differences in the paradigms used in the initial stage of the experiment where the amount or the precision of information on the individual components, which are presented simultaneously in the second stage of the experiment, was determined. In the studies by Moore *et al.* (1984) and Gockel *et al.* (2007), the individual components (harmonics), whose FDLs were to be determined, were presented within the remainder of the complex tone. Especially for short durations, this method might lead to an underestimate of the precision with which component frequency is represented in the auditory system because it might rely on subjects hearing out the individual component, whose FDL is measured, from the remainder of the complex. In contrast in the present study, the individual parts of the combined sound, tones A and B, were presented alone when performance for F0 discrimination for the parts was determined. If, in the present study, F0 discrimination performance had been determined for each of the two tones in the presence of the other tone—that is, in the PDI paradigm, corresponding to the measurement used in the initial stage by Moore *et al.* (1984) and Gockel *et al.* (2007)—then predictions for the combined stimulus would have been lower, and maybe similar to the observed performance levels, at least for the 400-ms duration. For the short duration, the predictions probably would be below the observed performance in the combined condition.

The second reason for the different pattern of results observed in the present study and those by Moore *et al.* (1984) and Gockel *et al.* (2007) could be related to the differences in *what* exactly was estimated in the initial stage of the experiment. In the present study, the prediction for performance in F0 discrimination of the combined stimulus was derived from performance in F0 discrimination of complex tones, i.e., perception of the same attribute—F0—was measured in the combined case and in the initial stage of the experiment. In contrast, in the previous studies, the attributes measured in the initial stage and in the combined case were not identical. The initial stage measured FDLs of tones, while in the combined case, perception of F0 was measured. The latter could be a higher stage process, using information from the initial stage. Combination of information at the same level (present study) might follow different rules/restrictions from combination of information for a higher stage process (previous studies).

Optimal combination of information across frequency regions, following Eq. (1), has also been reported by Buell and Hafter (1991). They measured sensitivity to ITDs of low-frequency stimuli. Stimuli consisted of either one, two, or three sine tones. They found that the observed d' values in the combined conditions, where two or three sine tones with identical ITDs were presented simultaneously, were predicted well assuming optimal combination of ITD information across frequency. This was true irrespective of whether the frequencies in the combined conditions were harmonically or inharmonically related to each other. Buell and Hafter (1991) did not specifically investigate the effect of stimulus duration; they used a short stimulus with a 50 ms raised-cosine envelope. It is important to point out that the combination of binaural information across frequency observed by them was optimal assuming independent internal noises, rather than a common noise as the main factor limiting performance.

In a second experiment, Buell and Hafter (1991) presented two-frequency complexes, in which one component, the target, contained the ITD which had to be detected, while the other component, the interferer, was presented diotically. This paradigm is analogous to that used in the PDI studies (Gockel *et al.*, 2004, 2005, 2009a, 2009b; Micheyl and Oxenham, 2007) mentioned above. In this paradigm, optimal combination of information requires assigning zero weight to the (non-relevant) information arising from the interferer. Buell and Hafter (1991) found that, for inharmonically related components, performance in the "combined" conditions was equal to that observed for targets presented alone, while for harmonically related components, performance was impaired. The finding of unimpaired performance with inharmonically related components suggested segregation of the target and interferer into separate auditory objects based on (in)harmonicity (Moore *et al.*, 1985b; Hill and Darwin, 1996). In contrast, with the harmonically related components, harmonics seemed to be grouped together and ITD information from the target and the interferer was combined, thus lowering performance.

The results of the present study on combination of pitch information across frequency largely conform with those of Buell and Hafter (1991) on combination of ITD information across frequency. When combination of information across frequency was advantageous, both studies showed optimal combination across frequency for short stimuli. Longer duration tones were not tested by Buell and Hafter (1991), so it is unclear whether ITD information is combined optimally across frequency for long tones as well. In addition, when combination of information across frequency was disadvantageous, Buell and Hafter's (1991) second experiment showed impaired performance when the tones were harmonically related, but optimal combination of information across frequency when the two tones were clearly segregated due to inharmonicity. Similarly for PDI, Gockel *et al.* (2004; 2009b) reported that the impairment was markedly reduced when the difference between the F0s of target and interferer was increased, leading to clearer segregation of the two com-

plex tones. While one would expect larger PDI for shorter stimuli, future studies may show the exact effects of stimulus duration in the PDI paradigm.

So far in the discussion we have concentrated on predictions for the combined condition that were derived from Eq. (1), based on the assumption that the noises that affected F0 discrimination of the complexes in the two frequency regions were statistically independent. However, as described in the results sections (III C, IV C, VI C, VII C), by assuming partial correlation between the noises and optimal combination of information otherwise, it is possible to estimate correlation coefficients such that the predicted d' values for the combined condition equal the observed values. The correlation coefficients estimated for experiment V (mean of 0.16) were markedly smaller than those estimated for the experiments using longer stimulus durations (mean of 0.54 across experiments I, II, and IV). While this is a consequence of performance in the combined condition being closer to optimal (assuming independent noises) for the short than for the long duration, it means that the assumed component of the noise that is common to both "channels" decreases relative to the independent component with decreasing duration.

According to Durlach *et al.* (1986), partial correlation between peripheral internal noises might be caused, for example, by respiratory or circulatory processes. It is not obvious why such a common noise component would decrease with decreasing duration. On the contrary, one might expect the relative contribution of a circulatory noise component to increase with decreasing duration. On the other hand, it could be that the component of the noise that is independent across channels decreases with increasing duration, due, for example, to temporal integration, while the part of the noise that is common across channels does not decrease. This could happen if the source of the common noise was located at a stage of processing after temporal integration. Although this is possible, it is not obvious what the source of this "semi-peripheral" noise would be. Alternatively, one could assume independent peripheral noises and a central noise at the decision stage that decreases with decreasing duration due, for example, to memory limitations in the time-frequency space. The latter description is just another way of saying that combination of information was more optimal (assuming independent noises) for the short than for the long duration. The present data do not allow one to distinguish between these two descriptions (or combinations thereof), but the latter seems more parsimonious.

IX. SUMMARY AND CONCLUSIONS

The combination of F0 information across spectral regions was investigated in five experiments using a 2AFC task in which subjects had to indicate the stimulus with the higher pitch. Stimuli were two complex tones, A and B, in separate frequency regions. Tones A and B were either presented alone or simultaneously. Performance in the combined condition was compared to predicted performance, assuming optimal combination of F0 information across spectral regions. Following signal-detection theory, predictions were derived based on the performance observed when tones A and B were presented alone, assuming independent peripheral noises for A and B as the limiting factor. The results showed the following.

(1) When 400-ms tones A and B contained only unresolved harmonics, were separated in spectral region by one octave, and were presented monaurally, performance in the combined condition was poorer than predicted assuming optimal combination of information (experiment I). The relative timing of envelope peaks in tones A and B had no significant effect on performance in the combined condition.
(2) When 400-ms tones A and B contained only unresolved harmonics and were filtered into two contiguous spectral regions, performance in the combined condition was unaffected by whether A and B were presented monaurally or dichotically (experiment II), and was very similar to that observed for experiment I, indicating that peripheral masking was probably not the reason for the observed sub-optimal performance.
(3) When tones A and B were presented simultaneously but differed in F0 in both intervals of the 2AFC task (in one randomly chosen interval the F0 of tone A was increased, while that of tone B was decreased, and in the other interval it was the other way around), subjects' pitch judgments were equally determined by the F0 change in the two spectral regions (experiment III). Thus, the nonoptimal combination of information observed in experiments I and II cannot be explained by subjects "listening" consistently to one specific frequency region.
(4) When 400-ms tones A and B contained at least some resolved harmonics, performance in the combined condition was poorer than predicted, assuming optimal combination of F0 information across spectral regions (experiment IV). The ratio of observed to predicted performance in the combined condition was similar to that observed in experiments I and II for complex tones containing only unresolved harmonics, indicating that the limitation in combination of F0 information across spectral regions was not limited to unresolved harmonic complexes.
(5) When the duration of the tones was shortened to 50 ms, keeping other stimulus parameters similar to those used in experiment I, observed performance in the combined condition was not significantly different from that predicted, assuming optimal combination of information and independent noises (experiment V). As for the longer duration, the relative timing of envelope peaks in tones A and B had no significant effect on performance in the combined condition.

Overall, the results indicate that F0 information can be combined across spectral regions in a optimal way, when the stimulus duration is short. They may give another example of the difficulty human listeners have with integrating information simultaneously across frequency and time.

ACKNOWLEDGMENTS

This work was supported by Wellcome Trust Grant No. 088263. We thank Brian Moore for comments on an earlier version of this paper. We also thank two reviewers, Laurent Demany and Christophe Micheyl, for helpful comments.

APPENDIX

In this appendix the method for predicting d'_c is derived, assuming partly correlated internal peripheral noises and optimal combination of information. Following van Trees (1968, pp. 96–99) assuming optimal combination of information across n Gaussian-distributed random variables (RVs) leads to the following prediction for d' in the combined condition:

$$d'^2_c = D^T K^{-1} D, \tag{A1}$$

where d'_c is the value of the d' for the combined condition, and D^T is the transpose of D, with $D^T = (\Delta_1 \ \Delta_2 \ \Delta_3 \ \cdots \ \Delta_n)$. The value of each Δ_i specifies the difference between the expected values of the ith RV, x_i, for the signal distribution and for the noise distribution, and K^{-1} is the inverse of the variance-covariance matrix K.

If one assumes that the individual RVs are all statistically independent, except for the addition of a common noise variable, R, to each, where R has expected value zero and variance σ_R^2, then

$$K = \begin{pmatrix} \sigma_1^2+\sigma_R^2 & \sigma_R^2 & \cdots & \sigma_R^2 & \sigma_R^2 \\ \sigma_R^2 & \sigma_2^2+\sigma_R^2 & \sigma_R^2 & \cdots & \sigma_R^2 \\ \sigma_R^2 & \sigma_R^2 & \ddots & \sigma_R^2 & \sigma_R^2 \\ \vdots & \vdots & & \sigma_{n-1}^2+\sigma_R^2 & \vdots \\ \sigma_R^2 & \sigma_R^2 & \cdots & \sigma_R^2 & \sigma_n^2+\sigma_R^2 \end{pmatrix}, \tag{A2}$$

where σ_i is the standard deviation of the ith RV before the addition of the common noise. For the current case of $n=2$, the inverse of K is especially simple with

$$K^{-1} = \frac{1}{(\sigma_1^2+\sigma_R^2)(\sigma_2^2+\sigma_R^2)-\sigma_R^4} \begin{pmatrix} \sigma_2^2+\sigma_R^2 & -\sigma_R^2 \\ -\sigma_R^2 & \sigma_1^2+\sigma_R^2 \end{pmatrix}. \tag{A3}$$

Substituting into Eq. (A1), this gives

$$d'^2_c = \frac{1}{(\sigma_1^2+\sigma_R^2)(\sigma_2^2+\sigma_R^2)-\sigma_R^4}[\Delta_1^2(\sigma_2^2+\sigma_R^2) + \Delta_2^2(\sigma_1^2+\sigma_R^2) - 2\Delta_1\Delta_2\sigma_R^2]. \tag{A4}$$

Substituting $d'_A = \Delta_1/\sqrt{(\sigma_1^2+\sigma_R^2)}$ and $d'_B = \Delta_2/\sqrt{(\sigma_2^2+\sigma_R^2)}$ into Eq. (A4) gives

$$d'^2_c = \frac{1}{(\sigma_1^2+\sigma_R^2)(\sigma_2^2+\sigma_R^2)-\sigma_R^4} \cdot [d'^2_A(\sigma_1^2+\sigma_R^2)(\sigma_2^2+\sigma_R^2) + d'^2_B(\sigma_2^2+\sigma_R^2)(\sigma_1^2+\sigma_R^2) - 2d'_A d'_B\sqrt{(\sigma_1^2+\sigma_R^2)}\sqrt{(\sigma_2^2+\sigma_R^2)}\sigma_R^2], \tag{A5}$$

which simplifies to

$$d'^2_c = \frac{1}{1-\dfrac{\sigma_R^4}{(\sigma_1^2+\sigma_R^2)(\sigma_2^2+\sigma_R^2)}} \cdot \left(d'^2_A + d'^2_B - 2d'_A d'_B \frac{\sigma_R^2}{\sqrt{(\sigma_1^2+\sigma_R^2)(\sigma_2^2+\sigma_R^2)}} \right). \tag{A6}$$

The correlation coefficient r between two random variables z_1 and z_2 is defined as the covariance of z_1 and z_2, divided by the product of the standard deviations of z_1 and z_2, so here we can replace the term $\sigma_R^2/\sqrt{(\sigma_1^2+\sigma_R^2)(\sigma_2^2+\sigma_R^2)}$ by r which gives the final result,

$$d'^2_c = \frac{1}{1-r^2}(d'^2_A + d'^2_B - 2d'_A d'_B r). \tag{A7}$$

Equation (A7) can be rewritten as

$$r^2 - r\frac{2d'_A d'_B}{d'^2_c} + \frac{d'^2_A + d'^2_B - d'^2_c}{d'^2_c} = 0. \tag{A8}$$

There exist two solutions for r:

$$r_{1/2} = \frac{d'_A d'_B}{d'^2_c} \pm \left[\left(\frac{d'_A d'_B}{d'^2_c} \right)^2 - \frac{d'^2_A + d'^2_B - d'^2_c}{d'^2_c} \right]^{0.5}. \tag{A9}$$

In the present study, only the smaller of the two solutions for r was used because the objective was to assume the smallest value of the common noise variable possible that would predict the d' values in the combined condition.

[1]It is commonly, and here, assumed that the internal noises in the processing can be represented by Gaussian noises. The use of d' is based on this assumption.

[2]Throughout the paper, if appropriate, the Huynh-Feldt correction was applied to the degrees of freedom (Howell, 1997). In such cases, the original degrees of freedom and the corrected significance value are reported.

Bernstein, J. G., and Oxenham, A. J. (**2003**). "Pitch discrimination of diotic and dichotic tone complexes: Harmonic resolvability or harmonic number?," J. Acoust. Soc. Am. **113**, 3323–3334.

Broadbent, D. E., and Ladefoged, P. (**1957**). "On the fusion of sounds reaching different sense organs," J. Acoust. Soc. Am. **29**, 708–710.

Buell, T. N., and Hafter, E. R. (**1991**). "Combination of binaural information across frequency bands," J. Acoust. Soc. Am. **90**, 1894–1900.

Carlyon, R. P. (**1994**). "Detecting pitch-pulse asynchronies and differences in fundamental frequency," J. Acoust. Soc. Am. **95**, 968–979.

Carlyon, R. P., and Shackleton, T. M. (**1994**). "Comparing the fundamental frequencies of resolved and unresolved harmonics: Evidence for two pitch mechanisms?" J. Acoust. Soc. Am. **95**, 3541–3554.

Dai, H. (**2000**). "On the relative influence of individual harmonics on pitch judgment," J. Acoust. Soc. Am. **107**, 953–959.

Durlach, N. I., Braida, L. D., and Ito, Y. (**1986**). "Towards a model for discrimination of broadband signals," J. Acoust. Soc. Am. **80**, 63–72.

Gockel, H., Carlyon, R. P., and Moore, B. C. J. (**2005**). "Pitch discrimination interference: The role of pitch pulse asynchrony," J. Acoust. Soc. Am. **117**, 3860–3866.

Gockel, H., Carlyon, R. P., and Plack, C. J. (**2004**). "Across-frequency interference effects in fundamental frequency discrimination: Questioning evidence for two pitch mechanisms," J. Acoust. Soc. Am. **116**, 1092–1104.

Gockel, H., Moore, B. C. J., and Patterson, R. D. (**2002**). "Asymmetry of masking between complex tones and noise: The role of temporal structure and peripheral compression," J. Acoust. Soc. Am. **111**, 2759–2770.

Gockel, H. E., Carlyon, R. P., and Plack, C. J. (**2009a**). "Further examination of pitch discrimination interference between complex tones containing resolved harmonics," J. Acoust. Soc. Am. **125**, 1059–1066.

Gockel, H. E., Hafter, E. R., and Moore, B. C. J. (**2009b**). "Pitch discrimination interference: The role of ear of entry and of octave similarity," J. Acoust. Soc. Am. **125**, 324–327.
Gockel, H. E., Moore, B. C. J., Carlyon, R. P., and Plack, C. J. (**2007**). "Effect of duration on the frequency discrimination of individual partials in a complex tone and on the discrimination of fundamental frequency," J. Acoust. Soc. Am. **121**, 373–382.
Goldstein, J. L. (**1973**). "An optimum processor theory for the central formation of the pitch of complex tones," J. Acoust. Soc. Am. **54**, 1496–1516.
Green, D. M., and Swets, J. A. (**1966**). *Signal Detection Theory and Psychophysics* (Wiley, New York).
Hafter, E. R., Dye, R. H., Wenzel, E. M., and Knecht, K. (**1990**). "The combination of interaural time and intensity in the lateralization of high-frequency complex signals," J. Acoust. Soc. Am. **87**, 1702–1708.
Hill, N. I., and Darwin, C. J. (**1996**). "Lateralization of a perturbed harmonic: Effects of onset asynchrony and mistuning," J. Acoust. Soc. Am. **100**, 2352–2364.
Houtgast, T. (**1987**). "On the significance of spectral synchrony for signal detection," in *Auditory Processing of Complex Sounds*, edited by W. A. Yost and C. S. Watson (Erlbaum, Hillsdale, NJ).
Howell, D. C. (**1997**). *Statistical Methods for Psychology* (Duxbury, Belmont, CA).
ISO 389-8 (**2004**). Acoustics—Reference zero for the calibration of audiometric equipment—Part 8: Reference equivalent threshold sound pressure levels for pure tones and circumaural earphones (International Organization for Standardization, Geneva).
Kaernbach, C., and Bering, C. (**2001**). "Exploring the temporal mechanism involved in the pitch of unresolved harmonics," J. Acoust. Soc. Am. **110**, 1039–1048.
Laneau, J., Wouters, J., and Moonen, M. (**2006**). "Improved music perception with explicit pitch coding in cochlear implants," Audiol. Neuro-Otol. **11**, 38–52.
Macmillan, N. A., and Creelman, C. D. (**1991**). *Detection Theory: A User's Guide* (Cambridge University Press, Cambridge, England).
Micheyl, C., and Oxenham, A. J. (**2007**). "Across-frequency pitch discrimination interference between complex tones containing resolved harmonics," J. Acoust. Soc. Am. **121**, 1621–1631.
Miyazono, H., and Moore, B. C. J. (**2009**). "Perceptual learning of frequency discrimination for tones with low fundamental frequency: Learning for high but not for low harmonics," Acoust. Sci. & Tech. **30**, 383–386.
Moore, B. C. J., Glasberg, B. R., and Baer, T. (**1997**). "A model for the prediction of thresholds, loudness and partial loudness," J. Audio Eng. Soc. **45**, 224–240.
Moore, B. C. J., Glasberg, B. R., Flanagan, H. J., and Adams, J. (**2006**). "Frequency discrimination of complex tones; assessing the role of component resolvability and temporal fine structure," J. Acoust. Soc. Am. **119**, 480–490.
Moore, B. C. J., Glasberg, B. R., and Peters, R. W. (**1985a**). "Relative dominance of individual partials in determining the pitch of complex tones," J. Acoust. Soc. Am. **77**, 1853–1860.
Moore, B. C. J., Glasberg, B. R., and Shailer, M. J. (**1984**). "Frequency and intensity difference limens for harmonics within complex tones," J. Acoust. Soc. Am. **75**, 550–561.
Moore, B. C. J., and Ohgushi, K. (**1993**). "Audibility of partials in inharmonic complex tones," J. Acoust. Soc. Am. **93**, 452–461.
Moore, B. C. J., Peters, R. W., and Glasberg, B. R. (**1985b**). "Thresholds for the detection of inharmonicity in complex tones," J. Acoust. Soc. Am. **77**, 1861–1867.
Oxenham, A. J., Micheyl, C., and Keebler, M. V. (**2009**). "Can temporal fine structure represent the fundamental frequency of unresolved harmonics?" J. Acoust. Soc. Am. **125**, 2189–2199.
Patterson, R. D. (**1987**). "A pulse ribbon model of monaural phase perception," J. Acoust. Soc. Am. **82**, 1560–1586.
Plomp, R. (**1964**). "The ear as a frequency analyzer," J. Acoust. Soc. Am. **36**, 1628–1636.
Plomp, R. (**1965**). "Detectability thresholds for combination tones," J. Acoust. Soc. Am. **37**, 1110–1123.
Plomp, R., and Mimpen, A. M. (**1968**). "The ear as a frequency analyzer II," J. Acoust. Soc. Am. **43**, 764–767.
Ritsma, R. J. (**1967**). "Frequencies dominant in the perception of the pitch of complex sounds," J. Acoust. Soc. Am. **42**, 191–198.
Shackleton, T. M., and Carlyon, R. P. (**1994**). "The role of resolved and unresolved harmonics in pitch perception and frequency modulation discrimination," J. Acoust. Soc. Am. **95**, 3529–3540.
Siebert, W. M. (**1970**). "Frequency discrimination in the auditory system: Place or periodicity mechanisms," Proc. IEEE **58**, 723–730.
Summerfield, Q., and Assmann, P. F. (**1991**). "Perception of concurrent vowels: Effects of harmonic misalignment and pitch-period asynchrony," J. Acoust. Soc. Am. **89**, 1364–1377.
van den Brink, W. A. C., and Houtgast, T. (**1988**). "Across-frequency integration in signal detection," in *Basic Issues in Hearing*, edited by H. Duifhuis, J. W. Horst, and H. P. Wit, (Academic Press, London).
van den Brink, W. A. C., and Houtgast, T. (**1990a**). "Efficient across-frequency integration in short-signal detection," J. Acoust. Soc. Am. **87**, 284–291.
van den Brink, W. A. C., and Houtgast, T. (**1990b**). "Spectro-temporal integration in signal detection," J. Acoust. Soc. Am. **88**, 1703–1711.
van Trees, H. L. (**1968**). *Detection, Estimation, and Modulation Theory* (Wiley, New York).
Vandali, A. E., Sucher, C., Tsang, D. J., McKay, C. M., Chew, J. W. D., and McDermott, H. J. (**2005**). "Pitch ranking ability of cochlear implant recipients: A comparison of sound-processing strategies," J. Acoust. Soc. Am. **117**, 3126–3138.

Revision, extension, and evaluation of a binaural speech intelligibility model

Rainer Beutelmann,[a] Thomas Brand, and Birger Kollmeier
Medizinische Physik, Carl-von-Ossietzky-Universität Oldenburg, 26111 Oldenburg, Germany

(Received 31 July 2008; revised 29 September 2009; accepted 31 December 2009)

This study presents revision, extension, and evaluation of a binaural speech intelligibility model (Beutelmann, R., and Brand, T. (2006). J. Acoust. Soc. Am. **120**, 331–342) that yields accurate predictions of speech reception thresholds (SRTs) in the presence of a stationary noise source at arbitrary azimuths and in different rooms. The modified model is based on an analytical expression of binaural unmasking for arbitrary input signals and is computationally more efficient, while maintaining the prediction quality of the original model. An extension for nonstationary interferers was realized by applying the model to short time frames of the input signals and averaging over the predicted SRT results. Binaural SRTs from 8 normal-hearing and 12 hearing-impaired subjects, incorporating all combinations of four rooms, three source setups, and three noise types were measured and compared to the model's predictions. Depending on the noise type, the parametric correlation coefficients between observed and predicted SRTs were 0.80–0.93 for normal-hearing subjects and 0.59–0.80 for hearing-impaired subjects. The mean absolute prediction error was 3 dB for the mean normal-hearing data and 4 dB for the individual hearing-impaired data. 70% of the variance of the SRTs of hearing-impaired subjects could be explained by the model, which is based only on the audiogram. [DOI: 10.1121/1.3295575]

PACS number(s): 43.66.Pn, 43.71.An, 43.55.Hy, 43.71.Ky [RYL] Pages: 2479–2497

I. INTRODUCTION

The task of understanding speech in the presence of other concurrent talkers was termed the "cocktail party problem" by Cherry (1953). The cocktail party problem is determined by several factors, including the location of speech and interferer sources, room acoustics, the type of interferer, and a potential hearing impairment of the listener. The ability to use binaural information in order to segregate the target signal and the interferer assists in solving the cocktail party problem. Binaural hearing decreases the signal-to-noise ratio (SNR) necessary to achieve 50% speech intelligibility in noise by up to 12 dB (Bronkhorst, 2000). A comprehensive model of speech intelligibility in complex situations, which might help to understand the underlying mechanisms, should incorporate as many of the involved factors as possible, especially binaural hearing. Furthermore, such a model could support diagnostic measurements in audiology and could serve as a tool for room acoustical planning and evaluation of binaural hearing-aid and audio algorithms.

Beutelmann and Brand (2006) presented a binaural model of speech intelligibility, which combined the equalization-cancellation (EC) model by Durlach (1963) with the standard speech intelligibility index (SII) (ANSI, 1997) based on the work by vom Hövel (1984). The model by Beutelmann and Brand (2006) predicted speech reception thresholds (SRTs) of sentences in steady state noise very well for different noise source locations, different room acoustics, and different degrees of hearing loss. The predictions were based on the binaural speech and noise signals and individual audiograms of the subjects. This study presents a revision of the EC/SII model. The model was mathematically simplified, which facilitates identifying the role of common binaural signal parameters in the operation of the model, such as the interaural cross correlation. The revision also increased the computational efficiency of the model. Furthermore, the model was extended for predicting SRTs also for modulated interferers. In order to evaluate this extension with experimental data, SRTs were measured with normal-hearing and hearing-impaired subjects in 36 conditions comprising different spatial separations of target and interferer, different reverberation times, and different interferer modulation depths. In order to distinguish between the different model versions, the original model from Beutelmann and Brand (2006) was abbreviated "EC/SII" model, the revised model was called binaural speech intelligibility model (BSIM), and the extended model for modulated interferers was called short-time BSIM (stBSIM).

A. Revision of binaural speech intelligibility model

The original EC/SII model was a straightforward implementation of the EC principle as a signal-processing front-end for the SII. It was a purely functional model without being explicitly related to physiology—a "black box" model according to the categories of Colburn (1996). However, in order to help understanding the mechanisms underlying binaural speech intelligibility at least a link to physiology should be found on the long term. This means to identify stages on the physiological pathways that correspond to stages of the model and to validate intermediate results between the model stages with empirical data measured at the corresponding physiological stages. An advantage of the EC/

[a]Author to whom correspondence should be addressed. Electronic mail: rainer.beutelmann@uni-oldenburg.de

SII model was that the EC stage could—in principle—deal with arbitrary signals, including nonspeech, although the validity of predictions has only been tested for speech in a restricted set of conditions so far. The binaural configuration (i.e., the directions or interaural relations of target and interferers, as well as room acoustics) did not have to be known explicitly because the model estimates the optimal equalization parameters by maximizing the SNR. Human inaccuracy was modeled in the EC/SII model with the help of a Monte-Carlo simulation, which assessed the effect of artificially imperfect binaural processing on the final result of the model. This Monte-Carlo simulation made the EC/SII model probabilistic and was computationally rather inefficient.

After the EC processing, actual waveforms were reconstructed from the frequency bands because a different frequency band division had to be used for the SII. The EC stage used overlapping gammatone filters and the SII standard assumed rectangular frequency bands, which was another limitation of the original EC/SII model. The revision of the EC/SII, resulting in BSIM, is a first step toward a link to physiology. The role of binaural signal parameters is revealed in the mathematical description of the model. A second aim of the revision is to preserve the independence from explicit information beyond the input signals and the individual audiogram, while making the model deterministic and improving efficiency by analytical simplification. The calculation scheme of the SII was adapted to the frequency bands of the EC stage. This saves the reconstruction procedure after the EC process and the SNRs can now be computed directly within the frequency bands without an intermediate step.

B. Extension for modulated interferers

Monaural speech intelligibility in modulated or speechlike interferers has been investigated in a number of studies: An early study by Miller and Licklider (1950) investigated the masking effect of interrupted broadband noise and noise bursts on speech reception compared to stationary noise. They found an increase in intelligibility for interrupted noise compared to stationary noise, which was dependent on the frequency of interruption and the SNR during the noise bursts. The largest increase was found for interruption frequencies between 4 and 10 Hz. Other studies have also shown that there is a decrease in SRT for modulated noises or for speech maskers compared to stationary noise (Dubno *et al.*, 2002; Gustafsson and Arlinger, 1994; Festen and Plomp, 1990; Wagener, 2003). In theses studies, the SRT decrease was up to 10 dB, depending on the modulation frequency, the modulation depth, and the type of modulation (broadband or frequency-dependent, regular or random). The release from masking due to fluctuations in the masker is significantly lower or absent for hearing-impaired subjects (Festen and Plomp, 1990; Gustafsson and Arlinger, 1994; Peters *et al.*, 1998; Wagener and Brand, 2006), and there is an additional effect of age which is not related to the hearing threshold (Dubno *et al.*, 2002; Peters *et al.*, 1998; Festen and Plomp, 1990). There is also evidence that linear amplification does not restore the release from masking due to fluctuations in the masker (Peters *et al.*, 1998; Gustafsson and Arlinger, 1994). Possible reasons for the detriment of hearing-impaired subjects are reduced temporal resolution and reduced comodulation masking release (Festen and Plomp, 1990; Hall *et al.*, 1984; Lorenzi *et al.*, 2009). However, the amount of comodulation masking release appears to be small in the case of speech recognition as opposed to speech detection (Festen, 1993; Grose and Hall, 1992). For diagnostic purposes, fluctuating maskers have the advantage that hearing-impaired subjects show larger interindividual differences in modulated noise than in stationary noise (Wagener and Brand, 2006; Versfeld and Dreschler, 2002; Smits and Houtgast, 2007). These interindividual differences could be used to distinguish between subjects with different hearing losses although their audiograms may be very similar.

Other studies have additionally taken effects of binaural hearing into account. Especially the interaction between the binaural release from masking and the beneficial effect of modulated maskers is of interest, for both normal-hearing and hearing-impaired subjects. Generally, it has been found that there is a combined benefit of location and modulation of the masker for normal-hearing subjects, but the individual effects interact. The difference between the combined effect and the sum of the single effects depends on the spatial distribution and number of interferers as well as their degree of comodulation (Hawley *et al.*, 2004; Peissig and Kollmeier, 1997; Duquesnoy, 1983). Hearing-impaired subjects gain little or no benefit from masker fluctuations, even if they can benefit from binaural release from masking (Bronkhorst and Plomp, 1992; Duquesnoy, 1983; Peissig and Kollmeier, 1997).

In some studies (Festen and Plomp, 1990; Peters *et al.*, 1998; Dubno *et al.*, 2002), the articulation index (AI) (ANSI, 1969), a predecessor of the SII (ANSI, 1997), has been used to make approximative first order predictions of speech intelligibility results. The focus was on an estimation of the influence of audibility for hearing-impaired subjects, but the effect of modulated or speechlike maskers was not included in the modeling. Models that were especially aimed at the prediction of speech intelligibility in modulated interferers were presented by Wagener (2003), Rhebergen and Versfeld (2005), and Rhebergen *et al.* (2006). Wagener (2003) included the noise level dependence of the SRT (Plomp, 1978) and a context model for phonemes and words in order to accurately predict the sentence intelligibility of normal-hearing and hearing-impaired listeners in fluctuating noise. Rhebergen *et al.* (2006) extended the SII (ANSI, 1997) for modulated noises by framewise calculation and subsequent averaging of the results per frame. The framewise calculation principle was also used in this study.

The extension of the BSIM is based on the ideas of Rhebergen and Versfeld (2005). The BSIM is repeatedly calculated in short time frames, and the resulting SRTs are averaged across all frames. This is a rather simple approach and does not include frequency band dependent frame lengths or forward masking (Rhebergen *et al.*, 2006). These additions would require fundamental changes in the binaural part of the model and were thus not considered in this study, but should be included in future versions of the BSIM, be-

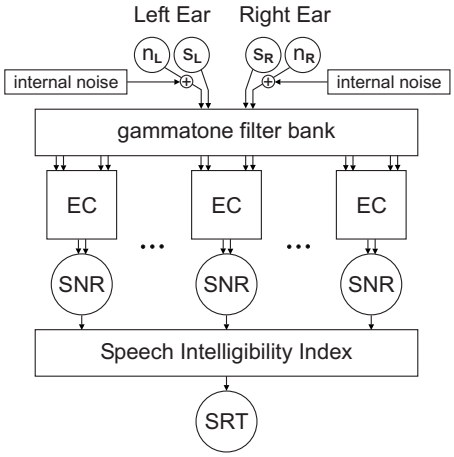

FIG. 1. Schematic diagram of the binaural speech intelligibility model. For a detailed description, refer to the text. The abbreviations s_L and n_L denote the speech and noise signals at the left ear of the subject, respectively, and s_R and n_R the same for the right ear. EC stands for the equalization-cancellation process, which results in estimated SNRs in each frequency band. The speech intelligibility index transforms the SNRs into a SRT.

cause they model the frequency dependence and the time asymmetry of gap detection in fluctuating maskers more accurately.

C. Evaluation of extended model

The predictions of the stBSIM were evaluated with perceptual data. For this purpose, a set of reference data was measured from 8 normal-hearing and 12 hearing-impaired subjects. The three factors target-interferer separation, room, and noise modulation depth were varied across conditions. In order to facilitate examining the interactions between the factors, all combinations of factor values (three noise azimuths, four rooms, and three noise types) were used, resulting in a total of 36 conditions. The hypotheses were that (1) SRTs decrease with increasing target-interferer separation due to increasing binaural release from masking, (2) SRTs decrease with increasing modulation depth of the noise due to the beneficial effect of noise fluctuations, (3) the effect of modulation depth decreases with increasing reverberation time due to temporal smearing of the noise fluctuations by the room impulse response, and (4) the effects of azimuth and noise interact especially in combination with room acoustics.

Other factors, such as "informational" masking (Kidd *et al.*, 2007), fundamental frequency differences between target and masker speaker (see Hawley *et al.*, 2004), or inter-individual cognitive differences not related to the auditory periphery, were excluded from this study. Although they are definitely important in certain situations, they are still very difficult to model and too complex to be included at the current state of the model presented here.

II. REVISION AND EXTENSION

A. Fundamental principle of the models

The basic principle of all three binaural speech intelligibility models is displayed in Fig. 1. The model receives the signals at the left and right ears of the subject as input. Independent masking noises are added to the left and right noise signals, respectively. These masking noises simulate internal noise in the auditory system and were adjusted to model the hearing threshold of each individual subject based on measured audiograms. Each of the four input signals is filtered into 30 frequency bands by a gammatone filter bank (Hohmann, 2002). The bandwidths and center frequencies are distributed between 140 Hz and 9 kHz according to the ERB scale by Glasberg and Moore (1990). The filtered input signals are processed by an EC stage (Durlach, 1963) (for a detailed explanation of the EC principle see Sec. II B), which models the binaural release from masking and searches for the maximal possible SNR with the given interaural differences of speech and noise in this frequency band. This maximal SNR is adapted to human binaural processing by artificial inaccuracies, the "binaural processing errors." The frequency-dependent SNRs, which were improved by the EC stage, serve as input for the monaural SII. The SII includes an importance weighting of frequencies and transforms the SNRs into an estimate of speech intelligibility in percent. Finally, the SRT (the broad-band SNR of the input signals that results in a speech intelligibility of 50%) is calculated.

The speech and noise signals are processed separately for a reliable estimate of SNR. The binaural process itself does not depend on separated speech and noise signals. The actual speech signal was replaced by a speech-simulating noise with the same long-term frequency spectrum as the speech because the intrinsic variance of speech would require very long signals and/or multiple predictions with different speech signals in order to make the variability of the predicted SRT independent of the specific speech sample.

B. Revision of the EC/SII model

The input signals $x_k(t)$ of the binaural speech intelligibility model (with $k \in \{L,R\}$ representing the left or right ear, respectively) are assumed to be a linear superposition,

$$x_k(t) = s_k(t) + n_k(t), \tag{1}$$

of the target speech signals $s_k(t)$ and the noise signals $n_k(t)$. This assumption is valid as long as nonlinearities in the transmission paths from the sound sources to the ears can be neglected, which is especially true for natural sound sources in reverberant rooms or their simulation via head-related transfer functions. The noise signals are assumed to be a superposition,

$$n_k(t) = \nu_k(t) + \mu_k(t), \tag{2}$$

of the external noise signals $\nu_k(t)$ and internal masking noises $\mu_k(t)$. The latter simulate the hearing threshold for the left and right ears, respectively. The interaural cross-correlation function of the internal masking noises is assumed to be exactly zero between $\mu_L(t)$ and $\mu_R(t)$, and so is the cross-correlation function between $\mu_k(t)$ and each other input signal. Thus, the internal masking noises cannot be eliminated by the binaural processing. This is a mathematical simplification because a physiological source of noise may actually include a component which is correlated between the ears.

The basic idea of the EC mechanism is to attenuate the external noise signal, if possible, by destructive interference between the left and right channels. For this purpose, a residual signal,

$$x_{\mathrm{EC}}(t) = \alpha x_L(t+\tau) - x_R(t), \tag{3}$$

is calculated from the input signals by applying an attenuation factor α and a relative time shift τ to one of the signals and subtracting the other signal, thus eliminating signal components with amplitude ratio α and time difference τ.

Equation (3) is symmetric in the sense that $x_L(t)$ and $x_R(t)$ may be swapped, if α is replaced by α^{-1} and τ by $-\tau$, resulting only in a sign change of $x_{\mathrm{EC}}(t)$. This can be expressed more clearly by symmetrizing Eq. (3), which gives

$$x_{\mathrm{EC}}(t) = e^{\gamma/2} x_L(t+\tau/2) - e^{-\gamma/2} x_R(t-\tau/2) \quad \text{with} \quad \alpha = e^{\gamma}. \tag{4}$$

The level equalization factor $e^{\gamma/2}$ is restricted to positive values, which represents the assumption that a simple addition of the left and right channels is impossible. This assumption was originally made by Durlach (1963) in order to explain the differences in binaural masking level difference (BMLD) between a π-phase-shifted pure tone in diotic noise and a diotic pure tone in π-phase-shifted noise.

For pure tone signal detection, modeling BMLDs usually only requires a single auditory filter band centered on the target signal to be examined—contrary to speech reception, where the bandwidth of the target signal is almost always larger than a single auditory frequency band. It has been shown that the binaural system is able to evaluate frequency-dependent interaural time and level differences (Akeroyd, 2004; Edmonds and Culling, 2005; Beutelmann *et al.*, 2009), suggesting independent binaural processing in different frequency bands. Within a single auditory filter, however, it is typically assumed (e.g., Durlach, 1972) that the interaural parameters of a binaural model may be considered to be constant. The conclusion for this model is that the input signals $x_L(t)$ and $x_R(t)$ are filtered into B narrow auditory frequency bands with center frequencies Ω_b, where $b \in [1,B]$. The transfer function magnitudes of the auditory filters are assumed to be negligible beyond a certain bandwidth β_b around Ω_b. In each frequency band, the SNR is maximized using an independent EC process with a separate set of equalization parameters $\alpha_b = e^{\gamma_b}$ and τ_b.

The following derivations are performed in the frequency domain and represent the output of *one* of the B auditory filters, without loss of generality. In order to avoid overly complex expressions, the index b was omitted. Upper case letters represent the filtered spectrum of time domain signals with respective lower case letters, for example, $X_L(\omega) = H(\omega)\mathcal{F}\{x_L(t)\}$, etc., where $H(\omega)$ is the transfer function of the respective auditory filter and ω is the angular frequency.[1] The EC process in Eq. (4) expressed in the frequency domain is

$$X_{\mathrm{EC}}(\omega) = e^{\gamma/2 + i\omega\tau/2} X_L(\omega) - e^{-\gamma/2 - i\omega\tau/2} X_R(\omega). \tag{5}$$

In EC theory, the signals are assumed to be subject to uncertainties in level and time, expressed by normally distributed processing errors ϵ_k and δ_k. These processing errors have been adapted by vom Hövel (1984) from the concept by Durlach (1963). Every quantity derived from the residual signal,

$$X_{\mathrm{EC}}(\omega) = e^{\gamma/2 + \epsilon_L + i\omega(\tau/2 + \delta_L)} X_L(\omega) - e^{-\gamma/2 + \epsilon_R - i\omega(\tau/2 - \delta_R)} X_R(\omega), \tag{6}$$

especially the signal intensity $I(X_{\mathrm{EC}})$ (as defined in Eq. (8), see below), is assumed to be the expected value $\langle I(X_{\mathrm{EC}})\rangle_{\epsilon_L,\epsilon_R,\delta_L,\delta_R}$ of this quantity with respect to the distributions of the processing errors. The distributions of ϵ_k and δ_k have means of zero and standard deviations dependent on the actual equalization parameters: $\sigma_\epsilon(\alpha)$ and $\sigma_\delta(\tau)$.[2]

Speech intelligibility prediction using SII is based on the bandwise SNR:

$$\mathrm{SNR} = \frac{\langle I(S_{\mathrm{EC}})\rangle_{\epsilon_L,\epsilon_R,\delta_L,\delta_R}}{\langle I(N_{\mathrm{EC}})\rangle_{\epsilon_L,\epsilon_R,\delta_L,\delta_R}}, \tag{7}$$

with the intensity I of a band pass signal with center frequency Ω and bandwidth β defined in the frequency domain as

$$I(X) = \int_{\Omega-\beta/2}^{\Omega+\beta/2} |X(\omega)|^2 d\omega. \tag{8}$$

The monaural SNRs at each ear are defined as

$$M_L = \frac{I(S_L)}{I(N_L)} \quad \text{and} \quad M_R = \frac{I(S_R)}{I(N_R)}, \tag{9}$$

and the interaural level differences (ILDs) of speech and noise are defined as

$$\Delta_S = \frac{1}{2}\ln\left(\frac{I(S_L)}{I(S_R)}\right) \quad \text{and} \quad \Delta_N = \frac{1}{2}\ln\left(\frac{I(N_L)}{I(N_R)}\right), \tag{10}$$

respectively (except for a scaling factor, they are equivalent to the ILD in dB). The normalized cross-correlation function between the left and right ears for the speech signal is defined as

$$\rho_S(\tau) = \frac{2\pi}{\sqrt{I(S_L)I(S_R)}} \int_{\Omega-\beta/2}^{\Omega+\beta/2} S_L(\omega) S_R^*(\omega) e^{i\omega\tau} d\omega \tag{11}$$

and $\rho_N(\tau)$ is defined analogously for the noise.[3] A comprehensive derivation, which is carried out in detail in Appendix A, leads to a closed-form expression for the SNR,

$$\mathrm{SNR} = (M_L M_R)^{1/2} \frac{e^{\sigma_\epsilon^2}\cosh(\gamma+\Delta_S) - \lambda(\tau) * \mathrm{Re}(\rho_S(\tau))}{e^{\sigma_\epsilon^2}\cosh(\gamma+\Delta_N) - \lambda(\tau) * \mathrm{Re}(\rho_N(\tau))} \tag{12}$$

where $\mathrm{Re}(\rho)$ denotes the real part of ρ, and $*$ denotes the convolution. Both interaural cross-correlation functions are smoothed by convolution with a Gaussian window,

$$\lambda(\tau) = \frac{1}{\sigma_\lambda\sqrt{2\pi}} e^{-(1/2)\tau^2\sigma_\lambda^{-2}}, \tag{13}$$

whose width is defined by the standard deviation of the time processing errors $\sigma_\lambda = \sigma_\delta\sqrt{2}$. Note that this is equivalent to a

low-pass filter in the frequency domain (with a likewise Gaussian transfer function).

The aim of the EC process is to maximize the SNR given in Eq. (12). It can be easily shown by expanding the cosh functions that the SNR converges to the left monaural SNR M_L as γ goes to positive infinity and that the SNR converges to the right monaural SNR M_R as γ goes to negative infinity. This means that the case of "better ear listening," that is, the case where the optimal strategy would be using only the signal at the ear with the favorable SNR, is implicitly included in Eq. (12). However, depending on the properties of the input signals, the parameters γ and τ can be used to achieve an additional benefit exceeding the "better ear" SNR, that is, a true binaural release from masking. Gallun *et al.* (2007) found that it may not always be possible to only listen to the ear with the monaurally favorable SNR due to auditory grouping of ipsi- and contralateral signals or due to limited processing resources of the subject. These factors are not yet included in the BSIM, as they are primarily an issue of informational masking.

Since the cosh function is symmetric with a minimum value of 1 at zero in the argument, and because the absolute value of the cross-correlation terms (even after convolution with the normalized smoothing window) is always equal to or less than 1, the fraction in Eq. (12) is always equal to or greater than zero. Equality is only achieved, if σ_ϵ is zero and $\rho_S(\tau)$ is 1 for a certain value of τ. Otherwise, both numerator and denominator are always finite, so that only a finite benefit compared to the better ear SNR can be achieved. This corresponds to the purpose of the processing errors, that is, to restrict the performance of the EC process by preventing perfect cancellation of the noise signal. The internal masking noise $\mu_k(t)$ is another reason why the noise signal cannot be canceled out perfectly. Given that the internal masking noises $\mu_k(t)$ are independent of each other and that $\rho_N(\tau)$ is the interaural cross correlation of the sum of the noise signals $n_k(t)$ and the internal masking noises $\mu_k(t)$, $\rho_N(\tau)$ can never exactly be equal to 1 or -1. Details about the internal noise are specified in Sec. II A and further discussion of the parameters and their meaning can be found in Sec. IV A.

C. Implementation of BSIM

The practical implementation of the BSIM involved some aspects which are important to mention, because they concern essential parts of the model or contributed considerably to the reduction of computation time. These modifications of the original "EC/SII" model (Beutelmann and Brand, 2006) include a new frequency band scheme for the SII, the way how the internal threshold noise is included, and the search method for the optimal SNR in each band.

The number and bandwidth of the SII calculation bands were adapted to the gammatone filter bank (Hohmann, 2002) which was used to divide the input signals into auditory frequency bands. The basic calculation procedure of the SII was not changed. Only the band importance functions had to be adapted to the new center frequencies. Although this implies a deviation from the standard SII, it was considered to be more accurate than using a different filter bank for the binaural part of the model or interpolating the output SNR of the binaural part to one of the standard frequency schemes. Because the transfer function relating SII to percent intelligibility is dependent on the speech material and type of presentation, the SII corresponding to 50% intelligibility at the SRT needed to be normalized to a reference condition. The revised model's modified SII procedure was normalized to the monaural presentation of the original Oldenburg Sentence Test in noise (see Sec. III A 1) at 65 dB sound pressure level (SPL), which yields a SII of 0.2 at the reference SRT of -7.1 dB SNR (Wagener *et al.*, 1999c). This differed from the procedure of Beutelmann and Brand (2006), which was normalized to a quasidiotic anechoic condition, in which both speech and noise came from the front.

The hearing threshold was simulated by adding a pair of constant intensity values corresponding to 1 dB above the hearing level to the noise intensities used for the calculation of Δ_N and the normalization of ρ_N in each frequency band. This replaced the actual internal noise signals that were added to the external noise signals in the original model of Beutelmann and Brand (2006). Those internal noise signals were spectrally shaped in such a way that the noise energy in an auditory filter band was 4 dB above the energy of a pure tone at the band center frequency with the respective hearing level at that frequency (see Breebaart *et al.*, 2001). The threshold criterion of 1 dB instead of 4 dB was chosen because it provided a better correlation between the predicted and the observed SRTs of the reference data from Beutelmann and Brand (2006).[4] A summary comparison of the predictions by the EC/SII model, BSIM, and stBSIM for the reference data from Beutelmann and Brand (2006) can be found in Appendix B and Table IV.

The optimal γ in Eq. (12), that is, the γ leading to the best SNR for a given τ, can be calculated analytically if the error variances are both set to zero. The optimal τ is searched for each band independently by calculating the interaural cross-correlation functions in Eq. (12) with a two step procedure. First, a coarse estimate is calculated with the help of a fast Fourier transform of the whole input signal (BSIM) or the current frame (stBSIM). This estimate is restricted to τ values at integer multiples of the sample period. Intersample interpolation was achieved by quadratic approximation at the maximum of Eq. (12) with respect to τ. The overall range of τ values was restricted to ± 10 ms in order to avoid numerical errors due to the finite length of the signal samples.

D. Extension of BSIM for modulated noises

The "EC/SII" model Beutelmann and Brand (2006) used long signals (between 1 and 3 s, i.e., about the length of a test sentence, see Sec. III A 1) to calculate a single SRT with a single set of EC parameters. This has the advantage that the result is not dependent on the (residual) signal statistics of the stationary interferer and that the EC parameters can be estimated very reliably if the binaural parameters of the input signals are constant. For modulated interferers, however, the SNR and hence potentially also the choice of optimal EC parameters vary over time. Thus, the signal level statistics need to be considered explicitly. In a first approach, we

therefore applied BSIM to short-time frames of the input signals and averaged across the framewise SRTs in order to obtain the final SRT prediction. Rhebergen and Versfeld (2005) showed that this approach is sufficient for good predictions of monaural SRT data in modulated noise, even with a fixed frame length across all frequency bands. A frame length of 1024 samples at 44 100 Hz sampling rate was used with a Hann window and a frame shift of half the frame length. Considering that the equivalent rectangular duration of a Hann window is only half of its full length, the effective frame length of this model is about 12 ms, which is close to the best fitting frequency-independent frame length found by Rhebergen and Versfeld (2005). The extended model is called stBSIM in the following. It is rather a proof of concept than an elaborate model for the combination of binaural speech intelligibility and fluctuating noise and may be refined with knowledge from monaural models (Rhebergen *et al.*, 2006; Plomp, 1978) in future studies. In this study, the masker was only (diotically) modulated in its envelope, but for nonstationary binaural cues, the EC part of the stBSIM will most likely need an additional time window with a length in the order of 100 ms simulating binaural "sluggishness" in future versions (see Culling and Summerfield, 1998; Culling and Colburn, 2000; Kollmeier and Gilkey, 1990).

III. EVALUATION WITH MODULATED INTERFERER

A. Methods

1. Sentence test procedure

The speech intelligibility measurements were carried out using the HörTech Oldenburg Measurement Applications (OMA), version 1.2. As speech material, the Oldenburg Sentence Test in noise (Wagener *et al.*, 1999a, 1999b, 1999c) convolved with room impulse responses was used. Except for the convolution with binaural room impulse responses, the signals complied with the commercial version. Each sentence of the Oldenburg Sentence Test consists of five words with the syntactic structure "name verb numeral adjective object." For each part of the sentence, ten alternatives are available, each of which occurs exactly twice in a list of 20 sentences, but in random combination. This results in syntactically correct but semantically unpredictable sentences. The subjects' task was to repeat each word they recognized after each sentence as closely as possible. The subjects' responses were analyzed using word scoring. An instructor marked the correctly repeated words on a touch screen display connected to a computer, which adaptively adjusted the speech level after each sentence to measure the SRT level of 50% intelligibility. The step size of each level change depended on the number of correctly repeated words of the previous sentence and on a "convergence factor" that decreased exponentially after each reversal of presentation level. The intelligibility function was represented by the logistic function, which was fitted to the data using a maximum-likelihood method. The details of this procedure have been published by Brand and Kollmeier (2002) (A1 procedure). A test list of 20 sentences was selected from 45 such lists to obtain each observed SRT value. Two sentence lists with 20 sentences each were presented to the subjects prior to each measurement session for training purposes. At the beginning of the first session, three training lists were presented to each subject. The test lists were balanced across subjects and conditions, and all measurements except for the training lists were performed in random order.

The noise signals used in the speech tests will be described in detail in Sec. III A 2. The noise token, with its starting point randomly selected within the whole noise signal, was presented simultaneously with the sentences. It started 500 ms before and stopped 500 ms after each sentence, including 50 ms Hann ramps at onset and offset. The noise level was kept fixed at 65 dB SPL for the normal-hearing subjects. For the hearing-impaired subjects, the noise levels were adjusted to their individual hearing loss. The noise level was first set to 55 dB SPL plus half the individual hearing loss averaged across 500 Hz and 4 kHz (in steps of 5 dB). No level was set lower than 65 dB SPL or higher than 85 dB SPL. The subjects were asked whether the level was uncomfortably loud during the first training sentence and the noise level was decreased in steps of 5 dB until a comfortable level was reached if necessary.

The headphones (Sennheiser HDA 200) were free-field equalized according to international standard (ISO/DIS 389-8), using a finite impulse response filter with 801 coefficients. The measurement setup was calibrated to dB SPL using a Brüel & Kjær (B&K) 4153 artificial ear, a B&K 4134 1/2 in. microphone, a B&K 2669 preamplifier, and a B&K 2610 measuring amplifier.

2. Interferer noises

Three different noise types were used in the measurements: stationary speech-shaped noise ("stationary"), 20-talker babble noise ("babble"), and a single-talker modulated noise ("single-talker"). As stationary speech-shaped noise, the original noise from the Oldenburg Sentence Test was used. It has been generated by randomly superimposing the speech material waveforms of the sentence test. Therefore, the long-term spectrum of this noise is very close to the mean long-term spectrum of the speech material. The multi-talker babble noise was taken from the Auditec CD "CD101RW2" (Auditec, 2006) and is a mixture of 20 speakers simultaneously reading different passages. The single-talker modulated noise is based on the "ICRA5" noise

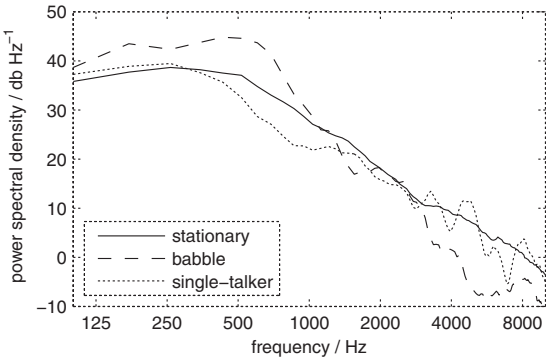

FIG. 2. Long-term frequency spectra of the interferer noises (stationary: solid line; babble: dashed line; single-talker: dotted line) used in this study. The overall level was identical for all three noises.

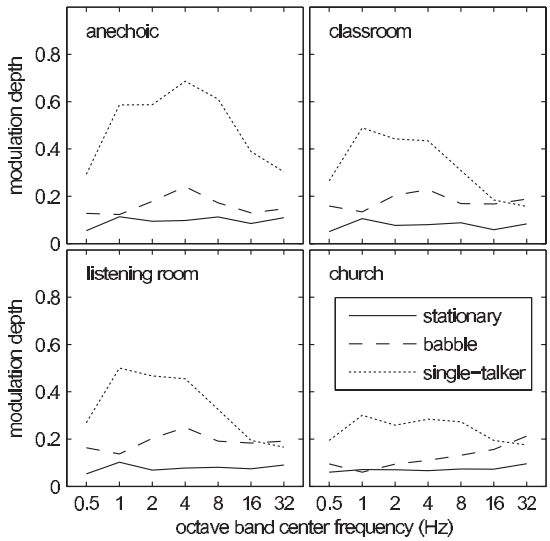

FIG. 3. Modulation octave band spectra for the three interferer noises (stationary: solid line; babble: dashed line; single-talker: dotted line) used in this study in each of the rooms. The room is denoted in the top left corner of the panel.

(Dreschler *et al.*, 2001), which has been created to eliminate intelligibility and fundamental frequency of the speaker as far as possible while preserving the modulation features of a single speaker in multiple frequency bands. The speech pause durations in this noise have been limited to 250 ms (Wagener and Brand, 2006). The long-term spectra of stationary noise and the single-talker noise are similar, as shown in Fig. 2, but the babble noise was attenuated by about 16 dB at frequencies higher than 5 kHz with a slope of about 5 dB/oct between 500 Hz and 5 kHz. Although this was originally due to a missing headphone equalization, it was kept because this was a way to test the model with substantially differing speech and noise spectra. The modulation spectra of the three noises, dependent on the room condition, are shown in Fig. 3. The modulation spectra were generated by calculating the Hilbert envelope of the signal, dividing the envelope by its mean, and filtering the result in octave bands between 0.5 and 32 Hz center frequencies. The power within each band is displayed as the modulation depth of the respective band.

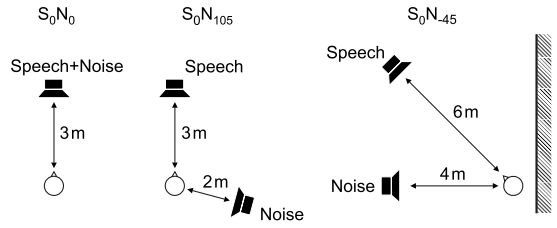

FIG. 4. Speech and noise source locations in the three setups used in the measurements. In the third setup, the subject was always placed very close to a wall at the right side.

3. Rooms and setups

Room acoustics and sound source locations were realized using virtual acoustics over headphones. The stimuli were prepared by convolving the original sentence material as well as the noise signals with binaural room impulse responses, which had been calculated using the ODEON software, Version 8.0 (Christensen, 2005). Four simulated rooms were used for the measurements: an anechoic room, a listening room ($7.8\times5\times3$ m^3, approximately 115 m^3), a typical classroom ($9.7\times6.9\times3.2$ m^3, approximately 210 m^3), and a church (outer dimensions: $63\times32\times22$ m^3, approximately 22.000 m^3). The listening room was designed according to IEC 268-13 (IEC, 1985). The church was a model of Grundtvig's Church in Copenhagen. Table I lists basic room acoustic parameters[5] of the three realistic (i.e., nonanechoic) rooms. The spatial setups used in the experiments included two different distances (3 and 6 m) between speech source and subject. The parameters shown in Table I were calculated for these two distances.

In each room, three different spatial setups were used: S_0N_0 (i.e., the speech source at 0° and the noise source at 0°), S_0N_{105}, and S_0N_{-45}. The configurations are shown in Fig. 4. In the S_0N_{-45} situation in each room (except for the anechoic case), the subject was positioned very close to a wall opposite to the noise source, as illustrated in Fig. 4. This was done to include the potentially disturbing effect of the direct reflections from the wall in this situation. (Beutelmann and Brand, 2006) showed that a reflecting surface close to

TABLE I. Basic room acoustic parameters of the three realistic (nonanechoic) rooms used in the measurements for two distances (3 and 6 m) between the speech source and an omnidirectional receiver at the subjects' position. The listed parameters[5] are the reverberation time (T_{30}), the early decay time (EDT), the "clarity" (C80), the "definition" (D50), and the STI. All values are averages across octave bands from 63 Hz to 8 kHz calculated by the ODEON software. The STI values only include the reduction in the modulation transfer function due to room acoustics but not due the noise interferers used in this study.

Room	Distance (m)	T_{30} (s)	EDT (s)	C80 (dB)	D50	STI
Listening room	3	0.40	0.35	13.2	0.88	0.81
	6	0.40	0.41	11.4	0.82	0.77
Classroom	3	0.94	0.48	10.1	0.83	0.77
	6	0.92	0.62	8.1	0.77	0.72
Church	3	8.78	7.38	2.8	0.57	0.60
	6	8.69	7.91	0.9	0.48	0.52

TABLE II. Summary of hearing losses of the hearing-impaired subjects and individual noise levels that were used in the SRT measurements. The PTAs are the mean hearing thresholds in dB HL across the audiometric frequencies from 125 to 750 Hz (PTA low), from 1 to 3 kHz (PTA mid), and from 4 to 8 kHz (PTA high). The subjects are grouped by similarity of their hearing losses.

		Left ear			Right ear			
Group	Subject	PTA low	PTA mid	PTA high	PTA low	PTA mid	PTA high	Noise level (dB SPL)
Low	1	8	13	20	10	12	27	70
Matched	2	6	29	63	10	35	63	70
	3	15	49	85	17	49	73	80
	4	34	49	67	24	49	68	75
	5	26	46	62	28	48	67	75
	6	33	51	62	34	55	62	75
	7	18	52	57	22	45	55	70
	8	33	53	57	30	48	45	70
	9	43	60	68	29	53	65	75
High	10	53	59	77	55	63	73	80
	11	64	50	37	53	53	38	80
	12	58	61	70	66	66	60	85

the listener may increase the SRT significantly in certain spatial configurations because the reflection creates a secondary virtual noise source.

4. Subjects

A total of 8 normal-hearing and 12 hearing-impaired subjects participated in the measurements. The age of the normal-hearing subjects ranged from 25 to 31 years (median: 26.5 years) and the age of the hearing-impaired subjects ranged from 36 to 80 years (median: 67 years). None of the hearing levels of the normal-hearing subjects exceeded 10 dB hearing loss (HL) at audiometric frequencies between 125 Hz and 8 kHz, inclusive. All hearing-impaired subjects had mostly symmetrical hearing losses (the maximal difference of pure tone average as reported in Table II was below 15 dB). Thus, only the means of the left and right ears are shown in Fig. 5. Eight of the hearing-impaired subjects had similar, moderately sloping hearing losses, as summarized in the left panel of Fig. 5. The remaining four subjects had various shapes and degrees of hearing loss, which are shown for each individual subject in the right panel of Fig. 5. The measurement and prediction data of all subjects are reported in Sec. III B. However, only the data of the matched group in the left panel of Fig. 5 were included in the subsequent statistical analyses. Table II lists the pure tone averages and the individually adjusted noise levels (see Sec. III A 1) used in the measurements. The frequencies for the calculation of the pure tone averages (PTAs) have been chosen according to the principal component analysis of audiograms by Smoorenburg (1992). They were 125, 250, 500, and 750 Hz for the low-frequency component, 1, 1.5, 2, and 3 kHz for the midfrequency component, and 4, 6, and 8 kHz for the high-frequency component. All subjects were paid for their participation.

5. Statistical analysis

The statistical significance of the measured effects was analyzed by means of multiway analyses of variance (ANOVAs) of the observed SRTs. For the normal-hearing subjects, the ANOVA was calculated with the three factors azimuth (three levels), room type (four levels), and noise type (three levels). A second ANOVA was calculated from the combined data of normal-hearing subjects and the matched group of hearing-impaired subjects with an additional factor hearing impairment (two levels, normal-hearing and hearing-impaired). The significance level was set to 5%. *Posthoc* pairwise comparisons were performed using Scheffé's procedure (Scheffé, 1963) for contrasts between all combinations of factor levels.

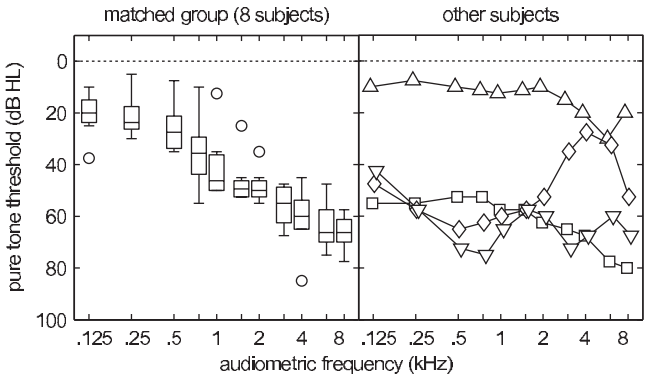

FIG. 5. Pure tone audiograms of the hearing-impaired subjects. All hearing losses were symmetrical, thus only the means of left and right ears are shown. The box plot in the left panel summarizes the audiograms of eight subjects with very similar hearing losses. The right panel shows the individual audiograms of the remaining four subjects. Only the data of the subjects in the left panel were included in the later statistical analyses. The box plots include the median (center line), the upper and lower quartiles (upper and lower box limits), and the extreme value within 1.5-times the interquartile range above of below the quartiles (whiskers). Outliers (i.e., values above or below the whiskers) are marked by a circle.

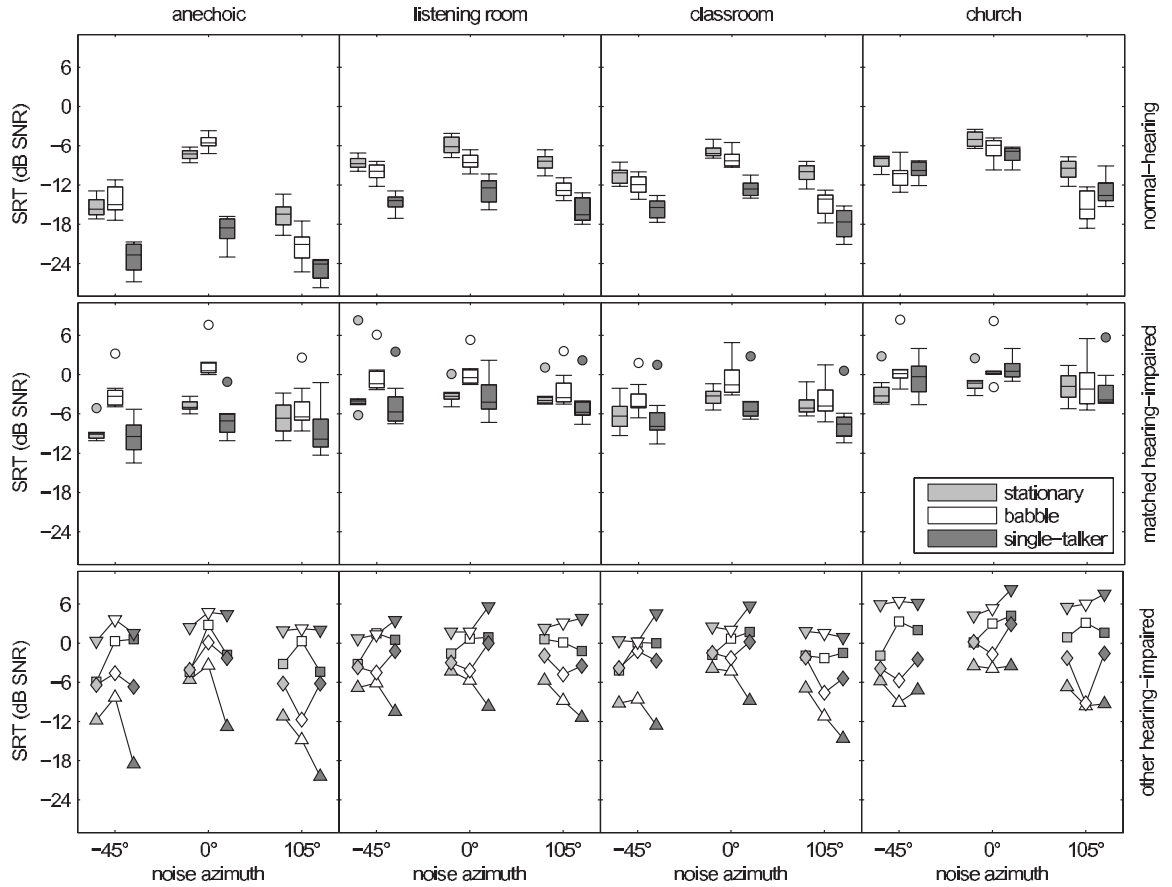

FIG. 6. Box plots of observed SRTs of the normal-hearing subjects (top row) and the matched group of hearing-impaired subjects (middle row). The bottom row shows individual data of the four separated hearing-impaired subjects with symbols corresponding to the audiograms in the right panel of Fig. 5. Each panel displays observed SRTs for one of the room conditions (labeled by the title at the top of each column of panels). Within each panel, the box plots are grouped by noise azimuth. The noise type is indicated by the shading of the box or symbol. The box plots include the median quartiles, extreme values, and outliers in the same way as in Fig. 5.

B. Results and discussion

1. Normal-hearing subjects

The top row of Fig. 6 shows the observed SRTs of the normal-hearing subjects. A three-way ANOVA of the normal-hearing subjects' data (as described in Sec. III A 5) found a significant main effect of azimuth ($p<0.0001$), indicating that an overall spatial release from masking was present. *Posthoc* contrasts (significance level $p<0.05$) showed that the spatial release from masking was larger in the 105° condition than in the −45° condition. This effect is most pronounced in the anechoic condition, where no wall reflection is present. This meets the expectation that the spatial release from masking increases with increasing spatial separation between speech and noise source. A significant main effect of room type was also found ($p<0.0001$), with a rank order from low to high SRTs of anechoic, classroom, listening room and church. The rank order of listening room and classroom is remarkable, because all room acoustical measures in Table I suggest a better speech intelligibility in the listening room than in the classroom. The main effect of noise type was likewise significant ($p<0.0001$), with the single-talker noise yielding the lowest SRTs, followed by babble noise, and stationary noise yielding the highest SRTs. This indicates that speech intelligibility was positively correlated with the modulation depth of the interferer noise in this study.

The room type has an influence on the spatial release from masking, indicated by a significant interaction between the factors azimuth and room type ($p<0.0001$). The spatial release from masking is generally reduced in the three reverberant rooms (listening room, classroom, and church) with respect to the anechoic conditions. A significant interaction was found between the factors room and noise type ($p<0.0001$). This is mainly due to the fact that the difference between babble and single-talker noise is nonsignificant in the church condition, which can be attributed to the long reverberation that reduces the modulation depth of the single-talker noise, thus making it less beneficial to the subject. Although the SRT at 0° for babble noise in anechoic conditions (upper left panel in Fig. 6) stands out noticeably against the other noise types, this is not a significant effect. A possible reason for the apparent trend has not been found. The interaction between the factors azimuth and noise type was also found to be significant ($p<0.0001$). The difference between the −45° conditions and the 105° conditions that occurs in the main effect of azimuth is significant only for babble and single-talker noise.

2. Hearing-impaired subjects

The observed SRTs of the hearing-impaired subjects are shown in Fig. 6 in the middle and bottom rows. The middle

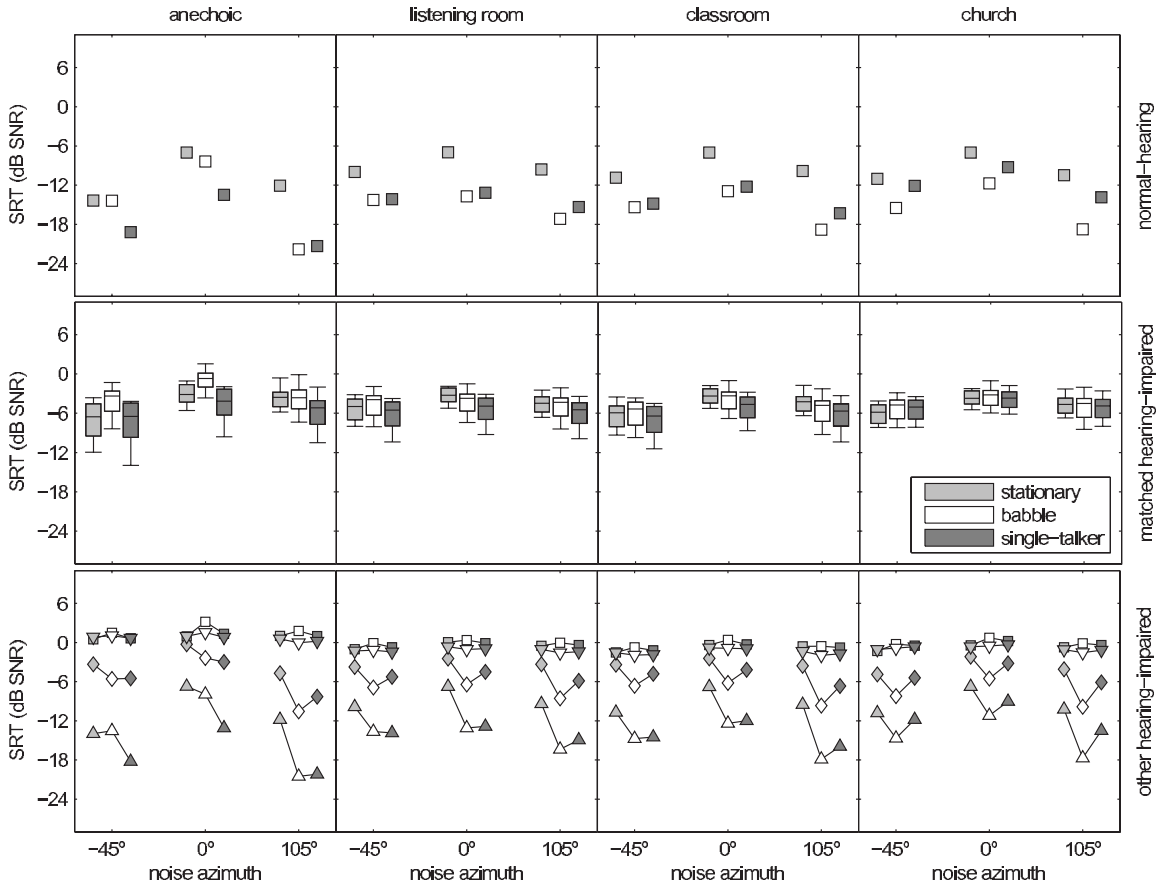

FIG. 7. Predicted SRTs for the normal-hearing subjects (top row) and the matched group of hearing-impaired subjects (middle row). The bottom row shows individual predictions of the four separated hearing-impaired subjects with symbols corresponding to the audiograms in the right panel of Fig. 5. The interindividual ranges of the predictions for the normal-hearing subjects in the top row are all below 0.7 dB, thus no box plots were drawn but single symbols. The display of predictions in the middle and bottom rows is identical to the display of observed data in Fig. 6.

row shows box plots of the matched group data (as described in Sec. III A 4) and the bottom row shows individual data from the other four hearing-impaired subjects. A four-way ANOVA of the combined data of normal-hearing and matched group subjects found a significant main effect of group ($p<0.0001$), that is, the hearing-impaired subjects generally had higher SRTs than the normal-hearing subjects. All other main effects and their respective *posthoc* contrasts are consistent with the analysis of the normal-hearing subjects' data, except for a nonsignificant overall difference between the SRTs for stationary noise and in babble noise. The latter fact appears to be due to an interaction between the group and noise type factors. Hearing-impaired subjects benefit much less from a large masker modulation depth than normal-hearing subjects, which is reflected in the results of the statistical analysis: No significant difference was found for the hearing-impaired subjects between SRTs in stationary and in single-talker noise, while the SRTs in babble noise are significantly higher. This is remarkable but can be explained by the different long-term spectra of stationary and single-talker noise, on the one hand, and babble noise, on the other hand. The babble noise has a low-pass characteristic compared to the other two noise types and thus caused a relatively low SNR in the low-frequency range and a relatively high SNR in the high-frequency range. Subjects with a high-frequency hearing loss have to use the information transmitted in the low-frequency range and benefit less from the high SNR in the high-frequency range than the normal-hearing subjects. A comparison between two of the individually displayed subjects (bottom row of Fig. 6 and right panel of Fig. 5) shows high SRTs in babble noise for high-frequency dominated hearing loss (square symbols) and low SRTs in babble noise for low-frequency dominated hearing loss (diamond symbols). The hearing-impaired subjects benefit less from spatial release from masking than the normal-hearing subjects, as indicated by a significant interaction between the factors azimuth and group ($p<0.0001$). This is especially noticeable in the anechoic conditions, where normal-hearing subjects have the largest benefit due to spatial release from masking compared to the other room conditions, while a pronounced difference between the room conditions is not present in the hearing-impaired subjects' data.

3. Model predictions

The model predictions are shown in Fig. 7 analogously to Fig. 6. The correlation between the observed data and predictions of stBSIM and BSIM are shown in Fig. 8 and summarized in Table III. The prediction quality was mainly analyzed by means of two parameters: first, the squared correlation coefficient R^2 (coefficient of determination), an estimator for the fraction of the observed variance that can be

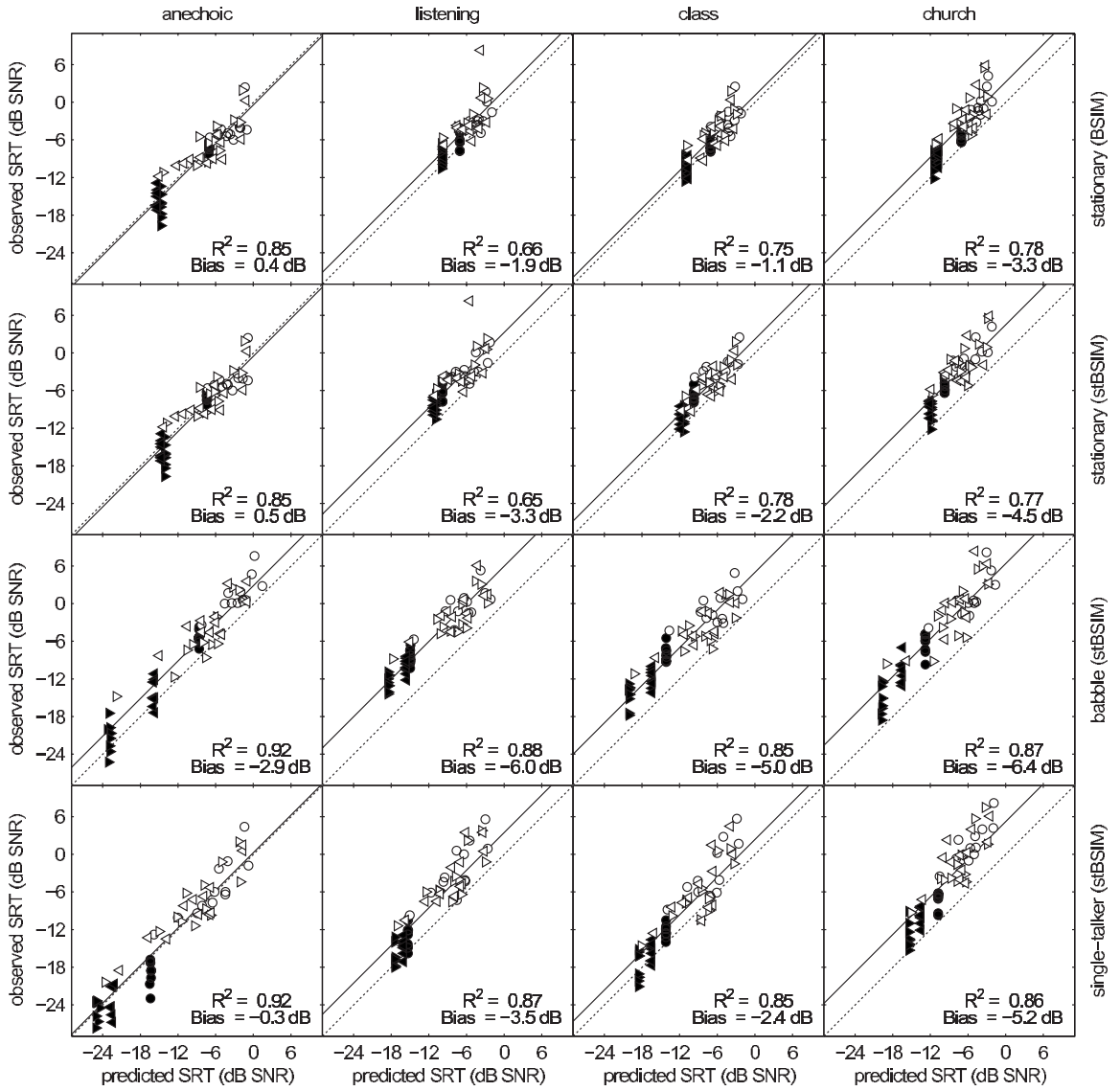

FIG. 8. Scatter plots of observed SRTs against predicted SRTs. Each panel contains the data of a combination of room (column, label on top) and noise type (row, label at the right). The top row shows predictions with BSIM, and all other rows with stBSIM. The data from normal-hearing subjects are plotted with filled symbols and the data from hearing-impaired subjects with open symbols. The noise azimuths are indicated by symbol type (circle: 0°, left-pointing triangle: −45°, right-pointing triangle: 105°). Within each panel, the squared correlation coefficient R^2 (coefficient of determination) and the bias (mean difference between predicted and observed SRTs) are specified in the lower right corner. The dashed lines mark identity between predictions and observations. The solid lines are lines of unity slope, which were least-squares fitted to the data in the panel. Their offset from the identity line is equal to the bias.

explained by the model, and second, the bias, that is, the mean of the signed prediction error (difference between predicted and observed SRTs). The overall R^2 is 0.78 and the overall bias is −3.4 dB, that is, the predicted SRTs are lower than the observed SRTs. The overall standard deviation of the prediction error is 3.0 dB. We did not compensate for the overall bias (which would be possible by simply shifting the predicted SRTs), because this would be inconsistent with the prediction of monaural SRTs and with the data of Beutelmann and Brand (2006). Comparing Fig. 7 with Fig. 6 generally shows a good agreement between predictions and observations, with only few noticeable deviations. The effect of noise type is well predicted for the difference between single-talker and stationary noise. However, all predicted SRTs for babble noise are too low (see Table III, bias of babble noise). This might be due to the spectral difference between babble noise and speech, and is probably a shortcoming of the SII rather than the EC part of the model, because the frequency band weighting of the SII is linear and does not include correlations between adjacent or synergistic effects between remote frequency bands. The overall effect of hearing loss is predicted well, except for the outliers in Fig. 6 (middle row). This might indicate a hearing impairment which is not well described only by the audiogram, such as a reduced sensitivity to temporal fine structure (Lorenzi *et al.*, 2009). The effect of noise azimuth is also well predicted, except for a constant bias for different azimuth values given in Table III. The first two rows of Fig. 8 present the same observed data and predictions using BSIM (top row) and using stBSIM (second row) for the respective conditions. The results of BSIM and stBSIM match closely, if the noise is not modulated. Figure 8 also shows that the prediction error is relatively homogeneously distributed within the different conditions and similarly across condi-

TABLE III. Squared correlation coefficient R^2 (coefficient of determination) and bias (mean difference) between predicted and observed SRTs pooled by different factors. R^2 indicates the fraction of explained variance within each factor and differences of the bias between factors represents discrepancies of the prediction between the factors (see text for details). In addition to the total set of data, the values are specified for the normal-hearing and the matched hearing-impaired subject groups.

Subject group		All		NH		Matched HI	
Pooled by		R^2	Bias (dB)	R^2	Bias (dB)	R^2	Bias (dB)
Room	Anechoic	0.89	−0.9	0.85	0.0	0.61	−1.1
	Listening room	0.78	−4.3	0.57	−3.6	0.29	−4.7
	Classroom	0.78	−3.2	0.58	−2.7	0.31	−3.2
	Church	0.82	−5.4	0.64	−4.1	0.25	−6.2
Azimuth	0°	0.68	−3.8	0.51	−3.2	0.22	−4.0
	105°	0.83	−3.1	0.68	−2.1	0.30	−3.4
	−45°	0.76	−3.4	0.65	−2.5	0.27	−4.1
Noise type	Stationary	0.65	−2.4	0.65	−1.8	0.13	−2.7
	Babble	0.84	−5.1	0.74	−4.7	0.33	−5.3
	Single-talker	0.86	−2.8	0.83	−1.3	0.36	−3.4

tions. This holds especially for the widespread individual observed SRTs of the normal-hearing subjects. This variance is apparently not related to the audiogram and consequently it is not predicted by the model. The prediction errors of the hearing-impaired subjects are similarly distributed, except for the most severe hearing losses. Possibly, the remaining variance is not related to the hearing threshold, but to other factors such as age, suprathreshold deficits, or central processing disorders.

IV. GENERAL DISCUSSION

A. BSIM

The BSIM is a complete revision of the EC/SII model presented in Beutelmann and Brand (2006). The EC/SII model combined a gammatone filter bank, an independent EC process in each frequency band, a resynthesis of the filter bands into broadband waveforms (speech and noise), and the SII. The EC/SII model was implemented in a straightforward way as a signal-processing device and provided good predictions of binaural speech intelligibility in spatial noise conditions including different room acoustics (Beutelmann and Brand, 2006). However, this approach was rather technical and disguised some of the underlying principles of binaural modeling. For example, the binaural processing errors, which were used to adjust the EC stage to match imperfect human binaural processing, were implemented using Monte-Carlo simulations. This stochastic approach made it difficult to interpret the binaural processing errors in psychoacoustical terms such as temporal resolution or representation of intensity. A further disadvantage of this stochastic approach is that slightly different results were obtained each time the model was run for the same input condition. On a rather technical level, another disadvantage was that the numerical search for optimal equalization parameters, the Monte-Carlo simulation, and the resynthesis were extremely time consuming, making the model hardly useful for practical applications, such as online evaluation of room acoustical simulations.

The analytical revision of the EC/SII model resulted in the BSIM presented here. It eliminated the above-mentioned disadvantages and combined technical improvement with a much more obvious relation to psychoacoustics. BSIM predicts the data used for validation of the EC/SII model (Beutelmann and Brand, 2006) at least as well as the original model and still remains independent of explicit *a priori* knowledge of parameters other than the speech and noise signals and the individual hearing threshold. The optimal equalization parameters (γ and τ) leading to the maximal SNR at the output of the model are automatically estimated from the input signals. Equation (12) directly relates the estimated SNR to interaural parameters calculated from the signals [i.e., the interaural level differences of speech and noise, Δ_S and Δ_N, and the interaural cross-correlation functions of speech and noise, $\rho_S(\tau)$ and $\rho_N(\tau)$]. Numerator and denominator of Eq. (12) each comprise separate parts for the influence of level differences (the cosh term) and time differences [the convolution of $\lambda(\tau) * \mathrm{Re}\{\rho(\tau)\}$] on the SNR. If the interaural level difference of speech or noise is large, the cosh term dominates the result of Eq. (12). This includes the limit case of better ear listening (i.e., using only one ear, if the SNR at this ear is favorable), for which γ approaches positive or negative infinity. The τ-dependent term becomes important, if either cosh term results in a value close to 1, that is, if the interaural level difference Δ is equalized by an opposite γ. In this case, the SNR strongly depends on $\rho(\tau)$. The interaural cross-correlation function $\rho(\tau)$ includes both deterministic decorrelation due to interaural time differences and stochastic decorrelation due to, for example, reverberation. The weighting between the level- and time-dependent terms as well as the maximally achievable SNR with perfectly correlated input signals is controlled by the binaural error terms. The gain error ($e^{\sigma_\epsilon^2}$) controls the overall balance

between the level- and time-dependent terms. The delay error ($e^{-\omega^2\sigma_\delta^2}$) reduces the influence of the interaural cross correlation on the SNR at high frequencies, which can be interpreted as a very simple model of the decreasing phase coherence on the auditory nerve toward high frequencies (Johnson, 1980). This is in line with similar low-pass filters in more physiological models (Dau *et al.*, 1996; Heinz *et al.*, 2001) and with the fact that BMLDs decrease with increasing target tone frequency (Hirsh and Burgeat, 1958). The binaural processing error variances (σ_ϵ^2 and σ_δ^2) have been taken from vom Hövel (1984), who derived them from predictions of pure tone BMLD data (Langford and Jeffress, 1964; Blodgett *et al.*, 1962; Egan, 1965). The analytic expressions for the binaural processing errors replaced the Monte-Carlo simulation and made the model completely deterministic.

In literature (Durlach, 1963, 1972; Sieben, 1979), expressions similar to Eq. (12) have already been derived, but mostly for certain binaural configurations and limited to tonal target signals, while the mathematical prerequisites for Eq. (12) are less restricted. Equation (12) can be transformed into the expression that Durlach (1963) derived for the "EC factor" f_j [Eq. (6) on p. 1210 in Durlach, 1963], because they are based on the same principle. For this purpose, the target signal is assumed to be a pure tone and the noise signal to be white Gaussian noise passed through an auditory filter centered at the target signal frequency. Both target and noise signals have time-invariant (but not necessarily equal) ILDs and ITDs, and γ and τ are set to equalize the ILD and ITD of the noise signal. Although the amplitude errors are expressed in a different form in this paper ($e^{\sigma_\epsilon^2}=1.03$) and by Durlach (1963) ($1+\sigma_\epsilon^2=1.06$), their values are very similar and $1+\sigma_\epsilon^2$ can be regarded as the first order series approximation of $e^{\sigma_\epsilon^2}$.

The SII was used with a modified frequency band scheme in order to align the center frequencies of the gammatone filter bank and of the SII bands. Although this was a deviation from the standard, the gammatone filters are a better representation of auditory filters than the rectangular filters assumed in the SII standard. The results of this study indicate that this modification is feasible.

The improved efficiency of the BSIM compared to the EC/SII model reduced the computing time for a SRT from minutes to seconds so that the model is now usable for practical applications beyond scientific interest.[6] It also made the development of stBSIM possible, which needs to calculate the model multiple times for a single SRT.

The two model stages, EC and SII, operate separately. First, the EC stage calculates the improved SNR, and then the SII determines the speech intelligibility. Culling *et al.* (2004) measured the amount of binaural unmasking for pure tones in noise in different spatial configurations of target and interferer sources and at different target frequencies. They then used the results to successfully predict the increase of speech intelligibility in speech-shaped noise in the same spatial configuration by calculating the expected SNR increase from the binaural masking level differences. Therefore, the EC front end might in theory be replaced by other models of BMLD (e.g., Breebaart *et al.*, 2001; Osman, 1971; Zerbs, 2000; Nitschmann and Verhey, 2007). The speech intelligibility prediction back-end might be replaced by another speech intelligibility predictor, for example, the speech transmission index (STI) (IEC, 1998; van Wijngaarden and Drullman, 2008), the speech recognition sensitivity (SRS) (Müsch and Buus, 2001), or speech intelligibility prediction based on automatic speech recognition (Holube and Kollmeier, 1996). A combination of the binaural model by Zerbs (2000) and the (monaural) speech intelligibility model by Holube and Kollmeier (1996), similar to the speech intelligibility model by Jürgens *et al.* (2008), could thus be a future step toward a more physiologically oriented model. Both are based on the same auditory preprocessing model, and the binaural part of the model by Zerbs (2000) is based on EC theory, but it would require some fundamental modifications of the speech intelligibility prediction part, if open-set sentence intelligibility test results, as measured in this study, need to be predicted.

B. Binaural speech intelligibility in modulated noise

The main focus of this study, apart from the model revision, was on investigating binaural speech intelligibility combined with other detrimental factors. The interaction of the spatial release from masking with various modulation depths of the interferer noise was of particular interest. The two other factors room acoustics and hearing impairment, which had already been examined in an earlier study (Beutelmann and Brand, 2006), were additionally included.

A main effect of spatial release from masking was found. The binaural intelligibility level difference (i.e., the difference between respective S_0N_0 and S_0N_{105} or S_0N_{-45} conditions) is, in the comparable anechoic conditions, in line with the earlier study (Beutelmann and Brand, 2006) and other similar experiments (see Bronkhorst, 2000; Platte and vom Hövel, 1980; Plomp and Mimpen, 1981; Bronkhorst and Plomp, 1988). The interaction between room acoustics and spatial release from masking is as expected from the mentioned studies: a large reverberation time generally leads to a small spatial release from masking, but in detail, the room size and the amount of pronounced early reflections also have to be taken into account. Strong early reflections of the interferer appear as virtual, additional sound sources. According to the interpretation of the EC model as an adjustable directional microphone, only a limited range of spatial directions can be suppressed. If the virtual sound source created by an early reflection is outside this range, it reduces the spatial release from masking considerably. In contrast to the cafeteria conditions of Beutelmann and Brand (2006), the reflecting wall in the S_0N_{-45} conditions in this study did not cause such a remarkable increase of the SRT. However, this point could only be evaluated in detail if the same condition without the wall was measured additionally.

The room acoustical measures clarity (C80), definition (D50), and STI in Table I are often used as a predictor of speech intelligibility in rooms; high values (C80$>$0 dB, D50 and STI$>$0.6, see Bradley, 1986; IEC, 1998) indicate good speech intelligibility. However, the lower SRTs in the

classroom compared to the listening room are inconsistent with the values in Table I, possibly because the room acoustical measures typically refer to speech without additional interferers and because the effect of room on the noise interferer dominates the results of this study (see Lavandier and Culling, 2007). The masking of reverberated speech on itself seems to play a less important role. Nevertheless, the results presented here probably overinterpret real-life situations, because the situation with a single, localized noise source is quite artificial.

The different noise modulation depths had a large effect on the observed SRTs of normal-hearing subjects: The SRTs in single-talker noise were up to 15 dB lower than the respective SRTs in stationary noise. The largest differences were found in anechoic conditions at 0° noise azimuth. The median difference for normal-hearing subjects in this condition was 11.2 dB. This value may be compared with the results of Wagener and Brand (2005), who used the same stationary noise ("olnoise") and a similar single-talker noise ("icra5"). The single-talker noise used by Wagener and Brand (2005) contained longer speech pause durations than the single-talker noise used in this study (see Wagener and Brand, 2006, and Sec. III A 2). Wagener and Brand (2005) reported about 2–3 dB larger SRT differences between stationary and single-talker noise for normal-hearing subjects compared to this study, which is probably due to the longer speech pauses. Festen and Plomp (1990) reported less benefit from similar speechlike maskers in normal-hearing subjects (6–8 dB), but the single-talker noise used in this study had a larger modulation depth that could explain this discrepancy. The benefit due to noise modulation in normal-hearing subjects is considerably reduced in the reverberant rooms, above all in the church, which is due to the reduction of actual modulation depth by the tail of the room impulse response, as is documented in Fig. 3. The interaction of the noise and azimuth effects may partly be due to the fact that the conditions with −45° noise azimuth additionally implied a doubled distance between the subject and both sound sources compared to the other noise azimuths. This results in an increased reduction in modulation depth because of the increased amount of reverberation at larger distances. The spatial release from masking seems to be reduced for the single-talker noise in anechoic conditions, but this is not necessarily due to a reduced binaural benefit in single-talker noise. The instantaneous noise level at troughs of the masker modulation may be so low that the hearing threshold limits the spatial release from masking. Hall and Harvey (1984) showed that pure tone BMLDs decrease for low spectrum levels of the noise. Apart from these two details, only little interaction was found between noise modulation and spatial release from masking. Apparently, these two effects are mostly independent in the conditions examined in this study. The effects of modulation are less pronounced for the babble noise than for the single-talker noise. This could be expected from the considerably lower modulation depths of babble noise compared to single-talker noise shown in Fig. 3, and is also in line with the results of Bronkhorst and Plomp (1992), who found that the largest difference of SRT due to the number of speechlike maskers occurs between one and six maskers, and that the SRT difference between six speechlike maskers and stationary noise is rather small (about 1 dB).

All effects found in normal-hearing subjects are reduced or absent in the hearing-impaired subjects: The spatial release from masking, which is especially large for normal-hearing subjects in anechoic conditions (up to 9 dB), is reduced for most hearing-impaired subjects, with the exception of subject 1 (see Table II, upward pointing triangle in Figs. 5–7). Some hearing-impaired subjects even have a small disadvantage of 1–2 dB in conditions with spatially separated speech and noise sources. Most hearing-impaired subjects in this study do not benefit from noise modulation: A significant difference of SRTs between stationary and single-talker noise was not found within the matched group. The results in babble noise conditions show an interesting behavior: In most hearing-impaired subjects, the SRTs in babble noise are considerably higher than the respective SRTs in stationary or single-talker noise. Subject 11 (symbol: diamonds) stands out against these results, because the babble noise SRTs of this subject are lower than the SRTs in stationary or single-talker noise in most of the cases. The reason is that all hearing thresholds, except that of subject 11, increase with increasing frequencies, while the hearing loss of subject 11 is predominantly in the low-frequency range. The babble noise spectrum has less energy in the high-frequency range than the other two noise spectra. Therefore, the SNR of speech in babble noise is relatively low in the low-frequency range and relatively high in the high-frequency range, compared to the other noise types. This is unfavorable for subjects with a high-frequency hearing loss. The results of the subject with the overall lowest hearing loss (upward triangles in Figs. 5 and 6) are comparable with the results of the normal-hearing subjects.

C. Prediction of binaural speech intelligibility in modulated noise

Regarding the results of this study, stBSIM, the extension of BSIM for modulated interferers, appears to be a successful approach. The intention of stBSIM was a proof of concept with simple implementation, which may be developed further. Nevertheless, this first approach is promising because it already yielded reasonable predictions of the data. The predictions for SRTs in stationary and in single-talker noise are equally good. However, a large bias difference exists between these two noise types and the babble noise group in Table III, although the R^2-value of the babble noise group suggests good within-group predictions, which is confirmed by the babble noise scatter plots in Fig. 8. A probable reason for this bias might be the difference between the long-term frequency spectra of the babble noise and the speech. The long-term frequency spectrum of the speech is equivalent to the stationary noise spectrum. The relatively high SNR in the high-frequency range seems to be overinterpreted by the SII and might be less useful for a human subject. Furthermore, there might be an additional perceptual difference between stationary noise and babble noise beyond the modulation depth that is not accounted for by the stBSIM.

The combined effects of room acoustics and spatial separation of sound sources can be well predicted by the EC principle, as long as the influence of room acoustics on the noise dominates the results, because the interaural decorrelation of the noise by reverberation and virtual noise sources created by early reflections directly affects the interaural cross-correlation function of the noise in Eq. (12). Principally, it is not possible with the present model to predict the detrimental effect of reverberation on the speech source itself, because the speech signal is not divided into useful and detrimental parts, which is a nontrivial problem. This is probably the cause of the differing bias values of the rooms in Table III. The principle of the STI (IEC, 1998) could be a promising way to solve this problem. It evaluates the reduction in speech modulation due to reverberation and noise instead of the SNR (as it is done in the SII) and is very successful in predicting of the influence of room acoustics on speech in quiet. Van Wijngaarden and Drullman (2008) presented a successful functional approach of predicting binaural consonant-vowel-consonant intelligibility scores using the STI, which could serve as basis for further development of BSIM concerning the effect of reverberation on the target speech.

Apparently, the hearing threshold alone is already a good predictor for the variance in SRTs due to hearing impairment in the experimental conditions of this study. The prediction of the influence of the hearing threshold is mainly a feature of the SII, but bilaterally asymmetric hearing thresholds are combined by the EC process by choosing the ear with the favorable SNR in each frequency band. Nevertheless, a remaining variance in both normal-hearing and hearing-impaired subjects could not be predicted. This unpredicted variance is especially noticeable in the vertical structures of the filled symbols in Fig. 8. They arise from the fact that the observed SRTs of normal-hearing subjects have a much larger variance than the respective predicted SRTs. The normal-hearing subjects had naturally very similar audiograms. Thus, this large observed variance likely results from other differences between individual subjects, including nonauditory factors, such as, the ability to concentrate on the task. It is remarkable that the unexplained variance of the hearing-impaired subjects is not substantially larger than the unexplained variance of the normal-hearing subjects. This might indicate that there is a variance in SRTs which could not be predicted, even if further measures of the hearing loss (e.g., loss of peripheral compression or substantially reduced temporal/spectral resolution) were incorporated into the model.

The predictions of BSIM and stBSIM for SRTs in stationary noise match closely but are not completely identical. A difference in bias occurs between SRTs in the reverberant rooms, which may be attributed to the fact that BSIM calculates the interaural parameters of Eq. (12) across relatively long input signals, while stBSIM estimates the parameters repeatedly from short time frames. Although the interaural level and time differences in the signals were fixed on long-term average, they fluctuate stochastically between short-time frames. A possible future extension of the stBSIM as mentioned in Sec. II D, an additional time window in order to simulate binaural "sluggishness," may eliminate also this misinterpretation of stochastic time and level difference by the model.

V. CONCLUSIONS

The binaural speech intelligibility model (Beutelmann and Brand, 2006) was analytically simplified and expressed more concisely. Thus, along with numerical optimizations, the practical use of the model was considerably accelerated (by a factor of about 60), while maintaining equivalent predictions as compared with the original model. The correlation coefficients between predictions of the revised model and the observed SRTs are larger than the correlation coefficients of the original "EC/SII" model. The root-mean-squared prediction error of the "BSIM" (normal-hearing subjects: 1.3 dB, hearing-impaired subjects: 1.9 dB) was less than for the original "EC/SII" model (NH: 1.7 dB, HI: 2.3 dB).

The binaural processing errors of the EC stage are mathematically equivalent to a low-pass filter reducing the interaural fine structure correlation for high frequencies. This is analogous to the low-pass filter in more physiological (hair cell) models.

In situations with modulated noise interferer, a large SRT benefit of up to 15.5 dB relative to unmodulated noise was measured for normal-hearing subjects. The benefit decreases to zero with increasing reverberation time, but the interaction with sound source location was rather small as compared with the overall size of the effect. Hearing-impaired subjects generally had less benefit; in certain cases, they were even disturbed by modulated interferers and their SRTs were higher than with stationary interferers.

Binaural speech intelligibility in modulated noise interferers can, in principle, be predicted by calculating the model in short time frames and averaging the resulting SRTs. The overall squared correlation coefficient R^2 between predicted and observed SRTs is 0.78 and the overall standard deviation of the prediction error (difference between predicted and observed SRTs) is 3.0 dB.

About 70% of the variance in SRTs of hearing-impaired subjects relative to the mean SRT of the normal-hearing subjects in the same condition can be predicted with the binaural model presented here based on the audiogram alone. The remaining variance presumably requires a more detailed model of hearing loss that includes more factors than just the hearing threshold. This applies also to the unpredicted variance of the individual normal-hearing subjects, which even more is larger than what could be assumed from the very small differences in the audiograms of the normal-hearing subjects.

ACKNOWLEDGMENTS

This research project was supported by grants from the European Union FP6, Project No. 004171 HEARCOM, and by the collaborative research center SFB/TRR 31 Das aktive Gehőr. The authors wish to thank the editor Ruth Litovsky, Quentin Summerfield, and three anonymous reviewers for their thorough and helpful reviews, and Claus Lynge from

Œrsted DTU, Acoustic Technology, Technical University of Denmark for providing the binaural room impulse responses.

APPENDIX A: DETAILED DERIVATION

The EC process described in Eq. (5) is a linear operation on the input signals. Together with Eq. (1) and the assumption that the speech and external noise signals are available separately, the residual signal after the EC process,

$$X_{\mathrm{EC}}(\omega) = S_{\mathrm{EC}}(\omega) + N_{\mathrm{EC}}(\omega), \tag{A1}$$

can be split up into the residual speech signal and the residual noise signal.

In order to compute the SNR that is needed for the SII [Eq. (7)], the overall intensity of the residual speech and noise signals has to be calculated. In the following, the derivation is only shown for the speech signal, because it is performed analogously for the noise signal. By using $|x-y|^2=|x|^2+|y|^2-2\,\mathrm{Re}(xy^*)$ on Eq. (6) inserted into the definition of the intensity [Eq. (8)], the absolute square in the integral can be expanded

$$I(S_{\mathrm{EC}}) = \int_{\Omega-\beta/2}^{\Omega+\beta/2} |S_{\mathrm{EC}}(\omega)|^2 d\omega \tag{A2}$$

$$= \int_{\Omega-\beta/2}^{\Omega+\beta/2} |e^{\gamma/2+\epsilon_L} e^{+i\omega(\tau/2+\delta_L)} S_L(\omega) - e^{-\gamma/2+\epsilon_R} e^{-i\omega(\tau/2+\delta_R)} S_R(\omega)|^2 d\omega \tag{A3}$$

$$= e^{\gamma+2\epsilon_L} \int_{\Omega-\beta/2}^{\Omega+\beta/2} |S_L(\omega)|^2 d\omega + e^{-\gamma+2\epsilon_R} \int_{\Omega-\beta/2}^{\Omega+\beta/2} |S_R(\omega)|^2 d\omega - 2e^{\epsilon_L+\epsilon_R} \times \mathrm{Re}\left(\int_{\Omega-\beta/2}^{\Omega+\beta/2} S_L(\omega) S_R^*(\omega) e^{i\omega(\delta_L+\delta_R)} e^{i\omega\tau} d\omega \right) \tag{A4}$$

into three summands. The first two summands are only dependent on the overall intensity of the left and right channels, respectively, while the third summand is a cross-correlation term, which is strongly dependent on the phase information available in the signals. As described in Sec. II B, the EC processing errors are incorporated by calculating the expectation value of the intensity with respect to processing error variables. With $\langle e^{2\epsilon}\rangle_\epsilon = e^{2\sigma_\epsilon^2}$ and $\langle e^{\epsilon}\rangle_\epsilon = e^{\sigma_\epsilon^2/2}$ for normally distributed ϵ follows that

$$\langle I(S_{\mathrm{EC}})\rangle_{\epsilon_L,\epsilon_R,\delta_L,\delta_R} = e^{2\sigma_\epsilon^2} e^{\gamma} I(S_L) + e^{2\sigma_\epsilon^2} e^{-\gamma} I(S_R) - 2e^{\sigma_\epsilon^2} \times \mathrm{Re}\left(\int_{\Omega-\beta/2}^{\Omega+\beta/2} S_L(\omega) S_R^*(\omega) e^{-\omega^2\sigma_\delta^2} e^{i\omega\tau} d\omega \right), \tag{A5}$$

leading to a Gaussian low-pass filter $e^{-\omega^2\sigma_\delta^2}$ on the cross-correlation term, that is, on the phase information available as a function of frequency. The cross-correlation term can be normalized by extracting the square root of the product of both channel intensities

$$\langle I(S_{\mathrm{EC}})\rangle_{\epsilon_L,\epsilon_R,\delta_L,\delta_R} = 2e^{\sigma_\epsilon^2} \sqrt{I(S_L) I(S_R)} \left[e^{\sigma_\epsilon^2} \frac{1}{2} \left(e^{\gamma} \sqrt{\frac{I(S_L)}{I(S_R)}} + e^{-\gamma} \sqrt{\frac{I(S_R)}{I(S_L)}} \right) - \mathrm{Re}\left(\frac{1}{\sqrt{I(S_L) I(S_R)}} \times \int_{\Omega-\beta/2}^{\Omega+\beta/2} S_L(\omega) S_R^*(\omega) e^{-\omega^2\sigma_\delta^2} e^{i\omega\tau} d\omega \right) \right], \tag{A6}$$

leaving a symmetric expression for the first two summands, which can be transformed into a cosh function

$$\langle I(S_{\mathrm{EC}})\rangle_{\epsilon_L,\epsilon_R,\delta_L,\delta_R} = 2e^{\sigma_\epsilon^2} \sqrt{I(S_L) I(S_R)} \left[e^{\sigma_\epsilon^2} \cosh \times \left(\gamma + \ln \sqrt{\frac{I(S_L)}{I(S_R)}} \right) - \mathrm{Re}\left(\frac{1}{\sqrt{I(S_L) I(S_R)}} \times \int_{\Omega-\beta/2}^{\Omega+\beta/2} S_L(\omega) S_R^*(\omega) e^{-\omega^2\sigma_\delta^2} e^{i\omega\tau} d\omega \right) \right]. \tag{A7}$$

The argument of the cosh is simplified with the definition of Δ_S [see Eq. (10)] for the interaural level difference of the signal. The low-pass function $e^{-\omega^2\sigma_\delta^2}$ can be extracted from the cross-correlation term by using the convolution theorem of the Fourier transform,

$$\langle I(S_{\mathrm{EC}})\rangle_{\epsilon_L,\epsilon_R,\delta_L,\delta_R} = 2e^{\sigma_\epsilon^2} \sqrt{I(S_L) I(S_R)} \left[e^{\sigma_\epsilon^2} \cosh(\gamma + \Delta_S) - \frac{\sqrt{\pi}}{\sigma_\delta} e^{-\tau^2/4\sigma_\delta^2} * \mathrm{Re}\left(\frac{1}{\sqrt{I(S_L) I(S_R)}} \times \int_{\Omega-\beta/2}^{\Omega+\beta/2} S_L(\omega) S_R^*(\omega) e^{i\omega\tau} d\omega \right) \right]. \tag{A8}$$

The inverse Fourier transform of the cross-correlation term is then also carried out, resulting in the normalized cross-correlation function in the time domain. Because of the convention used for the normalization of the Fourier transform pair, a factor of $(2\pi)^{-1}$ arises, which is included in the definition of the low-pass filter or Gaussian smoothing window $\lambda(\tau)$ [see Eq. (13)],

$$\langle I(S_{\mathrm{EC}})\rangle_{\epsilon_L,\epsilon_R,\delta_L,\delta_R} = 2e^{\sigma_\epsilon^2} \sqrt{I(S_L) I(S_R)} [e^{\sigma_\epsilon^2} \cosh(\gamma + \Delta_S) - \lambda(\tau) * \mathrm{Re}(\rho_S(\tau))]. \tag{A9}$$

Together with the same derivation for the noise intensity, this results in Eq. (12).

APPENDIX B: PREDICTION OF REFERENCE DATA

Predictions for the conditions which had originally been used by Beutelmann and Brand (2006) in order to evaluate the EC/SII model were performed with BSIM and stBSIM.

TABLE IV. Squared correlation coefficients R^2 (coefficient of determination) between predicted and observed SRTs and root-mean-squared prediction errors ε in dB for the EC/SII model from Beutelmann and Brand (2006), for the revised model (BSIM) and the modified, short-time model (stBSIM). R^2 is an estimate of the variance in the data explained by the model. The reference SII was set to 0.2 according to Sec. II C. The subject group "NH" are individual normal-hearing subject data, "NH mean" are averaged normal-hearing subject data, and "HI" are individual hearing-impaired subject data and their respective predictions.

	EC/SII		BSIM		stBSIM	
Subject group	R^2	ε (dB)	R^2	ε (dB)	R^2	ε (dB)
All	0.91	2.1	0.92	1.7	0.91	1.8
NH	0.83	1.7	0.87	1.3	0.86	1.4
NH mean	0.94	1.2	0.99	0.5	0.98	0.6
HI	0.85	2.3	0.88	1.9	0.87	2.0

The reference SRTs had been measured with the Oldenburg Sentence Test in noise (see Sec. III A 1), with the speech source always in front of the subject and a single, stationary speech-shaped noise source at one of eight azimuths. The measurements were performed in three different simulated room acoustical conditions. The rooms had reverberation times (T_{60}) of 0 s ("anechoic"), 0.6 s ("office"), and 1.3 s ("cafeteria"). The subjects taking part in the original study included 8 normal-hearing and 15 hearing-impaired subjects with different degrees and types of hearing loss (see Beutelmann and Brand, 2006, for further details). The predictions with the BSIM were calculated with a frame length of about 2.9 s to test the agreement with the original model. Additionally, the predictions for the same data were calculated with the "stBSIM" using a frame length of about 12 ms in order to assess if the model for modulated noises yields the same results as the original model for stationary noise data. Table IV gives an overview of the product-moment correlation coefficients and root-mean-squared prediction errors of the original "EC/SII" model from Beutelmann and Brand (2006), of the long-frame BSIM and the short-time stBSIM. Despite the already high correlation coefficients and low mean absolute prediction errors in the original EC/SII model, the predictions of both revised models show higher correlations and lower prediction errors than the original model does. The small deviations of the stBSIM compared to the long-frame BSIM are probably due to a larger variance of level and time parameters across the short-time frames.

[1]The normalization factors $(2\pi)^{-1/2}$ for the Fourier transform when using ω as the frequency variable are applied to both the transform and the inverse transform.

[2]The standard deviations of the processing errors are defined as $\sigma_\epsilon(\alpha)=\sigma_{\epsilon 0}[1+(|\alpha|/\alpha_0)^p]$ and $\sigma_\delta(\tau)=\sigma_{\delta 0}[1+(|\tau|/\tau_0)]$ with $\sigma_{\epsilon 0}=1.5$, $\alpha_0=13$ dB, $p=1.6$, $\sigma_{\delta 0}=65$ μs, and $\tau_0=1.6$ ms. These values have been fitted to pure tone BMLD measurement data (Blodgett *et al.*, 1962; Langford and Jeffress, 1964; Egan, 1965; vom Hövel, 1984; Beutelmann and Brand, 2006).

[3]S^* denotes the complex conjugate of S throughout this paper.

[4]This may partly be due to the fact that the assumption of perfectly uncorrelated internal noise channels, and internal and external signals, respectively, has to be relaxed (see Diercks and Jeffress, 1962; Osman, 1971).

[5]The reverberation time T_{30} is twice the decay time of the room impulse response from −5 to −35 dB below the level of the direct sound. The EDT is six times the decay time of the first 10 dB of the decay curve. Thus, both values are directly comparable to the (standard) reverberation time T_{60}, whose measurement is often impracticable, because it requires an extremely high SNR. C80 ("clarity") and D50 ("definition") are measures which are related to the balance between early and late arriving sound energy in the room impulse response. C80 is the ratio between the energy arriving within the first 80 ms and the energy arriving later than 80 ms expressed in dB. D50 is the fraction of the total energy of the room impulse response arriving in the first 50 ms (cf. CEN, 2000). STI denotes the speech transmission index (IEC, 1998).

[6]A BSIM demonstration package is available for download from http://hearcom.eu/prof/RoomAcoustics/BSIMDescription.html

Akeroyd, M. A. (**2004**). "The across frequency independence of equalization of interaural time delay in the equalization-cancellation model of binaural unmasking," J. Acoust. Soc. Am. **116**, 1135–1148.

ANSI (**1969**). "Methods for the calculation of the articulation index," American National Standard S3.5-1969 (Standards Secretariat, Acoustical Society of America).

ANSI (**1997**). "Methods for the calculation of the speech intelligibility index," American National Standard S3.5-1997 (Standards Secretariat, Acoustical Society of America).

Auditec (**2006**). CD101RW2, Audio CD, Auditec, St. Louis, MO, 2515 www.auditec.com (Last viewed 09/21/09).

Beutelmann, R., and Brand, T. (**2006**). "Prediction of speech intelligibility in spatial noise and reverberation for normal-hearing and hearing-impaired listeners," J. Acoust. Soc. Am. **120**, 331–342.

Beutelmann, R., Brand, T., and Kollmeier, B. (**2009**). "Prediction of binaural speech intelligibility with frequency-dependent interaural phase differences," J. Acoust. Soc. Am. **126**, 1359–1368.

Blodgett, H. C., Jeffress, L. A., and Whitworth, R. H. (**1962**). "Effect of Noise at One Ear on the Masked Threshold for Tone at the Other," J. Acoust. Soc. Am. **34**, 979–981.

Bradley, J. S. (**1986**). "Predictors of speech intelligibility in rooms," J. Acoust. Soc. Am. **80**, 837–845.

Brand, T., and Kollmeier, B. (**2002**). "Efficient adaptive procedures for threshold and concurrent slope estimates for psychophysics and speech intelligibility tests," J. Acoust. Soc. Am. **111**, 2801–2810.

Breebaart, J., van de Par, S., and Kohlrausch, A. (**2001**). "Binaural processing model based on contralateral inhibition. I. Model structure," J. Acoust. Soc. Am. **110**, 1074–1088.

Bronkhorst, A. W. (**2000**). "The cocktail party phenomenon: A review of research on speech intelligibility in multiple talker conditions," Acust. Acta Acust. **86**, 117–128.

Bronkhorst, A. W., and Plomp, R. (**1988**). "The effect of head-induced interaural time and level differences on speech intelligibility in noise," J. Acoust. Soc. Am. **83**, 1508–1516.

Bronkhorst, A. W., and Plomp, R. (**1992**). "Effect of multiple speechlike maskers on binaural speech recognition in normal and impaired hearing," J. Acoust. Soc. Am. **92**, 3132–3139.

CEN (**2000**). "Messung der Nachhallzeit von Räumen mit Hinweis auf andere akustische Parameter (Measurement of the reverberation time of rooms with reference to other acoustical parameters)," European Standard EN ISO 3382 (Europäisches Komitee für Normung).

Cherry, E. C. (**1953**). "Some experiments on the recognition of speech, with one and with two ears," J. Acoust. Soc. Am. **25**, 975–979.

Christensen, C. L. (**2005**). ODEON, room acoustics modeling software v8.0, ODEON A/S, www.odeon.dk (Last viewed 09/21/09).

Colburn, H. S. (**1996**). *Computational Models of Binaural Processing*, Springer Handbook of Auditory Research Vol. **6** (Springer, New York), Chap. 8, pp. 332–400.
Culling, J. F., and Colburn, H. S. (**2000**). "Binaural sluggishness in the perception of tone sequences and speech in noise," J. Acoust. Soc. Am. **107**, 517–527.
Culling, J. F., Hawley, M. L., and Litovsky, R. Y. (**2004**). "The role of head-induced interaural time and level differences in the speech reception threshold for multiple interfering sound sources," J. Acoust. Soc. Am. **116**, 1057–1065.
Culling, J. F., and Summerfield, Q. (**1998**). "Measurements of the binaural temporal window using a detection task," J. Acoust. Soc. Am. **103**, 3540–3553.
Dau, T., Püschel, D., and Kohlrausch, A. (**1996**). "A quantitative model of the 'effective' signal processing in the auditory system: I. Model structure," J. Acoust. Soc. Am. **99**, 3615–3622.
Diercks, K. J., and Jeffress, L. A. (**1962**). "Interaural phase and the absolute threshold for tone," J. Acoust. Soc. Am. **34**, 981–984.
Dreschler, W., Verschuure, H., Ludvigsen, C., and Westermann, S. (**2001**). "ICRA noises: Artificial noise signals with speech-like spectral and temporal properties for hearing instrument assessment," Audiology **40**, 148–157.
Dubno, J. R., Horwitz, A. R., and Ahlstrom, J. B. (**2002**). "Benefit of modulated maskers for speech recognition by younger and older adults with normal hearing," J. Acoust. Soc. Am. **111**, 2897–2907.
Duquesnoy, A. J. (**1983**). "Effect of a single interfering noise or speech source upon the binaural sentence intelligibility of aged persons," J. Acoust. Soc. Am. **74**, 739–743.
Durlach, N. I. (**1963**). "Equalization and Cancellation Theory of Binaural Masking-Level Differences," J. Acoust. Soc. Am. **35**, 1206–1218.
Durlach, N. I. (**1972**). *Binaural signal detection: Equalization and Cancellation Theory* (Academic, New York), Vol. **II**, Chap. 10, pp. 371–462.
Edmonds, B. A., and Culling, J. F. (**2005**). "The spatial unmasking of speech: evidence for within-channel processing of interaural time delay," J. Acoust. Soc. Am. **117**, 3069–3078.
Egan, J. P. (**1965**). "Masking-level differences as a function of interaural disparities in intensity of signal and of noise," J. Acoust. Soc. Am. **38**, 1043–1049.
Festen, J. M. (**1993**). "Contributions of comodulation masking release and temporal resolution to the speech-reception threshold masked by an interfering voice," J. Acoust. Soc. Am. **94**, 1295–1300.
Festen, J. M., and Plomp, R. (**1990**). "Effects of fluctuating noise and interfering speech on the speech-reception threshold for impaired and normal hearing," J. Acoust. Soc. Am. **88**, 1725–1736.
Gallun, F. J., Mason, C. R., and Gerald Kidd, J. (**2007**). "The ability to listen with independent ears," J. Acoust. Soc. Am. **122**, 2814–2825.
Glasberg, B. R., and Moore, B. C. J. (**1990**). "Derivation of auditory filter shapes from notched noise data," Hear. Res. **47**, 103–138.
Grose, J. H., and Hall, J. W. (**1992**). "Comodulation masking release for speech stimuli," J. Acoust. Soc. Am. **91**, 1042–1050.
Gustafsson, H. Å., and Arlinger, S. D. (**1994**). "Masking of speech by amplitude-modulated noise," J. Acoust. Soc. Am. **95**, 518–529.
Hall, J. W., Haggard, M. P., and Fernandes, M. A. (**1984**). "Detection in noise by spectro-temporal pattern analysis," J. Acoust. Soc. Am. **76**, 50–56.
Hall, J. W., and Harvey, A. D. G. (**1984**). "N_0S_0 and N_0S_π thresholds as a function of masker level for narrowband and wideband masking noise," J. Acoust. Soc. Am. **76**, 1699–1703.
Hawley, M. L., Litovsky, R. Y., and Culling, J. F. (**2004**). "The benefit of binaural hearing in a cocktail party: Effect of location and type of interferer," J. Acoust. Soc. Am. **115**, 833–843.
Heinz, M. G., Colburn, H. S., and Carney, L. H. (**2001**). "Evaluating auditory performance limits: I. One-parameter discrimination using a computational model for the auditory nerve," Neural Comput. **13**, 2273–2316.
Hirsh, I. J., and Burgeat, M. (**1958**). "Binaural effects in remote masking," J. Acoust. Soc. Am. **30**, 827–832.
Hohmann, V. (**2002**). "Frequency analysis and synthesis using a Gammatone filterbank," Acust. Acta Acust. **88**, 433–442.
Holube, I., and Kollmeier, B. (**1996**). "Speech intelligibility prediction in hearing-impaired listeners based on a psychoacoustically motivated perception model," J. Acoust. Soc. Am. **100**, 1703–1716.
IEC (**1985**). "Sound systems equipment, Listening tests on loudspeakers," International Standard 26-13 (International Electrotechnical Committee, Geneva).
IEC (**1998**). "Sound system equipment—Part 16: Objective rating of speech intelligibility by speech transmission index," International Standard IEC 60268-16 (International Electrotechnical Committee, Geneva).
Johnson, D. H. (**1980**). "The relationship between spike rate and synchrony in responses of auditory-nerve fibers to single tones," J. Acoust. Soc. Am. **68**, 1115–1122.
Jürgens, T., Brand, T., and Kollmeier, B. (**2008**). "Sprachverständlichkeitsvorhersage für Normalhörende mit einem auditorischen Modell (Speech intelligibility prediction for normal-hearing subjects with an auditory model)," *11. Annual Meeting of the German Audiological Society* (Deutsche Gesellschaft für Audiologie e.V., Kiel).
Kidd, G., Mason, C., Richards, V., Gallun, F., and Durlach, N. (**2007**). "Informational masking," in *Auditory Perception of Sound Sources*, Springer Handbook of Auditory Research Vol. **29**, edited by A. N. P. William, A. Yost, and R. R. Fay (Springer, New York), Chap. 6, pp. 143–189.
Kollmeier, B., and Gilkey, R. H. (**1990**). "Binaural forward and backward masking: Evidence for sluggishness in binaural detection," J. Acoust. Soc. Am. **87**, 1709–1719.
Langford, T. L., and Jeffress, L. A. (**1964**). "Effect of noise crosscorrelation on binaural signal detection," J. Acoust. Soc. Am. **36**, 1455–1458.
Lavandier, M., and Culling, J. F. (**2007**). "Speech segregation in rooms: Effects of reverberation on both target and interferer," J. Acoust. Soc. Am. **122**, 1713–1723.
Lorenzi, C., Debruille, L., Garnier, S., Fleuriot, P., and Moore, B. C. J. (**2009**). "Abnormal processing of temporal fine structure in speech for frequencies where absolute thresholds are normal," J. Acoust. Soc. Am. **125**, 27–30.
Miller, G. A., and Licklider, J. C. R. (**1950**). "The intelligibility of interrupted speech," J. Acoust. Soc. Am. **22**, 167–173.
Müsch, H., and Buus, S. (**2001**). "Using statistical decision theory to predict speech intelligibility. I. Model structure," J. Acoust. Soc. Am. **109**, 2896–2909.
Nitschmann, M., and Verhey, J. L. (**2007**). "Experimente und Modellrechnungen zur binauralen spektralen Selektivität (Experiments and model calculations on binaural spectral selectivity)," *Proceedings of the Annual Meeting of the German Acoustical Society* (Deutsche Gesellschaft für Akustik e.V., Berlin), pp. 371–372.
Osman, E. (**1971**). "A correlation model of binaural masking level differences," J. Acoust. Soc. Am. **50**, 1494–1511.
Peissig, J., and Kollmeier, B. (**1997**). "Directivity of binaural noise reduction in spatial multiple noise-source arrangements for normal and impaired listeners," J. Acoust. Soc. Am. **101**, 1660–1670.
Peters, R. W., Moore, B. C. J., and Baer, T. (**1998**). "Speech reception thresholds in noise with and without spectral and temporal dips for hearing-impaired and normally hearing people," J. Acoust. Soc. Am. **103**, 577–587.
Platte, H.-J., and vom Hövel, H. (**1980**). "Zur Deutung der Ergebnisse von Sprachverständlichkeitsmessungen mit Störschall im Freifeld (On the interpretation of speech intelligibility measurement results in noise in free-field conditions)," Acustica **45**, 139–150.
Plomp, R. (**1978**). "Auditory handicap of hearing impairment and the limited benefit of hearing aids," J. Acoust. Soc. Am. **63**, 533–549.
Plomp, R., and Mimpen, A. M. (**1981**). "Effect of the orientation of the speaker's head and the azimuth of a noise source on the speech-reception threshold for sentences," Acustica **48**, 325–328.
Rhebergen, K. S., and Versfeld, N. J. (**2005**). "A speech intelligibility index-based approach to predict the speech reception threshold for sentences in fluctuating noise for normal-hearing listeners," J. Acoust. Soc. Am. **117**, 2181–2192.
Rhebergen, K. S., Versfeld, N. J., and Dreschler, W. A. (**2006**). "Extended speech intelligibility index for the prediction of the speech reception threshold in fluctuating noise," J. Acoust. Soc. Am. **120**, 3988–3997.
Scheffé, H. (**1963**). *The Analysis of Variance* (Wiley, New York).
Sieben, U. (**1979**). "Binauraale Mithörschwellen bei aus Tönen und Rauschen Zusammengesetzten Maskierern (Binaural masking thresholds with maskers composed of tones and noise)," Ph.D. thesis, Georg-August-Universität zu Göttingen, Göttingen.
Smits, C., and Houtgast, T. (**2007**). "Recognition of digits in different types of noise by normal-hearing and hearing-impaired listeners," Int. J. Audiol. **46**, 134–144.
Smoorenburg, G. F. (**1992**). "Speech reception in quiet and in noisy conditions by individuals with noise-induced hearing loss in relation to their tone audiogram," J. Acoust. Soc. Am. **91**, 421–437.
van Wijngaarden, S. J., and Drullman, R. (**2008**). "Binaural intelligibility

prediction based on the speech transmission index," J. Acoust. Soc. Am. **123**, 4514–4523.
Versfeld, N. J., and Dreschler, W. A. (**2002**). "The relationship between the intelligibility of time-compressed speech and speech in noise in young and elderly listeners," J. Acoust. Soc. Am. **111**, 401–408.
vom Hövel, H. (**1984**). "Zur Bedeutung der Übertragungseigenschaften des Außenohrs sowie des binauralen Hörsystems bei gestörter Sprachübertragung (On the importance of the transmission properties of the outer ear and the binaural auditory system in disturbed speech transmisson)," Ph.D. thesis, RTWH, Aachen.
Wagener, K. (**2003**). "Factors influencing sentence intelligibility in noise," Ph.D. thesis, Carl-von-Ossietzky-Universität Oldenburg, Oldenburg.
Wagener, K., Brand, T., Kühnel, V., and Kollmeier, B. (**1999a**). "Entwicklung und Evaluation eines Satztests für die Deutsche Sprache I: Design des Oldenburger Satztests (Development and evaluation of a sentence test for the German language I: Design of the Oldenburg Sentence Test)," Z. Fuer Audiologie, Audiological Acoust. **38**, 4–15.
Wagener, K., Brand, T., Kühnel, V., and Kollmeier, B. (**1999b**). "Entwicklung und Evaluation eines Satztests für die Deutsche Sprache II: Optimierung des Oldenburger Satztests (Development and evaluation of a sentence test for the German language II: optimization of the Oldenburg Sentence Test)," Z. Fuer Audiologie, Audiological Acoust. **38**, 44–56.
Wagener, K., Brand, T., Kühnel, V., and Kollmeier, B. (**1999c**). "Entwicklung und Evaluation eines Satztests für die Deutsche Sprache III: Evaluation des Oldenburger Satztests (Development and evaluation of a sentence test for the German language III: evaluation of the Oldenburg Sentence Test)," Z. Fuer Audiologie, Audiological Acoust. **38**, 86–95.
Wagener, K. C., and Brand, T. (**2005**). "Sentence intelligibility in noise for listeners with normal hearing and hearing impairment: Influence of measurement procedure and masking parameters," Int. J. Audiol. **44**, 144–156.
Wagener, K. C., and Brand, T. (**2006**). "The role of silent intervals for sentence intelligibility in fluctuating noise in hearing-impaired listeners," Int. J. Audiol. **45**, 26–33.
Zerbs, C. (**2000**). "Modelling the effective binaural signal processing in the auditory system," Ph.D. thesis, Carl-von-Ossietzky-Universität Oldenburg, Oldenburg.

Benefits of knowing who, where, and when in multi-talker listening

Pádraig T. Kitterick,[a] Peter J. Bailey, and A. Quentin Summerfield
Department of Psychology, University of York, York YO10 5DD, United Kingdom

(Received 19 May 2009; revised 8 December 2009; accepted 25 January 2010)

The benefits of prior information about who would speak, where they would be located, and when they would speak were measured in a multi-talker spatial-listening task. On each trial, a target phrase and several masker phrases were allocated to 13 loudspeakers in a 180° arc, and to 13 overlapping time slots, which started every 800 ms. Speech-reception thresholds (SRTs) were measured as the level of target relative to masker phrases at which listeners reported key words at 71% correct. When phases started in pairs all three cues were beneficial ("who" 3.2 dB, "where" 5.1 dB, and "when" 0.3 dB). Over a range of onset asynchronies, SRTs corresponded consistently to a signal-to-noise ratio (SNR) of −2 dB at the start of the target phrase. When phrases started one at a time, SRTs fell to a SNR of −8 dB and were improved significantly, but only marginally, by constraining "who" (1.9 dB), and not by constraining "where" (1.0 dB) or "when" (0.01 dB). Thus, prior information about "who," "where," and "when" was beneficial, but only when talkers started speaking in pairs. Low SRTs may arise when talkers start speaking one at a time because of automatic orienting to phrase onsets and/or the use of loudness differences to distinguish target from masker phrases. © *2010 Acoustical Society of America.* [DOI: 10.1121/1.3327507]

PACS number(s): 43.66.Rq, 43.66.Pn, 43.71.Gv, 43.66.Dc [MW] Pages: 2498–2508

I. INTRODUCTION

Listeners face considerable challenges in multi-talker environments. They may need to divide attention between several talkers, alternate attention from one talker to another, and attend selectively to a single talker while resisting distraction from competing talkers. Prior knowledge of who will speak, where they will be located, and when they will speak may be beneficial. This paper reports experiments that measured the advantages gained from these three cues to the accuracy of speech perception in multi-talker environments.

A. Benefits of knowing where to listen

Directing auditory attention to the location of a stimulus can improve performance on listening tasks, both when stimuli are presented with headphones and in a sound field. For example, cueing the ear in which a tone will be presented reduces the latency with which the tone is detected (Simon, 1967). Similarly, cueing the hemifield to which a pair of clicks will be lateralized increases the accuracy with which a difference in inter-aural time difference (ITD) between the clicks is detected (Sach *et al.*, 2000). Also, the ability to identify the rhythm of a sequence of target tones in the presence of a sequence of distracter tones varies as a function of the difference in ITD between the two sequences, forming a spatial attentional "tuning curve" (Sach and Bailey, 2004).

Evidence for spatial attentional tuning has also been found when stimuli are presented in a sound field. For example, the latency of discriminating pure tones from complex tones declines with increasing angular distance between the stimulus and a cued location (Mondor and Zatorre, 1995). Similarly, the accuracy of identifying the direction of pitch changes across a sequence of target tones in the presence of sequences of distracter tones declines with increasing angular distance between the expected and actual locations of the target sequence (Arbogast and Kidd, 2000). The results of both experiments are compatible with the conclusion of Mondor and Zatorre (1995) that the "density of attentional resources" is distributed around the expected location, creating a spatial attentional filter (Mondor and Zatorre, 1995, p. 404).

The concept of a spatial attentional filter has also been invoked to explain listening performance in multi-talker environments. Specifically, cueing the spatial location of a target talker can aid the process of extracting a single speech stream from a mixture of streams (Kidd *et al.*, 2005; Best *et al.*, 2007, 2009). Kidd *et al.* (2005) presented three simultaneous phrases from the coordinate response measure (CRM) (Bolia *et al.*, 2000), i.e., one target phrase and two masker phrases, from three locations. The accuracy of reporting the key words in the target phrase improved significantly by 25 percentage points with increasing certainty about where the target would be presented. Best *et al.* (2007) presented stimuli from five locations in five time slots on each trial. One of the 25 combinations of a location and a time slot contained a target sequence of five digits, which listeners attempted to identify. The other combinations contained continuous speech maskers. Visually cueing the location of the digit sequence throughout each trial improved performance significantly by 12 percentage points.

Thus, knowing where to direct attention can confer ad-

[a]Author to whom correspondence should be addressed. Electronic mail: p.kitterick@psych.york.ac.uk

 0001-4966/2010/127(4)/2498/11/$25.00

vantages in detecting and discriminating sounds, and in hearing what one person is saying when other people are speaking at the same time.

B. Benefits of knowing who to listen to

Even brief prior exposure to a target talker can increase the accuracy of reporting words spoken by that talker in a mixture of talkers by 10 to 12 percentage points, particularly when the mixture includes talkers of the opposite gender (Brungart *et al.*, 2001). Moreover, familiarity with a masking talker can improve the intelligibility of a target talker (Brungart and Simpson, 2004; Johnsrude *et al.*, 2008). Thus, knowledge of vocal characteristics can enhance the ability both to attend to a target talker and to ignore distracters.

C. Benefits of knowing when to listen

Best *et al.* (2007), in another condition of the experiment described in Sec. I A, found that visually cueing the onset time of the digit sequence did not significantly improve the accuracy with which the sequence was reported. Gatehouse and Akeroyd (2008) presented a visual cue 1 s before the onset of a target word within a continuous stream of speech and speech-shaped noise. Identification performance improved significantly by 2 percentage points compared to a condition in which no cue was presented. Thus, knowing when to listen can result in a modest improvement in the intelligibility of a target talker in a multi-talker environment.

D. The present experiments

The main aim was to establish the relative benefits of the three cues—"where," "who," and "when"—in hearing out a target talker in the midst of competing talkers. The results of Kidd *et al.* (2005), Best *et al.* (2007), Brungart *et al.* (2001), and Gatehouse and Akeroyd (2008) suggest that prior knowledge about "where" and "who" is more beneficial than knowledge about "when." However, these studies used different methodologies, and no single study measured the benefits of all three cues. As a result, comparisons of the size of benefits across studies are confounded with differences in the ways in which the cues were provided and in the stimuli used. The present experiments avoided these problems.

Two ways of presenting cues involved in the control of attention can be distinguished (Mondor and Bryden, 1991). Cues provided at or close to the location of a target and/or briefly before the onset of the target can be said to act as "pull" cues. They are likely to be processed involuntarily (Yantis and Jonides, 1990). The "when" cues of Gatehouse and Akeroyd (2008) and Best *et al.* (2007) are examples of this type of cue. In contrast, the "where" cues of Best *et al.* (2007) and Kidd *et al.* (2005), and the "who" cues of Brungart *et al.* (2001), were more similar to "push" cues. They were provided prior to the start of each trial, allowing the listener time to process the cue and act on it in a volitional manner (Yantis and Jonides, 1990). In the present experiments, all cues were provided as push cues to facilitate the estimation of their relative benefits, while acknowledging that the effects of push cues may be influenced by the strategies of individual participants (Mondor and Bryden, 1991).

The present experiments addressed a further issue. In previous studies of the benefits of prior information about "who" and "where," target and masker phrases not only overlapped but started simultaneously (Kidd *et al.*, 2005; Brungart *et al.*, 2001). It is not clear, therefore, whether prior information is also beneficial when phrases overlap, but do not start at the same time, as is usually the case in everyday life. Experiments 1 and 2 addressed that distinction. In experiment 1, the target phrase co-occurred with competing phrases, but did not start at the same time as any of them ("non-simultaneous" conditions). In experiment 2, the target phrase also co-occurred with competing phrases, but started at the same time as one of them ("simultaneous" conditions). Experiments 3 and 4 explored the relationship between the simultaneous and non-simultaneous conditions by manipulating the onset *asynchrony* between the target phrase and a paired masker phrase. An issue in interpreting the results of the four experiments is whether the intelligibility of target phrases is determined entirely by the level of masking energy, or whether explanations involving cognitive processes of attention and distraction need also to be invoked. An acoustic analysis of the stimuli was conducted to inform that issue. Finally, two control experiments were run to establish whether biases had been introduced by the methods used to constrain parameters of target phrases.

II. GENERAL METHODS

A. Participants

Forty-one paid listeners between the ages of 18 and 27 years (mean of 21, standard deviation of 2.2) participated, eight in experiments 1–3, nine in experiment 4, and eight in a control experiment. Participants had lived in Britain or Ireland for at least 10 years, spoke English as their native language, and had pure-tone sensitivity better than 20 dB hearing level (HL) at octave frequencies from 250 to 8000 Hz, inclusive, tested in accordance with BS EN ISO 8253-1 (British Society of Audiology, 2004).

B. Apparatus

The experiments were conducted in a 5.3×3.7 m^2 single-walled audiology test room (Industrial Acoustics Co., NY) located within a larger sound-treated room. Stimuli were presented through an array of 13 loudspeakers (Bose Acoustimass 3 Series IV, MA) spaced at 15° intervals around half the perimeter of a circular stage with a diameter of 3.3 m. This arrangement defined a range of spatial locations from −90° to +90° azimuth, where 0° was directly in front of the listener and positive azimuths were to the listener's right. The axes of the loudspeakers were 104 cm above the floor of the stage. The array was calibrated by measuring the intensity of an octave band of white noise centered on 1 kHz from each loudspeaker at the center of the stage with a Brüel & Kjær 0.5-inch microphone (Type 4189) and sound level meter (Type 2260 Investigator) (Brüel & Kjær, Nærum, Denmark) The output of individual loudspeakers was adjusted to give the same level, within ±0.1 dB.

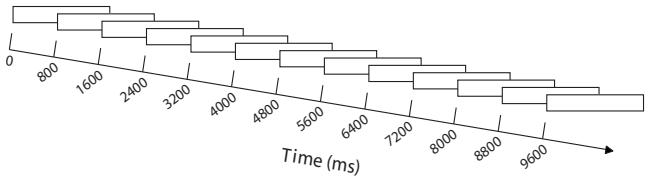

FIG. 1. The sequence of time slots that defined each trial of the experiments. Each sequence comprised 13 overlapping time slots (white rectangles). One or more phrases were allocated to each time slot. Each sequence contained one target phrase.

C. Stimuli

Stimuli were phrases from the CRM (Moore, 1981). The phrases were similar to those described by Bolia *et al.* (2000), except that they were spoken by native British-English talkers. Phrases had the form "Ready CALL-SIGN go to COLOUR NUMBER now," with eight call-signs ("arrow," "baron," "charlie," "eagle," "hopper," "laker," "ringo," and "tiger"), four colors ("blue," "green," "red," and "white"), and the numbers one to eight, inclusive, giving 256 different phrases. Phrases were spoken by four male and four female adult talkers, producing a corpus of 2048 phrases. Recordings were made in a carpeted sound-attenuated room using a Sennheiser (Wedemark, Germany) K3N/ME40 microphone, whose output was digitized at a sampling rate of 44.1 kHz with 16-bit amplitude quantization using a Lynx-ONE soundcard (Lynx Studio Technology Inc., CA). The recording of each phrase was edited to remove leading and trailing silences. The average duration of the edited phrases was 2.5 s. The levels of the digitized phrases were normalized to the same total root mean square (RMS) power. When presented from the loudspeaker at 0°, the variation in the peak A-weighted level among the phrases measured with the calibration equipment at the listening position using a 1-s integration time was ±2.5 dB. The gain in the system was set such that the average level of individual phrases was 62.5 dB (A) at the listening position.

D. Phrase Sequences

In all experiments, on each trial, phrases were presented in a sequence of 13 overlapping time slots, which were assigned randomly to the 13 loudspeakers and started at intervals of 800 ms (Fig. 1). This interval was chosen so that the initial part of the phrases containing the call-sign "Ready CALL-SIGN…" was not interrupted by the onset of a new phrase. Each sequence included one target phrase, containing the call-sign "baron," and masker phrases containing other call-signs.

E. Varying Uncertainty

Three parameters of the target phrase were either constrained within a block of trials or were varied randomly from trial to trial: The talker who spoke the target phrase ("who"), the loudspeaker from which the phrase was presented ("where"), and the time slot occupied by the phrase in the sequence of slots ("when").

When the "who" parameter was constrained, the identity of the target talker did not change within a block of trials. Otherwise, the identity varied randomly from trial to trial. When the "where" parameter was constrained, the target phrase was presented at 0°. Otherwise, it was presented from any of the 13 loudspeakers. The position of the target phrase in the sequence of phrases (the "when" parameter) was either constrained to the seventh (middle) time slot or was assigned randomly to one of the fourth to tenth time slots. In this way, the target phrase was always overlapped by at least three preceding and three following phrases.

To reduce confusion between target and masker phrases, restrictions were imposed on the phrases within the six time slots that partly overlapped the slot containing the target phrase. These surrounding phrases differed in talker and call-sign from each other and from the target phrase. In addition, none of them contained the specific combination of color and number that defined the coordinate of the target phrase, although they could include either the color or the number. The target coordinate could occur in phrases which did not overlap the target phrase.

F. Threshold Measurement

Listeners were instructed to report the color and number key words in the target phrase. Performance was measured as the level of the target phrase relative to the average level of the individual masker phrases at which accuracy was 71% correct. This threshold was measured by varying the level of the target phrase with a 2-down, 1-up adaptive procedure. Blocks of trials started at a target-to-masker ratio of +12 dB. A correct response was defined as one in which both the color and the number key words were identified correctly. The step size was 6 dB for the first three reversals and 2 dB for the next 12 reversals (experiments 1 and 2) or six reversals (experiments 3 and 4). A speech-reception threshold (SRT) was estimated by averaging the mid-points of the even-numbered runs in the phase with 2-dB steps (Levitt, 1971).

G. General Procedure

Participants sat in the middle of the stage and were instructed to face straight ahead for the duration of the experiment. Responses were made using a touch-screen. Participants touched buttons corresponding to the color and number key words in the phrase containing the call-sign "baron" on each trial. Feedback on the accuracy of responses was given by a change in the color of the buttons when pressed. A 1-s inter-trial interval began after the color and number responses had been registered.

III. EXPERIMENT 1

This experiment measured the benefits of constraining who would speak a target phrase, where it would be spoken from, and when it would be spoken. It was expected that constraining "who" and "where" would allow information within the target phrase to be heard out at lower target-to-masker ratios compared to when no information about the target phrase was available. Any advantage arising from constraining "when" was likely to be smaller.

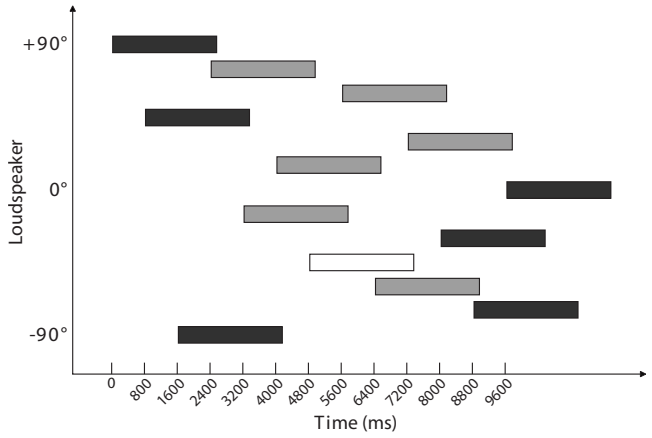

FIG. 2. Schematic illustration of the sequence of phrases from one trial of experiment 1. One phrase was placed in each slot. The target phrase appeared either in the center slot (white) or in one of the surrounding slots (light gray). Masker phrases were placed in the remaining 12 slots.

A. Procedure

Thirteen phrases from the CRM corpus were selected on each trial: A target phrase containing the call-sign "baron" and maskers phrases containing other call-signs. Each phrase was allocated a unique time slot (Fig. 2) and loudspeaker.

Eight conditions were defined by the factorial combination of three target parameters (who, where, and when) with two states (constrained or randomized). Prior to each block of trials, listeners were informed which parameters of the target phrase were constrained, what their values were, and which parameters would vary from trial to trial.

Each participant completed four sessions. Each session comprised eight blocks of trials, one for each of the eight conditions. The order of the conditions was counterbalanced across participants and sessions using a first-order Williams design (Williams, 1949). A different target talker was selected from a sub-set of four (see Sec. VIII A) in each session for the conditions in which the "who" parameter was constrained, in an order that was counterbalanced across participants.

B. Training

Participants completed four blocks of trials prior to the first session. In two of the blocks, all three target parameters varied randomly from trial to trial. In the other two blocks, the three parameters were constrained. The order of the training blocks was counterbalanced across participants. In addition, one of each type of training block was completed at the start of each subsequent session.

C. Results

Figure 3 shows group-mean and individual SRTs in the eight conditions. A repeated-measures analysis of variance (ANOVA) assessed the effects of constraining the three target parameters (who, where, and when factors) and of practice effects (session factor) on SRTs. By constraining who, participants could hear out the color-number coordinate at a SNR that was 1.9 dB less favorable on average compared to conditions in which the target talker varied from trial to trial

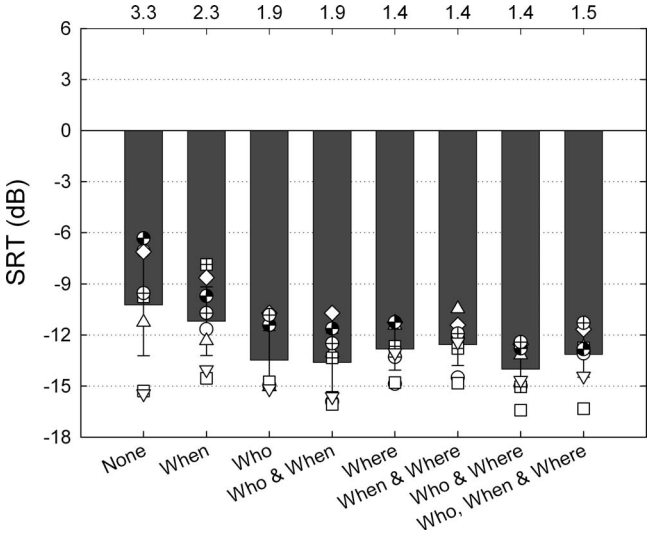

FIG. 3. Group mean (bars) and individual (symbols) SRTs for each condition in experiment 1. Error bars show 95% confidence intervals. Labels on the horizontal axes indicate between-subject standard deviations of SRTs (top) and the parameters of the target phrase, which were constrained in each condition (bottom).

[$F(1,7)=31.457$, $p<0.01$, $r=0.90$]. The improvements from constraining where [mean benefit of 1.0 dB; $F(1,7)=3.515$, $p>0.05$, $r=0.58$] and when [mean benefit of 0.01 dB; $F(1,7)=0.001$, $p>0.05$, $r=0.01$] were not significant. The main effect of session was not significant [$F(3,21)=1.07$, $p>0.05$, $r=0.22$]. None of the interactions was significant.

D. Discussion

Constraining "where" and "when" did not improve thresholds significantly; constraining "who" improved thresholds by an average of only 2 dB. While the results do not follow the pattern of benefits predicted by previous studies, they are compatible with the experience of some participants. They reported that two mechanisms—one seemingly automatic, the other volitional—were available to them to hear out the target phrase, irrespective of who spoke, or where or when they spoke. First, the onset of each phrase, if audible, oriented their attention. Second, they deduced that color and number key words, which were quieter than the words in other phrases, had to belong to target phrases. This cue could be used even if the onset of the target phrase and its call-sign had not been heard. Experiment 2 was designed to reduce the opportunity for benefiting from these two mechanisms.

IV. EXPERIMENT 2

A. Introduction

If the onset of a new talker orientates attention automatically, a masker phrase that starts at the same time as the target phrase should be particularly distracting. The requirement to monitor talkers who start to speak at the same time increases task demands compared to monitoring a single talker (Shafiro and Gygi, 2007). Kidd *et al.* (2005) suggested that "perhaps the role of spatial focus of attention is revealed more readily when the listening task is very demanding"

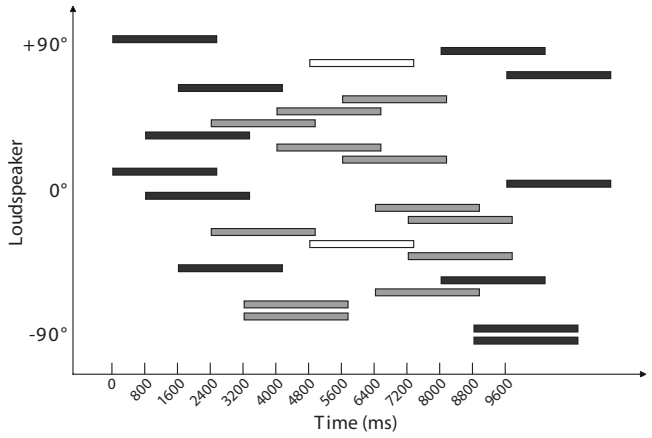

FIG. 4. Schematic illustration of the sequence of phrases from one trial of experiment 2. Two phrases with simultaneous onsets were placed in each slot. Twelve of the 13 slots contained two masker phrases, one at at a level of 62.5 dB (A) and one at a level of 52.5 dB (A). The target phrase was allocated either to the center slot (white) or one of the surrounding slots (light gray), together with a masker phrase at 62.5 dB (A).

(Kidd *et al.*, 2005, p. 3805). Accordingly, constraining "where," "who," and "when" may be beneficial when the target phrase is paired with a simultaneous masker.

B. Procedure

The sequences of phrases presented in experiment 2 were similar to those of experiment 1, except that each time slot was occupied by a pair of phrases with simultaneous onsets (Fig. 4), one spoken by a man and the other spoken by a woman. One phrase in each pair was presented at 62.5 dB (A). The level of the other phrase in slots that did not contain the target phrase was 10 dB lower. These manipulations meant that the slot containing the target phrase could not be distinguished from the other slots either because it contained less energy or because it was the only slot containing two phrases.

As the number of phrases in the sequence was greater than the number of loudspeakers, it was not possible to present each phrase from a unique loudspeaker. Instead, the phrases within each pair were allocated to different loudspeakers, chosen randomly with the constraint that they differed from those of the preceding phrase pair. The manipulation of prior information about parameters of the target phrase and the training regime were the same as in experiment 1.

C. Results

Figure 5 shows group-mean and individual SRTs in each condition. To determine whether constraining parameters of the target phrase had a significant effect on performance, and whether learning occurred, a repeated-measures ANOVA was performed with four within-subjects factors: who, where, when, and session. The effects of who [mean benefit of 3.2 dB; $F(1,7)=407.352$, $p<0.001$, $r=0.99$], where [mean benefit of 5.1 dB; $F(1,7)=363.432$, $p<0.001$, $r=0.99$], and when [mean benefit of 0.3 dB; $F(1,7)=31.121$, $p<0.01$, $r=0.90$] were significant. The effect of session was not significant [$F(3,21)=0.561$, $p>0.05$, $r=0.16$]. There was a significant interaction between who and where [$F(1,7)=11.360$, $p<0.05$, $r=0.79$]. Figure 6 shows the estimated mean benefits from constraining each of the three parameters of the target phrase in experiments 1 and 2.

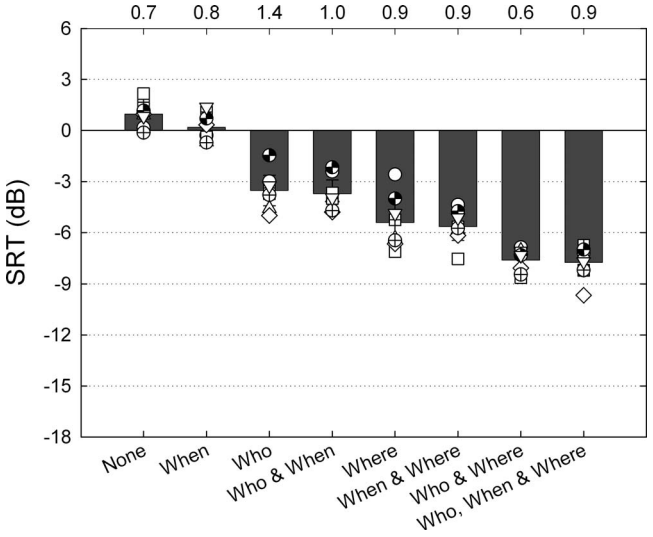

FIG. 5. Group mean (bars) and individual (symbols) SRTs for each condition in experiment 2. Error bars show 95% confidence intervals. Labels on the horizontal axes indicate between-subject standard deviations of SRTs (top) and the parameters of the target phrase which were constrained in each condition (bottom).

D. Discussion

When "who," "where," and "when" were not constrained, target phrases had to be more intense than masker phrases for participants to identify the color-number coordinate with an accuracy of 71%. This result is compatible with the idea that attention is oriented by the more intense of two voices that start at the same time (Webster and Thompson, 1954). Indeed, the orienting of attention was sufficiently complete to mean that participants contended that no target phrase had been presented on many trials when the target phrase was less intense than the paired masker.

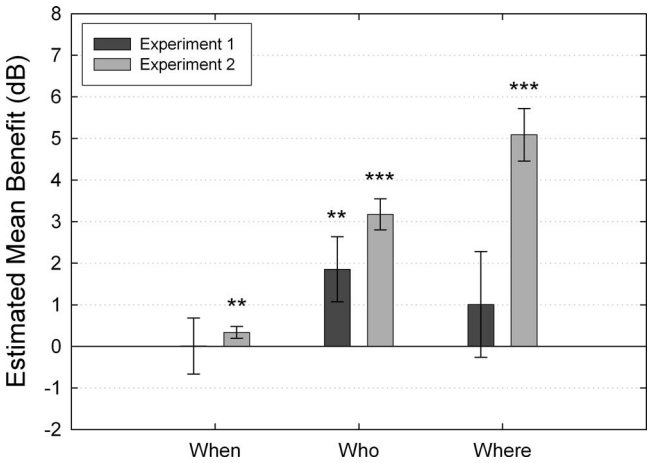

FIG. 6. Estimated mean benefits from constraining the who, where, and when parameters of the target phrase in experiments 1 (dark gray) and 2 (light gray). Error bars show 95% confidence intervals ($^{**}p<0.01$, $^{***}p<0.001$).

Performance improved when any or all of the target parameters were constrained. The relative benefits followed predictions from previous studies, with significantly larger benefits from constraining "where," than "who," than "when," as indicated by the non-overlapping confidence intervals in Fig. 6. The interaction between "who" and "where" arose because the benefit from constraining both cues together was less than the sum of the benefits from constraining the two cues individually.

In experiments 1 and 2, performance did not vary significantly across sessions. Participants showed little difficulty in learning the task. Performance had stabilized by the end of the training blocks.

V. EXPERIMENT 3

A. Introduction

The results of experiment 2 raise the question of whether a masker phrase elevates the SRT of a concurrent target phrase only when its onset is precisely synchronized with the onset of the target phrase. Experiments 3 and 4 examined the temporal extent of the influence of a masker phrase by manipulating the onset asynchrony between the masker phrase and a paired target. In experiment 3, the paired masker was isochronous with the other maskers, while the onset time of the target was manipulated. In experiment 4, the target was isochronous with the sequence of maskers, while the onset time of the paired masker was manipulated.

B. Procedure

The conditions of experiment 3 were derived from the condition of experiment 1 in which the three target parameters ("who," "when," and "where") were varied randomly from trial to trial. A masker phrase, presented at the same level as the other masker phrases, was added to the time slot containing the target phrase. The onset of this masker phrase was always aligned to the start of the time slot, i.e., 800 ms after the onset of the previous masker phrase.

The onset of the target phrase was manipulated to create nine asynchronies relative to the onset of the paired masker phrase: −320, −160, −80, −40, 0, +40, +80, +160, and +320 ms, with negative values indicating that the target started before the masker (Fig. 7). Zero and nonzero asynchronies define "simultaneous" and "non-simultaneous" conditions, respectively. An additional condition in which the paired masker phrase was omitted (identical to the "None" condition in Fig. 3) was also included.

The ten conditions were presented in an order that was partially counterbalanced across the eight participants by ensuring that each participant completed the conditions in a unique order. Each participant completed two repetitions of each condition across two sessions. Participants were reminded of the experimental task before each block of trials, but they were not informed whether the target phrase would occur before, simultaneously with, after the paired masker phrase, or alone. Participants completed a single training block of the 0-ms asynchrony condition at the start of each session.

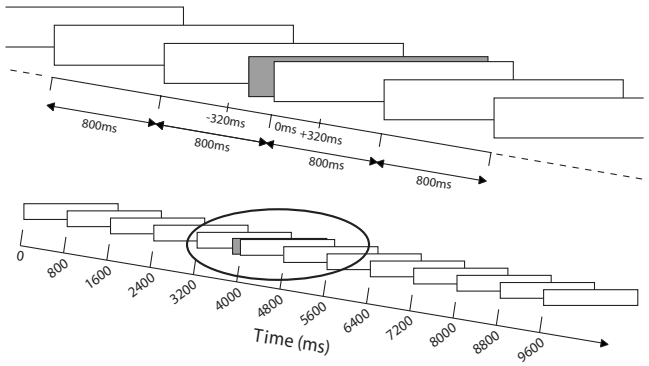

FIG. 7. An expanded section (top) of the sequence of time slots (bottom) in experiment 3. The target phrase (gray) was paired with a masker phrase within a sequence of other masker phrases (white). The onset of the paired masker occurred 800 ms after the onset of the previous masker. The onset of the target phrase was varied so that it preceded or followed the onset of the time slot containing the paired masker by up to 320 ms.

Bonferroni corrections were applied because multiple comparisons were made with the data from the condition in which the paired masker phrase was omitted. The adjusted probabilities are denoted by p_{bf}.

C. Results and Discussion

Figure 8 shows group-mean and individual SRTs in each condition. For the conditions in which the paired masker phrase was present, a repeated-measures ANOVA with a single within-subjects factor of asynchrony showed that main effect was not significant [$F(8,56)=0.605$, $p>0.05$, $\omega^2=0$].

Thresholds in the 0-ms asynchrony condition (mean SRT of 0.7 dB) did not differ significantly from the corresponding condition in experiment 2 ["None" in Fig. 5; mean SRT of 1.0 dB; $t(14)=0.584$, $p>0.05$, $r=0.15$]. Thresholds in the condition in which the paired masker was omitted were significantly lower than 0 dB [mean SRT of −6.6 dB;

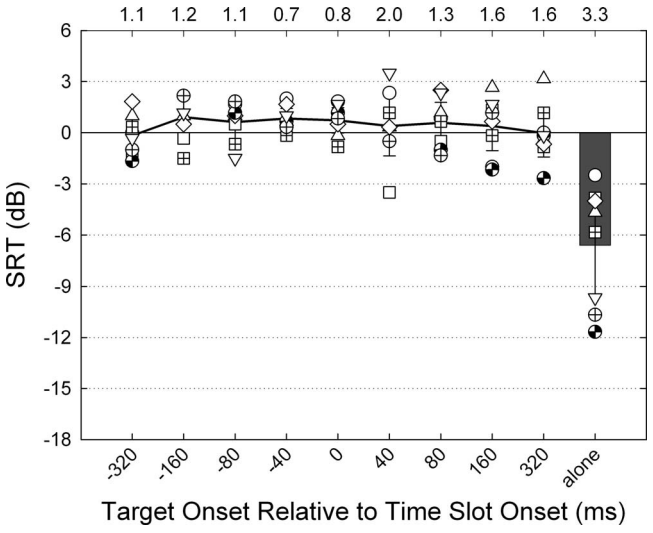

FIG. 8. Group mean (solid line) and individual (symbols) SRTs for the range of target-masker onset asynchronies used in experiment 3. In the "alone" condition (bar) the masker was omitted, making it identical to the "None" condition of experiment 1 (Fig. 3). Error bars show 95% confidence intervals, and numbers above the upper horizontal axis are between-subject standard deviations of SRTs.

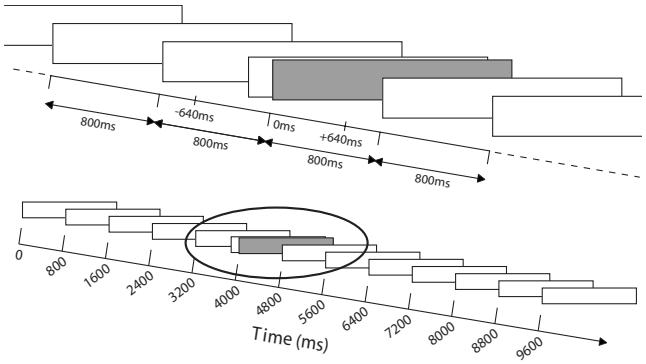

FIG. 9. An expanded section (top) of the sequence of time slots (bottom) in experiment 4. The target phrase (gray) was paired with a masker phrase within a sequence of other masker phrases (white). The onset of the target phrase occurred 800 ms after the onset of the previous masker. The onset of the paired masker phrase was varied so that it preceded or followed the onset of the time slot containing the target phrase by up to 640 ms.

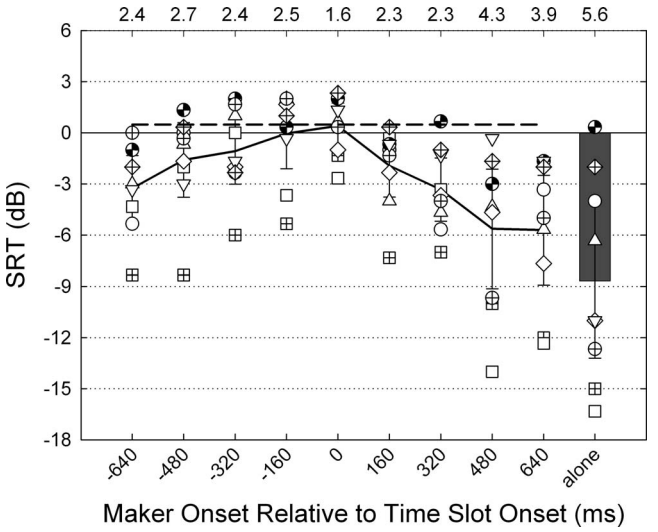

FIG. 10. Group mean (solid line) and individual (symbols) SRTs for the range of target-masker onset asynchronies used in experiment 4. The dashed line shows mean performance across the asynchrony conditions from experiment 3. In the "alone" condition (bar) the masker was omitted, making the condition identical to the corresponding condition in experiment 3 and the "None" condition of experiment 1 (Fig. 3). Error bars show 95% confidence intervals, and numbers above the upper horizontal axis are between-subject standard deviations of SRTs.

$t(7)=-5.294$, $p_{bf}<0.01$, $r=0.89$], and did not differ significantly from the identical condition in experiment 1 ["None" in Fig. 3; mean SRT of −10.2 dB; $t(14)=-2.041$, $p_{bf}>0.05$, $r=0.48$].

In summary, SRTs for target phrases did not vary significantly across target-masker onset asynchronies ranging from −320 ms to +320 ms, but fell significantly when the paired masker was removed.

VI. EXPERIMENT 4

A. Introduction

In experiment 3, the masker was isochronous with the sequence of masker phrases while the target was anisochronous. In experiment 4, the isochrony relationship was reversed. The experiment examined the effect of target-masker asynchrony while keeping the target isochronous with the sequence of phrase onsets.

B. Procedure

On each trial, the target phrase was synchronized with the sequence of phrases, i.e., it started 800 ms after the onset of the previous phrase in the sequence. Nine asynchronies of −640, −320, −160, 0, +160, +320, +480, and +640 ms were created by displacing the onset of the paired masker phrase (Fig. 9). A condition in which the paired masker phrase was omitted was included. Other aspects of the procedure were the same as in experiment 3.

C. Results

Figure 10 shows group-mean and individual SRTs. Data from the conditions containing the paired masker were subjected to a repeated-measures ANOVA with a single within-subjects factor of asynchrony. Mauchly's test indicated that the assumption of sphericity had been violated [$\chi^2(35)=58.068$, $p<0.05$]; therefore, Greenhouse–Geisser estimates of sphericity were used to correct the degrees of freedom ($\hat{\varepsilon}=0.32$). Asynchrony had a significant effect on performance [$F(2.53,20.26)=10.061$, $p<0.001$, $\omega^2=0.30$].

Planned contrasts between the simultaneous condition and each of the non-simultaneous conditions revealed that performance improved significantly when the masker preceded the target phrase by 480 ms [$F(1,8)=6.646$, $p<0.05$, $r=0.67$] or 640 ms [$F(1,8)=19.890$, $p<0.01$, $r=0.84$]. Performance also improved significantly when the masker onset followed the target onset with asynchronies of 160 ms [$F(1,8)=9.140$, $p<0.05$, $r=0.73$], 320 ms [$F(1,8)=25.360$, $p<0.01$, $r=0.87$], 480 ms [$F(1,8)=31.705$, $p<0.001$, $r=0.89$], and 640 ms [$F(1,8)=50.000$, $p<0.001$, $r=0.93$].

SRTs in the simultaneous condition did not differ significantly from the identical condition in experiment 3 [$t(15)=-0.470$, $p_{bf}>0.05$, $r=0.12$] or from the corresponding condition in experiment 2 ["None" in Fig. 5; $t(11.1)=-0.883$, $p_{bf}>0.05$, $r=0.26$]. When the paired masker was omitted, SRTs did not differ significantly from the identical condition in experiment 3 [$t(15)=-0.860$, $p_{bf}>0.05$, $r=0.22$] or from the corresponding condition in experiment 1 ["None" in Fig. 3; $t(15)=0.649$, $p_{bf}>0.05$, $r=0.17$; Fig. 11]. The mean benefit from the target phrase preceding the paired masker phrase by 320 ms was significantly larger in experiment 4 (3.7 dB) compared to the corresponding condition in experiment 3 (0.9 dB) [$t(12.1)=-3.468$, $p<0.01$, $r=0.71$].

D. Discussion

In contrast to experiment 3, performance improved with the introduction of an asynchrony between the onsets of the target and paired masker phrases. For example, a significantly larger benefit occurred in experiment 4 when the target preceded the masker phrase by 320 ms (mean benefit of 3.1 dB), compared to the corresponding condition of experiment 3 (mean benefit of 0.9 dB). A possible explanation for the difference might be based on the fact that the target phrase was isochronous with the rhythm of phrase onsets in

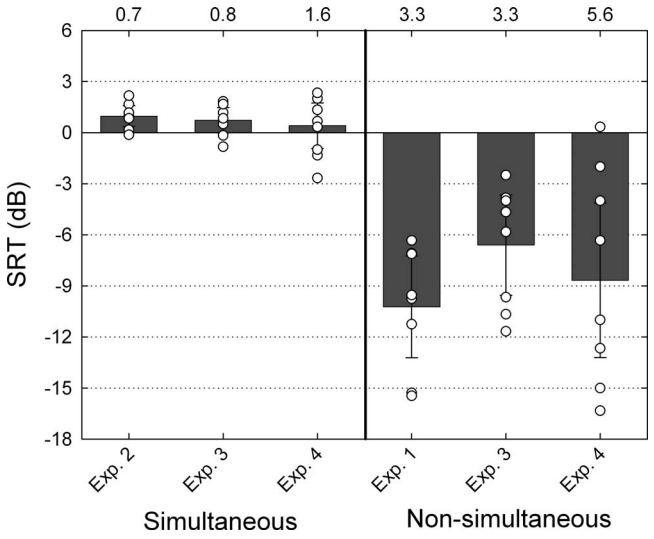

FIG. 11. Group mean (bars) and individual (symbols) SRTs for simultaneous and non-simultaneous conditions. The three bars on the left correspond to the "None" condition in experiment 2 and the simultaneous conditions in experiments 3 and 4. The three bars on the right refer to the "None" condition in experiment 1 and the conditions in experiments 3 and 4, in which the paired masker was omitted. Error bars show 95% confidence intervals, and numbers above the upper horizontal axis are between-subject standard deviations of SRTs.

experiment 4 but anisochronous in experiment 3. If a temporally regular pattern of stimuli creates attentional expectancies, which modulate vigilance levels over time (Jones *et al.*, 2002), then better performance might be expected when targets occur at expected times (in experiment 4) than at unexpected times (in experiment 3). Alternatively, the variation in SRTs with asynchrony in experiment 4, and the lack of variation in experiment 3, might be explained entirely by differences in masker energy. This explanation is examined in Sec. VII.

VII. PHYSICAL MEASUREMENTS

We made physical measurements of the stimuli to establish the extent to which SRTs were related to the level of energy available to mask each key word in the target phrases. A head and torso simulator (Brüel & Kjær HATS, Type 4128C) with microphones (Brüel & Kjær Type 4158/9C) in its ear canals was placed at the listening position facing 0°. One hundred trials were presented with the target phrase omitted in each of a sub-set of the conditions of the four experiments. For experiments 1 and 2, the sub-sets were the "None" conditions. For experiment 3, the sub-set was the conditions with asynchronies of −320, −160, 0, +160, and +320 ms. For experiment 4, the sub-set was the conditions with asynchronies of −640, −320, 0, +320, and +640 ms. The output of the microphones was recorded at a sampling rate of 44.1 kHz with 16-bit amplitude quantization. Average RMS levels were calculated for each ear within four 300-ms rectangular windows. The first window began at the time when the word "ready" in the target phrase would have started. The second to fourth windows began at the average times at which the call-sign, color, and number would have started. In addition, average RMS levels in 300-ms windows aligned with the onsets of the word "ready" and the call-sign, color, and number key words were measured in 100 target phrases presented in isolation with no attenuation. The measured levels of these key words were then adjusted by the amount of attenuation required to bring target phrases to the SRT in each condition. Finally, the levels of both masking and target energy were converted to dB sound pressure level (SPL). Differences in average level between the ears were less than 1 dB in all conditions. Accordingly, levels were averaged over the ears.

The resulting averages are plotted in Fig. 12. In panel A, open symbols plot the level in the "ready" window when isolated target phrases were presented at the SRT in each condition. Filled symbols plot the level of masking energy in the 300-ms window aligned with the moment when the word "ready" would have started in the target phrase. Thus, the difference in decibels between corresponding filled and unfilled symbols is the signal-to-noise ratio (SNR) in the "ready" window at the SRT in each condition. With the exception of the "None" condition in experiment 1 (plotted as circles), the correspondence is tight. Excluding the "None" condition of experiment 1, the SNR, calculated as the RMS

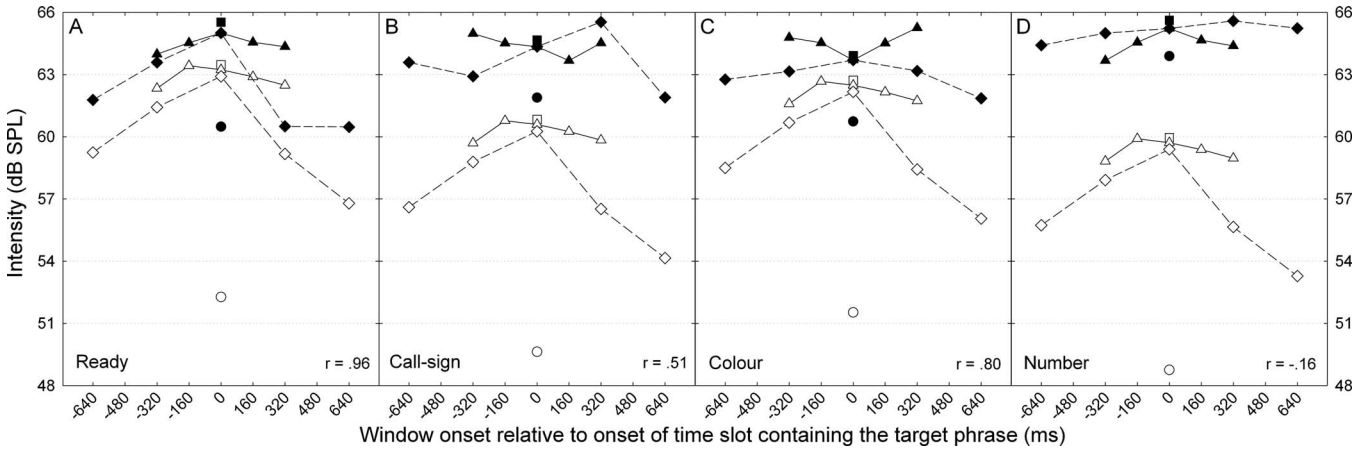

FIG. 12. A comparison of the levels of the target phrase at threshold (open symbols) and the masking energy (closed symbols) in each of four windows aligned at the start of key words in the target phrase. Data are shown for the "None" condition of experiments 1 (circles) and 2 (squares), and the asynchrony conditions of experiments 3 (triangles) and 4 (diamonds).

difference between corresponding filled and open symbols, is −2.1 dB and the product-moment correlation coefficient between the points is 0.96 ($p<0.01$).

Panels B–D in Fig. 12 plot results for the windows aligned with the start of the call-sign, color, and number key words. Correspondence between the level of masking energy (filled symbols) and the level of the key word at the SRT (open symbols) is weaker than for the "ready" window, and is shown by smaller correlation coefficients, although the coefficient for the number window is significant. The SNRs and correlation coefficients for the three windows are as follows: −5.5 dB and 0.51 ($p>0.05$) for the call-sign, −3.3 dB and 0.80 ($p<0.01$) for the color, and −7.2 dB and −0.16 ($p>0.05$) for the number.

These results suggest that SRTs in the sampled conditions of experiments 2–4 were determined primarily by the audibility of the word "ready" at the start of the target phrase, as evidenced by the highest SNR and highest correlation coefficient.

VIII. CONTROL EXPERIMENTS

A. Selection of talkers when constraining "who"

In those conditions of experiments 1 and 2 in which "who" was not constrained, target phrases were spoken by any of eight talkers. In conditions where "who" was constrained, target phrases were spoken by a sub-set of four of the talkers. Those talkers had been selected because they had the same average intelligibility as the group of eight talkers. Three experienced listeners had provided a separate SRT in the "who" condition of experiment 1 with each of the eight talkers acting as the target in turn. SRTs did not differ significantly across the eight talkers [$F(7,14)=1.315$, $p>0.05$, $r=0.40$]. The four talkers who where chosen (two males and two females) gave an average SRT of −13.5 dB (range of −12.8 to −14.1 dB) that was within 0.5 dB of the mean of the eight talkers (−13.1 dB, range of −11.9 to −14.5 dB).

B. Selection of locations when constraining "where"

In those conditions of experiments 1 and 2 in which "where" was not constrained, target phrases were presented from locations ranging from −90° to +90°. In conditions in which "where" was constrained, the target phrase was always presented from 0°. Phrases presented from this location could have been easier to hear out than phrases presented from other locations (because they came from straight ahead) or harder to hear out (because the average angular distance to masker phrases was smaller). In order to assess the direction and size of any bias, the participants from experiment 1 completed a supplementary experiment in which "where" was constrained with targets presented from either −90°, −45°, +45°, or +90°. Average SRTs were −14.8, −13.3, −13.8, and −15.9 dB, respectively. Compared to the condition in which "where" was constrained to 0°, SRTs were significantly lower at +90° (mean benefit of 3.1 dB) [$t(7)=3.6$, $p_{bf}<0.05$, $r=0.81$] and fell marginally short of significance at −90° (mean benefit of 2.0 dB) [$t(7)=3.3$, $p=0.013$ ($p_{bf}>0.05$), $r=0.78$]. We estimated SRTs for the remaining eight locations by interpolation. The average of the resulting 13 SRTs was −13.9 dB, compared with a measured SRT of −12.8 dB when "where" was constrained to 0°. It is possible, therefore, that the benefit of constraining "where" in experiment 1 was underestimated by about 1 dB.

As a further check, we decoupled constraining "where" from constraining the location of the target phrase in a supplementary version of experiment 2. Eight new listeners provided SRTs in three conditions. The "None" and "where" conditions of experiment 2 were repeated. In a third condition ("cued"), the stimuli from the "None" condition were presented, but the location of the target talker was cued by illuminating a light at the target location throughout each trial. Thus, the "cued" condition recreated the demands of the "where" condition, but used the configuration of phrases from the "None" condition. Mean SRTs were 0.4 ("None"), −4.8 ("where"), and −5.3 dB ("cued"). The mean advantage of restricting the target location to 0° (5.2 dB) did not differ from the mean advantage of cueing the target location (5.7 dB) [$t(7)=0.754$, $p>0.05$, $r=0.27$]. Thus, any bias in estimating the benefit of constraining "where" in experiment 2, introduced by presenting the target phrase only from 0°, was small in relation to the size and variability of the benefit.

IX. GENERAL DISCUSSION

The ability of listeners to hear out the color and number key words in target phrases differed between experiments 1 and 2. In experiment 1, the target phrase overlapped masker phrases but started at a separate time from them. Even when no parameters of the target phrase were constrained, listeners could hear out the color and number key words when the target phrase was 10 dB less intense than individual masker phrases. However, the benefits of constraining parameters of the target phrase were small. SRTs improved by less than 2 dB when "who," "where," or "when" were constrained. In experiment 2, the target phrase overlapped masker phrases but started at the same time as one of them. When no parameters of the target phrase were constrained, listeners required the target phrase to be 1 dB more intense than the accompanying masker phrase in order to hear out the color and number key words. Constraining each parameter improved SRTs significantly, though the benefit from constraining "when" was small ("where" of 5.1 dB, "who" of 3.2 dB, and "when" of 0.3 dB). This ordering of effectiveness was predicted by a comparison of previous studies (Brungart *et al.*, 2001; Kidd *et al.*, 2005; Best *et al.*, 2007; Gatehouse and Akeroyd, 2008). The present study adds to those results by quantifying the effectiveness of the three cues in a single experiment using a consistent methodology and stimuli.

One strategy for hearing out the color and number key words in target phrases was to attend to each new phrase as it started, interrogate its call-sign, and then either to focus attention on the phrase while resisting distraction from the next masker phrase or to allow attention to switch to the next phrase. We refer to this strategy as the "orienting" strategy. Subjectively, it was easy to attend to the onset of a new phrase, provided that the word "ready" at the start of the phrase was audible. If that requirement was met, the word

"ready" appeared to attract attention largely automatically. The experience was akin to the experience in vision where the abrupt onset of a new stimulus has a high likelihood of reorienting attention (Yantis and Jonides, 1984, 1990). In some conditions, an additional strategy could be used. If a cue was provided, or could be deduced, that distinguished the target phase from the masker phases, then color and number key words that possessed the characteristic that was cued could be attributed to the target phase even if the target call-sign had not been heard. We refer to this as the "cueing" strategy. The following paragraphs assess the extent to which the results of the experiments can be explained by the combined use of the orienting and cueing strategies.

A. Evidence for the importance of phrase onsets

Two pieces of evidence point to the importance of the audibility of the target phrase in determining SRTs in experiments 3 and 4 and in the "None" condition in experiment 2. First, SRTs were more closely associated with the SNR of the word "ready" than the SNRs of the other key words. Second, in conditions in which the target phrase started at the same time as a paired masker phrase, the SNR of the word "ready" corresponded to a level of the target that was more intense than the level of the paired masker. This result is compatible with the subjective experience that the word "ready" in the target phrase had to be more intense than the word "ready" in the paired masker phrase if the target phrase, rather than the masker, was to orient attention. Presumably, provided that the word "ready" was audible, the orienting strategy would have allowed listeners to tune into the target phrase so that they could then perform the task, despite the call-sign, color, and number key words being at more adverse SNRs than the word "ready" itself. This result may be related to the demonstration of Allen *et al.* (2008) that the advantage for intelligibility from the spatial separation of concurrent CRM phrases is achieved even when only the initial words of the phrases are presented from separate locations.

B. Difference in SRTs between experiments 1 and 2

SRTs were 11 dB lower in the "None" condition of experiment 1 than the "None" condition of experiment 2. Three effects may have contributed to this difference. First, there was 5 dB less energy masking the word "ready" at the start of the target phrase in experiment 1 than in experiment 2 (Fig. 12). Second, the fact that phrases started individually in experiment 1 but not in experiment 2 meant that the orienting strategy was available for listeners to use in experiment 1. Third, once use of the orienting strategy had reduced the level of target phrases below the level of masker phrases, differences in loudness between the target phrase and the surrounding masker phrases may have allowed listeners to use the cueing strategy. Brungart (2001) showed that the accuracy of reporting the color and number key words in the less intense of two concurrent CRM phrases was nearly constant as the relative level of the phrases was changed from 0 to −12 dB. Brungart argued that the difference in level itself provided a cue that could be used to hear out the less intense phrase despite the increase in masking energy. In experiment 1, color and number key words that were quieter than words in masker phrases could have been attributed to the target phrase, even if the listener had not heard the word "ready" or the call-sign at the start of the target phrase. The fact that the between-subject standard deviation of SRTs was larger in the "None" condition of experiment 1 than the "None" condition of experiment 2 is compatible with the idea that an extra cue was available (the difference in loudness between target and masker phrases), but that subjects differed in their ability to recognize its value or to exploit it.

C. Benefits of constraining cues in experiment 1

Although average SRTs were low in the "None" condition of experiment 1, prior knowledge of the identity, but not the location or timing, of the target talker lowered SRTs further. Possibly, use of the orienting strategy set the spatial attentional filter, and no improvement in its selectivity rose from explicit information about the location of the talker. The small, but significant, benefit from constraining "who" may have risen because the filter cannot perfectly isolate the target phrase. For example, Kidd *et al.* (2005) found that color-number identification accuracy was not perfect (92%) even when the location of the target phrase was known, and phrases were separated by 60°. In these circumstances, it may be advantageous for listeners to set up an attentional filter either for the target voice or for voices of the target gender (Brungart *et al.*, 2001). Use of that filter might help listeners to sustain attention on the target talker or, alternatively or additionally, to use the cueing strategy.

Two explanations can be offered for the lack of an effect of constraining "when." First, the experiment was not a sustained vigilance task and participants may have had little difficulty in sustaining arousal throughout the 12-s duration of each trial. Second, the study that has shown significant benefits of cueing when to listen (Gatehouse and Akeroyd, 2008) presented visual cues shortly before the start of the target words. Such pull-style cues may modulate arousal more effectively than the push-style cue for when to listen in experiment 1, which was provided at the start of each block of trials.

While listeners who performed poorly in the "None" condition of experiment 1 may have failed to exploit loudness differences as a cue to the identity of the target phrase, nonetheless, those listeners may have benefited from cues that were provided to them explicitly. To test this idea, we examined the relationship between a listener's level of performance in the "None" condition and the benefits that they derived from constraining parameters of the target phrase. In order to avoid the problem of mathematical coupling (Oldham, 1962) (i.e., overestimating the strength of relationships because participants who perform poorly by chance in one condition are likely to show larger differences with respect to another condition), we estimated correlations between the average SRT of a pair of conditions ("None" condition and another condition) and the difference in SRT between the conditions ("None" condition − another condition). Strong correlations were found for four of the six pairs of

conditions: "None" and "where" [$r=0.73$, $p<0.05$], "None," and "where and when" [$r=0.72$, $p<0.05$], "None," and "where and who" [$r=0.78$, $p<0.05$], "None," and "who, when, and where" [$r=0.80$, $p<0.05$]. Thus, subjects who performed poorly in the "None" condition improved their performance disproportionately when they were given explicit cues, particularly the "where" cue. In further experiments, it would be valuable to establish whether poor performers also improve their performance if they are alerted explicitly to the value of the loudness cue.

D. Benefits of constraining cues in experiment 2

In experiment 2, constraining both "who" and "where" was beneficial. Focusing a spatial attentional filter on the location of the target phrase (Kidd *et al.*, 2005), or focusing a vocal attentional filter on characteristics of the target talker (Brungart *et al.*, 2001), may help overcome masking by competing talkers. Each filter may help listeners to hear out the word "ready" at the start of the target phrase. Each filter, additionally, may allow color and number key words that match the filter to be attributed to the target phrase, even if the word "ready" and the call-sign were not detected. It would be interesting to confirm that listeners can, indeed, perform in this way by constraining "who" and "where" in a version of experiment 2 in which the role of the call-sign was neutralized by including the same call-sign in every phrase. Knowing when to listen had a significant but very small effect on performance. Constraining "when" may have allowed participants to increase their level of arousal during the slot containing the target phrase.

X. CONCLUSIONS

These experiments suggest that mechanisms related both to masking and attention play roles during speech perception in multi-talker environments. The importance of masking was shown by the close relationship between speech-reception thresholds and the SNR at the onset of target phrases in conditions in which target and masker phrases started simultaneously, or near simultaneously, and listeners did not know who would speak the target phrase, when they would speak, or where they would be located. The importance of attention was shown by the significant advantages from providing listeners with knowledge of the identity and location of the target talker in conditions where target and masker talkers started speaking at the same time.

ACKNOWLEDGMENTS

P.T.K. was supported by a studentship from the Royal National Institute for Deaf People. Research facilities were supported by The Laing Foundations, The Goodricke Appeal Fund, Deafness Research U.K., and the MRC Institute of Hearing Research.

Allen, K., Carlile, S., and Alais, D. (**2008**). "Contributions of talker characteristics and spatial location to auditory streaming," J. Acoust. Soc. Am. **123**, 1562–1570.

Arbogast, T. L., and Kidd, G. J. (**2000**). "Evidence for spatial tuning in informational masking using the probe-signal method," J. Acoust. Soc. Am. **108**, 1803–10.

Best, V., Marrone, N., Mason, C. R., Kidd, G., and Shinn-Cunningham, B. G. (**2009**). "Effects of sensorineural hearing loss on visually guided attention in a multitalker environment," J. Assoc. Res. Otolaryngol. **10**, 142–149.

Best, V., Ozmeral, E. J., and Shinn-Cunningham, B. G. (**2007**). "Visually-guided attention enhances target identification in a complex auditory scene," J. Assoc. Res. Otolaryngol. **8**, 294–304.

Bolia, R. S., Nelson, W. T., Ericson, M. A., and Simpson, B. D. (**2000**). "A speech corpus for multitalker communications research," J. Acoust. Soc. Am. **107**, 1065–1066.

British Society of Audiology (**2004**). "Recommended procedure: Pure tone air and bone conduction threshold audiometry with and without masking and determination of uncomfortable loudness levels," http://www.thebsa.org.uk/docs/bsapta.doc. Last viewed October 1, 2006.

Brungart, D. S. (**2001**). "Informational and energetic masking effects in the perception of two simultaneous talkers," J. Acoust. Soc. Am. **109**, 1101–1109.

Brungart, D. S. and Simpson, B. D. (**2004**). "Within-ear and across-ear interference in a dichotic cocktail party listening task: Effects of masker uncertainty," J. Acoust. Soc. Am. **115**, 301–310.

Brungart, D. S., Simpson, B. D., Ericson, M. A., and Scott, K. R. (**2001**). "Informational and energetic masking effects in the perception of multiple simultaneous talkers," J. Acoust. Soc. Am. **110**, 2527–2538.

Gatehouse, S. and Akeroyd, M. A. (**2008**). "The effects of cueing temporal and spatial attention on word recognition in a complex listening task in hearing-impaired listeners," Trends Amplif. **12**, 145–161.

Johnsrude, I. S., Mackey, A., Alexander, E. M., Macdonald, H., and Carlyon, R. P. (**2008**). "Effects of voice familiarity and age on perceptual organization of sound from two competing talkers (A)," J. Acoust. Soc. Am. **123**, 3566.

Jones, M. R., Moynihan, H., MacKenzie, N., and Puente, J. (**2002**). "Temporal aspects of stimulus-driven attending in dynamic arrays," Psychol. Sci. **13**, 313–319.

Kidd, G. J., Arbogast, T. L., Mason, C. R., and Gallun, F. J. (**2005**). "The advantage of knowing where to listen," J. Acoust. Soc. Am. **118**, 3804–3815.

Levitt, H. (**1971**). "Transformed up-down methods in psychoacoustics," J. Acoust. Soc. Am. **49**, 467–477.

Mondor, T. A., and Bryden, M. P. (**1991**). "The influence of attention on the dichotic REA," Neuropsychologia **29**, 1179–1190.

Mondor, T. A., and Zatorre, R. J. (**1995**). "Shifting and focusing auditory spatial attention," J. Exp. Psychol. Hum. Percept. Perform. **21**, 387–409.

Moore, T. J. (**1981**). "Voice communications jamming research," in Proceedings of the AGARD Conference 331: Aural Communication in Aviation, Neuilly-Sur-Seine, France, Vol. **2**, pp. 1–6.

Oldham, P. D. (**1962**). "A note on the analysis of repeated measurements of the same subjects," J. Chronic Dis. **15**, 969–977.

Sach, A. J., and Bailey, P. J. (**2004**). "Some characteristics of auditory spatial attention revealed using rhythmic masking release," Percept. Psychophys. **66**, 1379–1387.

Sach, A. J., Hill, N. I., and Bailey, P. J. (**2000**). "Auditory spatial attention using interaural time differences," J. Exp. Psychol. Hum. Percept. Perform. **26**, 717–729.

Shafiro, V., and Gygi, B. (**2007**). "Perceiving the speech of multiple concurrent talkers in a combined divided and selective attention task," J. Acoust. Soc. Am. **122**, EL229–EL235.

Simon, J. R. (**1967**). "Ear preference in a simple reaction-time task," J. Exp. Psychol. **75**, 49–55.

Webster, J. C., and Thompson, P. O. (**1954**). "Responding to both of two overlapping messages," J. Acoust. Soc. Am. **26**, 396–402.

Williams, E. J. (**1949**). "Experimental designs balanced for the estimation of residual effects of treatments," Aust. J. Sci. Res., Ser. A **2**, 149–168.

Yantis, S., and Jonides, J. (**1984**). "Abrupt visual onsets and selective attention: Evidence from visual search," J. Exp. Psychol. **10**, 601–21.

Yantis, S., and Jonides, J. (**1990**). "Abrupt visual onsets and selective attention: Voluntary versus automatic allocation," J. Exp. Psychol. **16**, 121–34.

Auditory temporal-order processing of vowel sequences by young and elderly listeners[a)]

Daniel Fogerty,[b)] Larry E. Humes, and Diane Kewley-Port
Department of Speech and Hearing Sciences, Indiana University, Bloomington, Indiana 47405

(Received 5 March 2009; revised 20 January 2010; accepted 21 January 2010)

This project focused on the individual differences underlying observed variability in temporal processing among older listeners. Four measures of vowel temporal-order identification were completed by young ($N=35$; 18–31 years) and older ($N=151$; 60–88 years) listeners. Experiments used forced-choice, constant-stimuli methods to determine the smallest stimulus onset asynchrony (SOA) between brief (40 or 70 ms) vowels that enabled identification of a stimulus sequence. Four words (pit, pet, pot, and put) spoken by a male talker were processed to serve as vowel stimuli. All listeners identified the vowels in isolation with better than 90% accuracy. Vowel temporal-order tasks included the following: (1) monaural two-item identification, (2) monaural four-item identification, (3) dichotic two-item vowel identification, and (4) dichotic two-item ear identification. Results indicated that older listeners had more variability and performed poorer than young listeners on vowel-identification tasks, although a large overlap in distributions was observed. Both age groups performed similarly on the dichotic ear-identification task. For both groups, the monaural four-item and dichotic two-item tasks were significantly harder than the monaural two-item task. Older listeners' SOA thresholds improved with additional stimulus exposure and shorter dichotic stimulus durations. Individual differences of temporal-order performance among the older listeners demonstrated the influence of cognitive measures, but not audibility or age.
 [DOI: 10.1121/1.3316291]

PACS number(s): 43.66.Sr, 43.71.Rt [KWG] Pages: 2509–2520

I. INTRODUCTION

It is clear that as adults age, the likelihood that they encounter difficulties with speech understanding increases. While the concurrence of peripheral damage due to hearing loss plays the most significant role in decreased speech-understanding abilities in older adults (e.g., Dubno and Schaefer, 1992, 1995; Humes and Christopherson, 1991; Humes, 1996, 2002, 2005; van Rooij and Plomp, 1992), older adults have deficits that remain even after audibility of the speech message is restored (Humes, 2007). One form of processing that has been attributed to part of this continued impairment is temporal processing (e.g., Gordon-Salant and Fitzgibbons, 1993, 1999; Schneider and Pichora-Fuller, 2000; Pichora-Fuller, 2003). This is consistent with repeated findings that older adults perform more poorly on a variety of auditory temporal processing tasks, particularly involving complex sequences (Fitzgibbons and Gordon-Salant, 1996, 1998). However, it remains unclear the extent to which the speech-communication deficits of older adults are related to peripheral or central auditory deficits, or to more general cognitive declines, an area that has been identified as a priority in auditory aging research for 20 years (Working Group on Speech Understanding and Aging, 1988). The nature of the underlying impairment could have profound implications for the treatment of speech-understanding deficits in the elderly. In order to investigate this issue, Humes (2005) outlined two primary techniques to use for the delineation of the underlying impairment: (1) concurrent study in multiple modalities and (2) correlational analysis with cognitive functioning. This paper reports the results of an ongoing investigation that is examining the cognitive, sensory, and temporal processing abilities for a large group of older adults across multiple modalities (see Humes *et al.*, 2009). In this report, we explored the auditory temporal-order processing abilities of older and younger adults for brief vowel sequences and analyzed individual differences to further identify related abilities in older adults.

There have been a number of age-related neurophysiological changes associated with aging, including declines in dopamine receptors, demyelination, cell loss, decreased cerebral blood flow, and increased inefficient dendritic branching which have been attributed to processing-speed deficits (e.g., Park *et al.*, 2001). Changes in the auditory system due to insult or degeneration, combined with global neural changes associated with aging, may result in a generalized decreased ability to process rapid acoustic events. Indeed, deficits in some form of processing speed may underlie many age-related cognitive declines (Salthouse, 1996). Findings such as these suggest a "common cause hypothesis" of cognitive aging (Baltes and Lindenberger, 1997; Lindenberger and Baltes, 1994) which proposes that an underlying amodal neural change results in widespread cognitive declines (for a review, see Hofer *et al.*, 2003) and concomitant sensory deficits. Processing time has been demonstrated as a crucial indicator of cognitive decline with aging and may be related to many of the persistent speech-understanding difficulties that

[a)] Portions of the data were presented at the 153rd, 155th, and 157th Meetings of the Acoustical Society of America (J. Acoust. Soc. Am., 121, 3188; 123, 3716; 125, 2722) and at the 2007 Aging and Speech Communication: An International and Interdisciplinary Research Conference, Bloomington, IN.

[b)] Author to whom correspondence should be addressed. Electronic mail: dfogerty@indiana.edu

older adults face, even with appropriate compensation for inaudibility associated with hearing loss. Therefore, in order to understand and potentially treat these lingering difficulties to improve communication and quality of life, it is essential to understand if and how auditory temporal processing deficits are manifest in older adult listeners.

Fluent speech is characterized by rapid acoustic changes that represent the information necessary to extract meaning. These dynamic acoustic changes likely play a facilitatory role (Dorman *et al.*, 1975). However, most temporal-order research has used non-speech stimuli, such as tone sequences. Trainor and Trehub (1989) inferred that age-related temporal-order deficits might underlie some of the speech-understanding difficulties that older listeners face. While Humes and Christopherson (1991) concluded that audibility is the primary predictor of age-related differences across a variety of auditory processing tasks, the four tasks that discriminated between young and old listeners had a temporal component, two of which were the temporal-order discrimination of tones and of syllables. Indeed, older listeners are less able to distinguish tone sequences with contrasting order regardless of whether the task requires discrimination or identification (Trainor and Trehub, 1989). While "normal" performance is sometimes maintained for simple patterns, processing generally breaks down at faster processing rates and for more complex patterns (Fitzgibbons and Gordon-Salant, 1998). However, the effects of age remain regardless of various stimulus characteristics, such as stimulus duration, interval spacing, or sequence timing characteristics (Fitzgibbons *et al.*, 2006; Shrivastav *et al.*, 2008). Age-related differences have also been described as being resistant to practice effects (Trainor and Trehub, 1989). While age differences in performance have sometimes not been observed for temporal-order judgments between two stimuli presented to opposite ears (Szymaszek *et al.*, 2006; Kołodziejczyk and Szelag, 2008), even here age differences become prominent for the very old (95–103 years) when compared to either young (19–25 years) or older (65–67 years) adults.

The auditory temporal-order processing deficits in older listeners appear to result from processing-speed declines. Fitzgibbons and Gordon-Salant (1998) suggested an auditory processing rate limitation underlies the deficits in temporal-order processing observed in older adults. These processing limitations appear to be associated with more general difficulties in higher-level perceptual and cognitive processing (Fitzgibbons *et al.*, 2006). Humes *et al.* (2007) also observed modality-specific deficits in auditory processing speed in older adults, as measured with both time-compressed speech and an auditory speeded-spelling task. Modality specificity of this processing deficit was confirmed through the use of a parallel visual speeded-spelling task in these same listeners. In support of auditory speed-of-processing deficits, corresponding measures of auditory evoked potentials have suggested the involvement of the P2 component which also correlated with behavioral performance (Lewandowska *et al.*, 2008). The results clearly demonstrate impaired temporal-order processing in older adults at higher central auditory levels that likely involve contributions from attentional (i.e., cognitive) resources (Szelag *et al.*, 2009).

The current study explored temporal-order identification for vowel sequences using three stimulus conditions: (1) monaural two-item sequences, (2) monaural four-item sequences, and (3) dichotic two-item sequences. The dichotic two-item stimulus condition was used for two different tasks: vowel-sequence identification and ear-sequence identification. All told, there were four primary dependent measures of temporal-order identification in this study. These stimulus conditions and tasks were motivated by several considerations. Comparison of performance for the monaural two-item and monaural four-item sequences, for example, may shed light on the contributions of memory to the identification of brief word-length sequences. Comparison of performance on the monaural and dichotic two-item tasks, on the other hand, may provide insight into the limitations posed by peripheral sensory processes, such as forward masking, or central auditory factors involved with this task. Finally, it is important to note that these tasks required judgment of both temporal-order and vowel identifications; thus, these tasks require a higher cognitive load than temporal-order tasks that can be made on the bases of, for example, pitch ordering (e.g., Fitzgibbons and Gordon-Salant, 1998) or ear ordering (e.g., Kołodziejczyk and Szelag, 2008). The inclusion of the ear-sequence identification task provided the ability to examine temporal-order identification without requiring concurrent vowel identification. Thus, comparison of performance for the two dichotic tasks, vowel-sequence identification vs ear-sequence identification, enables examination of the role played by phonological processing (i.e., stimulus categorization).

Additional experiments reported here also explored the effect of stimulus duration, ear randomization, and stimulus exposure effects regarding the performance of older adults. Few studies have addressed individual differences among older adult listeners related to temporal processing, although several have discussed the large variability among older adults (Moore *et al.*, 1992; Schneider *et al.*, 1994; Snell, 1997; Snell and Frisina, 2000). A primary objective of this series of experiments was to obtain temporal-order data from a large group of older adults to examine individual differences in detail. In the analyses presented here, individual differences in performance were explored to determine correlations between different auditory temporal-order tasks, age, audibility, and general measures of cognitive functioning (WAIS-III; Weschsler, 1997). That is, aside from comparisons of the group data from young and older adults, this study also explored individual differences in temporal processing among older listeners and correlations with cognitive tasks.

II. EXPERIMENT 1: MONAURAL AND DICHOTIC TEMPORAL ORDER

This first experiment was designed to meet two specific aims. First, group differences in temporal-order identification for vowel sequences were examined between young and older adults. Second, with the substantial number of older listeners tested, individual differences in performance among the older individuals were explored.

A. Listeners

Two groups of listeners participated in this study. The first group consisted of 35 young adult listeners (11 males, 24 females) with a mean age of 23 years (range: 18–31 years). The second group was comprised of 151 older adults (68 males, 83 females) with a mean age of 71 years (range: 60–88 years). Participants were recruited through advertisements in the local newspaper, in flyers for local community centers, and posted at various locations on the Bloomington campus of Indiana University.

Selection criteria for this study included age (18–35 or 60–89 years), a Mini-Mental Status Exam (Folstein *et al.*, 1975) score ≥25, and specific hearing sensitivity requirements. Maximum hearing thresholds for air conducted pure tones were not to exceed the following limits in at least one ear: 40 dB hearing loss (HL) (American National Standards Institute, 2004) at 250, 500, and 1000 Hz; 50 dB HL at 2 kHz; 65 dB HL at 4 kHz; and 80 dB HL at 6 and 8 kHz. It was also required that there be no evidence of middle ear pathology (air-bone gaps <10 dB and normal tympanograms). A pure-tone average (PTA) for the frequency range of the test stimuli used in this study was calcuated over 500, 1000, 1500, and 2000 Hz. Young listeners had mean PTA thresholds at 8 dB HL (SD=4 dB) and 8 dB HL (SD=5 dB) for right and left ears, respectively. Older listeners had mean PTA thresholds at 21 dB HL (SD=13 dB) and 20 dB HL (SD=11 dB) for right and left ears, respectively. Participants were paid for their participation. Due to the long testing duration of the entire multimodality project, there was some attrition across tasks resulting in a loss of approximately one participant in each age group for each task.

B. Stimuli

Stimuli were recorded by a male Midwestern talker in a sound-attenuating booth using an Audio-Technica AT2035 microphone. Four confusable vowel stimuli (i.e., from a restricted vowel space) /ɪ, ɛ, a, ʊ/ were spoken rapidly in a /pVt/ context in a carrier phrase "The first word is__now." The words pit, pet, pot, and put were digitally edited to remove voiceless sounds, leaving only the voiced pitch pulses. Productions of four vowels that had the shortest duration, F2<1800 Hz, and good identification by two young normal-hearing listeners, one older normal-hearing listener, and one older hearing-impaired listener during final pilot testing were selected for stimuli. Stimuli were modified in MATLAB using STRAIGHT (Kawahara *et al.*, 1999) to be 70 ms long with a fundamental frequency of 100 Hz. Stimuli were low-pass filtered at 1800 Hz and normalized to the same rms level. Low-pass filtering was used to minimize the influence of the high-frequency hearing loss of the older adults on their vowel-identification performance.

C. Calibration

Stimuli were presented via Tucker-Davis Technologies (TDT) System III hardware using 16 bit resolution at a sampling frequency of 48 828 Hz. The output of the TDT D/A converter was passed through a programmable attenuator (PA-5), headphone buffer (HB-7), and then to an ER-3A insert earphone. The earphone was calibrated in a 2 cm^3 coupler using a Larson Davis model 2800 sound level meter with linear weighting. The system was calibrated using a calibration vowel of the same rms amplitude as the test stimuli, but with a duration of 3 s. A single stimulus presentation measured 83 (±2) dB sound pressure level (SPL) and a presentation of two overlapping stimuli measured 86 (±2) dB SPL. Output levels were checked electrically at the beginning of each day of data collection and were verified acoustically with the sound level meter and 2 cm^3 coupler at monthly intervals throughout the study.

D. Procedure

All participants passed an identification screening of the four vowel stimuli in isolation with at least 90% accuracy on one of no more than 20-trial blocks in their test ear. This was to ensure that listeners would be able to complete the subsequent auditory temporal-order measures which were targeting identification performance of either 50% or 75% correct (see below). If participants did not reach this 90% identification accuracy criterion during screening, they were rescreened on a separate day. Participants ultimately unable to reach this criterion were dismissed from further auditory testing. Only five older adults were excluded from the study because of their failure to identify the brief vowel stimuli in isolation with at least 90% accuracy. In addition, all participants completed a full cognitive assessment using the WAIS-III (Weschsler, 1997) prior to data collection.

At the first auditory temporal-order experimental session listeners completed, a stimulus familiarization task which consisted of listening to each vowel stimulus in isolation while receiving orthographic feedback as to which stimulus was presented. In addition, prior to each new experimental task, listeners completed a demonstration of that task for 12 different temporal-order sequences. Correct responses were displayed with no response required on behalf of the listeners. Demonstrations were repeated for a total of 24 stimulus presentations prior to each task. Listeners were offered additional repetitions of the demonstration, although only 8% of listeners requested additional presentations.

All participants completed four tasks in the following order: Monaural two-item Identification (Mono2), Monaural four-item Identification (Mono4), Dichotic two-item Vowel Identification (Dich2), and Dichotic two-item Location (or Ear) Identification (DLoc). The first task, Mono2, required participants to identify the order of two vowels presented monaurally to the test ear. The right ear was the test ear for all monaural measurements in this study, except for six older listeners who were tested using their left ear due to right ear thresholds exceeding the inclusion criteria. The second task, Mono4, presented a sequence of four vowels to the test ear. Two dichotic tasks were also completed. Dich2 was analogous to Mono2 with the exception that each of the two vowels was presented to a different ear, with the ear that was presented first randomized from trial to trial. DLoc used the same stimulus presentation as Dich2, except listeners were only required to identify the location (i.e., ear) that received

the first stimulus. In this way, a direct comparison of performance between identification and location measurements could be made.

All auditory testing was completed in an IAC sound-attenuating booth with listeners seated in the sound booth either individually or in pairs. Each participant was seated comfortably in front of a touch-screen display (Elo Model 1915L). For all four tasks, the same vowel was never repeated twice in a row. The Mono4 task had the additional stipulation that each sequence must contain at least three of the four vowel stimuli. Thus, a single vowel could occur twice within a sequence, which was implemented to avoid the possibility of correctly guessing the identity of the fourth vowel based on the three preceding vowels. For the three vowel-identification tasks, responses were collected using columns consisting of four buttons labeled "pVt" on the screen, each column corresponding to the interval during which the stimulus was presented. Thus, for Mono2 and Dich2, there were two columns of four buttons displayed on the touch screen, and, for Mono4, there were four columns of four buttons displayed from left to right. Listeners were required to identify the correct vowel sequence exactly for the response to be judged correct. The location task, DLoc, only had two buttons (labeled "Right" and "Left") for the listener to identify which ear was stimulated first. Orthographic feedback showing the correct sequence was provided on all trials.

The dependent variable measured was the stimulus onset asynchrony (SOA) between the presented vowels. The minimum SOA value was $\geqslant$2 ms to ensure a sequential presentation for the stimuli. Given stimulus durations of 70 ms, SOA values less than 70 ms resulted in the stimuli overlapping in time. All tasks used the method of constant stimuli to measure the psychometric function relating percent-correct identification performance to SOA. For the three vowel-sequence identification tasks, threshold was defined as 50% correct, whereas 75% correct was defined as threshold for DLoc because chance performance was 50% for this ear-sequence task. Extensive piloting was completed to determine the appropriate starting SOA test intervals for young and older listeners in general. Due to the large variability of performance between older listeners, a single set of SOA values could not be used for all participants. Therefore, experimental testing was conducted in two phases. The first phase consisted of a preliminary wide-range estimate of SOA threshold (i.e., using a large step size, 25 ms), while the second phase consisted of narrow-range testing (i.e., using a smaller step size, 10 or 15 ms) to provide the actual SOA threshold estimates reported in the results. Table I lists the SOA test values used during initial wide-range testing across the four tasks for the young and older listeners. From this initial block of trials, the participant's identification accuracy at each SOA value was fitted by a psychometric function (Weibull) and a preliminary threshold at 50% was estimated (75% for DLoc). Next, narrow-range testing for that same task was completed using an initial SOA that was 30 ms (40 ms for Dich2) less than the wide-range threshold estimate and a 10 ms (15 ms for Dich2) step size over six steps. This was designed to result in about three performance estimates below the targeted performance level and three estimates above this performance level.

TABLE I. Wide-range starting test values across the four experimental tasks. Values for older adult listeners are listed (values for young listeners are in parentheses if different).

	Mono2	Mono4	Dich2	DLoc
Starting SOA (ms)	10	85 (35)	45	100 (20)
No. of trials	72	96	144	144

In the event that a threshold was not obtained by the wide-range task, a threshold was estimated based on visual inspection of the listener's performance graph and the wide-range was rerun with a starting SOA 30 ms below the threshold estimated by visual inspection. Narrow-range estimates were only considered valid if the threshold could be estimated without extrapolation beyond the range of performance measured. If this was not the case, the results were considered invalid. In this case, the narrow-range was adjusted to include the new estimated threshold and the narrow-range measurements were repeated. In the end, each threshold estimate for each task was based on three valid narrow-range estimates for a total of 216 (Mono2), 288 (Mono4), or 432 (Dich2, DLoc) trials. Typically, all three narrow-range thresholds for a given task were obtained over the same SOA test range.

Breaks were always available to listeners between test blocks, were verbally offered after about 1 h of testing, and were prompted on screen for the two longer dichotic tasks midway through a test block to avoid possible fatigue. Test sessions were no longer than 2 h. Listeners returned for three to four testing sessions. A few listeners scheduled more sessions due to difficulty obtaining reliable threshold estimates to begin the task or a slower rate of completing the tasks.

E. Results

1. Data reliability

Across each of the four tasks, three threshold estimates were obtained. To test the reliability and stability of these measures, Pearson-r correlations across the three blocks for each of the four experimental tasks were completed separately for both age groups. All correlations were significant at $p<0.01$, thereby demonstrating similar performance across blocks, with one exception for the young group (block 1 vs block 3 of Dich2, $r=0.33$). As a test of the stability of the threshold estimates, eight repeated-measures general linear model analyses were completed, one for each dependent measure and each group. Results showed no significant main effect of block number for any dependent measure or group ($p>0.01$), thus demonstrating no learning effect across blocks. Based on these results, threshold estimates from all three blocks appear to be reliable and stable estimates of performance for both age groups. Therefore, the default calculation of final threshold estimates for each task and participant was the average of three (narrow-range) threshold estimates.

TABLE II. Number of participants unable to achieve a threshold for each experimental task.

	Mono2	Mono4	Dich2	DLoc
Young	0	1	0	1
Old	1	21	6	6

As a further check for within-subject outliers across blocks, the standard deviation was calculated across the three blocks for each listener. Any listener that had a standard deviation greater than three times the average three-block standard deviation for the respective age group was judged to have an unreliable threshold estimate. In these cases, the two closest threshold estimates were used to calculate the final threshold estimate. A few listeners did not have at least two threshold estimates that fell within three standard deviations, and were therefore treated as missing data (about 1 participant per group per task). Reliable data points having been identified, threshold estimates averaged across all three blocks (or two blocks, 6% of cases) were used in subsequent analyses.

Of particular interest in this study are not only the listeners who perform well enough on the experimental tasks to yield valid threshold estimates but also those who perform poorly or otherwise could not complete the experimental testing. Table II lists the number of participants unable to complete experimental testing for each task. Only six of these participants were unable to complete two tasks (typically the two dichotic tasks). Inspection of the data in Table II reveals that older adults were unable to complete the temporal-order identification tasks than younger adults, especially for Mono4. In order to include these individuals in subsequent analyses and not bias the data by excluding them, their performance was coded as extreme values (maximum recorded threshold plus one standard deviation) and medians were used for group analyses. Such nonparametric analyses are more resistant to violations of normality and allowed inclusion of all participants.

2. Data analysis

Table III displays the descriptive statistics for each group. In order to test the difference between groups for each experimental task, a Bonferroni-adjusted Mann–Whitney test was used for pairwise comparisons and demonstrated significant ($p<0.001$) between-group differences for all three vowel-sequence identification tasks, as shown in Fig. 1. However, no significant difference between age groups was achieved for the dichotic ear-sequence identification task (Bonferroni-adjusted $p=0.032$). A Wilcoxon Signed-Ranks Test was used to compare performance within a group across experimental tasks (see Table IV). For both age groups, SOA thresholds for Mono2 were significantly shorter than SOA thresholds for the other three tasks. For older adults, SOA thresholds for Mono4 differed significantly from SOA thresholds for both dichotic conditions. This was not the case, however, for younger adults. The performance of older adults did not differ significantly between the two dichotic tasks, whereas the performance of the young adults did differ significantly between these two tasks.

TABLE III. Descriptive statistics for experiment 1; IQ range=interquartile range.

	Older adult listeners			Young adult listeners		
	N	Median	IQ range	*N*	Median	IQ range
Mono2	150	49.1	35.4	35	15.8	15.7
Mono4	129	154.1	142.5	33	90.3	90.54
Dich2	143	116.0	37.4	34	96.5	28.8
DLoc	142	121.2	41.6	32	109.1	36.3

F. Discussion and extension of results

The significant intertask differences demonstrate that these four temporal-order identification tasks tap into different processing demands. Clearly, the shortest SOAs were observed for both age groups in the Mono2 stimulus condition, with threshold SOA values being about 80–100 ms shorter for this condition than the others. Apparently, it is easier for both age groups to perform this task when the vowel sequence is presented to the same ear and is comprised of only two stimuli. Keeping the stimuli in one ear but doubling the number of items in the sequence (Mono4) resulted in sizable increases in SOA thresholds (i.e., greater than a factor of 3) relative to the SOA thresholds for the Mono2 condition. The differences in chance performance between Mono2 (8%) and Mono4 (1%) do result in a difference in task difficulty. In order to equate d' between the two tasks, new thresholds were calculated for the Mono4 task at a conservative 25% correct using conversion tables from Hacker and Ratcliff (1979). Significant differences remained for the Mono4 condition, both between young and older listeners ($p<0.001$) and between Mono2 and Mono4 tasks ($p<0.001$). However, Mono4 d' adjusted thresholds were significantly better than Dich2 thresholds, further highlighting the additional demands of dichotic processing.

If limitations in vowel identification influenced performance on the monaural tasks (rather than some other factors related to temporal-order judgment), then, the longer sequence in Mono4 would compound this factor, thereby reducing the probability of correctly selecting the vowel sequence. However, while younger listeners did perform better overall when identifying vowels in isolation than older listeners ($p<0.05$), vowel-identification performance in isolation did not significantly correlate with performance on either the Mono2 ($r=-0.05$) or Mono4 ($r=-0.07$) tasks. This indicates that the sizable increases in threshold for Mono4 were not due to vowel-identification limitations, but more likely due to task (e.g., sequential processing) and/or cognitive (e.g., memory) factors.

Considering dichotic presentations, separating the stimuli by presenting one to each ear resulted in considerably longer SOA thresholds relative to Mono2. No difference between dichotic tasks was found for older listeners. This provides further evidence that vowel identification was not a

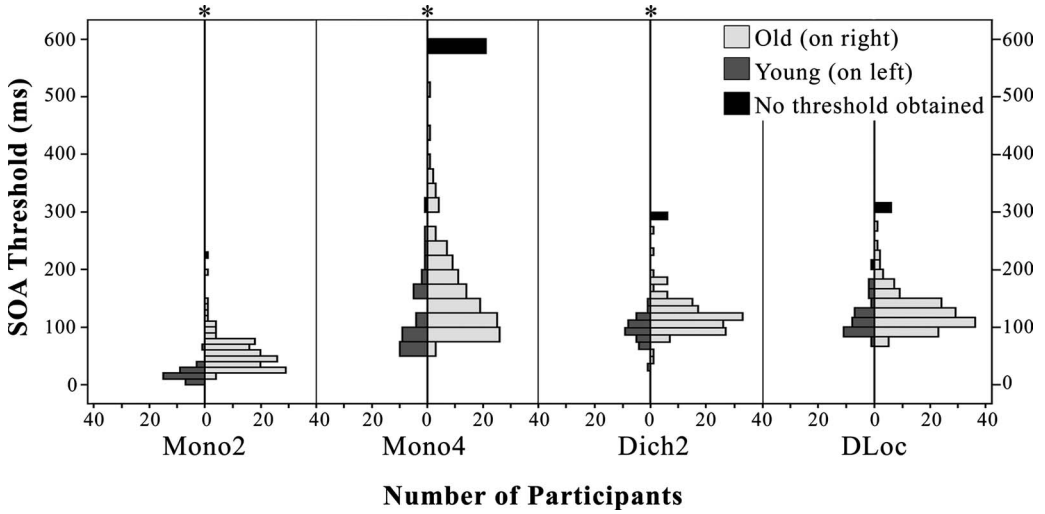

FIG. 1. Young and older adult performance distributions for the temporal-order tasks of experiment 1, $^*p<0.001$.

limiting factor for vowel-sequence tasks as no difference in performance was obtained for older listeners on the ear-identification task which did not involve vowel identification. Instead, it is likely that general temporal-order abilities limited performance on both vowel- and ear-identification tasks. However, one way of noting the processing demands of these tasks is by comparison to young performance. In agreement with previous studies of temporal-order for tones (Szymaszek *et al.*, 2006; Kołodziejczyk and Szelag, 2008), no age differences were obtained for the dichotic ear-sequence identification task (DLoc), indicating that the processing requirements that underlie this task may be preserved with age. It may be that the simpler task requirements for the ear-sequence identification (DLoc) measures, as compared to the parallel vowel-sequence identification measures (Dich2), resulted in similar performance between groups, as it has been consistently found that age group differences in temporal processing often become apparent as the complexity of the task increases (Fitzgibbons and Gordon-Salant, 1995, 1998). The DLoc task is simpler than the Dich2 task, in part, because there is no need to identify the phonological composition of the stimuli, simply to determine their location or laterality. In addition, the DLoc task is simpler than the Dich2 task because there were only two response alternatives for DLoc (right vs left), whereas Dich2 measures were comprised of 12 possible response sequences. However, while the DLoc task complexity is less, the threshold SOA values measured indicate that the demands of the task were significantly greater for young adults. At least for younger listeners, phonetic labeling was easier than remembering to which ear the stimulus had been presented first. Vowel identification appears to have actually aided performance for these young listeners.

TABLE IV. Wilcoxon Signed-Ranks Test for comparison between tasks, Z scores listed.

	Group	Mono2	Mono4	Dich2
Mono4	Old	−10.3*		
	Young	−5.1*		
Dich2	Old	−10.3*	−7.1*	
	Young	−5.1*	−1.6	
DLoc	Old	−10.3*	−5.4*	−1.4
	Young	−5.1*	−0.9	−4.0*

$^*p<0.001$.

Regarding group differences, older listeners perform significantly poorer across all three vowel-sequence identification tasks. Given that all listeners had normal or near-normal hearing within the frequency range of the stimuli (below 1800 Hz) and that a high presentation level (83 dB SPL) was used, group differences cannot be accounted for in terms of differences in audibility. Indeed, the PTA did not correlate significantly with vowel identification ($r=0.11$), suggesting that simple audibility did not influence identification performance. Across all tasks, older listeners demonstrated large variability, yet many older listeners performed within the performance range of the young adults. This is consistent with other age group differences found for other measures of auditory temporal processing (Moore *et al.*, 1992; Schneider *et al.*, 1994; Snell, 1997; Snell and Frisina, 2000; Humes *et al.*, 2009).

As noted, the large differences in SOA thresholds for both young and older listeners between the two-item monaural and two-item dichotic tasks were striking. This difference occurs even though the task requirements were identical: the only difference was presenting the sequence to one ear vs two ears, one stimulus per ear. Several possible factors could underlie this difference, including the obvious differences in physiological processing (i.e., central auditory processing) as well as cognitive explanations. First, Shrivastav *et al.* (2008) found that both presentation rate (i.e., SOA) and stimulus duration influence the performance of older listeners, with shorter tone durations leading to poorer discrimination performance. Given that experiment 1 only used one stimulus duration, it is not clear whether these performance patterns would persist with a different stimulus duration. Therefore, experiment 2 compared performance on these two-item identification tasks with 70 and 40 ms stimuli [40 ms stimuli were also used by Humes *et al.* (2010)]. Second, task performance differences may have been related to the relative demands due to divided-attention. Experiment 2 also examined how this factor might mediate monaural performance with

40 ms vowels. Finally, experiment 2 also examined test-retest learning, as it is not clear whether the performance observed in experiment 1 represents a maximal ability or an ability that can be enhanced with additional exposure to the stimuli and temporal-order tasks.

III. EXPERIMENT 2: ADDITIONAL FACTORS FOR OLDER LISTENERS

Experiment 2 used subsets of older listeners to investigate three additional phenomena: stimulus duration, stimulus-ear uncertainty (randomization), and test-retest learning. It has been reported that stimulus duration can have an impact on monaural temporal-order discrimination, most substantially for older adults (Shrivastav *et al.*, 2008). As stimulus duration is an important dimension that can influence temporal-order performance, it is not clear whether the performance patterns observed in experiment 1 will persist for other stimulus durations. Therefore, experiment 2 compared the difference in performance for vowel-sequence identification tasks comprised of 40 ms or 70 ms stimuli. It is possible that dichotic thresholds would be more influenced by duration than monaural threshold due to the longer processing time required.

Second, experiment 1 demonstrated a large difference in SOAs between monaural and dichotic two-item sequences for both young and older listeners. The second purpose of experiment 2 was to explore one possible processing difference between the Mono2 and Dich2 tasks: divided attention. In the dichotic testing, listeners were required to switch attention between the two presentation ears, while listeners only needed to attend to one ear in the monaural task. That is, for the Dich2 task, the ear receiving the first stimulus of the two-item sequence varied randomly from trial-to-trial such that the listener did not know where to listen or where the sequence would be initiated. This was not the case for the Mono2 task. To examine the impact of this possible demand on attention, this experiment randomized the ear to which the two monaural stimuli were presented, such that on any given trial the two vowels could both be presented to either the right or left ear. This helped to match the level of location uncertainty across trials between the monaural and dichotic tasks.

Third, listeners in this study completed a large number of tasks throughout the course of the study in multiple modalities (55 h of testing). The conditions presented in this final experiment occurred after significant exposure to the stimulus materials in experiment 1, as well as completion of eight different temporal-masking conditions using the same 40 ms vowel stimuli (reported in Humes *et al.*, 2010). All participants completed the same tasks and on average, participants completed about 12 h of testing with these vowel stimuli prior to participating in experiment 2. Thus, participants had considerable opportunity to learn stimulus and task-specific information prior to the measures completed in experiment 2. Perhaps some of the difference observed between age groups in experiment 1 reflects age-related differences in learning the task or the stimuli. The question explicitly tested here examined whether learning did occur for older adults. It may be that temporal-order processing abilities in older listeners are constrained by factors (e.g., physiological) not susceptible to learning.

A. Listeners

Two groups of older adult listeners from experiment 1 volunteered to complete a portion of the conditions from experiment 2. A subset (Group A) of 43 older listeners, 24 female and 19 male, ranging in age from 60–87 years (mean=70 years) from experiment 1 completed the measures investigating stimulus duration and test-retest learning. A second subset (Group B) of 24 older listeners, 16 females and 8 males, ranging in age from 62–83 years (mean =70 years) from experiment 1 completed the measures investigating the effect of ear randomization.

B. Methods

Five tasks were completed. Two tasks used the 70 ms vowels and were the same as those used in experiment 1: monaural two-item identification (Mono2_70) and dichotic two-item identification (Dich2_70). An additional three tasks used 40 ms versions of the stimuli used in experiment 1 excised from the middle portion of the 70 ms vowels. These three tasks were monaural two-item identification (Mono2_40), dichotic two-item identification (Dich2_40), and monaural two-item identification with randomization of the stimulus presentation ear across trials (M2Rand_40). Procedures were identical to those outlined in experiment 1 for the monaural and dichotic tasks. M2Rand_40 consisted of 144 trials, allowing for 72 trials to be presented to each ear. Group A completed shortened stimulus duration tasks Mono2_40 and Dich2_40 and the retest Mono2_70 and Dich2_70 tasks. Monaural versions were always tested prior to dichotic versions. Testing order of the two stimulus durations was counterbalanced across listeners. Group B completed the three 40 ms tasks (Mono2_40, Dich2_40, and M2Rand_40) to examine ear randomization as a possible factor in the larger dichotic thresholds.

Prior to completing the tasks in experiment 2, all older participants in both groups completed an additional screening task for the identification of these shortened vowels in isolation. Given the targeted threshold performance level of 50% for these two tasks, all participants were required to complete this screening with at least 60% accuracy in each ear to continue with experiment 2. Identification accuracy during screening actually ranged from 77.5%–100% with a mean of 95.2% (SD=6.2%) for the right ear and ranged from 62.5%–100% with a mean of 94.6% (SD=7.8%) for the left ear. Thus, most listeners (77%) identified the short 40 ms vowels in isolation with at least 90% accuracy, just as they had the longer 70 ms vowels used in experiment 1. Task demonstrations were provided prior to presenting any new experimental task and were analogous to those in experiment 1.

C. Results and discussion

The same data-reduction procedures as experiment 1 were used to obtain three-block averages to be used for an

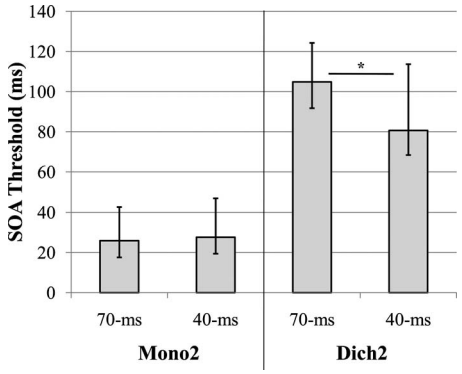

FIG. 2. Effect of stimulus duration; SOA thresholds from older adults in experiment 2, error bars=interquartile range, $^*p<0.001$.

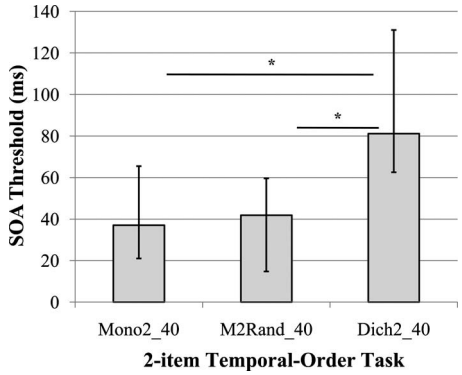

FIG. 3. Effect of ear randomization; SOA thresholds from older adults in experiment 2, error bars=interquartile range, $^*p<0.001$.

individual listener's SOA threshold estimate. Four older participants were unable to complete one or two tasks. Mono2_70 and Dich2_40 each had two missing values, and Mono2_40 and Dich2_70 each had one missing value. The only participant in this data set who had an ear with hearing thresholds beyond the audiometric criteria for this study did not complete either dichotic test. Missing data for these four participants were entered as extreme value outliers. As a result, medians were computed for group values and nonparametric tests were again used for analysis. Pursing correlations between performance on each task with mid-frequency hearing thresholds ($p>0.05$) and vowel identification in isolation ($p>0.05$) were not significant, suggesting that individual differences in performance are not attributable to simple audibility or vowel-identification abilities.

1. Stimulus duration

Group A completed the tasks for the investigation of stimulus duration. A paired-sample Kruskal Wallis test was used to examine the effect of test order between stimulus durations (e.g., M2_70 first vs M2_40 first). Results did not differ significantly across the task orders ($p>0.05$). Therefore, data for counterbalanced conditions were pooled in subsequent analyses for stimulus duration.

Figure 2 shows the median SOA values for the four stimulus conditions in this experiment. Comparisons between analogous tasks using different stimulus durations were tested using Wilcoxon Signed-Ranks tests. Results demonstrated no significant difference between the SOAs for the Mono2_70 (median=25.9 ms, IQ range=25.1 ms) and Mono2_40 (median=27.6 ms, IQ range=28.3 ms) tasks completed in experiment 2 ($p>0.05$). However, a significant effect of stimulus duration ($p<0.001$) was obtained for the dichotic task comparison of Dich2_70 (median=104.8 ms, IQ range=32.5 ms) and Dich2_40 (median=80.7 ms, IQ range=45.9 ms). This indicates that while no difference in SOA occurred between stimulus durations for monaural conditions, shorter stimulus durations actually lead to better SOA values for the older listeners in dichotic testing. However, while SOA thresholds decreased substantially for the shorter stimulus duration (40 ms) in the dichotic task, another measure, the interstimulus interval (ISI), was more similar (median ISI for Dich2_70 was 34.5 ms and for Dich2_40 was 40.4 ms). Nonetheless, all listeners had longer ISIs for the 40 ms stimuli (median difference=7.0 ms, IQ range=14.1 ms), which was significantly larger by means of a Wilcoxon Signed-Ranks test ($Z=-3.7$, $p<0.001$). Thus, using ISI as an index, it may be that 40 ms vowels are more difficult, requiring a larger temporal separation between the stimuli. Two older listeners had thresholds that led to a temporal overlap of the two 70 ms vowels (and therefore, no ISI or temporal separation), indicating that a silent interval is not required for successful performance on the dichotic task using 70 ms vowels. However, in general, it appears that additional processing for dichotic sequences occurs after the stimulus offset and that the processing requirements are somewhat greater for the shorter 40 ms stimuli.

2. Ear uncertainty

Group B completed these measures to determine if ear uncertainty resulted in the large differences between Mono2 and Dich2 tasks observed. Median SOA values for these 24 older adults appear in Fig. 3. Wilcoxon Signed-Ranks tests demonstrated significant (Bonferroni-adjusted $p<0.001$) differences between Dich2_40 (median=81.1 ms, IQ range =68.5 ms) and each monaural task ($p<0.001$), again demonstrating large differences between monaural and dichotic presentations, now for 40 ms stimuli. However, no differences were found between Mono2_40 (median=37.0 ms, IQ range=44.5 ms) and M2Rand_40 (median=41.9 ms, IQ range=44.8 ms), indicating that differences between the monaural and dichotic tasks for 40 ms vowels was not a result of attentional demands related to stimulus-ear uncertainty from trial-to-trial. Rather, differences appear to be related to inherent physiological (i.e., central auditory) differences between monaural and dichotic processing involved in the comparison of stimuli across ears.

3. Test-retest learning

Group A also completed the retest 70 ms versions of experiment 1 to investigate if performance improved for older listeners with additional exposure. Figure 4 illustrates the effect of the repeated exposures to stimuli and tasks between experiments 1 and 2. Comparisons were again tested using Wilcoxon Signed-Ranks tests. The comparison of SOAs between the first and second completion of Mono2_70 indicated a significant 39% improvement ($p<0.001$). The SOA values for Dich2_70 also improved significantly fol-

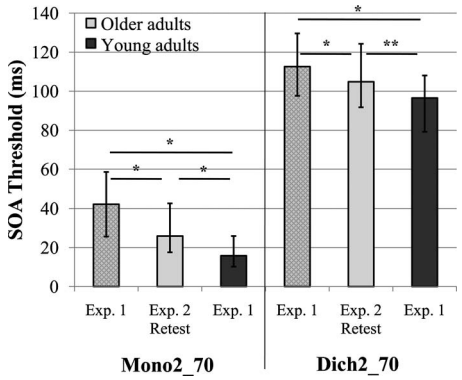

FIG. 4. Effect of stimulus exposure: Older adult performance for experiment 1 (before exposure, cross-hatched light gray) and experiment 2 (after exposure, solid light gray) in comparison to young performance for experiment 1 (before exposure, solid dark gray). Error bars=interquartile range, $^{*}p<0.001$, $^{**}p<0.025$.

lowing longer periods of exposure to the stimuli and tasks ($p<0.001$), but only with a 7% improvement. Thus, the older listeners were able to improve their performance on these vowel temporal-order identification tasks with increased exposure to the stimuli. Of particular interest is whether older listeners were able to approach the performance of young listeners after such exposures or whether older listener performance is limited by certain factors (i.e., physiological) and represents a maximal ability not susceptible to training. Therefore, comparisons between the SOAs from Mono2_70 and Dich2_70 conditions for older listeners obtained after repeated exposures in experiment 2 were compared to the results of the young listeners for the same tasks but from experiment 1 (Fig. 4). Results of the between groups Mann–Whitney tests still indicated a significant age group difference comparing the second testing of older listeners to the first testing of the young listeners for the two-item monaural task ($Z=-4.02$, $p<0.001$) and the two-item dichotic task ($Z=-2.30$, $p=0.022$). Thus, although the additional exposures to the brief vowel stimuli and the procedures in this study narrowed the gap (literally) in SOAs between the older adults and the young adults on these two measures of temporal-order identification, it was not enough to eliminate significant group differences. We are investigating whether young adults also improve over time, and currently partial results are available. Data from 42 young listeners indicate significant improvements with additional exposure (Bonferroni-adjusted $p<0.025$). Median SOAs went from 13.9 and 97.4 ms for the Mono2 and Dich2 tasks, respectively, to 7.3 and 85.7 ms following repeated exposures to the stimuli and tasks. Thus, it appears that the performance of young adults may also improve with exposure to a similar degree as older listeners (about 10–20 ms improvement across tasks and age groups).

IV. GENERAL DISCUSSION

A. Group differences

Overall, the results from this set of experiments demonstrate that older listeners have a significant difficulty identifying the order of rapid temporal events relative to young listeners. This difficulty becomes apparent and more pronounced as the cognitive complexity of the task increases, such as from identifying two-item sequences vs four-item sequences. One significant finding from experiment 1 was the substantially elevated SOA thresholds in the two-item dichotic tasks compared to the two-item monaural task. Differences between dichotic and diotic processing have also been noted previously (Szymaszek *et al.*, 2006). Results from randomizing the presentation ear for monaural sequences in experiment 2 demonstrated that this difference could not be accounted for by increased demands on divided-attention resources, at least for 40 ms stimuli. Indeed, Tun *et al.* (1992) noted a speech rate by age interaction for recall of spoken passages that was independent of the attention processing demands of the task. Instead, performance differences appear related to the physiological processing of dichotic vs monaural sequences, where dichotic presentations require integration of temporal events across hemispheres.

Experiment 2 also highlighted two other substantial findings related to temporal-order identification for older listeners. These results refer to the effects of stimulus duration and stimulus exposure on the performance of older listeners. With regard to exposure, the initial measurements in experiment 1 do not represent best performance—older listeners were able to improve temporal-order identification performance with extended exposure to stimulus information. This is contradictory to previous results for the discrimination of tonal sequences that have suggested no learning effect for older listeners (Trainor and Trehub, 1989). However, Szymaszek *et al.* (2006) reported an effect of practice on temporal-order identification thresholds after one session. Although older listeners did improve performance on our tasks, they still did not reach the monaural performance of the young listeners from experiment 1. Comparison to a second set of young listeners with equivalent additional exposure demonstrates approximately equal improvements in SOA for both age groups. This either suggests that older listeners would require additional and more focused training to achieve performance thresholds near that of younger listeners or that older performance is somehow limited by a factor that maintains age group differences. It should also be noted that considerable care was taken in establishing the SOA thresholds in experiment 1, including the use of several demonstration trials to familiarize the listeners to the stimuli and tasks, use of initial wide-range constant-stimuli trial blocks that essentially served as additional practice, and then basing each threshold estimate (for most listeners) on three blocks of trials that did not significantly vary from each other. Despite these efforts to obtain stable performance estimates, older listeners clearly continued to improve their performance with repeated exposures to these brief vowel stimuli (i.e., 12 h of testing). It also is important to note that this additional exposure to the stimuli did not involve substantial additional exposure to temporal-order identification. Rather, as noted previously, extended exposure to these stimuli was in the form of identification of one of the four target vowels serving as the signal in various temporal-masking tasks. Thus, any learning that has taken place from repeated exposures to the stimuli is more of an implicit nature rather than explicit and certainly would not be considered to be any

form of "training" temporal-order performance. For now, we can conclude that older adults do improve their thresholds with repeated exposures to the stimuli but not enough to eliminate differences in median SOA thresholds between the two age groups. Therefore, older adult abilities remain plastic and susceptible to learning, but significant age-related factors remain that inhibit performance.

The effect of stimulus duration also revealed an interesting result. Shorter stimulus durations did not adversely affect the performance of older adults. While resulting in no difference for monaural presentations (Fig. 2), shorter durations actually resulted in smaller SOA thresholds for dichotic sequences. On the surface this appears counterintuitive, as elevated thresholds for duration discrimination with shorter reference durations are well documented among older listeners (Fitzgibbons and Gordon-Salant, 1995) at least for tonal signals. Cullinan *et al.* (1977) presented diotic sequences of four vowels continuously to young listeners and found that performance on temporal-order identification improved as the stimulus length increased, although this was also confounded with slowing the rate of presentation. In contrast, for monaural presentations of three tone sequences, Fitzgibbons *et al.* (2006) reported an effect of rate with no contribution of stimulus duration. Shrivastav *et al.* (2008) found similar results for young normal-hearing participants listening to two-tone sequences with flanker tones using uniform duration and rate. Older listeners only demonstrated an effect of duration for stimuli less than 40 ms in that study. This is, in fact, what we found for our two-item monaural task: an effect of rate with no effect of duration (at least for the 70 and 40 ms vowels tested here).

However, it appears that stimulus duration does influence temporal-order identification performance for dichotic presentations. One possible reason for this advantage could be related to the larger silent interval between the offset of one stimulus and the onset of the next that shorter stimuli provide. This silent interval may be beneficial by providing more time for recovery (less masking) or processing; thereby, actually leading to shorter (better) SOA thresholds when shorter duration stimuli were used. Indeed, while SOA values improved, this silent duration, the ISI, significantly increased for shorter stimulus durations. It is important to note that the results for shorter stimulus durations were obtained only after significant exposure to the stimuli.

B. Individual differences among older listeners

This study was designed with a large sample size to explore individual differences among the older listeners, along with exploring a variety of task- and stimulus-specific variables that influence the temporal-order performance of older listeners in these experiments. First, correlations among the temporal-order tasks of experiment 1 were examined to determine if performance on one task was related to a listener's performance on another task. Only older listeners with threshold estimates (N and correlations shown in Table V) were included in these correlations. Results indicate significant Pearson correlations among all measures ($p<0.01$), with the highest agreement between the two-item identification measures (Mono2, Dich2; $r=0.59$).

TABLE V. Experiment 1 task correlations for data from older adults only, excluding participants who were unable to achieve a threshold value (N in parentheses).

	Mono2	Mono4	Dich2
Mono4	0.46* (128)		
Dich2	0.59* (142)	0.28* (121)	
DLoc	0.30* (141)	0.25* (120)	0.34* (140)

*$p<.01$.

In order to determine if age, pure-tone audiometry, or cognitive measures were able to predict an older listener's temporal-order identification performance, a second set of analyses were completed. Redundancy among the sets of audiometric and cognitive measures obtained for all participants was first reduced using principal component (PC) analysis with varimax rotation. Results of this analysis extracted three orthogonal PCs out of the 18 audiometric measures (Table VI), corresponding to low-frequency hearing thresholds in the right ear, the left ear, and bilateral high-frequency hearing thresholds. Four orthogonal PCs were extracted for the 15 cognitive measures (Table VII) based on the raw scores from the WAIS-III and corresponded roughly to verbal, performance, free recall/pairing, and symbol-search measures. These seven audiometric and cognitive components were entered, along with age, as possible predictors in four multiple linear-regression analyses, one for each of the four temporal-order tasks [Table VIII(a)]. Results indicate that cognitive measures of the WAIS, component 1 (verbal) and component 2 (performance), serve as the primary predictors of variance across the four experimental

TABLE VI. Audiogram principal component analysis: % variance accounted for in parentheses. Weights <0.4 removed for simplicity. R=right ear, L=left ear.

Frequency (kHz)	Bilateral high-frequency (33.9%)	Right low-frequency (23.2%)	Left low-frequency (20.7%)
0.25 R		0.82	
0.5 R		0.89	
1 R		0.84	
1.5 R		0.77	
2 R	0.51	0.66	
3 R	0.80	0.43	
4 R	0.86		
6 R	0.84		
8 R			
0.25 L			0.81
0.5 L			0.88
1 L			0.79
1.5 L			0.71
2 L	0.58		0.53
3 L	0.81		
4 L	0.88		
6 L	0.87		
8 L	0.75		

TABLE VII. WAIS-III principal component analysis: % variance accounted for in parentheses. Weights <0.4 removed for simplicity.

Variable	WAIS1 (25.5%)	WAIS2 (19.9%)	WAIS3 (13.8%)	WAIS4 (7.0%)
Information	0.83			
Vocabulary	0.80			
Similarities	0.75			
Comprehension	0.73			
Arithmetic	0.61			
Letter-number sequencing	0.51			
Picture arrangement	0.52	0.54		
Matrix reasoning	0.41	0.69		
Digit span		0.46		
Picture completion		0.66		
Block design		0.66		
Digit-symbol coding		0.75		
Pairing			0.99	
Free recall			0.99	
Symbol search				0.95

tasks. Therefore, cognitive status (i.e., the level of an individual's cognitive skills) appears to account for between 8% and 29% of the variance in performance among the older participants. Additional variance was not accounted for by either audiometric status or age.

Of interest is how much variance can be accounted for by a basic measure of temporal-order identification ability (Mono2). Running the regression analyses a second time to include Mono2 as a possible predictor [Table VIII(b)] resulted in Mono2 becoming the primary predictor variable across all tasks, accounting for over 20% and 34% of variance for Mono4 and Dich2 tasks, with cognitive measures only entering into consideration for DLoc. This suggests that Mono4 and Dich2 tasks are not predicted by other WAIS-III cognitive measures not already accounted for by Mono2.

Overall, tests of individual differences among these older listeners suggest that cognitive measures are related to an older listener's temporal-order identification ability for vowels, while audiometric status does not serve as a predictor. This latter finding is not surprising given that we low-pass filtered the vowel stimuli at 1800 Hz and used a relatively high presentation level to minimize the role of audibility. Thus, it appears plausible that general age-related cognitive declines may influence temporal processing abilities for vowels.

V. CONCLUSIONS

Four measures of temporal-order processing using speech stimuli were obtained among a large group of older adult listeners and compared to the performance of young listeners. As expected, results indicated age group differences for three measures of temporal-order identification with older listeners performing more poorly and with noticeably greater variability. However, the older group maintained a large overlap in performance with the young listeners. Increasing the length of the stimulus sequence from two to four vowels significantly degraded performance, possibly resulting from additional cognitive demands (i.e., memory). A large difference in performance between monaural and dichotic presentations occurred for both age groups and stimulus durations. This difference was not related to attentional demands created by stimulus presentation uncertainty across ears (at least for 40 ms vowels) and therefore appears to be specific to processing requirements. The manipulation of stimulus duration demonstrated that older listeners with substantial exposure to the stimuli had better SOA values with shorter stimuli for dichotic presentations; however, all listeners required a longer silent interval between stimuli to complete this task with shorter vowels, possibly indicating a need for more processing time. No difference in thresholds between vowel durations was obtained for monaural presentations. Older listeners also demonstrated improvement in temporal-order identification with significant additional exposure to the test stimuli, yet performance still did not match the performance of young listeners.

A major goal of this research project is to determine causes for individual differences in performance among the elderly, as large variability in performance among older listeners has been consistently noted in the literature. One notable result showed that verbal and performance measures of cognition predicted some of the variance associated with each of the four temporal-order vowel-identification measures. It should be noted that the stimuli here were speech, and perhaps verbal cognitive measures are more strongly as-

TABLE VIII. Linear regression: (a) age, 4 WAIS-PCs, 3 audiogram-PCs as predictors; (b) with Mono2 also included as a predictor.

Task variable	% total variance	Predictor variable	β coefficient	F (df)	p
(a) Mono2	14.5	WAIS2	−0.38	29.877 (2, 147)	<0.001
	14.4	WAIS1	−0.38		
Mono4	3.4	WAIS1	−0.184	4.44 (1, 127)	0.037
Dich2	6.1	WAIS1	−0.247	9.674 (2, 140)	<0.001
	6.0	WAIS2	−0.246		
DLoc	8.3	WAIS2	−0.288	12.682 (1, 140)	0.001
(b) Mono4	20.9	Mono2	0.457	33.224 (1, 126)	<0.001
Dich2	34.3	Mono2	0.586	73.207 (1, 140)	<0.001
DLoc	9.0	Mono2	0.224	9.928 (2, 138)	<0.001
	3.6	WAIS2	−0.203		

sociated with the temporal-order judgment of these vowels than might be found for analogous nonspeech stimuli. Nevertheless, the present results demonstrated that cognitive measures were able to account for some of the differences in temporal processing among older listeners, while no contributions of audibility or age were found among this group of older listeners.

ACKNOWLEDGMENTS

The authors would like to thank Thomas A. Busey and James C. Craig for their significant contributions to this project. They would also like to thank Dana Kinney as well as several graduate research assistants involved with this project. This work was supported, in part, by NIA Grant No. R01 AG022334 and by NIH-NIDCD Training Grant No. T32-DC00012.

American National Standards Institute (**2004**). Specifications for audiometers (ANSI S3.6-2004) (ANSI, New York).

Baltes, P. B., and Lindenberger, U. (**1997**). "Emergence of a powerful connection between sensory and cognitive functions across the adult lifespan: A new window to the study of cognitive aging?," Psychol. Aging **12**, 12–21.

Cullinan, W. L., Erdos, E., Schaefer, R., and Tekieli, M. E. (**1977**). "Perception of temporal order of vowels and consonant-vowel syllables," J. Speech Hear. Res. **20**, 742–751.

Dorman, M. F., Cutting, J. E., and Raphael, L. (**1975**). "Perception of temporal order in vowel sequences with and without formant transitions," J. Exp. Psychol. Hum. Percept. Perform. **1**, 121–129.

Dubno, J. R., and Schaefer, A. B. (**1992**). "Comparison of frequency selectivity and consonant recognition among hearing-impaired and masked normal-hearing listeners," J. Acoust. Soc. Am. **91**, 2110–2121.

Dubno, J. R., and Schaefer, A. B. (**1995**). "Frequency selectivity and consonant recognition for hearing-impaired and normal-hearing listeners with equivalent masked thresholds," J. Acoust. Soc. Am. **97**, 1165–1174.

Fitzgibbons, P. J., Gordon-Salant, S., and Friedman, S. (**2006**). "Effects of age and sequence presentation rate on temporal order recognition," J. Acoust. Soc. Am. **120**, 991–999.

Fitzgibbons, P. J., and Gordon-Salant, S. (**1995**). "Age effects on duration discrimination with simple and complex stimuli," J. Acoust. Soc. Am. **98**, 3140–3145.

Fitzgibbons, P. J., and Gordon-Salant, S. (**1996**). "Auditory temporal processing in elderly listeners," J. Am. Acad. Audiol. **7**, 183–189.

Fitzgibbons, P. J., and Gordon-Salant, S. (**1998**). "Auditory temporal order perception in younger and older adults," J. Speech Lang. Hear. Res. **41**, 1052–1062.

Folstein, M. F., Folstein, S. E., and McHugh, P. R. (**1975**). "Mini-mental state: A practical method for grading the cognitive status of patients for the clinician," J. Psychiatr. Res. **12**, 189–198.

Gordon-Salant, S., and Fitzgibbons, P. J. (**1993**). "Temporal factors and speech recognition performance in young and elderly listeners," J. Speech Hear. Res. **36**, 1276–1285.

Gordon-Salant, S., and Fitzgibbons, P. J. (**1999**). "Profile of auditory temporal processing in older listeners," J. Speech Hear. Res. **42**, 300–311.

Hacker, M. J., and Ratcliff, R. (**1979**). "A revised table of d′ for M-alternative forced choice," Percept. Psychophys. **26**, 168–170.

Hofer, S. M., Berg, S., and Era, P. (**2003**). "Evaluating the interdependence of aging-related changes in visual and auditory acuity, balance, and cognitive functioning," Psychol. Aging **18**, 285–305.

Humes, L. E. (**1996**). "Speech understanding in the elderly," J. Am. Acad. Audiol. **7**, 161–167.

Humes, L. E. (**2002**). "Factors underlying the speech-recognition performance of elderly hearing-aid wearers," J. Acoust. Soc. Am. **112**, 1112–1132.

Humes, L. E. (**2005**). "Do 'auditory processing' tests measure auditory processing in the elderly?," Ear Hear. **26**, 109–119.

Humes, L. E. (**2007**). "The contributions of audibility and cognitive factors to the benefit provided by amplified speech to older adults," J. Am. Acad. Audiol. **18**, 590–603.

Humes, L. E., Burk, M. H., Coughlin, M. P., Busey, T. A., and Strauser, L. E. (**2007**). "Auditory speech recognition and visual text recognition in younger and older adults: Similarities and differences between modalities and the effects of presentation rate," J. Speech Lang. Hear. Res. **50**, 283–303.

Humes, L. E., Busey, T. A., Craig, J. C., and Kewley-Port, D. (**2009**). "The effects of age on sensory thresholds and temporal gap detection in hearing, vision, and touch," Percept. Psychophys. **71**, 860–871.

Humes, L. E., and Christopherson, L. (**1991**). "Speech-identification difficulties of the hearing-impaired elderly: The contributions of auditory-processing deficits," J. Speech Hear. Res. **34**, 686–693.

Humes, L. E., Kewley-Port, D., Fogerty, D., and Kinney, D. (**2010**). "Measures of hearing threshold and temporal processing across the adult lifespan," Hear. Res. In press.

Kawahara, H., Masuda-Kastuse, I., and Cheveigne, A. (**1999**). "Restructuring speech representations using a pitch-adaptive time-frequency smoothing and an instantaneous frequency-based F0 extraction: Possible role of a repetitive structure in sounds," Speech Commun. **27**, 187–207.

Kołodziejczyk, I., and Szelag, E. (**2008**). "Auditory perception of temporal order in centenarians in comparison with young and elderly listeners," Acta Neurobiol. Exp. (Warsz) **68**, 373–381.

Lewandowska, M., Bekisz, M., Szymaszek, A., Wrobel, A., and Szelag, E. (**2008**). "Towards electrophysiological correlates of auditory perception of temporal order," Neurosci. Lett. **437**, 139–143.

Lindenberger, U., and Baltes, P. B. (**1994**). "Sensory functioning and intelligence in old age: A strong connection," Psychol. Aging **9**, 339–355.

Moore, B. C. J., Peters, R. W., and Glasberg, B. R. (**1992**). "Detection of temporal gaps in sinusoids by elderly subjects with and without hearing loss," J. Acoust. Soc. Am. **92**, 1923–1932.

Park, D. C., Polk, T. A., Mikels, J. A., Taylor, S. F., and Marshuetz, C. (**2001**). "Cerebral aging: Integration of brain and behavioral models of cognitive function," Dialogues Clin. Neurosci. **3**, 151–166.

Pichora-Fuller, M. K. (**2003**). "Processing speed and timing in aging adults: Psychoacoustics, speech perception, and comprehension," Int. J. Audiol. **42**, 59–67.

Salthouse, T. A. (**1996**). "The processing-speed *theory* of adult age differences in cognition," Psychol. Rev. **103**, 403–428.

Schneider, B. A., and Pichora-Fuller, M. K. (**2000**). "Implications of perceptual deterioration for cognitive aging research," *The Handbook of Aging and Cognition* (Lawrence Erlbaum, Mahwah, NJ), pp. 155–219.

Schneider, B. A., Pichora-Fuller, M. K., Kowalchuk, D., and Lamb, M. (**1994**). "Gap detection and the precedence effect in young and old adults," J. Acoust. Soc. Am. **95**, 980–991.

Shrivastav, M. N., Humes, L. E., and Aylsworth, L. (**2008**). "Temporal order discrimination of tonal sequences by younger and older adults: The role of duration and rate," J. Acoust. Soc. Am. **124**, 462–471.

Snell, K. B. (**1997**). "Age-related changes in temporal gap detection," J. Acoust. Soc. Am. **101**, 2214–2220.

Snell, K. B., and Frisina, D. R. (**2000**). "Relationships among age-related differences in gap detection and word recognition," J. Acoust. Soc. Am. **107**, 1615–1626.

Szelag, E., Dreszer, J., Lewandowska, M., and Szymaszek, A. (**2009**). "Neural representation of time and timing processes," in *Neural Correlates of Thinking*, edited by E. Kraft, B. Gulyás, and E. Pöppel (Springer-Verlag, Berlin, Heidelberg), pp. 187–199.

Szymaszek, A., Szelag, E., and Sliwowska, M. (**2006**). "Auditory perception of temporal order in humans: The effect of age, gender, listener practice and stimulus presentation mode," Neurosci. Lett. **403**, 190–194.

Trainor, L. J., and Trehub, S. E. (**1989**). "Aging and auditory temporal sequencing: Ordering the elements of repeating tone patterns," Percept. Psychophys. **45**, 417–426.

Tun, P. A., Wingfield, A., Stine, E. A. L., and Mecsas, C. (**1992**). "Rapid speech processing and divided attention," Psychol. Aging **7**, 546–550.

van Rooij, J. C. G. M., and Plomp, R. (**1992**). "Auditive and cognitive factors in speech perception by elderly listeners. III. Additional data and final discussion," J. Acoust. Soc. Am. **91**, 1028–1033.

Weschsler, D. (**1997**). *Wechsler Adult Intelligence Scale*, 3rd ed. (WAIS-III) (The Psychological Corporation, San Antonio, TX).

Working Group on Speech Understanding and Aging (**1988**). "Speech understanding and aging," J. Acoust. Soc. Am. **83**, 859–895.

Measurement of hearing aid internal noise[a)]

James D. Lewis,[b)] Shawn S. Goodman, and Ruth A. Bentler
Department of Communication Sciences and Disorders, University of Iowa, Iowa City, Iowa 52242

(Received 14 October 2009; revised 25 January 2010; accepted 27 January 2010)

Hearing aid equivalent input noise (EIN) measures assume the primary source of internal noise to be located prior to amplification and to be constant regardless of input level. EIN will underestimate internal noise in the case that noise is generated following amplification. The present study investigated the internal noise levels of six hearing aids (HAs). Concurrent with HA processing of a speech-like stimulus with both adaptive features (acoustic feedback cancellation, digital noise reduction, microphone directionality) enabled and disabled, internal noise was quantified for various stimulus levels as the variance across repeated trials. Changes in noise level as a function of stimulus level demonstrated that (1) generation of internal noise is not isolated to the microphone, (2) noise may be dependent on input level, and (3) certain adaptive features may contribute to internal noise. Quantifying internal noise as the variance of the output measures allows for noise to be measured under real-world processing conditions, accounts for all sources of noise, and is predictive of internal noise audibility.
 [DOI: 10.1121/1.3327808]

PACS number(s): 43.66.Ts, 43.50.Yw, 43.58.Ry [BLM] Pages: 2521–2528

I. INTRODUCTION

The continual improvement of digital technology has made possible the implementation of many innovative signal processing algorithms in hearing aids (HAs). Many of these algorithms are adaptive, altering their processing based on an ongoing analysis of the temporal and spectral properties of incoming sound. With these new processing schemes, additional methods of quantifying hearing aid performance may be necessary, including the measurement of internal noise, which is currently defined as equivalent input noise (American National Standards Institute, 2004).

Internal noise is not present in the acoustic input signal, but is added by the HA itself as an unintentional by-product of its design and/or processing. Internal noise is added to any external signal processed by the HA, potentially degrading the fidelity of the sound. Internal noise can arise anywhere along the HA processing path, including at the microphone, the analog-to-digital converter (ADC), the processing algorithms, the digital-to-analog converter (DAC), and the receiver. As used here, the term "processing algorithms" refers to the application of frequency- and level-dependent gain, as well as adaptive features, such as digital noise reduction (DNR), microphone directionality, and acoustic feedback control. It has been suggested that the primary source of internal noise is the microphone, specifically, random motion of electrons in the conductors, air molecules, and the particles in the diaphragm (Thompson *et al.*, 2002). It is not unreasonable, however, to consider other components of the HA as significant contributors to internal noise as well (Stuart, 1994).

Figure 1 shows a simple model of HA internal noise. In this model, it is assumed that environmental noise is negligible, so that the only input to the HA is an acoustic signal (s). Additive internal noise can occur both before (n_1) and after (n_2) the application of gain (G). The output (L_{out}) of the HA is

$$L_{out} = G(s + n_1) + n_2. \quad (1)$$

In the United States, the current standard for quantifying HA internal noise is equivalent input noise (EIN), defined as

$$\text{EIN} = L_0 - \text{HFAG50}, \quad (2)$$

where L_0 is the level of the HA output (in dB) with no acoustic input signal present, and HFAG50 is the average gain (in dB) at 1.0, 1.6, and 2.5 kHz when the input is a 50 dB sound pressure level (SPL) pure-tone (American National Standards Institute, 2004). EIN is measured with the hearing aid at the reference test gain setting (to ensure saturation of the amplifier/compressor does not occur) and with all features (e.g., noise reduction, microphone directionality, feedback control) disabled. EIN is typically measured in a 2 cm^3 coupler seated in a test box using a swept pure-tone stimulus.

An important assumption of the EIN measurement is that the primary source of internal noise is located prior to amplification (e.g., at the microphone), and any internal noise added after amplification is negligible. If this is the case, the n_2 term in Eq. (1) equals to zero. Since EIN is measured with no acoustic input signal (L_0), Eq. (1) reduces to

$$L_{out} = Gn_1. \quad (3)$$

Removal of the gain is then appropriate because it allows the internal noise to be evaluated independently of the gain of the HA. As noted earlier, however, other components of the HA may contribute significant amounts of noise, in which

[a)]Portions of this work were presented at the annual convention of the American Acoustical Society, Scottsdale, Arizona, March 2008.
[b)]Author to whom correspondence should be addressed. Electronic mail: james-lewis@uiowa.edu

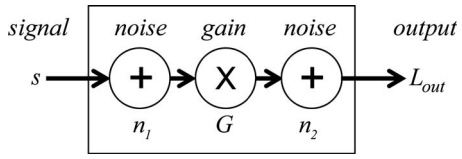

FIG. 1. Model of HA internal noise. To an acoustic signal s at the input of the hearing aid, noise (n_1) is added prior to the application of gain (G), and noise (n_2) is also added after gain.

case EIN will underestimate the internal noise of the HA. In terms of the noise model in Fig. 1, the equivalent input noise measure is arrived at by dividing both sides of Eq. (1) by the gain of the HA, resulting in

$$\mathrm{EIN} = n_1 + \frac{n_2}{G}. \tag{4}$$

Thus, when calculating EIN, noise added after amplification (n_2) is reduced by the gain term, resulting in an underestimation of the internal noise level. From a quality control standpoint, this implies that EIN primarily evaluates microphone noise, and not noise from later-occurring sources.

The sole utility of EIN in quantifying internal noise is not only questionable from a quality control standpoint, but also in clinical utility, as EIN was not intended to measure the audibility of HA internal noise. The audibility of a HA's internal noise is dependent on the circuit noise amplitude spectrum, low-level gain, and the listener's auditory thresholds (Killion, 1976; Agnew, 1997; Thompson, 2003). The loudness or annoyance of such noise may be dependent upon the spectral shape of the noise and, thus, cannot be described by a single value (Hellman and Zwicker, 1987). Relatively limited attention in the literature is directed toward the audibility and annoyance of HA internal noise; however, investigations have typically employed 1/3 octave-band analysis of generated noise to simulate the internal noise produced by a hearing aid.

Agnew (1997) demonstrated that hearing aid internal noise becomes audible to the listener when the 1/3 octave-band level of the noise exceeds the hearing threshold at the corresponding 1/3 octave-band frequency. Furthermore, noise detection was generally the result of 500 Hz energy, presumably due to preserved hearing sensitivity, and became objectionable to some listeners at only 4 dB above threshold. Significantly, the EIN does not include 500 Hz noise in its calculation, but is limited to 1.0, 1.6, and 2.5 kHz.

Lee and Geddes (1998) investigated both audible and objectionable levels of noise among normal and hearing-impaired listeners, and concluded that designing microphones with noise levels at or below the "just-objectionable level" of the normal hearing group may be excessive, since this level is probably not audible, and certainly not objectionable, to hearing-impaired individuals. However, depending on the frequencies with the highest noise energy, individuals with certain hearing losses may be more susceptible to the audibility of internal noise than others, specifically, those with better low- and mid-frequency hearing sensitivity.

Other research suggests that the amount of background noise an individual can tolerate or judges as acceptable, defined as the acceptable noise level (ANL), may be an important predictor of successful hearing aid use (Nabelek *et al.*, 1991, 2006). Additionally, relatively small changes in the ANL can have significant effects on the probability for success with hearing aids. Nabelek *et al.* (2006) found that if a subject's ANL decreases by 4 dB, the probability for success with hearing aids can increase from 45% to 92% (for an individual with an initial ANL of 10 dB). The presence of HA internal noise may also be a contributing factor to lack of success with HAs, especially if judged to be at unacceptable levels.

If a clinician encounters a patient with complaints about either background noise or the noise produced by their hearing aid, the complaint may be difficult to evaluate because a method for quantifying internal noise in a way that has perceptual relevance does not exist. Using EIN to confirm these complaints presents three main difficulties: (1) Even if noise is present at the microphone only, EIN quantifies the noise as an average at only three frequencies and does not take into account the whole audiogram; (2) if noise is not isolated to the microphone, any noise that might be present after gain is applied is not accurately evaluated by EIN; and (3) the internal noise in real-world processing conditions is not evaluated by EIN. Without other resources for measuring noise, some clinicians might be tempted to compare HAs from different manufacturers, based on EIN measures; however, such a decision may not be justified or be expected to result in a HA with the least audible internal noise.

Finally, clinicians typically use the EIN measure as a diagnostic indicator of HA performance: EIN values exceeding tolerance suggest that the aid is "out of specs" and may need repair. In-house measures according to American National Standards Institute (2004) suggest considerable variability in the EIN measure (Fig. 2). This variability was apparent across three different measurement systems, including a custom laboratory set-up in a sound-treated booth, a Frye Electronics Fonix system, and an AudioScan Verifit system. The EIN measure will erroneously label a HA as malfunctioning nearly one-third of the time.

The current study proposes and evaluates a novel method of measuring the internal noise of HAs that may be predictive of audibility to the user. The new measure may also have application as a quality control standard. The measurement quantifies the internal noise as the variance in the HA output across multiple measurement trials for a calibrated speech-like test signal. The measurement is made during hearing aid processing of the test signal, and is expected to be sensitive to all potential sources of internal noise. Internal noise is assessed across a broad range of frequencies and stimulus intensity levels, which may be beneficial when predicting noise audibility.

II. METHODS

A. Stimuli

The International Speech Test Signal (ISTS; IEC, 2008) was used as the stimulus. This 60-s recording is composed of speech segments from six different languages concatenated to yield a signal with temporal and frequency characteristics

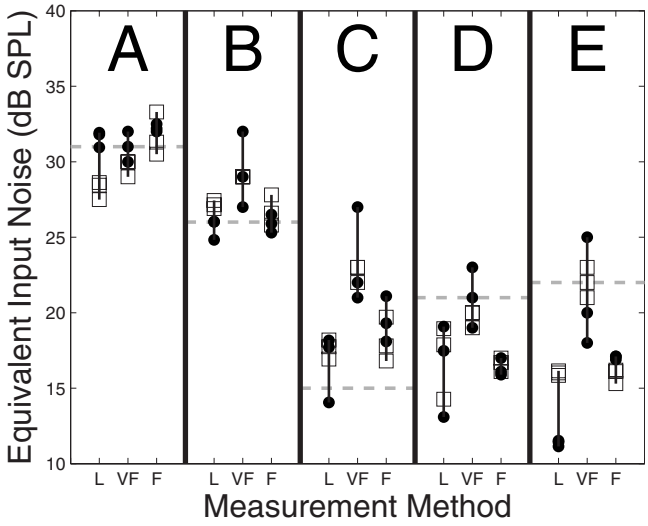

FIG. 2. Variability in clinical EIN measurements. Each panel (A–E) indicates HA model from one of six different manufacturers. EIN values are shown for two HAs of each model (filled circles, open squares). EIN values were computed using three different measurement systems (L—custom laboratory set-up, VF—AudioScan Verifit, F—Fonix 6500). Measurements were repeated three times with complete setup and takedown for each measurement. Dashed gray lines show manufacturer-reported EIN values plus 3 dB (ANSI tolerance). All HAs exceeded the ANSI tolerance of 3 dB above the manufacturer specified EIN level on at least one measurement.

representative of speech in numerous languages. ISTS was selected as a stimulus instead of the more traditional ICRA speech noise because the temporal structure of normal speech is preserved in the ISTS stimulus, decreasing the likelihood that certain noise canceling features of HAs would be activated during testing, thereby treating the signal as if it were unwanted noise.

B. Measurement paradigm

Stimulus delivery and response acquisition were controlled using a personal computer, custom software, and a sound card (Lynx L22, 24-bits, 44.1 kHz sample rate). The output of the sound card was routed through a power amplifier (ADCOM GFA 5002) to a loudspeaker (Tonoy System 800) positioned 1 m from a Knowles Electronics Manikin for Acoustic Research (KEMAR) at 0° azimuth relative to the geometric center of the head. KEMAR, as opposed to a 2 cm^3 coupler, was used to allow for more accurate predictions of internal noise audibility, as measured levels would be more representative of those encountered in the human ear canal. Hearing aid output was measured with a G.R.A.S. IEC-711 ear simulator attached to the right ear of the manikin. Multiple measurements were taken, with recording of the hearing aid output time-locked with acoustic stimulus presentation.

Responses were collected from HAs from each of the six major manufacturers. For each manufacturer, the HA model with the most advanced signal processing algorithms was selected for evaluation. The hearing aids were all set to default manufacturer ("first-fit") settings for a user with a sloping high-frequency hearing loss (thresholds were 10, 10, 30, 45, 60, and 75 dB HL at 0.25, 0.5, 1, 2, 4, and 8 kHz, respectively). Measurements were made in a sound booth, with additional acoustic treatment to reduce echoes and standing waves. All features (e.g., acoustic feedback control, noise reduction, directionality) were enabled or disabled as a parameter of testing.

Prior to recording the HA output for analysis, the 60-s ISTS noise was presented continuously for 8 min. This allowed the HA time to "settle," i.e., to reach a point where it would produce the same output for a given speech input. In practice, this length of time was never needed for a HA to reach steady state (longest required was 3 min); the 8-min length was simply chosen as a very conservative value. Immediately following the settling period, a 1.4-s segment of the 60-s ISTS noise sample was selected and consecutively presented 32 times. The same segment was used for all measurements and allowed for numerous recordings to be made within a relatively short period of time. The procedures just described were repeated for two HA conditions (adaptive features enabled and disabled), at seven stimulus input levels (20–80 dB SPL in 10-dB steps), and once with no stimulus. The order of presentation was always silence first, then stimulus level from lowest to highest. All measurements were completed on two hearing aids of each model to determine measurement reliability.

C. Calculation of internal noise

Data were analyzed using custom MATLAB software. For each condition, $K=32$ independent buffers of data were collected (where one buffer represents the waveform recorded in response to a single presentation of the speech-1.4 s stimulus). Each buffer was of length $N=61\,740$ samples (1.4 s at 44.1 kHz sampling rate). The data were filtered using a high-pass finite impulse response (FIR) filter (354 Hz cutoff, 5.7 ms group delay).

Discrete Fourier transforms were computed on each buffer,

$$X_k[m] = \sum_{n=0}^{N-1} x_k[n] e^{-j2\pi nm/N}, \tag{5}$$

where x_k is the waveform in the k-th buffer, and $X_k[m]$ is the DFT of the k-th buffer and the m-th frequency bin. In the frequency domain, the signal was taken as the (coherent) average complex spectrum,

$$\bar{X}[m] = \frac{1}{K} \sum_{k=1}^{K} X_k[m]. \tag{6}$$

The energy in the (mean) signal is therefore

$$|\bar{X}[m]|^2 = \frac{1}{K^2} \left| \sum_{k=1}^{K} X_k[m] \right|^2. \tag{7}$$

Noise was defined as any part of the measured waveform which was not repeatable (i.e., it did not phase lock to the stimulus). By this definition, the energy in the hearing aid noise floor is equivalent to the variance of the measurements,

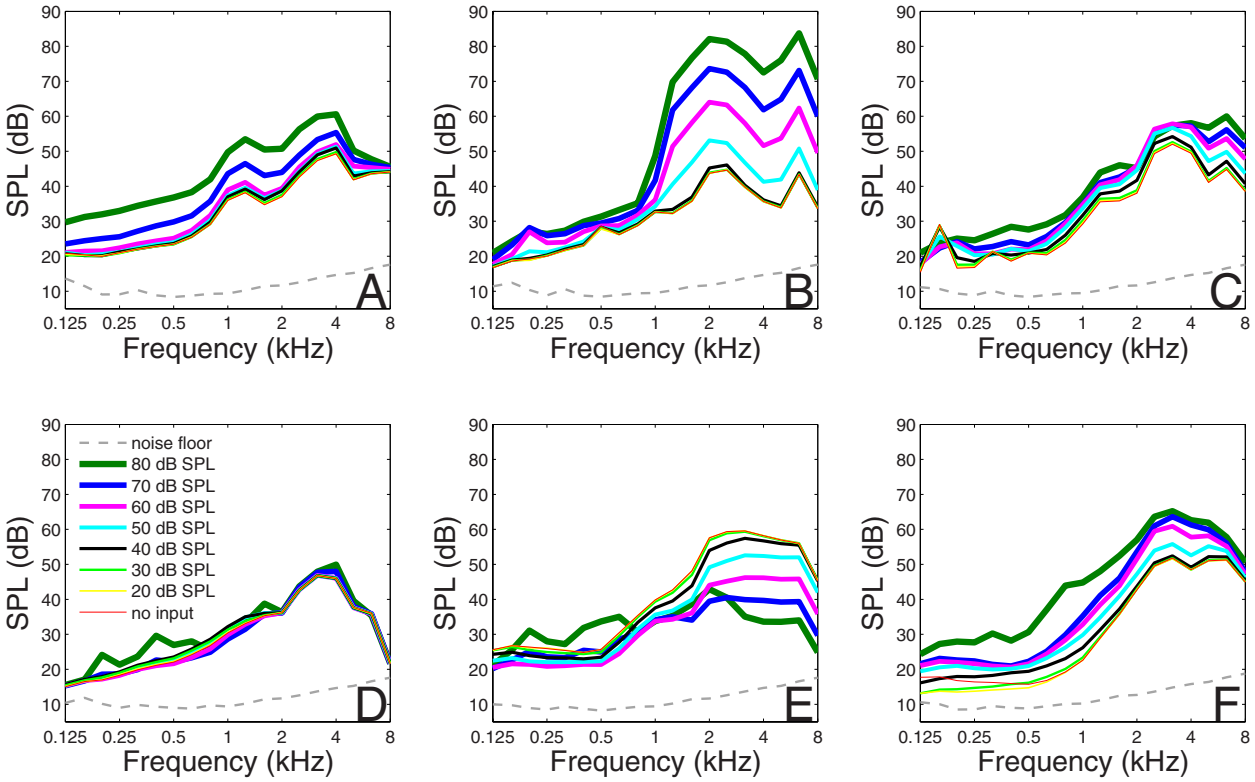

FIG. 3. (Color online) Measured internal noise (variance) as a function of frequency at various input levels for hearing aids A–F. Measurements show the internal noise generated by each hearing aid for inputs ranging from no-input (thinnest lines) to 80 dB SPL (thickest lines). The noise floor of the measurement system is plotted as the thin broken gray line.

$$S^2[m] = \frac{1}{K-1}\sum_{k=1}^{K}(X_k[m]-\bar{X}[m])(X_k[m]-\bar{X}[m])^*, \quad (8)$$

where * denotes the complex conjugate. Defining the reference pressure as $P_{\text{ref}}=20$ μPa, the spectral sound pressure levels of the signal and noise defined from frequency bins $m=1$ up to $N/2-1$ are

$$\text{SPL}_{\text{signal}} = 10\log_{10}\left(\frac{2}{N^2}\frac{|\bar{X}[m]|^2}{P_{\text{ref}}^2}\right) \quad (9)$$

and

$$\text{SPL}_{\text{noise}} = 10\log_{10}\left(\frac{2}{N^2}\frac{S^2[m]}{P_{\text{ref}}^2}\right). \quad (10)$$

An advantage of defining noise in this way is that the noise floor of a hearing aid can be measured while the aid is processing a signal and providing varying amounts of gain, for example, under compression or expansion schemes. Further, harmonic distortion or distortion products produced by the hearing aid are not calculated as noise, so long as they are exactly reproducible across repeated presentations of the same stimulus.

One potential disadvantage of defining noise in this way is the inability to distinguish between variability arising from intrinsic circuit noise versus variability in a hearing aid's amplification strategy. That is, if a hearing aid applies an algorithm that changes its response over time, the varying output will show up as increased variance, and therefore, "noise," even though this variability is too slow to be perceived by human users as noise. This potential problem can be overcome if some metric of output level is plotted over time. Should the hearing aid alter its processing, this will show up as a slow drift in the output level over time, and the measurement paradigm can be altered to avoid this confound.

III. RESULTS

A. Adaptive features enabled

Internal noise as a function of frequency, with adaptive features enabled, is plotted in Fig. 3 for hearing aids A–F. The lines indicate measurements made at different stimulus levels. In all measurements, the internal noise levels of the aids were greater than the noise floor of the system and testing environment (broken, light gray line). Three basic patterns of noise can be seen in the data: (1) The internal noise increases as the stimulus level increases (Fig. 3, A, B, C, and F); (2) the internal noise is constant across stimulus levels (Fig. 3, D); and (3) the internal noise decreases as stimulus level increases (Fig. 3, E).

Based on the noise model in Fig. 1, two general patterns of noise growth were expected. When the dominant source of internal noise is located prior to gain [$n_1 \gg n_2$ in Eq. (1)], the measured noise will vary with input level. Assuming the gain decreases as input level increases, and that the internal noise is constant, the noise measured at the HA output will also decrease as level increases. When the HA has significant levels of constant internal noise both before and after the gain [$n_1=n_2$ in Eq. (1)], the same pattern is seen. The mea-

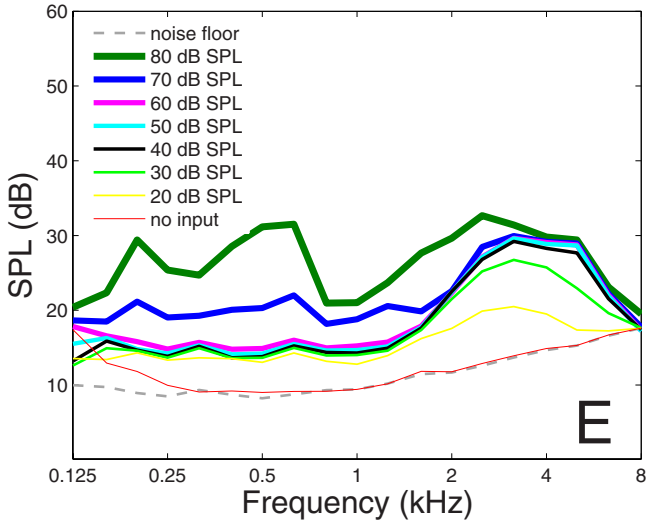

FIG. 4. (Color online) Internal noise as a function of input level for HA-E after removal of gain. Line thickness indicates level from lowest level (thinnest) to highest (thickest). The noise floor of the measurements system is plotted as the thin broken gray line.

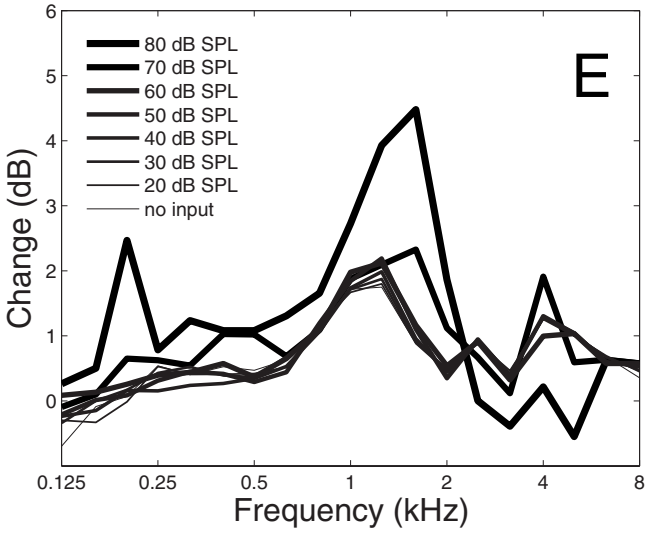

FIG. 5. Difference in internal noise levels across two hearing aids of the same model (HA-E) when tested individually and programmed for the same hearing loss. Line thickness indicates level from lowest level (thinnest) to highest (thickest).

sured noise will decrease with level, but the noise will be shifted upward by a constant amount, n_2. Of the six HAs tested, only HA-E (Fig. 3, E) showed this pattern. It may be possible to distinguish between $n_1 \gg n_2$ and $n_1 = n_2$ by removing the gain from the noise measurements. When this is done, a system characterized by $n_1 \gg n_2$ will show noise that is constant with level, while a system characterized by $n_1 = n_2$ will show noise that varies with level. Figure 4 shows the internal noise of HA-E with the gain removed. The noise with the gain removed is fairly constant through the midrange of input levels, but not at the lower and higher levels. These results are most consistent with noise being present both before and after amplification.

The second pattern of expected noise growth occurs when the dominant source of internal noise is located after the gain [$n_1 \ll n_2$ in Eq. (1)]. In this case, the measured noise will be constant with input level, again assuming that the internal noise is constant. Hearing aid D (Fig. 3, D) showed this pattern of noise. At all but the highest two levels, HA-A (Fig. 3, A) also showed this pattern.

The remaining three HAs (B, C, and F) showed an increase in internal noise as input level increased (and as gain decreased). The cause of this pattern is unclear. One possibility is that the internal noise is not constant as a function of level. In particular, it appears that the internal noise increases as input level increases. As noted earlier, this increase noise was measured as an increase in the variance of the HA output, so that this increase is not expected to reflect an increase in harmonic or other distortion at high levels. It is possible that the patterns of noise growth are caused by a complex interaction between noise occurring before gain (n_1) and noise occurring after gain (n_2).

Figure 5 shows the change in internal noise level across two HAs of the same model (HA-E). Measured noise levels varied by approximately 2 dB across this HA model with the exception of the most intense input level where a difference of nearly 5 dB was observed. These results were typical of the reliability across hearing aids of the same model for the remainder of the groups.

B. Adaptive features disabled

Figure 6 shows the change in internal noise levels when adaptive features were disabled, relative to adaptive features enabled. Each panel shows a different frequency. Results suggested that enabling features such as feedback cancellation, directionality, and digital noise reduction made only a small contribution to the internal noise of the majority of the HAs (as tested in a quiet room with a single sound source).

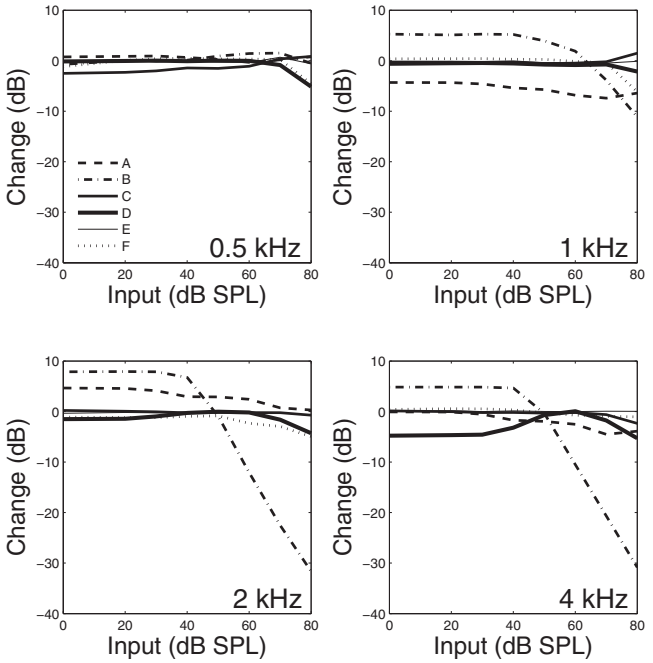

FIG. 6. Change in variance when adaptive features are disabled as a function of input level. Each panel represents a different frequency. Each line in a panel represents a different HA.

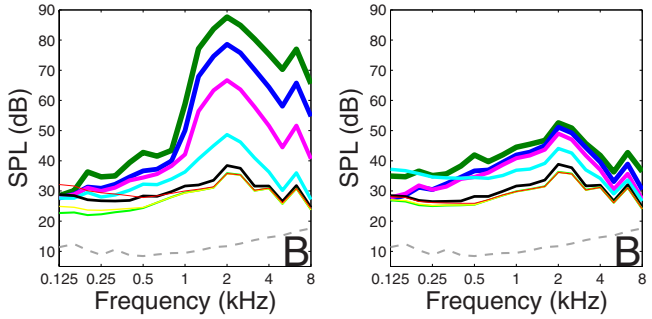

FIG. 7. (Color online) Internal noise of HA-B with adaptive features enabled (left panel) and with feedback management disabled (right panel) for each input level. Line thickness indicates level from lowest level (thinnest) to highest (thickest). The thin gray broken line indicates measurement system noise floor.

Except for HA-B, noise levels with features disabled remained within 5 dB of levels measured with features enabled. When adaptive features were enabled, the internal noise in HA-B grew nearly linearly with higher intensity levels at frequencies above 1 kHz (Fig. 3, B). When adaptive features were disabled in HA-B, noise levels were reduced by as much as 30 dB. Figure 7 shows the internal noise of HA-B with adaptive features enabled (left panel) and adaptive features disabled (right panel). With features disabled, noise levels were similar to the other HAs tested (Fig. 3). Further testing revealed that it was specifically the acoustic feedback cancellation feature that was the cause of this noise. This particular HA used a phase modulation algorithm to control feedback. Because the variance method of measuring noise is phase sensitive, it is probable that activation of the algorithm during the measurement process led to an increase in the measured noise.

C. Audibility of internal noise

The noise levels of HA-B generated for the 80 dB SPL input approach nearly 90 dB SPL when quantified by the variance in the measurements; however, listening tests carried out by the authors suggested that such levels are not perceived by human listeners. The discrepancy between perceived and measured noise appears to be due to the phase sensitivity of the variance method for calculating noise and the general phase insensitivity of the human auditory system. Further research is needed regarding users perception of such phase-altering algorithms and their relationship to noise measurements.

The most likely condition in which hearing aid users will hear the internal noise of the HA is a quiet environment. The HA internal noise levels, measured in a sound-treated booth, ranged from 15–60 dB SPL across the frequency range of 0.125–8 kHz (Fig. 3). Figure 8 compares the noise levels in quiet and the audiometric thresholds of the hearing loss for which the HAs were programmed. Wherever the thresholds (solid lines) fall below the noise level (broken lines), the noise was predicted to be audible to a listener having the same audiometric thresholds. The internal noise levels of all aids were predicted to be audible, with the exception of HA-F. In all cases where the noise was audible, noise levels exceeded hearing thresholds in the frequency range of 0.5–1.5 kHz.

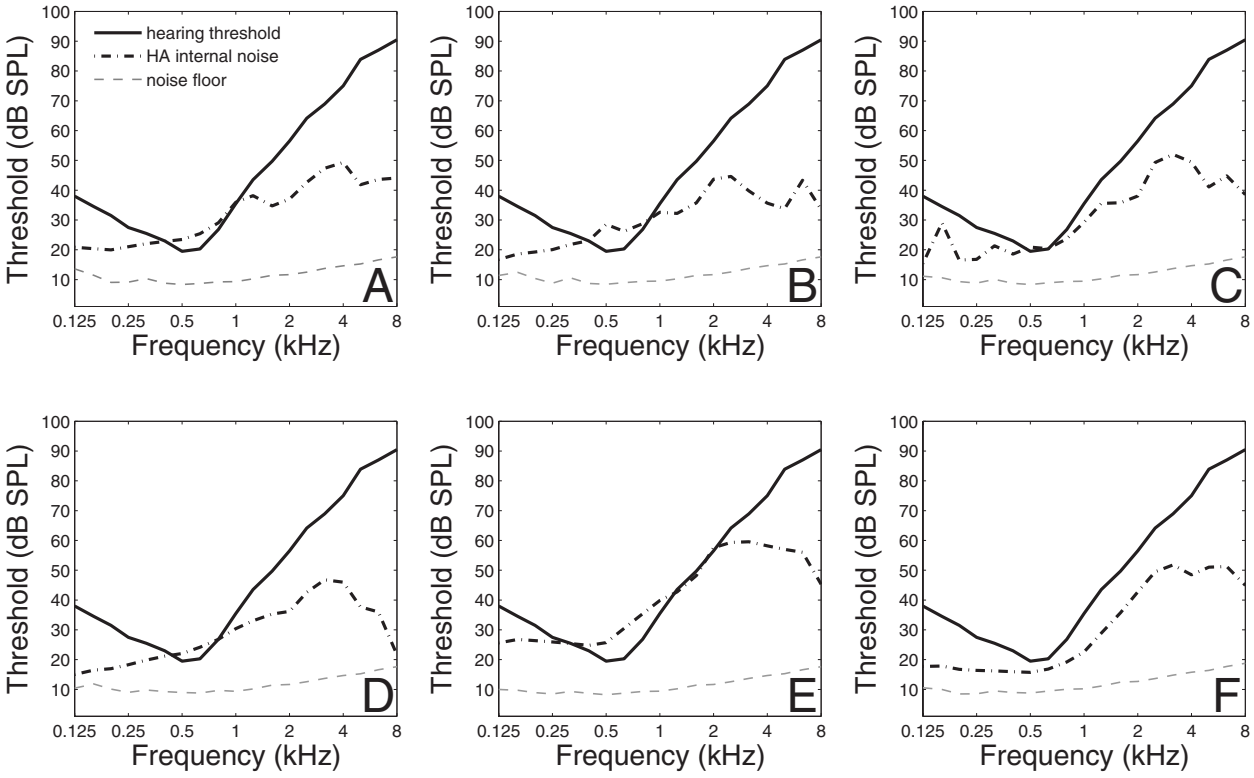

FIG. 8. Internal noise in quiet (dark broken lines) and programmed audiometric thresholds (solid lines) for each HA. Internal noise is predicted to be audible where the noise level is equal to or greater than the associated hearing threshold.

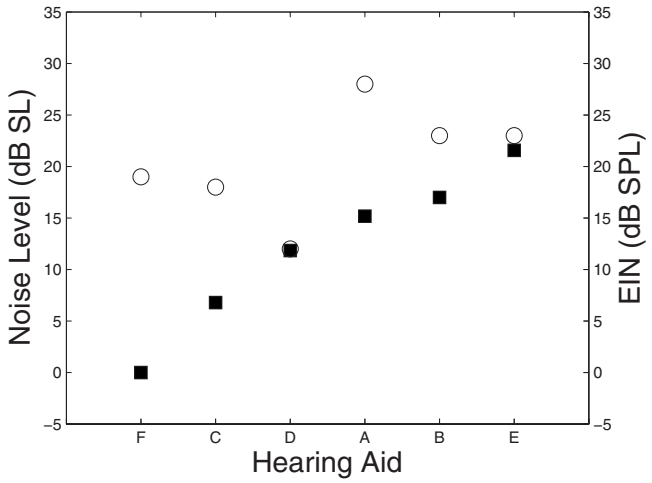

FIG. 9. Total audibility levels (filled squares) and manufacturer specified EIN values (open circles) for each hearing aid.

The "total audibility" for each aid was determined by subtracting the hearing threshold (dB SPL) from the noise level (dB SPL) at each 1/3 octave frequency where the noise was predicted to be audible. The differences at each frequency were converted into linear units, summed and converted back into decibels. Figure 9 compares the total audibility levels (filled squares) of the six HAs (arranged in order of increasing total audibility) and the manufacturers' reported EIN levels (open circles). Since the noise of HA-F was not predicted to be audible, a level of 0 dB SPL was assigned to it for display purposes only. This figure demonstrates that, although a particular HA may have a very low EIN value as quantified by American National Standards Institute (2004), the actual audibility of the internal noise to the hearing-impaired user may be higher than similar HAs with higher EIN values. For example, HA-D had the lowest reported EIN value (12 dB SPL), but two other HAs (F and C) were predicted to have internal noise levels that are less audible. As expected, the results reinforce the fact that EIN was never meant to indicate audibility. Further testing should be done to see if the relative audibility predictions based stemming from the variance measurements of internal noise are psychophysically valid.

IV. DISCUSSION

The current EIN calculation assumes a model of internal noise where the dominant noise source is located prior to the application of gain. When this is the case, internal noise measured at the output of the receiver and quantified as the variance across repeated trials is expected to change in proportion to the gain. As the input level of the stimulus increases, less gain will be applied and the noise will decrease accordingly. This pattern of noise was only apparent for one of the six hearing aids tested (HA-E). A model in which internal noise is primarily located after amplification is consistent with the measurements for HA-D, while a model with internal noise sources located both before and after gain is possible for the remaining four HAs.

Noise generated prior to amplification logically stems from the microphone (Thompson *et al.*, 2002); however, noise generated following amplification may result from several different mechanisms. One possible source of internal noise is the processing algorithms employed by the hearing aid, including acoustic feedback management, microphone directionality, and DNR. All six HAs used in this study included these specific features and are representative of nearly all modern hearing aids today. With one exception (HA-B), the results of this study suggested that these features do not significantly contribute to the internal noise of a HA. However, the testing environment used in the current study should be considered. All measurements were made in a quiet, sound-attenuating booth using a single sound source. Features such as directionality and digital noise reduction are designed to only be active in noisy environments, and may therefore not have been engaged by the processing of the hearing aid. Depending on the coupling between the hearing aid and KEMAR, feedback management may or may not have been engaged throughout testing.

The observation of internal noise changing due to activation of adaptive features for HA-B demonstrates both a strength and weakness of the proposed method to measure internal noise. It is apparent from these results that certain processing algorithms do contribute to the HA internal noise, and may or may not reduce the fidelity of the signal presented to the user. This is not something that can be determined by the current EIN calculation since it is calculated following measurements of hearing aid output in the absence of a complex input. The advantage then of quantifying the internal noise of the aid as the variance across multiple stimulus presentations is that the noise present in the processed complex signal is known.

Accordingly, the noise levels measured in terms of output variance provide insight into the auditory perception of the noise experienced by a HA user under normal-use conditions. Each hearing aid, except HA-F, was predicted to have noise levels audible to an individual with a high-frequency sensorineural hearing loss. The frequency distribution of the internal noise was similar for all the aids, and whenever noise was predicted to be audible, it was generally associated with energy around 750 Hz, due to the preservation of hearing sensitivity. The broad range of "total audibility" levels across the six HAs implies that the internal noise levels of some HAs may be significantly less than that of other HAs when programmed for an identical loss. For example, the total audibility for HA-E was predicted to be nearly 20 dB greater than the value calculated for HA-C (Fig. 9). In light of the research suggesting HA user intolerance to noise levels only slightly above threshold (Agnew, 1997), and the impact of background noise on successful hearing aid use (Nabelek *et al.*, 2006), quantifying noise as the output variance could be beneficial to clinicians in selecting a "quiet" hearing aid for a patient who is either a poor HA user or who is expected to be a poor user. As demonstrated in Sec. III, the EIN calculation is not an accurate predictor of noise audibility and should not be used as such. Further research is needed to verify the audibility predictions of the internal noise measurement method proposed in this paper.

In the case of the six aids assessed, HA-F would seem to be the obvious choice for a patient who is particularly sensitive to noise with an associated high ANL. However, it should be kept in mind that the measurements reported in the present study were obtained after each aid was programmed to its manufacturer's first-fit algorithm. Each manufacturer employs different amplification strategies, and therefore each aid amplified the test stimuli using different amounts of gain. From a quality control standpoint, to accurately compare aids, it would first be necessary to ensure all aids are providing equal gain. From a clinical standpoint, however, first-fit algorithms are commonly used, and gain differences often exist across aids despite similar audiograms, unless care is taken to match output levels using real ear verification.

As noted earlier, a potential short-coming to using output variance to quantify internal noise is that phase manipulations performed by a HA will add to, and may even dominate the noise measurement. This is undesirable if one of the goals of the measure is to predict noise audibility. It seems likely that such phase inconsistencies in processing are inconsequential, although it also seems that consistent processing of identical stimuli is desirable. This is a topic for further studies.

V. CONCLUSIONS

The current study described a method of quantifying the internal noise of hearing aids as the output variance across repeated trials. Internal noise levels were measured at stimulus input levels ranging from 20–80 dB SPL, and also in the absence of an input. Patterns of internal noise level as a function of stimulus level (and therefore gain) challenge the basic assumption of the current EIN calculation that the noise floor of a hearing aid is dominated by the microphone's contribution. Of the six aids tested, only one aid (HA-E) was consistent with the EIN model of internal noise. One aid (HA-D) had noise levels consistent with a primary noise generator following amplification. The remaining aids demonstrated more complicated models of non-constant internal noise that may have been generated, both prior to and following amplification.

In contrast to the EIN, calculating internal noise as the output variance across repeated trials allows for measurements of noise concurrent with HA processing of real-world stimuli. This may provide insight into the contribution of processing algorithms to the overall noise floor. One caveat is that phase manipulations, which contribute to the variance, may not be perceived by listeners.

Quantifying the noise as the variance permits predictions of noise audibility to be made, and may be beneficial from the standpoint of both quality control and clinical utility.

ACKNOWLEDGMENTS

The investigators thank the National Institutes of Health and the American Auditory Society (AAS) for funding the presentation of this study at the AAS 2008 Annual Convention (Mentored Doctoral Student Research Poster Session Grant). Additionally, the investigators thank the following manufacturers for providing the hearing aids used in this study: Phonak, Unitron, Widex, Starkey, Siemens, and Oticon.

Agnew, J. (**1997**). "Audible circuit noise in hearing aid amplifiers," J. Acoust. Soc. Am. **102**, 2793–2799.

American National Standards Institute (**2004**). *American National Standards Specification for Audiometers (ANSI S3.6–1996)* (American National Standards Institute, New York).

American National Standards Institute (**2004**). *American National Standards Specification of Hearing Aid Characteristics (ANSI S3.22–2004)* (American National Standards Institute, New York).

Hellman, R., and Zwicker, E. (**1987**). "Why can a decrease in dB (A) produce an increase in loudness?," J. Acoust. Soc. Am. **82**, 1700–1705.

International Electrotechnical Commission (**2008**). Electroacoustics-Hearing Aids—Part 15: Methods for characterizing signal processing in hearing aids (IEC 60118–15) (International Electrotechnical Commission, Geneva, Switzerland).

Killion, M. C. (**1976**). "Noise of ears and microphones," J. Acoust. Soc. Am. **59**, 424–433.

Lee, L. W., and Geddes, E. R. (**1998**). "Perception of microphone noise in hearing instruments," J. Acoust. Soc. Am. **104**, 3364–3367.

Nabelek, A. K., Freyaldenhoven, M., Tampas, J., and Burchfield, S. (**2006**). "Acceptable noise level as a predictor of hearing aid use," J. Am. Acad. Audiol **17**, 626–639.

Nabelek, A. K., Tucker, F. M., and Letowski, T. R. (**1991**). "Toleration of background noises: Relationship with patterns of hearing aid use by elderly persons," J. Speech Hear. Res. **34**, 679–685.

Stuart, J. R. (**1994**). "Noise: Methods for estimating detectability and threshold," J. Audio Eng. Soc. **42**, 124–140.

Thompson, S. C. (**2003**). "Internal noise in hearing aid microphones: Its causes and consequences," Hear. J. **56**, 46–47.

Thompson, S. C., LoPresti, J. L., Ring, E. M., Nepomunceno, H. G., Beard, J. J., Ballad, W. J., and Carlson, E. V. (**2002**). "Noise in miniature microphones," J. Acoust. Soc. Am. **111**, 861–866.

Wind noise in hearing aids with directional and omnidirectional microphones: Polar characteristics of custom-made hearing aids

King Chung[a)]
Department of Allied Health and Communicative Disorders, Northern Illinois University, DeKalb, Illinois 60115

Nicholas McKibben
Department of Mechanical Engineering, Purdue University, West Lafayette, Indiana 47907

Luc Mongeau
Department of Mechanical Engineering, McGill University, Montreal, Quebec H3A 2K6, Canada

(Received 2 July 2009; revised 24 November 2009; accepted 3 December 2009)

The purpose of this study was to examine the characteristics of wind noise at the output of in-the-ear, in-the-canal, and completely-in-the-canal hearing aids. The hearing aids were programed to have linear amplification with matching flat frequency responses for directional (DIR) and omnidirectional (OMNI) microphones. The microphone output was then recorded in a quiet wind tunnel when the Knowles electronic manikin for acoustic research (KEMAR) head was turned from 0° to 360°. The overall, 125, 500, and 2000 Hz one-third octave band flow noise levels were calculated and plotted in polar patterns. Correlation coefficients, average differences, and level differences between DIR and OMNI were also calculated. Flow noise levels were the highest when KEMAR was facing the direction of the flow and angles between 190° and 250°. The noise levels were the lowest when the hearing aids were facing the direction of the flow. The polar patterns of DIR and OMNI had similar shapes and DIR generally had higher levels than OMNI. DIR, however, could have lower levels than OMNI in some angles because of its capability to reduce noise in the far field. Comparisons of polar characteristics with behind-the-ear hearing aids, and clinical and engineering design applications of current results are discussed.
 [DOI: 10.1121/1.3277222]

PACS number(s): 43.66.Ts, 43.60.Fg, 43.38.Kb, 43.38.Hz [BLM] Pages: 2529–2542

I. INTRODUCTION

Wind induced noise can be a nuisance and/or a debilitating masker to hearing instrument users, especially for those who spend time outdoors and/or enjoy outdoor activities. Although hearing aid manufacturers implement wind noise reduction algorithms in their hearing aids, there is very little published on the reasons behind these strategies. A survey indicates that only 49% of hearing aid users are satisfied with the performance of their hearing aids in wind (Kochkin, 2005). In this study, the characteristics of wind noise at the output of several custom hearing aids were examined, and strategies to reduce wind noise interferences were also derived.

Local, flow-induced turbulent flow fluctuations over microphones are often referred to as "wind noise," "flow noise," "aerodynamic near field noise," or "pseudo-sound" (National Committee for Fluid Mechanics Films, 1972). It is generated when a turbulent air flow impinges on the microphone diaphragm. The wind noise problem for hearing instrument users can be exacerbated by the use of directional microphones, which are implemented in many high-performance digital hearing aids and some cochlear implants. Directional microphones have gained popularity in hearing instruments in recent years because they can reduce background noise and increase speech recognition in environments with low reverberation (Studebaker *et al.*, 1980; Hawkins and Yacullo, 1984; Valente *et al.*, 1995; Killion *et al.*, 1998; Ricketts and Dhar, 1999; Ricketts, 2000; Valente *et al.*, 2000; Amlani, 2001; Ricketts and Henry, 2002; Bentler *et al.*, 2004; Chung *et al.*, 2004; Chung *et al.*, 2006; Spriet *et al.*, 2007).

First-order directional microphones employ either one microphone with two ports (single-cartridge design) or two omnidirectional microphones (dual-microphone design) to sense the pressure difference or gradient between two points in space. They are often referred to as pressure gradient microphones in the engineering literature (Carlson and Killon, 1974; Eargle, 2004; Baumhaur and Marcus, 1997). Most directional microphones implemented in digital hearing aids utilize the dual-microphone design for its flexibility.

In the dual-microphone design, one microphone (front microphone) is placed closer to the front of the user's face relative to the other (rear microphone). The distance between the microphones (d) determines the external delay of the directional microphone, which is the time for sound waves to travel the distance d. The signal generated at the rear micro-

a)Author to whom correspondence should be addressed. Electronic mail: kchung@niu.edu

phone is delayed by an internal delay network and then subtracted from the signal generated by the front microphone. The resulting signal is the directional microphone output. In general, small microphone distances are associated with higher directivity in the high frequency region than the low frequency region. Directional microphones with large microphone distances also yield greater directional effects than those with small microphone distances (Ricketts, 2001).

Frontal incident sound waves reach the front microphone earlier than the rear microphone. As the signal in the rear microphone is delayed by the external and internal delays, the level of the signal from the front microphone is minimally affected when the signal from the rear microphone is subtracted. Directional microphones, therefore, have high sensitivity to sounds from the front (assumed to be speech or the desired signal).

Sound waves from the back, however, reach the rear microphone before the front microphone. If the internal and external delays are equal, a sound from 180° would lead to perfect cancellation (i.e., the null). The sensitivity of the directional microphone to other sounds from the back (assumed to be background noise) is also greatly reduced. The sensitivity of the directional microphone to sounds from different directions can be varied by changing the ratio of the internal and external delays to yield cardioid, dipole, hypercardioid, supercardioid, or other directivity patterns. As the most effective subtraction occurs when the amplitude of the signals received from the front and rear microphones are similar, the two omnidirectional microphones used to form the directional microphone need to have matching phases and sensitivity across frequency regions (Valente, 1999; Ricketts, 2001; Chung, 2004).

One of the disadvantages of directional microphones is that they generate higher noise levels than omnidirectional microphones in wind due to the incoherent sound source effect and the proximity effect (Beard and Nepomuceno, 2001; Thompson and Dillon, 2002; Chung *et al.*, 2009). When wind flows pass an obstacle (e.g., the head or the pinna), eddies are generated downstream of the obstacle. Small eddies are also formed locally over each microphone, creating large *random* pressure changes on the diaphragm of each microphone, thus yielding incoherent microphone signals. As the signal from the rear microphone is subtracted from that of the front microphone, the *directional microphone* output varies between the sum (i.e., when one signal is positive and the other one negative) and the difference (when both signals are positive or negative) of the two omnidirectional microphone outputs. Large amplitude fluctuations are, therefore, generated at the directional microphone output and the associated peak-to-peak fluctuations are greater than those of the individual omnidirectional microphone outputs.

In the presence of an eddy that is large enough to affect both omnidirectional microphones, the eddy acts as a near field sound source for the directional microphone. Sounds in the near field of hearing aids are sources located within 10–20 cm of the microphones (Thompson, 2002). The proximity effect or near field effect generally refers to a rise in the low frequency output of directional microphones. While it is common for singers and broadcasters to take advantage

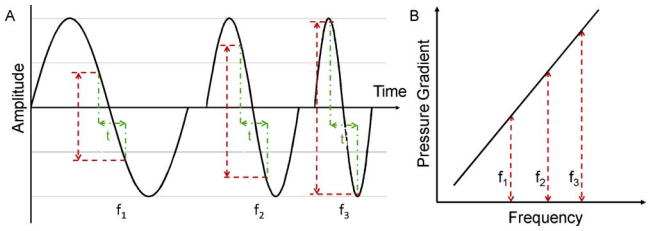

FIG. 1. (Color online) (A) The pressure gradient generated by low frequency sounds with different frequencies ($f_1 < f_2 < f_3$). Time (t) is the combination of the time for sound waves to travel the microphone distance (d) and the internal delay. (B) The pressure gradient obtained in (A) plotted as a function of frequency.

of the proximity effect to create warmth and to increase the fullness of their voices (Barlett and Barlette, 2001; Eargle, 2004; Gibson, 2007), the effect can also significantly increase wind noise levels in hearing aids.

Several factors contribute to the proximity effect. For *any sound* in the environment, the level of the directional microphone output depends on two components: (1) the pressure gradient generated by the phases of the sound wave in the two omnidirectional microphones (i.e., *phase difference*); and (2) the *intensity difference* which is inversely proportional to the square of the distance between the sound source and the microphone (i.e., the inverse-square law $1/r^2$).

The phase component is frequency *dependent*. For low frequency sounds in the far field (e.g., 100 Hz), the wavelength of the signal (wavelength=velocity of sound/frequency=3.43 m) is much longer than the microphone spacing of the directional microphone (e.g., microphone spacing=1 cm=0.01 m). As the two omnidirectional microphones sense the sound wave at similar phase and amplitude, the pressure gradient is small. Thus, the amplitude of the directional microphone output is low after the subtraction (Dillon, 2001; Ricketts, 2001).

As the frequency of the sound increases, the wavelength decreases and the phase difference increases, resulting in higher pressure gradient between the two omnidirectional microphones and higher directional microphone output. The directional microphone output frequency response, therefore, exhibits a characteristic 6 dB/octave slope in the low frequency region [Fig. 1(B)]. The frequency response, then, increases slowly to a peak value and then falls off at higher frequencies (Bauer, 1941; Carlson and Killon, 1974).

The intensity of a spherical sound wave and the intensity received by each omnidirectional microphone are governed by the inverse square law. They are frequency *independent* (Eargle, 2004; Shure, 2009). At a distance far away from the sound source (e.g., 1 m), the root mean square (rms) sound pressure level (SPL) differences between the two omnidirectional microphones are similar because the effective microphone distance (d=0.01 m) is much smaller than the distance from the sound source. The rms SPL difference between the two microphones is negligible [i.e., $10\log(r_1^2/r_2^2)=20\log(1.01/1)=0.09$ dB]. When the phase and intensity components are added together, the overall pressure at the directional microphone output is dominated

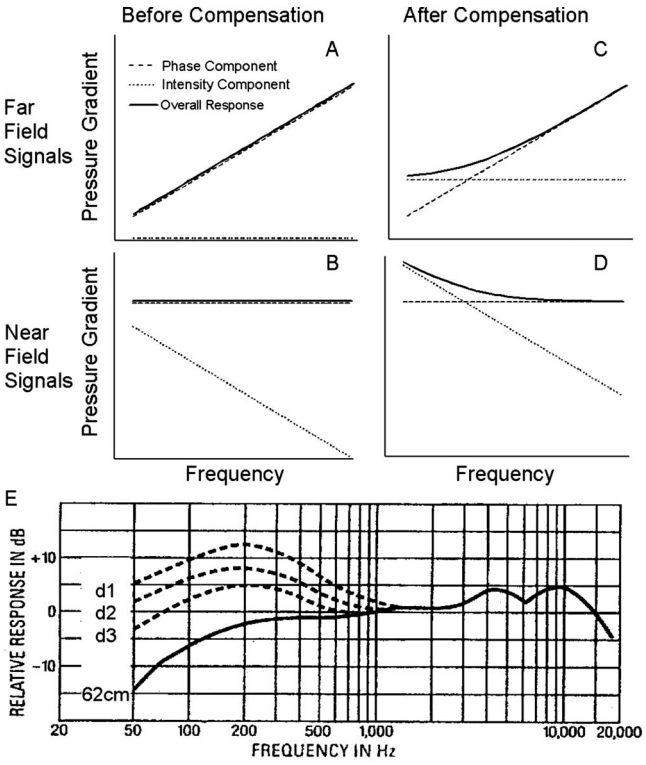

FIG. 2. The relationship between the phase component and the intensity component (A) in far field, and (B) in near field before low frequency compensation. The relationship of the components (C) in far field and (D) in near field after low frequency compensation. (E) The low frequency response of a microphone increases as the distance between the sound source and the microphone decreases (where d1<d2<d3<62 cm = far field response, figure modified from Eargle, 2004). Note: only low frequency responses are shown in (A)–(D).

by the phase component and exhibits the characteristic 6 dB/octave low frequency roll-off [Fig. 2(A)].

At a distance close to the sound source (i.e., in the near field), however, the rms SPL difference between the two microphones can be significantly larger [Fig. 2(B)]. If one of the microphones is 1 cm from the sound source and the other is 2 cm from the sound source, the SPL at the front microphone would be 6 dB higher than that of the rear microphone [i.e., $10\log(r_1^2/r_2^2)=20\log(0.02/0.01)=6$ dB]. As the sound source gets closer to the microphones (e.g., 0.5 and 0.15 cm), the intensity component gets even larger [i.e., $10\log(r_1^2/r_2^2)=20\log(0.015/0.005)=9.5$ dB]. The effect of the intensity component on the directional microphone, therefore, becomes more dominant and offset the phase component as the distance between the sound source and the microphone decreases. In some cases, the characteristic +6 dB/octave slope in the low frequency region can even disappear and become flat [Fig. 2(E), Eargle, 2004].

Notice that, in the above example, frontal incidence of sound waves and zero internal delay were assumed. In real life, eddies can form in any direction relative to the directional microphones. Depending on the length of the internal delay applied to the rear microphone and the distance between the eddies and each of the microphones, the relative contribution of the phase and the intensity components to the proximity effect can vary. Nevertheless, the end-result is similar: the phase component increases as frequency decreases in the low frequency region and the intensity component becomes more prominent as the distance between the microphones and the sound source decreases.

Furthermore, a common practice in hearing aids and audio microphones is to compensate for the 6 dB/octave low frequency roll-off in directional microphones so that both directional and omnidirectional modes have the same sensitivity to sounds in the far field [Fig. 2(C)]. While this compensation is needed because speech may sound "tinny" otherwise and some hearing aid users need low frequency amplification, this practice greatly increases the low frequency dominated wind noise in directional microphones. After the compensation, the intensity component becomes the dominant contributor to the overall signal in the low frequency region for near field signals [Fig. 2(D)], which results in an increase in low frequency responses [Fig. 2(E), Reedyk, 1973; Eargle, 2004; Shure, 2009]. For a hearing aid directional microphone that has a cut-off frequency of 1000 Hz, this low frequency boost can be as much as 18 dB at 125 Hz (which is three octaves down from 1000 Hz).

Omnidirectional microphones generally yield much lower noise levels in wind than directional microphones because they only have one microphone. There is no incoherent sound source effect or proximity effect. Flow noise generated at the omnidirectional microphone output is solely due to the turbulence impinging on the microphone diaphragm.

In a previous study, the authors recorded flow noise at the output of two behind-the-ear (BTE) hearing aids in a quiet wind tunnel (Chung *et al.*, 2009). Notice that the term "flow" is used here to refer to the air flow generated in wind tunnels instead of "wind," which usually refers to naturally occurring atmospheric air motion. Chung *et al.* (2009) showed that the highest flow noise levels were measured when the flow was coming from the front or back for both directional and omnidirectional microphones. Relatively low noise levels were measured when the hearing aid was facing the direction of the flow or facing downstream. These patterns were consistently observed over time and in the two behind-the-ear hearing aids tested, although the two hearing aids had different physical shapes and were made by different manufacturers.

In addition, Chung *et al.* (2009) reported that directional microphones generated higher noise levels than omnidirectional microphones at the hearing aid output for most angles at higher flow velocities (i.e., 9.0 and 13.5 m/s). At 4.5 m/s, however, directional microphones exhibited lower noise levels than omnidirectional microphones when the hearing aids were facing the direction of the flow. This was because the directional microphones were close to the point of stagnation for the flow and they reduced background noise in the far field.

Thompson and Dillon (2002) reported that the relative flow noise levels were different for different styles of hearing aids when the Knowles electronic manikin for acoustic research (KEMAR) head was turned to 0°, 30°, 50°, and −50°. Their results indicated that behind-the-ear hearing aids often yielded higher flow noise levels than in-the-canal (ITC), or completely in the-canal (CIC) hearing aids, which in turn yielded higher flow noise levels than in-the-ear (ITE) hearing

aids. These findings suggest that flow noise levels at the microphone output varied with hearing aid style and microphone location. The authors reported flow noise levels at four head angles and at a flow velocity of 5 m/s. Data on flow noise patterns at other angles and other flow velocities are needed.

In another study, Beard and Nepomuceno (2001) measured the flow noise level from 0° to 360° at the output of directional and omnidirectional microphones mounted in an in-the-ear hearing aid shell. The authors also reported that directional microphones, with either single-cartridge design or dual-microphone design, generally yielded higher flow noise levels than omnidirectional microphones at flow velocities of 2.1 and 5.0 m/s. In polar plots, the highest flow noise levels for the ITE hearing aids were reported to occur for frontal incidence and when KEMAR faced angles between 190° and 230°. This confirmed that the microphone sensitivity polar patterns in flow were different for in-the-ear and behind-the-ear hearing aids.

The purpose of this study is to measure and compare the flow noise characteristics at the output of an in-the-ear (i.e., ITE), an in-the-canal (i.e., ITC), and a completely-in-the-canal (i.e., CIC) hearing aid at various flow velocities. The goal was to develop strategies to reduce wind noise in amplification and hearing protection devices.

II. METHODS

Three hearing aids were custom-made for the large pinna of a KEMAR (Burkhard and Sachs, 1975) in the right ear. As there is a general lack of literature on wind noise in hearing aids, this study aimed at gaining a basic understanding of flow noise characteristics at hearing aid outputs without the influence of vents or other signal processing algorithms. The effects of signal processing algorithms (e.g., wide dynamic range compression and modulation-based noise reduction algorithms) on flow noise at the hearing aid output will be the subject of future investigations.

Each hearing aid was programmed in an anechoic chamber while worn on KEMAR. The frequency responses were matched between the directional and omnidirectional microphone modes and among the hearing aids. All other signal processing features (e.g., noise reduction and feedback reduction algorithms) were disabled. None of the hearing aids had a wind noise detection or management algorithm.

The KEMAR head and the hearing aid were then transported to a nearby quiet wind tunnel for flow noise measurements (Brown and Mongeau, 1995). After flow tests, the KEMAR head and the hearing aid were transported back to the anechoic chamber for calibration. The hearing aid remained in KEMAR's ear during the entire process. Flow noise levels were later analyzed using MATLAB. The methods used in this study were similar to those used by Chung *et al.* (2009).

A. Hearing aid characteristics

The hearing aids were 16-channel digital hearing aids made by the same manufacturer. When programed to OMNI, the front microphones were enabled and the rear microphones were disabled. The input-output functions of the hearing aids had a low-level expansion region and a mid-level compression region in each frequency channel, and a high-level broad-band output limiting region. According to the manufacturer's specifications, the expansion algorithm had a threshold of 42 dB in each frequency channel. For levels below the expansion threshold, the hearing aid provided less gain to lower level sounds (e.g., 10 dB SPL) than higher level sounds (e.g., 20 dB SPL). The mid-level region was programed to have linear amplification (i.e., compression ratio=1:1) so that the hearing aid output was not affected by the wide dynamic range compression algorithm. The 1:1 compression ratio also allowed level comparisons among hearing aids.

The output limiting region was controlled by a broad-band automatic gain control output limiting algorithm that limited the hearing aid maximum output to a value below the receivers' saturation level to prevent harmonic and intermodulation distortions of high-level outputs. Note that as output=input+gain for any hearing aid, the threshold of the automatic gain control algorithm was different depending on the gain settings of the hearing aid. In general, higher gain settings reduced the input level required to reach the threshold of the automatic gain control algorithm (i.e., maximum output level). In addition to the automatic output limiting algorithm, the maximum output levels of the hearing aids were limited by the input dynamic range of the microphone and the digital signal processing chip (see more details in Sec. II D).

The hearing aids were programed to achieve relatively flat frequency responses and linear amplification in an anechoic chamber when worn on KEMAR. A 75 dB SPL pink noise with a bandwidth of 1 to 8000 Hz was presented at 0° to KEMAR. Pink noise was used as the stimulus because it had a flat frequency response when analyzed in one-third octave band scales. The hearing aid output was received by a 1.27 cm microphone (ER-11 $\frac{1}{2}$ in. microphone, Etymotic Research) placed at the medial opening of a Zwislocki coupler. The microphone output was sent to its pre-amplifier (ER-11 pre-amplifier), an external sound card (Sound Blaster Extigy), and a computer. The ER-11 pre-amplifier was set to flat frequency response and −10 dB sensitivity so that it could measure undistorted input up to 140 dB SPL. The computer input was analyzed in real time using SPECTRAPLUS, which displayed the one-third octave band of the hearing aid output levels.

The frequency response (spectrum) of the hearing aid output was compared to the spectrum of the original pink noise. The gain settings of the hearing aid were adjusted using the NOAH programming interface to match the spectrum of the hearing aid output to that of the pink noise as closely as possible. Additionally, the gain of each hearing aid at different channels was set to be as low as possible to obtain matching flat frequency responses (less than 10 dB, when possible). This practice was utilized to increase the dynamic range of the flow noise measurement, defined as the input level at which the maximum output level was reached minus the noise floor of the wind tunnel. The frequency responses of ITE and ITC were also matched between the DIR and OMNI modes. The CIC was programed in the OMNI

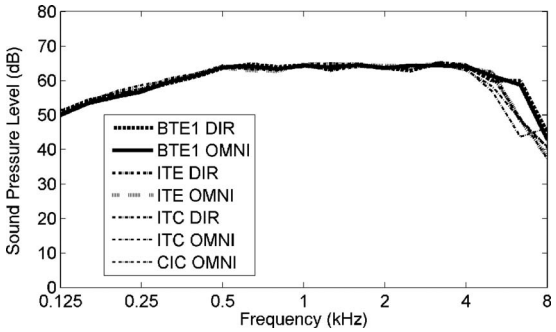

FIG. 3. Frequency responses of the custom hearing aids and KEMAR's ear canal.

mode because it did not have a directional microphone.

The frequency responses between the DIR and OMNI modes of ITE and ITC were matched within 1 dB from 100 to 4000 Hz and within 5.5 dB from 5000 and 8000 Hz. In addition, the frequency responses for all the hearing aids, including CIC OMNI, were matched within 2.0 dB between 100 and 4000 Hz and within 9 dB between 5000 and 8000 Hz (Fig. 3).

B. Wind tunnel characteristics

The wind tunnel was an Eiffel type tunnel measuring 10.36 m long. It had a honeycomb flow straightener and several layers of wire mesh at the wind tunnel inlet to break down large flow structures into fine-grained turbulence. A smooth contracting section followed to gradually accelerate the flow into the Plexiglas walled test section. Two progressive diffusers were also implemented upstream and downstream of the fan to reduce noise and to ensure stable flow.

The fan speeds to generate flow velocities of 0, 4.5, 9.0, and 13.5 m/s were calibrated using Pitot tube measurements and a linear regression equation. The 0 m/s flow velocity was included to measure the ambient noise in the wind tunnel in the absence of flow. The ambient noise in the wind tunnel was measured using an ER-11 microphone shielded with an ellipsoidal windscreen (B&K UA 0781). The one-third octave band levels of the ambient noise in the wind tunnel are reported in Chung *et al.*, 2009.

C. Flow noise measurements

1. Custom hearing aids

Flow noise was measured at the hearing aid output at flow velocities of 0, 4.5, 9.0, and 13.5 m/s, which correspond to 0, 3 (gentle breeze), 5 (fresh breeze), and 6 (strong breeze) on the Beaufort scale, respectively. The velocity of 4.5 m/s was the average wind speed recorded in cities in United States on a typical non-windy day (National Climate Data Center, 2006) and 13.5 m/s is the threshold for the National Weather Services to issue a wind advisory. Higher flow velocities are not included in this study because Chung *et al.* (2009) showed that the limiters in hearing aids limited the maximum flow noise levels recorded at the hearing aid output. At 13.5 m/s, the flow noise levels, especially for the DIR mode, reached the maximum output levels of the hearing aids at almost all head angles, and the polar patterns were nearly circular in shape.

The equipment used in the flow noise measurements was identical to that used in the hearing aid programming process. The hearing aid output was picked up by an ER-11 microphone placed in a Zwislocki coupler, and the microphone signal was fed to the external sound card and recorded in a computer using audio recording and editing software (AUDITION 1.0).

Prior to making recordings, the recording level of the sound card was set with caution so that the upper dynamic range was used but the maximum input level of the sound card was not exceeded. The hearing aid was programed to the DIR mode first and the KEMAR head was turned slowly from 0° to 360° in the presence of a flow at 13.5 m/s (i.e., the highest flow velocity). The angle with the highest flow noise output was identified and the KEMAR head was turned to that angle. The recording level of the sound card was adjusted so that the highest flow noise level was 10 dB below the maximum input level of the sound card. This process was carried out at the highest flow velocity, which ensured that the maximum flow noise level would never exceed the maximum input level of the sound card for the particular hearing aid. In other words, no peak-clipping or limiting was generated by the ER-11 microphone unit or the computer sound card.

After setting the recording level of the sound card, 30-s recordings were made at flow velocities of 0, 4.5, 9.0, and 13.5 m/s by turning the KEMAR head relative to the direction of the flow. The recording for each angle at each flow velocity was saved as a separate digital. wav file using AUDITION. KEMAR's head and the hearing aid were then transported back to the anechoic chamber for calibration measurements. Physical contact with KEMAR's pinnae was avoided during transportation to and from the wind tunnel to ensure the hearing aid settings used in the flow noise measurements were identical to those in the anechoic chamber.

The above procedures were repeated for each hearing aid.

2. KEMAR's open canal

To shed light on flow noise experienced by non-hearing aid users, flow noise was recorded in KEMAR's ear canal without the hearing aid. Prior to flow noise measurements, the recording level of the sound card was set to avoid peak-clipping or limiting by the ER-11 microphone unit or the sound card. 30-s flow noise measurements were made from 0° to 360° at the four flow velocities. The open canal recordings were different from the hearing aid recordings because there was no limiter in the recording path for flow noise levels lower than 140 dB SPL (i.e., the limits of the ER-11 microphone and its pre-amplifier).

D. Calibration measurements

1. Custom hearing aids

The levels of the flow noise recorded in the computer depended on the flow noise level at the microphone input as

well as on the gain/attenuation settings of the whole recording path (i.e., the gain of the hearing aid, the sensitivity of the ER-11 microphone and its pre-amplifier, and the recording level of the sound card). The hearing aid output in response to a 75 dB SPL pink noise presented at 0° was recorded in the anechoic chamber using identical equipment and volume control settings as in the flow noise recordings for the DIR and the OMNI modes of each hearing aid. The voltage of the calibration file for each microphone mode was then used as the reference for 75 dB SPL to calculate the overall and one-third octave band levels of the flow noise recordings.

Because output=input+gain for any audio system, by setting the level of the hearing aid output in response to a 75 dB SPL input to be 75 dB SPL would essentially set the gain of the whole recording path to 0 dB, i.e.,

$$\text{output(in response to a 75 dB SPL input)} = \text{input(equals 75 dB SPL)} + \text{gain(equals 0 dB)}.$$

This calibration method has the advantage of estimating the flow noise level at the microphone input without the influence of the hearing aid gain. If, however, only the gain/attenuation of the ER-11 microphone, its pre-amplifier, and the sound card was set to 0 dB (see the calibration procedures for the KEMAR open canal), the calculated flow noise level would have depended on the gain of the hearing aid. Another advantage was that, as gain equaled 0 dB, the highest flow noise level calculated in the recordings equaled the maximum output level of the hearing aid, which, in turn, equaled the *input level* at which the maximum output level was reached. In other words, the maximum output level =0 dB gain+input level at which the maximum output level was reached. Beyond this input level, further increase in flow noise level at the microphone would not cause further increase in the hearing aid output.

The following are the maximum output levels of the hearing aids when their gains were set to 0 dB:

(a) ITE DIR=110.5 dB, OMNI=108.5 dB;
(b) ITC DIR=100.7 dB, OMNI=100.9 dB; and
(c) CIC OMNI=107.3 dB.

Figure 3 shows the spectra of the calibration noises for the DIR and OMNI modes of each hearing aid when the overall levels of the calibration noises were equalized to 75 dB SPL. These spectra also represented the hearing aids' frequency responses, which were programed using the pink noise presented at 0°. Although there were slight differences between the spectra of the calibration noises in some frequency regions, the voltage differences for the calibration noises of the DIR and OMNI modes were within 0.2 dB for all hearing aids, indicating that the overall levels of the DIR and OMNI modes were well-matched. Additionally, the level differences of all the spectra/frequency responses were matched within 1.3 dB at 125, 500, and 2000 Hz one-third octave band. This matching of the frequency responses allowed direct comparison of the flow noise levels among the hearing aids.

2. KEMAR's open canal

For calibration purposes, the ER-11 microphone was removed from KEMAR's ear and mounted on a long wooden pole 1 cm in diameter. It was set at the same height as the center of the loudspeaker diaphragm and 1 m from the loudspeaker. The microphone output in response to a 75 dB SPL pink noise presented in sound field was recorded and then served as the 75 dB SPL reference for the estimation of flow noise levels in KEMAR's ear canal.

The above calibration procedures were adopted for two reasons.

(a) The hearing aid was absent so it was not necessary to account for the gain of the hearing aid (i.e., only needed to account for the gain/attenuation of the ER-11 microphone, its pre-amplifier, and the sound card).
(b) The ear canal had a resonance with flat frequency responses below 1500 Hz and a resonance of >10 dB between 2000 and 6300 Hz.

Setting the recorded calibration noise level (output of the recording equipment) in response to a 75 dB SPL input to equal 75 dB SPL eliminated the gain of the recording equipment and preserved the ear canal resonance. This allowed the calculation of the flow noise level inside KEMAR's ear canal and shed light on the flow noise levels experienced by non-hearing aid users.

III. RESULTS

Figures 4–6 show the polar patterns of the overall level and the 125, 500, and 2000 Hz one-third octave band levels of the custom hearing aids and the KEMAR open canal recordings. In flow noise discussions, angles are referred to in the clockwise direction. Flow *from the front* generally refers to angles between 320° and 40°. Flow *from the back* generally refers to angles between 140° and 220°. In addition, *hearing aid facing the direction of the flow* refers to the flow blowing from the side of the hearing aid (i.e., KEMAR turned between 50° and 130° for hearing aids worn on the right ear). *Hearing aid facing downstream* refers to the flow coming from the opposite side of the hearing aid (i.e., between 230° and 310°).

A. Custom hearing aid comparison

1. Similarities

The following characteristics were generally true for all custom hearing aids tested.

(a) At 4.5 m/s, the overall and the one-third octave band levels were generally the highest when the flow blew from the front and when the KEMAR was turned to angles between 200° and 250° relative to the direction of the flow.
(b) At flow velocities of 9.0 or 13.5 m/s, higher flow noise levels spread to a wider range of angles. The overall flow noise levels were the same at 9.0 and 13.5 m/s (e.g., ITE DIR at angles between 330° and 30° in Fig. 4). This phenomenon occurred because the flow noise levels reached the maximum output level of the hearing aids.

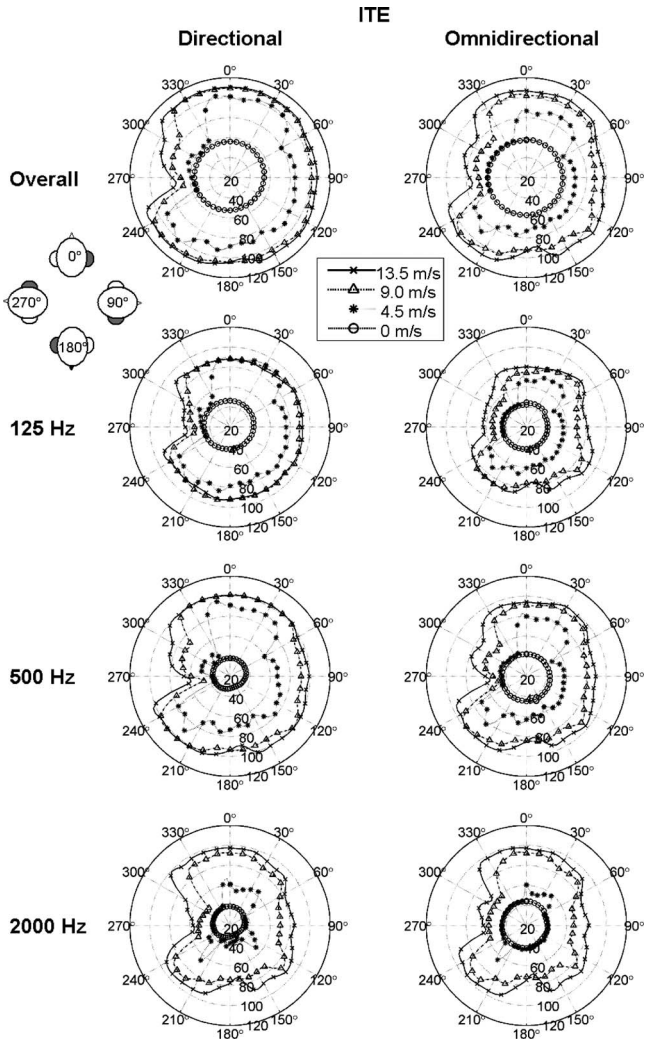

FIG. 4. The overall, 125, 500, and 2000 Hz one-third octave band levels of flow noise measured at the output of ITE, which was set to the directional (DIR) and omnidirectional (OMNI) modes. The four aerial views of the head with a darkened ear indicated the hearing aid locations at various angles. The high-level flow noise was reduced in some head angles by the limiters in the hearing aid (see text for details).

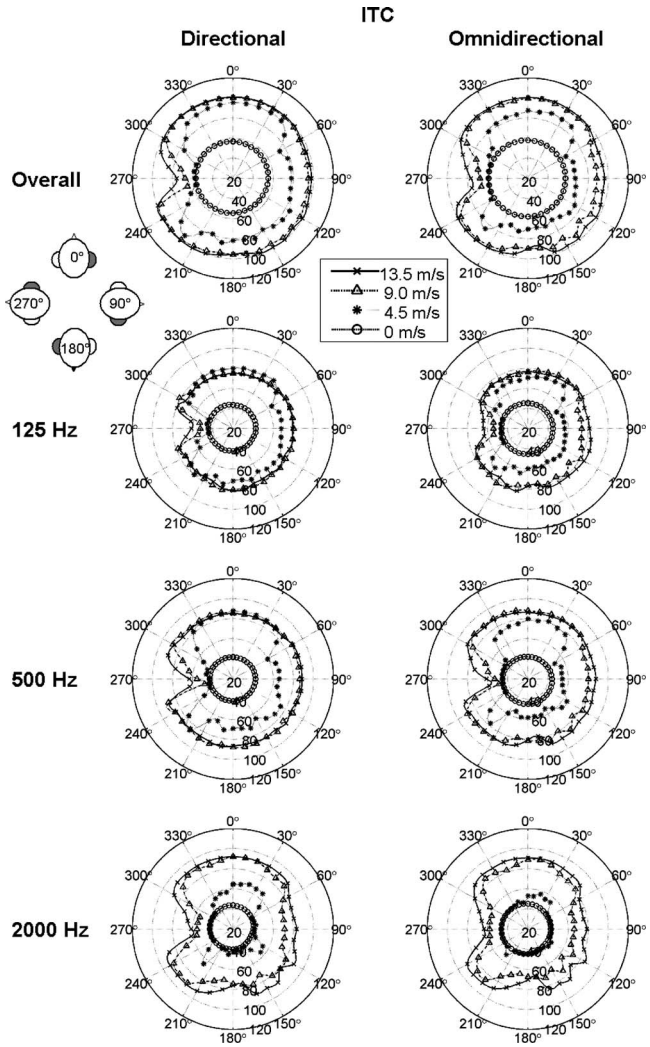

FIG. 5. The overall, 125, 500, and 2000 Hz one-third octave band levels of flow noise measured at the output of ITC, which was set to the directional (DIR) and omnidirectional (OMNI) modes.

Notice that the recordings made in KEMAR's open ear canal showed that the flow noise levels were all below 140 dB SPL, and they continued to increase from flow velocities of 9.0 to 13.5 m/s (i.e., the KEMAR's open canal data were recorded without limiting, Fig. 6). This result indicates that the cessation of the level increase in some hearing aid recordings (especially in DIR conditions at angles around 0°) was due to the actions of the limiters in the hearing aids.

(c) At angles where the overall level of the hearing aids reached their maximum output levels, two signs of limiting were observed: (1) the overall or one-third octave band polar patterns show larger arcs with similar values (e.g., the overall levels of ITE DIR between 330° and 30° were the same in Fig. 4), and (2) flow noise levels at lower velocities have higher levels than at higher velocities in the one-third octave band polar patterns at a wider range of angles (e.g., the flow noise levels obtained at 4.5 m/s were higher than those at 9.0 and 13.5 m/s at 125 Hz one-third octave band between 330° and 30° in Fig. 4). See detailed explanations in Chung *et al.*, 2009.

(d) The lowest flow noise levels were generally found when the hearing aid was facing the direction of the flow (e.g., at 260° and/or 270°).

(e) The flow noise levels when hearing aids faced downstream generally fell between the highest and the lowest flow noise levels.

2. Differences

Different styles of custom hearing aids also have individual characteristics.

(a) At 4.5 m/s, the angles with the highest wind noise levels for ITE tend to be narrower than other custom hearing aids. The highest levels occur between 340° and 50° (70° span) for ITE, whereas those for ITC and CIC occur between 310° and 50° (100° span). The overall, 125, and 500 Hz one-third octave band levels for ITE were only slightly higher than the ambient noise levels at angles

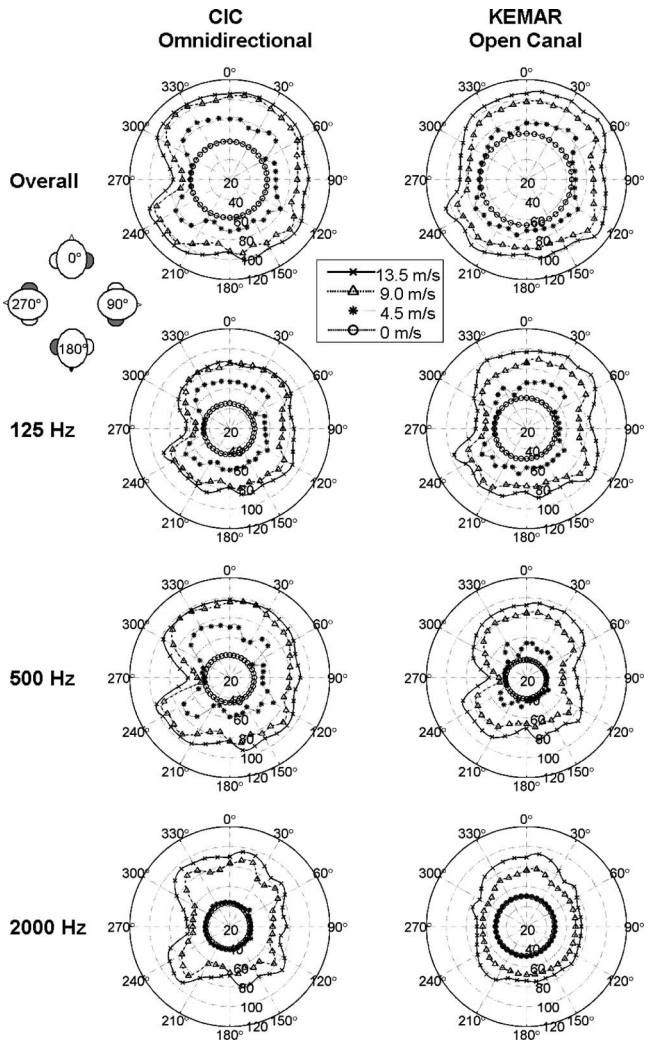

FIG. 6. The overall, 125, 500, and 2000 Hz one-third octave band levels of flow noise measured at the output of CIC OMNI and in KEMAR's ear canal.

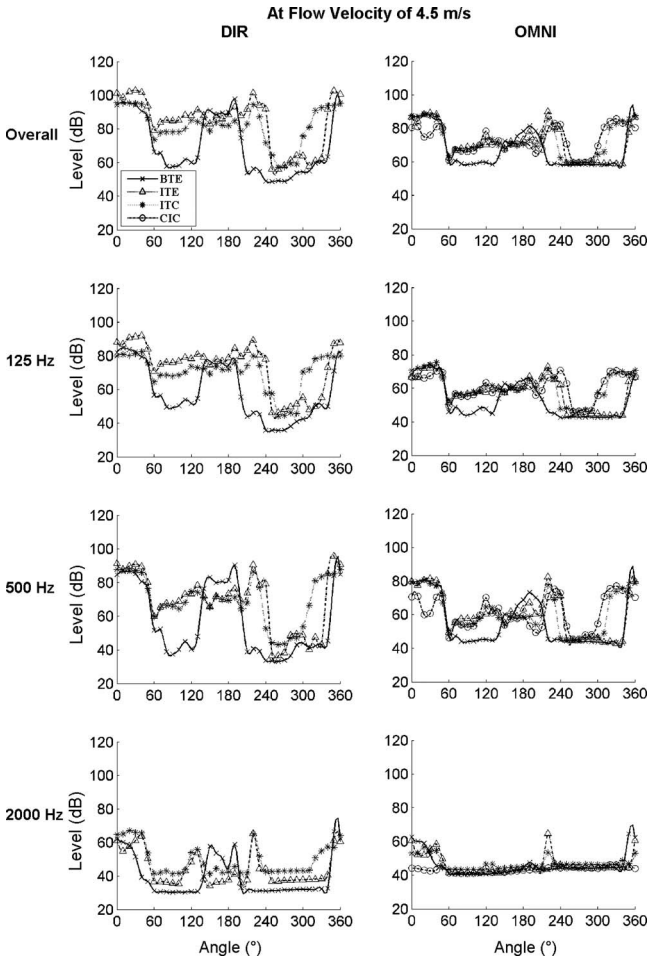

FIG. 7. A comparison of the overall, 125, 500, and 2000 Hz one-third octave band levels of flow noise measured at the output of ITE, ITC, CIC, and BTE1 at a velocity of 4.5 m/s.

between 310° and 330°, whereas those of ITC and CIC were much higher than the ambient noise level at the same angles.

(b) At 2000 Hz one-third octave band at 4.5 m/s, both CIC and KEMAR's open canal recordings showed that the noise levels were either the same or slightly above the ambient tunnel noise (Fig. 6). Those of ITE and ITC, however, had relatively higher levels between 350° and 40°, and at 220° (Figs. 4 and 5).

(c) Hearing aids with lower maximum output levels were more likely to show signs of limiting at lower flow velocity. For example, ITE had higher maximum output levels than ITC (Figs. 4 and 5). The polar patterns of the overall levels of ITE DIR at flow velocities of 9.0 and 13.5 m/s had the same values between 330° and 30° (a 70° span) but those of ITC DIR had the same values between 330° and 50° (a 90° span).

B. Behind-the-ear and custom hearing aid comparisons

In previous studies, Fortune and Preves (1994) and Thompson and Dillon (2002) compared the flow levels for different hearing aid styles at several discrete angles. No reports compared the flow noise levels of hearing aids from 0° to 360°. The data collected in this study provide an opportunity to compare wind noise in hearing aids with different styles because (1) the data from Chung *et al.*, 2009 and this study were collected using identical experimental procedures, (2) all measurements were carried out when the hearing aids were worn on KEMAR's right ear, and (3) the frequency responses of BTE1 in Chung *et al.*'s (2009) study and the custom hearing aids were matched within 1.3 dB at 125, 500, and 2000 Hz and matched within 1.9 dB from 100 to 4000 Hz (Fig. 3). This allowed direct comparisons of the flow noise levels among different hearing aid styles.

Figure 7 shows the flow noise levels at 4.5 m/s at the input of BTE1 and the custom hearing aids. Flow noise levels recorded at higher flow velocities were not plotted because flow noise levels reached the hearing aids' maximum output levels at some head angles. Several characteristics are observed in Fig. 7.

(a) The lowest levels in a plot reflected the ambient noise levels in the wind tunnel. The lowest levels in the OMNI plots generally had similar values among different hearing aids. The lowest levels in the DIR plots, however, are somewhat lower than those of the OMNI plots because

the directional microphones differed in their ability to reduce background noise in the far field. Further, if the ambient noise levels at the directional microphone output were lower than the expansion threshold (42 dB SPL), the noise levels would be further reduced by the expansion algorithm.

(b) BTE1 DIR and OMNI yielded lower levels in a wide range of angles than the custom hearing aids. They consistently had low noise levels between 60° and 130° and between 200° and 340° (a 140° span). The custom hearing aids generally had much higher noise levels than BTE1 at angles between 60° and 130°, and they only had low noise levels from 240° to 300° (a 60° span).

(c) At angles around 180°, BTE1 had higher noise levels than custom hearing aids, especially at higher frequencies (i.e., 500 and 2000 Hz one-third octave bands).

(d) At angles around 270° (i.e., when the hearing aid was facing the direction of the flow), all hearing aids generated the lowest flow noise levels in both DIR and OMNI modes.

(e) At angles between 0° and 50°, CIC OMNI consistently yielded lower flow noise levels than OMNI of other hearing aids, which generally had similar overall, 125, and 500 Hz one-third octave band levels. The DIR plots, however, showed that ITE generally displayed higher levels than those of BTE1 and ITC.

C. KEMAR's open canal

Figure 6 shows the polar patterns for the overall, 125, and 500 Hz one-third octave band levels of the KEMAR ear canal recordings. Their shapes were generally similar to the OMNI polar patterns of the custom hearing aids. The KEMAR's open canal polar patterns in the 2000 Hz one-third octave band, however, were distinctively different from those of custom hearing aids.

(a) The ambient noise levels of the KEMAR ear canal recordings were much higher than those of the hearing aids because of the pinna and ear canal resonances (Fig. 6).

(b) The polar patterns of the KEMAR ear canal looked somewhat circular with slightly higher levels at angles between 320° and 30° at 9.0 m/s, angles between 290° and 50°, and angles between 210° and 240° at 13.5 m/s. The patterns of the custom hearing aids, however, showed considerably higher noise levels and distinctively more level variations at 9.0 and 13.5 m/s.

D. DIR vs OMNI

The similarities and differences between DIR and OMNI of the ITE and ITC were analyzed. The CIC data were not analyzed because CIC did not have a DIR mode. Correlation coefficients were calculated by correlating the noise levels obtained at the same head angles in the DIR and OMNI modes of the same hearing aid. Average differences between the microphone modes were calculated using the absolute values of the DIR minus OMNI level differences so that either positive or negative differences were treated as variations in the measurements.

The correlation coefficients were used as a quantitative indication of the similarity in the shapes of the polar patterns for two data sets, and the average differences were used to infer the magnitude of the level difference between the two data sets. A high coefficient with a small average difference indicates that the two data sets have similar shapes and amplitudes. A high coefficient with a large average difference indicates that the two data sets had similar polar pattern shapes but had a relatively constant difference in amplitude. A low coefficient indicates that the shapes of the polar patterns were different for the two data sets. The lower the coefficients are, the fewer angles at which the levels rose and fell in unison.

In addition, the level differences of DIR minus OMNI (DIR-OMNI) at 4.5 m/s were calculated at each angle and plotted in Fig. 8. The DIR-OMNI differences at higher flow velocities, however, were not calculated because the flow noise levels reached the hearing aids' maximum output levels at some angles.

1. Correlation coefficients

The correlation coefficients and the average differences between DIR and OMNI of the same hearing aid are shown in Table I. Although the flow noise levels reached the maximum output levels of the hearing aids in some angles at higher flow velocities, the correlations are moderately high to very high (i.e., between 0.78 and 0.96), indicating that the polar patterns between DIR and OMNI generally had similar shapes.

2. DIR-OMNI differences and average differences

The DIR-OMNI level differences from 0° to 360° for ITE and ITC are shown in Fig. 8. In the absence of a flow (i.e., 0 m/s), DIR typically yielded lower noise levels than OMNI at the hearing aid output due to its directional effects. In the presence of a flow, the majority of the DIR-OMNI level differences were positive (Fig. 8) and the average differences were large (Table I), indicating that DIR generated much higher flow noise levels than OMNI. The DIR-OMNI differences and average differences, however, decreased as the flow velocity increased. The DIR-OMNI differences sometimes became zero or negative. Several factors could have contributed to this phenomenon: First, DIR usually reached its maximum output level at a lower flow velocity than OMNI. If the level of DIR was being limited but the level of OMNI continued to grow as flow velocity increased, then the DIR-OMNI difference decreased (e.g., the overall levels of ITE around 0° at 9.0 and 13.5 m/s in Figs. 4 and 8). Second, recall that when the overall levels are severely limited, the one-third octave band levels might show lower levels at higher flow velocities. The one-third octave band levels of OMNI, however, continued to increase with flow velocity, resulting in a negative DIR-OMNI difference (e.g., the 125 one-third octave band levels of ITC around 0° at 9.0 m/s in Figs. 5 and 8). Third, if the levels in both modes reached the maximum output levels, which are the same for OMNI and DIR, the DIR-OMNI level difference became zero (e.g., the overall levels of ITC around 0° at 13.5 m/s in Figs. 5 and 8).

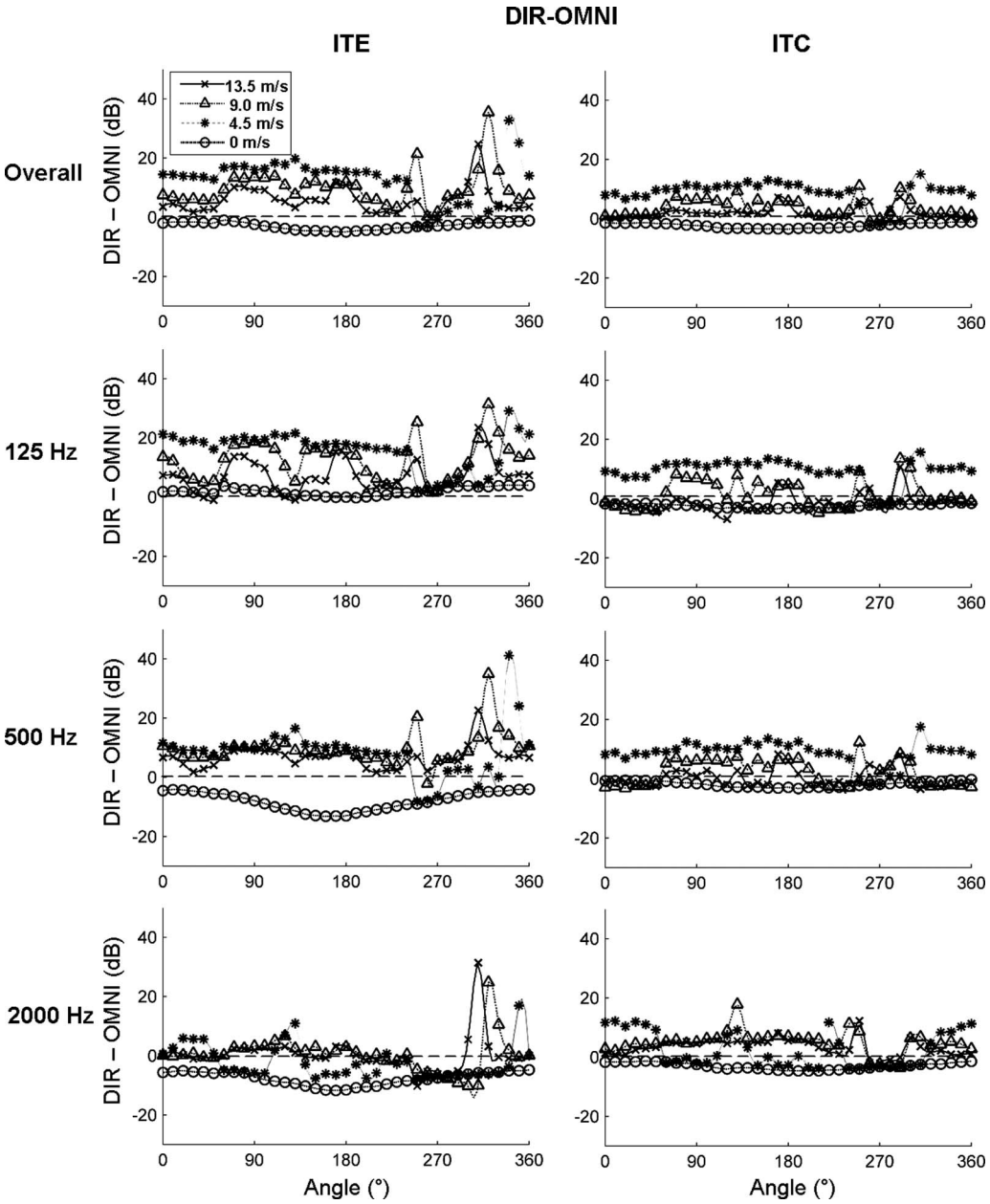

FIG. 8. Overall and one-third octave band level differences calculated by subtracting the noise levels of the omnidirectional microphone (OMNI) from its corresponding directional microphone (DIR) for ITE and ITC hearing aids.

Fourth, if flow noise levels were lower than the ambient noise levels in the wind tunnel, DIR would yield lower levels than OMNI because of its ability to reduce ambient noise in the far field. The DIR-OMNI differences, thus, become negative (e.g., the 500 Hz one-third octave band levels of ITE from 0° to 360° at 0 m/s).

IV. DISCUSSION

A. Custom hearing aid comparison

Custom hearing aids generally had the highest noise levels when the flow came from the front or when the head turned to angles between 190° and 250° at low velocities (Figs. 4–7). The lowest flow noise levels were recorded when the hearing aid was facing the direction of the flow at angles between 260° and 270°. The flow noise levels recorded when the hearing aid was facing downstream of the flow usually yielded intermediate levels.

Regarding the differences, ITE generated relatively lower levels between 300° and 330° at 4.5 m/s compared to ITC and CIC in both DIR and OMNI modes (Fig. 7). The flow noise levels generated by ITE were similar to the ambient noise levels between 300° and 340° whereas both ITC and CIC yielded flow noise levels much higher than the ambient noise levels (e.g., the overall levels in Figs. 4–6).

The polar patterns of ITE obtained in the present study bear remarkable resemblance to the ones reported by Beard and Nepomuceno (2001). In Beard and Nepomuceno, 2001, the authors measured flow noise levels every 10° from 0° to 360° at the output of microphones mounted on an ITE shell worn on KEMAR's left ear. They reported the ambient noise

TABLE I. The correlation coefficients and average differences between DIR and OMNI at three flow velocities for an ITE and ITC hearing aids. All the correlation coefficients were statistically significant ($p<0.01$).

	Correlation coefficient			Average difference (dB)		
	4.5 m/s	9.0 m/s	13.5 m/s	4.5 m/s	9.0 m/s	13.5 m/s
			Overall level			
ITE	0.89^	0.87*	0.88*	12.9	9.9	5.8
ITC	0.94^	0.94*	0.95*	9.0	3.8	2.0
			125 Hz one-third octave band level			
ITE	0.94^	0.82*	0.78*	15.9	12.8	7.3
ITC	0.93^	0.79*	0.79*	9.6	3.9	2.9
			500 Hz one-third octave band level			
ITE	0.89^	0.91*	0.93*	9.9	9.7	6.8
ITC	0.96^	0.89*	0.89*	8.9	4.3	2.4
			2000 Hz one-third octave band level			
ITE	0.84^	0.91	0.86*	5.4	3.7	3.0
ITC	0.89^	0.94*	0.94*	5.3	5.6	3.7

The asterisks (*) mark the entries calculated from data set with overall levels reached the maximum output levels at least at three angles and the ^ mark the entries calculated from data sets with flow noise levels that fell below the ambient noise levels at least three angles.

levels and polar patterns of flow noise levels at 100, 200, 500, and 1000 Hz at flow velocities of 2.1 and 5.0 m/s. When the 500 Hz one-third octave band results obtained in the present study at 4.5 m/s were compared to that of Beard and Nepomuceno (2001), which is obtained at 5.0 m/s, the polar plots in the present study had similar shapes but slightly lower levels than those obtained in Beard and Nepomuceno, 2001 due to the lower flow velocity. In addition, the shapes of polar plots obtained at 100 and 1000 Hz one-third octave bands in Beard and Nepomuceno, 2001 also had similar shapes as those measured in the present study at 125 and 2000 Hz. These results indicated that the flow noise patterns are highly repeatable across studies.

B. BTE1 and custom hearing aid comparison

When the flow was coming from the front (i.e., at angles around 0°), the flow noise levels were the highest regardless of the hearing aid style. These results are consistent with other studies (Beard and Nepomuceno, 2001; Thompson and Dillon, 2002). The difference was that at 4.5 m/s, the angles with the highest flow noise levels tended to be between 340° and 50° for BTE1 and ITE (Fig. 8), whereas those for ITC and CIC were between 300° and 50° (a wider span). At higher flow velocities, angles with the highest flow noise levels expanded to adjacent angles for all hearing aids.

Additionally, ITE DIR and OMNI consistently had higher levels than BTE1 and other custom hearing aids, except at 2000 Hz (Fig. 7). This was likely because the protrusion of the pinna from the head further increased the flow velocity. The ITE microphones' proximity to this area of faster flow caused the highest levels among the hearing aids tested.

When the overall and one-third octave band levels of all the hearing aids were compared, CIC OMNI tended to have the lowest levels between 0° and 50° (Fig. 8). These results agree with those of Fortune and Preves (1994) measured at 0°. In addition, CIC tended to yield the lowest noise levels in the 2000 Hz one-third octave band. The output levels at 4.5 m/s were either equal to or slightly higher than the ambient noise levels, likely because the microphone was shielded from direct air flow impingement. The advantage of CIC at 2000 Hz, however, seemed to disappear as the flow velocity increased. This result could be because of a high amount of turbulence generated in the vicinity of the microphone (i.e., in the concha bowl, Thompson and Dillon, 2002) and/or a shift in the location of the flow separation point.

At angles between 60° and 130°, BTE1 yielded much lower flow noise levels than the custom hearing aids (Fig. 7). This pattern was likely due to turbulent fluctuations in the wake of the KEMAR head acting on the hearing aid microphones. As the pinna protruded from the surface of the head and disrupted the streamlined air flow, additional turbulence could be generated in the vicinity of the custom hearing aid microphones. Custom hearing aids, thus, yielded higher flow noise levels than BTE1, which was close to the surface of the KEMAR head. When the hearing aid was facing downstream (i.e., at angles around 90°), the pinna should not have created any additional disruption to the streamlined air flow. Yet, custom hearing aids still had higher flow noise levels than BTE1. This phenomenon was likely because the pinna (with custom hearing aids) protruded into the turbulent flow in the wake of the KEMAR head, whereas BTE1 was much closer to the surface of the head and away from the turbulence.

When the flow came from the back (i.e., at angles around 180°), BTE1 tended to have higher flow noise levels than custom hearing aids (Fig. 7). This could be because BTE1 was immersed in the flow, whereas the custom hearing aids were shielded from the flow at 180°. Custom hearing aids, however, tended to have higher levels between 200° and 250° than BTE1 when the hearing aid was slightly

turned to the downstream side. This phenomenon was likely because the pinna protrusion increased the local flow velocity and turbulence was formed close to the hearing aid microphones.

When the hearing aids were facing the direction of the flow (i.e., at angles around 270°), the flow noise level was usually the lowest for all hearing aids because the hearing aid microphones were closest to the theoretical point of stagnation (Chung *et al.*, 2009). The difference was that, at 4.5 m/s, BTE1 had a relatively wider range of angles having low overall, 125, and 500 Hz one-third octave band flow noise levels than custom hearing aids. The angles with low levels ranged from 220° to 340° for BTE1 (a 130° span, Fig. 8), from 250° to 330° for ITE (a 90° span), from 240° to 310° for ITC (an 80° span), and from 250° to 300° for CIC (a 60° span).

Caution must be taken in interpreting the above results. Although hearing aids with the same styles generally have similar shapes in their polar patterns (Chung *et al.*, 2009), individual level differences do exist among the same styles of hearing aids (Grenner *et al.*, 2000). In addition, although the results of the present study showed that the behind-the-ear hearing aid either generated comparable or lower levels than custom hearing aids, Thompson and Dillon (2002) reported that a behind-the-ear hearing aid yielded higher flow noise levels than custom hearing aids at 0° and 30°. It is unclear if the differences were due to individual hearing aid differences, the signal level averaging scale differences (present study: one-third octave bands vs Thompson and Dillon (2002): log scale), or other unknown differences in the experimental setup. Future studies are needed to shed light on this issue.

C. KEMAR's open canal

Flow noise levels at the output of the hearing aids and in KEMAR's open canal are affected by their relative frequency responses. For example, KEMAR's open ear canal resonances produced a flat frequency response at low frequencies (i.e., between 100 and 500 Hz), whereas typical hearing aid frequency responses usually have a roll-off in the same frequency region. The open canal recordings, therefore, yielded a higher level at 125 Hz at 0 m/s than the hearing aid recordings even though the two systems were responding to a constant noise in the background (i.e., the ambient noise).

If comparisons of the increase in flow noise levels at different flow velocities are desirable, the comparisons should be made relative to the ambient noise level. For example, at 0° of 125 Hz one-third octave band at 4.5 m/s in Fig. 6, both CIC OMNI and KEMAR's open ear canal yielded a flow noise level of 68 dB. The ambient noise level of CIC OMNI was 45 dB at 0° but that of the open canal was 51 dB. Thus, flow noise level increase in CIC OMNI were greater than in KEMAR's open canal when the flow velocity increased from 0 to 4.5 m/s.

Compared to CIC OMNI, the shapes of the KEMAR's open canal polar patterns were very similar at 125 and 500 Hz (Fig. 6). The polar patterns of overall levels and 2000 Hz, however, did not exhibit the characteristic drop in flow noise levels at angles around 270°. This was likely because the microphone was shielded from direct flow impingement in the open canal recordings resulting in much lower flow noise in the high frequency region (e.g., 2000 Hz) than CIC OMNI (i.e., from 220° to 250° and from 290° to 60°).

Another use of the KEMAR open canal recordings is to demonstrate the flow noise growth patterns in conditions where no limiters were present in the recording path (i.e., from ear canal→ER-11 microphone and its pre-amplifier →computer sound card). The data obtained with KEMAR's open ear canal supported that (1) flow noise levels continued to increase as flow velocities increased from 9.0 to 13.5 m/s, and (2) the similar flow noise levels at flow velocities of 9.0 and 13.5 m/s in some angles for ITC and CIC recordings (i.e., around 0°) were due to the limiters in the hearing aids. These conclusions were also supported by the "microphone on cylinder" data in Chung *et al.*, 2009.

D. DIR vs OMNI

The correlation coefficients between the directional and omnidirectional microphone modes of the same hearing aids generally showed a moderately high to high correlation (i.e., above 0.78) although there were differences in the flow noise levels (i.e., from 2.0 to 9.6 dB, Table I). These results indicate that the flow noise levels were different between the DIR and OMNI modes but the magnitude generally rose and fell in unison from 0° to 360° (i.e., the shapes of the polar patterns were similar).

In the absence of a flow, directional microphones generally yielded lower noise levels than omnidirectional microphones (i.e., the negative DIR-OMNI values in Fig. 8) because of their ability to reduce background noise. The exception was at 125 Hz one-third octave band, the directional microphone was not effective because directional microphones with small microphone differences often have minimum or no directional effect for sounds in far field at low frequencies (Chung, 2004).

In addition, the exceptionally high negative DIR-OMNI for ITE at 500 Hz one-third octave band at 0 m/s was likely due to a combination of two factors: (1) The directional microphone was very effective in reducing noise, and (2) the noise level at the microphone output was below the expansion threshold (i.e., 42 dB SPL). The lower the input levels, the less gain was provided by the expansion algorithm. As a result, the DIR-OMNI calculations yielded large negative values in Fig. 8 (Chung *et al.*, 2009). Similar phenomenon was not found in ITC, likely because ITC had a smaller microphone distance than ITE. As the microphone distance reduces, the directional effect of a directional microphone generally lessens (Ricketts, 2001). The microphone output of the ITC, therefore, was not further reduced by the expansion algorithm, resulting in much smaller negative DIR-OMNI values.

In the presence of a flow, directional microphones had higher noise levels in most angles at low flow velocities (Fig. 8). As the frequency responses of the DIR and OMNI modes were matched, the higher flow noise levels in the directional microphones could be attributed to both incoherent source

effect and proximity effect. When the hearing aid was facing upstream, however, directional microphones consistently yielded lower noise levels at all flow velocities (i.e., angles around 270° had the negative DIR-OMNI values in Fig. 8). This phenomenon was created because the hearing aid was close to the theoretical point of stagnation. Although directional microphones usually generated more flow noise than omnidirectional microphones, directional microphones were able to reduce the ambient noise in the far field. The directional microphone output for the flow noise combined with the ambient noise was still lower than the omnidirectional microphone output. Similar level differences between the directional and omnidirectional microphones are also observed in the data obtained in the Beard and Nepomuceno (2001) and Thompson and Dillon (2002) studies.

At higher flow velocities (13.5 m/s), the limiters in the hearing aids limited the maximum output level of the hearing aids. As the outputs of directional microphones usually reach the maximum output level at a lower flow velocity than those of omnidirectional microphones, the average difference was reduced and more negative DIR-OMNI differences were obtained as flow velocity increased (see more details in Sec. III).

The above results on directional and omnidirectional microphones were generally consistent with those obtained in Chung *et al.*, 2009 on behind-the-ear hearing aids. The difference was that negative DIR-OMNI values were consistently obtained not only at angles around 270° but also around 90° in behind-the-ear hearing aids (Fig. 8).

E. Applications

1. Clinical applications

Currently, there is no consensus on how to fit or use hearing aids based on users' amplification needs in outdoor activities. Comparing hearing aids with different styles, BTE1 was found to have the largest range of angles with the lowest flow noise levels (Fig. 7). It also had comparable or lower levels than other custom hearing aids at other angles, except around 180°. Similar patterns were also observed on another behind-the-ear hearing aid in Chung *et al.*, 2009. Behind-the-ear hearing aids, therefore, appear to be the most desirable hearing aids for outdoor activities because it is more likely for the user to experience low noise levels in wind.

On the other hand, the flow noise comparisons in the 2000 Hz one-third octave band suggested that putting the microphone into the ear canal can reduce flow noise in the 2000 Hz one-third octave band (Figs. 4–6). In addition, CIC OMNI tended to have the lowest flow noise levels at a large range of angles compared to ITE and ITC at 4.5 m/s. It might, therefore, be beneficial for clinicians to recommend using completely-in-the-canal hearing aids if a user will often need to function in environments with low wind velocities.

Further, custom hearing aids had a narrow range of angles having the lowest flow noise levels (i.e., close to angles at 270°). Monaural custom hearing aid users, therefore, are recommended to position their hearing aids to directly face the direction of the wind. On the other hand, bilateral custom hearing aid users can position the better ear to face the direction of the wind and to either reduce the gain or turn off the second hearing aid to reduce binaural interference. Turning down the gain or turning off the hearing aid can be especially beneficial for hearing aid users who experience binaural interference as described in Walden and Walden, 2005 because they can understand more speech with monaural than binaural hearing aids in background noise.

2. Engineering and design applications

Monaural and binaural automatic microphone switching algorithms can be designed to take advantage of the wind noise differences between the directional and omnidirectional modes. Many high-performance digital hearing aids are designed to automatically switch to the omnidirectional mode across all frequency regions or only in the low frequency regions when incoherent/wind noise is detected. This, however, may not always be the most effective at reducing wind noise.

The results of the present study and several previous studies indicated that directional microphones could generate lower noise levels when the flow comes from the front and/or when the hearing aid was facing downstream at low flow velocity (Beard and Nepomuceno, 2001; Thompson and Dillon, 2002; Chung *et al.*, 2009). Even if flow noise was detected, the superposition of flow noise and background noise in a frequency channel can still be lower in the directional than in the omnidirectional microphone mode. A monaural automatic microphone switching algorithm, therefore, can be designed to monitor the output difference between the two microphone modes in each frequency channel and adapt to the mode with the lowest output levels.

Binaural automatic microphone switching algorithms can also be designed to monitor the presence of speech in the environment and hearing aid output in both ears. When a large level difference is detected between two hearing aids, the algorithms can automatically reduce the overall and/or the low frequency gain of the hearing aid with significantly lower signal-to-noise ratio. For users with confirmed severe binaural interference, the algorithms can be programed to turn off the hearing aid with higher noise output. Making use of binaural communication of hearing aids to combat wind noise can potentially enhance users' hearing aid satisfaction.

It should be noted that the results of this series of studies were obtained using a KEMAR manikin with a bold head and no shoulder. The effects of hair styles, headwear, shoulders, and clothing were not examined. In addition, the data were collected using hearing aids with many signal processing algorithms turned off (e.g., noise reduction algorithms and wind noise reduction algorithms). Further studies are needed to test the effects of these factors on flow noise characteristics.

ACKNOWLEDGMENTS

Many thanks are expressed to Paloma Mejia, Jong Beom Park, the Herrick Laboratories staff, and Dr. Kaibao Nie for their technical assistance. We would also like to thank Sonic

Innovations for donating a set of custom hearing aids to the study, and Michael Nilsson and Gerald Wilson for providing technical details of the hearing aids.

Amlani, A. M. (**2001**). "Efficacy of directional microphone hearing aids: A meta-analytic perspective," J. Am. Acad. Audiol. **12**, 202–214.

Barlett, B., and Barlette, J. (**2001**). *Practical Recording Techniques*, 3rd ed. (Focal Press, Burlington, MA).

Bauer, B. B. (**1941**). "Uniphase unidirectional microphones," J. Acoust. Soc. Am. **13**, 41–45.

Baumhaur, J. C., and Marcus, L. A. (**1997**). "Noise cancelling gradient microphone assembly," U.S. Patent No. 438826.

Beard, J., and Nepomuceno, H. (**2001**). "Wind noise levels for an ITE hearing aid," Knowles Engineering Report No. 128, Revision A, Knowles Electronics, Itasca, IL.

Bentler, R. A., Tubbs, J. L., Egge, J. L. M., Flamme, G. A., and Dittberner, A. B. (**2004**). "Evaluation of an adaptive directional system in a DSP hearing aid," Am. J. Audiol. **13**, 73–79.

Brown, D. V., and Mongeau, L. M. (**1995**). "The design, construction, and validation of a small, low-speed, quiet wind tunnel with application to noise from the flow over a cavity," Internal Report Nos. 204 and HL95-9, Herrick Laboratories, Purdue University, West Lafayette, IN.

Burkhard, M. D., and Sachs, R. M. (**1975**). "Anthopometric manikin for acoustic research," J. Acoust. Soc. Am. **58**, 214–222.

Carlson, E., and Killon, M. (**1974**). "Subminiature directional microphones," J. Audio Eng. Soc. **22**, 92–96.

Chung, K. (**2004**). "Challenges and recent developments in hearing aids Part I: Speech understanding in noise, microphone technologies and noise reduction algorithms," Trends Amplif. **8**, 83–124.

Chung, K., Mongeau, L., and McKibben, N. (**2009**). "Wind noise in hearing aids with directional and omnidirectional microphones: Polar characteristics of behind-the-ear hearing aids," J. Acoust. Soc. Am. **125**, 2243–59.

Chung, K., Zeng, F.-G., and Acker, K. N. (**2006**). "Effects of directional microphone and adaptive multichannel noise reduction algorithm on cochlear implant performance," J. Acoust. Soc. Am. **120**, 2216–2227.

Chung, K., Zeng, F.-G., and Waltzman, S. (**2004**). "Utilizing hearing aid technologies as pre-processors to enhance cochlear implant performance," Cochlear Implants Int. **5**, 192–195.

Dillon, H. (**2001**). *Hearing Aids* (Thieme, New York).

Eargle, J. (**2004**). *The Microphone Handbook*, 2nd ed. (Elsevier, New York/Focal Press, Burlington, MA).

Fortune, T., and Preves, D. (**1994**). "Effects of CIC, ITC, and ITE microphone placement on the amplification of wind noise," Hear. J. **47**, 23–27.

Gibson, B. (**2007**). *The Ultimate Live Sound Operator's Handbook* (Hal Leonard, New York).

Grenner, J., Abrahamsson, U., Jernberg, B., and Lindblad, S. (**2000**). "A comparison of wind noise in four hearing instruments," Scand. Audiol. **29**, 171–174.

Hawkins, D. B., and Yacullo, W. S. (**1984**). "Signal-to-noise ratio advantage of binaural hearing aids and directional microphones under different levels of reverberation," J. Speech Hear. Disord. **49**, 278–286.

Killion, M. C., Schulien, R., Christensen, L., Fabry, D., Revit, L., Niquette, P., and Chung, K. (**1998**). "Real world performance of an ITE directional microphone," Hear. J. **51**, 24–38.

Kochkin, S. (**2005**). "MarkeTrak VII: Customer satisfaction with hearing instruments in the digital age," Hear. J. **38**, 30–37.

National Climate Data Center (**2006**). "Minimum wind noise," http://www.ncdc.noaa.gov/oa/climate/online/ccd/avgwind.html (Last viewed 6/1/2006).

National Committee for Fluid Mechanics Films (**1972**). *Illustrated Experiments in Fluid Mechanics: The NCFMF Book of Film Notes*, 2nd ed. (MIT, Cambridge, MA).

Reedyk, C. W. (**1973**). "Noise-cancelling electret microphone for light weight telephones," J. Acoust. Soc. Am. **53**, 1609–1615.

Ricketts, T. A. (**2000**). "Impact of noise source configuration on directional hearing aid benefit and performance," Ear Hear. **21**, 194–205.

Ricketts, T. A. (**2001**). "Directional hearing aids," Trends Amplif. **5**, 139–176.

Ricketts, T. A., and Dhar, S. (**1999**). "Aided benefit across directional and omni-directional hearing aid microphones for behind-the-ear hearing aids," J. Am. Acad. Audiol. **10**, 180–189.

Ricketts, T. A., and Henry, P. (**2002**). "Evaluation of an adaptive directional-microphone hearing aid," Int. J. Audiol. **41**, 100–112.

Shure, Pro Audio (**2009**). "Proximity effect," available at http://shure.custhelp.com/cgi-bin/shure.cfg/php/enduser/std_adp.php?p_faqid=2844&p_created=1037811455&p_sid=Vf8vxsqi&p_lva=38&p_sp=cF9zcmNoPTEmcF9zb3J0X2J5PSZwX2dyaWRzb3J0PSZwX3Jvd19jbnQ9MTEzMSZwX3Byb2RzPTAmcF9jYXRzPTAmcF9wdj0mcF9jdj0mcF9zZWFyY2hfdHlwZT1hbnN3ZXJzLnNlYXJjaF9mbmwmcF9wYWdlPTEmcF9zZWFyY2hfdGV4dD1wcm94aW1pdHkgZWZmZWN0&p_li=&p_topview=1 (Last viewed 6/1/2009).

Spriet, A., Van Deun, L., Eftaxiadis, K., Laneau, J., Moonen, M., van Dijk, B., van Wieringen, A., and Wouters, J. (**2007**). "Speech understanding in background noise with the two-microphone adaptive beamformer BEAM™ in the Nucleus Freedom™ cochlear implant system," Ear Hear. **28**, 62–72.

Studebaker, G., Cox, R., and Formby, C. (**1980**). *Acoustical Factors Affecting Hearing Aid Performance: The Effect of Environment on the Directional Performance of Head-Worn Hearing Aids* (University Park Press, Baltimore, MD).

Thompson, S. (**2002**). *Microphones, Receivers, and Telecoils in Hearing Aids: Standards, Options, and Limitations*, edited by M. Valente (Thiemes, New York).

Thompson, S., and Dillon, H. (**2002**). *Wind Noise in Hearing Aids*, presented at the American Academy of Audiology Convention, Philadelphia, PA.

Valente, M. (**1999**). "Use of microphone technology to improve user performance in noise," Trends Amplif. **4**, 112–135.

Valente, M., Fabry, D. A., and Potts, L. G. (**1995**). "Recognition of speech in noise with hearing aids using dual microphones," J. Am. Acad. Audiol. **6**, 440–9.

Valente, M., Schuchman, G., Potts, L. G., and Beck, L. B. (**2000**). "Performance of dual-microphone in-the-ear hearing aids," J. Am. Acad. Audiol. **11**, 181–189.

Walden, T. C., and Walden, B. E. (**2005**). "Unilateral versus bilateral amplification for adults with impaired hearing," J. Am. Acad. Audiol. **16**, 574–84.

The effect of oral articulation on the acoustic characteristics of nasalized vowels

Panying Rong and David P. Kuehn
Department of Speech and Hearing Science, University of Illinois at Urbana-Champaign, Champaign, Illinois 61820

(Received 26 December 2008; revised 21 October 2009; accepted 23 December 2009)

To study the acoustic characteristics of nasalized vowels, the effects of velopharyngeal opening and oral articulation are considered. Based on vocal tract area functions for one American English speaker, spectral evolutions for the nasalization of three English vowels /a/, /i/, and /u/ were studied by simulating transfer functions for vowels with only velar movement, and for different nasal consonant-vowel utterances, which include both velar and oral movements. Simulations indicate extra nasal spectral poles and zeros and oral formant shifts as a result of the velopharyngeal opening and oral movements, respectively. In this sense, if oral articulation is coordinated with velar movement in such a way that nasal acoustic features are prominently attenuated, corresponding compensatory articulation can be developed to reduce hypernasality. This may be realized by (1) adjusting the articulatory placement for isolated nasalized vowels or by (2) changing the relative timing of coarticulatory movements for dynamic speech. The results demonstrate the effect of oral articulation on the acoustics of nasalized vowels. This effect allows oral articulation to compensate for velopharyngeal dysfunction, which may involve a constellation of speech production disorders resulting from anomalous velopharyngeal closure and which is usually accompanied by hypernasality and nasal emission of air. © *2010 Acoustical Society of America.*
[DOI: 10.1121/1.3294486]

PACS number(s): 43.70.Bk, 43.70.Aj, 43.72.Ar [DAB] Pages: 2543–2553

I. INTRODUCTION

Nasalization is the production of a sound while the velum is lowered, so that some air escapes through the nose during the production of the sound through the mouth. Vowels that are adjacent to nasal consonants (/m/, /n/, and /ŋ/ in English) tend to be at least partially nasalized because of the opening of the velopharyngeal port. Previous studies have used volumetric imaging techniques such as magnetic resonance imaging (MRI) to explore the structural characteristics of the vocal tract (Baer *et al.*, 1991; Dang *et al.*, 1994; Demolin *et al.*, 2003; Moore, 1992; Serrurier and Badin, 2008; Story *et al.*, 1996). Other studies have summarized the acoustic cues of vowel nasalization based on the anatomical structures of the oropharyngeal and nasal tract (Chen, 1997; Feng and Castelli, 1996; Kataoka *et al.*, 2001; Pruthi *et al.*, 2007). Transmission line modeling of the vocal tract has been used as an effective approach to correlate anatomical structures with the acoustic outputs of vowel nasalization (Feng and Castelli, 1996; Pruthi *et al.*, 2007). The majority of previous studies considered the effect of velopharyngeal opening (VPO) on vowel nasalization by correlating velar movement with the spectral evolutions for nasalized vowels in the absence of oral movement. Other studies have shown that oral articulation makes a difference in the pole/zero locations (Pruthi *et al.*, 2007). This difference was, however, not shown in the simulation. With regard to the variability of oral cavity shape for vowel production, oral articulatory placement can be quite flexible for nasalized vowel production. Specifically, the vocal tract profile for the same vowel in different vowel-nasal consonant (VN) or nasal consonant-vowel (NV) utterances can vary with nasal contexts due to the effect of coarticulation.

Volumetric imaging enables direct three-dimensional (3D) representation of the vocal tract shape by acquiring a series of image slices, in one or more anatomical planes, through a desired volume of the human body. MRI serves as an attractive imaging technique to obtain the 3D volume of the vocal tract with regard to its low hazard to human subjects. Story *et al.* (1996) measured static vocal tract shapes of a subject for different vowels and consonants by MR imaging and simulated the corresponding acoustics based on a transmission line model of the vocal tract.

Dang *et al.* (1994) analyzed the morphologic and acoustic properties of the nasal and paranasal cavities through MR imaging of the 3D geometry of the nasal and paranasal cavities in the coronal orientation, and the main vocal tract (oropharyngeal tract) in the sagittal orientation during sustained production of nasal consonants. The nasal and paranasal cavities differ from the oral cavity in (1) static acoustic structure, (2) complexity of morphology, (3) covering of mucosal layers, and (4) the existence of paranasal cavities. The area function derived from the image data indicated that the nasal tract could be divided into the posterior, middle, and anterior portions, each of which is characterized by a shape factor $S_f = S/\sqrt{4\pi A}$ (where S_f is the shape factor, S is a cross-sectional circumference, and A is a cross-sectional area of the tract). The nasal tract was considered as a side branch coupled to the main vocal tract, whereas the paranasal sinuses were regarded as Helmholtz resonators coupled to the nasal passages.

Pruthi *et al.* (2007) simulated the spectral properties of vowel nasalization based on the area functions derived from the MRI data in Story (1995) and Story *et al.* (1996) through a computer vocal tract model, VTAR (Zhang and Espy-Wilson, 2004). Both transfer functions and susceptance plots for nasalized vowels with different VPOs were simulated to obtain the pole-zero evolutions and order of principal cavity affiliations, where the pole-zero evolution means the change in spectral pole-zero patterns with the increase or decrease in velopharyngeal opening area. The acoustic characteristics of nasalized vowels were summarized from the simulation as (1) extra poles and zeros, (2) reduction in first formant amplitude, (3) increase in bandwidth of all poles affiliated with the nasal cavity, (4) spectral flatness in the low-frequency range, (5) movement of the low-frequency center-of-gravity toward a neutral vowel configuration, (6) reduction in the overall intensity of the vowel, and (7) shifts in pole frequencies due to the switch of affiliation from the oral cavity to the nasal cavity.

In order to characterize acoustic properties of nasal vowels, Feng and Castelli (1996) introduced a /ɳ/-like target for nasal vowels corresponding to the pharyngonasal tract realized when the velum is completely lowered. A nasal vowel was considered as a dynamic trend toward the nasal target. The evolutions of transfer function for 11 French nasal vowels were simulated through a two-branched-parallel L-C($-R$) electrical circuit model as trends from the oral vowels to their corresponding pharyngonasal configurations. Three categories of spectral pattern, represented by the three corner vowels /i/, /u/, and /a/, were summarized as (1) acquisition of a high pole (1000 Hz) and disappearance of $F2$ (second formant) for the /i/ category; (2) lowering of $F1$ and/or elevation of $F2$ for the /u/ category; and (3) acquisition of a low pole (250–300 Hz), disappearance of $F1$ and lowering of $F2$ for the /a/ category.

The limitation of most previous studies lies in that only the relationship between VPO and the acoustics of nasalized vowels has been simulated. Oral articulation, although mentioned in some studies to influence vowel nasalization by changing the resonant properties of the vocal tract, has not been correlated directly with the spectral patterns of nasalized vowels in simulation. For example, Pruthi *et al.* (2007) showed theoretically in Eq. (6) that both velopharyngeal opening and oral cavity configuration could affect the characteristics of nasalized vowels. Such an effect of oral articulation in shaping nasalized vowel spectra, although not systematically simulated in their study, raises the probability of developing proper oral articulation to compensate for the spectral effects of velopharyngeal opening, which may have potential clinical application in treating velopharyngeal dysfunction. This probability is further reinforced in Demolin *et al.*, 2003, which demonstrated the specific organization of oral articulation in French nasal vowel production.

So the purpose of this study is first to simulate the effect of articulatory placement on nasalized vowel spectra through transmission line modeling of the vocal tract. In this sense, the transfer function evolutions for NV utterances are simulated. If given the effect of oral articulation on shaping nasalized vowel spectra, the second purpose is to develop appropriate oral articulation to compensate for VPO in terms of attenuating nasal spectral features and preserving oral formant structures, which are realized in either of the two approaches: (1) optimizing the articulatory placement for isolated nasalized vowels or (2) adjusting the relative timing of coarticulatory movements for NV utterances to compensate for VPO.

II. METHODS

A. Transmission line modeling of the main vocal tract

A transmission line model of the main vocal tract (oropharyngeal tract) was constructed based on the vocal tract area functions for different oral vowels measured by Story *et al.* (1996). The model is sampled at a frequency of 44 100 Hz so that the entire vocal tract is divided into 44 cylindrical tubes, each with a length equal to the entire vocal tract length divided by the number of sections (i.e., 44) and a cross-sectional area depending on the articulatory placement. The transmission line model of each tube is represented by a L-C-R electrical circuit (Zhang and Espy-Wilson, 2004), in which the equivalent electrical parameters are determined by the cross-sectional area and length of the tube.

B. Modeling of the nasal tract

Modeling of the nasal tract is also based on the transmission line model but includes some additional considerations because of its structural complexity in (1) larger surface area of the nasal cavities, (2) coupling of paranasal sinuses and asymmetry of the nasal tract, and (3) irregularity of the nasal tract shape and mucosal covering. To model the nasal tract, it is necessary to take into account all these complexities. Specifically, the complexity of nasal cavity shape is described by a shape factor $S_f = S/\sqrt{4\pi A}$, where S is a cross-sectional circumference and A is a cross-sectional area of the tract. Dang *et al.* (1994) suggested that the shape factor was of the orders of 1, 4, and 2 for the posterior, middle, and anterior portions of the nasal passages, respectively. The sphenoidal and maxillary sinuses are modeled as Helmholtz resonators coupled to the main nasal tract, whereas the frontal sinus is not considered due to the unavailability of morphologic data and its negligible influence on the low-frequency spectrum. The parameters of the two nasal passages and paranasal sinuses are collected from the same subject (Story, 1995) whose vocal tract imaging data were used to develop the transmission line model.

C. Coupling of the oral and nasal tracts

Coupling of the oral and nasal tracts is achieved by opening the velopharyngeal port, which serves as the critical mechanism of nasal sound production. Complexity of the velopharyngeal mechanism is attributed to velar movement, which results in different degrees of nasalization and various velopharyngeal geometries. Although a 3D articulatory model of the velum and nasopharyngeal wall has been established by Serrurier and Badin (2008), current MRI data for this study are not sufficient to develop such a 3D model. Instead, a distributed coupling method is selected to model

the velopharyngeal port, where the first section of the velopharynx is set to a desired coupling area, and the remainder of the velopharynx is linearly interpolated to obtain a smooth variation in areas, resulting in a corresponding reduction in the areas of the oral cavity. Pruthi *et al.* (2007) compared the distributed coupling method with the trap door coupling method in modeling the velopharynx and found that for the trap door coupling method the zeros in the simulated transfer functions did not change with a change in the coupling area and therefore the order of principal cavity affiliations for the poles is fixed. Contrastively, the distributed coupling method can be performed in a more realistic way such that the order of principal cavity affiliations for the poles of the coupled system changes with a change in the coupling area. More advantages of the distributed coupling method are found by Maeda (1982b), who suggested that the reduction in the oral cavity area is very important to produce natural sounding nasalized vowels. Similarly, Feng and Kotenkoff (2006) stated that the decrease in oral area might play an important role in nasalization. Furthermore, Serrurier and Badin (2008) described the influence of velar movement on the oral area function based on their 3D articulatory model of the velopharyngeal port and observed the covariation of the areas of oral and nasal tracts when the velum moves.

D. Derived transfer functions from the transmission line model of the entire vocal tract

Transfer functions for different vowels can be calculated based on the transmission line model of the entire vocal tract (oropharyngeal and nasal tracts). For oral vowels, a transfer function is defined as the ratio of oral to glottal volume velocity, which is calculated by multiplying the transfer function of each tubular section within the vocal tract. For nasalized vowels, a transfer function is defined as the sum of oral and nasal volume velocities divided by the glottal volume velocity. The model of the entire vocal tract is obtained by coupling the nasal tract as a side branch to the main vocal tract through a three-port connection, namely, the velopharyngeal port.

III. SIMULATION

The transfer functions for the three corner vowels /a/, /i/, and /u/ are simulated and plotted in MATLAB (V.7.0). The effect of velopharyngeal opening on the acoustic characteristics of nasalized vowels is considered by simulating the transfer functions for nasalized vowels with different velopharyngeal openings and no other articulatory movement. Then the effects of both velopharyngeal opening and oral articulation are considered by simulating the spectral evolutions for NV utterances, where the velum and oral articulators move concomitantly from the initial nasal position to the final oral position. As long as the effect of oral articulation on the acoustics of nasalized vowels is specified, the relative timing of coarticulatory movements for NVs is adjusted to attenuate nasal spectral features and preserve oral formant structures. Furthermore, in order to accommodate such articulatory adjustment to different speech samples, the articulatory synthesis function of a MATLAB package (*Childer, Speech Processing and Synthesis Toolboxes*) is used to derive the optimal articulatory parameters such that the characteristic spectral features (the first four formant frequencies) for the nasalized vowel are adjusted to approach the oral counterparts. The spectra for the compensated nasalized vowels are then compared with the corresponding spectra for nasalized vowels without articulatory compensation.

A. Area functions and transfer functions for oral vowels

The area functions for the oral vowels /a/, /i/, and /u/ are derived from the MRI data of the vocal tract images in the study by Story *et al.* (1996) and depicted as the final targets of area function evolutions in Figs. 1(a), 1(c), and 1(e), respectively. The corresponding transfer functions are calculated through the transmission line model of the vocal tract and plotted as the bottom lines in Figs. 2(a)–2(c), respectively.

B. Transfer function evolutions for nasalized vowels with different VPOs

The effect of VPO on nasalized vowel spectra is considered by assuming that oral articulators remain in static position during the nasalization of vowels. Although oversimplified, this assumption still provides information on the relationship between VPO and spectral characteristics of nasalized vowels. The transfer functions for nasalized vowels /a/, /i/, and /u/ with a variation of velopharyngeal opening areas from 1 to 90 mm^2 are shown in Figs. 2(a)–2(c), respectively. In order to clearly depict the subtle spectral changes in nasalized vowels with small VPO, the transfer function evolutions are obtained by increasing velopharyngeal opening area from 1 to 10 mm^2 in 1 mm^2 steps, and from 10 to 90 mm^2 in 10 mm^2 steps in Figs. 2(a)–2(c), where the lowest line in each panel corresponds to the transfer functions for the oral vowels /a/, /i/, and /u/, respectively. The dashed bold horizontal line separates each panel into two parts such that the transfer functions below correspond to a variation of VPO area from 1 to 10 mm^2 in 1 mm^2 steps, and those above represent the transfer functions for nasalized vowels with VPO area varying from 10 to 90 mm^2 in 10 mm^2 steps. The amplitudes of the transfer functions within each panel are increased in 15 dB steps from the bottom to the top to be better distinguished. Figures 2(d)–2(f) compare the transfer functions for the nasalized vowels /a/, /i/, and /u/ (dotted line) with a VPO area of 60 mm^2 and their oral counterparts (dashed line), respectively.

C. Transfer function evolutions for NV utterances

Although the effect of velopharyngeal opening on the nasalized vowel spectrum has been revealed in Fig. 2, the assumption of static oral cavity shape during vowel nasalization is oversimplified. To better simulate real speech, the effect of not only velopharyngeal opening but also other concomitant oral articulatory movement needs to be considered. In this sense, NV utterances are chosen as the targets with regard to the coordinated articulatory movements. From a

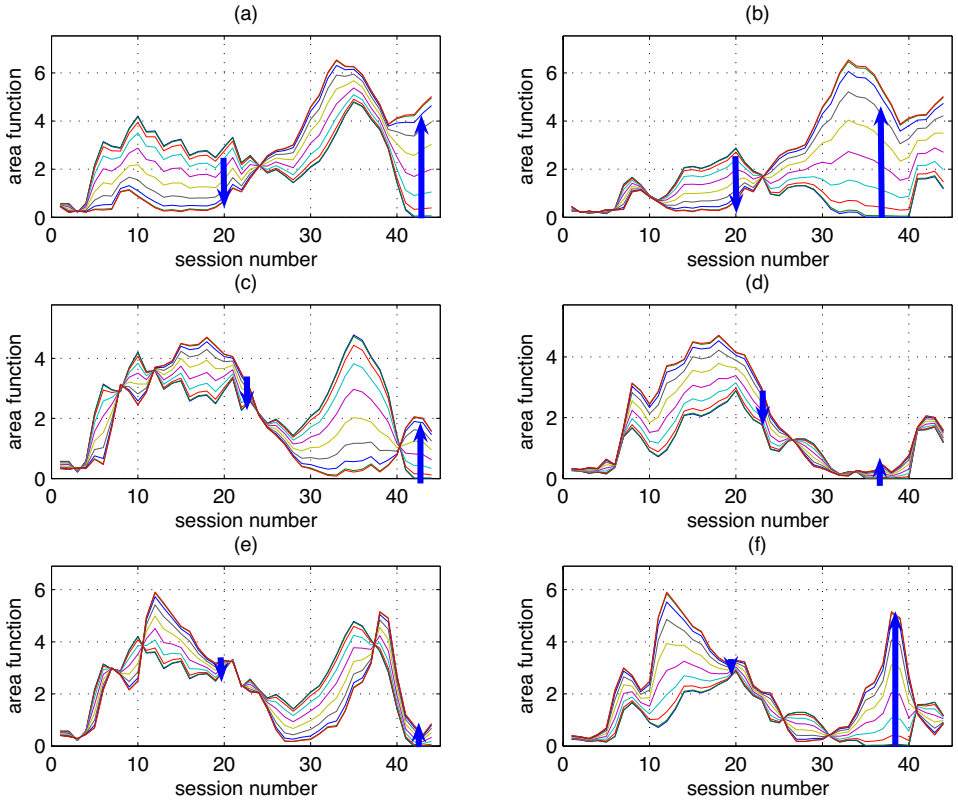

FIG. 1. (Color online) Oral area function evolutions for the NV utterances, where the up arrows mark the dominant oral articulatory movements and the down arrows point out the evolutions of the oral area at the velopharyngeal port. (a)–(f) show the area function evolutions for /ma/, /na/, /mi/, /ni/, /mu/, and /nu/, respectively.

morphologic view, a time-variable vocal tract profile changing from the initial shape for the nasal consonant to the final shape for the oral vowel is represented as an evolution of area functions by a mathematical function $u(t)=u_o+(u_f-u_o)(10(t/T)^3-15(t/T)^4+6(t/T)^5)$ for $0\le t\le T$ (*), where u_o and u_f are the area functions for the initial and final phonemes and T is the duration of the utterance. Since this mathematical function produces a "minimum jerk" movement (Story, 2005), the area function at any time t $(0<t<T)$ within the syllable can be approximately simulated from this function. The evolutions of area functions for six NV utterances (/ma/, /na/, /mi/, /ni/, /mu/, and /nu/) are depicted in Figs. 1(a)–1(f), respectively, where the up arrows mark the evolutions of the area corresponding to the critical articula-

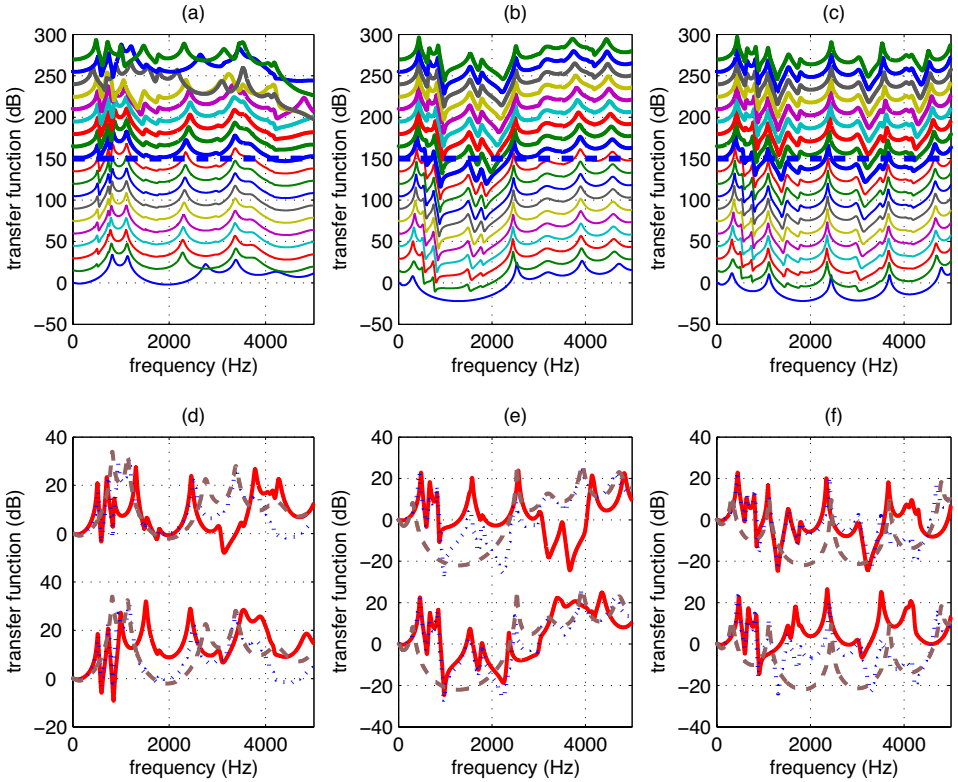

FIG. 2. (Color online) (a)–(c) show the transfer function evolutions for nasalized vowels /a/, /i/, and /u/ with a variation of velopharyngeal opening area (1) from 1 to 9 mm^2 in 1 mm^2 steps, represented by the next lowest line to the line right below the dashed bold horizontal line, and (2) from 10 to 90 mm^2 in 10 mm^2 steps, shown as the lines above the dashed bold horizontal line. The lowest lines in (a)–(c) represent the transfer functions for the corresponding oral vowels as references, and the amplitudes for the remainder of transfer functions are increased in 15 dB steps from the bottom to the top to be better distinguished. (d)–(f) compare the transfer functions for nasalized vowels /a/, /i/, and /u/ with a VPO area of 60 mm^2 (dotted lines) with the transfer functions for the nasalized vowels with the same VPO in /mV/ [solid lines in the upper panels of (d)–(f)] and in /nV/ [solid lines in the lower panels of (d)–(f)], where "V" represents /a/, /i/, and /u/ for (d), (e), and (f), respectively.

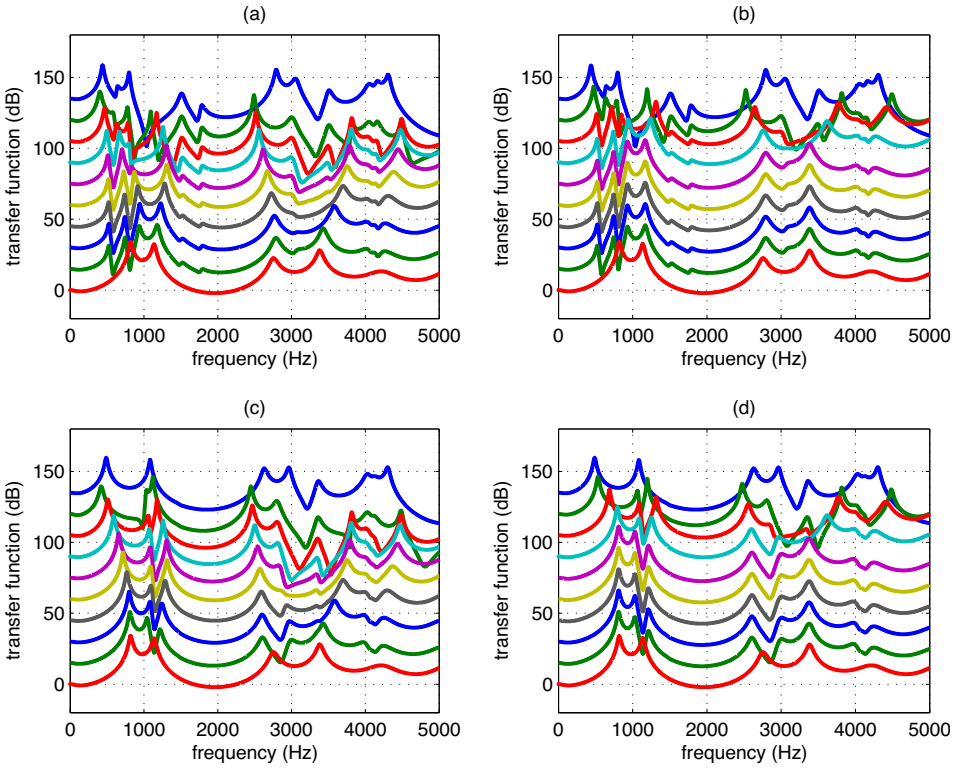

FIG. 3. (Color online) Transfer function evolutions for /ma/ (a) based on the vocal tract model with paranasal sinuses, (b) based on the vocal tract model with paranasal sinuses and with timing adjustment of coarticulation (oral articulators move in a faster pattern than the velum as specified in the text), (c) based on the vocal tract model with no paranasal sinuses, and (d) based on the vocal tract model with no paranasal sinuses and the same pattern of timing adjustment of coarticulation as described in (b). In each of (a)–(d), the transfer functions evolve from the nasal consonant /m/ at the top to the oral vowel /a/ at the bottom in ten equal time intervals. In each panel of the figure, the amplitudes of the transfer functions are increased from the bottom to the top in 15 dB steps to be better distinguished.

tory movement (labial movement for /mV/ and tongue tip movement for /nV/), and the down arrows point out the oral area evolutions at the velopharyngeal port.

However, this method of specifying the time variation of the vocal tract configuration is still oversimplified to some extent because all the articulators (including the velum, lips, and different parts of the tongue) are hypothesized to move in the same pattern as represented by the function, which is not the case for real speech with consideration to the relatively rapid movement of the tongue tip, lower lip, and slower movement of the tongue dorsum and velum (Kuehn, 1976; Kuehn and Moll, 1976). Moreover, the timing of the coarticulatory movements is set to be fixed in this fashion, which is obviously against the flexibility of coarticulatory timing in real speech. However, at this point, this simplified approach, due to the lack of dynamic MRI data for natural speech, still serves the purpose of demonstrating the effects of articulatory placement and VPO on vowel nasalization. The transfer functions for nasalized vowels in NV utterances are drawn and compared with their oral and simplified nasalized (same VPO, no oral movement) counterparts in Figs. 2(d)–2(f). The solid line in the upper part of each of (d)–(f) shows the transfer function for the nasalized vowel in /mV/, whereas the solid line in the lower part corresponds to the transfer function for the nasalized vowel in /nV/, where "V" represents the three vowels /a/, /i/, and /u/, respectively, for (d), (e), and (f). The two nasal consonant contexts are included to reflect the variation of spectral characteristics for different articulatory placements (i.e., bilabial constriction for /m/ and alveolar constriction for /n/). Figures 3(a), 4(a), 5(a), 5(c), 6(a), and 6(c) show the evolutions of transfer functions in ten equal time intervals for each of the following six NV utterances: /ma/, /na/, /mi/, /ni/, /mu/, and /nu/, respectively. Figures 3(c) and 4(c) show the simulated transfer function evolutions for /ma/ and /na/ based on a simplified vocal tract model with no paranasal sinuses as a comparison to Figs. 3(a) and 4(a).

D. Transfer function evolutions for NV utterances with timing adjustment

As mentioned above, the actual articulatory velocities of tongue, lips, and velum are different so that the relative timing of the articulatory movements can be adjusted to simulate different acoustic outcomes. With regard to the purpose of this study, the coordination between velar and other oral articulatory movements is of interest, and hence is explored by adjusting the timing of oral movements to compensate for velopharyngeal opening movement in a sense that the nasal acoustic features become less prominent and oral spectral features are largely preserved in the resultant spectrum. Since oral articulators such as tongue tip and lips normally move faster than the velum, it is reasonable to hypothesize that the oral area functions evolve in a faster pattern than the velopharyngeal area evolution in the production of NV utterances. Figures 3(b), 4(b), 5(b), 5(d), 6(b), and 6(d) show the transfer function evolutions for NV utterances (/ma/, /na/, /mi/, /ni/, /mu/, and /nu/, respectively) with a timing adjustment of oral movements such that the time for the oral area to evolve from the initial profile for the nasal consonant to the final profile for the oral vowel is half of the time for the velar area to decrease from the nonzero value for the nasal consonant to zero for the oral vowel. In this sense, the oral articulators move roughly twice as fast as the velum, so the oral area stays constant in the second half of the entire duration of the /NV/ syllable while the velar movement is still

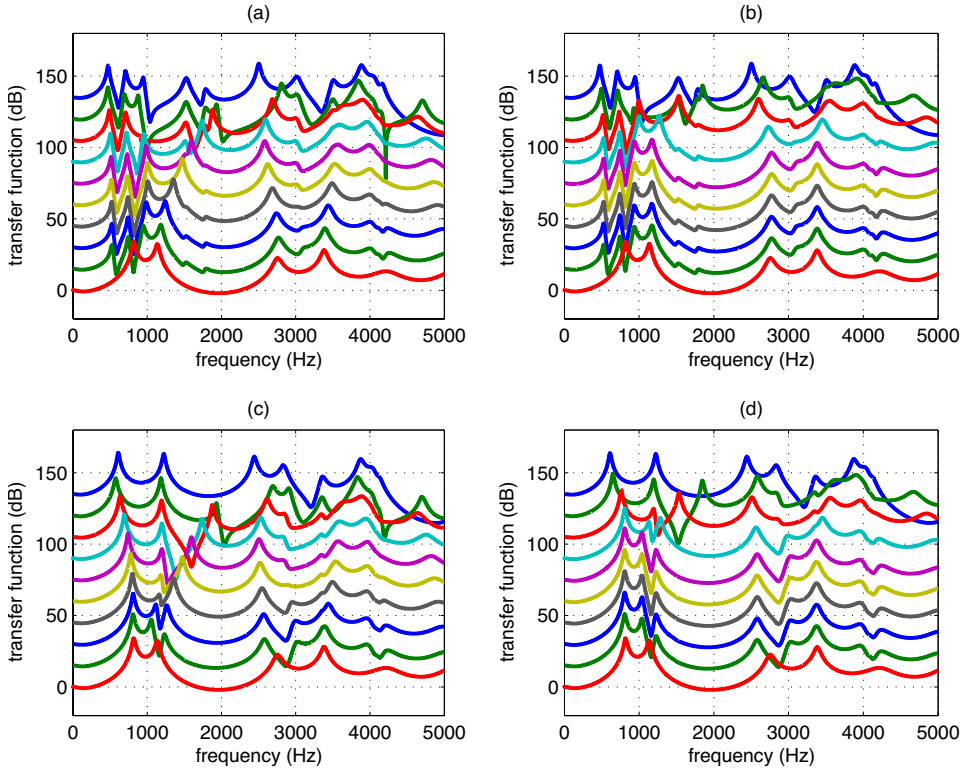

FIG. 4. (Color online) Transfer function evolutions for /na/, where (a), (b), (c), and (d) give the simulated results based on the four conditions as described in Figs. 3(a)–3(d), respectively.

continuing. Figures 3(d) and 4(d) show the corresponding timing-adjusted transfer function evolutions based on the vocal tract model with no paranasal sinuses.

E. Spectra of oral vowel and nasalized vowel without/with compensatory articulation

The timing adjustment of NV utterances allows oral articulation to compensate for VPO from a dynamic view, whereas the static oral articulatory placement can be adjusted to compensate for VPO in terms of attenuating nasal spectral features and preserving oral spectral structures. However, such an articulatory adjustment cannot be determined arbitrarily because the articulatory placement must follow some universal patterns to produce a specific speech sound, although minor variations are allowed to generate individual differences. In order to guarantee that the adjusted articulatory placement can be realized in real speech, a computer-implemented articulatory synthesizer (*Childer, Speech Processing and Synthesis Toolboxes*) is used to optimize such oral articulatory adjustments that the principal spectral characteristics (first four formant frequencies) of the resultant nasalized vowel are as close to the oral counterparts as possible. Given the target acoustic features (formant frequencies in this case), the articulatory synthesizer first optimizes the articulatory placement by adjusting a set of control articulatory parameters to generate such a vocal tract area function/midsagittal profile that the resultant acoustic features corresponding to the vocal tract model approximate the target with minimal error. Then the corresponding speech samples are synthesized based on the optimized vocal tract area function and an excitation source specified by the users. In this fashion, three types of vowels are synthesized based on the same acoustic inputs (first four formant frequencies) for comparison. The first type is an oral vowel, with the VPO parameter set to zero. The second one is a nasalized vowel without compensatory articulation, which follows the same articulatory pattern as the oral vowel except that the VPO is set to be a nonzero value. The third type is a nasalized vowel with compensatory articulation, which has its VPO set to the same value as the second type and all other articulatory parameters readjusted to optimize the acoustic outputs (the first four formant frequencies) to compensate for VPO. The effect of compensatory articulation then can be inferred by comparing the spectral features of the two nasalized vowels. Figures 7(a)–7(c) give the spectra and spectral envelopes for three such synthetic /i/ vowel samples. Specifically, Fig. 7(a) is the spectrum for oral /i/, and Figs. 7(b) and 7(c) are the spectra for nasalized /i/ without and with compensatory articulation, respectively. Figures 7(d)–7(i) give another two sets of synthetic /i/ vowel samples (each set includes three types of /i/ vowel as described above), based on the corresponding two sets of acoustic inputs. Altogether, three sets of /i/ vowel samples are exemplified in Fig. 7.

IV. RESULTS

A. Comparison of the transfer functions for oral and nasalized vowels

Figures 2(d)–2(f) show the transfer functions for the oral vowels /a/, /i/, and /u/ (dashed lines) as references and their nasalized counterparts (dotted lines) with a velopharyngeal opening area of 60 mm^2. The nasalized vowels are distin-

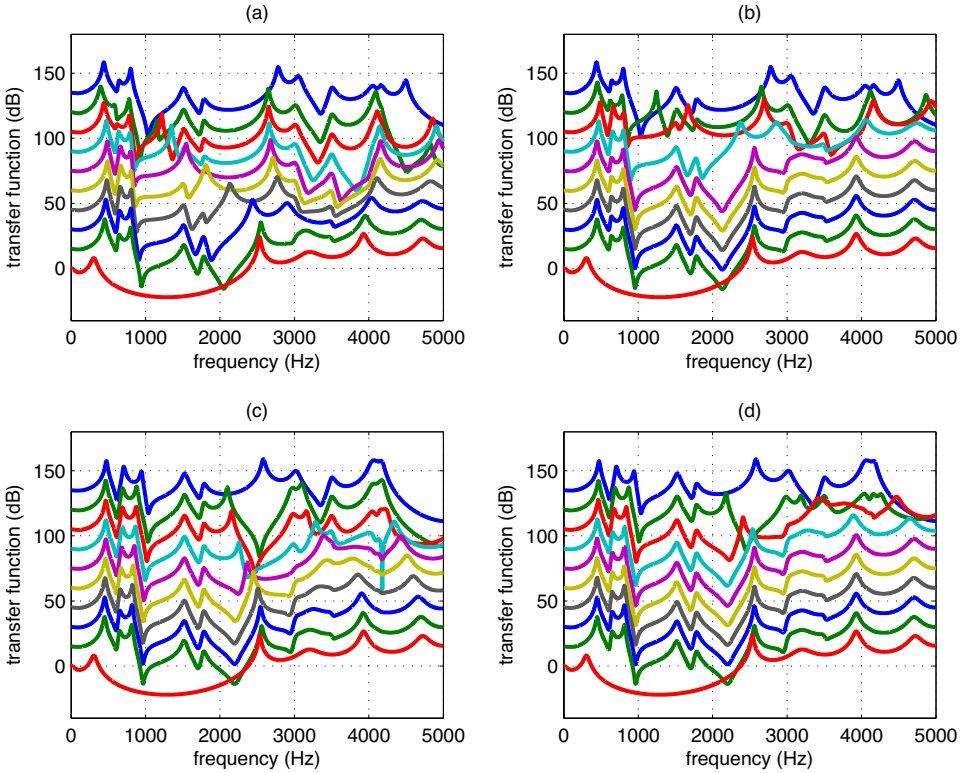

FIG. 5. (Color online) Transfer function evolutions for (a) /mi/, (b) /mi/ with timing adjustment of coarticulation (oral articulators move in a faster pattern than the velum as specified in the text), (c) /ni/, and (d) /ni/ with the same timing adjustment of coarticulation as for (b).

guished from the oral counterparts in more spectral peaks and valleys, especially in the low-frequency domain. This is consistent with previous studies such as Chen (1997) and Pruthi *et al.* (2007), who also found many spectral peaks and dips due to the paranasal sinuses and low-frequency pole-zero pairs due to the maxillary sinuses in the nasalized vowel spectra. Specifically, nasalization of the low-back vowel /a/ introduces two pole-zero pairs below the first formant. In contrast, coupling of the nasal tract introduced multiple pole-zero pairs between the first and second formants in the transfer function for the high-front vowel /i/, whereas for the mid-back vowel /u/, there are extra pole-zero pairs between $F1$ and $F2$, as well as between $F2$ and $F3$.

B. Transfer function evolutions for nasalized vowels with different VPOs

The resonant properties of the nasal and paranasal cavities are represented acoustically as extra poles and zeros in the transfer function. However, since only velar movement is considered in this model, the change in VPO does not have a large influence on transfer function evolutions, especially when the velopharyngeal opening area is small. This is attributed to structural stability of the nasal and paranasal cavities and ignoring the influence of oral articulatory movement. For nasalized vowels with larger VPOs, i.e., from 10 to 90 mm^2, the nasal spectral characteristics become more prominent for all three vowels, although the transfer function evolutions reveal different patterns for low and non-low vowels, specified as a larger spectral variation for the low vowel /a/ than for the non-low vowels /i/ and /u/, especially when VPO is larger than 50 mm^2, as shown in Figs. 2(a)–2(c). Such a difference is possibly due to the different distributions of low-frequency nasal poles and zeros relative to the oral $F1$. Specifically, the two pole-zero pairs introduced by the paranasal sinuses appear below $F1$ for nasalized /a/, but above $F1$ for nasalized /i/ and /u/. While the VPO increases, the nasal peaks become more isolated and more prominent with larger amplitude so that the second nasal zero approaches the oral $F1$ for /a/ but deviates the $F1$ for /i/ and /u/. For nasalized /a/ with a VPO larger than 50 mm^2, the second nasal zero is close enough to cancel out the first oral formant and results in a relatively flattened low-frequency response in the $F1$ region and a change in order of principal cavity affiliation for $F1$. The pole affiliation is defined to follow the convention set forth by Pruthi *et al.* (2007), who stated that a pole in the coupled system is affiliated with the nasal tract if a nasal pole with a lower frequency in the uncoupled nasal system moves to the frequency of the new pole when the coupling area increased, while the pole is referred to be affiliated with the vocal tract if an oral pole with a lower frequency in the uncoupled oral system moves to the frequency of this new pole as the coupling area increases. In this sense, the order of principal cavity affiliation can be changed as the coupling area increases, and the associated merging of the two resonances at the same frequency might therefore account for the larger variation of spectral evolution pattern for the low vowel /a/ than for the non-low vowels /i/ and /u/. Specifically, the principal cavity affiliation for $F1$ changes from the oral tract to the nasal tract during the nasalization of /a/, but remains affiliated with the oral tract for nasalized /i/ and /u/ when VPO increases. The $F2$ for all three vowels remain affiliated with the oral tract

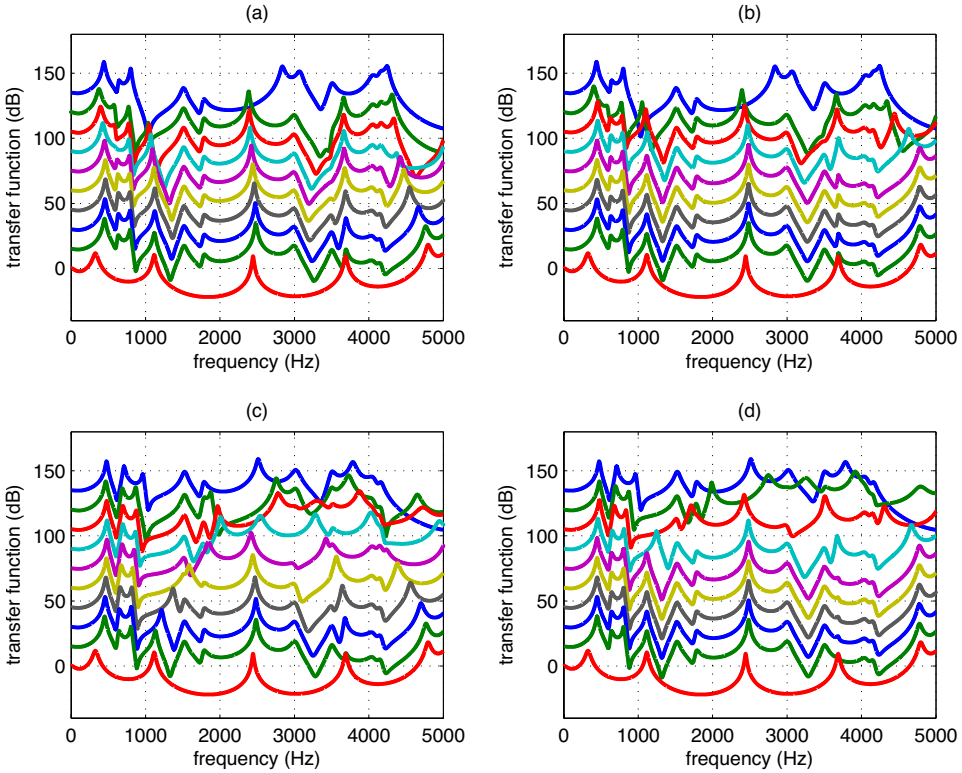

FIG. 6. (Color online) Transfer function evolutions for (a) /mu/, (b) /mu/ with timing adjustment of coarticulation (oral articulators move in a faster pattern than the velum as specified in the text), (c) /nu/, and (d) /nu/ with the same timing adjustment of coarticulation as for (b).

during nasalization. The nasal poles without intervention with oral formants in general become more prominent as VPO increases, but there is also an exception regarding the first nasal pole for nasalized /i/ and /u/. This nasal pole becomes more distinct when VPO increases from 1 to 9 mm^2 but degenerates for VPOs varying from 10 to 30 mm^2 and then becomes distinguished again when VPO keeps increasing.

C. Comparison of the transfer functions for oral and nasalized vowels in NV

From Figs. 2(d)–2(f), the spectral differences of oral versus nasalized vowels with and without other oral movements can be discriminated as formant shifts and amplitude modification. The solid line in the upper part of Fig. 2(d) shows the transfer function for nasalized /a/ in /ma/, which is defined as a transitional state between /m/ and /a/ with a velopharyngeal opening area of 60 mm^2 based on the velar area transition, and which reveals a reduction in $F1$ and $F2$ amplitudes and an increase in $F2$ frequency compared to the oral transfer function (dashed line) and nasalized counterpart with the same VPO (i.e., 60 mm^2) and no oral movement (dotted line). The solid line in the lower part of Fig. 2(d) corresponds to the transfer function for nasalized /a/ in /na/ with the same VPO of 60 mm^2, but is distinguished from the counterpart in /ma/ in relatively larger amplitude in the low-frequency domain and a further increase in $F2$ frequency. The spectral differences between /ma/ and /na/ clearly reveal that the oral articulatory adjustment superimposed on the area function for the vowel corpus has a distinct effect on vowel nasalization, which raises the possibility of developing appropriate oral articulation to compensate for velopharyngeal dysfunction (VPD) in a sense that the acoustic outcomes, such as nasal spectral peaks and oral formant shifts brought up by VPD, are attenuated. This compensatory articulation can be applied clinically as a speech treatment for VPD, because individuals with velopharyngeal dysfunction, which is defined to be a malfunction of velopharyngeal mechanism, and which is often accompanied by hypernasality and nasal emission of air, usually cannot close the velopharyngeal port fully as necessary and may hence require other speech strategies to compensate for the velopharyngeal deficiency.

By comparing the upper and lower parts of Fig. 2(e), the transfer function for /i/ in /mi/ (solid line in the upper part) reveals relatively larger amplitude in the low-frequency domain than that for /ni/ (solid line in the lower part), although both have similar spectral characteristics of extra poles and zeros between $F1$ and $F2$. However, the low-frequency spectral characteristics reveal only slight differences between nasalized vowel /i/ in /ni/ (solid line in the lower part) and its nasalized counterpart without oral movement (dotted line in the lower part). This probably can be attributed to the similar vocal tract profiles for the vowel /i/ and the nasal consonant /n/, i.e., an expanded pharyngeal cavity and a constricted oral cavity. When the nasal consonant /n/ is superimposed on the vocal tract profile for the vowel /i/, the resonant properties of the vocal tract have only slight changes such that the corresponding transfer function exhibits no prominent alteration in the low-frequency region.

For /mu/ and /nu/, a prominent difference between the upper and lower parts of Fig. 2(f) lies in that the $F2$ for /u/ in

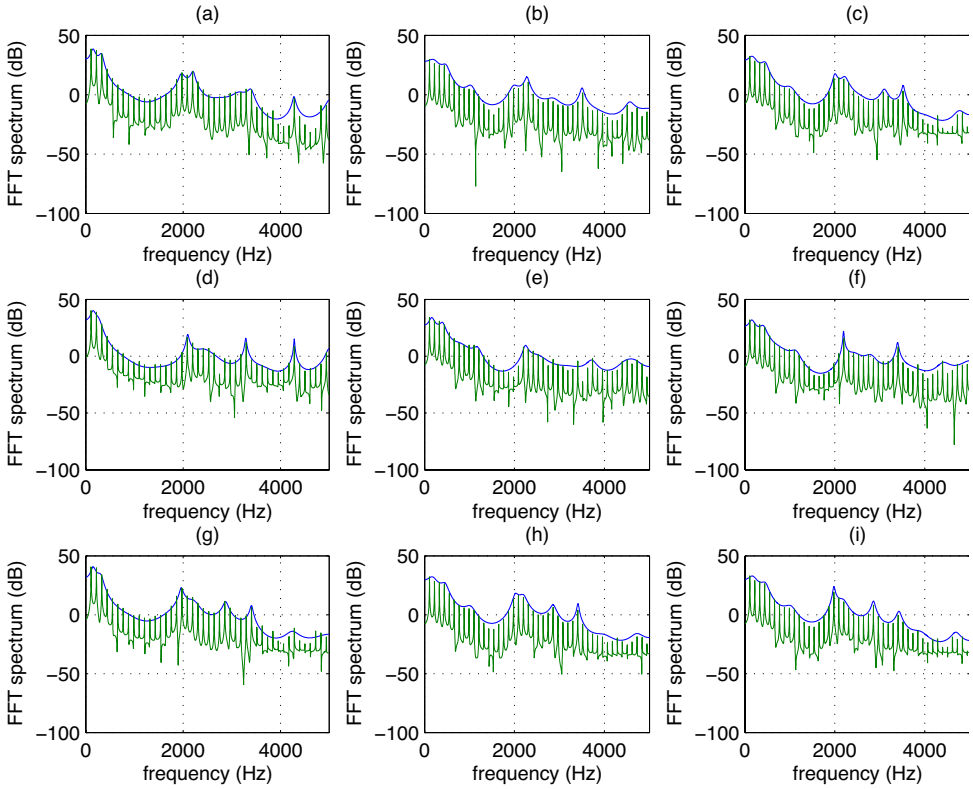

FIG. 7. (Color online) Spectra derived from Fast Fourier Transform (FFT) for three sets of synthetic /i/ vowel examples and the corresponding spectral envelopes. As the first set of examples, (a)-(c) correspond to the spectra for the oral /i/ and the two nasal /i/ vowels without/with compensatory articulation. (d)-(f) and (g)-(i) correspond to the other two sets of synthetic /i/ vowel examples.

/nu/ is substantially attenuated due to the vicinity of a nasal zero, whereas the $F2$ for /u/ in /mu/ remains stable as for the oral vowel. The upper part reveals only a small spectral difference between the nasalized vowel /u/ in /mu/ (solid line) and its nasalized counterpart without oral movement (dotted line), which is due to the similar vocal tract profiles for /u/ and /m/, just like the previous case of /ni/.

The spectral differences between each nasalized vowel pair with and without oral movement can only be attributed to the effect of oral articulation, because the effect of VPO has been controlled by setting the opening areas to the same value (i.e., 60 mm^2).

D. Evolutions of nasal poles and zeros and oral formant shifts for NV

Figures 3–6 show the transfer function evolutions for NV utterances. These transfer functions reveal the evolutions of nasal poles and zeros and oral formant shifts in terms of time. Compared to Figs. 2(a)–2(c), the spectral differences between two adjacent transfer functions for NV utterances are much more prominent, regarded as the effect of oral articulatory movements on modifying the acoustic correlates of velar movement. For the nasalization of /a/ in /ma/, the first oral formant is obscured by two extra nasal pole-zero pairs below $F1$, resulting in a relatively flattened response in the $F1$ region, whereas the second formant frequency exhibits a gradual increase when VPO increases. For /na/, a significant spectral difference from /ma/ is that the $F2$ frequency increases much more rapidly when VPO increases, as a result of different places of articulation in producing the nasal consonants /n/ and /m/.

For /mi/ and /ni/, both Figs. 5(a) and 5(c) reveal a slight increase in oral $F1$ frequency and several extra nasal poles and zeros between oral $F1$ and $F2$ while VPO increases. However, the evolution of $F2$ indicates a prominent difference: The $F2$ frequency for /i/ in /mi/ decreases much more rapidly than that for /ni/ when the VPO area increases. As a result, the $F2$ for nasalized /i/ in /mi/ is canceled out by an adjacent nasal zero between the original oral $F1$ and $F2$ after about four intervals, whereas the nasalized /i/ in /ni/ is not canceled out until the seventh interval.

For /mu/ and /nu/, Figs. 6(a) and 6(c) show a slight increase in $F1$ frequency and extra poles and zeros between $F1$ and $F2$, but again the $F2$ region reveals a prominent difference: The $F2$ frequency for /u/ in /mu/ decreases slightly while VPO increases, whereas the oral $F2$ for /u/ in /nu/ is eventually canceled out by an adjacent nasal zero of /n/ such that the principal cavity affiliation for $F2$ is switched from the oral tract to the nasal tract, resulting in a prominent increase in $F2$ frequency when VPO increases.

Figures 3(c) and 4(c) show the transfer function evolutions for /ma/ and /na/ based on a simplified vocal tract model with no paranasal sinuses. The most prominent difference between (a) and (c) in Figs. 3 and 4 lies in the nasal pole-zero distributions. Specifically, more spectral poles and zeros brought up by resonances of the paranasal sinuses and the branching of nasal tract are distinguished in the nasalized

vowel transfer functions with the paranasal sinuses, whereas for the model without side cavities the most prominent spectral feature is the resonance of the main nasal tract (nasal passages) at around 1000 Hz, which appears universally in the transfer functions for different nasalized vowels.

E. Effect of articulatory timing adjustment on the transfer function evolutions of NV

By adjusting the timing of the coordinated articulatory movements for NV utterances such that the oral articulators move faster than the velum, the transfer functions in Figs. 3(b)–6(b) reveal the corresponding spectral changes. In Figs. 3–6, each transfer function in the right panel corresponding to the same VPO as the counterpart in the left panel and with adjusted articulatory placement shows less prominent nasal spectral peaks and more distinctive oral formants.

F. Effect of compensatory articulation on the spectral features of nasalized vowels

Figures 7(a)–7(c) show the first example of the spectra for three synthetic /i/ vowel samples, where (a), (b), and (c) correspond to the oral vowel, and nasalized vowels without/ with compensatory articulation, respectively. In this example, both *F*1 and *F*2 formants are prominently attenuated in (b) compared to (a), whereas *F*2 is mostly preserved in (c). This effect of compensatory articulation on preserving oral *F*2 formant structure is revealed as well in the other two examples in (d)–(f) and (g)–(i). Another effect as exemplified in the second example in (d)–(f) is that the prominence of the nasal peak between *F*1 and *F*2 is attenuated in (c) compared to (b). Apart from formant amplitude reduction, bandwidth widening is another common effect of nasalization, which is exemplified in (h), where the *F*2 amplitude is largely attenuated and the bandwidth is widened compared to (g), but the *F*2 for the nasalized /i/ after compensatory articulation in (i) is well-preserved with a relatively narrow bandwidth and large amplitude comparable to the oral correspondences.

V. DISCUSSION

Velopharyngeal opening introduces extra poles and zeros affiliated with the nasal and paranasal cavities into the nasal/nasalized vowel spectra. Specifically, (1) for the nasalization of /a/, multiple nasal pole-zero pairs are introduced below *F*1 as well as between *F*2 and *F*3; (2) for the nasalized vowel /i/, extra nasal pole-zero pairs are introduced between *F*1 and *F*2; and (3) for the nasalization of /u/, introduction of nasal pole-zero pairs is between *F*1 and *F*2 as well as between *F*2 and *F*3. As a result, the transfer functions for nasalized vowels are characterized by a relatively flattened low-frequency response caused by the distribution of nasal poles and zeros in the *F*1, *F*2, and *F*3 regions. Apart from these overall acoustic characteristics of vowel nasalization, individual formants are also influenced by the coupling of the nasal tract in terms of changes in pole affiliation, which is defined to follow the convention in Pruthi *et al.*, 2007. When VPO increases, the nasal poles and zeros become more distinctive so that a nasal zero close enough to an adjacent oral formant may attenuate or even cancel out the formant and therefore changes the formant affiliation, such as the *F*1 evolution for nasalized /a/, which reveals a dramatic change in spectral pattern when the VPO area is larger than 70 mm^2, distinguished as the top three dashed lines in Fig. 2(a). For /i/ and /u/, the increase in VPO also makes nasal poles and zeros more distinctive, but instead of approaching *F*1, the first nasal pole (FN1) deviates from *F*1 when VPO increases because the oral *F*1 for both vowels have relatively low frequency such that FN1 becomes more isolated and therefore distinguished as prominent peaks for an opening of 40 mm^2 and above, marked as the dashed lines in Figs. 2(b) and 2(c).

Oral articulation affects the acoustic characteristics of nasalized vowels by shifting oral formants. The effect of oral articulation is demonstrated acoustically by the different spectral characteristics for nasalized vowel pairs with the same VPO and different articulatory placements. Oral formant shifts caused by oral articulation, as well as nasal poles and zeros introduced by VPO, together determine the spectral characteristics of nasalized vowels, which are revealed by the transfer function evolutions for NV utterances in Figs. 3–6. Specifically, (1) the *F*2 frequency for /na/ decreases more rapidly than that for /ma/ while VPO decreases, so from a view of nasalization, the oral *F*2 is preserved and the frequency is increased for /na/ but is attenuated by an adjacent nasal zero and decreases in both amplitude and frequency for /ma/; (2) the *F*2 frequency increases much more rapidly for /mi/ than for /ni/ as VPO decreases, since during the nasalization of /i/ the oral *F*2 for /mi/ is canceled out by an adjacent nasal zero between *F*1 and *F*2, resulting in a change in *F*2 affiliation from the oral to the nasal tract, whereas the oral *F*2 for /ni/ is preserved with a slight frequency decrease; and (3) since the resonant properties of the vocal tract have no prominent change while the nasal consonant /m/ is superimposed on the vowel /u/, the oral formants remain relatively stable for /mu/ during nasalization until an adjacent nasal zero becomes close enough to cancel out *F*2, whereas the oral *F*2 frequency for /nu/ is increased, resulting in a larger distance from the adjacent nasal zero.

Such an effect of oral articulation on the acoustic characteristics of nasalized vowels raises the possibility of developing appropriate oral articulation to compensate for velopharyngeal inadequacy in terms of attenuating nasal spectral features and preserving oral spectral structures. By adjusting the timing of the coarticulatory movements for NV utterances in such a way that the oral articulators move faster than the velum, the transfer functions result in less prominent nasal spectral poles and zeros and better-preserved oral formant structures (with less frequency shifts and less amplitude reduction) even with the same VPO as the correspondences without timing adjustment. The comparisons between the transfer function evolutions in the left and right panels in Figs. 3–6 clearly reveal such an effect of compensatory articulation. Specifically, for a given time interval (e.g., the fifth time interval), the transfer function for the timing-adjusted coarticulated nasalized vowel in the right panel of Figs. 3–6 is clearly a better approximation of the oral reference than its counterpart without timing adjustment in the left panel of Figs. 3–6.

More generally, compensatory articulation should be developed to accommodate individual differences in such a sense that each individual nasalized vowel can be properly compensated through oral articulation without changing the velopharyngeal mechanism. This is exemplified by optimizing the articulatory placement for the nasalized /i/ vowel using an articulatory synthesizer, which fixes the VPO and adjusts other articulatory parameters to maximally preserve the first four formant structures of the resultant nasalized vowel. Although they differ in spectral characteristics, the three sets of examples in Fig. 7 reveal in the same way that the spectra of nasalized vowels after articulatory compensation have less prominent nasal features and better-preserved oral spectral structures.

VI. CONCLUSION

This study demonstrated the effect of oral articulation and velopharyngeal opening on the acoustic characteristics of nasalized vowels by vocal tract modeling and transfer function simulation. Some low-frequency spectral characteristics of nasalized vowels are summarized for three corner vowels in different NV utterances as the effect of oral articulation on shaping nasalized vowel spectra. Such an effect of oral articulation is further revealed by the spectral characteristics of (1) the nasalized vowels in NV utterances with timing adjustment, and (2) the isolated nasalized vowels with articulatory placement compensation. It is possible that the compensatory effects of oral articulation on VPO might be learned spontaneously by individuals with hypernasal speech to reduce their level of hypernasality. Moreover, such compensatory effects raise the possibility of developing compensatory articulation to treat velopharyngeal dysfunction in therapy. Further research is needed to investigate these possibilities.

The limitations of this study lie in that (1) the MRI data of the vocal tract geometry are based on only one male subject (Story, 1995; Story *et al.*, 1996), (2) the NV utterances are simulated by a mathematical function due to the lack of dynamic MRI data for connected speech, (3) only three corner vowels are considered, which needs to be supplemented by studying other vowels, such as the large group of middle vowels, and (4) only the /i/ vowels are synthesized to exemplify the effect of compensatory articulation due to the intrinsic limitation of the articulatory synthesizer, which models the nasal tract in a simplified way as a single cavity without any side branches such that the critical nasal spectral features for low vowels are excluded. Future study should include more subjects (both males and females) to obtain the vocal and nasal tract profiles for various vowels, consonants, and NV utterances. The articulatory synthesizer should be improved to include paranasal sinuses and the asymmetry of two nasal passages in the nasal tract model, which will enable the synthesis of other vowels in a more realistic way to generalize the effect of compensatory articulation.

ACKNOWLEDGMENTS

We would like to express our gratitude to C. Shih and R. Shosted for their discussions and valuable comments. We would like to thank B. H. Story for generously sharing the MRI data with us.

Baer, T., Gore, J., Gracco, L. C., and Nye, P. W. (**1991**). "Analysis of vocal tract shape and dimensions using magnetic resonance imaging: Vowels," J. Acoust. Soc. Am. **90**, 799–828.

Chen, M. (**1997**). "Acoustic correlates of English and French nasalized vowels," J. Acoust. Soc. Am. **102**, 2360–2370.

Dang, J., Honda, K., and Suzuki, H. (**1994**). "Morphological and acoustical analysis of the nasal and the paranasal cavities," J. Acoust. Soc. Am. **96**, 2088–2100.

Demolin, D., Delvaux, V., Metens, T., and Soquet, A. (**2003**). "Determination of the velum opening for French nasal vowels by magnetic resonance," J. Voice **17**, 454–467.

Feng, G., and Castelli, E. (**1996**). "Some acoustic features of nasal and nasalized vowels: A target for vowel nasalization," J. Acoust. Soc. Am. **99**, 3694–3706.

Feng, G., and Kotenkoff, C. (**2006**). "New considerations for vowel nasalization based on separate mouth-nose recording," in Interspeech 2006-ICSLP, Pittsburgh, PA, pp. 2242–2245.

Kataoka, R., Warren, D., Zajaz, D. J., Mayo, R., and Lutz, R. W. (**2001**). "The relationship between spectral characteristics and perceived hypernasality in children," J. Acoust. Soc. Am. **109**, 2181–2189.

Kuehn, D. P. (**1976**). "A cineradiographic investigation of velar movement variables in two normals," Cleft Palate J. **13**, 88–103.

Kuehn, D. P., and Moll, K. L. (**1976**). "A cineradiographic study of VC and CV articulatory velocities," J. Phonetics **4**, 303–320.

Maeda, S. (**1982b**). "The role of the sinus cavities in the production of nasal vowels," Proceedings of the ICASSP, pp. 911–914.

Moore, C. A. (**1992**). "The correspondence of vocal tract resonance with volumes obtained from magnetic resonance imaging," J. Speech Hear. Res. **35**, 1009–1023.

Pruthi, T., Espy-Wilson, C. Y., and Story, B. H. (**2007**). "Simulation and analysis of nasalized vowels based on magnetic resonance imaging data," J. Acoust. Soc. Am. **121**, 3858–3873.

Serrurier, A., and Badin, P. (**2008**). "A three-dimensional articulatory model of the velum and nasopharyngeal wall based on MRI and CT data," J. Acoust. Soc. Am. **123**, 2335–2355.

Story, B. H. (**1995**). "Physiologically-based speech simulation using an enhanced wave-reflection model of the vocal tract," Ph.D. thesis, University of Iowa, Iowa.

Story, B. H. (**2005**). "A parametric model of the vocal tract area function for vowel and consonant simulation," J. Acoust. Soc. Am. **117**, 3231–3254.

Story, B. H., Titze, I. R., and Hoffman, E. A. (**1996**). "Vocal tract area functions from magnetic resonance imaging," J. Acoust. Soc. Am. **100**, 537–554.

Zhang, Z., and Espy-Wilson, C. Y. (**2004**). "A vocal tract model of American English /l/," J. Acoust. Soc. Am. **115**, 1274–1280.

Dependence of phonation threshold pressure and frequency on vocal fold geometry and biomechanics

Zhaoyan Zhang[a)]
UCLA School of Medicine, 31-24 Rehabilitation Center, 1000 Veteran Avenue, Los Angeles, California 90095-1794

(Received 24 July 2009; revised 2 December 2009; accepted 9 January 2010)

Previous studies show that phonation onset occurs as two eigenmodes of the vocal folds are synchronized by the interaction between the vocal folds and the glottal flow. This study examines the influence of the geometrical and biomechanical properties of the vocal folds on this eigenmode-synchronization process, with a focus on phonation threshold pressure and frequency. The analysis showed that phonation threshold pressure was determined by the frequency spacing and coupling strength between the two natural modes that were synchronized by the fluid-structure interaction. The phonation frequency at onset was the root mean square value of the two natural frequencies plus a correction due to the added stiffness of the glottal flow. When higher-order modes of the vocal fold structure were included, more than one group of eigenmodes was synchronized as the system moved toward phonation onset. Changes in vocal fold biomechanics may change the relative dominance between different groups and cause phonation onset to occur at a different eigenmode, which was often accompanied by an abrupt change in onset frequency. Due to the synchronization of multiple pairs of eigenmodes and the mode-switching possibility, a complete and accurate description of vocal fold biomechanical properties is needed to determine the final synchronization pattern and obtain a reliable calculation of the dependence of phonation threshold pressure and frequency on vocal fold geometry and other biomechanical properties.
 [DOI: 10.1121/1.3308410]

PACS number(s): 43.70.Bk, 43.70.Gr [AL] Pages: 2554–2562

I. INTRODUCTION

Phonation threshold pressure is defined as the minimum lung pressure that initiates self-sustained vibration of the vocal fold (Titze, 1988, 1992). Due to its theoretical and potentially practical importance (Titze *et al.*, 1995), phonation threshold pressure and its dependence on vocal fold properties have been investigated in many previous studies (Ishizaka, 1981, 1988; Titze, 1988, 1992; Titze *et al.*, 1995; Chan *et al.*, 1997; Lucero and Koenig, 2005, 2007). Using a linear stability analysis, Ishizaka (1981, 1988) derived conditions of phonation onset in the two-mass model. By numerically solving for the eigenmodes of the coupled airflow-vocal fold system, he showed that two natural modes of the vocal folds degenerated into a single mode as a consequence of aerodynamic coupling at a threshold flow rate, beyond which oscillation can be self-sustained. This eigenmode synchronization led to a phase difference in the motion of the upper and lower masses. Recognizing the importance of this phase difference in sustaining vocal fold vibration, Titze (1988) proposed a mucosal wave model, in which he related the phonation threshold pressure to the so-called mucosal wave velocity:

$$P_{th} = (2k_t/T)Bc\xi_{01}{}^2/(\xi_{01} + \xi_{02}), \quad (1)$$

where k_t is a transglottal pressure coefficient, B is the mean damping coefficient, c is the mucosal wave velocity, ξ_{01} and ξ_{02} are the prephonatory glottal half-widths at the upper and low margins of the medial surface, and T is the medial surface thickness. Equation (1) reveals the relation between the presence of the mucosal wave (or phase difference, as represented by the mucosal wave velocity c) and the energy transfer between the vocal folds and glottal flow (as represented by the phonation threshold pressure). As the mucosal wave can be directly observed in humans, this equation lays a theoretical foundation for many diagnostic measures of voice based on quantifying the mucosal wave motion using either stroboscopic or high-speed recordings of human vocal fold vibration. However, like the phonation threshold pressure, the mucosal wave velocity itself is a dynamic variable of the coupled airflow-vocal fold system and cannot be determined *a priori*. Therefore, a direct link between vocal fold biomechanics and phonation threshold pressure is still missing. Clinically, such a link would allow us to better predict the consequence of surgical manipulation of the vocal folds properties (e.g., geometry and stiffness of the multilayers of the vocal folds) and therefore help surgeons to better plan and evaluate possible treatment options.

Recently, Zhang *et al.* (2007) extended the linear stability analysis to a continuum model of the vocal folds, and the same eigenmode-synchronization phenomenon as in Ishizaka, 1981 was observed (Fig. 1). Further studies using the same model (Zhang, 2008, 2009) showed that details of the eigenmode-synchronization process determined the characteristics of phonation onset (threshold pressure, frequency, and vocal fold vibration pattern). A slight change in the eigenmode-synchronization pattern, as induced by changes in properties of the vocal system, may lead to qualitatively different vocal fold vibration and abrupt changes in phona-

a)Author to whom correspondence should be addressed. Electronic mail: zyzhang@ucla.edu

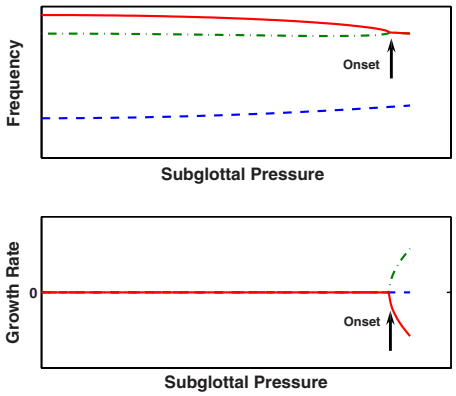

FIG. 1. (Color online) A typical eigenmode-synchronization pattern. Phonation onset occurs as two modes of the vocal folds are synchronized by the glottal flow. The figure shows the frequency (top) and growth rate (bottom) of the first three eigenmodes of the vocal folds as a function of the subglottal pressure. As the subglottal pressure increases, the frequencies of the second and third modes gradually approach each other and, at a threshold subglottal pressure, synchronize to the same frequency. At the same time, the growth rate of the second mode becomes positive, indicating the coupled airflow-vocal fold system becomes linearly unstable and phonation onset.

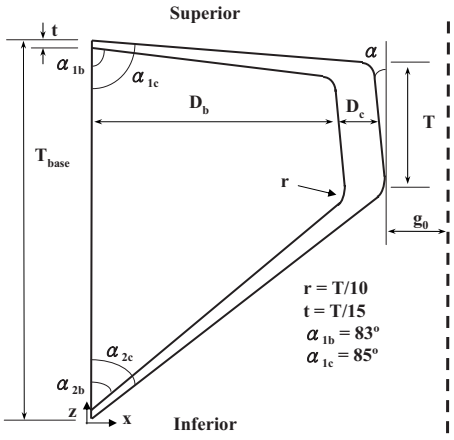

FIG. 2. The two-dimensional vocal fold model and the glottal channel. The coupled airflow-vocal fold system was assumed to be symmetric about the glottal channel centerline, and only the left half of the system was considered in this study. T and T_{base} are the thicknesses of the vocal fold in the flow direction at the medial surface and the lateral base, respectively; D_b and D_c are the depths of the vocal fold body and cover layers at the center of the medial surface, respectively; g_0 is the minimum glottal half-width of the glottal channel at rest. The divergence angle α is the angle formed by the medial surface of the vocal fold with the z-axis. Other control parameters include the thickness of the cover layer at the base of the vocal fold, t, the rounding fillet (for smoothing of the otherwise sharp corners) radius, r, and the glottal exit angles of the body and cover layers. The dash line indicates the glottal channel centerline.

tion onset frequency. Therefore, it seems that a better insight into the physics of phonation onset can be obtained by examining how vocal fold biomechanics affect the eigenmode-synchronization process, from which the influence of vocal fold biomechanics on phonation onset characteristics can be identified.

This study aims to identify the geometrical and biomechanical factors that affect phonation threshold pressure and frequency. This is achieved by first studying phonation threshold pressure and frequency in an idealized case of zero damping (both structural and flow-induced) and assuming a two-mode representation of the vocal fold motion (Sec. II). Such simplifications allow the phonation threshold pressure and frequency to be analytically investigated, in which way the factors underlying the eigenmode-synchronization process can be revealed. In the second part of the paper (Sec. III), numerical simulations were used to further illustrate the physical concept developed in Sec. II (Sec. III A). The simplifications made in Sec. II were then relaxed and influence of higher-order modes (Sec. III B), glottal opening (Sec. III C), and damping (Sec. III D) was examined. In contrast to the lumped-mass model used in Ishizaka, 1988, a continuum model of the vocal folds (Zhang *et al.*, 2007; Zhang, 2009) was used in this study so that the phonation threshold pressure and frequency were related to directly measurable parameters of the vocal system, such as vocal fold geometry and stiffness.

II. THEORY

A. Continuum vocal fold model

Figure 2 shows the continuum vocal fold model used in this study. A body-cover idealization as suggested by Hirano (1974) was used. The geometric control parameters of the model include the vocal fold thickness at the lateral base T_{base}, the medial surface thickness T, the depths of the body and cover layers D_b and D_c, respectively, the divergence angle of the medial surface from the glottal centerline α, the angles of the glottal exit of the body and cover layers, and the minimum glottal half-width at rest g_0. Left-right symmetry in system dynamics about the glottal centerline was assumed so that only half of the system was considered in this study. The vocal folds were modeled as a two-dimensional, plane-strain elastic body. Each layer has distinct density and Young's modulus. No vocal tract was included in this study. A constant flow rate Q was imposed at the glottal entrance. A potential-flow description was used for the glottal flow up to the point of flow separation, beyond which the pressure was set to the atmospheric pressure. The flow was assumed to separate from the glottal wall at a point downstream of the minimum glottal constriction whose width was 1.2 times the minimum glottal width.

B. Linear stability analysis

Phonation onset can be studied by examining how the eigenmodes and eigenvalues of the coupled airflow-vocal fold system vary as the glottal flow rate Q is increased from zero. Phonation onset occurs when the growth rate (real part of the eigenvalue) of one of the eigenvalues first becomes positive, indicating that the coupled system becomes linearly unstable. A brief description of the analysis procedure is given below. For details of the derivation of the system equations and the procedure of the linear stability analysis, readers are referred to the original papers of Zhang *et al.* (2007) and Zhang (2009). The analysis consists of two steps. In the first step, a steady-state problem was solved for the static deformation of the vocal fold structure for a given glottal flow rate Q (Zhang, 2009). In the second step, a linear stability analysis (Zhang *et al.*, 2007) was performed on the deformed state of the airflow-vocal fold system. The governing equations of the eigenvalue problem were derived from

Lagrange's equations as

$$(M-Q_2)\ddot{q}+(C-Q_1)\dot{q}+(K-Q_0)q=0, \tag{2}$$

where q is the generalized coordinate vector, M, C, K are the mass, damping, and stiffness matrices of the vocal fold structure, and the three matrices Q_0, Q_1, Q_2 are the flow-induced stiffness (proportional to vocal fold displacement), flow-induced damping (proportional to vocal fold velocity), and flow-induced mass (proportional to vocal fold acceleration) matrices, respectively. All three matrices (Q_0, Q_1, Q_2) are functions of the jet velocity U_j, which was calculated in the steady-state problem using the imposed subglottal flow rate and the resting vocal fold geometry. Equation (2) was solved as an eigenvalue problem by assuming a solution form of $q=q_0e^{st}$, where s is the eigenvalue and q_0 is the corresponding eigenmode. The two-step procedure was repeated until the flow rate was increased to a point that phonation onset was detected. The phonation threshold pressure would then be the subglottal pressure at onset, and the phonation onset frequency would then be given by the imaginary part of the corresponding eigenvalue.

Zhang *et al.* (2007) showed that the flow-induced stiffness term Q_0 played a dominant role in the eigenmode-synchronization process. When the other two flow-induced terms (Q_1 and Q_2) and structural damping are excluded, Eq. (2) becomes

$$M\ddot{q}+(K-Q_0)q=0. \tag{3}$$

The flow-induced stiffness matrix Q_0 is (Zhang *et al.*, 2007)

$$Q_{0,ij}=\frac{2\rho_f U_j^2}{H_s}\int_{l_{fsi}}\left[\left(\frac{H_s^3}{H_0^3}\varphi_{j,x}-\varphi_{j,x}^*\right)\varphi_{i,x}n_x+\left(\frac{H_s^3}{H_0^3}\varphi_{j,x}-\varphi_{j,x}^*\right)\varphi_{i,z}n_z)\right]dl, \tag{4}$$

where $[\varphi_{i,x},\varphi_{i,z}]$ is the ith normal mode of the vocal fold structure, ρ_f is the density of air, U_j is the mean jet velocity at the point of flow separation, H_0 is the glottal channel width as a function of the coordinate z, which is along the flow direction, H_s is the glottal channel width at the point of flow separation ($H_s\approx 2\times g_0\times 1.2$ in this study), and l_{fsi} denotes the portion of the vocal fold surface from the glottal inlet to the point of flow separation. The asterisk denotes that the function is evaluated at the point of flow separation.

C. Two-mode approximation

Equation (3) was further simplified by assuming a two-mode approximation of the vocal fold motion, i.e., the vocal fold displacement $[\xi,\eta]$ (displacement in the medial-lateral and inferior-superior directions, respectively) was approximated as the linear combination of the first two normal modes of the vocal fold structure:

$$\xi=q_1\varphi_{1,x}+q_2\varphi_{2,x},\quad \eta=q_1\varphi_{1,z}+q_2\varphi_{2,z}. \tag{5}$$

Substitution of Eqs. (5) into Eq. (3) yields

$$\begin{bmatrix}1&0\\0&1\end{bmatrix}\begin{bmatrix}\ddot{q}_1\\\ddot{q}_2\end{bmatrix}+\begin{bmatrix}\omega_{0,1}^2+\gamma a_{11}&\gamma a_{12}\\\gamma a_{21}&\omega_{0,2}^2+\gamma a_{22}\end{bmatrix}\begin{bmatrix}q_1\\q_2\end{bmatrix}=0, \tag{6}$$

where $\omega_{0,i}$ is the natural frequency of the ith natural mode of the vocal fold structure, and

$$\gamma=\frac{1}{2}\rho_f U_j^2,\quad a_{ij}=\frac{-4}{H_s}\frac{\int_{l_{fsi}}\left[\left(\frac{H_s^3}{H_0^3}\varphi_{j,x}-\varphi_{j,x}^*\right)\varphi_{i,x}n_x+\left(\frac{H_s^3}{H_0^3}\varphi_{j,x}-\varphi_{j,x}^*\right)\varphi_{i,z}n_z)\right]dl}{\int_V\rho_{vf}(\varphi_{i,x}^2+\varphi_{i,z}^2)dV}. \tag{7}$$

Note that γ is related to the subglottal pressure by a geometric factor:

$$P_s=\gamma\left(1-\frac{H_s^2}{H_{\text{inlet}}^2}\right), \tag{8}$$

where H_{inlet} is the glottal width at the glottal inlet. For convenience, the variable γ and the subglottal pressure P_s are used interchangeably in the rest of this paper. Assuming $q=q_0e^{st}$, Eq. (6) was solved as an eigenvalue problem for the eigenvalue s and the eigenmodes q_0. The characteristic equation of the eigenvalue problem is

$$s^4+[(\omega_{0,1}^2+\gamma a_{11})+(\omega_{0,2}^2+\gamma a_{22})]s^2+[(\omega_{0,1}^2+\gamma a_{11})\times(\omega_{0,2}^2+\gamma a_{22})-\gamma^2 a_{12}a_{21}]=0. \tag{9}$$

The solution to Eq. (9) is

$$s^2=\frac{-[(\omega_{0,1}^2+\gamma a_{11})+(\omega_{0,2}^2+\gamma a_{22})]\pm\sqrt{[(\omega_{0,1}^2+\gamma a_{11})-(\omega_{0,2}^2+\gamma a_{22})]^2+4\gamma^2 a_{12}a_{21}}}{2}. \tag{10}$$

Equation (10) shows that the effect of the flow-induced stiffness Q_0 is twofold. The diagonal terms (a_{11} and a_{22}) introduce additional stiffness to each corresponding eigenmode. [This can be seen by setting the off-diagonal terms (a_{12} and a_{21}) to zero, in which case the two solutions become ${\omega_{0,1}}^2+\gamma a_{11}$ and ${\omega_{0,2}}^2+\gamma a_{22}$.] The off-diagonal terms couple the two relevant modes and therefore allow the frequencies of the two modes to either approach (for negative value of $a_{12}a_{21}$) or diverge (for positive value of $a_{12}a_{21}$) from each other (see further discussion below). For positive values of $a_{12}a_{21}$, Eq. (10) shows that the eigenvalue s is either purely imaginary or real, indicating the system is either neutrally stable or becomes linearly unstable at a zero frequency (or static divergence, in which the amplitude of the disturbance would grow monotonically with time, in contrast to an oscillatory increase in flutter instability). As we were concerned with nonzero-frequency instability, a negative value of $a_{12}a_{21}$ was assumed in the following derivation.

At onset, the real part of the eigenvalue s becomes zero so that the eigenvalue is purely imaginary, which occurs at the following condition:

$$[({\omega_{0,1}}^2+\gamma a_{11})-({\omega_{0,2}}^2+\gamma a_{22})]^2+4\gamma^2 a_{12}a_{21}=0. \quad (11)$$

Solving Eq. (11) yields the value of γ at onset (by requiring γ to be positive and, if both two solutions were positive, choosing the smaller of the two solutions):

$$\gamma_{th}=\frac{{\omega_{0,2}}^2-{\omega_{0,1}}^2}{a_{11}-a_{22}+2\sqrt{-a_{12}a_{21}}}=\frac{{\omega_{0,2}}^2-{\omega_{0,1}}^2}{\beta}, \quad (12)$$

where β is defined as the coupling strength between the two modes due to aerodynamic coupling. Note that a similar expression was also derived by Auregan and Depollier (1995) in a linear stability analysis of the soft palate under the influence of inspiratory flow. Substituting Eq. (12) into Eq. (10), the frequency at onset is

$$\omega_{th}=\sqrt{\frac{{\omega_{0,1}}^2+{\omega_{0,2}}^2+\gamma_{th}(a_{11}+a_{22})}{2}} \quad (13)$$

or the phonation threshold pressure can be written as a function of phonation onset frequency:

$$\gamma_{th}=\frac{1}{a_{11}+a_{22}}(2{\omega_{th}}^2-{\omega_{0,1}}^2-{\omega_{0,2}}^2). \quad (14)$$

Equation (12) shows that the phonation threshold pressure depends on two factors: the frequency spacing and the coupling strength between the two natural modes that are being synchronized. Refer to Fig. 1, small frequency spacing indicates a small frequency difference that the two modes have to overcome to merge with each other and therefore a lower threshold pressure; and for the same frequency spacing, a strong coupling indicates that less airflow is required to synchronize the two modes.

The coupling strength, β, as defined in Eq. (12), again depends on two effects: the first is the relative frequency change due to the diagonal terms of the Q_0 matrix ($a_{11}-a_{12}$) and the second is the relative frequency change due to the coupling effect of the off-diagonal terms. When the two off-diagonal terms are large and of opposite sign (positive coupling strength), the coupling effect would dominate and the two modes would be synchronized to a same frequency. When the off-diagonal terms are of the same sign (coupling strength is complex) or when they are of opposite sign but their product much smaller than the difference of the second and first diagonal terms (negative coupling strength), the frequencies of the two modes would diverge from each other and mode synchronization is then not possible. Note that, for a given glottal half-width and a known flow separation point, the coupling strength, β, depends solely on the properties of the vocal fold structure, and therefore can be readily calculated for any given geometry and material properties of the vocal folds.

When synchronization occurs, the frequency at onset is the root mean square of the two natural frequencies with a correction due to the diagonal terms of the flow-induced stiffness matrix, as shown in Eq. (13). When the correction term is small, the phonation frequency at onset would then be a value in between the natural frequencies of the two modes being synchronized.

D. Flutter versus static divergence

As briefly mentioned before, two types of instabilities can occur in Eq. (6): one occurs at a zero frequency (static divergence) and the other at a nonzero frequency (flutter). For positive values of $a_{12}a_{21}$ or negative coupling strengths, static divergence is the only possible instability. For negative values of $a_{12}a_{21}$ and positive coupling strengths, which instability occurs first depends on properties of the given system. Refer to Eq. (13), a zero threshold frequency ω_{th} is only possible when the sum ($a_{11}+a_{22}$) is negative, in which case the diagonal terms of the flow-induced stiffness Q_0 lower the frequency of the corresponding eigenmode. By requiring the onset frequency [Eq. (13)] to be greater than zero, we have, after substitution of Eq. (12),

$$\frac{{\omega_{0,2}}^2-{\omega_{0,1}}^2}{a_{11}-a_{22}+2\sqrt{-a_{12}a_{21}}}<\frac{{\omega_{0,2}}^2+{\omega_{0,1}}^2}{-(a_{11}+a_{22})}. \quad (15)$$

Equation (15) is the condition the system has to satisfy to have a nonzero-frequency instability (or flutter). The physical meaning of Eq. (15) is clear: the frequencies of the two modes have to be brought together by the off-diagonal terms before they reach zero by the stiffness-lowering effect of the diagonal terms (see, e.g., Figs. 2(a) and 2(c) in Zhang, 2008). In other words, the threshold pressure for the system to reach flutter onset has to be lower than the threshold associated with static divergence.

III. SIMULATIONS

In this section, the influence of varying medial surface thickness T was investigated as an example to further illustrate the concept of coupling strength, frequency spacing, and eigenmode synchronization. The variation in the medial surface thickness was achieved by adjusting the entrance angles of the vocal folds accordingly, while keeping other control parameters (the vocal fold thickness at the lateral base, the depths of the body and cover layers, the exit angles of the vocal folds, and the divergence angle) constant. The

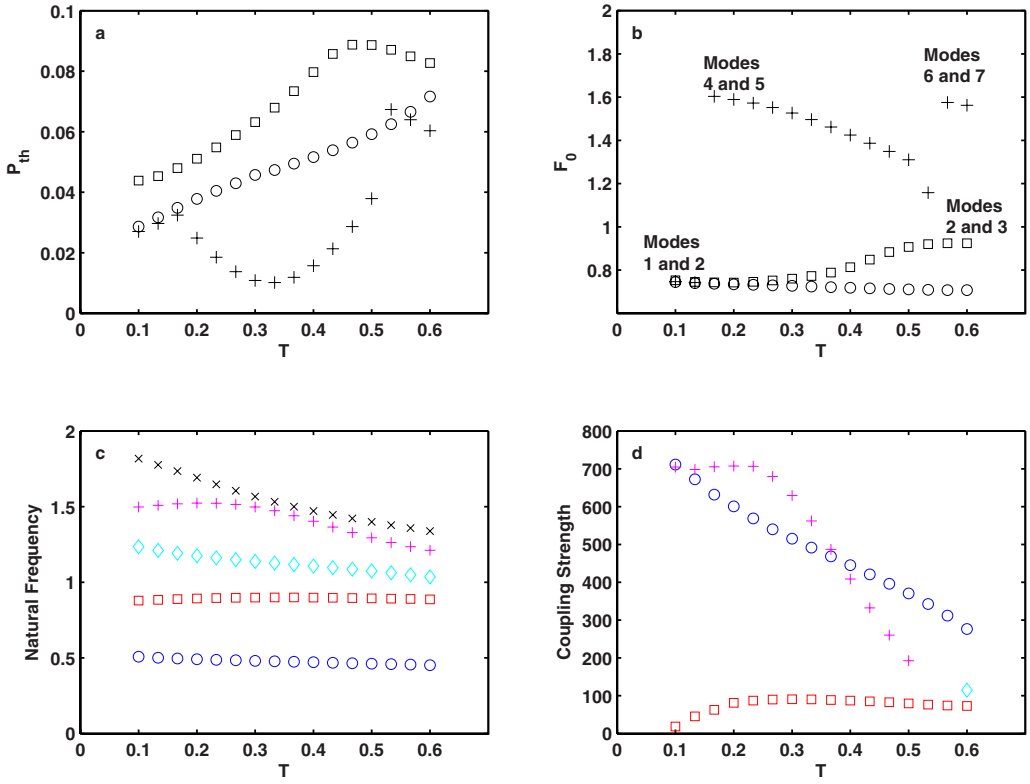

FIG. 3. (Color online) (a) Phonation threshold pressure P_{th} and (b) phonation onset frequency F_0 as a function of the medial surface thickness T. In (a) and (b), the symbol ○ denotes results obtained when Eq. (6) was solved with two modes only and no damping; + denotes results obtained when Eq. (3) was solved with the first ten modes included and no damping; □ denotes results obtained when Eq. (2) was solved with the first ten modes included and with a structural loss factor σ=0.4. (c) Natural frequencies of the first five modes (in ascending order) of the vocal fold structure as a function of the medial surface thickness T. (d) Coupling strength between the first and second modes (○), second and third modes (□), third and fourth modes (◇), and fourth and fifth modes (+) as a function of the medial surface thickness T. A convergent geometry was used with α=−5° and g_0=0.02. Coupling strengths for other pairs of modes were either negative or complex and are not shown.

phonation threshold pressure and frequency were numerically calculated following the procedure described in Sec. II B and in previous studies (Zhang *et al.*, 2007; Zhang, 2009). Section III A focuses on the idealized case as discussed in Sec. II C. The effects of higher-order modes, glottal opening, and damping are then discussed in Sec. III B, Sec. III C, and Sec. III D, respectively.

For the simulations below, a nondimensional formulation of system equations was used as in previous studies (Zhang, 2009). The vocal fold thickness at the lateral base $\bar{T}_{\text{base}}$, the cover layer density $\bar{\rho}_c$, and the wave velocity of the vocal fold cover layer $\sqrt{\bar{E}_c/\bar{\rho}_c}$ were used as the reference scales of length, density, and velocity, respectively. For the results presented below, unless otherwise stated, the following values of the model parameters were used:

$$D_b = 0.667,\ D_c = 0.167,\ g_0 = 0.02,\ \alpha = -5^\circ,$$

$$E_b = 10,\ \rho_b = 1,\ \rho_f = 0.00117. \quad (16)$$

For a vocal fold thickness of 9 mm at the lateral base, Eq. (16) gives a vocal fold body depth of 6 mm, a cover depth of 1.5 mm, and a 0.18 mm minimum glottal half-width at rest. For a cover stiffness of 5 kPa and a cover density of 1030 kg/m^3, Eq. (16) gives a body stiffness of 50 kPa, and a reference frequency scale of 244 Hz.

Note that in this study the reference length scale was the vocal fold thickness at the lateral base, rather than the medial surface thickness as in previous studies (Zhang *et al.*, 2007; Zhang, 2008, 2009). Due to this different choice of reference length scale, for the same frequency variables, the values in this study were generally larger than in previous studies.

A. Two-mode approximation and no damping

Figures 3(a) and 3(b) (circle symbols) show the phonation threshold pressure and frequency as a function of the medial surface thickness T. In this case, Eq. (6) was solved numerically for a convergent glottis with a divergence angle of −5°. Also shown in the figure are the natural frequencies [Fig. 3(c)] and the coupling strength β [Fig. 3(d), circle symbols] as a function of the medial surface thickness T. Figure 3 shows that, in this case, the variation in the medial surface thickness had little effect on the natural frequencies of the first two modes. Consequently, the resulting phonation onset frequency stayed nearly constant with increasing T. However, the increase in the medial surface thickness did significantly lower the coupling strength, leading to an increase in phonation threshold pressure.

B. Effects of higher-order modes

The continuum vocal folds have an infinite number of modes. Like the first two modes, other modes may also be synchronized by the glottal flow. Therefore, when higher-order modes are included, there is more than one pair of

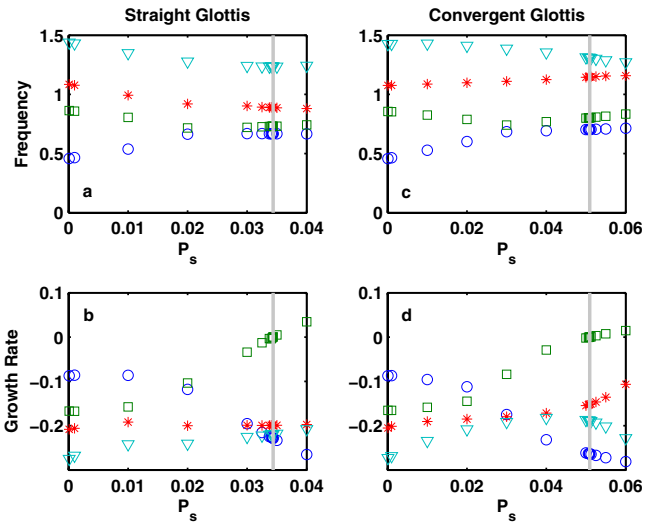

FIG. 4. (Color online) Frequency (top) and growth rate (bottom) of the first four modes of the coupled system as a function of the subglottal pressure, for vocal folds with a straight glottis (left column) and a convergent glottis (right column). The vertical line indicates the point of onset. $T=0.3$, $g_0=0.01$, $\sigma=0.4$, and other parameters are given by Eq. (16). Equation (2) was solved with the first ten modes included. Interaction between the first three modes helped to lower the phonation threshold pressure in the straight-glottis case.

modes being synchronized. Phonation onset may occur at higher-order modes if the synchronization of the higher-order modes leads to a lower threshold pressure. Similarly, changes in the model parameters may change the relative dominance between different pairs of modes, causing phonation onset to occur at a different mode. Such switching between modes is often accompanied by a sudden change in phonation onset frequency.

Figures 3(a) and 3(b) (symbols +) show the phonation threshold pressure and frequency when the first ten modes were included, other conditions remaining the same (i.e., zero damping). As the medial surface thickness increased, a switch in phonation onset between modes occurred from synchronization between the first and second modes to that between the fourth and fifth modes. This mode switching occurred because, for the fourth and fifth modes, the frequency spacing decreased significantly as T increased, while the coupling strength stayed higher than that between the first and second modes. Note that, in this case after the switching, the phonation threshold pressure did not vary monotonically with the onset frequency, due to the opposite trends of the frequency spacing and the coupling strength with increasing medial surface thickness T.

A less obvious effect of inclusion of higher-order modes is demonstrated in Fig. 4. Figure 4 shows that mode synchronization is affected by the presence of other modes. To illustrate this effect, a structural damping of $\sigma=0.4$ was used, and Eq. (2) was solved with the first ten modes included. The two cases in Fig. 4 had the same model parameter values except the divergence angle was different: one was 0° (straight glottis) and the other −5° (convergent glottis). For the straight-glottis case, due to the influence of the third eigenmode, the phonation threshold pressure was much lower than that in the convergent-glottis case, even though phonation onset in both cases occurred due to the synchronization between the first and second eigenmodes. Note that the frequencies of the first and second eigenmodes approached each other but did not merge. This was caused by the introduction of structural damping which prevents the exact merging of the two eigenmodes (Kuznetsov, 2004). However, the underlying mechanism still remained to be the coupled-mode flutter between the two modes (Zhang *et al.*, 2007).

C. Effects of glottal opening

Equations (12) and (7) show that increasing glottal opening reduces coupling strength, which generally raises phonation threshold pressure. Figure 5 shows the phonation threshold pressure and frequency as a function of the resting glottal half-width for a convergent glottal geometry ($\alpha=-5°$, $T=0.5$). The glottal half-width was varied from 0.01 to 0.1, which corresponds to a range between 0.2 and 2 mm glottal openings for a 10 mm vocal fold thickness at the lateral base. The results (circle symbols) were obtained by solving Eq. (3) with the first ten modes included. Figure 5(a) shows that phonation threshold pressure increased with increasing glottal half-width, due to the reduced coupling strength. However, Fig. 5(d) shows that the degree of this reduction effect was eigenmode dependent: it was the largest for the coupling strength between the first and second eigenmodes, and much smaller for the coupling strength between the second and third eigenmodes. This is because that the glottal half-width g_0 (through the variable H_s) also appears in the numerator of Eq. (7) as a weighting coefficient inside the integral. Due to this differential reduction effect on coupling strength, a mode switching was observed as the glottal opening was increased. For small glottal half-widths ($g_0<0.04$), phonation onset still occurred as the fourth and fifth eigenmodes were synchronized, consistent with the results in Sec. III B. For larger values of the glottal half-width, phonation onset occurred due to the synchronization of the second and third eigenmodes as the coupling strength between the fourth and fifth eigenmodes was reduced at a much faster rate than that between the second and third eigenmodes.

When damping was included (square symbols in Figs. 5(a) and 5(b)), phonation onset occurred at the second and third eigenmodes even for the range of small glottal half-widths for which phonation occurred at the fourth and fifth eigenmodes when no damping was included, due to a penalizing effect of the specific structural damping model used in this study (see further discussion in Sec. III D).

D. Effects of damping

In the simulations presented below, a proportional structural damping was assumed for the vocal fold material so that the structural damping and mass matrices were related by

$$C=\sigma\omega M, \tag{17}$$

where σ is the constant structural loss factor and ω is the angular frequency.

When structural damping is included, phonation onset is generally delayed to a higher threshold pressure, as more

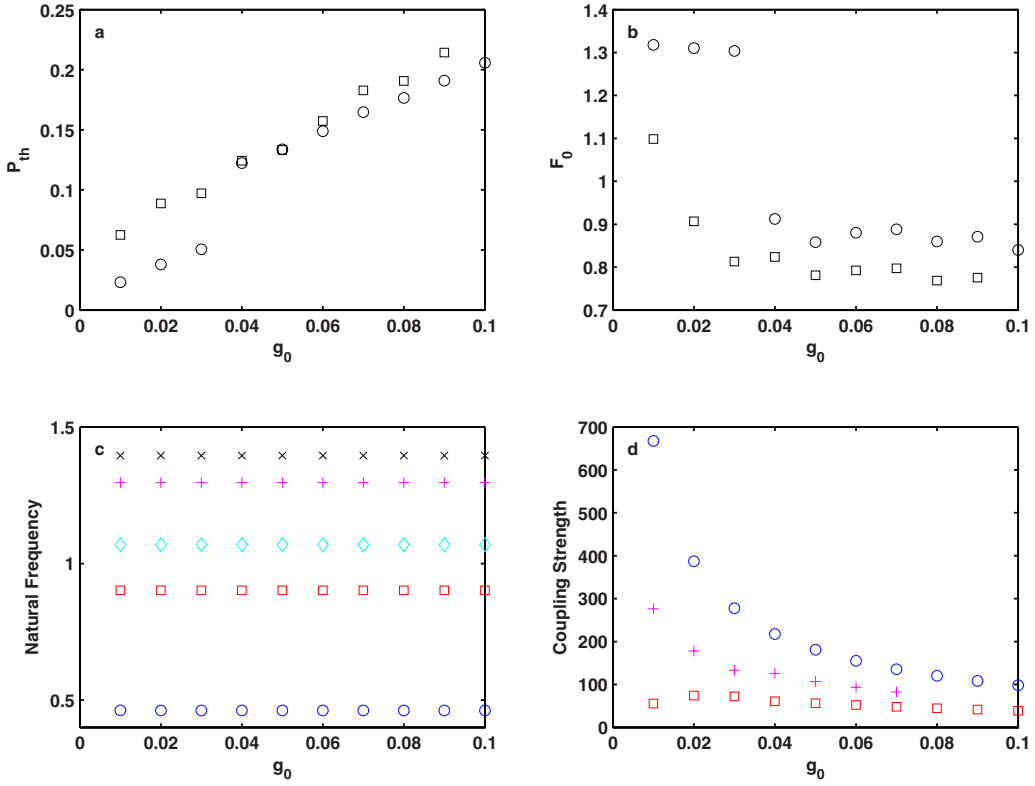

FIG. 5. (Color online) (a) Phonation threshold pressure P_{th} and (b) phonation onset frequency F_0 as a function of the resting glottal half-width g_0. In (a) and (b), the symbol ○ denotes results obtained when Eq. (6) was solved with two modes only and no damping; □ denotes results obtained when Eq. (2) was solved with the first ten modes included and with a structural loss factor σ=0.4. (c) Natural frequencies of the first five modes (in ascending order) of the vocal fold structure as a function of the resting glottal half-width g_0. (d) Coupling strength between the first and second modes (○), second and third modes (□), and fourth and fifth modes (+) as a function of the glottal half-width g_0. A convergent geometry was used with α=−5° and T=0.5. Coupling strengths for other pairs of modes were either negative or complex and are not shown.

energy is needed to overcome the extra structural dissipation. Figure 6 shows the phonation threshold pressure and frequency as a function of the structural loss factor for a convergent glottis (α=−5°, T=0.3). Equation (2) was solved with the first ten modes included. The value of the loss factor was varied from 0 to 2.0, which roughly covers the physiological range as measured by Chan and Rodriguez (2008) and Chan and Titze (1999). Due to increasing dissipation, phonation threshold pressure increased with increasing structural loss factor [Fig. 6(a)].

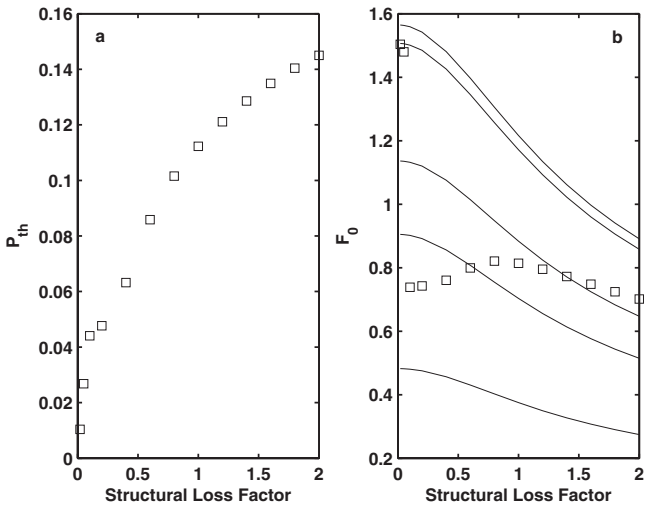

FIG. 6. Phonation threshold pressure (left) and onset frequency (right) as a function of the structural loss factor σ, for a convergent vocal fold geometry (α=−5°). T=0.3, and other parameters are given by Eq. (16). Equation (2) was solved with the first ten modes included. The solid lines in Fig. 6(b) denote the first five eigenfrequencies (in ascending order) of the damped vocal fold structure.

Figure 6 also shows that, for small values (σ =0.1−0.3) of the structural loss factor, phonation onset occurred due to the synchronization between the first and second eigenmodes, instead of between the fourth and fifth as discussed above in Sec. III B and Fig. 3. This is because that, for the type of damping used in this study [a constant loss factor as in Eq. (17)], dissipation increases linearly with frequency so that higher-order modes need to overcome more dissipation to reach onset. In other words, the structural damping tends to delay the onset of higher-order modes more than lower-order modes. As a result, the synchronization between the first and second eigenmodes was able to reach onset at a lower subglottal pressure than that between the fourth and fifth modes, causing a sudden decrease in phonation onset frequency with increasing structural loss factor [Fig. 6(b)].

However, the inclusion of structural damping does not completely rule out the possibility of phonation onset at higher-order modes. Figure 6 shows that, as structural damping increased, phonation onset gradually changed to involve the third and even the fourth eigenmodes for a loss factor as large as 2.0. Indeed, for large values of structural loss factor,

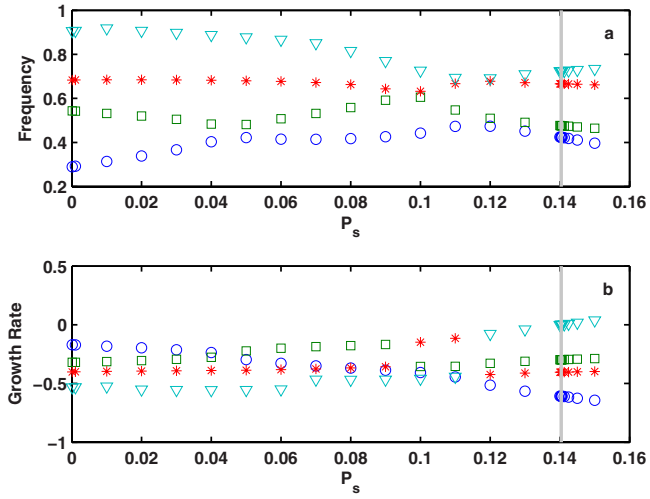

FIG. 7. (Color online) Frequency (top) and growth rate (bottom) of the first four modes of the coupled system as a function of the subglottal pressure, for vocal folds with a convergent glottis. $\alpha=-5°$, $T=0.3$, $\sigma=1.8$, and other parameters are given by Eq. (16). Equation (2) was solved with the first ten modes included. The vertical line indicates the point of onset. Phonation onset at large values of the structural loss factor often involves the interaction between more than two modes.

phonation onset often involved the interaction between more than two eigenmodes, as shown in Fig. 7 for a condition of $T=0.3$ and $\sigma=1.8$. Note that, as different modes were involved in phonation onset, vocal fold vibration patterns were quite different between the case of $\sigma=2.0$ and the case of $\sigma=0.1$, although the phonation onset frequency was similar for these two cases.

To compare with the prediction from the two idealized cases discussed in Secs. III A and III B, Figs. 3(a) and 3(b) (square symbols) also show the phonation threshold pressure and frequency obtained for a loss factor $\sigma=0.4$. Compared to the two idealized cases, phonation threshold pressure in this case was consistently higher, due to the inclusion of structural damping. In the lower end of the range of medial surface thickness, phonation onset occurred as the first and second modes were synchronized. This is similar to the case when only two modes and no damping were considered, but for a much larger range of T. For large values of T, phonation onset occurred as the second and third modes were synchronized. This is different from either one of the two idealized cases, demonstrating the effects of both higher-order modes (Sec. III B, more than one pair of modes being synchronized) and damping (Sec. III D).

IV. DISCUSSION AND CONCLUSIONS

In Zhang *et al.* (2007), a scaling relation between the phonation threshold pressure and the *in vacuo* eigenfrequencies of the vocal fold structure was proposed by requiring a balance or matching between the structural stiffness and the flow-induced stiffness. In this study, Eq. (12) further clarifies that it is the frequency spacing rather than the absolute eigenfrequencies or stiffness of the vocal fold (although the frequency spacing does generally increase with increasing stiffness) that determines phonation onset. Indeed, as shown in Sec. II D, a complete matching between the vocal fold stiffness and the flow-induced stiffness would lead to static divergence, rather than flutter instability of the coupled airflow-vocal fold system. Clinically, this suggests that one of the goals of phonosurgery would be to reduce the frequency spacing and enhance coupling between the first few eigenmodes of the vocal fold structure, by either changing the stiffness differential between different layers of the vocal folds, modifying the vocal fold geometry, or a combination of both. Although the final synchronization pattern and phonation threshold depend on other biomechanical properties, calculation of the frequency spacing and coupling strength does provide a quick and direct evaluation of how such changes in vocal fold biomechanics would affect mode synchronization. Both the frequency spacing and the coupling strength depend mainly on the natural modes of the vocal fold structure, which can be easily calculated for given vocal fold geometry and stiffness. Such calculations may be able to provide a first-order evaluation of the possible treatment options in phonosurgery, when detailed information of the vocal fold biomechanical properties is not available.

This study also shows that, as more than one pair of modes is synchronized by the glottal flow, changes in vocal fold biomechanical properties may change the relative dominance between different pairs of modes and cause phonation onset to occur at a different mode (Sec. III B and III C; also see Zhang, 2008, 2009). Similar concept of mode-switching has been used by Tokuda *et al.* (2007) to explain the abrupt chest-falsetto register transitions in excised larynx experiments. Due to the coupled-mode-flutter nature of phonation onset, the presence of structural damping and large glottal opening delays but does not seem to completely rule out the possibility of phonation onset at higher-order modes and therefore mode switching as observed in this study. Experiments are currently under way to verify these predictions. On the other hand, the excitation of higher-order modes and the mode-switching possibility suggest that a complete and accurate description of vocal fold biomechanical properties is needed to determine the final synchronization pattern and obtain an accurate prediction of phonation threshold pressure and frequency. For phonation modeling, this also suggests that higher-order modes need to be included, in particular, for small glottal openings and large structural dampings for which phonation onset often involves interaction among more than two modes, as shown in Fig. 7.

Although this study considered geometric changes in the vocal folds, changes in synchronization pattern can be equally induced by stiffness changes (Zhang, 2009), or a combination of both, all of which affect the frequency spacing and coupling strength, and therefore phonation threshold. This multivariable dependence of phonation threshold implies that it may be unrealistic to expect a simple relationship between phonation threshold pressure and onset frequency in experiments in which biomechanics of the vocal folds and their variations are either not controlled or unknown. This includes, for example, measurement of phonation threshold pressure and frequency in human subjects, in which it is impossible to control or monitor "the subtle vocal fold posturing or other performance variables in participating humans" (Solomon *et al.*, 2007). This is particularly the case

when mode switching as shown in this study is involved. Indeed, in our simulations, phonation threshold pressure was observed to be able to increase, decrease, or stay approximately constant with increasing phonation onset frequency, depending on which biomechanical property was varied in the simulations.

On the other hand, this multivariable dependence also suggests that experimental results should be interpreted with caution. For example, this study shows that an increase in medial surface thickness T led to an increase in phonation threshold pressure. Preliminary experiments in our laboratory using a rubber physical model (Zhang *et al.*, 2006) and implementing the exactly same geometric changes confirmed this prediction. This seems to contradict with the prediction of Eq. (1) and experimental observation by Chan *et al.* (1997). This discrepancy is likely due to the multivariable dependence of phonation threshold: phonation threshold pressure may vary differently with the medial surface thickness T if changes in T were achieved in different ways (e.g., using different geometric control parameters or different body-cover layer configurations). In this study, variation in the medial surface thickness T was achieved by varying the glottal entrance angles of the body and cover layers, while keeping other control parameters constant. The physical model used in Chan *et al.* (1997) is quite different from the geometries used in this study. Such differences in models used may at least partially contribute to the discrepancy here. Further experiments are needed to clarify this discrepancy.

The simulations of this study were obtained with some assumptions made to simplify the underlying physics (Zhang *et al.*, 2007). These include neglecting viscous loss in the airflow model, which is expected to play an important role for small glottal openings. For normal phonation, the larynx is often postured so that the two vocal folds are at least partially in contact. Future work will include modeling these effects and experimental validation of the results of this study.

ACKNOWLEDGMENTS

This study was supported by research Grant Nos. R01 DC009229 and R01 DC003072 from the National Institute on Deafness and Other Communication Disorders, the National Institutes of Health, and a UCLA Faculty Research Grant.

Auregan, Y., and Depollier, C. (**1995**). "Snoring: Linear stability analysis and in-vitro experiments," J. Sound Vib. **188**, 39–53.

Chan, R., Titze, I. R., and Titze, M. (**1997**). "Further studies of phonation threshold pressure in a physical model of the vocal fold mucosa," J. Acoust. Soc. Am. **101**, 3722–3727.

Chan, R. W., and Rodriguez, M. L. (**2008**). "A simple-shear rheometer for linear viscoelastic characterization of vocal fold tissues at phonatory frequencies," J. Acoust. Soc. Am. **124**, 1207–1219.

Chan, R. W., and Titze, I. R. (**1999**). "Viscoelastic shear properties of human vocal fold mucosa: Measurement methodology and empirical results," J. Acoust. Soc. Am. **106**, 2008–2021.

Hirano, M. (**1974**). "Morphological structure of the vocal cord as a vibrator and its variations," Folia Phoniatr (Basel) **26**, 89–94.

Ishizaka, K., "Equivalent lumped-mass models of vocal fold vibration," in *Vocal Fold Physiology*, edited by K. N. Stevens and M. Hirano, (University of Tokyo, Tokyo, **1981**), pp. 231–244.

Ishizaka, K., "Significance of Kaneko's measurement of natural frequencies of the vocal folds," in *Vocal Physiology: Voice Production, Mechanisms and Functions*, edited by O. Fujimara, (Raven, New York, **1988**), pp. 181–190.

Kuznetsov, Y. A., *Elements of Applied Bifurcation Theory* (Springer-Verlag, New York, **2004**).

Lucero, J. C., and Koenig, L. L. (**2005**). "Phonation thresholds as a function of laryngeal size in a two-mass model of the vocal folds," J. Acoust. Soc. Am. **118**, 2798–2801.

Lucero, J. C., and Koenig, L. L. (**2007**). "On the relation between the phonation threshold lung pressure and the oscillation frequency of the vocal folds," J. Acoust. Soc. Am. **121**, 3280–3283.

Solomon, N. P., Ramanathan, P., and Makashay, M. J. (**2007**). "Phonation threshold pressure across the pitch range: preliminary test of a model," J. Voice **21**, 541–550.

Titze, I. R. (**1988**). "The physics of small-amplitude oscillation of the vocal folds," J. Acoust. Soc. Am. **83**, 1536–1552.

Titze, I. R. (**1992**). "Phonation threshold pressure: A missing link in glottal aerodynamics," J. Acoust. Soc. Am. **91**, 2926–2935.

Titze, I. R., Schmidt, S., and Titze, M. (**1995**). "Phonation threshold pressure in a physical model of the vocal fold mucosa," J. Acoust. Soc. Am. **97**, 3080–3084.

Tokuda, I. T., Horacek, J., Svec, J. G., and Herzel, H. (**2007**). "Comparison of biomechanical modeling of register transitions and voice instabilities with excised larynx experiments," J. Acoust. Soc. Am. **122**, 519–531.

Zhang, Z. (**2008**). "Influence of flow separation location on phonation onset," J. Acoust. Soc. Am. **124**, 1689–1694.

Zhang, Z. (**2009**). "Characteristics of phonation onset in a two-layer vocal fold model," J. Acoust. Soc. Am. **125**, 1091–1102.

Zhang, Z., Neubauer, J., and Berry, D. A. (**2006**). "The influence of subglottal acoustics on laboratory models of phonation," J. Acoust. Soc. Am. **120**, 1558–1569.

Zhang, Z., Neubauer, J., and Berry, D. A. (**2007**). "Physical mechanisms of phonation onset: A linear stability analysis of an aeroelastic continuum model of phonation," J. Acoust. Soc. Am. **122**, 2279–2295.

Data-driven automated acoustic analysis of human infant vocalizations using neural network tools

Anne S. Warlaumont,[a] D. Kimbrough Oller, and Eugene H. Buder
School of Audiology and Speech-Language Pathology, The University of Memphis, 807 Jefferson Avenue, Memphis, Tennessee 38105

Rick Dale
Department of Psychology, The University of Memphis, 202 Psychology Building, Memphis, Tennessee 38152

Robert Kozma
Department of Mathematical Sciences, The University of Memphis, 373 Dunn Hall, Memphis, Tennessee 38152

(Received 25 January 2009; revised 19 January 2010; accepted 22 January 2010)

Acoustic analysis of infant vocalizations has typically employed traditional acoustic measures drawn from adult speech acoustics, such as f_0, duration, formant frequencies, amplitude, and pitch perturbation. Here an alternative and complementary method is proposed in which data-derived spectrographic features are central. 1-s-long spectrograms of vocalizations produced by six infants recorded longitudinally between ages 3 and 11 months are analyzed using a neural network consisting of a self-organizing map and a single-layer perceptron. The self-organizing map acquires a set of holistic, data-derived spectrographic receptive fields. The single-layer perceptron receives self-organizing map activations as input and is trained to classify utterances into prelinguistic phonatory categories (*squeal*, *vocant*, or *growl*), identify the ages at which they were produced, and identify the individuals who produced them. Classification performance was significantly better than chance for all three classification tasks. Performance is compared to another popular architecture, the fully supervised multilayer perceptron. In addition, the network's weights and patterns of activation are explored from several angles, for example, through traditional acoustic measurements of the network's receptive fields. Results support the use of this and related tools for deriving holistic acoustic features directly from infant vocalization data and for the automatic classification of infant vocalizations. [DOI: 10.1121/1.3327460]

PACS number(s): 43.70.Ep, 43.70.Jt, 43.72.Bs [AL] Pages: 2563–2577

I. INTRODUCTION

Over the course of their first year of life, human infants' vocalizations become progressively more speech-like in their phonation, articulation, timing, and in other respects (Stark, 1980; Oller, 1980, 2000; van der Stelt, 1993). The exploration of the sound-making capability by infants, the formation of new contrastive categories of sound, and the systematic use of these categories in vocal play and in flexible expression of emotional states appear to form a critical foundation for speech (Koopmans-van Beinum and van der Stelt, 1986; Vihman *et al.*, 1985). In fact, failure to reach milestones of vocal development is associated with hearing impairment and other medical conditions as well as with slower vocabulary development (Roe, 1975; Stoel-Gammon, 1989; Eilers and Oller, 1994; Oller *et al.*, 1999). However, in the first months of life, infant sounds bear little resemblance to speech and thus their description presents unique methodological challenges.

Acoustic analysis is central to the study of prelinguistic vocalization development. Since recordings of infant vocalizations constitute high-dimensional time series data, their acoustic analysis presents a challenge of data reduction. It is necessary to represent the signal in terms of the most significant features, the ones around which development is fundamentally organized. Some of the acoustic measures that have been applied to infant vocalizations include duration, f_0 means, peaks, standard deviations, contours, formant frequencies, spectral concentration/standard deviation, and degree of tremor (as measured by within-syllable f_0 and amplitude modulation) (Kent and Murray, 1982; Robb and Saxman, 1988; Papaeliou *et al.*, 2002). Such measures are inspired by *a priori* assumptions rooted in acoustic phonetic theory. They are usually treated as independent, with relatively limited attention paid to possible interactions. This is likely an oversimplification, since vocal categories are based on interactive, multivariate acoustic features in mature speech (Repp, 1982), and it seems likely that early infant sounds are also composed of acoustic features in interactive ways. Further, the traditional approach assumes that the selected *a priori* acoustic measures represent the fundamental dimensions of vocal development, exploration, and manipulation. There is a need for methods that address the multivariate and high-dimensional acoustic properties of infant vocalizations directly.

In addition, the need for automated analysis of infant vocal development is rapidly growing. Samples involving

[a]Author to whom correspondence should be addressed. Electronic mail: awarlmnt@memphis.edu

millions of utterances from thousands of hours of all-day audio recordings are being collected and analyzed (Zimmerman *et al.*, 2009). It is important to develop a set of automated acoustic analysis tools appropriate for such infant vocalization data, which would be impractical to analyze manually.

Here a method is presented for reducing high-dimensional samples of infant vocalizations to a smaller set of holistic acoustic features derived directly and automatically based on the patterns exhibited by a set of infant vocalizations. The approach makes relatively few *a priori* assumptions and is intended to complement research using more traditional acoustic measures derived from speech science principles. It utilizes a computational algorithm that would be suitable as an automated analysis method for application to large sets of infant utterances from naturalistic recordings.

Infant vocalizations are first analyzed using a type of unsupervised artificial neural network, the self-organizing map (SOM). The SOM derives a set of 16 holistic spectrographic features based on clusters detected in an input corpus consisting of spectrograms of infant utterances. Then a type of supervised neural network, the single-layer perceptron, is used to classify utterances on the basis of the SOM's derived acoustic features. The classification types are (1) prelinguistic vocal categories (*squeals*, *vocants*, and *growls*), (2) when in the first year of life the utterances were produced, and (3) the identity of the individual who produced a given utterance.

The relationship between the SOM's features and vocal categorizations, age, and individual differences is explored by looking at the patterns of activations across the SOM features and through some simple acoustic measurements (spectral mean, spectral standard deviation, and duration) made on the SOM features and the perceptron's weightings of those features. The perceptron's performance is also evaluated quantitatively and is compared to performance by a prominent neural network classifier, the multilayer perceptron (MLP). Note that the SOM and perceptron neural networks can be used either (1) purely for statistical analysis purposes or (2) as models of human perception and classification. The present study falls into the first category of usage, with the second being a potential future direction.

Section I A below provides background on prelinguistic vocal categories, developmental changes, and individual differences. This is followed in Sec. I B by a brief review of previous work that has used SOMs or perceptrons to analyze vocalization data.

A. Three areas of investigation in infant prespeech vocalization research

1. Prelinguistic phonological categories

The fact that vocalizations produced during the first year exhibit some of the characteristics of adult speech yet are still in many respects immature poses a challenge to phonological description. It is clear that phonetic transcription at the phonological segment level is not appropriate for early infant vocalizations (Lynip, 1951). As an alternative, some researchers have identified prelinguistic vocal categories, termed "protophones" (Oller, 2000), that seem to appear relatively universally during development across the first months of life (Stark, 1980; Nathani and Oller, 2001).

Some protophone categories relate to the purposeful variation of phonatory characteristics, especially pitch and voice quality. One such category is squeal, which includes utterances that are high in pitch and often accompanied by pitch variation, loft (falsetto) quality, and/or harshness (Nathani *et al.*, 2006). Another category is growl, which includes utterances with low pitch, harshness, creaky voice, and/or pulse register (Buder *et al.*, 2008). Perhaps the most frequently occurring protophone is the vocant, which refers to vowel-like utterances (Martin, 1981; Kent and Bauer, 1985). Vocants have intermediate pitch and relatively normal phonation. Purposeful variation of pitch and vocal quality usually appears by at least 4 months of age and continues to be explored throughout the first year and beyond (Stark, 1980). Although other protophone categories address maturation in the timing of syllable production (*marginal* and *canonical syllables*; Oller, 1980) and the capacity to produce multisyllabic utterances of various sorts (*reduplicated* and *variegated babbles*; Smith *et al.*, 1989), the present study focuses only on the early emerging phonatory protophones—squeal, growl, and vocant—as an illustration of how our method can be applied to the acoustic analysis of protophone categories.

Protophone categories have an inherent element of subjectivity, since they are seen as protophonological constructs that form the basis for interpretation of emotional states and intentions by caregivers (Papaeliou *et al.*, 2002; Scheiner *et al.*, 2002). Their validity is supported by the fact that squeals, growls, and vocants are often spontaneously reported by parents when asked to identify sounds their babies produce (vocants being called "vowels;" Oller *et al.*, 2001). Laboratory research involving these categories primarily uses trained adult listeners' perceptual judgments (Nathani and Oller, 2001).

Little relevant acoustic data on the key categories have been published for the squeal, vocant, and growl protophones. However, a primary acoustic correlate has been proposed to be fundamental frequency (f_0) (Nathani *et al.*, 2006; Oller, 1980; Stark, 1980). A goal of the present study is to explore the acoustic correlates of human listeners' protophone judgments via inspection and visualization of neural network weights and activations. The present study also lays a foundation for the development of automatic protophone classification. This is important because protophone classification is otherwise a costly and time-consuming procedure, involving prior training of analysts and repeated careful listening to individual utterances.

2. Developmental changes across the first year

Because during most or all of the first year of life infants do not produce recognizable words, their prelinguistic vocalizations are the main means of assessing the development of speech- and language-related production capabilities. While ethologically oriented auditory studies of changes in vocalizations across the first year have been informative in deter-

mining stages of vocal development and the protophones that emerge with each stage (Holmgren *et al.*, 1986; Koopmans-van Beinum and van der Stelt, 1986), developmental patterns have also been studied using acoustic phonetic methods. For example, Kent and Murray (1982) tracked a number of acoustic measurements, including duration, mean f_0, f_0 intonation contours, first and second formant frequencies, and a variety of glottal and supraglottal quality characteristics such as fry, tremor, and the spectral concentration of noise, in a cross-sectional study of 3-, 6-, and 9-month-old infants' vocalizations. Across age, they found changes in formant frequency values (see also Lieberman, 1980 and Kuhl and Meltzoff, 1996) as well as in amount of tremor.

Despite the important contributions of such research, it does not address the possibility that the changes in such acoustic measures across development are not independent of each other. For example, increases in duration and decreases in phonatory variability may emerge in coordination with each other, driven by common physiological and cognitive maturation that lead to increased control over the larynx. Unsupervised statistical analysis may help to address this concern, either (1) by reducing the large number of acoustic measures to a smaller number of component dimensions that are weighted on each of those acoustic parameters or (2) by deriving a limited number of new, holistic acoustic measures directly from relatively unprocessed recordings of infant vocalizations. The present study takes the second approach.

An aim of this work is to develop potential methods for automatic measurement of the acoustic maturity of infant utterances. This goal is motivated by fact that "language age" or "age-equivalence" is commonly used as an index of language development status in both research and clinical assessment of children older than 1 year (e.g., Stevenson and Richman, 1976; Thal *et al.*, 2007). Automatic classification of vocalization maturity is already being pursued with some success using statistical algorithms incorporating automatic calculation of more traditional acoustic measures, such as duration, and automatic detection of phonetic features, such as bursts, glottal articulations, sonorant quality, and syllabicity (Fell *et al.*, 2002). The method presented here lays groundwork for the automatic measurement of the maturity of an utterance on the basis of holistic, data-driven features, which could prove a worthwhile addition to current methods for automatic detection of utterance maturity.

3. Individual differences

The ordering of phonological stages of vocal development appears to be robust across infants, even those from different language environments, with differing socioeconomic status, and in large measure with differences in hearing function (Oller and Eilers, 1988). However, reports of notable individual differences are also common in literature on infant vocal development (Stark, 1980; Vihman *et al.*, 1986; Nathani Iyer and Oller, 2008). These individual differences appear to be associated with differences in later language styles and abilities. For example, Vihman and Greenlee (1987) found that the degree of use of true consonants (consonants other than glottals and glides) in babble and words at 1 year of age predicted phonological skill at 3 years. It is important to be able to quantify individual differences in preverbal vocalizations within normally developing infants as this might be used to predict later differences in speech and language ability and usage. The study of individual differences in typical infants also sets the stage for the study of infant vocalizations across groups, e.g., across various language or dialect environments, genders, and populations with hearing, language learning, or cognitive impairments.

As with the study of age differences, the study of individual differences is likely to benefit from the introduction of data-driven acoustic measures that convert high-dimensional acoustic input to a smaller number of essential holistic features. In this study, the problem of characterizing and quantifying individual differences among infants is addressed through exploration of differences across infants in the presence of such holistic features. Automatic detection of infant identity provides groundwork for future detection of differences in the vocalization patterns across different infant populations of clinical significance.

B. Previous applications of neural networks to related problems

Neural networks are often used as tools for statistical pattern analysis and are particularly appropriate for high-dimensional data that are suspected of having nonlinear cluster or class boundaries (Bishop, 1995). The networks are typically trained through exposure to data exemplars. They can be used both in cases where the classes in a data set are known and used to provide explicit feedback to the network (supervised networks), or when they are unknown and discovered without explicit supervision (unsupervised networks).

The perceptron is perhaps the most commonly used supervised neural network. It consists of an input layer, an output layer, and zero or more hidden layers. Each layer except the output has a set of weights that describes the strength of the connections between its nodes and the nodes of the following layer. Activation from the input is propagated to the hidden layers (if there are any) and then to the output. The network's output activations are then compared to the known classifications for that input, and the network's error is determined. Based on that error, the network's weights are adjusted, typically using the delta rule, or with backpropagation if there are any hidden layers (Bishop, 1995).

A common unsupervised network is the SOM (also known as Kohonen network). SOMs are typically used for unsupervised cluster analysis and visualization of multidimensional data (Kohonen, 2001; Ritter, 2003; Xu and Wunsch, 2005). A SOM consists of an input layer and an output layer and a set of connection weights between them. The nodes of the output layer are arranged spatially, typically on a two-dimensional (2D) grid. When an input is presented, each of the output nodes is activated to varying extents depending on the input and its connection weights from the input layer. The output node with the highest activation is the winner. It and, to a lesser extent, its neighboring nodes have

their connection weights strengthened so that their receptive fields (i.e., their preferred inputs) more closely resemble the current input stimulus. The result after training is that the output nodes' receptive fields reflect the patterns found in the input and that the receptive fields are topographically organized; i.e., nearby nodes have similar patterns of weights from the input layer.

There appear to be few, if any, previous applications of neural networks to recordings of infant prespeech non-cry vocalizations. However, neural networks have been used to analyze recordings of vocalizations produced by songbirds, disordered and normal adult human voice, and infant crying. Many of these applications were developed in response to a need to represent high-dimensional, complex acoustic signals in a data-driven way. For example, Janata (2001) used a SOM to cluster spectrographic representations of segments of juvenile zebra finch song into 200 topographically arranged holistic spectrogram prototypes. The visualizations of the loadings of features across 30 consecutive days represented a map of the developmental pathways by which adult songs emerged. In addition to permitting data-driven detection of song features, Janata (2001) pointed out that the SOM provides automated acoustic analysis and classification of a very large set of vocalization data, permitting the study of a data set that would have been unrealistic to attempt to score manually.

In another application of neural networks to avian vocalizations, Nickerson *et al.* (2007) used a single-layer perceptron, a type of supervised neural network, to discover the acoustic features most relevant to the distinction between three different note types in black-capped chickadee (*Poecile atricapillus*) "chick-a-dee" calls (notes being the primary units of these calls). The network received seven frequency- and duration-related acoustic features as input and learned to predict the note type for these inputs. Testing the network with systematically modified inputs enabled them to determine which acoustic features were most important in discriminating note types.

SOMs or SOM-inspired networks have also been used in a number of studies to model the perception and classification of speech sounds of one's native language. For example, Guenther and Gjaja (1996) trained an unsupervised network on formant frequency inputs. They then showed that the distribution of learned receptive fields exhibited the perceptual magnet effect humans exhibit in the perception of the vowels of their native language. Another example is a study by Gauthier *et al.* (2007) that used a SOM to successfully classify Mandarin tones based on the first derivative of f_0 contours. This classification was robust in the face of the surface variability present in the multiple speakers' connected speech from which the inputs were taken.

SOMs have also been applied to the study of disordered adult human voices. In one study, Leinonen *et al.* (1992) trained a SOM on short-time spectra from 200 Finnish words. They then provided the network input from both normal and dysphonic speakers and tracked the trajectory of winning SOM nodes for the vowel [a:]. Normal and dysphonic voices differed in the amount of area on the SOM that was visited by these vowel trajectories. The work illustrates that a SOM tool can discriminate between normal and dysphonic voices, and that acoustic differences for these two populations can be portrayed topographically. Callan *et al.* (1999) also used a SOM to study normal and dysphonic voices. However, instead of raw spectra, their inputs were scores on six acoustic measures that had previously been used in studies of dysphonia (e.g., amplitude perturbation quotient, first cepstral harmonic amplitude, and standard deviation of f_0). After training, they marked each SOM node according to which clinical group activated it the most. The SOM was able to reliably classify voices according to group. Output node activations and weights from the input (the six acoustic measures) were also visualized.

Finally, in an application of a neural network to the study of infant vocalizations, Schönweiler *et al.* (1996) used a SOM to cluster recordings of cries by normal and deaf infants. The input consisted of 20-step Bark spectra. It was noted that different individuals' cries mapped onto different areas of the SOM, which is in agreement with the idea that different infants produce identifiably different cries.

The results of the studies reviewed in this section suggest that neural networks, including the unsupervised SOM and the supervised perceptron networks, are appropriate and useful tools for visualization, feature-extraction, and classification purposes in the study of acoustic vocalization data. Thus, it seems fitting to explore the application of neural networks to study infant vocal development.

II. METHOD

A. Participants

Data from six typically developing human infant participants, four female and two male, are used in this study. Participants were recruited for a study of both interactive and spontaneously produced vocalizations and were recorded longitudinally from early in the first year until age 30 months (see Buder *et al.*, 2008 for additional details on participants and recording setup and procedures). The present study focuses on a subset of those recordings spanning three age intervals across the first year of life: 3;0–5;4, 6;0–8;4, and 9;0–11;4.

B. Recording

Infants were recorded for two to three 20-min sessions on each day of recording. For each infant, two of the 20-min sessions were selected from each age interval for use in the present study. The selections were made from among available recordings based on there being a relatively high vocal activity level of the infant and a relative lack of crying.

Recordings took place in a minimally sound-treated room furnished with soft mats and toys while the parent was present. Siblings were sometimes present during recordings as well. Infants and their mothers interacted relatively naturalistically although some periods of time were dedicated to an oral interview between laboratory staff and the parent while the infant played nearby. Both mother and infant wore wireless microphones [Samson Airline ultra high frequency (UHF) transmitter, equipped with a Countryman Associates low-profile low-friction flat frequency response

TABLE I. Number of vocalizations of each vocal type for each infant at each age.

	Age 3;0–5;4			Age 6;0–8;4			Age 9;0–11;4			
Infant	Vocant	Squeal	Growl	Vocant	Squeal	Growl	Vocant	Squeal	Growl	Total
1	73	2	23	53	5	40	77	6	15	294
2	72	21	5	67	15	16	70	22	6	294
3	79	14	5	72	19	7	74	23	1	294
4	68	20	10	78	7	13	80	3	15	294
5	71	0	27	66	0	32	84	1	13	294
6	71	2	25	91	1	6	75	11	12	294
Total	434	59	95	427	47	114	460	66	62	1764

MEMWF0WNC capsule, sending to Samson UHF AM1 receivers]. The infant's was sewn into a custom-built vest adapted from models designed by Buder and Stoel-Gammon (2002). The microphone capsule was housed within a velcro patch to locate the grill at a distance of approximately 5–10 cm from the infant's mouth. Using TF32 (Milenkovic, 2001) operating a DT322 acquisition card (Data Translation, Inc., Marlboro, MA), signals were digitized at 44.1–48.1 kHz after low-pass filtering at 20 kHz via an AAF-3 anti-aliasing board. Microphone signals were concurrently sent to digital video recorders via separate UHF receivers to eliminate contamination to the signals that would otherwise have been transmitted from the video monitors via direct cables. The recordings for infant 1 are an exception to this procedure. This infant's recordings were made according to an earlier laboratory protocol in which audio from the infant's and mother's microphones were compressed in mp3 format as part of an mpeg recording file that combined audio with video. These recordings were subsequently extracted from mp3 format to wav format. Based on detailed inspection of these wav files, the only noticeable compression-based difference between the mp3-based wav file and those for infants 2–6 was that mp3 compression eliminated frequency components above about 12 kHz. To ensure signal comparability across all the recordings, only frequencies 12 kHz or lower are included in the signals processed by the neural networks in this study.

C. Utterance location and coding by human analysts

Prior to analysis by the neural networks, recordings underwent two types of processing by trained adult human analysts: (1) location of infant utterances within recording session files and (2) labeling these utterances according to protophone categories. Infants' utterances were located within each recording using the spectrographic display feature of action analysis coding and training (AACT) software (Delgado, 2008), marking the beginning and end of each utterance. In addition to listening to the recordings, analysts were permitted to consult spectrograms, waveform views, rms contours, and videos for both the infant and the caregiver as they performed this localization task. An utterance was defined as a vocalization or series of vocalizations perceived as belonging to the same breath group (Oller and Lynch, 1992). Crying and other distress vocalizations as well as vegetative sounds were excluded. The first 49 utterances from each 20-min session are used in this study. Since 49 was the minimum total number of utterances produced in a session, this ensures equal representation of recording sessions, infants, and ages (see Table I).

After locating infants' utterances, analysts then coded each utterance as one of the following protophones: vocant, squeal, or growl. Analysts were encouraged during training to use intuitive auditory judgments rather than strict criteria. They were told that generally squeals are perceived as high pitched (beyond the range of habitual pitch for the individual) and can be dysphonated as well. Growls were portrayed as often having low pitch (again out of the range of habitual pitch) and as often being harsh or dysphonated, but it was noted that they are sometimes within the habitual pitch range with harsh or rough voice quality. Vocants were portrayed as the kinds of sounds that fit within the normal pitch of the infant, with relatively little deviation from normal phonation. Analysts were encouraged to attend to the most salient aspects of utterances in making squeal and growl judgments. For example, an utterance was not required to be high pitched throughout to be categorized as squeal; a brief but salient high pitched event could form the basis for the categorization. These instructions were designed to encourage coders to mimic the discriminatory behavior presumed to underlie the categorizations reflected in reports of caregivers regarding these kinds of sounds in their infants (Stark, 1980; Oller *et al.*, 2001). The coding procedures are similar to those used by Nathani *et al.*'s (2006) V (vocant) and SQ (squeal) categories. The difference was that in this study there is an additional growl category (see Buder *et al.*, 2008) and classifications regarding vocal type category were made independently of any syllabicity judgment. Table I provides a summary of the number of utterances in each protophone category for each infant at each age.

D. Preprocessing of utterances

Processing of utterances from this point on was done in MATLAB using the signal processing and neural networks toolboxes (MathWorks, 2008). Each utterance was extracted from the digital recording for the session during which it was recorded. As all inputs to a standard SOM (see following description) must be the same length, only the first second of each utterance was used (utterances were therefore aligned at the beginning). Longer utterances were truncated and shorter utterances were zero-padded. A spectrogram was obtained

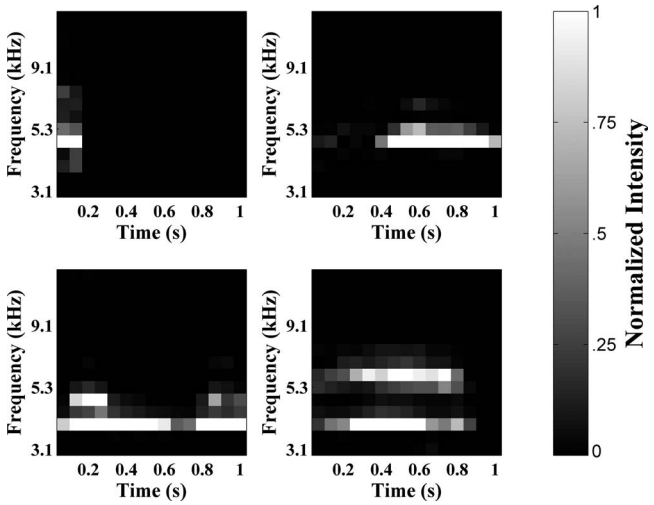

FIG. 1. Four examples of inputs provided to the SOM. Inputs are 225-pixel Bark-scaled spectrograms of utterances produced by infants recorded naturalistically. All inputs are 1 s long, with longer utterances truncated and shorter utterances zero-padded. White indicates high intensity and black indicates zero intensity. All spectrograms are normalized to the value of the highest intensity pixel. Clockwise, from top-left: a vocant produced by infant 1 at 3;2, a squeal produced by infant 2 at 4;1, a growl produced by infant 4 at 6;2, and a vocant produced by infant 3 at 10;2.

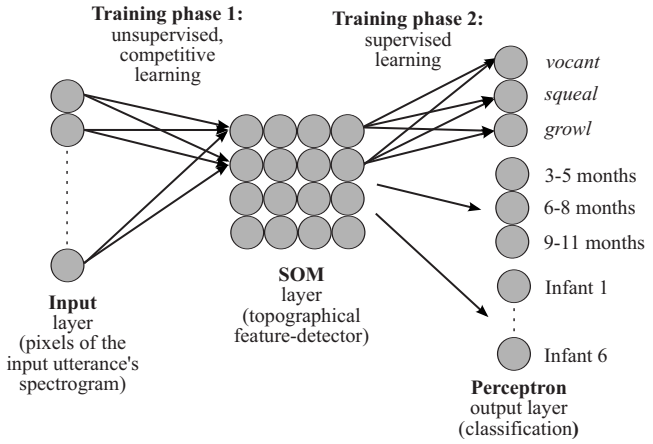

FIG. 2. Schematic of the neural network used in the present study. The network is a hybrid of a SOM and a single-layer perceptron. Pixels of an utterance are presented first to the SOM. Activations of the SOM nodes are then sent to the perceptron output nodes for classification according to protophone, age, and infant identity. The weights from the input layer to the SOM layer are trained first. After this first phase of training, weights to the SOM are frozen and the perceptron's weights are trained.

for each utterance using the fast Fourier transform (FFT)-based *spectrogram* function. Fifteen time bins were used, each with 50% overlap and a maximum frequency of 22 kHz. The frequency scale of this spectrogram was converted to a 15-bin sine-wave approximation of the Bark scale (Zwicker, 1961), and the maximum frequency was capped at 12 kHz using Ellis's (2007) inverse hyperbolic sine approximation algorithm from the RASTAMAT toolbox. For each utterance, the power spectral density values represented by this spectrogram were normalized to the maximum power spectral density magnitude within that utterance. Each utterance was thus represented as 225 spectrogram pixels corresponding to the normalized power spectral density at each frequency bin for each time bin. Figure 1 illustrates some examples of the spectrographic representations of infant utterances in our data set.

E. Neural network architecture

In this section, the architecture of the neural networks and the functions of each component are described. Section II F will describe neural network training. This will be followed by a description of how the infant utterance data were divided into a set for training and a set for testing each network in Sec. II G.

The main type of neural network used in this study is a hybrid architecture with two components (Fig. 2). The first component is a SOM consisting of 16 nodes arranged on a 4×4 grid. The choice of number of nodes and their arrangement was made on the basis of pilot analyses using various configurations, considering ease of visualization and balance between specificity and over-fitting of data. The SOM receives utterance spectrograms as input, transformed into a vector with the time-slice columns of the spectrogram laid end-to-end. Note that this is a common procedure for formatting neural network input data (e.g., see Janata, 2001), and that the transformation has no effect on the function of the SOM since the SOM algorithm does not take the location of input nodes into account. The SOM categorizes these utterances according to learned holistic features extracted based on a set of training utterances, as described in Sec. II F. Learning in the SOM is unsupervised and involves changing the weights from the input layer to each of the SOM nodes over the course of training. Eventually, these weights come to represent the nodes' ideal inputs (or receptive fields), and neighboring nodes end up having similar ideal inputs (topographic organization). This SOM component of the hybrid architecture thus serves as a data-driven holistic feature detector, reducing the 225-pixel spectrographic input to 16 learned features. It also serves as a means for visualizing utterance features topographically (Kohonen, 2001; Ritter, 2003; Xu and Wunsch, 2005). The SOM component was implemented using functions custom written for this study in MATLAB.

The second component is a set of three single-layer perceptrons, which are used to read the output from the SOM in order to obtain a quantitative measure of the learned SOM features' relevance to various classification tasks, to actually perform those classifications, and to determine which SOM nodes best distinguish different classes of utterances from each other. The perceptron is a type of supervised classifier and in single-layer form it essentially performs a logistic linear regression (Bishop, 1995). Each perceptron receives activations of the SOM layer nodes (produced in response to a single utterance input to the SOM) as input (see Kuang and Kuh, 1992, for another example of a perceptron trained on SOM activations). Based on the product of these SOM activations and the perceptron's weights (which can be either positive or negative) from the SOM layer to its output nodes, the perceptron classifies a given utterance according to its perceived protophone type as judged by trained human analysts, the age at which an utterance was produced, and the identity of the infant who produced it. Thus, the supervised

perceptrons relate the features learned by the unsupervised SOM to known protophone, age, and identity classifications. The output layer of each of these perceptrons was constructed to have one node for each class of utterances. The vocal type protophone perceptron thus has three output nodes: one for squeals, a second for vocants, and a third for growls. The age-predicting perceptron has three output nodes: one for utterances produced at age 3;0–5;4, a second for utterances produced at age 6;0–8;4, and a third for utterances produced at age 9;0–11;4. Finally, the identity-predicting perceptron has six output nodes, one for each infant in our data set. The perceptron component was implemented using the feed-forward network functions in MATLAB's neural network toolbox (Demuth *et al.*, 2006). Logistic activation functions were used for the output nodes of the perceptron classifiers, and default values were used for all other parameters in initializing the network (further details can be found in Demuth *et al.*, 2006).

To compare the hybrid SOM-perceptron classifier to the MLP, which is probably the most popular neural network used in supervised classification (Bishop, 1995), we also trained a set of MLPs to perform the age and vocal type classifications using the leave-one-infant-out training data. These MLPs were run using the same procedures and parameter settings as for the single-layer perceptrons described above. The number of hidden layer nodes was set to 16, which is the same as the number of nodes in the SOM layer of our SOM-perceptron hybrid. Thus, the numbers of weights (i.e., free parameters that the networks adjust during training) are roughly similar. We then compared the MLP's classification performance to that of our SOM-perceptron hybrid. In addition, we trained a single-layer perceptron to predict age on the basis of protophone-trained MLP's hidden layer activations. Likewise, we trained a single-layer perceptron to predict protophones on the basis of age-trained MLP's hidden layer activations. Comparing classifications of these perceptrons to classifications from the SOM-perceptron hybrid assesses whether using the SOM layer is truly critical to obtaining a task-general hidden layer.

F. Neural network training

For the SOM-perceptron hybrid, training was conducted in two phases. During the first phase, only the SOM component was involved. Prior to training, its weights were set to random values with a different randomization for each of the 15 SOM runs. The SOM training algorithm was adapted from Berglund and Sitte's (2006) parameterless SOM algorithm. This algorithm takes three parameters (β, Θ, and ε), which determine the behavior of the SOM during training. The following parameter values were used: $\beta=1$, method 2 for calculating Θ, and ε multiplied by a factor of 0.5. The exact roles of β, Θ, and ε are described in Berglund and Sitte (2006). In essence, training involved presenting an utterance as input (randomly chosen from the set of training utterances, discussed in Sec. II G) to the SOM, finding the SOM's node whose weights to the input layer are the most similar to that input (as measured by the Euclidean distance between the input vector and the vector representing weights from the input to a given output node), and then updating that node's weights and (to a lesser extent) its neighbors' weights to make them even more similar to the input. This procedure was repeated 1407 times. This was the number of utterances per session times the number of sessions times the reciprocal of the scaling factor for ε in the SOM training algorithm. This amount of training was more than sufficient for the network's performance to stabilize as judged by the mean squared distances between testing set inputs and their winning node's weights and by visual inspection of changes in network weights across training.

After completion of this first phase of training, the weights from the input layer to the SOM nodes remained fixed during the next training phase. This second phase of training the SOM-perceptron hybrid involved only the perceptron component. Perceptrons were trained using the delta rule with regularization using MATLAB's *trainbr* function. This is a variation on the traditional delta rule algorithm that balances reduction in classification error against parsimony of network weight. This method (sometimes also referred to as "learning with forgetting") has been shown to produce good generalization of performance to previously unseen data and increases the interpretability of network weights (Foresee and Hagan, 1997; Kasabov *et al.*, 1998; Demuth *et al.*, 2006). In essence, this training algorithm involves presenting training set examples, which are the SOM node activations produced in response to an infant utterance, one at a time. After presentation of each example, the network's classification predictions are calculated, and then, based on the difference between these classification predictions and the correct classifications, the weights from the SOM layer to each of the perceptrons' output nodes are updated so as to reduce this error (as measured by the squared error) in classifying subsequent inputs while also maintaining parsimony of network weights. All parameters other than the training method (*trainbr*) and the activation transfer function (*logsigmoid*) were set to default values. Further details can be found in the MATLAB documentation and in Demuth *et al.* (2006).

The MLPs were trained in mostly the same way as the perceptron described above but with the following exceptions: The MLP was trained directly on the spectrographic input and was done in a single phase. Training was performed using the same MATLAB training method (trainbr), but since there were two layers instead of just one, backpropagation was involved in addition to the delta rule (Bishop, 1995).

G. Partitioning of data into training and testing sets

In order to train the SOM, perceptron, and MLP while also allowing for testing the networks' generalization abilities, the infant utterance data were divided into two subsets: one for training the network and the other for evaluating the network's classification performance. From each recording session (of which there were two for each child at each age), 37 of the 49 utterances (approximately 75%) were randomly chosen to be used in training; the remaining 12 utterances (approximately 25%) were reserved for testing the network

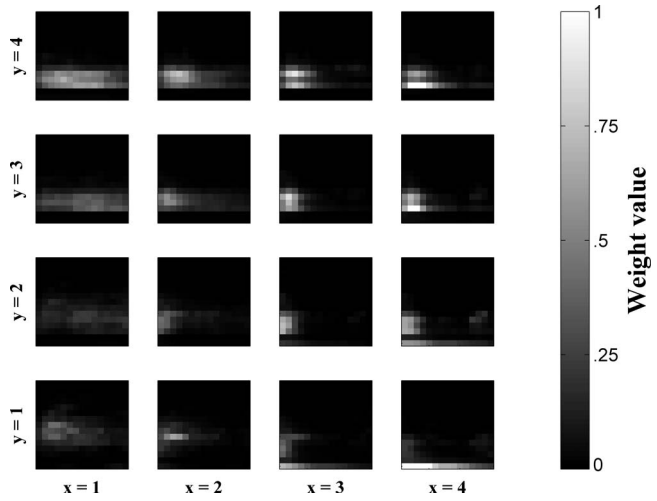

FIG. 3. Weights from the input layer to each SOM node for a network trained on the full set of utterances. Each spectrogram represents the input preference for that node. Note that input preferences are holistic spectrographic features and represent complex acoustic patterns. Also note the topographic organization of these inputs. White represents high weight (high intensity preference for that pixel on the input layer), and black represents zero weight.

(discussed in Sec. II I). This random partitioning was done 15 times and the SOM-perceptron hybrid was run 15 times, each corresponding to a different random partitioning. The means and standard deviations presented in Sec. III were computed over these 15 runs.

In a variation on this training procedure, an alternative leave-one-infant-out method of partitioning the data into training and testing sets was applied to a second set of 36 networks, wherein all the utterances produced by five infants were used in training and the utterances from the sixth remaining infant were reserved for use in testing only. Across these 36 networks, each infant was used as the test infant six times. As with the perceptron, means and standard deviations were computed over these 36 runs. The MLP simulations were trained and tested using the leave-one-infant-out method, although only 6 simulations (rather than 36) were run due to the long time it took for MLP runs to complete. Each infant was used exactly once in testing.

In addition, a SOM-perceptron hybrid was trained on all utterances from all recordings for the purpose of visualizing the trained network weights and activations. This network was used for generating Figs. 3–5 but was not included in any of the quantifications of network performance.

H. Adjusting for unequal representation of protophone categories

When training and testing the perceptrons and MLPs responsible for predicting protophone judgments, it is a concern that vocants occur much more frequently than squeals and growls (see Table I). This inequality inflates the percent correct that would be expected by chance, since with unequal numbers, the baseline strategy would be to give all utterances the classification corresponding to the most frequent category. With such a strategy, if 70% of the utterances were vocants, the baseline percent correct would be 70%. This

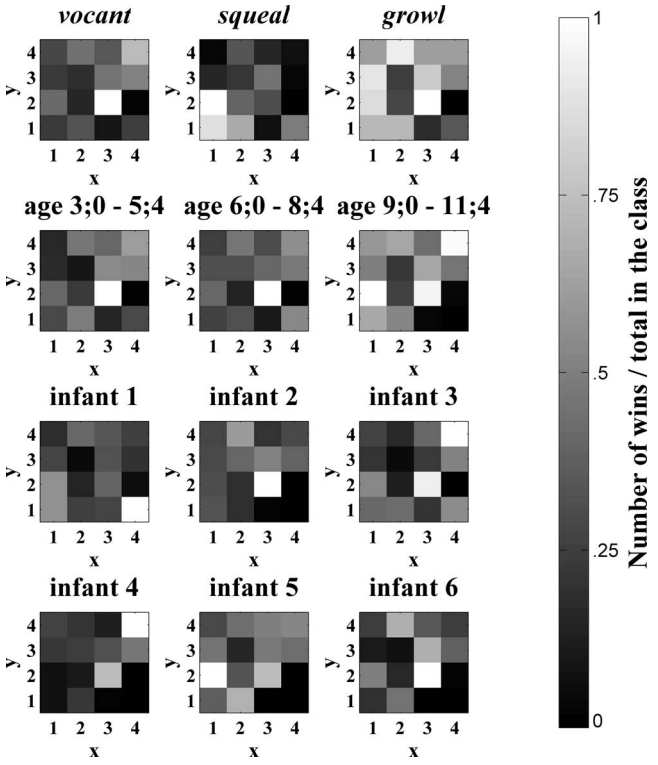

FIG. 4. Activations of the SOM layer by utterances with different protophone labels, produced at different ages, and produced by different infants. Bright indicates that a SOM node was often the winner and black indicates that a node was never the winner. Each 4×4 map corresponds to nodes of the SOM shown in Fig. 3. Note that the number of utterances belonging to each protophone category was not uniform; there were more vocants than squeals and more squeals than growls.

would be very difficult for even a "smart" classifier making use of acoustic information to outperform. We thus ran the perceptron component two ways: once without any adjustment for unequal numbers of vocal types and once with an adjustment. To adjust for the frequency bias, exemplars from the squeal and growl categories were repeated as many times as was necessary for their numbers to equal the number of vocants.

I. Evaluating the network's performance

After training the hybrid network, the network's performance was assessed (1) through visualization and descriptive acoustic measurement of network weights and activations and (2) through quantitative evaluation of classification performance. The visualizations are of the weights from the spectrographic input layer to the SOM output grid and from the SOM's grid to the perceptron classifier nodes. We also visualized the winning SOM nodes (an illustration of SOM activations) for utterances with different protophone judgments, from different ages, and from different individuals.

To supplement the visualizations, we made 3 theoretically derived acoustic measurements for each of the 16 SOM receptive fields. The first measure was the mean of the time-averaged spectrum and the second was the standard deviation of this spectrum, both measured in absolute frequency. These correspond to the first and second spectral moments computed by Forrest *et al.* (1988). The third measure was the

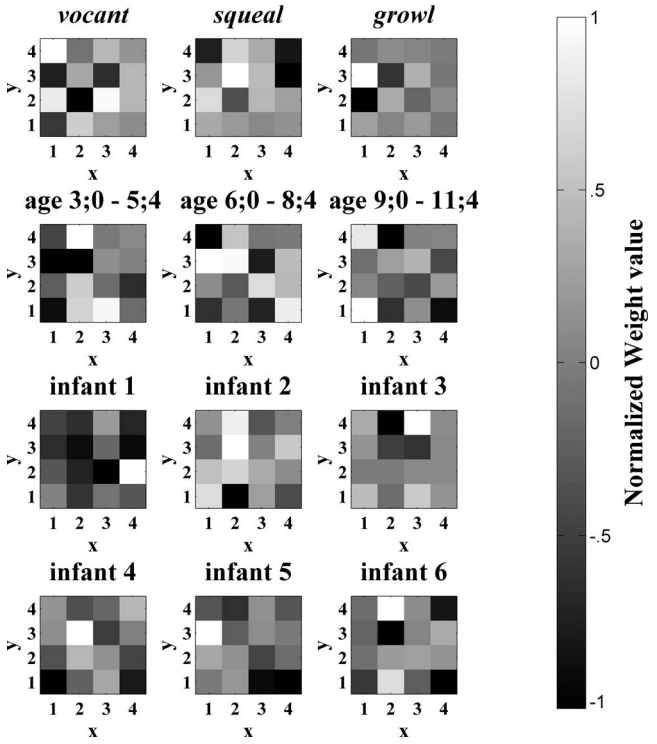

FIG. 5. Weights from the SOM layer to each perceptron output node. Bright indicates a large positive weight from the SOM node to that perceptron output node, black indicates a large negative weight, and gray indicates a near-zero weight. Each 4×4 map corresponds to the SOM nodes shown in Fig. 3. Note that for protophones, the weights are based on training the perceptron on a set of utterances that was adjusted to be balanced across vocant, squeal, and growl protophones by randomly repeating exemplars from the less frequent categories.

median point in time of the frequency-averaged intensity contour. This should give a rough measure of the preferred duration of the receptive field. After calculating these three values for each SOM node, we calculated each perceptron output node's preferred value for each of the three acoustic measures by finding the average SOM receptive field values weighted by the perceptron output node's weights from the SOM layer.

Quantitative evaluation involved feeding the networks' utterances from the set that were reserved for testing. The networks' classifications regarding the protophone, age group, and infant identity for each of these test utterances were then obtained, and an overall mean percentage correct for each type of classification for each type of network was computed. Cohen's κ reliability statistics and their corresponding probabilities were computed using Cardillo's (2009) MATLAB function, in order to evaluate the magnitude and significance of the agreement between each network's classifications and the correct classifications.

III. RESULTS

A. Visualization and descriptive acoustic measurement of network weights and activations

Each of the SOM's output nodes can be thought of as a holistic spectrographic feature formed by the SOM based on the training inputs. This is illustrated in Fig. 3, where the weights from the input layer to each node of the SOM are visualized as spectrograms representing the preferred spectrographic input for that node (white indicates a high value for a given weight and black indicates a zero value). Each node's spectrogram of weights can be thought of as a receptive field, specifying a particular preferred holistic feature derived from the input infant utterance data via the SOM's training algorithm. Note that these preferred inputs are arranged topographically; that is, neighboring nodes have similar preferred inputs. This is one of the characteristic properties of SOMs. Also note that, because the SOM nodes adjust their preferred inputs (i.e., their weights from the input layer) on the basis of exemplars from the training set of utterances, the nodes of the SOM come to represent global features of a complex nature such as would occur in an actual infant utterance. Thus, it seems that these features have a complex relationship with more basic acoustic features, such as duration and spectral compactness versus diffuseness. For example, the receptive fields for the SOM nodes pictured in the leftmost column ($x=1$) of Fig. 3 appear to exhibit long duration. In addition, the bottom two nodes of that leftmost column ($x=1$, $y=1-2$) have relatively high spectral means and spectral standard deviations. These observations are supported by measurements of the frequency-averaged intensity contours' median times, the time-averaged spectral means, and the time-averaged spectral standard deviations given in Table II.

Figure 4 illustrates how often each node of the SOM was the winning node (defined as the node with the highest activation) for utterances of each perceived protophone type, age group, and individual. This method of visualization provides a way of mapping from global features learned by the SOM to different utterances classes.

For example, it appears in the figure that growls may span a broader set of global features in the acoustic space represented by the SOM, as evidenced by the large number of relatively bright squares (bright indicates high activation) for this protophone category. To quantify the diffuseness of

TABLE II. Acoustic properties of the SOM receptive field spectrograms.

Spectral means[a]				Spectral standard deviations[a]				Temporal medians[b]			
0.7	0.7	0.7	0.6	0.7	0.7	0.7	0.6	7	5	4	4
0.7	0.8	0.7	0.6	0.8	0.8	0.7	0.7	9	4	3	3
1.3	1.1	0.7	0.5	1.3	1.8	0.9	0.8	8	4	2	3
1.7	1.3	0.6	0.3	1.6	1.3	1.1	0.9	6	4	3	5

[a]In kilohertz.
[b]In number of time bins (each bin is 66 ms).

activation across the SOM for a given utterance class, we first calculated for each node the number of inputs for which that node was the winner, divided by the total number of inputs belonging to that class. Then the median of these proportion values was computed. These medians were compared across the three protophone categories. Indeed, the median was higher for growls (0.24) than for vocants (0.18) or for squeals (0.15). This indicates that the winning nodes for this category are distributed more evenly across the map than for the other categories.

Another observation that is evident in Fig. 4 is the overlap between utterance classes. While there is some distinctness across protophones, as indicated, for example, by there being different most highly activated nodes for squeals (the node at $x=1$, $y=2$) than for vocants and growls (the node at $x=3$, $y=2$), there is also a high degree of overlap in the SOM node activations, as indicated by numerous nodes that show gray activation for all three protophone types.

Figure 5 illustrates the weights from the SOM to the perceptron output nodes for each age, infant, and protophone prediction. Recall that the goal of the perceptron is differentiation of categories (protophone type, age, and infant) via positive and negative weights. Thus for Fig. 5 the scaling is different from that of Fig. 4. In Fig. 5, white indicates high positive weight, black indicates high negative weight, and mid-gray indicates near-zero weight. The weights indicate which of the SOM's holistic features are informative for classification purposes, highlighting the differences between utterance classes and ignoring features that are common to all classes.

The visualizations in Figs. 4 and 5 exhibit both similarities and differences. This is evident in the correlation coefficients between a given class's SOM activations (Fig. 4) and the weights from the SOM to its perceptron node (Fig. 5). The mean, across all class types, of these correlation coefficients is $r=.31$ where r was always positive, ranging from 0.03 to 0.58. As an example of a specific similarity between activation and weight patterns, the SOM nodes located at ($x=1$, $y=4$), ($x=4$, $y=4$), and ($x=4$, $y=3$) are very dark for squeals in both figures. This indicates that these SOM nodes are both infrequent (Fig. 4) and negatively associated characteristics (Fig. 5) of squeals. An example of a difference between the two figures is that, while the SOM node located at ($x=4$, $y=4$) is the second highest activated for vocants as shown in Fig. 4, it does not have a very large positive weight to the perceptron vocant node, as indicated in Fig. 5. Differences between Figs. 4 and 5 are due to the fact that Fig. 4 indicates the frequency with which features were observed whereas Fig. 5 highlights the particular SOM nodes that, when activated at least partially by an utterance, distinguish utterances of one class (e.g., vocants) from utterances of other classes (e.g., squeals and growls).

Recall the discussion of duration, spectral mean, and spectral standard deviation from the discussion of the SOM receptive field spectrograms (Fig. 3). It was observed that the leftmost column was associated with long duration and that the bottom two nodes of that column also had high spectral means and standard deviations. Interestingly, this leftmost column appears both in Fig. 4 and in Fig. 5 to be associated more (as evidenced by light-colored pixels in this column) with the older two age groups than with the younger age group. This suggests that increase in duration is associated with increase in age. In addition, the bottom two nodes of that leftmost column are associated with the oldest age group. This suggests that the oldest age group is associated also with increase in spectral mean and standard deviation. Combining information about the acoustic properties of SOM weights and the values of the weights from the SOM layer to each of the perceptron output nodes, it is possible to explore whether these acoustic features are present in the nodes that distinguish between different ages. Table III shows the spectral mean, spectral standard deviation, and temporal duration properties for each age, protophone type, and infant. Indeed, the spectral duration of perceptron weights appears to increase across the three age groups, and the spectral mean and standard deviation are highest for the oldest age group.

TABLE III. Acoustic properties of the perceptron weights from the SOM layer, given the acoustic features of the SOM nodes (shown in Table II).

		Spectral mean[a]	Spectral SD[a]	Temporal median[b]
Age	3;0–5;4	0.80	0.91	4.11
	6;0–8;4	0.75	0.89	4.67
	9;0–11;4	0.87	0.95	4.84
Protophone	Vocant	0.78	0.89	4.49
	Squeal	0.85	0.96	4.69
	Growl	0.80	0.91	4.68
Infant	Infant 1	0.81	0.94	4.55
	Infant 2	0.83	0.93	4.62
	Infant 3	0.82	0.94	4.69
	Infant 4	0.77	0.87	4.47
	Infant 5	0.89	0.95	5.12
	Infant 6	0.84	0.92	4.41

[a]In kilohertz.
[b]In number of time bins (each bin is 66 ms).

Table III also reveals interesting patterns with respect to the three protophones' acoustic properties. Squeals have the highest spectral mean and spectral standard deviation. This is in accordance with previous descriptions of this category as high pitch often accompanied by harshness and/or pitch variation. However, growls do not differ from vocants in either mean or spectral standard deviation. Perhaps the high harshness/pulse/creaky-voice combine with the low pitch of growls to yield moderate spectral mean values. Thus, although the differentiating acoustic properties of squeals fit with their previous perceptual descriptions, the differentiating acoustic properties of growls may be less straightforwardly defined in this neural network.

B. Classification performance

1. Protophone-classification performance

When predicting human-judged protophone categories after equated-frequency training, the 15 hybrid networks had a mean percent correct on the previously unseen test utterances (selected randomly at the recording session level) of

TABLE IV. Classification task performance of the SOM-perceptron hybrid neural network.

	Protophones		Ages		Identities
Type of test set	25% per recording	100% of one infant[a]	25% per recording	100% of one infant	25% per recording
Mean % correct	54.4 (chance=33.3)	55.0 (chance=33.3)	42.8 (chance=33.3)	35.6 (chance=33.3)	32.4 (chance=16.7)
Standard deviation	3.2	6.5	1.4	4.7	1.9
Mean Cohen's κ	0.316	0.325	0.142	0.034	0.189
Mean p	<0.001	<0.001	<0.001	0.146	<0.001

[a]With adjustment for unequal category sizes. When there is no adjustment and one infant is reserved for testing, the mean percent correct is 73.4 (chance =74.9) with a standard deviation of 5.4.

54.4% (see the first column of Table IV). Since there were three protophone types, each of which was equally represented in both the training and the testing utterance sets, the classification performance that would be expected for a classifier performing at chance is 33.3%. The vocal-type-predicting networks' 54.4% correct performance was significantly better than chance, $\kappa=0.316$, $p<0.001$.

Recall that 36 additional hybrid networks were trained on utterances from five infants and tested on the sixth remaining infant's utterances. Each infant was used for testing for exactly 6 of the 36 networks. The purpose of this variation on the method for partitioning utterances into training and testing sets was to see if classification of protophones would generalize across infants. Mean classification performance for these networks was 55.0% correct, where chance level performance would have been 33.3% (see the second column of Table IV). This was statistically better than chance, $\kappa=0.325$, $p<0.001$. This shows that for protophone prediction, performance did not differ from when the session-level train-test partition method was used to when the leave-one-infant-out method was used. Thus, it appears that the network's protophone-classification capabilities are based on features of utterances that are generalizable even to infants the network has never previously encountered.

When no adjustment was made for the inequality in the number of exemplars in each protophone category, the percentage correct was 73.4% where the baseline percent correct for an algorithm that always guessed vocant would be 74.9%.

For the six MLPs that were trained using a leave-one-infant-out data partition to predict protophones (where the numbers of protophones were adjusted to give equal representation of all categories), the mean percent correct was 45.9% (see the first column of Table V). This was not quite as high as performance of the SOM-perceptron hybrid, although across runs, this performance was within a standard deviation of the SOM-perceptron hybrids. When no adjustment was made for the inequality in the number of exemplars for each protophone category, the percentage correct was 65.3% where the baseline percent correct for an algorithm that always guessed vocant would be 74.9%. When six MLPs were trained using the same leave-one-infant-out method to predict age and then a single-layer perceptron layer was trained to take those MLPs' hidden layer activations as input and produce protophone classifications as output, performance was 46.6% correct (see the second column of Table V). This was lower than the SOM-perceptron hybrid by more than eight percentage points. These combined results of the MLP networks suggest that while a MLP trained to perform protophone prediction may perform similarly to the SOM-perceptron hybrid, the hidden layer of other MLP trained on a different classification task (age-prediction) is not as good as the general-purpose unsupervised SOM layer. Furthermore, the MLP did not fare any better than the SOM when there was no adjustment for the overrepresentation of vocants.

2. Age classification performance

For the 15 hybrid networks trained to predict infant age with a session-level training-test data partition, the mean percent correct was 42.8% (see the third column of Table IV). This was significantly better than the 33.3% that would have been expected by chance, $\kappa=0.142$, $p<0.001$. Mean classification performance for the 36 additional hybrid networks that were trained on utterances from five infants and tested on the sixth was approximately 35.6% correct, where chance level performance would have again been 33.3% (see the fourth column of Table IV). This did not reach statistical significance, $\kappa=0.034$, $p=0.146$.

TABLE V. Classification task performance of the MLP neural network. All data are for leave-one-infant-out partitioning of utterances.

	Protophones		Ages	
Type of hidden layer	Protophone-predicting[a]	Age-predicting	Age-predicting	Protophone-predicting
Mean % correct	45.9 (chance=33.3)	46.6 (chance=33.3)	35.1 (chance=33.3)	36.1 (chance=33.3)
Standard deviation	10.3	5.7	3.6	3.0
Mean Cohen's κ	0.191	0.200	0.026	0.041
Mean p	<0.001	<0.001	0.118	0.018

[a]With adjustment for unequal category sizes. When there is no adjustment and one infant is reserved for testing, the mean percent correct is 65.3 (chance =74.9) with a standard deviation of 6.9.

The six MLPs that were trained using a leave-one-infant-out data partition to predict age had a mean percent correct of 35.1% (see the third column of Table V). This was very similar to the performance of the SOM-perceptron hybrid. When six MLPs were trained using the same leave-one-infant-out method to predict protophones (numbers adjusted for equal representation of protophone categories) and then a single-layer perceptron layer was trained to take those MLPs' hidden layer activations as input and produce age classifications as output, performance was 36.1% correct (see the fourth column of Table V). This was again very similar to the performance of the SOM-perceptron hybrid. These combined results of the two MLP variations suggest that both a MLP and the SOM-perceptron hybrid are approximately equally suited to the task of predicting age, though neither does very well when forced to generalize to an infant it has never previously encountered before.

3. Infant identity classification performance

For the 15 hybrid networks trained to predict the identity of the infant who produced an utterance (with session-level training-test data partition), the mean percent correct was approximately 32.4% correct (see the fifth column of Table IV). Compared to the 16.7% correct that would be expected had the networks been performing at chance, this performance was statistically significant, $\kappa=0.189$, $p<0.001$.

IV. DISCUSSION

A. Visualization of network weights and activations

One of the main advantages of the SOM-perceptron hybrid is its usefulness for data visualization purposes. By plotting the weights from the input layer to the SOM (Fig. 3), it is possible to visualize the range of holistic spectrographic features exhibited by the vocalizations in the present data set. These holistic features are extremely complex, which can be seen as both an advantage, in that they retain the complexity of prototypical utterances, and as a disadvantage, in that they are difficult to interpret. By plotting the activations of each SOM node according to protophone, age, and identity, and by plotting the weights from each SOM node to each perceptron node, it is also possible to explore the relationship between the holistic spectrographic features learned by the SOM and different categories of utterances.

One method that was used to quantitatively interpret the trends observed in the figures was to get the median number of wins per SOM node for a specific utterance type (e.g., for each of the protophone types) to see which tended to occupy more of the SOM's representational space. Using this method, it was found that growls had more diffuse activation of the SOM than squeals or growls, suggesting that growls have a larger range of acoustic variability.

In another approach to interpreting the trained network we showed that since the SOM's receptive fields take the same form as their inputs, which in this case are coarse-grained spectrograms, more traditional acoustic descriptions, such as spectral mean, spectral standard deviation, and temporal median (related to duration) can be gotten. As observed in Sec. III, the leftmost column of SOM nodes in Fig. 3 had long durations and the bottom two nodes of that column had high spectral mean and standard deviation. These nodes also had a tendency to be activated more by utterances from the older two age groups (6;0–11;4) than by utterances from the youngest age group (3;0–5;4), as evidenced by their lighter colorings in Figs. 4 and 5. Thus, a hypothesis for future investigation might be that utterances produced at older ages are not only longer in duration but also higher in spectral mean and variance.

B. Classification performance

The hybrid neural network, consisting of a perceptron classifier operating on the SOM's holistic spectrographic features, is able to reliably classify 1-s-long utterance samples according to vocal type protophones, ages at which they were produced, and the identities of the individuals who produced them. Reliable performance on these classification tasks provides support for the validity of the SOM's learned utterance features, suggesting that they reflect meaningful acoustic variation in infants' vocal productions. One of the most important possible applications of the work represented here may be in contributing to the rapidly growing field of automated analysis of vocalization. MLPs trained on the same classification tasks also performed well, so when the goal is purely classification, and comparison of holistic features across different classifications is not important, MLPs may also be a good choice of tool.

It should be emphasized that the most critical issue for the future of automated vocal analysis is that reliability be significant, not necessarily that it be high. With very large data sets, relatively low kappa values do not necessarily present an important problem. If a signal is consistently (even though at low levels) detectable, it can become highly discernible at high Ns. This principle is widely recognized, for example, in the field of averaged evoked potentials (Burkard and Secor, 2002). It should also be noted that, although the methods used in the present study did involve some processing by human analysts, this was only in order to perform utterance extraction and protophone labeling. An automated infant utterance extraction method has already been developed for very large vocalization data sets taken from day-long recordings (see Zimmerman *et al.*, 2009), and such a method could be substituted for the manual utterance extraction performed here. As for protophone labeling, for model training and evaluation, the use of human judgments in establishing gold-standard classifications is unavoidable. However, for automated analysis of large data sets, training and evaluation of a network using manually labeled utterances need not be done on the entire large data set, but only on a sample of data large enough to ensure satisfactory network performance and generalization.

The ability to reliably classify utterances according to protophone is of considerable interest. At present, protophone categories are widely used in studies of infant speech development in both typically and atypically developing children (e.g., Hardin-Jones *et al.*, 2003; Salas-Provance *et al.*, 2003; Iverson and Wozniak, 2007; Goldstein and Schwade, 2008) as well as in tools that use infants' vocaliza-

tions in their assessment of infants' communicative function (e.g., Bryson *et al.*, 2008). The ability to predict trained analysts' perceptual judgments suggests that neural networks and other data-driven statistical tools have the potential to be used for automatic classification of protophone categories (although a workaround for the issue of frequency imbalance across categories would have to be devised). This would be useful in many research and clinical settings where coding by trained analysts is costly or difficult. In the future, it would be interesting to apply either the SOM-perceptron-hybrid or a MLP to the classification of other protophones, such as *marginal syllable* and *canonical syllable*—categories related to the articulation timing of syllables that have been shown to be of particular importance as indicators of normal development (Oller, 2000).

The ability to identify age, combined with the network's ability to identify the individual who produced a given utterance, suggests that neural networks and related approaches have the potential for future use in classifying utterances produced by delayed or disordered individuals. Prediction of infant identity also lays groundwork for future work that might attempt to classify utterances produced by infants from different cultural or linguistic backgrounds and by female versus male infants.

C. Future development

1. Manipulating the network's input

The SOM-perceptron architecture is highly flexible with regard to the type of information it can be given as input. Although 225-pixel spectrograms of 1-s-long utterance samples were used in this study, such an input representation was chosen primarily for its computational efficiency and because it involved relatively little preprocessing of data. It is possible that other formats of input would yield better performance or additional insights. Future studies might compare features learned by SOMs trained on different types of input, be they relatively raw input (e.g., raw waveforms, spectrograms of various frequencies and time resolutions), more traditional acoustic measures (e.g., f_0 means, formant frequency means, amplitude means, durations), or measures that represent intermediate amounts of preprocessing (e.g., f_0 contours, formant frequency contours, and amplitude contours).

In discussing the visualizations afforded by the SOM-perceptron hybrid, reference was made to how these visualizations might be related to acoustic patterns described in more traditional terms. For example, it was noted that the SOM features' duration preferences appear to increase with increasing age. Although beyond the scope of the present study, this hypothesis could be tested by comparing the present SOM-perceptron hybrid (trained on raw spectrographic input) with a SOM-perceptron hybrid network trained on duration alone. That is, rather than providing the network with pixels of spectrograms as input, one could provide the network with a single value representing an utterance's duration. If such a network trained on utterance durations also performs significantly well, this would indicate that changes in utterance duration are indeed associated with increasing age. One could then train a SOM-perceptron network on input consisting of a spectrogram plus an additional feature representing the utterance's duration. If this network performed better than the network trained only on spectrograms (e.g., as measured by a hierarchical regression), this would imply that duration changes systematically with development but was not adequately represented by the SOM trained only on spectrograms. On the other hand, if the two networks perform equally well, this might suggest that the SOM had already encoded the relevant duration information in its features. This type of approach could provide a means for parsing out the role of various acoustic measures in how well they predict the age (or identity, protophone category, etc.) of infant utterances.

Finally, it would be highly desirable to explore input representations that deal more flexibly with temporal aspects of vocalizations. Infant utterances vary in length and often have prosodic and syllabic components that vary in their timing. The current static spectrograms used as input do not adequately deal with this fact. A better solution might be one in which small time segments of spectrograms (or other acoustic features) of infant utterances are presented in sequence. The network would then make classifications at each time point or at the conclusion of the entire sequence. A change of this sort in the temporal nature of the input would, however, require changes in the network architecture. Some possibilities are proposed as part of Sec. IV C 2.

2. Alternative architectures and algorithms

The choice of a SOM-perceptron hybrid architecture was motivated by the fact that its components had been previously applied to related problems involving the visualization and classification of acoustic vocalization data, including avian song, disordered adult voice, and infant crying. The choice of a SOM as the first element of this architecture was also motivated by studies suggesting that SOMs can produce results that are comparable to other statistical clustering and visualization methods (Flexer, 2001; de Bodt *et al.*, 2002). Choosing a SOM for the first component of the two-component hybrid network also has the advantage that the same first component is used regardless of the classification task performed by the subsequent perceptron component. Thus, the middle layer activations and weights can be compared across different classification tasks (e.g., the SOM node activations and weights for younger utterances can be compared to the SOM node activations and weights for vocants, squeals, and growls). Finally, the biologically inspired features of the SOM, notably its topographical self-organization and incremental learning algorithm, are also seen as advantages (see Sec. IV C 3 below on future modeling directions; Miikkulainen, 1991; Kohonen and Hari, 1999; Ritter, 2003).

Nevertheless, exploration of other architectures could yield better performance or additional information. For example, a two-layer perceptron may be worth using for situations where classification performance and differentiation between classes is the primary goal. Furthermore, non-neural-network statistical models, such as mixtures of Gaussians, k-nearest-neighbors analysis (Xu and Wunsch, 2005), and

possibly even linear discriminant analysis and regression techniques could potentially yield as good or better clustering and classification performance, respectively. Future work could compare such methods on their performance on a specific visualization or classification task.

In addition, recurrent neural networks are often considered better for temporal sequence processing than networks that take static input (Elman, 1990). Thus, given that infant vocalizations are temporal patterns occurring in temporal sequences, it would be worthwhile to explore recurrent versions of the SOM (e.g., Euliano and Principe, 1996) when unsupervised analysis is desired, or the simple recurrent network (SRN) (Elman, 1990), when classification or prediction is the primary goal. Perhaps even a hybrid of the recurrent SOM and the SRN could be used, which would be analogous to the static SOM-perceptron hybrid explored in the present study. Moving to such temporal architectures would involve changing the nature of the network's input representation as discussed in Sec. IV C 1. A fixed moving window of spectral input would be appropriate.

Finally, variations on the SOM that allow for uncertainty in the number of features/categories or that allow for hierarchical organization of features/categories (Carpinteiro, 1999; Rauber *et al.*, 2002) might also prove useful and informative. The SOM-perceptron hybrid presented in this early study is thus only one of a number of statistical and neural network options.

3. Modeling the perception and production of infant vocalizations

The SOM is a neural network inspired in large part by biological considerations, namely, the self-organizing topographic nature of its feature representations and unsupervised learning in response to stimulus exposure (Miikkulainen, 1991; Kohonen and Hari, 1999; Ritter, 2003). Although the present study focuses solely on acoustic analysis and classification applications, this work provides a potential foundation for future modeling of the perception of infant vocalizations by humans, including learning through exposure to such vocalizations.

Caregivers are commonly infants' primary communication partners, responding and providing feedback to infants. Furthermore, much of the current research on infant vocal development relies critically on naturalistic judgments by laboratory personnel. It is therefore important to understand how adults perceive infant vocalizations and to understand what acoustic features are relevant to adult communication partners. There are several ways in which the ability of the SOM to model adult humans' perceptions of infant utterances might be assessed. One way would be to have human participants perform tasks directly matched to those the SOM-perceptron hybrid performed. Another possibility would be to compare the topography of features on the SOM to listeners' similarity judgments.

ACKNOWLEDGMENTS

This study was supported by a Department of Energy Computational Science Graduate Fellowship (A.S.W.), by NIH Grant No. R01 DC006099-04 (D.K.O., PI, and E.H.B., Co-PI), and by the Plough Foundation. R.D. (PI) was supported by NSF Grant Nos. BCS-0720322 and BCS-0826825. The authors wish to thank Lesya Chorna, Kyounghwa Kwon, Elisabeth Callihan, Courtney Jacks, the University of Memphis Infant Vocalization Laboratory analysts, and the infant participants and their caregivers.

Berglund, E., and Sitte, J. (**2006**). "The parameterless self-organizing map algorithm," IEEE Trans. Neural Netw. **17**, 305–316.
Bishop, C. M. (**1995**). *Neural Networks for Pattern Recognition* (Oxford University Press, New York).
Bryson, S. E., Zwaigenbaum, L., McDermott, C., Rombough, V., and Brian, J. (**2008**). "The autism observation scale for infants: Scale development and reliability data," J. Autism Dev. Disord. **38**, 731–738.
Buder, E. H., Chorna, L. B., Oller, D. K., and Robinson, R. B. (**2008**). "Vibratory regime classification of infant phonation," J. Voice **22**, 553–564.
Buder, E. H., and Stoel-Gammon, C. (**2002**). "American and Swedish children's acquisition of vowel duration: Effects of identity and final stop voicing," J. Acoust. Soc. Am. **111**, 1854–1864.
Burkard, R. F., and Secor, C. (**2002**). "Overview of auditory evoked potentials," in *Handbook of Clinical Audiology*, edited by J. Katz, R. F. Burkard, and L. Medwetsky (Lippincott Williams & Wilkins, Baltimore, MD), pp. 233–248.
Callan, D. E., Kent, R. D., Roy, N., and Tasko, S. M. (**1999**). "Self-organizing map for the classification of normal and disordered female voices," J. Speech Lang. Hear. Res. **42**, 355–366.
Cardillo, G. (**2009**). Cohen's kappa, http://www.mathworks.com/matlabcentral/fileexchange/15365-cohens-kappa (Last viewed Nov. 13, 2008).
Carpinteiro, O. A. s. (**1999**). "A hierarchical self-organising map model for sequence recognition," Neural Process. Lett. **9**, 209–220.
de Bodt, E., Cottrell, M., and Verleysen, M. (**2002**). "Statistical tools to assess the reliability of self-organizing maps," Neural Networks **15**, 967–978.
Delgado, R. E. (**2008**). "Action analysis coding and training software (AACT)," computer software, Intelligent Hearing Systems Corp., Miami, FL.
Demuth, H., Beale, M., and Hagan, M. (**2006**). *Neural Network Toolbox for Use With MATLAB* (The Mathworks, Inc., Natick, MA).
Eilers, R. E., and Oller, D. K. (**1994**). "Infant vocalizations and the early diagnosis of severe hearing impairment," J. Pediatr. **124**, 199–203.
Ellis, D. P. W. (**2007**). PLP and RASTA (and MFCC, and inversion) in MATLAB, http://www.ee.columbia.edu/~dpwe/resources/matlab/rastamat/ (Last viewed 1/21/2008).
Elman, J. L. (**1990**). "Finding structure in time," Cogn. Sci. **14**, 179–211.
Euliano, N. R., and Principe, J. C. (**1996**). "Spatio-temporal self-organizing feature maps," Proceedings of the IEEE International Conference on Neural Networks, Vol. **4**, pp. 1900–1905.
Fell, H. J., MacAuslan, J., Ferrier, L. J., Worst, S. G., and Chenausky, K. (**2002**). "Vocalization age as a clinical tool," in the Proceedings of the 7th International Conference on Spoken Language Processing (ICSLP '02), Denver, CO, pp. 2345–2348.
Flexer, A. (**2001**). "On the use of self-organizing maps for clustering and visualization," Intell. Data Anal. **5**, 373–384.
Foresee, D. F., and Hagan, M. T. (**1997**). "Gauss-Newton approximation to Bayesian learning," Proceedings of the IEEE International Conference on Neural Networks, Vol. **10**, pp. 1930–1935.
Forrest, K., Weismer, G., Milenkovic, P., and Dougall, R. N. (**1988**). "Statistical analysis of word-initial voiceless obstruents: Preliminary data," J. Acoust. Soc. Am. **84**, 115–123.
Gauthier, B., Shi, R., and Xu, Y. (**2007**). "Learning phonetic categories by tracking movements," Cognition **103**, 80–106.
Goldstein, M. H., and Schwade, J. A. (**2008**). "Social feedback to infants' babbling facilitates rapid phonological learning," Psychol. Sci. **19**, 515–523.
Guenther, F. H., and Gjaja, M. N. (**1996**). "The perceptual magnet effect as an emergent property of neural map formation," J. Acoust. Soc. Am. **100**, 1111–1121.
Hardin-Jones, M., Chapman, K. L., and Schulte, J. (**2003**). "The impact of cleft type on early vocal development in babies with cleft palate," Cleft

Palate Craniofac J. **40**, 453–459.
Holmgren, K., Lindblom, B., Aurelius, G., Jalling, B., and Zetterstrom, R. (**1986**). "On the phonetics of infant vocalization," in *Precursors of Early Speech*, edited by B. Lindblom and R. Zetterstrom (Stockton, New York), Chap. 5, pp. 51–63.
Iverson, J. M., and Wozniak, R. H. (**2007**). "Variation in vocal-motor development in infant siblings of children with autism," J. Autism Dev. Disord. **37**, 158–170.
Janata, P. (**2001**). "Quantitative assessment of vocal development in the zebra finch using self-organizing neural networks," J. Acoust. Soc. Am. **110**, 2593–2603.
Kasabov, N. K., Kozma, R., and Watts, M. (**1998**). "Phoneme-based speech recognition via fuzzy neural networks modeling and learning," Inf. Sci. (N.Y.) **110**, 61–79.
Kent, R. D., and Bauer, H. R. (**1985**). "Vocalizations of one-year-olds," J. Child Lang **3**, 491–526.
Kent, R. D., and Murray, A. D. (**1982**). "Acoustic features of infant vocalic utterances at 3, 6, and 9 months," J. Acoust. Soc. Am. **72**, 353–365.
Kohonen, T. (**2001**). *Self-Organizing Maps*, 3rd ed. (Springer, New York).
Kohonen, T., and Hari, R. (**1999**). "Where the abstract feature maps of the brain might come from," Trends Neurosci. **22**, 135–139.
Koopmans-van Beinum, F. J., and van der Stelt, J. M. (**1986**). "Early stages in the development of speech movements," in *Precursors of Early Speech*, edited by B. Lindblom and R. Zetterstrom (Stockton, New York), Chap. 4, pp. 37–50.
Kuang, Z., and Kuh, A. (**1992**). "A combined self-organizing feature map and multilayer perceptron for isolated word recognition," IEEE Trans. Signal Process. **40**, 2651–2657.
Kuhl, P. K., and Meltzoff, A. N. (**1996**). "Infant vocalizations in response to speech: Vocal imitation and developmental change," J. Acoust. Soc. Am. **100**, 2425–2438.
Leinonen, L., Kangas, J., Torkkola, K., and Juvas, A. (**1992**). "Dysphonia detected by pattern recognition of spectral composition," J. Speech Hear. Res. **35**, 287–295.
Lieberman, P. (**1980**). "On the development of vowel productions in young children," *Child Phonology, Vol. 1: Production*, edited by G. Yeni-Komshian, J. Kavanagh, and C. Ferguson (Academic, New York), Chap. 7, pp. 113–142.
Lynip, A. W. (**1951**). "The use of magnetic devices in the collection and analysis of the preverbal utterances of an infant," Genet. Psychol. Monogr. **44**, 221–262.
Martin, J. A. M. (**1981**). *Voice, Speech, and Language in the Child: Development and Disorder* (Springer-Verlag, New York).
MathWorks (**2008**). MATLAB (Version R2008a), computer software, The Mathworks, Inc., Natick, MA.
Miikkulainen, R. (**1991**). "Self-organizing process based on lateral inhibition and synaptic resource redistribution," *Proceedings of the ICANN'91, International Conference on Artificial Neural Networks*, edited by T. Kohonen, K. Mäkisara, O. Simula, and J. Kangas (North-Holland, Amsterdam), Vol. **I**.
Milenkovic, P. (**2001**). TF32, computer program, University of Wisconsin-Madison, Madison, WI. Available online at http://userpages.chorus.net/cspeech (Last viewed 11/4/2009.
Nathani, S., Ertmer, D. J., and Stark, R. E. (**2006**). "Assessing vocal development in infants and toddlers," Clin. Linguist. Phonetics **20**, 351–369.
Nathani, S., and Oller, D. K. (**2001**). "Beyond ba-ba and gu-gu: Challenges and strategies in coding infant vocalizations," Behav. Res. Methods Instrum. Comput. **33**, 321–330.
Nathani Iyer, S., and Oller, D. K. (**2008**). "Fundamental frequency development in typically developing infants and infants with severe to profound hearing loss," Clin. Linguist. Phonetics **22**, 917–936.
Nickerson, C. M., Bloomfield, L. L., Dawson, M. R., Charrier, I., and Sturdy, C. B. (**2007**). "Feature weighting in 'chick-a-dee' call notes of poecile atricapillus," J. Acoust. Soc. Am. **122**, 2451–2458.
Oller, D. K. (**1980**). "The emergence of the sounds of speech in infancy," *Child Phonology, Vol. 1: Production*, edited by G. Yeni-Komshian, J. Kavanagh, and C. Ferguson (Academic, New York), Chap. 6, pp. 93–112.
Oller, D. K. (**2000**). *The Emergence of the Speech Capacity* (Lawrence Erlbaum Associates, Mahwah, NJ).
Oller, D. K., and Eilers, R. E. (**1988**). "The role of audition in infant babbling," Child Dev. **59**, 441–449.
Oller, D. K., Eilers, R. E., and Basinger, D. (**2001**). "Intuitive identification of infant vocal sounds by parents," Dev. Sci. **4**, 49–60.
Oller, D. K., Eilers, R. E., Neal, A. R., and Schwartz, H. K. (**1999**). "Precursors to speech in infancy: The prediction of speech and language disorders," J. Commun. Disord. **32**, 223–245.
Oller, D. K., and Lynch, M. P. (**1992**). "Infant vocalizations and innovations in infraphonology: Toward a broader theory of development and disorders," in *Phonological Development: Models, Research, Implications*, edited by C. A. Ferguson, L. Menn, and C. Stoel-Gammon (York, Timonium, MD), Chap. 18, pp. 509–536.
Papaeliou, C., Minadakis, G., and Cavouras, D. (**2002**). "Acoustic patterns of infant vocalizations expressing emotions and communicative functions," J. Speech Lang. Hear. Res. **45**, 311–317.
Rauber, A., Merkl, D., and Dittenbach, M. (**2002**). "The growing hierarchical self-organizing map: Exploratory analysis of high-dimensional data," IEEE Trans. Neural Netw. **13**, 1331–1341.
Repp, B. (**1982**). "Phonetic trading relations and context effects: New experimental evidence for a speech mode of perception," Psychol. Bull. **92**, 81–110.
Ritter, H. (**2003**). "Self-organizing feature maps," in *The Handbook of Brain Theory and Neural Networks*, 2nd ed., edited by M. A. Arbib (MIT, Cambridge, MA), pp. 1005–1010.
Robb, M. P., and Saxman, J. H. (**1988**). "Acoustic observations in young children's non-cry vocalizations," J. Acoust. Soc. Am. **83**, 1876–1882.
Roe, K. V. (**1975**). "Amount of infant vocalization as a function of age: Some cognitive implications," Child Dev. **46**, 936–941.
Salas-Provance, M. B., Kuehn, D. P., and Marsh, J. L. (**2003**). "Phonetic repertoire and syllable characteristics of 15-month-old babies with cleft palate," J. Phonetics **31**, 23–38.
Scheiner, E., Hammerschmidt, K., Jürgens, U., and Zwirner, P. (**2002**). "Acoustic analyses of developmental changes and emotional expression in the preverbal vocalizations of infants," J. Voice **16**, 509–529.
Schönweiler, R., Kaese, S., Möller, S., Rinscheid, A., and Ptok, M. (**1996**). "Neuronal networks and self-organizing maps: New computer techniques in the acoustic evaluation of the infant cry," Int. J. Pediatr. Otorhinolaryngol. **38**, 1–11.
Smith, B. L., Brown-Sweeney, S., and Stoel-Gammon, C. (**1989**). "A quantitative analysis of reduplicated and variegated babbling," First Lang. **9**, 175–189.
Stark, R. E. (**1980**). "Stages of speech development in the first year of life," *Child Phonology, Vol. 1: Production*, edited by G. Yeni-Komshian, J. Kavanagh, and C. Ferguson (Academic, New York), Chap. 5, pp. 73–92.
Stevenson, J., and Richman, N. (**1976**). "The prevalence of language delay in a population of three-year-old children and its association with general retardation," Dev. Med. Child Neurol. **18**, 431–441.
Stoel-Gammon, C. (**1989**). "Prespeech and early speech development of two late talkers," First Lang. **9**, 207–223.
Thal, D., Desjardin, J. L., and Eisenberg, L. S. (**2007**). "Validity of the MacArthur-Bates Communicative Development Inventories for measuring language abilities in children with cochlear implants," Am. J. Speech Lang. Pathol. **16**, 54–64.
van der Stelt, J. M. (**1993**). *Finally a Word: A Sensori-Motor Approach of the Mother-Infant System in its Development Towards Speech* (Uitgave IFOTT, Amsterdam).
Vihman, M. M., Ferguson, C. A., and Elbert, M. (**1986**). "Phonological development from babbling to speech: Common tendencies and individual differences," Appl. Psycholinguist. **7**, 3–40.
Vihman, M. M., and Greenlee, M. (**1987**). "Individual differences in phonological development: Ages one and three years," J. Speech Hear. Res. **30**, 503–521.
Vihman, M. M., Macken, M. A., Miller, R., Simmons, H., and Miller, J. (**1985**). "From babbling to speech: A re-assessment of the continuity issue," Language **61**, 397–445.
Xu, R., and Wunsch, D., II (**2005**). "Survey of clustering algorithms," IEEE Trans. Neural Netw. **16**, 645–678.
Zimmerman, F., Gilkerson, J., Richards, J., Christakis, D., Xu, D., Gray, S., and Yapanel, U. (**2009**). "Teaching by listening: The importance of adult-child conversations to language development," Pediatrics **124**, 342–349.
Zwicker, E. (**1961**). "Subdivision of the audible frequency range into critical bands (frequenzgruppen)," J. Acoust. Soc. Am. **33**, 248.

Acoustic characteristics of phonation in "wet voice" conditions

Shanmugam Murugappan[a)]
Department of Otolaryngology, Head and Neck Surgery, University of Cincinnati Medical Center, 231 Albert B. Sabin Way, Cincinnati, Ohio 45267-0528

Suzanne Boyce
Department of Communication Science and Disorders, French East Building, University of Cincinnati, 3202 Eden Avenue, Cincinnati, Ohio 45267-0379

Sid Khosla
Department of Otolaryngology, Head and Neck Surgery, University of Cincinnati Medical Center, 231 Albert B. Sabin Way, Cincinnati, Ohio 45267-0528

Lisa Kelchner
Department of Communication Science and Disorders, French East Building, University of Cincinnati, 3202 Eden Avenue, Cincinnati, Ohio 45267-0379

Ephraim Gutmark
Department of Aerospace Engineering and Engineering Mechanics and Department of Otolaryngology, Head and Neck Surgery, University of Cincinnati Medical Center, 231 Albert B. Sabin Way, Cincinnati, Ohio 45267-0528

(Received 11 May 2009; revised 11 January 2010; accepted 13 January 2010)

A perceptible change in phonation characteristics after a swallow has long been considered evidence that food and/or drink material has entered the laryngeal vestibule and is on the surface of the vocal folds as they vibrate. The current paper investigates the acoustic characteristics of phonation when liquid material is present on the vocal folds, using *ex vivo* porcine larynges as a model. Consistent with instrumental examinations of swallowing disorders or dysphagia in humans, three liquids of different Varibar viscosity ("thin liquid," "nectar," and "honey") were studied at constant volume. The presence of materials on the folds during phonation was generally found to suppress the higher frequency harmonics and generate intermittent additional frequencies in the low and high end of the acoustic spectrum. Perturbation measures showed a higher percentage of jitter and shimmer when liquid material was present on the folds during phonation, but they were unable to differentiate statistically between the three fluid conditions. The finite correlation dimension and positive Lyapunov exponent measures indicated that the presence of materials on the vocal folds excited a chaotic system. Further, these measures were able to reliably differentiate between the baseline and different types of liquid on the vocal folds.
 [DOI: 10.1121/1.3308478]

PACS number(s): 43.70.Gr, 43.60.Hj, 43.40.Ga, 43.60.Wy [AL] Pages: 2578–2589

I. INTRODUCTION

A. Background

Because a number of medical conditions affect the vibratory characteristics of the larynx, acoustic differences between normal and abnormal phonation have been of great interest to scientists and clinicians, as aids to diagnosis and treatment. Most of this work has been focused on conditions that result from normal versus abnormal physiology related to laryngeal disease. For instance, there is a long tradition of comparing normal voice production with that from patients with vocal folds polyps, cysts and nodules, vocal folds edema, spasmodic dysphonia, Parkinson disease, and surgical scarring, among others (Klingholtz, 1990, Kreiman *et al.*, 1993, Herzel *et al.*, 1994, Giovanni *et al.*, 1999a, Giovanni *et al.*, 1999b, Vieira *et al.*, 2002, Jiang *et al.*, 2006, Zhang *et al.*, 2005, Zhang and Jiang, 2004). One type of abnormal voice production that has not been well studied is the case of vocal fold vibration when foreign material is present in the laryngeal area. This phenomenon occurs frequently in patients with poor coordination of airway protection and swallowing, because solid and/or liquid food may enter the laryngeal vestibule during the pharyngeal phase on its way to the esophagus. It also is commonly found in patients who fail to clear mucosal secretions from the surface of the larynx by coughing, primarily because they have diminished sensory feedback due to disease. While foreign material of this kind does not prevent voice production, secretions, or food material passing through the glottis into the trachea (commonly referred to as aspiration) and thence to the lungs means that patients with these problems are at high risk for respiratory diseases. Thus, detection of foreign materials within the larynx and on the true vocal folds is potentially a useful clinical indicator of swallowing problems.

Patients with suspected swallowing disorders, who show a change in voice quality, are often described as demonstrat-

a)Author to whom correspondence should be addressed. Electronic mail: mugam@uc.edu

ing a wet or "gurgly" voice (Logemann 1998, Murray *et al.*, 1996, Warms and Richards, 2000). While this phenomenon is widely known among clinicians and often assumed to indicate aspiration risk when observed during a clinical evaluation or meal, few studies have addressed the phenomenon from an objective and/or quantitative point of view. In one of the two studies readily available in the literature, Ryu *et al.* (2004) compared phonation in 23 patients who had shown in an earlier videofluorographic study that they were at high versus low risk for laryngeal penetration of food materials. They found that patients in the high risk group showed some statistically significant differences in acoustic indices immediately after swallowing, when compared to low risk patients. However, they did not have independent evidence that the phonation behavior was linked simultaneously to the presence of foreign materials on the larynx. In a later study, Groves-Wright (2007) collected simultaneous recordings of phonation and digital fluorographic images of the vocal tract, including the larynx, from 78 patients. She compared patients *with* observable materials in the laryngeal vestibule to patients *without* such observable materials, and found statistically significant differences in acoustic measures [e.g., jitter, shimmer, noise-to-harmonic ratio (NHR)]. Thus, there are strong reasons to believe that foreign materials present in the larynx can induce acoustical changes in phonation. Further, the acoustical characteristics of phonation under such conditions may provide a clinical marker of swallowing dysfunction and disease.

In a real patient, it is impossible to fully control the amounts and total viscosity of the materials on the larynx, both because each swallow is different, and because the materials may mix with secretions already present. Thus, it is difficult to determine the relationship between amount and viscosity of materials, and the acoustical characteristics of voice production when materials are present. An excised larynx model, on the other hand, allows easy control of these factors. Excised larynx models have already contributed significantly to our understanding of laryngeal physiology and voice production (Berry *et al.*, 1996, Alipour *et al.*, 1997, Švec *et al.*, 1999, Jiang *et al.*, 2003, Ayache *et al.*, 2004, Khosla *et al.*, 2007).

B. Review of acoustic measures

Ryu *et al.* (2004) and Groves-Wright (2007) employed the classic measures of jitter, shimmer, NHR, relative average perturbation, voice turbulence index, and spectral tilt. In recent years, non-linear methods of analysis have been gaining popularity in the study of vocal folds acoustics (Mende *et al.*, 1990, Herzel *et al.*, 1994, Titze, 1994a, Steinecke and Herzel, 1995, Narayanan and Alwan, 1995, MacAuslan *et al.*, 1997, Giovanni *et al.*, 1999a, Giovanni *et al.*, 1999b, Švec *et al.*, 1999, Jiang *et al.*, 2003, Zhang and Jiang, 2004, Zhang *et al.*, 2005, Jiang *et al.*, 2006, Zhang and Jiang, 2008). This emphasis on non-linear methods is due to recognition that phonation involves a number of non-linear mechanisms, such as flow-pressure relations, source-tract interaction, flow turbulence, and stress-strain relations within the vocal fold tissue. Similar effects apply to the vocal folds in the course of collision. The presence of material on the larynx during phonation also fits the model of a non-linear system because the presence of foreign materials introduces the behavior of a dynamic load, which is subject to a large number of variables with high sensitivity and low predictability. For instance, fluid droplets due to secretions might remain in place or be flung far from their previous location as a result of small variations in the composition and tension (or motion) of the vocal folds tissue, the local viscosity of the fluid itself, temperatures differences at different points within the larynx, and variations in force exerted by the glottal airstream. Further, loss of the fluid onto other anatomical structures (e.g., aryepiglottic folds and posterior pharyngeal wall) or down into the larynx, subglottic region, and trachea (evaporation, impingement of the particles on each other, and fluid-dynamic instabilities, among other factors) may combine to affect the acoustic output.

The purpose of the current study is to conduct a series of experiments on an excised larynx model, with the aim of (1) methodically characterizing the acoustics and vibratory behavior of the larynx under controlled conditions due to differing viscosities of materials present during phonation, and (2) determining which acoustic measures are most highly correlated with changes in the vibratory behavior of the vocal folds due to foreign materials present during phonation.

II. METHODS

A. Experiment

Most previous *ex vivo* studies have used canine larynges, which resemble the human vocal anatomy tissue composition and angle relative to the trachea, but show some differences in size and vibratory characteristics. Recent data suggest that porcine larynges are anatomically similar to human larynges in most aspects, and show acoustical and vibratory behavior similar to that of humans (Jiang *et al.*, 2001), but differ in having a 40° angle from vocal process (higher) to anterior commissure (lower) relative to the trachea (Alipour and Jaiswal, 2009). For purposes of this study, which is focused on acoustical and vibratory characteristics, we chose the porcine model as most appropriate. It should be noted that the more angled anatomy of the porcine model may result in greater pooling and longer persistence of liquid on the vocal folds at the anterior commissure, relative to behavior in the human larynx.

Six excised porcine larynges were obtained within 4 h after sacrifice. Cartilage and soft tissue above the true vocal folds was removed. A "collar" or lip of a few millimeters (ranging between 1 mm and 4 mm) around the larynx was left in place. After the extraneous tissue and muscles were dissected, removed, and cleaned, the larynges were immediately placed in a normal saline solution (0.9% NaCl). The tracheas were 8–10 cm long. The average glottal length measured from the anterior commisure to the vocal process was 20.8 mm, and it varied from 19.6–22.9 mm between larynges. For all larynges, the inferior 4 cm of the trachea was placed over a rigid tube (inner diameter of 1/2 in. and outer diameter of 5/8 in.). The outer trachea wall was clamped to the tube to prevent air leaks. A stitch was used to adduct the

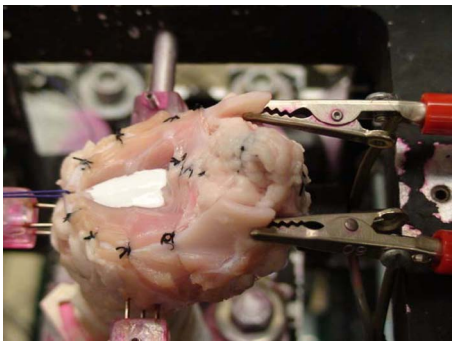

FIG. 1. (Color online) Photograph of the experimental setup.

vocal processes. Khosla placed one suture through both vocal processes at the same level with the aid of magnification. The stitch was tied with the minimal tension needed to have a prephonatory width between the vocal processes of 0 mm. Special care was taken to position the suture symmetrically in both the anterior-posterior and inferior-superior direction. The posterior glottis was completely closed with a suture. The larynx was fixed in space by using a square mounting apparatus that had four double prong pins on each side. Each pin was inserted into the thyroid cartilage (see also Fig. 1). Symmetry was monitored via video camera placed above the glottal exit. The flow that exited the rigid tube and entered the trachea was supplied by a blower, which could produce a maximum flow rate of 2500 cc/s at 35 psi. Pressure regulator, thermocouple, electronic pressure gauges, mass flow meter, and an electronic control valve were used to regulate the air upstream. The air was moistened using a humidifier with thermostat control (Conchatherm III, Hudson Respiratory Care Inc., Temecula, California).

Acoustic recordings were obtained by a Bruel and Kjaer freefield $\frac{1}{2}$ in. microphone (Model:4189), placed 12 cm above the glottal exit in such a way that it did not interfere with laryngeal airflow. The microphone has a sensitivity of 4 mV/Pa, a frequency bandwidth of 4 Hz–100 kHz (± 2 dB), and dynamic sensitivity of 28–164 dB. The response of this microphone is completely flat from 10 Hz–50 kHz and has 3% distortion for SPL$>$164 dB. The axis of the microphone was at 45° inward to the plane of the glottal exit. Of the various microphone settings, only the filter setting was changed to a low cut-off of 0.1 Hz and a high cut-off of 11 kHz. These settings were maintained for all the experiments. Static and dynamic subglottal pressure was recorded by a Honeywell pressure transducer (Model FPG1 WB) with sensitivity in the range of ± 24 cm H_2O relative to atmospheric pressure, a frequency response up to 2 kHz, and an accuracy of 0.1%. This pressure transducer was placed flushed on the walls of the rigid tube at a distance of 15 cm, below the vocal folds. Both the microphone and pressure transducers were calibrated before the start of every experiment. The EGG, acoustic and subglottal pressure signals recorded during phonation were each sampled at 20 kHz using a 16 bit NI data acquisition card (Model PCI 6259). A high-speed video camera (High Speed Phantom Version 7.1, sampled at 8 kHz) was placed approximately 30 cm above the glottal exit to visualize the vocal fold vibration and fluid motion on the laryngeal surface.

The experiments described in this paper used liquid of standardized viscosities as supplied by a manufacturer of Varibar barium (E-Z, EM, Inc.). The liquids used differed respectively by an order of magnitude: (1) Varibar "thin liquid," with a viscosity of 4 cP, (2) Varibar "nectar," with a viscosity of 300 cP, and (3) Varibar "improved honey," with a viscosity of 3000 cP. Our aims in using barium were: (a) because it can be obtained in standardized viscosity form; (b) it is opaque and easy to visualize by visible wavelength camera; and (c) it is routinely used during videofluorographic (VFSS) studies of human swallowing function. Although there may be reasons to suspect that VFSS tests using barium-mixed liquids are not fully representative of natural swallowing behaviors (Steele and Van Lieshout, 2005), barium as a contrast agent is always required for radiographic diagnostic imaging of swallow function (Logemann,1993, 1998). We reasoned that using barium in our *ex vivo* studies would be maximally comparable to this commonly used clinical test.

The same sequence of events was followed for each of the six larynges. There were four trials. Condition 1 consisted of a baseline trial (phonation with no fluid on the folds). Conditions 2, 3, and 4 involved the presence of materials on the larynx. The latter conditions will be referred to as the "viscosity" conditions. For each trial, a premeasured amount of liquid (0.3 ml) was placed on the larynx at a distance of approximately 1 cm above the glottal exit before the start of phonation by locating a syringe above the horizontal and vertical midline of the folds. Again for each trial, the larynx was set into vibration by increasing the subglottal pressure until the larynx began to sustain phonation. This pressure, i.e., the minimum pressure required to set the vocal folds into vibration, is commonly called phonation threshold pressure (PTP) (Titze, 1994b). Because it reflects various aspects of the physiology of the vocal folds (i.e., scar tissue, edema, bowing, among others) it is an important clinical parameter that appears to correlate well with speech system dysfunctions (Titze, 1988; Steinecke and Herzel, 1995; Lucero and Koenig, 2005, 2007; Tao and Jiang, 2008). We recorded the pressure at this point for each experimental condition.

The larynx was kept in vibration at PTP for 2 s. Before each experiment began, the larynx was cleaned of any remaining materials. The larynx was then removed from the apparatus and soaked in saline solution for 10 min before the start of the next condition. Images from the baseline condition were used to verify that the larynx was configured, within the apparatus, in the same manner for each of the conditions.

Observation of the high-speed images revealed that, during the 2-s period of the phonation experiment, each of the fluids (honey, nectar, and thin liquid) remained within the "collar" of tissue surrounding the vocal folds. All of the fluids were observed to slip gradually through the glottis, as the vocal folds opened and closed. We assumed evaporation to be negligible over this 2-s period.

B. Acoustic experiments

The first 500 ms of the acoustic recordings were extracted, and the following measurements were recorded: (1) average phonation frequency at PTP, (2) % jitter, (3) % shimmer, (4) correlation dimension (D_2), and (5) maximum Lyapunov exponent (L). In addition, we examined the signals using (6) conventional (CN) spectrograms, (7) time-corrected (TC) spectrograms, and (8) phase plots. % jitter, % shimmer, and average phonation frequency were calculated using the TF32 voice analysis software (Milenkovic, 2006). Jitter is defined as cycle to cycle variation in pitch period during voicing, and shimmer is variation between amplitudes in waveform cycles. In this study, we report both of these measures as percentages. The algorithm used to compute instantaneous pitch is that described by Milenkovic (1987).

Multibody dynamic systems such as those described here—i.e., liquid material lying on the surface of a vibrating vocal fold—are known to give rise to additional, nonharmonic frequencies. These frequencies are not well represented by conventional spectrograms, which tend to "smear" them. Accordingly, we evaluated the acoustic time series (x) with both conventional and time-corrected spectrograms (Fulop and Fitz, 2006). The later technique is a variant of the spectrogram reassignment method described in Fulop and Fitz (2006), as follows.

Given a spectrogram S_x, $S_x = \int_{-\infty}^{\infty}\int_{-\infty}^{\infty} W_x(s,\xi) W_h(t-s, \nu-\xi) ds d\xi$, which is defined as the two-dimensional convolution of the Wigner–Ville distribution (WVD), W_x and W_h, $W_x(t,\nu) = \int_{-\infty}^{\infty} x(t+(\tau/2)) x^*(t-(\tau/2)) e^{-j2\pi\nu\tau} d\tau$, and similarly, W_h is the WVD of the window function; superscript * denotes the complex conjugate.

Each point in time (t) and frequency (ν) space in the spectrogram (t,ν) is reassigned to another point (t',ν') in the time-corrected spectrogram. Mathematically,

$$\hat{t}(x;t,\nu) = \frac{\int_{-\infty}^{\infty}\int_{-\infty}^{\infty} s W_h(t-s,\nu-\xi) W_x(s,\xi) ds d\xi}{\int_{-\infty}^{\infty}\int_{-\infty}^{\infty} W_h(t-s,\nu-\xi) W_x(s,\xi) ds d\xi} \hat{\nu}(x;t,\nu)$$

$$= \frac{\int_{-\infty}^{\infty}\int_{-\infty}^{\infty} \xi W_h(t-s,\nu-\xi) W_x(s,\xi) ds d\xi}{\int_{-\infty}^{\infty}\int_{-\infty}^{\infty} W_h(t-s,\nu-\xi) W_x(s,\xi) ds d\xi}.$$

The reassigned spectrogram $S_x^{(r)}$ at any point (t',ν') is given as

$$S_x^{(r)}(t',\nu';h) = \int_{-\infty}^{\infty} S_x(t,\nu;h)\, \delta(t' - \hat{t}(x;t,\nu))\, \delta(\nu' - \hat{\nu}(x;t,\nu)) dt d\nu.$$

The reassignment can be thought of as a two step process: (1) smoothing using a window function, which dampens the oscillations that arises due to the cross interference terms; and (2) refocus the contributions that survived after smoothing. This method introduces a weighing function to t' and ν', such that the new time frequency coordinate better reflects the distribution of energy in the analyzed signal.

In order to allow better comparison between the conventional and TC spectrogram, the variables: (1) type of window (Hamming), (2) window size (256 samples), (3) overlap of the signal (50%), and (4) number of points of Fast Fourier Transform (FFT) (1024) were kept constant. Further, we observed from the high-speed video images that the liquid placed on the larynx tended to follow a cycle of collecting in pools, dispersing, and then collecting again. We suspected that this action of the material on the larynx might produce signals that were intermittent in nature.

C. Nonlinear methods

To investigate the nonlinear dynamics of the acoustic time series data $x(t_i)$, we employed three variables: (1) phase space methods, (2) correlation dimension, and (3) Lyapunov exponents (Heath, 2000; Kantz and Schreiber, 2000; Sprott, 2003). An m-dimensional phase space could be reconstructed as $y_i = \{x(t_i), x(t_i-\tau), \ldots, x(t_i-(m-1)\tau)\}$, where $x(t_i)$ represents a single sample at time instant t_i. The signal $x(t)$ is acquired at equal intervals, $dt = 1/\text{fs}$, where fs is the sampling frequency (fs=20 kHz in this study). These m-dimensional vectors, y_i, trace a trajectory in time, which eventually settle down on a path known as an attractor (Heath, 2000, Kantz and Schreiber, 2000, Sprott, 2003). The delay time τ and embedding dimension m are two fundamental parameters in the phase space reconstruction. Takens (1988) showed that when $m > 2D+1$, where D=Hausdorff dimension, the reconstructed phase space using the lagged coordinates is topologically equivalent to the original phase space. In this study, we employed the Takens method to estimate m. The time delay τ was identified according to the method of Fraser and Swinney (1986) as the first minimum corresponding to the least value of the mutual information S. Mathematically, $S = -\sum_{i,j} P_{ij}(\tau)^* \ln P_{ij}(\tau)/P_i P_j$, where P_i is the probability of finding a time series value in the ith interval and P_{ij} is the joint probability that (a) an observation falls on the ith interval and (b) after a delay τ, the same observation falls on the jth interval.

1. Correlation Dimension

The measure of correlation dimension D_2 is commonly used to study invariant characteristics of non-linear dynamical systems (Theiler, 1990). The higher the value of $D2$, the more complex the dynamical system, and the more degrees of freedom are needed to describe the dynamics of the system. In contrast, lower D_2 values require lesser states to describe the system. Mathematically, the correlation sum for a finite data set such as a time series is given as

$$C(N,\varepsilon) = \frac{2}{N(N-1)} \sum_{i=1}^{N} \sum_{j=i+1}^{N} \Theta(\varepsilon - \|x_i - x_j\|).$$

In this case, Θ is the Heaviside function, $\Theta(x)=0$ if $x <= 0$, and $\Theta(x)=1$ for $x>0$. The Theiler correction was applied to $C(N,\varepsilon)$ to discard data points that are strongly correlated in

TABLE I. *Post hoc* Tukey HSD Q values (critical Q at an alpha of 0.05 is 4.9).

	Q value (correlation dim)	Q value (Lyapunov exponent)	Q value (PTP)
Baseline versus thin liquid	5.85[a]	2.8	0.4
Baseline versus nectar	8.7[a]	8.6[a]	0.75
Baseline versus honey	12.7[a]	9.3[a]	8.12[a]
Nectar versus thin liquid	2.8	5.8[a]	0.4
Nectar versus honey	4.0	0.7	7.37[a]
Honey versus thin liquid	6.9[a]	6.4[a]	7.78[a]

[a]Statistically significant differences.

the phase space (Theiler, 1986, 1987). The modified formula is given as

$$C(N,\varepsilon,W) = \frac{2}{(N-W)(N+1-W)} \sum_{i=1}^{N} \sum_{j=i+1}^{N} \Theta(\varepsilon - \|x_i - x_j\|).$$

In this case, W is the number of closely spaced data points around x_i that are correlated. The correlation dimension D_2 is computed as the slope of logarithmic correlation sum to logarithmic distance ε,

$$d(N,\varepsilon) = \frac{\partial \ln C(N,\varepsilon,W)}{\partial \ln \varepsilon}$$

$$D_2 = \lim(\varepsilon \to 0)\lim(N \to \infty) d(N,\varepsilon)$$

In the current study, C was plotted as a function of ε for varying values of m. D_2 was estimated as the slope of the linear fit in the region where all the curves collapse for dimensional values greater than m (embedding dimension).

2. Lyapunov exponent

The Lyapunov exponent is another parameter that is used to describe the stability properties (i.e., sensitivity) of the dynamical system. A positive Lyapunov exponent L is an indication of the presence of chaos. The Lyapunov exponent expresses the relationship between positive and negative deviations from a trajectory in phase space. When deviations are damped over time, $L<0$. When deviations grow over time, $L>0$. A negative L is associated with stability of the dynamical system, while a positive L is associated with instability of the dynamical system (Wolfe *et al.*, 1985). In this study we used the Wolfe *et al.* (1985) method to compute the largest positive Lyapunov exponent L. The algorithm involves computing Euclidean distances between two neighboring points in the attractor over an "evolution time" T. The ratio of initial and final separation distances $d(0)$ and $d(T)$ is used to compute L, using the formula

$$L = \frac{1}{T}\left\langle \ln \frac{d(T)}{d(0)} \right\rangle,$$

where $\langle\ \rangle$ denotes average over several data points. The averaging procedure is performed over small separation distances d and along the most unstable direction (Wolfe *et al.*, 1985).

D. Statistical methods

A statistical significance level of $p=0.05$ was arbitrarily chosen in this study. A one-way analysis of variance (ANOVA) test was performed separately for each of the six different parameters (phonation threshold pressure, phonation frequency, % jitter, % shimmer, Lyapunov exponent, correlation dimension) across the four groups (baseline, thin liquid, nectar, and honey). ANOVA test is used to check the null hypothesis that different groups come from the same distribution (Dawson and Trapp, 2004). The ANOVA test assumes that data samples be drawn from normally distributed populations and that variances between the groups are similar. These two conditions were reasonably satisfied by the test data for the different computed parameters. A p value less than 0.05 indicates that a difference exist among different groups. For those parameters where the ANOVA results (from the parameter mean) were significant ($p<0.05$), a pairwise comparison was made among the groups using Tukey HSD *post hoc* analysis. A pairwise comparison involves comparing each of the possible pairs among the four groups (six possible pairs for four different groups, see also Table I). Stoline (1981) indicates that the Tukey HSD method is the most powerful and accurate method to make pairwise *post hoc* comparisons. MATLAB 7.6 (Mathworks) was used for statistical analysis.

III. RESULTS

A. Subglottal pressure experiments

The first set of experiments was conducted to determine a phonation threshold, i.e., the subglottal pressure required to initiate sustained phonation for each of the four conditions: (1) baseline, (2) thin liquid, (3) nectar, and (4) honey consistency. Thus, each larynx was set into vibration under each of the four conditions, and the subglottal pressure at which sustained vibration occurred was recorded. We expected that the addition of liquid would increase the aerodynamic load of the vocal folds, and thus, the subglottal pressure necessary for sustaining phonation. As Table II shows, the subglottal pressure for each of the six larynges did in fact increase under load. This difference was statistically significant with a p value of 0.00002 (see also Table III). Further, the pressure difference was related to the viscosity of the material; thus, the required pressure in the honey condition (3000 cP) was higher than the required pressure in the nectar condition (300 cP), and the pressure in the nectar condition was higher than the thin liquid (4 cP) condition.

TABLE II. PTP in cm of H_2O/phonation frequency (Hz) for baseline, "thin liquid" (4 cP), "nectar" (300 cP), and "honey"(3000 cP). Error in PTP $\pm$ 0.1%.

Viscosity	Larynx 1	Larynx 2	Larynx 3	Larynx 4	Larynx 5	Larynx 6
Baseline	6.4/278	6.9/260	6.3/266	7.2/269	7.8/274	6.1/274
4 cP	6.6/278	7/262	6.35/268	7.3/267	7.8/274	6.2/273
300 cP	6.6/282	7.1/268	6.4/269	7.35/269	8/271	6.45/272
3000 cP	8.5/283	9.0/268	8.9/268	9.1/272	10.2/272	8.0/277

B. Acoustic Experiments

It is interesting to consider what measures were consistent across conditions and larynges. Average phonation frequency ($F0$) at PTP for the baseline, thin liquid, nectar, and honey conditions was consistent across the three conditions and the six larynges, falling within a range of 266–283 Hz (see also Table II). The difference between the $F0$ for the different viscosity condition was statistically insignificant ($p=0.76$) at a p value of 0.05 (see also Table III) [for the baseline condition, the average $F0$ was 270 Hz (range =260–278 Hz), for the thin liquid condition, it was 270.3 Hz (range=262–278 Hz), for the nectar condition, it was 272(range=268–282 Hz), and for the honey condition, it was 273(range=268–283 Hz)]. Interestingly, this suggests that although the extra material on the vocal folds increased the subglottal pressure required to initiate phonation, it did not materially affect the rate of vocal fold vibration. Note that in a study of the effect of hydration, Ayache *et al.* (2004) found that adding viscous fluid to the surface of the vocal folds lowered the vibratory frequency. However, in the Ayache *et al.* study, as opposed to the current study, a very small amount of viscous fluid was swabbed onto the free margin of the fold. Further, the comparison condition involved vocal folds with no fluid applied. As such, the Ayache *et al.* study is less applicable than the current study to the conditions obtaining for patients with swallowing disorders. For instance, the methodology of the Ayache *et al.* study makes it possible that the fluid in question was absorbed by the dehydrated vocal folds internally, rather than resting on the surface during phonation.

Overall, as the experiments progressed, less and less materials remained on the vocal folds. Accordingly, the time trace of the subglottal pressure showed major differences between the baseline and the "viscosity" conditions. An example comparison is shown in Figs. 2(a) and 2(b), which contrast time traces of the subglottal pressure during phonation for the baseline no fluid condition [seen in Fig. 2(a)] and the highest viscosity honey condition [seen in Fig. 2(b)] for Larynx 1. As the figure shows, when we compare the baseline versus honey condition, there is a clear difference in the pressure peak-to-peak amplitude and pitch-pitch variation between cycles, with the baseline condition exhibiting a periodic signal with nearly constant peak-to-peak amplitude, and the honey condition showing wide variation in peak-to-peak amplitude. The honey condition also shows irregular kinks/humps that vary with time [see Fig. 2(b)]. Further, the average baseline PTP for this larynx was higher in the honey condition (6.4 cm of H_2O in the baseline condition, and 8.5 cm in the honey condition), while the average peak-peak amplitude of the signal was lower (2.89 cm H_2O versus 2.1 cm H_2O, respectively). In other words, as noted above, the mean PTP increased when fluid was added, and the increase was proportional to the change in viscosity (see also Table II). In contrast, the mean peak-peak amplitude of subglottal pressure decreased proportionately as viscosity increased during phonation.

Note that in all cases, the PTP and $F0$ values were consistent with those produced by normal human females using their habitual speaking voice. Figure 3 shows an FFT spectrum of the signal calculated across the entire 2-s experiment for Larynx 1, in each of the three baseline, thin liquid, nectar, and honey conditions. Distinct peaks can be observed at the average fundamental (278 Hz) and its harmonics. Consistent with our earlier observation (see also Table II), the change in average fundamental frequency between the three viscosity conditions was negligible.

Each of the effects described above are consistent with the characteristics of an unsteady dynamical system consisting of the combined vocal fold vibration and motion of fluid on the surface of the vocal folds. To further characterize the behavior of the system, we plotted the spectral density over time of the acoustic signals for each combination of condition and larynx, using CN and TC versions. Figure 4 shows an example of these measures for Larynx 1. The baseline condition is shown in Figs. 4(a) and 4(b), thin liquid condition in Figs. 4(c) and 4(d), the nectar condition in Figs. 4(e) and 4(f), and the honey condition in Figs. 4(g) and 4(h).

Both CN and TC spectrograms show distinct lines at the fundamental (first harmonic) and second harmonic (2^*F0) in the time frequency plots for all cases. The conventional spectrogram shows clear evidence of energy smearing (or broadening) at the fundamental (278 Hz) and second harmonic

TABLE III. p, F values from one-way ANOVA test for different metrics.

	PTP	Phonation frequency	% jitter	% shimmer	L	D_2
p value	0.00002[a]	0.76	0.14	0.07	0.004[a]	0.001[a]
F value, $df=3,20$	15.08	0.39	2.44	3.52	10.2	14.3

[a]Statistically significant differences ($p<0.05$).

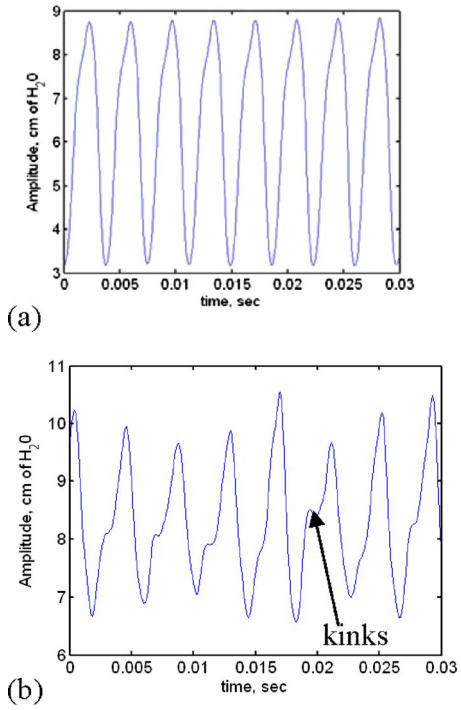

FIG. 2. (Color online) Acoustic time traces of phonation (a) baseline, no fluid on folds, and (b) honey condition for Larynx 1.

(556 Hz) for all cases. Some resolution is added by the TC spectrograms, such that we observe the presence of secondary frequencies between the fundamental and second harmonic. The presence of higher amplitude intermittent low frequencies (lower than $F0$) can also be clearly observed for the case with honey in both the conventional and TC spectrograms. Both CN and TC spectrograms show intermittent low frequencies for the load conditions, and a distinct dampening in the higher harmonics (834, 1112, 1390, 1668 Hz), but this dampening is much greater in the honey condition than in the nectar condition.

The presence of frequencies lower than the fundamental (i.e., the phonation frequency), the generation of high frequencies, the spectral broadening, and intermittent nature of these elements are classic signs of a non-linear system. Figures 5(a)–5(d) show the phase portraits of the baseline and the three viscosity conditions. The phase reconstruction is the plot of the acoustic phonation signal in delayed coordinates (Heath, 2000, Kantz and Schreiber, 2000, Sprott,

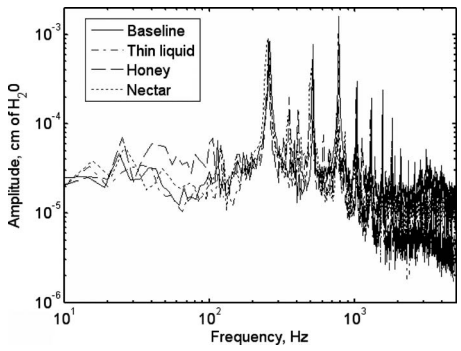

FIG. 3. Fast Fourier transform of the acoustic signal for baseline, thin liquid, nectar, and honey condition for Larynx 1.

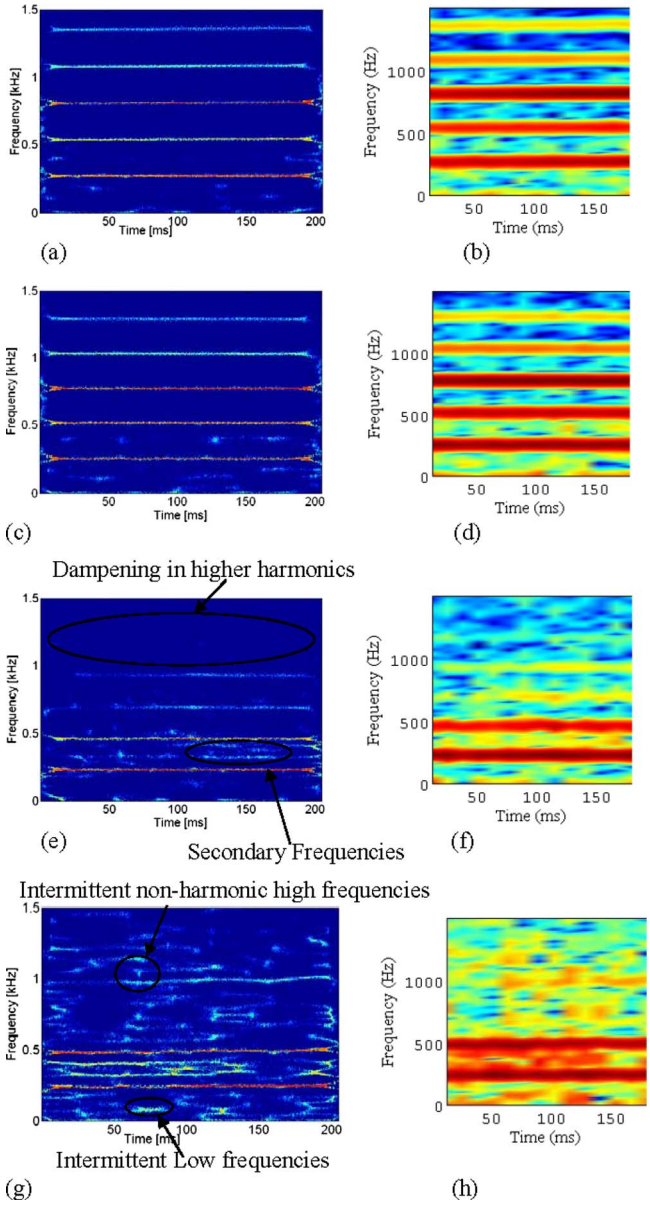

FIG. 4. (Color online) (a,c,e,g) Time corrected and (b,d,f,h) conventional acoustic spectrogram for (a,b) baseline, no fluid on folds, (c,d) thin liquid on folds, (e,f) nectar on folds, and (g,h) honey on vocal folds for Larynx 1.

2003). For the baseline condition, the signal is periodic, and shows the presence of a well-defined, i.e., regular, closed loop trajectory [see Fig. 5(a)]. The greatest contrast is shown by the honey condition, indicating an irregular pattern confirming the characteristics observed in the CN and TC spectrogram plots [see Fig. 5(d)]. The thin liquid and nectar conditions are intermediate in nature, showing a closed loop trajectory with less complex behavior, as compared with the honey condition. Note that the baseline condition and the nectar and thin liquid conditions differ in the attractor trajectory, which is seen in the thickness of the difference between the inner and outer boundaries of the loop. This in part arises due to the large variation in amplitudes between cycles in the thin liquid and nectar condition (also seen by large shimmer values, Fig. 6).

For purposes of quantifying the behavior observed in the phase plot, we computed the mean and standard error of the

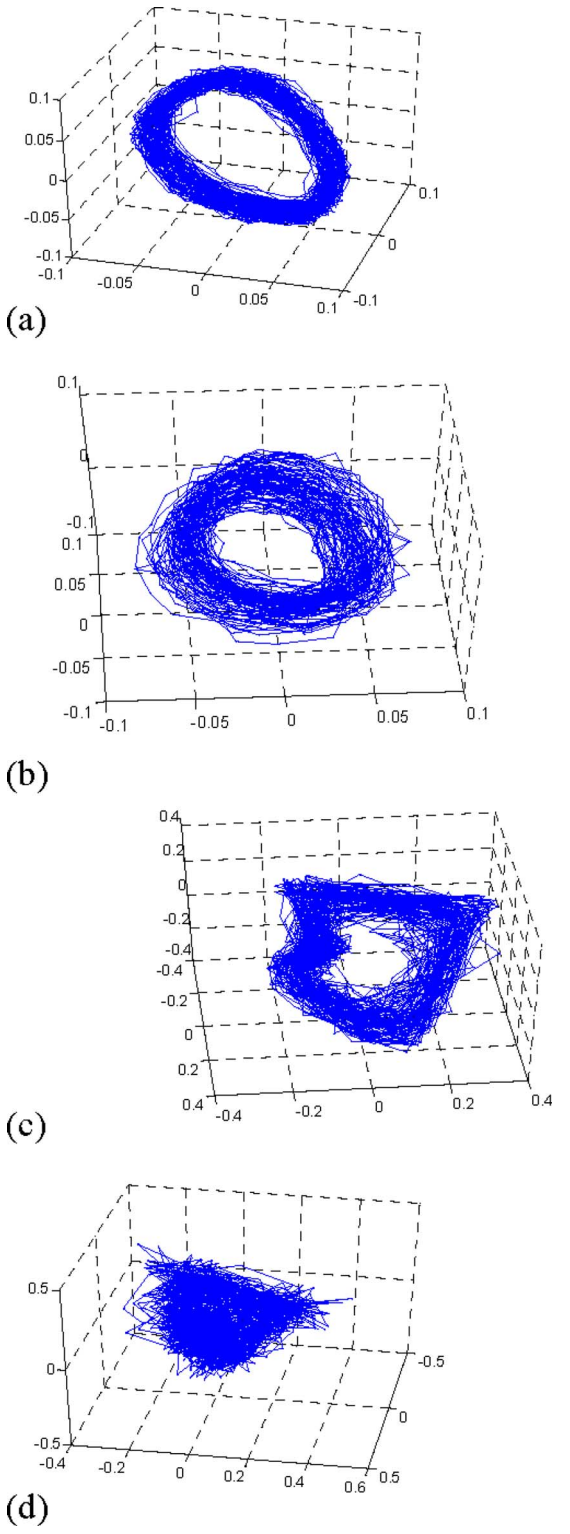

FIG. 5. (Color online) Phase portraits for (a) baseline, no fluid on folds, (b) thin liquid condition, (c) nectar condition, and (d) honey condition for Larynx 1.

correlation dimension (D_2), and the maximal Lyapunov exponent (L). In addition, we computed the conventional measures of % jitter and % shimmer. These are plotted in Fig. 6 for the six larynges, and for each of the four conditions. The vertical bars represent the standard error computed over all six larynges.

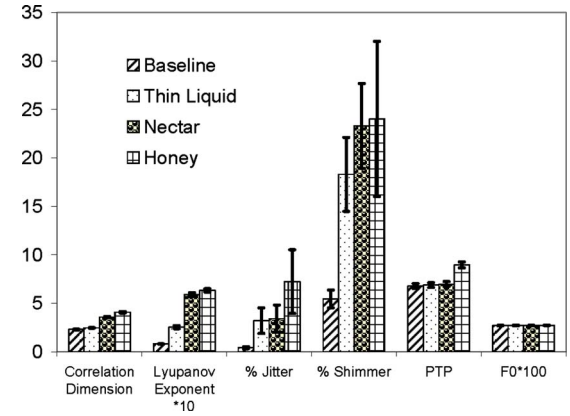

FIG. 6. (Color online) Bar plot of correlation dimension, Lyapunov exponent*10, % jitter, % shimmer, PTP, and $F0$ for the baseline, thin liquid, nectar, and honey condition. The vertical bars represent the standard error computed over all six larynges for each parameter.

In all of the cases, we observed a positive value for L, which suggests that the system exhibits chaotic behavior. However, a more stringent test to distinguish a random data from that of a chaotic data is the surrogate analysis (Theiler *et al.*, 1992). This test was performed in the current study. The surrogate data has the same power spectra as the original data set. A surrogate test involves subjecting both the original and surrogate data to the same type of non-linear analysis. This test has already been used in experimental data (Grassberger, 1986, Gober *et al.*, 1992, Kurths and Herzel, 1987, Narayanan and Alwan, 1995). If the results from the surrogate data are significantly different from those of the original data, then the null hypothesis that the original data arises from a random process can be rejected. One method of generating surrogate data is to take the Fourier transform of the original data, randomize phases, and then inverse Fourier transform to obtain the surrogate data set. This method was adopted in our study. We performed this analysis on two of the fluid conditions in Larynx 1. A plot of the correlation dimension and maximal Lyapunov exponent as a function of the embedding dimension is shown in Fig. 7. It can be seen that with increasing embedding dimension, the original data sets converged to a fixed correlation dimension and

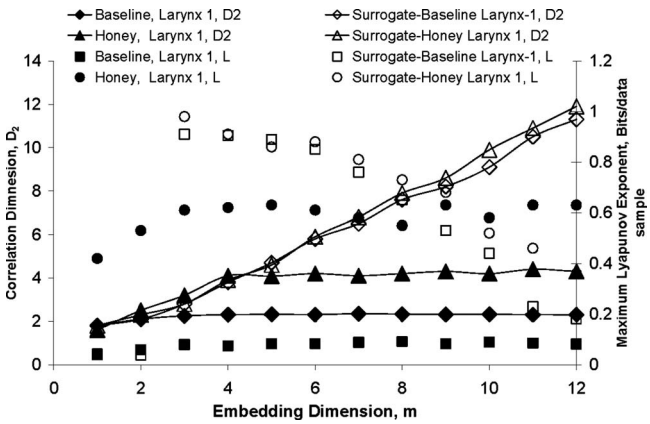

FIG. 7. Plot of correlation dimension and maximum Lyapunov exponent as a function of the embedding dimension, m for original and surrogate acoustic data for thin liquid and honey condition for Larynx 1.

TABLE IV. Range of % jitter, shimmer, correlation dimension, and maximal Lyapunov exponent for all the six larynges.

	Baseline	Thin liquid	Nectar	Honey
% jitter	0.38–0.58	2.6–4	1.5–6.7	3.8–11.39
% shimmer	3.6–6.4	17.6–18.9	14–29	9–26
Correlation dimension, D_2	2.28–2.4	3.0–3.34	3.4–3.7	3.9–4.17
Maximal Lyapunov exponent, L	0.05–0.1	0.19–0.32	0.58–0.595	0.625–0.637

Lyapunov exponent, whereas the surrogate data sets does not achieve a fixed value. The value of the Lyapunov exponent for the surrogate data sets is found to decrease with increasing embedding dimension, but never converges to a fixed value; whereas the value of correlation dimension steadily increases with increasing m. This test indicates that the surrogate data sets represent characteristics of a stochastic system. Additionally, the convergence of D_2 and L from the fluid conditions to a fixed value signifies that the data arose from a chaotic process.

Table IV shows mean and range for (1) % jitter, (2) % shimmer, (3) Lyapunov exponent, and (4) correlation dimension for the baseline and different viscosity conditions in all the six larynges. The p value and F statistic from the ANOVA test is summarized in Table III. For the non-linear metrics (correlation dimension and maximal Lyapunov exponent), p values were less than 0.05, indicating that there was a statistical difference between the baseline and three different viscosity conditions. In contrast, the classical measures showed a non-significant difference ($p>0.05$). Furthermore, no differences were identified in the phonation frequency between the different conditions, whereas a statistically significant difference was observed in the phonation threshold pressure between the different conditions.

The above finding suggests that the classic perturbation measures of jitter and shimmer cannot reliably identify differences between the baseline and different load conditions. Note that increased jitter and shimmer are sometimes found, but do not seem to be a consistent indicator of material on the vocal folds [this finding is consistent with the study of Ramig *et al.* (1990), which showed increased shimmer in some, but not all amyotrophic lateral sclerosis patients who presented with a wet sounding voice].

A *post hoc* analysis was performed using the Tukey HSD method to identify differences between the different conditions for PTP and the two nonlinear metrics, D_2 and L. The studentized range statistic Q is given in Table I for each different comparison of the baseline and viscosity conditions. To reach statistical significance at the 0.05 level, the necessary Q value for alpha is 4.9 (degrees of freedom=6 and number of treatments=4); that is, values of $Q>4.9$ indicate that there is a statistical difference. As Table I shows, all comparisons between baseline and viscosity conditions were significant for D_2. In contrast, the Lyapunov exponent was unable to detect a significant difference between baseline and thin liquid conditions, but was able to identify differences between nectar and thin liquid. D_2 did not detect reliable differences between thin liquid and nectar, or nectar and honey conditions. All three measures (PTP, D_2 and L) were able to identify differences between thin liquid and honey conditions.

It should be noted that the computation of correlation dimension and Lyapunov exponent in finite experimental data has several limitations. Some of these limitations include the presence of noise, stationarity of the signal, finite signal length, and influence/presence of auto-correlation effects. In this study, we attempted to obtain reliable estimates and validate them in the following manner. For instance, external noise perturbations were kept to a minimum during the measurements (this can be seen in Fig. 4, where the acoustic amplitude of the fundamental was at least 15 times higher the background noise level). The operational definition of stationarity used here was that proposed by Theiler (1991). In the current study, the spectral plot of the baseline and load conditions show amplitude at (frequencies $<$fundamental), which are at least an order of magnitude lower than the dominant frequencies (see Fig. 3). Narayanan and Alwan (1995) and Herzel (1993) imposed durational constraints on voice sounds in their non-linear analysis. The rationale behind this approach was that a large number of pitch cycles could then provide stationary time series segments. In their data, a duration of as little as 100 ms was found to be sufficient for the purpose. In the current study, we computed D_2 and L in four equal segments (500 ms) over the entire 2 s phonation period. The variations between D_2 and L between segments in all cases were within 3%. Using the formula given by Eckmann and Ruelle (1992), the upper bound for D_2 for a signal length of $N=5000$ (time segment*sampling frequency=500 ms*10 000) is 7.4. For both the baseline and viscous load conditions in all the six larynges, the value of D_2 was less than 7.4. This indicates that N was long enough for reasonable estimates of D_2. To minimize the possibility that the auto-correlation effects might result in spurious dimension estimates due to loss of scaling behavior in the correlation integral (Theiler, 1987), we employed the mutual information method for computation of τ (Narayanan and Alwan, 1995).

IV. DISCUSSION AND CONCLUSION

Overall, the results of this study document the following three characteristics of vocal fold vibration under liquid load.

(1) Phonation with liquid material on the vocal folds shows characteristics of irregular and aperiodic phonation.
(2) The non-linear measures tested were more sensitive to differences between viscosity conditions than were the classic measures of % jitter and % shimmer.

(3) Differences across conditions were consistent with the prediction that the effect of increasing liquid viscosity on the vocal folds is to increase the PTP, % jitter, and % shimmer, and reduce the peak-peak amplitude of subglottal pressure.

There are a number of similarities between our results and the results of studies on abnormal phonation in pathological voice conditions involving edema, vocal folds polyps, nodules, and cysts, among others (Herzel *et al.*, 1994, Berry *et al.*, 1996, Titze, 1994a, Giovanni *et al.*, 1999a, Giovanni *et al.*, 1999b, Švec *et al.*, 1999, Jiang *et al.*, 2003, Zhang and Jiang, 2004, Zhang *et al.*, 2005, Jiang *et al.*, 2006, Zhang and Jiang, 2008). As in the Jiang *et al.* (2003) excised experiments, we found that the acoustic signal showed signs of irregular phonation, and that non-linear methods worked better than classic perturbation methods for characterizing baseline versus viscosity conditions. Similarly, Jiang *et al.* (2003), Zhang *et al.* (2005), and Zhang and Jiang (2008) found that perturbation metrics such as jitter and shimmer were less effective than non-linear measures at characterizing differences between pathological voices, or at documenting change as a result of clinical intervention. In general, jitter and shimmer as measures are dependent on accurate extraction of the pitch period. One possible explanation for the relative insensitivity of these measures to our data may be explained by the fact that the viscosity conditions showed a number of characteristics that are challenging for typical pitch extraction algorithms. These characteristics include the generation of intermittent low and high frequencies in the proximity of the phonation frequency and its harmonics.

A similar explanation may apply to the pathological voices examined by Herzel *et al.*, 1994, Berry *et al.*, 1996, Titze, 1994a, Giovanni *et al.*, 1999a, Giovanni *et al.*, 1999b, Švec *et al.*, 1999, Jiang *et al.*, 2003, Zhang and Jiang, 2004, Zhang *et al.*, 2005, Jiang *et al.*, 2006, and Zhang and Jiang, 2008.

In addition, we found that the non-linear measures were particularly sensitive to differences in viscosity. For example, both correlation dimension and the Lyapunov exponent were able to identify difference between thin liquid and honey. Additionally, the Lyapunov exponent was able to detect differences between thin liquid and nectar, whereas correlation dimension did not (it should be pointed out that neither metric was sensitive to the difference between honey versus nectar). This result suggests that non-linear analysis of voice after swallowing in patients who show signs of swallowing disorder may be useful in assessing the presence of foreign materials. It might also be useful in assessing difference between different viscosity liquids present on the vocal folds (thick versus thin mucous/secretions or food material) in patients who fail to clear secretions or patients who present with a high risk of aspiration on a certain viscosity food material.

Our finding that liquid load on the vocal folds increases the subglottal pressure necessary for phonation (PTP) is not unexpected, simply because it takes a higher pressure to move a greater mass. Additionally, the presence of liquid on the vocal folds reduces the peak to peak subglottal pressure amplitude. We speculate that the presence of fluid on the folds dampens vibrations and mucosal waves on the surface. Higher viscosity fluids can be thought of inducing greater damping force on the vibrations, which could lead to higher PTP and lower peak-peak subglottal pressure amplitude in all the six larynges. Larger variation in subglottal pressure amplitude was also observed with the presence of liquid, which could be possibly attributed to dynamic motion of the liquid and its subsequent loss into the glottis opening. The finding of irregular and aperiodic components in the phonatory signal is also not surprising. The dampened vibrations generated due to presence of liquid on the vocal folds surface act to decrease the amplitude of sound production. In addition, the fluid may come into contact with the glottal airflow as a consequence of its motion on the surface of the vocal folds. Contact of this nature may well generate a multitude of effects related to fluid evaporation and fluid inertial behaviors (e.g., pooling on the surface of the larynx and into adjacent structures, spilling below the vocal folds, impinging on the walls of the supraglottal structures, and breaking up/atomization into smaller fluid particles). Various aeroacoustic mechanisms can cause generation of sound when the air flow is occasionally interrupted or comes in contact/impinges with the liquid during glottal opening. For example, the interaction of glottal air flow with liquid/food material on the vocal fold surface presumably will generate a fluctuating pressure, which in turn produces a new dipole source or modification of the rate of change in airflow Q at glottis, dQ/dt (Zhao *et al.*, 2002). Such effects may explain the intermittent acoustic events that were observed in the TC spectrograms [see Figs. 4(c)–4(h)].

This study focuses on only a few of the variables involved in evaluating vocal fold phonation under load. For instance, fluid mass affects the total load on the vocal fold. While in the present study, we employed a constant fluid volume for liquids of different viscosity, the behavior of different volumes is another dimension of variation, which arises commonly in clinical swallow studies. Many patients with swallowing difficulties also present with laryngeal pathologies, and it will be important to determine how these different pathologies affect the behavior of the material on the vocal folds, and their acoustic consequences. Additional work in the area of spatio-temporal vocal fold characteristics and liquid-phonatory airflow-vocal folds vibratory structure coupling will also be required to understand the complex interaction and its effect on non-linear metrics. Future work should also involve comparing these results with clinical endoscopic evaluations (flexible endoscopic swallowing study) of larynx in patients with swallowing disorders. Studies should also include comparing these data to other *ex vivo* tissue models (e.g., canine) and evaluate the effect that arises due to geometrical differences (e.g., sloping glottis).

The overall direction of these studies will be twofold. In the one case, the analysis of acoustic signals produced by vocal folds under different load conditions may provide a supplementary tool for use in the differentiation and monitoring of phonatory behavior during diagnosis and treatment of swallowing disorders. In the other case, if we can establish accurate identification of swallowed material on the vocal

folds during phonation via acoustic analysis, then this may help in estimating the threat of these conditions on lower airway protection and respiratory health.

ACKNOWLEDGMENTS

The authors would like to thank Raghav Lakhamraju for his help with experimental setup and data collection. They would also like to thank the two anonymous reviewers and the associate editor, Dr. Anders Lofquist, for taking extra care in providing valuable comments and suggestions that have enabled us to improve the quality of the article. The authors would also like to thank Kathy Groves-Wright and Bernice Klaben for inspiring this study, and Joel MacAuslan from STAR Analytical Services for providing insightful comments. They are grateful for the support received from the University of Cincinnati Research Council to conduct this work.

Alipour, F., and Jaiswal, S. (**2009**). "Glottal airflow resistance in excised pig, sheep, and cow larynges," J. Voice **23**, 40–50.

Alipour, F., Scherer, R. C., and Finnegan, E. (**1997**). "Pressure-flow relationships during phonation as a function of adduction," J. Voice **11**, 187–194.

Ayache, S., Ouaknine, M., Dejonkere, P., Prindee, P., and Giovanni, A. (**2004**). "Experimental study of the effects of surface mucus viscosity on the glottic cycle," J. Voice **18**, 107–115.

Berry, D. A., Herzel, H., Titze, I. R., and Story, B. H. (**1996**). "Bifurcations in excised larynx experiments," J. Voice **10**, 129–138.

Dawson, B., and Trapp, R. G. (**2004**). *Basic and Clinical Statistics*, 4th ed. (McGraw-Hill, New York).

Eckmann, J. P., and Ruelle, D. (**1992**). "Fundamental limitations for estimating dimensions and Lyapunov exponents in dynamic systems," Physica D **56**, 185–187.

Fraser, A. M., and Swinney, H. L. (**1986**). "Independent coordinates for strange attractors from mutual information," Phys. Rev. A **33**, 1134–1140.

Fulop, S. A., and Fitz, K. (**2006**). "Algorithms for computing the time-corrected instantaneous frequency (reassigned) spectrogram, with applications," J. Acoust. Soc. Am. **119**, 360–371.

Giovanni, A., Ouaknine, M., Guelfucci, B., Yu, P., Zanaret, M., and Triglia, J.-M. (**1999a**). "Nonlinear behavior of vocal folds vibrations: The role of coupling between vocal folds," J. Voice **13**, 465–476.

Giovanni, A., Ouaknine, M., and Triglia, J.-M. (**1999b**). "Determination of largest Lyapunov exponent of the vocal signal: Application to unilateral laryngeal analysis," J. Voice **13**, 341–354.

Gober, M., Herzel, H., and Graf, H.-F. (**1992**). "Dimension analysis of El Nino/southern oscillation time series," Ann. Geophys. **10**, 729–734.

Grassberger, P. (**1986**). "Do climatic attractors exist?," Nature (London) **323**, 609–612.

Groves-Wright, K. (**2007**). "Acoustics and perception of wet vocal quality in Identifying penetration/aspiration during swallowing," Ph.D. thesis, Communication Sciences and Disorders, University of Cincinnati, Ohio.

Heath, R. (**2000**). *Nonlinear Dynamics: Techniques and Applications in Psychology* (Lawrence Erlbaum Associates, Publishers, Mahwah, New Jersey).

Herzel, H. (**1993**). "Bifurcations and chaos in voice signals," Appl. Mech. Rev. **46**, 399–413.

Herzel, H., Berry, D., Titze, I. R., and Saleh, M. (**1994**). "Analysis of vocal disorders with methods from nonlinear dynamics," J. Speech Hear. Res. **37**, 1008–1019.

Jiang, J., Zhang, Y., and Ford, C. N. (**2003**). "Non-linear dynamics of phonation in excised larynx experiments," J. Acoust. Soc. Am. **114**, 2198–2205.

Jiang, J., Zhang, Y., and McGilligan, C. (**2006**). "Chaos in voice, from modeling to measurement," J. Voice **20**, 2–17.

Jiang, J. J., Raviv, J. R., and Hanson, D. G. (**2001**). "Comparison of the phonation related structures among pig, dog, white-tailed deer, and human larynges," Ann. Otol. Rhinol. Laryngol. **110**, 1120–1125.

Kantz, H., and Schreiber, T. (**2000**). *Nonlinear Time Series Analysis* (Cambridge University Press, Cambridge, England).

Khosla, S., Murugappan, S., Gutmark, E., and Scherer, R. (**2007**). "Vortical flow field during phonation in an excised canine larynx model," Ann. Otol. Rhinol. Laryngol. **116**, 217–228.

Klingholtz, F. (**1990**). "Acoustic recognition of voice disorders: A comparative study of running speech *versus* sustained vowels," J. Acoust. Soc. Am. **87**, 2218–2224.

Kreiman, J., Gerratt, J. B., Kempster, G. B., Erman, A., and Berke, G., (**1993**). "Perceptual evaluation of voice quality review, tutorial, and a framework for future research," J. Speech Hear. Res. **36**, 21–40.

Kurths, J., and Herzel, H. (**1987**). "An attractor in solar time series," Physica D **25**, 165–172.

Logemann, J. A. (**1993**). *Manual for the Videofluorographic Study of Swallowing*, 2nd ed. (Pro:Ed, Austin, Texas).

Logemann, J. A. (**1998**). *Evaluation and Treatment of Swallowing Disorders*, 2nd ed. (Pro:Ed, Austin, Texas).

Lucero, J. C., and Koenig, L. L. (**2005**). "Phonation thresholds as a function of laryngeal size in a two-mass model of the vocal folds," J. Acoust. Soc. Am. **118**, 2798–2801.

Lucero, J. C., and Koenig, L. L. (**2007**). "On the relation between the phonation threshold lung pressure and the oscillation frequency of the vocal folds," J. Acoust. Soc. Am. **121**, 3280–3283.

MacAuslan, J., Chenausky, K., Juda, J., and Manev, I. (**1997**). "Identifying laryngeal attractor changes from periodicity diagrams," Proceedings of the Nonlinear Signal and Image Processing Conference, Mackinac, MI.

Mende, W., Herzel, H., and Wermke, K., (**1990**). "Bifurcations and chaos in newborn cries," Phys. Lett. **145**, 418–424.

Milenkovic, P. (**1987**). "Least mean square measures of voice perturbation," J. Speech Hear. Res. **30**, 529–538.

Milenkovic, P. H. (**2006**). TF32Voice Reference Manual, Department of Electrical and Computer Engineering, University of Wisconsin-Madison, http://userpages.chorus.net/cspeech/ (Last viewed May, 2009).

Murray, J., Langmore, S. E., Ginsberg, S., and Dostie, A. (**1996**). "The significance of oropharyngeal secretions and swallowing frequency in predicting aspiration," Dysphagia **11**, 99–103.

Narayanan, S., and Alwan, A. (**1995**). "A nonlinear dynamical systems analysis of fricative consonants," J. Acoust. Soc. Am. **97**, 2511–2524.

Ramig, L. O., Scherer, R. C., Klasner, E. R., Titze, I. R., and Horii, Y. (**1990**). "Acoustic analysis of voice in amyotrophic lateral sclerosis: A longitudinal case study," J. Speech Hear Disord. **55**, 2–14.

Ryu, J. S., Park, S. R., and Choi, K. H. (**2004**). "Prediction of laryngeal aspiration using voice analysis," Am. J. Phys. Med. Rehabil. **83**, 753–757.

Sprott, J. C. (**2003**). *Chaos and Time Series Analysis* (Oxford University Press, New York).

Steele, C. M., and Van Lieshout, P. H. H. M. (**2005**). "Does barium influence tongue behaviors during swallowing?," Am. J. Speech Lang. Pathol. **14**, 27–39.

Steinecke, I., and Herzel, H. (**1995**). "Bifurcations in an asymmetric vocal fold model," J. Acoust. Soc. Am. **97**, 1874–1884.

Stoline, M. R. (**1981**). "The status of multiple comparisons: Simultaneous estimation of all pairwise comparisons in one-way ANOVA designs," Am. Stat. **35**, 134–141.

Švec, J. G., Schutte, H. K., and Miller, D. G. (**1999**). "On pitch jumps between chest and falsetto registers in voice: Data from living and excised human larynges," J. Acoust. Soc. Am. **106**, 1523–1531.

Takens, F., (**1988**). "Limit capacity and Hausdorff dimension of dynamically defined cantor sets," *Dynamical Systems* (Springer, Berlin), Vol. **1331**, pp. 196–212.

Tao, C., and Jiang, J. J. (**2008**). "The phonation critical condition in rectangular glottis with wide prephonatory gaps," J. Acoust. Soc. Am. **123**, 1637–1641.

Theiler, J. (**1986**). "Spurious dimension from correlation algorithms applied to limited time series data," Phys. Rev. A **34**, 2427–2432.

Theiler, J. (**1987**). "Efficient algorithm for estimating the correlation dimension from a set of discrete points," Phys. Rev. A **36**, 4456–4462.

Theiler, J. (**1990**). "Estimating fractal dimension," J. Opt. Soc. Am. A **7**, 1055–1073.

Theiler, J. (**1991**). "Some comments on correlation dimension of $1/f^{\alpha}$ noise," Phys. Lett. **155**, 480–493.

Theiler, J., Eubank, S., Longtin, A., Galdrikian, B., and Farmer, J. D. (**1992**). "Testing for nonlinearity in time series: The method of surrogate data," Physica D **58**, 77–94.

Titze, I. R. (**1988**). "The physics of small-amplitude oscillation of the vocal folds," J. Acoust. Soc. Am. **83**, 1536–1552.

Titze, I. R. (**1994a**. "Summary statement," Proceedings of the Workshop on

Acoustic Voice Analysis, NCVS, Denver, CO, Feb. 17 and 18.
Titze, I. R. (**1994b**). *Principles of Voice Production* (Prentice-Hall, Englewood Cliffs, NJ).
Vieira, M. N., McInnes, F. R., and Jack, M. A. (**2002**). "On the influence of laryngeal pathologies on acoustic and electroglottographic jitter measures," J. Acoust. Soc. Am. **111**, 1045–1055.
Warms, T., and Richards, J. (**2000**). "Wet voice as a predictor of penetration and aspiration in oropharyngeal dysphagia," Dysphagia **15**, 84–88.
Wolf, A., Swift, J. B., Swinney, H. L., and Vastano, J. A. (**1985**). "Determining Lyapunov exponents from a time series," Physica D, **16**, 285–317.
Zhang, Y., and Jiang, J. (**2004**). "Chaotic vibrations of a vocal folds model with a unilateral polyp," J. Acoust. Soc. Am. **115**, 1266–1269.
Zhang, Y., and Jiang, J. (**2008**). "Acoustic analysis of sustained and running voices with laryngeal pathologies," J. Voice **22**, 1–9.
Zhang, Y., Jiang, J., and Rahn, D., III (**2005**). "Studying vocal folds vibrations in Parkinson's disease with a nonlinear model," Chaos **15**, 033903.
Zhao, W., Zhang, C., Frankel, S. H., and Mongeau, L. (**2002**). "Computational aeroacoustics of phonation, Part 1: Computational methods and sound generation mechanisms," J. Acoust. Soc. Am. **112**, 2134–2146.

The effect of whisper and creak vocal mechanisms on vocal tract resonances

Yoni Swerdlin, John Smith,[a] and Joe Wolfe
School of Physics, University of New South Wales, Sydney, New South Wales 2052, Australia

(Received 12 May 2009; revised 20 January 2010; accepted 21 January 2010)

The frequencies of vocal tract resonances estimated using whisper and creak phonations are compared with those in normal phonation for subjects who produced pairs of these phonations in the same vocal gesture. Peaks in the spectral envelope were used to measure the frequencies of the first four resonances ($R1-R4$) for the non-periodic phonations, and broadband excitation at the mouth was used to measure them with similar precision in normal phonation. For resonances $R1-R4$, whispering raises the average resonant frequencies by 255 Hz with standard deviation 90 Hz, 115 ± 105, 125 ± 125, and 75 ± 120 Hz, respectively. A simple one dimensional model of the vocal tract is presented and used to show how an effective glottal area can be estimated from shifts in resonance frequency measured during the same vocal gesture. Calculations suggest that the effective glottal area thus defined increases to 40 ± 30 mm^2 during whispering. Creak phonation raised significantly only the first and third resonant frequencies, by 45 ± 50 and 65 ± 120 Hz respectively. It thus appears possible to use creak phonation to determine resonances with more precision than is available from the spectral envelope of voiced speech, and this supports its use in teaching resonance tuning to singers. © *2010 Acoustical Society of America.* [DOI: 10.1121/1.3316288]

PACS number(s): 43.70.Gr, 43.70.Aj, 43.70.Bk [CHS] Pages: 2590–2598

I. INTRODUCTION

The acoustic resonances (Ri) of the human vocal tract are of interest for several reasons. When excited by various mechanisms, these resonances give rise to peaks in the spectral envelope of the output sound (e.g., Fant, 1970). In speech, the peaks in the spectral envelope with the two lowest frequencies usually identify the vowels in Western languages and contribute to regional accents. Further, their variation in time is important to the identification of many consonants. The peaks in the spectral envelope that occur at higher frequencies are important in determining the timbre and identity of the voice (e.g., Fant, 1973; Clark *et al.*, 2007).

The resonances are also important in music, for reasons not directly related to phonetics (Wolfe *et al.*, 2009). Following suggestions by Sundberg (Lindblom and Sundberg, 1971; Sundberg, 1977), it has been demonstrated that some singers "tune" the lowest resonance to a frequency near the fundamental (f_0) of the note sung (Joliveau *et al.*, 2004a, 2004b), thereby obtaining extra output power for a given vocal effort. Other singers have been shown to tune the first resonance to the second harmonic (Henrich *et al.*, 2007). Furthermore, it is proposed that these resonances can also influence the vibratory behavior of the vocal folds (Titze 1988, 2004, 2008). Indeed it is possible that composers have aided the acoustics of the soprano voice at high pitch when setting text to music by appropriately matching sung pitch to resonance frequency (Smith and Wolfe, 2009). Vocal tract resonances also play an important role in determining the timbre or pitch of wind instruments, e.g., the didjeridu (Tarnopolsky *et al.*, 2005, 2006), the saxophone (Chen *et al.*, 2008), and the clarinet (Chen *et al.*, 2009). Indeed, experienced musicians have been observed to play with the relatively small glottis (Mukai, 1992) that would enhance vocal tract resonances.

The frequencies of the resonances may be estimated in a number of ways. The spectral maxima in the output sound will occur at frequencies close to those of the tract resonances that produce them, so one method involves estimating the resonances from the sound spectrum of speech or song. In normal phonation, however, the tract is predominantly excited by periodic vibration of the vocal folds. Consequently, the frequency domain is sampled at multiples of the fundamental frequency f_0, so it is difficult to determine unambiguously the frequencies of the resonances with a resolution much finer than $f_0/2$. f_0 is typically 100–300 Hz in conversational speech, but may be considerably higher in singing where the resolution is correspondingly much worse (Monsen and Engebretson, 1983). The estimation of resonance frequencies from spectral peaks in normal phonation is further complicated by the frequency dependence of the source function at the glottis, which is in general unknown.

One possible method of improving the frequency resolution involves vibrating the neck near the glottis using a broadband mechanical source (Coffin, 1974; Sundberg, 1977; Pham Thi Ngoc and Badin, 1994). This has the advantage that it stimulates the tract from an area near the glottis, but its disadvantages are that the transfer functions between the mechanical signal and the acoustical signal at the glottis are unknown, and that it involves perturbing the subjects.

A potentially more precise method of estimating the frequencies of resonances of the tract during normal phonation involves exciting it with a known, external, acoustic flow at the mouth (Epps *et al.*, 1997; Dowd *et al.*, 1998). A broadband source of acoustic flow and a microphone are posi-

[a]Author to whom correspondence should be addressed. Electronic mail: john.smith@unsw.edu.au

 0001-4966/2010/127(4)/2590/9/$25.00

tioned at the subject's lower lip. During normal phonation, the microphone pressure signal is the sum of the widely spaced harmonics of the periodic voice signal and the pressure produced by the injected acoustic flow interacting with the vocal tract and the radiation field. However, it has the disadvantages that the tract is measured from the mouth rather than the glottis, and it is measured in parallel with the external radiation field.

Another method of estimating resonances involves exciting the tract by a non-periodic vocal mechanism, thereby producing a spectrum whose peaks may be determined with greater precision than is possible for normal speech. Whispered speech is produced by turbulent flow through a relatively small, nearly constant aperture formed between the vocal folds. In creak phonation, also called the creak voice, vocal fry or mechanism 0, the vocal folds open in an aperiodic way (Hollien and Michel, 1968; Gobl, 1989). Researchers in acoustic phonetics have used whisper or creak phonation to obtain information about the resonances, with potential relevance to normal speech. Another practical use of creak phonation concerns the use of resonance tuning in singing: Singers may use spectral analysis of their creak phonation to learn to tune a resonance of the vocal tract (Miller *et al.*, 1997).

The whisper and creak methods have a possible limitation in that the different phonation types involve changes in the geometry of the tract around the glottis. Further, even if the geometry of the entire tract (glottis excepted) were fixed, the frequencies of the resonances should vary due to different average areas of the glottis. It is thus possible that the resonance frequencies are different for the different modes of phonation. Consequently, measurements of Ri made during whisper or creak phonation might not be exactly comparable with normal phonation.

Indeed, researchers have found that, on average, the resonances of whispered speech usually occur at significantly higher frequencies than those of normally phonated speech (Kallail and Emanuel, 1984a, 1984b; Jovocic, 1998; Matsuda and Kasuya, 1999). In contrast, the resonances produced by creak and normal phonations have been found to be similar (e.g., Miller *et al.*, 1997), although Ladefoged *et al.* (1988) and Ananthapadmanabha (1984) reported slight increases in $R1$ during creak phonation and Moosmüller (2001) found that, for women, $R2$ is slightly lowered in the creaky voice.

The above measurements are subject to the limitation that, while the resonances associated with whispered speech and creak phonations can be determined precisely from the spectral peaks in the sound, this is not usually possible for normal phonation, as explained above. Further, the studies cited above all compare averages of the resonance frequencies measured in separate vocalization gestures.

In the present study, using ten young Australian women as subjects, the resolution of such studies is increased by introducing two experimental improvements. The first is to use acoustical excitation at the mouth to estimate the acoustical resonances of the vocal tract more precisely during normal phonation. The second is to compare them with estimates of the resonances using whisper or creak phonation in the same vocal gesture. Finally a simple mathematical model is developed to estimate the increase in effective glottal area during these phonation modes. Some of the experimental results given have been briefly presented earlier (Swerdlin *et al.*, 2008).

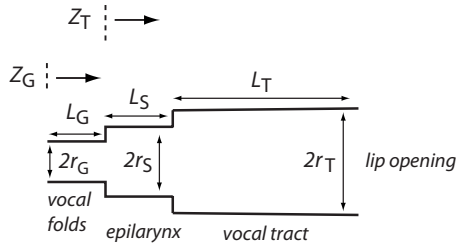

FIG. 1. A schematic (not to scale) indicating the simple 1D cylindrical model of the vocal tract. Arrows indicate the planes corresponding to the impedances Z_G and Z_T.

II. THEORY

A. Simple one dimensional model

In normal speech, the vocal tract is open at the lips and alternately closed and slightly open at the glottis as the vocal folds vibrate. In whispering, the glottis is permanently partly open. Barney *et al.* (2007) used a mechanical model in addition to an equivalent circuit model and showed that increased glottal opening raised the frequency of $R1$. One might explain this qualitatively as follows: A closed glottis produces a node in the acoustic flow. Provided that the subglottal tract has no strong resonances at the frequencies of interest, a slightly open glottis behaves approximately as an inertance in the frequency range of interest and so reflects a wave with phase changes in pressure and flow that are, respectively, slightly greater than 0 and slightly less than 180°. This displaces the node of acoustic flow toward the mouth, raising the resonant frequency. Because of the inertia of the air in the glottis, the effect decreases with increasing frequency: At sufficiently high frequency, the air in the glottis acts to "seal" the glottis and thus turns the slight opening into a termination that is effectively closed. Hence one expects that the increase in frequency will be greatest for the lowest resonance.

A very simple one dimensional (1D) model is shown in Fig. 1. To simplify the mathematical treatment, the vocal tract is modeled as a simple cylinder of effective length L_T and radius r_T. The radiation impedance at the lip opening is incorporated by including an end correction in L_T. The impedance Z_T looking from the junction of tract and glottal region is given by

$$Z_T = jZ_{T0}\tan(kL_T), \tag{1}$$

where $k=2\pi f/c$, f denotes the frequency, and c denotes the speed of sound. Wall losses will be neglected. The cross-sectional area S_T of the tract is given by $S_T=\pi r_T^2$. The characteristic impedance Z_{T0} of the tract is given by $Z_{T0}=\rho c/S_T$, where ρ is the density of air. The constricted region between the vocal folds is also modeled as a simple cylinder of effective length L_G and effective radius r_G. Again, end effects are incorporated in the effective length. The effective radius includes the open quotient and the influence of the subglottal region via the glottis. Initially the epilaryngeal region is ne-

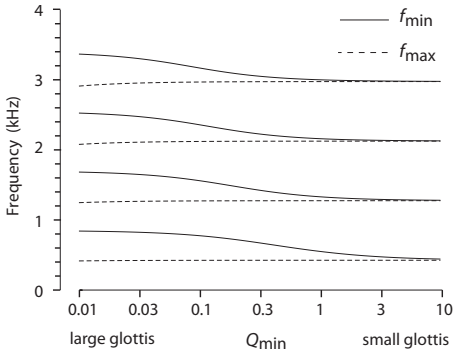

FIG. 2. A semi-logarithmic plot of the dependence of the frequencies f_{min} and f_{max} on the parameter Q_{min} $(=(r_T^2/r_G^2)(L_G/L_T))$. The frequencies f_{min} and f_{max} are those where minima and maxima, respectively, will occur in Z_G, the impedance looking out from the vocal folds toward the lip opening. Curves were calculated by solving Eq. (5) or Eq. (7), and assuming that $L_T=200$ mm.

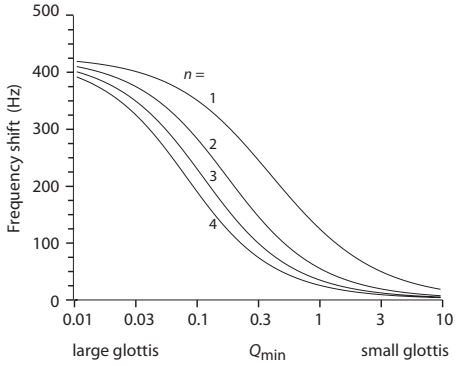

FIG. 3. A semi-logarithmic plot of the shift in resonance frequency from its value with a closed glottis as a function of the parameter Q_{min} $(=(r_T^2/r_G^2)\times(L_G/L_T))$. n indicates the order of the resonance Rn. Curves were calculated by solving Eq. (5) and assuming that $L_T=200$ mm.

glected. The impedance Z_G seen from the glottis through the constricted vocal folds would then be given by

$$Z_G = Z_{G0}\frac{Z_T\cos(kL_G)+jZ_{G0}\sin(kL_G)}{Z_{G0}\cos(kL_G)+jZ_T\sin(kL_G)}, \tag{2}$$

where the characteristic impedance of the vocal fold constriction is given by $Z_{G0}=\rho c/S_G$ and the glottal cross-sectional area is given by $S_G=\pi r_G^2$. The frequency of the nth minimum is determined primarily by the Z_T terms and will occur when $kL_T\approx n\pi$. For the situation considered here $L_G \ll L_T$. Then $kL_G \ll 1$ for small n and consequently $\sin(kL_G)\approx kL_G$ and $\cos(kL_G)\approx 1$. Equation (2) then simplifies to

$$Z_G \approx jZ_{G0}\frac{Z_{T0}\tan(kL_T)+Z_{G0}kL_G}{Z_{G0}-Z_{T0}\tan(kL_T)kL_G}. \tag{3}$$

Z_G will exhibit minima when

$$Z_{T0}\tan(kL_T) = -Z_{G0}kL_G. \tag{4}$$

After the substitution $x=kL_T$, Eq. (4) can be written in the form

$$\tan x = -Q_{min}x, \tag{5}$$

where

$$Q_{min} = (r_T^2/r_G^2)(L_G/L_T). \tag{6}$$

Similarly Z_G will exhibit maxima when

$$\tan x = Q_{max}/x, \tag{7}$$

where

$$Q_{max} = (r_T^2/r_G^2)(L_T/L_G) = Q_{min}(L_T^2/L_G^2). \tag{8}$$

These transcendental equations determine x, and thus the frequencies f_{min} and f_{max} at which the extrema occur in Z_G. The tan function is periodic, and Eqs. (5) and (7) will thus exhibit multiple solutions that correspond to the various resonances of the system—see Fig. 2. The minima in Z_G will correspond to maxima in the transfer function between the glottis and the mouth, and will consequently be associated with peaks in the spectral envelope of the output sound.

A new value of Q_{min} can thus be calculated from a change in the resonance frequency. Q_{min} depends on the relative areas and lengths of the glottis and vocal tract [see Eq. (6)]. Small values of Q_{min} correspond to a glottis whose area is a larger fraction of the vocal tract area and/or whose effective length is a smaller fraction of the vocal tract length. For very small values of Q_{min}, corresponding to a cylinder that was ideally open at the glottis, the maxima and minima would be evenly distributed with frequency at the expected harmonic frequencies. If Q_{min} increases due to a decrease in glottal effective area, the frequency f_{min} decreases and eventually becomes very similar to f_{max} for large values of Q_{min} (Fig. 2).

An increase in the effective glottal area from its low value in normal speech will thus cause an increase in the resonance frequencies. The value of Q_{min} at which a given shift in f_{min} occurs moves to lower values of Q_{min} as the order of the resonance increases—see Fig. 3. This figure also shows that the frequency shift due to a decrease in Q_{min} associated with a small glottis is predicted to become smaller as the order of the resonance increases. Similarly a decrease in the effective glottal length will cause an increase in the resonance frequencies.

The effect of changes in the geometry of the epilaryngeal region can now be included in the mathematical treatment using the same approach and approximations as that used above. Q_{min} and Q_{max} can then be replaced with Q'_{min} and Q'_{max} and are given by

$$Q'_{min}\frac{r_T^2}{L_T}\left(\frac{L_G}{r_G^2}+\frac{L_S}{r_S^2}\right), \tag{9}$$

$$Q'_{max} = r_T^2\left(\frac{L_S}{L_T}\frac{1}{r_S^2}+\frac{L_T}{L_G}\frac{1}{r_G^2}\right), \tag{10}$$

where the epilaryngeal region has an effective length L_S and radius r_S. In general the second term in Eq. (9) will be less important. However, Eq. (9) does predict that a decrease in r_S (while other parameters remain constant) will increase Q'_{min} and thus decrease the resonance frequencies.

III. MATERIALS AND METHODS

A. The subjects

Ten Australian women, aged between 20 and 30 years, volunteered to participate. All were native speakers of Australian English, were judged to have similar Australian accents, and none reported or showed evidence of speech problems or abnormalities. Nine had lived in Australia for all their lives, and the other for half her life. Each subject was given a brief explanation of the University's ethics policy, signed a consent form, and was then given a lesson (typically 3 min) on how to produce creak phonation. The instruction "Hum your lowest note and then go lower" began the instruction, and the experimenter gave demonstrations and feedback. One subject was not able to produce the creak voice reliably and consequently only her results for the whisper were recorded.

Women were chosen as subjects because their higher fundamental frequency generally improves the precision of resonance estimates using external broadband excitation. This is because it is then easier to separate the speech signal from the response to the broadband signal. This is the opposite result to methods that use the speech signal alone, where the precision decreases with increasing fundamental frequency.

B. Resonance frequencies in different phonation modes

The technique reported by Epps *et al.* (1997) and Dowd *et al.* (1998) was used to estimate the vocal tract resonances using broadband external excitation. The excitation signal was synthesized from harmonics of a signal with a frequency of 5.383 Hz (i.e., 44 100 Hz/2^{13}). The harmonics that fell between 200 Hz and 4.5 kHz were summed, with relative phases chosen to improve the signal to noise ratio (Smith, 1995). This signal was amplified and delivered to an enclosed loudspeaker (150 mm diameter), which was attached to an exponential horn of 600 mm length and coupled to a flexible tube (300 mm length with inner radius 6 mm), and which contained acoustic fiber to reduce resonances—see Fig. 4. This source of acoustic flow was placed at the subject's lower lip. Next to the source, a small electret microphone (Optimus 33-3013) recorded both the sound of the voice, and the sound of the acoustic source interacting with the subject's vocal tract and the radiation field.

In an initial calibration stage, a measurement is made with the subject's mouth closed, i.e., when the measurement device is effectively loaded only by the impedance of the radiation field Z_{rad} at the lips and baffled by the subject's face. The relative amplitude of harmonics in the synthesized signal is then adjusted so that the measured pressure signal at the lips is independent of frequency. Measurements are then made during vocalization with the mouth open. The impedance measured is then $Z_{\|}$, the impedance of the vocal tract Z_{tract}, in parallel with Z_{rad}. The variable γ, the ratio of the pressure measured during vocalization to that measured with the mouth closed, in response to the same acoustic flow, is

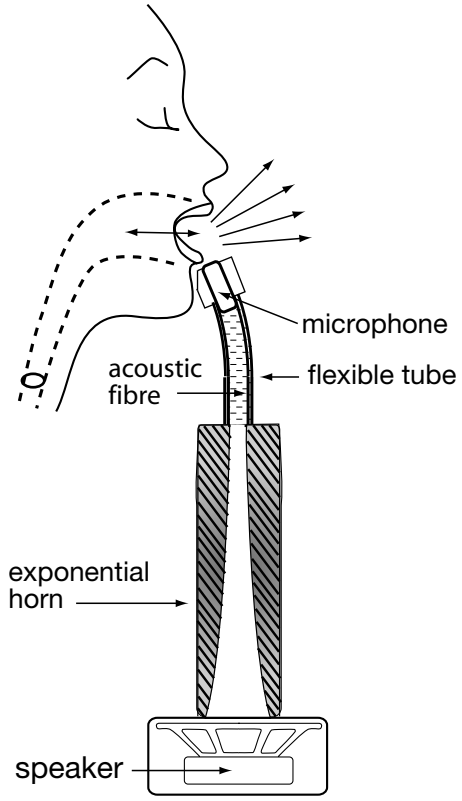

FIG. 4. Schematic (not to scale) showing how an external broadband signal is used to estimate the resonance frequencies of the vocal tract. The vocal tract is measured in parallel with the external radiation field. The microphone (8 mm diameter) is located immediately adjacent to the source of acoustic flow. It thus measures not only the sound produced by the subject, but also the response to the broadband signal interacting with the vocal tract. Initial calibration measurements are made with the subject's mouth closed.

then calculated. Because the output impedance of the acoustic flow source is large, this ratio equals the ratio of the impedances in the two cases; i.e.,

$$\gamma = Z_{\|}/Z_{rad} = Z_{tract}/(Z_{tract} + Z_{rad}). \quad (11)$$

At resonance, the imaginary components of Z_{tract} and Z_{rad} are equal and opposite, so the denominator is very small and maxima in γ identify resonances. The relationship between maxima in the transfer functions from glottis to external radiation field and maxima in the impedance measured just outside the lips is complicated, but they generally agree for our experimental conditions (Smith *et al.*, 2007). Experiments with simple physical models of the vocal tract suggest that a resolution around ± 20 Hz is possible.

For whisper and creak phonations, the power spectra were calculated using a window of 8192 points and a sampling rate of 44.1 kHz, and edited and displayed using the program AUDACITY (http://audacity.sourceforge.net). Resonance frequencies were estimated visually from the maxima in the spectral envelope. Examples are shown in Fig. 5.

C. The experimental sessions

The sessions were conducted in a "quiet room" inside the acoustics department. It was designed specifically for acoustic experiments. The walls and ceiling are treated to

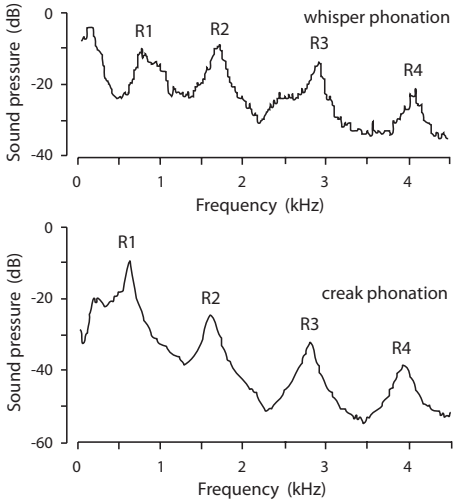

FIG. 5. Examples of measurements showing the spectra measured for the vowel in heard using whisper phonation (top) and creak phonation (bottom).

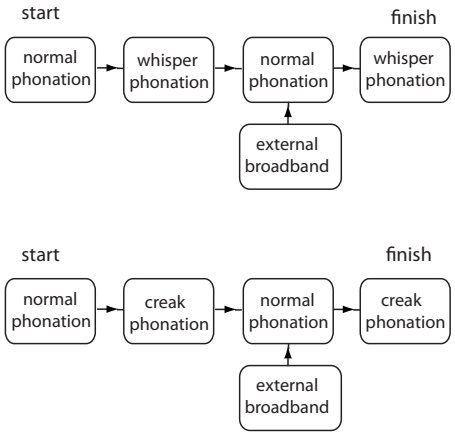

FIG. 6. Schematic showing the sequences used to compare whisper or creak phonation with normal phonation in a single vocal gesture.

reduce external sounds by around 30 dB and surfaces treated to reduce reverberation. Background noise was always below 35 dBA.

Subjects were asked to produce one of five vowels, being those in the English words "head" (ɛ), "hard" (ɑ), "who'd" (u), "hoard" (ɔ), and "heard" (ɜ). The desired vowel was indicated to the subject by showing one of these words on a card.

The estimated values of resonance frequencies for a particular vowel are not important to the primary aim, which is to determine, for a given vowel gesture, the differences among the frequencies of the resonances during normal phonation, creak phonation, and whisper phonation. The context of the vowel was completely artificial: Subjects produced a particular vocal tract articulation and held it constant for several seconds. This would be a limitation in a study of accent, but here it is not a disadvantage. Rather, it allows the subject to concentrate on using the same articulation for each mechanism.

Each example of each vowel was produced in the order normal-whisper-normal-whisper or normal-creak-normal-creak. Subjects were asked to take a deep breath and, in a single gesture, to produce about 2.5 s of each of the four phonations without changing the position of tongue and mouth—see Fig. 6. During the second normal phonation, the vocal tract resonances were measured by broadband excitation. The whole gesture was digitally recorded and a 2 s sample of each of the whisper or creak segments was subsequently analyzed.

All subjects were able to perform this procedure comfortably. None reported being perturbed by the broadband signal, which had a sound level of about 70 dBA at the subject's ears, or by having the flexible tube touch their lower lip.

Once the resonances of each of the five vowels had been measured using both whisper and creak phonations, the sequence of measurements was repeated twice, giving a total of 30 vocal gestures for each subject. Our method involving external broadband excitation means that the impedance of the tract is measured in parallel with the external radiation field and consequently a weak tract resonance may not always be capable of resolution at low frequencies. It was also occasionally difficult to identify a particular resonance from the recorded sound in whisper and creak phonations. Both problems reduced the number of samples available for analysis.

IV. RESULTS AND DISCUSSION

A. Phonetic values

The average values of the first four resonances $R1$–$R4$ for the normal voice are given in Table I. They agree with those given by Donaldson *et al.* (2003) for young Australian women. Because the vowels studied were sustained, they are not necessarily the same as ordinary spoken vowels. How-

TABLE I. The measured resonant behavior of the tract for the ten subjects during normal, whisper, and creak phonations. Data in this and subsequent tables are presented as mean ± standard deviation (number of samples).

Vowel	$R1$ (Hz)	$R2$ (Hz)	$R3$ (Hz)	$R4$ (Hz)
		Normal phonation		
Head	605 ± 55 (53)	1860 ± 133 (52)	2800 ± 220 (55)	3960 ± 345 (52)
Hard	780 ± 95 (41)	1370 ± 45 (53)	2895 ± 130 (48)	3950 ± 150 (53)
Who'd	435 ± 70 (50)	1480 ± 355 (53)	2695 ± 95 (35)	3755 ± 200 (37)
Hoard	590 ± 60 (55)	1135 ± 80 (55)	2910 ± 100 (45)	3865 ± 215 (55)
Heard	625 ± 60 (52)	1555 ± 100 (54)	2810 ± 65 (48)	3910 ± 330 (53)
		Whisper phonation		
Head	875 ± 55 (50)	1960 ± 235 (50)	2915 ± 260 (52)	4015 ± 365 (51)
Hard	1010 ± 60 (55)	1520 ± 120 (48)	2990 ± 120 (54)	4000 ± 130 (50)
Who'd	755 ± 230 (19)	1655 ± 395 (49)	2840 ± 120 (45)	3905 ± 150 (42)
Hoard	885 ± 80 (41)	1200 ± 65 (51)	3035 ± 190 (54)	3930 ± 205 (56)
Heard	870 ± 60 (52)	1700 ± 105 (58)	2905 ± 180 (54)	3945 ± 355 (56)
		Creak phonation		
Head	665 ± 65 (52)	1890 ± 140 (51)	2870 ± 105 (51)	4040 ± 190 (43)
Hard	800 ± 60 (50)	1365 ± 70 (50)	2975 ± 113 (50)	3965 ± 185 (48)
Who'd	480 ± 55 (50)	1440 ± 325 (49)	2750 ± 145 (50)	3800 ± 250 (48)
Hoard	640 ± 70 (52)	1126 ± 80 (52)	3000 ± 145 (52)	3845 ± 220 (50)
Heard	665 ± 75 (51)	1550 ± 120 (51)	2850 ± 100 (52)	3925 ± 240 (51)

ever, this study is concerned with how the values of Ri depend on the phonation mechanism, rather than their absolute values.

The average values of the resonance frequencies $R1-R4$ for creak phonation given in Table I are similar to the average values for the normal voice. However, the average values of $R1-R4$ for whisper phonation were always higher than the average $R1-R4$ for the normal voice. The difference for the first resonance between whisper and normal phonations was large; when averaged across all vowels, the difference was 270 Hz and the frequency ratio of whisper to normal was 1.45. The effect was reduced for the second resonance; the difference being 125 Hz and the ratio 1.09. These values are similar to those found by Jovocic (1998) for Serbian vowels, with the exception of /u/ where Jovocic (1998) found that the resonance frequencies decreased significantly during whispering. Although the average values of $R3$ and $R4$ for whispering were always slightly higher than those for the normal voice, the differences are not often substantially larger than the experimental uncertainties.

These differences between the average values of the resonance frequency for whispered and normal phonations are either similar (Jovocic, 1998) or somewhat larger than some reported previously (Kallail and Emanuel 1984a, 1984b; Matsuda and Kasuya, 1999), and also show a similar decrease for higher resonances. Where comparison is possible, the absolute values for the increase in $R1-R3$ with whispering are consistent with an earlier study on female subjects (Kallail and Emanuel, 1984a), except that a considerably higher value for the shift in $R1$ in who'd using whisper phonation was found. However, the difference might be partly because Kallail and Emanuel rejected over 30% of their samples because of incorrect identification by a listening panel, whereas this project is primarily concerned with acoustical rather than perceptual aspects.

B. Stability of vocal tract configuration

Sensitive comparisons between the tract resonances in the different phonation modes can be made using data measured during the same vocal gesture. Consequently, it is important to confirm first that the tract remained effectively in the same configuration during each sequence. Table II shows the average differences between pairs of resonance frequencies estimated "before" and "after" the period of whispering in the same vocal gesture. Some differences were negative and some positive. A paired t-test was applied to these pairs of data to determine whether there was a statistically significant difference between the before and after measurements. Of the values in the table, two values ($R2$ for head and who'd) are significantly different from zero at the 5% level, which is a little more than one would expect in 20 tests. ($R2$ for these two vowels was also significantly different for creak phonation.) It is therefore possible that there is a slight non-random variation in the value of $R2$ (by tens of hertz or a few percent) between the initial and final whispers in each sequence. The very good reproducibility for whispering is perhaps because subjects would be experienced in occasionally making transitions between whispered and normal speech in various conversations.

TABLE II. The stability of vocal gestures. The table presents the average difference between the pairs of resonance frequencies (for either whisper or creak phonation) that were measured immediately before and after each normal phonation within each sustained vocal gesture. The symbol * indicates that the difference was significant at the 5% level or lower as indicated by a paired t-test.

Vowel	$\Delta R1$ (Hz)	$\Delta R2$ (Hz)	$\Delta R3$ (Hz)	$\Delta R4$ (Hz)
		Whisper phonation		
Head	-5 ± 40 (23)	60 ± 85 (23)*	20 ± 75 (24)	-20 ± 75 (25)
Hard	0 ± 25 (27)	-10 ± 80 (23)	-10 ± 80 (25)	-5 ± 75 (22)
Who'd	-5 ± 15 (8)	85 ± 235 (24)*	-15 ± 95 (22)	10 ± 125 (20)
Hoard	-5 ± 35 (19)	-15 ± 40 (25)	5 ± 100 (25)	-25 ± 85 (27)
Heard	-5 ± 45 (25)	20 ± 75 (29)	20 ± 70 (27)	5 ± 75 (27)
All vowels	0 ± 35 (102)	30 ± 125 (124)*	5 ± 85 (123)	-10 ± 85 (121)
		Creak phonation		
Head	-10 ± 20 (26)*	60 ± 55 (25)*	25 ± 60 (25)*	20 ± 70 (19)
Hard	0 ± 15 (25)	10 ± 30 (25)*	30 ± 70 (25)*	-10 ± 70 (23)
Who'd	-10 ± 35 (25)	55 ± 55 (24)*	-30 ± 70 (25)*	-20 ± 80 (24)
Hoard	-10 ± 20 (26)*	-10 ± 40 (26)	15 ± 75 (26)	0 ± 75 (25)
Heard	-5 ± 25 (25)	0 ± 60 (25)	-5 ± 70 (26)	-15 ± 60 (25)
All vowels	-5 ± 25 (127)*	25 ± 55 (125)*	5 ± 70 (127)	-5 ± 70 (116)

Table II also shows the changes between pairs of resonance frequencies for creak phonation made during the same vocal gesture. Here there are larger differences, again with both positive and negative signs, and an increased number are significantly different at the 5% level. This is perhaps a consequence of the subjects being less familiar with creak phonation than whisper phonation. The differences are still relatively small, of the order of 10 Hz for $R1$, which is around the limit of resolution of the resonance estimates.

Are the resonances for normal speech different in our sequences when immediately preceded by whisper or creak phonation in the same vocal gesture? This was tested for each subject and vowel by comparing the average values of Ri measured for the normal speech in each sequence involving whispering with those involving creak phonation—see Table III. The differences in Ri associated with an intervening segment of whispering vs creak phonation are not significant. When averaged over all resonances, the difference was only $0.3\pm7.3\%$ (168): The effect of context was small.

TABLE III. The influence of the immediately preceding phonation mode on normal phonation. The table presents the fractional difference in average resonance frequency measured during normal phonations immediately before and after a whisper vs a creak phonation for a particular subject/vowel combination. Data were normalized by dividing by the average resonance frequency for that subject/vowel combination.

$\Delta R1/R1$	$\Delta R2/R2$	$\Delta R3/R3$	$\Delta R4/R4$
0.011 ± 0.094 (44)	0.012 ± 0.050 (45)	-0.002 ± 0.06 (39)	0.010 ± 0.072 (40)

TABLE IV. The estimated difference $\Delta R1$ in the first resonance frequency of the ten different subjects when changing from normal to whispered phonation, or from normal to creak phonation, measured in the same vocal gesture. Results from the five vowels studied have been combined. Subject No. 10 was not able to produce a satisfactory creak phonation.

	$\Delta R1$ (Hz)	
Subject	Normal to whisper	Normal to creak
1	255 ± 75 (12)	75 ± 50 (14)
2	185 ± 45 (9)	10 ± 20 (15)
3	235 ± 130 (5)	35 ± 45 (13)
4	260 ± 65 (9)	85 ± 30 (14)
5	235 ± 85 (7)	25 ± 30 (15)
6	215 ± 60 (13)	55 ± 35 (13)
7	290 ± 70 (12)	50 ± 45 (15)
8	235 ± 90 (4)	25 ± 70 (10)
9	360 ± 135 (12)	50 ± 50 (12)
10	245 ± 25 (9)	···

C. Resonance shifts due to whispering

Comparison between the average values for resonance frequencies measured during whispering and the average values measured during normal phonation (Table I) shows that $R1$ for whispering is distinctly higher than $R1$ for normal speech for all vowels. However, it is not immediately apparent that the other Ri are significantly higher during whispering. It is now possible to make use of the facts that pairs of estimates of the resonance frequencies for both normal and whispered phonations were made during the same vocal gesture, and that Table II indicates that the only properties of the tract that changed significantly over time during a vocal gesture were those associated with the change in phonation. The resonance frequencies for whispering in each individual gesture are taken to be the average of the values measured immediately before and immediately after each normal phonation in that gesture. The value of $R1$ measured during whispering was always found to be higher than the value of $R1$ measured during normal phonation in each individual vocal gesture; this was true for all subjects and vowels studied—see Table IV. The situation was similar for $R2$ with the value for whisper being higher than that for normal phonation for 115 of the 119 vocal gestures studied. $R3$ was higher for whisper than normal phonation in 94 of the 109 gestures, and $R4$ was higher for whisper in 88 of 118 gestures.

Table V shows the average values of the difference between pairs of values of the resonance frequency measured during whispering and during normal phonation, when measured during the same vocal gesture. It can be seen that all the resonance frequencies of the tract are significantly higher during whispering, and that the difference usually decreased for the higher resonances.

When averaged across subjects, the differences are always positive and always statistically significant at the 5% level for all vowels and all resonances, according to paired t-tests. Further, the magnitude of the difference decreases with the order of the resonance as predicted by Eq. (5)—see Fig. 3. (Shifts due to creak phonation are discussed later.)

D. Effective glottal dimensions during whispering

The estimated resonance frequencies for normal and whispered speech measured during the same vocal gesture can be used to estimate changes in glottal dimensions. For example, r_{GW}, the effective glottal radius during whispering, can be estimated. In the absence of appropriate information, the calculation presented here first assumes that the effective glottal length remains unaltered. Equations (5) and (6) can be rearranged to allow calculation of the effective length of the

TABLE V. The average differences ΔR in resonance frequency between whisper and normal phonations, or creak and normal phonations, measured in the same vocal gesture. The symbol * indicates that the difference was significant at the 5% level as indicated by a paired t-test.

Vowel	$\Delta R1$ (Hz)	$\Delta R2$ (Hz)	$\Delta R3$ (Hz)	$\Delta R4$ (Hz)
		Whisper phonation		
Head	255 ± 65 (21)*	140 ± 95 (20)*	145 ± 130 (24)*	105 ± 135 (25)*
Hard	220 ± 75 (20)*	155 ± 100 (23)*	120 ± 165 (22)*	45 ± 90 (22)*
Who'd	330 ± 190 (8)*	55 ± 140 (23)*	120 ± 105 (18)*	125 ± 150 (17)*
Hoard	280 ± 80 (19)*	70 ± 55 (25)*	115 ± 115 (20)*	45 ± 115 (27)*
Heard	250 ± 70 (24)*	150 ± 65 (28)*	110 ± 95 (25)*	75 ± 95 (27)*
All vowels	255 ± 90 (92)*	115 ± 105 (119)*	125 ± 125 (109)*	75 ± 120 (118)*
		Creak phonation		
Head	60 ± 45 (26)*	35 ± 80 (25)*	40 ± 95 (25)*	20 ± 85 (19)
Hard	40 ± 55 (21)*	−5 ± 50 (24)	60 ± 155 (23)*	25 ± 105 (22)
Who'd	45 ± 40 (24)*	20 ± 40 (24)*	−60 ± 145 (16)*	25 ± 170 (18)
Hoard	40 ± 45 (26)*	−15 ± 50 (26)	90 ± 105 (22)*	10 ± 110 (25)
Heard	35 ± 50 (24)*	10 ± 70 (25)	70 ± 90 (23)*	−10 ± 85 (24)
All vowels	45 ± 50 (121)*	10 ± 60 (124)	65 ± 120 (109)*	15 ± 110 (108)

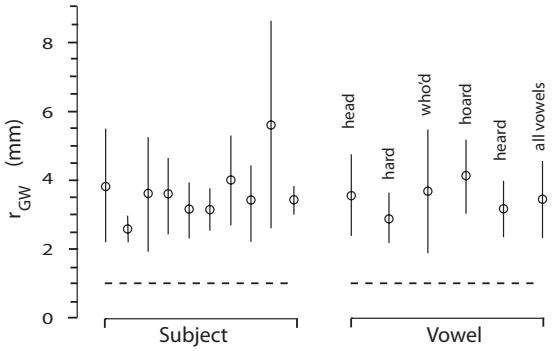

FIG. 7. Values of r_{GW}, the "effective" glottal radius during whispering for different subjects and vowels. They were calculated using the resonance frequencies for normal speech and whispering measured during individual vocal gestures. Values were calculated using Eqs. (10) and (11), assuming that r_T=15 mm and L_G=3 mm. The effective glottal radius in normal speech, r_{GN}, was assumed =1 mm as (indicated by the dashed lines on the figure). Error bars indicate standard deviations.

vocal tract (not including the glottis) in normal speech from the measured resonance frequency. Thus for the nth resonance of the tract

$$L_T = \tan^{-1}(-k_N r_T^2 L_G / r_{GN}^2)/k_N, \tag{12}$$

where $k_N = 2\pi f_N / c$ and f_N is the nth resonance frequency measured in normal speech. This requires that values have to be assumed for r_T, L_G, and also r_{GN}, the effective glottal radius in normal speech. Providing that L_T does not change during the transition to and from whispering, then

$$r_{GW} = [-k_W r_T^2 L_G / \tan(k_W L_T)]^{1/2}, \tag{13}$$

where $k_W = 2\pi f_W / c$ and f_W is the nth resonance frequency measured during whispering.

Thus, if estimates are available for the lowest resonance frequency in two different phonation modes, assumption of the geometry in one mode allows an estimate of the effective glottal area in the other mode. This estimation, based on the simple cylindrical model described above, also assumes that the rest of the tract geometry remains unchanged. Certainly, different vowels will produce different values of r_T for the upper vocal tract; however, the simple model is primarily concerned with the transition from glottis to the lower vocal tract, where r_T does not vary substantially from vowel to vowel.

Figure 7 presents the values of r_{GW} calculated from the measured values of $R1$ during a single vocal gesture using Eqs. (12) and (13). With one exception, the values were consistent across all ten subjects. The data for this one subject (subject 9—second from the right) were atypical (see Table IV) and were not used in further calculations of glottal radius. Figure 7 also indicates that a similar range of values of r_{GW} was associated with each of the five vowels studied; the average value being $3.4 \pm 1.1(79)$ mm. The increased glottal opening is consistent with observations made via laryngeal endoscopy (Matsuda and Kasuya, 1999). The glottal area during whispering was thus found to be $40 \pm 30(79)$ mm^2, a range that is consistent with directly measured glottal areas (Sundberg *et al.*, 2009).

The calculated values of r_{GW} will of course depend on the values assumed for r_T, L_G, and r_{GN}. However, the values used for the calculations shown in Fig. 7 produce a value of $Q_{min} \approx 4$, where the dependence of frequency shift on Q_{min} (and thus on the initial assumptions of r_T, L_G, and r_{GN}) is relatively small—see Fig. 3.

There is also evidence that the supra-glottal region is constricted during whispering (Tsunoda *et al.*, 1997; Matsuda and Kasuya, 1999). The inclusion of such supra-glottal narrowing would lead to a smaller estimated value for r_{GW}—see Eq. (9).

The values shown in Fig. 7 assumed that the effective length of the glottis remained unchanged during the transition to whispering. In practice, for most tract geometries, an increase in r_{GW} is likely also to increase the effective L_G because of an increase in the end effect associated with a larger aperture. Thus a given change in frequency will be associated with a greater change in r_{GW}. To model this effect properly would require a more detailed model of the glottal geometry. However, an estimate may be obtained by continuing the simple cylindrical model and incorporating an end effect at the glottis/tract boundary by replacing L_G with $L_G + 0.85 r_{GN}$ in Eq. (12) and $L_G + 0.85 r_{GW}$ in Eq. (13). This produces a quadratic equation in r_{GW}.

$$L_T = \tan^{-1}[-k_N r_T^2 (L_G + 0.85 r_{GN}) / r_{GN}^2]/k_N, \tag{14}$$

$$\tan(k_W L_T) r_{GW}^2 + 0.85 k_W r_T^2 r_{GW} + k_W r_T^2 L_G = 0. \tag{15}$$

As expected, this approach yields an appreciable larger value; $r_{GW} = 6.3 \pm 3.5(79)$ mm. For geometries lacking circular symmetry, the influence of end effects is likely to be smaller.

In terms of this very simplified model the measured increase in estimated resonance frequency from normal phonation to whispering is consistent with a plausible increase in glottal aperture. The real anatomy is obviously much more complicated, but changes of similar order would be expected.

E. Resonance shifts due to creak phonation

The average values for resonance frequencies measured during creak phonation are slightly higher than the average values measured during normal phonation for all vowels (Table I). However, the standard deviations in $R1$ are large. The differences in the averages are smaller for the higher resonances, while the standard deviations remain large. However, it is again possible to examine pairs of resonances for different phonation modes measured during the same vocal gesture. (The resonance frequencies for creak phonation in each individual gesture are taken to be the average of the values measured immediately before and immediately after each normal phonation in that vocal gesture.)

Table V shows that the average frequency shift from normal phonation to creak is positive, small, and significant for the first and third resonances, the exception being the third resonance of who'd. The differences are usually not significant for the second and fourth resonances. The values of $R1$, $R2$, $R3$, and $R4$, measured during a single vocal gesture, were found to increase from normal to creak phonation in 84%, 59%, 81%, and 64%, respectively, of the gestures

measured. The differences are generally positive, and this is consistent with the results of Ladefoged *et al.* (1988) and Ananthapadmanabha (1984), and inconsistent with the (small) decreases reported by Moosmüller (2001). However, these researchers used the peaks in the spectral envelope of normal phonation to estimate the resonances, which implies additional imprecision in the estimate of the resonance.

The observed average small increase in resonance frequency can be associated with a decrease in $Q_{\min}$ during glottal phonation, and this is consistent with a decrease in the ratio of glottal length to glottal area.

V. CONCLUSIONS

The resonance frequencies for whispered phonation for all subjects and vowels were found to be substantially higher than for the normal voice measured during the same vocal gesture, although the difference was greater than that found by other investigators. The increases are largest for $R1$ and decrease with increasing frequency. Calculations using a simple cylindrical model of the vocal tract, and assuming that the effective radius of the glottis is 1.0 mm for normal speech, yield a reasonable value of 40 ± 30 mm^2 for the effective glottal area during whispering. The lowest resonance frequencies of creak phonation were found to differ from those of normal speech by an average of 45 ± 50 Hz. This difference will usually be smaller than half of the fundamental frequency f_0, and then creak phonation might determine resonances with more precision than is available from the peaks in the spectral envelope of voiced speech, and be useful in teaching resonance tuning to singers (Miller *et al.*, 1997).

ACKNOWLEDGMENTS

We thank our volunteer subjects and the Australian Research Council for support. We would also like to thank Maëva Garnier and the reviewers for their comments on the manuscript.

Ananthapadmanabha, T. V. (**1984**). "Acoustic analysis of voice source dynamics," Speech Transm. Lab. Q. Prog. Status Rep. **25**, 1–24.
Barney, A., De Stefano, A., and Henrich, N. (**2007**). "The effect of glottal opening on the acoustic response of the vocal tract," Acta Acust. Acust. **93**, 1046–1056.
Chen, J. M., Smith, J., and Wolfe, J. (**2008**). "Experienced saxophonists learn to tune their vocal tracts," Science **319**, 776.
Chen, J. M., Smith, J., and Wolfe, J. (**2009**). "Pitch bending and *glissandi* on the clarinet: Roles of the vocal tract and partial tone hole closure," J. Acoust. Soc. Am. **126**, 1511–1520.
Clark, J., Yallop, C., and Fletcher, J. (**2007**). *An Introduction to Phonetics and Phonology* (Basil Blackwell, Oxford).
Coffin, B. (**1974**). "On hearing, feeling and using the instrumental resonance of the singing voice," NATS Bulletin **31**, 26–30.
Donaldson, T., Wang, D., Smith, J., and Wolfe, J. (**2003**). "Vocal tract resonances: A preliminary study of sex differences for young Australians," Acoust. Aust. **31**, 95–98.
Dowd, A., Smith, J. R., and Wolfe, J. (**1998**). "Learning to pronounce vowel sounds in a foreign language using acoustic measurements of the vocal tract as feedback in real time," Lang Speech **41**, 1–20.
Epps, J., Smith, J. R., and Wolfe, J. (**1997**). "A novel instrument to measure acoustic resonances of the vocal tract during speech," Meas. Sci. Technol. **8**, 1112–1121.
Fant, G. (**1970**). *Acoustic Theory of Speech Production* (Mouton, The Hague).
Fant, G. (**1973**). *Speech Sounds and Features* (MIT, Cambridge, MA).
Gobl, C. (**1989**). "A preliminary study of acoustic voice quality correlates," STL-QPSR **30**, 9–22.
Henrich, N., Kiek, M., Smith, J., and Wolfe, J. (**2007**). "Resonance strategies used in Bulgarian women's singing style: A pilot study," Logoped. Phoniatr. Vocol. **32**, 171–177.
Hollien, H., and Michel, J. F. (**1968**). "Vocal fry as a phonational register," J. Speech Hear. Res. **11**, 600–604.
Joliveau, E., Smith, J., and Wolfe, J. (**2004a**). "Tuning of vocal tract resonance by sopranos," Nature (London) **427**, 116.
Joliveau, E., Smith, J., and Wolfe, J. (**2004b**). "Vocal tract resonances in singing: The soprano voice," J. Acoust. Soc. Am. **116**, 2434–2439.
Jovocic, S. T. (**1998**). "Formant feature differences between whispered and voiced sustained vowels," Acustica **84**, 739–743.
Kallail, K. J., and Emanuel, F. W. (**1984a**). "Formant-frequency differences between isolated whispered and phonated vowel samples produced by adult female subjects," J. Speech Hear. Res. **27**, 245–251.
Kallail, K. J., and Emanuel, F. W. (**1984b**). "An acoustic comparison of isolated whispered and phonated vowel samples produced by adult male subjects," J. Phonetics **12**, 175–186.
Ladefoged, P., Maddieson, I., and Jackson, M. (**1988**). *Investigating Phonation Types in Different Languages* (Raven, New York).
Lindblom, B. E. F., and Sundberg, J. E. F. (**1971**). "Acoustical consequences of lip, tongue, jaw, and larynx movement," J. Acoust. Soc. Am. **50**, 1166–1179.
Matsuda, M., and Kasuya, K. (**1999**). "Acoustic nature of the whisper," in Proceedings of the Eurospeech '99, pp. 133–136.
Miller, D. G., Sulter, A. M., Schutte, H. K., and Wolf, R. F. (**1997**). "Comparison of vocal tract formants in singing and non-periodic phonation," J. Voice **11**, 1–11.
Monsen, R. B., and Engebretson, A. M. (**1983**). "The accuracy of formant frequency measurements: A comparison of spectrographic analysis and linear prediction," J. Speech Hear. Res. **26**, 89–97.
Moosmüller, S. (**2001**). "The influence of creaky voice on formant frequency changes," Forensic Linguistics **8**, 100–112.
Mukai, M. S. (**1992**). "Laryngeal movement while playing wind instruments," in Proceedings of the International Symposium on Musical Acoustics, Tokyo, Japan, pp. 239–242.
Pham Thi Ngoc, Y., and Badin, P. (**1994**). "Vocal tract acoustic transfer function measurements: Further developments and applications," J. Phys. IV **C5**, 549–552.
Smith, J., Henrich, N., and Wolfe, J. (**2007**). "Resonance tuning in singing," 19th International Conference on Acoustics, Madrid, Spain, Paper No. MUS-06-003-IP.
Smith, J., and Wolfe, J. (**2009**). "Vowel-pitch matching in Wagner's operas: Implications for intelligibility and ease of singing," J. Acoust. Soc. Am. **125**, EL196–EL201.
Smith, J. R. (**1995**). "Phasing of harmonic components to optimize measure signal-to-noise ratios of transfer functions," Meas. Sci. Technol. **6**, 1343–1348.
Sundberg, J. (**1977**). "The acoustics of the singing voice," Sci. Am. **236**, 82–91.
Sundberg, J., Scherer, R., Hess, M., and Müller, F. (**2009**). "Whispering—A single subject study of glottal configuration and aerodynamics," J. Voice
Swerdlin, Y., Smith, J., and Wolfe, J. (**2008**). "How whisper and creak phonation affect vocal tract resonances," J. Acoust. Soc. Am. **123**, 3242.
Tarnopolsky, A. Z., Fletcher, N. H., Hollenberg, L. C. L., Lange, B. D., Smith, J., and Wolfe, J. (**2005**). "The vocal tract and the sound of the didgeridoo," Nature (London) **436**, 39.
Tarnopolsky, A. Z., Fletcher, N. H., Hollenberg, L. C. L., Lange, B. D., Smith, J., and Wolfe, J. (**2006**). "Vocal tract resonances and the sound of the Australian didjeridu (yidaki): I. Experiment," J. Acoust. Soc. Am. **119**, 1194–1204.
Titze, I. R. (**1988**). "The physics of small-amplitude oscillations of the vocal folds," J. Acoust. Soc. Am. **83**, 1536–1552.
Titze, I. R. (**2004**). "Theory of glottal airflow and source-filter interaction in speaking and singing," Acta Acust. Acust. **90**, 641–648.
Titze, I. R. (**2008**). "Nonlinear source-filter coupling in phonation: Theory," J. Acoust. Soc. Am. **123**, 2733–2749.
Tsunoda, K., Ohta, Y., Soda, Y., Niimi, S., and Hirose, H. (**1997**). "Laryngeal adjustment in whispering: Magnetic resonance imaging study," Ann. Otol. Rhinol. Laryngol. **106**, 41–43.
Wolfe, J., Garnier, M., and Smith, J. (**2009**). "Vocal tract resonances in speech, singing and playing musical instruments," Human Frontier Science Program Journal **3**, 6–23.

A psychoacoustic method to find the perceptual cues of stop consonants in natural speech

Feipeng Li,[a] Anjali Menon, and Jont B. Allen
Department of Electrical and Computer Engineering, University of Illinois at Urbana-Champaign, Urbana, Illinois 61801

(Received 11 February 2009; revised 2 October 2009; accepted 31 December 2009)

Synthetic speech has been widely used in the study of speech cues. A serious disadvantage of this method is that it requires prior knowledge about the cues to be identified in order to synthesize the speech. Incomplete or inaccurate hypotheses about the cues often lead to speech sounds of low quality. In this research a psychoacoustic method, named three-dimensional deep search (3DDS), is developed to explore the perceptual cues of stop consonants from naturally produced speech. For a given sound, it measures the contribution of each subcomponent to perception by time truncating, highpass/lowpass filtering, or masking the speech with white noise. The AI-gram, a visualization tool that simulates the auditory peripheral processing, is used to predict the audible components of the speech sound. The results are generally in agreement with the classical studies that stops are characterized by a short duration burst followed by a F2 transition, suggesting the effectiveness of the 3DDS method. However, it is also shown that /ba/ and /pa/ may have a wide band click as the dominant cue. F2 transition is not necessary for the perception of /ta/ and /ka/. Moreover, many stop consonants contain conflicting cues that are characteristic of competing sounds. The robustness of a consonant sound to noise is determined by the intensity of the dominant cue.
 [DOI: 10.1121/1.3295689]

PACS number(s): 43.71.Es [ADP] Pages: 2599–2610

I. INTRODUCTION

Speech sounds are characterized by time-varying spectral patterns called acoustic cues. When a speech wave propagates on the basilar membrane (BM), unique perceptual cues (named *events*), which define the basic units for speech perception, become resolved. The relationship between the acoustic cues and perceptual units has been a key research problem for speech perception (Fletcher and Galt, 1950; Allen, 1996, 2005a).

Bell Labs (1940): The first search for acoustic cues dates back to 1940s at Bell Laboratories, when Potter *et al.* (1966) began their *visible speech* project, with the goal of training the hearing-impaired to read spectrograms. Five normal hearing (NH) and one hearing-impaired (HI) listeners participated in the study. Following a series of lectures on the spectrograph and its use on isolated syllables and continuous speech, the subjects were successfully trained to "read" speech spectrographs. Even though the acoustic cues identified by visual inspection were not very accurate, this pioneering work laid a solid foundation for subsequent quantitative analysis.

Haskins Laboratories (1950): Cooper *et al.* (1952), along with other researchers at the Haskins Laboratories over the following decade, conducted a series of landmark studies on the acoustic cues of consonant sounds. A speech synthesis system, called the *Pattern Playback*, was created to convert a spectrograph into (low quality) speech. Based on the spectrographs of real speech, it was postulated that stop consonants are characterized by an initial burst and the following consonant-vowel transition. In this 1952 study (Cooper *et al.*, 1952), the authors investigated the effect of center frequencies of the burst and the second formant (F_2) transition, on the percept of unvoiced stop consonants, by using a set of "nonsense" consonant-vowel (CV) speech sounds synthesized from 12 bursts followed by seven F_2 formant frequencies. The subjects were instructed to identify the stimulus as /p/, /t/, or /k/ (a closed-set task). Results show that most people hear /t/ when the burst-frequency is higher than the F_2 frequency; when the two frequencies are close, most listeners report /k/; otherwise they hear /p/. In a following study (Delattre *et al.*, 1955), the authors dropped the burst and examined the effect of F_2 transition only on the percept of stop consonants. It was found that stimuli with rising F_2 transition were identified as /b/, those with F_2 emanating from 1.8 kHz were associated with /d/ and those with a falling transition were reported as /g/.

Follow-up studies (1960–1990): These early Haskins studies have had a major impact on the research of speech perception. Since then speech synthesis has become a standard method for feature analysis. It was used in the search of acoustic correlate for stops (Blumstein *et al.*, 1977), fricatives (Hughes and Halle, 1956; Heinz and Stevens, 1961), nasals (Malécot, 1973; Liberman, 1957; Recasens, 1983), as well as distinctive and articulatory features (Blumstein and Stevens, 1979, 1980; Stevens and Blumstein, 1978). Similar approach was taken by Remez *et al.* (1981) to generate highly unintelligible "sine-wave" speech, and then concluded that the traditional cues, such as bursts and transitions, are not required for speech perception.

[a]Author to whom correspondence should be addressed. Electronic mail: fli2@illinois.edu

The *status quo* is extremely confusing in that most people strongly believe that the stop consonants are defined by the bursts and transitions (Cooper *et al.*, 1952; Delattre *et al.*, 1955), yet still argue that modulation is the key to understand speech perception (Drullman *et al.*, 1994a, 1994b; Shannon *et al.*, 1995; Elliott and Theunissen, 2009). They failed to point out that the two views are actually in conflict.

The argument in favor of the speech synthesis method is that the features can be carefully controlled. However, the major disadvantage of synthetic speech is that it requires prior knowledge of the cues being sought. This incomplete and inaccurate knowledge about the acoustic cues has often led to synthetic speech of low quality, and it is common that such speech sounds are unnatural and barely intelligible, which by itself is a strong evidence that the critical cues for the perception of target speech sound are poorly represented. For those cases, an important question is "How close are the synthetic speech cues to those of natural speech?" Another key issue is the *variability* of natural speech, due to the talker (Hazan and Rosen, 1991), accent, masking noise, etc., most of which are well beyond the reach of the state-of-the-art speech synthesis technology. To answer questions such as "Why /ba/s from some of the talkers are confused with /va/, while others are confused with /ga/?" or "What makes one speech sound more robust to noise than another?," it is necessary to study the acoustic cues of naturally produced speech, not artificially synthesized speech.

This study explores a psychoacoustic method for isolating speech cues from natural CV speech. Rather than making assumptions about the cues to be identified, each natural speech utterance is modified by (1) adding noise of variable type and degree, (2) truncation of the speech from the onset, and (3) highpass and lowpass filtering the speech with variable cutoff frequencies. For each of these modifications, the identification of the sound is judged by a large panel of listeners. We then analyze the results to determine where in time, frequency, and at what signal to noise ratio (SNR) the speech identity has been masked and we characterize the confusion. In this way we triangulate on the location of the speech cues and the events, along the three independent dimensions. This procedure is thus called the three-dimensional deep search (3DDS) method.

A. Principle of the 3DDS

Speech sounds are characterized in three dimensions: time, frequency, and intensity. Event identification involves isolating the speech cues along these three dimensions. In the past studies, confusion test on nonsense syllables has long been used for the exploration of speech features. For example, Fletcher and colleagues investigated the contribution of different frequency bands to speech intelligibility using highpass and lowpass filtered CV and CVC syllables (Fletcher and Galt, 1950; French and Steinberg, 1947), resulting in the articulation index (AI) model. Furui (1986) examined the relationship between dynamic features and the identification of Japanese syllables modified by initial and final truncations. More often masking noise was used to study consonant (Miller and Nicely, 1955; Wang and Bilger, 1973) and vowel (Phatak and Allen, 2007) recognition. Régnier and Allen (2008) successfully combined the results of time truncation and noise-masking experiments for the identification of /ta/ events. However, it has remained unclear how many speech cues could be extracted from real speech by these methods. In fact, there seems to be high skepticism within the speech research community as the general utility of any proposed methods.

In the present investigation, we have integrated the three types of tests, thus proposing the "3DDS" method for exploring the events of consonants from natural speech. To evaluate the acoustic cues along the three dimensions, speech sounds are truncated in time, highpass/lowpass filtered, and masked with white noise, as illustrated in Fig. 1, and then presented to NH listeners for identification. Small close set tasks are avoided because of their inherent bias.

Imagine that an acoustic cue, critical for speech perception, has been removed or masked. Would this degrade the speech sound and reduce the recognition score significantly? For the sound /t/, Régnier and Allen (2008) answered this question: The /t/ event is entirely due to a single short ≈20 ms burst of energy, between 4 and 8 kHz. To estimate the importance of individual speech perception events for sounds other than /t/, the 3D approach requires three independent experiments for each CV utterance. The *first* experiment determines the contribution of various time intervals, by truncating the consonant into multiple segments of 5, 10, or 20 ms per frame, depending on the sound and its duration. The *second* experiment divides the fullband into multiple bands of equal length along the BM and measures the score in these different frequency bands. Once the time-frequency coordinates of the event have been identified, a *third* experiment assesses the strength of the speech event by masking the speech at various signal-to-noise ratios. This experiment determines the score as a function of the SNR, as required for an AI calculation. To reduce the length of the experiments, the three dimensions, i.e., time, frequency, and intensity, are independently measured. The identified events have been further verified by a special software package designed for the manipulation of acoustic cues (Allen and Li, 2009) based on the short-time Fourier transform (Allen, 1977; Allen and Rabiner, 1977).

In order to understand continuous speech, it is necessary to first identify the acoustic correlates of the individual phonemes, for which the movement of the articulators are more easily interpretable (Fant, 1973). For this reason, as in the 1950 Haskins studies, we first look at the normal events of individual consonants in isolated CV syllables. The interaction between the events in continuous speech must be addressed in future studies. Finally, the 3DDS method has been successfully applied to all of the 16 Miller–Nicely consonants followed by three vowels /i, ɑ, u/, but for both space and pedagogical reasons, the discussion here has been limited to the six stop consonants /p, t, k, b, d, g/ preceding vowel /a/. Brief summaries of portion of this study have been presented in Allen *et al.*, 2009 and Allen and Li, 2009. The work was done as part of the Ph.D. thesis of Li.

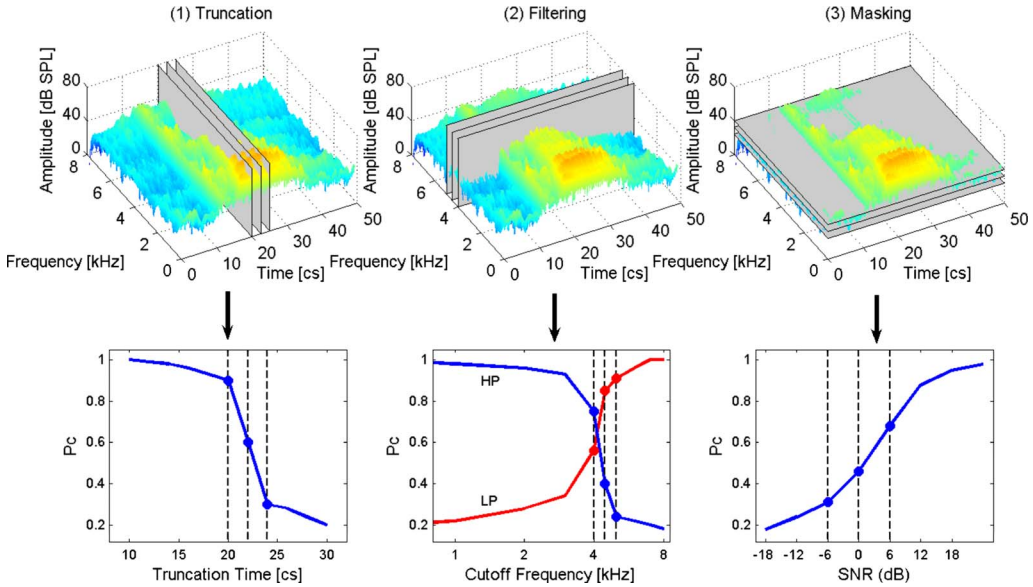

FIG. 1. (Color online) The 3D approach for the identification of acoustic cues: (1) to isolate the cue along the time, speech sounds are truncated in time from the onset with a step size of 5, 10, or 20 ms, depending on the duration and type of consonant; (2) to locate the cue along the frequency axis, speech sounds are highpass and lowpass filtered before being presented to normal hearing listeners; and (3) to measure the strength of the cue, speech sounds are masked by white noise of various signal-to-noise ratio. The three plots on the top row illustrate how the speech sound is processed. Typical correspondent recognition scores are depicted in the plots on the bottom row.

II. METHODS

The detail of the time-truncation (TR07), highpass/lowpass filtering (HL07), and noise-masking "Miller–Nicely (2005)" (MN05) experiments are described below. Each abbreviation gives the experiment type followed by the year the experiment was executed. An analysis of the MN05 experiment (also known as experiment: MN16R, publication: PLA08) has since been previously published (Phatak *et al.*, 2008), and results of HL07 can be found in Allen and Li (2009).

A. Subjects

In all, 61 listeners were enrolled in the study, of which 19 subjects participated in HL07, 19 in TR07. One subject participated in both of the experiments. The rest of the 24 subjects were assigned to experiment MN05 (Phatak *et al.*, 2008). The large majority of the listeners were undergraduate students, while the remaining were mothers of teenagers. No subject was older than 40 years, and all self-reported no history of speech or hearing disorder. All listeners spoke fluent English, with some having slight regional accents. Except for two listeners, all the subjects were born in the United States with their first language (L1) being English. The subjects were paid for their participation. University IRB approval was obtained.

B. Speech stimuli

A significant characteristic of natural speech is the variability of the acoustic cues. Thus we designed the experiment by manually selecting six different utterances per CV consonant based on the criterion that the samples be representative of the corpus. This decision was based on the scores from MN05. In retrospect this was a minor tactical mistake, as the most is learned from the sounds having 100% scores in quiet.

Six talkers saying the 16 Miller and Nicely (1955) (MN55) CVs /pa, ta, ka, fa, θa, sa, ʃa, ba, da, ga, va, ða, za, ʒa, ma, na/ were chosen from the University of Pennsylvania's Linguistic Data Consortium (LDC) LDC2005S22 "Articulation Index Corpus," which is used as the common speech source for the three experiments. This corpus is described in some detail by Fousek *et al.* (2004). Briefly, the speech sounds were sampled at 16 kHz using a 16 bit analog to digital converter. Each CV was spoken by 20 talkers of both genders. Experiment MN05 uses 18 talkers $\times$16 consonants. For the other two experiments (TR07 and HL07), six talkers, half male and half female, each saying each of the 16 MN55 consonants, were manually chosen for the test. These 96 (6 talkers$\times$16 consonants) utterances were selected such that they were representative of the speech material in terms of confusion patterns and articulation scores based on the results of two earlier speech perception experiments (Phatak and Allen, 2007; Phatak *et al.*, 2008).

The speech sounds were presented diotically (same sounds to both ears) through a Sennheisser "HD 280 Pro" headphone, at each listener's "most comfortable level" (MCL) (i.e., between 75 and 80 dB sound pressure level, and calibrated using a continuous 1 kHz tone into a homemade 3 cm^3 flat-plate coupler, as measured with a Radio Shack sound level meter). All experiments were conducted in a single-walled IAC sound-proof booth. Typically the room holding the booth had the door shut and people in the room were instructed to speak softly, so that their speech would not distract with the subject in the booth.

C. Conditions

Three independent experiments were performed, denoted TR07, HL07, and MN05. All three experiments included a common condition of fullband speech at 12 dB SNR in white noise, as a control.

Experiment TR07 evaluates the temporal property of the events. Truncation starts from just before the beginning of the utterance and stops at the end of the consonant. The starting, stopping, and truncation times were manually chosen, such that the duration of the consonant was divided into nonoverlapping consecutive intervals of 5, 10, and 20 ms. An adaptive scheme was applied for the calculation of the sample points. The basic idea was to assign more points where the speech changed rapidly, and fewer points where the speech was in a steady condition, in a manner consistent with the findings of Furui (1986). Starting from the end of the consonant, near the consonant-vowel transition, 8 frames of 5 ms were allocated, followed by 12 frames of 10 ms, and as many 20 ms frames, as needed, until the entire interval of the consonant was covered. To make the truncated speech sounds more natural and to remove possible minor onset truncation artifacts, white noise was used to mask the speech stimuli, at a SNR of 12 dB.

Experiment HL07 investigates the frequency properties of the events (Li and Allen, 2009). Nineteen filtering conditions, including one full-band (250–8000 Hz), nine highpass, and nine lowpass conditions, were included. The cutoff frequencies were calculated using Greenwood function (Greenwood, 1990) so that the full-band frequency range was divided into 12 bands, each having equal length along the basilar membrane. The highpass cutoff frequencies were 6185, 4775, 3678, 2826, 2164, 1649, 1250, 939, and 697 Hz, with an upper limit of 8000 Hz. The lowpass cutoff frequencies were 3678, 2826, 2164, 1649, 1250, 939, 697, 509, and 363 Hz, with the lower limit being fixed at 250 Hz. Note that the highpass and lowpass filtering share the same cutoff frequencies over the middle range. The filters were implemented in MATLAB© (The Mathworks Inc.) via a sixth order elliptical filter, with a stop band of 60 dB. White noise having a 12 dB SNR was added, to assure that the modified speech has no audible out-of-band component.

Experiment MN05 assesses the strength of the event in terms of noise robust speech cues, under adverse conditions of high noise. Besides the quiet condition, speech sounds were masked at eight different SNRs: −21, −18, −15, −12, −6, 0, 6, and 12 dB, using white noise. The results reported here are a subset of the Phatak and Allen (2007) study, which provides the full details.

D. Procedures

The three experiments employed similar procedures. A mandatory practice session was given to each subject at the beginning of each experiment. The stimuli were fully randomized across all variables when presented to the subjects, with one important exception to this rule being MN05 where effort was taken to match the experimental conditions of Miller and Nicely (1955) as closely as possible (Phatak *et al.*, 2008). Following each presentation, subjects responded to the stimuli by clicking on a button labeled with the CV that they heard. In case the speech was completely masked by the noise, the subject was instructed to click a "noise only" button. If the presented token did not sound like any of the 16 consonants, the subject were told to either guess 1 of the 16 sounds, or click the noise only button. To prevent fatigue, listeners were told to take frequent breaks, or break whenever they feel tired. Subjects were allowed to play each token for up to three times before making their decision, after which the sample was placed at the end of the list. Three different MATLAB programs were used for the control of the three procedures. The audio was played using a SoundBlaster 24 bit sound card in a standard PC Intel computer, running Ubuntu Linux.

III. MODELING SPEECH RECEPTION

The cochlea decomposes each sound through an array of overlapping nonlinear (compressive), narrow-band filters, splayed out along the BM, with the base and apex of BM being tuned to 20 kHz and 20 Hz, respectively (Allen, 2008). Once a speech sound reaches the inner ear, it is represented by a time-varying response pattern along the BM, of which some of the subcomponents contribute to speech recognition, while others do not. Many components are masked by the highly nonlinear forward spread (Duifhuis, 1980; Harris and Dallos, 1979; Delgutte, 1980) and upward spread of masking (Allen, 2008). The purpose of event identification is to isolate the specific parts of the psychoacoustic representation that are required for each consonant's identification (Régnier and Allen, 2008).

To better understand how speech sounds are represented on the BM, the AI-gram (see Appendix A) is used. This construction is a signal processing auditory model tool to visualize audible speech components (Lobdell, 2006, 2008; Régnier and Allen, 2008). The AI-gram is thus called, due to its estimation of the speech audibility via Fletcher's AI model of speech perception (Allen, 1994, 1996), was first published by Allen (2008), and is a linear Fletcher-like critical band filter-bank cochlear simulation. Integration of the AI-gram over frequency and time results in the AI measure.

A. A preliminary analysis of the raw data

The experimental results of TR07, HL07, and MN05 are presented as *confusion patterns* (CPs), which display the probabilities of all possible responses (the target and competing sounds), as a function of the experimental conditions, i.e., truncation time, cutoff frequency, and signal-to-noise ratio.

Notation: Let $c_{x|y}$ denote the probability of hearing consonant /x/ given consonant /y/. When the speech is truncated to time t_n, the score is denoted $c^T_{x|y}(t_n)$. The scores of the lowpass and highpass experiments at cutoff frequency f_k are indicated as $c^L_{x|y}(f_k)$ and $c^H_{x|y}(f_k)$. Finally, the score of the masking experiment as a function of signal-to-noise ratio is denoted $c^M_{x|y}(\mathrm{SNR}_k)$.

The specific example of Fig. 2 is helpful to explain the 3DDS method and to show how speech perception is affected by the events. It depicts the CPs of a /ka/ produced by

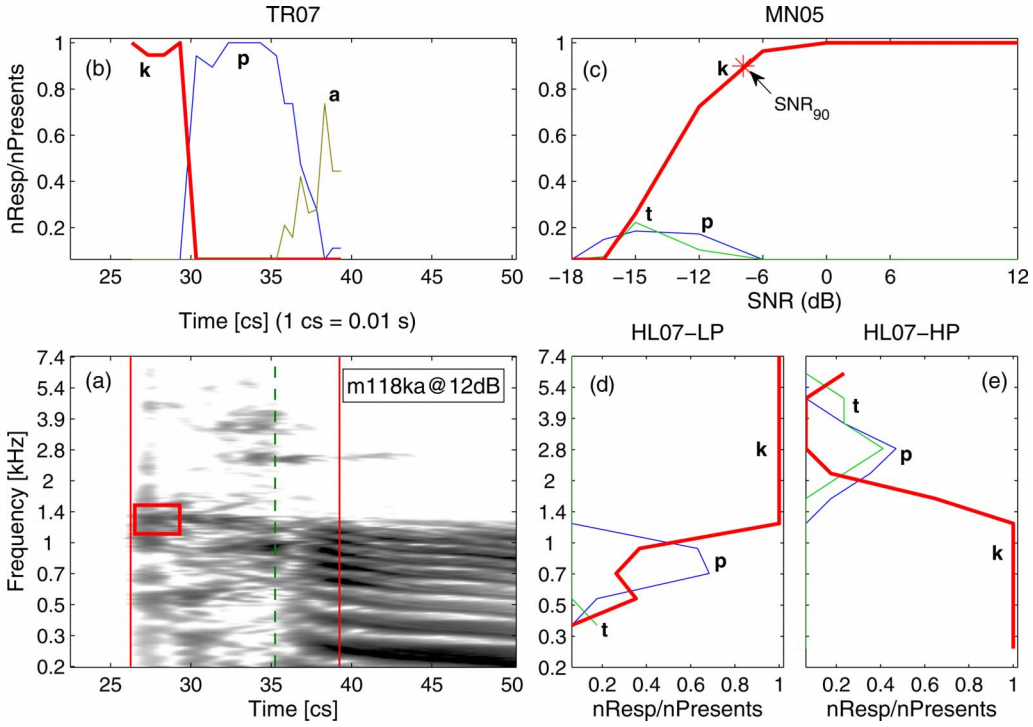

FIG. 2. (Color online) Various CPs of /ka/ spoken by talker m118 under various experimental conditions. (a) AI-gram at 12 dB SNR. The left and right vertical lines denote the start and end times for truncation. The middle line denotes the time of voice (sonorant) onset. (b) The temporal truncation CP as a function of truncation time from experiment TR07. (c) CP as a function of SNR for experiment MN05. The SNR_{90} point indicated by $*$ is at -8 dB SNR. Finally, the (d) low and (e) high CPs as a function of cutoff frequency for HL07. The text provides further details.

talker m118 (utterance m118_ka). The lower-left panel (a) shows the AI-gram. The results of the time-truncation experiment (TR07) is given in upper-left panel (b), lowpass/highpass of HL07 in lower-right panels [(d) and (e)], and MN05 in upper-right panel (c). To facilitate the integration of the three experiments, the AI-gram and the three scores are aligned in time t (in centiseconds) and frequency (along the cochlear place axis, in kilohertz) and thus depicted in a compact and uniform manner. Note that 1 cs=10 ms=0.01 s.

The CP of TR07 [Fig. 2(a)] shows that the probability of hearing /ka/ is 100% for $t \leq 26$ cs, where no speech component are removed. At 29 cs where the /ka/ burst has been completely truncated, the score for /ka/ drops sharply to 0%, within a span of 1 cs. For truncation times greater than 29 cs, only the transition region is heard, and 100% of the listeners report hearing a /pa/. Once the transition region is truncated ($t > 35$ cs), listeners report hearing only the vowel /a/.

A related conversion occurs in the lowpass and highpass experiment HL07 for /ka/ [Figs. 2(d) and 2(e)], in which both the lowpass score $c^L_{k|k}$ and highpass score $c^H_{k|k}$ abruptly plunge from 100% to less than 10% at a cutoff frequency of f_k=1.4 kHz, thereby precisely defining the frequency location of the /ka/ cue. For the lowpass case, listeners reported a morphing from /ka/ to /pa/ with score $c^L_{p|k}$ reaching 70% at 0.7 kHz, and for the highpass case, /ka/ morphed to /ta/, but only at the $c^H_{t|k}$=0.4 (40%) level. To reduce clutter, the remaining confusions are not shown.

The MN05 masking data [Fig. 2(d)] show a fourth CP. When the masker level increases from quiet to 0 dB SNR, the recognition score of /ka/ is close to 1 (i.e., 100%), signifying the presence of a robust cue. At SNR_{90}=−8 dB, the score sharply drops to chance performance where it is confused with /t/ and /p/.

IV. RESULTS

In this section we demonstrate how the events of stop consonants are identified by applying the 3DDS method. Again the results from the three experiments are arranged in an abbreviated and even more compact form. In Fig. 3(a) panel 1 (middle left) shows the AI-gram of the speech sound at 18 dB SNR. Each event hypothesis is highlighted by a rectangular box. The middle vertical dashed line denotes the voice-onset time, while the two vertical solid lines on either side of the dashed line denote the starting and ending points for the time-truncation experiment (TR07). Directly above the AI-gram, panel 2 shows the scores from TR07, while to the right, panel 4 shows the scores from HL07. Panel 3 (upper right) depicts the scores from experiment MN05. The CP functions are plotted as solid (lowpass) or dashed (highpass) curves, with competing sound scores with a single letter identifier next to each curve. The $*$ in panel 3 indicates SNR_{90}=−2 dB where the listeners just begin to confuse the sound in MN05, while the $\star$ in panel 4 indicates the intersection point (1.3 kHz) of the highpass and lowpass scores. The six small figures along the bottom show partial AI-grams of the consonant region, delimited in panel 1 by the solid lines, at −12, −6, 0, 6, 12, and 18 dB SNRs. A box in any of the seven AI-grams of panel 1 or 5 indicates a hypothetical event region, and for panel 5, indicates its audible threshold predicted by the AI-gram model.

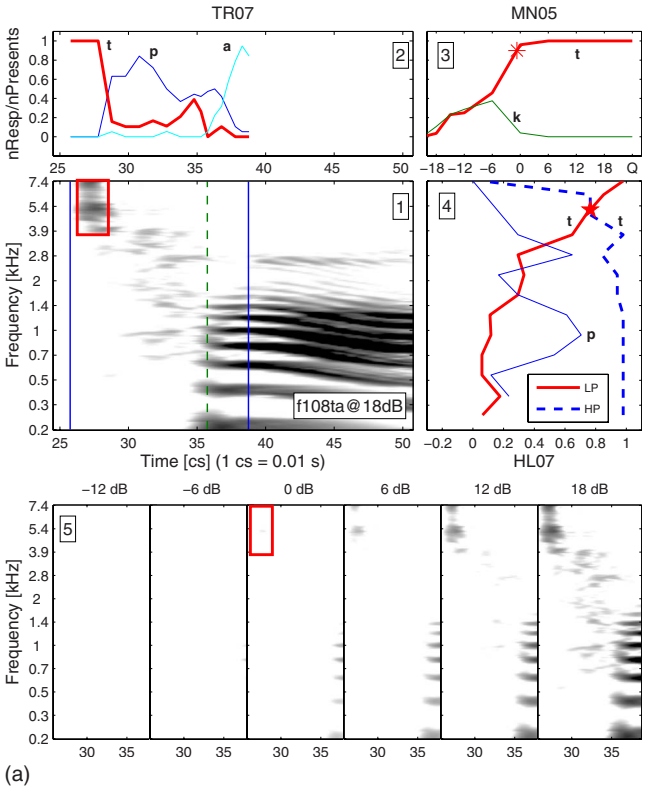

(a)

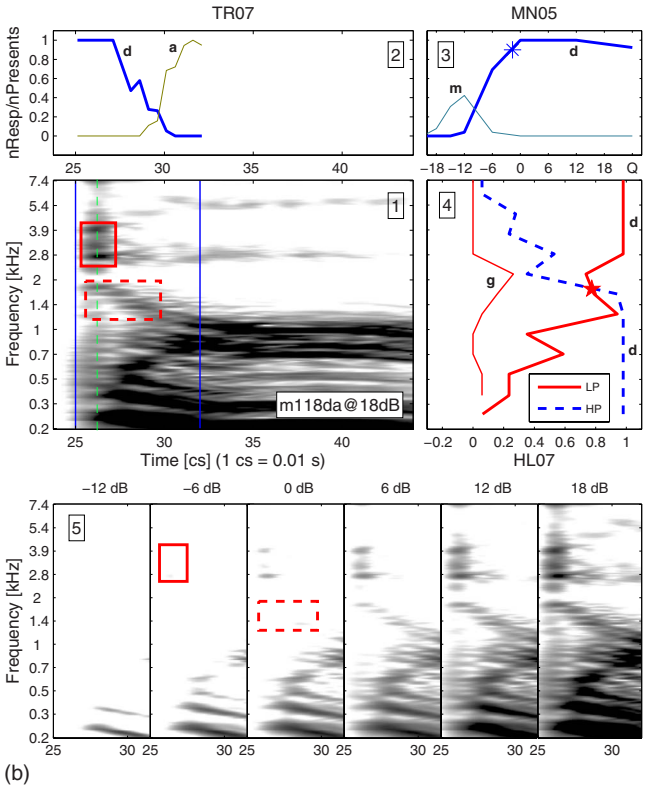

(b)

FIG. 3. (Color online) Hypothetical events for high-frequency stop consonants /ta/ and /da/. The multiple panels in each subfigure are [1] AI-gram. A dashed vertical line labels the onset of voicing (sonorance), indicating the start of the vowel. The solid and dashed boxes indicate the dominant and minor events, respectively. [2] CPs as a function of truncation time t_n. [3] CPs as a function of SNR_k. [4] CPs as a function of cutoff frequency f_k. [5] AI-grams of the consonant region (defined by the solid vertical lines on panel [1]) at −12, −6, 0, 6, 12, and 18 dB SNRs.

In Secs. IV A–IV C, we study the six stop consonants /t/, /d/, /k/, /g/, /p/, and /b/ followed by vowel /a/ as in "father." For each consonant, the six token utterances were analyzed by the members of our research group, and the most representative example was subjectively chosen to be presented, since it is impossible to publish all the data. An extensive attempt was made to automatically quantify the measures objectively; however, eventually this approach was abandoned, as it seriously obscured the raw data. Thus for this initial presentation of the 3DDS method, we decided to stick with a raw data presentation.

A. /ta/ and /da/

/ta/: Results of the three experiments (TR07, HL07, and MN05) clearly indicates that the /ta/ event [refer to Fig. 3(a) for a /ta/ from talker f105] is a high-frequency burst above 3 kHz, 1.5 cs in duration and 5–7 cs prior to the vowel. Panel [1] shows the AI-gram of the sound at 18 dB SNR in white noise with the hypothetical /ta/ event being highlighted by a rectangular frame. Above, panel [2] depicts the results of the time-truncation experiment. When the burst is completely removed at 28 cs, the score for the time-truncated /t/ drops dramatically from 1 to chance, and listeners start reporting /pa/, suggesting that the high-frequency burst is critical for /ta/ perception. This is in agreement with the highpass and lowpass data of panel [4]. Once the high-frequency burst has been removed by the lowpass filtering (solid curve), the /ta/ score $c^L_{t|t}$ drops dramatically and the confusion with /pa/ increases significantly. The intersection of the highpass and the lowpass perceptual scores (indicated by the ⋆) is ≈5 kHz, consistent with a high-frequency burst dominant cue. These results are then confirmed by the noise-masking experiment. From the AI-grams in panel [5], we see that the high-frequency burst becomes inaudible when the SNR is lower than 0 dB, as a consequence, the recognition score drops sharply at −1 dB SNR (labeled by a ∗ in panel [3]), proving that the perception of /ta/ is dominated by the high-frequency burst.

Of the six /ta/ sounds, five morph to /pa/ once the /ta/ burst was truncated, while one morphs to /ka/ (m112ta). For this particular sound, it is seen that the /ta/ burst precedes the vowel only by around 2 cs as opposed to 5–7 cs as is the case for a typical /ta/. This timing cue is especially important for the perception of /pa/, as we will discuss later in Sec. IV C.

/da/: Consonant /da/ [Fig. 3(b)] is the voiced counterpart of /ta/. It is characterized by a high-frequency burst above 4 kHz and a F_2 transition near 1.5 kHz, as shown in panel [1]. Truncation of the high-frequency burst (panel [2]) leads to an immediate drop in the score of $c^T_{d|d}$ from 100% at 27 cs to about 70% at 27.5 cs. The recognition score keeps decreasing until the F_2 transition is removed completely at 30 cs. From the highpass and lowpass data (panel [4]), it is seem that subjects need to hear both the F_2 transition and the high-frequency burst to get a full score of 100%, Lack of the burst usually leads to the /da/ → /ga/ confusion, as shown by the lowpass confusion of $c^L_{g|d}$=30% at f_c=2 kHz (solid curve labeled "g" in panel [4]), meaning that both the high-frequency burst and F_2 transition are important for the iden-

tification of a high quality /da/. This is confirmed by the results of the noise-masking experiment. From the AI-grams (panel 5), the F_2 transition becomes masked by noise at 0 dB SNR; accordingly the /da/ score $c^M_{d|d}$ in panel 3 drops quickly at the same SNR. When the remnant of the high-frequency burst is finally gone at −6 dB SNR, the /da/ score $c^M_{d|d}$ decreases even faster, until $c^M_{d|d}=c^M_{m|d}$ at −10 dB SNR; namely, the /d/ and /m/ scores are equal.

Some of the /da/'s are much more robust to noise than others. For example, the SNR_{90}, defined as the SNR where the listeners begin to lose the sound ($P_c=0.90$), is −6 dB for /da/-m104, and +12 dB for /da/-m111. The variability over the six utterances is impressive, yet the story seems totally consistent with the requirement that both the burst and the F_2 onset need to be heard.

B. /ka/ and /ga/

/ka/: Analysis of Fig. 4(a) reveals that the event of /ka/ is a mid-frequency burst around 1.6 kHz, articulated 5–7 cs before the vowel, as highlighted by the rectangular boxes in panels 1 and 5. The truncation data in panel 2 show that once the mid-frequency burst is truncated at 16.5 cs, the recognition score $c^T_{k|k}$ jumps from 100% to chance level within 1–2 cs. At the same time, most listeners report /pa/. The highpass score $c^H_{k|k}$ and the lowpass score $c^L_{k|k}$ (panel 4) both label 1.6 kHz with a sharp intersection, suggesting that the perception of /ka/ is dominated by the mid-frequency burst. Based on the AI-grams (panel 5), the 1.6 kHz burst is just above its detection threshold at 0 dB SNR, accordingly the recognition score of /ka/ $c^M_{k|k}$ (panel 3) drops dramatically below 0 dB SNR. Thus the results of the three experiments seem in perfect agreement in identifying a $\frac{1}{2}$ octave wide burst around 1.6 kHz as the single dominant cue of /ka/.

The identified /ka/ burst is consistent across all talkers. Four of the six /ka/ sounds morph to /pa/ once the /ka/ burst was truncated. Two have no morphs, remaining a very weak /ka/ (m114ka, f119ka).

/ga/: Consonant /ga/ [Fig. 4(b)] is the voiced counterpart of /ka/. Like /ka/, it is represented by a $\frac{1}{2}$ octave burst from 1.4 to 2 kHz, immediately followed by a F_2 transition between 1 and 2 kHz, all highlighted with boxes in panel 1. According to the truncation data (panel 2), the recognition score of /ga/ $c^T_{g|g}$ starts to drop once the mid-frequency burst is truncated beyond 21 cs. By 23 cs, a /ga/ → /da/ confusion appears with $c^T_{d|g}=40\%$. The highpass and lowpass scores (panel 4) fully overlap at 1.6 kHz, where both show a sharp decrease of more than 60%, consistent with the time-truncation data for /ga/. Based on the AI-grams in panel 5, the F_2 transition is masked by 0 dB SNR, while $SNR_{90}\approx-2$ dB, as labeled by a * in panel 3. When the mid-frequency burst is fully masked at −6 dB SNR, /ga/ becomes confused with /da/, suggesting that the perception of /ga/ is dominated by the mid-frequency burst.

All six /ga/ sounds have well defined bursts between 1.4 and 2 kHz. Most of the /ga/s (m111, f119, m104, and m112) have a perfect score of $c^M_{g|g}=100\%$ at 0 dB SNR. The other two /ga/s (f109 and f108) are a few dB weaker.

It is interesting to note that these two mid-frequency sounds all have conflicting cues that are characteristic of competing sounds. For example, the /ka/ sound [Fig. 4(a)] also contains a high-frequency burst around 5 kHz and a low-frequency burst around 0.5 kHz that that could be used as a perception cue of /ta/ and /pa/, respectively. As a consequence, listeners hear /ta/ when the highpass cutoff frequency is higher than the upper limit of /ka/ burst (2 kHz). In the lowpass experiment, people hear /pa/ when the lowpass cutoff frequency is smaller than 1.2 kHz, the lower limit of /ka/ cue. Similarly the /ga/ also contains a high-frequency burst above 4 kHz that promotes the confusion of /da/.

C. /pa/ and /ba/

/pa/: The AI-gram in Fig. 5(a) 1 for /pa/ spoken by female talker f103 reveals that there could be two different potential events: (1) a wide band click running from 0.3 to 7.4 kHz, maskable by white noise at 6 dB SNR and (2) a formant resonance at 1–1.4 kHz, maskable by white noise at 0 dB SNR. Panel 2 shows the truncated /p/ score $c^T_{p|p}(t_n)$. It starts at 100%. Once the wide band click spanning 0.3–7 kHz is truncated at ≈22–23 cs, the score drops out of saturation. Once the transition is removed at 27 cs it further drops to chance (1/16). The lowpass and highpass scores (panel 4) start at 100% at each end of the spectrum, and drop around the intersection point between 1.4 and 2 kHz. This broad intersection (indicated by a ⋆) appears to be a clear indicator of the center frequency of the dominant perceptual cue, which is at $F_2\approx0.7-1.0$ kHz and before 22–26 cs. The recognition score of noise-masking experiment (panel 3) drops dramatically at $SNR_{90}\approx=-1$ dB SNR (denoted by a *). From the six AI-grams (panel 5), we can see that the predicted audible threshold for the F_2 transition is at 0 dB SNR, the same as SNR_{90} (*) in panel 3 where the listeners just begin to lose the sound. Thus both the wide band click and the F_2 onset contribute to the perception of /pa/.

Stop consonant /pa/ is characterized as having a wide band click, as seen in this /pa/ example, but not in the five others we have studied. For most /pa/'s, the wide band click diminishes into a low-frequency burst. When the click is partially removed by filtering, the score remains at 100% as long as the F_2 region is audible. The click appears to contribute to the overall quality of /pa/. The 3D displays of other five /pa/s are in basic agreement with that of Fig. 5(a), with the main difference being the existence of the wideband burst at 22 cs for f103, and slightly different highpass and lowpass intersection frequencies, ranging from 0.7 to 1.4 kHz. The required duration of the F_2 energy before the onset of voicing (around 3–5 cs) is consistently critical for all the /pa/ utterances.

/ba/: Identifying the perceptual events for /ba/ are perhaps the most difficult of the six stops. For the 3DDS method to work well, 100% scores in quiet are required. Among the six /ba/ sounds, only the one in Fig. 5(b) has 100% scores at 12 dB SNRs and above. Based on the analysis of the AI-gram of Fig. 5(b), the potential features for /ba/ is a wide band click in the range of 0.3–4.5 kHz. Once the wide band click is completely truncated by $t_n=27$ cs, the /ba/ score $c^T_{b|b}$ [Fig. 5(b) 2] drops dramatically from 80% to chance, at the

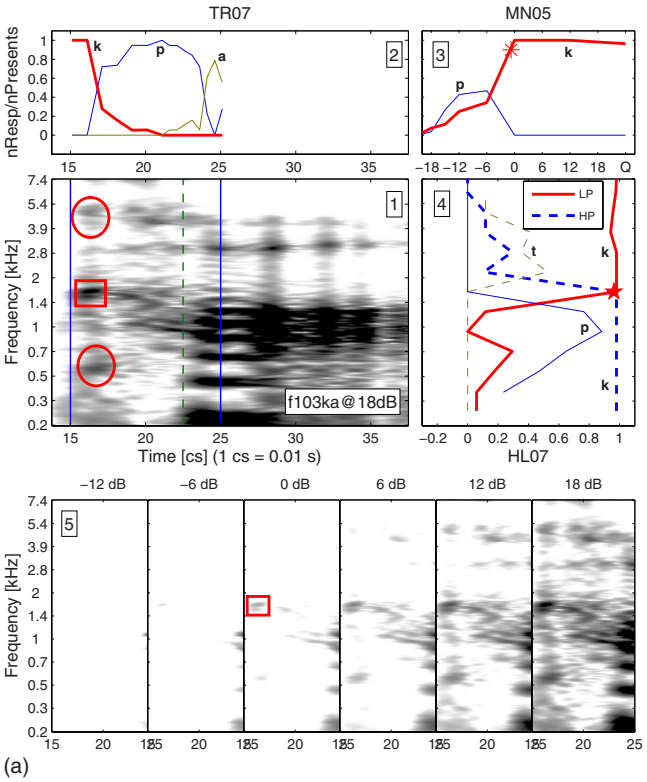

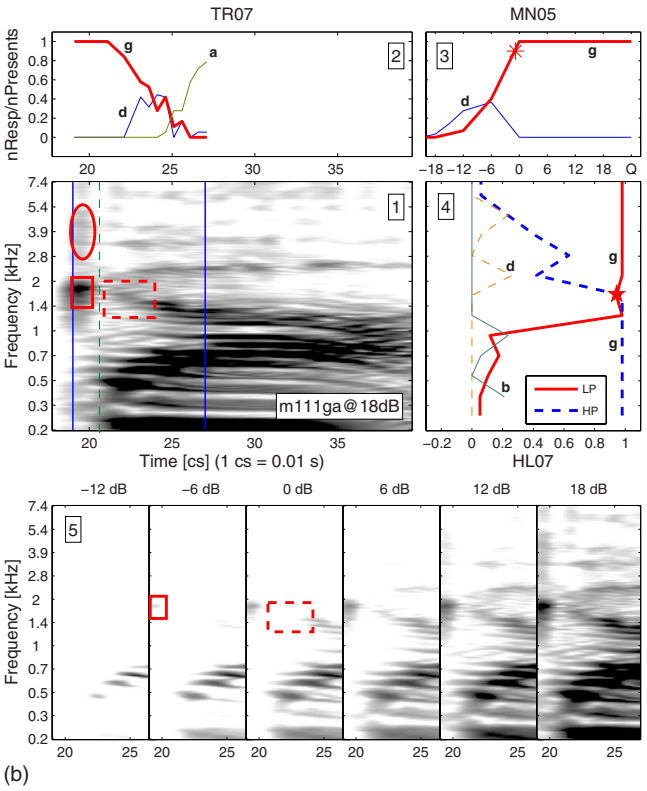

FIG. 4. (Color online) Hypothetical events for mid-frequency stop consonants /ka/ and /ga/. The multiple panels in each subfigure are 1 AI-gram. A dashed vertical line labels the onset of voicing (sonorance), indicating the start of the vowel. The solid and dashed rectangular boxes indicate the dominant and minor events, respectively. The ellipses denote the conflicting cues that cause the confusions. 2 CPs as a function of truncation time t_n. 3 CPs as a function of SNR_k. 4 CPs as a function of cutoff frequency f_k. 5 AI-grams of the consonant region (defined by the solid vertical lines on panel 1) at −12, −6, 0, 6, 12, and 18 dB SNRs.

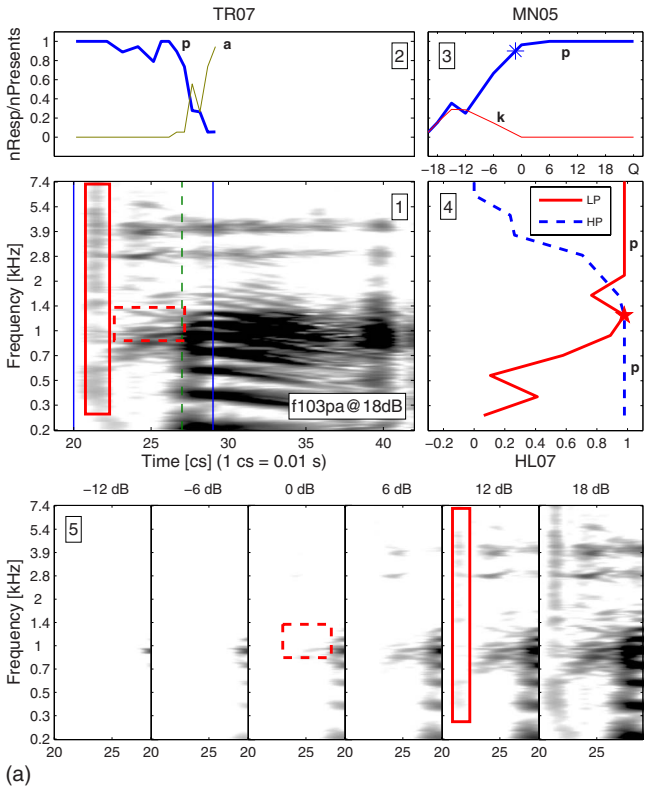

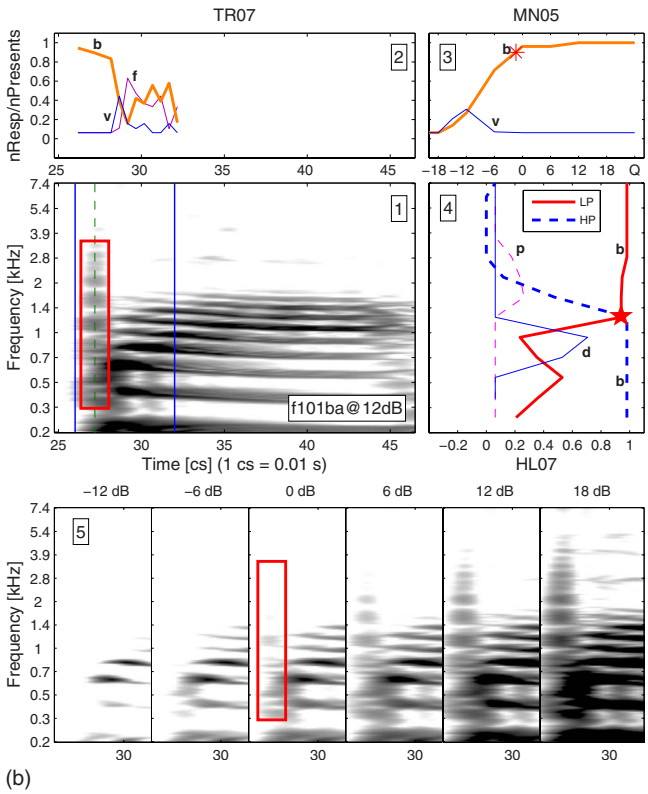

FIG. 5. (Color online) Hypothetical events for low-frequency stop consonants /pa/ and /ba/. The multiple panels in each subfigure are 1 AI-gram. A dashed vertical line labels the onset of voicing (sonorance), indicating the start of the vowel. The solid and dashed boxes indicate the dominant and minor events, respectively. 2 CPs as a function of truncation time t_n. 3 CPs as a function of SNR_k. 4 CPs as a function of cutoff frequency f_k. 5 AI-grams of the consonant region (defined by the solid vertical lines on panel 1) at −12, −6, 0, 6, 12, and 18 dB SNRs.

same time the /ba/ → /va/ confusion $c^T_{v|b}$ for and /ba/ → /fa/ confusion $c^T_{f|b}$ rapidly increase, indicating that the wide band click is important to distinguish of /ba/ from the two fricatives /va/ and /fa/. Panel [4] shows that the highpass and lowpass scores cross each other at 1.3 kHz, the center frequency of F_2 and change abruptly, indicating that the listeners need to hear both F_2 and a significant segment of the wide band click to decide the stimulus as a /ba/. From the AI-grams in panel [5], the wide band click becomes masked by the noise somewhere below 0 dB SNR. Accordingly the listeners begin to lose /ba/ sound at the same SNR, as represented by an ∗ in panel [3]. Once the wideband click has been masked, the confusions with /va/ increase and become equal to /ba/ at −12 dB SNR with a score of 40%.

There are only three LDC /ba/ sounds out of 18 with 100% scores at and above 12 dB SNR, i.e., /ba/ from f101/ shown here, and /ba/ from f109 and m120, all have a salient wide band click at the beginning. The remaining /ba/ utterances have /va/ confusions between 5% and 20%, in quiet. These nonzero quiet errors are the main difficulty in identifying the /ba/ event with certainty since the 3DDS method requires 100% in quiet for its proper operation. We do not know if it is the recordings in the LDC database that are responsible for these low scores, or if /ba/ is inherently difficult. A few high-error consonants with error rates greater than 20% were observed in LDC by Phatak and Allen (2007). From unpublished research, and not fully described here, we have found that in order to achieve a high quality /ba/ (defined as 100% identification in quiet), the wide band burst must exist over a wide frequency range. For example, a well defined 3 cs click from 0.3 to 8 kHz will give a strong percept of /ba/, which if missing or removed, may likely be heard as /va/ or /fa/.

D. Event variability

A significant characteristic of natural speech is the large variability of the acoustic cues across utterances. Typically this variability is characterized using the spectrogram. For this reason, we designed the experiment by manually selecting six utterances to have their natural variability, representative of the corpus. Since we did not, at the time, know the exact acoustic features, this was a design variable.

The center frequency of the burst (click) and the time difference between the burst and voicing onset for the 36 utterances are depicted in Fig. 6. Only the /ba/ from talker f101 is included because others do not have a wide band click and therefore highly confused with /va/ even in quiet. The figure shows that the burst times and frequencies for stop consonants are generally separated across the six different consonants.

E. Robustness

We have shown that the robustness of each consonant, as characterized by SNR_{90} is determined mainly by the strength of a single dominant cue. It is common to see the 100% recognition score drops abruptly within 6 dB, when the masking noise reaches the threshold of the dominant cue. The same observation was reported by Régnier and Allen (2008) that the 90% threshold (SNR_{90}) is directly proportional to the audible threshold of the /t/ burst based on the prediction of the AI-gram. This simple rule generalizes to the remaining five stop consonants. Figure 7 is the scatter plot of SNR_{90} versus the audibility threshold of the dominant cue. For a particular utterance (a point on the plot), the psychological threshold SNR_{90} is interpolated from the PI function), while the threshold of audibility for the dominant cue is estimated from the AI-gram. The two sets of threshold are nicely correlated over a 20 dB range, indicating that the recognition of each stop consonant is mainly dependent on the audibility of the dominant cue. Speech sounds with stronger cues are easier to hear in noise than weaker cues because it takes more noise to mask them.

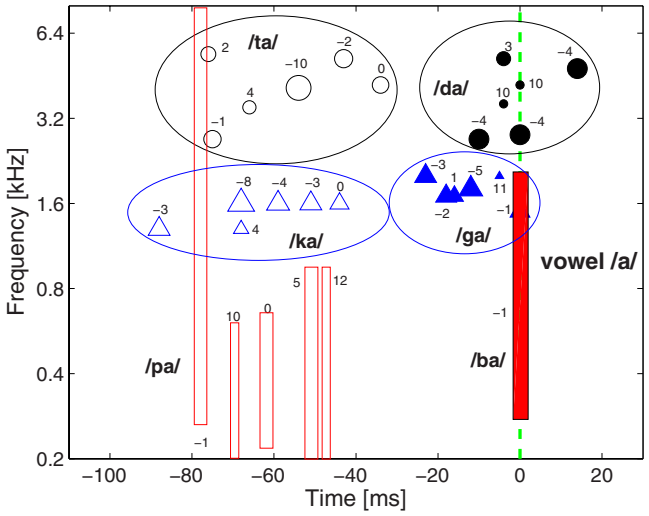

FIG. 6. (Color online) Variability of the bursts for stop consonants from multiple talkers. The strength of a burst, measured by the detection threshold (dB SNR) in white noise, is denoted by the neighboring digit.

F. Conflicting cues

It is interesting to see that many speech sounds contain conflicting cues. Take f103ka [Fig. 4(a)], for example. In

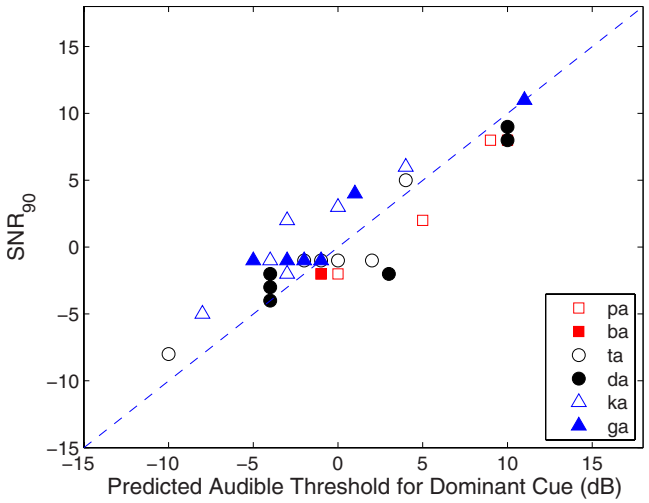

FIG. 7. (Color online) Correlation between the threshold of consonant identification and the predicted audible threshold of dominant cues based on the AI-gram.

addition to the mid-frequency /ka/ burst, it also contains two bursts in the high- and low-frequency ranges that greatly increase the probability of perceiving the sound as /ta/ and /pa/, respectively. When the dominant cue becomes masked by noise, the target sound is easily confused with other consonants within the same group. The conflicting cues have little impact on speech perception when the dominant cue is available. However, when the dominant cue is masked, the conflicting cues can cause the sound morph to another consonant. The masking range of a feature is typically 6 dB, and not more. Thus event detection is an all or nothing binary task. The spread of the event threshold is 20 dB, not the masking of a single cue. The existence of conflicting cues could make automatic speech recognition much more difficult, especially during training, because the training must sort out these false cues from the true target cues.

V. GENERAL DISCUSSION

The speech events are the perceptual information bearing aspects of the speech code. From what we have found, the density of the acoustic cues that support the events has a very low density in time-frequency space.

It was shown by Shannon (1948a, 1948b) that the performance of a communication system is dependent on the code of the symbols to be transmitted. The larger the "distance" between two symbols, the less likely the two will be confused. Shannon's proof of this principle equally applies to the case of human speech perception. For example, the /pa, ta, ka/ have common perceptual cues, i.e., a burst followed by a sonorant vowel. Once the burst is removed or masked by noise, the three sounds are highly confusable.

In all the speech perception tests, /pa, ta, ka/ commonly form a confusion group. This can be explained by the fact that the stop consonants share the same type of event patterns. The relative timing for these three unvoiced sounds is nearly the same. The major difference lies in the center frequencies of the bursts, with /pa/ having a click or low-frequency burst, /ka/ burst in the mid-frequency, and /ta/ burst in the high frequency. Similar confusions are observed for the voiced stop consonants /da/ and /ga/.

An especially interesting case is the confusions between /ba/ and /va/ [Fig. 5(b)]. Traditionally these two consonants were attributed to two different confusion groups based on their articulatory and distinctive features. However, in our experiments, we find that consonants with similar events tend to form a confusion group. Thus /ba/ and /va/ are highly confusable with each other because they share a common F_2 transition. This is strong evidence that events, not distinctive features, are the basic units for speech perception.

A. Summary

The six stop consonants are defined by a short duration burst (e.g., 2 cs), characterized by its center frequency (high, medium, and wide band), and the delay to the onset of voicing. This delay, between the burst and the onset of sonorance, is a second parameter called "voiced/unvoiced."

There is an important question about the relevance of the wide band click at the onset of the bilabial consonants /p/ and /b/. For /pa/ this click *appears* to be an option that adds salience to the sound. For /ba/ our source data are clearly insufficient because the /ba/ sounds that we chose were of poor quality; we hypothesize based on all the available data that the click is the key to a high quality /ba/ event, without which the unvoiced bilabial /ba/ is often confused with the fricatives /v/ and /f/, seen in many CPs.

In contrast, /ta/ and /ka/ are dominated by the burst frequency and delay to the sonorant onset. The voiced and unvoiced stops differ in the duration between the burst and the voicing onset. Confusion is much more common between /g/ and /d/ than with /t/ and /k/.

In other experiments, we have tried shifting the burst along the frequency axis, reliably morphing /ka/ into /ta/ (or *vice versa*). When the burst of /ka/ or /ta/ is masked or removed, the auditory system is sensitive to residual transitions in the low frequency, which cause the sound to morph to /pa/. Similarly we can convert /ga/ into /da/ (or vice versa) by using the same technique. The unvoiced stop consonants /p, t, k/ can be converted to their voiced counterpart /b, d, g/ by reducing the duration between the bursts and the onset of sonorance.

The timing, frequency, and intensity parameters may change, to a certain degree, in conversational speech, depending on the preceding and following vowels, and other factors. In a recent experiment, we investigate the effect of coarticulation on the consonant events. Instead of using vowel /a/, multiple vowels on the vertexes of the vowel triangle were selected for the study. Compared to the identified events for stops preceding vowel /a/, the identified bursts generally shift up in frequency for high vowels such as /i/ but change little for low vowels such as /u/. These recent results will be presented in a future paper.

B. Limitations of the method

It is important to point out that the AI-gram is imperfect, in that it is based on a linear model which does not account for cochlear compression, forward masking, upward masking, and other well known nonlinear phenomena seen in the auditory-nerve responses. These important nonlinearities are discussed in length in many places, e.g., Harris and Dallos (1979); Duifhuis (1980); Delgutte (1980); Allen (2008). A major extension of the AI-gram is in order, but not easily obtained. We are forced to use the linear version of the AI-gram until a fully tested time-domain nonlinear cochlear model becomes available. The model of (Zilany and Bruce, 2006) is a candidate for such testing.

Nevertheless, based on our many listening tests, we believe that the linear AI-gram generates a useful threshold approximation (Lobdell, 2006, 2008; Régnier and Allen, 2008). It is easy (trivial) to find cases where time-frequency regions in the speech signals are predicted audible by the AI-gram, but when removed, results in a signal with inaudible differences. In this sense, the AI-gram contains a great deal of "irrelevant" information. Thus it is a gross "overpredictor" of audibility. There are rare cases where the AI-gram "underpredicts" audibility, namely, where it fails to show an audible response, yet when that region is removed, the modi-

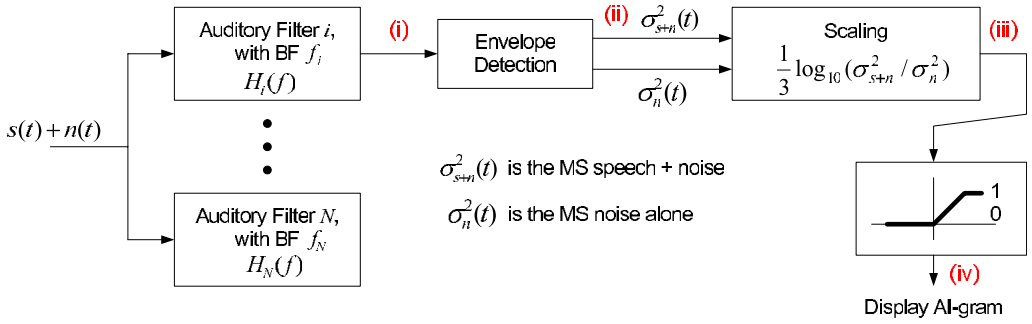

FIG. 8. (Color online) Block diagram of AI-gram [modified from (Lobdell, 2008), with permission].

fied signal is audibly different. Such cases, to our knowledge, are rare, but when discovered, are examples of serious failures of the AI-gram. This is more common below 1 kHz.

Finally, and perhaps most important, the relative strengths of cues can be misrepresented. For example, it is well know that onsets are strongly represented in neural responses due to adaptation (Delgutte, 1980). Such cues are not properly present in the AI-gram, and this weakness may be easily fixed, using existing hair-cell and neural models.

ACKNOWLEDGMENTS

The authors wish to express their appreciation to Bryce E. Lobdell, Andrea Trevino, Abhinauv Kapoor, Len Pan, Roger Serwy, and other members of the HSR group at University of Illinois, Urbana. A very small portion of this research has been supported by the NIH under Grant No. RDC009277A, awarded on 07/31/2008. This study represents a part of the Ph.D. thesis work of the first author (F.L.). They would like to acknowledge Etymotic Research and Phonak for their generous support.

APPENDIX A: THE AI MODEL

Fletcher's AI model is an objective appraisal criterion of speech audibility. The basic concept of AI is that every critical band of speech frequencies carries a contribution to the total index, which is independent of the other bands with which it is associated and that the total contribution of all bands is the sum of the contribution of the separate bands.

Based on the work of speech articulation over communication systems (Fletcher and Galt, 1950; Fletcher, 1995), French and Steinberg developed a method for the calculation of AI (French and Steinberg, 1947).

$$\mathrm{AI(SNR)} = \frac{1}{K}\sum_{k=1}^{K} \mathrm{AI}_k, \tag{A1}$$

where AI_k is the *specific* AI for the kth articulation band (Kryter, 1962; Allen, 2005b), and

$$\mathrm{AI}_k = \min\left[\frac{1}{3}\log_{10}\left(\frac{\sigma^2_{s+n}}{\sigma^2_n}\right), 1\right], \tag{A2}$$

where $\sigma^2_{s+n}/\sigma^2_n$ is the mean-square speech+noise over noise power ratio in the kth frequency band (French and Steinberg, 1947).

Given AI(SNR) for the noisy speech, the predicted average speech error is (Allen, 1994, 2005b)

$$\hat{e}(\mathrm{AI}) = e_{\min}^{\mathrm{AI}} \cdot e_{\mathrm{chance}}, \tag{A3}$$

where $e_{\min}$ is the maximum full-band error when AI=1, and e_{chance} is the probability of error due to uniform guessing (Allen, 2005b).

APPENDIX B: THE AI-GRAM

The AI-gram is the integration of the Fletcher's AI model and a simple linear auditory model filter-bank [i.e., Fletcher's SNR model of detection (Allen, 1996)]. Figure 8 depicts the block diagram of AI-gram. Once the speech sound reaches the cochlea, it is decomposed into multiple auditory filter bands, followed by an "envelope" detector. Fletcher audibility of the narrow-band speech is predicted by the formula of specific AI [Eq. (A2)]. A time-frequency pixel of the AI-gram (a two-dimensional image) is denoted $\mathrm{AI}(t,f)$, where t and f are the time and frequency, respectively. The implementation used here quantizes time to 2.5 ms and uses 200 frequency channels, uniformly distributed in place according to the Greenwood frequency-place map of the cochlea, with bandwidths according to the critical bandwidth of Fletcher (1995).

The average of the AI-gram over time and frequency, and then averaged over a phonetically balanced corpus, yields a quantity numerically close to the AI as described by Allen (2005b). An average across frequency at the output of the AI-gram yields the *instantaneous* AI

$$a(t_n) \equiv \sum_k \mathrm{AI}(t_n, f_k) \tag{B1}$$

at time t_n.

Given a speech sound, the AI-gram model provides an approximate "visual detection threshold" of the audible speech components available to the central auditory system. It is silent on which component is relevant to the speech event. To determine the relevant cues, it is necessary to directly relate the results of speech perception experiments (events) with the AI-grams (or perhaps some future nonlinear extensions of the AI-gram).

Allen, J. B. (**1977**). "Short time spectral analysis, synthesis, and modification by discrete Fourier transform," IEEE Trans. Acoust., Speech, Signal Process. **25**, 235–238.
Allen, J. B. (**1994**), "How do humans process and recognize speech"?,"

IEEE Trans. Speech Audio Process. **2**, 567–577.
Allen, J. B. (**1996**). "Harvey Fletcher's role in the creation of communication acoustics," J. Acoust. Soc. Am. **99**, 1825–1839.
Allen, J. B. (**2005a**), *Articulation and Intelligibility* (Morgan and Claypool, LaPorte, CO).
Allen, J. B. (**2005b**). "Consonant recognition and the articulation index," J. Acoust. Soc. Am. **117**, 2212–2223.
Allen, J. B. (**2008**). "Nonlinear cochlear signal processing and masking in speech perception," in *Springer Handbook on Speech Processing and Speech Communication*, edited by J. Benesty and M. Sondhi (Springer, Heidelberg, Germany), Chap. 3, pp. 1–36.
Allen, J. B., and Li, F. (**2009**). "Speech perception and cochlear signal processing," IEEE Signal Process. Mag. **29**, 117–123.
Allen, J. B., and Rabiner, L. R. (**1977**). "A unified approach to short-time Fourier analysis and synthesis," Proc. IEEE **65**, 1558–1564.
Allen, J. B., Régnier, M., Phatak, S., and Li, F. (**2009**). "Nonlinear cochlear signal processing and phoneme perception," in *Proceedings of the 10th Mechanics of Hearing Workshop*, edited by N. P. Cooper and D. T. Kemp (World Scientific, Singapore), pp. 95–107.
Blumstein, S. E., and Stevens, K. N. (**1979**). "Acoustic invariance in speech production: Evidence from measurements of the spectral characteristics of stop consonants," J. Acoust. Soc. Am. **66**, 1001–1017.
Blumstein, S. E., and Stevens, K. N. (**1980**). "Perceptual invariance and onset spectra for stop consonants in different vowel environments," J. Acoust. Soc. Am. **67**, 648–662.
Blumstein, S. E., Stevens, K. N., and Nigro, G. N. (**1977**). "Property detectors for bursts and transitions in speech perceptions," J. Acoust. Soc. Am. **61**, 1301–1313.
Cooper, F., Delattre, P., Liberman, A., Borst, J., and Gerstman, L. (**1952**). "Some experiments on the perception of synthetic speech sounds," J. Acoust. Soc. Am. **24**, 597–606.
Delattre, P., Liberman, A., and Cooper, F. (**1955**). "Acoustic Loci and translational cues for consonants," J. Acoust. Soc. Am. **27**, 769–773.
Delgutte, B. (**1980**). "Representation of speech-like sounds in the discharge patterns of auditory-nerve fibers," J. Acoust. Soc. Am. **68**, 843–857.
Drullman, R., Festen, J. M., and Plomp, R. (**1994a**). "Effect of temporal envelope smearing on speech reception," J. Acoust. Soc. Am. **95**, 1053–1064.
Drullman, R., Festen, J. M., and Plomp, R. (**1994b**). "Effect of reducing slow temporal modulations on speech reception," J. Acoust. Soc. Am. **95**, 2670–2680.
Duifhuis, H. (**1980**). "Level effects in psychophysical two-tone suppression," J. Acoust. Soc. Am. **67**, 914–927.
Elliott, T. M., and Theunissen, F. E. (**2009**). "The modulation transfer function for speech intelligibility," PLOS Comput. Biol. **5**, e1000302.
Fant, G. (**1973**). *Speech Sounds and Features* (MIT, Cambridge, MA).
Fletcher, H. (**1995**), "Speech and hearing in communication," in *The ASA Edition of Speech and Hearing in Communication*, edited by J. B. Allen (Acoustical Society of America, New York), pp. A1–A34 and 1–487.
Fletcher, H., and Galt, R. (**1950**). "Perception of speech and its relation to telephony," J. Acoust. Soc. Am. **22**, 89–151.
Fousek, P., Svojanovsky, P., Grezl, F., and Hermansky, H. (**2004**), "New nonsense syllables database—Analyses and preliminary ASR experiments," in Proceedings of the International Conference on Spoken Language Processing (ICSLP).
French, N. R., and Steinberg, J. C. (**1947**). "Factors governing the intelligibility of speech sounds," J. Acoust. Soc. Am. **19**, 90–119.
Furui, S. (**1986**). "On the role of spectral transition for speech perception," J. Acoust. Soc. Am. **80**, 1016–1025.
Greenwood, D. D. (**1990**). "A cochlear frequency-position function for several species—29 years later," J. Acoust. Soc. Am. **87**, 2592–2605.
Harris, D. M., and Dallos, P. (**1979**). "Forward masking of auditory nerve fiber responses," J. Neurophysiol. **42**, 1083–1107.
Hazan, V., and Rosen, S. (**1991**). "Individual variability in the perception of cues to place contrasts in initial stops," Percept. Psychophys. **59**(2), 187–200.
Heinz, J., and Stevens, K. (**1961**). "On the perception of voiceless fricative consonants," J. Acoust. Soc. Am. **33**, 589–596.
Hughes, G., and Halle, M. (**1956**). "Spectral properties of fricative consonants," J. Acoust. Soc. Am. **28**, 303–310.
Kryter, K. D. (**1962**). "Methods for the calculation and use of the articulation index," J. Acoust. Soc. Am. **34**, 1689–1697.
Liberman, A. (**1957**). "Some results of research on speech perception," J. Acoust. Soc. Am. **29**, 117–123.
Lobdell, B. E. (**2006**), "Information theoretic tool for investigating speech perception," MS thesis, University of Illinois at Urbana-Champaign, Urbana, IL.
Lobdell, B. E. (**2008**), "Information theoretic comparisons between speech intelligibility predictors and human phone perception with applications for feature extraction," Ph.D. thesis, University of Illinois at Urbana-Champaign, Urbana, IL.
Malécot, A. (**1973**). "Computer-assisted phonetic analysis techniques for large recorded corpuses of natural speech," J. Acoust. Soc. Am. **53**, 356.
Miller, G. A., and Nicely, P. E. (**1955**). "An analysis of perceptual confusions among some English consonants," J. Acoust. Soc. Am. **27**, 338–352.
Phatak, S., and Allen, J. B. (**2007**). "Consonant and vowel confusions in speech-weighted noise," J. Acoust. Soc. Am. **121**, 2312–2326.
Phatak, S., Lovitt, A., and Allen, J. B. (**2008**). "Consonant confusions in white noise," J. Acoust. Soc. Am. **124**, 1220–1233.
Potter, R. K., Kopp, G. A., and Kopp, H. G. (**1966**). *Visible Speech* (Dover, New York).
Recasens, D. (**1983**). "Place cues for nasal consonants with special reference to Catalan," J. Acoust. Soc. Am. **73**, 1346–1353.
Régnier, M. S., and Allen, J. B. (**2008**). "A method to identify noise-robust perceptual features: Application for consonant /t/," J. Acoust. Soc. Am. **123**, 2801–2814.
Remez, R., Rubin, P., Pisoni, D., and Carrell, T. (**1981**). "Speech perception without traditional speech cues," Science **212**, 947–949.
Shannon, C. E. (**1948a**), "The mathematical theory of communication," Bell Syst. Tech. J. **27**, 379–423.
Shannon, C. E. (**1948b**), "A mathematical theory of communication," Bell Syst. Tech. J. **27**, 623–656.
Shannon, R. V., Zeng, F. G., Kamath, V., Wygonski, J., and Ekelid, M. (**1995**). "Speech recognition with primarily temporal cues," Science **270**, 303–304.
Stevens, K. N., and Blumstein, S. E. (**1978**). "Invariant cues for place of articulation in stop consonants," J. Acoust. Soc. Am. **64**, 1358–1369.
Wang, M. D., and Bilger, R. C. (**1973**). "Consonant confusions in noise: A study of perceptual features," J. Acoust. Soc. Am. **54**, 1248–1266.
Zilany, M., and Bruce, I. (**2006**). "Modeling auditory-nerve responses for high sound pressure levels in the normal and impaired auditory periphery," J. Acoust. Soc. Am. **120**, 1446–1466.

The role of formant amplitude in the perception of /i/ and /u/

Michael Kiefte,[a] Teresa Enright, and Lacey Marshall
School of Human Communication Disorders, Dalhousie University, Halifax, Nova Scotia B3H 1R2, Canada

(Received 11 September 2009; revised 9 February 2010; accepted 11 February 2010)

Although recent evidence reconfirmed the importance of spectral peak frequencies in vowel identification [Kiefte and Kluender (2005). J. Acoust. Soc. Am. **117**, 1395–1404], the role of formant amplitude in perception remains somewhat controversial. Although several studies have demonstrated a relationship between vowel perception and formant amplitude, this effect may be a result of basic auditory phenomena such as decreased local spectral contrast and simultaneous masking. This study examines the roles that local spectral contrast and simultaneous masking play in the relationship between the amplitude of spectral peaks and the perception of vowel stimuli. Both full- and incomplete-spectrum stimuli were used in an attempt to separate the effects of local spectral contrast and simultaneous masking. A second experiment was conducted to measure the detectability of the presence/absence of a formant peak to determine to what extent identification data could be predicted from spectral peak audibility alone. Results from both experiments indicate that, while both masking and spectral contrast likely play important roles in vowel perception, additional factors must be considered in order to account for vowel identification data. Systematic differences between the audibility of spectral peaks and predictions of perceived vowel identity were observed. © *2010 Acoustical Society of America.* [DOI: 10.1121/1.3353124]

PACS number(s): 43.71.Es, 43.71.An [RSN] Pages: 2611–2621

I. INTRODUCTION

The experiments described in the present paper examine the role of formant amplitude in vowel perception while factoring out the effects of simultaneous masking and local spectral contrast. It is widely believed that the frequencies of the first two or three lowest formants are the most important for vowel perception (Peterson and Barney, 1952), and that secondary spectral properties such as formant bandwidth, global spectral tilt, or formant amplitude are relatively unimportant for preserving vowel identity (Klatt, 1982). However, the inability to predict listeners' identification of vowel-like stimuli on the basis of formant frequency alone with a high degree of accuracy has led to several alternative models of vowel perception (see Rosner and Pickering, 1994 for a review).

Some authors suggest that formant frequency models are overly simplistic and that broadly defined global spectral properties must be considered instead (Bladon and Lindblom, 1981; Miller, 1984; Ito *et al.*, 2001). In support of this view, Zahorian and Jagharghi (1993) found that spectral shape parameters in the form of cosine series coefficients were superior to any combination of formant and fundamental frequencies in an automatic classification task. Spectral shape parameters also corresponded better to error patterns in listeners' identifications.

Spectral shape models are completely agnostic with respect to the relative importance of atomic spectral properties such as formant frequencies or, more generally, the frequencies of local spectral maxima. However, spectral shape models can be criticized for lacking succinctness. An intermediate position is that a secondary perceptual analysis of vowel stimuli results in an integration of spectral peaks over a broad frequency range, which may obscure the relationship between raw formant frequencies and perceived vowel quality. Although the final perceptual representation of vowels in such models is still based on perceived peaks, these peaks do not correspond directly to formants. Following previous work on the equivalent second formant (F_2'; Carlson *et al.*, 1970, 1975; Bladon and Fant, 1978), Chistovich *et al.* (1979) suggested that formant peaks closer than 3–3.5 bark are merged into a single perceived spectral prominence (see also Chistovich and Lublinskaya, 1979). In this model, additional spectral properties such as formant amplitude may alter perceived vowel quality by influencing local spectral balance, thereby causing a shift in the perceived spectral peak. Hermansky (1990) offered an explicit computational model that includes this broadband processing of spectra, which effectively smears narrowly spaced spectral peaks.

Although this model proposes a role for formant amplitude under certain conditions, Assmann (1991) found little or no effect for formant amplitude on perceived vowel identity across a range of ±6 dB, even when formants were within 3 bark. One source for this discrepancy may be the use of perceptual matching tasks (Chistovich *et al.*, 1979; Chistovich and Lublinskaya, 1979), which may measure psychoacoustic similarity rather than actual phonetic distance (Klatt, 1982). While it is known that changes in formant amplitude can be perceived independently of changes in formant frequency (Bernstein, 1981) and that global spectral shape or loudness density patterns are good correlates to psychoacoustic distance (Bladon and Lindblom, 1981), it has been claimed that variations in formant amplitude have otherwise no effect on phonetic quality (Lindblom *et al.*, 2009).

Only a few studies have systematically examined the role of formant amplitude in vowel identification (Lindqvist and Pauli, 1968; Carlson *et al.*, 1970; Ainsworth and Millar, 1972; Aaltonen, 1985; Schwartz and Escudier, 1989). Miller (1953) found changes in listeners' identifications of synthetic

[a]Author to whom correspondence should be addressed. Electronic mail: mkiefte@dal.ca

vowels with variation in relative formant amplitude: As amplitude of the second formant (F_2) peak was lowered, there was a tendency toward back vowel responses in two-formant stimuli. Similarly, Chistovich and Chernova (1986) also showed that variations in relative formant amplitude can transform a high-front vowel into a high-back vowel as F_2 level was reduced in synthetic, two-formant stimuli. Hedrick and Nabelek (2004) varied F_2 amplitude across a range of 20 dB within a /u/–/i/ continuum and showed that this range of variation was sufficient to shift the perceived phonetic boundary. Jacewicz (2005) also found that variations in level of F_2 affected identification of the vowels /i/ and /ɪ/.

Aaltonen (1985) manipulated F_2 amplitude over a range of 20 dB; reduction by as little as 5–10 dB increased the number of /i/ identifications in an /i/–/y/ continuum, irrespective of formant frequencies. Aaltonen suggested that this change in response pattern was due to the perception of the F_3 peak as F_2 with decrease in relative F_2 amplitude. Nábělek *et al.* (1992) arrived at an analogous conclusion, following an experiment in which listeners misidentified /u/ as /i/ when presented against speech-spectrum noise—i.e., they speculated that F_2 at low amplitudes may be masked by noise, resulting in the misidentification of the F_3 peak as F_2.

While it has been argued that these results could also be due to a secondary broadband integration of vowel spectra (Chistovich *et al.*, 1979; Chistovich and Lublinskaya, 1979), it is also possible that basic psychoacoustic processes such as simultaneous masking may be involved. For example, Ainsworth and Millar (1972) concluded that F_2 frequency is independent of formant amplitude in perception of two-formant stimuli when the F_2 peak is no more than 28 dB below that of F_1. Below this threshold, listeners' responses resemble those to one-formant stimuli—i.e., similar to results reported by Miller (1953) and Chistovich and Chernova (1986), listeners largely perceive back vowels (Delattre *et al.*, 1952). In support of this conclusion, Nearey and Levitt (1974) and Rand (1974) found that F_1 peak can mask higher formants and that dichotic presentation provides a release from this masking.

Other basic psychoacoustic processes may also play a role in vowel perception that confound the relationship between formant amplitude and vowel identification. For example, Kiefte and Kluender (2005) found that the perceptual effects of formant amplitude may be exaggerated in isolated synthetic monophthongs, which differ from naturally produced tokens by virtue of the absence of natural vowel-inherent spectral change (Nearey and Assmann, 1986; Hillenbrand *et al.*, 1995). Kiefte and Kluender (2008) also found that the effects of spectral tilt or relative formant level could be exaggerated by a contrast effect with its surrounding acoustic context if the latter were filtered to enhance this contrast. Conversely, they found that the effects of spectral tilt or formant level were largely eliminated in synthetic monophthongs when they were presented with an unprocessed carrier phrase, which served as a spectrally neutral reference—i.e., the effect for spectral tilt was largely mitigated, even with unfiltered context sentences. These contrast effects are supported by observations by Lindqvist and Pauli (1968) and Lea and Summerfield (1994), who found that, for stimuli that were not blocked by signal manipulation, there was a larger effect for formant level presumably due to across-trial contrast effects.

Despite evidence that formant amplitude may provide additional phonetic information in vowel perception, it has been observed that the relationship between formant frequency and amplitude is entirely lawful and predictable in naturally produced speech. Given that formant amplitudes can be deduced largely from formant frequencies and that formant bandwidth also varies lawfully as a function of formant frequency in naturally produced speech (Fant, 1956, 1972; Stevens, 1998), it would seem that formant amplitude provides no more information regarding vowel identity than formant frequencies themselves. Jacewicz and Fox (2008) found that naturally occurring variation in formant amplitude corresponds well to predicted patterns. In addition, with the exception of /u/, which showed very large context effects on both formant frequency and amplitude, they found that naturally occurring variation in formant amplitude was much smaller than those changes that have been previously shown to induce a change in perceived vowel quality (Miller, 1953; Carlson *et al.*, 1970; Ainsworth and Millar, 1972; Aaltonen, 1985). In naturally occurring speech in ideal acoustic environments, one would not expect that significant gains could be made in predicting vowel perception through the addition of formant amplitude information.[1]

One might expect perceptual trading relations between formant frequency and amplitude in cases where one property is either distorted or ambiguous. However, other factors beyond formant frequency can have an even stronger effect on formant level. For example, de Cheveigné and Kawahara (1999) and Lindblom *et al.* (2009) point out that fundamental frequency (f_0) has a highly nonlinear effect on formant amplitude that can result in deviations much larger than those observed between vowel categories—especially for high fundamental frequencies. In addition, Jacewicz and Fox (2008) found that consonantal context has a significant effect on the amplitudes of individual formants. Due to this variation, formant amplitude may instead be a particularly *unreliable* correlate to vowel identity.

It was noted above that some effects of formant amplitude may be due to simultaneous masking—e.g., where F_1 peak masks that of F_2 (e.g., Ainsworth and Millar, 1972). If the F_2 peak is inaudible or masked by F_1, the F_3 peak may instead be perceived as F_2, resulting in a misidentification (or, if there is no F_3 peak, a back vowel may instead be heard). Alternatively, if the level of the F_2 peak is low, relative to the immediately surrounding harmonics, the peak may not be prominent enough to alter the perceived identity of a vowel; while lowering the amplitude of a formant may result in masking by a lower spectral peak, it is also possible that the lowered spectral peak may not have enough local spectral contrast to be perceived as such (e.g., Fig. 1).

Some studies have shown that a spectral peak does not have to be substantially higher in level than surrounding harmonics to have a perceptual effect. Lea and Summerfield (1994) found that the contrast threshold for a formant peak was 1.2–1.5 dB, which also agrees with results obtained in spectral enhancement studies (Summerfield *et al.*, 1987;

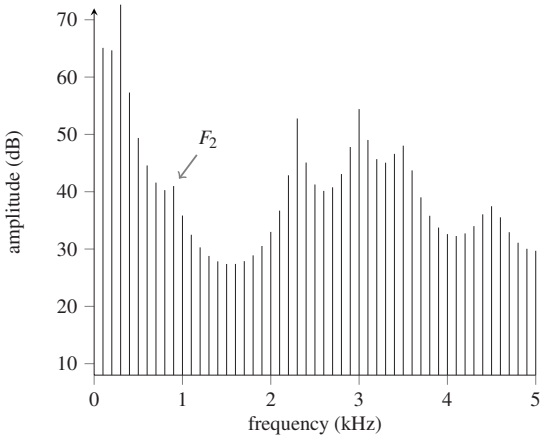

FIG. 1. Do listeners hear /u/ or /i/ when presented with the stimuli represented by the spectrum above? Formant frequencies are appropriate for /u/ while spectral tilt is intermediate between that for /i/ and /u/. However, F_2 amplitude is very low and the peak is not prominent relative to the surrounding harmonics. Second formant peak could either be masked by that of F_1 or it may not have sufficient local spectral prominence to be audible.

Leek *et al.*, 1987). However, formants in these studies consisted of only two harmonics presented against a flat complex periodic spectrum. When stimuli that resemble naturally produced vowels more closely are used, somewhat larger thresholds for the perception of a spectral notch between formants were found (Turner and Van Tasell, 1984).

The relatively small amount of spectral contrast required for perception of a distinct peak is likely due to suppression effects, and the effective increase in peak level can be as much as 15 dB (Moore and Glasberg, 1983a,1983b). Additionally, Assmann and Summerfield (1989) and Lea and Summerfield (1994) suggested that even spectral shoulders could serve the same role as spectral peaks in perception, suggesting that listeners are sensitive to even small perturbations of vowel spectra.

Evidence of suppression effects were demonstrated indirectly by Kakusho *et al.* (1971) and Chistovich and Lublinskaya (1979), who showed that formant peaks largely mask surrounding harmonics. Kakusho *et al.* additionally concluded that only two or three harmonics near each formant frequency are sufficient to obtain 100% correct identification rates, as well as preserve vocalic pitch—a result that was also demonstrated by Assmann and Nearey (1987) for F_1. Kakusho *et al.* also found that decreases in the amplitude of harmonics far from formants were largely inaudible, and therefore, could have no effect on phonetic identity.

In summary, several factors could account for observed effects of formant amplitude on vowel perception: global spectral tilt—the effects of which are exaggerated by acoustic context (Kiefte and Kluender, 2005, 2008); simultaneous masking of a formant peak by a lower-frequency formant (Nearey and Levitt, 1974); and degree of local spectral prominence or the amplitude of a peak relative to nearby spectral energy (Turner and Van Tasell, 1984). However, the use of full-spectrum vowels such as that illustrated by Fig. 1 in studies of formant amplitude does not allow the experimenter to distinguish two different types of basic auditory effects: When F_2 amplitude is low, the peak may be masked by lower formant peaks, or it may simply lose local spectral contrast.

Therefore, to factor out these effects, the present experiments use the following two sets of stimuli for listener identification:

1. *Full spectrum* (normally produced via cascade formant synthesis): With these stimuli, effects for formant amplitude may be the result of either peripheral masking effects or effects of local spectral contrast.
2. *Incomplete spectrum* (only harmonics at or adjacent to formant peaks preserved; Kakusho *et al.*, 1971; Assmann and Nearey, 1987): Observed perceptual effects of formant amplitude with these stimuli cannot result from reduced local spectral contrast as this property is effectively maximized.

Two types of experiments are described here: a basic vowel perception task, as well as a detection task, which probes whether the presence of the F_2 peak in the spectrum has a perceptual effect. In all experiments, the amplitudes of both F_2 and all higher formants are varied in a fully crossed design in order to factor out the perceptual effect of spectral tilt, which may be a potential confound (Kiefte and Kluender, 2005, 2008). Similar to Hedrick and Nabelek (2004), the endpoint vowel stimuli for these experiments were /i/ and /u/.

II. EXPERIMENT 1

The purpose of the first experiment was to examine the influence of formant amplitude on vowel perception and to examine the effects of local spectral contrast, simultaneous masking, and global spectral tilt separately. Previously, Hedrick and Nabelek (2004) have shown that formant amplitude does have an effect on vowel perception in an /i/–/u/ continuum, in which the second formant peak of /u/ is manipulated. Like the previous study, when the amplitude of F_2 approaches a level at which the amplitudes of harmonics close in frequency to the formant peak are not emphasized, we expect more /i/ responses. However, in the current study, two sets of stimuli are presented to listeners for identification: one with all harmonics present (full-spectrum) and another set in which each formant peak is represented by only three harmonics (incomplete-spectrum), thereby ensuring maximum local spectral contrast. Significant differences in response patterns between the full-spectrum and incomplete-spectrum stimuli would indicate that local spectral contrast plays an important role in the relationship between formant amplitude and vowel perception, as local spectral contrast is effectively maximized in the incomplete-spectrum stimuli.

A. Participants

Participants were 14 native speakers of Canadian English with normal hearing. Eligibility was determined using pure-tone audiometry to establish thresholds bilaterally at standard octave-spaced audiometric frequencies between 500

and 4000 Hz, as well as at 1500 and 3000 Hz. All subjects had hearing thresholds at or below 15 dB HL across all tested frequencies.

B. Stimuli

Forty-nine synthetic vowel-like stimuli were created in a two-way continuum ranging from /u/ to /i/ in both global spectral tilt and amplitude of the F_2 peak of /u/ (which was absent for the /i/ endpoint) in a fully crossed 7×7 design. The cascade branch of a flexible implementation of the KLATT80 speech synthesizer written for MATLAB was used to create the /i/ and /u/ endpoints (Klatt, 1980; Kiefte *et al.*, 2002). Fundamental frequency (f_0) was 100 Hz for all stimuli. The frequencies of F_1-F_6 were held constant at 300, 900, 2300, 3000, 3500, and 4500 Hz, respectively. For the /i/ endpoint, the 900 Hz parameter was skipped, and the remaining frequencies were reassigned to the next lower formant synthesis parameter (i.e., /i/ only had five formants with F_2 at 2300 Hz—henceforth, the amplitude of F_2 will be defined as the amplitude of the harmonic at 900 Hz irrespective of whether a spectral peak is actually present at that frequency or not). To generate an initial one-dimension series, the levels of the resultant harmonics were interpolated linearly in decibels from the spectra of the two endpoints, /i/ and /u/, in seven equal steps to create variations in both the amplitude of F_2 and spectral tilt (i.e., relative amplitude of higher formants). Unwrapped phase was also interpolated linearly. Waveforms were then created from the spectra via inverse Fourier transform. The range in F_2 amplitude (i.e., amplitude of the 900-Hz harmonic) between /u/ and /i/ was 21.4 dB.

Stimuli were 245 ms in duration and normalized on the basis of F_1 amplitude. Formant values of stimulus endpoints were similar to those recommended by Hillenbrand *et al.* (1995) while making formant frequencies constant across the series. Endpoints of the continuum were judged to be an appropriate representation of either /i/ or /u/.

Because synthesis resulted in spectral variation in both F_2 level and spectral tilt, amplitude variations for spectral tilt (i.e., relative amplitude of peaks at 2300, 3000, 3500, and 4500 Hz) were further manipulated in the same manner as Kiefte and Kluender (2005): A filter analogous to that used by the KLSYN88 speech synthesizer was used to impose a dB/octave difference between F_1 and F_3 peaks on the target stimuli in order to adjust source tilt (i.e., the TL parameter in KLSYN88; Klatt and Klatt, 1990). The spectral tilt (defined as the difference between amplitudes of peaks at 300 and 2300 Hz in dB/octave) of each stimulus in the initial one-dimensional series was adjusted to match that of every other stimulus in the series for a total of 49 stimuli. For stimuli that required an increase in spectral tilt rather than a decrease, a single-zero filter was used instead of a single-pole. A recursive algorithm was used to determine the level of attenuation or amplification of the 2300 Hz peak. The total range of spectral tilts was -9.6 to -3.9 dB/octave.[2]

Presentation of each stimulus was preceded by the phrase "You will now hear the vowel…," which was recorded from a male speaker of Canadian English (MK), sampled at 10 kHz, analyzed via 11-coefficient LPC, and resynthesized with 100 Hz f_0 to match that of the following target vowel. This phrase acted as a perceptual anchor to reduce the effect of spectral tilt on vowel identification that has been observed in studies using isolated synthetic vowels (Kiefte and Kluender, 2008).

In addition to the full-spectrum stimuli just described, incomplete-spectrum stimuli were also generated. These consisted of three harmonics centered at each of the six formant frequencies above (Fig. 2). The amplitudes of each of the three harmonics around each formant are unchanged from the original stimuli. The stimulus at the /i/ endpoint of the incomplete-spectrum continuum also has harmonics at and around 900 Hz in the incomplete-spectrum condition, even though this does not represent a formant for /i/. These harmonics, which correspond to the F_2 of /u/, have the same amplitudes as those around 900 Hz for the original /i/ endpoint. If there is no masking of this peak by F_1 and formant level has only a minor impact on vowel perception, one might expect a much larger number of /u/ responses with the incomplete-spectrum series due to the presence of these harmonics at 900 Hz.

Subjectively, it was judged that there was a not a substantial perceptual difference between the incomplete and full-spectrum stimuli and informal reactions from subjects suggested the same conclusion (cf., Kakusho *et al.*, 1971; Assmann and Nearey, 1987).

C. Procedure

Following hearing screening, eligible participants completed a two-alternative forced-choice (2AFC) vowel identification task with both sets of stimuli—full- and incomplete-spectrum—which were blocked into two separate sessions. Session order was counterbalanced across participants. After listening to each stimulus, participants pressed one of two buttons labeled "ee" or "oo." Each of the 49 stimuli was presented in random order to each participant with eight repetitions of each stimulus.

Stimuli were presented at an average level of 72 dB sound pressure level (SPL) through circumaural Beyer Dynamic DT 150 headphones in a sound-attenuated booth. Stimulus presentation and response collection were controlled by a Tucker-Davis RP 2.1 digital signal processor. Data were collected from up to two subjects simultaneously and stored on a desktop computer. Stimulus order was randomized separately for each subject. The task took approximately 60 min to complete.

D. Results

Responses to both full- and incomplete-spectrum conditions were each pooled across subjects and are presented in Fig. 3 as a function of both F_2 peak amplitude and spectral tilt (i.e., the difference between F_3 and F_1 amplitude in dB/octave). As expected, as the amplitude of the F_2 peak is reduced in either condition, there is an increase in the number of /i/ responses. However, there is also an increase in the number of /i/ responses as the spectral tilt is increased—i.e., with an increase in the relative amplitudes of F_3 and higher spectral peaks. Comparison of the two figures reveals that

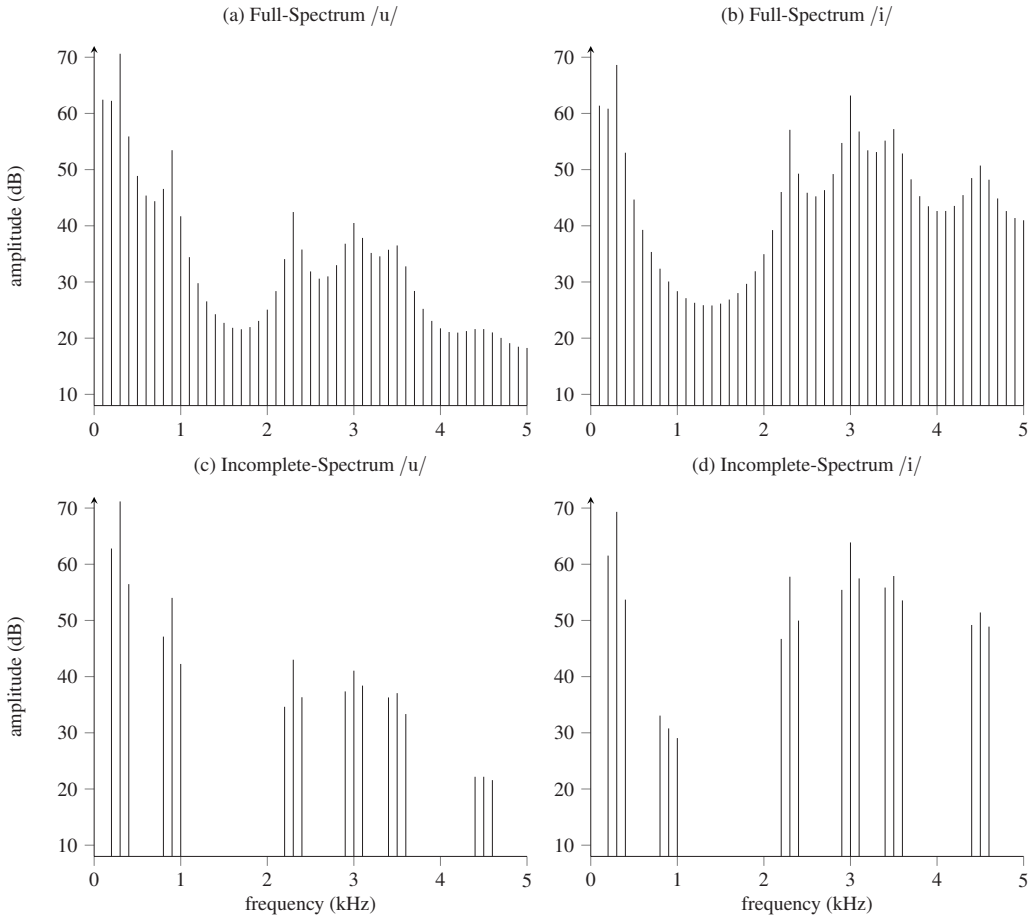

FIG. 2. Schematized spectra of stimuli at the (a) F_2 amplitude and (b) spectral tilt endpoints for both (c) full and (d) incomplete spectrum stimuli. Note that the (d) incomplete-spectrum /i/ has a peak around 900 Hz, consisting of harmonics with the same levels as those in the full-spectrum /i/.

the effect for F_2 amplitude was stronger for the full-spectrum stimuli [i.e., there is a wider range of responses across levels of F_2 amplitude in Fig. 3(a) than in Fig. 3(b)].

Each listener's responses to both identification tasks were analyzed via two-way logistic regression (McCullagh and Nelder, 1989) and regression coefficients across listeners were subjected to *t*-tests to determine if there was a significant effect for either changes in F_2 amplitude or spectral tilt, both within and between the full- and incomplete-spectrum conditions (Gumpertz and Pantula, 1989).

For the full-spectrum condition, changes in F_2 amplitude were highly significant ($p<0.001$; $d=2.27$), as were changes in spectral tilt ($p<0.001$; $d=3.43$). For the incomplete-spectrum condition, changes in F_2 amplitude and spectral tilt were also both highly significant ($p<0.001$; $d=3.03$ and 4.03, respectively).

A comparison of regression coefficients between the two conditions revealed that there was no significant difference for changes in the amplitude of higher peaks (spectral tilt) across the two conditions ($p=0.56$). A significant difference

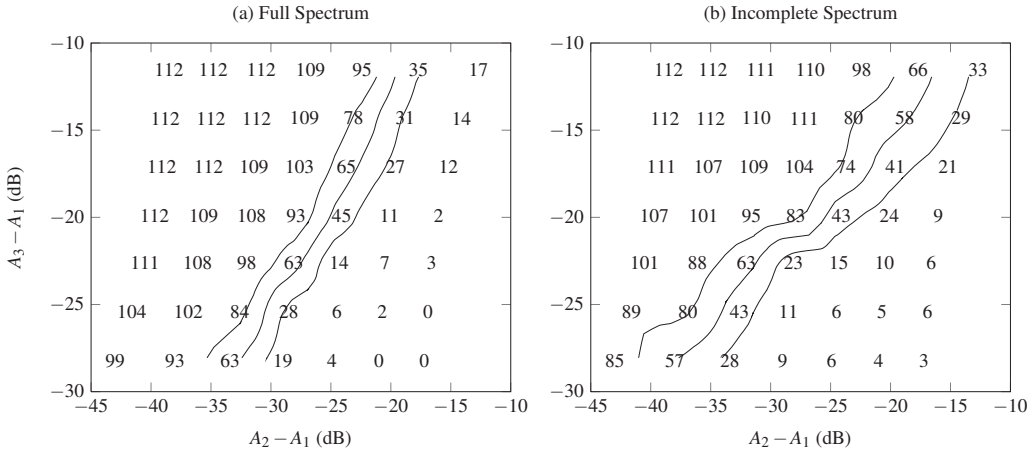

FIG. 3. Total /i/ responses to (a) full- and (b) incomplete-spectrum stimuli as a function of F_2 amplitude (A_2-A_1) and F_3 amplitude (A_3-A_1) (which is a linear function of spectral tilt). Amplitude measurements were calculated at formant frequencies via Fourier transform of the stimuli. Maximum possible number of responses is 112 for each condition. Lines give the 30%, 50%, and 70% crossovers in responses as determined via cubic interpolation.[2]

for changes in F_2 amplitude across the conditions was found, however ($p=0.001$), with an effect size of $d=1.15$. The sign of the difference indicates that F_2 amplitude had a significantly larger effect in the full-spectrum condition. Given the differences between stimuli in the two continua, this suggests that local spectral contrast may play some role in the effect of F_2 amplitude; some full-spectrum stimuli with low-amplitude F_2 peaks were more likely to be heard as /i/ than the corresponding incomplete-spectrum stimuli, which have greater spectral contrast.

E. Discussion

Although masking may play some role in vowel identification in both conditions, differences in responses between the two conditions could be attributed to a reduction in spectral contrast in the full-spectrum condition as F_2 peak level is reduced. In addition, there are several instances where a majority of participants identified incomplete-spectrum stimuli as /i/, even though a spectral local maximum was clearly present at 900 Hz, which is the frequency of the F_2 of /u/. Therefore, simultaneous masking effects may still also play a role in the perception of these stimuli.

It is surprising that there was a significant effect for gross spectral tilt in these stimulus sets. This contradicts results obtained by Kiefte and Kluender (2008), who used similar stimuli. However, Kiefte and Kluender did not also vary amplitude of F_2 in their study. It is possible that with higher levels of the F_3 peak, there is greater perceptual masking of F_2—i.e., with shallower spectral slope, the boundary between /i/ and /u/ is shifted toward higher levels of F_2 amplitude.

If it is true that simultaneous masking can account for much of the response patterns presented here, then it should be the case that eliminating the peak at 900 Hz (i.e., F_2 of /u/) entirely should not have any effect on the perception of many of the stimuli identified as /i/. Likewise, if it is true that local spectral contrast plays a role in the perception of full-spectrum stimuli, then excising the F_2 peak should also not be detectable for many stimuli identified as /i/ in the full-spectrum condition. In the following experiment, listeners are asked if they can detect the elimination of this peak and responses are compared with categorization data.

III. EXPERIMENT 2

The purpose of the second experiment was to determine whether vowel identification can be predicted solely on the basis of whether the presence or absence of the peak at 900 Hz (i.e., F_2 of /u/) can be detected auditorily. Subjects are asked to detect differences between stimuli that are identical, except for the presence/absence of a spectral peak at 900 Hz. If subjects largely identify a stimulus as /u/ when the peak at 900 Hz is detectable, and as /i/ otherwise, this would suggest that much of the relationship between formant amplitude and vowel perception can be attributed to peripheral auditory processes.

A. Participants

Participants were 24 speakers of English with normal hearing. Eligibility criteria were identical to those in experiment 1. No subject participated in both experiments 1 and 2.

B. Stimuli

Stimuli similar to those used in the identification task were presented in pairs that were spectrally identical, except as noted. In two-thirds of the pairs, the F_2 peak around 900 Hz was removed from one of the two stimuli (Fig. 4). Three different pairings were used: (1) identical, unaltered stimuli (*same* trials); (2) one unaltered stimulus followed by one altered stimulus (*different* trials); and (3) one altered stimulus followed by one unaltered stimulus (*different* trials). The stimuli were separated by 250 ms of silence. Presentation of each pair of stimuli was preceded by the phrase "You will now hear the vowel…" identical to that used in experiment 1. The distribution of pairs presented to listeners was equal (i.e., 33.3%).

For incomplete-spectrum stimuli, the altered stimulus was missing the three harmonics around 900 Hz. For full-spectrum stimuli, harmonic levels between 300 (F_1) and 2300 Hz (F_3) were taken from the spectrum of /i/ at the appropriate spectral tilt. At the lowest extreme of F_2 peak amplitude, there is no spectral peak at 900 Hz, and thus, there is no difference between the altered and unaltered stimuli. Responses to these pairs were always recorded as *correct rejection* or *false alarm*.

C. Procedure

Following hearing screening, eligible participants were assigned to one of two conditions: either incomplete- or full-spectrum. Subjects in both conditions completed two tasks: 2AFC vowel identification and difference detection. Presentation of the two tasks were counterbalanced across subjects. The 2AFC task was identical to that in experiment 1, except that each stimulus was presented only six times.

The detection task was given to determine if participants were able to hear the presence versus absence of the F_2 peak at 900 Hz. Participants were asked whether stimuli were *same* or *different*. Each pair of stimuli was presented randomly to the participant once per each of all possible pairings (one *same* and two *different* pairings per stimulus in the 7×7 continuum). Subjects were asked to respond by pressing one of two buttons marked "same" or "diff."

The stimuli were presented at an average level of 72 dB SPL with a roving amplitude of ±1.5 dB through circumaural headphones in a sound-attenuated booth. Both the identification and detection tasks took a total of approximately 60 min to complete. In the detection task, subjects received feedback regarding the correct response via a light above the corresponding button.

D. Results

Results for the identification task in experiment 2 were very similar to those in experiment 1, and are not presented here, except indirectly in Fig. 6. Total number of *hits* across

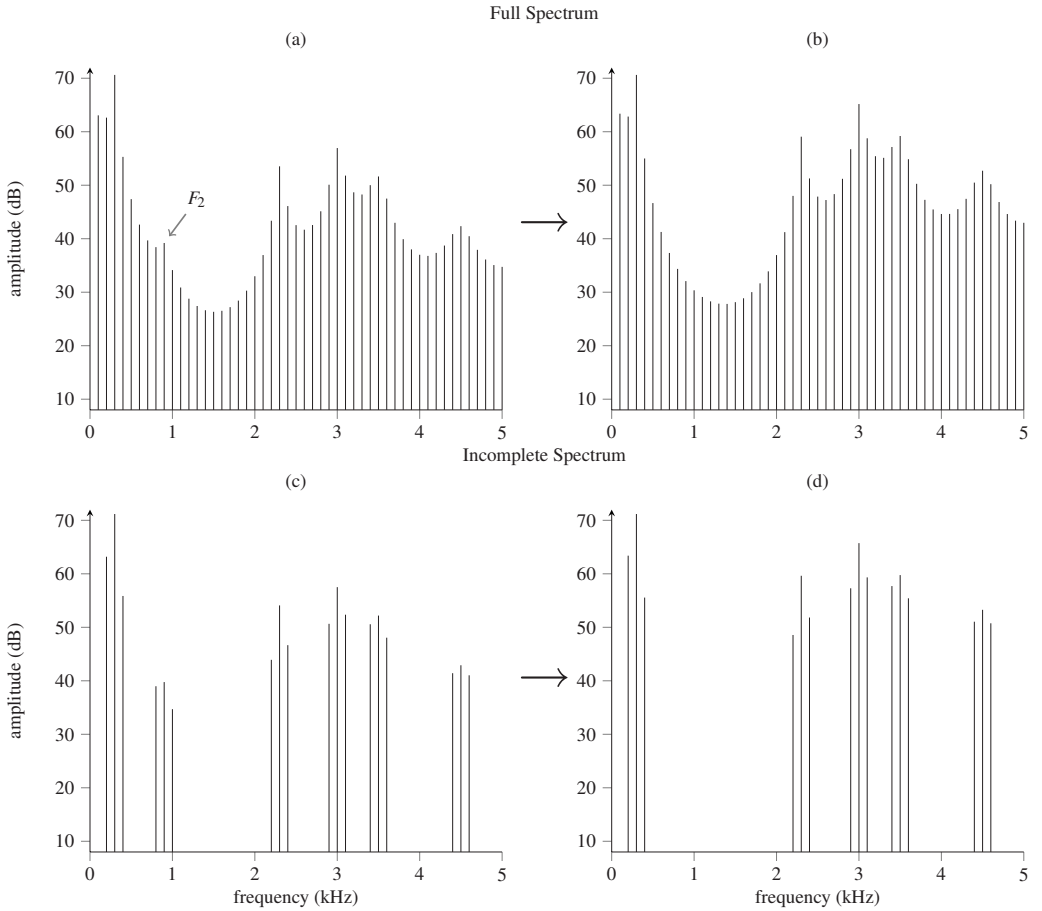

FIG. 4. Spectra of stimuli used in Exp. 2. (a) and (b) have a peak at 900 Hz, while in (b) and (d), the peak has been excised.

subjects for the detection task are represented in Figs. 5(a) and 5(b) for both the full- and incomplete-spectrum stimuli, respectively.

It was impossible to calculate d'-scores (Green and Swets, 1966) from the results as the false-alarm rate was very low (approximately 10% for both groups), resulting in a large number of zeros for *false-alarm*. This suggests that: (a) step sizes were not small enough to obtain an estimate of the slope of the psychometric function; (b) there were not enough trials; and/or (c) there was a substantial conservative bias toward *same* responses. Given that false-alarm rates were very similar for both tasks (9.8% and 10.6% for the full- and incomplete-spectrum condition, respectively), and that the distribution of *false alarms* was roughly uniform across the independent variables, it may be assumed that any response bias is roughly the same for both conditions and not stimulus-dependent. This is also supported by the fact that the data in Fig. 5 are subjectively very similar. In addition, this potential bias effect has no effect on the conclusions regarding the importance of F_2 peak amplitude in vowel perception discussed below.

Similar to the categorization task, hits in the detection

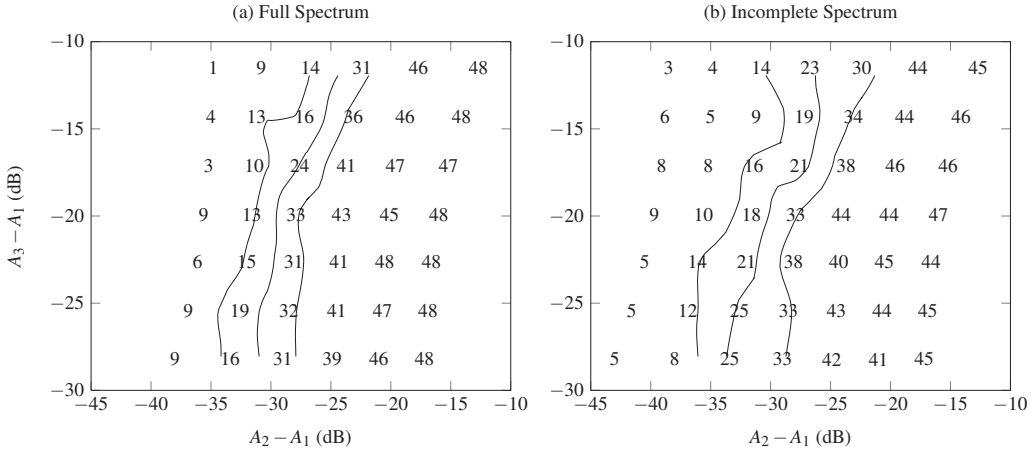

FIG. 5. Total *hits* to (a) full- and (b) incomplete-spectrum stimuli in Exp. 2 as a function of both F_2 amplitude (A_2-A_1) and spectral tilt (A_3-A_1). The left-most column of responses is missing from (a) as there was no F_2 peak at 900 Hz in the unmodified stimulus (i.e., /i/ endpoint). Maximum possible number of responses is 48 for each condition. Lines give the 30%, 50%, and 70% crossovers in responses as determined by cubic interpolation.

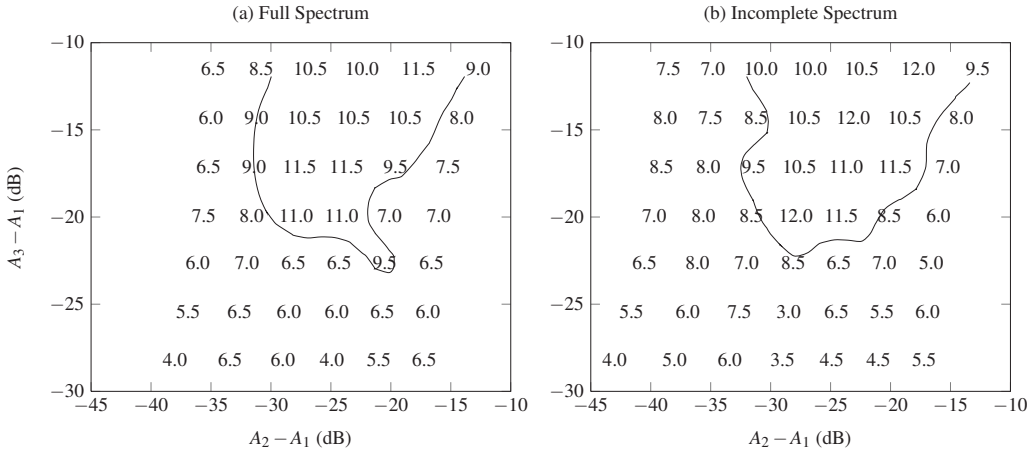

FIG. 6. Total number of subjects for whom hit rate was greater than the proportion of /u/ responses for (a) full- and (b) incomplete-spectrum stimuli in Exp. 2—i.e., the number of subjects who detected the F_2 peak at 900 Hz in the detection task more frequently than they labeled the corresponding stimulus as /u/ in the identification task as a function of both F_2 peak level (A_2-A_1) and spectral tilt (A_3-A_1). Ties were recorded as 0.5. The left-most column of responses is missing from (a) as there was no 900-Hz F_2 peak in the unmodified stimulus. Maximum possible is 12 subjects for each condition, while the expected value, given the null hypothesis, is 6. The contour line delineates the minimum value (9) with which the null hypothesis would be rejected at the $\alpha=.05$ level of significance using a sign test. The opposite hypothesis—that listeners were less likely to detect the F_2 peak at 900 Hz than to identify the corresponding stimulus as /u/—was not significant for any stimulus (maximum value of 3).

task were analyzed using logistic regression, and the coefficients were then subjected to *t*-tests. For both the full- and incomplete-spectrum conditions, there was a significant effect for the amplitude of the F_2 peak at 900 Hz ($p<0.001$ for both conditions; $d=2.9$ and $d=2.3$, respectively). There was also a significant effect for spectral tilt for both conditions ($p<0.001$; $d=1.4$ and $d=1.1$, respectively).

A significant difference was found between the full-spectrum condition and the incomplete-spectrum condition for F_2 amplitude ($p=0.03$, $d=0.94$), indicating that the effect for level was significantly stronger for the full-spectrum condition. No significant difference was found between conditions for changes in spectral tilt ($p=0.40$).

For the majority of stimuli, if a listener successfully responded with *different* for a given stimulus pair (i.e., one stimulus had a spectral peak at 900 Hz and the other did not), they identified the token which had the F_2 peak as /u/ in the identification task. In the full-spectrum condition, data from the signal-detection task could be used to predict 76% of the identification responses. Similarly, the responses from the incomplete-spectrum signal-detection task could be used to predict 71% of responses in the identification task.

Figure 6 gives a graphical representation of the predictability of vowel identification responses, based on the hit rate for corresponding stimuli as a function of both the amplitude of F_2 peak and spectral tilt (which is a linear function of F_3 amplitude). Data in the figures give the total number of subjects for whom the percent hit rate exceeded the total proportion of /u/ responses—i.e., stimuli for which the presence/absence of the F_2 peak at 900 Hz was detected more often than the corresponding stimulus was identified as /u/. The contours in the figures delineate those stimuli that showed statistically significant deviations from predictability (>9)—i.e., subjects identified those stimuli as /i/ significantly more often than would be predicted from the F_2-peak-detection data. As can be seen from the figures, there were a large number of stimuli with F_2 levels between −32 and −15 dB, which were identified as /i/, even though a peak appropriate for the F_2 of /u/ was detectable. This generally was the case when the spectral tilt was relatively shallow—i.e., with higher levels of F_3 and higher formants.

E. Discussion

The signal-detection task provides some evidence that basic psychoacoustic phenomena such as masking and local spectral contrast may play important roles in vowel perception. It is likely that many of the responses in the 2AFC task are attributable to the audibility of the F_2 peak at 900 Hz.

Given the significant difference in the effect of F_2 amplitude between full- and incomplete-spectrum continua in the detection task, it is likely that reduced local spectral contrast plays some role in the detection of spectral peaks in this experiment. Masking also likely plays a role given the large number of misses in the signal-detection task with incomplete-spectrum stimuli, which always contained a peak at 900 Hz, due to the absence of surrounding harmonics.

However, the predictability of categorization data from the detection data is lower than one might expect, given a very strict formant frequency model of vowel identification, in which every spectral peak is assigned to a formant. The present data show that, for a large number of stimuli, listeners identified a stimulus as /i/, even when a peak appropriate for the F_2 of /u/ was clearly audible (Fig. 6). This was generally true for stimuli with extremely shallow spectral slope. This was also true despite the possible conservative bias toward *same* responses in the signal-detection task. Similar results were also obtained for incomplete-spectrum stimuli.

IV. GENERAL DISCUSSION

Using stimuli similar to those used in the present experiments, Hedrick and Nabelek (2004) revealed that reduction in F_2 amplitude for /u/ resulted in an increase in the number of /i/ responses in normal hearing listeners. However, like similar studies (Ainsworth and Millar, 1972; Aaltonen, 1985), only the level of a single formant peak was manipu-

lated. In addition, the full-spectrum stimuli used by Hedrick and Nábělek did not permit separate analysis of the effects of simultaneous masking and local spectral contrast.

The present results show that simultaneous masking and local spectral contrast likely both play some role in vowel perception. Differences in responses between the full- and incomplete-spectrum conditions can possibly be attributed to the effects of local spectral contrast, given that this property was maximized in the incomplete-spectrum stimuli through the absence of harmonics surrounding formant peaks. Identification of some incomplete-spectrum stimuli as /i/ indicates that masking also likely plays a role, given that a peak appropriate for the F_2 of /u/ was present in all such stimuli irrespective of its amplitude. The view that simultaneous masking and local spectral contrast play roles in vowel perception is at least partially supported by the observation that many of the responses in the identification tasks could be predicted by responses to the detection task in experiment 2.

By using two sets of stimuli, the current study was able to provide more information regarding the specific factors responsible for changes in vowel identification with changes in formant amplitude. However, results from the identification and detection tasks revealed that changes in vowel perception cannot be attributed only to simultaneous masking or reduced local spectral contrast. Although both processes may be important in vowel perception, they did not predict the identification of several stimuli used here.

Several stimuli were identified by a majority of listeners as /i/, despite the fact that they could detect a peak at 900 Hz, which should instead predict a majority of /u/ responses. This appears to contradict the relatively narrow view that the frequencies of audible formant peaks are the primary predictors of vowel identity. There was also a very strong effect for spectral tilt in all these stimuli; an increase in the levels of F_3–F_5 of /u/ resulted in an increase in the number of /i/ responses, irrespective of the perceived presence/absence of a peak at 900 Hz. This further contradicts the observation made by Kiefte and Kluender (2008), who found that spectral tilt played a very minor role in similar stimuli. However, it should be noted that only two of the present stimuli (the /i/ and /u/ endpoints of the full-spectrum continuum) are the same as those used in the study by Kiefte and Kluender.

A similar result regarding the role of higher formant level, or spectral tilt, was obtained by Bonneau and Laprie (1998), who found that raising the level of F_3 of /u/ by 20 dB resulted in a majority of /i/ or /e/ responses. The results in the present study were not obviously as drastic, however. Over a range of 16.6 dB in F_3 level, no change in spectral tilt resulted in a majority of /i/ responses for an unattenuated F_2 of /u/ (i.e., F_2 level between −17.2 and −12.7 dB—the far right column of each figure in Fig. 3). However, /e/ was not given as a possible response category in the present experiments. Nevertheless, there were statistically significant effects for spectral tilt in all conditions in both experiments, indicating that the conclusions made by Bonneau and Laprie are basically correct.

The most immediate conclusion that can be drawn from this is that some spectral shape information is important in the perception of synthetic monophthongs; it is possible that the relationship between formant frequency and vowel quality is spurious and that vowel perception is more directly related to global spectral details, which necessarily include spectral peak information (Bladon and Lindblom, 1981). Another possibility is that more general spectral properties are an important factor in the psychoacoustics of peak-detection in that the perceived frequency of a formant peak is determined by multiple factors, including formant amplitude (Chistovich *et al.*, 1979; Chistovich and Lublinskaya, 1979). Given the present data, however, the relationship between perceived formant frequency and physical vowel spectrum is much more complicated than the center-of-gravity hypothesis would predict. For example, although the two peaks corresponding to F_1 and F_2 of /u/ may be merged perceptually, the theory does not explain why an increase in the amplitude of F_3 of /u/ would result in an increase in the total number of /i/ responses. In addition, the peaks corresponding to the F_1 and F_2 of /u/ in this study are 4.8 bark apart—well beyond the 3.5 bark window of integration proposed by Chistovich and colleagues.

Alternatively, from the point of view of a formant frequency model of vowel perception, it is clear that some mechanism of filtering out spurious spectral peaks must be included. In systems for automatic identification of formant frequencies (e.g., automatic speech recognition), spectral peaks are frequently pruned, prior to assignment to vowel formants. Although such peaks may result from overspecified linear-prediction models (McCandless, 1974), they can also occur via direct spectral analysis (Schafer and Rabiner, 1970). Given that even spectral shoulders influence perception (Assmann and Summerfield, 1989; Lea and Summerfield, 1994), a spectral analysis would need to be relatively liberal with respect to identification of possible formant candidates. However, human listeners must use some criterion for segregating spurious acoustic properties in perception. It has been noted that, "outside of the soundproof, anechoic chamber, properties of the recorded soundwave will not correspond in a simple way with properties of the spoken sound wave" (Darwin, 1984). Some perceptual mechanism must exist that segregates such spurious peaks.

One strategy for excluding such peaks from analysis is formant tracking (McCandless, 1974). While similar phenomena may be observed in human perception (Darwin, 1981; Bregman, 1990), it is not relevant here due to the stationary nature of the target stimuli. However, Schafer and Rabiner (1970) use the relationships between formant levels in selecting spectral peaks. For example, a peak is not assigned to F_2 if it falls below some threshold determined from an empirical analysis of spectra from male speakers that is a function of both F_1 and F_2 frequency. From their data, F_2 amplitude should be no less than −21.5 dB relative to F_1 amplitude for F_1 and F_2 frequencies of 300 and 900 Hz, respectively.[3] Interestingly, this agrees with Ainsworth and Millar (1972), who found that perception of two-formant stimuli changed markedly when F_2 level was more than 20 dB below that of F_1. The results of experiment 1 suggest that such a model may be appropriate for perception of the present stimuli with one addition: This threshold must also be modulated by the relative balance between low- and high-

frequency energy (i.e., spectral tilt), or the amplitude of the F_3 peak. It should be noted that this threshold has nothing to do with the *audibility* of a spectral peak, however.

Another explanation for the pattern of data—i.e., that a majority of listeners identified several stimuli as /i/ when they could detect the absence of a spectral peak at 900 Hz when excised—is that the *psychoacoustic* difference between stimuli in many stimulus pairs in the detection task may not be large enough to trigger a *phonetic* difference in the vowel identification task (Klatt, 1982). While this phenomenon could still be related to the peak-selection problem described above, it could also be more subtle as, for example, in a case where no vowel-like spectral peak is heard, yet a change in timbre is still perceived.

One phenomenon that has received little attention in speech-perception research, and which may explain some of the present results, is the perception of simultaneous vowels with same fundamental frequency. For example, Zwicker (1984) and Assmann and Summerfield (1989) found that listeners can identify two simultaneous vowels with identical f_0 with an accuracy much better than chance. Summerfield and Assmann (1989) found that listeners perceive concurrent vowels as consisting of a "dominant" vowel against a background of a second vowel. It is possible that listeners in the present experiment actually heard concurrent /i/ and /u/, but gave responses on the basis of a perceived dominant stimulus. This possibility is also supported by the fact that summation of the /i/ and /u/ endpoints would result in a stimulus with a high-amplitude peak at 2300 Hz (corresponding to the F_3 of /u/ and the F_2 of /i/), and a lower-amplitude peak at 900 Hz corresponding to the F_2 of /u/. It is expected, therefore, that listeners in this study would associate a clearly audible peak at 900 Hz with the F_2 of a background /u/ and still respond on the basis of the perceived foreground vowel /i/, especially when the spectral slope was relatively shallow (i.e., elevated high-frequency formants).

In modeling listeners' responses to concurrent vowels, Assmann and Summerfield (1989) found that models that emphasize spectral peaks and shoulders gave the best fit to their data. Although the best model tested de-emphasized properties such as spectral tilt and relative formant amplitude, it was not completely insensitive to these properties. In addition, a spectral peak-based model that includes formant amplitude more explicitly was never tested. Their finding that listeners could identify concurrent vowels in the absence of any formant amplitude information does not preclude the possibility that this information does indeed help in segregating them perceptually, when natural covariation of formant frequency and amplitude is present.

In the absence of differing source characteristics, it is possible that the amplitudes of formants can help segregate competing vowels by virtue of the established relationships between formant frequency and amplitude (Fant, 1956, 1972; Stevens, 1998). Listeners' experience with this natural variation can aid in what Bregman (1990) refers to as schema-based segregation, which is based on learned patterns as opposed to fundamental psychoacoustic processes. It is known that this type of natural covariation across multiple stimulus properties contributes to the resilience of perception in the face of extreme signal degradation (Kluender and Kiefte, 2006), and it is not unbelievable that formant amplitude can aid in signal segregation in this manner.

Finally, it is not known whether similar effects would be observed in more natural-sounding dynamically specified vowels. For example, Kiefte and Kluender (2005) found that effects of spectral tilt were largely mitigated in stimuli with changing formant frequencies, and it is possible that the effects of formant amplitude observed here may be likewise attenuated in stimuli with inherent spectral change.

In summary, additional evidence is presented that formant amplitude does play a role in vowel perception. This effect is likely related to three factors: simultaneous masking of spectral peaks, local spectral contrast near spectral peaks, and a third factor not at all related to peripheral auditory phenomena. This third factor could include auditory segregation of spectral peaks that fall below some threshold, which is determined by listeners' experience with natural variation between formant frequency and amplitude in naturally produced speech.

ACKNOWLEDGMENTS

This research was supported by a grant to the first author from the Social Sciences and Humanities Research Council of Canada. The authors would also like to thank Terrance M. Nearey, Peter F. Assmann, the associate editor Rochelle S. Newman, and two anonymous reviewers for comments and suggestions on earlier versions of this manuscript.

[1]Nearey and Kiefte (2003) found that adding relative formant amplitude information significantly improved model fit to vowel perception data, and that such models compared favorably to models of global spectral shape (Hermansky, 1990). These results are surprising, as stimuli used in these experiments were generated via cascade synthesis with constant formant bandwidths—i.e., formant amplitude was guaranteed to be predictable on the basis of formant frequency. These results suggest that synthesis parameters for formant frequency are inadequate for predicting listeners' responses and that some auditory processing must be accounted for in a model of vowel perception.

[2]The relationship between F_2 amplitude and spectral tilt is not orthogonal. The full range in F_2 amplitude in the original series is 21.4 dB, while the full range of F_2 amplitude change due solely to the effect of manipulation of spectral tilt was approximately 4.5 dB within each level of F_2 amplitude (empirical measurements from Fourier transform). The effect of the spectral tilt filter on F_2 peak amplitude is roughly half of that predicted by the dB/octave relationship, as the second formant peak is close to the spectral tilt filter corner frequency. All analyses for the effect of F_2 amplitude use empirical amplitude measurements as covariates.

[3]This takes into account their spectrum equalizing curve as well as first formant frequency.

Aaltonen, O. (**1985**). "The effect of relative amplitude levels of F2 and F3 on the categorization of synthetic vowels," J. Phonetics **13**, 1–9.

Ainsworth, W. A., and Millar, J. B. (**1972**). "The effect of relative formant amplitude on the perceived identity of synthetic vowels," Lang Speech **15**, 328–341.

Assmann, P. F. (**1991**). "The perception of back vowels: Center of gravity hypothesis," Q. J. Exp. Psychol. **43A**, 423–448.

Assmann, P. F., and Nearey, T. M. (**1987**). "Perception of front vowels: The role of harmonics in the first formant region," J. Acoust. Soc. Am. **81**, 520–534.

Assmann, P. F., and Summerfield, Q. (**1989**). "Modeling the perception of concurrent vowels: Vowels with the same fundamental frequency," J. Acoust. Soc. Am. **85**, 327–338.

Bernstein, J. (**1981**). "Formant-based representation of auditory similarity among vowel-like sounds," J. Acoust. Soc. Am. **69**, 1132–1144.

Bladon, R. A. W., and Fant, G. (**1978**). "A two-formant model and the cardinal vowels," Speech Transm. Lab. Q. Prog. Status Rep. **1**, 1–8.
Bladon, R. A. W., and Lindblom, B. (**1981**). "Modeling the judgement of vowel quality differences," J. Acoust. Soc. Am. **69**, 1414–1422.
Bonneau, A., and Laprie, Y. (**1998**). "The effect of modifying formant amplitudes on the perception of French vowels generated by copy synthesis," in Proceedings of the Fifth International Conference on Spoken Language Processing, Paper No. 260.
Bregman, A. S. (**1990**). *Auditory Scene Analysis: The Perceptual Organization of Sound* (MIT, Cambridge, MA).
Carlson, R., Fant, G., and Granström, B. (**1975**). "Two-formant models, pitch, and vowel perception," *Auditory Analysis and Perception of Speech* (Academic, London), pp. 55–82.
Carlson, R., Granström, B., and Fant, G. (**1970**). "Some studies concerning perception of isolated vowels," Speech Transm. Lab. Q. Prog. Status Rep. **11**, 19–35.
Chistovich, I. A., and Chernova, E. I. (**1986**). "Identification of one- and two-formant steady-state vowels: A model and experiments," Speech Commun. **5**, 3–16.
Chistovich, L. A., and Lublinskaya, V. V. (**1979**). "The 'center of gravity' effect in vowel spectra and critical distance between the formants: Psychoacoustical study of the perception of vowel-like stimuli," Hear. Res. **1**, 185–195.
Chistovich, L. A., Sheiken, R. L., and Lublinskaja, V. V. (**1979**). "Centres of gravity and spectral peaks as the determinants of vowel quality," *Frontiers of Speech Communication Research*, edited by B. Lindblom and S. Öman, (Academic, London), pp. 143–156.
Darwin, C. J. (**1981**). "Perceptual grouping of speech components differing in fundamental frequency and onset-time," Q. J. Exp. Psychol. **33A**, 185–207.
Darwin, C. J. (**1984**). "Perceiving vowels in the presence of another sound: Constraints on formant perception," J. Acoust. Soc. Am. **76**, 1636–1647.
de Cheveigné, A., and Kawahara, H. (**1999**). "Missing-data model of vowel identification," J. Acoust. Soc. Am. **105**, 3497–3508.
Delattre, P., Liberman, A. M., Cooper, F. S., and Gerstman, L. J. (**1952**). "An experimental study of the acoustic determinants of vowel color: Observations on one- and two-formant vowels synthesized from spectrographic patterns," Word **8**, 195–210.
Fant, C. G. M. (**1956**). "On the predictability of formant levels and spectrum envelopes from formant frequencies," in *For Roman Jakobson: Essays on the Occasion of His Sixtieth Birthday*, edited by M. Halle, (Mouton, The Hague), pp. 109–120.
Fant, G. (**1972**). "Vocal tract wall effects, losses, and resonance bandwidths," Speech Transm. Lab. Q. Prog. Status Rep. **13**, 28–52.
Green, D. M., and Swets, J. W. (**1966**). *Signal Detection Theory and Psychophysics* (Krieger, Huntington, NY).
Gumpertz, M., and Pantula, S. G. (**1989**). "A simple approach to inference in random coefficient models," Am. Stat. **43**, 203–210.
Hedrick, M. S., and Nabelek, A. K. (**2004**). "Effect of F2 intensity on identity of /u/ in degraded listening conditions," J. Speech Lang. Hear. Res. **47**, 1012–1021.
Hermansky, H. (**1990**). "Perceptual linear predictive (PLP) analysis of speech," J. Acoust. Soc. Am. **87**, 1738–1752.
Hillenbrand, J., Getty, L. A., Clark, M. J., and Wheeler, K. (**1995**). "Acoustic characteristics of American English vowels," J. Acoust. Soc. Am. **97**, 3099–3111.
Ito, M., Tsuchida, J., and Yano, M. (**2001**). "On the effectiveness of whole spectral shape for vowel perception," J. Acoust. Soc. Am. **110**, 1141–1149.
Jacewicz, E. (**2005**). "Listener sensitivity to variations in the relative amplitude of vowel formants," ARLO **6**, 118–124.
Jacewicz, E., and Fox, R. A. (**2008**). "Amplitude variations in coarticulated vowels," J. Acoust. Soc. Am. **123**, 2750–2768.
Kakusho, O., Hirato, H., and Kato, K. (**1971**). "Some experiments of vowel perception by harmonic synthesizer," Acustica **24**, 179–190.
Kiefte, M., and Kluender, K. R. (**2005**). "The relative importance of spectral tilt in monophthongs and diphtongs," J. Acoust. Soc. Am. **117**, 1395–1404.
Kiefte, M., and Kluender, K. R. (**2008**). "Absorption of reliable spectral characteristics in auditory perception," J. Acoust. Soc. Am. **123**, 366–376.
Kiefte, M., Kluender, K. R., and Rhode, W. S. (**2002**). "Synthetic speech stimuli spectrally normalized for nonhuman cochlear dimensions," ARLO **3**, 41–46.
Klatt, D. H. (**1980**). "Software for a cascade/parallel formant synthesizer," J. Acoust. Soc. Am. **67**, 971–995.
Klatt, D. H. (**1982**). "Prediction of perceived phonetic distance from critical-band spectra: A first step," IEEE Trans. Acoust., Speech, Signal Process. **7**, 1278–1281.
Klatt, D. H., and Klatt, L. C. (**1990**). "Analysis, synthesis, and perception of voice quality variations among female and male talkers," J. Acoust. Soc. Am. **87**, 820–857.
Kluender, K. R., and Kiefte, M. (**2006**). "Speech perception within a biologically realistic information-theoretic framework," *Handbook of Psycholinguistics*, 2nd ed., edited by M. A. Gernsbacher and M. Traxler, (Elsevier, London), pp. 153–199.
Lea, A. P., and Summerfield, Q. (**1994**). "Minimal spectral contrast of formant peaks for vowel recognition as a function of spectral slope," Percept. Psychophys. **56**, 379–391.
Leek, M. R., Dorman, M. F., and Summerfield, Q. (**1987**). "Minimum spectral contrast for vowel identification by normal-hearing and hearing-impaired listeners," J. Acoust. Soc. Am. **81**, 148–154.
Lindblom, B., Diehl, R., and Creeger, C. (**2009**). "Do 'dominant frequencies' explain the listener's response to formant and spectrum shape variations?," Speech Commun. **51**, 622–629.
Lindqvist, J., and Pauli, S. (**1968**). "The role of relative spectrum levels in vowel perception," Speech Transm. Lab. Q. Prog. Status Rep. **9**, 12–15.
McCandless, S. S. (**1974**). "An algorithm for automatic formant extraction using linear prediction spectra," IEEE Trans. Acoust., Speech, Signal Process. **22**, 135–141.
McCullagh, P., and Nelder, J. A. (**1989**). *Generalized Linear Models*, 2nd ed. (Chapman and Hall, London).
Miller, J. D. (**1984**). "Auditory processing of the acoustic patterns of speech," Arch. Otolaryngol. **110**, 154–159.
Miller, R. L. (**1953**). "Auditory tests with synthetic vowels," J. Acoust. Soc. Am. **25**, 114–121.
Moore, B. C. J., and Glasberg, B. R. (**1983a**). "Masking patterns for synthetic vowels in simultaneous and forward masking," J. Acoust. Soc. Am. **73**, 906–917.
Moore, B. C. J., and Glasberg, B. R. (**1983b**). "Suggested formulae for calculating auditory-filter shapes and excitation patterns," J. Acoust. Soc. Am. **74**, 750–753.
Nábělek, A. K., Czyzewski, Z., and Krishnan, L. A. (**1992**). "The influence of talker differences on vowel identification by normal-hearing and hearing-impaired listeners," J. Acoust. Soc. Am. **92**, 1228–1246.
Nearey, T. M., and Assmann, P. F. (**1986**). "Modeling the role of inherent spectral change in vowel identification," J. Acoust. Soc. Am. **80**, 1297–1308.
Nearey, T. M., and Kiefte, M. (**2003**). "Comparison of several proposed representations of vowel spectra," in Proceedings of the 15th International Congress of Phonetic Sciences, pp. 1005–1008.
Nearey, T. M., and Levitt, A. G. (**1974**). "Evidence for spectral fusion in dichotic release from upward spread of masking," Haskins Laboratories: Status Rep. Speech Res. **SR-39**, 81–89.
Peterson, G. E., and Barney, H. L. (**1952**). "Control methods used in a study of the vowels," J. Acoust. Soc. Am. **24**, 175–184.
Rand, T. C. (**1974**). "Dichotic release from masking for speech," J. Acoust. Soc. Am. **55**, 678–680.
Rosner, B. S., and Pickering, J. B. (**1994**). *Vowel Perception and Production* (Oxford University Press, Oxford).
Schafer, R. W., and Rabiner, L. R. (**1970**). "System for automatic formant analysis of voiced speech," J. Acoust. Soc. Am. **47**, 634–648.
Schwartz, J.-L., and Escudier, P. (**1989**). "A strong evidence for the existence of a large-scale integrated spectral representation in vowel perception," Speech Commun. **8**, 235–259.
Stevens, K. N. (**1998**). *Acoustic Phonetics* (MIT, Cambridge, MA).
Summerfield, Q., and Assmann, P. F. (**1989**). "Auditory enhancement and the perception of concurrent vowels," Percept. Psychophys. **45**, 529–536.
Summerfield, Q., Sidwell, A., and Nelson, T. (**1987**). "Auditory enhancement of changes in spectral amplitude," J. Acoust. Soc. Am. **81**, 700–708.
Turner, C. W., and Van Tasell, D. J. (**1984**). "Sensorineural hearing loss and the discrimination of vowel-like stimuli," J. Acoust. Soc. Am. **75**, 562–565.
Zahorian, S. A., and Jagharghi, A. J. (**1993**). "Spectral-shape features versus formants as acoustic correlates for vowels," J. Acoust. Soc. Am. **94**, 1966–1982.
Zwicker, U. T. (**1984**). "Auditory recognition of diotic and dichotic vowel pairs," Speech Commun. **3**, 265–277.

Influence of viscoelastic and viscous absorption on ultrasonic wave propagation in cortical bone: Application to axial transmission

Salah Naili[a] and Mai-Ba Vu
Laboratoire Modélisation et Simulation Multi-Échelle, Université Paris-Est, UMR 8208 CNRS, 94010 Créteil Cédex, France

Quentin Grimal and Maryline Talmant
UPMC Univiversité Paris 6, UMR 7623 CNRS, LIP, F-75005 Paris, France and Laboratoire d'Imagerie Paramétrique, F-75005 Paris, France

Christophe Desceliers and Christian Soize
Laboratoire Modélisation et Simulation Multi-Échelle, Université Paris-Est, UMR 8208 CNRS, 77454 Marne la Vallée Cédex 2, France

Guillaume Haïat
Laboratoire de Recherches Orthopédiques, Université Paris 7, UMR 7052 CNRS, B2OA, 75010 Paris, France

(Received 24 July 2009; revised 6 February 2010; accepted 9 February 2010)

Cortical bone and the surrounding soft tissues are attenuating and heterogeneous media, which might affect the signals measured with axial transmission devices. This work aims at evaluating the effect of the heterogeneous acoustic absorption in bone and in soft tissues on the bone ultrasonic response. Therefore, a two-dimensional finite element time-domain method is derived to model transient wave propagation in a three-layer medium composed of an inhomogeneous transverse isotropic viscoelastic solid layer, sandwiched between two viscous fluid layers. The model couples viscous acoustic propagation in both fluid media with the anisotropic viscoelastic response of the solid. A constant spatial gradient of material properties is considered for two values of bone thicknesses (0.6 and 4 mm). In the studied configuration, absorption in the surrounding fluid tissues does not affect the results, whereas bone viscoelastic properties have a significant effect on the first arriving signal (FAS) velocity. For a thin bone, the FAS velocity is governed by the spatially averaged bone properties. For a thick bone, the FAS velocity may be predicted using a one-dimensional model. © *2010 Acoustical Society of America.* [DOI: 10.1121/1.3353091]

PACS number(s): 43.80.Ev, 43.20.Mv, 43.20.Px, 43.40.Rj [CCC] Pages: 2622–2634

I. INTRODUCTION

Different metabolic diseases such as osteoporosis may affect bone quality (WHO Study Group, 1994), resulting in a decrease in bone mass and micro-architectural deterioration of bone tissue, which implies an increase in bone fragility. The diaphysis of long bones such as radius and femur is mainly constituted of cortical bone. Investigating cortical bone quality is of interest (Rico, 1997) because it accounts for about 80% of the skeleton, supports most of the load of the body, and is mainly involved in osteoporotic fractures (Seeley *et al.*, 1991). Moreover, cortical bone quality has recently been shown to be determinant for bone mechanical stability (Mayhew *et al.*, 2005) at the femur neck.

In axial transmission (AT) technique (which is particularly adapted to cortical long bone evaluation), both ultrasound emitter and receivers, are placed in the same side of the investigated skeletal site, along a direction close to the long bone axis. The earliest event or wavelet (usually called first arriving signal, FAS) of the multicomponent signal recorded by the receivers has been the most widely investigated. The wave velocity associated with this signal, which is measured in the time domain, can be used to discriminate healthy subjects from osteoporotic patients, and is therefore considered as a relevant index of bone status (Hans *et al.*, 1999; Muller *et al.*, 2005; Stegman *et al.*, 1995; Talmant *et al.*, 2009; Weiss *et al.*, 2000). Both experimental (Bossy *et al.*, 2004c; Raum *et al.*, 2005) and simulation studies (Bossy *et al.*, 2004b) have shown that the FAS velocity was related to different bone properties (bone mineral density, cortical thickness and bone elastic properties). Numerical simulations have been employed to show that when the cortical thickness is comparable or larger than the wavelength, the type of wave contributing to the FAS corresponds to a lateral wave, whereas when the wavelength is larger than the cortical thickness divided by four, the received signal corresponding to the FAS comes from the first symmetric Lamb wave mode (S_0) guided by the cortical thickness (Bossy *et al.*, 2002).

Cortical bone is a complex medium from a biomechanical point of view. Its elastic behavior has been described as transverse isotropic in different works (Dong and Guo, 2004;

[a]Author to whom correspondence should be addressed. Electronic mail: salah.naili@univ-paris-est.fr

 0001-4966/2010/127(4)/2622/13/$25.00

Haïat *et al.*, 2009). At the macroscopic scale, porosity in the radial direction (which is associated with the cross-section of the bone) is heterogeneous at all ages and for both genders (Bousson *et al.*, 2001; Thomas *et al.*, 2005): the mean porosity in the endosteal region (inner part of the bone) is significantly higher than in the periosteal region (outer part of the bone). Moreover, cortical bone is affected by age-related bone resorption and osteoporosis. It undergoes a thinning of the cortical shell, as well as an increase in porosity, mainly in the endosteal region (Bousson *et al.*, 2001). An increase in porosity is likely to affect bone material properties (mass density and elasticity) (Fritsch and Hellmich, 2007), which may in turn impact bone quality (Ammann and Rizzoli, 2003). Similarly, a thinning of the cortical shell is an important indicator of decreasing bone strength and of fracture risk (Turner, 2002). Moreover, cortical bone is a strongly attenuating medium where ultrasonic propagation occurs with losses (Han *et al.*, 1996; Lakes *et al.*, 1986; Langton *et al.*, 1990; Lees and Klopholz, 1992; Serpe and Rho, 1996). Ultrasonic attenuation may be due to the viscoelastic behavior of the bone matrix, as well as to the presence of the pores (through scattering effects of the ultrasonic wave) (Sasso *et al.*, 2007, 2008). The feasibility of frequency dependent attenuation coefficient measurements has been demonstrated in bovine cortical bone samples of a scale of the centimeter (Sasso *et al.*, 2007). Interestingly, broadband ultrasonic attenuation (BUA, defined as the slope of the curve of the frequency dependent attenuation coefficient) measurements have recently been shown to be significantly related to the microstructure, as well as to bone physical properties such as mass and bone mineral densities (Sasso *et al.*, 2008). Therefore, BUA has been evoked as a suitable parameter for cortical bone quality estimation. Similarly, human soft tissues such as skin, fat, and muscles (between the transducers and bone) or bone marrow (inside cortical bone) are also media where ultrasonic attenuation has been measured.

The potential advantage of numerical simulation tools over experimental approaches is that it can be used to determine the influence of each bone property independently, which is difficult when working with real samples, as all bone geometrical and mechanical properties evolve in parallel. Modeling the FAS in AT experiment is a time-domain elasto-acoustic problem. Time-domain analytical methods have been used in the past to solve the elasto-acoustic wave system in simple AT models (Grimal and Naili, 2006; Macocco *et al.*, 2005, 2006). Bossy *et al.* (2004b) have assessed the influence of a gradient of longitudinal wave velocity due to a heterogeneous distribution of porosity on the FAS velocity. More recently, our group has determined [using the COMSOL Multiphysics software (COMSOL Multiphysics, 2005)] the effect of heterogeneous material bone properties on the ultrasonic response, and more specifically, on the FAS velocity using 2-D finite element model (FEM) (Haïat *et al.*, 2009). Most models of AT developed in the past have considered cortical bone and the surrounding soft tissues as an elastic material. However, the influence of ultrasonic attenuation (in bone and/or in the surrounding soft tissues) on the ultrasonic response of the investigated anatomical site in the framework of the AT device remains unclear. Studying the influence of attenuation in bone on the FAS velocity is of particular interest since BUA has been suggested as a potential indicator of bone status. In addition, the determination of the sensitivity of the ultrasonic response of bone to attenuation variations may be considered as a first step toward the resolution of the inverse problem.

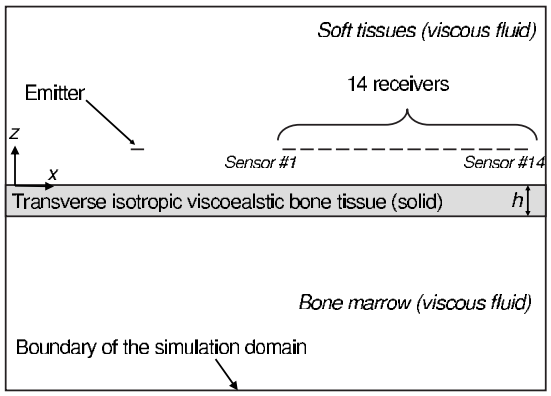

FIG. 1. Schematic representation of the simulation domain corresponding to a three-layer medium. The emitter and receivers are indicated by indents.

The aim of this paper is to assess the effect of the viscoelastic nature of cortical bone and of the viscous nature of the surrounding soft tissues on the ultrasonic response obtained with an AT device. Here, bone is modeled as an anisotropic (transverse isotropic) heterogeneous (a gradient of material properties in the radial direction is considered) viscoelastic material, and the surrounding soft tissues are modeled as homogeneous viscous liquids. More specifically, we aim at investigating the potentiality of 2-D finite element numerical simulation tools to assess the sensitivity of the FAS velocity to variations of different viscoelastic parameters.

With this introduction as background, a 2-D finite element model briefly described in Sec. II is used to compute the dependence of the FAS velocity on all viscoelastic coefficients of cortical bone at the organ level, as well as on the viscous nature of the surrounding soft tissues. The models used for the viscoelastic tensor are presented and discussed. Section III describes (i) the sensitivity of the FAS velocity to changes of each viscoelastic coefficient for homogeneous material properties, (ii) the effect of a constant gradient of each viscoelastic coefficient affecting the FAS velocity, and (iii) the effect of a constant gradient of porosity. Results are then discussed in Sec. IV.

II. METHOD

A. Simulation of the axial transmission configuration

The geometrical configuration used in the present study is the same as the one used by Haïat *et al.* (2009), and readers are referred to this previous study for details on the configuration. Briefly, cortical bone is modeled as a two-dimensional multilayer medium composed of one heterogeneous viscoelastic transverse isotropic solid layer, sandwiched between two homogeneous viscous fluid layers, as shown in Fig. 1. The cortical thickness is denoted h and the direction z corresponds to the bone radial direction.

In the simulation, a pressure source is positioned in the fluid and the excitation signal is a Gaussian pulse with a center frequency of 1 MHz, identical to the one given and plotted by Desceliers *et al.* (2008). The geometrical arrangement shown in Fig. 1 mimics that of the probe developed by the "Laboratoire d'Imagerie Paramétrique" (France) (Bossy *et al.*, 2004a). The FAS velocity is then determined following the procedure used in experiments with the actual probe (Bossy *et al.*, 2004a). Signals are collected for each one of the 14 receivers located in the soft tissue. The time t_i of the first maximum of each of the 14 signals recorded at the sensor #i was then determined using a thresholding method. The FAS velocity estimate is then given by the slope of the position of each sensor #i versus t_i, obtained through a least-square linear regression.

Moreover, we also consider the dependence of the amplitude of the first maximum of the signal recorded at the sensor #i as function of i, in order to assess the effect of viscoelasticity on the amplitude of the FAS.

In both fluid media, the formulation is written in terms of pressure. The equation of propagation in the viscous fluid is given by

$$\rho_f \ddot{p} = \eta_f \Delta \dot{p} + K \Delta p, \tag{1}$$

where $p(\mathbf{x};t)$ denotes the pressure field, ρ_f mass density, K the fluid compressibility, and η_f the bulk viscosity of the fluid. The acoustic wave velocity c_f in absence of viscosity ($\eta_f=0$) is given by $c_f=\sqrt{K/\rho_f}$.

In the solid media, the formulation is written in terms of displacement. Neglecting body forces, the momentum conservation equation writes

$$\text{div}\ \boldsymbol{\sigma} = \rho_s \ddot{\mathbf{u}}, \tag{2}$$

where $\boldsymbol{\sigma}(\mathbf{x};t)$ is the stress tensor, ρ_s is the bone mass density, and $\mathbf{u}(\mathbf{x};t)$ is displacement vector.

Cortical bone is modeled as an heterogeneous material using the linear theory of viscoelastic without memory. In this theory, the stress tensor $\boldsymbol{\sigma}$ is linearly related to the strain tensor $\boldsymbol{\epsilon}(\mathbf{x};t)$ and to the rate-of-deformation tensor $\dot{\boldsymbol{\epsilon}}(\mathbf{x};t)$

$$\boldsymbol{\sigma} = \mathbb{C}\boldsymbol{\epsilon} + \mathbb{E}\dot{\boldsymbol{\epsilon}}, \tag{3}$$

where $\mathbb{C}(\mathbf{x})$ is the stiffness tensor and $\mathbb{E}(\mathbf{x})$ is the viscoelastic tensor. For a 2-D transverse isotropic medium (in the plane defined by (x,z)), the stiffness tensor writes

$$\mathbb{C} = \begin{pmatrix} C_{11}(z) & C_{13}(z) & 0 \\ C_{13}(z) & C_{33}(z) & 0 \\ 0 & 0 & C_{55}(z) \end{pmatrix}, \tag{4}$$

where all stiffness coefficients only depend on z because only the heterogeneity in the radial direction is modeled, similarly as what was done by Haïat *et al.* (2009).

Cortical bone has been shown to be a significantly anisotropic medium in terms of ultrasonic attenuation, as BUA values measured in the axial direction are significantly smaller than BUA values obtained in the radial and tangential directions (Lakes *et al.*, 1986; Lees and Klopholz, 1992; Sasso *et al.*, 2007). Therefore, we have considered an anisotropic (transverse isotropic) tensor $\mathbb{E}$ to describe the bone dissipative behavior. In order to retrieve a physiological range of variation for the attenuation in cortical bone, we have used a study carried out with bovine cortical bone samples (Sasso *et al.*, 2007) because we could not find in the literature a sufficient amount of data in human cortical.

Moreover, BUA values depend significantly on bone mineral density and on mass density (Sasso *et al.*, 2008), which are two quantities closely related to the porosity. As the spatial distribution of porosity is heterogeneous in cortical bone (Bousson *et al.*, 2001), the viscoelastic properties of cortical bone are also expected to be spatially dependent. Therefore, we have considered an heterogeneous behavior of the viscoelastic tensor $\mathbb{E}$, similar to the one given in Eq. (4), and the viscoelastic tensor $\mathbb{E}$ writes

$$\mathbb{E} = \begin{pmatrix} \eta_{11}(z) & \eta_{13}(z) & 0 \\ \eta_{13}(z) & \eta_{33}(z) & 0 \\ 0 & 0 & \eta_{55}(z) \end{pmatrix}, \tag{5}$$

where all viscoelastic coefficients, written using the Voigt notation, only depend on z.

The boundary conditions at the edges of the simulation domain are identical to the one used by Desceliers *et al.* (2008). At both interfaces between the fluid layers and the solid layer, the boundary conditions in terms of displacement and normal stresses are taken into account. The model therefore fully describes the fluid-structure interaction between the three sub-domains. For each computation, around 186 000 triangular elements are used, resulting in about 393 000 degrees of freedom. The simulation software is the 3.5 version of COMSOL Multiphysics (2005).

The physiological variations of the different material properties are indicated in Appendix.

B. Lamb and bulk wave modes

When the thickness h is smaller than the wavelength λ (typically $h/\lambda < 0.25$), the FAS velocity tends toward the so-called plate velocity, which is the phase velocity of the first symmetric Lamb wave mode S_0 in the large wavelength limit (Bossy *et al.*, 2002, 2004b; Haïat *et al.*, 2009), with the expression

$$v_p = \sqrt{\frac{C_{11}}{\rho_s} \times \left(1 + \frac{C_{13}^2}{C_{11} \times C_{33}}\right)}, \tag{6}$$

which is only valid in the case of an elastic material.

When the thickness h is large compared to wavelength, the FAS velocity tends toward the bulk longitudinal wave velocity inside the material constituting the solid layer:

$$v_b = \sqrt{\frac{C_{11}}{\rho_s}}, \tag{7}$$

which is again only valid in the case of an elastic material.

In the present study, simulations were performed with two different solid layer thicknesses, $h=0.6$ mm and $h=4$ mm, because these two values of h correspond to cases where the behavior of the FAS velocity can be explained in terms of guided and bulk waves, respectively. Considering the dominant frequency of the broadband ultrasonic pulse

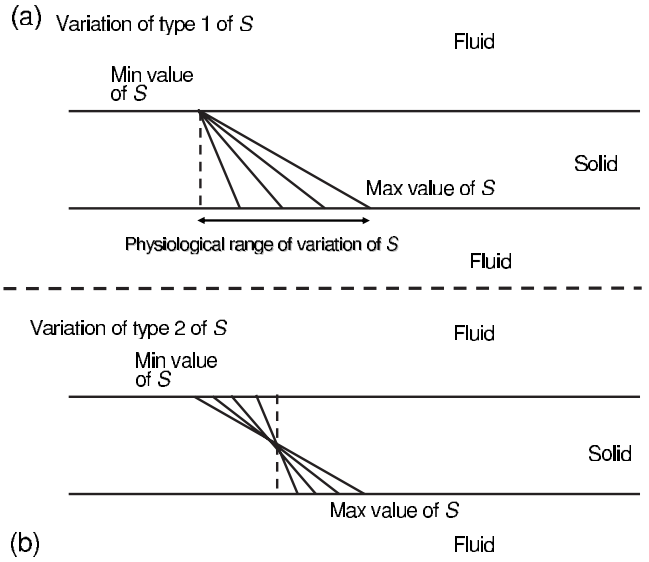

FIG. 2. Schematic representation of the two types of spatial variation considered for the material property S corresponding the viscoelastic coefficient. The lines in the solid layer indicate the spatial dependence of S. The dotted line indicates homogeneous material properties corresponding the reference material properties. The variation in type 1 (respectively, 2) shown in (a) [respectively, (b)] corresponds to a constant value at the bone-soft tissues interface (respectively in the middle of the bone).

and the range of variation in C_{11}, it means that h/λ varies in the intervals defined from 0.14 to 0.19, and from 0.96 to 1.25, respectively, for the thin and thick solid layers.

For the thinnest layer, the propagation in the solid layer is analyzed on the basis of the propagation of S_0 wave in an immersed homogeneous plate after adjustment of the material properties. Therefore, roots associated with the characteristic equation of the S_0 wave for homogenous transverse isotropic plate are calculated in the limit of large wavelengths.

C. Gradient of material property

Similarly, as what was done by Haïat *et al.* (2009), the impact of a controlled gradient vector $\boldsymbol{\delta}$ of a given material property S on the FAS velocity is investigated. In what follows, the scalar S corresponds to one of the viscoelastic coefficients η_{ij} defined in Eq. (5). In each set of simulations, all the material properties (stiffness and viscoelastic coefficients) are constant and equal to their reference value, while S is subjected to a gradient defined below.

The gradient vector $\boldsymbol{\delta}=\text{grad}\, S=\delta\mathbf{z}$ is assumed to be independent of x in all cases, where $\mathbf{z}$ is a unit vector along the z-axis and grad is the gradient operator acting on a scalar field. The quantity δ is always taken as negative because attenuation increases with porosity (Sasso *et al.*, 2008), and porosity is higher in the endosteal part than in the periosteal part of the bone. Moreover, only the simple situation of affine spatial variations of S is considered, corresponding to a constant value of δ. This affine spatial variation in S is chosen because the actual physiological spatial dependence of S remains unknown. Two different affine spatial dependences of the studied viscoelastic property are considered and are illustrated in Fig. 2. The associated gradient δ will be referred to as type 1 or 2, and corresponds to simple description of the spatial dependence of material properties. We choose this linear variation because the precise spatial variations of bone material properties remain poorly documented.

Type 1. The gradient of type 1 is such that the physical property S takes the same value S_m at the upper interface $z=0$ of the solid plate for all values of the gradient δ. The quantity $S(z)$ is therefore given by

$$S(z) = S_m + \delta \times z, \tag{8}$$

where S_m corresponds to the minimal value of the material property S considered. The minimal value δ_m of δ (which corresponds to its maximum in absolute value as $\delta<0$) is chosen so that $S(-h)$ is equal to S_M, where S_M is the maximal value of S. The gradient δ_m is given by

$$\delta_m = \frac{(S_m - S_M)}{h} < 0. \tag{9}$$

Type 2. The gradient of type 2 is such that S takes the same value at the middle of the solid plate ($z=-h/2$) for all values of gradient δ. Furthermore, the mean value of the property S is identical for all δ, and the quantity $S(z)$ is given by

$$S(z) = \frac{(S_m + S_M)}{2} + \delta \times \left(z + \frac{h}{2}\right). \tag{10}$$

The minimal value of δ is also given by Eq. (9) so that all values of $S(z)$ are again always comprised between S_m and S_M.

For both types of spatial variation, five different values of δ regularly distributed between δ_m and 0 are arbitrarily considered for each layer thickness. In what follows, the notations δ_{11}, δ_{13}, δ_{33}, and δ_{55} correspond to δ when S is defined by η_{11}, η_{13}, η_{33}, and η_{55}, respectively.

D. Gradient of porosity

In the case of bone, all material properties (mass density, stiffness, and viscoelastic coefficients) are expected to exhibit coupled spatial variations because they are all related to porosity, which increases from the periosteal to the endosteal part (Bousson *et al.*, 2001). When porosity increases, the values of the homogenized elastic constants and of mass density are expected to decrease, having opposite and competing effects on the wave velocity. In addition, the viscoelastic constants are expected to increase with porosity (Sasso *et al.*, 2008). Here, spatial variations of types 1 and 2 are considered for the porosity (noted P), with the minimum and maximum values of porosity P_m and P_M equal, respectively, to 3 and 15%. In the case of a spatial variation in types 1 and 2, the porosity writes, respectively,

$$P(z) = P_M + \delta_P \times z, \tag{11}$$

$$P(z) = \frac{(P_m + P_M)}{2} + \delta_P \times \left(z + \frac{h}{2}\right). \tag{12}$$

The dependence of mass density and of the stiffness coefficients is similar to what has been done by Haïat *et al.*

(2009), and is briefly recalled in what follows. Following a simple rule of mixture, a variation in porosity induces an affine variation in mass density given by

$$\rho_s(z) = \rho_m + \delta_\rho \times (P-3). \quad (13)$$

Here, we choose ρ_m in order to obtain a variation in mass density from 1.753 to 1.66 g cm^{-3} when P varies from 3% and 15%, which leads to $\delta_\rho = 7.7 \times 10^{-3}$ g cm^{-3}. These values correspond to a mass density equal to 1.722 g cm^{-3} when $P=7\%$.

The variations in all material properties with porosity are taken from the literature. Affine dependence of diagonal components of $\mathbb{C}$ with porosity was derived from Baron *et al.* (2007), where a variation of porosity between 3% and 15% corresponds approximately to a change of C_{11} and C_{33} of 7.8 and 4 GPa, respectively,

$$C_{11}(z) = C_{11}^m + \delta_C \times (P-3), \quad C_{33}(z) = C_{33}^m + \delta'_C \times (P-3). \quad (14)$$

The variations of C_{11} and C_{33} are centered on their reference value. Therefore, C_{11}^m and C_{33}^m are respectively equal to 19.7 and 16.85 GPa; the quantities δ_C and δ'_C are respectively equal to 0.65 and 0.33 GPa. Note that taking into account a slight nonlinear variation in C_{11} and C_{33} as a function of porosity should not modify significantly our results. Similarly as what was done by Haïat *et al.* (2009), we did not consider any variation in C_{13}, which was taken to be equal to its reference value.

Although BUA has been shown to increase when mass density and bone mineral density (which are both negatively correlated with porosity) decrease (Sasso *et al.*, 2008), the precise relationship between porosity and attenuation remains unknown. Therefore, for each viscoelastic constant η_{ij}, we assume (i) a linear relation between the corresponding attenuation at 1 MHz and porosity, and (ii) that the ultrasonic attenuation value at P_m (respectively P_M) corresponds to its minimal (respectively maximal) value within the physiological range. This approach constitutes a simple mean of investigating the effect of viscoelasticity variations due to heterogeneous porosity.

III. RESULTS

A. Physiological material properties

The same approach as the one described by Haïat *et al.* (2008a) is used to derive the attenuation coefficient α_f in bone marrow (see Appendix). We assumed that the bone marrow viscosity is similar to that of soft tissues, and the range of variation used for α_f is shown in Table I. The corresponding values of η_f were obtained using Eq. (A2).

TABLE I. Mean, maximum, and minimum values of the attenuation coefficient at 1 MHz and of the corresponding viscosity of bone marrow and of soft tissues considered in the present study. These values are taken from Dussik and Fritch (1956); Goss *et al.* (1978); Lehman and Johnson (1958).

Physical property	α_f (1 MHz) (dB cm^{-1})	η_f (Pa s)
Mean value (reference)	1	1.97
Minimum value	0	0
Maximum value	2	3.94

TABLE II. Mean, maximum, and minimum values of the four homogenized elastic constants and of mass density affecting the ultrasonic propagation in the framework of the 2D model of Fig. 1.

Mechanical quantity	C_{11} (GPa)	C_{13} (GPa)	C_{33} (GPa)	$C_{55}=G_L$ (GPa)	ρ_s (g cm^{-3})
Mean value (reference)	23.05	8.7	15.1	4.7	1.722
Minimum	17.6	5.1	11.8	3.3	1.66
Maximum	29.6	11.1	25.9	5.5	1.753

The values used for the stiffness tensor of cortical bone are the same as the ones given by Haïat *et al.* (2009) and are shown in Table II.

The values of the longitudinal attenuation coefficients associated with the axial and radial directions ($\alpha_{L,x}$ and $\alpha_{L,z}$, respectively) at 1 MHz were obtained from the axial and radial BUA values, respectively, assuming a linear frequency dependence of the attenuation coefficients within the entire frequency bandwidth. The mean value of the attenuation coefficient α_t (see Appendix) indicated in Table III was taken from Garcia *et al.* (1978). The corresponding value of η_{55} was obtained using Eq. (A5) by considering the reference values of the material properties indicated in Table II.

B. Analytical validation of the finite element model

In order to validate our simulation code in the framework of a viscoelastic constitutive law, the results obtained numerically in a simple geometrical situation (planar propagation) are compared to analytical results. Therefore, a through transmission experiment was simulated using the numerical simulation tool in order to verify that the material properties used as input parameters could be retrieved by analyzing the simulation results. Briefly, a 2-D plane wave propagation was considered in a rectangular simulation domain (10×5 mm^2) in the x-axis. A linear emitter was positioned at $x=0$, generating a broadband ultrasonic signal similar to that described by Desceliers *et al.* (2008). A linear receiver is located at the other end of the simulation domain (at $x=10$ mm) to record the ultrasonic wave after its propa-

TABLE III. Average, minimum, and maximum values of attenuation and corresponding viscoelastic coefficient taken for cortical bone. The values of $\alpha_{L,x}$ and $\alpha_{L,z}$ were taken from Table 1 of Sasso *et al.* (2007). The mean value of α_T was taken from Garcia *et al.* (1978). The corresponding values of η_{55} was obtained using Eq. (A5) by considering the reference values of the material properties indicated in Table II. The mean value of η_{13} was obtained using Eq. (A7) and the maximum and minimum values of η_{13} were obtained by verifying that the thermodynamical stability condition given by Eq. (A8) is always respected when η_{11} and η_{33} vary within their physiological range.

Mechanical quantity	$\alpha_{L,x}$ (dB cm^{-1})	$\alpha_{L,z}$ (dB cm^{-1})	α_T (dB cm^{-1})	η_{11} (Pa s)	η_{33} (Pa s)	η_{55} (Pa s)	η_{13} (Pa s)
Mean value (reference)	3.2	4.2	4	157	109	18	121
Minimum	0.8	1.7	0	39	44	0	39
Maximum	10.6	12.8	8	521	334	36.2	131

gation in the viscoelastic domain where the stiffness (respectively viscoelastic) coefficients correspond to the mean values indicated in Table II (respectively Table III). Longitudinal and transverse wave modes were successively tested by considering a time-dependent displacement in the x and z directions at the emitter as boundary conditions.

Meanwhile, the propagation of a longitudinal ultrasonic wave in water was simulated using the formulation in terms of pressure, leading to the reference signal, which is similar in shape to the input signal (data not shown). The reference signal is necessary in the framework of a through transmission configuration to derive the phase velocity. The black solid lines in Figs. 3(a) and 3(b) [respectively Figs. 3(c) and 3(d)] show the behavior of the frequency dependent attenuation coefficient (respectively of the phase velocity) within the frequency bandwidth of interest, obtained using the ratio of the spectra of the reference signal and of the signal transmitted in the simulation domain for the longitudinal and transverse wave modes (Haïat *et al.*, 2008b; Sasso *et al.*, 2008).

These last simulation results were compared to analytical results obtained by considering a plane wave propagation in a viscoelastic medium under the same assumptions of relatively weak absorption given in Appendix3, where (i) the attenuation coefficient varies has a f-square dependence, as indicated by Eqs. (A3) and (A5), and (ii) the longitudinal and transverse phase velocities $v_{L,x}^{\phi}$ and v_T^{ϕ} vary as a second order polynomial as a function of frequency, as indicated by Eqs. (A4) and (A6). The gray dashed lines in Fig. 3 show the frequency dependences of the attenuation coefficient and of phase velocity obtained using the analytical model described above. A good agreement between analytical and numerical results is obtained for the frequency dependences of $\alpha_{L,x}$ and α_T as the maximum difference between the two results is equal to 0.01 dB cm^{-1} for $\alpha_{L,x}$ and 0.012 dB cm^{-1} for α_T. Slightly more important discrepancies are obtained between the analytical and the numerical results for the frequency dependence of phase velocity as the difference between the two results slightly increases with frequency, and its maximum value is equal to 0.7 m s^{-1} for $v_{L,x}^{\phi}$ and to 0.3 m s^{-1} for v_T^{ϕ}. These discrepancies may be explained by effects related to numerical error in the scheme of the spatio-temporal discretization, which have been pointed out for example in Warren and Scott (1996), and are known to be due to the discretization. This numerical error is not due to the distortion effects during the pulse propagation related to dispersion, which has been detailed by Haïat *et al.* (2006) when the velocity is measured using a time marker such as the first zero crossing. Figure 3 thus constitutes a validation of the simulation method and an estimation of the error.

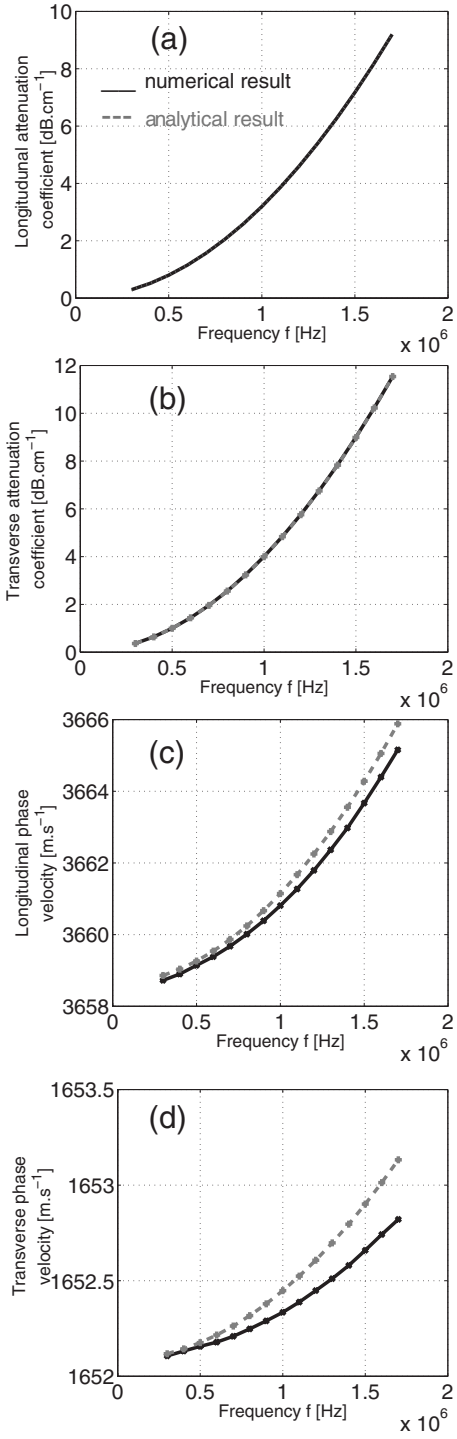

FIG. 3. Comparison between numerical (black solid lines) and analytical (gray dashed lines) results obtained for a plane wave propagation through an homogeneous transverse isotropic viscoelastic medium. [(a) and (b)] Attenuation coefficient of the longitudinal (transverse) wave mode. [(c) and (d)] Phase velocity of the longitudinal (transverse) wave mode. All velocities are plotted within the bandwidth of interest.

C. Effect of absorption on the first wavefront amplitude

In order to assess the qualitative effect of viscous properties of both fluids and of the viscoelastic properties of the solid on the FAS, Fig. 4 shows the amplitude of the first maximum of each signal recorded by the 14 receivers corresponding to the computation of the FAS velocity for a bone thickness equal to 4 mm. The amplitude of the signal at the first sensor with no attenuation was used to normalize the signals recorded at all the sensors in the elastic and viscoelastic case. The values of the components of the stiffness tensor were taken equal to their reference value indicated in Table II. The solid line corresponds to the normalized amplitude of the signal obtained without any absorption neither in the fluids nor in the solid. The dashed line corresponds to the

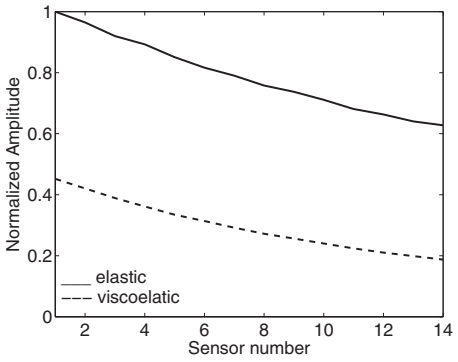

FIG. 4. Variation in the amplitude of the first arriving wave front as a function of the sensor number (increasing number corresponds to sensors farther to the emitter). The amplitude of the signal at the first sensor with no attenuation was used to normalize the signals recorded at all the sensors in the elastic and viscoelastic case. The values of the components of the stiffness tensor are equal to the reference values indicated in Table I. The solid line indicates the results when no absorption was accounted for and the dashed line indicates the case where viscous losses are considered in both surrounding fluids as well as in the solid (reference values indicated in Table III are used for viscous and viscoelastic parameters).

normalized amplitude of the signal obtained by considering absorption in both fluids and in the solid, the viscous and viscoelastic parameters being equal to their reference values given in Tables I and III.

The difference between the dashed and solid lines illustrates the influence of viscous and viscoelastic effects on the amplitude of the FAS. For both configurations (elastic and viscous cases), the amplitude of the signal is shown to decrease as a function of the position of the receiver, which can be explained by the fact that the wave radiates in fluid while it propagates in the bone structure, leading to a loss of energy. As shown in Fig. 4, including viscous and viscoelastic absorptions in the simulation model leads to a decrease in the amplitude of the first arriving wavefront.

When the reference material properties are considered, the FAS velocity obtained without absorption is equal to 3484 m s^{-1}, whereas it is equal to 3733 m s^{-1} when absorption is taken into account. The difference between these two values is significant, compared to the precision of the probe, and will be investigated in what follows.

D. Dependence of the FAS velocity to absorption in the surrounding fluids

From the analysis of numerical simulations, the variation in the FAS velocity due to changes of viscous properties of the soft tissues and of bone marrow within a realistic range was assessed for $h=0.6$ and 4 mm, and for homogeneous material properties. The material properties of cortical bone were taken equal to their reference values, as given in Table II for the stiffness tensor $\mathbb{C}$, and in Table III for the viscoelastic tensor $\mathbb{E}$. The minimal (m) and maximal (M) values of η_f are tested for the soft tissues and for bone marrow; the other material properties remaining equal to their reference values.

Table IV shows that the FAS velocity is independent of the viscous properties of the soft tissues, as well as of marrow within the physiological range. Therefore, the soft tissues and bone marrow will be considered as nonviscous fluids in what follows.

TABLE IV. Sensitivity of the FAS velocity to changes of the viscous properties of the soft tissues and of bone marrow for two values of the cortical thickness and homogeneous bone material properties. The computed FAS velocity is indicated for the minimal and maximal values of each variable corresponding to the realistic range of variation shown in Table II.

Material property S	η_f in soft tissues (Pa s)		η_f in bone marrow (Pa s)	
Cortical thickness h (mm)	0.6	4	0.6	4
FAS velocity for S_m (m s^{-1})	3483	3731	3484	3731
FAS velocity for S_M (m s^{-1})	3484	3732	3484	3731

E. Dependence of the FAS velocity to homogeneous viscoelastic absorption in cortical bone

The variation in the FAS velocity due to changes of the viscoelastic parameters of cortical bone within a realistic range was assessed for $h=0.6$ and 4 mm, and for homogeneous material properties, in order to determine which viscoelastic parameters play a role in the FAS velocity and must thus be considered to have spatial variations. Therefore, the material properties of the surrounding soft tissues and of the stiffness tensor were taken equal to their reference values, as indicated in Tables I and II. The minimal (m) and maximal (M) values of each component of the viscoelastic tensor $\mathbb{E}$ of cortical bone indicated in Table III were tested; the other material properties remaining equal to their reference values, except for C_{13}, which was taken equal to its minimum value when considering variations of C_{11} and C_{33} (in order to satisfy the thermodynamical stability conditions for all values, see Appendix). Table V shows the FAS velocity corresponding to a variation of each material property.

According to the value of h and to the considered viscoelastic property S, two situations may be distinguished: the difference of the FAS velocities obtained when considering the maximum and minimum values of S may be relatively "large" (above 67 m s^{-1}) or relatively "small" (lower than 3 m s^{-1}). Considering the thick solid layer ($h=4$ mm), Table V shows that small differences of the FAS velocity are obtained, when η_{13}, η_{33}, and η_{55} take their minimum or maximum values defined above. On the contrary, the FAS

TABLE V. Sensitivity of the FAS velocity to changes of the viscoelastic properties of cortical bone for two values of the cortical thickness and homogeneous bone material properties. The computed FAS velocity is indicated for the minimal and maximal values of each variable corresponding to the realistic range of variation shown in Table II.

Material property S	η_{11} (Pa s)		η_{13} (Pa s)		η_{33} (Pa s)		η_{55} (Pa s)	
Cortical thickness h (mm)	0.6	4	0.6	4	0.6	4	0.6	4
FAS velocity for S_m (m s^{-1})	3456	3654	3543	3738	3544	3732	3484	3734
FAS velocity for S_m (m s^{-1})	3787	3956	3475	3735	3469	3734	3484	3733

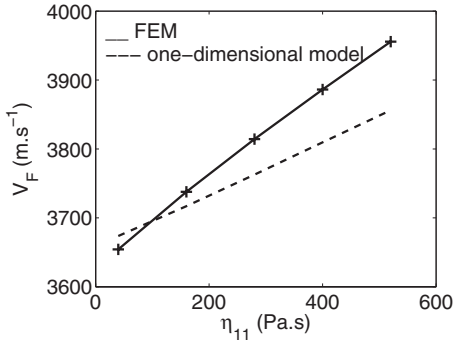

FIG. 5. Case of thick solid layer h=4 mm. Variation in the FAS velocity (v_F) versus η_{11} for homogeneous bone properties, the other material properties remaining equal to their reference value. The solid (respectively dashed) line indicates the results obtained using the finite element model (respectively the one-dimensional model described in subsection IV A)

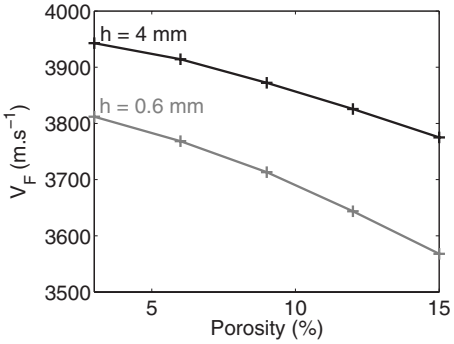

FIG. 7. Variation in the FAS velocity (v_F) versus porosity for homogeneous bone material properties. The black (respectively gray) solid line corresponds to the case of a thick (respectively thin) solid layer of h=4 mm (respectively, h=0.6 mm)

velocity varies significantly when η_{11} varies within the limits defined above. The solid line in Fig. 5 shows the variation in the FAS velocity as a function of η_{11} in the case of homogeneous bone properties; the other components of $\mathbb{E}$ and $\mathbb{C}$ remaining constant and equal to their reference value. The FAS velocity is shown to be an increasing function of η_{11} within the physiological range.

When considering the thin solid layer (h=0.6 mm), changes in η_{55} weakly affect the FAS velocity, while variations of η_{11}, η_{13}, and η_{33} lead to significantly larger changes of the FAS velocity. As shown in Fig. 6, the FAS velocity is an increasing function of η_{11} and η_{33}, and a decreasing function of η_{13} within the physiological range. The components of the viscoelastic tensor (η_{11}, η_{13}, and η_{33}), which influence the FAS velocity are the same than the components of the stiffness tensor (C_{11}, C_{13}, and C_{33}) having an effect on the FAS velocity (Haïat *et al.*, 2009) and determining the plate velocity v_p [see Eq. (6)].

Figure 7 shows the variation in the FAS velocity for homogeneous cortical bone where the porosity is assumed to vary within the physiological range, inducing a simultaneous variation in mass density and of all components of $\mathbb{C}$ and of $\mathbb{E}$. The results shown in Fig. 7 indicate that the FAS velocity is a decreasing function of the porosity for thick and thin bone widths, and that the dependence of the FAS velocity on the porosity is approximately similar for both thickness values.

In what follows, the effect of a gradient of each viscoelastic property playing a role in the determination of the FAS velocity will be investigated for both values of the bone thickness.

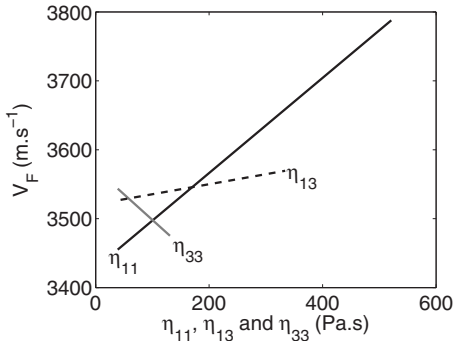

FIG. 6. Case of thin solid layer h=0.6 mm. Variation in the FAS velocity (v_F) *versus* η_{11} (black solid line), η_{13} (black dashed line) and η_{33} (gray solid line) for homogeneous bone properties, the other material properties remaining equal to their reference value.

F. Gradient of bone viscoelastic properties

1. A thick solid layer

Figure 8 shows the dependence of the FAS velocity on the gradient of η_{11} in the case of a thick solid layer (h=4 mm). For a gradient of type 1, the FAS velocity increases when δ_{11} increases, whereas for gradient of type 2, the FAS velocity slightly decreases with δ_{11}. The dashed lines of Fig. 8 describe the FAS velocity obtained for a constant value of η_{11} equal to its spatially averaged values, which corresponds to the value of η_{11} at z=−0.5h. The dashed lines of Fig. 8 were derived from the results shown in Fig. 5. The results indicate that in the case of a thick bone width with heterogeneous bone properties, an important dis-

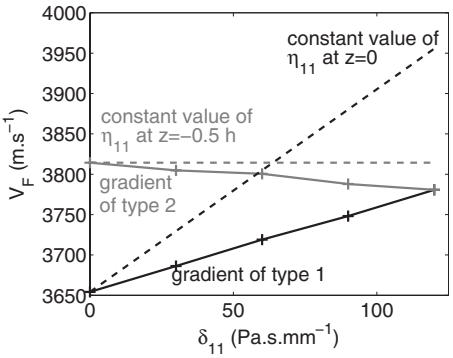

FIG. 8. Case of thick solid layer h=4 mm. Variation in the FAS velocity (v_F) *versus* δ_{11}. The black lines correspond to the variation in type 1 (constant value of η_{11} at z=0) and the gray lines correspond to the variation in type 2 (constant value of η_{11} at z=−0.5h). The continuous lines indicate the results obtained with the finite element model. The dashed lines correspond to the FAS velocity obtained with homogeneous spatially averaged viscoelastic properties (corresponding to the value at z=−0.5h) obtained from Fig. 5.

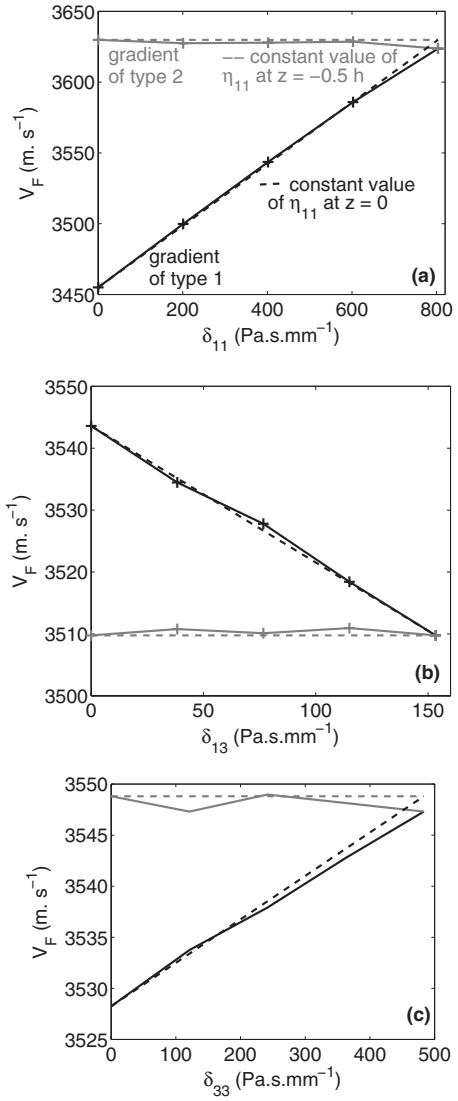

FIG. 9. Case of thin solid layer h=0.6 mm. Variation in v_F versus (a) δ_{11}, (b) δ_{33} and (c) δ_{13}. The black lines correspond to the variation in type 1 (constant value of η_{11}, η_{33} and η_{13} at z=0) and the gray lines correspond to the variation in type 2 (constant value of η_{11}, η_{33} and η_{13} at z=−0.5h). The continuous lines indicate the results obtained with the finite element model. The dashed lines correspond to the FAS velocity obtained with homogeneous spatially averaged viscoelastic properties (corresponding to the value at z=−0.5h)

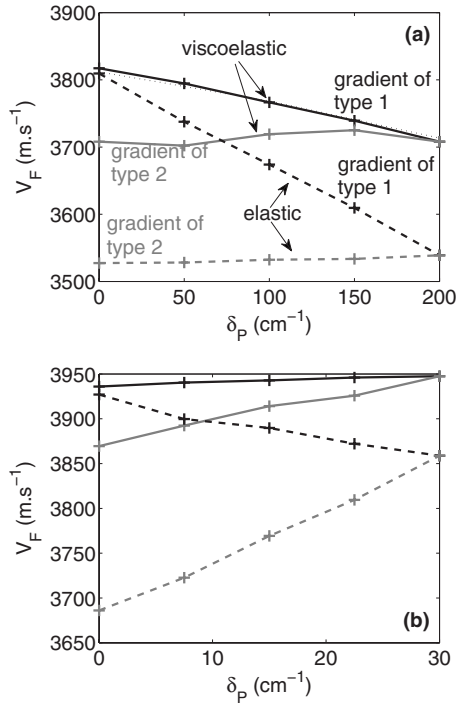

FIG. 10. Variation in v_F versus porosity for (a) h=0.6 mm and (b) h=4 mm. The black lines correspond to the variation in type 1 (constant value of P at z=0) and the gray lines correspond to the variation in type 2 (constant value of P at z=−0.5h). The solid lines indicate the results obtained when considering a simultaneous variation in mass density and of the stiffness and viscoelastic coefficients. The dashed lines indicate the results obtained when considering a simultaneous variation in mass density and of the stiffness coefficients only, bone being considered as an elastic material (see Haïat *et al.* (2009)). The thin dotted line in Fig. 10(a) shows the FAS velocity obtained when considering a constant value of the porosity equal to its spatially averaged values, which corresponds to the value of the porosity at z=−0.5h. (This line is very near to the black line.)

crepancy is obtained when comparing the numerical results and the FAS velocity obtained by spatially averaging η_{11} across the bone width.

2. A thin solid layer

When considering the thin solid layer (h=0.6 mm), the effect of a gradient of η_{11}, η_{13}, and η_{33} was investigated according to the results presented in Sec. III E. The results are shown in Fig. 9.

For a gradient of type 1, the FAS velocity is shown to increase when δ_{11} and δ_{33} increase, whereas it decreases when δ_{13} increases. For a gradient of type 2, the FAS velocity stays approximately constant with δ_{11}, δ_{13}, and δ_{33}.

The dashed lines of Fig. 9 show the FAS velocity obtained for a constant values of η_{11}, η_{33}, and η_{13} equal to their spatially averaged values, which correspond to the values of η_{11}, η_{33}, and η_{13} at z=−0.5h. The dashed lines of Fig. 9 were derived by considering the results shown in Fig. 5. For both types of gradient, the FAS velocity is accurately predicted by considering the spatially averaged values of η_{11}, η_{33}, and η_{13}, which shows that in the case of a thin bone width with heterogeneous bone properties; the FAS velocity is governed by the spatially averaged values of the viscoelastic properties η_{11}, η_{13}, and η_{33}.

G. Gradient of porosity

Figures 10(a) and 10(b) show the variation in the FAS velocity obtained for h=0.6 and 4 mm, respectively, when considering a gradient of porosity δ_P. The black and gray solid lines show the FAS velocity obtained numerically for a gradient of porosity of types 1 and 2, respectively. Note that the porosity induces a variation in mass density, as well as of the stiffness and viscoelastic coefficients, as described in Sec. II D. The dashed lines of Fig. 10 are the results described by Haïat *et al.* (2009), corresponding to the results obtained by only accounting for variations of stiffness coefficients and of mass density due to changes of porosity (elastic case).

As shown in Fig. 10, the viscoelastic behavior of cortical bone induces an increase in the FAS velocity compared to the elastic case. In the case of a thin bone width [Fig. 10(a)],

the FAS velocity does not depend on δ_P for a gradient of type 2, which is a result similar to what has been obtained in the elastic case. However, for a gradient of type 1, the FAS velocity decreases with δ_P with a slope approximately divided by 2, compared to the elastic case. The dashed line in Fig. 10(a) shows the FAS velocity obtained for a constant value of the porosity equal to its spatially averaged values, which corresponds to the value of the porosity at $z=-0.5h$. A good agreement is obtained between the results found with a gradient and with spatially averaged material properties, which confirms that in the case of a thin bone width with heterogeneous porosity, the FAS velocity is governed by the spatially averaged values of the porosity.

In the case of a thick bone width [see Fig. 10(b)], the FAS velocity increases with δ_P for a gradient of type 2, with a slope slightly lower than what is obtained in the elastic case. However, for a gradient of type 1, the FAS velocity slightly increases with δ_P, whereas it decreases with δ_P in the elastic case.

IV. DISCUSSION

To the best of our knowledge, this study is the first one to focus on the effect of ultrasonic attenuation on the FAS velocity estimated with an axial transmission configuration for different solid layer thicknesses.

The present study shows that in the studied geometrical configuration, ultrasonic attenuation effects related to the surrounding soft tissues are not likely to modify the results compared to the case with no losses. However, as shown in Fig. 4, attenuation effects strongly influence the amplitude of the signal associated with the FAS velocity. Our results show that in the case of bone with strong attenuation, the amplitude of the FAS may be significantly reduced compared to the elastic case (a factor of 3 may be expected). In some situations of strong bone attenuation, this decrease might lead to wrong estimation of the time of the FAS if the FAS amplitude does not cross the threshold used for the determination of the FAS, which is more likely for the receivers located far from the emitter because losses of amplitude are comparatively more important.

The results shown in Table V suggest that the effect of changes of viscoelastic properties within their estimated physiological range may be of the same order of magnitude as the effect of changes of the stiffness coefficients or mass density within the physiological range (Haïat *et al.*, 2009). These results indicate that attenuation is an important property, which should be accounted for when modeling the ultrasonic propagation in cortical bone in the context of axial transmission. Moreover, for both thin and thick bone widths, the components of the viscoelastic tensor affecting the FAS velocity are the same as the components of the elastic tensor influencing the value of the FAS velocity found in Table II of Haïat *et al.* (2009).

A. A one-dimensional model

To understand the results shown in Figs. 5 and 6, a one-dimensional model using linear filters similar to what has been developed by Haïat *et al.* (2006) has been applied. This model corresponds to a 1-D model in a viscoelastic medium where bone thickness is not taken into account. The approach is based on results obtained in trabecular bone showing that speed of sound values measured using a time marker in the early part of the signal increases when BUA increases (Haïat *et al.*, 2005, 2006; Wear, 2000, 2001).

Briefly, we employed a linear filter with a quadratic frequency dependent attenuation coefficient in order to generate 14 radio frequency signals on which the FAS velocity will be estimated using the model described in Sec. II A. Signal simulation was performed in order to understand the effects of the frequency dependent attenuation coefficient on the velocity measurements. For a given quadratic frequency dependent attenuation coefficient in bone $\alpha(f)=\beta f^2$, a transfer function was determined so that the effect of the propagation in bone could be modeled as a quadratic filter. In this last relation, β is a constant, consistently with the constant value of the viscoelastic coefficients.

In the model, the simulated signal $s_s(t)$ [with Fourier transform $S_s(f)$], corresponding to a propagation in bone over a distance of L, was obtained using the emitted signal $e(t)$ [Fourier transform $E(f)$] through

$$S_s(f) = E(f)\exp(-\beta f^2 L)\exp\left(-2i\pi f\frac{L}{v_{L,x}^{\phi}(f)}\right), \tag{15}$$

where the transfer function $H_1(f)=\exp(-\beta f^2 L)$ accounts for the attenuation in bone (attenuation in water was taken to be negligible as it does not impact the FAS velocity), and $H_2(f)=\exp(-2i\pi f(L/v_{L,x}^{\phi}(f)))$ accounts for the time delay corresponding to the propagation in bone. Following Eqs. (A3) and (A4) (see Appendix), together with the expression of the attenuation coefficient, we have

$$v_{L,x}^{\phi}(f) = c_{L,x}\left(1+\frac{3}{8\pi^2}c_{L,x}^2\beta^2 f^2\right). \tag{16}$$

For each value of β, the approach described above allows to construct a set of 14 signals by varying the value of L accordingly to the position of the receivers. A value of $L=0$ was arbitrarily chosen for the receiver located at the left of Fig. 1. Note that choosing another value would not impact the results presented below, as the FAS velocity is derived from the comparison between the 14 receivers and does not depend on the shape of the first signal. The FAS velocity was derived, following the same method, as described in Sec. II A.

The relationship between the parameter β and the bone viscoelastic properties depends on the bone thickness considered. In the case of a large bone thickness, the situation is relatively simple because only η_{11} impacts the FAS velocity, and using Eq. (A3) leads to

$$\beta = 2\pi^2\frac{\eta_{11}}{c_{L,x}C_{11}}. \tag{17}$$

The dashed line of Fig. 5 shows the variation in the FAS velocity as a function of η_{11} in the case of the 1-D model described above. The dashed line of Fig. 5 does not correspond to the "correct value" of the FAS velocity, and the solid line (results obtained with the 2-D simulation method)

reflects more closely the reality. Despite the strong approximation performed in the 1-D model (dashed line) compared to the 2-D model (solid line), a reasonable agreement is obtained between both methods as the maximum difference between both velocities is equal to 100 m s^{-1}. The distortion due to dispersion and the use of the time at which the peak of the FAS occurs is included in both 1-D and 2-D models. Note that similar results are obtained in the case of a thin bone width (data not shown) when considering an isotropic behavior ($\mathbb{C}$ and $\mathbb{E}$ isotropic tensors), which is necessary in order to derive an analytical relationship between β and the bone material properties.

B. Limitations

This study has limitations. First, the determination of homogenized viscoelastic material properties of cortical bone is a complex problem due to the multiscale nature of bone. Bone material properties depend on the microstructure (*e.g.* porosity, shape, and distribution of the pores), as well as on the material properties of the bone matrix at smaller scales (*e.g.* mineralization, orientation of collagen fibrils, etc.). Both porosity and material properties of bone tissue may depend on the radial position in bone and result in a gradient of all components of $\mathbb{C}$, $\mathbb{E}$, and in ρ_s. Therefore, multiscale models, coupled with structural and stiffness measurements at lower scales 9such as nanoindentation (Zysset *et al.*, 1999) or scanning acoustic microscopy (Raum *et al.*, 2006)] are needed in order to derive more realistic spatial variations in homogenized material properties.

Second, although the range of variation chosen for each component of the viscoelastic tensor was determined from the experimental results obtained by the group of some of the authors (Sasso *et al.*, 2007, 2008) for bovine cortical bone samples at 4 MHz, the precise relationship between the attenuation coefficient and porosity in human cortical bone around 1 MHz remains poorly understood. The values of η_{11} and η_{33} were obtained by considering BUA values measured at 4 MHz, and a linear dependence of the attenuation coefficient between 0 and 4 MHz. However, the dependence of the attenuation coefficient has been shown to be slightly nonlinear over a wide frequency bandwidth [see Fig. 5 of Sasso *et al.* (2007)]. Moreover, as shown by Eq. (A3), our time model approximation leads to a f-square dependence of the attenuation coefficient, which is not necessarily the case for real cortical bone samples. In order to account for other frequency dependence of the attenuation coefficient in the framework of a time-domain model, would need to be used, similarly as what was done in fluids using a fractional time derivative (Wismer, 2006) or a causal convolution wave equation (Cobbold *et al.*, 2004). However, the frequency dependence of the attenuation coefficient in cortical bone remains poorly understood. Ultrasonic attenuation has been shown to be related to scattering effects due to the presence of the pores (Sasso *et al.*, 2008). However, viscoelastic properties of the bone matrix are also expected to influence ultrasonic attenuation, but this dependence remains to be quantified. The coupling of scattering and viscous absorption effects makes the prediction of the frequency dependence of the attenuation coefficient difficult. The development of homogenization models capable of predicting bone attenuation and/or dispersive effects would be of great interest to predict the evolution of bone ultrasonic response with material properties or thickness.

Third, this study was performed in two dimensions, and this analysis would need to be validated in 3D and taking into account also the heterogeneity of cortical thickness and true varying 3D shape of the bone. However, it has been shown by Bossy *et al.* (2004b) that 2-D and 3-D simulations give qualitatively similar results.

Fourth, the linear dependence of the material properties as a function of the position (gradient of types 1 and 2) in the bone cross-section chosen in this study corresponds to a simple situation compared to the physiological situation. We choose this linear variation because the precise spatial variations of bone material properties remain poorly documented. Moreover, this model constitutes a first step toward the determination of the effect of more realistic spatial dependence of material properties. In a forthcoming paper, we have used homogenization models, coupled with high resolution imaging techniques to show that each material property varies approximately linearly as a function of the radial position. Further work should use the results obtained in this way to account for more realistic spatial variations of bone material properties.

ACKNOWLEDGMENT

This study was supported by the "Agence Nationale de la Recherche" (Contract BoneChar No. BLAN06-2_144779).

APPENDIX: PHYSIOLOGICAL MATERIAL PROPERTIES

1. Attenuation in the surrounding soft tissues

The mechanical properties of both fluid layers (soft tissues and bone marrow) were considered to be homogeneous. We assumed constant values for the mass density $\rho_f = 1$ g cm^{-3} and the compressibility $K = 2.25 \times 10^9$ Pa corresponding to an acoustic wave velocity c_f of 1 500 m s^{-1} in the absence of viscosity ($\eta_f = 0$) (El Sariti *et al.*, 2006).

The attenuation coefficient α_f is assumed to have a square frequency dependence, and writes (Auld, 1973; Royer and Dieulesaint, 2000)

$$\alpha_f = \frac{1}{2}\frac{\eta_f}{c_f K}\omega^2, \tag{A1}$$

when the condition $\omega \gg \alpha_f c_f$ is fulfilled, where $\omega = 2\pi f$ is the angular frequency and f the frequency. Note that at the center frequency of 1 MHz, $\omega \sim 6.3 \times 10^6$ s^{-1} and $\alpha_f c_f \sim 1.4 \times 10^5$ s^{-1}. Moreover, the phase velocity v^ϕ is given by Auld (1973) or Royer and Dieulesaint (2000):

$$v^\phi = c_f\left(1 + \frac{3}{8}\frac{\eta_f^2}{K^2}\omega^2\right). \tag{A2}$$

2. Stiffness tensor of cortical bone

In order to define realistic numerical values for the different components of the stiffness tensor of cortical bone and for their variation, the same approach as the one described by Haïat *et al.* (2009) is used in the present work. Here, we assume that cortical bone is transverse isotropic, as this approximation has been shown to be realistic experimentally by different authors (Bossy *et al.*, 2004b; Dong and Guo, 2004; Haïat *et al.*, 2009; Protopappas *et al.*, 2007; Yoon and Katz, 1976a, 1976b). The values of the stiffness coefficients corresponding to the mean values of the bone mechanical properties are referred to as "reference" set of parameters in what follows. The porosity was assumed to vary between 3% and 15% (Bousson *et al.*, 2001; Dong and Guo, 2004), and a rule of mixture leads to the range of variation in mass density.

3. Attenuation in cortical bone

The attenuation coefficients $\alpha_{L,x}$ and $\alpha_{L,z}$ associated with the longitudinal mode are respectively given in the x-axis and z-axis by Auld (1973) or Royer and Dieulesaint (2000):

$$\alpha_{L,x} = \frac{1}{2}\frac{\eta_{11}}{c_{L,x}C_{11}}\omega^2, \quad \alpha_{L,z} = \frac{1}{2}\frac{\eta_{33}}{c_{L,z}C_{33}}\omega^2, \tag{A3}$$

when the conditions $\omega \gg \alpha_{L,x}c_{L,x}$ and $\omega \gg \alpha_{L,z}c_{L,z}$ are fulfilled, respectively, where $c_{L,x}=\sqrt{C_{11}/\rho_s}$ and $c_{L,z}=\sqrt{C_{33}/\rho_s}$. Note that at the center frequency of 1 MHz, $\omega \sim 6.3\times 10^6$ s^{-1} and $\alpha_{L,x}c_{L,x} \sim 8.3\times 10^4$ s^{-1}.

Under these conditions, the associated phase velocities $v_{L,x}^{\phi}$ and $v_{L,z}^{\phi}$ are respectively given by

$$v_{L,x}^{\phi} = c_{L,x}\left(1+\frac{3}{8}\frac{\eta_{11}^2}{C_{11}^2}\omega^2\right), \quad v_{L,z}^{\phi} = c_{L,z}\left(1+\frac{3}{8}\frac{\eta_{33}^2}{C_{33}^2}\omega^2\right). \tag{A4}$$

Similarly, the attenuation coefficient α_T associated with the transverse mode is given in the x-axis by Auld (1973) or Royer and Dieulesaint (2000):

$$\alpha_T = \frac{1}{2}\frac{\eta_{55}}{c_T C_{55}}\omega^2, \tag{A5}$$

when the condition $\omega \gg \alpha_T c_T$ is fulfilled, where $c_T=\sqrt{C_{55}/\rho_s}$. Note that at the center frequency of 1 MHz, $\omega \sim 6.3\times 10^6$ s^{-1} and $\alpha_T c_T \sim 1.7\times 10^4$ s^{-1}.

Under this condition, the transverse phase velocity v_T^{ϕ} is given by

$$v_T^{\phi} = c_T\left(1+\frac{3}{8}\frac{\eta_{55}^2}{C_{55}^2}\omega^2\right). \tag{A6}$$

The values of η_{11}, η_{33}, and η_{55} are assumed to be constant within the frequency bandwidth of interest and determined by the value of α_f when $f_0=1$ MHz. The approximation of constant values for the viscoelastic constants corresponds to a dispersive medium, as indicated by Eqs. (A6) and (A4).

We could not find in the literature a simple way to determine the value of η_{13}. Therefore, the reference value of η_{13} is derived from the mean values of η_{11} and η_{55} by assuming an isotropic behavior of viscoelasticity, which leads to the relation

$$\eta_{13} = \eta_{11} - 2\eta_{55}. \tag{A7}$$

In addition, the minimum and maximum values of η_{13} were obtained by verifying that the following positive-definiteness properties (so-called thermodynamical stability conditions) (Ohayon and Soize, 1998):

$$\eta_{11} > 0, \quad \eta_{33} > 0, \quad \eta_{55} > 0, \quad -\eta_{13}^2 + \eta_{11}\eta_{33} > 0, \tag{A8}$$

is always respected when varying each material property independently within the physiological range. This approach constitutes a simple way of determining a realistic range of variation for η_{13}. The physiological ranges of variation in the other viscoelastic constants (η_{11}, η_{33}, and η_{55}, respectively) are obtained by considering the different values of ultrasonic attenuation coefficient measured in the literature, and using Eqs. (A3) and (A5), respectively. So, we have considered a spatial variation in the different viscoelastic properties within this range of variation.

Ammann, P., and Rizzoli, R. (**2003**). "Bone strength and its determinants," Osteoporosis Int. **14**, S13–S18.

Auld, B. A. (**1973**). *Acoustic Fields and Waves in Solids* (Wiley Interscience, New York).

Baron, C., Talmant, M., and Laugier, P. (**2007**). "Effect of porosity on effective diagonal stiffness coefficients (c_{ii}) and anisotropy of cortical at 1 MHz: A finite-difference time domain study," J. Acoust. Soc. Am. **122**, 1810–1817.

Bossy, E., Talmant, M., and Laugier, P. (**2002**). "Effect of bone cortical thickness on velocity measurements using ultrasonic axial transmission: A 2D simulation study," J. Acoust. Soc. Am. **112**, 297–307.

Bossy, E., Talmant, M., and Laugier, P. (**2004a**). "Bi-directional axial transmission can improve accuracy and precision of ultrasonic velocity measurement in cortical bone: A validation on test material," IEEE Trans. Ultrason. Ferroelectr. Freq. Control **51**, 71–79.

Bossy, E., Talmant, M., and Laugier, P. (**2004b**). "Three-dimensional simulations of ultrasonic axial transmission velocity measurement on cortical bone models," J. Acoust. Soc. Am. **115**, 2314–2324.

Bossy, E., Talmant, M., Peyrin, F., Akrout, L., Cloetens, P., and Laugier, P. (**2004c**). "An *in vitro* study of the ultrasonic axial transmission technique at the radius: 1-MHz velocity measurements are sensitive to both mineralization and intracortical porosity," J. Bone Miner. Res. **19**, 1548–1556.

Bousson, V., Meunier, A., Bergot, C., Vicaut, E., Rocha, M. A., Morais, M. H., Laval-Jeantet, A. M., and Laredo, J. D. (**2001**). "Distribution of intracortical porosity in human midfemoral cortex by age and gender," J. Bone Miner. Res. **16**, 1308–1317.

Cobbold, R., Sushilov, N., and Weathermon, A. (**2004**). "Transient propagation in media with classical or power-law loss," J. Acoust. Soc. Am. **116**, 3294–303.

COMSOL Multiphysics (**2005**). Model library, Grenoble (France).

Desceliers, C., Soize, C., Grimal, Q., Haïat, G., and Naili, S. (**2008**). "Three dimensional transient elastic waves in multilayer semi-infinite media solved by a time-space-spectral numerical method," Wave Motion **45**, 383–399.

Dong, X. N., and Guo, X. E. (**2004**). "The dependence of transversely isotropic elasticity of human femoral cortical bone on porosity," J. Biomech. **37**, 1281–1287.

Dussik, K., and Fritch, D. (**1956**). "Determination of sound attenuation and sound velocity in the structure constituting the joints, and of the ultrasonic field distribution with the joints of living tissues and anatomical preparations, both in normal and pathological conditions," Technical Report, Progress Report to Public Health Service, National Institutes of Health Project A454, Bethesda, MD.

El-Sariti, A., Evans, J., and Truscott, J. (**2006**). "The temperature dependence of the speed of sound in bovine bone marrow at 750 kHz," Ultra-

sound Med. Biol. **32**, 985–989.
Fritsch, A., and Hellmich, C. (**2007**). "'Universal' microstructural patterns in cortical and trabecular, extracellular and extravascular bone materials: Micromechanics-based prediction of anisotropic elasticity," J. Theor. Biol. **244**, 597–620.
Garcia, B. J., Cobbold, R. S. C., Foster, F. S., and McNeill, K. G. (**1978**). "Ultrasonic attenuation in bone," in *Proceedings of the IEEE Ultrasonic Symposium* (IEEE, Cherry Hill, NJ), pp. 327–330.
Goss, S., Johnston, R., and Dunn, F. (**1978**). "Comprehensive compilation of empirical ultrasonic properties of mammalian tissues," J. Acoust. Soc. Am. **64**, 423–457.
Grimal, Q., and Naili, S. (**2006**). "A theoretical analysis in the time-domain of wave reflection on a bone plate," J. Sound Vib. **298**, 12–29.
Haïat, G., Lhemery, A., Renaud, F., Padilla, F., Laugier, P., and Naili, S. (**2008a**). "Velocity dispersion in trabecular bone: Influence of multiple scattering and of absorption," J. Acoust. Soc. Am. **124**, 4047–4058.
Haïat, G., Naili, S., Grimal, Q., Talmant, M., Desceliers, C., and Soize, C. (**2009**). "Influence of a gradient of material properties on ultrasonic wave propagation in cortical bone: Application to axial transmission," J. Acoust. Soc. Am. **125**, 4043–4052.
Haïat, G., Padilla, F., Barkmann, R., Dencks, S., Moser, U., Glüer, C., and Laugier, P. (**2005**). "Optimal prediction of bone mineral density with ultrasonic measurements in excised human femur," Calcif. Tissue Int. **77**, 186–92.
Haïat, G., Padilla, F., Cleveland, R., and Laugier, P. (**2006**). "Effects of frequency dependent attenuation and dispersion on different speed of sound measurements on human intact femur," IEEE Trans. Ultrason. Ferroelectr. Freq. Control **53**, 39–51.
Haïat, G., Sasso, M., Naili, S., and Matsukawa, M. (**2008b**). "Ultrasonic velocity dispersion in bovine cortical bone: An experimental study," J. Acoust. Soc. Am. **124**, 1811–1821.
Han, S., Rho, J., Medige, J., and Ziv, I. (**1996**). "Ultrasound velocity and broadband attenuation over a wide range of bone mineral density," Osteoporosis Int. **6**, 291–296.
Hans, D., Srivastav, S. K., Singal, C., Barkmann, R., Njeh, C. F., Kantorovich, E., Gluer, C. C., and Genant, H. K. (**1999**). "Does combining the results from multiple bone sites measured by a new quantitative ultrasound device improve discrimination of hip fracture?," J. Bone Miner. Res. **14**, 644–651.
Lakes, R. S., Yoon, H. S., and Katz, J. L. (**1986**). "Ultrasonic wave propagation and attenuation in wet bone," J. Biomed. Eng. **8**, 143–148.
Langton, C. M., Ali, A. V., Riggs, C. M., Evans, J. A., and Bonfield, W. (**1990**). "A contact method for the assessment of ultrasonic velocity and broadband attenuation in cortical and cancellous bone," Clin. Phys. Physiol. Meas. **11**, 243–249.
Lees, S., and Klopholz, D. Z. (**1992**). "Sonic velocity and attenuation in wet compact cow femur for the frequency range 5 to 100 MHz," Ultrasound Med. Biol. **18**, 303–308.
Lehman, J., and Johnson, E. (**1958**). "Some factors influencing the temperature distribution in thighs exposed to ultrasound," Arch. Phys. Med. Rehabil. **39**, 347–356.
Macocco, K., Grimal, Q., Naili, S., and Soize, C. (**2005**). "Probabilistic modelling of an ultrasonic setup: Calculation of the dispersion on wave speed measurements," C. R. Mec. **333**, 565–573.
Macocco, K., Grimal, Q., Naili, S., and Soize, C. (**2006**). "Elastoacoustic model with uncertain mechanical properties for ultrasonic wave velocity prediction; application to cortical bone evaluation," J. Acoust. Soc. Am. **119**, 729–740.
Mayhew, P. M., Thomas, C. D., Clement, J. G., Loveridge, N., Beck, T. J., Bonfield, W., Burgoyne, C. J., and Reeve, J. (**2005**). "Relation between age, femoral neck cortical stability, and hip fracture risk," Lancet **366**, 129–135.
Muller, M., Moilanen, P., Bossy, E., Nicholson, P., Kilappa, V., Timonen, J., Talmant, M., Cheng, S., and Laugier, P. (**2005**). "Comparison of three ultrasonic axial transmission methods for bone assessment," Ultrasound Med. Biol. **31**, 633–642.
Ohayon, R., and Soize, C. (**1998**). *Structural Acoustic and Vibration* (Academic, San Diego).
Protopappas, V. C., Kourtis, I. C., Kourtis, L. C., Malizos, K. N., Massalas, C. V., and Fotiadis, D. I. (**2007**). "Three-dimensional finite element modeling of guided ultrasound wave propagation in intact and healing long bones," J. Acoust. Soc. Am. **121**, 3907–3921.
Raum, K., Cleveland, R. O., Peyrin, F., and Laugier, P. (**2006**). "Derivation of elastic stiffness from site-matched mineral density and acoustic impedance maps," Phys. Med. Biol. **51**, 747–758.
Raum, K., Leguerney, I., Chandelier, F., Bossy, E., Talmant, M., Saied, A., Peyrin, F., and Laugier, P. (**2005**). "Bone microstructure and elastic tissue properties are reflected in QUS axial transmission measurements," Ultrasound Med. Biol. **31**, 1225–35.
Rico, H. (**1997**). "The therapy of osteoporosis and the importance of cortical bone," Calcif. Tissue Int. **61**, 431–432.
Royer, D., and Dieulesaint, E. (**2000**). *Elastic Waves in Solids. I: Free and Guided Propagation* (Springer-Verlag, Berlin).
Sasso, M., Haïat, G., Yamato, Y., Naili, S., and Matsukawa, M. (**2007**). "Frequency dependence of ultrasonic attenuation in bovine cortical bone: An in vitro study," Ultrasound Med. Biol. **33**, 1933–1942.
Sasso, M., Haïat, G., Yamato, Y., Naili, S., and Matsukawa, M. (**2008**). "Dependence of ultrasonic attenuation on bone mass and microstructure in bovine cortical bone," J. Biomech. **41**, 347–355.
Seeley, D. G., Browner, W. S., Nevitt, M. C., Genant, H. K., Scott, J. C., and Cummings, S. R. (**1991**). "Which fractures are associated with low appendicular bone mass in elderly women? The Study of Osteoporotic Fractures Research Group," Ann. Intern Med. **115**, 837–842.
Serpe, L., and Rho, J. (**1996**). "The nonlinear transition period of broadband ultrasound attenuation as bone density varies," J. Biomech. **29**, 963–966.
Stegman, M. R., Heaney, R. P., Travers-Gustafson, D., and Leist, J. (**1995**). "Cortical ultrasound velocity as an indicator of bone status," Osteoporosis Int. **5**, 349–353.
Talmant, M., Kolta, S., Roux, C., Haguenauer, D., Vedel, I., Cassou, B., Bossy, E., and Laugier, P. (**2009**). "*In vivo* performance evaluation of bi-directional ultrasonic axial transmission for cortical bone assessment," Ultrasound Med. Biol. **35**, 912–919.
Thomas, C. D., Feik, S. A., and Clement, J. G. (**2005**). "Regional variation of intracortical porosity in the midshaft of the human femur: age and sex differences," J. Anat. **206**, 115–125.
Turner, C. H. (**2002**). "Biomechanics of bone: determinants of skeletal fragility and bone quality," Osteoporosis Int. **13**, 97–104.
Warren, G., and Scott, W. (**1996**). "Numerical dispersion of higher order nodal elements in the finite-element method," IEEE Trans. Antennas Propag. **44**, 317–320.
Wear, K. A. (**2000**). "The effects of frequency-dependant attenuation and dispersion on sound speed measurements: applications in human trabecular bone," IEEE Trans. Ultrason. Ferroelectr. Freq. Control **47**, 265–273.
Wear, K. A. (**2001**). "A numerical method to predict the effects of frequency-dependent attenuation and dispersion on speed of sound estimates in cancellous bone," J. Acoust. Soc. Am. **109**, 1213–1218.
Weiss, M., Ben-Shlomo, A., Hagag, P., and M., R. (**2000**). "Reference database for bone speed of sound measurement by a novel quantitative multi-site ultrasound device," Osteoporosis Int. **11**, 688–696.
WHO Study Group (**1994**), "Assessment of fracture risk and its application to screening for postmenopausal osteoporosis," WHO Technical Report No. 843, World Health Organization, Geneva, Switzerland.
Wismer, M. (**2006**). "Finite element analysis of broadband acoustic pulses through inhomogenous media with power law attenuation," J. Acoust. Soc. Am. **120**, 3493–502.
Yoon, H. S., and Katz, J. L. (**1976a**). "Ultrasonic wave propagation in human cortical bone—I. Theoretical considerations for hexagonal symmetry," J. Biomech. **9**, 407–412.
Yoon, H. S., and Katz, J. L. (**1976b**). "Ultrasonic wave propagation in human cortical bone—II. Measurements of elastic properties and micro hardness," J. Biomech. **9**, 459–464.
Zysset, P., Guo, X., Hoffler, C., Moore, K., and Goldstein, S. (**1999**). "Elastic modulus and hardness of cortical and trabecular bone lamellae measured by nanoindentation in the human femur," J. Biomech. **32**, 1005–12.

Effect of lithotripter focal width on stone comminution in shock wave lithotripsy

Jun Qin,[a] W. Neal Simmons, Georgy Sankin, and Pei Zhong[b]
Department of Mechanical Engineering and Materials Science, Duke University, Durham, North Carolina 27708

(Received 30 July 2009; revised 8 January 2010; accepted 8 January 2010)

Using a reflector insert, the original HM-3 lithotripter field at 20 kV was altered significantly with the peak positive pressure (p_+) in the focal plane increased from 49 to 87 MPa while the −6 dB focal width decreased concomitantly from 11 to 4 mm. Using the original reflector, p_+ of 33 MPa with a −6 dB focal width of 18 mm were measured in a pre-focal plane 15-mm proximal to the lithotripter focus. However, the acoustic pulse energy delivered to a 28-mm diameter area around the lithotripter axis was comparable (~120 mJ). For all three exposure conditions, similar stone comminution (~70%) was produced in a mesh holder of 15 mm after 250 shocks. In contrast, stone comminution produced by the modified reflector either in a 15-mm finger cot (45%) or in a 30-mm membrane holder (14%) was significantly reduced from the corresponding values (56% and 26%) produced by the original reflector (no statistically significant differences were observed between the focal and pre-focal planes). These observations suggest that a low-pressure/broad focal width lithotripter field will produce better stone comminution than its counterpart with high-pressure/narrow focal width under clinically relevant *in vitro* comminution conditions.
 [DOI: 10.1121/1.3308409]

PACS number(s): 43.80.Gx [CCC] Pages: 2635–2645

I. INTRODUCTION

The design of shock wave lithotripters has evolved significantly since the introduction of the original Dornier HM-3 in the early 1980s, which instantaneously revolutionized the surgical management for kidney and upper urinary stone diseases (Chaussy and Fuchs, 1989; Rassweiler *et al.*, 2005). The original HM-3 (first-generation lithotripter) was designed based on electrohydraulic principle using an underwater spark discharge for shock wave generation and a truncated ellipsoidal reflector for wave focusing. Patients were immersed in a large water tub filled with degassed/deionized water (37 °C) for acoustic coupling. Stone location was realized with bi-planar fluoroscopy. The initial success of the HM-3 prompted several manufacturers to introduce a number of second-generation lithotripters in the late 1980s, using different techniques for shock wave generation, wave focusing, and patient coupling (Rassweiler *et al.*, 1992; Lingeman, 1997). Representative second-generation lithotripters include the Siemens Lithostar, which uses an electromagnetic generator with an acoustic lens, both enclosed in a water cushion (i.e., "dry" lithotripter); and the Richard Wolf Piezolith-2300 that utilizes a self-focusing piezoelectric generator placed at the bottom of a small water basin. The primary changes in the design of the second-generation lithotripters are the increased aperture angle of the shock wave source and reduced acoustic output energy (Coleman and Saunders, 1989), enabling shock wave lithotripsy (SWL) to be performed under intravenous sedation rather than regional or general anesthesia as used for the HM-3 (Lingeman *et al.*, 2003). Continued evolution in lithotripter design in the 1990s led to the introduction of the third-generation lithotripters, which are characterized by high peak pressure with small focal width (or beam size; these two terms are used interchangeably hereinafter), increased energy output, as well as multifunctional use of the lithotripter system for SWL, ureteroscopic, and percutanous procedures (Lingeman, 1997; Rassweiler *et al.*, 2005). However, it should be noted that the technical improvements in the second- and third-generation lithotripters were largely made based on empirical experience, practical concerns for user convenience, and the desire for multifunctionality of the system rather than a rigorous understanding of the working mechanisms of SWL (Lingeman *et al.*, 2003; Zhou *et al.*, 2004; Zhong, 2007).

Previous studies have suggested that the progressive disintegration of kidney stones in SWL is produced by dynamic fatigue (Lokhandwalla and Sturtevant, 2000) under the influence of lithotripter shock wave (LSW) induced stress waves (e.g., by squeezing) inside the stone (Eisenmenger, 2001; Cleveland and Sapozhnikov, 2005) and cavitation bubbles in the surrounding fluid (Coleman *et al.*, 1987; Crum, 1988; Sass *et al.*, 1991; Zhong and Chuong, 1993; Zhong *et al.*, 1993; Pishchalnikov *et al.*, 2003). When stone phantoms of spherical geometry are used, the initial fracture of a stone may be enhanced by spallation at the posterior surface of the stone due to acoustic impedance mismatch and geometric focusing (Gracewski *et al.*, 1993; Xi and Zhong, 2001) and/or shear stresses produced by quasi-static or dynamic squeezing (Xi and Zhong, 2001; Cleveland and Sapozhnikov, 2005; Sapozhnikov *et al.*, 2007). It has been shown that stress wave-induced fracture is important for the initial dis-

[a]Present address: College of Engineering, Southern Illinois University Carbondale, Carbondale, IL 62901.
[b]Author to whom correspondence should be addressed. Electronic mail: pzhong@duke.edu

integration of kidney stones while cavitation is necessary to produce small and dischargeable fragments that are critical for the clinical success of SWL (Zhu *et al.*, 2002). Stress waves and cavitation interact synergistically to produce effective stone fragmentation during SWL (Zhu *et al.*, 2002; Sapozhnikov *et al.*, 2007; Zhong, 2007).

A growing number of clinical studies have demonstrated that compared to the original HM-3 lithotripter, the second- and third-generation lithotripters are often less effective in stone comminution yet have a higher propensity for tissue injury and stone recurrence (Graber *et al.*, 2003; Lingeman *et al.*, 2003; Gerber *et al.*, 2005). Among multiple potential contributory factors, a distinct change in the lithotripter design that has often been speculated to link with the reduced effectiveness of the third-generation lithotripters is the significantly increased peak pressure with concomitantly decreased beam size (Lingeman *et al.*, 2003).

In the past few years, there is a renewed interest in lithotripters with broad beam size, which is motivated primarily by the clinical success of Eisenmenger *et al.*'s (2002) "wide-focus and low-pressure" electromagnetic shock wave lithotripter that produces a peak positive pressure of 25 MPa and a −6 dB beam size of 18 mm. It should be noted that a low pulse repetition frequency (PRF) of 0.3 Hz was used in this initial series of clinical studies, which might contribute to the effective comminution outcome (Sapozhnikov *et al.*, 2002; Pishchalnikov *et al.*, 2006). Moreover, based on numerical model calculations, Cleveland and Sapozhnikov (2005) demonstrated that the peak principal stresses inside a stone increase significantly with the −6 dB focal width of the lithotripter. However, investigation of the effect of beam size on stone comminution using different lithotripters is problematic because of the inherent differences in the acoustic field, coupling method, stone localization technique, and output setting used by different lithotripters (Cleveland and McAteer, 2007). Much more work is still needed to better understand the effect of beam size on stone comminution and to define the optimal beam size for producing effective stone comminution with less tissue injury in SWL.

In this study, we have developed a method to modify the reflector geometry of the original HM-3 to produce a lithotripter field with high peak pressure and narrow beam size. Using this design, the effect of beam size on stone comminution can be compared in the same lithotripter using identical energy source, focusing technique, and coupling and stone localization methods, thus eliminating the inherent variations when such a comparison is performed using different lithotripters. Moreover, we have designed a new stone holder that allows us to mimic more closely the characteristics of stone fragmentation *in vivo*. Our results suggest that under the same effective acoustic pulse energy, a lithotripter field with low peak pressure and broad beam size produces significantly better stone comminution than its counterpart of high peak pressure and narrow beam size when stone fragments are allowed to disperse laterally as typically occurred *in vivo* during clinical SWL.

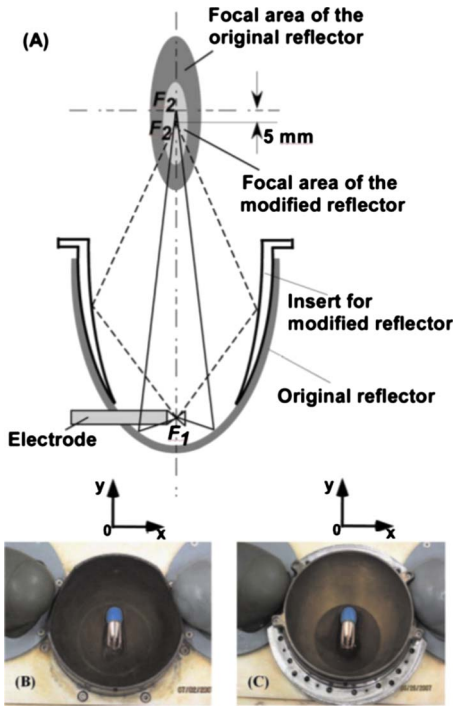

FIG. 1. (Color online) A schematic illustrating the original and modified reflector configurations in an HM-3 lithotripter (A), and photos of the original (B) and modified (C) reflectors.

II. MATERIALS AND METHODS

A. Lithotripter

The experiments were carried out in an original HM-3 lithotripter with an 80-nF capacitor and a truncated ellipsoidal brass reflector with a semi-major axis $a=138$ mm, a semi-minor axis $b=77.5$ mm, and a half-focal length $c=114$ mm. The HM-3 was operated at a representative clinical output setting of 20 kV with 1 Hz PRF.

To produce an acoustic field with high peak pressure and narrow beam size, a thin shell ellipsoidal brass reflector insert ($a'=134.4$ mm, $b'=75$ mm, and $c'=111.5$ mm) was fabricated and fitted snugly into the original HM-3 reflector (Fig. 1). The reflector insert shares the same first focus (F_1) with the original HM-3 reflector, yet its second focus (F_2') is located 5 mm pre-focally from the focus (F_2) of the original HM-3 reflector (Zhong and Zhou, 2001). The interpulse delay time Δt between the leading shock wave produced by the reflector insert and the second shock wave produced by the uncovered bottom surface of the original reflector can be determined by

$$\Delta t = \frac{2[(a-a')-(c-c')]}{c_0}, \tag{1}$$

where c_0 is the sound speed in water. Using the geometry of this new reflector insert [which is different than the one reported previously (Zhong and Zhou, 2001)], Δt is estimated to be about 1.5 μs. Because of nonlinear wave propagation, the leading shock wave and the second shock wave merge as they propagate toward the lithotripter focus, leading to the formation of an acoustic field with high peak pressure and narrow beam size (Zhou and Zhong, 2006).

B. Pressure measurements, energy density, and acoustic pulse energy calculations

The acoustic field and pressure distribution produced by the HM-3 using the original reflector in the focal plane ($z=0$ mm) and a pre-focal plane ($z=-15$ mm), as well as using the modified reflector in the focal plane, were determined by using a light spot hydrophone (LSHD-2, University of Erlangen-Nuremberg, Erlangen, Germany), which has a bandwidth of 40 MHz, a sensitivity of 10 mV/MPa, and spatial resolution of 100 μm, based on manufacturer's specification. The optical head of the LSHD (a $90\times60\times30$ mm^3 in $L\times W\times H$ glass block) was attached to a three-dimensional (3D) translation stage (Velmex, Bloomfield, NY) with the front surface of the glass block aligned perpendicular to the lithotripter axis. Alignment of the LSHD with F_2 was aided by a mechanical pointer. Using a LABVIEW program, the LSHD was scanned orthogonally from -14 to $+14$ mm in the measurement plane along the x- and y-axis, respectively (Fig. 1). The x-axis is defined by the left to right direction, and the y-axis is defined by the head to foot direction of the patient placed in the HM-3 tub. A step size of 1 mm was used between -6 and 6 mm, and a step size of 2 mm was used otherwise. At least six pressure waveforms at each selected position were recorded by using a digital oscilloscope (LeCroy 9314M, Chestnut Ridge, NY) operated at a sampling rate of 100 MHz. The oscilloscope was triggered by the spark discharge at the tip of the HM-3 electrode. To avoid cavitation interference, a long interpulse delay of 120 s was used for pressure measurement. Based on the measured pressure waveforms, several characteristic parameters of the lithotripter fields were calculated following the IEC 61846 Standard (IEC-Standard, 1998), unless otherwise specified. The -6 dB beam size in each measurement plane was determined by the focal width at half maximum of the peak positive acoustic pressure (p_+).

The energy density (ED) (or the derived pulse-intensity integral) of the lithotripter field at each measurement point is calculated by

$$\mathrm{ED}=\frac{1}{Z}\int_T p^2dt, \tag{2}$$

where $Z(=\rho c_0)$ is the acoustic impedance of the medium and ρ is the density of water, T is the total temporal integration limits ranging from the start to the end of the pressure waveform of the LSW, and p is the acoustic pressure that varies with time (t).

The derived acoustic pulse energy (E_R) of the LSW can be calculated by

$$E_R=\frac{1}{Z}\int_S\int_T p^2dtds=\int_S EDds, \tag{3}$$

where S is the measurement area. To determine E_R in different focal areas in each measurement plane, the integration was carried out over circular areas of 6-, 12-, and 28-mm diameters, respectively.

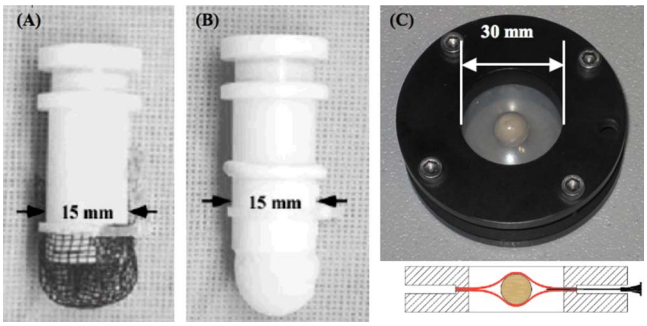

FIG. 2. (Color online) Pictures illustrating three different types of stone holders: (A) a mesh holder, (B) a finger cot holder, and (C) a membrane holder together with a schematic of its cross-sectional view. A 22 G needle (Becton Dickinson, Franklin Lakes, NJ) was sandwiched between the two silicone sheets in the membrane holder to equalize the pressure inside the exposure chamber with the fluid in the test tank.

C. Cavitation assessment

Cavitation activity produced in the lithotripter field was characterized using several established methods, including measurements by a 2.25-MHz focused hydrophone aligned confocally with F_2, by a pressure transducer (119B, PCB Piezotronics Inc., Depew, NY) placed in the measurement plane along the lithotripter axis, and by high-speed imaging using a phantom camera (Phantom v. 7.3, Vision Research, Wayne, NJ) at a framing rate up to 20 000 frames/s and an exposure time of 6 μs. The detailed description of these measurements can be found in our previous studies (Zhong *et al.*, 1997, 2001; Sankin *et al.*, 2005). In addition, cavitation potential in a lithotripter field (Iloreta *et al.*, 2007) was calculated using the Gilmore model assuming spherical symmetry in bubble geometry

$$R\left(1-\frac{U}{C}\right)\frac{dU}{dt}+\frac{3}{2}\left(1-\frac{U}{3C}\right)U^2=\left(1+\frac{U}{C}\right)H+\frac{1}{C}\left(1-\frac{U}{C}\right)R\frac{dH}{dt}, \tag{4}$$

where R and U are radius and velocity of the bubble wall, and C and H are the speed of sound in the liquid at the bubble wall and the enthalpy difference between the liquid at pressure on bubble wall and pressure at infinity. The numerical calculation was described previously (Zhu and Zhong, 1999).

D. Stone fragmentation tests

1. Stone holders

As shown in Fig. 2, three different types of stone holders were used in this study: (1) a 15-mm mesh holder, (2) a 15-mm finger cot holder, and (3) a 30-mm membrane holder. The mesh holder [Fig. 2(A)] is made of a plastic-mesh with 2-mm grids, which is fastened on a 15-mm plastic tube. During SWL, small fragments can fall through the 2-mm grids, while large residual fragments are kept within a relatively small area near the bottom of the mesh. The finger cot holder consists of a finger cot made of disposable rubber (QRP, Tucson, AZ), which is attached to the 15-mm tube [Fig. 2(B)]. Using the finger cot holder, stone fragments during

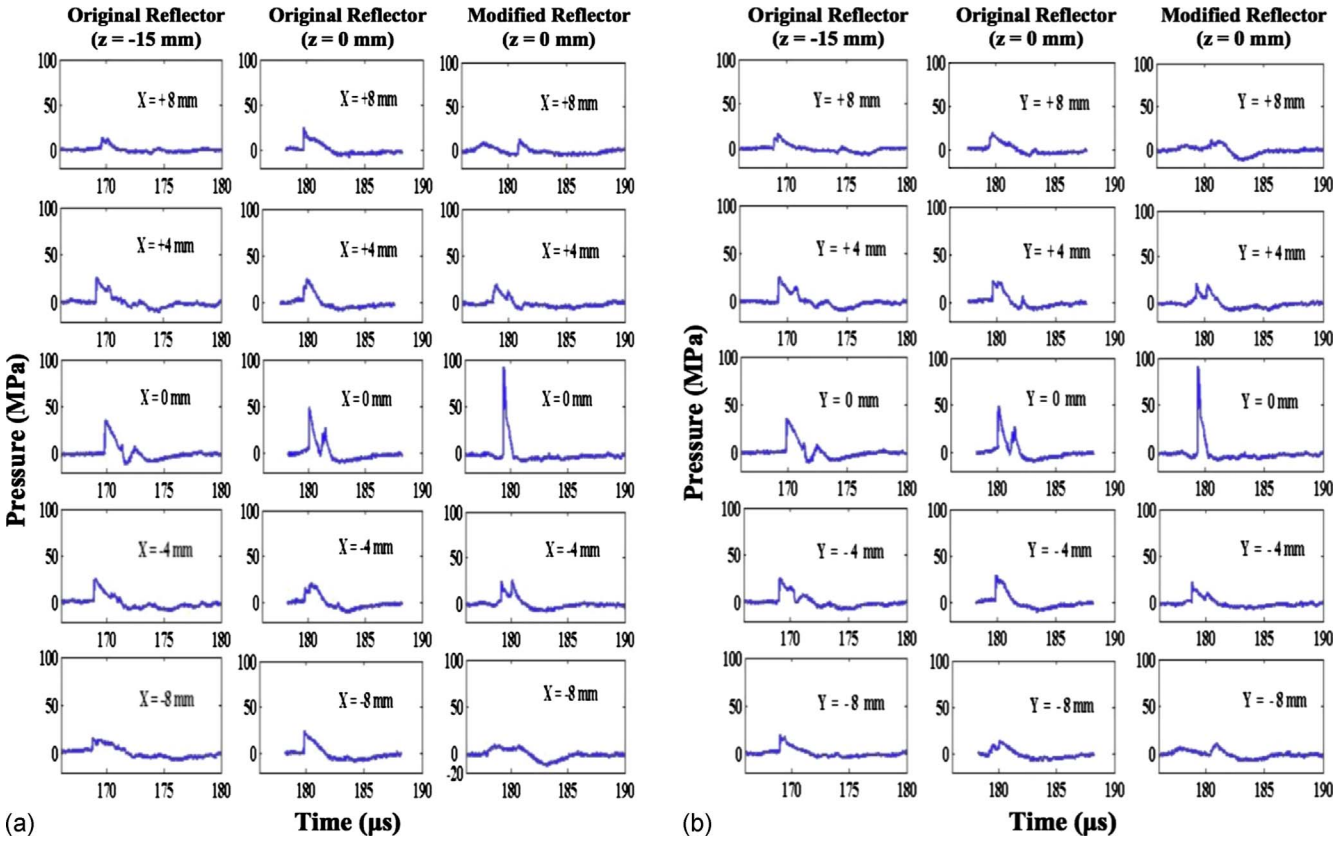

FIG. 3. (Color online) Representative pressure waveforms measured along the x-axis (A) and y-axis (B) in the focal (z=0 mm) and pre-focal (z=−15 mm) planes of the HM-3 lithotripter at 20 kV using either the original or modified reflector.

SWL will be retained and accumulated in a relatively small volume around the lithotripter focus. Overall, the mesh holder and finger cot represent idealized targeting of the stone during SWL.

The membrane holder consists of two Noryl polyphenylene oxide (PPO) plastic rings with an inner diameter of 30 mm, which compress two 0.5-mm thick transparent silicone rubber membranes (Product No.: 86915 K12, McMaster-Carr, Santa Fe Springs, CA) to sandwich a stone at the center of the holder [Fig. 2(C)]. The membrane holder allows stone fragments to disperse laterally, and thus mimicking more closely the lithotripsy procedures *in vivo*. An added benefit of the membrane holder is that the dynamic process of stone fragmentation during SWL can be recorded for further analysis.

2. Comminution tests

Spherical stone phantoms (D=10 mm) made of Begostone with a powder to water mixing ratio of 5:1 by weight (Liu and Zhong, 2002) were used. For comminution tests, a sample size of n=6 was used in each group. Before shock wave treatment, each stone phantom was weighed in dry state, and then immersed in degassed water for at least 4 h. Next, the stone phantom was placed into the selected holder filled with degassed water (O_2 concentration <3 mg/l), and aligned to F_2 under the guidance of bi-planar fluoroscopy. For treatment in the pre-focal plane, the stone phantom was first aligned to F_2, and then translated by 15 mm toward the shock wave source along the lithotripter axis using a 3D stage. After the shock wave treatment, all residual fragments were carefully collected, and then let dry in air for 24 h. Finally, the dry fragments were sieved sequentially through a series of grids of 2, 2.8, and 4 mm, respectively, and weighed thereafter. The efficiency of stone comminution was determined by the percent of fragments less than 2 mm.

III. RESULTS

A. Lithotripter fields

1. Pressure waveforms

Representative pressure waveforms measured on the beam axis and at ±4 and ±8 mm along the x- and y-axis in the three selected measurement planes are shown in Fig. 3. For the original reflector, the LSW arrives at the pre-focal location (z=−15 mm) on the beam axis in about 170 μs and at F_2 (z=0 mm) in about 180 μs after the spark discharge. A dual-peak structure in the leading compressive wave is observed at both locations, which is presumably caused by the truncation in the lateral sides of the ellipsoidal reflector to facilitate the bi-planar fluoroscopic imaging for stone localization (Zhou and Zhong, 2003). In comparison, the LSW produced by the modified reflector arrives at F_2 in about 179 μs after the spark discharge and its pressure waveform has a single peak with high pressure in the leading compressive wave. Away from F_2, two positive peaks can be observed in the LSW profile, and the peak pressure drops quickly along both the x- and y-axis. Specifically, p_+ produced by the modified reflector at F_2 nearly doubles the

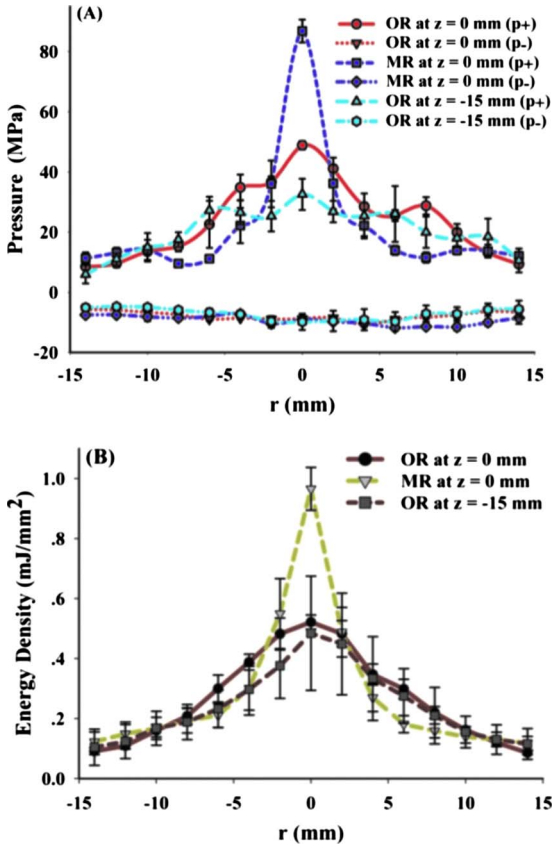

FIG. 4. (Color online) Peak pressure (A) and energy density (B) distribution of the shock waves produced by the HM-3 lithotripter at 20 kV using the OR in both the focal (z=0 mm) and pre-focal (z=−15 mm) planes, and the MR in the focal plane (z=0 mm).

value produced by the original reflector. However, at 4-mm lateral distance from F_2, the modified reflector produces a lower peak positive pressure than the original one [p =0.002 based on data shown in Fig. 4(A)].

Figure 4(A) shows the lateral distribution of p_+ and peak negative pressure (p_-) produced by the original reflector (OR) in the focal plane (z=0 mm) and in the pre-focal plane (z=−15 mm), as well as by the modified reflector (MR) in the focal plane of the HM-3 at 20 kV. The peak pressure at each radial distance was determined by the arithmetic mean of the corresponding values measured on the x- and y-axis at the same radial distance. In the focal plane and at a small radial distance from F_2 (i.e., −2 to 2 mm), the modified reflector produces much higher p_+ than the corresponding value of the original reflector, both of which are higher than the p_+ produced by the original reflector in the pre-focal plane (z=−15 mm). However, moving further away from F_2, p_+ of the modified reflector was found to be significantly lower than the corresponding values produced by the original reflector in both the z=0 mm and z=−15 mm planes. Specifically, the mean value of p_+ produced by the modified reflector at F_2 was measured to be 86.9 MPa, which is significantly higher than the corresponding value of 48.9 MPa produced by the original reflector ($p<0.001$). In the pre-focal plane, p_+ produced by the original reflector is further reduced to 32.6 MPa. In contrast to the significant change in p_+, the values of p_- were found to be similar, which are −10.6 MPa for the modified reflector in the focal plane, and −10.7 MPa in the focal plane and −9.8 MPa in the pre-focal plane for the original reflector. More importantly, the modified reflector produces the narrowest −6 dB beam size of 3.6 mm, while the original reflector produces a broad beam size of 10.9 mm in the focal plane, and the broadest beam size of 17.8 mm in the pre-focal plane.

2. Energy density and acoustic pulse energy

The distribution of energy density produced by the original and modified reflectors in the three aforementioned measurement planes is shown in Fig. 4(B). In general, the profiles of energy density variation produced by the two reflectors are similar to those in the peak positive pressure distribution [Fig. 4(A)]. One feature worth noting is that with the significant change in p_+ at F_2, the maximum energy density is increased from 0.52 $\mathrm{mJ/mm^2}$ produced by the original reflector to 0.97 $\mathrm{mJ/mm^2}$ produced by the modified reflector.

The acoustic pulse energy (E_R) is an important parameter of the lithotripter field that correlates closely with stone comminution in SWL (Granz and Kohler, 1992; Delius *et al.*, 1994). Based on pressure measurement data, E_R was calculated in three different cross-sectional areas of 6, 12, and 28 mm in diameter, respectively. It was found that E_R delivered to the three aforementioned measurement planes (i.e., 121.7, 115.9, and 116.1 mJ) is approximately the same in the area with 28-mm diameter, which covers essentially the area of the membrane holder. For the acoustic pulse energy that covers the 10-mm spherical stone (i.e., E_R in the 12-mm diameter area), the value produced by the original reflector in the focal plane (42.9 mJ) is slightly higher than the value (36.4 mJ) in the pre-focal plane, and that produced by the modified reflector in the focal plane (37.4 mJ). In comparison, near the beam axis (i.e., E_R in the 6-mm diameter area), the modified reflector produces the highest acoustic pulse energy (15.5 mJ), followed by the original reflector in the focal plane (13.0 mJ) and the pre-focal plane (11.2 mJ), respectively. Altogether, these results indicate that while the total acoustic pulse energy delivered to the membrane holder (i.e., E_R in the 28-mm diameter area) is essentially the same, the energy density and energy distribution can change significantly depending on the reflector configuration and the measurement plane. Overall, the modified reflector produces a narrow beam size and concentrates more acoustic energy around the beam axis, while the original reflector has a broad beam size with a comparably more uniform energy density distribution. The characteristic parameters of the acoustic fields produced by the original and modified reflectors in the three aforementioned measurement planes are summarized in Table I.

B. Cavitation activities produced in different lithotripter fields

1. Collapse time of bubble cluster

Using the 2.25-MHz focused hydrophone or the PCB transducer, the collapse time (t_c) of bubble cluster induced around F_2 or near the beam axis in the pre-focal plane was determined by the time delay between the arrival of the LSW

TABLE I. Characteristic parameters of the acoustic fields produced by an HM-3 lithotripter with the original and modified reflectors (the geometry of the reflector is given in Sec. II).

	Original reflector at $z=-15$ mm	Original reflector at $z=0$ mm	Modified reflector at $z=0$ mm
Peak positive pressure (MPa)	32.6 ± 5.2	48.9 ± 1.3	86.9 ± 3.8
Peak negative pressure (MPa)	-9.8 ± 2.7	-10.7 ± 0.4	-10.6 ± 0.6
−6 dB focal width (mm)[a]	17.8	10.9	3.6
Acoustic pulse energy (mJ) (6-mm diameter)[a]	11.2	13.0	15.5
Acoustic pulse energy (mJ) (12-mm diameter)[a]	36.4	42.9	37.4
Acoustic pulse energy (mJ) (28-mm diameter)[a]	115.9	121.7	116.1

[a]Data were calculated based on the arithmetic mean of the value measured on the x- and y-axes.

and the peak pressure in acoustic emission signals produced by the violent collapse of cavitation bubbles (Coleman *et al.*, 1987; Zhong *et al.*, 1997). In free field, t_c for bubble clusters produced by the original reflector at F_2 is 324.9 ± 19.0 μs (mean $\pm$ standard derivation), which is comparable to that produced by the modified reflector at F_2 (318.0 ± 32.3 μs), while the corresponding value for the original reflector in the pre-focal plane is slightly higher (365.7 ± 42.6 μs). Near the boundary of the PCB transducer, the values for t_c of the bubble cluster produced by the original reflector are 659.0 ± 30.4 μs at F_2 and 698.1 ± 35.9 μs in the pre-focal plane. The corresponding value for the modified reflector at F_2 is 636.6 ± 12.1 μs. Overall, there is no statistical difference ($p > 0.10$) between the values of t_c for bubble clusters produced at the three aforementioned positions either in free field or near a solid boundary.

2. High-speed imaging of bubble dynamics

Representative high-speed imaging sequences of the bubble dynamics produced in degassed water (O_2 concentration about 2.4 mg/l) by a single shock using either the original or modified reflector are shown in Fig. 5. Following the passage of the LSW at F_2 (~180 μs), a cluster of bubbles was observed that expanded rapidly, and some individual bubbles near the lithotripter beam axis coalesced with each other during the maximum expansion of the bubbles between 385 and 495 μs. Subsequently, the bubbles collapsed violently to a minimal size, followed by a few rebounds. Based on images from 25 individual sequences, no statistically significant differences were observed in terms of the maximum bubble radius produced by the original and modified reflectors at the center of the three measurement planes (see inset in Fig. 6).

3. Gilmore model calculation of bubble dynamics

Based on the pressure waveforms measured at different radial distances from the beam axis, the Gilmore model was used to calculate the maximum bubble radius (R_{max}) at the corresponding positions. It was found that the values of R_{max} predicted by the Gilmore model in the three measurement planes are comparable on the beam axis (i.e., ~1.1 mm), which is confirmed by the experimental measurements based

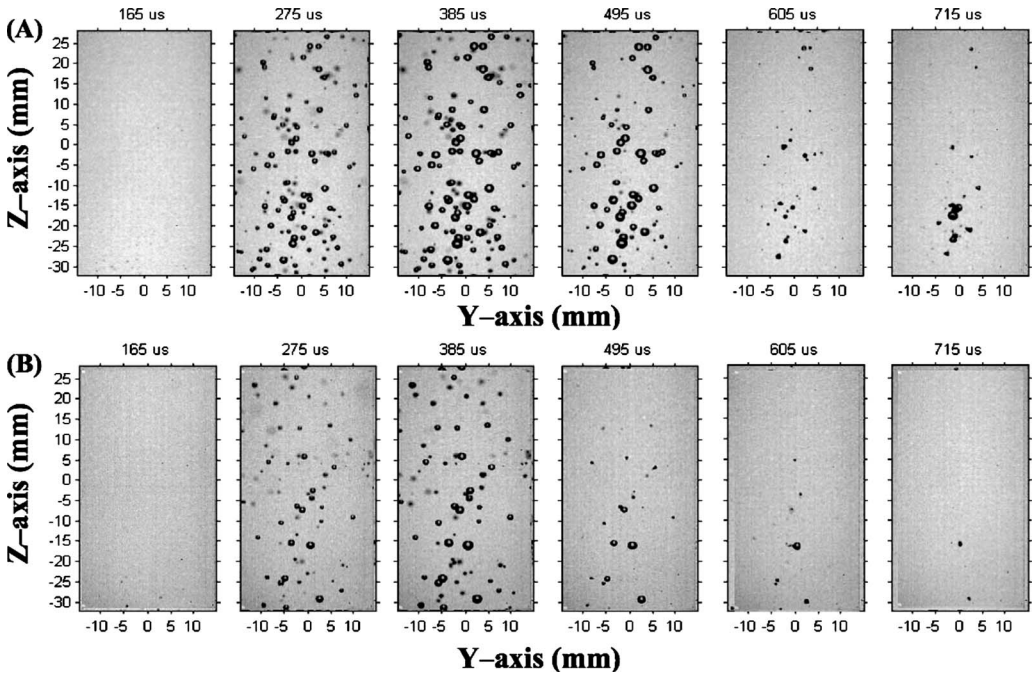

FIG. 5. Representative sequences of high-speed images of bubble dynamics in water produced by the HM-3 lithotripter at 20 kV using either the original (A) or the modified (B) reflector. The lithotripter focus is located at the origin of the coordinate system, frame size=60×30 mm^2 ($H \times W$), interframe time =110 μs, and O_2 concentration in water=2.4 mg/l. Time zero of the image sequence coincides with the spark discharge of the HM-3 electrode.

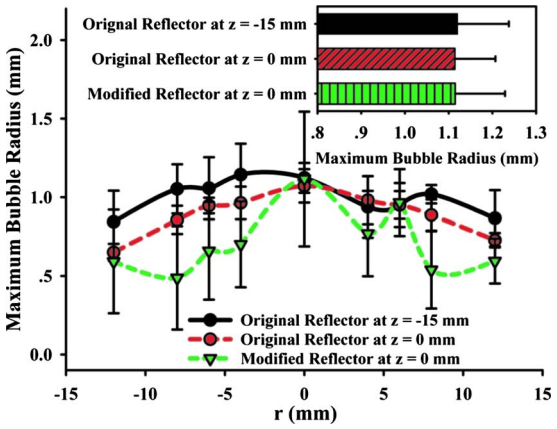

FIG. 6. (Color online) The maximum bubble radius predicted by the Gilmore model at different lateral distances from the central axis of the HM-3 lithotripter at 20 kV. The model calculation was carried out based on the pressure waveforms measured in the HM-3 lithotripter field using either the original or modified reflector. Inset shows the measured maximum bubble radius (mean ± standard derivation) from high-speed imaging sequences.

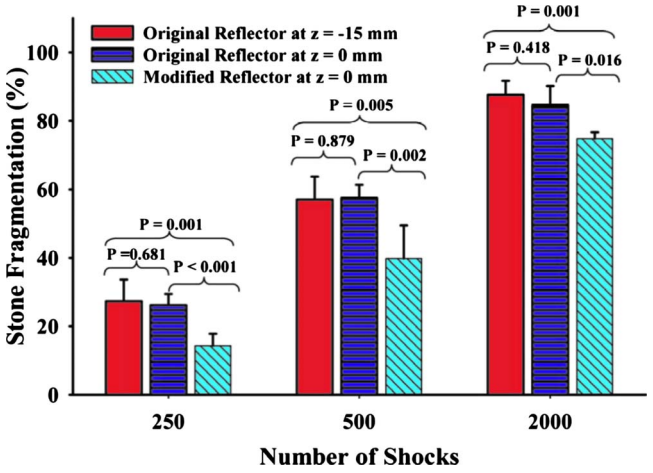

FIG. 8. (Color online) Dose-dependence of stone fragmentation in the membrane holder in the focal (z=0 mm) and pre-focal (z=−15 mm) planes produced by the HM-3 lithotripter at 20 kV using either the original or modified reflector.

on high-speed imaging (see inset in Fig. 6). Furthermore, for the original reflector, R_{max} was predicted to decrease slightly away from the beam axis both in the focal and pre-focal planes. In comparison, for the modified reflector, R_{max} was predicted to decrease significantly off the beam axis in the focal plane, although large standard deviations were observed.

C. Stone fragmentation

Stone comminution after 250 shocks produced by using either the original or modified reflector was evaluated in three different holders (Fig. 7). Overall, the efficiencies of stone fragmentation are the highest in the mesh holder, followed by in the finger cot, and the lowest values were obtained in the membrane holder. These differences can be attributed to the effects of LSW attenuation by the residual

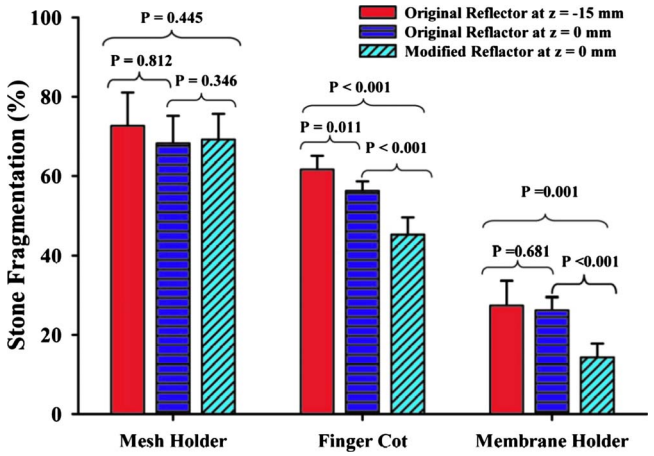

FIG. 7. (Color online) Stone fragmentation in the focal (z=0 mm) and pre-focal (z=−15 mm) planes after 250 shocks produced by the HM-3 lithotripter at 20 kV using either the original or modified reflector. The comminution tests were carried out in three different holders.

fragments in the finger cot (Zhu *et al.*, 2002) and the significant lateral spreading of stone fragments in the membrane holder (see Fig. 9).

In the mesh holder, no statistical differences in stone fragmentation were observed between the original reflector either in the focal or pre-focal plane and the modified reflector in the focal plane. In contrast, in the finger cot or in the membrane holder, the efficiencies of stone fragmentation produced by the modified reflector in the focal plane were found to be significantly lower (by more than 20%) than the corresponding values produced by the original reflector either in the focal or pre-focal plane. The differences are statistically significant ($p<0.001$). Altogether, these findings suggest that lithotripter beam size will not influence comminution outcome when small fragments (<2 mm) are filtered out and large fragments (>2 mm) are concentrated in a small volume around F_2 (as in the case of mesh holder). However, when residual fragments are accumulated inside the holder and/or spread to a large area (as in the case of finger cot and/or membrane holder), a lithotripter field with a broad beam size will produce better stone comminution than its counterpart with a narrow beam size under the same acoustic pulse energy.

Furthermore, the dose-dependency of stone comminution in the membrane holder was evaluated (Fig. 8). From 250 to 2000 shocks, the efficiencies of stone comminution produced by the original reflector both in the focal and pre-focal planes were found to be significantly higher than the corresponding values produced by the modified reflector in the focal plane ($p<0.02$). In comparison, there is no statistical difference ($p>0.4$) in stone fragmentation produced by the original reflector between the results obtained in the focal and pre-focal planes.

Figure 9(A) shows representative photographic sequences of stone comminution produced by the original reflector in the focal and pre-focal planes and by the modified reflector in the focal plane. These images were taken by a digital camera (Homeconnect 0770, 3Com, Marlborough, MA) mounted directly above the membrane holder, aiming at

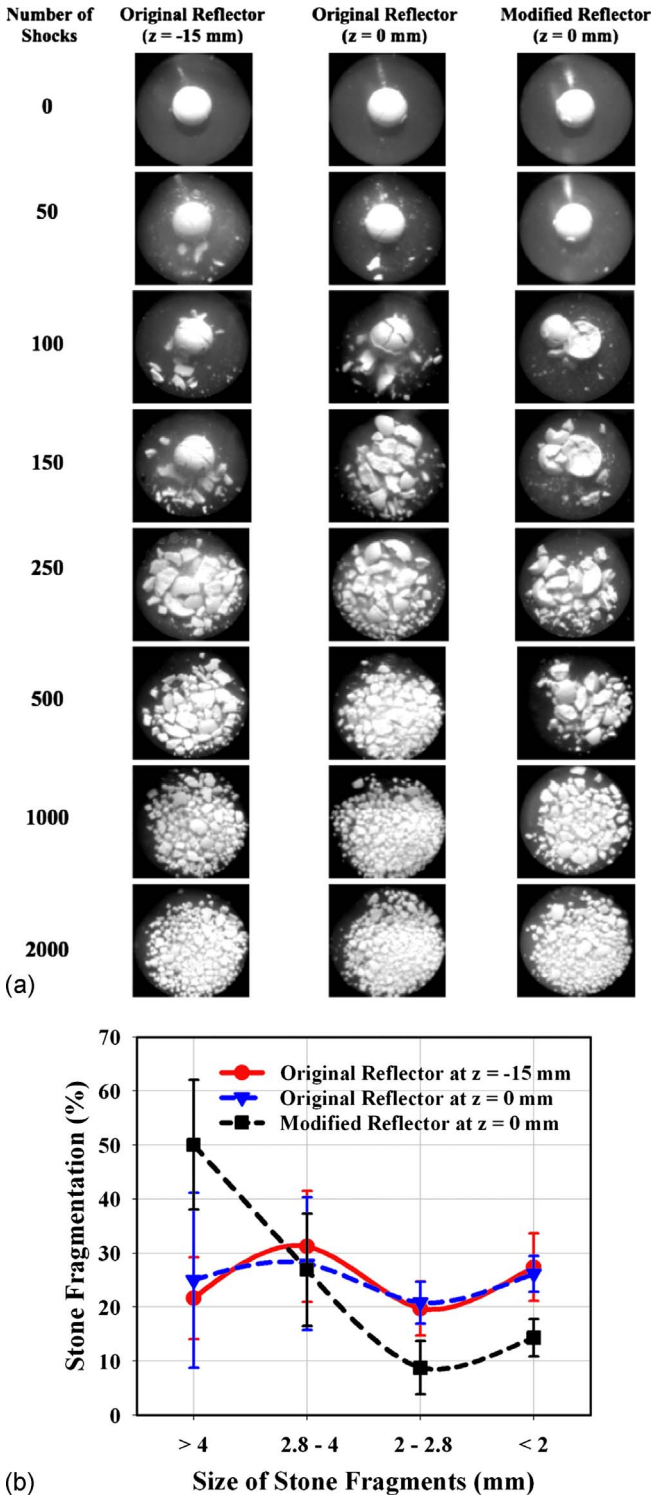

FIG. 9. (Color online) Representative images of the progressive stone comminution process from 0 to 2000 shocks (A) and fragment size distribution after 250 shocks (B) in the membrane holder in the focal (z=0 mm) and pre-focal (z=−15 mm) planes produced by the HM-3 lithotripter at 20 kV using either the original or modified reflector. Lithotripter shock waves were propagating in the direction out of the page.

the posterior surface of the stone. Several interesting features can be observed. First, using the original reflector, the initial fragmentation was observed to occur at the anterior side of the stone facing the incident LSW (see images after 50 shocks where multiple small pieces came off). With the membranes initially in contact with the spherical stone, cavitation damages such as the formation of deep craters centered around the lithotripter axis at the LSW entrance and exit sites, as often reported in free field (Pishchalnikov *et al.*, 2003), were not observed. Instead, the stone was crumbled from multiple sites into a cluster of fragments with relatively homogenous size distribution after 250 shocks [Fig. 9(B)]. In contrast, using the modified reflector, the initial fragmentation occurred primarily on the posterior side of the stone, with one or a few large pieces popping off from the backside of the stone within 100 shocks. In addition, the disintegration process was uneven and the resultant fragments have a relatively heterogeneous size distribution after 250 shocks, with a high percent of large fragment (>4 mm) with a concomitantly low percent of small fragment [<2.8 mm, see Fig. 9(B)]. This difference in the initial fragmentation of the stone produced by the original and modified reflectors may be related to the differences in pressure distribution and shock wave-bubble interaction produced by these two reflector configurations. Second, using the original reflector, the initial stone disintegration was observed to occur through multiple fracture planes (see images after 100 shocks in z=0 mm plane). In addition, because of the reduced peak positive pressure, the initiation of a significant disintegration of the stone in the pre-focal plane was slightly delayed compared to that in the focal plane. In comparison, using the modified reflector, the stone was fractured initially across a plane perpendicular to the beam axis into two large cap-like pieces, which were difficult to break in the subsequent 50 shocks (see images after 100 and 150 shocks in z=0 mm plane). Overall, the initial fragmentation process produced by the modified reflector in the focal plane is significantly slower than its counterparts produced by the original reflector both in the focal and pre-focal planes. Third, between 250 and 2000 shocks, large residual fragments were gradually broken up and spread over the entire area of the membrane holder in all three groups. Because of the higher pressure and stronger shock wave-bubble interaction, fragments located in the central area of the membrane holder were disintegrated much more easily than those located in the outer rim. Fourth, significant mixing of the fragments inside the membrane holder was observed during the treatment. Some fragments in the outer rim region were observed to migrate back to the central region and subsequently disintegrated, while other fragments were moved away from the central area and remained almost unchanged in the outer rim region. However, the mixing effect was not quantified. Overall, the characteristics of stone disintegration and fragment size distribution observed in these photographic sequences are consistent with the quantitative stone comminution results shown in Fig. 8.

IV. DISCUSSION

Since the introduction of the first-generation HM-3 lithotripter in the early 1980s, evolution in SWL technology has bought several significant changes in the design of modern lithotripsy systems (Lingeman, 1997; Rassweiler *et al.*, 2005). One of the most critical design changes in the second- and third-generation lithotripters is the increased aperture

and aperture angle of the shock wave source with concomitantly decreased beam size of the lithotripter field (Coleman and Saunders, 1989; Rassweiler *et al.*, 2005). Although it has been widely speculated that this dramatic reduction in beam size (by 50% or more) may significantly influence the effectiveness of stone comminution in SWL, an objective investigation of this topic using various lithotripsy devices is difficult. This is because of the inherent dissimilarities in the acoustic field, coupling method, stone localization technique, and output setting used by different lithotripters (Cleveland and McAteer, 2007). Ideally, such a study should be carried out in the same lithotripter to eliminate these inherent variations between different machines. Recently, the encouraging clinical results from Eisenmenger's "wide-focus and low-pressure" lithotripter (Eisenmenger, 2001; Eisenmenger *et al.*, 2002) and the introduction of "dual focus" design in clinical lithotripters (Leistner *et al.*, 2007) have further heightened the interest and urgency in addressing this critical issue.

To overcome the aforementioned limitation, we have developed a reflector insert for the HM-3 so that we can generate a significantly different lithotripter field with a high peak pressure (~87 MPa) and narrow beam size (~4 mm) compared to the original HM-3 lithotripter (49 MPa and 11 mm). These two distinctively different acoustic fields in the geometric focal plane ($z=0$ mm) of the HM-3 lithotripter are produced by using the same shock wave source and under the same output setting (i.e., 20 kV). Moreover, we have characterized the acoustic field produced by the original reflector in a pre-focal plane ($z=-15$ mm), which has an even lower peak pressure (~33 MPa) yet broader beam size (18 mm). Despite these differences, the effective acoustic pulse energies (i.e., E_R in the 12- and 28-mm diameter areas) produced by the original or modified reflector in the three aforementioned measurement planes are similar to each other within the uncertainty of the pressure measurements. Since acoustic pulse energy has been shown to correlate closely with stone comminution (Granz and Kohler, 1992; Delius *et al.*, 1994; Eisenmenger, 2001), our experimental system and study design provide a well-controlled test configuration to evaluate the effect of lithotripter beam size on stone comminution while avoiding potential confounding issues when such a comparison is made across different lithotripters.

Another critical limitation of previous *in vitro* studies is that stone is often placed either in a mesh holder or in a finger cot in which fragments smaller than certain size (e.g., 2 mm) are filtered out from the holder or confined within a small volume around the lithotripter focus. These phantom systems, while convenient and useful for quality control by the manufacturers to ensure adequate output of clinical lithotripters, do not capture some important characteristics of stone comminution *in vivo*, such as dispersion of fragments in the renal collecting system. To overcome this limitation, we have developed a membrane holder that allows stone fragments to be accumulated and also spread laterally within the holder ($D=30$ mm) during SWL. This membrane holder can also be used to record in real time the entire stone fragmentation process during SWL, providing valuable insights into the factors that may impact treatment outcome.

Using these phantom systems, we have observed that, using the same energy source and under comparable effective acoustic pulse energy, stone comminution produced in the mesh holder ($D=15$ mm) is similar and independent of the beam size. Because the stone was originally aligned with F_2 and, following each shock wave exposure, fragments less than 2 mm were filtered out from the mesh holder, the energy of ensuing LSWs could be delivered directly to residual fragments larger than 2 mm, leading to effective stone comminution (see Fig. 7). In contrast, when stone fragments were retained and confined within the finger cot ($D=15$ mm), the overall comminution efficiency was reduced substantially from the corresponding values in the mesh holder. Moreover, the largest reduction was observed with the modified reflector, which, because of its high $p+$, might experience the strongest attenuation of the LSW by residual small fragments accumulated at the bottom of the finger cot (Zhu *et al.*, 2002). It is also interesting to note that using the original reflector, stone comminution in the pre-focal position is slightly but significantly higher than that produced in the focal plane, which is interpreted as the result of stronger cavitation and more synergistic interaction between the stress waves and cavitation (Zhu *et al.*, 2002) produced in the finger cot at the pre-focal position than at the lithotripter focus. This finding is also consistent with the observation from a previous study (Sokolov *et al.*, 2002). Finally, stone comminution in the membrane holder was further reduced from the corresponding values in the mesh holder and in the finger cot. In comparison, the modified reflector produced significantly lower stone comminution than the original reflector, which, however, did not show a statistically significant difference between the results in the focal and pre-focal planes. These differences in stone comminution produced by the original and modified reflectors and the similarities between the focal and pre-focal planes in the original lithotripter field were further confirmed at various shock wave doses (see Fig. 8). Altogether, these findings suggest that when fragments are dispersed to a large area ($15\ \text{mm} < D < 30$ mm) during SWL, the original HM-3 with a broad beam size will produce better stone comminution than its counterpart of a narrow beam size produced by the modified reflector. However, further increase in the beam size (from 11 to 18 mm) with concomitantly reduced peak positive pressure (from 49 to 33 MPa) does not alter the resultant stone comminution in the membrane holder, indicating that an optimal beam size may exist that leads to effective stone comminution.

For the same effective acoustic pulse energy, why does a lithotripter field with a broad beam size (of ~11 mm) produce better stone comminution than its counterpart with a narrow beam size (of ~4 mm) under clinically relevant test conditions? Several interesting observations of the differences in stone fragmentation produced by the two contrasting lithotripter fields may be worth noting. First, a low-pressure/broad beam size lithotripter field breaks up stone initially on the anterior surface of the stone and the damage propagates through multiple fracture planes, resulting in fragments with a relatively homogeneous size distribution [see Fig. 9(B)]. This observation is consistent with other

studies using low-pressure and broad beam size lithotripters (Eisenmenger, 2001; Eisenmenger *et al.*, 2002). In contrast, a high-pressure/narrow beam size lithotripter field breaks up stone initially from the posterior side of the stone. This initial damage may be caused by the high pressure at the center and low pressure surrounding the periphery of the stone through a combination of spallation (Gracewski *et al.*, 1993; Xi and Zhong, 2001) and quasi-static or dynamic squeeze (Eisenmenger, 2001; Cleveland and Sapozhnikov, 2005; Sapozhnikov *et al.*, 2007) mechanism that causes an uneven fracture of the stone (see Fig. 9). Once the original spherical geometry of the stone is destroyed by the initial fracture, the residual large fragments with irregular geometry become much more resistant to subsequent shock waves, and the fragments produced by additional 150–200 shocks are heterogeneous in size distribution [see Fig. 9(B)]. Second, the radiation force exerted by the incident LSW may cause lateral displacement of stone fragments. This feature was observed but not quantified in this study. Especially, because of the high peak pressure and pressure gradient along the beam axis of the modified reflector, large residual fragments may be dispersed further away from the high-pressure and high ED region at the center of focal region. Significant lateral dispersion of the fragments may impact more negatively on stone comminution produced by the modified reflector because of its small effective fragmentation zone. However, significant mixing was observed in the membrane holder in the later stage of the stone comminution process, during which some fragments in the outer rim region could move back to the central area or vise versa. This mixing effect might affect stone fragmentation outcome in the membrane holder when a large number of shock waves were delivered. Nevertheless, the extent by which this mixing effect may occur *in vivo* is not known. Third, there are subtle differences in cavitation potential and bubble dynamics produced by the two lithotripter fields. Based on the results of high-speed imaging (Fig. 5) and model calculations (Fig. 6), the maximum bubble sizes produced by the two lithotripter fields are similar along the beam axis. However, at off-axis locations, the original reflector with a broad beam size may generate stronger cavitation than the modified reflector (see Fig. 6). Combined with the characteristics of pressure distribution [Fig. 4(A)], these observations suggest that a high-pressure/narrow beam size lithotripter field will be effective in comminuting stones that are accurately aligned to the lithotripter focus, and when the residual fragments are also confined in a small volume around the beam focus under the influence of minimal respiratory motion. In comparison, a low-pressure/broad beam size lithotripter field will be more effective when stones are less accurately aligned with the beam focus, and when residual fragments are dispersed or moved away from the lithotripter axis due to significant respiratory motion.

It has been argued that with high-pressure and high-energy output, a small beam size lithotripter may produce the same effective fragmentation zone based on an absolute pressure threshold (e.g., $p_+ = 10$ MPa) for stone comminution, compared to a low-pressure and broad beam size lithotripter such as the HM-3 (Wess, 2005). This argument, however, is primarily based on stone fragmentation data obtained under idealized test conditions such as in a mesh holder or finger cot placed at the lithotripter focus (Teichman *et al.*, 2000). In addition, the output settings used by different lithotripters in those previous studies are not the same, with significantly higher acoustic pulse energy delivered by the high-pressure and narrow beam size third-generation lithotripters, leading to better treatment output under idealized test conditions (Teichman *et al.*, 2000). In contrast, under clinically relevant *in vitro* test conditions such as stone fragmentation in the membrane holder as described in this study, which accounts for dispersion of stone fragments, or in a setup that mimics the respiratory motion of the stone (Cleveland *et al.*, 2004), the comminution efficiency produced by a lithotripter field with high peak pressure and narrow beam size has been found to be greatly reduced. These factors (i.e., dispersion of stone fragments and respiratory motion of the stone) may also contribute to the reduced comminution efficiency with concomitantly increased stone recurrence rate observed clinically in the third-generation lithotripters with high pressure and narrow beam size (Lingeman *et al.*, 2003; Gerber *et al.*, 2005). Furthermore, comparison of stone comminution based on absolute pressure threshold (instead of effective acoustic pulse energy delivered to the patient) without considering the adverse effects of high-energy shock waves on renal tissues should not be recommended for guiding the clinical practice of SWL. Similar to stone comminution, it is well known that tissue injury in SWL increases with the output energy of the lithotripter (Evan *et al.*, 1998).

In summary, we have developed a method to modify the reflector geometry of the original HM-3 lithotripter so that a distinctively different acoustic field with high pressure and narrow beam size can be produced using the same energy source and output setting. For the same effective acoustic pulse energy, a lithotripter field with low peak pressure and broad beam size produces significantly better stone comminution than its counterpart of high peak pressure and narrow beam size when stone fragments are dispersed laterally as frequently occurs *in vivo* during clinical SWL. A high-pressure and narrow beam size lithotripter field produces efficient comminution when stone and residual fragments are well constrained near the lithotripter focus. On the other hand, their fragmentation power decreases rapidly at off-axis positions. In contrast, a low pressure and broad beam size, lithotripter field produces effective stone comminution over a large area and the resultant fragments are relatively homogeneous and small in size.

ACKNOWLEDGMENTS

This work was supported in part by NIH through Grant Nos. R01-DK052985 and S10-RR16802. The authors are also grateful to W. Eisenmenger, M. Delius, and R. Nanke for their critical reading of the manuscript and helpful discussions.

Chaussy, C. G., and Fuchs, G. J. (**1989**). "Current state and future-developments of noninvasive treatment of human urinary stones with extracorporeal shock-wave lithotripsy," J. Urol. (Baltimore) **141**, 782–789.

Cleveland, R. O., Anglade, R., and Babayan, R. K. (**2004**). "Effect of stone motion on in vitro comminution efficiency of Storz Modulith SLX," J. Endourol **18**, 629–633.

Cleveland, R. O., and McAteer, J. A. (**2007**). "The physics of shock wave lithotripsy," in *Smith's Textbook of Endourology*, edited by A. D. Smith, G. H. Badlani, D. H. Bagley, H.Demetrius, R. V. Clayman, S. G. Docimo, and G. H. Jordan (BC Decker, Hamilton, ON, Canada), pp. 317–332.

Cleveland, R. O., and Sapozhnikov, O. A. (**2005**). "Modeling elastic wave propagation in kidney stones with application to shock wave lithotripsy," J. Acoust. Soc. Am. **118**, 2667–2676.

Coleman, A. J., and Saunders, J. E. (**1989**). "A survey of the acoustic output of commercial extracorporeal shock wave lithotripters," Ultrasound Med. Biol. **15**, 213–227.

Coleman, A. J., Saunders, J. E., Crum, L. A., and Dyson, M. (**1987**). "Acoustic cavitation generated by an extracorporeal shockwave lithotripter," Ultrasound Med. Biol. **13**, 69–76.

Crum, L. A. (**1988**). "Cavitation microjets as a contributory mechanism for renal calculi disintegration in ESWL," J. Urol. (Baltimore) **140**, 1587–1590.

Delius, M., Ueberle, F., and Gambihler, S. (**1994**). "Destruction of gallstones and model stones by extracorporeal shock-waves," Ultrasound Med. Biol. **20**, 251–258.

Eisenmenger, W. (**2001**). "The mechanisms of stone fragmentation in ESWL," Ultrasound Med. Biol. **27**, 683–693.

Eisenmenger, W., Du, X. X., Tang, C., Zhao, S., Wang, Y., Rong, F., Dai, D., Guan, M., and Qi, A. (**2002**). "The first clinical results of 'wide-focus and low-pressure' ESWL," Ultrasound Med. Biol. **28**, 769–774.

Evan, A. P., Willis, L. R., Lingeman, J. E., and McAteer, J. A. (**1998**). "Renal trauma and the risk of long-term complications in shock wave lithotripsy," Nephron **78**, 1–8.

Gerber, R., Studer, U. E., and Danuser, H. (**2005**). "Is newer always better? A comparative study of 3 lithotriptor generations," J. Urol. (Baltimore) **173**, 2013–2016.

Graber, S. F., Danuser, H., Hochreiter, W. W., and Studer, U. E. (**2003**). "A prospective randomized trial comparing 2 lithotriptors for stone disintegration and induced renal trauma," J. Urol. (Baltimore) **169**, 54–57.

Gracewski, S. M., Dahake, G., Ding, Z., Burns, S. J., and Everbach, E. C. (**1993**). "Internal stress wave measurements in solids subjected to lithotripter pulses," J. Acoust. Soc. Am. **94**, 652–661.

Granz, B., and Kohler, G. (**1992**). "What makes a shock wave efficient in lithotripsy?," J. Stone Dis. **4**, 123–128.

IEC-Standard (**1998**). "International Standard: Pressure pulse lithotripters—Characteristics of fields," IEC 61846.

Iloreta, J. I., Zhou, Y. F., Sankin, G. N., Zhong, P., and Szeri, A. J. (**2007**). "Assessment of shock wave lithotripters via cavitation potential," Phys. Fluids **19**, 086103.

Leistner, R., Wendt-Nordahl, G., Grobholz, R., Michel, M. S., Marlinghaus, E., Kohrmann, K. U., Alken, P., and Hacker, A. (**2007**). "A new electromagnetic shock-wave generator 'SLX-F2' with user-selectable dual focus size: Ex vivo evaluation of renal injury," Urol. Res. **35**, 165–171.

Lingeman, J. E. (**1997**). "Extracorporeal shock wave lithotripsy. Development, instrumentation, and current status," Urol. Clin. North Am. **24**, 185–211.

Lingeman, J. E., Kim, S. C., Kuo, R. L., McAteer, J. A., and Evan, A. P. (**2003**). "Shockwave lithotripsy: Anecdotes and insights," J. Endourol **17**, 687–693.

Liu, Y., and Zhong, P. (**2002**). "BegoStone—A new stone phantom for shock wave lithotripsy research," J. Acoust. Soc. Am. **112**, 1265–1268.

Lokhandwalla, M., and Sturtevant, B. (**2000**). "Fracture mechanics model of stone comminution in ESWL and implications for tissue damage," Phys. Med. Biol. **45**, 1923–1940.

Pishchalnikov, Y. A., McAteer, J. A., Williams, J. C., Pishchalnikova, I. V., and Vonderhaar, R. J. (**2006**). "Why stones break better at slow shockwave rates than at fast rates: In vitro study with a research electrohydraulic lithotripter," J. Endourol **20**, 537–541.

Pishchalnikov, Y. A., Sapozhnikov, O. A., Bailey, M. R., Williams, J. C., Jr., Cleveland, R. O., Colonius, T., Crum, L. A., Evan, A. P., and McAteer, J. A. (**2003**). "Cavitation bubble cluster activity in the breakage of kidney stones by lithotripter shockwaves," J. Endourol **17**, 435–446.

Rassweiler, J., Henkel, T. O., Kohrmann, K. U., Potempa, D., Junemann, K. P., and Alken, P. (**1992**). "Lithotripter technology—Present and future," J. Endourol **6**, 1–13.

Rassweiler, J. J., Tailly, G. G., and Chaussy, C. (**2005**). "Progress in lithotriptor technology," EAU Update Series **3**, 17–36.

Sankin, G. N., Simmons, W. N., Zhu, S. L., and Zhong, P. (**2005**). "Shock wave interaction with laser-generated single bubbles," Phys. Rev. Lett. **95**, 034501.

Sapozhnikov, O. A., Khokhlova, V. A., Bailey, M. R., Williams, J. C., McAteer, J. A., Cleveland, R. O., and Crum, C. A. (**2002**). "Effect of overpressure and pulse repetition frequency on cavitation in shock wave lithotripsy," J. Acoust. Soc. Am. **112**, 1183–1195.

Sapozhnikov, O. A., Maxwell, A. D., MacConaghy, B., and Bailey, M. R. (**2007**). "A mechanistic analysis of stone fracture in lithotripsy," J. Acoust. Soc. Am. **121**, 1190–1202.

Sass, W., Braunlich, M., Dreyer, H. P., Matura, E., Folberth, W., Preismeyer, H. G., and Seifert, J. (**1991**). "The mechanisms of stone disintegration by shock waves," Ultrasound Med. Biol. **17**, 239–243.

Sokolov, D. L., Bailey, M. R., Crum, L. A., Blomgren, P. M., Connors, B. A., and Evan, A. P. (**2002**). "Prefocal alignment improves stone comminution in shockwave lithotripsy," J. Endourol **16**, 709–715.

Teichman, J. M., Portis, A. J., Cecconi, P. P., Bub, W. L., Endicott, R. C., Denes, B., Pearle, M. S., and Clayman, R. V. (**2000**). "In vitro comparison of shock wave lithotripsy machines," J. Urol. (Baltimore) **164**, 1259–1264.

Wess, O. (**2005**). "Shock wave lithotripsy (SWL) and focal size," in *Therapeutic Energy Applications in Urology—Standards and Recent Developments*, edited by D. J. Ch. Chaussy, G. Haupt, K. U. Kohrmann, and D. Wilbert (Georg Thieme Verlag KG, Stuttgart, Germany), pp. 26–35.

Xi, X., and Zhong, P. (**2001**). "Dynamic photoelastic study of the transient stress field in solids during shock wave lithotripsy," J. Acoust. Soc. Am. **109**, 1226–1239.

Zhong, P. (**2007**). "Innovations in lithotripsy technology," in the 1st Annual International Urolithiasis Research Symposium, Indianapolis, IN, pp. 317–325.

Zhong, P., and Chuong, C. J. (**1993**). "Propagation of shock waves in elastic solids caused by cavitation microjet impact. I: Theoretical formulation," J. Acoust. Soc. Am. **94**, 19–28.

Zhong, P., Chuong, C. J., and Preminger, G. M. (**1993**). "Propagation of shock waves in elastic solids caused by cavitation microjet impact. II: Application in extracorporeal shock wave lithotripsy," J. Acoust. Soc. Am. **94**, 29–36.

Zhong, P., Cioanta, I., Cocks, F. H., and Preminger, G. M. (**1997**). "Inertial cavitation and associated acoustic emission produced during electrohydraulic shock wave lithotripsy," J. Acoust. Soc. Am. **101**, 2940–2950.

Zhong, P., and Zhou, Y. (**2001**). "Suppression of large intraluminal bubble expansion in shock wave lithotripsy without compromising stone comminution: Methodology and in vitro experiments," J. Acoust. Soc. Am. **110**, 3283–3291.

Zhong, P., Zhou, Y., and Zhu, S. (**2001**). "Dynamics of bubble oscillation in constrained media and mechanisms of vessel rupture in SWL," Ultrasound Med. Biol. **27**, 119–134.

Zhou, Y., Cocks, F. H., Preminger, G. M., and Zhong, P. (**2004**). "Innovations in shock wave lithotripsy technology: Updates in experimental studies," J. Urol. (Baltimore) **172**, 1892–1898.

Zhou, Y., and Zhong, P. (**2003**). "Suppression of large intraluminal bubble expansion in shock wave lithotripsy without compromising stone comminution: Refinement of reflector geometry," J. Acoust. Soc. Am. **113**, 586–597.

Zhou, Y., and Zhong, P. (**2006**). "The effect of reflector geometry on the acoustic field and bubble dynamics produced by an electrohydraulic shock wave lithotripter," J. Acoust. Soc. Am. **119**, 3625–3636.

Zhu, S., Cocks, F. H., Preminger, G. M., and Zhong, P. (**2002**). "The role of stress waves and cavitation in stone comminution in shock wave lithotripsy," Ultrasound Med. Biol. **28**, 661–671.

Zhu, S. L., and Zhong, P. (**1999**). "Shock wave-inertial microbubble interaction: A theoretical study based on the Gilmore formulation for bubble dynamics," J. Acoust. Soc. Am. **106**, 3024–3033.

Whistles emitted by Atlantic spotted dolphins (*Stenella frontalis*) in southeastern Brazil

Alexandre F. Azevedo[a)]
Departamento de Oceanografia, Laboratório de Mamíferos Aquáticos e Bioindicadores (MAQUA), Universidade do Estado do Rio de Janeiro, Rua São Francisco Xavier 524, Maracanã, Rio de Janeiro 20550-013, Brazil

L. Flach
Projeto Boto Cinza, Rua Sta Terezinha, 531 Muriqui, Mangaratiba, Rio de Janeiro 23870-000, Brazil

Tatiana L. Bisi, Luciana G. Andrade, Paulo R. Dorneles, and J. Lailson-Brito
Departamento de Oceanografia, Laboratório de Mamíferos Aquáticos e Bioindicadores (MAQUA), Universidade do Estado do Rio de Janeiro, Rua São Francisco Xavier 524, Maracanã, Rio de Janeiro 20550-013, Brazil

(Received 20 September 2009; revised 22 December 2009; accepted 11 January 2010)

The whistles of Atlantic spotted dolphins have been studied in a few localities of the North Atlantic Ocean and those studies revealed that the species emits whistles within a broad frequency range, with a high number of inflection points and presence of harmonics. In the South Atlantic Ocean, there is no information about the sounds produced by Atlantic spotted dolphins. A total of 1092 whistles emitted by free-ranging Atlantic spotted dolphins in Southeastern Brazilian coastal waters were analyzed. Whistles recorded in this study had a broad frequency range from 1.15 to 23.44 kHz. Whistles without harmonics were frequently emitted (N=701; 64.2%) and those signals with zero up to two inflection points corresponded to 94% of all whistles. Some differences in whistle characteristics (inflection points and duration) were found in relation to areas in North Atlantic Ocean and whistles were shorter and with a smaller number of inflection points in Brazil. Whistles produced by Atlantic spotted dolphins varied between the two behavioral states in which dolphins were engaged. Whistles were more frequently emitted when dolphins presented behaviors that included fast movement at surface, prey pursuit, aerial behavior, and physical contact. In these situations, whistles were on average longer and had higher frequency parameters than those emitted when animals were engaged in slowly and moderate traveling. The findings presented herewith reveal that dolphins modified whistle structures within behavioral states.
 [DOI: 10.1121/1.3308469]

PACS number(s): 43.80.Ka [WWA] Pages: 2646–2651

I. INTRODUCTION

Dolphins emit two broad categories of acoustic signals: pulsed and tonal sounds (Popper, 1980; Richardson *et al.*, 1998). Whistles are narrow-band frequency modulated sounds used primarily for communication between individuals (Tyack, 1998). These signals have been the focus of several bioacoustic studies on delphinids due to the numerous easily measured characteristics presented by them. In addition, they have been used for characterization and comparisons among groups and populations (e.g., Rendell *et al.*, 1999; Bazúa-Durán and Au, 2004; Azevedo and Van Sluys, 2005; May-Collado and Wartzok, 2009).

Atlantic spotted dolphins (*Stenella frontalis*) are found in warm temperate to tropical waters in Atlantic Ocean (Jefferson *et al.*, 2008). As most delphinids, this species is a highly vocal dolphin species that produces echolocation click trains, burst pulse sounds, and whistles related to behavioral activities (Perrin, 2002). Narrow-band signature whistles have been reported in Atlantic spotted dolphins both in captive (Caldwell *et al.*, 1973) and in the wild (Herzing, 1996). The whistles of Atlantic spotted dolphins have been studied in a few localities of the North Atlantic Ocean, especially in Bahamas and Gulf of Mexico (e.g., Wang *et al.*, 1995; Lammers *et al.*, 2003; Baron *et al.*, 2008). Those studies revealed that Atlantic spotted dolphins emit whistles with a high number of inflection points, duration between 0.08 and 2.07 s, as well as with minimum and maximum frequency average values of 7 and 16 kHz, respectively.

The Atlantic spotted dolphin is the only member of the genus *Stenella* that is frequently observed close to shore in Brazil (Moreno *et al.*, 2005). Group size is relatively small for *Stenella* species, being most of the times smaller than 50 individuals (Moreno *et al.*, 2005). Despite being commonly observed, there is no information available about acoustic signals of the species in the area. In this study, we describe the whistle acoustic structure of free-ranging Atlantic spotted dolphins and provide insights on whistle geographical variations by comparing our results with previous studies.

II. METHODS

Acoustic recordings of underwater sounds produced by Atlantic spotted dolphins were made at Ilha Grande

[a)]Author to whom correspondence should be addressed. Electronic mail: azevedo.alex@uerj.br

 0001-4966/2010/127(4)/2646/6/$25.00

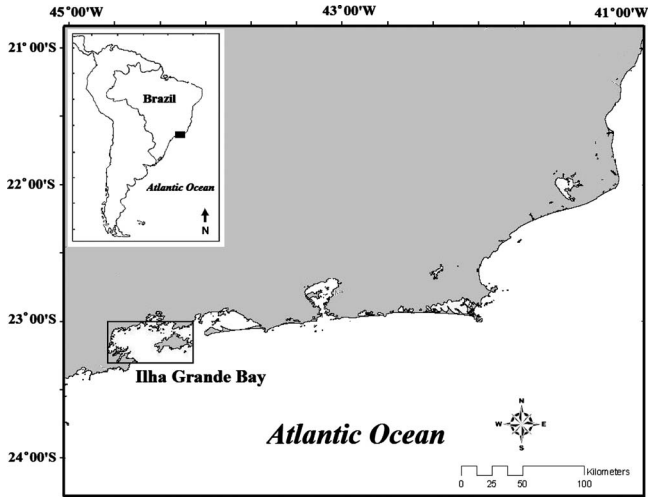

FIG. 1. Map of Rio de Janeiro coast, southeastern Brazil, where acoustic recordings of underwater sound produced by Atlantic spotted dolphins were made.

Bay (23°05′–23°14′ S; 44°05′–44°23′ W), southeastern Brazil, (Fig. 1), during one day in April 2007, two days in October 2007, and one day in December 2008. All surveys were carried out under similar weather conditions (Beaufort sea states ≤2), in a small inboard-powered boat about 8 m in length. In the four encounters, Atlantic spotted dolphins were in groups of 40–50 animals and calves corresponded to about 10%–15%. Besides group size and composition, the four herds had the same characteristics with individuals moving together in apparent association, engaged in same activity and rarely split out in a large area (Table I). Two distinct behavioral states were observed and associated with the acoustic recordings: (a) low surface activity: dolphins engaged in slowly and moderate traveling and short distances between individuals (less than 10 m), but no physical contact was observed; (b) high surface activities: dolphins engaged in socializing and foraging/feeding behaviors with fast move at surface, prey pursuit, aerial behavior, and physical contact between dolphins.

Acoustic recordings were made with the engine turned off and were monitored by headphones. Whenever dolphin sounds became weak, we stopped recording and repositioned the boat. The recording system consisted of a High Tech Inc. hydrophone (model HTI-96-MIN, frequency response: 5 Hz to 30 kHz ± 1.0 dB, −165 dB re 1 V/μPa) and a digital audio tape recorder Sony TCD-D8 with upper frequency limit of 24 kHz (sampling rate of 48 kHz). Whistles were defined as continuous, narrow-band sound emissions with or without harmonics (Popper, 1980). Whistles were analyzed using the RAVEN 1.1 program (Cornell Laboratory of Ornithology, New York) with a fast Fourier transform (FFT) size of 1024 points, an overlap of 50%, and using a 512 sample Hamming window.

The contour of each whistle was determined by visual analyses of the frequency modulation by at least two authors and was then categorized into the following broad classes: ascending (whistles rising in frequency and with no one inflection point), descending (whistles falling in frequency and with no one inflection point), ascending-descending (initial rising in frequency, one inflection point, and then falling in frequency), descending-ascending (initial falling in frequency, one inflection point, and then rising in frequency), constant (whistles which the frequency changes 1000 Hz or less during more than 90% of duration), and multi (more than one inflection point).

Nine acoustic parameters from fundamental component of each whistle were measured: starting frequency (SF), ending frequency (EF), minimum frequency (MinF), maximum frequency (MaxF), delta frequency (DF) [MaxF−MinF], duration (DUR), frequency at $\frac{1}{4}$ of duration $\left(F\frac{1}{4}\right)$, frequency at $\frac{1}{2}$ of duration $\left(F\frac{1}{2}\right)$, and frequency at $\frac{3}{4}$ of duration $\left(F\frac{3}{4}\right)$. Presence of harmonics and number of inflection points (defined as points where the whistle contour changed from ascending to descending or vice versa) were also determined. The frequency variables were measured in kilohertz and the duration in milliseconds. The mean frequency (MeF) was calculated as the average of SF, EF, MinF, and MaxF. These whistle parameters were chosen to be consistent with previous studies of Atlantic spotted dolphins (e.g., Wang *et al.*, 1995; Lammers *et al.*, 2003; Baron *et al.*, 2008) and other dolphin species (e.g., Bazúa-Durán and Au, 2004; Azevedo and Van Sluys, 2005). Only whistles for which all parameters of a spectral contour were distinctly measurable were used.

The descriptive statistics for all measured variables includes the minimum values, maximum values, means, and standard deviations. The paired-sample *t* test (Zar, 1999) was applied to verify if the mean of the end frequency of all whistles analyzed was significantly different from the start frequency. The frequency of whistles in each category was compared between the two behavioral states using Chi-square test ($P<0.01$) and Mann–Whitney test ($P<0.05$) was applied to investigate variation in whistle variables between the two behavioral states.

TABLE I. Aggregation size, percentual of calves, time observed, and total time of recording, in which Atlantic spotted dolphin whistles were recorded in study area.

Month	Aggregation size	Percentual of calves	Time observed (h)	Time recorded (min)
April 2007	55	10	2.5	56
October 2007	40	10	4	58
October 2007	50	15	4	90
December 2008	50	15	3.5	75

III. RESULTS

A total of 1745 whistles were recorded over 279 min. Five whistles were not analyzed because they were "cut off" by the upper frequency limit of the recording system. Of that total ($N=1745$), 1092 whistles had adequate signal quality for acoustical analyses. Pure tone whistles were the most frequent ones ($N=701$; 64.2%) and whistles with up to 14 inflection points were found, but those with zero up to two

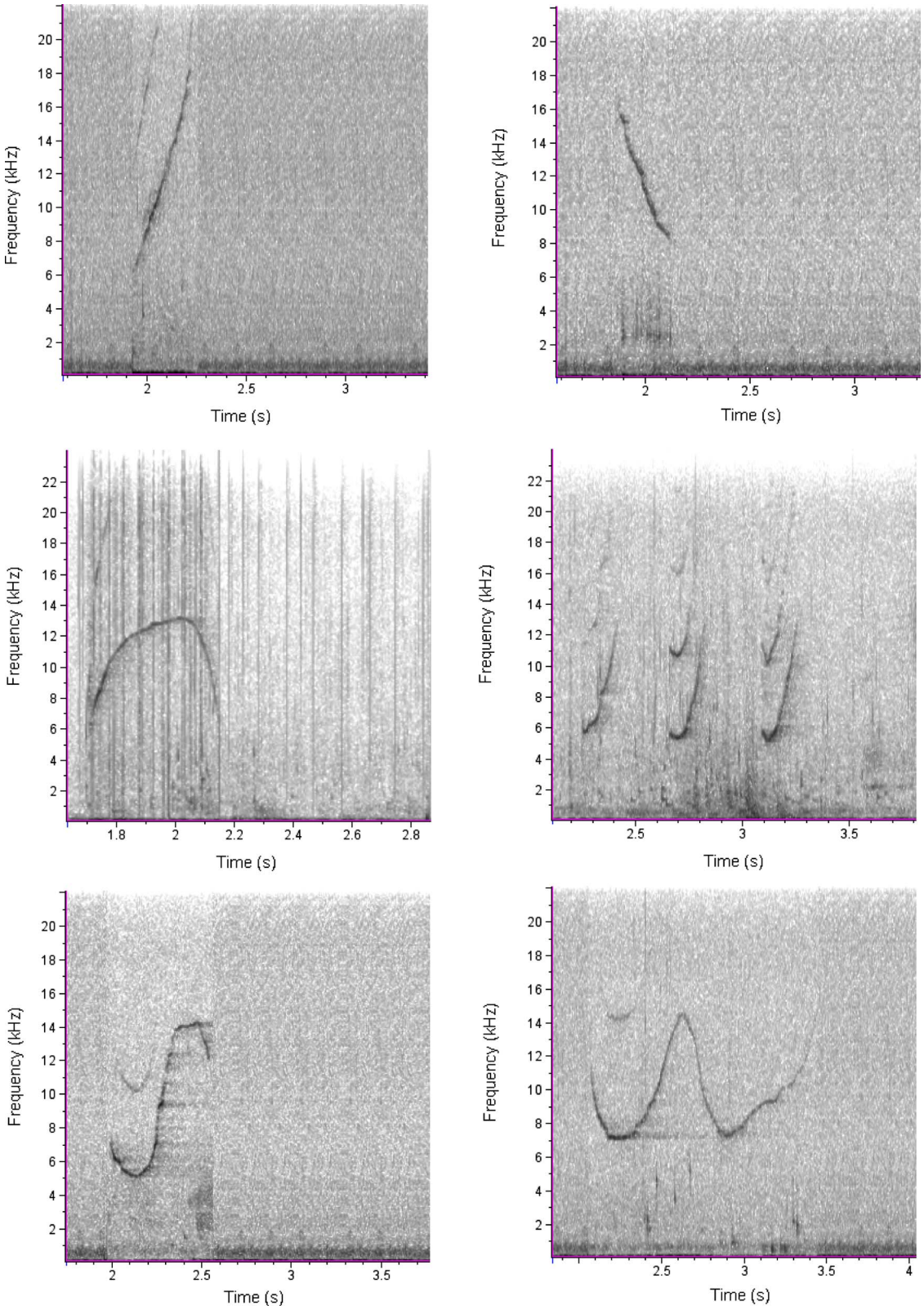

FIG. 2. (Color online) Examples of whistles emitted by Atlantic spotted dolphins in southeastern Brazil.

inflection points corresponded to 94% of all whistles. Whistles categorized as ascending were the most common and corresponded to 47.0% of all whistles. Those with more than one inflection point represented 16.5% and descending-ascending 15.5%. Ascending-descending (10.3%), descending (6.5%), and constant (4.2%) whistles were less frequent. Examples of whistles emitted by Atlantic spotted dolphins are presented in Fig. 2. There were significant differences for whistle contour distribution of the six categories between low and high activities, but ascending whistles were more frequently emitted in both behavioral states ($X^2=41.9$; df $=5$; $P<0.01$; Fig. 3).

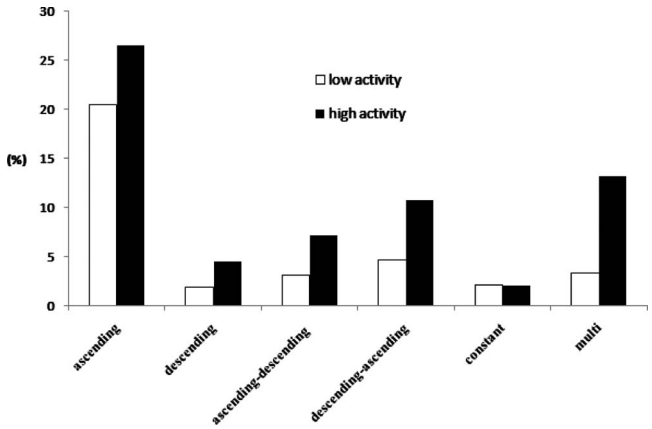

FIG. 3. Distribution of the six categories of whistles emitted by Atlantic spotted dolphins during low and high activities.

Whistle duration mean was 360.9 ± 293.2 ms and 97.6% of the whistles lasted less than 1 s. The average minimum frequency was 8.04 ± 2.51 kHz and maximum frequency averaged 13.58 ± 3.64 kHz. The mean of delta frequency was 6.25 ± 3.34 kHz. The average mean frequency was 10.81 ± 2.63 kHz and the whistles had MeFs ranging from 2.72 to 21.00 kHz. The end frequency (mean 12.76 ± 3.80 kHz) of the Atlantic spotted dolphin whistles was, on average, higher than the start frequency (mean 8.85 ± 3.21 kHz) (paired-sample t-test, $t=29.41$, df$=1091$, $P<0.01$). Descriptive statistics of all measured whistle parameters are shown in Table II.

Comparisons of acoustic whistle parameters recorded during low and high activities found significant differences in most of whistle variables. Averages of duration, starting frequency, maximum frequency, delta frequency, mean frequency, frequency at $\frac{1}{4}$ of duration, frequency at $\frac{1}{2}$ of duration, frequency at $\frac{3}{4}$ of duration, and number of inflections points of the whistles emitted during high activities were higher than those produced in low activities (Table II; Mann–Whitney test; $P<0.05$). Additionally, whistles were produced more frequently during high surface activities (9.2/min) than during low surface activities (3.9/min).

IV. DISCUSSION

Atlantic spotted dolphin emitted a varied repertoire of whistles simple in structure. Whistles with up to two inflections were more abundant. This is not in accordance with previous studies of free-ranging Atlantic spotted dolphins in North Atlantic Ocean. Wang *et al.* (1995) and Baron *et al.* (2008) reported that the species produced whistles with a higher number of inflection points (Table III). Wang *et al.* (1995) found a mean number of inflection points of 3.43 in Bahamas, and Baron *et al.* (2008) reported the value of 2.22 as the average in Gulf of Mexico, while we found 0.72 in southeastern Brazilian coast. These differences may be related to longer whistles reported by those authors, since they found whistles with mean values of duration 127% and 80% higher than in Rio de Janeiro coast. Differences between those characteristic whistles of Atlantic spotted dolphins from South Atlantic Ocean and other sites may be caused by adaptation to environmental conditions, social relationship, behavioral variation, as well as anatomical features related to sound production, as it has been suggested for other dolphin species (Steiner, 1981; Rendell *et al.*, 1999; May-Collado *et al.*, 2007a). Another whistle character that differs from

TABLE II. Descriptive statistics (mean ± standard deviation; minimum-maximum) for 11 acoustic parameters values of Atlantic spotted dolphin whistles in Rio de Janeiro coast, southeastern Brazil. The frequency variables were measured in kHz and the duration in s. Mann–Whitney test ($P<0.05$) results for variation in whistle variables among the two behavioral states.

Parameters	All ($N=1092$)	Low activity ($N=388$)	High activity ($N=704$)	Mann–Whitney test ($P<0.05$)
Duration	0.36 ± 0.29	0.34 ± 0.34	0.37 ± 0.26	Yes
	0.05–3.62	0.05–3.62	0.06–1.87	
Starting frequency	8.85 ± 3.21	8.00 ± 3.0	9.04 ± 3.31	Yes
	1.15–21.88	1.15–21.11	1.55–21.88	
Ending frequency	12.76 ± 3.80	12.50 ± 3.88	12.91 ± 3.75	No
	1.56–22.35	1.56–22.35	2.76–22.12	
Minimum frequency	8.04 ± 2.51	7.94 ± 2.47	8.10 ± 2.54	No
	1.15–20.09	1.15–20.09	1.55–18.90	
Maximum frequency	13.58 ± 3.64	13.07 ± 3.77	13.86 ± 3.54	Yes
	3.00–23.44	3.23–23.44	3.00–22.98	
Delta frequency	5.53 ± 3.52	5.13 ± 3.54	5.76 ± 3.50	Yes
	0.11–16.47	0.11–16.47	0.29–16.44	
Mean frequency	10.81 ± 2.63	10.50 ± 2.71	10.98 ± 2.58	Yes
	2.72–21.00	3.01–21.00	2.72–20.20	
Frequency at $\frac{1}{4}$ of duration	9.63 ± 3.00	9.12 ± 2.82	9.91 ± 3.05	Yes
	2.71–22.19	2.71–22.19	3.00–21.96	
Frequency at $\frac{1}{2}$ of duration	10.77 ± 3.04	10.36 ± 2.98	11.00 ± 3.05	Yes
	3.00–23.44	3.11–23.44	3.00–22.82	
Frequency at $\frac{3}{4}$ of duration	11.55 ± 3.02	11.26 ± 3.10	11.70 ± 2.97	Yes
	2.88–22.74	3.17–22.74	2.88–22.46	
Inflections	0.74 ± 1.30	0.47 ± 0.89	0.90 ± 1.45	Yes
	0–14	0–8	0–14	

TABLE III. Values of whistle parameters for Atlantic spotted dolphins reported in some studies cited in this paper.

Parameters	This study[a] (N=1092)	Wang *et al.* (1995)[b] (N=80)	Lammers *et al.* (2003)[c] (N=220)	Baron *et al.* (2008)[d] (N=27)
Duration	0.36 ± 0.29	0.82 ± 0.40	0.44 ± 0.30	0.65 ± 0.04
	0.05–3.62	0.08–2.07		
Starting frequency	8.85 ± 3.21	10.95 ± 3.21		9.08 ± 0.25
	1.15–21.88	5.47–19.13		
Ending frequency	12.76 ± 3.80	11.56 ± 3.66		13.13 ± 0.35
	1.56–22.35	6.25–19.79		
Minimum frequency	8.04 ± 2.51	7.91 ± 1.18	7.1 ± 1.5	7.51 ± 0.17
	1.15–20.09	5.00–11.09		
Maximum frequency	13.58 ± 3.64	16.04 ± 1.89	14.5 ± 2.5	15.84 ± 0.32
	3.00–23.44	9.92–19.79		
Mean frequency	10.81 ± 2.63		10.9 ± 2.0	ND
	2.72–21.00			
Delta Frequency	5.53 ± 3.52		7.4 ± 2.0	8.33 ± 0.31
	0.11–16.47			
Inflections	0.74 ± 1.30	3.43 ± 2.03		2.22 ± 0.14
	0–14	0–11		

[a]Frequency response of recording system: 24 kHz.
[b]Frequency response of recording system: 25 kHz.
[c]Frequency response of recording system: 130 kHz.
[d]Frequency response of recording system: 24 kHz.

those observed in previous studies was the presence of harmonics. Our findings revealed that Atlantic spotted dolphins preferentially produced whistles without harmonics, whereas Lammers *et al.* (2003) reported that the majority of the whistles produced by the species had one or more harmonics in Bahamas. However, these differences should be interpreted with caution because Lammers *et al.* (2003) used a broadband recording system that capture more of the whistles frequency range of this species.

Atlantic spotted dolphins have been shown to emit whistles within a broad frequency range (Wang *et al.*, 1995; Lammers *et al.*, 2003; Baron *et al.*, 2008). Whistles recorded in our study also had wide frequency range (1.15–23.44 kHz), revealing that the species in Atlantic South Ocean emits whistles in frequencies close to 1 kHz and higher than 20 kHz. Several odontocete species, including Atlantic spotted dolphin, emit whistles with fundamental frequency extending into the ultrasonic range (Lammers *et al.*, 2003; May-Collado *et al.*, 2007b). But, in fact, the usage of whistles with fundamental frequencies above 20 kHz seems to be not usual by Atlantic spotted dolphins. Our results revealed only 4.7% of whistles with fundamental frequency higher than 20 kHz and only five whistles with fundamental frequency higher than 24 kHz. Additionally, Lammers *et al.* (2003) reported 27.4 kHz as the highest maximum fundamental frequency measured for Atlantic spotted dolphin, in Bahamas, but only 3.6% of all whistles had fundamental frequencies above 20 kHz.

Based on the relationship between starting and ending frequencies, Bazúa-Durán and Au (2002) suggested that *Sotalia* spp., *Delphinus delphis, Stenella attenuata, S. clymene, S. longirostris*, and *Lagenorhynchus albirostris* share some of the characteristics of their whistles. Considering that hypothesis, the Atlantic spotted dolphin can be included in that group since our findings showed a clear predominance of ascending whistles and the ending frequency was, on average, higher than starting frequency. However, our analysis is simple and the similarity of the whistles between Atlantic spotted dolphin and other delphinids deserves further exploration.

Variations in whistle parameters of dolphins and whistling rate related to behavioral states have been usually reported for delphinids (e. g. Herzing, 1996; Van Parijs *et al.*, 2000; Bazúa-Durán and Au, 2004) and they seem to be related to whistle functions, which include to transmit emotional states and to coordinate dolphin activities (Tyack, 1998). Whistles produced by Atlantic spotted dolphins varied among the two behavioral states in which dolphins were engaged. When dolphins presented behaviors with fast movement at surface, prey pursuit, aerial behavior, and physical contact, the whistles were more frequently emitted and were, on average, longer and had higher frequency parameters than when animals were engaged in slowly and moderate traveling. Additionally, dolphins emitted whistles more complex in shape when engaged in high surface activities.

V. CONCLUSIONS

This is the first description of the whistles produced by Atlantic spotted dolphins in South Atlantic Ocean. Dolphins emitted whistles within a wide frequency range and some differences in signal characteristics were found in comparison to areas of North Atlantic Ocean. Additionally, dolphins modified whistle structures within behavioral states, maybe as a result of whistle communication functions.

ACKNOWLEDGMENTS

This study was funded by Conselho Nacional para o Desenvolvimento Científico e Tecnológico (CNPq-Brazil; Edital Universal No. 476255/2007-4). We particularly thank Adriana Nascimento Gomes, Sylvia Chada, and Sílvia Peixoto of the Estação Ecológica Tamoios (ESEC Tamoios-

ICMBio) and Faculdade de Oceanografia (UERJ) which provided logistical support. We also thank Mr. José Carlos to help us during all data collection. Dr. Azevedo has a research grant from CNPq (Grant No. 304826/2008-1). J.L.-B. is a researcher of "Prociência" Program-FAPERJ/UERJ. T.L.B. has a scholarship from CAPES. Being a team, the interns of the Laboratório de Mamíferos Aquáticos e Bioindicadores (MAQUA-UERJ) are acknowledged.

Azevedo, A. F., and Van Sluys, M. (**2005**). "Whistles of tucuxi dolphins (*Sotalia fluviatilis*) in Brazil: Comparisons among populations," J. Acoust. Soc. Am. **117**, 1456–1464.

Baron, S. C., Marinez, A., Garrison, L. P., and Keith, E. O. (**2008**). "Differences in acoustic signals from delphinids in the western North Atlantic and northern Gulf of Mexico," Marine Mammal Sci. **24**, 42–56.

Bazúa-Durán, M. C., and Au, W. W. L. (**2002**). "Whistles of Hawaiian spinner dolphins," J. Acoust. Soc. Am. **112**, 3064–3072.

Bazúa-Durán, M. C., and Au, W. W. L. (**2004**). "Geographic variations in the whistles of spinner dolphins (*Stenella longirostris*) of the main Hawaiian islands," J. Acoust. Soc. Am. **116**, 3757–3769.

Caldwell, D. K., Caldwell, M. C., and Miller, J. F. (**1973**). "Statistical evidence for individual signature whistles in the spotted dolphin, *Stenella plagiodon*," Cetology **16**, 1–21.

Herzing, D. L. (**1996**). "Vocalizations and associated underwater behavior of free-ranging Atlantic spotted dolphins, *Stenella frontalis* and bottlenose dolphins, *Tursiops truncatus*," Aquat. Mamm. **22**, 61–79.

Jefferson, T. A., Webber, M. A., and Pitman, R. L. (**2008**). *Marine Mammals of the World, A Comprehensive Guide to their Identification* (Elsevier, Amsterdam).

Lammers, M. O., Au, W. W. L., and Herzing, H. L. (**2003**). "The broadband social acoustic signaling behavior of spinner and spotted dolphins," J. Acoust. Soc. Am. **114**, 1629–1639.

May-Collado, L. J., Agnarsson, I., and Wartzok, D. (**2007a**). "Phylogenetic review of tonal sound production in whales in relation to sociality," BMC Evol. Biol. **7**, 136.

May-Collado, L. J., Agnarsson, I., and Wartzok, D. (**2007b**). "Reexamining the relationship between body size and tonal signals frequency in whales: A comparative approach using a novel phylogeny," Marine Mammal Sci. **23**, 524–552.

May-Collado, L. J., and Wartzok, D. (**2009**). "A characterization of Guyana dolphin (*Sotalia guianensis*) whistles from Costa Rica: The importance of broadband recording systems," J. Acoust. Soc. Am. **125**, 1202–1213.

Moreno, I. B., Zerbini, A. N., Danilewicz, D., Santos, M. C. O., Simões-Lopes, P. C., Lailson-Brito, J., Jr., and Azevedo, A. F. (**2005**). "Distribution and habitat characteristics of dolphins of the genus *Stenella* (Cetacea: Delphinidae) in the southwest Atlantic Ocean," Mar. Ecol. Prog. Ser. **300**, 229–240.

Perrin, W. F. (**2002**). "Stenella frontalis," Mamm. Species **702**, 1–6.

Popper, A. N. (**1980**). "Sound emission and detection by delphinids," in *Cetacean Behaviour: Mechanisms and Functions*, edited by L. M. Herman, (Wiley, New York), pp. 1–52.

Rendell, L. E., Matthews, J. N., Gill, A., Gordon, J. C. D., and MacDonald, D. W. (**1999**). "Quantitative analysis of tonal calls from five odontocete species, examining interspecific and intraspecific variation," J. Zool. **249**, 403–410.

Richardson, W. J., Greene, C. R. J., Malme, C. I., and Thomsom, D. H. (**1998**). *Marine Mammals and Noise* (Academic, New York).

Steiner, W. W. (**1981**). "Species-specific differences in pure tonal whistle vocalizations of five western North Atlantic dolphin species," Behav. Ecol. Sociobiol. **9**, 241–246.

Tyack, P. L. (**1998**). "Acoustic communication under sea," in *Animal Acoustics Communication: Sound Analysis and Research Methods*, edited by S. L. Hopp, M. J. Owen, and C. S. Evans (Springer, New York), pp. 163–219.

Van Parijs, S. M., Parra, G. J., and Corkeron, P. J. (**2000**). "Sounds produced by Australian Irrawaddy dolphins, *Orcaella brevirostris*," J. Acoust. Soc. Am. **108**, 1938–1940.

Wang, D., Wursig, B., and Evans, W. E. (**1995**). "Comparisons of whistles among seven odontocete species," in *Sensory Systems of Aquatic Mammals*, edited by R. A. Kastelien, J. A. Thomas, and P. E. Nachtigal, (De Spil, Woerden, The Netherlands), pp. 299–323.

Zar, J. H., *Biostatistical Analysis* (Prentice-Hall, Englewood Cliffs, NJ) (**1999**).

Whistle emissions of Indo-Pacific bottlenose dolphins (*Tursiops aduncus*) differ with group composition and surface behaviors

Elizabeth R. Hawkins[a] and Donald F. Gartside
Whale Research Centre, Southern Cross University, Lismore, New South Wales 2480, Australia

(Received 13 July 2009; revised 17 December 2009; accepted 11 January 2010)

The intricate and highly developed acoustic communication system of bottlenose dolphins reflects the complexities of their social organization. Indo-Pacific bottlenose dolphins (*Tursiops aduncus*) produce numerous types of acoustic emissions, including a diverse repertoire of whistles used for communicative purposes. The influence of group composition on whistle production and the function of different whistles produced by dolphins in wild contexts are relatively unknown. Recordings of acoustic emissions and behavior of dolphins were made concurrently during vessel-based surveys along the coast of northern New South Wales, Australia. Whistles were divided into five tonal classes (sine, rise, down-sweep, flat, and concave) and categorized into distinct whistle types. It is shown that while whistle repetition rate and whistle diversity was influenced by group composition, it is not influenced by behavior. Noncalf groups produced a significantly higher whistle repetition rate and whistle diversity than calf groups. In contrast, the types of whistles produced were related to the behavior in which the dolphins were engaged in: some tonal classes and distinct whistle types were related to different behavior states. Findings suggested that some whistle types may be used to communicate specific information on the behavioral context of the individuals involved. © *2010 Acoustical Society of America.* [DOI: 10.1121/1.3308465]

PACS number(s): 43.80.Ka [WWA] Pages: 2652–2663

I. INTRODUCTION

Darwin (1872) hypothesized that animal vocalizations were used to advertise an individual's level of arousal or motivational state and was primarily an "affective" communication system (Manser *et al.*, 2002; Seyfarth and Cheney, 2003). Bioacoustics research over the last 20 years has shown that animal vocalization can be both affective and referential where vocalizations relate to specific events or objects (Manser *et al.*, 2002; Seyfarth and Cheney, 2003). Specific types of animal vocalizations can be produced in a number of social contexts and ecological situations (Seyfarth and Cheney, 2003). Some vocalizations may be specific to particular stimuli, while others may be used in a variety of situations (Seyfarth and Cheney, 2003). The majority of vocalizations produced by animals are thought to be contact, alerting, and affiliative calls, while other vocalizations such as functionally referential signals make up the minority of vocalizations (Marler, 1975; Manser *et al.*, 2002). How social animals utilize acoustic emissions to communicate is a particularly important aspect of their ecology that needs to be understood in order to gain insight into their requirements for survival (Seyfarth and Cheney, 2003).

The complex social systems of bottlenose dolphins (*Tursiops spp.*) are underpinned by their intricate and adaptable acoustic, visual, and tactile communication systems (Marino *et al.*, 2007). For these animals that live in an aquatic environment where visual communication can be limited, acoustic communication is more reliable, efficient, and effective (Tyack, 2003). Bottlenose dolphins produce a variety of acoustic emissions that are broadly classified as whistles, clicks, and burst-pulse sounds (Caldwell and Caldwell, 1967; Caldwell *et al.*, 1990). Whistles produced by bottlenose dolphins are particularly important in the transfer of information between individuals and the maintenance of group cohesion (Caldwell *et al.*, 1990; Janik and Slater, 1998).

The rate of whistle production in bottlenose dolphins cannot only be influenced by environmental factors such as season and habitat but also group size and behavior (dos Santos *et al.*, 1990; Jacobs *et al.*, 1993; Cook *et al.*, 2004; Nowacek, 2005). Some research has reported that the number of whistles emitted per individual increases with larger group sizes (Jones and Sayigh, 2002; Cook *et al.*, 2004) while others have reported that fewer whistles are produced in groups with larger sizes (Quick and Janik, 2008). Whether the conflicting results were influenced by the composition of groups encountered is not clear.

Acevedo-Gutiérrez and Stienessen (2004) suggested that the rate of sounds produced by bottlenose dolphins may influence group size and be used as a technique to transmit information about the caller's activity and attract individuals to join in the activity. In Isla del Coco, Costa Rica, bottlenose dolphins increased whistle production when feeding to possibly attract other dolphins to join and aid in the cooperative herding of prey and defend against potential predators (Acevedo-Gutiérrez and Stienessen, 2004). The behavior of the dolphins can also contribute to the rate of whistles produced. During social behaviors, dolphins generally increase the repetition rate of whistles, compared to when they are

[a]Author to whom correspondence should be addressed. Electronic mail: elizabeth.hawkins@scu.edu.au

 0001-4966/2010/127(4)/2652/12/$25.00

traveling, and the repetition rate of whistles is significantly reduced (dos Santos *et al.*, 1990; Jacobs *et al.*, 1993; Cook *et al.*, 2004).

Variability in acoustic sequences and signals of bottlenose dolphins strongly suggests that they exchange organized information (Markov and Ostrovskaya, 1990). Earlier studies have broadly described some sounds produced by captive bottlenose dolphins that may be associated with specific behavioral displays. For example, sounds described as "yelps" are emitted during sexual behaviors in captive bottlenose dolphins and "bray" emissions during feeding behaviors of bottlenose dolphins in Moray Firth, Scotland (Wood, 1953; Janik, 2000). Bottlenose dolphins have a diverse whistle repertoire, yet there is little known about the purpose of many of these sound types and the relationship with the dolphins' behavior or activity. The fine-scale acoustic structures of the whistle are thought to play a significant role in the exchange of information between individuals (Kaznadzei *et al.*, 1977; Janik and Slater, 1998; Sayigh *et al.*, 1999). It has been hypothesized that bottlenose dolphins produce an individually distinct stereotyped "signature whistle" that may be used as a contact call to advertise identity and location of the signaler (Caldwell *et al.*, 1990; Tyack, 1997; Janik and Slater, 1998). The purpose of other types of whistles and how these sounds relate to the signaler's context or behavior remain unclear (Caldwell *et al.*, 1990; McCowan and Reiss, 1995; Janik and Slater 1998; Cook *et al.*, 2004).

Some terrestrial species that have sexually segregated fission-fusion societies similar to those of most bottlenose dolphin populations, such as chimpanzees (*Pan troglodytes*) and baboons (*Papio cynocephalus ursinus*), produce a variety of behaviorally specific calls that can be influenced not only by behavior but also the age and sex classes of the individuals involved (Mitani and Nishida, 1993; Price, 1998; Connor *et al.*, 2000; Rendall *et al.*, 2000; Fischer *et al.*, 2001). Variations in calls produced by groups differing in composition can be reflective of the varying roles of sex and age classes within the society. For example, female baboons use grunts to facilitate social interactions and to reconcile with opponents following a bout of aggression (Cheney *et al.*, 1995). In Rhesus macaques (*Macaca mulatto*), there are evident sex differences in the number of food related calls produced, with males producing fewer than females (Hauser and Marler, 1993). This raises the question whether a population of bottlenose dolphins may use certain whistle types to communicate specific information regarding the activity or context of the signaler, and if some whistles are utilized only by groups consisting of certain age and sex classes.

To increase the understanding of the communicative functions of whistles in a population of wild Indo-Pacific bottlenose dolphins (*Tursiops aduncus*), we examined whether specific whistle types (i.e., tonal class and distinct whistle types) were associated with varying behavior states and group compositions. We also investigated whether whistle production (i.e., repetition rate and diversity) was influenced by group size, group composition, or behavior.

II. METHODS

A. Data collection

Surveys of Indo-Pacific bottlenose dolphins (*Tursiops aduncus*) were undertaken in 226 km^2 area of coastal waters around Byron Bay, northern New South Wales, Australia (153°38′E, 28°38′S). The population consisted of approximately 865 dolphins (95% C.I. ± 861–869) and was typified by an apparent sexually segregated society with both resident and transient groups and individuals (Hawkins and Gartside, 2008).

Vessel-based surveys were conducted between March 2003 and January 2006 in seasonal (autumn, winter, spring, and summer) 2–4 week blocks. Vessel-based surveys were conducted over 4–8 h between 0700 h and 1500 h, depending on weather and tidal conditions (low tide affected the access points to coastal waters for the research vessels). Different vessels were used to undertake surveys: a 6 m aluminum motor vessel and a 12 m sailing yacht. A single research vessel was used per survey (day). Observations were made by four observers onboard the research vessel that traveled along predefined routes. Two observers recorded the behavior of the dolphins, another recorded the acoustics, and a fourth took dorsal fin photographs for the identification of individual dolphins. Surveys were not conducted in winds greater than 20 kts and a Beaufort scale of >3 (on a scale of 12).

B. Behavior, group composition, and individual identification

A group was defined as an aggregation of dolphins that was either engaged in the same behavior state, with an average of one to two dolphin lengths between individuals and within a 100 m radius (Mann, 2000; Shane, 1990). When a group of dolphins was sighted, the vessel would move from a predefined route and begin a 1 h group follow. The vessel remained within 50 m of the group for the duration of observations. For each group observed, the time, GPS location, group size, group composition, behavior, and acoustics were recorded. Groups were only included in the following analysis if there was only a single group visible from the survey vessel (i.e., within a radius of approximately 300 m) and remained together (i.e., there were no affiliations or disaffiliations) for the duration of the group follow. This was one of the methods used to ensure that whistle emissions recorded originated from individuals in the group being followed.

The size and composition of each group was determined by the number of adults, calves and dolphins of unknown age class. Adults were defined as full sized individuals (2–4 m) with moderate to heavy ventral speckling. Individuals were also identified as adults if they were accompanied by a calf (an individual no more than half the size of an adult) traveling in infant or "echelon" position (Smolker *et al.*, 1992). If any individual in a group could not be confirmed as an adult or a calf, it was labeled as an unknown. For the purposes of the following analysis, the group compositions were divided into those with calves and those without calves.

Continuous observations using scan sampling of the behavior "states" and "events" displayed by dolphins within

TABLE I. Ethogram of dolphin behavior states and "frequent" events (i.e., those recorded >20 times in association with whistle emissions)

Behavior state	Description
Traveling	Dolphin moves in a defined direction with regular and consistent dive intervals.
Socializing	Two or more dolphins are clearly interacting with each other by direct physical contact such as body rolls, petting, and tail slapping. Frequent splashes and disturbance at the surface may be observed.
Milling/resting	Group frequently changes travel direction (no consistent travel direction). Individuals may surface facing different directions. Dolphins have slow movements with variable, but frequent, dive intervals and often remain floating at the surface for a short amount of time between dives.
Feeding/foraging	Dolphins are actively pursuing prey and feeding (often confirmed by visual observation of fish or prey item). Usually associated with deep diving (fluke-up dives), fast swims, or porpoising, frequent changes in travel direction and inconsistent interbreath intervals. Group may be in a circular formation, spread over a wide area, and individuals' surface facing different directions.

the group were recorded (Altmann, 1974). Four behavior states were defined as milling (including resting), traveling, socializing, and feeding (Table I). Only groups where all individuals were engaged in the same behavior state at the surface were included in the subsequent analysis.

Photo-identification of individual dolphins was performed using photographs taken with a SLR Digital Nikon D100 camera with 70–300 mm lens (Hansen and Defran, 1990). Efforts were made to photograph the dorsal fin of each individual dolphin in a group during focal follows. Photographs of dorsal fins were allocated a photo-grade between 0 (poor) and 10 (excellent) based on the clarity (defined by the sharpness, contrast and angle) of the dorsal fin in the photograph. Each dolphin was categorized according to one of eight dorsal fin categories based on the pattern of nicks and notches on the trailing edge of the fin. An individual identification number was allocated to each identified dolphin. Details of individuals including the identification number, dorsal fin category, sex and age class, species, and distinguishing features were recorded into an Access 2000 (Microsoft Corp.) dolphin catalog. Information on each individual recorded in the catalog was: location, group behavior, group composition acoustic recordings, and other individuals present (i.e., other dolphins identified in the group). Around 78% of dolphins in the bottlenose dolphin population at Byron Bay showed distinct markings and could be individually identified (Hawkins, 2007). The photo-identification of individual dolphins was undertaken to ensure that a range of different dolphins were included in the study and that the samples were representative of the whole population.

C. Acoustic recordings

Two different hydrophone systems were used to record dolphin acoustics during group follows. The first was a CR-100–27 single hydrophone (frequency range 7 Hz–100 kHz; sensitivity −179 dB ± 5 dB re 1 V/μPa) with an HP-A1 amplifier (volume gain set between 7 and 10 dB; direct out 7 Hz–100 kHz ± 3 dB) (Burns Electronics Pty Ltd., Australia) powered by a 12 V dc battery. Signals were recorded using a Sony Digital Audio Tape recorder (sample rate of 44 kHz). This single hydrophone system allowed for rapid deployment and was the primary acoustic recording device. A second hydrophone system used was a two channel towed hydrophone array with 100 m of 14 mm cable and 10 m of sealed streamer tubing containing two hydrophones placed 3 m apart with preamplifiers (frequency range of 7 Hz–100 kHz; sensitivity of −169 dB ± 1.5 dB, and sample rate of 44–96 kHz). The hydrophone array was connected to a CR-MAX (Multiplexed Active Filter) amplifier (volume gain of 0–40 dB; frequency response of 7 Hz–450 kHz ± 3 dB; high pass gain rumble filter of 80 Hz 6 dB/octave within input range) (Burns Electronics Pty Ltd., Australia) powered by a 12 V battery. The hydrophone array system was attached to a connector block and Data Acquisition card (National Instruments) and Notino High Grade 3600s computer with SONAMON V 1.0 software for recording (Madry Technologies, Australia). Buoys were attached to the hydrophone streamer and cables at 10 m intervals to keep the hydrophone at a consistent depth of 2.5 m. This system was used to obtain directionality of acoustic emissions as a further check that the group being observed was creating the acoustic emissions being recorded. The hydrophone array was the secondary acoustic recording device as it required calm conditions and a long deployment time which was not practical for all groups observed. These hydrophone systems were not used simultaneously and recordings were made using only one hydrophone system at a time.

To record the acoustic emissions of focal groups, the vessel was positioned parallel and slightly ahead of the dolphins' direction of travel and the hydrophone was then deployed. Recordings were continued until any member of the group had moved more than 100 m from the vessel. This was to ensure that all the whistles emitted and at least most or all of the whistles produced by the focal group, could be recorded. This was to ensure that at least most or all of the whistles produced by the focal group could be recorded.

D. Whistle classification and analysis

Spectrograms (time versus frequency graphs) (Blackmann-Harris window; 256–512 band resolution; 2048 FFT size) were used to identify and classify whistles in COOLEDIT 2000 (Syntrillium Software). Using visual analysis techniques, each whistle was classified into one of five tonal classes based on the frequency modulations: sine (A), flat (B), down-sweep (C), concave (D), and rise (E) (Tyack, 1986; Azevedo and Sluys, 2005; Hawkins and Gartside, 2009a, 2009b). Distinct whistle types were given an identification number [e.g., 1A (the first sine whistle identified); 2C (the second down-sweep whistle identified)] and the acoustic parameters of each whistle: duration, start time, start frequency, end frequency, lowest frequency, and highest frequency were recorded together with the number of loops, breaks, and harmonics (Tyack, 1986; Rossi-Santos and Groupos, 2006). Distinct whistle types were considered to be

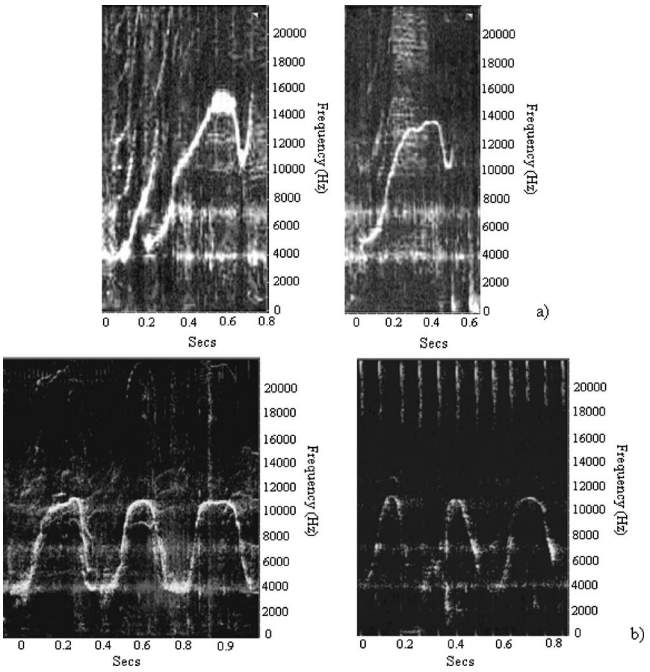

FIG. 1. Two examples of two different distinct whistle types from (a) rise tonal class and (b) sine tonal class, with frequency in (Hz) on the *y* axis and time (s) along the *x* axis. Representations of the degree of variation in the same distinct whistle types can be seen in each example. Note: example (a) is a distinct common whistle "26E."

looped if they were repeated within 0.3 s of the same preceding whistle. Measurements of the acoustic parameters for whistles along with tonal classes were used to match and define distinct whistle types. The 24 h time (h:min:s) that each whistle was emitted was also noted. Figure 1 shows examples of two distinct whistle types from rise and sine tonal classes and demonstrates the degree of variability observed in whistles. If a whistle had a poor signal to noise ratio or could not be confirmed as a specific whistle type, it was noted as a "poor resolution" (PR) whistle.

Four independent observers were used to validate and assess the accuracy of the observer method and whistle classification system used. Two of the observers were familiar with spectrographic analysis for bioacoustic sounds, one was inexperienced and another was the principal author. Thirty-two randomly selected whistles that consisted of a variety of different tonal classes were chosen and each observer categorized each whistle according to tonal class. Whistles were presented to observers in a random order. Matches between spectrograms were then made to identify distinct whistle types. Observers used spectrograms in RAVENLITE V. 1.0 (Cornell Laboratory of Ornothology) to categorize and identify whistles via visual and audible means. There was 95% similarity in the classification of whistles into each tonal class. For matching of distinct whistle types, there was 78% agreement between observers although this was likely to be higher with more experienced observers.

E. Statistical analysis

1. Group characteristics

The composition and characteristics were determined for each group recorded. The overall numbers of individuals observed and the number of individuals identified from photographs were determined. Groups were divided into two different categories, those with and without calves and the mean sizes of these groups were calculated. A T-test was performed to determine if there was a significant difference between the sizes of calf and noncalf groups.

2. Rate of whistle production

The repetition rate of whistles was calculated for each group. The whistle repetition rates were calculated by summing the total number of whistles recorded (including "PR" whistles) for each group and dividing this value by the duration (minutes) for which recordings of acoustics were made and the number of individuals in the group. As there were differences in the duration of recordings and the number of whistles from each group, this standardized the data set for analysis. Whistle diversity was calculated for each group as the number of distinct whistle types per dolphin per minute (dos Santos *et al.*, 2005). To account for the non-normal distribution of data, logged values of both whistle repetition and diversity rates were used in all statistical tests.

Correlation tests were used to examine if there was a relationship between group sizes and whistle repetition rate and whistle diversity. To provide adequate sample sizes for statistical analysis, group sizes were divided into clusters between 1 and 5, 6 and 10, 11 and 15, 16 and 20, 21 and 25, 26 and 30, 31 and 40, and 41 and 55. Group sizes with more than 31 individuals were aggregated into larger increments to minimize possible bias in tests caused by small sample sizes as there were fewer samples. Correlation tests were performed in Excel 2003 (Microsoft Corp.).

The range of whistle repetition rates and averages for calf and noncalf groups were calculated. Comparisons were made between groups of calf groups and noncalf of the same size using Mann–Whitney U-tests to examine relationships with group size and whistle repetition rates. To investigate if the number of distinct whistle types produced by dolphins was related to group size or composition, T-tests were used. These comparisons were limited to groups with sizes between 1 and 20 individuals as there were no groups without calves that contained >20 individuals. Statistical analyses were carried out in SPSS V 11.5 (SPSS Inc.).

Acoustic and behavior data were synchronized using the 24 h time (h:min:s) records for each focal group. These data were then be used in tests to examine the associations between behavior states and whistles. One-way analysis of variance (ANOVA) and Kruskall–Wallis tests were performed in SPSS V. 11.5 (SPSS Inc.) to investigate if there were differences in the repetition rate of whistles between group compositions, group sizes, and behavior states.

3. Production of different whistle types

The overall numbers and percentages of whistles from each tonal class were tallied for all recordings from each group. In order to account for any differences between groups, the rate of tonal class emissions per dolphin per minute for each group was calculated by summing the total number of whistles of each tonal class for each group and

dividing this by the number of individuals and the number of minutes of acoustic recordings made for the group. The logged values of the rates of tonal class emissions were then calculated to address the non-normal distribution of data. These logged tonal class rates were then compared between calf and noncalf groups. One-way ANOVA and Kruskall–Wallis tests were performed in SPSS V. 11.5 (SPSS Inc.) to investigate whether any tonal classes were associated with particular group compositions. The number of different distinct whistle types cataloged under each tonal class category was also noted. This was to show whether a particular tonal class contained more distinct whistle types than the other tonal classes.

Correspondence analyses using symmetrical normalization SPSS V. 11.5 (SPSS Inc.) were carried out to investigate the associations between tonal classes, distinct whistle types, and behavior states for groups with and without calves (Hawkins and Gartside, 2009a). This analysis allowed both broad and detailed assessments to be made of associations between whistles and behavior states.

Correspondence analysis, however, does not take into account group effects and is likely to be highly influenced by some groups that produced high numbers of whistles of a certain tonal class during a behavior state. We therefore used tonal class emission rates and Kruskal–Wallis tests to investigate if there were significant differences in the rate of tonal class emissions between behavior states. The rate of tonal class emissions was calculated for each group and are reported as the number of x (tonal class category) whistles per minute per dolphin.

Distinct "common" whistle types were identified and tested for associations with behavior states. Distinct common whistles were defined as those produced by more than one group on more than 1 day and recorded ≥ 40 times. To ensure that each group included in the analysis consisted of different individuals, results from photo-identification were used to reduce the effects of individuals. If an individual had been recorded more than once from a group where concurrent behavior and acoustic recordings were made, only one recording was used in the analysis examining associations between distinct common whistles and behaviors. This method was adopted ensure that the results on group composition were not being biased by over-representation of particular individuals in the sample.

To further examine any apparent associations between behaviors and distinct whistle types, a generalized multilevel statistical model with the whistle classes as a multinomial response, the individual whistles at level 1 and groups at level 2, was constructed following the exploratory correspondence analysis. Although this statistical model was a logical development in a study of this kind, it became apparent that this model was not valid in the present study because the set of data had many small sample sizes and because only one population was sampled. These are limitations of studies of this kind that would apply to other field studies of wild dolphins. The survey techniques used in this study also limited the ability to undertake multilevel models because individual callers could not be identified. Therefore, only group-level exploratory analysis could be undertaken.

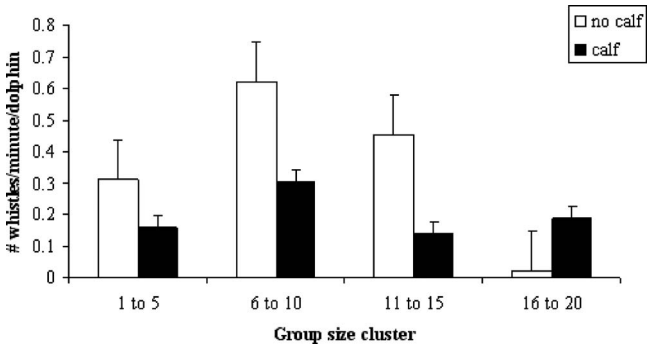

FIG. 2. Bar graph showing the mean whistle repetition rate and standard error bars of groups with and without calves within size clusters of 1–20 dolphins.

III. RESULTS

A. Survey effort

Forty-three vessel-based surveys were made between 2003 and 2006. Around 27 h of acoustic recordings were analyzed, the majority of which were made using the single hydrophone system with the exception of 1 h that was made using the hydrophone array. The duration of acoustic recordings per group varied between 1 and 77 min ($\bar{x}=19.1$ min; S.D. ± 17.6 min). Analyses of 4125 whistles were made resulting in 1713 whistles being classified into 186 distinct whistle types and the remaining 2412 as PR whistles.

B. Group characteristics

Acoustic recordings were made of 71 groups (1022 individuals): 41 groups with calves (788 individuals) and 30 without calves (234 individuals). There was a significant difference between the sizes of groups with and without calves (T-test $P<0.0001$; Df=31). The average size of groups with calves was larger ($\bar{x}=20.1$; S.D. ± 13.9; range 2–55) than those without calves ($\bar{x}=11.2$; S.D. ± 3.01; range 1–19). Four hundred individual dolphins were positively identified from photographs. An average of 10 individuals (S.D. ± 9) was identified per group.

C. Rate of whistle production

1. Repetition rate of whistles, group size, and composition

The repetition rate of whistles per group varied from 0.009 to 18.45 whistles/minute/dolphin ($\bar{x}=0.75$; S.D. ± 2.68). There was a significant relationship between the group size and whistle repetition rate, with the number of whistles emitted decreasing as the group sizes increased ($r=0.634$, Df=58, $P<0.05$). The mean repetition rates of whistles were higher in small groups of six to ten dolphins ($\bar{x}=0.40$; S.D. ± 0.38), and lower in larger groups of 41–55 individuals ($\bar{x}=0.02$; S.D. ± 0.01) (Fig. 2).

The whistle repetition rate also significantly differed between group compositions (i.e., calf and noncalf groups) (Mann–Whitney $U=164.00$; $P=0.006$; $N=52$). Groups with calves produced lower whistle repetition rates ($\bar{x}=0.18$; S.D. ± 0.20) compared to noncalf groups ($\bar{x}=1.58$; S.D. ± 4.52).

TABLE II. Summary table showing the number of minutes of acoustic recordings was made of each behavior state from noncalf and calf groups. Note TR=travelling; MI=milling; SOC=socializing; FE=feeding.

	Behavior (No. of minutes recorded)					
Group composition	*N* groups	TR	MI	SOC	FE	Total
Noncalf	30	70 (23%)	54 (18%)	63 (21%)	118 (39%)	305
Calf	41	479 (36%)	282 (21%)	338 (25%)	231 (17%)	1330
Total	71	549 (34%)	336 (21%)	401 (25%)	349 (21%)	1635

When the whistle repetition rate of calf and noncalf groups of the same size clusters were compared, there were significant differences found in groups between 6 and 10 and 16 and 20 dolphins (Fig. 2). Calf groups of 6–10 dolphins ($N=11$) and 16–20 dolphins ($N=9$) had significantly lower whistle repetition rates than noncalf groups of the same size ($N=7$; $N=4$, respectively; Mann–Whitney $U=17.00$; $P=0.02$; Mann–Whitney $U=4$; $P=0.01$, respectively). The whistle repetition rates of calf and noncalf groups with sizes of 1–5 ($N=4$; $N=3$, respectively) and 11–15 ($N=11$; $N=7$, respectively) were not significantly different (Mann–Whitney $U=6.00$; $P=0.50$; Mann–Whitney $U=4$; $P=0.124$, respectively).

2. Whistle diversity, group size, and composition

The diversity of whistles (i.e., the number of distinct whistle types) ranged between 0.13 and 0.98 whistle types/minute/dolphin ($\bar{x}=0.39$; S.D. ± 0.26). Correlation tests indicated that there was no relationship between the group size and whistle diversity ($r=0.218$; Df=9; $P>0.05$). However, there was a significant difference in the number of distinct whistle types emitted per minute/dolphin between groups with and without calves (T-test $P=0.007$; Df=99). Compared to calf groups ($\bar{x}=0.07$; $N=101$; S.D. ± 0.528), noncalf groups produced a significantly higher diversity of whistles per individual ($\bar{x}=0.729$; $N=11$; S.D. ± 1.48).

3. Rate of whistle production and behavior state

Table II shows that the number of minutes of acoustic recordings were made from dolphins engaged in the four different behavior states for calf and noncalf groups. Acoustic recordings were fairly evenly distributed across each behavior state, but more recordings were made from groups with calves that were traveling.

The highest mean repetition rate of whistles was recorded from dolphins that were socializing ($\bar{x}=1.3$ whistles/minute/dolphin; S.D. ± 1.9; range 0.01–18.5 whistles/minute/dolphin). The mean repetition rate of whistles during traveling was 0.5 whistles/minute/dolphin (S.D. ± 0.4; range 0.003–2.9 whistles/minute/dolphin). Feeding and milling had slightly lower whistle repetition rates ($\bar{x}=0.4$ whistles/minute/dolphin; S.D. ± 0.3; range 0.01–1.37 whistles/minute/dolphin and $\bar{x}=0.2$ whistles/minute/dolphin; S.D. ± 0.2; range 0.002–0.82 whistles/minute/dolphin, respectively). One-way ANOVA tests showed that there were no significant differences between the logged repetition rate of whistles and behavior state ($P=0.351$; $F_{3,56}=1.115$). There was also no significant difference in the logged number of distinct whistle types per minute per dolphin between behavior states (Kruskal–Wallis $\chi^2=0.379$; Df=3; $P=0.945$).

D. Production of different whistle types

1. Tonal class emissions

Rise (40%; $N=692$) and sine whistles (40%; $N=690$) were the most frequently recorded tonal classes. Flat (11%; $N=185$) and concave (7%; $N=123$) tonal classes were less common, and down-sweep whistles were rarely recorded (1%; $N=23$). There were different numbers of distinct whistle types in each tonal whistle class. One of the two most numerous whistle types, sine whistles, was also the most diverse class with the highest number of distinct whistle types identified (98). Rise whistles were also diverse with 51 distinct whistle types identified. Down-sweep (15), flat (15), and concave (7) whistles, were less diverse classes.

2. Tonal class emissions and group composition

The number of whistles that were produced from each tonal class per minute/dolphin was compared between noncalf and calf groups. The logged rates of flat and rise whistles were significantly different between calf and noncalf groups ($P=0.006$; $F_{1,10}=12.269$ and $P=0.001$; $F_{1,34}=13.456$, respectively). Although the number of noncalf groups where flat ($N=4$) and rise whistles ($N=4$) were recorded was low, the rate of emission of these tonal classes ($\bar{x}=0.67$ /minute/dolphin; S.D. ± 1.28 and 2.4/minute/dolphin; S.D. ± 4.55 respectively) was higher than in groups with calves ($\bar{x}=0.02$ /minute/dolphin; S.D. ± 0.40; $N=9$ and 0.20/minute/dolphin; S.D.=0.82; $N=24$ respectively). The rate of sine ($P=0.376$; $F_{1,34}=0.826$), down-sweep ($P=0.321$; $F_{1,6}=1.168$) and concave ($P=0.922$; $F_{1,7}=0.010$) emissions did not vary significantly between calf and noncalf groups. Table III summarizes the number of whistle types that were recorded from each tonal class according to group composition and behavior state.

3. Tonal class emissions, group composition, and behavior state

Correspondence analysis using symmetrical randomization was used to undertake an exploratory assessment of the associations between whistles and behavior states for calf and noncalf groups. The assumption that whistle tonal classes were related to behavior states was justified in both cases (noncalf groups $\chi^2=139.74$; $P=0.0001$, Df=12 and calf groups $\chi^2=266.83$; $P=0.0001$, Df=12). For calf groups, the first two dimensions accounted for 92% of the variance in the whistle and behavior matrix, where inertia values

TABLE III. Summary of the number of whistles recorded from each tonal class with the number of groups each tonal class was recorded from according for each group composition category. Percentages represent the proportion of each tonal class recorded from each behavior state. Note TR=travelling; MI=milling; SOC=socializing; FE=feeding; PR=poor resolution whistles.

			Behavior				
Group composition	Tonal class	*N* groups	TR	MI	SOC	FE	Total
Noncalf	Sine	8	10 (9%)	0 0	63 (53%)	45 (38%)	118
	Flat	4	2 (3%)	0 0	77 (97%)	0 0	79
	Down	1	2 (100%)	0	0	0	2
	Concave	3	2 (100%)	0	0	0	2
	Rise	4	0	0	273 (100%)	0	273
	Pr	21	24 (3%)	0	616 (66%)	290 (31%)	930
	Total		40	0	1029	335	1404
Calf	Sine	21	391 (68%)	22 (4%)	127 (22%)	32 (6%)	572
	Flat	10	82 (77%)	0	23 (22%)	1 (1%)	106
	Down	8	6 (29)	6 (29%)	1 (5%)	8 (38%)	21
	Concave	7	35 (29%)	17 (14%)	22 (18%)	47 (39%)	121
	Rise	25	302 (72%)	18 (4%)	58 (14%)	41 (10%)	419
	Pr	32	835 (61%)	59 (5%)	361 (22%)	227 (13%)	1482
	Total		1651	122	592	356	2721

showed that differences between milling (inertia=0.077) and socializing (inertia=0.040) accounted for most of the variance in the data. For noncalf groups, the first two dimensions accounted for 100% of the variance in the whistle and behavior matrix, where inertia values showed that the differences between socializing (inertia=0.102) and traveling (inertia=0.393) accounted for most of the variance in the data. The biplots in Figs. 3 and 4 show that there are some apparent differences in the strengths of associations of whistle tonal classes and behavior states between calf and noncalf groups.

Rise whistles were highly associated with social behaviors for noncalf groups but were more closely associated with traveling in calf groups. Flat whistles appear to be associated with social behaviors for both types of group compositions, although the association is stronger in noncalf groups. Sine whistles appear to be a "mutual" whistle type for noncalf groups and may be used during a number of different behaviors. For groups with calves, sine whistles were more associated with traveling behaviors. Concave whistles were associated with feeding behaviors in groups with calves but were not associated with any behavior for noncalf groups. Down-sweep whistles were also not associated with any behavior for either calf or noncalf groups. This may be due to the low number of concave and down-sweep whistles recorded from noncalf and calf groups.

In order to account for group affects, the rate of tonal class emissions for each behavior state was tested using Kruskal–Wallis analysis. Due to the low numbers of groups recorded and whistle classes for noncalf groups, the data for

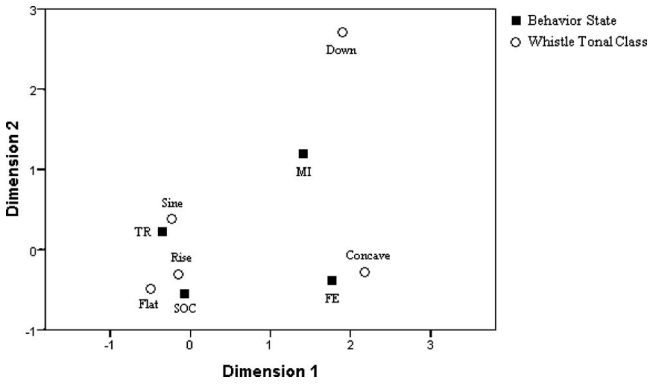

FIG. 3. Biplot displaying the association between whistle class and behavior states from groups with calves using correspondence analysis (inertia dimension 1=0.253; inertia dimension 2=0.042). (Note: the closer the dimension points are to one another in the biplot, the closer the association between the behavior state and whistle class). Behavior abbreviations: FE=feeding; MI=milling; SOC=socializing; TR=travelling.

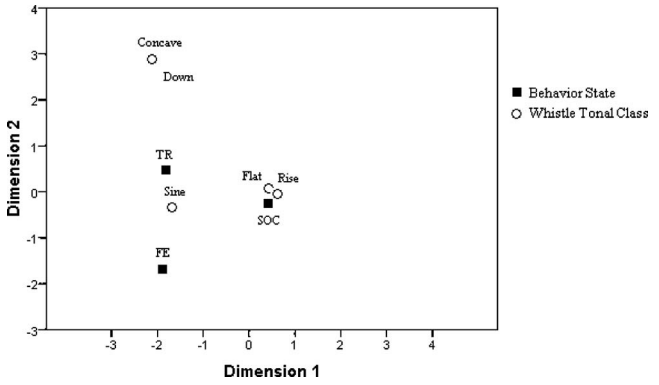

FIG. 4. Biplot displaying the association between whistle class and behavior states from noncalf groups using correspondence analysis (inertia dimension 1=0.631; inertia dimension 2=0.131). (Note: the closer the dimension points are to one another in the biplot, the closer the association between the behavior state and whistle class). Behavior abbreviations: FE=feeding; MI =milling; SOC=socializing; TR=travelling.

noncalf and calf groups were combined for this analysis. Results showed that the logged rate of flat whistles (χ^2 =8.598; Df=2; P=0.014), down-sweep (χ^2=9.643; Df=3; P=0.022), concave (χ^2=21.523; Df=3; P=0.0001), and rise (χ^2=9.819; Df=3; P=0.020) were significantly different between behavior states. The rate of sine (χ^2=1.504; Df=3; P=0.681) did not significantly differ between behavior states, consistent with the results of correspondence analysis, that these whistles are used in a variety of contexts.

The rate of emission of flat whistles was higher during socializing ($\bar{x}$=0.486/minute/dolphin; S.D.±0.71; N=6) than feeding behaviors ($\bar{x}$=0.003; N=2). The highest rate of down-sweep whistles occurred during milling ($\bar{x}$=0.046; SD=0.01; N=3) and the lowest during traveling ($\bar{x}$=0.01; S.D.±0.01; N=3). The number of samples for concave whistles was low, but the highest rate of concave whistles occurred during feeding ($\bar{x}$=0.041; N=2) and milling behaviors ($\bar{x}$=0.031; N=1) and least during socializing ($\bar{x}$=0.01; S.D.±0.003; N=3). For rise whistles, the rate of emission was highest during socializing ($\bar{x}$=0.51; S.D.=1.56; N=10) and least during milling and feeding ($\bar{x}$=0.08; S.D.=0.07; N=5; $\bar{x}$=0.05; S.D.=0.05; N=4, respectively) (Fig. 5).

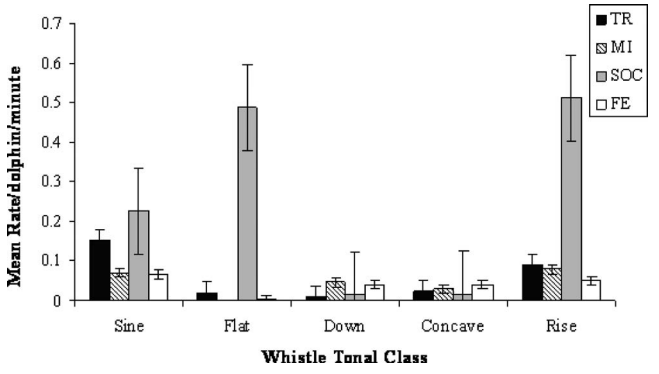

FIG. 5. Mean rate of whistle tonal class emissions per minute per bottlenose dolphin during each behavior state with standard error bars (rise N=692; sine N=690; flat N=185; concave N=123; down N=23).

These patterns are consistent with the general associations between tonal classes and behaviors found in correspondence analysis.

4. Distinct whistle types, group composition, and behavior state

To examine whether distinct types of whistles were more likely to be emitted during particular behaviors by calf and noncalf groups, we examined the associations of 15 distinct "common" whistles (i.e., those whistles emitted by more than one group on more than 1 day and recorded >40 times). Of the distinct common whistles, seven were from the rise tonal class, six from sine, two from flat, and two from concave. Table IV shows the numbers of distinct whistles emitted by calf and noncalf groups during each behavior state. The majority of distinct common whistles were recorded during socializing and traveling behaviors. Ten distinct common whistles were recorded from both calf and noncalf groups, while the remaining seven were only recorded from groups with calves. It therefore appears that nearly 50% of distinct common whistles are shared between groups with and without calves.

Due to the relatively small sample sizes, distinct common whistles from groups with calves and noncalf groups were combined for correspondence analysis tests. The assumption that common whistles were related to behavior states was justified (behavior states χ^2=1371.30, P=0.0001, Df=51; behavior events χ^2=200.81, P=0.0001, Df=48). In the first two dimensions, 92% of the variance in the matrix between common whistles and behavior states was accounted for. Inertia values indicated that the differences between milling (inertia=0.108) and feeding (inertia=0.484) contributed most to the overall variance of the data, suggesting that the whistles used during these behaviors were very different. Figure 6 displays the biplot from correspondence analysis showing the levels of associations between common distinct whistles and behavior states. These exploratory analyses suggest that some distinct common whistles are more likely to be, but not exclusively, emitted during particular behaviors. However, some group effects may also contribute to the strengths of associations, where one group may have emitted a large number of a distinct whistle type, while another emitted few. For this data set, further multivariate analyses that compensate group effects could not be taken into account due to the low numbers of samples of some distinct whistle types between groups. The low sample sizes for the data on differences in the rate of emission and type of whistle emissions during different behaviors precludes statistically rigorous assessment but suggests there are underlying associations.

IV. DISCUSSION

Earlier studies have reported that the rate of whistles increased with group size (Jones and Sayigh, 2002; Cook *et al.*, 2004). In contrast, our findings showed that the repetition rate of whistles decreased as the group size increased, with higher numbers of whistles being produced by group sizes between 5 and 9 individuals, and lower numbers in groups

TABLE IV. Occurrence of 15 distinct common whistles for each behavior state and the numbers of noncalf and calf groups from which each distinct common whistle was recorded.

			Behavior state			
Whistle No.	Group composition	*N* groups	Traveling	Milling	Socializing	Feeding
11B	No calf	1			42	
	Calf	2	1			1
21A	No calf	1	13			
	Calf	1			28	
29A	No calf	0				
	Calf	2	38			
3E	No calf	1			8	
	Calf	3	1		26	6
28A	No calf	0				
	Calf	2	45			
7E	No calf	0				
	Calf	3	1		47	
2D	No calf	1		2		
	Calf	3	20	8	8	6
4A	No calf	0				
	Calf	2	75			
21E	No calf	1			78	
	Calf	1		1		
9E	No calf	0				
	Calf	5	43		36	1
5E	No calf	1			7	
	Calf	6	13		50	18
20A	No calf	0				
	Calf	2	13		28	
10E	No calf	0				
	Calf	3	147	5		
4D	No calf	1				
	Calf	3	3		14	41
26E	No calf	1			299	
	Calf	1			15	
Total		47	413	16	686	73

between 41 and 55 individuals. Thus our findings show that in larger groups, individuals reduced the number of whistles they produced. These results were similar to those recently reported by Quick and Janik (2008) who found that the number of whistles produced per dolphin begins to decrease in group sizes of 10 or more. Our findings also show that there is a relationship between the whistle repetition rate and group composition. The presence or absence of calves may therefore be a contributing factor to these contrasting results.

Groups without calves had a significantly higher repetition rate and diversity of whistles compared to groups with calves. These differences may be related to sex and age classes of the dolphins present in the group as the population of bottlenose dolphins studied is characterized by a sexually segregated fission-fusion society (Hawkins and Gartside, 2008). Therefore, groups with calves were likely to have more females than males and noncalf groups were more likely to have more males than females. A number of factors

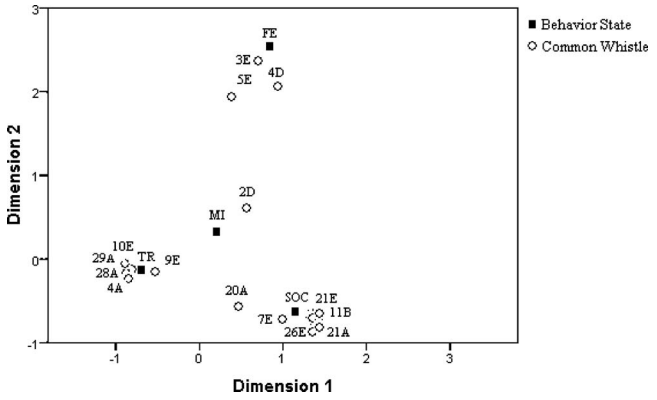

FIG. 6. Biplot of correspondence analysis of 15 associations between behavior state and common whistles ($N=859$) (inertia dimension 1=0.809; inertia dimension 2=0.572). The common whistles are shown by their catalog number, followed by a letter designating the class of whistle, e.g., 26E. (Note: the closer the dimension points are to one another in the biplot, the closer the association). Whistles containing A=sine, B=flat, C=down-sweep, D=concave, and E=rise. Behavior abbreviations: FE=feeding; MI=milling; SOC=socializing; TR=travelling.

may drive these differences in the rate and diversity of whistle production such as antimasking strategies (Quick and Janik, 2008). This may be of particular relevance to groups with calves where communication between mothers and their offspring is imperative (Smolker *et al.*, 1993). In addition, the reduction in whistle emissions by groups with calves may also be an antipredator strategy. In the study population, there have been several cases of predation by sharks on dolphins and a number identified from photo-identification data with evident scars from shark attacks. By reducing the rate of whistles, the risk of detection by potential predators may be reduced.

For noncalf groups, the increase in whistle repetition rate and diversity may be driven by a number of other factors. It is likely that the increase in whistle rate and diversity of noncalf groups is related to the individuals present and social context. In several species of marine mammals, such as humpback whales (*Megaptera novaeangliae*) (Payne and McVay, 1971) and Weddell seals (*Leptonychotes weddellii*) (Stirling and Thomas, 2003), males increase the use of specific call types and the level of vocalizations during breeding seasons to attract mates and defend territories. While there is no evidence that male bottlenose dolphins use vocal displays to attract mates, it seems unlikely that they would not give the highly developed social vocalization system of this species. In addition, the larger diversity of whistles in noncalf groups may also relate to males finding receptive females and a possible increase in associations with different individuals. Further division of group composition was not possible in this study; however, it would be interesting to assess whistle production patterns of female-female, male-female, and male-male associations with respect to known age classes.

Acevedo-Gutiérrez and Stienessen (2004) suggested that the rate of whistle production of bottlenose dolphins may be used to communicate information about a specific situation. In the Sado Estuary, Portugal, the number of distinct whistle types (stereotyped contours) produced by bottlenose dolphin per minute significantly differ between behavior states, particularly between traveling and feeding (dos Santos *et al.*, 2005). Jones and Sayigh (2002) also reported significant differences in the whistle repetition rate of bottlenose dolphins between behavior states, with the highest being produced during socializing. Our study did not find a significant difference in the repetition rate of whistles between behavior states. Our results show that dolphins are more likely to communicate specific information relating to their activity by producing particular types of whistles.

For some mammals, the behavioral context influences the production of specific types of vocalizations, for example, pan hoots in male chimpanzees (*Pan troglodytes*), contact calls of female baboons (*Papio cynocephalus ursinus*), and the alarm calls of California ground squirrels (*Spermophilus beecheyi*) (Owings and Virginia, 1978; Mitani and Nishida, 1993; Rendall *et al.*, 2000). Associations between different call types or whistle categories (similar to the tonal classes described here) and behaviors have been identified for killer whales (*Orcinus orca*) and North Atlantic pilot whales (*Globicephala melas*) (Morton *et al.*, 1986; Weilgart and Whitehead, 1990; Foote *et al.*, 2008). Our results, consistent with a small number of other studies, show that tonal classes and distinct whistle types are related to particular behavior states in bottlenose dolphins (Janik *et al.*, 1994; Cook *et al.*, 2004; Hawkins and Gartside, 2009a, 2009b). The production of some tonal classes also significantly differed between groups with and without calves. These tonal classes were rise and flat whistles, which were emitted at higher rates by noncalf groups. Due to the low number of samples, however, these findings should be considered preliminary.

In the present study, the majority of whistles of each tonal class were associated with the same behavior states for both calf and noncalf groups although the strengths of association slightly varied. Sine whistles were associated with traveling behaviors and may therefore be important in the advertisement of identity and location of individuals to maintain cohesion when moving between areas. In a group of provisioned dolphins at Tangalooma, Moreton Island, Australia, sine whistles appeared to be used as group contact calls (Hawkins and Gartside, 2009a). Our findings further support the suggestion that whistles of this tonal class may have a specific role in maintaining group cohesion.

Non-signature whistles of bottlenose dolphins identified by Cook *et al.* (2004) included a large percentage of rise whistles that were also more likely to be emitted during social behaviors. Rise whistles were also found to be associated with social behaviors in a group of provisioned dolphins at Tangalooma, Moreton Island, Australia, and interactive behaviors with vessels (e.g., bowriding) in Byron Bay, New South Wales (Hawkins and Gartside, 2009a, 2009b). In the population studied here, flat and rise whistles were associated with socializing behaviors. Therefore, it appears that in multiple populations of wild bottlenose dolphins, rise whistles are related to social behaviors where dolphins experience higher levels of arousal and activity. In contrast, concave whistles were associated with milling behaviors while

down-sweep whistles were infrequently recorded and were therefore likely to be emitted in limited contexts or situations.

Foote *et al.* (2008) distinguished between dominant call types of killer whales that function to identify a group and less common call types that were likely to be shared between social groups and produced more during social situations, particularly intergroup affiliations. In the present study, we demonstrated that in addition to tonal classes, some distinct whistle types were also associated with different behavior states in wild bottlenose dolphins. The distinct common whistles identified here were also likely to be shared between individuals and the majority were produced during social and feeding behaviors.

Our findings show that whistles may be used to communicate specific information to cohorts relating to the behavior and the situation of the caller (behavioral context). This is consistent with suggestions in other studies that dolphin whistles convey discrete information between cohorts to coordinate individuals and organize their behavior (Caldwell and Caldwell, 1967; Burdin *et al.*, 1975; Kaznadzei *et al.*, 1977). Some whistles that are produced by bottlenose dolphins in the wild may have referential purposes and function in the same manner as the referential signals of other highly social and intelligent species, such as chimpanzees (Slocombe and Zuberbuhler, 2005). Dolphins may therefore not only have developed an identity-labeling system through the development of "signature" whistles (Janik and Slater, 1998; Janik *et al.*, 2006) but also intricate method of communicating other important information through the development of a diverse whistle repertoire. Determining if the uses of common whistles remain stable over time is an essential element for future assessment and understanding of the biological significance of bottlenose dolphin whistles.

V. CONCLUSIONS

This study has shown that the repetition rate of whistles produced by bottlenose dolphins is related to both group size and composition but not behavior state. The diversity of whistles produced is also related to group composition. We have suggested that differences in the rate of whistle production may be associated with the age and sex classes of the individuals; however, further assessments are required to obtain a better understanding of the ecological need for such differences. We have further shown that there is an association between types of whistles and behavior. This strongly suggests that dolphins are transferring specific information about their activity. Further investigation that takes into consideration the identity of signalers will greatly further our understanding of the functions of whistle emissions in bottlenose dolphins.

ACKNOWLEDGMENTS

This work was supported by grants from the Sustainable Tourism Cooperative Research Centre, sponsorship from Baysail Pty Ltd. and the Dolphin Kayaking Co. The authors thank Max Egan and Iain McCabe for field support, Lyndon Brooks for analytical assistance, Peter Harrison, Neal Ryan, Susan Hawkins, David Newell, Megan Anderson, and the many project volunteers. Special thanks are due to the numerous reviewers for their helpful comments on earlier versions of this manuscript. This research was conducted under New South Wales National Parks and Wildlife Service Scientific License No. S10404 (2003–2007) and with Southern Cross University Animal Care and Ethics Committee approval Permit No. 03/11 (2003–2007).

Acevedo-Gutiérrez, A., and Stienessen, S. C. (**2004**). "Bottlenose dolphins (*Tursiops truncatus*) increase number of whistles when feeding," Aquat. Mamm. **30**, 357–362.

Altmann, J. (**1974**). "Observational study of behavior: Sampling methods," Behavior **49**, 227–266.

Azevedo, A. F., and Sluys, M. V. (**2005**). "Whistles of tucuxi dolphins (*Sotalia fluviatilis*) in Brazil: Comparisons among populations," J. Acoust. Soc. Am. **117**, 1456–1464.

Burdin, V. I., Reznik, A. M., Skornyakov, V. M., and Chupakov, A. G. (**1975**). "Communication signals of the Black Sea bottlenose dolphin," Sov. Phys. Acoust. **20**, 314–318.

Caldwell, M. C., and Caldwell, D. K. (**1967**). "Intraspecific transfer of information via the pulsed sound in captive Odontocete cetaceans," in *Animal Sonar Systems*, edited by R. G. Busnel (Laboratoire De Physiologie Acoustique, France), pp. 879–936.

Caldwell, M. C., Caldwell, D. K., and Tyack, P. L. (**1990**). "Review of the signature-whistle hypothesis for the Atlantic bottlenose dolphin," in *The Bottlenose Dolphin*, edited by S. Leatherwood and R. R. Reeves (Academic, London), pp. 199–235.

Cheney, D. L., Seyfarth, R. M., and Silk, J. B. (**1995**). "The role of grunts in reconciling opponents and facilitating interactions among adult female baboons," Anim. Behav. **50**, 249–257.

Connor, R., Wells, R. S., Mann, J., and Read, A. J. (**2000**). "The bottlenose dolphin—Social relationships in a fission-fusion society," in *Cetacean Societies—Field Studies of Dolphins and Whales*, edited by J. Mann, R. C. Connor, P. L. Tyack, and H. Whitehead (University of Chicago Press, Chicago), pp. 91–126.

Cook, M. L. H., Sayigh, L. S., Blum, J. E., and Wells, R. S. (**2004**). "Signature whistle production in undisturbed free-ranging bottlenose dolphins (*Tursiops truncatus*)," Proc. Biol. Sci. **271**, 1043–1049.

Darwin, C. (**1872**). *The Expression of the Emotions in Man and Animals* (Murray, London).

dos Santos, M. E., Caporin, G., Moreira, H. O., Ferreira, A. J., and Bento Coelho, C. J. L. (**1990**). "Acoustic behavior in a local population of bottlenose dolphins," in *Sensory Abilities of Cetaceans*, edited by J. Thomas and R. Kastelein (Plenum, New York), pp. 585–598.

dos Santos, M. E., Louro, S., Couchinho, M., and Brito, C. (**2005**). "Whistles of bottlenose dolphins (*Tursiops truncatus*) in the Sado Estuary, Portugal: Characteristics, production rates, and long-term contour stability," Aquat. Mamm. **31**, 453–462.

Fischer, J., Hammerschmidt, K., Cheney, D. L., and Seyfarth, R. M. (**2001**). "Acoustic features of female chacma baboon barks," Ethology **107**, 33–54.

Foote, A. D., Osborne, R. W., and Hoelzel, A. R. (**2008**). "Temporal and contextual patterns of killer whale (*Orcinus orca*) call type production," Ethology **114**, 599–606.

Hansen, L. J., and Defran, R. H. (**1990**). "A comparison of photo-identification studies of California coastal bottlenose dolphins," Rep. Int. Whal. Comm. **12**, 101–104.

Hauser, M. D., and Marler, P. (**1993**). "Food-associated calls in rhesus macaques (*Macaca mulatta*): I. Socioecological factors," Behav. Ecol. **4**, 194–205.

Hawkins, E. R. (**2007**). "Behavior and acoustics of bottlenose dolphins (Tursiops aduncus) in the Byron Bay region, NSW, Australia," PhD thesis, Southern Cross University, Lismore, Australia.

Hawkins, E. R., and Gartside, D. F. (**2008**). "Social and behavioral characteristics of Indo-Pacific bottlenose dolphins (*Tursiops aduncus*) in northern New South Wales, Australia," Aust. Mammal. **30**, 71–82.

Hawkins, E. R., and Gartside, D. F. (**2009a**). "Patterns of whistles emitted by wild Indo-Pacific bottlenose dolphins (*Tursiops aduncus*) during a Provisioning Program," Aquat. Mamm. **35**, 171–186.

Hawkins, E. R., and Gartside, D. F. (**2009b**). "Interactive behaviors of bottlenose dolphins (*Tursiops aduncus*) during encounters with vessels," Aquat. Mamm. **35**, 259–268.

Jacobs, M., Nowacek, D. P., Gerhart, D. J., Cannon, G., Nowicki, S., and Forward, R. B., Jr. (**1993**). "Seasonal changes in vocalizations during behavior of the Atlantic bottlenose dolphin," Estuaries **16**, 241–246.
Janik, V. M. (**2000**). "Food-related bray calls in wild bottlenose dolphins (*Turiops truncatus*)," Proc. R. Soc. London, Ser. B **267**, 923–927.
Janik, V. M., Dehnhardt, G., and Todt, D. (**1994**). "Signature whistle variations in a bottlenose dolphin, *Tursiops truncatus*," Behav. Ecol. Sociobiol. **35**, 243–248.
Janik, V. M., Sayigh, L. S., and Wells, R. S. (**2006**). "Signature whistle shape conveys identity information to bottlenose dolphins," Proc. Natl. Acad. Sci. U.S.A. **103**, 8293–8297.
Janik, V. M., and Slater, P. J. B. (**1998**). "Context-specific use suggests that bottlenose dolphin signature whistles are cohesion calls," Anim. Behav. **56**, 829–838.
Jones, G. J., and Sayigh, L. S. (**2002**). "Geographic variation in rates of vocal production of free-ranging bottlenose dolphins," Marine Mammal Sci. **18**, 374–393.
Kaznadzei, V. V., Kreichi, S. A., and Khakhalkina, E. N. (**1977**). "Types of dolphin communication and their organization," Sov. Phys. Acoust. **22**, 484–488.
Mann, J. (**2000**). "Unraveling the dynamics of social life—Long-term studies and observational methods," in *Cetacean Societies—Field Studies of Dolphins and Whales*, edited by J. Mann, R. C. Connor, P. L. Tyack, and H. Whitehead (University of Chicago Press, Chicago), pp. 45–64.
Manser, M. B., Seyfarth, R. M., and Cheney, D. L. (**2002**). "Suricate alarm calls signal predator class and urgency," Trends Cogn. Sci. **6**, 55–57.
Marino, L., Connor, R. C., Fordyce, R. E., Herman, L. M., Hof, P. R., Lefebvre, L., Lusseau, D., McCowan, B., Nimchinsky, E. A., Pack, A. A., Rendell, L., Reidenberg, J., Reiss, D., Uhen, M. D., Van der Gucht, E., and Whitehead, H. (**2007**). "Cetaceans have complex brains for complex cognition," PLoS Biol. **5**, e139.
Markov, V. I., and Ostrovskaya, V. M. (**1990**). "Organization of communication system in *Tursiops truncatus* Montagu," in *Sensory Abilities of Cetaceans*, edited by J. Thomas and R. Kastelein (Plenum, New York), pp. 599–622.
Marler, P. (**1975**). "On the origin of speech from animal sounds," in *The Role of Speech in Language*, edited by J. F. Kavanaughand J. E. Cutting (MIT, Cambridge), pp. 114–131.
McCowan, B., and Reiss, D. (**1995**). "Quantitative comparison of whistle repertoires from captive adult bottlenose dolphins (Delphinidae, *Tursiops truncatus*): A re-evaluation of the signature whistle hypothesis," Ethology **100**, 194–209.
Mitani, J. C., and Nishida, T. (**1993**). "Contexts and social correlates of long-distance calling by male chimpanzees," Anim. Behav. **45**, 735–746.
Morton, A. B., Gale, J. C., and Prince, R. C. (**1986**). "Sound and behavioral correlations in captive *Orcinus Orca*," in *Behavioral Biology of Killer Whales*, edited by B. C. Kirkevold and J. S. Lockard, (Alan R. Liss Inc., New York), pp. 303–333.
Nowacek, D. P. (**2005**). "Acoustic ecology of foraging bottlenose dolphins (*Tursiops truncatus*), habitat-specific use of three sound types," Marine Mammal Sci. **21**, 587–602.
Owings, D. H., and Virginia, R. A. (**1978**). "Alarm calls of California ground squirrels (*Spermophilus beecheyi*)," Z. Tierpsychol **46**, 58–70.
Payne, R. S., and McVay, S. (**1971**). "Songs of humpback whales," Science **173**, 585–597.
Price, J. J. (**1998**). "Family- and sex-specific vocal traditions in a cooperatively breeding songbird," Proc. R. Soc. London, Ser. B **265**, 497–502.
Quick, N. J., and Janik, V. M. (**2008**). "Whistle rates of wild bottlenose dolphins (*Tursiops truncatus*): Influences of group size and behavior," J. Comp. Psychol. **122**, 305–311.
Rendall, D., Cheney, D. L., and Seyfarth, R. M. (**2000**). ""Proximate factors mediating "contact" calls in adult female baboons (*Papio cynocephalus ursinus*) and their infants," J. Comp. Psychol. **114**, 36–46.
Rossi-Santos, M. R., and Groupos, J. (**2006**). "Latitudinal variation in whistle structure of the estuarine dolphin *Sotalia guianensis*," Behavior **143**, 347–364.
Sayigh, L. S., Tyack, P. L., Wells, R. S., Solows, A. R., Scott, M. D., and Irvine, A. B. (**1999**). "Individual recognition in wild bottlenose dolphins: A field test using playback experiments," Anim. Behav. **57**, 41–50.
Seyfarth, R. M., and Cheney, D. L. (**2003**). "Signallers and receivers in animal communication," Annu. Rev. Psychol. **54**, 145–173.
Shane, S. H. (**1990**). "Behavior and ecology of the bottlenose dolphin at Sanibel Island, Florida," in *The Bottlenose Dolphin*, edited by S. Leatherwood and R. R. Reeves (Academic, London), pp. 245–266.
Slocombe, K. E., and Zuberbuhler, K. (**2005**). "Functionally referential communication in a chimpanzee," Curr. Biol. **15**, 1779–1784.
Smolker, R., Mann, J., and Smuts, B. (**1993**). "Use of signature whistles during separations and reunions by wild bottlenose dolphin mothers and infants," Behav. Ecol. Sociobiol. **33**, 393–402.
Smolker, R. A., Richards, A. F., Connor, R. C., and Pepper, J. W. (**1992**). "Sex differences in patterns of association among Indian Ocean bottlenose dolphins," Behavior **123**, 38–69.
Stirling, L., and Thomas, J. A. (**2003**). "Relationships between underwater vocalizations and mating systems in phocid seals," Aquat. Mamm. **29**, 227–246.
Tyack, P. L. (**1986**). "Whistle repertoires of two bottlenosed dolphins, *Tursiops truncatus*: Mimicry of signature whistles?" Behav. Ecol. Sociobiol. **18**, 251–257.
Tyack, P. L. (**1997**). "Development and social functions of signature whistles in bottlenose dolphins *Tursiops truncatus*," Bioacoustics **8**, 21–46.
Tyack, P. L. (**2003**). "Dolphins communicate about individual-specific social relationships," in *Animal Social Complexity: Intelligence, culture and individualized societies*, edited by F. B. M. de Waal and P. Tyack, (Harvard University Press, Cambridge, MA), pp. 342–361.
Weilgart, L., and Whitehead, H. (**1990**). "Vocalizations of the Northern Atlantic pilot whale (*Globicephala melas*) as related to behavioral contexts," Behav. Ecol. Sociobiol. **26**, 299–402.
Wood, J. F. (**1953**). "Underwater sound production and concurrent behavior of captive porpoises, *Tursiops truncatus* and *Stenella plagiodon*," Bull. Mar. Sci. Gulf Caribb. **13**, 120–133.

Spatial location influences vocal interactions in bullfrog choruses

Mary E. Bates[a] and Brett F. Cropp
Department of Psychology, Brown University, Providence, Rhode Island 02912

Marina Gonchar
Program in Neuroscience, Lafayette College, Easton, Pennsylvania 18042

Jeffrey Knowles
Department of Neuroscience, Brown University, Providence, Rhode Island 02912

James A. Simmons
Department of Neuroscience, Brown University, Providence, Rhode Island 02912

Andrea Megela Simmons
Department of Psychology and Department of Neuroscience, Brown University, Providence, Rhode Island 02912

(Received 14 July 2009; revised 17 December 2009; accepted 11 January 2010)

A multiple sensor array was employed to identify the spatial locations of all vocalizing male bullfrogs (*Rana catesbeiana*) in five natural choruses. Patterns of vocal activity collected with this array were compared with computer simulations of chorus activity. Bullfrogs were not randomly spaced within choruses, but tended to cluster into closely spaced groups of two to five vocalizing males. There were nonrandom, differing patterns of vocal interactions within clusters of closely spaced males and between different clusters. Bullfrogs located within the same cluster tended to overlap or alternate call notes with two or more other males in that cluster. These near-simultaneous calling bouts produced advertisement calls with more pronounced amplitude modulation than occurred in nonoverlapping notes or calls. Bullfrogs located in different clusters more often alternated entire calls or overlapped only small segments of their calls. They also tended to respond sequentially to calls of their farther neighbors compared to their nearer neighbors. Results of computational analyses showed that the observed patterns of vocal interactions were significantly different than expected based on random activity. The use of a multiple sensor array provides a richer view of the dynamics of choruses than available based on single microphone techniques. [DOI: 10.1121/1.3308468]

PACS number(s): 43.80.Ka [WWA] Pages: 2664–2677

I. INTRODUCTION

Males of several different vertebrate groups, including anuran amphibians, orthopteran insects, and songbirds, aggregate into breeding choruses to vocally advertise their presence and willingness to mate (Gerhardt and Huber, 2002; Burt and Vehrencamp, 2005). Participation in a chorus can confer significant benefits on its residents, such as increased attraction of females and reduced predation risk; however, there are also disadvantages to such group mate attraction. Because males of many species are territorial, more physical competition may arise when males are closely spaced within chorusing groups. In addition, the high levels of noise generated in a chorus may mask the perception of an individual's vocalizations by both receptive females and rival males. Both senders and receivers of acoustic signals in a dense, noisy chorus must therefore devise some perceptual strategy for discriminating and then localizing particular signals of interest against a complex acoustic background.

Field and laboratory observations of patterns of calling behavior in males of different chorusing species have attempted to identify such strategies (reviewed in Klump and Gerhardt, 1992; Gerhardt and Huber, 2002). One way to reduce masking of one's own vocalizations by those of neighbors is to shift the timing of one's signal (either individual notes or entire multinote calls) so as to minimize overlap with those emitted by other callers. This strategy can result in a pattern of note-by-note alternation or call alternation between several individual chorusing males (Schwartz, 1987, 1993; Grafe, 1996, 1999; Moore *et al.*, 1989). As another strategy to reduce masking, males may physically space themselves within choruses so as to maintain some minimum distance between nearest neighbors (Brush and Narins, 1989; Schwartz and Gerhardt, 1989; Forrest and Green, 1991). Measurements of intermale distances and signal sound pressure levels suggest that call amplitude can mediate this spacing (Wilczynski and Brenowitz, 1988); visual cues and even physical interactions can also be important. These two general strategies may occur concurrently. In several species of chorusing insects and anurans, males time their own advertisement calls so as to actively avoid overlapping the calls of

[a]Author to whom correspondence should be addressed. Electronic mail: mary_bates@brown.edu

 0001-4966/2010/127(4)/2664/14/$25.00

only their nearest or loudest neighbors (Brush and Narins, 1989; Schwartz, 1993; Minckley *et al.*, 1995; Snedden *et al.*, 1998; Greenfield and Rand, 2000; Schwartz *et al.*, 2002). The temporal sequences of calling thus generated form rhythmic patterns of call alternation, or even call synchrony when local male density and calling rates are high. Such calling patterns have been modeled by the operation of an endogenous oscillator that can be reset by exogenous cues (Brush and Narins, 1989; Greenfield and Roizen, 1993; Greenfield and Schul, 2008). Presumably, acoustic interactions with chorus members outside of this local, restricted area occur randomly, such that the internal oscillator is not reset by the vocal activity of these far males.

Most of these studies of chorusing dynamics are based on vocal interactions occurring between small local groups of males located within a larger chorus. Very little is known about patterns of vocal interactions within a chorus as a whole (Grafe, 1997; Boatright-Horowitz *et al.*, 2000). This is because of the difficulty in recording and analyzing chorus activity based on the single or paired microphone recording techniques most commonly used to assess calling patterns. The real challenge of studying vocal interactions in animal choruses is the difficulty in accurately identifying, discriminating, and localizing large numbers of calling individuals and their locations, especially in dense assemblages when considerable numbers of acoustic signals temporally and spatially overlap. This is unfortunate, because the biological task faced by females approaching an insect or anuran chorus is just that—discriminating individual acoustic elements within a large, complex auditory scene (Bee, 2007). Recently, several techniques based on the use of multiple microphone arrays have been introduced to enable large scale analysis and modeling of chorusing activity (McGregor *et al.*, 1997; Hayes *et al.*, 2000; D'Spain and Batchelor, 2006; Mennill *et al.*, 2006; Mohan *et al.*, 2008; Simmons *et al.*, 2008; Jones and Ratnam, 2009). These techniques all attempt to automatically localize and discriminate many callers within a chorus based on both spatial location and the physical characteristics of their vocalizations. Although promising, these techniques have not been widely adopted for use on terrestrial choruses and so far have been tested on only a small number of animals within a larger chorus. Thus, they have not yet yielded a large amount of acoustic data that can elucidate biologically relevant patterns of natural vocal interactions in animal assemblages.

Previously, we described a technique for recording and analyzing chorus activity in the American bullfrog, *Rana catesbeiana*, using an array of multiple, closely spaced acoustic sensors (Simmons *et al.*, 2008). This methodology is based on computing the differences in arrival time of sounds at the sensors using a cross-correlation algorithm, and using these time differences to then estimate sound source by vector triangulation. We initially tested this technique by identifying and localizing a small number of individual callers within a single larger bullfrog chorus. Here, we extend this initial analysis by examining the large scale spatial and temporal organization of two separate bullfrog choruses on five different recording nights. Individual callers were identified by the acoustic characteristics (fundamental and first harmonic frequencies) of their advertisement calls, and their spatial locations were estimated. This method enabled us to discriminate and localize both overlapping and nonoverlapping advertisement calls produced by vocalizing males located at different sites within the chorus. Our data highlight the different kinds of vocal interactions in bullfrog choruses, related to the spatial distances and local group behavior of individual males, which have not been readily available from data based on single microphone techniques (Boatright-Horowitz *et al.*, 2000).

II. METHODS

A. Study sites and animals

We performed acoustic recordings at two different ponds between 2100 and 2400 h on five nights in June and July of 2005 and 2006. On 6/12/05 and 7/5/05, recordings were made at a pond [pond 1; 42 m long by 20 m wide; outline and orientation in Figs. 1(A) and 1(B)] located in a suburban neighborhood in Rhode Island (described previously in Boatright-Horowitz *et al.*, 2000). This pond was bordered on one side by thin, low vegetation and on three other sides by houses and a bike path. Due to development and to the construction of this bike path, the dimensions of this pond have changed since the site was first described in 2000. On 7/5/06, 7/6/06, and 7/9/06, we carried out recordings at another pond [pond 2; 40 m long by 15 m wide; outline and orientation in Fig. 1(C)] located on private property in central Massachusetts (described previously in Simmons *et al.*, 2008). This pond was surrounded on three sides by heavy vegetation and woods, and on another side by a small clearing and house. Both ponds supported populations of bullfrogs (6–14 active callers on any given night) and green frogs (*Rana clamitans*; number not censused). Because green frogs were not very vocally active during our recording times and they appeared to be present in only small numbers, we did not undertake a quantitative analysis of any acoustic partitioning between these two species. Air temperatures (measured using a thermometer) on recording nights ranged between 17.8° and 23.3 °C, relative humidity (obtained from www.nws.noaa.gov) was between 76% and 87%, and there was no precipitation. Recording times at the different nights ranged between 85 and 172 min, with an average of 118 min.

We set up the recording equipment approximately 30 min before the onset of any vocal activity by the bullfrogs. We did not capture or handle the animals for visual inspection or morphological measurements, and so did not disturb their natural behaviors. To correlate the directional estimates derived from the sensor array with actual spatial locations of individual bullfrogs, an observer periodically surveyed the pond during recordings and marked the location of each calling male on a scaled map. Spatial distances between these estimated locations were later verified by direct measurements using a surveying transit and with reference to aerial maps obtained using Google earth (see Simmons *et al.*, 2008). Our research protocol was approved by the Brown University Institutional Animal Use and Care Committee.

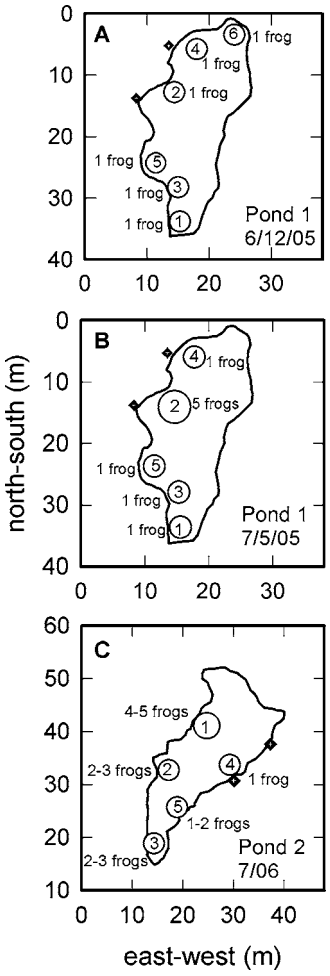

FIG. 1. Diagrams of the two chorusing sites. On each diagram, the two black square/white cross symbols outside of the pond outline indicate the position of the two acoustic sensors. (A) Map of pond 1 showing estimated locations and numbers of actively calling bullfrogs (designated by open circles with numbers) on the night of 6/12/05. Each circle is placed at the median of the vector intersection points derived from the computational model. Only one bullfrog was present at each indicated location. Locations are numbered in the order in which they were identified in the analysis. (B) Map of activity at pond 1 on the night of 7/5/05. Five vocalizing bullfrogs were now present at location 2. (C) Map of pond 2. The locations of bullfrogs were similar on all three nights (7/5/06, 7/6/06, and 7/9/06) at this site; the variability in numbers of animals at each location is indicated. On all three nights, location 4 contained only one bullfrog.

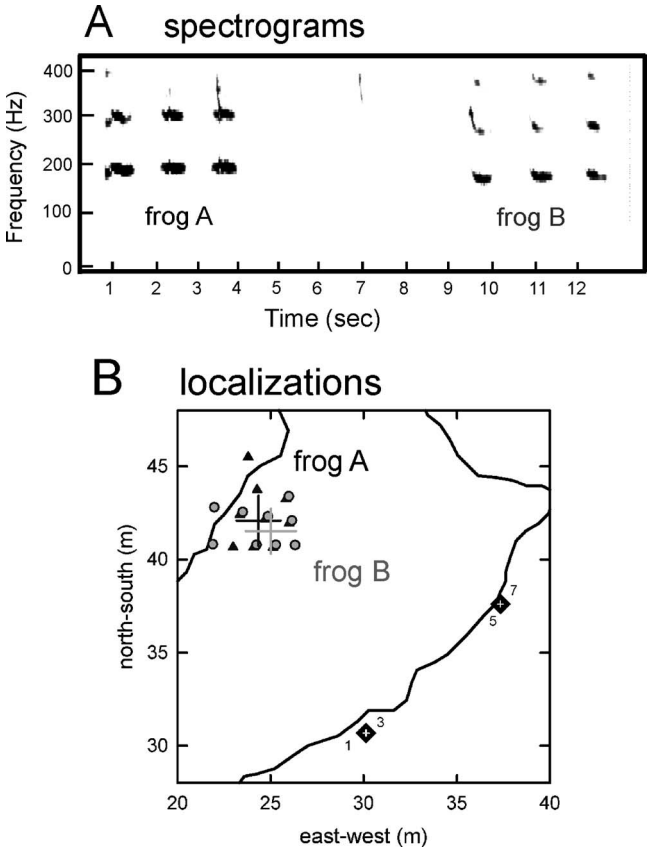

FIG. 2. Estimates of source locations for two bullfrogs belonging to the same cluster to illustrate the effective accuracy of localization. (A) Spectrograms to 400 Hz of three note advertisement calls produced by two individual male bullfrogs (frog A and frog B), calling sequentially over a 14 s time interval. For calculation of these and other spectrograms by ADOBE AUDITION, sounds were downsampled to 1500 Hz (Blackmann-Harris window, 512 frequency bands). The first harmonic frequencies of the notes in each bullfrog's advertisement call differ (190 Hz for frog A and 170 Hz for frog B). (B) Localization estimates derived from calls in A. The black square/white cross symbols outside the pond's outline show the locations of the two sensors. The active microphones (1, 3 and 5, 7) in each sensor are indicated. The symbols inside the pond outline show the points of vector intersection computed from the advertisement call notes of each individual male. Estimates for frog A are indicated by the black triangles, and estimates for frog B are indicated by the gray circles. The localization program provided 20 intersection points for the three notes emitted by frog A, and 28 intersection points for the three notes emitted by frog B. Although all of these points are plotted, not all are visible because many of their locations overlap. Variability is indicated by black and gray crossed lines for standard deviations in the east-west and north-south dimensions calculated from all location estimates for frog A and frog B, respectively. The intersection points of each cross designate the mean locations calculated from the intersection points for the two frogs. Frog A and frog B are separated by a mean diagonal distance of 1.68 m. The maximum dispersion between all intersection points for these two frogs, excluding the points outside the pond, is 3.5 m. Dispersion is due largely to effects of reverberation on each localization estimate.

B. Sensor array

We recorded the vocalizations of chorusing male bullfrogs using a sensor array previously described by Simmons *et al.* (2008). This array consists of two individual four-microphone sensors ("cubes," 3.3 cm), each mounted on top of a vertical aluminum rod and held in a position 0.6 m above the surface of the ground by an adjustable survey tripod. A sensitive, calibrated, omnidirectional electret condenser microphone (Knowles Electronics, Model FG3329, Itasca, IL) was placed in the center of each of the four vertical faces of each sensor. When in use, each sensor was covered by a spherical black foam windscreen 10 cm in diameter. At each recording site, the two sensors on their tripods were placed on one side of the pond, separated by 10 m (square/cross symbols alongside pond outlines in Figs. 1 and 2). They were set back about 0.5 m from the water's edge, in an area clear of vegetation, rather than in the center of the pond, which the cabling system prevented. Because the pond was entirely on one side of the array, so that front-back localization was not needed, data were collected from only two of the four microphones in each sensor. In the leftmost sensor, channels 1 (to the left) and 3 (to the right) were used, while in the rightmost sensor, channels 5 (to the left) and 7 (to the right) were used.

A full description of data handling and display can be found in Simmons *et al.* (2008). Acoustic signals picked up by the two active microphones in each sensor cube were amplified (10× gain) and recorded on four channels of a Sony SIR-1000W wideband digital instrumentation recorder (Sony Precision Technology America Corp., Lake Forest, CA). The sounds were digitized simultaneously in each recorder channel at 48 kHz sampling rate (16-bit accuracy). Binary files containing the four channels of data [two from the 1,3 (left) sensor and two from the 5,7 (right) sensor] were subsequently downloaded into a Pentium-3 PC using Sony PCSCAN programs supplied with the Sony recorder. Each night thus produced four digitized data streams lasting for the entire recorded epoch. For processing, these files were broken into two "stereo" data streams corresponding to the two microphone channels in each cube sensor (microphones 1 and 3 or 5 and 7). Each stereo stream, which covered the entire night's recording epoch for one sensor, then was subdivided into consecutive 10 s segments and low-pass filtered at 4 kHz to remove high frequency signals, using custom-written MATLAB routines (MathWorks, Natick, MA). For computational processing, these 10 s segments were further divided into shorter, overlapping 100 ms time segments (because overlap is 50%, there are 250 short segments in each longer 10 s stereo segment). Data were processed by a binaural computational model of the auditory system (available online at the Boston University EarLab website; Mountain *et al.*, 2007), which operated by bandpass filtering the acoustic signals from each sensor into 32 parallel overlapping frequency bands (60 Hz–5 kHz). Time-of-arrival differences (from −180 to +180 μs) were calculated in each of these frequency bands separately. When running the model, a threshold is set to prevent background noise or very low-level sounds from entering into the processed data. Time difference estimates are then pooled across all 32 frequency channels to generate a histogram (bin width 10 μs) of time differences in each consecutive 100 ms segment of the signal. The final estimate of the time difference for any one 100 ms time segment is determined from the peak of this histogram. The model then plots the peaks derived from successive histograms to give a running history of arrival time differences across all 100 ms segments of each 10 s long stereo signal. The result is a stream of up to 250 separate time difference estimates between the left and right microphones. The threshold setting determines how many of the potentially 250 estimates actually appear in the model's output.

All of the sequential arrival time difference streams for successive 10 s segments are concatenated to create a history of sound arrival time differences over the entire duration of the recorded session in each sensor cube (stereo pair). To locate the source of the sound on a map of the pond, the time difference estimates at each sensor are transformed into spatial angle estimates. Each sensor provides one directional estimate (vector) for each particular time difference in the data stream. Synchronized angle estimates from both sensors yield vector intersections that are used to estimate the location of the sound source. We computed the intersection point of the two vectors from each sensor using a custom-written MATLAB routine, and then plotted multiple intersection points obtained from consecutive segments of the recordings on a template of the pond. We calculated the median, mean, and standard deviations of these points to form an estimate of the location of the sound source. In the example in Fig. 2, two bullfrogs (frog A and frog B) are vocalizing one after the other during a 14 s segment of the chorus [spectrograms in Fig. 2(A)]. The diagram of the pond in Fig. 2(B) shows the position of the calculated points of intersection from the two sensors for the advertisement call notes of these two bullfrogs. The mean locations of the vector intersection points indicate that the two males are separated by a distance of 1.68 m. For bullfrog A, the standard deviation of its mean location is 1.36 m in the north-south dimension and 1.18 m in the east-west dimension. For bullfrog B, the standard deviation of its mean location is 1.21 m in the north-south dimension and 1.35 m in the east-west dimension. This example provides an indication of the accuracy of the localization program for processing real sound sources in a noisy natural environment.

There are several limitations of this sensor technique. One technical limitation is the relatively short aperture between the left and right microphones within each cube, which leads to higher variability in estimates of azimuth than if the aperture were larger. The size of each pond dictated a minimum spacing of 8–10 m between cubes to ensure that all of the bullfrogs were recorded, but the complexity of the natural situation, especially the presence of multiple sound-propagation paths due to irregular screens of vegetation around the ponds, caused decorrelation to occur in recordings of the same sounds at such widely spaced sensors. Use of two relatively small sensor units, each capable of estimating azimuth, combined with a wider spacing between sensors, proved to be an acceptable compromise. Another limitation is imposed by presence of vegetation around the recording sites, which was particularly thick and extended in depth on the far side of pond 2 [northwest side in Fig. 1(C)]. Sound sources emanating along this side of the pond were sometimes localized in the trees or outside the boundaries of the pond [Fig. 2(B)] because reverberation from the surrounding vegetation was especially strong from that direction. Another limitation emerged when two call notes arrived at the two sensors entirely simultaneously, with no brief interval of one note or the other being entirely separate from the other. Localization estimates for such completely overlapping notes could occur at places between the two actual calling bullfrogs. In cases of complete or near-complete note overlap, we used amplitude cues and knowledge of the first harmonic frequencies in the notes of particular known individuals when calling without interference, as well as visual inspections of the chorus site and field notes taken during recordings, to estimate the actual locations of these overlapping notes. This limitation means, however, that when two males are very closely spaced, as in Fig. 2(B), the estimated locations of overlapping notes could be between their actual locations. This problem becomes more acute when it is realized that bullfrogs, particularly those who are closely spaced, do not stay stationary during chorusing activity, but move around and often engage in physical aggressive interactions with other males in their immediate vicinity. Movements of

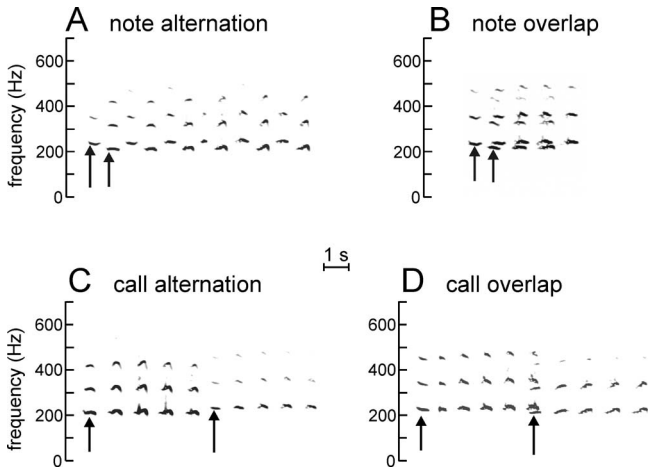

FIG. 3. Spectrogram examples of the four types of vocal interactions (bouts) identified in the recordings. Advertisement calls were low-pass filtered to show only the low frequency harmonics. Arrows indicate the first notes of each bullfrog's individual call. The relative darkness of the spectrograms provides an indication of the relative amplitude of each individual's call notes. (A) Note alternation, in which one bullfrog begins calling after the completion of the first note of another bullfrog's call and the two continue with their notes alternating in time. (B) Note overlap, in which more than one-half of the notes in the first bullfrog's call is overlapped by the call notes of another bullfrog. In this example, the second bullfrog does not begin calling until the completion of the first note in the leading bullfrog's call, but subsequent notes of both bullfrogs overlap considerably. (C) Call alternation, in which one bullfrog begins calling within 2 s after the completion of another bullfrog's call. (D) Call overlap, in which one bullfrog begins calling after the completion of more than one-half of the notes of another bullfrog's call. In this example, only the last note of the first bullfrog's call overlaps with the first note of the second bullfrog's call.

the sound source complicate the accuracy of localization. Finally, because the localization program also picked up and provided location estimates for advertisement calls of *R. clamitans* as well as for other sounds within the frequency range of bullfrog advertisement calls, we needed to identify these sounds by their spectrograms and then manually delete them from the processed data stream.

C. Acoustic analysis of bullfrog advertisement calls

Male bullfrogs emit complex advertisement calls consisting of 1–12 individual notes [croaks; Figs. 2(A) and 3]. Each note contains a number of harmonically related frequencies from about 200 to 2000 Hz, with a missing fundamental frequency around 80–125 Hz (Bee, 2004; Suggs and Simmons, 2005). The duration of the notes varies considerably between successive notes and between individuals, with the average duration about 550 ms and average internote interval around 530 ms (Simmons, 2004). The envelopes of these notes often contain amplitude modulations (AMs) that increase in number from one note to the next; these modulations are correlated with an increase in note duration (Suggs and Simmons, 2005). Bullfrogs exhibit relatively low calling rates, with intercall intervals as long as 16–36 s reported in some choruses (Emlen, 1976; Boatright-Horowitz *et al.*, 2000; Bee, 2004).

To determine the spectral content of each recorded bullfrog advertisement call, the four-channel binary files of raw sensor recordings were separated into two stereo.wav files, one for channels 1 and 3 (left sensor) and the other for channels 5 and 7 (right sensor). General acoustic characteristics of the calls (duration, duty-cycle, harmonic frequencies, and onset time) were analyzed with custom-written MATLAB routines and then displayed as spectrograms and sound pressure waveforms using ADOBE AUDITION V 1.5 (Adobe Systems Inc., San Jose, CA).

We first isolated advertisement calls of bullfrogs vocalizing individually (without any overlap or interference from other frogs and when the calls of individual males were separated by at least 2 s), and then estimated, using the model output, the locations of these animals on a map of the pond (Fig. 1). The locations of individual males were cross referenced against locations estimated from visual sightings of calling bullfrogs at the time of data collection. We then identified four types of multiple bullfrog vocal interactions (bouts) from the recorded spectrograms (Fig. 3) and estimated their source locations. Note alternation [Fig. 3(A)] was defined as one bullfrog beginning his call after the completion of the first note of another male's call, with the successive call notes of the two males distinctly alternating in time. Note overlap [Fig. 3(B)] occurred when more than one-half of the notes of the first caller were overlapped by the notes of another caller, resulting in overlap of successive notes. Several instances of note overlap consisted of bouts of three or more bullfrogs calling in near synchrony. In call alternation [Fig. 3(C)], one bullfrog began his call within 2 s of the completion of another male's entire call. We chose 2 s as the cut-off point between call alternation and individual calling based on the analysis of intercall intervals between identified individuals (or groups of bullfrogs who overlapped calls) during the three nights from pond 2. Plotting the distribution of all intercall intervals showed two peaks, one at intervals less than 1 s in all data sets and a broader peak at intervals between 5 and 12 s, depending on chorus size. Dividing the overall distribution into two separate distributions, using a clear trough located at 2 s between the modes of each distribution as a cut-off point, minimized the standard deviations of both distributions in all three data sets. Successive calls with an intercall interval of 2 s or less were categorized as call alternations, while calls separated by more than 2 s were labeled individual calls. Finally, in call overlap [Fig. 3(D)], one bullfrog initiated calling after the completion of more than one-half of the notes of another male's call, resulting in overlap of the last notes of the first caller and the first notes of the second caller. As with note overlap, some instances of call overlap reflected vocal responses of three or more bullfrogs calling in near synchrony. The sample spectrograms show that, even in cases of note overlap [Fig. 3(B)], at least one note from an individual and a portion of the note from the other individual (usually the first or last notes in each case) is free enough from interference that these portions can be analyzed to determine the first harmonic frequency of the note, as an indicator of individual identity (Bee, 2004). In practice, we first analyzed single, nonoverlapping call notes in multiple bullfrog interactions, and estimated the locations of these sound sources on the map. We found that, even in situations where notes overlapped com-

TABLE I. Events measured in simulated and empirical data.

Event type	Corresponding empirical category	Percentage of "individual call"
Individual call	Individual call	$\%=100$
Call alternation	Call alternation	$80\leq\%<100$
Call overlap	Call overlap	$50\leq\%<80$
Note alternation/overlap	Note alternation and note overlap	$0\leq\%<50$

pletely in time, they differed enough in spectral frequency that individual males could be separated acoustically.

For statistical analysis, data were categorized as representing one of the five types of acoustic events (individual calling and the four types of vocal bouts) and as spatial location (within or between clusters). We defined a cluster as a location where two or more vocalizing males were very closely spaced (in practice, intracluster spacing ranged up to 6.5 m, depending on the numbers of bullfrogs within that local area). The program UNCERT (Hailman and Hailman, 1993) was used to compute the frequencies and probabilities of these types of vocal interactions ("events," zero-order analysis) and the frequencies of transition from preceding to following events (first-order analysis) to determine the existence of any sequential calling patterns within a chorus. Chi-square tests were performed using SPSS V.16 (SPSS Inc., Chicago, IL) to analyze the relation between type of vocal interactions and spatial location of the callers, as well as to compare the frequency (rate) of observed calling events to the expected frequency (rate) if the bullfrogs were calling randomly. Due to the sometimes small number of call events, data were grouped together across recording sites to increase the power of analyses when appropriate.

D. Simulation of chorus activity

In order to model the calling behavior of the chorus residents, a custom-written MATLAB routine was used to simulate bullfrogs calling at the same rate as that observed in the natural choruses, but with each male vocalizing independently of its neighbors through a Poisson process. The simulation represented the bullfrogs as arrays of time bins in which silence was recorded as zeros and calls recorded as a series of ones. The initiation of calls was random, but each call lasted for the same duration as that observed in the natural chorus. The behavior of multiple bullfrogs could be assessed by summing the arrays together, and call interaction events were counted by logical filters that ran iteratively though the simulation epoch.

For each recording session, a simulation was run in which the same numbers of vocalizing bullfrogs were grouped into identical spatial locations (clusters) as determined from the empirical data, and each "male" generated calls at a rate that would produce an expected number of calls equal to that observed in the natural chorus. All bullfrogs in each simulation generated the same expected number of calls. Then, four different kinds of calling events were defined that corresponded to the five categories of events observed in the natural chorus. The events measured in the simulated data were individual calls, call alternation, and call overlap, which directly corresponded to the same categories in the empirical analysis, and note alternation/overlap, which grouped together the two categories of note alternation and note overlap that were measured in the empirical data. In the simulation, bouts were identified and then classed as one of these four events based on a measure of the percentage of the bout epoch during which only one bullfrog was vocalizing (Table I). These event definitions are mathematical approximations of the corresponding bout types observed in the empirical data based on the duration of overlap among calls from multiple bullfrogs. Although the simulated events were counted by logical filters whereas the empirical events were counted by observation, these definitions allow for a direct comparison between their occurrence in nature and at random.

Further, the identification and classification of bouts were performed both within spatial clusters (intracluster bouts) and between spatial clusters (intercluster bouts) as retrieved from the empirical calculations of location. Because a simulation was run to mirror the spatial arrangements observed in each of the recording sessions, direct comparison was possible between the intercluster and intracluster interactions observed in the natural chorus, and those that would occur if males were vocalizing at random. Because the quantity of each of these events in the simulation is a random variable, 50 trials of each simulation were run in order to generate a distribution of each output that could then be compared with the empirical data. Statistical differences between model output and empirical observations were analyzed by z-tests to generate the probability of each observation occurring in a population of randomly vocalizing bullfrogs.

III. RESULTS

A. Spatial location of vocalizing males

We analyzed five nights of chorus activity, two from pond 1 and three from pond 2. For the 6/12/05 recording from pond 1, bullfrogs were spaced out enough and calling activity was low enough that it was possible to clearly identify each active individual and his location based on both the field notes from that night and the localization program. In all the July recordings from both ponds, however, more vocalizing bullfrogs were present than on 6/12/05 and the close spacing of some of the males and the large number of overlapping calls made identification and localization of individuals more challenging. For these nights, clusters of closely spaced bullfrogs were identified, containing between two and five vocalizing males within a local area of the pond. Locations of individual calling bullfrogs at pond 1 on 6/12/05 and 7/5/05 are shown in Figs. 1(A) and 1(B), respec-

tively. Each circle on the map represents the median location estimate over the duration of each recording night; numbers within the circles are location/cluster number. On 6/12/05, each numbered location represents a single vocalizing male. The closest distance between individual males at this site on this night was 5 m (locations 3 and 5, measured as the difference between the mean location estimates). The caller at location 6 was missing from the chorus when the next recording was made at this site on 7/5/05 [Fig. 1(B)]. On this date, location 2 now consisted of a cluster of five actively vocalizing males, four of whom were not recorded during the earlier night. Within location 2, these five males were separated by at most 4.2 m, the maximum dispersion of all vector intersection points for this location. They were separated by 13.9 m from their nearest neighbors at location 4. At pond 2, the estimated locations of bullfrogs were similar on the three recording nights [Fig. 1(C)], although numbers of vocalizing individuals in a particular local area varied across the three nights. Four of the identified sound source locations contained between two and five vocalizing bullfrogs, with only one location containing an isolated individual. Within a cluster, vocalizing males could be separated by as little as 1.68 m [Fig. 2(B)]. The maximum dispersion of all intersection points within this particular cluster was 6.5 m. The closest distance between different clusters was 7 m (locations 3 and 5, on opposite sides of the pond).

B. Overall activity and types of vocal events

The relative amount of calling activity, expressed as calling rate (percent of call type over the length of that recording session), at the different sites is shown in Fig. 4. The relative rate of individual calling activity and of calling bouts (all acoustic interactions in which more than one bullfrog vocalized, including note overlap, note alternation, call alternation, and call overlap) varied between the June and the July nights [Fig. 4(A)]. On all four July nights, bullfrogs were significantly more likely to call in bouts than to call as individuals, while the opposite pattern holds for the night in June, $X^2(1)=339.8$, $N=1816$, $p<0.001$. The rate of the different kinds of calling events at both ponds on all five nights also varied. At pond 1 [Fig. 4(B)], the most common calling event on both nights was individual calling, whether or not the animals were located within a local cluster with other calling males. On 6/12/05, the rate of other calling events was low. Conversely, on 7/5/05, call alternation was the most frequent event after individual calling, followed by call overlap, note alternation, and note overlap, respectively. The pattern of calling activity from the three nights at pond 2 differed from that at pond 1, and also showed some differences between individual nights [Fig. 4(C)]. When the pond as a whole was sampled, note overlap was the most frequent event at all three nights, followed by individual calling. The relative amounts of call alternation, note alternation, and note overlap varied between nights, indicating the dynamic nature of interactions in choruses.

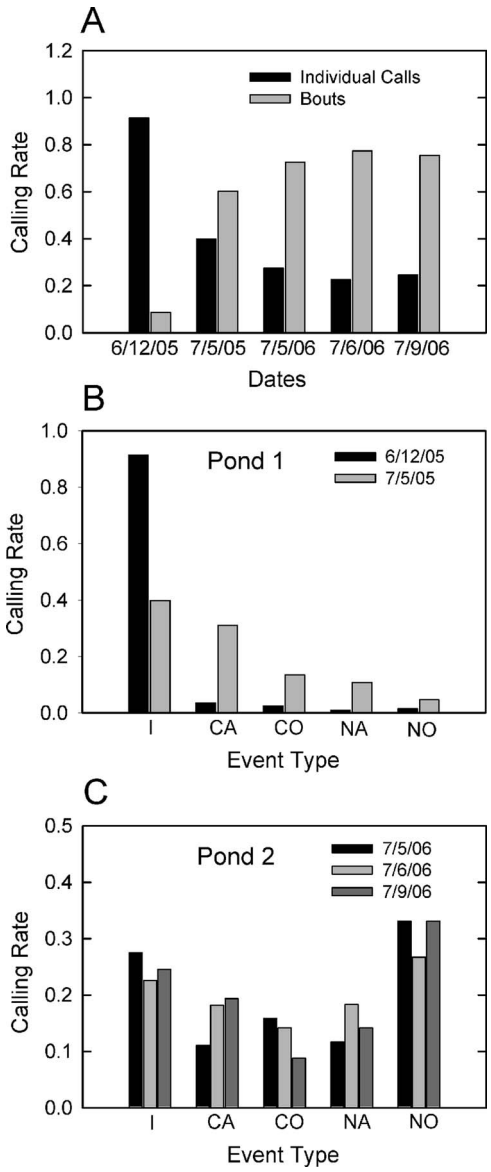

FIG. 4. Calling rates (normalized for the total numbers of calling events per night) at the two different chorusing sites. (A) Rate (y axis) of individual calls (black bars) and multiple frog interactions (bouts; gray bars) across all five nights (x axis) of chorus activity. The rate of multiple frog bouts was significantly higher in July than in June. (B) Rate of calling events at pond 1 on 6/12/05 (black bars) and 7/5/05 (gray bars). I=individual call; CA=call alternation; CO=call overlap; NA=note alternation; NO=note overlap. (C) Rate of calling events at pond 2 on 7/5/06 (black bars), 7/6/06 (gray bars), and 7/9/06 (dark gray bars). Note overlap was the most common type of multiple frog interaction on all three nights, but there were many instances of all types of calls and variability between the three nights.

C. Within- and between-cluster interactions

We next compared the frequency of the different kinds of bouts (regardless of the particular type of interaction) within and between identified local clusters of bullfrogs (Fig. 5). Data from 6/12/05 were eliminated from this analysis because there were no clusters of bullfrogs on this night. On 7/5/05, there were significantly more bouts between frogs in different clusters than between frogs within the same cluster, $X^2(1)=17.78$, $N=90$, $p<0.001$. However, on both 7/5/06 and 7/9/06, there were significantly more within-cluster interactions than between-cluster interactions [7/5/06: $X^2(1)=9.87$, $N=274$, $p=0.002$; 7/9/06: $X^2(1)=9.03$, $N=335$, p

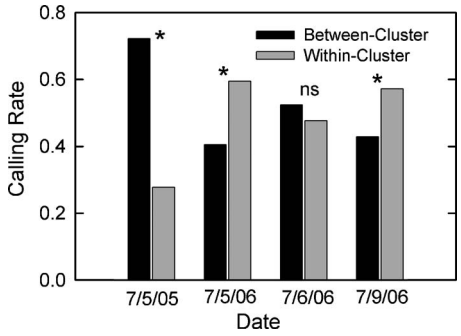

FIG. 5. Within-cluster and between-cluster calling rates on four nights at the two recording sites. Data show combined calling rates for all four types of acoustic interactions. Asterisks (*) denote statistical significance of comparisons of between-cluster and within-cluster rates on a given chorusing night. ns=not statistically significant. There was a significantly higher number of between-cluster than within-cluster interactions at pond 1 on 7/5/05. At pond 2, there were significantly more within-cluster interactions on two of the nights (7/5/06 and 7/9/06), but no difference on the third night (7/6/06).

$=0.003$]. The rate of within-cluster interactions and between-cluster interactions did not differ from chance on 7/6/06, $X^2(1)=1.77$, $N=508$, $p>0.05$.

Different kinds of vocal bouts predominated within compared to between clusters. At both ponds, bullfrogs located in different clusters or spatial locations were more likely to participate in call alternation or call overlap than were bullfrogs located within the same cluster [Figs. 6(A) and 6(B)]. Again, data from the June recording night are not shown because no clusters were present. On all four July nights, call alternation occurred between clusters significantly more often than it occurred within clusters [7/5/05: $X^2(1)=42.09$, $N=46$, $p<0.001$; 7/5/06: $X^2(1)=33.80$, $N=45$, $p<0.001$; 7/6/06: $X^2(1)=59.71$, $N=121$, $p<0.001$; 7/9/06: $X^2(1)=67.16$, $N=86$, $p<0.001$]. At pond 1, there was only one location which contained a cluster of males (location 2), and males within this cluster alternated calls with each other only one time over the entire recording session. The data from pond 2 also show that more call alternation occurred between compared to within clusters on all three recording nights [Fig. 6(A)]. Call overlap on all four July nights [Fig. 6(B)] also occurred between clusters significantly more than it occurred within clusters [7/5/05: $X^2(1)=17.19$, $N=21$, $p<0.001$; 7/5/06: $X^2(1)=41.67$, $N=60$, $p<0.001$; 7/6/06: $X^2(1)=27.27$, $N=103$, $p<0.001$; 7/9/06: $X^2(1)=24.64$, $N=39$, $p<0.001$]. At pond 1 on 7/5/05, the cluster of males in location 2 engaged in call overlap with each other only one time over the entire recording session. Call overlap within clusters at pond 2 occurred much less often than it did between clusters on all three recording nights.

While call alternation and call overlap were more common between bullfrogs in different clusters, note alternation and note overlap were more likely to occur between bullfrogs located within the same cluster [Figs. 6(C) and 6(D)].

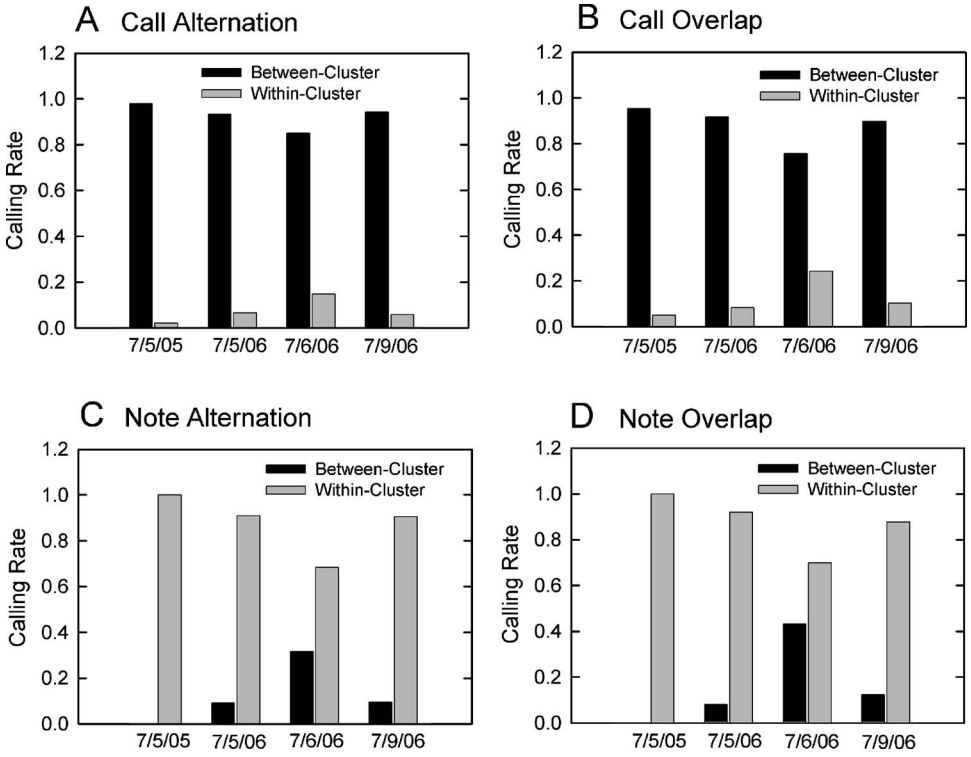

FIG. 6. Calling rates for the four different kinds of bouts for the four July chorus nights at the two chorus sites. (A) Rate of call alternation events. Call alternation was significantly more likely to occur between clusters compared to within clusters on all four nights. (B) Rate of call overlap events. The pattern of call overlap differed significantly between clusters compared to within clusters in all choruses. Call overlap was more likely to occur between clusters. (C) Rate of note alternation events. Note alternation occurred exclusively within clusters at pond 1 (7/5/05), so no statistical test could be performed on these data. At the other three choruses, note alternation was significantly more likely to occur within clusters than between clusters. (D) Rate of note overlap events. Note overlap was observed only within clusters and never between clusters at pond 1. At the other choruses, note overlap occurred significantly more often within clusters than between clusters.

Statistical analyses could not be performed on data from 7/5/05 (pond 1) because note alternation and note overlap occurred exclusively within clusters on this night. For all three nights at pond 2, note alternation was significantly more frequent within clusters than between clusters [7/5/06: $X^2(1)=29.45$, $N=44$, $p<0.001$; 7/6/06: $X^2(1)=16.13$, $N=120$, $p<0.001$; 7/9/06: $X^2(1)=41.29$, $N=63$, $p<0.001$]. Note overlap was significantly more likely to occur within rather than between clusters at this location as well [7/5/06: $X^2(1)=88.20$, $N=125$, $p<0.001$; 7/6/06: $X^2(1)=26.24$, $N=166$, $p<0.001$; 7/9/06: $X^2(1)=83.82$, $N=147$, $p<0.001$].

D. Patterns of sequential interactions

Patterns of sequential calling between males in different spatial locations were calculated using the UNCERT program. This analysis is based only on numbers of acoustic events, and not on their type (that is, individual calling and the four different kinds of calling bouts were not distinguished in the analysis). At pond 1 on 6/12/05, the most active callers were the bullfrogs at locations 3 and 6, and these two were also the most widely spaced [Fig. 7(A)]. Bullfrogs at locations 1 and 2 each called only one time during that recording session, so data from these males were not included in the sequential analysis. The probabilities of the male at location 6 vocalizing directly after its farthest vocalizing neighbors were 0.5556 (location 3) and 0.2917 (location 5), while the probability of vocalizing directly after its nearest neighbor, at location 4, was only 0.1129 [Fig. 7(A)]. The bullfrog at location 5 never vocalized directly after its nearest neighbor, location 3, but vocalized directly after the male at location 6 (probability of 0.1031) and location 4 (probability of 0.1774).

At pond 1 on 7/5/05, five bullfrogs aggregated into a cluster (location 2), and this cluster overall produced the most calls. Figure 7(B) shows the transition probabilities for this chorus. Location 2 showed the highest probabilities of calling directly after its three farthest neighbors, location 1 (0.4688), location 3 (0.5000), and location 5 (0.5714), and its lowest probability of calling after its nearest neighbor, location 4 (0.2667). Bullfrogs in cluster 2 vocalized after other bullfrogs in that same cluster with a probability of 0.3409.

Sequential probabilities of calling from one night (7/9/06) at pond 2 are shown in Fig. 7(C). For this analysis, each cluster is considered as a unit, and no attempt was made to separately identify the separate probabilities of vocalizations of the individual frogs within each cluster. Location 1, with four bullfrogs on this night, was the most active location. Animals at this location vocalized after another animal at the same location with a probability of 0.5347. When examining transitional probabilities of calling from location 1 to the other locations, bullfrogs in location 1 were found to vocalize least often after their closest neighbors, at location 4 (one bullfrog; probability of 0.7778) and location 2 (two bullfrogs, 0.6667). The probabilities of bullfrogs in cluster 1 vocalizing after their farthest neighbors, at location 3 (two bullfrogs, 0.8409) and location 5 (two bullfrogs, 0.9091), were higher. Data from the other two nights at this pond show similar trends, with the higher probabilities of sequential calling between locations occurring to farther, rather than nearer, clusters.

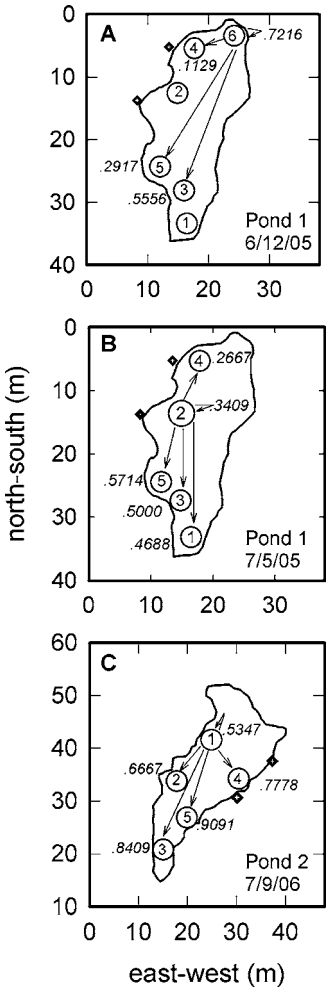

FIG. 7. Patterns of sequential calling in choruses, derived from first-order analysis in UNCERT. The numbers in italics on each pond diagram are the probability of that location (cluster) responding immediately after the most active location (cluster). Arrows represent the direction of interaction. The arrow that goes back onto itself shows the probability of the most active cluster (location) vocalizing immediately after itself. (A) Pond 1 on 6/12/05. The most active location on this night is location 6. The probability of the bullfrog at location 6 vocalizing immediately after itself is 0.7216. The bullfrog in location 6 was most likely to vocalize after the bullfrog in location 3 (0.5556), its farthest neighbor. Locations 1 and 2 were not included in the analysis, because the animals at these locations called only once during the recording session. (B) Pond 1 on 7/5/05. The chorus organization differed on this night than on the earlier night shown in (A). The animal in location 6 was absent from the chorus, and the most active location was now location 2. Numbers in italics show the probabilities that any bullfrog at location 2 followed the calls of any individuals at the other locations. The sequential probabilities of calling were similar to the three farthest neighbors (locations 5, 3, and 1) and lowest to the nearest neighbor at location 4. The bullfrogs in location 2 followed themselves with a probability of 0.3409. (C) Pond 2 on 7/9/06. The most active location at this night was location 1. Bullfrogs in this location followed themselves with a probability of 0.5347. The highest sequential probabilities of calling were to the farthest neighbors at locations 3 and 5.

E. Comparison to random simulation

A normal distribution was used to calculate the probability of each of the empirical results occurring under the ran-

dom conditions of the MATLAB simulation. When comparing the observed frequency of individual calls to the expected (chance) frequency (correcting for the length of the actual recording session), significantly fewer individual calls were observed than would be expected if the males were calling randomly and independently of each other (6/12/05: $z=19.42$, $p<0.0001$, one-tailed; 7/5/05: $z=99.18$, $p<0.0001$, one-tailed; 7/5/06: $z=190.25$, $p<0.0001$, one-tailed; 7/6/06: $z=213.01$, $p<0.0001$, one-tailed; 7/9/06: $z=50.41$, $p<0.0001$, one-tailed; all p values are adjusted according to the Bonferroni correction).

On all four July nights (excluding 6/12/05 because there were no clusters of bullfrogs at this night), call alternation within clusters occurred significantly less frequently than would be expected from chance (7/5/05: $z=21.48$, $p<0.0001$, one-tailed; 7/5/06: $z=31.39$, $p<0.0001$, one-tailed; 7/6/06: $z=26.46$, $p<0.0001$, one-tailed; 7/9/06: $z=32.95$, $p<0.0001$, one-tailed; all p values according to the Bonferroni correction). Call overlap was also less frequent within clusters than was predicted by the random model (7/5/05: $z=-32.67$, $p<0.0001$, one-tailed; 7/5/06: $z=-238.42$, $p<0.0001$, one-tailed; 7/6/06: $z=-184.08$, $p<0.0001$, one-tailed; 7/9/06: $z=-249.79$, $p<0.0001$, one-tailed; all p values according to the Bonferroni correction).

The MATLAB simulation grouped note overlap and note alternation events together. The random simulation predicted significantly fewer note overlaps and note alternations occurring within clusters than what was observed in the empirical data (7/5/05: $z=-32.67$, $p<0.0001$, one-tailed; 7/5/06: $z=-238.42$, $p<0.0001$, one-tailed; 7/6/06: $z=-184.08$, $p<0.0001$, one-tailed; 7/9/06: $z=-249.79$, $p<0.0001$, one-tailed; all p values according to the Bonferroni correction).

IV. DISCUSSION

Using a novel multiple sensor recording technique, we analyzed the acoustic and spatial patterns of vocalizations between groups of male bullfrogs at two natural chorusing sites. This technique has the advantages of being able to simultaneously record sounds of all vocalizing bullfrogs within the chorus and provides estimates of their individual locations and the acoustic characteristics of their calls. Disadvantages of the technique include its computational complexity and inaccuracies in its location estimates. In particular, spatial position of individual bullfrogs within a cluster can show considerable scatter, resulting from movements of the animals during chorusing activity, reverberations produced by the heavy vegetation surrounding some areas of the pond, and inclusion of sounds other than bullfrog advertisement calls in the recorded data. Addition of more sensors to the array should alleviate these problems.

Our data reveal both individual calling behavior and complex vocal interactions between males at these sites. First, we show individual bullfrogs are not evenly spaced throughout the chorus, but often aggregate into local clusters where they are in close spatial proximity with other calling males. Second, we show that aggregation into clusters affects the types of vocal interactions in which the animals engage. In particular, we show that the rates of note and call overlap differ in relation to the spatial distances between the callers. Third, we show that aggregation into clusters modifies, but does not eliminate, the near-far sequential pattern of advertisement calling described previously based on single microphone techniques (Boatright-Horowitz *et al.*, 2000). Clustering thus does not prevent animals from "paying attention to" the calls of noncluster residents. Fourth, we show that these patterns of vocal interactions differ from what is expected from a model in which advertisement calling occurs randomly and independently from that of other chorus residents. Finally, we show that the numbers of vocalizing male bullfrogs in a particular chorus is not stable, even over consecutive nights. Together, these results extend data from previous studies, based on visual observations and single microphone techniques, suggesting that choruses are dynamic, rather than static, assemblages (Emlen, 1976) in which individuals can change their calling strategies under particular circumstances and according to particular behavioral rules (Boatright-Horowitz *et al.*, 2000; Greenfield and Rand, 2000; Freeberg and Harvey, 2008).

A. Variability in bullfrog spacing

Spacing of males within chorusing assemblages can be highly variable between species (Gerhardt and Huber, 2002) and over the course of a breeding season within the same species (Emlen, 1976). Previous observations of bullfrog chorusing behavior (Emlen, 1976; Boatright-Horowitz *et al.*, 2000) indicated that males are highly territorial and individually spaced, with distances between nearest neighbors ranging widely, from as little as 3 to as many as 17 m, depending on chorus density and availability of calling sites. The data collected here show that vocalizing male bullfrogs, rather than maintaining distinct individual locations throughout the breeding season, often organize into smaller groups or clusters within the larger chorus. At both chorus sites, individuals within clusters are more closely spaced than single individuals in different locations, and intercluster distance is larger than spacing within a cluster. This spatial organization is defined based solely on data from vocalizing males; other studies based on visual surveys (Emlen, 1976) included nonvocalizing males in their location estimates. It is possible that nonvocalizing males are individually spaced and not part of a local cluster, but, given that these males are not vocalizing, they are not contributing to the acoustic scene of the chorus and have not been considered as part of these data. We did observe aggressive interactions (physical contact and aggressive vocalizations) between vocalizing bullfrogs within, but not between, clusters. Aggressive interactions did not appear to influence the overall chorus organization, at least over the length of our recording sessions, but, along with movements of individuals seemingly unrelated to aggressive encounters, they did complicate the accuracy of the program in pinpointing a unique location for each individual male within a cluster.

With an overall low density of chorus members (9–14 at the two ponds where clusters were observed), why would males space themselves close together, rather than making use of the entire chorusing site? One possibility is that clus-

ters may form in especially attractive spatial locations. Since female bullfrogs oviposit in the territory of their mates, several males may stake claim to a patch of high quality territory in order to increase their chances of breeding success. Similarly, there may be some local geographic or environmental characteristic, unrelated to female choice behavior, which makes some spots more attractive to vocalizing males than other spots within the same chorus. We currently have no data with which to assess either of these possibilities. Clustering may also arise due to spatial constraints at the chorusing site. Boatright-Horowitz *et al.* (2000) conducted a field experiment at pond 1 six years prior to the data collection for the present study and found a similar number of bullfrogs, but all individually located and separated by a minimum of 4 m (mean separation 28 m). They did not observe any clustering of vocalizing males at that site at any time during that field season. Six years later, human encroachment onto the chorusing site had grown: most noticeably, a bike path was constructed along one margin of the pond, and changes in drainage also served to shrink the pond dimensions. It is possible that the animals may now have responded to the reduced habitat by tolerating closer neighbors out of necessity, particularly during the height of the breeding season when more bullfrogs were present. It is also possible that some of the variability in spacing we observed is related to seasonal effects. At pond 1, two nights of chorusing activity were recorded approximately 1 month apart. The first night was in early June, at the very beginning of the breeding season, and the second was in early July, when the season was well underway and more animals were present. In June, each location contained just one bullfrog, while in July a cluster of five closely spaced males was present. We currently have no geographic explanation for the clustering behavior at pond 2, except to note that location 4, where only one bullfrog was found, is the location at this pond closest to a cleared backyard where children congregated.

Local clustering of males in a larger chorus could provide some biological benefits to the vocalizing males themselves, benefits to approaching females, or to both. If males are gathered into such local aggregations, then the cost of mate assessment by females could be lower, by attracting them to a more restricted area from which several potential mates are advertising. Females would have to expend more energy traveling to different sites within the chorus in order to evaluate males close-up if those males were widely dispersed (Gerhardt and Huber, 2002). Traveling to several different sites within the chorus could also make the females more susceptible to predation. Evidence for this explanation, summarized from results of female choice behavior in different species of chorusing anurans and insects, is equivocal (Gerhardt and Huber, 2002). Aggregations of males into smaller local areas could facilitate the production of synchronous calls, which might produce a more salient acoustic stimulus (Klump and Gerhardt, 1992).

Conversely, small spatial separations between vocalizing males could lead to masking of an individual's own advertisement call by the calls of the other males within that cluster. This in turn might negatively affect the female bullfrogs' ability to detect and localize specific individuals, by minimizing any spatial release from masking allowed by larger spatial separations (Schwartz and Gerhardt, 1989; Bee, 2007). We argue below that the clustering of males into local calling spots increases the temporal cues in a complex signal and thus indirectly can aid in sound localization by approaching females and by far chorus residents.

B. Variability in calling patterns

Besides the clustering of bullfrogs into closely spaced locations, our acoustic sensor technique introduces another novel finding, differences in the kinds of acoustic interactions between and within clusters. Our earlier data on the organization of bullfrog choruses (Boatright-Horowitz *et al.*, 2000), based on single microphone recordings, could not reliably distinguish between patterns of note overlap and call overlap, and so those kinds of complex vocal interactions were not identified or localized in that study. We show here that the aggregation of males into local clusters within a larger chorus affects the type of vocal interactions in which the males engage. In particular, alternation of entire advertisement calls and overlap between small proportions of calls are more common patterns of vocal interactions between farther-spaced males located in different clusters, while note alternation and note overlap are more commonly observed between closely spaced males located within the same cluster. The high occurrences of note alternation and note overlap within clusters suggest that male bullfrogs, like males of other anuran species (Brush and Narins, 1989; Schwartz, 1993; Greenfield and Rand, 2000; Schwartz *et al.*, 2002), do vocalize in response to their closest neighbors. But, in some other anuran species (Schwartz, 1993; Greenfield and Rand, 2000), vocalizing males are more likely to avoid overlap with near neighbors than with farther neighbors. Some of these differences in calling patterns may be related to the different acoustic structure of advertisement calls in different species. Bullfrog advertisement calls are long duration, multiple harmonic signals emitted at relatively slow rates, while advertisement calls of neotropical frogs such as *Hyla microcephala* (Schwartz, 1993) are pulselike in structure and are emitted at relatively high rates.

Our data also show that, when examining between-cluster vocal bouts made up of call alternation or call overlap, bullfrogs located within clusters preferentially respond to their farther neighbors [Figs. 7(B) and 7(C)], although the pattern is not as strong as that identified earlier in a chorus where clusters of vocalizing males were not present [Boatright-Horowitz *et al.*, 2000; see also Fig. 7(A)]. These comparisons again highlight the complex, dynamic patterns of vocal interactions that occur in natural choruses. As previously discussed (Boatright-Horowitz *et al.*, 2000), near-far sequential patterns of calling might provide approaching listeners with salient, easily localizable acoustic cues. If this is so, then it raises the question of why anurans often call in close temporal and spatial proximities in patterns that lead to substantial overlap of vocalizations.

Many species that rely on vocalizations to communicate actively avoid overlapping their signals with those of conspecifics (Gerhardt and Huber, 2002). Overlapping calls may

increase the difficulty faced by females in detecting and/or localizing individual males within a chorus, perhaps by disrupting or destroying fine temporal cues in the males' calls that are important for discrimination (Schwartz, 1987, 1993; Grafe, 1996). Calling as individuals and call alternation are common strategies to maintain acoustic space between advertising male frogs and to countervail these deleterious effects of overlap (Schwartz, 1987, 1993; Grafe, 1996). The distinction between these two different calling strategies (individual calling and call alternation) is a matter of definition (we used a 2 s intercall interval to distinguish them), but both result in one male's call having no acoustic interference from another male's call. Our data show a predominance of individual calls on all five nights analyzed, suggesting that bullfrogs, even those located in clusters, require some of their calls to be free from interference. Even when animals are localized into local clusters, call alternation and call overlap (defined here as an interaction when most of the notes in each male's call occur without interference) are the most common types of acoustic interaction occurring between these clusters. Together, these calling patterns may facilitate the female's ability to localize males by eliminating any masking produced by high amplitude signals spaced close together.

Choruses of orthopteran insects exhibit patterns of synchronous or near-synchronous calling in which calls or notes of neighbors can completely overlap (Greenfield and Roizen, 1993). No species of anuran amphibian exhibits the extreme synchrony of calling found in some of these insect choruses, but some species call in rhythmic bursts of activity in which one male's calls seem to stimulate calling by other males, resulting in extensive call or note overlap. The benefits of call synchrony include the maintenance and amplification of species-specific temporal patterns, facilitation of the detection of female acoustic replies, and reduction in the detectability or locatability of signalers by predators (Gerhardt and Huber, 2002). Call synchrony may emerge from the operation of an inhibitory-resetting pacemaker that generates a temporal rhythm and that assumes that males pay attention to acoustic cues (i.e., each other; Greenfield and Roizen, 1993; Greenfield and Schul, 2008). It may be the result of a strategy in which each male vies to be the leader in a calling bout, either because females prefer leading calls (Minckley *et al.*, 1995; Grafe, 1996) or in order to mask the calls of neighboring males (Grafe, 1999).

Our data show instances of note overlap, in which most of the notes of one bullfrog's call overlapped partially or completely with the notes of another bullfrog's call. Note overlap commonly occurred in the acoustic interactions of males located within the same cluster. The least common type of acoustic interaction we observed was note alternation, in which one bullfrog seemingly timed his notes to fall between the notes of another bullfrog. Although this could also be a strategy for avoiding masking, it may not be an efficient one for this species. Bullfrog calls consist of several notes that usually increase in duration from first to last note (Suggs and Simmons, 2005). Additionally, there is a great deal of individual variability associated with note duration and internote interval. One study reported individual note durations from nine male bullfrogs ranging from 370 to 970 ms, with a similar range for internote intervals (Simmons, 2004). The combination of variable note durations between bullfrogs and increasing note durations within each male's call may make timing notes to precisely alternate with those of another bullfrog very difficult. Analysis of spectrograms showed that instances of note alternation were likely to merge into patterns of note overlap as number of call notes and the number of vocalizing males increased. Thus, our data suggest that note overlap and note alternation may be part of the same general strategy, that of attempting near-synchronous calling patterns within a local cluster.

Spatial organization and vocal interactions may vary seasonally. In addition to changes in the individuals making up the chorus and their relative locations, the early and mid-season recordings from pond 1 also differed substantially in call activity. Early in the season, bullfrogs were much more likely to call individually than they were to engage in any type of multiple-male acoustic interaction. The opposite pattern held for the recording done in July, in which multiple-male vocal activity (across all four types of interactions) was greater than individual calling. This latter pattern was also observed on the three nights in July at pond 2, suggesting that individual calling may be more common in the early breeding season, but bouts of two or more bullfrogs calling simultaneously or in response to one another become more numerous as the season progresses. More data on seasonal variability in choruses are needed to address this issue.

C. Increased temporal cues in near-synchronous signals

Consistent with the hypothesis of Gerhardt and Huber (2002) regarding one function of call synchrony, note overlap (leading to note synchrony) could be a strategy for increasing the salience of species-specific temporal patterns of calling. Overlap could also increase the amplitude of the combined signal, providing another cue allowing increased salience. We examined these two possibilities by quantifying the relative amplitudes of the first harmonic frequency in notes made by individual identified bullfrogs (location 1, pond 2), both when these males called individually and when they called in note overlap with other males in that cluster. The calls showing note overlap between calls of different males were greater in amplitude, by a maximum of 3 dB, than calls by the same bullfrogs when they were calling individually. This 3 dB value is within the range of spatial release from masking observed in one study of *Hyla cinerea* (Schwartz and Gerhardt, 1989), but below that needed to produce the effect in *Hyla chrysoscelis* (Bee, 2007). In a field situation, the 3 dB increase in amplitude produced by note overlap may not be a reliable enough cue on which to base a perceptual decision.

Besides producing a signal greater in amplitude, the occurrence of note overlap also altered the time domain waveforms of the resultant combined signals (Fig. 8). As previously described (Suggs and Simmons, 2005), the envelopes of successive notes in advertisement calls of individual male bullfrogs progressively increase in the rate of slow AMs. We examined the changes in the AM produced in natural call

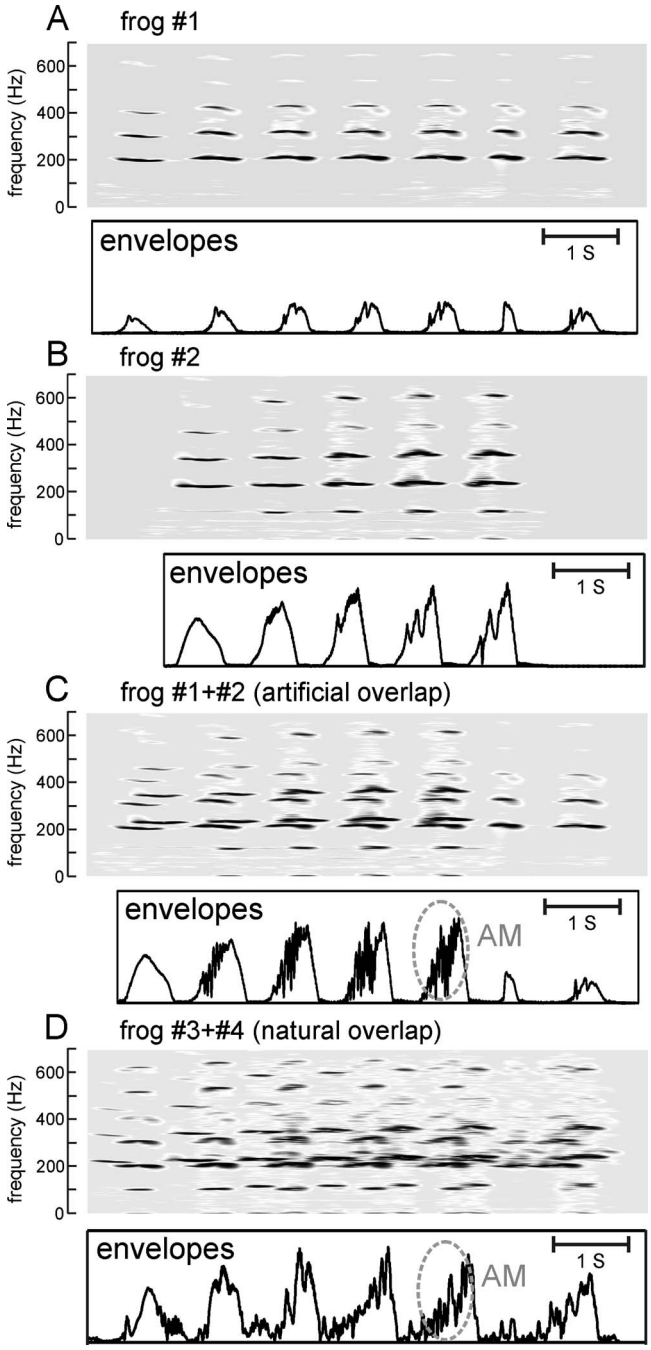

FIG. 8. Demonstration of how overlap of call notes results in increased AM due to interference between signals. (A) Spectrograms to 700 Hz and envelopes of the seven notes in an advertisement call of an individual bullfrog, frog 1, calling alone. (B) Spectrograms and envelopes of the five notes in an advertisement call of another bullfrog, frog 2, also vocalizing alone. (C) Spectrograms and envelopes of call notes from frog 1 and frog 2, which were artificially superimposed by aligning and mixing the calls to overlap their individual notes. (D) Spectrogram and envelopes of call notes from two other bullfrogs, frog 3 and frog 4, which the frogs themselves produced in an overlapping pattern. This is an example of actual note overlap occurring naturally. The overlapping advertisement call notes in (C) and (D) show more complex envelopes than the nonoverlapped call notes in (A) and (B). Most of the envelopes for the overlapped notes, whether artificial (C) or real (D), show roughly 10–30 cycles of AM (gray ovals) on top of the smoother envelope for the notes by themselves.

notes when these notes overlap. Figures 8(A) and 8(B) show spectrograms and envelopes of advertisement call notes from two bullfrogs (frog 1 and frog 2) calling individually. The envelopes of these notes are amplitude modulated, and the rate of AM is higher in later than in earlier notes. We then artificially overlapped these notes, producing the spectrograms and envelopes shown in Fig. 8(C). The overlap produced higher AM in the envelopes of the overlapped signal than seen in the envelopes of the nonoverlapped notes. Figure 8(D) shows an example of actual note overlap in the vocalizations of two other bullfrogs, frog 3 and frog 4. Again, more rapid AM is added to the envelopes of the overlapped notes, due to reinforcement and cancellation from interference caused by their frequency differences. Thus, overlapping of notes produces more AM. Physiological studies of the bullfrog's auditory system (Simmons *et al.*, 1996, 2000) show that AM rates of 10–100 Hz, which are within the AM range present in both individual and overlapped call notes, are robustly coded by phase-locked discharges in both the eighth nerve and the auditory midbrain. Phase locking is a reliable cue for coding and discriminating the periodicities of complex signals, and the increased AM of overlapping notes could expand the strength of phase locking of these signals. This pronounced AM might serve perceptually as a "supranormal" stimulus that attracts the female's attention to a general location in the chorus, even if it masks the unique location of specific individuals within that particular cluster. Once a female is attracted to the general vicinity of the cluster, males within that cluster may then compete for her with physical contests or by calling individually. Field studies of female bullfrog choice behavior would be necessary to determine the value of bouts between near neighbors and the perceptual salience of overlapped notes.

Overall, the dynamics of calling behavior that we observed suggest that chorusing bullfrogs may balance out their need to be individually heard by potential mates with the increased ease of detection that local aggregations within a chorus allows. Males thus may not only tolerate but also cooperate with very close neighbors in regulating calling activity. These data also show the importance of developing, perfecting, and implementing microphone array techniques for gathering a more comprehensive view of the strategies chorusing animals use to parse out a complex acoustic stream.

ACKNOWLEDGMENTS

Data collection and analyses were supported by the NIH Grant No. R01 DC05257 to Andrea M. Simmons and the ONR Contract No. N00014-04-1-0415 to James A. Simmons. M.G. was supported by the LEARN Program, Lafayette College. Preliminary versions of these results were presented at the Second International Conference on Acoustic Communication by Animals, Corvallis OR, Aug. 12–15, 2008, and at the 158th Meeting of the Acoustical Society of America [J. Acoust. Soc. Am. 126, 2270 (2009)].

Bee, M. A. (**2004**). "Within-individual variation in bullfrog vocalizations: Implications for a vocally mediated social recognition system," J. Acoust. Soc. Am. **116**, 3770–3781.

Bee, M. A. (**2007**). "Sound source segregation in grey treefrogs: Spatial release from masking by the sound of a chorus," Anim. Behav. **74**, 549–558.

Boatright-Horowitz, S. L., Horowitz, S. S., and Simmons, A. M. (**2000**).

"Patterns of vocal interaction in a bullfrog (*Rana catesbeiana*) chorus: Preferential responding to far neighbors," Ethology **106**, 701–712.

Brush, J. S., and Narins, P. M. (**1989**). "Chorus dynamics of a neotropical amphibian assemblage: Comparison of computer simulation and natural behavior," Anim. Behav. **37**, 33–44.

Burt, J. M., and Vehrencamp, S. L. (**2005**). "Dawn chorus as an interactive communication network," in *Animal Communication Networks*, edited by P. K. McGregor (Cambridge University Press, Cambridge, UK), pp. 320–343.

D'Spain, G. L., and Batchelor, H. H. (**2006**). "Observations of biological choruses in the Southern California Bight: A chorus at midfrequencies," J. Acoust. Soc. Am. **120**, 1942–1955.

Emlen, S. T. (**1976**). "Lek organization and mating strategies in the bullfrog," Behav. Ecol. Sociobiol. **1**, 283–313.

Forrest, T. G., and Green, D. M. (**1991**). "Sexual selection and female choice in mole crickets (*Scapteriscus*: Gryllotalpidae): Modeling the effects of intensity and male spacing," Bioacoustics **3**, 93–109.

Freeberg, T. M., and Harvey, E. M. (**2008**). "Group size and social interactions are associated with calling behavior in Carolina chickadees (*Poecile carolinensis*)," J. Comp. Psychol. **122**, 312–318.

Gerhardt, H. C., and Huber, F. (**2002**). *Acoustic Communication in Insects and Anurans: Common Problems and Diverse Solutions* (University of Chicago Press, Chicago, IL).

Grafe, T. U. (**1996**). "The function of call alternation in the African reed frog (*Hyperolius marmoratus*): Precise call timing prevents auditory masking," Behav. Ecol. Sociobiol. **38**, 149–158.

Grafe, T. U. (**1997**). "Costs and benefits of mate choice in the lek-breeding reed frog, *Hyperolius marmoratus*," Anim. Behav. **53**, 1103–1117.

Grafe, T. U. (**1999**). "A function of synchronous chorusing and a novel female preference shift in an anuran," Proc. Biol. Sci. **266**, 2331–2336.

Greenfield, M. D., and Rand, A. S. (**2000**). "Frogs have rules: Selective attention algorithms regulate chorusing in *Physalaemus pustulosus* (Leptodactylidae)," Ethology **106**, 331–347.

Greenfield, M. D., and Roizen, I. (**1993**). "Katydid synchronous chorusing is an evolutionarily stable outcome of female choice," Nature (London) **364**, 618–620.

Greenfield, M. D., and Schul, J. (**2008**). "Mechanisms and evolution of synchronous chorusing: Emergent properties and adaptive functions in Neoconocephalus katydids (Orthoptera: Telligoniidae)," J. Comp. Psychol. **122**, 289–297.

Hailman, E. D., and Hailman, J. P. (**1993**). UNCERT User's Guide, Zoology Department, University of Wisconsin, Madison, WI. Available at http://www.animalbehavior.org/Resources/CSASAB/#UNCERT (Last viewed 12/15/09).

Hayes, S. A., Mellinger, D. K., Croll, D. A., Costa, D. P., and Borsani, J. F. (**2000**). "An inexpensive passive acoustic system for recording and localizing wild animal sounds," J. Acoust. Soc. Am. **107**, 3552–3555.

Jones, D. L., and Ratnam, R. (**2009**). "Blind location and separation of callers in a natural chorus using a microphone array," J. Acoust. Soc. Am. **126**, 895–910.

Klump, G. M., and Gerhardt, H. C. (**1992**). "Mechanisms and function of call-timing in male-male interaction in frogs," in *Playback and Studies of Animal Communication*, edited by P. K. McGregor, (Plenum, New York), pp. 153–174.

McGregor, P. K., Dabelsteen, T., Clark, C. W., Bower, J. L., Tavares, J. P., and Holland, J. (**1997**). "Accuracy of a passive acoustic location system: empirical studies in terrestrial habitats," Ethol. Ecol. Evol. **9**, 269–286.

Mennill, D. J., Burt, J. M., Fristrup, K. M., and Vehrencamp, S. L. (**2006**). "Accuracy of an acoustic location system for monitoring the position of duetting songbirds in tropical forest," J. Acoust. Soc. Am. **119**, 2832–2839.

Minckley, R. L., Greenfield, M. D., and Tourtellot, M. K. (**1995**). "Chorus structure in tarbrush grasshoppers: Inhibition, selective phonoresponse and signal competition," Anim. Behav. **50**, 579–594.

Mohan, S., Lockwood, M. E., Kramer, M. L., and Jones, D. L. (**2008**). "Localization of multiple acoustic sources with small arrays using a coherence test," J. Acoust. Soc. Am. **123**, 2136–2147.

Moore, S. W., Lewis, E. R., Narins, P. M., and Lopez, P. T. (**1989**). "The call-timing algorithm of the white-lipped frog, *Leptodactylus albilabris*," J. Comp. Physiol. [A] **164**, 309–319.

Mountain, D., Anderson, D., Bresnahan, G., Brughera, A., Deligeorges, S., Hubbard, A. Lancia, D. and Vajda, V. (**2007**). EarLab: A virtual laboratory for auditory experimentation. Available at http://scv.bu.edu/SCV/vizgal/earlabnew/earlab.html (Last viewed 2/11/10).

Schwartz, J. J. (**1987**). "The function of call alternation in anuran amphibians: A test of three hypotheses," Evolution **41**, 461–471.

Schwartz, J. J. (**1993**). "Male calling behavior, female discrimination and acoustic interference in the Neotropical treefrog *Hyla microcephala* under realistic acoustic conditions," Behav. Ecol. Sociobiol. **32**, 401–414.

Schwartz, J. J., Buchanan, B. W., and Gerhardt, H. C. (**2002**). "Acoustic interactions among male gray treefrogs, *Hyla versicolor*, in a chorus setting," Behav. Ecol. Sociobiol. **53**, 9–19.

Schwartz, J. J., and Gerhardt, H. C. (**1989**). "Spatially mediated release from auditory masking in an anuran amphibian," J. Comp. Physiol. [A] **166**, 37–41.

Simmons, A. M. (**2004**). "Call recognition in the bullfrog, *Rana catesbeiana*: Generalization along the duration continuum," J. Acoust. Soc. Am. **115**, 1345–1355.

Simmons, A. M., Sanderson, M. I., and Garabedian, C. E. (**2000**). "Representation of waveform periodicity in the auditory midbrain of the bullfrog, *Rana catesbeiana*," J. Assoc. Res. Otolaryngol. **1**, 2–24.

Simmons, A. M., Shen, Y., and Sanderson, M. I. (**1996**). "Neural and computational basis for periodicity extraction in frog peripheral auditory system," Aud. Neurosci. **2**, 109–133.

Simmons, A. M., Simmons, J. A., and Bates, M. E. (**2008**). "Analyzing acoustic interactions in natural bullfrog choruses," J. Comp. Psychol. **122**, 274–282.

Snedden, W. A., Greenfield, M. D., and Jang, Y. (**1998**). "Mechanisms of selective attention in grasshopper choruses: Who listens to whom?" Behav. Ecol. Sociobiol. **43**, 59–66.

Suggs, D. N., and Simmons, A. M. (**2005**). "Information theory analysis of patterns of modulation in the advertisement call of the male bullfrog, *Rana catesbeiana*," J. Acoust. Soc. Am. **117**, 2330–2337.

Wilczynski, W., and Brenowitz, E. A. (**1988**). "Acoustic cues mediate intermale spacing in a neotropical frog," Anim. Behav. **36**, 1054–1063.

Sound production by singing humpback whales

Eduardo Mercado III[a)]
Department of Psychology, University at Buffalo, The State University of New York, Buffalo, New York 14260

Jennifer N. Schneider
Evolution Ecology and Behavior, University at Buffalo, The State University of New York, Buffalo, New York 14260

Adam A. Pack
Department of Psychology, University of Hawaii at Hilo, 200 West Kawili Street, Hilo, Hawaii 96720

Louis M. Herman
The Dolphin Institute, 91-117 Kekai Place, Kapolei, Hawaii 96707

(Received 2 June 2009; revised 8 January 2010; accepted 15 January 2010)

Sounds from humpback whale songs were analyzed to evaluate possible mechanisms of sound production. Song sounds fell along a continuum with trains of discrete pulses at one end and continuous tonal signals at the other. This graded vocal repertoire is comparable to that seen in false killer whales [Murray *et al.* (1998). J. Acoust. Soc. Am. **104**, 1679–1688] and human singers, indicating that all three species generate sounds by varying the tension of pneumatically driven, vibrating membranes. Patterns in the spectral content of sounds and in nonlinear sound features show that resonating air chambers may also contribute to humpback whale sound production. Collectively, these findings suggest that categorizing individual units within songs into discrete types may obscure how singers modulate song features and illustrate how production-based characterizations of vocalizations can provide new insights into how humpback whales sing.
 [DOI: 10.1121/1.3309453]

PACS number(s): 43.80.Ka, 43.80.Ev, 43.60.Uv, 43.25.Ts [WWA] Pages: 2678–2691

I. INTRODUCTION

The mechanisms of sound production used by an animal constrain the types of sounds that the animal can produce. Anatomical and physiological constraints on production may in turn limit the ways an animal can use sounds. For example, a smaller animal may not be able to generate the sound amplitudes or frequencies necessary for it to compete reproductively with larger conspecifics (Fitch and Hauser, 1995). Similarly, the amplitudes and frequencies produced by an echolocating animal limit the size and distance of the targets it can detect (Au, 1993). Knowing how a species physically produces sounds can thus provide a useful foundation for understanding the functions that vocalizations may serve, as well as for assessing physical features of the individual producing the sound. The purpose of this paper is to use acoustic data and models of phonation in terrestrial mammals to investigate sound production by singing humpback whales (*Megaptera novaeangliae*).

A. Anatomy of humpback whale respiratory structures

Most mammals produce sounds by forcing air from the lungs through the glottis, causing membranes (typically vocal folds) to pulsate (Keleman, 1963). Air oscillations or turbulence generated by these membranes are a primary source of sound. As the sound waves travel out of the animal's body, they are modified by the resonating properties of the structures they pass through or by. For example, the vocal tract can act as a resonator, filtering the sound to emphasize certain frequencies while dampening others. As a result, the final form of a produced sound depends on both the initial vibrations produced at the source, and the length, shape, and tissue composition of the vocal tract. Cetaceans produce sounds underwater, necessitating somewhat different mechanisms from those used by terrestrial mammals. Nevertheless, in the few cetacean species that have been studied, the source mechanism still appears to involve pneumatically driven membrane vibrations which travel through internal structures that may impact the acoustic properties of the emitted sound (Au, 1993; Cranford *et al.*, 1996; Cranford and Amundin, 2004). Air-filled chambers are thought to play little role in sound production by toothed whales (however, see Ridgway, *et al.*, 2001).

Humpback whales are the most vocally versatile of the great whales, well known for the long and elaborate songs produced by males during the winter breeding season (Payne and McVay, 1971; Winn *et al.*, 1970). The mechanisms that humpback whales use to internally generate sound are not well understood. Several researchers have postulated that humpbacks produce sounds by pushing an air stream over or through membranes in the larynx as terrestrial mammals do

[a)]Author to whom correspondence should be addressed. Electronic mail: emiii@buffalo.edu

(Purves and Pilleri, 1983; Quayle, 1991; Reidenberg and Laitman, 2007; Schevill, 1964; Sukhovskay and Yablokov, 1979; Reeb and Best, 1999). Anatomical examinations of the respiratory tracts of mysticetes have begun to provide a clearer picture of how humpback whales may produce sounds (Quayle, 1991; Schevill, 1964; Sukhovskay and Yablokov, 1979). Quayle (1991) noted similarities between the human larynx and the larynx of a humpback whale calf suggesting that this structure is capable of sound production. Reidenberg and Laitman (2007) identified a U-fold between the upper and lower respiratory systems as a possible source of vibrations. Unlike typical vocal folds in terrestrial mammals, the U-fold is oriented parallel to airflow. The U-fold borders the entrance of a large laryngeal sac, which may function as a resonance chamber or as a receptacle for air exhaled from the lungs (Reeb and Best, 1999; Reidenberg and Laitman, 2007). Sound may be produced when air flowing from the larynx passes the U-fold, causing vibrations in the air column within the larynx (or laryngeal sac). The vibrating air (or membranes) could then generate pressure fluctuations that are transferred through surrounding tissue into the water.

Singing humpback whales can produce sounds underwater for 15 min or more without any air escaping from either the blowhole or mouth (personal observations, A. A. P. and L. M. H.), suggesting that they recirculate air internally during sound production. How such recirculatory processes are coordinated with sound production is currently unknown.

B. Models of mammalian sound production

Most hypotheses about sound production by humpback whales are based on anatomical measurements because it is currently not possible to directly observe what humpbacks are doing internally while producing sounds. The dynamics of sound production can be indirectly observed, however, through examination of the acoustic features generated during production (Gaunt, 1983; Taylor and Reby, 2009). For example, techniques developed to describe human speech sounds have greatly increased our understanding of the dynamics of speech production, as well as the production of nonspeech sounds by primates (Owren *et al.*, 1997, Fitch, 1997; Rendall *et al.*, 1998), birds (Beckers *et al.*, 2004; Riede *et al.*, 2004), and deer (Reby *et al.*, 2005; Vannoni and McElligott, 2007). Comparable techniques for characterizing humpback whale sounds might similarly provide insights into the processes underlying their sound production.

One classical approach to modeling mammalian sound production (especially human speech) is a signal processing model called the source-filter model (Fant, 1960). In this model, the "source" simulates features of sound production related to vocal fold vibrations or air turbulence, and the "filter" simulates the transformative effects of the vocal tract. This model can be physically instantiated by combining a silicone vocal fold model with a PVC tube (Riede *et al.*, 2008). From a signal processing perspective, cetacean sound production can be characterized using a source-filter model just as it is for terrestrial mammals—the properties of the source and filter simply need to be adjusted to account for the differences in cetacean anatomy (e.g., see Altes *et al.*, 1975). Homologies between the sound production mechanisms hypothesized in humpback whales and those present in terrestrial mammals (Reidenberg and Laitman, 2007), increase the likelihood that the source-filter model can adequately characterize humpback whale sound production. For example, U-fold vibrations may be modeled in the same way as vocal fold vibrations, and the effects of the laryngeal sac and/or larynx on these vibrations can be modeled in the same way as vocal tract filtration.

Past analyses of animal sounds based on source-filter models of production have revealed that animals attend to information about vocal filters (Charlton *et al.*, 2007; Fitch and Fritz, 2006; Sommers *et al.*, 1992; Taylor *et al.*, 2008) and that resonant frequencies (called formants) may be used for individual identification and body size (reviewed by Taylor and Reby, 2009). Formant distribution is correlated with individual identity in grunt calls of chacma baboons (Owren *et al.*, 1997; Rendall, 2003) and coos and grunts of rhesus monkeys (Rendall *et al.*, 1998). Both formant features and fundamental frequency may be used for individual identification in fallow deer groans (Vannoni and McElligott, 2007) and African elephant rumbles (Soltis *et al.*, 2005). Formant distribution has been correlated with body size in rhesus macaques (Fitch, 1997), domestic dogs (Riede and Fitch, 1999), red deer (Reby and McComb, 2003), and southern elephant seals (Sanvito *et al.*, 2007). Development of comparable models for humpback whale sound production may similarly provide new ways of assessing individual differences in singing humpbacks.

C. Singing

Humpback whales produce sounds in a variety of contexts. Researchers have focused most of their attention, however, on sound production during singing. Humpbacks are described as singing when they rhythmically produce sounds (called units) in predictable sequences (Payne and McVay, 1971). The features of humpback whale songs and their constituent units are described in numerous papers (see e.g., Winn and Winn, 1978; Payne and Payne, 1985; Helweg *et al.*, 1998; Mercado *et al.*, 2005). The broad range of frequencies, durations, intensities, and spectrotemporal patterns that humpback whales produce within songs makes songs particularly useful for understanding the dynamics of production mechanisms. Additionally, the fact that songs are often produced by stably positioned, lone individuals makes it easier to obtain recordings of sufficient quality for decomposing units into production-related parameters.

In terrestrial mammals, singing behavior typically involves respiratory patterns and production modes that differ somewhat from nonsinging (Doscher, 1994; Miller, 1986). Nevertheless, the physical mechanisms engaged during singing are typically the same mechanisms used to produce nonsong sounds. For example, human song contains the same basic sounds present in speech. These sounds can be divided into three broad classes based on their periodicity: voiced, unvoiced, and mixed sounds. Voiced sounds (e.g., vowels) are quasiperiodic pulse trains generated when the vocal

folds vibrate in relaxed oscillations. Unvoiced sounds (e.g., most consonants) are aperiodic noise bursts generated by turbulence or an abrupt release of air. Mixed sounds have features of both voiced and unvoiced sounds. If humpback whales sing using vocal mechanisms analogous to those used by humans, then voiced components should be evident in their units.

D. Source vibrations

In the source-filter model, two main properties characterize the source: the fundamental frequency or pulse rate and the pulse shape. Voiced sounds are modeled as a periodic series of impulses, the rate of which is quantified using a single value for constant pulse rates, or as a time series for time-varying pulse rates. Pulse rate is determined by the tension of the vocal folds, as well as the pressure below the folds, and typically is perceived as the pitch of the sound. Pulse shape is more difficult to characterize and may be modeled using specific waveforms or spectra that are modified to simulate empirically measured features of individual pulses, some of which may be pulse rate dependent. Pulse shape reflects the degree of vocal fold closure during oscillation and contributes to the perceptual qualities (or timbre) of a voiced sound. In singing humans, pulse shape usually varies with pulse rate (Cleveland, 1994; Gregg, 1992). Acoustically characterizing the "source" of humpback whale sounds within a source-filter model thus entails measuring variability in periodicity, fundamental frequency, and waveform shape within and across units.

When human singers reach certain pitch thresholds, their vocal mechanisms shift into different modes of vibration (Cleveland, 1994; Titze, 2008a). These transitions divide the pitches of singers into four vocal registers: vocal fry, modal, falsetto, and whistle. The vocal fry register includes the slowest pulse rates that singers can produce (5–60 Hz). In this register, individual pulses are perceptually discriminable. The modal register is associated with slightly higher pitches (80–300 Hz). In this register, individual pulses are broadband giving rise to multiple harmonics. The falsetto register is associated with higher pitches (250–900 Hz) and pulses tend to be narrowband, giving rise to fewer harmonics (Miller, 1986). The whistle register includes very high-pitched sounds (850–2300 Hz) that have few harmonics. The full range of song sounds produced by human singers falls along a graded continuum, with sounds containing trains of discrete pulses at one end and sinusoidlike sounds at the other.

Most of the sounds produced by human singers are subjectively very different from those produced by cetaceans. Nevertheless, recent analyses of the acoustic structure of clicks, burst-pulse sounds, and whistles produced by false killer whales (*Pseudorca crassidens*) have revealed that these sounds fall along a similar graded continuum (Murray *et al.*, 1998). At one end of this continuum are trains of clicks that can be modeled as exponentially damped sinusoidal pulses. At the other end are whistles, which are highly similar to sinusoids. False killer whales often gradually modulate from click trains to whistles and can rapidly shift between signal types, for example, shifting immediately from a whistle to a click train without changing the frequency with peak energy across the transition. Such vocal dexterity is consistent with the proposal that toothed whales, like humans, generate sounds by using air to control the rate at which paired membranes vibrate (Cranford *et al.*, 1996; Brown, 2008).

The current study quantitatively assessed whether humpback whale song units are best described in terms of discrete sounds types, or as points along a graded acoustic continuum. Specifically, the current analysis tested the hypothesis that sounds described as ratchets, moans, and cries (e.g., Winn and Winn, 1978) within humpback whale songs represent points along a pulse rate (i.e., vocal fold tension) continuum. If the sounds of humpback whales fall along a similar continuum to that seen in humans and false killer whales, then this would provide support for Reidenberg and Laitman's (2007) proposal that humpbacks generate sounds by passing air over or through vocal folds.

E. Formants

Voiced sounds are categorized based on their spectral features, which are a result of the resonance properties of the vocal tract (i.e., the "filter"). Specifically, they are classified based on the positions and dynamics of regions of frequency enhancement called formants. Generally, about 4–5 formants are evident in sung sounds and in spoken vowels. For males the first formant is typically between 250–700 Hz, and the second formant is between 750–2500 Hz (Sundberg, 1977). The pattern of formants produced by human singers is highly pitch dependent (Rossing *et al.*, 1987; Sundberg, 1977). Lower pitched sounds tend to show more clustering of higher formants than higher pitched sounds. Singers may adjust their formant positions to facilitate the transmission of certain high-pitched sounds by changing the size of their mouth opening and jaw position (Cleveland, 1994; Schutte *et al.*, 1995; Titze, 1994). Some singers are also able to tune their formant regions to specific upper harmonics (called overtone singing) such that they emphasize different frequencies while maintaining a steady pulse rate (Boersma and Kovacic, 2006; Sundberg, 1977).

The prevalence and properties of formants within humpback whale sounds have not previously been analyzed in any detail. Analyses of spectral features of units provide a way to characterize the humpback whale "filter" in terms of formant dynamics and to determine the possible role of air chambers in humpback whale sound production. The current study examined the spectral properties of units to determine whether units contain formants. In terrestrial mammals, formants are the primary acoustic evidence that internal air chambers shape the features of vocalizations. Furthermore, the patterns of formants that distinguish certain classes of sounds (e.g., vowels) correlate with changes in the shape of the vocal tract, and also provide an indication of the length of the vocal tract. If air-filled chambers contribute to sound production by humpback whales, then the properties of these resonators should be evidenced by systematic formant patterns in units.

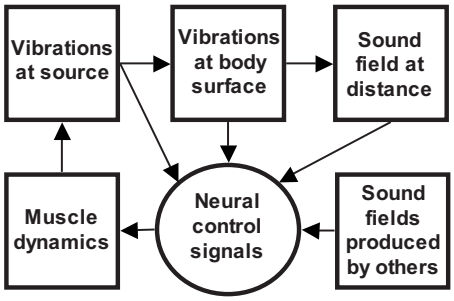

FIG. 1. Multiple internal and external mechanisms contribute to the signals recorded from vocalizing humpback whales. Production-based analyses decompose recorded sounds into acoustic components generated by different mechanisms. Humpbacks neurally control muscle dynamics that affect airflow as well as the tension of vibrating membranes that are the source of vocalizations. These vibrations are transformed as they travel through the whale's body such that emitted vibrations differ from those generated at the source. Sounds are further distorted as they travel through the ocean. Auditory and somatic sensations provide feedback about produced and received sounds that can potentially influence control mechanisms. By identifying acoustic components resulting from membrane vibrations, internal transformations, and environmental filtering, one can better understand which variations vocalizing humpback whales control and how they control them.

F. Study goals

The ultimate goal of the current analyses was to better understand how humpback whales sing. A first step in many past analyses of humpback whale song has been to categorize individual sounds into discrete types (often designated using letters or nominal labels) that are then used to describe the structure of songs or the vocal repertoire of singers. Such classifications emphasize the distinctive properties of "prototypical" units heard from a distance without considering what the singer is doing when it sings. In contrast, the production-based analyses reported here attempt to distinguish acoustic features that singers can potentially control from those that they cannot (Fig. 1). Decomposing recorded sounds into components attributable to source vibrations, the filtering effects of tissue transmission, or environmental filtering can help address questions such as the following: do singing whales use similar vocal actions to produce different sound features? If so, could apparent switching between discrete sound types actually reflect more gradual adjustments of vocal control mechanisms? How much control do whales have over the acoustic properties of sound sequences? Which, if any, properties of produced sounds are inadvertent? Knowing more about how singing humpback whales produce sounds can clarify appropriate techniques for describing the properties of songs as well as the vocal acts of singers.

II. MATERIALS AND METHODS

A. Study sites and subjects

Singing humpback whales were recorded in waters off the coast of the island of Hawaii between 1981 and 1995, and off the coast of Puerto Rico in 2009. Humpbacks in these two regions, as well as in other regions worldwide, are considered a single species. Recordings were collected during the winter months (February–April) when singing whales can be found in these areas. Singers in both regions are often separated by many kilometers, and although songs are typically produced at high source levels (Au *et al.*, 2006), in most of the recordings used for these analyses only a single singer was audible. Additionally, ambient noise levels in these waters are lower than in areas where numerous whales can be heard singing simultaneously (e.g., in waters off the island of Maui), and singing humpback whales often maintained a relatively stationary position while singing. Collectively, these features made it possible to collect high quality recordings of individual singing whales.

B. Recordings and acoustic analysis

All recordings were made from one or more hydrophones suspended approximately 10 m beneath a small boat located in relatively close proximity to the singer being recorded. Various configurations of hydrophones and recording systems were used across years. Recordings collected in Hawaii were made on analog cassette tapes, whereas recordings from Puerto Rico were stored digitally in .wav formatted files. All recordings were imported into the MATLAB programming environment as vectors representing time-domain waveforms. The sampling rate for digitization of Hawaiian songs was 8 kHz, and for Puerto Rican songs was 44 kHz. Signal processing techniques derived from both source-filter modeling, speech analyses, and prior analyses of human song sounds were applied to recordings using a combination of functions from MATLAB's Signal Processing Toolkit as well as customized MATLAB programs. Visual inspections of spectrograms and basic measures of spectrographic features were made using both MATLAB and RAVEN 1.3.

C. Source characteristics

All measurements of unit source characteristics were collected from a single, 54 min segment of a song session digitally recorded in Puerto Rico in 2009. This recording was selected because it was the highest fidelity recording available and because earlier analyses of lower fidelity recordings showed that the range of pulse rates within songs is relatively similar across individuals and years (Mercado *et al.*, 2005). Use of a single high quality sample controls for variability attributable to individual differences between singers, environmental conditions, time of recording, interference from other sound sources (including singers), and differences in recording systems. This approach is comparable to a case study of an individual human singer during a single performance and is not intended to represent the full vocal repertoire of humpback whales.

Short-term analyses of pulse rate in human speech generally are based on a 10–30 ms waveform sample, which includes three to five periods. Automated techniques developed to extract the pitch of speech can give erroneous results when applied to the full range of rates in units produced by singing whales because too few or too many periods are contained within a 10 ms sample frame; low pulse rate sounds are particularly problematic (Ishi *et al.*, 2008). For medium to high pulse rate sounds, pulse rate can be estimated from spectrograms or spectra by measuring the spacing of spectral bands (Watkins, 1967), but lower pulse rate

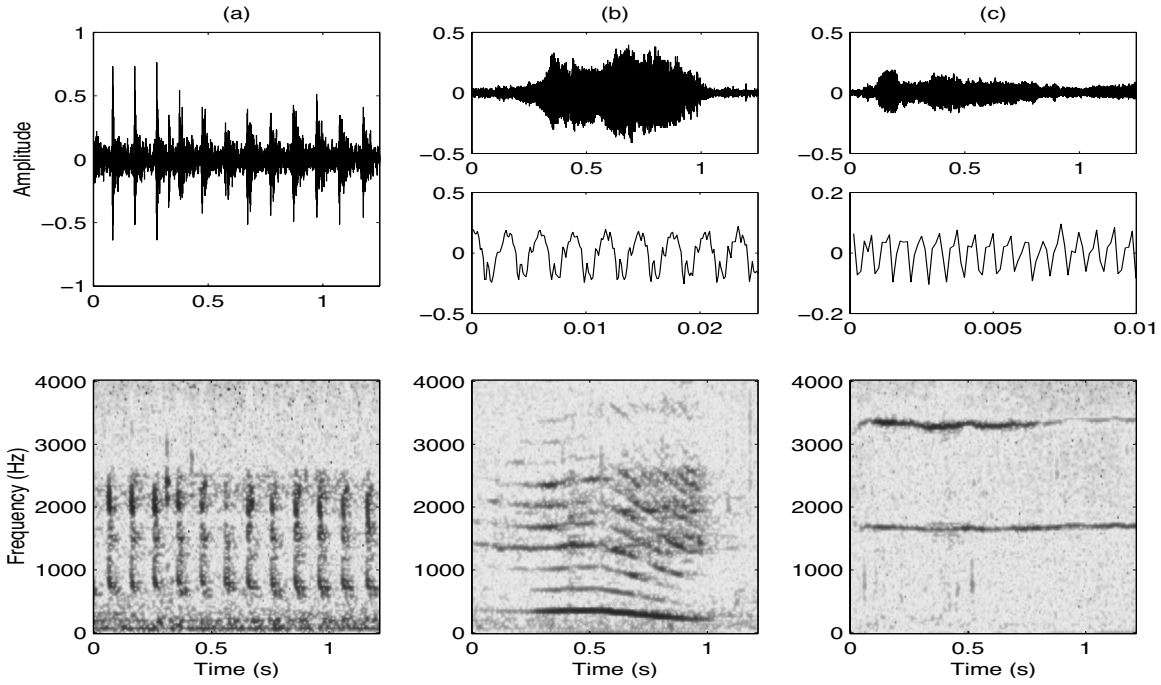

FIG. 2. (a) Low pulse rate units appear as discrete pulses in waveforms (top) and as a series of vertical lines in spectrograms (bottom). (b) Medium pulse rate units typically appear as a coherent increase in amplitude in low-resolution waveforms (top), as quasiperiodic, continuous signals similar to those of human vowels in high-resolution waveforms (middle), and as closely spaced horizontal bands in spectrograms (bottom). (c) High pulse rate units are typically indistinguishable from medium rate units in low-resolution waveforms (top), appear as continuous, sinusoid-, or sawtoothlike signals in high-resolution waveforms (middle), and as widely spaced horizontal bands in spectrograms (bottom). Fast Fourier transform (FFT) size=256 Hz for all spectrograms.

sounds often do not show clear bands without careful selection of the analysis window. In the current analyses, waveforms of individual units were visually inspected and dichotomously classified based on whether discrete repeating pulses were evident [as in Fig. 2(a)] or were not [as in Figs. 2(b) and 2(c)]. For units containing discrete pulses, short-term analyses were applied to nonoverlapping 200 ms sample frames. For all other units, 25 ms frames were used. A MATLAB function ("shrp") was used to estimate the pulse rate within frames based on the subharmonic-to-harmonic ratio (Sun and Xu, 2002).

In past work characterizing pulsed sounds produced by false killer whales, pulse shape was modeled as an exponentially damped sinusoid based on observations of recorded vocalizations (Murray *et al.*, 1998). The only published report of individual pulses produced by humpback whales shows a representative "megapclick" that is readily modeled as an exponentially damped sinusoid (Stimpert *et al.*, 2007). In the current study, visual inspection of unit waveforms revealed a much broader variety of pulse shapes than those seen in false killer whales (Fig. 2). Although some pulses within units were adequately modeled by damped sinusoids [Fig. 2(a)], others were more comparable to those seen in human speech [Fig. 2(b)]. Pulses within higher pulse rate units often were best modeled as one period of a triangle wave, sawtooth wave, or distorted sinusoid [Fig. 2(c)]. Developing a model of pulse shape that captures the full range of features present in units is beyond the scope of the current paper. Instead, duty cycle was used to characterize variability in waveform shape across units (Murray *et al.*, 1998). Duty cycle refers to the percentage of time a signal is on relative to the duration of the signal. The duty cycle measurement used here quantifies the similarity of the unit waveform to a sine wave as a value between 1 (a sine wave) and 0 (an impulse train). Duty cycle for units like the one shown in Fig. 2(a) would thus be lower than for the unit in Fig. 2(b), which would in turn be lower than the duty cycle of the unit in Fig. 2(c). Duty cycle was calculated for each sampled frame by rectifying the frame, converting all of its points to a percentage of the maximum value, averaging these percentages, and then normalizing this average relative to that of a sine wave by dividing the average by 0.636. The frequency with peak energy was also calculated for each frame.

D. Filter characteristics

Formants can be measured in human singers by having them produce broadband vocalizations such as frequency sweeps, vocal fry, or noisy vocalizations (e.g., see Titze, 2008b). This technique is comparable to using an impulse or sequence of sinusoids to determine the frequency response of a filter. As an initial test for formants in humpback whale sounds, power spectral density functions were calculated [using MATLAB's "psd" function, with a 128 point fast Fourier transform (FFT)] for units with acoustic features similar to those used to detect formants in human singers. Spectral analyses of these types of vocalizations provide the best opportunity for revealing resonance (and antiresonance) frequency regions, if they exist. Additionally, three standard methods of formant estimation were applied to 60 units sampled from five humpback whale songs recorded in Hawaii: wide-band spectral analysis, linear prediction spectra, and cepstrally smoothed spectra. This small sample of units was chosen simply to test the ease with which formants can

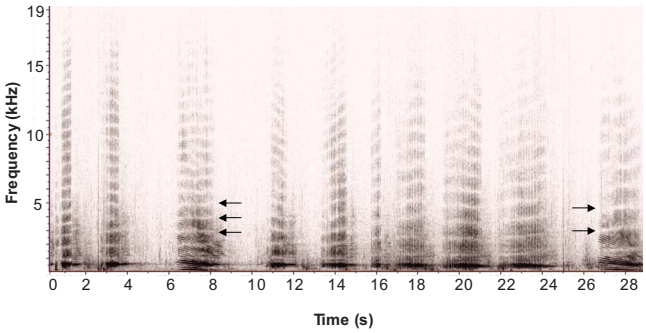

FIG. 3. (Color online) Interference resulting from shallow-water propagation can generate formants in units; the formants appear as dark bands separated by lighter bands (spectral gaps) in this spectrogram. Arrows indicate spectral gaps that are continuously shifting in frequency across units such that two acoustically similar units show different formant positions. The highly regular spacing of gaps across a broad band of frequencies also suggests that most of the formants visible in this spectrogram are environmentally generated. FFT size=1500 Hz.

be measured in units. Units were selected based on recording quality and signal-to-noise ratio, and so that units of different pulse rates were included.

Another technique used to analyze formants in human singers, called long-term average spectrum (LTAS) analysis, involves measuring the spectral content of whole songs. This technique can reveal spectral regions where the greatest energy is being produced, thereby providing not only an indication of prominent formant positions but also information about the spectral bands that singing humpback whales use most extensively. LTAS were created for songs and long segments (>10 min) of song sessions recorded in Hawaii between 1981 and 1995 by averaging the power density spectra (MATLAB's psd command, FTT=256) of adjacent, nonoverlapping, 625 ms frames across entire recordings. To further explore the origins of patterns observed in LTAS, the spectral content of units was calculated, and spectra from units were plotted in their order of occurrence to create spectral history plots for entire songs. This analysis normalized units in the time domain because spectra were calculated across the entire duration of each unit (i.e., differences in duration across units were converted into differences in spectral energy).

A problem arises in analyzing formants within humpback units that is seldom encountered when analyzing the vocalizations of terrestrial mammals, which is that mechanisms other than internal resonators can generate systematic patterns of spectral degradation and enhancement in song recordings. In the shallow-water environments frequented by singing humpback whales, sounds often reflect from the surface and bottom before reaching a recording sensor, leading to constructive and destructive interference patterns (Mercado and Frazer, 1999; Mercado *et al.* 2007; Thode, 2000). These interference patterns produce formants in recorded units with positions and properties that can be highly similar to those that would be generated by vocal tract filtering. Environmentally generated formants may change gradually over time depending on the source depth, receiver depth, and the distance between the source and receiver (see Fig. 3). Consequently, any pattern of formants observed in units potentially reflects filtering by both internal structures and the external environment.

To account for this confound, additional spectral measures of units beyond peaks and valleys were made. Specifically, nonlinearities within units called frequency jumps (Fitch *et al.*, 2002; Tyson *et al.*, 2007) were measured to further assess the role of air-filled chambers in humpback whale sound production. In human singers, nonlinear phenomena such as subharmonics and frequency jumps are sometimes observed when the pulse rate is similar to a vocal tract resonance frequency (Titze, 2008b). Titze (2008a) suggested that such instabilities reflect interactions between vocal fold vibrations and the resonance properties of the vocal tract. The standard source-filter model assumes that there are no interactions between the source and the filter (i.e., that they independently contribute to sound generation). However, if air-filled chambers in humpback whales do influence source vibrations, then one would expect that the likelihood of a frequency jump occurring within a unit would be related to the resonance properties of that chamber. In other words, as the pulse rate gets closer to a formant peak, the probability that a frequency jump occurs should increase. Because formant peaks are a function of the dimensions of the air space generating them, the probability of a frequency jump should be as well. Thus, the distribution of frequency jumps within songs can provide indirect evidence of formant positions. Patterns in the probability of frequency jumps should not be impacted by propagation effects, and thus can be combined with more traditional measures of formants to evaluate the extent to which directly measured formant patterns are distorted by environmental factors.

Measures of frequency jumps were collected by visually inspecting and manually measuring spectrograms of units (FFT size=1500) using RAVEN 1.3 to determine whether frequency jumps were more likely to occur near particular frequencies. Measures of frequency jumps were collected from 15 Hawaiian songs and 1 Puerto Rican song (the same one used in analyses of source characteristics). When frequency jumps were identified, the frequency of the lowest visible spectral band before and after the jump was measured (Fig. 4). For units containing multiple frequency jumps, only the three clearest jumps were measured. The number of times jumps occurred within particular frequency ranges was then determined.

E. Modeling humpback whale sound production

The original source-filter model developed to describe human speech production provides a useful tool for generating and testing specific predictions about physical constraints on humpback whale sound production and for describing recorded sounds in ways that are more closely tied to the processes that whales use to generate sounds. Nevertheless, this simple signal processing approach clearly does not capture all of the factors that determine the acoustic features generated by singing humpback whales. The standard source-filter model does not specify particular sound generating mechanisms, does not account for the possibility that source vibra-

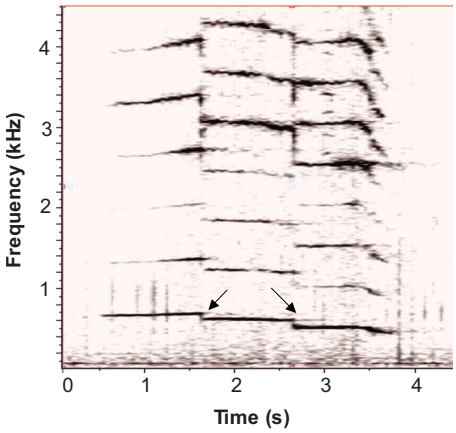

FIG. 4. (Color online) Frequency jumps within a unit appear as discrete vertical shifts in the positions of horizontal bands in spectrograms. Arrows indicate two frequency jumps. FFT size=1500 Hz.

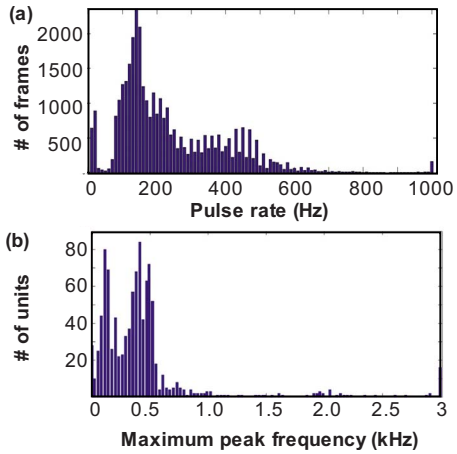

FIG. 5. (Color online) (a) Histogram showing the distribution of pulse rates measured in all unit frames analyzed (n=35 734); (b) Histogram showing the distribution of peak frequencies at the apex of the waveform envelope for all units (n=1019).

tions might be generated by both the inflow or outflow of air within a closed system, and assumes that the spectral features of produced sounds are largely determined by a single air-filled chamber (the vocal tract) that is weakly coupled to the source. The source-filter model also cannot account for nonlinear phenomena that are commonly produced by singing whales.

Simple geometric models of sound producing mechanisms (which are analogs of physical models) were developed to address some of these limitations. Specifically, patterns of spectral peaks and valleys in unit and LTAS analyses were modeled as the effects of filtering by an air-filled tube. Uniform, closed-end tubes have been used extensively to model the effects of the vocal tract on sound production by humans and other terrestrial mammals (Riede *et al.*, 2008). Such a tube resonates at frequencies that are odd multiples of a fundamental frequency, $F_o = c/4L$, where L is the length of the tube and c is the sound velocity. The closed-end tube model predicts that antiresonances should occur at even multiples of the fundamental resonating frequency of the tube. In the current study, this basic tube model was modified to account for internal air recirculation by humpback whales, as well as observed patterns in nonlinear frequency jumps.

III. RESULTS

A. Relationships between pulse rate, peak frequency, and duty cycle

Automated unit detection algorithms based on energy levels (see Green *et al.*, 2007) identified 1221 sounds within the 54 min recording of a single whale singing in Puerto Rican waters. Of these, 286 (23%) were subjectively classified as units containing discrete pulses, 733 (60%) were classified as units not containing discrete pulses, and 201 (16%) were not classified as units (e.g., boat noise, ambient noise, and unidentifiable low amplitude sounds). Unit pulse rate varied greatly, ranging from approximately 8 to 6000 Hz within and across units. Figure 5(a) shows the distribution of pulse rates across all 35 734 frames analyzed. The median pulse rates for units containing discrete pulses were 25 Hz (S.D.=17) on average and 230 Hz (S.D.=103) for units not containing discrete pulses. The acoustic characteristics of some units gradually shifted across repetitions. For example, Fig. 6 illustrates the gradual transformation of high pulse rate, short duration units (often described in the literature as chirps) into low pulse rate, and long duration units (ratchets) within a 2 min song segment.

The precise duration of units was difficult to measure because waveform envelopes typically showed gradual increases and decreases in amplitude at the beginning and end of the unit, respectively, and because ambient noise and water noises occasionally overlapped with the beginning or end of a unit. Automated measures of unit duration ranged from about 200 ms to 4.3 s. The median duration of all units was 1.2 s; the median duration for units containing discrete

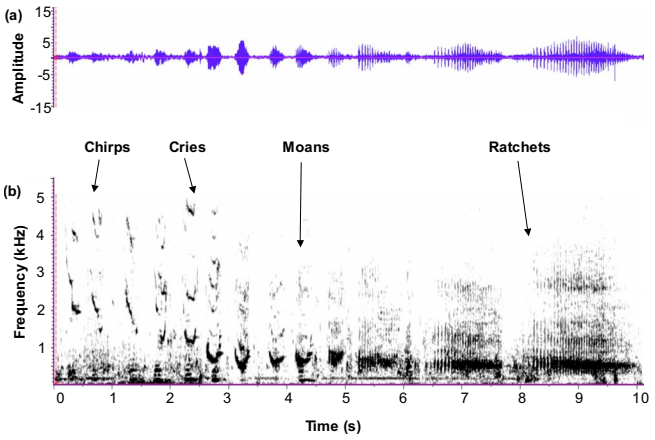

FIG. 6. (Color online) Example of units gradually shifting from being high pulse rate tonal sounds (chirps and cries) to medium rate units (moans), and finally to low pulse rate trains (ratchets). This spectrographic sequence was created by deleting units from a continuous, 2 min segment of song, leaving only a subset of units that were representative of transitions along the pulse rate continuum (i.e., the order of units within the sequence was preserved, but not all units and intervening silences are shown). In both the waveform (top) and spectrogram (bottom), the gradual emergence of discrete pulses is evident. This sequence also illustrates how pulse rate can change while peak frequencies remain stable.

pulses was 1.3 s, and for other units was 1.1s. The modal unit duration was 260 ms. Unit duration was not correlated with pulse rate ($r=-0.03$).

Peak frequencies ranged from a low of 0–29 Hz (the lowest bin in the spectral analysis) to a high of about 6000 Hz. For units containing discrete pulses, the average peak frequency was 320 Hz (S.D.=220 Hz), whereas for other units, it was 450 Hz (S.D.=480 Hz). The envelope of each unit corresponded to the energy of peak frequencies across consecutive samples. The distribution of peak frequencies at the apex of this envelope (the maximum peak frequency) across units is shown in Fig. 5(b). This apex occurred at 57% (S.D. 24%) of the duration of the unit on average (i.e., near the middle of the unit). Peak frequency at the apex was not correlated with duration ($r=-0.03$) or median pulse rate ($r=0.09$). Peak frequencies could be maintained across or within units despite changes in pulse rate (e.g., see Fig. 6).

Duty cycle measures ranged from a minimum of 0.04 to a maximum of 1.0. The average duty cycle across all frames was 0.52 (S.D.=0.15); the distribution was approximately Gaussian around this mean. For units containing discrete pulses, the average duty cycle was 0.22 (S.D.=0.07), whereas for other units it was 0.52 (S.D.=0.08). Average duty cycle was strongly correlated with median pulse rate ($r=0.69$, $p<0.001$), but not with peak frequency ($r=0.12$) or duration ($r=0.05$).

Collectively, results from source analyses were consistent with the hypothesis that the sound generator in humpback whales involves a pair of vibrating membranes (such as the U-folds) that are dynamically tensed to vary the rate at which they generate pulses. The relationship between pulse rate and waveform shape (quantified in terms of duty cycle) further suggests that techniques for characterizing glottal pulse shape within source-filter models may be appropriate for characterizing pulse features produced by singing humpback whales. Differences in pulse shape between humpback whales and other species may reflect differences in the physical properties of the vibrating membranes in humpbacks (e.g., the parallel orientation of the U-folds) or in how membrane position is controlled. More detailed measures of variability in pulse shape are needed to determine the range of pulses that humpback whales can generate and how pulse shape relates to other acoustic properties of units. Understanding the dynamics of pulse generation can potentially provide new insights into the functional properties of the U-folds.

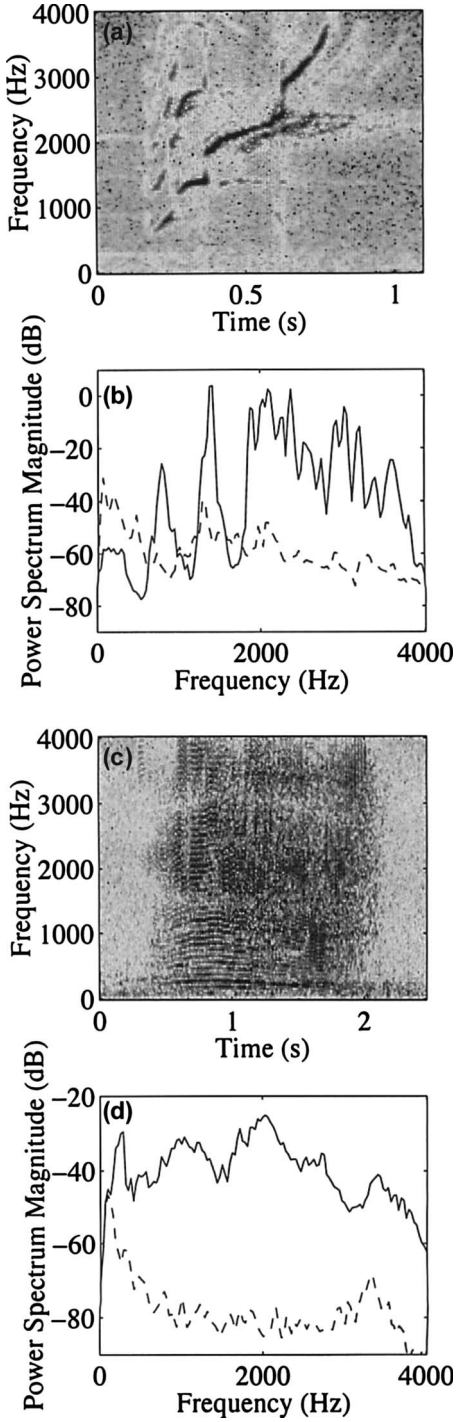

FIG. 7. Example broadband units revealing formants: (a) spectrogram of a frequency glide spanning four octaves; (b) peaks in the power spectral density plot for this unit show formants; (c) spectrogram of a relatively low pulse rate unit shows darker regions indicative of formants; (d) the power spectral density plot shows corresponding formant peaks. Dotted lines show the spectra of ambient noise. FFT size=256 Hz.

B. Spectral markers of resonating structures

Evidence of alternating enhanced and degraded spectral energy regions was found in each of the broadband units examined. Figure 7 shows example spectra for two units modulated across a broad frequency range: a frequency glide and a low pulse rate unit. The frequency glide shows narrow, harmonically related peaks and troughs for frequencies below 2 kHz, with broader peaks centered near 2.5 and 3.25 kHz. The low pulse rate unit shows one narrow peak near 300 Hz, and three or four broad, evenly spaced peaks at higher frequencies. Figure 8 shows the spectra of a very low pulse rate unit and of an aperiodic unvoiced unit.[1] Both reveal narrow low frequency peaks and broader higher frequency peaks. The number of formants extracted from song units ranged from 3–8. Eight frequency regions where formants were consistently detected across units were identified: 100–500, 600–900, 1000–1500, 1600–1900, 2000–2400, 2500–2900, 3000–3400, and 3500–3800 Hz. These

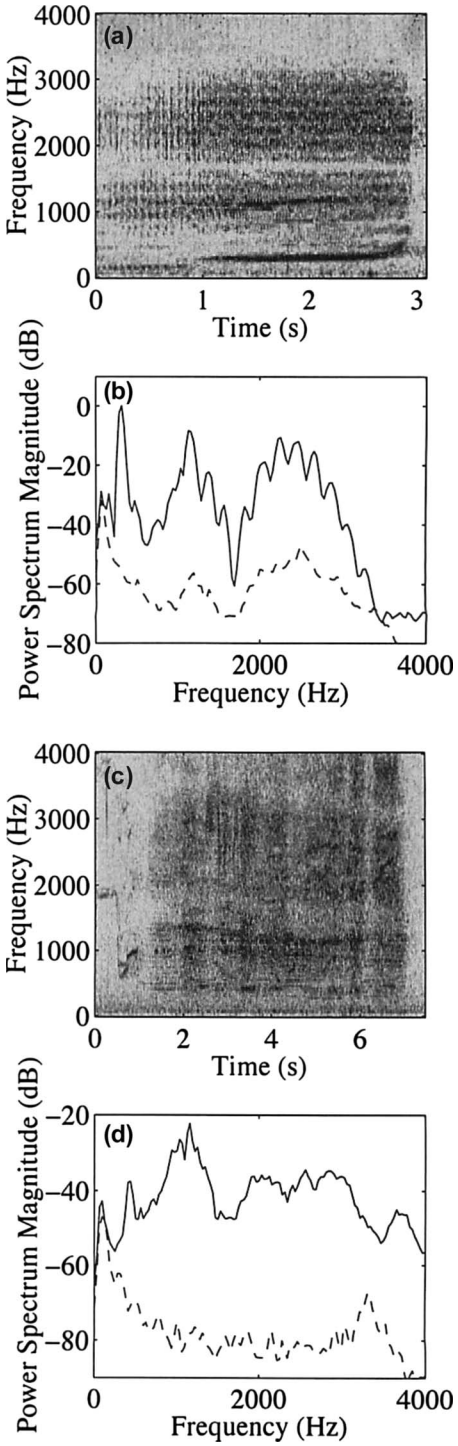

FIG. 8. Example broadband units revealing formants: spectrogram (a) and power spectral density plot (b) of a low pulse rate unit show formants that are narrow at lower frequencies and broader at higher frequencies—note also the regularly spaced peaks within the broad formants above 1 kHz; (c) spectrogram of a noisy, aperiodic unit shows stable darker bands which appear as broad peaks in the power spectral density plot of this unit (d). Dotted lines show the spectra of ambient noise. FFT size=256 Hz.

regions were bounded by narrower spectral regions in which formant peaks seldom occurred (e.g., 500–600 and 900–1000 Hz).

Results from LTAS analyses of Hawaiian songs and spectra of units showed consistent trends in peaks and valleys with peaks occurring between 150–450, 600–900, 1100–1600, 1700–2200, 2300–2700, and 2800–3100 Hz, and valleys occurring between 500–600, 1000–1100, 1600–1700, and 2100–2200 Hz (Fig. 9). These regions are similar to those identified above from spectral analyses of units.

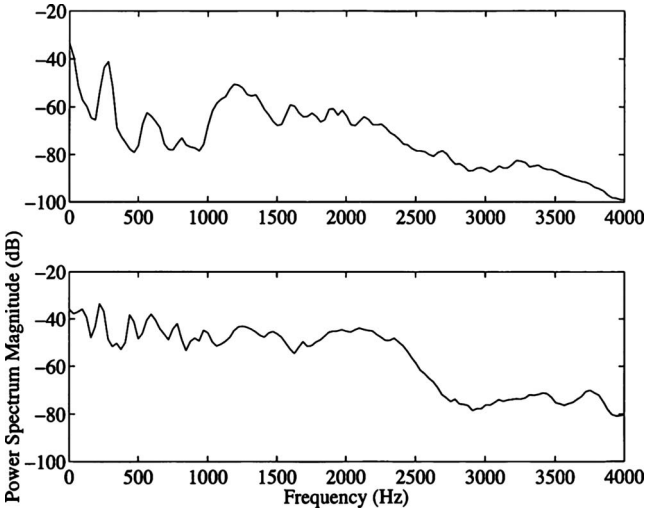

FIG. 9. LTASs for a 41 min segment of song session produced by a single whale, recorded off the coast of Hawaii on 2/16/95 (top), and for a 27 min segment of a song session recorded on 2/19/95 (bottom), show narrow formants at frequencies below 1000 Hz and broader formants above this frequency.

Spectral history plots of songs revealed that the patterns in LTAS reflected the cumulative spectral content of songs rather than formant patterns that were consistently present across units. For example, in Fig. 10 it is clear that narrow spectral peaks below 500 Hz are occurring in different sec-

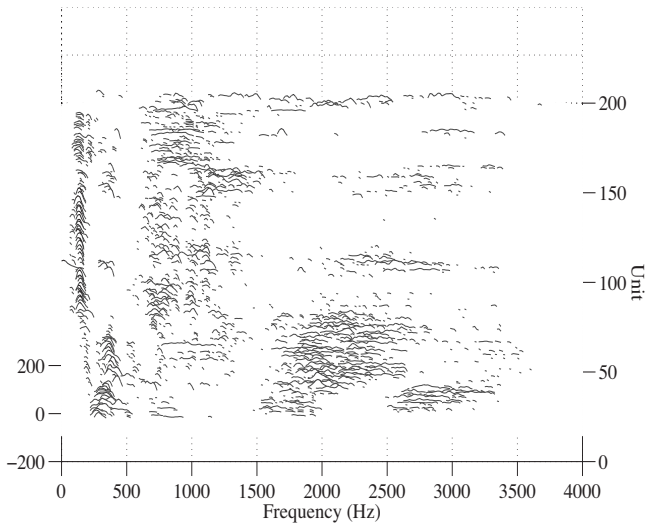

FIG. 10. Three-dimensional spectral history plot for a single humpback whale song recorded off the coast of Hawaii in 1981. Each horizontal trace shows the peaks of the power spectral density plot for a single unit (as in Figs. 7 and 8). The order of traces from the bottom of the plot to the top corresponds to the order of the units (approximately 200) within the song. Viewed as a topographical contour map, the closer peaks (at the bottom of the plot) are from sounds early in the song and the farther peaks (near the top of the plot) are from sounds later in the song. This plot reveals narrow, low frequency peaks and broader, higher frequency peaks that vary progressively throughout the song, but that are relatively stable for long portions of the song. Changes in narrow, low frequency formants are paralleled by changes in broader, higher frequency formants. FFT size=256.

tions of the song, and that broader peaks at higher frequencies are also prevalent at different times during the song. Spectral history plots also revealed that the spectral content of units showed continuity throughout the song. For example, the most prominent lower frequency peak (~200 Hz) evident in Fig. 10 shows a gradual increase in energy that coincides with a decrease in energy at a slightly higher frequency peak (~350 Hz). This lower frequency peak is associated with a broader region of enhanced frequencies (near 1000 Hz) that is evident throughout the song, despite changes in themes. These results are surprising because they suggest that resonant frequencies, if present, are not fixed, and that when singers "switch" to a new theme, the spectral features of units within the new theme are systematically related to those of the preceding theme.

Overall, spectral patterns within frames sampled from units, across whole units, and across songs were consistent with air-filled chambers impacting the features of at least some units. The systematic spectral peaks and valleys observed provide clear evidence that many units have formants. This property of units has not been noted in past studies of humpback whale songs, possibly because most efforts to classify units have focused on features that were clearly audible and easy to trace on spectrograms (e.g., pitch contours). Neither technique is conducive to the identification of formants. Another possibility is that researchers could not consistently distinguish formants produced by humpback whales from those generated by propagation (see also Gaunt, 1983; Watkins, 1967). Propagation-related formant patterns should vary as a function of distance, so that analyses of units recorded at varying distances would tend to reduce such effects, especially in LTAS analyses. Nevertheless, if both the singer and the boat from which recordings were collected were drifting in similar directions, then propagation-generated formants could contribute significantly to formant patterns. Furthermore, environmental formants can themselves be periodic as a function of range (Mercado and Frazer, 1999), so that even if the distance between the singer and hydrophone continuously varied, these formants could potentially overshadow those generated by the whale. In the current analyses of frames, units, and songs, observed spectral peaks varied in bandwidth, with lower frequency peaks being narrower than higher frequency peaks. It is not immediately clear how propagation-induced interference might generate such formant patterns. This trend in bandwidth variability is often observed in vocal tract resonances, however, where it is typically explained as resulting from the clustering of higher frequency formants.

As noted earlier, the closed-end tube model of mammalian sound production predicts that antiresonances should occur at even multiples of the fundamental resonating frequency of the tube. A common multiple within the range of observed spectral valleys in humpback whale units is 500 Hz, corresponding to a tube with a fundamental resonating frequency of approximately 250 Hz (assuming the size of the tract varies between whales, this value would likely vary across individuals). Based on this resonant frequency, the model predicts that a 34 cm long air-filled tube (twice the length of a human vocal tract) or similarly shaped chamber contributes to humpback whale sound production. Although the tube model is attractive because it is simple and adequately characterizes sound production by many terrestrial mammals, its application to humpback whale sound production is problematic. First, low pulse rate units should show the clearest evidence of formants, yet some of these units do not exhibit them (personal observation, E. Mercado). Second, unlike spoken and sung vowels, the number of formants present in a unit can vary considerably, and not many units show all the formants one might expect to be produced by a resonating tube (e.g., see Figs. 3 and 10). Finally, the distribution of dominant peak frequencies in the one recording from Puerto Rico analyzed here does not show a single peak near 250 Hz, but instead shows two peaks at frequencies surrounding this frequency [Fig. 5(b)]. These factors suggest that the closed-end tube approximation of the vocal tract is insufficient to characterize the spectral variability in units produced by humpback whales, and that if internal air spaces are involved in humpback whale sound production, their role differs somewhat from that seen in most terrestrial mammals.

TABLE I. Frequencies at which frequency jumps were most likely to occur (shown as peaks in the distribution in Fig. 11) and spacing between peaks (all values in Hz). Estimated formant positions were derived by identifying a distribution that was comparable to the measured distribution, and in which the spacing between formants was uniform and equal to the fundamental frequency (i.e., the frequency of the first peak). For formants above 1200 Hz, where regularity was less clear, the estimated formant position is the midpoint between the frequency jumped from and the frequency jumped to, as shown in Fig. 11.

Frequency jumped from	Difference from prior peak	Estimated formant position
163	⋯	127
263	100	254
363	100	381
488	125	508
613	125	635
738	125	762
888	150	889
1013	125	1016
1188	175	1143
1963	775	2000
2663	700	2800

C. Possible nonlinear source-filter coupling

A total of 5496 units from 16 recordings were visually examined for evidence of frequency jumps. From these, 827 units (15%) with one or more frequency jumps were identified. The proportion of units within a recording that contained frequency jumps varied considerably across recordings, ranging from 6% to 48%. Overall, the frequencies before and after 997 frequency jumps were measured. These measurements revealed harmonically related frequency regions in which the probability of a frequency jump peaked (Table I). These regions overlapped with those identified in formant analyses, but differed in several respects. In particular, there were a larger number of narrow peaks in the distribution of frequency jumps than was evident in formant analyses (Fig. 11). The spacing between these narrow peaks

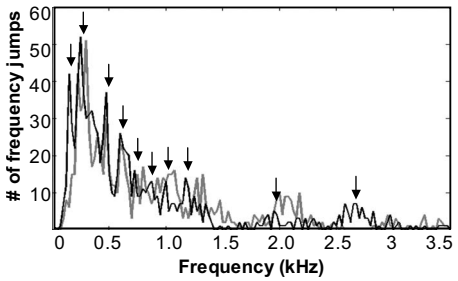

FIG. 11. Histogram showing the distribution of frequencies just before (black line) and after (gray line) a frequency jump occurred within a unit. Arrows show frequencies where jumps were most likely to occur.

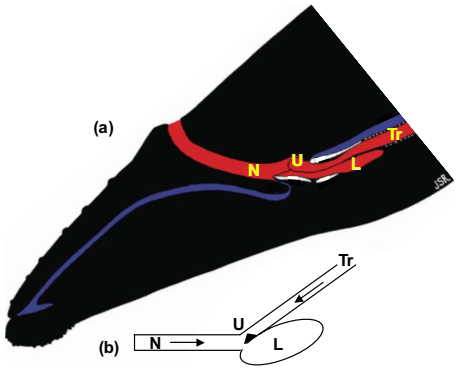

FIG. 12. (Color online) (a) Respiratory tract of a humpback whale showing major components hypothesized to be sound production mechanisms (adapted from Reidenberg and Laitman, 2007); N=nasopharynx, L=laryngeal sac, Tr=trachea; U=U-folds. (b) Egressive units may be produced when air from the lungs induces vibrations in the U-folds, generating airborne vibrations that resonate in the nasopharynx and laryngeal sac. Ingressive units may also be produced when air moves back into the lungs.

was regular across at least six consecutive peaks, making it highly unlikely that the pattern occurred by chance. Spacing between peaks above 1200 Hz was less clear, but also appeared to be nonrandom.

These results further suggest that filtering and resonance of source vibrations in humpback whales differs from what is typically observed in terrestrial mammals. Frequency jumps within sounds do not directly indicate filtration by air-filled resonators. However, recent work with human singers shows that vocal tract resonances can impact the likelihood that such nonlinear phenomena will occur (Titze, 2008b). In the current analysis, the likelihood of a frequency jump within a unit was tightly linked to the frequency content of the unit. The regular spacing of jump-prone regions suggests that modes of source vibration in humpback whales may be more tightly coupled to resonance features of internal structures than is the case in humans. Such coupling is more typical of musical instruments (e.g., brass and woodwinds). If regions where frequency jump probability is high are interpreted as likely formant regions, then the pattern of peak probabilities suggests that the fundamental frequency of the resonator is about 125 Hz rather than 250 Hz (the value indicated above by more traditional formant analyses). Furthermore, the observed pattern of peaks is more consistent with a 1.4 m tube with both ends closed, than it is with a 34 cm closed-end tube. Higher frequency (1200–3500 Hz) jump probabilities showed a different pattern that was more consistent with the closed-end tube model. In fact, the formant frequencies physically measured by Riede *et al.* (2008) from a 20 cm closed-end tube were 380, 1170, 1990, and 2560 Hz. These peaks are startlingly similar to estimated formant positions identified by analyses of unit frequency jumps (381, 1143, 2000, and 2800 Hz; see Table I).

A possible explanation for the discrepancy in formant patterns suggested by the different spectral analyses is that not all units are filtered by the same air-filled cavities. Figure 12 depicts one scenario in which production of different units might engage different resonators. This model of sound production assumes that humpback whales shuttle air bidirectionally while singing, and that they can produce units using air moving in either direction. The model predicts two broad classes of units that have similar source characteristics, but divergent formant features and nonlinear characteristics. Reidenberg and Laitman (2007) described sounds produced by air flowing from the lungs as "egressive vocalizations," and sounds produced by air flowing into the lungs as "ingressive vocalizations." In the proposed model, the lungs serve as the pneumatic force for egressive units, the U-folds as the vibratory source, and two chambers act as resonating filters: the laryngeal sac (a closed-end tube) and the nasopharynx (a tube closed at both ends). Air forced from the lungs gradually fills the nasopharynx, creating a resonant air space. Once this space is filled, air begins to inflate the laryngeal sac. This mode of production would account for the gradually increasing and decreasing envelope of units, the evidence suggesting that frequency jumps result from acoustic coupling between the vibrating source and a long air-filled tube, and the evidence of a much shorter closed-end tube generating broad higher frequency formants. During ingressive production, air escapes from the nasopharynx (possibly aided by buoyant forces), and to a lesser extent from the laryngeal sac, back into the lungs. The U-folds would again serve as the vibratory source, but the nasopharnyx would no longer resonate because of the air flowing from it. The laryngeal sac might (or might not) continue to resonate during ingressive production. Experiments with doves show that the resonance properties of air sacs in their throats are minimally affected by changes in the volume of the sacs (Riede *et al.*, 2004). Instead, the tissue lining the walls of the dove's sac appears to determine how it resonates (see also Riede *et al.*, 2008). This geometric model of humpback whale sound production can be instantiated within the source-filter framework by modeling filtration during egressive production as resulting from a uniform, "closed mouth" tube with an inflatable air sac attached as a side branch (Riede *et al.*, 2008) and filtration during ingressive production as resulting from the sac alone. However, more advanced nonlinear models such as those developed to describe sound production by birds (Amador and Mindlin, 2008; Fee *et al.*, 1998) may ultimately prove to be more suitable for modeling sound production by humpback whales.

IV. DISCUSSION AND CONCLUSIONS

The analyses of humpback whale songs and units described in this paper have revealed several phenomena rel-

evant to understanding how humpback whales produce sounds. First, many units could be characterized as graded, lying along a continuum with trains of discrete pulses at one end and continuous tonal signals at the other. This finding suggests that traditionally discrete categories of song units such as cries, moans, and ratchets may correspond to points along a continuum from high pulse rates to lower pulse rates (e.g., see Fig. 6), and that humpback whales may gradually modulate specific features of the sounds they produce while singing (e.g., pulse rate) rather than switching between discrete sound types selected from a fixed repertoire. Second, the observed correlation between unit pulse rate and duty cycle suggests that pulse shape may be a function of pulse rate, as is seen in human singers. This suggests that variability in the frequency content of units could reflect variations in the properties of the vibrating membranes that whales use to generate sounds. Third, units contained formants. These formants differed from the ones present in human vocalizations, however, and thus could not resolve the question of whether resonating air-filled chambers contribute to humpback sound production. In contrast, systematic patterns of nonlinear frequency jumps suggested acoustic coupling between a vibrating source and one or more resonant cavities within the respiratory tract, providing more convincing evidence that such cavities do play a role in sound generation.

Past analyses of cetacean vocalizations have often emphasized the differences between sounds produced by the larger baleen whales and those produced by delphinids. The current study suggests, however, that the acoustic structure of humpback whale sounds is similar in many respects to that seen in sounds produced by false killer whales (Murray *et al.*, 1998). Both species show the capacity to continuously modulate their sounds from low rate pulse trains to higher rate tonal sounds. These acoustic similarities indicate that similar analysis techniques should be adequate for characterizing the basic source characteristics of both species (see also Killebrew *et al.*, 2001). The sounds produced by the two species' seem to differ mainly in terms of the shapes and frequency content of individual pulses, and in that false killer whales can simultaneously produce two independent pulse rates (see also Brown, 2008). These differences likely reflect variations in the size and configuration of the membranes that are vibrating (phonic lips in false killer whales versus vocal folds in humpbacks) and the presence of two sets of membranes in false killer whales versus one in humpback whales. Pulse shape appears to be more variable in humpbacks than in false killer whales, suggesting that source membrane vibrations in humpback whales are more complex.

Most units were readily modeled as quasiperiodic pulse trains (see also Mercado and Kuh, 1998), acoustically analogous to the voiced sounds within human speech and song. The range of pulse rates produced by humpback whales was larger than that produced by humans, however. In fact, the range of unit pulse rates within the single recording analyzed covered the full range of registers producible by humans and extended it. Pulse rates were distributed relatively evenly throughout the range of measured rates, consistent with continuous gradations in pulse rate across units. The lowest pulse rate units identified in this analysis appear to correspond to surface ratchets (Winn *et al.*, 1970). These sounds are analogous to vocal fry in human singers, except that humpbacks use this mode of sound production much more extensively. Interestingly, nonhuman primates also appear to use the vocal fry register more extensively than humans do (Riede and Zuberbuhler, 2003). The overall distribution of unit pulse rates suggests a modal rate between 100 and 200 Hz, which falls within the modal register of human singers. Subjectively, higher pulse rate units have features similar to those of sounds produced by humans singing in the falsetto and whistle registers. These parallels suggest that constraints on vocal fold vibration in singing humans related to pitch range may also apply to the vibrations generated by singing humpback whales.

The graded structure of units within humpback whale songs has important implications for methods designed to sort units into discrete categories or to identify repeating patterns in songs. Consider, for example, the sequence of units shown in Fig. 6. Classification of these units by subjective aural or visual inspection, or by automated sorting of spectrograms, would invariably lead one to conclude that several unit "types" are present (e.g., chirps, cries, and ratchets). The analyses presented here suggest, however, that this sequence corresponds to a gradual decrease in the tension of the singing whale's vibrating membranes over time, analogous to a human singer gradually decreasing the pitch of her notes. In this production-based context, segregating these units into several types is as arbitrary as dividing a chromatic scale into several distinct categories of pitches.[2] It is possible that humpbacks perceive units as falling into discrete categories despite their graded structure, as humans do for vowels. If so, there is currently no way to determine how a whale's categories might map onto the categories that are salient for humans. Consequently, characterizing humpback whale songs in terms of the acoustic properties of their constituent units provides a more objective approach than analyses based on the visual and aural percepts that those sounds induce in human observers, or on similarities between arbitrarily chosen time-frequency representations of units.

Understanding the ways in which humpback whales produce sounds is also relevant to future investigations of humpback whale behavior and physiology. For example, measurements of vibrations at various positions on the head of a humpback whale (see Stimpert *et al.*, 2007) might provide higher quality signals with which to assess variations in pulse shape, which could provide additional information about vocal fold dynamics. Techniques for measuring air movements within the body of a singing whale (e.g., using high frequency active sonar) can potentially be used to examine air recirculation during sound production, which would clarify how physical constraints shape the structure of phrases within songs as well as the contributions of air-filled resonators to sound generation. Knowing how singing whales produce sounds could also provide new insights into the features of their sounds that are most likely to provide information about individual singers, such as their size, age, or identity. For example, more experienced singers might

exhibit more stable control of pulse dynamics, as evidenced by a reduction (or increase) in frequency jumps within their songs.

Finally, understanding how humpback whales sing may clarify why they sing and how their songs function. In the past, extensive variability in individual sounds has been cited as evidence that units are functionally impotent, and that sound patterns (i.e., whole songs, themes, or phrases) are instead more likely to be the functional units (Tyack, 1981). If singing humpback whales are precisely modulating the acoustic features of individual sounds, however, then this would suggest the opposite conclusion, namely, that individual sounds are the core functional units of songs (see, e.g., Frazer and Mercado, 2000). Although the current analyses do not show the extent to which humpback whales control the features of units, they do provide a more coherent model of how singing whales vary the sounds within their songs, which is an important first step toward identifying which of those variations they control.

ACKNOWLEDGMENTS

This work was supported in part by NSF Grant No. 0718004 and a fellowship from the Center for Advanced Studies in the Behavioral Sciences to E.M., as well as by a grant to L.H. from the Earthwatch Foundation. We thank A. Frankel for his efforts in collecting many of the Hawaiian recordings used in these analyses, as well as the numerous graduate students and volunteers of the Kewalo Basin Marine Mammal Laboratory who assisted with this work. We also thank J. Olsen for his technical assistance with recording equipment, and A. Hollins and P. Banks for their assistance in collecting recordings.

[1]More detailed analyses of "noisy," unvoiced components of units are warranted, given that these elements may result from nonlinear (e.g., chaotic) source vibrations (Tyson *et al.*, 2007).

[2]It could be argued that differences in time-varying frequency contours justify the categorization of units. For instance, the first units in Fig. 6 are downsweeps, later units are inverted chevrons, the last units are constant frequency, etc. If unit contours were stereotyped and stable over time, then this argument would have force. They are not. The contours of units are known to gradually change over time within songs, across songs, and across years (Payne and Payne, 1985). Even in Fig. 6, it is clear that when a single whale repeats a unit within a short period, frequency contours can change substantially.

Altes, R. A., Evans, W. E., and Johnson, C. S. (**1975**). "Cetacean echolocation signals and a new model for the human glottal pulse," J. Acoust. Soc. Am. **57**, 1221–1224.

Amador, A., and Mindlin, G. B. (**2008**). "Beyond harmonic sounds in a simple model for birdsong production," Chaos **18**, 043123.

Au, W. W. L. (**1993**). *The Sonar of Dolphins* (Springer-Verlag, New York).

Au, W. W. L., Pack, A. A., Lammers, M. O., Herman, L. M., Deakos, M. H., and Andrews, K. (**2006**). "Acoustic properties of humpback whale songs," J. Acoust. Soc. Am. **120**, 1103–1110.

Beckers, G. J. L., Nelson, B. S., and Suthers, R. A. (**2004**). "Vocal-tract filtering by lingual articulation in a parrot," Curr. Biol. **14**, 1592–1597.

Boersma, P., and Kovacic, G. (**2006**). "Spectral characteristics of three styles of Croatian folk singing," J. Acoust. Soc. Am. **119**, 1805–1816.

Brown, J. C. (**2008**). "Mathematics of pulsed vocalizations with application to killer whale biphonation," J. Acoust. Soc. Am. **123**, 2875–2883.

Charlton, B. D., Reby, D., and McComb, K. (**2007**). "Female perception of size-related formant shifts in red deer, *Cervus elaphus*," Anim. Behav. **74**, 707–714.

Cleveland, T. F. (**1994**). "A clearer view of singing voice production: 25 years of progress," J. Voice **8**, 18–23.

Cranford, T. W., and Amundin, M. (**2004**). "Biosonar pulse production in odontocetes," in *Echolocation in Bats and Dolphins*, edited by J. A. Thomas, C. F. Moss, and M. Vater, (University of Chicago Press, Chicago), pp. 27–35.

Cranford, T. W., Amundin, M., and Norris, K. S. (**1996**). "Functional morphology and homology in the odontocete nasal complex: Implications for sound generation," J. Morphol. **228**, 223–285.

Doscher, B. (**1994**). *The Functional Unity of the Singing Voice* (Scarecrow, Metuchen, NJ).

Fant, G. (**1960**). *Acoustic Theory of Speech Production: With Calculations Based on X-ray Studies of Russian Articulations* (Mounton and Co., Netherlands).

Fee, M. S., Shraiman, B., Pesaran, B., and Mitra, P. P. (**1998**). "The role of nonlinear dynamics of the syrinx in the vocalizations of a songbird," Nature (London) **395**, 67–71.

Fitch, W. T. (**1997**). "Vocal tract length and formant frequency dispersion correlate with body size in rhesus macaques," J. Acoust. Soc. Am. **102**, 1213–1222.

Fitch, W. T., and Fritz, J. B. (**2006**). "Rhesus macaques spontaneously perceive formants in conspecific vocalizations," J. Acoust. Soc. Am. **120**, 2132–2141.

Fitch, W. T., and Hauser, M. D. (**1995**). "Vocal production in nonhuman primates: Acoustics, physiology, and functional constraints on 'honest' advertisement," Am. J. Primatol **37**, 191–219.

Fitch, W. T., Neubauer, J., and Herzel, H. (**2002**). "Calls out of chaos: The adaptive significance of nonlinear phenomena in mammalian vocal production," Anim. Behav. **63**, 407–418.

Frazer, L. N., and Mercado, E., III (**2000**). "A sonar model for humpback whale song," IEEE J. Ocean. Eng. **25**, 160–182.

Gaunt, A. S. (**1983**). "On sonograms, harmonics, and assumptions," Condor **85**, 259–261.

Green, S. R., Mercado, E., III, Pack, A. A., and Herman, L. M. (**2007**). "Characterizing patterns within humpback whale (*Megaptera novaeangliae*) songs," Aquat. Mamm. **33**, 202–213.

Gregg, J. W. (**1992**). "From singing to speech: On glottal configuration," J. Sing. **53**, 47–50.

Helweg, D. A., Cato, D. H., Jenkins, P. F., Garrigue, C., and McCauley, D. (**1998**). "Geographic variation in South Pacific humpback whale songs," Behaviour **135**, 1–27.

Ishi, C. T., Sakakibara, K.-I., Ishiguro, H., and Hagita, N. (**2008**). "A method for automatic detection of vocal fry," IEEE Trans. Audio, Speech, Lang. Process. **16**, 47–56.

Keleman, G. (**1963**). "Comparative anatomy and performance of the vocal organ in vertebrates," in *Acoustic Behavior of Animals*, edited by R.-G. Busnel, (Elsevier, Amsterdam), pp. 489–521.

Killebrew, D. A., Mercado, E., III, Herman, L. M., and Pack, A. A. (**2001**). "Sound production of a neonate bottlenose dolphin," Aquat. Mamm. **27**, 34–44.

Mercado, E., III, and Frazer, L. N. (**1999**). "Environmental constraints on sound transmission by humpback whales," J. Acoust. Soc. Am. **106**, 3004–3016.

Mercado, E., III, Herman, L. M., and Pack, A. A. (**2005**). "Song copying by humpback whales: Themes and variations," Anim. Cogn. **8**, 93–102.

Mercado, E., III and Kuh, A. (**1998**). "Classification of humpback whale vocalizations using a self-organizing neural network," in Proceedings of the IJCNN '98, pp. 1584–1589.

Mercado, E., III, Schneider, J. N., Green, S. R., Wang, C., Rubin, R. D., and Banks, P. N. (**2007**). "Acoustic cues available for ranging by humpback whales," J. Acoust. Soc. Am. **121**, 2499–2502.

Miller, R. (**1986**). *The Structure of Singing: System and Art in Vocal Technique* (Collier Macmillan, London).

Murray, S. O., Mercado, E., and Roitblat, H. L. (**1998**). "Characterizing the graded structure of false killer whale (*Pseudorca crassidens*) vocalizations," J. Acoust. Soc. Am. **104**, 1679–1688.

Owren, M. J., Seyfarth, R. M., and Cheney, D. L. (**1997**). "The acoustic features of vowel-like *grunt* calls in chacma baboons (*Papio cyncephalus ursinus*): Implications for production processes and functions," J. Acoust. Soc. Am. **101**, 2951–2963.

Payne, K., and Payne, R. S. (**1985**). "Large scale change over 19 years in songs of humpback whales in Bermuda," Zeit. Tierpsychol **68**, 89–114.

Payne, R. S., and McVay, S. (**1971**). "Songs of humpback whales," Science **173**, 585–597.

Purves, P. E., and Pilleri, G. E. (**1983**). *Echolocation of Whales and Dolphins* (Academic, New York).
Quayle, C. J. (**1991**). "A dissection of the larynx of a humpback whale calf with a review of its functional morphology," Mem. Queensl. Mus. **30**, 351–354.
Reby, D., and McComb, K. (**2003**). "Anatomical constraints generate honesty: Acoustic cues to age and weight in the roars of red deer stags," Anim. Behav. **65**, 519–530.
Reby, D., McComb, K., Cargnelutti, B., Darwin, C., Fitch, W. T., and Clutton-Brock, T. (**2005**). "Red deer stags use formants as assessment cues during intrasexual agonistic interactions," Proc. Biol. Sci. **272**, 941–947.
Reeb, D., and Best, P. B. (**1999**). "The laryngeal apparatus of the pygmy right whale, *Caparera marginata* (Gray 1846)," J. Morphol. **242**, 67–81.
Reidenberg, J. S., and Laitman, J. T. (**2007**). "Discovery of the low frequency sound source in Mysticeti (baleen whales): Anatomical establishment of a vocal fold homolog," Anat. Rec. **290**, 745–759.
Rendall, D. (**2003**). "Acoustic correlates of caller identity and affect intensity in the vowel-like grunt vocalizations of baboons," J. Acoust. Soc. Am. **113**, 3390–3402.
Rendall, D., Owren, M. J., and Rodman, P. S. (**1998**). "The role of vocal tract filtering in identity cueing in rhesus monkey (*Macaca mulatta*) vocalizations," J. Acoust. Soc. Am. **103**, 602–614.
Ridgway, S. H., Carder, D. A., Kamolnick, T., Smith, R. R., Schlundt, C. E., and Elsberry, W. R. (**2001**). "Hearing and whistling in the deep sea: Depth influences whistle spectra but does not attenuate hearing by white whales (*Delphinapterus leucas*) (Odontoceti, Cetacea)," J. Exp. Biol. **204**, 3829–3841.
Riede, T., Beckers, G. J. L., Blevins, W., and Suthers, R. A. (**2004**). "Inflation of the esophagus and vocal tract filtering in ring doves," J. Exp. Biol. **207**, 4025–4036.
Riede, T., and Fitch, W. T. (**1999**). "Vocal tract length and acoustics of vocalization in the domestic dog (*Canis familiaris*)," J. Exp. Biol. **202**, 2859–2867.
Riede, T., Tokuda, I. T., Munger, J. B., and Thomson, S. L. (**2004**). "Mammalian laryngeal air sacs add variability to the vocal tract impedance: Physical and computational modeling," J. Acoust. Soc. Am. **124**, 634–647.
Riede, T., and Zuberbuhler, K. (**2003**). "Pulse register phonation in Diana monkey alarm calls," J. Acoust. Soc. Am. **113**, 2919–2926.
Rossing, T. D., Sundberg, J., and Ternstrom, S. (**1987**). "Acoustic comparison of soprano solo and choir singing," J. Acoust. Soc. Am. **82**, 830–836.
Sanvito, S., Galimbert, F., and Miller, E. H. (**2007**). "Vocal signaling of male southern elephant seals is honest but imprecise," Anim. Behav. **73**, 287–299.
Schevill, W. E. (**1964**). "Underwater sounds of cetaceans," in *Marine Bioacoustics*, edited by W. N. Tavolga, (Pergamon, New York), pp. 307–316.
Schutte, H. K., Miller, D. G., and Svec, J. G. (**1995**). "Measurement of formant frequencies and bandwidths in singing," J. Voice **9**, 290–296.
Soltis, J., Leong, K., and Savage, A. (**2005**). "African elephant vocal communication II: Rumble variation reflects the individual identity and emotional state of callers," Anim. Behav. **70**, 589–599.
Sommers, M. S., Moody, D. B., Prosen, C. A., and Stebbins, W. C. (**1992**). "Formant frequency discrimination by Japanese macaques (*Macaca fuscata*)," J. Acoust. Soc. Am. **91**, 3499–3510.
Stimpert, A. K., Wiley, D. N., Au, W. W. L., Johnson, M. P., and Arsenault, R. (**2007**). "'Megapclicks': Acoustic click trains and buzzes produced during night-time foraging of humpback whales (*Megaptera novaeangliae*)," Biol. Lett. **3**, 467–470.
Sukhovskay, L. I., and Yablokov, A. V. (**1979**). "Morpho-functional characteristics of the larynx in *Balaenopteridae*," in *Investigations on Cetacea*, edited by G. Pilleri (Brain Anatomy, Berne), pp. 205–214.
Sun, X., and Xu, Y. (**2002**). "Perceived pitch of synthesized voice with alternate cycles," J. Voice **16**, 443–459.
Sundberg, J. (**1977**). "The acoustics of the singing voice," Sci. Am. **236**(3), 82–91.
Taylor, A. M., and Reby, D. (**2009**). "The contribution of source-filter theory to mammal vocal communication research," J. Zool. **280**, 221–236.
Taylor, A. M., Reby, D., and McComb, K. (**2008**). "Human listeners attend to size information in domestic dog growls," J. Acoust. Soc. Am. **123**, 2903–2909.
Thode, A. (**2000**). "Source ranging with minimal environmental information using a virtual receiver and waveguide invariant theory," J. Acoust. Soc. Am. **108**, 1582–1594.
Titze, I. R. (**1994**). *Principles of Voice Production* (Prentice-Hall, Englewood Cliffs, NJ).
Titze, I. R. (**2008a**). "Nonlinear source-filter coupling in phonation: Theory," J. Acoust. Soc. Am. **123**, 2733–2749.
Titze, I. R. (**2008b**). "Nonlinear source-filter coupling in phonation: Vocal exercises," J. Acoust. Soc. Am. **123**, 1902–1915.
Tyack, P. (**1981**). "Interactions between singing humpback whales and conspecifics nearby," Behav. Ecol. Sociobiol. **8**, 105–116.
Tyson, R. B., Nowacek, D. P., and Miller, P. J. O. (**2007**). "Nonlinear phenomena in the vocalizations of North Atlantic right whales (*Eubalaena glacialis*) and killer whales (*Orcinus orca*)," J. Acoust. Soc. Am. **122**, 1365–1373.
Vannoni, E., and McElligott, A. G. (**2007**). "Individual acoustic variation in fallow deer (*Dama dama*) common and harsh groans: A source-filter theory perspective," Ethology **113**, 223–234.
Watkins, W. A. (**1967**). "The harmonic interval: Fact or artifact in spectral analysis of pulse trains," in *Marine Bioacoustics 2*, edited by W. N. Tavolga, (Pergamon, New York), pp. 15–43.
Winn, H. E., Perkins, P. J., and Poulter, T. C. (**1970**). "Sounds of the humpback whale," in Proceedings of the 7th Annual Conference on Biological Sonar and Diving Mammals, pp. 39–52.
Winn, H. E., and Winn, L. K. (**1978**). "The song of the humpback whale *Megaptera novaeangliae* in the West Indies," Mar. Biol. (Berlin) **47**, 97–114.

Psychophysical and electrophysiological aerial audiograms of a Steller sea lion (*Eumetopias jubatus*)[a)]

Jason Mulsow[b)]
Department of Ocean Sciences, Long Marine Laboratory, University of California, Santa Cruz, 100 Shaffer Road, Santa Cruz, California 95060

Colleen Reichmuth
Institute of Marine Sciences, Long Marine Laboratory, University of California, Santa Cruz, 100 Shaffer Road, Santa Cruz, California 95060

(Received 23 August 2009; revised 21 January 2010; accepted 25 January 2010)

A within-subject comparison of auditory steady-state response (ASSR) and psychophysical measurements of aerial hearing sensitivity was conducted with an individual of the largest otariid species, the Steller sea lion. Psychophysical methods were used to obtain an unmasked aerial audiogram at 13 frequencies, spanning a range of 0.125–34 kHz. The subject had a hearing range (frequencies audible at 60 dB_{rms} re 20 μPa) of about 0.250–30 kHz, and a region of best hearing sensitivity from 5–14.1 kHz. The psychophysical aerial audiogram of this Steller sea lion was remarkably similar to aerial audiograms previously obtained for California sea lions and northern fur seals, suggesting that the otariid pinnipeds form a functional hearing group. ASSR thresholds, measured at frequencies of 1, 2, 5, 10, 20, and 32 kHz, were elevated relative to corresponding psychophysical thresholds, ranging from +1 dB at 20 kHz, to +31 dB at 1 kHz. The ASSR audiogram accurately predicted the subject's high-frequency cutoff, and provided a reasonable estimate of hearing sensitivity at frequencies above 2 kHz. In testing situations where psychophysical methods are not possible, ASSR methods may provide an objective and efficient estimate of behavioral hearing sensitivity in otariid pinnipeds.
 [DOI: 10.1121/1.3327662]

PACS number(s): 43.80.Lb, 43.64.Ri [WWA] Pages: 2692–2701

I. INTRODUCTION

The otariid pinnipeds (family *Otariidae*, the sea lions and fur seals) lead an amphibious existence, foraging at sea, and carrying out reproductive functions in coastal haul-out areas. Aerial vocalizations are critical for communication among individuals in these crowded rookeries (see Schusterman and Van Parijs, 2003 for a review). For example, the vocalizations emitted by mature males are used to maintain breeding territories (Peterson and Bartholomew, 1969; Fernandez-Juricic *et al.*, 2001; Gwilliam *et al.*, 2008), and vocal interactions aid in the reunion of mothers and pups in crowded breeding colonies (Insley *et al.*, 2003).

Despite the importance of aerial acoustic cues to otariid reproductive behavior, aerial hearing sensitivity curves (audiograms) have been reported for only two of the 14 otariid species: the California sea lion (*Zalophus californianus*) and the northern fur seal (*Callorhinus ursinus*). Following the first otariid aerial audiogram obtained with a California sea lion (Schusterman, 1974), Moore and Schusterman (1987) conducted refined aerial hearing sensitivity measurements with one California sea lion and two northern fur seal subjects using psychophysical methods in a sound-attenuating booth. The audiograms of all three individuals displayed generally similar characteristics: a gradual increase in sensitivity from the low frequencies up to 2 kHz, best sensitivity near 8 to 16 kHz, and a sharp loss in sensitivity indicating an upper-frequency limit between 16 and 32 kHz. Babushina *et al.* (1991) reported a similar aerial audiogram for a northern fur seal with a range of best hearing sensitivity from 2–16 kHz.

In addition to providing comparative data on marine mammal auditory function, the few published investigations on aerial hearing in otariids have been important in designing criteria to mitigate the negative effects of anthropogenic noise in coastal marine environments (e.g., Southall *et al.*, 2007). However, the available data are limited to small sample sizes of captive individuals, making it difficult to form conclusions regarding the variability of hearing sensitivity among individuals within a population, as well as between otariid species. This lack of basic information has led to recommendations that the number of otariid individuals and species for which hearing data exists should be increased (National Research Council 2000, 2005).

A method which has shown promise for objectively estimating hearing sensitivity in an increased number of marine mammals is the recording of the auditory brainstem response (ABR), which comprises electrophysiological responses generated by the auditory system following acous-

[a)]Portions of this research were presented at the Second International Conference on Acoustic Communication by Animals in Corvallis, Oregon, August 12–15, 2008, and the 157th meeting of the Acoustical Society of America in Portland, Oregon, May 18–22, 2009.

[b)]Author to whom correspondence should be addressed. Current address: U.S. Navy Marine Mammal Program, Space and Naval Warfare Systems Center, San Diego, Code 71510, 53560 Hull Street, San Diego, California 92152. Electronic mail: jason.mulsow@gmail.com

tic stimulation. Hearing screening using ABR methods is a rapid and non-invasive procedure that does not require the training of subjects, and is now a standard procedure with newborn infants in the United States (see Hall, 2007). In order to extend ABR-based methods to pinnipeds, Wolski *et al.* (2003) measured aerial hearing sensitivity using both behavioral and ABR methods in an individual harbor seal (*Phoca vitulina*). The electrophysiological thresholds, defined as the lowest stimulus level for which an ABR elicited by tone bursts was visually detectable, were reasonable predictors of behavioral thresholds. Electrophysiological methods therefore appear to provide a means of efficiently estimating behavioral hearing sensitivity in pinnipeds.

The traditional methods of visually detecting ABRs in electrophysiological recordings are subjective, and may be prone to high variability as a result of inter-observer detection biases and extraneous electrical noise in recordings (e.g., Arnold, 1985; Vidler and Parker 2004). As a means of reducing such confounding effects in the detection of an ABR, objective statistical detection of an auditory evoked potential can be facilitated in the frequency domain through the measurement of the auditory steady-state response (ASSR). ASSRs can be recorded as rhythmic potentials generated by the auditory brainstem that are phase-locked to a modulation pattern (i.e., amplitude modulation) imposed on an acoustic stimulus (Kuwada *et al.*, 1986; Lins *et al.*, 1995, Kuwada *et al.*, 2002). Thus, an ASSR can be detected in the frequency-domain representation of the electrophysiological record as a spectral peak present at the stimulus modulation rate. The application of ASSR methods has recently proven to be useful for measuring the hearing sensitivity of odontocete cetaceans (dolphins and porpoises) in a number of settings where behavioral methods were not readily available (Nachtigall *et al.*, 2005, 2008a; Cook *et al.*, 2006; Houser *et al.*, 2008; Supin *et al.*, 2001).

In order to determine if ASSR methods can provide a useful prediction of behaviorally measured hearing sensitivity in otariids, we measured unmasked aerial hearing sensitivity in a 1-year-old male Steller sea lion (*Eumetopias jubatus*) using both psychophysical and ASSR methods. The Steller sea lion, the largest of otariid species, inhabits a range in the North Pacific from Japan to the central coast of California (Loughlin *et al.*, 1984; National Research Council, 2003). This species has garnered recent attention due to an 80% population decline over the last 3 decades, and its listing in 1997 as an Endangered Species under the United States Endangered Species Act (National Research Council, 2003). This study was completed while the Steller sea lion subject was temporarily housed at Long Marine Laboratory in Santa Cruz, California, prior to his transfer to a permanent captive facility. This opportunity allowed for the first measurements of aerial hearing sensitivity to be made for this endangered species, and enabled a direct comparison of hearing thresholds obtained using psychophysical and ASSR methods.

II. MATERIALS AND METHODS

A. Psychophysical audiogram

1. Subject

The subject of the study was a 1-year-old male Steller sea lion identified as "Astro" (NMFS Identification Number: NOA0006398). For the duration of the psychophysical study, the sea lion was housed in a saltwater pool with adjacent haul-out areas at Long Marine Laboratory, at the University of California, Santa Cruz. His diet consisted of a mix of fish (herring and capelin, 6.8 kg total per day), approximately one-third to one-half of which was provided during experimental sessions. The subject was previously naive to psychophysical research, but had participated in training for husbandry purposes. Training for audiometric sessions was initiated on January 1, 2008. Data collection took place during the period of January 14, 2008 to February 25, 2008, with one to two audiometric sessions conducted per day.

2. Experimental apparatus and testing environment

All sessions were conducted in a $4.0 \times 2.8 \times 2.4$ m^3 hemi-anechoic, sound-attenuating chamber (Eckel Industries), previously described by Holt *et al.* (2004a). The experimental apparatus consisted of a 52 cm tall PVC chin cup that served as a station, placed 1 m in front of the speakers used for test signal production (see Sec. II A 3 below), and a 9×9 cm^2 PVC response target placed 50 cm to the left of the chin cup. In order to indicate the time interval that delineated individual trials, a small "trial light" was placed immediately next to the speaker. A second speaker (Audiovox Advent AD570), used to produce a bell tone marking a correct response, was placed on the floor to the right of the subject, near the front wall of the chamber.

One of two trainers was present in the test chamber for all experimental sessions. During a session, the trainers wore headphones with sound-attenuating earmuffs that rendered them unable to hear test stimuli. The subject was therefore unable to gain information regarding the presence or absence of an acoustic signal, based on inadvertent cues from the trainer. The experimenter was located in an adjacent $1.3 \times 2.8 \times 2.4$ m^3 control room, and monitored the sessions using surveillance cameras and a monitor. Thus, both the subject and the trainer were out of visual and auditory contact with the experimenter during data collection.

3. Acoustic stimuli and calibration

Test stimuli were pure tones of 500 ms duration with a linear rise-fall time of 40 ms. This duration was chosen as it exceeds the temporal integration time constant for otariids, below which threshold is dependent on stimulus duration (Holt *et al.*, 2004b; Ghoul *et al.*, 2009). Stimuli were generated by a custom National Instruments LABVIEW virtual instrument, and sent through a National Instruments PXI-6229 data acquisition (DAQ) card with an attached National Instruments BNC-2120 breakout box. Signals were then attenuated with a Tucker–Davis Systems PA5 programmable attenuator, followed by band-pass filtering using a Krohn-Hite 3550 filter. In some cases (0.125, 0.25, 4, 28.2, and 34

kHz), outgoing stimuli were amplified using a Hafler Trans Ana P1000 power amplifier. The stimuli were projected using one of four speakers, depending on frequency: a JBL 2245H low frequency loudspeaker (0.125 kHz), JBL 2123H/J midrange transducer (0.250, 0.500, 1, 2, 4, and 5 kHz), JBL 2404H ultra-high frequency transducer (5, 10, and 14.1 kHz), or a Fostex FT96H Horn Super Tweeter (20, 28.2, 30, and 34 kHz).

Signals were calibrated before and after each audiometric session in the absence of the subject using either a Josephson engineering C550H microphone (0.02–20 kHz ± 2 dB) or an Aco-Pacific 7016 microphone (0.005–120 kHz ± 2 dB), placed at the position corresponding to the center of the subject's head during testing. The incoming calibration signal was band-pass filtered to prevent aliasing, amplified by 20 dB using a Krohn-Hite 3364 filter, and then sent through the BNC-2120 breakout box to the PXI-6229 DAQ card. Signal SPLs (dB_{rms} re 20 μPa) were calibrated in the LABVIEW virtual instrument using an averaged FFT with a flat top window. In addition to this standard calibration procedure, the sound field was measured at every frequency at three points in a 20 cm transect (10 cm increments approximating a line through the ears) to ensure that the calibration point was indicative of the subject's received levels. For all frequencies, except for 10 and 20 kHz, the levels measured at each location were within ±3 dB of the calibration location at the center of the chin station. Sound levels at 10 and 20 kHz differed from those at the center of the chin station by ±4 dB and ±6 dB, respectively.

Noise levels were measured in the testing chamber with a Brüel & Kjær 2250 sound level meter (1-min unweighted recording, 1/3-octave band analysis), placed at a position corresponding to the center of the subject's head. Noise measurements at frequencies higher than 20 kHz were not available due to limitations of the B&K 2250, however, some explorative measurements were made using the Aco-Pacific 7016 microphone and a spectrum analyzer.

4. Test procedure

The experimental task was a go/no-go procedure, in which the subject was trained to touch the response target, placed immediately to the left of the chin station when he perceived a signal as being present, and to remain motionless at the chin station when a signal was not detected. When the subject oriented toward the speaker with his head placed firmly within the chin station, the experimenter signaled the beginning of a trial by turning on the trial light located in front of the subject. Both signal-absent and signal-present trials were 4 s in duration, during which time the trial light remained on. In the case of a signal-present trial, the test tone was presented in an unpredictable fashion by varying the delay at which it was triggered within the 4 s window. If the subject touched the response target after the test tone was presented (a *hit*), the bell tone marking a correct response was played through the AD570 speaker, and the trainer rewarded the sea lion with one capelin. The subject was similarly rewarded for remaining motionless in the chin station for the entire 4 s duration of a signal-absent trial (a *correct rejection*). When the subject responded by touching the response target on a signal-absent trial (a *false alarm*), or failed to respond during the 4 s trial interval on a signal-present trial (a *miss*), the trial light was turned off, no reward was provided, and the following trial was initiated, following a short delay. In the case that the subject pressed the response target before the presentation of signal, the response was scored as a false alarm. The experiment was double-blind in nature, in that both the subject and the trainer did not have any *a priori* knowledge of the trial type.

An adaptive up-down descending methods of limits, or staircase, procedure was used to determine hearing thresholds at each frequency (Cornsweet, 1962). At the start of each session, initial signal levels were set to a "warm-up" level, approximately 25 dB above the subject's predicted threshold. The signal level was attenuated by 4 dB after each hit until the first miss. After this point, all signal level adjustments were made in 2 dB increments, with the signal level elevated by 2 dB following each miss and attenuated by 2 dB following each hit. Trials were conducted in this fashion until nine reversals (transitions from miss to hit, and vice versa) had occurred. After the ninth reversal, the signal was re-elevated to the starting level, and a "cool-down" phase consisting of six trials was conducted. Sessions typically comprised 45 to 50 trials and lasted approximately 10 min. Signal-present and signal-absent trials were generated in a pseudo-random order. The probability of a signal-present trial occurring was 50%, 60%, or 65% (adjusted between sessions over the course of the experiment in order to maintain a response bias corresponding to a false alarm rate between 0% and 30%).

5. Data analysis

Thresholds for individual sessions were calculated in the fashion of Dixon and Mood (1948) using signal-present trial data from the first through the ninth reversal. Data collection for a threshold was complete when the subject had reached a stable threshold (i.e., a standard deviation of less than or equal to 3 dB for three consecutive sessions at a given frequency), and the average false alarm rate of the three sessions was greater than 0% and less than 30%. Final thresholds were calculated as the mean of these three consecutive sessions. The threshold at 20 kHz was the only exception to these criteria; data collection at this frequency was completed with a false alarm rate of 0% due to time constraints.

The thresholds obtained in this experiment were compared to the results of a previous study of underwater hearing in one male and one female Steller sea lion reported by Kastelein *et al.* (2005). Comparisons were made, both using sound pressure and sound intensity (assuming plane-wave propagation) as the relevant metric of sound detection [see Kastak and Schusterman (1998), regarding aerial and underwater hearing comparisons in pinnipeds]. Pressure comparisons were made by converting underwater thresholds (reported originally in dB_{rms} re 1 μPa by Kastelein *et al.*) to dB_{rms} re 20 μPa. Sound intensity thresholds were estimated in W/m^2 using the following relationship for plane-wave propagation conditions:

$$I = p^2/\rho c, \quad (1)$$

where I is sound intensity in W/m^2, p is rms sound pressure in Pa, ρ is the density of the medium (estimated at values of $\rho=1.2$ kg/m^3 for air, $\rho=1030$ kg/m^3 for seawater), and c is the speed of sound in the medium (estimated at values of $c=340$ m/s for air, $c=1500$ m/s for seawater) (Kinsler *et al.*, 1982). It should be noted that the values for density and sound speed are estimates, and that plane-wave sound propagation conditions likely did not exist in the pool where the underwater pressure thresholds were obtained; thus, sound intensity thresholds can only be approximated.

B. ASSR audiogram

1. Testing environment and subject state

Collection of electrophysiological data took place three months after the completion of the psychophysical study, following the subject's transport to Mystic Aquarium and Institute for Exploration for permanent housing. ASSR recordings were obtained in a veterinary surgery room, following the completion of an unrelated surgical procedure. Prior to the surgical procedure, the subject was administered with an intra-muscular injection of 30 mg of diazepam, 19.5 mg midazolam, and 2.6 mg medetomidine. Following intubation, 1%–2% isoflurane was used to keep the subject unconscious for the surgery and subsequent ASSR data collection. He was positioned in ventral recumbence and monitored continuously by the attending veterinarian and veterinary technicians during the ASSR recording procedure.

2. Acoustic stimuli and calibration

Thresholds were determined for sinusoidally amplitude-modulated (SAM) pure tone stimuli with carrier frequencies matched to five of the data points from the psychophysical audiogram: 1, 2, 5, 10, and 20 kHz. During the ASSR experiment, 32 kHz was tested instead of 34 kHz, due to the limitations of the headphones and the calibration microphone used in the experiment (see below). The SAM tones were continuous on a given trial to avoid "stimulus-on" or "stimulus-off" neural potentials in the ASSR recordings, and the polarities of the waveforms alternated between positive and negative on successive presentations to reduce electrical artifacts in the ASSR records. The rate of amplitude modulation for the SAM tones was 153.9 Hz. Following generation using the Evoked Response Study Tool (EVREST) (Finneran, 2009) and digital-to-analog conversion by a USB-6251 DAQ card, the SAM signals were first passed through a Krohn-Hite 3C series low-pass filter module (-3 dB at 150 kHz), and then passed through a custom attenuator controlled by EVREST. The conditioned signals were sent binaurally to a pair of Telephonics TDH-39 headphones, which had been custom fit with sound-attenuating supra-aural "earmuffs" (3 to 17 dB of noise attenuation at test frequencies) designed to fit over the subject's ears without altering the natural orientation of the pinnae.

Signal calibration levels for the each of the tested frequencies were based on mean SPLs measured during electrophysiological testing of sea lion subjects conducted prior to this procedure using a similar experimental set-up. For these calibrations, an Etymotic ER-7C probe microphone (0.25–10 kHz $\pm$ 2.5 dB) was placed underneath a subject's headphone near the meeting of the pinna and the scalp. Incoming electrical signals from the microphone were low-pass filtered using a second Krohn-Hite 3C series filter module to prevent aliasing (-3 dB at 200 kHz), followed by analog-to-digital conversion with the USB-6251 card and subsequent recording and coherent averaging by EVREST. The frequency responses of the two headphones were similar there was less than 3 dB difference at all test frequencies. For frequencies above the nominal range of the ER-7C microphone, calibration values were corrected, based on the microphone's frequency response.

Ambient noise levels were measured immediately following data collection using a custom LABVIEW virtual instrument and the Etymotic ER-7C probe microphone placed underneath the subject's Telephonics TDH-39 headphones.

3. ASSR collection

ASSRs were recorded using a three-electrode montage comprising Grass F-E3M-72 12 mm $\times$ 30 gauge stainless steel subdermal needle electrodes. An active (non-inverting) electrode was placed on the dorsal midline of the subject's head, midway between the ears, a reference (inverting) electrode was placed on the subject's dorsal midline, just posterior to the nape of the neck and near the scapula, and a ground electrode was placed just posterior to the ribcage. Incoming electrophysiological signals were amplified 100,000 times and bandpass filtered (0.1 to 1 kHz, -6 dB at cutoffs) using a Grass IP511 differential bio-potential amplifier. Following amplification and filtering, electrophysiological signals underwent analog-to-digital conversion with the USB-6251 card. The EVREST software sampled ($F_s=5.618$ kHz), recorded, and averaged the ASSR waveforms over a 64.97 ms recording window. An FFT (rectangular window) of the averaged 64.97 ms window was used to transform the electrophysiological record into the frequency domain. The 64.97 ms duration of the window allowed for a frequency bin in the spectra that was centered at the 153.9 Hz modulation rate. Any recording window containing a voltage of absolute peak magnitude greater than 25 μV was considered to contain spurious electrical artifacts, and was therefore rejected without being included in the waveform average. The first four epochs at a given level were also automatically rejected from each record to avoid the inclusion of onset responses to the SAM signal.

Up to 2000 individual 64.97 ms epochs were coherently averaged in real time in order to eliminate extraneous electrical noise. At intervals of 250 epochs, a magnitude-squared-coherence (MSC) test was used to determine if an ASSR at the 153.9 Hz modulation rate was present in the record. The MSC test created 20 sub-averages from the grand average record, and provided a ratio of the power at the SAM modulation rate in the grand average to the average power at the modulation rate in the sub-averages (Dobie and Wilson, 1989, 1995). An ASSR was considered to be present if the MSC statistic was larger than a critical value at the level of $\alpha=0.01$ (critical values obtained from Amos and

TABLE I. Aerial hearing thresholds for a juvenile male Steller sea lion obtained using psychophysical methods. The mean thresholds are the average of the three consecutive session thresholds reported. Also shown are the average false alarm rates for each frequency and the order in which testing occurred for each frequency.

Frequency (kHz)	Mean threshold (dB re 20 μPa)	Session thresholds (dB re 20 μPa)	False alarm (%)	Testing order
0.125	66	68, 65, 67	25	10
0.25	55	54, 54, 57	17	8
0.5	43	45, 43, 40	13	7
1	21	22, 21, 20	25	5
2	29	29, 29, 29	24	3
4	20	22,19,18	26	9
5	8	7, 10, 8	12	1
10	7	7, 7, 7	6	2
14.1	14	16, 12, 15	17	11
20	29	29, 30, 29	0	4
28.2	39	38, 39, 39	25	12
30	54	52, 54, 56	12	6
34	81	79, 82, 82	15	13

Koopmans, 1963 and Brillinger, 1978). If an ASSR was not detected using the MSC test after 2000 averaged epochs, it was considered that no ASSR was present.

For threshold determination, SAM stimuli at each frequency were set to an initial level assumed to be above the subject's threshold. In the case of a hit at this level (an ASSR was detected using the MSC test), the signal for the subsequent trial was then attenuated 10 dB relative to the previous level. A miss was scored when a statistically significant ASSR was not detected after 2000 epochs. Following the first miss, a signal level 5 dB above the miss was tested. Thresholds at each frequency were defined as the signal level corresponding to the lowest detectable response. Before thresholds were accepted at a frequency, two misses at 5 and 10 dB below the lowest hit were collected to confirm that threshold had been reached. The total time for collection of the ASSR audiogram was approximately 70 min.

III. RESULTS

A. Psychophysical audiogram

The subject's aerial thresholds and false alarm rates at each frequency tested are provided in Table I, and the psychophysical audiogram is shown in Fig. 1. The audiogram had a U-shape with a shallow low frequency roll-off below 1 kHz, and a steep high-frequency roll-off above 28.2 kHz. The subject's hearing range (defined as the range of frequencies audible at 60 dB SPL) was about 0.250 kHz to 30 kHz. Maximum sensitivity of 7 dB SPL was found at 10 kHz, with a range of best hearing (defined as the range of frequencies audible at 10 dB above maximum sensitivity) of 5 to 14.1 kHz. The shape of the audiogram was remarkably similar to aerial audiograms previously obtained for two other otariid species (Fig. 2). A prominent feature of this Steller sea lion's audiogram was an increase in sensitivity at 1 kHz, relative to 0.500 kHz, followed by a decrease in sensitivity at 2 kHz.

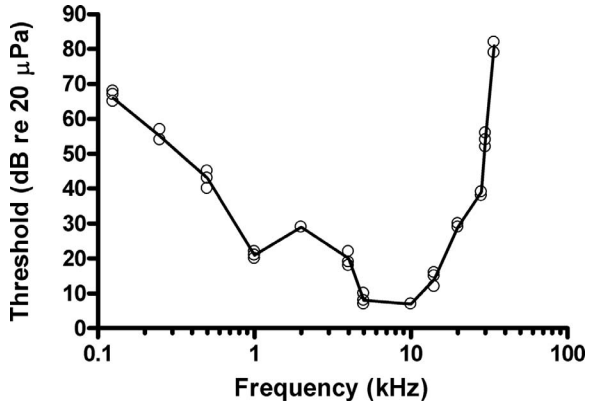

FIG. 1. Aerial audiogram for a juvenile male Steller sea lion obtained using psychophysical methods. Thresholds for three individual sessions per frequency (from Table I) are shown with open circles. The contour of the mean of the three session thresholds is shown by a solid black line.

Thresholds and false alarm rates among sessions for each frequency were fairly consistent and allowed for false alarm rate and threshold standard deviation criteria (see Sec. II above) to be met over the course of a few days of testing. A single exception to this occurred during testing at 20 kHz, where the subject's false alarm rate was consistently 0%. Due to the unusually conservative response bias at this frequency, the threshold value of 29 dB SPL at 20 kHz may be an underestimation of sensitivity relative to other frequencies.

Noise spectral density levels in the test chamber (Fig. 3(a)) decreased with increasing frequency; levels fell below 0 dB re (20 μPa)^2/Hz above 0.200 kHz, and were generally limited by the self-noise of the B&K 2250 (-20 dB re (20 μPa)^2/Hz) from 1.25–20 kHz. Explorative measurements with the Aco-Pacific 7016 microphone indicated that noise levels appeared to be sufficiently low to prevent masking of thresholds above 20 kHz.

The underwater thresholds obtained by Kastelein *et al.* (2005) are shown with the aerial audiogram from our Steller sea lion subject in Fig. 4. When comparisons are made in terms of sound pressure [Fig. 4(a)], all thresholds were lower in air with the exception of the highest frequencies tested by Kastelein *et al.* The underwater thresholds were lower than aerial thresholds at the low and high ends of the audiogram when sound intensity was used as the relevant metric of de-

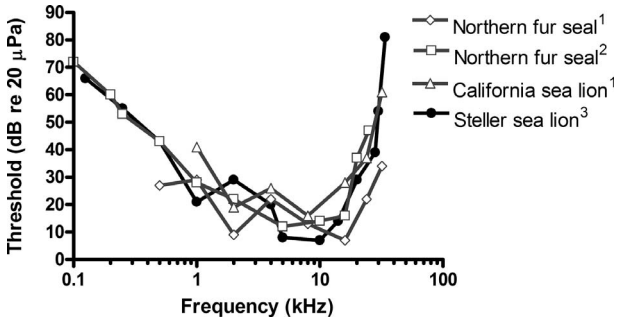

FIG. 2. Aerial audiograms for three species of otariid obtained using psychophysical methods: [1]Moore and Schusterman, 1987, California sea lion (n=1), northern fur seals (n=2); [2]Babushina *et al.*, 1991, northern fur seal (n=1); [3]this study.

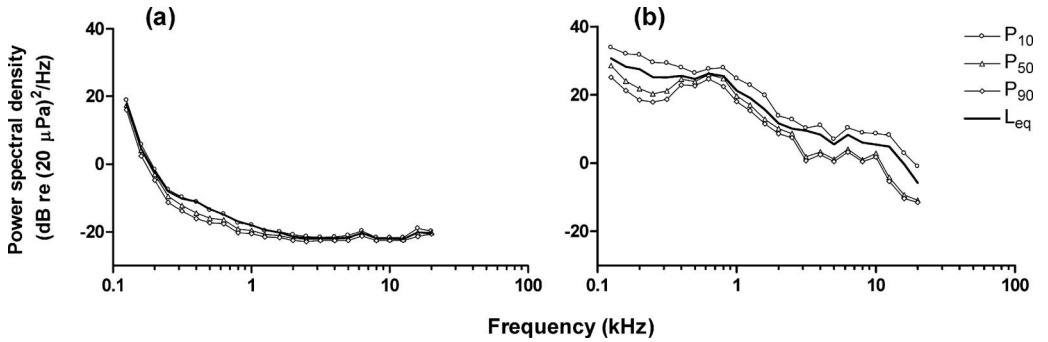

FIG. 3. Ambient noise in (a) the sound-attenuating chamber used for the behavioral audiogram and (b) the surgery room in which the ASSR audiogram was conducted. Noise levels for the ASSR audiogram were further attenuated by headphones placed over the subject's ears. Power spectral density levels are derived from 1-min unweighted recordings using 1/3-octave band analysis. The 10th, 50th, and 90th percentiles of the noise level distribution are shown in addition to the L_{eq}. Note the positive skew of the noise level distribution in the surgery room due to the intermittent activity of the anesthesia ventilator.

tection [Fig. 4(b)]. However, estimated aerial intensity thresholds were lower than estimated underwater intensity thresholds in the range of best hearing sensitivity (5–14.1 kHz) for the subject of the present study.

B. ASSR audiogram

The last detectable ASSR responses at each tested frequency, determined using the MSC test described in Sec. II (above), are provided in Table II. A comparison with the psychophysical audiogram obtained for this subject shows that there is a good agreement between thresholds obtained using the two methods (Fig. 5). All ASSR thresholds were elevated above psychophysical thresholds obtained at corresponding frequencies, although, to varying degrees: differences of greater than 10 dB were found at the lowest tested frequencies, 1 and 2 kHz, as well as at 10 kHz.

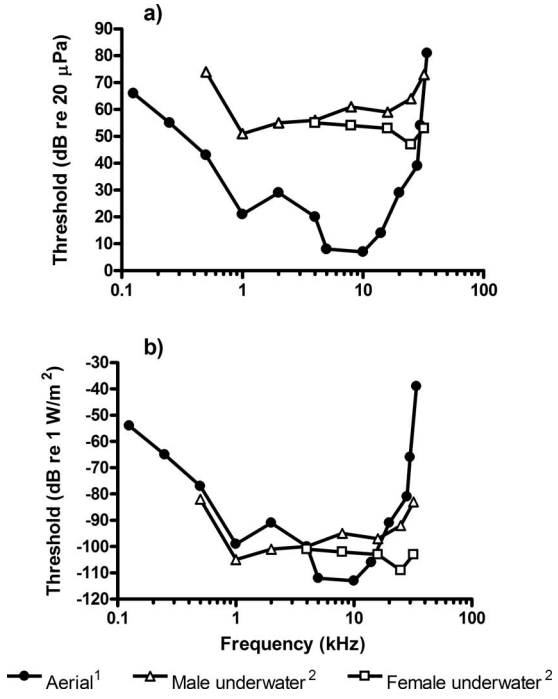

FIG. 4. A comparison of the aerial audiogram from a juvenile male Steller sea lion with underwater audiograms from one male and one female Steller sea lion (this study; Kastelein *et al.*, 2005). All audiograms were obtained using psychophysical methods. (a) Audiograms are compared in terms of sound pressure by converting the underwater thresholds to dB re 20 μPa. (b) Audiograms are compared in terms of estimated sound intensity by converting all sound pressure thresholds to dB re 1 W/m^2 (assuming plane-wave propagation conditions).

Noise spectral density levels measured under the subject's headphones decreased with increasing frequency up to 1 kHz, where levels were below 0 dB re (20 μPa)^2/Hz (61 Hz bin resolution). Above 1 kHz, noise levels were limited by the self-noise of the probe microphone, but it is a fair assumption that noise spectrum levels above 1 kHz were lower in amplitude than those measured at 1 kHz as the room was kept quiet during testing, with all doors closed and equipment use kept to a minimum. In order to further characterize the acoustic noise levels in the surgery room, noise measurements were made at a later date using a Brüel & Kjær 2250 sound level meter (1-min unweighted recording, 1/3-octave band analysis), in a testing configuration that approximated that of the ASSR experiment. Noise levels [Fig. 3(b)] decreased approximately linearly with increased log-frequency, with levels of 21 dB re (20 μPa)^2/Hz at 1 kHz, falling below 0 dB re (20 μPa)^2/Hz at 16 kHz. Intermittent sound generated by compression of the anesthesia ventilator (about 1 compression per 7 s) caused the noise distribution at most frequencies to be positively skewed (i.e., actual noise levels were generally less than the 1-min L_{eq} level during testing).

IV. DISCUSSION

A. Comparison of ASSR and psychophysical methods

The psychophysical thresholds obtained in the sound-attenuating chamber reliably depict the aerial hearing capa-

TABLE II. Aerial hearing thresholds for a juvenile male Steller sea lion, obtained using the ASSR method. Thresholds are defined as the last statistically detectable ASSR response.

Frequency (kHz)	ASSR threshold (dB re 20 μPa)	Testing order
1	52	2
2	44	4
5	15	5
10	22	1
20	30	3
32	82	6

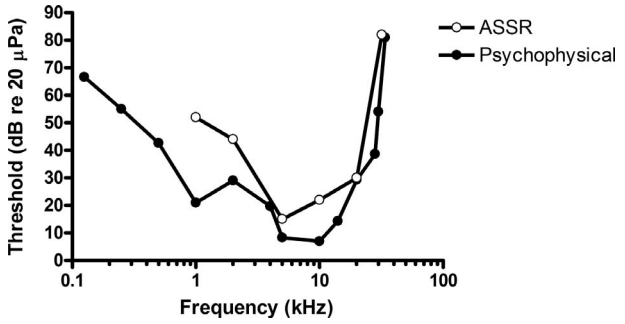

FIG. 5. A comparison of aerial hearing sensitivity measured using psychophysical and ASSR methods with the same juvenile male Steller sea lion.

bilities of this Steller sea lion. The audiogram is unmasked, based on the noise levels measured in the testing chamber and otariid critical ratios obtained for California sea lions (Southall *et al.*, 2003). The only data point for which the potential for masking exists is 14.1 kHz, as a result of ambient tonal noise at 15.7 kHz with amplitude below 20 dB SPL. This noise could potentially fall within the critical bandwidth for 14.1 kHz, assuming an otariid critical band of 25% of the center frequency (Southall *et al.*, 2003). However, any elevation of this data point due to masking is most likely minimal, as the 14.1 kHz threshold is similar in magnitude to thresholds at 10 and 20 kHz.

The correspondence between this psychophysical audiogram and the ASSR audiogram is qualitatively similar to the findings of similar studies with delphinid species (Yuen *et al.*, 2005; Finneran and Houser 2006; Schlundt *et al.*, 2007) and human subjects (see Picton *et al.*, 2003 for a review) in that thresholds obtained using the ASSR method are similar, although elevated, relative to psychophysical thresholds. Based on noise levels in the surgery room, which served as the testing environment, the potential for auditory masking by ambient noise must be considered in the interpretation of elevated ASSR thresholds. The surgery room was not designed for sound attenuation, and the ventilator that was used to administer gas anesthesia created intermittent broadband noise. Although it is difficult to quantitatively determine the influence of background noise on the ASSR thresholds, the greatest potential for masking exists at the lowest tested frequencies of 1 and 2 kHz, where noise levels were highest. This may have contributed to the marked elevation above behavioral thresholds at these frequencies (see, e.g., Lins *et al.*, 1996). The ASSR thresholds at frequencies higher than 2 kHz are relatively similar to the unmasked behavioral thresholds, and masking effects are most likely minimal. The ASSR threshold at 10 kHz is an exception to this trend and difficult to explain, based on the limited electrophysiological data from this study. It is possible that the discrepancy at this frequency is due to random error in the ASSR measurement, an issue which may be resolved by repeated within-subject threshold measurements in future studies.

An increased discrepancy between behavioral and ASSR measurements of underwater hearing sensitivity in a bottlenose dolphin (*Tursiops truncatus*) was also found at the lowest tested frequencies in a study by Schlundt *et al.* (2007). The authors attribute this to the fact that low frequency SAM stimuli are not especially effective at evoking ASSRs due to mechanical properties of the inner ear. Some effort should be put into resolving the problem of estimating hearing at low frequencies in future electrophysiological assessments of hearing in pinnipeds. The use of frequency-specific stimuli, such as trains of repeated tone bursts, which elicit higher-amplitude ASSRs than those elicited by SAM tone stimuli (Supin and Popov, 2007) and improved methods of extracting electrophysiological signals from noise, such as weighted averaging of epochs (Elberling and Wahlgreen, 1985), may allow for higher ASSR signal-to-noise ratios at low frequencies. Specially constructed, sound-attenuating testing environments for electrophysiological hearing procedures can additionally help by reducing the potential for auditory masking.

The use of different transducers (i.e., speakers in a direct field vs. headphones in the psychophysical and the ASSR experiments, respectively) presents a potential problem when comparing psychophysical and electrophysiological thresholds. A comparison of free-field aerial hearing thresholds and circumaural headphone thresholds in a pinniped species, the harbor seal (*Phoca vitulina*) (Holt *et al.*, 2001), failed to show any marked differences (although differences in head and ear structure between the harbor seal and the Steller sea lion should be noted). Large transducer-dependent threshold differences in our comparison thus seem unlikely, and in any case, the demonstration that the ASSR method provided a reasonable estimate of behavioral hearing sensitivity is of main importance.

The two-month time period required to obtain a reliable psychophysical audiogram demonstrates the utility of conducting psychological testing with stranded marine mammals who are housed in captive research facilities (see Nachtigall *et al.*, 2008b). In situations where the training of subjects is not feasible, ASSR methods may efficiently predict features of the audiogram such as range of best sensitivity and upper-frequency cutoff. One relevant application of ASSR methods is the detection of age-related hearing loss at the high-frequency end of the audiogram, which has been previously demonstrated in a California sea lion subject (Schusterman *et al.*, 2002). Additionally, the underwater and aerial upper-frequency limits of hearing in otariids appear to occur at similar frequencies (Schusterman *et al.*, 1975; Moore and Schusterman, 1987; Babushina *et al.*, 1991; Hemilä *et al.*, 2006), therefore, ASSR measurements of aerial hearing sensitivity may be of use in estimating otariid underwater audiograms.

B. Comparative otariid hearing

Although somewhat elevated above the absolute sensitivities of terrestrial carnivores (see Fay, 1988), the psychophysical hearing thresholds in the region of best hearing indicate acute aerial sensitivity in the Steller sea lion. The absolute sensitivities and frequency range of hearing of the Steller sea lion are especially similar to those of the California sea lion and northern fur seal. The close correspondence of these three species is remarkable, as the northern fur seal

is the most evolutionarily distinct of the living otariid species, belonging to the monophyletic group that diverged from all other extant otariid species more than 5 million years ago (see Heyning and Lento, 2002). It is therefore a reasonable assumption that the common ancestor of all extant otariids possessed hearing characteristics similar to the California and Steller sea lions and the northern fur seal, and that all extant otariids form a functional hearing group with similar aerial hearing characteristics. Further testing of a fur seal representing the *Arctocephalus* genus (for which no hearing data are currently available) would help to confirm the uniformity of otariid aerial hearing.

A feature similar to the decrease in sensitivity at 2 kHz relative to 1 kHz in the Steller sea lion audiogram is also present in audiograms for the two previously tested otariid species, the northern fur seal, and the California sea lion (Moore and Schusterman, 1987), as well as a phocid species, the harbor seal (Møhl, 1968). Noting the relationship between resonance frequency and the length of the human external auditory meatus found by Wiener and Ross (1946), Møhl suggested than an increase in sensitivity at 2 kHz in the harbor seal audiogram is a result of quarter length resonance in an external auditory meatus with an estimated length of 50–60 mm. It is conceivable that resonant properties of outer and/or middle ear structures could result in the "notches" of increased or decreased sensitivity in the mid-frequency region of otariid audiograms. The underwater audiograms of the otariids do not display such notches (Schusterman *et al.*, 1975; Moore and Schusterman, 1987; Babushina *et al.*, 1991; Kastelein *et al.*, 2005). This is congruent with the suggestion that these features are not cochlear in origin, but rather related to differences in the conformation of the outer and/or middle ear in aerial and underwater environments. Further description of the outer and middle ear structures of pinnipeds and their conformations, both in air and under water, would be of use in confirming this hypothesis.

The similarity of the aerial hearing capabilities in otariids is applicable in validating criteria designed to mitigate the impacts of anthropogenic noise in marine environments. For example, Southall *et al.* (2007) have generated *M*-weighting curves that are qualitatively similar to the *A* and *C* weighting functions used in human noise exposure regulation (see Kryter, 1994). *M*-weighting functions for a number of marine mammal functional hearing categories (e.g., high-frequency cetaceans, pinnipeds in air) are based on the audiograms of marine mammal species, and are designed to estimate the effects of anthropogenic noise as a function of noise amplitude and spectral characteristics. For example, a "pinniped in air" *M*-weighting function effectively eliminates frequency components below 50 Hz and above 50 kHz, as sound beyond these limits falls outside of the aerial hearing range of every tested pinniped species. Our findings suggest that the "pinniped in air" *M*-weighting function can be appropriately extrapolated to all otariids in conservatively estimating the effects of aerial anthropogenic noise.

Comparison of the aerial and underwater hearing capabilities determined for the Steller sea lion lend weight to the notion that otariid hearing is well adapted for aerial function (Kastak and Schusterman, 1998; Schusterman *et al.*, 2000). When comparisons are made based on acoustic pressure (which Kastak and Schusterman concluded to be the relevant metric of comparison for pinnipeds), the Steller sea lion's hearing is 30–50 dB better in air throughout the range of best sensitivity. Threshold comparisons, based on estimated sound intensity, would suggest that auditory sensitivity is essentially similar in air and under water at all, except for the highest frequencies in the hearing range of the Steller sea lion. When either sound pressure or estimated intensity is used as the metric of comparison, it appears that adaptations of the otariid ear for underwater function, such as modifications of osseous structures in the skull, cavernous tissue in the middle ear, and diminished tympanic membrane size relative to the oval window (Odend'hal and Poulter, 1966; Repenning, 1972) have resulted in a only a relatively small loss of aerial sensitivity relative to terrestrial carnivores.

A few caveats must be noted in the comparison of the aerial thresholds from the Steller sea lion in this study with the underwater thresholds reported by Kastelein *et al.* (2005). The comparisons were not made using the same subject or testing configuration, and the possibility exists that some of the differences between thresholds are based on inter-individual or methodological differences. Second, we have calculated intensity based on sound propagation in a free field, an assumption that is probably not valid for testing environments such as the small pool used by Kastelein *et al.* (2005).

The acute aerial hearing capabilities of the Steller sea lion should be considered in the context of the perception of vocal signals. The majority of Steller sea lion vocalizations have energy mainly below 3 kHz (Schusterman *et al.*, 1970; Campbell *et al.*, 2002; Park *et al.*, 2006). Although Steller sea lions appear to have good aerial hearing sensitivity within a wide range of frequencies between 1 kHz and 20 kHz, they are relatively insensitive below 1 kHz, where the dominant energy in many of their vocalizations occurs. Thus, the region of best hearing sensitivity in this species is not correlated with the dominant frequencies of vocalization. Harmonic components in the calls of Steller sea lions can extend to the mid-frequencies (Park *et al.*, 2006) where this species is especially sensitive, and these spectral components may be especially important in a Steller sea lion's perception of vocalizations by conspecifics. Future work including playback studies, field measurement of vocalization parameters, and psychophysical studies with captive subjects will provide insight on the relationship between the physical characteristics of vocal signals and detection and recognition by otariid species.

ACKNOWLEDGMENTS

This study would not have been possible without the involvement of Traci Kendall and Beau Richter, who conducted all animal training associated with psychophysical data collection. The authors also thank Frances Gulland, Terrie Williams, Tracy Romano, Lisa Mazzaro, and Mike Osborn for providing access to the subject, and Martin Haulena and the veterinary staff of Mystic Aquarium for providing

veterinary care. James J. Finneran developed the EVREST software used to collect the ASSR audiogram, and provided helpful technical support. Brian Lynn provided assistance during the evoked potential portion of the study. The authors gratefully acknowledge Ronald Schusterman and two anonymous reviewers for their critical comments on this manuscript. The electrophysiological portion of this study was supported in part by the NOAA Ocean Acoustics program in the National Marine Fisheries Service Office of Science and Technology. All research was conducted under NMFS Marine Mammal Permit No. 932-1489-09, and the authors thank Teri Rowles and the NMFS Office of Protected Resources for their participation in this effort. This study was approved by the Institutional Animal Care and Use Committees at the University of California, Santa Cruz and the Mystic Aquarium and Institute for Exploration.

Amos, D. E., and Koopmans, L. H. (**1963**). *Tables of the Distribution of the Coefficient of Coherence for Stationary Bivariate Gaussian Processes* (Sandia Corporation, Livermore, CA).

Arnold, S. A. (**1985**). "Objective versus visual detection of the auditory brain stem response," Ear Hear. **6**, 144–150.

Babushina, Y. S., Zaslavskii, G. L., and Yurkevich, L. I. (**1991**). "Air and underwater hearing characteristics of the northern fur seal: Audiograms, frequency and differential thresholds," Biophysics (Engl. Transl.) **36**, 909–913.

Brillinger, D. R. (**1978**). "A note on the estimation of evoked response," Biol. Cybern. **31**, 141–144.

Campbell, G. S., Gisiner, R. C., Helweg, D. A., and Millette, L. L. (**2002**). "Acoustic identification of female Steller sea lions (*Eumatopias jubatus*)," J. Acoust. Soc. Am. **111**, 2920–2928.

Cook, M. L. H., Varela, R. A., Goldstein, J. D., McCulloch, S. D., Bossart, G. D., Finneran, J. J., Houser, D., and Mann, D. A. (**2006**). "Beaked whale auditory evoked potential hearing measurements," J. Comp. Physiol. [A] **192**, 489–495.

Cornsweet, T. N. (**1962**). "The staircase method in psychophysics," Am. J. Psychol. **75**, 485–491.

Dixon, W. J., and Mood, A. M. (**1948**). "A method for obtaining and analyzing sensitivity data," J. Am. Stat. Assoc. **43**, 109–126.

Dobie, R. A., and Wilson, A. J. (**1989**). "Analysis of auditory evoked potentials by magnitude-squared coherence," Ear Hear. **10**, 2–13.

Dobie, R. A., and Wilson, A. J. (**1995**). "A comparison of *t* test, *F* test, and coherence methods of detecting steady-state auditory-evoked potentials, distortion-product otoacoustic emissions, or other sinusoids," J. Acoust. Soc. Am. **97**, 3042–3050.

Elberling, C., and Wahlgreen, O. (**1985**). "Estimation of auditory brainstem response, ABR, by means of Bayesian inference," Scand. Audiol. **14**, 89–96.

Fay, R. R. (**1988**). *Hearing in Vertebrates: A Psychophysics Databook* (Hill-Fay Associates, Winnetka, IL).

Fernandez-Juricic, E., Campagna, C., Enriquez, V., and Ortiz, C. L. (**2001**). "Vocal rates and social context in male South American sea lions," Marine Mammal Sci. **17**, 387–396.

Finneran, J. J. (**2009**). "Evoked response study tool: A portable, rugged system for single and multiple auditory evoked potential measurements," J. Acoust. Soc. Am. **126**, 491–500.

Finneran, J. J., and Houser, D. S. (**2006**). "Comparison of in-air evoked potential and underwater behavioral hearing thresholds in four bottlenose dolphins (*Tursiops truncatus*)," J. Acoust. Soc. Am. **119**, 3181–3192.

Ghoul, A., Holt, M. M., Reichmuth, C., and Kastak, D. (**2009**). "Auditory temporal summation in pinnipeds (A)," J. Acoust. Soc. Am. **125**, 2676.

Gwilliam, J., Charrier, I., and Harcourt, R. G. (**2008**). "Vocal identity and species recognition in male Australian sea lions (*Neophoca cinerea*)," J. Exp. Biol. **211**, 2288–2295.

Hall, J. W. (**2007**). *New Handbook of Auditory Evoked Responses* (Pearson Education, Boston, MA).

Hemilä, S., Nummela, S., Berta, A., and Reuter, T. (**2006**). "High-frequency hearing in phocid and otariid pinnipeds: Inertial and cochlear constraints," J. Acoust. Soc. Am. **120**, 3463–3466.

Heyning, J. E., and Lento, G. M. (**2002**). "The evolution of marine mammals," *Marine Mammal Biology: An Evolutionary Approach*, edited by A. Rus Hoelzel, (Blackwell, Oxford), pp. 38–72.

Holt, M. M., Schusterman, R. J., Southall, B. L., and Kastak, D. (**2004a**). "Localization of aerial broadband noise by pinnipeds," J. Acoust. Soc. Am. **115**, 2339–2345.

Holt, M. M., Southall, B. L., Kastak, D., Reichmuth Kastak, C., and Schusterman, R. J. (**2001**). "Aerial hearing sensitivity in pinnipeds: A comparison of free-field and headphone thresholds," in Proceedings of the 14th Biennial Conference on the Biology of Marine Mammals, Vancouver, BC, November 28–December 5.

Holt, M. M., Southall, B. L., Kastak, D., Schusterman, R. J., and Reichmuth Kastak, C. (**2004b**). "Temporal integration in a California sea lion and a harbor seal: Estimates of aerial auditory sensitivity as a function of signal duration (A)," J. Acoust. Soc. Am. **116**, 2531.

Houser, D. S., Gomez-Rubio, A., and Finneran, J. J. (**2008**). "Evoked potential audiometry of 13 Pacific bottlenose dolphins (*Tursiops truncatus gilli*)," Marine Mammal Sci. **24**, 28–41.

Insley, S. J., Phillips, A. V., and Charrier, I. (**2003**). "A review of social recognition in pinnipeds," Aquat. Mamm. **29**, 181–201.

Kastak, D., and Schusterman, R. J. (**1998**). "Low frequency amphibious hearing in pinnipeds: methods, measurements, noise, and ecology," J. Acoust. Soc. Am. **103**, 2216–2228.

Kastelein, R. A., Van Schie, R., Verboom, W. C., and de Haan, D. (**2005**). "Underwater hearing sensitivity of a male and a female Steller sea lion (*Eumetopias jubatus*)," J. Acoust. Soc. Am. **118**, 1820–1829.

Kinsler, L. E., Frey, A. R., Coppens, A. B., and Sanders, J. V. (**1982**). *Fundamentals of Acoustic*, 3rd ed. (Wiley, New York).

Kryter, K. D. (**1994**). *The Handbook of Hearing and the Effects of Noise: Physiology, Psychology, and Public Health* (Academic, San Diego, CA).

Kuwada, S., Anderson, J. S., Batra, R., Fitzpatrick, D. C., Teissier, N., and D'Angelo, W. R. (**2002**). "Sources of the scalp-recorded amplitude-modulation following response," J. Am. Acad. Audiol **13**, 188–204.

Kuwada, S., Batra, R., and Maher, V. L. (**1986**). "Scalp potentials of normal and hearing-impaired subjects in response to sinusoidally amplitude-modulated tones," Hear. Res. **21**, 179–192.

Lins, O. G., Picton, P. E., Picton, T. W., Champagne, S. C., and Durieux-Smith, A. (**1995**). "Auditory steady-state responses to tones amplitude-modulated at 80–110 Hz," J. Acoust. Soc. Am. **97**, 3051–3063.

Lins, O. G., Picton, T. W., Boucher, B. L., Durieux-Smith, A., Champagne, S. C., Moran, L. M., Perez-Abalo, M. C., Martin, V., and Savio, G. (**1996**). "Frequency-specific audiometry using steady-state responses," Ear Hear. **17**, 81–96.

Loughlin, T. R., Rugh, D. J., and Fiscus, C. H. (**1984**). "Northern sea lion distribution and abundance: 1956–80," J. Wildl. Manage. **48**, 729–740.

Møhl, B. (**1968**). "Auditory sensitivity of the common seal in air and water," J. Aud Res. **8**, 27–38.

Moore, P. W. B., and Schusterman, R. J. (**1987**). "Audiometric assessment of northern fur seals (*Callorhinus ursinus*)," Marine Mammal Sci. **3**, 31–53.

Nachtigall, P. E., Mooney, T. A., Taylor, K. A., Miller, L. A., Rasmussen, M. H., Akamatsu, T., Teilmann, J., Linnenschmidt, M., and Vikingsson, G. A. (**2008a**). "Shipboard measurements of the hearing of the white-beaked dolphin (*Lagenorhynchus albirostris*)," J. Exp. Biol. **211**, 642–647.

Nachtigall, P. E., Reichmuth, C., and Schusterman, R. J. (**2008b**). "Healthy stranded animals and laboratory research," Marine Mammal Sci. **24**, 746.

Nachtigall, P. E., Yuen, M. M. L., Mooney, T. A., and Taylor, K. A. (**2005**). "Hearing measurements from a stranded infant Risso's dolphin, *Grampus griseus*," J. Exp. Biol. **208**, 4181–4188.

National Research Council (**2000**). *Marine Mammals and Low-Frequency Sound: Progress Since 1994* (National Academy Press, Washington, DC).

National Research Council (**2003**). *Decline of the Steller Sea Lion in Alaskan Waters* (National Academy Press, Washington, DC).

National Research Council (**2005**). *Marine Mammal Populations and Ocean Noise: Determining When Noise Causes Biologically Significant Effects* (National Academy Press, Washington, DC).

Odend'hal, S., and Poulter, T. C. (**1966**). "Pressure regulation in the middle ear cavity of sea lions: A possible mechanism," Science **153**, 768–769.

Park, T., Iida, K., and Mukai, T. (**2006**). "Characteristics of vocalizations in Steller sea lions," in Proceedings of the 22nd Wakefield Fisheries Symposium, Sea Lions of the World: Conservation and Research in the 21st Century, edited by A. W. Trites, S. K. Atkinson, D. P. DeMaster, L. W. Fritz, T. S. Gelatt, L. D. Rea, and K. M. Wynne (Alaska Sea Grant Program, Anchorage, AK).

Peterson, R. S., and Bartholomew, G. A. (**1969**). "Airborne vocal communication in the California sea lion," Anim. Behav. **17**, 17–24.

Picton, T. W., John, M. S., Dimitrijevic, A., and Purcell, D. (**2003**). "Human auditory steady state responses," Int. J. Audiol. **42**, 177–219.
Repenning, C. A. (**1972**). "Underwater hearing in seals: Functional morphology," *Functional Anatomy of Marine Mammals*, edited by R. J. Harrison, (Academic, London), Vol. **1**. pp. 307–331.
Schlundt, C. E., Dear, R. L., Green, L., and Houser, D. S. (**2007**). "Simultaneously measured behavioral and electrophysiological hearing thresholds in a bottlenose dolphin (*Tursiops truncatus*)," J. Acoust. Soc. Am. **122**, 615–622.
Schusterman, R. J. (**1974**). "Auditory sensitivity of a California sea lion to airborne sound," J. Acoust. Soc. Am. **56**, 1248–1251.
Schusterman, R. J., Balliet, R. F., and St. John, S. (**1970**). "Vocal displays underwater by the gray seal, the harbor seal, and the Steller sea lion," Psychon. Sci. **18**, 303–305.
Schusterman, R. J., Barrett, B., and Moore, P. W. (**1975**). "Detection of underwater signals by a California sea lion and a bottlenose porpoise: Variation in the payoff matrix," J. Acoust. Soc. Am. **57**, 1526–1532.
Schusterman, R. J., Kastak, D., Levenson, D. H., Reichmuth, C. J., and Southall, B. L. (**2000**). "Why pinnipeds don't echolocate," J. Acoust. Soc. Am. **107**, 2256–2264.
Schusterman, R. J., Southall, B. L., Kastak, D., and Reichmuth Kastak, C. (**2002**). "Age-related hearing loss in sea lions and their scientists (A)," J. Acoust. Soc. Am. **111**, 2342–2343.
Schusterman, R. J., and Van Parijs, S. (**2003**). "Pinniped vocal communication: An introduction," Aquat. Mamm. **29**, 177–180.
Southall, B. L., Bowles, A. E., Ellison, W. T., Finneran, J. J., Gentry, R. L., Greene, C. R., Jr., Kastak, D., Ketten, D. K., Miller, J. H., Nachtigall, P. E., Richardson, W. J., Thomas, J. A., and Tyack, P. L. (**2007**). "Marine mammal noise exposure criteria: Initial scientific recommendations," Aquat. Mamm. **33**, 412–521.
Southall, B. L., Schusterman, R. J., and Kastak, D. (**2003**). "Auditory masking in three pinnipeds: Aerial critical ratios and direct critical bandwidth measurements," J. Acoust. Soc. Am. **114**, 1660–1666.
Supin, A. Ya., and Popov, V. V. (**2007**). "Improved techniques of evoked-potential audiometry in odontocetes," Aquat. Mamm. **33**, 14–23.
Supin, A. Ya., Popov, V. V., and Mass, A. M. (**2001**). *The Sensory Physiology of Aquatic Mammals* (Kluwer, Boston, MA).
Vidler, M., and Parker, D. (**2004**). "Auditory brainstem response threshold estimation: Subjective threshold estimation by experienced clinicians in a computer simulation of the clinical test," Int. J. Audiol. **43**, 417–429.
Wiener, F. M., and Ross, D. A. (**1946**). "The pressure distribution in the auditory canal in a progressive sound field," J. Acoust. Soc. Am. **18**, 401–408.
Wolski, L. F., Anderson, R. C., Bowles, A. E., and Yochem, P. K. (**2003**). "Measuring hearing in the harbor seal (*Phoca vitulina*): Comparison of behavioral and auditory brainstem response techniques," J. Acoust. Soc. Am. **113**, 629–637.
Yuen, M. M. L., Nachtigall, P. E., Breese, M., and Supin, A. Y. (**2005**). "Behavioral and auditory evoked potential audiograms of a false killer whale (*Pseudorca crassidens*)," J. Acoust. Soc. Am. **118**, 2688–2695.

ACOUSTICAL NEWS

Elaine Moran
Acoustical Society of America, Suite 1NO1, 2 Huntington Quadrangle, Melville, NY 11747-4502

Editor's Note: *Readers of this journal are encouraged to submit news items on awards, appointments, and other activities about themselves or their colleagues. Deadline dates for news and notices are 2 months prior to publication.*

New Fellows of the Acoustical Society of America

Oleg Lobkis—For contributions to diffuse-wave ultrasonics

Paul E. Nachtigall—For contributions to marine mammal acoustics

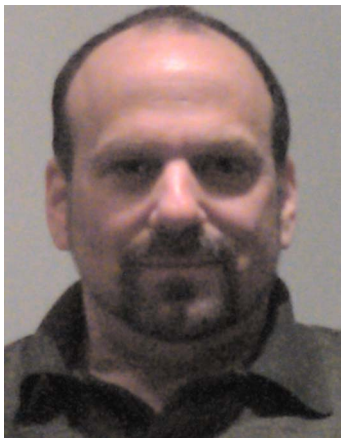

Peter J. Stein—For contributions to ocean acoustic instrumentation

Calendar of Meetings and Congresses

Compiled by the Information Service of the International Commission for Acoustics

2010

19–23 April	Baltimore, MD, USA. Joint meeting: 159th Meeting of the Acoustical Society of America and Noise-Con 2010. http://asa.aip.org/meetings.html
27–30 April	Ghent, Belgium. Institute of Acoustics/Belgian Acoustical Association Joint Meeting. http://www.ioa.org.uk/viewupcoming.asp
6–7 May	Paris, France. 2nd International Symposium on Ambisonics and Spherical Acoustics. http://ambisonics10.ircam.fr
10–12 May	Bergen, Norway. Baltic-Nordic Acoustics Meeting 2010. E-mail: sanordby@norsonic.com
9–11 June	Aalborg, Denmark. 14th Conference on Low Frequency Noise and Vibration. http://lowfrequency2010.org
13–16 June	Lisbon, Portugal. INTERNOISE2010. http://www.internoise2010.org
5–9 July	Istanbul, Turkey. 10th European Conference on Underwater Acoustics. http://ecua-2010-istanbul.org
18–22 July	Cairo, Egypt. 17th International Congress on Sound and Vibration (ICSV17). http://www.icsv17.org
23–27 August	Sydney, Australia. International Congress on Acoustics 2010. http://www.ica2010sydney.org
23–27 August	Seattle, USA. 11tth International Conference on Music Perception and Cognition.
29–31 August	Melbourne, Australia. International Symposium on Room Acoustics(ISRA2010). http://www.isra2010.org
14–18 September	Kyoto, Japan. 5th Animal Sonar Symposium. http://cse.fra.affrc.go.jp/akamatsu/AnimalSonar.html
15–18 September	Ljubljania, Slovenia. Alps-Adria-Acoustics Association Meeting joint with EAA. E-mail: mirko.cudina@fs.uni-lj.si
20–22 September	Leuven, Belgium, International Conference on Noise and Vibration Engineering (ISMA2010), http://www.isma-isaac.be
26–30 September	Makuhari, Japan. Interspeech 2010—ICSLP. http://www.interspeech2010.org
11–14 October	San Diego, Cal. USA. IEEE 2010 Ultrasonics Symposium. E-mail: b.potter@vectron.com
14–16 October	Niagara-on-the Lake, Ont., Canada. Acoustics Week in Canada. http://caa-aca.ca/E/index.html
11–14 October	San Diego, California, USA. IEEE 2010 Ultrasonics Symposium. E-mail: bpotter@vectron.com
13–15 October	Leon, Spain. 41st Spanish Congress of Acoustics and 6th Iberian Acoustics Congress. http://www.sea-acustica.es
18–22 October	Nagahama, Japan. 10th International Workshop on Railway Noise (IWRN10). http://www.rtri.or.jp/IWRN10/first.announcement.html
15–19 November	Cancún, Mexico. 2nd Pan-American Meeting on Acoustics http://asa.aip.org/meetings.html

 0001-4966/2010/127(4)/2702/2/$25.00

2011

22–27 May	Prague, Czech Republic. International Conference on Acoustics, Speech, and Signal Processing (IEEE ICASSP 2011). http://www.icassp2011.com
23–27 May	Seattle, WA, USA. 160th meeting of the Acoustical Society of America. http://asa.aip.org/meetings.html
27 June–1 July	Aalborg, Denmark. Forum Acusticum 2011. http://www.fa2011.org
24–28 July	Tokyo, Japan. 19th International Symposium on Nonlinear Acoustics (ISNA 19). http://www.isna19.com
27–31 August	Florence, Italy. Interspeech 2011. http://www.interspeech2011.org
4–7 September	Osaka, Japan. Internoise 2011. http://www.internoise2011.com
5–8 September	Gdansk, Poland. International Congress on Ultrasonics. http://icu2011.ug.edu.pl/index.html

2012

20–25 March	Kyoto, Japan. IEEE International Conference on Acoustics, Speech, and Signal Processing. http://www.icssp2012.com

2013

26–31 March	Vancouver, Canada. 2013 IEEE International Conference on Acoustics, Speech, and Signal Processing (ICASSP). http://www.icassp2013.com
2–7 June	Montréal, Canada. 21st International Congress on Acoustics (ICA 2013). http://www.ica2013montreal.org

REVIEWS OF ACOUSTICAL PATENTS

Sean A. Fulop
Dept. of Linguistics, PB92
California State University Fresno
5245 N. Backer Ave., Fresno, California 93740

Lloyd Rice
11222 Flatiron Drive, Lafayette, Colorado 80026

The purpose of these acoustical patent reviews is to provide enough information for a Journal reader to decide whether to seek more information from the patent itself. Any opinions expressed here are those of reviewers as individuals and are not legal opinions. Printed copies of United States Patents may be ordered at $3.00 each from the Commissioner of Patents and Trademarks, Washington, DC 20231. Patents are available via the internet at http://www.uspto.gov.

Reviewers for this issue:

GEORGE L. AUGSPURGER, *Perception, Incorporated, Box 39536, Los Angeles, California 90039*
ANGELO CAMPANELLA, *3201 Ridgewood Drive, Hilliard, Ohio 43026-2453*
JOHN ERDREICH, *Ostergaard Acoustical Associates, 200 Executive Drive, West Orange, New Jersey 07052*
JEROME A. HELFFRICH, *Southwest Research Institute, San Antonio, Texas 78228*
DAVID PREVES, *Starkey Laboratories, 6600 Washington Ave. S., Eden Prairie, Minnesota 55344*
CARL J. ROSENBERG, *Acentech Incorporated, 33 Moulton Street, Cambridge, Massachusetts 02138*
NEIL A. SHAW, *Menlo Scientific Acoustics, Inc., Post Office Box 1610, Topanga, California 90290*
ERIC E. UNGAR, *Acentech, Incorporated, 33 Moulton Street, Cambridge, Massachusetts 02138*
ROBERT C. WAAG, *Department of Electrical and Computer Engineering, University of Rochester, Rochester, New York 14627*

7,603,866

43.35.Ud THERMOACOUSTIC APPARATUS

Yoshiaki Watanabe and Shinichi Sakamoto, assignors to The Doshisha
20 October 2009 (Class 62/6); filed in Japan 26 March 2004

This patent discloses the use of thermoacoustic effects to pump heat from a cold body to a warmer one, i.e., to make a refrigerator that uses only a gaseous medium as its moving part. The apparatus consists of two vertical pipes, joined into a loop at the top and bottom as shown in the figure. Heat applied to the stack 3a on the lower left initiates an oscillation in the gas loop inside the pipes. The oscillation carries over into the right-hand vertical pipe, where it forces gas to shuttle through stack 3b on the upper right. The

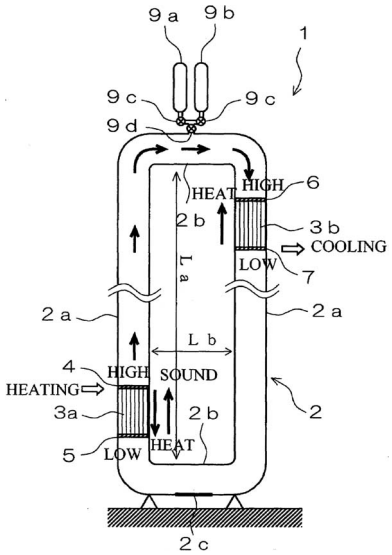

oscillatory motion of the gas, in conjunction with thermal and viscous penetration depth effects, causes the gas to pump heat from the bottom end 7 of stack 3b, where refrigeration occurs, to the bottom end 5 of stack 3a. The authors claim that the system will auto-excite, but mention that a loudspeaker or other source of sound can be used to speed up the initiation of the process. All of this has been described elsewhere in the literature, and is not particularly novel. Their principal claim for novelty lies in the use of two different gases to facilitate starting up the refrigerator. In the patent, the gases are introduced sequentially at the top of the loop via valve 9b, first helium to start the oscillation quickly, then argon to increase the cooling power.—JAH

7,471,028

43.35.Zc LIQUID EJECTION HEAD AND IMAGE FORMING APPARATUS

Sho Onozawa, assignor to Fujifilm Corporation
30 December 2008 (Class 310/313 R); filed in Japan 7 June 2006

Surface acoustic wave (SAW) ink ejection head 10 having reduced heat generation is claimed. Several SAW generators 30 project a SAW (dotted arrows) into substrate 16. SAW generators 30 are disposed in a circle

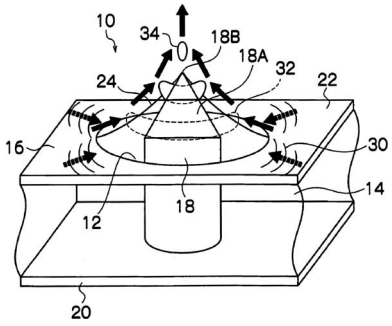

around pedestal 18, resulting in a converging SAW pattern around the pedestal 18A. SAWs are launched from interface 12 into the surface of ink 14 which propel that fluid (arrow trail) to converge toward tip 18B. The amplitude 32 of the fluid SAW near tip 18B increases to the extent that droplet (O) is ejected outward. Several ejection heads 10, activated by a graphics controller (not shown), can be assembled in an array to form a graphics printer head.—AJC

 0001-4966/2010/127(4)/2704/11/$25.00

7,602,267

43.38.Ar MEMS ACTUATOR AND RELAY WITH HORIZONTAL ACTUATION

Trevor Niblock *et al.*, assignors to National Semiconductor Corporation
13 October 2009 (Class 335/78); filed 25 May 2007

People have been trying to miniaturize the relay for decades, and the microelectronic mechanical systems (MEMS) community has, for at least 20 years, been plagued by an inability to improve upon what has been done using plain old wires and silicon steel, especially for currents of more than milliamperes. This patent shows how it can be done using CMOS-compatible MEMS techniques, and why it probably would not be. In a

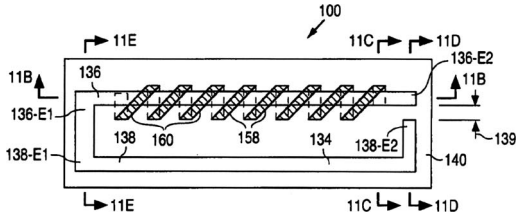

technical tour-de-force, the authors describe all of the steps necessary to fabricate a miniature relay out of copper, steel, gold and silicon. The resulting device (see figure) looks simple, but takes many deposition steps and results in a device that takes 20 mA at 2.5 V to operate. In return, one gets the excellent control-to-signal isolation of a mechanical relay with a little bit of speed increase. We will wait to see who starts producing this.—JAH

7,582,191

43.38.Dv PROCESS FOR PRODUCING LOUDSPEAKER DIAPHRAGM, LOUDSPEAKER DIAPHRAGM PRODUCED BY THE PROCESS, AND LOUDSPEAKER WITH THE DIAPHRAGM

Takashi Suzuki and Shinya Mizone, assignors to Panasonic Corporation
1 September 2009 (Class 162/218); filed in Japan 22 March 2005

To reduce the variation in pulp deposition and pulp fiber orientation in the manufacture of paper loudspeaker cones, pulp-making bath 21 is set in

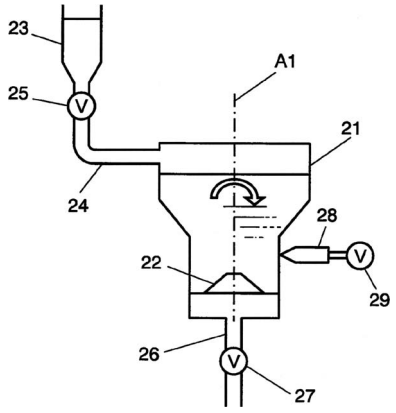

circular motion, or a "vortex" as described in the patent, by water nozzle 28 or by small plates that rotate around axis A1. The paper cone is formed on mold 22 when valve 27 of drain pipe 26 is opened. The vortex is assumed to impose a more uniform flow and therefore more uniform cones.—NAS

7,475,598

43.38.Fx ELECTROMECHANICAL FORCE TRANSDUCER

Mark William Starnes *et al.*, assignors to New Transducers Limited
13 January 2009 (Class 73/778); filed in United Kingdom 11 September 2003

Cell phone loudspeaker electromechanical force transducer 1 is claimed. A low stiffness plastic foam material (not shown) to damp resonance modes is fitted between piezoelectric beams 2 and 3, driven as a

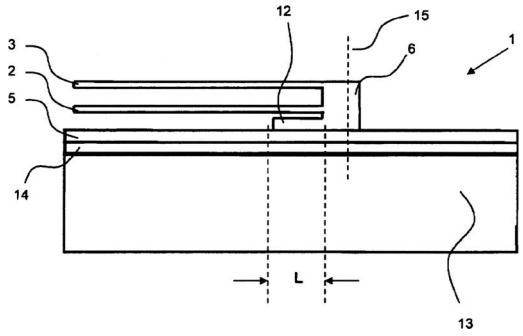

distributed mode actuator. Beams 2 and 3 connect to stub 6 having foot 12 of length L that transmits a linear force and a bending moment to cell phone case 5, driving it as a loudspeaker.—AJC

7,602,105

43.38.Fx PIEZOELECTRICALLY ACTUATED ULTRANANOCRYSTALLINE DIAMOND TIP ARRAY INTEGRATED WITH FERROELECTRIC OR PHASE CHANGE MEDIA FOR HIGH-DENSITY MEMORY

Orlando H. Auciello, assignor to UChicago Argonne, LLC
13 October 2009 (Class 310/324); filed 24 April 2007

This patent affords an interesting glimpse of new approaches to data storage. The author describes an approach to data storage in a "phase change medium" such as lead zirconate titanate. There are actually two methods discussed here, one involving a change in the polarization state of the material and the other involving a change in the resistivity of the material (evidently not lead zirconate titanate in this case). In either case, the process of storing the digital bits proceeds by using ultrananocrystalline diamond tips 44 (hence the tongue-twisting title of the patent) to contact the phase change medium at points that are addressed in (x, y) fashion by a crossed

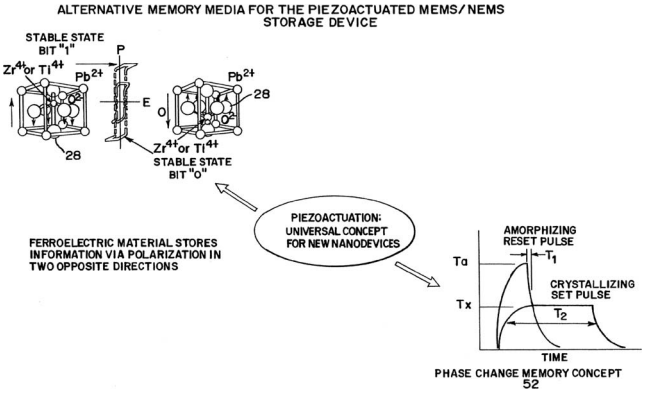

array of electrodes 40. The tip is driven downward by the action of piezoelectric backing 28, thus allowing current to pass from the tip to the conducting layer 20, which is presumably grounded. The local heating or voltage difference (depending on the case as discussed above) induces the desired phase change. Little space is given to discussion of how the bits are

actually read out. Speeds of nanoseconds per read/write of a bit are mentioned, but no speed claims are given.—JAH

7,601,763

43.38.Ja DIAPHRAGM FOR SPEAKER AND MANUFACTURING METHOD THEREOF

Satoshi Hachiya *et al.*, assignors to Pioneer Corporation
13 October 2009 (Class 521/142); filed in Japan 27 September 2005

Loudspeaker cones can be made of acrylic foam, but in its usual formulation the material readily absorbs moisture, making it unsuitable for use

	FOAMING MAGNIFICATION	DENSITY [kg/m³]	COMPRESSIVE STRENGTH[MPa]	SATURATED WATER ABSORPTION [wt%]
<COMPARATIVE EXAMPLE 1> MATERIALS (1) to (3)	15	80	2.02	–
<COMPARATIVE EXAMPLE 2> POLY(METH)ACRYLIMIDE	15	70	1.63	30.0
<THIS INVENTION> MATERIALS (1) to (5)	15	80	1.67	4.0

in humid environments. This patent describes alternative formulas that offer comparable compressive strength but much less water absorption. Although the patent claims are restricted to "a diaphragm for a speaker," there is no information about acoustical performance.—GLA

7,607,512

43.38.Ja SPEAKER ASSEMBLY FOR A STRUCTURAL POLE AND A METHOD FOR MOUNTING SAME

Ronald Paul Harwood, Farmington Hills, Michigan
27 October 2009 (Class 181/148); filed 23 August 2005

What seems to be patented here is not the idea of mounting a loudspeaker to the banner brackets of a pole, but rather the idea of designing a

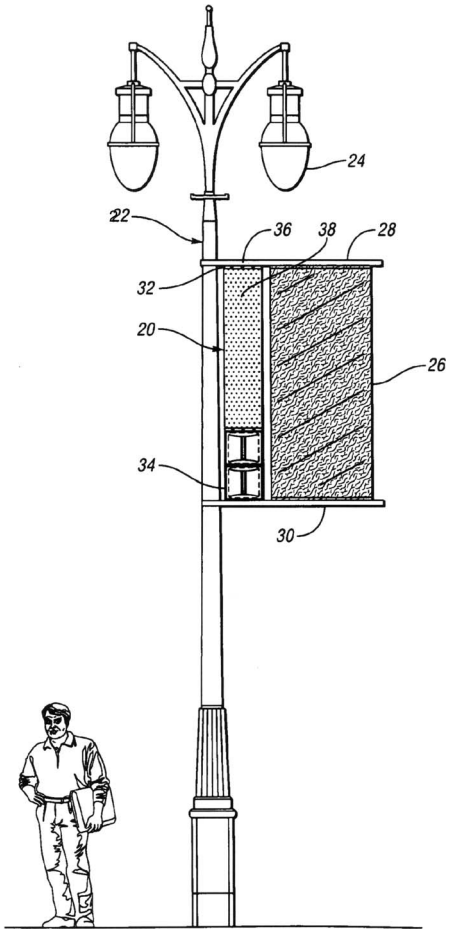

loudspeaker for the specific purpose of mounting it to the banner brackets of a pole. Novel features? Well, the housing is "elongated" and its height is "sized to match a height of a banner of the structural pole." Pretty exciting stuff.—GLA

7,610,991

43.38.Ja SPEAKER AND METHOD OF OUTPUTTING ACOUSTIC SOUND

Nobukazu Suzuki *et al.*, assignors to Sony Corporation
3 November 2009 (Class 181/153); filed in Japan 9 February 2006

In this invention, Sony's cylindrical glass tweeter is combined with a

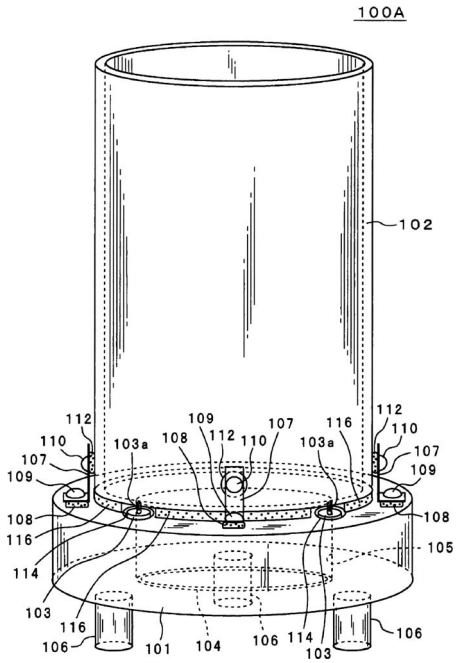

woofer to form a full-range loudspeaker system. Glass cylinder 102 is driven by magnetostrictive transducers 103. In one embodiment, the cylinder is divided by interior partitions so that two or more radiating areas can reproduce different signals. The cylinder is mounted to base assembly 101 which houses upward-firing woofer 104. The proportions of the illustration are not to scale; in reality the cylinder is about 1 m high but only 50–100 mm in diameter.—GLA

7,574,005

43.38.Md HOWLING FREQUENCY COMPONENT EMPHASIS METHOD AND APPARATUS

Mikio Tohyama *et al.*, assignors to Yamaha Corporation
11 August 2009 (Class 381/66); filed in Japan 30 March 2004

A method of detecting feedback that emphasizes the "howling frequencies," since they are said to exhibit a "transition in same phase," is used to

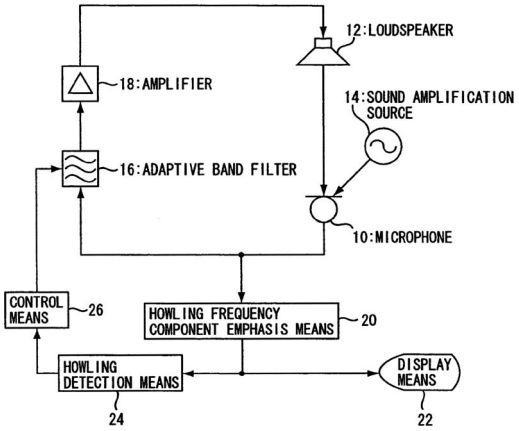

determine the pole (or poles) in the resulting transfer function. This information is then used to adjust adaptive filter sections.—NAS

7,603,080

43.38.Md MULTIPLE CHANNEL WIRELESS COMMUNICATION SYSTEM

Lawrence Richenstein, Brookville, New York et al.
13 October 2009 (Class 455/3.06); filed 12 April 2006

This is an update of earlier U.S. Patent No. 7,076,204, and it is still difficult to figure out exactly what has been patented. On the one hand, preferred embodiments are described in great detail. On the other hand, the

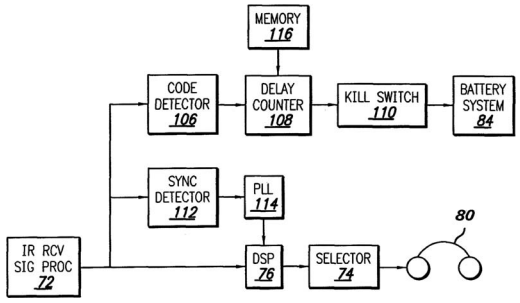

patent claims are much more general, setting forth a wireless headphone device or wireless headphone system that allows the user to select a desired program channel from a number of multiplexed audio streams. The basic description and most of the patent claims might just as well refer to any one of many available wireless translation systems.—GLA

7,613,306

43.38.Md AUDIO ENCODER AND AUDIO DECODER

Shuji Miyasaka *et al.*, assignors to Panasonic Corporation
3 November 2009 (Class 381/22); filed in Japan 25 February 2004

The patent explains that MPEG-2 audio files include two sets of encoded information. The first is a stereo program downmixed from an original multi-channel source. The second contains additional information required to restore the full multi-channel program. In this way, an inexpensive

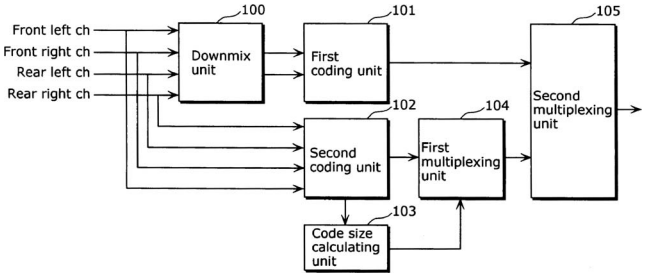

playback device can simply decode the stereo information and ignore the second bitstream. Unfortunately, a number of additional operations must be carried out to keep track of which is which. An improved system is proposed which includes code size information in the header section.—GLA

7,605,686

43.38.Si ALERTING SYSTEM FOR A COMMUNICATION DEVICE

Salomon Serfaty *et al.*, assignors to Motorola, Incorporated
20 October 2009 (Class 340/384.73); filed 16 November 2006

Most legal documents use well established terms and syntax to avoid ambiguity. In patents, however, the goal may be just the opposite, and this patent is a good example. Here, an overabundance of simple, everyday words are combined to form a shimmering image that never quite comes

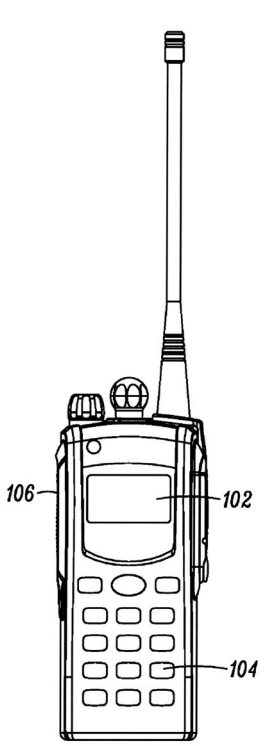

PRIOR ART

into focus. We have "a plurality of operating modes." We have "an electromechanical switch." We have "a transducer for transforming electrical impulses into vibrations and for transforming vibrations into electrical impulses." In one notable paragraph, more than 400 words are used to define an ordinary push-to-talk switch. The actual invention appears to be a communications device (mobile phone, two-way radio, etc.) in which a single audio transducer is used as both a microphone and a loudspeaker. This is well-established prior art. The novel feature is that the transducer motor is mechanically coupled to one membrane 104 when talking (microphone) and to a different membrane 102 when listening (earphone).—GLA

7,605,862

43.38.Si APPARATUS FOR A PORTABLE ELECTRONIC DEVICE

Chuan-Kung Hou, Yonghe City, Taipei County 234, Taiwan
20 October 2009 (Class 348/373); filed 20 January 2004

A cellular telephone or hand-held computer may include a camera, and

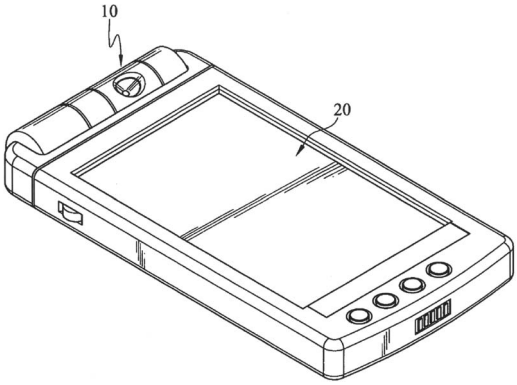

the camera may be mounted in a cylindrical cavity as shown. If so, and if the cavity has unused space available, then it can also house a miniature loudspeaker. That is the substance of this patent.—GLA

7,606,382

43.38.Si BTE/CIC AUDITORY DEVICE AND MODULAR CONNECTOR SYSTEM THEREFOR

Jim Feeley and Mike Feeley, assignors to Hear-Wear Technologies LLC
20 October 2009 (Class 381/330); filed 17 November 2006

A variety of behind-the-ear electronic devices 30 can be combined

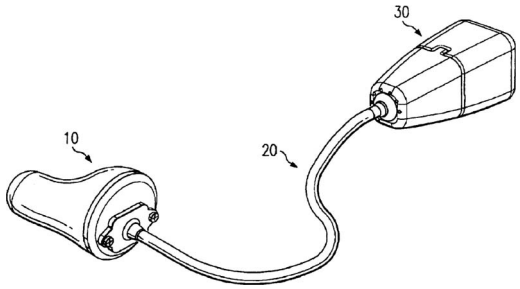

with an in-canal receiver 10. The two are connected by plug-in cord 20. The objective is to create a custom auditory device from a selection of modular components.—GLA

7,606,386

43.38.Si VIBRATION ACTUATOR

Dae Lyun Kang *et al.*, assignors to Samsung Electro-Mechanics Company, Limited
20 October 2009 (Class 381/396); filed in Republic of Korea 4 February 2005

The illustration shows a typical loudspeaker/vibrator used in cellular phones. At audio frequencies voice coil 4 drives diaphragm 3 as a normal

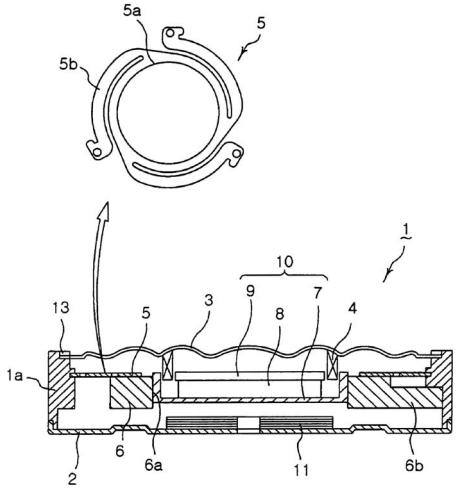

miniature loudspeaker. However, the entire motor structure is resiliently suspended and can be driven at its resonance frequency to generate tactile vibrations instead of sound. The resilient suspension is a stamped metal spider 5. This patent teaches that such a suspension is prone to fatigue, and that its stiffness is difficult to control. A coil spring is said to be a better choice. Numerous practical embodiments are disclosed in the patent.—GLA

7,609,844

43.38.Si NOISE ATTENUATING HEADSET

Wayne Lederer, Atlantic Beach, New York
27 October 2009 (Class 381/380); filed 7 September 2007

This patent explains that magnetic resonance imaging rooms can be very noisy, requiring operators to communicate through noise-attenuating

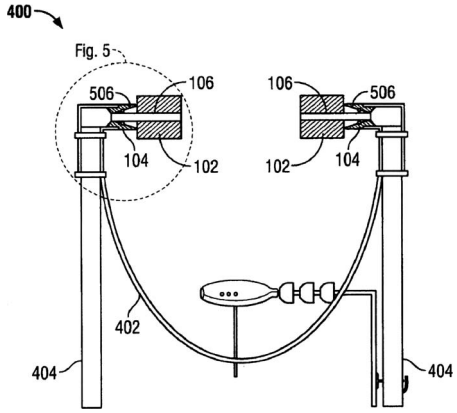

headsets. At the same time, all equipment in the vicinity of the machine must be non-magnetic. To meet these requirements, the inventor proposes a stethoscope-type headset made of non-magnetic components. A non-magnetic microphone may also be included. Any questions?.—GLA

7,613,315

43.38.Si CONFIGURABLE HEADSET

Peter Vestergaard Vaerum *et al.*, assignors to Sennheiser Communications A/S
3 November 2009 (Class 381/381); filed in the European Patent Office 4 March 2005

This over-the-ear headset includes a number of features intended to improve user comfort and provide better operation. The speaker unit 15 is

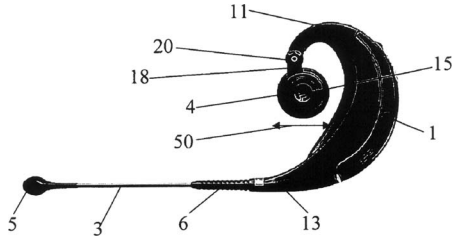

pivoted and has a detachable peripheral band 4 chosen to match the size of the user's ear. Once the proper band is installed, the headset can be worn on either ear.—GLA

7,606,377

43.38.Vk METHOD AND SYSTEM FOR SURROUND SOUND BEAM-FORMING USING VERTICALLY DISPLACED DRIVERS

John L. Melanson, assignor to Cirrus Logic, Incorporated
20 October 2009 (Class 381/97); filed 31 May 2006

This patent is a continuation of U.S. Patent No. 7,545,946 filed in 2006. Assume that the illustration shows the left speaker system of a stereo pair. The cabinet houses two speakers stacked vertically. (Additional woofers and tweeters are included in some variants.) In the range from about 200 Hz to 2 kHz, both speakers reproduce the front-left channel essentially in-phase, although delay can be used to tilt the in-phase axis slightly up or

down. In the same frequency range, the two speakers reproduce the surround-left channel in reverse polarity, producing a null along the listening

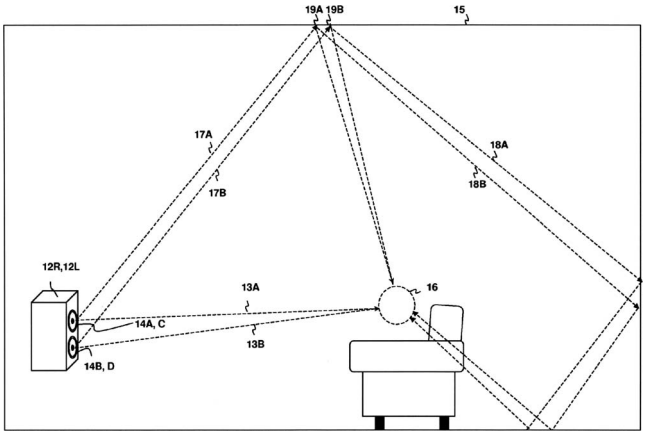

axis. Thus, scattered room reflections are used to convey surround information. Although the vertical array seems counterintuitive, it enables two cabinets to reproduce front-left, front-right, surround-left, and surround-right channels with appropriate localization. The method has no effect on the center channel, which may be a phantom center or a discrete loudspeaker.—GLA

7,606,380

43.38.Vk METHOD AND SYSTEM FOR SOUND BEAM-FORMING USING INTERNAL DEVICE SPEAKERS IN CONJUNCTION WITH EXTERNAL SPEAKERS

John L. Melanson, assignor to Cirrus Logic, Incorporated
20 October 2009 (Class 381/300); filed 28 April 2006

This is a companion patent to U.S. Patent No. 7,606,377 and is based on the same two-source array geometry. In this case, however, additional speakers and electronics are combined with existing internal speakers of a

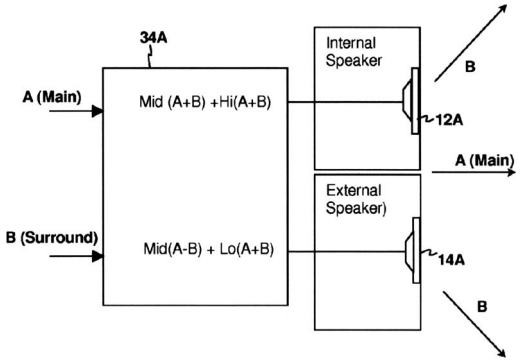

television receiver to create the beam-forming arrays. Obviously, one could just as easily augment existing freestanding speakers, but that application seems to be carefully avoided in the patent claims.—GLA

7,578,603

43.38.Yn ACOUSTIC WAVE INDUCED LIGHT EMITTING GOLF BALL

Chang-Hsiu Huang, Pusin Township, Changhua County 513 and Wei-Lung Chou, Sanchong City, Taipei County 241, both of Taiwan
25 August 2009 (Class 362/276); filed 10 August 2007

Battery powered light emitting device 30 is encapsulated within a transparent golf ball 10. Encapsulating material 41 cures at room temperature, thereby avoiding potential damage from thermoset or similar materials heretofore used in this part of the light emitting golf ball. The "acoustic

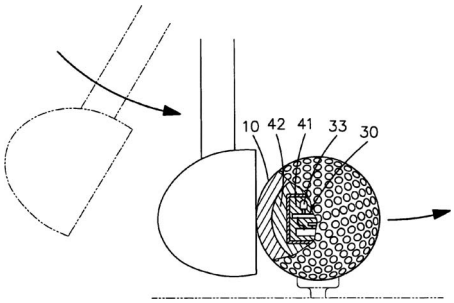

wave" transducer is a piezoelectric button, opposed to a spring in a hollow tube switch, which triggers a controller that flashes one or more light-emitting diodes. Your reviewer speculates that this type of ball may be used when playing golf at night.—NAS

7,468,085

43.40.Qi SYSTEM AND METHOD FOR CLEANING A FILTER

John D. Goddard, assignor to Caterpillar Incorporated
23 December 2008 (Class 55/385.3); filed 19 December 2005

A sonic method 10 to aid the clean-out of a diesel engine exhaust gas particulate filter is claimed. Sound source 14 projects intense sound of any suitable frequency into particulate filter 30. Exhaust gas from engine 18 passes through manifold 20 through normally open valve 24, into filtering

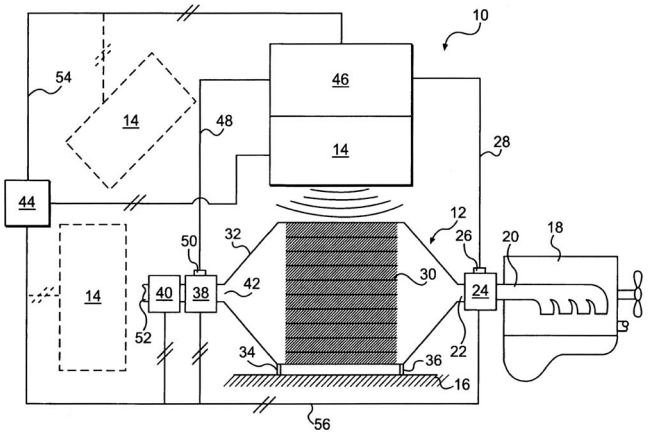

device 12, through particulate filter 30, and through valves 38 and 40 and exhaust pipe 52. Filter 30 may contain catalysts and any other material capable of removing pollutants such as soot, NO_x, sulfur compounds, etc. When clean-out is required, sound source 14 is activated to shake loose particulate matter that is then swept out or carried away by a fast moving gas stream. Several sweep-out strategies with and without the engine running are described.—AJC

7,252,157

43.40.Tm POWER TOOL

Yonosuke Aoki, assignor to Makita Corporation
7 August 2007 (Class 173/162.2); filed in Japan 1 April 2003

In this power hammer, a striker weight is made to reciprocate in the axial direction of the tool bit, causing that bit to reciprocate. The pressure in the striker housing is used to make a dynamic balancing weight move opposite to the striker, thus reducing the net force transmitted to the tool's handle.—EEU

7,575,523

43.40.Tm GOLF CLUB HEAD

Masatoshi Yokota, assignor to SRI Sports Limited
18 August 2009 (Class 473/332); filed in Japan 10 January 2006

Damper 3 can be made from various and sundry materials, or a combination of materials with different damping characteristics, so that the vi-

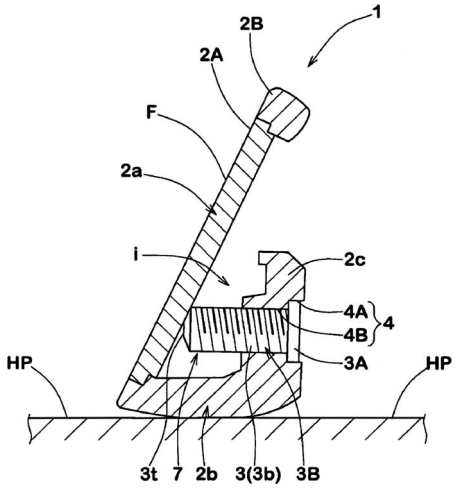

bration damping of club face plate 2A can be varied per the duffer's preference. The design of socket portion 4A and main portion 4B of hole 4 are said to be designed to fully ensure that the damper does not loosen with use.—NAS

7,600,945

43.40.Tm VACUUM FORMED CLADDING

Alan Burgess, assignor to Trelleborg CRP Limited
13 October 2009 (Class 405/216); filed in United Kingdom 12 September 2003

This patent pertains to spiral strakes that are to be attached to underwater pipes or cables in order to suppress vortex shedding and thereby to reduce vibrations induced in these structures. The strakes according to this patent are provided in part-tubular portions that can be placed around a tubular member and interconnected. This patent suggests polyethylene as a suitable material; it can be thermoformed in multiple layers and has a density similar to that of water, so that the strake assemblies are nearly neutrally buoyant.—EEU

7,604,259

43.40.Tm DAMPER ROOT RING

Dale O. Cipra, assignor to Pratt & Whitney Rocketdyne, Incorporated
20 October 2009 (Class 285/226); filed 15 August 2007

Flow-induced vibrations in a bellows-type expansion joint are suppressed by means of damper rings 14 that fit into the root regions on the

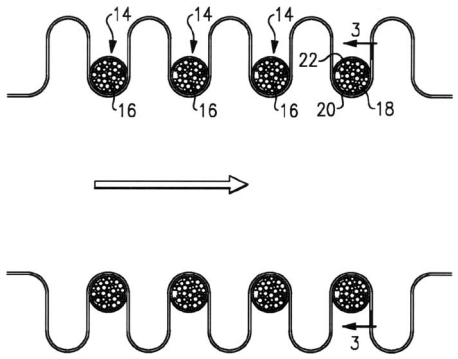

exterior of the bellows. The rings are hollow and filled with a damping medium 16, which may consist of fluids and/or particles.—EEU

7,613,540

43.40.Vn METHOD AND SYSTEM FOR VIBRATION AVOIDANCE FOR AUTOMATED MACHINERY

Francis Joseph Testa, assignor to Teknic, Incorporated
3 November 2009 (Class 700/187); filed 4 May 2007

It is desirable that machine elements in automatic machinery execute specific motions accurately and rapidly. As such elements are made to move, they are subject to vibrations, predominantly at their natural frequencies, and thus perform suboptimally. Suppression of vibrations at these frequencies can be accomplished by means of active control systems, but these change the motion of the elements. The present patent deals with reduction of the undesirable vibrations by adjustment of the motion time histories so that forcing at the offending frequencies is minimized. The motion history is developed in terms of a series of concatenated polynomial segments that are adjusted via an optimizing engine.—EEU

7,469,603

43.40.Yq ANGULAR VELOCITY DETECTOR, METHOD OF DETECTION OF ANGULAR VELOCITIES USING ANGULAR VELOCITY DETECTOR, AND METHOD OF FABRICATING ANGULAR VELOCITY DETECTOR

Masaya Nagata *et al.*, assignors to Sony Corporation
30 December 2008 (Class 73/862.325); filed in Japan 20 October 2003

A miniature angular velocity sensor that is sensitive on two axes is claimed. Angular rotation of the sensor causes Coriolis perturbations of a vibrating slotted plate which in turn vary the capacitances between selected segments and a fixed element.—AJC

7,465,151

43.50.Gf SHOCK-ABSORBENT STRUCTURE OF SERIALLY-CONNECTED FANS

Alex Hong and Ming Chien Wu, assignors to Sunonwealth Electric Machine Industry Company, Limited
16 December 2008 (Class 415/119); filed in Taiwan 4 July 2006

A coupled fan vibration resonance reduction method is claimed. Cool-

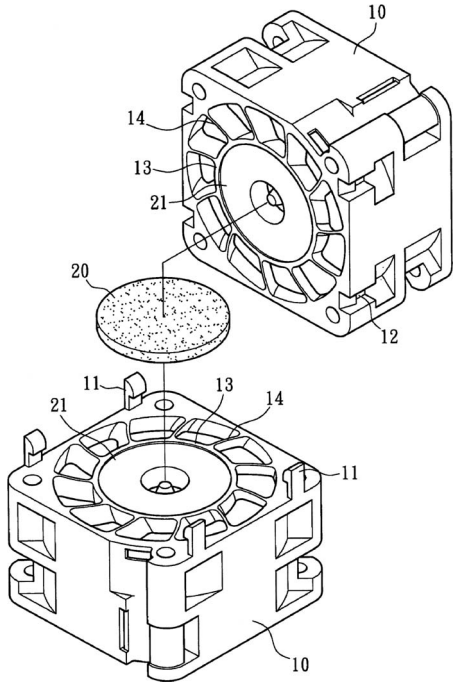

ing fans 10-10, rotating, respectively, at 14 000 and 15 000 rpm (233–

250 Hz), are normally attached together at faces 13 to double the air static pressure created with small air flows. Case vibration at 9 mm/s vibration velocity was found to occur. Addition of rubber or foam material 20 received in shallow depression 21 reduced the case vibration to 3 mm/s. This resulted in reduced system noise and should provide longer life of the fan and the cooled equipment. A ring of rubber or foam material at the rim outside ribs 14 serves the same purpose.—AJC

7,470,108

43.50.Gf AXIAL FLOW FAN

Masanori Watanabe *et al.*, assignors to Japan Servo Company, Limited
30 December 2008 (Class 415/207); filed in Japan 20 April 2004

Refrigerator freezer air circulation fan 4 having reduced noise and

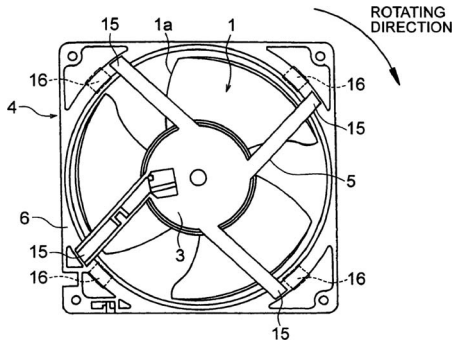

vibration is claimed. Inlet and outlet fairings are added. Air approach and departure angles are tailored for reduced air noise. Support spider legs 5 are canted to reduce the amplitude of the wake interference blade passage pressure pulse. Motor vibration transmission to the frame is reduced by pads 16.—AJC

7,476,079

43.50.Gf LOW-NOISE HVAC BLOWER ASSEMBLY

Eric Raymond Bartlett, assignor to Continental Automotive Systems US, Incorporated
13 January 2009 (Class 415/203); filed 5 May 2006

A quieter and more efficient automobile centrifugal blower is claimed.

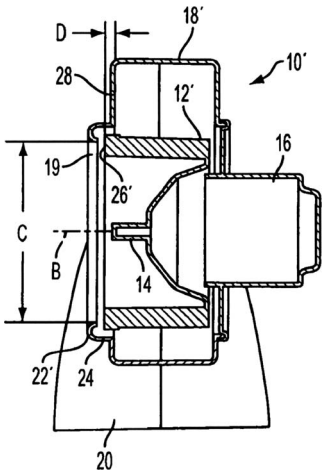

Fan rotor 12 rotating on axis *B* is improved with extension 26 to extend beyond discharge cavity 18–20 to reduce air recirculation and fan noise.—AJC

7,613,307

43.50.Ki ACTIVE SOUND REDUCTION APPARATUS AND ACTIVE NOISE INSULATION WALL HAVING SAME

Keizo Ohnishi *et al.*, assignors to Mitsubishi Heavy Industries, Limited
3 November 2009 (Class 381/71.1); filed in Japan 21 April 2000

The gist of this patent is a theme and variations. The theme is an active noise cancellation device on top of a barrier to cancel sound waves as they diffract over the barrier. The variations aim to expand the frequency range and reach of the cancellation devices by increasing the number of active control cells, by adding a "sound tube," by spacing several rows of active

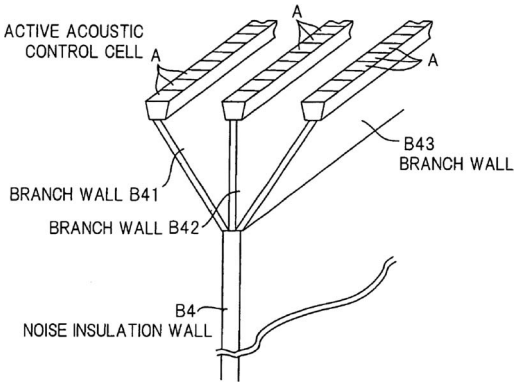

controls at varying distances from each other, by adding absorptive materials, by shifting the angle of the apparatus, and so on and so forth.—CJR

7,612,635

43.58.Kr MEMS ACOUSTIC FILTER AND FABRICATION OF THE SAME

Yongli Huang, assignor to Kolo Technologies, Incorporated
3 November 2009 (Class 333/186); filed 3 August 2006

The author discloses a set of ideas involving the application of capacitive micromachined ultrasonic transducers to problems of impedance matching of transducers to media and coupling of acoustic filter elements to each

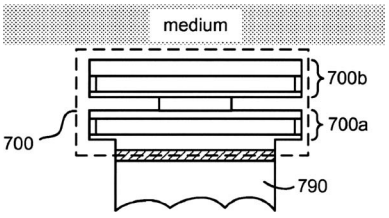

other. The structures discussed here are targeted for megahertz frequencies, probably useful in medical ultrasound and nondestructive evaluation of materials. The basic theme is that the impedance of a block of silicon (700a or 700b in the figure) can be controlled by dividing it up into an array of rectilinear voids, which can be readily fabricated by micromachining techniques. These blocks can be cascaded as shown to make filters, or used to impedance match transducers to media. The author claims further benefits can be obtained by cascading such elements in silicon using other micromachining techniques and by utilizing the medium as a distribution bus for multiplexing signals to other devices. There is not much in the way of analysis offered to justify the complexity of such a structure; with all of the junctions and internal structure, one suspects they would be plagued by parasitic resonances of various types.—JAH

7,578,200

43.60.Cg METHOD AND APPARATUS FOR MEASURING PAPER SAMPLE STIFFNESS

Denys Leveugle and Patrick Legrand, assignors to Georgia-Pacific France
25 August 2009 (Class 73/801); filed in France 31 May 2006

A method for measuring the rigidity of paper and other products made

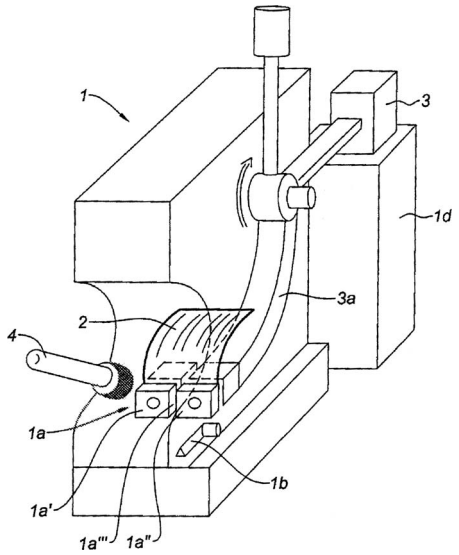

from cellulose fibers wherein the paper is torn and a digitized sound recording is made during the tearing process is then analyzed to determine the percentage of time during which characteristic frequencies are present during the tearing process. It has been found that this percentage correlates well with rigidity.—NAS

7,602,928

43.66.Ts TELEPHONE WITH INTEGRATED HEARING AID

Barbara Moo and Doree Duncan Seligmann, assignors to Avaya Incorporated
13 October 2009 (Class 381/315); filed 1 July 2002

Only three very general claims cover forming an audio signal to drive

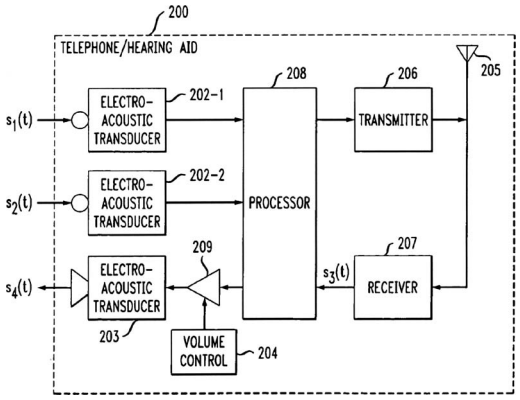

the hearing aid speaker based on the outputs of two microphones mixed with a received electromagnetic signal (from an antenna). The output of one of the microphones is transmitted (by the antenna) to pick up the user's voice during a telephone call. The system automatically adjusts the mixing ratio depending on whether or not the user is engaged in a telephone call.—DAP

7,602,930

43.66.Ts POWER-SAVING MODE FOR HEARING AIDS

Thomas Kasztelan, assignor to Siemens Audiologische Technik GmbH
13 October 2009 (Class 381/323); filed in Germany 30 July 2004

To conserve power, the charge status of the voltage source for the hearing aid is checked, and the low-frequency response of the hearing aid is adjusted accordingly. If the voltage source output voltage drops below a series of threshold values, the low-frequency response is attenuated in stages related to the threshold values by shifting a low-frequency cutoff to higher frequencies.—DAP

7,605,812

43.66.Ts INTELLIGENT MODELING METHOD AND SYSTEM FOR EARMOLD SHELL AND HEARING AID DESIGN

Fred McBagonluri and Joerg Bindner, assignors to Siemens Aktiengesellschaft
20 October 2009 (Class 345/420); filed 19 December 2006

This patent recommends combining into one knowledge-based automatic system the two separate software processes typically used for hearing

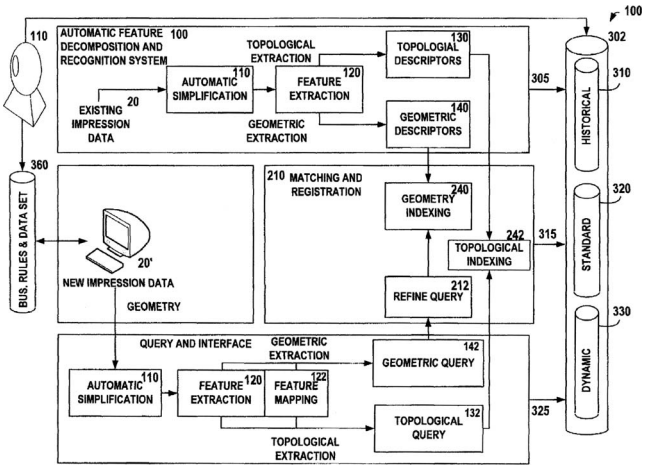

aid earmold shell design: detailing the earmold impression to the selected shell type and optimizing the shell model to add features and fit components. If a database query determines that a stored shell model matches the new undetailed shell model or one or more of the extracted features, previously stored rules are used. If no match is found, generalized binaural modeling rules are used to create the hearing aid shell.—DAP

7,609,259

43.66.Ts SYSTEM AND METHOD FOR PERFORMING A SELECTIVE FILL FOR A HEARING AID SHELL

Fred McBagonluri *et al.*, assignors to Siemens Audiologische Technik GmbH
27 October 2009 (Class 345/419); filed 18 October 2006

The boundary defining the fill region for a hearing aid shell is defined, checked for validity, stored, and displayed for operator modification to bet-

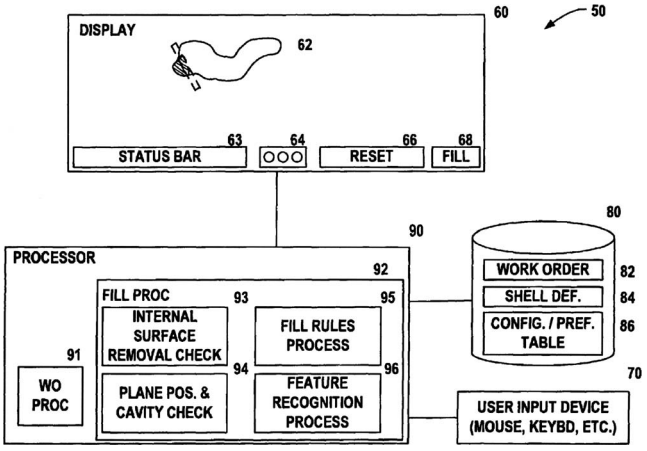

ter fit in components and help reduce electroacoustic feedback.—DAP

7,609,841

43.66.Ts FREQUENCY SHIFTER FOR USE IN ADAPTIVE FEEDBACK CANCELLERS FOR HEARING AIDS

Daniel J. Freed and Sigfrid D. Soli, assignors to House Ear Institute
27 October 2009 (Class 381/318); filed 4 August 2004

Frequency shifting for feedback oscillation reduction has traditionally produced undesirable audible artifacts. To reduce these artifacts, small positive and negative frequency shifts of approximately 0.3% are alternately applied only to the high frequency portion of the audio signal.—DAP

7,537,011

43.66.Vt HEARING PROTECTION DEVICE

Robert Falco, assignor to 3M Innovative Properties Company
26 May 2009 (Class 128/864); filed 10 December 2007

A triple flange earplug is described, with radial supports for the flex

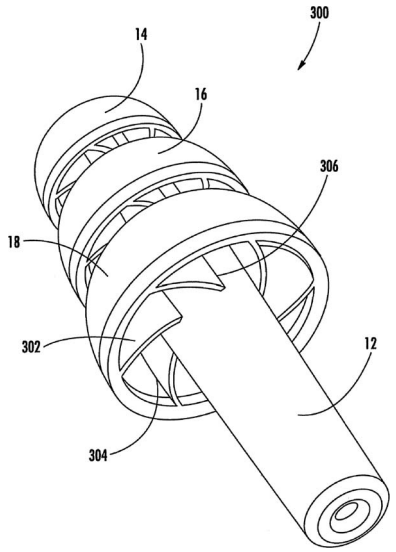

ible flanges 302 to resist deformation upon insertion. Also provided is a hollow stem 12 providing space for a stiffener to facilitate insertion.—JE

7,603,433

43.72.Ne IMS-BASED INTERACTIVE MEDIA SYSTEM AND METHOD

Thomas Paterik, assignor to Sprint Spectrum, L.P.
13 October 2009 (Class 709/217); filed 18 November 2005

A browser determines the location of an interactive application with a location server and the called telephone number, and invokes at least one

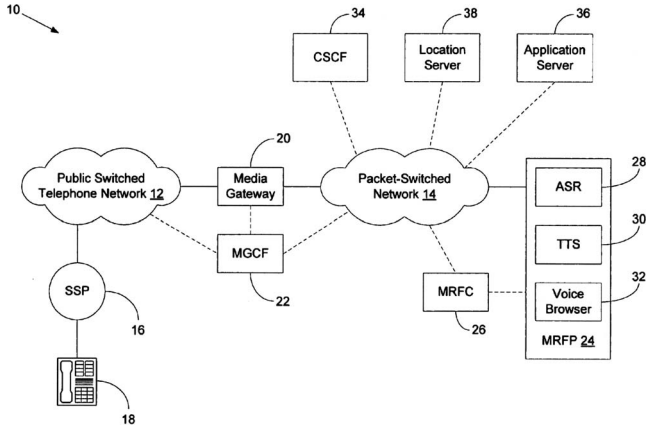

media resource from an application server via a media resource controller according to the desired interactive application.—DAP

7,601,121

43.80.Vj VOLUME RENDERING QUALITY ADAPTATIONS FOR ULTRASOUND IMAGING

Nikolaos Pagoulatos *et al.*, assignors to Siemens Medical Solutions USA, Incorporated
13 October 2009 (Class 600/443); filed 12 July 2004

The quality of volume rendering by an ultrasound imaging system is automatically adjusted as a function of ultrasound acquisition parameters that permit higher quality rendering for slower acquisitions of data.—RCW

7,604,594

43.80.Vj METHOD AND SYSTEM OF CONTROLLING ULTRASOUND SYSTEMS

Qian Zhang Adams *et al.*, assignors to General Electric Company
20 October 2009 (Class 600/437); filed 4 August 2004

Image data are processed to obtain a time-gain compensation curve. The curve can be used in conjunction with user-defined parameters. These include a time-gain compensation parameter and a dynamic-range parameter.—RCW

7,604,595

43.80.Vj METHOD AND SYSTEM FOR PERFORMING REAL TIME NAVIGATION OF ULTRASOUND VOLUMETRIC DATA

Erik Normann Steen *et al.*, assignors to General Electric Company
20 October 2009 (Class 600/437); filed 26 August 2004

A display processor successively accesses two volumes of data stored in an image buffer to produce a two-dimensional or a three-dimensional rendering based on display parameters. The first volume of data in the buffer is acquired using one set of scan parameters. The second volume of data is acquired using another set of scan parameters. Renderings are presented in real time by a navigation processor. The display can be changed to show different planes. A navigation view is modified to show the changes.—RCW

7,604,596

43.80.Vj ULTRASONIC SIGNAL PROCESSOR FOR A HAND HELD ULTRASONIC DIAGNOSTIC INSTRUMENT

Juin-Jet Hwang *et al.*, assignors to SonoSite, Incorporated
20 October 2009 (Class 600/443); filed 24 December 2003

The transducer array in this instrument contains an analog integrated-circuit transceiver for transmission and reception of ultrasound echoes. Also in the probe are digital integrated circuits that perform *b*-mode and Doppler signal processing. Further processing for display is performed in a back-end unit.—RCW

7,604,600

43.80.Vj ULTRASONIC IMAGING DEVICE

Shin-ichiro Umemura *et al.*, assignors to Hitachi Medical Corporation
20 October 2009 (Class 600/458); filed in Japan 17 March 2003

Ultrasonic imaging is performed using microbubbles injected to provide contrast. Transmitting-receiving operations are repeated N times ($N \geq 3$) by using transmitted pulses with a carrier phase given by $360/N$ degrees from one wave to another while the pulse envelope is the same. Echoes from the N transmit pulses are summed to obtain an image.—RCW

7,604,601

43.80.Vj DISPLAY OF CATHETER TIP WITH BEAM DIRECTION FOR ULTRASOUND SYSTEM

Andres Claudio Altmann and Assaf Govari, assignors to Biosense Webster, Incorporated
20 October 2009 (Class 600/463); filed 26 April 2005

A sensor in the tip of a catheter transmits signals that are used to determine the position of the catheter. An ultrasound transducer in the catheter is used to transmit pulses and receive echoes from which an image is formed. An image processor displays a catheter icon along with the image to show the orientation of the catheter.—RCW

7,608,044

43.80.Vj ULTRASONIC IMAGE DISPLAY METHOD AND ULTRASONIC DIAGNOSIS APPARATUS

Shunichiro Tanigawa, assignor to GE Medical Systems Global Technology Company, LLC
27 October 2009 (Class 600/441); filed in Japan 18 August 2004

An ultrasound image composed of a *b*-mode image and a bloodflow image is displayed with decreased weight of the *b*-mode image and increased weight of the bloodflow image as the intensity in the *b*-mode image increases.—RCW

7,610,078

43.80.Vj SYSTEM AND METHOD OF GRAPHICALLY GENERATING ANATOMICAL STRUCTURES USING ULTRASOUND ECHO INFORMATION

N. Parker Willis, assignor to Boston Scientific Scimed, Incorporated
27 October 2009 (Class 600/424); filed 26 August 2005

The distal end of an elongated probe containing an ultrasound transducer for transmission of pulses and reception of echoes is moved within the heart. Geometric shapes are defined using received echoes as the probe is moved. Based on the geometric shapes, at least part of the heart is represented graphically.—RCW

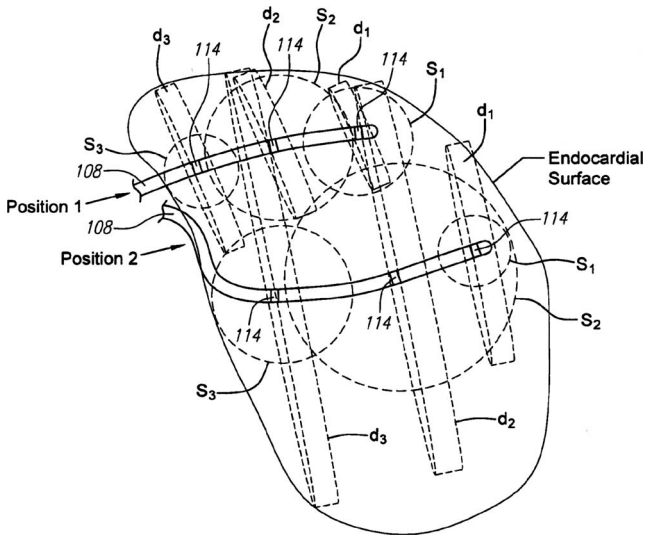

7,611,464

43.80.Vj METHOD FOR PROCESSING DOPPLER SIGNAL GAPS

Yong Li, assignor to Shenzhen Mindray Bio-Medical Electronics Company, Limited
3 November 2009 (Class 600/441); filed in China 16 August 2005

A continuous sequence of Doppler signal data is obtained by estimating signals to fill gaps in the data.—RCW

7,611,465

43.80.Vj RAPID AND ACCURATE DETECTION OF BONE QUALITY USING ULTRASOUND CRITICAL ANGLE REFLECTOMETRY

Peter P. Antich *et al.*, assignors to Board of Regents, The University of Texas System
3 November 2009 (Class 600/442); filed 30 July 2003

The coefficient of elasticity in a bone is found by simultaneously determining two or more critical-angle reflections of an ultrasound wave with a system that includes a transmitter and two or more receivers.—RCW